ISES and IEA SHC International Conference on Sustainable and Solar Energy for Buildings and Industry

26. - 30. August 2024
Limassol, Cyprus

EuroSun2024

Proceedings

ISES and IEA SHC International Conference on Sustainable and Solar Energy for Buildings and Industry

Conference of

ISES International Solar Energy Soci

SHC SOLAR HEATING & COOLING PROGRAMME INTERNATIONAL ENERGY AGENCY

Hosted by

Cyprus University of Technology

ΟΗΕ - Κύπρου - 1990

Proceedings

Proceedings of the EuroSun 2024 - ISES and IEA SHC International Conference on Solar Energy for Buildings and Industry in Limassol, Cyprus

Copyright © 2025 by the International Solar Energy Society
and the Authors

International Solar Energy Society
Wiesentalstr 50
79115
Freiburg
Germany

Tel + 49 761 45906 – 0
Fax + 49 761 45906 – 99
Email hq@ises.org
http://www.ises.org

ISBN 978-3-9826306-0-1

All rights reserved. No part of the publication may be reproduced, transmitted, in any form or by any means, electronic, mechanical, photocopying, recording or otherwise, without permission of the publisher, except in the case of brief quotations embodied in critical articles and review or where prior rights are preserved.
Produced by International Solar Energy Society

Notice

The International Solar Energy Society nor any one of the supporters or sponsors of the EuroSun 2024 conference make any warranty, expressed or implied, or accepts legal liability or responsibility for the accuracy, completeness or usefulness of any information, apparatus, product, or process disclosed, or represents that its use would not infringe privately on rights of others. The contents of articles express the opinion of the authors and are not necessarily endorsed by the International Solar Energy Society or supporters or sponsors of the conference. The International Solar Energy Society or any one of the supporters or sponsors of the EuroSun 2024 conference do not necessarily condone the politics, political affiliation and opinions of the authors or their sponsors.

Disclaimer

We cannot assume any liability for the content of external pages. The operators of those linked pages are solely responsible for their content. We make every reasonable effort to ensure that the content of this web site is kept up to date, and that it is accurate and complete. Nevertheless, the possibility of errors cannot be entirely ruled out. We do not give any warranty regarding the timeliness, accuracy or completeness of material published on this web site and disclaim all liability for (material or non-material) loss or damage incurred by third parties arising from the use of content obtained from the website.

Note from the Scientific Committee Co-Chairs

During the last week of August, the Cyprus University of Technology had the opportunity to welcome 200+ participants to Cyprus for EuroSun 2024, the ISES and IEA SHC International Conference on Sustainable and Solar Energy for Buildings and Industry. It was a pleasure and a privilege to host a conference of this caliber, dedicated to advancing renewable energy solutions and fostering collaboration across the international solar community.

Cyprus, like many island nations and regions with smaller energy systems, faces unique challenges and opportunities in implementing renewable energy technologies. Islands often have limited grid capacity, specific local resources, and higher dependencies on fossil fuels. These characteristics make them ideal testing grounds for pioneering renewable energy solutions that can be replicated and scaled elsewhere.

EuroSun 2024 has brought a diverse audience together to present the latest research and ideas across a range of renewable energy sources. As the Minister of Energy, Commerce and Industry of Cyprus, Mr Giorgos Papanastasiou, mentioned during his opening remarks, “Solar Energy plays, and will continue to play, a vital role, since it contributes to the enhancement of security of energy supply, it is cheap, and it can be extensively utilized.” From photovoltaics and solar thermal systems to energy communities and policy recommendations, the presentations and papers in these proceedings of EuroSun 2024 offer a holistic view of the integral role of renewables.

We are united by a shared commitment to address the pressing issue of decarbonization, a highly complex endeavor. Achieving it requires a combination of technical, political, and economic solutions tailored to each region's specific needs and resources. Only by bridging these domains together, we can hope to achieve a sustainable future.

With your innovative work and dedication, we are moving closer to a cleaner, more resilient world. Decarbonization is within reach, and together, we can make it happen. We hope you find these Proceedings of EuroSun 2024 of value to your own research and development activities. We look forward to continuing this journey with you during the Solar World Congress in Fortaleza, Brazil in 2025 and the next EuroSun conference in Freiburg, Germany in 2026.

Associate Professor Alexandros G. Charalambides, Cyprus University of Technology (Cyprus)

and

Dr. Corry de Keizer, TNO (Netherlands)

Committees

Conference Chair

Associate Professor Alexandros G. Charalambides | Cyprus University of Technology

International Organizing Committee

Associate Professor Alexandros G. Charalambides | Cyprus University of Technology

Dr. Corry de Keizer | Netherlands Organization for Applied Scientific Research (TNO)

Prof. Andreas Häberle | Eastern Switzerland University of Applied Science

Dr. Lucio Mesquita | Natural Resources Canada

Prof. Klaus Vajen | University of Kassel

Kerstin Krüger | Forschungszentrum Jülich GmbH

Pamela Murphy | IEA SHC

Arabella Liehr | International Solar Energy Society

Melina Hanhart | International Solar Energy Society

Local Organizing Committee

Associate Professor Alexandros G. Charalambides | Cyprus University of Technology

Dr. Polycarpos Polycarpou | Agricultural Research Institute of Cyprus

Scientific Committee

Chairs:

Dr. Corry de Keizer | Netherlands Organization for Applied Scientific Research (TNO)

Associate Professor Alexandros G. Charalambides | Cyprus University of Technology

Scientific Program Theme Chairs:

Prof. Salvatore Carlucci,

Dr. Caroline Hachem-Vermette, Concordia University

Dr. Fabrizio Fattori

Dr. Nicolas Christofides

Dr. Maria Herrando

Prof. Fabian Ochs

Prof. Ulrike Jordan

Prof. Soteris Kalogirou

Dr. Klaus Lichtenegger

Magdalena Berberich

Rosie Christodoulaki

Cristoph Brunner

Prof. Andreas Häberle

Dr. Venizelos Efthymiou

Brian Azzopardi

Assoc. Prof. Manolis Souliotis

Dr. Andreas Hauer

Dr. Abdulrahman Dahash

Dr. Vassiliki Drosou

Dr. Korbinian Kramer

Dr. Nestor Fylaktos

Prof. Uli Jakob

Salvatore Vasta

Prof. Denia Kolokotsa

Valerie Sejourne

Khalid Salmi

Prof. Andreas Kazantzidis

Scientific Review Committee Members

Zunaib Ali
Amín Altamirano
Chris Bales
Evangelos Bellos
Francisco Beltran
Franziska Bockelmann
John Boland
Christoph Bott
Jose Cardemil
Salvatore Carlucci
Rosa Christodoulaki
Alberto Coronas
Abdulrahman Dahash
Jiangtao Du
Ali Ehsan
Jianhua Fan
Jürgen Fluch
Andrea Frazzica
Hua Ge
Theodoros Glytsos
Alexis Gonnelle
Iker González Pino
Kuljeet Singh Grewal
Jean-Christophe Hadorn
Araceli Hernandez
Maria Herrando
Daniel Herrera
Adrian Hiel
Mercedes Ibarra
Ulrike Jordan
Valentin Kaisermayer
Andreas Kazantzidis
Corry Keizer
Felix Kriedemann
Chrysovalantou Lamnatou
Ana Lázaro
Markus Leeb
Klaus Lichtenegger
Luis M. Serra
Dirk Mangold
Shawn Martin
Diego Martínez-Plaza
Isaac Meir
Andreu Moia-Pol
Kristian Pagh Nielsen
Fabian Ochs
Philip Ohnewein
Monica Oliphant
Janybek Orozaliev
Konstantinos Oureilidis
Peter Paerisch
Felix Pag
Giorgos Panaras
George Papadakis
Spiros Papaefthimiou
Alan Pino
Jesús Polo
David Pozo-Vazquez
Efthymios Rallis
Alois Resch
Manuel Riepl
Agnieszka Rządkowska
Alessio Sapienza
Anne Schierenbeck
Thomas Schmidt
Christian Schweigler
Viacheslav Shemelin
Raquel Simón
Aaron Sprecher
Gerald Steinmaurer
Wolfgang Streicher
Onur Taylan
Danjana Theis
Elisabeth Thiele
Costas Travasaros
Christoph Trinkl
Elisavet Tsekeri
Loreto Valenzuela
Constantinos Vassiliades
Cristobal Villasante
Willy Villasmil
Valery Vuillerme
Werner Weiss
Carsten Wemhöner
Stefan Wilbert
Somil Yadav
Shunmin Zhu

Conference Themes

Energy Efficient Buildings

- Solar and Efficient Buildings, Energetic Renovation of Buildings, Daylighting, Digitalization and Industrial Renovation

Sustainable Heating and Cooling Systems for Buildings

- Solar Domestic Hot Water and Space Heating, Heat Pump Systems for Buildings, PV and PVT Systems, Solar Energy and Heat Pumps, Sustainable Air Conditioning for Buildings, Smart Control Systems

Solar and Efficient Districts

- Innovative District Heating and Cooling, Urban Planning of districts, Simulations, Digitalization and AI

Sustainable Process Heat for Industry

- High temperature Heat Pumps for Industry, Solar Energy and Heat Pumps, Simulations, Digitalization and AI, Heat Recovery, Water Purification through Renewable Energy

Sustainable Energy Infrastructure and Electrification

- Sector Coupling and Grid Stabilization, Electrification of the Heating Sector, Thermal Energy Storage for Grid Integration of RES

Thermal Energy Storage

- Season Thermal Energy Storage, Thermal Energy Storage in Applications, New Concepts in TES, Innovative Materials for TES

Solar Thermal and PVT Collectors and Solar Loop Components

- Solar Thermal and PVT collectors, Solar Loop Components, Testing and Certification

Solar Air Conditioning and Refrigeration

- Solar Cooling for the Sunbelt region, Solar refrigeration for Industry

Sustainable and Solar Energy Transition

- Renewable Energy Strategies, Scenarios, Financing and Policies, Renewable Energy Education, Citizens' Participation / empowering consumers, Carbon Neutral Regions, Sustainability and LCA

Solar Resources and Energy Meteorology

- Solar Resource Assessment, Solar Forecasting, Remote Sensing

Partners

Conference by

ISES International Solar Energy Society

SHC SOLAR HEATING & COOLING PROGRAMME INTERNATIONAL ENERGY AGENCY

Hosted by

Cyprus University of Technology

ΔΟΗΕ - Κύπρου - 1990

Sponsors

Silver Sponsor

Supporting Sponsors

Young ISES Sponsor

Scientific Program

01. Energy Efficient Buildings

Air-based BIPV/T for Low-arctic Applications
Baril, D., Athienitis, A., Ge, H. 1

Energy Building Sustainability by Optimized Daylight Tubes
Fernández, B.G., Fernández-Balbuena, A.A., Garcia, M.A., Jaureguizar, M., Vázquez-Moliní, D. 12

Enhancing Thermal Performance of Roofs Within Heavy-Weight Thermal Mass Residential Buildings in The Warm Mediterranean Climate of Lebanon
Geagea, T. 22

A Parametric Study: Impact of Thermal Mass on Summer Overheating for Residential Buildings in Germany
Gottkehaskamp, B., Auer, T., Hepf, C., Romero, J., Talke, M. 33

Integration of Weather and Emission Predictive Control (WEPC) into Building Energy Simulations
Gottkehaskamp, B., Auer, T., Chong, A., Hepf, C., Miller, C. 46

Model Predictive Control of a Heat Pump System Integrated with PVT Collectors and Ice Storage
Nienborg, B., Bampi, B.B., Frison, L., Khamidov, D. 58

Propane-based heat pump solutions for existing multi family houses – requirements and possible system solutions
Nienborg, B., Engelmann, P., Rodenbücher, B., Uhl, A. 70

Space Heating and Cooling Demand of Buildings in the Perspective of Climate Change in Cold and Hot Climates – Is this a Risk?
Ochs, F., Karsbergen, V.v., Streicher, W., Thür, A. 82

Occupant feedback on indoor humidity assessment
Papadopoulos, P., Carlucci, S., Kyprianou, I., Luparelli, A. 88

Deep Learning Techniques for Prediction of Non-visual Luminous Content of Cellular Offices
Potonik, J. 98

Thermal Characterization of Single Greening Components and Green Roofs
Reim, M., Brütting, M., Körner, W., Studtrucker, M., Weiglein, C.,
Weinläder, H., Weismann, S., Wolfrath, E. 110

A Review of the Coherence of Strategies to Optimize Photovoltaic Systems within the Built Environment in Nordic Countries
Valencia, S. 122

Thermal Characterization Of Living Wall Systems
Weinläder, H. 134

02. Sustainable heating and cooling systems for buildings

Techno-Economic Comparison of Different Solar Photovoltaic/Thermal (PVT) Absorber Designs for Ground Source Heat Pump (GSHP) Integration
Beltran, F., Sommerfeldt, N. 146

Energy concepts with high solar fraction for multi-family houses
Bockelmann, F., Peter, M. 154

Quantifying the effect of radiator capacity on hybrid heat pump performance using a hardware-in-the-loop setup
Bulut, Y., Dubhashi, V., Kemp, R., Wijhe, A.v. 165

Sizing an Electrical Storage in Combination with Thermochemical Storage for a PVT-Driven Energy System in a Residential Application
Coca-Ortegón, A., Belda, A., Lara, Y., Lozano, I., Martinopoulos, G.,
Nikolopoulos, N., Simón-Allué, R., Tsimpoukis, A. 176

Mathematical modelling of an Innovative Ice Storage system
Daborer-prado, N., Wagner, C. 187

Energy Performance and Environmental Impact of Solar Photovoltaic, Thermal and Hybrid PVT Panels in an Individual House
Fares, H., Chèze, D., Pierrès, N.L., Wurtz, E. 196

Providing Flexibility for District Heating Grids with Thermally Activated Building Structures in Residential Buildings
Gumhalter, M., Gradl, P. 208

Research And Analysis Of Solar Heat Pump Performance
Jiao, Q., Jiao, X. 216

Simulation of a Photovoltaic-Thermal (PV-T) Air Source Heat Pump (ASHP) System for Building Thermal Demands
Kasturi, P., Schwarz, J.S., Torio, H. 228

Potential thermal energy storage technologies for radiative cooling implementation in buildings
Marco, J.M., Castell, A., Cofré-Toledo, J., Medrano, M., Mselle, B., Solé, C., Vilà, R. 240

Solar Radiant Floor and Sub-Surface Ground Heat Exchanger Thermal Storage System: Feasibility and Performance Assessment
Mesquita, L., Djebbar, R., Thornton, J., Weiss, A. 250

Integrating Radiative Cooling and Chilled Ceilings in Buildings: A Simulation Study for Sustainable Cooling
Miró, R.V., Capiello, F.L., Cimmino, L., Martorell, I., Medrano, M. 262

Comparative study on small-scale HPs for decentral DHW preparation in multi-family buildings
Monteleone, W., Ochs, F. 273

Domestic hot water heating with direct electricity from PV panels and the grid
Nielsen, E., Fan, J., Furbo, S. 285

S.A.P.I.EN.T.E Experimental Test Facility For Full-Scale Testing Of New Configurations Of Collective Thermal Electric Self-Consumption From Renewable Sources. First Experimental Test With Thermo-Photovoltaic Collectors Plant
Nissim, R., Palma, A.L., Pietra, B.D., Segreto, M. ***297***

Monitoring an innovative cold district heating network with decentralized heat pumps and sewage water as heat source
Sauer, C., Georgii, M., Orozaliev, J., Schmelzer, C., Vajen, K., Werner, F. ***310***

Achieving Sustainable Buildings: Balancing Energy Efficiency and Comfort through Ventilation Management
Verma, R., Rakshit, D. ***322***

Investigation of the Influence of Instantaneous Water Heaters on the Efficiency of (Regenerative) Central Heating Systems in the Simulation Environment TRNSYS
Walter, J. ***334***

Development of a Hybrid Collector for an Innovative Energy Supply System Using Molecular Solar Thermal Energy Storage
Weismann, S. ***346***

03. Solar and Efficient Districts

Yearly thermal performances of Danish solar heating plants
Fan, J., Furbo, S., Nielsen, E. ***360***

Development of a new generation of cold district heating systems with water as heat transfer medium
Huber, P., Dott, R., Drück, H., Hafner, B. ***371***

Predictive Rule-Based Control Strategy for Optimizing the Operation of Solar District Heating Plants
Lichtenegger, K., Gölles, M., Unterberger, V. ***382***

Comparison of Solar Systems with Seasonal Storage for Renewable Heat Production for District Heating
Matuska, T., Sourek, B. ***391***

Integrating Concentrated Solar Thermal in District Heating - A Simulation Study in TRNSYS
Tamm, S., Berberich, M. ***398***

Evaluation of positive energy districts with district heating and heat pumps
Venturi, E., Dermentzis, G., Magni, M., Ochs, F. ***409***

Two case studies for renewable district heating with solar fraction 70 %
Volk, P., Jordan, U., Kusyy, O., Orozaliev, J., Schmelzer, C., Vajen, K. ***421***

Sensitivity Analysis of Solar District Heating Systems
Wagner, C., Dehner, H. ***432***

Improved Pre-calculation of Solar Thermal Production for Milp-based Optimization Problems
Wissocq, T., Lamaison, N. ***444***

04. Sustainable Process Heat for Industry

Parabolic Trough Collector Cost Update for Industrial Process Heat in The United States
Akar, S., Kurup, P. **457**

ASTEP Project: Status And Progress At 2024
Christodoulaki, R., Abbas, R., Androutsopoulos, A., Barbero, R.,
Barnetche, M., Ibarra, M., Muñoz, J., Rovira, A., Solano, J.P. **470**

Hybrid Steam Generation for Industry Using Linear Fresnel Solar Collectors and High Temperature Heat Pump
Famiglietti, A., Abbas, R. **478**

Pilot plant for hydrogen production using high-temperature solid oxide electrolyser and solar heat and power
Gonzalez-Aguilar, J., Barreto, G., Romero, M. **489**

Dynamic Energy Management Model: A Catalyst for Carbon Neutrality in Austrian Thermal Baths
Seidnitzer-Gallien, C., Bühne, X., Gradl, P., Gumhalter, M. **494**

05. Sustainable Energy Infrastructure and Electrification

Custom sizing and cost analysis of a PV-battery system: Dual-purpose application for residential load and agricultural water needs
Irandoostshahrestani, M., Rousse, D.R., Turcotte, P. ***505***

Techno-Economic Analysis of a Stationary Battery Storage Operating on Frequency Regulation Markets in a Church Powered with PV System
Koubar, M., Boork, M., Jalilzadehazhari, E., Munkhammar, J., Wessberg, M., Wikstrom, J. ***512***

Enhancing Energy Transition on Campus: Implementing Thermal Accumulation Mechanisms for Flexibility
Moll, V.M., Alonso, I., Bibiloni, P.A., Canals, V., Díaz-Torres, Y.,
Mas, B., Moià-Pol, A., Vidal, J. ***524***

Scenarios for Integration of Power to Heat Technology in Czech District Heating Systems
Pokorny, N., Safranek, J., Zavrel, V. ***536***

06. Thermal energy storage

Efficiency Analysis of An Integrated Cascade Sorption Energy Storage into A Solar DHW System
Aliyari, N., Fernandes, M.S., Gaspar, A.R. **547**

Assessment of Fin Thickness Influence on Melting and Solidification Processes Inside Longitudinally Finned Latent Thermal Energy Storage
Batista, J., Kirincic, M., Lenic, K., Trp, A. **559**

Pilot facility for the study of thermal energy storage: Experiments and Theoretical model
Castro, A., Babul, K., Camacho, M.J.A., Cano, M.S.R., Gil, B., López, A.M.P.,
Montesinos, J.A., Rosiek, S., Saldaña, J.L.B. **571**

Microwave Desorption for Flexible Sorption-Heat Storage Application
Daborer-prado, N., Issayan, G., Zettl, B. **580**

CFD analysis of a thermal storage tank driven by natural convection
Gonzalez-Aguilar, J., Barreto, G., Giaconia, A., Romero, M. **587**

State of charge estimation using regression models in a novel photovoltaic thermal storage system with macro-encapsulated phase change material
Krabben, Y., Palacios, A., Roos, P., Schäfer, F., Stamatiou, A., Sztranyovszky, L. **596**

Effect of zinc oxide-water nanofluids on the thermal efficiency of a flat plate solar collector – a comparative analysis of central composite design and box Behnken design
Nwaigwe, K.N., Budu, M.N.A.A. **604**

01. PV Cell Technologies

Extruded Water Adsorbent APO-Tric for Adsorption Thermal Battery Utilizing Solar Energy
Ristic, A., Helden, W.v., Hengel, F., Logar, N.Z., Mal, S., Mlakar, U., Stritih, U. ***613***

06. Thermal energy storage

Optimized Thermodynamics and Building Physics of large-scale Thermal Energy Storage
Tosatto, A., Hengel, F., Muser, C., Ochs, F. ***621***

07. Solar Thermal and PVT Collectors and Solar Loop Components

Modeling and Simulation of the National Solar Thermal Research Demonstration Facility in Gwalpahari
Alexopoulos, S., Arora, A., Mahdi, Z. **634**

Fins vs No Fins: A Comparative Experimental Analysis of Novel Box-Channel Photovoltaic/Thermal Collector Prototypes for Ground Source Heat Pump Integration
Beltran, F., Delachaux, V., Jaafar, M.A., Lopez, A.C., Nicholson, E.L., Sommerfeldt, N. **640**

Experimental Study on Heat Transfer from Ambient Air in Row-installed Photovoltaic-thermal (PVT) Solar Collectors on a Flat Roof
Delachaux, V., Jaafar, M.A. **651**

Energy Performance Simulation of the 52mW Minos Solar Tower Project
Drosou, V., Christodoulaki, R., Hysenj, S., Karagiorgas, M., Katsaros, V. **659**

Validation of a simulation model for parabolic trough collectors in a high-latitude district heating system
Fogelström, F., Ahlgren, B., Danielski, I., Gambardella, A., Nair, G., Nguyen, T. **670**

Comparative Numerical Analysis of Middle-Temperature and High Temperature versions of High-Vacuum Flat-Plate Collectors: Assessing Performance in the Field.
Gaudino, E. **681**

Performance Analysis of a Hybrid Solar-Geothermal Power Plant in México
González-Mora, E., Durán-García, M.D., Lentz-Herrera, Á.E. **690**

Computational Fluid Dynamics Optimization of a Heat Exchanger Design for Photovoltaic Thermal Retrofit Applications
Herrando, M., Acosta-Pazmiño, I.P., García, A.C., Gomes, J., Morales-Hernández, M., Murali, D., Santana, J.P. **699**

Numerical Study of the Effect of the System Specifications on the Performance of a Brine/Water Heat Pump in Combination with Photovoltaic Thermal Solar Collectors
Jaafar, M.A., Chhugani, B. **711**

Solar Thermal Collectors and their Components. Results of Long-term Exposure at Extreme Test Site
Kaltenbach, T., Heck, M., Mehnert, S., Platzer, W. **721**

Experimental Assessment of the Effects of Cold Climate Weather Patterns on Novel PVT Collector Designs for Low Temperature Heat Pump Integration
Lopez, A.C., Beltran, F., Delachaux, V., Jaafar, M.A., Nicholson, E.L., Sommerfeldt, N. **725**

Effect of Boundary Conditions on Glazed Flat-Plate Solar Collector Performance Test Results
Matuska, T., Shemelin, V. **737**

Experimental Investigation of Large-Area Transpired Solar Air Collectors
Mesquita, L., Breton, R., Harrison, S., Johnson, G. **747**

Performance Comparison of a Transpired Air Solar Collector with Low-E Surface Coating
Mesquita, L., Harrison, S., Johnson, G., Nguyen, A.K. ***758***

How does the thermal characteristics of PVT panels influence the performance of PVT heat pump systems
Nielsen, E., Dannemand, M., Furbo, S., Mikkelsen, S.E. ***766***

Estimation of Dust Accumulation in Parabolic trough Concentrators using Aerial Laser Reflection
Peña-Cruz, M., Robles-Velázquez, S., Sánchez-González, M. ***773***

Study of the Impact of Automatic Backflush on Direct SDHW Thermosyphon Systems
Stinson, B., Breton, J., Harrison, S., Nyugen, A.K. ***780***

Field Evaluation of Naked Energy's Virtu Solar Thermal and Hybrid PVT Collectors in Commercial Energy Systems
Zagorulko, M., Mellor, A., Murrell, A. ***788***

Quantifying The Environmental Implications Of Solar Thermal Technologies: A Comprehensive Examination Of Life Cycle Impacts And Payback Periods
Zagorulko, M., Mellor, A., Murrell, A. ***793***

08. Solar Air Conditioning and Refrigeration

First experimental investigations of a facade-integrated adsorption system for solar cooling
Boeckmann, O. **802**

Towards designing and evaluating solar cooling integrated façades in office buildings
Hamida, H., Beneito, L., Knaack, U., Konstantinou, T., Prieto, A. **812**

Modelling and Analysis of Building Optimisation and Solar thermal Cooling System in Nepal
Strobel, M., Jakob, U. **824**

Slurry Production for Solar-Ice Systems using Supercooling and a Flow-based Crystallizer
Thamm, A., Carbonell, D., Erb, K., Gurruchaga, I. **833**

Developing and demonstrating innovative solutions for renewable and waste heat-driven cooling technologies in industries: the RE-WITCH project
Vasta, S., Agirre, M.E., Baelz, A., Frazzica, A., Giganda, J.L.C.,
Jakob, U., Mittelbach, W., Papageorgiou, D., Sapienza, A., Schweigler, C., Ziegler, F. **846**

Solar Cooling for the Sunbelt Regions – Final results from IEA-SHC Task 65
Vasta, S., Jakob, U., Kohlenbach, P., Neyer, D., Weiss, W. **854**

09. Sustainable and Solar Energy Transition

Simulation model for autonomous energy planning for Milos island
Alexopoulos, S., Mathew, G. **867**

Critical Analysis on the Renewable Heating and Cooling plans in Croatia, Germany, Greece, Poland and Portugal
Christodoulaki, R., Doroti, H., Drosou, V., Ehrig, R., Fernandes, J., Micò, L., Tobiacelli, M. **874**

Evaluation of an Indirect Solar Dryer with Integrated Heat Exchanger
Davidsson, H., Andersson, M., Jamtsho, T., Om, D. **885**

Techno-Economic Evaluation For Joint Production Of Electricity And Green Hydrogen With Hybrid Concentrated Solar Power (CSP) And Photovoltaic (PV) Technologies Coupled With PEM Electrolyzers
Leiva-Illanes, R., Amador, G., Herrera, C., Tuñon, G.H. **894**

Solar Hydrogen Production: Techno-Economic Evaluation of Concentrated Solar Power Plant and High-temperature Electrolysis Integration
Martins, J.H.S., Monnerie, N., Roeder, T., Rosenstiel, A. **904**

Thermal performance of a solar box cooker with forced convection heating and sensible heat storage
Mawire, A., Mahavar, S. **917**

Quantum Dot as a Mechanism to Supress Charge Recombination in Polymer Solar Cell
Mola, G.T., Ogundelea, A.K. **923**

Optimizing energy and economic performance of solar-biomass systems for rural district heating: a technical and financial analysis
Pauletta, S., Duret, A., Jobard, X. **927**

Feasibility study of a solar desalination unit for small isolated communities
Rousse, D.R., Deblock, V., Irandoostshahrestani, M., Turcotte, P. **937**

Enhancement of a photovoltaic drinking water pumping system design software tool
Turcotte, P., Irandoostshahrestani, M., Rousse, D. **949**

10. Solar Resources and Energy Meteorology

Study of intra-hour direct normal irradiance variability effects on hourly WRF-Chem outputs
Astudillo, D.P., Bachour, D., Fountoukis, C. ***958***

Evaluation of aerosol optical depth for further assimilation into WRF-Chem simulations
Bachour, D., Fountoukis, C., Perez-Astudillo, D. ***966***

Climate Adjustment of Photosynthetically Active Radiation Estimates Using Site Adaptation Technique
Ferrera-Cobos, F., Gouveia, L., Llorens, M.N., Navarro, A.A., Popovich, C.,
Silva, G.H.R.d., Valenzuela, R.X., Wane, O., Zarzalejo, L.F. ***975***

The Aerosol Effect on Direct Normal Irradiance in a Dust-Rich Hot, Desert Climate
Fountoukis, C., Bachour, D., Perez-Astudillo, D. ***982***

Assessing the Impact of Diffuse Fraction Estimation on Ground Albedo Modeling
Rodríguez-Muñoz, J.M., Abal, G., Alonso-Suárez, R., Bove, I. ***987***

11. Solar Energy Advances

A minute-resolution downscaling algorithm for high-resolution global irradiance time series
Almpantis, D., Andersson, H.D.a.M. **1000**

Selective transmission and absorption in oxide-based nanofluid optical filters for PVT collectors
Barthwal, M., Rakshit, D. **1001**

Turning weakness into strength - A feasibility analysis and comparison of datacenter deployment in hot and cold climates
Chrysostomou, M., Christofides, N., Ioannou, S. **1002**

A quality control scheme for solar irradiance measurements on facades in urban environments
Köker, N.I., Desthieux, G., Gallinell, P., Giorio, M., Jelle, B.P., Lobaccaro, G., Manni, M. **1003**

Combining expansion turbines, heat pumps, and low-temperature solar heat for enhanced primary energy savings in gas pressure regulating stations
Louvet, Y., Ahlgrimm, S., Pag, F., Vajen, K. **1004**

Multisectoral decarbonisation strategies in Punta Arenas, Chile: A multi-renewable technologies approach
Muñoz, I., Fuentes, F. **1005**

Industrial solar heat potential in Chile: A technical-economic analysis
Naranjo, D., Fuentes, F., Muñoz, I. **1006**

Characteristic load curves of positive energy districts
Ochs, F., Breuss, S., Dermentzis, G., Magni, M., Tosatto, A., Venturi, E., Wemhoener, C. **1007**

Oversizing solar heating plants in industry: A cost-effective solution to increase solar fractions
Pag, F., Jesper, M., Jordan, U., Vajen, K. **1008**

Design and modeling of PV-integrated Double Skin Facades and application to retrofit buildings
Yadav, S., Desthieux, G., Jilani, M.N.H., Vermette, C. **1009**

01. Energy Efficient Buildings

AIR-BASED BIPV/T FOR LOW-ARCTIC APPLICATIONS

Daniel Baril[1], Andreas Athienitis[1], and Hua Ge[1]

1 Centre for Zero Energy Building Studies, Concordia University, 1455 De Maisonneuve Blvd. W, Montreal, Quebec, (Canada)

Abstract

The Arctic communities of Canada are almost completely dependent on fossil fuels for their energy needs. This dependence can lead to negative environmental consequences, such as fuel spills and harmful emissions as well as vulnerabilities during emergency situations. Alternative energy options are required in order to have a sustainable future for this region. One such promising system is the building integrated photovoltaic/thermal collector (BIPV/T), where not only electricity is generated but valuable heat is recovered and can be used for all seasons of the year in the Arctic. In this study a simulation model of the BIPV/T was created using design weather data for Iqaluit, Canada as the input to test the electricity generation and heat recovery for different configurations to maximize the energy performance for the area. It was seen that the best performing month was April, with outlet temperature increases of approximately 18°C, and daily heat recovery and electricity generation over 6.2 kWh and 8.7kWh respectively. Based on these initial simulations an experimental prototype has been designed and fabricated to test thermal enhancements in a solar simulator laboratory. Upon experimental testing, improvements are to be recommend for a field prototype to be deployed in a low-Arctic community of Canada.

Keywords: BIPV/T, fossil fuel reduction, Arctic renewable energy

1. Introduction

Canada has close to three hundred remote communities, as seen in Fig.1 (Hayne et al., 2023), that are almost totally dependant on fossil fuels for their electricity and heating needs. Electricity is generated in these locations from local microgrid diesel fired thermal power plants. In order to maximize the efficiency of the electricity produced all heating needs must be met from heating oil fired burners in each building. While well established and fairly dependable if properly maintained, there are many negative environmental consequences from fossil fuel energy systems (Taillard et al., 2022).

© 2024. The Authors. Published by International Solar Energy Society
Selection and/or peer review under responsibility of Scientific Committee
10.18086/eurosun.2024.01.01 Available at http://proceedings.ises.org

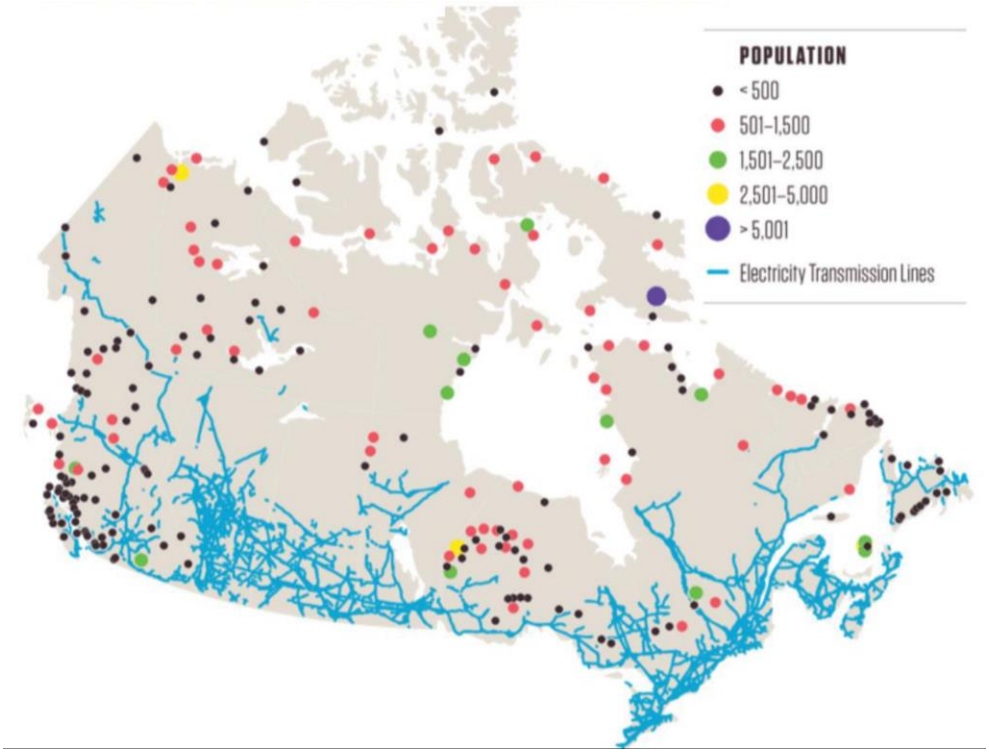

Fig.:1 Canada's Diesel Dependant Communities (Hayne et al., 2023)

On top of CO_2 emissions, fuel spills and leaks are major issues. Leaks inside buildings from poorly maintained heating equipment can lead to strong odors and vapors that significantly affect the indoor air quality and safety of the occupants (Paquet et al., 2021). Since heating oil is a light weight hydrocarbon it can easily be dispersed from the initial leakage area and spread throughout the building materials, and leak into the ground (Canadian Council of Ministers of the Environment, 2008), depriving soils of water and oxygen as well as vital nutrients (Mitter et al., 2021).

(a) Heating oil leakage from boiler (Photo taken by author)

(b) Heating oil leak from storage tank (Photo taken by Edua Jones)

Fig. 2: Heating oil leakage

The northern villages of Canada have several engineering challenges that must be taken into account when designing buildings for the region. As presented by (Baril et al., 2023) some of the main issues are the extreme cold climate, the remoteness of area causing long lead times for goods to be delivered, and shortage of skilled labor. Keeping these issues in mind on top of the need to reduce the fossil fuel usage, solar energy is seen as a viable option to the fossil fuel based energy systems. Several photovoltaic projects have taken place in the recent years to generate clean electricity, helping to avoid the extremely high electricity costs for the off-grid communities in the remote Arctic regions of Canada, such as the 940kW solar farm in small Arctic village of

Old Crow (Arctic Economic Council, 2022) and the 3.5MW solar power plant at the Diavik Mine in Canada's Northwest Territories (Rio Tinto, 2024). Both projects use traditional ground mounted PV arrays and are able to generate approximately 25% percentage of their energy needs, however large portions of lands must be developed for the PV structure and access roads. Other systems take advantage of the already developed land, by applying the PV systems to existing buildings (BAPV), such as the 100kW façade applied PV array on the arena in the northern village of Kuujjuaq (Tarquti, 2024). This system helps reduce the environmental impact on the land and delicate ecosystem as well as minimizing electrical cable and other material needs. Improving on the BAPV is the building integrated PV system (BIPV) that uses the PV system as an architectural element of the building serving such purposes as the rainscreen and UV barriers of the cladding or roofing materials, or incorporated into fenestration systems, such the BIPV roof of the Varennes Library in Quebec, Canada (Sigounis et al., 2023).

A higher level of integration is the building integrated photovoltaic/thermal collector (BIPV/T) in which heat is actively recovered from the PV panels; a cross section of an air-based BIPV/T system is shown in Fig.3. In the extreme cold regions of Canada's north over 80% of the energy costs are for heating purposes. The usage of BIPV/Ts are an effective way to maximize the energy benefits for the region and are deemed suitable for several reasons. This system serves multiple purposes, not only generating electricity but also recovering useful heat, cooling the PV modules, increasing PV efficiency and replacing the building cladding or roofing materials, acting as the rain and UV barriers. BIPV/T system typically have two types of heat transfer fluids, either liquid based or air based (Yang & Athienitis, 2016), (Dimitrios Rounis et al., 2022). While a liquid-based system can take advantage of the higher specific heat of the liquid to improve heat transfer, air as the heat transfer fluid eliminates the risk of damage from leaks that could occur when using a liquid-based system, reducing the maintenance requirements and improving the ease of construction. Air based systems can easily be integrated with a building's heating, ventilation and air conditioning system (HVAC) as seen in the successful projects in Montreal, Canada, such as the BIPV/T system at Concordia University which is used to preheat the fresh air for classrooms (Athienitis et al., 2011), as well as a portion of the roof at the Varennes Library used to pre-heat the air of an energy recovery ventilator (ERV) as well as an air to water heat pump (Amara et al., 2020).

In order to reduce heat losses through the building envelope in the extreme cold climate of the Canadian Arctic it is important to reduce the unintentional air infiltration and exfiltration to a minimum. Fresh air must then be provided by the use of a heat recovery ventilator (HRV) or energy recovery ventilator (ERV). However, when inlet temperatures drop below -5^{o}C to -10^{o}C frosting of the air exchange core occurs, resulting in a stoppage of fresh air during system defrost (Beattie et al., 2018). Simulation studies conducted in extreme cold climates concluded that pre-heated fresh air using a BIPV/T was seen to be useful to prevent frosting of a heat recovery ventilator (HRV) (Li et al., 2021), (Baril et al., 2021) or to improve the coefficient of performance (COP) of a heat pump (Ma et al., 2021). The focus of this project is to maximize the energy performance of a BIPV/T system for demonstration house in the low Arctic communities of northern Canada, (Berquist et al., 2021), as part of a greater project focused on renewable energy microgrid integration for remote off-grid cabins in Nunavut, Canada (CINUK, 2024).

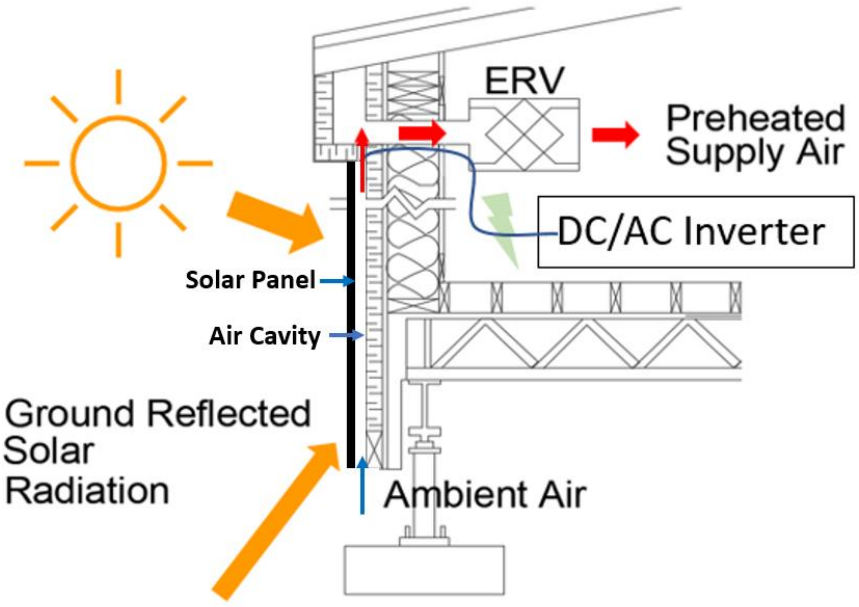

Fig.3: BIPV/T system cross section

2. Methodology

The first step in the BIPV/T design was a parametric study using a thermal network model of the system similar to the model created by (Candanedo et al., 2011) using local weather data. The cross-sectional thermal network of the BIPV/T cavity is shown in Fig. 4. By setting up an energy balance of the thermal resistive network at the key nodes of the PV panel, cavity air and cavity back surface, a system of equations was obtained. The equations were solved using an explicit finite difference control volume method with Canadian Weather Year for Energy Calculations (CWEC) monthly average hourly weather data for the city of Iqaluit, Nunavut, Canada, 63°N. The model was calibrated and validated using experimental data from (Yang & Athienitis, 2014).

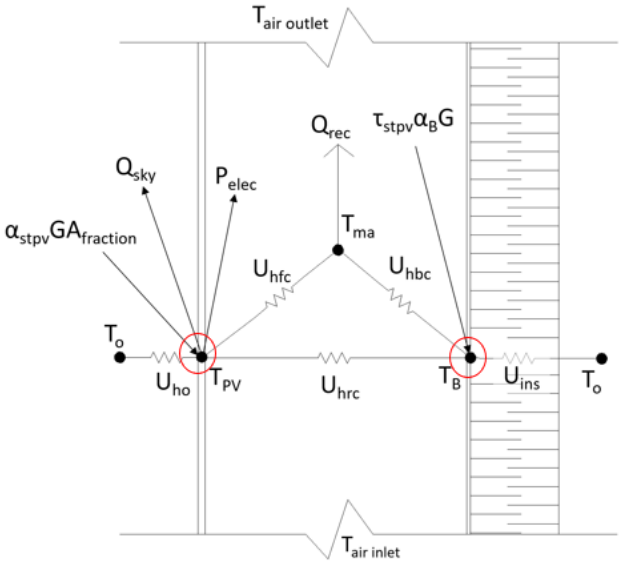

Fig. 4: BIPV/T thermal network

Due to the low solar altitude of Iqaluit , Canada a façade integration was chosen instead of the low sloped roof to maximize the solar irradiance received on PV panels and to take advantage of the ground snow reflectance,

and to better match the energy generation with the building's loads throughout the year. A roof integrated system could be advantageous if the building such as a hunting cabin is intended to be used primarily in the late spring and summer. Therefore, it is important to determine the intended usage and occupant schedule of the building and design the BIPV/T accordingly.

$$T_{air\ outlet} = \frac{T_{pv}+T_B}{2} + \left(T_{air\ inlet} - \frac{T_{pv}+T_B}{2}\right) * e^{\frac{-2L_{CV}}{A}} \quad \text{(eq.1)}$$

$$A = \frac{M*C_{p_air}*\rho_{air}}{W_{ch}*\frac{(hb+hf)}{2}} \quad \text{(eq. 2)}$$

$$T_B = \frac{U_{hbc}T_{ma} + U_{hrc}T_{PV} + U_{ins}T_O + A_{CV} * \alpha_B * G * \tau_{STPVG}}{U_{hbc} + U_{hrc} + U_{ins}} \quad \text{(eq.3)}$$

$$T_{pv} = \frac{T_o U_{ho} + A_{CV} * \alpha_{STPV} * G * A_{fraction} - P_{elec} - q_{sky} * A_{CV} + T_{ma}U_{hf} + T_B U_{hr}}{U_{hr} + U_{ho} + U_{hf}} \quad \text{(eq.4)}$$

$$Q_{rec} = \dot{m} * C_{p_air} * (T_{outlet} - T_O) \quad \text{(eq.5)}$$

$$P_{elec} = \eta_{pv} * \alpha_{pv} * G * A_{pv} \quad \text{(eq.6)}$$

$$Q_{sky} = e_1 * \sigma * (T_{PV} + 273.15)^4 - \left(T_{sky} + 273.15\right)^4 \quad \text{(eq.7)}$$

Semi-transparent photovoltaic (STPV) modules with a transparent glass between the solar cells, were selected to allow for a portion of the irradiance to reach the back cavity surface, reducing heat losses from the PV surface and increasing heat recovery. A packing factor of 0.9 is used. The PV properties are listed in Table 1 (Prism Solar, 2023) along with the assumed BIPV/T material properties listed in Table 2.

Table 1: PV Specifications (Prism Solar, 2023)

Model	**Prism Solar BI60-381BSTC**
Type	Mono-crystalline
Exterior Glass Dimensions	985 X 1696mm (1.67m^2) X 6.4mm
Module Efficiency	18.1%
Power Temperature Coefficient	-0.376%/C
STC Temperature	25°C
STC Power	300W

Table 2: Parameters assumed for BIPV/T

BIPV/T
STPV Absorptance=0.85
Back cavity surface absorptance= 0.9
Packing factor of STPV=0.893
Emissivity of Glass=0.9
Emissivity of Insulation= 0.6

3. Results

The airflow through the BIPV/T is assumed to be via a residential HRV with a range of volumetric air flow of 15.5L/s to 40.5L/s. Major outputs from the simulation were the BIPV/T outlet air temperature, the heat recovered and the electricity generation. As shown in eq. 1, eq. 2, and Fig. 5, the peak daily outlet temperature for April, follows an exponential decay trend dependent on the cavity length. Since a typical single-story house has a usable façade height of approximately 2 m to 3m it can be seen that the outlet temperature does not

approach its peak for either the high or low flow rates at these heights. The asymptote can be seen in Fig. 5 to occur between cavity heights of 8m to 13m, therefore, a C-shaped cavity was designed, as seen in Fig 6, which increases the cavity length to approximately 10m.

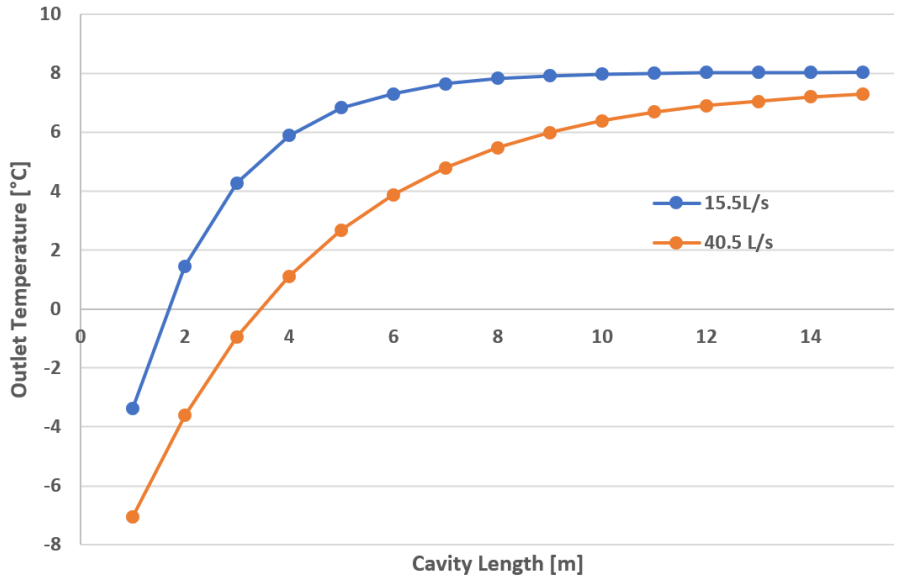

Fig. 5: BIPV/T Peak daily outlet temperature in April vs cavity length for Iqaluit, Canada

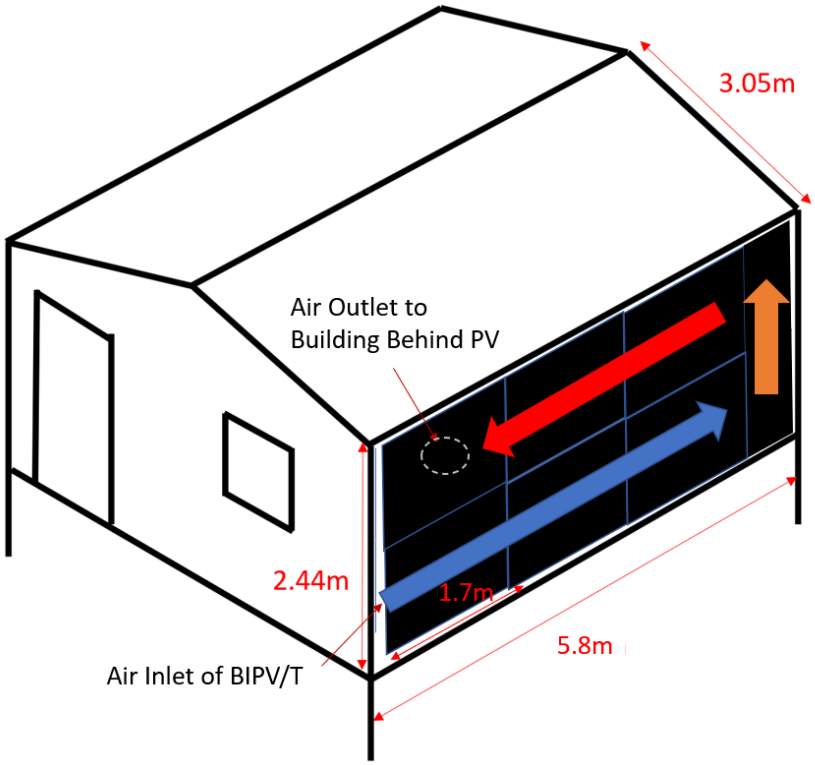

Fig. 6 C-Shaped BIPV/T

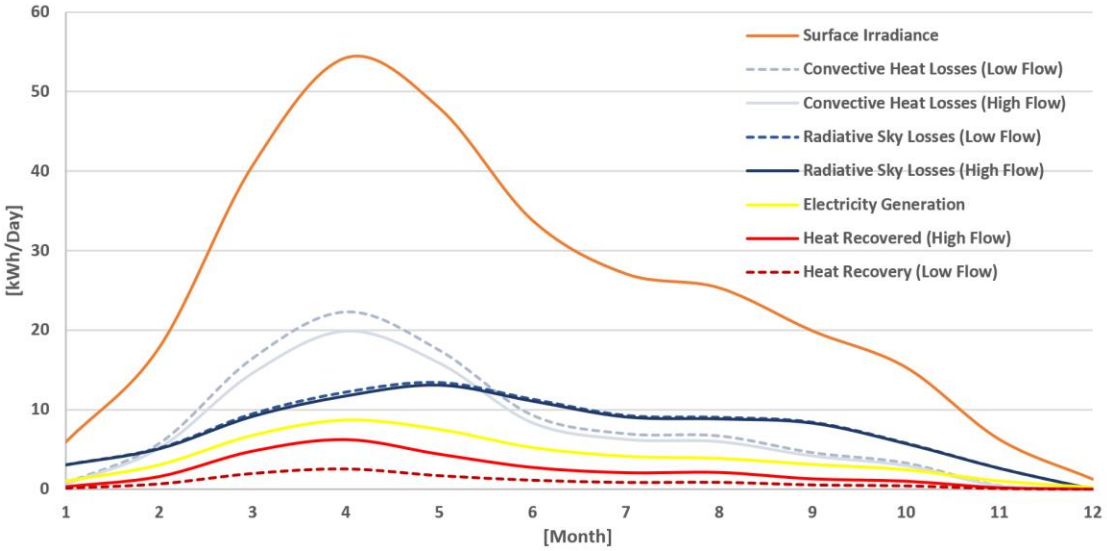

Fig.7: Solar energy conversion for 15.5L/s and 40.5L/s air flows using 10m cavity length

The surface solar irradiance is either reflected, converted to electricity, heat, or transmitted. The breakdown of the surface irradiance for the high air flow of 40.5 L/s and the low air flow of 15.5L/s is shown in Fig.7. Several strategies are available to decrease heat losses to the environment, such as increasing the cavity air flow rate, thus recovering more of the heat. As shown in Fig.7, as the air flow rate is increased from 15.5L/s to 40.5L/s, the convective and radiative losses are reduced and the heat recovered is increased. However, the increase of airflow rate reduces the air temperature rise through BIPV/T. As shown in Fig.8, the highest daily outlet temperature increases occur in April with a temperature increase of over 18°C at the low flow rate of 15.5L/s, while a delta T close to 14°C at the highest flow rate of 40.5L/s.

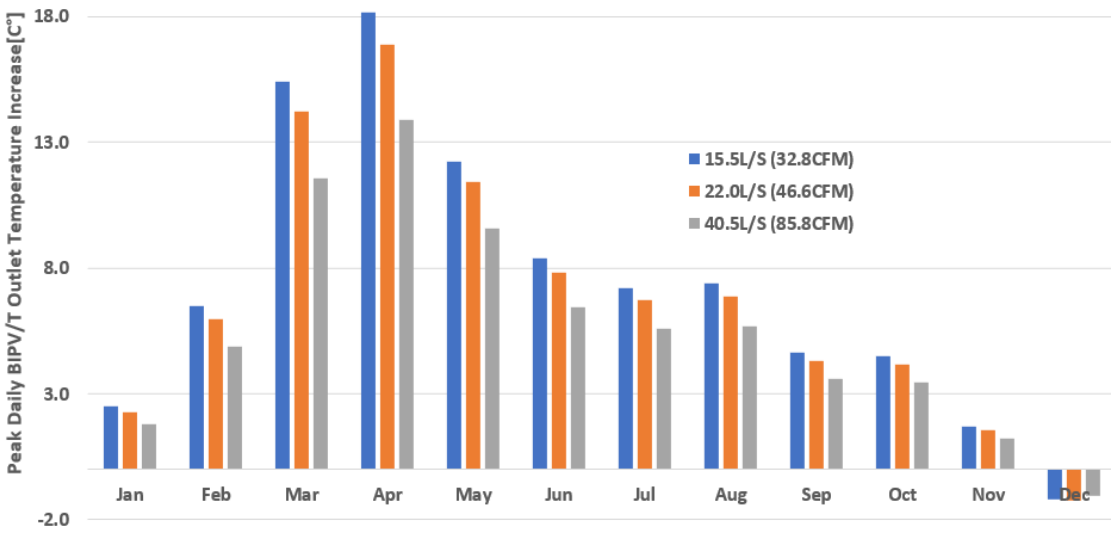

Fig.8 Daily peak BIPV/T outlet air temperatures increase

However more strategies are needed to increase the heat recovery, such as increasing the convective heat transfer from the back cavity surface U_{hbc}. As studied by (Nghana et al., 2023) it was seen that adding transverse ribs to the air cavity helped increase the air turbulence thus increasing the convective heat transfer from the cavity surfaces to the air, reducing the PV temperature, increase PV efficiency. To study the thermal enhancements for a BIPV/T, an experimental prototype has been designed (shown in Fig.9), similar to the curtain wall BIPV/T system developed by (Rounis et al., 2021), and will be tested in a solar simulator and environmental chamber lab (Fig.10), with the objective to validate the simulation model for the C- shaped cavity as well as testing the heat transfer enhancements such as alternative cavity back surfaces to increase convective heat transfer U_{hbc} by increasing the air turbulence from the cavity back surface. Other experimental objectives include testing of air flow control strategies to maximize heat recovery when applicable, and

improving durability of the design to withstand the harsh Arctic environment. Upon completion of these objectives a field prototype will be fabricated and shipped to a northern village for installation on a demonstration house for continuous field monitoring to evaluate the performance of the system throughout all seasons of the year.

(a) Back Cavity Surface (b) Integrated STPV and flow path

Fig. 9 BIPV/T Prototype

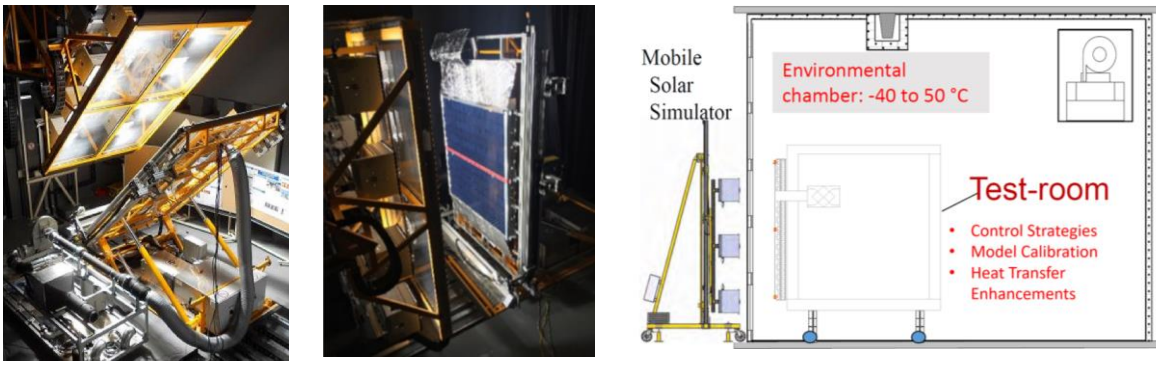

(a) Solar simulator test bed (b) Mobile solar simulator lamp field (c) Environmental chamber experimental set up

Fig.10: Concordia's Solar Simulator and Environmental Chamber Lab

4. Discussion

The average monthly peak daily outlet temperatures can be seen in Figure 11. The peak values are seen to occur in July and August when the outdoor air temperatures are the highest with values over 16°C at the lowest flow rate. As these average peak annual values are well under the typical room set point temperature of 20-22°C, the pre-heated air from the BIPV/T can be assumed to be of value almost all year round without risk of over heating the indoor space. However for periods of time when outlet temperature values are greater than 20°C are encountered then a control strategy can be implemented to increase the air flow rate, thus decreasing the outlet temperature and recovering additional heat while there is no need for HRV defrosting. Another option is the integration of the BIPV/T with an air to water heat pump, which allows for coupling with the building's hydronic heating system and leads to the possibility of thermal storage. By

controlling the airflow rate the optimal balance between outlet temperature and heat recovery can be used to boost the coefficient of performance (COP) of the heat pump and facilitates thermal storge of excess heat in water tanks or thermal mass.
Other unique thermal enhancement opportunities in the extreme cold Arctic climate is the addition of low-emissivity coatings to the inside of the outer glass surface to reduce the radiative heat losses, as well as the possibility to add an additional glazing cover to reduce the convective wind losses. While an increase in PV temperature can reduce the PV efficiency and lifespan of the module, the cold outdoor temperatures reduces the risk of over heating and when used with airflow control the air speed can be modulated to maximize the balance between PV generation and heat recovery, resulting in a increased electrical and thermal efficiency.

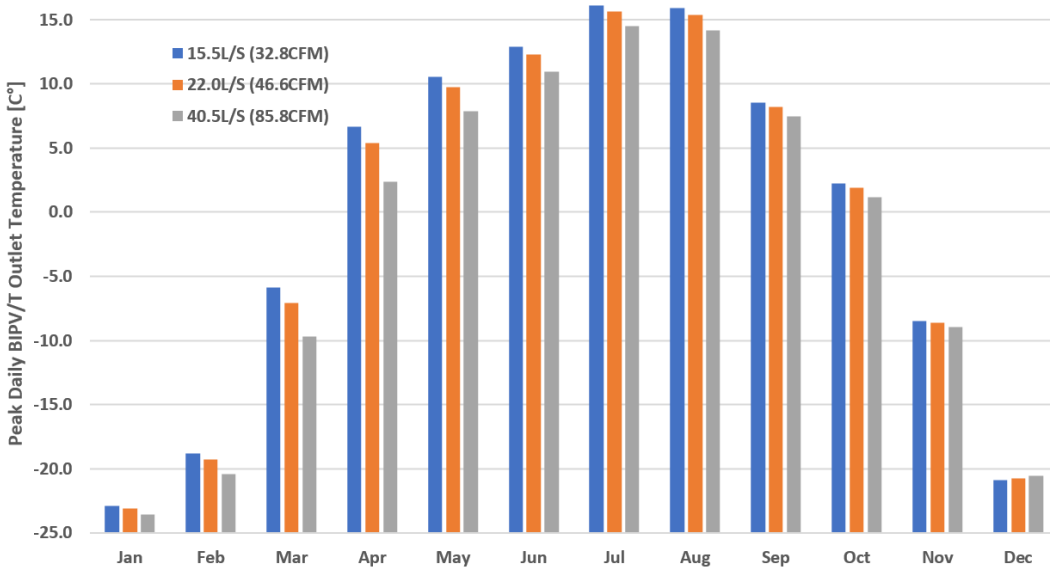

Fig. 11 Daily peak BIPV/T outlet temperature

5. Conclusions

An air-based BIPV/T system design project for a low-Arctic residential application has been started. From initial simulation modelling, the 2.4m air cavity length using the one story demonstration house needed to be increased to maximize the outlet air temperature, therefore an alternative C-Shaped channel design was chosen to increase the cavity length to 11m. The increased cavity length resulted in outlet temperature increases up to 18°C in April and more than 6.2kWh of heat recovery per day and approximately 1436kWh/year of electricity and 814kWh/year of heat. An experimental prototype has been designed and fabricated to be tested in a solar simulator and environmental lab to validate the simulation model as well as to test heat transfer improvements, using an alternative back cavity surface material to increase turbulence and convective heat transfer for improved thermal efficiencies, as well as to test air flow control strategies to prepare for a field monitoring project in a low-Arctic community of Canada.

6. Nomenclature

α_{STPV} –Absorptance of STPV
α_B –Absorptance of cavity back surface
$A_{fraction}$-Surface area of PV, m^2
Cp_{air} -Specific heat of air, kJ/kgK
hb-Cavity back convective heat transfer coefficient, W/(m^{2}K)
G – Incident irradiance, W/m^2
L_{cv}-Length of control volume, m
M – Volumetric flow rate, m^3/s
ρ_{air} -Density of air, kg/m^3
P_{elec}-Electrical energy generated, W
Q_{rec}-Heat recovered, W/m^2
T_{ma}-Cavity air mass temperature, °C
T_O - Outdoor Dry Bulb Temperature, °C
$T_{Air\ Inlet}$ – BIPV/T Inlet Temperature, °C
$T_{Air\ Outlet}$ – BIPV/T Outlet Temperature, °C
T_{pv}-PV Module temperature, °C
Uhf-Cavity front convective heat transfer coefficent, W/(m^{2}K)
Uhb-Cavity back convective heat transfer conductivity, W/(m^{2}K)
Uhf- Cavity front convective heat transfer conductivity, W/(m^{2}K)

Q_{sky}-Heat losses to sky, W/m^2
τ_{STPV} –Transmittance of STPV
T_B- Cavity back surface temperature, °C
Uho- Exterior convective heat transfer conductivity, W/(m^{2}K)
$Uhrc$- Cavity radiative heat transfer conductivity, W/(m^{2}K)
U_{ins}-Wall thermal conductivity, W/(m^{2}K)
W_{ch}-Width of cavity, m

7. Acknowledgments

This project has been funded in part by CINUK and the CFREF grant “Electrifying Society: Towards Decarbonized Resilient Communities”.

8. References

Amara, F., Dermaridiros, V., & Athienitis, A. K. (2020). Energy Flexibility Modelling and Implementation for an Institutional Net-zero Energy Solar Building and Design Application. *ACEEE Summer Study 2020 Conference on Energy Efficiency in Buildings*.

Arctic Economic Council. (2022). A small, isolated village in Arctic Canada becomes a green energy producer. In *https://arcticeconomiccouncil.com/news/a-small-isolated-village-in-arctic-canada-becomes-a-green-energy-producer/*.

Athienitis, A. K., Bambara, J., O’Neill, B., & Faille, J. (2011). A prototype photovoltaic/thermal system integrated with transpired collector. *Solar Energy*, *85*(1). https://doi.org/10.1016/j.solener.2010.10.008

Baril, D., Athienitis, A., & Ge, H. (2021). BIPV/T for arctic residential applications. *Journal of Physics: Conference Series*, *2069*. https://doi.org/10.1088/1742-6596/2069/1/012227

Baril, D., Ge, H., & Athienitis, A. (2023). Simulation Study of ERV Pre-heating for Arctic Residential Applications. *Environmental Science and Engineering*. https://doi.org/10.1007/978-981-19-9822-5_225

Beattie, C., Fazio, P., Zmeureanu, R., & Rao, J. (2018). Experimental study of air-to-air heat exchangers for use in arctic housing. *Applied Thermal Engineering*, *129*, 1281–1291. https://doi.org/10.1016/j.applthermaleng.2017.10.112

Berquist, J., Banister, C., & Krys, D. (2021). Performance of an advanced heat recovery ventilation system in the Canadian Arctic. *International Journal of Ventilation*, *20*(3–4), 183–192. https://doi.org/10.1080/14733315.2020.1777009

Canadian Council of Ministers of the Environment. (2008). *CANADA-WIDE STANDARDS for PETROLEUM HYDROCARBONS (PHC) IN SOIL*.

Candanedo, L. M., Athienitis, A., & Park, K. W. (2011). Convective heat transfer coefficients in a building-integrated photovoltaic/thermal system. *Journal of Solar Energy Engineering, Transactions of the ASME*, *133*(2). https://doi.org/10.1115/1.4003145

CINUK. (2024). *REMIROCaN*. https://www.cinuk.org/projects/remirocan/

Dimitrios Rounis, E., Ioannidis, Z., Sigounis, A. M., Athienitis, A., & Stathopoulos, T. (2022). “A novel approach for the modelling of convective phenomena for building

integrated photovoltaic thermal (BIPV/T) systems." *Solar Energy*, *232*, 328–343. https://doi.org/10.1016/j.solener.2021.12.058

Hayne, H., Carsen Banister, P., & Martinussen, N. (2023). Renewables for Decarbonization and Resiliency of Remote and Arctic Communities in Canada: Policy and Economics Review. *ASHRAE and Scanvac HVAC Cold Climate Conference*.

Li, J., Zmeureanu, R., & Ge, H. (2021). Simulation of energy impact of an energy recovery ventilator in Northern housing. *E3S Web of Conferences*, *246*. https://doi.org/10.1051/e3sconf/202124610005

Ma, L., Ge, H., Wang, L., & Wang, L. (2021). Optimization of passive solar design and integration of building integrated photovoltaic/thermal (BIPV/T) system in northern housing. *Building Simulation*, *14*(5), 1467–1486. https://doi.org/10.1007/s12273-021-0763-1

Mitter, E. K., Germida, J. J., & de Freitas, J. R. (2021). Impact of diesel and biodiesel contamination on soil microbial community activity and structure. *Scientific Reports*, *11*(1). https://doi.org/10.1038/s41598-021-89637-y

Nghana, B., Tariku, F., & Bitsuamlak, G. (2023). Numerical Study of the Impact of Transverse Ribs on the Energy Potential of Air-Based BIPV/T Envelope Systems. *Energies*, *16*(14). https://doi.org/10.3390/en16145266

Paquet, A., Cloutier, G., & Blais, M. (2021). Renewable energy as a catalyst for equity? Integrating inuit interests with nunavik energy planning. *Urban Planning*, *6*(4), 338–350. https://doi.org/10.17645/up.v6i4.4453

Prism Solar. (2023). *60-CELL BIFACIAL SERIES BN60-305*. www.prismsolar.com

Rio Tinto. (2024, July 2). *Rio Tinto completes construction of its solar power plant at Diavik Diamond Mine*. Rio Tinto completes construction of its solar power plant at Diavik Diamond Mine

Rounis, E. D., Athienitis, A. K., & Stathopoulos, T. (2021). BIPV/T curtain wall systems: Design, development and testing. *Journal of Building Engineering*, *42*. https://doi.org/10.1016/j.jobe.2021.103019

Sigounis, A. M., Vallianos, C., & Athienitis, A. (2023). Model predictive control of air-based building integrated PV/T systems for optimal HVAC integration. *Renewable Energy*, *212*. https://doi.org/10.1016/j.renene.2023.05.059

Taillard, V., Martel, R., Pasquier, L. C., Blais, J. F., Gilbert, V., & Mercier, G. (2022). Diesel spills under stilted buildings in Canadian Arctic villages: what is the best remediation method? *Polar Research*, *41*. https://doi.org/10.33265/polar.v41.7724

Tarquti. (2024). *Tarquti - Tarquti*. https://tarquti.ca/communities/kuujjuaq/

Yang, T., & Athienitis, A. K. (2014). A study of design options for a building integrated photovoltaic/thermal (BIPV/T) system with glazed air collector and multiple inlets. *Solar Energy*, *104*, 82–92. https://doi.org/10.1016/j.solener.2014.01.049

Yang, T., & Athienitis, A. K. (2016). A review of research and developments of building-integrated photovoltaic/thermal (BIPV/T) systems. In *Renewable and Sustainable Energy Reviews* (Vol. 66, pp. 886–912). Elsevier Ltd. https://doi.org/10.1016/j.rser.2016.07.011

Energy Building Sustainability by Optimized Daylight Tubes

Berta García-Fernandez[1], Antonio Álvarez Fernandez-Balbuena[2], Mikel Jaureguizar[3], Miguel Angel Garcia[3] and Daniel Vazquez-Moliní[2]

[1] ETSI Montes, Forestal y del Medio Natural, Dpto. de Ingeniería y Gestión Forestal y Ambiental, Centro de I+D+i para la Conservación de la Biodiversidad y el Desarrollo Sostenible (CBDS) Universidad Politécnica de Madrid, Madrid (Spain)

[2] Facultad de Óptica y Optometría, Departamento de Óptica Universidad Complutense de Madrid, Madrid (Spain)

[3] Normagrup, Asturias (Spain)

Abstract

New interest in Innovative Daylight Systems has emerged strongly because energy consumption must be reduced, and human environment conditions improved. Light propagated through prismatic films, exhibits a characteristic behavior optimal for energy savings, sustainability and environmental conservation. These optical particularities and capabilities can be useful for multiple applications in areas such as architectural lighting, automotive lighting, and display technology. Therefore, it is essential to consider the optical properties of these singular light guiding systems to control light energy and thus, accurate simulations and modeling are necessary to improve the designs. In this study, the application of Fresnel's equations is compared with basic Snell's law showing the angular propagation differences and the influence of defects in peak's prism is quantified. In this framework, a prototype in real scale has been developed and tested.

Keywords: Energy saving, Innovative Daylighting Systems, Daylighting, Light guides, Sustainability

1. Introduction

Saving energy is key to fighting climate change and reducing the energy dependency. Energy efficiency improvements could reduce not only CO_2 emissions, but also the bill for energy imports (Energy saving: EU action). Demand for lighting is continued increasing driven by strong growth in many fields like buildings or display technologies. Within this context, improving energy saving is essential by means of efficient lighting systems, which implies a truly exhaustive study of the optimal optical components of lighting systems for proper use. The use of natural light in buildings is very valuable because energy consumption can be reduced and human environment conditions can be improved (Sharp, 2014). Innovative Daylighting Systems (IDS) have been developed over the last few decades to increase daylight levels within buildings where it is not possible with simple windows or domes (Littlefair, 1994; Mayhoub, 2014; Kim, 2010). They improve and control daylight, minimize glare and reduce energy consumption. Hollow Light Guides (HLG) are IDS that channels light into the core of the buildings through long distances (Garcia-Fernandez, 2023; Osama Omar, 2018; Nair, 2014), they can transmit high-diameter light beams in daylight and artificial lighting applications without relevant losses. Hollow Prismatic Light Guides (HPLG) are made from a plastic transparent prismatic film with a plane surface on the inner side and prisms with right angle on the outer side. Prismatic films are especially valuable for their performance in light guiding and is used for multiple applications in areas such as daylight in architecture, lighting, solar concentrator systems, automotive illumination and displays (Xie B, 2015; Wang, 2015). Light introduced into the light guide at the appropriate angle range will be retained inside the guide and guided long distances due to the phenomenon of Total Internal Reflection (TIR) (García-Fernández, B, 2015). The multiple reflections of light existing in these optical guiding elements and their interaction with surface defects cause uncontrolled light that leaves the ideal optical ray pattern and increases exponentially with the distance travelled. Simulate accurately prismatic lighting systems performance is a complex task due to the amount of computation necessary to represent data of light paths. Thus, as a rule, calculations are usually made by the simple method based on approximations of the law of Snell, this procedure don't consider partial reflections or transmissions defined by Fresnel equations (Dupertuis, 1994; De Greve, 2006; Born, 2013). Within this context, this study presents a detailed analysis applied Snell's Law and Fresnel equations for all incident angles and shows the influence of a curved apex of the prism which simulates defects in corners. The defects in corners have been meassured by Scanning Electron Microscopy (SEM) based image analysis. Firstly, a theoretical study of optical properties was made using the Snell's law and Fresnel's equations. Secondly the defects in corner as key element of

© 2024. The Authors. Published by International Solar Energy Society
Selection and/or peer review under responsibility of Scientific Committee
10.18086/eurosun.2024.01.02 Available at http://proceedings.ises.org

efficiency in guiding were tested by a ray-tracing software TracePro. Finally, experimental measurements were made to compare the simulated result with measured data.

2. Theoretical context Snell's law versus Fresnel equations

Snell's law gives the relationship between the incidence angle and refraction θ (or reflection θ') for a ray impinging on an interface between two media with different refraction index n (Fig.1). The Snell's Law is expressed as:

$$n \sin\theta = n' \sin\theta', \quad \text{(eq. 1)}$$

The vector form of Snell's Law is used for calculating the direction of transmitting light in software simulations by a coordinate-free formalism based on vector algebra.

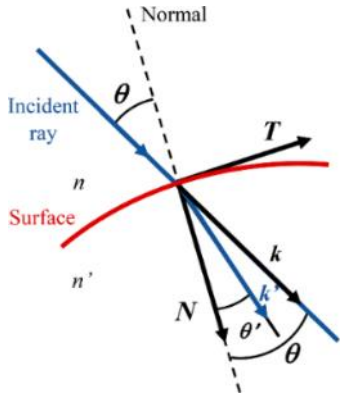

Figure. 1. Refractive optical surface represented by tracing vector rays

Writing Snell's law using the direction vectors of the incident and refracted rays' $\boldsymbol{k}$ and $\boldsymbol{k}'$ and the surface normal vector $\boldsymbol{N}$. These vectors are coplanar, so that both k and k 'may be expressed as a linear combination of two vectors in the plane of incidence, the normal $\boldsymbol{N}$ and the tangent vector $\boldsymbol{T}$. In figure 1, the incident ray is defined by a vector $\boldsymbol{k}$ with an angle of incidence θ. After refraction at the surface, the refracted ray is defined by a vector $\boldsymbol{k'}$ with an angle of refraction θ'. The normal to the surface at the point of intersection of the ray with the surface is denoted by a vector $\boldsymbol{N}$. We can define a vector in the plane of $\boldsymbol{k}$, $\boldsymbol{k'}$, and $\boldsymbol{N}$, and parallel to the surface at the point of incidence. This unit vector is denoted by $\boldsymbol{T}$. From Fig. 1 we can see that:

$$\boldsymbol{k} = \cos\theta\, \boldsymbol{N} + \sin\theta\, \boldsymbol{T}, \quad \text{(eq. 2)}$$

Hence, the vector in the direction of propagation is given by:

$$\boldsymbol{k}' = \cos\theta'\, \boldsymbol{N} + \sin\theta'\, \boldsymbol{T}, \quad \text{(eq. 3)}$$

Equation 2 can be combined with 3 to give

$$\boldsymbol{T} = \frac{\boldsymbol{k} - \boldsymbol{N}\cos\theta}{\sin\theta} = \frac{\boldsymbol{k'} - \boldsymbol{N}\cos\theta'}{\sin\theta'}, \quad \text{(eq. 4)}$$

Therefore,

$$(\boldsymbol{k} - \boldsymbol{N}\cos\theta)\sin\theta' = (\boldsymbol{k}' - \boldsymbol{N}\cos\theta)\sin\theta, \quad \text{(eq. 5)}$$

and, using Snell's law,

$$(\boldsymbol{k} - \boldsymbol{N}\cos\theta)n = (\boldsymbol{k}' - \boldsymbol{N}\cos\theta)n', \quad \text{(eq. 6)}$$

Finally, we can summarize with the general expression of Snell´s law written in vector form, which is given by the expression,

$$n'\boldsymbol{k}' - n\boldsymbol{k} = \boldsymbol{N}(n'\cos\theta' - n\cos\theta). \quad \text{(eq. 7)}$$

$$\boldsymbol{k}' = \frac{n\boldsymbol{k} + \boldsymbol{N}(n'\cos\theta' - n\cos\theta)}{n'}. \quad \text{(eq. 8)}$$

TIR occurs whenever the incident beam in the optically denser medium strikes the boundary at an angle of incidence equal to, or grater tan a critical angle given by:

$$\sin\theta_c = \frac{n_2}{n_1}. \quad \text{(eq. 9)}$$

The condition was defined purely geometrically by setting,

$$\theta' = \frac{\pi}{2} \quad \text{(eq. 10)}$$

Total Internal Reflection occurs whenever the incident beam in the optically denser medium strikes the boundary at an angle of incidence equal to, or grater tan a critical angle given by setting sin $\theta'=\theta$. In calculations, Fresnel reflection is based on refractive index and the complex index of refraction is defined by,

$$\check{n} = n + ik\,, \quad \text{(eq. 11)}$$

where k is the extinction coefficient defined as,

$$k = \frac{\lambda\alpha}{4\pi}. \quad \text{(eq. 12)}$$

λ is the wavelength and α is the absorption coefficient.

Fresnel equations describe the ratios of the reflected and transmitted waves' electric fields to the incident wave's electric field [14]:

$$t_s = \frac{2n\cos\theta}{n\cos\theta + n'\cos\theta'}, \quad \text{(eq. 13}$$

$$r_s = \frac{n\cos\theta - n'\cos\theta'}{n\cos\theta + n'\cos\theta'}, \quad \text{(eq. 14)}$$

$$r_p = \frac{n\cos\theta' - n_2\cos\theta}{n\cos\theta' + n_2\cos\theta}, \quad \text{(eq. 15)}$$

$$t_p = \frac{2n\cos\theta}{n\cos\theta' + n'\cos\theta}, \quad \text{(eq. 16)}$$

Power reflectivity and transmission is then calculated as,

$$R_{s,p} = \left|r_{s,p}\right|^2, \quad \text{(eq. 17}$$

$$T_{s,p} = \frac{n'\cos\theta'}{n\cos\theta}\left[t_{s,p}\right]^2. \quad \text{(eq. 18)}$$

The unpolarized case is computed as an average between *S* and *P* polarizations.

3. Application of Snell's law and Fresnel's equations for light propagation in prismatic dielectric films.

In this section, we report a computer simulation analysis of light transmission and reflexion in prisms comparing the results applying the Snell's law and the Fresnel's equations. Fresnel equations show a more detailed explanation of the process of light refraction and refraction at a boundary than Snell's law. The behavior of the right-angle prism as a function of the incident angles along the base of the prism has been studied by three-dimensional simulations performed in a non-sequential optical raytracing called TracePro [15]. The transparent optical material used is defined as continuous, homogeneous, perfect transmitter and non-absorbing. The incident light is assumed to consist of a plane wave of infinite extent. In simulations, the light rays enter through the base of a PMMA (Polymethylmethacrylate) prismatic structure and undergo TIR and refractions on the inner surfaces of the prism. Firstly, data processing was performed to evaluate light patterns. Secondly, a curved prismatic peak is developed and examined to assess the importance it can have in ray patterns and thus in transmission efficiency and guide of light.

The prismatic optical structure with an apex angle of a right-angle is characterized by polycarbonate material with a refractive index of 1.59 without consideration of absorption. Seven discrete equidistant quarter spheres (P1-P7) are inserted in the prismatic base to analyze the full angular range of light incidence and the flux ratio of light rays in several positions. The light source emits in the full angular range at a wavelength of 550 nm. The coordinate system

used defines the angles α and β are the direction cosines of the departing ray in X and Y axis. Rays emitted are propagated through the prism, undergoing refractions and reflections on the inner surfaces of the extruded prism. After analyzed ray behavior, the definite patterns of internal reflections and refractions within the material are computed. Figure 2 represents, at each position, the ray pattern obtained. The internal directionality happens through different patterns after the first refraction of a ray through the base of the prism. Firstly, a Double TIR of light (DTIR) occurs as is shown in Fig. 2 (a), in this case the light beam is guided along the interior material by means of two TIR following the Snell's law, and it returns to the base of the prism. In this pattern, some rays found are directed towards the left side (L) and other rays are directed towards the right side (R), depending on the internal surface on which ray effect. Secondly, a Multiple Internal Reflection (MTIR) occurs, in which one of the angles of the reflected ray is reversed (compare it with an ordinary specular reflection), in this case the beam undergoes three TIRs, as shown in Figure 2 (b). Finally, there are two patterns in which the rays are expelled to the outer upper surface. In one pattern, the beam is expelled after only one refraction through the prism side, Transmission 1 (TA1) shown in Figure 2(c). In the other pattern, the beam undergoes first a TIR and later, comes out by refraction through the prismatic side, Transmission 2 (TA2) (Fig. 2 (d)). From the point of view of the efficiency of a light pipe, TA1 and TA2 are considered the negative cases, since the necessary condition for guiding is not met. The prisms of Figure 2 represent the principal ray defined by Snell's law. There are reflected rays with lower energy which carry on the DTIR or MTIR pattern on the exit surface. This energy will be calculated by applying the Fresnel equations.

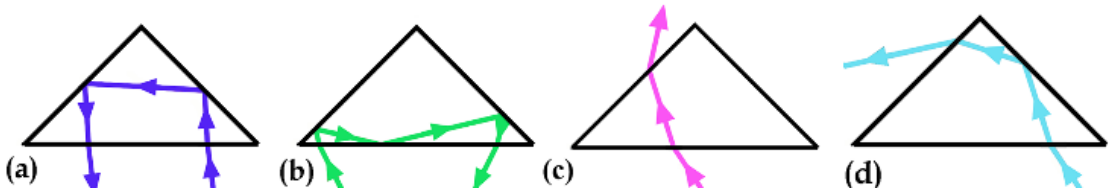

Figure. 2. Prism ray patterns evaluated; the arrows indicate the direction of the light beam. In the first figure (a), rays experience Double TIR (DTIR). In the second figure (b), the ray undergoes Multiple Internal Reflection (MTIR). Finally, in the last two patterns, the rays are expelled to the outside by Transmission (TA1) (c), and by TIR plus Transmission (TA2) (d)

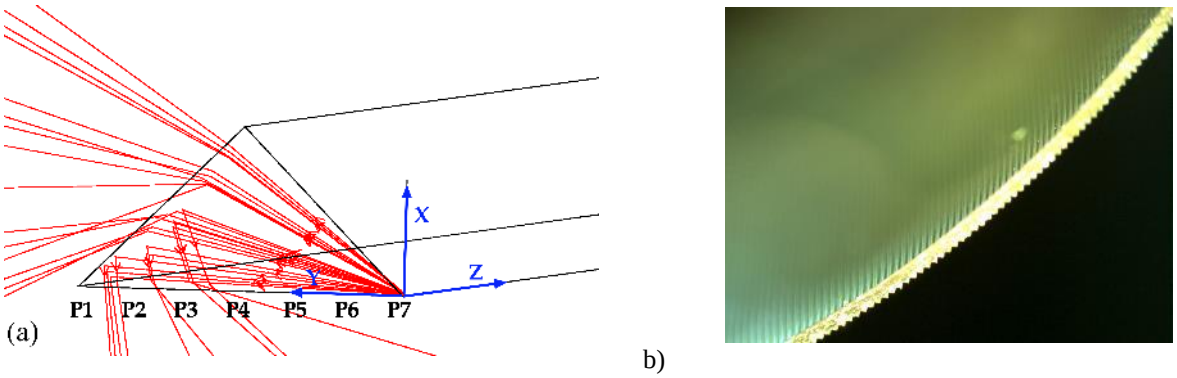

Figure. 7. Ray positions in Prismatic structure: P1, P2, P3, P4, P5, P6 and P7 (a). Perspective view of prismatic film (b). The ray flux is obtained for each pattern (Ro) defining the angular behaviors of each ray position (Fig. 7(a)). Figure 7 (b) shows a perspective view of the prismatic film.

2. 1. Snell's law versus Fresnel equations, ray path analysis in the prismatic structure

The optimization of light guidance is required in order to obtain more efficient lighting systems. Fresnel equations show a more detailed explanation of the process of light refraction and refraction at a boundary than Snell's law. Optical simulations were performed by the meaning of Snell' Law and Fresnel equations to make comparisons by processing the ray path information in MATLAB software.

Results of calculations are presented in Fig. 3, Fig. 5, Fig. 7. Figure 3 shows the angular range in degrees where TIR is produced by means of director angles (DTIR and MTIR), the positive directions of the coordinate axes are defined by alpha α, determined by the angle formed with the direction of the x axis, and beta β, defined as the angle formed with the positive direction of the y axis. By applying Snell's Law, the total flux of transmission (TA1 plus TA2) has constant values of 67.88%. Those who suffer TIR (MIR plus DTIR) are guided internally, add up to a value of 32.12 %. There is an angular range in which light acts by the phenomenon of TIR and will fulfill the condition to be transmitted internally in prismatic hollow guidance systems by numerous internal reflections. The boundary angle

condition (see Fig. 3 left) defines the angular range limit of TIR and within which rays are guided along the prism system.

Fresnel losses (Fig. 3 right) had been considered in simulations to improve accuracy. A new distribution appears, setting the angular range of rays that suffer internal reflections superimposing the previous ones. When comparing the coefficients of reflection and transmission obtained by applying the Fresnel Equations from an external incidence and comparing them with the transmittance and reflectance pattern calculated by applying Snell's Law, the amount of light transmitted outside (TA1 plus TA2) decreased from 67.88 % to ~51.56 %. Thus, results indicated a significant increase in light rays that suffer reflection plus TIR from 32.12 to ~ 48.32 %.

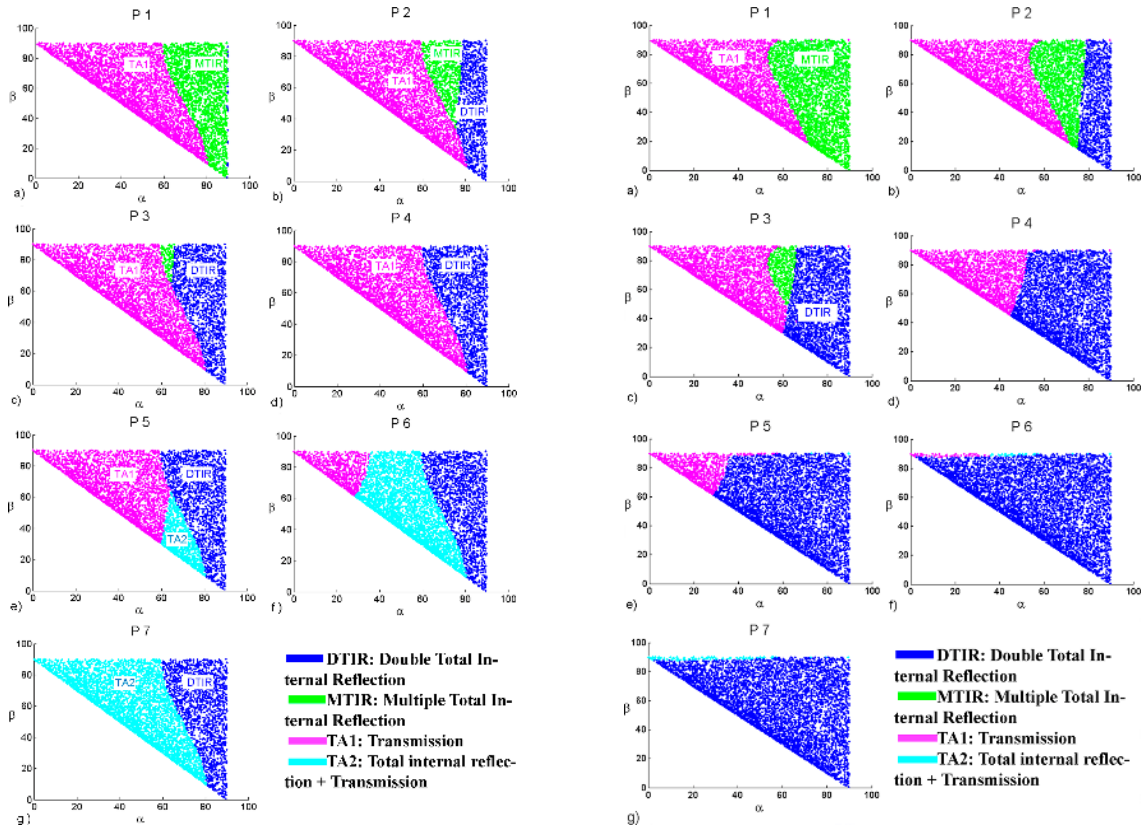

Figure. 3. (a) Graphs show the operation of light rays (P1-P7) in a perfect right angle prism by using a model based on the Snell's law (left) and Fresnel equations (right)

2.2. Scanning Electron Microscopic analysis, roughness influence

The defects were studied using Scanning Electron Microscopic (SEM-Tescan Mira 3). The image processing allows us to estimate a defect width of ~5-10 μm by measuring changes in surface roughness, which represents about 4.7% of prismatic surface. Defects in the surface have been identify in corners and defined by a curved region in simulations to compute the influence of corner defects in light guidance. Figure 4 shows the image of a prismatic peak obtained with Scanning Electronic Microscopy (SEM; Mira3 TESCAN).

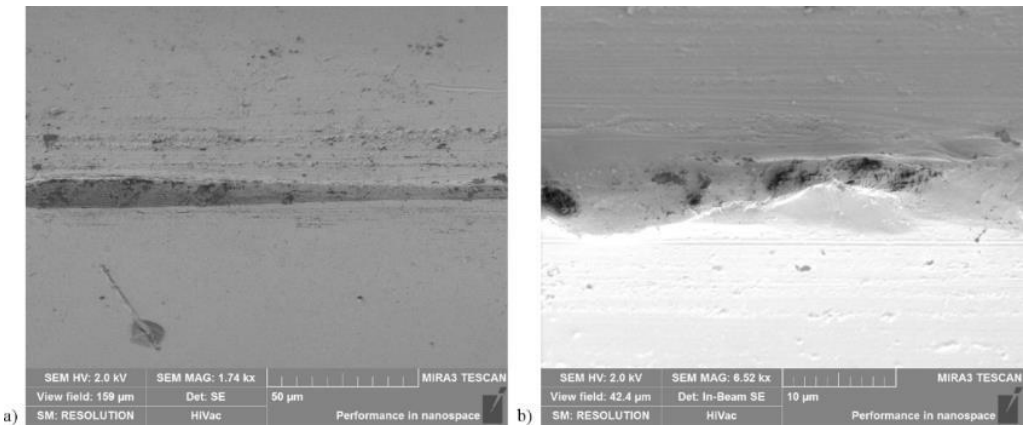

Figure. 4. Low (1.74 kX) (a) and high (6.52 kX) (b) magnification Scanning Electron Microscope (SEM) images of the

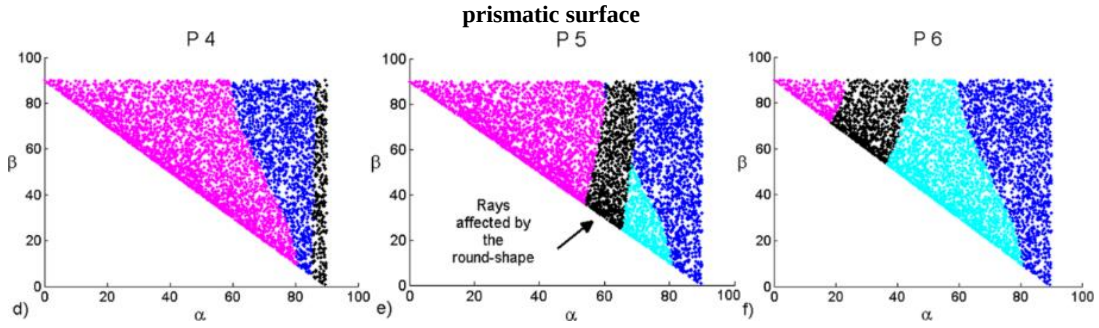

Figure. 5. Patterns of refracted and reflected rays located in positions P4, P5, P6 affected by rounded peaks (CP) in black color

Figure 5 shows in black color (CP) the rays affected by the round shape. The existence of the curved area on the peak of the prism modifies the optical path in positions P4, P5 and P6 and therefore the rays that impact over the rounded peak is redirected to other directions undergoing multiple internal reflections. In this case, many mixed patterns appear and some of those light rays are directed through the internal prism structure undergoing by multiple TIRs in the inner surfaces. Positions P1, P2, P3 and P4 are not affected by the rounded peak because no light strikes this surface. The influence of peak defects causes changes in behavior of rays. Thus, control the influence of defects on surfaces and objectify improvements in manufacturing processes are basic parameters in prismatic guidance systems.

2.3. Pattern classification ratio

Results are computed considering the angular distribution of a 90º quadrant (Fig. 8 (a)) and the total amount affected by a hemisphere emission range of 180 degrees (Fig. 8 (b) defined as.

$$R = \frac{R_o}{R_i} \quad , \qquad \text{(eq. 19)}$$

where Ri is the input flux and Ro represents the output flux.

The ratio associated with defined patterns for each position Figure 3 (left) and Figure 5 is given in Figure 8. The flux ratio obtained from patterns DTIR, TA1 and TA2, shows lower values than those found with perfect right angle peaks due to the rounded peak. The ratio of the rounded peak encompasses different light behaviors and rays that strike the inner surfaces of the prism and guide through the interior of the material.

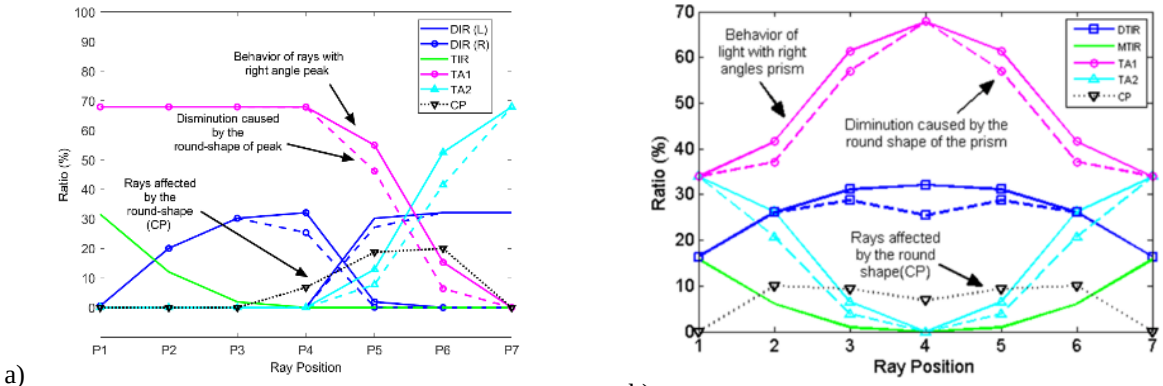

Figure 8. Patterns in a perfect prism for seven positions evaluated (continuous line). the angular behaviors of the rays considering an angular quadrant emission range (a) and the total amount affected by a hemisphere emission range of 180 degrees (b).

Tab. 1: Percentage of patterns affected by the perfect right angle prism and the curved right-angle prism

	Perfect Right Angle Prism	Curved Right Angle Prism
DTIR	25	24
MTIR	7	7
TA1	49	46
TA2	19	17

CP	-	7

4. Polar Intensity Distribution

The polar intensity distributions of the perfect right angle prism by applying Snell and Fresnel equations are shown in Figure 9 (a) and (b) and the light distribution produced in a rounded right angle prism simulating defects in apex is represented in Figure 10 (a) and (b). The Polar Luminous Intensity Graph illustrates the distribution of luminous intensity, in candelas, for the transverse (blue line) and axial (red line) planes of the luminaire. The curve in Figures 8 and 9 (a) shown the type of distribution expected from the prism acting as light source with side emitting pattern of peak intensity in 50º and semi-indirect. The curve in Figures 8 and 9 (b) shows the type of distribution expected from the prism with a rounded in peak.

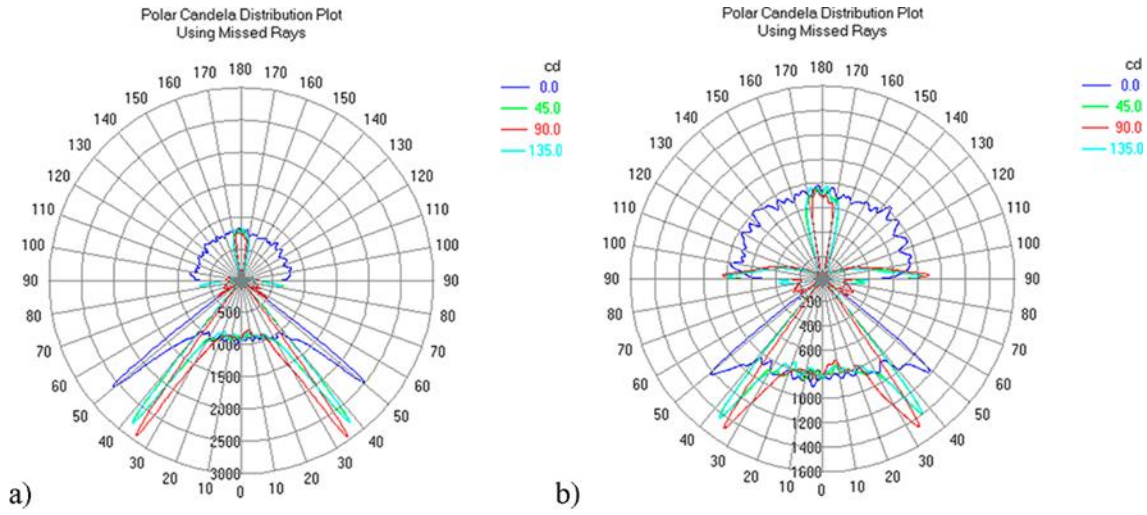

Figure. 9. Intensity distribution curves generated by applying Snell (a) and Fresnel (b) equations in a perfect right angle prism

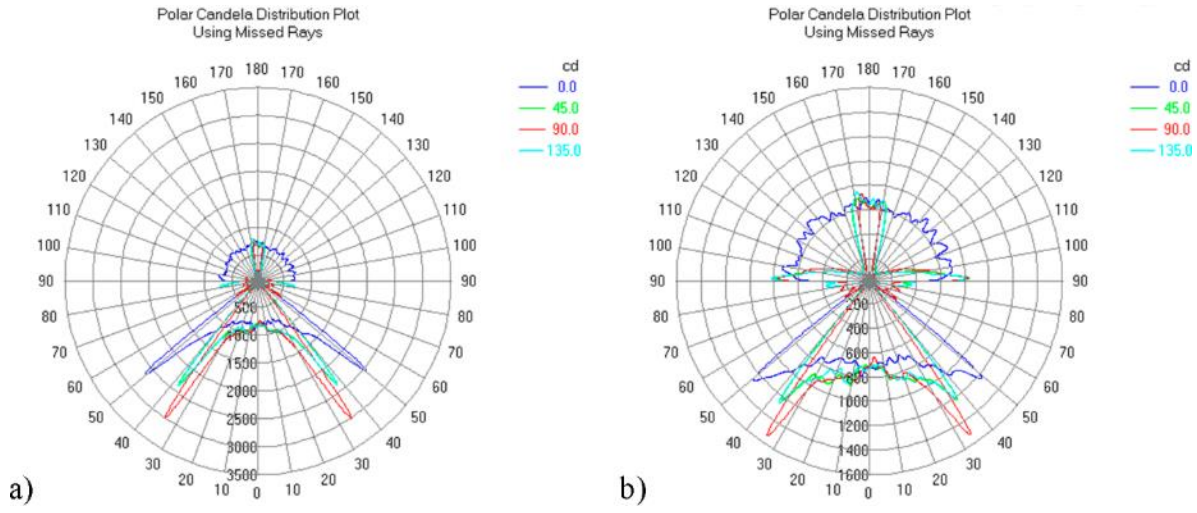

Figure 10. Intensity distribution curves generated by applying Snell (a) and Fresnel (b) equations with a rounded in peak

5. Hollow Light Guide Prototype: Laboratory Testing

This section shows an experimental model consisting of a 1:5 scale Hollow Prismatic Light Guide (HPLG), designed to illuminate a 47.52 m2 office space with natural light. The rectangular light guide has 2 m length, and the aperture side is 0,1 m, this HPLG simulates a big one of 10 m length and 0,5 m the aperture side, this corresponds to an aspect ratio of 20. Figure 11 shows a Schematic representation of the light pipe illumination device in section (a) front elevation (b) floor plant (c) and the first state of the prototype experimental mock-up (d).

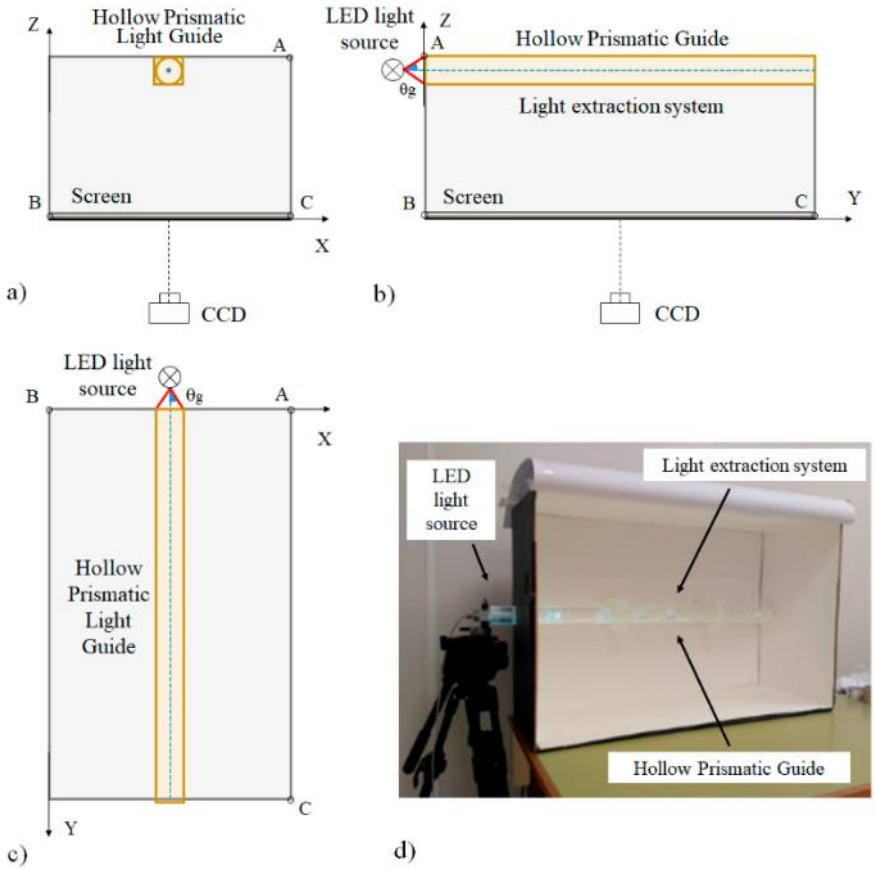

Figure 11. Schematic representation of the light pipe illumination device. (a) Section (b) Front elevation (c) Floor plant (d) Experimental mock-up. (b)

Figure 12 (a) shows the lateral view of the specified light pipe configuration. Figure 12 (a.1) illustrates the light distribution along the guide based on the characteristic exponential decay of the HPLG [11]. Figure 12 (a.2) represents the light behavior of a HPLG by optimizing light distribution along the guide with a light extraction system. Figure 12 (b) shows the cross-section of a Rectangular HPLG (b.1) and Cylindrical HPLG (b.2). The HPLG prototype with a rectangular light pipe (Fig. 12 (c)), a hemispherical screen collects the flux through a diaphragm appointed by a diaphragm designed to determine the light distribution. The luminous intensity distribution obtained is represented by Dialux software (Fig. 12 (d)). Figure 12 (e) shows the light distribution obtained in a square screen of the experimental mock-up. The light source is a LED which provides white uniform lambertian lighting within an angular acceptance of semiangle cone θg 30º according to the prismatic guide acceptance angle. Figure 12 (f) shows the illuminance map obtained in the experimental setup.

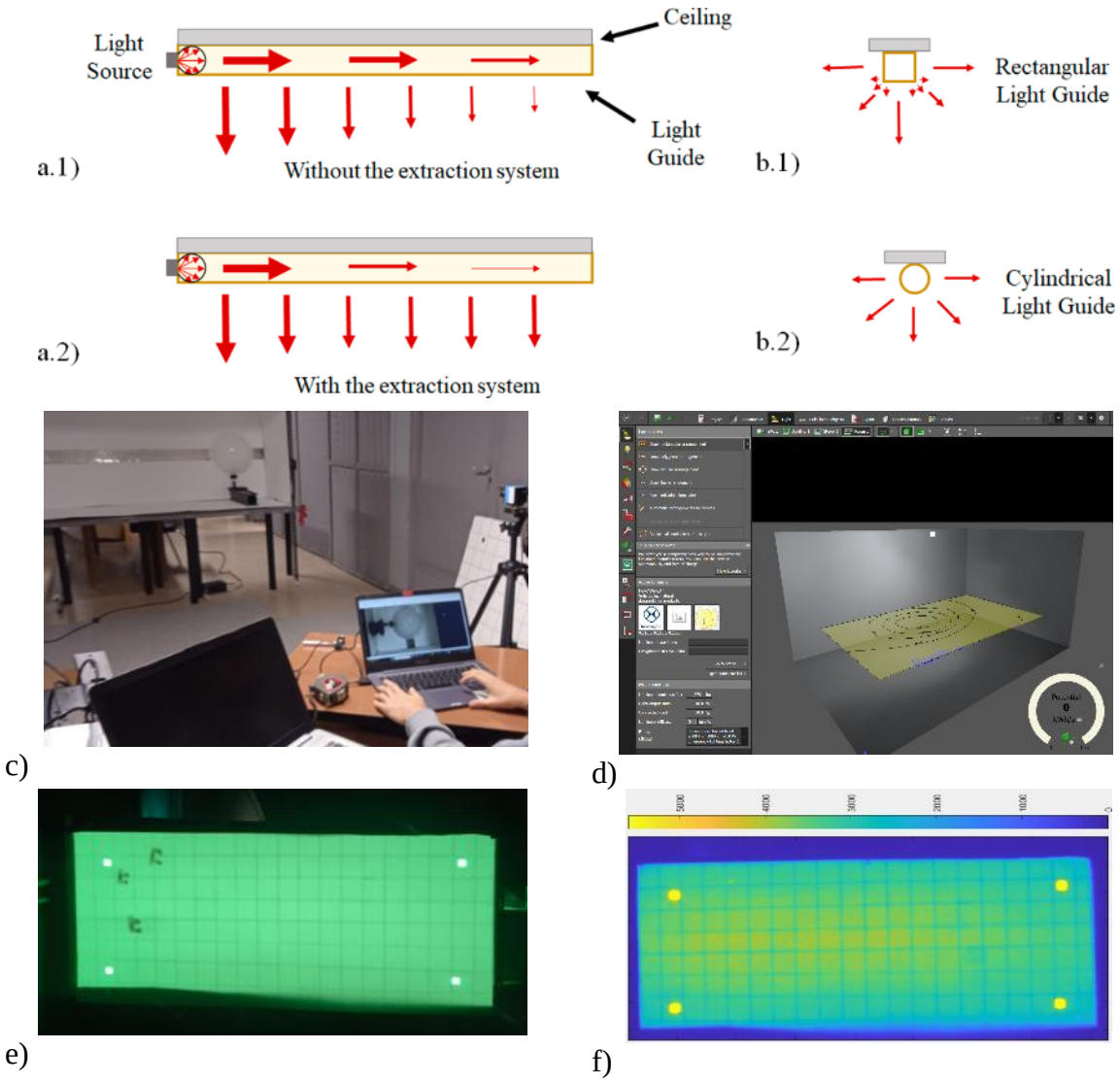

Figure 12. HPLG without extraction system (a.1) and with extraction system (a.2). The cross-section of a Rectangular HPLG (b.1) and Cylindrical HPLG (b.2). The experimental mock-up of a rectangular HPLG for photopic characterizing (c). Luminous Intensity distribution by Dialux software (d). Experimental setup image, illuminance measurement plan (e). Illuminance map of experimental setup.

6. Conclusions

Prismatic films are optical elements widely used due to its many practical applications as panel displays, renewable and green energy solutions and lighting. In this paper is presented the photometric characterization of prismatic film used in Hollow Prismatic Light Guides used to improve lighting, control daylight, minimize glare and reduce energy consumption through a new way to establish boundary conditions. The present study shows a novel classification of light transmission and the reflection properties in right angle dielectric prism by comparison of the flux rate calculated using Snell's law and Fresnel equations as a function of incidence angle and position in the prism base. Results based on Fresnel equations show a significant increase in light rays that suffer reflection plus TIR, so the total flux ratio goes from 32.12 % (Snell) to ~48.32 % (Fresnel). Scanning electron microscopy analysis shows the defects in prism's surfaces mainly located in peaks. Analysis shows that peak irregularities cause changes in behavior of rays of the order of 7% in the case of 4.7% width, this percentage is exponentially increasing due to multiple reflections in light guiding. Hence, control the influence of defects on surfaces and objectify improvements in manufacturing processes would be very advantageous for prismatic guidance performance. In this framework, a light guide in real scale has been developed and tested obtaining a uniform light distribution in the measurement plane according to the photometry of the prismatic guide.

7. Acknowledgments

This work has been funded by Normagrup and the Economic Development Institute of the Principality of Asturias: PID-1-II-23-006

8. References

Sharp, F., et al., 2014. The use and environmental impact of daylighting. *Journal of Cleaner Production*, *85*, 462-471. https://doi.org/10.1016/j.jclepro.2014.03.092

Littlefair, P. J., et al. 1994. The performance of innovative daylighting systems, Renewable Energy 5.5-8: 920-934. https://doi.org/10.1016/0960-1481(94)90113-9

Mayhoub, M. S. 2014. Innovative daylighting systems' challenges: A critical study. Energy and buildings 80: 394-405. https://doi.org/10.1016/j.enbuild.2014.04.019

Kim, J. T., & Kim, G., 2010. Overview and new developments in optical daylighting systems for building a healthy indoor environment. Building and environment, 45(2), 256-269. https://doi.org/10.1016/j.buildenv.2009.08.024

Garcia-Fernandez, B., & Omar, O., 2023. Integrated innovative solar lighting system for optimization of daylight utilization for public library in Alexandria, Egypt. Ain Shams Engineering Journal, 14(1), 101819. https://doi.org/10.1016/j.asej.2022.101819

Osama Omar, et al., 2018. Optimization of Daylight Utilization in Energy Saving, Application on the Library in Faculty of Architecture, Design and Built Environment, Beirut Arab University, Alexandria Engineering Journal, 57(4), 3921-3930, ISSN: 1110-0168. https://doi.org/10.1016/j.aej.2018.10.00

Nair, M. G., et al., 2014. Classification of indoor daylight enhancement systems. Lighting Research & Technology, 46(3), 245-267. https://doi.org/10.1177/1477153513483299

Xie B. et al., 2015. Design of a brightness-enhancement-film-adaptive freeform lens to enhance overall performance in direct-lit light-emitting diode backlighting, Applied optics, 54(17), 5542-5548. https://doi.org/10.1364/AO.54.005542

Wang Y.J: et al. 2015. High directional backlight using an integrated light guide plate, Optics Express 23.2 1567-1575. https://doi.org/10.1364/OE.23.001567

García-Fernández, B., et al. 2015. Light losses in hollow, prismatic light guides related to prism defects: a transmittance model. Chinese Optics Letters, 13(9), 092201. http://dx.doi.org/10.3788/COL201513.092201

Dupertuis, M. A et al. 1994. Generalization of complex Snell–Descartes and Fresnel laws. JOSA A, 11(3), 1159-1166. https://doi.org/10.1364/JOSAA.11.001159

De Greve, B. 2006. Reflections and refractions in ray tracing. Retrived Oct, 16, 2014.

Born, M. & Wolf. E. 2013. Principles of optics: electromagnetic theory of propagation, interference and diffraction of light. Elsevier. ISBN 0-08-026482. https://doi.org/10.1063/1.1325200

Energy saving: EU action to reduce energy consumption. https://www.europarl.europa.eu (Accessed: November 12, 2024)

TracePro® Opto-Mechanical Design Software. https://lambdares.com/tracepro (Accessed: November 12, 2024)

Enhancing Thermal Performance of Roofs Within Heavy-Weight Thermal Mass Residential Buildings in The Warm Mediterranean Climate of Lebanon

Tony L. Geagea[1]

[1]G Design, Zouk Mekael (Lebanon)

Abstract

The research aims to analyze the thermal performance of the common practice roof construction types in fully exposed heavy-weight buildings in the coastal warm zone of Lebanon. Two roof types in one residential house, are monitored simultaneously during the summer of 2023, one with a reinforced concrete slab and the other with a steel structure covered by red clay tile. Once the house was simulated using Insight 360 software, results were compared to the recorded data of every room's indoor dry bulb temperature during the day and night. This is followed by further shading and spatial manipulation to enhance the construction materials' thermal properties, giving an in-depth overview of the thermal performance of those materials. The research concludes with practical design recommendations and solutions for keeping with the same construction material yet considerably reducing the annual cooling load and relying on scarce non-renewable energy. However, enhancing the roofs' thermal performance can decrease 56% of the energy used for indoor cooling.

Keywords: Thermal simulation, Thermal mass, Warm climate, Summer indoor cooling.

1. Introduction

The residential sector is responsible for 40% of global energy consumption (UNDP, 2022). This is due to the large heating and cooling loads that rely on scarce non-renewable energy resources to ensure indoor thermal comfort (Hooyberghs et al., 2017). Implementing measures to reduce carbon footprint and energy consumption is essential to mitigate the negative impact on the environment (Hachem-Vermette et al., 2019). While implementation of energy efficiency measures in residential buildings enables a decrease of 35% according to (ASHRAE, 2024). The energy used for cooling a building in a warm climate can be decreased through effective passive design techniques, choice of construction material, and enhancing the building envelope's thermal performance (Amaripadath, D et al., 2022). Lebanon relies on air-conditioning powered by diesel fuel oil electricity as a source of indoor cooling (Melki & Radan, 2005). Since Lebanon suffers from a daily power shortage. Thus, the supply cannot meet the demand.

In response to the increase of awareness on energy consumption overwhelming scarce non-renewable resources, numerous strategies and recommendations are available in Lebanon for buildings' envelope to reduce energy demands and consumption for each climatic zone issued by local and international bodies, targeting the development of low energy housing in warm climates (MOE/UNDP/GEF, 2015). It recommends highly insulated construction materials equivalent to a low U-value external envelope (external walls and roof). Moreover, the "Building Energy Codes Program" recommends thermal properties for each envelope within the four climatic zones of Lebanon that can reduce energy consumption and demand caused by cooling (Aznabaev et al., 2016). Thus, insulation is being used for hot climatic zones to reduce heat transfer and reduce heating loads (International Energy Conservation Code, 2011). However, the literature review does not support the use of insulation in hot and warm climates. Heavyweight construction materials such as concrete and their derivates are the common choice in warm environments to reduce internal temperature (ASHRAE, 2004). When it comes to the built-up fabric of Lebanon in all climatic zones combined, roofs are mainly made out of

© 2024. The Authors. Published by International Solar Energy Society
Selection and/or peer review under responsibility of Scientific Committee
10.18086/eurosun.2024.01.03 Available at http://proceedings.ises.org

materials such as reinforced concrete or steel structures roof covered by red roof clay tile cladding.

The research studies the thermal performance of roof construction materials in Lebanon. Although Lebanon has 4 different climatic zones, the paper deals with the coastal warm zone which has cool and short winters, and hot, humid, and long summers (UNDP, 2005). The common roof construction type in Lebanon has reinforced concrete slabs and an optional steel-pitched roof covered by red clay tiles. These materials are labeled as heavyweight materials or thermal mass due to their capacity to absorb, store, and release heat (UNDP, 2005).

Del col Diaz et al. (2010) studied the concrete as a construction material to achieve an efficient thermal resistance in warm climates without an effective insulation property. The insulation has its impact on air flow within the unit's modeled interior space. Where it increases the thermal performance of the concrete. This research showed an increase of 42% through insulation. They showed the difference between insulated and non-insulated concrete slab. The next paper by Pierquet P. et al. (1998) compares eleven different slab systems to the lightweight insulated construction such as steel construction, and concrete construction. Concrete construction shows the best long-term energy performance compared to other construction materials in warm climate. Several studies have tackled the issue of reducing energy consumption by minimizing the demand for cooling in warm and hot climates (Visser et al., 2013), (Bretz et al., 1998), and (Prado et al., 2013). Their research outlined the reliance on passive strategies switching to being independent of fossil fuels. These strategies are natural ventilation, passive cooling, and reducing heat gain from the roof. Retrofitting has been addressed to improve indoor comfort conditions and reduce energy demand and consumption. (Blázquez et al., 2019) proposed retrofitting strategies for improving ventilation and adding insulation layers on 218 housing units. (Suárez et al., 2015) applied to retrofit strategies for a 68-apartment unit in a residential building in Cordoba, Spain. Results show that this reduced 38% of the total energy demand. (Suárez et al., 2015) highlighted a significant envelope improvement as increasing insulation and night ventilation. This led to a reduction of 27% of energy for indoor cooling. (Panayi, 2004) Investigated the impacts of different passive strategies for retrofitting on cooling energy consumption as insulation, glazing, thermal mass, and orientation of a house in Nicosia, Cyprus. The analysis was conducted through simulation software. Results showed that the most effective measure is double glazing, 25 mm of wall insulation, thermal mass, and roof insulation. (Florides et al., 2000) studied a house in Cyprus analyzing its cooling load throughout the year. Results showed that roof insulation reduces cooling demand by up to 57%.

This study investigates a building's roof as an external envelope by comparing two common construction materials in Lebanon to study their thermal properties during the summer of 2023. The aim is to monitor the internal dry bulb temperature of every room to assess each roof construction material's impact under the same conditions. Where, rooms are identical in windows' type and size, walls, construction materials, shutters, surroundings, and occupancy. The duration of the monitoring allowed weekly comparisons between results to experiment with random changes. The purpose was to test the behavior of each material during the day and night. Following an overview of previous studies that deal with temperature monitoring of each of the cited construction materials.

The research aims to assess the potential of decreasing energy consumption by enhancing the thermal properties of the roof's construction materials used in Lebanon to minimize cooling loads that depend on scarce non-renewable energy.

2. Methodology

This research is carried out on a residential house located in Jounieh area (33.9843° N, 35.6344° E), 20 km northeast Beirut, 60 m above sea level (Figure 1), monitoring its internal temperature for a period from August 2023 till September 2023 (summer of 2023). It is a two-floor residential house having two different external envelopes: limestone 30 cm for the external and internal walls and concrete masonry unit (CMU) 10 cm for the rooms that have been added lately. Part of the roof is a 15cm reinforced concrete, while the other part has a steel slab covered by clay roof tiles (Figure 2). The slab between the ground floor and the first floor is a steel structure covered with ceramic tiles. All the internal walls are plastered and painted, and the windows are single glazed with a wooden frame (Figure 4).

The house has two balconies, one towards the north (14 sq. m), while the other is towards the southeast and is closed with single-glazed curtain glass. The closed balcony is 25 sq. m, and its roof is made of steel structure covered with red roof tiles. The ground floor sums up to 113 sq. m, while the first floor is 37 sq. m. The living area and the dining area on the ground floor have a double height of 6 m. The bedrooms on the ground floor are covered with corrugated sheet shading elements to use the space underneath them as a storage area.

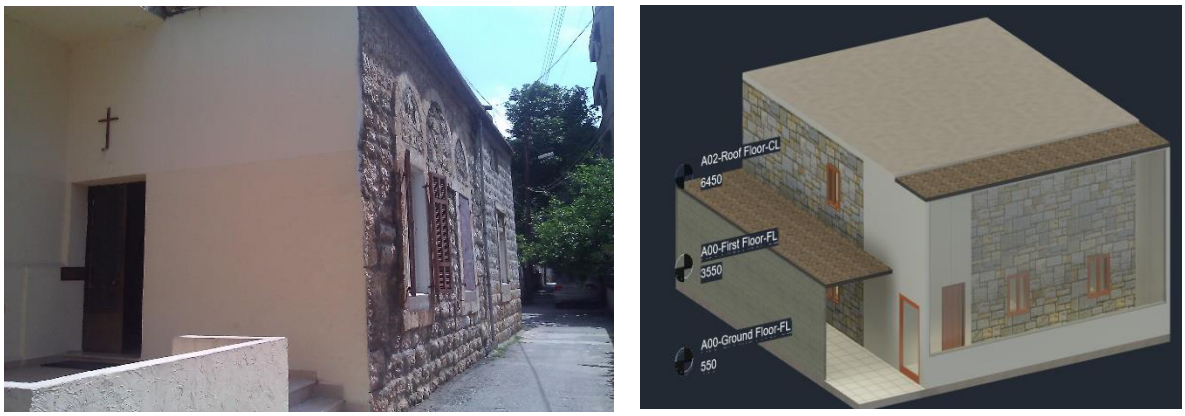

Fig. 1: Picture and isometric view showing the studied house. Source: Author.

The observation was divided into two categories. The first one (category A) is the rooms that had the reinforced concrete roof. While the second category (B) contains the rooms that have steel structure with red roof tiles. The AC in both categories work according to the availability of electricity. This is due to Lebanon suffering from daily power shortages. Affected by the high demand for electricity and the inefficiency of power plants. According to (Fardoun et al. 2012, p.317), There is a lack of electricity to meet market demands, where the demand increases while the supply decreases.

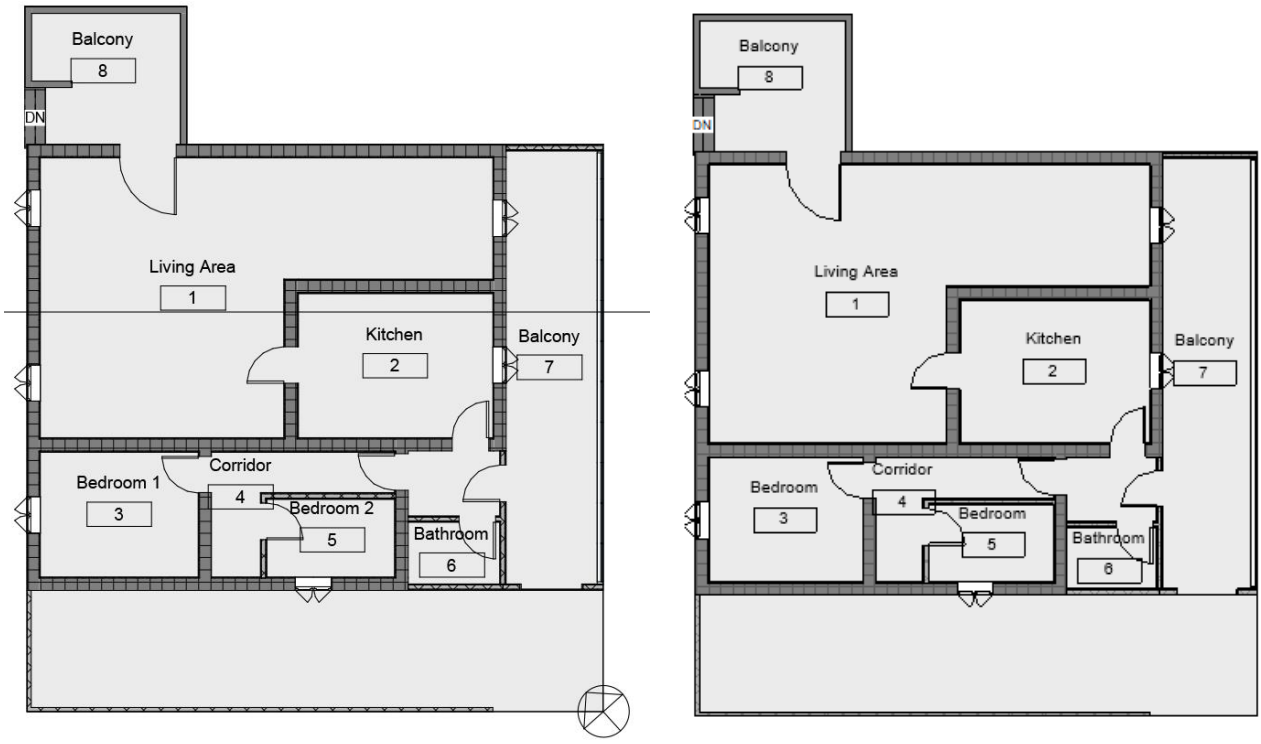

Fig. 2: Ground Floor and First Floor Plans of the Studied House. Source: Author through Revit Autodesk 2020

The current situation depends on the private sector supplying the required energy through diesel generator. The energy used for the residential sector shows that the main consumption is summer indoor cooling (MOEW/GEF/UNDP, 2015, p. 19).

Recorded temperature shows that peak temperature occurs after mid-day hottest peak when the solar radiation is directly hitting the room's roof. Also, the temperature within the most exposed rooms to the sun is constantly

higher than in the other rooms. This was shown during the observed period where the inside temperature is above the comfort band. This is in clear contrast with the recorded rooms that were least exposed to solar radiation where it was within the comfort band.

Fig. 3: Photos showing the instruments used for dry bulb data collection. Source: Author on August 2023.

In addition, the monitoring instruments consist of a Davis weather station which was installed on a nearby building's roof to record the outdoor air temperature and solar radiation at hourly intervals in °C. Also, Tiny Tag data loggers were installed in each room of the house recording the dry bulb temperature at the hour in °C. All of these values are used in the analysis to compare internal and external temperatures. Moreover, a single-phase energy meter was installed to record the air-conditioning consumption in terms of electricity in Wh.

Fig. 4: Isometric Section showing the inner space of the House. Source: Author through Revit Autodesk 2020.

Furthermore, the house was modeled by using Revit Autodesk 2020 as thermal simulation software (Figure 5). Results were compared to the recorded temperature data. Subsequently, the model was constructed and simulated by retrofitting the roof in terms of enhancing the external envelope's thermal properties to minimize cooling demand and adding shading devices. Insight 360 (Autodesk) and Green Building Studio (GBS) are energy simulation software that allows designing, analyzing, predicting, and evaluating energy consumed in models in a specific location, orientation, and climatic conditions (Fasi et al., 2015). The simulation allows a clear understanding of the impact of the building design, including retrofitting measures for existing buildings on energy consumption. A calibration was done to insure the correlation between the actual recorded data with the software simulation data. Adding to that, the simulation included the enhancement in the construction

materials' thermal performance such adding insulation and reducing sun radiation exposure to the roof surface. This resulted to have an overview of the results that will occur in case of enhancement. Reaching 222 kWh/m^2/yr which is below the benchmark set by AHRAE 90.1 (252 kWh/m^2/yr).

The research uses also the method of degree hours of overheating above 30^{o}C to establish performance ranking of the various cases.

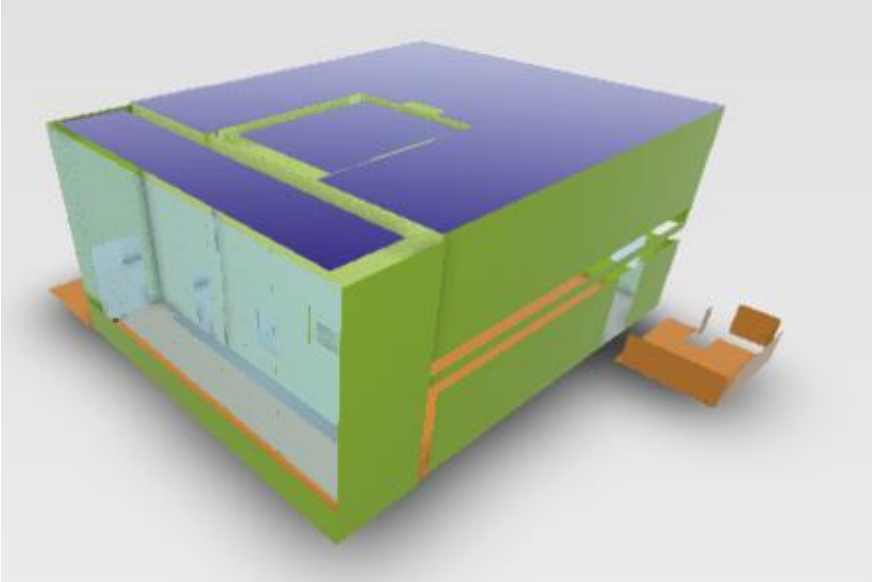

Fig. 5: Isometric Section showing the modelled House through Insight 360. Source: Author.

3. Results

The monitoring period showed that each room performed differently with significant day and night temperature differences, and with exposure to solar radiation (Figure 6). During the day, bedroom #4 (1st floor) had the highest indoor dry bulb temperature and recorded the hottest peak between the other rooms, while bedroom #2 (ground floor) recorded the warmest score and maintained the coolest (Figure 6).

Initially, during days 239 and 240 on the 27th and 28th of August 2023 (Figure 5), the highest outdoor temperature trend was recorded during daytime 32.8°C. This is reflected in the inner temperature of bedroom #4 where it recorded a peak temperature of 38.3°C. As soon as the air-condition (A/C) was turned on, the internal temperature of the room dropped to reach 27.8°C (day 239). Once the A/C was turned on (day 240), the room kept cooler than the previous day and reached a maximum of 34.9°C which is lower than day 239.

Observation showed that during day 239, the A/C was turned on for 12 hours simultaneously. While, during day 240, the A/C was turned on for 17 hours simultaneously. This reflects the indoor temperature of the room that differs between these two days while having almost the same outdoor temperature and solar radiation. According to figure 5, the A/Cs consumed 50 kWh at day 239 while on day 240 it consumed 56 kWh. Although,

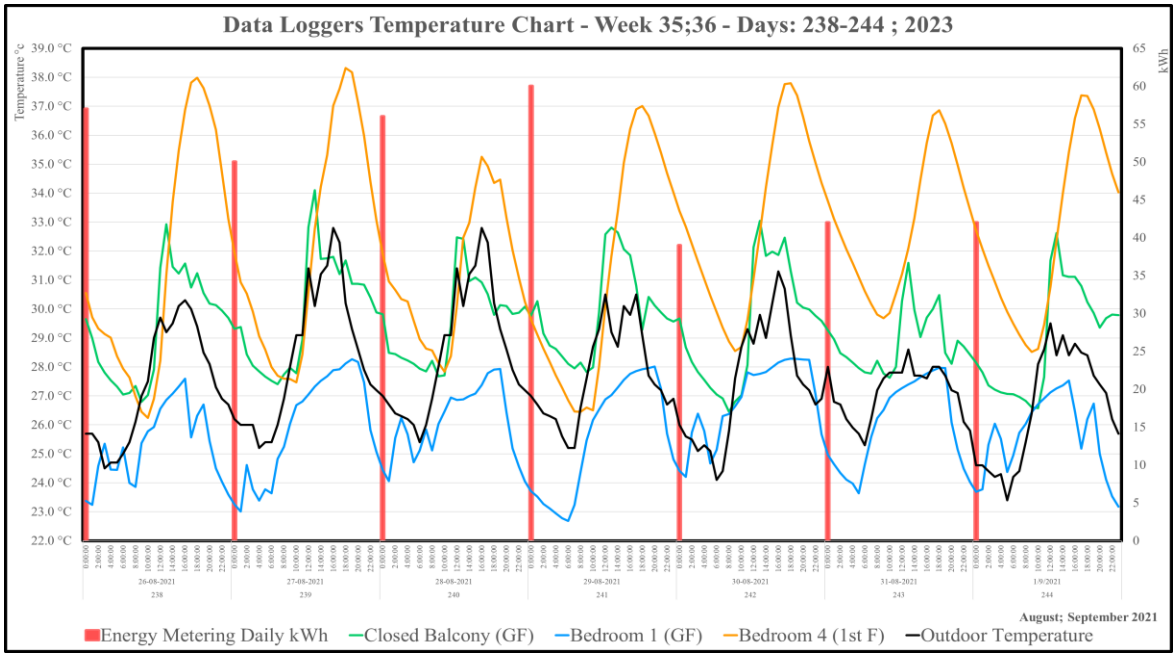

Fig. 6: Comparison between indoor and outdoor Temperature. Source: Author.

having an A/C running more than half of the day, the temperature of bedroom #4 did not drop below the outdoor temperature.

The observation of the closed balcony showed that during noon, the internal temperature started increasing. This is due to the orientation of the room which is towards the southeast (Figure 6). This was evident during the study period, where temperature started increasing until it reacheed its peak during the day. This is where the A/C was turned on and started decreasing the internal temperature. Accordingly, with a minimum of 12 hours of A/C running, also the closed balcony did not reach a temperature below the outdoor temperature during the day.

Internal peaks and fluctuation happened at various times during the day; this occurred due to the electricity blackout. As shown in figure 6, when the electricity is cut off, the internal temperature of the closed balcony increases rapidly. Bedroom #1 (below bedroom #4 on the ground floor) has the coolest temperature compared to the rooms that use an A/C in the house.

Observation shows that during day and night, this room had its inner temperature below the outdoor temperature. The daily temperature peaks sharply afternoon. This is due to the orientation of the bedroom towards the west. When the internal temperature starts rising, the A/C was turned on to decrease the room

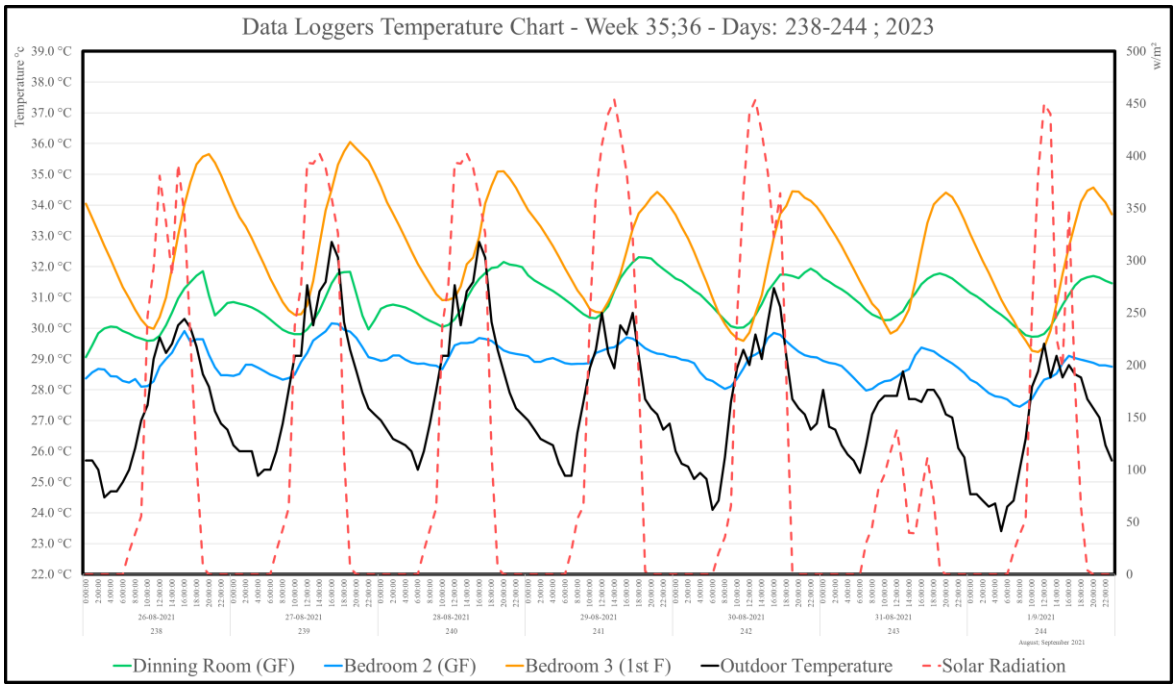

Fig. 7: Comparison between indoor and outdoor Temperature. Source: Author.

temperature. Accordingly, the temperature drops until the A/C was shot-off. Internal peaks and valleys happened at various times; as a general trend, they occurred due to electricity blackout with a malfunction of the A/C. So far, these three rooms showed that the direct exposure of the solar radiation on the roof highly affect the indoor temperature. In order to assess the impact of the external envelope on the internal temperature, a comparison of bedroom #2 which is situated on the ground floor, where the solar radiation doesn't hit the room due to the shading platform on its elevation, and bedroom #3 which is situated on the first floor where its roof is totally exposed to the solar radiation during the day (Figure 7).

Days 239 and 240 recorded the highest temperature during the studied period compared to day 243 which has the lowest temperature recordings and lowest solar radiation at that week. Figure 6 shows that bedroom #2 has almost a daily repetitive fluctuation of 1.5°C temperature difference between day and night. While bedroom #3 has a difference of 5.7°C between day and night. Subsequently, when the outdoor temperature reaches its lowest recording which is 24.5°C, the internal temperature of bedroom #2 drops to reach 28.1°C. Yet bedroom #3 recorded a 30°C. However, when the outdoor temperature reaches its daily peak which is 32.8°C, the internal temperature of bedroom #2 records 29.6°C while bedroom #3 reaches a 35.7°C. It is noticeable that the internal temperature of bedroom #2 does not exceed the external temperature where it

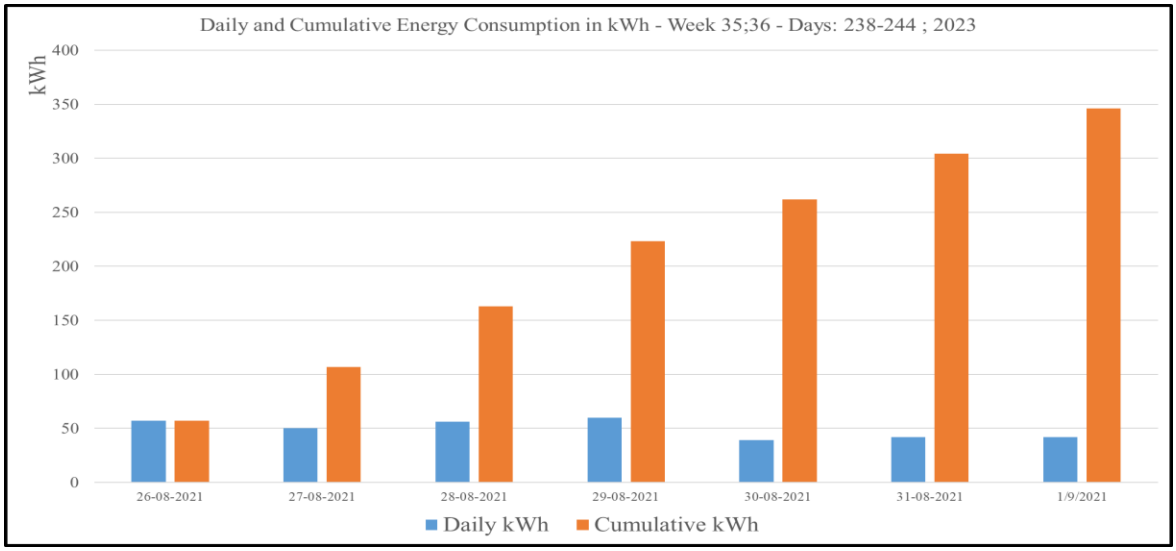

Fig. 8: Comparison between daily and cumulative energy consumption. Source: Author.

fluctuates at a constant temperature. Whereas the lowest temperature recorded in bedroom #3 is higher than the outdoor temperature.

Besides, the dining room temperature monitoring showed that internal temperature is affected by the solar radiation hitting its roof. The gap between the lowest and the highest internal temperature is around 2°C difference. Observation shows that the peak internal temperature occurred in the afternoon, this is due to the external envelope facing the west orientation and exposure to the sun radiation. This can be shown during each day of the studied period. Throughout days 238 and 239 (Figure 7), the temperature at 12:00 pm recorded 29.9°C. The internal temperature starts increasing until reaching an indoor temperature of 31.9°C as a peak

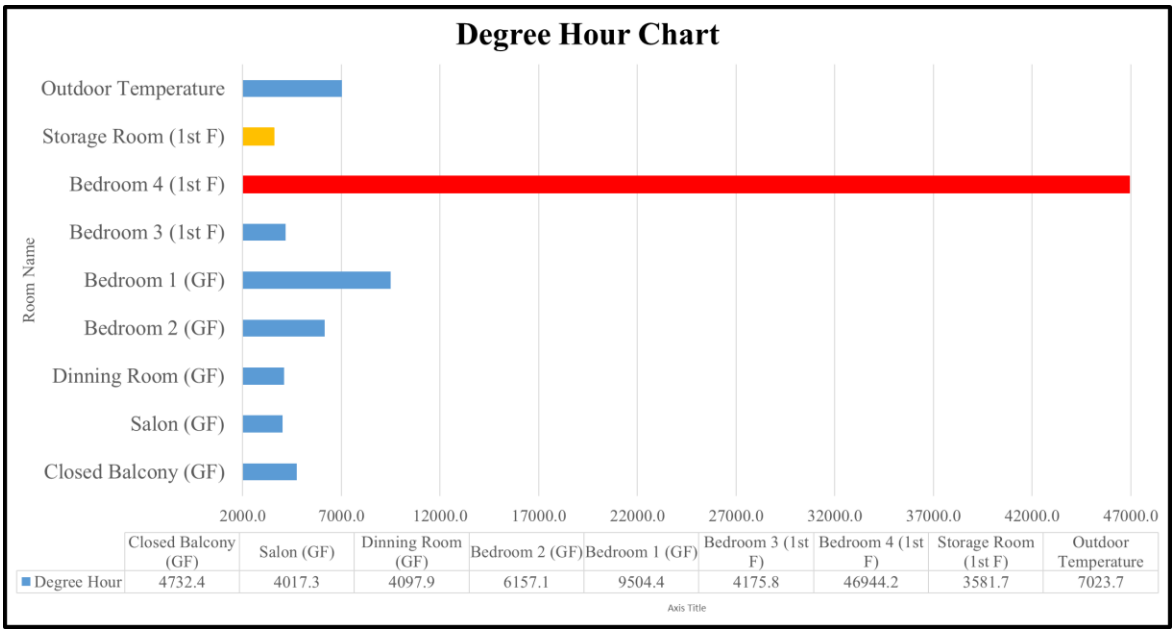

Fig. 9: The recorded degree hour. Source: Author.

dry-bulb temperature at 7:00 pm. this is when the sunset during the summer season. After this action, a decrease in internal temperature occurred until reaching a temperature of 30°C.

To establish the performance ranking of the various studied rooms, degree hour method was implemented. It shows the proper situation in such context that has the higher thermal properties in providing coolest internal temperature among all rooms.

Saleh P. (2019) emphasized that degree hour is more relevant to such study. Where the purpose of such method is to use a benchmark temperature to compare the overheating hours. In this study, the benchmark is taken 30 ^{o}C due to insure of having a wide difference between the minimum accepted by the publication, where according to UNDP (2005), temperature in the coastal area of Lebanon should not fall above 24 ^{o}C.

The outdoor temperature degree hour of the studied area according to the weather station is 7023.7 Dh during the study period based on a selected benchmark 30 °C. Also, the bedroom #4 which is situated on the 1st floor, where it is exposed directly to the solar radiation recorded the hottest degree hour between all studied rooms which is 46,944 Dh of overheating above 30^{o}C. Followed by bedroom #1 which recorded 9,504 Dh. Then, bedroom # 2, closed balcony, bedroom #3, dining room, and salon recorded respectively 6,157 Dh, 4,732 Dh, 4,175 Dh, 4,098 Dh, 4,017 Dh. It can be observed that there is a huge gap between the room that has the hottest Dh compared to the other rooms (Figure 9).

4. Discussion

So far, house monitoring has shown the impact of solar radiation exposure and roof construction materials' actual thermal properties on the internal dry bulb temperature. Observation showed that the room with no

exposure to solar radiation has the coolest internal day and night peaks and temperature, whereas the more the solar radiation hits the roof, the more the room is warmer.

The source of energy requirement for summer indoor cooling is based only on electricity. Figure 6 shows an overview of the current situation. The effect of the high internal temperature required an average of 50 kWh of daily electricity consumption to decrease the internal dry bulb temperature in only three rooms which constitute 58 sq. m. This leads to energy consumption of 0.86 kWh/m² (for each m²). Whereas, projecting this number on the studied house which is 150 sq.m. if it was cooled during summer will end up consuming 129 kWh daily electricity (multiplying the energy consumption of each m² by the total house area).

Given that the thermal performance of the house was directly affected by the solar radiation and the absorbance of the roof. Therefore, the model simulation depends mainly on installing shading elements and enhancing the external envelope's thermal properties to reduce heat gain to help the cooling process.

In the enhancement of the current situation thermal and energy consumption of the studied house, the construction is altered to insulated construction method to increase thermal resistance and minimize heat loss. In addition to these alterations, an increase in the ventilation also was proposed to regulate the internal temperature was also simulated.

To begin with the construction material enhancement, the roof thermal properties where improved. Where it was a 15 cm reinforced concrete roof. Thermal insulation was added on top of the slab with a 50 cm earth to have a green roof. This enhanced its U value from 5.4 kWh/m²/year to 1.3 kWh/m²/year which is 76%. By this, the elimination of solar radiation hits the roof surface. In addition, insulation was added to the roof cladding construction material to prevent heat transfer to the inside and increase the indoor temperature.

By doing such enhancements and changes and according to the simulation software, the energy use intensity (EUI) of the house was reduced by 56% from 506 kWh/m²/year to 222 kWh/m²/year. Insight 360 gives results in EUI (Energy Use Intensity) per unit of the built area. It means that this software provides an evaluation of the building's annual energy consumption according to the gross floor area. This process is applied to all types of energy used in the building, such as space heating, and space cooling. For this reason, these measurements should be taken into consideration while selecting the external envelope building's material according to the benchmark set by Insight 360, which is ASHRAE 90.1.

The positive impact of minimizing solar radiation contact with the roof and enhancing the house envelope thermal components on both the electricity consumption and the energy use intensity. Furthermore, it shows the impact of the reducing cooling load. The values of the above for the indoor cooling electricity consumption changed from 350 kWh as an average in a warm and hot week to 194 kWh after the retrofitting enhancements. While for the EUI, it dropped from 506 to reach 222 kWh/m²/year which is a decrease of 56%. The benchmark set by Insight 360 is 257 kWh/m²/year.

The external envelope varies considerably within the different parts of the house which affects the needed energy for indoor cooling. Whereas, whenever the house area increases, the cooling load increases. Accordingly, the need for energy will increase. The energy simulation of the house indicates that retrofitting could achieve a sufficient energy status by enhancing the envelope's thermal properties and using the roof only for electricity generation, under the given climate conditions.

5. Conclusion

This research made an investigation into all aspects of heavyweight thermal mass roof with comparison to the red roof tile and the impact of solar radiation and effect of each construction material on the internal temperature through data recording of the internal dry bulb temperature and through software simulation in the warm Mediterranean coastal area of Lebanon reaching the following key conclusions:

The first factor deals with enhancing the thermal properties of the external envelope can decrease energy consumption and cooling load. The second factor is to incorporate shading devices to protect the envelope from direct solar radiation. These two strategies showed that 56% of cooling demand could be reduced.

6. References

Ali Ahmad, Muzna Al-Masri, Hassan Hrajli, Alix Chaplain, Jamil Moawad, et al.. Models for tackling Lebanon's electricity crisis. 2021

Blázquez, T.; Simone, F.; Rafael, S.; José, S.J. Adaptive approach-based assessment of a heritage residential complex in southern Spain for improving comfort and energy efficiency through passive strategies: A study based on a monitored flat. Energy 2019, 181, 504–520.

Del Coz Díaz, J.J., García Nieto, P.J., Martín Rodríguez, A., Martínez-Luengas, A.L., and Betegón Biempica, C. (2010). "Nonlinear Thermal Analysis of Light Concrete Hollow Brick Wall by the Finite Element Method and Experimental Validation."

Fardoun, F., Ibrahim, O., Younes, R., & Louahlia-Gualous, H. (2012). Electricity of Lebanon: Problems and Recommendations. Energy Procedia, 19, 310-320. doi: 10.1016/j.egypro.2012.05.211

Fasi, M. A., & Budaiwi, I. M. (2015). Energy performance of windows in office buildings considering daylight integration and visual comfort in hot climates. Energy and Buildings, 108, 307-316. doi: 10.1016/j.enbuild.2015.09.024

Friess, W.A. and Rakhshan, K. (2017) "A review of passive envelope measures for improved building energy efficiency in the UAE," Renewable and Sustainable Energy Reviews, 72, pp. 485–496. Available at: https://doi.org/10.1016/j.rser.2017.01.026.

F. Visser, A. Yeretzian, Energy Efficient Building Guidelines for MENA Region: Energy Efficiency in the Construction Sector in the Mediterranean, MED-ENEC, Cairo, 2013.

G.A. Florides, S.A. Tassou, S.A. Kalogirou, L.C. Wrobel, Modeling of the modern houses of Cyprus and energy consumption analysis, Energy 25 (2000) 915–937.

Green Building Studio Validation | Search | Autodesk Knowledge Network. (2020). Retrieved 7 August 2020, from https://knowledge.autodesk.com/searchresult/caas/ClouDelp/clouDDelp/ENU/BPA-Help/files/GUID-EF68E7D5-C0A54805-BFE5-7C74C57B712E-html

Gyamfi, S., Krumdieck, S. and Urmee, T. (2013) "Residential Peak Electricity Demand Response—highlights of some behavioural issues," Renewable and Sustainable Energy Reviews, 25, pp. 71–77. Available at: https://doi.org/10.1016/j.rser.2013.04.006.

Isaac, M. and van Vuuren, D.P. (2009) "Modeling global residential sector energy demand for heating and air conditioning in the context of climate change," Energy Policy, 37(2), pp. 507–521. Available at: https://doi.org/10.1016/j.enpol.2008.09.051.

MoE/UNDP/GEF (2015). National Greenhouse Gas Inventory Report and Mitigation Analysis for the Energy Sector in Lebanon. Beirut, Lebanon.

Panayi, P. (2004) "Prioritising energy investments in new dwellings constructed in cyprus," Renewable Energy, 29(5), pp. 789–819. Available at: https://doi.org/10.1016/j.renene.2003.07.010.

Pierquet, P., Boywer, J., & Huelman, P. (2020). THERMAL PERFORMANCE AND EMBODIED ENERGY OF COLD CLIMATE WALL SYSTEMS. Forest Products Journal, 48(6), 53-51.

R.T.A. Prado, F.L. Ferreira, Measurement of albedo and analysis of its influence the surface temperature of building roof materials, Energy Build. 37 (4) (2005) 295–300.

S. Bretz, H. Akbari, A. Rosenfeld, Practical issues for using solar-reflective materials to mitigate urban heat islands, Atmos. Environ. 32 (1) (1998) 95–101.

Silvero, F.; Sergio, M.; Fernanda, R.; Enrico, S.; Humberto, V. Energy retrofit solutions for heritage buildings located in hot-humid climates. In Proceedings of the XIV International Conference on Building Pathology and Constructions Repair (CINPAR), Florence, Italy, 20–22 January 2018.

Smith, P. (2005) Architecture in a climate of change.

Suárez, R.; Jessica, F. Passive energy strategies in the retrofitting of the residential sector: A practical case study in dry hot climate. Build. Simul. 2015, 8, 593–602.

UNDP. (2005). Climate and Comfort: Passive design strategies for Lebanon. Prime Design, 1, 13-42. Retrieved on October 28, 2018 from: http://primedesignpea.com/pdf/2005,ClimateandComfort.pdf.

Ürge-Vorsatz, D. et al. (2015) “Heating and cooling energy trends and drivers in buildings,” Renewable and Sustainable Energy Reviews, 41, pp. 85–98. Available at: https://doi.org/10.1016/j.rser.2014.08.039.

A Parametric Study: Impact of Thermal Mass on Summer Overheating for Residential Buildings in Germany

Juan Romero[1], Mai-Khanh Talke[2], Ben Gottkehaskamp[1], Christian Hepf[1] and Thomas Auer[1]

[1] Technical University of Munich, Chair of Building Technology and Climate Responsive Design, Munich (Germany)

[2] Technical University of Munich, Chair of Building Physics, Munich (Germany)

Abstract

Rising average temperatures and the increasing frequency of heatwaves as a result of climate change make effective passive measures for indoor overheating mitigation urgently needed. This paper evaluates the future thermal performance of 2,880 building variants, focusing on material- and design-related parameters, using climate data sets intended to represent future conditions. The study shows that future climate datasets (TRY-45) for all three summer climate regions in Germany only represent current summer conditions, emphasizing the need for additional climate data to simulate future scenarios. Based on the parametric simulation outputs, the statistical analysis suggests that window-to-floor ratio, sun shading, and thermal mass of exterior walls have the greatest impact on overheating hours in residential buildings. The assessment of a reduced set of variants, that comply with both thermal and visual comfort, indicates that façade configurations with medium- and high bulk density materials offer a larger degree of design freedom for window sizing than lightweight configurations.

Keywords: parametric simulation, thermal mass, overheating hours, thermal comfort, visual comfort

1. Introduction

High temperature anomalies are getting more severe and occurring more often. This problem has become even more acute in the last years with constant new record braking-temperatures registered worldwide. Recently, the global average surface temperature surpassed in 1.48 °C the 1850-1900 reference value (Copernicus, 2024). With this, the past nine years have been the warmest on record globally (Umweltbundesamt, 2024).

Global warming can be largely attributed the emission of greenhouse gases, where the building sector plays a major role (Levermore G, 2008). Despite existing pacts to limit global warming, such as the Paris Agreement, it is likely that the threshold of 1.5 °C above preindustrial levels will be surpassed by 2030, rather than by 2100 as initially intended. This rapid trend implies irreversible effects on ecosystems and further acceleration of climate change (Armstrong McKay, D. I. et al., 2022).

Europe exhibits temperatures that are rising twice as fast as the global average since the 1980s (EEA, 2024). More frequent and intense heat extremes are taking place in Germany, where the number of Summer Days with a maximum temperature of at least 25 °C has more than doubled since the 1950s, while the number of Hot Days with a maximum temperature of at least 30 °C has nearly tripled. (DWD, 2024)

Recurring elevated outdoor temperatures lead to more frequent high indoor temperatures, causing thermal discomfort. Furthermore, high indoor temperatures can trigger cardiovascular health problems, as well as cognitive impairments, among other issues (Cicci et al., 2022; Khan et al., 2021). The use of air conditioning is a countermeasure; however, they rely on energy-intensive systems typically powered by fossil resources, which generate additional CO_2 emissions and further exacerbate the problem. Passive design strategies are a better approach to mitigate indoor overheating. The German standard DIN 4108-2establishes a general framework with minimum requirements for summer heat protection promotes such passive strategies and measures. These measures aim to prevent high room temperatures during the summer in buildings without mechanical cooling.

This research explores a set of passive measures for residential buildings and evaluates their effectiveness in improving thermal comfort. In addition, for a selected future scenario, daylighting conditions are evaluated to establish minimum window-to-floor ratio values. The assessment of both, thermal and visual comfort reveals

© 2024. The Authors. Published by International Solar Energy Society
Selection and/or peer review under responsibility of Scientific Committee
10.18086/eurosun.2024.01.04 Available at http://proceedings.ises.org

dependencies between external wall types and window ratio. The study aims to address the following research questions: What passive design strategies in Central Europe are effective in reducing overheating in residential buildings? Which of the construction types offer advantages regarding flexible window sizing configurations?

2. Methodology

To reach the formulated objective, a parametric study was set up using dynamic building simulations at a detailed room level. The parametric study assessed a total of 2,880 variants and it is performed using TRNLizard (Transsolar Software Engineering, 2017), which allows automated input parameter variations for thermal simulations with TRNSYS via additional scripts. The evaluation of all performed simulations was rated using automated scripts with statistical functions.

Each simulated variant is assessed according to the thermal comfort band for operative room temperature defined by DIN EN 16798-1 and the number of overtemperature hours (OTH [Kh a^{-1}]). Consequently, results of OTH lead to corresponding exceedance frequencies (EF [%]) during occupancy or usage time. Since the study focuses only on residential buildings without mechanical cooling, we use the adaptive comfort band within Category II as a realistic framework for the assessment.

The study is divided into three analysis stages, each building upon previous results. First, Test Reference Years (TRY) datasets from the German Weather Service (DWD) are compared against measured weather data for all three summer climate regions. This comparison is intended to verify the suitability of TRY datasets for subsequent investigations. In the second stage, a parametric study is conducted, and its results are statistically rated to identify the most effective passive measures. In the third stage, certain combinations of measures are selected to compare them according to their thermal- and visual comfort performance. Plotting the results for both comfort categories elucidates the degree of design freedom enabled by each configuration.

3. Modeling and Simulation

3.1. Climate Analysis (Stage One)

Using future weather data in thermal building simulations is essential due to the long lifespan of buildings, typically 50 to 100 years, during which significant climate changes are expected. Considering future conditions ensures that currently built spaces will remain comfortable and energy-efficient in the future (Cellura et al., 2018). Moreover, future climatic conditions will greatly impact heating and cooling demands. Studies, such as those by Cellura et al. (2018) indicate that while heating energy demand will decrease, cooling energy demand will increase drastically.

To verify whether the future weather data provided by the German Weather Service (DWD) is suitable for our study, test reference years for the present (TRY-15) and future (TRY-45) were compared with measured weather data for the respective locations.

The impacts of climate change vary regionally. Vukadinovic et al. (2020) and Cellura et al. (2018) highlight that urban areas may be more affected by summer overheating than rural regions. The urban heat island effect causes cities to have higher temperatures and longer heat periods. The study of Vukadinovic et al. (2020) also shows that the differences in Gh26 values (excess temperature degree-hours over 26 °C) are so significant that a differential consideration of the summer climate regions is necessary. When considering summer thermal protection in Germany, the standard DIN 4108-2 distinguishes between three different summer climate regions. Table 1 shows representative locations commonly used.

Tab. 1: Summer Climate Regions

Summer climate region		Indoor temperature ref. value	Location
A	cool	25 °C	Rostock
B	temperate	26 °C	Potsdam
C	warm	27 °C	Mannheim

3.2. Parametric Analysis (Stage Two)

The study starts with the "small multi-family building" by Klauß and Maas (2010) as reference for the studied space because of its comprehensive inclusion of various building types and frequent use in other studies (Doleski, 2020; Schlitzberger et al., 2017). The model building was slightly adapted, and the two critical rooms shown in Figure 4 were chosen to perform the simulation.

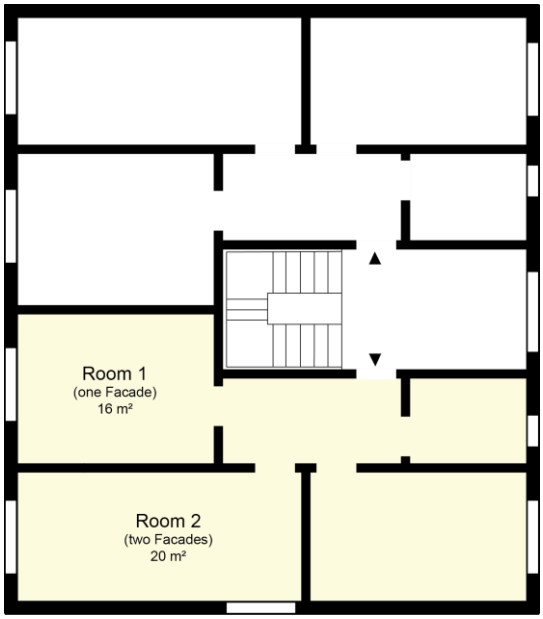

Fig. 4: Floor plan of the modified model building (own illustration based on Schlitzberger et al. (2017))

Table 2 summarizes the general boundary conditions to perform the thermal simulation. These values are based on established German standards, specifically DIN 4108-2:2013-02 and DIN V 18599-10:2018-09.

Tab. 2: Boundary Conditions for Thermal Simulation

Boundary Condition	Value
Room set temperature	$20\ °C \leq \theta_i \leq 25\ °C$
Night setback	$\Delta\theta_{i,NS} = 4\ K$
Annual usage days	$365\ d\ a^{-1}$
Daily heating operating time	6 a.m. – 11 p.m.
Base air exchange rate	$n = 0{,}5\ h^{-1}$
Increased day/night air exchange rate	$n = 3\ h^{-1}$ and $n = 5\ h^{-1}$ (depending on occupancy schedule)
Sun protection control based on threshold irradiance I_{lim}	NE, NW: $I_{lim} \geq 200\ W\ m^{-2}$ Other orientations: $I_{lim} \geq 300\ W\ m^{-2}$
Active cooling	None
Ventilation unit	None

DIN 4108-2, defines that for thermal simulations, all internal heat loads caused by occupants, electronic devices, and artificial lighting are combined into a continuous load of 100 Wh m^{-2} d^{-1} or about 4.16 W m^{-2}. Since we chose a more detailed approach, values and profiles for each internal heat source are based on Annex C of DIN EN 16798-1. The following table summarizes the implemented occupancy schedules.

Tab. 3: Day Profiles for each Internal Heat Load

Internal Heat Load	Schedule
Occupants	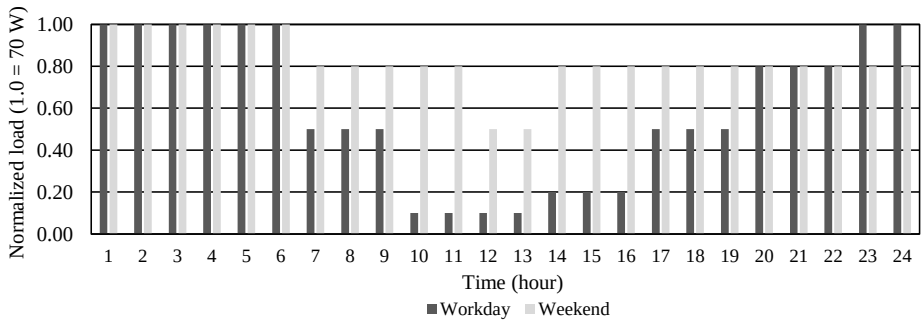
Electronic equipment	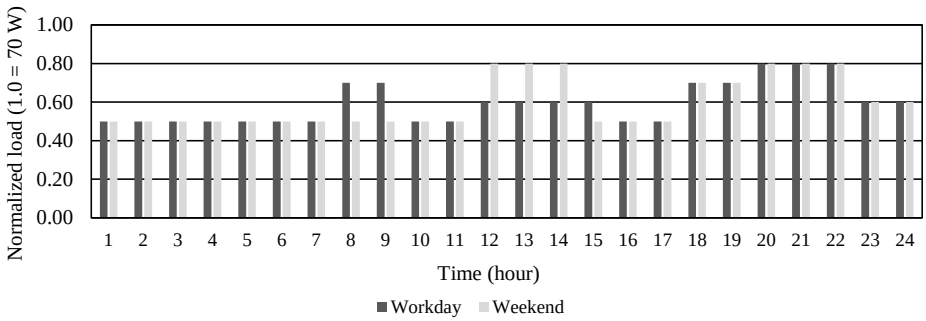
Light	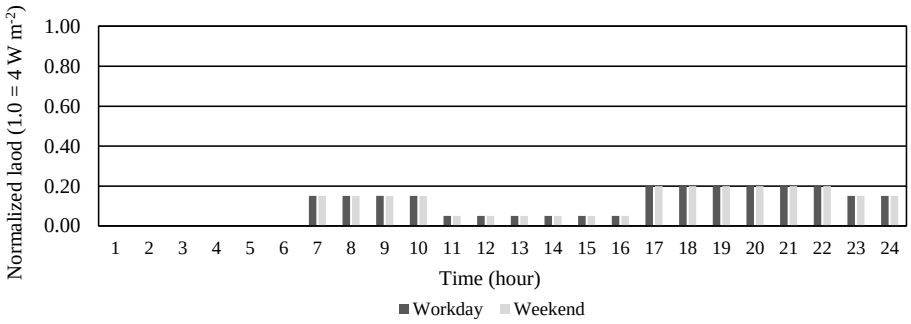

A minimum air exchange rate of 0.5 h^{-1} was defined as a baseline. In addition, elevated air exchange rates can be expected when windows are opened. In this case, an increased value up to 3.0 h^{-1} was defined for a standard room (openable window in one facade) and up to 5.0 h^{-1} for a corner room (openable windows in two facades). We assumed no automated window opening system in residential buildings; therefore, windows are only opened during occupancy, i.e. from midnight to 8 a.m. and from 6 p.m. to midnight. Window opening only occurs when the indoor air temperature exceeds 23 °C and is higher than the outdoor air temperature (DIN 4108-2:2013-02).

The total number of simulations is derived from building variations, namely: exterior wall types, slab types, room types, ceiling heights, room orientations, window-to-floor ratio, and shading types. The variant matrix is shown in Table 4.

Tab. 4: Variant matrix

Parameter	**Levels**					**Total**
Room type	One facade		Two facades			2
Sun shading	No shading		Ext. shading			2
Location	Rostock		Potsdam		Mannheim	3
Room height	2.4 m		2.8 m		3.2 m	3
Orientation	NO		SW			2
Window-to-floor ratio	0.12	0.18	0.25	0.30	0.34	5
Exterior wall	AW0 (timber)	AW1 (ρ = 600 kg m^{-3}) Insulating Brick	AW2 (ρ = 1200 kg m^{-3}) Perforated Brick	AW3 (ρ = 1800 kg m^{-3}) Sand-Lime Brick		4
Slab	Timber		Concrete			2
						2880

The façade serves as the primary interface between outdoor and indoor conditions. Therefore, most of the studied parameters are related to the building envelope. The size of the window is a relevant parameter in our research. Hereby the size of the window is defined as the window area ratio relative to the usable floor area, or short “window-to-floor ratio”.

The variation in exterior wall types focuses on different bulk densities. Additionally, room-enclosing elements (interior walls) are categorized into two groups (Table A2) and assigned based on the material type used in the façade. An overview of these components, including their material properties, is provided in Table A1 and Table A2 in the Appendix. Four different exterior wall constructions with low to high bulk densities were examined. The bulk density values, as indicated in kg m^{-3}, are grouped into bulk density classes (BDC) for simplification:

- AW0: Timber frame construction
- AW1: Insulating brick with a BDC of 0.6
- AW2: Perforated brick with a BDC of 1.2
- AW3: Sand-Lime brick with a BDC of 1.8

Variants AW2 and AW3 are constructed as double-leaf exterior walls. The outer leaf, made of an insulating brick (e.g., Poroton-WDF-180), functions similarly to an external thermal insulation composite system (ETICS), while the inner load-bearing wall leaf with a bulk density class of 1.2 or 1.8 acts as a thermal storage layer.

In addition, the massive timber slab appears to gain greater relevance in the near future and is therefore contemplated in our study. As a viable alternative to components with CO_2-intensive production processes, the massive timber slab offers both ecological and economic advantages (Abed et al., 2022) compared to the standard reinforced concrete slab, which is also analyzed in our study.

3.3. Degree of Design Freedom (Stage Three)

Each parameter combination in the given matrix yields a different result regarding overheating hours. The implementation of certain measures enables thermal comfort without compromising the degree of flexibility in design-related parameters. Based on the results of the previous section (stage two), the passive measures with the most influence on heat mitigation are further analyzed by plotting their occurrence of overheating hours. These results show parameter configurations that enable extended design flexibility while complying with thermal and visual comfort requirements.

In order to filter the 2,880 variants and establish a reduced set of relevant scenarios, the following assumptions are considered:

- The political commitment to achieve decarbonization goals in Germany is expected to increase the market relevance of timber products. Therefore, mass timber slabs are likely to replace a significant portion of the currently dominant reinforced concrete.
- A room height of 2.8 m is considered representative of both currently built and future residential spaces.
- Although sun protection in glazed surfaces plays a major role in mitigating indoor overheating, this section (stage three) focuses only on results with a g_{tot} = 0.6 (total energy transmittance value). Sun-protective glazing is excluded from the study as it reduces solar gains during winter and significantly limits daylight conditions during the same period. Manually operated external shading is a common configuration in current projects, however, a correct and consistent operation (user-dependent) cannot be guaranteed. This leads to several user behavior scenarios that are beyond the scope of this study.

To establish threshold values for both thermal and visual comfort, we refer to the standards outlined in German regulations. The selected metric to assess summer thermal comfort is the “Frequency of Excess Temperature” also known as Over Temperature Hours (OTH), whereas visual comfort is evaluated using the Daylight Factor (DF).

The term "frequency of excess temperature" encompasses all hours during which the adaptive comfort ranges are exceeded. A certain number of overheating hours should not compromise human thermal comfort and are therefore tolerated. Values of 3 % (equivalent to 259 hours per year) and 5 % (equivalent to 432 hours per year) during the occupancy period in residential buildings are considered acceptable thresholds established in DIN EN 15251, the preceding norm to DIN EN 16798-1. These thresholds have been also used in building certification systems such as DGNB (2018).

The German standards catalog offers well-defined daylight thresholds for office and other working spaces; however, such thresholds are not established for residential spaces. This study uses recommendations in DIN EN 17037 based on calculations under a covered sky with a diffuse horizontal illuminance of approximately 14,000 lux (DIN EN 17037, 2019). An appropriate level of illumination is achieved when DF exceeds 2 % on a horizontal plane at a height of 0.85 m above the floor over at least 50 % of the room area, and DF is also above 0.7 % for more than 95 % of the room area. These values approximately correspond to illuminance levels of 300 lux and 100 lux, respectively, and when fulfilling both conditions, the space is considered well-lit.

4. Results and Discussion

4.1. Climate Analysis (Stage One)

Besides average dry-bulb temperatures, the DWD defines other indicators such as “Climatological Reference Day” (*Klimatologischer Kenntag* in German). A "Climatological Reference Day" refers to a day on which a specific threshold of a climatic parameter is met or exceeded. Summer Days, Hot Days, and Tropical Nights are suitable for summer climate assessment. A Summer Day is defined by a maximum temperature of at least 25.0 °C, while a Hot Day is characterized by a maximum temperature of at least 30.0 °C. Conversely, Tropical Nights are defined by a minimum temperature that does not fall below 20.0 °C (Deutscher Wetterdienst, 2023).

Figure 5 shows the annual values for average temperatures, Hot Days, and Tropical Nights. The orange columns represent the average measured data from 2016 to 2021, whereas the blue columns display values from the Test Reference Year (TRY) datasets: TRY-15 (light blue) and TRY-45 (dark blue). The locations of the weather stations correspond to the locations of the TRY datasets, enabling a direct comparison between measured and reference data.

The results indicate that the TRY-15 datasets do not accurately reflect current climatic conditions. In contrast, the TRY-45 datasets provide a more accurate representation of all climate regions, particularly in terms of the above-mentioned Climatological Reference Day categories. Since our focus is on future climate projections and the German Weather Service does not provide datasets beyond TRY-45, we selected the dataset RCP 4.5 2080 (Representative Concentration Pathway, a moderate climate scenario for the year 2080, defined by the IPCC) retrieved from Meteonorm as a representative weather dataset for future climate conditions.

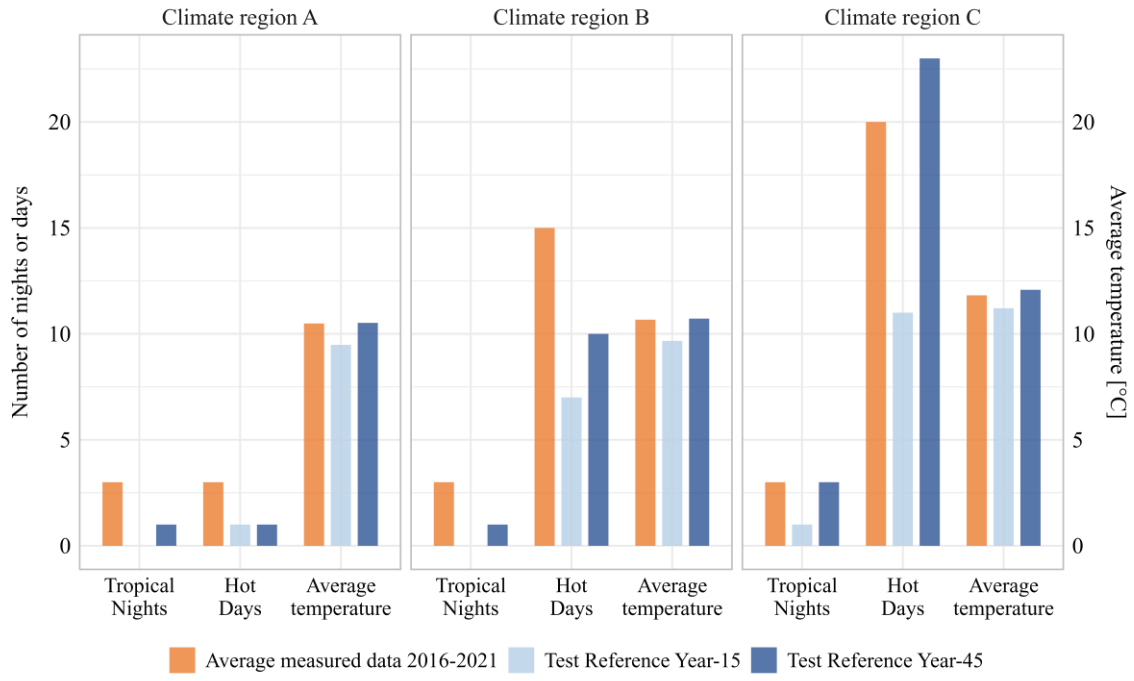

Fig. 5: Climatological reference days: Comparison between measured data and available reference data (TRY)

4.2. Parametric Analysis (Stage Two)

To identify which parameter has the most significant impact on overheating hours, we employed the Spearman correlation coefficient to determine the effect size, given its suitability for non-parametric and ordinal data. This method allows us to effectively measure the strength and direction of the association between each parameter and overheating hours. Figure 6 depicts the correlation coefficient between the analyzed parameters and overheating hours. Focusing on the strength of the effect, we considered the absolute values of the correlation coefficients, making it easier to compare the magnitudes of the relationships, as the direction of the correlation does not play a significant role in this analysis. According to Cohen's (1992) guidelines for interpreting effect sizes, the correlation coefficients are categorized as follows: small (0.1 to < 0.3), medium (0.3 to < 0.5), and large (≥ 0.5).

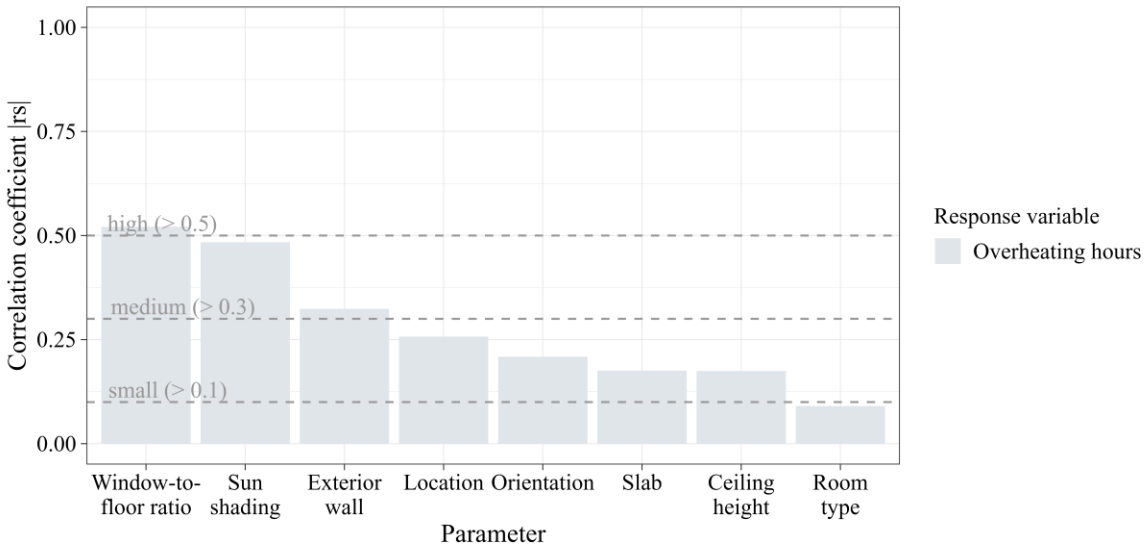

Fig. 6: Comparison of the effect size (correlation coefficient) of the analyzed passive strategies

Here, it can be observed that the window-to-floor area ratio, the sun shading, and the exterior wall have the greatest influence on the overheating hours. In contrast, the room type (room with one façade or with two facades) has the smallest influence. Surprisingly, when the timber frame structure is excluded from the statistical analysis, the influence of the exterior wall shifts from being the third most significant factor to the least significant. This suggests that medium- and high-density exterior wall constructions yield similar results in terms of overheating hours.

4.3. Degree of Design Freedom (Stage Three)

Building on the previous findings, this section focuses on the overheating hours for the four studied exterior wall types in relation to increasing window area ratios. The 5 % OTH threshold in combination with a minimum threshold for daylighting indicates different degrees of flexibility in facade design.

Figure 7 shows two scenarios with performance differences in wall types. Solid lines represent the results for a room with a concrete slab and one façade opening, located in climate region C. Dashed lines correspond to results with the same setup, except for the slab being built in massive timber.

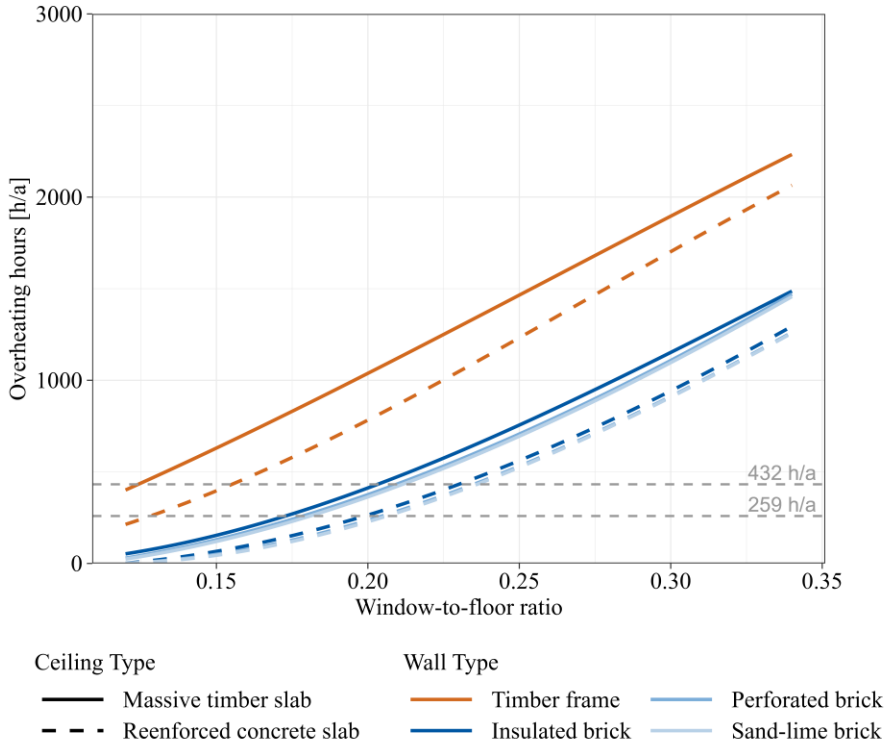

Fig. 7: Overheating hours with increasing window-to-floor ratio for reference room

The overlapping lines for Perforated- and Sand-lime brick suggest that there are no significant performance differences for exterior walls with bulk densities between 1200 kg m^{-3} and 1800 kg m^{-3}. Lightweight constructions may cause overheating issues in the future, even with a low window-to-floor ratio of approximately 16 %. Exterior walls with a bulk density of 600 kg m^{-3} reach this threshold at approximately 22.5 % window-to-floor ratio. In contrast, exterior walls with a bulk density above 1200 kg m^{-3} do not cause overheating issues as long as the window-to-floor area ratio remains below 23.5 %.

When the concrete slab is replaced with a mass timber slab, the suggested 5 % thermal threshold is reached at a window-to-floor ratio of 12.5 % for lightweight façade constructions, 20 % for exterior walls with a density of 600 kg m^{-3}, and 21 % for the other two categories.

Figures 8 and 9 depict the daylight factor results for window-to-floor area ratio of 12 % and 16 % respectively. The daylight recommendation (DF > 0.7 % for more than 95 % of the room) is achieved with a fenestration ratio of at least 15 %. To fulfill the second condition (DF > 2 % for more than 50 % of the room) the window-to-floor area ratio must be of at least 19.5 %. For this study we will take the first stated condition as the absolute minimum daylight requirement to be fulfilled.

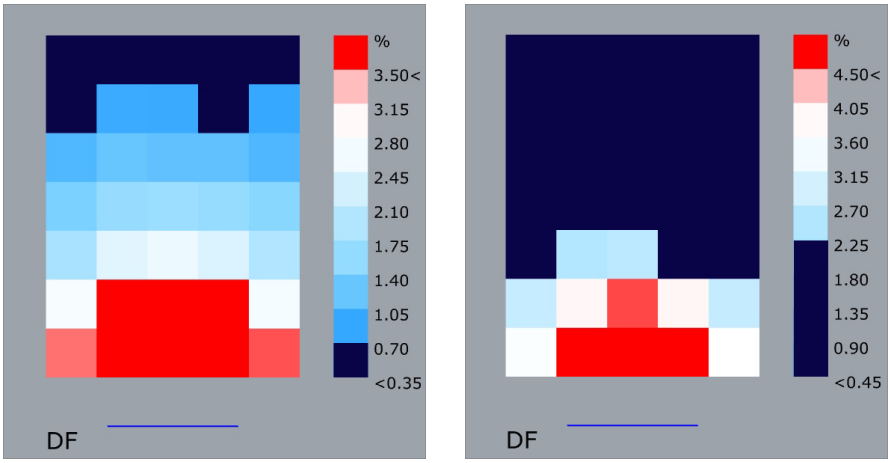

Fig. 8: Daylight performance with DF 0.7% (left) and DF 2% (right) for ref. room with window-to-floor area ratio of 12%

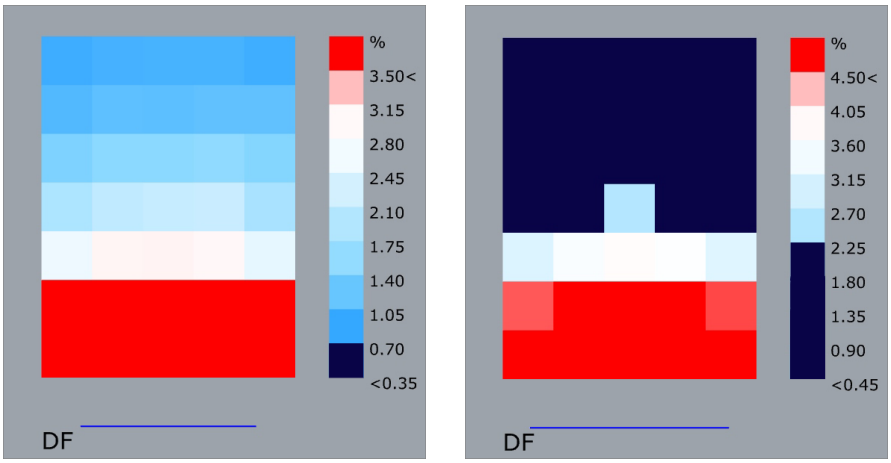

Fig. 9: Daylight performance with DF 0.7% (left) and DF 2% (right) for ref. room with window-to-floor area ratio of 16%

The combination of both (thermal and visual) thresholds defines the degree of design freedom for the planner in terms of flexibility in fenestration ratio, without limiting comfort either due to excessive overheating or the scarcity of natural light in the room. Figure 10 depicts the combination of the reference case with concrete slab presented at the beginning of this section. Evidently, in this case, the lightweight construction offers a reduced fenestration ratio scenario whereas walls with a bulk density of 600 kg m^{-3} and ≥ 1200 kg m^{-3} allow a larger fenestration ratio selection of 15 % and 22.5 %, respectively. In the case of mass timber slab implementation, the design freedom is restricted for all external wall types, mainly affecting results for the timber frame construction as shown in Figure 11.

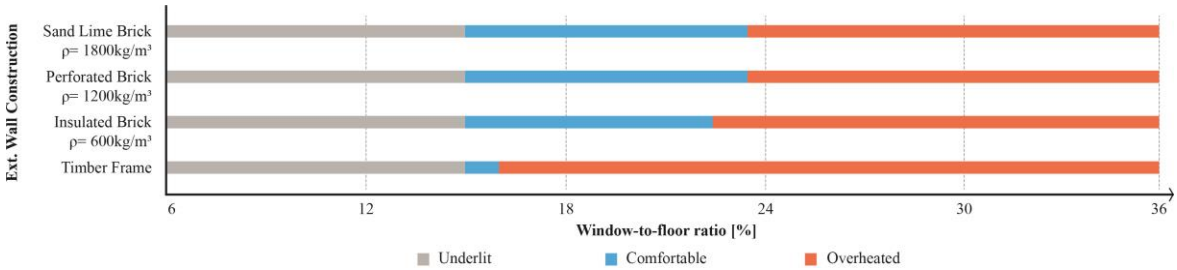

Fig. 10: Degree of Design Freedom by external wall type – Reinforced concrete slab

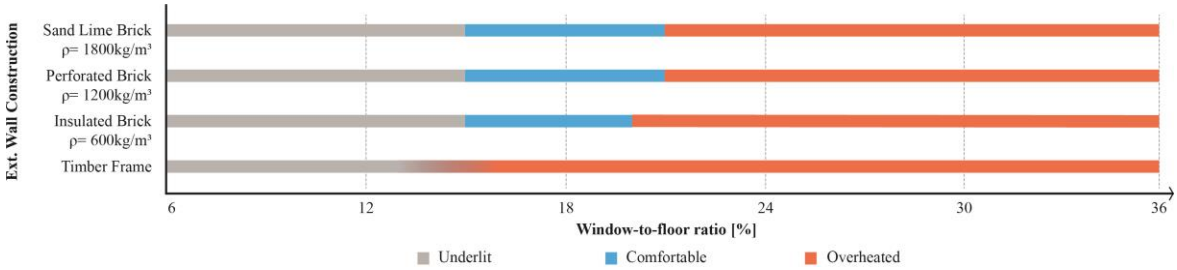

Fig. 11: Degree of Design Freedom by external wall construction type – Massive timber slab

5. Conclusion and Outlook

Within the current and future dynamics of climate change, the summer thermal performance of buildings is becoming increasingly important and is expected to play an even greater role in the future. This study investigated the effectiveness of passive design strategies for summer heat protection in terms of thermal comfort using suitable climate data sets for the future. Following multiple simulated scenarios, evidence was provided that in the future summer heat protection can be achieved within the adaptive comfort range of DIN EN 16798-1 without mechanical cooling. However, this is achievable only with specific passive measure configurations and applying a 5 % Frequency of Exceedance threshold.

The statistical analysis shows that the most effective passive measures, considering minimal energy demand, include reduced window-to-floor area ratio, sun shading, and the mass of the external wall. Nevertheless, thermal storage mass can also be achieved through mass in internal components or through phase change materials. The thermal and visual comfort analysis for specific configurations of thermal mass in relation to window-to-floor ratio indicates that medium- to high-bulk-density facade constructions offer greater design flexibility compared to lightweight solutions. This applies within a contextual scenario where external shading is either not implemented or not properly operated by users.

Although mass in exterior wall constructions offer an advantage in terms of design flexibility for the façade, the decarbonization goals imply a further evaluation of the studied construction types. Environmental aspects (e.g. Global Warming Potential (GWP) or recyclability) have to be also assess and included in upcoming studies.

The analysis of 2,880 simulated variants suggests that, without additional passive cooling measures, lightweight constructions with massive timber slabs and correspondingly low proportions of embodied energy may soon require effective sun protection measures or additional thermal storage to avoid active cooling during summer. Construction elements made of materials with a bulk density of approximately 900 kg m^{-3} or higher provide more leeway regarding additional measures to prevent overheating. However, with respect to improving summer heat protection, no significant differences or further enhancements are observed beyond a bulk density of 1200 kg m^{-3}.

Future research should address relevant aspects beyond the scope of this study. First, although natural ventilation was considered in the assessment, different natural night ventilation scenarios would yield a variety of results relevant to expanding the findings of this study. Second, despite the limited emphasis on natural daylighting in residential buildings, remote work practices have increased over the past four years since the onset of the COVID-19 pandemic and are likely to remain a staple of modern working culture. Therefore, a more detailed daylight study is necessary to establish thresholds for residential buildings. Third, sun shading is an effective strategy for mitigating heat. However, a realistic representation of its operation in residential buildings is challenging and requires an in-depth analysis of user behavior. Building on the current findings, future studies should address these challenges.

6. Acknowledgments

The research reported in this paper was funded by the German Federal Institute for Research on Building, Urban Affairs and Spatial Development (BBSR) as part of the research initiative “Zukunft Bau” (FWD–10.08.17.7-21.07). We also thank the “Bundesverband der Deutschen Ziegelindustrie e. V.” for their support.

7. References

Abed, J., Rayburg, S., Rodwell, J. & Neave, M., 2022. A review of the performance and benefits of mass timber as an alternative to concrete and steel for improving the sustainability of structures. Sustainability, 14(9):5570.

Armstrong McKay, D.I., Staal, A., Abrams, J.F., Winkelmann, R., Sakschewski, B., Loriani, S., Fetzer, I., Cornell, S.E., Rockström, J., Lenton, T.M., 2022. Exceeding 1.5°C global warming could trigger multiple climate tipping points. Science (New York, N.Y.), 377(6611), eabn7950. https://doi.org/10.1126/science.abn7950

Cellura, M., Guarino, F., Longo, S., Tumminia, G., 2018. Climate change and the building sector: Modelling and energy implications to an office building in southern Europe. Energy for Sustainable Development, 45, 46–65. https://doi.org/10.1016/j.esd.2018.05.001

Cicci, K.R., Maltby, A., Clemens, K.K., Vicedo-Cabrera, A.M., Gunz, A.C., Lavigne, É., Wilk, P., 2022. High temperatures and cardiovascular-related morbidity: A scoping review. International Journal of Environmental Research and Public Health, 19(18), 11243. https://doi.org/10.3390/ijerph191811243

Cohen, J., 1992. A power primer. Psychological Bulletin, 112(1), 155-159.

Copernicus, 2024. Global Climate Highlights 2023. Retrieved from https://climate.copernicus.eu/copernicus-2023-hottest-year-record

DIN 4108-2:2013-02. Thermal protection and energy economy in buildings - Part 2: Minimum requirements to thermal insulation. Beuth Verlag GmbH, Berlin.

DIN EN 16798-1:2022-03. Energy performance of buildings - Ventilation for buildings - Part 1: Indoor environmental input parameters for design and assessment of energy performance of buildings addressing indoor air quality, thermal environment, lighting and acoustics. Beuth Verlag GmbH, Berlin.

DIN EN 15251:2012-12. Indoor environmental input parameters for design and assessment of energy performance of buildings addressing indoor air quality, thermal environment, lighting and acoustics. Beuth Verlag GmbH, Berlin.

DIN EN 17037:2019-03. Daylight in buildings. Beuth Verlag GmbH, Berlin.

DGNB, 2018. DGNB System – Kriterienkatalog Gebäude Neubau. Version 2018. Hg. v. Deutsche Gesellschaft für Nachhaltiges Bauen. Retrieved from https://www.dgnb.de/de/zertifizierung/das-wichtigste-zur-dgnb-zertifizierung/nutzungsprofile.

Doleski, O.D. (Ed.), 2020. Realisierung Utility 4.0 Band 1: Praxis der digitalen Energiewirtschaft von den Grundlagen bis zur Verteilung im Smart Grid. 1st ed. Springer Fachmedien Wiesbaden GmbH, Wiesbaden.

DWD, 2023. Wetter- und Klimalexikon. Retrieved from https://www.dwd.de/DE/service/lexikon/Functions/glossar.html

DWD, 2024. Klimatologischer Rückblick auf 2023: Das bisher wärmste Jahr in Deutschland.

EEA, 2024. European Climate Risk Assessment. Retrieved from https://www.eea.europa.eu/publications/european-climate-risk-assessment

Klauß, S., Maas, A., 2010. Entwicklung einer Datenbank mit Modellgebäuden für energiebezogene Untersuchungen, insbesondere der Wirtschaftlichkeit. Forschungsinitiative ZukunftBau: SF – 10.08.17.7-09.27.

Levermore, G.J., 2008. A review of the IPCC Assessment Report Four, Part 1: the IPCC process and greenhouse gas emission trends from buildings worldwide. Building Services Engineering Research and Technology, 29(4), 349–361. https://doi.org/10.1177/0143624408096263

Schlitzberger, S., Kempkes, C., Maas, A., Schäfers, M., 2017. Einfluss der Wärmespeicherfähigkeit auf Heizwärmebedarf und thermischen Komfort. Bauphysik, 39(1), 57–63. https://doi.org/10.1002/bapi.201710008

Transsolar Software Engineering, 2017. TRNSYS 18 - TRNLizard. Retrieved from https://trnsys.de/static/d5760da45b4c0b4585b20a4b29e6bdb9/170307_T18_flyer_TS_TRNLizard_de.pdf

Umweltbundesamt, 2024. Trends der Lufttemperatur. Retrieved from https://www.umweltbundesamt.de/daten/klima/trends-der-lufttemperatur#steigende-durchschnittstemperaturen-weltweit

Vanova, R., Stompf, P., Stefko, J., Stefkova, J., 2021. Environmental impact of a mass timber building – A case study. Forests, 12(11), 1571. https://doi.org/10.3390/f12111571

Vukadinovic, M., Kempkes, C., Maas, A., 2020. Auswirkungen klimatischer Veränderungen auf die Überhitzung von Gebäuden, in: BauSim Conference, Proceedings of BauSim Conference 2020: 8th Conference of IBPSA-Germany and Austria. IBPSA-Germany and Austria, pp. 227–233. https://doi.org/10.3217/978-3-85125-786-1-26

Appendix

Tab. A1: Exterior wall constructions

	Material	Thickness [m]	Thermal conductivity [W m^{-1} K^{-1}]	Bulk density [kg m^{-3}]	Specific heat capacity [J kg^{-1} K^{-1})]	U-value [W m^{-2} K^{-1}]
AW0						0.18
	Larch wood external wall cladding	0.024	0.155	600	1600	
	Spruce wood battens offset (30/50; 30/80) - ventilation	0.030	0.120	450	1600	
	Fibreboard (MFD)	0.015	0.140	600	1700	
	Construction timber	0.22	0.12	600	1100	
	Mineral wool	0.22	0.04	33	1030	
	Vapour barrier	-	-	1000	-	
	Gypsum fibre board	0.015	0.32	1000	1003	
AW1						0.17
	Lime cement plaster	0.02	0.87	1800	1000	
	Thermal insulation brick	0.425	0.075	600	1000	
	Gypsum plaster	0.01	0.7	1400	1000	
AW2						0.25
	Lime cement plaster	0.02	0.87	1800	1000	
	Poroton-WDF-180	0.18	0.055	400	1000	
	Hollow brick 1.2	0.24	0.5	1200	1000	
	Gypsum plaster	0.01	0.7	1400	1000	
AW3						0.27
	Lime cement plaster	0.02	0.87	1800	1000	
	Poroton-WDF-180	0.18	0.055	400	1000	
	Calcium silicate brick	0.175	1	1800	1000	
	Gypsum plaster	0.01	0.7	1400	1000	

Tab. A2: Interior wall constructions

	Material	Thickness [m]	Thermal conductivity [W m^{-1} K^{-1}]	Bulk density [kg m^{-3}]	Specific heat capacity [J kg^{-1} K^{-1})]
IW0					
	Gypsum plasterboard	0.0125	0.25	800	1050
	Gypsum plasterboard	0.0125	0.25	800	1050
	Construction timber (60/100) with wood fiber insulation	0.01	0.039	45	1600
	Gypsum plasterboard	0.0125	0.25	800	1050
	Gypsum plasterboard	0.0125	0.25	800	1050
IW1					
	Gypsum plaster	0.01	0.7	1400	1000
	Hollow brick	0.175	0.58	1400	1000
	Gypsum plaster	0.01	0.7	1400	1000

Integration of Weather and Emission Predictive Control (WEPC) into Building Energy Simulation

Ben Gottkehaskamp[1], Christian Hepf[1], Clayton Miller[2], Adrian Chong[2], Thomas Auer[1]

[1] Chair of Building Technology and Climate Responsive Design, TUM School of Engineering and Design, Technical University of Munich, Munich (Germany)

[2] Department of the Built Environment, National University of Singapore, Singapore (Singapore)

Abstract

Buildings contribute significantly to global carbon emissions, highlighting the urgent need for improved sustainable operational practices. Enhanced efficiency promises cost savings amid climate concerns and digitalization and electrification trends. Intelligent controls are vital for integrating buildings into energy grids, crucial for achieving the EU's target of carbon neutrality by 2050 effectively managing the expanding availability of renewable energy sources. This paper aims to present a simulation-based framework for integrating Weather and Emission Predictive Control (WEPC) into building energy simulations, detailing how weather and emission forecast are simply incorporated to optimize control strategies.

Keywords: weather-and-emission predictive control; dynamic emission; thermal storage; electrical storage; thermal inertia; intelligent control strategy

1. Introduction

At the Paris Climate Agreement in December 2015, nearly 190 parties committed to limiting global warming to 1.5°C, attributing manmade greenhouse gas emissions as the primary drivers of global warming (United Nations Environment Programme and Global Alliance for Buildings and Construction, 2024). The United Nations Environment Programme (UNEP) identifies the building sector as responsible for 38% of carbon emissions, encompassing emissions from both building operations (28%) and the production of building materials, notably concrete and steel. This underscores the urgency for action to mitigate emissions. Additionally, factors such as climate change, the increase of renewable energy sources like photovoltaic (PV) and wind energy, and the electrification of building technology, as noted by the Fraunhofer Institute for Solar Energy Systems, introduce fluctuations in both energy supply and demand. Consequently, power grids experiences daily and seasonal variability in emissions (Fraunhofer Institute for Solar Energy Systems, 2020). Within the current existing building norms and codes, a constant annual static emission factor serves as a parameter for assessing emission balances.

Various concepts and data-driven control strategies, based on model predictive control, deep learning, weather forecast, or artificial intelligence, have been developed in the last decade, outlining energy- and CO_2-saving potentials (Drgoňa et al., 2020; Halhoul Merabet et al., 2021; Hepf et al., 2022; Jia et al., 2019; Thieblemont et al., 2017). Thereby, a few hurdles make it difficult to transform the concept into practice: data-intense algorithms, the creation of digital twins, or the necessity of highly educated employees to manage building technology. Standard building users or building operation managers are not data science experts and cannot apply these concepts to the built world.

Hence these dynamics, particularly concerning emission balance boundaries in building operations, the conventional concept of a static emission factor warrants scrutiny. This underscores the imperative to incorporate dynamic control factors to better address fluctuating emissions associated with building operations. Thus, this paper presents an integration of weather and emission forecasts in building energy simulations aiming to optimize energy consumption.

This paper integrates weather and emission forecasts into building energy simulations to optimize energy consumption and emissions , with Figure 1 summarizing how these predictions influence shading, ventilation,

© 2024. The Authors. Published by International Solar Energy Society
Selection and/or peer review under responsibility of Scientific Committee
10.18086/eurosun.2024.01.05 Available at http://proceedings.ises.org

heating, cooling, and energy evaluation parameters within an integrated feedback loop.

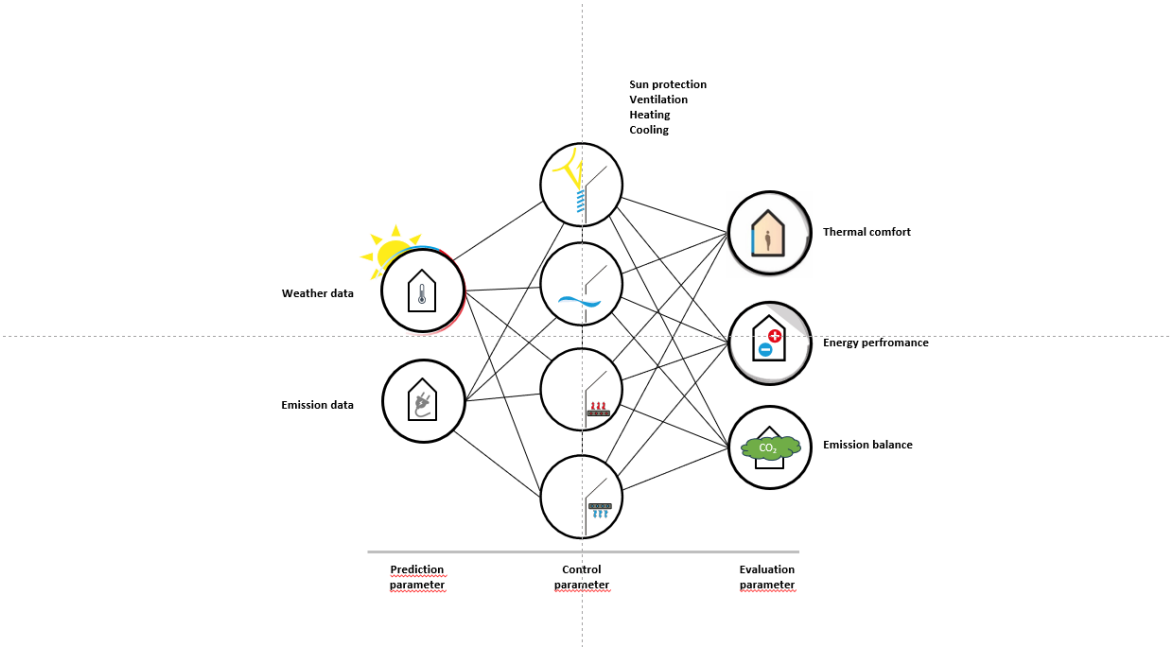

Fig. 1: General Overview

2. Review

As the focus of this paper is the workflow of the weather and emission predictive control, this review outlines the current state of literature in the fields of intelligent building control strategies and the concept of dynamic emissions.

2.1 Intelligent Building Control

Various control methodologies have been proposed, ranging from traditional to advanced systems, aiming to enhance energy efficiency and maintain thermal comfort in buildings. The widely adopted On/Off control method regulates building technology systems primarily based on room temperature thresholds, employing a straightforward three-position controller. Its simplicity and minimal data requirement facilitate practical implementation, especially with thermal building mass. However, other studies suggest that reliance on building thermal mass alone may lead to thermal discomfort, particularly without considering room heat gains or feedback from thermal zones (Gwerder et al., 2009). In contrast to On/Off control, proportional–integral–derivative controllers (PID) provide continuous regulation, utilizing feedback loops to adjust system outputs based on past and present conditions (Deutsches Institut für Normung e.V, 2018). Although PID controllers generally outperform On/Off systems in terms of energy efficiency, they can still result in thermal discomfort due to their inability to handle simultaneous heating and cooling demands and dynamic disturbances like solar radiation changes and internal heat gains (Schmelas, 2017).

Weather-dependent control strategies adjust supply temperatures according to ambient conditions, using heating and cooling curves to define operational thresholds (Bollin et al. 2021). This method optimizes energy consumption by deactivating systems within specified temperature ranges. However, this approach lacks direct feedback on room conditions, necessitating additional systems to ensure thermal comfort. Model predictive controllers (MPC) anticipate future disturbances and system behaviors to optimize responses, aiming to minimize energy consumption and costs while enhancing thermal comfort (Thieblemont et al. 2017). A reasonable number of projects show significant energy savings and improved efficiency when employing MPC strategies (Halhoul Merabet et al., 2021). Despite its effectiveness, MPC requires substantial computational resources and complex modeling, limiting its potential application in the built world. Researchers explore intelligent control strategies based on reinforcement learning (RL) to address the limitations of MPC and other conventional methods. These adaptive systems offer flexibility in adapting to diverse building conditions and optimizing operational parameters, while promising, implementing RL-based strategies requires advanced technical expertise and significant initial investments, restricting their widespread adoption in conventional

building settings (Zoltan 2023). It is highlighted that various control strategies for optimizing building performance, emphasizing the trade-offs between complexity, efficiency, and practical implementation (Lee, 2002). Future research should focus on developing simplified yet effective intelligent control approaches that mitigate the challenges posed by current methodologies.

2.2 Dynamic Emissions

The concept of the dynamic emission factor is not new. In Germany, the Agora Enegiewende provides hourly data to the public (Dambeck, 2021) on a national level. On a global scale, the "Electricity Maps" tool provides hourly electricity and emissions data for over 230 regions, covering past, present, and future periods. This platform includes information on CO_2 emissions factors, electricity production, and consumption. (Electricity Maps, 2024). In their research "*Dynamic CO_2 Emission Factors for the German Electricity Mix*," authors P. Wörner, A. Müller, and D. Sauerwein emphasize the need for hourly emission factors as a more realistic evaluation method compared to static emission factors. They argue that static emission factors cannot accurately reflect the future state of an electrified and volatile energy system. Motivated by this, they developed a methodology to calculate a quarter-hourly emission dataset for the electricity mix, which can be incorporated into dynamic simulations. In 2019, authors A. Müller and P. Wörner expanded upon their previous research by calculating future emission factors for the years 2030 and 2050 (Wörner et al., 2019). The article "*Dynamic Prospective Average and Marginal GHG Emission Factors—Scenario-Based Method for the German Power System until 2050*", N. Seckinger and P. Radgen outline a methodology for calculating and evaluating future greenhouse gas (GHG) emission factor. The GHG emissions from electricity generation are based on combustion emissions, excluding upstream emissions. The model also accounts for electricity trade (import and export), storage, and grid losses, making electricity consumption the reference for hourly emission factors (Seckinger, 2021).

In their research "*Plus minus zero: carbon dioxide emissions of plus energy buildings in operation under consideration of hourly German carbon dioxide emission factors for past, present, and future*", A. Studniorz et al. discuss using hourly CO_2 emission factors for evaluating building operations in Germany. They find that grid electricity is primarily used when emission factors are high (winter) and fed back into the grid when emission factors are low (summer). (Studniorz et. al., 2022) In their research "*Impact of a Weather Predictive Control Strategy for Inert Building Technology on Thermal Comfort and Energy Demand*" C. Hepf et al. aim to develop an intelligent, improved, yet simple weather predictive control strategy for thermally inert buildings. They find increased comfort in buildings of heavy and medium construction, although the energy balance improves only marginally. The authors suggest extending the research internationally to various climate zones and including CO_2 emissions as an evaluation criterion. (Hepf et al. 2022). The research potential for calculating future dynamic emission factors is further highlighted in the work of C. Hepf, B. Gottkehaskamp, C. Miller, and T. Auer titled "*International Comparison of Weather and Emission Predictive Building Control*". At five international locations, the authors compare weather and emission predictive control strategies to standard control methods for the years 2020 and 2050. They test the hypothesis that a simple control approach can harness potential energy and emission savings. The authors emphasize the need for intelligent control strategies due to future changes in the power grid from the increase in renewable energy and the need to meet European climate neutrality goals. (Hepf et. al., 2024) This work connects to the previous study and describes the weather and emission predictive control strategy methodology in detail.

3. Methodology

3.1 WEPC Integration

This paper describes a framework to integrate WEPC into thermal dynamic simulations, which is designed to optimize building thermal performance by integrating dynamic simulations utilizing weather data and emission calculations. This approach considers emissions, factoring in the availability of renewable energy sources, and the buildings storage capacities and powers output of the supply systems. This framework is designed to be adaptable to various building technology configurations, though specific adjustments required for different setups are not detailed in this paper. The approach presented was tested and used using TrnSys18. A detailed overview of the process is depicted in Figure 3, showing the multistep process. The process can be broken down into:

- Conduct Initial Thermal Dynamic Simulation: Perform the initial simulation using current weather data to compute the Solar Heat Gains (SHG) and other relevant thermal metrics for each thermal zone.
- Transpose Simulation Results: Calculate future weather conditions by transposing the initial simulation results, incorporating forecast data for ambient temperature and solar radiation.
- Adjust Control Strategies: Modify shading, ventilation, heating, and cooling control strategies based on the transposed future data to optimize energy use and maintain comfort.
- Run Second Thermal Dynamic Simulation: Perform a second simulation that includes the effects of the future data and the adjusted control strategies to predict the system's performance.
- Incorporate Emission Control: Integrate hourly emission data and energy performance metrics into the simulation to evaluate and manage the environmental impact of the building's energy use.

Detailed thermodynamic simulations typically utilize hourly timesteps to numerically verify thermal comfort and calculate energy consumption. This approach is in alignment with ASHRAE 90.1 (Halverson et al., 2014), a widely recognized standard, which often employs hourly simulations. Commonly used simulation engines like EnergyPlus and TRNSYS also default to hourly timesteps. Crawley and Barnaby (2019) indicated that hourly resolution weather data is sufficient for design and code compliance, offering adequate granularity for accurate simulations. While higher resolutions can yield more detailed results, they are often not readily available.

In the context of electricity consumption and carbon intensity, hourly data becomes is necessary as exemplary data is depicted in Figure 3 from Agora. The carbon intensity of consumed electricity can differ significantly from that of produced electricity, especially when imports constitute a substantial share of the consumed electricity. Therefore, it is essential to adopt a consumption-based perspective to accurately capture the carbon footprint of electricity use within a specific zone and time. This can be achieved through flow tracing methodologies that trace the origin of electricity and calculate its carbon intensity (Soimakallio & Saikku, 2012, Bialek, J. (1996). To determine the source of electricity and calculate its carbon intensity, Agora employs a flow tracing methodology. (Trnberg et al., 2019) Figure 2 exemplarily depicts such hourly emission values.

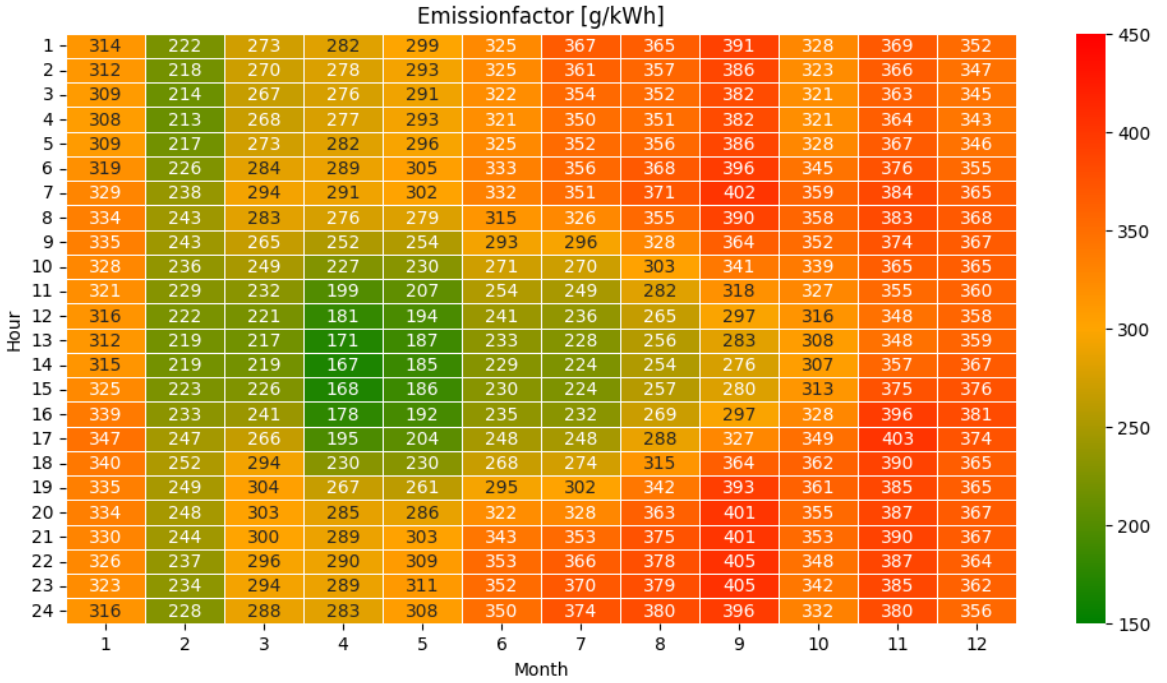

Fig. 2: Exemplary hourly Emissions data from Agora for Munich, Germany for the TRY 2020

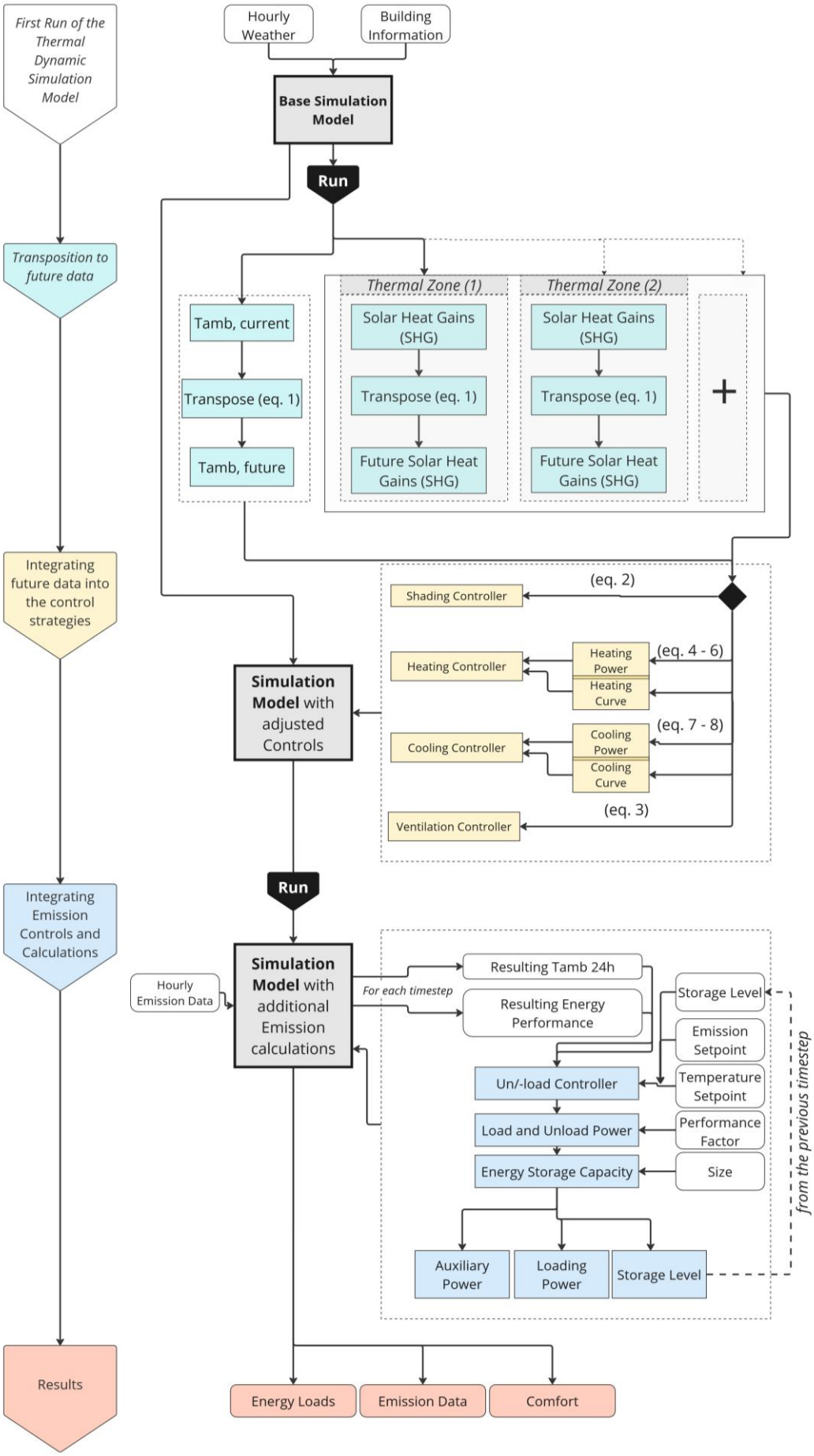

Fig. 3: Detailed Framework Flowchart for Weather and Emission predictive control (WEPC)

3.2 Computation of future data

The initial thermal dynamic simulation utilizes weather data to compute the Solar Heat Gains (SHG), which describe the total solar radiation transmitted through external windows for each thermal zone at each time step. It is recommended to use hourly time steps, though more detailed intervals can be adopted depending on the resolution of the weather data and emissions. Lower resolution data can reduce the accuracy of predictions.

The ambient air temperature from the provided weather file, along with the SHG, is then transposed to describe future conditions. This transposition process involves using data from the current simulation step and incorporating forecast values for future steps. The forecast horizon can vary, typically they have been set between 12 or 24 hours. Weather forecasts tend to lose accuracy the further ahead they predict environmental variables, hence this framework recommends adhering close to this range for good accuracies, but it has not been further investigated. For each future step, the influence of the prediction is reduced by a factor, alpha, to account for the decreasing accuracy of weather forecasts over longer time periods.

Equation 1 describes the transposition of the future data, hence computes an exponentially weighted sum of input variables over a specified number of future timesteps t. In this functi1on, a is a parameter that controls the rate of exponential decay, ensuring that more recent inputs have a greater influence. Each input z_k is weighted by a_k, and the overall sum is scaled. This formulation allows the function to adapt to different numbers of input terms, making it useful for scenarios that require weighted sums over multiple future timesteps.

$$f(a, z_0, z_1 \dots z_t) = (1 - a) \sum_{k=0}^{t} (a^k * z_k) \qquad \text{(eq. 1)}$$

with

- $f(a, z_0, z_1 \dots z_t)$: Exponentially weighted sum of input variables over *t* future timesteps.
- *a*: Decay parameter controlling the rate of exponential decay, with $0 \leq a < 10$
- z_k: Input variables at each timestep *k* (where *k* ranges from 0 to *t*).
- *t*: Total number of future timesteps considered.

3.3 Controller Adjustments

The future data for SHG and ambient temperature is than utilized to adjust the heating, cooling, shading and ventilation controls for the initial thermal dynamic simulation to perform a second run, to calculate the hourly energy performance for each zone.

Shading greatly influences the solar heat gains transmitted into the thermal zone, hence adjusting the shading controller, for better temperature control and its impacts on the heating and cooling system to maintain indoor comfort and lower energy consumptions. Shading controllers are often activated based on an ambient temperature setpoint or time based, which could be, with the setpoint sometimes being controlled by a schedule, allowing to adapt to seasonal changes. The adapted equation (eq. 2) also utilizes a setpoint for the ambient temperature, the current solar heat gains and future solar heat gains to print out an active signal.

$$ShadController = \begin{Bmatrix} 1 & if\ T_{amb,current} > 14 \\ 1 & if\ SHG_{current} > 200 \\ 1 & if\ SHG_{future} > 150 \\ 0 & otherwise \end{Bmatrix} \quad \text{(eq. 2)}$$

with

- *ShadController*: Control signal for the shading device, equal to 1 if the shading should be activated, and 0 otherwise.
- $T_{amb,\ current}$: Current Ambient temperature [∘C]
- $SHG_{current}$: Current solar radiation [W/m2].
- SHG_{future}: Forecasted solar radiation for t timesteps ahead [W/m2].

To maintain thermal comfort, temperature control must minimize energy losses or maximize energy gains. This requires controlling air exchange based on transposed future data. Air exchange can be managed using various strategies, such as day and night cooling, different setpoints for varying intensities, and schedules. However, the general concept of integrating future data remains consistent. By incorporating an additional statement that utilizes the Ambient Future Temperature, we can further enhance a Simple Controller.

Equation 3 demonstrates a controller designed to output a specific airflow rate at a certain temperature range. This formular is then used in a greater formular with combined other Airflow formular to control the specific airflow rate for other temperature ranges to a final specific airflow rate.

Temperature is chosen as the primary parameter because temperature control systems are already widely established and integrated into most building HVAC systems (Rehrl and Horn, 2011), making it cost-effective and practical to leverage existing infrastructure. Additionally, temperature is easily measurable and can be accurately predicted using ambient temperature forecasts, allowing the controller to anticipate changes and adjust airflow rates proactively, thus enhancing both comfort and energy efficiency.

$$ACH_gt23 = \begin{Bmatrix} 3 & Schedule\ if\ T_{air} > T_{amb,\ current}\ and\ T_{amb,\ future} > 23 \\ 0 & otherwise \end{Bmatrix} \quad \text{(eq. 3)}$$

with

- ACH_gt23: Is a specific airflow rate [m s-1]
- Schedule: An optional schedule, equal to 1 if activated, and 0 otherwise.
- T_{air}: Current Zone Air temperature [∘C]
- $T_{amb,\ current}$: Current Ambient temperature [∘C]
- $T_{amb,\ future}$: Futurue transposed Ambiant Temperature [∘C]

After managing passive strategies for shading and ventilation, heating and cooling methods are also adjusted to maintain comfort with low energy consumptions. Both heating and cooling controllers are typically defined by specific curves, which include a supply temperature and a power output. To enhance these controllers, future data is integrated into their formulas. Instead of using the current ambient temperature, the heating or cooling curve incorporates the future ambient temperature (eq. 4). Additionally, future solar radiation is factored into the supply temperature adjustments to reduce energy consumption (eq. 4, 5).

Future solar radiation impacts the power output of the heating and cooling systems: it reduces the heating power output and increases the cooling power output (eq. 6). This adjustment ensures that the systems respond

appropriately to anticipated solar gains. The influence of future solar radiation and ambient temperature on these adjustments depends on the specific location, as different regions experience varying solar intensities and weather patterns.

$$T_{sup,\ HT} = \max\left(25.4 - 0.27 * T_{amb,\ future}, 22\right) \quad \text{(eq. 4)}$$

$$\delta T_{soltr,\ future} = \frac{Q_{soltr,future}}{\frac{m_{spec} * c_W}{3.6}} \quad \text{(eq. 5)}$$

$$P_{HT,\ future} = \max\left(P_{HT,\ max} - Q_{soltr,\ future}, 0\right) \quad \text{(eq. 6)}$$

with

- $T_{sup,\ HT}$: Representing the Supply Temperature for the Heating Curve [∘C]
- $T_{amb,\ future}$: Transposed Future Ambient Temperature [∘C]
- $T_{soltr,\ future}$: Transposed incoming solar radiation referring at the area $[\frac{W}{m^2}]$
- m_{spec}: specific mass flow $[\frac{kg}{hm^2}]$
- c_w: specific heat capacity of water $[\frac{KJ}{hm^2}]$
- $P_{HT,\ future}$: Resulting Power Heating Output considering the future data [W]
- $P_{HT,\ max}$: Maximum Power Heating Output [W]

$$T_{sup,\ CL} = \min\left(25.4 - 0.27 * T_{amb,\ future}, 18\right) \quad \text{(eq. 7)}$$

$$P_{CL,\ future} = \max\left(P_{HT,\ max} - Q_{soltr,\ future}, 90\right) \quad \text{(eq. 8)}$$

with

- $T_{sup,\ CL}$: Representing the Supply Temperature for the Cooling Curve [∘C]
- $T_{amb,\ future}$: Transposed Future Ambient Temperature [∘C]
- $T_{soltr,\ future}$: Transposed incoming solar radiation referring at the area $[\frac{W}{m^2}]$
- $P_{CL,\ future}$: Resulting Power Cooling Output considering the future data [W]
- $P_{CL,\ max}$: Maximum Power Cooling Output [W]

Using the adjusted Zone Model, which incorporates controls for shading, ventilation, heating, and cooling, the second simulation run results can describe thermal comfort and provides the energy balance. The Energy balance is then used as an input for the pseudo-predictive post-simulation processing, which incapsulates the CO_2 calculation based on some given parameters named the System Model calculations.

3.4 System Model for Emission calculations

The System Model utilizes the hourly energy balance output from the second run of the thermal dynamic simulation, including 24-hour average ambient temperature and an hourly emissions dataset. This model incorporates various building technologies for heating, cooling, and auxiliary consumptions (equipment, electrical, etc.), as well as electrical storage capacities, loading and unloading powers, efficiencies, and the overall dimensions of the system as depicted in Figure 2. This results compute into CO_2 emission with loading and unloading times as well as storage capacity levels.

Complex control strategies are modeled using a pseudo-predictive approach. Instead of developing an algorithm for real-time data prediction, the model assumes that the future data is already known, since the thermal dynamic simulation has already provided all necessary results. Hence, it is possible to identify minimal values within specific periods (typically 1-2 days) and schedules the charging period around these minimal

values. Thus, the model:

- Specifies the periods during which storage systems are charged based on the minimum energy requirements identified.
- Determines the timeframe for loading and unloading operations is determined based on the 24-hour average ambient temperature, energy performance loads and low CO_2 emissions. This helps ensure that the system operates efficiently and maintains optimal thermal comfort.

Also, both thermal storage (heating and hot water) and battery storage are modeled using a simple input-output approach. The discharge power required by the storage (e.g., for heating demand) must be available within the storage capacity. If the storage is "empty," the required energy is supplied externally during defined charging periods.

The following equations to define how storage loading capacity and supplementary power are processed, determining the energy purchased from the grid (eq. 9). This energy is subsequently used, along with emission data and the Annual Performance Factor, to compute the system's resulting dynamic CO_2 emissions (eq. 10).

$$\rho_{grid}(t) = \sum_{t=1}^{8760} \left(\frac{\rho_{ld}(t) + p_{xlr}(t)}{JAZ} \right) \qquad \text{(eq. 9)}$$

$$E_{dyn} = \sum_{t=1}^{8760} \left(\rho_{grid}(t) * \frac{ef(t)}{1000} \right) \qquad \text{(eq. 10)}$$

with

- $\rho_{grid}(t)$: Grid volume of purchased energy [kWh]
- $\rho_{ld}(t)$: Storage loading capacity [kWh]
- $p_{xlr}(t)$: Supplementary Power [kWh]
- JAZ: Annual Performance Factor
- E_{dyn}: Resulting dynamic CO_2-Emissions [kg CO_2]
- $ef(t)$: Emission factor [g CO_2/kWh]

This System Model framework offers a streamlined approach to integrating thermal and electrical storage, enabling efficient emission calculations and providing a foundation for future enhancements. The model does not simulate complex physical processes such as temperature stratification in thermal storage. With a pseudo-predictive the solar radiation data could be precomputed in the first simulations runs of the thermal dynamic simulations, or in a separate solar radiation study, to additionally incorporate the effects of Photovoltaics into the loading and unloading methods.

4. Discussion

The workflow developed in this study demonstrates both potential and limitations when considering its applicability in thermal models and its transferability to real-world building systems. While the workflow's simplicity in utilizing basic mathematical equations and widely available weather data allows for easy implementation in thermal simulations, it faces challenges in direct application to the built environment.

Firstly, the workflow, though simplified, still requires some level of computational power and understanding of HVAC systems. This makes it unsuitable for a straightforward application in real-world scenarios without the support of a computational unit such as a computer or smart controller. Additionally, basic knowledge in HVAC engineering is necessary to comprehend and apply the process, creating a barrier for non-specialists. These factors highlight the complexity that remains despite attempts to simplify, making the direct transfer of the workflow into built environments challenging.

On the other hand, the low technological requirements and the simplicity of the equations used suggest that the workflow could be implemented using basic devices, such as smartphones or low-cost controllers. This broadens the potential for integration into building systems, offering a path for easier connectivity and application in various settings. Moreover, the availability of weather data for any location further supports the feasibility of using this workflow in real-world applications. However, the lack of granular emissions data, available only at a national level, could potentially limit the precision of the workflow when applied to specific local contexts.

In terms of its relevance to ongoing climate change and adaptation strategies, the workflow presents a mixed case. The need for optimization remains significant, especially as the integration of renewable energies and the stability of the grid become increasingly important. The workflow effectively delivers energy savings, emissions reductions while sustaining thermal comfort, aligning with objectives to enhance energy efficiency and support grid stability. This paper focuses on presenting the framework, while prior studies by Hepf et al. (2022, 2024) have implemented this approach. The 2022 study evaluated four configurations, showing energy savings between 3.5% and 11%, impacted by variations in thermal and battery storage. In 2024, the analysis expanded internationally, covering diverse climate zones and reporting emissions reductions of 5% to 25% across various building types. However, the current framework does not consider humidity, which is one of the driving factors in energy consumption, particularly in humid climates where dehumidification significantly impacts energy usage. This limits the workflow's effectiveness in tropical climates.

Additionally, the long-term effectiveness of this approach is debatable. As emission factors decrease in line with European and governmental targets, the impact of further optimization may diminish, reducing the necessity for such workflows. Furthermore, focusing on sufficiency improvements might offer more substantial benefits than efficiency improvements alone. Despite these considerations, in large building energy systems where HVAC management is crucial, the simplicity of this workflow could offer significant benefits by streamlining complex optimization processes.

In conclusion, while the workflow offers promising advantages in certain scenarios, its broader application in the built environment and its alignment with long-term climate strategies require careful consideration. Its success will depend on the specific context, particularly in terms of technological capability, data availability, and the evolving priorities of energy and emission management.

5. References

Bollin, E., Schmelas, M., 2021. TABS – Thermoaktive Bauteilsysteme: Selbstlernendes und vorausschauendes Steuern mit AMLR. Wiesbaden: Springer Fachmedien.

Crawley, D. B., & Barnaby, C. S., 2019. Weather and climate in building performance simulation. In Building Performance Simulation for Design and Operation (pp. 191-220). Routledge.

Dambeck, H., Ess, F., Falkenberg, H., Kemmler, A., Kirchner A., Kreidelmeyer, S., Koepp, M., Lübbers, S., Piégsa, A., Scheffer, S., Spillmann, T., Thamling, N., Wünsch, A., Ziegenhagen, I., Böttcher, H., Görz, W., Hennenberg, K., Matthes, F.C., Scheffler, M., Wiegmann, K., Schneider, C., Holtz, G., Saurat, M.., Tönjes, A., Lechtenböhmer, S., 2021. Klimaneutrales Deutschland 2045 - Wie Deutschland seine Klimaziele schon vor 2050 erreichen kann.

Drgoňa, J., Arroyo, J., Cupeiro Figueroa, I., Blum, D., Arendt, K., Kim, D., Ollé, E. P., Oravec, J., Wetter, M., Vrabie, D. L., & Helsen, L., 2020. All you need to know about model predictive control for buildings. Annual Reviews in Control, 50, 190–232. https://doi.org/10.1016/j.arcontrol.2020.09.001

Electricity Maps, 2024. Carbon Intensity Data (Version January 17, 2024). Electricity Maps Data Portal, https://www.electricitymaps.com/data-portal (Accessed: 16.08.2024)

Fraunhofer Institute for Solar Energy Systems., 2020. Wege zu einem klimaneutralen Energiesystem—Die deutsche Energiewende im Kontext gesellschaftlicher Verhaltensweisen; Fraunhofer-Institut für Solare Energiesysteme ISE: Freiburg, Germany. https://doi.org/10.24406/publica-fhg-300232

Gwerder, M., Tödtli, J., Lehmann, B., Dorer, V., Güntensperger, W., Renggli, F., 2009. Control of Thermally Activated Building Systems (TABS) in Intermittent Operation with Pulse Width Modulation. Applied Energy 86(9):1606–16. https://doi.org/10.1016/j.apenergy.2009.01.008

Halhoul, M.G., Essaaidi, M., Ben Haddou, M., Qolomany, B., Qadir, J., Anan, M., Al-Fuqaha, A., Abid, M.R., Benhaddou, D., 2021. Intelligent Building Control Systems for Thermal Comfort and Energy-Efficiency: A Systematic Review of Artificial Intelligence-Assisted Techniques. Renewable and Sustainable Energy Reviews 144:110969. https://doi.org/10.1016/j.rser.2021.110969

Halverson, M.A., Hart, R., Athalye R.A., Rosenberg, M.I., Richman, E.E., Winiarski, D.W., ANSI/ASHRAE/IES Standard 90.1-2013 Determination of Energy Savings: Qualitative Analysis. United States: N. p., 2014. https://doi.org/10.2172/1159790

Hepf, C., Bausch, K., Lauss, L., Koth, S.C., Auer, T., 2022. Impact of Dynamic Emission Factors of the German Electricity Mix on the Greenhouse Gas Balance in Building Operation. Buildings 12(12):2215. https://doi.org/10.3390/buildings12122215

Hepf, C., Gottkehaskamp, B., Miller, C., Auer, T., 2024. International Comparison of Weather and Emission Predictive Building Control. Buildings 14(1):288. https://doi.org/10.3390/buildings14010288.

Jia, R., Jin, M., Sun, K., Hong, T., Spanos, C., 2019. Advanced Building Control via Deep Reinforcement Learning. Energy Procedia, 158, 6158–6163. https://doi.org/10.1016/j.egypro.2019.01.494

Lee, J.-Y., Yeo, M.-S. and Kim, K.-W., 2002. Predictive control of the radiant floor heating system in apartment buildings, Journal of Asian architecture and building engineering, 1(1), pp. 105–112. https://doi.org/10.3130/jaabe.1.105.

Nagy, Z., Henze, G., Dey, S., Arroyo, J., Helsen, L., Zhang, X., Chen, B., Kadir Amasyali, Kuldeep Kurte, Zamzam, A., Zandi, H., Ján Drgoňa, Quintana, M., McCullogh, S., June Young Park, Li, H., Hong, T., Brandi, S., Pinto, G. and Capozzoli, A. (2023). Ten questions concerning reinforcement learning for building energy management. Building and Environment, 241, pp.110435–110435. https://doi.org/10.1016/j.buildenv.2023.110435

Rehrl, J., Horn, M., 2011. Temperature Control for HVAC Systems Based on Exact Linearization and Model Predictive Control. Pp. 1119–24. IEEE International Conference on Control Applications (CCA), Denver, Colorado, USA, 28-30 September.

Schmelas, M., 2017. Entwicklung und Evaluierung eines adaptiv-prädiktiven Algorithmus' für thermoaktive Bauteilsysteme. Doctoral thesis, Albert-Ludwigs-Universität Freiburg: Breisgau, Germany. https://doi.org/10.6094/UNIFR/13892

Seckinger, N., and Radgen, P., 2021. Dynamic Prospective Average and Marginal GHG Emission Factors—Scenario-Based Method for the German Power System until 2050. Energies 14(9):2527. https://doi.org/10.3390/en14092527

Soimakallio, S., Saikku, L., 2012. CO_2 Emissions Attributed to Annual Average Electricity Consumption in OECD (the Organisation for Economic Co-Operation and Development) Countries. Energy 38(1):13–20. https://doi.org/10.1016/j.energy.2011.12.048

Studniorz, A., Wolf, D., Kiessling, N., Fahrich, R., Banhardt, C., Tsatsaronis, G., 2022. Plus Minus Zero: Carbon Dioxide Emissions of plus Energy Buildings in Operation under Consideration of Hourly German Carbon Dioxide Emission Factors for Past, Present and Future. IOP Conference Series: Earth and Environmental Science 1078(1):012048. Berlin, Germany, 20-23 September. https://doi.org/10.1088/1755-1315/1078/1/012048

Thieblemont, H., Haghighat, F., Ooka, R., Moreau, A., 2017. Predictive control strategies based on weather forecast in buildings with energy storage system: A review of the state-of-the art. Energy and Buildings, 153, 485–500. https://doi.org/10.1016/j.enbuild.2017.08.010

Tranberg, B., Corradi, O., Lajoie, B., Gibon, T., Staffell, I. and Andresen, G.B., 2019. Real-time carbon accounting method for the European electricity markets. Energy Strategy Reviews, 26, p.100367.

https://doi.org/10.1016/j.esr.2019.100367

United Nations Environment Programme (UNEP), Global Alliance for Buildings and Construction, 2024. Global Status Report for Buildings and Construction: Towards a Zero-emission, Efficient and Resilient Buildings and Construction Sector. https://doi.org/10.59117/20.500.11822/45095

Wärmeschutz und Energie-Einsparung in Gebäuden: 1–11, 4108; Deutsches Institut für Normung e.V., 2018: Berlin, Germany, 2013.

Wörner, P., Müller, A., Sauerwein, D., 2019. Dynamische CO_2-Emissionsfaktoren Für Den Deutschen Strom-Mix. Bauphysik 41(1):17–29. https://doi.org/10.1002/bapi.201800034

Model Predictive Control of a Heat Pump System Integrated with PVT Collectors and Ice Storage

Daler Khamidov[1], Bruno B. Bampi[1], Lilli Frison[1], Björn Nienborg[1]

[1] Fraunhofer Institute for Solar Energy Systems (ISE), Freiburg (Germany)

Abstract

This paper focuses on optimizing a building heating system consisting of a heat pump, photovoltaic collectors (PVT), an ice storage tank, and a buffer tank. The aim is to assess the potential of using Mixed-Integer Nonlinear Model Predictive Control (MI-NMPC) in a novel heat pump system with dual heat sources—PVT collectors and ice storage, along with buffer storage. The paper investigates dynamic interactions, algorithm development, and performance evaluation, emphasizing energy efficiency, cost-effectiveness, and demand response. We find that control-oriented dynamic simulation accurately captures the system's behavior. The application of NMPC in this context highlights its potential for advanced control strategies in hybrid (switched) energy systems. The simulation results demonstrate the improved performance of the system using the MI-NMPC strategy compared to a reference Rule-Based Control (RBC) strategy. This improvement is reflected in a 17.4% reduction in electricity costs over the heating season and a 15.4% decrease in net costs, including revenue from selling excess energy to the grid. In addition, the MI-NMPC strategy increases the self-consumption rate of the generated PV power to 38.2%, further improving the economic and energy efficiency of the system. The application of MI-NMPC in this context underscores its potential for advanced control strategies in hybrid energy systems, particularly in multi-source heat pump systems.

Keywords: Multi-Source Heat Pump, Ice Storage, Mixed-Integer NMPC, PVT, Control-oriented modelling.

1. Introduction

To achieve a sustainable future, it is essential to address the limitations of finite resources, especially fossil fuels. Integrating renewable energy sources into the building sector is a critical part of this transition. Today, buildings account for approximately 30 percent of global final energy consumption and 26 percent of global energy emissions (International Energy Agency, 20/23). About 80 percent of households in Germany still rely on traditional heating systems based on fossil fuels (Bundesverband der Deutschen Heizung- und Warmwasserindustrie, 20/24). Modernization efforts have already helped avoid about 3 million tons of CO2 emissions by 2023 (Umweltbundesamt, 2023). Achieving greenhouse gas neutrality by 2045 and the interim goal of a 65 percent reduction in emissions by 2030 will require a shift to cleaner technologies such as heat pumps. Optimizing heat pump performance when combined with renewable energy requires moving beyond traditional control strategies. Traditional heat pump controllers, which usually rely on a heating curve, fail to consider factors like solar radiation and internal gain (Rolando and Madani, 2013). Complex systems, such as heat pump systems with different sources can benefit from advanced methods of predictive control (Parisio et al., 2020). In addition, strategies such as MPC can account for variable electricity prices. This offers residential customers the opportunity to reduce costs by scheduling operations during periods of lower electricity prices.

1.1 Solar-assisted heat pump system

Heating, Ventilation, and Air Conditioning (HVAC) systems play a critical role in indoor comfort and energy efficiency. The integration of renewable energy sources with conventional systems, such as solar-assisted heat pump (SAHP) systems, has gained attention for its ability to utilize sustainable energy sources (Sezen and Gungor, 2023), improve system efficiency (Hengel et al., 2020), and support the transition to greener technologies. An effective control strategy is essential to optimize efficiency, reduce operating costs, and minimize the environmental footprint, especially in the SAHP system (Perella et al., 2024). In this context, MPC, the focus of this paper, has emerged as a promising approach to optimizing the performance of HVAC systems. The primary objectives of MPC have traditionally included minimizing energy consumption, maximizing comfort, and reducing energy expenses. These goals have been achieved through various methods such as optimal operation with storage systems, implementation of zone temperature control, and optimal

© 2024. The Authors. Published by International Solar Energy Society
Selection and/or peer review under responsibility of Scientific Committee
10.18086/eurosun.2024.01.06 Available at http://proceedings.ises.org

operation of heat pumps, among others (Drgoňa et al., 2020; Afram and Janabi-Sharifi, 2017; Frison et al., 2019).

1.2 Related work

In Multi-Source Heat Pumps (MSHP) systems, supervisory controllers fall into two main categories: MPC and RBC (Pean and Costa-Castello, 2008). These controllers regulate MSHP operation by setting parameters based on factors like solar irradiance, temperatures, and energy storage. RBC, though more advanced than traditional heating curves, lacks MPC's clear objective formulation (Pean and Costa-Castello, 2008) and can become complex with increasing system components. MPC is attractive in HVAC systems for its ability to integrate predictive data from renewable sources and model dynamics, thus improving energy efficiency (Serale et al., 2018). The concept of optimal control for SAHP systems dates to the 1980s (Molyet et al., 2020). Fiorentini et al. (2015) investigated a similar system with PVT collectors, a PCM storage tank, and a heat pump, using Hierarchical Model Predictive Control (HMPC) with a suboptimal two-level control scheme: a high-level controller for a 24-hour horizon and a low-level controller for 1-hour intervals, which may not always yield optimal performance. Hierarchical control strategies are often used in HVAC systems to simplify complex problem formulations and handle nonlinearities, splitting the control into a high-level convex problem and a low-level heuristic-based problem. Switched dynamics in MSHP systems lead to challenging Mixed-Integer Nonlinear Programming (MINLP) formulations, which are managed through techniques like convexification and linearization, transforming problems into Mixed-Integer Linear Programming (MILP) formulations (Atam and Helsen, 2015). Derivative-free methods such as Genetic Algorithms (GA) (Xia et al., 2018) and Particle Swarm Optimization (PSO) (Beghi et al., 2013) are also used. However, GA may yield suboptimal performance if mode selection relies on heuristics rather than being optimally chosen. This work focuses on addressing MINLP problems in MSHP systems, utilizing the Combinatorial Integral Approximation (CIA) technique, previously applied to solar thermal systems (Bürger et al., 2021) and heating networks (Frison et al., 2024).

1.3 Contributions

This paper presents a detailed analysis of MPC applied to an advanced solar-assisted MSHP system that integrates PVT collectors, ice storage, a heat pump, and a buffer storage tank. The optimization of this system is complicated by nonlinearities in the model, such as heat transfer interactions between components, hybrid behaviors arising from various operation modes, and the phase change properties of ice storage. These challenges, typically addressed using discrete variables, result in a complex mixed-integer nonlinear optimization problem. To address this, we investigate a real-time control approach using Mixed-Integer Nonlinear MPC (MI-NMPC), offering practical insights into its implementation. Our analysis compares the effectiveness of MPC with an RBC strategy in minimizing energy costs while maintaining indoor comfort. The results reveal that the RBC strategy, as implemented in this study, faces significant difficulties in rule selection and is less effective than MPC.

1.4 Paper outline

In this paper, we first outline the heating system description, followed by a mathematical model describing each component and the interactions between them. Section 3 provides a detailed MPC formulation and our solution to the arising optimal control problem. Next, in Section 4, we present and discuss the results obtained from simulations.

2. Model development

This section begins with a brief description of the system, followed by a detailed mathematical description of the system model, which is essential for developing the control strategy. The system under consideration is modeled using state-space representation, a method that effectively captures its dynamics.

2.1 System description

Figure 1. shows a simplified schematic of an elaborate heating system that integrates photovoltaic thermal (PVT) collectors, an ice storage tank, a heat pump, and a buffer storage tank. At the core of this system is a brine/water heat pump with a rated thermal capacity of 12.1 kW (B0W35, with a 0°C brine source and a 35°C

sink). This heat pump consists of four main components: the evaporator, which absorbs heat from the source fluid; the condenser, which transfers the absorbed heat to the buffer tank; the compressor, which pumps the refrigerant through the system; and the expansion valve, which regulates the refrigerant flow. On the left side of the heat pump, referred to as the source side, the evaporator is connected to PVT collectors and an ice storage tank. The PVT collectors capture solar energy and convert it into thermal and electrical energy. The ice storage tank stores thermal energy. In this work the ice storage is buried underground, and it is not insulated. Thus, it can gain heat from the ground or lose heat to the ground. The ice fraction in the ice storage cannot exceed 70% in this study. The source side of the heat pump system operates in four different modes, visually illustrated in Figure 2. In Mode 1, solely the ice storage serves as the heat source for the evaporator, with brine circulating between them. Conversely, Mode 2 activates only the PVT collectors, directing brine circulation between the collectors and the evaporator. The Parallel mode (Mode 3) combines both sources, efficiently delivering heat to the refrigerant. Lastly, Mode 4 involves the regeneration of the ice storage tank by the PVT collectors during periods when the heat pump is inactive. These modes provide versatility in managing heat sources for optimal system performance. On the right side of the heat pump, called the sink side, the condenser exchanges heat with the buffer tank, which provides heat to the house. The buffer tank plays a crucial role in storing and regulating the heat delivered to the house. The heating system in the house, which includes radiators, uses hot water from the buffer tank to provide consistent and efficient heating. In cases where the heat pump is unable to generate enough heat to reach the set flow temperature of the heating circuit, the auxiliary heating system is activated to provide the required heat.

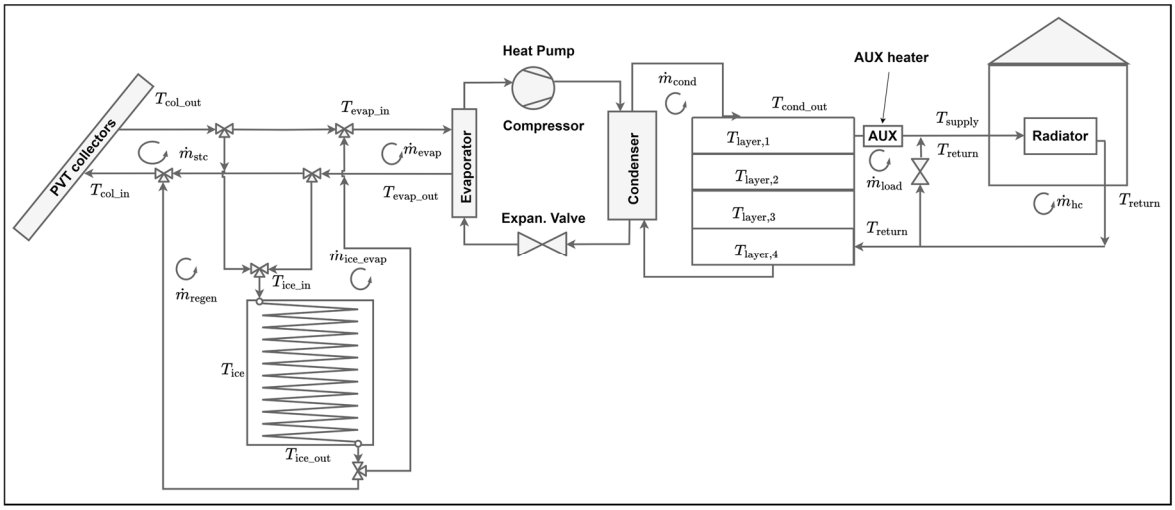

Fig. 1: Simplified scheme of the system

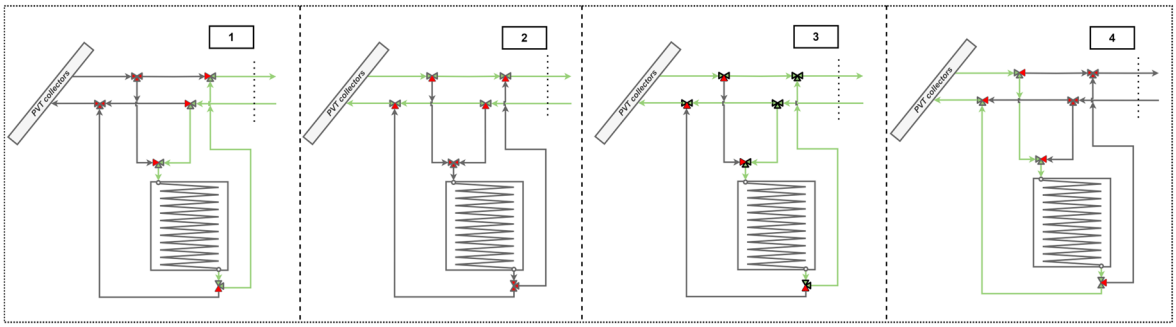

Fig. 2: Operating modes of the source side of the system

2.2 System model

The system under consideration is modeled using a state space representation. This approach captures the dynamics of the system through differential equations that describe the temperatures at different levels of the system components. The state variables listed in Table 1, are critical for describing the thermal dynamics of the system. The differential equations governing the system states are derived from energy balance principles

applied to the system components.

Tab. 1 Notation of state variables

Symbol	Description	Bounds
$T_{\text{col_out}}$	Temperature of the brine leaving the PVT collectors	[-15, ∞],(°C)
T_{ice}	The heat stored in the ice storage	[-∞, 15],(°C)
$T_{\text{ice_out}}$	The ice storage hex outlet source fluid temperature	[-∞,∞],(°C)
$T_{\text{layer,i}}$	The temperature of layer *i* in the buffer storage tank	[0,80],(°C)

Besides the state variables, the system model includes control variables (see Table 2.), disturbances or time-varying parameters (see Table 3.) and finally in Table 4. the model parameters (constants) are given. The control variables can be divided into discrete ones, which describe the modes of the source side, and continuous ones, which describe the power consumption of the compressor and the auxiliary heater.

Tab. 2 Notation of control variables

Symbol	Type	Description	Bounds
$P_{\text{el_comp}}$	Continous	Compressor electrical power consumption	[0, 6000],(W)
P_{aux}	Continous	Auxilary heater electrical power consumption	[0, 6000],(W)
b_{i}	Binary	Binary variable for mode i ∈ {1,2,3,4}	{0,1},(-)

Tab. 3 Notation of time-varying parameters

Symbol	Description
T_{amb}	The ambient temperature (°C)
T_{supply}	The supply temperature of the heating circuit (°C)
T_{return}	The return temperature of the heating circuit (°C)
G_{tot}	Solar irradiance (W/m^2)
C_{el}	The price of electricity from the grid (EUR/WΔt)
$\dot{Q}_{\text{load}}$	The thermal load of the building (W)

Tab. 4 Notation constant parameters

Symbol	Description	Value	Unit
c_{eff}	Effective thermal capacity of PVT collectors	7879	J/(m ^{2} · K)
h_{hx}	Heat transfer coefficient of heat exchanger	80	W/(m ^{2} · K)
A_{hx}	Heat exchange area of hex	30	m ^{2}
$U_{\text{ice_storage}}$	Heat transfer coefficient of the ice tank walls to the ground	4	W/(m ^{2} · K)
ρ_{ice}	Density of ice	920	kg/m ^{3}
ρ_{w}	Density of water	1000	kg/m ^{3}
L_{ice}	The latent heat of fusion for ice	335	kJ/kg
$T_{\text{amb_ice}}$	Surroundings temperature (ice tank)	5	°C
$\dot{m}_{\text{regen}}$	Mass flow rate during regeneration mode	0.35	kg/s
$\dot{m}_{\text{evap}}$	Evaporator mass flow	1	kg/s
$\dot{m}_{\text{stc}}$	Mass flow at PVT collectors	1	kg/s
$\dot{m}_{\text{ice_evap}}$	Mass flow rate at ice storage	1	kg/s
$\dot{m}_{\text{combined}}$	Mass flow rate during combined mode	0.5	kg/s
R_{ice}, V_{ice}	The radius and volume of tank (ice storage)	1, 5.2	m, m ^{3}
c_{br}	Brine specific heat capacity	3595	J/kg/K
c_{w}	Water specific heat capacity	4181	J/kg/K
ρ_{br}	Brine density	1000	kg/m ^{3}
A_{pvt}	PVT collector area	40	m ^{2}
V_{buffer}	Volume of tank (buffer storage)	1	m ^{3}
l_{buffer}	Height of tank (buffer tank)	1	m
$T_{\text{amb_buffer}}$	Surroundings temperature (buffer tank)	20	°C
h_{buffer}	Heat transfer coefficient (buffer tank walls)	0.4	W/(m ^{2} · K)

We have developed a control-oriented model that represents the dynamics of the multisource heat pump system. This model includes equations for the heat pump, PVT collectors, ice storage tank, and buffer tank.

For the thermal part of a PVT system, the energy balance on the absorber plate is given by:

$$\frac{\mathrm{d}}{\mathrm{dt}}T_{\mathrm{col_out}}(t) = \frac{1}{C_{\mathrm{stc}}}(\dot{Q}_{\mathrm{col}}(t) - b_2(t)\dot{m}_{\mathrm{stc}}c_{\mathrm{br}}(T_{\mathrm{col_out}}(t) - T_{\mathrm{evap_out}}(t)) - b_3(t)\dot{m}_{\mathrm{combined}}c_{\mathrm{br}}(T_{\mathrm{col_out}}(t) - T_{\mathrm{evap_out}}(t)) - b_4(t)\dot{m}_{\mathrm{regen}}c_{\mathrm{br}}(T_{\mathrm{col_out}}(t) - T_{\mathrm{ice_out}}(t))) \quad \text{(eq. 1)}$$

Where $C_{\mathrm{stc}} = c_{\mathrm{eff}}A_{\mathrm{pvt}}$ and $\dot{Q}_{\mathrm{col}}$ is the total heat gain:

$$\dot{Q}_{\mathrm{col}} = \eta_{\mathrm{col}}A_{\mathrm{pvt}}G_{\mathrm{tot}} \quad \text{(eq. 2)}$$

Here η_{col} is the efficiency of collector, which for a flat plate collector can be approximated by the polynomial:

$$\eta_{col} = \alpha_1 - \alpha_2\frac{T_{\mathrm{col_out}} - T_{\mathrm{amb}}}{G_{\mathrm{tot}}} - \alpha_3\frac{(T_{\mathrm{col_out}} - T_{\mathrm{amb}})^2}{G_{\mathrm{tot}}} \quad \text{(eq 3)}$$

where $\alpha_1, \alpha_2, \alpha_3$ are parameters of solar thermal collector (-), $(\frac{\mathrm{W}}{\mathrm{Km^2}})$, $(\frac{\mathrm{W}}{\mathrm{K^2m^2}})$.

The electrical power generated by the PV system is:

$$P_{\mathrm{pv_gen}} = \eta_{\mathrm{pv}}A_{\mathrm{pvt}}G_{\mathrm{tot}} \quad \text{(eq. 4)}$$

The electrical efficiency of the PV panel calculated using the following equation (Zondag et al., 2003):

$$\eta_{\mathrm{pv}} = \eta_0 \cdot (1 - 0.0045(T_{\mathrm{cell}} - T_{\mathrm{ref}})) \quad \text{(eq. 5)}$$

where η_0 electrical the efficiency of pv at reference temperature T_{ref} = 25 °C, T_{cell} is the temperature of the solar cell.

For the ice storage model, we first define the ice fraction as a sigmoid function:

$$f = \frac{1}{(1 + e^{2(T_{ice} - Tm)})} \quad \text{(eq. 6)}$$

The energy balance equation for the ice storage is:

$$\frac{\mathrm{d}}{\mathrm{dt}}T_{\mathrm{ice}}(t) = \frac{1}{m_{\mathrm{ice}}\left(c_{\mathrm{p}} + L_{\mathrm{ice}}\frac{\mathrm{d}f(T)}{\mathrm{d}T}\right)}(b_4(t)c_{\mathrm{br}}\dot{m}_{\mathrm{regen}}(T_{\mathrm{col_out}}(t) - T_{\mathrm{ice_out}}(t)) - b_1(t)c_{\mathrm{br}}\dot{m}_{\mathrm{ice_evap}}(T_{\mathrm{ice_out}}(t) - T_{\mathrm{evap_out}}(t)) - b_3(t)c_{\mathrm{br}}\dot{m}_{\mathrm{combined}}(T_{\mathrm{ice_out}}(t) - T_{\mathrm{evap_out}}(t)) - UA_{\mathrm{ice_storage}}(T_{\mathrm{ice}}(t) - T_{\mathrm{amb_ice}})) \quad \text{(eq. 7)}$$

To determine the output temperature of the fluid in a heat exchanger immersed in the ice storage system, the energy balance is applied. The rate of change of the brine outlet temperature can be expressed as:

$$\frac{\mathrm{d}}{\mathrm{dt}}T_{\mathrm{ice_out}}(t) = \frac{1}{V_{\mathrm{hx}}}(b_1(t)\left(\frac{\dot{m}_{\mathrm{ice_evap}}}{\rho_{\mathrm{br}}}(T_{\mathrm{evap_out}}(t) - T_{\mathrm{ice_out}}(t)) - \frac{\dot{Q}_{\mathrm{net,1}}}{\rho_{\mathrm{br}}c_{\mathrm{br}}}\right) + b_3(t)\left(\frac{\dot{m}_{\mathrm{combined}}}{\rho_{\mathrm{br}}}(T_{\mathrm{evap_out}}(t) - T_{\mathrm{ice_out}}(t)) - \frac{\dot{Q}_{\mathrm{net,3}}}{\rho_{\mathrm{br}}\cdot c_{\mathrm{br}}}\right) + b_4(t)\left(\frac{\dot{m}_{\mathrm{regen}}}{\rho_{\mathrm{br}}}(T_{\mathrm{col_out}}(t) - T_{\mathrm{ice_out}}(t)) - \frac{\dot{Q}_{\mathrm{net,4}}}{\rho_{\mathrm{br}}\cdot c_{\mathrm{br}}}\right)) \quad \text{(eq. 8)}$$

Then $\dot{Q}_{\mathrm{net,i}}$ is given as follows:

$\dot{Q}_{\mathrm{net,i}} = U_{\mathrm{hx}}A_{\mathrm{hx}}\Delta T_{\mathrm{MTD,i}}$, where *i* refers to the mode of operation, and $\Delta T_{\mathrm{MTD,i}}$ is given as a mix of geometric and arithmetic mean temperatures . (eq. 9)

The buffer storage tank is modeled as a stratified tank divided into *n* (*n*=4) layers based on Eicker (2003). From the energy balance equations applied to each layer, the rate of temperature change for each layer is derived. For the intermediate layer *i*, it is given as:

$$\frac{\mathrm{d}}{\mathrm{dt}}T_{\mathrm{layer,i}} = \frac{1}{m_{\mathrm{layer,i}}c_{\mathrm{w}}}\begin{pmatrix} -UA_{\mathrm{lat}}\left(T_{\mathrm{layer,i}} - T_{\mathrm{amb}}\right) - UA_{\mathrm{layer}}\left(T_{\mathrm{layer,i}} - T_{\mathrm{layer,i+1}}\right) \\ +UA_{\mathrm{layer}}\left(T_{\mathrm{layer,i-1}} - T_{\mathrm{layer,i}}\right) \\ +\dot{m}_{\mathrm{cond}} \cdot c_{\mathrm{w}}\left(T_{\mathrm{layer,i-1}} - T_{\mathrm{layer,i}}\right) - \dot{m}_{\mathrm{load}}c_{\mathrm{w}} \cdot \left(T_{\mathrm{layer,i}} - T_{\mathrm{i+1}}\right) \end{pmatrix} \quad \text{(eq. 10)}$$

Here UA_{lat}, UA_{layer} represent the overall transfer coefficients for lateral-to-ambient transfer and transfer between layers, respectively and $m_{\mathrm{layer,i}}$ represents the mass of each layer.

In total, Equations (1), (7), (8), (10), and three equations for the remaining layers based on Equation (10) are the differential equations describing the evolution of the system's states. In these equations, the thermal power output of the heat pump is defined by:

$$\dot{Q}_{\mathrm{th_cond}}(t) = P_{\mathrm{el_comp}}(t)(b_1(t) \cdot \mathrm{COP}_1(t) + b_2(t) \cdot \mathrm{COP}_2(t) + b_3(t) \cdot \mathrm{COP}_3(t)) \quad \text{(eq. 11)}$$

For each mode COP_i (i corresponding to mode $i \in \{1,2,3\}$), it is defined by a function with corresponding inlet temperature of evaporator and temperature at sink side This approach avoids double multiplication of the binary control variable, so only the outer multiplication of a binary variable is carried out. The condenser mass flow is calculated by:

$$\dot{m}_{\mathrm{cond}}(t) = \frac{\dot{Q}_{\mathrm{th_cond}}(t)}{c_{\mathrm{w}}(\Delta T_{\mathrm{condenser}}(t))} \quad \text{(eq. 11)}$$

We assume a constant temperature difference between the inflow and outflow from the condenser:

$$\Delta T_{\mathrm{condenser}}(t) = T_{\mathrm{cond_out}}(t) - T_{\mathrm{layer,4}}(t) = 5 \quad \text{(eq. 12)}$$

In this paper, COP and the maximum thermal output of the heat pump are estimated using a polynomial function that depends on the temperatures of the source and sink sides.

2.3 Assumptions

To simplify the system model for optimization, several key assumptions were made. First, mass flow rates are assumed to be constant across all operational modes, which reduces the number of dynamic variables in the system. Additionally, the power of the compressor is treated as a continuous variable, avoiding the complexities associated with discrete power levels. Concerning the sink side, a constant temperature difference is assumed, and heat losses to the environment from both the evaporator and condenser are considered negligible. Ambient temperature around the ice storage and buffer tanks is also assumed to be constant, which simplifies the boundary conditions. Furthermore, the densities and viscosities of the brine and water are treated as constant, eliminating the need to account for temperature-dependent variations. The model maintains mass balance by ensuring that the mass flow rates entering and exiting each control volume are equal. Lastly, both the source and sink fluids are considered incompressible, which simplifies the fluid dynamics equations.

2.4 Boundary conditions

In terms of MPC, the boundary conditions are given in the form of a disturbance vector, which partially includes calculated variables. In our case, ambient temperature, solar irradiance, and the price of electricity are predicted variables, while the heating demand, supply, and return temperatures of the heating circuit are calculated. The predicted variables are provided for the simulated period. For simulation purposes, dynamic pricing is used, with data obtained from the European Energy Exchange (EEX), visually shown in Figure 3. The calculated variables in the disturbance vector are derived using the house parameters and the predicted variables.

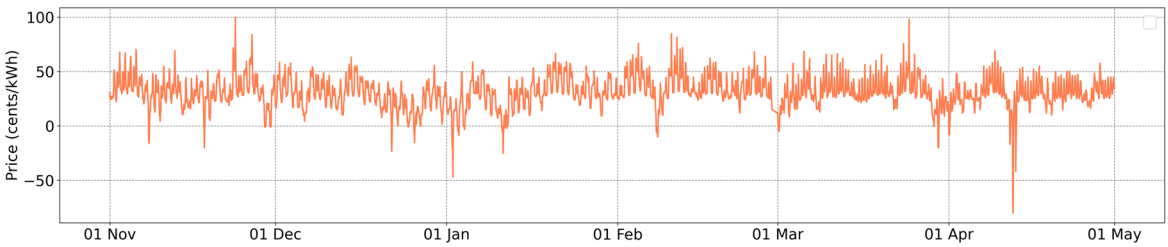

Fig. 3: The price of the electricity used in the simulations

Since the current project develops the control strategy for a house in Ulm, Germany, the house parameters and

the disturbance vector are specific to this house and location. The calculated variables represent the operating parameters of a heating system designed to maintain a comfortable indoor environment. This includes maintaining an indoor temperature of 20°C. At a nominal outdoor temperature of -13°C, the heating system should provide heat to the house, and have a supply (flow) temperature of 45°C and a return temperature to the heat exchangers (radiators) of 35°C. These calculations are performed for the actual house with the goal of developing a cost- and energy-efficient control strategy. By integrating the predicted variables with the house parameters, the control strategy aims to optimize the performance of the heating system while minimizing energy consumption and costs.

3. Model predictive control formulation

Model Predictive Control (MPC) is a widely used optimization-based control strategy in process engineering. This approach uses a mathematical model of the controlled system to predict its future behavior over a finite time horizon, known as the prediction horizon. In our system, the mathematical model is defined by the differential equations described in the previous section. MPC solves an optimization problem to determine the optimal trajectory of the system states, producing control inputs that meet the desired objectives while satisfying the constraints. MPC considers future disturbances, such as weather conditions, demand and electricity prices, as detailed in the previous section. Predictions of these disturbances are provided for this study. For more realistic results, the control data from the optimization is applied on the system with disturbances, including random noise. This approach introduces discrepancies between the model and the actual system to better capture real world scenarios.

3.1 Optimal control problem formulation

Given the previously defined states $x \in \mathbb{R}^{n_x}$ ($n_x = 7$) as described in Table 1, and the differential equations are given in the previous section, the OCP is formulated. The controls include continuous variables $u \in \mathbb{R}^{n_u}$ ($n_u = 2$) and binary variables $b \in \mathbb{R}^{n_b}$ ($n_b = 4$), time-varying parameters $p \in \mathbb{R}^{n_p}$ ($n_p = 6$), and slack variables $s \in \mathbb{R}^{n_s}$ ($n_s = 1$). The objective function aims to minimize the cost of electricity consumed, maximize the utilization of solar energy, and minimize the use of the auxiliary heating system (see Equation 13, where W_i is a weighting coefficient for each component of the objective function). Additionally, it includes quadratic penalty terms for the slack variables. Constraints are then defined, leading to the formulation of the OCP.

$$\min J = \int_0^{tf} \sum_{i=1}^{4} b_{\mathrm{i}}(t) \left(W_{\mathrm{el}} \cdot C_{\mathrm{el}}(t) \cdot P_{\mathrm{el,comp}}(t) - W_{\mathrm{el},2} P_{\mathrm{el,comp}}(t) G_{tot}(t) \right) + W_{\mathrm{aux}} P_{\mathrm{aux}}(t) + W_{\mathrm{s,q}} s^2(t) dt \quad \text{(eq. 13)}$$

s.t.

$$x(t_0) = x_0 \quad \text{(eq. 14)}$$

$$\dot{x}(t) = f(x(t), u(t), p(t)) + \sum_{i=1}^{4} b_i(t) f_b(x(t), u(t), p(t)) \quad \text{(eq. 15)}$$

$$\sum_{i=1}^{4} b_{\mathrm{i}}(t) \leq 1 \quad \text{(eq. 16)}$$

$$T_{\mathrm{hc_supply}}(t) \leq T_{\mathrm{layer},1}(t) + s(t) \quad \text{(eq. 17)}$$

$$P_{\mathrm{el_comp}}(t) COP(t) \leq Q_{\mathrm{th,max}}(t) \quad \text{(eq. 18)}$$

$$P_{\mathrm{el_comp,MIN}} \sum_{i=1}^{3} b_i(t) \leq P_{\mathrm{el_comp}}(t) \quad \text{(eq. 19)}$$

$$P_{\mathrm{el_comp}}(t) \leq \sum_{i=1}^{3} b_{\mathrm{i}}(t) M \quad \text{(eq. 20)}$$

$$P_{\mathrm{el_comp}}(t) \leq (1 - b_4(t)) M \quad \text{(eq. 21)}$$

$$x(t) \in [x_{\mathrm{lb}}, x_{\mathrm{ub}}]^{n_{\mathrm{x}}} \quad \text{(eq. 22)}$$

$$u(t) \in [u_{\mathrm{lb}}, u_{\mathrm{ub}}]^{n_{\mathrm{u}}} \quad \text{(eq. 23)}$$

$$b(t) \in \{0,1\}^{n_{\mathrm{b}}} \quad \text{(eq. 24)}$$

Eq. (14) ensures that the system starts from a specified initial state. The system's evolution is described by the differential equations in Eq. (15). The binary constraint in Eq. (16) guarantees that only one mode is active at any given time. Eq. (17) involves the tank temperature and supply temperature to consistently meet the house's heat demand. By introducing a slack variable, this constraint is relaxed, allowing for more solver flexibility, though it results in a minor negative temperature deviation, which is penalized in the objective function. Eq. (18) pertains to heat pump operation, stating that the electric power consumed by the heat pump, multiplied by

the COP, cannot exceed the maximum possible thermal power output. Eq. (19) defines the minimum input of the heat pump in terms of the electric power of the compressor, which is active in one of the operational modes when the heat pump is on. Conversely, Eq. (20) ensures that when the heat pump is off, its electric power input is zero. Finally, Eq. (21) ensures that when the regeneration mode is active, the electric input to the compressor is zero. In these equations, *M* refers to the Big M method. Eqs. (22, 23, and 24) constrain the lower and upper bounds for the state variables, continuous control variables, and binary control variables, respectively.

3.2 Solution approach

The following is the methodology used to solve the Optimal Control Problem (OCP) described in Eqs. (13-24). The OCP includes both continuous and discrete control variables, where the discrete variables are binary. This results in a Mixed Integer Optimal Control Problem (MIOCP). To solve the continuous-time OCP, the problem is discretized using the direct collocation method, which converts the infinite-dimensional optimization problem into a Mixed-Integer Nonlinear Programming (MINLP) problem. While solvers such as BONMIN (Bonami et al., 2008) can handle MINLP problems, they are often impractical for real-world applications due to their long computation times and the need to satisfy real-time constraints, especially when dealing with large problems at each time step. In this study, the Combinatorial Integral Approximation (CIA) technique, as described by Sager et al. (2011) and practically demonstrated by Bürger et al. (2021), is employed. This algorithm consists of three main steps, which are outlined in Algorithm 1.

Algo. 1 Algorithm for Solving the MIOCP

1. Solve the relaxed discretized MIOCP (MINLP) with $b_i \in [0, 1]$
2. Solve the CIA problem to obtain $b_i \in \{0, 1\}$
3. Solve the discretized MIOCP (MINLP) with $b_i \in \{0, 1\}$

Output: *x, u, b*

In the closed loop simulation, the obtained control variables are applied to the system after step 3 in Algorithm 1. The system is simulated using the fourth-order Runge-Kutta (RK4) integration scheme. To improve computational efficiency, warmstarting is used to transfer solution information from the previous MIOCP problem to the current one as an initial guess. According to Rawlings et al. (2017), shift initialization is particularly beneficial for systems with time-varying parameters in their dynamics. In this technique, the solution of the previous MINLP problem is shifted to the next one and adapted to the next time step. We apply the shift initialization technique specifically to the relaxed MIOCP problem.

All the computations were carried out on a desktop PC equipped with an Intel(R) Core(TM) i5-9500 @ 3.00 GHz CPU and 16 GB of RAM, running on the Windows 10 operating system. The CasADi symbolic framework (version 3.6.3) (Andersson et al., 2019), which provides algorithmic differentiation capabilities, was used to formulate and solve the (MIOCP) problems. IPOPT (3.14.11) (Wächter and. Biegler, 2006) has been used for solving the sparse NLP problems using the linear solver MUMPS (5.4.1.) (Amestroy et al., 2001). For solving the CIA (Sager et al., 2011) problems, the open-source package pycombina (Bürger et al., 2020) was used, with MILPs solved using the branch-and-bound algorithm. All code was written in Python.

4. Results

4.1 Overview of controllers

To evaluate the performance of the MI-NMPC strategy, a reference control strategy was needed. This work included the implementation of the RBC strategy, which is based on simple heuristics. These heuristics were partially derived from observations of the MI-NMPC simulation. The RBC strategy utilizes solar energy when it is available.

4.2 Case study: Heating season simulation

This section presents and analyzes the outcomes of closed-loop simulations comparing the MI-NMPC strategy to the RBC strategy for the heating heat pump system during a heating season. A sampling time for MI-NMPC is $\Delta T = 900$ seconds, and RBC inputs are updated every 900 seconds. To begin with, there is a notable disparity in the utilization of the auxiliary heater when comparing RBC and MI-NMPC control strategies. Specifically,

the MI-NMPC strategy reduces auxiliary heater usage by a factor of 4.3, compared to RBC. In percentage terms, the auxiliary heater accounts for 4.3% of the total heat delivered when the system is controlled by the RBC strategy, versus only 1% with MI-NMPC.

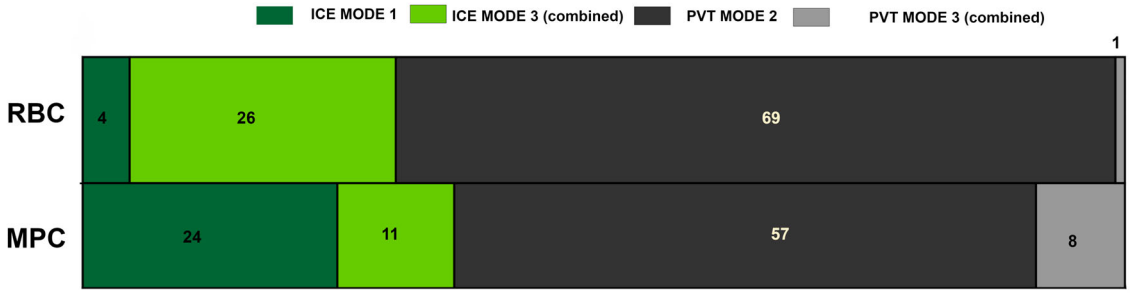

Fig. 4: Heat flow (in percent, %) from PVT and ice storage in each mode

Next, Figure 4. demonstrates the amount of heat delivered to the evaporator from each source and during each mode when controlled by MI-NMPC and RBC strategies and Figure 5. shows the ice fraction, temperature inside the ice storage tank, and the thermal power output of the auxiliary heater throughout the simulation period for both MI-NMPC and RBC strategies. The utilization of ice storage is lower for the RBC strategy due to the depletion of ice storage, with the ice fraction achieving its maximum allowed value. In contrast, the MI-NMPC strategy better utilizes ice storage in mode 1, with 24% utilization compared to 4% for RBC. During the combined mode with MI-NMPC, the PVT collectors contributed 8% of the total heat, compared to 1% with RBC over the entire simulation period. In total, solar thermal energy (PVT) accounts for more than 65% of the total heat source for both controllers. This high proportion is likely due to the under sizing of the ice storage system for this application. When the ice storage tank is depleted, both strategies employ the auxiliary heater. However, MI-NMPC reduces utilization to 0.25 MWh compared to 1.08 MWh for RBC. In addition, the economic analysis revealed that with MI-NMPC, the electricity bill is 1776 EUR, with a PV feed-in revenue of 233 EUR, resulting in net expenses of 1543 EUR. In contrast, for RBC, the electricity bill is 2151 EUR, with a PV feed-in revenue of 327 EUR, indicating less PV self-consumption. Economically, MI-NMPC results in net expenses of 15.4% less compared with RBC, further demonstrating its superior cost performance. Figure 7. illustrates the cumulative cost of electricity for both cases over the simulated period. From an energy management perspective, MI-NMPC optimizes the operation of the heat pump, resulting in better energy consumption management and significant cost savings. The utilization of solar energy is notably more effective with MI-NMPC, showcasing a higher self-consumption of generated PV electricity, with 38.2% compared to 34.5% for RBC.

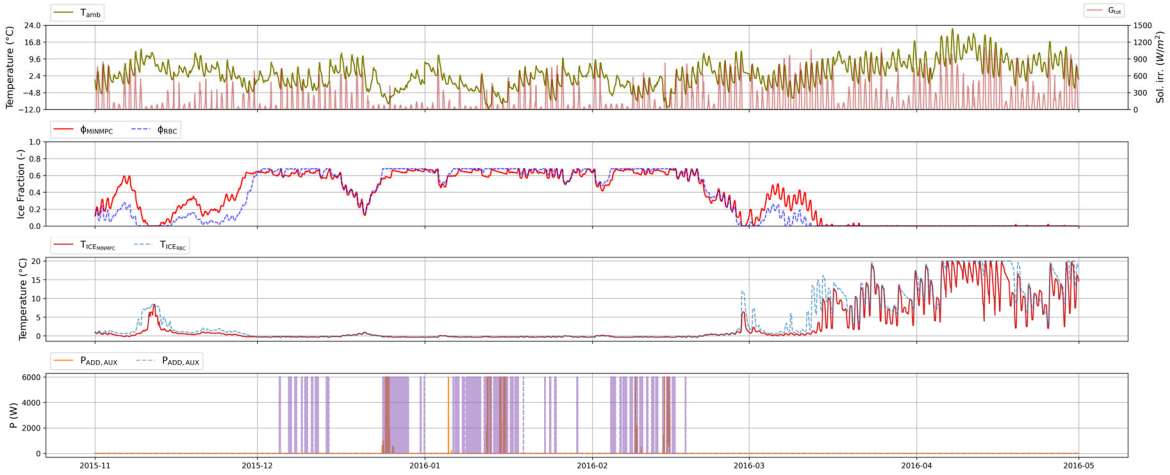

Fig. 5: Ice fraction, temperature inside ice storage, activation of auxiliary heating system for both MINMPC and RBC controlled cases

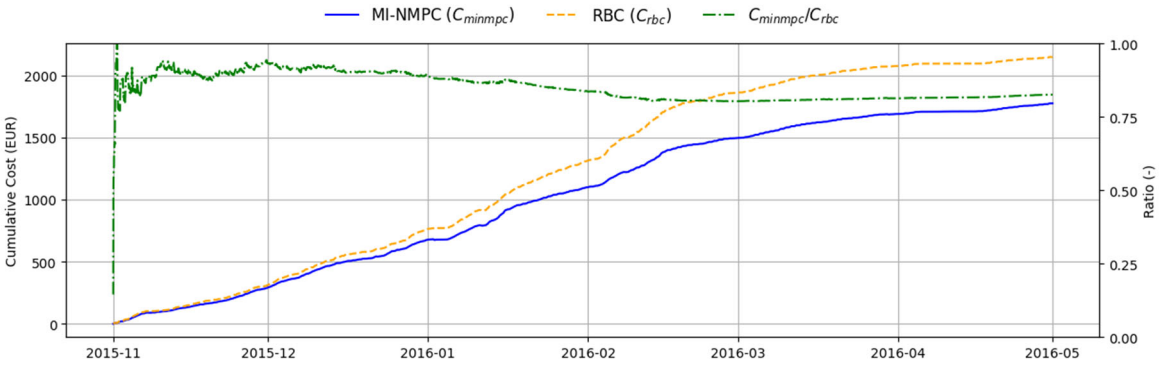

Fig. 6: Cumulative electricity costs over simulated time

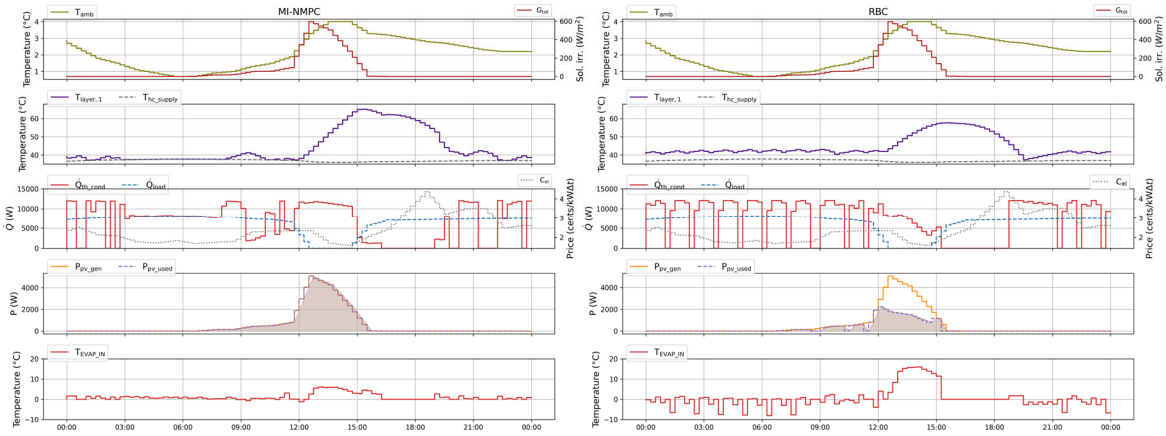

Fig. 7: Simulation Results: Detailed visualization of key parameters and operational aspects under MI-NMPC (left) and RBC (right) control strategies.

To provide a detailed analysis, we look at the results of a one-day simulation. While a general overview of the entire heating season was provided, the detailed one-day simulation results offer insights into the specific operational differences of MI-NMPC. The sampling time for MI-NMPC is $\Delta T = 900$ seconds, and RBC inputs are updated every 900 seconds. Figure 8. presents plot of the simulation results from 00:00 to 00:00 the following day for both control strategies, with MI-NMPC on the left and RBC on the right. The first subplot displays changes in temperature and solar irradiance levels over the day, with the average ambient temperature on the selected day above 0°C. The second subplot shows the temperature of the top layer of the tank and the supply temperatures, with both controllers meeting the heating demand. The third subplot illustrates the heat pump's thermal output and demand changes over a 24-hour period, with the electricity price on another y-axis. The fourth subplot demonstrates that MI-NMPC charges the buffer tank when electricity is cheap or PV generation is available, consuming 100% of PV-generated electricity compared to 48.5% with RBC. The last subplot illustrates the input temperatures of the evaporator, with MI-NMPC maintaining higher, steadier temperatures, leading to fewer mode changes compared to RBC.

Several observations can be made based on the simulation results. The MI-NMPC strategy effectively meets heating demand while minimizing electricity costs, dynamically adapting to changing conditions, and optimizing storage utilization. This adaptability shows potential in dynamic pricing scenarios. The study also highlights the benefits of combining expertise from different fields to address complex HVAC and energy management challenges.

5. Conclusion

In conclusion, this study confirms the effectiveness of the MI-NMPC strategy in meeting heating demands while minimizing electricity costs. The MI-NMPC strategy significantly reduces auxiliary heater utilization and demonstrates superior economic performance, with electricity costs reduced by up to 17.4% over the entire heating season and net costs lowered by 15.4%, including income from electricity sold back to the grid. Additionally, the MI-NMPC strategy optimizes energy consumption, achieving a higher self-consumption rate

of 38.2% for generated PV electricity. The research contributes to control-oriented modeling and implementation of MI-NMPC strategies and paves the way for future research in MPC for multi-source heat pump systems. Overall, the MI-NMPC strategy shows superior performance in terms of demand satisfaction, cost minimization, and energy efficiency compared to the RBC strategy.

6. Acknowledgments

D. Khamidov would like to acknowledge Prof. Dr. Moritz Diehl and Prof. Dr. Hans-Martin Henning for their support and guidance throughout this project. He also extends his gratitude to Fraunhofer ISE and co-authors Dr. L. Frison, B.B. Bampi, and B. Nienborg for the opportunity to work on this project.

The study presented in this paper received funding from the German Federal Ministry of Economic Affairs and Climate Action (BMWK) under the grant agreement number FKZ 03EN4016A (HPPVT40).

7. References

Afram, A., Janabi-Sharifi, F., 2017. Supervisory model predictive controller (MPC) for residential HVAC systems: Implementation and experimentation on archetype sustainable house in Toronto. Energy and Buildings, 154, 268-282.

Andersson, J. A. E., Gillis, J., Horn, G., Rawlings, J. B., Diehl, M., 2019. CasADi: a software framework for nonlinear optimization and optimal control. Mathematical Programming Computation, 11(1), 1-36.

Atam, E., Helsen, L., 2015. A convex approach to a class of non-convex building HVAC control problems: Illustration by two case studies. Energy and Buildings, 93, 269-281.

Beghi, A., Cecchinato, L., Rampazzo, M., Simmini, F., 2013. Modeling and control of HVAC systems with ice cold thermal energy storage. In 52nd IEEE Conference on Decision and Control, pp. 4808-4813.

Bonami, P., Biegler, L.T., Conn, A.R., Cornuéjols, G., Grossmann, I.E., Laird, C.D., Lee, J., Lodi, A., Margot, F., Sawaya, N., Wächter, A., 2008. An algorithmic framework for convex mixed integer nonlinear programs. Discrete Optimization, 5(2), pp.186-204.

Bürger, A., Bull, D., Sawant, P., Bohlayer, M., Klotz, A., Beschütz, D., Altmann-Dieses, A., Braun, M., Diehl, M., 2021. Experimental operation of a solar-driven climate system with thermal energy storages using mixed-integer nonlinear model predictive control. Optimal Control Applications and Methods, 42(5), 1293-1319.

Bürger, A., Zeile, C., Hahn, M., Altmann-Dieses, A., Sager, S., Diehl, M., 2020. pycombina: An open-source tool for solving combinatorial approximation problems arising in mixed-integer optimal control. IFAC-PapersOnLine, 53(2), 6502-6508.

Bundesverband der Deutschen Heizungsindustrie (BDH), 2024. Pressemitteilung: Heizungsindustrie: Rekordabsatz in turbulentem Marktumfeld. Available online: https://www.bdh-industrie.de/fileadmin/user_upload/Pressemeldungen/PM_BDH_Jahresbilanz_Gesamtmarkt_19022024.pdf [Accessed: 11 August 2024].

Drgoňa, J., Arroyo, J., Cupeiro Figueroa, I., Blum, D., Arendt, K., Kim, D., Ollé, E.P., Oravec, J., Wetter, M., Vrabie, D.L., Helsen, L., 2020. All you need to know about model predictive control for buildings. Annual Reviews in Control, 50, 190-232.

Eicker, U., 2003. Solar Technologies for Buildings. Chichester: John Wiley & Sons Ltd.

Federal Association of the German Heating Industry, 2024. Available online: https://www.bmwsb.bund.de [last accessed: 07 August 2024].

Fiorentini, M., Cooper, P., Ma, Z., Robinson, D.A., 2015. Hybrid model predictive control of a residential HVAC system with PVT energy generation and PCM thermal storage. Energy Procedia, 83, 21-30.

Frison, L., Kleinstück, M., Engelmann, P., 2019. Model-predictive control for testing energy flexible heat pump operation within a Hardware-in-the-Loop setting. Journal of Physics: Conference Series, 1343(1), 012068.

Frison, L., Kollmar, M., Oliva, A., Bürger, A., Diehl, M., 2024. Model predictive control of bidirectional heat transfer in prosumer-based solar district heating networks. Applied Energy, 358, 122617. https://doi.org/10.1016/j.apenergy.2023.122617.

Hengel, F., Heschl, C., Inschlag, F., Klanatsky, P., 2020. System efficiency of PVT collector driven heat pumps. International Journal of Thermofluids, 5-6, 100034.

International Energy Agency, 2023. Tracking clean energy progress 2023. Available online: https://www.iea.org/reports/tracking-clean-energy-progress-2023. Licence: CC BY 4.0.

Molyet, R.G., Eltimsahy, A.H., Jones, M.L., 1980. Optimal control of solar heating systems utilizing a dual source heat pump. Proc. Annu. Meet. - Am. Sect. Int. Sol. Energy Soc.; (United States).

Parisio, A., Fabietti, L., Molinari, M., Varagnolo, D., Johansson, K.H., 2014. Control of HVAC systems via scenario-based explicit MPC. In 53rd IEEE Conference on Decision and Control, pp. 5201-5207.

Pean, T.Q., Salom, J., Costa-Castello, R., 2019. Review of control strategies for improving the energy flexibility provided by heat pump systems in buildings. Journal of Process Control, 74, 35-49.

Perrella, S., Bisegna, F., Bevilacqua, P., Cirone, D., Bruno, R., 2024. Solar-assisted heat pump with electric and thermal storage: The role of appropriate control strategies for the exploitation of the solar source. Buildings, 14(1).

Rawlings, J.B., Mayne, D.Q., Diehl, M., 2017. Model Predictive Control: Theory, Computation, and Design (2nd ed.). Nob Hill Publishing.

Rolando, D., Madani, H., 2018. Smart control strategies for heat pump systems. Available online: https://varmtochkallt.se/wp-content/uploads/Projekt/EffsysExpand/P18_Project_Report_final_reviewed.pdf [Accessed: 8 August 2024].

Sager, S., Jung, M., Kirches, C., 2011. Combinatorial integral approximation. Mathematical Methods of Operations Research, 73, 363-380.

Sezen, K., Gungor, A., 2023. Comparison of solar assisted heat pump systems for heating residences: A review. Solar Energy, 249, 424-445.

Serale, G., Fiorentini, M., Capozzoli, A., Bernardini, D., Bemporad, A., 2018. Model predictive control (MPC) for enhancing building and HVAC system energy efficiency: Problem formulation, applications and opportunities. Energies, 11, 631.

Umweltbundesamt, 2023. Modernisierungsmaßnahmen zur Emissionsreduktion. Available online: https://www.umweltbundesamt.de/emissionsreduktion-2023. Licence: CC BY 4.0.

Wächter, A., Biegler, L., 2006. On the implementation of an interior-point filter line-search algorithm for large-scale nonlinear programming. Mathematical Programming, 106, 25-57.

Xia, L., Ma, Z., Kokogiannakis, G., Wang, S., Gong, X., 2018. A model-based optimal control strategy for ground source heat pump systems with integrated solar photovoltaic thermal collectors. Applied Energy, 228, 1399-14

Zondag, H.A., de Vries, D.W., van Helden, W.G.J., van Zolingen, R.J.C., van Steenhoven, A.A., 2003. The yield of different combined PV-thermal collector designs. Solar Energy, 74(3), pp.253-269. https://doi.org/10.1016/S0038-092X(03)00121-X.

Propane-based heat pump solutions for existing multi family houses – requirements and possible system solutions

Björn Nienborg*, Beatrice Rodenbücher, Annette Uhl, Peter Engelmann

Fraunhofer ISE, Freiburg, Germany

*Corresponding author: bjoern.nienborg@ise.fraunhofer.de

Abstract

Approximately 40% of the living area in Germany can be attributed to multi-family houses, a large share of which are existing buildings heated with fossil fuels. To decarbonize these with heat pumps, the housing industry needs standardized solutions for refurbishment. Therefore, this study compiles essential boundary conditions from the housing stock such as

- required capacity for heating and domestic hot water preparation
- required condenser outlet temperatures
- available installation space
- permissible acoustic emissions
- safety measures

On this basis three different heat pump solutions based on the future-proof low-GPW refrigerant propane (R290) are outlined:

- apartment-wise heating systems (currently typically consisting of wall-hung gas boilers)
- central heating systems, heat pump installed indoors
- central heating systems, air-source heat pump installed outdoors (direct evaporation)

Keywords: heat pump, multi family houses, requirements, heat sources, R290

1. Introduction

Heat pumps are expected to contribute strongly to decarbonizing residential space heating. The German government aims to have 6 million units installed by 2030, with continued installations in the subsequent decade. This ambitious goal necessitates a substantial increase in production, planning, and installation capacities. To achieve long-term greenhouse gas neutrality, it is crucial to avoid lock-in effects, especially regarding the choice of refrigerants. Therefore, natural refrigerants with low GWP should be utilized.

While heat pumps have become the favored heating technology in new single-family houses (SFH) in recent years and are increasingly common in existing ones, the existing stock of multi-family houses (MFH) still presents a challenge for this technology. High supply temperatures, limited installation space, and constraints in source availability in densely populated areas are significant barriers to its widespread adoption. Additionally, solid data on the performance of heat pumps in existing MFH is scarce. Lämmle et al. (2023) report seasonal performance factors (SPF, including backup heating rod, before buffer storage) of heat pump systems in small MFH from 1.5 to 4.7, averaging 3.5.

As a result, the majority of market-available products are designed for the SFH sector. Heat pumps with higher capacities (>15 kW) that use future-proof refrigerants and are specifically designed for refurbishing heating

© 2024. The Authors. Published by International Solar Energy Society
Selection and/or peer review under responsibility of Scientific Committee
10.18086/eurosun.2024.01.07 Available at http://proceedings.ises.org

systems in MFH are limited (Oltersdorf et al., 2024a). To support new developments, the goal of this study is to compile typical requirements for heat pump systems in MFH and to derive generic solutions. Propane (R290) is the favored refrigerant in this context as it allows for high condensing temperature required for domestic hot water (DHW) preparation and bears no environmental risks such as high global warming potential (GWP=3) or persistent degradation products (PFAS).

2. Methodology

The compilation of requirements for propane heat pump solutions in multi-family houses is primarily based on literature research. This involves combining data from various sources to obtain clear and comprehensive information. The validity of these findings is cross-checked with stakeholders from both the housing and heat pump industry. To achieve this, an advisory board comprising over 15 heat pump manufacturers and 5 housing companies (collectively owning over 30,000 residential units) has been consulted in frame of the German development project LCR290[1]. For detailed case studies, six buildings from this stock have been selected as "example buildings," representing different scenarios and boundary conditions (such as central and decentral space heating, year of construction, urban environment, etc.).

3. Results

An extensive study on the availability of typical ambient heat sources has been conducted in recent years. Using simplified technical specifications of different source technologies combined with available GIS and statistical data, heat demands and source availability were determined for Germany. The resulting potential of promising low grade heat sources for heat pumps to supply the building stock is presented in Figure 1. This analysis does not differentiate between single and multi-family houses. Additionally, the results can only be regarded as indicative due to the simplifications in the methodology. Nevertheless, it becomes obvious that all regarded sources can contribute significantly. By including further sources, combining and adapting them, there is a good chance to increase the potential further.

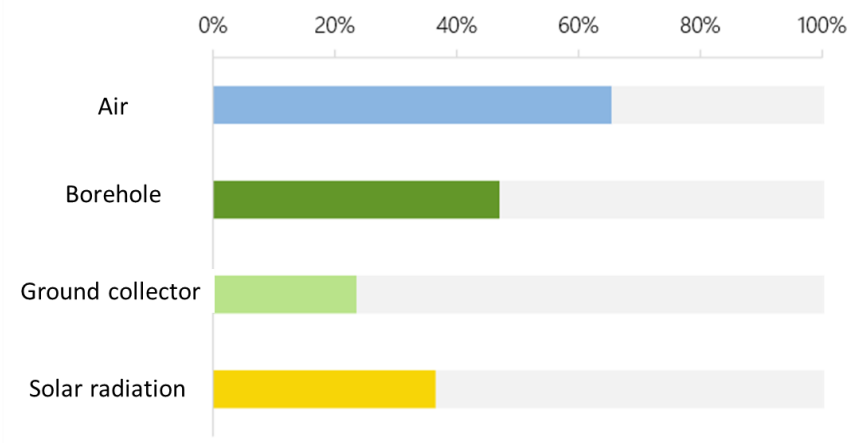

Figure 1: Share of residential building stock which can be supplied with heat pumps by sources according to (Greif, 2023)

3.1 Required heating capacities

3.1.1 Central heating systems

The basis for this analysis is a frequency distribution of buildings' areas based on data from the project partners' portfolio of buildings (see Figure 2 left). In total 3.3 Mio multi family houses exist in Germany. A crosscheck with the German residential building typology, which distinguishes by number of apartments instead of heated surface gives a good general agreement (Loga et al., 2015). Another basic

[1] https://lcr290.eu/

source is a frequency distribution of energy efficiency classes in German multi family houses which was gathered from the information of approximately 75000 energy certificates buildings (see right) (Krieger 2018). While the efficiency classes correspond to ranges of specific consumption (kWh/m²/a) an average (or typical) specific peak heating power (in W/m², defining the required capacity of the heating device) can be attributed to each of the energy efficiency classes. When the two sources are combined, multiplying the areas with the specific heating powers and weighting their occurrence accordingly a frequency distribution as shown in figure 2 results.

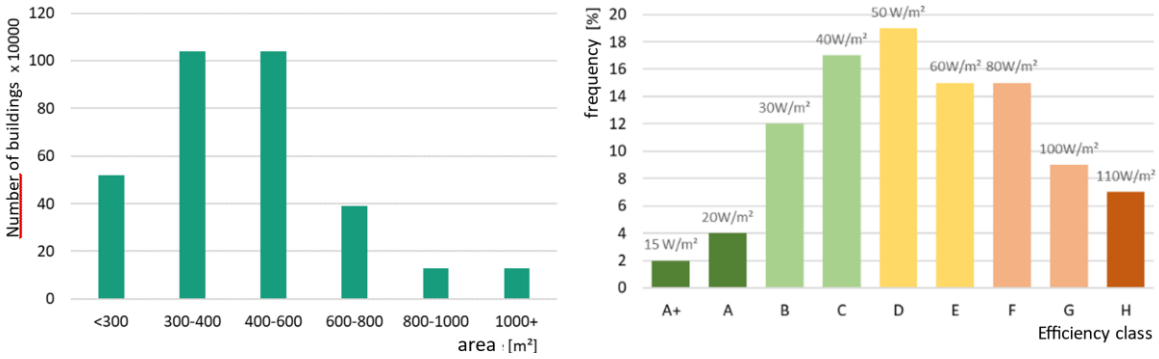

Figure 2: Data basis for an estimation of performance classes for central heat generators: the frequency distribution of flat sizes based on data from the project partners[2] building portfolio and the distribution of efficiency classes of multi-family buildings in Germany (Krieger 2018).

A large variety of heat pumps with R290 up to 15kW can be found on European market already. However, for the dominant capacity range of 16 to 35 kW the market availability of heat pumps is limited. Therefore, the recommendation is to concentrate on heat pump development in this capacity range. Higher capacities can be supplied by cascading various appliances.

3.1.2 Decentralized heating systems

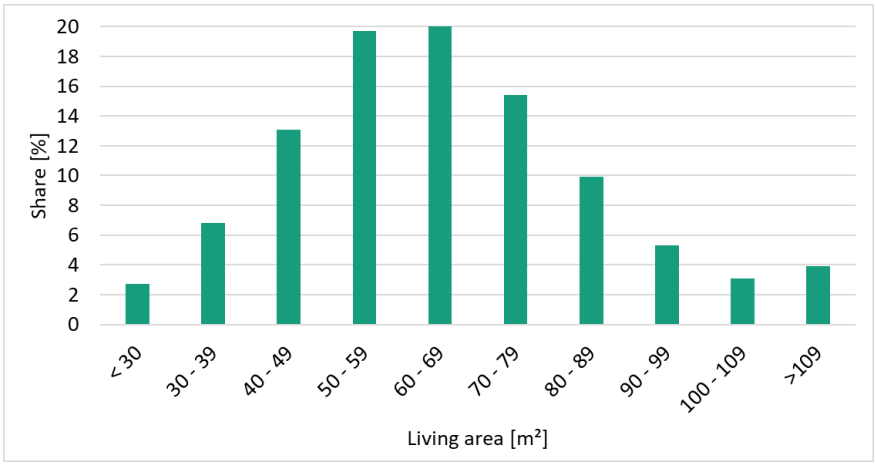

Figure 3: Frequency distribution of living areas in the German rental multi family house stock (Statistische Ämter des Bundes und der Länder, 2011)

A similar procedure as for the central heating systems has been applied to determine the required heating capacity of apartment wise decentralized heating systems. The frequency distribution of living areas in the German multi family house stock as shown in Figure 3 serves as data source in this case. Combining it with the efficiency classes and the related specific heating capacities yields (as in figure 2, right graph) a distribution

[2] The European Energy Performance of Buildings Directive 2010 requires buildings to have an energy performance certificate which specifies its final energy demand for heating and domestic hot water. Efficiency classes from A+ to H correspond to certain ranges of energy demand.

of required heating capacities as shown in Figure 4.

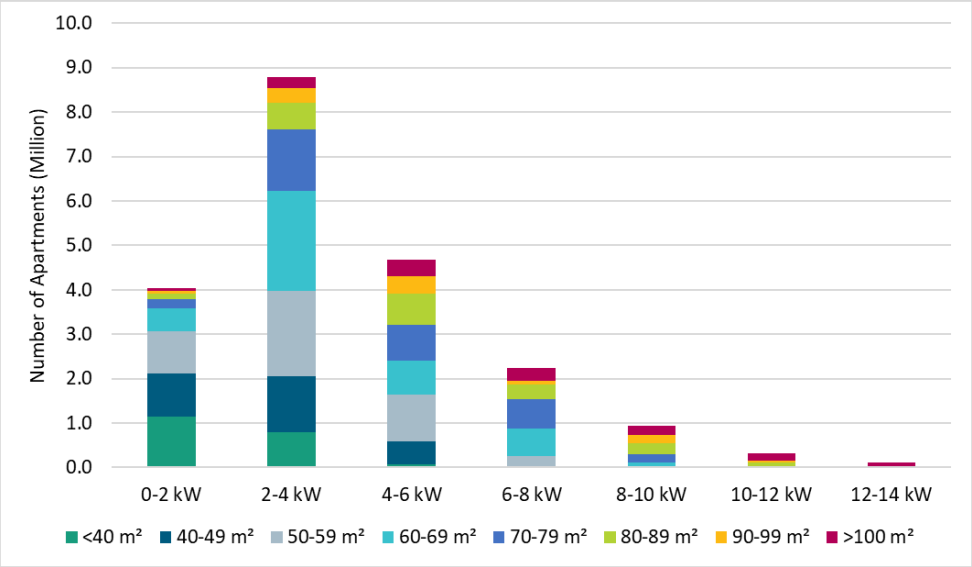

Figure 4: Derived frequency distribution of heating capacities of apartments in German multi-family houses

As a result, 60% of the flats have heating loads below 4 kW and 80% below 6 kW. Inaccuracies in this estimate result e.g. from

- the allocation of one average area-specific heating loads to each energy efficiency class, independently of the building size etc.
- the homogeneous application of the allocation of energy efficiency classes to all residential areas
- the fact that the frequency distribution of living space only relates to the rental housing stock

Nevertheless, it can be assumed that the majority of the housing stock has heating loads in the low to mid single-digit range.

3.2 Required hot water temperature

3.2.1 Space heating

Existing buildings in Germany and central Europe are typically heated by hydronic radiators. Typical design temperatures in existing buildings were 90/70°C (supply/return) or 75/65°C, which is the design point for radiators according to the European Standard EN 442-2.

To achieve decent seasonal performances with heat pumps which allow CO2-savings over fossil alternatives, a design temperature of 55°C has been found reasonable (Lämmle et al., 2022b). As radiators were oversized frequently in the past and based on a review of the radiator dimensioning of approximately 130.000 multi-family houses, it was estimated that the design heating supply temperature can be decreased to this value in approximately 50% of the German multi family houses without any adaptions to the distribution system (Techem Energy Services GmbH, 2023). In approximately 10% of the studied buildings the temperature could be decreased to even lower temperatures without the need for changes in the distribution system. The same study claims that another 40% of the stock can be refurbished to this temperature by a (partial) exchange of the radiators by products with higher capacity but the same cross section. An example for such a transformation is a building in Karlsruhe-Durlach (Germany), where the temperature could be decreased to 55°C from formerly 75°C by exchanging 7% of the radiators (11 out of 150) (Lämmle et al., 2022a).

3.2.2 Centralized domestic hot water preparation

To avoid the risk of legionella growth, central domestic hot water (DHW) systems in German multi-family houses need to supply a temperature of 60°C to all tapping locations (DIN 2012; DVGW 2004). The buildings also need to have a circulation line which prevents the cooling of the water (with subsequent potential legionella growth) in times without demand. The minimum temperature is required to be at least 55°C in the circulation return to the heat generator.

Typical system configurations for DHW preparation with heat pumps in MFH contain a storage to be able to cover peaks in demand. There is always a heat exchanger to separate the heating water circulating in the heat pump from the DHW. To overcome this heat resistance a temperature gradient is necessary, so a heat pump needs to be able to supply at least 65°C for such a system. A review of ~2500 market available heat pump models which received the Heat Pump Keymark (see (Jardin, 2024)) by (Lämmle et al., 2023) reveals that this required high temperature is a strong argument for using R290 as refrigerant. The median maximum temperature over the 94 listed products with this refrigerant is 70°C. The other common refrigerants R32 and R410A have median maximum temperatures of 55°C and 60°C, respectively (with 1478 and 818 listed products, respectively).

3.2.3 Decentralized domestic hot water preparation

DHW installations with a water volume of less than 3 liters between the heat generator and the most distant tapping location count as “small systems” in Germany (DVGW 2004). For these, there is no mandatory minimum temperature. 60°C are recommended and temperatures below 50°C “should be avoided” to hinder growth of legionella.

Yet, as space is limited in typical apartments with decentralized heating (see the chapter 3.3) and a substantial storage capacity is needed to cover demand peaks, it may not be possible to use this potential for decreasing the set temperature for heat pumps: the storage capacity is directly linked to its temperature. E.g. assuming a cold water temperature of 10°C, a tapping temperature for the DHW of 40°C and a perfectly mixed storage, decreasing its set temperature from 60°C to 50°C requires a 25% higher storage volume to achieve the same capacity. As the DHW will be prepared by heat exchanger, a temperature range up to 65°C is recommendable also for this application.

3.3 Available installation space

3.3.1 Centralized heat pump systems

According to current legislation in Germany for heating systems with a nominal output of more than 28 kW, the area of the installation room must be at least 7.5 m². The analysis of a small sample of MFH basement plan supplied by housing companies accompanying the project, proves that typical sizes are around 10 m² and no influence of building size can be observed (see Figure 5). As the buildings are typically heated with central gas boilers, which are compact up to a capacity of ~200kW, and DHW is provided by one central storage tank this is reasonable. The outlier with a surface of 32m² is a building heated by an oil boiler, so the area includes the space for a building integrated oil tank.

Switching to heat pumps will lead to a higher space requirement as the appliances themselves are larger and because systems are typically designed with higher storage volumes for robust operation and DHW supply. Additional space can typically be found in existing buildings’ basements, possibly at the cost of reducing the size of the tentants’ storage cellars. Therefore, new heat pump solutions should be compact and allow a wide modulation range to minimize the storage volume required for stable operation.

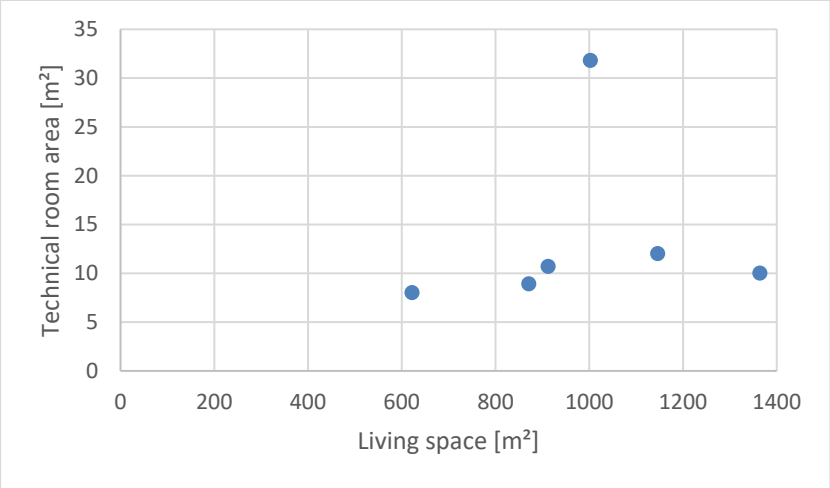

Figure 5: Area of 6 technical rooms compared to the heated living area in the sample buildings.

3.3.2 Decentralized heat pump systems

Wall-hung gas boilers typically have dimensions in the order of 450x750x350 mm (WxHxD). An overview of the dimensions of appliances from 7 manufacturers serving the European market is shown in Figure 6. In principle, the appliances can supply domestic hot water and heating without an additional storage cylinder. In some cases, however, they are installed with an additional domestic hot water tank in order to a) ensure comfort even when tapping at several points at the same time and b) enable simultaneous heating and domestic hot water utilization.

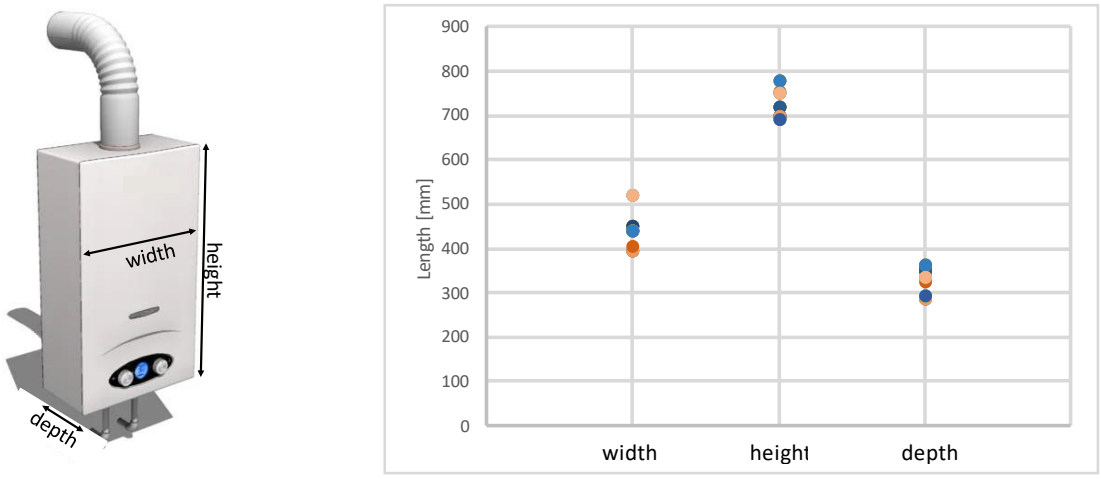

Figure 6: Dimensions of 27 wall-hung gas boilers from 7 manufacturers; only core appliance without hydronic, gas and flue-gas connections; source of image: Sketchup Warehouse

From the point of view of the housing industry, it would be desirable for heat pump solutions to have the same dimensions as a gas boiler. This is challenging due to the domestic hot water storage tank required for heat pumps. E.g. a storage for a 3-person household (a realistic number of tenants for an apartment with 50....70m²) requires a capacity of at least 82 liters if dimensioned according to EN 15450 and a set temperature of 60°C. The storages of market available heat pump systems suitable for apartments typically have higher volumes in the range of 120 to 180 liters. Therefore, the dimensions shown in Figure 7 should be considered.

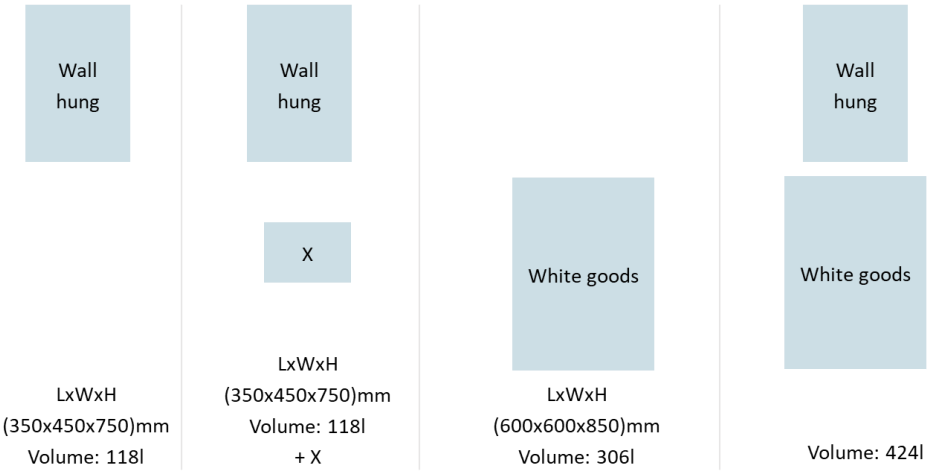

Figure 7: Design options of heat pump solutions for replacing decentralized gas boilers

3.4 Bivalence point of air source heat pumps

Multifamily houses typically have electric connection powers above 30 kW if design according to the corresponding standard DIN 18015-1, as illustrated by Figure 8. Above this value grid operators in Germany can pass part of the cost for extending the connection capacity to the owner(s) of the building. If a new electric transformation station is required to cover additional electricity load, the resulting costs can amount to several ten thousands of Euros. Therefore, the required connection power is relevant when switching to heat pumps.

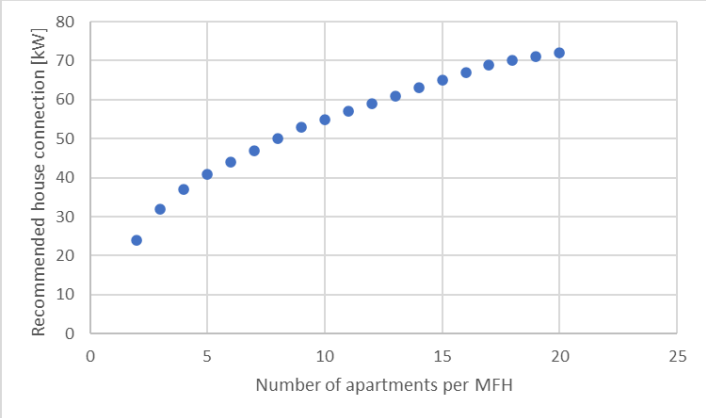

Figure 8: Recommended capacities for the electric house connection for MFH without direct electric DHW preparation according to German standard DIN 18015-1:2020 (DIN 2020)

The required connection power for a heat pumps system is primarily determined by the buildings heat demand and the bivalence point. The bivalence point defines the ambient temperature at which the heat pump reaches its maximum capacity. At lower temperatures it needs support of an (electric) backup heater to meet the heating load. A low bivalence point allows a high load coverage by the heat pump at the cost of a larger (and more expensive) appliance. The bivalence point also affects the required electric connection power for the heat pump system. Figure 9 visualizes this for an exemplary building with 25kW design heating load at -10°C ambient temperature. For a monovalent system (-10°C bivalence point) no backup heater is required. A typical air source heat pump which reaches 40% of the Carnot efficiency will require ~12.4kW electric power at this point (P_el_HP = P_el_sum; adopting the 55°C heating supply temperature from above, resulting in a COP of 2.02). As the bivalence point increases the required connection power also rises. E.g. a system with a bivalence point of -4°C will require a maximum of 16.6kW electric power (P_el_sum), half of which will be used by the direct electric heating rod (P_el_HR).

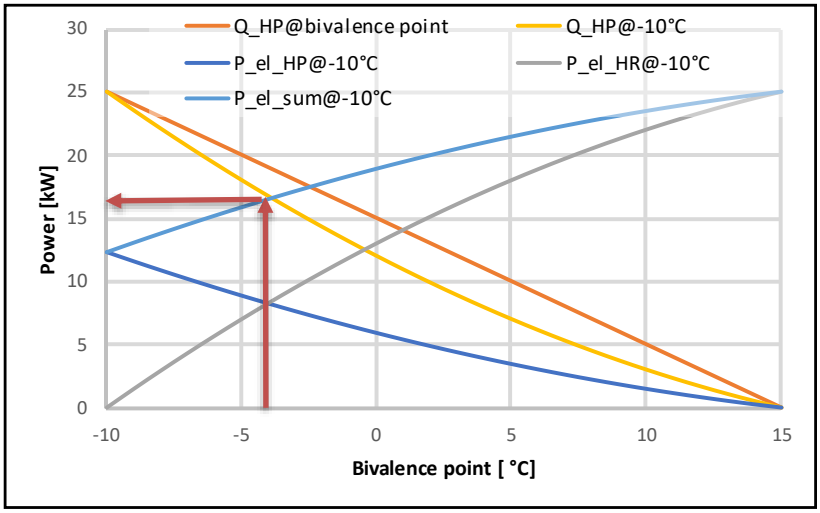

Figure 9: Influence of the bivalence point on the required electric power of a heat pump (HP), the backup heating rod (HR) and the resulting sum for an exemplary load case with 25kW design heat load at -10°C; Q: thermal power, P_el: electric power

Assuming that the 25kW design heat load corresponds to a rather average MFH with a living area of 500m², the frequently occurring energy class D (50W/m², see Figure 2) and is distributed over 8 apartments. According to the applicable standard for the dimensioning of the electricity supply this house should have an electric house connection of at least 50kW (excluding heat pump, see Figure 8). Assuming the electric connection was implemented exactly according to the standard (no over-dimensioning e.g. due to restrictions in available cable diameters) a monovalent heat pump with 12,4 kW electric power demand at -10°C will therefore need an increase of the connection power by 25%, the system with -4°C bivalence point even by 33%.

As the number of electric appliances increased in the past decades, the required connection capacity in older versions (the standard was first issued in 1955) may have been lower. Therefore, the relative additional capacity for heat pumps may be higher for older buildings.

3.5 Acoustics

This part focusses on indoor acoustics, as requirements on acoustics for air-source heat pumps placed outside the buildings are considered implicitly in chapter 3.1 (if restrictions on outside acoustic emissions are high, air is regarded as a non-available source).

Central heat pumps usually are not located inside an apartment, so it is not possible to actually specify limits for the heat pumps themselves. Limits typically apply for the immisions inside the inhabited space.

In the German standard DIN 4109-1989, a sound pressure level of max. 30 dB(A) in living rooms and bedrooms and 33 dB(A) in kitchens is recommended. For the wall-mounted gas boilers surveyed above, the sound power level is between 27 and 47 dB(A) at partial load and 41 and 52 dB(A) at full load. For wall-hung installation (hemispherical sound propagation), a sound pressure level 8 dB(A) below the sound power level can be assumed at a distance of 1 meter, i.e. between 19 and 39 dB(A) at partial load and 33 dB(A) and 44 dB(A) at full load. As living rooms/sleeping rooms are not generally used as installation locations for heat generators, 33 dB(A) is used as the target value for the sound pressure level at a distance of 1 m under nominal conditions. This corresponds to a sound power level of 41 dB(A) for the appliance.

3.6 Safety due to flammable refrigerant

As propane is a flammable refrigerant, specific safety measures apply for heat pumps with this refrigerant. For systems with a charge of maximum 152g, these can be solved by relatively simple measures such as

hermetically sealed refrigerant circuit, as it is being done for typical household refrigerators in Europe. This approach seems feasible for decentralized heat pumps as first products on the market indicate. For higher capacities, safety measures need to be more extensive. A comprehensive overview can be found in a recently presented publication by Fraunhofer ISE (Oltersdorf et al., 2024b).

4. OUTLINE OF SYSTEM SOLUTIONS

Figure 10 visualizes major implementation options for (propane) heat pump solutions. These depend strongly on the heating system to be replaced. E.g. a central boiler will surely be replaced by another central heating solution, in our case a propane heat pump placed inside or outside the building. This decision is strongly influenced by the required safety measures on the one hand and the feasibility of air as heat source on the other hand.

Decentralized wall-hung gas boilers can either be replaced by decentralized solutions. This option is especially attractive if the refurbishment is not planned for all apartments at once but stepwise, e.g. only when the existing boiler breaks. Alternatively the building could switch to a central heating system, which implies major (and cost intensive) changes but may be attractive under the aspect of maintenance.

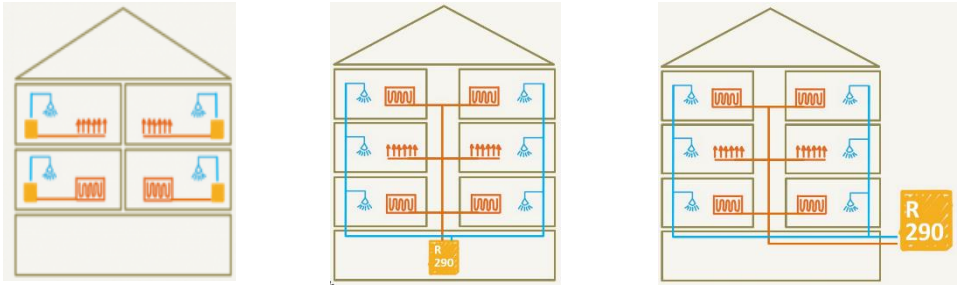

Figure 10: Left: decentralized heat pump solutions; center: central indoor heat pump; right: central outdoor heat pump; source: https://heatpumpingtechnologies.org/annex62/solution-matrix/

Table 1: Overview on possible options for implementation; A: Air, B: Brine, DHW: domestic hot water, HR: heating rod, HP: heat pump, HX: heat exchanger, SH: space heating, W: water, *: no or only few products available on the market with propane but development focus in the German project LCR290; ** no products available on the market with propane

Decentralized (~5kW)		**Centralized Indoor (>25kW)**		**Centralized Outdoor (>25kW)**	
SH	**DHW**	**SH**	**DHW**	**SH**	**DHW**
A/A-HP**	HR	A/W-HP*	HR	A/W-HP*	HR
A/A-HP**	as SH** (condensing storage)	A/W-HP*	as SH	A/W-HP*	as SH
A/W-HP	HR	B/W-HP*	HR		
A/W-HP	as SH	B/W-HP*	as SH		
A/B-HX + B/W-HP*	HR	W/W-HP*	HR		
A/B-HX + B/W-HP*	as SH	W/W-HP*	as SH		
Central source + B/W-HP*	HR	A/B-HX + B/W-HP*	HR		
Central source + B/W-HP*	as SH	A/B-HX + B/W-HP*	as SH		

Table 1 gives an overview on possible heat pump system solutions for the different options shown in figure 10. The availability of suitable heat pumps with propane as refrigerant is market with an asterisk. Only small capacity air-water products are available in significant amount[3].

The decision between the outlined solutions depends on many aspects, some of them shall be briefly discussed here:

- As space is very limited in existing apartments, it may be an option to only have a heat pump for space heating (SH) and prepare domestic hot water (DHW) with a direct electric heating rod. The negative implications are the much lower efficiency and thus higher electricity costs and the higher required electric connection power, which may not be available in existing buildings.
- Air-air heat pumps (multi-split systems) have low investment costs, can work efficiently in heating mode and also provide cooling in summer. Yet, their extensive installation may lead to problems with noise from numerous outdoor units, also maintenance is challenging. Additionally, indoor comfort may be affected by air circulation and noise from the indoor units; further on, split systems with propane are not really available on the market currently and all synthetic refrigerants currently used in systems below 12 kW will be banned by the F-gas regulation
- Small capacity B/W-heat pumps with R290 are currently being introduced on the market; they typically have a refrigerant charge below 152g and therefore require no complex safety concept (similar to household refrigerators, which typically use R600a/Iso-Butane as refrigerant in Europe)
- Small capacity monoblock A/W-solutions are readily available on the market; as the have refrigerant charges above 152g, they typically require safety distances from window openings and electric sockets; this may hinder their installation on facades/balconies. Brine-split systems, consisting of an air-brine heat exchanger installed outdoors and a B/W heat pump indoor, may be a workaround.
- Central heat pump solutions require higher heating capacities which lead to higher refrigerant charges. For systems using the flammable refrigerant propane this imposes additional safety measurements. As a consequence, heat pump manufacturers showed restraints concerning such products until now; one objective of the project LCR290 is the provision of generic and scalable safety concepts to overcome this limitation.
- Central DHW preparation requires the continuous circulation of water at temperatures above 55°C, as described in chapter 3.2.2. Especially in existing buildings the hot water piping may be poorly insulated which results in high losses. Therefore it may be an option to use central heat pumps for heating only and rely on direct electric heating rods for DHW – at the cost of a higher electric connection power.

5. CONCLUSIONS

In this paper we compile different categories of requirements for heat pumps for the refurbishment of multi-family homes. For central systems a heating capacity of ~30 kW at 55°C hot water temperature seems reasonable. For the replacement of wall-hung boilers in single apartments the capacity should be around 5 kW. As the existing fossil heat generators usually are significantly more compact than heat pump solutions which generally require larger storage volumes and space is limited, the development of compact appliances is recommendable. During system design it should also be considered that the electric power connection may be a limiting factor. An overview on possible system solutions with a brief discussion of their advantages and drawbacks is given.

[3] As of March 2024, the German list of heat pumps eligible for funding (“BAFA Liste”) reports 324 R290 air-water heat pumps with a capacity up to 8 kW at A7/W55 but only 18 products with more than 25 kW.

6. ACKNOWLEDGEMENTS

The authors greatly acknowledge the funding for this work in frame of the project LCR290 (grant number 03EN4046) by the German Federal Ministry for Economic Affairs and Climate Action and the support by Project Office Jülich.

7. REFERENCES

2011. Statistische Ämter des Bundes und der Länder. Auswertung Wohnungsgröße - Wohnungen nach Art des Gebäudes, Art der Wohnungsnutzung und weitere Merkmale für Deutschland. Ergebnis des Zensus 2011 zum Berichtszeitpunkt 9. Mai 2011. https://ergebnisse.zensus2011.de/#dynTable:statUnit=WOHNUNG;absRel=ANZAHL;ags=00;ag.

DIN German Institute for Standardization, 2012. DIN 1988-200: Codes of practice for drinking water installations - Part 200: Installation Type A (closed system) - Planning, components, apparatus, materials; DVGW code of practice 93.025.

DIN German Institute for Standardization, 2020. DIN 18015-1 - Electrical installations in residential buildings - Part 1: Planning principles. Beuth Verlag GmbH, Berlin, Germany 91.140.50.

DVGW Deutscher Verein des Gas- und Wasserfaches e. V. - Technisch-wissenschaftlicher Verein, 2004. DVGW W 551: Drinking water heating and drinking water piping systems - Technical measures to reduce Legionella growth - Design, construction, operation and rehabilitation of drinking water installations. DVGW.

Greif, S., 2023. Räumlich hoch aufgelöste Analyse des technischen Potenzials von Wärmepumpen zur dezentralen Wärmeversorgung der Wohngebäude in Deutschland. Dissertation. Munich, 195 pp.

Jardin, D., 2024. Heat Pump Keymark - Certified Products. https://keymark.eu/en/products/heatpumps/certified-products (accessed 10 June 2024).

Krieger, O. 2018. Preparatory studies for the development of a long-term renovation strategy in accordance with Art 2a of the EU Buildings Directive Directive 2018/844 (EPBD): supplement to the final report. Deutsche Energie-Agentur GmbH, 134 pp. (accessed 2 May 2024).

Lämmle, M., Bongs, C., Wapler, J., Günther, D., Hess, S., Kropp, M., Herkel, S., 2022a. Performance of air and ground source heat pumps retrofitted to radiator heating systems and measures to reduce space heating temperatures in existing buildings. Energy 242, 122952. https://doi.org/10.1016/j.energy.2021.122952.

Lämmle, M., Bongs, C., Wapler, J., Günther, D., Hess, S., Kropp, M., Herkel, S., 2022b. Performance of air and ground source heat pumps retrofitted to radiator heating systems and measures to reduce space heating temperatures in existing buildings. Energy 242, 122952. https://doi.org/10.1016/j.energy.2021.122952.

Lämmle, M., Metz, J., Kropp, M., Wapler, J., Oltersdorf, T., Günther, D., Herkel, S., Bongs, C., 2023. Heat Pump Systems in Existing Multifamily Buildings: A Meta-Analysis of Field Measurement Data Focusing on the Relationship of Temperature and Performance of Heat Pump Systems. Energy Tech 11, 2300379. https://doi.org/10.1002/ente.202300379.

Loga, Tobias, Stein, Britta, Diefenbach, Nikolaus, Born, Rolf, 2015. Deutsche Wohngebäudetypologie: Beispielhafte Maßnahmen zur Verbesserung der Energieeffizienz von typischen Wohngebäuden ; erarbeitet im Rahmen der EU-Projekte TABULA - « Typology approach for building stock energy assessment », EPISCOPE - « Energy performance indicator tracking schemes for the continous optimisation of refurbishment processes in European housing stocks », 2nd ed. IWU, Darmstadt, 281 pp.

Oltersdorf, T., Garashli, E., Wapler, J., Fugmann, H., Schnabel, L., 2024a. Heat pump product and market data – Tools and Analysis. 16th IIR Gustav Lorentzen Conference on Natural Refrigerants.

Oltersdorf, T., Methler, T., Colbourne, D., Kreuz, M., Fugmann, H., 2024b. A try to close more knowledge

gaps in R290 heat pump safety testing. 16th IIR Gustav Lorentzen Conference on Natural Refrigerants.

2023. Techem Verbrauchskennwerte 2022 -: Wärme: Erhebungen und Analysen zum Energieverbrauch und zur CO2-Emission für Heizung und Warmwasser in deutschen Mehrfamilienhäusern., 152 pp. (accessed 2 May 2024).

SPACE HEATING AND COOLING DEMAND OF BUILDINGS IN THE PERSPECTIVE OF CLIMATE CHANGE IN COLD AND HOT CLIMATES – IS THIS A RISK?

Wolfgang Streicher[1], Vincent van Karsbergen[1], Alexander Thür[1] and Fabian Ochs[1]

[1] Unit of Energy Efficient Building, University of Innsbruck (Austria)

Abstract

The global rise in temperature due to climate change is undisputed today. This will lead to a decrease in space heating demand in winter but to an increase in cooling demand in summer. In the following contribution, the space heating and cooling demand of a residential building for climates of Innsbruck and Rome for different climate scenarios (IPCC (2014), RCP Scenarios) and time horizons are calculated and analyzed. Required changes for building codes and standards as for climate change are sketched. In conclusion, the increase of the cooling demand can be met with slightly oversized cooling systems in hot climates (e.g., Rome), whereas in cold climates (e.g. Innsbruck) the increase can be kept very low by passive measures. The increase in electricity demand for cooling in summer coincides with the comparable high summer-production of PV. The reduction of energy demand in winter will help in reducing the gap of low PV electricity production in winter. This is also valid for mountainous countries like Austria with high hydro power availability in summer due to snow melt.

Keywords: climate change, scenarios, building heating demand, building cooling demand

1. Introduction

The global rise in temperature due to climate change is undisputed today. For buildings in Central and South Europe, this means that the need for space cooling will increase. On the other hand, space heating requirements in winter will be reduced also in northern Europe or is even not needed any more in Middle Europe. Electricity will be one of the main energy carriers in future energy systems. By the use of heat pumps for heating and cooling for a fossil free energy system the electricity will be used highly efficient.

Sufficient photovoltaic electricity will be available in summer if the current strong installation increase is carrying on. In winter, electricity from wind energy will be available in Europe due to expected massive expansion of installations in the North Sea, but photovoltaics naturally will only make a small contribution. Hydropower tends to be at its maximum in end of spring due to snow melt and at its minimum at the end of winter due to snow fall during winter. Therefore, shifting the energy demand from heating energy in winter to cooling energy in summer should not be classified as a risk in climate change impact studies. In the following contribution, the space heating and cooling demand of a residential building for climates of Innsbruck and Rome for different climate scenarios (IPCC (2014), RCP Scenarios) and time horizons are calculated and analyzed and proposals for changes for building codes and standards according to expected climate change are sketched.

2. Boundary conditions for the simulation

2.1. Building definition

The residential building used in this study was defined in detail in Dott et al (2013) for IEA SHC Task 44 / HPP Annex 38 as SFH45 (Single Family House with approx. 45 kWh/m^{2}a space heating demand in 2020 Innsbruck climate) and is widely used in scientific case studies. It represents a 2-storey single family building with about 140 m² net area with about current new or renovated German and Austrian insulation standards (U-

© 2024. The Authors. Published by International Solar Energy Society
Selection and/or peer review under responsibility of Scientific Committee
10.18086/eurosun.2024.01.08 Available at http://proceedings.ises.org

values: external wall 0.29 W/m²K, roof ceiling 0.20 W/m²K, ground floor 0.17 W/m²K, windows 1.1 W/m²K and g-value of 0.62) and an air exchange rate of 0.4 h^{-1}. All windows in the buildings are equipped with venetian blinds (shading coefficient 0.25) which are activated, if all of the following conditions are fulfilled:

- *the global horizontal irradiation exceeds 300 W/m²,*
- *the indoor room temperature is higher than 22.8°C and*
- *the 24 hour moving average ambient temperature is greater than 12°C.*

A free driven night ventilation mode for passive cooling, realized by tilted windows, is activated for all buildings if all of the following conditions are met:

- *time between 9 p.m. and 8 a.m.,*
- *average ambient temperature of the last 24 hours above 12°C,*
- *room temperature above 24°C*
- *and actual ambient temperature at least 2K below the actual room temperature.*

Schedules for occupancy and electric gains were defined. The set temperature for space heating was 21°C and for cooling 26°C. The building was simulated using TRNSYS 17 (2014). Figure 1 shows a schematic drawing of the building.

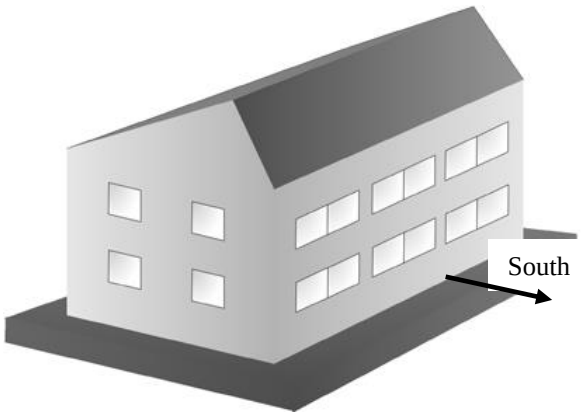

Fig. 1 Simple view of the simulated house (showing South and West facades)

2.2. Climate definition

The two different locations of Innsbruck/Austria (cold climate) and Rome/Italy (hot climate) have been used to represent a climate span from middle to southern Europe. Using the software [Meteonorm 8.2.0, 2020] the building simulations were carried out for today's climate and the three different Scenarios of the Intergovernmental Panel on Climate Change, scenarios RCP 2.6, RCP 4.5 and RCP 8.5 for the year 2050 IPCC (2014). Additionally, calculations for the RCP scenario 8.5 for the year 2080 as extreme condition, with higher yearly average temperature of 4.3°C in Innsbruck and 3.9°C in Rome, were done. In the RCP 4.5 and RCP 8.5 scenarios the temperature will still rise after 2080. Figure 2 shows the annual emissions and the prognosed temperature rise of the different scenarios until the year 2100. RCP means Representative Concentration Pathway and describes several possibilities, how the emission of greenhouse gases will develop. The current worldwide development is close to the higher RCP scenarios.

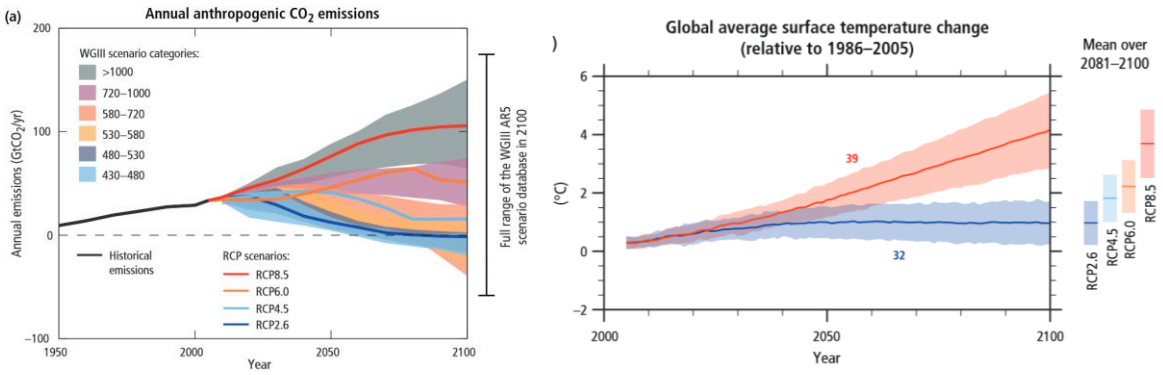

Fig. 2 Anthorpogenic (human made) CO2 emissions and global average earth surface temperature rise for the different RCP scenarios (IPCC, 2014)

3. Results and Analysis

Figure 3 (Innsbruck) and Figure 4 (Rome) and Table 1 show the results for the specific heating and cooling energy demand in kWh/m²a as well as the maximum load (power demand, size of heating and cooling device) for both climates in kW. The energy demand is responsible for the operating costs and the heat/cooling load for the sizing of the heating/cooling devices and therefore the investment costs. Additionally, in the legend of Figure 3 and Figure 4 the seasonal temperature rise compared to today is given for every calculation.

It can be seen that for the cold climate example of Innsbruck, the specific space heating demand (kWh/m²a) is decreasing more than the cooling demand increases with increasing seasonal temperatures. Until 2050 there is more or less the same reduction of space heating demand by 7 kWh/m²a (or about 15%) for all climate scenarios. The space cooling demand is increasing between 1–4 kWh/m²a. Here the percentage increase is very high, as only very low cooling occurs in the current climate. Even in 2050 the cooling demand still is more or less negligible, because only a few days are affected where the room temperature becomes higher than 26°C. Of course, if night ventilation and shading as described in chapter 2.1 are not used, the cooling demand would be much higher. For the RCP 8.5 scenario for the year 2080, the cooling demand is already at about 10 kWh/m²a and active cooling is possibly needed. The maximum space heating load in the different scenarios reduces slightly from 4.4 kW to 3.9 kW as the cooling load increases from 0.7 kW to 2.0 kW.

Both demands can be covered by the same reversible heat pump, that can switch from heating to cooling. For this ratio of heating and cooling demand the size of the heat pump is defined by the heating load, it's cooling capacity is lower for the same heat source and heat sink temperatures, but the needed cooling power is even lower (ref. to equation1).

$$\dot{Q}_{cooling} = \dot{Q}_{heating} \cdot \left(\frac{(COP_{heating}-1)}{COP_{heating}}\right) = \dot{Q}_{heating} \cdot \left(\frac{COP_{cooling}}{COP_{heating}}\right) \quad \text{(eq. 1)}$$

$$COP_{heating} = \frac{\dot{Q}_{heating}}{P_{el}}; \; COP_{cooling} = \frac{\dot{Q}_{cooling}}{P_{el}}$$

with

$\dot{Q}_{cooling}$	[kW]	Maximum Cooling Load
$\dot{Q}_{heating}$	[kW]	Maximum Heating Load
P_{el}	[kW]	Electricity demand for the maximum heat load
$COP_{heating}$	[-]	Heating Coefficient of Performance
$COP_{cooling}$	[-]	Cooling Coefficient of Performance

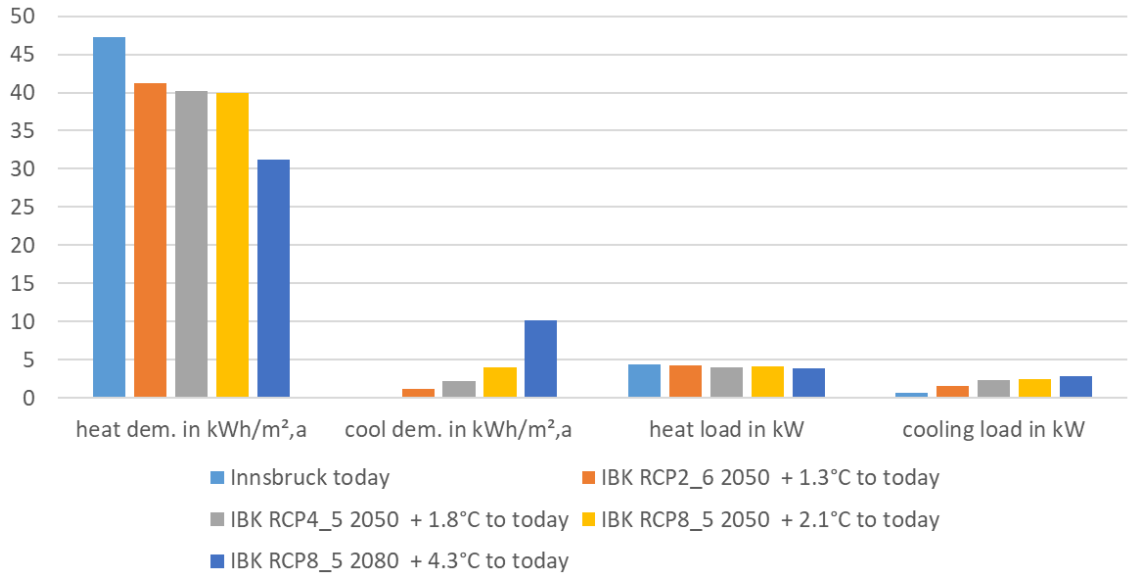

Fig. 3 Innsbruck, residential building 140 m², specific heating/cooling energy demand and load for different climate scenarios. Today: spec. heating demand 47.3 kWh/m²a, spec. cooling demand 0.1 kWh/m²a

For the hot climate (Figure 4 and Table 1), the space heating demand is reduced from 12.2 kWh/m²a to 3.0 kWh/m²a for RCP 8.5 in the year 2080, which means nearly no need for space heating any more. The cooling demand increases from 18 to 40 kWh/m²a. The cooling demand increases more than the heating demand reduces. The heating load reduces insignificantly from 2.2 kW to 1.5 kW and the cooling load increases from 2.6 to 3.5 kW (increase of 34%, RCP 8.5, 2080). To match the 2050 cooling demand for all climate scenarios, cooling machines bought today should be oversized by about 20 % to account for climate change until 2050 with a cooling load of around 3.1 kW. Reversible heat pumps used for space heating and cooling should be sized according the cooling load.

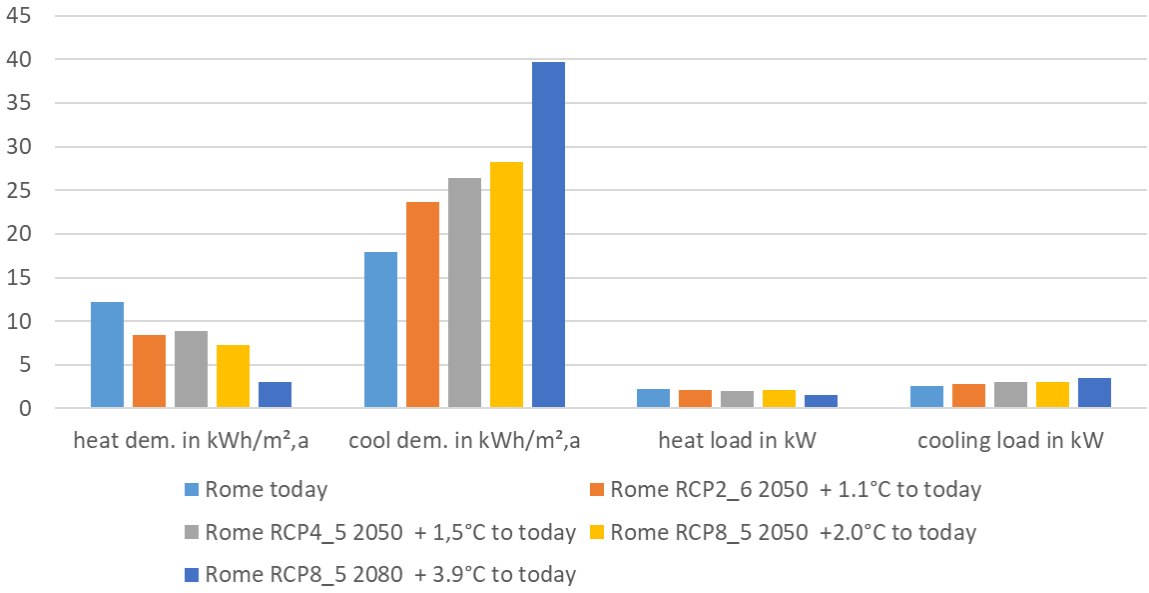

Fig. 3 Rome, residential building 140 m² specific heating/cooling energy demand and load for different climate scenarios. today: spec. heating demand 12.2 kWh/m²a, spec. cooling demand 18.0 kWh/m²a

Tab. 1: Heating and Cooling demand and maximum load for the different climates and the locations Innsbruck and Rome

Loation/	Climate	Heating	Cooling
		Spec. demand / max. load kWh/m²a / kW	Spec. demand / max load kWh/m²a / kW
Innsbruck	**Today**	**47.3 / 4.4**	**0.1 / 0.7**
	RCP 2.6, 2050	41.2 /4.2	1.3 / 1.5
	RCP 4.5, 2050	40.2 / 4.0	2.2 / 2.3
	RCP 8.5, 2050	39.9 / 4.0	4.0 / 2.5
	RCP 8.5, 2080	31.3 / 3.9	3.9 / 2.9
Rome	**Today**	**12.2 / 2.2**	**18.0 / 2.6**
	RCP 2.6, 2050	8.4 / 2.1	23.7 / 2.8
	RCP 4.5, 2050	8.4 / 2.1	26.4 / 3.0
	RCP 8.5, 2050	7.2 / 2.1	28.2 / 3.1
	RCP 8.5, 2080	3.0 / 1.5	39.8 / 3.5

The primary focus for all climates is on the use of passive measures. For the heating period a very good thermal insulation and three pane windows, main window areas facing south are keeping their importance. In the cooling period, external gains from the sun should be kept out of the building by a good insulation of roofs and facades as well as active movable shading systems (in the south also overhangs may help, but they increase space heating demand in winter) and night ventilation (as being used in the simulation). Such passive measures have to be kept or, if currently not there they have to be included, in the building codes to keep the cooling demand low despite of rising temperatures due to climate change.

To keep costs low for the building owners/users, the dual use of a system for heating and cooling, both in terms of generation and delivery to the buildings, are needed (e.g. reversible heat pump with space heating/cooling ceiling for water driven systems or combined ventilation/space heating and cooling outside air systems as split or multi-split systems). Heating systems based on fossil fuels (oil, natural gas) will be forbidden in most of the countries. If biomass driven or direct electric heating systems are used, additional cooling systems have to be installed thus increasing the costs. If radiators or floor heating systems are used for room heating, additional cooling delivery systems have to be installed, again increasing the HVAC investment costs. The cheapest solution would be integrated ventilation/heating/cooling all-in-one systems which are under development. They can be used especially in energetically well designed (see above) buildings either centrally or decentralized.

The building codes and standards of HVAC systems have to be adapted accordingly, in order to build climate-fit cheap systems already today. Planners and HVAC installers have to be trained to assure high quality and low cost systems.

In conclusion the climate change is not causing mayer problems in building energy demand, as long as passive and active measures to reduce the demand are consequently applied in the buildings. The increase of the very low space cooling demand in cold climates can be met with reversible heat pumps sized on current heating demand. Additionally, in cold climates the increase of cooling load still can be handled by consequent use of passive measures in residential buildings, offices and hotels. The heating demand in hot climates will be reduced but the cooling demand will be increased by a larger extend. However, the increase in electricity demand for cooling in summer coincides with the production of PV or partly hydro power. In winter, the reduction of the space heating demand will help in reducing the energy demand.

4. References

IPCC, 2014: Climate Change 2014. Synthesis Report. Contribution of Working Groups I, II and III to the Fifth Assessment Report of the Intergovernmental Panel on Climate Change [Core Writing Team, R.K. Pachauri and L.A. Meyer (eds.)]. IPCC, Geneva, Switzerland, https://www.ipcc.ch/site/assets/uploads/2018/02/SYR_AR5_FINAL_full.pdf.

Dott, R., Haller, M.Y., Ruschenburg, J., Ochs, F., Bony, J., 2013, The Reference Framework for System Simulations of the IEA SHC Task 44 / HPP Annex 38, Part B: Buildings and Space Heat Load, A technical report of subtask C, https://w.iea-shc.org/Data/Sites/1/publications/T44A38_Rep_C1_B_ReferenceBuildingDescription_Final_Revised_130906.pdf

TRNSYS 17, 2014, https://www.trnsys.com

Meteonorm 8.2.0, 2020, Meteotest AG, Bern, Switzerland. https://meteonorm.com/

Appendix: Nomenclature

HPP	Heat Pump Programme of the International Energy Agency
IEA	International Energy Agency
IPCC	Intergovernmental Panel on Climate Change
RCP	Representative Concentration Pathway, Names of IPCC scenarios
SFH	Single Family House
SHC	Solar Heating and Cooling Program of the International Energy Agency

Occupant feedback on indoor humidity assessment

Panayiotis Papadopoulos[1], Antonio Luparelli[2], Ioanna Kyprianou[1] and Salvatore Carlucci[3]

[1] The Cyprus Institute, Nicosia (Cyprus)

[2] Centro di Ricerche Europeo di Tecnologie Design e Materiali (CETMA), Brindisi (Italy)

[3] University of Insubria, Varese (Italy)

Abstract

Heating, ventilation, and air conditioning systems can adjust indoor temperature, air quality, and humidity levels, regulating occupants' comfort. In this study, we focus on humidity, a parameter whose regulation is energy-intensive, and research is limited compared to thermal regulation. Research focuses on new technologies and materials to improve energy efficiency in humidity control; here, we study how it affects building occupants and the conditions in which they are affected. Using statistical tools on a sample of post-occupancy evaluation questionnaires, we investigate whether building occupants can assess indoor humidity effectively through three lenses: judgment, perception, and subjective preference. We show that while occupants can determine their preference in temperature, interpretation error is detected when it comes to humidity. Through exploratory and confirmatory analysis, it appears that humidity preference might be subject to greater variability in occupants' responses, calling for further investigation to verify the consistency of these observations across different populations. By confirming ineffective subjective assessment of indoor humidity, the existing comfort levels could be extended, and significant energy savings could be achieved.

Keywords: Humidity, building occupants, feedback, confirmatory factor analysis

1. Introduction

People spend a lot of time indoors, and to create suitable conditions, buildings consume energy that takes a considerable share of the world's demand - approximately one-third of global final energy use is directed towards buildings, which emit a slightly smaller share of global energy-related greenhouse gas emissions (UN Environment and International Energy Agency 2017). These proportions are even greater when it comes to densely populated cities, where modern comfort standards set higher energy demands. Heating, ventilation, and air conditioning (HVAC) systems ensure that building occupants are comfortable by regulating indoor conditions related to temperature, humidity, and indoor air quality. However, they require energy; for instance, while in general, there have been reports of HVAC systems consuming roughly 40% of the primary energy consumed by buildings when considering the residential building stock, air conditioning can climb over 50% in tropical climates (Chua et al. 2013). In the European Union, where most of the building stock is ageing and inefficient, space heating can reach 80% of the average specific consumption (Martinopoulos, Papakostas, and Papadopoulos 2018). HVAC systems, therefore, present an area with great potential for energy savings, contributing to decreased carbon footprints as well.

Addressing humidity through HVAC systems is key to achieving thermal comfort in buildings, but regulating this parameter requires considerable amounts of energy. In particular, the process of removing humidity is energy intensive; a study has shown that raising humidity setpoints by 30% can decrease energy consumption almost by half (Xu et al. 2023). Beyond decreasing the setpoints for humidity, dehumidification (removing humidity) is a field of ongoing research; from the commonly used cooling coils to the more advanced liquid desiccant dehumidification technologies (Gao and Lu 2024). Through these advancements, studies have shown a considerable potential for energy savings through improvement in the efficiency of processes or equipment. For instance, Che et al. explored how a retrofitted HVAC system can create comfortable indoor conditions while reducing energy consumption and used dehumidification as a key feature; the overall reduction of energy

© 2024. The Authors. Published by International Solar Energy Society
Selection and/or peer review under responsibility of Scientific Committee
10.18086/eurosun.2024.01.09 Available at http://proceedings.ises.org

use reached 50% while maintaining adequate levels of indoor thermal comfort (Che et al. 2019). Mumtaz et al. adopted new combinations of novel technologies (membrane dehumidification and dewpoint evaporative cooling), achieving up to 50–90% energy savings and up to 50% reduced GHG emissions (Mumtaz et al. 2023). It, therefore, seems possible to maintain thermal comfort in buildings and achieve energy savings through retrofits, but the investment and running costs of the required systems constitute a great expense and possibly extra control strategies (Vakiloroaya et al. 2014).

Research on the topic of humidity and how it can be managed through HVAC systems is evolving, introducing new materials, technologies, and approaches. What is disputed in the literature is whether indoor humidity specifically affects building occupants and in which conditions. Up to now, research has regarded humidity within thermal comfort assessments but not as an individual component (Alaidroos and Mosly 2023; Cho et al. 2023).

With this study, we aim to fill this gap and determine whether building occupants are able to assess indoor humidity effectively. To do this, a dataset of post-occupancy evaluations accompanied by field measurements is used. The employment of consolidated statistical methods and Confirmatory Factor Analysis (CFA) is used for its exploration.

2. Methods

2.1. Data sample and sites

The dataset used for the analysis consisted of answers to post-occupancy evaluations (POEs) questionnaires distributed in different living spaces. In particular, the case study involves fourteen buildings that are either public, commercial, or private and located in four countries (Norway, France, Cyprus, and Italy), covering a variety of climatic regions across Europe and different building types and typologies. Table 1 presents the demographics of the case study buildings, including name, type, total area of the building, and number of zones participating in this study.

Table 1. Demographics of case study buildings

Country	Building name	Building type	Area (m^2)	Number of zones in which indoor environmental conditions are monitored
Norway	Eidet Omsorgsenter	Health care centre	7039	5
	Ellingsøy Idrettshall	Sports center	2610	2
	Flisnes Barneskole	Elementary school	4477	2
	Hatlane Omsorgsenter	Health care centre	5980	5
	Moa Helsehus	Medical center	2700	6
	Spjelkavik Ungdomsskole	High school	9700	5
	Tennfjord Barneskole	Elementary school	2490	7
France	Green'ER building (G2Elab)	Campus building	700	8
Cyprus	Guy Ourisson Building (GOB)	Campus building	2020	9
	Graduate School (GS)	Campus building	580	6
	Novel Technologies Laboratory (NTL)	Campus building	2440	4

Italy	C2 Tower	Residential Apartments	1250	4
	C3 Tower	Residential Apartments	1250	4
	C4 Tower	Residential Apartments	1250	4

From the dataset, non-numerical values (NAN) were filtered out and then randomly divided into two subsets. The first subset was used for exploratory factor analysis. The second subset was used for confirmatory factor analysis. The responses were treated as ordinal variables. This approach allows levels of agreement or intensity to be recognised without assuming a uniform distance between different levels of agreement or intensity.
In the present study, factor analysis was applied to the data collected to obtain a preliminary understanding of the underlying factor structure. This methodological choice was primarily aimed at assessing the effectiveness of the items used in the questionnaire in measuring the theoretical construct of interest, which is subjective thermal comfort. Through this approach, it was possible to identify the main underlying factors and ascertain the relevance of the questionnaire scales in the specific study.

2.2. Factor analysis configuration

Factor analysis is divided into two main techniques: exploratory and confirmatory. Exploratory factor analysis (EFA) is mainly used to uncover the underlying factor structure by associating one or more latent factors with a group of observed items (Woods and Edwards 2007). CFA is utilised to confirm whether the hypothesised factor structure is present in the survey data and to validate the hypothesised relationships between the observed variables and their underlying latent constructs from a background theory (DeVellis and Thorpe 2021; Mueller and Hancock 2015). The purpose of CFA is to test the factor structure suggested by the previous exploratory factor analysis (EFA) by establishing an explicit and direct connection between the theoretical constructs and the measured variables. Based on the results of EFA analysis, in CFA, these three latent factors are being configured:

I. **Temperature judge factor**: This factor can hence be interpreted as a construct relating to how individuals find and judge the air temperature.
II. **Temperature Preference Factor**: This factor represents a combination of preference and subjective perception relating to air temperature and/or humidity.
III. **Humidity Assessment Factor**: This factor can be interpreted as a construct derived from the evaluative, judgmental and preference responses of individuals in relation to humidity.

3. Results

3.1. Observations of responses over field measurements

This section presents a statistical analysis of occupants' responses on preference for both temperature and humidity in comparison with their respective field measurements. By associating occupants' responses about their preference (i.e., "lower", "without change", or "higher") on humidity and temperature with their corresponding field measurements, i.e., indoor relative humidity (%) and indoor air temperature (°C), at the time of the completion of the questionnaire, we can identify if there is a pattern that relates occupants' responses and indoor environmental measurements. In particular, this exercise can provide some insights into how indoor conditions such as relative humidity and air temperature affect human preferences.

The graphs in Figure 1 show the probability distribution of each preference response collected during the field campaign. Note that violin plots can depict distributions of numeric data for one or more categories using density curves (width is approximately equal to the frequency). Statistical information such as median, 1st and 3rd quartile, min, and max values are presented as well. For temperature preference, as presented in Fig. 1(a), occupants prefer "lower" temperature with a median indoor air temperature of 22.95 °C, "without change" at 22.24 °C and "higher" temperature at 21.7°C. Hence, the temperature preference question could characterise the indoor air temperature on average. On the other hand, for the humidity preference question, as presented in Figure 1(b), occupants prefer "lower" humidity with median indoor relative humidity at 43.4%, "without

change" at 44.6% and "higher" humidity at 35%. This indicates that building users expressed different preferences on humidity, i.e. lower and without change, even if humidity values were similarly distributed. Differently, they expressed the willingness to have higher relative humidity when it was lower. From these results, it appears that people are more sensitive to lower values of relative humidity (Q1 equal to 15%) and properly require an increase in it. In comparison, higher values of relative humidity (Q3 equal to 73%) do not trigger a clear preference.

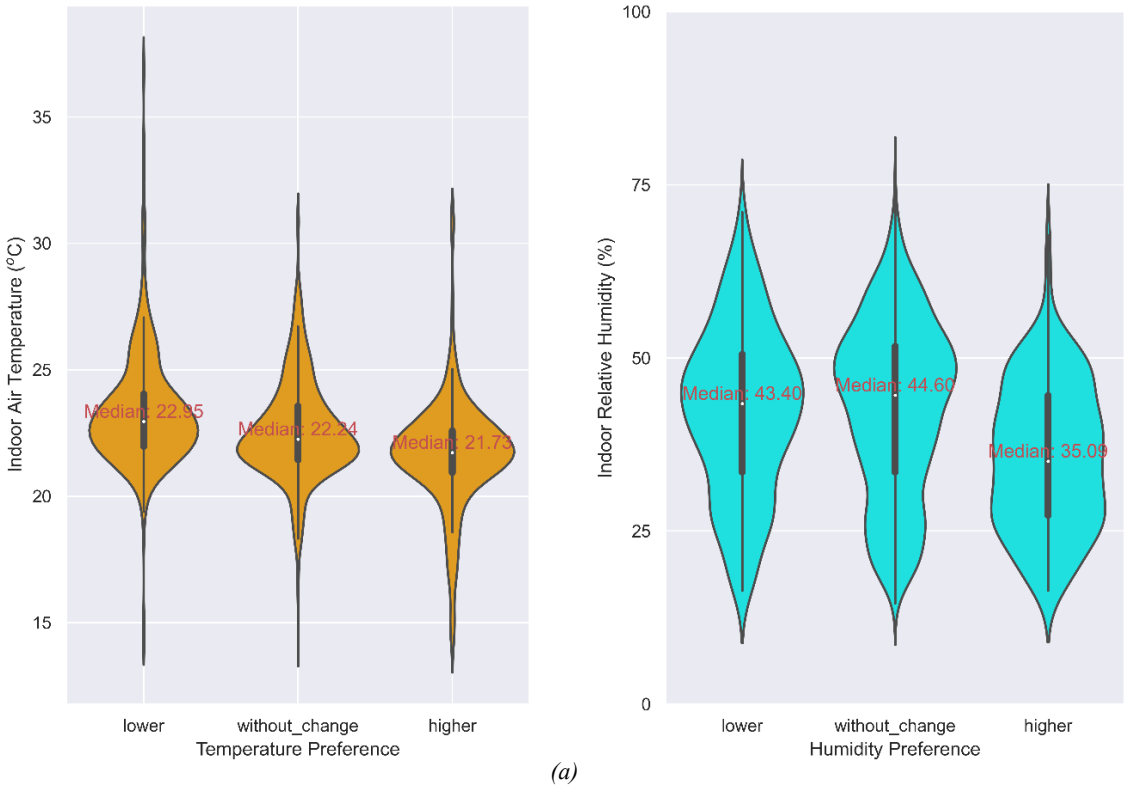

Figure 1: Violin plots of occupants' responses on preference for (a) temperature and (b) humidity for their corresponding indoor measurements

3.2. CFA

In this section, exploratory and confirmatory factor analysis (EFA/CFA) techniques are used to investigate, test and validate latent factors related to occupants' preferences for temperature and humidity. EFA helps to identify potential underlying factor structures in the data, while CFA is used to confirm and validate these structures, ensuring that the relationships between observed variables and latent factors are valid and reliable. To conduct EFA/CFA analyses, a total of 2188 answers (including NaN values) were collected and analysed. The data consists of the answers to the Post Occupancy Evaluation (POE) questionnaire related to thermal comfort with regard to temperature and humidity items. The data came from different living spaces, such as classrooms, single or shared offices, private flats and laboratories. The participants were children (584), young (536), adults (987) and elderly (62). Data was further divided into country-specific subsets for Norway (1202) and Cyprus (762).

Pre-processing involved removing missing values and dividing the dataset into two parts, one for exploratory factor analysis (EFA) and the other for confirmatory factor analysis (CFA) for independent validation of the factor structure. Furthermore, all variables were ensured to be coded in the same direction. Finally, the responses were treated as ordinal variables. The choice to treat the data as ordinal allows for the identification of levels of agreement or intensity without assuming a uniform distance between different levels of agreement or intensity. This type of approach is crucial because it influences the choice of estimation methods and the interpretation of results in the CFA.

The factorial structure that emerged without applying any level of aggregation confirms the presence of several components of the latent thermal comfort construct represented by judgement, perception and subjective

preference for humidity and temperature (Figure 1). The latent factors specified in the CFA fit the observed data well, as demonstrated by the Comparative Fit Index (CFI) and Tucker-Lewis Index (TLI) values, which are above the commonly accepted threshold of 0.95 (Xia and Yang 2019). While the Root Mean Square Error of Approximation (RMSEA) and the Standardized Root Mean Square Residual (SRMR) are below the acceptable thresholds of 0.05 for RMSEA and 0.08 for SRMR, respectively (Shi, Maydeu-Olivares, and Rosseel 2020). Considering the factorial loadings, most items converge well with their factor, indicating a clear association with the respective constructs, *except for the humidity preference item*, which shows a factorial loading below the threshold of 0.7 (Cheung et al. 2023). On the other hand, correlations between the factors are weak to moderate; none of the correlations exceed the critical value of 0.85 (Henseler, Ringle, and Sarstedt 2015), confirming adequate discrimination between the factors examined.

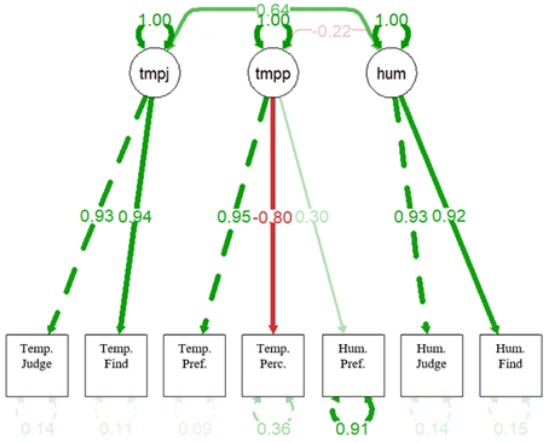

Figure 2: CFA factor loadings

The CFA was conducted separately on two countries (Norway and Cyprus) by frequency of responses, confirming the factorial structure, although with differences in the way the items are interpreted or evaluated by the participants, in particular, the humidity preference item seems to be subject to different interpretations by the participants.

In Norway (Figure 3(a)), where the answers come predominantly from primary school classes, the humidity preference item is grouped in the latent factor of temperature perception. Consequently, the humidity preference item is dissociated from how people judge and find humidity rather than finding its place in the context of temperature preferences and perceptions. Within this factor, humidity preference moves in the same direction as temperature preference, and both show an inverse relationship with temperature perception. In short, when the temperature is perceived as cold, the preference for temperature and humidity is that both are higher and vice versa. However, the humidity preference item has a low significance for the latent factor of which it is a part, an indication that it does not tie in well with the rest of the scale and that the answers given to this specific item could be subject to random error.

In Cyprus (Figure 3(b)), on the other hand, where the responses come predominantly from adults in single or shared offices and from tertiary school classes, the humidity preference item is not related to temperature preference but is associated with and moves in the opposite direction from items that measure how people actually judge and find humidity. In short, when humidity is found and judged as excessively high, the preference for humidity is lower, and vice versa. It should be noted, however, that although the humidity preference item has a discrete significance for the latent factor of which it is a part, with a factorial loading of -0.65, it is still just below the commonly accepted threshold of 0.7.

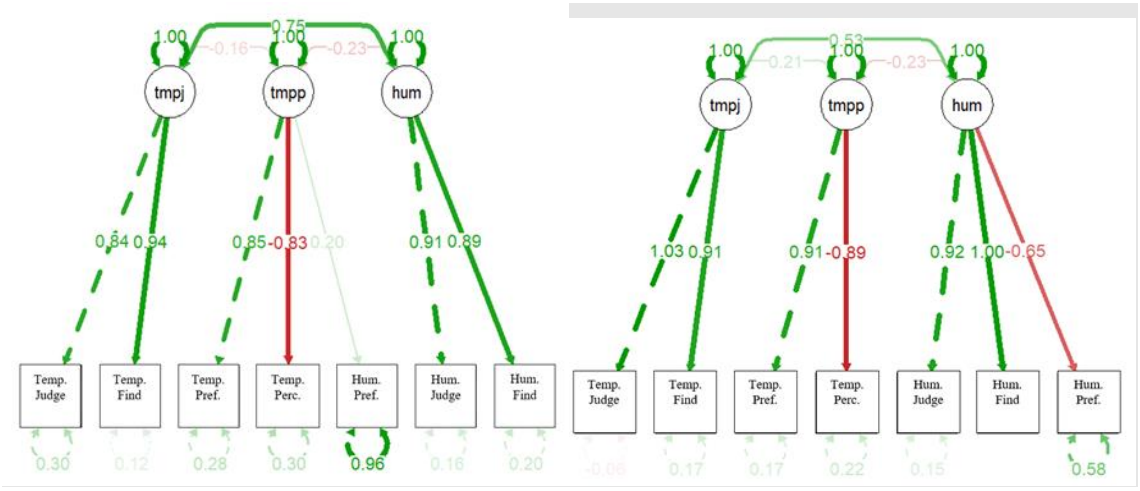

(a) *(b)*

Figure 3 CFA factor loadings for Norway (a) and Cyprus (b)

Compared to the other items of the same construct and the items of the other constructs whose factorial loadings exceed the reference threshold, the preference for humidity, however, seems to be subject to greater variability in the subjective assessment of the respondents.

Based on these results, EFA showed that factors appear to be related to several aspects of thermal comfort from the temperature and humidity items, such as judgement, preference and perception, indicating that the questionnaire items effectively capture multiple dimensions within these constructs. CFA validated the suggested latent factor structure, showing, however, that some areas of the questionnaire need attention to improve convergent and discriminant validity. The overall reliability of the thermal comfort questionnaire was adequate, with potential for improvement through in-depth evaluation of individual items (in this case, the humidity preference items) and implementation of necessary adjustments.

As a limitation, it is important to note that the analysis conducted did not include the temporal dimension despite the longitudinal nature of the data. The decision to treat the responses as independent, despite the possible overlap between participants on different days, is a pragmatic choice given the complex nature of the data. Consequently, although factor analysis provides useful initial insights, it is emphasised that an in-depth exploration of changes in the underlying factors, both in terms of qualitative significance and quantitative changes in factor levels over time and by levels of aggregation, would require analytical approaches specifically geared towards longitudinal data processing (Corballis and Traub 1970; Henseler, Ringle, and Sarstedt 2015).

4. Concluding remarks

The evaluation of subjective and objective data for both indoor air temperature and relative humidity on the dimension of occupants' preference shows that humans can assess more clearly variations in temperature rather than variations in humidity.

Although the results of the CFA analysis demonstrated a solid factorial structure for temperature-related preferences, the same was not found for humidity-related preferences. The CFA, conducted for the overall data sample and separately for the highest sample size pilots (Cyprus and Norway), showed that humidity preference presented high variability between those two groups compared to the remainder of the items. This suggested that the humidity-related preferences might be influenced by different interpretative frameworks or subjective biases of the participants, etc.

In summary, the subjective evaluation of occupants on humidity preference shows indications of unreliability that could create issues in the design of an occupant feedback-based control system. Therefore, in the development of thermal comfort evaluation or control algorithms, we suggest to avoid humidity-related occupant feedback that is subjective.

5. References

Alaidroos, Alaa, and Ibrahim Mosly. 2023. "Preventing Mold Growth and Maintaining Acceptable Indoor Air Quality for Educational Buildings Operating with High Mechanical Ventilation Rates in Hot and

Humid Climates." *Air Quality, Atmosphere & Health* 16(2): 341–61.

Che, Wen Wei et al. 2019. "Energy Consumption, Indoor Thermal Comfort and Air Quality in a Commercial Office with Retrofitted Heat, Ventilation and Air Conditioning (HVAC) System." *Energy and Buildings* 201: 202–15.

Cheung, Gordon W., Helena D. Cooper-Thomas, Rebecca S. Lau, and Linda C. Wang. 2023. "Reporting Reliability, Convergent and Discriminant Validity with Structural Equation Modeling: A Review and Best-Practice Recommendations." *Asia Pacific Journal of Management*.

Cho, Seonghun et al. 2023. "Wireless, AI-Enabled Wearable Thermal Comfort Sensor for Energy-Efficient, Human-in-the-Loop Control of Indoor Temperature." *Biosensors and Bioelectronics* 223(August 2022): 115018.

Chua, K.J., S.K. Chou, W.M. Yang, and J. Yan. 2013. "Achieving Better Energy-Efficient Air Conditioning – A Review of Technologies and Strategies." *Applied Energy* 104: 87–104.

Corballis, M. C., and R. E. Traub. 1970. "Longitudinal Factor Analysis." *Psychometrika* 35(1): 79–98.

DeVellis, Robert F., and Carolyn T. Thorpe. 2021. *Scale Development: Theory and Applications*. SAGE.

Gao, Yu, and Lin Lu. 2024. "Performance Characteristics of a Compact Self-Circulating Liquid Desiccant Air Dehumidification System Coupled with a Heat Pump: A Comprehensive Parametric Study." *Applied Thermal Engineering* 236(March 2023): 121640.

Henseler, Jörg, Christian M. Ringle, and Marko Sarstedt. 2015. "A New Criterion for Assessing Discriminant Validity in Variance-Based Structural Equation Modeling." *Journal of the Academy of Marketing Science* 43(1): 115–35.

Martinopoulos, Georgios, Konstantinos T. Papakostas, and Agis M. Papadopoulos. 2018. "A Comparative Review of Heating Systems in EU Countries, Based on Efficiency and Fuel Cost." *Renewable and Sustainable Energy Reviews* 90(February): 687–99.

Mueller, Ralph O., and Gregory R. Hancock. 2015. "Factor Analysis and Latent Structure Analysis: Confirmatory Factor Analysis." In *International Encyclopedia of the Social & Behavioral Sciences*, Elsevier, 686–90.

Mumtaz, Maisha et al. 2023. "Hybrid Membrane Dehumidification and Dewpoint Evaporative Cooling for Sustainable Air Conditioning." *Energy Conversion and Management* 294(July): 117547.

Shi, Dexin, Alberto Maydeu-Olivares, and Yves Rosseel. 2020. "Assessing Fit in Ordinal Factor Analysis Models: SRMR vs. RMSEA." *Structural Equation Modeling: A Multidisciplinary Journal* 27(1): 1–15.

UN Environment and International Energy Agency. 2017. *Towards a Zero-Emission, Efficient, and Resilient Buildings and Construction Sector. Global Status Report 2017*.

Vakiloroaya, Vahid, Bijan Samali, Ahmad Fakhar, and Kambiz Pishghadam. 2014. "A Review of Different Strategies for HVAC Energy Saving." *Energy Conversion and Management* 77: 738–54.

Woods, Carol M., and Michael C. Edwards. 2007. "12 Factor Analysis and Related Methods." In , 367–94.

Xia, Yan, and Yanyun Yang. 2019. "RMSEA, CFI, and TLI in Structural Equation Modeling with Ordered Categorical Data: The Story They Tell Depends on the Estimation Methods." *Behavior Research Methods* 51(1): 409–28.

Xu, Yifang et al. 2023. "Simulation-Based Trade-off Modeling for Indoor Infection Risk of Airborne Diseases, Energy Consumption, and Thermal Comfort." *Journal of Building Engineering* 76(June).

Appendix: Post-Occupancy Evaluation Questionnaire

This section provides the Post-Occupancy Evaluation (POE) questionnaire used to collect occupants' feedback from the 14 pilot buildings.

The questionnaire is fully anonymized, and the experimental design is randomized, therefore NO data is related to the individual person. Therefore, every time you answer this questionnaire, we need to acquire few information to contextualize your feedback. Thank you for your understanding and precious support.

SECTION 1: Personal information

Purpose: understanding potential differences in thermal comfort perception and/or use of systems

1. Hello! Who are you?

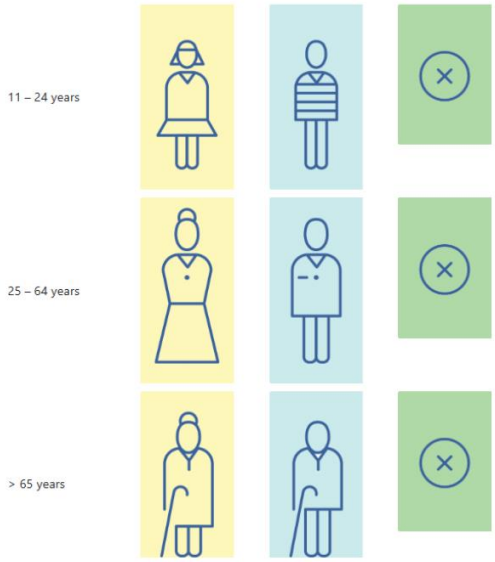

2. How would you describe your body dimension? Please, make your best guess

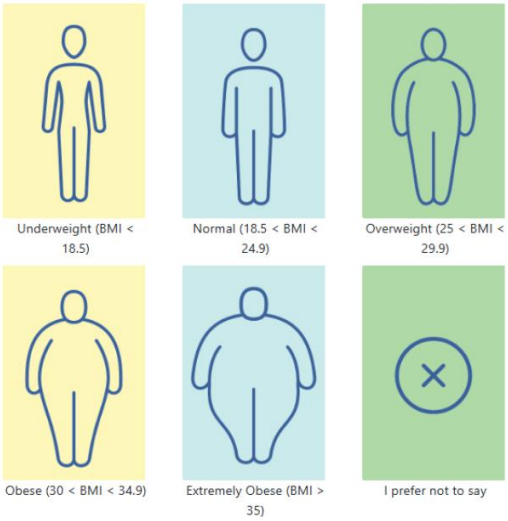

SECTION 2: Personal factors

Purpose: understanding if personal factors may affect the thermal response of a person.

3. Which ensemble best describe your clothing right now?

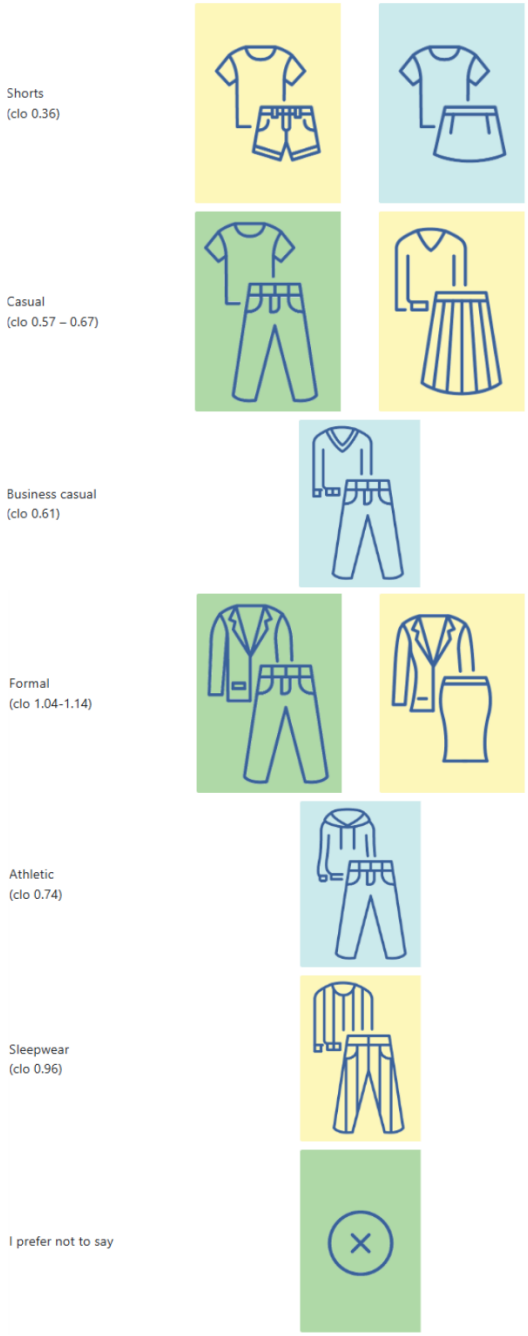

4. Which activity better describes what you are doing now?

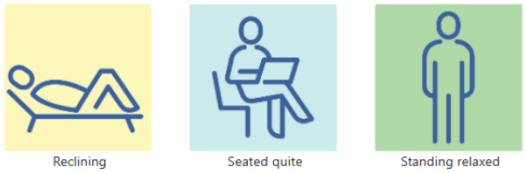

5. Are you alone in this moment?

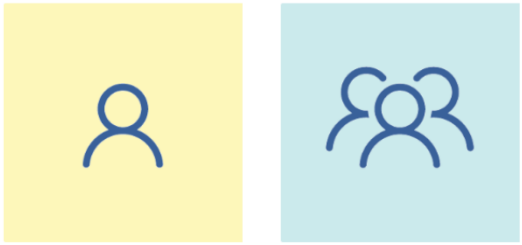

SECTION 3: Thermal comfort assessment

Purpose: assessment of the thermal environment.

6. How do you feel now?

7. At this precise moment, would you prefer the room temperature to be ... ?

8. At this precise moment, how do you judge the room temperature on a personal level?

9. At this precise moment, how do you find the room temperature?

10. At this precise moment, how do you perceive the room temperature?

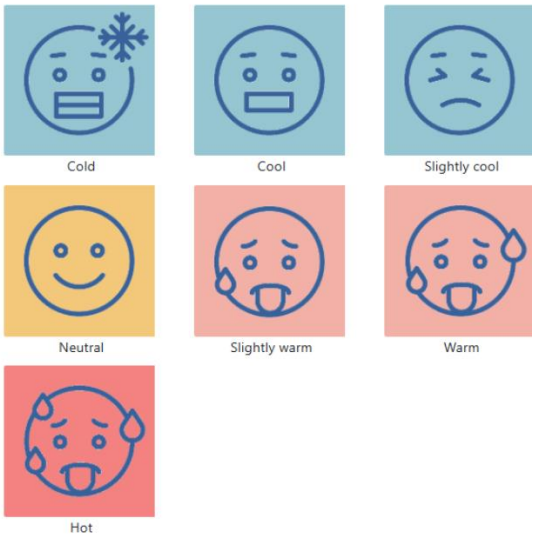

10. At this precise moment, how do you perceive the room temperature?

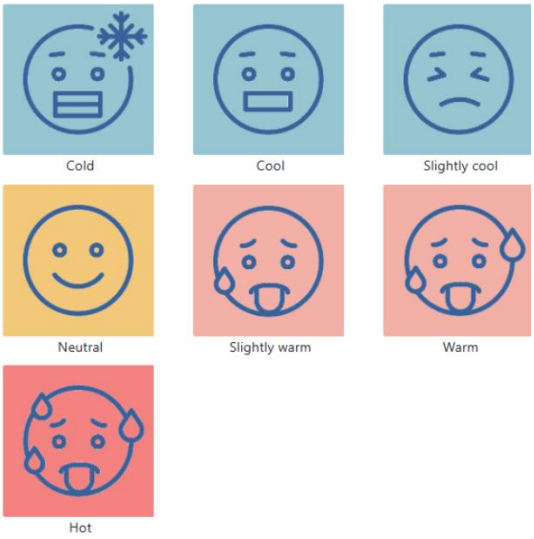

11. At this precise moment, would you prefer the humidity in the air of the room to be ...?

12. How do you judge, on a personal level, the humidity in the air of the room?

13. At this precise moment, how do you find the humidity in the air of the room?

14. Are all windows and doors closed at the moment?

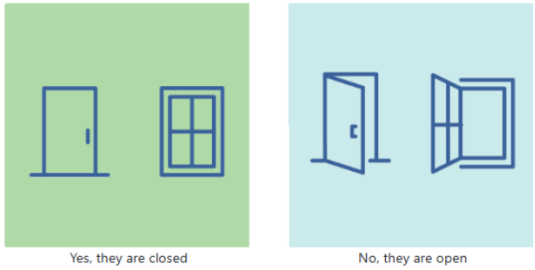

DEEP LEARNING TECHNIQUES FOR PREDICTION OF NON-VISUAL LUMINOUS CONTENT OF CELLULAR OFFICES

Summary

Simulation evaluation of non-image-forming (NIF) effects of daylight in the built environment necessitates using computationally demanding and specialised software. Therefore, this study introduces an alternative approach by exploring the potential of implementing Artificial Neural Networks (ANNs) to predict NIF effects in unilaterally daylit rectangular office spaces. The ANN models were trained on a dataset generated by simulating 349,445 cases of various office geometric configurations, optical material properties, location, sky types, and time of day in a year. The Circadian Stimulus model achieved the best ANN regression model performance with R^2 of 0.965, while the melanopic Equivalent Daylight Illuminance model predicted compliance with minimum requirements with 96.7 % accuracy. The results show the practical implications of ANN models for fast prediction of NIF effects in the built environment, significantly reducing the time and effort required for such evaluations and particularly suited for early-stage design phases.

Keywords: Non-image forming effects, Neural networks, Prediction, Parametric study, Daylight

1. Introduction

Over the past two decades, scientific findings have established that daylight is the primary synchroniser of the circadian rhythms in almost all organisms on Earth. The discovery of Intrinsically Photosensitive Retinal Ganglion Cells (ipRGC) introduced a new dimension to our understanding of light's effect on humans. These cells contain the photopigment melanopsin, which has a maximum sensitivity to light between 460 and 480 nm (Bailes and Lucas, 2013). The impact of light on the circadian system is also substantially influenced by the intensity and temporal characteristics of light stimuli. Evaluating light from a non-image-forming (NIF) perspective is, therefore, much more complex than evaluating the visible effects of light. Unlike the visual effects of daylight, which are usually determined on a horizontal plane at a height of 0.85 m (at the level of desk work), the circadian aspects of daylight are evaluated on a vertical plane at 1.2 m above the ground, which matches the average cornea height of a seated occupant. Furthermore, the received spectral power distribution (SPD) may differ significantly with the orientation of the gaze despite identical positioning in the space (Potočnik and Košir, 2021).

Several metrics have been established in the literature to describe light from the perspective of the circadian system. One key metric is the equivalent α-opic lux, which describes light based on the efficacy curves of each photopigment and follows a methodology comparable to the calculation of photometric lux. Equivalent Melanopic Lux (EML) is commonly used to quantify circadian influence among equivalent α-opic metrics(Lucas et al., 2014). This methodology was also adopted by the International Commission on Illumination – CIE(CIE S 026/E, 2018). The CIE, furthermore, proposed two additional metrics: the melanopic Equivalent Daylight Illuminance (mEDI), which depicts the measured source's equivalent of non-image-forming effect relative to the D65 illuminant, and the Equivalent Melanopic Irradiance (EMI), which represents a melanopically weighted irradiance. A scientific consensus was achieved in 2022 by Brown et al. (2022) that 250 lx (mEDI) during daytime indoors is the recommended target quantity of light for optimal physical and mental health and performance. Rea et al. (2005, 2010), proposed an alternative method for assessing the circadian aspects of light the Circadian Light (CLA). CLA considers the contribution of all photoreceptors involved in NIF light perception. CLA of 1000 represents the effect of 1000 lx of standard CIE illuminant A on the NIF system. Moreover, the CLA method is directly linked to the Circadian Stimulus (CS) metric, where the CS represents the intensity of suppression of nocturnal melatonin. CS of 0.3 means 30 % suppression of nocturnal melatonin and corresponds to 275 CLA. The value of 0.3 CS has been confirmed by several studies (Figueiro and Rea, 2016; Figueiro, 2017; Figueiro et al., 2018) as effective in reducing fatigue and drowsiness

© 2024. The Authors. Published by International Solar Energy Society
Selection and/or peer review under responsibility of Scientific Committee
10.18086/eurosun.2024.01.10 Available at http://proceedings.ises.org

and improving attention and alertness in human subjects.

To accurately assess the NIF daylight conditions through simulations, software capable of multi-spectral simulations is necessary so that the SPD of light can be calculated at a given point. However, established approaches and tools for visible light simulations, which calculate light in three channels (R, G, B), are inadequate for this task. Currently, LARK (Inanici and LLP, 2015) and ALFA (LLC Sollemma, 2020) are the two most used software tools for simulating NIF effects in buildings. Of these, only ALFA utilises the built-in libRadtran (Emde et al., 2016) solar radiative transfer library to evaluate spectral radiation data of the climate-conditioned sky in determination of indoor SPD. Both tools, however, require significant computation time, suitable hardware, and high user input.

Both daylight and circadian simulations are computationally demanding and time-consuming, making them less appealing to practitioners who face iterative design on a daily basis (Ayoub, 2020). However, in the last decade, we have witnessed the expansion of artificial intelligence (AI), which enables faster acquisition of results based on predictive models offered within the vast field of AI predictive techniques. In the past decade, machine learning and deep learning techniques, such as Artificial Neural Networks (ANN), have been increasingly used in daylighting and lighting applications (Ngarambe et al., 2022). Between 2006 and 2023, over 30 relevant studies on machine learning applications in daylighting have been published (Liu et al., 2023), pointing to a growing interest in the subject. Machine learning has been employed to predict light levels and control various machine-controlled building components such as shades (Xie and Omidfar Sawyer, 2021) or automatic control of luminaires (Park et al., 2019) to ensure the appropriate indoor light levels. Machine learning and deep learning techniques offer an alternative to traditional simulation methods. They can be used to develop models that replace complex simulation tools, particularly in the early design stages. However, these approaches rely on robust databases for training the models. Many machine learning techniques are currently known, and approaches such as support vector machines – (SVM) are most commonly used in the literature for logical control. However, the most commonly used method reported in the literature for predicting the luminous environment is back propagation neural network (BPNN) (Liu et al., 2023), which is a type of ANN. Liu et al. (2023) have identified BPNN as the most efficient method for the regression of light quantity in the built environment. However, these studies addressed only the visual aspects of daylight (Ahmed et al., 2011), artificial illumination (Bellochio et al., 2011) or daylight in combination with building energy performance (Wu et al., 2024). Typically, annual daylight metrics such as Useful Daylight Illuminance (UDI), spatial Daylight Autonomy (sDA), and Annual Sunlight Exposure (ASE) are predicted. For example, Han et al. (2021) have developed an early-stage design framework for BIM, which, based on the data available in the BIM model, can predict the UDI using BPNN techniques. Tests on a single room have shown high accuracy of the model with mean average percentage error (MAPE) under 10 %. Similarly, using BPNN, Lin and Tsay (2021) have predicted the ASE and sDA of different façade designs using the novel concept of pre-processor and intermediary features, which enabled the expansion of the model's application scope. Li et al. recently demonstrated (2024) that absolute values of daylight illuminance can also be predicted using ANN. They used a Generative Adversarial Network to generate daylight predictions, which saved 73 % of the computational time compared to the time required by the simulations with a mean average percentage error of 0.135.

Although significant advancements have been made in applying ML and ANN algorithms for daylight prediction, our literature review revealed that no ML or ANN models currently predict the NIF aspects of daylight. This study aims to address this gap by creating a spectral simulation database and developing ANN models based on that database. In this study, we aim to develop the following models:

- An ANN model for predicting Equivalent Melanopic Illuminance – EML regression model.
- An ANN model for predicting melanopic Equivalent Daylight Illuminance – mEDI regression model.
- An ANN model for predicting Circadian Stimulus – CS regression model.
- Classification ANN models for predicting compliance with EDI or CS requirements – CS and mEDI classification models.

2. Methodology

To achieve the research objectives of environment developing predictive models for NIF environment, the

study implemented the following phases (Fig. 1): 1. Simulation model definition; 2. Data generation; 3. Feature selection /engineering; 4. ANN development and evaluation.

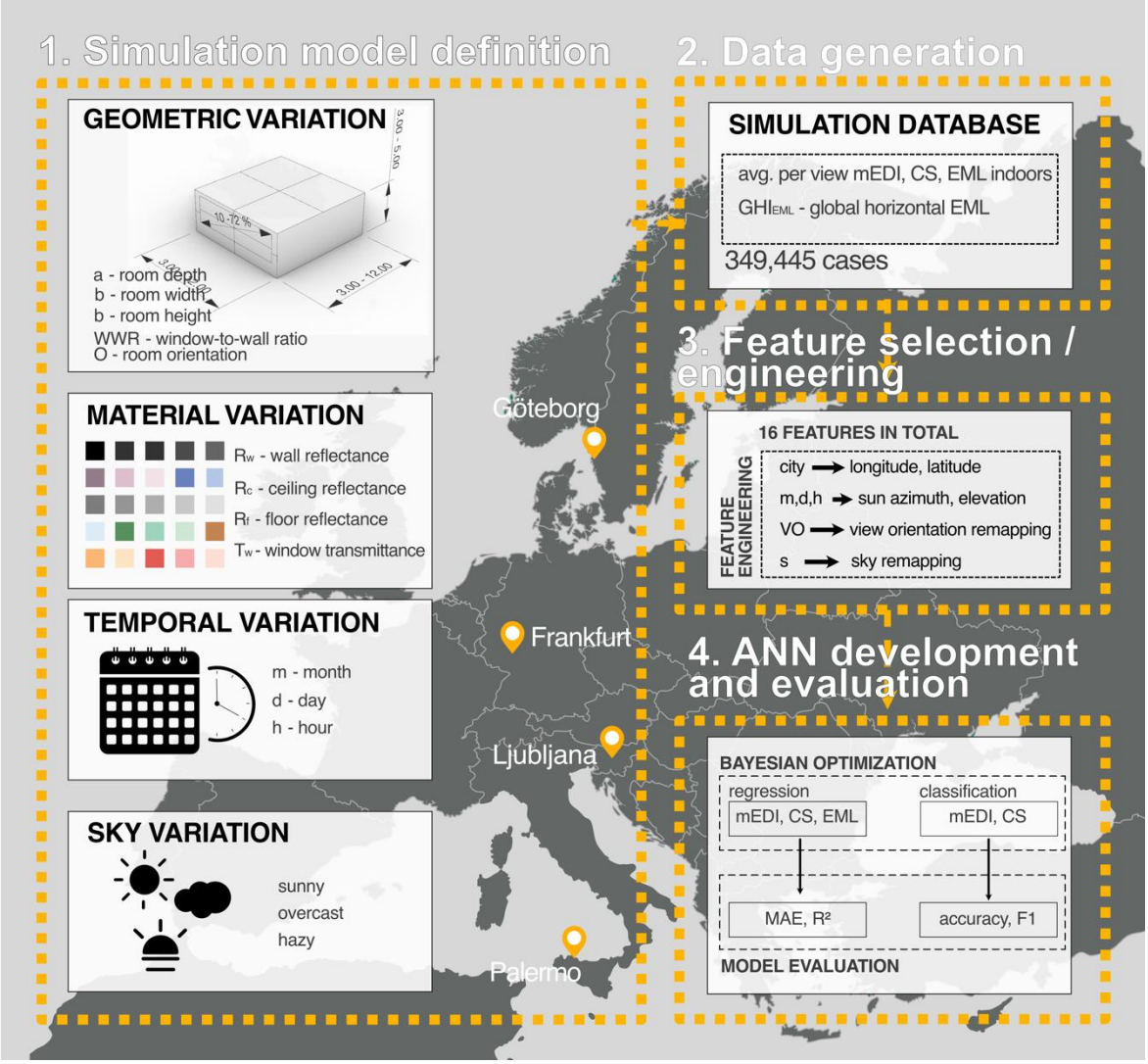

Fig. 1: Workflow diagram of developed prediction models.

2.1. Simulation Model Definition

To provide a universal model, it was first necessary to determine the appropriate input parameters and their range for the simulation database upon which the ANN models were trained. Simulation models were created upon variation of 15 simulation variables. They can be divided into five main categories (see Tab. 1). The first category includes geometric parameters. The prediction models were limited to rectangular floor plans with unilateral façade openings. Consequently, the geometry of the space can be described by four parameters: depth (a), width (b), and height (h) of the space, as well as Window-to-Wall-Ratio (WWR). The window was fixed at a parapet height of 0.85 m, while cardinal directions of east, south, west and north were considered for its orientation (O). The last geometric parameter was the view orientation (VO) of the considered hypothetical occupant at a corneal height of 1.2 m above the finished floor. The hypothetical occupant positions were placed on a grid with 0.5 x 0.5 m spacing and an offset of 0.25 m from the walls. The grid size depends on the variation of the a and b parameters (see Tab 1). The second category included optical properties of the considered geometric elements. The melanopic reflectivity of walls ($R_{w\text{-}m}$), ceiling ($R_{c\text{-}m}$) and floor ($R_{f\text{-}m}$) were modified. Similarly, the melanopic ($T_{w\text{-}m}$) transmittance of glazing was varied. The third category of temporal parameters included the variation of the month (m), days (d) and hours in a day (h), while only the daylit part was considered. The last category included climate variables of location and sky type variation. Sky was modelled as sunny, hazy, and overcast, and the locations considered were Göteborg (57.71° N, 11.97° E), Frankfurt (50.11° N, 8.68° E), Ljubljana (46.05° N, 14.51° E), and Palermo (38.12° N, 13.36° E).

Tab. 1: Simulation model variables.

Group	Parameter	Min	Max	Step
Geometric parameters	Depth - a [m]	3	12	2.25
	Width - b [m]	3	12	2.25
	Height - c [m]	3	12	2.25
	WWR [%]	10	72	varies
	View orientation - VO [°]	0	270	90
	Room orientation - O [°]	0	270	90
Temporal parameters	Month - m	1	11	2
	Day – d	1	30	15
	Hours in a day - h [h]	7	21	varies
Optical parameters	$R_{w\text{-}m}$ [%]	10	100	varies
	$R_{f\text{-}m}$ [%]	10	100	varies
	$R_{c\text{-}m}$ [%]	10	100	varies
	$T_{g\text{-}m}$ [%]	10	100	varies
Group	**Parameter**	**Categorical input**		
Climate parameters	Location	Frankfurt, Ljubljana, Göteborg, Palermo		
	Sky type	clear sky, hazy sky, overcast sky		

2.2. Data Generation

All potential simulation parameter variations would result in over 1 x 10^9 cases. Therefore, a random selection script was run on all possible parameter permutations to select 349,445 cases to be modelled, simulated and included in the simulation database. The required geometric models were created using a custom script in Grasshopper and baked into layers in Rhinoceros accordingly. The geometry from Rhinoceros was then fed to the multispectral simulations, which were performed using the multispectral raytracing software plugin for Rhinoceros ALFA (LLC Sollemma, 2020). ALFA is a well-established and reliable simulation tool for multispectral simulations of daylight (Diakite-Kortlever and Knoop, 2021; Potočnik and Košir, 2022). The mentioned software uses libradtran (Emde et al., 2016), a radiative transfer calculation software package for calculating the spectral sky according to the geographic location. It can calculate four different sky types: clear, hazy, overcast and heavy rain cloudy from the atmospheric profile for midlatitude locations. Since ALFA does not offer a batch function to simulate numerous study cases, a Python script with PyAutoGUI for graphical user interface automation was used to automate simulations by controlling the computer mouse pointer and keyboard input. The automation script and the simulation models were deployed to 25 individual computers connected to a common network, which simultaneously calculated the simulations and built a database of all simulation outcomes. The spectral daylight calculations were performed at the following settings for each case: ambient bounces – (ab) 8, limit weight (lw) 0.001 at 200 passes for each simulation. Default ALFA results include data such as SPD, EML, and lx. For this study's ANN regression models, the photopic illuminance data was discarded, and SPD was used to calculate the mEDI and CS values. Afterwards, average values per case variation and occupant view orientation were calculated for each of the selected metrics. In the end, for the classification models, the average values mentioned before were evaluated according to the NIF requirement criteria for mEDI of $\geq$ 250 lx and $\geq$ 0.3 CS and output into the binary output of 0, meaning it does not meet the criteria, and 1, meaning the value meets the criteria.

2.3. Feature engineering and selection

In total, 14 properties (see Tab. 1) defined the simulation iterations performed to obtain the simulation data; however, for the ANN training, 16 variables were selected/derived (Fig. 2). All the input variables were coded as continuous. Sky was transformed from a categorical to a continuous variable where clear = 1, hazy = 0.5

and overcast = 0. Room orientation with window facing north equalled to 0°, the east oriented room was coded to 90° etc., in a clockwise direction. View orientation was coded so that the 0° view was always facing the window with other views coded in 90° increments clockwise accordingly. The location property was coded into longitude and latitude. The input combination of longitude, latitude, hour, day and month was used to calculate sun azimuth and elevation. Global horizontal EML (GH_{EML}) data were gathered directly from the database. Other variables were input directly from the simulation model development. As can be seen in the correlation matrix in Fig. 2, no multicollinearity was present in the predictors. A stronger correlation of 0.81 between sun altitude and GH_{EML} was present, but the GH_{EML} was not dropped since it directly affects indoor illuminance – higher/lower outdoor illuminances translate directly to higher/lower indoor illuminances.

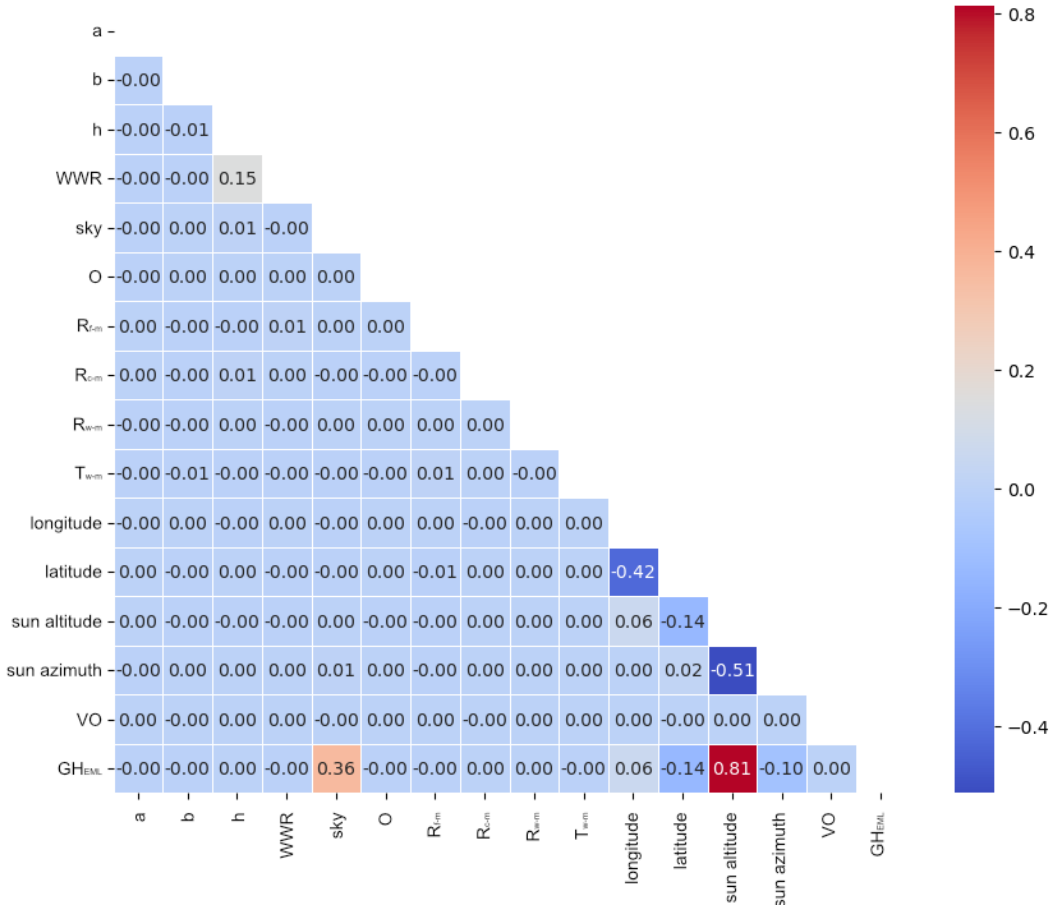

Fig. 2: Correlation matrix of input variables for ANN models.

2.4. Neural Network Model Development

Neural networks are computational models inspired by the human brain's structure and functioning, designed to recognise patterns, learn from data and make predictions. They consist of nodes – neurons that receive input data – signal, process it, and produce an output. The nodes are usually connected using connections-weights, which are adjusted during learning and influence the signal's strength and direction to the next neuron. The connections between neurons are transformed using non-linear transformations. These functions introduce non-linearity into the network to learn complex patterns. Two different non-linear transformation functions, rectified linear unit function (ReLU) and hyperbolic tangent function (tanh), were explored for the regression of ANN models, and three different functions, ReLU, tanh and sigmoid, were explored for the classification ANN models.

The neurons of an ANN model are organised into layers. First is the input layer, which matches the number of input variables used for the predictive model. For this study, each developed model had 16 input variables and one output layer. In between, an optimal number of hidden layers (hl) was determined for each developed model simultaneously with the number of neurons per hidden layer (n). The data input to the model follows

the principle of forward propagation, meaning that the input data is fed into the network, and the computations proceed layer by layer from input to output, producing a final prediction. To minimise the difference between the network's prediction and actual target values, a backpropagation learning algorithm was used, where the principle of gradient descent is used to propagate the error backwards through the network to minimise the loss function (i.e. mean average error – MAE for regression tasks and binary cross-entropy for the classification tasks) using an optimisation algorithm that updates the model parameters. Two different optimisation algorithms were explored in the development of ANNs for this study Root Mean Square Propagation (RMSProp) and Adaptive Moment Estimation (ADAM), which are controlled by the learning rate (lr). The learning rate determines the step size at each iteration while moving towards the minimum of the loss function. Two general types of ANN models for predicting non-visual luminous environments were developed for this study. The first model type are regression ANN models, developed for the prediction of EML, CS and mEDI, expressing the absolute NIF luminous content. The second type of ANN model was the classification model, which predicted whether the average CS and mEDI of the space passed their respective requirements.

ANN's ability to learn depends on the structure and other hyperparameters. Furthermore, the optimal hyperparameters vary from case to case. There are three most commonly used methods to determine the optimal structure of an ANN: random search (James Bergstra and Yoshua Bengio, 2012), grid search (Pontes et al., 2016) or hyperparameter optimisation using Bayesian optimisation (Snoek et al., 2012). The first two methods are brute force principles, which demand the calculation of a large pool of different parameter combinations to find the optimal model performance. In this study, a substantial amount of training data (349 445) was collected to build the ANN models. Consequently, a large average calculation time was expected to be required to train a single ANN model. Therefore, the Bayesian optimisation of hyperparameters was used to find the optimal models. Bayesian optimisation uses a surrogate model, a Gaussian Process, to approximate the objective function of hyperparameters. It utilises an acquisition function to decide which hyperparameters to evaluate next, balancing exploration and exploitation. This process iterates until the optimal hyperparameters are found or a stopping criterion is met, making it a highly efficient method for hyperparameter tuning in ANNs (Snoek et al., 2012). In the search for the optimal models, we have identified six hyperparameters, which would be optimised using Bayesian optimisation. As shown in Tab. 2, the chosen hyperparameters to be optimised were: number of hidden layers (hl), number of neurons per layer (n), batch size (bs), optimiser (opt), activation function (a_f) and learning rate (lr). The Bayesian optimisation was applied to TensorFlow models using the Bayesian optimisation API (Nogueira, 2014).

Tab. 2: Results of the performed ANN regression models.

Hyperparameter name	Optimization pool
hl	1 – 6 hidden layers
n	16 – 128 neurons
bs	32 – 256 samples
opt	ADAM, RMSProp,
a_f	RELU, tanh , sigmoid
l_r	0.00001-0.001

Data used for the training of models was split into training, validation and test datasets in a ratio of 70/20/10 %. All models were configured to train for up to 300 epochs, with the training process governed by an early-stopping algorithm. The patience parameter was set to 10 epochs, meaning the algorithm would wait for 10 epochs for any improvement in the model's validation metric. The training would halt if no improvement was observed within these ten epochs. This approach effectively prevented the potential overfitting of the models. The algorithm was set to select the best training weights along this process.

2.5. Model evaluation

Both regression and classification models were evaluated using commonly used evaluation metrics in machine learning. Regression models were evaluated using mean average error (MAE) presented in eq. 1 and coefficient of determination (R^2).

$$MAE = \frac{1}{n}\sum_{i=1}^{n}|y_i - \hat{y}_i| \qquad \text{(eq. 1)}$$

Classification models were evaluated using Accuracy rating (eq. 2), which is the ratio of correctly predicted instances (TP – true positive and TN – true negative values) to the total of instances (including FP – false positive and FN – false negative values), the ratio of 1 presents a perfect score. Additionally, models were tested using the F1 score (eq. 5), which, in addition to Precision rate (accuracy of positive predictions – eq. 4), evaluates recall rate (false positive occurrence – eq. 3), a value of 1 presents perfect F1 score.

$$Accuracy = \frac{TP+TN}{TP+TN+FP+FN} \qquad \text{(eq. 2)}$$

$$Recall = \frac{TP}{TP+FN} \qquad \text{(eq. 3)}$$

$$Precision = \frac{TP}{TP+FP} \qquad \text{(eq. 4)}$$

$$F1 = 2 \times \frac{Precision \times Recall}{Precision+Recall} \qquad \text{(eq. 5)}$$

3. Results

3.1. Dataset results

The dataset contains calculated values for the NIF environment simulations obtained from the ALFA simulations. Fig. 3, presents the simulation data distribution used to train the model. Most EML values ranged from 240 EML (Q1) to 1869 EML (Q3), with a median value of 707 EML and an average of 1788 lx. Similarly, the mEDI values ranged from 217 lx (Q1) to 1693 lx (Q3), with a median value of 640 lx and an average of 1620 lx. The CS values are defined on a logarithmic scale between 0 and 0.7. The database yielded a median value of 0.48 CS, with most data falling between 0.29 CS (Q1) and 0.61 CS (Q2) and an average of 0.44 CS.

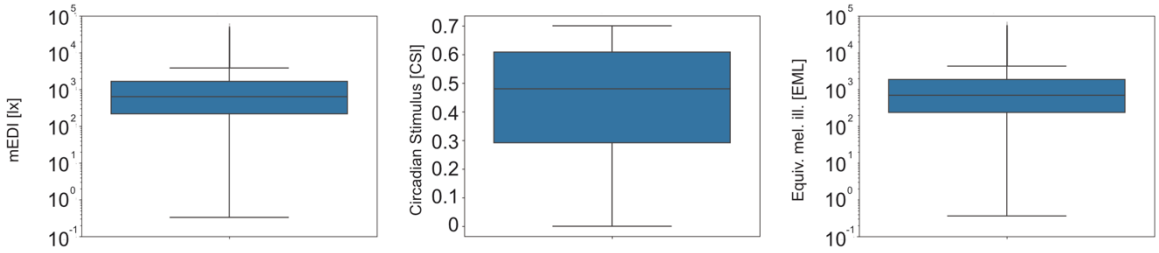

Fig. 3: Data gathered for the EML, CS and mEDI prediction models.

3.2. ANN regression model results

Based on the dataset's calculated NIF values presented in section 3.1, three ANN regression models were developed using the Bayesian optimisation process. The optimal hyperparameters and resulting prediction accuracy are shown in Tab. 3. The Bayesian optimisation has effectively tuned the models, with the CS regression model emerging as the most effective in explaining variance (R^2). The CS model reached the best performance in terms of R^2 score (0.965), indicating it explains 96.5 % of the variance, which can be considered an excellent result. In addition, it is also worth mentioning that the CS model required the least complex structure among presented models, namely four hidden layers with 96 neurons each were required by the optimal CS regression model. In contrast, both EML and mEDI required five hidden layers with 120 and 123 neurons for EML and mEDI regression models respectively. Despite having a more complex structure, the regression models performed excellently with 91.1 % and 91.2 % of variance explained for the EML and EDI models, respectively.

Tab. 3: Results of the performed ANN regression models.

ANN regression models

M	#f	h-l	n	b_s	a_f	opt	lr	MAE_{train}	MAE_{val}	MAE_{test}	R^2

EML	14	5	120	46	RELU	RMSProp	0.001	186.4	188.9	181.1	0.911
CS	14	4	96	123	RELU	ADAM	0.001	0.0117	0.0126	0.0135	0.965
EDI	14	5	123	49	RELU	ADAM	0.0009	163.32	168.13	165.5	0.912

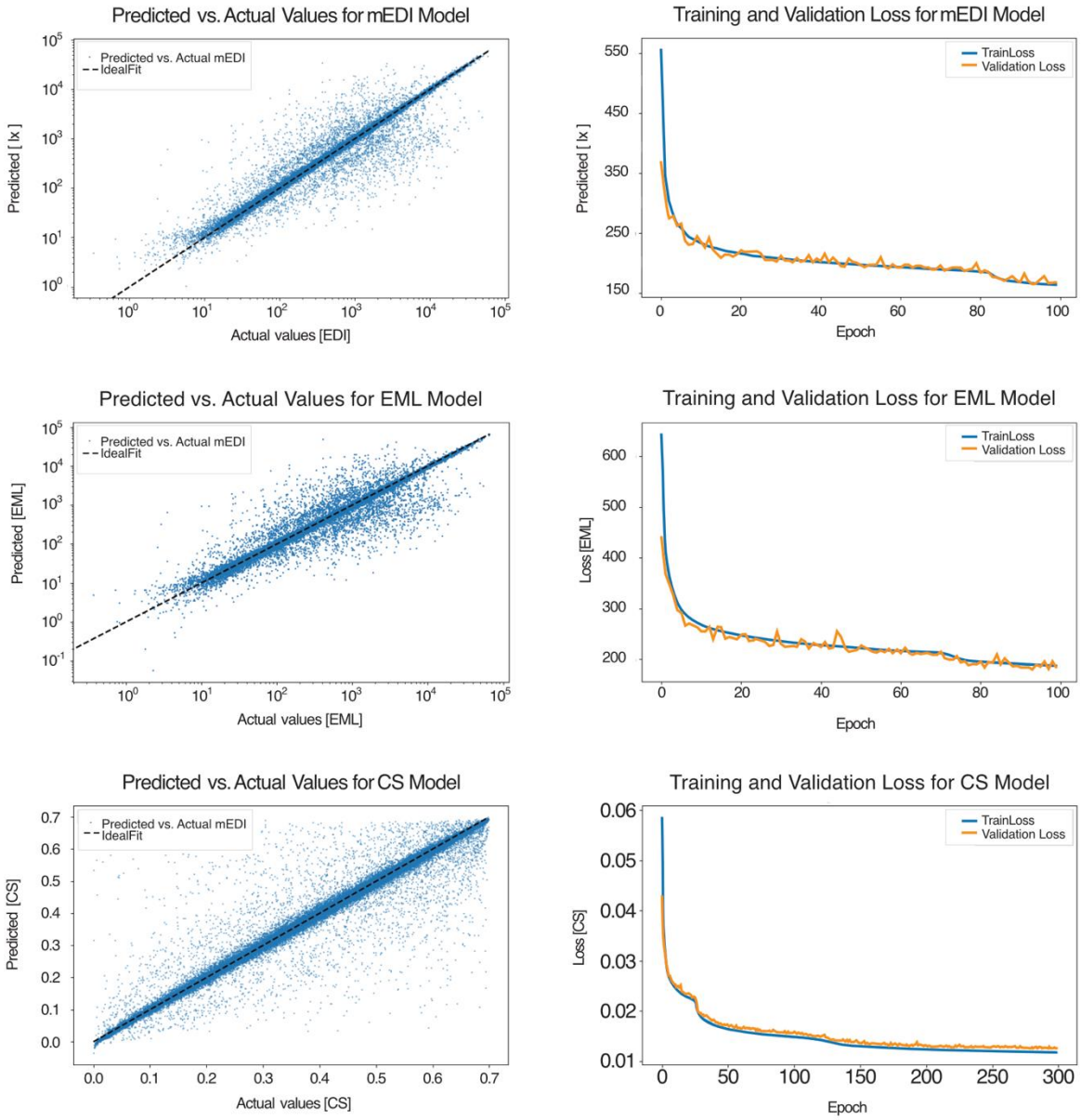

Fig. 4: Performance and training process of regression ANN regression models.

Each regression model shows consistent performance and good generalisation ability, which is expressed by slight differences in performance between training (MAE_{train}), validation (MAE_{val}), and test (MAE_{test}) datasets (Tab. 3). The small difference in MAE_{test} is particularly significant, as it describes the model's performance on unseen data. If the model were overfit, the MAE_{test} would result in considerably higher errors. As shown in Fig. 4. all models learned well, with good convergence and stable training performance. No major deflection of validation loss (orange lines in Fig. 4) can be detected for either of the models, which would indicate overfitting. Both mEDI and EML models stopped at the 98th epoch, while the CS model's training was stopped at the 287th epoch. Predicted vs. actual values plots of models in Fig. 4 show the best performance for the mEDI regression model in the range between 10^1 and 10^2 mel lx and approximately 10^4 and 10^5 mel lx. A similar is true for the EML regression model. Meanwhile, the CS model shows almost consistent performance throughout the entire range, with slightly higher inaccuracy between 0.6 and 0.7 CS.

3.3. ANN classification model results

The optimal model architecture and hyperparameter values for the ANN classification models performed in this study are shown in Tab. 4. As seen from the table, these data introduced much less complexity than the data for regression models (see Tab. 3) and required considerably simpler model architectures. CS compliance classification prediction model required two hidden layers with 32 neurons using a sigmoid activation function with a 0.0002 learning rate and a batch size of 32 samples. The model performed excellently, as expressed by the 96.7 % accuracy on the training dataset (acc_{train}). Tests on validation data (acc_{val}) and test data (acc_{test}) also expressed excellent performances with a difference in performance on validation and test dataset compared to the training dataset with only 0.3 percentage points (pp) for each respective dataset. When testing the model's performance by evaluating false positive and false negative predictions, the F1 score showed that the model performed at an even higher precision rating of 97 % on the test dataset. mEDI compliance classification model's structure, similar to the CS model, required lower complexity than the regression models to achive optimal performance. The optimal architecture of the model was found at six hidden layers with 16 neurons per layer at a learning rate of 0.0006 and 123 batch sample size. Similarly, to the CS classification model, mEDI used a sigmoid activation function and ADAM optimiser. The model resulted in even higher accuracy on the train data set of 97 % with acc_{val} and acc_{test} with comparable accuracy (Tab. 4) and the difference to the acc_{train} performance of only 0.1 pp and 0.3 pp, respectively. The F1 score of 97.7 % is almost the same as for the CS classification model, indicating robust performance.

Tab. 4: Results of the performed ANN classification models.

	Classification models										
M	**#f**	**hl**	**n**	**b_s**	**a_f**	**opt**	**lr**	**acc_{train}**	**acc_{val}**	**acc_{test}**	**F1**
CS	14	2	32	32	sigmoid	ADAM	0.0002	0.967	0.964	0.964	0.970
mEDI	14	6	16	123	sigmoid	ADAM	0.0006	0.970	0.969	0.967	0.977

Fig.5 shows the training process of the presented CS and mEDI classification prediction models. Both models show good convergence with no possible overfitting of the models, and no notable deflection between the accuracy and validation loss was detected with the models. CS model's early stopping algorithm stopped the learning at the 53rd epoch, while mEDI's early stopping algorithm halted the training at the 74th epoch, thus prohibiting possible overfitting of the model. As mentioned before, minute differences in acc_{train}, acc_{val} and acc_{test} express that overfitting is not present. Therefore, we can say the model generalises well.

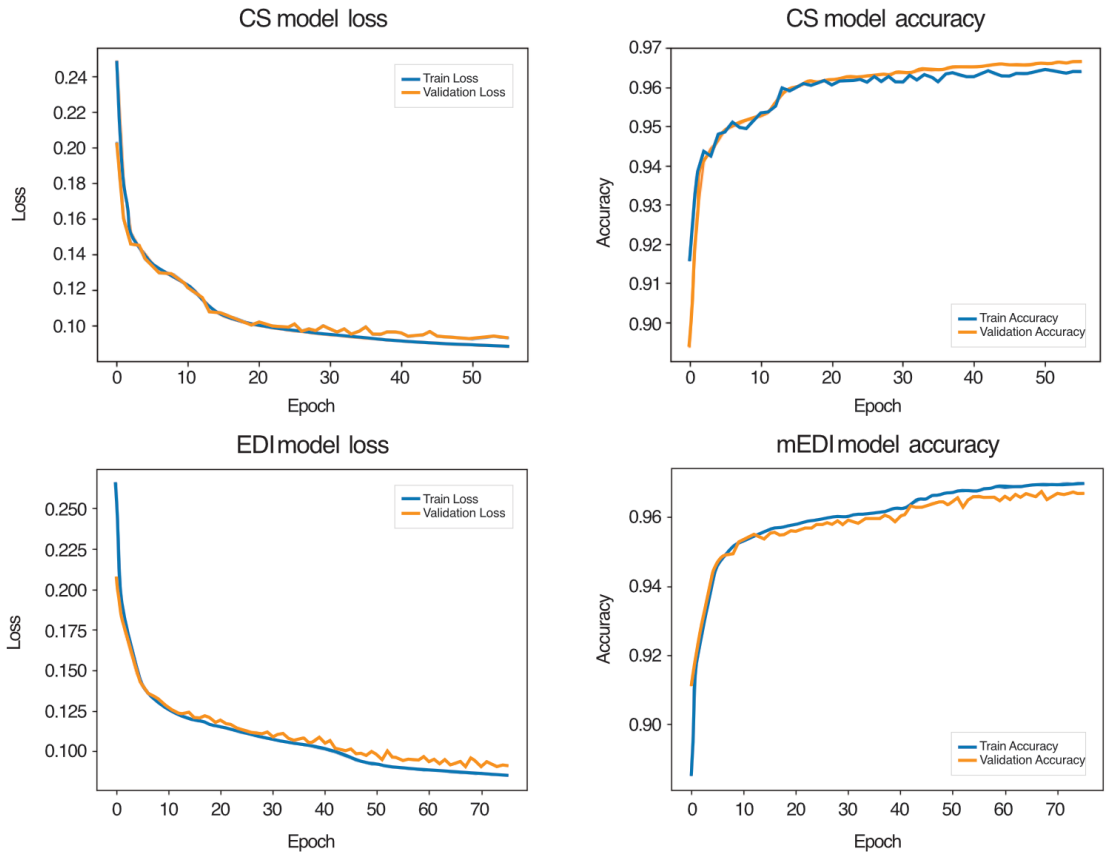

Fig. 5: Performance of classification ANN models.

4. Discussion and Conclusion

The presented study introduced a novel framework for predicting the NIF indoor potential of unilaterally lit spaces. We have successfully developed an NIF simulation database, which served as a training basis for the development of predictive Artificial Neural Networks, using backpropagation algorithms. The Bayesian Optimisation methodology of hyperparameter optimisation was successfully applied to the framework, where model hyperparameters were optimised to develop accurate prediction models of the NIF environment. The best-performing model among regression models was the Circadian Stimulus (CS) model, whose predictions were able to explain 96.5 % of the variance. The Equivalent Melanopic Illuminance (EML) and melanopic Equivalent Daylight Illuminance (mEDI) models also performed well, with over 91 % of explained variance in the test predictions. Additionally, two classification models were trained using the ANN methodology. The same Bayesian Optimisation algorithm was applied to the models to find the optimal architecture of the models. As a result, models could discern the compliance of the average CS or mEDI requirements for healthy luminous environments. Both model's accuracy was exerted at over 97 %.

The results have shown that the NIF properties of indoor environments can be predicted using the principles of deep learning, specifically Artificial Neural Networks. Results from the trained models can be used by the practitioners for early-stage building design checking in regard to the designed space NIF luminous aspects. They can also be used as an informative tool by property managers or occupants to assess the NIF potential of their properties without the need for complex and lengthy simulations. Such models, due to their fast performance (1 input into ANN predictive model is calculated in 850 µs), could potentially, in future studies, be used on annual weather data, which would enable the prediction of yearly NIF potentials of the validated unilaterally lit spaces.

Nevertheless, it is essential to recognise that the study's findings are confined to average room values and do not account for spatial variations in the space. Moreover, the current model is restricted to rooms daylit through a single window on one façade and rectangular room geometries. Currently, the models were developed based

on data from just four locations. For more accurate predictions at other latitudes, it would be necessary to include data from additional locations. Future efforts should aim to develop models capable of predicting NIF daylight potential based on specific sensor positions within a room, enabling the evaluation of the spatial distribution of daylight within the considered space. In addition, further research is needed to assess prediction accuracy in spaces illuminated from multiple directions.

5. Acknowledgments

The presented research resulted from a project, *Calculation of Yearly Circadian Potential in Buildings Using Deep Learning Techniques—YCPdeep* (project No. J2 – 3036), funded by the Slovenian Research and Innovation Agency (project No. J2 – 3036). The authors also acknowledge the financial support from the Slovenian Research and Innovation Agency research core funding No. P2 – 0158.

6. References

Ahmed, A., Otreba, M., Korres, N.E., Elhadi, H., Menzel, K., 2011. Assessing the performance of naturally day-lit buildings using data mining. Advanced Engineering Informatics 25, 364–379. https://doi.org/10.1016/j.aei.2010.09.002

Ayoub, M., 2020. A review on machine learning algorithms to predict daylighting inside buildings. Solar Energy 202, 249–275. https://doi.org/10.1016/J.SOLENER.2020.03.104

Bailes, H.J., Lucas, R.J., 2013. Human melanopsin forms a pigment maximally sensitive to blue light (λmax ≈ 479 nm) supporting activation of Gq/11 and Gi/o signalling cascades. Proc. R. Soc. B 280, 20122987. https://doi.org/10.1098/rspb.2012.2987

Bellochio, F., Ferrari, S., Lazzaroni, M., Cristaldi, L., Rossi, M., Poli, T., Paolini, R., 2011. Illuminance prediction through SVM regression, in: IEEE Workshop on Environmental Energy and Structural Monitoring Systems. Milan, Italy, pp. 1–5. https://doi.org/10.1109/EESMS.2011.6067051

Brown, T.M., Brainard, G.C., Cajochen, C., Czeisler, C.A., Hanifin, J.P., Lockley, S.W., Lucas, R.J., Münch, M., OHagan, J.B., Peirson, S.N., Price, L.L.A., Roenneberg, T., Schlangen, L.J.M., Skene, D.J., Spitschan, M., Vetter, C., Zee, P.C., Wright, K.P., 2022. Recommendations for daytime, evening, and nighttime indoor light exposure to best support physiology, sleep, and wakefulness in healthy adults. PLoS Biol 20, e3001571. https://doi.org/10.1371/JOURNAL.PBIO.3001571

CIE S 026/E:2018, 2018. CIE System for Metrology of Optical Radiation for ipRGC-Influenced Responses to Light CIE S 026/E:2018.

Diakite-Kortlever, A.K., Knoop, M., 2021. Forecast accuracy of existing luminance-related spectral sky models and their practical implications for the assessment of the non-image-forming effectiveness of daylight: Lighting Research & Technology 53, 657–676. https://doi.org/10.1177/1477153520982265

Emde, C., Buras-Schnell, R., Kylling, A., Mayer, B., Gasteiger, J., Hamann, U., Kylling, J., Richter, B., Pause, C., Dowling, T., Bugliaro, L., 2016. The libRadtran software package for radiative transfer calculations (version 2.0.1). Geosci Model Dev 9, 1647–1672. https://doi.org/10.5194/gmd-9-1647-2016

Figueiro, M., Rea, M., 2016. Office lighting and personal light exposures in two seasons: Impact on sleep and mood. Lighting Research & Technology 48, 352–364. https://doi.org/10.1177/1477153514564098

Figueiro, M.G., 2017. Disruption of Circadian Rhythms by Light During Day and Night. Curr Sleep Med Rep 3, 76–84. https://doi.org/10.1007/s40675-017-0069-0

Figueiro, M.G., Nagare, R., Price, L.L.A., 2018. Non-visual effects of light: How to use light to promote circadian entrainment and elicit alertness. Lighting Research & Technology 50, 38–62. https://doi.org/10.1177/1477153517721598

Han, Y., Shen, L., Sun, C., 2021. Developing a parametric morphable annual daylight prediction model with improved generalization capability for the early stages of office building design. Build Environ 200, 107932. https://doi.org/10.1016/J.BUILDENV.2021.107932

Inanici, M., LLP, Z.A., 2015. Lark Spectral Lighting [WWW Document]. URL http://faculty.washington.edu/inanici/Lark/Lark_home_page.html (accessed 10.30.20).

James Bergstra, Yoshua Bengio, 2012. Random Search for Hyper-Parameter Optimization. Journal of

Machine Learning Research 13, 281–305.

Li, X., Yuan, Y., Liu, G., Han, Z., Stouffs, R., 2024. A predictive model for daylight performance based on multimodal generative adversarial networks at the early design stage. Energy Build 305, 113876. https://doi.org/10.1016/J.ENBUILD.2023.113876

Lin, C.H., Tsay, Y.S., 2021. A metamodel based on intermediary features for daylight performance prediction of façade design. Build Environ 206, 108371. https://doi.org/10.1016/J.BUILDENV.2021.108371

Liu, Q., Chen, Y., Liu, Y., Lei, Y., Wang, Y., Hu, P., 2023. A review and guide on selecting and optimizing machine learning algorithms for daylight prediction. Build Environ 244, 110822. https://doi.org/10.1016/J.BUILDENV.2023.110822

LLC Sollemma, 2020. ALFA - Adaptive Lighting for Alertness [WWW Document]. URL https://www.solemma.com/Alfa.html (accessed 10.30.20).

Lucas, R.J., Peirson, S.N., Berson, D.M., Brown, T.M., Cooper, H.M., Czeisler, C.A., Figueiro, M.G., Gamlin, P.D., Lockley, S.W., O'Hagan, J.B., Price, L.L.A., Provencio, I., Skene, D.J., Brainard, G.C., 2014. Measuring and using light in the melanopsin age. Trends Neurosci 37, 1–9. https://doi.org/10.1016/j.tins.2013.10.004

Ngarambe, J., Adilkhanova, I., Uwiragiye, B., Yun, G.Y., 2022. A review on the current usage of machine learning tools for daylighting design and control. Build Environ 223, 109507. https://doi.org/10.1016/J.BUILDENV.2022.109507

Nogueira, F.M.F., 2014. BayesianOptimization.

Park, J.Y., Dougherty, T., Fritz, H., Nagy, Z., 2019. LightLearn: An adaptive and occupant centered controller for lighting based on reinforcement learning. Build Environ 147, 397–414. https://doi.org/10.1016/j.buildenv.2018.10.028

Pontes, F.J., Amorim, G.F., Balestrassi, P.P., Paiva, A.P., Ferreira, J.R., 2016. Design of experiments and focused grid search for neural network parameter optimization. Neurocomputing 186, 22–34. https://doi.org/10.1016/J.NEUCOM.2015.12.061

Potočnik, J., Košir, M., 2022. ASSESSMENT OF MULTISPECTRAL SIMULATION TOOLS FOR THE EVALUATION OF THE CIRCADIAN LUMINOUS ENVIRONMENT. Gradbeni vestnik 111–125.

Potočnik, J., Košir, M., 2021. Influence of geometrical and optical building parameters on the circadian daylighting of an office. Journal of Building Engineering 42, 102402. https://doi.org/10.1016/j.jobe.2021.102402

Rea, M.S., Figueiro, M.G., Bierman, A., Bullough, J.D., 2010. Circadian light. J Circadian Rhythms 8. https://doi.org/10.1186/1740-3391-8-2/METRICS/

Rea, M.S., Figueiro, M.G., Bullough, J.D., Bierman, A., 2005. A model of phototransduction by the human circadian system. Brain Res Rev 50, 213–228. https://doi.org/10.1016/j.brainresrev.2005.07.002

Snoek, J., Larochelle, H., Adams, R.P., 2012. Practical Bayesian Optimization of Machine Learning Algorithms. Adv Neural Inf Process Syst 25.

Wu, C., Pan, H., Luo, Z., Liu, C., Huang, H., 2024. Multi-objective optimization of residential building energy consumption, daylighting, and thermal comfort based on BO-XGBoost-NSGA-II. Build Environ 254, 111386. https://doi.org/10.1016/J.BUILDENV.2024.111386

Xie, J., Omidfar Sawyer, A., 2021. A simplified open-loop control strategy for integrated shading and lighting systems using machine learning. https://doi.org/10.26868/25222708.2021.30629

Thermal Characterization of Single Greening Components and Green Roofs

Michaela Reim[1], Helmut Weinläder[1], Christian Weiglein[1], Werner Körner[1], Elias Wolfrath[1], Marvin Studtrucker[1], Michael Brütting[1] and Stephan Weismann[1]

[1] Center for Applied Energy Research e.V. (CAE), Würzburg (Germany)

Abstract

The aim of the project is to develop and evaluate measurement methods for the thermal characteristics of green roof and façade systems and their individual parts. These measurement methods provide a scientifically sound basis for the development of industrial standards for the physical characterization of such components and systems. A large number of measurements were carried out in the laboratory on plants, substrates and system structures to characterize their physical parameters, evaporation performance, effective thermal conductivity, heat capacity and heat transfer coefficient. In addition, various roof and façade greening systems were measured outdoors under real conditions. The results for green roof systems are presented in this paper.

Keywords: green roofs, thermal behavior, heat flux, evaporation, cooling, retention

1. Introduction

Green roofs improve the quality of stay and surroundings, balance the temperature in buildings and improve air quality in inner-city areas. In addition to these benefits, they also help to avoid heat islands and contribute to cooling the building in the summer months through shading and evaporation, furthermore there is an insulating effect in winter time.

The study from (Ketut Acwin Dwijendra et al., 2023) is based on simulations and compared the thermal performance of roof coverings in non-insulated and insulated buildings across climates in Medan, Indonesia; Najaf, Iraq; and Moscow, Russia. Green roofs significantly reduce cooling loads in hot humid environments, cutting energy demand by 31 %, and lower heating loads by up to 71 % due to increased thermal resistance. Green roofs are less effective in dry climates. Insulation reduces energy consumption for cooling but increases air conditioning operation at night.

A very good overview of "The effectiveness of green roofs in reducing building energy consumptions across different climates" is provided by the literature study by Bevilacqua (Bevilacqua, 2021) with a summary of 121 literature sources. Besir (Besir and Cuce, 2018) provides a comprehensive review of roof and façade greening with 157 literature sources. For mediterranean climates, Koroxenidis (Koroxenidis and Theodosiou, 2021) carries out a comprehensive energy demand analysis, the results of which are incorporated into an environmental life cycle analysis and an economic life cycle analysis in order to compare and evaluate two different green roofs with a conventional roof. In a study by Yang (Yang et al., 2021), measurements of a green roof at the Onondaga County Convention Center in Syracuse (USA) for both summer and winter conditions are compared with simulations which consider both energy and water balancing to describe the thermal dynamic behaviour of the green roof. Bevilacqua (Bevilacqua et al., 2020) calculates the temperatures and heat flows of an extensive green roof on a real building at the University of Calabria (Italy) using the transient dynamic code TRNSYS and compares these results with real experimental data from 2016 and 2017.The measurements of the year-round energy balance of an existing green roof and an ungreened reference roof in Italy are compared with simulations using a Finite Element Model (FEM) code for obtaining equivalent thermophysical properties (Guattari et al., 2020). In a living laboratory in Italy, lightweight extensive green roof for building renovation is being investigated for different roof orientations and sky orientations for the summer case (Salvalai et al., 2023). Schade (Schade et al., 2021) measured the performance of a green roof compared with a black roof on a highly insulated building in a subarctic climate in Kiruna, Sweden. Yildirim (Yıldırım et al., 2023) measures the temperature curves over a year for three differently planted roof structures on the island of Cyprus in Nicosia (TRNC). Richter and Dickhaut (Richter and Dickhaut, 2023) investigated various blue-green roofs in Hamburg and compared the hydrological effectiveness of retention roofs with extensive green roofs without rainwater retention and established the positive effect on both the vegetation and the evaporation

© 2024. The Authors. Published by International Solar Energy Society
Selection and/or peer review under responsibility of Scientific Committee
10.18086/eurosun.2024.01.11 Available at http://proceedings.ises.org

capacity.

Previous studies of green roofs and façades have mostly been based on individual cases only. In order to move away from individual case studies or simulations and to be able to make a comprehensive statement about the thermal effect of green roofs and façades on buildings, the U-green project was launched. As part of the public-funded research project U-green, commercially available roof and façade greening systems are systematized into classes and both the individual components and the overall systems are thermally characterized. The project contributes to the holistic recording of all thermal effects of greening systems. In particular, the dynamic thermal behavior of façade and roof greening systems is to be considered. This opens up the possibility of reliably determining the thermal insulation effect and evaporative cooling performance of greening components and systems. The transpiration performance of different plants and the stationary and dynamic thermal behavior of green roofs and façades are also analyzed. Overall, this results in a register of measurement data that is published online without barriers and thus made freely accessible to the interested public.

For this purpose, a large number of different laboratory measurements as well as measurements in the field are carried out. This paper presents results of various laboratory measurements on substrates for green roofs and, in addition, outdoor measurements on six different roof structures.

2. Laboratory Measurements

2.1 Plant transpiration

In order to ensure a holistic recording of the thermal processes in the various greening systems and to establish a comprehensive data basis, we measured the transpiration rate of a number of different plants under defined conditions in a climate chamber. For this purpose, the different plants were each placed in three pots on a scale in the climate chamber with three lamps, whose spectrum is specially designed for plants, type DL2 from RVG LICHT. The substrate was covered with foil so that only the transpiration of the plants themselves was determined. The temperature was set to 25 °C, the humidity to 50 % and the illumination intensity to 70 kLux (center area). The measurements were taken under water saturation. The measurement setup is shown in Figure 1.

Fig. 1: Measurement setup in the climate chamber to determine the transpiration of different plants. The plants were placed on a scale and illuminated with three lamps, whose spectrum is specially designed for plants, type DL2 from RVG LICHT.

Figure 2 shows the transpiration rates of the plants used in the green roof systems for the outdoor measurements (see section 3).

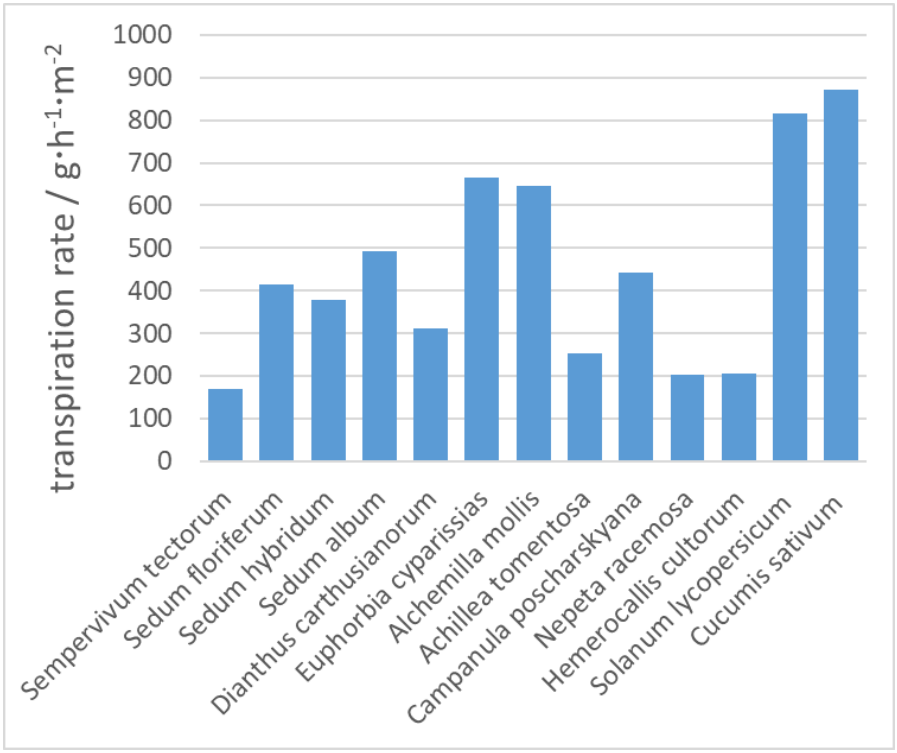

Fig. 2: Measured transpiration rate per ground area of different plants typically used in the green roof systems.

2.2 Moisture-dependent heat capacity and thermal conductivity of substrates for greening systems

In addition, the heat capacity and thermal conductivity of different substrates were measured as a function of water content.

The resulting heat capacity and effective thermal conductivity of three different roof substrates as a function of water content are shown in Figure 3. The measurements show the typical linear increase in heat capacity with increasing water content. The effective thermal conductivities show the typical S-shaped curves with a slow increase for low water contents, an extensive linear range, and a saturation range for high water contents. Measurement data for the Optigrün substrate are still pending. The substrates are used in the green roof systems for the outdoor measurements.

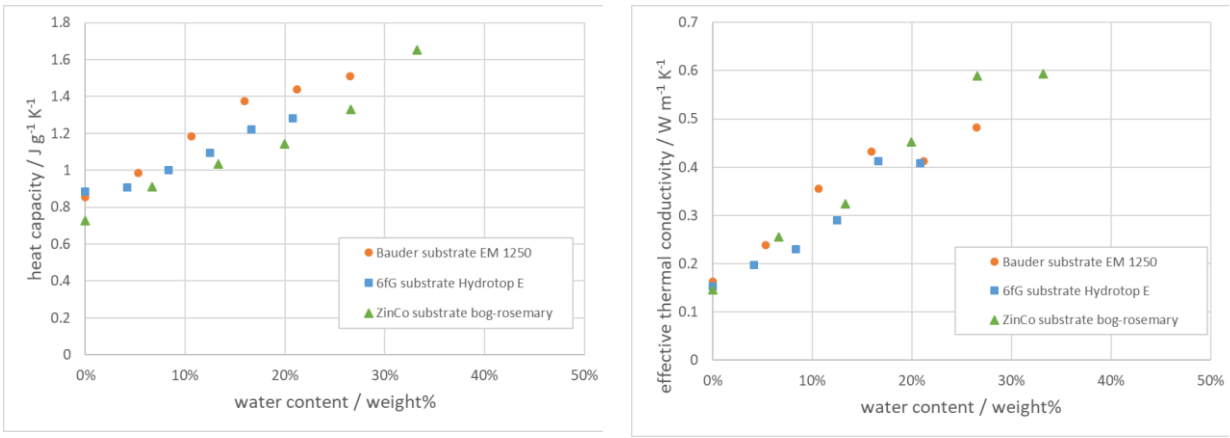

Fig. 3: Thermal heat capacity and effective thermal conductivity as a function of water content for three different green roof substrates: Bauder substrate EM 1250; 6 fürs Grün substrate Hydrotop E; ZinCo substrate bog-rosemary.

3. Outdoor Measurements

3.1 Measurement setup

Six different roof structures were installed in the open field next to the CAE institute building in Würzburg (Germany). Each roof structure is located in an inner box with an area of 120 cm x 100 cm, which is surrounded by a thermally insulated and weatherproof outer box for thermal separation and weather protection. The inner box is placed on load cells to record the evapotranspiration rate. The area below the inner box is temperature-controlled and reproduces the conditions that would occur in a room below the roof structure. Various sensors measure the temperatures T and humidity Φ_{soil} at different points in the roof structure as well as the heat flow Φ_q directly into the simulated room under the roof structure. In addition, the amount of water flowing off that cannot be completely absorbed by the substrate is measured. The weather data (air temperature and humidity, solar radiation, atmospheric longwave radiation, wind direction and speed, and amount of rain) are recorded at the weather station at CAE. The schematic measurement setup is shown in Figure 4.

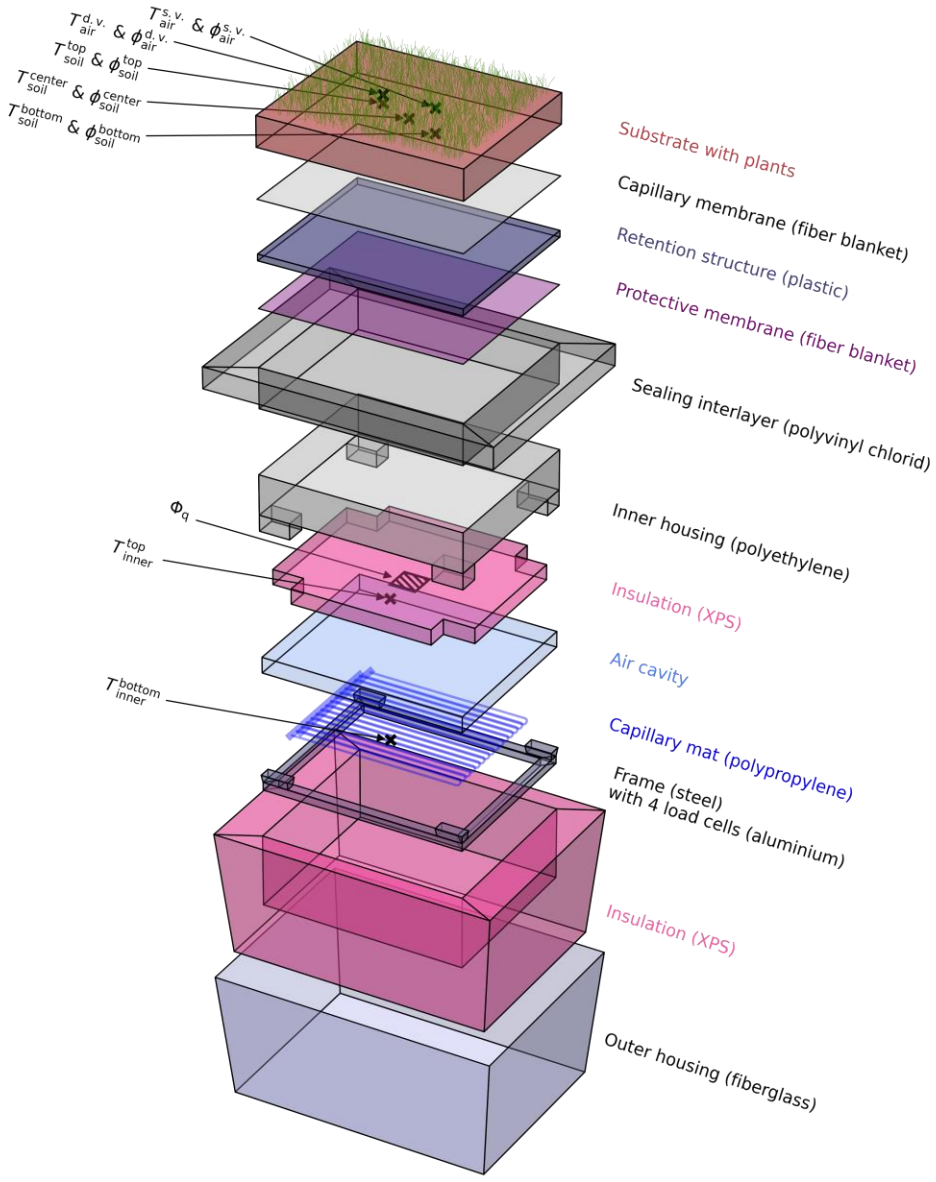

Fig. 4: Exploded view of the outdoor measurement setup for the roof constructions. Various sensors are placed at different points in the roof structure, temperature T, humidity Φ_{soil} and the heat flow Φ_q.

A gravel roof with a fill thickness of 6 cm is chosen as a reference field. Five green roof structures according to Table 1 were also installed. A picture of the roof systems is shown in Figure 5.

Tab. 1*: Planting list of green roof systems for outdoor measurements.*

Name	**System manufacturer**	**Plants**
Extensive 6 cm	6 fürs Grün GmbH, Germany	Sempervivum tectorum Sedum floriferum `Weihenstephaner Gold` Sedum hybridum `Immergrünchen` Sedum album `Coral Carpet`
Extensive 10 cm no retention	Paul Bauder GmbH & Co. KG, Germany	Sedum floriferum `Weihenstephaner Gold` Sedum album `Coral Carpet` Dianthus carthusianorum Euphorbia cyparissias
Extensive 10 cm plus 4 cm retention	Paul Bauder GmbH & Co. KG, Germany	Sedum floriferum `Weihenstephaner Gold` Sedum album `Coral Carpet` Dianthus carthusianorum Euphorbia cyparissias
Intensive 20 cm plus 7.5 cm retention	Optigrün international AG, Germany	Summer: Alchemilla mollis Achillea tomentosa Nepeta racemosa `Senior` Hemerocallis cultorum `Stella d´oro` Winter: Alchemilla mollis Campanula poscharskyana Nepeta racemosa `Senior` Hemerocallis cultorum `Stella d´oro`
Intensive 25 cm plus 4 cm retention	ZinCo GmbH, Germany	Summer: Solanum lycopersicum Cucumis sativum Hemerocallis cultorum `Stella d`oro` Winter: Alchemilla mollis Campanula poscharskyana Nepeta racemosa `Senior` Hemerocallis cultorum `Stella d`oro`

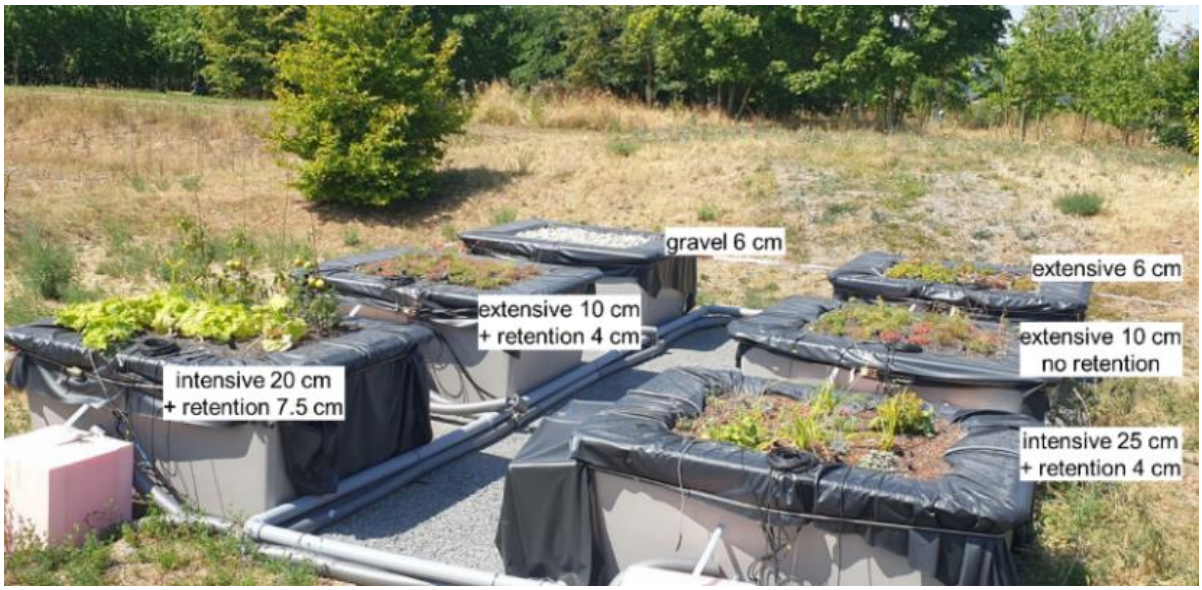

Fig. 5: External measurement setup for five different green roof structures and a reference field (6 cm gravel) on July 19, 2023.

The area under each roof construction is kept at constant temperature by a thermostat via capillary tube mats. The results for the heat flow into the simulated room below the system are presented for both a summer and a winter period. Additionally, water inflow and outflow as well as the amount of rain and the amount of evapotranspiration from the superstructure were recorded.

3.2 Summer measurements of green roof systems

The planting was carried out on June 21, 2023 by the project partner Bavarian State Institute for Viticulture and Horticulture (LWG) located in Veitshöchheim (Germany) and was individually adapted for the different structures. The substrate also differed for the individual structures, as each manufacturer used his own substrate (see Table 1). Only the two extensive setups with a substrate thickness of 10 cm use identical substrates. The superstructures exhibit systematic differences, but thus reflect the behavior of the manufacturers' original systems. Four of the green roof systems are not watered automatically, but are watered manually if necessary, e.g. during long periods of drought. Only for the system “Intensive 25 cm with 4 cm retention” a drip hose was inserted into the substrate and the automatic watering system prepared. However, the automatic watering system was off during the measurement period described here.

The green roof structures are insulated at the bottom with a 10 cm thick layer of extruded polystyrene (XPS), which corresponds to a U-value of 0.35 $W \cdot m^{-2} \cdot K^{-1}$. The superstructures therefore correspond to a moderately to well insulated roof structure.

The measurements were evaluated for the summer period from 2023/08/17 - 2023/09/24, with the “room” temperature set to 24 °C. During this period, there were two dry hot spells with daily maximum temperatures sometimes well above 30 °C (2023/08/17 – 2023/08/24 and 2023/09/4 – 2023/09/17) and two cooler periods with some precipitation (2023/08/25 – 202309/03 and 2023/09/18 – 2023/09/24).

The heat flows on the bottom of the roof towards the "room" were measured using a heat flux plate, as these directly reflect the heat inputs and losses through the roof structure. In addition, the evapotranspiration performance of the systems was recorded by weighting. The data from the load cells was averaged hourly and the difference from midnight to midnight was then determined for each day. Days with rain were usually not taken into account, as unreasonable values often resulted despite recording the rain and runoff volume. Furthermore, the soil moisture was analyzed and correlated with the evapotranspiration quantities and heat inputs. For this purpose, three soil moisture sensors were installed at a depth of 5 cm and their values were averaged. The results are shown in the following figures.

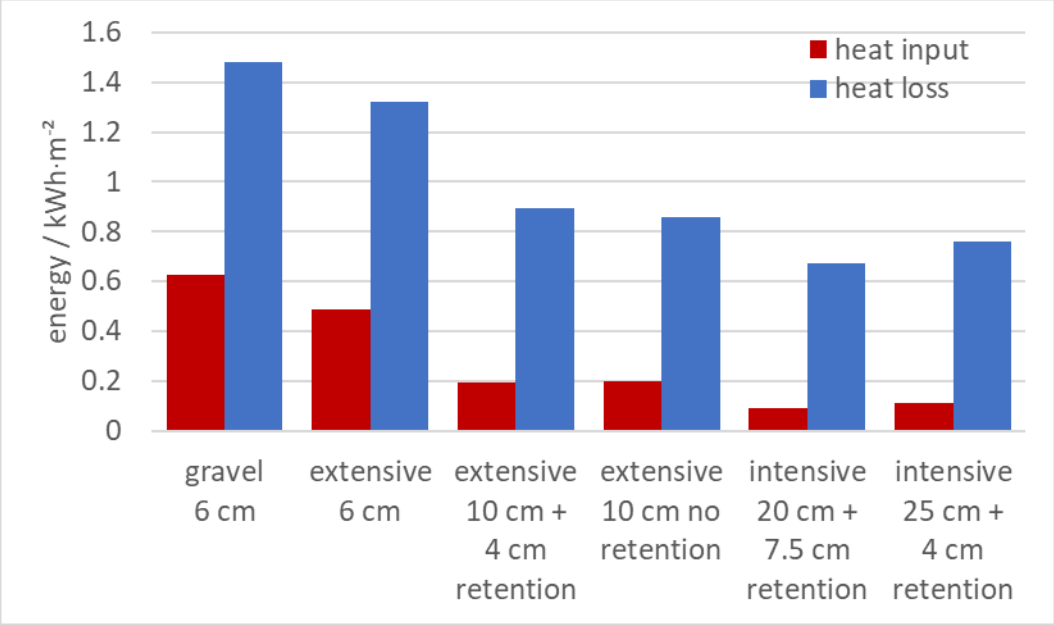

Fig. 6: Total heat inputs and losses of the green roof systems for the measurement period from August 17 to September 24, 2023.

The total heat input can be drastically reduced in some cases by the green roof systems (see Figure 6). The thicker the substrate layer of the structure, the greater the reduction. A retention layer also has a positive effect, but this effect appears to be only slightly pronounced.

In addition to heat input, green roof systems also reduce heat losses, which makes it more difficult for the roof structure to cool down the room below, e.g. on clear summer nights. Overall, the heat losses predominate during the measurement period, so that the net balance of the green roof systems is worse than that of the reference roof. Green roof systems thus reduce cooling load peaks, but can possibly lead to a higher base load if there is no option for night ventilation. However, the exact impact of this effect on the room below and its cooling balance can only be determined using a more precise dynamic analysis (thermal building simulation).

Figure 7 shows the relative daily heat input of the six roof structures for a hot and dry week without any rain in August 2023. The data for the reference roof are set to 100 %. When the substrate dries out during the first five days, the heat input reduction potential of the green roofs is strongly reduced. This occurs especially at the thinner green roof constructions with the 6 cm extensive green roof having even higher heat inputs than the reference roof from August 19. The soil moisture of this green roof construction drops to values close to 0 % (not shown in the graph), meaning that the substrate dries out almost completely. After the soil moisture is raised again by manual irrigation on August 22, the heat inputs then drop again to values that are significantly below those of the reference roof. A sufficient cooling effect of green roof systems can therefore only be achieved with sufficient soil moisture.

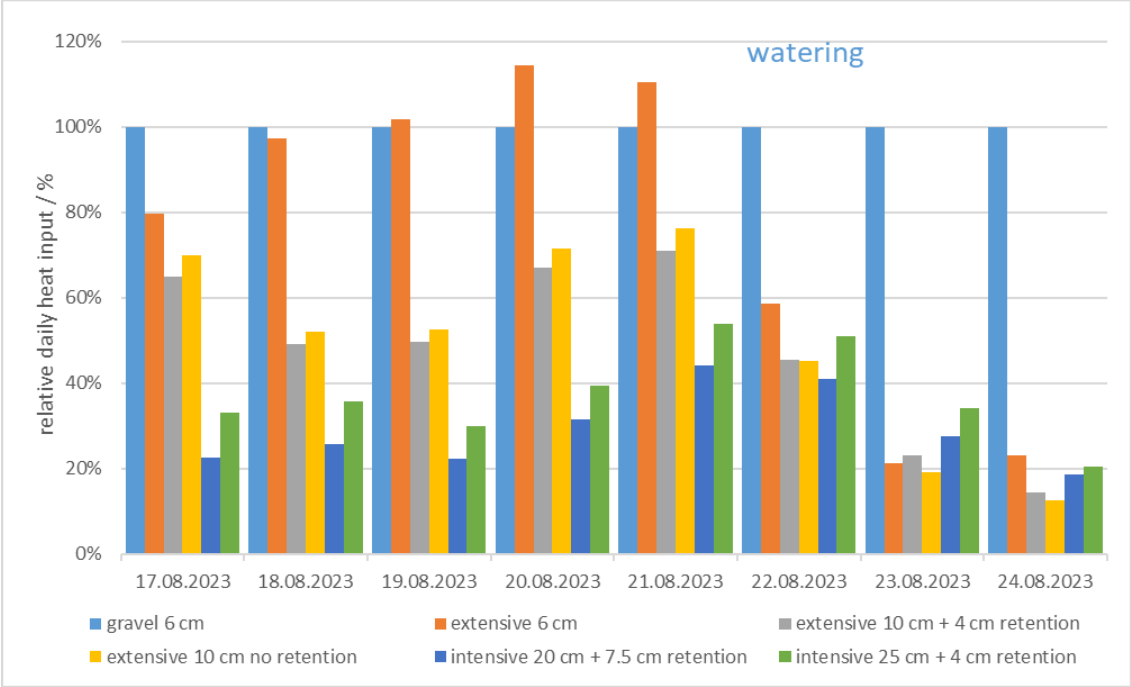

Fig. 7: Daily heat input relative to the reference field with 6 cm gravel for five different green roof structures.

The average soil moisture at 5 cm depth of the different green roof structures for the entire measurement period is shown in Figure 8. The structure with a substrate thickness of only 6 cm shows the lowest average soil moisture and the greatest fluctuations. A retention volume favors a higher average soil moisture and a higher minimum soil moisture (cf. the two structures with 10 cm substrate thickness). A thicker substrate layer also has a positive effect on maintaining soil moisture during dry periods, although this effect only becomes visible after longer periods. While the roof structure with a substrate thickness of 6 cm dries out completely during this period and the structures with a substrate thickness of 10 cm fall to values below 40 %, the average soil moisture in the thicker intensive structures remains at values of 60 - 70 %. The higher soil moisture levels are always found in the two intensive structures with 20 cm substrate thickness and 7.5 cm retention layer. The thickness of the retention layer therefore appears to have a greater influence than the substrate thickness.

The mean daily evapotranspiration of the roof constructions is shown in Figure 9.

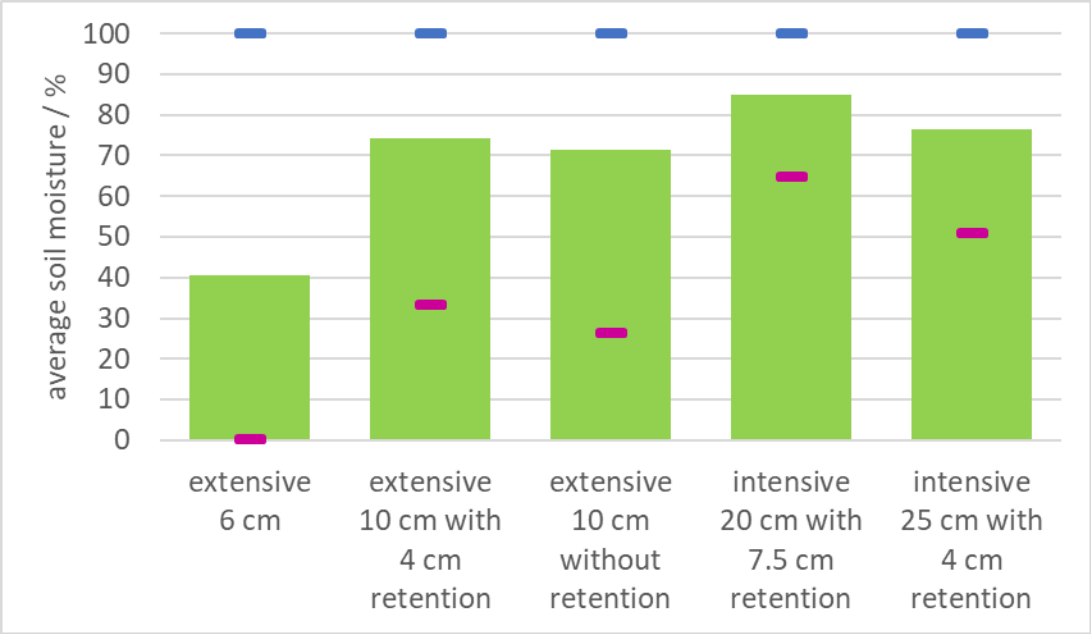

Figure 8: Measured mean values of soil moisture with minimum (pink bars) and maximum (blue bars) values at a soil depth of 5 cm for the green roof systems for the measurement period from August 17 to September 24, 2023.

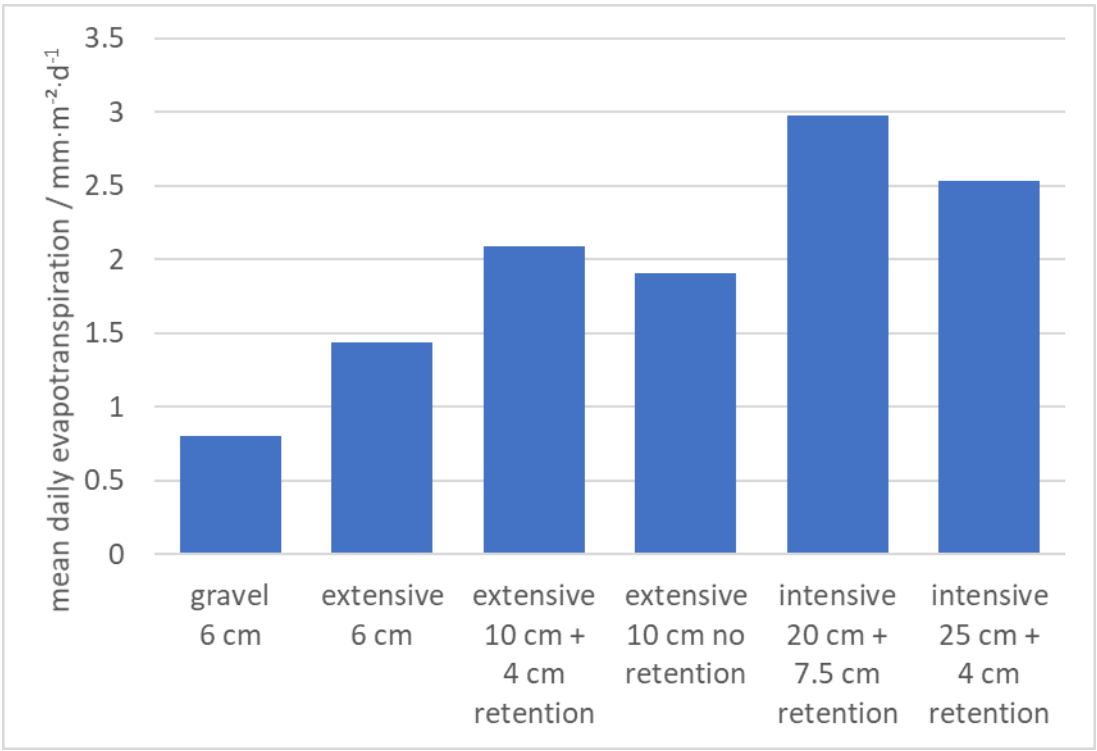

Figure 9: Measured mean daily evapotranspiration of the green roof systems for the measurement period from August 17 to September 24, 2023.

There is a clear correlation between the amount of evapotranspiration, which significantly determines the cooling effect of the roof structures and is directly associated with the reduction in heat input (see Figure 7), and the substrate thickness. The superstructure with a substrate thickness of 6 cm evapotranspirates approx. 1.5 $mm \cdot m^{-2} \cdot d^{-1}$, the superstructures with 10 cm around 2 $mm \cdot m^{-2} \cdot d^{-1}$, and the superstructures with 20 cm or 25 cm 2.5 – 3 $mm \cdot m^{-2} \cdot d^{-1}$. The positive influence of the retention layer is also clearly recognizable. It is interesting to note that a certain amount of evaporation can also be observed on the reference roof with 6 cm of gravel.

Thermography was used to determine how the different structures affect the surface temperatures and therefore the microclimate in the surrounding area. Although the surface temperature is also measured using temperature sensors, these were often exposed to the sun during the measurement period due to the still relatively low growth density of the vegetation. The thermographic images are shown in Figure 10.

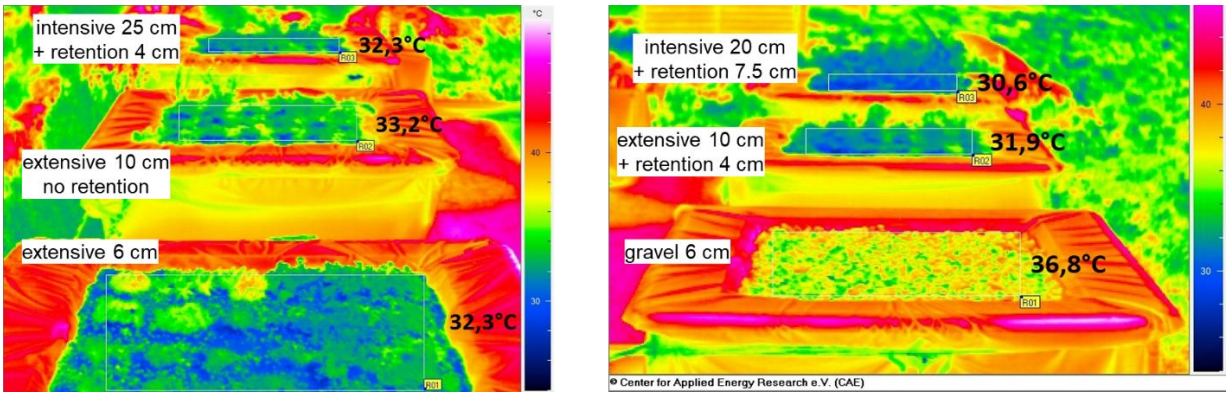

Fig. 10: Thermographic images of the six roof structures shortly after installation.

Although the plant growth directly after planting is still low, the green roof structures show a reduction in surface temperatures of 3 – 6 °C compared to the reference roof with gravel.

3.3 Winter measurements of green roof systems

Before the start of the measurements in winter, the plants in the two intensive green roof structures were partially replaced by the LWG so both fields now have identical plants, but still have different substrates.

The winter measurements were analyzed for the period from October 15, 2023 to April 04, 2024, with the thermostat temperature set to 21 °C. This period was characterized by strong temperature fluctuations and included periods with very cold, but also relatively warm days for winter conditions. Until the beginning of January, the weather was very humid with almost daily precipitation. It was not until January 5, 2024 that a dry period began with average daily temperatures dropping below freezing for several days.

Heat inputs did not play a role or were not present in the period shown. The evapotranspiration performance of the systems was not analysed over the winter, as the measured data often did not show meaningful values due to the persistent rain. The soil moisture was analysed, whereby some of the soil moisture sensors were repositioned before the start of the winter measurements. In the extensive roof structures with 6 cm and 10 cm, all three soil moisture sensors remained at a depth of 5 cm; in the roof structure with 20 cm, one sensor was relocated to a depth of 10 cm; in the roof structure with 25 cm, one sensor was relocated to a depth of 10 cm and another to a depth of 15 cm. In the two thicker intensive structures, it was thus possible to record a moisture profile over the soil depth (not part of this paper). The results are shown in the following figures. The relative heat losses in percent related to the reference roof are shown in Figure 11.

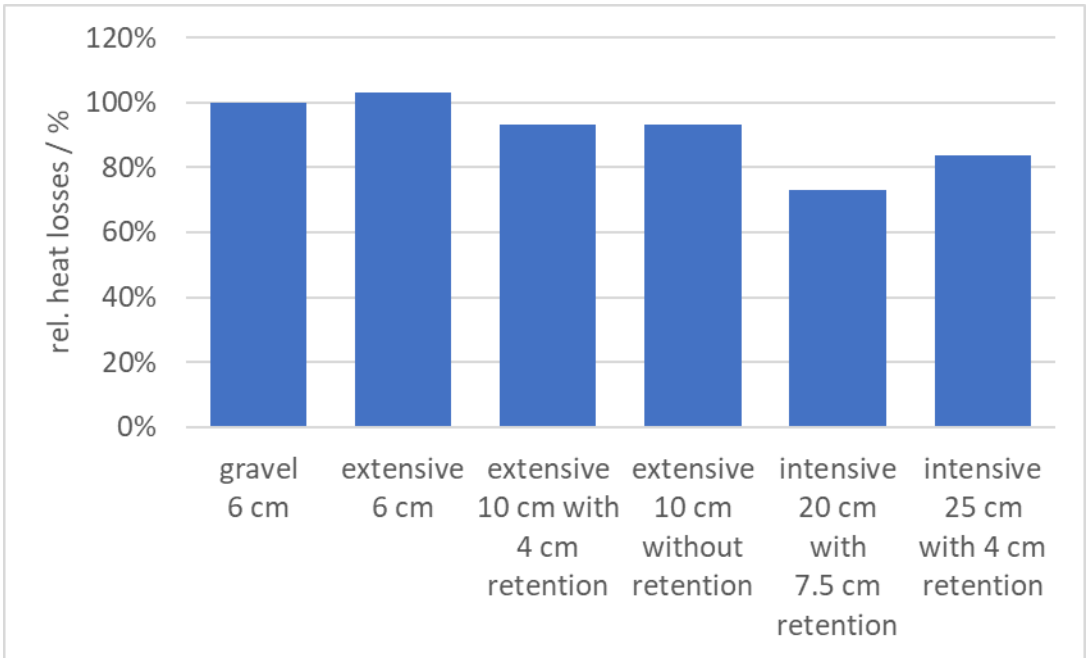

Figure 11: Measured relative heat losses of the green roof systems related to the heat input of the reference roof (set to 100 %) for the measurement period from 2023/10/15 – 2024/04/04.

Due to slightly different internal temperatures of the measurement boxes, the heat flows for the evaluation of the winter measurements were corrected using the average temperature differences between the measurement boxes and the outside air. The results show that certain heat loss reductions can be achieved with the thicker green roof structures. These are 7 % for the two structures with 10 cm substrate thickness, 27 % for the structure with 20 cm substrate thickness and 7.5 cm retention, and 16 % for the structure with 25 cm substrate thickness and 4 cm retention. The structure with a substrate thickness of 6 cm shows a slight increase in heat losses of 3 % compared to the reference roof. With an appropriate structure, green roofs can therefore contribute to a significant reduction in heating demand in winter. In residential buildings, the proportion of heat loss via the roof is generally between 15 % and 30 %. With an optimised green roof, savings in heating consumption by installing a green roof of approx. 3 – 7 % should therefore be achievable.

The soil moisture data show relatively high mean values, as was to be expected due to the persistent precipitation during the measurement period. However, the minimum values, some of which are surprisingly low, are striking. This is due to the start and mid times of the measurement period. At the beginning of the measurements, the ground was still dry from the summer, while in the mid of the measurement period the roof structures were probably partially affected by ground frost, so that the moisture sensors no longer showed a signal. Some moisture sensors showed strange signals even after the frost period, therefore the soil moisture was only evaluated from October 20, 2023 to January 7, 2024 (see Figure 12). The data show the expected high mean values of around 80 % for the structure with a substrate thickness of 6 cm and more than 90 % for all other systems. The minimum values reflect the water storage capacity of the superstructures and are 16 % for the thin superstructure, 54 % and 62 % for the other two extensive superstructures and 62 % and 68 % for the thicker intensive superstructures.

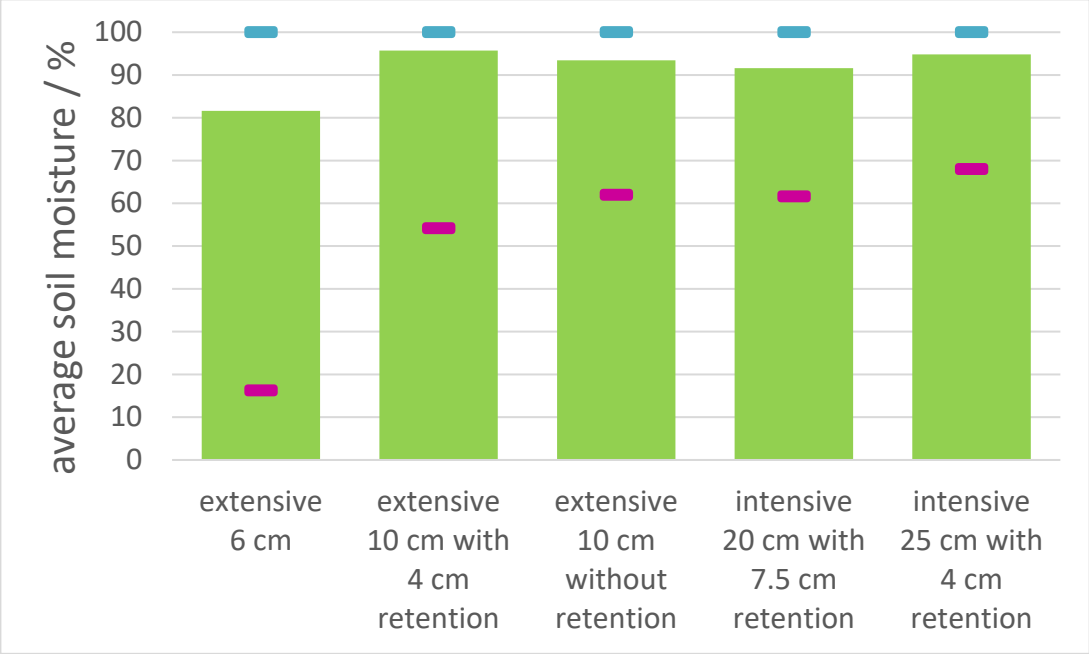

Figure 12: Measured mean values of soil moisture with minimum (red bars) and maximum (blue bars) values at a soil depth of 5 cm for the green roof systems for the shortened measurement period from October 20, 2023 to January 7, 2024.

4. Conclusions

Measurements taken outdoors in the summer months in the temperate Central European climate zone (Würzburg, Germany) show that green roofs have a cooling effect if the substrate moisture is sufficient. Green roof structures with a higher substrate thickness with additional retention exhibit lower fluctuations in moisture content and therefore also in the cooling effect. Retention volumes in green roof structures are not only suitable for storing rainwater and intercepting heavy rainfall events, but are also able to bridge long periods of drought and increase the evapotranspiration capacity of the overall system. By reducing the maximum surface temperatures, green roofs have a positive effect on the microclimate in city centers. On the building level, a green roof means reduced heat input and therefore lower cooling load peaks during the day, but the green roof also reduces night-time cooling via the roof.

During the winter period, green roof structures with a substrate thickness of 10 cm or more reduce heat losses through the roof. We measured maximum reductions in heat losses of 27 % for an intensive green roof with 20 cm substrate plus 7.5 cm retention. Thinner green roof constructions show no energy savings potential or can even increase the heat losses slightly, as was measured for an extensive green roof with 6 cm substrate and an increase in heat losses of 3 % compared to a reference roof with 6 cm gravel.

Acknowledgements

The work in the project “U-green - Building physics assessment of green façade and green roofs“ is supported by the Federal Ministry of Economic Affairs and Climate Action (BMWK), based on a resolution of the German Parliament. FKZ 03EN1045A.

We also like to thank our project partners Bayerische Landesanstalt für Weinbau und Gartenbau Veitshöchheim (LWG), especially Dr. Nadja Stingl-Sinn, and Technische Universität Berlin (TUB), Dr. Karin Hofmann and Dr. Thomas Nehls, for the great co-working and also Bundesverband Gebäudegrün (BuGG) and the Bayerische Architektenkammer (ByAk).

We would especially like to thank our colleague Leslie Ullerich for her tireless commitment to the U-green project and her excellent care and support of all the plants.

The roof systems were supplied without any charge by

- 6 fürs Grün GmbH, Kanalstr. 2, 66130 Saarbrücken, Germany, Handelsregister: HRB 11753
- Paul Bauder GmbH & Co. KG, Korntaler Landstraße 63, 70499 Stuttgart, Germany, Handelsregister: HRA 2178
- Optigrün international AG, Am Birkenstock 15-19, 72505 Krauchenwies-Göggingen, Germany, Handelsregister: HRB 711009
- ZinCo GmbH, Lise-Meitner-Straße 2, 72622 Nürtingen, Germany, Handelsregister: HRB 789793

References

Besir, A.B., Cuce, E., 2018. Green roofs and facades: A comprehensive review. Renewable and Sustainable Energy Reviews 82, 915-939.

Bevilacqua, P., 2021. The effectiveness of green roofs in reducing building energy consumptions across different climates. A summary of literature results. Renewable and Sustainable Energy Reviews 151, 111523.

Bevilacqua, P., Bruno, R., Arcuri, N., 2020. Green roofs in a Mediterranean climate: energy performances based on in-situ experimental data. Renewable Energy 152, 1414-1430.

Guattari, C., Evangelisti, L., Asdrubali, F., De Lieto Vollaro, R., 2020. Experimental Evaluation and Numerical Simulation of the Thermal Performance of a Green Roof. Applied Sciences 10(5), 1767.

Ketut Acwin Dwijendra, N., Muda, I., Milanes, C.B., Bharath Kumar, N., Abosinnee, A.S., Akhmadeev, R., 2023. How do green roofs affect per capita energy consumption in residential buildings under various climate conditions? Sustainable Energy Technologies and Assessments 56, 103127.

Koroxenidis, E., Theodosiou, T., 2021. Comparative environmental and economic evaluation of green roofs under Mediterranean climate conditions – Extensive green roofs a potentially preferable solution. Journal of Cleaner Production 311, 127563.

Richter, M., Dickhaut, W., 2023. Long-Term Performance of Blue-Green Roof Systems—Results of a Building-Scale Monitoring Study in Hamburg, Germany. Water 15(15), 2806.

Salvalai, G., Marrone, G., Maria Sesana, M., Imperadori, M., 2023. Lightweight extensive green roof for building renovation: Summer performance analysis and application in a living laboratory. Energy and Buildings 298, 113589.

Schade, J., Lidelöw, S., Lönnqvist, J., 2021. The thermal performance of a green roof on a highly insulated building

in a sub-arctic climate. Energy and Buildings 241, 110961.

Yang, Y., Davidson, C.I., Zhang, J., 2021. Evaluation of thermal performance of green roofs via field measurements and hygrothermal simulations. Energy and Buildings 237, 110800.

Yıldırım, S., Özburak, Ç., Özden, Ö., 2023. Green Roofs, Vegetation Types, Impact on the Thermal Effectiveness: An Experimental Study in Cyprus. Sustainability 15(3), 2807.

A Review of the Coherence of Strategies to Optimize Photovoltaic Systems within the Built Environment in Nordic Countries

Santiago Valencia G.[1,2], Xingxing Zhang[1,2], Joakim Munkhammar[3], Andreas Theocharis[4]

[1] Department of Energy and Construction Engineering, Dalarna University, 79188 Falun (Sweden)

[2] Sustainable Energy Research Centre, Dalarna University, 79188 Falun (Sweden)

[3] Built Environment Energy Systems Group (BEESG), Division of Civil Engineering and Built Environment, Department of Civil and Industrial Engineering, Uppsala University, SE-751 04, Uppsala (Sweden)

[4] Karlstad University, Engineering and Physics Department, 65635 Karlstad (Sweden)

Abstract

Climate change is often cited in renewable energy research by stating motives in environmental, technical, social, and economic categories, which can be linked to metrics that are called key performance indicators (KPIs). Furthermore, these indicators can be set as a target for an optimization model and become optimization objectives. This paper critically reviews the motives, optimization objectives, and KPIs selected in studies of solar photovoltaic (PV) systems with energy storage within the built environment in Nordic countries. A subset of 36 scientific articles, sorted as relevant from a selection of 349, was analyzed to make the review. The results reveal that even when environmental motives are expressed by 75% of the authors, only 8% focus on optimizing with environmental indicators. This imbalance suggests that the environmental problems intended to be addressed with the optimization model could be left unchanged or even exacerbated by the strategic choices made during the energy modeling. In addition to this, there is a lack of consistency in the way the different indicators are calculated, especially for environmental indicators where the impacts of materials and manufacturing were not included. Furthermore, in the economic and technical categories, the economic volatility and peak power motives do not have a matching indicator within the articles analyzed. Therefore, it is recommended to conduct comprehensive optimization studies that align with carefully considered motives.

Keywords: photovoltaic, optimization, key performance indicators, Nordic

1. Introduction

The decision to invest in renewable energy technologies, including PV, has different motives behind it. According to Bergek and Mignon (2017) the most significant factors are environmental concerns, interest in technology, access to renewable resources, and economic benefits. In their study, the survey participants assessed the environmental benefit with the highest importance. Similarly, the individual motives and decision paths of residential energy supply systems have been studied by Matschegg et al. (2023). Their results show that more than 90% of survey respondents had technical motives. Environmental performance was also highly valued, whereas financial aspects were considered less important. To aim for motives, they can be related to indicators which can be set as targets for performance.

A useful way to improve the performance of an energy system is to use optimization (Lund, 2018). An optimization process is used to identify the best possible solution to a mathematical problem (to determine the maximum or minimum value achievable for a function). This can be applied to both the design and operation of an energy system (Xu et al., 2020). During the design phase, it can determine the optimal capacities and configurations of various subsystems. In the operational phase, it coordinates energy flows between subsystems, such as PV and energy storage systems. A review of the optimization process in planning PV and battery systems was performed by Khezri et al. (2022), they focused on methods including the optimization function (objectives) and constraints. These are the variables selected to be part of the optimization method.

Other reviews of metrics for evaluating the performance of energy systems refer to key performance indicators (KPIs), a metric whose performance is evaluated regarding some objective (Costa et al., 2019). For example, a review

© 2024. The Authors. Published by International Solar Energy Society
Selection and/or peer review under responsibility of Scientific Committee
10.18086/eurosun.2024.01.12 Available at http://proceedings.ises.org

of KPIs for PV systems with storage was performed by (Kourkoumpas et al., 2018) and gives a detailed description of environmental and energy KPIs, grouped according to the interests of different stakeholders. One of their conclusions was the need for replicable and scalable environmental and energy performance indicators. Another review of the optimization of energy systems by Klemm and Wiese (2022) published a set of indicators for optimizing sustainable urban energy systems. In that study, the main conclusion is the recommendation of multi-criteria optimization approaches.

This set of decisions, which includes motives, optimization objectives, and KPIs can be considered a strategy for optimization. First, the motives are stated. Afterward, the optimization objectives and constraints are defined taking indicators that match the defined motives. Finally, the performance of the optimization process is assessed using KPIs. Despite existing literature on optimization strategies and KPIs for solar PV systems, there is a lack of reviews that standardize the process of defining motives, optimization objectives, and KPIs. Therefore, investigating the coherence between these strategic choices could enhance the effectiveness of results and better align them with stakeholders' interests. In this review, this set of choices made during the optimization process is thus termed the optimization strategic framework, as illustrated in Figure 1.

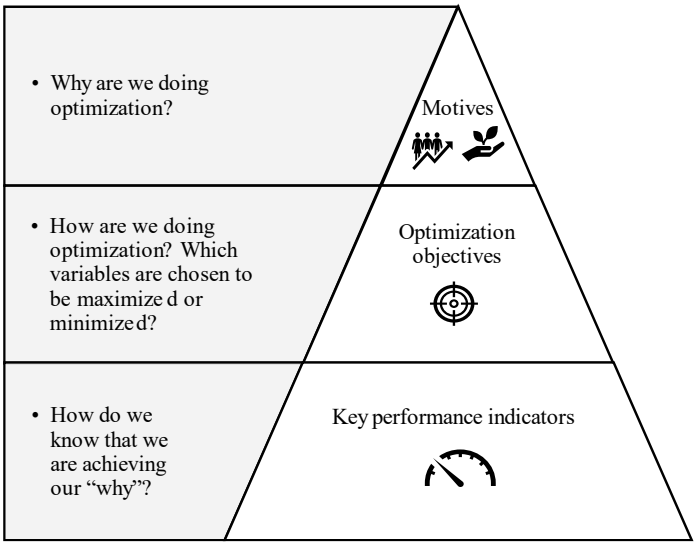

Figure 1. The proposed strategic framework.

The need for this framework is particularly evident in the context of solar PV systems within the built environment in the Nordic countries. Here, solar irradiation is low, and a building's energy consumption is relatively high during winter (Paatero and Lund, 2007). To reconcile this disparity the use of optimized energy systems equipped with storage capabilities is a possible solution (Lund, 2018). In consequence, this review analyzes the indicators and alignment between the motives, optimization objectives, and key performance indicators (KPIs) used in solar PV systems for the built environment within the Nordic countries by aiming to answer the following research questions:

- What indicators are being selected to be used as part of optimization models?
- What is the distribution of the selection of motives, optimization objectives, and KPIs among the environmental, technical, and economic categories?
- Are there matching indicators for the expressed motives?

The focus is on the coherence of the strategic framework presented previously. The analysis is divided into environmental, technical, and economic categories. In the first part, the distribution of choices for the different categories is shown. It is followed by a table with the categories found in each journal paper analyzed. Afterward, a general description of each of the categories of strategic framework plus the mathematic definition of a selection of the indicators found is shown. Finally, the paper discusses current limitations and possible future directions.

2. Method

The analysis uses collected and filtered peer-reviewed journal articles based on the following method. The search engines IEEE Xplore, Scopus, and Web of Science were used to gather scientific articles. The search string used is shown in Figure 2. These searches yielded a total of 349 journal articles. To filter the results, the relevance of each article was assessed by examining the abstract. Specifically, the articles were filtered for the following characteristics: optimization, PV system, built environment, energy storage, and Nordic locations studied. After the sorting process,

36 relevant scientific articles were selected. The graphic summary of the search, filtering, and sorting method is presented in Figure 2.

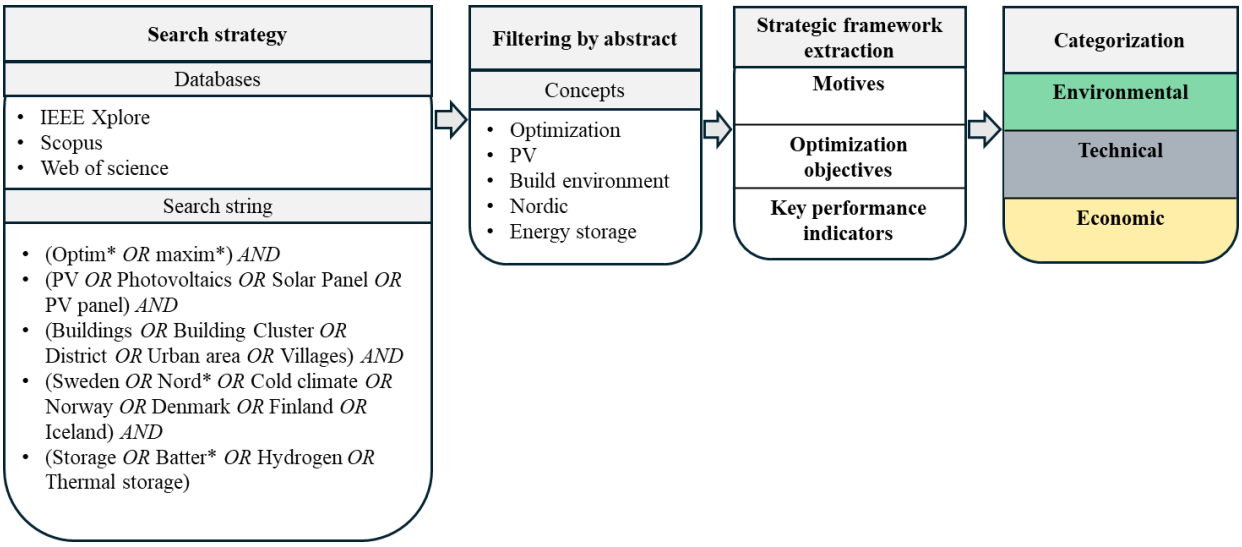

Figure 2. Method for the review.

The selected articles are analyzed based on their optimization strategic framework. Each feature from the strategic frameworks is extracted and assigned into environmental, technical, and economic categories. For this review, the motives refer to the collective goals mentioned by the authors and are extracted from the introduction section of the articles, the optimization objective is typically found in the methodology section and the KPIs are extracted from the results section. In addition, to give a general overview, the percentage of articles that chose a certain category is quantified and compared among the categories.

3. Results

3.1. General distribution of strategic choices per category: environmental, technical, and economic

Figure 3 presents the distribution of various categories across the strategic choices in the analyzed journal articles. Technical motives are prevalent, appearing in over 90% of the studies. Similarly, environmental motives are found in 75% of the articles. In contrast, economic motives are mentioned in less than half of the studies. When it comes to optimization objectives, most articles focus on economic variables, while a small fraction (8%) utilizes environmental optimization objectives. In terms of key performance indicators (KPIs), most scientific articles feature KPIs from the technical and economic categories. However, only 11% of the articles present their results using environmental indicators.

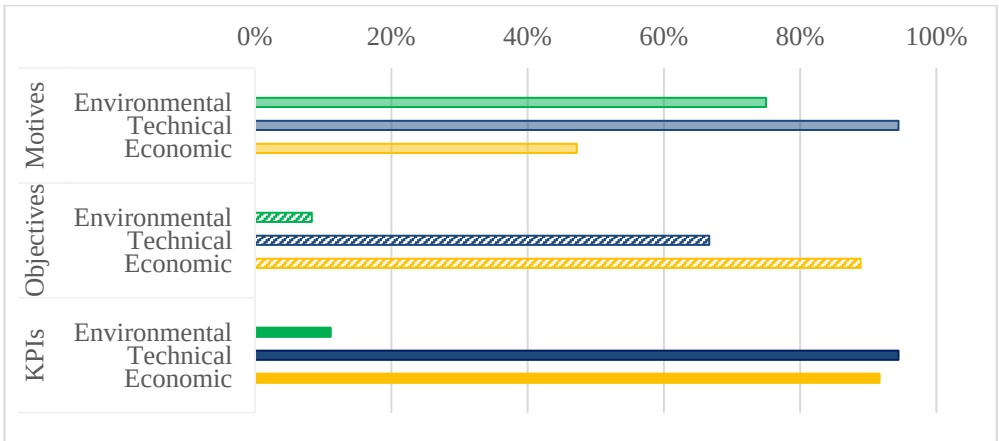

Figure 3. Percentage of articles distributed per strategic choice.

The strategic choices in an individual article are not exclusive to a single category. Table 1 shows that most articles simultaneously demonstrate motives from different categories. Motives as well as objectives from the three above-mentioned categories were studied by Kharseh and Wallbaum (2019). The same was found for the optimization

objectives. Environmental, technical, and economic objectives are set in multi-objective optimization models in two studies (Arabkoohsar et al., 2021b; Behzadi and Sadrizadeh, 2023). Similarly, multiple key performance indicators are commonly used in a single study. For example, the results in all environmental, technical, and economic indicators were shown to assess the performance of an optimization for a residential district (Yuan et al., 2022). The strategies used in these articles are complex and comprehensive, built up from multiple individual choices of motives and indicators.

Table 1. The strategic choices in the analyzed articles were distributed per category.

Reference	Environmental			Technical			Economic		
	Mot.	Obj.	KPI	Mot.	Obj.	KPI	Mot.	Obj.	KPI
(Salpakari et al., 2016) , (Hirvonen et al., 2018), (Rehman et al., 2018), (Perera et al., 2019),(Arabkoohsar et al., 2021a)	✓			✓	✓	✓		✓	✓
(Salpakari and Lund, 2016), (Hirvonen et al., 2017), (Hirvonen and Sirén, 2018), (Psimopoulos et al., 2019), (Huang et al., 2019) (Huang et al., 2019), (Mbuwir et al., 2020)				✓	✓	✓		✓	✓
(Nyholm et al., 2016)				✓	✓	✓			
(Nyholm et al., 2016),(Rehman et al., 2019), (Kharseh and Wallbaum, 2019), (Carli et al., 2020), (Srithapon and Månsson, 2023)	✓			✓	✓	✓	✓	✓	✓
(Kharseh and Wallbaum, 2017), (Huang et al., 2020), (Rikkas and Lahdelma, 2021), (Savolainen and Lahdelma, 2022), (Meriläinen, A. et al., 2023), (Meriläinen, Altti et al., 2023)	✓			✓		✓	✓	✓	✓
(Azaza and Wallin, 2017)	✓				✓	✓	✓	✓	✓
(Koskela, J. et al., 2019), (Hajiaghapour-Moghimi et al., 2023)	✓			✓			✓	✓	✓
(Andersen and Lindberg, 2021)	✓	✓		✓		✓		✓	✓
(Rabani et al., 2021), (Fachrizal et al., 2024)	✓			✓	✓	✓			
(Arabkoohsar et al., 2021b), (Behzadi and Sadrizadeh, 2023)	✓	✓	✓	✓	✓	✓	✓	✓	✓
(Fachrizal et al., 2024)	✓			✓		✓		✓	✓
(Goop et al., 2021)						✓	✓	✓	✓
(Huang et al., 2022)	✓			✓	✓	✓			✓
(Yuan et al., 2022)	✓		✓	✓	✓	✓		✓	✓
(Berg et al., 2024)			✓	✓		✓		✓	✓

3.2. Environmental Strategic Framework in the analyzed studies

The environmental category is mainly focused on climate change concerns. Broad expressions of motives, such as “Environmental issues” providing context for an energy-sharing study, are found in some articles (Huang et al.,

2022). Another instance of environmental motives is the potential reduction of "Greenhouse gas emissions of buildings by adopting renewable-based hybrid energy systems" (Savolainen and Lahdelma, 2022). A more specific and quantifiable motive is "Zero emission building" (Andersen and Lindberg, 2021). Moving on to the optimization objectives and constraints, all of them are related to climate change. All the environmental optimization objectives identified aim to minimize greenhouse gas emissions, such as the objective to minimize the direct emissions from a biomass boiler (Behzadi and Sadrizadeh, 2023). Climate change is also the focus of environmental constraints, with "Zero emission building" being selected for one of the models found (Andersen and Lindberg, 2021). In the same way, in the articles analyzed, the environmental KPIs only quantified the global warming potential. This consistency around global warming led to a closer analysis of the indicators.

A more detailed analysis of the environmental indicators in Table 2 reveals a variation regarding the scope of the quantified impacts. For instance, Equation 1 shows an indicator used to assess the global warming potential for a district hybrid energy optimization model that only includes direct emissions from a biomass boiler, even though the model has grid electricity. Another indicator estimates the "Carbon dioxide emission reduction rate" to compare two energy models, as shown in Equation 2. It accounts for the operation emissions from the grid electricity and the heat from the district heating network. In a solar energy system study, exported energy is considered negative emissions (see equation 4). Similarly, the emissions from the grid and district heating are estimated, as shown in (Yuan et al., 2022). However, unlike the two previously shown indicators, the estimation made for the grid had a variable emissions index with monthly resolution, see equation 5. Lastly, the total yearly equivalent greenhouse gas emissions are estimated to assess the performance of an operation cost optimization model, as shown in (Berg et al., 2024). In this study, the emissions from grid-imported electricity are estimated with an hourly resolution (see equation 6). In conclusion, all the models aim to estimate the global warming potential Despite this, the scope and resolution are different.

Table 2. The mathematical definitions for environmental indicators are shown.

Reference	Indicator name	Mathematical definition
(Behzadi and Sadrizadeh, 2023)	"CEI (CO_2 emission index)"	$CEI = \frac{CO_2\ emitted\ to\ the\ atmosphere}{\dot{E}_{Solar} + \dot{C}_{Chiller} + \dot{Q}_{Space\ heating} + \dot{Q}_{Hot\ water}}$ (eq. 1)
		CEI: Carbon Emission Index (kg/MWh) CO_2 emitted to the atmosphere: "Considering the carbon dioxide emitted from the biomass heater"(kg) $\dot{E}_{Solar}$: Electricity generated via photovoltaic thermal Panels (MWh) $\dot{C}_{Chiller}$: Cooling generated via absorption chiller (MWh) $\dot{Q}_{Space\ heating}$: Heating supplied for space heating (MWh) $\dot{Q}_{Hot\ water}$: Heating for domestic hot water (MWh)
(Arabkoohsar et al., 2021b)	"Carbon dioxide emission reduction Rate"	$CDERR = \frac{CDE^{SP} - CDESolar}{CDE^{SP}} \times 100$ (eq. 2)
		$\mathrm{CDE^{SP}} = \dot{\mathrm{E}}_{\mathrm{Demand}} \times \lambda_{\mathrm{electricty}} + \dot{\mathrm{Q}}_{\mathrm{Demand}} \times \lambda_{\mathrm{heat}}$ (eq. 3)
		$\mathrm{CDE^{Solar}} = \left(\dot{\mathrm{E}}_{\mathrm{Bought}} - \dot{\mathrm{E}}_{\mathrm{Sold}}\right) \times \lambda_{\mathrm{electricty}} + \left(\dot{\mathrm{Q}}_{\mathrm{Bough}} - \dot{\mathrm{Q}}_{\mathrm{Sold}}\right) \times \lambda_{\mathrm{heat}}$ (eq. 4)
		CDERR: Carbon dioxide emission reduction rate $\mathrm{CDE^{SP}}$: Carbon dioxide emission Separation production (kg) $\mathrm{CDE^{Solar}}$: Carbon dioxide emission of the solar-based systems(kg) $\dot{E}$: Electricity from the grid (kWh) $\dot{Q}$: Heat from district heating network (kWh) λ: Carbon dioxide emission coefficient (kg/MWh)

(Yuan et al., 2022)	"Life Cycle CO_2 emissions"	$LC_{CO2} = \sum_t E_{e,import,t} \times CO2_{El} + \sum_t E_{DH,import,t} \times CO2_{DH}$	(eq. 5)
		LC_{CO2}	Life Cycle CO_2 emissions, ($\times 10^3\ ton$)
		$E_{e,import}$	Electricity imported from the grid (MWh)
		$CO2_{El}$	Monthly emission factor for electricity production (MWh)
		$E_{DH,import}$	Heat energy imported from DH (MWh)
		$CO2_{DH}$	Constant emission factor for district heating (g/kWh)
(Berg et al., 2024)	Annual "CO_2 emission equivalents"	$Tot.em_{year} = \sum_{h=1}^{8760} CO_{2eq}(h) \cdot p_t^{imp}(h)$	(eq. 6)
		$Tot.em_{year}$	Annual "CO_2 emissions from imported electricity", ($kgCO_2$)
		CO_{2eq}	Hourly "CO_2 emission equivalents" (gCO_2eq/kWh)
		p_t^{imp}	"Grid import" (kWh)

3.3. Technical strategic framework found in the analyzed studies

The technical motives and indicators found in the scientific articles can be classified into five main categories: production/demand imbalance, energy efficiency, energy storage, reliability/flexibility, and well-being. The main motive in the imbalance group is to make as much use of renewable energy onsite as possible. The equations related to the main technical indicators are shown in Table 3. The indicators related to the production/demand imbalance are self-consumption (eq. 7) and self-sufficiency (eq. 8). Moving on to the energy efficiency category, there are some specific examples (eq. 9). However, the definition from (Patterson, 1996) as the ratio of the useful output and the energy input can be used to generalize them. The concept of efficiency also applies to energy storage, equation 10 shows an indicator to evaluate a seasonal storage system performance. Furthermore, the temperature variation of thermal storage is used to assess the performance of the storage (eq. 11). Batteries are another way to store energy in the articles being analyzed. Some of its characteristics are affected by the degradation (Lin et al., 2023), which depends on the number of cycles. Therefore, the number of cycles is an indicator used when batteries are being integrated into the energy system, see equation 12. The reliability motive is related to minimizing the power interruptions (Azaza and Wallin, 2017). The indicator related to this motive is Loss of power supply probability (eq. 13). Sharing energy within a community is addressed by the indicator shown in equation 14. The last subcategory that was included within the technical framework is the well-being of building occupants shown in equations 15 and 16.

Table 3. The mathematical definitions for technical indicators are shown.

Reference	**Indicator name**	**Mathematical definition**	
(Nyholm et al., 2016)	"Self-consumption"	$\varphi_{SC} = \frac{\int_{t=t_1}^{t_2} \mathrm{M(t)dt}}{\int_{t=t_1}^{t_2} \mathrm{P(t)dt}}$	(eq. 7)
	"Self-sufficiency"	$\varphi_{SS} = \frac{\int_{t=t_1}^{t_2} \mathrm{M(t)dt}}{\int_{t=t_1}^{t_2} \mathrm{L(t)dt}}$	(eq. 8)
		M(t)	Generated electricity used inhouse in every instance (kW)
		P(t)	Instantaneous PV electricity generation (kW)
		$S(t)$	Instantaneous household electricity load (kW)
(Behzadi and Sadrizadeh, 2023)	"Energy efficiency"	$\eta = \frac{\dot{E}_{Solar} + \dot{C}_{Chiller} + \dot{Q}_{Space\ heating} + \dot{Q}_{Hot\ water}}{\dot{Q}_{Sun} + Q_{Biomass} + \dot{E}_{Chiller} + \dot{E}_{Heat\ pump} + \dot{E}_{Tank}}$	(eq. 9)
		$\dot{E}$	Electricity (MWh)
		$\dot{Q}$	Heat (MWh)

		$\dot{C}$	Cooling (MWh)
		$(\dot{E}_{Solar} + \dot{C}_{Chiller} + \dot{Q}_{Space\ heating} + \dot{Q}_{Hot\ water})$	Useful output (MWh)
		$(\dot{Q}_{Sun} + Q_{Biomass} + \dot{E}_{Chiller} + \dot{E}_{Heat\ pump} + \dot{E}_{Tank})$	Energy input (MWh)
(Hirvonen et al., 2018)	"Efficiency of a seasonal energy storage system"	$\eta_{BTES} = \frac{E_{discharge}}{E_{charge}}$	(eq. 10)
		$E_{discharg}$	Annual energy taken out of the borehole thermal energy storage (BTES) (MWh)
		E_{charge}	Energy injected into the storage (MWh)
(Yuan et al., 2022)	"Annual temperature variation BTES"	$\Delta T_{BTES} = T_{\text{year n+1}} - T_{\text{year n}}$	(eq. 11)
		$T_{\text{year n}}$	Temperature of the BTES on a given year (°C)
		$T_{\text{year n+1}}$	Temperature of the BTES on the immediately next year (°C)
(Meriläinen, Altti et al., 2023)	"Battery energy system (BESS) cycles"	$\mathrm{N} = \sum_{\mathrm{t=1}}^{\mathrm{T}} C_{\mathrm{t}}$	(eq. 12)
		N	Total number of cycles
		C_t	Number of cycles in a given time
		T	Time period
(Azaza and Wallin, 2017)	"Loss of power supply probability (LPSP)"	$\mathrm{LPSP} = \frac{\sum P_L - P_{PV} - P_{WT} + P_{SOC,min} + P_D}{\sum P_L}$	(eq. 13)
		P_L	Power load (kW)
		P_{PV}	Power from photovoltaic panels (kW)
		P_{WT}	Power from wind turbines (kW)
		$P_{SOC,min}$	Minimum state of charge of the battery storage (kW)
		P_D	Power from diesel generator (kW)
(Huang et al., 2022)	"Energy Sharing Ratio (ESR)"	$r_{share} = \frac{\sum_{\mathrm{i=1}}^{8760} \mathrm{P}_i^{share}}{\sum_{\mathrm{j=1}}^{\mathrm{N}} \sum_{\mathrm{i=1}}^{8760} \max(P_{j,i}^{d}, P_{j,i}^{s},)}$	(eq. 14)
		P_i^{share}	Power shared in the i[th] hour (kWh)
		$P_{j,i}^{d}$	Power demand of the j[th] building in the i[th] hour (kWh)
		$P_{j,i}^{s}$	Power supply of the j[th] building in the i[th] hour (kWh)
(Rabani et al., 2021)	"Weighted Discomfort Hours"	$\mathrm{W_DH}_{26} = \frac{\sum_{\mathrm{k=1}}^{\mathrm{N}} A_{\mathrm{k}} \cdot DH26_k}{\sum_{\mathrm{k=1}}^{\mathrm{N}} A_{\mathrm{k}}}$	(eq. 15)
	"Weighted Predicted Percentage Dissatisfied"	$\mathrm{W_PPD} = \frac{\sum_{\mathrm{k=1}}^{\mathrm{N}} A_{\mathrm{k}} \cdot PPDavg_k}{\sum_{\mathrm{k=1}}^{\mathrm{N}} A_{\mathrm{k}}}$	(eq. 16)
		N	Total number of zones in the building
		k	Index to denote a specific zone
		A_{k}	Area of the k[th] zone (m^2)
		$DH26_k$	Discomfort hours in the k[th] zone where the indoor operative temperature exceeds 26°C during occupancy. (h)
		$PPDavg_i$	Average Predicted Percentage Dissatisfied in the k[th] zone (%)

3.4. Economic strategic framework in the analyzed studies

The motives found in the literature are mainly related to cost, feasibility, volatility and some general economic

concerns. Continuing with the indicators for optimization and for assessing the economic performance of the energy systems (shown in Table 4), they can be grouped depending on the analyzed life cycle stage. In some studies, like in (Rehman et al., 2018) only the investment cost was estimated, see equation 17. On the other hand, other studies analyzed the operation cost. For example, in (Salpakari and Lund, 2016) the yearly electricity cost was optimized and analyzed for a single-family building. Another example of an operational cost indicator is found in Equation 20. In this case, it is used to analyze community-level optimization. Furthermore, other studies take a more comprehensive approach from the lifecycle perspective and integrate different stages of the energy system lifespan. In (Campana et al., 2017) a scope from initial investment to salvage value is taken to analyze the lifecycle cost and levelized cost of electricity of a community energy system optimization. Another example that involves investment and operation costs can be seen in equations 23 to 26. In this study, the cumulative cash flow is used to analyze the payback performance of an energy system in a residential building.

Table 4. The mathematical definitions for economic indicators are shown.

Reference	Indicator name	Mathematical definition
(Rehman et al., 2018)	"Overall investment cost"	$\mathrm{IC} = C_{ST} + C_{PV} + C_{BTES} + C_{WT} + C_{HT} + C_B$ (eq. 17)
	"Building investment costs"	$\mathrm{C}_B = C_{Wins} + C_{Rins} + C_{Fins} + C_{WIND} + C_{HR}$ (eq. 18)
		C_{ST} Investment cost of Solar collectors C_{PV} Investment cost of Photovoltaic C_{BTES} Investment cost of borehole C_{WT} Investment cost of warm tank C_{HT} Investment cost of hot tank C_{Wins} Investment cost insulation material, wall C_{Rins} Investment cost insulation material, roof C_{Fins} Investment cost insulation material, floor C_{WIND} Investment cost of windows C_{HR} Investment cost, building heat recovery
(Salpakari and Lund, 2016)	"Yearly electricity bill"	$\mathrm{J}_{year} = \sum_{\mathrm{k}=1}^{\mathrm{N}} g_{\mathrm{k}}(x_{\mathrm{k}} + u_{\mathrm{k}} + w_{\mathrm{k}})$ (eq. 19)
		N End of optimization horizon g Time-step cost x State vector u Control vector w External data vector
(Huang et al., 2022)	"Electricity costs"	$Cost = \sum_{\mathrm{i}=1}^{8760} P_{ex}^{cm,i} \times \tau \times X_{\mathrm{i}}, \begin{cases} X_i = X_{buy}, if P_{mis}^{c,i} > 0 \\ X_i = X_{sell}, if P_{mis}^{c,i} \leq 0 \end{cases}$ (eq. 20)
		$P_{ex}^{cm,i}$ Community hourly power exchanges with the grid τ Charging duration in hours X_{buy} Energy injected into the storage X_{sell} Feed-in-tariff X_i $P_{mis}^{c,i}$ Aggregation of the community power mismatches

(Campana et al., 2017)	"Lifecycle Cost of the renewable based hybrid power system"	$\mathrm{LCC}_{ren} = ICC_{ren} - \sum_{n=1}^{N} \frac{d_t}{(1+i)^n} tr + \sum_{t=1}^{N} \frac{a_t}{(1+i)^n}(1-tr) - \frac{s}{(1+i)^n}$	(eq. 21)
		ICC_{ren} Initial capital cost of the renewables based system	
		N The lifetime of the project (years) d_t Annual depreciation i Interest rate tr Tax rate a_t Annual costs s Salvage value	
	Levelized cost of electricity	$LCOE = \frac{LCC_{pv} + LCC_{bapv} + LCC_{wt} + LCC_{batt}}{EP \sum_{n=1}^{N} \frac{r_t}{(1+i)^n}}$	(eq. 22)
		LCC_{pv} Lifecycle cost of the ground-based PV systems LCC_{bapv} Lifecycle cost of the building attached PV systems LCC_{wt} Lifecycle cost of the Wind turbine LCC_{batt} Lifecycle cost of the Battery r_t Degradation rate	
(Kharseh and Wallbaum, 2019)	"Cumulative cash flow (CCF)"	$\mathrm{CCF}_j = \frac{C_{net}}{(1+d)^j} - C_{inv}$	(eq. 23)
	"Discount rate"	$d = (1+g) \cdot (1+ir) - 1$	(eq. 24)
	"Up-front cost"	$C_{inv} = (0.340 \cdot P_{nominal} + C_{panel}) \cdot N$	(eq. 25)
	"Net income of year ´j´"	$C_{net,j} = (\sigma \cdot P_e \cdot E_d - P_e - P_{e,fed}) \cdot E_{fed}) \cdot (1 + er)^j - C_{O\&M,j}$	(eq. 26)
		g Inflation rate ir Interest rate 0.340 Labor costs factor $P_{nominal}$ Nominal capacity of a PV panel C_{panel} Cost of a PV panel N Number of PV panels σ Annual saving target (%) P_e Current electricity price E_d Required annual electricity $P_{e,fed}$ Feed-in tariff E_{fed} Generated electricity that is fed into the utility grid er Annual escalation rate of electricity price $C_{O\&M,j}$ Operation and maintenance cost	

4. Discussion

The quantification of the indicators in different categories across the strategic choices revealed that while most indicators in the analyzed articles focus on technical and economic aspects, environmental objectives and KPIs are considered less frequently. This presents a drawback for the environmental motives expressed in most of the articles, as they will not directly optimize and quantitatively express how much the environmental impact is reduced by the

proposed optimization. On the other hand, as seen in several of the equations, the environmental and economic variables are dependent on technical performance. This means technical indicators can indirectly pass information about the performance in the other two categories. Furthermore, environmental and economic performances depend on the social and economic conditions of a location and the timeframe for the study. Therefore, if technical indicators are not used, the comparability of the different studies will be sacrificed. In consequence, multi-objective optimization can provide solutions that minimize the risk of deteriorating other variables related to the initial motives as it is also addressed in (Klemm and Wiese, 2022). They recommend multi-criteria approaches to enable more holistic optimization and planning of sustainable urban energy systems.

Another aspect of the optimization process for sustainability is the lack of a comprehensive approach in the lifecycle scope. According to (Nugent and Sovacool, 2014), there are four basic lifecycle assessment stages for PV and wind energy systems: material cultivation and fabrication, construction, operation, and decommissioning. From these stages, only the operation is considered to account for the greenhouse gas emission within the studies reviewed. This implies not considering the material extraction and manufacturing, despite having PV area or power installed as a decision variable. This could cause an underestimation of the environmental impact given that this lifecycle stage represents around 70% of the greenhouse gas emissions of a PV system (Nugent and Sovacool, 2014). This contrasts with some of the economic indicators that include the initial stage as investment costs.

A deeper analysis of the economic and technical indicators suggests that some motives shown in these two categories could not be assessed. For example, energy price volatility is mentioned in (Hajiaghapour-Moghimi et al., 2023) to set the context for an optimization study about demand response and energy storage for a PV system in Finland. However, an indicator that aims to quantify this motive is not found within this or in the other articles analyzed. Similarly, the importance of decreasing the peak power is mentioned in (Koskela, Juha et al., 2019). Despite this, there are no indicators that evaluate the intensity and/or frequency of the power peaks in the results. This situation opens the opportunity to propose indicators that cover the motives that are currently not covered by indicators for this field. Furthermore, the social strategic choices are not covered in the present review. However, the well-being indicators displayed in the results under the technical category can be viewed as a group of social indicators. Despite this, there is a significant potential for future studies around social motives and indicators.

The present review has other limitations. To start with, the analyzed indicators are limited to the subset of studies mentioned in the method. There could be additional motives and indicators in literature outside the scope of study that can be useful to fill the gaps found. Another limitation is that the motives of the optimizations are assumed to be in the introduction, stated as the societal context. It is likely that in some of the studies, the motives are more specific, such as comparing two different methods therefore they do not need comprehensive optimization. Nevertheless, the strategic framework proposed can be a useful way to define the indicators to be used in an optimization energy model.

From the previous discussion, it can be concluded that possible future research could be: (1) an analysis of the impact on environmental indicators if an optimization model only focuses on technical or economic objectives; (2) replicable indicators that quantify and help to compare the risk that economic volatility poses on energy systems investment; (3) a replicable indicator that quantifies the frequency and intensity of peaks in the power of energy systems; (4) An analysis of the consequences of considering or not material extraction and manufacturing when optimizing the design of an energy system with environmental objectives; (5) A review of indicators can be useful to match collective social sustainability motives for energy systems; (6) A review of the coherence of strategies to optimize energy systems in other regions.

5. Conclusions

The review process revealed the coherence of a group of strategic frameworks applicable to optimizing energy systems. This overview facilitates strategic decision-making, ensuring alignment between the optimization process and stakeholders' motives. Furthermore, it showed that even when environmental motives are expressed by most of the authors, a relatively low portion of the scientific articles focused on optimizing environmental objectives and quantifying environmental performance. Furthermore, the renewable energy systems' raw material extraction and manufacturing stage is not being considered in the optimization studies reviewed. This could cause an underestimation of the environmental impact of the energy system in the model, which can lead to a suboptimal design solution. These inconsistencies show the need for more comprehensive studies into the optimization of energy systems in the Nordic built environment, aiming to contribute to the solutions for environmental issues related to the solar PV energy systems in the built environment.

Another key finding is that certain objectives highlighted in the literature are not currently addressed by any existing

indicators. To bridge this gap, it would be beneficial to introduce new indicators. These could monitor periods of peak energy production and demand, and measure the instability of energy prices. These indicators could provide a more comprehensive understanding of the technical risks and energy market dynamics and help stakeholders make informed decisions. They could also contribute to the development of strategies for managing the risks associated with power peaks and energy price volatility.

6. Acknowledgments

The authors acknowledge the financial support received from the Swedish Energy Agency through the project “The Solar Electricity Research Centre (SOLVE)”, grant number 52693-1.

7. References

Andersen, I.M., Lindberg, K.B., 2021. Optimal Investment Decisions for a Zero Emission Building under Uncertainty: Stochastic BUTLER. 2021 International Conference on Smart Energy Systems and Technologies (Sest).
Arabkoohsar, A., Behzadi, A., Alsagri, A.S., 2021a. Techno-economic analysis and multi-objective optimization of a novel solar-based building energy system; An effort to reach the true meaning of zero-energy buildings. Energy Conversion and Management 232.
Arabkoohsar, A., Behzadi, A., Nord, N., 2021b. A highly innovative yet cost-effective multi-generation energy system for net-zero energy buildings. Energy Conversion and Management 237, 17.
Azaza, M., Wallin, F., 2017. Multi objective particle swarm optimization of the hybrid micro-grid system: A case study in Sweden. Energy 123, 108-118.
Behzadi, A., Sadrizadeh, S., 2023. Grid-tied solar and biomass hybridization for multi-family houses in Sweden: An optimal rule-based control framework through machine learning approach. Renewable Energy 218, 17.
Berg, K., Hernandez-Matheus, A., Aragüés-Peñalba, M., Bullich-Massagué, E., Farahmand, H., 2024. Load configuration impact on energy community and distribution grid: Quantifying costs, emissions, and grid exchange. Applied Energy 363.
Bergek, A., Mignon, I., 2017. Motives to adopt renewable electricity technologies: Evidence from Sweden. Energy Policy 106, 547-559.
Campana, P.E., Quan, S.J., Robbio, F.I., Lundblad, A., Zhang, Y., Ma, T., Karlssona, B., Yan, J.Y., 2017. Optimization of a residential district with special consideration on energy and water reliability. Applied Energy 194, 751-764.
Carli, R., Dotoli, M., Jantzen, J., Kristensen, M., Ben Othman, S., 2020. Energy scheduling of a smart microgrid with shared photovoltaic panels and storage: The case of the Ballen marina in Samsø. Energy 198, 117188.
Costa, L., Ribeiro, M., Miranda, I., Leite, H., 2019. Integrating Hybrid Off-grid Systems with Battery Storage: Key Performance Indicators. Ieee Pes Innov Smart.
Fachrizal, R., Qian, K., Lindberg, O., Shepero, M., Adam, R., Widén, J., Munkhammar, J., 2024. Urban-scale energy matching optimization with smart EV charging and V2G in a net-zero energy city powered by wind and solar energy. Etransportation 20, 20.
Goop, J., Nyholm, E., Odenberger, M., Johnsson, F., 2021. Impact of electricity market feedback on investments in solar photovoltaic and battery systems in Swedish single-family dwellings. Renewable Energy 163, 1078-1091.
Hajiaghapour-Moghimi, M., Hajipour, E., Hosseini, K.A., Tavakkoli, M., Fattaheian-Dehkordi, S., Vakilian, M., Lehtonen, M., 2023. Hedging Investments of Grid-Connected PV-BESS in Buildings Using Cryptocurrency Mining: A Case Study in Finland. Ieee Access 11, 66327-66345.
Hirvonen, J., Rehman, H.U., Deb, K., Sirén, K., 2017. Neural network metamodelling in multi-objective optimization of a high latitude solar community. Solar Energy 155, 323-335.
Hirvonen, J., Rehman, H.U., Sirén, K., 2018. Techno-economic optimization and analysis of a high latitude solar district heating system with seasonal storage, considering different community sizes. Solar Energy 162, 472-488.
Hirvonen, J., Sirén, K., 2018. A novel fully electrified solar heating system with a high renewable fraction - Optimal designs for a high latitude community. Renewable Energy 127, 298-309.
Huang, P., Han, M., Zhang, X., Hussain, S.A., Jayprakash Bhagat, R., Hogarehalli Kumar, D., 2022. Characterization and optimization of energy sharing performances in energy-sharing communities in Sweden, Canada and Germany. Applied Energy 326, 120044.
Huang, P., Lovati, M., Zhang, X., Bales, C., 2020. A coordinated control to improve performance for a building cluster with energy storage, electric vehicles, and energy sharing considered. Applied Energy 268, 114983.
Huang, P., Lovati, M., Zhang, X., Bales, C., Hallbeck, S., Becker, A., Bergqvist, H., Hedberg, J., Maturi, L., 2019. Transforming a residential building cluster into electricity prosumers in Sweden: Optimal design of a coupled PV-heat pump-thermal storage-electric vehicle system. Applied Energy 255, 113864.
Kharseh, M., Wallbaum, H., 2017. The effect of different working parameters on the optimal size of a battery for grid-connected PV systems. Enrgy Proced 122, 595-600.
Kharseh, M., Wallbaum, H., 2019. How Adding a Battery to a Grid-Connected Photovoltaic System Can Increase its Economic Performance: A Comparison of Different Scenarios. Energies 12(1), 19.

Khezri, R., Mahmoudi, A., Aki, H., 2022. Optimal planning of solar photovoltaic and battery storage systems for grid-connected residential sector: Review, challenges and new perspectives. Renewable and Sustainable Energy Reviews 153, 111763.
Klemm, C., Wiese, F., 2022. Indicators for the optimization of sustainable urban energy systems based on energy system modeling. Energy Sustain. Soc. 12(1).
Koskela, J., Rautiainen, A., Järventausta, P., 2019. Using electrical energy storage in residential buildings - Sizing of battery and photovoltaic panels based on electricity cost optimization. Applied Energy 239, 1175-1189.
Koskela, J., Rautiainen, A., Järventausta, P., 2019. Using electrical energy storage in residential buildings – Sizing of battery and photovoltaic panels based on electricity cost optimization. Applied Energy 239, 1175-1189.
Kourkoumpas, D.S., Benekos, G., Nikolopoulos, N., Karellas, S., Grammelis, P., Kakaras, E., 2018. A review of key environmental and energy performance indicators for the case of renewable energy systems when integrated with storage solutions. Applied Energy 231, 380-398.
Lin, Z., Li, D., Zou, Y., 2023. Energy efficiency of lithium-ion batteries: Influential factors and long-term degradation. Journal of Energy Storage 74, 109386.
Lund, P.D., 2018. Capacity matching of storage to PV in a global frame with different loads profiles. Journal of Energy Storage 18, 218-228.
Matschegg, D., Carlon, E., Sturmlechner, R., Sonnleitner, A., Fuhrmann, M., Dissauer, C., Strasser, C., Enigl, M., 2023. Investigation of individual motives and decision paths on residential energy supply systems. Energy 281.
Mbuwir, B.V., Paridari, K., Spiessens, F., Nordström, L., Deconinck, G., 2020. Transfer learning for operational planning of batteries in commercial buildings, 2020 IEEE International Conference on Communications, Control, and Computing Technologies for Smart Grids (SmartGridComm). pp. 1-6.
Meriläinen, A., Montonen, J.-H., Kosonen, A., Lindh, T., Ahola, J., 2023. Cost-optimal dimensioning and operation of a solar PV–BESS–heat pump-based on-grid energy system for a Nordic climate townhouse. Energy and Buildings 295, 113328.
Meriläinen, A., Montonen, J.H., Hopsu, J., Kosonen, A., Lindh, T., Ahola, J., 2023. Power balance control and dimensioning of a hybrid off-grid energy system for a Nordic climate townhouse. Renewable Energy 209, 310-324.
Nugent, D., Sovacool, B.K., 2014. Assessing the lifecycle greenhouse gas emissions from solar PV and wind energy: A critical meta-survey. Energy Policy 65, 229-244.
Nyholm, E., Goop, J., Odenberger, M., Johnsson, F., 2016. Solar photovoltaic-battery systems in Swedish households - Self-consumption and self-sufficiency. Applied Energy 183, 148-159.
Paatero, J.V., Lund, P.D., 2007. Effects of large-scale photovoltaic power integration on electricity distribution networks. Renewable Energy 32(2), 216-234.
Patterson, M.G., 1996. What is energy efficiency?: Concepts, indicators and methodological issues. Energy Policy 24(5), 377-390.
Perera, A.T.D., Nik, V.M., Wickramasinghe, P.U., Scartezzini, J.L., 2019. Redefining energy system flexibility for distributed energy system design. Applied Energy 253, 18.
Psimopoulos, E., Bee, E., Widen, J., Bales, C., 2019. Techno-economic analysis of control algorithms for an exhaust air heat pump system for detached houses coupled to a photovoltaic system. Applied Energy 249, 355-367.
Rabani, M., Bayera Madessa, H., Nord, N., 2021. Achieving zero-energy building performance with thermal and visual comfort enhancement through optimization of fenestration, envelope, shading device, and energy supply system. Sustainable Energy Technologies and Assessments 44, 101020.
Rehman, H.U., Hirvonen, J., Kosonen, R., Sirén, K., 2019. Computational comparison of a novel decentralized photovoltaic district heating system against three optimized solar district systems. Energy Conversion and Management 191, 39-54.
Rehman, H.u., Hirvonen, J., Sirén, K., 2018. Influence of technical failures on the performance of an optimized community-size solar heating system in Nordic conditions. Journal of Cleaner Production 175, 624-640.
Rikkas, R., Lahdelma, R., 2021. Energy supply and storage optimization for mixed-type buildings. Energy 231, 13.
Salpakari, J., Lund, P., 2016. Optimal and rule-based control strategies for energy flexibility in buildings with PV. Applied Energy 161, 425-436.
Salpakari, J., Mikkola, J., Lund, P.D., 2016. Improved flexibility with large-scale variable renewable power in cities through optimal demand side management and power-to-heat conversion. Energy Conversion and Management 126, 649-661.
Savolainen, R., Lahdelma, R., 2022. Optimization of renewable energy for buildings with energy storages and 15-minute power balance. Energy 243, 13.
Srithapon, C., Månsson, D., 2023. Predictive control and coordination for energy community flexibility with electric vehicles, heat pumps and thermal energy storage. Applied Energy 347, 121500.
Union, T.E.P.a.t.C.o.t.E., 2018. DIRECTIVE (EU) 2018/2001 OF THE EUROPEAN PARLIAMENT AND OF THE COUNCIL of 11 December 2018 on the promotion of the use of energy from renewable sources (recast), in: Union, O.J.o.t.E. (Ed.). Official Journal of the European Union.
Xu, Y., Yan, C., Liu, H., Wang, J., Yang, Z., Jiang, Y., 2020. Smart energy systems: A critical review on design and operation optimization. Sustainable Cities and Society 62, 102369.
Yuan, X., Heikari, L., Hirvonen, J., Liang, Y., Virtanen, M., Kosonen, R., Pan, Y., 2022. System modelling and optimization of a low temperature local hybrid energy system based on solar energy for a residential district. Energy Conversion and Management 267, 115918.

Thermal Characterization of Living Wall Systems

Helmut Weinläder[1], Michaela Reim[1], Leslie Ullerich[1], Werner Körner[1] and Stephan Weismann[1]

[1] Center for Applied Energy Research e.V. (CAE), Würzburg (Germany)

Abstract

The energetic impact of several Living Wall Systems (LWS) was measured in the laboratory and in an outdoor test facility in Würzburg, Germany. It was found, that the usual rear ventilation of the systems reduces their thermal benefits in winter. When estimating the energy savings potential of LWS, the solar absorptance of the façade has to be taken into account. When installed on facades with medium to high solar absorptance values, LWS can even increase the heat losses in winter. In summer, the cooling potential of LWS is higher on facades with high solar absorptance values while it is strongly reduced on façades with low solar absorptance. However, when considering solar absorptance on walls to regulate heat losses in winter and heat gains in summer, this needs opposite measures, while LWS show their advantages equally in both seasons.

Keywords: façade greening, Living Wall System, thermal performance, energy savings, U-value

1. Introduction

Façade greening has a number of positive effects such as improving the air quality, decreasing the heat island effect, enhancing biodiversity, decreasing the noise level, and improving thermal behavior of buildings (Ogut et al. 2022). While the first points are good for the environment, the last point in particular is important for building operators and users, as any savings in cooling or heating energy pay off directly for them. While façade greening incorporates different kinds of systems, like Green Walls where the plants are planted in the ground, according to Mann et al. (2023), an increasing market for façade greening is Living Wall Systems (LWS) that use modular structures with substrate layers in a curtain wall construction.

While the effects of LWS regarding their temperature reduction potential have been widely studied, much less publications investigate their energetic effects. Susca et al. (2022) reviewed the number of articles dealing with specific topics: they found 5 articles dealing with heating energy, 13 articles for cooling energy, and 30 articles investigating surface temperature effects. Since several of the articles use simulations only, the numbers show a need for experimental work in this field. The following passages discuss some of the relevant results already published.

Bianco et al. (2017) investigated a newly developed LWS in a test cell in Turin, Italy, with a south facing wall with a U-value of 0.4 W m^{-2} K^{-1}. They found a reduction in heat losses during winter conditions of 56 % to 58 % for the LWS compared to the reference wall. During summer conditions, the LWS performed worse than the reference wall. According to the authors, the heat fluxes during summer were very small and in the range of error of the heat flux meter. The paper does not mention the solar absorptance of the reference wall, however, according to the pictures, the reference wall looks bright white.

The same LWS was measured in a real-scale demonstration mock-up (Serra et al. 2017). The reference wall had an additional insulation layer of 3 cm extruded polystyrene foam (XPS) to give both constructions an effective U-value of 0.3 W m^{-2} K^{-1}. An equivalent thermal transmittance of 0.29 W m^{-2} K^{-1} was measured for the wall with LWS while 0.25 W m^{-2} K^{-1} was measured for the reference wall.

Djedjig et al. (2017) investigated the thermal performance of a west façade with LWS in La Rochelle, France. The setup used empty concrete tanks as scaled-down buildings. A block without LWS with a façade solar reflectance of 0.64 was used as reference. The 5 cm concrete walls had no insulation. The LWS reduced heat

© 2024. The Authors. Published by International Solar Energy Society
Selection and/or peer review under responsibility of Scientific Committee
10.18086/eurosun.2024.01.13 Available at http://proceedings.ises.org

gains by 97 % and heat losses by about 30 % in summer. In winter, heat gains were reduced by 40 % whereas heat losses were reduced by about 80 %. This study differs from the others listed here in that the indoor temperatures in winter were free floating.

Tudiwer and Korjenic (2017) measured two different LWS at two buildings in Vienna, Austria, during winter. They compared the measured heat fluxes of the greened façade with a non-greened part of the façade as reference. The two wall constructions without LWS had U-values of 0.75 to 0.79 W m^{-2} K^{-1} and 0.35 to 0.37 W m^{-2} K^{-1}, respectively. With LWS, the authors found an overall reduction in U-value of 20 % to 22 % for the first wall construction and of 17 % to 22 % for the second.

Fox et al. (2022) measured the energetic effect of a LWS on a non-insulated building during winter in Plymouth, UK. They found an improvement in insulation by the LWS of 31.4 % compared to the reference wall with a U-value of 1.12 W m^{-2} K^{-1}.

All these publications provide indications of the positive effect of LWS for improving the energy efficiency of buildings, which could lead to the following assumptions:

- LWS generally reduce heat gains of walls in summer (Bianco et al. 2017 got different results, however, they attributed this to the measurement uncertainty due to the small heat flows),
- LWS generally reduce heat losses of walls in winter,
- the higher the U-value of the wall, the greater the effect of the LWS.

While the last conclusion is in accordance to building physics, the first two conclusions seem to miss one important aspect of the energy balance of walls: the shading effect of the LWS. Since LWS cover the wall completely due to the opaque back layer – even if the plants shed their leaves in winter – the solar absorptance of the wall should play an important role in the energy balance. In this sense, the LWS must be understood not only as a thermal insulation system but also as a solar shading system even in winter. None of the above listed articles, apart from Djedjig et al. (2017), however, do mention the solar absorptance or at least the brightness of the reference wall.

In order to clarify this, the thermal performance of façade greening is being systematically investigated and quantified in the project U-green. This includes laboratory measurements in a Hot-Box system to determine the stationary U-value, as well as dynamic outdoor measurements on test façades. The long-term goal of the project is to determine calculation methods for the energy assessment of façade greening in standards and building energy laws.

2. Laboratory Measurements

Several Living Wall Systems (LWS) were measured in a computer-controlled Hot-Box system (see Figure 1) in accordance with ASTM C236-89 (1989) to determine their heat transmission coefficient in steady state. In the Hot-Box system a sample is installed between two compartments with different temperatures and the heat flow density is determined via the energy supply in the heated compartment needed to maintain the steady state. The thermal coefficients are calculated with the environmental conditions selected using the heat flow density and the temperature difference.

The LWS were mounted onto a reference wall construction that was measured separately. The LWS sample size ranged from 0.9 m^{-2} for the gabion system and modular system 2 up to 1.7 m^{-2} for the tray system and modular system 1. The results were corrected for the different sample sizes. By comparing the U-values of the reference wall with LWS U_{LWS} with the U-value of the reference wall without LWS U_{ref}, the thermal resistance of the LWS R_{LWS} was calculated according to eq. 1:

$$R_{LWS} = \frac{1}{U_{LWS}} - \frac{1}{U_{ref}} \qquad \text{(eq. 1)}$$

Living Wall Systems usually have an air gap for rear ventilation. The measurements in the Hot-Box were therefore also carried out with an air gap. The wind speed in the cold chamber was 1.6 m s^{-1} for the reference wall, while some LWS reduced the wind speed to values as low as 0.3 m s^{-1}. Additional measurements with a closed air gap show the influence of this rear ventilation on the thermal performance. The results are shown in Table 1.

Fig. 1: Hot-Box system (top left), reference wall (top mid), and LWS samples: gabion system (top right), tray system (bottom left), modular system 1 (bottom mid), and modular system 2 (bottom right).

Tab. 1: U-values of different kinds of LWS measured in a Hot-Box system.

System	U-value [W m^{-2} K^{-1}]	ΔU [%]	R_{LWS} [m^2 K W^{-1}]
Reference wall	0.83 ± 0.02	0	-
LWS (gabion system) rear ventilated	0.75 ± 0.02	10	0.13 ± 0.02
LWS (tray system) rear ventilated	0.74 ± 0.02	11	0.15 ± 0.02
LWS (modular system 1) rear ventilated	0.74 ± 0.02	11	0.15 ± 0.02
LWS (modular system 2) rear ventilated	0.72 ± 0.02	13	0.18 ± 0.02
LWS (gabion system) air gap closed	0.58 ± 0.02	30	0.52 ± 0.02
LWS (tray system) air gap closed	0.68 ± 0.02	18	0.27 ± 0.02
LWS (modular system 1) air gap closed	0.69 ± 0.02	17	0.24 ± 0.02
LWS (modular system 2) air gap closed	0.64 ± 0.02	23	0.36 ± 0.02

With rear ventilation, the measured R-values of the Living Wall Systems are equivalent to 4 to 7 mm expanded polystyrene foam (EPS) insulation, ranging from 0.13 to 0.18 m² K W^{-1}, and almost identical, regardless of the system structure. With suppressed rear ventilation, the values are much higher – 0.24 to 0.52 m² K W^{-1} or equivalent to 8 to 18 mm EPS – and there are bigger differences between the systems. Some manufacturers use very thick substrate layers, e.g. gabion system, or thin insulation layers in their systems, e.g. modular system 2. However, their thermal advantages can only be utilized if the LWS will be installed without rear ventilation.

These values provide an initial indication that LWS can have a certain energy savings effect on poorly insulated walls, but their thermal impact on better insulated walls or new buildings is limited.

3. Outdoor Measurements

Since the Hot-Box measurements in the laboratory exclude important solar thermal effects of LWS like shading, we used an outdoor test facility for additional measurements. The test facility is a container with a floor area of 6 m x 3 m and a height of 3 m. The 10 cm concrete walls are insulated with 18 cm mineral wool, which gives a U-value of 0.2 W m^{-2} K^{-1}. The inside is temperature-controlled by an air conditioning unit. We used the south and west façade to investigate the thermal effect of different kinds of LWS. A sketch of the setup is depicted in Figure 2. The two façades were divided into separate wall sections, four on the south and six on the west façade (see Figure 2 right). Each wall section can accommodate a LWS or serve as a reference field without greening. Due to some problems with the setup on the west façade, we focus in this paper on the results for the south façade only.

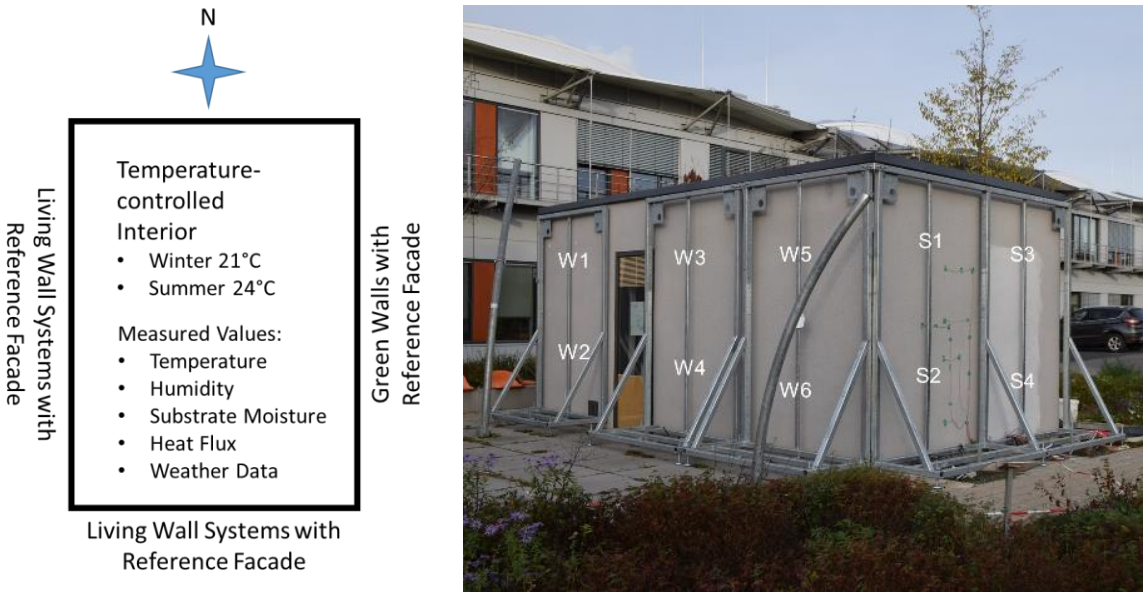

Fig. 2: Sketch of the measurement setup for LWS on our outdoor test facility (left) and southwest view of the test facility with frames for the LWS and designations for the wall sections (right).

As can be seen in Figure 2 right, sections S3 and S4 have a brighter plaster than the other sections. A solar reflectance measurement of the two plaster samples yielded a solar absorptance α_S of 0.6 for the medium and 0.24 for the bright plaster. The medium plaster therefore is a good reference, because a solar absorptance of 0.6 is a typical value for building façades according to the German standard DIN V 18599-2 (2018), which gives a range of 0.4 to 0.8 for bright and dark façade surfaces, respectively, and it uses a standard value of 0.6 if more precise values are not known.

The energetic impact of the LWS was measured via heat flux sensors positioned on the inside wall surface of every wall section. The heat flux therefore directly gives the heat gains and losses of the room through the respective wall section.

3.1 Summer Measurements

In a first measurement period from July 11 to September 5, 2023 we investigated the summer performance of

two LWS on the south façade (S3, S4) while the two wall sections S1 and S2 had no LWS and were used as reference wall. The room temperature was set to 24°C. Pictures of the façade at the beginning and after the measurement period are shown in Figure 3 and a list of the installed LWS is given in Table 2. All LWS use the same substrate (DG EXT Dachgartensub.extensiv, Patzer Erden, Germany) and the same plant mix (see Table 3). An automatic irrigation system with individual parameters for each wall section ensures a consistently high level of humidity in all systems. The LWS are mounted on holders and stand in front of the façade without any direct contact. The distance between LWS and facade is about 5 cm and the sides are all open to wind and rain.

Fig. 3: South façade with two different LWS at the beginning of the measurement period on July 20, 2023 (left) and after the measurement period on September 20, 2023 (right). In the right picture, there's already a new system installed on S2 for the winter measurements; this was not measured during summer.

Tab. 2: Description of the LWS used in the summer measurements.

Wall Section	System	Company	Façade area
S1, S2	Reference without LWS	-	1.84 m² / 2.57 m²
S3	greencityWALL	floor-design Wand GmbH, Germany	2.57 m²
S4	Tray system	Tech Metall Erzeugungs Handel und Montage GmbH, Austria	1.84 m²

Tab. 3: Plant mix used in the LWS.

Description	Botanical Name
Mix sunny	Stachys monnieri `Hummelo` Campanula poscharskyana Heuchera villosa var. macrorrhiza Bergenia cordifolia `Rosi Klose` Fragaria vesca semperflorens `Alexandria` Thymus praecox `Minor` Potentilla thurberi `Monarch`s Velvet` Origanum vulgare `Compactum`

The heat flux sensors are HFP01 from the company Hukseflux, Netherlands, with a relative uncertainty of ± 3 %. The measurement data are recorded by Agilent data loggers at one-minute intervals and stored in a SQL database. The weather data is recorded at a weather station about 50 meters away and also exported into the SQL database. All raw data is then exported with the Monisoft[1] evaluation software in precisely timed 5-minute steps for further analysis in Excel.

Figure 4 left shows the weather data and Figure 4 right depicts the summarized heat gains and losses through

[1] https://fbta.ieb.kit.edu/monisoft.php

the wall sections for the summer measurement period. The weather was mixed with several cold periods with maximum daily temperatures below 20°C but also with some hot periods with maximum daily temperatures of more than 30°C.

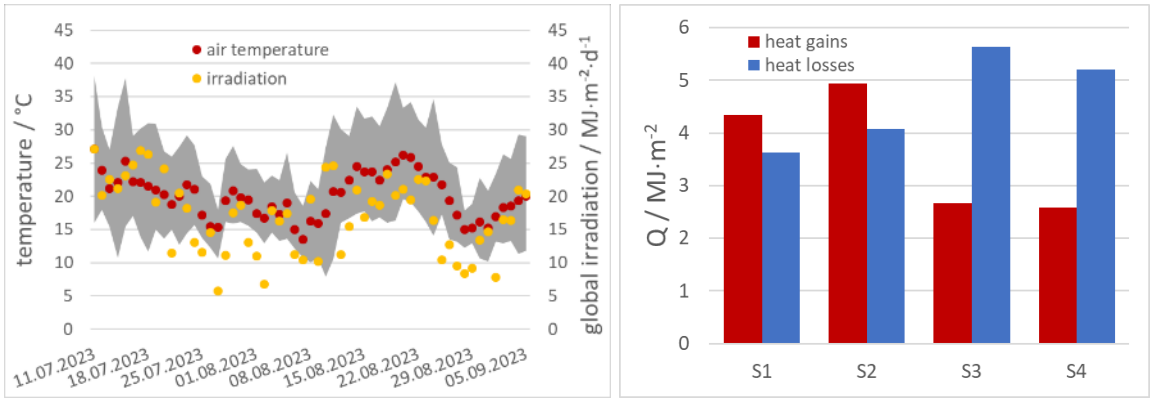

Fig. 4: Measured daily mean air temperature (red dots), minimum and maximum daily air temperature (grey area), and horizontal solar global irradiation (left); summarized heat gains and losses through the wall sections S1 and S2 without and S3 and S4 with LWS (right).

The measured data show some slight differences between the two reference walls S1 and S2 with S2 having 14 % higher heat gains and 12 % higher heat losses than S1. For the reference walls, the heat gains are higher than the heat losses. The walls with LWS have significantly lower heat gains than the reference walls, the reduction is 38 % to 40 % if compared to S1 and 46 % to 48 % if compared to S2. The heat losses of the walls with LWS on the other hand are much higher than that of the reference walls. This indicates, that LWS on the south façade reduce heat gains through walls with a solar absorptance of 0.6 while they do not prevent the room from cooling down through the wall. On the south façade, such walls without LWS show a negative energy balance with regard to heat input (more gains than losses), while the balance is clearly shifted into positive region (more losses than gains) with a LWS.

3.2 Influence of solar absorptance in summer

To estimate the influence the solar absorptance of the wall has on this effect, we determined the heat gains and losses of the walls with LWS compared to a reference wall with bright plaster with a solar absorptance α_S of 0.24. To do this, we measured all four wall sections without LWS. This was done between May 23 and June 11, 2023, before the LWS were installed. Since we wanted to focus on the effect α_S has on the heat gains, we set the room temperature to 21°C. Figure 5 shows the weather data as well as the heat gains and losses. The heat losses are just for information and are not used further.

The data show a clear reduction in heat gains for the wall sections S3 and S4 with lower α_S. The heat gains seem to be systematically lower in the top sections S1 and S3 while the heat losses are higher, which indicates temperature stratification in the room.

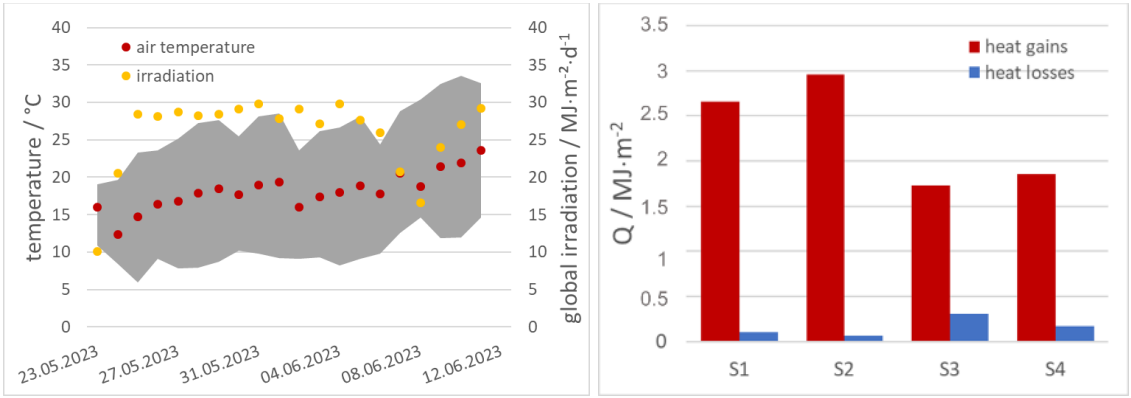

Fig. 5: Measured daily mean air temperature (red dots), minimum and maximum daily air temperature (grey area), and horizontal solar global irradiation (left); summarized heat gains and losses through the wall sections without LWS (right).

With these data we determined the heat gains for the wall sections S1 and S2 with hypothetical bright plaster

according to equations 2 and 3:

$$Q_{S1,bright} = \frac{Q_{S3}}{Q_{S1}} \cdot Q_{S1,medium} \qquad \text{(eq. 2)}$$

$$Q_{S2,bright} = \frac{Q_{S4}}{Q_{S2}} \cdot Q_{S2,medium} \qquad \text{(eq. 3)}$$

Q_{Si} are the heat gains from the measurements of S1 to S4 in this section (red bars in Figure 5 right), $Q_{Si,medium}$ are the heat gains of S1 and S2 from the measurements in section 3.1, and $Q_{Si,bright}$ are the hypothetical heat gains of S1 and S2 for the summer measurements in section 3.1 if the wall sections had a bright plaster. This estimate can be made under the assumption that the weather boundary conditions during both measurement periods are similar. The mean outside air temperature for the measurement period in section 3.1 is 20.1°C while that for section 3.2 is 18.1°C. However, the room air temperature in section 3.1 is 24°C while that in section 3.2 is 21°C, which should equalize the differences somewhat. The mean daily solar irradiance on the south façade for section 3.1 is 8.922 ± 0,446 MJ m^{-2} d^{-1} while that for section 3.2 is 11.748 ± 0,587 MJ m^{-2} d^{-1}. These values show that there are some differences especially regarding the solar irradiation, which is higher in section 3.2. This could lead to relatively more heat gains for the wall sections with medium plaster compared to those with bright plaster in section 3.2, which in turn would underestimate the heat gains $Q_{Si,bright}$. Nevertheless, this estimation should give a feeling for the effects of the solar absorptance.

Table 4 gives an overview of the data used and the results. Figure 6 shows a comparison of the heat gains.

Tab. 4: Measured heat gains for the wall sections S1 and S2 with medium plaster as well as S3 and S4 with bright plaster and estimated heat gains for S1 and S2 with bright plaster. All wall sections are without LWS.

Wall section	Heat gain [MJ m^{-2}]	Description and measurement period
Q_{S1}	2.658 ± 0,080	Medium plaster, section 3.2, measured
Q_{S2}	2.956 ± 0,089	Medium plaster, section 3.2, measured
Q_{S3}	1.728 ± 0,052	Bright plaster, section 3.2, measured
Q_{S4}	1.859 ± 0,056	Bright plaster, section 3.2, measured
$Q_{S1.medium}$	4.335 ± 0,130	Medium plaster, section 3.1, measured
$Q_{S2.medium}$	4.942 ± 0,148	Medium plaster, section 3.1, measured
$Q_{S1.bright}$	2.818 ± 0,085	Bright plaster, section 3.1, estimated
$Q_{S2.bright}$	3.107 ± 0,093	Bright plaster, section 3.1, estimated

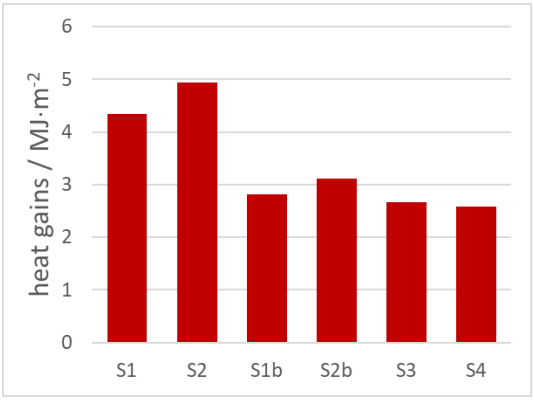

Fig. 6: Comparison of the summarized heat gains through the wall sections: S1 and S2 are measured values without LWS and with medium plaster (α_S = 0.6), S1b and S2b are estimated values without LWS and with bright plaster (α_S = 0.24), S3 and S4 are measured values with LWS.

The data in Figure 6 show that the bright plaster in wall sections S1b and S2b reduces the heat gains to almost the same level as the LWS (S3 and S4). While the LWS reduce the heat gains compared to a medium plastered wall with α_S = 0.6 by 38 % to 48 %, they show a much slighter reduction of 5 % to 17 % compared to a bright plastered wall with α_S = 0.24.

3.3 Winter Measurements

In a second measurement period from November 22, 2023, to April 5, 2024, we investigated the winter performance of three LWS on the south façade. Pictures of the façades are shown in Figure 7 and a list of the installed LWS is given in Table 5.

Fig. 7: South façade with three different LWS before the measurement period on September 20 2023 (left) and near the end of the measurement period on February 2 2024 (right).

Tab. 5: Description of the LWS used in the winter measurements.

Wall Section	System	Company	Façade area
S1	Reference without LWS	-	1.84 m²
S2	fytotextile	Verticalgreendesign GmbH, Germany	2.57 m²
S3	greencityWALL	floor-design Wand GmbH, Germany	2.57 m²
S4	Tray system	Tech Metall Erzeugungs Handel und Montage GmbH, Austria	1.84 m²

As in the summer measurements, all LWS use the same substrate and the same plant mix. During winter the LWS were not irrigated. The holders have no direct contact to the façade with a distance of about 5 cm and the sides are all open to wind and rain.

As there were signs of temperature stratification in the room, additional temperature sensors were installed to measure the inside air temperature directly in front of each wall section. With the mean temperature of the inside air $\bar{T}_i$, the mean temperature of the outside air $\bar{T}_o$, the summarized heat losses Q_{loss}, and the duration t of the measuring period, an effective U-value U_{eff} was determined for each wall section according to equation 4:

$$U_{eff} = \frac{Q_{loss}}{(\bar{T}_i - \bar{T}_o) \cdot t} \qquad \text{(eq. 4)}$$

This evaluation via U_{eff} corrects for differences in the internal air temperature T_i between the individual wall sections. The heat gains measured in winter are so small that they are not considered further. Figure 8 left shows the weather data and Figure 8 right depicts the calculated U_{eff} values of the wall sections for the winter measurement period. The weather was mostly moderate with daily mean temperatures between 5 to 10°C and one longer frost period in January. It was rainy with very little sunshine until the beginning of March.

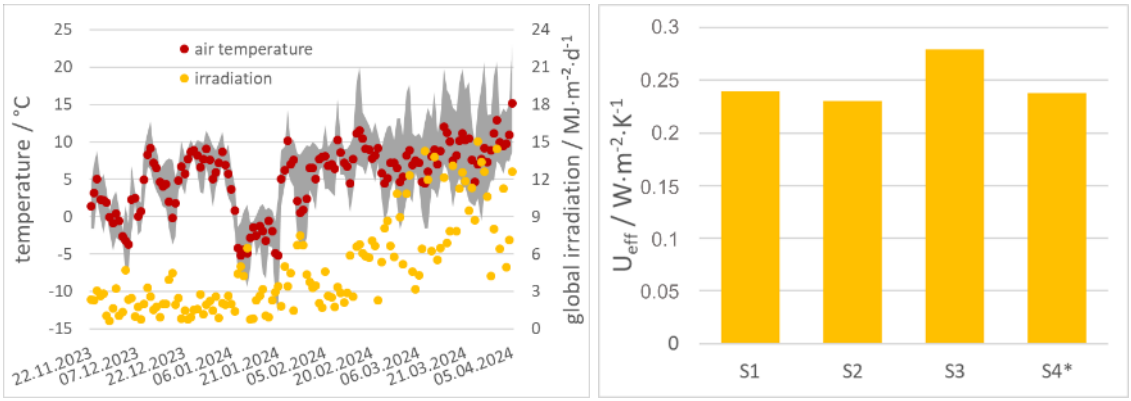

Fig. 8: Measured daily mean air temperature (red dots), minimum and maximum daily air temperature (grey area), and horizontal solar global irradiation (left); U_{eff} values for the wall section S1 without and the wall sections S2 to S4 with LWS (right). *Due to problems with the inside air temperature sensor of S4 only data for the following periods are considered: November 22-29, 2023; December 5-6, 2023; December 9 2023 – February 12 2024; March 12-26, 2024.

On the south façade, the LWS do not improve U_{eff} very much compared to a reference wall with a solar absorptance of 0.6. While LWS S2 and S4 show a slight reduction of 4 % and 1 %, respectively, the U_{eff} of LWS S4 is even 16 % higher compared to the reference wall S1. This is a first indication that LWS can lead to greater heat losses, especially when compared to walls with medium to high solar absorptance. Of course, facades with medium to high solar absorptances instead have disadvantages in summer.

3.4 Influence of solar absorptance in winter

To estimate the influence of the solar absorptance, we estimated the heat losses and U_{eff} of the reference wall S1 for a bright plaster with a solar absorptance α_S of 0.24 as described in section 3.2. A measurement of S1 and S3 without LWS between March 17 and May 3 2023 was used as reference. The room temperature was set to 21°C. Figure 9 shows the weather data as well as the heat gains and losses. The heat gains are just for information and are not used further.

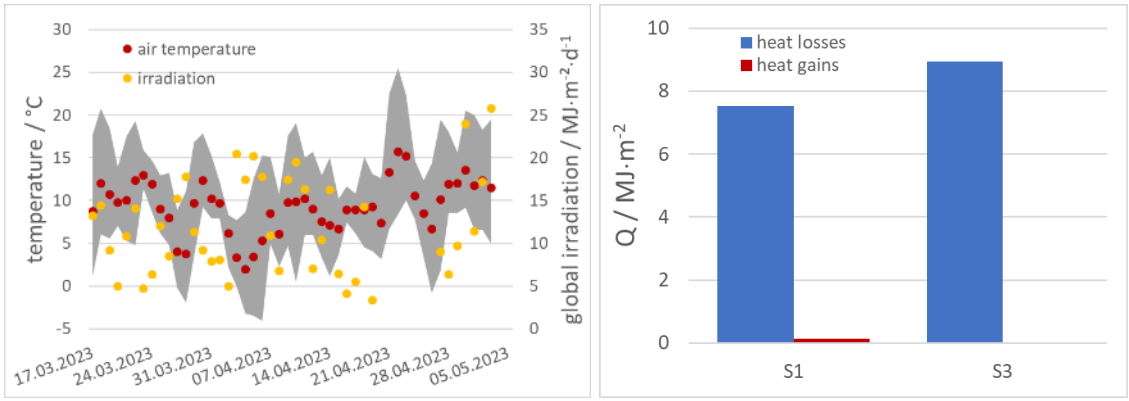

Fig. 9: Measured daily mean air temperature (red dots), minimum and maximum daily air temperature (grey area), and horizontal solar global irradiation (left); summarized heat gains and losses through the wall sections without LWS (right).

$Q_{S1.bright}$ was calculated according to equation 2. Table 6 gives an overview of the data used and the results. Figure 10 shows the U_{eff} values of the south wall sections S2 to S4 of Figure 8 compared to the U_{eff} value for S1 with a bright plaster.

Due to the bright plaster, the U_{eff} value of S1b is about 19 % higher than that of S1. Consequently, the effect of the LWS changes accordingly when compared to S1b instead of S1. While S3 now shows a slight reduction in U_{eff} value of 2 %, the U_{eff} values of S2 and S4 are lower by 19 % and 17 %, respectively.

Tab. 6: Measured heat losses for wall section S1 with medium plaster and S3 with bright plaster and estimated heat losses for S1 with bright plaster. All wall sections are without LWS.

Wall section	Heat loss [MJ m^{-2}]	Description and measurement period
Q_{S1}	7.513 ± 0.225	Medium plaster, section 3.4, measured
Q_{S3}	8.936 ± 0.280	Bright plaster, section 3.4, measured
$Q_{S1.medium}$	46.17 ± 1.39	Medium plaster, section 3.3, measured
$Q_{S1.bright}$	54.91 ± 1.65	Bright plaster, section 3.3, estimated

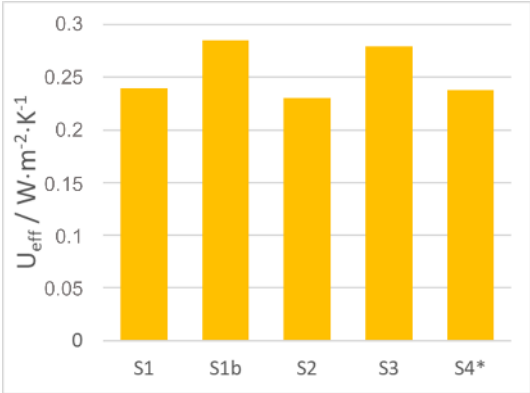

Fig. 10: Comparison of the U_{eff} values of the wall sections: S1 is measured without LWS and with medium plaster (α_S = 0.6), S1b is estimated without LWS and with bright plaster (α_S = 0.24), S2 to S4 are measured values with LWS. *Due to problems with the inside air temperature sensor of S4 only data for the following periods are considered: November 22-29, 2023; December 5-6, 2023; December 9 2023 – February 12 2024; March 12-26, 2024.

4. Conclusions and Outlook

Measurements on different kinds of LWS were performed in the laboratory as well as on a test façade. The laboratory measurements in a Hot-Box system show reduced U-values for all investigated LWS. When rear ventilated, the different kinds of LWS perform almost identical with reductions in U-value of 10 % to 13 %. Without rear ventilation, the U-value reduction is much bigger ranging from 17 % to 30 % and the LWS perform differently, dependent on their design.

The results on the test façade are considerably more varied. With solar radiation effects included, the performance of the LWS on the thermally well-insulated test façade depend strongly on the solar absorptance of the reference wall. Compared to a south wall with a medium plaster with α_S = 0.6, the three investigated LWS show only small reductions of a few percent or in one case even lead to 16 % higher heat losses in winter. Compared to a reference wall with a bright plaster with α_S = 0.24, all three LWS show reductions of 2 % up to 19 %.

In summer, the LWS reduce the heat gains through the wall. The effect of the solar absorptance of the reference wall is reversed here. While a high solar absorptance helps reduce heat losses in winter it generates high heat gains in summer. On the south façade, the two investigated LWS reduced the heat gains by 38 % to 48 % compared to a reference wall with medium plaster but only by 5 % to 17 % for a bright plastered reference.

The positive effects of LWS, lower heat losses in winter and lower heat gains in summer, can also be achieved by adjusting the solar absorption of the wall. However, a high solar absorption value in summer leads to undesirably high heat gains, while a low value in winter increases heat losses. An LWS shows its advantages in both seasons.

The results also show significant differences between the LWS with some performing better than others. Favorable design criteria here appear to be the use of very thick substrate layers, as in the gabion system, and

carrier materials with low thermal conductivity, such as foams as in the Fytotextile system.

An important fact to mention is that the LWS are elevated in front of the façade, so that no thermal bridge effects due to retaining structures or screws are included in the measurement data. These thermal bridges have to be taken into account for they can reduce or even overcompensate any savings effects (Tudiwer et al. 2019), especially on well insulated façades.

In a next step, a simulation model shall be validated by the measurements to calculate the energetic effect of LWS on different kinds of buildings.

Acknowledgements

The work in this project is supported by the Federal Ministry of Economic Affairs and Climate Action (BMWK), based on a resolution of the German Parliament.

References

ASTM C236-89, 1989. Standard test method for steady-state thermal performance of building assemblies by means of a guarded hot box.

Bianco, L., Serra, V., Larcher, F., Perino, M., 2017. Thermal behaviour assessment of a novel vertical greenery module system: first results of a long-term monitoring campaign in an outdoor test cell. Energy Efficiency 10, 625–638, https://doi.org/10.1007/s12053-016-9473-4.

DIN V 18599-2, 2018. Energy efficiency of buildings – Calculation of the net, final and primary energy demand for heating, cooling, ventilation, domestic hot water and lighting – Part 2: Net energy demand for heating and cooling of building zones.

Djedjig, R., Belarbi, R., Bozonnet, E., 2017. Experimental study of green walls impacts on buildings in summer and winter under an oceanic climate. Energy and Buildings 150, 403-411, https://doi.org/10.1016/j.enbuild.2017.06.032.

Fox, M., Morewood, J., Murphy, T., Lunt, P., Goodhew, S., 2022. Living wall systems for improved thermal performance of existing buildings. Building and Environment 207 Part A, https://doi.org/10.1016/j.buildenv.2021.108491.

Mann, G., Gohlke, R., Haase, D., 2023. BuGG-Marktreport Gebäudegrün 2023 - Dach-, Fassaden- und Innenraumbegrünung Deutschland. Bundesverband GebäudeGrün e.V. (BuGG), ISSN 2750-3763.

Ogut, O., Tzortzi, N.J., Bertolin, C., 2022. Vertical Green Structures to Establish Sustainable Built Environment: A Systematic Market Review. Sustainability 14(19), 12349, https://doi.org/10.3390/su141912349.

Serra, V., Bianco, L., Candelari, E., Giordano, R., Montacchini, E., Tedesco, S., Larcher, F., Schiavi, A., 2017. A novel vertical greenery module system for building envelopes: The results and outcomes of a multidisciplinary research project. Energy and Buildings 146, 333-352, https://doi.org/10.1016/j.enbuild.2017.04.046.

Susca, T., Zanghirella, F., Colasuonno, L., Del Fatto, V., 2022. Effect of green wall installation on urban heat island and building energy use: A climate-informed systematic literature review. Renewable and Sustainable Energy Reviews 159, 112100, https://doi.org/10.1016/j.rser.2022.112100.

Tudiwer, D., Korjenic, A., 2017. The effect of living wall systems on the thermal resistance of the façade. Energy and Buildings 135, 10-19, https://doi.org/10.1016/j.enbuild.2016.11.023.

Tudiwer, D., Teichmann, F., Korjenic, A., 2019. Thermal bridges of living wall systems. Energy and Buildings 205, 109522, https://doi.org/10.1016/j.enbuild.2019.109522.

02. Sustainable heating and cooling systems for buildings

Techno-Economic Comparison of Different Solar Photovoltaic/Thermal (PVT) Absorber Designs for Ground Source Heat Pump (GSHP) Integration

Francisco Beltran, Nelson Sommerfeldt

KTH Royal Institute of Technology, Stockholm (Sweden)

Summary

This study assesses the performance of a PVT+GSHP system using four different PVT collectors, each with unique design features, for a multi-family building in Stockholm. Thermal performance coefficients are obtained through outdoor testing of each collector under low-temperature conditions, and incorporated into a comprehensive dynamic system model in TRNSYS. The study varies the design and array size of the PVT collectors and evaluates their impact on the techno-economic performance of the system, considering traditional and undersized borehole fields. Technical performance metrics include annual thermal energy output, seasonal performance factor and back-up heater utilization, and economic performance is assessed with total life cycle cost (TLCC). The results show that when integrating PVTs with GSHP systems, lower collector costs should be prioritized over enhanced thermal performance. Despite the finned designs exhibiting a higher thermal yield (up to 10%) this only improves the seasonal performance factor by 0.6% compared to non-finned designs, but can increase TLCC by up to 5.2%.

Keywords: Solar heat pumps, techno-economic analysis, PVT plus GSHP, borehole regeneration

1. Introduction

The integration of photovoltaic-thermal (PVT) collectors with ground source heat pumps (GSHP) has been shown to reduce borehole length and spacing, significantly decreasing the land area required for the ground heat exchanger (Chhugani et al., 2023; Sommerfeldt & Madani, 2019). One of the key advantages of PVT collectors in this context is the low temperature of the working fluid. This characteristic not only facilitates the simultaneous cooling of the PV cells, thereby enhancing their electrical efficiency, but also improves the thermal performance of the system through increased heat transfer with ambient air (Giovannetti et al., 2019). This has led to the investigation and market development of PVT collectors aimed at improving heat transfer with ambient air, such as by expanding the heat transfer area with the addition of fins. Additionally, the lower temperatures within a GSHP circuit enable the utilization of polymeric materials. However, despite these advancements, there remains a gap in the literature regarding the techno-economic comparison of PVT collectors with different design features for integration with GSHP systems. Existing studies have predominantly focused on performance metrics in isolation, without a comprehensive assessment of the trade-offs between enhanced thermal output, overall system efficiency, and total life cycle cost. Addressing this gap is crucial for informing the design and development of PVT collectors that are optimally suited for GSHP applications. The results of this study are anticipated to enhance the understanding of how PVT collectors should be designed for this particular application, with a focus on technical and economic metrics.

2. Objectives

The objective of this study is to identify the techno-economic optimal PVT collector design for integration into GSHP systems in the Nordic region. This is achieved by answering the following research questions:

- How does PVT design impact thermal energy generation in a PVT+GSHP system?
- How is the technical system performance impacted by the various PVT designs?
- Is there an economically preferred design approach for PVT as applied to GSHP?

© 2024. The Authors. Published by International Solar Energy Society
Selection and/or peer review under responsibility of Scientific Committee
10.18086/eurosun.2024.02.01 Available at http://proceedings.ises.org

3. Methods

This study employs a comprehensive dynamic system modeling approach to evaluate the integration of different PVT absorber designs with a ground source heat pump (GSHP) system. The methodology begins with outdoor testing to obtain empirical thermal performance coefficients for the studied PVT designs. These coefficients are then incorporated into a TRNSYS simulation model tailored to represent a multi-family building in Stockholm. By simulating various configurations of PVT arrays and borehole fields, the model assesses both the technical and economic performance of the system. This ensures that the analysis captures the nuanced trade-offs between thermal energy output, system efficiency, and total life cycle costs across different design scenarios.

The case study for the dynamic modelling is based on the PVT + GSHP TRNSYS model developed by Sommerfeldt & Madani, (2019), as shown in Fig. 1. It represents a typical multi-family house in Stockholm built between the years 1985 and 2005 with 2,000 m^2 of heated floor area. The building's energy needs are 125 kWh/m^2-yr for space heating, 38 kWh/m^2-yr for domestic hot water, and 30 kWh/m^2-yr for electricity. The system includes a variable-speed ground source heat pump with a capacity of 52 kW (B0/W35) at 3600 RPM. The baseline ground heat exchanger consists of 12 parallel U-tube boreholes, each 300 meters long and spaced 15 meters apart. The PVT array features 48, 96, and 144 (maximum array size assumed to fit on the roof) connected in a series/regenerative configuration with the GSHP. The PVT collectors are modeled using Type 203 (Chhugani et al., 2021), which relies on the empirical thermal performance coefficients of the collectors.

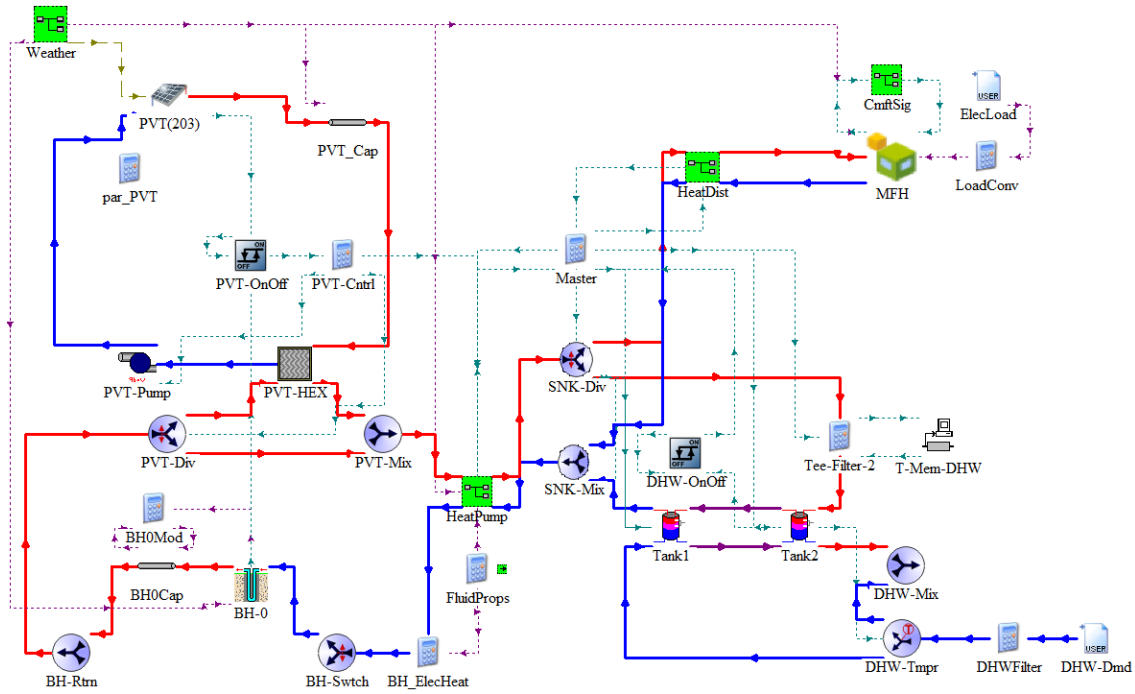

Fig. 1. PVT + GSHP simulation model in TRNSYS

The studied collectors are a sheet and tube (S&T), box-channel polypropylene (BC-PP), finned-tube (FT), and box-channel aluminum with 20 mm fins (BC-AL-20), which are described in detail in (Beltrán et al., 2024). A representation of the different PVT designs can be seen in Fig. 2. The collectors are evaluated based on four key metrics: specific annual thermal energy output (in kWh/m^2-yr), seasonal performance factor (SPF_{4+}), utilization rate of direct electric backup heater (in percentage of total thermal energy delivered), and total life cycle cost (TLCC) in Euros. These results are benchmarked against a baseline GSHP system with a borehole field comprising 12 boreholes, each 300 m deep, spaced 15 meters apart and without PVTs. Additionally, the same PVT systems are coupled with an undersized borehole field of 6x300 m boreholes and 5 m spacing to evaluate if the cost-benefit balance changes.

The seasonal performance factor is calculated according to eq.1, following the methodology established by Sommerfeldt and Madani (Sommerfeldt & Madani, 2019). The SPF_{4+} metric used in this study is a hybrid of

SPF4, as defined by Nordman et al. (Nordman et al., 2012), and SHP+, as presented by the IEA's T44A38 program (Hadorn, 2015).

$$SPF_{4+} = \frac{Q_{sh}+Q_{dhw}}{E_{hp}+E_{p,src}+E_{p,snk}+E_{bb}+E_{b,dhw}+E_{p,pvt}} \quad \text{(eq. 1)}$$

The total life cycle cost is used to compare the economic performance of the PVT+GSHP systems and is described by eq. 2. The main components of the TLCC are investments (I_x), operations and maintenance (OM_x), and residual value (RV_x). The nomenclature for both equations can be found in Tab. 1, whereas the economic boundary conditions are presented in Tab. 2.

$$TLCC_{PVT+GSHP} = I_{HP} + I_{BH} + I_{PVT} + OM_{EL} + OM_{EQ} - RV_{PVT} - RV_{BH} \quad \text{(eq. 2)}$$

Tab. 1: Nomenclature for equations 1 and 2

Parameter	Symbol	Unit
Thermal energy for space heating	Q_{sh}	kWh_{th}
Thermal energy for domestic hot water	Q_{dhw}	kWh_{th}
Electric energy for heat pump compressor	E_{hp}	kWh_{el}
Electric energy for borehole circuit pump (source)	$E_{p,src}$	kWh_{el}
Electric energy for heat delivery pump (sink)	$E_{p,snk}$	kWh_{el}
Electric energy for backup heat pump heater	E_{bb}	kWh_{el}
Electric energy for backup tank heater	$E_{b,dhw}$	kWh_{el}
Electric energy for PVT circulation pump	$E_{p,pvt}$	kWh_{el}
Investment costs – heat pump	I_{HP}	€
Investment costs – boreholes	I_{BH}	€
Investment costs - PVT	I_{PVT}	€
Operation and maintenance – electricity purchases	OM_{EL}	€
Operation and maintenance – system equipment	OM_{EQ}	€
Residual value - PVT	RV_{PVT}	€
Residual value - boreholes	RV_{BH}	€

Tab. 2: Economic boundary conditions

Parameter	Unit	Value
Purchase electricity price	€/kWh	0.14
Wholesale electricity price	€/kWh	0.052
Heat pump cost (w/VAT)	€	32,586
S&T PVT cost	€/m²	312.3
BC-PP PVT cost	€/m²	393.0
FT PVT cost	€/m²	524.1
BC-AL-20 cost	€/m²	356.4
PVT fixed cost	€	11,300
PVT variable cost	€/collector	260.8

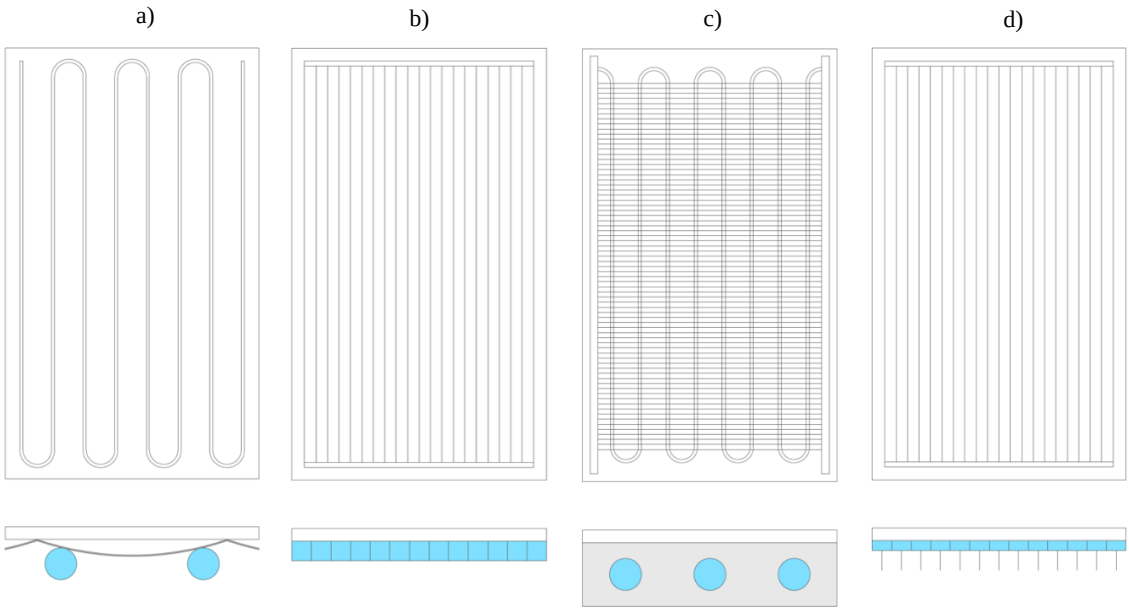

Fig. 2. Representation of a) S&T b) BC-PP c) FT d) BC-AL-20 (Beltrán et al., 2024)

The thermal performance coefficients of the studied PVT collectors are derived at an outdoor testing facility in Stockholm, as described in Beltrán et al., (2024). The thermal output of the PVT collectors is measured under a wide range of operating and weather conditions, and a linear multivariable regression analysis is used to derive the empirical thermal performance coefficients of each collector according to eq. 3, a simplified form of the ISO 9806:2017 standard equation for liquid heating collectors (ISO, 2017). The zero-loss efficiency (η_0), first-order thermal loss coefficient (c_1), the wind dependence of the heat loss coefficient (c_3), and the wind dependence of the zero-loss efficiency (c_6) for each PVT collector design are presented in Tab. 3. T_a is the ambient temperature, T_m the mean fluid temperature, G the global irradiance on the plane of the array and u the wind velocity.

$$\dot{q}_{th} = \eta_0 G - c_1(T_m - T_a) - c_3 u(T_m - T_a) - c_6 u G \qquad \text{(eq. 3)}$$

Tab. 3: Thermal performance characteristics of the different PVT collectors

Coefficients	S&T	BC-PP	F&T	BC-AL-20
Area [m^2]	1.67	1.88	1.99	1.95
η_0	0.410	0.490	0.428	0.566
c_1 [W/(m^2.K)]	13.345	13.925	34.502	27.105
c_3 [J/(m^3.K)]	4.012	4.026	6.066	5.637
c_6 [s/m]	0.027	0.021	0.027	0.017

4. Results

Fig. 3A shows the average specific annual thermal energy output of the different collector designs throughout the 20-year time span, for varying PVT array sizes. As expected, the finned designs provide a higher thermal energy output than the non-finned designs due to the enhanced heat capture from ambient air. When compared with the S&T, the FT and BC-AL-20 absorbers generate 7.4% and 10.0% higher specific annual thermal energy output respectively, for the 48 PVT array size. The thermal output of the BC-PP is higher than the S&T thanks to a higher contact area between the fluid and rear side of the PV panel, but lower than the finned designs due to a lower heat exchange area with ambient air. As the array size increases, there are diminishing returns on

the thermal output due to the increased borehole temperature, and with 144 collectors the specific annual output is similar across designs.

Fig. 3B shows that the addition of 48 PVT of the S&T design can improve the seasonal performance factor by 1.9% compared to the case with no PVTs, while the finned designs can improve SPF by 2.5%. This shows that the effect of the different PVTs on SPF is similar, regardless of the absorber design. Increasing the PVT array size to 96 or 144 collectors shows additional improvements in SPF but with diminishing returns (improvement of 1.5% and 0.9% respectively for the S&T design). A similar effect is seen in the back up heater use, as shown in Fig. 3C. By adding 48 of the S&T PVTs, the back-up heater use is negligibly reduced from 2.21% to 2.01% of the total space heating demand. By changing to FT or BC-AL-20, a minimum value of 1.96% is achieved. Due to the low impact that PVT collectors have on the overall system efficiency with the baseline borehole field, the TLCC of a PVT+GSHP system is higher than that of a GSHP-only system for all the considered PVT designs (Fig. 3D).

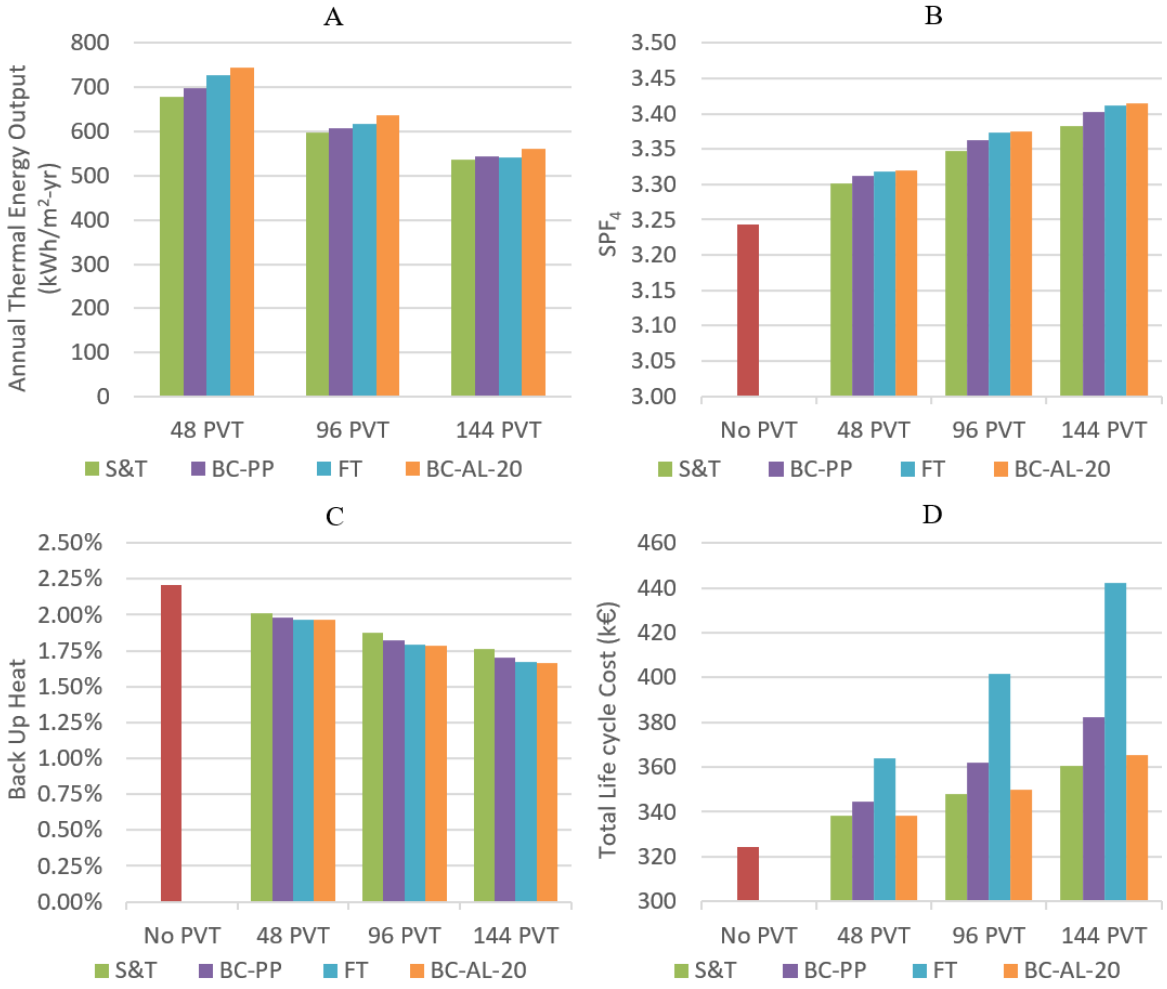

*Fig. 3. A) Annual thermal energy output B) SPF C) Back up heater use and D) TLCC of the different PVT collector designs for varying array sizes and the baseline borehole field. *(note that y-axis does not start at zero for SPF and TLCC)*

Since one of the main benefits of PVTs on GSHP systems is the potential to reduce borehole field size and/or regenerate degraded borehole fields, an undersized borehole field of 6x300 m boreholes with 5 m spacing is also simulated. The results in Fig. 4A show that the specific thermal energy output of the PVT collectors connected to an undersized borehole field is 40-45% higher than for the baseline borehole field. This can be explained by the fact that in an undersized borehole field, the temperatures in the ground are lower, and therefore the heat capture potential of the collector is considerably higher, as seen in Fig. 5. In terms of PVT yields for the 48 PVT case, the S&T produces 1,030 kWh/m^2-yr, with the FT and BC-AL-20 producing 1,068 kWh/m^2-yr and 1,078 kWh/m^2-yr respectively. The specific thermal production is almost equal among the different designs since the less efficient PVT collectors result in lower ground temperatures, increased temperature differences between ambient and fluid, and therefore comparable thermal generation. It is also

worth noting how the thermal production drops as array sizes increase. The specific thermal yield of 144 PVTs with an undersized borehole field is lower than that of the baseline borehole field with 48 PVTs

The impact on SPF and back up heater use is higher in the case of an undersized borehole field, as can be observed in Fig. 4B and Fig. 4C. The addition of 48 PVTs of the S&T collectors can improve the seasonal performance factor by 7.7% and reduce back up heat from 6.0% to 4.7% of the total space heating supply. As observed for the case of the baseline borehole field, there is a negligible difference in system efficiency between the different designs, with all SPFs between 2.83 and 2.88, and back up heat supply between 4.7% and 4.4%. Increasing the array size to 96 and 144 PVT collectors has diminishing returns, with the SPF of a system with 96 of the BC-AL-20 (187 m^2) being almost equal to that of a system with 144 of the S&T or BC-PP collectors (240-244 m^2).

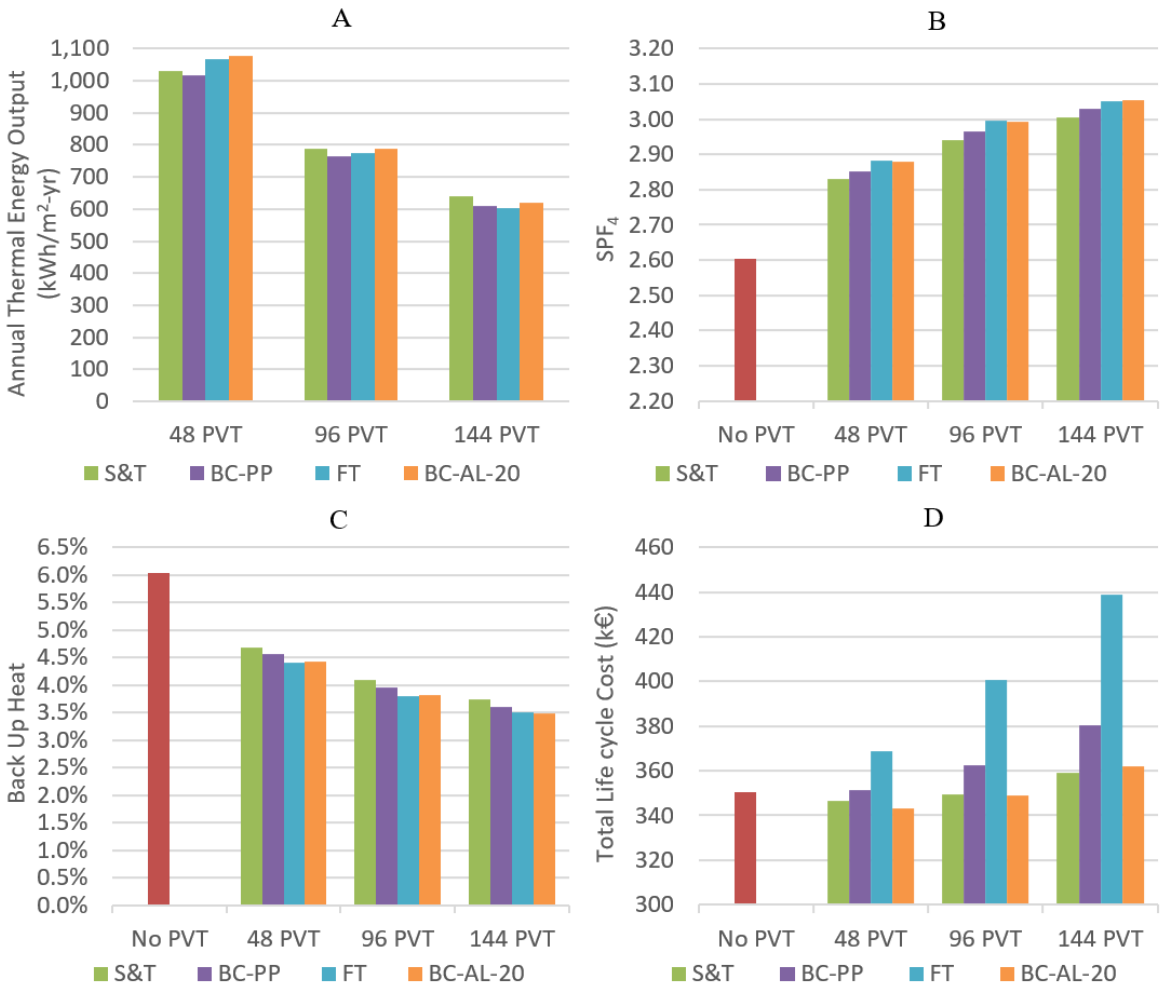

*Fig. 4. A) Annual thermal energy output B) SPF C) Back up heater use and D) TLCC of the different PVT collector designs for varying array sizes and an undersized borehole field. *(note that y-axis does not start at zero for SPF and TLCC)*

There is a clear shift in the economic balance when adding PVT collectors to a GSHP system with an undersized borehole field. Fig. 4D shows that the TLCC of a system without PVT is the same as for a system with 48 of the BC-PP PVT collectors. If we consider adding 48 of the S&T or BC-AL-20 collectors, TLCC can be reduced by 1.2% and 2.0%, making it economically more attractive than the case without PVT. However, the more expensive manufacturing process of the FT design is not cancelled out by the higher thermal energy output and SPF improvement, which results in a TLCC 5.2% higher than for the case without PVT. Lower costs are achieved for the S&T and BC-AL-20 designs when considering 96 PVTs, but in all other cases the PVT + GSHP system ends up being more expensive than the GSHP-only. The lowest cost system overall is the traditionally sized GSHP without PVT.

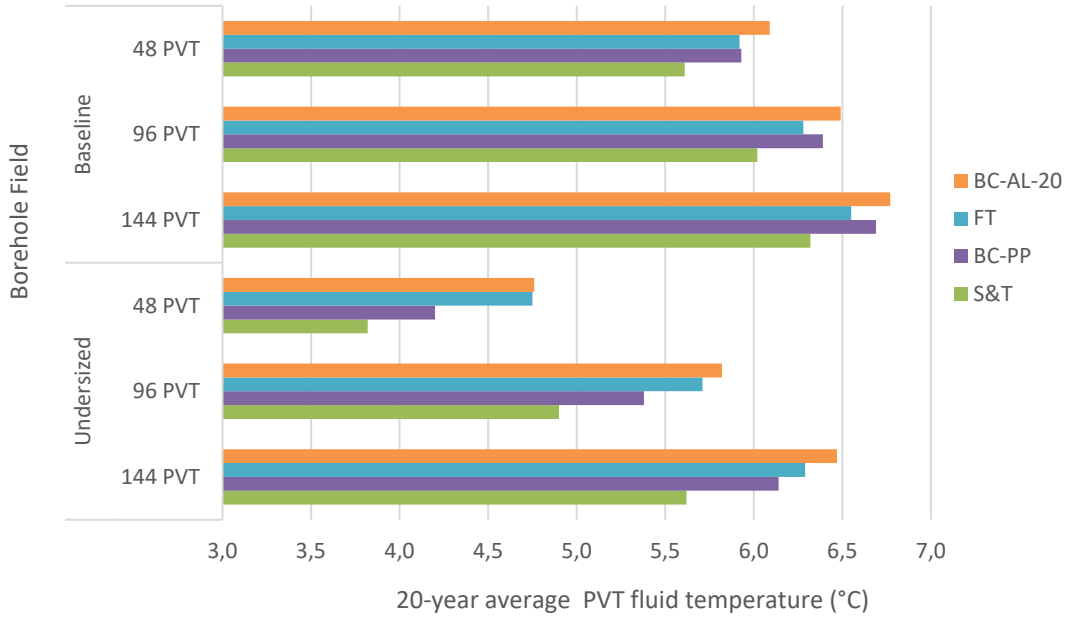

Fig. 5. 20-year average fluid temperature in the PVT collectors for baseline and undersized borehole fields across different PVT array sizes (48, 96, and 144 PVTs).

5. Conclusions

The results of this work show that when integrating PVT collectors with ground source heat pump systems it is necessary to prioritize lower capital costs over enhanced thermal performance. Although the finned designs yield a higher annual thermal energy output, it does not translate to an equivalent improvement in system efficiency. Fins are a positive feature for this application, only if they can be added at a low cost, as is the case of the BC-AL-20.

It has also been shown that there is no need for large PVT arrays since the best economic results were achieved with the lowest array size due to the higher specific heat output. Besides, considering only technical performance, increasing the array size has diminishing returns on SPF improvement and back up heat reduction.

Another important aspect to consider is material selection. The only plastic absorber considered in the study is the BC-PP, and the annual thermal energy output is higher than for the non-finned metallic counterparts, but it comes at a higher manufacturing cost. However, it is still a cheaper option than the finned designs.

Finally, it is confirmed that there is a greater potential for PVT to be integrated into systems with undersized borehole fields than there is in new systems with a well-dimensioned ground heat exchanger. Adding PVT collectors can yield positive economic results in those cases.

6. Acknowledgements

This study was conducted as part of the *Smart Renovation Strategies for Sustainable Electrification* project (SmartReno SE - Project No. P2023-01509), funded by the Swedish Energy Agency under the ReBygg Program. The authors also gratefully acknowledge the financial support provided by Nordic Energy Research, which facilitated an exchange to the Norwegian University of Science and Technology (NTNU), where an important portion of this work was carried out.

7. References

Beltrán, F., Sommerfeldt, N., Eskola, J., & Madani, H. (2024). Empirical investigation of solar photovoltaic-thermal collectors for heat pump integration. *Applied Thermal Engineering*, *248* (December 2023). https://doi.org/10.1016/j.applthermaleng.2024.123175

Chhugani, B., Pärisch, P., Helmling, S., & Giovannetti, F. (2023). Comparison of PVT - heat pump systems with reference systems for the energy supply of a single-family house. *Solar Energy Advances*, *3* (December 2022), 100031. https://doi.org/10.1016/j.seja.2022.100031

Chhugani, B., Pärisch, P., Kirchner, M., Littwin, M., Lampe, C., & Giovannetti, F. (2021). *Model Validation and Performance Assessment of Unglazed Photovoltaic-Thermal Collectors with Heat Pump Systems*. 1–12. https://doi.org/10.18086/eurosun.2020.05.13

Giovannetti, F., Lampe, C., Kirchner, M., Littwin, M., Asenbeck, S., & Fischer, S. (2019). Experimental investigations on photovoltaic-thermal arrays designed for the use as heat pump source. *Proceedings of the ISES Solar World Congress 2019 and IEA SHC International Conference on Solar Heating and Cooling for Buildings and Industry 2019*, 177–188. https://doi.org/10.18086/swc.2019.05.03

Hadorn, J. (2015). *Solar and Heat Pump Systems for Residential Buildings*.

ISO. (2017). *ISO 9806:2017 Solar energy - Solar thermal collectors - Test methods*.

Nordman, R., Kleefkens, O., Riviere, P., Nowak, T., Zottl, A., Arzano-Daurelle, C., Lehmann, A., Polyzou, O., Karytsas, K., Riederer, P., Miara, M., Lindahl, M., Andersson, K., & Olsson, M. (2012). *SEasonal PErformance factor and MOnitoring for heat pump systems in the building sector SEPEMO-Build: FINAL REPORT*.

Sommerfeldt, N., & Madani, H. (2019). In-depth techno-economic analysis of PV/Thermal plus ground source heat pump systems for multi-family houses in a heating dominated climate. *Solar Energy*, *190*, 44–62. https://doi.org/10.1016/j.solener.2019.07.080

Energy concepts with high solar fraction for multi-family houses

Franziska Bockelmann[1] and Markus Peter[1,2]

[1] Steinbeis-Innovationszentrum (siz) energieplus, Braunschweig (Germany)

[2] dp-quadrat, Soest (Germany)

Abstract

In most cases, the heat and power supply of buildings is still planned and realized separately, including the use of renewable energies like photovoltaic and solar thermal. By means of a simulation study, this approach is to be changed and holistic solar-based supply concepts for residential buildings are targeted and developed. As single family houses, multi-family houses offer potentials for the implementation of solar-based energy supply concepts, however they have to be evaluated in terms of the space requirements and the number of stories. Based on various solar energy systems and the boundary conditions from building and construction, energy supply concepts and design specifications for multi-family houses are derived. The results of a simulation study show, that for the building and the measures under investigation a total solar fraction of up to 70 % can be achieved. The most suitable area-ratio of solar thermal to photovoltaic is 20/80 to 50/50.

Keywords: multi-family houses, high solar fraction, simulation, photovoltaic, solar thermal, energy concepts

1. Introduction

More than half of the final-energy demand in Germany is related to heating, cooling and air conditioning of buildings. On the other hand, there is high potential of solar energy that can be gained directly at the buildings, usable to cover major parts of their energy demand. Commonly solar energy concepts for buildings are set-up separately for heat and electricity by different designers, planners and installers. Therefore, the market has developed to concepts focusing either the thermal aspects or the electrical part of the buildings. On the one hand, large solar thermal collector areas and large hot water stores with high thermal capacities are implemented to cover high thermal solar fractions of the heat demand. On the other side, for high electricity gains large PV-systems are integrated aiming to generate as much electricity as possible and/or to realize a surplus in the annual balance of the building demand and production of electricity. Electricity-based concepts increasingly often use PV produced electricity to provide heat. In Germany, depending on the remuneration for feeding PV produced electricity into the public grid and energy costs, a few years ago, PV systems on buildings almost exclusively feed electricity into the grid. By changing in the boundary conditions, gradually PV electricity has been used to cover household and operating electricity requirements of the buildings. Nowadays the use of PV electricity to provide heat - usually in combination with heat pumps - is a growing trend.

Generally, in most cases at best there is a slight interaction of both concepts – although there is high need to achieve cost-effective high solar fractions with acceptance of the investor in both, heat and electricity, to reduce costs for non-renewable energy supply. Solar thermal energy and photovoltaics are by no means mutually contradictory technologies. In order to counteract this widespread opinion and to provide necessary background and recommendations for holistic system solutions aiming for ecologically and economically reasonable solar-based heat and power supplies for residential buildings, as a part of the presented simulation study, corresponding concepts have been developed.

2. Solar Energy Buildings and Key Performance Indicators

A significant reduction of the fossil energy use of buildings can be achieved by utilizing solar thermal (ST) and photovoltaic (PV) energy for their operation. IEA SHC Task 66 focus on the development of economic energy supply concepts with high solar fractions for single-family houses, multi-story residential buildings and

© 2024. The Authors. Published by International Solar Energy Society
Selection and/or peer review under responsibility of Scientific Committee
10.18086/eurosun.2024.02.02 Available at http://proceedings.ises.org

building blocks or distinguished parts of cities (communities) for both, new buildings and existing buildings after comprehensive refurbishment. The central component to achieve real Solar Energy Buildings (SEB) is the active and passive use of solar energy.

The feasible solar thermal and solar electrical fractions depend significantly on the clime in that the building is located. For central European climate conditions and for households employing e-mobility, according to Task 66 the following solar fractions should be achieved:

- at least 85 % of the heat demand,
- 100 % of the cooling demand and
- at least 60 % of the electricity requirements.

Ahead of achieving these solar fractions by intensive use of solar thermal and solar electric (photovoltaic) energy, the focus must be on reducing the energy demand of the buildings.

To describe, evaluate and/or to compare buildings, so-called Key Performance Indicators (KPIs) are used. They can be applied to

- evaluate and compare different buildings/blocks/communities,
- evaluate and compare different concepts in one building/block/community,
- optimize components of the buildings in terms of energy use/flows, economics, ecology etc.

Note: The aim is to optimize the overall performance of a building. Therefore, all numbers and fractions are evaluated from the view of production and not from consumption. Doing so, also heat losses of stores and other hidden consumer are considered. By this, in some cases, lower rates as expected might result.

With respect to the different solar fraction used by Task 66, the following Key Performance Indicators (KPIs) are most relevant (nomenclature see chapter 8):

Total solar fraction $f_{sol,tot}$
Fraction of self-generated and self-used PV electricity and useful solar thermal heat referred to the total energy used for household and technical purposes in the form of electricity and heat.
In other words: Energy supplied by the solar part (PV and ST) of a system divided by the total load (electrical and thermal).

$$f_{sol,tot} = \frac{E_{PV,tot} - E_{PV,grid} + Q_{ST,tot} - Q_{ST,grid}}{E_{PV,tot} - E_{PV,grid} + E_{grid} + Q_{ST,tot} - Q_{ST,grid} + Q_{grid} + Q_h - Q_{h,el}} \text{ [\%]} \quad \text{(eq. 1)}$$

Thermal solar fraction $f_{sol,th}$
Fraction of solar-generated useful heat referred to the total heat consumption. Solar thermal as well as solar electric heat generation (heat pumps based on photovoltaic power) are considered.
In other words: Thermal energy supplied by the solar thermal part of the system and heat supplied by heat pumps using PV produced electricity divided by the total thermal load.

$$f_{sol,th} = \frac{Q_{ST,tot} - Q_{ST,grid} + Q_{sol,PVHG}}{Q_{ST,tot} - Q_{ST,grid} + Q_{grid} + Q_h} \text{ [\%]} \quad \text{(eq. 2)}$$

Electrical solar fraction $f_{sol,el}$
Fraction of electricity generated by a photovoltaic system referred to the total electricity consumption.
In other words: Energy supplied by the solar electrical part of a system divided by the total electrical load.

Note that also electricity from PV that is used for heat generation, e. g. by heat pumps or resistance heaters, is included.

$$f_{sol,el} = \frac{E_{PV,tot} - E_{PV,grid}}{E_{PV,tot} - E_{PV,grid} + E_{grid}} \text{ [\%]} \quad \text{(eq. 3)}$$

3. Numerical system simulation - boundary conditions and variants

In front of the simulation study, the building and construction, building physics and boundary conditions for the technical system of the multi-family house and the variants chosen to be examined, are defined. In the case on hand a building, which has been monitored by the corresponding author, is used as reference. For this building with regard to the KPIs variants and changes have been developed and implemented in numerical simulations. The analysis and evaluation of the results focus on the solar fractions and the CO_2 emissions. Representing the major focus and objectives of Task 66, in this paper only solar fractions and energy values are discussed.

In addition to technical aspects, in order to determine a holistic picture of solar-based buildings, also the building requirements will be considered. For heat generation only heat pumps are used. Compared to heat pumps, gas boilers or other heat sources that base on combustion hardly require any electric energy and therefore does not draw notable renewable electricity from a PV system and/or an electrical storage. Thus, for the combustion of fuels, for operation virtually no (renewable) electricity is required - and by this the achievable solar fraction will be low.

3.1. Boundary conditions

In the simulations, only the technologies for producing heat and electricity are varied. The way distributing and transferring the energy for space heating and domestic hot water preparation within the building remain unchanged.

As the reference building has not and German regulations do not provide for cooling in the planning and design of residential building, cooling is not implemented. Furthermore, e-mobility is not taken into account. Self-evident this additional load would significantly reduce the solar fraction related to the building.

Building data (Bockelmann, 2019):

- Multi-family house consisting of two buildings with three floors each, in total 12 apartments. The entire net floor area of both buildings amount to 1,140 m².
- The thermal standard of the entire block is 46.3 kWh/(m²a) (see Figure 2). The buildings have flat roofs and are orientated 24.3° south-east (orientation of the long building side).
- Technology: From the architectural point of view, the PV system and the solar thermal collectors should have the same tilt angle; considering the performance of the solar thermal collector to serve for space heating, the angle is set at 65°. The orientation equals to that of the buildings (24.3° south-east).
- The building is located in Potsdam (Germany), see weather data in Figure 3 (Meteonorm, 2018).

Note: In the following the singular term building always mean and refer to the building data given above.

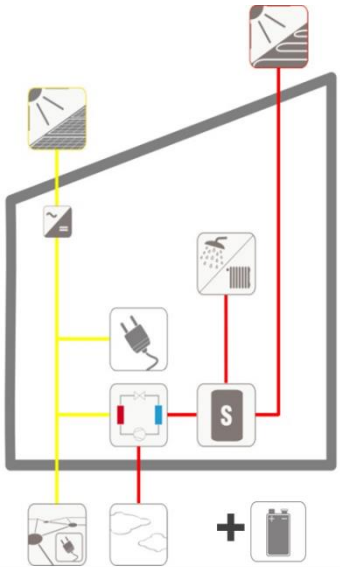

Fig. 1: Energy concept for multi-family house

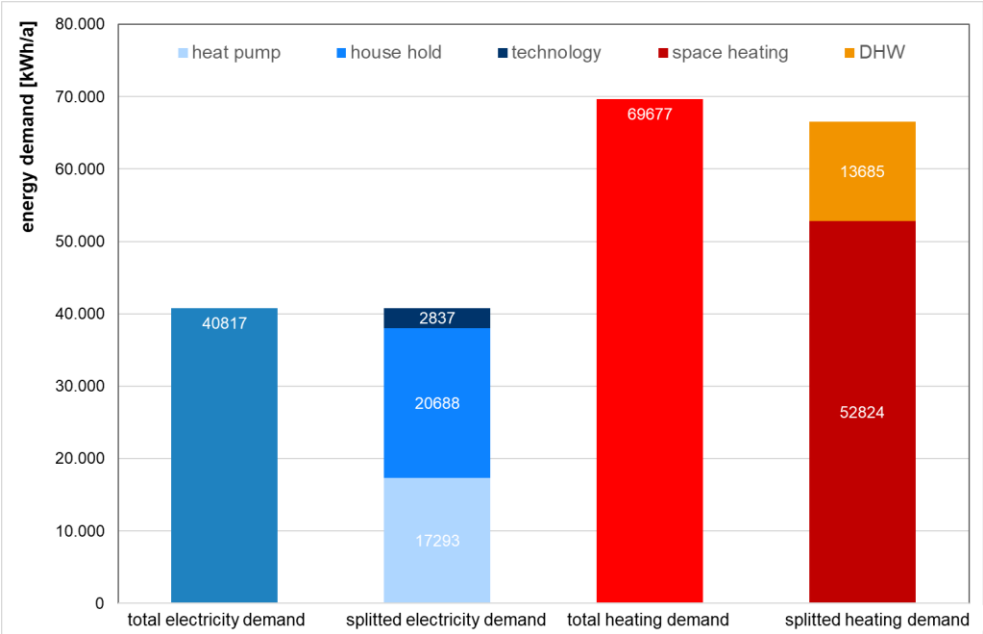

Fig. 2: Electricity demand and demand of thermal energy of the building

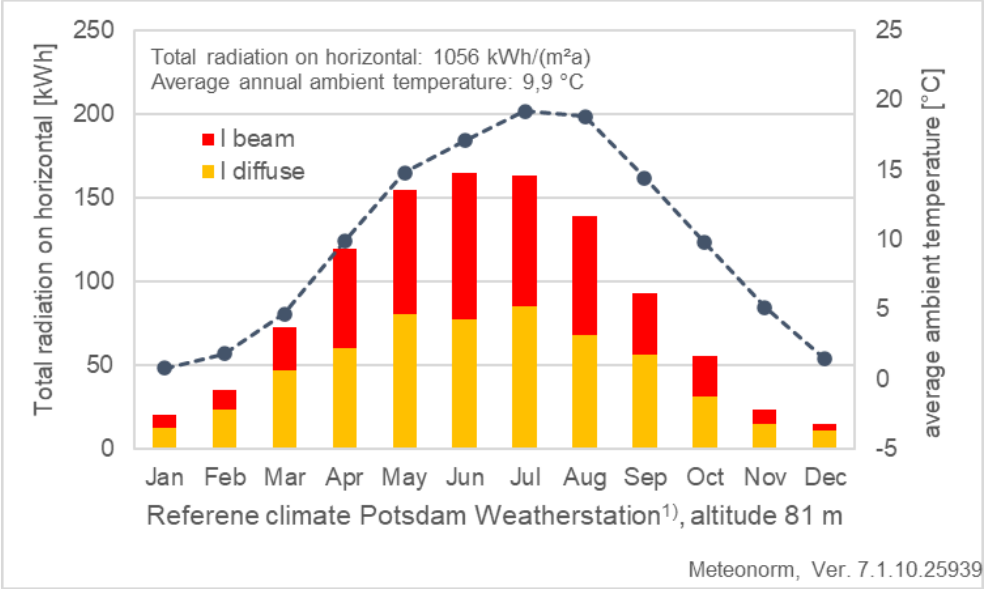

Fig. 3: Weather data Potsdam (Germany), average ambient temperature and solar radiation on horizontal

3.2. Simulation variants

With regard to the regenerative cover factor of the entire energy demand (solar thermal and solar electric), the simulation study determines the variant for which, by a complementary distribution of the shares of solar thermal and photovoltaics on the available roof area, the renewable energy used in the building is maximized. In addition to the varying proportions of solar thermal collectors and PV area, the influences of the different ratios combined with unlike thermal and/or electrical storage have been investigated. Since the influence of selected building physics is also to be evaluated, the thermal insulation of the building, in addition to the technical variants, is altered. (see Table 1)

The key data for the variants examined are summarized in the following table.

Tab. 1: Simulation variants

Variation	Starting point	Changes/ adaptions
thermal building standard	as build, no changes apart from insulation and heat recovery of air change for the passive house	"average"– 46.3 kWh/(m²a) = as build (GEG) "good" – 30 kWh/(m²a) "very good" = passive house – 15 kWh/(m²a)
orientation of the building	orientation of PV and ST similar to building	rotation: 0°, 30°, 60° and 90°
varying storage size	as build	50, 100 and 150 l/m² referred to aperture area of the thermal collector 0, 0.5, 1.0 and 2.0 kWh/kW_p (usable capacity of electrical energy storage)
expansion of the area available / solar active area	initial area 108 m² (as build)	add 50 % (new area 162 m²) correspond to approx. 80 % of the roof area
varying the area shares of PV and ST	PV and ST (entire area as build)	0 %/100 % to 100 %/0 % (10 % steps) as shown by the first simulations with the system as build, a high total solar fraction is reached in a range between 20/80 and 80/20 -> used for further simulations
orientation of PV and ST	building orientation south PV and ST tilt angle 65°	orientation PV east / west and ST south
varying the tilt angel of PV	building orientation south	ST – unchanged, tilt angle 65°, orientation south PV –tilt angle 30°, orientation south PV – tilt angle 10°, orientation east/west (tilt angle according to pre-study)
varying efficiency (better components)	initial situation (as build) PV - 16,1 % ST – conventional plate collector	PV – 24 % (very good) (source: technology radar Subtask D, (Task 66, 2024)) ST – high performance CPC-collector

4. Results of the parameter study

The parameter study shows that not one single concept is best. Rather more, depending on the respective evaluation parameter, different variants have advantages and disadvantages.

However, as a goal of the Task 66 the evaluation of the simulations focuses on solar fractions and also on the energy demand, following the question: "How far can fossil energy consumption be reduced?". It should be noted that the results and conclusions given subsequently refer to the building investigated in this study. However, most results have general character and will apply to other multi-family buildings too.

4.1. Influence of electrical and thermal storage sizes (pre-study)

When considering the capacity of an electrical energy storage, it was found, that the in practice widely used capacity of 0.5 to 1.0 kWh/kW_p has a noticeable influence on the overall system performance and increases the solar-electric fraction. The capacity of 2.0 kWh/kW_p has a significantly higher influence but also the financial outlay increases significantly as well.
As the design value for the simulations on hand a value of 1.0 kWh/kW_p was implemented.

With regard to the specific volume of the hot water store, for the multi-family house under investigation a

sensitivity analysis including a flat plate collector results in a reasonable value of 100 l/m², referred to the aperture area of the thermal collector. In that case a specific storage volume of more than 100 l/m² does not lead to a significant increase in the performance of the solar thermal system. On the other hand, a specific volume of 50 l/m² decreases the solar fraction of the system by around 5 percentage points, compared to that with 100 l/m².

4.2. Influence of thermal insulation and orientation of the building

Of course, the better the thermal building standard, the less energy for space heating and by this less electricity for the heat pump is needed. Furthermore, it is clear that the further the house is turned from south orientation to west (or east), due to decreasing passive solar gains, the more energy for space heating is required.

With better thermal insulation of the building (lower energy demand for space heating), the orientation to south results in higher solar fractions. Moreover, the ratio between produced energy and energy demand increases.

By enhancing the thermal insulation of the building and turning the building to the south, a total solar fraction of up to 45 % can be achieved (Figure 4). In this case the maximum thermal solar fraction amount to 45 % (interpolated) and the electrical solar fraction (PV) to 40 % (interpolated) (Figure 5).

Outcome of the variants for reaching SEB: A low energy building (15 kWh/(m²a)) with orientation south is advantageous.

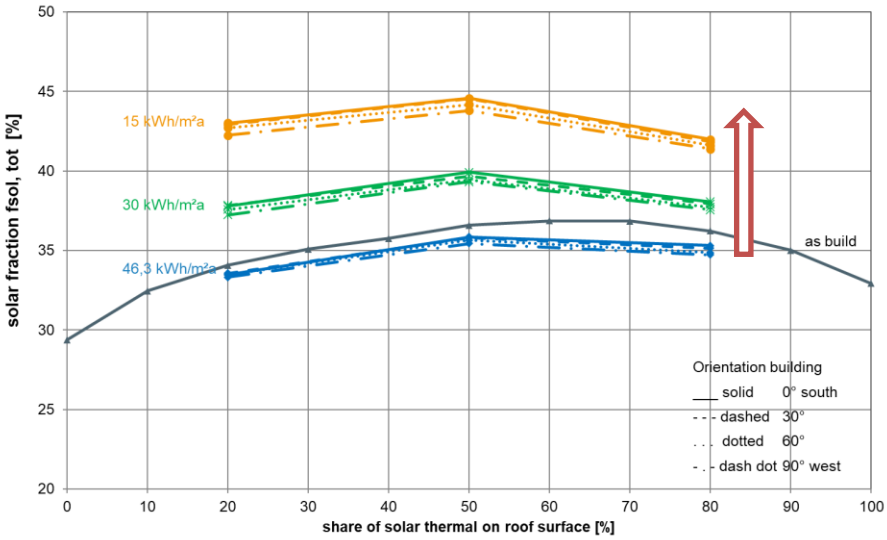

Fig. 4: Total solar fraction – thermal insulation and orientation of building

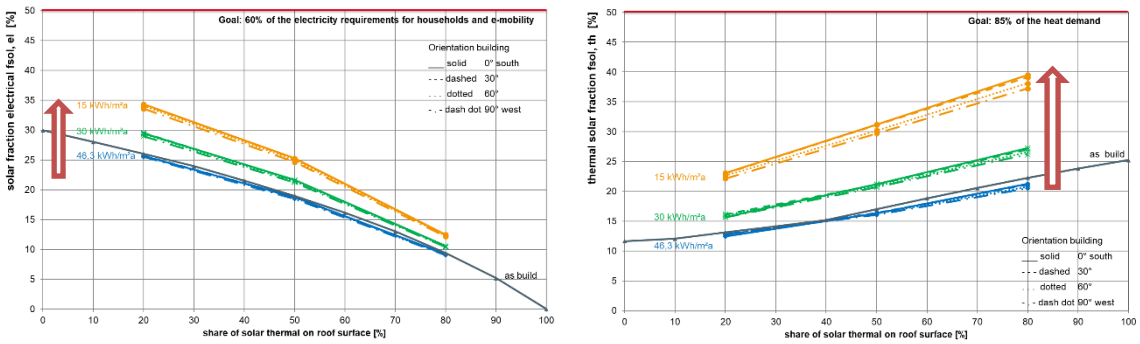

Fig. 5: Electrical solar fraction (left) and thermal solar fraction (right) – thermal insulation and orientation of building

4.3. Influence of orientation und tilt angle on the system performance (PV and ST)

An orientation to south provides the highest solar irradiation and therefore, at first glance, the highest yield. If the tilt angle of a south oriented PV module and a thermal solar collector is adapted to archive the highest yield, of course the highest solar fraction will be reached.

By orienting the systems to south and modify the tilt angle (starting point see Table 1), a total solar fraction of up to 45 % can be achieved (Figure 6). The maximum thermal solar fraction amount to 45 % (interpolated) and the electrical solar fraction to 42 % (interpolated) (Figure 7).

Outcome of the variants for reaching SEB: PV modules and solar thermal collectors should be oriented to south. PV should have a tilt angle of 30°, while the tilt angle of solar thermal collectors should be 65°.

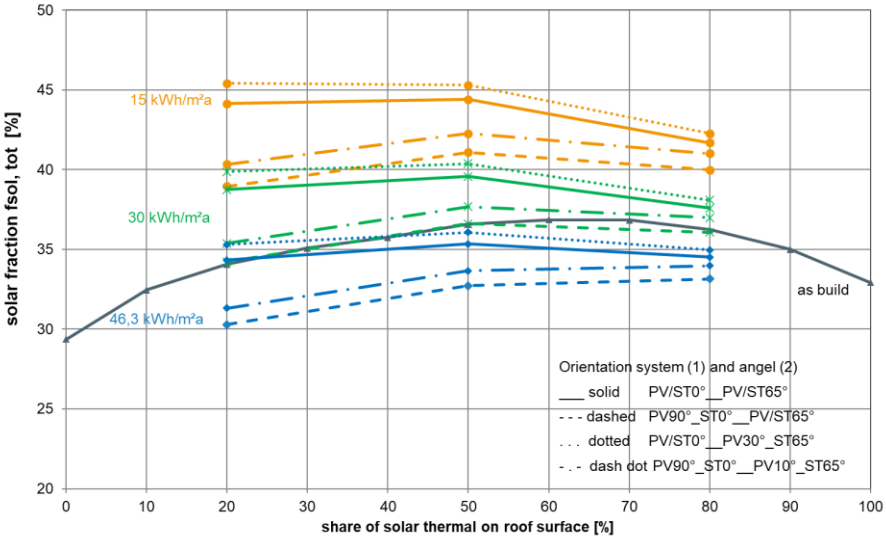

Fig. 6: Total solar fraction – orientation and tilt angle of solar appliances

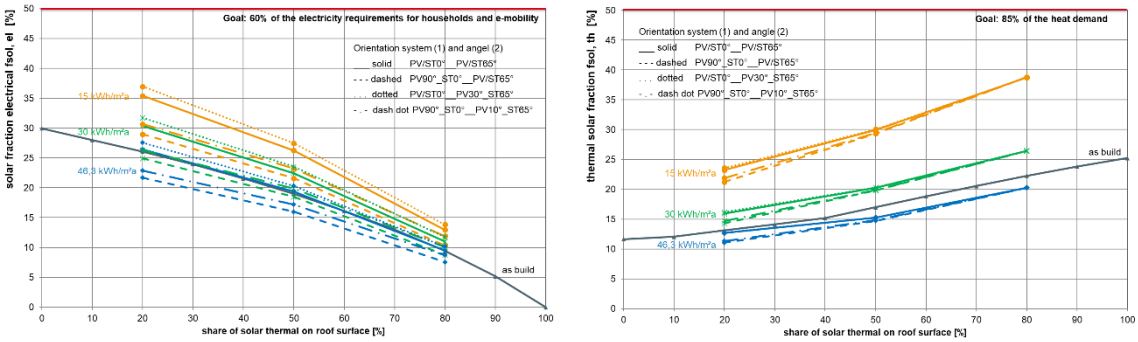

Fig. 7: Electrical solar fraction (left) and thermal solar fraction (right)– orientation and tilt angle of solar appliances

4.4. Influence of efficiency and area of solar applications (PV and ST)

Self-evident the higher the efficiency and the area of solar applications, the more energy can be generated and the higher the solar fraction will be.

By altering the efficiency and the area of solar applications in a range that is feasible for the given building (starting point see Table 1), a total solar fraction of up to 70 % can be achieved (Figure 8). The maximum thermal solar fraction amount to 70 % and the electrical solar fraction to 72 % (Figure 9).

Outcome of the variants for reaching SEB: The efficiency and area of PV and ST should be as high as possible. To approach and reach the goals stated in Task 66 for the given building (see Figure 8 and 9), the ratio of the net floor area to the area of solar applications (PV and ST) for the 15 kWh/(m²a) building must not be larger than 7. The 30 kWh/(m²a) building is approaching the Task 66 target, while the 46.3 kWh/(m²a) building needs much more solar area.

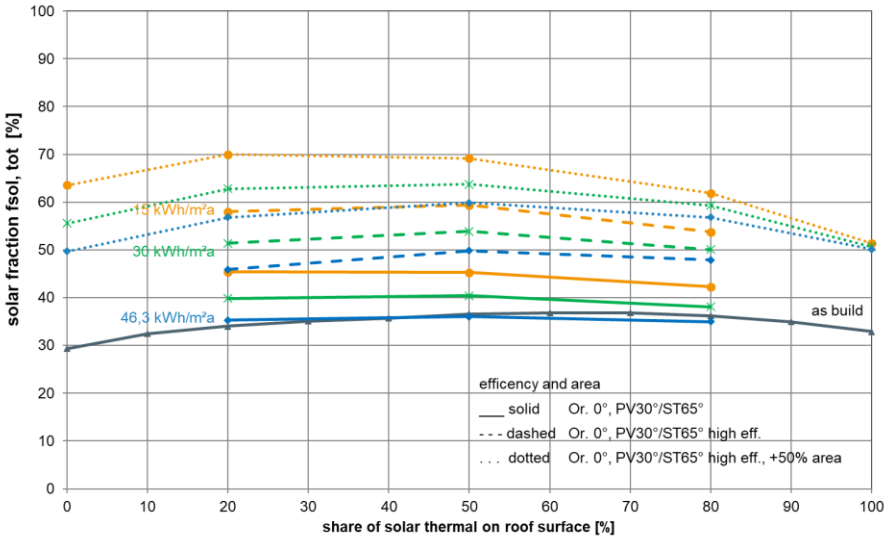

Fig. 8: Total solar fraction – efficiency and area of solar appliances

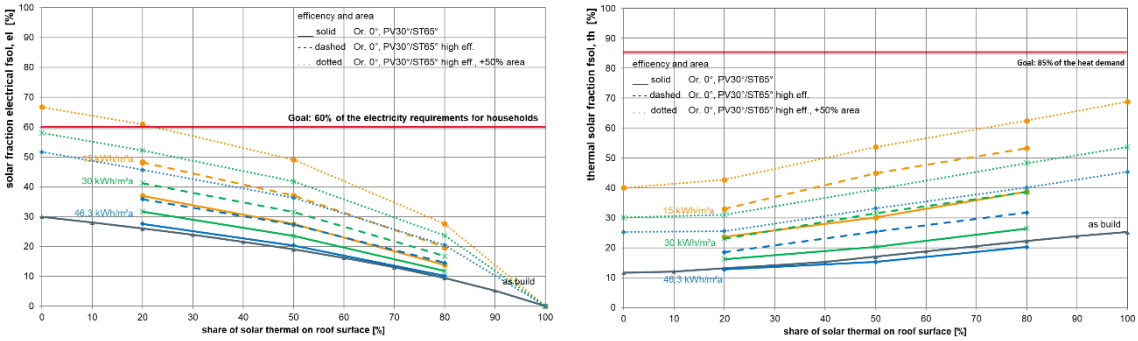

Fig. 9: Electrical solar fraction (left) and thermal solar fraction (right) – efficiency and area of solar appliances

4.5. Energy production, feed-in and electricity purchase from the local grid

The adaptations of the supply concept and system components mostly result in different energy productions in terms of electricity and heat. By improving the system, the yields generally increase (Figure 10). If the concepts are adapted according to the mentioned outcomes, the electricity production increases by 144 % that of heat by 48 %.

Since the reduction of the use of fossil fuels was a goal underlying the strive to reach high solar fractions, the results show that some adjustments in parallel lead to reduced electricity purchase from the grid. Electricity purchase from grid can be reduced by up to 30 %, depending on the measures implemented. At the same time, the feed-in of surplus electricity into the public grid increases by 267 %. This can support increasing the share of renewable energy in the grid and might in addition have network-friendly effects. (Figure 11)

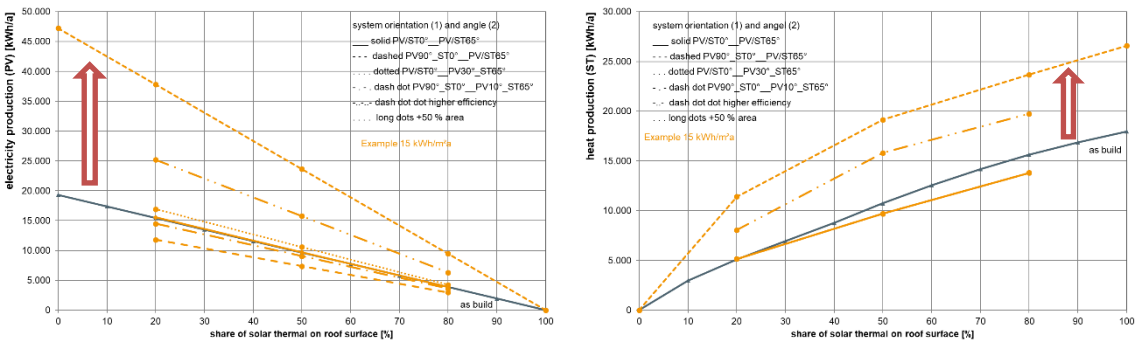

Fig. 10: Electricity production (PV) (left) and heat production (ST) (right)

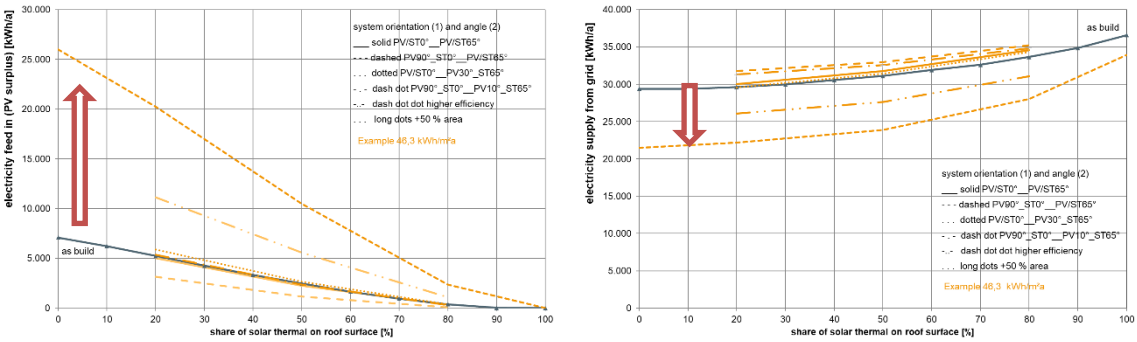

Fig. 11: Electricity feed in the grid (left) and grid supply (right)

5. Conclusions

Using an existing example of a multi-family house in Germany, by means of system simulation solar energy supply concepts have been investigated systematically. With focus on technical and energy efficiency, various building designs and technical systems have been analyzed and compared with each other. The aim was to show which concepts and approaches for integrating solar thermal and photovoltaic systems can be used to achieve high solar fractions and thus most climate-neutral energy concepts.

The study was based on the definitions and objectives of IEA SHC Task 66. The aims defined in Task 66 announce thermal solar fraction larger than 85 % and electric solar fraction above 65 %.

The evaluation of the results of the simulations show that there is not one best concept. Depending on the respective parameter different system designs and variants have advantages and disadvantages.

The results documented in this paper are valid for the specified building including the defined insulation standards and a thermal store of 100 l per square meter aperture area of a thermal collector. With respect to the photovoltaic system an electrical storage with a useful capacity of 1 kWh/kW$_p$ has been implemented.

The following findings have been derived:

- For the building under investigation and the mentioned measures, the goal for renewable electricity production, given by Task 66, can be achieved - for thermal energy it cannot.
- Measures to achieve a high solar fraction in a multi-family house are
    - Building insulation standard and orientation: Reduce the energy demand as much as possible -> very good thermal building standard -> 15 kWh/(m²a) is needed.
    - Orientation and tilt angle of solar applications: All systems should be orientated south. PV should have a tilt angle of 30°, solar thermal collectors should have a tilt angle of 65°.
    - Efficiency of the systems: Very good component and system efficiency are needed.
    - Area of system: Ratio between net floor area and area of solar applications (PV and ST) for the 15 kWh/(m²a) building should not be greater than 7. The 30 kWh/(m²a) building is approaching the Task 66 target, while the 46.3 kWh/(m²a) building needs much more solar area.
- The feed-in of surplus PV electricity into the public grid decreases with an increase in the size of the solar thermal system because less PV electricity is produced.
- Enhancing the system might lead to a reduction of electricity supply from the grid. The electricity supply for the building can be reduced by up to 30 %.
- At the same time the feed-in of surplus electricity into the public grid increases by more than 250 %. This can support increasing the share of renewable energy in the grid and might in addition have network-friendly effects.

With regard to the solar fractions (with all measures included) the following results can be presented:

- Total solar fraction: → up to 70 %
  Variants with high total solar fraction range from a ratio between ST and PV of around 20/80 to 50/50. The total solar fraction increases with the size of the solar thermal collector, but in order to be able to cover household electricity, a minimum proportion of photovoltaics should be available.

- Thermal solar fraction: → up to 70 %
  It is evident that electricity-oriented heat generation benefits from PV systems. As the PV system becomes smaller, this fact of an electricity-oriented concepts is reduced. On the other hand, due to its greater area efficiency, a solar thermal application may overcompensate this effect. Of course, the maximum thermal solar fraction is generated by a ratio of ST to PV of 100/0.

- Electrical solar fraction: → up to 65 %
  The smaller the PV area, the lower the share of solar electricity coverage. Self-evident the maximum electrical solar fraction is generated by a ratio of ST to PV of 0/100. To reach the target for the 15 kWh/(m²a) building the ratio between net floor area and PV area should around 7. For building with higher energy demand ratio lower than 7 are mandatory.

6. Acknowledgments

The research project “SolSys” (0325558A/B) were funded by the German Federal Ministry for Economic Affairs and Energy (BMWi). We would like to thank all building owner and operator as well as our project partner for their help and support as well as providing measurement data and information about the buildings.

As well as we would like to thank IEA Solar Heating and Cooling Technology Collaboration Program (SHC TCP) for developing and disseminating the project and the results of Task 66.

7. References

Bockelmann, F., Peter, M., Oliver, A. Bestenlehner, D., Drück, H., 2019. Final report “Solsys - Analyse und Optimierung solarer Energieversorgungssysteme (Wärme/Strom) für Gebäude“, BMWi Fkz 0325558A/B

IEA SHC Task 66, 2024. Task 66 – Solar Energy Buildings, Integrated solar energy supply concepts for climate-neutral buildings and communities for the "City of the Future”

Meteonorm® 7, 2018, Global Meteorological Database for Engineers, Planners and Education, Version 7.1.10.25939, Meteotest, Bern (CH)

TRNSYS 17, TRaNsient SYstem Simulationprogramm, Version 17.02.0004, Solar Energy Laboratory, University of Wisconsin-Madison

8. Nomenclature

Symbol	Definition	Unit
E_{grid}	energy (electric), electricity from grid	kWh
$E_{PV,grid}$	energy (electric), generated by photovoltaics, feed into grid	kWh
$E_{PV,tot}$	energy (electric), generated by photovoltaics on site, total (AC)	kWh
GEG	Gebäudeenergiegesetz Act on Energy Conservation and the Use of Renewable Energies for Heating and Cooling in Buildings (Germany)	
KPI	Key Performance Indicator	
PV	Photovoltaic	
Q_{grid}	energy (thermal), delivered from a thermal grid, e.g. a district heating system	kWh
$Q_{h/c}$	energy (thermal), generated from a heating/cooling system; space heating as well as domestic hot water	kWh

Symbol	Definition	Unit
$Q_{h,el}$	energy (thermal), generated through electrical energy e.g. heat from a heat pump or a heating element	kWh
$Q_{sol,PVHG}$	energy (thermal) based on solar-electric heat generation powered by photovoltaics in combination with e.g. electrical heating elements or heat pumps	kWh
$Q_{ST,grid}$	energy (thermal), generated by a solar thermal collector, feed into a thermal grid / District Heating System	kWh
$Q_{ST,tot}$	energy (thermal), generated by solar thermal collector/systems in total	kWh
SEB	Solar Energy Building	
ST	Solar thermal	

Quantifying the effect of radiator capacity on hybrid heat pump performance using a hardware-in-the-loop setup

Yasin Bulut[1], Andries van Wijhe[1], Richard Kemp[1] and Ved Dubhashi[1]

[1]TNO, Delft (The Netherlands)

yasin.bulut@tno.nl

Abstract

Heat pumps achieve higher efficiency (COP) if the water temperature at which they reject heat is lower. A method to lower this temperature is by increasing the capacity of the hydronic heating system. A larger heating system can deliver the same amount of heat at a lower water temperature compared to a smaller system. However, the relationship between heating capacity and COP varies depending on the system. To quantify this for a hybrid air-to-water heat pump, a hardware-in-the-loop method was employed. The heat pump was tested in a climate chamber, connected to a virtual house and hydronic radiator heating system. Tests were repeated with upgraded radiators (from Type 22 to Type 33) and finally with a revised weather compensation curve. The case study demonstrated that the increased radiator capacity and adjusted weather compensation curve resulted in a COP increase of approx. 0.4 (approx. 10%).

Keywords: (hybrid) heat pump, hardware-in-the-loop (HIL), COP, hydronic radiator, weather compensation curve, emulator

1. Introduction

The relationship between heat pump supply water temperature and radiator capacity is a fundamental aspect of heating systems. Understanding the complexity between these two parameters is essential for optimising heating system performance, achieving thermal comfort, and minimising energy consumption. It is generally known that with larger radiators, the heat pump can operate at a lower water temperature while maintaining the desired indoor temperature. This increases the heat pump's efficiency, potentially leading to lower energy consumption and reduced operating costs.

The hybrid air-to-water heat pump, a system that combines a conventional heat pump with an (existing) gas boiler, offers an effective retrofit solution for homes in the Netherlands, where most households are already equipped with gas boilers. This study therefore focuses on hybrid air-to-water heat pumps and examines the impact of radiator capacity on their performance. Testing was conducted at TNO's Heat Pump Application Centre (HPAC) in the Netherlands, where actual water-based hardware, such as air-to-water heat pumps, can be tested in a simulated outdoor environment, paired with a fully dynamic house model, including a heating system. This approach combines the modeled load with actual hardware, providing better insights into how a hybrid heat pump performs under real-world conditions compared to static testing methods or purely model-based approaches - especially when interactions are complex to model.

In addition to providing more realistic system dynamics, the setup is well-suited for parametric measurements which enable the investigation of the radiator capacity effect under the same conditions - this is normally very challenging with standard field measurements in practice. Consequently, this paper explains how this setup, called hardware-in-the-loop (HIL), uses these parametric studies to quantify the impact of radiator capacity on hybrid heat pump performance.

2. Method

As part of a government-funded research program in the Netherlands, the performance of hybrid heat pumps is measured in a hardware-in-the-loop (HIL) setup. The general idea of the HIL is that the tested (hybrid) heat pump does not 'know' that it is in a test environment. This is achieved by bilaterally coupling the (hybrid) heat pump to a house model with a heating system running in real-time. The general structure of the HIL is shown schematically in Figure 1. The interaction between the hardware and software is represented by dashed lines.

© 2024. The Authors. Published by International Solar Energy Society
Selection and/or peer review under responsibility of Scientific Committee
10.18086/eurosun.2024.02.03 Available at http://proceedings.ises.org

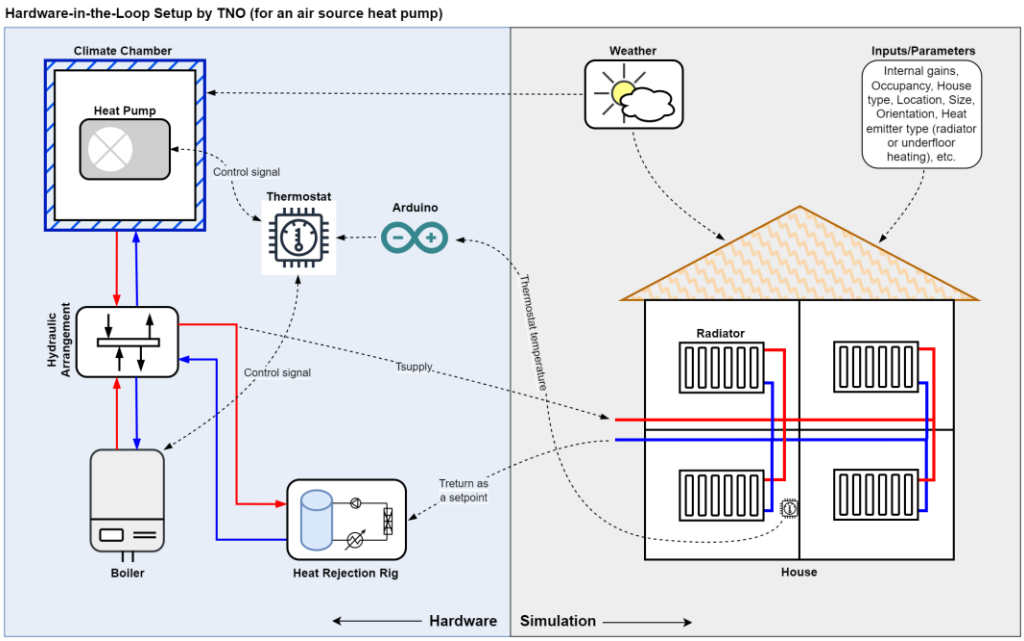

Fig. 1: Description of test setup. Left: hardware environment with climate chamber, heat rejection rig and thermostat. Right: software environment with house, radiators and weather scenario. Dashed lines are data connections.

The typical operation of the HIL setup is as follows: The climate chamber provides time-dependent ambient conditions, i.e. temperature and humidity, based on a predefined reference weather profile. The heat pump operates according to its internal control logic. The generated heat is then transferred to the heat emitter model (e.g. radiator or underfloor heating) in the house model. The room thermostat and heating system water temperatures are calculated based on the dynamic heat balance equation in the models. The calculated return water temperature is sent to the heat rejection rig as a setpoint so the heat pump. Finally, the heat rejection rig conditions the water and sends it to the heat pump back.

2.1. House model

A dynamic multi-zone house model was developed using the Type 56 within TRNSYS 18 (Klein, 2017), representing a terraced Dutch housing typology of the late 1980s to early 1990s. These houses typically have three floors. The ground floor includes the living room, kitchen, and entrance. The first floor comprises the bathroom, hallway, and all three bedrooms. The top floor is attic space, assumed to be unheated. The useful area, excluding the attic, is 109 m² (SenterNovem, 2007). Each space in the house was defined as a thermal zone, leading to a total of 9 zones.

Typical thermal resistance properties (Rc/U values) of this housing typology were obtained from (Agentschap NL, 2011). To accurately model the thermal mass, specific attention was paid to determine the typical construction details of the building envelope, interior walls and floors, but also the presence of furniture. Additionally, an advanced ventilation model was integrated into the house model using TRNFlow in TRNSYS 18 (Transsolar Energietechniek GmbH, 2009). TRNFlow allows modelling air exchange through the building envelope and between thermal zones, considering driving forces such as wind pressure and buoyancy. Only natural ventilation is present in the house model. Therefore, air is primarily supplied via ventilation grilles and extracted by passive exhaust ducts in the kitchen, bathroom, and toilet, according to the requirements from the Dutch Building Code (Nederlands Normalisatie Instituut, 1975; 2001). Infiltration was also implemented into TRNFlow based on a qv;10 value (the infiltration flow at a pressure differential between inside and outside of 10 Pa) of 222 dm3/s based on NTA 8800 (Nederlands Normalisatie Instituut, 2019) and it was distributed over the building envelope based on (Vereniging Leveranciers Luchttechnische Apparaten, 2019).

The main sources of internal heat gain are occupancy, appliances, and lighting. For occupancy, a two-person household with one child was assumed. Occupancy profiles per person per room were obtained from (Vereniging Leveranciers Luchttechnische Apparaten, 2019) and the same daily profile was iterated in the

simulation. In order to incorporate the heat gain released by the appliance and lighting, the yearly electricity consumption of approx. 3300 kWh was assumed. The daily appliance and lighting schedules were created based on the defined occupancy profile and the monitored cases of multi-occupancy houses with a child (Zimmermann et al., 2012). Not all electrical use was assumed to result in room heating, for example, a washing machine and dishwasher use a significant amount of electricity, rejecting most of the heat via the sink.

The nominal heat load (peak load) of 6 kW was calculated under design conditions (an ambient temperature of -10°C, a wind speed of 5 m/s, and no solar or internal gains) for this house. The annual heat demand for space heating was estimated to be between 7.3 and 7.9 MWh, which is equivalent to Label B, based on the CBS gas consumption data (Centraal Bureau voor de Statistiek, 2021).

2.2. Radiator model

The modelled house is heated using only radiators as heat emitters. Since the radiators are coupled to the (hybrid) heat pump, their behaviour is crucial for the system's performance. Each radiator in the house is modelled separately and coupled to the house model. The model follows the EN442 standard (Nederlands Normalisatie Instituut, 2014) for characterizing radiator thermal performance, with added thermal inertia to capture dynamic responses. Validation of the model was carried out against extensive measurements conducted on panel radiators.

Thermal output and heat pump defrosting

If an air source heat pump defrosts via a reverse cycle, heat is removed from the radiator circuit. In practice, this means that the water inlet temperature of the radiator drops below the water outlet temperature. Radiators do not work optimally if the hot water inlet is connected to the bottom and the cold water outlet is connected to the top. The buo yancy of the water normally stratifies the internal volume with the hot water at the top. Temporarily reversing the connections thus short-cuts the radiator. This results in only a small fraction of the thermal inertia of the water being used and the temperature at the water outlet of the radiator drops much faster than is expected based on the full radiator volume. The effect of this shortcutting can be seen in Figure 2, by a drop in temperature of the radiator body on the connection side during the defrost. After the defrost the temperature recovers again and the stratification resumes. This phenomenon was integrated into the radiator model and validated through extensive testing.

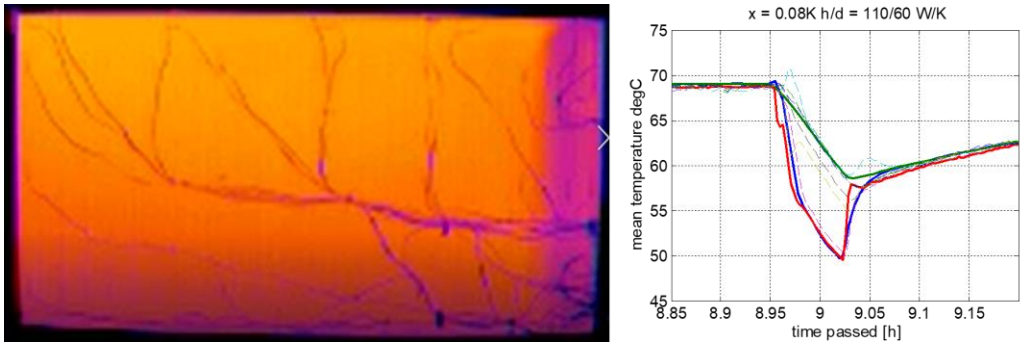

Fig. 2: Left: Thermal image of a panel radiator during a heat pump defrost (reverse) cycle. The hydronic connections are on the right side. The purplish (colder) area on the right side indicates shortcutting of water flow. The black veins' are thermocouple wires. Right: The graph displays the results of the radiator model with and without defrost logic. The red line shows the measured mean inlet and outlet temperatures of the radiator, compared with the model results: with defrost logic (blue) and without defrost logic (green).

Thermostatic radiator valves

Thermostatic radiator valves (TRVs) are a common means of controlling room temperatures outside the zone containing the main heating system thermostat. Therefore, it was assumed in the modelled house that each room radiator (except for the living room) is equipped with a TRV. In the model, TRV setpoints of 20°C for the kitchen, 22°C for the bathroom, and 18°C for the bedrooms, hallway, and entrance were used. These values are based on ISSO 51 (ISSO Kennisinstituut voor de Installatiesector, 2009).

The TRV model was created based on EN215 (Nederlands Normalisatie Instituut, 2014) including the physics of the measuring body's time constant, valve hysteresis and the effect of water temperature on the sensed temperature of the body. It senses the room air temperature and adjusts the valve with proportional control. The model then calculates water flow resistance for the heating system circulation pump and allocates flow distribution between radiators. In the tested heat pump this effect is achieved by adjusting a calibrated flow control valve in the heat rejection rig, ensuring the connected hybrid heat pump experiences the same flow resistance as the modelled heating system.

2.3. Heat rejection rig

The heat generated in the form of warm water is typically delivered to a heating circuit in the house, such as radiators or underfloor heating. To emulate this connection, a purpose-built rig is used. This rig adjusts the temperature of the return water to the heat generator by means of cooling or heating. This way the entering water temperature of the physical heat pump is equal to the temperature calculated by the computer model of the heating circuit. Additionally, the hydraulic resistance of the heat rejection rig is controlled using a motorized valve to mimic the variation caused by thermostatic radiator valves in the model.

2.4. Hybrid heat pump

The HIL tests were conducted using a commercially available hybrid heat pump, selected by the manufacturer as a suitable match for the modelled house described in Section 2.1. The thermal specifications of the unit based on the manufacturer's catalogue are presented in Table 1.

Tab. 1: Thermal specifications of the unit based on the manufacturer's catalogue

HP thermal capacity [kW]	5.5	at 2 °C ambient and 35°C leaving water
HP thermal capacity [kW]	4.8	at -10 °C ambient and 35°C leaving water
HP SCOP [-]	3.3	with 55 °C leaving water temperature for an average climate
Boiler thermal capacity [kW]	25	at 80 °C leaving and 60 °C return water temperatures

The unit was hydraulically connected in accordance with the manufacturer's recommendations for the modelled house type. As shown in Figure 3, the air-to-water heat pump is located in the laboratory's climate chamber and all indoor parts of the hybrid (gas boiler, indoor unit, etc.) are located in the general lab area. The indoor unit contains a header, mixing valve, and circulation pump, enabling controlled mixing of the gas boiler and heat pump circuits (note that the header and mixing valve are not drawn in Figure 3).

The tested unit offers several configuration settings to tune system performance, such as the weather compensation curve[1], the switch-over point[2] between the heat pump and boiler, and room thermostat compensation[3]. For these settings, the manufacturer's recommendations for the selected house type were followed to mimic the unit's performance in a real-world application. Additionally, the living room thermostat was set at 20 °C without a night setback.

[1] It is the process of adjusting the heating water temperature with the outdoor temperature. It is typically set via selection of pre-set curves, or by manual definition of the line. In the Netherlands, the maximum heating water temperature of the curve is set at -10°C ambient temperature (design condition).

[2] It is a function for blocking the boiler and heat pump operation with respect to outdoor temperatures and/or COP threshold (e.g., the boiler does not operate above x°C and the heat pump does not operate below y°C, or heat pump does not operate below certain COP).

[3] It is about how the room thermostat temperature influences the target water temperature. Some units include functions that adjusts the target water temperature based on room temperature. However, it was not always clear what the function is doing. Some of these settings include numerical input values, others include an option to switch on/off a feature or to select a correction method via a choice of correction type.

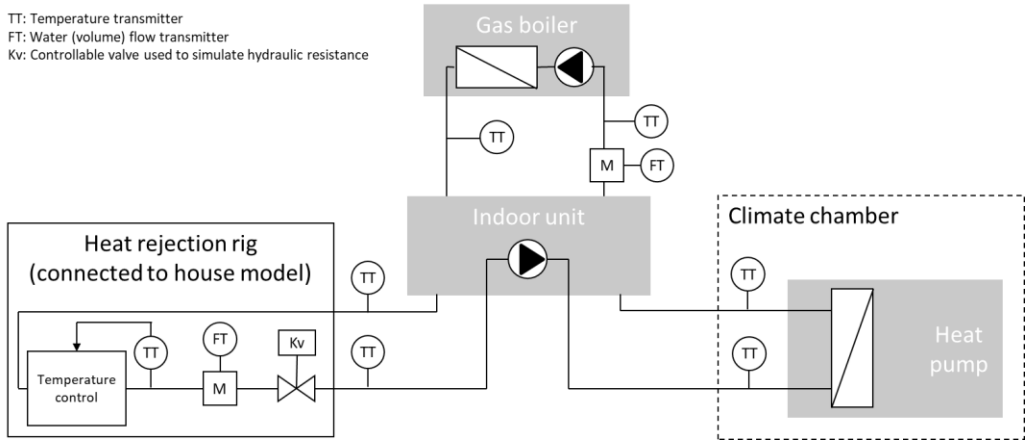

Fig. 3: Hydraulic configuration of the test setup

It should be emphasized that there was no additional information regarding the systems' control other than that available from the product manual because there was no interaction with the product design engineers or software programmers during the project, therefore, the control logic of the unit was essentially black box. In the following sections, some commentary is therefore made regarding notable operational characteristics of the unit.

2.5. Interface with the room thermostat

The heat pump controller usually uses the room thermostat temperature as a control feedback. To ensure proper operation of the system, the thermostat should read the correct room temperature. In the HIL setup, the real reference sensor is removed and replaced by a virtual sensor, which emulates a temperature coming from the house model at the assumed thermostat location.

2.6. Data acquisition

The setup was extensively instrumented with calibrated instruments, as illustrated in Figure 3. Data acquisition was performed using in-house data acquisition software and hardware, with a sampling interval of 10 seconds. On the hydraulic side, water temperatures at the inlet and outlet of each heating system component were measured, along with all water flow rates. On the air side of the heat pump, sensors for air temperature (in and out) and relative humidity were installed. Additionally, electrical power is measured individually for each component of the hybrid (heat pump, gas boiler and indoor unit) as well as boiler gas consumption. The flow measurement combined with calculated density and the temperature difference across different components is used to calculate generated or absorbed heat. These instruments combined provide full information on the energy balance of each component.

2.7. Reference weather days

As the HIL tests are conducted in real-time, it is impractical and undesirable to extend the testing period excessively. Therefore, six reference days (-5, -1, 2, 4, 7, and 12-degree days) were derived from NEN5060 (Nederlands Normalisatie Instituut, 2008). These days are selected to cover a range of average daily temperatures throughout the heating season, ensuring that the conclusions are applicable across the entire period.

The reference year was sorted into days with the same daily average dry bulb temperature when rounded as an integer (referred to as temperature bins in various sources). Taking the average hourly temperatures of the days within the integer bins results in a somewhat flattened temperature profile so the difference between the hourly values and the daily average was scaled (increased) to match the median standard deviation of the days within the bin. The relative humidity (RH) of all hours in the year was correlated with the dry bulb temperature. Using

this correlation, hourly values of RH were assigned according to dry bulb temperature in the weather files of the 6 reference days. A solar radiation profile per average temperature day was needed, so using the same bin method as for dry bulb temperature the average solar radiation per hour was used for each reference test day.

2.8. Preconditioning and an actual test day

Since the test days are analogous to "snapshot" days in a heating season, it is important to precondition the house model with similar weather days. This ensures that the various construction elements reach appropriate temperatures at the start of the actual HIL test, thereby minimising the thermal buffering effect. This was achieved by running a preconditioning period of house and heating system simulation for 4 simulation days[1] with a looped reference weather day before the actual HIL became operational, as illustrated in Figure 4. For this period, a fictitious and simplified heat generator and a control were included.

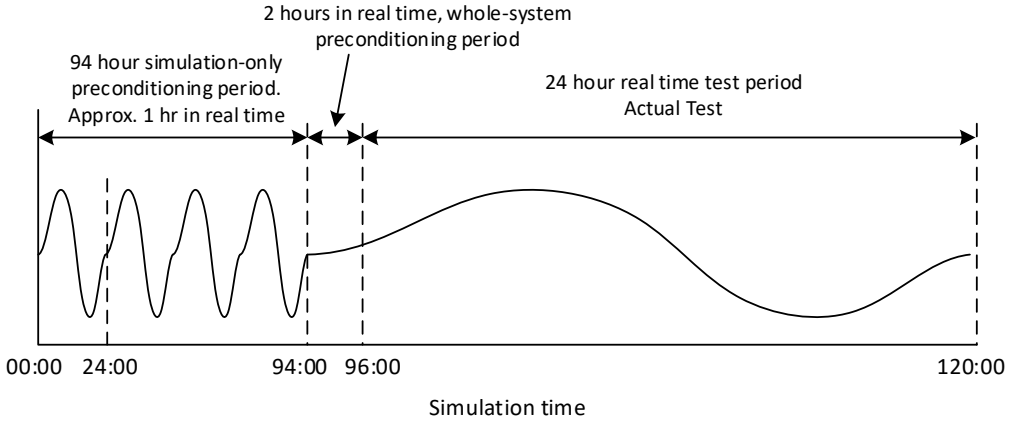

Figure 4: Arrangement of preconditioning and actual test day

This period was followed by the actual HIL for a simulated time from 94:00 to 96:00, allowing for some preconditioning time for the hardware (e.g., heat pump, boiler, heat pump controller, and heat rejection rig) as well. Finally, the actual test ran for a 24-hour period, beginning at 96:00 simulation time, which corresponds to 00:00 clock time at the start of the test day, as illustrated in Figure 4.

3. Parametric study: Radiator capacity

The HIL setup is not only useful for obtaining more realistic system dynamics but also quite suitable for parametric measurements in which the radiator capacity effect can be investigated purely while other factors remain the same. However, this is very challenging with standard field measurements in practice. In the HIL setup, there is full control over the model and the parameters can be adjusted easily. Simply said, the setup allows us to install larger radiators in the modelled house without any plumbing work.

Using this advantage of the setup, three test cases were defined, as shown in Table 1. While the hybrid heat pump and the house model remained the same, the radiator capacity and the weather compensation curve were varied. The initial case (Case 0) was conducted as a baseline scenario with the original radiator capacity of 9 kW at 75/65/20°C[2] and a maximum water temperature of 55°C[3] on the weather compensation curve at an outdoor temperature of -10°C. All radiators were assumed Type 22 which is with 2 plates and 2 convectors. Then, in Case 1, while keeping the dimensions (length and height) the same, the radiators were upgraded from Type 22 to Type 33 (3 plates and 3 convectors) which brings approximately a 50% capacity increase (Radson, 2020). During this case, the weather compensation curve was kept the same as the base case. Upgrading the

[1] The number of days depends on house type (heavy/lightweight) and other conditions such as night setback, heated/unheated attic, etc. Therefore, each house model used in the HIL setup needs to be analysed carefully before starting the test.
[2] It is the typical Dutch radiator design condition, representing the radiator inlet, outlet and room temperatures respectively.
[3] The weather compensation curve was set by the installer according to standard practices for the similar type of houses.

radiators could be done with underfloor heating, low-temperature convector, radiator booster fan, etc. However, the purpose of the article is not to do a techno-economic analysis on retrofitting the heating emitters, but rather to show the impact of the radiator capacity on the (hybrid) heat pump performance. Finally, the maximum water temperature of the weather compensation curve was reduced to 50°C in Case 2 while keeping the radiator capacity the same as in Case 1.

Tab. 1: Cases for the parametric study

Parameters	Case 0	Case 1	Case 2
Radiator	Type 22 9 kW nominal capacity at 75/65/20°C	Type 33 13.6 kW nominal capacity at 75/65/20°C	Type 33 13.6 kW nominal capacity at 75/65/20°C
Weather compensation curve	Maximum water temperature of 55°C at an outdoor temperature of -10°C	Maximum water temperature of 55°C at an outdoor temperature of -10°C	Maximum water temperature of 50°C at an outdoor temperature of -10°C

An important factor in this study is the original design capacity of the radiator: non-representative estimations may lead to misleading conclusions. Defining a realistic installed radiator capacity, however, is challenging due to a lack of availability of past building regulations[1] for existing Dutch buildings. There are reasons to expect radiators to be oversized, for example, related to design safety margins, allowances for intermittency and risk aversion with respect to underheating. Therefore, to estimate the radiator capacity in the modelled house, a sizing factor of 1.5 was applied to the nominal heat load (6 kW) of the house under design conditions (an ambient temperature of -10°C, a wind speed of 5 m/s, and no solar or internal gains). This is equivalent to a nominal capacity of 9 kW at 75/65/20°C.

A recent field measurement done with a representative dwelling sample[2] concludes that 80% of existing radiator systems can provide the required heating at the nominal condition with a supply temperature of 60°C and is largely independent of building type, construction period or specific annual heat demand (Pothof et al, 2022; 2023). Note that the study presumably includes some houses that have been renovated with heat loss reduction measures. This will also make the radiators “oversized”, but doesn’t mean the original system was, or at least not by as much as the analysis might suggest. Nevertheless, the sizing factor is considered to be a reasonable sizing estimate but is still subject to some uncertainty.

4. Test results

All cases defined in the previous section were tested in the HIL setup over 3 reference weather days with average ambient temperatures of -1, 2 and 4°C. These days account for a significant part of the heating season in the Dutch climate (Nederlands Normalisatie Instituut, 2008). This section will present some observed results of the parametric study as well as the control characteristics of the unit.

4.1. Control characteristics of the unit

The setup allows for highly detailed monitoring of the performance of the tested unit. Figure 5 illustrates the measurements of temperature (thermostat, supply, and return temperatures), flowrate (main circuit and boiler circuit), and power (thermal and electrical) for Case 0 on a reference weather day of 4°C. Also, the weather compensation curve is shown in the figure and it was calculated based on a linear correlation, which slightly differs from the unit's set curve but still serves as a good indicator.

When the unit switches on, it controls in such a way that the heat pump leaving water temperature targets the temperature calculated from the weather compensation curve (Figure 5, plot 2). Initially, it requires a high

[1] The first known regulation on this topic was ISSO51 (ISSO Kennisinstituut voor de Installatiesector, 2009).
[2] A sample of 187 dwellings distributed over building typology (detached, corner, terraced, apartment, etc.) and construction period (before 1974, 1974-1992 and after 1992).

output to achieve this, since the heating water was cold from the heat pump being off before. Note that some heat pumps have a start-up sequence for returning oil to the compressor resulting in medium to high heat output.

During the period from 12:00 to 24:00 hours, the unit is periodically switching on and off. Since the required heat output of the unit is lower than the capacity at minimum modulation it runs in a type of pulse width modulation. During a colder period from 00:00 to 12:00 hours, the unit operates at minimum capacity for an extended period, even though the supply temperature and thermostat are consistently under. Various settings on how the room temperature affects the working of the heat pump are provided by the manufacturer. These were all set to default as it was commissioned by an installer appointed by the manufacturer and not reviewed in this work.

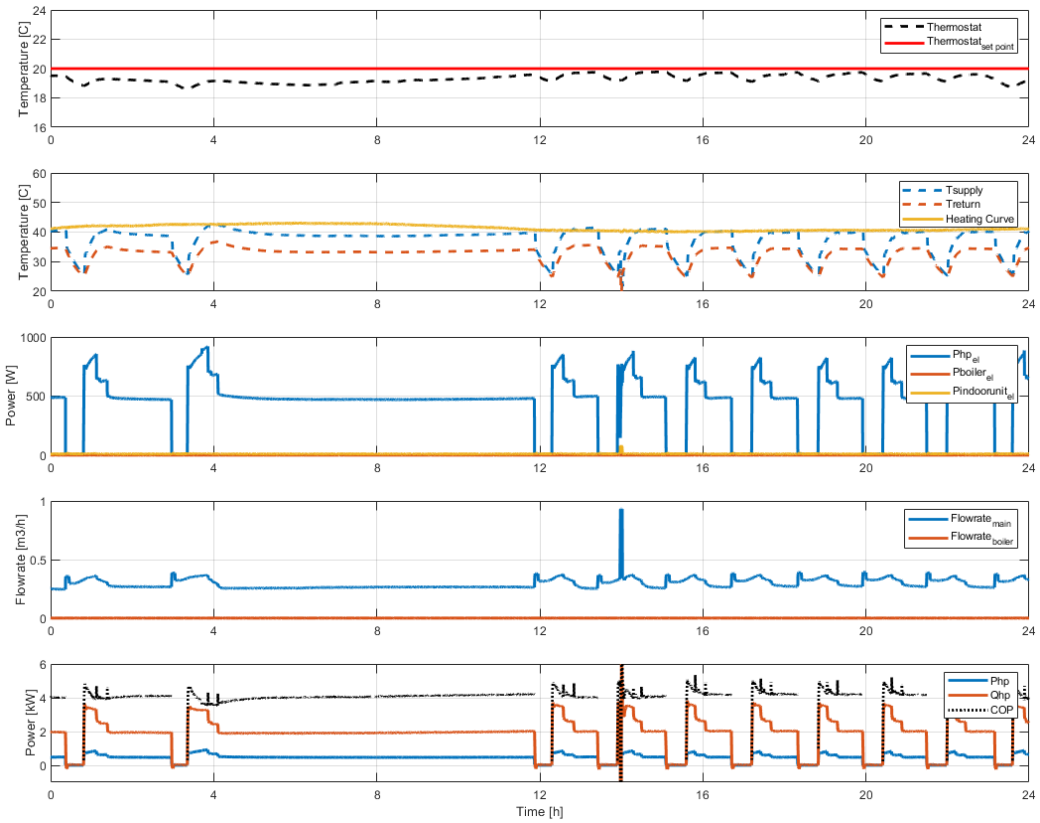

Fig. 5: The typical operation of the unit. The measurements of Case 0 on a reference weather day of 4°C.

It is important to note that there is no boiler operation during this test. The unit utilizes the boiler primarily during defrost periods, which is evident on reference weather days with temperatures of -1°C and 2°C. During defrost, the boiler reaches a maximum capacity of around 20-25 kW, causing a sudden increase in the supply temperature, followed by an overshoot in the room thermostat temperature.

4.2. The results of the parametric study

Figure 6 illustrates the daily average water temperature, COP, and thermostat temperature for each test day. Initially, radiator capacity was increased by replacing the radiators from T22 with T33 while keeping the weather compensation curve the same (from Case 0 to Case 1). As expected, increasing the radiator capacity increases the heat output of the radiators at lower supply temperatures. This heat output is actually higher than needed, as the room thermostat temperature averaged over the 3 days is above 20°C, and approximately 0.6°C higher than in Case 0. With this change, only a limited increase in COP was achieved as most of the benefit of increased radiator capacity was in improving comfort (room temperature closer to the setpoint) which was at times a bit low for case 0.

Therefore, the maximum water temperature of the weather compensation curve was adjusted from 55°C to 50°C at -10°C outdoor temperature in order to optimise the system performance (from Case1 to Case2). After

lowering the weather compensation curve, the thermostat temperature remained around 20°C with a lower supply water temperature. Consequently, the COP of the system increased by approx. 0.4 (approx. 10 %) on average due to increasing radiator capacity and adjusting the weather compensation curve. In fact, the heat emitted to the house was still greater (as shown by the daily average thermostat temperature) than in the base case.

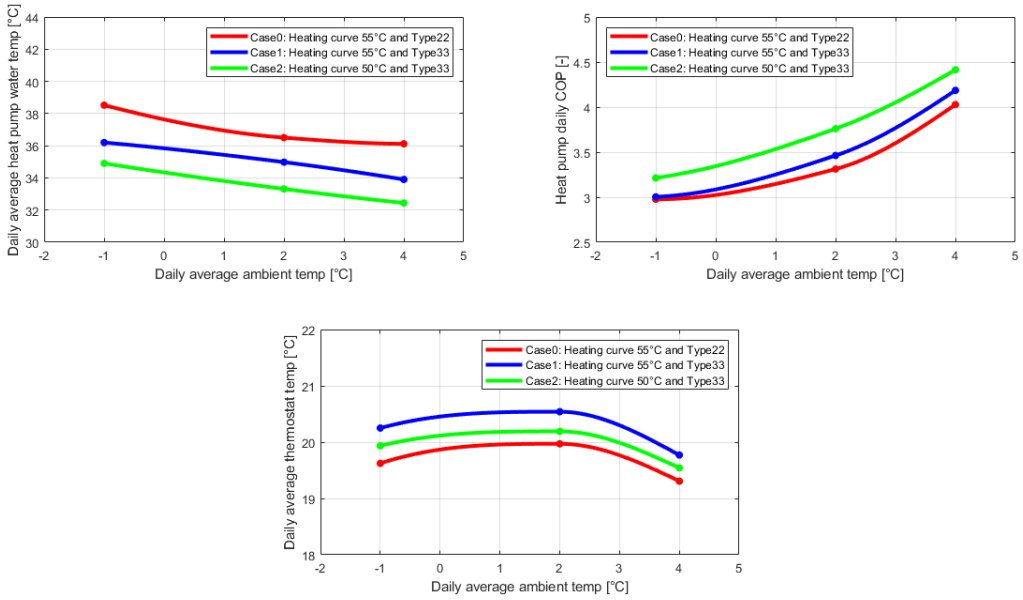

Fig. 6: Result of the parametric study; top left: daily average heat pump water temperature, top right: Heat pump daily COP, bottom: daily average thermostat temperature.

This indicates that lowering the maximum water temperature of the weather compensation curve from 55°C to 50°C (from Case1 to Case2) was not sufficient to compensate for the increase in radiator size (from Case0 to Case1). Based on these numbers it can be estimated that lowering the maximum water temperature of the weather compensation curve by another 2-3°C will increase the COP difference between Case 0 and Case 2 and will show the isolated effect of upgrading the radiator system to be higher than the found 10%.

It is worth emphasising here that these parametric measurements were carried out for -1, 2, and 4°C reference weather days only. These represent a significant part of the heating season in the Dutch climate (Nederlands Normalisatie Instituut, 2008). Therefore, it provides valuable insights into what is the impact of radiator capacity on heat pump performance. However, it is not enough to draw a conclusion about the seasonal performances. Besides, the control mechanism of this particular (hybrid) heat pump primarily relied on the weather compensation curve. The influence of the room thermostat compensation was not noticeable. Consequently, the unit conditioned the house at different room temperatures for the same reference weather day, depending on the specified weather compensation curve temperature and the defined radiator capacity. For instance, in Case 2, the thermostat temperature is higher than in Case 0. This led to more heat being transferred to the house however with better performance (COP). Therefore, directly comparing energy consumption between these cases can be misleading. With a better room thermostat compensation, the unit can maintain approximately the same thermostat temperature across all cases, allowing for a more accurate comparison of energy consumption.

Additionally, the impact of an incorrectly set weather compensation curve can be inferred indirectly from the results. In Case 0, a low weather compensation curve causes a reduction of the room thermostat temperature, which could lead to thermal comfort issues. Also, the most significant increase in the coefficient of performance (COP) occurs between Case 1 and Case 2 (approx. 7 %). This indicates that simply upgrading the heat emitter is insufficient; the weather compensation curve must be adjusted as well. This demonstrates the substantial influence of the installer on the unit's performance, especially for units without or with weak room thermostat compensation.

5. Discussion and Conclusion

The work presented in this paper demonstrates the successful creation of a HIL setup that can be used not only for obtaining more realistic system dynamics but also for facilitating comprehensive parametric studies. The repeatable nature of the setup allows for parametric studies to be performed, which is normally very challenging with standard field measurements in practice. In the HIL setup, there is complete control over the systems, meaning that the parameters can be adjusted, and the test can be run under the same conditions.

Through parametric studies, the HIL setup quantifies the impact of radiator capacity on hybrid heat pump performance. The results show that for a house with a 6 kW design heating load and a 9 kW radiator capacity at 75/65/20°C, upgrading the radiators from Type 22 to Type 33 (approximately a 50% increase in capacity) results in an increase in the performance of the hybrid heat pump by more than 10%, based on the average of three reference weather days (-1, 2, and 4°C).

An increase in the COP can indirectly influence the gas consumption in the hybrid heat pump. Typically, hybrid heat pumps switch from the heat pump to a gas-fired boiler based on the available heat pump capacity and a switchover COP, which is determined by economic or ecological considerations. Increasing the COP by lowering the water temperature thus reduces the use of gas-fired boilers and can also reduce the overall gas consumption in hybrid heat pumps.

Although this study shows that the HIL setup is quite useful in providing valuable insights into the influence of radiator capacity on heat pump performance, the test cases represent an example of a specific situation with limited weather conditions. For that reason, it is not sufficient to establish a more general conclusion between radiator capacity and the (hybrid) heat pump performance. Future work will therefore focus on extending the current study to include different construction years and insulation levels of the house, as well as varying radiator sizes (undersized, perfectly sized, and oversized) and different heat pump capacities. Additionally, the work will involve designing usable tools for assisting with techno-economic choices such as upgrading radiators.

Ultimately, more insight into this relationship can help homeowners and installers to make well-founded decisions related to selecting the (hybrid) heat pump system and changing/upgrading the heat emitter system in an existing dwelling. A financial trade-off can then be made between the costs of upgrading heat emitters and potential energy savings due to higher system efficiency.

6. Acknowledgements

The authors would like to thank the Rijksdienst voor Ondernemend Nederland, the Dutch Ministry of Economic Affairs and Climate Policy and the Dutch Ministry of the Interior and Kingdom Relations for subsidizing this research through the MMIP subsidy scheme.

7. References

Agentschap NL. (2011). Voorbeeldwoningen. Bestaandebouw. Sittard.

Centraal Bureau voor de Statistiek. (2021, May 12). Aardgasleveringvanuit het openbare net; woningkenmerken. Retrieved from http://statline.cbs.nl/statweb/

ISSO Kennisinstituut voor de Installatiesector. (2009). ISSO-publicatie 51: Warmteverliesberekening voor woningen en woongebouwen . Rotterdam: ISSO.

Klein, S. A. (2017). TRNSYS18: A transient system simulation program. Madison, USA: Solar Energy Laboratory, University of Wisconsin.

Nederlands Normalisatie Instituut. (1975). NEN1087 Ventilatie van woongebouwen. Delft: NEN.

Nederlands Normalisatie Instituut. (2001). NEN1087 Ventilatie van woongebouwen. Delft: NEN.

Nederlands Normalisatie Instituut. (2008). NEN 5060 Hygrothermal performance of buildings - climatic reference data. Delft: NEN

Nederlands Normalisatie Instituut. (2014). NEN442 Radiators and convectors. Delft: NEN.

Nederlands Normalisatie Instituut. (2014). NEN215 Thermostatic radiator valves - requirements and test methods. Delft: NEN.

Nederlands Normalisatie Instituut. (2019). Nederlandse technische afspraak (NTA) 8800. Delft: NEN.

Pothof, I., Vreeken, D., & van Meerkerk, M. (2023). Data-driven method for optimized supply temperatures in residential buildings. Energy, 284, 129183.

Pothof, I., Vreeken, T. & van Meerkerk, M. (2022). Field measurements on lower radiator temperatures in existing buildings. Report of the WarmingUP project.

Radson. (2020). Technische Fiche Paneelradiatoren Compact

SenterNovem. (2007). Referentiewoningen Nieuwbouw.

Transsolar Energietechniek GmbH. (2009). A module of an air flow network for coupled simulation with type 56 (multi-zone building of TRNSYS) - version 1.4. Stuttgart.

Vereniging Leveranciers Luchttechnische Apparaten. (2018). VLA methodiek gelijkwaardigheid voor energiebesparende ventilatieoplossingen in woningen (versie 1.3). VLA.

Zimmermann, J., Evans, M., Griggs, J., King, N., Harding, L., Roberts, P., & Evans, C. (2012). R66141 Final Report Issue 4. Household Electricity Survey. A study of domestic electrical product usage. Intertek testing and certification Ltd.

Sizing an Electrical Storage in Combination with Thermochemical Storage for a PVT-Driven Energy System in a Residential Application

Adriana Coca-Ortegón[1], Raquel Simón-Allué[1], Alberto Belda[2], Ismael Lozano[2], Georgios Martinopoulos[3], Alexandros Tsimpoukis[3], Nikolaos Nikolopoulos[3], Yolanda Lara[1]

[1] ENDEF Solar Solutions, Zaragoza (Spain)

[2] Fundación CARTIF, Valladolid (Spain)

[3] Centre for Research & Technology Hellas / Chemical Process and Energy Resources Institute, Thessaloniki (Greece)

Abstract

This work is focused on sizing electrical storage based on Li-ion batteries in combination with a thermochemical (TCM) storage for a system, driven by photovoltaic thermal (PVT) collectors coupled to a vapor compression heat pump, that provides heating, cooling, domestic hot water (DHW) and electricity in residential buildigs.

A sensitivity analysis of the electrical storage system is performed considering two sizes for the TCM storage to minimize the electrical requirement from the grid. The analysis is conducted through a simplified model implemented in the dynamic simulation software TRNSYS. This model uses as input the base electrical load profiles for the building and the TCM subsystem.

The electrical profiles linked to the TCM components are obtained from a more detailed model developed in Aspen and MATLAB, which considers the thermal loads in the building, and the internal TCM system configuration.

Keywords: Photovoltaic-Thermal collectors, PVT system, thermochemical storage, electrical storage

1. Introduction

Energy efficiency and the decarbonization of the building sector are the main objectives of energy policy worldwide. Currently, final energy consumption in buildings is mainly due to thermal uses, including space heating, water heating and cooking which represent 33%, 13% and 8%, respectively, followed by electrical appliances with a 16% share. Cooling is also a thermal use that currently represents 6% of overall final consumption, but this figure is expected to grow considerably by 2050, especially in developed countries (IEA, 2023a).

To achieve the energy policy objectives at European level, it is necessary to combine different strategies, such as the integration of renewable energies in buildings, the electrification of the thermal demand through efficient technologies such as heat pumps and the use of effective energy storage systems.

Among the renewable technology options, solar technology stands as one of the most promising for application at the building level, due to the ease of installation and integration. Particularly, the use of solar photovoltaic-thermal (PVT) technology has been growing in recent years (IEA, 2022), as it produces thermal and photovoltaic energy in a single device, with better overall efficiency than individual photovoltaic technology (Tiwari et al., 2023; Zondag, 2008).

The use of energy storage is also a key point to be included in the building energy systems' design. Within thermal storage technologies, the most common option used in buildings is sensible heat storage through water tanks (Fan and Luo, 2018; Koçak et al., 2020), followed by latent heat storage based on phase change materials (PCM) (Dincer and Rosen, 2011; Jouhara et al., 2020). Another thermal storage option with a higher energy density is the thermochemical (TCM) storage (Jarimi et al., 2019; Salgado-Pizarro et al., 2022), which is currently implemented in buildings mainly at the demonstration level. Electrical storage with electrochemical technology based on Li-ion batteries is another option that has been growing in the building sector in recent

© 2024. The Authors. Published by International Solar Energy Society
Selection and/or peer review under responsibility of Scientific Committee
10.18086/eurosun.2024.02.04 Available at http://proceedings.ises.org

years linked to the increment of self-consumption PV installations. The Li-ion battery price is still high, although it is expected that costs will decrease, thereby gaining a more competitive position (Kebede et al., 2022; MI (Mordor Intelligence), 2022; Xu et al., 2022).

This paper focuses on the sizing of an electrical storage system (ESS) based on Li-ion batteries for two sizes of TCM storage (17.5 and 30 kWh). These energy storage technologies are integrated into a building energy system, driven by a PVT-solar system in combination with an air-to-water vapor compression heat pump (HP). This energy system will provide thermal and electrical energy to an 80 m^2 building located in Santiago de Compostela (Spain). The objective is to define suitable ESS sizes that minimize the electrical dependency on the grid.

2. Methodology

2.1 Overall system description

The energy system analyzed consists of three main systems: i) the PVT-HP energy generation system, in charge of producing electricity and thermal energy through a hybrid PVT solar field and an air source HP, including an ESS based on Li-ion batteries; ii) the MiniStor system, where the thermal energy is stored through a thermochemical (TCM) storage in combination with a small heat pump and phase change materials (PCM) vessels; iii) the building's demand, which is met using the existing energy generation system, as well as the energy supply from the MiniStor system. Figure 1 shows the overall energy system scheme.

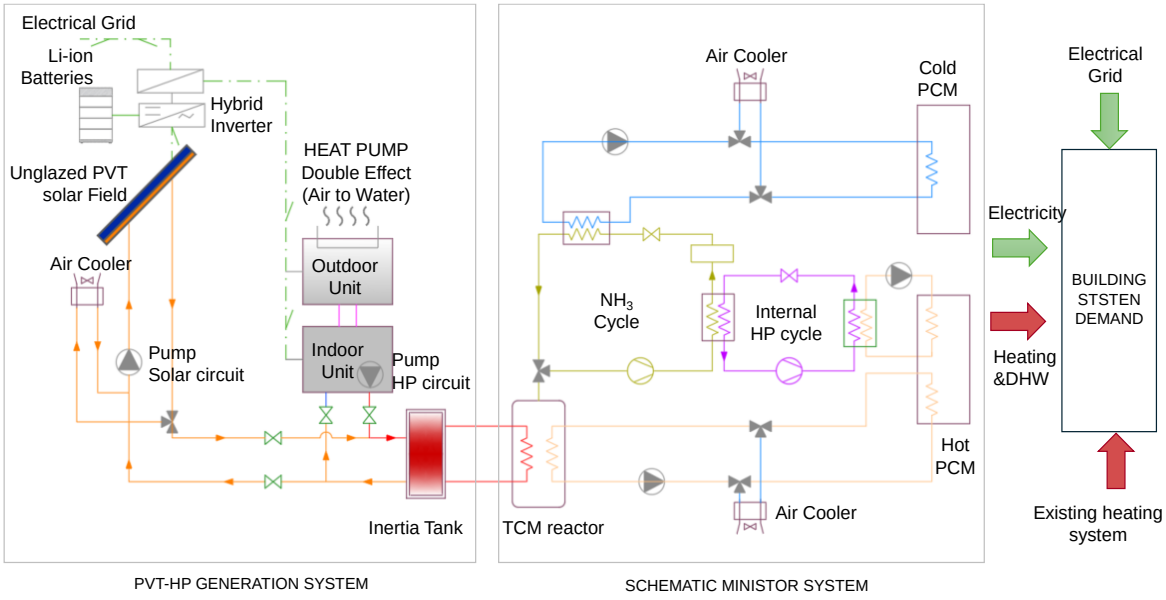

Fig. 1: Overall energy system scheme

The PVT-HP generation system includes a 39.2 m^2 solar field with unglazed liquid-based PVT collectors (nominal electrical power 7.80 kWp), which are hydraulically integrated, using a parallel configuration through an inertia tank (Lazzarin, 2020), with an air-to-water vapor compression HP (nominal capacity 11 kW in heating). The PVT electrical production is dedicated firstly to run the air-to water HP, with any excess being used to cover the building electrical demand or stored in the ESS. The PVT thermal production is used to pre-heat the inertia tank, which the air-to-water HP uses to provide thermal energy for the MiniStor system.

The MiniStor system included several subsystems: i) a TCM reactor containing ammoniated $CaCl_2$ salts, ii) an ammonia refrigeration cycle with a liquid ammonia storage tank, iii) a complementary small ammonia-to-water HP and iv) PCM units, through which the connection of MiniStor with the building is realized. (Tsimpoukis et al., 2024).

During the winter, in the TCM reactor operates by performing a solid-gas sorption process, that stores heat energy efficiently and at a high density. During the charging phase, it is used heat (44 to 70 °C) to produce a gaseous ammonia stream (NH_3) which is compressed, condensed and stored in a tank. Next, the condensation heat is used by the internal small heat pump, to charge a hot PCM vessel or cover the heating needs in the

building. During the discharging phase, the NH_3 stored as liquid in the tank is used. If the reactor equilibrium pressure is lower than the evaporation pressure, the material flows into the evaporator and evaporates at a temperature set by the surrounding environment. The gaseous ammonia is adsorbed in the reactor and since this is an exothermic reaction, the excess heat is used to cover the thermal demand.

During summer, the previous procedure is slightly modified. Because the heating thermal demand is negligible, the operation of the water-to-water HP during the charging phase is not necessary. The heat produced by the PVT-HP system is sufficient for covering the DHW loads, and thus the ammonia condensation heat is rejected to the ambient. The MiniStor system also provides cooling by exploiting the NH_3 evaporation, during the discharging mode; however, this effect is not required in the case of the analyzed building.

2.2 Energy demand estimation

The energy demand at the building includes the thermal loads (heating and DHW), as well as the electrical loads linked to the different lights and equipment used inside the building.

For the heating demand, a load profile is estimated following the EN 12831:2017 Standard (CEN and CENELEC, 2017) . The DHW demand is estimated following the Spanish Technical Building Code (Ministry of Development of Spain, 2019), which indicates that the average daily DHW demand in a residential building can be estimated at 28 liters per person produced at 60 °C. Considering the two previous reference norms and four people in the building, the overall thermal load profiles were defined for a typical day according to the season: extreme winter, average winter, autumn-spring and summer season.

The electrical demand considers three different load profiles: i) the electrical loads in the building, ii) the electrical loads of the air-to-water HP and iii) the electrical demand linked to the MiniStor system. The electrical load profile in the building was defined by studying the building inhabitant's behavior and monthly consumption data. The electrical load of the HP is obtained from a TRNSYS simulation model, by activating the equipment on a limited schedule during the day taking into consideration the average monthly PVT-electrical production. Finally, the load electrical profiles for the MiniStor system are obtained for defined typical days using a MATLAB/Simulink - ASPEN model, where the MiniStor system is modelled in detail (Zisopoulos et al., 2021).

2.3 Simulation model

The energy system that supplies thermal and electrical energy to the building is simulated using a simplified model implemented in the dynamic simulation software TRNSYS (SEL (Solar Energy Laboratory), 2018). This model has three main purposes, to simulate the PVT electrical and thermal production, to simulate the air-to-water HP thermal production as well as the corresponding electrical consumption, and finally to size the ESS. Internally the TRNSYS model included four main subsystems: (i) the PVT-HP generation subsystem, (ii) the electrical subsystem, (iii) the simplified thermal demand subsystem and (iv) the weather data subsystem. The implemented model is shown in Figure 2.

The PVT-HP generation sub-system includes the PVT solar field with the solar loop as well as the air-source HP with the corresponding hydraulic circuit. the PVT solar field is arranged in two groups of of 10 PVT collectors; within each group, the PVT collectors are hydraulically connected in parallel, and both groups are connected, to each other, in series. To simulate the PVT collectors type 50 b is used, the HP is simulated using type 541, which is activated using a pre-defined schedule. Finally, the inertia tank, that integrates the PVT and HP, is simulated with type 534. The corresponding performance curves provided by the HP manufacturer (Hitachi) were included in type 534's configuration. Other components in the solar and HP hydraulic circuits are the circulation pumps, the air cooler, the hydraulic pipes and valves.

The electrical production from the PVT solar field is sent to the electrical subsystem. The main components in this subsystem are a hybrid inverter (Fronius Gen 24 Plus, 8kW) and the Li-ion batteries (BYD, LVS models). The hybrid inverter manages the electrical production to use it directly to meet the electrical demand, or to store the excess in the batteries for later use. The battery models use LFP (Li-Iron-Phosphate) chemestry, which offers better power density, safety performance and higher lifetime compared to other chemistries available on the market; their round-trip efficiency is 96% and they support a maximum Depth of Discharge (DOD) of 90%.

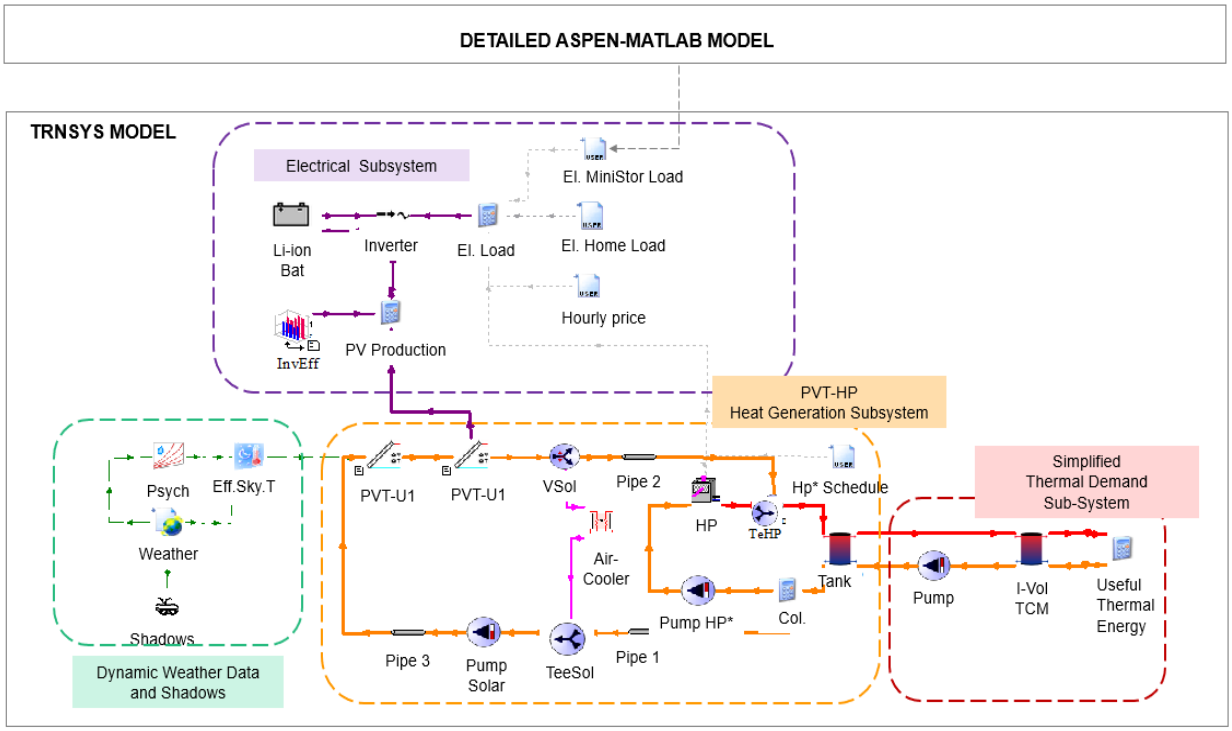

Fig. 2: Model layout implemented in TRNSYS software

To simulate the inverter and batteries types 48b and 47a are used. Additionally, the inverter uses a dynamic efficiency. Considering the previously mentioned battery models, specific commercial sizes (10.24, 12.8, 16.56 and 20.48 kWh) were used to perform a sensitivity analysis to select the optimal battery size.

The electrical subsystem requires as inputs the electrical load profiles for the MiniStor system and the building, which were obtained for typical days as section 2.2 described. Particularly, the electrical load profiles for the MiniStor system were estimated using a detailed ASPEN - MATLAB/Simulink model previously developed (Zisopoulos et al., 2021). These electrical loads were defined for two TCM reactor sizes (30 and 17.5 kWh).

The thermal production from the PVT-HP subsystem is sent to the MiniStor system, represented as a simplified thermal demand subsystem, which includes a hydraulic circuit between the inertia tank and the TCM reactor, a circulation pump to discharge the inertia tank, the inertia volume in the TCM reactor (type 534). The thermal demand of the TCM is simulated in a simplified way using an auxiliary calculation element, assuming a ΔT of 5 °C when the PVT-HP generation system sends thermal energy to the reactor. Table1 summarizes the different types used in the TRNSYS simulation model.

Tab. 1 : Summary of components used in the implemented TRNSYS Model

Subsystem	Component	Type /Library
PVT-HP subsystem	Unglazed PVT Collectors	Type 50b / Standard
	Air-to water HP	Type 941 / TESS
	Inertia tank, Air-cooler	Type 91 / Standard
	Inertia tank	Type 534 /TESS
Electrical subsystem	Hybrid inverter	Type 48b / Standard
	Li-ion batteries	Type 47a / Standard
	Dynamic efficiency hybrid inverter	Type 581 / TESS
Simplified thermal subsystem	Inertia TCM volume	Type 534 Standard
	Circulation pump TCM loop	Type 110 / Standard
	Complementary calculations	Equa
Weather data subsystem	Reading weather and external data	Type 15-3, 9 /Standard

	Psychrometric calculations	Type 33 /TESS
	Sky temperature calculations	Type 69 / Standard

2.4 PVT solar hybrid collector characterization

As stated was stated in the previous section, the simulation model uses a liquid-based unglazed PVT collector. This PVT collector corresponds to a prototype which was characterized in a test rig in accordance with the European Norm EN ISO- 9806 (CEN and CENELEC, 2014) and following the procedure applied in other studies where PVT collectors are also characterized and analysed (Simón-Allué et al., 2022).

$$\eta_{th} = \eta_0(1 - b_u u) - (b_1 + b_2 u)\left(\frac{T_m - T_a}{G^{"}}\right) \qquad \text{(eq. 1)}$$

This standard indicates that the thermal efficiency (η_{th}) for this PVT collector type has a linear behavior, dependent on incident solar radiation, fluid temperature, ambient temperature and wind speed, as Equation 1 indicates, where u corresponds to the wind velocitythe, η_0 represents the optical efficiency of the collector, b_u is a coefficient dependent on wind speed that affects the optical efficiency of the PVT collector; b_1 is the first thermal loss coefficient, and b_2 is the second thermal loss coefficient, also dependent on wind velocity; T_m corresponds to the mean fluid temperature in the PVT collector, T_a is the ambient temperature, $G^{"}$ is the net irradiance.

Tab. 2: Technical characteristics of the PVT solar collector

Description		Unit	Value
General characteristics	Dimensions: Length x Width x Height	[mm]	1719x1140x35
	Gross area	[m^2]	1.96
	Weight	[kg]	22
Main electrical characteristics STC	Cell type	[-]	Si-monocrystalline, PERC
	Efficiency STC (1)	[%]	19.9
	Power at maxim power point (PMPP)	[W]	390
	Temperature NOTC (2)	[°C]	42.3±2
	Power temperature coefficient	[% . K^{-1}]	-0.34%
Main thermal characteristics	Absorber type	[-]	Sheet & tubs
	Absorber materials	[-]	Aluminum and cooper
	Optical efficiency η_0	[-]	0.405
	Coefficient: b_u	[s/m]	0.0175
	First thermal loss coefficient: b_1	[W. m^{-2}. K^{-1}]	8.52
	Second thermal loss coefficient: b_2	[W. s. m^{-3}. K^{-1}]	0.275

(1) STC: Standard Testing Conditions; (2) Normal Operation Temperature Cell

2.5 Performance indicators

A set of performance indicators was defined to assess the effect of battery size on the solar fraction and grid system dependency (Alanne, 2023; IEA, 2023b). The corresponding applied formulation is presented below.

The Solar thermal fraction (SF_{th}) corresponds to the monthly thermal energy produced by the PVT solar field (Q_{PVT}), sent to the inertia tank, divided by the total thermal energy produced by the PVT-HP system (Zenhäusern et al., 2020)., as Equation 2 shows, where Q_{HP} represents the air-source HP thermal production

$$SF_{th} = \frac{Q_{PVT}}{Q_{PVT} + Q_{HP}} \qquad \text{(eq. 2)}$$

Similarly, the solar electrical fraction (SF_{el}) is calculated as the relation between the monthly electricity produced by the PVT solar field (E_{PVT}) divided by the electrical loads (E_L), according to Equation 3. In this case, the electrical loads considered are due to the air-source HP ($E_{L,Hp}$) and the MiniStor system ($E_{L,Ms}$).This solar fraction is assumed to range 0 to 1; therfore, values above 1 were normalized to 1 . Values above 1 means that there is an electricity excess, which can be either stored in the batteries for later use or fed into the grid.

$$SF_{el} = \frac{E_{PVT}}{E_{L,Hp} + E_{l,Ms}} \quad \text{(eq. 3)}$$

To evaluate the influence of the battery size on the electrical grid dependency, the grid fraction (GF) is used, which is calculated as the ratio between the electricity taken from the grid (E_{grid}) and the electrical loads (E_L), using Equation 4. For this indicator, three different scenarios are considered: i) loads due to the air-source HP; ii) loads due to the air-source HP and the MiniStor system; iii) loads due to the air-source HP, the MiniStor system and the building.

$$GF = \frac{E_{grid}}{E_L} \quad \text{(eq. 4)}$$

3. Results and Discussion

3.1 Annual energy demand

The annual thermal demand in the building is 7940 kWh, with 72% attributable to the heating and the remaining 28%, to DHW. Figure 3 (a) shows the monthly evolution for the thermal demand. During the winter period the demand is higher with monthly values between 793 and 1750 kWh, while during the summer and intermediate seasons the demand decreases drastically with monthly values from 169 to 189 kWh, which are linked exclusively to the DHW.

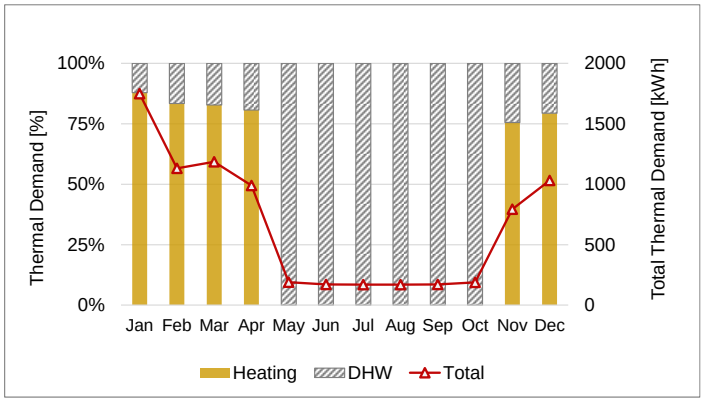

(a) Thermal demand

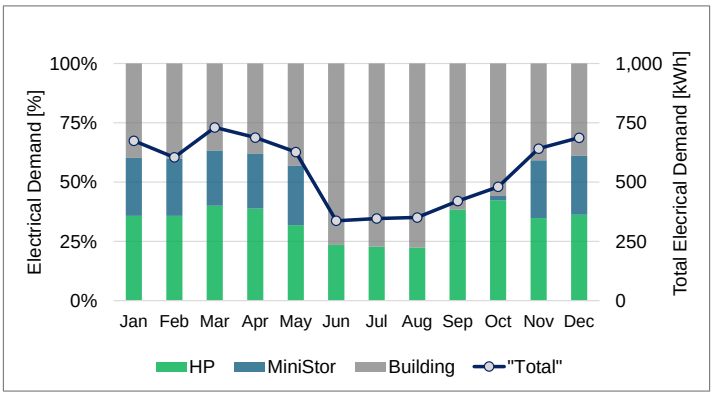

(b) Electrical demand

Fig. 3: Monthly thermal and electrical demand by type of use

Regarding the electrical demand, Figure 3(b) shows the electrical loads by use when the TCM storage has a capacity of 30 kWh. The annual electrical consumption is 6588 kWh, with 48.0% due to the building, 34.8% to the HP and 17.2% to the internal components of the MiniStor system. When the TCM capacity is 17.5 kWh the annual electrical consumption is slight higher (0.35%) with a similar share values by use (47.8% due to the building, 32.2% to the HP and 20% to the MiniStor system). These values indicate that the use of MiniStor system represents a high increment in the electrical demand. Therefore, the system control strategy for the HP and MiniStor system activation is based on a limited schedule, defined according to the electrical production

from the PVT solar field, in order to drive the MiniStor system using mainly renewable energy resources.

3.2 Sensitivity analysis of the battery size on the grid dependency

The sensitivity analysis of battery size on the grid dependency was performed for the two defined TCM storage capacities (30 and 17.5 kWh) and considered four commercial sizes for the ESS (10.24, 12.8, 16.56 and 20.48 kWh). The first TCM capacity (30 kWh) is closer to the daily building heating demand, therefore the Li-ion batteries provide a complementary energy storage capacity to cover the overall building energy demand (electrical and thermal). The second TCM capacity (17.5 kWh) is lower than the daily heating demand, so in this case the Li-ion batteries are focused on also covering the thermal building demand.

To size the electrical batteries as maximum value for the Grid Factor of 0.3 was assumed to limit the system grid dependency, besides SF_{el} above 0.80 on monthly basis were verified once the batteries were sized . Figure 4 shows the results for the three scenarios describe in section 2.5, considering different electrical load profiles during the winter months.

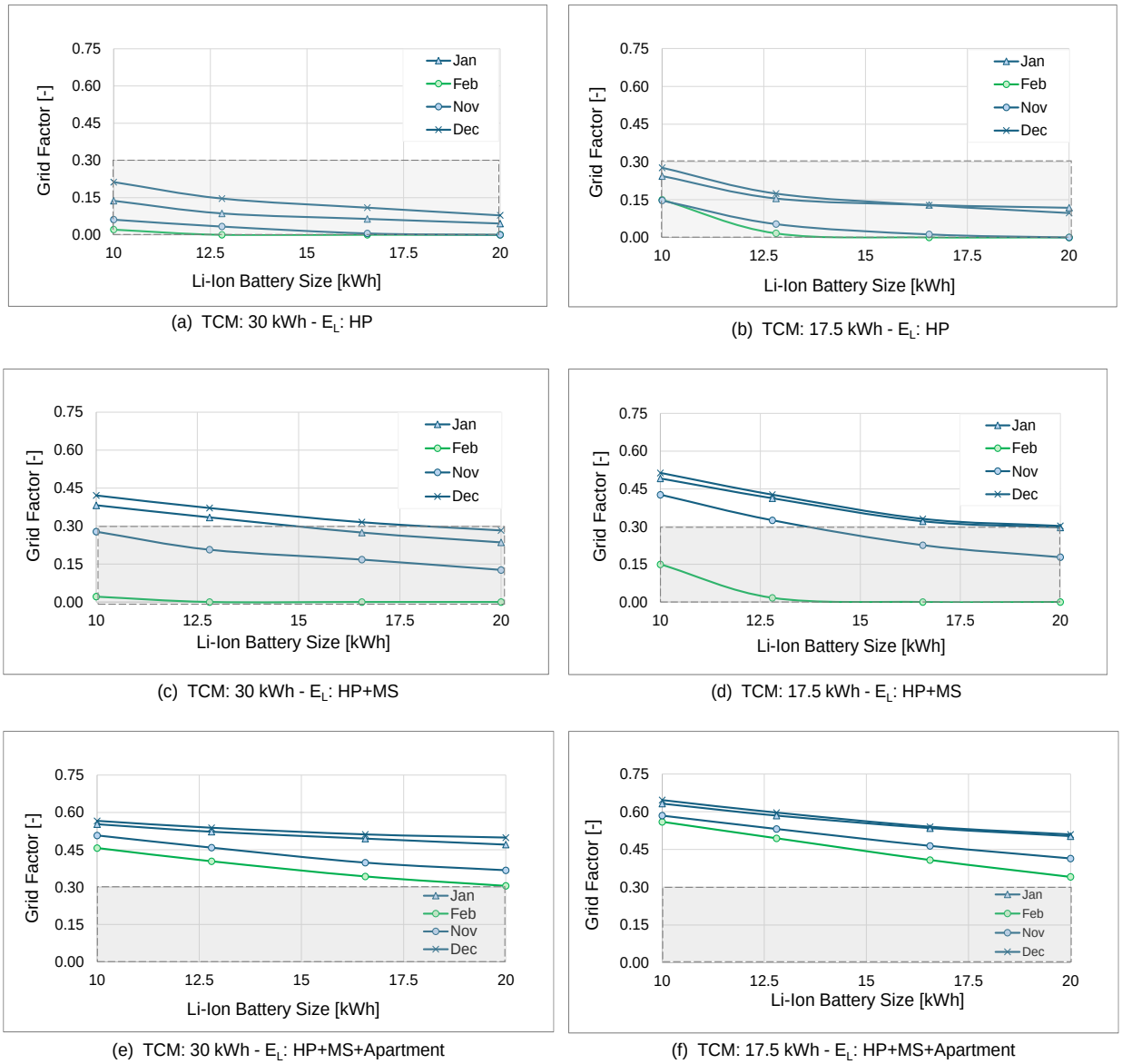

(a) TCM: 30 kWh - E_L: HP

(b) TCM: 17.5 kWh - E_L: HP

(c) TCM: 30 kWh - E_L: HP+MS

(d) TCM: 17.5 kWh - E_L: HP+MS

(e) TCM: 30 kWh - E_L: HP+MS+Apartment

(f) TCM: 17.5 kWh - E_L: HP+MS+Apartment

Fig. 4: Electricity taken from the grid for different energy storage sizes.

The first scenario includes the electrical loads due to the air-source HP (Figures 4.a and 4.b). In this scenario, for all battery sizes, the GF is below the target value. When the electrical battery size has the minimal simulated capacity (10.24 kWh), the maximum monthly value for the GF is 0.21 for the TCM capacity of 30 kWh and 0.28 if the TCM capacity is reduced to 17.5 kWh . Therefore, in this scenario, the grid dependency improves

when the TCM capacity is higher, that indicates a better interaction between the HP electrical load profile and the battery storage.

The second scenario considers the electrical loads due to the HP as well as the MiniStor system (Figures 4.c and 4.d). In this scenario, the GF is close to the target value, when an electrical battery size of 16.56 kWh is considered. Specifically, the GF is 0.32 and 0.33 for the TCM capacities of 30 and 17.5 kWh respectively; therefore, in this scenario, there is not a significant impact on the grid dependency, due to the additional capacity in the TCM.

Finally, the third scenario includes the electrical loads due to the HP, the MiniStor system and the building (Figure 4.e and 4.f). In this scenario, the GF target value is not achieved for any simulated battery size, because the electrical loads due to the building are bigger than loads linked to the HP and MiniStor system. For the maximum simulated battery size (20.48 kWh), the maximum GF values are 0.50 and 0.51 for the TCM capacities of 30 and 17.5 kWh.

Considering the above, when the HP and the MiniStor loads are included (second scenario),, the suitable capacities for the TCM and the electrical storage are 17.5 kWh and 16.56 kWh respectively, since the GF factor associate to these values is close to the target value of 0.30. There is no significant reduction in the GF factor when a higher TCM size is used. The final energy storage sizes must also consider other relevant variables such as the system and electricity costs.

3.3 Solar fractions

This subsection presents the PVT energy production with the solar fractions for the second scenario, using 17.5 and 16.56 kWh sizes for the TCM storage and Li-ion batteries respectively. Regarding the PVT electrical performance (Figure 5.a), the system achieves an annual production of 8732 kWh , which exceeds the overall annual electrical demand by 30%, including the air-source HP, the MiniStor system as well as the building.

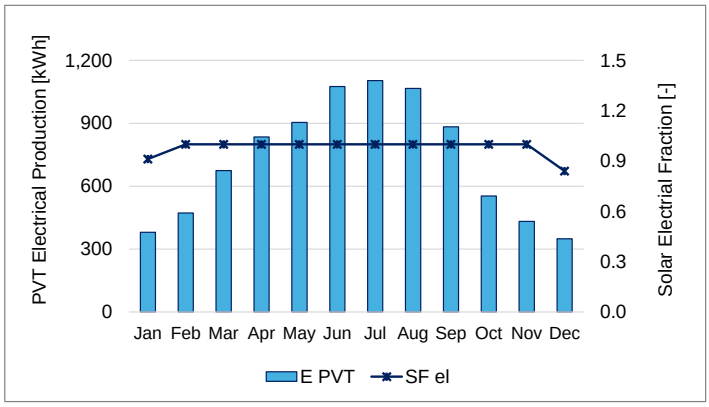

(a) PVT electrical production

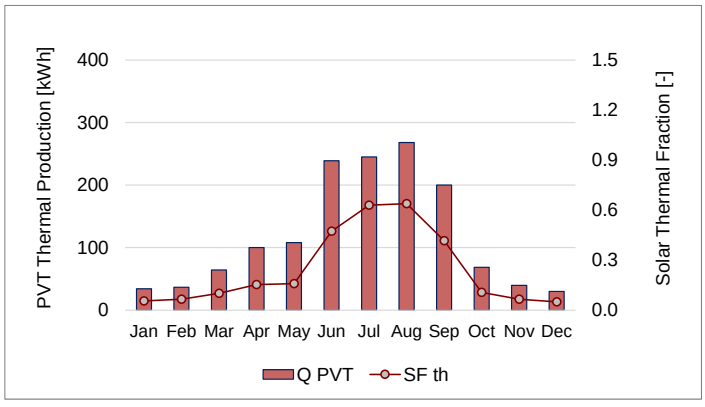

(b) PVT thermal production

Fig. 5: Monthly thermal and electrical demand by type of use.

Considering the HP and the MiniStor loads, the SF_{el} is high throughout the year with a minimal value of 0.84

in December and 0.91 in January; for the rest of the months, this fraction reaches values of 1.0. These high fractions suggest that the GF factor obtained (0.33) could be improved by implementing additional actions based on demand response strategies.

In relation to the PVT thermal performance (Figure 5.b), the annual production is 1434 kWh. The corresponding SF_{th} gets values between 0.06 and 0.11 in winter, so the effective solar thermal contribution to the thermal demand is relatively low in winter. On the contrary, during summer the SF_{th} achieves values between 0.42 and 0.64 indicating a high contribution to the DHW deman . Despite the low SF_{th}in winter, the SF_{el} and the GF show good performance, which guarantees that the MiniStor system will contribute to the thermal building demand using mainly solar energy.

4. Conclusions

The previous analysis revised the grid dependency of the considered energy system, including two types of energy storages (ESS based on Li-ion batteries and thermochemical (TCM)). The results lead to the following main conclusions:

The grid factor, as an indicator, helps to optimally define the sized combination of these two energy storage technologies. For the analyzed system, there is a similar grid factor (0.32 and 0.33) when an ESS of 16.5 kWh is used together with either TCM sizes (30 and 17.5 kWh). To complete the optimization a complementary analysis must be carried out, considering different cost factors such as investment, maintenance, and useful life, as well as other factors such as the availability of materials to manufacture these technologies at local and global levels.

Regarding the solar thermal fraction, the PVT technology achieves higher values in summer than in winter in winter. This performance is mainly due to the high temperature required by the TCM in the MiniStor system and the system's demand in winter. To achieve better performance, other technologies can be evaluated in the overall energy system such glazed PVT as well as solar thermal technology.

The thermal energy produced by the PVT-HP system primarily comes from renewable sources, as the activation of the HP uses a limited schedule linked to the PVT electrical production. Thanks to this control strategy, the system achieves higher solar electrical fractions and lower grid factors to cover the electrical loads for the HP and the MiniStor system.

These grid factors can potentially be improved considering that the solar electrical fraction reaches values above 0.84 on a monthly basis, when the electrical loads include the air-source HP and the MiniStor system. To achieve this improvement the HP activation should be optimized by obtaining a more accurate forecast for the expected PVT electrical production and implementing complementary demand response strategies.

5. Acknowledgments

This paper was prepared in the context of the European Union's Horizon 2020 research and innovation program through grant agreement No 869821 (Minimal Size Thermal and Electrical Energy Storage System for In-Situ Residential Installation - MiniStor). The authors also express their gratitude to the Universidad de Santiago de Compostela for supplying the data required to estimate the thermal and electrical energy demand for the analyzed case.

6. References

Alanne, K., 2023. Study on reducing the grid dependency of urban housing in Nordic climate by hybrid renewable energy systems. Renew. Energy Focus 46, 1–15. https://doi.org/10.1016/j.ref.2023.05.006

CEN, CENELEC, 2017. EN 12831-1 Energy performance of buildings - Method for calculation of the design heat load - Part 1: Space heating load, Module M3-3 18-22+95.

CEN, CENELEC, 2014. Solar energy. Solar thermal collectors -Test methods. EN-ISO 9806:2013.

Dincer, I., Rosen, M.A., 2011. Thermal energy storage. Systems and applications, 2nd ed. Wiley. A John Wiley and Sons, Ltd., UK.

Fan, Y., Luo, L., 2018. Energy Storage by Sensible Heat for Buildings, in: Wang, R., Zhai, X. (Eds.), Handbook of Energy Systems in Green Buildings. Springer, Berlin, Heidelberg. https://doi.org/https://doi.org/10.1007/978-3-662-49088-4_40-1

IEA, 2023a. World Energy Outlook 2023.

IEA, 2023b. Electricity Grids and Secure Energy Transitions. https://doi.org/10.1787/455dd4fb-en

IEA (International Energy Agency), 2022. Solar Thermal Market Records Year of Growth. SOLARUPDATE. Newsl. IEA Solar-Heating Cool. Program. 75, 1–29.

Jarimi, H., Aydin, D., Yanan, Z., Ozankaya, G., Chen, X., Riffat, S., 2019. Review on the recent progress of thermochemical materials and processes for solar thermal energy storage and industrial waste heat recovery. Int. J. Low-Carbon Technol. 14, 44–69. https://doi.org/10.1093/ijlct/cty052

Jouhara, H., Żabnieńska-Góra, A., Khordehgah, N., Ahmad, D., Lipinski, T., 2020. Latent thermal energy storage technologies and applications: A review. Int. J. Thermofluids 5–6, 100039. https://doi.org/10.1016/j.ijft.2020.100039

Kebede, A.A., Kalogiannis, T., Van Mierlo, J., Berecibar, M., 2022. A comprehensive review of stationary energy storage devices for large scale renewable energy sources grid integration. Renew. Sustain. Energy Rev. 159, 112213. https://doi.org/10.1016/j.rser.2022.112213

Koçak, B., Fernandez, A.I., Paksoy, H., 2020. Review on sensible thermal energy storage for industrial solar applications and sustainability aspects. Sol. Energy 209, 135–169. https://doi.org/10.1016/j.solener.2020.08.081

Lazzarin, R., 2020. Heat pumps and solar energy: A review with some insights in the future. Int. J. Refrig. 116, 146–160. https://doi.org/10.1016/j.ijrefrig.2020.03.031

MI (Mordor Intelligence), 2022. Global Enery Storage System Market.

Ministry of Development of Spain, 2019. Technical building Code - Basic Energy Saving Document (CTE-DB-HE). Código Técnico de la Edificación -Documento Básico Ahorro de Energía (CTE-DB-HE).

Salgado-Pizarro, R., Calderón, A., Svobodova-Sedlackova, A., Fernández, A.I., Barreneche, C., 2022. The relevance of thermochemical energy storage in the last two decades: The analysis of research evolution. J. Energy Storage 51. https://doi.org/10.1016/j.est.2022.104377

SEL (Solar Energy Laboratory), 2018. TRNSYS 18 - A Trnsient Syste, Simulation Program. Volume 8 - Weater Data.

Simón-Allué, R., Guedea, I., Coca-Ortegón, A., Villén, R., Brun, G., 2022. Performance evaluation of PVT panel with phase change material: Experimental study in lab testing and field measurement. Sol. Energy 241, 738–751. https://doi.org/10.1016/j.solener.2022.05.035

Tiwari, A.K., Chatterjee, K., Agrawal, S., Singh, G.K., 2023. A comprehensive review of photovoltaic-thermal (PVT) technology: Performance evaluation and contemporary development. Energy Reports 10, 2655–2679. https://doi.org/10.1016/j.egyr.2023.09.043

Tsimpoukis, A., Martinopoulos, G., Nikolopoulos, N., 2024. Analysis of a novel compact integrated thermal energy storage system (MiniStor) in European sites, in: 12th International Conference on Improving Energy Efficiency ICommercial Buildings and SmartCommunities. European Union, pp. 3–14. https://doi.org/10.2760/716916

Xu, Y., Pei, J., Cui, L., Liu, P., Ma, T., 2022. The Levelized Cost of Storage of Electrochemical Energy Storage Technologies in China. Front. Energy Res. 10, 1–16. https://doi.org/10.3389/fenrg.2022.873800

Zenhäusern, D., Gagliano, A., Jonas, D., Tina, G.-M., Hadorn, J.-C., Lämmle, M., Herrando, M., 2020. Key performance indicators for PVT Systems. IEA SHC, Task 60 PVT Systems, Report D1. https://doi.org/10.18777/ieashc-task60-2020-0007

Zisopoulos, G., Nesiadis, A., Atsonios, K., Nikolopoulos, N., Stitou, D., Coca-Ortegón, A., 2021. Conceptual design and dynamic simulation of an integrated solar driven thermal system with thermochemical energy storage for heating and cooling. J. Energy Storage 41. https://doi.org/10.1016/j.est.2021.102870

Zondag, H.A., 2008. Flat-plate PV-Thermal collectors and systems: A review. Renew. Sustain. Energy Rev. 12, 891–959. https://doi.org/10.1016/j.rser.2005.12.012

Mathematical modelling of an Innovative Ice Storage System

Nayrana Daborer-Prado[1], and Christian Wagner[1]

[1] University of Applied Sciences Upper Austria – Research group ASIC, Wels (Austria)

Abstract

Ice storage systems are important applications for heating and cooling due to its ability to efficiently store thermal energy for later use, reducing reliance on conventional energy sources during peak demand periods. In combination with heat pumps and solar collectors, ice storages present a large advantage in comparison with other conventional heating and cooling systems. In this work, the mathematical modelling of an innovative ice storage system will be presented. The energy storage in this system, happens in innovative spiral flat registers created by the company ECOTHERM, where internal and external melting can be used as required. The mathematical model will then be further integrated in an overall system and a yearly simulation of its performance will be carried out. In the scope of this study, just the heating performance of the ice storage system were analyzed, while the combined use of the ice storage for heating and cooling will be carried out in the subsequent phases of the project. The results focus on the State of Charge (SOC) and the temperature of the ice storage during the simulated year as well as the energy accumulated in the same period. Moreover, the seasonal performance factor (SPF) of the whole system is also presented. The results obtained with the simulations, were later compared to literature data and present a fair equivalence.

Keywords: ice storage, heat storage, mathematical modelling, state of charge

1. Introduction

Substantial progress has been achieved in the last decade in the application of renewable energies, from different sources, to improve energy-storage technologies with the objective of balancing energy supply and demand (Gan et al. 2020). Phase change thermal storage systems, play an important role in this scenario due to its high thermal storage capacity and small volume variation. Phase change materials (PCM) are substances which absorb or release a significant amount of energy during its phase transition, in a process at nearly constant temperature. Even though the large amount of PCM types available, ice is a favored choice in view of its low-cost, high-energy density and its melting temperature (Dincer, I., Rosen, M. 2011).

Ice storage, when integrated with heat pumps and solar collectors, represents a significant advancement in efficient energy management and sustainability within the realm of heating, ventilation, and air conditioning (HVAC) systems. This innovative combination offers several key advantages over conventional heating and cooling systems. For instance, in places where boreholes cannot be drilled, the ice storages can be used instead of ground source systems. Also, the ice storage systems can be a replacement of air source-based concepts, in cases when noise problems or efficiency are to be considered (Carbonell et al., 2015). A few examples of ice thermal storage systems being used in different types of industries, including air conditioning, food processing and building energy conservation can be found in (Zhao et al. 2020), (Sidik et al. 2018), (Bayrak et al. 2017) and (Sheikholeslami et al. 2021).

Mathematical modeling plays a crucial role in understanding and optimizing ice storage systems, offering insights into their thermodynamic behavior, performance characteristics, and operational efficiency. These models typically incorporate equations derived from principles of heat transfer, fluid dynamics, and thermodynamics to simulate the complex interactions within the system. One key aspect of mathematical modeling involves predicting the thermal behavior of ice storage mediums, such as water or phase change materials, during charging and discharging cycles (Buchner, Sebastian 2005). This includes analyzing heat transfer mechanisms, phase change phenomena, and energy storage capacity under varying operating conditions.

In the scope of this study, a mathematical model for an ice storage system will be presented and later, further integrated in an overall system containing, a single-family house, a heat pump and a solar thermal collector field. The simulations will be performed using MATLAB/Simulink (The MathWorks, Inc. 2024). The mathematical model

© 2024. The Authors. Published by International Solar Energy Society
Selection and/or peer review under responsibility of Scientific Committee
10.18086/eurosun.2024.02.05 Available at http://proceedings.ises.org

used in the simulations presents some simplifications to enable a faster simulation time, without losing the accuracy. In the further sections the overall system as well as the mathematical model for the ice storage will be presented and detailed. Also, the results achieved using the ice storage in the overall system, as the State of Charge (SOC) and the temperature of the ice storage will be calculated and discussed. Finally, the conclusions and the outlook for the project will be presented.

2. Methods and methodology

2.1 System overview

Figure 1 presents an overview of the entire system used in this work. It consists of an ice storage device, a buffer storage tank, a solar collector (i.a. PVT collector) and a heat pump. The evaporator of the heat pump is connected to the ice storage tank via a hydraulic circuit. The energy required for vaporization is therefore provided by the ice storage. The heat generated from the heat pump is transferred to a buffer storage, from which energy is supplied for domestic heating and domestic hot water (DHW) needed in a single-family house. Regeneration of the ice storage is done via the solar circuit. However, if there is sufficient solar radiation, the buffer storage can also be charged directly via the solar circuit. In summer, the ice storage can also be used for cooling applications. For this purpose, the energy in form of ice is used directly from the ice storage, without the use of a conventional cooling unit. Therefore, the ice storage is connected to the building's cooling distribution system via another hydraulic circuit, including an additional heat exchanger. In this work the focus is on the mathematical modelling of the ice storage system (highlighted in the blue dotted square), which will be further described in the next section.

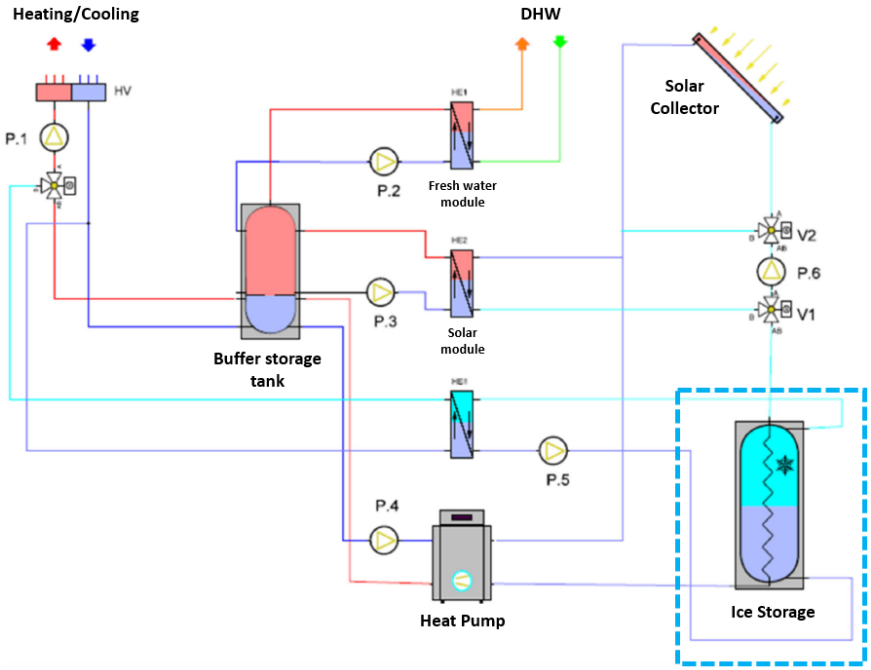

Figure 1: Overview diagram of heat pump system with ice storage and solar regeneration

2.2 Mathematical model of ice storage system

In order to develop a mathematical model for an ice storage system, it is important to understand the dynamics of it. The relationship between the media temperatures and the speed of ice formation affects the cost-effectiveness of the ice storage. Hence, although the ice formation will happen in a faster pace at low temperatures, low coefficients of performance (COP) are to be expected for the heat pumps in this condition. Another important factor is that the ice formation is a transient process, representing a heat conduction problem in which a phase change of the fluid occurs. This problem is usually referred to in the literature as Stefan-Problem, which is characterized by the fact that the heat flows occur as a result of transient heat conduction and also are directly linked to the phase change enthalpies (Dohmann 2016).

The formation of an ice layer in the system considered in this paper, happens in a thin-walled layer of stainless steel, which separates two media from each other, in this case, water and glycol. A cold flow of glycol (cooling medium) is separated from the wall of water, which is already at a solidification temperature. The growth of the ice layer is one-dimensional and occurs along the spatial coordinate x, as it can be observed in Figure 2. The layer of ice

represents a transport resistance for the heat flow between the water and the glycol.

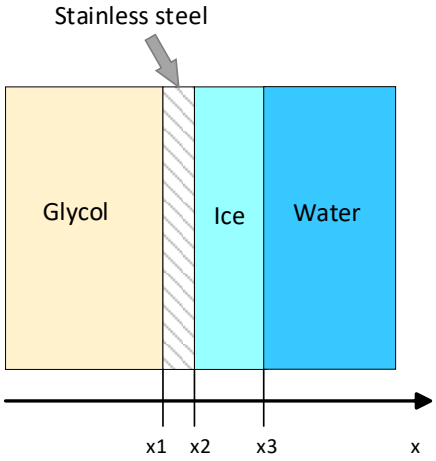

Figure 2: Example of ice formation in a heat exchanger of an ice storage system

It is also important to observe that the temperature of the ice storage depends on the heat flows to the wall and the heat flows due to the heat exchangers. For the first phase of the project, the mathematical modelling using a simpler model will be implemented in MATLAB/Simulink. In this model, the formation of ice on the heat exchangers will be calculated through the enthalpy H. This is a lumped capacitance model, meaning that the temperature inside the ice storage is assumed to be homogeneous (Winteler C. et al. 2014).

$$H_{ice} = \int \frac{1}{m_{ice}} \left(\sum_i \left(\dot{Q}_{2ice} \right)_i + UA_{tank}(T_{wall} - T_{ice}) \right) \quad (1)$$

Where, m_{ice} (kg) represents the mass of liquid in the ice storage, $\left(\dot{Q}_{2ice} \right)_i$ (W/m²) describes the heat flows through heat exchangers, A_{tank} (m²) is the area of the storage tank and T_{wall} and T_{ice} (°C) are the temperatures of the storage wall and the ice, respectively.

The ice storage temperature T_{ice} is calculated by means of a linear interpolation from the values in Table 1, which depends on the enthalpy (H). In the table, cp_{ice} and cp_w (J/kg K) represent the specific heat capacity of the ice and water, respectively, while q_{fice} is the specific heat of freezing water-ice.

$$T_{ice} = T_{tabelle}(H_{ice}) \quad (2)$$

Table 1: Interpolation values for temperature calculation

Temperature [°C]	Enthalpy [J/kg]
-10	-10 * cp_{ice}
-3	-3 * cp_{ice}
0	q_{fice}
10	$10 * cp_w + q_{fice}$

Using the enthalpy, the thermal energy stored during the melting phase transition and the thermal energy released in the solidification phase transition, can be taken into consideration.

In order to solve the Equation (1), the initial enthalpy value has to be calculated according to Equation (3):

$$H_{init} = (1 - f_{ice}) * 3.35 * 10^{-5} + \Theta(-f_{ice}) * 4182 * T_{init} \quad (3)$$

Where, f_{ice} (-) represents the initial fraction of ice inside the storage tank and T_{init} (°C) is the initial storage temperature, both values are user-defined initial parameters. Here, the $\Theta(z)$ is the Heaviside function, a step function which has the value of zero for a negative z and assumes a value of one for $z \geq 0$.

Further steps

In a subsequent second phase of this project, a more detailed mathematical approach will be used to describe the ice storage system. The mathematical model for the ice storage will be derived from the solution of the energy conservation law applied to the water of the storage integrated over several control volumes, as can be observed in Equation (4) (Carbonell et al. 2014), (Carbonell et al, 2015). In order to simplify the calculations, the following assumptions will be considered:

- The forced convection heat transfer between control volumes is neglected.
- Physical properties are constant in the control volumes.
- The solid phase will remain always at the same temperature.
- The viscous dissipation, radial fluid flow, compressibility, external forces and axial heat conduction are neglected.

$$\rho c_p \frac{\partial T_w}{\partial t} + \left(\rho c_p\right)_{ice} \frac{\partial T_{ice}}{\partial t} = \frac{\partial}{\partial y}\left(\lambda \frac{\partial T}{\partial y}\right) + \frac{h_f}{V} \frac{\partial\, m_{ice}}{\partial t} + \dot{q}_{ext} + \dot{q}_{hx} \tag{4}$$

In Equation (4), t is time (s), y is the coordinate along the height of the storage, T_w (°C) is water temperature, V (m³) is the water volume of the storage, λ (W/mk) and ρ (kg/m³) are the heat conductivity and density of water respectively, c_p (J/kg K) is specific heat capacity of water, h_f (J/kg) is enthalpy of fusion, m_{ice} (kg) is mass of ice and $\dot{q}_{ext}$ and $\dot{q}_{hx}$ (W/m³) are the heat fluxes per unit volume between the storage fluid and the surroundings and heat exchanger respectively.

The first and second terms of Equation (4) are the accumulated sensible heat of the fluid and solid ice. On the right-hand side, the first term represents the heat of conduction between control volumes, the second is the latent heat of solidification and melting, and the last terms are the heat from the surroundings and heat exchangers respectively.

The heat loss to the surroundings through the external surface area of the tank (A_{ext} in m²), is calculated as follows:

$$\dot{Q}_{ext} = U_{ext} A_{ext} (T_w - T_{ext}) \tag{5}$$

In Equation (5), T_{ext} (°C) is the temperature of the surroundings, U_{ext} (W/m²K) is a heat transfer coefficient and $\dot{Q}_{ext} = \dot{q}_{ext} V$.

Regarding the heat transfer from heat exchanger to storage fluid, it can be calculated using the following equation,

$$\dot{Q}_{hx} = -\dot{m} c_p (T_{f,o} - T_{f,i}) \tag{6}$$

Where, $\dot{m}$ represents the mass flow rate (kg/s) of cooling fluid, $T_{f,o}$ and $T_{f,i}$ (°C) are the fluid temperature of the heat exchanger at the outlet and inlet, respectively. In order to get to Equation (6), a constant heat transfer coefficient through the fluid path, has to be considered.

3. Results and discussion

3.1. Ice Storage description

The simulation model for the ice storage is performed to represent the ECOTHERM Ice Memory System. In this system, 12 spiral flat coil cooling bundles are connected in parallel. Figure 3 presents the ice storage system and the internal view of one of the spirals (marked in red) is amplified in the left-hand side. The storage tank is made of stainless steel, with a height of 2,9 meters, a volume of 5000 liters, and a weight of ca. 4800 kg. The total storage capacity can reach a maximum of 425 kWh at approximately 65% of icing. During the simulations, a system with 10 m³ was used, combining in parallel two of the former mentioned Ice Memory System. The material properties of water and glycol were determined using the CoolProp add-in tool in MATLAB (Bell et al., 2014).

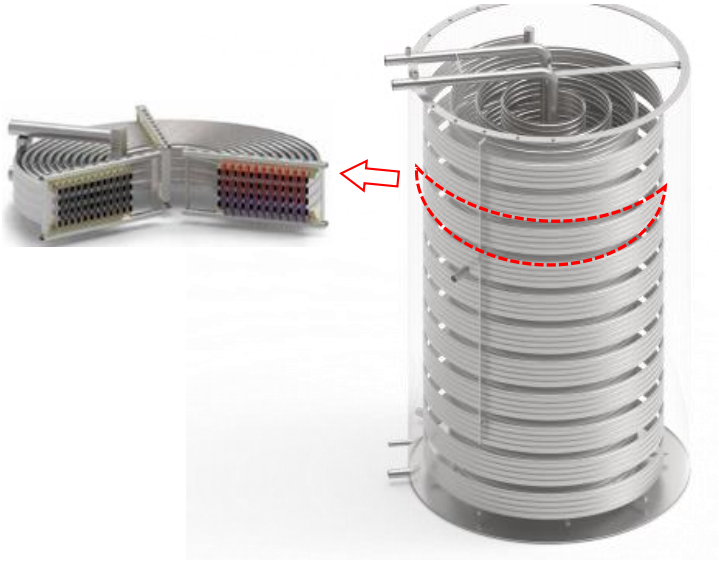

Figure 3: Ice storage system (right) and internal view of one of the cooling bundles (left)

3.2. Complete system

As previously mentioned, the ice storage model developed in this project will be integrated in a comprehensive system. Figure 4 presents the overview of the system created in Simulink, where the ice storage is the blue block outlined in red. The simulation is carried out using the Carnot Toolbox (CARNOT Toolbox, 2024), which is used to analyze the performance of the ice storage. In general, ice storages can be used for both heating and cooling. Nevertheless, in the course of this work, the performance of the ice storage only for heating purposes is analyzed. For this reason, a complete heating system is simulated in Simulink. The system consists of a single-family house, an ice storage, a heat pump and a solar thermal collector field. The heat demand of the single-family house is met by the heat pump. The ice storage is used to provide the thermal energy required for the heat pump process and consequently, the water in the ice storage decreases its temperature and freezes due to the associated heat flux. Thus, the ice storage must be regenerated. The energy required for regeneration is supplied by the solar thermal collector field. The regeneration process is controlled via the temperature difference between the collector outlet and the temperature of the medium in the ice storage. If the temperature difference is greater than 5 K, the solar pump is switched on and the ice storage is regenerated, whereas the solar pump is switched off at a temperature difference less than 1K.

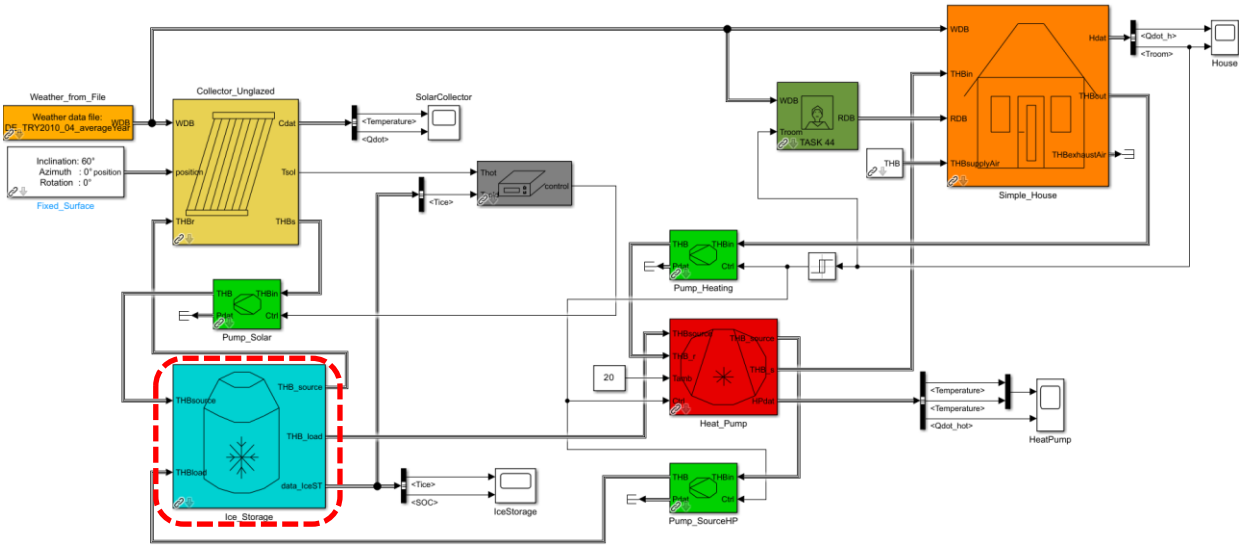

Figure 4: Simulink view of the complete system

The system parameters used in the simulation are listed in Table 2:

Table 2: Simulation parameters

Parameter	Value
Single family house	Specific heat demand 45 kWh/(m²a), 120 m² heated living surface
Ice storage	10 m³
Thermal insulation surface ice storage	50 mm, 0.05 W/(m K)
Heat pump	7 kW nominal heat output
Solar thermal collector field	20 m² unglazed

The ice storage model in the Carnot Toolbox is designed for use with underground ice storage systems. However, the ice storage under consideration in this work is intended for installation within a building. In consequence, the corresponding ice storage model has been modified so that the ice storage is now surrounded by air, as opposed to soil. The calculation of heat losses or gains to the surrounding air is computed according to Equation (5). In order to prevent condensation occurring on the exterior surface of the ice storage walls, a 50 mm layer of thermal insulation is applied to the model.

Subsequently, an annual simulation of the entire system is conducted in accordance with the previously mentioned system parameters (Table 2). Figure 5 shows the State of Charge (SOC) of the ice storage. The SOC describes how much thermal energy is stored in the ice storage, related to the energy content of the phase change. For example, a SOC of 1 indicates that the entirety of the water within the ice store is in a liquid state at 0°C. By contrast, a SOC of 0 means that all the water in the storage is ice at 0°C. Since the water can also reach temperatures above 0°C, for example during regeneration, it is possible that the SOC of the ice storage can reach values above 1. According to Figure 5, this is particularly the case in summer, as the heat pump is not in operation at this time. Due to the expansion of the ice and the associated blasting effect during the icing process, the ice storage and the thermal collector field have been designed in such a way that the degree of icing does not exceed 80%. Therefore, the minimum possible SOC is 20%. The simulation indicates that this threshold will only be reached by the end of January. Figure 5 clearly shows that, with the specified configuration of the components, the SOC reaches a value between 0.2 and 1 during the heating period. This indicates that the energy associated with the phase change of the water is optimally utilized during this period. Following the heating period, the temperature within the ice storage may reach a maximum of 30°C (Figure 6). Since the heat pump is not operating during this period, only the heat losses to the surrounding air need to be covered by the solar thermal collector. For this reason, the temperature of the ice storage varies between 20°C and 30°C during the summer. At the beginning of the heating period in autumn, the temperature in the ice storage drops accordingly as the heat pump starts up and initially ranges between 10°C and 0°C. Towards the end of the year, the water begins to freeze again. The SOC now reaches constant values below 1.

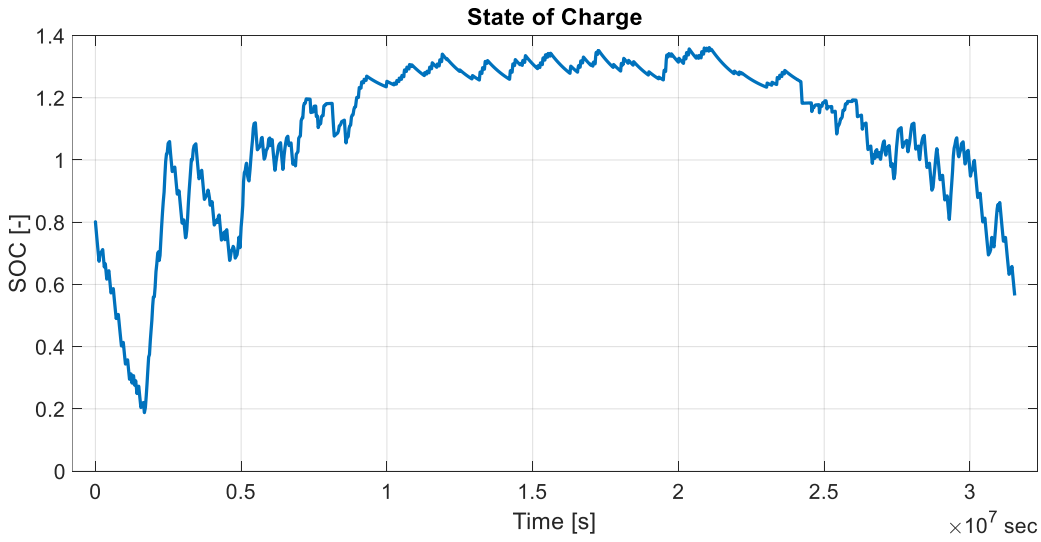

Figure 5: State of charge of ice storage

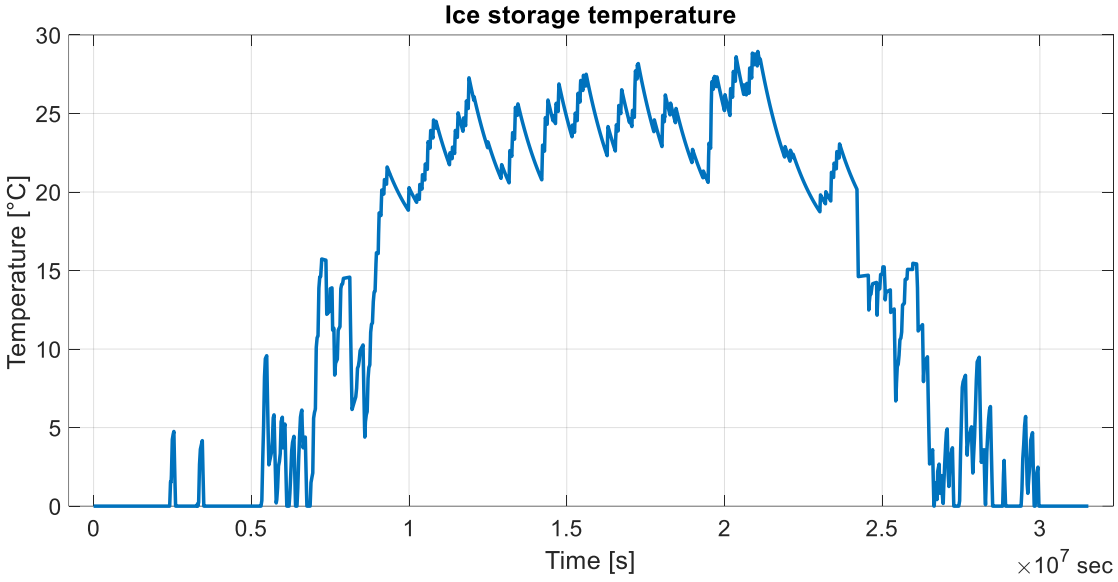

Figure 6: Temperature of ice storage

The energy input from the ice storage to the heat pump is shown in Figure 7. In total, the ice storage provides almost 6000 kWh of thermal energy to the heat pump. In the first half of the year, approximately 3300 kWh and in the second half of the year, 2700 kWh are delivered to the heat pump. The cumulated energy curve can be employed to ascertain the mean thermal power delivered by the ice storage to the heat pump. During the first part of the heating period, this equates to approximately 1.36 kW, while during the second part of the heating period, an average of 1.15 kW is observed.

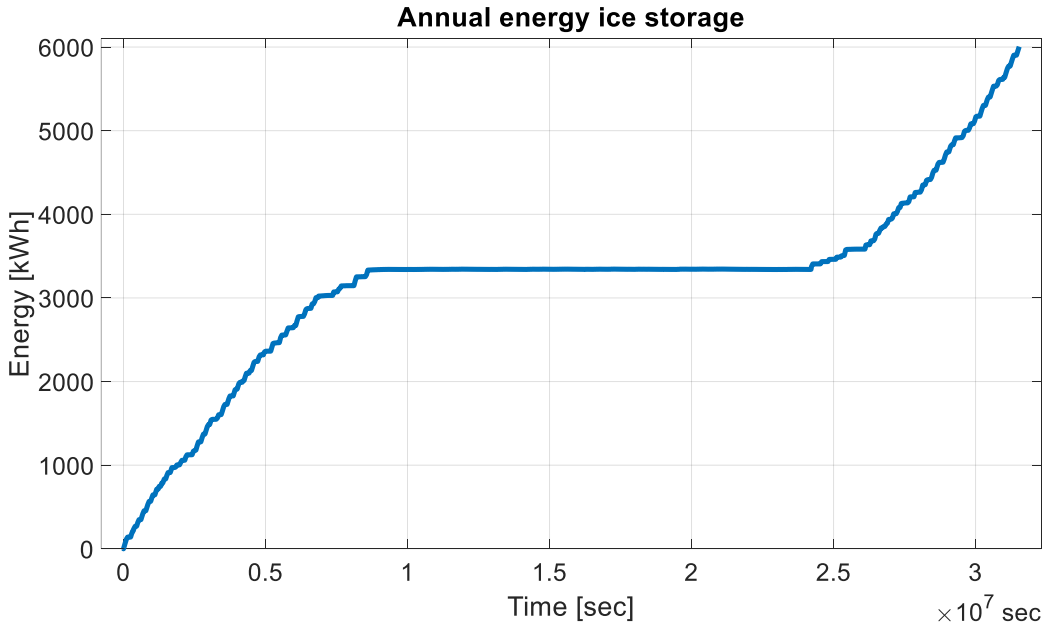

Figure 7: Cumulated energy curve of the ice storage

Several key figures are used to describe the efficiency and performance of the whole system and the individual components. The efficiency of the heat pump is described by the Seasonal Coefficient of Performance (SCOP):

$$SCOP_{HP} = \frac{Q_{H,HP}}{W_{el,HP}} \tag{8}$$

Where the $SCOP_{HP}$ is the seasonal coefficient of performance (-), $Q_{H,HP}$ (kWh) is the annual thermal energy which is supplied by the heat pump and finally $W_{el,HP}$ (kWh) is the annual electrical energy which is consumed by the heat pump.

In accordance with the parameters established for this simulation, the $SCOP_{HP}$ attains a value of 4.54. However, this value only reflects the efficiency of the heat pump and does not include other electrical consumers such as various

circulation pumps. For this reason, the performance of the overall system is described with the Seasonal Performance Factor (SPF). The SPF is defined as follows (Malenkovic et al., 2013):

$$SPF = \frac{\int \left(\dot{Q}_H + \dot{Q}_{DHW} + \dot{Q}_C\right) dt}{\int \sum P_{el}\, dt} \tag{9}$$

Where the SPF (-) is the seasonal performance factor, $\dot{Q}_H$ (kW), $\dot{Q}_{DHW}$ (kW) $\dot{Q}_C$ (kW) are the thermal powers for heating, domestic hot water and cooling, respectively, and finally $\sum P_{el}$ (kW) describes the overall power consumption of all components.

In this work, only the heating case is considered, consequently the corresponding energy for domestic hot water and cooling are zero. The overall system's SPF is 4.34, which is slightly below the $SCOP_{HP}$. This is due to the fact that all electrical consumers are taken into account in the SPF. To illustrate, the pumps utilized for regeneration of the ice storage or the circulation pump between the ice storage and the heat pump are incorporated into the calculations. Moreover, the previously mentioned energy quantities refer to the demand of the building and not to the energy quantities supplied by the components. The SPF therefore also includes the heat losses that occur in the system. The results achieved in these simulations were compared to the literature (Malenkovic et al., 2013) and it was possible to notice that they present a good fit.

4. Conclusions and outlook

This work presented a mathematical model for an ice storage system with spiral type heat exchangers. The model was performed to represent the ECOTHERM Ice Memory System. In this system, 12 spiral flat coil cooling bundles are connected in parallel. After the development of an ice storage model, it was then included in a complete heating system containing a simple house with a heating demand of 45 kWh/(m²a) and 120 m² heated living surface, a solar collector field with 20 m² of unglazed collectors and a heat pump with 7 kW of nominal heat output. As previously mentioned, the work done so far corresponds to the first phase of the project. Based on the results obtained during the simulations it was possible to observe that the mathematical model implemented, although simple in comparison with the model to be used in the next phase, presents reliable results when compared with literature data. As formerly explained, due to the expansion of the ice and the associated blasting effect during the icing process, the ice storage and the thermal collector field were designed to allow a maximum degree of icing of 80%. Therefore, the minimum possible SOC is 20%, which could also be observed in the results. The state of charge is an important parameter to consider when calculating the efficiency of the ice storage.

In order to assess the performance of the system, the Seasonal coefficient of performance of the heat pump and the Seasonal Performance Factor of the whole system were calculated. The SCOP of the heat pump presented a final value of 4.54, while the SPF had a value of 4.34. The difference between the values can be explained by the fact that in the SPF all the electrical consumers and the losses in the system are taken into consideration.

On the second phase of the project a more detailed mathematical model will be implemented using MATLAB/Simulink. The model will be based on the work of (Carbonell et al. 2014) and (Brandstätter 2023), which divide the system into several control volumes to perform the calculations. A few important assumptions in this model are that the physical properties are constant in the control volumes and that the forced convection heat transfer between control volumes is neglected. These assumptions simplify the calculations while maintaining the accuracy of the model leading to faster simulation times. This subsequent mathematical model will also be able to predict the amount of ice formed in the coil heat exchangers inside the ice storage system at a given time (icing degree), which is an important parameter to determine the efficiency of the ice storage and the complete system. Moreover, regarding the complete system, the ice storage will be used to provide not only heating during winter, but also cooling during summer to the single-family house.

In conclusion, as a last step in this project, experiments with a prototype made of stainless steel will be performed using different materials for the shell and heat exchangers, as well as different types of cooling media substances, as for example, the triethylenglycol. Based on these experiments results and the results of similar existent models in the literature, the mathematical model developed will be further on validated.

5. Acknowledgments

This work has been supported by the Government of Upper Austria in the project 'COMPESTO – comprehensive energy storage', Research Grant Wi-2022-600132/7-Au and in the project 'ICE4H&C – ICE Heating and Cooling for SFH and MFH' (FET-Future energy technologies call).

6. References

Bayrak, Fatih; Abu-Hamdeh, Nidal; Alnefaie, Khaled A.; Öztop, Hakan F. (2017): A review on exergy analysis of solar electricity production. In *Renewable and Sustainable Energy Reviews* 74, pp. 755–770. DOI: 10.1016/j.rser.2017.03.012.

Bell, I.H., J. Wronski, S. Quoilin and V. Lemort. Pure and Pseudo-pure Fluid Thermophysical Property Evaluation and the Open-Source Thermophysical Property Library CoolProp [online]. Industrial & engineering chemistry research, 2014, 53(6), 2498-2508. ISSN 0888-5885. Available at: doi:10.1021/ie4033999

Brandstätter, Felix 2023. Solare Eisspeicherung zur Milchkühlung. University of Applied Sciences Upper Austria. Available at https://search-fho.obvsg.at/

Buchner, Sebastian 2005. Eine Auslegungsmethodik für Eisspeicheralagen. Ohm Fachhochschule Nürnberg Fachbereich Maschinenbau und Versorgungstechnik. Available at: https://www.grin.com/document/418349

Carbonell, D.; Philippen, D.; Haller, M. Y.; Frank, E. (2014): Development and Validation of a Mathematical Model for Ice Storages with Heat Exchangers that can be De-iced. In Energy Procedia 57, pp. 2342–2351. DOI: 10.1016/j.egypro.2014.10.242.

Carbonell, D., Philippen, D., Haller, M. Y., and Frank, E. (2015). Modeling of an ice storage based on a de-icing concept for solar heating applications. Solar Energy, 121:2-16.

CARNOT Toolbox Ver. 8. 02, 06/2024, für Matlab/Simulink R2021b, © Solar-Institut Jülich

Dincer, I., Rosen, M. (2011): Thermal energy storage: systems and applications. West Sussex: Wiley.

Dohmann, Joachim (2016): Thermodynamik der Kälteanlagen und Wärmepumpen. Berlin, Heidelberg: Springer Berlin Heidelberg.

Gan, Lu; Jiang, Pengyan; Lev, Benjamin; Zhou, Xiaoyang (2020): Balancing of supply and demand of renewable energy power system: A review and bibliometric analysis. In Sustainable Futures 2, p. 100013. DOI: 10.1016/j.sftr.2020.100013.

Malenkovic, I., Eicher, S., und Bony, J. (2013), Definition of Main System Boundaries and Performance Figures for Reporting on SHP Systems, A technical report of Subtask B, Deliverable B1.1, Final Document, IEA SHC Task 44 / HPP Annex 38, http://www.iea-shc.org/task44

Sheikholeslami, M.; Jafaryar, M.; Said, Zafar; Alsabery, Ammar I.; Babazadeh, Houman; Shafee, Ahmad (2021): Modification for helical turbulator to augment heat transfer behavior of nanomaterial via numerical approach. In Applied Thermal Engineering 182, p. 115935. DOI: 10.1016/j.applthermaleng.2020.115935.

The MathWorks, Inc. (2024). *MATLAB version: 24.1.0.2628055 (R2024a) Update 4*. Accessed: August 15, 2024. Available: https://www.mathworks.com

Sidik, Nor Azwadi Che; Kean, Tung Hao; Chow, Hoong Kee; Rajaandra, Aravinthan; Rahman, Saidur; Kaur, Jesbains (2018): Performance enhancement of cold thermal energy storage system using nanofluid phase change materials: A review. In International Communications in Heat and Mass Transfer 94, pp. 85–95. DOI: 10.1016/j.icheatmasstransfer.2018.03.024.

Winteler C.; Dott R.; Afjei T.; Hafner B. (2014): HEAT PUMP, SOLAR ENERGY AND ICE STORAGE SYSTEMS - MODELLING AND SEASONAL PERFORMANCE.

Zhao, Y.; Guo, Q.; Lin, T.; Cheng, P. (2020): A review of recent literature on icing phenomena: Transport mechanisms, their modulations and controls. In *International Journal of Heat and Mass Transfer* 159, p. 120074. DOI: 10.1016/j.ijheatmasstransfer.2020.120074.

Energy Performance and Environmental Impact of Solar Photovoltaic, Thermal and Hybrid PVT Panels in an Individual House

Hafsa Fares[1,2], Nolwenn Le Pierrès[1], David Chèze[2] and Étienne Wurtz[2]

[1] Laboratoire procédés énergie bâtiment (LOCIE) – CNRS : UMR5271, Université Savoie Mont Blanc, Savoie Technolac, Le Bourget-du-Lac (France)

[2] Univ. Grenoble Alpes, CEA, LITEN, campus INES, Le Bourget-du-Lac (France)

Abstract

The solar energy market has experienced significant fluctuations due to technological advancements, economic considerations, and regulatory dynamics. Despite widespread efforts, integrating solar technologies into buildings still faces some challenges. An important question in this context is the choice between electrical and thermal recovery systems, which depends on specific building requirements where there is a clear demand for both types of energy. Therefore, the objective of this work is to assess the performance of diverse building integrated solar solutions, i.e. photovoltaic, solar thermal and hybrid photovoltaic and thermal collectors, by defining key performance indicators that encompass both electricity and heat aspects, considering both energy efficiency and environmental impact, and using metrics that follow first and second law of thermodynamics, primary energy and energy equivalence. From an energy performance perspective, exergy and energy equivalence, which evaluates the systems based on their ability to produce useful work or heat-equivalent energy, allows a fairer comparison. From the environmental impact assessment point of view, the study concludes that while solar thermal is the most efficient and environmentally friendly option overall and photovoltaic excels in material efficiency for heat-equivalent energy, the analysis of photovoltaic and thermal is limited as it is based on only one industrial reference, unlike the average panels used for the two other panels.

Keywords: Photovoltaic, solar thermal, hybrid PVT, energy performance, Life cycle assessment, primary energy, exergy, coefficient of performance, building.

1. Introduction

1.1. Solar photovoltaic, thermal and hybrid PVT in building application :

With the word facing a severe climate change crisis and the important demand for energy in the building sector, which amounts to more than 30% worldwide and causes more than 26% of global greenhouse gas emissions, implementing renewable energy sources within the building represents one of the key actions to reduce their environmental impact and greenhouse gas emissions. Among the renewable energy sources, solar energy stands out as a promising candidate offering abundant and clean energy potential.

Active solar panels, which include photovoltaic (PV), solar thermal (ST), and hybrid photovoltaic and thermal (PVT) systems, offer a versatile solution to meet building energy needs. These three solar technologies are primarily used for building applications, unlike concentrated solar power (CSP) technology, which is typically associated with large-scale power generation in solar thermal power plants rather than residential or commercial buildings. PV panels convert sunlight into electricity, addressing the global demand for power that is projected to rise by 30% by 2030. ST systems capture solar heat for building heating and hot water production, crucial aspect given that heating accounts for about 47% of energy use in residential buildings. Hybrid PVT systems combine the benefits of both PV and ST, providing both thermal and electrical energy, and represent a comprehensive approach to achieving energy independence and reducing reliance on traditional power sources. Furthermore, in its renewable energy report in Abdelilah et al. (2023), the International Energy Agency (IEA) predicts that global heat consumption in the building sector will remain stable from 2023 to 2028. However, modern renewable energy sources for space and water heating are expected to grow by nearly 40%, increasing their share of the building sector's heat consumption from 15% in 2023 to 21% in 2028. The IEA highlights that renewable electricity will be the fastest-growing renewable heat source in buildings, expanding by two-thirds globally and accounting for almost 40% of the increase in renewable heat consumption.

On the one hand, the presence of heat and electricity in building use complicates the adoption of solar technologies. Buildings do not only require electricity for lighting and appliances but also rely heavily on heat for space and water heating. On the other hand, the diversity of solar technologies available, from PV systems to solar thermal collectors ST and hybrid solutions PVT, producing either electricity and/or heat, adds a layer of complexity.

© 2024. The Authors. Published by International Solar Energy Society
Selection and/or peer review under responsibility of Scientific Committee
10.18086/eurosun.2024.02.06 Available at http://proceedings.ises.org

Understanding how these technologies perform in terms of energy generation and environmental impact is crucial for making informed decisions regarding their implementation.

1.2. Insights from previous research : KPI used to compare different solar panels

1.2.1. Energy performance evaluation

Evaluating the energy performance of solar technologies requires robust and standardized key performance indicators (KPI). In recent years, several studies have focused on defining these KPI to better assess the efficiency of solar energy systems. This section presents insights from the IEA Task 66 in Bockelmann et al. (2022), specifically highlighting three main KPI from an energy performance perspective: load cover factor (LCF), supply cover factor (SCF), and on-site energy ratios (ER). The LCF is defined as the ratio between the solar self-used electricity and heat, and the total energy used for household and technical purposes in the form of heat and electricity. The SCF is the percentage of solar energy used on-site by the building over the total solar energy production. The on-site ER is the solar production response to the building's consumption.

1.2.2. Environmental impact assessment

Assessing the environmental performance of solar energy systems, including PV panels, ST, and hybrid PVT systems, focuses on key indicators such as CO2 emissions, Cumulative Energy Demand (CED), Energy Payback Time (EPBT) and materiel investment (Me), that are the most recurrent in the literature. Life Cycle Assessment (LCA) is the standardized tool used to evaluate the environmental impact of these systems, examining all life stages from material extraction to manufacturing, transportation, installation, operation, and recycling, furnishing the outputs that allows quantifying the KPI. The following aims to present a brief state of the art of studies that used LCA to quantify the four KPI chosen for the present work.

Kavian et al. (2020) used as indicator CO2 emissions of different types of PV panels: polycrystalline, monocrystalline, and thin-film cells, coupled with a ground source HP. The experimental data of the Fthenakis and Alsema (2006) study was used which indicated that the amount of climate change potential for the polycrystalline, silicon thin film, and monocrystalline are 37, 30 and 45 gCO2eq/kWh, respectively. In Nikolic et al. (2022), the CO2 emissions from photovoltaics are 50 g CO2 per kWh of generated electricity, whereas CO2 emissions from solar collectors are 72 g CO2 per kWh of generated thermal energy.

The CED is defined as the total primary energy consumed during the manufacturing, distribution and installation of the solar panel, defined in Frischknecht et al. (2015), with a distinction between non-renewable and renewable primary energy forms. From this value and the energy production of the solar panels, energy payback times are calculated. According to Bhandari et al. (2015), the average EPBT for various PV module types ranged from 1 to 4.1 years. The ranking of module types, from shortest to longest EPBT, is as follows: cadmium telluride (CdTe), copper indium gallium diselenide (CIGS), amorphous silicon (a-Si), polycrystalline silicon, and monocrystalline silicon. The work of Bany Mousa et al. (2019) revealed that the EPBT of PV and ST panels ranged from 1.2 to 15 years across the various geographical locations considered. Additionally, the results indicate that a ST collector system has a lower EPBT in regions with high direct normal irradiation compared to a monocrystalline PV system.

Finally, a KPI named material investment, defined in Olivès et al. (2022) as the total quantity of material invested in the manufacturing and installation of the solar panel, is also evaluated in this work. According to their calculations using LCA and literature data, the material investment for an on-roof PV panel is approximately 5800 t/TWh. PV panels were compared to other energy production sources, such as solar power plants that require more than 9000 t/TWh of materials to generate electricity.

1.3. Research gap and motivation of the paper :

Comparing the performance of different solar technologies, especially concerning heat and electricity generation, using the energy metrics, may not adequately capture the full spectrum of their impacts, leading to incomplete assessments and potentially misguided conclusions. To avoid this problematic, three other metrics are used when trying to compare heat and electricity simultaneously, which are exergy, primary energy and energy equivalence, and each of these shows certain advantages and limitations. Concerning the environmental impact assessment, the normalized tool is the LCA, and solar technologies can be compared one to another by defining a functional unit (FU) usually taken as the kWh of energy produced, or the square meter. Following the first case leads to fall into the same problematic of dealing with both heat and electricity and comparing them in the same level.

The aim of this study is to address these challenges by evaluating the energy performance and environmental

impact of the three solar technologies by establishing clear criteria and comparing the different ways of dealing with both heat and electricity. A case study application illustrates the assessment wherein PV, ST and hybrid PVT are evaluated and compared within the context of an individual house integration.

2. Method and development

2.1. Case study description :

2.1.1. Meteorological data

In this study, the solar panels are installed on an individual house's roof in the city of Chambéry in the south-east region of France. According to the Köppen climate classification, Chambéry experiences a mountain climate characterized by dry, hot summers and moderate winters. For the weather data, files are retrieved from the Meteonorm (2023) database v7.3.3 that uses interpolated data from other locations for both temperature and solar irradiation.

2.1.2. Solar panels technical and environmental description :

The selection of solar panels for this study was primarily based on the availability of detailed data sheets necessary for conducting energy simulations on TRNSYS, as well as the presence of environmental product declarations (EPD) required for environmental modeling on SimaPro. The EPD information was sourced from the French INIES (2023) database, which includes several PV panel references. For the solar ST collectors, only one EPD sheet was available, describing a generic flat-plate solar collector based on an analysis of eight commercial references. Since there was no EPD sheet available for a PVT panel in the INIES database, the international EPD system was consulted where only one reference for PVT was found.

The studied PV panel is a monocrystalline, monofacial, phosphorus-doped (P-type) module. Key characteristics summarized in tab.1 below, including nominal power, module efficiency, area, weight excluding mounting support and packaging, power temperature coefficient, lifespan, and degradation coefficient, were derived from the manufacturer's data sheets. Additional details such as wafer sizes and thickness, cell number, front and back sheet types, encapsulant, and frame material were obtained from the EPD of the PV panel available in the INIES database.

Tab. 1: Solar panels characteristics for energetic and environmental modeling

PV	
Nominal power at STC	450 W_p
Efficiency at STC	20.85 %
Gross area	2.16 m²
Total weight	24.20 kg
Power temperature coefficient	-0.35 %/K
Lifespan	25 years
Degradation coefficient 1st year	2 %
Degradation coefficient over lifespan	0.55 %
Wafer size	M10
Wafer thickness	150 μm
Cell type	Mono crystalline
Number of cells	60
Front sheet	Glass 3.2 mm
Encapsulant	EVA
Back sheet	PET
Frame	Aluminum

The flat plate solar collector consists of a flat absorber plate with liquid circulation that captures solar radiation, which is then transferred to the heat transfer fluid. This fluid circulates through the collector, transferring the absorbed heat for various applications. Its energy performance and environmental characteristics retrieved from the manufacturer and the INIES database respectively, are displayed in tab.2.

Tab. 2: Solar panels characteristics for energetic and environmental modeling

ST	
Nominal power	1364 W
Optical efficiency	77 %
Gross area	2.16 m²
a_1	3.71 $W.m^{-2}.K^{-1}$
a_2	0.015 $W.m^{-2}.K^{-2}$
Total weight	52.21 kg
Lifespan	50 years
Absorber	Aluminum / Steel
Tube network	Copper, coil
Frame	Aluminum
Insulation	Rock-wool
Working fluid	Brine

The PVT panel chosen is a second-generation PVT panel that offers a cutting-edge solution for simultaneously generating hot water and electricity. Featuring advanced technology, the panel maximizes solar radiation absorption and efficiently transfers heat through its lattice-like copper tube network. The 72-cell PV laminate produces electricity alongside thermal energy, while a transparent insulating cover and rock wool-insulated metal case minimize heat loss. The characteristics taken from the manufacturer and the EPD international system are summarized in tab.3 below.

Tab. 3: Solar panels characteristics for energetic and environmental modeling

PVT	
Nominal power at STC	350 W_p
Efficiency at STC	17.8 %
Gross area	1.96 m²
Total weight	52 kg
Power temperature coefficient	-0.36 %/K
Lifespan	25 years
Degradation coefficient 1st year	3 %
Degradation coefficient over lifespan	0.71 %
Wafer size	M2
Wafer thickness	210 μm
PV module	Laminate
Number of cells	72
Front sheet	Glass 3.2 mm
Optical efficiency	70 %
a_1	5.98 $W.m^{-2}.K^{-1}$
a_2	0 $W.m^{-2}.K^{-2}$
Absorber	Copper
Tube network	Copper, lattice-like
Frame	Aluminum
Insulation	Rock-wool
Working fluid	Brine

2.1.3 Building's energy loads :

The case study's building is a single-family detached house, modeled using the TRNSYS Type 56 building model as shown in figure 1. The house has a total area of 170 m², with 90 m² of heated space and a solar roof area potential of 16.6 m². It is assumed that two people live in the house, with a domestic hot water (DHW) consumption of 104 liters per day. From the simulations, the DHW annual needs reach $\boldsymbol{Q_{DHW} = 1478\ kWh}$ annually. The specific electricity profile was assessed using the CREST model v2.2.1 from McKenna and Thomson [2016], assuming an annual specific electricity needs $\boldsymbol{E_{elecspec}}$ **= 2280 kWh**. The air infiltration rate was set at 0.685 vol/h for the living rooms and 1.1 vol/h for the attic. The heating needs, that correspond to keeping a set point temperature of the heated

areas at 19°C during winter and inter season, are equal to $\boldsymbol{Q_{SH}}$ **= 12492 kWh** in Chambéry.

In order to make full use of the whole roof's surface, the solar panels installation cover all the 16.6 m^2 available area. Since each the PV and ST panels have a gross area of 2.16 m^2, the total number of panels installed for the two configurations is seven. The number of PVT installed is eight panels of 1.96 m^2 each. Regarding the house's energy systems, it is equipped with an air-to-water heat pump (HP), which serves as the sole heating system. Two storage tanks for the heating and DHW loops are connected to the heat pump and the heat exchanger of the ST and PVT panels. It is also assumed that the house is connected to the local electricity grid. Since the HP satisfies the heating loads, the energy consumption of the house when the solar energy produced is not sufficient is 100% electric and furnished by the grid $\boldsymbol{E_{grid}}$, and corresponds to the electrical consumption of the HP $\boldsymbol{E_{HPcons}}$ and $\boldsymbol{E_{elecspeccons}} = \boldsymbol{E_{elecspec}}$ the specific electricity consumption, with $\boldsymbol{E_{HPcons}} = \boldsymbol{6854, 6190\ and\ 6426\ kWh}$ annually in the three solar configuration, ie. PV, ST and PVT respectively.

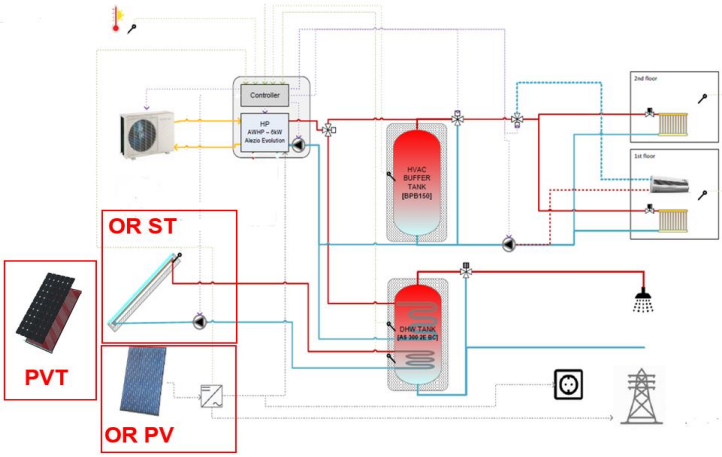

Figure 1: Building's energy systems configuration

2.2. Energy performance evaluation using the four metrics :

2.2.1. Solar self-produced and self-consumed energy :

From the TRNSYS simulations are retrieved the solar self-produced and self-consumed energy. The solar self-produced energy $\boldsymbol{E_{solar,tot}}$ corresponds to the total electricity and heat generated by the PV, ST and hybrid PVT. The solar self-consumed $\boldsymbol{E_{solar,used}}$ is the part of this produced energy that is locally used by the building to meet its demands. In the case of this study, the solar electricity is used to satisfy the specific electricity demand of the house when both the solar production and demand match. Solar electricity is also used to power the HP to satisfy the temperature set-points of the DHW and Buffer tanks. The solar over produced electricity is fed to the grid, which is not the case for the solar produced heat. The solar used heat is considered as the one stored in the two storage tanks, considering the thermal losses occurring in the primary solar circuit and the installation efficiency.

The three KPI from an energy perspective introduced in 1.2.1 and applied to the case study are defined following the equations 1, 2 and 3, and using the building's energy loads described in section 2.1.3 and the solar self-produced and self-consumed energy.

$$LCF_{En} = \frac{E_{solar,used} + Q_{solar,used}}{E_{solar,used} + E_{grid}} \quad \text{(eq. 1)}$$

$$SCF_{En} = \frac{E_{solar,used} + Q_{solar,used}}{E_{solar,tot}} \quad \text{(eq. 2)}$$

$$ER_{En} = \frac{E_{solar,tot}}{E_{elecspeccons} + Q_{SH} + Q_{DHW}} \quad \text{(eq. 3)}$$

2.2.2 Exergy evaluation :

The First Law of Thermodynamics allows combining different energy forms, but energy conversions and losses must be considered. The Second Law of Thermodynamics, introducing entropy, shows that not all energy transformations are reversible, causing inefficiencies.

Exergy is a state function that measures the maximum useful work that can be obtained from a system as it interacts with its environment. For the electrical part, exergy is equal to energy because electrical energy is seen as

pure exergy. Whereas for the thermal part, exergy is defined as the maximum useful work derived from a system using the Carnot factor, which indicates the fraction of energy that can be converted into useful work in an ideal Carnot engine, where T is the temperature at which energy in heat form is supplied and T_{ref} is the reference temperature. Exergy depends on constant reference conditions like ambient pressure and temperature. However, for solar exergy evaluation, ambient conditions fluctuate, leading to different approaches in the choice of the reference temperature. In this work, exergy is evaluated on a daily basis, so the daily minimum temperature is taken as the reference temperature $T_{ref} = min(T_a(t))$ as in the work of Pons (2019).

$$\dot{E}x_{heat} = \dot{Q}\left(1 - \frac{T_{ref}}{T}\right) \quad \text{(eq. 4)}$$

Thermal exergy is assessed at many systems level. First is the solar heat exergy of the solar thermal and PVT heat production. The temperature T of the available solar heat production is the temperature at the outlet of the heat exchanger of the ST or PVT panel. For the heat produced by the heat pump, it is the outlet temperature at the condenser. For the space heating and domestic hot water heating loads, the available temperature is taken as the average temperature of the Buffer and DHW thermal storage tanks.

From these statements, the three KPI from an exergy perspective introduced in 1.2.1 and applied to the case study are defined following the equations 5, 6 and 7.

$$LCF_{Ex} = \frac{Ex_{solar,used}}{Ex_{solar,used} + E_{grid}} \text{ (eq. 5)}$$

$$SCF_{Ex} = \frac{Ex_{solar,used}}{Ex_{solar,tot}} \text{ (eq. 6)}$$

$$ER_{Ex} = \frac{Ex_{solar,tot}}{E_{elecspeccons} + Ex_{SH} + Ex_{DHW}} \text{ (eq. 7)}$$

2.2.3 Primary energy factor :

The main purpose of primary energy factors (PEF) is to provide a standard reference for calculating and comparing different energy sources, allowing diverse energy carriers like coal, natural gas, electricity, biomass, and uranium to be brought to a common basis as stated in Hirzel and al. (2023). In this work, PEF is used to convert the electricity from the grid into heat in the context of the french electricity mix. In France, the PEF for electricity is set at $\boldsymbol{\eta_{grid} = 2.3}$, this means that for 1 kWh of electricity in final energy, 2.3 kWh of primary energy are consumed on average. When it comes to renewable energy including solar energy, the PEF is equal to one.

Therefore, the three KPI introduced in 1.2.1 and applied to the case study are defined following the equations 8, 9 and 10, with the electricity imported from the local grid converted to the primary energy form using $\boldsymbol{\eta_{grid}}$.

$$LCF_{PE} = \frac{E_{solar,used} + Q_{solar,used}}{E_{solar,used} + E_{grid} * \eta_{grid}} \text{ (eq. 8)}$$

$$SCF_{PE} = \frac{E_{solar,used} + Q_{solar,used}}{E_{solar,tot}} \text{ (eq. 9)}$$

$$ER_{PE} = \frac{E_{solar,tot}}{E_{elecspeccons} * \eta_{grid} + Q_{SH} + Q_{DHW}} \text{ (eq. 10)}$$

2.2.4 Energy equivalence using the COP :

Another way to convert electricity into heat form, is to use a coefficient of energy equivalence that takes into account the use made of the solar produced electricity. The advantage of converting this solar electricity into heat will demonstrate the benefit of storing this electricity, for example in an electric car, through thermal inertia, or as in this case study, in hot water through the use of a HP. In this case study, solar electricity is used to fulfil the specific electricity needs of the house when both the solar electricity production and electricity needs match, and is also used to store hot water in the tanks for the DHW and heating needs through the use of a HP. The COP of the actual heat pump installed in the house is used to convert the part of the solar electricity into the heat form it is converted into by the HP. The COP is retrieved dynamically from the TRNSYS simulations as the ratio between the heat delivered and the electricity produced by the solar panels and consumed by the HP at every step of the simulation.

Therefore, the three KPI introduced in 1.2.1 and applied to the case study are defined following the equations 11, 12 and 13, with the solar electricity produced converted to the heat form using the COP of the HP.

$$LCF_{EE} = \frac{E_{solar,used} * COP + Q_{solar,used}}{E_{solar,used} + E_{grid}}$$ (eq. 11)

$$SCF_{EE} = \frac{E_{solar,used} * COP + Q_{solar,used}}{E_{solar,tot}}$$ (eq. 12)

$$ER_{EE} = \frac{E_{solar,tot} * COP}{E_{elecspeccons} + Q_{SH} + Q_{DHW}}$$ (eq. 13)

2.3 Environmental impact evaluation using SimaPro :

Life Cycle Assessment (LCA) is now a standardized approach for assessing environmental impacts of a product. The process starts with defining the goal and scope, which includes setting the purpose, boundaries, impact assessment method, and functional unit (FU) for the product under study. The next step involves conducting an inventory analysis by collecting data on the inputs and outputs throughout the product's life cycle stages. This is followed by an impact assessment, which converts the inventory data into environmental impacts. Finally, the results are synthesized and interpreted.

2.3.1 Goal and scope :

The goal of the LCA simulation is to provide the environmental footprint of the selected solar panel references, intended for installation in an individual house. This footprint assessment focuses on Global Warming Potential (GWP), Cumulative Energy Demand (CED), and material investment (Me) throughout the manufacturing, distribution, installation, and use phases. The SimaPro software and the Ecoinvent database v3.9 are utilized for this purpose. SimaPro and Ecoinvent are the most accurate tools in LCA due to their comprehensive database and rigorous data collection methods, ensuring reliable environmental impact assessments.

Among the various impact assessment methods available in LCA calculations, the environmental footprint (EF) reference package 3.1 is employed. This approach aligns with the EU Commission's recommendation 2021/2279, which aims to measure and indicate the environmental performance of products and organizations throughout their life cycle. The EF3.1 method uses the global warming potential over a 100-year time horizon (GWP100) to describe climate change potential. This indicator, expressed in kg.CO2-equivalent, is essential for assessing the environmental footprint of a system or product, as it evaluates its contribution to changes in global average surface-air temperature and subsequent impacts on climate parameters such as storm frequency, rainfall intensity, and flooding frequency. The CED is assessed using the abiotic depletion potential (ADP): fossil fuels indicator from the EF3.1 method, which considers only non-renewable energy resources in their fossil fuel form. Material investment, part of the LCA modelling, involves the materials utilized in manufacturing and installing the PV panels and excludes the material used for packaging. These materials are included in the life cycle inventory, which will be detailed subsequently.

The FU in which the LCA results are calculated in the LCA simulations is 1 kW of heat and electricity production capacity for the PV and ST panels whereas for the PVT, the LCA modelling is conducted for a FU of 1 module due to the data availability in the EPD sheet.

The final FU used to quantify the KPI and evaluate the impact of the solar panels as recommended is 1 kWh of heat and electricity produced. The initial FU in 1 kW is converted to kWh using the heat or electricity produced during the lifespan from the TRNSYS simulations following equations respectively. For the electricity generation, a degradation coefficient is taken into account with a maximum of 2% of production the first year and 0.55% the remaining years based on reference lifetime of 25 years with a mono crystalline PV panel. For the PVT panel, the degradation coefficient is equal to 3% the first year and 0.71% the remaining years until the lifespan of 25 years. No degradation coefficient is considered for the heat production of the ST and PVT systems. The lifespan of the ST system is considered 50 years. The scope of the LCA modelling takes into account an inverter replacement after 15 years as well as all the other equipment that come alongside a PV installation, i.e. the BOS.

$$E_{solar,lifespan} = E_{solar,tot} * D_{1^{st}year} * (1 + \sum_{n=1}^{Lifespan-1}(1 - D_{Lifespan-1})^{n})$$ (eq. 16)

$$Q_{solar,lifespan} = Q_{solar,tot} * Lifespan$$ (eq. 17)

Then, the second FU is 1kWh of useful produced solar exergy, which as stated in section 2.2.2 is the total

solar electricity produced during the lifespan $E_{solar,lifespan}$ since electricity is pure exergy. For the solar thermal part, $Ex_{solar,lifespan}$ is calculated following equation 4. The last FU corresponds to 1kWh of equivalent produced solar electricity using the COP from the HP as explained in section 2.2.4. Note that it is unnecessary to study a FU of PE, since as mentioned above the primary energy factor for solar energy is equal to 1.

2.3.2 Life cycle inventory :

At this stage, all processes necessary to create the final product are integrated to design the product stage. This involves selecting processes for the manufacturing phase, followed by the processes related to distribution and installation, as well as compiling an inventory of materials invested in the manufacturing and installation mi, both displayed in tab.4 and tab.5 respectively.

Tab. 5: Solar panel's manufacturing processes

Solar technology	LCA step	Ecoinvent process	Location
PV	Polysilicon	Siemens process	Germany
	Ingots	Czochralski purification	Norway
	Wafers	Diamond wire cutting	Norway
	Cell	PERC process	China
	Module assembly	Monofacial	France
	Distribution	Lorry	Chambéry
	Installation	Neglected	Chambéry
ST	Absorber	Laminated + Laser welding	France
	Frame	Laminated	France
	Coil	High pressure tube twisting	France
	Collector assembly	Manually	France
	Distribution	Lorry	Chambéry
	Installation	Neglected	Chambéry
PVT	PV module	PV laminate	China
	ST heat exchanger	Same process as ST	Spain
	Assembly	Manually	Spain
	Distribution	Lorry	Chambéry
	Installation	Neglected	Chambéry

Tab. 4: Material invested mi in kg per functional unit.

PV		**ST**		**PVT**	
Silver	0.014	Aluminium	19.4	PV laminated	17.80
Copper	2.7	Steel	7.4	Heat recovery system	4.65
Aluminium	18.1	Copper	2.1	Steel (Housing)	9.4
Steel	0.62	Silicone	0.72	Rock-wool	2.88
Silicon	2.6	SMC	1.2	Glass	15.10
Glass	39.2	PELD	0.26	EVA	0.64
Plastic	6.7	Polyester	0.19	PVC	6.12
		PVC	0.07	Silicone	0.83
		EPDM	0.26		
		EPS	0.13		
		PA66	0.06		
		Glass	13.6		
		Rock-wool	2.2		
Total (kg)	**69.9**	Total (kg)	**47.6**	Total (kg)	**57.4**

The manufacturing scenario of the PV panel described is retrieved from internal CEA database and is typical in the market, where the silicon manufacturing phases are carried out in Germany and Norway, given the presence of plants specializing in these processes in these countries as said in Norman, (2023). Most PV panel cell assemblies

are still commonly done in China due to the cost advantages offered by Chinese manufacturers. Finally, to cater to local markets, the assembly of the PV module is conducted in the installation country. Note that the transport between the different manufacturing is taken into account in the PV panel modeling. The materials comprising the PV panel include those used in both the manufacturing of the panel and its installation on the roof. Tab. 4 displays the quantity of materials per functional unit of 1 kW. The quantities of aluminum, steel, and copper used for mounting and roof installation of the PV panels are sourced from Underwood et al. (2022), using the average of the ranges considered for roof-mounted modules for each material. Glass constitutes the largest share of material use in a PV panel since the module considered is dual glass, enhancing its toughness and resistance. The second most used material is aluminum, utilized for the frame, support, and mounting structures. Plastic is used for both the encapsulant and back sheet. Copper is used for interconnecting the cells, in the junction boxes that are part of the BOS, in the inverter's composition, and for module-to-module cabling. Additionally, the inverter contains steel, and silver is used in the cell for its conductive properties.

Solar thermal collectors have the advantage of requiring simpler industrial processes than PV, which leads to their entire manufacturing in Europe. For the solar thermal collector selected in this study, all manufacturing and assembly stages are carried out in a factory in France, where all the collector's parts, i.e. the absorber in the form of rolled aluminum plate, the copper tubes for the exchanger, and the glass, are shipped. Raw materials extraction and pre-processing is included in the materials inventory, with materials of European origin considered whenever possible as in the case of aluminum, or by default a global or rest-of-the-world origin is considered.

The PVT manufacturing comprises both the PV part that consists of a laminated PV module, the heat recovery part for the thermal production that is constituted the same way as the flat plate collector of an aluminum absorber where copper twisted tubes are welded on. The PV laminate originates from China where it is manufactured, and the heat recovery part is manufactured in a factory in Spain. The two parts are then brought and assembled together in a Spanish factory and shipped to the installation place in France.

2.3.3 Life cycle impact assessment (LCIA) :

The LCA outputs from the SimaPro simulations and that are discussed in the following are the global warming potential (GWP) in kg.CO2eq and the non-renewable cumulative energy demand (CED) in MJ and are displayed for the whole manufacturing, distribution and installation phases, per initial FU of 1 kW for the PV and ST, and a FU of 1 module for the PVT.

Tab. 6 : LCA simulation outputs for the FU.

Per FU = 1kW of PV/ST, or 1 PVT module	PV	ST	PVT
GWP in kg.CO_2eq	943	385	724
CED in MJ	11723	4610	13664

These simulation output results are intermediate results that will allow to quantify the environmental KPI described in the following :

- The energy payback time (EPBT) expressed in years is a frequently used indicator. It refers to the period it takes for a solar panel to generate the same amount of energy that was spent in its manufacturing, transportation, installation, and maintenance processes. Therefore, the EPBT is expressed as follows in equation 14 :

$$EPBT = \frac{CED}{E_{solar,tot}} \quad \text{(eq. 14)}$$

- The quantity of materials Me employed to deliver 1 kWh of electricity and/or heat for the solar panels is equal to the ratio between the total quantity of material invested in the manufacturing and installation obtained from the LCA in the inventory analysis mi and the energy production over the lifespan of the panel following equation 15.

$$Me = \frac{m_i}{E_{solar,lifespan}} \quad \text{(eq. 15)}$$

2.4 KPI quantification : application to the case study

2.4.1 Energy performance KPI:

The energy performance KPI introduced in section 1.2.1, ie. the load and supply cover factors and the on site energy ratio, are quantified following the case study of the individual house with the three different solar

configurations coupled with an air-to-water HP. In literature, it was seen that the three KPI are defined mixing heat and electricity as in equations 2, 3 and 4. The objective of this work is to define these KPI also using either exergy or converting electricity to heat form using either the french PEF or the COP of the studied HP. The different definitions are displayed following equations 5 to 13. In table 8 are displayed the results of the KPI quantification in the three solar configurations and using the four metrics, ie. Energy (En), exergy (Ex), primary energy (PE) and energy equivalence (EE).

Tab 8. : Energy performance KPI quantification applied to the case study

	LCF [%]			SCF [%]			ER [%]		
	PV	**ST**	**PVT**	**PV**	**ST**	**PVT**	**PV**	**ST**	**PVT**
En	15.3	30.4	30.1	34.7	89.1	54.2	22.3	22.4	33
Ex	15.3	25.4	26.6	34.7	89.1	51.7	16.9	13.6	22.5
PE	5.7	16	13	34.7	89.1	54.2	11	11.6	16.6
EE	15	17.4	21	46.1	89.1	57.5	18.5	12.3	22.1

The solar panels scored LCF equal to 15.3%, 30.4% and 30.1% for the PV, ST and PVT respectively in the energy definition, meaning that the solar energy used is up to 30% for PVT and ST of the total energy used on site, which consists of electricity imported from the grid when solar energy is not sufficient. What justifies these values is that the ST and PVT solar used energy is higher than the PV due the solar heat storage. When using the exergy definitions, the ST and PVT LCF are lower because of the maximum useful work that can be extracted from the solar heat produced and stored, still their LCF is higher than the PV. When converting the electricity from the grid into its primary energy form in the denominator, the LCF values for all the three solar panels is reduced. Finally, in the case of converting the electricity produced by the PV and PVT panels into heat via the heat pump, the LCF values are increasingly close for all three panels, suggesting that this metric could enable a fairer comparison.

The SCF values, meaning the share of solar energy produced that was consumed on site, show that the ST offers the most solar self-consumed energy reaching 89.1% because the heat is stored in the thermal tanks, in the four definitions since the temperatures involved are the same in the case of the produced heat and the consumed one. In the PV case, the SCF reached 34.7%, meaning that only this share was used to respond to the specific electricity demand when it matched the electricity production, and the demand of the HP. The rest is injected into the local electricity grid. This valued remained the same for the three definitions, ie. the energy, exergy and primary energy factor one, since electrical energy is pure exergy and the PEF of solar PV electricity is equal to one. As for the energy equivalent definitions, that reached 46.1%, it is due to the conversion of the PV electricity used by the HP to the actual heat produced by the HP using the COP dynamically. The PVT panel's score in SCF falls between both the PV and ST thanks to its ability to combine flexible electrical generation and storable heat.

Unlike the LCF, the on-site ER, or solar fraction as it is known in many studies, accounts for the contribution of solar energy in its response to the building's energy needs. In this case study, the building's needs consists of the space heating, the DHW and specific electricity needs. In the nominator, the 16.6 m^2 of the PV and ST panels produced almost the same amount of electricity and heat, resulting in a LCF nearly equal to 22.3 and 22.4% respectively. The PVT produces 30% more energy than the PV and ST for the same surface, resulting in an ER of 33%. In terms of exergy, the same tendency is observed, which devalues heat in comparison to electricity due to their different exergetic nature and content. The values of on-site ER all decrease in the case of the primary energy and energy equivalence definitions, because the electricity imported from the grid and converted to heat form, whether using the primary energy factor or the COP, is greater.

2.4.2 Environmental impact assessment KPI :

The environmental impact KPI results are displayed in table 9, for the three solar solar panels, and per FU of 1kWh of produced energy, useful exergy and energy equivalence.

In terms of energy, the ST collectors scored the lower GWP equal to 17.7 of kg.CO_2eq per kWh of heat produced, against 31.1 for PV and 52.3 for PVT. ST require manufacturing processes that are less energy consuming and occurring in Europe, unlike PV and PVT modules which are produced in China. When using the exergy metric, the impact of ST and PVT are increased, but ST still does not exceed PV. By considering the share of solar electricity converted into heat by the heat pump and stored, as the production actually served by PV and PVT panels, their

environmental impact in terms of all the environmental KPI is further reduced. In summary, ST is the most environmentally and energetically efficient system overall, but PV offers a material efficiency advantage in heat-equivalent applications. PVT, while offering both electricity and heat, tends to have the highest environmental and material costs, indicating that it may not be the best option unless its dual-output capabilities are highly valued.

Tab 9. : Environmental impact KPI quantification

Per FU = 1kWh	**GWP [kg.CO_2eq]**			**CED [MJ]**			**EPBT [years]**			**Me [t/TWh]**		
	PV	ST	PVT	PV	ST	PVT	PV	ST	PVT	PV	ST	PVT
En	31.1	17.7	52.3	0.39	0.21	0.66	0.8	0.5	1.4	2306	2184	2510
Ex		22.7	59.2		0.27	0.74		0.6	1.6		2803	2843
EE	23.8	17.7	46.1	0.29	0.21	0.58	0.6	0.5	1.3	1762	2184	2212

While the analysis highlights Solar Thermal (ST) as the most efficient and environmentally friendly option overall, and Photovoltaic (PV) as the most material-efficient for heat-equivalent energy, it is important to acknowledge a limitation in the study. The PVT system analyzed represents only one industrial reference, whereas the PV and ST systems are based on average panels. This means that the performance of PVT in this study might not fully reflect the diversity of PVT technologies available on the market, which could potentially offer different efficiency and environmental profiles. Therefore, the conclusions drawn about PVT may be limited in scope and may not capture the full potential or variability of this technology.

3. Conclusion and perspective

In the context of global climate crisis, using solar energy in residential buildings emerges as a crucial solution due to resource availability and technological maturity. To compare various solar technologies fulfilling the building needs, a standardized assessment of their energy and environmental performance is imperative. This study focuses on evaluating active solar panels' energy and environmental performance, considering their electricity and heat outputs, and compares different metrics of defining the KPI based on energy, exergy, primary energy, and energy equivalence. While primary energy reduction factor is commonly used, it remains dependent on the location when choosing the electricity to heat conversion factor. The second law of thermodynamics introduces exergy as a key metric, dependent on the choice of reference temperature, and allows considering the quality of the energy compared to first law of thermodynamics. Converting solar energy production and building loads using energy system's COP reveals promising comparisons, necessitating further investigation concerning the choice of the energy system. Integrating both energy forms facilitates future comparisons across economic, technical, and social criteria, paving the way for informed solar panel selection in building applications.

4. Acknowledgment

This work has benefited of a grant from French Alternative Energies and Atomic Energy Commission (CEA), Université Savoie Mont Blanc (USMB) and Conseil Savoie Mont-Blanc (CSMB).

5. References

Inies. Reference environmental and health data for buildings and RE2020. https://www.inies.fr/en/ , visited 2023-11-14, 2023.

The international EPD system. https://www.environdec.com/home , visited 2024-07-30.

Meteonorm. Worldwide irradiation data. https://www.meteonorm.com , visited 2022-09-19, 2023

Abdelilah Y., Bahar A., Bojek P., Briens F. Criswell T., Moorhouse J., and Martinez L-M. (2023). Renewables 2023 Analysis and forecast to 2028. International energy agency. www.iea.org

Bany Mousa, O. and Kara, S. and Taylor, R., 2019. Comparative energy and greenhouse gas assessment of industrial rooftop-integrated PV and solar thermal collectors. Applied Energy, doi : 10.1016/j.apenergy.2019.03.052

Bhandari K., Collier J., Ellingson R., and Apul D.. Energy payback time (EPBT) and energy return on energy invested (EROI) of solar photovoltaic systems: A systematic review and meta-analysis. Renewable and Sustainable Energy Reviews, 47:133–141, July 2015. ISSN 1364-0321. doi: 10.1016/j.rser.2015.02.057.

Bockelmann, F., Gauer, T., Späte, F., 2022. Final list of KPIs. International Energy Agency, SHC Task 66: Solar Energy Buildings. Filename of deliverables: Task66_D.A2_Final list of KPIs_1.3. Report number D.A2, DOI.

Delisle V. and Kummert M. A novel approach to compare building-integrated photovoltaics/thermal air collectors to side-by-side PV modules and solar thermal collectors. Solar Energy, 100:50–65, February 2014. ISSN 0038092X. doi: 10.1016/j.solener.2013.09.040

Dimri N. and Ramousse J. Thermoeconomic optimization and performance analysis of solar combined heating and power systems: A comparative study. Energy Conversion and Management, 244, 2021. ISSN 01968904. doi: 10.1016/j.enconman.2021.114478

Frischknecht, R., Wyss, F., Büsser Knöpfel, S., Lützkendorf, T., Balouktsi, M., 2015. Cumulative energy demand in LCA: the energy harvested approach. Int J Life Cycle Assess. 20, 957–969.

Fthenakis V. and Alsema E., 2006 Photovoltaics energy payback times, greenhouse gas emissions and external costs: 2004–early 2005 status. Progress in Photovoltaics: Research and Applications, 14(3):275–280, 2006. ISSN 1099 159X. doi: 10.1002/pip.706.

Gazbour, N., 2019. Intégration systémique de l'éco-conception dès la phase de R&D des technologies photovoltaïques. PhD thesis, Université Grenoble Alpes.

Hirzel, S.; Rohde, C.; Barkhausen, R.; Durand, A. (2023). ENERGY EXPLAINED - Primary Energy Factors. Karlsruhe: Fraunhofer ISI. https://doi.org/10.24406/publica-999

Kavian S., Aghanajafi C., Jafari Mosleh H.and Nazari A., 2020. Exergy, economic and environmental evaluation of an optimized hybrid photovoltaic-geothermal heat pump system. Applied Energy, 276:115469, October 2020. ISSN 0306-2619. doi: 10.1016/j.apenergy.2020.115469.

Kim M-H., An Y., Joo H-J., Lee D-W., and Yun J-H. Self-Sufficiency and Energy Savings of Renewable Thermal Energy Systems for an Energy-Sharing Community. ENERGIES, 14(14), July 2021. doi:10.3390/en14144284

McKenna E. and Thomson M. High-resolution stochastic integrated thermal–electrical domestic demand model. Applied Energy, 165:445–461, March 2016. ISSN 0306-2619. doi: 10.1016/j.apenergy.2015.12.089

Nikolic D., Skerlic J., Radulovic J., Miskovic A., Tamasauskas R., Sadauskien J., 2022. Exergy efficiency optimization of photovoltaic and solar collectors' area in buildings with different heating systems. Renewable Energy, doi: 10.1016/j.renene.2022.03.075.

Norman W. A renaissance within the Solar PV industry in Europe: 30GW of PV manufacturing by 2025 possible with legislation - ESIA. PV Tech, 2023. https://www.pv-tech.org/a-renaissance-within-the-solar-pv-industry-in-europe-30gw-of-pv-manufacturing-by-2025-possible-with-legislation-esia/ , visited 2024-01-11.

Olives, R., Ribeiro, E., Py, X.,2022. Matériaux pour la transition énergétique : importance du recyclage. Congrès SFGP 2022, Toulouse, France. hal-03859923.

Pons M. Exergy Analysis and Process Optimization with Variable Environment Temperature. Energies, 12(24): 4655, December 2019. ISSN 1996-1073. doi: 10.3390/en12244655.

Underwood R., Kim M., Drury S., Zhang Y., Wang L., Chan C., and Hallam B. Abundant Material Consumption Based on a Learning Curve for Photovoltaic toward Net-Zero Emissions by 2050. Solar RLL, 2022. doi: 10.1002/solr.202200705

Zampori L. and Pant R. Suggestions for updating the product environmental footprint (pef) method, eur 29682 en. Publications Office of the European Union, Luxembourg, ISBN 978-92-76- 00654-1., 2019. Doi:10.2760/424613, JRC115959

PROVIDING FLEXIBILITY FOR DISTRICT HEATING GRIDS WITH THERMALLY ACTIVATED BUILDING STRUCTURES IN RESIDENTIAL BUILDINGS

Michael Gumhalter[1], Philipp Gradl[1]

[1] AEE INTEC, Gleisdorf (Austria)

Abstract

For the urban housing sector's ongoing decarbonization efforts, district heating solutions stand as fundamental components. However, scaling up district heating systems presents significant challenges in grid extension and the integration of renewable heat sources. Demand peaks and generation mismatch pose operational hurdles which can be alleviated by using heat storages and demand flexibilities. This study evaluates the utilization of Thermally Activated Building Structures within residential complexes, employing model-based predictive controllers, to aid energy suppliers and grid operators in navigating operational challenges. Through a simulation study conducted for a real use case in the city of Vienna, this research demonstrates the efficacy of the proposed system in effectively mitigating grid peaks by leveraging thermal mass to offset non-shiftable demands, such as domestic hot water usage. The results show a peak load reduction of 27 % during the coldest week of the year and a 30 % reduction for an average winter week while keeping indoor comfort boundaries unviolated. The proposed technology therefore holds the potential to reserve grid capacity for additional buildings or to reduce the demand for peak load generation which is often based on fossil technologies.

Keywords: Thermally Activated Building Structures, District Heating Grids, Model Predictive Control

1. Introduction

For the ongoing decarbonization of heat supply in the urban housing sector, District Heating (DH) solutions are one of the main pillars. At the same time, major challenges for new and existing DH-systems are caused by a combination of growing grid size, more volatile renewable generation, lower temperature levels and high costs for peak load generation. This work proposes and evaluates a concept for the utilization of Thermally Activated Building Systems (TABs) to provide flexibility for grids and energy suppliers to overcome operational and system design challenges. Based on operational data from a real DH grid, and the conceptual data for a planned residential building project in the city of Vienna, Austria a simulation study is conducted to answer the following question.

How can TABs employing advanced Demand Side Management (DSM) strategies through Model Predictive Control (MPC) be optimized to support DH grid expansion by mitigating demand peaks, particularly by compensating for non-shiftable Domestic Hot Water (DHW) demand peaks, thereby ensuring new buildings are grid-supportive?

2. State of the art

Reynders et al. (2013) stated that the load shifting potential increases with the thermal mass of a building. This refers to the ability of materials within the structure to store heat. Studies indicate that in-floor heating, which directly utilizes the floor slab as thermal mass, offers a higher peak shaving potential compared to traditional radiators. However, it is crucial to acknowledge the potential trade-off between increased thermal mass activation and overall energy efficiency. While activating thermal mass enhances load shifting capabilities, it may also lead to higher energy consumption. Therefore, optimizing the utilization of thermal mass is essential to minimize unnecessary energy losses.

While Rijksen et al. (2010) have demonstrated a 50% reduction in peak cooling capacity for office buildings using concrete core activation, these results cannot be directly extrapolated to residential settings with heating systems.

Le Dreau and Heiselberg (2016) have shown that low-energy houses offer significant potential for load shifting, a strategy for managing energy demand by strategically moving consumption to off-peak periods. However, achieving this benefit requires robust control systems to prevent overheating issues. The effectiveness of load shifting in these houses is heavily influenced by the level of insulation. Buildings with good insulation have a reduced modulation potential, yet they offer an extended time frame for adjusting heat demand, which can surpass 24 hours. Simulations

© 2024. The Authors. Published by International Solar Energy Society
Selection and/or peer review under responsibility of Scientific Committee
10.18086/eurosun.2024.02.07 Available at http://proceedings.ises.org

indicate that load shifting can be an effective strategy in single-family low-energy homes for managing electricity consumption.

The literature review delivers evidence that the desired results for grid operation can be achieved with TABs. However, a multifamily residential building with TABs has not been used for load shifting to the benefit of a thermal grid in any of the sources.

3. Methodology

The methodology of this study revolves around evaluating the feasibility of shifting heating demand to smooth the overall load curve of a district heating grid, particularly in scenarios where non-shiftable assets like DHW constitute a significant portion of the delivered energy and contribute to load peaks. Two distinct variants, as outlined in Tab. 1, are defined for analysis, including a baseline variant featuring rule-based control with ambient temperature dependent heating curves and one system variant which is dynamically optimized by Model Predictive Control (MPC). The simulation experiments are conducted for the complete heating season and results are focused on the coldest week of the year (Feb 12th to Feb 18th) and one average winter week (March 18th to March 24th) within an ASHRAE sample climate for the city of Vienna, Austria. Evaluation methods such as comparison of duration diagrams for heat demand, and time series data of occurring room temperatures including deviations are employed to compare the simulation variants. To assess the model fidelity of the used MPC method a residual analysis for room temperature predictions is used.

Tab. 1: Simulation variants

Name	Technologies	Explanation
Standard control	TABs; Return temperature control; Individual zone temperature control; Ambient temp. dependent feed temperatures	This variant serves as a baseline showing how a conventional control system would affect the heat demand of the TABs system in the examined building.
MPC	TABs; Return temperature control; Individual zone temperature control; Ambient temp. dependent feed temperatures; MPC	The standard control of the building is extended by a supervisory MPC control which can manipulate room temperature setpoints and can set aggregated heating power for the building by manipulating the feed temperatures. The MPC is utilizing knowledge of future external boundary conditions like weather, DHW and household electricity demand and has the objective to reduce heat demand peaks of the building including the DHW demand.

The core of the used method is a comprehensive energy simulation conducted on the sample building via the software IDA ICE by EQUA (2023). This building model was first implemented by Stipsits (2024) based on planning data for the residential housing project in the city of Vienna, Austria. A 3-D Depiction of the building geometry can be found in Fig. 1.

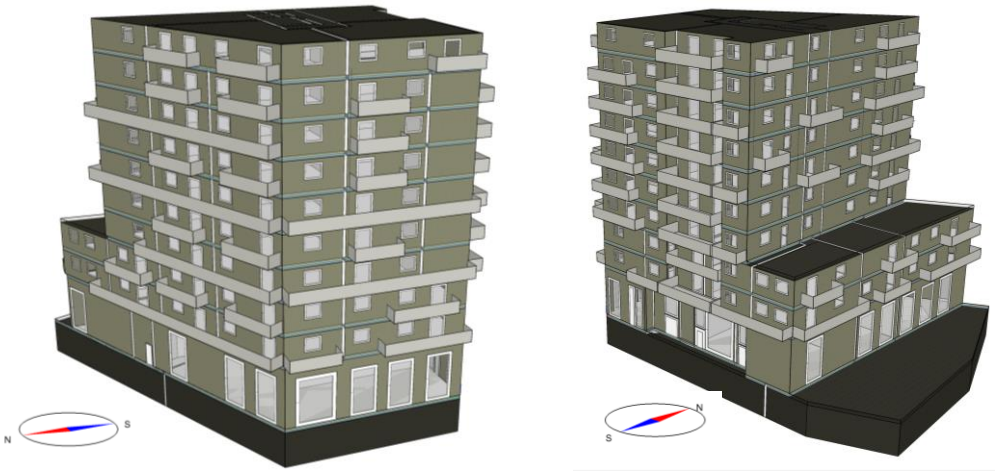

Fig. 1: 3-D views of the examined planned residential Building (left: view from northwest, right: view from southeast) (Source: Stipsits (2024))

For the applied MPC and Moving Horizon Estimation (MHE) a semi-physical model was initially devised for the application in a prior study, as outlined in Putz et al. (2023). Expanding upon this model, the proposed system incorporates a district heating connection and is displayed in its RC-equivalent form in Fig. 2 and the associated symbol description in Tab. 2. The control objective is to reduce heat demand peaks of the building including the DHW demand which is implemented by using a power dependent heat tariff. Subsequently, a co-simulation is conducted, coupling the model-based control method with the highly detailed building and system model within IDA ICE. This co-simulation involves optimizing daily load shifting tasks for the building through MPC control, while concurrently executing MHE operations to perform classical parameter estimation based on dynamic data from the IDA ICE simulation. Additionally, a state observer is employed within the controller to estimate the building structural temperature. Furthermore, the IDA ICE simulation provides essential data regarding thermal zone comfort and the hydronic system, including TABS return temperature and heat flux. The MPC Framework is implemented using the dynamic modelling and optimization package GEKKO in Python (Beal et al., 2018; Hedengren et al., 2014).

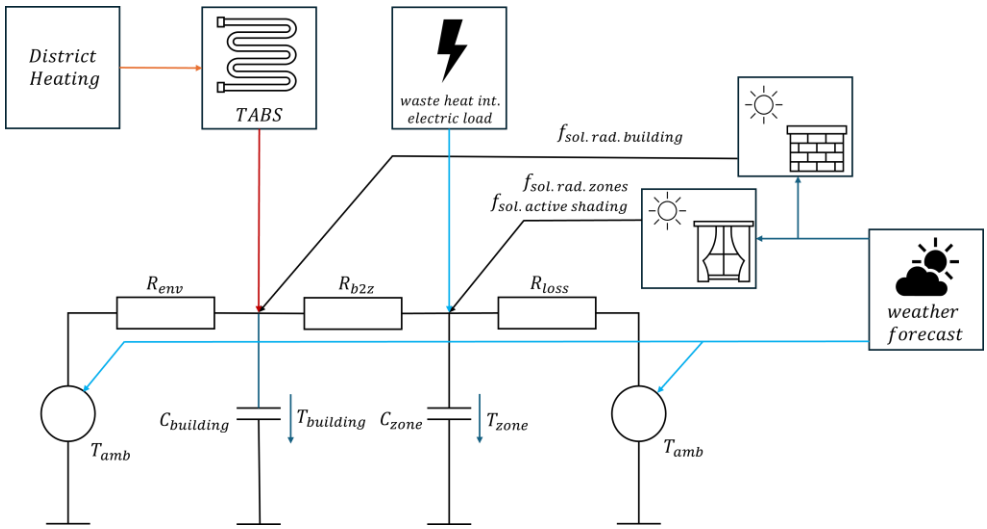

Fig. 2: RC-representation of the semi physical building model used in MPC and MHE

Tab. 2: Description of parameter symbols for the semi physical building model used in MPC and MHE

Parameter	Description
$T_{building}$	Average temperature of building masses
T_{zone}	Average air temperature of building zones
T_{amb}	Ambient air temperature
R_{env}	Thermal resistance of the building envelope part 1
R_{loss}	Thermal resistance of the building envelope part 2 and other leaks
R_{b2z}	Thermal resistance from the building structure to the thermal zone
C_{zone}	Aggregated thermal capacity of the thermal zones
$C_{building}$	Thermal capacity of the building structure
$f_{sol.rad.building}$	Multiplication factor to estimate heat flux into building structure based on solar radiation
$f_{sol.rad.zones}$	Multiplication factor to estimate heat flux into building zones based on solar radiation
$f_{sol.active\ shading}$	Time dependent multiplication factor to estimate impact of active window shading on the heat flux into building zones based on solar radiation

4. Results

In this study, the analysis of results is presented in two distinct sections to capture the variability in weather conditions during the winter season. The first section focuses on the coldest week of the year, characterized by extreme temperatures, which allows for an examination of the effects on the highest expectable peak loads. The second section presents data from an average winter week, providing a baseline for comparison and highlighting the typical conditions experienced during the season.

The coldest week of the simulated year is Feb 12th to Feb 18th. For the implemented standard control, the lowest occurring outdoor temperature of -14.6 °C leads to a space heating peak demand of 140 kW. Fig. 3 shows that using MPC for load shifting under consideration of the DHW demand, leads to lower and time shifted peaks. The total heat demand of the building is the sum of the heating power used in the TABS for space heating and the heat demand for DHW consumption plotted in Fig. 4. The total heat demand in this week is compared for the standard control and MPC in the duration diagrams in Fig. 5. It is shown that the highest occurring demand peak can be reduced by 27 % which is a significant decrease considering that this is the coldest week of the year. Comparing sum of shifted energy from times of high demand to times with lower demand, it can be observed, that lowering the peak demand comes at the cost of overall higher energy consumption. This increase amounts to 12.7 % for the coldest week scenario and 6.3 % for the average winter week. This significant increase is mainly cause by two effects. First, by comparing the achieved room temperatures for the variant with standard control (Fig. 6) and the variant with MPC based load

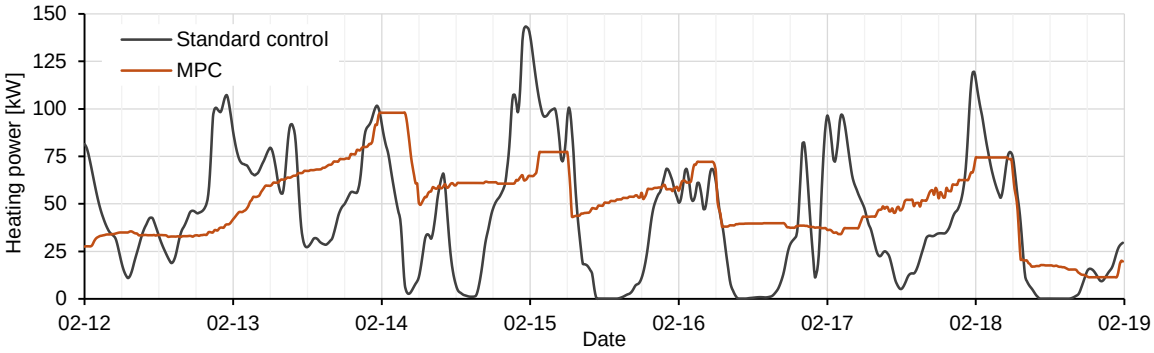

Fig. 3: Heating power of the TABs system in comparison for standard control and MPC during the coldest week of the year.

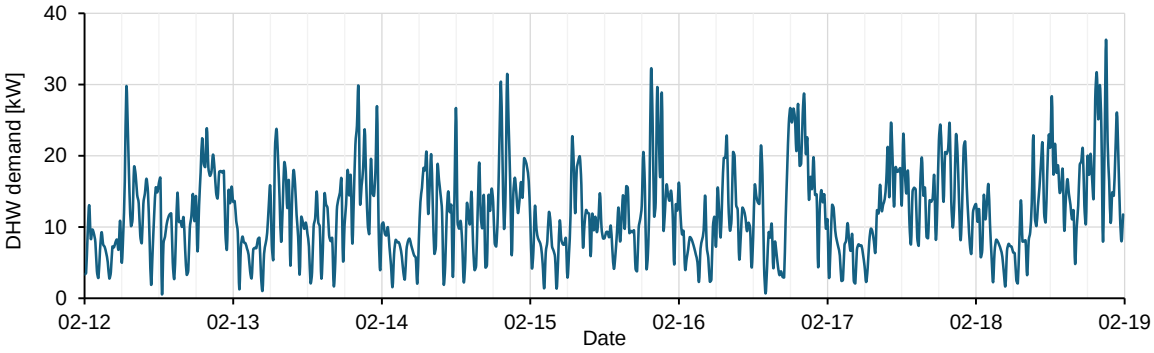

Fig. 4: Defined DHW demand of the building during the coldest week of the year.

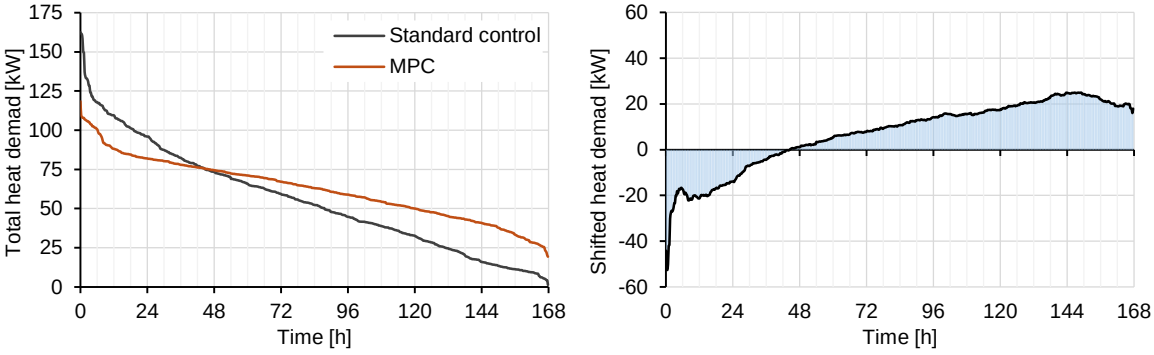

Fig. 5: Duration curves of total heat demand including TABS and DHW for standard control and MPC variant in the coldest week of the year (left). Difference between the duration curves representing the peak load reduction and the shifted energy (right).

shifting (Fig. 7) it can be seen that the MPC variant performs superior in maintaining the room temperature setpoint of 22 °C and never breaches the lower comfort limit of 21 °C. The building using standard control without predictive components struggles to maintain setpoint temperatures due to the high latencies in the thermal building dynamics. The higher energy demand of the variant with MPC is therefore caused by higher envelope losses while achieving higher temperature comfort. Secondly, the slight preheating of concrete structures raises heat losses through the building envelope and thermal bridges which can be interpreted as actual storage losses.

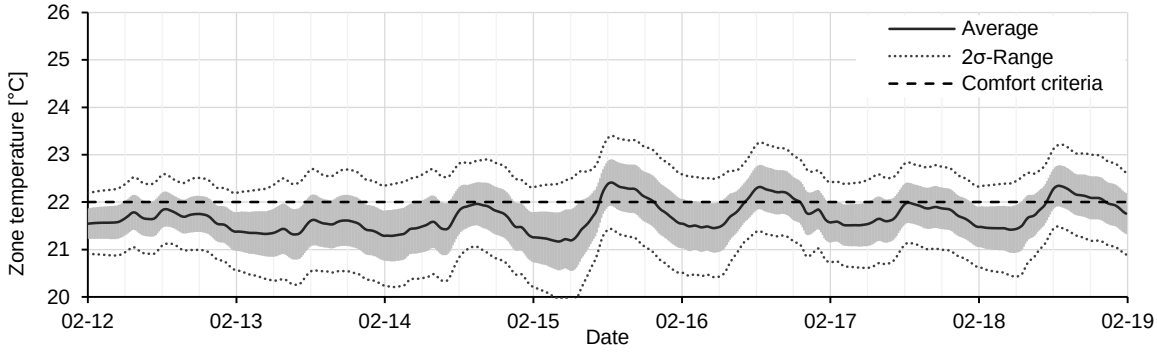

Fig. 6: Average building zone temperature and standard deviation for the coldest week of the year and standard control.

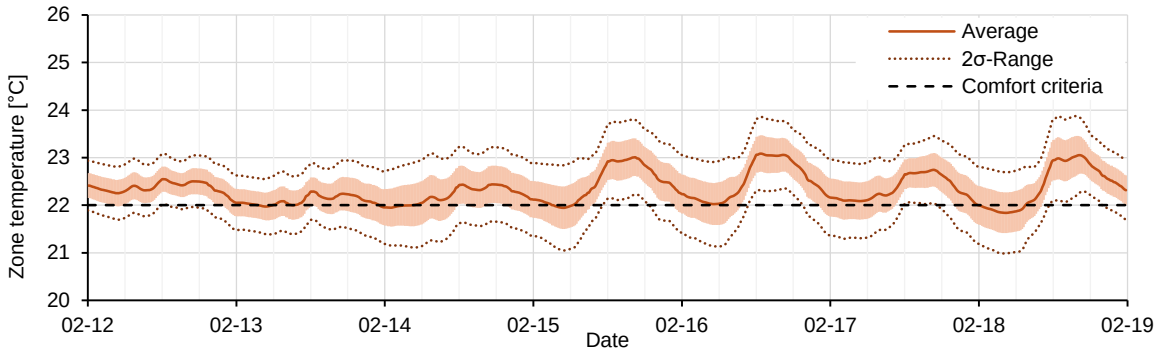

Fig. 7: Average building zone temperature and standard deviation for the coldest week of the year and MPC.

The implemented semi physical building model performs sufficiently for the load shifting task and offers a coefficient of determination of 0.95 for predicting the average room air temperature in the building. The results of a residual analysis performed for the coldest week of the year are shown in Fig. 8.

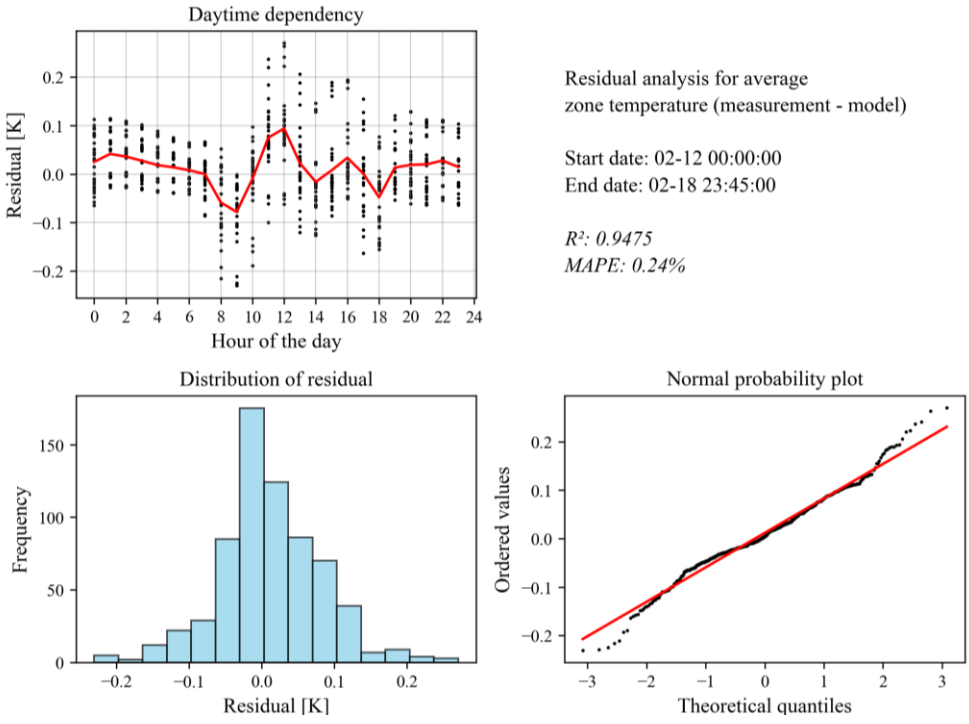

Fig. 8: Statistical evaluation of the residual of the predicted average zone temperature for the coldest week of the year.

The evaluation of results for the average winter week (March 18th to March 24th) was conducted using the same methodology as applied to the coldest week of the year. Also, in this case the use of MPC for peak load reduction is highly effective as Fig. 9 shows how the heat demand is shifted from otherwise high demand times to low demand times. Together with the heat demand for DHW consumption plotted in Fig. 10 the resulting total heat demand is calculated and shown in duration curves in Fig. 11. In this average winter week the heat demand peak can be reduced by 30 %.

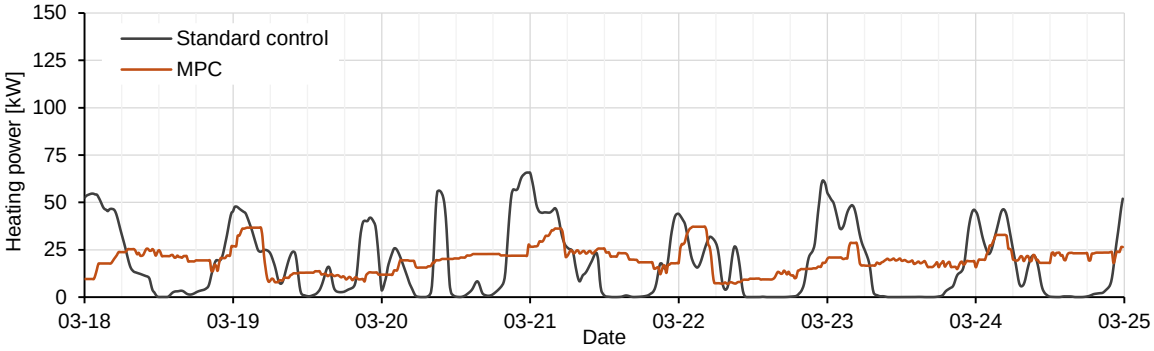

Fig. 9: Heating power of the TABs system in comparison for standard control and MPC for an average winter week.

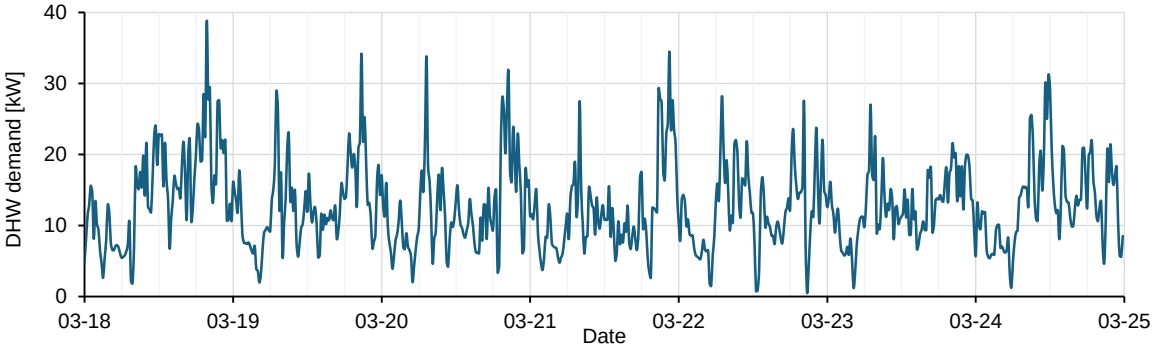

Fig. 10: Defined DHW demand of the building for an average winter week.

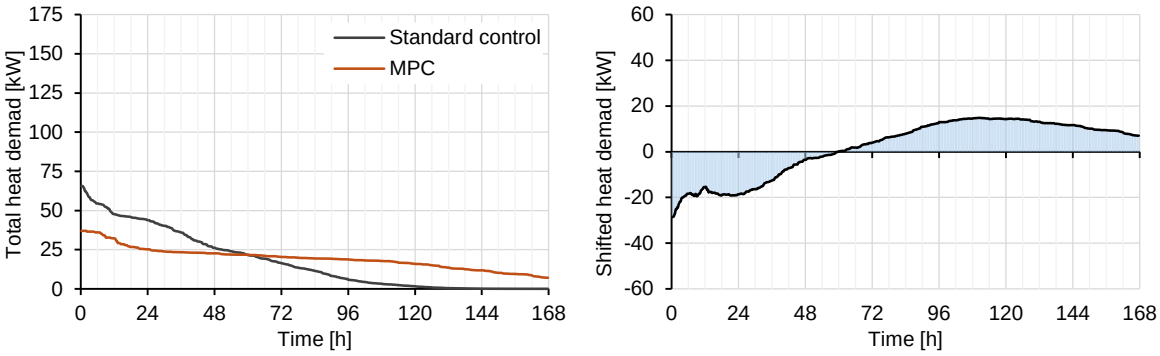

Fig. 11: Duration curves of total heat demand including TABS and DHW for standard control and MPC variant for the average winter week (left). Difference between the duration curves representing the peak load reduction and the shifted energy (right).

The MPC internal semi physical building model also performs positively in this week and offers a coefficient of determination of 0.93 for predicting the average room air temperature in the building. The results of a residual analysis performed for this average winter week are shown in Fig. 12.

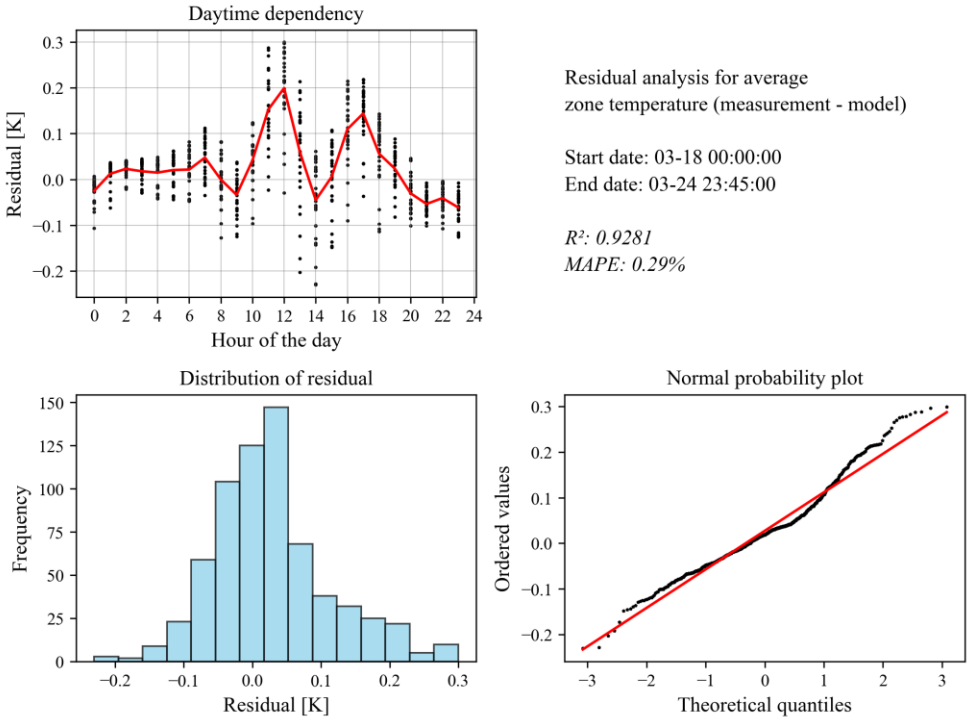

Fig. 12: Statistical evaluation of the residual of the predicted average zone temperature for the average winter week.

5. Conclusion

The study has shown that even during the coldest week of the year grid peaks can be effectively reduced. Manipulating the generally low flow temperatures of TABS together with targeted room temperature setpoint adaption enables the possibility to use the studied building for load shifting even in times of peak heat demand without compromising the tenant's thermal comfort. The utilization of supervisory MPC strategies on a building level is a key enabler for the derived results and ensures effective use of the activated thermal mass by balancing indoor comfort, heating losses and grid objectives. In the conducted simulation study this model-based control system also caused an increase in total energy consumption compared to the reference scenario which can be attributed to better compliance with temperature comfort boundaries and actual storage losses caused by the load shifting. Thus, causing overall higher energy consumption, it does so in times of lower demand which potentially can reduce the CO_2 emissions and cost. Depending on the utilized heat sources in the respective DHW grid, using more energy at times where renewable sources are available can have significant advantages over using energy from mostly fossil fuel based peak load generation.

Low order differential equation models can be sufficient to predict the thermal dynamics of large volume residential buildings sufficiently accurate to perform optimization calculations. The quality of model fitment achieved in this study can be classified with a coefficient of determination (R^2value) larger 0.9 which indicates strong correlation and is sufficient for the underlying use case. This has the potential to ease the expansion and operation of DH grids and therefore speed up the transition from fossil energy based heat supply in urban areas to more climate friendly alternatives.

6. Acknowledgments

The reference building has been defined, simulated and evaluated within the Hybrid LSC project, supported by the Austrian Federal Ministry of Climate Action, Environment, Energy, Mobility Innovation and Technology [FFG project number 880768]. The development of the Building MPC component was supported by the European Union's Horizon 2020 research and innovation program LC-EEB-03-225 2019 - New developments in plus energy houses (IA) under the Project EXCESS "FleXible user-CEntric Energy poSitive houseS" [grant number 870157]. The publication is supported by the national participation project of the international IEA Annex 83 – Positive Energy

Districts [FFG project number FO999890451].

7. References

G. Reynders, T. Nuytten, D. Saelens, Potential of structural thermal mass for demand-side management in dwellings, Building and Environment, Volume 64, 2013, Pages 187-199, ISSN 0360-1323, https://doi.org/10.1016/j.buildenv.2013.03.010

D.O. Rijksen, C.J. Wisse, A.W.M. van Schijndel, Reducing peak requirements for cooling by using thermally activated building systems, Energy and Buildings, Volume 42, Issue 3, 2010, Pages 298-304, ISSN 0378-7788, https://doi.org/10.1016/j.enbuild.2009.09.007.

J. Le Dréau, P. Heiselberg, Energy flexibility of residential buildings using short term heat storage in the thermal mass, Energy, Volume 111, 2016, Pages 991-1002, ISSN 0360-5442, https://doi.org/10.1016/j.energy.2016.05.076.

EQUA, 2023 IDA ICE simulation software for indoor climate and environment. EQUA Solution AB, Sweden, https://www.equa.se/de/ida-ice

Stipsits A. 2023; Regelkonzepte zur Lastverschiebung bei fernwärmeversorgten Gebäuden mit thermischer Bauteilaktivierung; Master Thesis; Gebäudetechnik und Gebäudemanagement; FH-Burgenland; Pinkafeld; Austria

Putz, D., Gumhalter, M. & Auer, H., 2023. The true value of a forecast: Assessing the impact of accuracy on local energy communities. Sustainable Energy, Grids and Networks, Issue 33; https://doi.org/10.1016/j.segan.2022.100983.

Hedengren, J. D. and Asgharzadeh Shishavan, R., Powell, K.M., and Edgar, T.F., 2014, Nonlinear Modeling, Estimation and Predictive Control in APMonitor, Computers and Chemical Engineering, Volume 70, pg. 133–148, 2014, DOI: 10.1016/j.compchemeng.2014.04.013.

Beal, L.D.R., Hill, D., Martin, R.A., and Hedengren, J. D., 2018, GEKKO Optimization Suite, Processes, Volume 6, Number 8, 2018, doi: 10.3390/pr6080106.

Research and Analysis of Solar Heat Pump Performance

Xuefeng Jiao[1], Zixuan Xu[2], Qingtai Jiao[2], Gang Xu[2], Daojin Xu[2], Jingshan Zhang[2], Kaichun Li[2], Bo Wang[2]

[1] University of Pennsylvania, Philadelphia (USA)

[2] Sunrain Group Co., Ltd, Lianyungang (China)

Abstract: Solar energy is a kind of inexhaustible, clean energy and the heat pump has high efficiency in energy utilization. If solar energy and heat pumps are combined and developed into a solar heat pump system, it will produce greater economic and social benefits. This experiment develops and designs three different solar heat pump water heater systems: solar direct-expansion heat pump water heater, solar and air dual-source heat pump water heater, and PVT heat pump water heater. Moreover, the performance of three kinds of solar heat pump water heater systems is preliminarily tested and verified under different solar irradiation. The problems found in the testing process are analyzed and demonstrated, which lays a foundation for the future commercial development of solar heat pump water heater systems.

Keywords: solar heat pump water heater; solar direct-expansion heat pump water heater; solar and air dual-source heat pump water heater; PVT heat pump water heater; overall COP

1. Introduction

Solar energy is a kind of inexhaustible and clean energy. The most comprehensive application of solar heat utilization is using the solar collector to convert the solar energy into the internal energy of the water or other medium to increase the temperature of the medium [1], which is used in water heating, heating supply, and industrial fields [2]. While air energy is used through the reverse Carnot cycle. The consumption of a share of energy in the air will transfer more than one share of heat to water or other media, which is an efficient way of using energy [3]. Air energy can also be used in water heating, heating supply, and industrial fields [4]. If solar and air energy are combined and developed into a solar heat pump system, it will produce greater economic and social benefits [5]. This research explores three innovative solar heat pump water heater systems: solar direct-expansion heat pump water heater, solar and air dual-source heat pump water heater, and PVT heat pump water heater.

2. Principle of solar heat pump water heater systems

The first system is the solar direct-expansion heat pump water heater system, and the operating principle is shown in Figure 1. The characteristics of the system are that the solar collector is the only heat source. The refrigerant becomes a high-temperature and high-pressure gas refrigerant after being compressed by the compressor. The high-temperature and high-pressure gas refrigerant heats the water in the hot water storage tank through the heat exchanger. The heat exchanger condenses the high-temperature and high-pressure gas refrigerant into the high-pressure and low-temperature liquid refrigerant. The high-pressure and low-temperature liquid refrigerant is depressurized by the electronic expansion valve to the low-pressure and low-temperature liquid refrigerant. The low-temperature and low-pressure liquid refrigerant flows through the solar collector. When there is solar radiation, the front of the solar collector absorbs the heat from the solar energy, and the back of the solar collector absorbs heat from the air, vaporizing the low-temperature and low-pressure

© 2024. The Authors. Published by International Solar Energy Society
Selection and/or peer review under responsibility of Scientific Committee
10.18086/eurosun.2024.02.08 Available at http://proceedings.ises.org

liquid refrigerant into the low-temperature and low-pressure gas refrigerant. After being compressed by the compressor, it becomes a high-temperature and high-pressure gas refrigerant to heat the heat storage tank. This cycle will continue until the water in the heat storage tank reaches the target temperature. Without solar radiation, the solar collector will absorb heat from the air through the front and back.

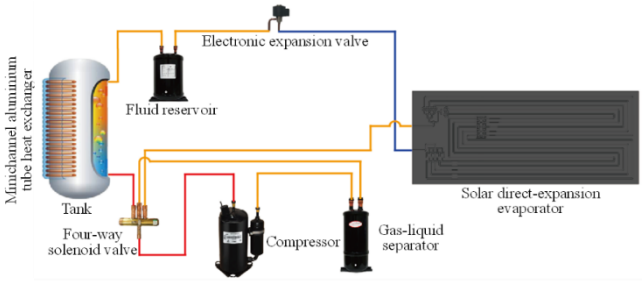

Fig. 1: Solar direct expansion heat pump water heater system

The second system is the solar and air dual-source heat pump water heater system, which is shown in Figure 2. The feature of the system is that the solar collector and the finned heat exchanger are in parallel and serve as the evaporator of the heat pump to provide thermal energy for the heat pump water heater system. The refrigerant becomes a high-temperature and high-pressure gas refrigerant after being compressed by the compressor. The high-temperature and high-pressure gas refrigerant heats the water in the heat storage box through the heat exchanger. The high-temperature and high-pressure gas refrigerant is condensed into the high-pressure and low-temperature liquid refrigerant through the heat exchanger. Low-temperature liquid refrigerant flows through the solar collector and the finned heat exchanger. When there is solar radiation, the front of the solar collector absorbs the heat from the solar energy. At the same time, the back of the solar collector absorbs heat from the air and vaporizes the low-temperature and low-pressure liquid refrigerant flowing through the solar collector into the low-temperature and low-pressure gas refrigerant. At the same time, the finned heat exchanger will also absorb heat from the air, and the low-temperature and low-pressure liquid refrigerant flowing through the finned heat exchanger is vaporized into low-temperature and low-pressure gas refrigerant. After being compressed by the compressor, it becomes a high-temperature and high-pressure gas refrigerant to heat the heat storage tank. This cycle will continue until the water in the heat storage tank reaches the target temperature. Without solar radiation, the solar collector will absorb heat from the air through the front and back, while the finned heat exchanger will also absorb heat from the air.

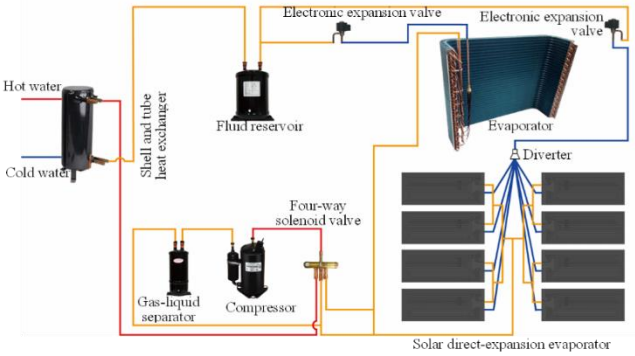

Fig. 2: Solar and air dual-source heat pump water heater

The third system is the PVT heat pump water heater system, which is shown in Figure 3. The characteristics of the system are that the heat absorbent part of the integrated photovoltaic module (PVT) is used as the evaporator of the heat pump to provide thermal energy for the heat pump water heater system, and

the photovoltaic part can generate electricity at the same time, which can be used to drive the DC load and grid-tie inverter, and charge the battery. The refrigerant becomes a high-temperature and high-pressure gas refrigerant after being compressed by the compressor. The high temperature and high-pressure gas refrigerant heats the water in the heat storage box through the heat exchanger. The high-temperature and high-pressure gas refrigerant is condensed into the high-pressure and low-temperature liquid refrigerant through the heat exchanger. The low-temperature and low-pressure liquid refrigerant flows through the back channel of the solar photovoltaic thermal integrated module. When there is solar radiation, the front side can absorb the heat generated by the photovoltaic panel while generating electricity. At the same time, the back side of the PVT will absorb heat from the air, which will vaporize the low-temperature and low-pressure liquid refrigerant flowing through the PVT channel into the low-temperature and low-pressure gas refrigerant. After being compressed by the compressor, it becomes a high-temperature and high-pressure gas refrigerant to heat the heat storage tank. This cycle will continue until the water in the heat storage tank reaches the target temperature. Without solar radiation, the solar collector will absorb heat from the air through the front and back.

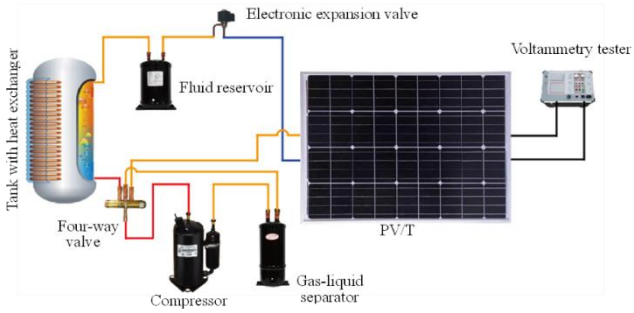

Fig. 3: PVT heat pump water heater

3. Testing method

The testing method for system 1 is illustrated below.

Fig. 4: Prototype of the solar direct-expansion heat pump water heater system

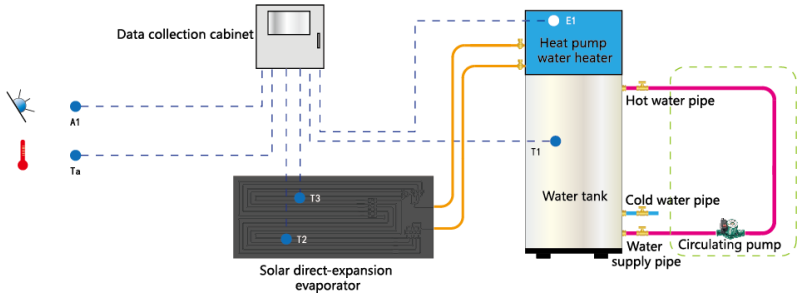

Fig. 5: Schematic diagram of the solar direct-expansion heat pump water heater system

Tab 1: Testing parameters of the solar direct-expansion heat pump water heater

	Testing parameters	Instrument for testing	Note
1	Tank temperature T1	PT100 sensor	
2	Heat pump power consumption E	Digital electricity meter	
3	Water tank capacity M	Scale of electron	Measuring water tank capacity by weighing method
4	Irradiation intensity H	Irradiation meter	Same angle as solar heat absorption panel (75°)
5	Ambient temperature	PT100 sensor	
6	Ambient humidity	Humidity meter	
7	Ambient wind speed	Wind speed instrument	
8	Rainfall	Rain gauge	

1. Testing Preparation

1) Fill the tank with water, circulate the pump to mix water, and record the starting temperature T1.

2) Record the initial electricity quantity E1 of the electricity meter.

2. Testing Process

1) Start the heat pump system and set the final temperature at 55 degrees Celsius. During the experiment, the data acquisition system will automatically record the parameters of irradiation, water tank temperature, wind speed, and real-time electricity.

2) After the heat pump reaches the temperature and stops, start the external mixed water pump until the water temperature from the mixed water to the tank does not change, then record the water temperature T2 as the final water temperature.

3) Record the final reading of the digital electricity meter: E2. C is the specific heat capacity of water; M is the mass of water, COP is the Coefficient of Performance.

3. Data Processing

1) Heat gain of the water tank:

$$Q = CM(T2 - T1) \quad \text{(Eq. 1)}$$

2) Power consumption of heat pump system:

$$E = E2 - E1 \quad \text{(Eq. 2)}$$

3) For the heat pump system:

$$COP = Q/E \quad \text{(Eq. 3)}$$

The testing method for system 2 is illustrated below.

Fig. 6: Prototype of the solar and air dual-source heat pump water heater system

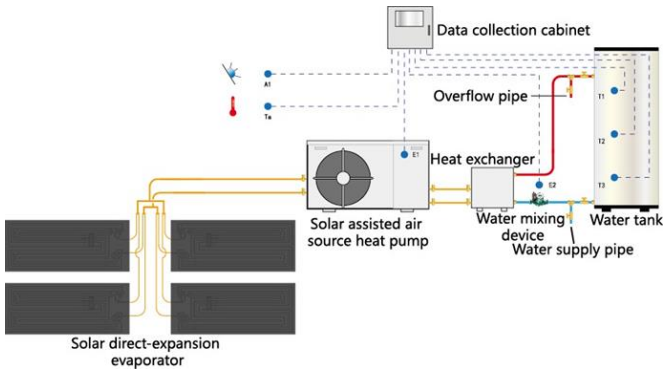

Fig. 7: Schematic diagram of the solar and air dual-source heat pump water heater system

Tab 2: Testing parameters of the solar and air dual-source heat pump water heater system

	Testing parameters	**Instrument for testing**	**Note**
1	Tank temperature T1	PT100 sensor	
2	Heat pump power consumption E	Digital electricity meter	
3	Water tank capacity M	Scale of electron	Measuring water tank capacity by weighing method
4	Irradiation intensity H	Irradiation meter	Same angle as solar heat absorption panel (75°)
5	Ambient temperature	PT100 sensor	
6	Ambient humidity	Humidity meter	
7	Ambient wind speed	Wind speed instrument	
8	Rain	Rain Gauge	

The testing steps, testing process, and data processing of system 2 are same with system 1.

The testing method for system 3 is illustrated below.

Fig. 8: Prototype of the PVT heat pump water heater system

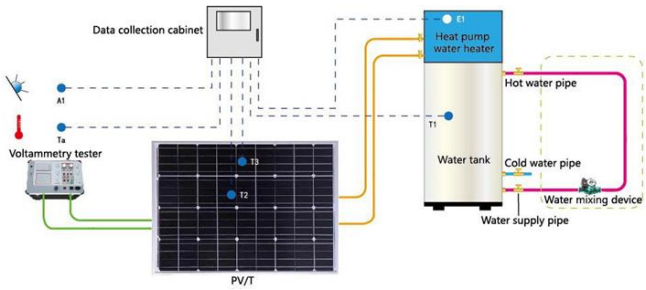

Fig. 9: Schematic diagram of the PVT heat pump water heater system

Tab 3: Testing parameters of the PVT heat pump water heater system

	Testing parameters	**Instrument for testing**	**Note**
1	Tank temperature T1	PT100 sensor	
2	Heat pump power consumption E	Digital electricity meter	
3	Water tank capacity M	Scale of electron	Measuring water tank capacity by weighing method
4	Irradiation intensity H	Irradiation meter	Same angle as solar heat absorption panel (75°)
5	Ambient temperature	PT100 sensor	
6	Ambient humidity	Humidity meter	
7	Ambient wind speed	Wind speed instrument	
8	Rain	Rain Gauge	

For system 3, we record the electricity generation of PVT as E3, and we can use Equation 4 to calculate

the COP of the photothermal heat pump system. For the PVT heat pump system:

$$COP = Q/(E - E3) \quad \text{(Eq. 4)}$$

4. Testing results and analysis

Similar external conditions are selected during the test for three systems. For solar direct-expansion heat pump water heaters and solar and air dual-source heat pump water heaters, the COP of the system is tested respectively with and without solar irradiation.

For the PVT heat pump water heater, the test includes the heat pump COP with solar irradiation and the power generation of the photovoltaic panel. The testing results of three solar heat pump water heater systems are shown below. The followings are the results and analysis for the first system: solar direct-expansion heat pump water heater system.

Tab 4: Testing results of the solar direct-expansion heat pump water heater

Test Date	Time	Inclined plane irradiation (W/m^2)	Horizontal plane irradiation (W/m^2)	Ambient temp. (℃)	Wind speed (m/s)	Heat gain of water tank (kWh)	Power consumption of heat pump (kWh)	COP
2022/6/14	21:06	0	0	20.9	0.27	6.44	2.04	3.16
2022/6/15	19:23	0	0	24.2	1.79	6.19	1.66	3.73
2022/6/14	14:56	64	122	27.4	1.02	6.08	1.75	3.47
2022/6/15	14:02	184	470	32.8	2.12	5.78	1.43	4.04
2022/6/17	13:45	212	551	39.9	1.62	5.84	1.26	4.63
2022/6/16	13:46	231	565	33.7	2.35	6.02	1.31	4.6
2022/6/17	8:39	459	744	32	2.08	6.2	1.32	4.7
2022/6/18	11:50	466	898	38.9	1.86	5.82	1.21	4.81
2022/6/16	8:33	475	778	33.3	1.12	6.52	1.35	4.83
2022/6/21	9:23	518	870	32.5	1.46	5.77	1.23	4.69
2022/6/15	9:21	524	891	33.1	1.52	6.24	1.4	4.46
2022/6/20	10:42	532	912	33.4	2.37	5.91	1.21	4.89

It can be seen from the testing results that the COP of the solar direct-expansion heat pump water heater is about 3.16 when the average ambient temperature is 21℃ without irradiation. At this time, the heat obtained by the tank is mainly achieved by the heat exchange between the evaporator and the surrounding air and heat absorption and work done by the compressor.

With the increase of ambient temperature and irradiation, the COP of the system increases significantly. When the irradiation of the inclined plane reaches 532 W/m^2, the COP of the system reaches 4.89. It can be seen that the irradiation has an obvious effect on the heating performance of solar direct-expansion heat pump water heaters. The average COP of the solar direct-expansion heat pump water heater is 4.33 throughout the testing period.

In order to study the effect of rain on the performance of the solar direct-expansion heat pump water heater system, the difference of COP between the system in the rain and no rain is tested, as shown in Table 5.

Tab 5: Effect of rain on COP of solar direct-expansion heat pump water heater

Ambient temperature（℃）	COP without rain or irradiation	COP in the rain but no irradiation (Average rainfall: 4 mm/h, heavy rain)	Improvement of COP caused by rain
22.3	3.58	4.05	13.13%

With the other environmental conditions being the same, the COP of the system is 4.05 when it rains, while the COP is only 3.58 when there is no rain. The COP of the solar direct-expansion heat pump water heater increases by 13.13% due to rain. Solar heat pump water heater systems can obtain heat from the sun, air, and rain with a diverse energy source. The COP is higher during the daytime. And the system does not depend on a fan to run, which is required by traditional air heat exchangers, thus reducing the operating noise. This system needs to absorb heat from sunlight and air through solar panels, which needs enough area to install the panels. For civil high-rise buildings, this system can be installed with balconies.

The followings are the results and analysis for the second system: solar and air dual-source heat pump water heater system.

Tab 6: Testing results of the solar and air dual-source heat pump water heater

Testing date	Time	Inclined plane irradiation (W/m^2)	Horizontal plane irradiation (W/m^2)	Ambient temp. (℃)	Wind speed (m/s)	Heat gain of water tank (kWh)	Power consumption of heat pump (kWh)	COP
2022/6/14	19:58	0	0	23	0.66	11.52	3.07	3.75
2022/6/14	23:25	0	0	20.7	0.32	11.84	3.21	3.69
2022/6/15	19:32	0	0	24.9	1.77	11.38	2.66	4.28
2022/6/15	23:30	0	0	22.5	1.73	11.56	2.8	4.13
2022/6/14	15:03	137	151	31.1	1.22	10.91	2.6	4.19
2022/6/13	13:40	217	282	32.8	1.27	10.58	2.33	4.54
2022/6/12	14:37	249	324	31.1	2.04	11.26	2.47	4.56
2022/6/17	13:22	336	608	38.9	1.83	11.27	2.32	4.86
2022/6/17	8:47	342	557	28.7	1.99	11.4	2.39	4.77
2022/6/14	9:17	355	597	27	0.92	11.8	2.82	4.18
2022/6/20	14:07	357	760	34.2	2.58	9.66	2.02	4.78
2022/6/12	9:43	431	711	30	1.68	11.26	2.56	4.4
2022/6/16	13:03	435	765	35	1.92	11.05	2.19	5.04
2022/6/16	8:46	448	770	31.2	1.11	11.72	2.8	4.19
2022/6/13	10:35	466	769	33.1	1.29	11.49	2.49	4.61
2022/6/15	9:20	480	792	32	1.63	11.67	2.52	4.63
2022/6/15	12:37	525	893	35.5	1.23	12.03	2.38	5.05
2022/6/18	11:28	559	916	35.2	2.08	11.07	2.09	5.30

Compared with the solar heat pump water heater, the solar and air dual-source heat pump has two kinds of evaporator: solar heat collector and finned heat exchanger, so the dual-source heat pump can operate more efficiently when there is no irradiation. According to the testing data, the average COP reaches 3.96 during the testing period without irradiation. With the increase of ambient temperature and irradiation, the COP of the system increases significantly. When the irradiation of the inclined plane reaches 559 W/m^2, the COP of the system reaches 5.30. The average COP of the solar heat pump water heater is 4.50 throughout the testing period.

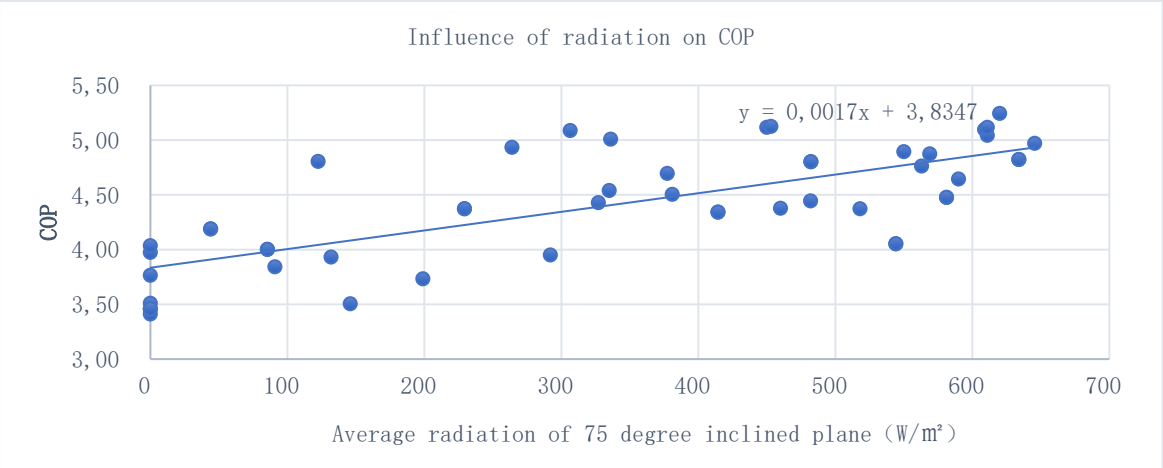

Fig. 10: Effect of irradiation on the performance of the solar and air dual-source heat pump

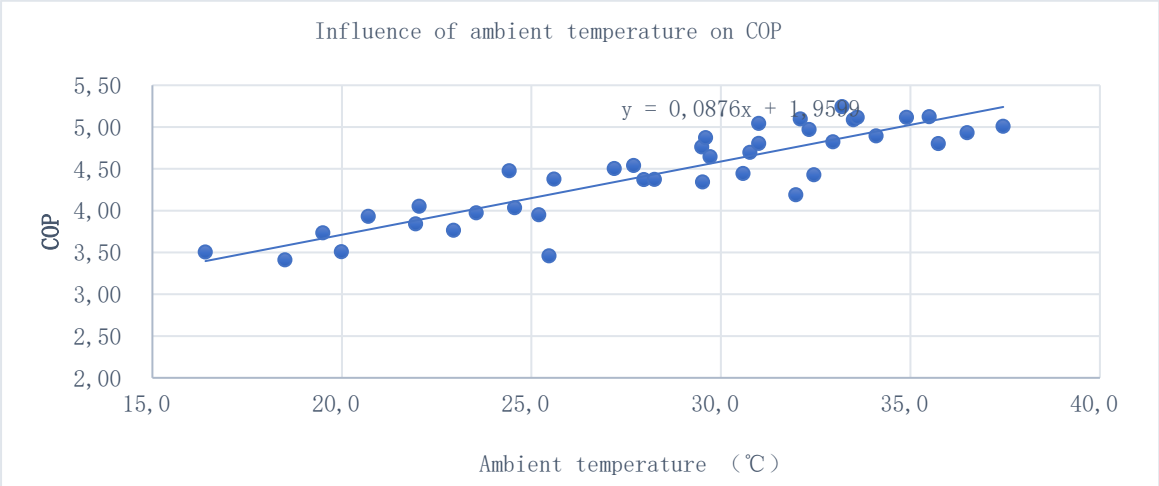

Fig. 11: Effect of temperature on the performance of the solar and air dual-source heat pump

According to the testing data, the linear regression equation of COP with irradiation and temperature during the testing period is obtained by using mathematical statistics theory:

$$COP = 2.164119 + 0.000649\,G + 0.074948\,T \qquad \text{(Eq. 5)}$$

Where G is the solar irradiation intensity (W/m^2), T is the ambient temperature (°C). The ratio of the ambient temperature coefficient (0.074948) to the irradiation coefficient (0.000649) is about 115. Under this system configuration and the external environmental conditions during the testing period, the influence of the ambient temperature increment of 1°C is basically close to that of the COP increment caused by the irradiation increment of 115W/m^2. For the solar and air dual-source heat pump water heater, there is a distinct influence of ambient temperature and irradiation on COP. However, the influence of temperature is more obvious.

To study the influence of the solar heat transfer side and air heat transfer side on the system performance at night, the COP of the system at different ambient temperatures with and without a solar heat collector

evaporator is tested separately. The testing results are as follows: ambient dry bulb temperature during the test: 35℃, 30℃, 25℃, 20℃, 15℃, 10℃, 5℃, 0℃, -5℃, -10℃; System operating water temperature: 41℃.

Tab 7: Testing results of COP for solar and air dual-source heat pump water heater with/without solar heat collector evaporator

Ambient temperature (℃)	COP with a solar heat collector	COP without solar heat inflator
-10	0.637	1.597
-5	1.071	1.912
0	1.582	2.589
5	2.054	2.908
10	2.526	3.236
15	2.988	3.521
20	3.458	3.776
25	3.989	4.171
30	4.394	4.663
35	4.83	5.206

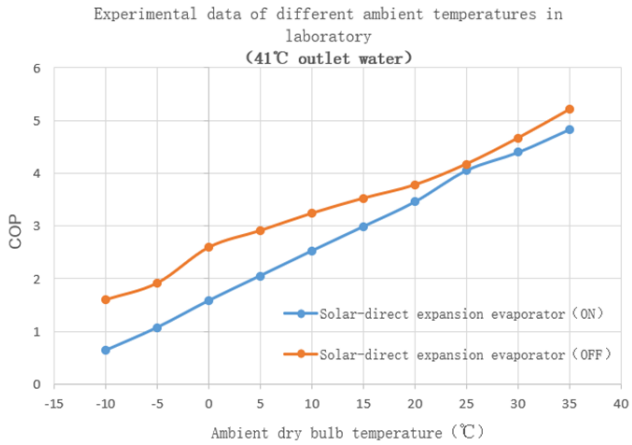

Fig. 12: COP for solar and air dual-source heat pump water heater with/without solar heat collector evaporator

The testing results show that the COP of the system is higher when the solar collector is turned off than when the solar collector is turned on. Under normal circumstances, it is believed that when the solar collector panel is turned on, the area of the evaporator for the heat pump system increases. Even without irradiation, the solar side can absorb heat from the air, thus playing a positive role in increasing the energy efficiency of the heat pump system. However, the experimental results indicate the opposite. The possible reasons are as follows. The control logic does not reach the optimal, and the electronic expansion valve fails to adjust the two refrigerants to the appropriate flow rate according to the overheating, resulting in excessive refrigerant retained in the inflator plate. Moreover, the air evaporator refrigerant quantity is small, resulting in a decrease in heat exchange efficiency, thus affecting the COP. Optimizing the control logic and adjusting the distribution of refrigerant in different working conditions is the key to optimizing the performance of the solar and air dual-source heat pump water heater system. The followings are the results and analysis for the third system: the PVT heat pump water heater system.

Tab 8: Testing results of the COP for the PVT heat pump water heater system

	Inclined plane irradiation (W/m^2)	Horizontal plane irradiation (W/m^2)	Average temp. (℃)	Average wind speed (m/s)	COP of the heat pump	Power generation of the PVT (kWh)	Power consumption of the PVT (kWh)	Overall power consumption of the PVT system (kWh)	Overall COP of the heat pump system
1	527	783	35.9	1.7	3.54	0.791	1.83	1.039	6.23
2	568	832	36.9	1.3	4.01	0.665	1.46	0.795	7.36
3	450	678	35.6	1.6	3.79	0.759	1.63	0.759	7.1

This test only studies the system operating during the daytime with solar irradiation. From the results, when the irradiation of the PVT heat pump water heater is installed at an angle of 45° and the inclined plane irradiation of 515 W/m^2, the COP of the heat pump system is about 3.78 without considering the photovoltaic power generation. However, the PVT heat pump water heater differs from the other two systems. During the heat pump heating stage, the PVT module can on average generate 0.738 kWh of electricity. If the heat pump offsets this part of electricity, the average COP of the PVT heat pump water heater system is 6.90.

5. Conclusion

Under similar working conditions, the testing results of the three systems are summarized in Table 9.

Tab 9: Summarized testing results of the COP for three heat pump water heater system

System	Average COP during the test	Note
Solar direct-expansion heat pump water heater	4.33	
Solar and air dual-source heat pump water heater	4.50	
PVT heat pump water heater	6.90	Overall COP

The comparison results show that the solar direct-expansion heat pump water heaters use solar panels as the evaporator, and the energy efficiency is affected by solar radiation. It is more suitable for collecting heat during the daytime and using heat at night. At the same time, the capacity of the water tank is generally 100-300 Liters. The installation of the heat collection plate requires a particular plane or building facade, so it is more practical to provide rural and urban domestic households with hot water.

The solar and air dual-source heat pump water heater has high energy efficiency, whether under irradiation or not. However, under different working conditions, the two evaporators will directly interfere with each other. Therefore, it is necessary to optimize the refrigerant charging amount and operation logic and further improve the system's adaptability under different working conditions. Similarly, installing heat collection plates and units requires a specific surface. The system can work with a single machine or multiple machines in series and parallel. The volume of the system can be both large and small. It is usually suitable for domestic and commercial usage to get hot water, heating, and drying under various working conditions in solar-rich areas.

PVT solar heat pump water heaters can combine photothermal and photovoltaic to achieve a higher solar energy utilization rate. In the process of heat pump heating, PVT solar heat pump water heater can also reduce the temperature of photovoltaic panels and improve the efficiency of photovoltaic power generation. However,

the industrialization of PVT photovoltaic thermal modules is not mature, the structure is complex, and the initial investment is high. It is not widely used in some areas.

The emission coating on the backside of the solar panel can significantly improve efficiency. Meanwhile, the coating can improve the anti-corrosion performance of the panel and extend the system's service life. Using selective solar absorption coating on the front of the solar panel helps to improve the solar heating efficiency of the system. However, there are some problems such as complex processing technology, poor weather resistance, and high cost, which should be further studied.

More projects of this solar fresh air system should be built to conduct a more comprehensive study on the solar heating efficiency of the system, the economy of actual use, and the improvement of indoor air quality to get better guidance on the development and utilization of this solar fresh air system.

6. Acknowledgments

We would like to express our sincere gratitude to Sunrain Group for providing the technical support and resources necessary for the development and testing of the comprehensive residential clean energy solutions.

7. References

[1] D. Wang, B. Fan, Y. Chen, Y. Han, Y. Liu, Y. Wang, H. Liu, and X. Jiao, “Comparative analysis of heat loss performance of flat plate solar collectors at different altitudes,” Solar Energy, vol. 244, 2022.

[2] Q. Jiao and T. Xu, “Performance of a high solar fraction district heating system,” Proceedings of the ISES Solar World Congress 2021, 2021.

[3] R. Z. Wang, M. Li, Y. X. Xu, and J. Y. Wu, “An energy efficient hybrid system of solar powered water heater and adsorption ice maker,” Solar Energy, vol. 68, no. 2, pp. 189–195, 2000.

[4] S. Lu, R. Liang, J. Zhang, and C. Zhou, “Performance improvement of solar photovoltaic/thermal heat pump system in winter by employing vapor injection cycle,” Applied Thermal Engineering, 2019.

[5] J. Ji, K. Liu, T.-T. Chow, G. Pei, and H. He, “Thermal analysis of PV/T evaporator of a solar-assisted heat pump,” International Journal of Energy Research, vol. 31, no. 5, pp. 525–545, 2007.

Simulation of a Photovoltaic-Thermal (PV-T) Air Source Heat Pump (ASHP) System for Building Thermal Demands

Pranay Kasturi[1,2], Dr. Herena Torio[2,3] and Jan Sören Schwarz[1,2]

[1] OFFIS Institute for Information Technology, Oldenburg (Germany)

[2] University of Oldenburg, Oldenburg (Germany)

[3] DLR Institute of Networked Energy Systems, Oldenburg (Germany)

Abstract

The coupling of photovoltaic-thermal (PV-T) collectors with heat pumps improves both the electrical and thermal performance of the heat pumps. The main objective of this study is to investigate the potential efficiency improvements resulting from the combined operation of an air PV-T system with an air source heat pump (ASHP). We simulate the said combined operation of the system for meeting building thermal demands (space heating and domestic hot water production), using models developed for this study. Different configurations of the PV-T collector system (from 2 to 12 panels in series) are simulated, and the configuration with 4 panels in series is identified as the most suitable one in this context. This configuration of the PV-T ASHP system has better electrical performance as compared to the baseline case of only a photovoltaic (PV) ASHP system with the same configuration, with a 6.61% increase in the seasonal COP of the heat pump. The presented simulation methodology builds the base for further investigation of other types of PV-T collector systems and heat pumps.

Keywords: Heat pumps, PV-T collectors, co-simulation, open-source modelling, Python

1. Introduction

Heat pumps will play a crucial role in reducing the carbon emissions of the buildings sector, as they provide the largest electrification opportunity, displacing heating from fossil fuel boilers (Cozzi and Gould, 2021). Coupling the heat pumps with renewable energy sources will be critical for decarbonization. In this context, photovoltaic thermal (PV-T) collectors are increasingly being used to assist the heat pumps. In addition to generating electrical energy that can be self-consumed, the PV-T collectors also generate thermal energy that can be used as a heat source for the heat pump, resulting in higher source temperatures, and thereby higher efficiency, enhancing the decarbonization potential and grid-friendly operation of heat pumps. The main objective of this study is to investigate the efficiency improvements resulting from the coupling of air PV-T systems with air-source heat pumps (ASHP). For this, we simulate the combined operation of PV-T and ASHP systems for building thermal demands (space heating and domestic hot water production) and compare its performance with a reference case consisting of a photovoltaic (PV) system coupled with an ASHP system. Based on the results, we identify the optimal size of the PV-T system for the demands in consideration and evaluate the benefits that can be achieved with the said combined operation.

2. Methodology

2.1 Basis for the scenario simulations

The basis for the system simulations is the building thermal demand, available as separate profiles for space heating and domestic hot water, for two buildings from the Energetisches Nachbarschafts-Quartier (ENaQ) project (WWW1), for the year 2020. The total annual domestic hot water and space heating demands are 73081 kWh and 35921 kWh respectively. The heating system configuration for the baseline scenario consists of an ASHP, coupled with a hot water tank between the ASHP and the consumer. For the PV-T ASHP system, an indirect expansion

© 2024. The Authors. Published by International Solar Energy Society
Selection and/or peer review under responsibility of Scientific Committee
10.18086/eurosun.2024.02.09 Available at http://proceedings.ises.org

configuration is chosen, with an air PV-T collector system added in parallel to the external air source of the baseline scenario configuration. The proposed system schematic is shown in the figure 1. In the cases where the demand cannot be met by the system, back up electrical heaters are considered to supply the demands.

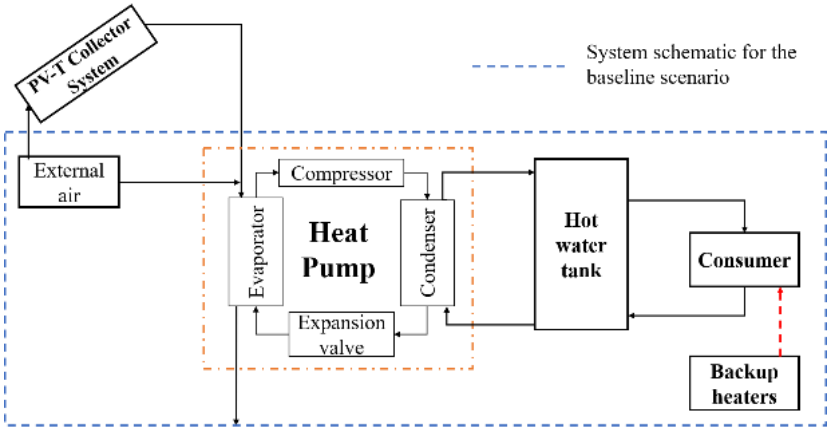

Figure 1: Proposed schematic for the heating system

System design data, shown in table 1, has been obtained from project planning of the energy cooperative Olegeno (WWW2). The weather data required for the simulations has been obtained from PVGIS (WWW3) for the year 2020. The temperature of the cold water replacing the domestic hot water in the tank is also necessary for the simulations, and is assumed to follow a sinusoidal curve (Heimrath, 2004).

Table 1: System design parameters

System Design Parameter	Value
Total peak heating demand (kW)	58
Total volume of hot water storage (Litres)	4000
Space heating supply temperature (°C)	35
Space heating circuit temperature drop (°C)	7
Domestic hot water supply temperature (°C)	40
Total building roof area (m^2)	642

2.2 Models used in the simulations

The different models required for the study have been developed in the Python programming language. The models for the heat pump, hot water tank and the controller, are available as a part of the *mosaik-heatpump* Python package (WWW4). These three models, first developed for a previous work (Barsanti et al., 2021), have been significantly extended for this study. The models are briefly described in this section and detailed documentation of the functionality of these models is available online (WWW5). Additionally, the PV-T system model has been developed for this work and the functionality of this model is described in this section as well.

Heat Pump Model

The combined operation of the PV-T and heat pump systems, lead to higher source temperatures for the heat pump, and therefore lower temperature lift conditions. The performance of heat pumps at such conditions is not trivial. Extrapolating the performance from the standard operation range in the data sheets, as done by simple parametric-fit equation-based models, may lead to errors in the calculated performance (Gasser et al., 2017). Thus, for this work, a detailed quasi-steady state modelling approach has been adopted based on the openly available TESPy library (Witte and Tuschy, 2020).

The performance of the heat pump is simulated by considering the energy and mass balances in the individual *components* of the heat pump – condenser, evaporator, compressor, expansion valve, heat exchangers and pumps

– and the state of fluids in the *connections* between these *components*. The *connections* and *components* together form a topological *network* that is represented and solved as a system of equations. The model is parametrized for the study based on an actual heat pump available in the market, the LW 300L heat pump from ait-deutschland (WWW6), due to its suitability to meet the peak demands mentioned in table 1. The operating conditions, i.e. source air temperature and the condenser water inlet temperature, are provided as inputs to the model. The model then provides the heating capacity, the electrical power consumption, the coefficient of performance (COP), the mass flowrate of water in the condenser and the condenser water outlet temperature as the outputs. The different steps taken to develop the heat pump model (shown in figure 2) based on the LW 300L heat pump are detailed below.

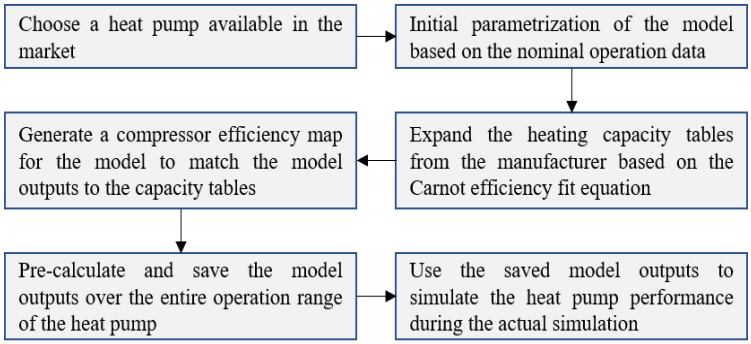

Figure 2: Methodology of heat pump model development

First, an initial calculation of the system network in the *design* calculation mode is performed. The key parameters for the different *components* and *connections* are set based on the nominal operating point data obtained from the manufacturer's datasheet, shown in table 2. All the parameters in the table, except the electrical power, are set as inputs. Since the refrigerant R448A is not available in TESPy, R404A has been used in the model due to the similarity in their properties (Mota-Babiloni et al., 2015). A temperature difference of 5°C is assumed for the water in the condenser. The electrical power consumption of the heat pump is estimated as per the equation 1, where P is the power consumption of the compressor, $\dot{m}_{in}$ is the mass flow in the compressor, $(h_{out,s} - h_{in})$ is the enthalpy change in an isentropic compression process, and η_s is the isentropic efficiency of the compressor. For given operating conditions, η_s is the parameter that affects the power consumption the most and has to be set as an input. Since this value is not available in the datasheet, it is changed on a trial-and-error basis to match the power consumption calculated by the model to that from the datasheet.

$$P = \frac{\dot{m}_{in} \cdot (h_{out,s} - h_{in})}{\eta_s} \qquad \text{(eq. 1)}$$

Table 2: Nominal operating point data of the heat pump

Parameter	Value	Units
Condenser outlet temperature	35	°C
Source air temperature	7	°C
Mass flow of air in evaporator	7800	m^3/h
Heating capacity	32.5	kW
Electrical Power	8.56	kW
Refrigerant	R448A	-

While the initial *design* mode calculation is only for the nominal operating point, the actual operational range of the heat pump varies from -20°C to 35°C for the source air, and 15°C to 65°C for the condenser water outlet temperatures, with varying maximum heating capacities and power consumption. The performance of the heat

pump at these other operating conditions is estimated by the *offdesign* calculation mode of TESPy, which uses the initial design calculation along with generic characteristic curves of the components available in the library. Instead of using the generic curve for η_s over the entire operation range, a series of design points (table 3) are identified where the η_s is changed as done in the initial design point calculation explained earlier.

Table 3: Design point conditions

Parameter	Values
Source air temperature (°C)	-20, -15, -12, -10, -7, -2, 2, 7, 10, 12, 15, 20, 25, 30, 35
Condenser outlet temperatures (°C)	15, 20, 25, 30, 35, 40, 45, 50, 55

From the table 3, every pair of source air and condenser water temperatures forms an operating point at which the maximum heating capacity and power consumption are required for the design point calculation. The manufacturer's datasheet contains the respective curves for the entire range of temperatures of source air, but only for two specific condenser water outlet temperatures (35°C & 55°C). Therefore, the maximum heating capacity and power consumption have to be estimated for the missing condenser water outlet temperatures. The maximum heating capacity is strongly influenced only by the source air temperature and the average of the capacities at the two available condenser water outlet temperatures is assumed for all the missing points. The corresponding power consumption, however, is influenced strongly by both the source air temperature as well as the condenser water outlet temperature, and hence has been estimated using an approach based on the Carnot effectiveness fit equation.

For all the operating points at which the power consumption is known, the temperature lift (T_{lift}) and ideal COP (COP_{ideal}) are calculated according to equations 2 & 3 respectively, where T_h is the condenser water outlet temperature and T_c is the source air temperature. The Carnot effectiveness (η_{carnot}) is then calculated according to equation 4, using the real COP of the heat pump (COP_{real}). A second order polynomial equation is fit to the η_{carnot} vs. T_{lift} curve. For the operating points with missing power consumption data, this fit equation is used to estimate the Carnot effectiveness, which in turn is used to estimate the power consumption. The network calculations in the *design* mode are then made for each of the operating points and the compressor isentropic efficiency is changed to match the power consumption calculated by the model with the estimated values, there by generating the so-called compressor efficiency map. The *offdesign* mode with the generic curve for η_s is then used only in the smaller ranges between the different design points.

$$T_{lift} = T_h - T_c \qquad \text{(eq. 2)}$$

$$COP_{ideal} = \frac{T_h}{T_h - T_c} \qquad \text{(eq. 3)}$$

$$\eta_{carnot} = \frac{COP_{real}}{COP_{ideal}} \qquad \text{(eq. 4)}$$

The model is then finally developed to estimate the heat pump performance over the entire operation range, with a 1°C resolution for both the inputs of the model, the source air and condenser water inlet temperatures. For each set of inputs, assuming a rise of 5°C for the water in the condenser, the model identifies the closest design point, and first runs the design point calculation using the respective values for the maximum heating capacity and η_s from the map. The model then uses the *offdesign* calculation mode to estimate the performance at the input conditions, assuming the same heating capacity as in the design point and using the generic curve for η_s. The condenser water outlet temperature, the mass flow rate of water, the power consumption and the COP of the heat pump, are all calculated by the model and provided as outputs. The inputs and corresponding outputs of the model are saved. During the scenario simulations, the saved inputs that are closest to the input data are identified, and the saved output data for these points are used to calculate the outputs of the model, rather than performing the actual *design* and *off-design* calculations. Though the granularity of the model is reduced, there is a significant improvement in the simulation duration.

PV-T collector system model

The PV-T collector system model has been developed as a combination of two separate models for the thermal and photovoltaic components of the collector, once again following a quasi-steady state modelling approach. The tilted plane irradiance (E) and the temperature of the air at the inlet of the PV-T field, which is the same as the ambient temperature (T_{amb}), are provided as inputs to the model. The outlet temperature of air from the PV-T field which is used as the source air in the heat pump, and also the electricity generated by the PV-T field which can be self-consumed by the heat pump, are calculated as the outputs of the model.

The thermal performance has been modelled based on the solar collector component available in the TESPy library. The equations for steady state energy balance (equations 5 & 6) are applied to each collector panel, where ($h_{out} - h_{in}$) is the enthalpy change of the fluid in the collector and T_m is the mean temperature of the fluid in the collector panel. The inlet temperature for each panel (T_{in}), T_{amb} and E are provided as inputs, to calculate the temperature of the fluid in the outlet *connection* (T_{out}) of the panel. While T_{amb} is used as the T_{in} for the first panel in series, the T_{out} from the previous panel is used as the T_{in} for the next panel in series. The relevant parameters - collector area (A), optical efficiency (η_{opt}), linear thermal loss coefficient (α_1), quadratic thermal loss coefficient (α_2), and mass flow of air ($\dot{m}$)- have been obtained from literature for a reference glazed type PV-T air collector (Tonui and Tripanagnostopoulos, 2007), and are summarized in table 4. The outlet temperature from the final panel is series is used as the source air temperature in the heat pump. A mixing strategy has been implemented to ensure that this temperature is within the limits of operation of the heat pump. The temperature of the source air in the heat pump should be lower than both the maximum temperature limit (35°C) and the condenser water inlet temperature of the heat pump. In case the outlet temperature of air from the PV-T system is higher than either of these, the outlet air is mixed with ambient air to bring down the temperature to the lower value of the two.

$$\dot{m} * (h_{out} - h_{in}) = A * (E * \eta_{opt} - \alpha_1 * (T_m - T_{amb}) - \alpha_2 * (T_m - T_{amb})^2 \quad \text{(eq. 5)}$$

$$T_m = \frac{T_{out} + T_{in}}{2} \quad \text{(eq. 6)}$$

Table 4: Thermal parameters of the collector

Parameter	Value	Units
Operating fluid	Air	
$\dot{m}$	0.02	kg/s
A	0.4	m^2
η_{opt}	0.364	-
α_1	4.79	W/K-m^2
α_2	0	W/K^2-m^2

The PV performance has been modelled as a standalone PV panel, considering just the effect of panel temperature on its efficiency. The electrical power output of the PV module (P) is calculated using eq. 7. The electrical efficiency (η_{el}) of the collector varies with the temperature of the PV module (T_{PV}) and is calculated as shown in eq. 8, where the reference electrical efficiency ($\eta_{el,ref}$) at standard test conditions (STC – 25°C) and the temperature coefficient (β_0) have been obtained from literature for a reference glazed type PV-T air collector (Tonui and Tripanagnostopoulos, 2007), and are shown in table 5.

$$P = \eta_{el} * E * A \quad \text{(eq. 7)}$$

$$\eta_{el} = \eta_{el,ref} * (1 - \beta_0 * (T_{PV} - 25)) * E * A \quad \text{(eq. 8)}$$

When the thermal component of the PV-T collector was being operated, to supply air to the heat pump, the temperature of the PV module (T_{PV}) is assumed to be the mean temperature of the air inside the collector (Kramer, 2020), as calculated by eq. 6. For the systems with multiple collector panels in series, the mean temperature in each

panel varies, leading to a varying production of electricity.

Table 5: Photovoltaic parameters of the PV-T collector

Parameter	Value	Units
$\eta_{el,ref}$	0.13	-
β_0	0.006	1/K
$T_{PV,NOCT}$	43	^{0}C
$T_{amb,NOCT}$	20	^{0}C
E_{NOCT}	800	W/m^2
$T_{PV,ref}$	25	^{0}C
$\tau\alpha$	0.83	-

However, in the cases when the heat pump is turned off, the thermal component of the PV-T collector is not operated, and the temperature of the PV module is calculated using the PV cell temperature equation available in the HOMER simulation software (WWW7), as shown in eq. 9. $T_{PV,NOCT}$ is the nominal operating cell (PV module) temperature (NOCT), $T_{amb,NOCT}$ is the ambient temperature at NOCT, E_{NOCT} is the tilted plane irradiance at NOCT, $T_{PV,ref}$ is the PV module temperature at the reference STC conditions, τ and α are the solar transmittance and the solar absorptance of the PV module. All of these parameters have also been obtained from literature for a reference glazed type PV-T air collector (Tonui and Tripanagnostopoulos, 2007), and are summarized in table 5. All the temperatures have been converted to the Kelvin scale before being used in the equation. In these cases, the electricity generated by all the individual panels in the system is assumed to be the same. The electricity generation of only the PV system, is also estimated using the same equations (7 & 8), with the cell temperature always calculated using the eq. 9.

$$T_{PV} = \frac{T_{amb}+\left(T_{PV,NOCT}-T_{amb,NOCT}\right)*\left(\frac{E}{E_{NOCT}}\right)*\left(1-\frac{\eta_{el,ref}*(1-\beta_0*T_{PV,ref})}{\tau\alpha}\right)}{1+\left(T_{PV,NOCT}-T_{amb,NOCT}\right)*\left(\frac{E}{E_{NOCT}}\right)*\left(\frac{\beta_0*T_{PV,ref}}{\tau\alpha}\right)} \qquad \text{(eq. 9)}$$

For the PV-T collector field, the number of panels in parallel are calculated to be 133, considering the need to maintain a fixed mass flow rate within each panel (0.02 kg/s) and to supply the required mass flow of air to the heat pump (2.65 kg/s). Each of the 133 strings can have a maximum of 12 panels in series, considering the panel area of 0.4 m^2 (from table 1) and the available building roof area of 642 m^2, as mentioned in section 2.1.

Hot water tank model

The hot water tank model developed for another project (Gerster et al., 2016), is used in this work to act as a buffer in between the heating device and the heat consumer. It is a multinode stratified thermal tank model (Saloux and Candanedo, 2019), where the tank volume is divided into a specified number of layers (nodes) of equal volume, each characterized by a specific temperature. A traditional density distribution approach is adopted where the water flowing into the tank enters the layer that best matches its density (i.e., temperature). The model assumes that the fluid streams are fully mixed before leaving each of the layers and the flows between the layers follow the law of mass conservation. Heat transfer to the surrounding environment from the walls of the tank, and the heat transfer between the layers have been considered.

The schematic of the hot water tank model is shown in figure 3. The dimensions of the tank are specified in terms of its volume and height. The storage volume required is 4000L (table 1). The height of the tank is calculated assuming a height to diameter ratio of 3:1. Based on the literature for the optimum number of nodes in the tank (Saloux and Candanedo, 2019), especially its impact on long term simulations (Arias et al., 2008), the tank is parametrized to contain six layers. The initial temperature of all the layers at the beginning of the simulation is set to 20°C.

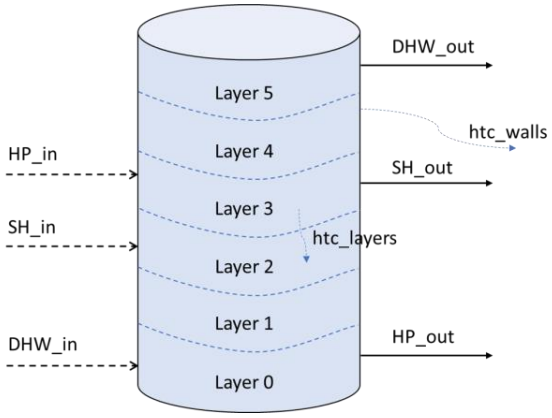

Figure 3: Schematic representation of the hot water tank model

The flows into and out of the tank are specified as the connections of the hot water tank model. The flow going to the heat pump (*HP_out*), the space heating demand (*SH_out*), and the domestic hot water demand (*DHW_out*) are connected to the bottom layer, the fourth layer and the top layer respectively. As described above, the corresponding flows coming into the tank (*HP_in*, *SH_in*, and *DHW_in*) are not connected to a fixed layer in the tank. They are connected to the layer with a temperature closest to that of the flow. The heat transfer coefficient of the walls of the tank (*htc_walls*) is assumed to be 0.28 W/m^2 - K (Heimrath, 2004). The heat transfer coefficient for the heat transfer between the layers of the tank (*htc_layers*) is assumed to be 1.5 times the thermal conductivity of water (Heimrath, 2004). The value is calculated as 0.897 W/m-K, considering the thermal conductivity of water to be 0.598 W/m-K (WWW8).

Controller model

The controller model used in this work utilizes simple Boolean logic to match the heating demands with the supply from the hot water tank/back up heaters. The controller is initialized with the set points mentioned in table 1. Based on the heat demands, the controller calculates the necessary mass flows for the hot water tank model. For the domestic hot water demand, the supplied water is replaced by the cold water. Additionally, if the supply temperature is higher than the set point, the flow is adjusted by mixing with the cold water to bring the temperature down to the set point. For the space heating demand a constant temperature drop of 7°C in the circuit is assumed. For both the demands, if the supply temperatures are lower than the set points, the controller calculates the additional heat that must be supplied by the backup heaters, assuming 100% efficiency for the heaters.

The controller model also controls the operation of the heat pump with a control strategy based on the temperatures of both the bottom and top layers of the tank. The fifth layer of the hot water tank is considered as the top layer instead of the sixth layer, in order to ensure a higher temperature in the actual top layer for periods of high demands. The top layer of the tank is controlled against the higher set point of 43°C, i.e., the heat pump is turned on when the temperature in the top layer of the tank falls below the higher set point. The bottom layer of the tank is controlled against the lower set point of 37°C, i.e., the heat pump is turned off only when the temperature in the bottom layer of the tank is greater than the lower set point. In this case, the temperature of the top layer is expected to be greater than the higher set point due to stratification inside the tank. The heat pump continues to remain turned off and turns back on only when the temperature of the top layer falls below the higher set point again.

The controller model can also adapt the control strategy during the photovoltaic-thermal (PV-T) collector operation. When operating the photovoltaic-thermal (PV-T) collector along with the heat pump, an advanced control strategy has been implemented in an attempt to extend the operation of the heat pump during the daytime when the source air for the heat pump is available at a higher temperature. The set points for the heat pump operation are increased by the value of the temperature difference of the air inside the PV-T system. This increase is limited to a maximum of 7°C, in order to not heat up the tank much higher than that required for the domestic hot water supply.

2.3 Co-simulation

The stand-alone models for heat pump, hot water tank, photovoltaic thermal (PV-T) system and controller are dependent on the information from each other that only becomes available over the course of the simulation, as shown in figure 4. This type of joint simulation of models is called co-simulation. In this work, the co-simulation framework mosaik (Steinbrink et al., 2019) has been used to couple the independent models. The models have been implemented with the mosaik component application programming interface (API) to allow coupling with mosaik. Additionally, the scenario API provided by mosaik has been used to specify data flows between the coupled models in the scenario definition and execute the co-simulation. The input and output data for all the models is handled by mosaik-csv (WWW9), a tool available in mosaik that operates as a pseudo simulator to handle data in the CSV (comma separated values) data format. The co-simulation of all the models is done at a time step of 1 minute, with the information being exchanged between all the models after each time step of the simulation.

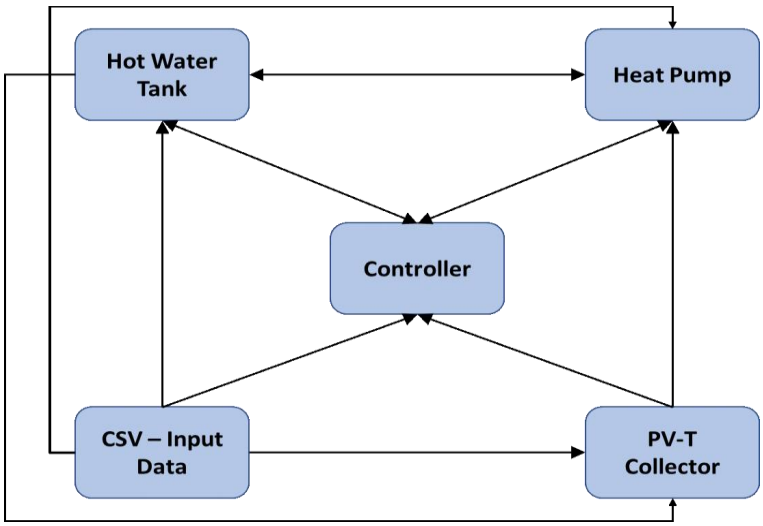

Figure 4: The flow of information between the different models

2.4 Scenarios

The system simulations are performed for the PV-T ASHP system, for a range of configurations of the PV-T field, with 2,4,6,8,10 and 12 PV-T collector panels connected in series, limited by the roof area available as explained earlier. The system performance for the different configurations are compared to the baseline of PV ASHP system with corresponding configurations of the PV field. The annual energy supply, seasonal COP of the heat pump, self-consumption of electrical energy by the heat pump, and grid electrical energy consumed by the system are used as indicators for the system performance comparison. Based on the comparison, the PV-T collector field configuration that is most appropriate for the building thermal demands in consideration is identified. This configuration of the PV-T ASHP system is finally simulated with the advanced control strategy described earlier.

3. Results

The simulations are performed for all the scenarios described in section 2.4 and the performance of the system is evaluated using the key performance indicators (KPIs) shown in table 6. While the results for only two configurations of the PV-T/PV field (4 and 12 panels in series) of both the PV-T ASHP and PV ASHP systems are shown in the table, additional plots with results from the simulations of the other configurations are also shown and discussed in section 3.1. The configuration with 4 panels in series is identified as the optimal one for the thermal demands in consideration and is simulated with the advanced control strategy described in the ‘Controller model’ part of section 2.2. The performance of the system from this simulation is evaluated again using the same KPIs, as shown in the table 6, and the results are discussed with an additional plot in section 3.2.

Table 6: Comparison of KPIs for different configurations of PV-T/PV ASHP Systems (annual for 2020) (TE- thermal energy; EE- electrical energy; HP- heat pump; HWT- hot water tank; ACS – advanced control strategy)

System configuration / System performance KPIs	PV ASHP	PV-T ASHP	PV ASHP	PV-T ASHP	PV-T ASHP	Units
	4 panels in series		12 panels in series		ACS	
TE - system (kWh)	110221.04	110223.50	110221.04	110218.41	110326.79	kWh
EE - system (kWh)	31476.52	29534.94	31476.52	28358.63	30035.28	kWh
EE - HP (kWh)	30779.48	28883.05	30779.48	27638.69	29497.40	kWh
TE/EE - backup heaters (kWh)	697.03	651.88	697.03	719.93	537.87	kWh
HWT mean temperature (°C)	40.47	40.52	40.47	40.40	43.12	°C
HP seasonal COP	3.56	3.79	3.56	3.96	3.72	-
PV/-T EE generation (kWh)	35162.48	35548.81	105487.45	104885.85	35613.28	kWh
PV/-T EE self-consumption (kWh)	10367.27	8684.37	15142.88	12045.50	10331.44	kWh
EE from grid (kWh)	21109.24	20850.56	16333.64	16313.13	19703.83	kWh

3.1 Performance evaluation of the system with different configurations of PV/-T field

As seen from the table 6, the total thermal energy for all the cases is almost the same and the thermal energy supplied by the backup heaters is significantly lower with a maximum share of 0.65% of the total thermal energy observed for the '12 panels in series' configuration of the PV-T system. The thermal energy is mostly supplied by the heat pump and consequently most of the electrical energy consumed by the system is that of the heat pump. For the PV-T ASHP system, having higher number of panels in series results in higher temperatures for the source air of the heat pump and therefore results in lower electrical energy consumption/higher COP. However, these KPIs remain same for the PV ASHP system irrespective of the number of panels in series, as the source air for the heat pump is available just at the ambient temperature, as can be seen from table 6.

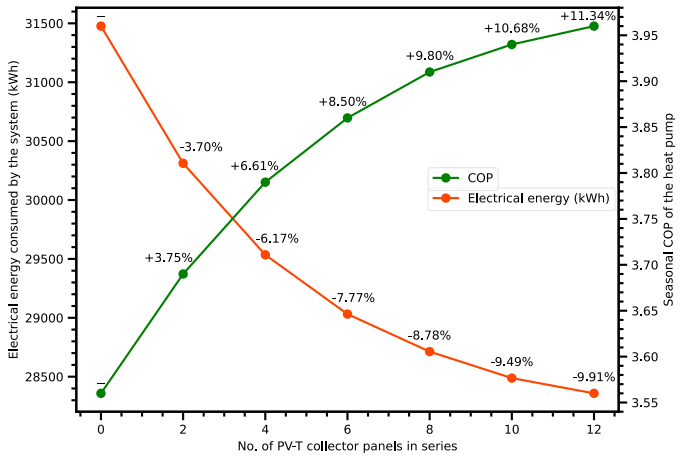

Figure 5: Comparison of system electrical performance for the different configurations of the PV-T collector system

Figure 5 shows the comparison of the electrical performance of all the configurations of the PV-T ASHP system and the PV ASHP system (labelled 0 panels). With an increase in the number of panels in series, the rate of increase/decrease in the COP/total electrical energy consumed reduces. For the PV-T system with 4 panels in series, the COP increases by 6.61%, and by increasing the number of panels in series to 12, the COP is improved further only by an additional 4.73%. As expected, a similar trend can also be seen for the electrical energy consumed by the system. Considering these trends, the PV-T ASHP system configuration with 4 panels in series

for the PV-T field, is identified as the most suitable one for the building thermal demands in consideration.

The electrical energy generated by the PV-T or the PV field, the self-consumption of this electrical energy by the system and the additional electrical energy required from the grid, are influenced by the number of panels in series as can be seen from table 6. For the '4 panels in series' configuration, the total electrical energy generated by the PV-T system is higher than the energy generated by the corresponding PV system, as the heat extracted by the PV-T collector reduces the cell temperature, thereby increasing the electrical efficiency of the PV-T system. However, for the '12 panels in series' configuration, the total electrical energy generated by the PV-T system is lower than that of the corresponding PV system, due to the very high temperatures reached inside the panels which reduce the electrical efficiency.

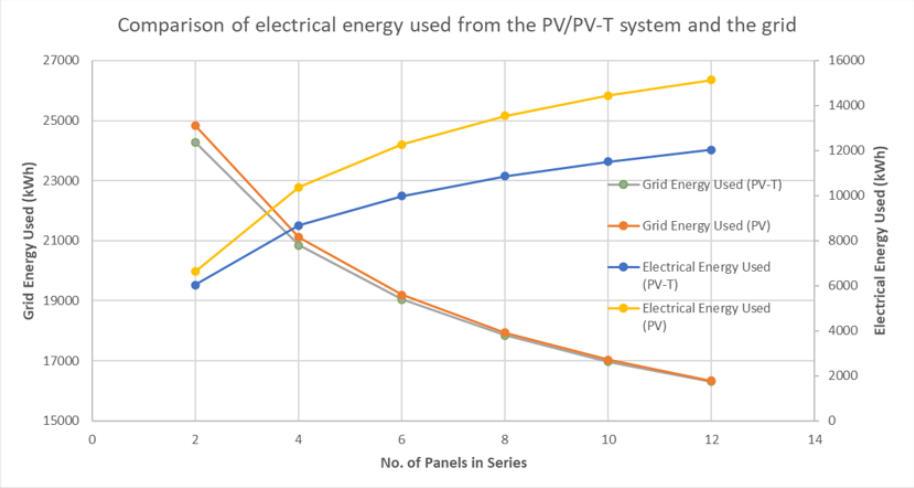

Figure 6: Comparison of the electrical energy used from the PV/PV-T field and the grid for different configurations of PV/PV-T field

Figure 6 shows the comparison of the self-consumption of electrical energy generated by the PV-T/PV field and the electrical energy from the grid, for all the configurations simulated. The self-consumption of electrical energy generated by the PV-T ASHP system is always lower than that of the PV ASHP system, due to the lower operation duration of the PV-T ASHP system as a result of the higher heating capacities of the heat pump at the higher source air temperatures. However, due to lower total electrical energy consumption by the PV-T ASHP system, the grid energy used is lower than that used by the PV ASHP system for all the configurations.

3.2 Advanced control strategy

The configuration of the PV-T collector with 4 panels in series, which has been identified as the most suitable one for the building thermal demands, has been simulated with the advanced control strategy which extends the operation of the system during the daytime by increasing the control set points for the hot water tank. This is reflected in the higher HWT mean temperature of 43.12°C as can be seen in table 6. The total electrical energy consumed by the system, and that consumed by the heat pump increase by 1.7% (500 kWh) and 2.1% respectively, with the COP of the heat pump decreasing by 1.9%. This happens due to the higher temperatures in the condenser of the heat pump, with the increase in the temperatures inside the hot water tank at higher control limits. At the same time, the self-consumption of the electrical energy generated by the PV-T system increases by 19% (1647 kWh), due to the synchronised operation of the heat pump and the PV-T system, resulting in a 5.5% (1100 kWh) reduction in the grid electrical energy used.

In order to study the effect of the advanced control strategy, the performance of the system is observed over a shorter time frame of a week in August with high irradiance, as shown in figure 7. The results from the case with the normal control strategy are shown on the left and the results from the case with the advanced control strategy are shown on the right. The temperature of the air at the inlet and the outlet of the PV-T system, labelled '*Air – PV-T inlet*' and '*Air - PV-T outlet*' respectively, the source air temperature for the heat pump, labelled '*Air – HP*

inlet', temperatures of the top and the bottom layers of the hot water tank, labelled '*HWT – Top layer*' and '*HWT – Bottom layer*' respectively, and the heat supplied by the heat pump during day time and night time, labelled '*HP Heat Supply – Day*' and '*HP Heat Supply – Night*' respectively, are shown.

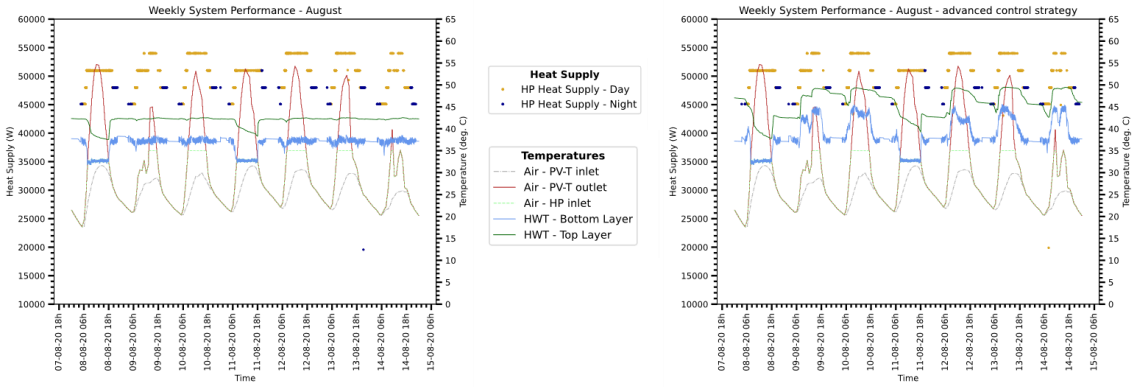

Figure 7: Weekly analysis of the PV-T ASHP system – normal vs advanced control strategy

In the plots on the right-hand side, the increase in the hot water tank temperatures, as compared to the corresponding plot on the left, can be seen during the day time operation of the heat pump. The temperatures for the '*HWT – Top layer*' reach around 50°C in the plot on the right, and is limited to less than 43°C in the plot on the left. It can be observed from both the plots that the '*Air – HP inlet*' is restricted to the heat pump operation limit of 35°C, despite the 'Air – PV-T outlet' temperature being reaching up to 50°C, as a result of the mixing strategy explained in the 'PV-T collector system model' part in section 2.2. This explains the reducing improvement in the system performance as the number of panels in series in the PV-T field increase beyond 4 panels in series. The PV-T outlet temperatures already breach the temperature limit of operation for the heat pump at time with high irradiance. Thus, with more panels in series, though the PV-T field achieves higher outlet temperatures for air, the heat pump cannot utilize it.

4. Conclusions

PV-T collectors are a suitable low temperature source to increase the performance of a decentralized HP when no other low temperature sources (like waste or geothermal heat) are available. Based on the energy performance analysis the PV-T collector field configuration with 4 panels in series is found to be the most suitable one for the building thermal demands in consideration. This configuration of the PV-T ASHP system has better electrical performance as compared to the PV ASHP system with the same configuration, with a 6.61% increase in COP. Consequently, the PV-T ASHP system has lower grid electrical energy consumption. Though the advanced control strategy resulted in a 1.9% decrease in the COP of the heat pump, an increase of 19% in the self-consumption of the electrical energy generated by the PV-T system resulted in a 5.5% decrease in the grid electrical energy used by the system. While these results show the potential improvement in the system performance that can be achieved by connecting an air PV-T collector system in an indirect expansion configuration with an ASHP system, the presented simulation methodology can be extended to research other types of PV-T collector systems, heat pumps and configurations for combined operation. Furthermore, including an analysis of the costs for investment and operation would shed additional light on the optimal design, sizing and control of such system configurations.

5. Acknowledgments

This research was funded by the Lower Saxony Ministry of Science and Culture under grant number 11-76251-13-3/19–ZN3488 (ZLE) within the Lower Saxony "SPRUNG" of the Volkswagen Foundation. It was supported by the Center for Digital Innovations (ZDIN).

6. References

Arias, D.A., McMahan, A.C., Klein, S.A., 2008. Sensitivity of long-term performance simulations of solar energy systems to the degree of stratification in the thermal storage unit. Int J Energy Res 32, 242–254. https://doi.org/10.1002/ER.1344

Barsanti, M., Schwarz, J.S., Gérard Constantin, L.G., Kasturi, P., Binder, C.R., Lehnhoff, S., 2021. Socio-technical modeling of smart energy systems: a co-simulation design for domestic energy demand. Energy Informatics 4, 1–13. https://doi.org/10.1186/S42162-021-00180-6/TABLES/2

Cozzi, L. (International E.A., Gould, T. (International E.A., 2021. World Energy Outlook 2021 1–386.

Gasser, L., Flück, S., Kleingries, M., Meier, C., Bätschmann, M., Wellig, B., 2017. O.1.4.5 High efficiency heat pumps for low temperature lift applications - HPT - Heat Pumping Technologies, in: 12th IEA Heat Pump Conference.

Gerster, J., Blank, M., Stern, K., Sonnenschein, M., 2016. Intelligentes Heimenergiemanagement – Nutzung der Synergiepotentiale bei der thermischen und elektrischen Objektversorgung durch modellbasierte und prädiktive Betriebsführungsstrategien - Tagungsbeiträge - VDE VERLAG, in: VDE-Kongress 2016 - Internet Der Dinge. VDE VERLAG GMBH, Berlin, Offenbach.

Heimrath, R., 2004. Simulation, Optimierung und Vergleich solarthermischer Anlagen zur Raumwärmeversorgung für Mehrfamilienhäuser. Institut für Wärmetechnik.

Kramer, K., 2020. Status Quo of PVT Characterization. https://doi.org/10.18777/ieashc-task60-2020-0004

Mota-Babiloni, A., Navarro-Esbrí, J., Peris, B., Molés, F., Verdú, G., 2015. Experimental evaluation of R448A as R404A lower-GWP alternative in refrigeration systems. Energy Convers Manag 105, 756–762. https://doi.org/10.1016/J.ENCONMAN.2015.08.034

Saloux, E., Candanedo, J.A., 2019. Modelling stratified thermal energy storage tanks using an advanced flowrate distribution of the received flow. Appl Energy 241, 34–45. https://doi.org/10.1016/J.APENERGY.2019.02.075

Steinbrink, C., Blank-Babazadeh, M., El-Ama, A., Holly, S., Lüers, B., Nebel-Wenner, M., Acosta, R.P.R., Raub, T., Schwarz, J.S., Stark, S., Nieße, A., Lehnhoff, S., 2019. CPES testing with MOSAIK: Co-Simulation planning, execution and analysis. Applied Sciences (Switzerland) 9. https://doi.org/10.3390/APP9050923

Tonui, J.K., Tripanagnostopoulos, Y., 2007. Air-cooled PV/T solar collectors with low cost performance improvements. Solar Energy 81, 498–511. https://doi.org/10.1016/J.SOLENER.2006.08.002

Witte, F., Tuschy, I., 2020. TESPy: Thermal Engineering Systems in Python. J Open Source Softw 5, 2178. https://doi.org/10.21105/JOSS.02178

Web references

WWW1- Projekt – ENaQ – Energetisches Nachbarschaftsquartier Fliegerhorst Oldenburg [WWW Document], n.d. URL https://www.enaq-fliegerhorst.de/teilprojekte/ (accessed 08.18.24).

WWW2- Home | Olegeno Oldenburger Energie-Genossenschaft eG [WWW Document], n.d. URL https://www.olegeno.de/ (accessed 08.18.24).

WWW3- JRC Photovoltaic Geographical Information System (PVGIS) - European Commission [WWW Document], n.d. URL https://re.jrc.ec.europa.eu/pvg_tools/en/tools.html#PVP (accessed 08.18.24).

WWW4- Kasturi, P., Schwarz, J.S., n.d. mosaik-heatpump [WWW Document]. URL https://gitlab.com/mosaik/components/energy/mosaik-heatpump (accessed 08.18.24).

WWW5- mosaik-heatpump — mosaik 3.3.0b1 documentation [WWW Document], n.d. URL https://mosaik.readthedocs.io/en/latest/ecosystem/components/mosaik-heatpump/overview.html (accessed 08.18.24).

WWW6- LW Serie | alpha innotec [WWW Document], n.d. URL https://www.alpha-innotec.com/de/warmepumpen/luft-wasser-warmepumpen/lw-serie (accessed 08.18.24).

WWW7- How HOMER Calculates the PV Cell Temperature [WWW Document], n.d. URL https://www.homerenergy.com/products/pro/docs/3.15/how_homer_calculates_the_pv_cell_temperature.html (accessed 08.18.24).

WWW8- Water - Thermal Conductivity vs. Temperature [WWW Document], n.d. URL https://www.engineeringtoolbox.com/water-liquid-gas-thermal-conductivity-temperature-pressure-d_2012.html (accessed 08.18.24).

WWW9- mosaik / components / data / mosaik-csv · GitLab [WWW Document], n.d. URL https://gitlab.com/mosaik/components/data/mosaik-csv (accessed 08.18.24).

Potential thermal energy storage technologies for radiative cooling implementation in buildings

Jesús Monterrubio[1], Boniface Mselle[1], Roger Vilà[1], Marc Medrano[1], Albert Castell[1], Jonathan Cofré-Toledo[1,2] and Cristian Solé[1]

[1] Sustainable Energy, Machinery and Buildings (SEMB) Research Group, INSPIRES Research Centre, Universitat de Lleida, Pere de Cabrera 3, 25001 Lleida (Spain)

[2] Departamento de Ingeniería Mecánica, Facultad de Ingeniería, Universidad de Santiago de Chile, Avenida Libertador Bernardo O'Higgins Nº 3363, Estación Central, Santiago (Chile)

*Corresponding author: marc.medrano@udl.cat

Abstract

Radiative cooling (RC), a passive cooling strategy of bodies to release heat to the sky, has shown promise in alleviating cooling energy demands. Since it does not use refrigerants, does not impose urban heating, and has low dependency on electricity, it catches an eye as a potential sustainable technology to slow down greenhouse gas emissions. Buildings' cooling energy profile demonstrates an intermittent nature leading to the core need of coupling with energy storage technologies. Therefore, this study evaluates prevalent thermal energy storage (TES) technologies, including sensible thermal energy storage and latent thermal energy storage using Phase Change Materials (PCM). It aims to provide valuable insights into selecting the most suitable TES solution for optimal integration with RC systems. Our results indicate that water tanks provide extended cooling demand coverage compared to PCM tanks. On average, they are also capable of storing more energy. Regarding thermal levels, the temperatures achieved by the end of the night are very similar in both types of tanks.

Keywords: Radiative cooling, Thermal energy storage, Phase Change Materials, Numerical simulation, TRNSYS

1. Introduction

Global energy consumption is rising as a result of the energy needs of modern society. It is acknowledged that the building industry has a significant impact on both the World's energy consumption and greenhouse gas emissions (Allouhi et al., 2015). Moreover, it is specified that approximately 40% of the World's energy is consumed by residential and commercial buildings, while 30% of greenhouse gas (GHG) emissions worldwide are attributable to the building sector (Atmaca and Atmaca, 2022).

To meet thermal energy demands, the utilization of green renewable energy aims to reduce GHG emissions. Solar collectors harness solar radiation to fulfil heating needs. In recent years, research for renewable cooling has been focusing on radiative cooling (RC). RC is the process by which a surface lowers its temperature by utilizing the transparency of the infrared atmospheric window at specific wavelengths, from 8 to 13 μm (Vall and Castell, 2017). Thus, using RC, it is feasible to cool down below the ambient temperature because of the low effective temperature of the space (Granqvist and Hjortsberg, 1981).

Heating and cooling can be achieved in a single device, known as Radiative Collector and Emitter (RCE). The RCE is capable of producing hot water during the day and cold water at night (Vall et al., 2020b). During the day, the water that flows through the equipment is heated, and at night, it is cooled. To operate, specific optical properties are required for each functionality. A blackbody absorber emitter can provide both functionalities, but differentiated covers are required (high transparency to solar radiation and low transparency in the atmospheric window for solar collection to provide greenhouse effect, and high transparency to the atmospheric window for radiative cooling to allow infrared radiation to pass through). For this reason, the RCE incorporates a movable cover for switching between solar collection and radiative cooling modes. The RCE cold power production per unit area, q_{net} ($\mathrm{W\,m^{-2}}$), can be determined with eq. 1.

© 2024. The Authors. Published by International Solar Energy Society
Selection and/or peer review under responsibility of Scientific Committee
10.18086/eurosun.2024.02.10 Available at http://proceedings.ises.org

$$q_{net} = \sigma\left(\varepsilon_s \cdot T_s^4 - \alpha_s \cdot \varepsilon_{sky} \cdot T_a^4\right) - q_{cond} - q_{conv} \qquad \text{(eq. 1)}$$

Where σ is the Stefan-Boltzmann constant (5.67·10-8 W m^{-2} K^{-4}), ε_s is the average emissivity of the RCE surface in the infrared (IR) range (-), T_s is the surface temperature of the RCE (K), α_s is the average absorptivity of the RCE surface in the IR (-), ε_{sky} is the average emissivity of the sky in the IR (-), T_a is the ambient temperature (K), and q_{cond} and q_{conv} are the conduction and convection heat fluxes of the RCE (W m^{-2}), respectively.

The RCE produces heat and cold, but they are not coincident in time with the demand. Thus, thermal energy storage (TES) is required to compensate for the mismatch between demand and production times. The temperature of the fluid flowing through the RCE directly affects the cooling potential of RC. As this fluid cools down, the cooling power decreases (as it depends on the fourth power of the surface temperature, which in turn decreases with decreasing fluid temperature). Therefore, latent heat energy storage using Phase Change Materials (PCM) could maintain RC power higher by keeping the temperature more constant while storing the same amount of cold. However, a balance between power increase and temperature usefulness must be kept, as higher temperatures may be less useful for cooling purposes. Several investigations have been conducting research on the use of PCM in solar thermal collection applications (Abuşka et al., 2019; Ma et al., 2021; Solé et al., 2008). However, there has not been much research done on the pairing of RC and PCM.

PCM can be used as a storage medium to increase the amount of energy stored and maintain a more constant temperature (Zalba et al., 2003). These materials utilize latent heat to store energy at nearly constant temperatures with small storage volumes by experiencing a phase change (often solid-liquid) at a chosen temperature.

Therefore, in this study we explore the integration of TES systems with RC systems to address the intermittent nature of building cooling demands through a numerical simulation, using TRNSYS software. We compare the traditional sensible energy storage, using water, with latent energy storage, using PCM systems. The study aims to identify the most suitable solution for optimal RC integration.

2. Data acquisition and methodology

We used Meteonorm v7.2 (Remund et al., 2019), a database with more than 8000 weather stations, to download weather information, hereby selecting Lleida city in Spain. This city is characterized by high heating and cooling demands. Situated in southern Europe, Lleida exhibits high RC power potential, as indicated in the maps developed by Vilà et al. (2023), making it an ideal location for our study.

To delve into the coupling of radiative cooling technology and thermal energy storage (TES) technologies in buildings, we used TRNSYS simulation studio v18. The evaluation included sensible thermal energy storage (water), and latent thermal energy storage (PCM systems). The modelling was carried out as in Fig. 1 to offer valuable insights for the optimal integration in energy-efficient buildings of TES with RC systems.

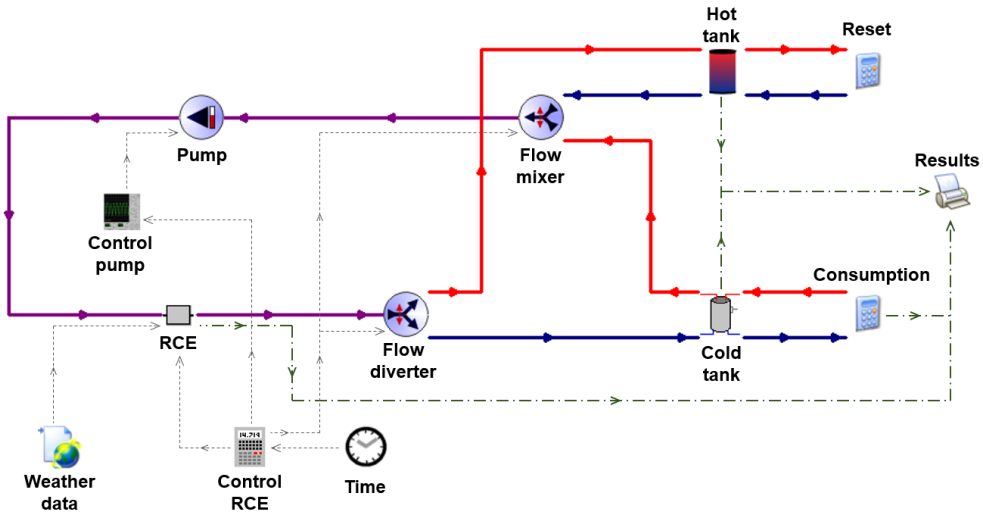

Fig. 1: Schematic diagram to assess thermal energy storage technologies for radiative cooling in buildings

Usually, tanks with heat exchangers are used to store hot water to separate the production from the demand. In this case, instead, a tank without heat exchanger has been used because the solar collection mode is not the focus of this

study, and we aimed to prevent heat production from impacting the cooling production. In fact, for these simulations we used a tank with a very large volume and a high flow rate in the solar collection mode. Thus, the temperature at the inlet of the RCE remains nearly stable along the time.

TRNSYS works with Types which represent different components of the system modelled. These Types may include control algorithms, calculations, performance metrics, post-processing, sensitivity analysis, etc.

Different components were used to fulfil the planned objectives, as shown in Fig. 1. For climate data input, TRNSYS Type 15 was employed to integrate the weather data downloaded from Meteonorm, encompassing solar radiation, atmosphere infrared radiation, ambient temperature, dew point temperature, wind velocity, and opaque sky cover specifics for the location under scrutiny. The Type that simulates the RCE was also incorporated. This component was previously developed and validated by Vall et al. (2020a). In this analysis, a single RCE device of 2 m^2 was implemented. For the cooling energy storage, a vertical tank model developed by Moser et al. (2022) was integrated. This model was used to simulate both a sensible and latent energy storage tank (water and PCM). For the heating energy storage, a vertical tank without heat exchanger was included (Type 158). Additional models were needed to consider both configuration modes of the RCE: the flow diverter and mixer valves (Type 11) to change from one storage tank to another and a variable speed pump model (Type 110) to adapt the water flow rate for each configuration mode. The component “Control RCE” enabled to change the cover material between modes (solar collection mode and radiative cooling mode) as a function of the hour of the day, while the component “Control pump” allowed to switch the water flow rate from one working mode to the other (solar collection or radiative cooling). TRNSYS Type 25 facilitated the acquisition of the desired outputs for further analysis.

2.1. PCM properties

For the study of latent thermal energy storage, we used two ideal PCMs. Their phase changes occur from 16.0ºC to 17.0ºC and from 16.5ºC to 17.5ºC, temperatures achievable by the RCE for summer nights in Lleida. This temperature range allows for the cooling of spaces via chilled ceilings, systems which can operate with low temperature differences. Both PCMs follow the same trend, so here we present the enthalpy curve for the material with a phase change between 16.0ºC and 17.0ºC (Fig. 2). The curves for the PCM with a phase change between 16.5ºC and 17.5ºC are identical to those in Fig. 2 but shifted 0.5ºC to the right.

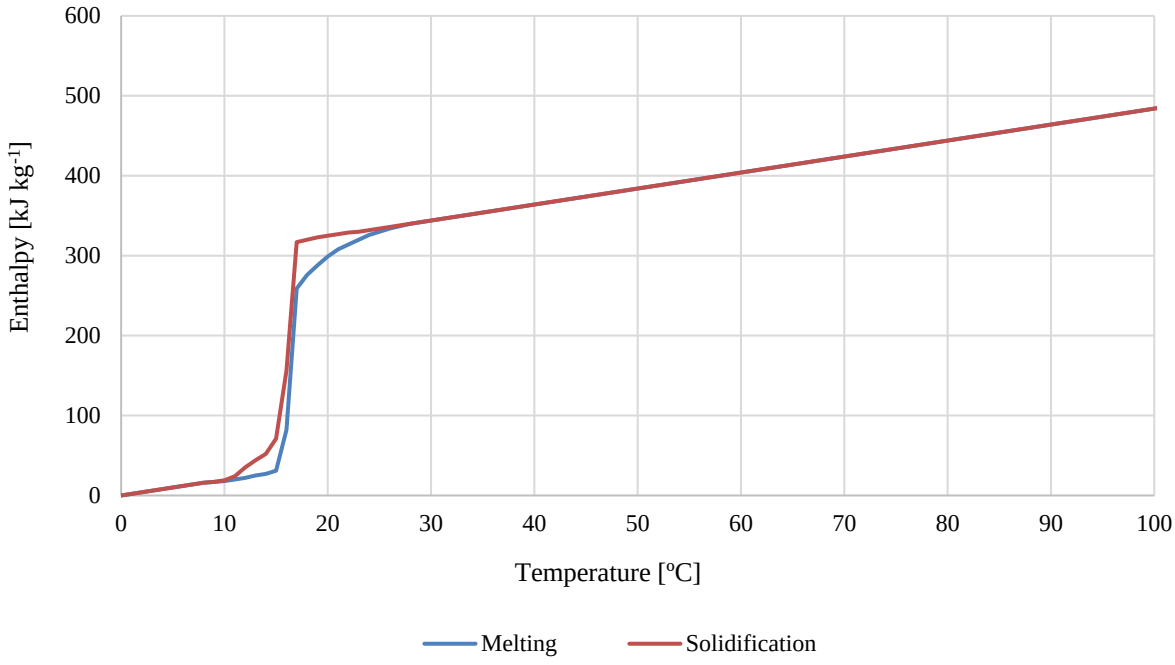

Fig. 2: Enthalpy curves for melting and solidification of the PCM. Phase change occurs between 16.0ºC and 17.0ºC. The reference temperature is 0ºC

As it can be seen, no subcooling was considered. The most important data related to the designed Phase Change Materials are presented in Table 1. These PCMs, with a conductivity similar to water, outstand by their high phase change enthalpy in a little range of temperatures. Considering that the density is not much higher than that of water, this high storage capacity allows for the use of smaller tanks, capable of accumulating the same amount of energy.

Tab. 1: Properties of the PCM designed for this study

Property	Value
Phase change enthalpy	237 kJ kg^{-1}
Solid density	1100 kg m^{-3}
Liquid density	1200 kg m^{-3}
Heat conductivity	0.6 W m^{-1} K^{-1}
Specific heat capacity	2000 J kg^{-1} K^{-1}

2.2. Sizing of tanks

The hot tank of the simulated facility was used as a heat sink capable to absorb the energy produced in the RCE during the solar collection mode. The flow rate and volume were sufficiently high to ensure that the solar heating mode had no effect on the results of the cooling mode. All the tanks started at a temperature of 20ºC. The cold tank decreased its temperature, while the hot tank's temperature remained nearly stable over time, thanks to its high volume and high flow rate in the solar heating mode.

On the other hand, the water flow rate pumped during the cooling mode was 665 kg h^{-1}. This flow rate was used for both the water tank and the PCM tank. However, the volumes of the analyzed tanks were different. For the base case, the volume of the water tank was 70 L, while for latent storage we used a tank with 5.78 L of PCM and 9.18 L of water. The cylindrical water tank had a height of 0.63 m, while the dimensions of the PCM tank were modified to include 7 modules of PCM along with water, while maintaining the same height-to-diameter ratio (Fig. 3). Detailed dimensions of each tank are provided in Table 2 and Table 3.

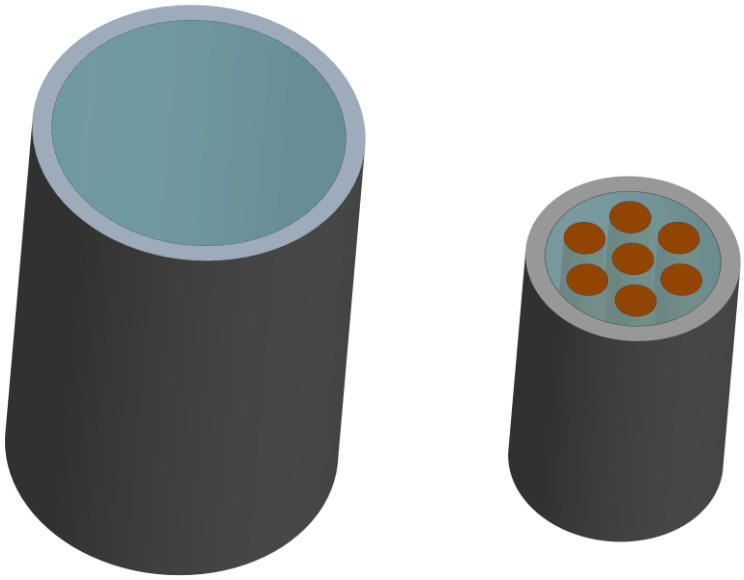

Fig. 3: 3D visualization of the interior of the water tank (left) and the PCM tank (right)

Tab. 2: Dimensions of the water tank

Characteristic	Value
Volume of the tank	0.070 m^3
Height of the tank	0.625 m
Interior diameter of the tank	0.377 m
Total volume of water	0.070 m^3

Tab. 3: Dimensions of the tank with PCM

Characteristic	Value
Volume of the tank	0.015 m^3
Height of the tank	0.374 m
Interior diameter of the tank	0.226 m
Interior diameter of a PCM module	0.053 m
Thickness of a PCM module	0.0015 m
Height of a PCM module	0.335 m
Total volume of PCM	0.0058 m^3
Total volume of water	0.0092 m^3

To determine the volume of PCM (V_{PCM} $[m^3]$), we first calculated with Eq. 2 the mass of Phase Change Material (m_{PCM} $[kg]$) capable of storing the same amount of energy as the average energy accumulated each night with the cold tank of water (E_w $[J]$), by considering only the phase change enthalpy (Δh_{PCM}). Then, we used the density of the PCM in solid state to obtain the required volume (higher result than if we considered the liquid density). E_w was determined with Eq. 3. As shown in the results section, the mean temperature difference of the water tank due to radiative cooling along the studied period (ΔT_w) was 5.2ºC, the mass of water (m_w) was 70 kg (assuming an average density of 1000 kg m^{-3}) and the specific heat of water (c_w) was 4180 J kg^{-1} K^{-1}.

$$m_{PCM} = \frac{E_w}{\Delta h_{PCM}} \quad \text{(eq. 2)}$$

$$E_w = m_w \cdot c_w \cdot \Delta T_w \quad \text{(eq. 3)}$$

2.3. Energy consumption

One of the parameters analyzed in this study is the operational time of the chilled ceiling. That is to say, the number of hours during which the chilled ceiling could operate with the energy stored during the previous night. Fig. 4 shows an example of the facility which could be coupled to the cold tank to take profit of the cold stored in it. To simulate this cooling consumption, we assumed a temperature difference of 1.5ºC between the supply (outlet temperature of the storage unit) and the return of the chilled ceiling. The pumped flow rate was 54 kg/h, resulting in a cooling power of 94 W. This power is achievable by an RCE of 2 m^2 considering the potential maps of nocturnal radiative cooling in Spain (Vilà et al., 2020).

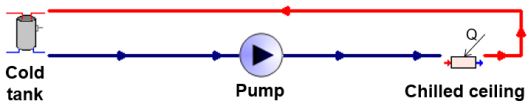

Fig. 4: Scheme of the energy consumption of the cold tank

There must be a temperature difference between the setpoint temperature of the refrigerated volume and the water used for cooling. Thus, the pump stopped when the outlet temperature of the refrigerated volume reached 20ºC or higher. We measured each day the number of operating hours of the pump supplying cold water to the chilled ceiling.

2.4. Storage Coefficient of Performance

The Storage Coefficient of Performance (SCP [%]) indicates the amount of energy the tank has stored at the end of the cooling mode (E_{tank} $[J]$) relative to the total energy produced with the RCE (E_{RCE} $[J]$), as presented in Eq. 4. This parameter was calculated for each day and helped analyze the unused energy in both storage types. Higher storage temperatures are expected to increase the cooling production with the RCE while also increasing the heat losses.

$$SCP = \frac{E_{tank}}{E_{RCE}} \cdot 100 \quad \text{(eq. 4)}$$

The cooling energy stored in the tank (E_{tank}) is obtained daily as the difference between the energy at the beginning and the end of the RC mode. This energy accounts for both the water and the PCM in the case of the latent storage tank. On the other hand, the energy produced with the RCE (E_{RCE}) is calculated with Eq. 5.

$$E_{RCE} = \sum_{i=1}^{n} \dot{m}_{RCE} \cdot c_w \cdot \Delta T_{RCE_i} \quad \text{(eq. 5)}$$

Where $\dot{m}_{RCE}$ is the water flow rate of the RCE, ΔT_{RCE_i} is the temperature difference between the inlet and outlet of the RCE each timestep and n is the number of timesteps of 5 minutes during which we produce cooling each night.

3. Results

Table 4 summarizes the analyzed parameters of the energy simulations. In all the cases, the reduction in the average tank temperature is almost the same, exceeding a decrease of 5ºC. The sensible storage contains more water but maintains it at a higher temperature. Regarding the operational time of the chilled ceiling, the same flow rate can circulate longer in the case of sensible storage. Although the PCM units were designed to have the same energy storage capacity as the water tank, water can store more cooling energy thanks to its direct use.

Tab. 4: Average daily results observed in the cold tanks over the period studied

Type of storage	Phase change temp. [ºC]	Temp. reduction of the water [ºC]	Temp. reduction of the PCM [ºC]	Temp. reduction of the tank [ºC]	Chilled ceiling operational time [h]	Energy produced [Wh]	Energy stored [Wh]
Sensible storage (water)	-	5.1	-	5.1	4.33	448.6	418.3
Latent storage (PCM)	16.0-17.0	5.4	4.6	5.2	2.73	305.0	267.4
	16.5-17.5	5.3	4.5	5.1	2.95	322.0	285.2

Comparing the two storages with PCM, although the temperature change is slightly lower in the case with phase change between 16.5ºC and 17.5ºC, both the replacement time and the stored energy are significantly better. Therefore, from now on, we will compare the storage using this PCM with that of water.

An SCP of 92.8% is observed in sensible storage, whereas in PCM storage, this value decreases to 88.6%, indicating that less energy produced by the RCE is stored.

Annually, the RCE produces 40.4 kWh of useful cooling when it is used in combination with the tank of water. Its production decreases to 29.0 kWh when it is combined with the tank of PCM. Despite one of the PCM's objectives was to maintain the inlet temperature of the RCE as high as possible to maximize the cooling power, it has been demonstrated that cooling production decreases when PCM modules are implemented. This is primarily because the latent storage tank contains less water, having a lower height and including cylindrical modules as indicated in Fig. 3. This results in a fast temperature reduction of the water, thereby reducing the energy dissipated by the radiative collector and emitter.

The PCM does not solidify every day. In fact, solidification is only achieved on 19.6% of the analyzed days. Therefore, its full storage capacity is not utilized. This value shows an increase of 3.3% when compared to the PCM with a phase change interval of 16.0-17.0ºC. Increasing the days of PCM solidification could be achieved by raising the phase change temperatures. However, this approach would lead to an increase of the final tank temperature after the cooling process, thereby reducing the temperature difference with the setpoint temperature and limiting the usefulness of the water tank for cooling purposes.

Fig. 5 depicts the levels of temperatures and the cooling consumption on the day with the highest temperature reduction (June 8th). The replacement flow rate refers to the water flowing through the chilled ceiling for cooling purposes.

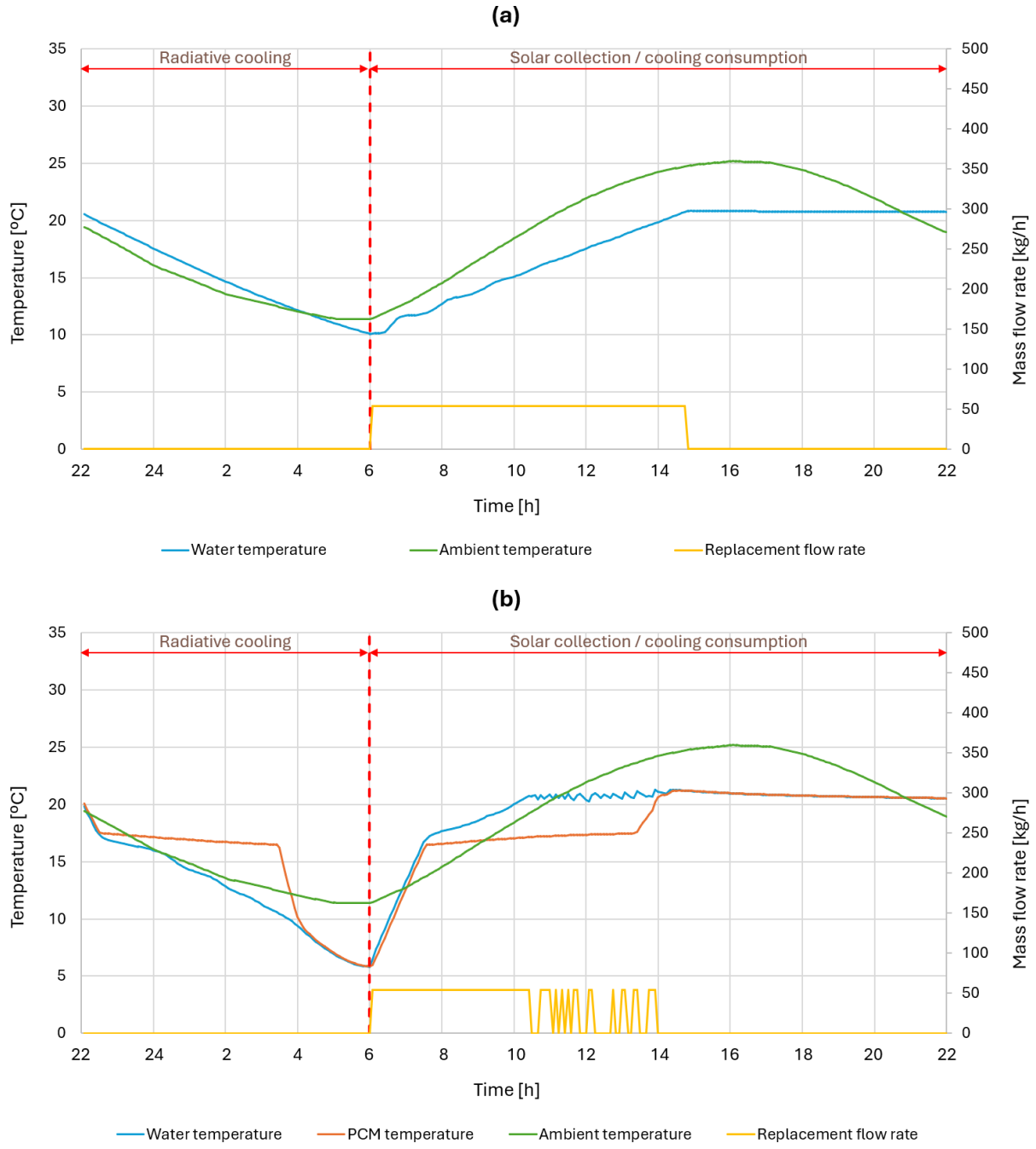

Fig. 5: Evolution of the temperatures and cooling consumption by the chilled ceiling on June 8th. (a) sensible storage, (b) latent storage

The water temperature decrease due to radiative cooling is greater with the PCM tank, reaching nearly 5ºC. The PCM solidifies after 4 hours, and during the day it melts while capturing energy released by the water. Subambient temperatures are achieved faster in the PCM tank. There is an extended operating time for the chilled ceiling when using sensible energy storage. It is also noteworthy that the PCM tank exhibits intermittent flow. This occurs because when the outlet water from the cold tank reaches 20ºC, the chilled ceiling ceases its operation. If the PCM is at a lower temperature, it absorbs the heat released by the water, reducing its temperature and allowing the chilled ceiling to resume its operation.

We present additional graphs (Fig. 6) to illustrate the behavior of both tanks the day with the lowest reduction of the tank temperature (August 25th).

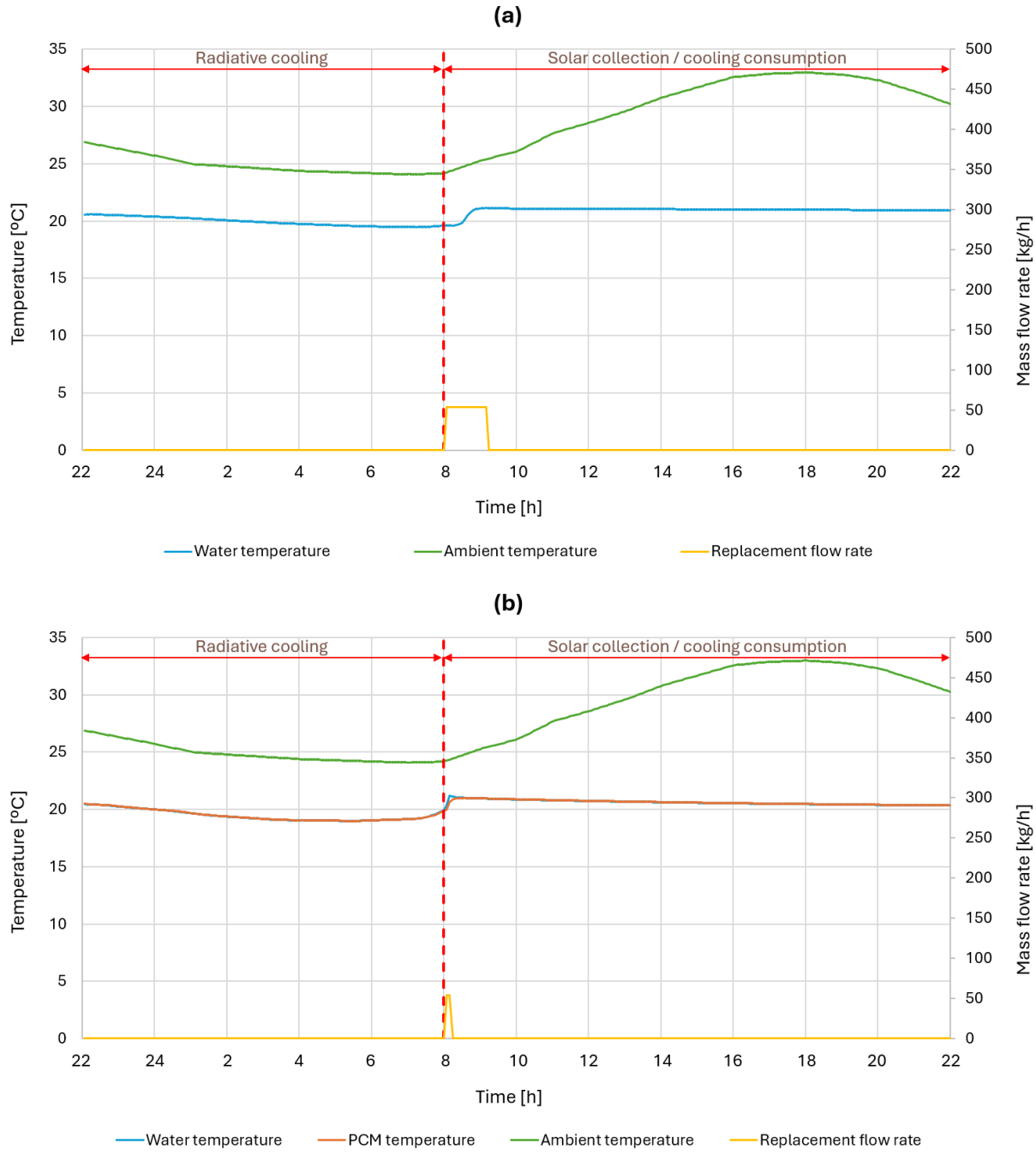

Fig. 6: Evolution of the temperatures and water consumption by the chilled ceiling on August 25th. (a) sensible storage, (b) latent storage

In this case, the PCM does not solidifies, as ambient conditions result in a minor reduction in the temperature. Since there is no phase change, the PCM temperature remains nearly the same as the water temperature. The PCM tank reaches its maximum temperature faster due to its lower mass. The flow rate through the chilled ceiling can last longer with the water tank, although it lasts significantly less than on June 8th.

Table 5 summarizes the main results obtained for both tanks on June 8th and August 25th. Although the use of the tank with PCM was intended to improve cooling production with the RCE, the opposite is observed. On both days, the energy produced by the RCE and the energy stored in the tank are higher when using sensible storage. Focusing on June 8th, in radiative cooling mode, the water temperature is lower in the PCM tank due to its smaller water volume, which results in a lower cooling power of the RCE.

Tab. 5: Main results of the simulations performed on June 8th and August 25th

Day	Type of storage	Minimum water temp. [ºC]	Minimum PCM temp. [ºC]	Chilled ceiling operational time [h]	Energy produced [Wh]	Energy stored [Wh]
June 8th	Sensible (water)	10.1	-	8.75	895.9	846.4
	Latent (PCM)	5.8	5.8	6.00	626.8	583.2
August 25th	Sensible (water)	19.6	-	1.17	91.0	78.0
	Latent (PCM)	19.8	19.7	0.17	36.8	10.6

4. Conclusions

In this study, we have conducted a comparison between two thermal energy storage systems to determine the preferred solution when used with radiative cooling systems. While the PCM tank can reach lower temperatures because of its lower volume, this type of tank performs worse in the other aspects studied. On average, the water tank can store over 500 kJ/day more, and the chilled ceiling can operate 1.38 hours longer. It is interesting to note that the PCM does not solidify every day, so increasing the phase change temperature of the PCM improves both the stored energy and the duration of the chilled ceiling operation. If the temperature of the PCM is lower than that of the water, when the outlet temperature reaches 20ºC, the replacement flow rate becomes intermittent because the PCM absorbs the heat dissipated by the water.

Future work will involve performing simulations with Phase Change Slurry (PCS) tanks to include them in the comparison presented in this study. Additionally, we will also modify the PCM modules (shape, dimensions and conductivity) to improve heat transfer. Changes in the amount of water in the PCM tank will also be done to increase the operational time of the chilled ceiling.

5. Acknowledgments

This publication is part of the grant PDC2022-133215-I00, funded by CIN/AEI/10.13039/501100011033/ and by the "European Union NextGenerationEU/PRTR". This publication is also part of the grant TED2021-131446B-I00, funded by MCIN/ AEI/10.13039/501100011033/ and by the "European Union NextGenerationEU/PRTR" The authors would like to thank Generalitat de Catalunya for the project awarded to their research group (2021SGR 01370). Jesús Monterrubio would like to thank the grant FPU22/01304 funded by MICIU/AEI/10.13039/501100011033 and by "ESF+".

6. References

Abuşka, M., Şevik, S., Kayapunar, A., 2019. Experimental analysis of solar air collector with PCM-honeycomb combination under the natural convection. Sol. Energy Mater. Sol. Cells 195, 299–308. https://doi.org/10.1016/j.solmat.2019.02.040

Allouhi, A., El Fouih, Y., Kousksou, T., Jamil, A., Zeraouli, Y., Mourad, Y., 2015. Energy consumption and efficiency in buildings: current status and future trends. J. Clean. Prod., Special Issue: Toward a Regenerative Sustainability Paradigm for the Built Environment: from vision to reality 109, 118–130. https://doi.org/10.1016/j.jclepro.2015.05.139

Atmaca, A., Atmaca, N., 2022. Carbon footprint assessment of residential buildings, a review and a case study in Turkey. J. Clean. Prod. 340, 130691. https://doi.org/10.1016/j.jclepro.2022.130691

Granqvist, C.G., Hjortsberg, A., 1981. Radiative cooling to low temperatures: General considerations and application to selectively emitting SiO films. J. Appl. Phys. 52, 4205–4220. https://doi.org/10.1063/1.329270

Ma, Y., Tao, Y., Wu, W.L., Shi, L., Zhou, Z., Wang, Y., Tu, J.Y., Li, H.R., 2021. Experimental investigations on the performance of a rectangular thermal energy storage unit for poor solar thermal heating. Energy Build. 111780. https://doi.org/10.1016/j.enbuild.2021.111780

Moser, C., Heinz, A., Schranzhofer, H., 2022. TRNSYS Type 840: Simulation model for PCM/water storage tanks (Version 3.0). https://doi.org/10.3217/F1K4A-GG440

Remund, J., Müller, S., Kunz, S., Huguenin-Landl, B., Studer, C., Cattin, R., 2019. Meteonorm. Meteotest, Switzerland.

Solé, C., Medrano, M., Castell, A., Nogués, M., Mehling, H., Cabeza, L.F., 2008. Energetic and exergetic analysis of a domestic water tank with phase change material. Int. J. Energy Res. 32, 204–214. https://doi.org/10.1002/er.1341

Vall, S., Castell, A., 2017. Radiative cooling as low-grade energy source: A literature review. Renew. Sustain. Energy Rev. 77, 803–820. https://doi.org/10.1016/j.rser.2017.04.010

Vall, S., Johannes, K., David, D., Castell, A., 2020a. A new flat-plate radiative cooling and solar collector numerical model: Evaluation and metamodeling. Energy 202, 117750. https://doi.org/10.1016/j.energy.2020.117750

Vall, S., Medrano, M., Solé, C., Castell, A., 2020b. Combined Radiative Cooling and Solar Thermal Collection: Experimental Proof of Concept. Energies 13, 893. https://doi.org/10.3390/en13040893

Vilà, R., Rincón, L., Medrano, M., Castell, A., 2023. Potential maps for combined nocturnal radiative cooling and diurnal solar heating applications in Europe. Sustain. Energy Technol. Assess. 59, 103381. https://doi.org/10.1016/j.seta.2023.103381

Vilà, R., Rincón, L., Medrano, M., Castell, A., 2020. Radiative Cooling Potential Maps for Spain, in: Radiative Cooling Potential Maps for Spain. Presented at the Eurosun 2020 Conference, Eurosun 2020 Conference.

Zalba, B., Marín, J.M., Cabeza, L.F., Mehling, H., 2003. Review on thermal energy storage with phase change: materials, heat transfer analysis and applications. Appl. Therm. Eng. 23, 251–283. https://doi.org/10.1016/S1359-4311(02)00192-8

Solar Radiant Floor and Sub-Surface Ground Heat Exchanger Thermal Storage System: Feasibility and Performance Assessment

Angela Weiss[1], Jeff Thornton[1], Lucio Mesquita[2] and Reda Djebbar[2]
[1]Thermal Energy System Specialists, LLC, Madison (USA)
[2] Natural Resources Canada, CanmetENERGY-Ottawa, Ottawa (Canada)

Abstract

Solar seasonal thermal energy storage (SSTES) has long been studied and implemented as a viable means of satisfying the thermal demands of both commercial and residential buildings. This paper introduces an SSTES system with the flexibility to direct thermal energy between a solar collector array, a hydronic radiant floor space heater, and/or a sub-surface ground heat exchanger storage medium, depending on the demands on and resources within the system. This SSTES system was modeled in TRNSYS, and the results demonstrated that the system balanced thermal storage charging and discharging over the year quite well, achieving a very high solar fraction (0.96). The SSTES system was then compared to five alternate space heating systems using conventional technologies such as boilers, air source heat pumps, and ground source heat pumps; while the COP of the SSTES system far exceeded the COP of any of the alternate conventional systems, the temperature control of the space was overall tighter for the conventional systems. Parametric studies of insulation thickness over the storage volume and solar collector array type were performed to assess the impact of these variables on system performance. Results demonstrated that both adequate insulation and quality solar collectors with some thermal loss protection (either via glazing or evacuated tubes) are necessary components of a high performance SSTES system.

Keywords: thermal storage, seasonal storage, space heating, solar heating

1. Introduction

A solar seasonal thermal energy storage (SSTES) system utilizes solar collectors to heat a fluid, phase-change material, or other thermal storage medium whenever sufficient solar radiation is available. With adequate production and storage capacity, the system can store enough solar energy in the peak solar summer months to offset or eliminate auxiliary thermal demands over the winter months. In recent years, research has focused transitioning the technology from large-scale (primarily commercial) to smaller-scale (primarily residential) applications, as well as on improving numerical modeling techniques for these systems.

Several studies in recent years have investigated proposed implementations of SSTES in smaller-scale applications, such as for single-family residences and smaller commercial buildings. Studies investigating using water as the thermal storage medium include Villasmil et al (2021), who compared alternative insulation materials and using building-integrated versus buried underground storage to cost-optimize installation of a hot-water tank and solar collector array system in a retrofit multifamily building. Their study ultimately concluded that external buried underground storage was more cost-effective for existing buildings than building-integrated storage, even after accounting for excavation costs and increased thermal losses. Pinamonti et al (2021) also studied using water tanks for seasonal thermal storage; their study integrating modulating water-water heat pumps into a solar system with a water tank for seasonal storage found that solar fraction was improved by approximately five percentage points by including the heat pumps, as compared to a reference system without the heat pumps.

While water is a viable thermal storage medium, most studies (including the current investigation) focus on sand, soil, and other common foundation and ground solids as the storage medium. Alkhalidi et al (2021) modeled a variation on solar thermal seasonal storage in which a composite thermal storage medium of sand, stone, and copper mesh was installed between the underground foundation pillars of a hypothetical four-story hotel. The system was modeled in three different climates, and the findings showed the systems' coverage of annual heat demand varied from 56% in a moderate climate (Potsdam, Germany) to 84% in a warm climate (Doha, Qatar). Using a fluidized rock bed as the storage medium, Sweet (2010) modeled SSTES radiant floor systems in six conceptual single-story houses in Richmond, VA, USA, ranging in size from 800 ft^2 (74.3 m^2) to 2400 ft^2 (223 m^2) to assess performance

© 2024. The Authors. Published by International Solar Energy Society
Selection and/or peer review under responsibility of Scientific Committee
10.18086/eurosun.2024.02.11 Available at http://proceedings.ises.org

and optimal design parameters for a typical residence, such as storage bed size and solar collector area. The research found that, with 80% of the south-facing roof covered in solar collectors and an optimal storage bed size of 15 m3, the systems achieved comparable temperature profiles to homes without SSTES and satisfied 64%-77% of the annual heating demand.

Studies incorporating data gathered from implemented SSTES systems have also confirmed promising results. In the realm of water thermal storage systems, Meister and Beausoleil-Morrison (2021) reviewed long-term experimental results on a two-story research house in Ottawa, Canada that has long utilized a 36 m3 buried water tank for solar seasonal thermal storage and built a model simulation validated with the site data. By modeling simple improvements on the existing system, such as increased insulation and higher-performance solar collectors, their research demonstrated that solar fractions of 86%-100% were feasible. With regard to foundation and ground solids storage systems, Naranjo-Mendoza et al (2018a) and Naranjo-Mendoza et al (2019) ran several analyses of an installed system at a two-story, 70 m^2 floor area house in Leicester, UK, consisting of seven photovoltaic-thermal (PVT) collectors connected in series with an array of sixteen shallow (1.5-m deep) vertical boreholes. Using the vertical borehole array as an 'earth energy bank' for solar thermal storage for domestic heating, the experimental system performed well in offsetting the building's winter space heating needs after over one and a half years, resulting in a near net-zero building, though analysis did show that in addition to utilizing the energy stored from solar, heat extraction from the ground surrounding the storage contributed in part in meeting the building's energy demands. Hailu et al (2017) conducted a 14-week experimental study of an evacuated tube solar array and sand-bed thermal energy storage system at a home in Palmer, Alaska. The proof-of-concept study demonstrated excellent results, with sand-bed storage temperatures steadily increasing over the 14-week period in close agreement with system models, and it established sand-bed thermal storage as a viable option for regions with long periods of freezing temperatures. Following the initial study, Hailu et al (2019) revisited the system to conduct longer-term experiments and observations, presenting over a year of monitored data from the site. Comparison of site data to the authors' simulation models showed comparable to conservative performance estimates from the simulation model as compared to the site data, again asserting the viability of SSTES in cold climates.

With respect to modeling techniques, Naranjo-Mendoza et al (2018b) ran studies of sinusoidal, semi-infinite, and finite-difference method (FDM) models of soil temperatures at shallow depths (0.75-m to 2.75-m) compared to hourly measured data at a site in Leicester, UK. The results favored FDM with air temperature as a boundary condition as the most accurate modeling approach for both short- and long-term applications. Naranjo-Mendoza (2020) also showed preference for FDM as a faster and more accurate model than conventional infinite-line source and infinite cylindrical source analytical models for studying the thermal response of very shallow boreholes. Loveridge et al (2020) studied numerical modeling and field testing of a variety of geostructures for thermal storage. Sweet (2010) also studied models of an SSTES system in the ground with no load attached and found that the models reached steady state after 1.5 years to 5 years of simulation, with systems with high loss coefficients requiring longer to reach steady state operation than systems with lower loss coefficients.

Informed by this research and by prior modeling experience, this paper investigates a solar seasonal thermal storage system for a cold-climate warehouse. The heating system's components include an array of evacuated tube solar thermal collectors (the source), radiant floor heating in the warehouse (the load), and a modified horizontal ground heat exchanger in the building sub-surface (the thermal storage). An auxiliary boiler is integrated prior to the radiant floor supply to boost the supply temperature as needed. An innovative control algorithm balances the competing loads of the radiant floor and the underground storage, directing any solar resource available to its most effective load while also prioritizing discharging from underground storage over running the auxiliary boiler.

The current investigation models the ground using three-dimensional FDM models with building heat flux as the boundary condition between the soil and the building and a sinusoidal ambient air temperature as the soil boundary condition between the soil and the air. The coupling between the sub-surface soil model and the building model solves simultaneously for both boundary temperatures and heat flux between building and soil, meaning the integrated system is a function of the boundary temperature as well as the heat flux. The system is modeled for a three-year period, with steady-state behavior in the second and third year visually confirmed by temperature plots. All results are reported from the final twelve months of simulation.

2. Configuration of Radiant Floor and Sub-Surface SSTES System

The target building in the current investigation is a single-story, single-zone warehouse located in Calgary, Alberta, Canada. The warehouse has a footprint of about 464 m^2 and an overall air volume of just over 2,500 m^3. The building

has no active cooling and is heated solely by a hydronic radiant floor heating system, which is comprised of a network of 28 parallel serpentine pipes evenly distributed within the warehouse floor. The warehouse thermostat maintains the space at 21 °C (± 0.55 °C) and calls for auxiliary if the space temperature drops below 19.5 °C. The minimum supply temperature set-point for the radiant floor system is 30 °C, or 33 °C if the thermostat calls for auxiliary heating. If the solar array and/or the ground thermal storage are insufficient to meet the heating demand, the system is modeled with an auxiliary boiler of infinite capacity and perfect thermal efficiency to maintain the minimum supply temperature set-points as specified. The circulation pump for the radiant floor only runs when the warehouse thermostat calls for heating.

The primary heat source of the system is an array of 60 fixed-position, evacuated tube solar thermal collectors in parallel, with a total collector surface area of 240 m^2. A variable-speed circulation pump for the solar array modulates speed as needed to maintain a desired set-point of 35 °C when the floor heating is active, or to maintain a temperature difference of 10 °C above the return temperature from the ground heat exchanger when the floor heating is inactive and the ground storage system is charging. The solar array pump will turn off if the collector array outlet temperature falls below the array inlet temperature.

The sub-surface ground directly beneath the warehouse provides thermal storage for the system. The storage volume's footprint matches that of the warehouse (464 m^2) and extends 2.25-m below the ground surface, for a total storage volume of 1,037 m^3. Within the storage volume, a system of 26 parallel serpentine pipes is buried in two layers about 0.8-m and 1.7-m, respectively, below the ground surface. The storage volume is insulated with 7.6-cm (3 inches) of insulation on the top surface and 31-cm (12 inches) of insulation on the bottom surface and its four vertical side surfaces. The system may charge the ground heat exchanger when the solar array outlet temperature exceeds the return temperature from the ground heat exchanger by 5 °C or more. Once the system is in charge mode, it remains in charge mode until the difference between the solar collector outlet temperature and the return temperature from the ground heat exchanger reduces to 2 °C or less. The system discharges to the radiant floor when the return temperature from the ground heat exchanger exceeds the return temperature from the building radiant floor by 1.66 °C. Once the system is in discharge mode, it remains in discharge mode until the difference between the ground heat exchanger temperature and the radiant floor return temperature reduces to 0.55 °C or less. A minimum run-time and minimum reset time of 15 minutes each are enforced by the model to prevent short cycling of the pumps. Table 1 below summarizes the equipment sizing of the investigated system.

Table 1. Equipment Specifications, Radiant Floor and Sub-Surface SSTES System

System Specifications		
Solar Collector System	**Value**	**Units**
Evacuated tube solar collection area	240	m^2
Solar array pump rated power	900	W
Solar array pump rated flow rate	3.78	$l.s^{-1}$
Warehouse and Radiant Floor System	**Value**	**Units**
Building footprint	464	m^2
Building volume	2.548	m^3
Building capacitance	30.582	kJ/K
Floor heating pump rated power	900	W
Floor heating pump rated flow rate	3.78	$l.s^{-1}$
Auxiliary heater capacity	Infinite	W
Auxiliary heater efficiency	100	%
Sub-Storage Ground HX System	**Value**	**Units**
Total ground storage volume	1.037	m^3
Ground storage footprint	464	m^2
Insulation thickness, top	0.076	m
Insulation thickness, sides and bottom	0.3048	m
Ground heat exchanger pump rated power	900	W
Ground heat exchanger pump rated flow rate	3.78	$l.s^{-1}$

3. Modeling and Controls of the Radiant Floor and Sub-Surface SSTES System

The warehouse building, solar collector array, and sub-surface ground storage system were all modeled as an integrated system within the TRNSYS transient system simulation software. The Type 56 multi-zone building model from the standard TRNSYS model library was used to model the warehouse and its radiant floor heating, and Types 1345 and 1268 from the TESS model library were used to model the solar collector array and sub-surface ground storage system, respectively.

Figure 1 through Fig. 3 depict the major flow paths and connections in the TRNSYS model, highlighting the following three primary flow paths for the thermal fluid: serving the space heating load from solar (Fig. 1), charging the sub-surface thermal storage from solar (Fig. 2), and discharging from the sub-surface thermal storage to serve the space heating load (Fig. 3). Note that these figures do not represent the complete or full expression of the TRNSYS model, as several piping, controls, and output components have been removed or hidden in these views for clarity.

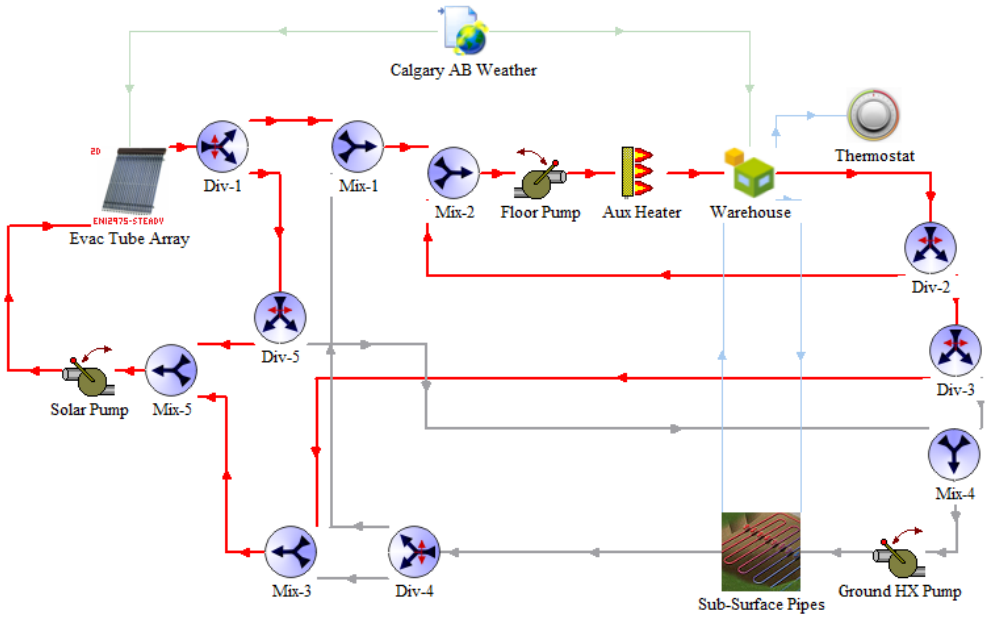

Fig. 1: TRNSYS model of radiant floor and sub-surface SSTES system, highlighting flow paths (in red) when the system is serving the space heating load from the solar array.

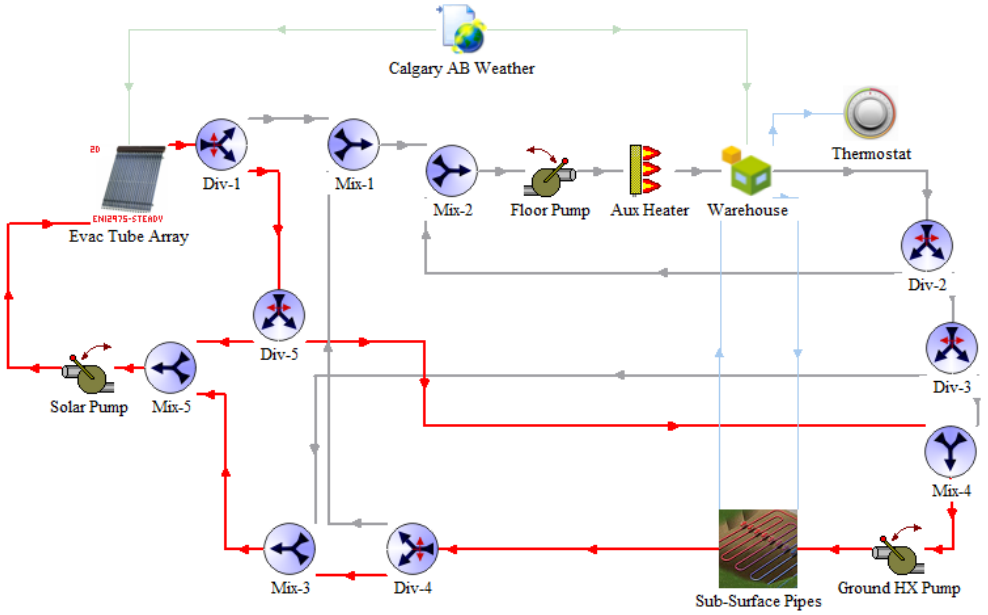

Fig. 2: TRNSYS model of radiant floor and sub-surface SSTES system, highlighting flow paths (in red) when the system is charging the sub-surface thermal storage from the solar array.

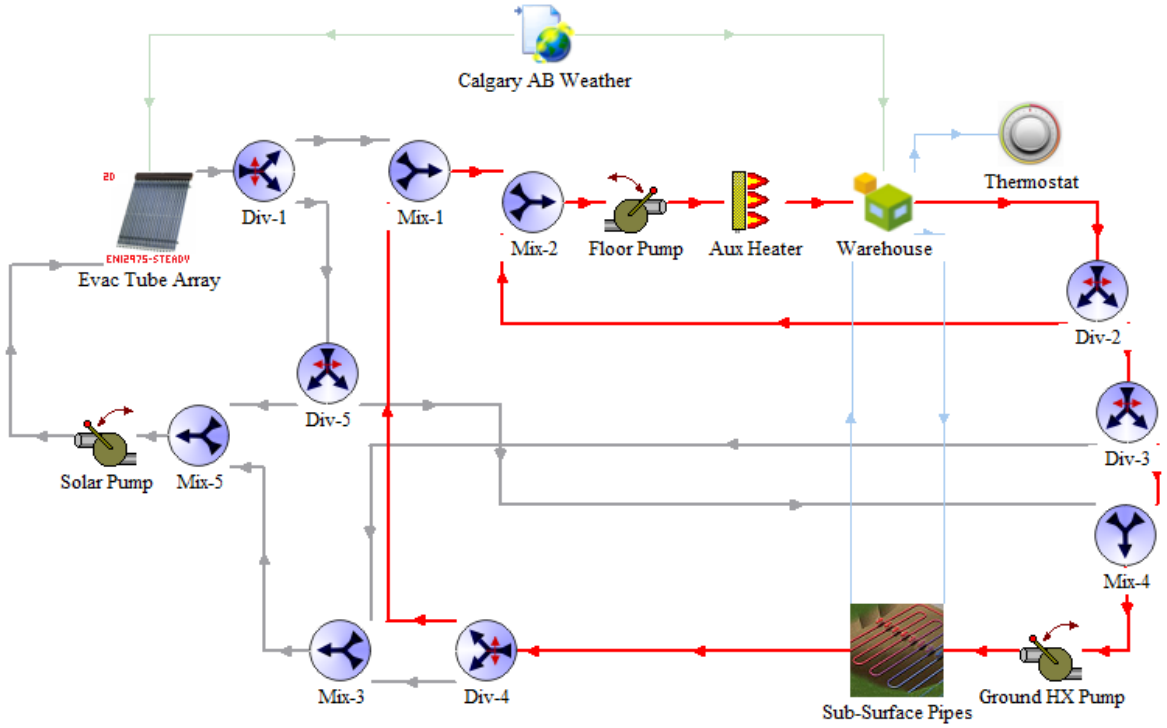

Fig. 3: TRNSYS model of radiant floor and sub-surface SSTES, highlighting flow paths (in red) when the system is discharging the sub-surface thermal storage to serve the space heating load.

In addition to the flow paths illustrated in the TRNSYS model screen captures in Fig. 1 through Fig. 3, the system may operate in some combination of these service modes; for example, the system may use the solar array to both serve the space heating load and charge the sub-surface thermal storage, or it may use both the solar array and discharge from the sub-surface thermal storage to serve the space heating load. In all, the controls algorithm allows the system to operate in any of the following eight 'modes,' depending on the solar resource available, the demand of the radiant floor, and the thermal balance in the ground storage system:

1. If the ground temperature is low, there is very good solar available, and the warehouse thermostat is not calling for heat, the system may send up to 100% of the fluid out of the solar array directly to the sub-surface ground heat exchanger for thermal storage.

2. If the ground temperature is high, there is very good solar available, and the warehouse thermostat calls for heat, the system will satisfy the thermal load of the radiant floor system from solar energy.

3. If the ground temperature is low, there is very good solar available, and the warehouse thermostat also calls for heat, the system will both satisfy the radiant floor load and charge the ground storage.

4. If there is no solar available, the warehouse thermostat calls for heat, and the ground temperature is high, the system will discharge from the ground storage to satisfy the radiant floor load.

5. If there is no solar available, the warehouse thermostat calls for heat, and the ground temperature is low, the system will run the radiant floor heat loop using only the auxiliary boiler for source heat, bypassing both the underground storage and the solar array.

6. If there is fair solar available, the warehouse thermostat calls for heat, and the ground temperature is neutral, the system will satisfy the thermal load of the radiant floor system from solar energy as much as possible.

7. If there is fair solar available, the warehouse thermostat calls for heat, and the ground temperature is low, the system will prioritize serving the radiant floor heat and use any additional thermal resource to charge the ground storage.

8. If there is very little solar available, the warehouse thermostat calls for heat, and the ground temperature is high, the system will use both solar and discharge from the underground storage to serve the radiant floor system.

Table 2 below summarizes the eight control modes available, as well as the general resource criteria and flow paths for each scenario.

Table 2. Control Mode Summary for Radiant Floor and Sub-Surface SSTES System

Scenario	Solar Resource	Underground State of Charge	Warehouse Call Heat?	Solar Flow	Flow to Floor?	Flow to Charge?	Flow to Discharge?
1	High	Low	No	High	No	Yes	No
2	High	High	Yes	High	Yes	No	No
3	High	Low	Yes	High	Yes	Yes	No
4	None	High	Yes	None	Yes	No	Yes
5	None	Low	Yes	None	Yes	No	No
6	Low	High	Yes	Low	Yes	No	No
7	Low	Low	Yes	Low	Yes	Yes	No
8	Low	High	Yes	Low	Yes	No	Yes

4. Comparable Alternate (Non-Solar Assisted) Heating System Configurations

To provide a reference point for performance metrics, the modeled radiant floor and sub-surface SSTES system was compared against models of the following five alternate warehouse space heating systems:

(a) Represents a conventional boiler-fed radiant floor heating system. The boiler is modeled as a theoretical heating source with infinite capacity and no thermal or conversion losses. The thermostat set-points, floor supply temperature set-points, and pump controls are the same as those described for the radiant floor and sub-surface SSTES system.

(b) Represents a 2-stage cold-climate air-source heat pump (CCASHP) system. The air-source heat pump modeled in this investigation is a Daikin 2-stage cold climate air source heat pump with a rated high-speed capacity and power draw of 175 kBtu/hr (51.3 kw) and 12.4 kW, respectively. The heat pump also has two auxiliary heat stages with rated capacities of 75 kW each. A three-stage thermostat commands the heat pump either at low speed, at high speed, or at high speed with auxiliary heat, depending on how long the building has been below the desired setpoint of 21 °C. The air conditioning feature of this heat pump is not used in this application.

(c) Represents the same radiant floor and sub-surface heat exchanger layout as the SSTES system, only the heating load is met from one of two water-water heat pumps (WWHP), using the sub-surface heat exchanger as the heating source. The two single-stage water-water heat pumps modeled are each Water Furnace Envision NDW180 units with a rated heated capacity and rated heating power of 222.7 kBtu/hr (65.3 Kw) and 13.6 kW, respectively. The units are staged by a 2-stage thermostat controller such that only one runs if the building temperature falls below 21 °C, but the second will turn on if the temperature falls below 20 °C. An auxiliary boiler runs as needed to maintain the supply temperature to the sub-surface and ground heat exchanger at or above -3.88 °C.

(d) Represents the same radiant floor and water-water heat pumps as system (c), only the system utilizes a conventional vertical ground heat exchanger as the heat source for the heat pumps. The vertical ground heat exchanger modeled here is a 20-borehole system with a bore depth of 100 meters, with insulation over the top surface of the borefield. In this system, without the size constraint of the building footprint, the ground heat exchanger may be sized as needed to adequately meet the building load.

(e) Same as system (d), only using a conventional horizontal ground heat exchanger instead of a vertical borefield ground heat exchanger. The horizontal heat exchanger is modeled as two layers of 50 pipes at 30.47 meters in length. The layers are buried at very shallow depths of 1-m and 2-m, respectively, and have no insulation surrounding the heat exchanger system.

For consistency, all systems model the building sub-surface with the same composition and thermal contacts as for the SSTES system; however, with the exception of system (c), there are no buried pipes in the ground and no actively managed energy exchange between the building and its sub-surface.

Figure 4 through Fig. 6 depict the TRNSYS models of these alternate systems and Table 3 summarizes key technologies and use of the ground use (if any) in the SSTES system and the five alternate modeled systems.

Table 3. Summary of Technology and Ground Use, SSTES versus Alternate Systems

	SSTES	Boiler *(a)*	CCASHP *(b)*	WWHP, sub-surf HX *(c)*	WWHP, vertical GHX *(d)*	WWHP, horizontal GHX *(e)*
Building heat conveyance	radiant floor	radiant floor	forced air	radiant floor	radiant floor	radiant floor
Primary heating technology	Evac tube solar	Boiler	Air-source heat pump	Water-water heat pumps	Water-water heat pumps	Water-water heat pumps
Auxiliary heating technology	Boiler	N/A	Heat pump auxiliary	Boiler	N/A	N/A
Heat pump source	N/A	N/A	Ambient air	Building sub-surface ground	Ground uncoupled from building	Ground uncoupled from building
Thermal storage	Horizontal ground heat exchangers	N/A	N/A	Horizontal ground heat exchangers	Vertical ground heat exchanger	Horizontal ground heat exchanger
Thermal storage location	Building sub-surface ground	N/A	N/A	Building sub-surface ground	Ground uncoupled from building	Ground uncoupled from building

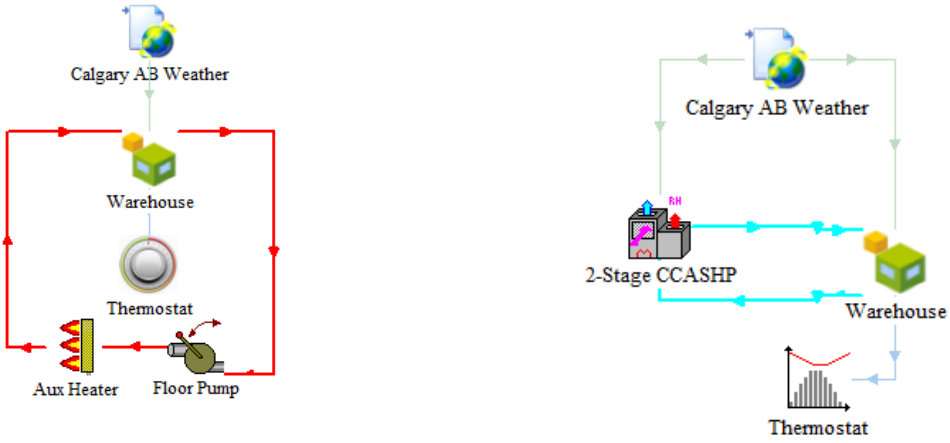

Fig.1: TRNSYS models of conventional boiler-fed radiant floor heating system *(a)* and conventional 2-stage cold-climate air-source heat pump *(b)*.

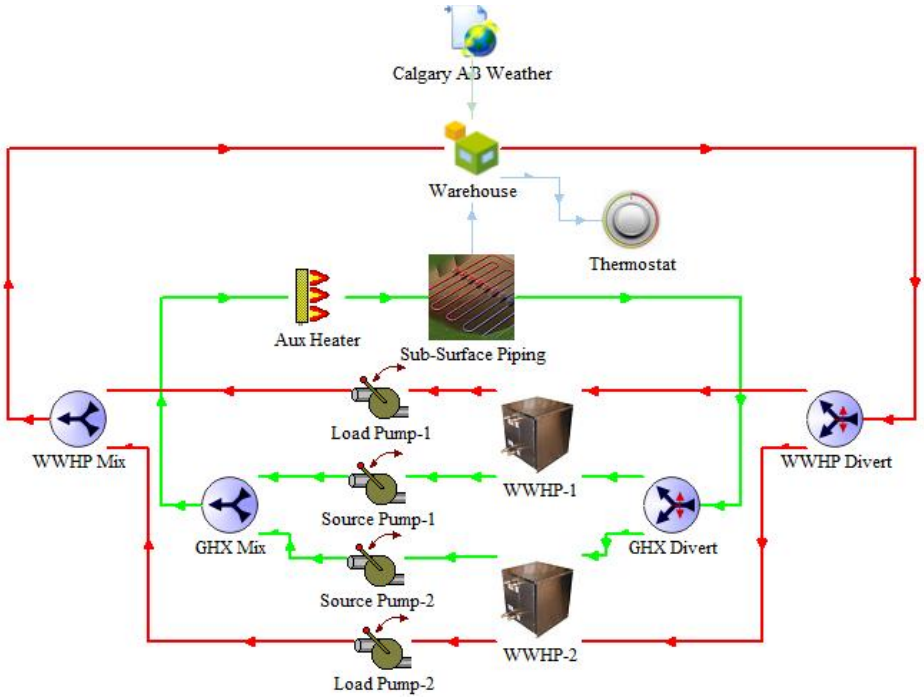

Fig. 5: TRNSYS model of conventional water-water heat pump heating system using the sub-surface ground as the heat source (c).

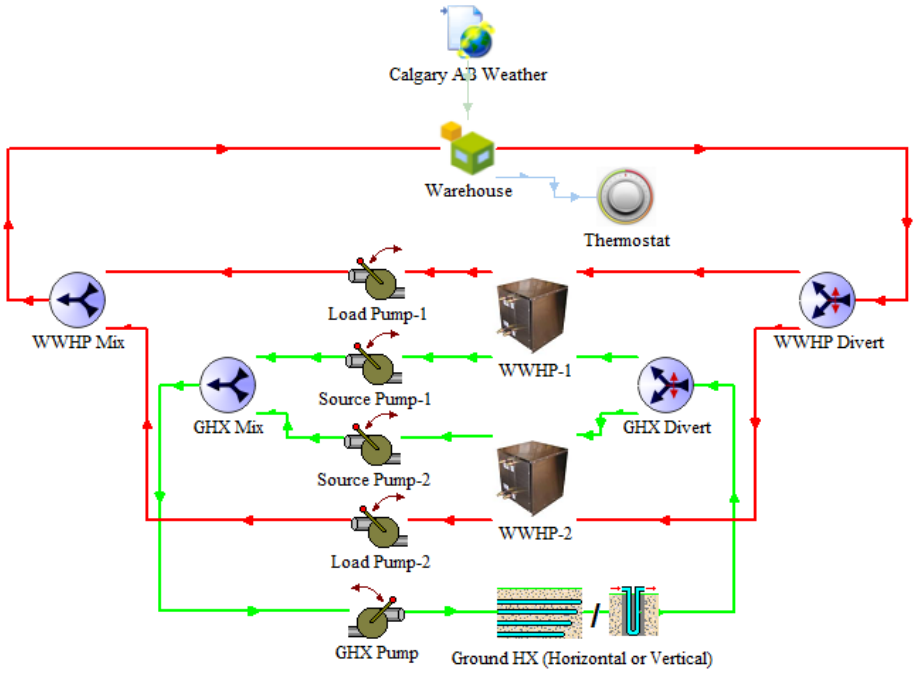

Fig. 6: TRNSYS model of conventional dual water-water heat pump heating system, using either a vertical (d) or horizontal (e) ground heat exchanger as the heat source.

5. Simulation Results

5.1. Thermal Delivery, Power Consumption, and Coefficients of Performance

Table 2 compares the net thermal energy delivery of the SSTES system and each of the five alternate heating systems, including equipment gains to load and net thermal exchange with the farfield ground (if applicable). All annual values represent totals from the last twelve months of the three-year simulation.

Table 2. Thermal Energy Delivery, By System

	Thermal energy delivered [MWh/yr]					
Gains To Load	SSTES	Boiler	CCASHP	WWHP – sub-surf HX	WWHP – vertical GHX	WWHP – horizontal GHX
Solar Array	114.93	-	-	-	-	-
Boiler	4.00	86.31	-	15.59	-	-
CCASHP - heat pump	-	-	64.72	-	-	-
CCASHP- auxiliary	-	-	13.05	-	-	-
WWHP 1	-	-	-	85.49	79.72	76.73
WWHP 2	-	-	-	7.89	5.26	6.10
System pumps (all)	1.63	0.38	-	-	-	-
Total:	**120.55**	**86.69**	**77.77**	**108.98**	**84.99**	**82.84**
Exchange With Surroundings	SSTES	Boiler	CCASHP	WWHP – sub-surf HX	WWHP – vertical GHX	WWHP – horizontal GHX
System piping (all)	-19.52	-0.89	-	3.46	2.74	7.25
From ground farfield	-0.01	-	-	-	26.42	38.48
Total:	**-19.53**	**-0.89**	**0.00**	**3.46**	**29.16**	**45.73**
Net Total:	**101.02**	**85.80**	**77.77**	**112.43**	**114.14**	**128.56**

As shown in Table 4, the net thermal gain of the systems modeled varies from 77 to 128 MWh/yr, with the SSTES representing the middle of the range. With only 4.00 MWh/year of thermal energy supplied from the boiler in the SSTES system, the solar fraction for the SSTES system is 0.96, or near net-zero thermal system performance over the year. The SSTES loses about 19.5 MWh/yr to the surroundings, or about 17% of its net gains from the solar collector array, though very little of this is due to leakage from the ground storage volume to the farfield ground.

Note that the alternate ground-source water-water heat pump systems (d) – (e) draw net energy from the farfield ground of 26 to 38 MWh/yr, with the less-insulated and shallower horizontal GHX system drawing almost 50% more energy from the farfield as compared to the deeper vertical GHX system with surface insulation. Net draws of this magnitude from the farfield suggest the systems would be unsustainable over several years of operation without better insulation or ground use design. Also note that the alternate system with the sub-surface ground source (c) required 15.59 MWh/year from the auxiliary boiler to maintain the ground temperature, or almost one-fifth of the auxiliary boiler's annual energy use when meeting the radiant load directly.

Table 5 compares the power consumption of the SSTES and the alternate systems by equipment, as well as the overall coefficient of performance (COP) of each system.

Table 3. Power Consumption and COP, By System

	Power consumption of system [MWh/yr]					
Equipment	SSTES	Boiler	CCASHP	WWHP – sub-surf HX	WWHP – vertical GHX	WWHP – horizontal GHX
Solar array pump	1.18	-	-	-	-	-
Floor heating pump	2.06	1.26	-	-	-	-
Ground HX pump	2.19	-	-	-	0.00*	0.00*
Boiler	4.00	86.31	-	15.59	-	-
CCASHP - compressor	-	-	17.17	-	-	-
CCASHP - fans	-	-	4.89	-	-	-
CCASHP - auxiliary	-	-	13.05	-	-	-
WWHP1	-	-	-	34.38	29.95	30.19
WWHP2	-	-	-	3.79	2.43	2.95
WW Source Pump 1	-	-	-	1.31	1.11	1.13
WW Source Pump 2	-	-	-	0.13	0.08	0.10
WW Load Pump 1	-	-	-	1.31	1.11	1.13
WW Load Pump 2	-	-	-	0.13	0.08	0.10
Total:	**9.42**	**87.57**	**35.11**	**56.65**	**34.76**	**35.60**
Thermal to load (from Table 4)	101.02	85.80	77.77	108.98	84.99	82.84
COP, system:	**10.73**	**0.98**	**2.21**	**1.92**	**2.44**	**2.33**

**The ground HX pump was modeled with a rated power of 0 W in these systems.*

Total auxiliary and parasitic power consumption for the SSTES system are 9.42 MWh/year, including the auxiliary boiler, solar field pump, floor heat pump, and ground heat exchanger pump. The SSTES system obtains a coefficient of performance of 10.7 as compared to the net thermal energy delivered by the SSTES system, or 9.1 as compared to the thermal energy delivered by the conventional boiler system (the nearest directly comparable system). In other words, the SSTES system returns 9.1-10.7 MWh of thermal energy for every MWh of energy consumed to operate the system. Compare this to the COPs of the five alternate systems, which range from 0.98 for the auxiliary boiler system to 2.44 for the water-water heat pump system with the vertical borefield ground source, the best of the four heat pump-powered systems.

5.2. Solar Ground Storage Charge, Discharge, and Net Storage

The ultimate goal of the SSTES design is to store solar heat when it is seasonally available and use it over the rest of the year to offset or eliminate auxiliary heating from fossil fuel sources. Fig. *2* shows the net energy stored in (or

discharged from) the radiant floor and sub-surface SSTES system, by month, over the last 12 months of the simulation.

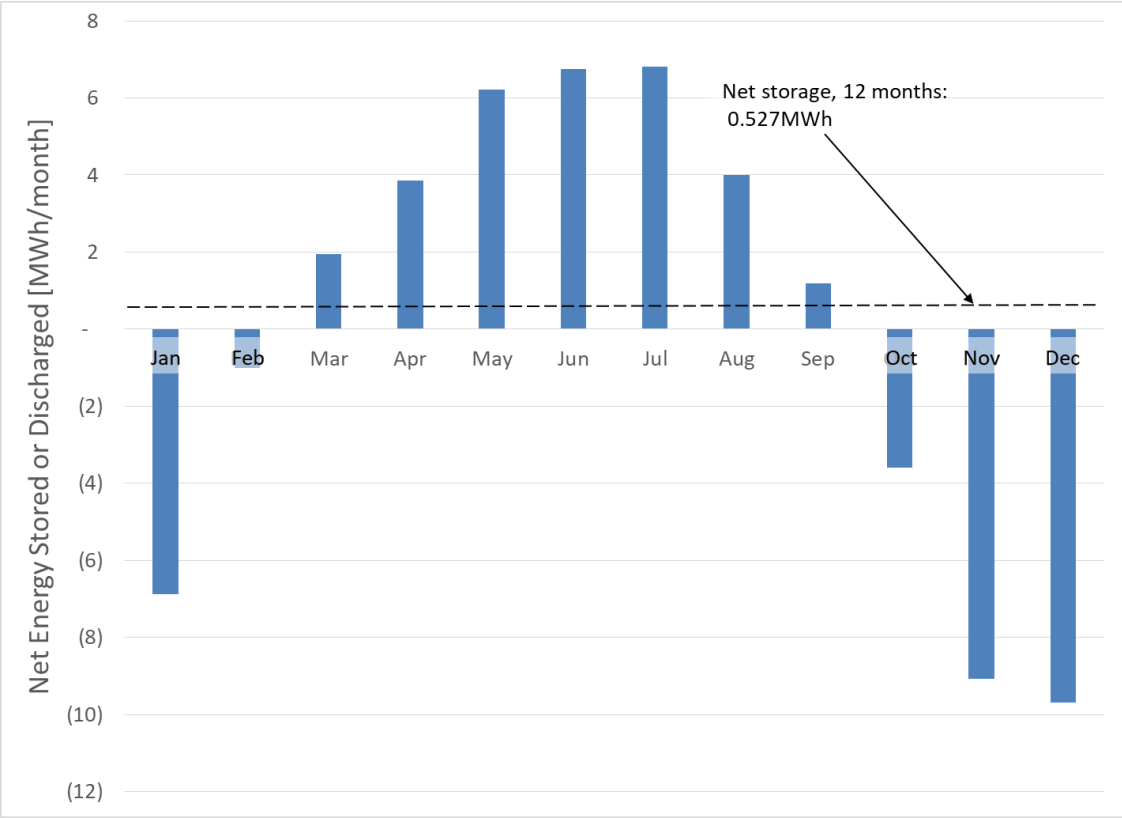

Fig. 2: Net energy stored or discharged by SSTES system, by month

5.3. Temperature Control

All six systems had a desired space heating set-point of 21 °C (± 0.55 °C). Table 4 compares the performance of the six systems in satisfying the space heating set-point over the year. With respect to temperatures well above set-point, recall that the building has no active cooling and some 'float' above set-point is expected, especially in the summer months.

Table 4. Annual Hours By Temperature Bin At, Above, or Below Set-Point, By System

Hours	SSTES	Boiler	CCASHP	WWHP – sub-surf HX	WWHP – vertical GHX	WWHP – horizontal GHX
Above 23.5°C	38%	25%	8%	23%	24%	25%
23.5°C to 22.5°C	11%	15%	5%	13%	15%	14%
22.5°C to 21.556°C	13%	26%	7%	18%	19%	19%
21.556°C to 20.444°C	**21%**	**32%**	**78%**	**36%**	**35%**	**34%**
20.444°C to 19.5°C	9%	2%	1%	10%	7%	8%
19.5°C to 18.5°C	4%	0%	0%	1%	0%	0%
Below 18.5°C	3%	0%	0%	0%	0%	0%

As evidenced in Table 4, the cold-climate air source heat pump (CCASHP) system provided noticeably tighter temperature control than either the SSTES or any of the alternate systems, maintaining a temperature range between 21.556 °C and 20.444 °C for over 78% of the year and only falling below 20.444 °C for about 1% of the year. It is the only system of those studied that did not use the radiant floor for space heating, and it is also the only system for which the space was above 22.5 °C for only 13% of the year, as compared to 49% for the SSTES system and 36%-40% for the other alternate systems. This observation suggests the radiant floor system, regardless of its heat source, cannot be as thermally responsive as the CCASHP system and favors overheating in this application. The boiler system and the three water-water heat pump systems all performed comparably to each other in satisfying the space, though the boiler-fed radiant floor system did not under-heat nearly as often as the three water-water heat pump systems. The SSTES system maintains the space within the desired range only 21% of the year, is overheated 62% of the year, and is under-heated 16% of the year. Notably, it is also the only system that ever falls below 18.5 °C and one of only two systems out of the six that ever falls below 19.5 °C.

5.4. Effects of Insulation and Collector Technology on Radiant Floor and Sub-Surface SSTES System

Modeling of the baseline radiant floor and sub-surface SSTES system began with best-practice or best-available technologies to the extent possible, including using an evacuated tube array for the solar field and very good insulation on all sides of the thermal storage medium. To assess the impact of these design choices on the performance of the system, the baseline SSTES model was compared against models with the following design adaptations:

1) Double the baseline insulation is applied on the six surfaces of the thermal storage volume.
2) Half the baseline insulation is applied on the six surfaces of the thermal storage volume.
3) A glazed flat plate array of the same area is substituted for the evacuated tube array.
4) An unglazed flat plate array of the same area is substituted for the evacuated tube array.

Table 5 compares the net thermal energy delivered and power consumed in the baseline SSTES system and in the four design-adapted systems.

Table 5. SSTES Thermal Delivery and Power Consumption vs Insulation and Collector Type

	Thermal energy delivered to system [MWh/yr]				
Equipment	SSTES - baseline	SSTES – double insul	SSTES – half insul	SSTES – glazed FP	SSTES – unglazed FP
Solar Field	114.93	110.44	119.56	121.75	18.92
Boiler	4.00	0.17	11.13	24.70	76.79
Total:	**118.92**	**110.60**	**130.69**	**146.45**	**95.71**
	Power consumption of system [MWh/yr]				
Equipment	SSTES - baseline	SSTES – double insul	SSTES – half insul	SSTES – glazed FP	SSTES – unglazed FP
Solar array pump	1.18	1.13	1.23	0.66	0.08
Floor heating pump	2.06	2.02	2.14	0.82	1.41
Ground HX pump	2.19	1.77	2.43	0.97	0.08
Boiler	4.00	0.17	11.13	24.70	76.79
Total:	**9.42**	**5.08**	**16.93**	**27.14**	**78.37**

As shown in Table 5, increasing the insulation to twice its baseline value decreased auxiliary boiler use by more than 95%, from 4 MWh/year to only 0.17 MWh/year, and reduced parasitic pump power use by about 10% as well. When the insulation was decreased by half from its baseline value, the overall parasitic pump power use increased by about 7%, and the auxiliary boiler use increased over 275%, from 4 MWh/yr to over 11 MWh/yr. The results demonstrate the magnitude by which insulation affects the auxiliary support required to meet the same heating load. Adequate insulation surrounding the storage volume, therefore, must be part of the optimal SSTES system. Both the glazed flat plate collector system and the unglazed flat plate collector system underperformed as compared to the baseline evacuated tube collector system, with the glazed flat plate system and the unglazed flat plate system requiring about 600% and 1900% more auxiliary boiler use, respectively, than the baseline system. The glazed flat plate collector modeled has higher efficiency at lower temperatures as compared to the evacuated tube collector, but also higher thermal losses as the collector temperature rises above the ambient air temperature, as well as a very different incidence angle modification (IAM) profile, making it somewhat difficult in the absence of a full simulation to anticipate which collector will perform better overall in different scenarios. In this case, it appears the evacuated tube collector system is preferable for thermal performance to the glazed flat plate collector system, though the glazed flat plate system may be more cost-effective once capital costs are considered. The unglazed flat plate array performed poorly.

6. Conclusions

A solar seasonal thermal energy storage (SSTES) system consisting of a solar collector array, a hydronic radiant floor space heater, and a sub-surface ground heat exchanger, has been demonstrated via simulation to successfully balance thermal storage charging and discharging over the year for a warehouse in a cold climate, achieving a very high solar fraction (0.96). Comparison of the SSTES system to alternate conventional systems showed some trade-off between system COP and temperature control of the space, with the excellent COP of the SSTES system coming at the cost of a somewhat wider temperature range in the conditioned space over the year. For applications with loose

to moderate temperature control requirements (such as the lightly-occupied warehouse of this investigation), this may be more than adequate; further investigation is needed to assess the extent to which temperature control may be improved. Modeling different insulation thicknesses and solar collector array types demonstrated that both adequate insulation and quality solar collectors with some thermal loss protection (either via glazing or evacuated tubes) are necessary components of a high performance SSTES system.

7. Acknowledgments

The authors gratefully acknowledge the financial support of Natural Resources Canada through the Office of Energy Research and Development – Energy Innovation Program (EIP).

8. References

Alkhalidi, A., Al Khatba, H., Khawaja, M.K., 2021.Utilization of Buildings' Foundations for a Seasonal Thermal Energy Storage Medium to Meet Space and Water Heat Demands. International Journal of Photoenergy, Vol. 2021.

Hailu, G., Hayes, P., Masteller, M., 2017. Seasonal Solar Thermal Energy Sand-Bed Storage in a Region with Extended Freezing Periods: Part I Experimental Investigation. Energies, Vol. 10.

Hailu, G., Hayes, P., Masteller, M., 2019. Long-Term Monitoring of Sensible Thermal Storage in an Extremely Cold Region. Energies, Vol 12.

Loveridge, F., McCartney, J. S.; Narsilio, G. A., Sanchez, M., 2020. Energy geostructures: a review of analysis approaches, in situ testing and model scale experiments. Geomechanics for Energy and the Environment, Vol. 22.

Meister, C., Beausoleil-Morrison, I., 2021. Experimental and modelled performance of a building-scale solar thermal system with seasonal storage water tank. Solar Energy, Vol. 222.

Naranjo-Mendoza, C., Greenough, R.M., Wright, A.J., 2018a. Are shallow boreholes a suitable option for inter-seasonal ground heat storage for the small housing sector? IGSHPA Research Track, Stockholm.

Naranjo-Mendoza, C., Wright, A. J., Oyinlola, M.A., Greenough, R.M., 2018b. A comparison of analytical and numerical model predictions of shallow soil temperature variation with experimental measurements. Geothermics, Vol. 76.

Naranjo-Mendoza, C.; Oyinlola, M. A.; Wright, A. J.; Greenough, R. M., 2019. Experimental study of a domestic solar-assisted ground source heat pump with seasonal underground thermal energy storage through shallow boreholes. Applied Thermal Engineering, Vol. 162.

Naranjo-Mendoza, C., 2020. An investigation into the performance of a very shallow borehole thermal energy store for a solar-assisted ground source heat pump. De Montfort University Institute of Energy and Sustainable Development Doctoral Thesis, 2020.

Pinamonti, M., Beausoleil-Morrison, I., Prada, A. Baggio, P., 2021. Water-to-water heat pump integration in a solar seasonal storage system for space heating and domestic hot water production of a single-family house in a cold climate. Solar Energy, Vol. 213.

Sweet, Marshall. "Numerical Simulation of Underground Solar Thermal Energy Storage, 2010." Virginia Commonwealth University Scholars Compass Graduate School MSc Thesis.

Villasmil, Willy; Troxler, Marcel; Hendry, Reto; Schuetz, Philipp; Worlitschek, Jörg, 2021. "Parametric Cost Optimization of Solar Systems with Seasonal Thermal Energy Storage for Buildings." Cold Climate HVAC & Energy. Vol. 246.

9. List of Acronyms

CCASHP	cold-climate air-source heat pump	**PVT**	photovoltaic-thermal
FDM	finite-difference method	**SSTES**	solar seasonal thermal energy storage
GHX	ground heat exchanger	**WWHP**	water to water heat pump

INTEGRATING RADIATIVE COOLING AND CHILLED CEILINGS IN BUILDINGS: A SIMULATION STUDY FOR SUSTAINABLE COOLING

Roger Vilà[1], Francesco L. Capiello[2], Luca Cimmino[2], Marc Medrano [1], Ingrid Martorell [1]

[1] Universitat de Lleida, Lleida (Spain)

[2] Università degli Studi di Napoli Federico II, Napoli (Italy)

Abstract

The Radiative Collector and Emitter (RCE) is a device that combines the functionalities of radiative cooling and solar heating to cool down or warm up water, respectively. This study present a first approximation of the integration of RCE systems with chilled ceilings to provide sustainable cooling solutions for buildings. The research focuses on a multifamily building in Lleida, Spain, and employs TRNSYS 18 for simulation during the summer months. The RCE system leverages the natural process of radiative cooling, emitting infrared radiation into space to dissipate heat and reduce temperatures with minimal electricity consumption. The combined system's performance was compared against a commercial air conditioner system, demonstrating energy savings for cooling demand of approximatively 140 kWh during the observed period, along with enhanced occupant comfort. The RCE system achieved a mean net radiative cooling power of 30.34 $W \cdot m^{-2}$ and an efficiency of 42.3%, reducing the storage tank temperature by an average of 3.29°C nightly. The chilled ceiling system operated autonomously 87.74% of the time, maintaining comfortable indoor temperatures.

Keywords: Radiative Cooling, Chilled Ceiling, Building Modelling, Numerical Simulation, TRNSYS

1. Introduction

Energy consumption in buildings is estimated to be 40% of final energy consumption in Europe, accounting for 36% of CO_2 emissions (Eurostat, 2019). The largest portion of this energy (80%) is utilized to meet the needs of space conditioning, which includes domestic hot water (DHW), cooling, and heating. Space cooling, in particular, is a major contributor to the rise in electricity consumption, with CO_2 emissions related to space cooling increasing by 2% annually. Worldwide projections show that by 2050, the energy demand for space cooling will have tripled, being necessary the installation of more air-conditioning units (IEA, 2019).

In the last decade, technologies based on the radiative cooling (RC) phenomenon have emerged as promising renewable solutions to address the growing energy needs related to cooling in buildings. RC is a natural process in which a surface emits infrared radiation into outer space, thereby dissipating heat and cooling down (Vilà et al., 2021). The peaks of radiation are in the wavelength range of 7 μm to 14 μm, which falls within the atmospheric window, the region of the electromagnetic spectrum where Earth's atmosphere is highly transparent. This transparency allows the radiation to escape into outer space, leading to a significant temperature reduction below ambient levels at the surface, with minimal or no electricity consumption (Chen et al., 2020).

The operation of radiative cooling, despite being opposite to solar heating, is entirely analogous and can be combined. Researchers at the University of Lleida have developed a device of 2 m^2, named Radiative Collector and Emitter (RCE) (Vall et al., 2020a), that combines both solar heating and radiative cooling functionalities to heat up water, during the day, or cool down water in contact with a radiative cooling surface, during the night. The RCE includes a grid of pipes through which water flows, such pipes are installed on a highly emissive/absorptive plate within the infrared spectrum. In solar collection mode, during the day, the RCE absorbs solar radiation to heat the water. In cooling mode, the plate emits infrared radiation towards the sky, cooling the water below ambient temperature.

© 2024. The Authors. Published by International Solar Energy Society
Selection and/or peer review under responsibility of Scientific Committee
10.18086/eurosun.2024.02.12 Available at http://proceedings.ises.org

Despite the notable growth in radiative cooling research (Su et al., 2023), the integration of radiative cooling technologies with the built environment has not been thoroughly explored (Kousis and Pisello, 2023; Vilà et al., 2020). One explanation for this gap in the literature can be found in the limitation of nighttime radiative cooling devices, such as the RCE systems, which have a relatively low cooling density power, averaging only 50 W/m² (Vall et al., 2020b). This limitation results in that RCE achieves a temperature few degrees below the nocturnal ambient temperature, diminishing its power with the temperature reduction. For this reason, such devices cannot behave like conventional terminal units, like fan-coils, operating at 6-7 ºC. However, there is promising potential for these devices to be coupled with cooling technologies operating at higher temperatures, such as chilled ceilings, thereby broadening their applicability and enhancing their efficiency in the built environment.

Chilled ceilings are cooling systems designed to regulate the inside temperature of a space. These systems typically operate with a temperature difference close to 2 ºC between the water inlet and outlet (Jin et al., 2020), with an operating inlet temperature a few degrees above the dew point. Combining radiative cooling for cooling production with chilled ceilings for cooling delivery to buildings appears to be a practical option due to the similarity in operating temperature levels (Yuan et al., 2018). This study is a first approach to combine RCE with chilled ceilings. The paper specifically studies the radiative cooling functionality of the RCE, as it is the innovative solution and the one lacking result in literature, by simulating the thermal performance of an integrated systems (RCE + Chilled Ceiling) in a multifamily building in Lleida (Spain). The study seeks to assess the energy savings and thermal performance of these integrated systems, offering new insights into the applicability of radiative cooling technologies in the built environment, contributing to close the literature gap.

2. Methods

This section details the numerical simulations conducted to assess the energy-saving potential of integrating radiative cooling technology with building cooling systems. This study compares a reference case using a traditional air-to-water heat pump and chilled ceiling system with an improved case employing the Radiative Collector and Emitter (RCE) combined with chilled ceilings. The section includes descriptions of the multifamily building in Lleida, Spain, and the computational models used for both scenarios. Additionally, it outlines the mathematical model employed to simulate the radiative cooling performance of the RCE.

2.1. Conditions of Simulation

The transient behaviour of the systems was simulated using TRNSYS 18 for the warmest months in Lleida, Spain, spanning from May to September, both included. A timestep of 5 minutes was used in the simulations in TRNSYS.

Meteorological data for Lleida was sourced from Meteonorm's database (Remund et al., 2019), providing essential parameters such as solar radiation, ambient temperatures, humidity levels, and wind speeds, needed to simulate the behaviour of the RCE. Atmospheric radiation calculations (eq. 1) assumed the Walton correlation for sky emissivity (eq. 2), where T_{db} represents the dry bulb temperature in Kelvins, and N denotes the opaque sky cover in tenths.

$$R_{atm} = \varepsilon_{sky} \cdot \sigma \cdot T_{db}^4 \quad (1)$$

$$\varepsilon_{sky} = (0.787 + 0.764 \cdot \ln\left(\frac{T_{dp}}{273}\right) \cdot (1 + 0.0224 \cdot N - 0.0035 \cdot N^2 + 0.00028 \cdot N^3) \quad (2)$$

The net cooling power on the surface is defined as the difference between the radiation emitted by the surface (at the surface temperature of the RCE, T_s) and the incoming atmospheric infrared radiation absorbed by the surface (eq. 3).

$$R_{net} = \varepsilon_s \cdot \sigma \cdot T_s^4 - \alpha_s \cdot R_{atm} \quad (3)$$

2.2. Description of the Building

The building selected as a case study to analyse the performance of the Radiative Collector and Emitter (RCE) is a two-floor multifamily building located in Lleida, Spain. The thermophysical features of the building envelope are listed in **Table 1**, while **Fig 1** shows the occupancy profiles. The characteristics of the building, both in terms of geometry and materials, are selected based on the fact that 55% of buildings in Spain are older than 1980, with the average building age in Lleida being 33 years (Ministerio para la Transición Ecológica y el Reto Demográfico, n.d.). The selected values for the envelope fall between the first building normative in Spain (NBE-CT) (Presidencia del Gobierno, 1979) and the initial Technical Building Code (CTE) established in 2006 (Ministerio de Vivienda, 2006).

The building is divided into two floors, each representing an apartment and, therefore, a thermal zone in the developed system. In each apartment, the number of occupants is four (two adults and two children), each with different occupancy profiles. These profiles are crucial for determining when the cooling system should be activated to create comfortable indoor conditions and whether the heat gains are on or off.

Table 1: Features of the building envelope.

Building element	U (W/m^{2}K)	Thickness (m)	ρ_s (–)	ε (–)
Roof	0.509	0.373	0.4	0.9
Façades	0.904	0.225		
Ground floor	0.742	0.360		
Adjacent ceiling	0.904	0.225		
Windows glass	1.10	0.006/0.016/0.006	0.13	0.18

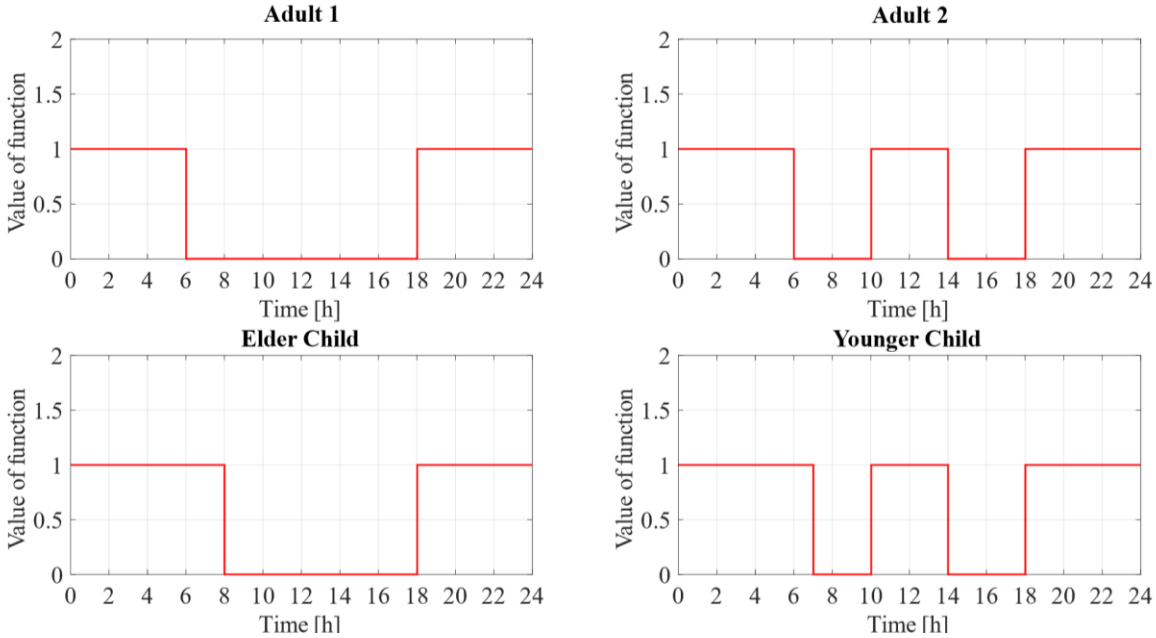

Fig 1: Occupation scheduling for the types of users of the multifamily building.

A set point temperature of 27ºC was established; any temperature exceeding this threshold was considered to induce discomfort. Consequently, if there was occupancy in the room, cooling systems were activated to restore comfort levels. The specific cooling systems utilized in the simulations are described in subsequent sections. However, a general control strategy was implemented, including a free cooling approach. This strategy leverages outdoor air to reduce indoor temperatures, reducing the needs of mechanical cooling when the outdoor air temperature was below the set point temperature. This free cooling strategy was scheduled to occur during specific hours: from 6:00 AM to 8:00 AM and from 4:00 PM to 10:00 PM.

2.3. Description of the Facility for the Improved Case (RCE + Chilled Ceiling)

This section describes the facility setup for the improved case, which integrates the Radiative Collector and Emitter (RCE) with chilled ceilings on the first floor of the building to enhance energy savings and cooling performance compared to the reference case.

The facility simulated in this study features a rooftop field of 45 Radiative Collector and Emitter (RCE) units covering 90% of the building's rooftop area, replacing the traditional air-to-water heat pump of the reference case (**Fig 2**). These units operate during nighttime hours to cool the water inside a 3.5 m³ storage tank. In this simulation, the tank is assumed to be adiabatic. The generation of cold occurs at night, while most of the cold is utilized during the day. Therefore, a storage tank was necessary to effectively manage and dispatch the cooling capacity as required.

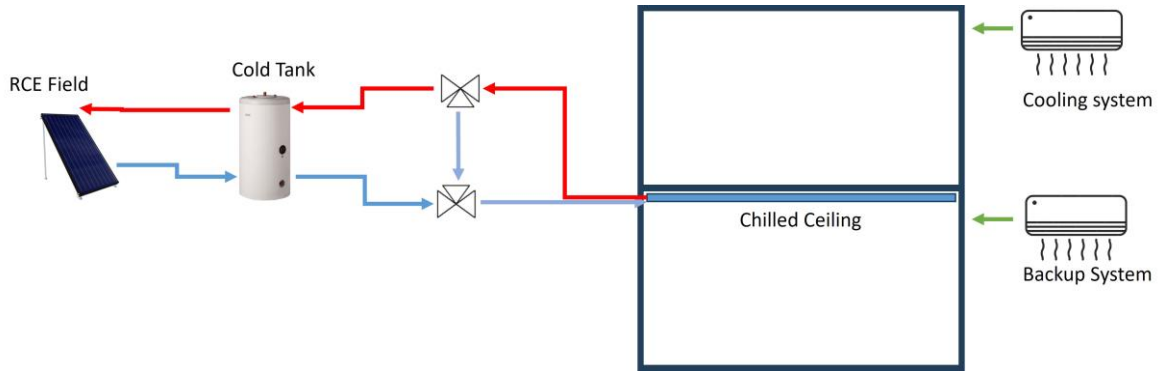

Fig 2. Schematic representation of the RCE + Chilled Ceiling facility.

During the daytime, the chilled ceiling system on the first floor operates with an inlet temperature range of 17-19 ºC, optimized to achieve indoor cooling. In the best scenario, the RCE field can cool down the tank to 12 ºC. The chilled ceiling has been modelled according to Uponor units, which are preassembled commercial panels of 1 m² (Uponor, n.d.). The geometric characteristics of the chilled ceiling are detailed in **Tab. 2**. To maximize the utilization of the cold stored generated by the RCE, the chilled ceiling system's inlet temperature is regulated to 18 ºC. This is achieved through a recirculation process where a portion of the water from the chilled ceiling's outlet is mixed with water from the storage tank. This mixing arrangement enhances thermal comfort while optimizing cooling discharge of the tank.

Table 2: Geometric and operational characteristics of the Chilled Ceiling on the first floor

Parameter	Description	Value	Unit
t_p	Pipe spacing	0.015	m
d_p	Pipe inside diameter	0.01	m
m_S	Specific normalized mass flow	0.5	$l \cdot min^{-1} m^{-2}$
P_S	Specific normalized power	80	$W \cdot m^{-2}$

In scenarios where additional cooling capacity is needed beyond what the chilled ceiling system can provide, typically when the storage tank temperature rises above 20 ºC due to increased cooling demand, the backup air conditioner system with a capacity of 4 kW on the first floor is activated to supplement cooling requirements. This backup system ensures continuous comfort conditions for occupants, seamlessly integrating with the overall cooling strategy. On the second floor, cooling is managed separately through a traditional air conditioner system, highlighting the contrast with the innovative integrated approach employed on the first floor.

2.3. Description of the Facility for the Reference case

Fig 3. shows the facility configuration used for the reference case, which includes a traditional air-to-water heat pump and chilled ceiling system. This setup serves as the baseline for comparison against the improved case incorporating the Radiative Collector and Emitter (RCE) combined with chilled ceilings. Similarly to the previous facility, this hydronic system developed to meet the cooling demand of the building is based on a 6 kW commercial air-to-water heat pump integrated with a 3.5 m³ water tank that stores the cooling energy.. To compare the cooling performance of the RCE and the heat pump, the same control strategy was used for both heat generation systems. The heat pump operates to provide cooling energy to the tank only during the night, the time window in which the RCE operates in cooling mode. This approach ensures that the comparison between the two systems is as similar as possible. Additionally, the heat pump operates only to decrease the temperature of the tank to 15°C. This control strategy reduces the consumption of the heat pump by operating with a small ΔT and therefore with a high Energy Efficiency Ratio (EER), allowing for a fair comparison of the systems under the same conditions.

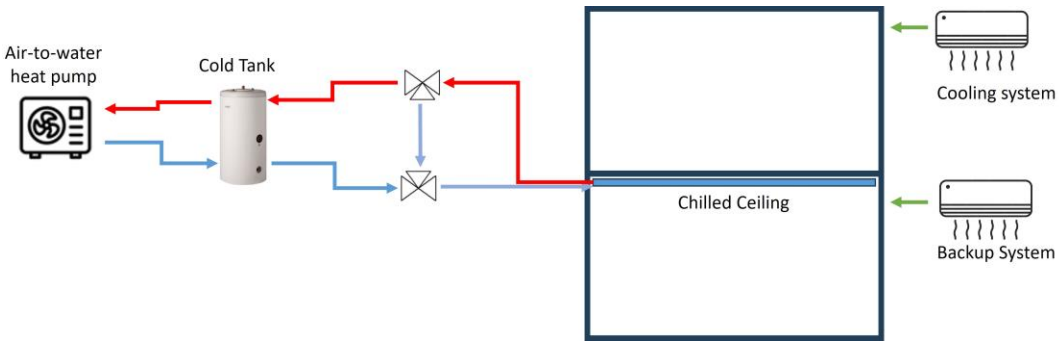

Fig 3: Schematic representation of the reference facility.

2.5. RCE Model

This research uses the numerical model of the RCE developed, and experimentally validated, by Vall et al. (Vall et al., 2020a). The implementation in TRNSYS v18 involved a comprehensive energy balance, designed considering the interactions between the RCE, ambient air, the sky, and the building. To develop a model not so heavy from the computational point of view, the RCE model was discretized into nodes using a one-dimensional electrical analogy (1D) approach. Two-dimensional effects were incorporated through detailed simulations using COMSOL Multiphysics. Radiative balance calculations were performed for four distinct wavelength ranges (0-4 μm, 4-7 μm, 7-14 μm, and >14 μm), with a specific emphasis on the infrared atmospheric window (7-14 μm). Solving energy balance equations, which are ordinary first-order differential equations, was achieved numerically using Euler's implicit method.

Tab.3: Parameters of the RCE.

Parameter	Description	Value	Unit
A_{RCE}	Useful surface	2	m^2
n_{pipe}	Nº parallel pipes	9	-
l_{pipe}	Pipe length	1.886	m
t_{pipe}	Distance between pipes	0.125	m
d_{pipe}	Pipe diameter	0.008	m
ε_{RCE}	Radiator emissivity	0.95	-
τ_{RCE}	Cover transmissivity	0.80	-
$\dot{m}_{RCE}$	Flowrate	4.5	$l \cdot min^{-1} m^{-2}$

3. Results and Discussion

3.1. Performance of the Radiative Collector and Emitter (RCE)

The simulations indicate that, on average, the RCE had the power to cool the storage tank by 3.29°C each night over the simulation period, with peak values equal to 7.82ºC. The daily temperature at the end of the night was 18ºC on average. During its operation, the chilled ceiling warmed the tank 2.98ºC. This indicates that RCE field was able to compensate the increasing of temperature derived from the chilled ceiling system. The average energy cooled by the RCE during the operational days was 12.38 kWh, cooling a total of 879 kWh in the simulated period.

The overall mean net radiative cooling power of the RCE was 30.34 $W \cdot m^{-2}$, with peak values reaching up to 97.04 W/m^2. The average efficiency of the RCE, defined as the ratio between the cooling power in the pipes and the net radiative cooling power, was determined to be 42.3%, which is considered a good performance for this type of system. **Fig 4** shows the thermal evolution during three consecutive nights in July (from 10/07 at 00:00 to 13/07 at 23:55). During the day, a constant flow through the RCE has been simulated to maintain the emitter at a temperature below or close to the ambient. The energy stored in the tank is used in the chilled ceiling during the day, increasing its temperature above 23ºC. During the night, the RCE field is able to cool down the tank below 19 ºC. On the first and second nights, it was able to cool the water in the RCE 2 ºC below ambient temperature, and almost 2 ºC below ambient temperature in the tank in the second night. On the third night, it cooled it down only a few tenths of a degree below the ambient temperature. Powers up to 50 $W \cdot m^{-2}$ were reached.

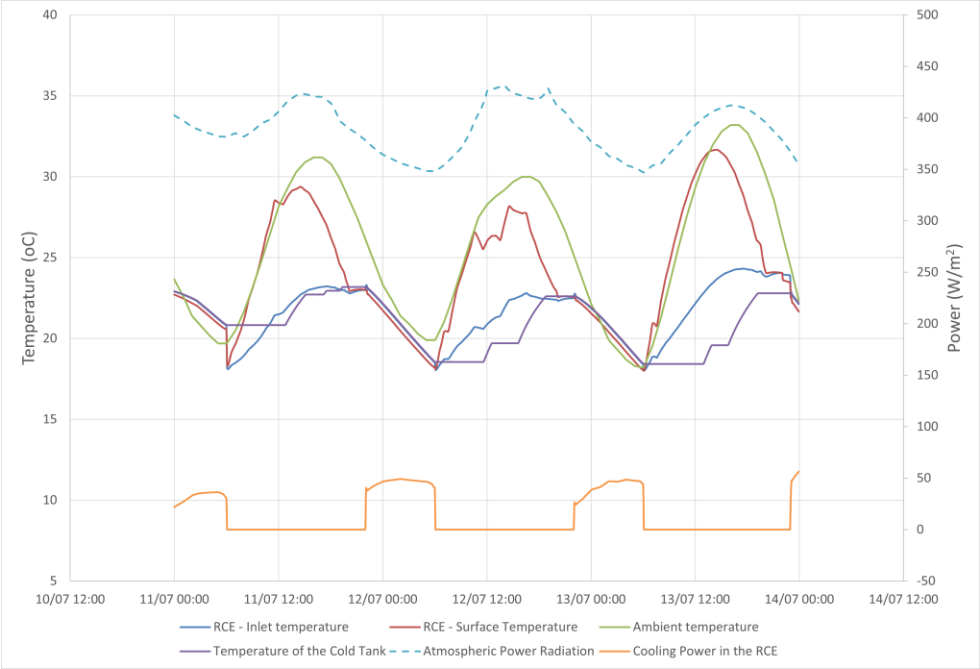

Fig 4. Thermal evolution of the RCE field between the days July 10th at noon and July 13th at 23:55.

Fig 5 shows the daily cooling energy produced by the RCE versus the energy absorbed by the chilled ceiling to cool down the first floor.

The RCE facility remained unused on many occasions. This suggests that in the unused nights, the RCE could have been used to renewably meet part of the second-floor demands. The figure also indicates that for 6 nights, the RCE system delivered negative cooling energy, warming the water instead of cooling it. These nights coincided with high atmospheric infrared radiation, highlighting the need for better optimization of the RCE control in future research.

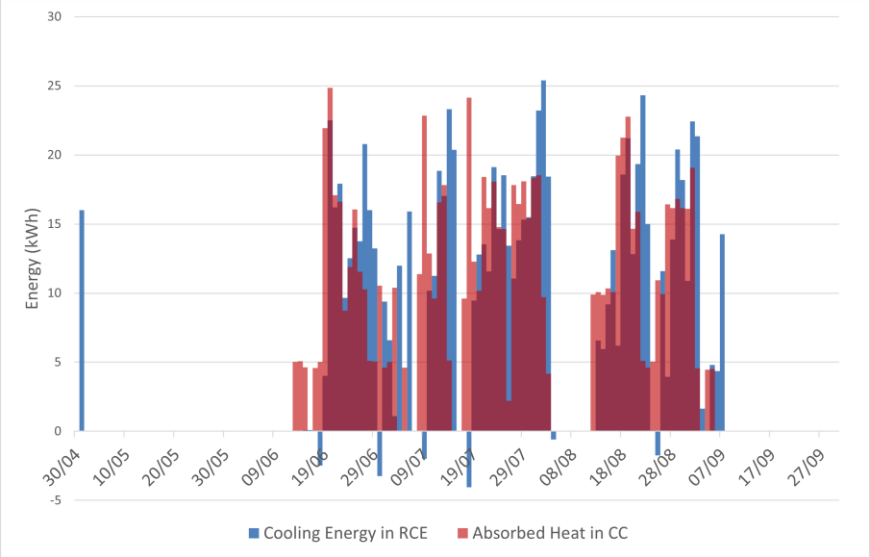

Fig 5. Visual comparison between the cooling energy produced in the RCE and the cooling energy consumed in the chilled ceiling.

3.2. Chilled Ceiling Performance

The chilled ceiling system was operational for 70 out of the 152 days simulated, working between 3 to 6.5 hours per day on average during half of the operational days. The total cooling energy load absorbed by the water in the chilled ceiling was on 859 kWh.

Fig 6 shows the cooling energy delivered by the chilled ceiling system and the backup system, air conditioner, over the simulation period. During its operational period, the chilled ceiling system functioned autonomously 87.74% of the time. The backup system was active for the remaining 12.26 % of the time. Notably, the backup system had to work for more than 50 % of the time on only three days (22/07, 23/07, and 24/07). The performance of the integrated system during the critical period from July 22 to July 25 is illustrated in **Fig 7** . The peak ambient temperature rises above 35 ºC, being the warmest days of the simulation. As a result, the temperature in the cold tank quickly rises above 23 ºC to compensate the warm days.

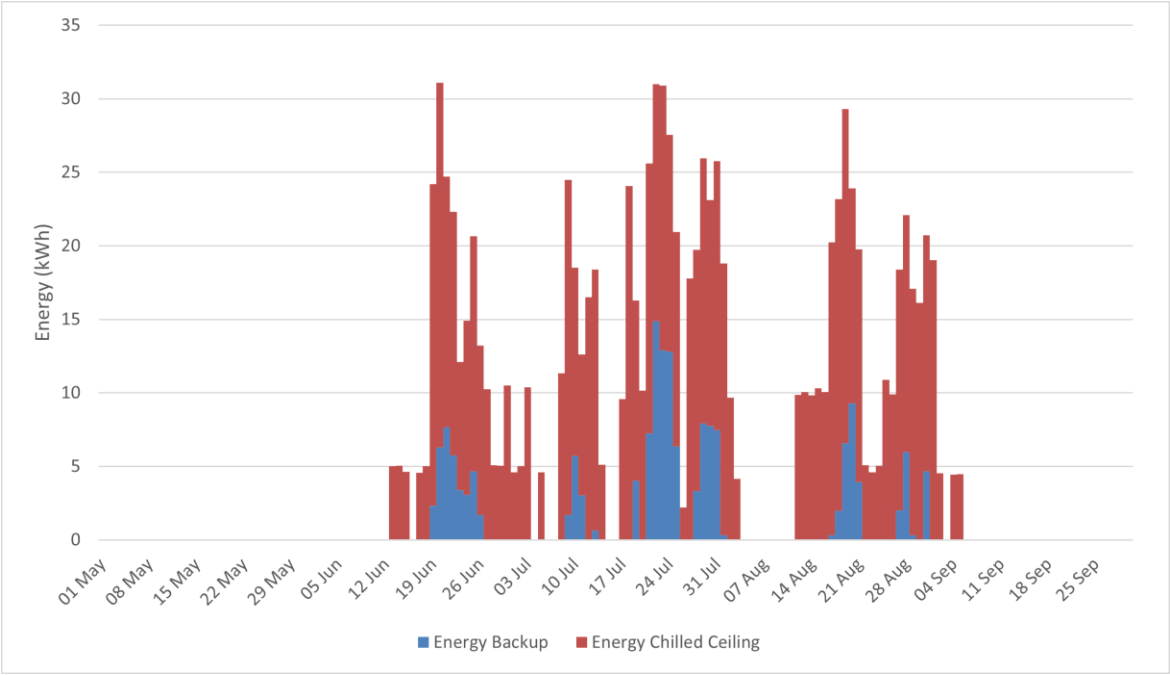

Fig 6. Difference between the energy contribution by the chilled ceiling and the backup system on the first floor.

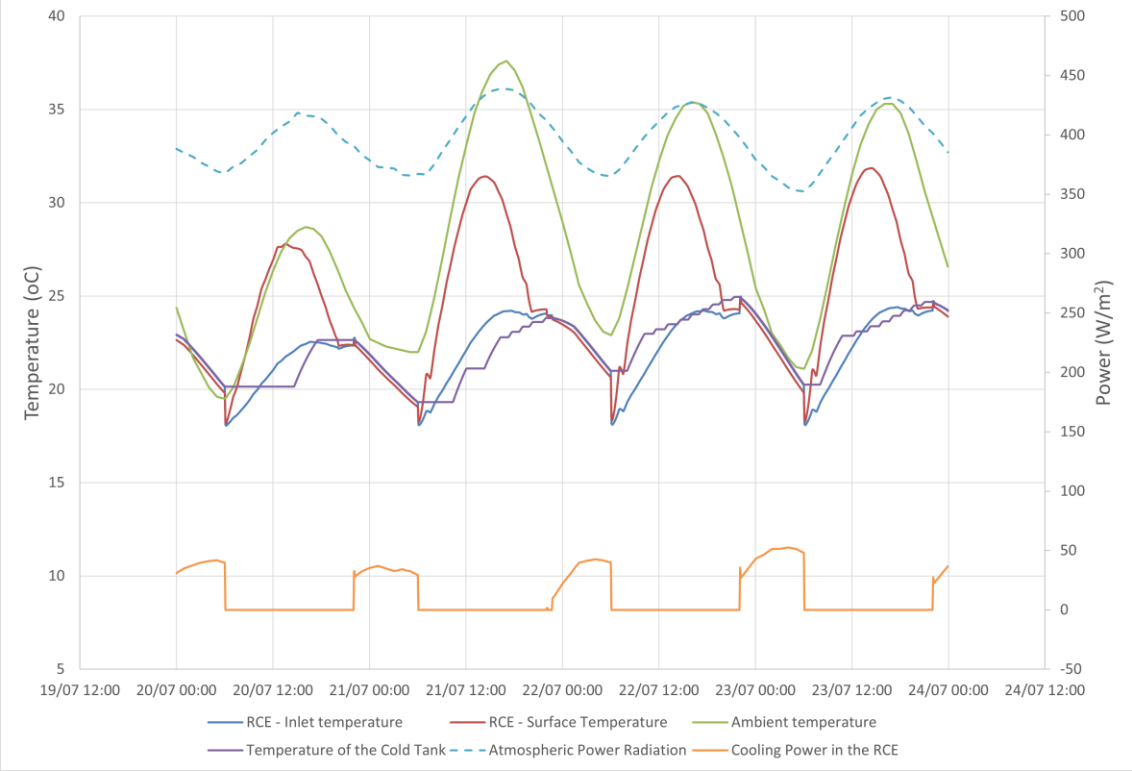

Fig 7. Performance of the RCE during the critical period from July 22nd to July 25th.

3.3. Comfort and Discomfort Analysis

Fig 8 and **Fig 9** show the room temperature (in blue) in the first and second floor, respectively; the green columns indicate when the cooling system (chilled ceiling or back up in the first floor) can be activated.

Comfort levels were analysed for the periods when the conditioning systems (free cooling, cooling system or backup) were designed to operate (represented by the green line in the graphics). Most of the time, the temperature of the floors is in the desired range. The first-floor experienced discomfort for only 0.8% of the time, with an average discomfort level of 0.21 °C and a maximum discomfort of 0.29 °C. In contrast, the second floor, which relied on a commercial air conditioner system, experienced discomfort for 5.76 % of the time, with an average discomfort level of 1.1 °C.

This discomfort observed on the second floor is specific to the sizing and control strategy used in this study. It is important to note that the use of a chilled ceiling with the RCE is not the sole determinant of comfort levels. However, these findings support the idea of utilizing underused cooling capacity from the RCE to partially meet the cooling needs on the second floor too, potentially reducing the occurrence of the discomfort observed.

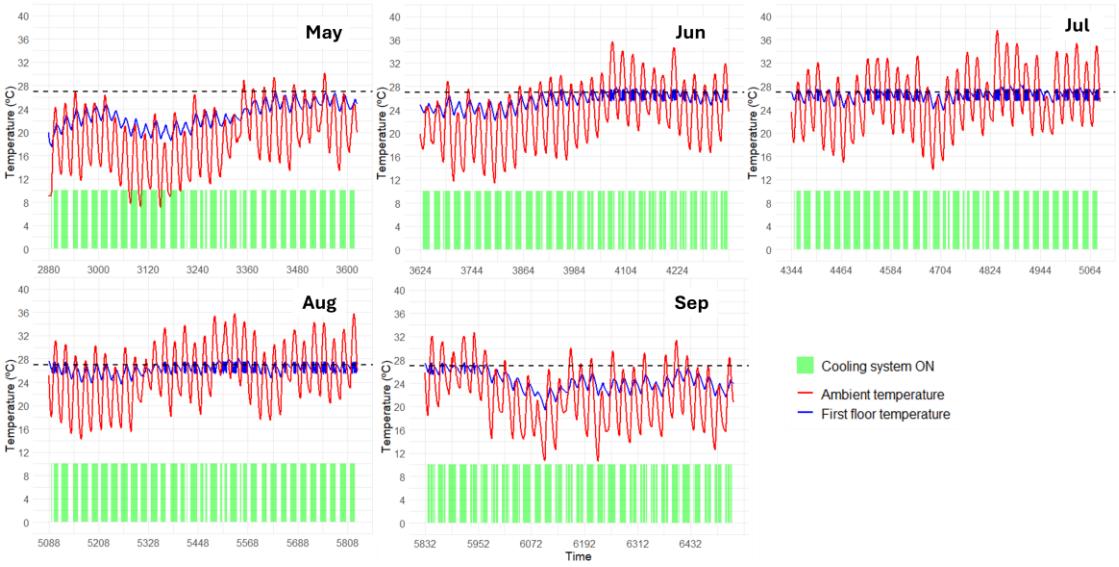

Fig 8. Thermal evolution in the first floor over the simulations months. The green line indicates when the cooling systems can operate.

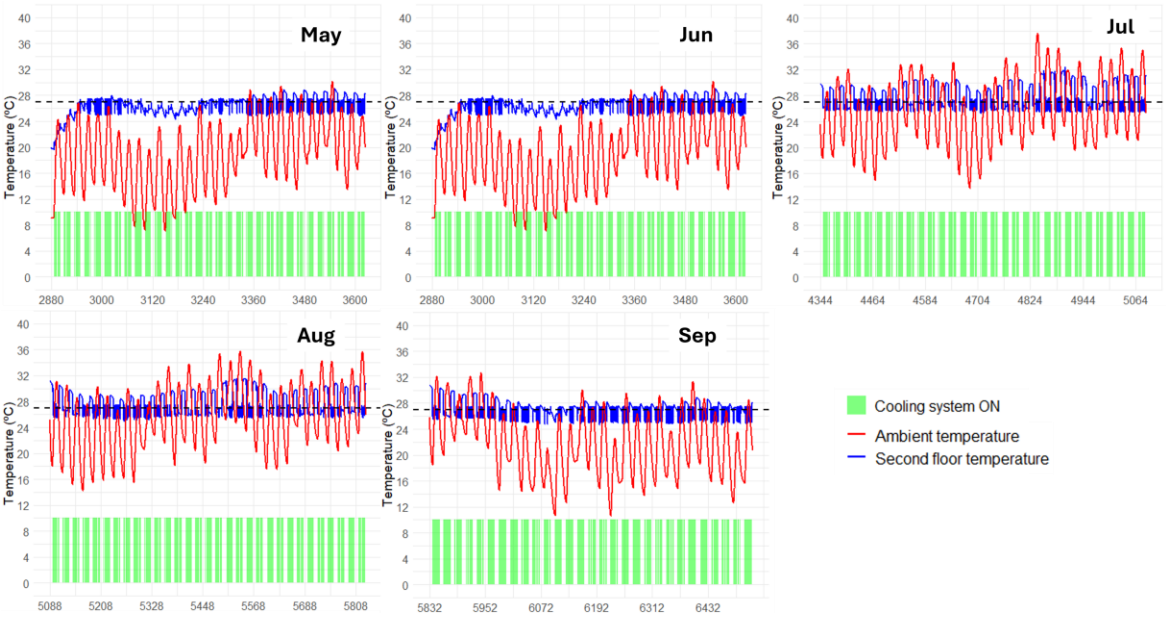

Fig 9. Thermal evolution in the second floor over the simulations months. The green line indicates when the cooling systems can operate.

3.4. Energy savings. Comparison with the reference case

The energy consumption of the reference system is due to the electricity needed by the heat pump to achieve the meet the cooling demands in the first floor. The distribution system is identical in both the reference and proposed cases, utilizing a hydronic system to supply cold to the user. **Fig 10** shows the electricity consumption of the heat pump over three consecutive days in July (from 10/07 at 00:00 to 13/07 at 23:55). The electricity consumption for heating is not considered since it is out of the scope of analysis for this study.

Regarding the electricity demand for cooling, shown in **Fig 10**, the electricity consumption is limited to a few hours, with the control strategy aiming to cool the water flow until the cold tank temperature drops to 15 °C.

In the RCE+CC case, the total electricity consumption is 1540 kWh, which accounts for the electricity consumption of both air conditioners (the backup system and the one on the second floor). The reference case shows a total electricity consumption of 1680 kWh, which includes the energy used by the air conditioners and the air-to-water heat pump. The total electricity savings in the improved system throughout the season is

approximately 140 kWh due to the use of the RCE field.

It should be noted that this analysis does not include the electricity consumption of other hydronic components, such as the pumps that circulate water through the RCE field and the chilled ceiling. As a result, the actual energy savings achieved may differ to those reported in this study, as the additional electricity consumption from these hydronic components was not accounted for in the calculated savings.

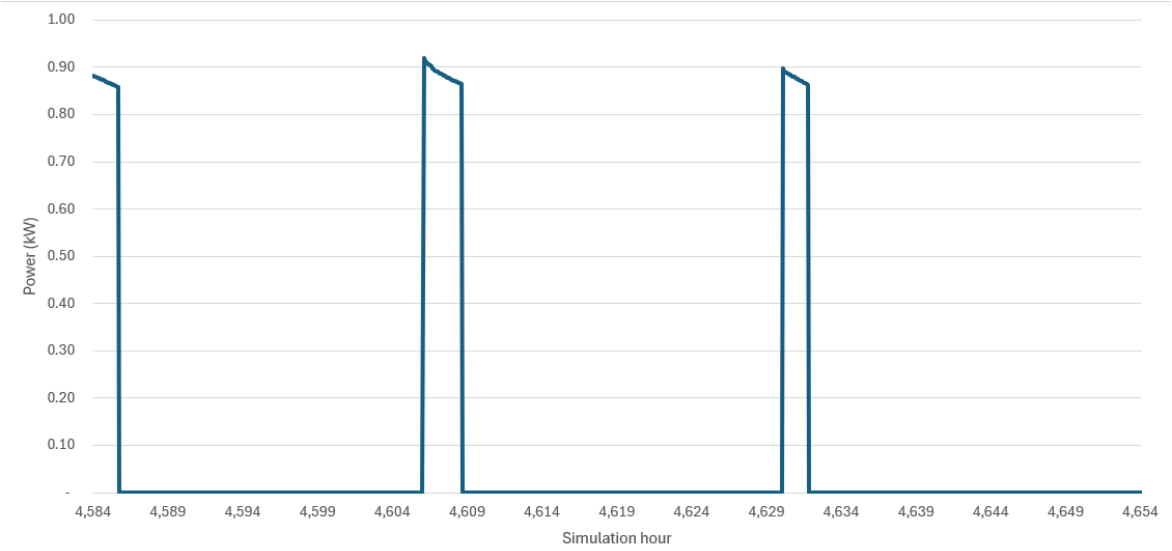

Fig 10. Electric energy consumption for cooling due to the heat pump between the days July 10th at noon and July 13th at 23:55.

4. Conclusions

This paper presented a first evaluation of the performance of an integrated Radiative Collector and Emitter system combined with chilled ceilings in cooling a multifamily building in Lleida, Spain. Using TRNSYS 18 for simulations over the summer months, key findings are as follows:

The RCE system's mean net radiative cooling power was 30.34 $W \cdot m^{-2}$ with an average efficiency of 42.3%. The chilled ceiling system operated efficiently and autonomously 87.74% of the time, rarely needing the backup system. The system demonstrated modest electricity savings for cooling demand of approximatively 140 kWh during the observed period compared to the reference case. In terms of indoor comfort, the first floor, using the integrated system, experienced minimal discomfort (0.8% of the time with an average discomfort of 0.21°C).

The RCE system reduced the storage tank temperature by an average of 3.29°C each night, with peak nights up to 7.82°C, while the chilled ceiling increased the tank temperature by 3°C during its operation

The findings from this study suggest that integrating radiative cooling technologies with chilled ceilings can lead to energy savings while maintaining occupant comfort in buildings. However, the RCE system still requires further improvement to achieve significant and consistent energy savings. The demonstrated performance highlights its potential for widespread application in sustainable building designs, but additional research is needed to refine the system's efficiency. Future studies should focus on optimizing the sizing and control strategies for these integrated systems and explore their performance across different climatic regions.

5. Acknowledgments

This publication is part of the grant PDC2022-133215-I00, funded by CIN/AEI/10.13039/501100011033/ and by the "European Union NextGenerationEU/PRTR". This publication is also part of the grant TED2021-131446B-I00, funded by MCIN/ AEI/10.13039/501100011033/ and by the "European Union NextGenerationEU/PRTR". The authors would like to thank Generalitat de Catalunya for the project awarded to their research group (2021SGR 01370).

6. References

Chen, L., Zhang, K., Ma, M., Tang, S., Li, F., Niu, X., 2020. Sub-ambient radiative cooling and its application in buildings. Build. Simul. 13, 1165–1189. https://doi.org/10.1007/s12273-020-0646-x

Eurostat, 2019. Energy consumption in households. URL https://ec.europa.eu/eurostat/statistics-explained/index.php?title=Energy_consumption_in_households#Use_of_energy_products_in_households_by_purpose

IEA, 2019. Global energy demand rose by 2.3% in 2018, its fastest pace in the last decade. IEA. URL https://www.iea.org/news/global-energy-demand-rose-by-23-in-2018-its-fastest-pace-in-the-last-decade (accessed 1.23.20).

Jin, W., Ma, J., Jia, L., Wang, Z., 2020. Dynamic variation of surface temperatures on the radiant ceiling cooling panel based on the different supply water temperature adjustments. Sustainable Cities and Society 52, 101805. https://doi.org/10.1016/j.scs.2019.101805

Kousis, I., Pisello, A.L., 2023. Toward the Scaling up of Daytime Radiative Coolers: A Review. Advanced Optical Materials 11, 2300123. https://doi.org/10.1002/adom.202300123

Remund, J., Müller, S., Kunz, S., Huguenin-Landl, B., Studer, C., Cattin, R., 2019. Meteonorm.

Su, W., Cai, P., Darkwa, J., Hu, M., Kokogiannakis, G., Xu, C., Wang, L., 2023. Review of daytime radiative cooling technologies and control methods. Applied Thermal Engineering 235, 121305. https://doi.org/10.1016/j.applthermaleng.2023.121305

Uponor, n.d. Build on Uponor with Varicool Eco S. URL https://e-cooling.cz/wp-content/uploads/2018/12/EN_Varicool-Eco-S.pdf (accessed 7.15.24).

Vall, S., Johannes, K., David, D., Castell, A., 2020a. A new flat-plate radiative cooling and solar collector numerical model: Evaluation and metamodeling. Energy 202, 117750. https://doi.org/10.1016/j.energy.2020.117750

Vall, S., Medrano, M., Solé, C., Castell, A., 2020b. Combined Radiative Cooling and Solar Thermal Collection: Experimental Proof of Concept. Energies 13, 893. https://doi.org/10.3390/en13040893

Vilà, R., Garcia, M., Medrano, M., Martorell, I., Castell, A., 2020. Combining Radiative Collector and Emitter with Compression Heat Pump: Numerical Analysis, in: Proceedings of the ISES EuroSun 2020 Conference – 13th International Conference on Solar Energy for Buildings and Industry. Presented at the EuroSun 2020, International Solar Energy Society, Athens (Greece), pp. 1–7. https://doi.org/10.18086/eurosun.2020.06.01

Vilà, R., Martorell, I., Medrano, M., Castell, A., 2021. Adaptive covers for combined radiative cooling and solar heating. A review of existing technology and materials. Solar Energy Materials and Solar Cells 230, 111275. https://doi.org/10.1016/j.solmat.2021.111275

Yuan, J., Zhang, K., Zhao, D., Yin, X., Yang, R., Tan, G., 2018. Energy saving analysis of a metamaterial-based radiative cooling system for low-rise residential buildings by integrating with radiant floor, in: Proceeding of 3rd Thermal and Fluids Engineering Conference (TFEC). Presented at the 3rd Thermal and Fluids Engineering Conference (TFEC), Begellhouse, Fort Lauderdale, USA, pp. 1747–1750. https://doi.org/10.1615/TFEC2018.nbe.022313

Comparative study on small-scale HPs for decentral DHW preparation in multi-family buildings

William Monteleone[1], Fabian Ochs[1]

[1] Unit for Energy Efficient Building, University of Innsbruck, Austria

Abstract

In renovated multi-family buildings, domestic hot water preparation is still predominantly supplied by gas-fired or electric boilers. Where centralized solutions cannot be adopted, flat-wise compact heat pump solutions can contribute substantially to the decarbonization of the building stock and reduce the invasiveness of the installation, but an experiments-based comparative study of different decentral hydronic concepts is missing in the literature. Within this work, three heat pumps based solutions for decentral domestic hot water preparation were tested and their dynamic behavior with a predefined tapping pattern was observed. The results highlighted that the use of a mantle heat exchanger in common boiler heat pumps results in longer charging intervals and increased electricity consumption. Through simulations, the monthly performance of the air-source systems was evaluated and indicated a mini-split solution as the most efficient, with a yearly performance factor of 2.5.

Keywords: Decentral DHW preparation, Compact heat pumps, serial renovation, multi-family buildings

1. Introduction

Space heating (SH) and domestic hot water (DHW) preparation in multi-family buildings (MFBs) are still heavily based on fossil fuels or inefficient technologies (IEA, 2022). To achieve the climate-neutrality targets of the European Union (EU) concerning the building stock by 2050 (European Commission, 2021), an increase in the renovation rate is required as well as a swift transition to efficient and sustainable heating systems. Heat Pumps (HPs) will play a decisive role in the decarbonization of the building sector (IEA, 2022) but their implementation in MFBs often faces technical and non-technical challenges, among them source-accessibility, installation space requirements, noise as well as invasiveness (Cozza et al., 2022). Where centralized HPs cannot be adopted, flat-wise HP solutions for DHW preparation are promising candidates to replace gas-fired boilers or E-boilers but their investment costs are usually higher than traditional technologies (Gustafsson et al., 2017). Within this work, three HP-based solutions for decentral DHW preparation will be evaluated, consisting of a façade-integrated mini-split air-to-water HP (Monteleone et al., 2024), a air-source boiler HP and a return flow water-to-water HP. The first solution was investigated within the research projects "FitNeS" (FFG (Austrian Research Promotion Agency), 2023) and "PhaseOut" (FFG (Austrian Research Promotion Agency), 2024), while the others are commercial solutions already available on the market. Prefabricated façade elements allow on one hand the improvement of the building envelope and on the other hand a fast, cost-effective replacement of fossil-based technologies. First, the three solutions are tested in the laboratory over a cycle of 24 hours and variable heat source temperature to assess their dynamic performance. Based on the measurements, performance maps depending on source and sink temperature were obtained for the air-source HPs and a yearly simulation was performed for the climate of Innsbruck in the Simulink environment with the use of the Carnot Toolbox (Solar-Institut Juelich FH Aachen, 2018). Out of the simulations, a yearly system performance factor was calculated for the two air-based solutions, as well as the peak photovoltaic (PV) power necessary to cover 50% of the yearly HP electric consumption.

2. Methodology

The hydronic systems which will be analyzed within this work are depicted schematically in Figure 1 to Figure 3. Figure 1 shows a semi-central system with a central HP supplying the SH demand of the building and a decentral air-source boiler HP for DHW preparation. The heat source (air) can be either room air or outside air

© 2024. The Authors. Published by International Solar Energy Society
Selection and/or peer review under responsibility of Scientific Committee
10.18086/eurosun.2024.02.13 Available at http://proceedings.ises.org

by means of a duct. In Figure 2 a system with a central HP for SH and a decentral return flow HP for DHW is shown. The return flow HP uses the return of the SH as a heat source to heat up a storage tank (integrated within the HP casing). Then, in Figure 3, the decentral DHW preparation is provided by means of a 1.5 kW façade-integrated split air-to-water HP, as the one described in (Monteleone et al., 2024; Ochs et al., 2022). With focus only on DHW preparation, all three systems have been replicated and tested in the hydraulics laboratory of the University of Innsbruck and their dynamic behavior has been observed.

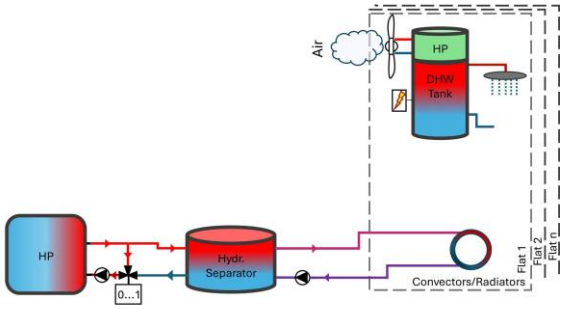

Figure 1: Conceptual scheme of a hydronic system with central HP for SH and decentral ambient air HP for DHW preparation.

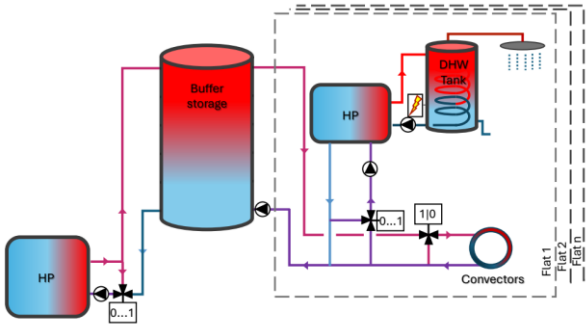

Figure 2: Conceptual scheme of a hydronic system with central HP for SH and decentral return flow HP for DHW preparation (and optionally for cooling).

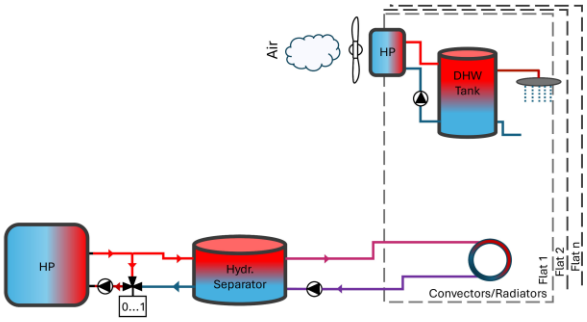

Figure 3: Conceptual scheme of a hydronic system with central HP for SH and decentral façade-integrated split air-to-water HP for DHW preparation.

2.1. Experiments

The HP-based solutions mentioned in the previous sections were tested in a double-room climate chamber. Each test room is 200 cm x 250 cm x 280 cm and is insulated with 8 cm polyurethane. Heating and cooling in each room are provided by means of water-based fan coils. The test duration is 15 hours, during which the tapping profile “M” is applied to replicate the hot water consumption of a medium-small flat (CEN/TC 113, 2017). Table 1 gives an overview of the boundary conditions applied during the measurements to each decentral HP concept for DHW preparation. The required source temperature for all air-source HP concepts is guaranteed by means of the fan coils installed in the test rooms, while a 5000 Liters water storage tank is used

as heat source for the return flow HP. The water is delivered from the heat source (i.e. 5000 Liters hot water storage tank) to the test specimen by means of an unpressurised manifold, with the possibility to control the flow rate and supply temperature by means of a mixing valve and a variable speed pump, as shown in Figure 4(a). For the ambient air-to-water boiler HP concept, the unit is installed in a room where the indoor air temperature corresponds to the requested source temperature. The tested ambient air and return flow HP are commercial units available on the market and share the same HP layout. For their test procedures, the setup depicted in Figure 4(b) was adopted.

Table 1: Boundary conditions applied during the measurements for each decentral HP concept.

Ambient air-to-water HP	
Source temperature (Room air) / [°C]	10….15….20
Source (air) volume flow / [m^3/h]	160
Storage tank size / [Liters]	150
Return flow HP	
Source temperature (SH return) / [°C]	25….30….35 (Manufacturer's limitations)
Source (water) volume flow / [l/min]	5
Storage tank size / [Liters]	150
Façade-integrated split air-to-water HP	
Source temperature (Outdoor air) / [°C]	10….15….20
Source (air) volume flow / [m^3/h]	350
Storage tank size / [Liters]	120

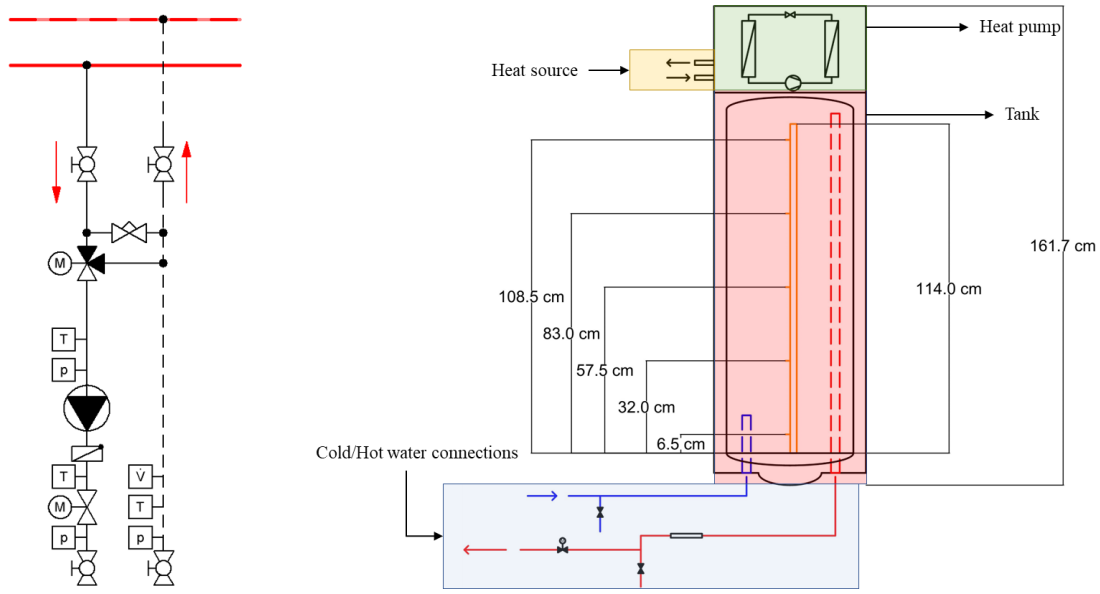

(a) (b)

Figure 4: (a) Test infrastructure for the control of source temperature level and flow rate in the measurement of the return flow HP and (b) Test layout for the measurement of ducted air-source HP and return flow HP. The probe with 5 Pt100 sensors inside the storage tank is also shown.

Water is heated up by means of a mantle heat exchanger installed between the tank lining and the insulation layer. Inside the water tank, a rod carrying 5 Pt100 temperature sensors is installed in order to monitor the thermal stratification. Both HP models are provided with an electric back-up heater, which however is disconnected during the measurements. To apply the tapping profile, a magnetic 2-way valve is used. The (tapped) water volume flow is detected by means of a magnetic flow meter (MFM). The measurement starts with a fully charged storage with a setpoint temperature of 55 °C and the tapping cycle is initiated 30 seconds afterwards. After the completion of the full tapping cycle, the measurement is stopped. In the case of the mini-split air-to-water HP, the outdoor unit is placed in the room replicating the outdoor air conditions, while the remaining infrastructure is placed in the ambient room at a temperature of 20 °C. The test layout highlighted in Figure 5 is adopted, similar to the one used for the previous HP concepts. Three temperature sensors are installed within the DHW storage, 5 cm, 36 cm and 64 cm from the top edge of the tank respectively. The flush valve on the cold water side is kept open for the whole duration of the test to guarantee a possibly constant

freshwater temperature. Figure 6(a), (b) and (c) depict the double room climate chamber used for the measurements, the outdoor unit of the tested mini-split air-to-water HP and its layout when integrated in a test façade.

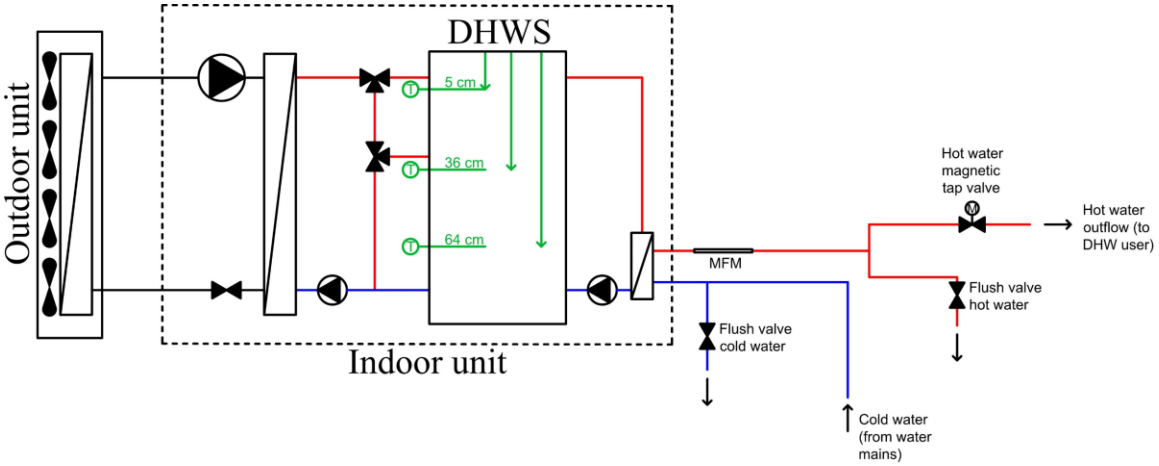

Figure 5: Test setup for a mini-split air-to-water HP with integrated DHW storage.

(a) (b) (c)

Figure 6: (a) Double-room insulated climate chamber used for the testing of air-to-water and water-to-water HPs, (b) Outdoor unit of the tested (façade-integrated) mini split air-to-water HP in the chamber and (c) outdoor unit of the mini split HP integrated in a test façade.

The performance of each HP concept is evaluated by means of the following definition of COP:

$$COP_{DHW} = \frac{Q_{DHW}}{Q_{el,HP}} \qquad \text{(eq. 1)}$$

Where Q_{DHW} is the energy delivered to the DHW user in [kWh_{th}] and $Q_{el,HP}$ the electricity supplied to the HP during the whole measurement cycle in [kWh_{el}].

To produce the performance maps for each HP, first the measurement data from the HP refrigerant cycle are retrieved. For ambient air and for the return flow HPs, the measurement setup represented in Figure 7(a) was available, with four temperature sensors installed within the refrigerant cycle, at the entrance and at the exit of condenser and evaporator respectively. Additionally, the electric power consumption of the compressor is measured, as well as the source and sink temperatures. For the mini-split HP, a more detailed setup (see Figure 7(b)) was used.

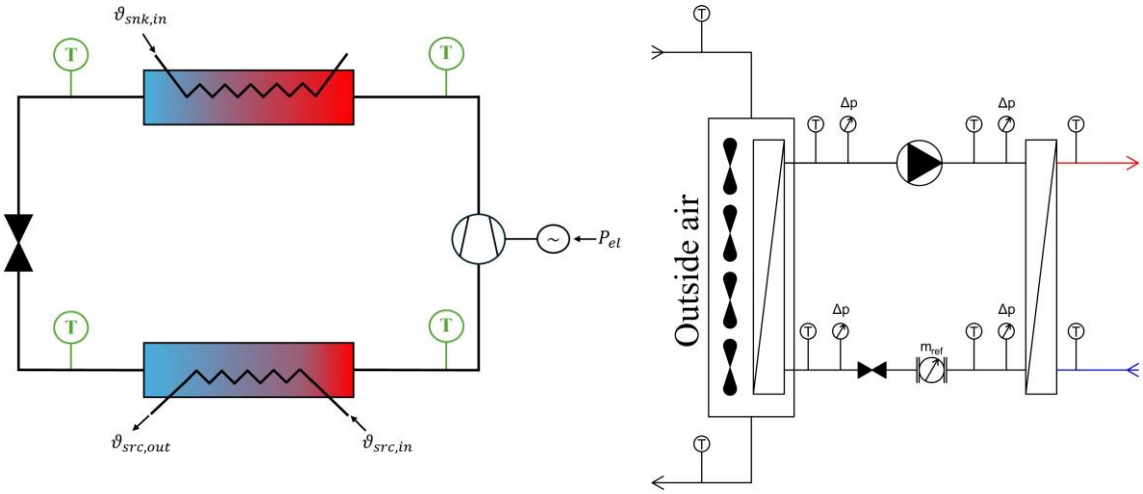

(a) (b)

Figure 7: Schematic representation of the refrigerant cycle of a generic HP with the position of the temperature sensors.

For the tests involving the façade-integrated split HP, the pressure levels and the refrigerant mass flow are also available. The measured data are then fed to the refrigerant cycle model described in (Monteleone et al., 2024) to complete the missing information and generate the performance maps for each HP concept. The ambient air HP, as well as the return flow HP, feature the same vertical rotary-type single-speed compressor with a displacement volume of 5.6 cm^3. On the other hand, the mini-split HP uses a horizontal rotary-type single-speed compressor but with a displacement volume of 12.7 cm^3.

2.2. Simulations

For the DHW preparation in minimal invasive renovations, the HP concepts of Figure 1 and Figure 3 were further investigated in a dynamic simulation study within the simulation environment of MATLAB+Simulink (Mathworks, 2022) with the use of the CARNOT toolbox (Solar-Institut Juelich FH Aachen, 2018). The aim of the simulation study is to evaluate the annual performance of the investigated systems for a single flat in the climate of Innsbruck, Austria. However, instead of considering ambient air as heat source for the system in Figure 1, a ducted variant (with outdoor air as heat source) was selected for the simulation study. This was done in order to guarantee the same ambient boundary conditions to both simulated systems and focus more on the dynamic performance of the presented HP concepts. A daily "M" tapping profile was assumed for all the simulation studies, with a storage temperature setpoint of 55 °C and freshwater temperature equal to 13 °C. The same tank sizes presented in Table 1 were adopted for the simulation study. The heat transfer coefficient of the storage envelope was chosen to obtain a tank with energy efficiency class ErP "B" (The European Parliament and the Council of the European Union, 2009). In the modelled system shown in Figure 8(a) (ducted air-source DHW HP), one temperature sensor is used to turn on and off the HP, positioned at 70% of the storage height. The HP is turned on when the temperature measured by the sensor is 8 K lower than the setpoint and turns off when the sensor temperature is 2 K above the setpoint. In Figure 8(b) the system with a façade-integrated mini-split air-to-water HP is illustrated. The system features a façade-integrated outdoor unit housing the evaporator and four parallel axial fans, while the indoor unit includes the compressor, the condenser, the expansion valve and a 120 litres DHW storage. An 8-kW electric post-heater is considered and the delivery of the DHW demand takes place through a freshwater station. During the startup phase of the HP, the temperature of the water supplied to the storage would be lower than the temperature in the tank. For this reason, the top mixing valve in Figure 8(b) is closed entirely and water is recirculated in a loop until the temperature sensor T0 detects a water temperature higher than 52 °C. Once the water supply temperature has reached the setpoint, the HP begins to charge the top part of the storage to guarantee comfort in case of short-term taps. Once the reserve volume of the storage is charged, the tank is heated up via the intermediate charging point. Similarly to the system presented in Figure 8(a), the HP in Figure 8(b) is controlled by means of a hysteresis controller based on the temperature sensors T1 and T2. The HP is thus turned on when the sensor T1 detects a temperature 5 K lower than the setpoint and turns off when the sensor T2 measures a temperature equal to the setpoint plus 1 K. The temperature sensors T1 and T2 are placed at 32% and 84% of the storage height respectively. On the secondary side the speed-controlled pump is modulated by means of a PID

controller to reach a comfort temperature for the DHW user of 45 °C (temperature sensor T3). For both air-source HPs, minimum and maximum operational time intervals are assigned. If the air temperature is higher than 7 °C, the HP is assigned a minimum run time of 3 minutes while there is no maximum run time. If the air temperature falls below 7 °C, a maximum run time of 80 minutes is considered, after which the HP is stopped for 10 minutes to allow for the defrosting. The degradation of the performance of the heat exchanger due to ice formation, as well as the additional electricity consumption for defrosting, are not considered within this model.

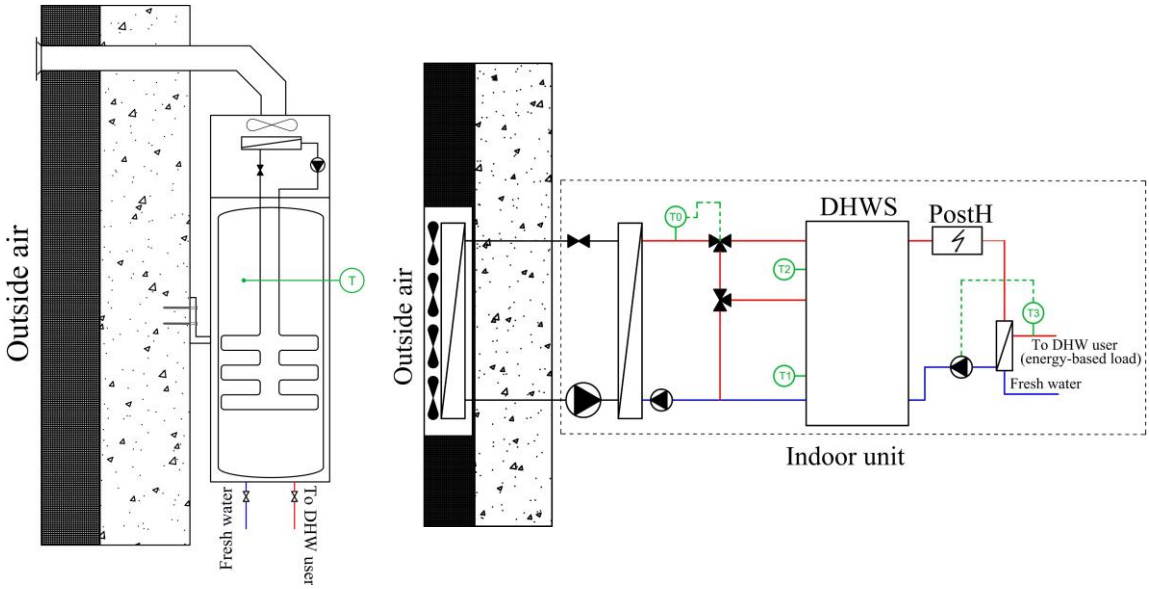

(a) (b)

Figure 8: Modelled (a) ducted air-source DHW HP with integrated 150 litres tank and (b) façade-integrated mini-split HP with 120 litres tank, 8 kW post-heater and freshwater station.

For the evaluation of the electricity consumption covered by PV, a reference building, subjected to renovation, is considered. The reference building consists of a ground floor and four upper floors, with two-room apartments with an area of 44.0 m^2 and one-room apartments with an area of 37.3 m^2, for a total of ten flats (with reference floor plane shown in Figure 9). It is assumed that hot water consumption for each flat is the same and corresponds to the "M" profile according to the norm. While the instantaneous hot water consumption varies considerably during the day for each flat the in the building, it is assumed that the monthly hot water consumption for the entire building is simply the single flat consumption in a month multiplied with the number of flats. For all simulated variants, the properties of the PV system are indicated in Table 2. The electricity consumption of the appliances as well as for circulation pumps is discarded for this study and for the evaluation of the PV coverage.

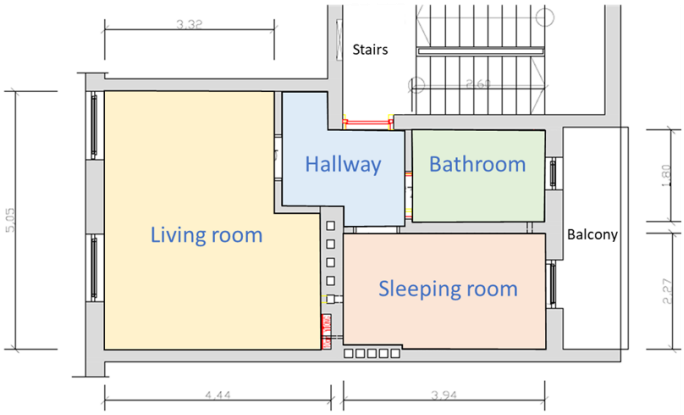

Figure 9: Floor plane of one of the one-room apartments subjected to renovation, with a floor area of 37.3 m^2.

Table 2: Assumptions used for the modelling of the PV system in the simulations.

Installed PV [kWpeak]	5 kW
Location	Roof

Slope of PV modules [°]	30 °
Azimuth [°]	0 ° (South)
Inverter efficiency [%]	96 %
Inverter standby power [W]	2 W
Maximum AC power for PV [kW]	3.8 kW

The performance of the HP concept has been evaluated for each month of the year by means of a performance factor (PF) defined as:

$$PF_{HP} = \frac{Q_{th,HP}}{Q_{el,HP} + Q_{el,PostH}} \qquad \text{(eq. 2)}$$

Where $Q_{th,HP}$ represents the heat delivered from the HP to the DHW storage in [kWh$_{th}$], $Q_{el,HP}$ the electricity consumed by the compressor and by the HP control in [kWh$_{el}$] and $Q_{el,PostH}$ the electricity consumption of the electric post-heater (if available) in [kWh$_{el}$].
The PV coverage is defined in turn as:

$$f_{PV,cover} = \frac{Q_{el,PV,AC}}{n_{flats}\,(Q_{el,HP} + Q_{el,PostH})} \qquad \text{(eq. 3)}$$

Where $Q_{el,PV,AC}$ represents the AC PV yield in [kWh$_{el}$] and n_{flats} the number of flats in the building.

3. Results and discussion

3.1. Experiments

In Figure 10 the measurement results for the ambient air HP at source temperature of 10 °C are shown. The top diagram depicts the profile of the temperatures detected by the 5 Pt100 sensors inserted in the probe. ϑ_5 represents the top sensor, ϑ_1 the lowest one. Then the middle diagram shows the measured HP electric power consumption, while the bottom diagram shows the tapping profile with the respective measured water volume flows.

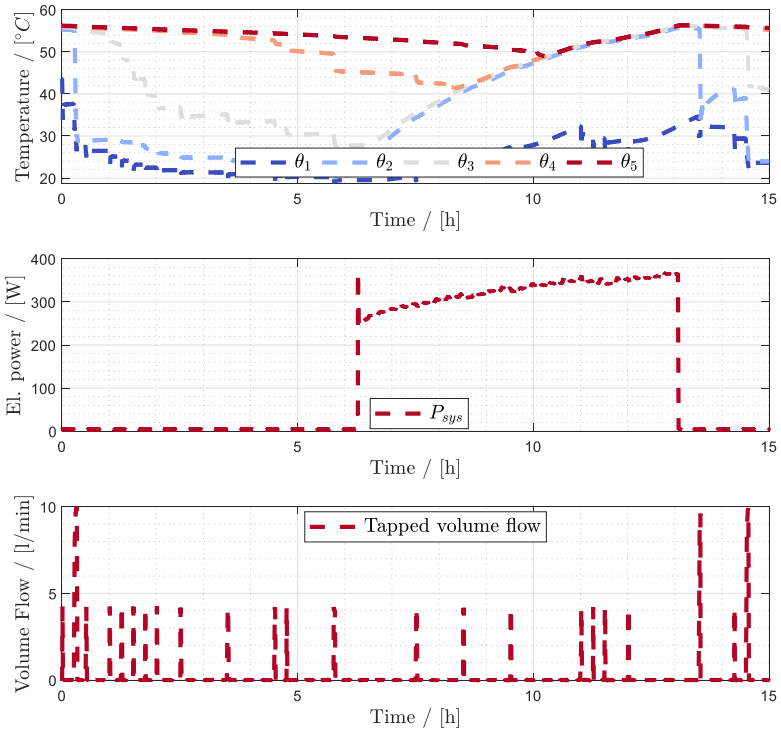

Figure 10: Dynamic test results for the ambient air HP with 10 °C ambient temperature and "M" tapping profile.

During the 15 hours of the measurement, only one charging cycle is performed by the HP which lasts for about 7 hours with an average electric power consumption of 320 W. When the charging starts, the storage is

homogeneously heated from the bottom to the top due to the presence of the mantle heat exchanger, which results in longer charging intervals and increased electricity consumption. This leads to a COP_{DHW} of 1.28, as also illustrated in Table 3. At an air temperature of 15 °C, the COP_{DHW} reaches 1.53 while it jumps to 2.85 at an air temperature of 20 °C. This behaviour was expected, since the thermal losses attributed to the storage tank are much lower at 20 °C then at 15 or 10 °C. As a consequence, the charging intervals are shorter and the electricity consumption drops from 4.03 kWh_{el} to 2.17 kWh_{el} for the whole tapping cycle.

Table 3: Summary of measurement results for the ambient air HP for DHW preparation. The cold water temperature equals 13 °C.

ϑ_{source} /[°C]	10	15	20
$Q_{DHW}/[kWh_{th}]$	6.15	6.15	6.18
$Q_{el,HP}/[kWh_{el}]$	4.83	4.03	2.17
COP_{DHW} /[−]	1.28	1.53	2.85

Figure 11 illustrates the measurements of the return flow HP at a source temperature of 25 °C. For this type of HP concept, the charging cycles are much shorter than in an ambient-air HP. In fact, in the diagrams presented in Figure 11, the charging interval lasts for less than 3 hours. Therefore, the resulting electricity consumption equals 1.09 kWh_{el}, as shown in Table 4. The resulting COP_{DHW} at 25 °C corresponds to 5.61, while it equals 5.84 and 6.24 at source temperatures of 30 °C and 35 °C respectively.

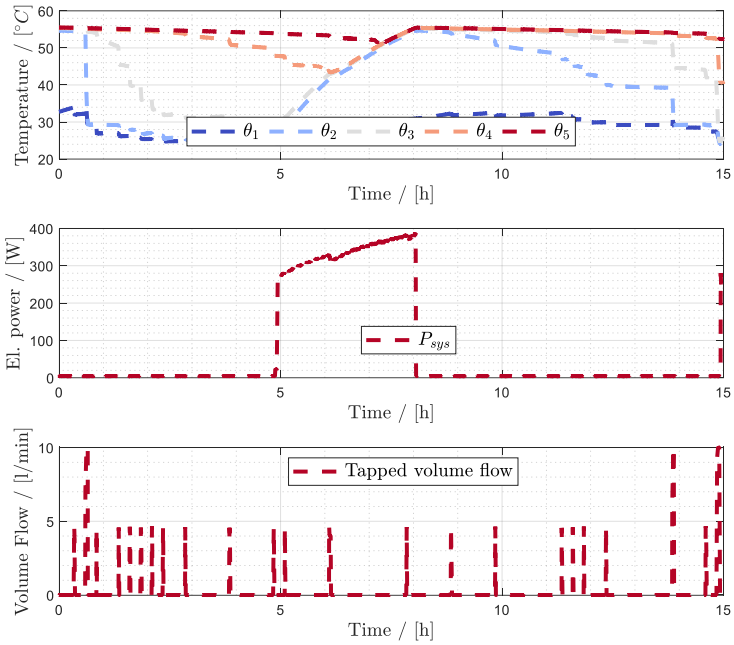

Figure 11: Dynamic test results for the return flow HP with 25 °C source temperature and “M” tapping profile.

Table 4: Summary of measurement results for the return flow HP for DHW preparation. The cold water temperature equals 13 °C.

ϑ_{source} /[°C]	25	30	35
$Q_{DHW}/[kWh_{th}]$	6.11	6.11	6.11
$Q_{el,HP}/[kWh_{el}]$	1.09	1.05	0.98
COP_{DHW} /[−]	5.61	5.84	6.24

Figure 12 shows then the measurement results at 10 °C air temperature for the developed mini-split air-to-water HP. During the measurement cycle, three charging cycles were observed, with a duration of about 1.5 hours each and average electric power consumption of 630 W. Since the water heated up in the condenser is directly supplied to the DHW storage (i.e. without the use of internal heat exchangers, see also Figure 5), the charging phase is also characterized by increased mixing, which causes a perturbation in the temperature of upper and medium layers. The smaller hysteresis selected for the HP control (i.e. 5 K) leads to more frequent charging cycles. Nevertheless, the electricity consumption at 10 °C air temperature corresponds to 2.12 kWh_{el}, resulting in a COP_{DHW} of 2.82 (see also Table 5). At 15 °C an electricity consumption of 1.99 kWh_{el} is detected

while at 20 °C it slightly decreases to 1.96. The resulting COP_{DHW} are therefore 3.06 and 3.11, at 15 and 20 °C respectively.

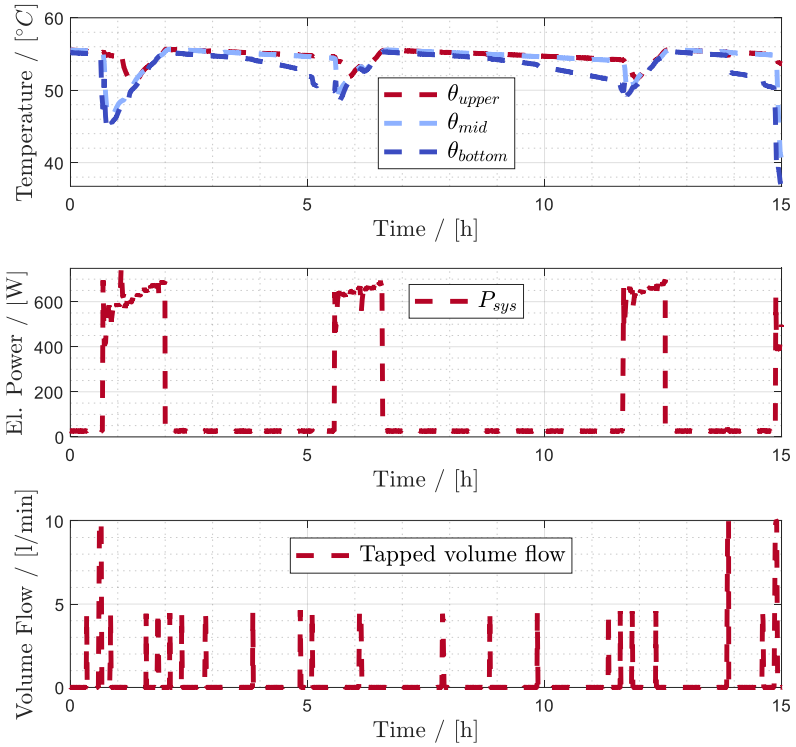

Figure 12: Dynamic test results for the mini-split HP with 10°C source temperature and "M" tapping profile.

Table 5: Summary of measurement results for the mini-split air-to-water HP for DHW preparation. The cold water temperature equals 13 °C.

ϑ_{source} /[°C]	10	15	20
$Q_{DHW}/[kWh_{th}]$	5.98	6.10	6.10
$Q_{el,HP}/[kWh_{el}]$	2.12	1.99	1.96
COP_{DHW} /[−]	2.82	3.06	3.11

Based on the measurements and through the use of the refrigerant cycle model presented in (Monteleone et al., 2024), the performance maps presented in Figure 13 to Figure 15 were generated. In Figure 13 it is possible to remark that the heating capacity of the ambient air HP is lowest among the analysed HP concepts, with about 900 W being delivered at A20W55. The best performance is obtained, as expected, for the return flow HP, with HP COPs well above 2.5 for source temperatures between 25 and 35 °C (see Figure 14(b)). The heating capacity however is lower than the one shown in Figure 15(a) for the mini-split HP, which in turn exhibits lower electric power consumption for the compressor and therefore lower COPs.

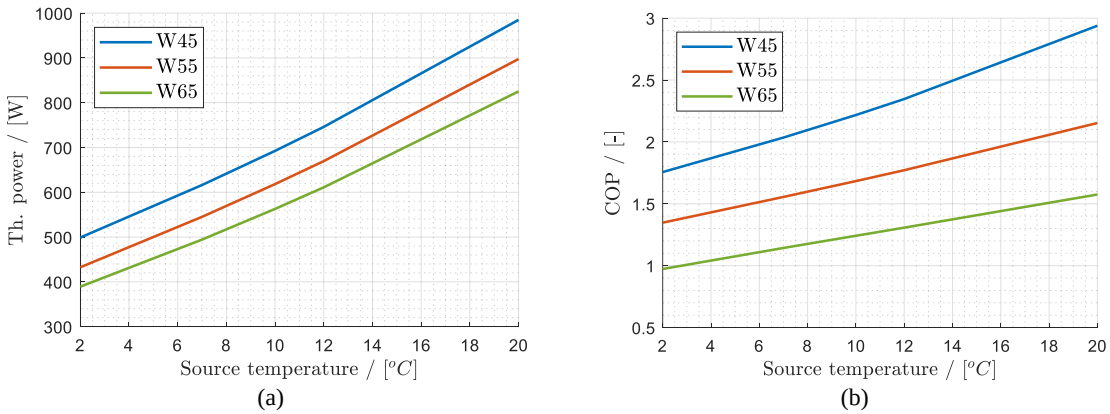

(a) (b)

Figure 13: Performance maps of (a) condenser power and (b) COP based on measurements and refrigerant cycle model (based on (Monteleone et al., 2024)) for the ambient-air HP.

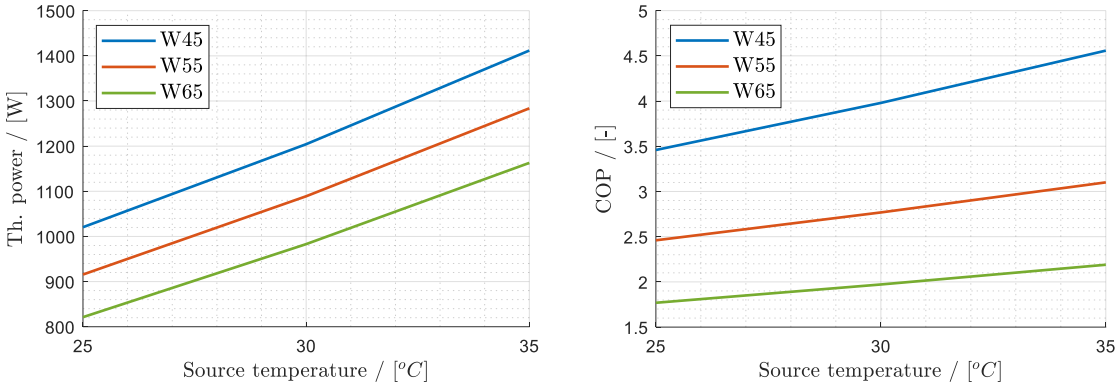

(a) (b)

Figure 14: Performance maps of (a) condenser power and (b) COP based on measurements and refrigerant cycle model (based on (Monteleone et al., 2024)) for the return-flow HP.

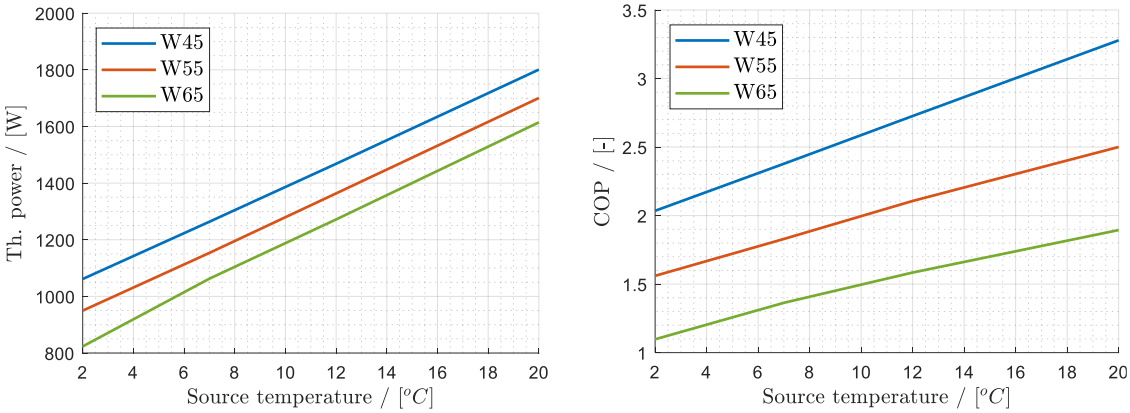

(a) (b)

Figure 15: Performance maps of (a) condenser power and (b) COP based on measurements and refrigerant cycle model (based on (Monteleone et al., 2024)) for the mini-split air-to-water HP.

3.2. Simulations

Figure 16 shows the monthly variation of the simulated PF for DHW preparation (defined according to eq. (2)) for a system with a mini-split façade-integrated air-to-water HP (FIHP) and for a system with a ducted air-source HP (AAHP). As highlighted also in the previous section, the low capacity of air-source boiler HPs results in longer charging intervals and therefore increased electricity consumption and worse yearly performance compared to the mini-split HP. The yearly PF for a mini-split HP reaches a value of 2.50, with a maximum of 2.84 in July and a minimum of 2.11 in January. During the whole year, no post-heater operation was detected. On the other hand, for the ducted air-source HP a yearly PF of 1.99 was obtained, with a maximum of 2.49 in July and a minimum of 1.47 in January.

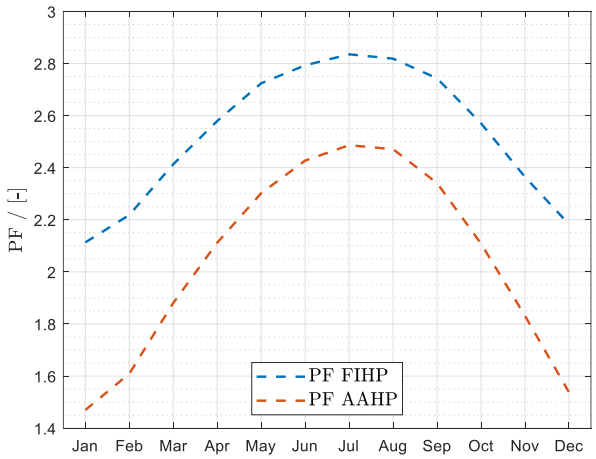

Figure 16: Simulated monthly performance factor for DHW preparation for a mini-split façade-integrated HP and for a ducted air-source HP.

The evaluation of the monthly PV yield with respect to the monthly HP electricity consumption for the reference building (see also section 2.2) yielded the results illustrated in Figure 17(a) and (b), for the mini-split HP and for the ducted air-source HP respectively. During the warmer months, the 5 kW PV supplies up to 68% of the HP electricity demand for the mini-split HP and up to 57% for the ducted boiler HP. However, a yearly coverage factor $f_{PV,cover}$ of 46% is obtained for the first, while a value of 37% is obtained for the second. Therefore, with a slightly larger PV size (if the location and the angle of each panel remain unaltered) the goal of 50% coverage can be easily reached for the mini-split HP but not for the ducted air-source HP.

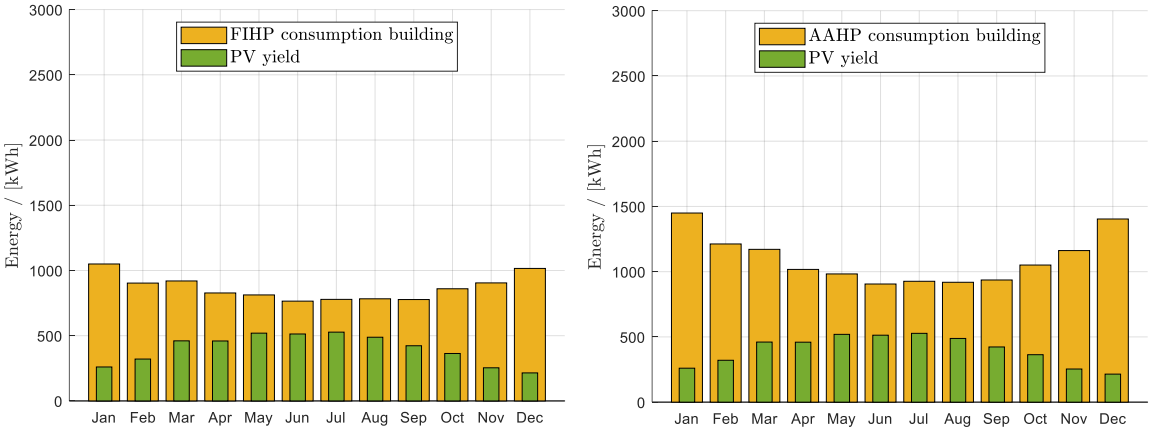

Figure 17: Simulated monthly electricity consumption for DHW preparation in the reference building and PV yield for (a) a mini-split façade-integrated HP and (b) a ducted air-source HP.

4. Conclusions

In this work, a comparative analysis of decentral systems for DHW preparation was performed. The results of the experiments indicated that common air-source boiler HPs available on the market have reduced heating capacities, which result in longer charging intervals and increased electricity consumption. Moreover, if such HPs are used as ambient air HPs, thermal losses further decrease the overall performance, with a COP_{DHW} of 1.28 at 10 °C ambient air temperature, 1.53 at 15 °C and 2.85 at 20 °C. An improvement can be reached with a return flow HP, which uses the return of the space heating as heat source. For this HP concept a COP_{DHW} ranging between 5.61 and 6.24 was measured for source temperatures of 25 and 35 °C respectively. However, this solution is highly dependent on the level of renovation of the heating system, which in turn has a huge impact on the invasiveness. A mini-split façade-integrated HP developed within the FFG-funded research projects *FitNeS* and *PhaseOut* can be a promising and efficient solution in renovated flats. For a source temperature of 10 °C a COP_{DHW} of 2.82 was measured, while at 15 °C and 20 °C COPs of 3.06 and 3.11 were reached, indicating a clear advantage compared to ambient air HPs. A simulation study was conducted to assess the yearly performance of the mini-split air-to-water HP compared to a ducted air-source boiler HP in a reference building with 10 renovated flats. A yearly PF of 2.50 was observed for the solution with the mini-split HP, while a PF of 1.99 was obtained for the solution with the ducted air-source HP. The gap in the performance is once again to be attributed to the lower heating capacity of the ducted air-source HP, which leads to longer charging intervals and larger electricity consumption. With a 5 kW peak PV system, a yearly coverage factor of about 50% could be reached for the system with the mini-split HP, while a coverage factor of only 37% was obtained for the ducted air-source HP with the same PV size. From these analyses, it can be concluded that the developed mini-split façade-integrated HP can be a viable and efficient solution in renovated multi-family buildings, where no disruptive construction works can be carried out and has a better performance than conventional air-source boiler HPs available on the market. In future work, the simulation study will be extended to the return-flow HP, for which the achieve building quality and the renovation degree of the SH system are crucial and for which different renovation scenarios will be evaluated. Furthermore, the optimal PV size to cover 50% and 60% of the electricity consumption for DHW will be investigated for all three presented HP concepts by means of parametric analyses.

5. Acknowledgments

This work has been part of the research projects “FitNeS” (FFG-Nr. 867327) and “PhaseOut” (FFG-Nr. 999895470) funded by the FFG (Austrian Research Promotion Agency) in the “Stadt der Zukunft” program. Our thanks go to the project partners Drexel und Weiss, Drexel Reduziert, Element Design, Winter, Rothbacher, Kulmer Holzbau and IIG.

6. References

CEN/TC 113, 2017. EN 16147. Heat pumps with electrically driven compressors - Testing, performance rating and requirements for marking of domestic hot water units. https://doi.org/https://dx.doi.org/10.31030/2513808

Cozza, S., Chambers, J., Bolliger, R., Tarantino, M., Patel, M.K., 2022. Decarbonizing residential buildings with heat pumps: Transferability of front-runner experiences from Swiss Cantons. Energy Reports 8, 14048–14060. https://doi.org/10.1016/j.egyr.2022.09.141

European Commission, 2021. Proposal for a Directive of the European Parliament and of the Council on the energy performance of buildings (recast). Official Journal of the European Union 0426.

FFG (Austrian Research Promotion Agency), 2024. PhaseOut - Wärmepumpentechnologien in der Bestandssanierung [WWW Document]. URL https://projekte.ffg.at/projekt/4499093 (accessed 7.17.24).

FFG (Austrian Research Promotion Agency), 2023. FitNeS - Façade-integrated modular split heat pumps for new builduings and refurbishments [WWW Document]. URL https://projekte.ffg.at/projekt/3037619 (accessed 8.8.24).

Gustafsson, M., Dipasquale, C., Poppi, S., Bellini, A., Fedrizzi, R., Bales, C., Ochs, F., Sié, M., Holmberg, S., 2017. Economic and environmental analysis of energy renovation packages for European office buildings. Energy Build 148, 155–165. https://doi.org/10.1016/j.enbuild.2017.04.079

IEA, 2022. The Future of Heat Pumps. The Future of Heat Pumps. https://doi.org/10.1787/2bd71107-en

Mathworks, 2022. MATLAB [WWW Document]. URL https://de.mathworks.com/products/matlab.html

Monteleone, W., Ochs, F., 2023. Simulation-assisted development of a mini-split air-to-water façade-integrated heat pump for minimal invasive renovations. 14th IEA Heat Pump Conference, Chicago.

Monteleone, W., Ochs, F., Dermentzis, G., Breuss, S., 2024. Simulation-assisted design of a silent façade-integrated R290 mini-split heat pump. Appl Therm Eng 243, 122520. https://doi.org/10.1016/j.applthermaleng.2024.122520

Ochs, F., Monteleone, W., Dermentzis, G., Siegele, D., Speer, C., 2022. Compact Decentral Façade-Integrated Air-to-Air Heat Pumps for Serial Renovation of Multi-Apartment Buildings. Energies (Basel) 15. https://doi.org/10.3390/en15134679

Solar-Institut Juelich FH Aachen, 2018. CARNOT Toolbox.

The European Parliament and the Council of the European Union, 2009. DIRECTIVE 2009/125/EC of the European Parliament and of the Council of 21 October 2009 establishing a framework for the setting of ecodesign requirements for energy-related products (recast) (OJ L 285 31.10.2009, p. 10). Official Journal of the European Union 1–40.

Domestic hot water heating with direct electricity from PV panels and the grid

Elsabet Nielsen, Simon Furbo and Jianhua Fan

Technical University of Denmark, Department of Civil and Mechanical Engineering, Kgs. Lyngby (Denmark)

Abstract

A solar domestic hot water tank with direct electrical heating is investigated experimentally. The investigations are carried out from January to June 2024 under Danish weather conditions. The tank has five electrical heating foils on the outside vertical tank surface. The tank is well insulated, and thermal bridges are avoided by having all the pipe connections at the bottom. The different electrical foils are supplied with electricity from PV panels or the grid. A semi-smart controller allows the tank to be heated with electricity from the grid at night to establish the energy needed to cover the demand the following day. The investigations show that the domestic hot water system can supply all the energy needed for domestic hot water at a levelized cost of heat of 0.28 €/kWh. The levelized cost of heat can be directly compared to the electricity price users pay for purchasing electricity from the grid.

Keywords: PV heated tank, control strategy, levelized cost of energy

1. Introduction

Fossil fuels dominate the heating sector. Apart from the use of traditional biomass, only 11% of the global heating needs were met by modern renewables in 2021, Solar-Heat-Worldwide-2023.pdf (iea-shc.org). Countries worldwide have committed to reducing their CO_2 emissions by significantly increasing their share of renewable energy by 2030. Worldwide, the operation of buildings accounts for about 40 % of the primary energy consumption and approximately 25 % of the greenhouse gas emissions. In Europe, buildings are responsible for 40 % of the energy consumption and 36 % of CO_2 emissions, of which water heating accounts for around 16 % of the energy consumption and 14% of CO_2 emissions, IEA-EnergyEnd-usesandEfficiencyIndicatorsdatabase-HighlightsNovember2023.xlsb (live.com).

The energy consumption for heating and cooling of buildings can be significantly reduced by building envelope improvements in existing buildings and clever design of new buildings. Still, such measures do not affect the energy demand for hot water. Therefore, decentralized solutions with individual storage tanks and solar energy collectors will be needed in the city of the future, interacting with existing grid infrastructures in the best possible way.

In recent years, photovoltaic technologies have taken over the dominant position of solar thermal water heaters in installed renewable capacity globally, Renewables 2023 (windows.net). Direct electric heating with PV panels is a robust technology because there is no circulation pump, and the requirements for maintenance are minimal. Reduced installation costs are expected because of the system's lower complexity than traditional solar thermal water heaters. Further, smart and adaptive control systems can interface with the household's energy consumption for water heating, lighting, household machinery, and possible electrical vehicles, optimize the use of the produced energy, and maximize the efficiency and profitability of the system.

The system types utilizing PV panels for heating are referred to as PV2heat or Power2heat systems and are already widely used, especially in combination with heat pumps. However, system solutions utilizing PV electricity directly are also on the market. For example, in Germany, the company NEXOL Photovoltaic AG (https://www.nexol-ag.net) offers retrofit solutions with one or two heating elements and controller for existing hot water tanks if the tank has one or two available 1.5-inch E-sleeves located at suitable heights in the tank.

In this project, electrically heating foils mounted on the outside surface of the tank supplied with electricity from PV panels or the grid are investigated experimentally. This approach is well-suited for new or retrofit systems that do not have available E-sleeves.

© 2024. The Authors. Published by International Solar Energy Society
Selection and/or peer review under responsibility of Scientific Committee
10.18086/eurosun.2024.02.14 Available at http://proceedings.ises.org

2. Aim and scope

The research aims to develop a cost-effective PV-heated domestic hot water system with a standard hot water tank, a smart control system, and a good interplay with the electrical grid. The suitability of the system will be elucidated. Hot water tanks can significantly reduce the non-renewable energy consumption of buildings by using energy more efficiently. Further, hot water tanks can help to balance the grid, as they provide a storage capacity for a surplus of electricity.

3. Method

The solar domestic hot water system comprising an electrical heated hot water tank, PV panels, and inverter is installed in a test facility at the Technical University of Denmark (Lat. 55.79°, Lon. -12.52°).

The PV panels and the inverter are referred to as the PV system in this paper.

The domestic hot water tank is a standard hot water tank, type 42002, with a volume of 196 liters from METRO THERM, the PV panels are type MG230, Racell BLACK Diamond from RACELL, the inverter is type PIKO MP plus 2.5-1 kW from Kostal solar electric, and the electrical heated foils (EHF) are type HSSD/C from SAN Electro Heat A/S.

The temperatures inside the tank are measured at five different levels. The temperature sensors, copper/constantan, type TT, are arranged in a glass tube inserted into the tank through the bottom (Figure 1 and Figure 2).

Fig. 1: Glass tube with temperature sensors (T1-T5) for temperature measurements inside the tank

The tank is equipped with five electrically heated foils of a maximum of 1000 W each. The electrical heating foils cover the complete vertical tank surface. The tank is well insulated with 100 mm of mineral wool on the side and 200 mm on the top. The bottom is insulated with molded flamingo. Thermal bridges are avoided by having all the pipe connections in the bottom of the tank (Figure 2).

Six photovoltaic panels with a total gross area of 8.928 m^2 are installed on the test facility's 45° tilted south-facing roof (Figure 3).

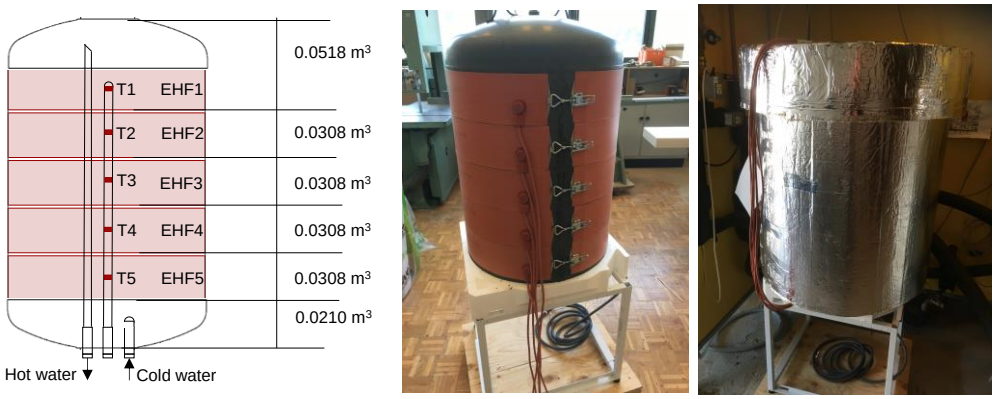

Fig. 2: Tank design

Fig. 3: PV panels on the roof of the test facility (left) and the inverter (right)

The five electrical heating foils are supplied with electricity from PV panels or the grid. The tank is heated sequentially from the top to a usable temperature. Since only one foil operates at a time, thermal stratification is established in an excellent way in the hot water tank. The electricity produced by the PV panels can also be used to cover the electricity consumption in the building and/or be sold to the grid.

Ideally, the use of electricity from the grid is optimized by forecasts of consumption, electricity prices, and PV production based on weather forecasts, and electricity from the grid would only be used in low-cost electricity periods where the PV panels could not cover the demand. However, consumption, weather, and electricity price forecasts are not included in the control of the investigated system.

4. Operation conditions and evaluation method

The control strategy is designed in LabVIEW, Bitter et al. (2006), and it provides that the tank is heated sequentially from the top with electricity from PV panels or the grid. Only if the electrical energy produced by the PV system exceeds 1000 W, which is the maximum power of each electrical heating foil, are two neighboring heating foils activated simultaneously. In this case, the first heating foil used 1000 W, and the second foil used the rest.

During nighttime, from midnight until 6 am, the tank is heated by electrical energy from the grid to establish the energy to cover the daytime heating demand, if not already present. The tank is heated until the temperature of the three upper layers (T1, T2, T3) exceed 55 °C. The energy amount established is sufficient to cover the domestic hot water demand without considering the solar energy supplied to the tank during the daytime. Incoming solar heat from the day can reduce the energy supplied to the tank from the grid the following night.

During the daytime, all electrical power produced by the PV system is supplied to the tank, and no electrical energy from the grid is exchanged with the grid. The tank is heated layer by layer from the top until the temperature in each layer reaches 90 °C.

The solar radiation measurements are obtained from the DTU climate station (https://weatherdata.construct.dtu.dk) located on the roof of a 3-story building next to the test facility. The test facility is a 1-story building surrounded by other buildings and trees. Consequently, the PV panels may be shaded in periods where there are no shades affecting the climate station. This is mainly a problem in the morning and the evening. Therefore, such periods are excluded when determining the efficiency of the PV system.

The daily hot water consumption is 100 liters heated from 10 °C to 50 °C. Hot water is tapped from the top of the tank through a PEX pipe inserted through the bottom of the tank. Tapping takes place at 7 am, noon, and 7 pm in three equal portions with a volume flow rate of about 2.5 l/min.

Measured data are obtained with a time resolution of 1-minute. Data of the used measurement equipment is shown in Table 1.

Tab. 1: Measurement equipment

Equipment	Type	Location	Accuracy
Flow sensor	Clorius Combimeter 1.5 EPD	DHW loop	± 2-3 %

Temperature sensor	Copper/constantan, type TT	DHW loop, Tank	± 0.5 K
Pyranometer	Kipp & Zonen CMP11	DTU Climate station	± 1.4 %
Pyrheliometer	Kipp & Zonen CHP1	DTU Climate station	± 1 %
Ambient temperature	Vaisala weather transmitter WXT520	DTU Climate station	± 0.3 K

The electrical energy amounts from the grid and the PV system (Q_{grid} and Q_{PV}) are measured directly with an energy meter, while the tapped energy (Q_{tap}) is calculated from the measured hot and cold water temperatures and the volume flow rate. The energy change in the tank (Q_{change}) is calculated from the measured temperatures (T1, T2, T3, T4, T5) and the respective volume each temperature sensor represents, see Figure 2. The energy balance is used to determine the heat loss of the tank (Q_{loss}):

$$Q_{grid} + Q_{PV} - Q_{tap} - Q_{loss} + Q_{change} = 0 \quad \text{(eq. 1)}$$

$$Q_{loss} = Q_{grid} + Q_{PV} - Q_{tap} + Q_{change} \quad \text{(eq. 2)}$$

$$Q_{change} = Q_{tank.start} - Q_{tank.end} \quad \text{(eq. 3)}$$

The total solar radiation on the PV panels (Q_t) is determined with measurements from the DTU climate station (https://weatherdata.construct.dtu.dk). The measured solar irradiance data are direct normal irradiance (DNI), global irradiance (G), and horizontal diffuse irradiance (G_d). The total irradiance on the PV panels (G_t) is determined in the following way, assuming an isotropic distribution of the diffuse irradiance (Liu and Jordan, 1963) and a reflectance coefficient (ρ) of 0.2:

$$G_{bt} = DNI \cdot \cos \Theta, i \quad \text{(eq. 4)}$$

$$G_{dt} = G_d \cdot \left(\frac{1+\cos\beta}{2}\right) + G \cdot \rho \cdot \left(\frac{1-\cos\beta}{2}\right) \quad \text{(eq. 5)}$$

$$G_t = G_{bt} + G_{dt} \quad \text{(eq. 6)}$$

$$Q_t = G_t \cdot A_{PV} \quad \text{(eq. 7)}$$

The efficiency of the PV system (η_{PV}) is determined in the following way:

$$\eta_{PV} = \frac{Q_{PV}}{Q_t} \quad \text{(eq. 8)}$$

5. Results

The measurements were obtained from January to June 2024, and Table 2 shows the availability of measurements.

Tab. 2: Periods with available measurements

Month	January	February	March	April	May	June
Measurement days	1-31	1-18	1-31	1-30	1-31	1-28

5.1 Weather conditions

Figure 4 shows the monthly beam and diffuse solar radiation on the PV panels as well as the monthly average ambient temperature. About 50% of the energy comes from the beam radiation, except for January and May, where the beam radiation accounts for about 65%.

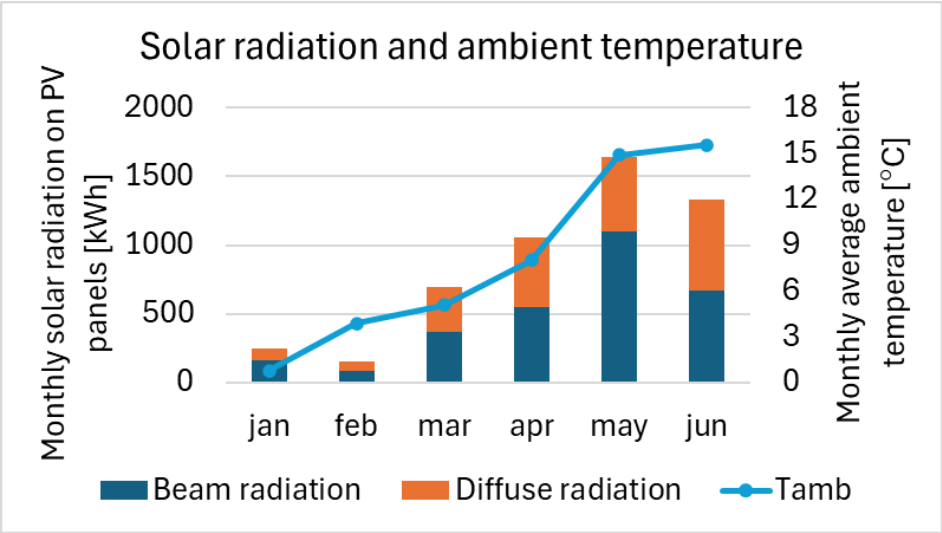

Fig. 4: Solar radiation and ambient temperature

5.2 Domestic hot water consumption

Figure 5 shows the energy tapped from the tank. There are only small variations in the daily tapped energy.

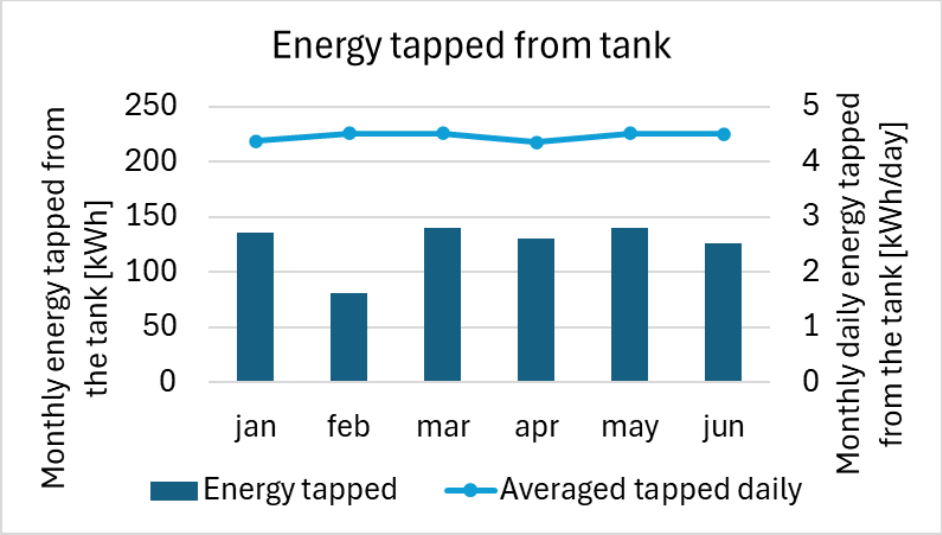

Fig. 5: Energy tapped from the tank

5.3 Tank temperatures and heat losses

Figure 6 shows the weighted average tank temperature and the heat loss from the tank. The tank temperature is the lowest in January and February when the contribution from the PV system is limited. As the tank temperature increases, the heat loss increases. In June, the tank heat loss is higher than in May, even though the average tank temperature is higher in May.

The test facility where the tank is located is a light building highly affected by weather conditions such as ambient temperature, solar radiation, wind speed, and wind direction. During the daytime, the temperature in the test facility is higher, especially when the sun is shining, and during nighttime, the temperature is lower.

When the tank is heated at night with electricity from the grid, the electrical power supplied to the electrical heating foils is always 1000 W. Consequently, the temperature of the tank wall is the highest while the temperature in the test facility is the lowest.

When the tank is heated during the day by electricity from the PV system, all the electricity is supplied to the heating foils. The electrical power rarely exceeds 1000 W. In case the power exceeds 1000 W, the excess power is supplied to the next electrical heating foil. Consequently, the temperature of the tank wall is lower most of the time compared to the nighttime conditions, while the temperature in the test facility is highest.

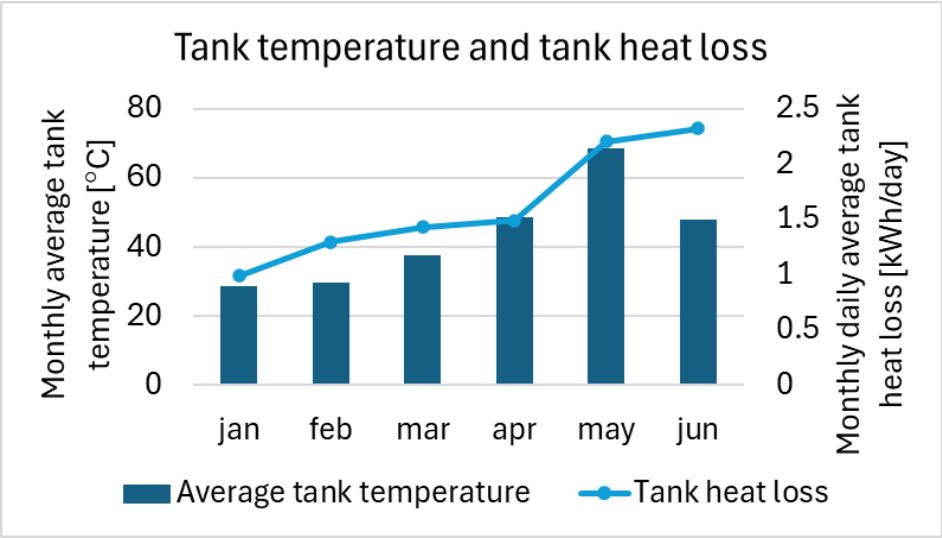

Fig. 6: Tank temperatures and tank heat loss

Figure 7 shows the temperature variations in the test facility from January to June 2024.

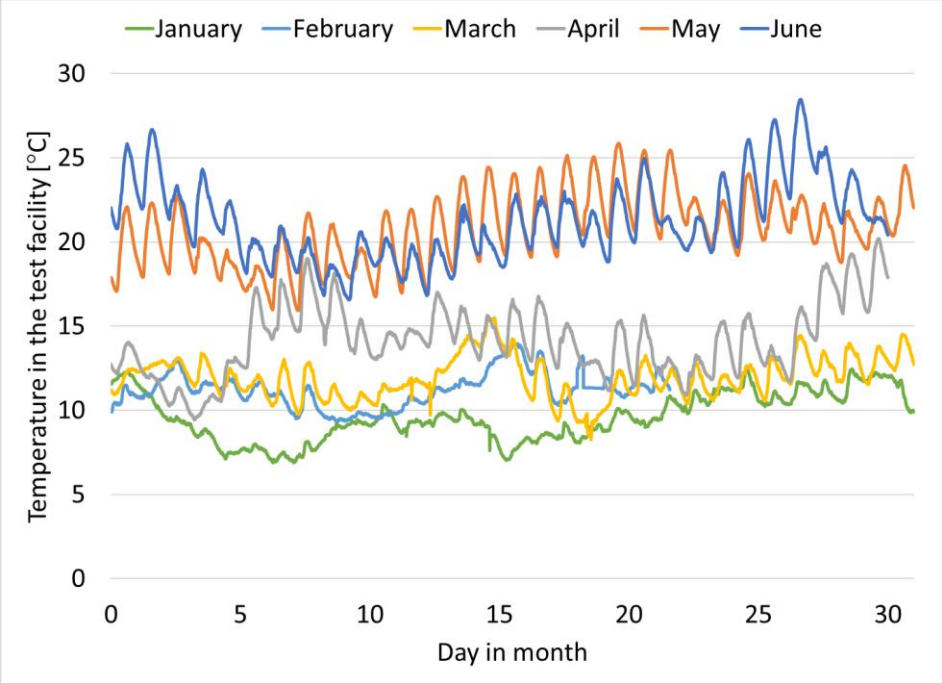

Fig. 7: Temperatures in the test facility

The temperature difference between the tank wall and the water in the tank at the same level is less than 10 K when the electric heating foil is operated with the full power of 1000 W and lower when the power is lower. The tank wall temperature is only measured at the upper heating element, EHF1. Figure 8 shows the tank temperatures during a night period with 1000 W heating through the electric heating foils and the tank wall temperature at the level of the upper heating foil. The tank wall temperature difference between the tank wall and the water at the upper level is high at the beginning of the heating period. This is explained by the water velocity along the inside of the tank wall being downward in periods without heating and upward in periods with heating. At the beginning of the heating period, while the water velocity switches direction, the heat transfer is lowest. This process takes about 10 minutes. The heat transfer from the hot tank wall to the water increases as the upward water velocity develops and reaches its maximum when the water velocity profile is fully developed after about 30 minutes.

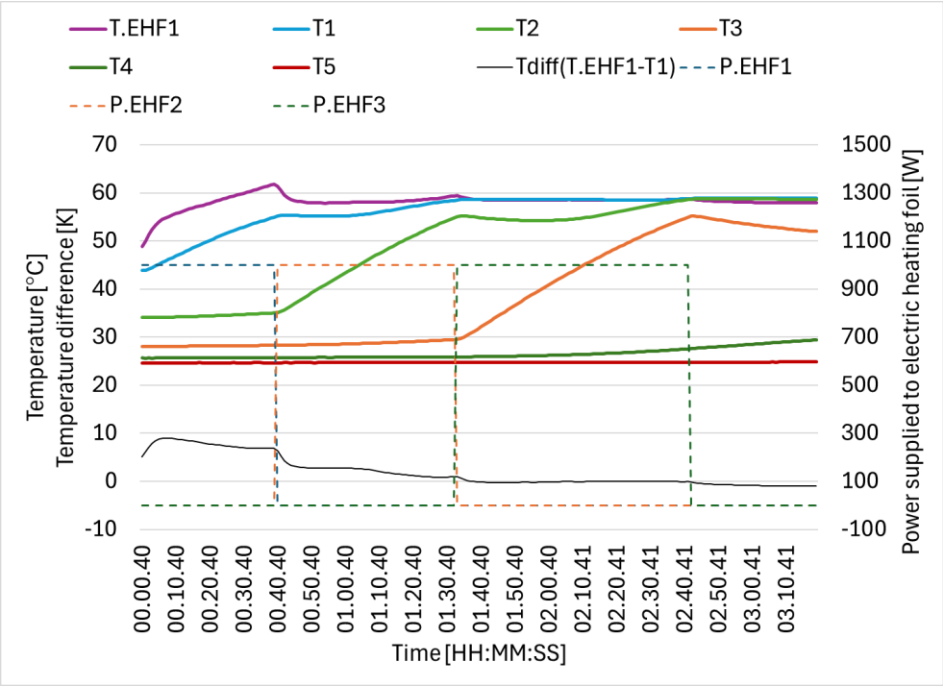

Fig. 8: Temperatures in the tank during heating at night on June 24, 2024

5.4 Electrical energy supply

Figure 9 shows the monthly energy supply to the tank from the grid and the PV panels, as well as the average efficiency of the PV system. The monthly average PV system efficiency increases slightly from 12.7% in January to 13.6 % in June. March stands out with the highest efficiency of 14 %. The reason for the highest efficiency in March is that the ambient temperature is still low while the solar radiation is high.

The hourly PV system efficiency as a function of the total solar radiation on the PV panels is displayed in Figure 10. There are some outliers in January, February, and March. These are due to snow laying on the PV panels or the pyranometer of the climate station. The outliners in May are due to obstacles casting shading on the PV panels while not on the climate station. The PV system efficiency has a maximum when the solar radiation is about 2 – 4 kWh/h. For low solar radiation, the share of diffuse radiation is high, resulting in low efficiency. For high solar radiation, the PV cell temperature is relatively high, resulting in low efficiency.

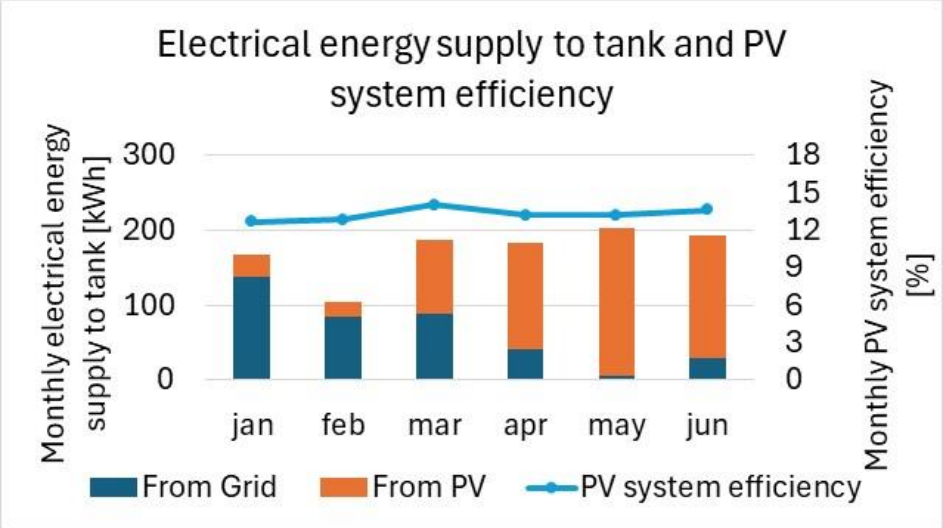

Fig. 9: Electrical energy supplied to the tank and PV system efficiency

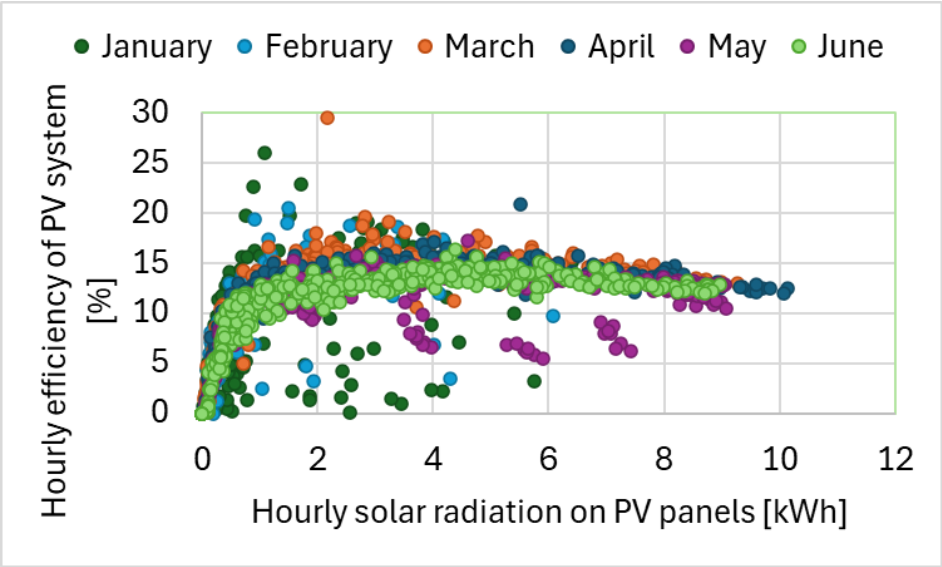

Fig. 10: PV system efficiency versus solar radiation on PV panels (8.928 m^2)

Figure 11 shows the monthly energy supply to the tank during nighttime, where the energy comes from the grid, and Figure 12 shows the monthly energy supply to the tank during daytime, where the energy comes from the PV panels.

The PV system and the grid use the upper electric heating foils (EHF1, EHF2, EHF3), and the two lowest foils (EHF4, EHF5) are only used by the PV system.

The number of hours the individual heating foils are utilized can be seen in Figure 13. The upper electric heated foil (EHF1) is utilized about 60 % of the total operation time, while the next two foils (EHF2, EHF3) are utilized about 15 % of the time. The two lowest-located foils (EHF4, EHF5) are only utilized about 4% of the time. Utilization of the individual electrically heated foils is a direct consequence of the control strategy and the climate under which the system operates.

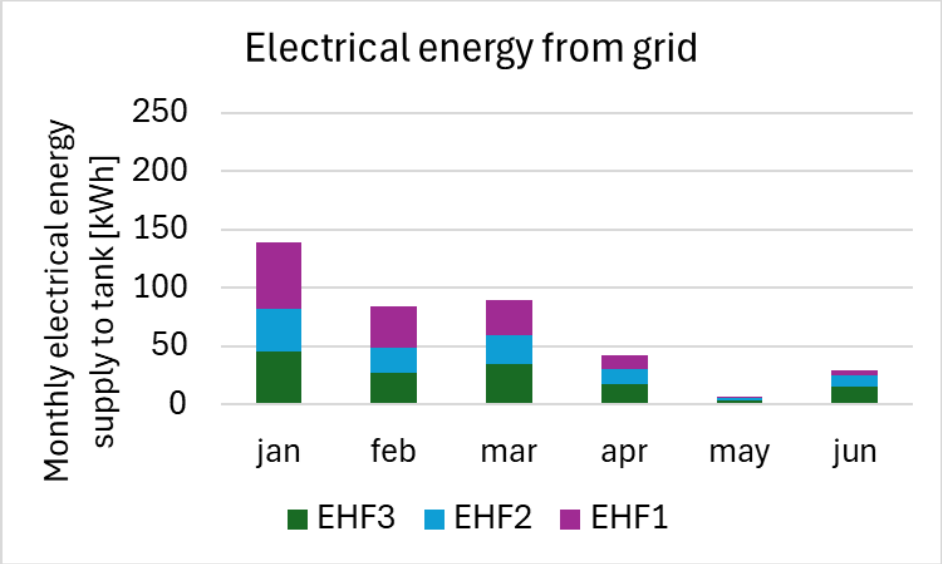

Fig. 11: Electrical energy from the grid

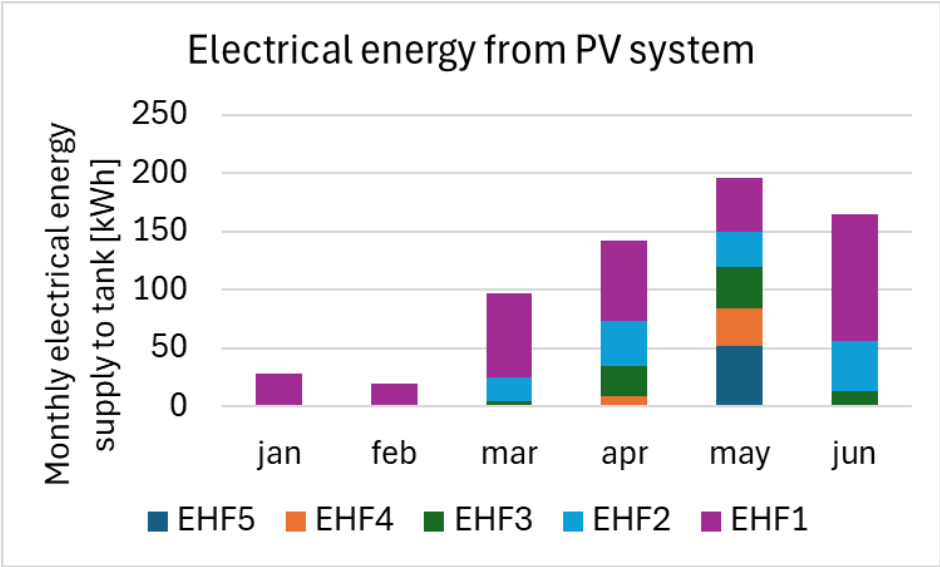

Fig. 12: Electrical energy from the PV system

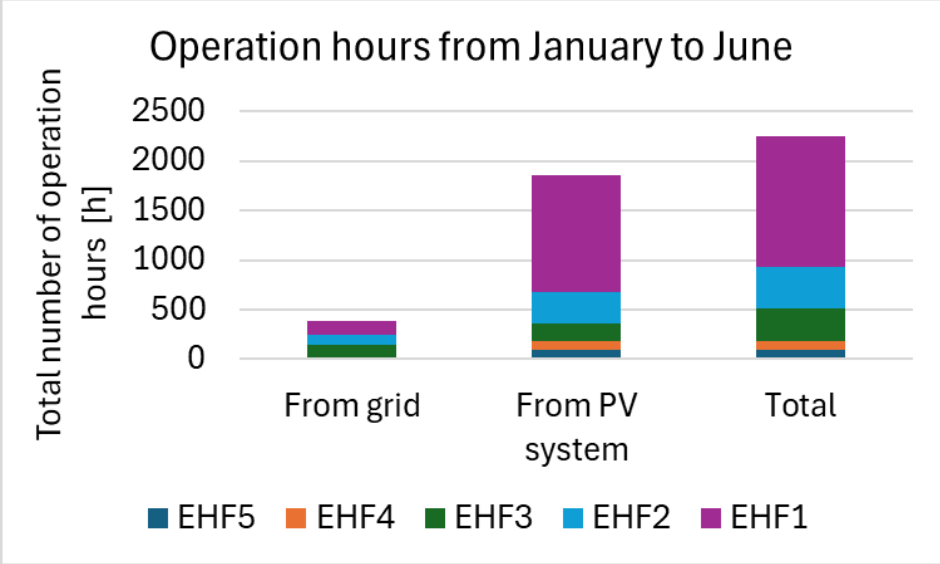

Fig. 13: Operation hours

5.5 Economy

The cost of the investigated system is compared to the cost of a conventional heating system comprising a domestic hot water tank heated by an electrical heating element with electric energy from the grid and a controller always keeping the usable temperature in the tank. Only the extra costs for the investigated domestic hot water system over the cost for the conventional domestic hot water system are included in Table 3. The prices include VAT. The lifetime of the system is estimated to be 20 years, during which only the anode used to protect the tank from corrosion needs replacement approximately every five years. The owner can easily replace a flexible anode through the top of the tank. If the tank is well maintained, an exchange of the PV modules and the electric heating foils will result in another 20-year system lifetime at a low cost. However, in this paper, only a lifetime of 20 years is considered.

Tab. 3: System costs

PV panels and inverter	2,800 €
Electrical heating foils	1,900 €
Domestic hot water tank	270 €

Control system	270 €
Installation	1500 €
Total system costs, incl. installation	6,740 €

The levelized cost of heat can estimate the cost of providing domestic hot water with the investigated system type, LCoH (Louvet et al., 2019):

$$LCoH = \frac{I_0 - S_0 + \sum_{t=1}^{T} \frac{C_t(1-TR) - DEP_t \cdot TR}{(1-r)^t} - \frac{RV}{(1-r)^T}}{\sum_{t=1}^{T} \frac{E_t}{(1-r)^t}} \quad \text{(eq. 9)}$$

The application is for residential use. No subsidies or operation and maintenance costs are included for the expected lifetime of the system of 20 years. Therefore, equation 9 can be simplified:

$$LCoH = \frac{I_0}{\sum_{t=1}^{T} Q_t} \quad \text{(eq. 10)}$$

$$E_t = Q_{conv}^{ref} - Q_{grid} \quad \text{(eq. 11)}$$

The energy demand of a conventional heating system (Q_{conv}^{ref}) is estimated in the following way:

$$Q_{conv}^{ref} = Q_{tap} + Q_{loss}^{ref} \quad \text{(eq. 12)}$$

The tapped energy (Q_{tap}) is estimated as the average energy amount tapped each month from the investigated system times the number of days in the month. The tapped energy (Q_{tap}) and the energy supplied by the grid (Q_{grid}) are then multiplied by two to account for the whole year. The heat loss of the conventional heating system (Q_{loss}^{ref}) is estimated to be 1 kWh/day during the whole year.

LCoH is calculated to be 0.28 €/kWh and can be directly compared to the electricity price from the grid.

The electricity price from the grid is made up of the raw electricity production price, electricity tax, transmission network tariff, system tariff, and costs to the grid company. Figure 14 shows the monthly average electricity prices hour by hour during the days of the months of January to June 2024. The electricity prices are lowest at night when the load on the grid is low, but they are also low during the daytime in the spring and summer months due to an increasing number of installed large-scale PV systems that feed electricity into the grid. In the evening, when the load on the grid is highest, the electricity prices are also the highest.

Whether the investigated system as presented here is economically attractive compared to a conventional system depends on how the conventional system with an electrically heated domestic hot water tank draws electricity from the grid and how the electricity prices will vary in the future.

A smart control that draws electricity from the grid based on forecasts of electricity prices, solar radiation, and consumption patterns could optimize electricity use further. Furthermore, the system cost could be lower if the system was sold as a complete plug-and-play unit. Both actions would result in a reduction in LCoH.

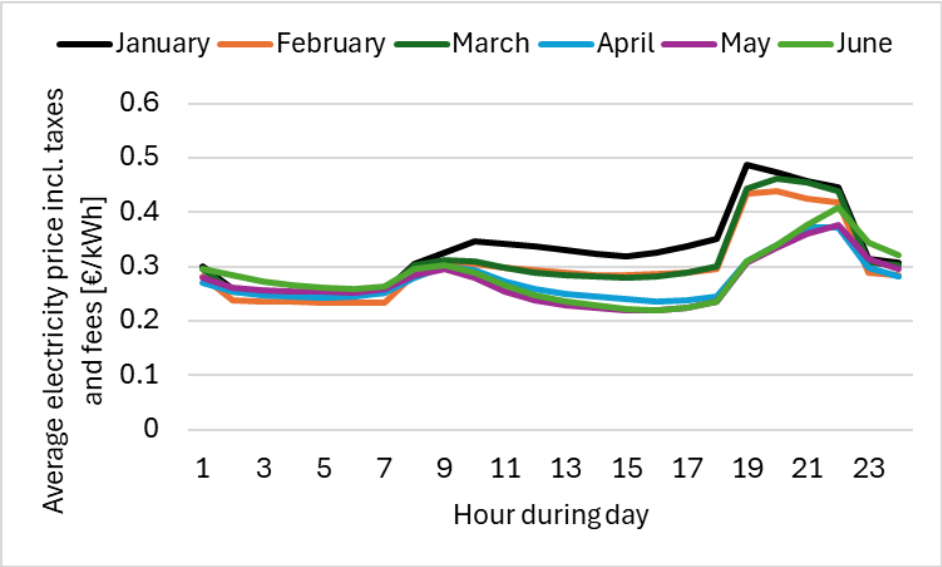

Fig. 14: Electricity prices, incl. electricity tax, transmission network tariff, system tariff, and costs to the grid company

6. Perspectivation

The investigations showed that a PV-based domestic hot water system with electrical heating foils placed on the surface of the tank walls and with backup from the electric grid could work and cover the total hot water consumption. The system can both be economically attractive for consumers and provide a good interplay with the energy system. It is therefore suggested to start research to elucidate the suitability of similar PV-based heating systems with backup from the electric grid, which can cover the total yearly heat demand of buildings. Among other things, the following questions should be answered for different buildings:

- What is the best design and size of the system from an economical point of view?
- Under which conditions is it favorable to include a heat pump or an electric battery in the system?
- How much can a smart control system optimizing purchases and sales of electricity to/from the electric grid improve the system?
- Are the optimal system solutions more suitable than other solutions, such as heat pump systems, solar heating systems, etc., from an economical point of view?

7. Conclusions

A 196-liter domestic hot water system heated by electricity from 8.928 m^2 PV panels and the grid is experimentally investigated. The tank is heated by five electric heating foils mounted on the vertical tank surface under the tank insulation. The system is tested under Danish weather conditions from January to June 2024.

The investigation shows that the domestic hot water system can supply all the energy needed at a levelized cost of heat of 0.28 €/kWh. The levelized cost of heat can be directly compared to the electricity price users pay for purchasing electricity from the grid, which varies during the day and the year.

The investigation also showed that the temperature of the tank wall is less than 10 K compared to the temperature inside the tank when the power supplied to the electric heating foil is the maximum of 1000 W. The heat transfer between the electric heating foil and the tank water is lowest in the first 10 minutes of a heating period, where the water velocity along the inside tank wall changes direction from downward to upward and reaches its maximum after about 30 minutes when the upward water velocity is fully developed.

8. Acknowledgments

This research project was funded by the Bjarne Saxhof Foundation through the project "Energy supply systems for buildings based on PV panels" and by the Danish Energy Agency through the project "EUDP 2022-I3 IEA SHC Smart Solar Hot Water for 2030", EUDP program grant no: 134223-495988.

9. Nomenclature

Quantity	Symbol	Unit
Energy from the grid	Q_{grid}	kWh
Energy from the PV system	Q_{PV}	kWh
Energy tapped from the domestic hot water tank	Q_{tap}	kWh
Energy loss of domestic hot water tank	Q_{loss}	kWh
Energy change in the domestic hot water tank	Q_{change}	kWh
Energy content in the domestic hot water tank at the start	$Q_{tank.start}$	kWh
Energy content in the domestic hot water tank at the end	$Q_{tank.end}$	kWh
Energy demand of the conventional heating system	Q_{conv}^{ref}	kWh
Energy loss from the conventional heating system	Q_{loss}^{ref}	kWh
Total energy on the PV panels	Q_t	kWh
Global irradiance	G	W m^{-2}
Diffuse irradiance on horizontal	G_d	W m^{-2}
Beam irradiance on the PV panels	G_{bt}	W m^{-2}
Diffuse irradiance on the PV panels	G_{dt}	W m^{-2}
Direct normal irradiance	DNI	W m^{-2}
Incidence angle on PV panels	Θ, i	°
Tilt of PV panels	β	°
Reflectance coefficient	ρ	-
Efficiency of PV system	η_{PV}	-
Area of PV panels	A_{PV}	m^2
Initial investment	I_0	€
Subsidies and incentives	S_0	€
Operation and maintenance costs	C_t	€ y^{-1}
Corporate tax rate	TR	%
Asset depreciation	DEP_t	€ y^{-1}
Residual value	RV	€
Saved final energy	E_t	J y^{-1}
Discount rate	r	%
Period of analysis or temperature	T,t	Years or °C

10. References

Bitter, R., Mohiuddin, T., Nawrocki, M., 2006. *LabVIEW: Advanced programming techniques*. Crc Press.

Climate station at DTU, https://weatherdata.construct.dtu.dk

IEA Energy End-uses and Efficiency Indicators database (November 2023 edition), Highlights, IEA-EnergyEnd-usesandEfficiencyIndicatorsdatabase-HighlightsNovember2023.xlsb (live.com)

Liu, B.Y.H., Jordan, R.C., 1963. The Long-Term Average Performance of Flat-Plate Solar Energy Collectors. Solar Energy, Vol. 7, No. 2, 1963 53-74.

Louvet, Y., Fischer, S., Furbo, S., Giovannetti, F., Helbig, S., Köhl, M., Mugnier, D., Philippen, D., Veynandt, F., Vejen, K., 2019. Economic comparison of reference solar thermal systems for households in five European countries. Solar Energy, 193 (2019) 85-94. https://doi.org/10.1016/j.solener.2019.09.019

NEXOL Photovoltaic AG, https://www.nexol-ag.net

Renewables, 2023, Renewables 2023 (windows.net)

Solar Heat Worldwide, 2023 Edition, Solar-Heat-Worldwide-20231.pdf (iea-shc.org)

S.A.P.I.EN.T.E. Experimental Test Facility For Full-Scale Testing Of New Configurations Of Collective Thermal Electric Self-Consumption From Renewable Sources. First Experimental Test with Thermo-photovoltaic Collectors Plant

Ruggero Nissim[1], Alessandro Lorenzo Palma[1], Biagio Di Pietra[1] and Maria-Anna Segreto[1]

[1] ENEA, Rome (Italy)

Abstract

The European Renewable Energy Directive (RED) promotes the adoption of Renewable Self-Consumption strategies for local production and shared consumption of energy. In this paper, the authors illustrate S.A.P.I.EN.T.E., an experimental facility consisting of several generation sections, energy storage and distribution systems designed to simulate energy communities and related experimental tests focused on maximizing self-consumption of locally produced renewable energy. We demonstrate, through experimental tests, the benefits in terms of energy self-consumption and self-sufficiency that such a system architecture can achieve. We show the results of the first experimental tests conducted on the Thermo-photovoltaic collectors **(**PVT) system installed in S.A.P.I.EN.T.E.

Keywords: *Self-consumption, Self-sufficiency, TPV, renewable energy*

1. Introduction

In addressing the challenges posed by climate change and the energy crisis, the Renewable Energy Directive and its recent update (EU/2018/2001 - EU/2023/2413) encourage the proliferation of Renewable Energy Communities (REC) and Jointly Acting Renewable Self-Consumers. These initiatives promote local energy production and shared consumption as viable alternatives to traditional centralized energy systems. However, transitioning to these new system architectures introduces complexities, particularly regarding the stability and reliability of electrical grids due to the intermittent and uncertain output of renewable energy sources. Additionally, the growing and variable energy demand of consumers further compounds these challenges. To maximize the efficiency of REC, it is imperative to implement demand side management strategies, such as load shifting facilitated by storage systems, to prioritize self-consumption and self-sufficiency. [1-8]

We show the plant structure, operating logics and control systems. We demonstrate how the storage systems belonging to such a plant maximize self-consumption of locally produced energy through experimental test results. The plant named S.A.P.I.EN.T.E. (Sistema di Accumulo e Produzione Integrata di ENergia Termica ed Elettrica - integrated thermal and electrical energy storage and production plant), installed at the ENEA Casaccia Research Center, is an experimental facility composed of four different sections: energy generation, energy storage, distribution system and energy utilities. A control system based on a Programmable Logic Controller (PLC) is used to manage energy flows and implement demand side management strategies.

2. S.A.P.I.EN.T.E.

2.1. Description of the facility

The energy generation section is composed by a photovoltaic (PV) plant provides the plant with a peak power production of 11.6 kW. A thermo-photovoltaic collectors (PVT) plant consisting of 20 panels, each with a nominal thermal output of 770 W and a nominal electrical power of 320 W (for a total of 6.4 kWp), is also

© 2024. The Authors. Published by International Solar Energy Society
Selection and/or peer review under responsibility of Scientific Committee
10.18086/eurosun.2024.02.15 Available at http://proceedings.ises.org

present. An air/water Heat Pump (HP) provides a maximum thermal power of 30.4 kW. A simplified schematic of the S.A.P.I.EN.T.E. system is shown, distinguishing the thermal section with dashed lines and the electrical section with continuous lines shown in Figure 1.

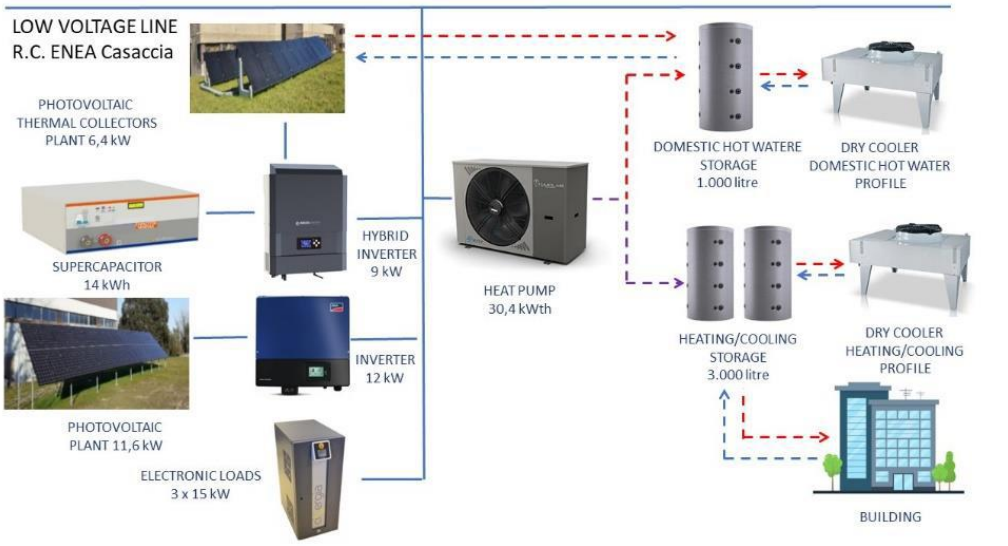

e

Figure 1: S.A.P.I.EN.T.E. system schematic. Continuous lines represent electrical connections, dashed lines thermal connections.

The electrical section of the PVT powers a hybrid inverter, to which are connected 4 supercapacitors with a total capacity of 14 kWh, representing electrical storage section of S.A.P.I.EN.T.E. The thermal storage section consists of two thermal storage tanks for heating or cooling with a total capacity of 3.000 liters. Another 1.000 liters storage tank for domestic hot water (DHW) is present. The load section is composed by devices that can emulate thermal and electrical loads. Two 70 kW dry coolers are present, one connected to the heating and cooling tanks and the other to the DHW tank, that act as thermal load emulation section. The distribution system is equipped with solenoid valves, controlled by the PLC, which allow switching the load between the dry cooler, used for emulating the thermal load, and 9 fan-coils from 9 rooms in the nearby office building, acting as a real thermal load.

The electrical load emulation section consists of three regenerative electronic loads (15 kVA each) capable of emulating electrical load profiles. If needed, these can be also used to emulate power generators.

2.2. Coefficient of Self-Consumption and Self-Sufficiency

In the context of REC, the coefficients of self-consumption (SC) and self-sufficiency (SS) are key indicators for assessing the efficiency and effectiveness of energy production and consumption within the community. The SC is expressed as a percentage and represents the fraction of energy produced from renewable sources that is used directly by the energy community, instead of being fed into the power grid, compared to the total energy generated from renewable sources.

This coefficient can be defined through the following formula:

$$SC = \frac{SCE}{TEP} \qquad \text{(eq. 1)}$$

Where:

- SCE = Self Consumed Energy is the energy produced and consumed directly within the community.

- TEP = Total Energy Produced is the total energy generated from renewable sources in the community.

A high self-consumption coefficient indicates that a large proportion of the energy produced is used directly within the community, reducing energy losses due to transmission and improving overall system efficiency.

The SS indicates the ability of the energy community to meet its energy needs through local renewable energy production, without having to depend on energy from the external power grid. It is expressed as a percentage

and refers to the amount of self-consumed energy generated from renewable sources relative to the total energy consumed, including electricity taken from the grid.

This coefficient can be defined through the following formula:

$$SS = \frac{SCE}{TEC} \qquad \text{(eq. 2)}$$

Where:

- SCE = Self Consumed Energy is the energy produced and consumed directly within the community.

- TEC = Total Energy Consumed is the total energy used by the community, including energy taken from the grid.

A high coefficient of self-sufficiency shows that the community can meet a large part of its energy needs through local production, reducing dependence on the electricity grid and increasing energy resilience.

These coefficients are crucial for:

- Assessing the energy performance of renewable energy communities.
- Plan and optimize energy production and consumption.
- Promote sustainability and energy independence.
- Incentivize energy policies that encourage the use of renewable energy and the creation of energy communities.

Optimizing SC and SS brings to environmental, economic, and social benefits. It helps reducing greenhouse gas emissions and improving environmental sustainability, while also leading to economic savings for members of the energy community or collective self-consumption group. It improves the quality of life for participants through increased energy independence.

3. Control system and experimental strategies

3.1. PLC Management strategies

We implemented proportional-integral-derivative (PID) control to convert a portion of the electrical energy produced by the PV system to thermal energy. This consists of tracking the electrical energy produced by the photovoltaic system and using this exact amount to power the heat pump, therefore realizing a power-to-heat (P2H) strategy. The PID receives as inputs the power produced by the PV and the electrical power consumed by the HP and adjusts its output to minimize the difference between the inputs, controlling the speed of the HP compressor. By adopting this strategy, all the energy produced by the PV is used to power the HP, increasing the SC. In addition, our system shows the ability to meet thermal needs of the load, decreasing the need to draw electricity from the grid, therefore increasing the SS. PID regulation operates within a configurable range of HP operating temperatures, determined by low and high temperature setpoints that can be configured both for the thermal and DHW tanks. The electrical energy in excess is stored in the supercapacitors.

When the heat pump compressor starts operating, high peak power absorption can occur, which may exceed the instantaneous PV power production. The supercapacitors are used to instantly compensate for electrical power demand peaks. The load is managed through the PLC, which allows setting the thermal power profiles to be emulated with the dry cooler. The system parameters are monitored through a network of electrical and thermal sensors connected to the PLC.

Following these logics, the electrical power absorbed by the heat pump is limited by the signal generated by the PID to match power produced by the PV, so that the two profiles overlap. When the storage temperature reaches the high temperature setpoints, the control system deactivates PV tracking, turning off the heat pump. When the storage tank temperature falls below the low temperature setpoints, photovoltaic tracking is reactivated to feed the HP. The PID saturates the generated signal to its maximum value until the electrical power generated by the PV falls below the maximum power the heat pump can absorb, which is influenced by the coefficient of performance (COP) and the outdoor temperature.

In case wind power is used together with photovoltaic, the heat pump will go in tracking of the power produced by photovoltaic and wind power.

3.2. Experimental tests: boundary conditions

In this work, we conduced experimental tests focusing mainly in the summer season, producing and storing cold thermal energy and DHW. The load profile was designed proportionally to the electricity, central cooling, and DHW needs of an apartment building consisting of four units. This choice is mainly agreed upon as a function of the dimensions of the PV, storage tanks, and HP of S.A.P.I.EN.T.E.

The load profile of electrical energy, DHW and cooling load were kept constant throughout the experiment. This is to limit the number of variables and to be able to focus on the variation of SC and SS coefficients in relation to the diversification of renewable sources used such as PVT, PV and wind.

The figure 2 with the reference building cooling load and the reference DHW load is shown below. A higher peak is observed in the morning for both cooling and DHW load.

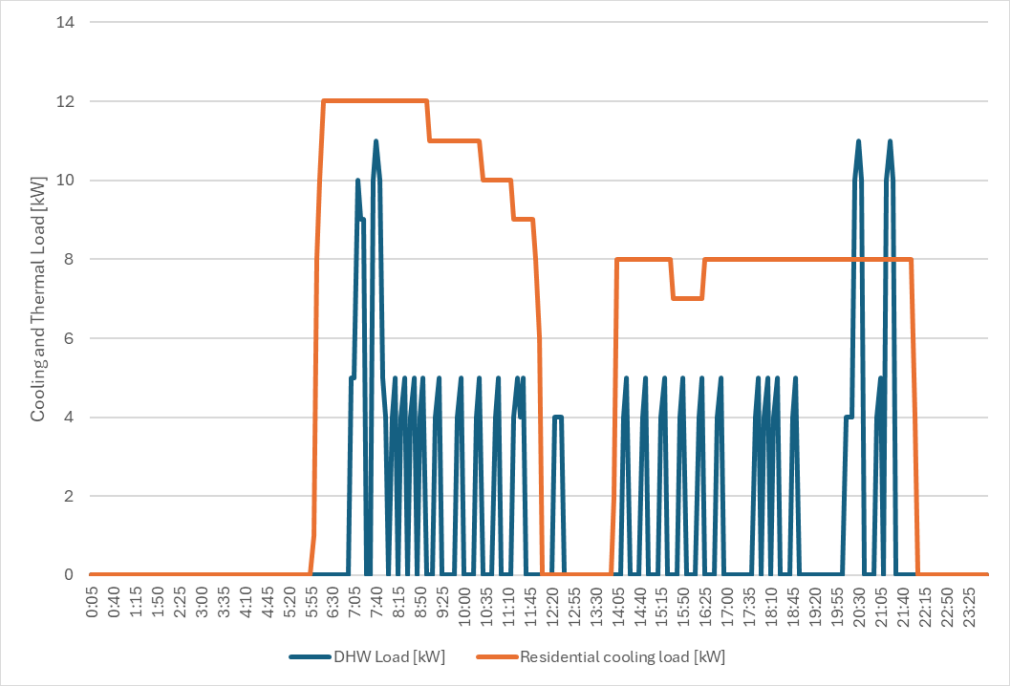

Figure 2 DHW and residential cooling load

Two loads are considered, the first domestic hot water and the second for cooling the building. The loads are taken constant to reduce the number of variables and emphasize the aspects of self-consumption and self-sufficiency. We considered standard DHW and cooling load profiles, not investigating the exact typology, but focusing on the plant behavior. We focused on the weekly load trends and leave the weekend analysis for further discussion

Regarding generation from renewable sources, a characteristic day of a summer month was chosen to be replicated in the experiments. Analyses were made on the contribution of PVT in meeting the DHW load. Finally, analyses were made substituting PV generation with PVT and wind-power generation. The peak power of the PV and wind system remained the same as that of the PV system alone. Through a Montecarlo method [9], we generated the electrical load profile of the building, shown in figure 3 together with the PV generation profile.

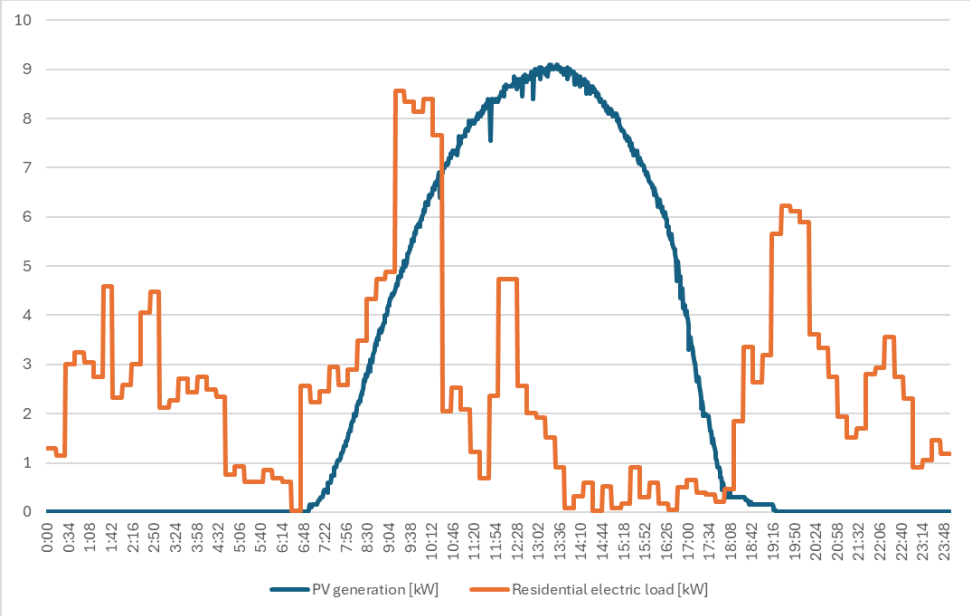

Figure 3 Residential electrical load and summer photovoltaic generation curve

The benefits of the supercapacitor storage system were analyzed in previous publications related to the S.A.P.I.EN.T.E. system [10], supercapacitors are a viable and effective alternative to lithium-ion batteries in the context of REC, since these can be very useful for handling peak loads that exceed the PV generation curve. In fact, the application of these devices resulted in a 10 % increase in SC compared to the case where they were not used.

A scenario with produced wind energy is also considered. This scenario is developed from wind detection data that occurred in the research center and simulated in the software, virtually. Thus, the wind generation is simulated and not real but follows a pattern consistent with the climatic conditions at the location where the S.A.P.I.EN.T.E. system is installed.

Wind generation is introduced to see how self-consumption and self-sufficiency coefficients can be affected by diversified generation.

Between the case in which the wind curve is predicted and the case in which the wind profile is not predicted, the installed capacity of renewables is considered constant, and thus PV has a trend with installed capacity of exactly half, as it is replaced by the installed capacity from wind.

Finally, everything was systematized and summarized through tables.

4. Experimental

In the first experimental session we focused on the contributions of the PVT system to DHW. Finally, we highlighted the overall test results in the wind plus PV mode.

4.1. PVT in DHW

Four days of energy production were compared, in which PVT thermally powered the DHW storage. No thermal load was applied. In the first case, we operated the PVT circulator without any special external condition; in the second case, the storage was kept at a temperature of 30 °C to maximize the thermal performance. On the next two days, the PVT was kept off and we analyzed how the water circulation would affect the efficiency of the PV section of PVT.

Below is the summary table of the tests carried out showing the type of operation considered, in our case the type of operation is for domestic hot water production, the thermal and electrical source refers to the same PVT system. In cases A and B the thermal source is used, turning on the circulator, in case C and D on the other hand it is kept off with the idea of raising the temperature on the panels and see how this aspect can affect the electrical efficiency.

In this section we focus on the electrical efficiency of PVT and look at how, in this system, the electrical production performance can be affected by the conditions in which the PVT thermal collectors are set to work.

Table 1 Schematic summary of the tests performed on the PVT

Case	A	B	C	D
Type of operation	DHW	DHW	DHW	
DHW Thermal Source	PVT	PVT	OFF	
Electric Source	PVT	PVT	PVT	
Storage System	DHW Storage	DHW Storage	DHW Storage	
Thermal profile	None	Storage temperature at 30 °C	None	

The first two cases (A) and (B) showed the potential of the PVT system and how its contribution to the heat generation in DHW is maximized when the DHW load is continuously operating. It can contribute to important savings in the industrial and commercial sectors where heat absorption is continuous and programmable.

From the following figure 4 one can see the thermal efficiencies in the cases where the circulator is kept on. Case B, the one with the storage tank kept at the constant temperature of 30 °C has the best thermal efficiency and for the longest time.

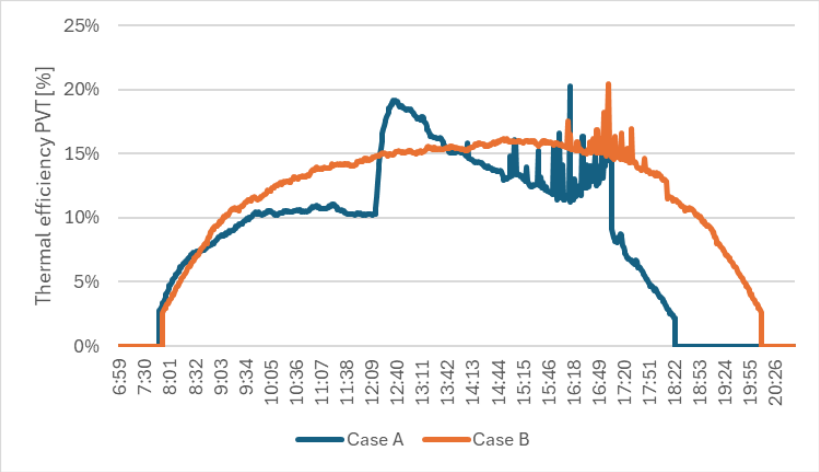

Figure 4 PVT thermal efficiency case A and B as represented in the table

From the latest tests, represented by figure 5, it is shown that the electrical output during the day is not affected by temperature if the temperature remains within ten degrees, rappesented by figure 6.

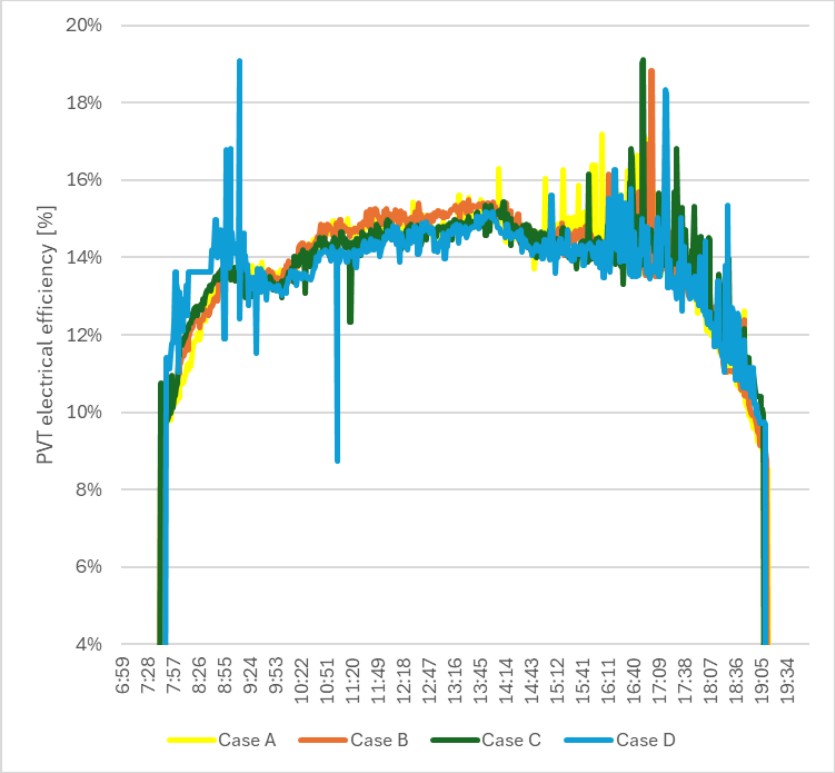

Figure 5 Electrical efficiency in the four cases described in the table

Below in the figure 6, note the trend of reference water temperatures inside the PVT panels in the four different cases. The first two with circulator on and the last two with circulator off.

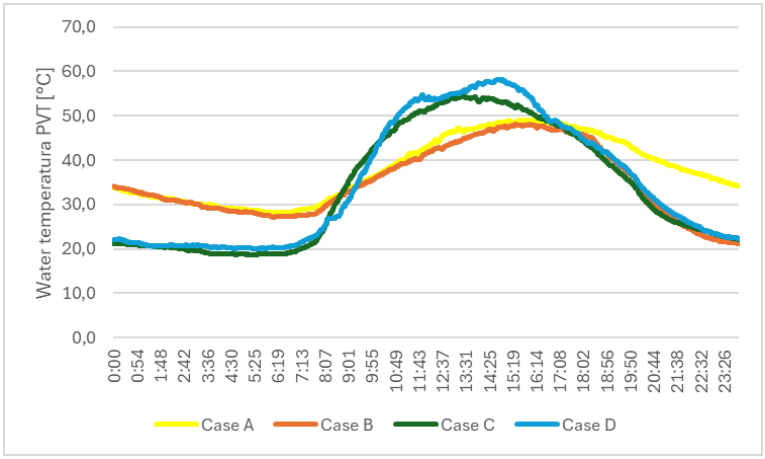

Figure 6 Water temperature of PVT in the four cases described in the table

If we zoom in, we can see that the hydraulic circuits at lower temperature have a higher electrical efficiency of PVT during peak hours. This interesting behavior will be investigated with further experiments, to evaluate how lower input temperatures can affect the electrical efficiency of our PVT, while producing heat for the DHW storage.

4.2. Production of cold thermal energy

In experiments conducted producing cold thermal power, two typical days were compared, maintaining the same residential cooling load. In the first case, the HP worked by providing comfort according to its own logic. In the second case, the HP was employed in the P2H strategy. This logic is realized to maximize SC, being able to have a few degrees of adjustment depending on the storage temperature. Below we summarize the boundary conditions in Table 2 in which the two tests were done, which differ only regarding the HP control strategy.

Table 2 Summary data of experiments for summer cooling case E to F

Case	E	F
Type of operation	Cooling	Cooling
Thermal Source	HP	HP
Electric Source	Grid and PV summer profile	Grid and PV summer profile
Thermal profile	Residential cooling load	Residential cooling load
Electrical profile	Residential electric load	Residential electric load
HP control strategy	No	PV profile tracking

In the first case (E), the HP followed its internal logics while providing thermal comfort following the thermal load demand, independently from the PV curve. In the second case (F), we applied the P2H strategy to control the HP. It can be seen from Figure 7 how the HP operates independently of the photovoltaic bell.

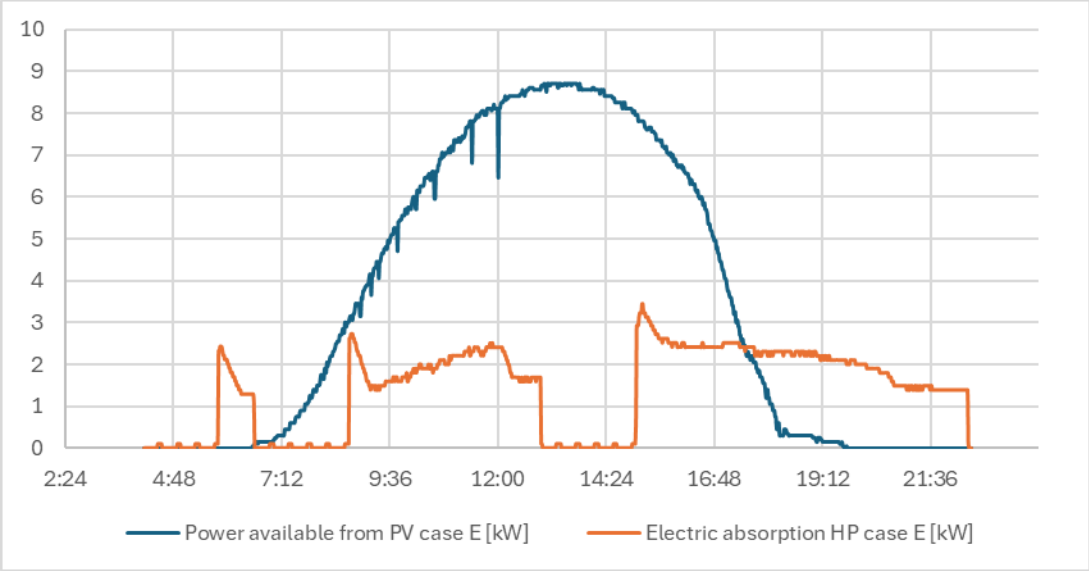

Figure 7 Power available from PV and Electrical Absorption of HP (case E)

From Figure 8 below, it is clear how the heat pump strategy goes in tracking of the PV bell by limiting the maximum absorption to renewable production.

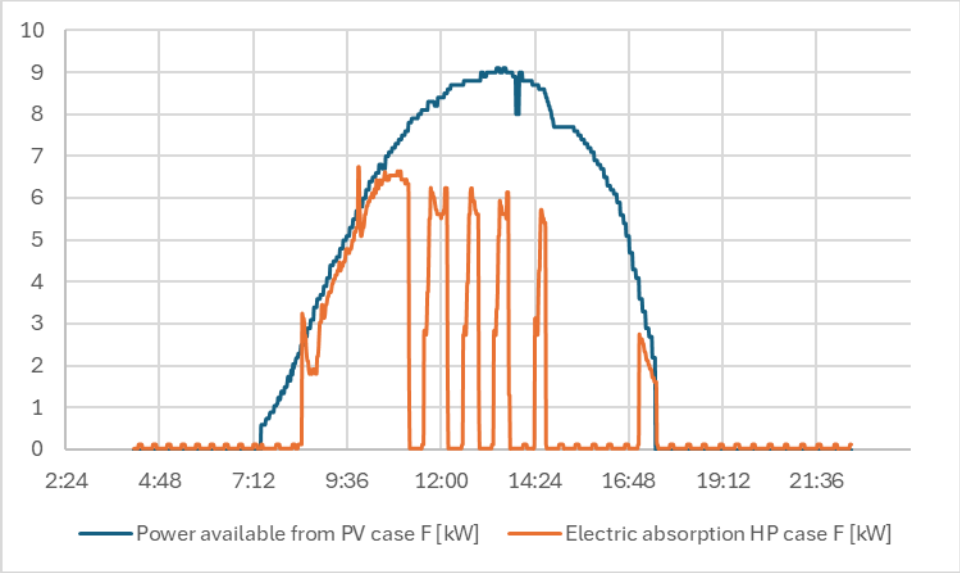

Figure 8 Power available from PV and Electrical Absorption of HP (case F)

Then, we report the results summarized in Table 3 emphasizing the different energies that are considered for the calculation of the coefficients. In (F) case, the performance indices reach very high values. We calculated the energy coefficients from the experimental results shown above.

Table 3 Summary parameters of experimental tests E and F

Case	E	F	
Electricity produced by PV	64	64	kWh
Electrical energy absorbed by the HP in total	26	23	kWh
Electrical energy absorbed by the HP in self-consumption	15	22	kWh
Thermal energy produced by the HP	121	107	kWh
Electricity self-consumed utilities	3	5	kWh
Electricity taken from the utility grid	56	54	kWh
Electricity fed into the grid	47	37	kWh
Calculation Energy Coefficients			
SC	0,27	0,42	-
SS	0,21	0,32	-
Daily COP	4,7	4,6	-

The table shows that in the second case SC and SS are increased mainly because the energy absorbed by the HP is used during the PV generation hours, therefore minimizing the energy absorptions outside from the PV production curve.

4.3. Wind and PV Energy

In this case, a scenario of cooling and DHW in a residential setting were compared. The sources were PV and wind power. The electrical load is considered. The only difference between the two systems is the use in the second case of the PVT, so the heat load related to DHW consumption has an advantage in that it is no longer met by the HP alone but by the HP plus the PVT. Below is Table 4 summarizing the boundary conditions of the last two tests, which differ only from the use of PVTs as the thermal source in the (AB) case.

Table 4 Summary parameters of experimental tests with photovoltaic and wind generation

Case	AA	AB
Type of operation	DHW + Cooling	DHW + Cooling
DHW Thermal Source	HP	PVT + HP
Electric Source	PV + Wind	PV + Wind
Thermal profile	Residential cooling and DHW heat load	Residential cooling and DHW heat load
Electrical profile	Residential electrical load	Residential electrical load

In Figure 9 the generation curve (PV + wind) and the residential electrical load are shown, during the daylight hours, when the PV production is available. The four curves shown are related to the electrical load of the building and the wind and photovoltaic renewable sources, and finally, the fourth curve is the sum of the individual contributions of wind and photovoltaics.

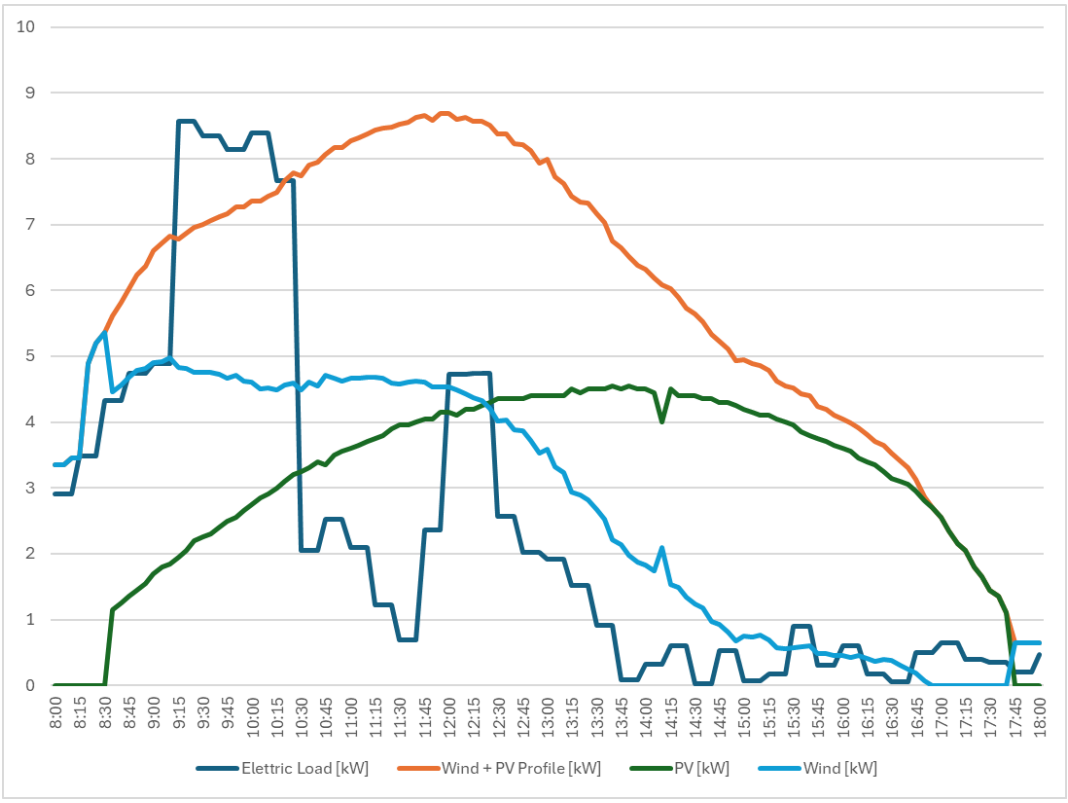

Figure 9 PV and wind power generation profile together with residential electrical profile.

The peak power of the PV and wind power system is the same as in previous cases where only PV was evaluated

In Figure 10 below, note how the HP followed the PV and wind generation curve until the evening when to meet the thermal load of cooling and DHW it left the tracking logic and entered a comfort logic. We show the graph obtained while the HP was used in P2H strategy, following the wind + PV curve to ensure the maximum possible absorption during generation hours, therefore maximizing SC.

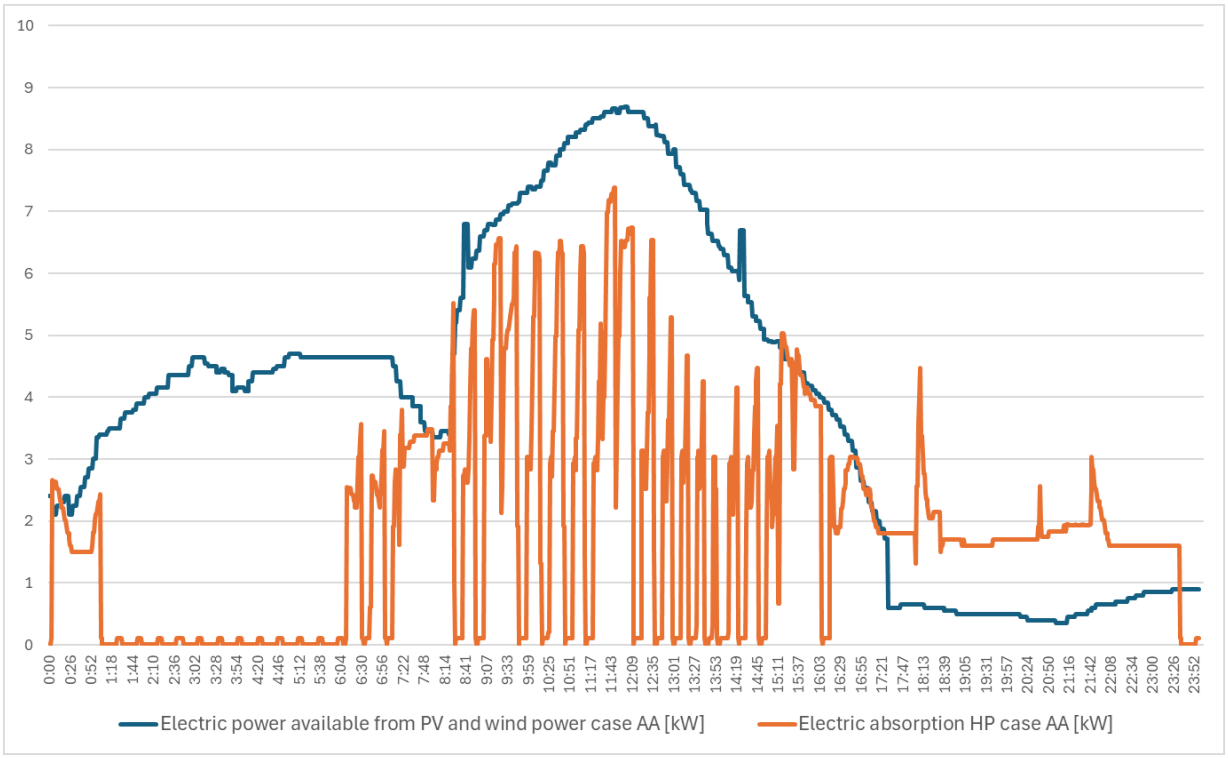

Figure 10 Electric power available from PV and wind power and power absorbed by HP (case AA)

Figure 11 below shows the performance of the heat pump in the case where, in addition to having PV and wind as electrical sources, there is also PVT as thermal contribution. The heat pump followed the PV and wind generation profile until the evening when the pdc exited the tracking logic and entered the comfort logic to ensure the comfort of the users.

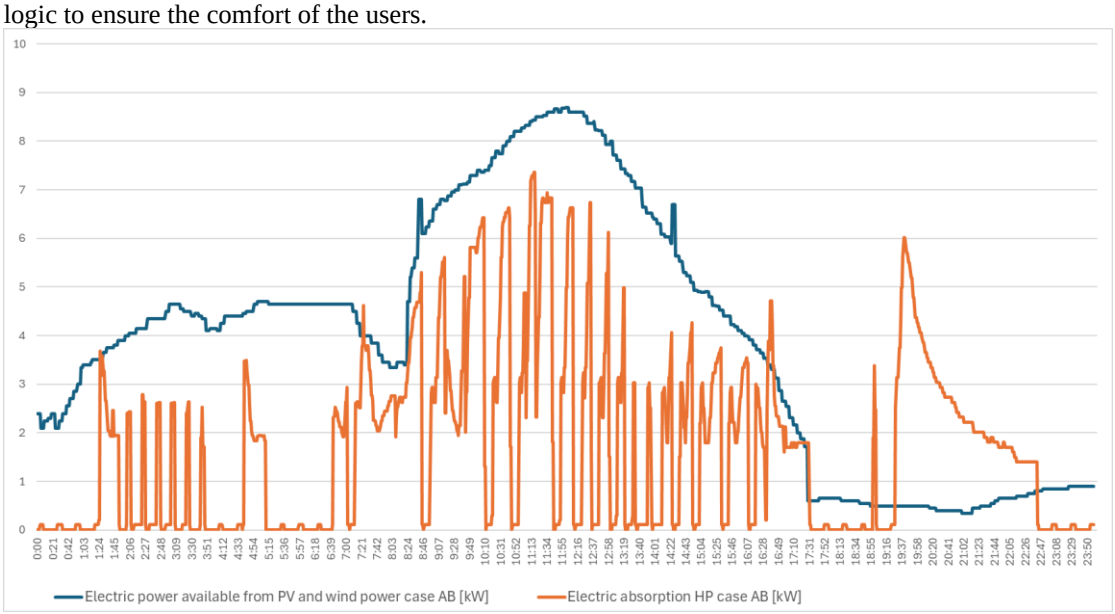

Figure 11 Electric power available from PV and wind power and power absorbed by HP (case AB)

No strong evidence is remarked upon from these graphs, in fact even the results summarized in the table 5 below underscore these aspects, the only factor that emerges is a slight increase in the SS factor. Further testing will be needed to obtain clearer data. Table 5 shows the energies considered in the calculation of the coefficients and the calculation of the SC and SS coefficients. In the (AB) case where PVT are used as thermal sources, there is a SS three percentage points higher than in the (AA) case.

Case	AA	AB	
Electricity produced by PV plus Wind	94,9	94,9	kWh
Electrical energy absorbed by the HP in total	43,7	40,1	kWh
Electrical energy absorbed by the HP in self-consumption	29,4	30,5	kWh
Thermal energy produced by the HP	194,0	170,9	kWh
Electricity self-consumed utilities	9,3	8,6	kWh
Electricity taken from the utility grid	25,6	26,2	kWh
Electricity fed into the grid	56,2	55,8	kWh
Calculation Energy Coefficients			
SC	0,41	0,41	-
SS	0,49	0,52	-
Daily COP	4,4	4,3	-

Table 5 Summary parameters of experimental tests AA and AB

Note how SC remains constant between the two cases while SC has a slight increase in the second case. This data is not very significant; the contribution of PVT is sensitive and difficult to quantify. Having a PV + wind generation curve results in a higher SS than the case of using only PV.

Comparing these two trials where wind power is used versus the previous two cases (E) and (F) where only PV is used, it can be seen that diversifying renewable sources can increase benefits compared to SS because it allows you to meet consumption for more time during the day but the SC remains constant because the difficulty of using all the energy that is produced remains almost constant.

5. Conclusion

Realizing RECs that show high self-consumption and self-sufficiency rates by sharing the energy locally produced from renewable sources not only follows the recent EC directives, but also have a direct impact on the global environment. In this work, we demonstrated effective resource management and control methods to enhance SC and SS in the context of RECs, adopting P2H and load shifting strategies. Moreover, we demonstrated how diversifying generation capabilities, making the power production available throughout the whole day can have a beneficial impact. We also shown how converting electrical power into thermal power by means of a HP can enhance the energy coefficients, while also warrantying thermal comfort to the RECs users. Finally, we demonstrated that the thermal section of a PVT plant, if used in the right context, can improve system performance.

6. References

[1] G. Gowrisankaran, S. S. Reynolds, and M. Samano, "Intermittency and the Value of Renewable Energy," J. Pol. Econ., vol. 124, no. 4, pp. 1187-1234, 2016.

[2] S. Gyamfi, S. Krumdieck, and T. Urmee, "Residential peak electricity demand response—Highlights of some behavioural issues," Renewable and Sustainable Energy Reviews, vol. 25, pp. 71-77, 2013.

[3] N. Mlilo, J. Brown, and T. Ahfock, "Impact of intermittent renewable energy generation penetration on the power system networks – A review," Technology and Economics of Smart Grids and Sustainable Energy, vol. 6, no. 1, p. 25, 2021.

[4] C. W. Gellings, "The Concept of Demand-Side Management for Electric Utilities," Proc. IEEE, Article vol. 73, no. 10, pp. 1468-1470, 1985.

[5] G. Strbac, "Demand side management: Benefits and challenges," Energy Policy, vol. 36, no. 12, pp. 4419-4426, 2008.

[6] H. J. Jabir, J. Teh, D. Ishak, and H. Abunima, "Impacts of Demand- Side Management on Electrical Power Systems: A Review," Energies, vol. 11, no. 5, p. 1050, 2018.

[7] R. Luthander, J. Widén, D. Nilsson, and J. Palm, "Photovoltaic selfconsumption in buildings: A review," Appl. Energy, vol. 142, pp. 80-94, 2015.

[8] A. Ciocia, A. Amato, P. Di Leo, S. Fichera, G. Malgaroli, F. Spertino, and S. Tzanova, "Self-Consumption and Self-Sufficiency in Photovoltaic Systems: Effect of Grid Limitation and Storage Installation," Energies, vol. 14, no. 6, p. 1591, 2021.

[9] A. Campoccia, S. Favuzza, E. R. Sanseverino and G. Zizzo, "Reliability analysis of a stand-alone PV system for the supply of a remote electric load," SPEEDAM 2010, pp. 158-163, 2010.

[10] A. L. Palma, L. L. Notte, B. D. Pietra, and R. Nissim, "Supercapacitors as a system-level solution for enhanced self-consumption strategies," in 2024 24th EEEIC International Conference on Environment and Electrical Engineering

Monitoring an innovative cold district heating network with decentralized heat pumps and sewage water as heat source

Christian Sauer1, Florian Werner1, Christoph Schmelzer1, Matthias Georgii1, Janybek Orozaliev1, and Klaus Vajen1

[1] University of Kassel, Institute of Thermal Engineering, Department of Solar and Systems Engineering, Kassel (Germany)

Abstract

The innovative heating network of a new development area in the city of Wiesbaden (**Germany**) is presented. The system uses waste heat from a sewer as the only source for heating via a cold heating network. Decentralized heat pumps in the buildings are used to raise the temperature level and electrical heating elements provide back-up. Possible advantages include high efficiency due to consistent wastewater temperatures and minimal noise and visual impact. The 2023 monitoring results are presented, showing that the heat pump systems provided 343 MWh to 5 multi-family buildings. Due to a leakage-related outage of the wastewater heat exchanger lasting several months and various problems in the operation of the heat pumps, the efficiency goals could not yet be fully achieved in operation. The total electricity consumption for heat supply in 2023 was 128 MWh. The average Seasonal Performance Factor (SPF) ranged from 2.7 (including network shutdown and use of electric heating elements) to 4.1 (fault-free operation).

Keywords: Renewable District Heating, Heat Pump, Sewage, Wastewater Heat, Ultra-low Temperature District Heating

1. Introduction

In the Germany city of Wiesbaden, a new development area is supplied with heat via a cold heating network and decentralized heat pumps. The development of the site is not yet completed. In 2023, five apartment buildings were built and have been supplied by the heating supply system in regular operation. When fully developed, the system is expected to provide up to 500 MWh/a of heat. A distinctive feature of this system is the utilization of high and relatively stable wastewater temperatures throughout the year as heat source, which is expected to significantly enhance the efficiency of the heat pump systems. Furthermore, the system presents several other advantages: it minimizes noise pollution compared to conventional air-to-water heat pumps, reduces fuel delivery traffic (e.g. wood pellets), and avoids adverse impacts on the densely developed urban landscape, such as visible plant technology installations. Cold district heating networks also offer potential advantages over conventional district heating systems. Operating at very low temperatures reduces or even eliminates heat losses which is especially significant while supplying high efficiency housing with low energy demand. Also, the decentralized nature over the systems offers flexibility and scalability in the development of the supply area. For this reasons, local cold district heating networks with decentralized heat pumps are an innovative heat supply system that has become increasingly popular in recent years.

Various publications deal with the operational evaluation of cold district heating networks. Ruesch et al. (2015) examine a low-temperature district heating network in Zurich, Switzerland, serving over 400 households and validating dynamic simulation models with operational data with a focus on pumping power prediction. The main heat source of the system is a datacenter. Four large decentralized heat pumps provide heat with an average COP of 3.7. Vetterli et al. (2017) presents the monitoring results of a one-year operational period of an ultra-low-temperature heating network in the district "Suurstoffi," located in central Switzerland. The study focuses on the first development phase of a new residential area with a design heat

© 2024. The Authors. Published by International Solar Energy Society
Selection and/or peer review under responsibility of Scientific Committee
10.18086/eurosun.2024.02.16 Available at http://proceedings.ises.org

demand of 1.2 GWh. The heat sources for the system include a geothermal borehole field and photovoltaic-thermal system. The heat pumps achieve a COP of 4.4, meeting the design expectations. However, the electricity consumption for auxiliary equipment, circulating pumps and electric heating, was higher than anticipated. Calixto et al. (2021) analyzed different modeling approaches for an existing cold temperature-temperature district heating network in Ospitaletto. Heat sources included industrial waste heat and aquifer wells. Year-round monitoring revealed efficient operation and alignment between different simulation model approaches. The decentralized heat pumps were maintaining stable performance and COPs between 4.2 and 4.5. Zeh and Stocking (2022) describe the long-term monitoring of a cold district heating network in Bad Nauheim, Germany with an 11.000 m²- geothermal ground collector system that supplies 400 residential units. The COP of the considered heat pumps is 3.9. It is pointed out that the 6 km long, uninsulated cold district heating network itself also acts as a form of geothermal collector and thus serving as an additional heat source.

Despite many publications and realized projects, there is still only limited information available on detailed real-life operating experience and the potential problems and challenges that can arise when operating a cold district heating network especially in the combination with a wastewater heat exchanger. This paper aims to provide a comprehensive overview of the system's structure and functionality, including the wastewater heat exchanger, the heating network, and the decentralized heat pump systems. Additionally, the monitoring concept and the results of the operational monitoring for the year 2023 are presented. The analysis covers the operating behavior of the wastewater heat exchanger and the performance of the decentralized heat pumps. Furthermore, the paper discusses the challenges malfunctions and outages observed during the operational monitoring, along with lessons learned and potential optimization approaches for the systems.

2. Design and function of the heat supply system

Structure and function of the heat supply system

At the periphery of a new real estate development area, heat is extracted from a passing sewer at a low temperature level (approx. 14°C) with an internal heat exchanger. The thermal energy is distributed via a cold local heating network and raised to a temperature level that can be used for domestic hot water and space heating purposes (30°-60°C) with decentralised heat pump system in the buildings. The cold heating network is designed without a central pump system. Circulation in the network is ensured entirely via pumps at the decentralized heat pump systems. Fig. 1 shows the structure schematically.

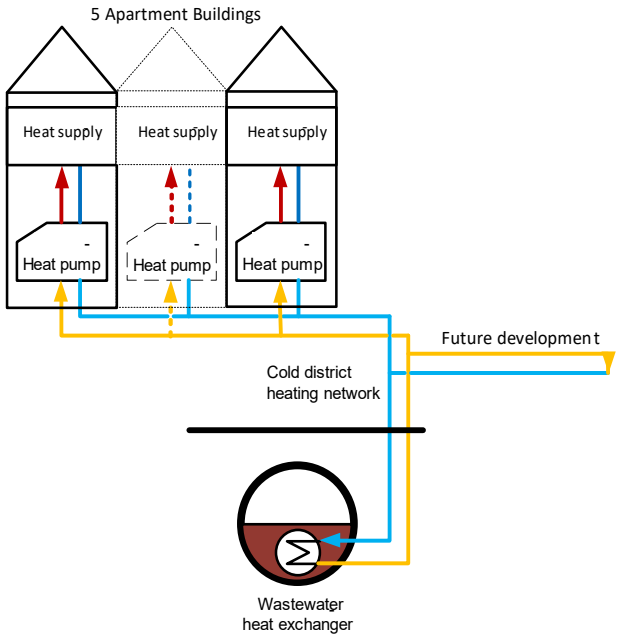

Fig. 1: Schematic representation of the heat supply system

District heating supply area

The cold local heating network supplies a new development area of around 2.5 hectares, which is divided into different construction phases. Only construction phase 1 is already fully completed. It comprises of five apartment buildings with a total of 67 residential units and a total living space of around 5000m². The buildings are constructed according to low energy standards with a specific design heat requirement < 30 kWh/(m²a) and low temperature underfloor heating systems. The total design heat demand for the buildings is 280 MWh/a with a peak load of 250 kW. Typically for high-efficiency multi-family houses, a high proportion of the heat requirement is needed for hot water preparation. A share of 42 % of the total heat requirement was projected here. As the project progresses, it is planned to connect a further 10 semi-detached houses (total design heat demand 220 MWh/a) and multiple single-family houses (maximum additional heat demand 80 MWh/a in total).

Waste water heat exchanger and cold district heating network

The wastewater heat is extracted from a larger channel (DN1500) that acts as a collector sewer for the adjacent urban area (not just the newly developed area) to the sewage treatment plant. For this purpose, a channel heat exchanger design was installed during ongoing sewer operation.

The heat exchanger is made from modular stainless-steel elements, which were installed as a retrofit solution via the existing shaft infrastructure. The heat exchanger has a length of 112 m, a transfer area of 151 m² and is designed for an extraction capacity of 340 kW. Fig. 3 shows a schematic representation of the heat exchanger including the measurement equipment (A), a 3D-illustration of the heat exchanger channel design (B), as well as a picture of the actual installation situation in the sewer (C).

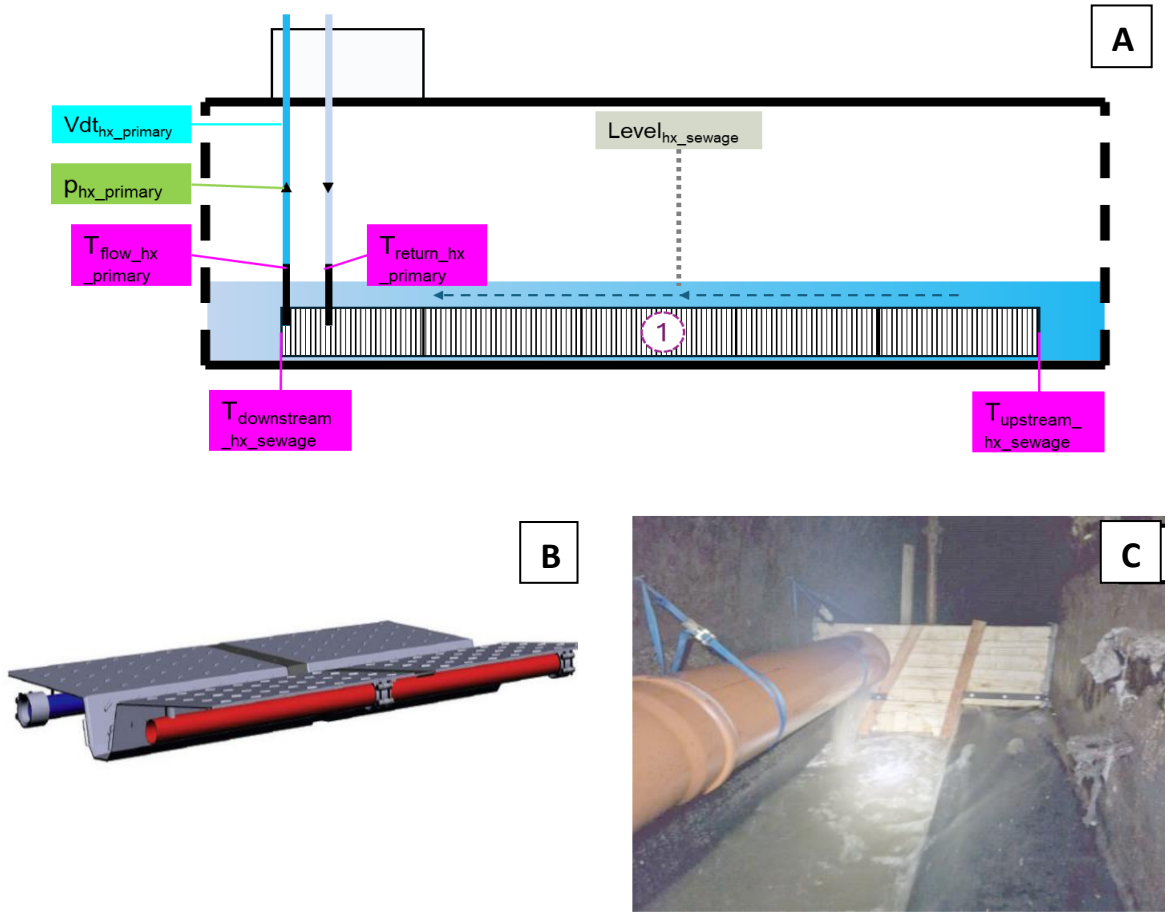

Fig. 2: A: Schematic illustration of waste water heat exchanger
B: 3D Illustration of the heat exchanger [UHRIG 2023]
C: On-site installation situation with wastewater bypass during a repair operation [UHRIG 2023]

The heat transfer fluid of the heating network flows directly through the primary side of the heat exchanger. A mixture of water and organic corrosion inhibitors is used. In terms of its thermal properties, it has no significant differences to pure water. It therefore also has no antifreeze protection. In the initial design phase of the system a heat transfer medium based on propylene glycol was planned. But because of local water protection regulations this had to be changed in the process.

The heating network is made of uninsulated PE pipes and is designed as a classic two-pipe system. The trench length in the current expansion status is only about 500 m. The different parts of the development area supplied by main lines that can be shut off individually. To minimize pressure losses, the main line in the multi-family house section is dimensioned in DN180 and the branches to the buildings in DN110.

The entire network and the heat exchanger are designed as completely passive elements. There are no pumps, actuators or an active control system in the heating network. There is also no permanent circulation in the network, the volume flow in the network is solely generated on demand by the decentralized source pumps at the heating systems of the individual buildings.

Heat Pump Systems

Each multi-family house has its own identically designed heating system. The centrepiece of each system is a water/water heat pump with a thermal output of 65 kW (B7/W50 according to EN14511). The heat pump is an on/off device with a fixed compressor speed without the ability to actively modulate the output power. Fig. 3 shows the layout of the system schematically

The source pump (1) feeds the heat transfer fluid from the network directly to the evaporator of the heat pump (2). For efficiency reasons and to avoid freezing, the heat transfer fluid is only allowed to cool down 5°K. Due to this low temperature difference, a high-volume flow is required to provide the required source energy for the heat pump. In order to match the resulting pressure losses in the network and heat exchanger, a sufficiently powerful source pump must be used (nominal flow rate: 18.7 m³/h, nominal head: 18.3 m). The pumps are designed without external speed control and deliver a constant flow rate during operation. The storage charging pump (3) transports the heating water through the condenser of the heat pump where it is heated by a small temperature range (approx. 5°K) each time it passes through. A 3-way motor valve (4) is used to control whether the storage charging pump loads the 1000 l domestic hot water buffer storage tank (5) or the 1500 l space heating buffer storage tank (6).

From the buffer storage tanks, heat is transferred to the building. With domestic hot water (DHW) preparation, this is done indirectly. For this purpose, cold tap water is heated from around 8°C to 60°C via a temperature-controlled heat exchanger installation, a freshwater station (7). Also, the thermal losses of the DHW-circulation are compensated. For hygiene reasons, the DHW-buffer itself does not contain any domestic hot water.

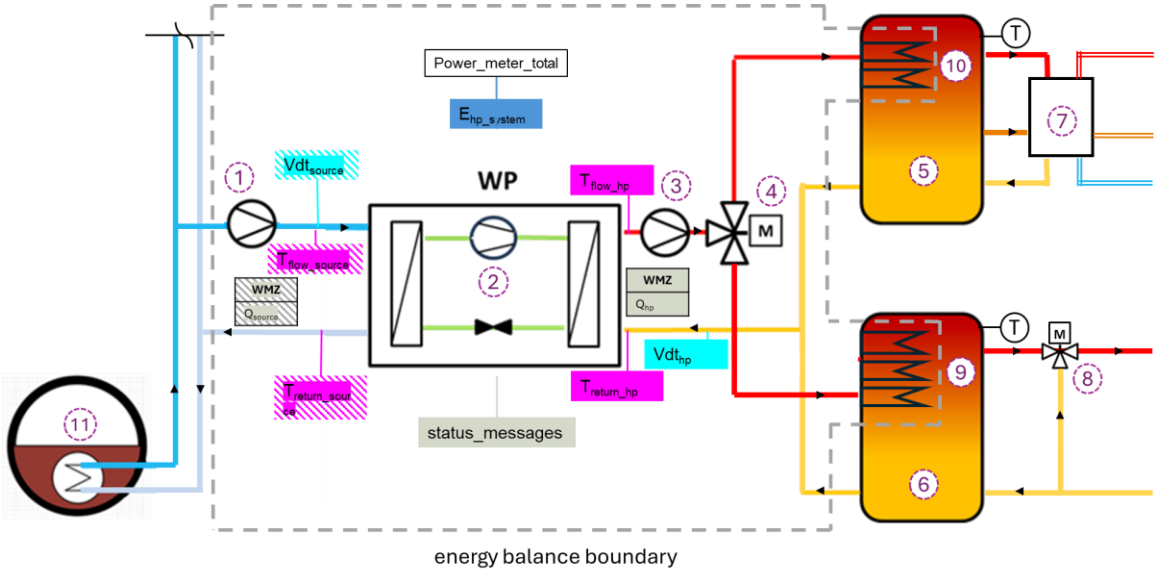

Fig. 2 Schematic diagram of heat pump system with measurement locations and energy balance boundary.

The heating buffer storage tank is hydraulically connected directly to the underfloor heating circuit of the building. The temperature is regulated to the required heating temperature via a circuit mixer (8).

The heat pump is controlled by a hysteresis-based control scheme with a temperature sensor in each of the buffer tanks and a temperature sensor in the return flow of the heat pump. As the temperature of the heating water is only increased by a few kelvins with each "pass-through" the storage volume may has to be circulated several times for complete charging. DHW-preparation has a higher priority than heating operation, i.e. loading of the heating buffer storage tank is interrupted when DHW is required and resumed when the required DHW temperature is reached.

The heat pump systems and the heating network are sufficiently dimensioned to ensure that the building's heating requirements can be supplied by the heat pump alone at the design temperatures (-15°C). As backup in the event of an outages, electric heating elements (HE) are installed in both buffer storage tanks as alternative heat generators. The DHW-HE (9) has an output of 12 kW (2x6 kW) and the heating-HE (10) has an output of 27 kW (3x9 kW).

3. Data acquisition and monitoring

The focus of this study is on the wastewater heat exchanger, the section of the heating network that supplies the completed construction area and the decentralized heat pump systems in the five multi-family houses. principle of monitoring the innovative heat supply system is to view it as a whole and from a system perspective. The internal processes of the individual components, e.g. the cooling circuit functionality of the heat pumps, are not examined.

Fig. 2 A shows the various sensos in the heat exchanger. The temperatures in the heat exchanger flow and return on the network side (primary) as well as the flowrate in the network, the absolute pressure in the network, and the pressure drop across the heat exchanger are measured. In the wastewater flow, the wastewater temperatures upstream and downstream of the heat exchanger are measured. For cost considerations, the flowrate of the wastewater is not measured directly. Instead, the water level of the wastewater channel is measured using an ultrasonic level measurement, from which qualitative conclusions about the wastewater volume flow can be derived.

All temperatures are measured with PT100 class A sensors. A robust thermal flow-velocity sensor is used to measure the flowrate in the network. However, the sensor has a high measurement uncertainty of +-17% in the occurring measurement range due to very low flow velocities. This high measurement uncertainty is propagated in the measurement chain for thermal power and energy.

In the decentralized heat pump systems, the combined electrical power consumption of the heat pump, source pump, storage charging pump as well as the auxiliary power consumption, and the power consumption of the HE are measured with an electric power meter. Due to its specific load profile, the electricity demand of the HE can be isolated from the total electricity demand.

The flow and return temperatures, volume flows, and the resulting thermal energy and power at the output of the heat pumps are determined via heat meters. The stationary measurement technology is supplemented by mobile ultrasonic flow meters and clamp-on temperature sensors, which are used to measure the flowrates as well as the flow and return temperatures of some heat pump sources for selected time periods. The system measurement data is supplemented by automatically generated error and status messages from the heat pumps and by weather data from the German Weather Service for the location. In fig. 3 all sensor positions can be seen.

Also shown in fig. 3 is the boundary for the energy balance and the performance assessment of the heat pump systems. The cut off-point for the heat supply lies directly behind the heat meter at the outlet of the heat pumps. For technical reasons, the electric heating elements are located behind the heat meter in the buffer storage tanks but could be allocated to the energy balance as heat generators according to their electricity consumption. (An electricity-to-heat conversion rate of 100% is assumed). Heat losses in the buffer storage or in the DHW circulation pipes or, are not considered in the balancing.

The key evaluation parameter for a heat pump system is the coefficient of performance (COP). It describes the ratio of electrical energy used to heat generated. The annual average coefficient of performance is also called seasonal performance factor (SPF).

Typically, two different balance sheet limits are used. For COP1 electrical power consumption of the heat pump, the source pump, the storage charging pump and other auxiliary power consumption for control systems etc. is taken into account (eq.1). The HEs are not considered here. COP2 also includes the electricity demand and heat generation of HEs (eq.2)

$$\mathrm{COP1} = \frac{Q_{HP}}{E_{hp}+E_{pump,source}+E_{pump,sink}+E_{aux}} \quad \text{(eq.1)} \qquad \mathrm{COP2} = \frac{Q_{HP}+Q_{HE}}{E_{hp}+E_{pump,source}+E_{pump,sink}+E_{aux}+E_{HE}} \quad \text{(eq.2)}$$

4. Assessment of the wastewater heat exchanger

In 2023, a total of 160 MWh of wastewater heat was extracted from the sewer and fed into the heating network, see fig. 4. The low/absent heat extraction between April and July is due to a network outage caused by a heat exchanger leakage. Therefore, the total heat energy delivered does not correspond to a typical operating year. The high measurement uncertainty is mainly caused by the thermal flow velocity sensor.

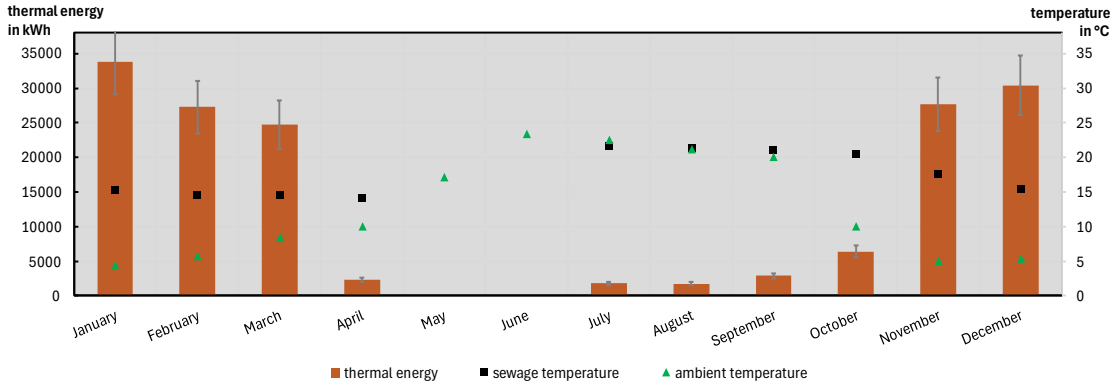

Fig. 3. Monthly heat extraction from the wastewater heat exchanger and average monthly ambient air and wastewater temperature (right y-axis)

Wastewater temperatures

The average monthly wastewater temperature and the average outdoor temperature are plotted on the secondary axis in fig. 4. In July to September, the average wastewater temperature is almost identical to the outdoor temperature. However, the seasonal variations in wastewater temperature are much less pronounced than the variation of the ambient air temperature. During the heating period from 1st October to 30th April, the average wastewater temperature is 9 °C higher than the outdoor temperature. The average monthly wastewater temperature ranges from 14.5 °C in February to 21.6 °C in July. The average wastewater temperature over the entire observation period is 16.2 °C.

A more suitable approach for examining the wastewater temperature than the average temperature over time is the average temperature level at which the thermal energy is actually extracted. The histogram in 5 shows what proportion of the total thermal energy is extracted at certain temperature level of the wastewater.

The largest proportion of the extracted energy, just under 90 % or 141 MWh, is extracted at temperatures between 12 °C and 18 °C. Especially low temperatures of <10 °C are extremely rare, with a share of < 1 % of the extracted energy. Around 5 % of the energy is transferred at particularly high temperatures of >18 °C. Both, very high and very low temperatures can cause problems with heat pump operation.

The energetic average temperature level is 13.7 °C, this is significantly lower than the time average temperature. This is of course due to the fact that periods with above-average heat demand correlate with below-average wastewater temperatures.

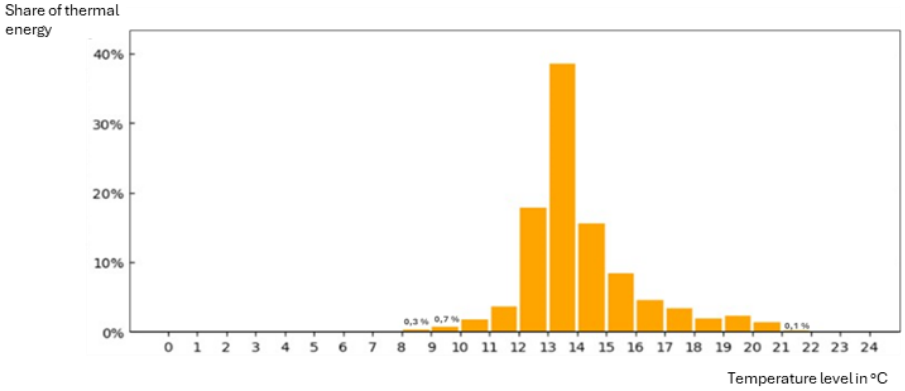

Fig. 4 Distribution of the temperature level of waste heat utilisation

Precipitation-related temperature drop in the wastewater temperature

Normally, the wastewater temperature is relatively stable and is subject only to slow diurnal and seasonal changes. However, sudden drops in the otherwise relatively constant wastewater temperature could be observed sporadically. Fig. 6 shows an exemplary representation of this behavior. The wastewater temperature (brown) drops from 15.6°C to 7.4°C within a short period of time. This behavior is due to the design of the local sewer, which is a mixing sewage system. During heavy rainfall, rainwater and wastewater are discharged together through the sewer. Very high precipitation (blue) leads to a sharp increase in the wastewater level (purple) due to the inflow of cold surface water. In combination with low outside temperatures (green), this leads to a significant drop in the wastewater temperature. After the end of the precipitation, the temperature normalizes again within a day. The minimum observed wastewater temperature can drop to 7.2 °C in similar cases. Very pronounced drops in wastewater temperature, cause some of the decentralized heat pump systems to repeatedly experience outages.

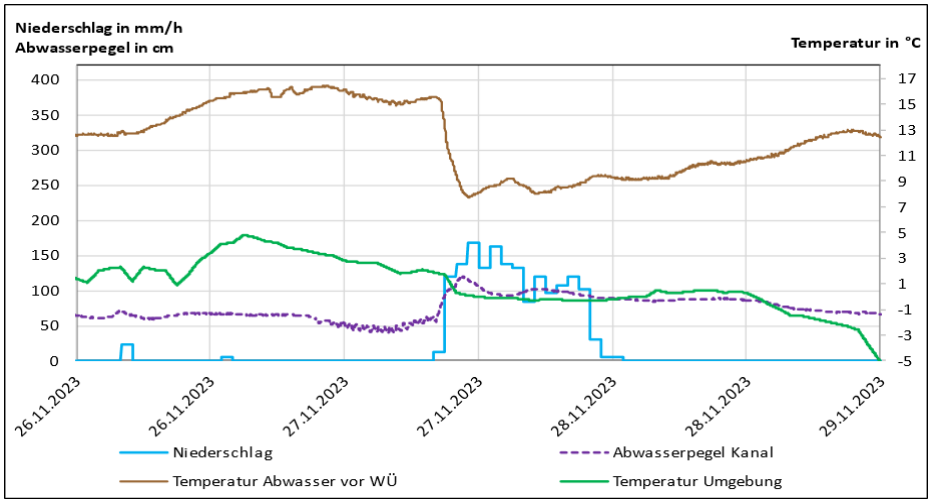

Fig. 5 Temperature drop in wastewater - correlation between precipitation, wastewater level and outside temperature

Heat exchanger operation

The heat extraction rate from the heat exchanger is rather fluctuating, as the network flow rate varies greatly. Depending on the operation of the decentralized heat pumps the flow rate is between 16 m³/h (for one active heat pump) and approx. 102 m³/h (for all active heat pumps). The average network flow rate during operation is 20 m³/h. The average heat extraction rate during operation is 54 kW, with a maximum stationary extraction

rate of 390 kW in peak conditions. The average temperature reduction of the wastewater during operation is only 0.2 °K (within the measurement uncertainty range of the sensors). The same applies to the coarseness of the heat exchanger (temperature difference between the wastewater and primary side at the heat exchanger outlet). with 0.3 °K during operation. This means that the flow temperature in the cold local heating network is essentially identical to the wastewater temperature.

Typically, sediments and the development of a biofilm (fouling), can lead to a significant reduction in the thermal conductivity of a wastewater heat exchanger surface. However, due to the very small temperature differences (in the range of the measurement uncertainty), no significant reduction in the heat transfer coefficient/heat transfer capacity (UA-value) could be determined.

Network outage caused by heat exchanger leakage

In early April 2023, an unexpected pressure drop occurred in the local heating network, accompanied by a simultaneous malfunction of all heat pump systems. The cause was identified as a leak in the channel heat exchanger, which led to an outage of the entire heating network. The manufacturer's investigation suggested that the most likely cause for the damage were concrete drilling debris from an unknown construction site upstream. Extensive repairs were required after locating the fault. Since the damage was below the water level, the wastewater channel had to be dewatered without disrupting wastewater transport. In coordination with the local authorities, a dam plate was installed and a bypass line was laid within the channel. Subsequently, damaged modular heat exchanger components were replaced. The network was fully operational again by mid-July. The total network outage lasted 91 days. During this period, the heating demand of the connected buildings (primarily for domestic hot water preparation) was met using the HEs

5. Operational assessment of heat pump systems

In this section, the operating behavior of the heat pump system is presented. Fig. 7 shows the typical operation over 24 hours for a selected sample system. In the top panel the electrical power consumption (green) and the thermal power output (yellow) of the heat pump could be seen. The source temperature of the heat pump (flow temperature of the cold heating network) is plotted in blue on the right y-axes. The flow temperature of the heat pump is shown in red. In the bottom panel the current operating mode of the heat pump is shown.

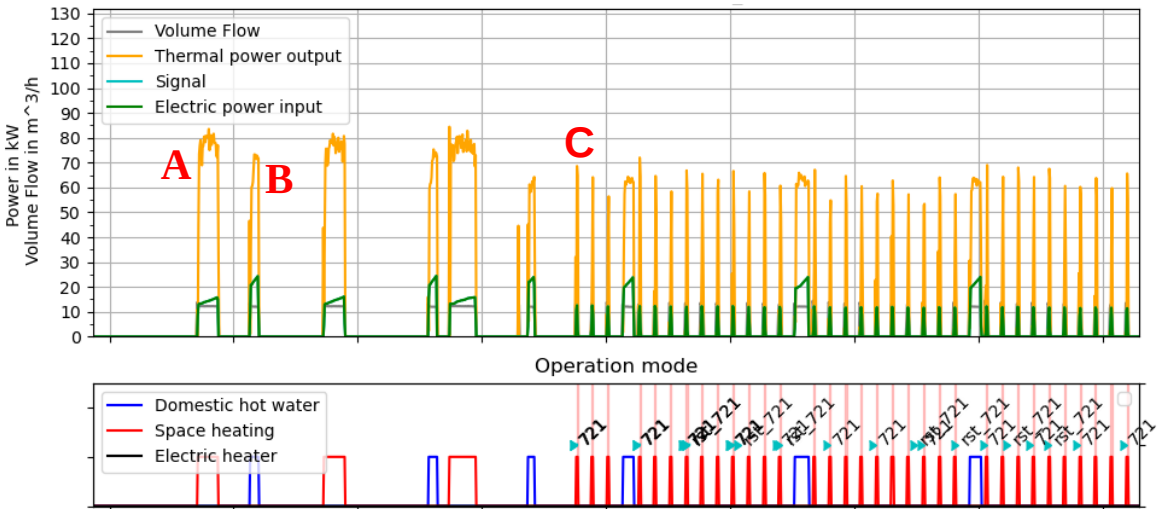

Fig. 6 Heat pump operation. Top: Electrical and thermal power
Bottom: Operation mode

Space heating and drinking hot water preparation

Marking A flags a typical heating operation phase of the heat pump. With the start of the compressor, the electrical power consumption (green) rises to approx. 15 kW. At the same time, the thermal output power (yellow) rises to around 75 kW. The flow temperature increases till the target temperature is reached (heating curve dependent on the outside temperature) and the heating buffer storage tank is fully charged.

For all heat pump systems in 2023, the average flow temperature in space heating operation is 42°C. In steady state space heating operation, without consideration of the start-up and shut-down process the heat pump systems reach a $COP1_{Space\ heating}$ of 5.1

In a DHW-preparation phase (marking B), the flow temperature rises to the fixed target temperature of 65°C degrees. Due to the higher temperature difference between the source temperature and the sink temperature, a higher compression rate and therefore a higher electrical power demand of the heat pump compressor is required than in space heating mode. For all heat pump systems, the average $COP1_{DHW}$ for DHW preparation in steady state conditions is 2.6.

Operating faults - aborted operating phases:
From 09:00, there is a significant drop in the flow temperature of the cold district heating network (blue). This was caused by a strong reduction in the temperature of the wastewater due to heavy precipitation as described in the previous chapter. This drop in source temperature triggers an abnormal behavior of the heat pump. The heating operation phases last only a few minutes without reaching the target flow temperature.

The operation is aborted due a low-pressure fault status of the heat pump (code 721). A low-pressure fault or a low-pressure cut-out is an operating pressure shortfall on the low-pressure side (evaporator/heat source) in the refrigerant circuit of a heat pump.

Individual low-pressure faults are typically not considered critical. The fault does not necessitate an immediate response from the plant operator and typically has no significant impact on the operation of the heat pump. The heat pump restarts after a brief blocking period. However, a more concerning issue is the occurrence of a heavy clustering of faults over an extended duration. This can result in the heat pumps being unable to maintain normal heating operations over an extended period. In order to prevent an undersupply, the electrical backup heating element must then be activated.

In total, over 1,000 operating phases of the five heat pump systems were aborted due to faults in 2023. In 10 cases, the HE had to switch on to providing backup heat generation for several days at a time.

In addition, one heat pump had a breakdown due to a defect in the evaporator and had to be substituted with the backup HE for over two months. Overall, the five backup HE were required to operate for over 800 hours due to direct faults/breakdowns of the five heat pump systems (not including the outage of the district heating network from April-July)

The underlying cause of the many aborted operation phases of the heat pumps is still under investigation. While the temperature drops in the wastewater play an important role, they are not considered the sole cause. Particularly because only some of the heat pump systems are affected by a high number of low-pressure faults. Other systems show no conspicuous behavior. Although all heat pump systems have identical hydraulics and share the same network temperature. The issues also arise despite the source volume and temperatures being within the permitted operating parameters for the heat pumps.

Possible causes that are under consideration are: Deposits on the evaporator that reduce heat transfer, insufficient refrigerant quantity or malfunctions in the refrigeration circuit control of the heat pumps, and air or undissolved gases in the heating transfer fluid of the cold district heating network. Deposits on the evaporator that reduce heat transfer, malfunctions in the refrigeration circuit control of the heat pumps, insufficient refrigerant quantity and air /undissolved gases in the heat transfer fluid of the cold district heating network.

Operating time and cycle behaviour
The number and length of the operating cycles and thus the number of compressors starts is an important parameter for evaluating heat pump operation. Frequent instationary operating states (start-up and shutdown processes) have a negative influence on the efficiency of heat pumps. Experimental and simulation-based research indicate that frequent on/off switching can lead to efficiency losses of up to 20% an minimum operating cycle times should not be below 15 (Uhlmann und Bertsch 2010) and 20 minutes (Waddicor et al. 2016) to avoid exceeding efficiency losses. Furthermore, a high number of compressor starts could lead to a reduced service life of the heat pump.

During the observation period, the five heat pumps on average run 730 full operating hours and complete an average of 2243 operating cycles each. This equates to an average of just 22 minutes per cycle.

In Fig. 8 the typical distribution of duration cycle duration of a heat pump system for one month can be seen. In space heating operation the heat pump system have running periods of 26-60 minutes (38 minutes average for all systems). DHW preparation phases are much shorter with average cycle duration of only 14 minutes, DHW preparation is also responsible for 62 % of all compressor starts. The quite short operating cycle duration of the DHW preparation indicates that the heat pump is slightly oversized for the existing DHW buffer storage. Although not optimal, the operating cycle duration and the cycle behavior of the heat pumps in regular/fault-free operation are still within an acceptable range. Much more critical is the high number of very short operating phases that are aborted due fault conditions of the heat pumps. In some heat pump systems, these account for a considerable proportion of compressor starts (up to 18 %).

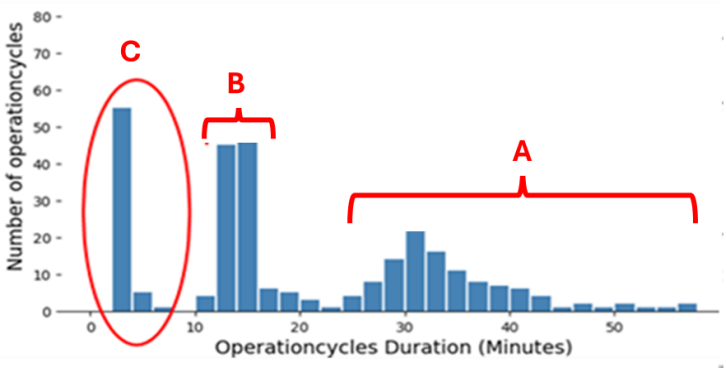

Fig. 7: Distribution of the operating cycle duration

6. Energetic assessment of heat pump systems

The five heat pump systems in the multi-family houses delivered 343 MWh of thermal energy in 2023. The average amount of heat supplied for each building is slightly varying and lies between 55 and 72 MWh. Fig. 9 shows the monthly distribution across the individual buildings.

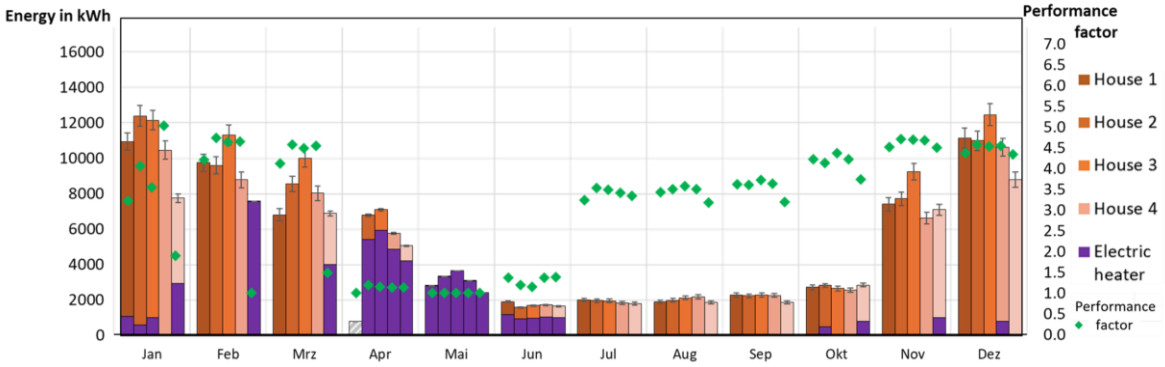

Fig. 8 Monthly heat quantities provided by the heat pumps and electric heating elements (shaded). Monthly average COP (right y-axes)

The heat requirement for DHW-preparation is similar for all houses and averages 26 MWh (39% of the total heat supply) From June to September, the heat requirement can be fully allocated to DHW preparation.

The purple area of the bars represents the amount of heat that had to provided by the backup electric heating elements. In the months of April-June, the electric heating elements had to take over a large part or all of the heat supply due to the described outage of the cold district heating network. During the outage period from 04/13/2023 to 07/12/2023, the electric heating elements produced 42 MWh of heat There were also several occasions when the HE had to provide the load due to problems directly related to the heat pumps. From mid-January to March, the heat pump in house 5 failed due to a defect in the evaporator. The other HE operation cases were caused by a cluster of heat pump operation faults, as described in the previous section. Over the year 59 MWh of heat hat to be provided by the backup HE (17% of the total heat supply)

A total of 128 MWh of electricity, including the consumption of the backup HE was used to generate the required heat. The right y-axis in Fig. 9 shows the corresponding monthly average COP2 for each heat pump system. Again, the heating network outage between April and June is clearly visible. During this period, heat had to be supplied exclusively by the electric HE, which convert electricity directly into heat (COP=1).

The use of HE during the heat pump related outages also has a significant impact on the corresponding COP2 of these heat pump systems. In the second half of the year, the COP is much more stable. There was only a very low usage of the HE in this time period. With the start of the heating period, the average monthly COP for all heat pumps rise from 3.4 in July to around 4.6 in November. This can be attributed to the increasing demand for space heating and the resulting decrease in the proportion of DHW preparation in the overall heating demand. Due to the lower temperature spread, the heat pumps work correspondingly more efficiently.

As a result of the various outages of the network and the heat pumps and the resulting need to use the inefficient HEs, the overall average seasonal performance factor (SPF2) for all heat pump systems is relatively low at 2.7. If the period with the heating network outage is not considered the average SPF2 rises to 3.5. If the complete HE operations are excluded the SPF1 rises to 4.1.

7. Conclusion and summary

The scientific monitoring of the cold district heating network with decentralised heat pumps and sewage water as heat source for the year 2023 illustrates the many challenges that can arise while operating an innovative and complex heat supply system.

The evaluation confirms the basic function and efficiency of the wastewater heat exchanger for supplying the cold local heating network. It was possible to extract 160 MWh of energy from the waste water at relatively high temperatures of 13.7 °C on average. The heat capacity flow of the wastewater is sufficiently large so that there is no significant cooling of the wastewater in the current state of expansion of the district heating network. Also, the heat transfer capacity is more than sufficient for the current heat requirement. No negative effects of deposits (fouling) on the heat exchanger are currently detectable. Sudden drops in temperature (~8 °C) that occur after heavy precipitation must be regarded as normal operating behaviour but could trigger unexpected faults conditions in the decentralised heat pump systems.

The leakage of the heat exchanger and the associated failure of the network must be regarded as "force majeure". The authors are not aware of any comparable incident with a similar system. However, the incident also highlights some of the fundamental challenges of wastewater heat exchanger systems. The environment of the sewer and the composition of the wastewater flow cannot be fully controlled. Work and repairs can be very time consuming. They often have to be carried out during ongoing sewer operation and must therefore be closely coordinated with the sewer operators and implemented with substantial interventions in the wastewater infrastructure.

In addition to the prolonged outage of the district heating network, a high number of direct heat pump-related faults meant that 17 % of the required heat energy had to be provided by the electrical backup heating elements. This led to an increased electricity requirement and a low overall seasonal performance factor (SPF1) of 2.7. Furthermore, an unfavourable operating behaviour of the heat pumps in the form of a high number of compressors starts and aborted operation phases caused by fault conditions in the refrigeration cycle could be observed. However, in regular operation (not taking into account the use of the backup heating elements during outages) an average seasonal performance factor (SPF1) of 4.1 could be reached.

The high efficiency values achieved during certain periods highlight the potential of the overall system. However, they also show that complex heat supply systems often require intensive monitoring and optimization over an extended period following commissioning to ensure sustained operational performance. Several optimization measures are currently under development, and their implementation will be monitored and evaluated in the next phase.

8. Acknowledgments

The authors would like to thank State Energy Agency Hessen (LEA Hessen) for funding the accompanying scientific research and the owner and operator of the monitored system ESWE Versorgungs AG for their excellent cooperation.

9. References

Calixto, Selva; Cozzini, Marco; Manzolini, Giampaolo (2021): Modelling of an Existing Neutral Temperature District Heating Network: Detailed and Approximate Approaches. In: Energies 14 (2), S. 379. DOI: 10.3390/en14020379.

Ruesch, Florian; Rommel, Matthias; Scherer, Jakob (2015): Pumping power prediction in low temperature district heating networks. DOI: 10.5075/epfl-cisbat2015-753-758. Online available: https://infoscience.epfl.ch/entities/publication/7d0eedf1-9680-4e1c-87b5-31951d94073d/conferencedetails (last checked 20.08.2024)

Uhlmann, Michael; Bertsch, Stefan (2010): Measurement and Simulation of Startup and Shut Down of Heat Pumps. In: International Refrigeration and Air Conditioning Conference. Paper 1008. Online available https://docs.lib.purdue.edu/cgi/viewcontent.cgi?article=2007&context=iracc (last checked 20.08.2024)

Vetterli, Nadège; Sulzer, Matthias; Menti, Urs-Peter (2017): Energy monitoring of a low temperature heating and cooling district network. In: Energy Procedia 122, S. 62–67. DOI: 10.1016/j.egypro.2017.07.289.

Waddicor, David A.; Fuentes, Elena; Azar, Marc; Salom, Jaume (2016): Partial load efficiency degradation of a water-to-water heat pump under fixed set-point control. In: Applied Thermal Engineering 106, S. 275–285. DOI: 10.1016/j.applthermaleng.2016

Zeh, Robin; Stockinger, Volker (2022): Monitoring of a large-scale geothermal collector system and a 5GDHC in Bad Nauheim. In: European Geothermal Congress,Berlin. Online available: https://www.researchgate.net/publication/369039743_Monitoring_of_a_largescale_geothermal_collector_system_and_a_5GDHC_in_Bad_Nauheim. (last checked 20.08.2024)

Achieving Sustainable Buildings: Balancing Energy Efficiency and Comfort through Ventilation Management

Rahul Verma, Dibakar Rakshit

Indian Institute of Technology Delhi (India)

Abstract

Proper ventilation management is essential for balancing energy requirements and limiting indoor CO_2 concentration. A high continuous ventilation rate ensures safe indoor CO_2 levels but significantly increases energy consumption. The high energy demand often leads building owners and occupants to prioritize meeting thermal requirements while neglecting the importance of indoor air quality. To optimize energy demand while maintaining thermal comfort and safe CO_2 limits, intermittent ventilation or reduced ventilation rates must be employed. Based on this study, different occupant densities provide varying ventilation time gaps to maintain CO_2 concentration within safe limits and offer an opportunity to save energy. For occupant densities higher than 50 m^3/person, a maximum ventilation gap of 250 minutes can be utilized, and the ventilation gap depends on the outdoor CO_2 level. For safe CO_2 levels at occupant densities above 20 m^3/person, continuous ventilation of 1.0 ACH suffices, while higher densities necessitate intermittent ventilation to cut energy demand. Energy use increases with higher ventilation rates and occupant densities, ranging from 1.25 to 2.28 times compared to the base case for 10 m^3/person to 90 m^3/person, respectively. Continuous ventilation at 2.0 and 3.0 ACH is required for lower occupant densities of 20 m^3/person and 10 m^3/person, which escalates energy use. So, it is recommended that lower occupant densities be avoided in indoor spaces. Tailored ventilation strategies can achieve approximately 50% energy savings in building operations.

Keywords: CO_2 concentration, intermittent ventilation, energy saving, occupant density, ventilation gap

1. Introduction

Human society is facing a lot of serious trouble in terms of environmental air pollutants and way of life. Indoor air quality (IAQ) is essential to enhance the quality of life, given that people spend most of their time in indoor spaces. Environmental pollution stands as a consequential and irreversible outcome of heightened energy consumption and the consequent combustion of fossil fuels. The International Environmental Agency reported that the rise in electricity demand on a global level in 2021 is 5%, which is almost met by fossil fuels (IEA, 2021). Total energy-related emissions increased by around 900 Mt between 2019 and 2023 with the growing development of major clean energy technologies such as solar PV, nuclear, wind, electric cars, and heat pumps. Otherwise, the expected increase in CO_2 emissions would have been threefold of emissions during the same period (IEA, 2023). In the year 2022, the global demand for air conditioning devices reached approximately 117.8 million units, marking the highest figure of the past decade and surpassing the peak recorded in 2019, which stood at around 116 million units (Statista, 2022). The global air quality based on the CO_2 concentration range underlined is in a good category 86% of the time. However, the Asia–Pacific (APAC) region belongs to the risk category approximately 10% of the time. The average CO_2 distribution highlighted in the Figure 1 for different regions. This data analysis is a collective representation of both the number of occupants present and ventilation. However, relying on simple statistics may not provide a comprehensive picture of the indoor air quality because occupancy densities play a vital role in CO_2 accumulation ("IAQ Data Benchmarks for 2023: What are Average Levels of PM2.5, CO_2, and TVOC in Different Regions?," n.d.). As shown in Figure 2 ("Press Release Ifrma Page: Press Information Bureau," n.d.), the AQI index can significantly impact ventilation requirements and underscores the limitation of relying solely on statistics for a comprehensive guideline. Figure 2 (a) illustrates the AQI distribution over the years based on the number of days, while Figure 2 (b) shows the monthly AQI distribution for various years.

© 2024. The Authors. Published by International Solar Energy Society
Selection and/or peer review under responsibility of Scientific Committee
10.18086/eurosun.2024.02.17 Available at http://proceedings.ises.org

Figure 1: Global CO_2 concentration across all regions (a) percentage bar (b) daily indoor air distribution

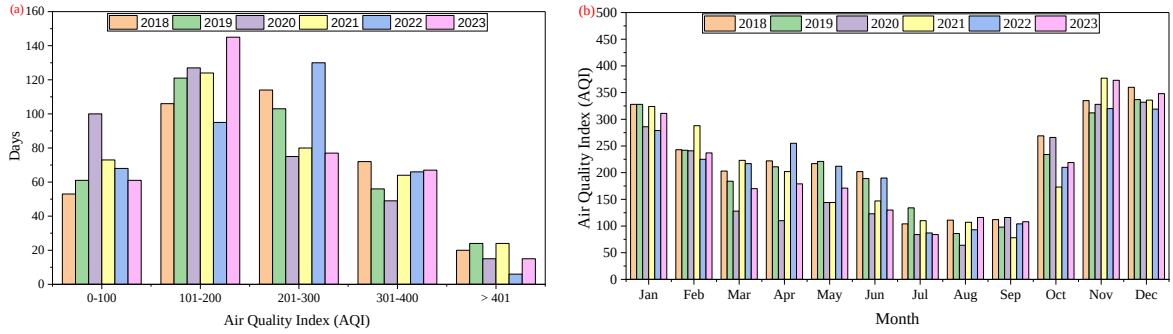

Figure 2: Delhi air quality index for different years (a) index division into days (b) monthly AQI level

A study was presented by (Baghoolizadeh et al., 2023) with the objective of achieving thermal comfort and improving CO_2 concentration through the optimization of genetic algorithms in residential buildings. Optimization results revealed that thermal comfort improved from 52% to 80%, and concentration of CO_2 improved, ranging from 17% to 30%. (Sakamoto et al., 2022) has been calculated CO_2 emissions rate per person and measured CO_2 concentrations in the control environment once it has reached to steady state. The emission rates per person varied from 14.1 to 17.8 L/h for sedentary work: higher emissions calculated in the afternoon might be because metabolism increases after diet. (Franco and Leccese, 2020) were estimated indoor occupancy through CO_2 concentration measurement for different types of activities. (Hussin et al., 2017) CO_2 measurements were observed in the university laboratory for 10 air-conditioned buildings and highlighted inadequate ventilation because CO_2 concentrations exceeded the limit of 1000 ppm. (Lawrence and Braun, 2006) have presented models for predicting indoor CO_2 concentrations, taking into account people as internal sources of emission. (Shriram and Ramamurthy, 2019) have emphasized that as recommended by ASHRAE, continuous ventilation results in high energy demand. (Salthammer, 2024) stressed the use of carbon dioxide as an air quality index because of fatal poisoning associated with it, and in indoor surveys, this substance receives less attention. (Krawczyk et al., 2016) conducted a CO_2 measurement in school buildings situated in Bialystok and Belmez and found that with medium occupancy, CO_2 concentration exceeded recommended values. (Borowski et al., 2022) experimentally observed in the occupant thermal comfort and indoor air quality of the hotel building. The analysis in a hotel building revealed that most of the time, occupants feel thermally comfortable; however, CO_2 concentration temporarily exceeded 2000 ppm. (Mahyuddin and Essah, 2024) considered CO_2 concentrations as a parameter to explore the ventilation strategies and design guidelines for classrooms. The research documented standard classrooms may have occupant densities in the range of 1.8- 2.4 m^2/ person. (Wargocki et al., 2002) unraveled indoor air quality improvement by enhancing air change rates; however, energy consumption for cooling and heating increased depending on the location and season. (Bakó-Biró et al., 2007) aimed to establish a link between occupant cognitive performance and air quality using a classroom atmosphere. By performing in-situ experimental measurements and considering CO_2 as an air quality indicator, the investigation revealed that low ventilation rates significantly decrease vigilance, attention, memory, and concentration. (Lu et al., 2010) developed a model for individual space for calculating CO_2 generation and ventilation rates in mechanically ventilated buildings. (Kim and Choi, 2019) inquired about the impact of increased outdoor CO_2 on the ventilation rate for buildings located in Shanghai, China. The research unveiled that to maintain indoor CO_2 levels with an increase in outdoor CO_2 levels, the outdoor flow

rate needs to be increased.

The current amount of literature has extensively explored the challenges posed by the accumulation of CO_2 in indoor environments. Further research has also unveiled the potential for energy saving as a result of optimizing indoor air quality and thermal comfort. The comprehensive determination of ventilation cycle time or minimum ventilation requirement is imperative for the efficient operation of mechanical ventilation in spaces equipped with ductless air conditioning systems. Previous recommendations have resulted in high energy demand, emphasizing the need for accurate calculations to optimize energy consumption. By utilizing the ventilation cycle time, occupants can effectively reduce accumulated CO_2 concentrations in indoor spaces without the necessity of installing expensive sensors. The aim of this research is to evaluate the ventilation cycle time and potential of energy saving compared to recommended ventilation for different occupant densities and ambient CO_2 concentrations.

The analysis, detailed through numerical results and experimental model validation, includes the following objectives:

- Measuring indoor CO_2 concentration in the actual environment to validate the numerical model in office space.
- Analysing indoor CO_2 concentration levels based on outside concentration levels and indoor occupant densities.
- Determining the impact of ventilation rate on energy consumption and indoor CO_2 level for numerous occupant’s densities.

2. Methodology

In several research studies, CO_2 as indoor air quality presented a concern for occupants; however, some denied the potential concern and stressed the other indoor quality parameters. The effect of other air quality parameters might have a strong potential to deteriorate the occupant's health compared to CO_2 concentrations. However, this research is focused on maintaining the CO_2 concentrations within the safe limit because other indoor air quality parameters have less concentration change in most indoor spaces than CO_2 levels. The variation in outdoor CO_2 concentration provides an understanding of the season and the effect of locations. To analyze the indoor CO_2 concentrations, a constant occupancy schedule was considered between 8:00 to 18:00 hours, and except this time, there is no occupancy associated with the building spaces. As a case study, we developed a two-story building (627.25 m^2) model through Design Builder located at the Indian Institute of Technology in Delhi (IITD), India. The main methodologies for this study were categorized in part:

- Measurement of indoor CO_2 concentration in an actual indoor environment to validate the numerical model.
- Calculation of the CO_2 concentration by numerical modeling for specific occupancy duration with constant building infiltration.
- Comparison of the impact of continuous ventilation rate on building energy demand and indoor CO_2 concentration.

Numerical modeling examines how insufficient air circulation can lead to elevated CO_2 levels, potentially compromising occupants' well-being. By exploring various occupant densities and outdoor CO_2 levels, the study investigates the impact of the continuous replacement of indoor air on energy consumption and indoor CO_2 regulation. The study also proposes intermittent ventilation operation as a strategy to effectively mitigate CO_2 concentrations tailored to different space dimensions and occupancy levels. The research aims to recommend optimal ventilation rates and operational time for different occupant densities to maintain thermal comfort and acceptable CO_2 levels while reducing energy usage. Additionally, it analyzes the patterns of CO_2 accumulation and dissipation over time across different outdoor CO_2 levels. The investigation scrutinizes a ventilation system's ventilation rate or operational intervals across different outdoor CO_2 levels and indoor occupant densities, as delineated in Table 1. The study evaluated through a building model based

on the assumption of an infiltration rate of 0.2 ACH, attributing to leakage through cracks, and the occupant CO_2 generation rate of 4.16×10^{-8} m^3/s-W. The ACH is basically a unit of measurement of air circulation or replacement in a space, which stands for air changes per hour. The circulation or replacement of air in space can happen in controlled and uncontrolled ways. The transient air mass balance equation (eq. 1) calculates carbon dioxide concentration in zone air (EnergyPlusTM Version 22.1.0 Documentation Engineering Reference, 2022). The two-story building model at IIT Delhi is being considered for the analysis of energy-saving potential and validation purposes, as depicted in Figure 3. The details of the building dimensions, orientation, and envelope material properties are streamlined (Verma et al., 2023). The building space and envelope thermal properties important for building energy modeling have been delineated in Table 2 and Table 3, respectively.

Table 1: The numerical study parameters and variations

Parameter	Range
Outside CO_2 concentration (ppm)	150, 250, 350, 450
Occupant density (m^3/person) or (m^3/p)	10, 20, 30, 40, 50, 60, 70, 80, 90
Exhaust ventilation rate (ACH)	1.0, 2.0, 3.0
Infiltration (ACH)	0.2

Table 2: Overall building envelope and space information

Item	Description
Total conditioned area (m^2)	627.25
Overall window-to-wall ratio (WWR)	0.2
Number of floors	2
Floor to floor height(m)	3.5
Floor to ceiling height (m)	3.0
Window-sill height (m)	0.8

Table 3: Building envelope thermal properties

Building Element	Component layer	Component material	Material Thickness (m)	U-value (W/m^2K)
Exterior wall	Layer 1(outside)	Plaster	0.0125	
	Layer 2	Brick	0.225	1.566
	Layer 3(inside)	Plaster	0.0125	
Roof	Layer 1(outside)	Lime sand render	0.1	
	Layer 2	Reinforced Concrete	0.1	
	Layer 3	Cast Concrete	0.2	1.36
	Layer 4	Air gap	0.5	
	Layer 5(inside)	Gypsum (false ceiling)	0.01	
Ground Floor	Layer 1(outside)	Medium weight concrete	0.075	
	Layer 2	Brick	0.075	
	Layer 3	Concrete, Reinforced (with 2% steel)	0.0250	2.181
	Layer 4	Cement screed	0.025	
	Layer 5(inside)	Ceramic/clay tiles	0.025	
Internal partition	Layer 1(outside)	Cellulosic insulation	0.001	
	Layer 2	Plywood (Heavyweight)	0.025	2.180
	Layer 3(inside)	Cellulosic insulation	0.001	

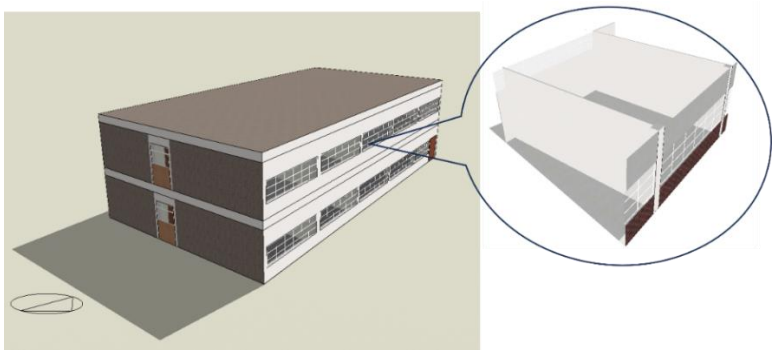

Figure 3: Building model used to calculate energy consumption and CO_2 concentration.

$$\rho_{air} V_z C_{CO2} \frac{dC_z^t}{dt} = \sum_{i=1}^{N_{sl}} kg_{mass_{sched\ load}} \times 10^6 + \sum_{i=1}^{N_{zone}} \dot{m}_i (C_{zi} - C_z^t) + \dot{m}_{inf}(C_\infty - C_z^t) + \dot{m}_{sys}(C_{sup} - C_z^t) \quad \text{(eq.1)}$$

Where $\sum_{i=1}^{N_{sl}} kg_{mass_{sched\ load}}$ indicates internal CO_2 load due to occupancy (kg/s), $\sum_{i=1}^{N_{zone}} \dot{m}_i (C_{zi} - C_z^t)$ denotes CO_2 transfer due to interzone air mixing (ppm-kg/s), $\dot{m}_{inf}(C_\infty - C_z^t)$ represents CO_2 transfer due to ventilation and infiltration of ambient air (ppm-kg/s), $\dot{m}_{sys}(C_{sup} - C_z^t)$ indicates CO_2 transfer due to system supply (ppm-kg/s). Furthermore, the terms $C_\infty, C_z^t, C_{zi}, C_{sup}$ represents the CO_2 concentration of outdoor zone air, the CO_2 concentration at the current time, the CO_2 concentration being transferred into this zone, and the CO_2 concentration in the supply air stream by the system, respectively, measured in parts per million (ppm). In addition, C_{CO2} indicates CO_2 capacity multiplier and V_z denotes zone volume (m^3).

This study simulated indoor CO_2 levels for various outdoor CO_2 concentrations and different air change rates per hour over a period of 10 hours, from 8:00 AM to 6:00 PM on a typical weekday. Generally, the indoor CO_2 concentration increased starting at 8:00 AM and continued to rise until 6:00 PM due to constant occupancy during this period. After these spaces were vacated, the CO_2 concentration began to decrease, continuing until the start of occupancy the following day. Atmospheric CO_2 levels vary with the time of day and exhibit seasonal fluctuations in any given location. Therefore, we considered different atmospheric CO_2 levels in the present study, which cover variations across seasons and locations. In all cases, the indoor CO_2 concentration was calculated for an infiltration rate of 0.2 ACH.

The numerical building model for CO_2 concentration was validated through experimental monitoring of indoor CO_2 levels. These concentrations were measured using a carbon dioxide probe connected to a microclimatic datalogger (HD32.1), as shown in Figure 3. The CO_2 sensor operates on the non-dispersive infrared (NDIR) principle with a dual-source configuration. The measurement uncertainty of the sensors is specified as ± (50 ppm + 3% of the reading) under standard conditions of 20°C, 50% relative humidity, and 1013 hPa. The validation results of the building model presented in Figure 5. The model was validated for building space known as the Thermal Devices Testing Laboratory (TDTL) at the Department of Energy Science and Engineering, IIT Delhi. The two-story building where the laboratory is located has a total area of 627.25 m², with the TDTL occupying approximately 30.79 m². A numerical analysis was performed to validate indoor CO_2 concentration by monitoring occupancy variations and the operation of the ventilation system from 10:00 to 16:30. The ventilation system was activated one hour prior to the experiment, at 09:00, to equalize the indoor CO_2 concentration with that of the ambient environment. During this period, the indoor space was maintained without occupancy and without the air-conditioning system in operation. The variations in occupancy and the switching on/off of the exhaust ventilation system are illustrated in Figure 5. Furthermore, the numerical and experimental results were presented, showing a strong agreement. The variation in numerical results fell within the uncertainty range of the carbon dioxide sensor measurements.

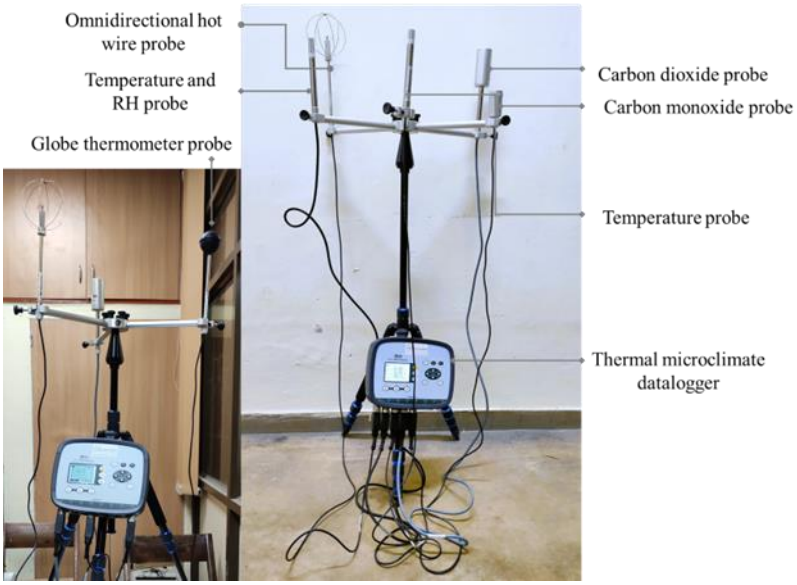

Figure 4: Thermal microclimatic datalogger HD32.1

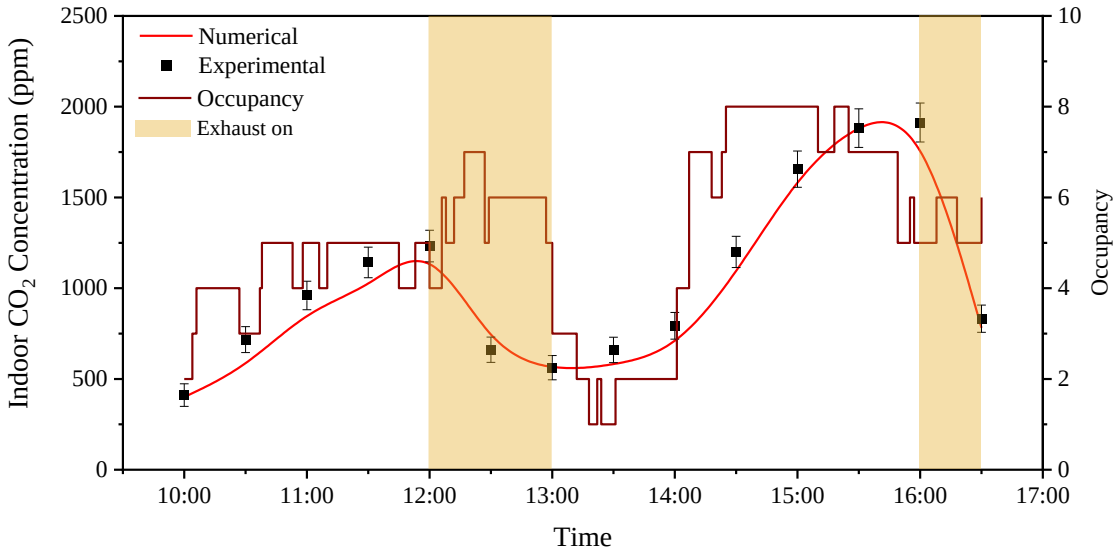

Figure 5: Model validation for CO_2 concentration

3. Results and Discussion

The calculation of CO_2 concentration for various occupant densities, ranging from 10 to 90 m^3/person, and different outdoor concentrations was performed using computational modeling with Design Builder and Energy Plus. The study considered a 10-hour occupancy period from 08:00 to 18:00, during which the CO_2 concentration was monitored starting at 08:00, as accumulation began with the onset of occupancy. After the unoccupied period starting at 18:00, the CO_2 levels began to decrease due to building infiltration alone, as illustrated in Figure 6. The study has been conducted for occupant densities varying from 10 m^3/person to 90 m^3/person during the occupied period from 08:00 to 18:00. The safe CO_2 concentration limit considered 1,000 ppm, as highlighted in Figure 6 since exposure to concentrations above this threshold has been linked to neurophysiological symptoms such as headaches, fatigue, and difficulty concentrating (Muscatiello et al., 2015). In addition, Figure 5 illustrates the variation in indoor CO_2 concentration over time as a function of occupant density under different outdoor CO_2 concentrations. The four outdoor CO_2 concentrations analyzed in the study were 150 ppm, 250 ppm, 350 ppm, and 450 ppm. Unintentional infiltration occurred through cracks in the building envelope as well as through doors and windows. This infiltration significantly impacts

both energy consumption and indoor CO_2 concentration levels. To address this, the study assumed a constant infiltration rate of 0.2 ACH for both occupied and unoccupied periods. Maintaining a lower infiltration rate helps to minimize energy consumption while ensuring thermal comfort for occupants during occupied periods.

Figure 6 (a) illustrates the accumulation of indoor CO_2 concentrations at varying occupant densities, assuming an outdoor CO_2 concentration of 150 ppm. For occupant densities exceeding 80 m^3/person, CO_2 levels remain below 1000 ppm during the 10-hour occupied period. However, lower occupant densities result in CO_2 concentrations surpassing safe limits. Occupant densities below 50 m^3/person are particularly critical, as indoor CO_2 concentrations increase rapidly, exceeding 2000 ppm. A decrease in occupant density results in faster CO_2 accumulation. In scenarios without ventilation, indoor CO_2 concentration exceeds the safe limit within the occupied period for all mentioned occupant densities. Specifically, for occupant densities of 40 m^3/person and below, the safe CO_2 limit is surpassed within 200 minutes of occupancy duration. For occupant densities above 50 m^3/person, mandatory ventilation is not required until 250 minutes of occupancy duration. In spaces with an occupant density of 10 m^3/person, CO_2 concentration rapidly exceeds the safe level, necessitating mandatory ventilation within 60 minutes of occupancy. Similarly, for an occupant density of 20 m^3/person, ventilation is required within 90 minutes of occupancy to maintain a safe CO_2 level. Furthermore, for occupant densities of 10 m^3/person, ventilation is needed at the beginning of the next occupancy period to release accumulated CO_2, as an infiltration rate of 0.2 ACH is insufficient to reach outdoor CO_2 levels. Therefore, it is advisable to provide ventilation before the start of the next occupancy period for occupant densities below 20 m^3/person, which will also help in saving energy. Furthermore, the accumulation of indoor CO_2 concentration for numerous occupant densities for different ambient CO_2 levels has been illustrated in Figure 6 (b, c, d). As outdoor CO_2 concentration increases, the occupant densities cross the safer limit of CO_2 concentration in less time. This signifies that outdoor CO_2 concentration levels are crucial in ventilation requirements and energy consumption. Moreover, the detailed ventilation gap analysis for all outdoor CO_2 concentrations and occupant densities has been outlined in Table 4.

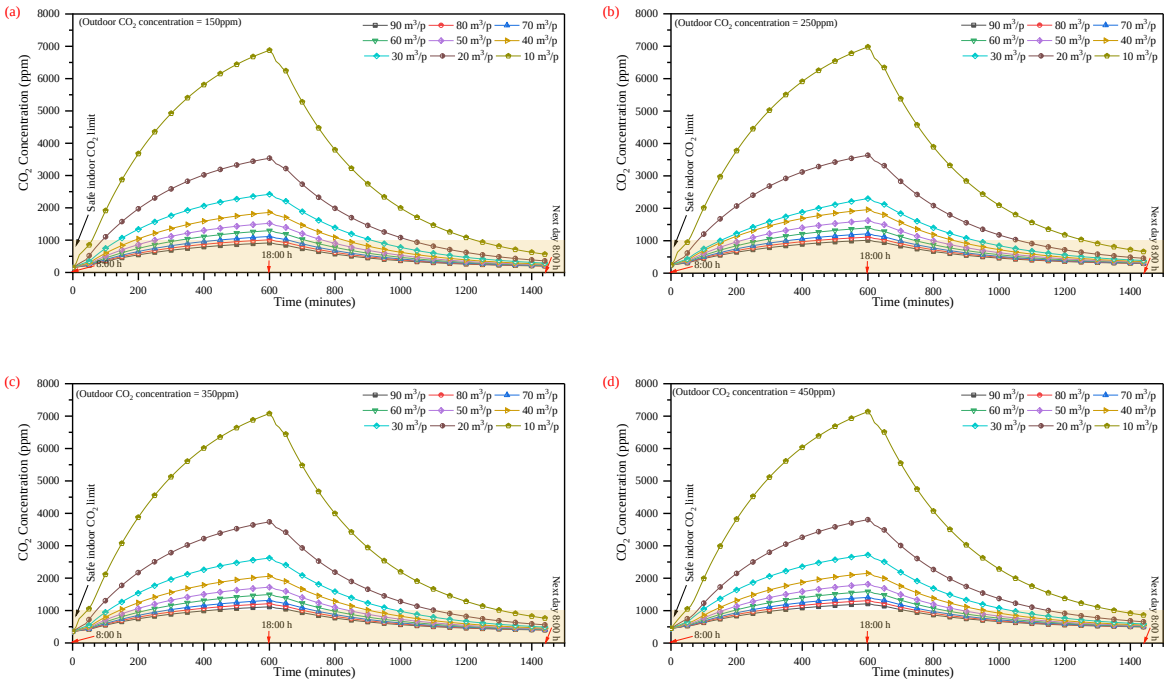

Figure 6: The impact of occupant density on indoor CO_2 concentration in case of no ventilation for outdoor concentrations (a) 150 ppm, (b) 250 ppm, (c) 350 ppm, (d) 450 ppm.

Table 4: Ventilation gap analysis for indoor space for different ambient CO_2 level

Ambient CO_2 concentration	Occupant densities (m^3/person)								
	90	80	70	60	50	40	30	20	10

(ppm)	Approximate time (minutes) to cross indoor CO_2 concentration above the safer limit								
150		580	450	330	250	190	150	90	60
250	570	440	350	270	210	170	140	85	55
350	410	335	285	220	180	140	110	80	45
450	320	270	245	190	160	125	95	80	45

Ventilating indoor air to the outdoors helps reduce indoor CO_2 concentration by introducing lower-pollutant outdoor air into building spaces. However, this process also increases the building's energy consumption due to the influx of hot or cold ambient air into indoor spaces. The energy consumption is influenced by both the ventilation rate and the surrounding environmental conditions. This study conducted calculations with ventilation rates ranging from 1.0 ACH to 3.0 ACH in intervals of 1.0 ACH. Atmospheric conditions significantly affect building energy consumption, and for the purpose of comparison, the environmental conditions were kept constant across all cases. Energy consumption varies substantially throughout the year due to fluctuations in the building's thermal load, with the highest thermal loads occurring during the summer. This study provides a comparative analysis of the annual energy consumption related to both cooling and heating requirements. Figure 7 presents a comparison of energy consumption in relation to variations in occupant density and ventilation rates. As illustrated in Figure 7, higher occupant densities result in lower energy consumption compared to lower occupant densities. Notably, energy demand increases significantly when occupant density falls below 30 m^3/person for the same ventilation rate. The lower occupant densities necessitate higher energy consumption because the present location belongs to a cooling-dominated region. The reduced occupant density leads to greater indoor heat accumulation due to the metabolic rate of individuals. Additionally, increasing ventilation rates in response to elevated atmospheric CO_2 concentrations further exacerbates energy consumption. The energy consumption changes with the ventilation rate, and the comparison of the energy requirement is calculated as depicted in Figure 8 for different ventilation rates with the base case (no ventilation). The energy consumption for the building in the case of a 1.0 ACH ventilation rate varies from 1.25 to 1.54 times higher than the base case scenario (no ventilation) for occupant densities 10 m^3/person to 90 m^3/person. The increase in energy consumption is higher for higher occupant densities than in comparison with no-ventilation. For the ventilation rate 3.0 ACH, the energy consumption increased from 1.66 and 2.28 times for occupant densities 10 m^3/person and 90 m^3/person as compared to no ventilation case. However, the increase in energy consumption may discourage building owners from providing continuous ventilation in indoor spaces.

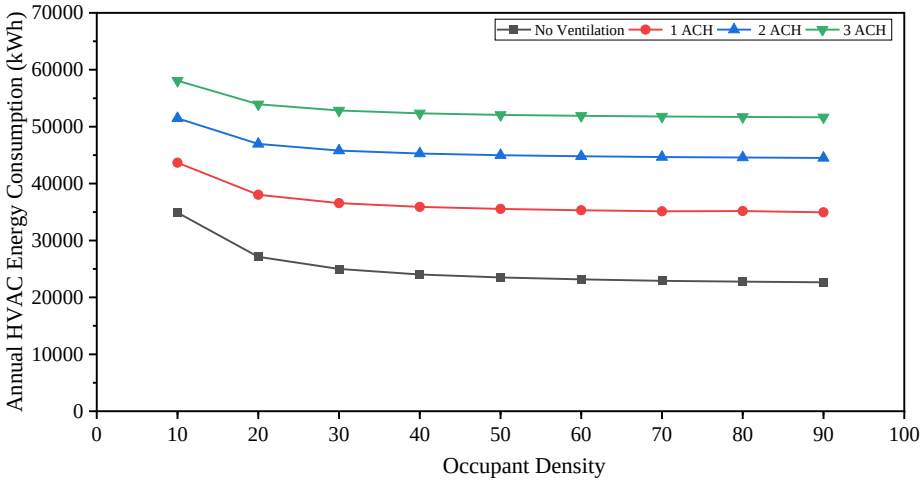

Figure 7: Annual energy consumption of building to maintain thermal comfort

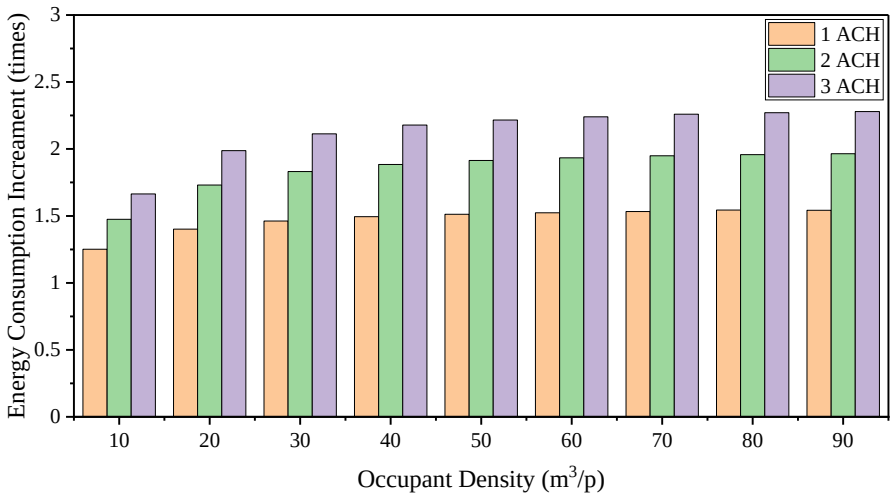

Figure 8: Comparison of energy consumption with no ventilation

Based on the different continuous ventilation rates, indoor CO_2 concentration presented in Figure 9 for outdoor CO_2 concentration of 450 ppm. Ventilation was provided during the occupied period only, and indoor CO2 concentration diffusion happened during the remaining time due to the building's infiltration of 0.2 ACH. The continuous ventilation rate of 1 ACH, as illustrated in Figure 9 (a) occupant densities of 10 m3/person and 20 m^3/person crosses safe indoor limits. Furthermore, 2.0 ACH continuous ventilation maintains indoor CO_2 concentrations for all occupant densities except 10 m^3/person. The spaces with occupant density 10 m^3/person required a continuous ventilation rate of 3 ACH. A continuous ventilation rate of 3 ACH is sufficient to maintain safe indoor CO_2 concentrations. For higher occupant densities above 50 m^3/person, intermittent ventilation can provide significant energy savings. Furthermore, the ventilation rate must be controlled according to the outdoor AQI level because severe AQI regions might worsen indoor air quality due to the exchange of indoor air with outdoor air. As illustrated in Figure 2 Delhi's air quality index reaches severe conditions that require avoidance of ventilation in these days.

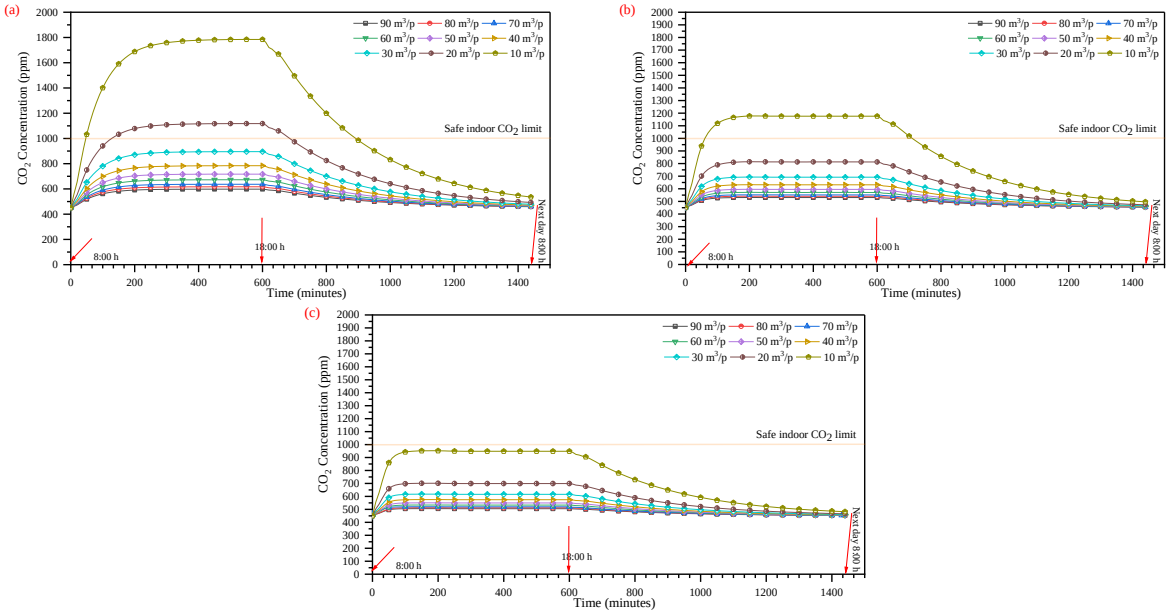

Figure 9: Indoor CO_2 concentration for 450 ppm outdoor CO_2 level with ventilation (a) 1.0 ACH (b) 2.0 ACH (c) 3.0 ACH

4. Conclusions

In this study, indoor CO_2 concentration was evaluated for numerous outdoor CO_2 levels and occupant densities. Based on the two-story building model, a detailed analysis has been done to compare the energy consumption to maintain thermal comfort and air quality for different scenarios. The present study reinforces

that inadequate ventilation diminishes indoor air quality by accumulating CO_2 released by occupants. The annual energy consumption can be reduced by controlling the ventilation rate based on indoor occupant densities. The main objective of the research was to enhance indoor air quality and control energy consumption by assessing mandatory ventilation requirements for different occupancy scenarios. The findings revealed that adapting different ventilation rates for different occupant densities provides less energy losses. The conclusions of this work are outlined below:

- Energy consumption escalates with increased ventilation rates and occupant densities, ranging from 1.25 to 2.28 times the base case (no ventilation). Specifically, at 1.0 ACH, energy consumption rises between 1.25 and 1.54 times, while at 3.0 ACH, it increases from 1.66 to 2.28 times in comparison with the base case for occupant densities ranging from 10 m^3/person to 90 m^3/person respectively. Therefore, optimizing ventilation is crucial for balancing energy efficiency and indoor air quality.
- Occupant densities exceeding 20 m^3/person require a maximum continuous ventilation rate of 1.0 ACH to maintain a safe indoor CO_2 concentration limit of 1000 ppm. For higher occupant densities, intermittent ventilation, as outlined in Table 4, can be utilized to maintain safe CO_2 levels and ensure thermal comfort, thereby further reducing energy demand.
- This analysis indicated that maintaining a safe CO_2 concentration at an occupant density of 20 m^3/person requires a continuous ventilation rate of 2.0 ACH, while a density of 10 m^3/person necessitates 3.0 ACH. This escalation in ventilation rates results in an increased energy demand, ranging from 1.17 to 1.27 times higher for 2.0 ACH and 1.33 to 1.47 times higher for 3.0 ACH, compared to a baseline of 1.0 ACH. Consequently, it is recommended that building owners limit occupant density to above 20 m^3/person to optimize energy efficiency and maintain indoor air quality.
- After a nighttime occupancy gap, indoor CO_2 levels were near the ambient level for most of the occupant densities. At the start of occupancy in the morning, low CO_2 levels in indoor spaces can be leveraged to save energy by delaying the operation of the ventilation system. Without ventilation, indoor CO_2 levels exceed the safe limit after 45 minutes of occupancy at a density of 10 m^3/person. This time frame extends with higher occupant densities and can be strategically utilized based on building operation scenarios.
- Implementing tailored ventilation strategies based on specific building scenarios can save up to 50% of building energy. Post-night occupancy, leveraging ambient CO_2 levels can also save further energy.

This research will assist policymakers and building owners with specific requirements in developing a comprehensive roadmap for optimizing energy efficiency and maintaining safe indoor air quality under varying occupancy and outdoor conditions. Furthermore, this study was based on constant occupant densities over a 10-hour duration, considering an infiltration rate of 0.2 ACH. However, actual building spaces may experience fluctuations in occupant density over short timeframes. These variations may not significantly impact energy demand, but further research is needed to determine more precise ventilation time. Moreover, a detailed analysis might be helpful in more accurate ventilation interval analysis for different types that represent different infiltration.

5. Acknowledgments

The authors acknowledge the necessary resources provided through the research grants by the Department of Science and Technology, Government of India "Different Energy Vector Integration for Storage of Energy" - Grant number- TMD/CERI/MICALL19/2020/03(G), Ministry of Education, Scheme for Promotion of Academic and Research Collaboration (SPARC) “Advancing Sustainable Building Practices: A Comprehensive Investigation into Estimation Techniques for Thermal Load of Buildings”- Grant number- P3094 and Border Road Organisation (BRO) “Comprehensive Research on Sustainable Infrastructure For CPLs Working In HAA”- Grant Number IITD/IRD/RP04651G.

6. Reference

Baghoolizadeh, M., Rostamzadeh-Renani, M., Hakimazari, M., Rostamzadeh-Renani, R., 2023. Improving CO_2 concentration, CO_2 pollutant and occupants' thermal comfort in a residential building using genetic algorithm optimization. Energy Build 291. https://doi.org/10.1016/j.enbuild.2023.113109

Bakó-Biró, Z., Clements-Croome, D.J., Awbi, H.B., Williams, M.J., 2007. Ventilation Rates in Schools and Learning Performance.

Borowski, M., Zwoli, K., Czerwi, M., 2022. An Experimental Study of Thermal Comfort and Indoor Air Quality — A Case Study of a Hotel Building.

EnergyPlus™ Version 22.1.0 Documentation Engineering Reference, 2022.

Franco, A., Leccese, F., 2020. Measurement of CO_2 concentration for occupancy estimation in educational buildings with energy efficiency purposes. Journal of Building Engineering 32. https://doi.org/10.1016/j.jobe.2020.101714

Hussin, M., Ismail, M.R., Ahmad, M.S., 2017. Air-conditioned university laboratories: Comparing CO_2 measurement for centralized and split-unit systems. Journal of King Saud University - Engineering Sciences 29, 191–201. https://doi.org/10.1016/j.jksues.2014.08.005

IAQ Data Benchmarks for 2023: What are Average Levels of PM2.5, CO_2, and TVOC in Different Regions? [WWW Document], n.d. URL https://learn.kaiterra.com/en/resources/iaq-data-benchmarks-for-2023-what-are-average-levels-of-pm2.5-co2-and-tvoc-in-different-regions (accessed 7.26.24).

IEA, 2023. CO_2 Emissions in 2023.

IEA, 2021. Electricity Market Report.

Kim, M.K., Choi, J.H., 2019. Can increased outdoor CO_2 concentrations impact on the ventilation and energy in buildings? A case study in Shanghai, China. Atmos Environ 210, 220–230. https://doi.org/10.1016/j.atmosenv.2019.04.015

Krawczyk, D.A., Rodero, A., Gładyszewska-fiedoruk, K., Gajewski, A., 2016. CO_2 concentration in naturally ventilated classrooms located in different climates — Measurements and simulations. Energy Build 129, 491–498. https://doi.org/10.1016/j.enbuild.2016.08.003

Lawrence, T.M., Braun, J.E., 2006. Evaluation of simplified models for predicting CO_2 concentrations in small commercial buildings. Build Environ 41, 184–194. https://doi.org/10.1016/j.buildenv.2005.01.003

Lu, T., Knuutila, A., Viljanen, M., Lu, X., 2010. A novel methodology for estimating space air change rates and occupant CO_2 generation rates from measurements in mechanically-ventilated buildings. Build Environ 45, 1161–1172. https://doi.org/10.1016/j.buildenv.2009.10.024

Mahyuddin, N., Essah, E.A., 2024. Spatial distribution of CO_2 Impact on the indoor air quality of classrooms within a University. Journal of Building Engineering 89, 109246. https://doi.org/10.1016/j.jobe.2024.109246

Muscatiello, N., Mccarthy, A., Kielb, C., Hsu, W.H., Hwang, S.A., Lin, S., 2015. Classroom conditions and CO_2 concentrations and teacher health symptom reporting in 10 New York State Schools. Indoor Air 25, 157–167. https://doi.org/10.1111/ina.12136

Press Release Ifrma Page: Press Information Bureau [WWW Document], n.d. URL https://pib.gov.in/PressReleaseIframePage.aspx?PRID=1991970 (accessed 8.17.24).

Sakamoto, M., Li, M., Kuga, K., Ito, K., Bekö, G., Williams, J., Wargocki, P., 2022. CO_2 emission rates from sedentary subjects under controlled laboratory conditions. Build Environ 211. https://doi.org/10.1016/j.buildenv.2021.108735

Salthammer, T., 2024. Carbon monoxide as an indicator of indoor air quality. Environmental Science: Atmospheres 4, 291–305. https://doi.org/10.1039/d4ea00006d

Shriram, S., Ramamurthy, K., 2019. Assessment of CO_2-based demand controlled ventilation requirement for a flexible work environment with ductless split air conditioners. Sci Technol Built Environ 25, 805–818. https://doi.org/10.1080/23744731.2019.1569458

Statista, 2022. Air conditioning demand worldwide 2012-2022 [WWW Document]. URL https://www.statista.com/statistics/871534/worldwide-air-conditioner-demand/ (accessed 3.12.24).

Verma, R., Kumar, S., Rakshit, D., Premachandran, B., 2023. Design and Optimization of Energy Consumption for a Low-Rise Building With Seasonal Variations Under Composite Climate of India. J Sol Energy Eng 145. https://doi.org/10.1115/1.4054831

Wargocki, P., Bakó-Biró, Z., Clausen, G., Fanger, P.O., 2002. Air quality in a simulated office environment as a result of reducing pollution sources and increasing ventilation.

Investigation of the Influence of Instantaneous Water Heaters on the Efficiency of (Regenerative) Central Heating Systems in the Simulation Environment TRNSYS

Jonathan Walter[1], Jonas Keuler[1], Christoph Büttner[1] and Peter Pärisch[1]

[1] Institute for Solar Energy Research Hamelin (ISFH), Emmerthal (Germany)

Abstract

The use of central instantaneous water heaters enables the use of buffer storage systems for domestic hot water provision. No hygiene requirements need to be observed for buffer storages, so a larger temperature stratification with lower temperatures at the bottom is permissible than for potable water storage tanks. This leads to energy benefits, as the efficiency of temperature-sensitive heat generators such as solar thermal and heat pump systems can be increased by lowering the mean storage temperature.

This study examines the influence of instantaneous water heaters on the efficiency of three different (partially) regenerative central heating systems. They are considered large-scale systems and must comply with the relevant regulations in Germany. The results are compared with a reference system with a focus on the CO_2 emissions during operation and the associated energy costs. For this purpose, a parameter variability study is conducted using the TRNSYS simulation environment. Instantaneous water heaters with different performance levels, the influence of a return flow distribution using various mechanisms at different actuating times and the influence of the tapping and circulation load were investigated. Furthermore, the storage setpoint temperature was minimized for each combination option.

Keywords: potable water hot, buffer storage, instantaneous water heater, efficiency, regenerative combi systems

Final energy consumption	FEC	Gas boiler	GB
Potable water hot	PWH	Instantaneous water heater	IWH
Potable water hot, circulation return	PWH-C	Electric instantaneous water heater	El.IWH
Potable water cold	PWC	Buffer storage	BS
Heat pump	HP	Apartment building	AB
Solar thermal	ST		

1. Introduction

Within the last 10 years, FEC per capita in Germany has fallen slightly and was around 28 MWh (100 GJ) in 2022. Just over half of this is accounted for by the heating sector. One focus is on space heating and PWH in the residential sector, which accounts for around a third of the total FEC. The FEC share for potable water heating has remained relatively constant at around 5 % over the last 10 years. The largest share of this, 4.47 % points, was accounted for by private households in 2022. In the same year, the share of renewable energies in total potable water heating was only 12.6 %. (AGEB 2023)

The energy modernization of existing buildings makes it possible to reduce the flow temperature level for heating. This is in contrast to the PWH supply. Hygienic requirements pose a challenge in particular for large systems, especially for temperature-sensitive heat generators such as HP and ST systems. Therefore, the focus of science is increasingly on efficient and hygienic potable water heating. (Pärisch et al. 2020a)

The use of central IWH enables the use of BS. With BS, no hygiene requirements need to be observed, allowing for a wider temperature range, including lower temperatures, compared to PWH storage. This leads to energy benefits, as the efficiency of temperature-sensitive heaters such as ST and HP can be increased by creating a cold preheating zone. (Pärisch et al. 2020b)

© 2024. The Authors. Published by International Solar Energy Society
Selection and/or peer review under responsibility of Scientific Committee
10.18086/eurosun.2024.02.18 Available at http://proceedings.ises.org

In Germany, 53 % of homes are in apartment buildings (AB), which therefore account for a significant proportion of the FEC (Statistisches Bundesamt 2023). Therefore, more efficient PWH systems in AB are particularly relevant for the FEC in Germany.

In order to design the domestic hot water systems more efficiently, this study investigates the influence of technical properties of IWH on the efficiency of three different (renewable) central heating systems in AB. The heat centers each supply an AB with 8 residential units with PWH. They are therefore considered to be large systems for which hygiene regulations according to the generally acknowledged rules of technology must be observed. This means that a temperature of 60 °C must be maintained at the IWH outlet and the temperature of the circulating water (PWH-C) must not be less than 55 °C.

The results are compared with a reference system with a gas boiler (GB) and PWH storage. For this purpose, a parameter variation study is carried out in the TRNSYS simulation environment. A particular focus is placed on the potential savings in energy costs and CO_2-equivalent emissions. This study serves as a continuation of the earlier investigations by Pärisch et al., see (Pärisch et al. 2020b; Pärisch et al. 2020a; Keuler et al. 2022), in which the influence of other parameters and heat centers is investigated.

2. System models

This chapter presents the four systems examined. The most important TRNSYS types used and their key parameters are:

- Modulating GB: Type 204 (Glembin et al., eds. 2013) with 28.5 kW, water content 7.3 l and efficiency of 96.6 %;
- Modulating HP: Cascade of three Types 401 (Afjei and Wetter 1997) and interpolation with a typical thermal output of 20 kW;
- ST: Type 832v600 (Haller et al. 2012) with 32 m² and an inclination angle of 45° and inversion factor of 0.81 and coefficient of loss of lin. 3.757 and quadr. 0.0147, which represents a flat-plate collector;
- BS: Type 340 (Drück 2006) with energy efficiency labeling according to (EU-Verordnung Nr. 812/2013 2013) and (EU-Verordnung Nr. 814/2013 2014).

The investigations in this study are carried out in TRNSYS 18 (version 18.04.0001) for an AB with 8 residential units. Annual simulations with a time resolution of 5 s are carried out. To reduce the simulation time, the dynamic coupling of the system technology with the building is dispensed with and only the PWH load profile is used. We consider this to be justified when using a separate heat storage for potable water heating with a PWH priority circuit of the heat generator. An ambient temperature is required for the individual components, which is set to 15 °C for all components in the boiler room. The storage connection positions are specified from 0 to 1 as a relative height. The 4 systems shown in Figure 1 are described below.

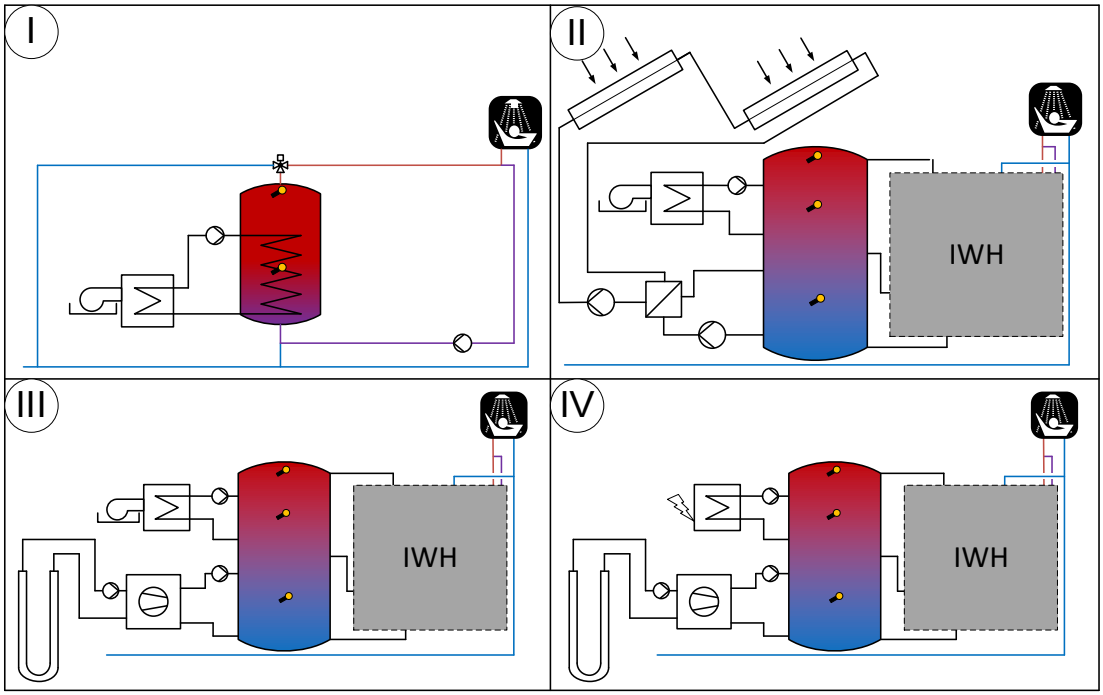

Figure 1: Hydraulic plans of the four systems: I Reference system; II Solar thermal & gas boiler system; III Heat pump & gas boiler system; IV Heat pump & electrical instantaneous water heater.

Description System 1: Gas boiler with PWH storage

In the reference system, heat is generated by a gas condensing boiler, which heats a PWH storage monovalently. A PWH storage supplies the AB with PWH. The PWH outlet is at a height of 1, whereas PWC and the PWH-circulation (PWH-C) enter the storage from below, i.e. at a relative height of 0. Due to the size of the system, a circulation pipe must be installed. This is connected to the PWC pipe just before the storage inlet. The GB transfers the energy to the potable water via an immersed pipe heat exchanger with an inlet height of 0.55 and an outlet at 0.05. This means that the storage has four connections. They are equipped with heat siphons to minimize losses. As a result, the storage has an average UA value of 2.25 W/K with a volume of 600 l. A thermostatic control unit with a temperature sensor is used to control the GB. This is positioned centrally between the flow and return of the GB. It is switched on at a temperature below 65 °C and switched off at over 70 °C.

Description of system 2: Solar thermal & gas boiler

In the second system, a ST and a GB are used as heat generators (ST&GB-system). They bivalent parallel heat a BS with 1600 l. The BS supplies the IWH with heating water. If required, this heats the potable water for the AB. The flow of the IWH is located at the top at a relative height of 1. During hot water draw-off, the cold heating water is fed in at the bottom. In circulation operation, it can be fed in at a relative height of 0.55. The BS has a volume of 1600 l and a total of seven connections. All of them are equipped with heat siphons to avoid pipe-internal circulation losses. The BS therefore has an average UA value of 4.1 W/K. The flow of the GB is at a height of 0.8, the return at 0.6. The GB is controlled by means of thermostatic regulation with a temperature sensor. This is positioned in the middle between the flow and return. The GB is switched off at 5 K above the set temperature (part of the parameter variation). In addition, there is a protective control which stops the GB and the ST as soon as the temperature sensor at the top of the BS registers over 95 °C. The flow of the ST is at a height of 0.5, the return flow at 0.03. As suggested in (Mercker and Arnold 2017), an area of 4 m² is used for each apartment. This results in a total area of 32 m². The heat is transferred via an external heat exchanger with a UA value of 100 W/K per m² collector area (VDI 2014). It is also controlled via a centrally positioned temperature sensor between the flow and return. If the collector temperature is 15 K higher than the lower BS area, the primary pump is started. It is stopped when the temperature falls below 5 K. The secondary pump starts as soon as the temperature in the flow of the primary side of the heat exchanger exceeds the BS temperature by 7 K and stops at a difference of less than 3 K. The pumps operate at 640 l/h in the low-flow range. As soon as the maximum BS temperature of 95 °C is reached, only the secondary pump is switched off. To protect the system components, the primary pump is switched off at collector temperatures above 130 °C.

Description of systems 3 and 4: Heat pump & gas boiler as well as heat pump & electric instantaneous water heater

The third system uses a HP and a GB as the heat generators (HP&GB-system), the fourth system uses a HP and an electric instantaneous water heater (El.IWH) (HP&El.IWH-system). As both systems are very similar, they are described in one chapter. They provide bivalent parallel heating for a BS with 1600 l. The storage connections of the IWH, as well as the number of connections and size, and the resulting UA value, are the same as for the ST&GB system. However, the heat generators are connected differently to the BS. The flow of the heat pump is at a height of 0.5, the return flow is at a height of 0.15. The flow of the El.IWH or GB is at a height of 0.8, the return flow at 0.6. The HP has a geothermal probe available as a heat sourcec. The control works by means of a thermostatic control with one temperature sensor each, which is positioned centrally between the respective flow and return. The heat pump is switched on at 55 °C and switched off at 60 °C so that the maximum heat pump temperature of 62 °C is not exceeded. The upper heat generator is switched off at 5 K above its set temperature, which is part of an optimization. The output of the GB and the El.IWH is 28.5 kW.

Location

The building location is the city of Zurich and represents a moderate, central European climate (Heimrath and Haller 2007). The weather data is provided by Meteonorm 8. The radiation data is based on the climate period from 1996 to 2015, the other parameters are based on the years 2000 to 2019. The PWC inlet temperature is calculated according to Task 32 (Heimrath and Haller 2007) using Eq.

$$\vartheta_{\mathrm{CW}} = \vartheta_{\mathrm{CW,Av}} + \mathrm{d}\vartheta_{\mathrm{CW,AMP}} \cdot SIN\left(360 \cdot \frac{TIME + 24 \cdot \left(273.75 - \mathrm{d}t_{\mathrm{CW,Shift}}\right)}{8760}\right). \quad \text{(eq. 1)}$$

The following applies to Zurich: the average temperature $\vartheta_{\mathrm{CW,Av}}\,[°\mathrm{C}] = 9.7$, the maximum amplitude $\mathrm{d}T_{\mathrm{CW,AMP}}\,[°\mathrm{C}] = 6.3$, and the shift $\mathrm{d}t_{\mathrm{CW,Shift}}\,[\mathrm{d}] = 60$. The time *TIME* is given in h and corresponds to the hour of the year. BHE is from an internal ISFH pre-simulation and is imported into this simulation in order to shorten the calculation time.

3. Object of investigation: instantaneous water heaters

The IWH heats the PWC to PWH with a plate heat exchanger in the flow. To provide the thermal energy, BS are used, which are heated directly by one or more heat generators. (Albers, ed. 2021)

The most important features of IWH in terms of energy efficiency are according to (Pärisch et al. 2020b):

1. The necessary excess temperature of the heating water compared to the desired PWH temperature.
2. The cooling of the return flow compared to the PWC temperature.
3. The changeover time of the return valve, or two pump solutions, for switching between circulation and tap operation so that temperature stratification can be maintained.

The UA value of the IWH was determined empirically in the lab of ISFH according to (Pärisch et al. 2020b) based on the quality of the heat exchanger and the mass flow rate according to

$$UA = f_{\vartheta} \cdot \left(-3\,\frac{\mathrm{W/K}}{(\mathrm{l/min})^2} \cdot \dot{V}^2_{\mathrm{secondary}} + 295\,\frac{\mathrm{W/K}}{(\mathrm{l/min})} \cdot \dot{V}_{\mathrm{secondary}}\right) \cdot f \quad \text{(eq. 2)}$$

with

$$f_{\vartheta} = \left(1{,}0395 - 0{,}008 \cdot \left(\vartheta_{\mathrm{P,in}} - 60\ °\mathrm{C}\right)\right). \quad \text{(eq. 3)}$$

The definition of the temperature correction factor f_{ϑ} (see eq. 3) is limited to primary inlet temperatures $\vartheta_{\mathrm{P,in}}$ between 60 and 90 °C. The specific heat transfer coefficient (*UA*) is obtained in W/K where the secondary side flow rate $\dot{V}_{\mathrm{secondary}}$ is in l/min. Various high-performance heat exchangers and station concepts (see Figure 2) are simulated by varying the factor f. The factor is varied in the range from 1.0 to 2.5. A factor range of 1.0 to 1.5 stands for a standard IWHs according to Concept I, which is more than sufficiently efficient for the above-mentioned tapping profile in AB. The factor range from 1.5 to 2.0 represents large modules for AB in accordance with Concept II or III with a circulation module in parallel. A factor of 2.5 stands for particularly powerful heat exchangers or Concept IV, in which two heat exchangers are connected in series.

The changeover time of the primary returns between the lower and middle storage area is examined with modeling

from 5 to 130 s, as well as without. The shortest changeover time of 5 s, which is the simulation time-step, is possible either with two pumps on the primary side or with fast-switching valves.

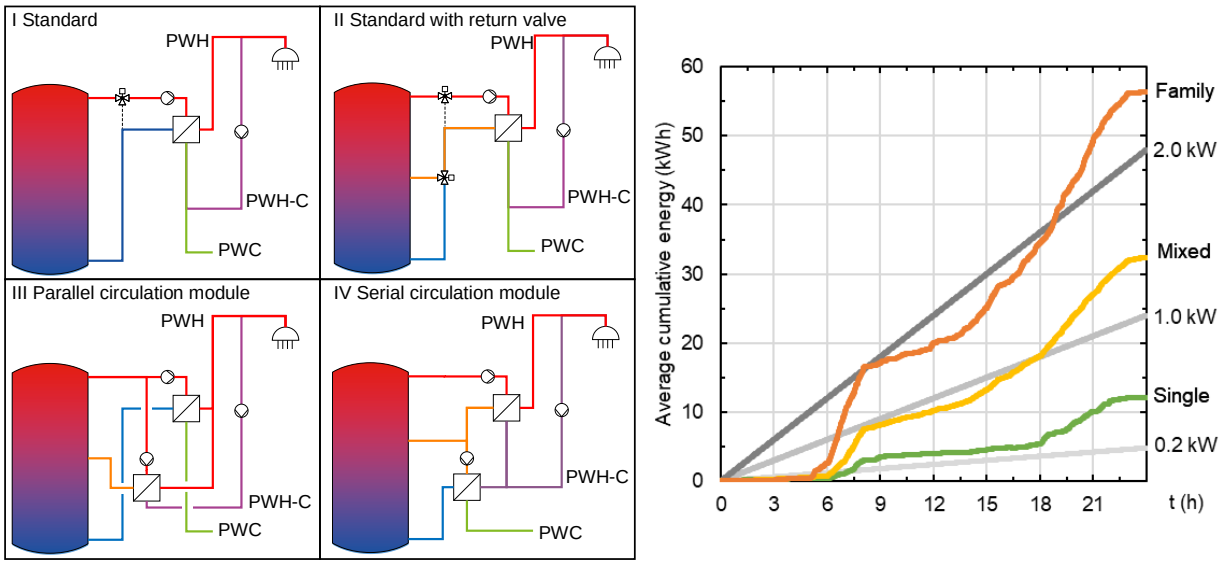

Figure 2: Left: Comparison of four different instantaneous water heaters according to (Pärisch et al. 2020b); Right: Average daily tapping and circulation demand (chapter 4).

4. Parameter variation

The parameter variations of the systems with IWH are listed in Table 1. There are 216 different possible parameter combinations per system. Including temperature minimization this results in 4536 possibilities. By using a binary search algorithm, however, significantly less simulation time is required to find the lowest setpoint temperature for each of the 216 different possible combinations.

Table 1: Parameter variation table of the (partially) regenerative systems.

UA factor *f* (IWH)	1.0, 1.5, 2.0, 2.5
Changeover time return valve (s)	5, 20, 65, 100, 130, without
Circulation load (kW)	0.2, 1.0, 2.0
Tapping profile	Family, Single, Mixed
Setpoint temperature (°C)	55, 56, …, 75

The aim is to find a minimum BS temperature for the respective variation case at which the PWH temperature never falls below 60 °C at the outlet of the IWH. The hard criterion makes it possible to compare the variants, as they all have the same level of comfort. This is achieved by varying the setpoint temperature, which is examined between 55 and 75 °C in 1 K steps. Setpoint temperature means that as soon as the temperature at the sensor falls below this temperature, the heater is switched on. In all cases, the heaters are operated with a hysteresis, i.e. the heaters are switched off again at a certain excess temperature. This is always the case at 5 K above the set temperature.

The variation of the circulation load is intended to cover different network topologies and insulation standards. The load of 0.2 kW stands for short insulated lines, 1 kW for long insulated lines and 2 kW for long uninsulated lines.

Unlike with the old studies, this study uses high-resolution 5 s tapping profiles according to (Distelhoff et al. 2022). These high-resolution tapping profiles are necessary to correctly map the IWH with changeover of the return valve. Furthermore, three tapping profile are created for the parameter variation. A low (only young singles (Single)), a medium (mixed house occupants (Mixed)) and a high consumption (only families with two children (Family)) are considered in order to cover the "normal case" and two "extreme" scenarios. Simultaneities were avoided by shifting the profiles by one week each when using identical tapping profiles. The average daily tapping and circulation requirements are shown in Figure 2. The maximum peak loads at the tapping point with 45 °C are 22.8 l/min for singles, 33.6 l/min for mixed households and 37.2 l/min for families.

The parameter variations of the reference system are listed in Table 2. The aim is to find a minimum storage volume for the 9 reference cases at which the PWH temperature does not fall below 60 °C at the outlet of the PWH storage. The results range from 200 l for the lowest to 800 l for the highest load.

Table 2: Parameter variation table of the reference system.

Circulation load (kW)	0.2, 1.0, 2.0
Tapping profile	Family, Single, Mixed
Storage volume (l)	200, 300, …, 1000

5. Evaluation

The key assessment parameters in this evaluation are the CO_2-equivalent emission and energy cost savings compared to the corresponding reference system. Firstly, the absolute values of the reference system and the systems with simple IWH (UA factor of 1 and without return valve) are compared with each other. Then the potential savings of the (regenerative) systems with IWH variation compared to the reference system are analyzed.

Various assumptions regarding energy costs and CO_2 equivalents are necessary for this comparison. Considering the upstream chain emissions, the values for Germany are shown in Table 3. However, these only represent a snapshot for Germany and are subject to fluctuations and trends. For Germany, the Climate Protection Act stipulates, that emissions in the electricity sector will fall from 257 Mt of CO_2 equivalents in 2022 to 108 Mt of CO_2 equivalents by 2030 (Agora Energiewende 2024). With a forecast electricity consumption of 658 TWh (Kemmler et al. 2021), this results in CO_2-equivalent emissions of 164 g/kWh without upstream chain emissions. If the upstream chain emissions for electricity are neglected, the ratio electricity/gas is already 0.71 in 2030 instead of 2.17 in 2022 and even heating directly with electricity emits fewer CO_2 equivalents than heating with gas.

Table 3: Energy costs and CO_2 equivalents for electricity and natural gas for Germany in 2022.

	Electricity	**Natural gas**	**Ratio**
Costs (€/kWh)	0.28 (Spiegel 2023)	0.0838 (Icha and Lauf 2023)	3.34
CO_2 equivalents (g/kWh)	498 (Statistische Bundesamt 2023)	230 (DVGW 2020)	2.17

The calculation of the CO_2 equivalent savings compared to the reference system with the same circulation load and tapping profile is carried out according to:

$$f_{\mathrm{save,CO_2}} = 1 - \frac{m_{\mathrm{CO_2}}}{m_{\mathrm{CO_2,Ref}}}. \quad \text{(eq. 4)}$$

Equivalently, the energy cost savings are calculated according to:

$$f_{\mathrm{save,K}} = 1 - \frac{K}{K_{\mathrm{Ref}}}. \quad \text{(eq. 5)}$$

The different ratio of emission factors and energy prices leads to a different weighting of the savings. The results based on costs and CO_2 equivalents can therefore also be applied to other assumptions. For example, a natural gas price of 13 ct/kWh leads to a ratio of 2.15 and the expected cost savings can be seen from the CO_2 equivalent savings.

In the calculations, only the heat pumps are considered, but not the pumps and control systems. However, these values are generally less than 1 % compared to the amount of heat transferred and it is assumed that they are the same in all systems.

Other parameters are important for the assessment: According to (VDI 2014), the solar fraction f_{sol} and the solar utilization factor η_{sol} are used to evaluate the ST&GB system. The solar fraction can also be transferred to the heat pump. The solar utilization factor is defined as the ratio of the amount of energy fed into the storage tank by the solar thermal system (system yield) Q_{sol} to the solar radiation energy H_{c}, which hits the collector surface A_{KF} within a year, to:

$$\eta_{\mathrm{sol}} = \frac{Q_{\mathrm{sol}}}{A_{\mathrm{KF}} \cdot H_{\mathrm{c}}}. \quad \text{(eq. 6)}$$

To determine the solar fraction f_{sol}, the quotient of the annual solar system yield Q_{sol} and the sum of Q_{sol} and the system yield of the gas boiler Q_{boiler} is calculated as follows

$$f_{\mathrm{sol}} = \frac{Q_{\mathrm{sol}}}{Q_{\mathrm{sol}} + Q_{\mathrm{boiler}}}. \quad \text{(eq. 7)}$$

According to (VDI 2019), the seasonal performance factor SPF_{HP} of the heat pump is determined from the ratio between the amount of heat generated Q_{use} and the electricity used for this W_{drive} within a whole year, to

$$SPF_{\mathrm{HP}} = \frac{Q_{\mathrm{use}}}{W_{\mathrm{drive}}}. \quad \text{(eq. 8)}$$

According to (Baehr and Kabelac 2016), the GB utilization factor ω_{boiler} is calculated as follows

$$\omega_{\mathrm{boiler}} = \frac{|Q_{\mathrm{n}}|}{m_{\mathrm{fuel}}^{\mathrm{to}} H_{\mathrm{s}}}. \quad \text{(eq. 9)}$$

$|Q_{\mathrm{n}}|$ is the usable heat supplied by the fuel input $m_{\mathrm{fuel}}^{\mathrm{to}}$ and the calorific value H_{s}.

To limit the scope, however, only isolated values are given.

Comparison of the systems

First of all, the results contain certain outliers. This has to do with the search for the lowest possible storage tank setpoint temperature. Due to unfavorable operating states, there is not one minimum storage setpoint temperature but sometimes several. Unfortunately, the use of the binary search means that the lowest minimum is not always found. This worked better with the ST&GB system than with the HP&GB and HP&EL.IWH system, as the temperatures there are often higher than the set temperature due to the solar thermal system.

For an initial overview, the 2022 CO_2 equivalents and the energy costs of the four systems above the circulation load and the tapping profile can be compared in Figure 3. To avoid giving the impression that the current installation of a heat pump with direct electric heating has even higher emissions over its lifetime than the reference system, the CO_2-equivalent emissions for the year 2030 are shown in the discussion in Figure 7. The next chapters will deal in detail with the savings that can be made by increasing the performance of the plate heat exchanger and the influence of the return flow distribution.

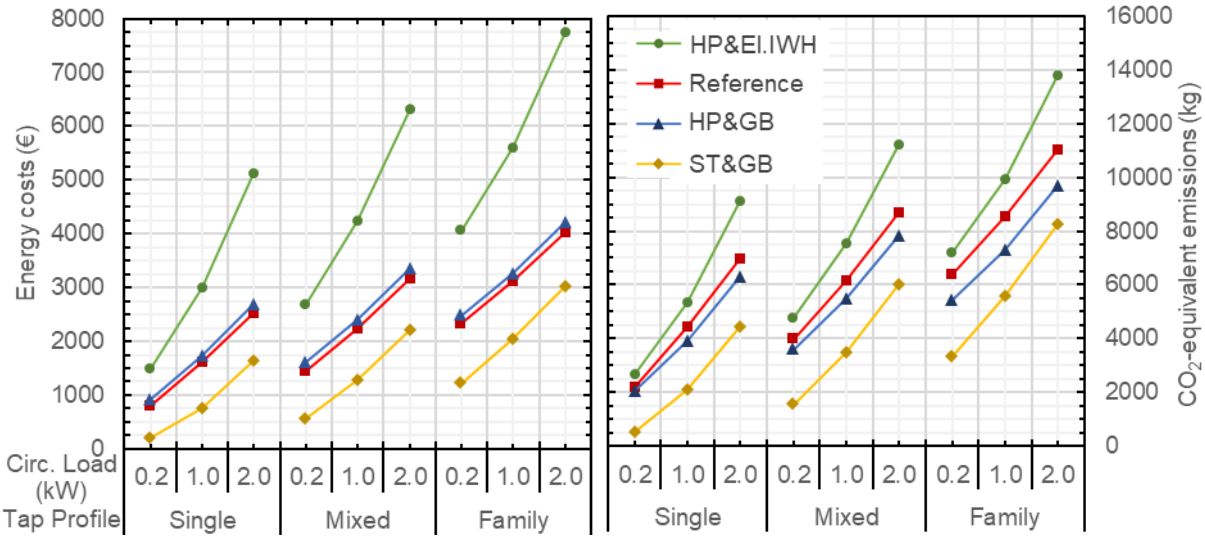

Figure 3: Comparison of the 2022 energy costs (left) and the 2022 CO_2-equivalent emissions (right) of the four systems over the circulation load and the tapping profile (with UA factor of 1 and without return valve).

The ST&GB system always has the lowest costs and emissions, as the radiation energy is free of emissions and costs. With low tapping profile and low circulation load, they can reach almost zero. However, the solar utilization rate then reaches its minimum at 18 %.

The emissions of the HP&GB system are slightly lower than those of the reference system, whereas the energy costs are slightly higher. This behaviour can be explained by the relationship between the energy costs and emissions of gas and electricity. In this system, the actual efficiency of the GB is between 0.7 and 0.8. Assuming an efficiency of 0.75, the ratio between gas and electricity is 2.5 for energy costs and 1.6 for emissions. The HP has an SPF of between 2.8 and 3.3, which means that emissions and energy costs are lower.

In the HP&El.IWH system, the El.IWH takes over the part of the gas boiler and operates with a significantly higher efficiency of 0.98. However, this cannot compensate for the approximately twice as high emissions and approximately three times higher energy costs of the electricity. As a result, the emissions are higher than with the reference system and the energy costs are significantly higher.

Solar thermal & gas boiler system

Figure 4 shows the potential savings of the ST&GB system with IWH variation in terms of CO_2 equivalents and

energy costs compared to the respective reference system. With this system, it is possible to show all variations clearly in one diagram, as the results of the individual variations are identical in terms of savings in energy costs and CO_2 equivalents. They are therefore summarized below and described as savings.

A higher UA factor always has a positive effect on the savings. It can increase the savings by up to 8 % points. This influence is to be expected, as the temperatures in the storage tank are lowered with a higher UA value and the ST system can therefore provide a higher proportion of the heat generation. The influence is greater the larger the hot water demand and the smaller the circulation load.

In general, the lower the specific demand of the solar collector (kWh/m²) (Family→Single, circulation load = 2.0→circulation load = 0.2), the higher the savings from the solar thermal system. With higher circulation load, the return valve can be assessed as consistently positive. It can increase the savings by up to 8 % points. The shorter the changeover time and the higher the tapping profile, the higher the savings. This behaviour is to be expected, as temperature stratification is possible due to the return valve and is improved by a fast changeover time. This allows a cold zone to form in the lower part of the BS, which improves the temperature level for the ST system.

However, with circulation load of 0.2 kW and especially with low UA values and large tapping profile, the savings are reduced with slow return valve. This is due to the significantly poorer efficiency of the GB, which becomes worse as soon as a return valve is used. This effect is compensated for at high circulation load by increasing the solar utilization factor. However, at low circulation load, the solar utilization factor stagnates over the changeover time. In addition, the storage losses tend to stagnate over the tapping profile for circulation load of 0.2 kW, whereas they can fall by over 300 kWh (1.08 GJ) from without return valve to short changeover time for high circulation load.

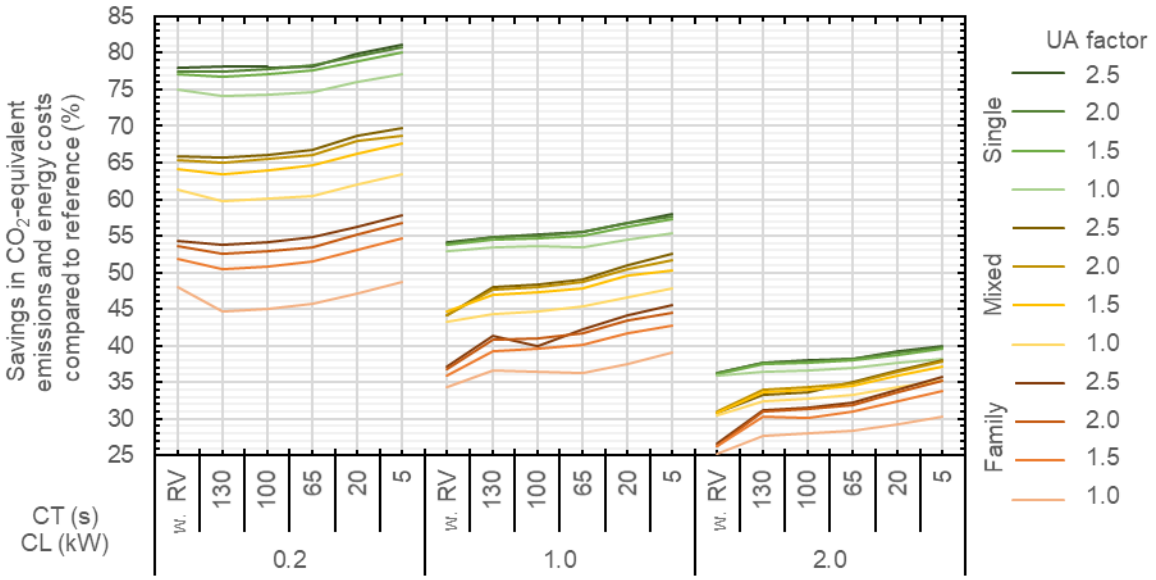

Figure 4: Illustration of the savings in CO_2-equivalent emissions and energy costs of the solar thermal & gas boiler system compared to the reference system via the changeover time (CT) of the return valve and the circulation load (CL) (w. RV: without return valve).

Heat pump & gas boiler system

Figure 5 shows the potential savings of the HP&GB system with IWH variation in terms of CO_2 equivalents and energy costs compared to the corresponding reference system.

The tapping profile has almost no influence on the CO_2 savings. For a better overview, only the tapping profile Family is therefore shown. With a low tapping profile and high circulation load, however, the savings from a higher UA factor are significantly smaller.

A higher UA factor always has a positive effect on the savings. It can increase the savings by up to 10 % points. The smaller the circulation load, the greater the impact. This influence is to be expected, as the temperatures in the BS are lowered with a higher UA value and the heat pump can therefore provide a higher proportion of the heat generation. In extreme cases, its share can be increased by up to 30 % points.

A return valve can minimize the savings with fast switching and low circulation load. If it switches slowly, however, it reduces the savings by up to 2.5 % points. Two effects work against each other here: The share of HP drops significantly with the introduction of a return valve (up to 25 % points), but then stagnates as the changeover time decreases. The SPF of the HP, on the other hand, increases continuously (by up to 0.25), while the degree of

utilization of the GB first increases (by around 0.01) and then stagnates.

When analysing the energy cost savings, the savings of the tapping profile Mixed are not shown for reasons of clarity, as they lie between those of the two others. A higher UA factor always has a positive effect on the savings. It can increase the savings by up to 8 % points. The smaller the circulation load, the greater the influence. This influence is to be expected, as the temperatures in the BS are lowered with a higher UA value and the HP can therefore provide a higher proportion of the heat generation. A return valve usually increases the savings by a few % points. The impact of the effect is different here than with CO_2 savings, as the difference in costs between the heat generators is minimal and the efficiency benefits are more important here. The efficiency of both heat generators increases with a return valve and the lower the changeover time, the better the efficiency of the HP.

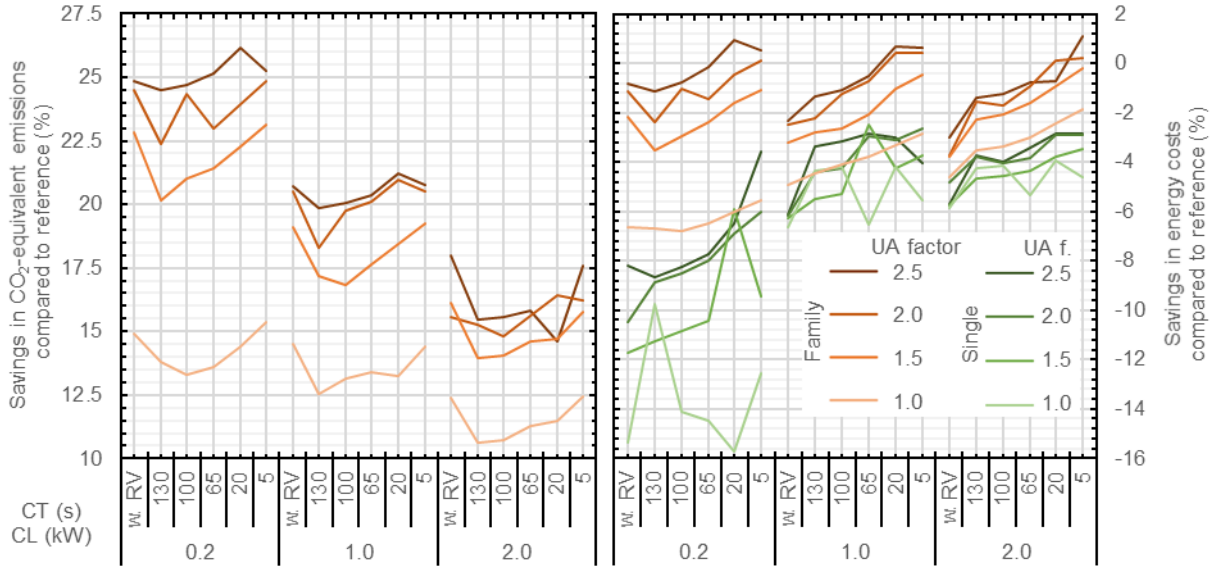

Figure 5: Illustration of the CO_2-equivalent savings (left) and the energy cost savings of the heat pump & gas boiler system compared to the reference system via the changeover time (CT) of the return valve and the circulation load (CL) (w. RV: without return valve).

Heat pump & electric instantaneous water heater system

Figure 6 shows the potential savings of the HP&El.IWH system with IWH variation in terms of CO_2 equivalents and energy costs compared to the reference system. The tapping profile has only a minor influence on the CO_2 savings. For a better overview, only the tapping profile Family is therefore shown. With a lower tapping profile and higher circulation load, however, the savings due to a higher UA factor are significantly smaller.

A higher UA factor always has a positive effect on savings. It can increase savings by up to 26 % points. The smaller the circulation load, the greater the influence. This influence is to be expected, as the temperatures in the BS are lowered with a higher UA value and the HP can therefore provide a higher proportion of the heat generation. In extreme cases, its share can be increased by up to 30 % points. The influence in this system is significantly higher than in the HP&GB system, where the HP already achieves more savings than the El.IWH from an SPF above 0.98.

A slow return valve usually reduces the savings significantly, in extreme cases by up to 10 % points. However, in the case of small circulation load, the savings can increase again with shorter changeover time, but usually not to the original level. Two effects work against each other here. The share of HP falls significantly with the introduction of a return valve (up to 25 %), but then stagnates as the changeover time decreases. On the other hand, the SPF of the HP increases continuously (by up to 0.25).

When analysing the energy cost savings, a higher UA factor always has a positive effect. Particularly in the case of small tapping profile, these can be very large and increase by up to 37 % points. This influence is to be expected, as the temperatures in the BS are lowered with a higher UA value and the HP can therefore provide a higher proportion of the heat generation.

A slow return valve usually reduces the savings significantly, in extreme cases by up to 15 % points. However, as the changeover time becomes shorter, they can increase again, but usually not to the level without return valve. The effect here is similar to that of emissions and contrary to the energy cost savings of the HP&GB system. Here it is always an advantage if the HP has a higher share of heat generation. The explained influences are significantly higher in this system than in the HP&GB system, as electricity performs significantly worse than gas in a direct comparison, even if the poorer efficiency of GB is considered.

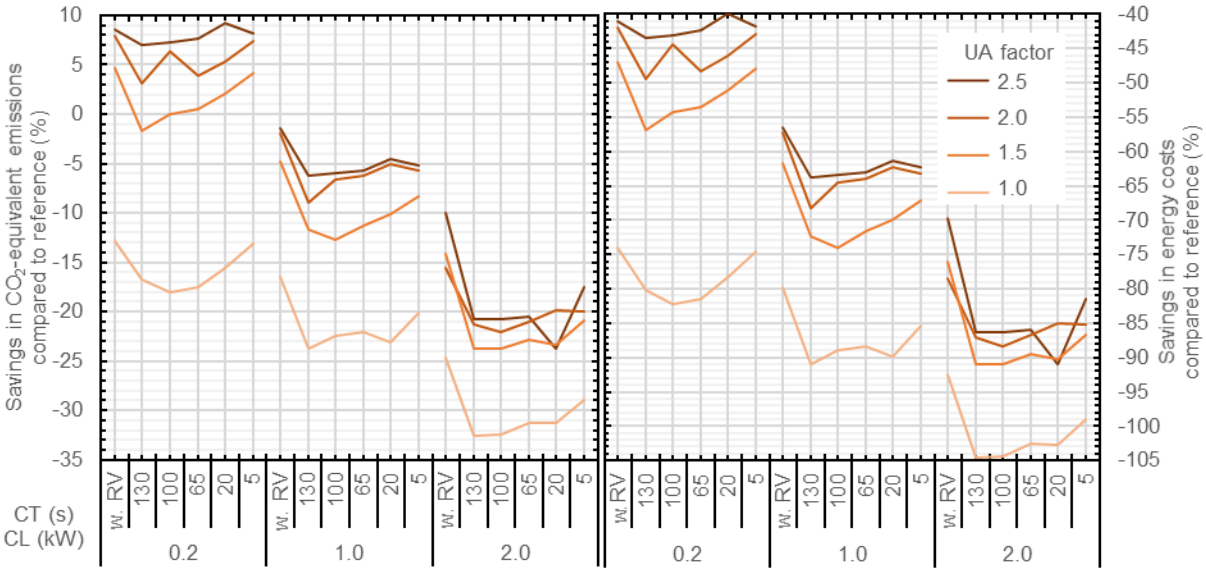

Figure 6: Illustration of the CO_2-equivalent savings (left) and the energy cost savings of the heat pump & electric instantaneous water heater system compared to the reference system via the changeover time (CT) of the return valve and the circulation load (CL) with tapping profile Family.

6. Summary

In this work, the influence of technical properties of IWH on the efficiency of three different (regenerative or hybrid) water heaters with BS was investigated. The central water heater supply 8-party apartment blocks with PWH. The results were compared with a fossil reference system.

In the reference system, the circulation load and the tapping profile were varied in three steps. In each case, the storage volume was minimized on a system-specific basis. For the three (regenerative) systems, the exact influence of the area-specific heat transfer coefficient (UA value) of the IWH and a return valve with variable changeover time was also analyzed. In addition, a minimization was carried out for the setpoint temperature in each case.

The focus of the analysis was on the savings in CO_2-equivalent emissions (ratio electricity/gas 2.17) and energy costs (ratio electricity/gas 3.34) of the hybrid systems compared to the reference system using higher-quality IWH in terms of UA value and a quicker return diversion with return valve or two pumps.

A higher UA value always has a positive influence on the savings. This is not the case for the return diversion.

In the case of solar thermal and gas boiler systems, a high UA value of the IWH can result in savings in emissions and costs of up to 8 % points. A return valve is advantageous at higher circulation load and can result in savings of up to 8 % points. Savings can also be reduced at lower circulation load. If a return valve is used, the lower the changeover time, the higher the savings.

The savings with the heat pump and gas boiler system can be increased by over 10 % points in terms of emissions by a high UA value, and by almost 7 % points in terms of costs. A slow return valve reduces the emission savings. return valves with short changeover time only have the same level as a IWH without return valve. However, the energy cost savings can be increased by a few % points with a fast return valve.

The heat pump and electric instantaneous water heater system can be significantly improved by a higher UA value of the IWH. The savings in emissions can be up to 26 % points, and in energy costs even up to 37 % points. A return valve, on the other hand, is always negative. The savings in emissions can be reduced by up to 10 % points and in energy costs by up to 15% points.

As this study could give the impression that the fossil reference system is better than the partially regenerative systems, the values for the year 2030 are shown in Figure 7. The figure shows that the HP&EL.IWH system will have the lowest emissions in just a few years, despite the direct electric heater. However, emissions from the HP&GB system will also fall significantly, while those from the other two systems will remain constant.

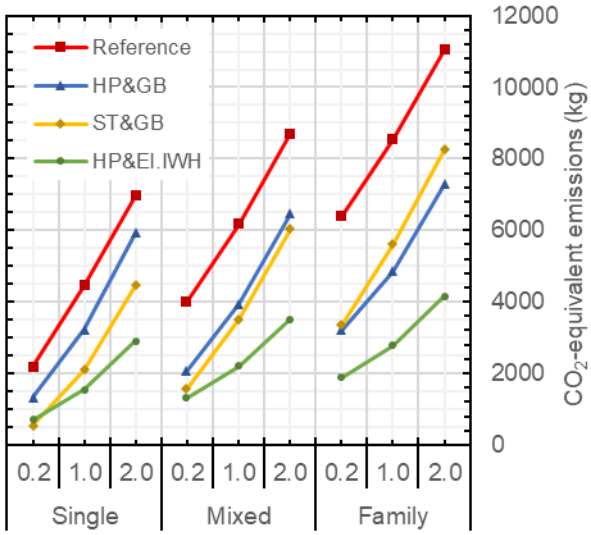

Figure 7: Comparison of the CO_2-equivalent emissions of the four systems over the circulation load and the tapping profile calculated with expected CO_2 emission factors for electricity in 2030 (with UA factor of 1 and without return valve).

In future, the linear search will be used to find the lowest target storage tank temperature. Although this requires more computing time, the global minimum will be found. The simulations are to be extended to include a monovalent heat pump system. Another relevant option in real life is the use of the roof area for PV to generate electricity for the heat pump. In further investigations, the systems are to be used to simulate real tapping profile for non-residential buildings. Possible optimization strategies will also be developed and tested.

References

Afjei, T., and Wetter, M. (1997), *Compressor heat pump including frost and cycle losses. Version 1.1 Model description and im-plementing into TRNSYS* <https://www.iea-shc.org/data/sites/1/publications/T44A38_Rep_C2_C_HeatPumpModels_Final_Draft_Revised_130610.pdf>, accessed 13 Aug 2024.

AGEB (2023), *Anwendungsbilanzen zur Energiebilanz Deutschland*: *Endenergieverbrauch nach Energieträgern und Anwendungszwecke*, Detaillierte Anwendungsbilanzen der Endenergiesektoren für 2021 und 2022 sowie <https://ag-energiebilanzen.de/wp-content/uploads/2023/01/AGEB_22p2_rev-1.pdf>, accessed 22 Feb 2024.

Agora Energiewende (2024), 'Die Energiewende in Deutschland: Stand der Dinge 2023. Rückblick auf die wesentlichen Entwicklungen sowie Ausblick auf 2024', 2024 <https://www.agora-energiewende.de/fileadmin/Projekte/2023/2023-35_DE_JAW23/A-EW_317_JAW23_WEB.pdf>, accessed 13 Aug 2024.

Albers, P. D.-I. K.-J. (2021) (ed.), *Taschenbuch für HEIZUNG+KLIMATECHNIK* (ITM InnoTech Medien GmbH). 978-3-96143-090-1.

Baehr, H. D., and Kabelac, S. (2016), *Thermodynamik*: *Grundlagen und technische Anwendungen* (16., aktualisierte Auflage, Berlin, Heidelberg: Springer Vieweg). 978-3-662-49567-4.

Distelhoff, M., Pärisch, P., and Lampe, C. (2022), 'Methodology for the development of temporally high-resolved and spatially accurate tapping profiles', CLIMA 2022 conference, 2022: CLIMA 2022 The 14th REHVA HVAC World Congress, 2022.

Drück, H. (2006), *Mathematische Modellierung und experimentelle Prüfung von Warmwasserspeichern für Solaranlagen* (Universität Stuttgart). 978-3-8322-6215-0.

DVGW (2020), *Methanemissionen Der Erdgas-Infrastruktur*: *Daten, Fakten und Initiativen der Gasbranche* (Bonn: DVGW Deutsche Vereinigung des Gas und Wasserfaches e. V.).

EU-verordnung Nr. 812/2013 (2013), 'Delegierte Verordnung (EU) Nr. 812/2013 der Kommission. zur Ergänzung der Richtlinie 2010/30/EU des Europäischen Parlaments und des Rates im Hinblick auf die Energieeffizienzkennzeichnung von Warmwasserbereitern, Warmwasserspeichern und Verbundanlagen aus Warmwasserbereitern und Solareinrichtungen', 2013.

EU-Verordnung Nr. 814/2013 (2014), 'Verordnung (EU) Nr. 814/2013 der Kommission. zur Durchführung der Richtlinie 2009/125/EG des Europäischen Parlaments und des Rates im Hinblick auf die Festlegung von Anforderungen an die umweltgerechte Gestaltung von Warmwasserbereitern und Warmwasserspeichern', 2014.

Glembin, J., Bertram, E., Rockendorf, G. et al. (2013) (eds.), *A New Easy-to-Parameterize Boiler Model for Dynamic Simulations* (ASHRAE).

Haller, M., Perers, B., Bale, C. et al. (2012), *TRNSYS Type 832 v5.00 „Dynamic Collector Model by Bengt Perers"*: *Updated Input-Output Reference* <https://backend.orbit.dtu.dk/ws/portalfiles/portal/51568914/121113_Collector%20Model%20Type%20832v500%20-%20Input-Output%20Reference.pdf>, accessed 13 Aug 2024.

Heimrath, R., and Haller, M. (2007), 'The Reference Heating System, the Template Solar System of Task 32. A Report of IEA Solar Heating and Cooling programme - Task 32 "Advanced storage concepts for solar and low energy buildings"', Report A2 of Subtask A, *Solar Heating & Cooling Programme (SHC)*, May 2007 <https://www.iea-shc.org/data/sites/1/publications/task32-Reference_Heating_System.pdf>, accessed 13 Aug 2024.

Icha, P., and Lauf, T. (2023), ‘Entwicklung der spezifischen Treibhausgas-Emissionen des deutschen Strommix in den Jahren 1990 - 2022’, 2023 <https://www.umweltbundesamt.de/publikationen/entwicklung-der-spezifischen-treibhausgas-9>, accessed 13 Aug 2024.

Kemmler, A., Wünsch, A., and Burret, H. (2021), ‘Entwicklung des Bruttostromverbrauchs bis 2030. Berechnungsergebnisse aus dem Szenario 1’, erstellt im Rahmen des Vorhabens Projektionen zu nationalen und, 2021 <https://www.bmwk.de/Redaktion/DE/Downloads/E/prognos-bruttostromverbrauch-2018-2030.pdf?__blob=publicationFile&v=2>, accessed 14 Aug 2024.

Keuler, J., Pärisch, P., and Büttner, C. (2022), ‘Energetic Comparison of Different Instantaneous Water Heater Concepts in a Solar Combi-System for a Multi-Family House with TRNSYS’, *ISES Solar World Congress*, 2022.

Mercker, O., and Arnold, O. (2017), ‘Abschlussbericht zum Vorhaben Ansätze zur Reduktion der konventionell erzeugten Wärmeverteilverluste in solar unterstützten Mehrfamilienhäusern’, 2017 <https://isfh.de/wp-content/uploads/2017/04/Abschlussbericht_MFH-re-Net_20170223_final_corr.pdf>, accessed 13 Aug 2024.

Pärisch, P., Büttner, C., Keuler, J. et al. (2020a), ‘Parameter study of four different instantaneous water heaters in a solar assisted multi-family-house with TRNSYS’, *Eurosun*, 2020.

Pärisch, P., Büttner, C., Keuler, J. et al. (2020b), ‘Warum sind Frischwasserstationen wichtig für die Dekarbonisierung großer Trinkwasserinstallationen?’, *Symposium Solarthermie und innovative Wärmesysteme*, 2020.

Spiegel (2023), *Kabinett beschließt 28-Cent-Preisbremse für Heizstrom*: *Wärmepumpen und Nachtspeicher* <https://www.spiegel.de/wirtschaft/soziales/waermepumpen-und-nachtspeicher-kabinett-beschliesst-heizstrom-preisbremse-von-28-cent-a-882cf2d8-f101-4b18-a239-2dc524f29e10>, accessed 28 Jun 2023.

Statistische Bundesamt (2023), ‘Erdgas-Strom-DurschnittsPreise’ <https://www.destatis.de/DE/Themen/Wirtschaft/Preise/Erdgas-Strom-DurchschnittsPreise/_inhalt.html#sprg421292>, accessed 27 Jun 2023.

Statistisches Bundesamt (2023), *43,4 Millionen Wohnungen in Deutschland zum Jahresende 2022*: *Pressemitteilung Nr. 297* <https://www.destatis.de/DE/Presse/Pressemitteilungen/2023/07/PD23_297_31231.html>, accessed 22 Feb 2024.

VDI (2014), *Solare Trinkwassererwärmung - Allgemeine Grundlagen - Systemtechnik und Anwendung im Wohnungsbau*: *VDI 6002 Blatt 1*.

—— (2019), *Berechnung der Jahresarbeitszahl von Wärmepumpenanlagen*: *Blatt 4650*.

Development of a Hybrid Collector for an Innovative Energy Supply System Using Molecular Solar Thermal Energy Storage

Stephan Weismann[1], Ronny Kastner[1], Sven Hippeli[1], Werner Körner[1], Cornelia Stark[1] and Elias Wolfrath[1]

[1] Center for Applied Energy Research e.V. (CAE), Würzburg (Germany)

Abstract

An innovative system for chemical heat storage using photo-induced isomerization will be presented. For this process, also known as molecular solar thermal energy storage (MOST), a special collector was developed. The initial small collector was scaled up to hybrid collector of a size of 0.5 m². This collector consists of a transparent front part for the photo-induced isomerization, but this process does only absorb a small spectral part within the UV region of the solar energy spectrum. Therefore, the back part of the hybrid collector is similar to a conventional flat plate solar collector to absorb the remaining solar energy. The paper covers the special requirements for materials and geometries for an optimum and most efficient operation. The biggest challenge in the development at the first stage of the project was the necessity to use of a solvent as a carrier for the molecules with the photo-induced isomerization properties which was not compatible to any usual materials. Furthermore, the paper describes the upscaling process, the testing and the installation of the first complete full-scale prototype of the hybrid collector in a complete MOST system, consisting of the collector, pumps, storage tanks, heat release device and heat exchangers.

Keywords: hybrid collector, molecular solar thermal energy storage, MOST, photo-induced isomerization, norbornadiene–quadricyclane, chemical heat storage

1. Introduction

Conventional solar thermal systems are state of the art for regenerative heat generation (Alexopoulos and Kalogirou, 2022; Stieglitz and Heinzel, 2013; Tiwari and Tiwari, 2016). The solar cover ratio, which is defined by the ratio of heat requirement e.g. of a building to solar generated heat is limited by the size of the collector, the size of the thermal heat storage and the maximum temperature of the fluid. The solar-generated heat is thereby stored as sensible heat. This means that there are always thermal losses in the thermal heat storage. This paper describes the development of a hybrid collector which design and requirements differ significantly from conventional solar thermal collectors. This collector is part of a new innovative system for solar energy generation using photo-induced isomerization for energy storage, which enables almost loss-free long-term energy storage.

A first concentrating solar collector with a reflector size of approx. 900 cm² for photo-induced isomerization is presented in (Wang et al., 2019). The idea of and the first lab scale prototype of a hybrid collector is described in (Orrego-Hernández et al., 2020). In this paper we describe the development of a full-scale hybrid collector which is almost ready to the market and embedded in a complete MOST system for outdoor tests under real conditions.

This innovative energy efficient energy storage has the potential to be a key technology for solar regenerative energy supply.

2. Photo-induced isomerization

The photo-induced isomerization process used here for chemical energy storage is based on norbornadiene–quadricyclane derivatives. These molecules absorb the UV part of the solar insolation and store this energy by

© 2024. The Authors. Published by International Solar Energy Society
Selection and/or peer review under responsibility of Scientific Committee
10.18086/eurosun.2024.02.19 Available at http://proceedings.ises.org

changing their molecular structure and were dispersed in an UV transparent liquid, together called MOST liquid (MOST = Molecular Solar energy Storage System). The energy storage density is up to 103 kJ mol^{-1} respectively 396 kJ kg^{-1}. After the photo-induces isomerization the MOST liquid can be stored in tanks for days or even weeks. The back reaction for the heat release can be triggered either using catalysts (Gimenez-Gomez et al., 2023; Magson et al., 2024) or a heat pulse. The energetic principle of this process is shown in Figure 1 (Dreos et al., 2017): by absorbing solar energy the parent molecule in Fig. 1 is lifted to an energetically excited intermediate state (parent* in Fig. 1) and then converts into a long-term stable photoisomer. When the isomer overcomes the energetic barrier ΔH^{++} (through the addition of heat or a catalyst), the back conversion to the original molecule takes place whereby $\Delta H_{storage}$ is released as heat.

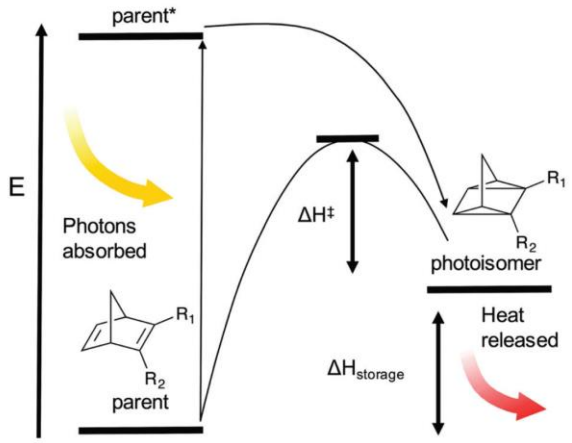

Figure 1: Schematic energy chart of the norbornadiene–quadricyclane molecular solar thermal energy storage system.

3. Principle of the molecular solar thermal energy storage system

A complete MOST system for renewable energy generation consists of a hybrid collector, the heat release device, a consumer and various storage units. A simplified representation of such a system is shown in Figure 2.

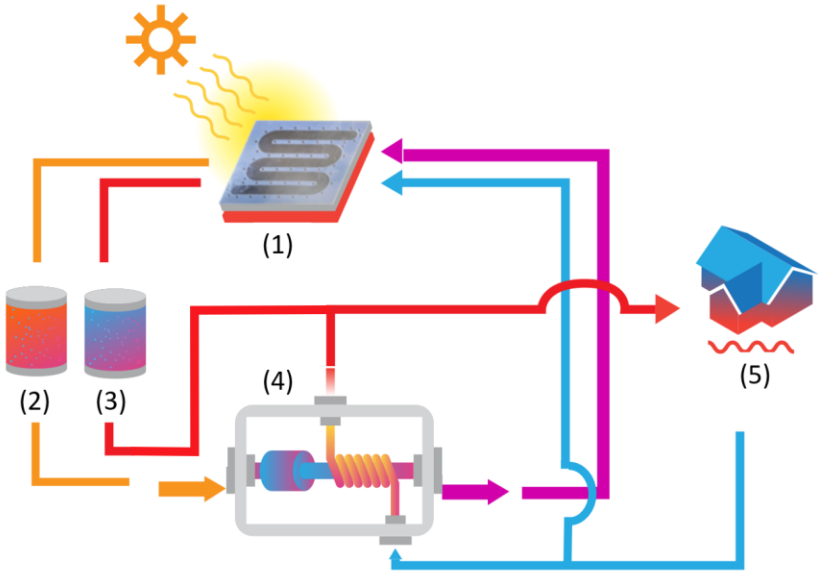

Figure 2: Simplified scheme of a MOST system, consisting of a hybrid collector (1), MOST storage (2), thermal storage (3), heat release device (4) and a heat consumer (5, building only as an example).

The aim is to develop and demonstrate an emission-free solar energy storage system. The MOST system is based on a molecular system that can store solar energy for very long periods of time. This corresponds to a closed cycle

of energy generation, storage and release.

In simple terms, the MOST system works as follows: In the hybrid collector (1 in Fig. 2), the UV spectrum of the solar irradiation stimulates photo-induced isomerism in the MOST liquid; the remaining solar irradiation is converted into heat in the rear part of the hybrid collector and dissipated by a thermal fluid. The MOST liquid and the thermal fluid are stored in separate tanks (2) and (3), whereby the MOST liquid can be stored over a long period of time without any heat losses. The heat can be utilised either directly from the thermal storage tank or via the MOST liquid, which is fed into the heat release device. In this device, the reverse reaction is triggered via a catalyst, the chemically stored heat is released again and dissipated via a heat exchanger. MOST liquid and thermofluid are then fed back into the collector.

As part of the MOST project, the molecular systems as well as the associated catalysts and other devices are being tailormade for this world first outdoor installation of a complete MOST System. Catalysts and devices will be developed beyond the state of the art.

4. Demonstration Stages

Four steps, so-called demonstration stages, were planned for the development of the overall system with hybrid collector (MOST collector + solar thermal collector) (see Figure 3). Since only part of the solar spectrum is absorbed for photo-induced isomerization, (typically wavelengths between 320 nm and 400 nm,), it is necessary to have a hybrid collector for a maximum solar efficiency as a development goal. This consists of two functional layers (demonstration stage III and IV): the first layer contains the MOST liquid and must be as transparent as possible for the entire solar spectrum. the second layer then utilizes the emitting spectrum and largely corresponds to a normal thermal flat plate collector.

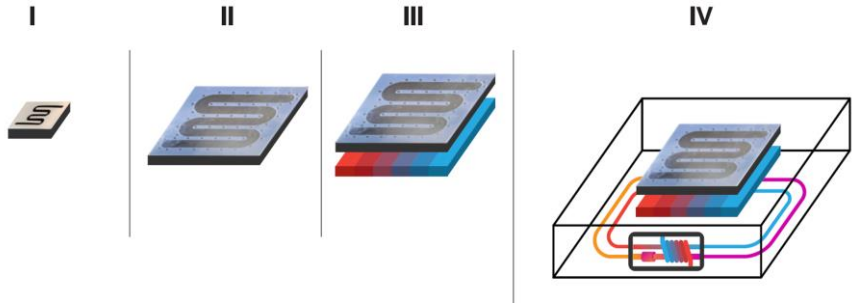

Figure 3: Device Development stages. I) Small "pre-devices", II) MOST devices in lab-size, III) Hybrid MOST-TES, still lab-size, IV) integrated system according to Figure 2 with hybrid collector in full size.

4.1 Stage I - Small pre-devices

First development step I were solar collectors with a size of approximately (2 x 2) cm², which is a standard size that fits into smaller lab-scale solar simulators to carry out first tests of the photo-induced isomerization. These pre-devices are of low complexity and should allow rapid screening of MOST materials and catalysts without consuming large amounts of material. The collectors were developed and constructed at the Center for Applied Energy Research, in Würzburg (Germany), the isomerization tests were carried out at the University of Copenhagen (Denmark) and University of La Rioja (Spain).

The following technical requirements and problems arose during the development:

The carrier material in which the MOST molecules are dissolved can have a considerable influence (usually negative) on the photoisomeric properties of the MOST molecules. At the beginning of development, toluene was used as a solvent. In addition to the easy flammability, there was the further problem that many of the materials required for the collector, (especially adhesives, sealants, hoses and connectors) are not compatible with toluene in the long term. Only metals, glass and a few plastics with fluorine content were usable for the implementation of the first laboratory scale prototype. Further research revealed that a special epoxy resin (EPO-TEC® 377) and a ceramic adhesive (RESBOND® 940 HE and RESBOND® 940) are resistant to toluene. This has opened up further possibilities to consider adhesive bonds as well as clamped bonds.

Because of the development aim of a hybrid collector as mentioned above, the glass panes of the collector should have the highest possible UV transmittance in the wavelength range of approximately 320 nm to 400 nm. For the subsequent application of a hybrid collector with solar thermal energy, the MOST collector should have a very high surface transmittance of the radiation in wavelengths above 400 nm, too.

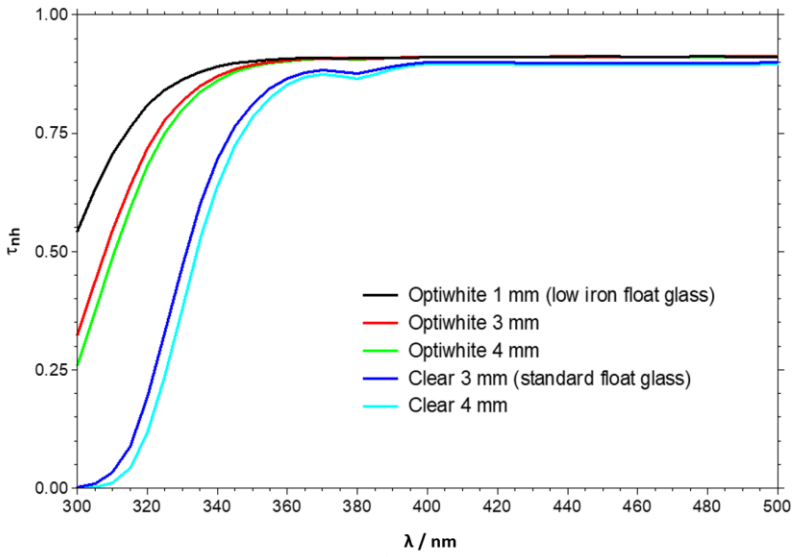

Figure 4: Overview of the wavelength-dependent normal-hemispherical transmittance τ of typical white glass panes and standard float glass panes at different glass thicknesses as a function of wavelength.

Usual plate glass (also known as float glass) with no special properties is not sufficiently suitable for this application due to its low UV transmittance in the wavelength range from 320 nm to 360 nm ("Clear 3 mm" and "Clear 4 mm" in Fig. 4 (IGDB, 2024)). White glass, produced using quartz sand with a low fraction of Fe_2O_3 (less than 0.03 % in mass) shows significantly higher transmittance values within the relevant wavelength range, even at a thickness of 3 mm to 4 mm (Optiwhite® in Fig. 4).

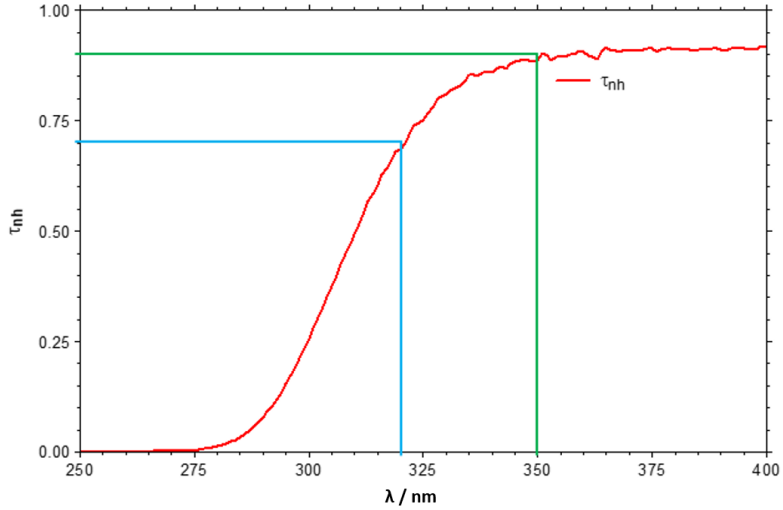

Figure 5 : Measurement of the normal-hemispherical transmittance τ_{nh} of a white glass pane "Guardian Optiwhite" with a thickness of 2.9 mm as a function of the wavelength λ within the relevant ultraviolet spectral range. A transmittance of approx. 70 % was measured at 320 nm and of approx. 90 % at 350 nm.

The commercially available white glass Guardian Optiwhite® from Guardian Industries Holdings (LLC) with a thickness of 2.9 mm confirmed the values in the database in the laboratory measurements (see Figure 5) and was

therefore suitable. A UV transmittance of approx. 70 % at 320 nm and 90 % at 350 nm was measured. This glass type was therefore used for almost all prototypes shown below. Even higher transmittances can only be achieved with pure quartz glass (laboratory glass). However, this glass is extremely expensive compared to white glass and only available in certain smaller sizes.

The toluene-resistant material PTFE (Polytetrafluoroethylene), also known as Teflon®, was used as the inlay for the prototype (Fig. 6). Further advantage of PTFE is the permanent temperature resistance until 260 °C. The use of an inlay in combination with extremely low flowrates ensures, that a uniform turbulent free flow is ensured, so that each part of the fluid absorbs the same amount of solar radiation. Laser processes were used for cutting the inlay. In some cases, the same results can be achieved with waterjet processes.

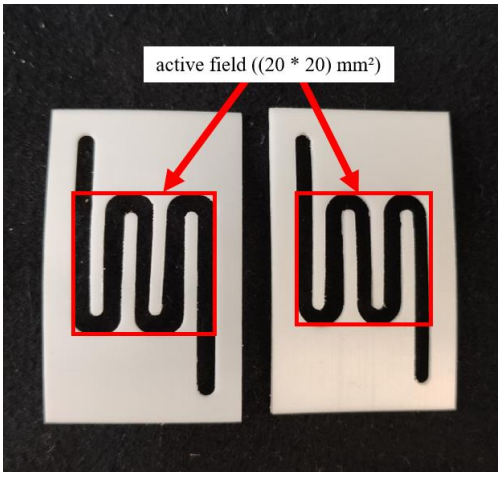

Figure 6: Lasered meander inlay made of PTFE (active field (20 x 20) mm²). Different layouts were tested, the right one has rounder bows.

A clamping method was realized as a very small laboratory scale collector (20 x 20) mm² in order to fixate the inlay between two panes of white glass. With the existing clamping process, due to the tolerances of the glass panes and the caused bending of the glass panes during the clamping, tightness could not be achieved.

The bonding process could be used for small laboratory scale collectors and larger prototypes. For smaller laboratory prototypes, edge bonding only should be sufficient.

For larger prototypes, a solution must be found to prevent the pane tolerances and deflections of the glass panes. In addition to glass edge bonding, the glass pane would also have to be bonded in the surface.

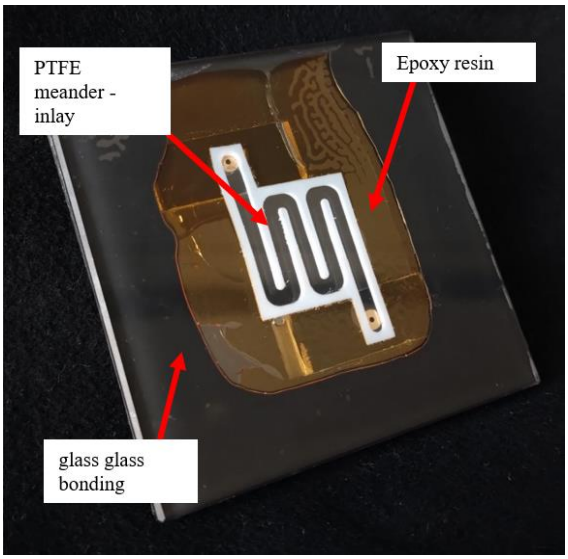

Figure 7: The first functional prototype resistant to the solvent toluene ((76 x 76) mm²) – active field (20 x 20) mm².

Figure 7 shows the first functional prototype filled with the solvent toluene. A meander inlay made of toluene-resistant PTFE was selected as the inlay in order to realize a very slow and uniform flow of the MOST fluid. The edge areas were bonded with a flexible glass-glass bonding. The prototype was then filled with epoxy resin around the meander inlay. The inlet and outlet connectors made of brass are at the back side. For safety, the filling side was then masked again with flexible glass-glass bonding. For testing it in lab scale sun simulators, the whole collector is covered with a metal mask so that only the active field in the middle is exposed to irradiation.

4.2 Stage II - MOST devices

In development stage II, the focus of the collector design was on functional testing of the systems and an initial performance evaluation (flow rates and photo-isomerisation conversion rates). This collector development had to be carried out with an intermediate step in the panel size 0.09 m² due to the change in the adhesive. Using toluene as a solvent, several bonding options, e.g., ceramic adhesives or indium compounds, were tested without permanent sealing success.

The next intermediate stage of the collector is larger and is dimensioned in such a way that two of them placed next to each other already reach the size of the last development stage.

Meanwhile, the project partners searched intensively for a different carrier fluid due to the design problems and the fire hazard of all organic solvents, especially toluene. It turned out that a commercially available thermal oil from the company Duratherm Extended Life Fluids (USA) was suitable as a carrier fluid. This opened up many new possibilities for collector bonding.

Instead of the opaque PTFE, now a transparent ETFE film (Ethylene tetrafluoroethylene from Nowofol Kunststoffprodukte GmbH & Co. KG, Germany) was used for the meander-shaped inlay, increasing the gain of the thermal part of the hybrid collector. The solar transmittance of this ETFE in a thickness of 500 µm is 83.3 % according to the manufacturer's datasheet. The film is specified by the manufacturer as resistant to toluene, but this requirement has been dropped in the meantime.

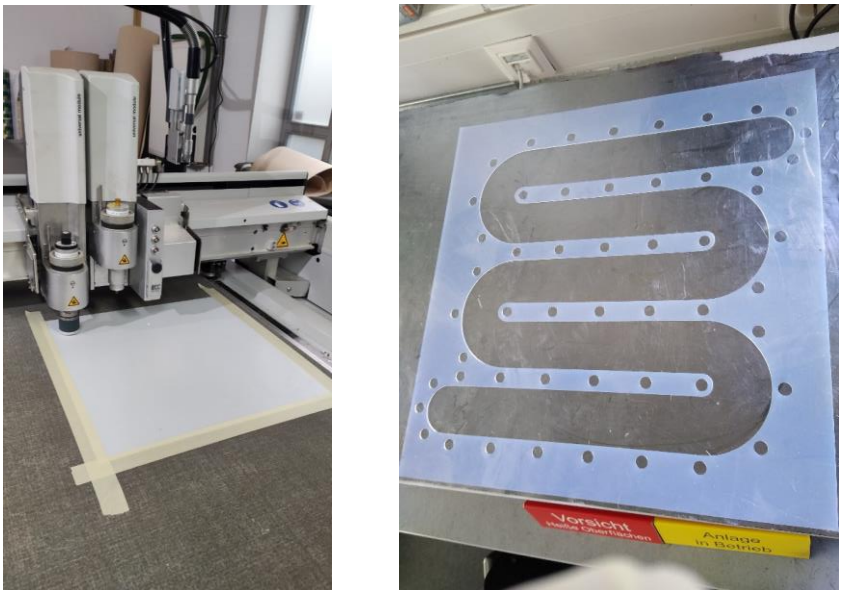

Figure 8: Left: Successful cut plotter tests with 500 µm Teflon film (PTFE); Right: ETFE film with very precisely cut out adhesive dot circles, again performed with a cut plotter.

Both films with a thickness of 500 µm could be accurately processed with the cut plotter (see Figure 8). However, the ETFE film was clearly easier to process due to its flat contact surface compared to the slightly wavy Teflon film.

Additionally, at this stage several adhesives/glues were tested (Fig. 9). Three of them passed the 8 weeks tightness test successfully (Tab. 1). Tests were carried out with glass specimens, consisting of two edge glued glass panes (76 x 76) mm² filled with the Duratherm oil.

The thermal test was 55 cycles of:

- stay for 20 minutes at 30 °C
- heat up to 80 °C within 20 minutes
- keep at 80 °C for 20 minutes
- cool down to 30 °C within 120 minutes

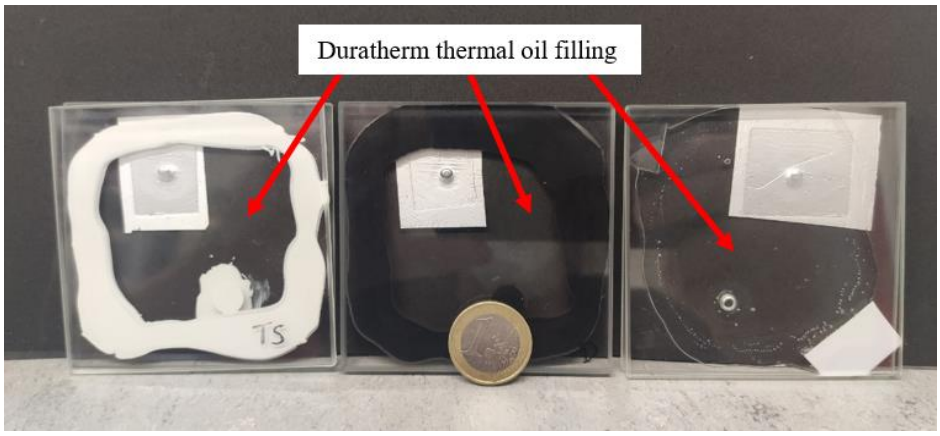

Figure 9: Test specimen of various adhesives with Duratherm oil filling. after 8 weeks with thermal cycle tests. Left: Torr Seal bonding, middle: DELO PUR 9694 bonding, right: transparent DELO PHOTOBOND GB368 bonding. All passed the testing.

Tab. 1: Manufacturer and product name of the adhesives which passed the test.

Manufacturer:	**Product name:**
Agilent Technologies, USA	Agilent Torr Seal Low Vapor Pressure Resin Sealant
DELO Industrie Klebstoffe GmbH & Co. KGaA, Germany	DELO® -PUR 9694
DELO Industrie Klebstoffe GmbH & Co. KGaA, Germany	DELO® PHOTOBOND® GB368

The two major changes in collector construction (partially transparent inlay and transparent bonding) significantly increased the solar transmission of the whole MOST collector. This will increase the performance of the hybrid collector (MOST + solar thermal collector) in the later stages of development.

For the search for new solvents, collector flow simulations with the dynamic viscosity as parameter was performed for the MOST collector. For the flow velocity a typical value of 0.035 mm * s^{-1} was chosen.

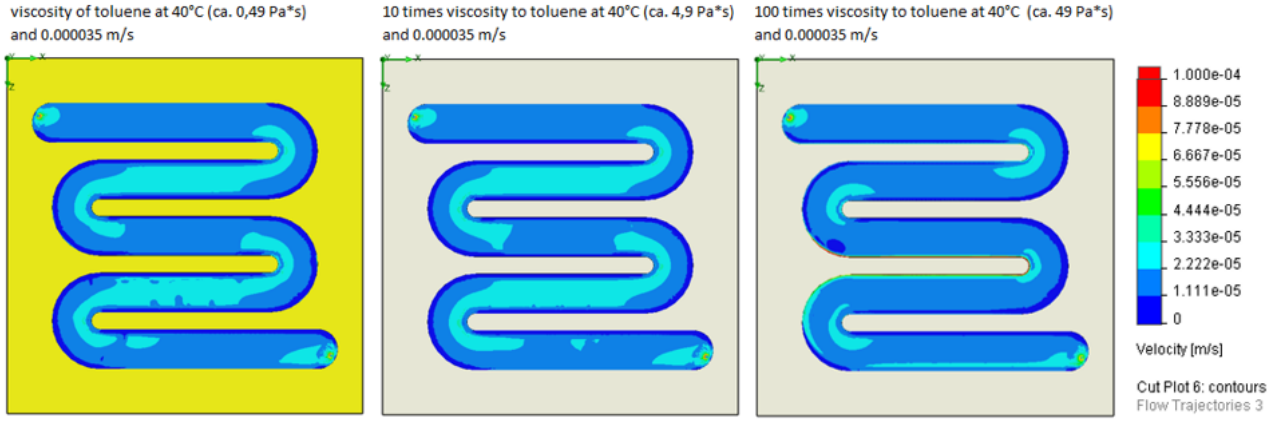

Figure 10: Volume flow simulation for the prototype at different viscosities of the MOST solvent.

The viscosity of Toluene (η = 0.49 Pa * s) was taken as the initial value, because the new solvent was not determined at this stage of the project, and the viscosity was increased by a magnitude each step (4.9 Pa * s and 49 Pa * s). There were only minor differences of the fluid velocity in the 45 mm wide channels of the meander shape. Thus, it can be concluded that the function of the collector is not affected at viscosities at least up to 49 Pa * s (see Figure 10). Further result is, that there are no dead edges with stagnation of the MOST fluid.

Figure 11: Almost fully transparent thermal oil resistant collector with DELO PHOTOBOND GB368. For better visibility, the edges of the collector are marked with a dotted line.

The MOST collector was tested for tightness with the new solvent Duratherm oil fluid over 3 months (see Figure 11). The very good transparency indicates a very high efficiency of the solar thermal collector (note the MOST logo behind the collector).

4.3 Stage III - Hybrid MOST collector

In development stage III, a hybrid collector was developed. This consists of a MOST collector as the outer layer and a thermal flat-plate collector underneath. The collector is an intermediate step with a square area of 0.09 m². The size was specified by the maximum dimensions of the solar simulator at the project partner University of Copenhagen. As thermal flat-plate collectors of this size are not commercially available, the entire hybrid collector was handmade, details are shown in Fig. 12.

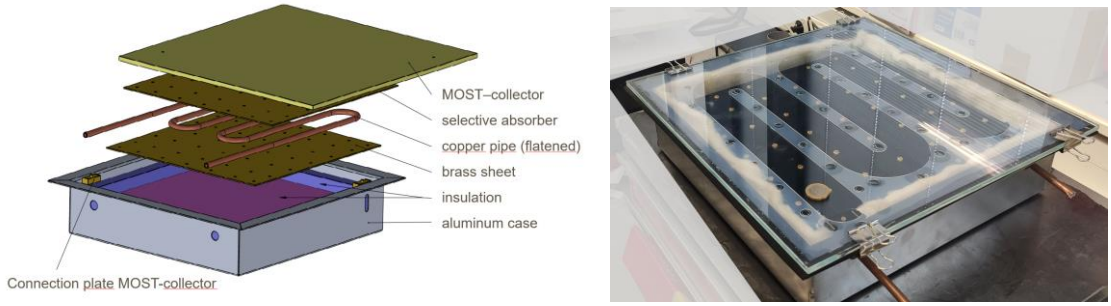

Figure 12: Left: Exploded view drawing of the first hybrid collector (MOST collector (top) + solar thermal collector (below); right: Picture of the finished hybrid collector.

An important point in the development was that even with a high thermal load, the temperature in the MOST collector does not rise to the temperature limit where the back reaction is thermally activated. The following tests were carried out to ensure this. The collector was exposed to an irradiation of around 1000 W * m^{-2} in a solar simulator. The temperature of the thermal collector was kept at 80 °C using a thermostat and then even at 90 °C.

The ambient temperature was kept at 35 °C and then at 36 °C. The temperature of the most collector was measured at three points (centre inside, centre outside, corner inside). In the first case (with 80 °C in the thermal collector), all temperatures in the MOST collector were approx. 54 °C, in the second case (with 90 °C in the thermal collector) at 57 °C (Fig. 13). This was still within the tolerable range as the critical temperature for triggering the back reaction is approx. 65 °C.

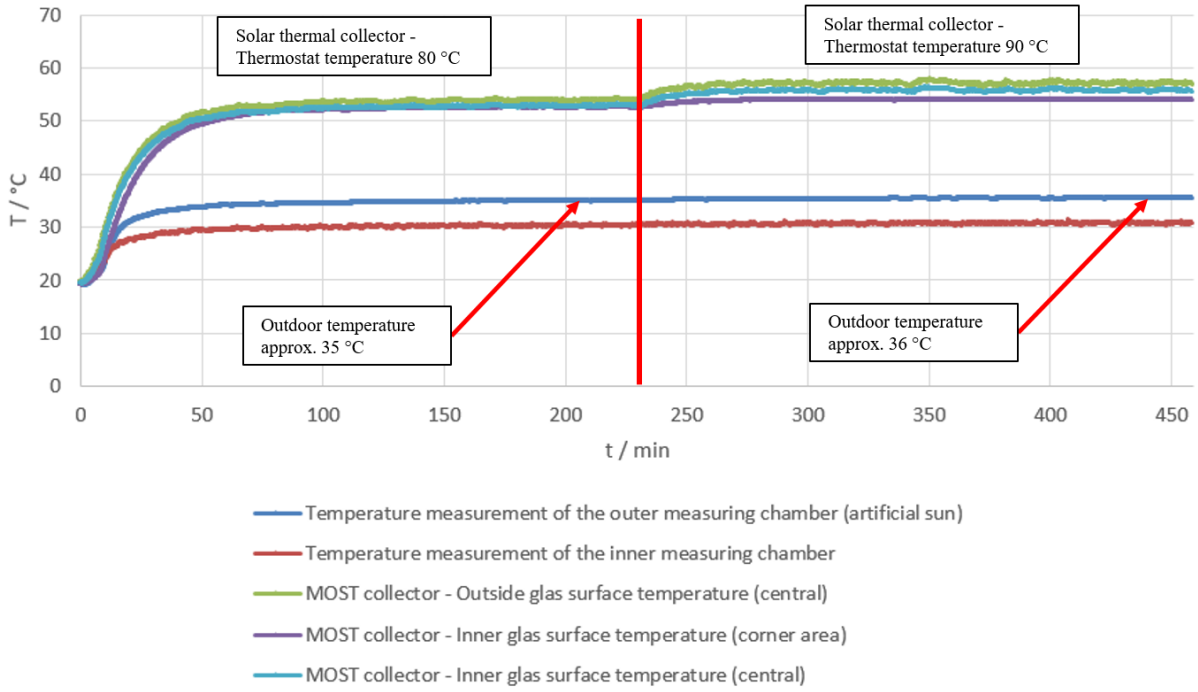

Figure 13: Temperature results of the solar simulator test for the hybrid collector.

The final stage of upscaling of the collector was a near-series hybrid collector with size of (50.8 * 105.5) cm² (Fig. 14 and 15). The size of the collector results to the use of a slightly modified commercially available flat plate collector for the thermal part of it (FK 8000 from GREENoneTEC Solarindustrie GmbH (Austria)).

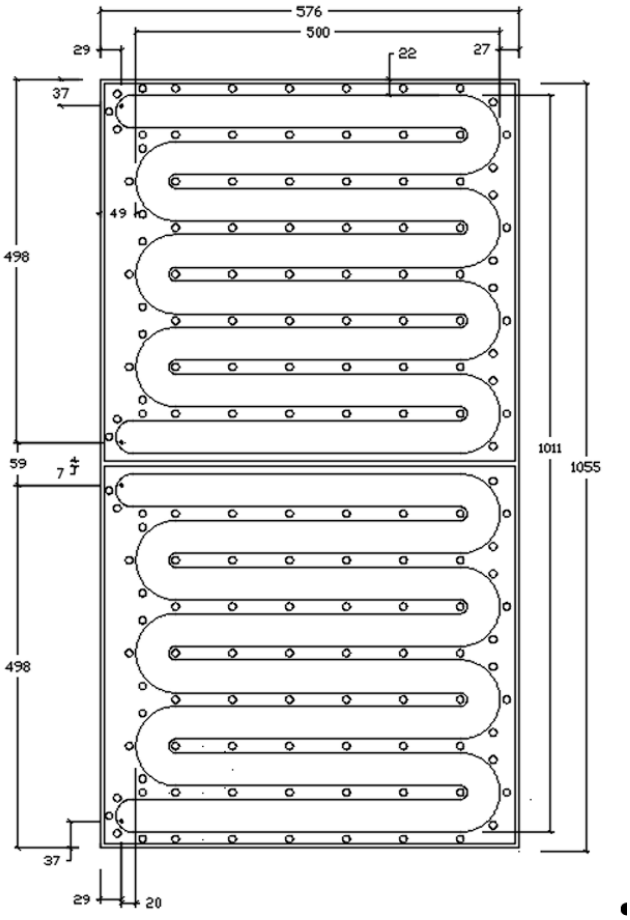

Fig. 14: Technical drawing of the final hybrid collector

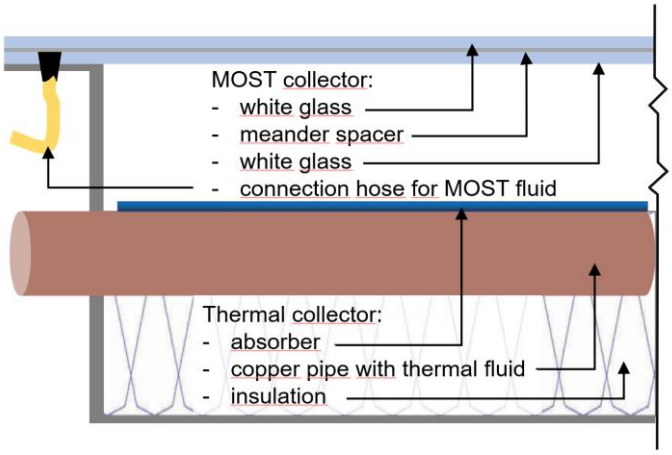

Fig 15: Cross section (schematic) of the final hybrid collector.

The MOST collector here is divided into two test areas of 0.25 m² each for mechanical reasons. Additional advantage of this is, that there are direct comparisons between different fluids, different flow rates or different operation modes possible. The design of the hybrid collector is almost close to series production, resistant to UV, storm and frost and for a high cycle capacity. The hybrid collector was extensively tested in an indoor solar simulator for tightness and stability for three weeks without intermission (Fig. 16). When performing the tests, water was flowing through the thermal part of the collector and Duratherm oil (without any photoisomeric molecules because there were not available in a sufficient amount at this stage of the project) was flowing through the MOST layer of the collector. The tests were therefore related to mechanical stability, tightness to water and

oil and thermal performance, especially testing that the MOST layer is not getting to hot which would trigger the back reaction inside the collector.

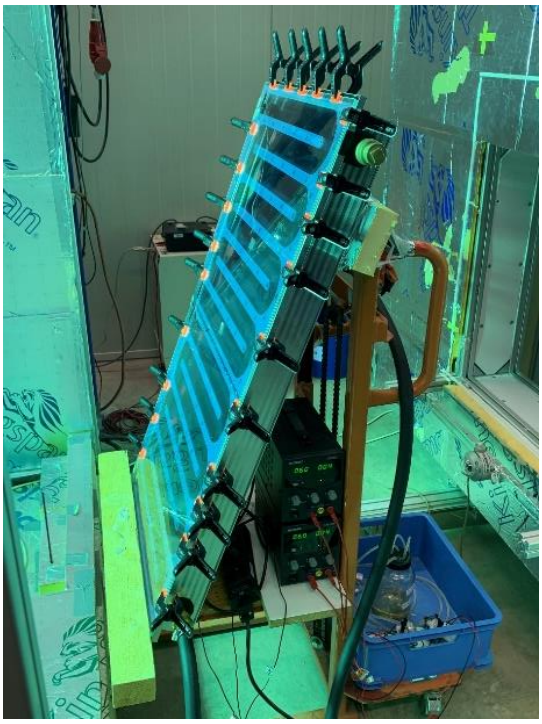

Figure 16: Sun simulator tests of the hybrid collector before the MOST-collector was finally bonded with the thermal collector. Instead, it was fixed with several clamps.

The testing was carried out at a surrounding temperature of 24 °C, the water in the thermal part of the collector was kept at 85 °C. Within the MOST layer the Duratherm oil was pumped through the MOST layer with a flow rate of approx. 5-10 ml/min.

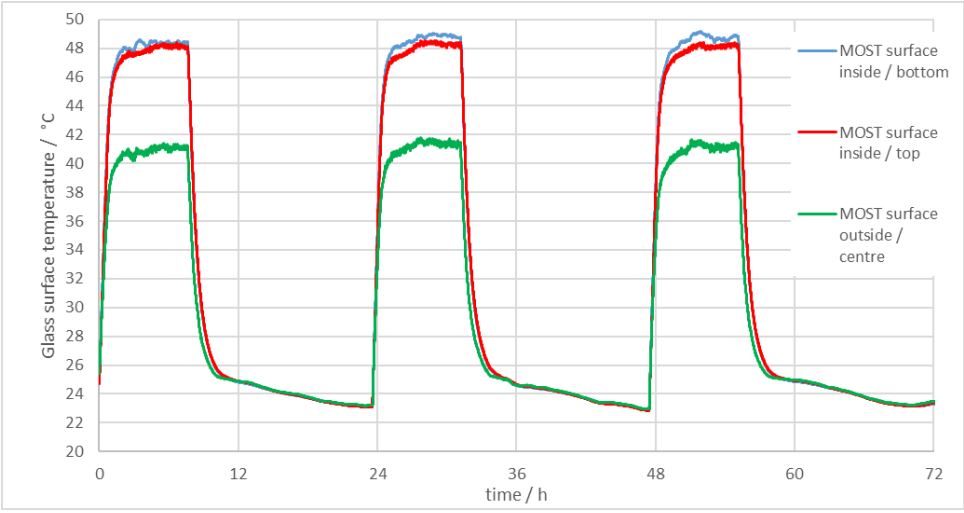

Figure 17: Glass surface temperatures of the MOST part (first collector-layer) when tested at the solar simulator. Red/blue line: temperature at the inside glass pane (pointing to the thermal collector); green line: temperature at the outside glass pane.

As a result, all parts or the collector stayed tight and the glass pane surface temperature of the MOST layer pointing to the solar thermal collector is approx. 48-49°C (see Fig. 17) which is not critical to trigger the back reaction.

The glass panes were glued in with special silicone for outdoor use. Experience from the small version with regard

to production processes and connections could be usefully incorporated here.

In January 2024, two hybrid collectors were shipped to the Universitat Politècnica de Catalunya in Barcelona (Spain) for real monitoring of the overall system in Stage IV.

4.4 Stage IV - Integrated system

In the final development stage, a complete MOST system is developed and constructed in accordance with Fig. 2 with all associated components. The setup is supplemented by a normal thermal flat-plate collector whose output is measured in parallel operation. The system is realized as an outdoor test stand on the roof of the Universitat Politècnica de Catalunya in Barcelona (Spain). The system is south oriented with a variable slope for the collectors. The Hardware setup is completed (Fig. 18), software for controlling the MOST system and data acquisition is under development by Fraunhofer ISE in Freiburg (Germany). The MOST system will go into operation under realistic conditions like changing insolation, changing outdoor temperature and changing heat demand (simulated with a chiller unit) in September 2024.

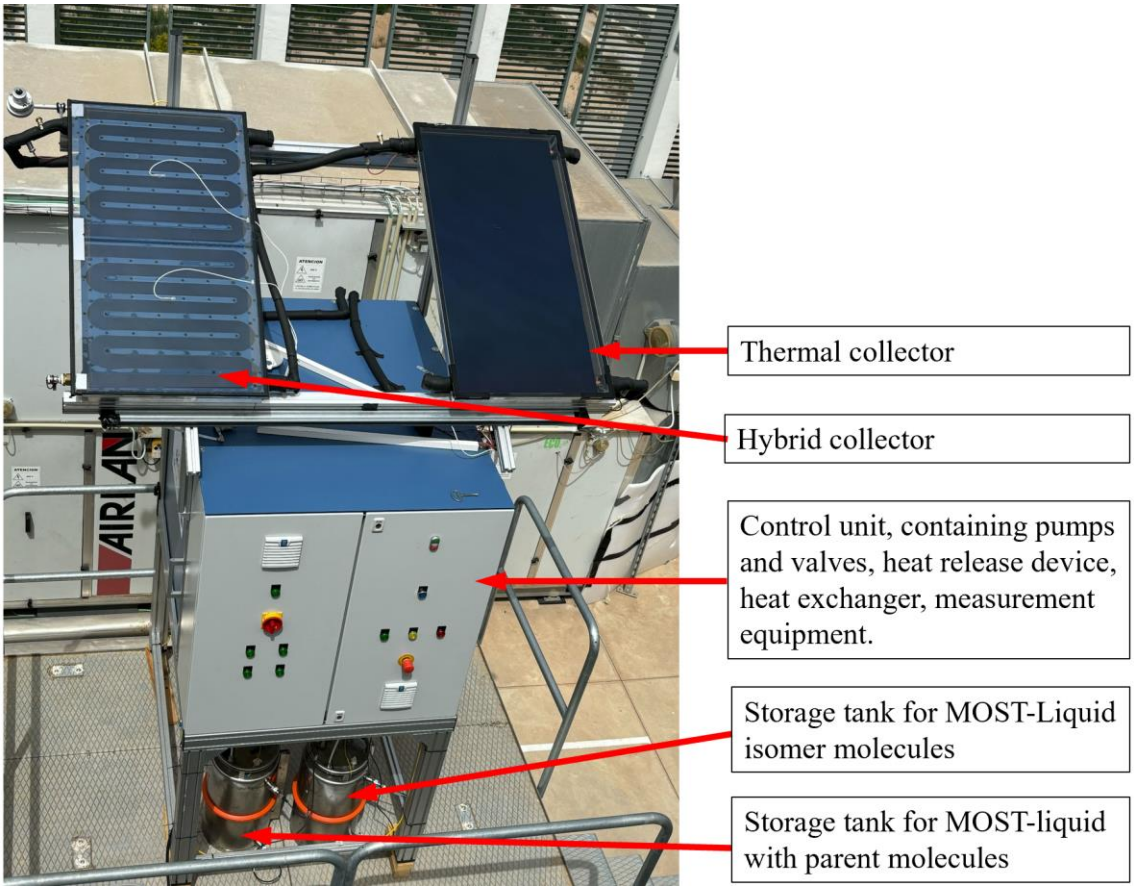

Figure 18: MOST-system at the roof of the Universitat Politècnica de Catalunya (UPC) - Barcelona Tech in Barcelona; on the left the hybrid collector (solar thermal + MOST) and on the right a normal solar thermal collector for comparison.

5. Summary

A small MOST collector was initially developed for the first laboratory-scale tests. This was scaled up in several stages into a near-series hybrid collector. The initial major problems with the choice of materials, caused by toluene as the carrier liquid, have now been solved. The hybrid collector has been tested for permanent leak-tightness and all components are UV-resistant.

The upper layer of the hybrid collector (the MOST collector) is almost completely transparent, so that as much of the energy of the solar spectrum as possible still reaches the second thermal collector layer.

The world's first complete MOST system with a close to series production collector has been installed at the Universitat Politècnica de Catalunya in Barcelona and will go into operation in September 2024.

6. Acknowledgments

This project has received funding from the European Union's Horizon 2020 research and innovation programme under grant agreement No 951801. Furthermore, we want to thank the company GREENoneTEC Solarindustrie GmbH (Austria) for the provision of important components of the thermal part of the hybrid collector. We would also like to thank the project consortium for the excellent cooperation: Chalmers University of Technology (Sweden), Fraunhofer-Institut für Solare Energiesysteme ISE (Germany), Johnson-Matthey (UK), Universitat Politècnica de Catalunya (Spain), University of Copenhagen (Denmark), University of Rioja (Spain).

Special thanks to our colleagues Leslie Ullerich, Thomas Will and Johannes Wachtel for contributing their skills to the construction of the different stages of the collector.

7. References

Alexopoulos, S., Kalogirou, S.A., 2022. Solar Thermal Energy. Springer.

Dreos, A., Börjesson, K., Wang, Z., Roffey, A., Norwood, Z., Kushnir, D., Moth-Poulsen, K., 2017. Exploring the potential of a hybrid device combining solar water heating and molecular solar thermal energy storage. Energy & Environmental Science 10(3), 728-734.

Gimenez-Gomez, A., Rollins, B., Steele, A., Hölzel, H., Baggi, N., Moth-Poulsen, K., Funes-Ardoiz, I., Sampedro, D., 2023. Unveiling the Potential of Heterogeneous Catalysts for Molecular Solar Thermal Systems. Chemistry – A European Journal 30(1), e202303230.

IGDB, 2024. International Glazing Database (IGDB), V98.0. https://windows.lbl.gov/igdb-downloads. (Accessed 27.07.2024 2024).

Magson, L., Hölzel, H., Aslam, A.S., Henninger, S., Munz, G., Moth-Poulsen, K., Knaebbeler-Buss, M., Funes-Ardoiz, I., Sampedro, D., 2024. Synthesis and Characterization of Carbon-Based Heterogeneous Catalysts for Energy Release of Molecular Solar Thermal Energy Storage Materials. ACS applied materials & interfaces.

Orrego-Hernández, J., Dreos, A., Moth-Poulsen, K., 2020. Engineering of Norbornadiene/Quadricyclane Photoswitches for Molecular Solar Thermal Energy Storage Applications. Accounts of Chemical Research 53(8), 1478-1487.

Stieglitz, R., Heinzel, V., 2013. Thermische Solarenergie: Grundlagen, Technologie, Anwendungen. Springer-Verlag.

Tiwari, G., Tiwari, A., 2016. Handbook of solar energy. Springer.

Wang, Z., Roffey, A., Losantos, R., Lennartson, A., Jevric, M., Petersen, A.U., Quant, M., Dreos, A., Wen, X., Sampedro, D., Börjesson, K., Moth-Poulsen, K., 2019. Macroscopic heat release in a molecular solar thermal energy storage system. Energy & Environmental Science 12(1), 187-193.

03. Solar and Efficient Districts

Yearly thermal performances of Danish solar heating plants

Elsabet Nielsen, Simon Furbo and Jianhua Fan

Department of Civil and Mechanical Engineering, Technical University of Denmark, Kgs. Lyngby, Denmark

Abstract

The number of Danish solar heating plants in district heating areas increased strongly from 16 plants in 2009 to 123 plants in 2019. Many of the plants were installed in district heating systems with natural gas boilers due to good economy. The thermal performance of most of the Danish solar heating plants have been measured for many years. The average yearly thermal performance for the solar heating plants for the period 2012-2023 is 459 kWh/m² solar collector and the yearly average utilization of the solar radiation for all the years is 40%.

Solar district heating plants are based on a simple, well proven and reliable technology. They supply heat with a relatively low cost of about 0.04 euro/kWh and the used solar collectors have a lifetime longer than 30 years. The solar heating plants provide about 2% of the total heat demand in Danish district heating areas.

In spite of the good experience from the plants, the Danish market for solar heating plants collapsed in 2020.

Solar heating plants are produced in Europe, the plants contribute to a global reduction of CO_2 emissions, even with a strong growth of installed systems. It is therefore hoped that the market for solar heating plants soon will be reestablished.

Keywords: Solar heating plants, measured thermal performances, district heating

1. Introduction

Solar heating plants in district heating areas consist of a high number of rows of serial connected solar collector panels. The rows are connected in parallel and the number of collector panels in each row can vary with up to 20 panels as shown in Figure 1.

Fig. 1: Solar district heating plant in Silkeborg (156,694 m²)

The technology for solar heating plants inclusive large solar collector panels was first developed in Sweden (Dalenbäck et al., 1981), and further developed and marketed in Denmark by Arcon Solvarme. The first Danish solar heating plant for district heating was installed in 1988 in Saltum (Jensen, 1990). The number of solar

© 2024. The Authors. Published by International Solar Energy Society
Selection and/or peer review under responsibility of Scientific Committee
10.18086/eurosun.2024.03.01 Available at http://proceedings.ises.org

heating plants in Danish district heating areas increased strongly from 16 to 123 within 10 years, in the period 2009-2019. The collector area of the Danish solar heating plants in operation during the period from 2005 to 2023 is shown in figure 2.

There has been a strong growth of Danish solar heating plants until 2019. Many of the solar heating plants were installed by district heating companies using natural gas boilers, since solar collectors in such systems were economically favorable. The Danish market for solar heating plants collapsed in 2020.

Almost all the solar heating plants are based on flat plate solar collectors with one or two cover plates. During the period 2002-2012 Arcon Solvarme and the Technical University of Denmark had a close cooperation on development of the large solar collector panels marketed by Arcon Solvarme (Fan and Furbo, 2007; Fan et al, 2009; Bava and Furbo, 2019). The collector efficiency was strongly improved, and a cost reduction of the solar collectors was achieved at the same time during the period.

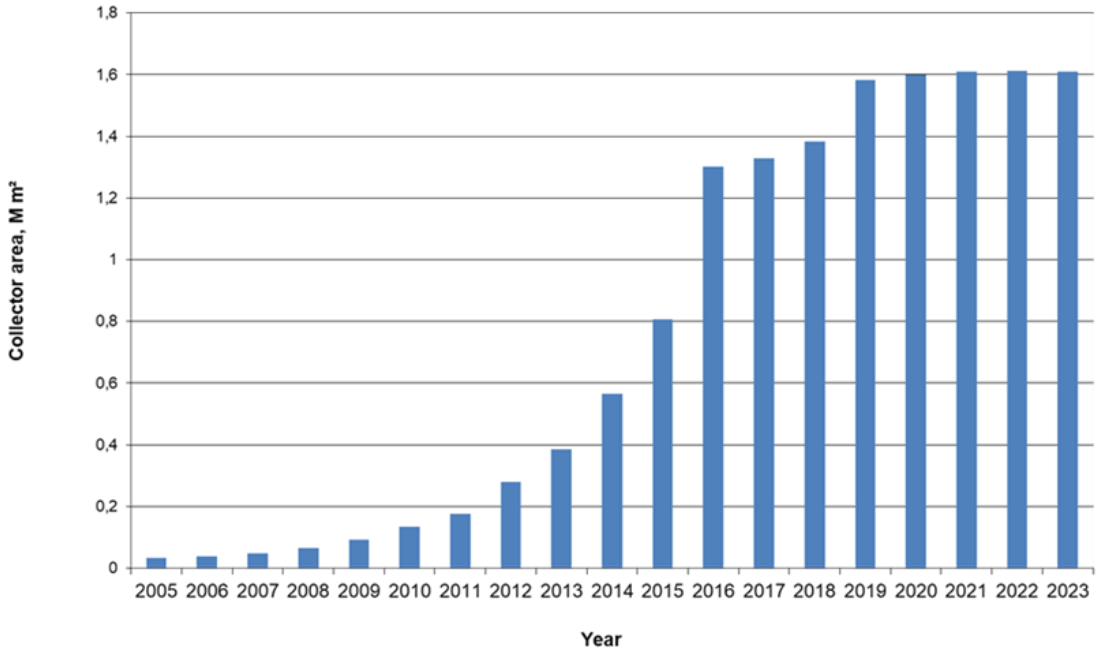

Fig. 2: Solar collector area of Danish solar heating plants during the period 2005-2023

2. Thermal performances of solar heating plants

The thermal performances of many Danish solar heating plants are available on the homepage (https://solvarmedata.dk/), (Furbo et al., 2018). Most of the plants are based on flat plate collectors from Arcon Solvarme, Sunmark or Arcon-Sunmark. In 2015, the two main producers of large flat plate collectors, Arcon Solvarme and Sunmark merged to form Arcon-Sunmark.

For the period 2012-2023 yearly thermal performances have been determined for 78 solar heating plants. The thermal performances are measured with energy meters on the water side of the heat exchangers in the solar collector loops. In this way the accuracies of the measurements are estimated to be about ±2%, and not influenced by the propylene glycol/water mixtures used as solar collector fluids. Further, the solar radiation on the solar collectors is measured with pyranometers. Often inexpensive pyranometers are used resulting in relatively high inaccuracies, about ±10%.

The collector areas of the investigated solar heating plants varied between 2970 m² and 156694 m². The tilts of the solar collectors varied between 30° and 45°, and the solar heating plants were installed between 1996 and 2021. Wang et al. (2012) suggested to divide Denmark in six different solar radiation regions as shown in figure 3. Table 1 shows the number of solar heating plants investigated in each solar radiation region.

Measured yearly thermal performances for the solar heating plants for the period 2012-2023 appear from table 2. The thermal performances are shown as kWh per m² aperture solar collector area. The number of plants, the

variations of thermal performances and the average yearly performance of the plants are shown for each year.

Tab. 1: Locations of 78 investigated solar heating plants

Region	1	2	3	4	5	6	Total
Number of plants	13	19	19	20	7	0	78

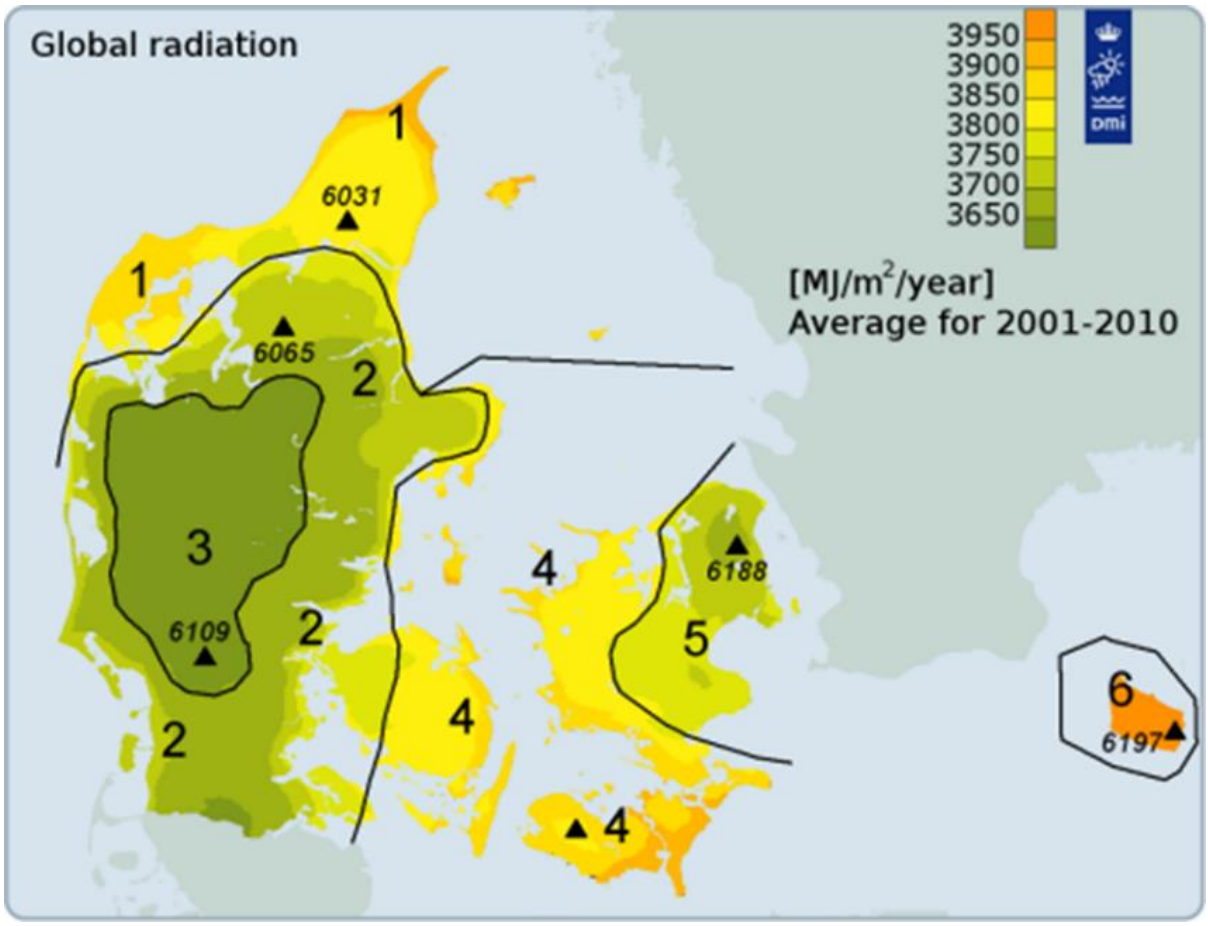

Fig. 3: Six Danish solar radiation regions

Tab. 2: Measured yearly thermal performances of Danish solar heating plants

Year	Number of solar heating plants	Yearly thermal performance, kWh/m²	Average yearly thermal performance, kWh/m²
2012	16	313 – 484	411
2013	21	389 – 493	450
2014	31	390 – 577	463
2015	36	322 – 518	439
2016	41	324 – 538	433
2017	54	318 – 495	407
2018	52	349 – 602	494
2019	55	378 – 616	454
2020	56	355 – 638	504
2021	33	332 – 585	445
2022	42	343 – 635	512
2023	42	359 – 617	490

Table 3 shows the yearly measured total solar radiation on the solar collectors and the utilization of the solar radiation for the investigated solar heating plants. The utilization is the ratio between the thermal performance and the total solar radiation on the collectors. The number of plants, the variations of the solar radiation and utilizations and the average yearly solar radiation and utilization of the plants are shown for each year.

Tab. 3: Measured solar radiation and utilization for Danish solar heating plants

Year	Number of solar heating plants	Yearly solar radiation, kWh/m²	Average yearly solar radiation, kWh/m²	Yearly utilization of solar radiation, %	Average yearly utilization of solar radiation, %
2012	16	942 – 1274	1102	28 – 45	37
2013	21	1039 – 1363	1135	31 – 46	40
2014	31	991 – 1474	1114	30 – 51	42
2015	36	876 – 1325	1101	31 – 47	40
2016	41	975 – 1444	1153	30 – 49	38
2017	54	848 – 1491	1133	26 – 48	36
2018	52	942 – 1479	1246	27 – 49	40
2019	55	913 – 1435	1179	29 – 58	39
2020	56	948 – 1625	1241	30 – 50	41
2021	33	891 – 1190	1095	30 – 55	41
2022	42	843 – 1300	1125	32 – 58	45
2023	42	866 – 1294	1154	30 – 52	42

Figure 4 shows yearly thermal performance as a function of the yearly solar radiation on the collectors for all investigated solar heating plants for all years. Each point corresponds to one year for one plant and the location of the plant is indicated as a specific solar radiation region.

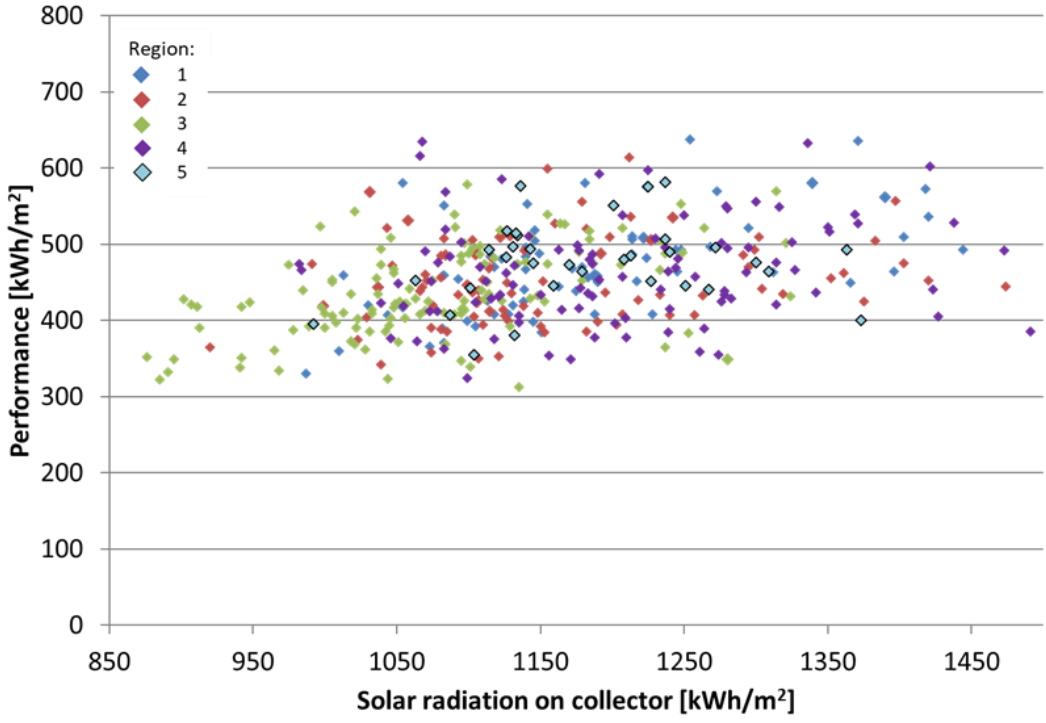

Fig. 4: Yearly thermal performance as function of solar radiation on solar collectors for Danish solar heating plants

There are large variations of the thermal performances and solar radiation from plant to plant and from year to

year. There are many reasons for the variations of the thermal performances. Among other things, the following reasons can be mentioned:

- Different temperature levels of the solar collector fluid in the solar collectors. The thermal performance will be high if the temperature level is low
- Different weather conditions. The thermal performance will be high if the solar radiation and ambient air temperature are high
- Different solar collectors and different designs of solar collector fields
- Different operation strategies inclusive different flow rates
- Different heat losses from pipes in solar collector loops
- Different tilts, shadow conditions, moisture conditions, snow conditions and dirt conditions on the glass covers for the collectors
- Some plants have long-term heat storages charged to high temperatures during summer. Consequently, the high temperature levels of the solar collector fluid in these plants will result in relatively low thermal performances per m² solar collector

Figures 5 and 6 show yearly average thermal performances and yearly average utilizations of solar radiation for the investigated solar heating plants year by year. The yearly average thermal performances variates between 407 kWh/m² and 512 kWh/m² and the yearly average utilizations vary between 36% and 45%. The average thermal performance for all years is 459 kWh/m² solar collector and the average utilization for all years is 40%.

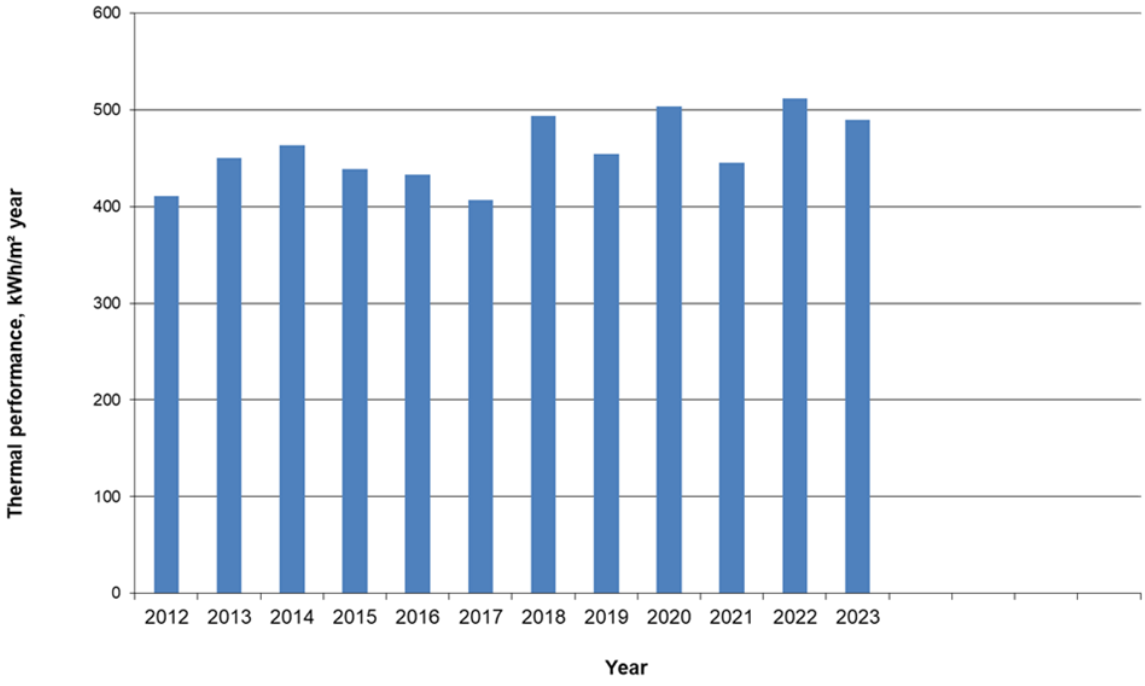

Fig. 5: Average yearly thermal performances of Danish solar heating plants

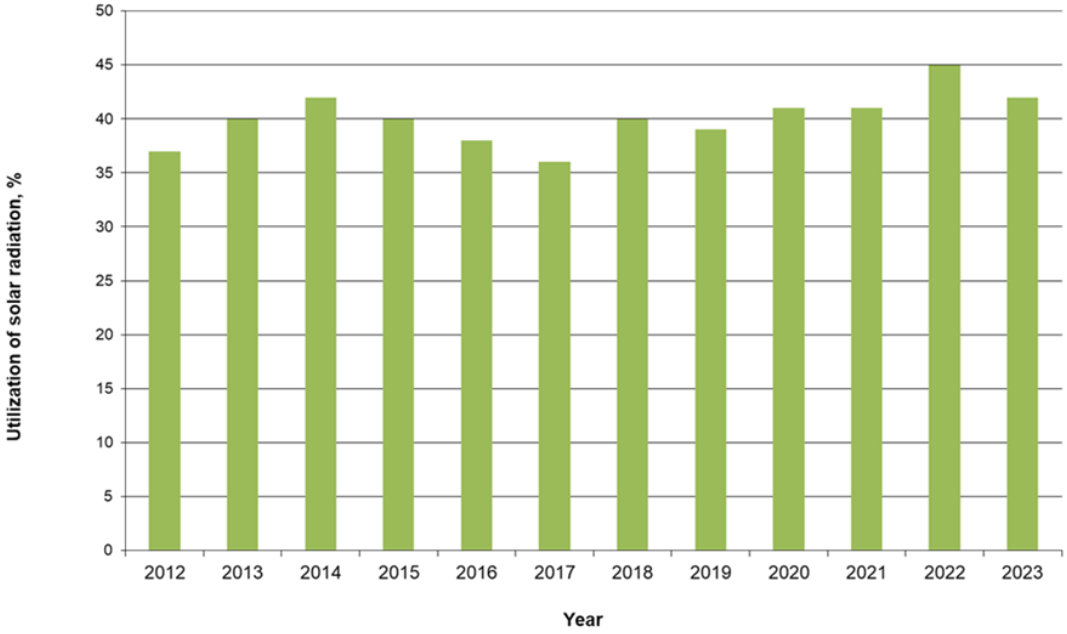

Fig. 6: Average yearly utilization of solar radiation of Danish solar heating plants

Figure 7 shows average yearly thermal performances of all Danish solar heating plants as well as yearly thermal performances of solar heating plants in solar radiation regions 1, 2, 3, 4 and 5. For most years the solar heating plants located in regions 1 or 5 perform best while the solar heating plants located in the "dark" region 3 perform worst. The average yearly thermal performance for all years for all solar heating plants is 459 kWh/m², and the average yearly thermal performances for the solar heating plants in regions 1, 2, 3, 4 and 5 are 477 kWh/m², 453 kWh/m², 435 kWh/m², 466 kWh/m² and 483 kWh/m² respectively. That is, the plants in sunny region 5 performs in average 11% better than the plants in region 3.

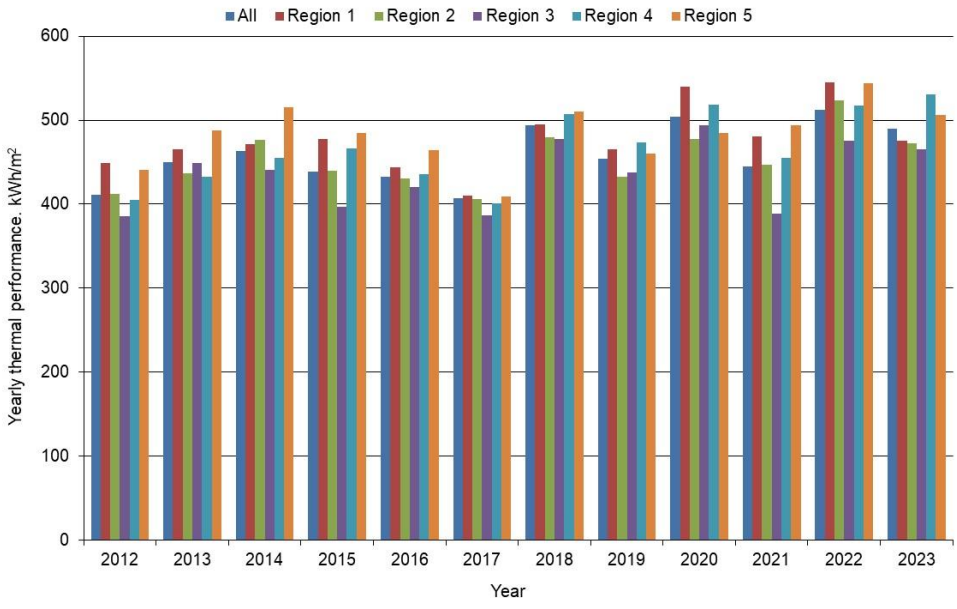

Fig. 7: Average yearly thermal performances of Danish solar heating plants in different solar radiation regions

Four of the solar heating plants in the investigations are equipped with large seasonal water pit storages: The solar heating plants in Marstal located in region 4, Dronninglund located in region 1 as well as Gram and Vojens, both located in region 2. These heat storages are charged to high temperatures of about 90°C during summer. This results in high temperature levels in the solar collector loops and relatively low collector

efficiencies during summer. Measurements show that the average yearly thermal performance of these plants for all years is about 10% lower than the average yearly thermal performance of all the plants.

3. Potential of solar heating plants

Table 4 shows approximate quantities of solar heating contribution from all Danish solar heating plants to the total Danish district heating consumption for the period 2011-2023. During the last 6 years solar heating plants have covered about 2% of the total heating demand in Danish district heating networks. Together with individual solar heating systems solar heating covers about 1% of the total energy consumption in Denmark.

Tab. 4: Solar heating contribution to Danish district heating consumption

Year	Total district heating, PJ/year	Solar district heating, PJ/year	Solar district heating, %
2011	132	0.33	0.3
2012	136	0.55	0.4
2013	135	0.68	0.5
2014	122	0.98	0.8
2015	130	1.26	1.0
2016	135	2.03	1.5
2017	136	1.93	1.4
2018	132	2.47	1.9
2019	131	2.59	2.0
2020	127	2.87	2.3
2021	142	2.58	1.8
2022	130	2.97	2.3
2023	135	2.84	2.1

There are 445 district heating systems in Denmark supplying heat to about 66% of all Danish buildings. 123 of the systems have solar heating plants. The energy mix covering the heat demand of the Danish district heating systems appear from figure 8 for the period 1990-2022. The share of fossil fuels has been strongly reduced during the last decades and replaced by renewables. Today 76% of the energy supply to district heating is considered to be renewable. Most of the renewable energy is, however, biomass, and most of the biomass is imported from abroad. Consequently, the district heating systems are emitting CO_2 and are not operated in a sustainable way. There is a need to transform district heating systems into truly sustainable systems. In this connection district heating companies have in the last five years installed large electrically driven heat pumps in high numbers because electricity costs for district heating companies are expected to be low in the future. Further, the installation of such heat pumps is supported economically by the government.

Our electricity demand is expected to increase strongly in the future. There are many reasons for this increase:

- The number of electric cars will increase strongly
- New Power-to-X systems for production of sustainable fuels, chemicals and materials based on green hydrogen will be installed
- New data centers with high electricity consumption will be installed
- Many buildings outside district heating areas will in the future be heated by electrically driven heat pumps

The strong growth of electricity consumption requires high investments and CO_2 emissions, both due to installation of new wind farms and new PV solar fields and due to the needed reinforcement of the electricity grid. Therefore, electricity savings should be a high priority in future energy plans. The use of solar heating systems is an efficient way to reduce electricity consumption in the future.

The following advantages of solar heating plants for district heating should be considered:

- The plants are based on a simple, well proven, and reliable technology
- High thermal performance of existing solar heating plants: About 460 kWh/m² year
- Long lifetime of marketed solar collectors, > 30 years
- Low heat price for solar heat, about 0.04 euro/kWh
- Low maintenance costs, 0.00027 euro/kWh (Bava et al, 2025)
- No unexpected solar heat costs
- Good interplay with the energy system, since the heat storages of the plants can be used by different energy systems
- Produced in Europe
- Limited heat loss from solar collectors to ambient air resulting in low contribution to increase of ambient temperature

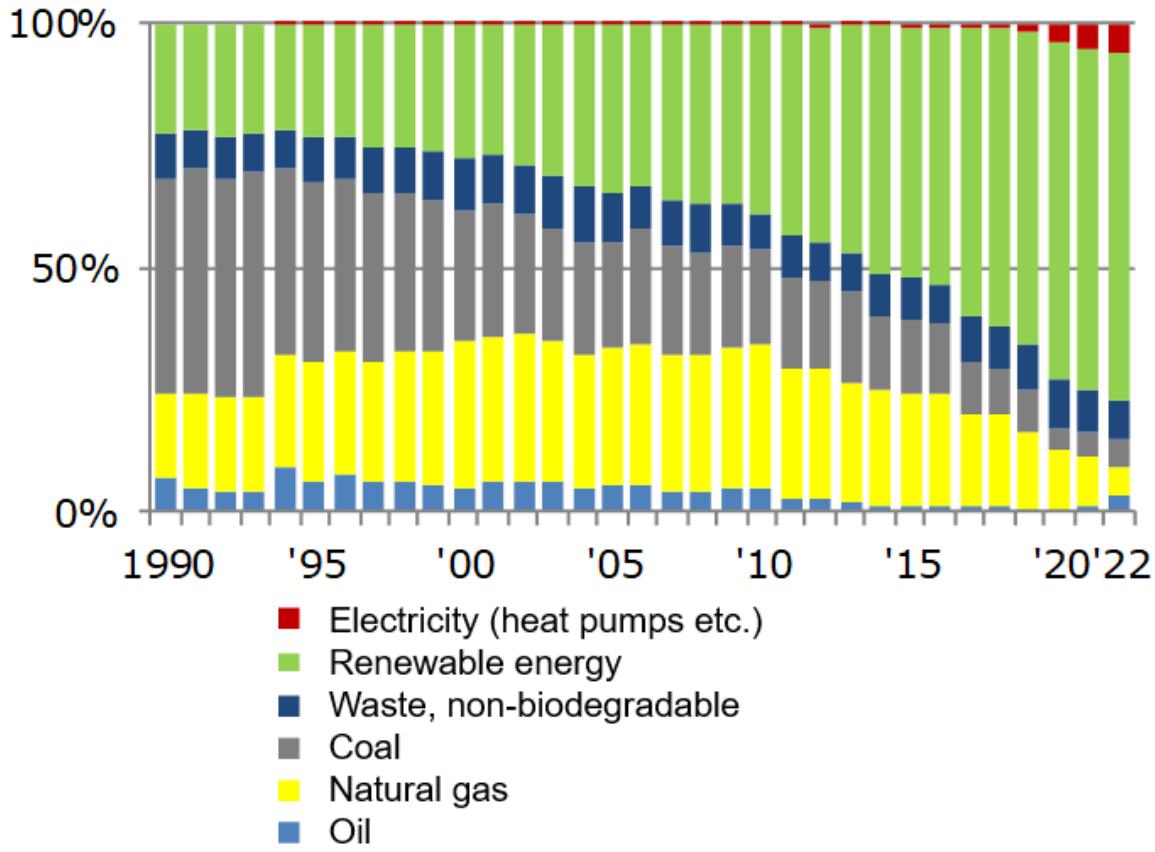

Fig. 8: Energy mix for Danish district heating systems

The strong growth of use of large electrically driven heat pumps in district heating systems is economically favorable. But, is it a sustainable solution for society?

To answer this question, a comparison on CO_2 emissions between a solar heating plant and a heat pump solution combined with a PV field is given in the following.

CO_2 emissions related to production of large solar collectors in Europe and PV panels with complete glass back sheets produced in Chine appear from table 5.

Tab. 5: CO_2 emissions from production of solar collectors in Europe and PV panels produced in China (Carlsson et al, 2014; Reichel et al, 2022)

Panel	Solar collector	PV panel
CO_2 emission	89 kg/m² panel	810 kg/kWp, corresponding to 178 kg/m² panel

CO_2 emissions from heat production from Danish district heating systems and from Danish electricity production are decreasing year by year. The CO_2 emissions for heat production in district heating systems was in 2022 in average 17 kg/GJ, corresponding to 61 g/kWh (https://ens.dk/service/statistik-data-noegletal-og-kort/noegletal-og-internationale-indberetninger) and for electricity production the CO_2 emissions was in 2023 81 g CO_2/kWh (https://energinet.dk/media/drikubl5/milj%C3%B8redeg%C3%B8relse-2023.pdf).

Based on the above mentioned CO_2 emissions and a yearly thermal performance of solar collectors of 459 kWh/m² in agreement with the average performance of the investigated solar heating plants and a yearly electricity production of PV panels of 200 kWh/m², the yearly CO_2 emission reduction is 28 kg CO_2/m² collector for solar collectors and the yearly CO_2 emission reduction is 16.2 kg/m² PV panel. That is: The number of panel operation years needed until the CO_2 emitted by the panel productions is saved is 3.2 year for solar collectors and 11 years for PV panels.

If the CO_2 emissions connected to transportation of the panels and the CO_2 emissions related to heat pump production were considered, the difference between the CO_2 emission pay back time for the two solutions will be even larger than mentioned above, even if a high SPF for the heat pump is assumed.

Further, it should be mentioned that a strong growth of yearly installed systems with a high CO_2 pay back time result in strongly increased global CO_2 emissions for society, until the growth is deceased.

It is concluded that from a CO_2 emission point of view solar heating plants produced in Europe is a much better solution for district heating systems than PV panels produced in China combined with heat pumps.

Consequently, it is hoped that the Danish market for solar heating plants soon will be reestablished.

4. Ups and downs for the market of solar heating plants

The strong growth of Danish solar heating plants until 2019 has many reasons. Besides the advantages mentioned in the previous section the following should be mentioned:

- Denmark has an ambitious energy plan. By 2050 the country must be independent of fossil fuels
- Denmark has a lot of district heating. Today 66% of all Danish buildings are heated by district heating
- Danish district heating systems operate with low temperature levels. A typical forward temperatureto towns is about 80°C and a typical return temperature from towns is about 40°C
- Danish district heating companies are often nonprofit cooperatives
- There are high taxes for fossil fuels in Denmark. Typical tax is about 0.035 euro/kWh produced heat
- The Danish energy system is decentralized
- There is a high share of wind energy for electricity production. In 2023, 54% of the Danish electricity consumption was produced by wind turbines
- The costs for marketed solar collector fields installed on the ground are relatively low, about 150 euro/m²
- In many cases relative low ground costs are available
- There is a good cooperation between solar heating plant owners. Among other things, regular meetings with experience exchange are arranged

In 2020 the Danish market for solar heating plants collapsed. There are several reasons for the collapse:

- There is no taxation on biomass fuels. Consequently, biomass fuels are used in large amounts by district heating companies.
- The taxation of electricity for district heating companies was reduced from the start of 2021 from 0.028 €/kWh to 0.0005 €/kWh.
- The Danish Energy Agency supports district heating companies on installation of large heat pumps in district heating systems economically and inexpensive electricity is foreseen in the future. Consequently, heat pumps are installed in high numbers by district heating companies due to good economy.
- In 2020 Arcon-Sumark was sold to GreenOneTec. Therefore, the most important actor in the field is no longer a Danish company.

5. Conclusions

The number of Danish solar heating plants in district heating areas increased strongly from 16 plants in 2009 to 123 plants in 2019. Many of the plants were installed in district heating systems with natural gas boilers due to good economy.

The average yearly thermal performance for the solar heating plants for the period 2012-2023 is 459 kWh/m² solar collector and the yearly average utilization of the solar radiation for all the years is 40%.

Solar district heating plants are based on a simple, well-proven, and reliable technology. They supply heat with a relatively low cost of about 0.04 euro/kWh, and the used solar collectors have a lifetime longer than 30 years. The solar heating plants provide about 2% of the total heat demand in Danish district heating areas.

Despite the good experience from the plants, the Danish market for solar heating plants collapsed in 2020, mainly because district heating systems are installing large electrically driven heat pumps.

Solar heating plants are produced in Europe and the plants contribute to a global reduction of CO_2 emissions, even with a strong growth of installed systems. It is therefore hoped that the market for solar heating plants will soon be re-established.

6. Acknowledgements

The investigations were funded by the Danish Energy Agency through the EUDP projects: IEA SHC Task 66 Solar Energy Buildings, grant no. 64020-1071 and IEA SHC Task 71 Life cycle and cost assessment for heating and cooling technologies, grant no. 134232-510332.

7. References

Dalenbäck, J.-O., Gabrielsson, E., Ludvigsson, B., 1981. Three Swedish group solar heating plants with seasonal heat storage: a summary of experience from Studsvik, Lambohov and Ingelstad plants up to the end of 1980. Swedish Council for Building Research.

Jensen, B., 1990. Måling på Saltum solvarmeanlæg. Nordvestjysk Folkecenter for Vedvarende Energi, PC-tryk, ISBN 87 88660 93 1.

Fan J., Furbo S., 2007. Optimering og afprøvning af solfanger til solvarmecentraler. Department of Civil Engineering, Technical University of Denmark. Report SR-07-06.

Fan J., Chen Z., Furbo S., Perers B., Karlsson B., 2009, Efficiency and lifetime of solar collectors for solar heating plants, ISES Solar World Congress 2009. Johannesburg, South Africa, p. 331-340.

Bava, F., Furbo, S., 2014. Comparative test of two large solar collectors for solar field application. EuroSun 2014: International Conference on Solar Energy and Buildings - Aix-les-Bains Congress Center, Aix-les-Bains, France.

Wang P.R., Scharling M., Nielsen K.P., 2012. 2001-2010 Design Reference Year for Denmark, beta.dmi.dk/fileadmin/Rapporter/TR/tr12-17.pdf, Technical Report 12-17, DMI, Copenhagen, Denmark

Carlsson B., Persson H., Meir M., Rekstad J., 2014. A total cost perspective on use of polymeric materials in solar collectors – Importance of environmental performance on suitability. Applied Energy 125, pp. 10-20.

Reichel C., Müller A., Friedrich L., Herceg S., Mittag M., Neuhaus D.H., 2022. WPPEC-8, 8th World Conference on Photovoltaic Conversion, 26-30 September 2022, Milan, Italy.

https://solvarmedata.dk/

https://ens.dk/service/statistik-data-noegletal-og-kort/noegletal-og-internationale-indberetninger

https://energinet.dk/media/drikubl5/milj%C3%B8redeg%C3%B8relse-2023.pdf

Development of a new generation of cold district heating systems with water as heat transfer medium

Peer Huber[1], Harald Drück[1], Bernd Hafner[2] and Ralf Dott[2]

[1] Institute for Building Energetics, Thermotechnology and Energy Storage (IGTE)
University of Stuttgart, Germany

[2] Viessmann Climate Solutions SE, Allendorf (Eder), Germany

Abstract

The purpose of cold district heating systems is to cover the heating and cooling demand of consumers connected to the district heating network. Generally, they consist of a thermal energy source, a thermal energy store, heat pumps and a cold district heating network for distribution. Some of these cold district heating systems use thermal energy sources like an ice store or solar thermal air-brine-collectors supplying temperatures below the freezing point of water and therefore in these conventional cold district heating systems a mixture of water and antifreeze as heat transfer medium is necessary. As the use of antifreeze leads to ecological and economic disadvantages, the development of a new generation of cold district heating systems with water as heat transfer medium is being performed. In this paper this new innovative system concept and a simulation model of this system concept is presented. Furthermore, an evaluation of the operation strategy of the ice store integrated into the overall system based on simulation results is presented. In addition, the results of a simulation study related to an energetic comparison of heat losses and gains between the new innovative cold district heating network using water and a conventional network using a mixture of water and antifreeze are introduced. In conclusion, the evaluations performed clearly show the important role of the ice store as a seasonal thermal energy store and the higher heat losses of the new innovative cold district heating network compared to the conventional network. It is expected that the new generation of cold district heating systems with water as heat transfer medium has ecological and economic advantages compared to conventional cold district heating systems. Demonstrating this is part of the ongoing research project "SolKaN2.0" related to the development of a new generation of cold district heating systems.

Keywords: Cold district heating system, cold district heating network, 5GDHC, heat transfer medium, antifreeze, ice store, solar thermal air-brine-collector, TRNSYS simulation

1. Introduction

Cold district heating systems are also known as the fifth generation of district heating and cooling (5GDHC) systems. During the evolution of district heating and cooling networks the temperatures in the network distributing the heat decreased continuously from generation to generation. As described by Lund et al. (2014) the first generation started with steam as heat transfer medium and temperatures up to 200 °C followed by pressurized hot water with temperatures mostly above 100 °C in the second generation. In the third generation the temperatures decreased often below 100 °C, whilst in the fourth generation they are between 30 and 70 °C. With the most recent fifth generation of cold district heating systems this evolution continues towards lower temperatures between −15 and 30 °C.

The main reason to use such systems with low temperatures is the reduction of heat losses to the environment. The use of relatively low temperatures is also supported by the continuously improving energetic building standard that makes it possible to use heating systems with relatively low flow temperatures. Furthermore, the usage of distribution temperatures below approx. 15 °C also offers the possibility to use the district heating network for both, heating and cooling. However, the supply of domestic hot water is challenging with relatively low temperatures.

© 2024. The Authors. Published by International Solar Energy Society
Selection and/or peer review under responsibility of Scientific Committee
10.18086/eurosun.2024.03.02 Available at http://proceedings.ises.org

2. State of the art of cold district heating systems

Generally, cold district heating systems consist of thermal energy sources such as solar thermal air-brine-collectors and a thermal energy store, e.g. an ice store, heat pumps and the cold district heating network for the distribution of the thermal energy. In Figure 1 the thermal energy sources are located on the left hand side, the heat demand of the decentral consumers can be seen on the right hand side and in between the cold district heating system and the substations with decentral heat pumps are positioned.

Some of these systems use thermal energy sources supplying temperatures below the freezing point of water. To perform a heat transfer between the thermal energy sources and the cold district heating network in conventional cold district heating systems the usage of a mixture of water and antifreeze as heat transfer medium is required. However as elaborated in the following chapter, the use of antifreeze results in ecological and economic disadvantages.

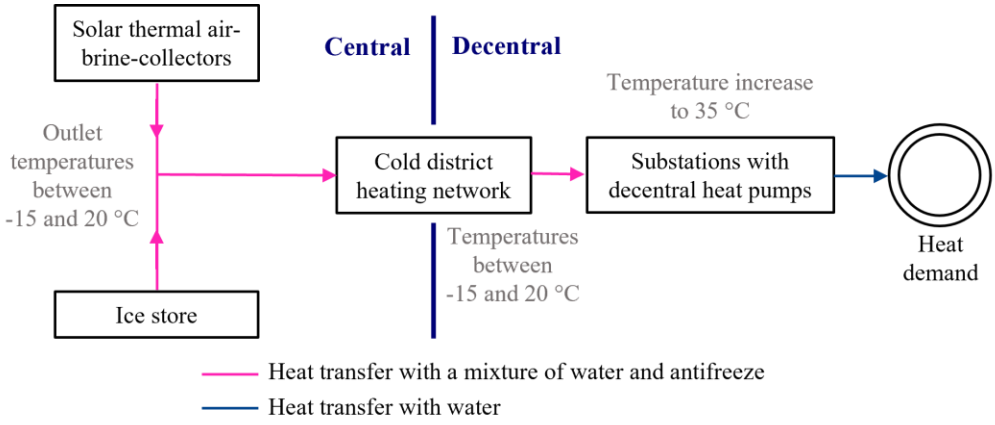

Fig. 1: Schematic set-up of a state of the art cold district heating system with solar thermal air-brine-collectors and an ice store as thermal energy sources and a mixture of water and antifreeze as heat transfer medium

3. Disadvantages using antifreeze in cold district heating systems

Major challenges of using antifreeze are several necessary security measures due to the classification of common antifreeze types as slightly water polluting. Therefore, depending on the individual requirements of the country, double-walled pipes and an automatic system for leakage detection must be implemented in the cold district heating network e. g. in Germany. Furthermore, the decentral substations which transfer the heat between the decentral heat pumps and the central cold district heating network must be equipped with collecting basins for the antifreeze medium in case of a leakage. These measures lead to increasing costs from an economic point of view on the one hand. On the other hand, the collecting basins require additional valuable space in the buildings and are therefore related to additional costs.

In addition, the viscosity of the mixture of water and antifreeze is higher, and the specific heat capacity is lower compared to pure water. This leads to an increased electric energy demand for the pumps installed in the different cycles operated with the mixture of water and antifreeze as heat transfer medium.

Moreover, the mixture of water and antifreeze is significantly more costly than water. From an ecological point of view, the production of the mixture is associated with additional greenhouse gas emissions.

To conclude, the replacement of the mixture of water and antifreeze with water is a reasonable improvement of cold district heating systems. Therefore, this is the key aspect of the development of a new generation of cold district heating systems, which is described in the following chapter.

4. New generation of cold district heating systems with water as heat transfer medium

In Figure 2 the schematic set-up of the new generation of a cold district heating system with water as heat transfer medium is shown. On the right side the heat demand of the decentral consumers is located. On the left side the solar thermal air-brine-collectors as thermal energy source and an ice store as thermal energy store are centrally positioned. Between the heat demand and the heat supply the cold district heating network distributes the heat using water as heat transfer medium.

Before the heat supplied by the thermal energy sources can be transferred into the cold district heating network a central heat pump is required to increase the temperature. This is necessary as the outlet temperatures of the solar thermal air-brine-collectors and the ice store can vary approximately between −15 to 20 °C. This also requires the use of a mixture of water and antifreeze for the heat transfer between the thermal energy sources and the central heat pump. But after the temperature increase by the central heat pump water can be used as heat transfer medium in the main part of the district heating network.

Additionally, decentral heat pumps are located in the respective buildings to cover the heat demand using the cold district heating network as their heat source. In this case the temperature is increased from around 5 to 15 °C to 35 °C which is suitable for floor heating systems.

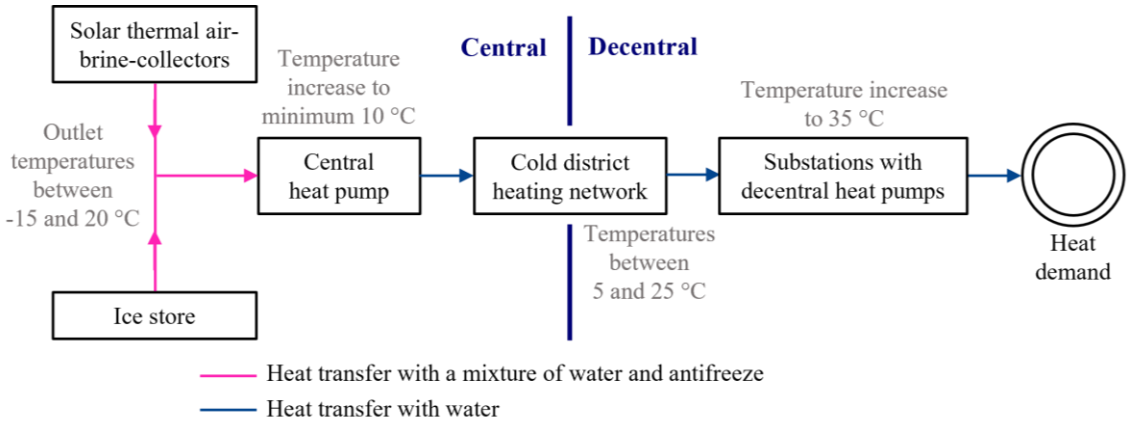

Fig. 2: Schematic set-up of the new generation of a cold district heating system supplying heat to the customers with water as heat transfer medium

Figure 2 and the previous explanation describe the heat supply by the cold district heating system in case of a space heating demand. Additionally, the system is suitable for the extraction of heat from the buildings for cooling purposes in summer. The extracted heat can then be stored in the ice store or dissipated by the solar thermal air-brine-collectors to the environment.

Unfortunately, e.g. for German weather conditions in times with cooling demand the temperatures of the ambient air are mostly too high to use the environment directly by the solar thermal air-brine-collectors as heat sink. Additionally, from an economic point of view the ice store capacity cannot be designed to store the cooling demand of the whole cooling season and will reach its maximum capacity at about 20 °C water temperature in the ice store within the first weeks of summer based on the experience from pilot plants which were part of the preceding research project ‘Development of integrated solar supply concepts for climate-neutral buildings for the “city of the future” (Sol4City)’. Therefore, in an additional operating mode the central heat pump can be used to actively extract heat from the buildings by using them as heat source, as shown in Figure 3. The resulting heat at a high-temperature level of about 40 °C is transferred to the environment by the solar thermal air-brine-collectors.

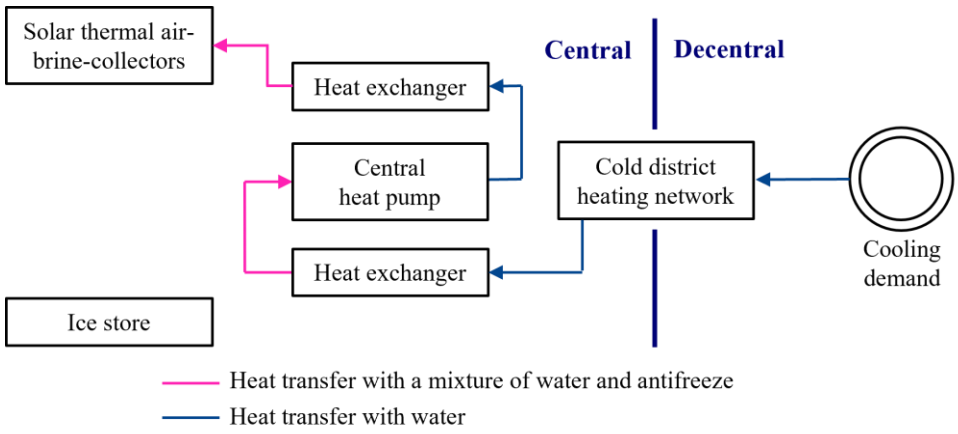

Fig. 3: Schematic figure of the new generation of a cold district heating system using the central heat pump to actively cool the decentral buildings and transfer the heat to the environment by the solar thermal air-brine-collectors

In addition, the central heat pump may actively cool the ice store at night and hence decrease the temperature of the water inside the store. The gained capacity for heat can then again be used as a heat sink for the cooling of the buildings by day. Compared to cooling the buildings via the central heat pump during the day directly, it is more efficient to operate the central heat pump during the night when the ambient temperatures are lower. Theoretically there is also the possibility to passively cool the ice store in nights with significantly lower ambient temperatures compared to the water temperature in the ice store. As those cold nights are rare in summer for German weather conditions, this passive precooling of the ice store is not often in use.

As described previously the ice store can be regenerated or heated respectively on the one hand with the extracted heat from the buildings for cooling purposes. On the other hand, heat gains from the solar thermal air-brine-collectors can be used to melt the ice and / or increase the temperature of the water inside the ice store.

In conclusion the main innovative aspect of this system is the use of water as heat transfer medium in the district heating network. However, this results in the need for an additional central heat pump. To assess this new innovative system, in chapter 6 and 8 various investigations are performed by means of numerical simulations with the software TRNSYS. This simulation model developed for this purpose is described in more detail in the following chapter 5.

5. Simulation model

The simulation model of the new innovative cold district heating system has been created with the simulation software TRNSYS. This software is commonly used for dynamic simulations of energy supply systems. To model the overall cold district heating system sub-models for every component are used. The most important sub-models are presented in the following.

For modeling the solar thermal air-brine-collectors the TRNSYS “Type 832” is used. The characteristic values for the collector type “SLK-600” which are used in this simulation to parameterize the collector model were determined by Fischer et al. (2021). Like other components of the system simulation this model receives weather data for a location near Stuttgart, Germany.

Both the central and the decentral heat pumps are modeled by the TRNSYS “Type 212” which was developed at the Institute for Building Energetics, Thermotechnology and Energy Storage (IGTE). This model determines the heat output and the electrical energy demand based on characteristic curves depending on the inlet temperature in the evaporator and a linear interpolation approach. Those characteristic curves are quadratic polynomials which are created based on performance data provided by the heat pump manufacturer.

Small hot water stores are used in this system to allow a consistent operation of the heat pumps and therefore increase their efficiency and also to hydraulically separate different parts of the cold district heating system from each other. To model those hot water stores the TRNSYS “Type 340” by Drück (2007) is implemented in the simulation model. These stores are directly charged and discharged without using a heat exchanger. In addition to thermal stratification inside the store the model also considers heat losses to the environment.

The cold district heating network is simulated with the TRNSYS “Type 710” and will be described further in chapter 7.

To simulate the ice store the TRNSYS “Type 343” developed by Hornberger (1994) is used. This model includes an underground storage tank with water as storage medium and pipe coils inside the store as heat exchanger. Inside these pipe coils a mixture of water and antifreeze must be used in order to generate ice inside the store. In addition, the model considers heat gains from the surrounding earth and offers the possibility to configure the store dimensions and material properties of the storage material, pipe coils, storage medium, heat transfer medium and the surrounding earth. In the following chapter 6 simulation results focusing on the ice store are presented.

6. Heat balance and state of charge of the ice store

The ice store has the ability of balancing seasonally varying heating and cooling demands over a long period of time. Additionally, heat gains by solar radiation can be stored in the ice store and used for heating demands if required. In the following the operation of the ice store is presented with a monthly heat balance and the state of charge for the time of one year based on results of the previously presented simulation model.

In Figure 4 heat inputs are represented with positive bars and heat outputs with negative bars. Heat inputs occur through regeneration with solar heat gains or with heat extracted from the buildings for cooling purposes and through heat gains from the earth surrounding the ice store. Heat outputs occur in times with heating demands from the buildings and therefore in this case the ice store is used as a heat source for the central heat pump. In addition, heat can be actively or passively extracted from the ice store to precool it during summer nights as described in chapter 4.

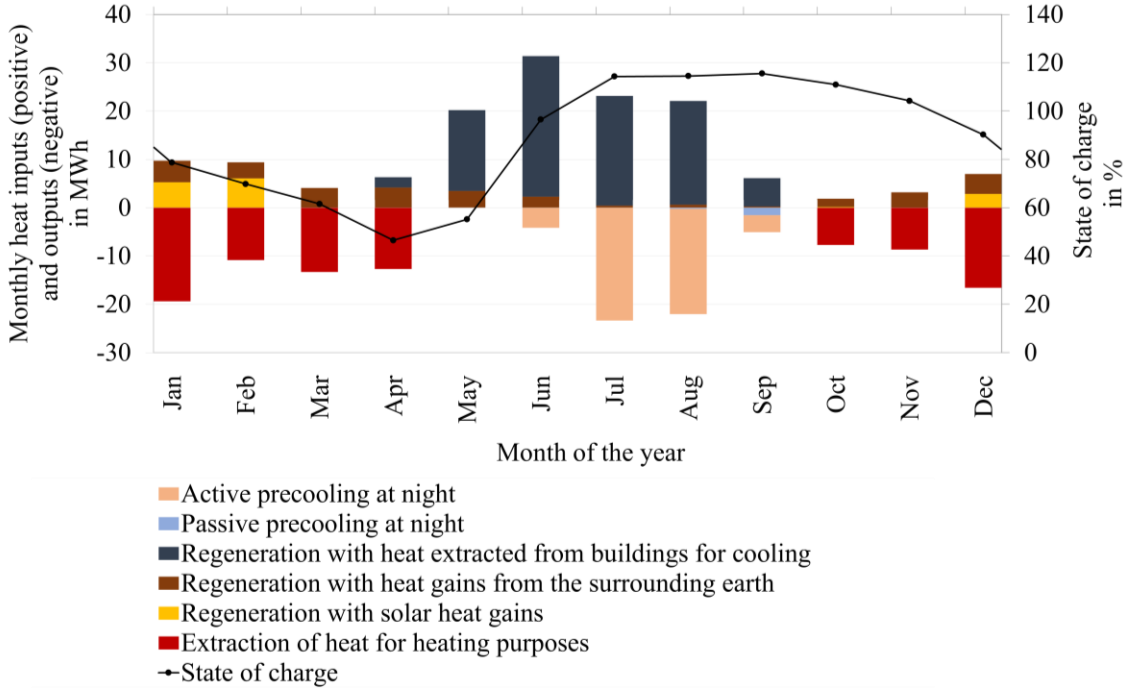

Fig. 4: Monthly heat balance and monthly average state of charge of the ice store over the period of one year

The development of the state of charge of the ice store is also shown in Figure 4. This state of charge is defined as 100 % for a state with only liquid water and a water temperature of 0 °C. With an increasing share of solid water or respectively ice, the state of charge is continuously decreasing below 100 %. Theoretically, at a state of charge of 0 % all liquid water would be solid ice. But the ice store is operated only until around a state of charge of 20 %, as with an increasing ice layer around the pipes of the heat exchanger the efficiency of the heat transfer is decreasing. Additionally, a completely frozen ice store would result in tensions in the material of the storage wall as ice has a higher volume than liquid water. With a rising water temperature above 0 °C the state of charge can increase above 100 % until the water reaches the maximum temperature of 20 °C. This maximum temperature is due to avoid material fatigue in the storage walls.

With the beginning of the heating season in October the state of charge is decreasing as more heat is extracted from the ice store compared to heat gains from the surrounding earth and the solar thermal air-brine-collectors. This continues throughout the whole heating season until April. Although regeneration through solar heat gains reduces the discharging of the ice store in some months the system control intentionally limits this regeneration to provide enough capacity for cooling purposes at the end of the heating season. With the beginning of the cooling season this capacity is used to store heat extracted from the buildings and thus the state of charge is increasing from May to July until it reaches its previously mentioned maximum. Then the active and on a small scale the passive precooling of the ice store at night ensures to provide storage capacity for cooling during the day. Since the extraction of heat at night and the insertion by day compensate each other, the state of charge remains constant from July to September.

The results of the system simulation presented in this chapter clearly shows the essential role of the ice store as a seasonal thermal energy store integrated into a cold district heating system with heating and cooling demands.

7. Validation of the cold district heating network model

For the simulation of the cold district heating network the TRNSYS model “Type 710” originally developed by the Institute for Solar Energy Research in Hameln (ISFH) for horizontal ground heat collectors is used. It can be configured to model only one horizontal pipe buried in a specified depth below the surface.

As described by Hirsch (2016) the model can consider the heat exchange between the earth directly surrounding the pipe and the undisturbed earth. Therefore, undisturbed earth temperatures are calculated based on the Kusuda correlation by Kusuda and Archenbach (1965) and depending on the time of the year, the depth below the surface, the ambient temperature and various properties of the earth. This undisturbed earth temperature is not influenced by the heat exchange with the fluid. In contrast the area of the disturbed earth around the pipe is influenced by the heat exchange with the fluid, the heat exchange between the earth’s surface and the ambient air by convection and the influence of solar and thermal radiation on the earth’s surface. Finally, the heat related to the phase change between liquid water and solid water or respectively ice included in the earth is considered.

To validate the simulation results of the TRNSYS model “Type 710” the simulation results of the heat gains and losses at the flow pipe in the new innovative cold district heating network are compared with the results of a simplified analytical calculation of the heat exchange between the fluid and the surrounding earth. Within every timestep of the simulation the heat exchange is calculated by the following equation 1.

$$Q_i = U_{d,\text{outer}} \cdot L \cdot P_{\text{outer}} \cdot \left(\vartheta_{\text{Earth},i} - \vartheta_{\text{Fluid},i}\right) \cdot t_i \qquad \text{(eq. 1)}$$

Q_i	Heat exchange between fluid and earth within the timestep i in J
$U_{d,\text{outer}}$	Heat transfer coefficient in relation to the outer diameter of the pipe in W m^{-2} K^{-1}
L	Pipe length in m
P_{outer}	Outer perimeter of the pipe in m
$\vartheta_{\text{Earth},i}$	Temperature of the surrounding earth in timestep i in °C

$\vartheta_{\text{Fluid},i}$ Temperature of the fluid in timestep i in °C

t_i Time duration of timestep i in s

The calculation of the heat transfer coefficient considers the convective heat transfer between fluid and pipe and the conductive heat transfer within the pipe. The convective heat transfer has been calculated with the Nusselt correlation for a fully developed turbulent flow by Gnielinski (1975) and a mass flow of 42,908 kg h^{-1}. The heat transfer between the pipe and the earth is assumed to be ideal. This results in a heat transfer coefficient of 0.259 W m^{-2} K^{-1} in relation to the outer diameter of the pipe.

Regarding the pipe a length of 420 m, an inner diameter of 141.8 mm and an outer diameter of 298.2 mm are assumed. There are inner pipe walls and outer pipe walls, both made of polyethylene with a thermal conductivity of 0.38 W m^{-1} K^{-1} and a thickness of 9.1 mm. In between the inner and the outer pipe walls an insulation with a thickness of 60 mm and a thermal conductivity of 0.022 W m^{-1} K^{-1} is assumed.

The time duration of one timestep amounts to 12 minutes.

Like in the TRNSYS model "Type 710" the temperature of the surrounding earth is calculated with the Kusuda correlation by Kusuda and Archenbach (1965), which was already described at the beginning of this chapter.

As fluid temperature the mean value of inlet and outlet temperature of the flow pipe is used and assumed to be constant over the whole pipe length.

In Figure 5 the resulting monthly heat gains and losses calculated analytically are shown as black line. The analytical calculation does not consider the effects due to solar and thermal radiation and the heat exchange with the ambient air. In order to compare the results, those effects were also ignored by the simulation model in the first step. The resulting continuous grey line is shown in Figure 5. In comparison the simulation results are close to the results of the analytical calculation. Although, in the first month and the last five months of the year a higher difference between the simulation results and the analytical calculation compared to the other months can be observed. In further investigations it was recognized that those differences mainly occur in the time periods without mass flow through the pipe. It is assumed that especially in those time periods the fluid temperature used for the analytical calculation differs from the fluid temperature used in the model.

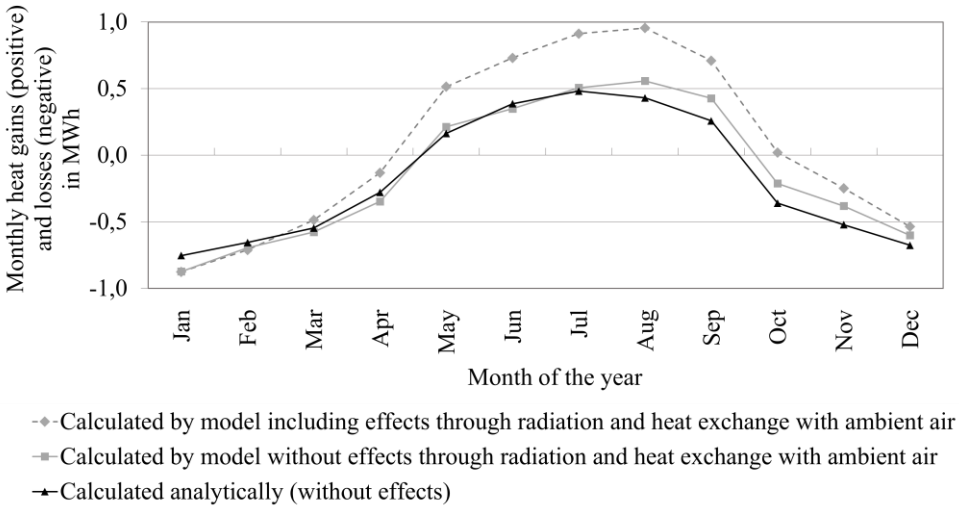

Fig. 5: Validation of the model of the innovative cold district heating network by comparison with analytical calculation results

In a second step the simulation results of the model including the effects by solar and thermal radiation and the heat exchange with the ambient air were calculated and are also shown in Figure 5 as a dashed grey line. In comparison to the simulation results without these effects and the analytical calculation the heat gains are mostly in the summer months higher. This is plausible as these are usually months with higher heat gains through solar radiation and hence higher earth temperatures in the area of the pipe. This also shows the

noticeable dependency of the heat gains and losses from impacts originating from the surface as the pipes of cold district heating networks are usually buried in a low depth of 1 to 2 m below the surface.

Overall, the comparison with the analytical calculation results shows that the simulation results by the model can be considered as valid with a high probability. To further support this assumption, an additional validation of the simulation model with measurement values of a real pilot plant of a cold district heating network is planned. Based on the results of that comparison with measurement values the configuration and if necessary, the programming of the model will be improved with the goal to model the heat gains and losses of a cold district heating network even more accurately.

8. Comparison of the innovative with a conventional cold district heating network

The cold district heating network is an essential part of the entire cold district heating system, as it connects the different components exchanging heat with the consumers to cover the heating or cooling demand. The change of the heat transfer medium from a mixture of water and antifreeze to only water has an effect on the fluid temperatures in the network and therefore on the heat gains and losses of the cold district heating network. The results of some investigations regarding these effects are described in this chapter.

Those investigations are based on system simulations performed with the developed simulation model described in chapter 5. For this purpose, both for the conventional and the innovative cold district heating system an adapted simulation model has been created. Additionally, both simulation models have the same boundary conditions based on a newly built district completed in May 2022. This district is located in the city of Ludwigsburg, about 15 km north of Stuttgart and therefore influenced by continental climate. It consists of nine multi-family houses and a kindergarten with three residential units above. In total, for the 107 residential units with a heated floor space of 8,567 m^2 an annual heating demand of 508 MWh and a cooling demand of 167 MWh is assumed. The supply of domestic hot water is not taken into account, as domestic hot water is provided by electric instantaneous water heaters. For the cold district heating network pipes with a length of 420 m each for flow and return and with the dimensions and material properties described in chapter 7 are used. Just like in the validation in chapter 7 those pipes are equipped with an insulation.

In Figure 6 the average inlet temperatures in the flow pipe and the return pipe of the cold district heating network are shown. In addition, the monthly heat gains of the cold district heating network through heat transfer from the surrounding earth are shown as positive bars and the heat losses as negative bars.

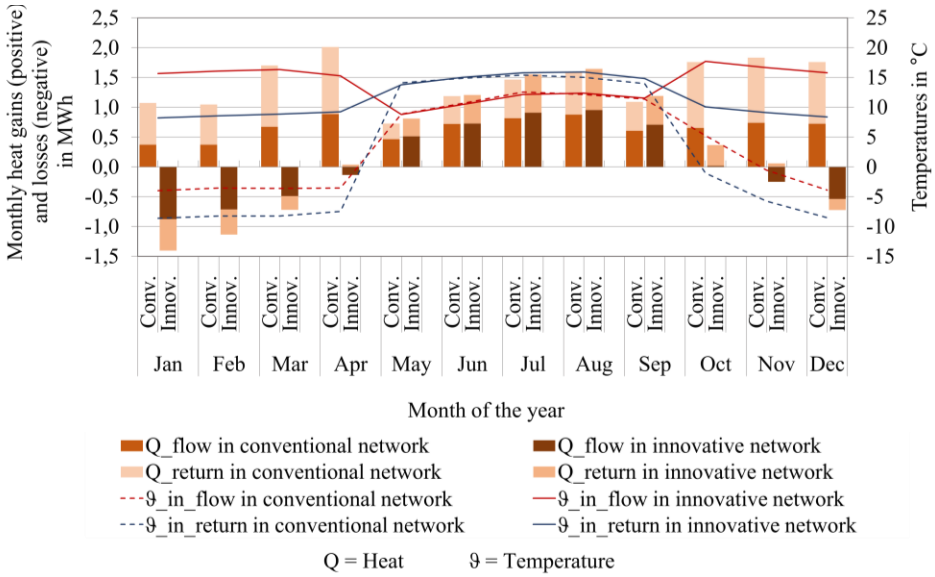

Fig. 6: Comparison between the conventional and innovative cold district heating network regarding temperatures and heat gains or losses respectively in the cold district heating network

Firstly, the average inlet temperatures of the innovative cold district heating network are significantly higher in the months with heat demand, compared to the temperatures of the conventional system. This can be explained by the additional central heat pump that is necessary to increase the temperatures for the usage of water as heat transfer medium. Due to the partly negative outlet temperatures of the solar thermal air-brine-collectors and the ice store the temperatures in the cold district heating network of the conventional system are accordingly below the freezing point during most of the time in the heating season.

Secondly, as a result of the higher temperatures in the innovative cold district heating network compared to the surrounding earth, heat losses occur from November to April. In contrast, there are heat gains in the conventional cold district heating network due to lower temperatures compared to the surrounding earth temperature. In relation to the overall heat supplied to the buildings there are significant heat gains in the conventional cold district heating network, in contrast to the low heat losses in the innovative network in the months with heating demand (as shown in table 1). In the months with cooling demand both the conventional and the innovative network have similar heat gains in relation to the overall heat removed from the buildings.

Tab. 1: Comparison of the heat gains and losses of the conventional and the innovative cold district heating network in relation to heat supplied and removed from the buildings

		Conventional	**Innovative**
Months with heating demand Oktober until April	Heat supplied to the buildings	507.7 MWh	507.7 MWh
	Heat gains or losses	11.2 MWh 2.2 % heat gains	3.9 MWh 0.8 % heat losses
Months with cooling demand May until September	Heat removed from the buildings	163.3 MWh	164.6 MWh
	Heat gains	6.1 MWh 3.7 % heat gains	6.4 MWh 3.9 % heat gains

Generally, heat gains in the months with heating demand can be rated positive as they can reduce the heat supplied by the ice store and therefore preserve its state of charge. Heat gains in the months with cooling demand are negative as they require additional electricity to remove the heat gains from the network.

In relation to the innovative cold district heating network the goal of the ongoing research project “SolKaN2.0” is to minimize the heat losses in the months with heating demand or even reach heat gains in those months. One approach to accomplish this goal is to reduce the fluid temperature in the network as much as possible by means of an optimized control of the central heat pump and the decentral heat pumps in the buildings. As shown in Figure 2 the average inlet temperatures in the flow and return pipes vary between 8 and 18 °C in the months with heating demand. As a minimal temperature of 3 °C is sufficient to avoid freezing of the water this offers a high potential for temperature reductions. Another approach is the use of a thermal insulation with a lower heat transfer coefficient or the insertion of the pipes at a greater depth below the surface. These measures would also decrease the heat gains in the months with cooling demand and therefore increase the efficiency of the system during periods with cooling demand.

9. Conclusion and outlook

In the research project “SolKaN2.0”, which started at the beginning of the year 2024, the development and implementation of a new generation of cold district heating systems with water as heat transfer medium in the cold district heating network is performed. The mainly ecological and economic reasons for changing the heat transfer medium from a mixture of water and antifreeze, which is commonly used in conventional cold district heating systems so far, to water were presented at the beginning of this paper. After that a concept of an energy supply system covering heating and cooling demands with the innovative aspect of water as heat transfer

medium in the cold district heating network was introduced. To realize this innovative system an additional central heat pump between the thermal energy sources and the cold district heating network is necessary.

In addition, as part of this research project, a simulation model for this innovative system was developed and the resulting simulation results were used to perform various investigations. For this paper monthly heat balances and the state of charge of the ice store over the period of one year were calculated and presented. Thereby the essential role of the ice store as a seasonal thermal energy store integrated in the cold district heating system was shown.

Besides the ice store the cold district heating network has been examined theoretically in more detail. Therefore, in a first step the used simulation model for the network was validated with analytical calculation results. In a second step numerical system simulations of a conventional and an innovative cold district heating network were carried out. The results showed higher heat losses in months with heating demand as a result of the higher fluid temperatures in the innovative network compared to a conventional network. As the reduction of those heat losses is one goal of the ongoing research project, ideas to achieve this were presented at the end.

In conclusion, although the heat losses in the cold district heating network can be rated negatively, it is expected that the ecological and economic advantages using water as heat transfer medium outweigh potential higher heat losses. The development and implementation of a new generation of cold district heating systems with water as heat transfer medium and to proof the functionality and advantages of this new innovative system concept is the central goal of the research project “SolKaN2.0”. In this context also a prototype of the central heat pump will be developed and tested together with a small ice store at the IGTE in Stuttgart in a first step. In a second step a pilot plant of the whole new innovative cold district heating system will be implemented in a real district in Germany and assessed technically, economically and with regard to environmental aspects based on detailed measurement data.

10. Acknowledgments

The research project “Second generation cold district heating” (SolKaN2.0) is funded by the German Federal Ministry for Economic Affairs and Climate Action (Bundesministerium für Wirtschaft und Klimaschutz “BMWK”), based on a decision of the German Bundestag by the project management organization PTJ Jülich, under grant number 03EN6033A/B/C. Also, the project ‘Development of integrated solar supply concepts for climate-neutral buildings for the “city of the future” (Sol4City)’ was funded by the German Federal Ministry for Economic Affairs and Climate Action (Bundesministerium für Wirtschaft und Klimaschutz “BMWK”), based on a decision of the German Bundestag by the project management organization PTJ Jülich, under grant number 03ETW019 A/B. The authors gratefully acknowledge this support and carry the full responsibility for the content of this publication.

Selected results of the project “Sol4City” are contributions to Task 66 ”Solar Energy Buildings” of the Solar Heating and Cooling program (SHC) of the International Energy Agency (IEA). Furthermore, the management of Task 66 is supported by the project “Sol4City” and “SolKaN2.0”. The authors also gratefully acknowledge this support.

11. References

Drück, H., 2007. Mathematische Modellierung und experimentelle Prüfung von Warmwasserspeichern für Solaranlagen. Bericht aus der Energietechnik, Shaker Verlag, Aachen.

Gnielinski, V., 1975. Neue Gleichungen für den Wärme- und Stoffübergang in turbulenten durchströmten Rohren und Kanälen. Forschung im Ingenieurwesen 41, 8-16.

Hirsch, H. et al., 2016. Erdwärmekollektoren in Kombination mit Solarkollektoren als Quelle für Wärmepumpensysteme. 26. Symposium Thermische Solarenergie 2016, Bad Staffelstein.

Hornberger, M., 1994. Solar unterstützte Heizung und Kühlung von Gebäuden. Forschungsberichte des Deutschen Kälte- und Klimatechnischen Vereins e.V. Nr. 47, Stuttgart, pp. 32-42.

Kusuda, T., Archenbach, P.R., 1965. Earth Temperature and Thermal Diffusivity at Selected Stations in the United States, ASHRAE Transactions, Vol. 71, Part 1.

Lund, H. et al., 2014. 4th Generation District Heating (4GDH). Energy, Vol. 68.

Lott, S. et al., 2022. Quasi-Dynamic Testing of Air-Brine-Collectors and Numerical Simulations of a Cold District Heating Network. ISES and IEA SHC International Conference on Solar Energy for Buildings and Industry - EuroSun 2022, Kassel.

Predictive Rule-Based Control Strategy for Optimizing the Operation of Solar District Heating Plants

Viktor Unterberger[1], Klaus Lichtenegger[1,2] and Markus Gölles[1,3]

[1] BEST – Bioenergy and Sustainable Technologies, Graz (Austria)

[2] FH JOANNEUM – University of Applied Sciences, Graz (Austria)

[3] Graz University of Technology, Institute of Automation and Control, Graz (Austria)

Abstract

For large-scale solar district heating plants, there is often the choice either to provide solar heat to on-site consumers or to feed it into a district heating grid. Plant operators get a better price if they sell the heat to the on-site consumers instead of to the grid. Current state-of-the-art control strategies typically decide on the basis of temperature thresholds on the mode of operation: if the heat should be stored for selling it later to the consumers or it should be fed into the district heating grid. Such strategies, however, can lead to frequent rapid mode switches throughout the day and sometimes the storage is loaded insufficiently, so that heat has to be bought back from the grid. If, the other way around, the storage tank is loaded to a higher extent than needed, this leads to increased storage losses. To address these problems, this contribution presents a predictive rule-based control strategy that takes information on the predicted future conditions into account. By doing so, it ensures that the storage is only loaded to an extend which can be sold to the on-site consumers, thus reducing storage losses, increasing efficiency and maximizing monetary profit for heat sales.

Keywords: profit optimization, predictive control strategy, rule-based control, solar district heating

1. Introduction

It is known since decades that the basis of our energy system has to be transformed from fossil fuels to renewable energy, and, with increasing impact of climate change, this need has become painfully obvious, (IPCC, 2021). Often, strategies for such a change focus on the electric sector, regarding all demands other demands, including heating, just as contributions to the load profile. But **#heatIsHalf**: Process heat and space heating are responsible for almost 50 % of the world end energy consumption, (REN21, 2023). At the same time, the electric grid is already often overstressed by current demand and fluctuating production, (Ghavi, 2024). Here, thermal solutions that do not rely heavily on electric energy can offer a solution.

Heating grids are particularly useful and versatile for providing renewable heat to households, and large-scale solar plants can be an important source of heat, in particular when combined with large-scale thermal storage (up to seasonal storage). Thus, optimal operation of such systems is an important task, but, as it is often the case with fluctuating renewable energy, a challenging one.

Beyond just the technical aspects, renewable energy systems are embedded in an economic framework as well, and at the moment, they have to compete with other energy sources that create enormous damage (called *negative externals* in economy) and are nevertheless often still subsidized by governments to a larger extent (though often less visible) than renewables, (EEA, 2023). This is a rather unfair competition, with emission trading systems and carbon taxes only slowly and slightly levelling the field. A more reasonable economic system would not require necessary measures for our survival to provide attractive interest rates for investors as well – but, at the moment, we have to live with what we have. Thus, also the economic performance of renewable energy systems has to be optimized as good as possible when designing operation strategies.

© 2024. The Authors. Published by International Solar Energy Society
Selection and/or peer review under responsibility of Scientific Committee
10.18086/eurosun.2024.03.03 Available at http://proceedings.ises.org

2. Description of the System and the Challenge

Large-scale solar district heating (SDH) plants, as sketched in Figure 1, often consist of a large-scale solar thermal field, a storage, on-site consumers and a direct connection to a local district heating grid (DHG).

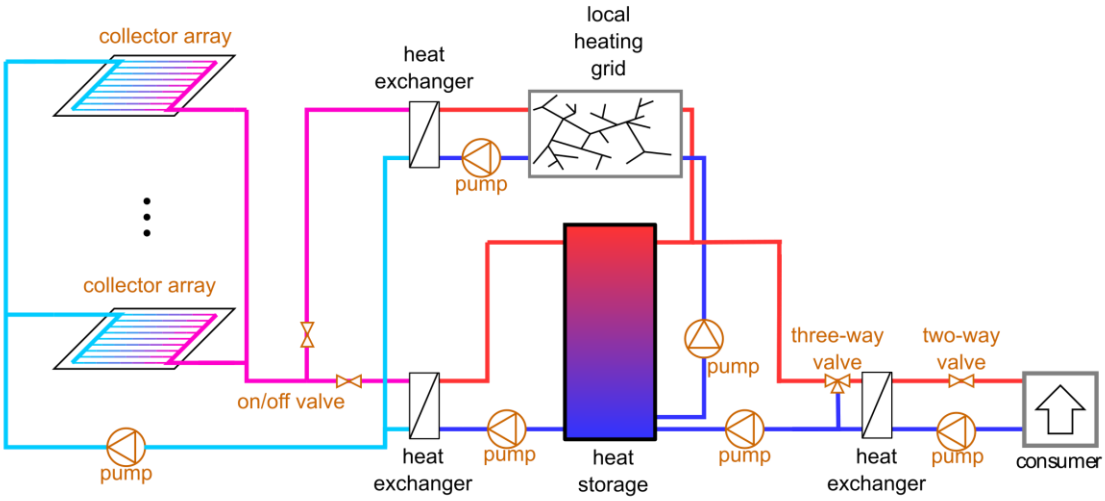

Figure 1: Schematic representation of a typical large-scale solar thermal plant as investigated in this contribution.

Via the connection to the DHG, the SDH plant can generate additional profit by feeding the solar heat into the grid in case the production exceeds the needs of the on-site consumers. Vice-versa, in case there is not enough solar heat available, the grid acts as auxiliary heating and additional heat can be purchased to avoid comfort losses for the on-site consumers. Therefore, simply speaking, this kind of SDH plants can run in two general operation modes:

- **`HSt`**: transfer the solar heat to the local heat storage in order to sell it to the on-site consumers.
- **`DHG:`** transfer the solar heat to the district heating grid to directly generate profit.

In order to decide on the operation mode, state-of-the-art high-level control strategies are based on simple state machines considering the loading state of the storage and the actual ambient temperature. The idea is that in case the ambient temperature falls below a certain threshold, the storage is loaded to a higher extend and vice versa. This strategy takes into account the fact that the heat demand is correlated with the ambient temperature; it also tries to keep the heated volume in the storage as small as reasonably possible.

While such strategies are simple and transparent, they can lead to *multiple mode switches*, which have a negative effect on the system, and to *profit losses* by a suboptimal storage management. For example, profit losses can occur for a sunny day followed by a cool night. Then a lot of solar heat is fed into DHG over the day since the ambient temperature is relatively high and the storage gets only partially loaded. During night, that heat has to be bought back from the DHG at a higher price in order to supply the consumers. Tackling this issue by loading the storage to a higher extend as default would in general lead to higher storage losses, which again reduce the monetary profit.

3. A Predictive Algorithm

A way to deal with issues of multiple mode switches and profit losses is to use a control strategy that also considers the *expected* solar heat output and heat demand of the consumers, (Gölles[+], 2021). Such predictive control strategies can be based on mathematical optimization, with an optimization problem often formulated as a mixed-integer linear program, (Moser[+], 2020). Such optimization-based approaches are both powerful and versatile, and for operation of trans-sectorial energy systems beyond a certain level of complexity, they are usually the best choice. This power, however, comes at a price, both the one-time effort of setting up the optimization problem and the computational resources required to repeatedly solve it. In addition, optimization-based decisions often lack explainability. For rather simple systems like the SDH-DHG interaction, a rule-based predictive approach can provide reasonable performance and transparent decisions, while requiring significantly less effort.

For this special case, we present such an algorithm, based on (Unterberger, 2021). The goal of the algorithm is to decide when to run in `mode = HSt` or `mode = DHG`. The number of mode switches is to be minimized, while the storage is managed in a way such so that

- the on-site demand can be satisfied with solar heat, if possible,
- no excess heat is sold to the DHG and has to be bought back later for a higher price,
- only heat really required is stored, in order to minimized storage losses.

In order to determine the optimal operation schedule, the following steps are executed for a forecast horizon of 24 hours (and periodically repeated to update the strategy in order to incorporate new information):

Step 1 – calculate available heat in the storage: The storage is separated in multiple volume elements (e.g. 100), each with a certain temperature. The temperature of the elements is obtained from a cubic interpolation between the measurements of the temperature sensors in the storage. The available heat in the storage is calculated with respect to a reference temperature for which the heat is still useful for the connected consumers.

Step 2 – calculate the forecasts for the expected solar heat output and heat demand: The expected solar heat output and the heat demand is calculated by using forecasting methods. Advanced methods, e.g. adaptive linear regression or machine learning models based on Bayesian regression or Recurrent Neural Networks, (Murphy, 2022), continuously adapt to latest measurements and take seasonal changes into account. The expected solar heat output is counted positive while the expected heat demand is counted negative.

Step 3 – set default mode to `HSt`: For all future time steps before sunrise and after sunset, the `optimal_MODE` array is set `HSt` for the respective indices. By doing so, a day is started and finished by loading the storage in order to use the heat for the on-site consumers at the earliest or latest time possible, which increases local consumption.

Step 4 – determine optimal time for switching to mode `DHG`: Ideally, during each day, there is only one transition from mode `HSt` to `DHG` and back. A supply-consumers-first policy is enforced by the algorithm, as the heat is only fed into the DHG in the case the demand of the on-site consumers is fully satisfied. The optimal switching time is determined in three sub-steps:

- First, the currently available heat is used to iteratively reduce the expected effective heat demand (i.a. predicted demand minus demand satisfied by the operation strategy) along the forecast horizon, by assuming to fully cover it by heat from the storage. This ensures that the storage is emptied quickly (reducing storages losses) and guarantees that no overloading of the storage occurs, as the storage is typically designed to store the heat of a full day of sunshine. If the current heat in the storage is sufficient to satisfy the heat demand for the next 24 h, all available solar heat can be fed into the DHG. Otherwise, it has to be decided along the forecast horizon at which time the solar heat should be fed into the storage or into the DHG in order to fully satisfy the demand.
- Second, the cumulative sum of the predicted demand, reduced by the heat from the storage, along the forecast horizon is calculated, in order find times where this effective demand is negative and therefore not fully satisfied. The index `idx` of the first element where the cumulative sum is negative determines the time for which part of the solar heat must be fed into the storage beforehand, in order to maximize self-consumption and minimize heat purchases from the grid. In order to find the best possible time to feed solar heat into the storage, it is evaluated if `idx` corresponds to a time between sunrise and sunset: In case the demand occurs after sunrise but before sunset, the first available solar heat after sunrise is used to reduce the effective heat demand. In case the demand occurs after sunset, the latest available solar heat before sunset is used to reduce the effective demand. This is done in order to reduce mode switches by extending the mode for feeding heat into the storage at the beginning or end of a day. The corresponding elements of the schedule are set to `HSt`.
- After this step, the remaining cumulative sum is re-calculated until it no longer shows any negative heat demand and the schedule is set to `DHG` for the remaining time.

Step 5 – apply mode to the system: Finally, the current mode of operation of the plant is set to the first value of the schedule.

The Algorithm is illustrated in Figure 2, and an example of its application is shown in Figure 3 and Figure 4.

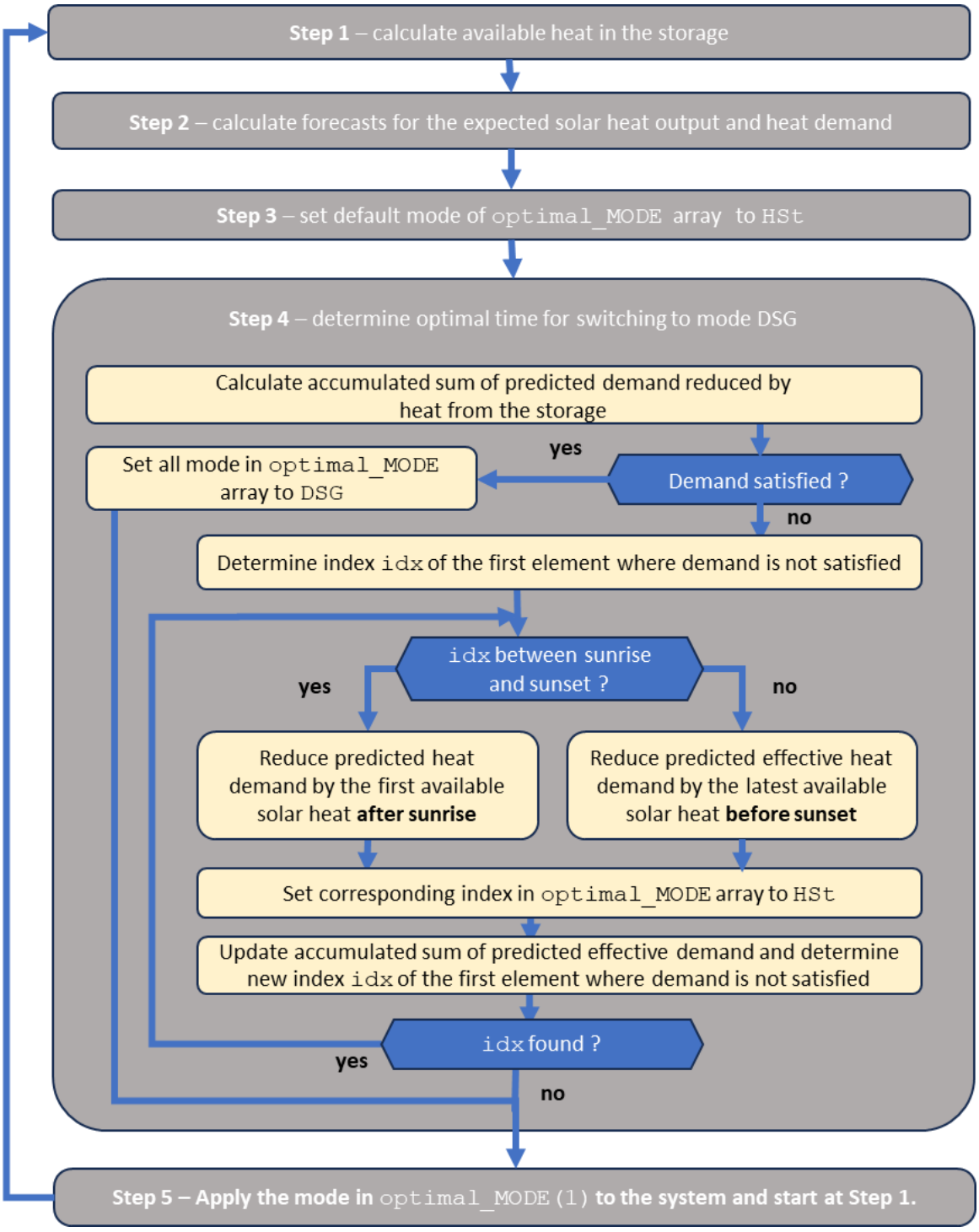

Figure 2: Flow-chart for the proposed algorithm, where the mode values `HSt` or `DHG` are stored in an array `optimal_MODE`

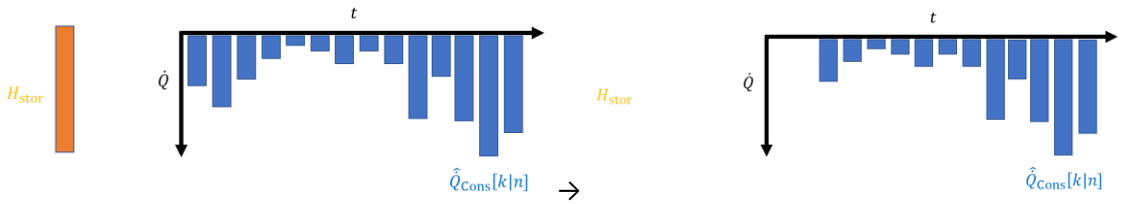

Figure 3: Example for the action of the proposed algorithm, Step 3 (all heat from storage is used to reduce the effective consumption as early as possible, in order to reduce storage losses)

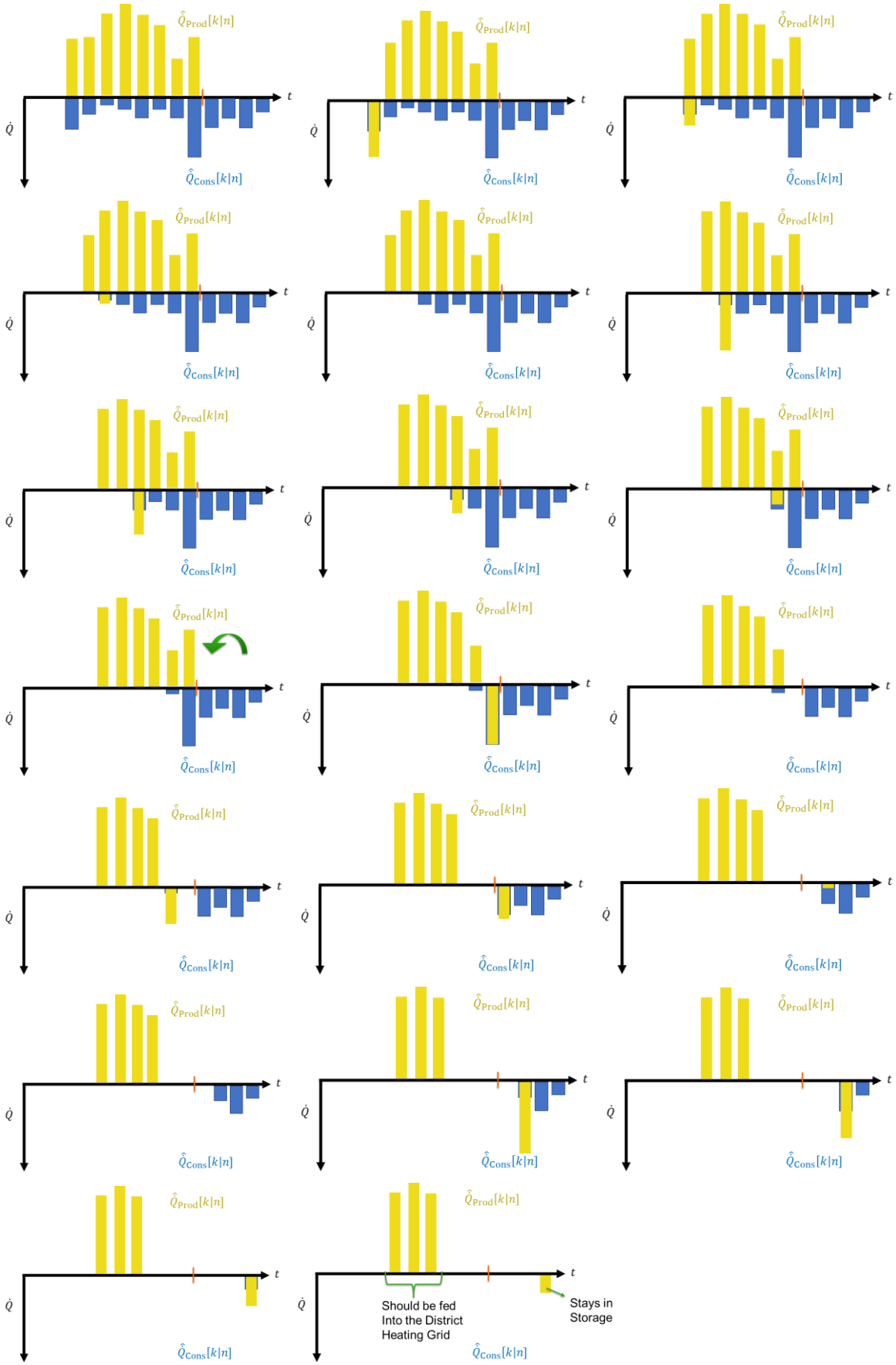

Figure 4: Example for the action of the proposed algorithm, Step 4 (predicted production $\hat{Q}_{\mathrm{Prod}}$ is matched against predictive consumption, in order to reduce the effective consumption $\hat{Q}_{\mathrm{Cons}}$)

4. Methodology for Validation of the Algorithm in a Simulation Study

A state-of-the-art control strategy, as described in Sec. 2, has been compared to one described in Sec. 3 in simulation studies for a representative week during transition time (the period between summer and winter), which is typically most sensitive to the quality of the control strategy, in particular the storage management. The study, described in more detail in (Unterberger, 2021), is based on data for a solar plant located in the south of Austria. The ambient conditions for the investigated week, regarding solar radiation on the collector surface $I_g´$ and the ambient temperature T_{amb} are shown in Figure 5.

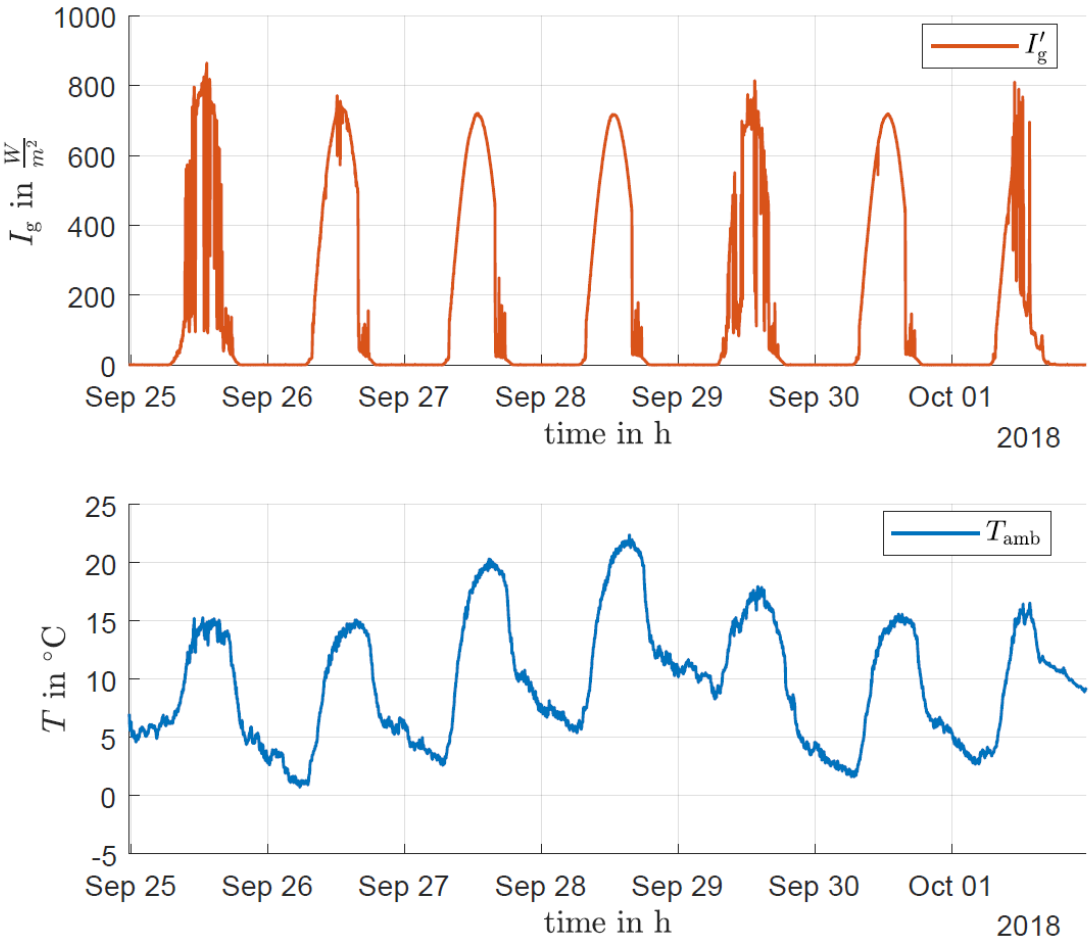

Figure 5: Ambient conditions, solar radiation $I_g´$ on the collector surface and ambient temperature T_{amb}, for a representative week in the transition period measured on site and used as input for the simulation studies.

The overall simulation model describing the plant has been implemented in MATLAB®/Simulink for a simulation step size of 1 min. For the different components like collector field, heat exchanger and storage, simulation-oriented models based on partial differential equations were used. The models for the different components had been verified with measurement data from the real plant. For the components of the hydraulic heat distribution system such as pumps and valves only static models had been used since their dynamic characteristics play a minor role for a step size of 1 min. These models had been parametrized by information from the data sheet as well as by measurement data from the plant.

For the low-level controllers, PI-Controllers have been used which have been extended by a static feedforward control in case of the collector field as it is state-of-the-art in such systems. Furthermore, switching between modes was assumed to take 1 minute until heat can be supplied again, which is based on the experience with the plant.

For the forecast of the future solar heat $\hat{\dot{Q}}_{\text{Sol}}$ and the predicted heat demand $\hat{\dot{Q}}_{\text{Con}}$, the adaptive forecasting methods from (Nigitz, 2019) and (Unterberger+, 2021) have been used with a forecast horizon of 1 day and with a sampling time of 15 min, considering the last past weeks of measurement for the parameterization.

For the state-of-the-art high-level controller that only considers the current state of the system, the parameters haven been taken from the real plant controller, which had been optimized by the plant operator for years leading to thresholds of $T_{\mathrm{HSt,warm}}$ = 15 °C and $T_{\mathrm{HSt,load,OFF}}$ = 72 °C. For the predictive high-level controller, additionally considering future information, the only parameter, the reference temperature for the evaluation of the heat in the storage (lowest usable temperature), was set to T_{ref} = 55 °C.

5. Results of Validation

The results for the state-of-the-art controller, only considering the current state of the system, are shown in Figure 6 and for the predictive high-level controller additionally considering future information in Figure 7. In each of the figures, the upper graph shows the different energy flows with $\dot{Q}_{\mathrm{Con}}$ as the heat demand of the on-site consumers, $\dot{Q}_{\mathrm{Sol,HSt}}$ as the solar heat fed into the heat storage, $\dot{Q}_{\mathrm{Sol,DHG}}$ as the solar heat fed into the DHG and $\dot{Q}_{\mathrm{Aux}}$ as the heat provided to the storage by DHG, which acts as an auxiliary heating system.

Additionally, in Figure 7 the predicted heat demand $\hat{\dot{Q}}_{\mathrm{Con}}$ and the predicted solar heat $\hat{\dot{Q}}_{\mathrm{Sol}}$ are shown as black dotted lines. The middle graph of each figure shows the mode, with `mode` = 1 in case heat is fed into the heat storage, while for `mode` = 2 the heat is fed into the DHG. The lower graph shows the temperature of the topmost temperature sensor $T_{\mathrm{HSt,upper}}$ inside the heat storage, together with the critical value $T_{\mathrm{HSt,crit}}$ indicating the threshold for loading the storage via the auxiliary heating. This means in the case that the most upper temperature sensor $T_{\mathrm{HSt,upper}}$ in the storage drops below $T_{\mathrm{HSt,crit}}$, the storage is heated up until $T_{\mathrm{HSt,upper}}$ is above $T_{\mathrm{HSt,crit}}$ plus a safety margin ΔT.

The state-of-the-art control strategy, based only on the current state of the system, has to heat up the storage by heat from the DHG three times during this week, at the beginning of September 30$^{\mathrm{th}}$. This happens even though the day before, September 29$^{\mathrm{th}}$, there would have been sufficient solar radiation available to heat up the storage to a higher extent. This is an undesirable behavior, since heat must be bought back at a higher price, which reduces the profit of the plant operator. In the middle graph of Figure 6, it can be seen that switching between modes happens rather often, in total 54 times.

In the first graph of Figure 7, it can be seen that no auxiliary heating is necessary. Furthermore, in the second graph, it can be seen that the modes switches are drastically reduced, in total only 14 times, even if the forecast especially for the solar heat output deviates for some days as can be seen in the first graph. In the third graph, it can be seen that the most upper temperature sensor never drops below the threshold, but also that the heat storage is better managed since the storage is always emptied close to the critical threshold in times before solar heat is expected. An economic analysis, using feed-in tariffs and heat consumption prices for the plant investigated in (Unterberger, 2021), yields a 3 % increase regarding the overall profit.

6. Conclusions and Outlook

The proposed algorithm has several important features, which may help to tap the full potential of SDH plants:

(1) *Performance*: The algorithm takes into account predictions and thus can outperform state-of-the-art approaches that are solely based on the current state of the system:

- *Reduction of storage losses:* By starting and ending a day with loading the storage as well as loading the storage only to the extend which is used by the consumers storage losses are minimized.
- *Reduction of mode switching:* The algorithm determines the optimal window when to feed into the grid and avoids repeated changes of the mode of operation.
- *Priority for supply of on-site consumer:* Heat is only fed into the DHG if the local demand of the consumers can be satisfied (according to the predictions)

(2) *Transparency and simplicity:* The algorithm is rule-based and thus transparent. It can be implemented even on rather simple controllers, which is in contrast to optimization-based control, which requires more computational resources and offers a lower level of explainability.

(3) *Automatic Adjustment:* When using adaptive forecasting methods, the algorithm automatically adapts to seasonal changes or changing consumer behavior, reducing parameterization efforts to a minimum.

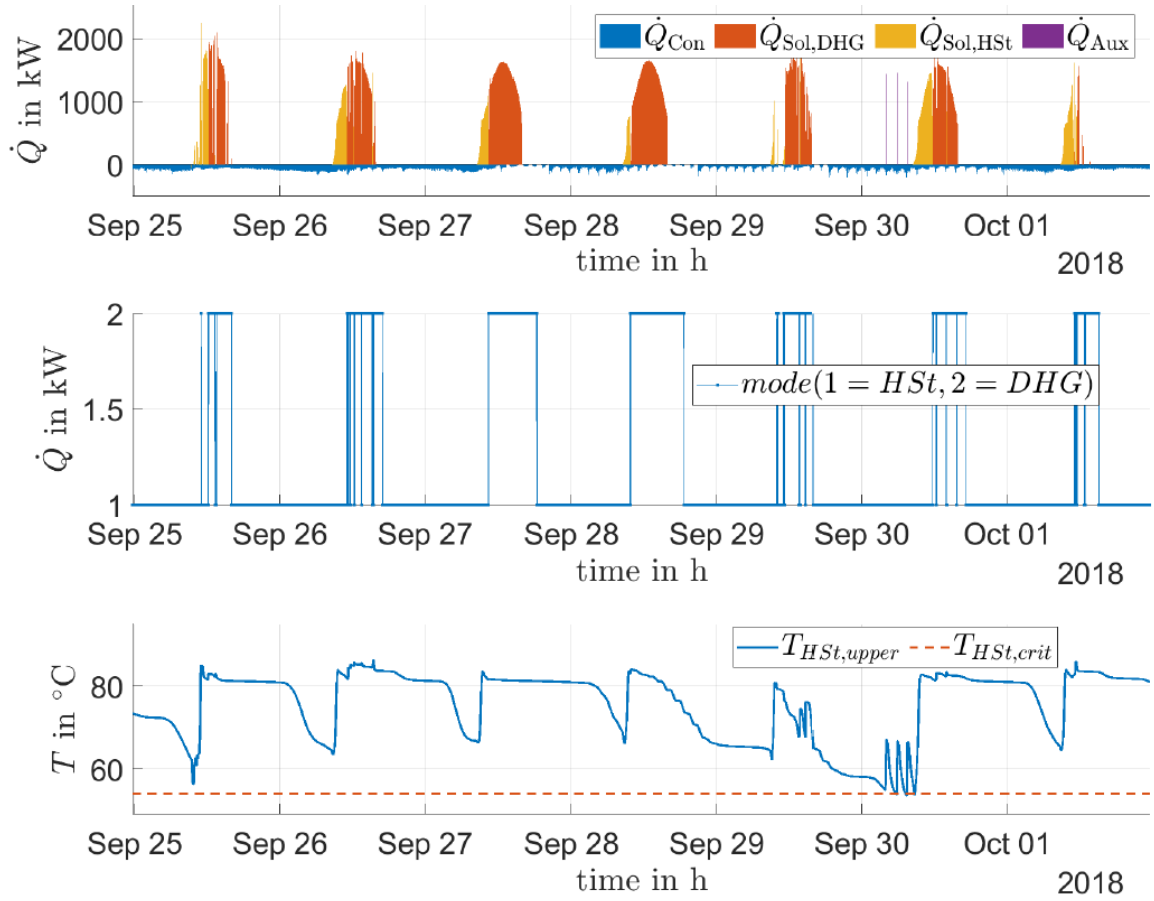

Figure 6: Simulation results for state-of-the-art control strategy

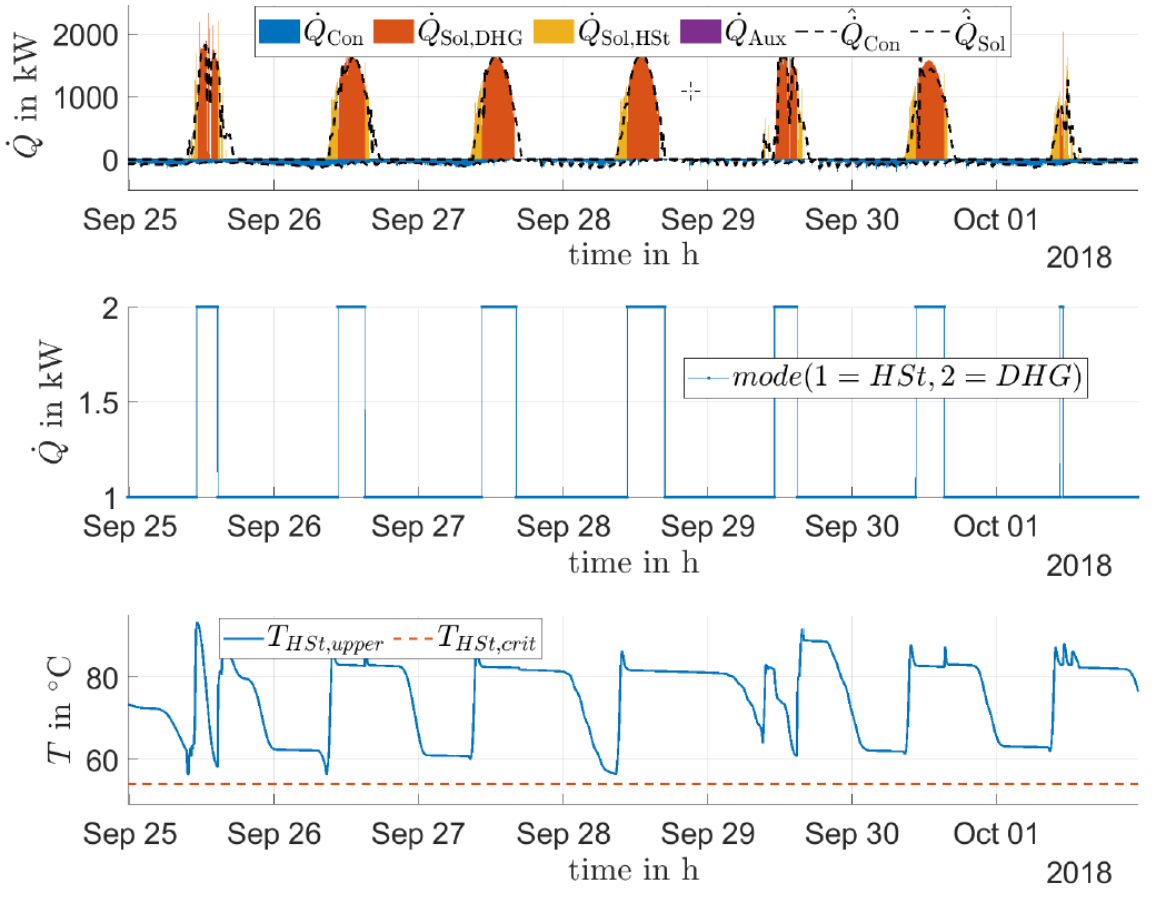

Figure 7: Simulation results for the proposed predictive rule-based control strategy

In simulation studies, the developed predictive rule-based control strategy leads to only one third of the number of mode switches and about +3 % regarding the overall profit.

As next steps, more extensive simulation studies (for several weeks, preferably even a whole year) with a more detailed analysis of contributions to the results, a consistent inclusion of storage losses, comparison also to optimization-based control and the test at a real SDH system are planned.

7. Acknowledgments

The research yielding these results received funding from the COMET program under Grant No. 869341, from the Horizon 2020 program under Grant No. 792276 (Ship2FAIR) and from the Austrian representation within IEA under Grant No. FO999890460 (IEA SHC Task 68) and Grant No. FO999890464 (IEA DHC Annex TS5).

The COMET program is managed by the Austrian Research Promotion Agency (FFG) and co-financed by the Republic of Austria and the Federal Provinces of Vienna, Lower Austria and Styria. Horizon 2020 was the research and innovation funding programme of the European Union (EU), 2014-2020. The Austrian representation within IEA is managed by the Austrian Research Promotion Agency (FFG) and financed by the Republic of Austria, represented by the Federal Ministry for Climate Action, Environment, Energy, Mobility, Innovation and Technology (BMK).

8. References

European Environment Agency (EEA). Nov 17th, 2023, *Fossil fuel subsidies*, available on https://www.eea.europa.eu/en/analysis/indicators/fossil-fuel-subsidies *(last access: July 31st, 2024)*

Ghavi, M. 2024. *Europe faces a €600bn power grids challenge by 2030 – here's how we can meet it*, available on https://www.rechargenews.com/energy-transition/europe-faces-a-600bn-power-grids-challenge-by-2030-heres-how-we-can-meet-it/2-1-1640726 *(last access: July 31st, 2024)*

IPCC, 2021. *Climate Change 2021: The Physical Science Basis. Contribution of Working Group I to the Sixth Assessment Report of the Intergovernmental Panel on Climate Change* [Masson-Delmotte, V., P. Zhai, A. Pirani et al. (eds.)]. Cambridge University Press, Cambridge, United Kingdom and New York, NY, USA, 2391 pp., doi:10.1017/9781009157896.

Moser, A., Muschick, D., Gölles M. et al., 2020. *A MILP-based modular energy management system for urban multi-energy systems: Performance and sensitivity analysis*, Applied Energy 261, 114342, p. 1-13, https://doi.org/10.1016/j.apenergy.2019.114342.

Murphy, K. P., 2022. *Probabilistic Machine Learning: An introduction*, MIT Press, https://probml.ai

Nigitz, T. & Gölles, M., 2019. *A generally applicable, simple and adaptive forecasting method for the short-term heat load of consumers*, Applied Energy. 241, p. 73-81, https://doi.org/10.1016/j.apenergy.2019.03.012

REN21, 2023. *Renewables 2023 Global Status Report collection, Renewables in Energy Supply*, available on https://www.ren21.net/gsr-2023/modules/energy_supply/01_energy_supply *(last access: July 31st, 2024)*

Unterberger, V., 2021. *Modelling and control of large-scale solar thermal systems*. PhD thesis, Graz University of Technology

Unterberger, V., Lichtenegger, K., Kaisermayer, V., Gölles, M., Horn., M., 2021. *An adaptive short-term forecasting method for the energy yield of flat-plate solar collector systems*. Applied Energy, 293, 116891, p. 1-13, https://doi.org/10.1016/j.apenergy.2021.116891

Gölles, M., Unterberger, V., Kaisermayer, V., Nigitz, T., Muschick, D., 2021. *Supervisory control of large-scale solar thermal systems*, IEA SHC Fact Sheet 55.A-D4, https://task55.iea-shc.org/fact-sheets

Comparison of Solar Systems with Seasonal Storage for Renewable Heat Production for District Heating

Tomas Matuska and Borivoj Sourek

Czech Technical University in Prague, Prague (Czech Republic)

Abstract

The use of solar energy for renewable heat production for supply to a low-temperature district heating system is compared for two solar system concepts: solar thermal system with photothermal collectors and system combining photovoltaic modules and air source heat pumps. Both systems are operated with identical seasonal heat storage within the borehole field. Renewable heat production and efficiency of seasonal heat storage are compared. The analysis shows that for the same area of collectors a system based on heat pumps powered only by electricity from photovoltaics has about 10 to 20 % higher production and supply of heat than solar thermal system depending on sizing.

Keywords: solar thermal collector, photovoltaic module, heat pump, seasonal heat storage

1. Introduction

Heat accounts for approximately half of the world's total energy consumption. Of this, approximately 46 % is consumed in buildings for space heating and hot water preparation (IEA, 2019). Decarbonisation of the heating sector is expected to play a key role in the transformation to future 100% renewable energy systems. In Europe, the transformation of district heating (DH) systems can significantly enable the application of renewable and waste-heat utilization technologies such as solar thermal systems, heat pumps, geothermal heat, excess heat from processes in industry and commercial buildings (e.g. supermarkets).

The temperature in modern or retrofitted DH systems usually ranges from 30 to 60 °C thanks to low temperature space heating systems in newbuilt buildings, however in the case of existing buildings this means a necessary reduction in energy demand through insulation, replacement of windows and energy-saving ventilation systems with heat recovery. Furthermore, 5th generation DH systems can also be encountered, where the concept of the DH system prefers the distribution of low-potential heat with a temperature level between 15 and 30 °C throughout the district to individual buildings, where decentralized “heat transformers” are installed, usually heat pumps, which on the one hand can take heat from the distribution system (cooling) or transfer it to the distribution system (heating) depending on the type of building or the time of year. The centralized supply of heat and cold is connected into one complex system of thermal energy shared within the cluster of buildings. In addition to the easy integration of renewable sources and waste heat, the advantages of such low temperatures are mainly the elimination of heat losses, a reduction in the level of thermal insulation of the distribution system, the possibility of using cheaper plastic pipes or significant use of seasonal storage of renewable heat (Lund et al. 2021).

2. SYNERGYS project

A unique infrastructure focused on research and testing of renewable energy sources is being realized within the SYNERGYS project (under Just Transition Fund) in city of Litoměřice in Czech Republic, including pilot systems for the production, storage and supply of renewable heat for district heating purpose. The SYNERGYS project combines the topic of using a deep geothermal source of energy and above-ground technologies using seasonal heat storage in the underground. The research infrastructure will be created to show possible ways of transforming Czech cities towards a carbon-free future in the field of building energy supply.

© 2024. The Authors. Published by International Solar Energy Society
Selection and/or peer review under responsibility of Scientific Committee
10.18086/eurosun.2024.03.04 Available at http://proceedings.ises.org

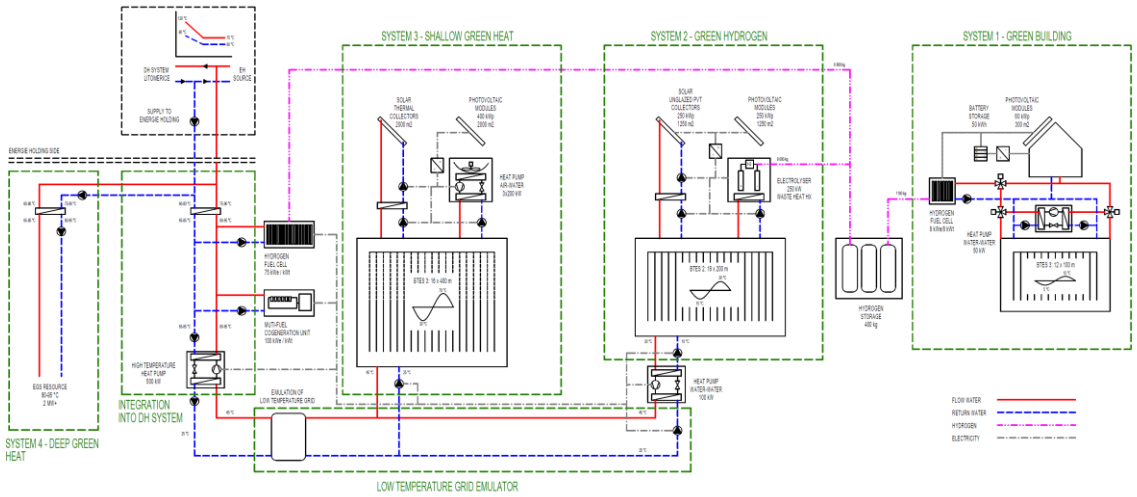

Fig. 1: Scheme of SYNERGYS project with 4 sub-systems

As a part of the technical study carried out in the planning phase using computer modeling a complex energy system consisting of four sub-systems has been designed (see Fig. 1). The core of the entire system is a deep geothermal heat source with a depth of 3.5 km and heat output in order of MW for the permanent heat supply at temperature level of 90 to 100 °C to the local district heating system. The other three systems use seasonal storage based on ground boreholes fields with different operating temperatures and depths (100, 200 and 400 m). For the annual production of up to 8 tons of green hydrogen an electrolyser with power input of 250 kW will be connected to photovoltaic-thermal (PVT) solar collectors with a peak electric output of 500 kW_p (system 2). Waste heat from hydrogen production and heat from cooling of photovoltaic cells will be stored within the borehole field in the summer and will be supplied to the DH system with use of a heat pump in winter. The building of the existing RINGEN research center will be heated and cooled by a ground source heat pump combined with a photovoltaic system and battery storage. Fuel cell will use part of the local hydrogen production from seasonal hydrogen storage (about 1 ton) to supply electricity and heat in winter for the building. The goal of the solution is to achieve a carbon neutral building operated in real time only with the help of local renewable energy (system 1). System 3 consists of large-scale solar thermal system with a collector area of 2000 m^2 with seasonal borehole storage, supplemented by air source heat pump (600 kW at A7/W35) powered only by PV system with an area of 2000 m^2. The systems 2 and 3 are interconnected by a low-temperature network 45/25 °C using heat from seasonal storage, and a high-temperature heat pump will transform the heat to the temperature level of the DH system in Litoměřice.

3. Solar systems

The presented analysis focuses on system 3 (green heat) designed as part of the SYNERGYS project to compare two renewable heat supply systems that will be connected to a common seasonal heat storage in the form of borehole field. The system SOLAR is solar thermal system, the system PV-HP is a combination of a PV and air source heat pumps for production of usable heat from the heat of ambient air using only renewable electricity from PV. The analysis thus compares a system with direct conversion of solar radiation into the heat, where the efficiency of solar collectors depends on the operating temperature and climatic conditions, and on the other hand, a system with direct conversion of solar radiation into electricity, which drives the air source heat pump, whose efficiency is also dependent on operating temperature and climatic conditions. Since both sources show a significant production of renewable heat in the period from spring to autumn, they are connected to seasonal storage with different layouts investigated.

The aim of the simulation analysis performed in TRNSYS was to compare the overall efficiency of heat production and supply from both systems, including the effect of seasonal storage, with the same installed area of solar collectors / photovoltaic modules, under the same climatic conditions and conditions of heat supply to a low-temperature DH system with a permanent load power of 500 kW (from October 1 to April 30) at the temperature level of 45/25 °C. The heat supply system is considered for preheating of the return water, with the fact that the required temperature of the supply water to the DH is not exceeded.

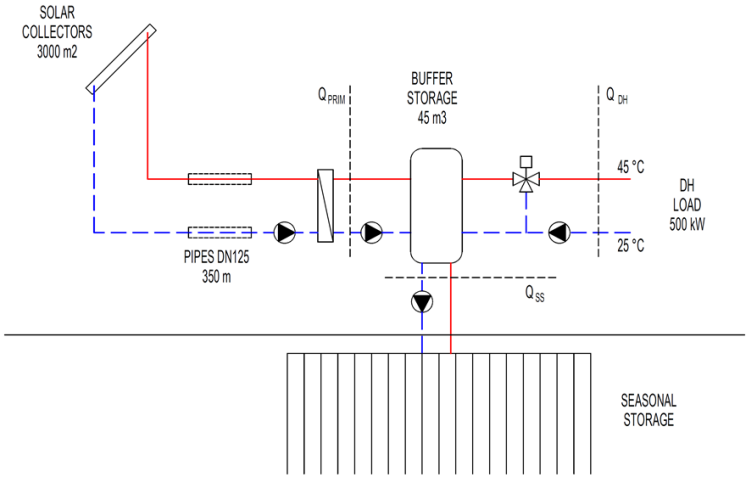

Fig. 2: Scheme of variant SOLAR

The basic SOLAR variant considers the solar thermal system with standard flat-plate solar collectors (η_0 = 0.75, a_1 = 3.8 W/m^{2}K, a_2 = 0.014 W/m^{2}K^2) with a total area of 3000 m^2, installed with slope of 45° and orientation to the south. The collector field is connected by DN125 pipe (length of distribution 350 m) to a buffer storage tank with a water volume of 45 m^3. A simplified scheme is shown in Fig. 2.

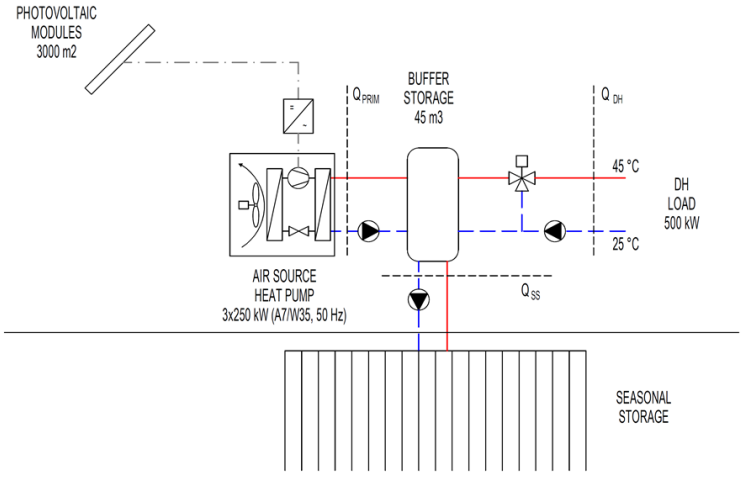

Fig. 3: Scheme of variant PV-HP

The basic PV-HP variant represents a combination of photovoltaic system and air source heat pump and is considered as an equivalent to the solar thermal system (see Fig. 3). The area of the photovoltaic modules is assumed to be the same 3000 m^2 with the same slope and orientation. With a reference efficiency of PV modules of 20 %, this practically means 600 kW$_p$ peak output of the PV field. The real operational efficiency of the entire system is at the level of 16 % (effect of module temperature, inverter efficiency, electric losses, etc.). The heat pump is considered as a cascade of three units at 250 kW (at A7/W35, 50 Hz), each with continuous power control of compressor from 30 to 120 Hz. The heat pump units are connected to a buffer storage tank with a water volume of 45 m^3. Based on the produced power of the PV system and the temperature in the buffer tank, the system controller determines how many heat pump units and with what compressor frequency they should be operated so that their electric power input is equal to the actual electric power of the PV system. This is to achieve that the heat pump does not consume any electricity from the grid and uses only renewable electricity. The simplified model for the controller uses an equation created from the detailed characteristics of given heat pump for different frequencies, temperature to the evaporator and temperature to the condenser. Fig. 4 shows an example of controlling the heat pump's electrical input according to the electrical output of the PV system in simulation. It is evident that the control is not perfect due to the inaccuracy of the simple model for controller. However, the inaccuracy of the control, expressed by the share of electricity

that the heat pump had to take from the grid during the whole year, is under 2%.

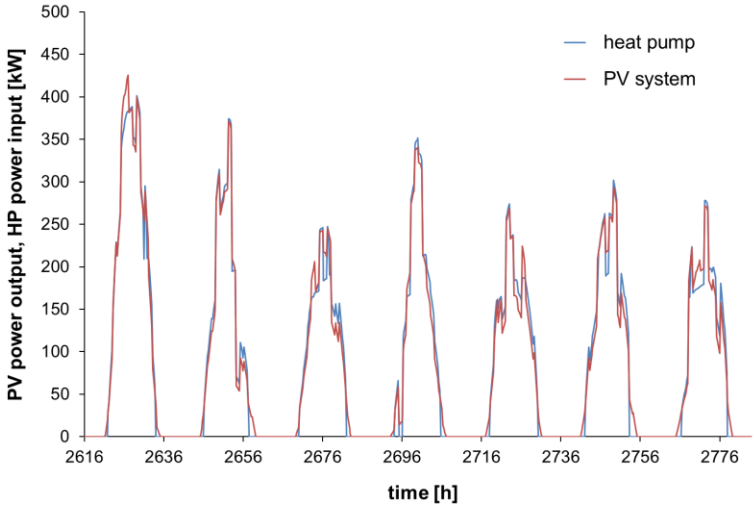

Fig. 4: Adaptation of power input of heat pumps to power output of PV system

For both systems, the same variants of seasonal storage were considered using a borehole field with a concentric tube and bentonite filling: a) 32 shallow boreholes with a depth of 200 m; b) 16 deep boreholes with a depth of 400 m, but with the upper 200 m filled with a heat-insulating mixture to prevent heat loss and eliminate the thermal influence of the upper layers of the subsoil with possible groundwater flow. The total active length of the ground boreholes is thus considered the same with generally comparable costs of the seasonal storage. In all cases, boreholes are considered with a spacing of 5 m. The rock profile up to a depth of 500 m was defined on the basis of a geological survey of the given SYNERGYS infrastructure site. An underground thermal energy storage with longer boreholes can count on a higher temperature of the massif, but its total storage volume is finally smaller than in the case of an underground storage with higher number of shorter boreholes. Thus, shallow borehole field has a larger active storage volume than in the case of deep boreholes, where the upper half of the boreholes is insulated for the heat transfer. It is clear from the scheme of both systems that the seasonal storage is used to store actual excess heat from the buffer tank. The renewable heat source supplies heat primarily to the buffer tank, and when the defined temperature 45 °C is exceeded, the seasonal storage charging pump is started.

4. Comparison

Due to the same area of solar collectors and photovoltaic modules and the same considered configurations of seasonal storage, it is possible to make a direct comparison of the total renewable heat delivered to the buffer storage from primary production side (Q_{PRIM}) and the usable heat transferred further to the low-temperature DH system (Q_{DH}) during the year. At the same time, the balance of the seasonal storage (Q_{SS}) is shown in all variants (input: in, output: out). The results of the comparison are presented in Tab. 1 for all variants with basic sizing (area of solar systems 3000 m^2).

Tab. 1: Annual energy balance of variants with solar collectors area 3000 m^2

Variant	Q_{PRIM} [MWh]	$Q_{SS,in}$ [MWh]	$Q_{SS,out}$ [MWh]	Q_{DH} [MWh]
SOLAR 400 m	1571	1259	722	1034
SOLAR 200 m	1580	1301	715	994
PV-HP 400 m	1869	1450	816	1235
PV-HP 200 m	1912	1526	831	1217

Comparison of solar energy systems (SOLAR, PV-HP) producing renewable heat shows that PV-HP

combination brings approximately 20 % higher heat gains both on the primary side of the system and in usable heat for low-temperature DH supply, despite the fact that the solar thermal system has relatively high specific heat gains of over 500 kWh/m^2.a. The heat pumps in PV-HP variant work with annual COP of 3.53 (400 m) and 3.61 (200 m), the photovoltaic system produces around 177 kWh/m^2 of module area (gross area) per year.

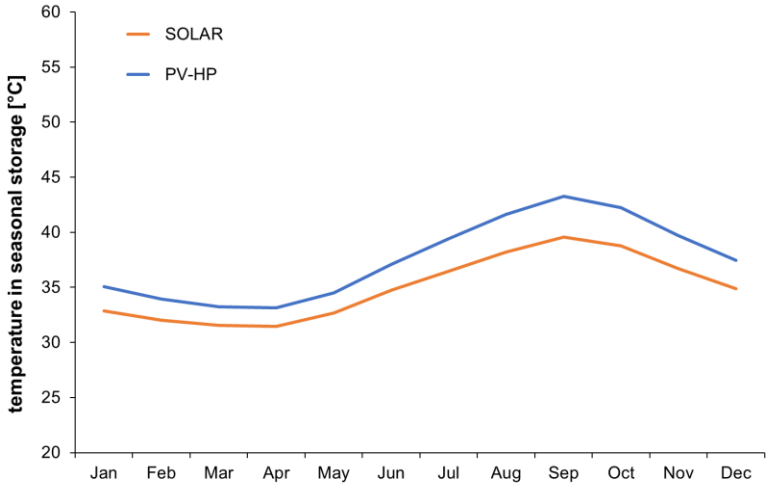

Fig. 5: Monthly average temperature of seasonal heat storage volume (borehole field)

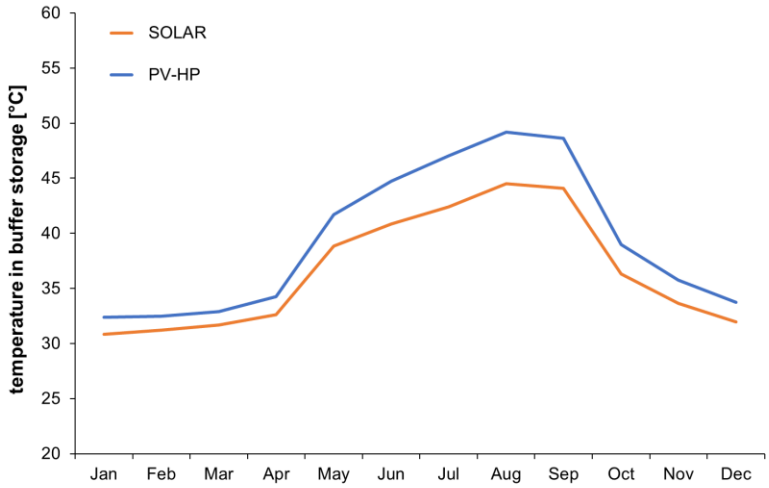

Fig. 6: Monthly average temperature of buffer water storage

Tab. 2: Comparison of performance indicators for variants

Collector area [m2]	SOLAR		PV-HP	
	Coverage [%]	Specific gains [kWh/m^2.a]	Coverage [%]	COP [-]
1500	15	564	23	4,1
3000	39	527	48	3,6
4500	61	498	65	3,3

Results also showed that the layouts of the seasonal storage do not differ much from each other. The efficiency of the heat storage as a ratio between the output and the input of the seasonal storage varies between 54 % and 57 %, as the seasonal storage in general is burdened by a significant share of heat losses. It follows that it is not economically advantageous to perform deep ground boreholes (400 m) with thermal insulation compared to conventional ground boreholes up to 200 m due to the need to use more expensive drilling technology. For

additional information, the graphs in Fig. 5 and Fig. 6 shows the temperature evolvement in the seasonal storage and in the buffer storage for both system variants with 200 m boreholes. The displayed temperature in the seasonal storage is the average temperature of the entire ground mass within the borehole field. The temperature is higher in the center and around the boreholes, and the temperature is lower then the average towards the edge of the borehole field. It is evident from the comparison of the temperature trends that the heat pumps, by giving more energy, also get the seasonal storage at a higher temperature. The highest temperatures are reached at the end of September, the lowest in March.

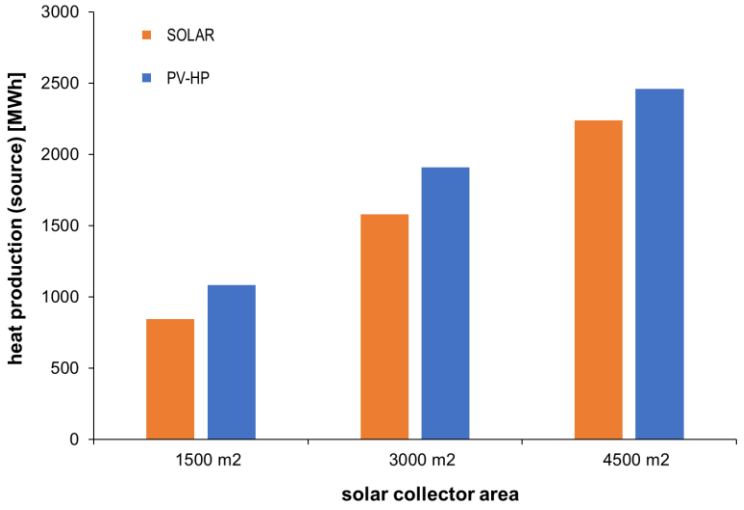

Fig. 7: Influence of sizing on heat source production

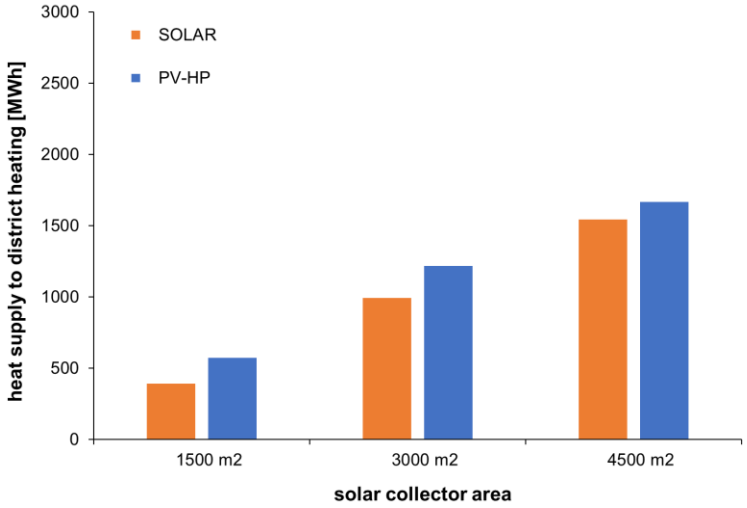

Fig. 6: Influence of sizing on heat supplied to district heating system

In addition to the basic variants of systems, sizing with 50 % larger (4500 m^2) and 50 % smaller (1500 m^2) area of solar thermal collectors and photovoltaic modules were also analyzed. As the area increased, the volume of the buffer storage tank was changed proportionally, in the case of the SOLAR variant, also the dimensions of the pipes, and in the case of the PV-HP variant, the nominal heat output of the heat pump units has been adapted. Seasonal storage with 32 ground boreholes with a depth of 200 m has been considered for all variants of sizing. The comparison of the total annual production of the heat source and the heat supply to DH system is shown graphically for the variants in Fig. 7 and Fig. 8. The resulting performance indicators of the technologies (coverage of heat consumption, specific heat gains, *COP* of the heat pump) are summarized in Tab. 2.

The results show that as the heat output of the heat source increases due sizing in both variants, the difference in performance between SOLAR and PV-HP variants decreases. In the case of variants with an area of 4500 m^2, the heat production of the PV-HP system is only 10 % higher compared to the SOLAR system, and the heat supply to the DH system is only 8 % higher.

5. Conclusion

Renewable heat sources connected to low-temperature heat supply systems will increasingly appear in district heating systems in future. Within the upcoming SYNERGYS project renewable heat production will be investigated theoretically and experimentally, using seasonal storage in the boreholes field. Presented analysis showed possible advantages of the combination of photovoltaic systems and heat pumps for (especially) summer heat production with significant efficiency. Compared to solar thermal systems, the combination of efficient PV modules with air source heat pumps shows a roughly 10 to 20 % higher heat supply with the same area of solar collectors. A certain uncertainty in the results arises from the fact that the effect of possible freezing (and therefore necessary defrosting) of the evaporator at outside air temperatures between 5 and 10 °C, typically during the transition period has not been taken into account within the simulations. Also the limitations of compressor envelope with frequency control were not included. This will be subject of further analyses.

The efficiency of seasonal heat storage was around 55 %, which is a relatively low value. The results and practical experience from other projects show that the efficiency increases with increasing collector area, with increasing storage size (compactness, lower proportion of heat loss compared to stored heat) and, naturally, with a lower temperature of intake to the distribution of centralized heat supply (low-temperature district heating systems). At the same time, it has been proven so far that the use of deeper boreholes and storage at greater depths (400 m) does not bring an advantage in the efficiency of heat storage compared to more affordable shallower boreholes up to 200 m. The results of the analysis will be used for the final design of both systems in the JTF SYNERGYS project, in which the effectiveness of the production and supply of renewable heat for the district heating will be verified in the real operation of the technologies.

6. Acknowledgments

Publication was created within the project „SYNERGYS - systems for energy synergies“ No. CZ.10.02.01/00/22_002/0000172, co-funded by the EU Operational programme Just Transition..

7. References

IEA, 2019. Renewables 2019: Analysis and forecast to 2024.

Lund, H., Østergaard, P.A., Nielsen, T.B. et al., 2021. Perspectives on fourth and fifth generation district heating. Energy 227 (2021), 120520.

TRNSYS 17, 2010. A Transient System Simulation Program. Solar Energy Laboratory, University of Wisconsin, Madison, USA.

INTEGRATING CONCENTRATED SOLAR THERMAL IN DISTRICT HEATING - A SIMULATION STUDY IN TRNSYS

Silas Tamm[1], Magdalena Berberich[1]

[1] Solites/ Steinbeis Research Institute for Solar and Sustainable Thermal Energy Systems, Stuttgart (Germany)

Abstract

Since concentrated solar collectors can deliver higher flow temperatures with higher efficiency compared to standard collectors such as high performance flat plate (HPFPC) and evacuated tube collectors, they are of interest for heating networks with supply temperatures above 100 °C. In addition, they can usually track the sun, which can increase the solar yield over the course of a day.

In this paper, different collector technologies and their properties are described. In addition, concentrated and non concentrated collectors are compared with each other on the basis of their Solar Keymark characteristics and in a simulation study for implementing in district heating systems.

The comparison and simulation of high performance flat plate collectors and parabolic trough collectors for heating networks shows that at higher network temperatures, parabolic trough collectors deliver higher yields at German locations. The parabolic trough collectors (PTC) investigated are especially interesting at locations with high direct radiation, as this can be better reflected and converted into heat than diffuse radiation.

This work is part of the German research project Pro-Sol-Netz, funded by the German Federal Ministry for Economic Affairs and Climate Action (BMWK). Pro-Sol-Netz aims to develop and evaluate technologies for the integration of parabolic trough collectors in district heating (DH) and process heat.

Keywords: concentrated solar thermal collectors, parabolic trough, collector technologies, district heating, TRNSYS, simulation study

1. Introduction

Solar thermal collectors are one important technology for the supply of renewable heat in DH and for industrial processes. Among other things, they can be integrated in DH and installed decentrally on detached houses and apartment buildings or industrial buildings (Mazhar et al. 2018). There is a great potential for solar thermal in DH in Germany, because around 14 % of homes were heated with district heating in 2019 (AGFW, 2022). Large-scale high performance flat plate collectors and evacuated tube collectors without and with CPC (compound parabolic concentrator) are the state of the art for the integration of solar heat into DH networks with supply temperatures up to 90 °C. These standard collector technologies are described e.g. in the AGFW's 'Solar thermal practice guide' (AGFW, 2021). However, existing heating networks, heating networks with large customers and industrial plants often require high transportation capacities or high temperatures respectively. In these cases, it can be important to be able to provide temperatures of around 100 to 140 °C economically using solar thermal energy (Agora Energiewende, 2019).

Other collector technologies, such as parabolic troughs (Figure 1) and Fresnel collectors, can provide supply temperatures above 100 °C with higher efficiency compared to standard collectors, therefore they are of interest for the decarbonization of existing DH networks. These collector technologies are new for utilities and other stakeholders in district heating.

Therefore, an analysis and comparison of collector technologies from various manufacturers is an important step towards encouraging the integration of solar thermal energy in heating networks. In this paper, the comparison of different solar thermal collector technologies is shown. In addition, a simulation case study comparing parabolic trough collectors and flat plate collectors in a DH network was carried out.

© 2024. The Authors. Published by International Solar Energy Society
Selection and/or peer review under responsibility of Scientific Committee
10.18086/eurosun.2024.03.05 Available at http://proceedings.ises.org

Figure 1 Photo of parabolic trough collectors (Solarthemen Media GmbH, 2021)

2. Collector technologies

Different collector technologies have various characteristics and specific features. Concentrated collectors are designed to focus the direct radiation of the sun onto a secondary absorber element, which considerably enhances the solar yield at high temperatures. Examples include evacuated tubes with CPC, parabolic troughs, and Fresnel collectors. In comparison to standard collectors such as flat plate collectors, evacuated tube collectors with and without CPC, which typically have a fixed collector slope angle, there are also collectors with tracking systems. Tracking systems allow the collectors to follow the sun, minimizing the angle of incidence and thereby maximizing the amount of irradiation received on the collector surface and the collector output. Tracking systems can be classified into single-axis and dual-axis types. To avoid damage from overheating, collectors can be tracked away from the sun, allowing for better regulation of thermal yield (Stahlhut et al. 1-2/2022).

Various heat transfer fluids are used in solar collectors based on the specific technology and application, as typically specified by the manufacturer. The most prevalent fluids include water, water-propylene glycol mixtures, thermal oil, and steam. When using water, the costs are generally low, and transferring from the solar circuit to a secondary circuit may not be necessary. However, a strategy to prevent freezing under any condition is essential. Water can be used for operating temperatures up to around 200 °C, but systems with temperatures exceeding 95 °C must be pressurized, which incurs additional costs. Alternatively, using water-propylene glycol mixtures can prevent freezing. These fluids can handle operating temperatures up to approximately 170 °C for short durations and up to 120 °C for extended periods (TYFOROP Chemie GmbH, 2015). Thermal oils are suitable for use at temperatures up to 400 °C, but some of these oils have a high viscosity at low temperatures. This can cause issues when starting a cold system. The environmental impact of high-temperature oils should also be considered (Therminol, 2022).

2.1. Flat plate collector

Flat plate collectors are typically utilized for low and medium temperature applications below 90 °C. As illustrated in Figure 2, these collectors have a large absorber surface, making diffuse radiation a significant factor in their heat yield. This feature allows flat plate collectors to generate heat effectively in cloudy, dusty, or humid conditions. They are generally constructed with a glass cover, copper tubes, absorber plates, thermal insulation, and an aluminum casing, which makes them relatively inexpensive to produce (Shamsul Azha, et al. 2020). To enhance performance, many manufacturers of high performance collectors use anti-reflective glass. Flat plate collectors can have either single or double glazing. Double-glazed collectors perform better at higher temperatures due to reduced heat loss, but they are more costly and heavier than single-glazed versions.

These double-glazed large-scale collectors are often used in DH applications.

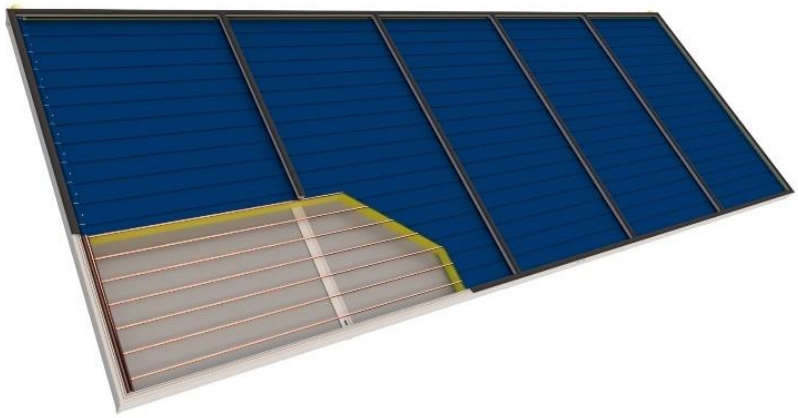

Figure 2 Structure of a flat plate collector for district heating (GREENoneTEC)

2.2. Evacuated tube collector without and with CPC

There are two main types of evacuated tube collectors: Sydney tube collectors and single glass tube collectors. Sydney tube collectors consist of double glass tubes with an inner absorber tube coated with a selective material, and the space between the tubes is evacuated. Single glass tube collectors consist of one evacuated tube with a conventional metallic absorber inside. The vacuum insulation in both types reduces heat loss and enhances performance at higher collector temperatures. An example of an evacuated tube collector with heat pipes is shown in Figure 3. It uses a trapezoidal plate with a high reflection factor, mainly reflecting diffuse radiation onto the vacuum tube.

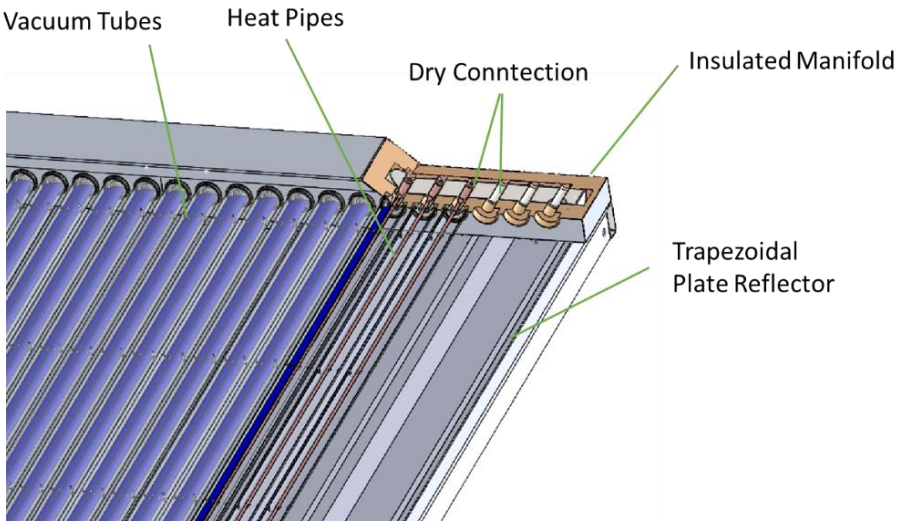

Figure 3 Main components of an evacuated tube collector without CPC (AKOTEC)

A specific design of this technology is the evacuated tube collector with CPC, which includes a parabolic mirror on the backside of the absorber tube (see Figure 4). This mirror geometry reflects direct radiation onto the absorber tube at any angle of incidence, eliminating the need for tracking and allowing for small row spacing due to minimal shading and the flat geometry. This design is highly area-efficient and can economically generate high temperatures (manufacturer information).

Figure 4 Main components of an evacuated tube collector with CPC, sectional view (Ritter Energie- und Umwelttechnik GmbH & Co. KG)

2.3. Parabolic trough collector

This technology features a large, curved mirror that focuses incoming radiation onto the absorber tube (see Figure 5). An electric servo motor can be used to adjust the angle of incidence in order to optimize solar radiation onto the collector plane during the day. Due to their large size, these collectors are typically tracked on a single-axis. A significant advantage of this design is comparatively low heat losses because of the small surface area of the absorber tube. Consequently, high temperatures exceeding 400 °C can be achieved efficiently through the concentration of direct irradiation. However, parabolic trough collectors are generally not stagnation safe, meaning that overheating protection is mandatory. Stagnation is typically prevented by rotating the collector out of direct sunlight. Most absorber tubes are enclosed by a protective glass tube, and many receiver tubes are vacuum-insulated, which can be re-evacuated during maintenance (W. Weiss, M. Rommel, 2008).

Figure 5 illustrates the schematic structure of a large parabolic trough collector, highlighting the key components and geometric parameters.

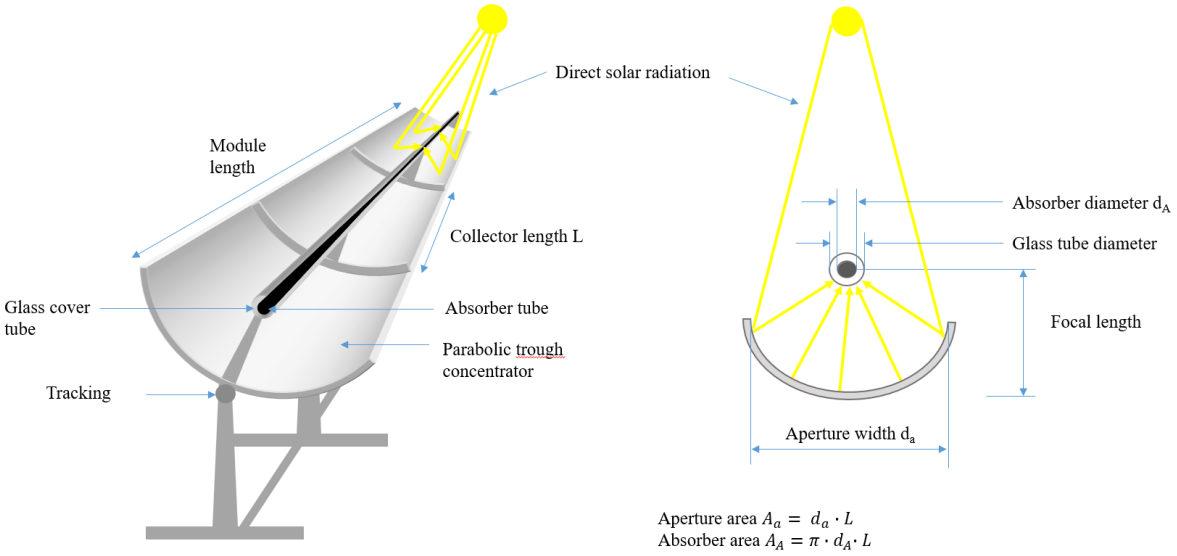

Figure 5 Large parabolic trough collector, perspective view and cross-sectional view (figure: Solites)

2.4. Fresnel lenses collector

The Fresnel lenses by a Danish manufacturer represents an innovative concentrated collector technology. This design focuses direct radiation onto the absorber surface behind the lenses, see Figure 6. Each module contains eight plastic lenses that act like magnifying glasses to concentrate light. Its compact design allows for two-axis tracking, which significantly increases solar yield. Additionally, there is no risk of glare, as the collector consistently reflects towards the sun due to the dual-axis tracking (datasheet, manufacturer information).

Figure 6 Photo of Fresnel lenses, Heliac in Denmark (Jensen et al. 2022)

3. Comparison of solar thermal collectors according to Solar Keymark

Most funding programs for collectors require that the collectors are certified, to have standardized performance parameters available. The most widely used certificate in Europe is the Solar Keymark certificate, which is also accepted in many countries outside Europe. Accredited test laboratories evaluate collectors according to the EN 12975 and EN ISO 9806 standards. The certification process also includes periodic monitoring of the manufacturing process and the product. Large parabolic trough collectors are hard to test in laboratories due to their size, but in-situ testing is a valid option under the Solar Keymark certification scheme (Solar Keymark, 2024).

Concentrated solar collectors focus the solar radiation onto a secondary element, from which the converted heat is extracted and, if necessary, converted again. In case of a parabolic trough collectors the radiation is directed and focused from the mirrors to the absorber tube. Compared to standard collectors such as flat plate collectors and evacuated tubes, the influence of diffuse radiation on parabolic trough collectors is low. This is due to the comparatively small surface area of the absorber (Weiss and Rommel, 2008).

The next Figure 7 shows the specific annual yields of three parabolic trough collectors with gross areas of 6 to 15 m² and a standard high performance flat plate collector according to their Solar Keymark certificate as a function of the average collector temperature. The mean temperature corresponds to the mean value of the supply and return temperatures of the collector. Solar Keymark provides specific annual yields for operating temperatures of 25 °C, 50 °C, and 75 °C at reference locations in Athens, Davos, Stockholm, and Würzburg. The following diagram shows values for Würzburg, Germany. Besides the standard temperatures, an additional operating temperature of 100 °C was calculated using the ScenoCalc tool, which is used to calculate the values for Solar Keymark certificates (ScenoCalc, 2024).

From collector mean temperatures above 55 °C, there is a yield advantage for concentrated collectors. The drop in specific yield at higher temperatures is not as steep as for the HPFPC. In this comparison concentrated collectors are therefore more suitable for high temperature applications.

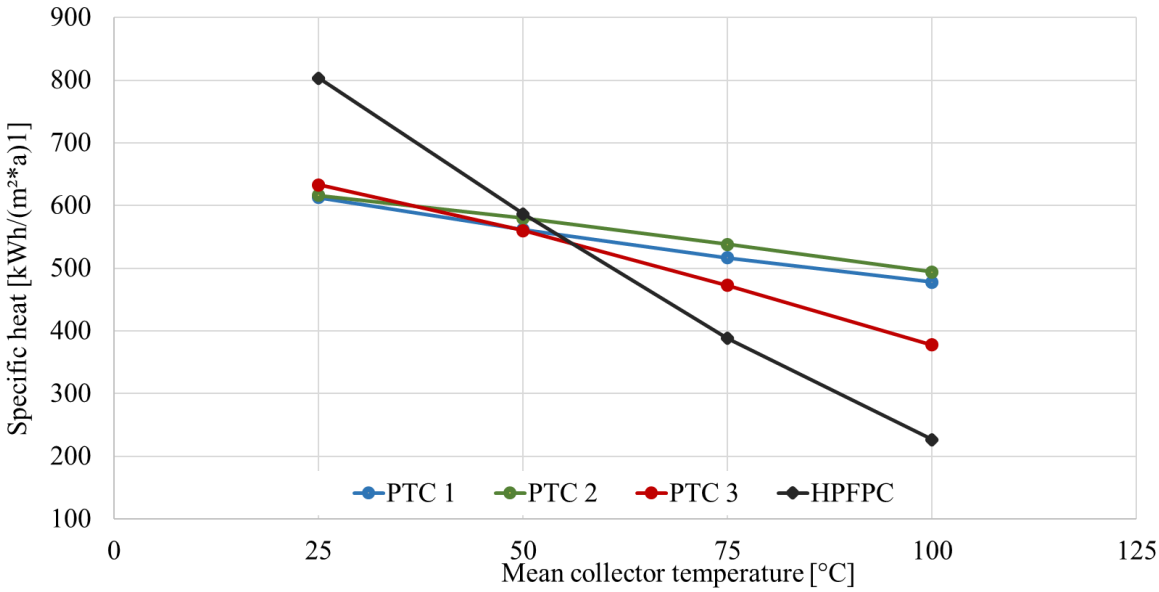

Figure 7 Specific annual heat yield of different small parabolic trough collectors (PTC) and a high performance flat plate Collector (HPFPC), related to the gross area, location Würzburg (Solar-Keymark) (ScenoCalc) (figure: Solites)

All preceding analyses and references are part of the report RA1 in IEA SHC Task 68, which will soon be available at (Task 68, 2024). Within this report, further collector technologies are analyzed Subsequent sections are based on additional investigations.

4. Case study

4.1 Parameterization

In a TRNSYS simulation case study, a heating network with supply temperatures of 140 °C in winter and 120 °C in summer and an annual heat demand of 6,150 MWh is fed by 2,250 m² aperture area of the PTC 1800 parabolic trough collector from the manufacturer Soliterm. There is also a buffer storage tank with 1,000 m³. Frankfurt am Main, Germany, is the reference location for the weather data used. The tracking axis is north-south, i.e. the collector tracks the sun from east to west. In addition, a stagnation prevention control is installed, which turns the collector out of the sun if the collector temperature is too high. The remaining heat requirement is covered by an additional heater. The results are compared with a high performance flat plate collector for solar district heating applications simulated in the same system. The main parameters of the case study are listed in Tab. 1 (TRNSYS, 2024)

Tab. 1 Parameterization of the case study

Parameter	Description
TRNSYS type / technology	Type 1357 / parabolic trough collector
Collector model, manufacturer	PTC 1800, Soliterm
Aperture area	2,250 m²
Row distance	4 m
Storage volume	1,000 m³
Maximum storage temperature	150 °C
Supply/return temperatures summer	120/70 °C
Supply/return temperatures winter	140/65 °C
Reference location	Frankfurt am Main, TRY 2015 (test reference year)
Source weather data	DWD (Deutscher Wetterdienst, German Weather Service)
Annual load	6,150 MWh/a
Feed in type	return-supply
Storage mode	Operation with charging to required supply temperature
Tracking	single-axis, north-south axis, tracking away when supply temperature of collector is 153 °C
Simulation period	1 year
Simulation time step	1 hour

4.1 Main results

The solar fraction of the parabolic trough is almost 20 %. Therefore, it generates almost 1,200 MWh heat per year while the high performance flat plate collector achieves less than 10 % solar coverage and 600 MWh per year heat. The specific solar yield shows the difference between the two technologies. The parabolic trough collector achieves 526 kWh/m² per year and the high performance flat plate collector 276 kWh/m² per year. The simulation results show that the parabolic trough collector can achieve supply temperatures of over 100 °C. The flat plate collector, on the other hand, produces significantly lower heat yields in this application. Tab. 2 gives an overview of the main results of the simulation study for both collector technologies. The solar yields of the PTC 1800 parabolic trough collector are at a high level from March to September inclusive. However, the yields in winter are not sufficient to supply the heating network, even on sunny days. Nevertheless, they are many times higher than the yields of the high performance flat plate collector. Proportionally higher heat losses from the storage tank are to be expected using the concentrated collector due to higher supply and storage temperatures. The pumps are switched on more often because more heat is supplied by the parabolic trough collector.

Tab. 2 Main results of the case study, comparison of parabolic trough and high performance flat plate collector

Output	Parabolic trough collector	Flat plate collector
Annual solar yield	1,157 MWh/a	600 MWh/a
Specific solar yield	526 kWh/(m²*a)	276 kWh/(m²*a)
Solar fraction	18.8%	9.8%
Number of pump switch-ons for the collector circuit	337	286
Number of pump switch-ons for the solar circuit	320	267
Number of stagnation days	5	0

4.2 Monthly solar yields

Figure 8 shows the monthly heat demand (Load) and the solar heat yield supplied by the parabolic trough collector (Solar). The remaining heat is supplied by an auxiliary heater (Aux). As there is more irradiation and a comparatively low heat demand in summer, the solar fraction is comparatively high from March to September. Due to the solar fraction of 100 % in July and August and 5 stagnation days, the collector area and buffer storage could be further optimized in their size.

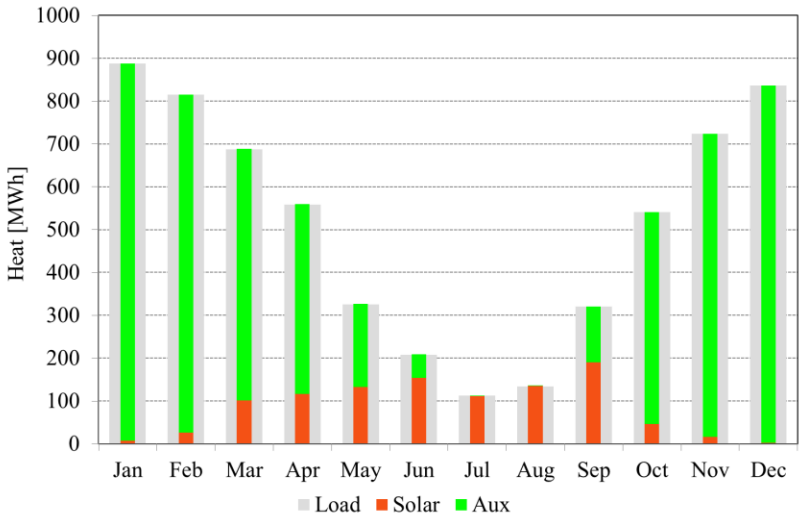

Figure 8 Monthly solar yield, parabolic trough collector

4.3 Temperature and radiation evaluation on a typical sunny day

The evaluation of day-dependent simulation results is an important measure for comparing the parabolic trough collector with the high performance flat plate collector. Based on the radiation data, identical days are selected and uniform diagrams are generated from the results, which are comparable for the respective day. A daily diagram is generated for both collectors, with simulation results provided at hourly intervals. Figure 9 illustrates the radiation values entering the collector level, represented by dashed lines. The horizontal axis indicates the time of day.

An example of this daily evaluation is shown in Figure 9, which presents the daily diagram of the parabolic trough and the HPFPC for 02. July, covering the period from 4 a.m. to 10 p.m. The high proportion of direct radiation at the collector level indicates a sunny day. The direct radiation in the collector plane of the PTC has a m-shaped curve. This is due to the single-axis tracking in east-west direction The parabolic trough collector is therefore able to deliver relatively constant solar yields over a longer period of the day. Constant energy yields throughout the day make it easier to control the pumps in the collector and solar circuit, as load demand is usually low at midday (12 am to 2 pm) and comparatively high in the morning and afternoon. In comparison to that, the direct radiation at the collector level of the HPFPC looks like a downwards facing parabola and is highest at midday (12 pm to 1 pm). This is due to the fixed collector slope which is 15°. At midday the direct radiation at the collector level of the HPFPC is higher than the direct radiation at PTC level. As the diffuse radiation for the HPFPC has an influence on heat generation, it is shown here.

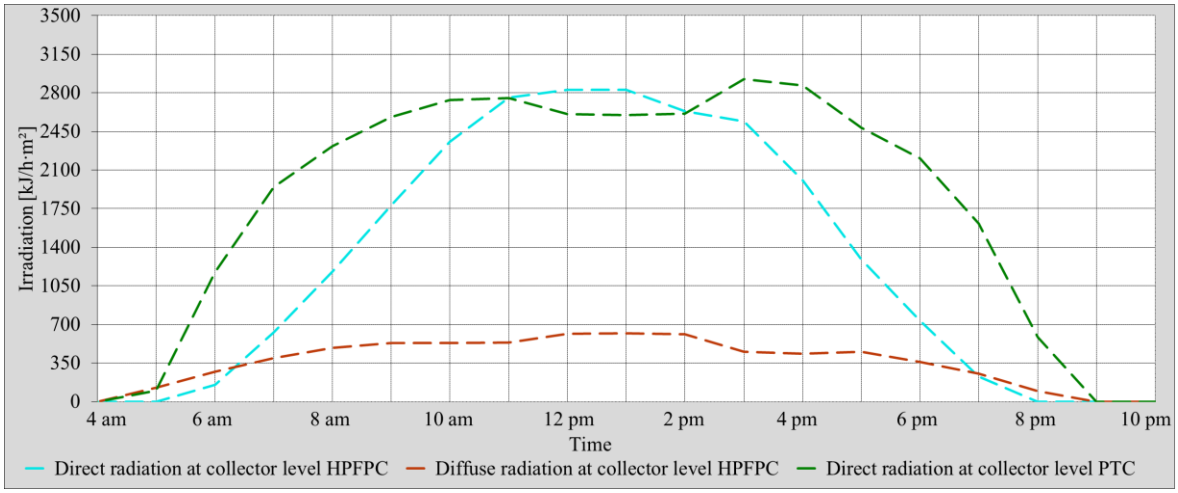

Figure 9 Daily diagram, 02. July, sunny day, parabolic trough collector (PTC) and high performance flat plate collector (HPFPC), relevant irradiation for heat generation

The following Figure 10 shows values that relate only to the parabolic trough collector on 02. July. The supply and return temperature (T_supply, T_return) of the PTC refer to the secondary vertical axis and are shown with solid lines. The scale of the radiation values can be seen, as in Figure 9 on the first vertical axis, which are shown with dashed lines. The total, direct and diffuse radiation entering the collector level are shown. In addition, the total horizontal radiation is shown in yellow. As previously mentioned, the irradiation in the collector plane has a m-shaped curve. This enables the PTC to supply constant temperatures to the DH system throughout the day. Due to transmission and storage losses, the collector delivers nearly 140 °C, even though the required supply temperature is 120 °C.

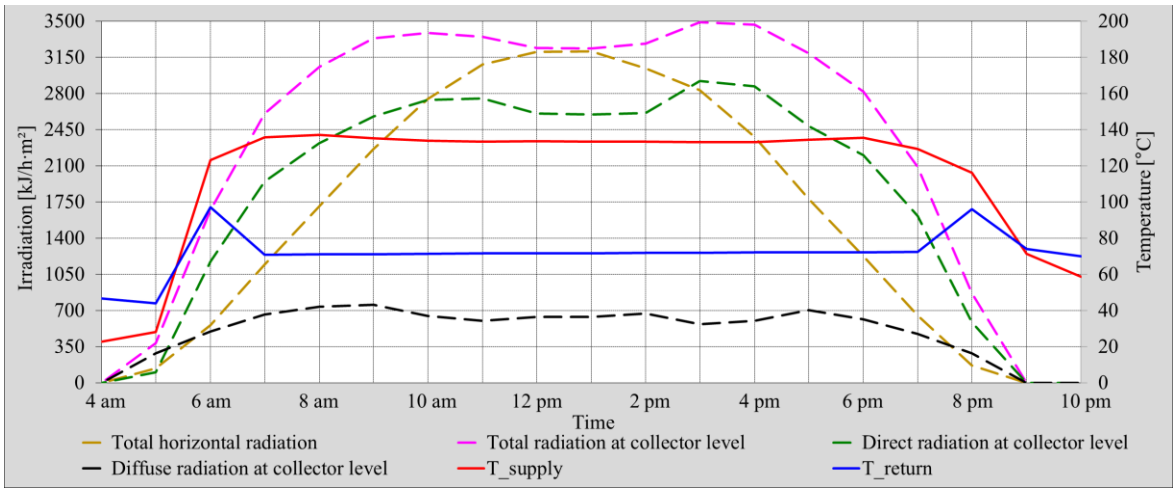

Figure 10 Daily diagram, 02. July, sunny day, parabolic trough collector, solid lines: temperatures, dotted lines: irradiation

4.4 Conclusion of the case study

On cloudy days, the solar yields of parabolic trough collectors are significantly lower than those of flat plate collectors as the parabolic trough has a comparatively small absorber surface, which is relevant for the yields from diffuse radiation. In the case study, the parabolic trough collector has a clear advantage overall. Due to the required heating network temperature of up to 140 °C, the flat plate collector is not able to supply heat efficiently.

A decisive advantage of parabolic trough collectors is the increased and adjustable solar yield due to tracking. The daily evaluations show that on sunny days, the direct radiation at the PTC level is relatively constant and there is no peak of direct radiation at the collector level at midday. This makes pump control easier, as the load demand is normally low at midday and higher in the morning and afternoon. Another advantage of parabolic trough collectors is the reduction of stagnation events which also results from tracking. However, it is also important to consider the row spacing of the parabolic trough collectors. When designing the system, care must be taken to ensure that the shading and area utilization are low and that the area efficiency is as high as possible.

While concentrated collectors are suitable for applications requiring higher temperatures when using solar energy, flat plate collectors remain a promising option, especially in applications where lower flow temperatures are sufficient. However, in addition to technological considerations, the economic feasibility of these technologies must also be thoroughly assessed, taking into account potential cost variations and uncertainties associated with real applications.

The studies and comparison that were carried out show that concentrated collectors such as parabolic troughs are interesting for heating networks in Germany and most probably in Central Europe and are useful in sunny locations. The use of these technologies needs to be investigated further.

5. Outlook

Further investigations will be carried out as part of the project Pro-Sol-Netz (May 2024 to April 2027) and IEA SHC Task 68 (April 2022 to March 2025). The TRNSYS simulation model and the assumptions made should be further optimized. In addition, different concentrated collector technologies can be compared with each other and further case studies can be carried out. In this described case study, mainly the parabolic trough collector PTC 1800 was investigated. The investigation of other parabolic trough collectors is also interesting. In addition, a comparison with other standard collectors, such as vacuum tube collectors, proves to be relevant.

Pro-Sol-Netz aims to provide developments and evaluations in order to successfully establish and use concentrated collectors in the markets for district heating systems and process heat in central Europe, both technically and economically. The availability of knowledge and calculation tools for municipal utilities and planning offices plays a central role in enabling them to plan and implement concentrated solar thermal systems.

The work in Pro-Sol-Netz focuses on carrying out the developments and evaluations, including the first pilot plants in Germany, in order to be able to use and establish concentrated collectors for heating networks and process heat successfully in the German markets, both technically and economically, once the project has been successfully completed. These solar collectors should not be seen as competition to other renewable energy technologies such as heat pumps, but as a necessary technology for process heat and heating networks. All scenarios for the future energy mix of a decarbonized Germany show a strong increase in heat pumps, geothermal energy and solar thermal energy. The project-specific conditions lead to the most economical selection of the technologies mentioned, with alternatives to heat pumps being required for supply temperatures above 95 °C in particular.

In Pro-Sol-Netz, the thermal yield of commercial parabolic trough systems is scientifically measured and monitored. The measurement data is used for validation and as practical proof of the performance of concentrated collectors in the future-oriented sectors of heating networks and process heat. Existing simulation tools for calculating and predicting system yields, such as SCFW and Greenius, are being further developed for use with concentrated collectors. The ROKA³ heating network calculation software is also being improved for the integration of solar thermal heat production, thereby supporting the validation and dissemination of research results (SCFW, 2024) (Greenius, 2024) (ROKA³, 2024).

In Pro-Sol-Netz Solites leads two work packages and supports other work packages by contributing expertise, carrying out modeling and simulations and developing simulation tools, among others. Solites is also active in the international exchange of knowledge in the parallel ongoing IEA SHC Task 68.

6. References

AGFW, 2022: Hauptbericht - Fakten und Antworten zu Fernwärme, available online at https://www.agfw.de/energiewirtschaft-recht-politik/energiewende-politik/ueberblick-fakten-und-antworten-zu-fernwaerme, accessed on 04.04.2024.

AGFW, 2021: Praxisleitfaden des AGFW, available online at https://www.agfw-shop.de/agfw-praxisleitfaden-solarthermie.html

Agora Energiewende, 2019: Wie werden Wärmenetze grün? Documentation of the discussion event on May 21, 2019 at the Berliner Energietage 2019, Page 5–6.

Greenius, 2024. available from https://elib.dlr.de/68570/

Mazhar, Abdur Rehman; Liu, Shuli; Shukla, Ashish, 2018: A state of art review on the district heating systems. In: Renewable and Sustainable Energy Reviews 96, Page. 420–439.

Jensen, A.R.; I. Sifnaios; G.P. Caringal; S. Furbo; J. Dragsted, 2022. Thermal performance assessment of the world's first solar thermal Fresnel lens collector field [online]. Solar Energy, 237, Page 447-455. https://doi.org/10.1016/j.solener.2022.01.067

ROKA³, 2024. available from https://www.roka3.de/

ScenoCalc, 2024. available from http://www.estif.org/solarkeymarknew/component/content/article/13-public-area/163-scenocalc

SCFW, 2024. available from https://www.scfw.de/

Shamsul Azha, N.I.; Hussin, H.; Nasif, M.S; Hussain, T, 2020. Thermal Performance Enhancement in Flat Plate Solar Collector Solar Water Heater: A Review Processes, 8(7), 1-14. https://doi.org/10.3390/pr8070756

Solar Keymark, 2024. available from https://solarkeymark.eu/

Solarthemen Media GmbH (Hg.), 2021: Solarthermie: Wärme aus Solaranlagen. Available online at https://www.solarserver.de/wissen/basiswissen/solarthermie-solaranlage-funktionsweise-typen/, accessed on 04.08.2023.

Stahlhut, M.; Ackermann, C.; Urbaneck, T.,1-2/2022. Exemplarische Untersuchung verschiedener Kollektoren zur Einbindung in Fernwärmenetze. EuroHeat&Power, Page 40-45.

Task 68, 2024. IEA SHC Task 68, available from https://task68.iea-shc.org/

Therminol, 2022. available online at: https://www.therminol.com/product/71093438?pn=Therminol-66-Heat-Transfer-Fluid, accessed on 08.05.2024

TRNSYS, 2024, TRNSYS-Transient System Simulation Tool, available from https://www.trnsys.com/

TYFOROP Chemie GmbH, 2015. Technische Information TYFOCOR HTL. Hamburg.

Weiss, Werner; Rommel, Matthias, 2008: Process Heat Collectors. State of the Art within Task 33/IV. Austria: AEE INTEC

Supported by:

Federal Ministry for Economic Affairs and Climate Action

on the basis of a decision by the German Bundestag

The project „Pro-Sol-Netz" has received funding from the German Ministry for Economic Affairs and Climate Action on the basis of a decision by the German Bundestag.

The sole responsibility for the content of this publication lies with the authors. It does not necessarily reflect the opinion of the funding organizations. Neither the funding organizations nor the authors are responsible for any use that may be made of the information contained therein.

Evaluation of positive energy districts with district heating and heat pumps

Elisa Venturi[1], Fabian Ochs[1], Mara Magni[1], Georgios Dermentzis[1]

[1] University of Innsbruck, Innsbruck, (Austria)

Abstract

The transformation of districts into Positive Energy Districts (PEDs) is one of the major EU goals on the path to a sustainable building stock. When connecting PEDs to district heating systems, which typically rely on non-renewable sources, the energy balance requires careful consideration. Methods for calculating the necessary photovoltaic energy to achieve a positive balance are not yet available. To consider different energy carriers, the energy demands have to be converted to primary energy or CO_2 emissions. In addition to the annual energy balance typically used in PED calculations, time-depending methods, i.e. monthly conversion factors, address the impact of seasonal variations on energy demand and supply. These methods are applied to a case study of a realized residential district in Austria. Alternative system concepts district heating (DH) and heat pumps (HP) and different combinations of DH and HP are investigated by applying different balancing methods. Insights into the challenges and feasibility of achieving PED for multi-family buildings in urban areas with DH are derived.

Keywords: Positive energy district, district heating, heat pump, CO_2 emissions, monthly conversion factors

1. Introduction and aim of the study

Numerous studies have extensively explored the concept of Positive Energy Districts (PEDs), providing a range of definitions and methodologies (Lindholm, et al., 2021), (Albert-Seifried, et al., 2021), (Guarino, et al., 2023), (Moreno, et al., 2021), (Walker, et al., 2018), (Shnapp, et al., 2020). Key performance indicators (KPIs), including primary energy (PE) (Guarino, et al., 2023), non-renewable (non-RE) PE (Moreno, et al., 2021), and carbon footprint (Guarino, et al., 2023), have been used in these investigations. The primary focus of these studies is on assessing the annual balance between energy demand and supply. However, annual methodologies overlook grid-related challenges arising from energy imbalances (i.e. energy demand peaks in winter and supply peaks in summer, the so-called winter gap).

The transformation of districts with multi-apartment buildings connected to a non-RE district heating (DH) system requires careful consideration of the balancing method, i.e. annual vs. monthly, PE vs. CO_2. Furthermore, it is important to address whether it is acceptable and if so, how to overcompensate the use of gas in the DH with an additional supply of photovoltaic (PV) energy. As shown in (Ochs, et al., 2022) for the DH in Vienna and Innsbruck, the gas demand in DH is particularly high during the winter months due to space heating (SH) needs. Hence, the future development of the DH system has to be considered, too.

This study aims to develop and compare methods for assessing the performance of PEDs connected to DH systems. The goal is to determine the necessary PV energy (i.e. PV area) to achieve a PED. The required PV area depends on the method employed for the calculation of the PE or CO_2 balance. Various methods will be developed and tested by means of a comprehensive case study of an existing residential district in Innsbruck, Austria. The study will use the design data of the existing system and expand the methods to explore alternative system concepts involving DH and heat pumps (HP). This approach aims to draw more general conclusions about the requirements for achieving PED with DH and HP. The alternative system concepts that will be investigated, include: 1) HP for space heating (SH), and DH for domestic hot water (DHW) (i.e., as built), 2) HP only (for both SH and DHW), 3) DH only (for both SH and DHW), and 4) DH for SH, and HP for DHW (i.e., opposite of as-built).

© 2024. The Authors. Published by International Solar Energy Society
Selection and/or peer review under responsibility of Scientific Committee
10.18086/eurosun.2024.03.06 Available at http://proceedings.ises.org

2. Case Study

The "Campagne-Areal" Smart City Quarter is a project involving 16 new buildings subdivided into four blocks (Figure 1, left). Predominantly residential, some buildings also accommodate non-residential facilities (e.g. supermarket and kindergarten). The first four buildings (i.e. the first block) have already been built and tenants have been moving in in late 2022, which is also the start of a three-year monitoring campaign. The total living area amounts to 22277 m^2. A common technical room accommodates the main components of the central heating system (Figure 1, right) for the entire quarter. The goal of the Smart City Quarter is the creation of a "Zero Emission Urban Region" and to contribute to the Energy Strategy Tyrol 2050, thus it can serve as an example of achieving PED in an urban environment with DH.

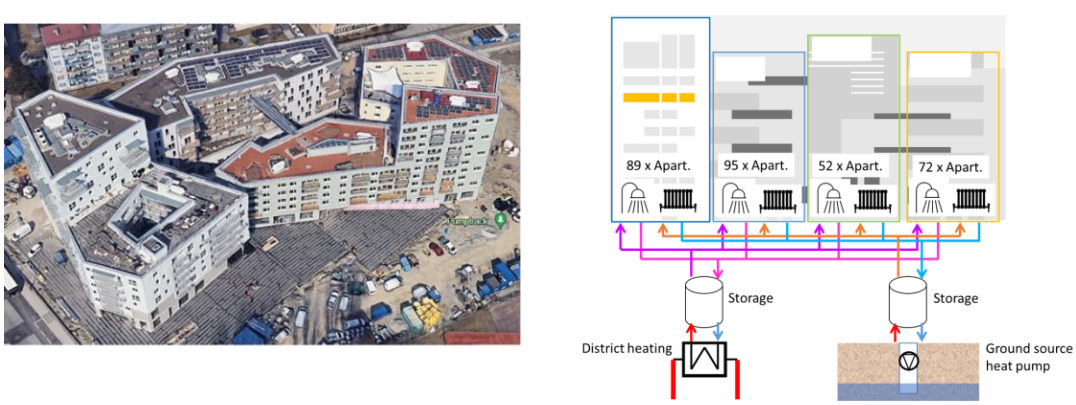

Figure 1: Left: Campagne Areal district (source: Google Earth). Right: Scheme of the energy system

The buildings were designed to meet the Passive House standard, with space heating demands ranging from 15 kWh/(m²a) to 21 kWh/(m²a). A mechanical ventilation system with heat recovery (MVHR) is installed. SH is provided by a ground source HP, while DHW is provided by the city DH. Storages for SH and DHW are integrated into the hydronic circuit. The Passive House Planning Package (PHPP) (Feist, et al., 2007) was used during the planning phase to design the four buildings. Energy demands for space heating, domestic hot water, auxiliaries and appliances are calculated on a monthly basis using PHPP. The monthly SH and DHW demands are calculated including distribution and storage losses. Monitoring data for the first two years of the districts are available on district-, building-, and apartment-level. A comparison between design results and monitoring data is carried out in (Venturi, et al., 2024). The annual electricity demand for the HP for SH amounts to 77 MWh_{el}, while the electricity demand for appliances is 392 MWh_{el}, and for auxiliaries (including the MVHR) is 153 MWh_{el}. The thermal demand from the DH system for DHW is 582 MWh_{th}. The monthly electric and thermal energy demands are shown in Figure 2.

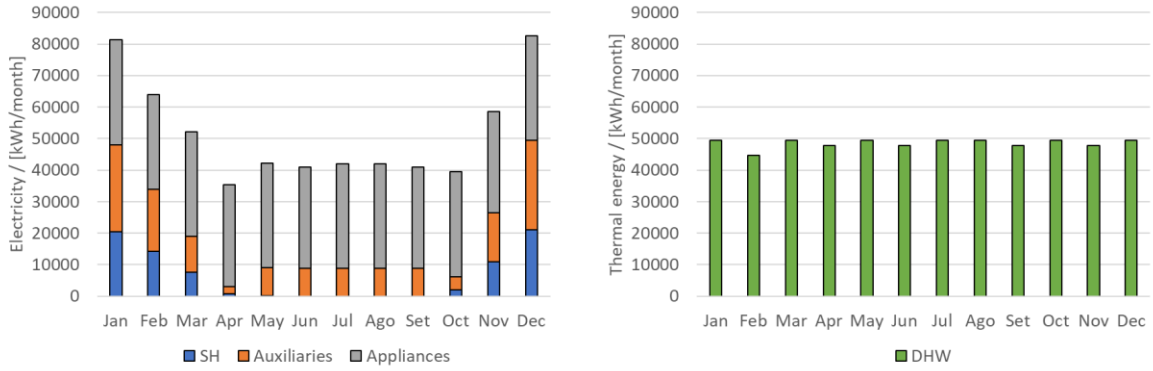

Figure 2: Left: Monthly electric energy required by HP (for SH), auxiliaries and appliances. Right: thermal energy required by DH (for DHW)

3. Methods

Several conversion factors and CO_2 balances are proposed in order to explore the necessary PV energy (i.e. PV area) to reach a positive energy balance. The conversion factors vary based on the balanced quantity (CO_2 or non-RE PE) and the type of conversion factor (annual or time-dependent). The CO_2 balances differ in the type of storage considered (grid as an ideal storage or hydrogen storage with losses). The methods are tested on the case study to assess the performance of PEDs connected to DH and HP. Additionally, different variants of heat generation are introduced, and the methods are applied to these variants accordingly.

3.1 Conversion factors

3.1.1 Balanced quantity

Primary energy (PE), non-renewable primary (non-RE PE) energy and CO_2 emissions are commonly used in the PED assessment. Since the goal of this study is to calculate the necessary PV area to offset the energy from non-renewable sources, the CO_2 and the non-RE PE conversion factors are relevant. The renewable part of PE is excluded, as it does not require offsetting with PV energy (as it already comes from renewable sources). In the case of absence of nuclear energy, CO_2 and non-RE PE conversion factors are the same. Therefore, for sake of simplicity, only the CO_2 conversion factor is considered in the current study, however, the method is valid with non-RE PE, too.

The quantity of equivalent CO_2 (in kg) produced by the energy (electric and thermal) demand is calculated according to eq. 1:

$$CO_2 = W_{el} \cdot f_{CO2eq,el} + Q_{DH} \cdot f_{CO2eq,DH} \quad \text{(eq. 1)}$$

Where:

- W_{el} is the electric energy demand from the electric grid [kWh_{el}]
- Q_{DH} is the thermal energy demand from the city district heating [kWh_{th}]
- $f_{CO2eq,el}$ is the CO_2 conversion factor for electricity [kg_{CO2}/kWh_{el}]
- $f_{CO2eq,DH}$ is the CO_2 conversion factor for DH [kg_{CO2}/kWh_{th}]

Since the energy mix for DH is highly dependent on the specific city or region, this study uses the energy mix specific to the DH of Innsbruck, rather than the Austrian national values. In contrast, the conversion factors for electricity are based on the Austrian national energy mix.

3.1.2 Type of conversion factor (annual and time-dependent)

In the current study both annual and time-dependent (i.e., monthly) conversion factors are used. The annual conversion factors represent the energy mix (electricity or DH) over the course of a year, providing a generalized average of the energy sources used in each month. In contrast, the monthly conversion factors, which vary throughout the year, reflect the energy mix for each individual month. These monthly variations occur due to the fluctuating availability of renewable sources throughout the year.

The annual values of the CO_2 conversion factor for electricity are country-specific and are documented in the literature, often provided in standards and norms. For example, the Austrian norm OIB 2023 (OIB, 2023) specifies the CO_2 conversion factor for electricity as $f_{CO2eq,el}$ = 156 g/kWh. The annual values used in the current paper for the DH of Innsbruck is $f_{CO2eq,DH}$ = 127 g/kWh (Ochs, et al., 2022), based on (Streicher, 2018). Although the data from (Streicher, 2018) refers to the year 2017, the annual values for 2023 from (TIGAS, 2024) confirm similar shares with only minor changes.

To account for the timing of energy demand and supply, it is necessary to assess the CO_2 conversion factor based on the time of the year (at least on monthly basis). In the current study, monthly conversion factors are considered. This approach, initially proposed by (Ochs & Dermentzis, 2018) and then applied by (Dermentzis, et al., 2021), allows for consideration of the so-called winter gap. Monthly conversion factors for the Austrian

electricity mix are available in (OIB, 2023), while those related to the Innsbruck DH system are derived by (Ochs, et al., 2022). It is important to note that the availability of monthly conversion factors depends on the country, or in case of DH on the specific city/region. Finding accurate monthly conversion factors for DH can be challenging and the assumptions used in their calculation can have a significant impact on the results.

The monthly and annual CO_2 conversion for electricity and DH are illustrated in Figure 3.

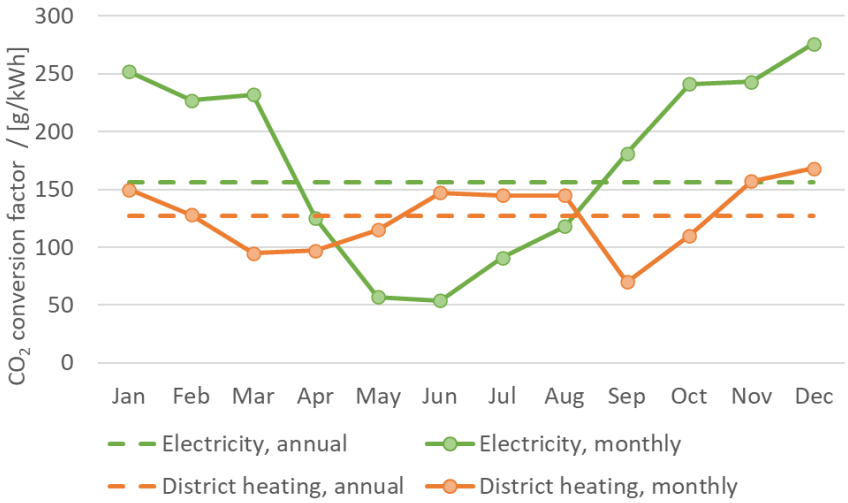

Figure 3: Annual (dotted line) and monthly (continuous line) CO_2 conversion factor for electricity (in green) and DH (in orange). Source for electricity: (OIB, 2023). Source for DH: (Ochs, et al., 2022)

The monthly conversion factor for electricity shows peaks during the winter months. In contrast, the monthly conversion factors for the DH system in Innsbruck have peaks in both winter and summer (June to August) when fewer renewable sources are utilized (Ochs, et al., 2022).

3.2 CO_2 balance

A CO_2 balance between the required energy and the produced energy by the PV system is necessary, regardless of the conversion factor used. The CO_2 balance means that the annual CO_2 emissions due to the energy demand must be offset by the annual CO_2 savings due to the PV production (see eq. 3).

$$\sum_{i=1}^{12} CO_{2,demand,i} = \sum_{i=1}^{12} CO_{2,supply,i} \quad \text{(eq. 3)}$$

Where:

- $CO_{2,demand,i}$ is the CO_2 emissions due to the energy demand in every month (i)
- $CO_{2,supply,i}$ is the CO_2 savings (or negative emissions) due to the PV production in every month (i)

Knowing the annual required CO_2 negative emissions, the necessary PV energy (i.e., PV area) to achieve a PED can be calculated. In the current study, two CO_2 balance approaches are used: one considers the grid as an "ideal storage" (i.e., no losses), and the other involves a seasonal storage system with losses (i.e., a more realistic approach), such as using hydrogen (H_2) technologies. These two possible balances are called: "Grid as ideal storage" and "Seasonal storage (H_2)" and are detailed in the following sections.

3.2.1 CO_2 balance: "Grid as ideal storage"

The most common balance used in the literature is the annual balance with the grid (here called "Grid as ideal storage"). In this scenario, the required PV energy to achieve PED can be produced during the summer months (when the PV production is high and the energy consumption is low) and used in winter. Since no losses are accounted for, the grid is considered as an ideal storage system. The required PV area for the case "Grid as

ideal storage" is calculated to have CO_2 balance according to eq. 4:

$$Area_{PV} = \frac{\sum_{i=1}^{12}\left(\frac{CO_{2,supply,i}}{f_{CO2,eq,i}}\right)}{\sum_{i=1}^{12} I_{sol,i} \cdot \eta_{PV}} \quad \text{(eq. 4)}$$

Where:

- $Area_{PV}$ is the required PV area
- $I_{sol,i}$ is the solar radiation in each month (i)
- η_{PV} is the efficiency of the PV panel
- Monthly CO_2 negative emissions ($CO_{2,supply,i}$) and monthly conversion factors ($f_{CO2,eq,i}$) are as described in section 3.2 and 3.1.1

The efficiency of the PV panels (η_{PV}) is assumed to be 22%. The monthly solar radiation is obtained from the standard weather data of Innsbruck provided in Passive House Planning Package (PHPP), see Table 1.

Table 1: Solar radiation in kWh/(m² month) for Innsbruck according to PHPP

Jan	Feb	Mar	Apr	May	Jun	Jul	Aug	Sep	Oct	Nov	Dec
58.5	70.9	106.2	134.6	139.2	125.8	137.3	129.0	113.9	96.7	50.5	49.8

It has to be noted that when the current method is applied using annual conversion factors, the balance is known as the so-called "net balance".

3.2.2 CO_2 balance: "Seasonal storage (H_2)"

Hydrogen can serve as an alternative method for storing electric energy produced during the summer months for later use in the winter months. This CO_2 balance accounts for the losses in the hydrogen storage process. The process includes: electrolyzer (efficiency $\eta = 70\%$ (Tosatto & Ochs, 2024)), H_2 storage (charging efficiency $\eta_{charge} = 89\%$ and discharging efficiency $\eta_{discharge} = 100\%$ (Tosatto & Ochs, 2024)), and fuel cells (efficiency $\eta = 50\%$). Consequently, the total roundtrip efficiency (η_{H2}) of the process is 31%, which affects the PV overproduction in the summer months (i.e., the electricity that can be stored).

The calculation of the required PV area must consider the energy self-consumption in each month (unlike in the "Grid as ideal storage" calculation where the process efficiency was assumed to be 100%). The required PV area is determined by solving the eq. 5, which is based on eq. 6, and further derived from eq. 7. The calculation necessitates an iterative process.

$$\sum_{i=1}^{12} W_{PVover,i} = 0 \quad \text{(eq. 5)}$$

$$\begin{cases} W_{PVover,i} = \left(W_{prod_{PV},i} - \frac{CO_{2,supply,i}}{f_{CO2,eq,i}}\right) \cdot \eta_{H_2} & when \left(W_{prod_{PV},i} - \frac{CO_{2,supply,i}}{f_{CO2,eq,i}}\right) > 0 \\ W_{PVover,i} = \left(W_{prod_{PV},i} - \frac{CO_{2,supply,i}}{f_{CO2,eq,i}}\right) & when \left(W_{prod_{PV},i} - \frac{CO_{2,supply,i}}{f_{CO2,eq,i}}\right) < 0 \end{cases} \quad \text{(eq. 6)}$$

$$W_{prod_{PV},i} = I_{sol.i} \cdot \eta_{PV} \cdot Area_{PV} \quad \text{(eq. 7)}$$

Where:

- $W_{PVover,i}$ is the PV overproduction in each month (i). $W_{PVover,i}$ is negative in months when the PV production is less than the required energy
- $W_{prod_{PV},i}$ is the produced energy by PV panels in each month (i)
- η_{H_2} is the roundtrip efficiency of the total H_2 process (electrolyzer, H_2 storage and fuel cells), which is 31%
- Monthly CO_2 negative emissions ($CO_{2,supply,i}$) and monthly conversion factors ($f_{CO2,eq,i}$) are as described in section 3.2 and 3.1.1. Monthly solar radiation ($I_{sol.i}$) and PV efficiency (η_{PV}) are as described in section 3.2.1

3.3 Methods for assessing the performance of PEDs

Four methods are derived from the combination of the type of conversion factors (section 3.1.2) and the CO_2 balance (section 3.2). These methods are illustrated by the white cells in Figure 4. The methods become eight when also the balanced quantity of the conversion factor (section 3.1.1) is changed (CO_2 and non-RE PE, in case of presence of nuclear energy in the grid). The comparisons of the possible methods are indicated by the colored arrows in Figure 4 and include:

- Comparison of the type of the conversion factor (green arrow), it will be presented in section 4.1.1 (i.e. annual vs. monthly conversion factor)
- Comparison of the CO_2 balance (orange arrow), it will be presented in section 4.1.2. (i.e. “Grid as ideal storage” vs. “Seasonal storage (H_2)”)

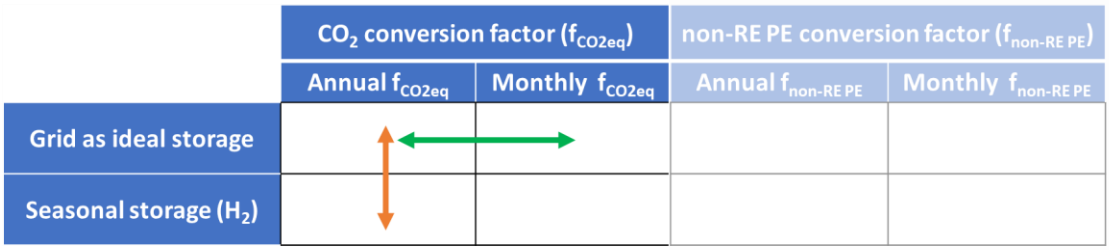

Figure 4: Schematic representation of the 4 methods (illustrated by the white cells) resulting from different combinations of conversion factors and CO_2 balances. The number of methods increases to 8 when the non-RE PE conversion factors are also considered

3.4 Variants of the heat generation

To draw more general conclusions on the requirements to achieve PEDs using DH and HP, several alternative system concepts are investigated. These variants combine different heat generations and are as follows:

1) HP for SH, and DH for DHW (i.e., as built),

2) HP only (for both SH and DHW),

3) DH only (for both SH and DHW),

4) DH for SH, and HP for DHW (i.e. opposite of as-built).

The electric and thermal energy demands for these four systems are calculated using PHPP. Electricity for auxiliaries and appliances is included. The energy demands are available on monthly basis.

4. Results

The methods are compared in section 4.1. Section 4.2 focuses on comparing the different heat generation's variants. The different methods are applied to the four heat generation's variants of the Campagne district, but for simplicity, results are presented using only the monthly CO_2 conversion factor.

4.1 Comparison of the methods

4.1.1 Comparison of the type of conversion factors

The influence of using the annual or the monthly conversion factor (green arrow of Figure 4) is discussed in the current section.

The monthly CO_2 emissions (due to the energy demand) are presented in Figure 5 with calculations using annual and monthly CO_2 conversion factors.

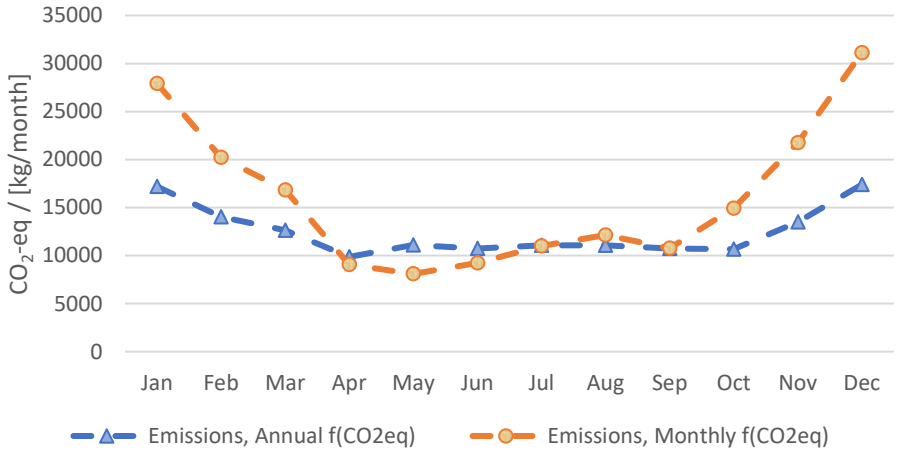

Figure 5: Equivalent CO_2 emissions calculated using the annual (blue line) and monthly (orange line) CO_2 conversion factors (based on the same energy demand)

The use of monthly conversion factors leads to higher CO_2 emissions during the winter months, reflecting the increased reliance on non-renewable sources during these months. In contrast, the annual conversion factor tends to underestimate these emissions. This discrepancy impacts the calculation of the required PV area: 3604 m^2 using the annual CO_2 conversion factor and 4518 m^2 using the monthly CO_2 conversion factor, according to the "Grid as ideal storage" CO_2 balance, which is commonly used in the literature. The PV production corresponding to these PV areas results in negative CO_2 emissions, shown in Figure 6 alongside the positive CO_2 emissions due to the energy demand (as depicted in Figure 5).

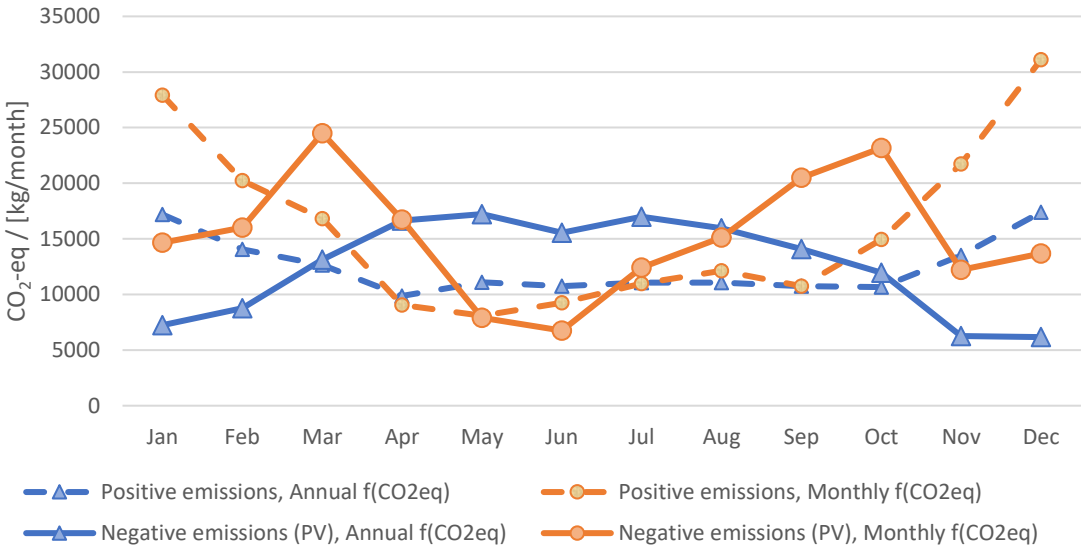

Figure 6: Positive CO_2-equivalent emissions (dotted lines) due to the energy demand and negative CO_2-equivalent emission (continuous lines) due to the PV production. Monthly emissions are presented using annual f_{CO2eq} (blue) and monthly f_{CO2eq} (orange)

As observed in Figure 5, the monthly conversion factors affect also the negative emissions associated with the PV production. The peaks in negative CO_2 emissions calculated using the monthly CO_2 conversion factor during the intermediate months (e.g., March and October) result from the combination of relatively high conversion factors (higher than the annual value, see Figure 3) and the relatively high PV production compared to the winter months (due to the higher solar radiation, see Table 1).

4.1.2 Comparison of the CO_2 balance

The impact of the ideal or seasonal storage in CO_2 balance (orange arrow of Figure 4) is discussed in the current section. The two CO_2 balances (i.e. "Grid as ideal storage" and "Seasonal storage (H_2)", as described in section 3.2) are calculated using monthly conversion factors.

Due to the losses associated with the "Seasonal storage (H_2)", the required PV area is 5623 m^2, which is 24% larger than the area calculated using the "Grid as ideal storage" (4518 m^2). The resulting monthly PV production is illustrated in Figure 7.

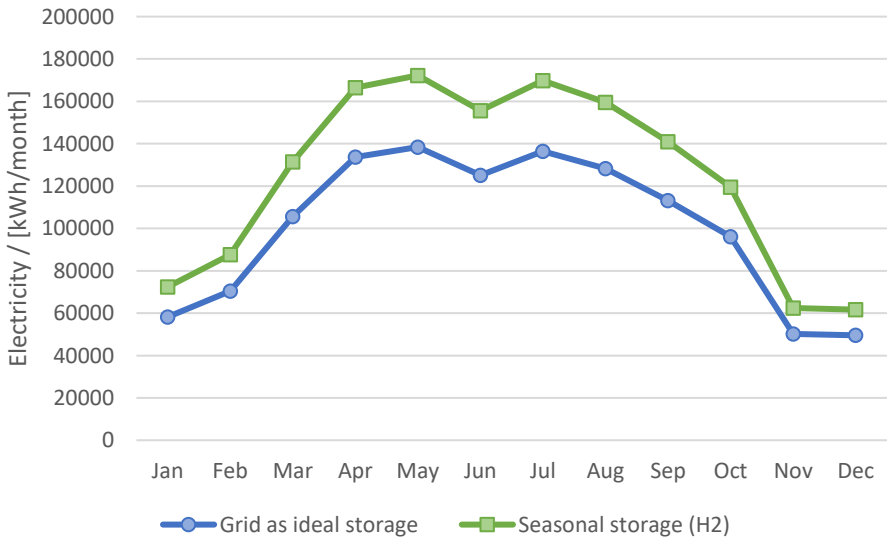

Figure 7: Electricity produced by the PV areas calculated according the two CO_2 balances. Calculations with monthly f_{CO2eq}

Figure 8 shows the equivalent CO_2 emissions, highlighting the positive emissions due to the energy demand (black line) and the negative emissions due to the PV production.

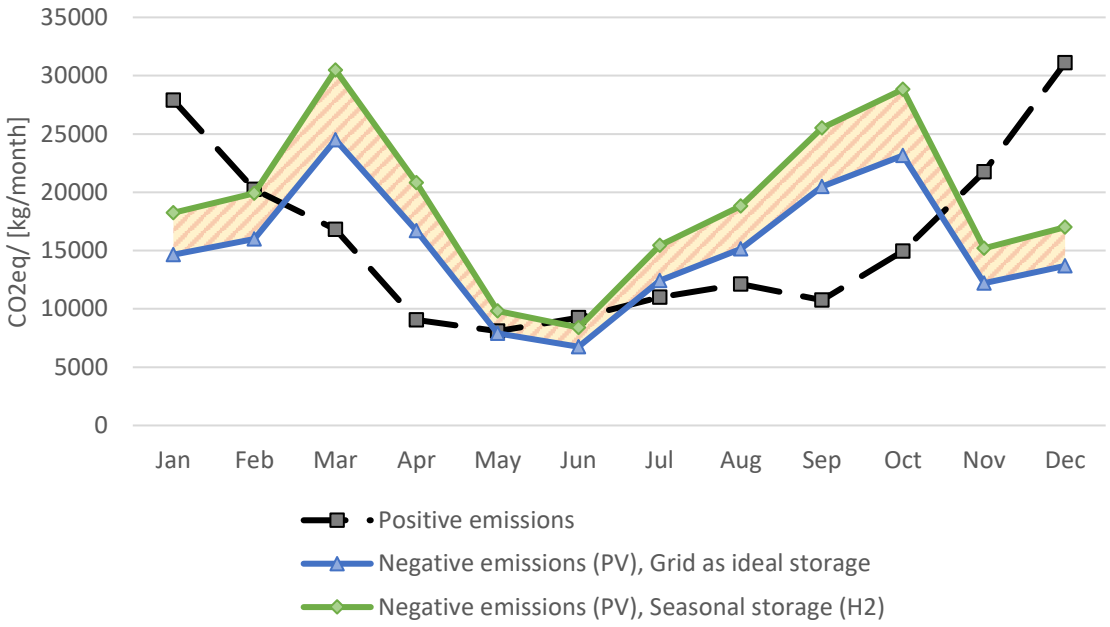

Figure 8: Monthly equivalent CO_2 emissions calculated with the monthly f_{CO2eq}. Positive emissions (black) are due to the energy demand, negative emissions are due to the PV production, based on the PV area calculated using the two CO_2 balances. The area between the two lines of negative emission represents the conversion losses associated with the H_2 storage process.

The areas under the black line (representing the CO_2 emissions) and the blue line (representing the CO_2 savings, calculated using the "Grid as ideal storage" balance) are identical. This indicates that the total annual CO_2 emissions and CO_2 savings due to the PV installation are equal, as defined by the "Grid as ideal storage" CO_2 balance. This implies that the overproduction of electricity during summer (characterized by high solar radiation and low energy demand) is shifted to the winter months without accounting for any associated losses. In contrast, the "Seasonal storage (H_2)" CO_2 balance exhibits a similar trend, but with increased required CO_2 negative emissions (i.e., increased PV production) because a part of these will be lost due to the H_2 storage process. The yellow area between the two lines of negative emissions represents the conversion losses associated with the H_2 storage process (roundtrip efficiency η_{H2} = 31%).

4.1.3 Comparison of the methods based on the required PV area

To summarize the comparison of methods discussed in the previous sections, the required PV area calculated using each method is presented in Table 2.

Table 2: Required PV area (in m^2) to achieve PED calculated according to the four different methods

	CO_2 conversion factor (f_{CO2eq})	
	Annual f_{CO2eq}	**Monthly f_{CO2eq}**
Grid as ideal storage	3604	4518
Seasonal storage (H_2)	4866	5623

The net balance (i.e. the combination of annual f_{CO2eq} and "Grid as ideal storage" balance) results in the smallest required PV area (3604 m^2). Conversely, using monthly conversion factor combined with the "Seasonal storage

(H_2)" balance yields the largest required PV area (5623 m^2), which is 56% more than the area determined by the net balance. The other combinations produce results that fall between these two cases.

4.2 Comparison of the heat generation variants

The four variants of the heat generation are compared using the monthly CO_2 conversion factors. The required PV area to reach PED is calculated using both CO_2 balances.

The required PV areas are presented in Figure 9, and Table 3 shows the increase in PV area relative to the "as built" case.

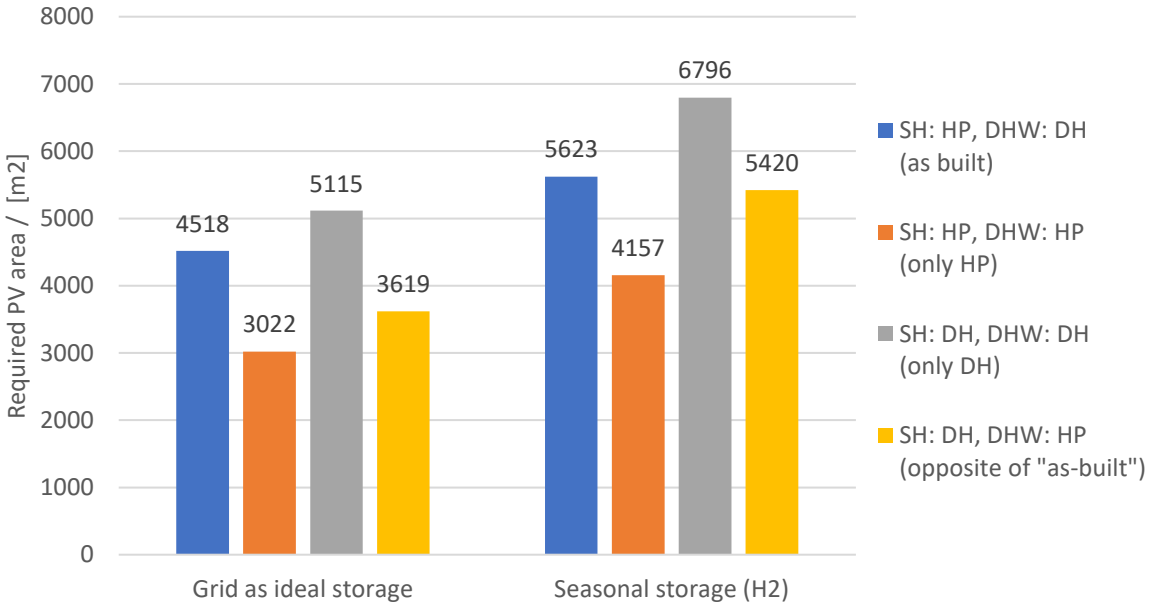

Figure 9: Required PV area (in m^2) to achieve PED for different heat generation variants and the two CO_2 balances. Calculation with monthly f_{CO2eq}

Table 3: Increase in the required PV area compared to the "as-built" case. Calculation with monthly f_{CO2eq}

	SH: HP DHW: DH (as-built)	**SH: HP DHW: HP (only HP)**	**SH: DH DHW: DH (only DH)**	**SH: DH DHW: HP (opposite of as-built)**
Grid as ideal storage	0%	-33%	13%	-20%
Seasonal storage (H_2)	0%	-26%	21%	-4%

Regardless of the CO_2 balance, the solution involving only the HP results in a reduced required PV area to reach PED, while the solution using only DH increases the required PV area. The "Grid as ideal storage" balance significantly reduces the required PV area for the "opposite of as-built" variant (-20%), while the "Seasonal Storage (H_2)" balance narrows the reduction to just -4%, making the two system concepts comparable in terms of PV area. Therefore, the choice of CO_2 balance can significantly impact the results and influence the evaluation of systems that implement different energy sources.

5. Discussion and conclusions

Various methods for calculating the necessary photovoltaic energy (i.e., required PV area) to achieve a positive CO_2 balance in PEDs with combinations of heat pump (HP) and district heating (DH) are investigated and compared. The methods differ for the type of conversion factors (annual or time-dependent, i.e., monthly), and the CO_2 balance, i.e., the use of "Grid as an ideal storage" or "Seasonal storage (H_2)". The methods are tested using an existing residential district in Innsbruck. To draw more general conclusions on the requirements to achieve PED with DH and HP, four system concepts are investigated, varying the heat generation: 1) HP for space heating (SH), and DH for domestic hot water (DHW) (i.e., as built), 2) HP only (for both SH and DHW), 3) DH only (for both SH and DHW), and 4) DH for SH, and HP for DHW.

As in case of absence of nuclear energy in the electric grid (as in the case of Austria), using CO_2 or non-RE PE conversion factors leads to the same conclusions, the analysis is carried out only by implementing the CO_2 conversion factors (f_{CO2eq}). Using monthly conversion factors results in higher CO_2 emissions during the winter months compared to annual conversion factors and provides a more accurate or "fair" representation of the available renewable sources throughout the year (which contrasts with the significantly higher demand in winter). In contrast, the use of annual conversion factors tends to underestimate this mismatch. However, obtaining monthly conversion factors could be challenging, especially for DH systems, which depend on the city/region and where often there is a lack of information about the time depending operation of the DH.

The net balance (i.e., the combination of annual f_{CO2eq} and "Grid as ideal storage" balance) leads to the smallest required PV area. Considering the grid as an ideal storage underestimated the required PV area because it assumes that the surplus of PV energy produced in summer can be used in the winter months without any loss. In contrast, implementing the seasonal storage (H_2 with roundtrip efficiency of 31%) in the CO_2 balance leads to a 23% increase of the required PV area (using monthly CO_2 conversion factor). The adoption of monthly CO_2 conversion factor and "Seasonal storage (H_2)" results in a 56% increase of the required PV area (5623 m^2) compared to the net balance.

Different heat generation variants are compared in terms of the required PV area against the "as-built" case. The choice of CO_2 balance method can significantly impact the results and even change the ranking of the systems implementing different energy sources. For the system with DH for SH and HP for DHW (opposite of "as-built"), the required PV has different trends (compared to the "as-built" case) depending on the CO_2 balance used. When using the "Grid as ideal storage", the required PV area significantly decreases (-20%), whereas with the "Seasonal storage (H_2)" balance, it slightly decreases (-4%), making the two variants comparable. Contrarily, the system concept with only HPs achieves the greatest savings in PV area independently of the use of storage in CO_2 balance (e.g. -26% with the "Seasonal storage (H_2)") and the case with only DH shows the largest increase in the required PV area (e.g. +21% with the "Seasonal storage (H_2)").

The results of the current study are influenced by the choice of the conversion factors, which are subject to change as the electric grid and the DH systems are supposed to undergo future decarbonization. The use of adapted conversion factors could significantly affect the results. Future studies should consider future scenarios of energy sources and the development of the load in particular in the building stock, such as e.g. in case of the electricity conversion factors suggested by (Ochs & Dermentzis, 2018). Challenging is the decarbonization of the DH, which will rely on high-temperature HPs and seasonal energy storage. To achieve a comprehensive assessment, it is also essential to consider the industry and mobility sectors, in particular electric vehicle charging. An open question that remains is, whether it is appropriate or justified at all to compensate non-renewable sources (e.g., natural gas in the DH) with renewable sources (e.g., PV), or whether a district relying on non-renewable energy sources can be considered a PED at all.

6. Acknowledgments

The project “Monitoring Innsbruck Campagne” is supported by Klima- und Energiefonds (FFG Österreichische Forschungförderungsgesellschaft Nr. 899823, 'IBK_Campagne'), Leuchttürme für resiliente Städte 2040 - Ausschreibung 2022.

The authors would like to thank NHT Neue Heimat Tirol, IIG Innsbrucker Immobiliengesellschaft and Stransky for the collaboration within the current project.

The outcomes of the Campagne-Areal project will contribute to the international projects IEA EBC A83 Positive Energy Districts, IEA HPT A61 Heat Pumps in Positive Energy Districts and IEA SHC T66 Solar Energy Buildings.

7. References

Albert-Seifried, V. et al., 2021. Definitions of Positive Energy Districts: A Review of the Status Quo and Challenges. *Sustainability in Energy and Buildings 2021,* pp. 493-506.

Feist, W. et al., 2007. *Passive House Planning Package 2007.* s.l.:s.n.

Guarino, F. et al., 2023. Renovation assessment of building districts: Case studies and implications to the positive energy districts definition. *Energy and Buildings,,* pp. Volume 296,.

Lindholm, O., Rehman, H. u. & Reda, F., 2021. Positioning Positive Energy Districts in European Cities. *Buildings,* pp. 11(1), 19.

Moreno, G. et al., 2021. How to Achieve Positive Energy Districts for Sustainable Cities: A Proposed Calculation Methodology. *Sustainability https://doi.org/,* Volume 13, no. 2: 710.

Ochs, F. & Dermentzis, G., 2018. *Evaluation of Efficiency and Renewable Energy Measures Considering the Future Energy Mix.* Syracuse, NY, s.n.

Ochs, F., Magni, M. & Dermentzis, G., 2022. Integration of Heat Pumps in Buildings and District Heating Systems—Evaluation on a Building and Energy System Level. *energies.*

OIB, Ö. I. f. B., 2023. *OIB-Richtlinie 6, Energieeinsparung und Wärmeschutz,* s.l.: s.n.

Ploß, M. et al., 2022. *Low-Cost nZEB, Paris-kompatible Mehrfamilienhäuser,* Dornbirn, Austria: s.n.

Shnapp, S., Paci, D. & Bertoldi, P., 2020. *Enabling Positive Energy Districts across Europe: energy efficiency couples renewable energy,* s.l.: s.n.

Streicher, W., 2018. *Fernwärmeverbundsystem der TIGAS für 2017 - Ermittlung des Primärenergiemix für das FW Verbundnetz der TIGAS für 2017 und weiteren Ausbau.,* s.l.: s.n.

TIGAS, 2024. *Fernwärmetransportschiene.* [Online]
Available at: https://www.tigas.at/produkte/fernwaerme/fernwaermetransportschiene/
[Accessed 14 08 2024].

Tosatto, A. & Ochs, F., 2024. Performance comparison of large-scale thermal energy storage and hydrogen as seasonal storage for achieving energy autarky in residential districts with different renovation levels. *Journal of Energy Storage,* Volume 98, Part A,.

Venturi, E. et al., 2024. *Campagne project: Passive houses to enable Positive Energy District.* Innsbruck, s.n.

Walker, S. et al., 2018. An assessment methodology of sustainable energy transition scenarios for realizing energy neutral neighborhoods. *Applied Energy,* Volume 228, pp. 2346-2360.

Two case studies for renewable district heating with solar fraction ≥ 70 %

Paul Volk, Christoph Schmelzer, Oleg Kusyy, Janybek Orozaliev, Ulrike Jordan, Klaus Vajen
University of Kassel, Department of Solar and Systems Engineering, Kassel (Germany)

Abstract

Two case studies of renewable district heating in rural areas with high solar fraction are presented. The first solar district heating system is currently under construction. Here, an approximately 8 km heating network will supply heat to 180 households. The main heat supply components are a large collector field (11,700 m²), a seasonal pit storage tank with 26,600 m³, two internal heat pumps (combined 1.5 MW thermal) to discharge the storage tank and raise the temperature for district heating, and a biomass boiler. The total energy demand of 3.6 GWh/a is supplied by solar thermal (67%) and biomass (26%). The rest is supplied by the internal heat pump (electricity 6%). The second district is smaller, with a total energy demand of 2.3 GWh/a for 100 buildings and a 5 km heating network. The demand is covered exclusively by solar thermal energy (87%) and an internal heat pump (electricity 13%). The main components of the second case study are 5,700 m² of collectors (flat plate and evacuated tube), one 15,000 m³ storage tank and the large heat pump (1 MW thermal). Both systems were modeled in TRNSYS and optimized by using numerical algorithms to achieve the lowest levelized cost of heat (LCoH).

Keywords: Solar District Heating, High Solar Fraction, Renewable District Heating

1. Introduction

Around 57 % of Germany's final energy consumption in 2022 was used to provide heating and cooling (33 % for space heating and hot water) with a renewable share of 17.5 % (German Association of Energy and Water Industries 2024; Umweltbundesamt 2024). In order to achieve a climate-neutral heat supply, local authorities in Germany are obliged to develop heating plans by 2028 (municipalities with more than 10,000 inhabitants by 2026) (German Federal Government 2023). These plans shall define how a climate-neutral heat supply for citizens and companies can be achieved in the respective municipalities by 2045 at the latest.

Based on previous experience and the guidelines of Baden-Württemberg (KEA Baden-Württemberg 2020) and Hesse (Landes Energie Agentur Hessen 2020), a special focus is put on heating networks. Various nationwide studies (Blesl and Eikmeier 2015; Gerbert et al. 2018; Gerhardt 2019) also predict a significant expansion of heating networks, as this can reduce the transformation costs and speed up the process for achieving a climate-neutral heat supply. Local heat sources (solar energy and environmental heat for heat pumps) are generally not sufficiently available to guarantee a comprehensive regenerative heat supply, especially in large cities with dense development (Hess et al. 2019). Fossil-free heating networks are therefore an important prerequisite for decarbonizing the heat supply in these areas. For rural areas, the main focus lies currently on extensive energy-efficient building refurbishment and a building-specific heat supply with individual heating systems (especially heat pumps). The share of heating networks in the future heat supply is less than 20% in the study of Gerhardt (Gerhardt 2019), for example. The reason for this is the low heat density of rural areas, which makes the implementation of heating networks more difficult. However, extensive building refurbishment is generally very cost intensive and also very time-consuming due to low refurbishment rates. In rural areas, this is exacerbated by the fact that the buildings have significantly lower market values compared to urban areas and the refurbishment costs increase relative to the value of the building, which makes implementation less likely. As a result, the challenges for the heating transition in rural areas are particularly large. On the other hand, there are also opportunities. For example, rural areas generally have larger undeveloped areas that represent

© 2024. The Authors. Published by International Solar Energy Society
Selection and/or peer review under responsibility of Scientific Committee
10.18086/eurosun.2024.03.07 Available at http://proceedings.ises.org

an important resource for the provision of renewable heat and can be used, for example, for large solar thermal fields, storage facilities and heating centers. Furthermore, the laying of pipelines in rural areas is significantly cheaper than in cities.

This paper examines initiatives to decarbonize the local heating supply in German villages based on two case studies in Rauschenburg-Bracht and Amöneburg-Rüdigheim. Decentralized solutions that include building-specific refurbishments and heat pumps are compared with centralized solar local heating systems that include extensive use of solar fields and thermal energy storage. The results of existing feasibility studies, simulation analyses and cost assessments will be analyzed to identify the most effective strategies to significantly reduce CO_2 emissions. The investigations will form the basis for the implementation of climate-neutral heat supply systems that are economically viable and can cover both current and future energy needs in order to show other villages possible future scenarios for a regenerative heat supply.

2. Case Study 1: Rauschenberg-Bracht

2.1. Boundary Conditions

The first case study focuses on the German village called Rauschenberg-Bracht (or in short “Bracht”) in northern Hesse. The village with around 860 inhabitants consists of 2 districts, which are around one kilometer apart, and has a total of 294 buildings. In 2013, a feasibility study was presented for solar local heating (solar coverage rate 100%) for the village at a citizens' meeting in order to make the village's heating supply CO_2 neutral and independent of fossil resources (Solarwaerme Bracht eG 2024). This concept envisaged a 12,000 m² solar field with a 45,000 m³ above-ground tank thermal energy storage (TTES) and did not include any other heat generators. As this concept turned out to be very costly and funding from the state of Hesse or the federal government was ruled out, the Department of Solar and Systems Engineering at the University of Kassel was asked to optimize the solar district heating system and to investigate whether an individual building refurbishment with decentralized heat supply (mainly via air-to-water heat pumps) or a central heat supply via a regenerative heating network would be the more cost-effective solution for a CO_2 saving of at least 80 %. To coordinate (and later finance) the implementation of a regenerative heat supply in the village, the people of Bracht have founded a citizens' cooperative that collected data on the heat supply and the conditions of the cooperative members' buildings. Based on current data, approximately 180 out of the 294 buildings in Bracht will be linked to the local heating network. This includes 156 current buildings and 24 new ones that are being built in the next years.

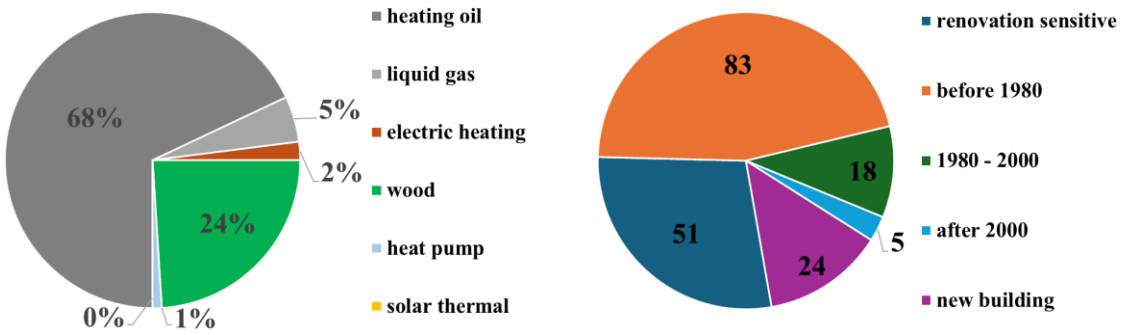

Figure 1: Relative distribution of heat generators in the analyzed buildings (left) and years of construction of the buildings divided into 5 categories (right) (Kelch et al. 2023).

Figure 1 shows the relative distribution of heat generators and the age structure of thes buildings in Bracht. More than 80 % of the buildings were constructed before 1980, with some being half-timbered. The category “renovation sensitive” refers to those half-timbered houses and buildings constructed before 1919. Additionally, a significant part of these predominantly single-family homes is heated using oil heaters or wood stoves, as Bracht is not connected to a natural gas network .

2.2. Centralized vs. dezentralized solution

Kelch et al. (Kelch et al. 2024) examined the refurbishment of buildings with decentralized supply via mainly air source heat pumps or the creation of a regenerative heating network as more cost-effective solution. Here, several assumptions were initially made to make them comparable. Firstly, in both scenarios, 180 potential consumers had to be supplied with heat, including space heating and hot water. Furthermore, the heat supply had to be achieved without the local use of fossil fuels and the use of biomass was not allowed to exceed level of the original state.

In the decentralized renovation scenario described in the paper, decarbonization is targeted through specific insulation measures in individual buildings. This involved using reference buildings in the village, for which detailed information was available, to estimate when building renovation measures would be necessary. For example, it was determined that all buildings that exceed a certain limit value in the heat transfer coefficient must be renovated in such a way that limit values for current funding programs are achieved. The number of underfloor and panel heating systems already installed in the buildings was also investigated. For the new buildings, it was assumed that these would be fitted exclusively with panel heating systems. In addition, new biomass boilers were only proposed for buildings with the highest heat demand that are difficult to renovate (half-timbered houses) or for buildings that already heat with biomass. All other buildings should be equipped with air heat pumps in that scenario. The result of these calculations was that once the insulation measures have been implemented, the total heat consumption of the buildings examined can be reduced by an average of 18%. This, coupled with heat generation using only biomass boilers and heat pumps, meant that CO_2e emissions in the buildings concerned could be reduced by 95%. The proportion of heat provided after the renovation measures is finally shown in Figure 2.

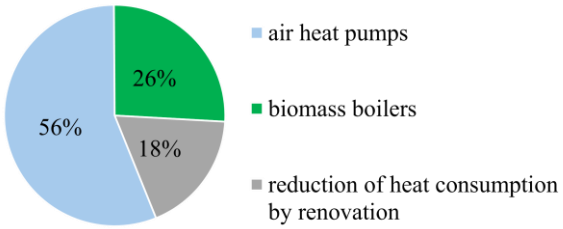

Figure 2: Reduction of heat consumption and shares of heat supply for decentralized renovation scenario in Bracht (Kelch et al. 2024).

The solar district heating scenario focused on a significant reduction in CO_2e emissions through the integration of renewable energy sources, primarily by solar thermal energy. This approach targeted the 156 existing buildings and focused on minimal renovation measures in the buildings (such as insulation of basement ceilings etc.). In this scenario, these measures reduced the heating requirement by around 2 %. The core components of the heating network scenario included an extensive solar thermal collector field coupled with a seasonal pit thermal energy storage system (PTES), coupled with an electric heat pump to cool the storage to about 31°C during the heating season. This cooling significantly reduces both the size and cost of the storage system compared to maintaining it at the higher temperatures traditionally required. As it was assumed that the proportion of biomass can remain the same compared to the original situation, but must not exceed this in future solutions, the concept also provided for the use of biomass boilers to cover the remaining heat demand. The system sizing was optimized using TRNSYS simulations over a period of 3.5 years, with a focus on the last year in which the system reached thermal equilibrium. The optimization aimed to achieve the lowest levelized cost of heat and involved configuring the sizes of the system components using GenOpt software. Of the various possible variants, all of which had similar costs, the variant that offered the greatest flexibility for the future, such as additional consumers connected to the heating network, was favored. This variant comprised a 13,000 m² flat-plate collector field, a PTE storage volume of 26,600 m³, 2 biomass boilers with a total power of 600 kW_{th} and a heat pump with 1.300 kW_{th}, which supply the network with heat via a 250 m³ short-term storage tank (Kelch et al. 2024). Taking into account the practical boundary condition, a collector area of

around 11,700 m², a heat pump output of 1.200 kW_{th} and a total biomass boiler output of 550 kW_{th} working on a 400 m³ buffer storage tank turned out to be the best solution, achieving net levelized costs of heat after subsidies of 104 $€_{net}$/MWh (213 $€_{net}$/MWh before subsidies) (Kelch et al. 2022). With this system (see Figure 3), which would have a solar fraction of almost 70 %, a CO_2 reduction of approx. 97 % could also be achieved.

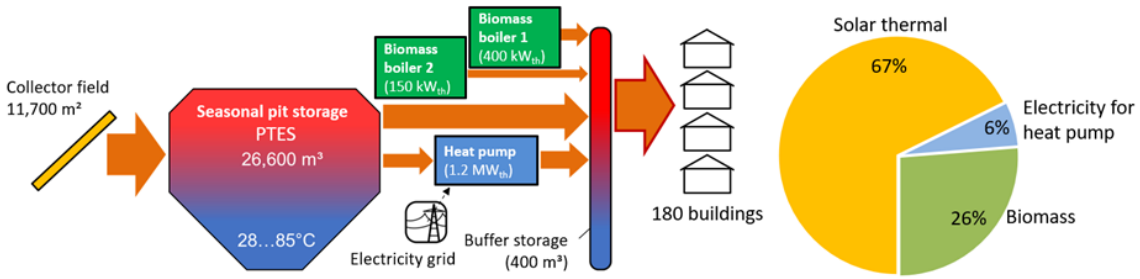

Figure 3: Components, their dimensioning and their share of the heat supply in the district heating solution for Bracht.

In a comparison of the two possible solutions for CO_2-neutral heat supply, Kelch et al. found that centralized solar heating and decentralized building refurbishment achieve the same full heating costs per building within the scope of the calculation accuracy (see Figure 4). However, the main difference between the two variants is that the centralized solution achieves the full CO_2 reduction in just a few years after commissioning, while the decentralized refurbishment takes significantly longer, considering realistic refurbishment rates of 2-3 %/a at most (figure 4, right).

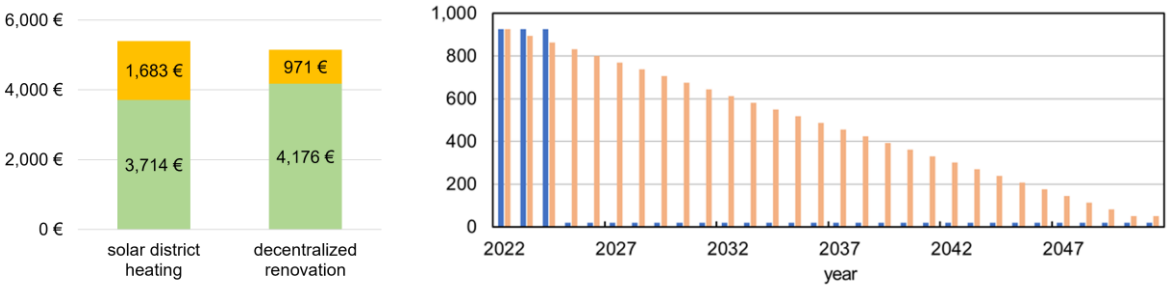

Figure 4: Annual heat costs per average building from solar district heating vs. decentralized solution in Bracht (left) and comparison of annual CO_2e emissions in t_{CO2}/a (right) (Kelch et al. 2024).

These investigations reinforced the citizens' cooperative's original goal of installing a renewable heating network in their village, so that they finally entered the implementation phase with the aim of setting up the system shown in Figure 3.

2.3. Implementation, current design and status

In the original concept developed by Kelch et al. (Kelch et al. 2024), all heat generators initially worked on the buffer storage tank. One of the reasons for this was that the heat pump did not have to provide heat at the network supply temperature. The goal was to increase the efficiency of the heat pumps by connecting them to the center of the storage tank, effectively pre-heating the water of the biomass boiler. In the project currently being implemented (Figure 6), however, the storage tank with a volume reduced to 200 m³ has more the function of a hydraulic switch. Both the biomass boiler (only one boiler in this concept) and the heat pumps can operate directly at the grid supply temperature. In addition, a total heat pump output of 1.5 MW is planned, which is slightly more than in the originally planned variant. This system is currently being modeled and investigated using simulations. However, no results are yet available.

Construction of the PTES (Figure 5) began in November 2023. The process was interrupted several times due to adverse weather conditions. However, the pit will be completely covered with liners by the end of July 2024, meaning that the PTES is likely to be filled by fall 2024. The availability of sufficient water to fill the PTES quickly continued to prove problematic in this area, but has now been resolved.

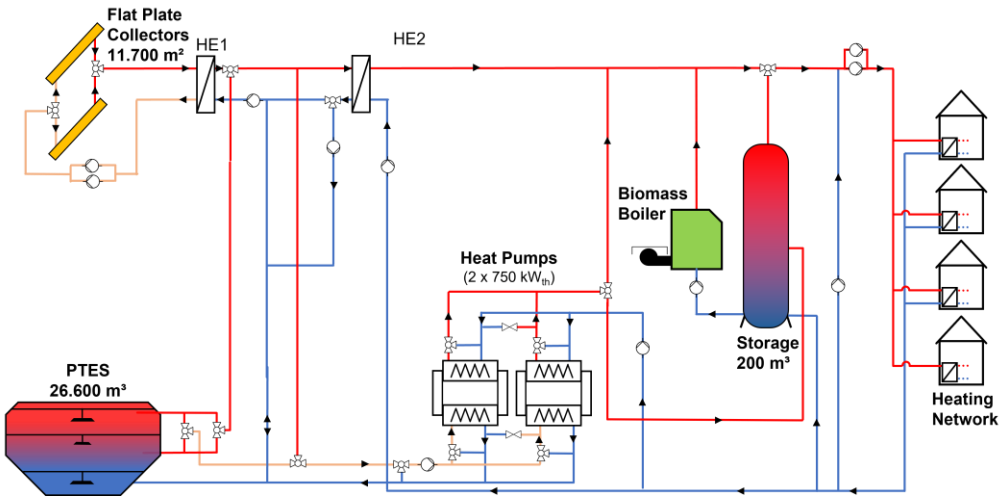

Figure 6: Schematic representation of the hydraulics in Bracht of the system expected to be implemented.

Figure 5: Construction progress of the PTES (image as of July 2024).

In order to check the technical performance of the system, the PTES is to be measured at several points. In addition to the sensors for monitoring the water temperature inside of the PTES, sensors for measuring the wall temperature and the ground temperature in the immediate vicinity of the PTES are also planned to be able to estimate the heating of the ground around the storage. There are also plans to measure the solar thermal field as well as all generators and the heating network to monitor the system and draw conclusions for similar, future projects.

3. Case Study 2: Amöneburg-Rüdigheim

3.1. Boundary Conditions

The second village considered in this paper is Amöneburg-Rüdigheim (Rüdigheim for short), located about 17 kilometers south of Bracht. A citizens' co-operative has also been set up to build a renewable heating network in the village and to provide district heating for about 100 houses, which corresponds to a connection rate of around 60 %. The initial aim was to achieve 100 % solar coverage using a seasonal storage system, mainly to be independent of biomass and fluctuating fuel prices. For this purpose, a planning office, together with a plant constructor and a manufacturer of tank thermal energy storages (TTES), has developed a concept in which the 100 houses with an estimated annual heat demand of 2,250 MWh/a can be supplied via a 5 km heating network. The concept, as shown in Figure 7, envisages a 7,000 m² solar thermal evacuated tube collector (ETC) field and two 15,000 m³ seasonal TTES. Special heat transfer stations, which can enable a return temperature of 40 °C according to the manufacturer (supply temperature approx. 68 °C), are intended to increase the storage capacity in this concept.

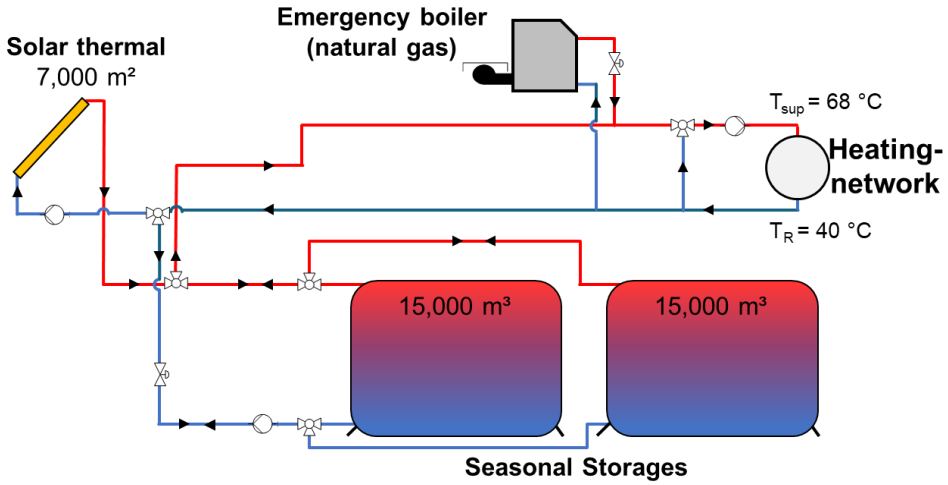

Figure 7: Schematic representation of the original concept in Rüdigheim with 2 TTES and a 7,000 m² evacuated tube collector field.

3.2. Re-simulation of the original variant

The federal subsidies used for the manufactures calculation are not offered any more and the assumed costs were based on rather low investment and operating costs. Additionally, a 100 % solar-powered heating network for the full supply of existing buildings has not yet been realized. For this reason, the University of Kassel, financially supported by the Energy Agency of Hesse (LEA), carried out an extended simulation study. The aim was to examine the technical feasibility and economic viability of the existing concept in more detail and, if necessary, to optimize it.

To ensure the technical functionality, the manufacturer's simulation model in the Polysun software (Vela Solaris), including the technical boundary conditions, was transferred to the TRNSYS simulation program as a first step, so that potential optimizations could be carried out using generic algorithms with GenOpt and Python. For its calculations, the manufacturer has assumed that the storage tanks and the collectors are connected directly to the network without heat exchangers. Furthermore, it was assumed that the heat consumption profile is constant over one month, with a constant demand (including network losses) between April and September and a constant demand from October to March. In the manufacturer's simulations, a value of 1,162 kWh/m²a was used as the annual irradiation at the collector level and the supply temperature of the solar field was simulated at 90 °C in matched flow operation, which has led to additional heat losses in the storage tank of 360 MWh/a. Assuming that the return temperature of 40 °C specified by the manufacturer can be achieved, the manufacturer's specifications regarding the energy balances could be confirmed in the TRNSYS calculations of the University of Kassel, as shown in Figure 8.

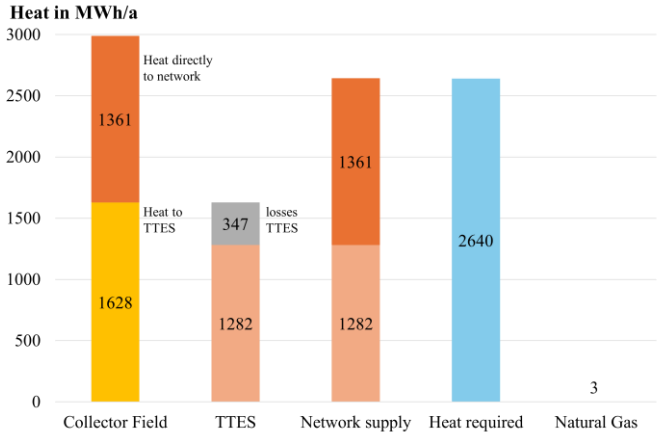

Figure 8: Results of the TRNSYS simulations for the energy balances of the manufacturer's concept.

In the second step, the costs of the original variant were updated and adapted to new subsidy schemes in Germany according to the new funding for efficient heating networks (German Federal Office for Economic Affairs and Export Control 2024), only the investment costs of the collectors can be subsidized in this concept. For example, the cost functions for the storage tank and the collectors were adjusted, the operating costs were increased and a price increase (for electricity consumption) was taken into account in the calculations. All other investment costs and cost functions were assumed by the manufacturer and updated to new boundary conditions as required. With these boundary conditions, an LCoH of 378 €$_{net}$/MWh (237 €$_{net}$/MWh after subsidies) was calculated for the original system design with 100 % solar fraction. This are relatively high costs compared to other regenerative heating networks, which, however, are mainly biomass-based. As implementation is unlikely under these circumstances and the function of a flagship project for other municipalities would be jeopardized, a simulation study was carried out with the aim of reducing costs. The simulations were also based on the assumption that the supply and return temperatures can be maintained as in the original concept and that TTES are used for heat storage. In addition, the heat requirement should still be covered without using fossil fuels, as favored by the citizens' cooperative.

3.3. Economic optimization of the system

Table 1 shows the results calculated with TRNSYS and GenOpt regarding the sizing of the main system components for the different variants studied. However, in variant 1b, without optimization in GenOpt, an attempt was first made to reduce costs by replacing two-thirds of the collector area with less expensive flat-plate collectors (FPC). The total collector area of 7,000 m² was to remain unchanged. Nevertheless, the simulations for this variant showed that the heat demand could not be covered, so the LCoH were not calculated for this variant.

Table 1: Results for collector area, storage tank size, thermal output of the heat pump of the optimized variants based on the initial variant 1 and the resulting LCOH according to Baez and Larriba Martinez (Baez and Larriba Martinez 2015).

Nr.	Variant description	Storage Size in m³	Collector Field (%ETC / %FPC) in m²$_{gross}$	Thermal Power Internal Heat Pump in kW$_{th}$	LCoH before funding in €$_{net,2022}$/MWh
1	original concept manufacturer	2 x 15,000	7,000 ETC only	-	378
1b	original concept, mix of collector types	2 x 15,000	7,000 (33 % / 67 %)	-	heat demand not covered
2	original concept, optimized in TNSYS GenOpt	2 x 14,600	7,600 (43 % / 57 %)	-	363
3	1 Storage	1 x 30,000	7,200 (29 % / 71 %)	-	327
4	1 storage, internal heat pump	1 x 24,000	6,500 (29 % / 71 %)	337	326
5	1 storage, internal heat pump (T_{sup} HP 69 °C)	1 x 23,800	6,600 (26 % / 74 %)	337	325
6	1 storage with manufacturers limitation, internal heat pump (T_{sup} HP 69 °C)	1 x 15,000	5,700 (23 % / 77 %)	1026	323

Starting with variant 2, the system was then optimized in the simulations. For this purpose, an hourly profile was used instead of a monthly, constant load profile. In addition, heat exchangers were included between the collector field and the TTES as well as between the TTES and the network, and the control of the overall system was adapted in order to optimize potential variants with internal heat pumps. The TRNSYS simulations were carried out over 2.5 years in six-minute increments, with only the last year being evaluated. The balance limit was the heating central including heat generators and TTES. The target function in GenOpt was the LCoH per kWh with full coverage of the heat demand, for which the global optimum was determined iteratively. The dimensioning of the main components, the proportion between flat-plate and evacuated tube collectors, the heat pump connection heights to the TTES and, in some cases, the control of the heat pumps, such as the switch-on temperature of the heat pumps, were varied.

Variant 2 shows the optimum LCoH for the case in which 2 TTES are still used in the system. The optimization for this case showed that the storage tanks can be slightly smaller than in the manufacturer's original variant, but the area of the solar thermal system must be around 9 % larger with a flat-plate collector share of around 60 %. In this case, the LCoH would fall by around 4 %, which still corresponds to a relatively high heat price.

To further reduce the costs, in variant 3 was that only one TTES (with twice the volume) used instead of the two originally planned. Due to economies of scale, this results in lower storage costs per m³ of storage volume. In addition, the use of only one storage tank reduces the volume-to-surface ratio, which decreases the storage losses. The result for this variant was that, as originally, 30,000 m³ of storage volume is required with a 3 % higher total collector area. However, this would be able to provide the necessary heat with 70 % flat-plate collectors, so that the heat price (with a solar fraction of still 100 %) could be reduced by around 10 % to a value of 327 €$_{net}$/MWh. An internal heat pump was integrated into the concept from variant 4 onwards. This is intended to cool the TTES below the return temperature of the heating network and thus increase the storage capacity due to the greater temperature spread. The storage volume can be reduced in this way, which may make realization easier due to lower construction heights and reduced space requirements. Under these boundary conditions, variant 4 resulted in a storage volume that is around 20 % smaller than variant 3 and a collector field that was 10 % smaller if a heat pump with 337 kW$_{th}$ is used to cool the TTES. Similar dimensioning resulted for variant 5, in which the heat pump control was selected so that it feeds heat into the storage tank at a maximum of 1 K above the supply temperature of the heating network, which leads to an average supply temperature of the heat pump of 69 °C. The LCoH for these variants are similar to variant 3 with a smaller area requirement and a smaller storage size, but a solar coverage rate of 100 % is no longer achieved here.

As the simulations are based on the boundary conditions of the manufacturer's special house transfer stations and the manufacturer is also expected to supply the TTES in this context, no TTES larger than 15,000 m³ can be provided (manufacturers limitation). Therefore, in variant 6, lowest costs were determined for a system in which the heat demand of the network can be covered with only one storage tank of the maximum size with an internal heat pump. In this system, around 15 % less collector area is required compared to variants 4 and 5 with about the same LCoH. However, the thermal heat pump capacity triples, which leads to a significantly higher electricity requirement and thus to a further reduction in the solar coverage rate. Since this variant nevertheless achieves one of the most cost-effective heat supplies and further dispenses with the use of fuel-based heat generators, this variant is currently being favored by the citizens' co-operative and has been submitted for funding.

3.4. Details of the favored concept

In order to be able to provide sufficient heat with the reduced collector area, the collectors in this variant are connected in series. The 4,400 m² (around 3/4 of the area) of flat-plate collectors are used to preheat the heat transfer fluid, which is then reheated in the 1,300 m² of evacuated tube collectors to the required temperature. Between November and May, the collectors are regulated to a maximum of 75 °C to increase collector efficiency. Despite the smaller collector field, the calculations show that stagnation cannot be prevented in this variant towards the end of the summer, so that stagnation protection is required. Assuming that the collector field losses amount to 3 %, the energy balance of the overall system can finally be taken from figure 9. As can be seen at 3 MWh/a, the fossil reheating requirement is negligible and the heat losses in the TTES, at 9 %, are only a third of the storage losses than in the originally planned variant.

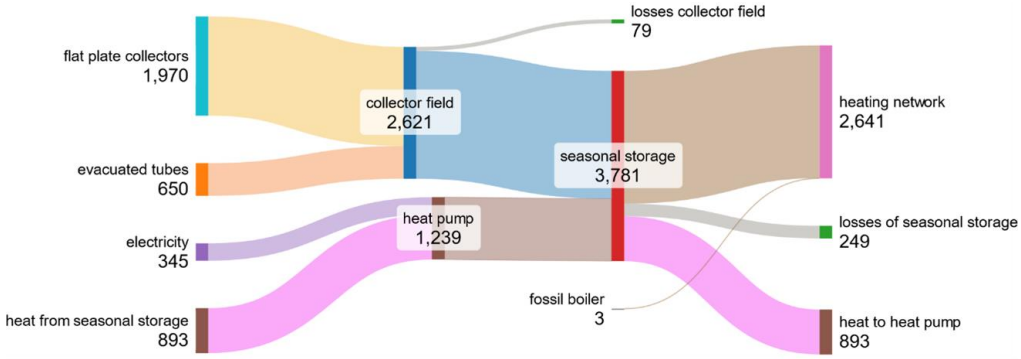

Figure 9: Energy balances of optimized system in Rüdigheim (numbers depict energies in MWh/a).

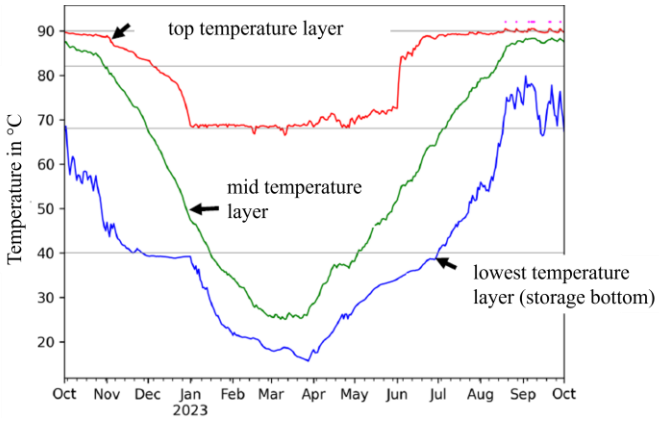

Figure 10: Simulated storage temperatures in 3 layers of the TTES.

As can be seen in figure 10, the average storage tank temperature over the course of a year ranges between around 88 °C and 25 °C. The top storage layer, on the other hand, is only for a few time steps below the network flow temperature. This indicates that the concept was designed to be cost-optimized, the solar fraction reaches almost 90 percent. Figure 11 shows in summary how the optimized system in Rüdigheim is schematically structured. Renewable district heating can be provided for existing buildings with only two different regenerative heat generators in combination with a TTES.

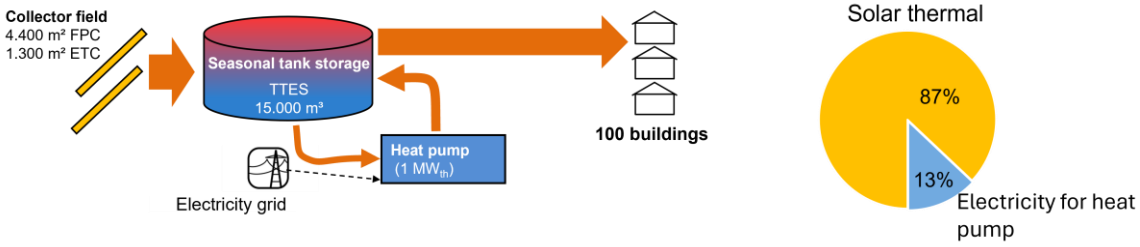

Figure 11: Components, their dimensioning and their share of the heat supply in the optimized system (variant 6) of Rüdigheim.

Table 2 summarizes once again how the Rüdigheim heating network will differ from the Bracht network. The high proportion of solar coverage is currently unique for existing areas. In contrast, however, Bracht has more competitive heating costs.

Table 2: Summary of the data from both case studies (network length incl. house connection pipes).

Locality	Heat Demand in GWh/a	Network length in km	Connected Households	Collector Field in m^2_{gross}	Solar fraction in %	Storage Size in m^3	LCoH before funding in $€_{net,2022}$/MWh
Bracht	3.6	8	180	11,700	70	26,600	213
Rüdigheim	2.3	5	100	5,700	87	15,000	323

4. Conclusion

This article showed that district heating can, despite low heat densities, lead to practicable and sustainable solutions for a climate-friendly central heat supply in rural areas in Germany due to existing open spaces and low infrastructure costs. Through the investigations in Rauschenberg-Bracht and Amöneburg-Rüdigheim, viable models were identified that maximize the use of renewable energies and minimize reliance on fossil resources. Using the example of Rauschenberg-Bracht, it was shown that central solar thermal heating networks in combination with seasonal thermal energy storages can compete economically with the individual heat supply of buildings, while reducing CO_2 emissions to almost zero after a very short time. In addition, the example of Amöneburg-Rüdigheim was used to show how such simulation-based system optimization can be used to reduce the high initial costs of 100 % renewable heating networks. The implementation of these solutions highlights the importance of dedicated citizen initiatives and government funding, which play a critical role in the implementation of renewable heating networks.

5. Acknowledgment

The authors would like to thank the Hesse State Ministry of Economy for long term committed support of the two solar district heating projects and for directly funding several studies as well as measurement equipment (FKZ: E/611/71690944). We also thank the Federal Ministry of Economics and Technology (BMWi) for funding the accompanying scientific research (“ruralHeat”, FKZ: 03EN6031). We are furthermore grateful to the respective energy cooperatives Sonnenwärme Rüdigheim eG and Solarwärme Bracht eG as well as cupasol GmbH and the associated project partner Viessmann Deutschland GmbH for the great co-operation.

References

Baez, M. J., Larriba Martinez, T., 2015. Technical Report on the Elaboration of a Cost Estimation Methodology. Work Package 3 - Estimating RHC energy costs. Madrid, Spain: Creara, URL: https://www.front-rhc.eu/wp-content/uploads/2014/11/FROnT_D3.1_elaboration-of-a-cost-estimation-methodology_2015.07.22.pdf, accessed November 14, 2020.

Blesl, M., Eikmeier, B., 2015. Die 70/70-Strategie. Konzept und Ergebnisse. URL: https://www.agfw.de/strategien-der-waermewende/perspektive-der-fw-7070-4040, accessed July 30, 2024.

Gerbert, P., Herhold, P., Burchardt, J., Schönberger, S., Rechenmacher, F., Kirchner, A., Kemmler, A., Wünsch, M., 2018. Klimapfade für Deutschland: The Boston Consulting Group (BCG); Prognos AG. URL: https://web-assets.bcg.com/e3/06/1c25c60944a09983526ff173c969/klimapfade-fuer-deutschland.pdf, accessed July 30, 2024

Gerhardt, N., Ganal, I., Jentsch, M., Rodriguez, J., Stroh, K., Buchmann, E.K., 2019. Entwicklung der Gebäudewärme und Rückkopplung mit dem Energiesystem in -95% THG-Klimazielszenarien. URL: https://www.iee.fraunhofer.de/content/dam/iee/energiesystemtechnik/de/Dokumente/Veroeffentlichungen/2019/2019_Feb_Bericht_Fraunhofer_IEE_-_Transformation_Waerme_2030_2050.pdf, accessed July 30, 2024

German Association of Energy and Water Industries (BDEW), 2024. Statusreport: Wärme. URL: https://www.bdew.de/service/publikationen/statusreport-waerme/, accessed July 9, 2024.

German Federal Government, 2023. Act for heat planning and the decarbonization of heating networks. URL: https://www.bmwsb.bund.de/SharedDocs/gesetzgebungsverfahren/Webs/BMWSB/DE/Downloads/waermeplanung/wpg-bgbl.pdf?__blob=publicationFile&v=2, accessed July 16, 2024.

German Federal Office for Economic Affairs and Export Control, 2024. Information sheet: Federal funding for efficient heating networks (BEW). URL: https://www.bafa.de/DE/Energie/Energieeffizienz/Waermenetze/Effiziente_Waermenetze/effiziente_waermenetze_node.html, accessed July 30, 2024

Hess, S., Vollmer, R., Wapler, J., Kleinstück, M., Bongs, C., Henning, H.-M., 2019. Ambient Heat Source Availability for Low-Ex Heating of Multi-Family Buildings. *ISES Solar World Congress 2019*. Santiago, 3-7 November

KEA Baden-Württemberg, 2020. Leitfaden Kommunale Wärmeplanung. URL: https://www.kea-bw.de/fileadmin/user_upload/Publikationen/094_Leitfaden-Kommunale-Waermeplanung-022021.pdf, accessed July 16, 2024.

Kelch, J., Kusyy, O.,Orozaliev, J., Vajen, K. 2022. Weiterentwicklung und Optimierung des Konzepts einer solaren Nahwärmeversorgung für ländliche Gebiete am Beispiel von Bracht-Dorf. Abschlussbericht eines Forschungsvorhabens, gefördert durch das Land Hessen und den Europäischen Fonds für regionale Entwicklung; FKZ: EF960 0039/2021 20008503. URL: https://www.uni-kassel.de/maschinenbau/index.php?eID=dumpFile&t=f&f=4844&token=5882c5c8243e420723571b4d64b2773b3579081b, accessed July 30, 2024

Kelch, J., Kusyy, O., Zipplies, J., Orozaliev, J., Vajen, K., 2023. Solar District Heating versus Renovation of Buildings as Measures for Decarbonization of Heat Supply in Rural Areas. *EuroSun 2022*. Kassel, 25-29 September

Kelch, J., Kusyy, O., Zipplies, J., Orozaliev, J., Vajen, K., 2024. Comparison of solar district heating and renovation of buildings as measures for decarbonization of heat supply in rural areas. Solar Energy Advances, 4:100060.

Landes Energie Agentur Hessen, 2020. Die Wärmewende voranbringen. Kommunale Wärmeplanung in Hessen gemeinsam gestalten, URL: https://redaktion.hessen-agentur.de/publication/2021/3443_LEA_Broschuere_Kommunale_Waermeplanung_212018.pdf, accessed July 16, 2024.

Solarwaerme Bracht eG, 2024. Aktueller Stand und Historie Solarwaerme Bracht. URL: https://www.solarwaerme-bracht.de/aktueller-stand-und-historie-solarw%C3%A4rme-bracht/, accessed July 15, 2024.

Umweltbundesamt, 2024. Erneuerbare Energien in Zahlen. URL: https://www.umweltbundesamt.de/themen/klima-energie/erneuerbare-energien/erneuerbare-energien-in-zahlen#waerme, accessed July 9, 2024.

VDI-Gesellschaft Bauen und Gebäudetechnik (GBG),2012. VDI 2067 Blatt 1/ Part 1: 2012-09, Wirtschaftlichkeit gebäudetechnischer Anlagen Economic efficiency of building installations. Grundlagen und Kostenberechnung, Fundamentals and economic calculation (2067 Blatt 1/ Part 1). Düsseldorf

Sensitivity Analysis of Solar District Heating Systems

Christian Wagner[1], Harald Dehner[1]

[1] University of Applied Sciences Upper Austria, Wels (Austria)

Abstract

The economic consideration of large-scale solar thermal systems to support district heating is often a challenge. Due to the necessary planning efforts and high investment costs of the solar thermal components, the solar-supported scenario is often ruled out. Therefore, the present work deals with a tool where an approximate economic sensitivity analysis can be carried out at the beginning stage of the planning process. This includes the calculation of the levelized cost of heat (LCoH) and the comparison with conventionally operated district heating systems. Further, by using cost functions of solar thermal systems and thermal energy storages, a preliminary calculation of the investment costs of solar supported district heating in different variations is made possible. The calculation of the LCoH considers the energy prices, lifetime of the components, costs for CO_2-emissions, increase of energy prizes, etc. By varying the mentioned parameters, a sensitivity analysis of the LCoH is performed and analyzed over the lifespan of the system. To validate the tool, results from completed projects were recalculated and interpreted. To do this, different scenarios are defined, LCoHs are calculated and a sensitivity analysis for each scenario is carried out. The results show a consistent correlation between the individual project results and the calculation methods.

Keywords: solar district heating, levelized cost of heat, sensitivity analysis

1. Introduction

Climate change presents new global challenges for our society. Both political and technical solutions are therefore being sought on a global scale. The European Union (EU) has established new benchmarks in climate policy with the introduction of the “Green Deal”. A central objective of the Green Deal is the reduction of greenhouse gas emissions by 55% by 2030. Additionally, the goal is to achieve complete climate neutrality by 2050 (European Commission, 2021). In order to achieve this goal, the energy sector in particular is facing major challenges, as it is responsible for 75% of the greenhouse gas emissions in the EU (European Commission, 2023a). It is evident that within the energy sector, heating and cooling (H&C) has the potential to play a pivotal role in decarbonizing the energy system. Given that H&C accounts for about 50% (European Commission, 2023b) of the final energy demand in the EU, it is clear that this must be a key focus for decarbonization efforts. Presently, the share of renewable energy sources utilized in the H&C sector in only marginally above 23%, and the majority of energy consumption is still reliant on fossil fuels (European Commission, 2023b).

The European Commission identifies district heating, including the integration of renewable energy sources, as a key technology for the decarbonization of the H&C sector (European Commission, 2022). For instance, the use of solar thermal district heating offers an obvious solution for integrating renewable energy sources into district heating systems. It is indisputable that the integration of solar systems in district heating networks can be technically and successfully implemented. A significant number of solar district heating systems are in operation, particularly in Denmark (Tian et al., 2019). Nevertheless, the share of solar thermal energy supplied to district heating systems in the EU is currently only 0.1% (European Commission, 2022). Consequently, the potential of solar district heating systems is far from being exploited.

A lack of information on the economy of solar-supported district heating systems could be one of the reasons for that. Due to the large number of parameters that have to be taken into account, which are often unknown at the beginning of the planning activities, it is extremely complex to be able to make well-founded statements about the economic viability of a solar-supported district heating systems. Therefore, the latter systems are often ruled out before the actual planning begins. In this work, a sensitivity analysis tool is developed where a comprehensive comparison between solar-supported and conventional district heating systems is carried out.

© 2024. The Authors. Published by International Solar Energy Society
Selection and/or peer review under responsibility of Scientific Committee
10.18086/eurosun.2024.03.08 Available at http://proceedings.ises.org

2. Methodology

The present tool is designed to quantify the economic efficiency of solar-supported district heating (SDH) systems compared to conventionally operated district heating (CDH) systems. The mentioned comparison is conducted in two principal stages:

1) Calculation of the Levelized Cost of Heat
    a. Calculation of the Levelized Cost of Heat for a SDH system
    b. Calculation of the Levelized Cost of Heat for a CDH system
2) Execution of the sensitivity analysis
    a. Comparison of the Levelized Cost of Heat
    b. Variation of individual parameters for sensitivity analysis

2.1 Calculation of the Levelized Cost of Heat

There are a number of methodologies that can be employed to calculate economic efficiency. To illustrate, there are static methods, such as the static amortization method, and dynamic methods that also consider the timing of incoming and outgoing payments, such as the annuity method or the internal rate of return method (Poggensee & Poggensee, 2021). Due to the large number of options for analyzing economic efficiency, it is often difficult to compare the individual results for different systems, therefore a standardized calculation method is also being sought in the solar thermal sector. In the course of IEA SHC Task 54 “Price reduction of solar thermal systems” the calculation method of “Levelized Cost of Heat” (LCoH) for solar thermal applications was finally introduced. The calculation of LCoH is based on the methodology of the “Levelized Cost of Energy” (Short et al., 1995), which has so far been used mainly in the electricity sector, for example in (Branker et al., 2011; Zakeri & Syri, 2015).

In essence, LCoH describes the capital utilization throughout the service life, divided by the supplied energy. The calculation method of LCoH, used in this work, was formulated within the collaborative work in IEA SHC Task 54 and is given in the equation below (Louvet et al., 2019):

$$LCoH = \frac{I_0 - S_0 + \sum_{t=1}^{T} \frac{C_t(1-TR) - DEP_t \cdot TR}{(1+r)^t} - \frac{RV}{(1+r)^T}}{\sum_{t=1}^{T} \frac{E_t}{(1+r)^t}} \qquad \text{(eq.1)}$$

Where $LCoH$ is the levelized cost of heat (€/kWh), I_0 is the initial investment (€), S_0 are subsidies and incentives (€), T is the period of analysis in year, C_t are operation and maintenance costs (€/a), TR is the corporate tax rate (%), DEP_t and E_t are asset depreciation (€/a) and final energy (kWh/a), RV is the residual value (€) and finally r is the discount rate (%).

In IEA SHC Task 54, a simplified formula was employed for the calculations, as the focus was on small, mainly residential solar thermal systems. For example, interest rates, corporate tax, asset depreciation and the residual value were often set at 0 (Louvet et al., 2019). As district heating systems are predominantly commercial or industrial, the complete formula, including corporate tax rate, asset depreciation and residual value, as outlined in eq.1, is employed for the calculation of LCoH in the course of this work.

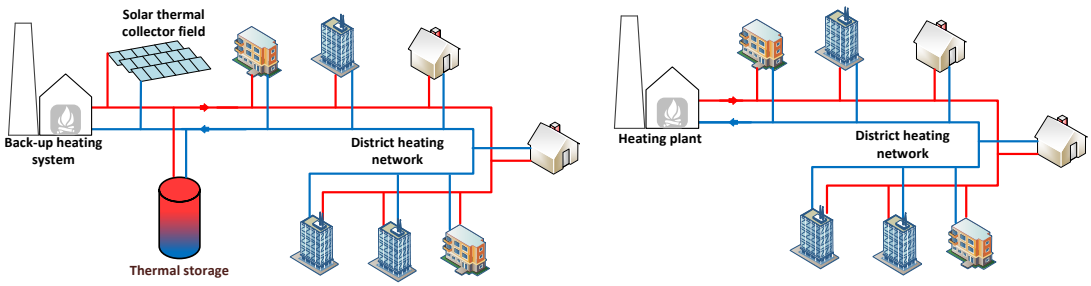

Fig. 1: Definition of solar-supported district heating system with back-up heating system (left) and conventionally heated solar district heating system (right) in scope of this work

As a basis for the sensitivity analysis, the LCoHs are calculated for both SDH and CDH systems. For the definition of the respective systems, see Fig. 1. As SDH generally does not have a solar fraction of 100 %, they require a back-up heating system which provides the remaining energy demand of the district heating system. It should be noted that, in scope of this work, the LCoH of the SDH also includes the costs associated with the supply of the residual energy demand that cannot be met by the solar thermal system.

The procedure for carrying out the calculation of LCoH and sensitivity analysis is shown in Fig. 2. The required main data for the analysis consists of the annual energy quantity of the district heating network, the utilized solar components, the solar energy yield, the heat generator, the energy source used, current energy prices and as well as general data such as the observation period, costs for CO_2-emissions and the corporate tax rate.

The initial step is to enter the annual energy demand of the district heating network. Subsequently, the solar thermal components are selected, including the solar field and thermal energy storage size, as well as type of the collectors and storage to be employed. Once the required solar thermal components have been selected, their investment costs are determined. Either the costs are already known, for example from a project-specific offer, they can be entered directly. However, in the absence of known costs, the costs are estimated using specific cost curves, both for solar thermal collectors, according to (Mauthner, 2016; VDI 3988, 2018) and for thermal energy storages, according to (Mauthner, 2016; Goeke, 2021). As the selection of the solar thermal components is made via drop-down menu, the cost curves are assigned automatically. Consequently, the investment costs are calculated based on the collector field area and thermal energy storage size and the specific costs according to the cost curves.

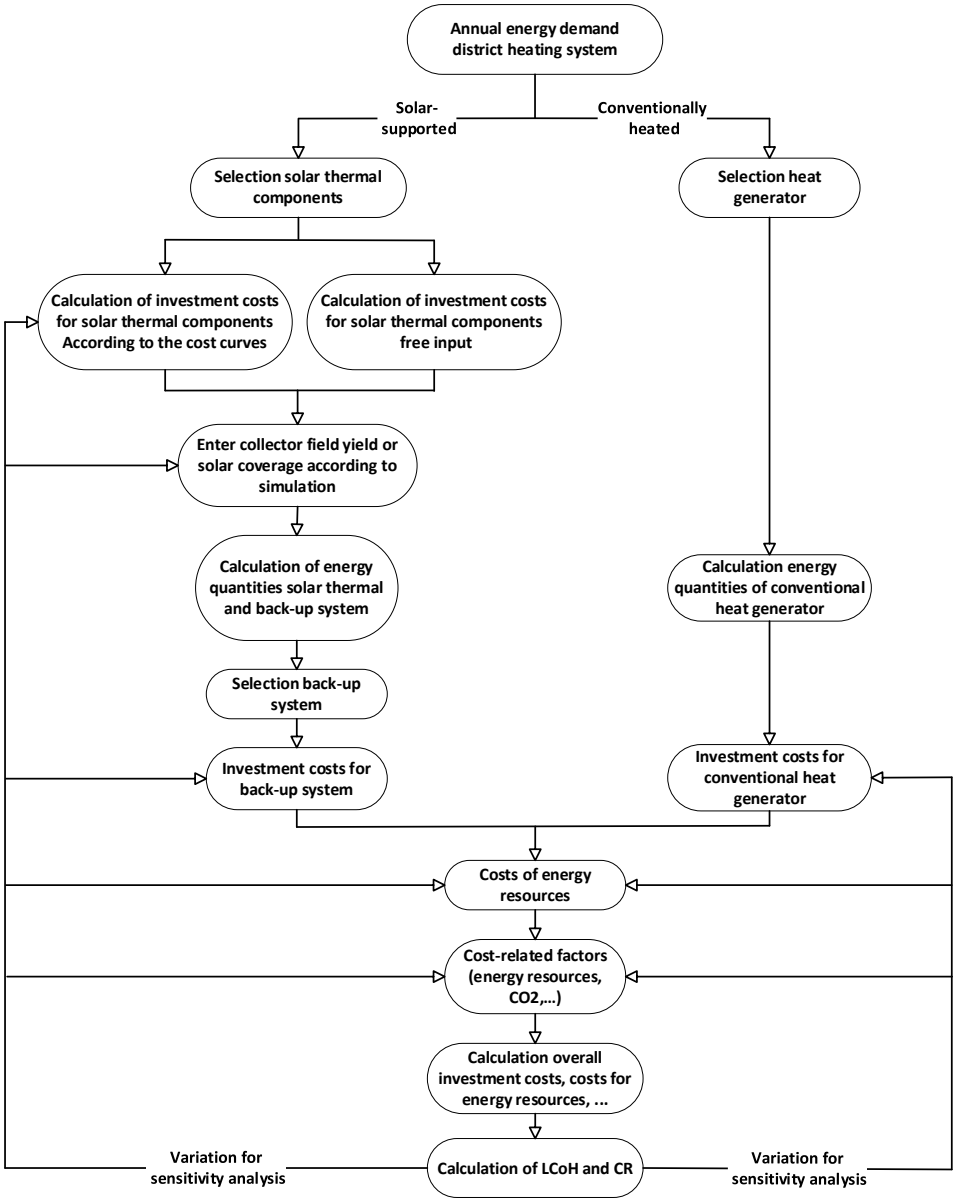

Fig. 2: Workflow for calculation of the LCoH and sensitivity analysis

Once the investment costs of the solar thermal parts have been calculated, the annual collector field yield is entered according to a simulation. Based on the entered annual energy demand and the annual solar energy yield, the amount of energy that must be provided by the back-up heating system is determined. Subsequently, a back-up heating system is selected. A variety of heat generators are available, including biomass boilers, oil and gas fired boilers or heat pumps. After entering the annual efficiency factor of the selected heat generator, the investment costs of the back-up heating system are calculated.

Next step is to enter the type of heat generator for the CDH system. As CDH systems does not have a solar thermal support, the entire annual energy demand of the district heating network must therefore be provided by the conventional heat source. After entering the investment costs of the conventional heat generator, the costs of energy resources, maintenance and operational costs, the LCoH are calculated in accordance with eq.1.

The LCoH can be calculated for any desired observation period. However, as the individual components, such as the solar thermal collectors or the conventional heat generator, have different estimated lifetimes, this is taken into account via replacement investments and the residual value. The replacement investments and the assumed lifespan of the mentioned components are calculated in accordance with the VDI 2067 "Economic efficiency of building installations – Fundamentals and economic calculation" (VDI 2067, 2012).

2.2 Execution of the sensitivity analysis

The sensitivity analysis includes the calculation of the LCoH, both for SDH and CDH systems, for a variety of scenarios. For each scenario, a selected parameter such as the change in energy prices, costs of CO_2 emissions or a change in investments costs, is altered and the resulting impact on the LCoH is observed. The ratio of the two LCoH (cost ratio = CR) is determined as the key figure for the economic sensitivity analysis (Neyer et al., 2016). The CR is defined as follows:

$$CR = \frac{LCoH_{SDH}}{LCoH_{CDH}} \qquad \text{(eq.2)}$$

Where CR is the Cost Ratio (-), $LCoH_{SDH}$ (€/kWh) is the levelized cost of heat for the solar-supported district heating system and $LCoH_{CDH}$ (€/kWh) is the levelized cost of heat for the conventional operated district heating system.

The CR thus represents the ratio of the LCoH of the two systems under consideration. If the CR is less than 1, the heat generation costs of the SDH system are less than those of the CDH system, indicating a more economical option.

The sensitivity analysis tool calculates the CR based on the entered and defined values. Subsequently, a single specific parameter is altered while all other parameters remain constant, resulting in a recalculation of the LCoH and respectively CR, see Fig. 2. This process is repeated for all defined parameters, and the results are then displayed graphically. This provides a clear visualization of which parameters exert a significant influence on the LCoH and which are negligible. Furthermore, the cumulative costs within the considered observation period of the two analyzed systems are shown graphically.

3. Results

In the following section, the sensitivity analysis tool is employed to assess the feasibility of two different district heating systems in Austria. This includes a consideration of a district heating network in an Austrian city with a planned collector area of almost 44000 m² and a small local district heating network with a collector area of 1590 m². In order to achieve this, the LCoHs are initially recalculated in accordance with the available data and then compared with the published data according to (Becke, 2021; Riebenbauer, 2022). Subsequently, a series of hypothetical scenarios and variants are calculated and a sensitivity analysis is conducted.

3.1 District heating network of an Austrian city

The first project considers the possibility of integrating a large-scale solar thermal system into an urban district heating network. A feasibility study has therefore already been carried out (Riebenbauer, 2022). The feasibility study is used to validate the sensitivity analysis carried out in this work. The selected scenarios and corresponding data required for the calculations are shown in Tab. 1. The objective of scenario A1 is to calculate and compare the LCoH in accordance with the feasibility study that has already been conducted. A1 also serves as a starting point for the subsequent scenarios. In scenario A2, the system considered in scenario A1 is compared with a conventional gas-fired district heating system. In scenario A3, the LCoH is calculated in the event that the solar thermal collector area and the thermal energy storage volume are reduced by 50%.

Tab. 1: Scenarios and given data for sensitivity analysis of a district heating network of an Austrian city

	Scenario A1 (starting point, data according to (Riebenbauer, 2022))	**Scenario A2**	**Scenario A3**
Gross collector area	44847 m²	44847 m²	22424 m²
Collector type	Flat plate	Flat plate	Flat plate
Thermal energy storage volume	2 x 50000 m³	2 x 50000 m³	1 x 50000 m³
Type of back-up heating	Biomass (exits already)	Biomass (wooden chips)	Biomass (wooden chips)
Annual energy demand	27707 MWh/a	27707 MWh/a	27707 MWh/a
Specific solar energy yield	334 kWh/(m²a)	334 kWh/(m²a)	428 kWh/(m²a)
Comparison with	-	Purely gas fired district heating system	Purely biomass fired district heating system (wooden chips)

The values presented in Tab. 1 were integrated into the developed tool and employed for the calculation of the LCoH of the SDH system. The following boundary conditions were established for the calculation:

- Observation period: 20 years
- Discounting factor: 1.035
- Corporate tax: 25%
- Annual efficiency factor for biomass boiler: 0.75 (VDI 3988, 2018)
- Factor for CO_2 emissions natural gas: 0.2008 kg_{CO2}/kWh (Quaschning, 2012)
- Price for biomass (wooden chips): 0.04 €/kWh
- Annual efficiency factor gas-fired boiler: 0.8 (VDI 3988, 2018)
- Price for natural gas: 0.08 €/kWh
- Price for CO_2 emissions: 45 €/t_{CO2}
- Factor for price increase: 1.02

The LCoH for scenario A1 has now been calculated using the shown values and assumptions and the sensitivity of the results is illustrated in Fig. 3. The calculated LCoH is 0.0674 €/kWh, which is markedly lower than the calculated LCoH of the feasibility study (Riebenbauer, 2022), which was 0.0936 €/kWh. One reason for this is the definition of total energy. The LCoH in this tool always refer to the total annual energy required by the district heating network, which consists of the LCoH of the solar thermal part and the LCoH of the back-up heating system. However, the LCoH calculated in (Riebenbauer, 2022) refer only to those of the solar thermal part. Since these are higher than the LCoH of the back-up heating system in this scenario, the LCoH to meet the total annual energy demand must be lower than that of the solar-only part. If only the solar-related LCoH were calculated the resulting costs would be 0.0855 €/kWh. The LCoH for the solar-thermal part only calculated with this tool is therefore within the range of the LCoH calculated in the feasibility study. The small difference can be explained by the different investment costs. The present tool calculates the investment costs on the basis of cost curves. In this scenario, these are likely to be slightly lower than those assumed in the feasibility study. In addition to the costs associated with the energy prices, investment costs for the thermal storage have the most significant impact on heat generation costs, which was also corroborated in (Riebenbauer, 2022).

In scenario A2, a hypothetical comparison is made between a SDH system with a biomass back-up heating system and a gas-fired CDH system. The data from scenario A1 is used as the foundation for this scenario. In both cases, it is assumed that the SDH and the CDH systems are completely new, therefore there is no availability of any of the components at the beginning of the observation period. The economic efficiency of the two systems is evaluated in relation to the CR, as illustrated in (eq.2). The sensitivity of the CR is shown in Fig. 4. It is clearly visible, that the CR with the preselected parameters is already below 1 and therefore the SDH system is already more econmomical than the gas-fired CDH system.

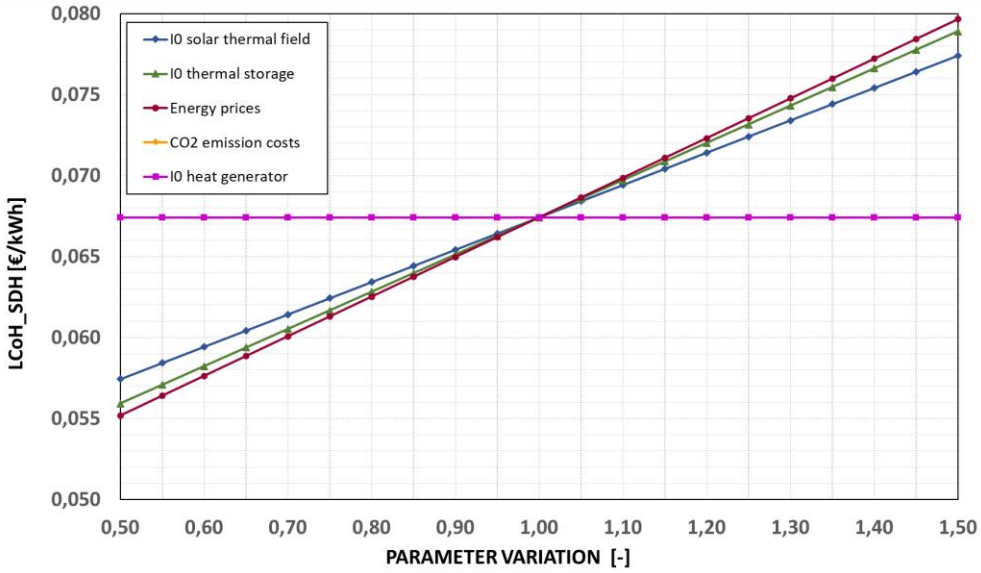

Fig. 3: Sensitivity of the calculated LCoH scenario A1

Moreover, it is evident that fluctuations in energy prices exert the most significant impact on the CR, whereas cost of CO_2-emissions, bases on an assumed value of 45 €/t_{CO2}, exert a comparatively minor influence. In contrast to scenario A1, the necessity of purchasing the biomass and gas-fired boiler has an impact on the CR, as these also require an investment. When considering the impact of investment costs in isolation, it is evident that the thermal energy storage has the most significant effect on the CR.

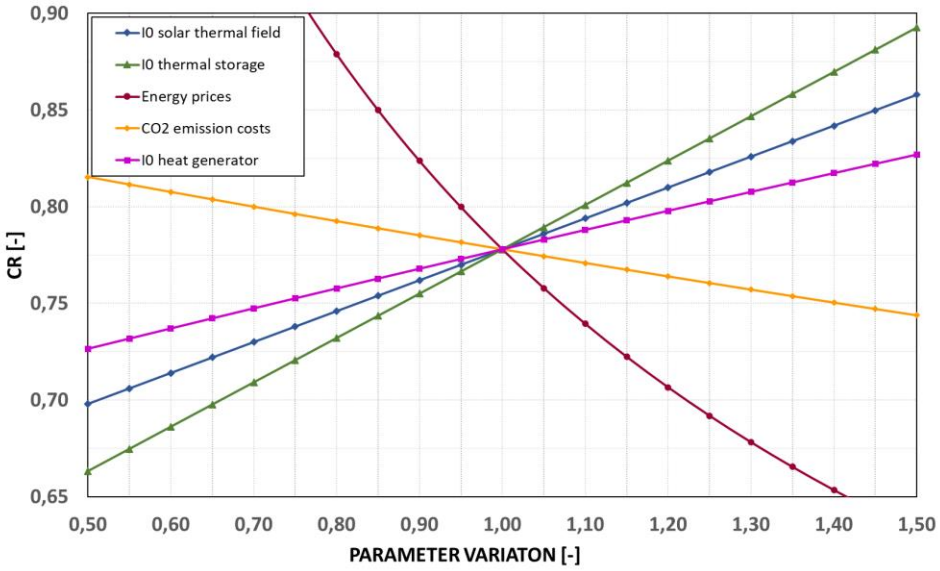

Fig. 4: Sensitivity of the calculated CR scenario A2

In addition to the LCoH and the CR, the cumulative costs are calculated over the observation period, see Fig. 5. As a consequence of the high investment costs associated with the solar thermal components, the SDH system exhibits significantly higher cumulative costs at the outset of the observation period, but after just 12 years the cumulated costs of the SDH system are already lower than those of the gas-fired CDH system. Due to the assumed lifespan of the biomass boiler of 15 years, a replacement investment is necessary. This is also evident in Fig. 5. Despite this replacement investment, when considering an observation period of 20 years, the SDH system is still more economical than the CDH system.

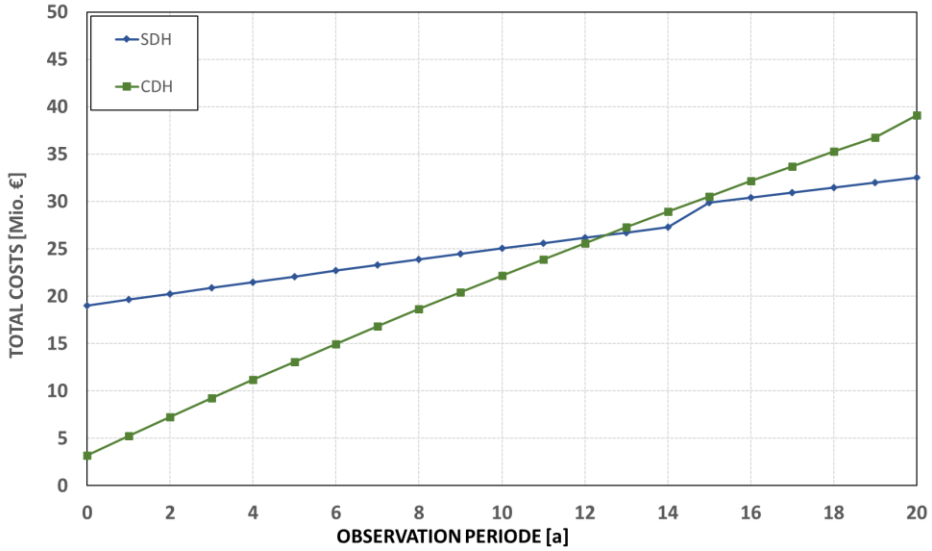

Fig. 5: Cumulative cost scenario A2

In scenario A3, the solar components are each reduced by 50% due to the high investment costs. The SDH system is now being compared with a conventional biomass-fired district heating system. Fig. 6 illustrates the sensitivity of the calculated CR for scenario A3. The calculated LCoH of the SDH system amount to 0.0654 €/kWh and those of the conventional system to 0.063 €/kWh, which results in a CR of 1.035. In (Riebenbauer, 2022), the LCoH was also calculated for the case of a 50% reduction in the solar thermal components. There, the LCoH amounted to 0.0746 €/kWh. However, these heat production costs again only relate to the solar-thermal heat production and not to the annual energy requirement, which needs to be covered. Fig. 6 also illustrates that a price reduction of approximately 20% for the thermal energy storage is sufficient to achieve a CR of 1. This indicates that the SDH and CDH system would have identical heat production costs. A similar outcome would be attained if the energy prices for the fuel were to rise by 15%. In this scenario, the costs associated with CO_2-emissions are not a factor, as both the SDH and CDH system utilize a biomass as energy source.

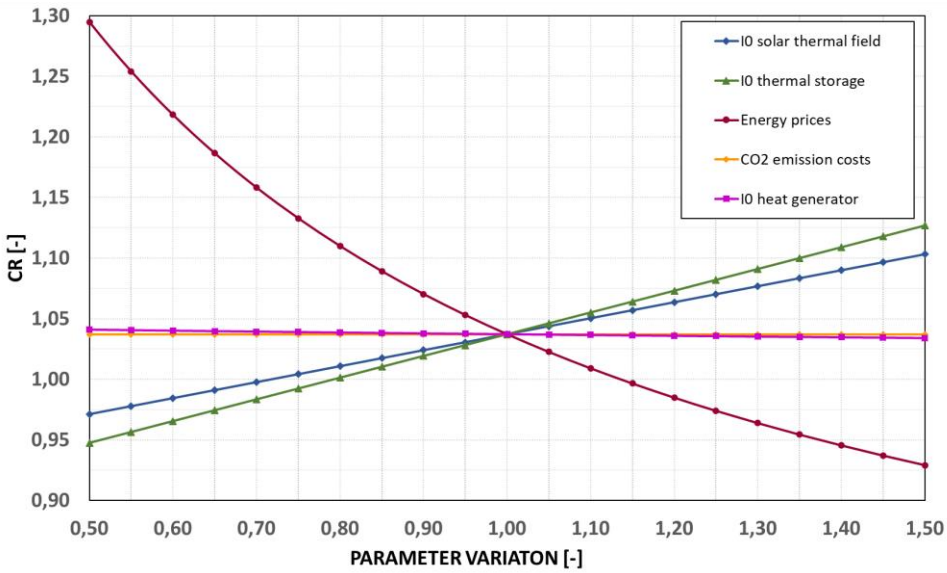

Fig. 6:Sensitivity of the CR scenario A3

3.2 Small local district heating system

In the second project, the developed tool will be applied to a local district heating network. To be able to compare and validate the LCoH of different variants, they are calculated once according to VDI 3988, “Solar thermal process heat” (VDI 3988, 2018) and once with the present tool. Scenario B1 uses the data from (Becke, 2021) to calculate the LCoH. It is assumed that the biomass-fired back-up heating system is already in place. Since this is a real existing system, it is not necessary to use cost curves as an input for the sensitivity analysis, but the known costs can be entered directly. The boundary conditions are the same as for the previous project. The different scenarios are listed below in Tab. 2.

Tab. 2: Scenarios and given data for sensitivity analysis of a local district heating network

	Scenario B1 (starting point, data according to (Becke, 2021))	**Scenario B2**	**Scenario B3**
Gross collector area	1590 m²	1590 m²	1590 m²
Collector type	Double glazed flat plate	Double glazed flat plate	Double glazed flat plate
Thermal energy storage volume	100 m³	100 m³	100 m³
Type of back-up heating	Biomass (exits already)	Biomass (wooden chips)	Biomass (exits already)
Annual energy demand	4509 MWh/a	4509 MWh/a	6493 MWh/a
Specific solar energy yield	458 kWh/(m²a) (simulated)	458 kWh/(m²a) (simulated)	664 kWh/(m²a) (measured)
Comparison with	Purely biomass fired district heating system (exists already)	Purely gas fired district heating system	Purely biomass fired district heating system (exists already)

Scenario B1 represents the realized state, using simulated data. As the CR here is just under 1, the SDH system is more economical that the CDH system, see Fig. 7. This is mainly due to the fuel savings resulting from the use of solar thermal energy. If the costs would decrease by 10% both the SDH and CDH system would have the same heat production costs. The LCoH calculated with the developed tool amount to 0.0504 €/kWh. These costs have been calculated for the SDH system and therefore include the costs of the solar-thermal part as well as the costs of the back-up system. For comparison, LCoH was also calculated according to VDI 3988, “Solar thermal process heat (VDI 3988, 2018). LCoH of 0.0516 €/kWh is specified here. Both calculated LCoH values are therefore in a similar range. If investment costs are considered on their own, the investment costs of the collector field have the greatest influence on the heat production costs in this project, while the thermal energy storage has only an insignificant influence.

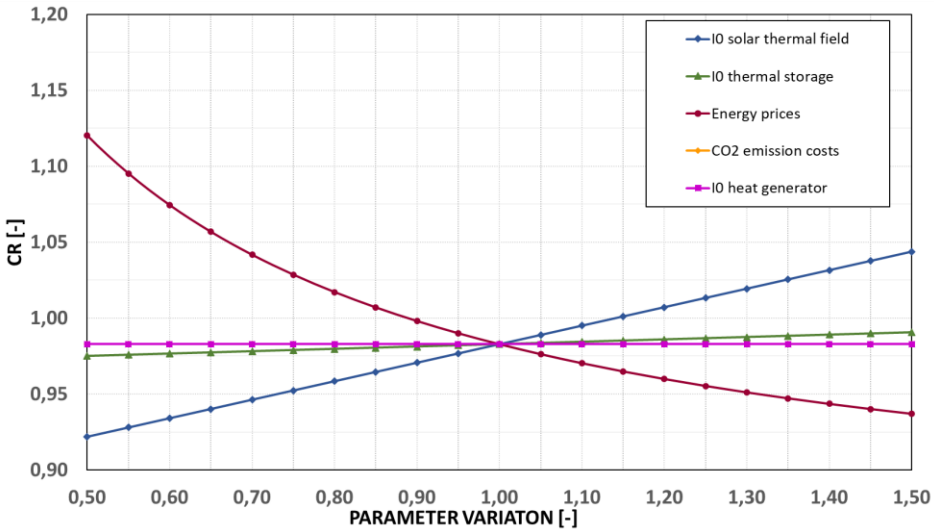

Fig. 7: Sensitivity of the CR of scenario B1

In scenario B2, as in scenario A1, a comparison is made between a SDH system with a biomass back-up heating system and a conventional gas-fired district heating system. In contrast to scenario B1, it is assumed that no heat generators are available yet and therefore all heat generators have to be purchased. The result of the sensitivity analysis of the CR of scenario B2 is shown in Fig. 8. Again, energy prices have the greatest impact on the CR.

Due to the comparison with a gas-fired district heating system, the cost of CO_2-emissions also has a significant impact. Looking only at the investment costs, those for the heat generators have the greatest influence in this scenario, while the investment costs for the thermal energy storage have almost no influence. This is mainly due to the fact that the investment cost of the 100 m³ thermal energy storage is only small part of the total investment cost. The cumulative cost for this project can also be displayed graphically. This is shown in Fig. 9. After just 3 years, the SDH system is already more cost-effective than the CDH system.

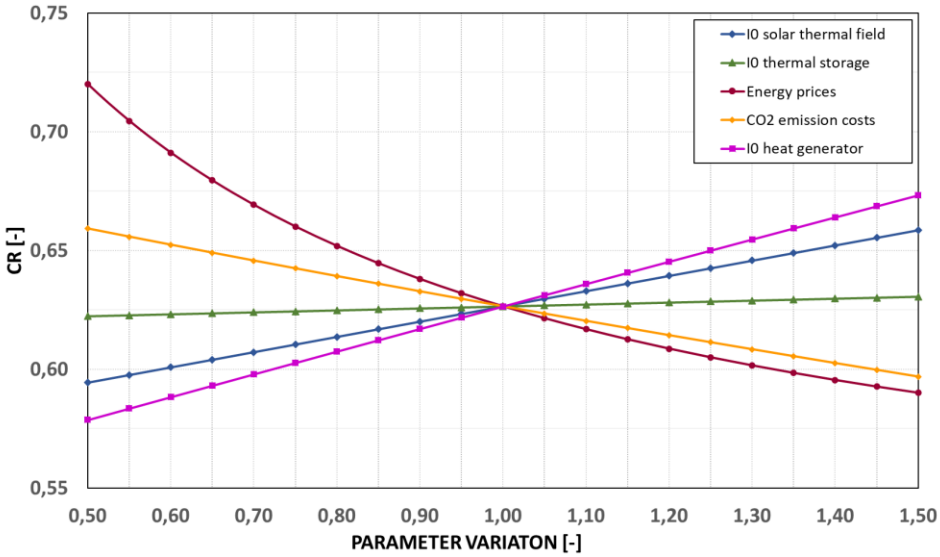

Fig. 8: Sensitivity of the CR scenario B2

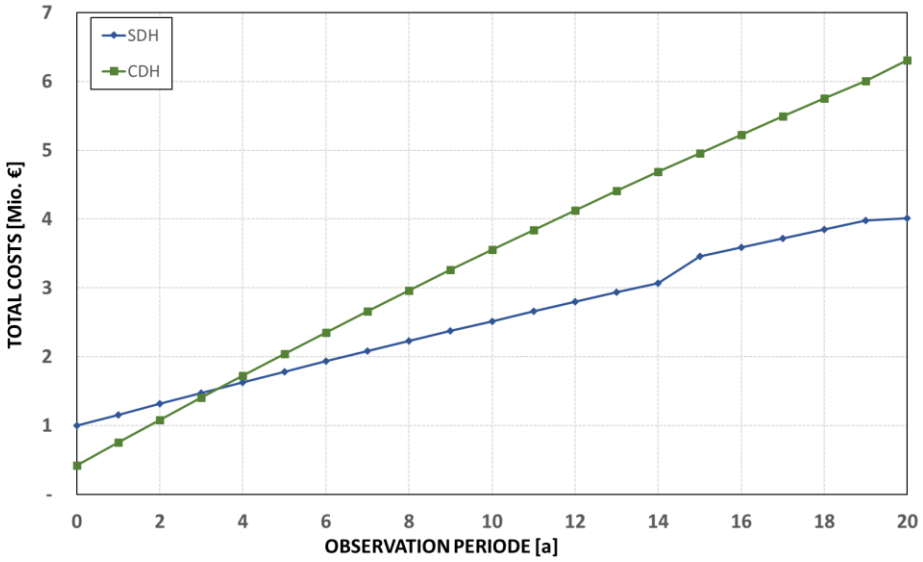

Fig. 9: Cumulative costs of scenario B2

As B1 is a realized project, a sensitivity analysis is conducted in scenario B3 using data collected in accompanying research. While the calculation in scenario B1 was based on simulated data, the sensitivity analysis in scenario B3 employs real measured data. In the simulation, an annual heat demand of 4509 MWh/a was assumed. However, the actual operation of the district heating network demonstrated a total heat demand of 6493 MWh/a. The latter resulted in a specific solar energy yield that was about 45% higher than that assumed in the simulation, as listed in Tab. 2. Subsequently, a sensitivity analysis was conducted for scenario B3 utilizing the measured data. The calculation of the LCoH for the SDH system yields in a value of 0.0482 €/kWh, whereas the costs of 0.0513 €/kWh are recorded for the CDH system. In comparison to scenario B1 there has been a reduction in the LCoH from 0.0504 €/kWh to 0.0482 €/kWh for the SDH system. This is a consequence of an increased annual heat demand and the resulting higher specific solar energy yield. The projected LCoH for the CDH system have been calculated to be 0.0513 €/kWh, which results in a CR of 0.93. The sensitivity of the CR is illustrated in Fig. 10. Scenario B2 exhibits comparable characteristics to that of scenario B1. However, CR is slightly diminished in comparison to that observed in scenario B1, predominantly due to the reduced LCoH of the SDH system.

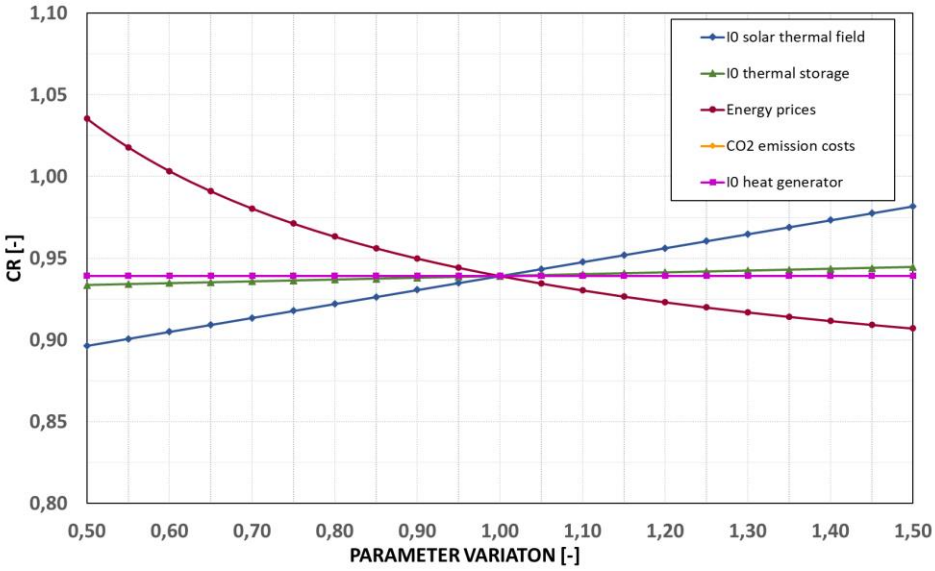

Fig. 10: Sensitivity of the CR scenario B3

3.3 Summary of the calculations performed

Previous chapters demonstrated the applicability of the developed tool in practical settings. Consequently, it is feasible to ascertain the economic viability of SDH systems at the outset of the planning phase. The results of the calculated LCoH and the LCoH from the validation data are listed in Tab. 3. In scenario A1 and scenario A3, it was established that the SDH system is not more cost-effective that the CDH system. This is primarily due to the high investment costs associated with the solar thermal components. In scenario A2, the SDH system would be the more economical option when compared to the CDH system. However, this is only because a conventional gas-fired district heating system was selected as the basis for comparison. A comparison of the LCoH with scenarios A1 and A2 reveals that the highest LCoH is still associated with scenario A2. A comparison of the validation data reveals that the calculated LCoH is markedly lower than those derived from existing validation data. However, this is largely attributable to the fact that the LCoH of the validation data was only calculated for the solar thermal part. Given the significant investment costs associated with these, the LCoH calculated exclusively for the solar thermal part is also considerably higher.

When analyzing the existing local heating network, the LCoH calculated within this work shows a good overlap with the LCoH calculated according to the VDI 3988, “Solar thermal process heat” (VDI 3988, 2018). In scenario B1, it was established that the SDH system is more cost-effective than the CDH system within the specified boundary conditions. This is primarily due to reduction of fuel consumption resulting from the utilization of solar thermal energy. In scenario B2, a further hypothetical comparison of two new systems was conducted. This scenario once more encompasses a SDH system with a biomass back-up boiler and a gas-fired CDH system. As with the previous scenario, the results demonstrated that the SDH system is considerably more cost-effective than the gas-fired district heating system. In scenario B3, actual measured values were employed on the calculation of the LCoH. As a consequence of the increased annual energy demand and the associated increase in the specific solar energy yield, a further reduction in the LCoH was observed in comparison to scenario B1.

Tab. 3: Comparison of the calculated results of the various scenarios and validation data

	Scenario A1	**Scenario A2**	**Scenario A3**	**Scenario B1**	**Scenario B2**	**Scenario B3**
LCoH_SDH (calculated with this tool)	0.0674 €/kWh	0.0767 €/kWh	0.0654 €/kWh	0.0504 €/kWh	0.0609 €/kWh	0.0482 €/kWh
LCoH_CDH (calculated with this tool)	0.0513 €/kWh	0.0986 €/kWh	0.0630 €/kWh	0.0513 €/kWh	0.0972 €/kWh	0.0513 €/kWh
LCoH (purely solar thermal, according to (Riebenbauer, 2022))	0.0936 €/kWh	-	0.0746 €/kWh	-	-	-
LCoH_SDH (according to (VDI 3988, 2018))	-	-	-	0.0516 €/kWh	0.0811 €/kWh	0.0493 €/kWh
LCoH_CDH (according to (VDI 3988, 2018))	-	-	-	0.0533 €/kWh	0.0889 €/kWh	0.0533 €/kWh

4. Conclusion and Outlook

In course of this work, a sensitivity analysis tool was developed with the objective of providing a simple and effective method for the analysis of economic efficiency in solar-supported district heating systems. The basis for the execution of the sensitivity analysis is the calculation of the LCoH. The latter is calculated once for a solar-supported district heating system and once for a conventional district heating system. The comparison of the two systems is carried out using the cost ratio of the LCoH. The essential data required for calculating the LCoH are the solar thermal collector area, the thermal energy storage volume, the annual energy demand of the district heating system and current energy prices. As investments costs for the solar thermal components are often unknown at the beginning of the planning activities, these can be estimated using cost curves provided. However, available project-specific costs can also be entered directly. The LCoH can be calculated for any observation period, as it takes into account replacement investments for solar thermal components and heat generators, as well as their residual values. This allows easy comparison with other methods of calculating LCoH.

In order to validate and verify results from the developed tool, the latter was applied to two different projects. These entailed the evaluation of a potentially solar-supported district heating system in an Austrian city, as well as an assessment of an existing local heating network. Three distinct scenarios were considered for each of the two projects, with scenario 1 representing the status quo as determined by the validation documents. In scenario 2, a hypothetical comparison was made between the construction of a new solar-supported district heating system and conventional gas-fired system. In scenario 3, the sensitivity analysis was carried out for a variation of scenario 1.

In the first project, heat production costs were already calculated as part of a feasibility study. Based on the available data, these were recalculated and compared using this tool. It was found that the heat production costs in the feasibility study were always higher than the costs calculated in this project. This is because the heat production costs in the feasibility study only referred to the solar thermal part, whereas the costs calculated with the present tool always referred to the total annual energy demand. The method used here, therefore also takes into account the cost of the back-up system. As the cost of the back-up is lower than the cost of the solar thermal part in the calculated cases, the calculated heat production costs of the whole system is lower than that of the solar thermal part only. For this reason, the differences that occurred were mainly due to the difference in the methods used to calculate heat production costs.

In the second project, validation was carried out using a comparative calculation with VDI 3988 “Solar thermal process heat”. A very good agreement was found between the calculation of heat production costs carried out according to VDI 3988 and those carried out with the tool at hand. As the second project is a real existing facility, the LCoH was calculated twice. The first calculation was based on the values from the simulation and the second on measured values from the plant. Due to the increase in the annual heat demand of the system and the associated increase in the specific solar energy yield, the LCoH of the measured scenario was again lower than those of the simulation scenario.

Next step is to integrate the effects of the district heating network, e.g. supply and return pipe temperature levels in winter and summer, proportion of summer load and its effect on the annual solar coverage, etc. into the sensitivity analysis tool. Thus, it is possible to consider various settings regarding network operation (especially temperature levels) of the district heating network in the sensitivity analysis.

5. Acknowledgments

This work has been supported by the government of Upper Austria in the projects “COMPESTO – comprehensive energy storage”, Research Grant Wi-2022-600132/7-Au, “Restore – Investigation of different energy storage technologies on the resilience of sector-coupled energy systems” and “Heat Highway” (reference number 880797, funding program “Vorzeigeregion Energie”), financed by the “Klima- und Energiefonds” and the government of Upper Austria.

Editing of the English language was performed by Gayaneh Issayan from the University of Applied Sciences Upper Austria.

6. References

Becke, W., 2021. Förderprogramm des Klima- und Energiefonds „Solarthermie – Solare Großanlagen“. Endbericht Nahwärme St. Ruprecht.

Branker, K., Pathak, M. & Pearce, J.M., 2011. A review of solar photovoltaic levelized cost of electricity. Renewable and Sustainable Energy Reviews 15, 4470–4482. https://doi.org/10.1016/j.rser.2011.07.104

European Commission, 2021. European Green Deal: Delivering on our targets. https://ec.europa.eu/commission/presscorner/detail/en/fs_21_3688, Accessed 21 June 2024. doi:10.2775/595210

European Commission, 2023a. Report from the commission to the European parliament, the council, the European economic and social committee and the committee of the regions, State of the Energy Union Report 2023. https://ec.europa.eu/commission/presscorner/detail/en/ip_23_5188, Accessed 11 July 2024.

European Commission, Directorate-General for Energy, Bacquet, A., Galindo Fernández, M., Oger, A. et al., 2022. District heating and cooling in the European Union – Overview of markets and regulatory frameworks under the revised Renewable Energy Directive, Publications Office of the European Union. https://data.europa.eu/doi/10.2833/962525, doi:10.2833/962525

European Commission, Directorate-General for Energy, Braungardt, S., Bürger, V., Fleiter, T. et al., 2023b. Renewable heating and cooling pathways – Towards full decarbonisation by 2050. Final report, https://data.europa.eu/doi/10.2833/036342, Accessed 24 June 2024, doi:10.2833/036342

Goeke, J., 2021. Thermische Energiespeicher in der Gebäudetechnik, Springer Vieweg, Wiesbaden.

Louvet, Y., Fischer, S., Furbo, S., Giovanetti, F., Köhl, M. & Mauthner, F. et al., 2019. Guideline for levelized cost of heat (LCoH) calculations for solar thermal applications. Info Sheet A0. Task 54 Price Reduction of Solar Thermal Systems. IEA Solar Heating and Cooling Programme.

Mauthner, F., Herkel, S., 2016. Technology and Demonstrators - Technical Report Subtask C - Part C1: Classification and benchmarking of solar thermal systems in urban environments. Task 52 Solar Heat and Energy Economics in Urban Environments. IEA Solar Heating & Cooling Programme.

Neyer, D., Neyer, J., Stadler, K., Thür, A., 2016. Energy-Economy-Ecology-Evaluation Tool T53E4-Tool. Tool Description and introductory Manual. Task 53 New Generation Solar Cooling & Heating. IEA Solar Heating & Cooling Programme.

Poggensee, K. & Poggensee, J., 2021. Investment Valuation and Appraisal: Theory and Practice. first ed. Springer Nature Switzerland.

Quaschning, V., 2012. Regenerative Energiesysteme: Technologie - Berechnung – Simulation, eighth ed. Hanser Verlag, München.

Riebenbauer, L., 2022. Förderprogramm des Klima- und Energiefonds "Solarthermie - Solare Großanlagen". Solare Großanlage - Machbarkeitsstudie Eisenstadt.

Tian, Z., Zhang, S., Deng, J., Fan, J., Huang, J. & Kong, W. et al., 2019. Large-scale solar district heating plants in Danish smart thermal grid: Developments and recent trends. Energy Conversion and Management. 189, 67–80. https://doi.org/10.1016/j.enconman.2019.03.071.

VDI 2067, 2012. Economic efficiency of building installations - Fundamentals and economic calculation. VDI-Richtlinie.

VDI 3988, 2018. Solar thermal process heat. VDI-Richtlinie.

W. Short, D. Packey, and T. Holt, 1995. A Manual for the Economic Evaluation of Energy Efficiency and Renewable Energy Technologies, National Renewable Energy Laboratory, Golden, Colorado.

Zakeri, B. & Syri, S., 2015. Electrical energy storage systems: A comparative life cycle cost analysis. Renewable and Sustainable Energy Reviews. 42, 569–596. https://doi.org/10.1016/j.rser.2014.10.011.

IMPROVED PRE-CALCULATION OF SOLAR THERMAL PRODUCTION FOR MILP-BASED OPTIMIZATION PROBLEMS

Thibaut Wissocq[1], Nicolas Lamaison[1]

[1] Univ. Grenoble Alpes, CEA, Liten, Campus Ines, 73375 Le Bourget du Lac (France)

Abstract

The decarbonisation of heat supply in district heating network can be achieved through solar thermal systems, providing a carbon-free and competitive energy. Their integration with large-scale thermal storage allows for enhancing solar fraction by utilizing summer heat during winter months. However, conventional optimization tools often treat solar thermal production as a simple input, potentially leading to miscalculations and neglecting the influence of storage behavior on the thermal solar production. The presence of a thermal storage especially influences both the temperature and the mass flow observed by the solar plant. In this context, a good prediction of solar production is crucial for a better computation of the system. We propose here a 6-step methodology based on simulation and optimization models to enhance solar thermal production pre-calculation. With this methodology, the predicted solar production has resulted in an average error of 3.4% compared to the final solar production obtained after convergence of optimization/simulation of the entire plant, on six district heating cases studies. The latter has to be compared with an average error of 10% when using a state-of-the-art approach for the solar production calculation.

Keywords: solar thermal, simulation, Dymola, Modelica, long-term storage, district heating.

1. Introduction

1.1. The role of solar thermal in district heating network

A major part of final energy consumption in European countries is dedicated to space heating and domestic hot water needs. District heating networks (DHNs) have emerged as a promising solution for reducing carbon emissions in heat supply. Notably, the 4th generation of district heating currently under development across Europe, focuses on lower temperature networks compared to older generations (2nd and 3rd generation). This evolution enhances the integration of renewable heat sources, such as heat pumps and solar thermal plants (Lund, 2014).

Solar district heating networks (SDH) are a specific type of district heating system that primarily relies on solar thermal plants as the main source of energy, aiming for a high solar fraction. Solar thermal systems offer several key advantages: they are renewable, carbon-free, and contribute to diversifying energy sources, thereby reducing dependency on fossil fuels and enhancing energy security.

A particularly significant advantages of solar thermal systems is their compatibility with large-scale thermal storage. By coupling solar thermal plants with thermal storage, excess heat generated during the summer months can be stored and then utilized during periods of lower solar availability, such as in the winter. This coupling not only increases the overall efficiency and solar fraction of the system but also ensures a more stable and reliable heat supply throughout the year. The ability to shift energy production across seasons makes solar thermal coupled with storage a particularly attractive option for sustainable district heating networks. The presence of thermal storages can also benefit other production methods by optimizing the overall system efficiency and reducing heat production costs

However, SDH are generally more complex than classical DHN. The inherent intermittency of solar resources adds further complexity to managing SDHs compared to traditional DHNs. Optimizing the operation of solar district heating (SDH) systems presents significant challenges due to the intricate interactions between various components, particularly when thermal storage is involved. Thermal storage operation affects both DHN temperature and mass flow rates. Since solar collectors are sensitive to operating temperatures, the behavior of thermal storage can significantly impact the overall system efficiency. Therefore, a deep understanding of the thermal-hydraulic behavior within these networks is crucial for optimizing their design, operation, and control strategies, to ensure maximum efficiency and reliability. To address these challenges, mathematical tools such as simulation or optimization models can help to address the intricate task of matching demand with supply in district heating networks.1.2. How SDH are modelled in the literature

© 2024. The Authors. Published by International Solar Energy Society
Selection and/or peer review under responsibility of Scientific Committee
10.18086/eurosun.2024.03.09 Available at http://proceedings.ises.org

In the literature, two main methods are used to model solar district heating network. The first approach involves simulation tools such TRNSYS (University of Wisconsin, 1975) or Modelica models (Brück, 2002). These methods employ expert rules such as plant priority settings for energy dispatch and are able to model non-linear equations, thus, offering a more accurate representation of solar production profiles (Giraud., 2014; Descamps, 2018; Renaldi 2019). However, while simulations can enhance the understanding of system behavior, they do not ensure optimal economic or environmental solutions, as thermal plants production profiles are predefined from rules rather than optimization computation. Therefore, optimization methods are often used for optimal dispatch.

Optimization methods involve modeling solar district heating (SDH) equations as constraints to minimize an objective function, which can be economic (e.g. operating costs), environmental (e.g. CO_2) or a combination of both. Scolan et al (2020) and Delubac et al (2021) developed a multi-period optimization tool to enhance the integration of solar thermal into district heating networks using a Mixed-Integer Non-Linear Programming (MINLP) approach. In their model, temperatures at the input and output of the solar field as well as mass flows are modeled as problem variables. Solar thermal power output is then computed based on global irradiance, ambient temperature, solar field temperature and DHN mass flows. As a result, thermo-hydraulic equations of the network are well modeled, thereby ensuring a comprehensive representation of the network, particularly regarding the impact influence of storage behavior on solar production. However, due to the large complexity and to avoid intractability issues, the MINLP problem is translated in NLP problem through the use of sigmoid functions, and representative days are used. The problem remains complex to solve and computationally expensive.

The other class of optimization problems is Mixed-Integer Linear Programming (MILP). MILP is commonly used for unit commitment problems to determine the optimal production plan for thermal plants to meet demand while minimizing costs or carbon emissions. In MILP models, mass flows and temperatures are treated as parameters rather than variables, as the thermo-hydraulic equations are linearized. This linearization enables the use of powerful linear solvers such as CPLEX, which provide stable solutions with guaranteed convergence, albeit with some approximations. Consequently, the model constraints in MILP are energy constraints like energy and power balances rather than temperature and flow rate balances. As a result, thermal solar production is often treated as a fixed input, computed solely based on solar radiation and solar field size (Buoro, 2014; Carpaneto 2015; Van Der Heijde, 2019). However, Lamaison et al (2018) highlighted the limitation of MILP models to get realistic trajectories noting that errors of several percent in the energy mix can arise, particularly due to oversimplification of storage modelling (i.e., the omission of temperature effects). Similarly, the oversimplification inherent in MILP models and neglecting temperature effects on plant performance can lead to an overestimation of solar production, as they fail to account for the impact of thermal storage, fluid inertia, and thermal losses in the solar field on overall system dynamics.

1.3. Aim of the paper

To address this gap, we propose a comprehensive six-step methodology designed to enhance the pre-calculation of solar thermal production for MILP optimization problems. By incorporating insights from the aforementioned studies, our methodology encompasses solar field and storage sizing, as well as a more precise computation of solar thermal production. Our methodology relies on efficient non-linear simulations with Modelica models and small optimization problems. The refined solar thermal production data can then be effectively utilized in classical MILP optimization problems for energy production, paving the way for more efficient and sustainable operation of Solar District Heating systems.

2. Methodology

The methodology is described in Figure 1 below and consists of six steps and an additional validation step.

- The first six steps represent the core of the methodology presented here. The objective is to improve the computation of solar thermal production by taking into account the behavior of thermal storage. It results in an improved thermal solar production trajectory Psol1.
- The six steps are based on Modelica models of increasing complexity (figure 2), alongside Python codes for sizing and optimization.
- The last 7th step involves a validation procedure. An iterative loop is established between a comprehensive Modelica model of the DHN plants, which generates a solar production profile called Psol[k]. This profile is then used in a MILP optimization model to determine optimal trajectories for biomass plant, gas plant and Pit Thermal Energy Storage (PTES). Convergence is assessed using the mean RMSE between two iterations Psol[k] and Psol[k+1].

- The inputs of the methodology are the external temperature, solar radiation, DHN temperatures and mass flow rate.
- The outputs are solar field area, pit thermal energy storage capacity and a more precise solar thermal power trajectory.

The different steps are detailed in the next subsections.

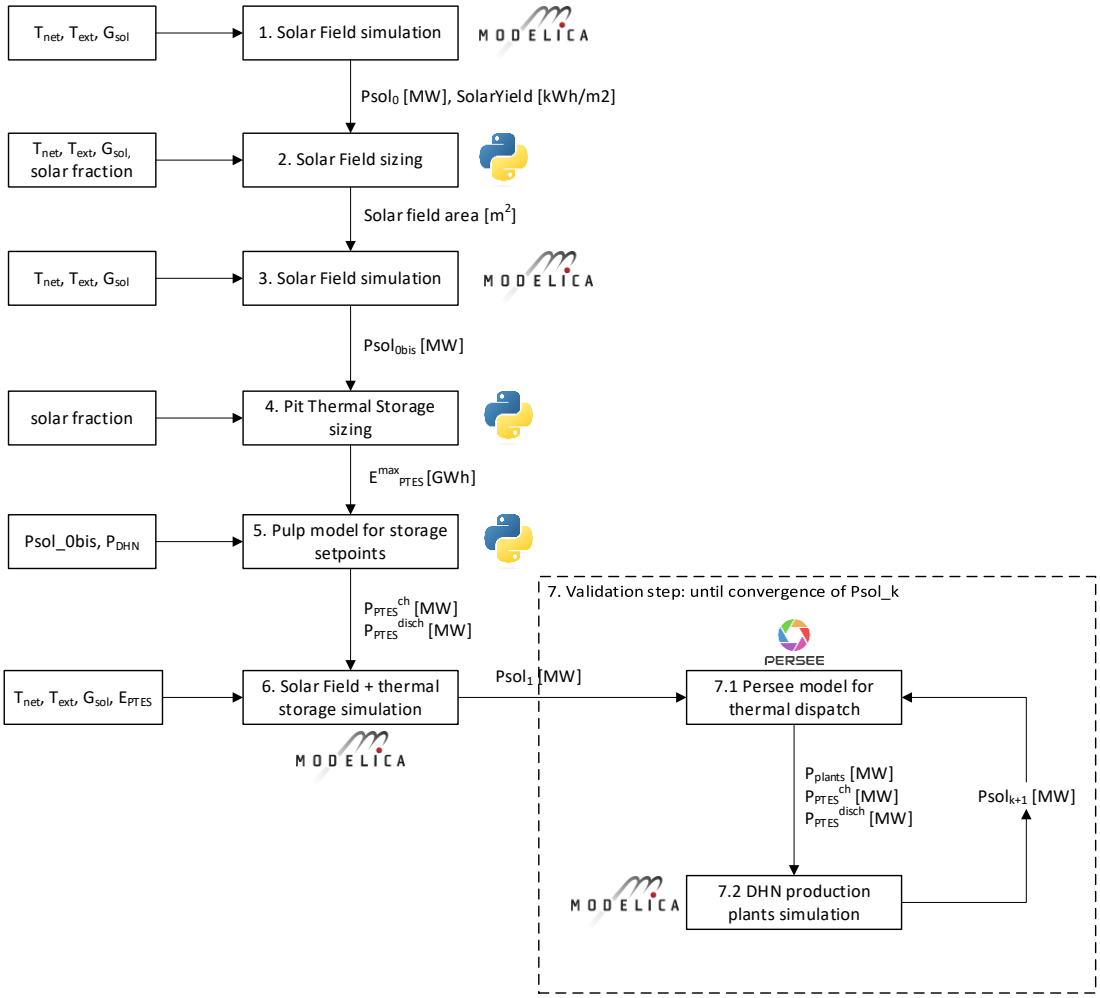

Figure 11- Methodology for precomputation of thermal solar production $Psol_1$ and validation procedures

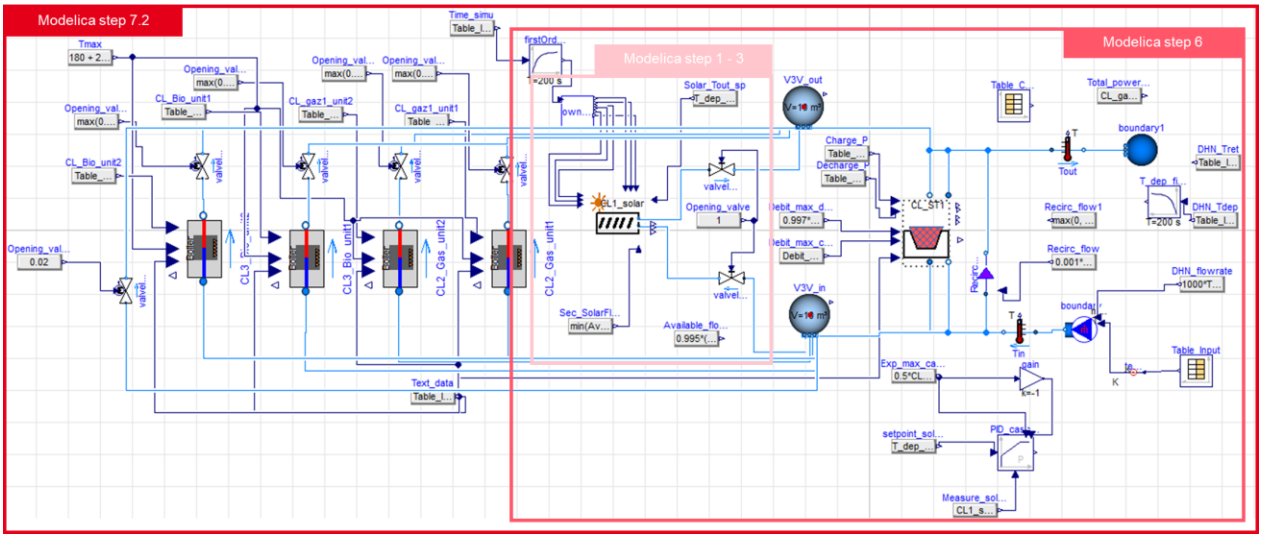

Figure 22 - Modelica models for step 1, 3, 5 and 7

2.1 Step 1: Solar field simulation for sizing

The first step involves a solar field Modelica model, developed using an in-house CEA Modelica library (Giraud, 2015). The objective of this simulation is to obtain a solar yield per unit area, in order to size the solar field to meet the system's solar energy requirements. The simulation is conducted using network temperature data (supply and return temperatures) and meteorological data (solar irradiation, ambient temperature). The simulation assumptions are the following:

- The return temperature of the network is set at the solar field heat exchanger secondary-side inlet.
- The solar field secondary flow rate is controlled to achieve the desired network supply temperature.
- The network flow rate is assumed to be unlimited so that all the energy from the solar field can be absorbed by the network

The outputs are time series of production in W/m² and annual $Solar_yield$ in kWh/m²/year). The resulting time series here obtained is denoted $Psol_0$.

2.2. Step 2: Solar field sizing

The size of the solar field is computed by the following equation:

$$area\ [m^2] = SolarFraction[-] \cdot \frac{\sum_t P_{DHN}(t)[kWh]}{Solar_yield\ [kWh/m^2]} \qquad (1)$$

Where $\sum_t P_{DHN}(t)$ is the DHN total annual energy and $Solar_producible$ is the solar energy yield per unit area, obtained from step 1.

The solar fraction is a SDH parameter and is computed by $SolarFraction[-] = \frac{\sum_t P_{sol}(t)[kWh]}{\sum_t P_{DHN}(t)[kWh]}$ where Psol is the solar production.

2.3. Step 3: Solar field simulation

In large district heating networks where solar production constitutes a significant portion, the solar field may be extensive (potentially several thousands of square meters). In such cases, the impact of thermal loss and field inertia may not be neglected as it affects solar production. Therefore, the same Modelica model of step 1 is resimulated but with a corrected area and coherent pipe diameter, corresponding to the desired solar fraction.

It results in a new solar production called Psol_0bis.

After step 3, the simulation provides a solar production for a solar field corresponding to the required solar fraction within the network. The next step involves sizing the seasonal thermal energy storage (PTES) to achieve this solar fraction effectively.

2.4 Step 4: Pit storage sizing

Solar production exhibits high intermittency with significant variations between nights and days. Peak production can exceed DHN demand during several time steps, especially during summer. Thus, to meet the desired solar fraction (computed based on annual energy production), coupling solar field with Pit Thermal Energy Storage (PTES) is essential. The critical question is determining the appropriate capacity for this thermal energy storage.

The process is explained in Figure 3. This figure depicts the evolution of the cumulated difference between DHN demand and solar production $\sum_{s \le t} P_{DHN}(s) - P_{sol}(s)$. At the beginning of the year, solar production is lower than DHN demand, causing the cumulative difference to increase until the day T0. At T0, solar production surpasses DHN demand indicating a production surplus that should be stored. This production surplus continues until TF, where cumulative DHN demand exceeds again solar production.

Therefore, storage size corresponds to the difference of cumulative energy between T0 and TF, as depicted in the figure. This approach accounts for daily variations in PTES loading and unloading.

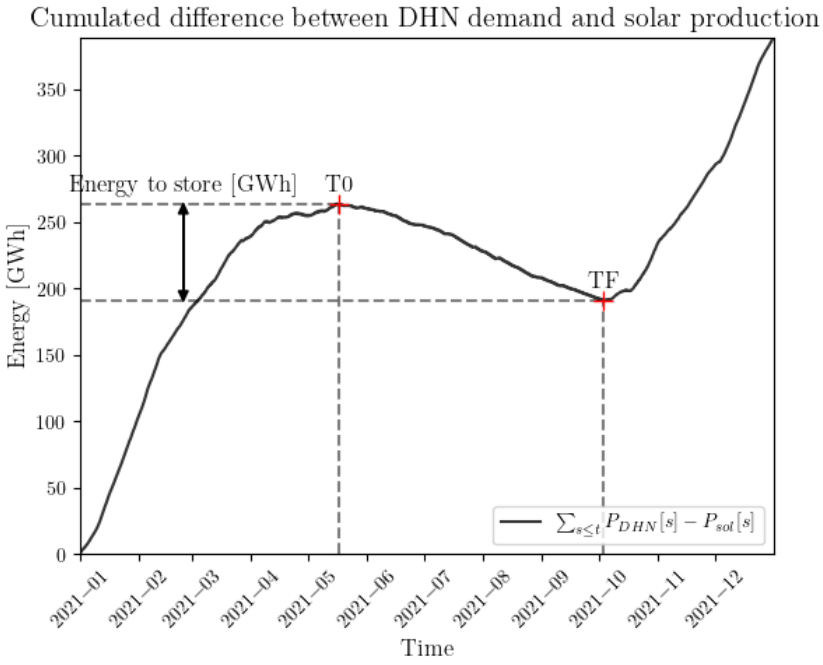

Figure 33 – Illustrative cumulated difference between P_{DHN} and P_{sol}

2.5 Step 5: MILP model for hypothetical charging and discharging profiles

The next step after PTES capacity design is to determine feasible charging and discharging profiles for the PTES. This is achieved through a small optimization problem formulated in PulP (Mitchell, 2011). The following assumptions to dispatch the energy are as follows:

- The charging power corresponds to the surplus of thermal solar production compared to DHN demand.
- The discharging power outside the period [T0-TF] should approximate a mean discharging value.

The optimization problem is the following (variables are shown in bold):

$$\min \sum_t \boldsymbol{\epsilon}^+[t] + \boldsymbol{\epsilon}^-[t] \qquad (2)$$

With the following constraints:

$$\boldsymbol{E}[0] = \boldsymbol{E}[T_{end}] \qquad (3)$$
$$\boldsymbol{E}[T0] = 0 \qquad (4)$$
$$\boldsymbol{E}[TF + 1] = E_{PTES}^{max} \qquad (5)$$

T0 and TF corresponds to the time steps where the storage is empty and fulfilled. These time steps are computed in step 2, simultaneously with the storage sizing.

From TF to T0, we want to approximate a mean discharging value :

$$\boldsymbol{P^{disch}}[t] = P_{mean}^{disch}[t] + \boldsymbol{\epsilon}^+[t] - \boldsymbol{\epsilon}^-[t] \qquad (6)$$

Where $\boldsymbol{\epsilon}^+$ and $\boldsymbol{\epsilon}^-$ represent deviations from the mean discharge value P_{mean}^{disch} which is computed from the following equation:

$$P_{mean}^{disch}[t] = \begin{cases} 0 \; when \; P^{ch}[t] > 0 \\ \frac{E^{max}}{\Delta t} \; else \end{cases} \qquad (7)$$

where Δt corresponds to the length of interval of time from TF to T0.

The discharging power must be less or equal to the DHN demand:

$$\boldsymbol{P^{disch}}[t] \leq P^{DHN}[t] \qquad (8)$$

Charging and discharging cannot occur simultaneously:

$$\boldsymbol{P^{disch}}[t] \cdot P^{ch}[t] = 0 \quad (9)$$

The energy balance of the storage is computed:

$$\boldsymbol{E}[t+1] - \boldsymbol{E}[t] = P^{ch}[t] - \boldsymbol{P^{disch}}[t] \quad (10)$$

The energy is the storage should remain positive within the storage capacity obtained in step 2:

$$\boldsymbol{E}[\boldsymbol{t}] \leq E_{PTES}^{max} \quad (11)$$

Note that we do not take into account thermal losses in the storage. The approach is to provide theoretical load profiles, matching with step-4 PTES sizing, close to a physical reality, rather than getting perfect loading and unload profiles matching the reality.

Solving this problem gives discharging profiles, close to a mean value during non-heating season. The optimization problem is linear, and does not involve any binary variables. A solution is then obtained in a few seconds.

2.6 Step 6: Simulation of a solar field model combined with thermal storage

After determining theoretical storage profiles, the next step is to assess the impact of these profiles on the solar field and overall district heating network. Therefore, a new Modelica model is developed, adapted from step 1 Modelica model including a PTES with loading/unloading setpoints and load-following thermal plant to meet DHN demand continuously. A simulation is performed with the following assumptions:

- The flow rate through the secondary side of the solar field heat exchanger is controlled in order to achieve the desired network supply temperature.
- The actual district heating network flow rates are considered.
- PTES operational setpoints (charge and discharge) from step 5 are used.

This new solar production is expected to be lower than Psol_0bis because of 1) the limited DHN mass flow (mass flow is no longer considered unlimited, and solar energy may need to be dissipated to prevent the solar field from overheating when the flow rate is restricted) and 2) the storage influence on the return temperature of the solar field heat exchanger when charging. Indeed, during PTES charging, network return temperature is mixed with PTES bottom temperature. The latter results in a higher temperature observed by the solar plant, compared to a simulation without storage. This can reduce the thermal solar output.

This simulation gives a new solar production Psol_1. The validity of this solar production is then assessed in an iterative loop between MILP optimization problem (to get optimal thermal plant trajectories satisfying heat demand) and a Modelica simulation model representing the whole district heating production plants.

2.7 Step 7: Validation

The validation step consists in an iterative loop and relies on two models:

- 7.1: a MILP optimization model based on the tool PERSEE (Ruby, 2024). This optimization model represents the district heating production plants, including the solar thermal plant and the PTES. Solar production $Psol_k$ is considered as fixed input profile. The objective is to satisfy heat demand while minimizing the operational costs. This step gives the production level plants P_{plants} and PTES profiles P_{PTES}^{ch} and P_{PTES}^{disch}.
- 7.2: A Modelica model representing the entire district heating production plants, including the solar field. The inputs are the production levels plants from PERSEE. This gives a revised solar production profile, noted $Psol_{k+1}$, k+1 corresponding to the $k+1^{th}$ iteration.

The convergence criteria is the mean root mean square difference between two iterations of Psol:

$$NRMSD = \frac{\sqrt{(\overline{Psol_k} - \overline{Psol_{k+1}})^2}}{\overline{Psol_k}} \quad (12)$$

The goal of this iterative loop is to align the production plant profiles with the solar production levels, thereby refining the optimization results to ensure they reflect a realistic and operationally feasible solar district heating system.

3. Results

3.1. Case study

The methodology presented here is applied on a hypothetical case study, representing a solar district heating network, with two different level of temperature (3rd and 4th generation district heating), with 3 different solar irradiances (corresponding to the meteorological areas H1, H2 and H3 in France). Network heat demand and supply/return temperatures are derived using the HeatPro tool (CEA Liten, 2024). The solar district heating network is composed of solar thermal plant, a pit thermal energy storage, biomass plants and gas plants. The desired solar fraction is 40%. (fig4)

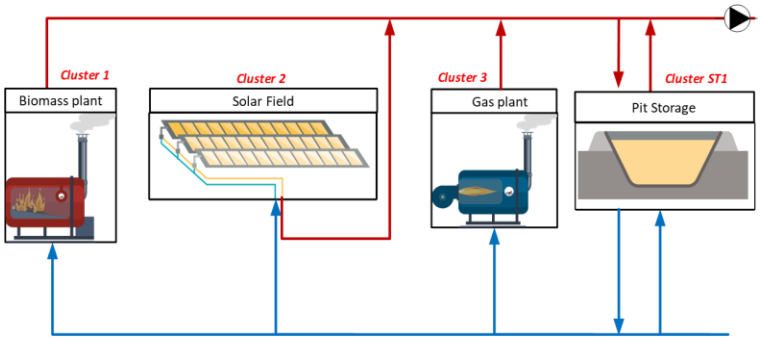

Figure 44 - DHN production plants

3.2. Solar precomputing production profile $Psol_1$

The following Table 1 presents the results of the precalculation methodology. It reports the difference between the corrected pre-calculated solar field production ($Psol_1$) with respect to the initial ideal simulation ($Psol_{0bis}$). It shows that $Psol_{0bis}$ overestimates the solar production level when storage is incorporated.

Table 1: Reduction in annual solar output between $Psol_{0bis}$ and P_{sol1} due to storage operation.

H1 3G	H1 4G	H2 3G	H2 4G	H3 3G	H3 4G
-11.6%	-10.8%	-11.3%	-10.5%	-7.4%	-8.3%

New solar fraction, recalculated using $Psol_1$ is shown in Table 2.

Table 2: Solar fraction computed with $Psol_1$. Desired solar fraction is 40%

H1 3G	H1 4G	H2 3G	H2 4G	H3 3G	H3 4G
35.3%	35.2%	35.7%	35.3%	36.7%	36.2%

As expected, solar fraction and annual solar output decrease when considering storage. This effect can be explained by Figure 5 representing the storage state of charge (right-axis) and the solar production $Psol_{0bis}$ (grey) and Psol1 (black) (left-axis). For clarity, solar production is represented as the maximum value over a one-week rolling window. As expected, solar production Psol1 is now lower than $Psol_{0bis}$. Several reasons can be identified:

- A limited mass flow of the solar field exchanger at the network side can lead to an overheating of the solar field, requiring to dissipate a part of the solar energy.
- At the beginning of the year, $Psol_1$ is lower than $Psol_{0bis}$ because of storage operation: PTES is discharging, thus limiting the mass flow available for the solar field. This limitation is more pronounced compared to $Psol_{0bis}$, which assumes unlimited mass flow rates to capture all potential solar production
- During summer, $Psol_1$ production levels are lower than $Psol_{0bis}$. This is also explained by storage operation: PTES is charging and its temperature is increasing. Thus, temperature observed by the solar field is higher than expected and solar production is reduced. This effect becomes even more pronounced at the end of summer when the storage is full.

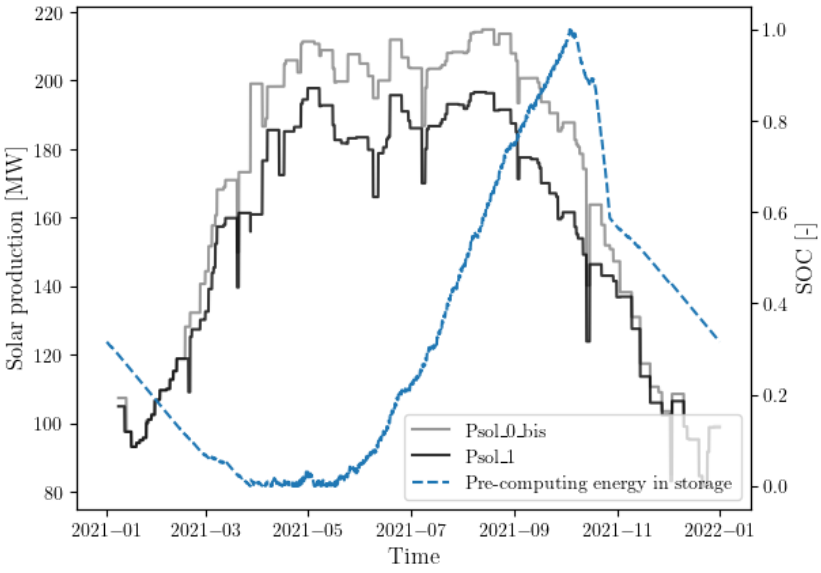

Figure 55 - Solar production and state of charge of H1 3G. Solar production is the max value over 1 week.

3.3. Validation step

Psol1 is generated using hypothetical storage profiles, which may not align with economically optimal profiles. To address this, an iterative loop between optimization and simulation is employed. PERSEE optimization model will generate optimal DHN plants trajectories to meet DHN demand over a year, with an hour time step precision. The objective function is the minimization of the operating costs. Then, Dymola simulation is conducted to generate actual solar production level when considering optimal discharging and charging profiles and the influence of other production plants. This iterative process not only refines the solar production profile but also highlights model mismatch between the simulation and optimization models. The validation loop is stopped after 6 iterations or if the convergence criteria (NRMSE) gets lower than 3%.

Figure 6 shows the RMSE evolution for the six different cases. Notably, for Montpellier 4G, NRMSE drops below 3% after three iterations at which point we consider that Psol has converged.

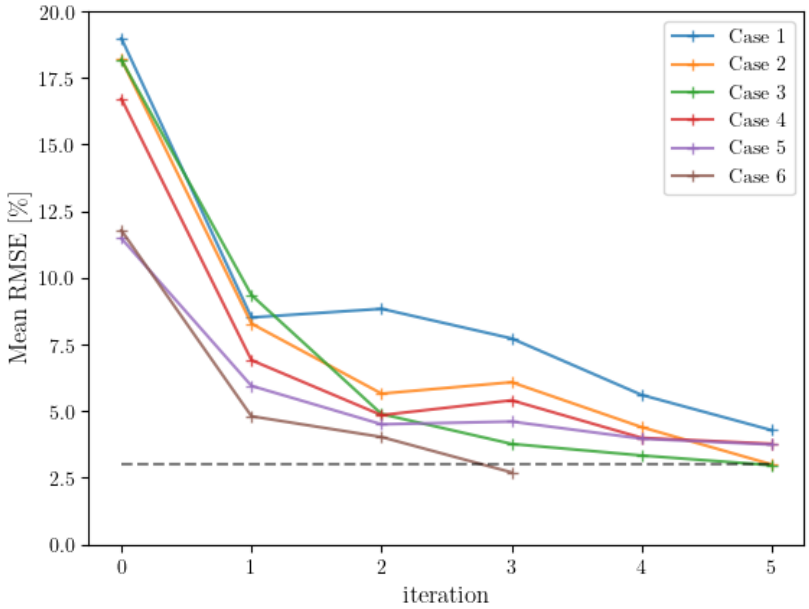

Figure 66 - Mean RMSE evolution

Throughout the iterative process, the solar production profiles gradually converge, as evidenced by the decreasing mean RMSE values across different iterations. The RMSE values, all of which are under 5%, indicate a high level of agreement between the optimization and simulation models. This suggests that the solar production profiles are becoming increasingly stable and consistent between these two models. However, perfect convergence is unattainable due to inherent model mismatches (e.g., different thermal loss models) and considering the fact that

MILP optimization can give multiple optimal solutions within an optimization gap (set here at 5%).

New solar fractions from solar production of the last iteration can be computed, presented in the Table 3.

Tab 3 - New solar fraction after convergence

H1 3G	H1 4G	H2 3G	H2 4G	H3 3G	H3 4G
36.5%	36.4%	37.2%	36.9%	37.8%	36.9%

New solar fractions are slightly higher than the ones obtained from Psol1 (they were around 35-36%). Actually the increase in solar production can be attributed to the modified storage behavior that results from considering economically optimal profiles.

Unlike in step 5 where only solar was able to be stored, step 7.1 considers the possibility of storing heat from biomass or gas plants (if it is economically profitable), which influences solar production profiles. As a result, charging and discharging profiles differs from those obtained in step5 (fig. 7). Storage is not used as expected and is maybe oversized as SOC in PERSEE (red continuous line) does not reach 1. In Psol1 (blue line), the storage is charged and discharged more frequently and for longer durations than in the full simulations. As a result, during charging periods, the maximum temperature is reached more quickly, thereby limiting solar production earlier ($Psol_1$). Additionally, with more frequent discharge periods, the flow rate is more often restricted, further limiting solar production. That explained the difference of solar production between Psol1 (black line) and Psol7 (the last iteration, red line), as seen in Figure 8.

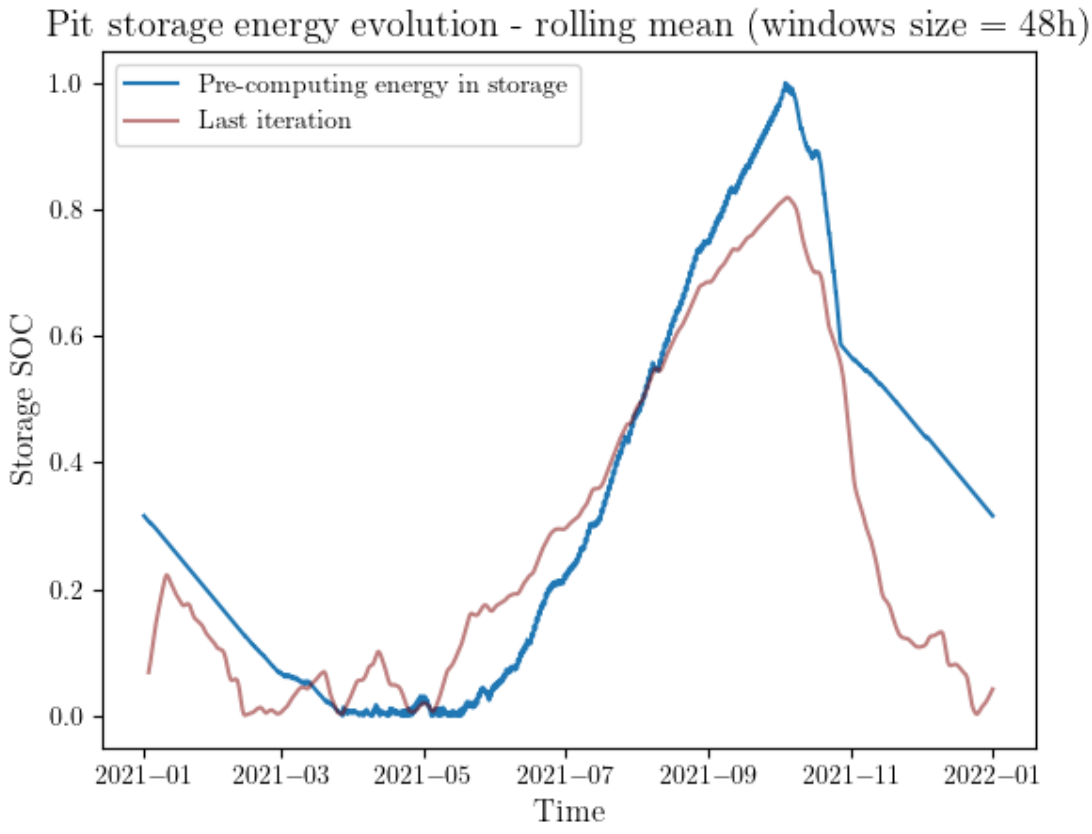

Figure 77 - Comparison of storage state of charge between Persee, Dymola and step 5 (H1 3G)

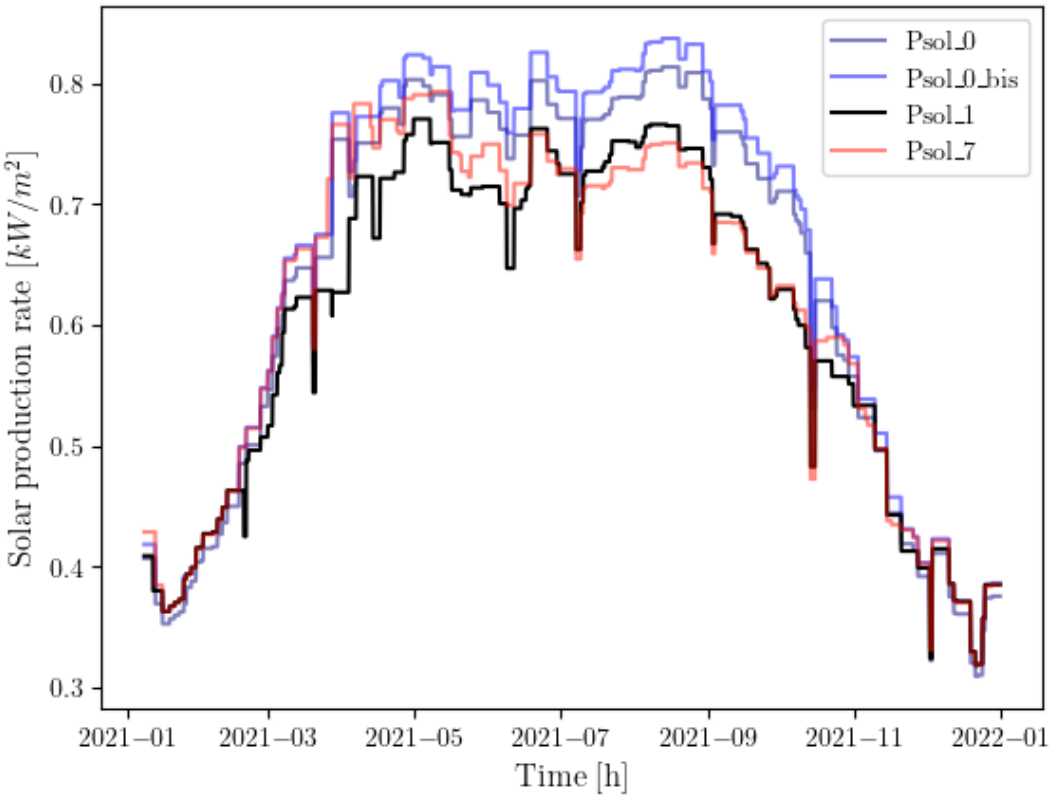

Figure 88 - Solar production rate in kW/m² for the first steps of the methodology and last iteration after convergence for H1 3G. Solar production is the max value over a week. (Solar production rate is shown to compare it with $Psol_0$ which is computed with a different surface)

Finally, Table 4 sums up the results and the difference on solar production and computation time for the methodology and the validation.

Table 4 - Methodology performance on precision and computation time

	H1 3G	**H1 4G**	**H2 3G**	**H2 4G**	**H3 3G**	**H3 4G**
$Esol_{0bis}$ [GWh]	260	252	200	192	137	134
$Esol_1$ [GWh]	230	225	177	172	127	123
Error on $Esol_{0bis}$ [%]	-11,6	-10,8	-11,4	-10,5	-7,4	-8,3
Esol after convergence [Gwh]	237	232	185	180	131	126
Error on $Esol_1$ [%]	3,26	3,30	4,25	4,33	3,12	2,06
Computation time : step 1->6 (sec)	418	394	374	369	348	383
Computation time: step 7 (sec)	7126	6100	4950	6069	7412	3322

While the average error between annual solar production of Psol1 (with estimated load profiles) and Psol0 (computation with solar field efficiency) was about -10%, the error between annual production of Psol1 and actual annual solar production after convergence is below 3.5%. However, the validation step is computationally intensive as it lasts from one hour to two hours, depending on the case. Moreover, the optimization step in PERSEE is costly, and we do not reach full optimality, the optimality gap was set at 5%. In contrast, steps 1 to 6 are very fast, with only few minutes to success 3 simulations (with simpler model than step 7.2) and an LP optimization. This seems to be a good compromise between accuracy and computational time for obtaining hourly solar production profiles and this within a methodology that is agnostic to other production sources.

4. Conclusion & perspectives

In conclusion, we present here a comprehensive methodology in order to enhance the pre-calculation of solar thermal production, particularly tailored for MILP-based optimization problems in Solar District Heating systems. By integrating solar field and pit thermal energy storage Modelica models with a LP optimization model for determining storage charging and discharging profiles, our approach offers a systematic framework for improving solar production pre-calculation levels.

These pre-calculated solar production levels are validated through a feedback loop utilizing in six different cases. Convergence between an optimization model (PERSEE), which fixed input solar thermal production to establish storage setpoints, and simulation models that account for the behavior of district heating plants and its influence on solar thermal production. After few iterations, our analysis revealed a final error rate of 3.4% between our pre-computed solar production and the actual solar production levels demonstrating the effectiveness of our methodology.

This method could be further refined to address model mismatches observed between the simulation and linear optimization, particularly in the representation of storage. Temperatures are not taken into account in MILP models, as a result, thermal losses are underestimated, and charging flow rates are overestimated. A potential solution could be to implement a rolling horizon approach within the validation loop. This approach would continuously update storage states in the optimization model based on non-linear simulation results, ensuring that charging flow rates and power outputs of other generators are more accurate as they are regularly updated by physical models. Consequently, the solar production calculated by Dymola would better account for the behaviors of other generators, leading to more precise results and fewer iterations in the validation loop. Such integration promises to refine the accuracy of our predictions and optimize system performance, thereby advancing the efficacy and sustainability of Solar District Heating systems

5. References

Brück, D., Elmqvist, H., Mattsson, S. E., & Olsson, H. (2002, March). Dymola for multi-engineering modeling and simulation. In Proceedings of modelica (Vol. 2002). Citeseer.

Buoro, D., Pinamonti, P., & Reini, M. (2014). Optimization of a distributed cogeneration system with solar district heating. Applied Energy, 124, 298-308.

Carpaneto, E., Lazzeroni, P., & Repetto, M. (2015). Optimal integration of solar energy in a district heating network. Renewable Energy, 75, 714-721.

CEA-Liten, District Heating load generator (2024). https://github.com/CEA-Liten/HeatPro [Access date 09-08-2024]

Descamps, M. N., Leoncini, G., Vallée, M., & Paulus, C. (2018). Performance assessment of a multi-source heat production system with storage for district heating. Energy Procedia, 149, 390-399.

Delubac, R., Serra, S., Sochard, S., Reneaume, J-M., 2021. A Dynamic Optimization Tool to Size and Operate Solar Thermal District Heating Networks Production Plants. Energies 14. 23, 8003

Giraud, Loïc & Bavière, R. & Paulus, Cédric. (2014). Modeling of solar district heating: a comparison between TRNSYS and MODELICA. 10.18086/eurosun.2014.19.06.

Giraud, L., Baviere, R., Vallée, M., & Paulus, C. (2015, September). Presentation, validation and application of the DistrictHeating Modelica library. In Proceedings of the 11th International Modelica Conference (Vol. 118, pp. 79-88). Linköping, Sweden: Linköping University Electronic Press.

Lamaison, N., Collette, S., Vallée, M., & Bavière, R. (2019). Storage influence in a combined biomass and power-to-heat district heating production plant. Energy, 186, 115714.

Lund, H., Werner, S., Wiltshire, R., Svendsen, S., Thorsen, J. E., Hvelplund, F., & Mathiesen, B. V. (2014). 4th Generation District Heating (4GDH): Integrating smart thermal grids into future sustainable energy systems. Energy, 68, 1-11.

Mitchell, S., OSullivan, M., & Dunning, I. (2011). Pulp: a linear programming toolkit for python. The University of Auckland, Auckland, New Zealand, 65, 25.

Renaldi, R., & Friedrich, D. (2019). Techno-economic analysis of a solar district heating system with seasonal thermal storage in the UK. Applied Energy, 236, 388-400.

Ruby, A., Crevon, S., Parmentier, P., Gaoua, Y., Lavialle, G. (2024). Persee, a single tool for various optimizations of multi-carrier energy system sizing and operation. In ECOS 2024-Efficiency, Cost, Optimization and Simulation of energy conversion systems and processes.

Saloux, E., & Candanedo, J. A. (2021). Model-based predictive control to minimize primary energy use in a solar district heating system with seasonal thermal energy storage. Applied energy, 291, 116840.

Salvestroni, M., Pierucci, G., Pourreza, A., Fagioli, F., Taddei, F., Messeri, M., & De Lucia, M. (2021). Design of a solar district heating system with seasonal storage in Italy. Applied Thermal Engineering, 197, 117438.

Scolan, S., Serra, S., Sochard, S., Delmas, P., & Reneaume, J. M. (2020). Dynamic optimization of the operation of a solar thermal plant. Solar Energy, 198, 643-657.

University of Wisconsin--Madison. Solar Energy Laboratory. (1975). TRNSYS, a transient simulation program. Madison, Wis. :The Laboratory,

Van Der Heijde, B., Vandermeulen, A., Salenbien, R., & Helsen, L. (2019). Representative days selection for district energy system optimisation: a solar district heating system with seasonal storage. Applied Energy, 248, 79-94.

04. Sustainable Process Heat for Industry

Parabolic Trough Collector Cost Update for Industrial Process Heat in The United States

Sertaç Akar[1] and Parthiv Kurup[1]

[1] National Renewable Energy Laboratory, Golden, Colorado (USA)

Abstract

Despite great potential, the worldwide adoption of concentrating solar thermal (CST) collectors for solar industrial process heat (SIPH) is modest. Industrial process heat (IPH) demands for heat and steam are typically below 300°C, where CST collectors can provide the needed heat. Parabolic trough collectors (PTCs) are the most deployed CST technology for SIPH applications. This paper is focused on the United States, and a summary of known operating parabolic trough plants is shown. A previous analysis of a modern PTC in 2016 found that for SIPH applications, the installed solar field cost could be \$200/m^2 (2016\$). Recent advances in PTC design and manufacturing have led to reduced cost per square meter of aperture area, and for a field of 510 solar collector assemblies (SCAs), the installed cost was \$120/m^2 (2020\$). On one hand, the results from this study showed that the solar field cost for large solar fields (510 SCAs or ~804,000 m^2) would increase to \$184/m^2 (2023\$) due to post pandemic inflation and increase in metal prices. On the other hand, medium SIPH sized fields (90 SCAs or ~142,000 m^2) cost analysis indicated an installed cost could be \$197/m^2 (2023\$). When small SIPH fields (12 SCAs or ~19,000 m^2) are considered, this jumps to \$297/m^2 (2023\$). These are cost estimates for the Installed Cost of the solar fields using the United States 2023\$ steel prices. When Chinese steel is used for comparison, the installed cost could be between \$162 - \$210/m^2 for the range of SIPH sizes.

Keywords: Concentrating Solar Thermal, Solar Industrial Process Heat, Parabolic Trough Collector

1. Introduction

Thermal energy and steam are ubiquitous needs in industrial process heating (IPH) applications. From the extraction of raw materials to food processing, heat is a vital part of the processing and manufacturing sectors. Globally, 53% of the final energy consumed by industrial processes is for heat such as heating fluids, processing materials, and reactions (IEA, 2023). In the United States, nearly 70% of the IPH demands are less than 300°C (McMillan et al., 2023). Linear concentrating solar thermal (CST) systems (i.e., parabolic troughs) can take heat transfer fluids (HTFs) and provide renewable heat for IPH up to 300°C (McMillan et al., 2021).

Global interest in using solar thermal for providing heat has been steadily increasing. Particularly in countries like China, Denmark, and Germany, solar thermal is used for solar water heating (SWH), solar district heating (SDH), and solar IPH (SIPH) applications. At present, flat plate collectors (FPCs) like glazed and unglazed collectors are widely used for SWH, and as of 2022 there were 542 gigawatts thermal (GWth) of global installed capacity. For SDH and SIPH, the installed capacities were 1.795 GWth and 0.856 GWth respectively (Weiss and Spörk-Dür, 2023). 75% of the total SIPH capacity (0.645 GWth), was installed at 494 sites. In 2022, 30 megawatts thermal (MWth) of SIPH capacity was installed (Weiss and Spörk-Dür, 2023).

When the number of SIPH systems is considered, parabolic trough collectors (PTCs) are used less than FPCs. There were 219 operating FPC sites for SIPH compared to 65 for PTCs, but the MWth installed is greater for PTCs i.e., 366 MWth compared to 219 MWth (Weiss and Spörk-Dür, 2023). There is significant potential for PTCs for SIPH applications. For example, when the Ma'aden Solar 1 site in Saudi Arabia is considered, it could be the largest SIPH plant at 1.5 GWth (Weiss and Spörk-Dür, 2023). This SIPH site would provide steam for alumina processing, which could reduce gas consumption by 12 million (MM) British Thermal Units (BTUs) per year and save 600,000 tonnes of CO_2 emissions per year (Glasspoint, 2023a). Whilst such large CST plants are very important to be deployed to reduce costs, such large projects may not be completed. For example the Miraah plant in Oman for solar thermal enhanced oil recovery was originally expected to be 1,021 MWth (Kraemer, 2017), and of that 330 MWth was finally constructed and is in operation (Glasspoint, 2023b).

Another technology suitable for SIPH are the Linear Fresnel Collectors (LFCs). Major advantages of LFCs are having potentially lower cost optical components due to its nearly flat shaped mirrors instead of curved mirrors, and potentially lower operating and maintenance (O&M) since the receiver tubes are fixed and so flexible

© 2024. The Authors. Published by International Solar Energy Society
Selection and/or peer review under responsibility of Scientific Committee
10.18086/eurosun.2024.04.01 Available at http://proceedings.ises.org

hoses or ball joints as used in PTCs are not needed (Pulido-Iparraguirre et al., 2019). The German company Industrial Solar (lately named PSE AG) used LFCs in several projects, such as the solar/gas cooling plant at the Engineering School of Seville, Spain (Haeberle et al., 2006). The most recent example of LFC SIPH application is the 4 MWth solar field that meets 10% of the steam demand at a Valencian brewery developed by HEINEKEN and CSIN (Solatom Indertec Company). This 4-MWth solar field has an aperature area of 6,000 m^2 and 182 Fresnel modules (HEINEKEN Spain, 2024).

This paper looks at the use of CST for SIPH applications at less than 300°C and is primarily focused on the United States and highlights PTC examples in the United States, a PTC installed cost update (in 2023$), and an analysis of the impact of global steel prices to PTC installed costs. It is worth noting, concentrating solar power (CSP) PTCs can be used for electricity generation and heat generation. Depending on the land availability and the heat generation needed, large aperture PTCs can be used for IPH applications.

2. PTC examples in the United States

There are only four SIPH plants installed using PTCs in the United States with a total capacity of 5.56 MWth (Tab. 11), of that 2.48 MWth is operational. To note, SkyFuel`s and Industrial Solar Technology (IST) Corp`s sites are not operating. The IST site was designed to deliver pressurized water from the solar field at 450 Fahrenheit (Walker et al., 2007), or 232°C. There have been reported issues of the solar field integration at the IST site, which included lower utilization of the energy used from the solar field than planned (86% instead of 100%), and higher soiling rates than expected (Kurup and Turchi, 2015). At the water desalination pilot site, the commercial readiness and performance of the electricity generation PTC and multiple effect distillation (MED) system was shown, though the electricity generation PTCs were underutilized in terms of the exit temperature of the solar field (180°C needed for the MED system compared to the PTC design of 390°C), and the cost of the treated water was expensive (Kurup and Turchi, 2015). There have been other CST demonstrations utilized for SIPH in the United States, such as LFCs (Kincaid et al., 2019; Kraemer, 2020).

Tab. 11. A summary of PTCs used for SIPH in the United States (*currently not operational)

Location	Developer	Application	Capacity (MW_{th})	HTF	Source
CA	Sunvapor	Almond Pasteurization	2.30	Water	(Epp, 2022)
CA	SkyFuel	Water Desalination*	0.48	Water & Glycol	(WaterFX, 2015)
AZ	Rackam	Sludge Drying	0.18	Synthetic Oil	(SPM, 2021)
CA	IST Corp	Food processing*	2.6	Pressurized water	(Walker et al., 2007)

2.1. Food Processing Application in California, USA

Sunvapor constructed and put into operation in 2022 a 2.3-MWth solar steam facility for almond pasteurization in Madera, California (CA) (Epp, 2022). The PTCs during the construction phase are shown in Figure 11 (Sunvapor, 2022), and water is heated through the PTCs to then produce steam with a solar steam boiler (Epp, 2022). The project is expected to achieve a 50% reduction in natural gas consumption per year, and a 100% reduction during clear sky conditions (Sunvapor, 2022).

Figure 11. 2.3 MWth solar steam facility for almond pasteurization in Madera, CA [(Epp, 2022), Image credit: Sunvapor]

2.2. Waste Management Application in Arizona, USA

Environmental laws require municipalities to treat wastewater sludge. There are many methods for decontaminating and disposing of sludge. Solar heat can be used to dry the sludge and prepare it for incineration or use as fertilizer. Solar heat can also be used in arid regions to distill and recover water-settling ponds. This gives two products with high added value, drinking water and fertilizer for crops. Rackam developed an innovative solar drying solution for sludge drying in City of Surprise, Arizona (AZ) (Figure 22) (SPM, 2021). Rackam proposed a dryer that combines solar heat generated by its PTCs and a ventilated greenhouse to evaporate water contained in the sludge with a very high efficiency (Rackam, 2024). The dryer is equipped with a feed system, a discharge system and multiple automated flipping tools that insure uniformity of the dried product. At full operation the goal is to reduce biosolid weight from 27 wet tonnes per day to 8 dry tonnes per day, approximately a 70% reduction by weight (SPM, 2021).

Figure 22. 175 kWth solar waste management system in City of Surprise, AZ (Image Credit: Rackam)

3. Global Market Analysis of Steel

CST solar fields that provide heat or generate electricity utilize significant quantities of commodity materials. These include steel, glass, cement, and aluminum, which can generally be locally sourced, leading to the development of an integrated supply chain (Chung et al., 2016; Turchi et al., 2015). Large PTC fields can have between 33% - 44% purchased components (Kurup et al., 2022). The majority of these specialized or purchased components such as mirrors and receivers, are typically bought from countries such as Germany or China.

For this paper, the PTC design utilized in the cost analysis (Section 4) is primarily steel based. For CST plants, typically low-carbon structural steel is used and then galvanized to allow for outdoor corrosion protection (Kurup et al., 2022; Turchi et al., 2015). A large PTC solar field can be approximately 31% carbon steel, iron, zinc and stainless steel by mass in metric tonnes (Turchi et al., 2015), as such changes in the raw steel price will fundamentally drive the solar field Installed Cost ($/m^2). This section looks at the global and U.S. markets for steel to highlight the significant impacts in steel price over the last 5 years.

3.1. Global steel analysis

Steel as a key commodity material, produced in many forms from hot rolled coil (HRC), structural plates, tubes and pipe, and rebar (SteelBenchmaker, 2024). Steel grades also vary by end-use from stainless steel to low-carbon steel. HRC is a typical and principal steel product, and an indicator of raw material, and overall market steel prices (Ryerson, 2020). Figure 33 shows the HRC price per metric tonne by country, and the fluctuations from 2014 to 2024. This highlights that United States domestically manufactured steel (in $/tonne), has over the last decade been significantly higher than Chinese and European steel. During the pandemic in 2020, significant price hikes for HRC in $/tonne increased from ~$500/tonne to nearly $2,000/tonne (4 times increase). HRC $/tonne prices saw sharp declines in 2023 (Figure 33). At present the United States HRC is approximately $777/tonne (SteelBenchmaker, 2024; Trading Economics, 2024).

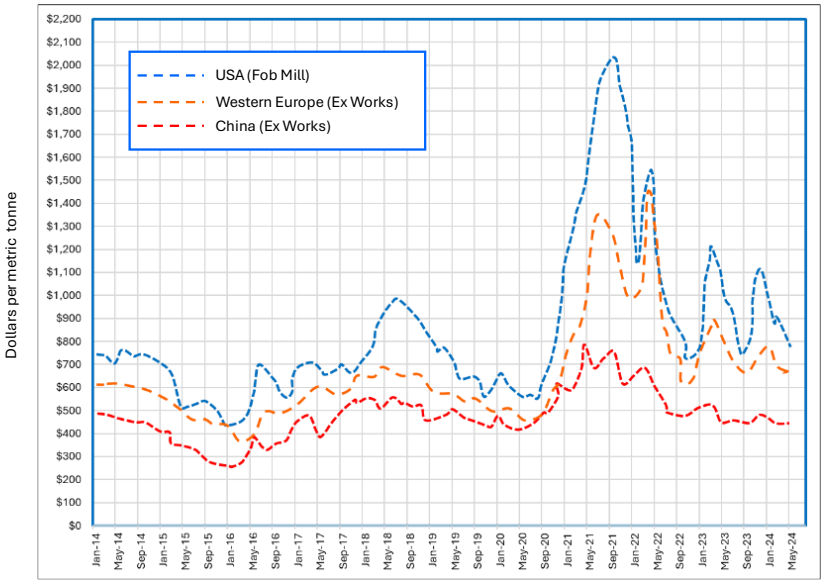

Figure 33. HRC steel prices (in dollar per tonne) for USA, Western Europe and China (SteelBenchmaker, 2024)

3.2. United States steel analysis

With the focus of this paper on the United States, the U.S. steel market is also shown. Steel for CST IPH applications is likely to be sourced in the United States to offer domestic benefits such as reduced transportation. Figure 44. **Total Steel Price Index from 1980 to 2024 (Ibis World, 2024)** shows the Total Price of Steel Index spanning from 1980 to 2024. Relative to 2020's 184.5, by 2023 the index was considerably higher at 319.9 i.e., a 73% increase (Ibis World, 2024). The Total Price of Steel is determined from the "producer price index for steel mill products, averaging the growth in price for various types of steel, including bars, sheets, strips, plates and wires, of the hot-rolled and cold-rolled varieties. The index has a base year of 1982" (Ibis World, 2024).

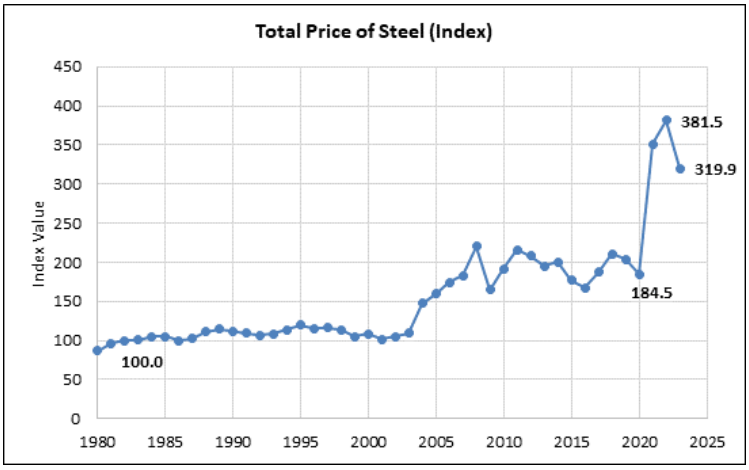

Figure 44. Total Steel Price Index from 1980 to 2024 (Ibis World, 2024)

4. Parabolic Trough Collector Cost Update Methodology

Previously an installed cost analysis and a manufacturing methodology for a state-of-the-art and a near-commercial parabolic trough solar collector assemblies (SCAs) was developed (Kurup et al., 2022; Turchi et al., 2016). An SCA is built of a string of PTC modules controlled by a single drive and represents the smallest unit of a functional parabolic trough solar field. In this context, an updated bill of materials (BOM) was provided by Solar Dynamics for the SunBeam™ 8-m aperture width mid-term collector (Figure 55). The cost of specialty components such as receiver tubes, drive systems, and glass mirror panels were based on quotes from representative suppliers. Design for Manufacturing and Assembly (DFMA®) software is used to calculate detailed manufacturing and assembly cost of the system at different manufacturing volumes. The DFMA® tool has detailed databases and allows the knowledgeable user to calculate a primary manufacturing cost for

each component and then assemble it within the overall product/assembly.

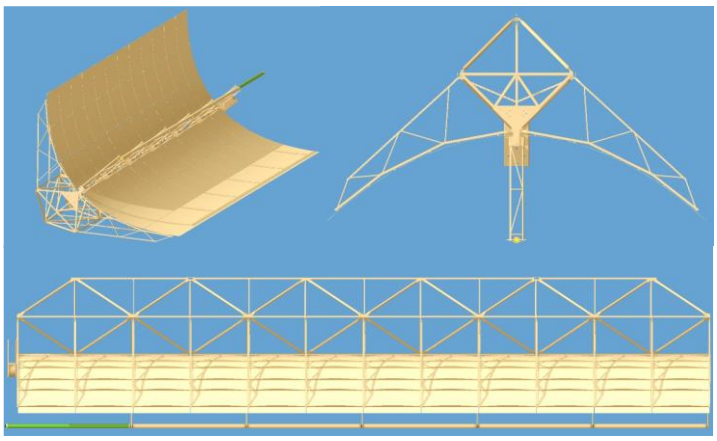

Figure 55. Schematics of SunBeam™ PTC Mid-term Design (Image Credit: Solar Dynamics)

The estimated solar field installed cost per square meter as a function of the number of SCAs built is given as (Eq. 1):

$$Solar\ Field\ Cost\ \left(\frac{\$}{m^2}\right) = \frac{Manufacturing\ Cost\ (\$) + Assembly\ Cost\ (\$)}{(Number\ of\ SCAs) * (Area\ per\ SCA)\ (m^2)} \quad \text{(eq. 1)}$$

The installed cost analysis for the PTC System includes manufacturing costs, in-house assembly costs, outsourced parts and field assembly cost. In the scope of this cost update first the BOM and manufacturing cost model is updated based on a medium size and a small system size which consists of 90 SCAs and 12 SCAs of SunBeam™ collectors respectively. The manufacturing costs are calculated by using the DFMA® software`s updated material and process libraries in version 2023a. The cost estimates purchased parts such as mirrors, drive hydraulics, control systems, fasteners, interconnected and electrical cabling are escalated to 2023 dollars by using the U.S. Consumer Price Index for urban customers (CPI-U) (BLS, 2024) and new price quates from vendors.

An earlier analysis found that the PTC solar field installed cost could be \$200/m^2 (2016\$) sized for SIPH applications with 10 SCAs (5MWth), and ~\$180/m^2 for approximately 500 SCAs (Turchi et al., 2016). In another analysis from 2020, the solar field cost was calculated as \$120/m^2 (2020\$) for a large CST system with 510 SCAs and ~1,570 m^2 aperture area per SCA (Kurup et al., 2022). The estimates for 2023 showed that the solar field cost for 510 SCAs could be 53% more than the 2020 results.

5. Results

5.1. Installed Cost Analysis

The installed cost for large size PTC system assuming a production volume of 510 SCAs, which is representative of a solar field of approximately ~800,000 m^2 is calculated as \$184/m^2 (Figure 66a). This solar field, which occupies approximately 1,000,000 m^2 of land area, is suitable for 225 MWth in Daggett, CA with a solar multiple (SM) of 2.3 and six hours of thermal energy storage (TES) (NREL, 2024). The manufacturing cost also includes an estimated \$934,000 investment cost to purchase tooling specific to the manufacturing of the steel components for the space frame, support arms, and receiver supports. When the total manufacturing tooling investment (i.e. stamping dies) is amortized over 510 SCAs, it adds \$1.2/m^2 to the manufactured cost.

The installed cost for medium size PTC system assuming a production volume of 90 SCAs, which is representative of a solar field of approximately ~142,000 m^2 is calculated as \$197/m^2 (Figure 66b). This solar field, which occupies approximately 177,000 m^2 of land area, is suitable for a 40 MWth solar field with the same SM and TES configuration. Total tooling investment is the same as large size PTC system and it adds \$6.2/m^2 to the manufactured cost when the total manufacturing tooling investment for stamping dies is amortized over 90 SCAs.

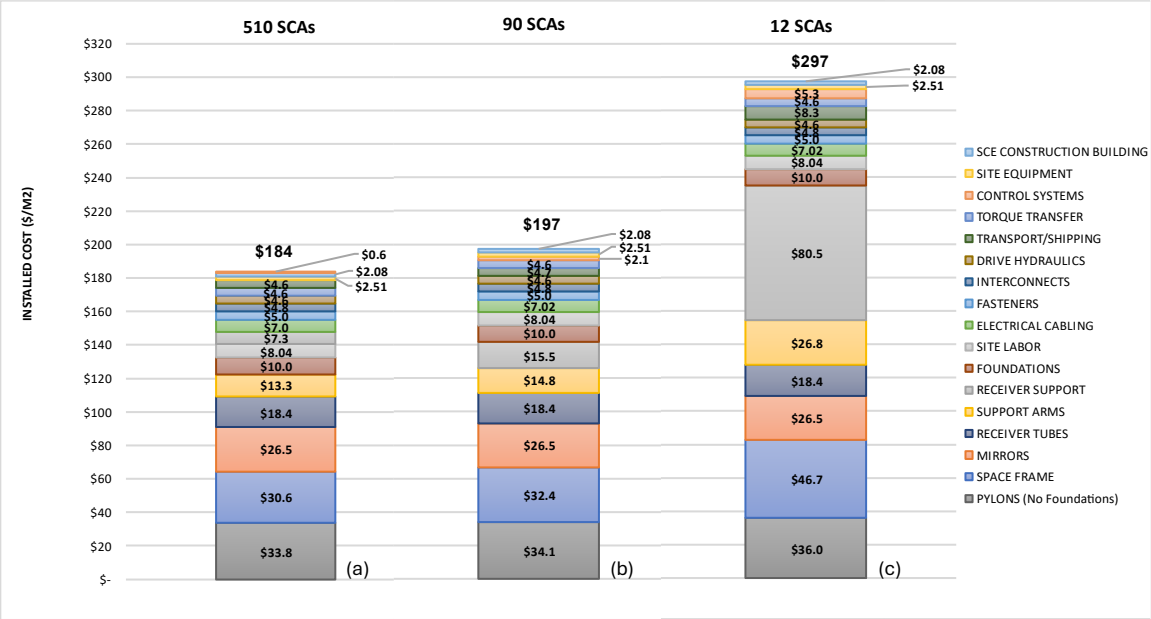

Figure 66. Installed cost breakdown by component for a) 510 SCAs SunBeam™ PTC, b) 90 SCAs SunBeam™ PTC, c) 12 SCAs SunBeam™ PTC

The installed cost for small size PTC system assuming a production volume of 12 SCAs, which is representative of a solar field of approximately ~19,000 m^2 is calculated as $297/$m^2$ (**Error! Reference source not found.**). This solar field, which occupies approximately 24,000 m^2 of land area, is suitable for a 5 MWth with the same SM and TES configuration. The manufacturing cost analysis of the small size PTC system includes machining, in-house assembly and purchased items, assuming a production volume of 12 SCAs. When the total manufacturing tooling investment is amortized over 12 SCAs, it adds $49.4/$m^2$ to the manufactured cost. In an earlier study, the installed cost of a similar sized 10 SCA, 5 MWth solar field in 2016$ was $200/$m^2$ (Turchi et al., 2016). When comparing this aluminum space frame design to the 12 SCA steel frame design, the installed solar field cost has increased to $297/$m^2$ (2023$). The current analysis indicates the steel components have the highest cost share followed by the mirror panels and the receiver. While unit cost steel components correspond to ~52-54% of the installed cost of 510 SCAs and 90 SCAs, this share can jump to 67% for the 12 SCAs (Figure 77).

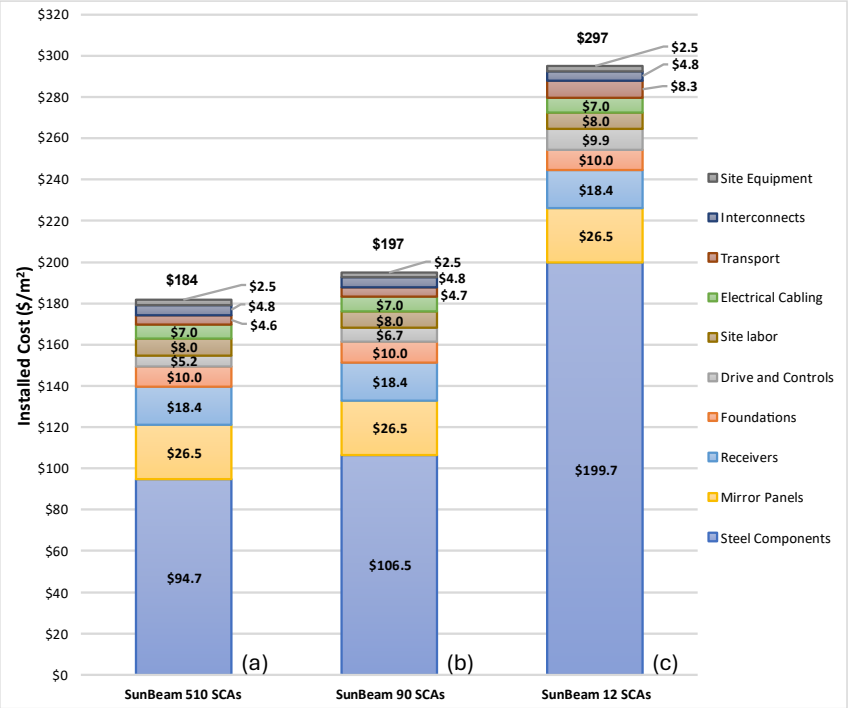

Figure 77. Cost share of steel components in a) 510 SCAs SunBeam™ PTC, b) 90 SCAs SunBeam™ PTC, c) 12 SCAs SunBeam™ PTC

5.2. Impact of Global Steel Prices

The DFMA® software has the option to select the material library which allows the user to select the sources of the material for concurrent costing. It can be either North American Origin, or Chinese origin materials. Using the 2023 databases, the analysis indicated that the large size PTC system can be 10% cheaper, the medium size PTC system can be 12% cheaper, and the small size PTC system can be 28% cheaper when Chinese origin steel is used as raw material for manufacturing processes (Figure 88). It is important to note that, while the material cost is taken from Chinese origin with estimated shipping cost, remaining cost items such as, the operation times, labor rates and energy costs are still representing the North American rates.

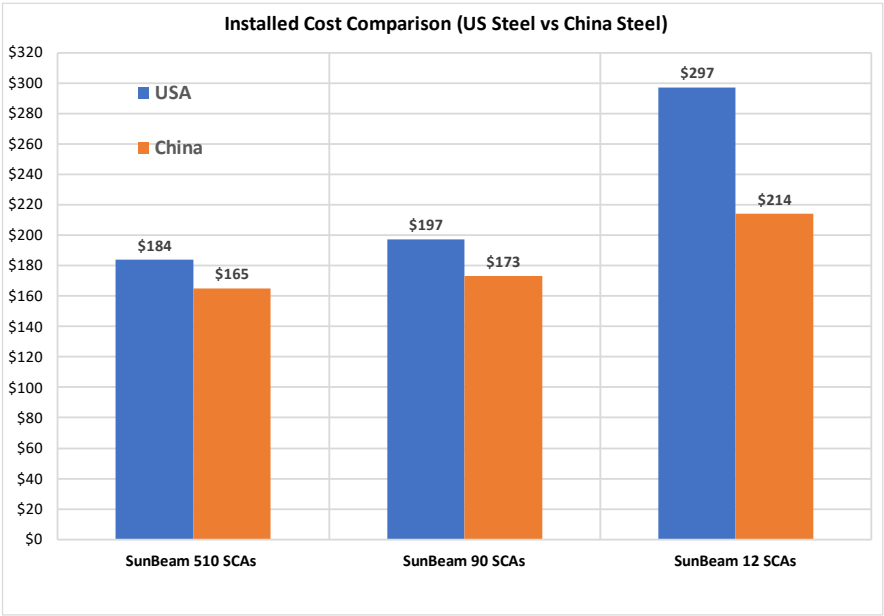

Figure 88. Comparison of the installed cost for large, medium and small field aperture area PTC systems with respect to the USA and Chinese origin steel as raw material.

The steel price analysis undertaken in this work has only looked at the relative price difference such as $297/m^2$ for the solar field installed cost compared to $214/m^2$ for the same 12 SCA design, which has utilized United

States or Chinese steel respectively. Estimated average cost of shipping for steel from China to the United States is $175/tonne (Basenton, 2024) which corresponds to a $3/m^2 cost adder to the total installed cost. Specific tariffs have not been considered, which aim to increase the competitiveness of U.S. Steel. For example, the current "tariff rate on certain steel and aluminum products under Section 301" is 0% – 7.5% (White House, 2024), has not been added. This same tariff has been announced to increase to 25% in 2024 (White House, 2024), with the impacts which would be seen in 2025 and later. The impact of tariffs has been excluded, as that requires specific project and supplier information, which was outside of this scope. The steel prices in the United States and China have been highlighted to help give perspective on the choice for companies looking to develop SIPH projects in the United States are likely to face higher CAPEX costs due to local steel being relatively higher than sourced from Europe or China.

5.3. Levelized Cost of Heat (LCOH) for SIPH applications in the United States

For an industrial site that is considering the use of SIPH, an important evaluation is whether to install a renewable heat solution such as a PTC solar field and the heat conversion hardware (i.e., HTF to steam generator) to integrate it into the site. This analysis assumes that a brownfield industrial site (i.e., with existing infrastructure), has two options: the site could install a PTC solar field adjacent to the site; or replace an existing natural gas burner. Industrial gas burners are commonly used to produce steam, and can range in cost such as $102 - $250/kWth (Akar et al., 2021; Karki et al., 2019). We have utilized a 5 MWth system capacity for the commercial natural gas boiler, operating at 83% efficiency (DOE FEMP, 2022a). Industrial steam boilers can operate for approximately 1,500 – 6,000 full load hours equivalent depending on the industry and use case (DOE FEMP, 2022b; Loes, 2019; Rissman, 2022). It is expected that the boiler would ramp up and down and have partial loads during operations. We have used 3,000 full load hours equivalent, based on 5,500 hours of annual operation (Cleaver Brooks, 2020), and a $234/kWth natural gas installation cost (Rissman, 2022).

Natural gas fuel costs are important to highlight in this analysis, as any industrial site would compare their natural gas costs due to operating their plant to the SIPH application. The SIPH application would save them costs, reduce volatility, and increase the security of their energy supply. 2023 U.S. and state level Industrial Price of gas ($ per thousand feet and converted to $ per MMBTU) have been used (EIA, 2024).

The LCOH is an important and convenient metric that shows the estimated lifetime cost of the PTC solar field and installation for SIPH and comparing it to the LCOH of replacing an existing natural gas steam boiler. The LCOH for SIPH is similar to the Levelized Cost of Electricity (LCOE), where renewable electricity generation technologies can be compared. The LCOH method used is from SAM (NREL, 2024; Short et al., 1995), and (Eq. 2) shows the LCOH calculation. The total installed project cost is the TIPC, the fixed charge rate is FCR, Annual O&M is the Annual Operating and Maintenance (O&M), and the annual thermal generation (which for simplicity is the same every year) is based on direct normal irradiance (DNI) at different places in the United States. The TIPC includes the solar field installed cost and additional hardware such as the HTF system to generate steam and heat exchanger, site preparation costs (i.e., $25/m^2), contingency on Direct Capital (CAPEX) Costs at 7% and Indirect CAPEX cost at approximately 10%. The SAM Industrial Process Heat Parabolic Trough model has been used to obtain the SIPH estimates relating to the solar field integration.

$$LCOH = \left(\frac{\$}{kWhth}\right) = \frac{(TIPC)*(FCR)+(Annual\ O\&M)}{Annual\ thermal\ generation} \quad \text{(Eq. 2)}$$

Figure 99 shows the LCOH for a range of installed solar field costs (not the total cost per m^2) at three different DNI levels that are representative of the United States, and the LCOH of a replacement 5 MWth natural gas boiler. For example, as can be seen the U.S. average LCOH for the natural gas boiler replacement was $0.025/kWhth and the CA average was approximately $0.059/kWhth. The LCOH for gas is based on 2023 industrial gas prices of $4.42/MMBTU for the United States, and $12.74/MMBTU for CA (EIA, 2024). A United States average industrial gas price of $4.42/MMBTU corresponds to $0.015/kWhth of natural gas price, and similarly $12.74/MMBTU in California corresponds to $0.043/kWhth. As seen in Figure 99, if the installed solar field cost is approximately $200/m^2 in an excellent solar resource area which has an average DNI of 7.5kWh/m^2/day (i.e., Daggett in CA has an average estimated daily DNI of 7.67 kWh/m^2/day (NREL, 2024), the LCOH of the PTC field could be approximately $0.025/kWth. In CA, which has a range of DNIs from 5.5 to over 7.5/kWh/m^2/day, natural gas costs are significantly higher than the U.S. average, and solar fields at $150 – 300/m^2 could yield an LCOH less than the natural gas system.

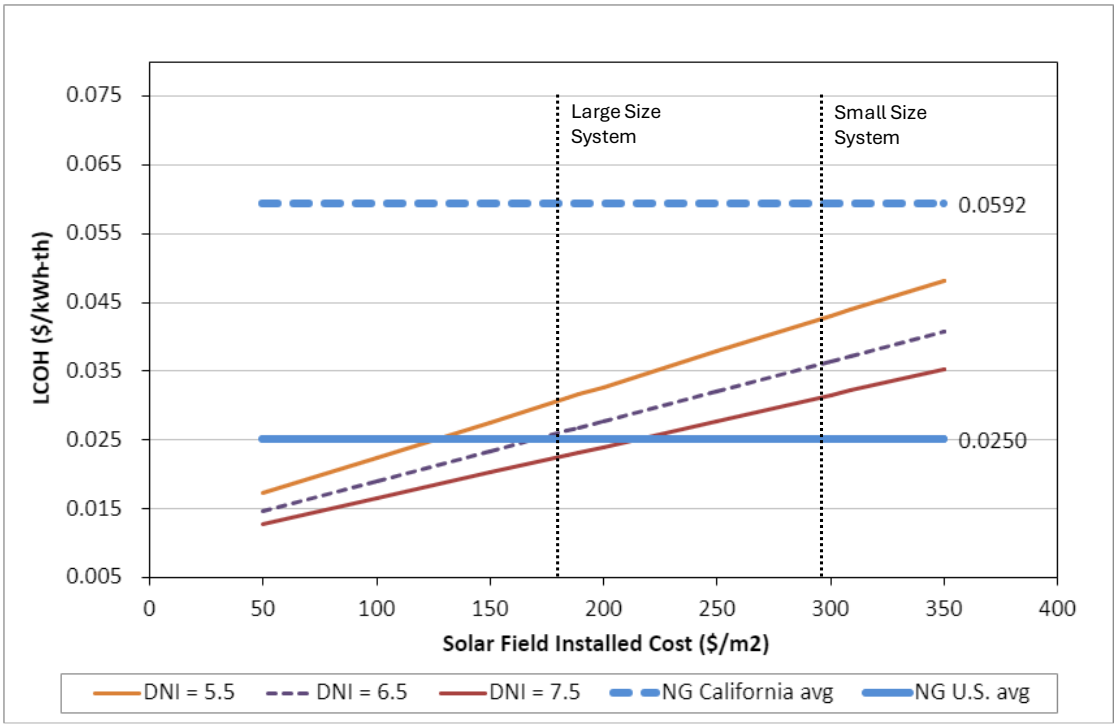

Figure 99. LCOH for a range of installed costs and three different solar resource levels that are representative of the United States.

Figure 1010 shows the range of the LCOH for a range of installed solar field costs across the 3 DNI resource levels, and with 3 different gas prices ranging from $5/MMBTU to $10/MMBTU. This in 2023 is representative of natural gas price for most states in the United States, as 11 states in the United States had natural gas prices over $10/MMBTU (a LCOH of $0.0479/kWth) (EIA, 2024). As expected, as the natural gas price decreases from $10/MMBTU to $7.5/MMBTU and then to $5/MMBTU, it becomes significantly more difficult for PTC SIPH fields to compete directly without subsidies or credits against low natural gas LCOHs. For example, if a site has $10/MMBTU natural gas pricing, even with a lower DNI of 5.5 kWh/m^2/day and $350/m^2 for the installed solar field cost, it can produce a competitive LCOH of approximately $0.0479/kWth. In a gas price environment of $7.5/MMBTU such as AZ, which also has very good to excellent DNI, installed solar fields costs up to $300/m^2 could have a LCOH lower than $0.0377/kWhth.

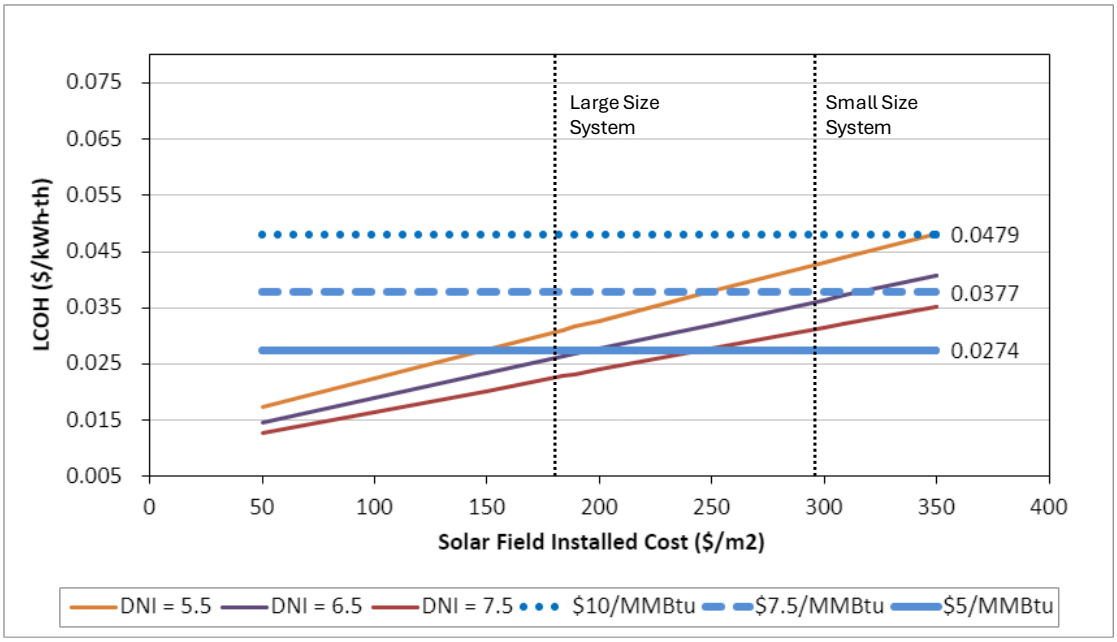

Figure 1010. LCOH across gas price ranges ($7.5/MMBTU in AZ)

6. Discussions

6.1. Volume of Manufacturing & Economies of Scale

The volume of manufacturing is the key for the parts to be economically feasible to manufacture in-house. While the manufacturing processes which do not require additional tooling such as laser cutting do not have a significant impact on the part cost, processes like heavy stamping which require significant tooling cost have a great impact on the unit cost of the part. The economic threshold varies by the type of material and the size of the part to stamp but on average 10,000 parts is the economic limit for a part to be stamped at low manufacturing cost (Figure 1111). While the average manufacturing volume for a large size PTC system (510 SCAs) could be ranging between 40,000 and 100,000 parts, it is as low as ~1,000 parts for a small size PTC system (12 SCAs). Thus, the economic threshold for the IPH application should be at least 9-10 projects at size of 12 SCAs per year.

A one SCA prototype is just for test purposes and does not represent a cost feasible IPH application (~0.4 MWth). The solar field installed cost of a one SCA prototype could be as high as $1,465/m^2 with North American steel and $750/m^2 with Chinese steel. Similarly, to make the one SCA IPH application economically feasible the manufacturer should have a project volume ranging between 90 and 100 PTC systems per year.

Design changes can have a positive impact on the installed solar field cost of the PTC systems. Considering 50-60% of the total installed solar field cost comes from the material cost, any design change that requires less parts and materials in the structural frame can lower the installed cost significantly. Another important factor that affects the cost of manufacturing is the change in process. As an example, replacement of stamping with roll forming or increased automation in manufacturing and assembly such as robotic arm riveting would reduce the total installed cost of the PTCs.

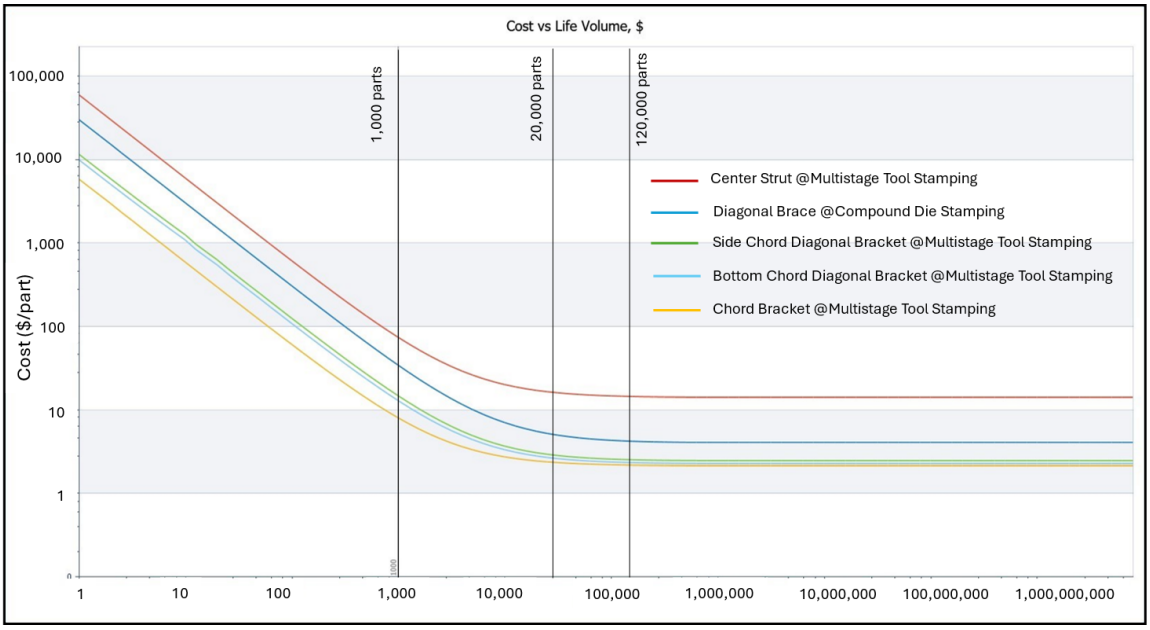

Figure 1111. Cost vs volume chart for parts manufactured by stamping processes which require additional tooling

6.2. LCOH Discussions

This study finds that CA represents a favorable environment for SIPH since the natural gas prices are typically significantly higher than the national average, and DNI values are excellent. CA typically also has strong incentive programs for renewable energy technologies. The LCOH for SIPH improves or reduces as the raw steel prices drop, the solar field integration costs decrease e.g., the piping and HTF to steam generator, and contingencies reduce as learnings increase and there are more solar field installations. When natural gas prices stay high, or a tax credit is applied for carbon emissions, the LCOH for SIPH applications becomes more competitive when compared to the heat generated by the existing natural gas systems. This study assumes a 5-MWth system capacity for the SIPH application, and as such would be higher than the LCOH of a medium size PTC system (40 MWth), which can utilize the volume of manufacturing, and economies of scale

highlighted earlier.

6.3. Global Examples of Small Aperture area PTCs for IPH

This analysis has highlighted large aperture PTCs, which have the potential to be utilized for SIPH applications (e.g., 5 MWth), if sufficient thermal load can be met by the field and there is land area adjacent to the industrial site. PTCs designed originally for electricity generation and then used for SIPH are operating, such as the 30 MWth PTC solar field integration at the Heineken España site (Epp, 2023). Typically SIPH applications utilize smaller PTCs such as 1-2 m of aperture width, which are suitable for rooftop applications (Figure 1212a), or ground mount for size constrained sites (Figure 1212b).

Figure 1212. a) Absolicon`s rooftop PTC for IPH application in Greece (RTC, 2023); b) Inventive Power's ground mount application in Mexico (Rosell, 2022). Image Credits: Absolicon and Inventive Power

7. Acknowledgments

NREL does not endorse the companies specified in this paper, and any mention is strictly for research purposes only. This work was authored by the National Renewable Energy Laboratory, operated by Alliance for Sustainable Energy, LLC, for the United States Department of Energy (DOE) under Contract No. DE-AC36-08GO28308. Funding is provided by the United States Department of Energy Office of Energy Efficiency and Renewable Energy's Solar Energy Technologies Office. The views expressed herein do not necessarily represent the views of the DOE or the United States Government. The United States Government retains and the publisher, by accepting the article for publication, acknowledges that the United States Government retains a nonexclusive, paid up, irrevocable, worldwide license to publish or reproduce the published form of this work, or allow others to do so, for United States Government purposes.

8. References

Akar, S., Kurup, P., McTigue, J., Boyd, M., 2021. Renewable Thermal Hybridization Framework for Industrial Process Heat Applications, in: AIP Conference Proceedings. Presented at the SolarPACES 2020, American Institute of Physics, Online Conference, p. 12.

Basenton, 2024. Guide to Importing and Shipping Steel Materials from China - Basenton [WWW Document]. URL https://www.basenton.com/guide-to-importing-and-shipping-steel-materials-from-china/ (accessed 8.16.24).

BLS, 2024. CPI for All Urban Consumers (CPI-U) [WWW Document]. US Bur. Labor Stat. URL https://beta.bls.gov/dataViewer/view/timeseries/CUSR0000SA0 (accessed 3.12.24).

Chung, D., Horowitz, K., Kurup, P., 2016. On the Path to SunShot: Emerging Opportunities and Challenges in U.S. Solar Manufacturing (No. NREL/TP-7A40-65788). National Renewable Energy Laboratory, Golden, CO.

Cleaver Brooks, 2020. Boiler Efficiency Guide.

DOE FEMP, 2022a. Purchasing Energy-Efficient Large Commercial Boilers [WWW Document]. Energy.gov. URL https://www.energy.gov/femp/purchasing-energy-efficient-large-commercial-boilers (accessed 7.18.24).

DOE FEMP, 2022b. Energy Savings Calculator for Commercial Boilers [WWW Document]. Energy.gov. URL https://www.energy.gov/femp/energy-savings-calculator-commercial-boilers (accessed 7.18.24).

EIA, 2024. Natural Gas Industrial Price [WWW Document]. Energy Inf. Adm. URL https://www.eia.gov/dnav/ng/ng_sum_lsum_a_EPG0_PIN_DMcf_a.htm (accessed 7.18.24).

Epp, B., 2023. Technical tour to Europe's largest solar industrial heat plant at Heineken Spain. Solarthermalworld.
Epp, B., 2022. 2.3 MW solar steam boiler for almond pasteurization in California. Solarthermalworld.
Glasspoint, 2023a. Ma'aden Solar I [WWW Document]. GlassPoint. URL https://www.glasspoint.com/projects/maaden-solar (accessed 3.6.24).
Glasspoint, 2023b. Miraah [WWW Document]. GlassPoint. URL https://www.glasspoint.com/projects/miraah (accessed 3.6.24).
Haeberle, A., Berger, M., Luginsland, F., Zahler, C., Rommel, M., Baitsch, M., Henning, H.M., 2006. Linear concentrating Fresnel collector for process heat applications; Linear konzentrierender Fresnel-Kollektor fuer Prozesswaermeanwendungen.
HEINEKEN Spain, 2024. HEINEKEN and CSIN open world's largest solar thermal plant with innovative Fresnel technology for industrial use in Spain [WWW Document]. HEINEKEN CSIN Open Worlds Larg. Sol. Therm. Plant Innov. Fresnel Technol. Ind. Use Spain. URL https://www.theheinekencompany.com/newsroom/heineken-and-csin-open-worlds-largest-solar-thermal-plant-with-innovative-fresnel-technology-for-industrial-use-in-spain/ (accessed 7.22.24).
Ibis World, 2024. Price of Steel (United States) [WWW Document]. URL https://www.ibisworld.com/default.aspx (accessed 6.29.24).
IEA, 2023. Renewables 2022. International Energy Agency.
Karki, S., Haapala, K.R., Fronk, B.M., 2019. Technical and economic feasibility of solar flat-plate collector thermal energy systems for small and medium manufacturers. Appl. Energy 254, 113649. https://doi.org/10.1016/j.apenergy.2019.113649
Kincaid, N., Mungas, G., Kramer, N., Zhu, G., 2019. Sensitivity analysis on optical performance of a novel linear Fresnel concentrating solar power collector. Sol. Energy 180, 383–390. https://doi.org/10.1016/j.solener.2019.01.054
Kraemer, S., 2020. Solar Heat for Cleaning Wastewater and Recovering Clean Water. SolarPACES. URL https://www.solarpaces.org/solar-heat-for-cleaning-wastewater-and-recovering-clean-water/ (accessed 7.16.24).
Kraemer, S., 2017. Glasspoint starts up 1 GW Solar Thermal EOR on Time and on Budget. SolarPACES. URL https://www.solarpaces.org/glasspoint-starts-1-gw-solar-thermal-eor-time-budget/ (accessed 3.6.24).
Kurup, P., Glynn, S., Akar, S., 2022. Manufacturing cost analysis of advanced parabolic trough collector. AIP Conf. Proc. 2445, 020006. https://doi.org/10.1063/5.0085663
Kurup, P., Turchi, C., 2015. Initial Investigation into the Potential of CSP Industrial Process Heat for the Southwest United States (No. NREL/TP-6A20-64709). National Renewable Energy Laboratory, Golden, CO. https://doi.org/10.2172/1227710
Loes, R., 2019. Technology Factsheet - Natural Gas STeam Boiler Industry. TNO, Netherlands.
McMillan, C., Kurup, P., Feldman, D., Wachs, E., Akar, S., 2023. Renewable Thermal Energy Systems: Systemic Challenges and Transformational Policies (Report 2) (No. NREL/TP-7A40-83020), Renewable Thermal Energy Systems: Report 2. Golden. https://doi.org/10.2172/1957765
McMillan, C., Schoeneberger, C., Zhang, J., Kurup, P., Masanet, E., Margolis, R., Meyers, S., Bannister, M., Rosenlieb, E., Xi, W., 2021. Opportunities for Solar Industrial Process Heat in the United States (No. NREL/TP-6A20-77760). National Renewable Energy Laboratory, Golden, CO. https://doi.org/10.2172/1762440
NREL, 2024. Download - System Advisor Model (SAM). Golden, CO.
Pulido-Iparraguirre, D., Valenzuela, L., Serrano-Aguilera, J.-J., Fernández-García, A., 2019. Optimized design of a Linear Fresnel reflector for solar process heat applications. Renew. Energy 131, 1089–1106. https://doi.org/10.1016/j.renene.2018.08.018
Rissman, J., 2022. Decarbonizing Low-Temperature Industrial Heat in the U.S. Energy Innovation.
Rosell, A.D., 2022. Zero CAPEX solar heat for Mexican industry. Solarthermalworld.
RTC, 2023. Case Study: Colgate-Palmolive Factory.
Ryerson, 2020. What is the Market Price of Steel? [WWW Document]. Ryerson. URL https://www.ryerson.com/resource/the-gauge/what-is-the-market-price-of-steel (accessed 6.29.24).
Short, W., Packey, D., Holt, T., 1995. A manual for the economic evaluation of energy efficiency and renewable energy technologies (No. NREL/TP-462-5173). National Renewable Energy Laboratory, Golden, CO. https://doi.org/10.2172/35391
SPM, 2021. Surprise Progress Magazine - Summer 2021 [WWW Document]. URL https://comm.surpriseaz.gov/ProgressMag/Progress_Summer_2021/#page=6 (accessed 3.6.24).
SteelBenchmaker, 2024. Price History.
Sunvapor, 2022. California Custom Processing - Madera, CA [WWW Document]. Sunvapor Inc. URL https://www.sunvapor.net/technologies/solar-steam (accessed 2.29.24).
Trading Economics, 2024. HRC Steel [WWW Document]. Trading Econ. URL https://tradingeconomics.com/commodity/hrc-steel (accessed 6.29.24).

Turchi, C., Kurup, P., Akar, S., Flores, F., 2015. Domestic Material Content in Molten-Salt Concentrating Solar Power Plants (No. NREL/TP--5500-64429, 1215314). https://doi.org/10.2172/1215314

Turchi, C.S., Kurup, P., Zhu, G., 2016. Revisiting Parabolic Trough Concentrators for Industrial Process Heat in the United States. Presented at the ASME 2016 Power Conference collocated with the ASME 2016 10th International Conference on Energy Sustainability and the ASME 2016 14th International Conference on Fuel Cell Science, Engineering and Technology, American Society of Mechanical Engineers Digital Collection. https://doi.org/10.1115/POWER2016-59621

Walker, A., Kutscher, C., Halvorsen, A., McKenna, C., Chambers, D., May, K., 2007. Design and Analysis of a Large Solar Industrial Heat Plant for Frito Lay in Modesto California, in: ES2007. Presented at the ASME 2007 Energy Sustainability Conference, American Society of Mechanical Engineers Digital Collection, Long Beach, CA. http://dx.doi.org/10.1115/ES2007-36050

WaterFX, 2015. California's First Commercial Solar Desalination Plant to Bring Freshwater to the Central Valley [WWW Document]. URL https://www.prnewswire.com/news-releases/californias-first-commercial-solar-desalination-plant-to-bring-freshwater-to-the-central-valley-300113489.html (accessed 3.6.24).

Weiss, W., Spörk-Dür, M., 2023. Solar Heat Worldwide Edition 2023. AEE Intec, Gleisdorf, Austria.

White House, 2024. FACT SHEET: President Biden Takes Action to Protect American Workers and Businesses from China's Unfair Trade Practices [WWW Document]. White House. URL https://www.whitehouse.gov/briefing-room/statements-releases/2024/05/14/fact-sheet-president-biden-takes-action-to-protect-american-workers-and-businesses-from-chinas-unfair-trade-practices/ (accessed 6.29.24).

ASTEP project: status and progress at 2024

Antonio Rovira[1]; Rubén Abbas[2]; Juan P. Solano[3]; Magdalena Barnetche[2]; José Muñoz[4]; Mercedes Ibarra[1]; Rubén Barbero[1], Andreas Androutsopoulos[5]

[1] Universidad Nacional de Educación a Distancia (UNED); [2] Universidad Politécnica de Madrid (UPM); [3] Universidad Politécnica de Cartagena (UPCT); [4] Universidad Miguel Hernández de Elche (UMH); [5] Centre for Renewable Energy Sources and Saving (CRES)

Abstract

Solar thermal energy for industrial processes (SHIP) is gaining relevance for meeting industrial thermal energy demands. This method offers a twofold advantage: reducing fossil fuel consumption and emissions while establishing a distinct market niche for solar technology. The ASTEP project, funded by the European Commission focuses on an innovative SHIP concept. Integrating modular designs—SunDial solar collectors from and phase-change material thermal storage—ASTEP employs a flexible control system. It aims to demonstrate its capability to fulfill a significant portion of industrial heat demand above 150 ºC in latitudes challenging for existing designs.

Keywords: Solar Heat for Industrial Processes (SHIP), Concentrating Solar Power (CSP), Thermal Storage System (TES).

1. Introduction

Solar thermal energy for industrial processes (SHIP) is gaining increasing importance as one of the ways to meet the high thermal energy demand required by industry. This implies a double benefit: firstly, by using a renewable energy source, fossil fuel consumption is reduced, and therefore, pollution and greenhouse gas emissions to the atmosphere are diminished; secondly, heat for industrial processes becomes a new market niche for solar technology, which can lead to a reduction in the cost of solar collectors through economies of scale in manufacturing and advances in the learning curve in implementation.

According to the National Renewable Energy Laboratory (NREL) of the United States (Kurup & Turchi, 2015), the European Union (EU) has been a leader in the use, development, implementation, and monitoring of SHIP plants over the past decade. However, to date, this has largely been limited to heat loads below 150 ºC. The next step in the large-scale adoption of solar process heating is to develop technologies and methodologies for the production of solar thermal energy applied to industrial processes reliably and above 150 ºC, which will expand the exploitation possibilities.

Currently, there are just over a hundred operational SHIP systems in Europe, according to the SHIP plant database of IEA Task 49 (http://ship-plants.info/), and only about twenty of them operate at temperatures above 150 ºC, and it can be achieved with parabolic trough or linear Fresnel collectors (Montes et al., 2018). The main objective of the ASTEP project (Application of Solar Thermal Energy to Processes) is to develop a new concept of solar energy applied to industry (SHIP) and demonstrate its viability at two relevant industrial demonstration sites located in two different climatic regions: Iasi in Romania and Corinth in Greece. To this end, two demonstrators of the technology are being built, able to supply thermal energy to meet heat demands above 150 ºC and cooling under the conditions required by the industrial processes of the respective industries.

The project objectives can be summarized into three:

1. Develop the various technologies involved in the ASTEP concept: the SunDial solar collector, the thermal storage system based on phase change materials, and the integration of the technologies along with the control system.
2. Demonstrate the ASTEP technology on a 25 kW scale at two relevant industrial sites. To this end, the concepts of the three main subsystems (SunDial, thermal storage, and integrated concept system) are being built and will be installed, tested independently in the laboratory, and sent to the end-users for technology

© 2024. The Authors. Published by International Solar Energy Society
Selection and/or peer review under responsibility of Scientific Committee
10.18086/eurosun.2024.04.02 Available at http://proceedings.ises.org

testing in integrated and relevant real operating conditions.

3. Evaluate the sustainability of the ASTEP concept. The benefits of the ASTEP technology cover not only environmental aspects but also political and socio-economic aspects. Various tools are used for its evaluation, such as life cycle analysis, calculation of CAPEX, OPEX, and Levelized Cost of Heat (LCOH), social life cycle analysis, and social acceptance.

The following sections briefly describe the main technologies of the project as well as the case studies in which they will be tested. Subsequently, the current state of the project and preliminary results are presented, and finally, the work to be carried out until the end of the project is outlined.

2. ASTEP project and case studies

2.1. SunDial, the rotatory Fresnel solar collector

Solar collectors for industrial processes are generally either flat type without concentration (or with small concentration), linear Fresnel collectors, and parabolic trough collectors. The latter two are able to reach temperatures well above 150 ºC but are adapted systems that come from the power generation technology, generally with a high maintenance cost. ASTEP proposes an innovative concept, the SunDial, whose main objective is to limit installation, maintenance, and operation requirements.

The SunDial is a rotating Fresnel collector consisting of a horizontal platform that rotates around a vertical axis, with a linear concentrator installed on the platform. The solar field consists of curved mirrors parallel to the receiver line that are used as a concentrator. To limit its cost and meet necessary requirements, these curved mirrors are derived from flat mirrors that are bent in situ, simplifying the installation.

Two designs of the SunDial device are considered, illustrated in Fig. 1. In the first, the working condition for this Fresnel system is that the sun must be in the symmetry plane of the concentrator, i.e., the system must rotate in the azimuth angle during the day. In this design, the mirrors are fixed to the structure. The compactness of the system and the fixed mirrors lead to a low-cost solution with high focusing accuracy.

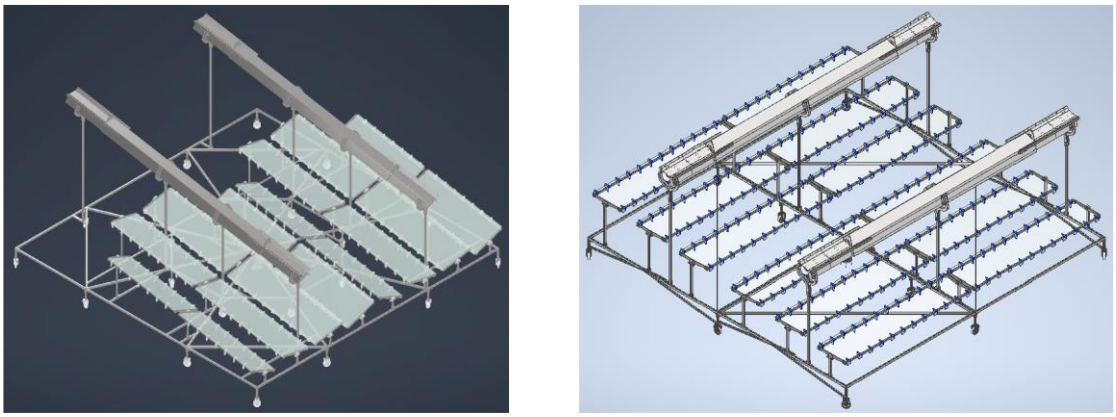

Fig. 1: CAD of the two versions of the SunDial with solar tracking system on one (left) and two (right) axes, for the Mandrekas and AMTP case studies, respectively

In the second design, the SunDial consists of several rows of rotating mirrors instead of fixed ones. The mirrors and the receiver are installed on the rotating platform that rotates around a vertical axis to keep the sun within the transversal plane of the collector. At the same time, the mirrors will rotate around their longitudinal axis to reflect towards the receiver as the sun's altitude varies. Thus, the system follows the sun using a two-axis tracking system, i.e., the platform rotates with the sun's azimuth angle, and the tilt angle of the mirrors changes following the solar altitude. This solution shares the previous one's advantages in terms of cost reduction, simplicity, and compactness. The additional tracking system (mirror tilt) introduces some complexity—and the corresponding cost—but provides higher performance, allowing the use of Fresnel technology at altitudes where conventional technologies cannot operate.

2.2. Thermal energy storage system

As a thermal energy storage (TES) system, a system based on phase change materials (PCM) with passive heat transfer enhancement inserts, in the form of fins, is being developed. The goal is to store excess solar thermal energy during peak solar resource hours and deliver it according to the end-user's demand under controlled power conditions.

The passive design includes the application of honeycomb structures located in a casing and shaped as multi-tubes with integrated elements that enhance heat transfer. The heat transfer fluid flows through the internal tubes, and the PCM is stored on the casing side, filling the structure created by the honeycomb.

The development of the system includes the selection of the phase change material, the design of the inserts, the method for their manufacture, the design of the accumulators, and the testing of thermal performance and potential corrosion. The accumulator and the inserts designs are shown in Fig. 2.

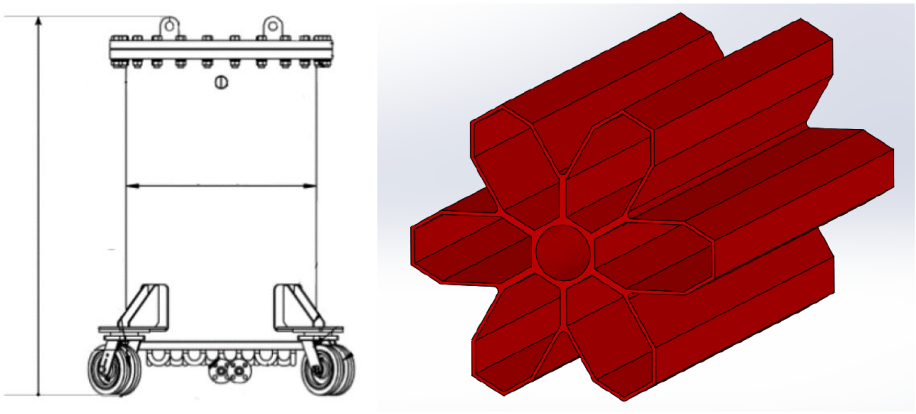

Fig. 2: CAD of the accumulators and the inserts of the TES

3. Case studies

2.3. Case studies

Mandrekas:

The company MANDREKAS is a dairy industry located in Corinth (latitude 37.93º N), thus near the so-called solar belt, where solar concentration systems can be installed at a lower cost. The industry produces all types of yogurt, dressings (tzatziki sauce), and dairy desserts. For their production, they need both steam generation at 8 bar (175 ºC) to pasteurize the milk and refrigeration to store their products at temperatures around 5 ºC.

The concentrator developed for this case study must be designed to minimize capital and maintenance costs. Therefore, the first design of SunDial is proposed, so that the vertical rotation axis belongs to the symmetry plane. The working condition for this Fresnel system is that the sun must be in the symmetry plane of the concentrator, i.e., the system must rotate in the azimuth angle during the day. Therefore, the platform must be placed on some sets of wheels that are guided in a circular motion.

The mirrors are fixed on a flat platform that rotates following the sun in the azimuth angle. The tilt of each mirror is defined in the reference position (when the receiver and the sun define the virtual symmetry plane of the system). By minimizing moving parts, maintenance and operation are also straightforward, achieving a robust and reliable system.

ArcelorMittal Tubular Products:

ArcelorMittal is the world's leading steel and mining company. In particular, ArcelorMittal Tubular Products – Iași (AMTP), which belongs to the European division of tubular products of ArcelorMittal, is dedicated to the manufacture of welded steel tubes for various applications. This industry is located in Iași (Romania), at a latitude of 47.1º N. One of the key finishes for AMTP products is the so-called color coating, which consists of a thin layer of colored protective/decorative material (epoxy, water-based, thermoplastic, etc.) that covers the entire outer surface of the tube. To apply this color coating, the tubes must be preheated to a temperature of 220 ºC.

In this case, the solar concentrator must be installed in locations with relatively high latitude, so the SunDial design with two-axis solar tracking will be used. In this case, the working condition for this Fresnel system is that the sun must be in the transverse plane of the concentrator, i.e., the system must rotate in the azimuth angle during the day so that the longitudinal component of the incident solar radiation is zero. Therefore, the platform must be placed on some sets of wheels that are guided in a circular motion.

Since the sun's altitude varies throughout the day and year, the mirrors must be installed on longitudinal rotation axes so that their transverse tilt adapts to the sun's altitude. This implies a higher cost compared to the single axis tracking system, but it eliminates both cosine factor losses and end losses. As a result, the variation of the incident thermal power will only be due to shading losses, which are less significant than cosine factor losses and end losses when the

sun's altitude is very low. Additionally, it eliminates the need for a fixed longitudinal tilt of the platform and transverse mirrors, which implies a cost reduction.

2.4. ASTEP concept for the case studies

Fig. 3 shows the proposed integrated system for Mandrekas. The storage system is arranged in series with the SunDial and the demand. The SunDial must generate between 2 and 20 kW of thermal power when there is solar irradiation, while the storage system must store or supply between 0 and 15 kW. To meet the thermal requirements of the industry, a heat exchanger that functions as an evaporator, with a power of 8 kW, and another exchanger that emulates the feed to an absorption chiller for cold production, with a power of 6 kW, are planned.

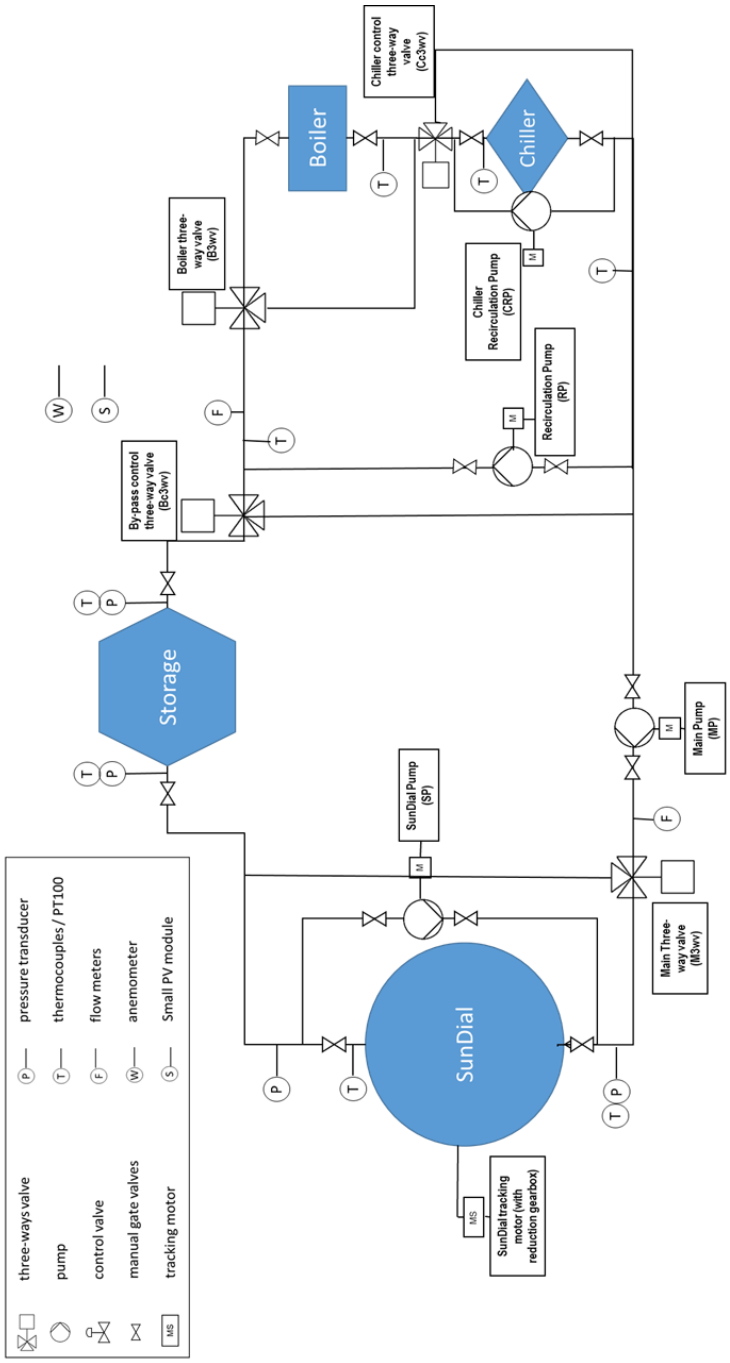

Fig. 3: Diagram of the ASTEP concept for the Mandrekas case study

Since the dairy industry does not operate on weekends, there is no heat demand on these days, but the cold demand remains unchanged. Therefore, the system must be able to operate with two demands, one of them for 24 hours, 7 days a week. The defined control strategy, with the systems arranged in series, provides enough margin to select the nominal power for the process heat. As a compromise solution, a nominal thermal power of 8 kW was selected, which will need to be operational from 9 am to 5 pm from Monday to Friday.

Finally, the control strategy must ensure the dispatch of energy not only in terms of energy utilization but also in

terms of selecting the type of load (process heat, cold, or both) to be covered at any given time, to minimize the impact of the hysteresis inherent in the thermal storage system and to accommodate possible uncertainties related to the received solar energy.

Likewise, Fig. 4 shows the proposed design for AMTP, which has storage in series with SunDial and the demand.

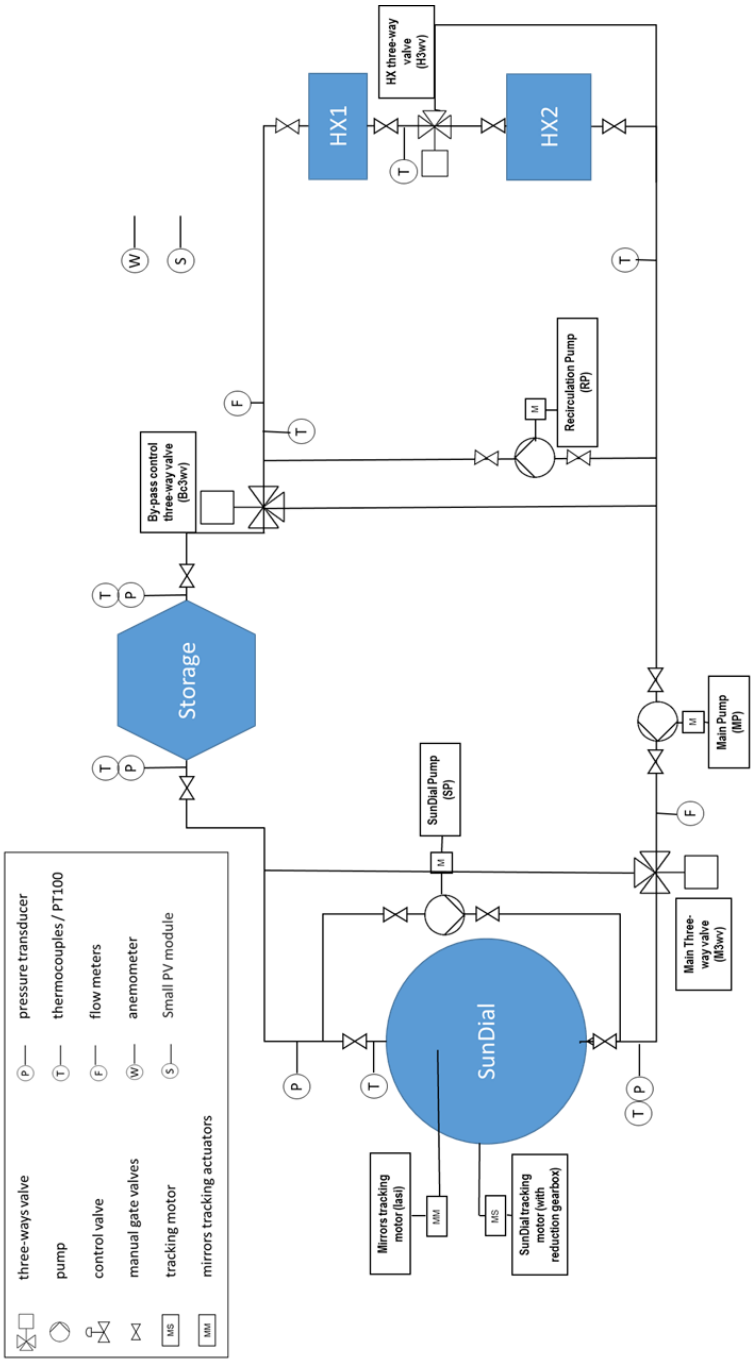

Fig. 4: Diagram of the ASTEP concept for the AMTP case study

The main differences between the Mandrekas and AMTP cases are the demand and location. Since solar irradiation at AMTP is reduced during the winter, the SunDial needs a second solar tracking system, which requires an additional motor per line of mirrors with its corresponding control system.

While the demand at Mandrekas consists of an evaporator and an absorption chiller, at AMTP it is composed of a furnace to preheat the steel tubes before coating them with paint. Similarly to the previous case, it was decided to incorporate two oil-oil heat exchangers of 7 kW each, which will feed this furnace. Thus, thanks to the defined control strategy, there is room to select the size of the heat exchangers and to minimize hysteresis in the storage system by modulating the use of one independently or both simultaneously. In this case, the industry operates 18 hours a day from Monday to Saturday.

4. Current state and preliminary results

During the initial stage of the project, the design, sizing, and selection of prototypes and the necessary components for implementation were carried out. During this first stage, numerous preliminary results were obtained to evaluate the designs. For example, Fig. 5 and Fig. 6 present some results from the simulation models.

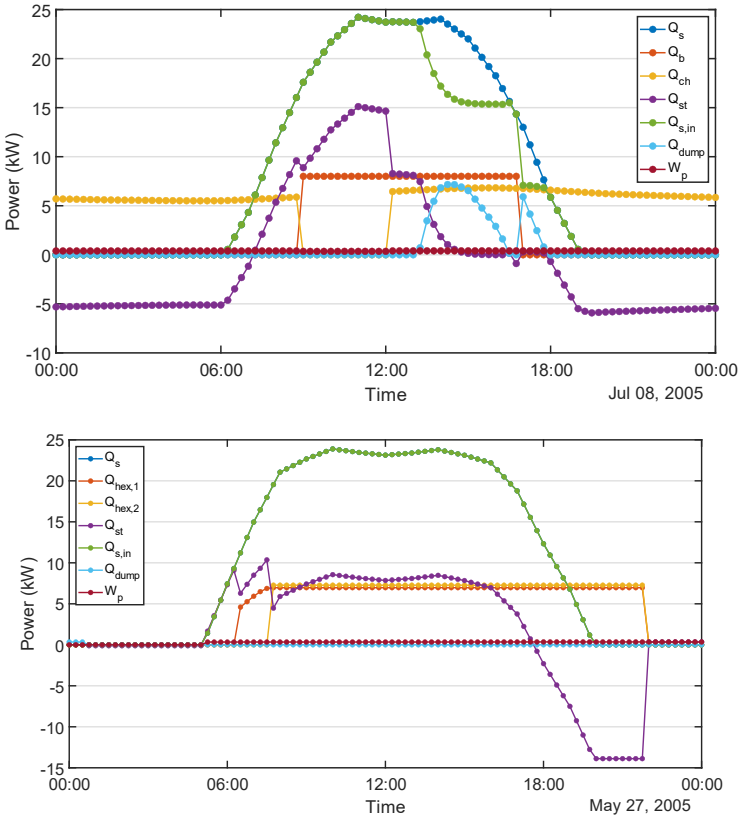

Fig. 5: Power flows in the SunDial, storage, and demand for a day with high solar resource in Mandrekas (up) and AMTP (down)

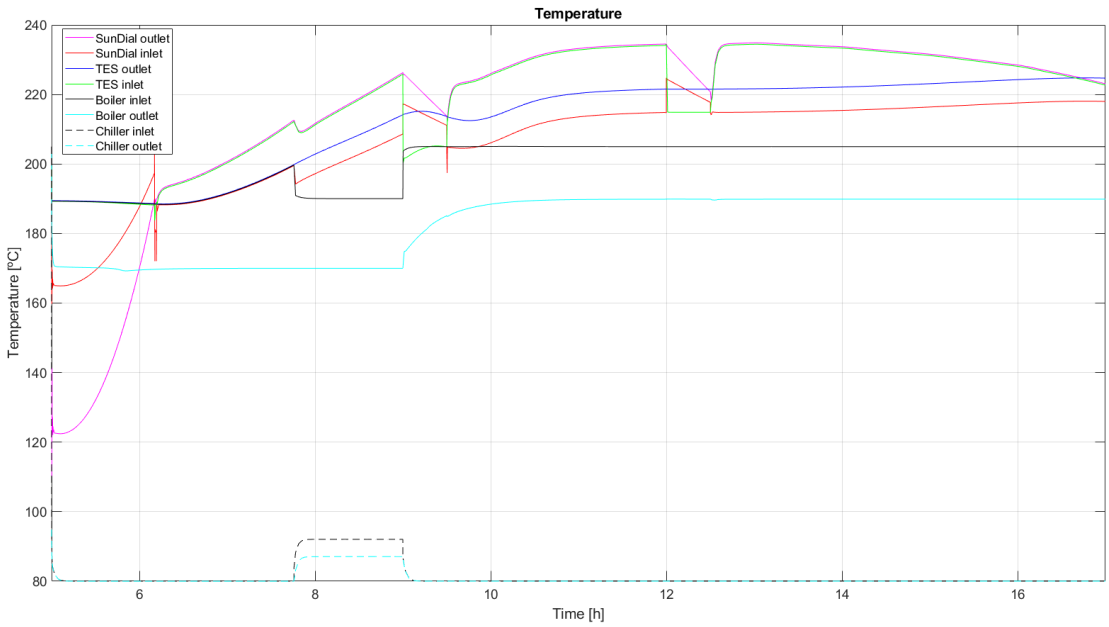

Fig. 6: Dynamic simulation of the ASTEP system for Mandrekas in a scenario with variable solar radiation due to cloud cover

After the design stage concluded, the SunDial and TES prototypes started construction in Madrid (UPM) and Cartagena (UPCT) & Wroclaw (Wroclaw University), respectively. Fig. 7 and Fig. 8 show the current construction status of the two SunDial collectors, while Fig. 9 shows one of the storage tanks.

As of today, the construction of the SunDials has been completed, and the control system is being fine-tuned, so there are no experimental results from the collectors yet. The three accumulators of the thermal storage system (one

for Mandrekas and two for AMTP, as it requires a more constant temperature demand) have been built, assembled, filled with PCM after preparation in the UPCT laboratory, the material has been melted, and testing has finished.

Fig. 7: SunDial with single axis tracking system for the Mandrekas case study, before (left) and after (right) placing the reflectors

Fig. 8: SunDial with two axis tracking system for the AMTP case study

Fig. 9: Accumulator of the storage system and detail of the inserts

Fig. 10 shows an example of the results of the system's charging and discharging process.

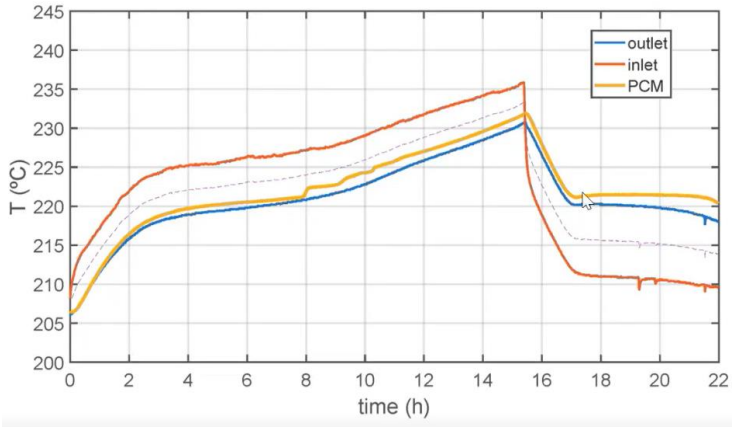

Fig. 10: Experimental results of the charging and discharging process of one of the storage system accumulators

Once all the systems: SunDial, storage system, and control system, are properly tested in the laboratory, the equipment will be disassembled and sent to the end-users, Mandrekas and AMTP. The remaining activities are shown in Table 1.

Tab. 1: Table captions (8 pt) should be centered and placed above the table

T7.1 - Implementation of Concept Design for 2 Test Cases	1-1-2021 a 30-11-2024
T7.2 - Installation & Commissioning on Site	1-8-2024 a 30-11-2024
T7.3 - Monitoring	1-2-2023 a 30-6-2025
T7.4 - Validation	1-12-2024 a 29-6-2025
T8.1 - Life Cycle Assessment (LCA)	1-10-2020 a 30-6-2025
T8.2 - Life Cycle Costing (LCC)	1-7-2021 a 30-6-2025
T8.3 - Social LCA	1-10-2020 a 30-6-2025
T8.4 - Social Acceptance	1-12-2021 a 30-6-2025
T8.5 - Exergy Analysis	1-5-2021 a 30-6-2025

A comprehensive list of results and publications from the project can be found in the ASTEP project community at Zenodo platform (https://zenodo.org/communities/astep/records).

5. Conclusions

This work presents the objectives and the current status of the ASTEP project. The main objective of the project is to develop a new concept of solar energy applied to industry and demonstrate its feasibility in two case studies: the Mandrekas dairy industry and the ArcelorMittal Tubular Products steel industry. In the first case, by producing process heat and cold, and in the second, by producing process heat at high latitude.

To achieve this, the technologies involved in the ASTEP concept have been developed: the rotatory Fresnel solar collector, SunDial; the thermal storage system, based on phase change materials; and the integration of the technologies according to a series layout, along with the control system. Once the designs were completed, the prototypes of the different systems were built and are currently being independently tested at the facilities of the Universidad Politécnica de Madrid (UPM) and the Universidad Politécnica de Cartagena (UPCT). After the tests are concluded, the equipment will be transferred to the end-users in Greece and Romania, where the integration of the ASTEP concept will be tested in an integrated manner and in a relevant environment with real operating conditions.

6. Acknowledgments

The ASTEP project has received funding from the European Union's Horizon 2020 Research and Innovation Programme under Grant Agreement No 884411. Disclosure: The present publication reflects only the author's views and the EU are not liable for any use that may be made of the information contained therein.

7. References

ASTEP project community at Zenodo platform, https://zenodo.org/communities/astep/records (accessed on 2-8-2024).

Database for applications of solar heat integration in industrial processes, http://ship-plants.info/ (accessed on 2-8-2024)

Kurup, P., Turchi, C., 2015 Technical Report No. NREL/TP--6A20-64709, 1227710.

Montes, M.J., Abbas, R., Barbero, R, Rovira, A., 2022. A new design of multi-tube receiver for Fresnel technology to increase the thermal performance. Applied Thermal Engineering 204 (2022) 117970.

Hybrid Steam Generation for Industry Using Linear Fresnel Solar Collectors and High Temperature Heat Pump

Antonio Famiglietti[1], Ruben Abbas[1]

[1]Thermal Energy for Sustainibility (TE4S) Group, Escuela Técnica Superior de Ingenieros Industriales, Departamento de Ingeniería Energética, Universidad Politécnica de Madrid, Madrid (Spain)

Abstract

Although the ongoing energy transition is dominated by renewable electricity production, most of industrial energy consumption remains in form of heat, mostly provided by fossil fuel combustion. Relevant industrial sectors as food and beverage, textile, chemical, pulp and paper, among others, present large heat consumption in the low and medium temperature range. Steam is used as heat transfer fluid in a large variety of processes.

Concentrating solar thermal technologies are suitable renewable heat sources able to replace fossil fuel and are recently receiving increasing attention and market share. Besides, electricity-driven Heat Pump are able to provide heat using either renewable or grid electricity whenever waste or unused low-grade heat is available. Although commercial industrial Heat Pumps are limited to low temperature applications, recent developments are bringing High Temperature Heat Pumps to market, able to provide heat above 150 °C up to 280 °C. In this study Linear Fresnel Solar Collectors and High Temperature Heat Pumps are considered as heat sources for steam generation for industrial process. Energetic and economic analysis is performed for different locations under various design constraints.

Keywords: Solar Heat for Industrial Processes, Steam Generation, High temperature Heat Pump, Thermal Energy Storage

1. Introduction

Decarbonization of the industrial sector is crucial to achieving sustainability goals and reducing industrialized economies' dependence on fossil fuels. According to IRENA (International Renewable Energy Agency), 74% of industrial energy demand is heat (85 EJ), mainly provided by consuming fossil fuels. Around 50% of industrial heat is required at low temperature (< 150 °C) and medium temperature (150-400 °C), consumed in a wide variety of industrial processes. ST Solar Thermal technologies can provide heat in different temperature ranges, with good performance and reasonable costs.

Linear concentrating solar technologies such as parabolic troughs and linear Fresnel collectors can operate in the medium temperature range with high efficiencies. They offer high performance and are available in different scales due to their modularity at decreasing costs. Despite their technological maturity and huge market potential, ST solar thermal technologies still play a marginal role as an industrial heat source. Among the barriers to the massive implementation of technology, economic competitiveness with conventional sources plays a fundamental role.

Solar photovoltaic (PV) energy is gaining market share at increasingly lower costs, being the dominant solar technology in the electricity sector. The application of photovoltaic energy in industry is intended to cover not only conventional electrical demand, but its applications to process heat are becoming more and more interesting. Furthermore, the electrification of industrial thermal demand is strategic in a context with high penetration of renewables in the electrical grid. “Power-to-heat” solutions, capable of efficiently using solar and renewable electricity for industrial heat supply today are extremely necessary and attractive. Although commercial industrial heat pumps are limited to low temperature applications, recent developments are bringing to the market High Temperature Heat Pumps (HT-HP) capable of providing heat above 150 °C

© 2024. The Authors. Published by International Solar Energy Society
Selection and/or peer review under responsibility of Scientific Committee
10.18086/eurosun.2024.04.03 Available at http://proceedings.ises.org

(Arpagaus et al., 2018).

This study analyzes the generation of steam for industrial use using Fresnel-type concentration technology and the high-temperature heat pump powered by photovoltaic solar energy. For this purpose, a reference industrial user is considered, characterized by the specifications of the steam network (saturated steam pressure, condensate return temperature, among others).

The integration scheme chosen for the study is the "indirect" generation of steam, in parallel to a conventional natural gas steam boiler. The indirect generation of solar steam implies the need for a BOP (Balance of Plant) system consisting of a "kettle reboiler Steam Generator (SG)" and auxiliary equipment. The kettle steam generator is fed by condensate from the industrial network while the heat is supplied through a primary heat transfer fluid. The saturated steam generated by the kettle is injected into the industrial distribution network. In this study, the Heat Transfer Fluid (HTF) is pressurized water, being a commonly used option in the expected temperature range (150-200 °C). Different configurations of solar heating of the primary fluid are analyzed. Concentrating Solar Thermal (CST) and high temperature Heat Pump (HP) powered by a Photovoltaic (PV) are considered as heat sources, either alone or combined in hybrid scheme.

The first option in Fig.1 uses a Concentrating Solar Thermal (CST) solar field as heat source. In the second scheme, shown in Fig. 2, a high temperature Heat Pump (HP) powered by a Photovoltaic (PV) solar field is the heat source. A comparative energetic and economic analysis is carried out considering the CST and PV-HP schemes through annual simulation on a large number of locations in European countries.

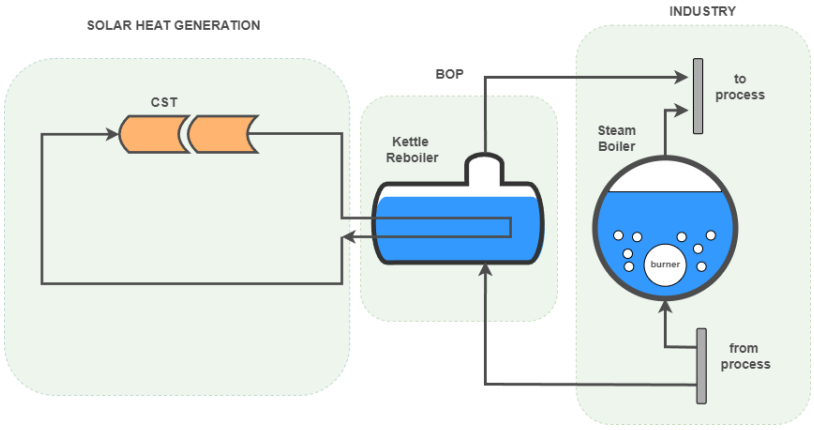

Fig.1: Indirect steam generation using CST as heat source.

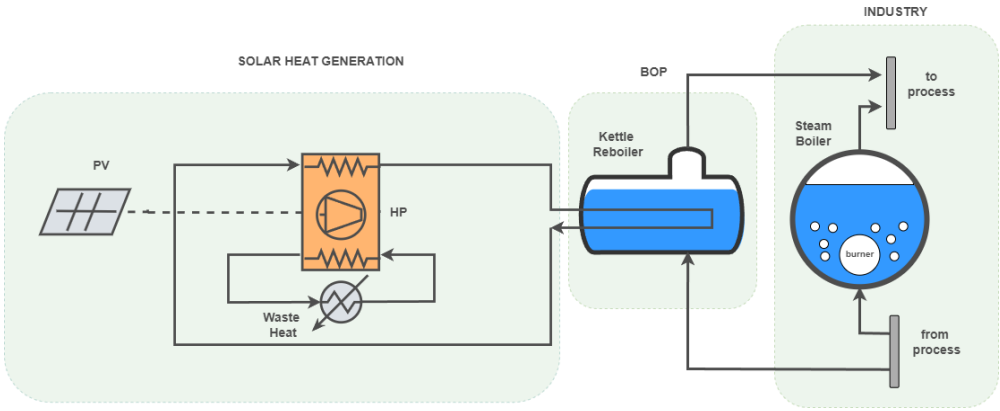

Fig.2: Indirect steam generation using PV-HP as heat source

Advanced hybrid scheme including either the CST and PV-HP as heat source and a sensible Thermal Energy Storage TES is analyzed, Fig.3. For the various configurations, hourly simulations are carried out across the typical meteorological year of the localities of interest, to evaluate the main energy indicators (annual solar fraction) and economic indicators (Levelized Cost of Heat, LCOH). A parametric analysis allows to establish the impact of the main design and operational parameters on energy and economic indicators.

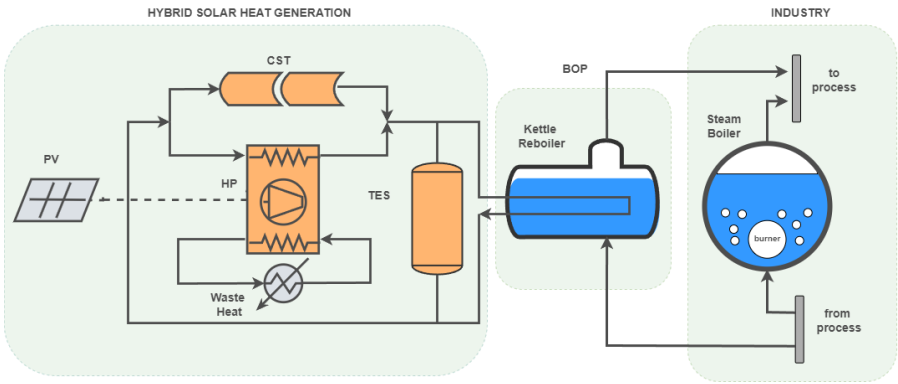

Fig.3: Hybrid scheme for indirect solar generation using CST and PV-HP as heat source including TES

2. Numerical model

The numerical models have been implemented in Python and include the SG vapor generation, the concentrating solar field CST, the photovoltaic solar field PV, the heat pump HP, the thermal storage TES, besides the control algorithm appropriate for each configuration. The economic model of the considered components is also implemented.

2.1. Steam generation SG

Solar steam generation is carried out in parallel with the main steam generator (Boiler, BO) via a kettle steam generator (SG). The steam pressure p_s and the temperature T_s are defined according to parameters of the boiler, as well as the water inlet temperature T_{cond} (condensate return). The steam flow rate $\dot{m}_s$ and the corresponding thermal power $\dot{Q}_s$ are obtained from the design values $\dot{m}_{s,d}$ and $\dot{Q}_{s,d}$ and the hourly profile of the industrial demand. Other design parameters of the SG are the inlet and outlet temperatures of the liquid side $T_{l,in}$, $T_{l,ou}$. The primary liquid is pressurized water. The pressure on the liquid side p_l is set above the saturation temperature to avoid two-phase flow, $p_l = p_{sat}\langle T_{l,in} + \Delta T_{safe}\rangle$. Outlet water temperature $T_{l,ou}$ is defined starting from steam temperature T_s as $T_{l,ou} = T_s + \Delta T_{HX}$, and $T_{l,in} = T_{l,ou} + \Delta T_l$.

The estimation of the installation costs C_{SG} of the SG steam generator is obtained starting from the area of the heat exchanger A_{SG}, considering a heat transfer reference value $U_{SG} = 1400\ \mathrm{Wm^{-2}K^{-1}}$. Corrective factors that consider the pressure F_P and the material F_M are applied to the base cost C_B, (Seider et al.).

$$C_{SG} = C_B F_P F_M C_{Eur} CE_{index} \quad \text{(eq. 1)}$$

$$C_B = exp\left(12.3310 - 0.8709 ln(A_{SG}) + 0.09005\left(ln(A_{SG})\right)^2\right) \quad \text{(eq. 2)}$$

$$F_P = 0.9803 + 0.018\left(\frac{p_{SG}}{100}\right) + 0.0017\left(\frac{p_{SG}}{100}\right)^2 \quad \text{(eq. 3)}$$

$$F_M = a + \left(\frac{A_{SG}}{100}\right)^b \quad \text{(eq. 4)}$$

with a=2.7 and b=0.07 of stainless steel, and C_{Eur} conversion factor USD to Eur , A_{SG} in ft^2 and pressure p_{SG} in $psig$. The CE_{index} accounts for inflation, according to CEPCI index (Maxwell).

2.2 Concentrating Solar Thermal CST

The CST field is defined based on the collector features, the configuration of the loops and their orientation. The collector is a commercial linear Fresnel collector LFC (Solatom), equipped with a single standard evacuated tube receiver, whose main technical data are reported in Tab.1.

Tab. 1. CST parameters and data

Length of the module	L_m	5.28 m
Aperture	W_a	5.00 m
Height	H_m	2.72 m
Active area of the module	A_m	26.40 m^2
Maximum optical efficiency	η_{op0}	0.632
Internal diameter receiver	D	0.066 m
External diameter receiver	D_{ex}	0.07 m

The solar field is defined by the number of LFCs assembled in series n_s in a straight row, while n_p rows are arranged in parallel. The LFC is modeled by calculating heat flux $\dot{q}_s$ concentrated on the receiver perimeter $P_{ex} = D_{ex}\pi$, by means of an optical efficiency η_{op} including the Incidence Angle Modifiers IAMs.

$$\dot{q}_s = \frac{G_{bn}\eta_{op}A_c}{A_r} = \frac{G_{bn}\eta_{op}W_a}{P_{ex}} = G_{bn}\eta_{op}C \quad \text{(eq. 5)}$$

$$\eta_{op} = \eta_{op0}\mathrm{IAM}_T\langle\theta_T\rangle\mathrm{IAM}_L\langle\theta_L\rangle \quad \text{(eq. 6)}$$

The thermal power $\dot{Q}_u$ generated by the fluid across a length L of the receptor is obtained according to (Duffie et al., 1985) using the collector efficiency factor F' and the heat dissipation factor F_R.

$$\dot{Q}_u = F_R L P_{ex}[\dot{q}_s - U_L(T_{in} - T_{amb})] = \dot{m}(he_{ou} - he_{in}) \quad \text{(eq. 7)}$$

$$F' = \left[1 + \frac{U_L P_{ex}}{h_l P}\right]^{-1};\ F_R = \frac{\dot{m}c_p}{LP_{ex}U_L}\left[1 - \exp\left(-\frac{LF'P_{ex}U_L}{\dot{m}\,c_p}\right)\right] \quad \text{(eq. 8)}$$

The global heat transfer coefficient of the receiver tube $U_L\langle T_w, T_{amb}\rangle$ is obtained by means of a polynomial expression obtained from experimental data (Burkholder & Kutscher, 2009). Internal heat transfer h_l coefficient is computed from Gnielinski correlation. The length of the receiver is discretized into n_e elements for increasing the accuracy.

The solar field area is sized based on the required peak power $\dot{Q}_{CST}$ which determine the solar multiple as $SM_{CST} = \dot{Q}_{CST}/\dot{Q}_{s,d}$. The number of loops n_p and their length L_d are adjusted to fit the required area.

The installation cost of solar field is obtained from an estimated cost per area $c_{CST} = 325$ Eur m^{-2}. This cost is retrieved from the manufacturer's simulation tool (Ressspi, 2018) implemented by (Solatom), for a solar field of 50 modules without integration, applying the CEPCI inflation correction factor (Maxwell). Peak irradiance is $G_{bn,peak} = 1000$ Wm^2.

$$A_{CST} = \frac{\dot{Q}_{CST}}{G_{bn,peak}\eta_{op0}} = L_d W_a n_p \quad \text{(eq. 9)}$$

$$C_{CST} = A_{CST}c_{CST} \quad \text{(eq. 10)}$$

2.3 Solar photovoltaic field PV

The solar field is defined according to the electrical power required by the heat pump in nominal conditions P_d. The orientation is horizontal, being the most common option on industrial rooftops. The conversion efficiency of the solar cell is $\eta_{PV} = 0.20$, and a reference system efficiency of η_{sys}=0.86, account for system losses such as losses in cables, power inverters, dirt on the modules, efficiency degradation with time. The

installation cost is obtained from the cost per kwp $c_{kWp} = 814$ €/KWp, (IRENA, 2022).

$$A_{PV} = \frac{P_{PV,d}}{G_{bn,peak}\eta_{PV}\eta_{BOP}} \quad \text{(eq. 11)}$$

$$C_{PV} = P_{PV,d}c_{kWp} \quad \text{(eq. 12)}$$

2.4 High Temperature Heat Pump

The high-temperature heat pump considered is a pre-commercial Stirling-type model manufactured by Enerin (*Enerin*, n.d.). The real COP_{HP} of the hat pump is obtained from the ideal COP_{Carnot}, according to the efficiency η_{COP} reported by (Høeg et al., 2023), as function of the average temperatures of the heat source temperature $T_{source,m}$ and the heat sink temperature $T_{sink,m}$.

$$COP_{HP} = \frac{Q_h}{P_{HP}} = \frac{Q_h}{Q_h - Q_c} = COP_{Carnot}\eta_{COP} \quad \text{(eq. 13)}$$

$$COP_{Carnot,h} = \frac{T_{sink,m}}{T_{sink,m} - T_{source,m}} \quad \text{(eq. 14)}$$

The heat transfer fluid is pressurized water on both low and high temperature sides, with a maximum temperature glide of 25 °C and 40 °C respectively. The maximum temperature drop (lift) is indicated by the manufacturer is 200°C, with a maximum heat sink temperature of 250 °C. The heat supply capacity is between 0.3 MW and 10 MW, (*Annex 58 Task 1*). The installation cost is calculated from the unitary cost $c_{HP} = 700\,\frac{€}{\text{kW}}$, as $C_{HP} = c_{HP}\dot{Q}_{HP}$. The HP is sized according to $\dot{Q}_{HP}$ and solar multiple $SM_{HP} = \dot{Q}_{HP}/\dot{Q}_{s,d}$.

2.5 Thermal energy storage TES

The sensible thermal storage considered in this study is of the thermally stratified tank filled with pressurized water. The TES volume is sized based on the required storage hours h_{TES} and the design temperatures T_h and T_c, for the hot and cold side respectively. The V_{TES} volume is divided into several n_{tanks} with a maximum admissible tank height $H_{tank,max}$ and a shape factor F_{Sh}.

$$V_{TES} = \frac{3600\,\dot{Q}_{s,d}h_{TES}}{\rho_l cp_l(T_h - T_c)} = V_{tank}n_{tank} \quad \text{(eq. 15)}$$

$$D_{tank} = \left(\frac{n_{tank}4}{\pi F_{sh}}\right)^{\frac{1}{3}};\ H_{tank} = F_{Sh}D_{tank} \quad \text{(eq. 16)}$$

Tank shell thickness e_{tank} is obtained from pressure and diameter, Eq (17), with $E = 0.85$, S and p_{tank} in psi, $S = 16000\ psi$ for stainless steel.

$$e_{tank} = \frac{p_{tank}D_{tank}}{2SE - 0.6p_{tank}}0.0254 \quad \text{(eq. 17)}$$

The cost of each tank is calculated considering the cost of the vessel C_{vessel}, of the liquid C_{liq}, thermal insulation C_{ins}, foundations C_{fou}, hydraulic and electrical equipment C_{AUX}, installation C_{inst} and overhead C_{oh}, elaborated starting from (Mostafavi Tehrani et al., 2017).

$$C_{PBTES} = C_{vessel} + C_{fluid} + C_{ins} + C_{fou} + C_{AUX} + C_{oh} + C_{inst}$$

Tab. 2: Economic parameters of TES

Vessel	C_{vessel}	4.5 €/kg
Insulation	C_{ins}	300 €/m^2
HTF	C_{fluid}	Agua 0.8 €/ m^3
Foundations	C_{fou}	1120 €/m^2
Electric and instrumentation, valves and fittings	C_{AUX}	390 €/m3
Overhead	C_{oh}	10% of total
Installation	C_{inst}	20% of total

2.6 Levelized Cost of Heat LCOH

The Levelized Cost of Heat (LCOH) is used as the main economic indicator in this study. The LCOH is the heat generation cost, also the minimum price that must be sold to recover the installation costs (CAPEX) and the operation and maintenance costs (OPEX) during its useful life of the plant. It is defined in a similar way to the Level of Energy Cost LCOE used for the financial analysis of electricity production.

According to Task 54 of the IEA, the LCOH can be estimated in the following way, considering constant annual discount, Eq (18). If we assume $r_{dis} = 0.05$, $n_y = 25$ years, $\mathrm{OPEX} = 0.02\ \mathrm{CAPEX}$.

$$\mathrm{CAPEX} = C_{CST} + C_{TES} + C_{PV} + C_{HP} + C_{SG} \quad \text{(eq. 18)}$$

$$\mathrm{LCOH} = \frac{I_0 + \sum_{n_y=1}^{N_y} \frac{\mathrm{OPEX}_{n_y}}{(1 + r_{dis})^{n_y}}}{\sum_{n_y=1}^{N_y} \frac{E_{n_y}}{(1 + r_{dis})^{n_y}}} \quad \text{(eq. 19)}$$

3. Methodology

The models allow to carry out annual simulations considering the typical meteorological year for each location considered. Hence the simulation considers time interval of 1 hr, according to meteorological data. The load time profile of industry is considered constant in this study (24/7). The design parameter used for the simulation are defined as in Tab. 3, assuming 8 bar steam pressure (170 °C), a condensate return line temperature of 150 °C, a steam flow rate $\dot{m}_s = 1\ \mathrm{kg/s}$. The inlet/outlet temperature of tube side of the kettle SG liquid is set to 210/180 °C working with pressurized water at 23.4 bar. Considering the PV-HP, the heat pump needs a low temperature source, which is assumed here to be waste heat at 70 °C available at the factory. Under the current assumptions, the HP operates with a $\mathrm{COP} = 2.07$.

Tab. 3: Design parameters for steam generation

Steam Pressure	8 bar
Steam Temperature	170 °C
Condensate Temperature	150 °C
Load Profile	24/7
Steam flow rate	1 kg/s
Load Thermal Power	2.14 MWh
ΔT_l	30°C
ΔT_{HX}	10°C
ΔT_{safe}	10°C
Orientation CST	N-S
Tilt PV	horizontal
Waste heat temperature HP	70 °C

Three main values obtained from the annual simulation are considered as KPIs in this study, being the annual solar fraction SF, the annual energy yield per unit of gross area occupied by solar field (either CST or PV) E_{area}, and the levelized cost of heat LCOH.

The analysis is first devoted to assessing the energetic and economic performance of CST and PV-HP steam generation scheme across European locations.

Then hybrid schemes are considered where both CST and PV-HP technologies are integrated to produce industrial steam according to layout in Fig.3. As design parameter, hybridization ratio R_{hy} is defined in this study to account for the proportions of installed power of CST and PV-HP respectively, Eq. (20). Hybrid solar multiple is defined for the hybrid scheme analogously to PV-HP and CST simple schemes, Eq.(21).

$$R_{hy} = \frac{\dot{Q}_{HP}}{\dot{Q}_{CST} + \dot{Q}_{HP}} \quad \text{(eq. 20)}$$

$$SM_{hy} = \frac{\dot{Q}_{CST} + \dot{Q}_{HP}}{\dot{Q}_{s,d}} \quad \text{(eq. 21)}$$

For $SM_{hy} = 1$ the thermal energy storage is not included in the layout. For higher SM_{hy} a proper TES volume is added in parallel to the PV-HP and CST heat generation.

In this study a criterion for TES sizing is implemented. First an attempt of sizing the volume V_{TES} is made on daily basis, defining the minimum volume $V_{TES,max}$ which allow to store the maximum daily energy excess. Then an economic criterion is applied to find and optimization factor F_{TES} which gives the minimum LCOH including the a $V_{TES} = V_{TES,max} F_{TES}$ in the scheme. In this study F_{TES} can assume discrete values from 0 to 2 with step of 0.20, in order to keep low computational cost.

4. Results

4.1 Comparative CST and PV-HP steam generation.

Annual simulations are carried out for the CST scheme as well for the PV-HP. The solar multiple is set to SM = 1 for both cases, so that no excess of energy is provided by the solar installation. The simulation is carried out for 50 random selected locations per each European country, for a total of 1350 locations. The results for the three selected KPIs are shown in Fig.4 as geographical heat maps. Moreover, the results are reported ordered by annual global horizontal irradiation (GHI) in Fig.4.

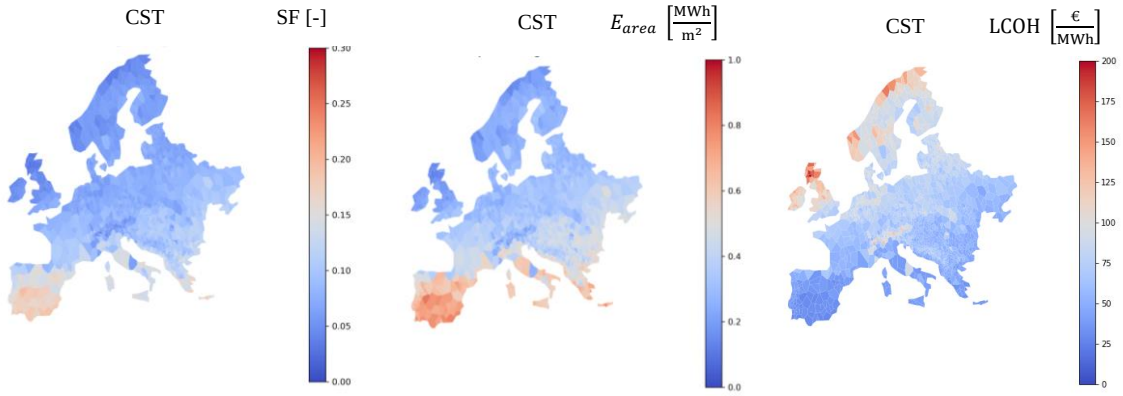

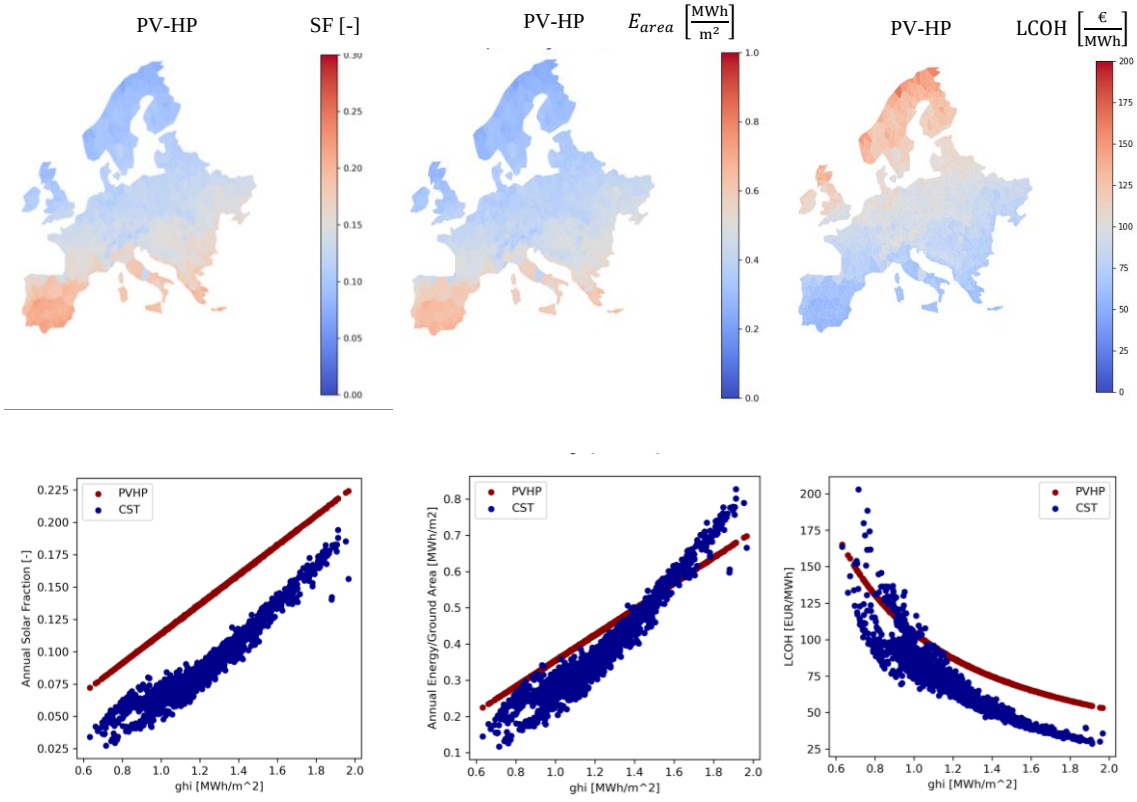

Fig.4: Comparative CST and PV-HP as heat sources for indirect steam generation in Europe.

For all the considered locations the PV-HP scheme provide higher solar fraction than CST, when assuming the same SM = 1. As expected solar fraction varies according with the GHI, increasing from 0.75 in the northern European locations up to 0.22 for southern locations for PV-HP, and from 0.03 to 0.20 for the CST case. As other energetic KPI it is worth to analyze the energy yield per unit of ground area. For high irradiance, GHI above 1.6 MWh/m^2, corresponding to southern European locations, CST provides better results than PV-HP. In northern Europe the trend is reversed, and PV-HP provides higher values of E_{area}. Considering economics, the LCOH also is remarkably affected by solar resource, clearly decreasing with GHI. As general trend the cost of PV-HP is higher than the CST, which results the most convenient option, reaching values lower than 50 €/MWh in southern European locations.

4.2 Hybrid configuration

Although having slightly difference in the energetic or economic performance both CST and PV-HP are viable technologies for industrial steam generation. Both can be integrated in a hybrid solar steam generation layout, as in Fig. 3.

Annual simulations of hybrid scheme are carried out for several values of R_{hy} varying between 0 and 1, where $R_{hy} = 0$ corresponds to CST only and $R_{hy} = 1$ corresponding to PV-HP. As locations, 20 European sites are considered, representative of different climatic conditions.

Fig. 5 shows the results for a $SM_{hy} = 1$, so that no excess of energy is provided and TES is not included in the scheme. The annual solar fraction is shown against the global horizontal irradiation. Varying the hybridization ratio from 0 to 1 intermediate values between the CST and PV-HP reference cases are obtained either for the SF as for the LCOH.

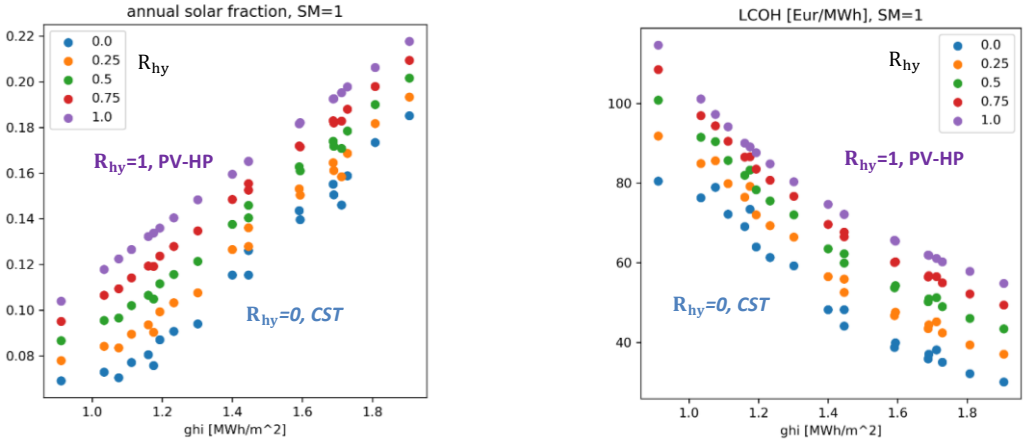

Fig.5: Hybrid scheme, with different hybridization ratios without TES

As previously mentioned, assuming the $SM_{hy} = 1$ limits the achievable solar fraction to relatively low values, having a top of 0.18-0.22 for high GHI locations in the south, and lower values going to northern sites. Increasing the solar multiple to $SM_{hy} > 1$ can lead to increased solar fraction but excess of energy appears in the central hours of the days especially in the summer season. The excess of energy, the energy provided by solar installation not absorbed instantaneously by the industrial process, can be stored if a proper TES is included into the layout as in Fig. 3. Depending on the TES size, the energy excess can be stored completely or partially, according to the installed storage capacity and the control strategy.

4.3 Hybrid configuration with TES

The results of TES sizing procedure are shown in terms of storage hours h_{TES}, Fig. 6, for $SM_{hy} = 3$ and for $SM_{hy} = 5$, for all the considered locations and hybridization ratio. For $SM = 3$ the h_{TES} varies from 0 to 6 according to location and hybridization ratio, as results of sizing procedure, while higher values up to h_{TES} =12 are obtained for $SM_{hy} = 5$.

The resulting SF and LCOH are shown accordingly in Fig.6. Highest values of solar fraction still are associated with PV-HP, reaching $SF = 0.6$ for high GHI locations. Conversely, the best economic performance are related to CST, with small or null TES.

Increasing the oversizing of solar installation, for $SM_{hy} = 5$ a solar fraction of $SF = 0.8$ is reached at high GHI with PV-HP, decreasing going to lower R_{hy} and lower GHI. The economic trend is similar to previous case discussed, but higher LCOH is shown according to the added cost of TES. The best economic performance are obtained for GHI =1.9 MWh/m^2 , with a $LCOH = 60 \div 85$ €/MWh with $SF = 0.67 \div 0.8$, with more than 10 hr of storage.

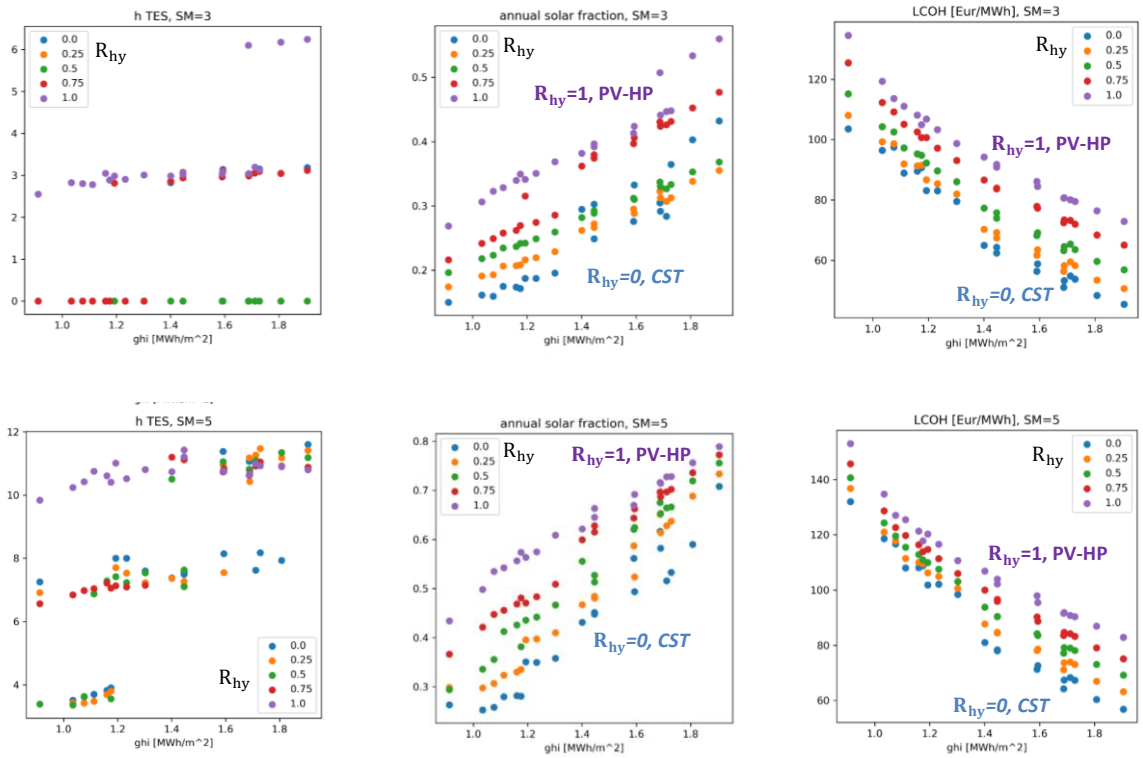

Fig. 6: Hybrid configuration with TES

5. Conclusions

An energetic and economic analysis is carried out on the industrial solar steam generation using linear Fresnel solar collectors (CST) and high temperature heat pump powered by dedicated photovoltaic (PV-HP). Steam production at 8 bar is analysed through numerical annual simulation for several locations in Europe. A comparative analysis between CST and PV-HP indicates that higher annual solar fraction can be obtained using PV-HP respect to CST, assuming a unitary solar multiple. Considering the actual cost of the technologies, a lower LCOH is shown by CST option.

Moreover, the possibility of implementing hybrid layout including either CST and PV-HP as heat source varying the main design parameters is analysed across European locations. The limitation of low annual solar fraction can be overcome by oversizing the solar installations and including a sensible thermal energy storage TES. According to the design criterion implemented in the study, simulations for different solar multiple are carried out as basis for an economic and energetic assessment. The hybrid scheme with TES allows high solar fraction with an increased cost associated with the cost of thermal storage.

6. Acknowledgments

This research was supported by the Industrial Ph.D. program of Comunidad de Madrid, Spain (BOCM Reference IND2017/ AMB7769), “Ayudas Juan de la Cierva Formación de Ministerio de Ciencia e Innovación” funded by MCIN/AEI/10.13039/501100011033 and European Union “NextGenerationEU”/PRTR, and Open-Seed Funds 2023 by Pontifica Universidad Catolica de Chile, Title: “Development of a simulation tool for yield assessment of solar heat for industrial processes coupled to thermal energy storage”.

7. References

Annex 58 Task 1. (n.d.). Retrieved July 15, 2024, from https://heatpumpingtechnologies.org/annex58/task1/

Arpagaus, C., Bless, F., Uhlmann, M., Schiffmann, J., & Bertsch, S. S. (2018). High temperature heat pumps: Market overview, state of the art, research status, refrigerants, and application potentials. In *Energy* (Vol. 152, pp. 985–1010). Elsevier Ltd. https://doi.org/10.1016/j.energy.2018.03.166

Burkholder, F., & Kutscher, C. F. (2009). Heat loss testing of Schott's 2008 PTR70 parabolic trough receiver. *NREL Technical Report, May*, 58. http://www.nrel.gov/docs/fy09osti/45633.pdf

Duffie, J. A., Beckman, W. A., & McGowan, J. (1985). Solar Engineering of Thermal Processes . In *American Journal of Physics* (Vol. 53, Issue 4). https://doi.org/10.1119/1.14178

Høeg, A., Løver, K., Asphjell, T.-A., & Lümmen, N. (2023). *Performance of a new ultra-high temperature industrial heat pump*. https://www.researchgate.net/publication/371192209

Enerin. Retrieved July 15, 2024, from https://www.enerin.no/

International Renewable Energy Agency (IRENA). (n.d.). www.irena.org

Maxwell, C. *Cost indices. 2024. URL: https://toweringskills.com/financial-analysis/cost-indices/; accessed: 2024.*

Mostafavi Tehrani, S. S., Taylor, R. A., Nithyanandam, K., & Shafiei Ghazani, A. (2017). Annual comparative performance and cost analysis of high temperature, sensible thermal energy storage systems integrated with a concentrated solar power plant. *Solar Energy*, *153*, 153–172. https://doi.org/10.1016/j.solener.2017.05.044

Solatom. *SOLAR STEAM FOR INDUSTRIAL PROCESSES*. http://www.solatom.com/

Pilot plant for hydrogen production using high-temperature solid oxide electrolyser and solar heat and power

Germilly Barreto, José González-Aguilar and Manuel Romero

High Temperature Processes Unit, IMDEA Energy, Avda. Ramón de la Sagra 3, 28935, Móstoles, Spain

Abstract

This work presents the design of a pilot plant for hydrogen production that integrates a high-temperature Solid Oxide Electrolyser (SOE) with solar heat and power. SOE operates at around 750 ºC and requires a balance of plant (BoP) to ensure this condition. Operating at high temperatures also requires less electricity, consequently making the SOE highly efficient. The process flow diagram (PFD) of the integrated plant consists of two main subsystems: (i) BoP of the SOE and (ii) BoP of the solar field. The coupling between these two systems is done in the steam generator. The heat from the solar field and the storage system is used to generate the steam supplied to the electrolyser, and the required electricity is from PV plant and electrical grid. The integrated plant was analysed for four operation models: full, partial, hot standby and night modes. The analysed plant uses a SOE with a capacity of 9 kWe, and at full load will consume 3.7 kg h^{-1} of steam, and produce 0.24 kg h^{-1} of hydrogen.

Keywords: green hydrogen, solid oxide electrolyser, solar thermal energy, thermal storage, balance of plant

1. Introduction

This work is part of the GREENH2-CM project [1], which is aligned with the strategic positioning of the Comunidad de Madrid in R&D&I for green hydrogen and fuel cells. Figure 1 shows the process flow diagram (PFD) developed for the pilot plant, integrating two main subsystems: (i) the balance of plant (BoP) of the Solid Oxide Electrolyser (SOE) and (ii) the BoP of the solar field. The BoP of the solar field primarily consists of the solar collectors, a thermocline storage tank, and two electrical heaters. The BoP of the SOE comprises the SOE itself, two heat exchangers, three electrical heaters, a blower, a mixer, and the conditioning of the hydrogen section. The connection between the BoP of the solar field and the BoP of the SOE occurs in the steam generator.

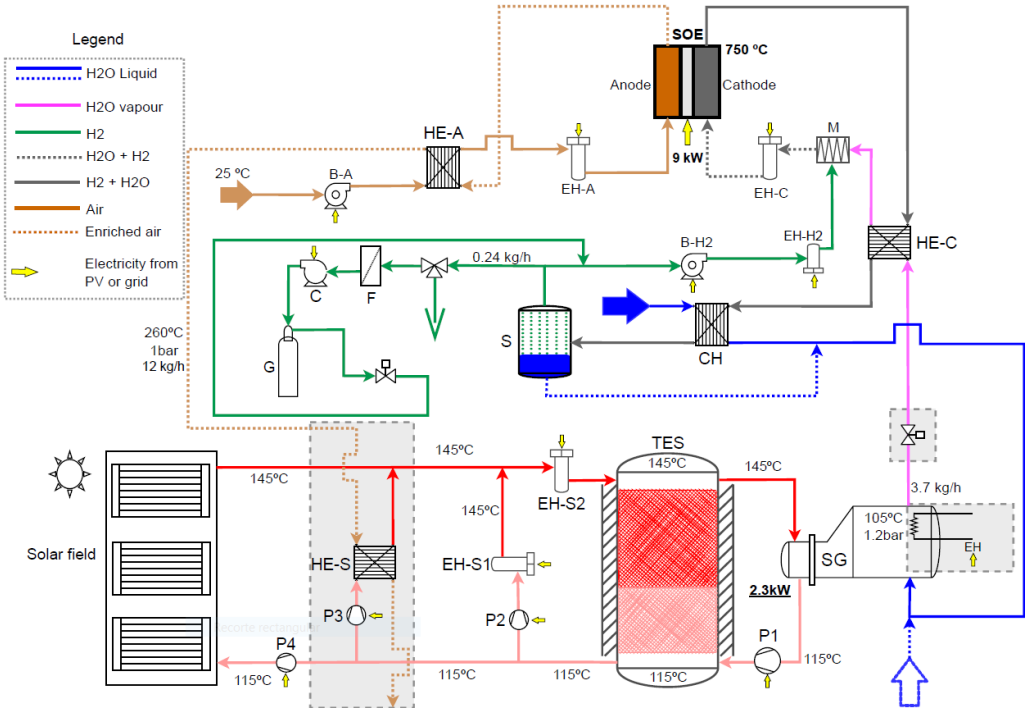

Fig. 1: PFD of the integrated system of high-temperature solid oxide electrolyzer and solar heat and power.

© 2024. The Authors. Published by International Solar Energy Society
Selection and/or peer review under responsibility of Scientific Committee
10.18086/eurosun.2024.04.04 Available at http://proceedings.ises.org

An efficient integration of SOE with solar heat and solar power leads to high sun-to-hydrogen efficiencies, thanks to the higher efficiencies of SOE. The main challenge of this project is to achieve an efficient integration of the non-programmable solar energy source with the SOE, which requires very stable operating conditions. This integration involves using solar concentration systems to supply heat to the steam generator and electricity from PV plants to power the SOE and the different components of the PFD. The plant will use an electrolyser with a capacity of 9 kWe manufactured by SolydEra, and at the design point (full load), it will consume 3.7 kg h^{-1} of steam and produce 0.24 kg h^{-1} of H_2. Table 1 summarizes the design conditions of the SOE. The thermal solar collectors are being manufactured and supplied by SEENSO, and the storage system is being developed by the IMDEA Energy Institute. Electric heaters are used when temperature adjustments are needed and when there is no available energy in the storage system. The prototype will be assembled at the IMDEA Energy premises in Móstoles, Madrid, Spain.

Tab. 1: Technical specifications of the SOE under design conditions (full load).

Technical specifications	Value
SOE power (kWe)	9.0
Steam conversion (%)	60%
Inlet temperature of the gases (°C)	771
Outlet temperature of the gases (°C)	751
Steam inlet flow rate (kg h^{-1})	3.70
Volume fraction of H_2 at inlet (%)	10
Air inlet flow rate	28
Operating temperature (°C)	760
Maximum working pressure (mbarg)	100

1.2. Solar collector

The solar collector analysed in this work consists of a combination of an evacuated tube solar collector and two north-south tracking mirrors, as described in Figure 2. The purpose of the mirrors is to provide a solar concentration of around 1.7 (depending on the time and season), which allows for higher temperatures for water evaporation. Since the solar concentration is low, it is also possible to utilize the diffuse radiation component. The collector has a normal incidence aperture area of 22.5 m² (absorber surface and the projection of the mirrors on the absorption plane), operates with a temperature difference of 30 °C (115 °C - 145 °C), and uses pressurized water at 4 bar as working fluid.

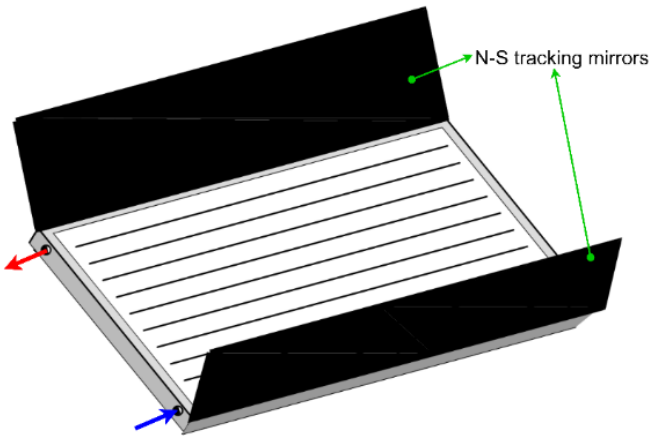

Fig. 2: Evacuated solar tube collector with N-S tracking mirrors.

1.2. Thermal storage system (TES)

The thermal storage system consists of a thermocline packed-bed with encapsulated phase change materials, as shown in Figure 3. In addition to storing heat, the storage tank also plays a crucial role in maintaining stable operation of the steam generator, a requirement imposed by the SOE.

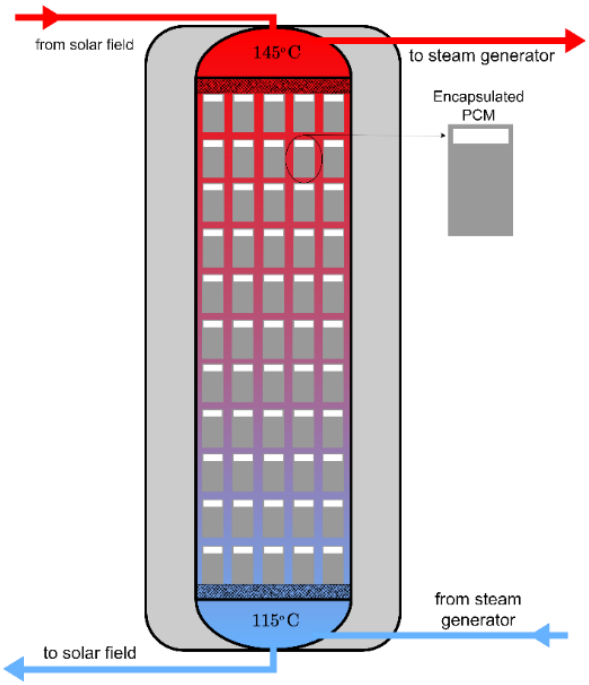

Fig. 3: Thermocline of a packed-bed with encapsulated phase change materials.

2. Methodology

To construct the prototype, it is necessary to size, test, and integrate all components. In this context, an initial step comprises conducting a numerical analysis of the demo plant to obtain energy and mass balances for all the components in the PFD (Figure 1). The numerical model is based on solving the mass and energy conservation equations for each component using EcosimPro software (v6.4) [2]. After validation of the simulation results, they were used as a reference for the sizing of the components. Furthermore, sizing considerations included four operation modes: full load, partial load, hot standby, and night modes.

3. Results

Table 2 and Table 3 present the energy and mass balance in the anode and cathode sides of the electrolyser, respectively, for full, partial, hot standby and night operation modes. In addition, the thermal and transport properties for all streams are also known, which are necessary for the design and sizing of the different components. Regarding the hot standby mode, the SOE stack is off (no power, no steam consumption, no hydrogen production), but it is maintained hot by circulating air and fuel. Regarding the night mode, the same working temperature of hot standby is considered in the night mode, but in the cathode side it is applied a mass flow rate of a mixture of Nitrogen and Hydrogen of 0.8 kg h^{-1}, which implicates changes in the BoP of cathode for this mode. Table 4 shows the thermal of electrical power consumed or dissipated in each component of the BoP of the electrolyser for the four operation modes.

Tab. 2: Energy and mass balance in the anode side of the electrolyser for the different operation modes.

	Full load		Partial load		Hot standby		Night mode	
	In	Out	In	Out	In	Out	In	Out
Temperature (°C)	771	751	726	701	726	701	726	701
Flow rate (kg h^{-1})	27.92	29.89	27.92	29.00	27.92	27.92	27.92	27.92
Composition	N_2 (78%) O_2 (22%)	N_2 (73%) O_2 (27%)	N_2 (78%) O_2 (22%)	N_2 (75%) O_2 (25%)	N_2 (78%) O_2 (22%)	N_2 (78%) O_2 (22%)	N_2 (78%) O_2 (22%)	N_2 (78%) O_2 (22%)

Tab. 3: Energy and mass balance in the cathode side of the electrolyser for the different operation modes.

	Full Load		Partial load		Hot standby		Night mode	
	In	Out	In	Out	In	Out	In	Out
Temperature (°C)	771	751	726	701	726	701	726	701
Flow rate (kg h^{-1})	3.75	1.77	1.75	0.67	0.65	0.65	0.80	0.80
Composition (%)	H_2O (90) H_2 (10)	H_2O (36) H_2 (64)	H_2O (90) H_2 (10)	H_2O (27) H_2 (73)	H_2O (90) H_2 (10)	H_2O (90) H_2 (10)	N_2 (80) H_2 (20)	N_2 (80) H_2 (20)

Tab. 4: Thermal/electrical power in each component for the different operating modes.

Component	Description	Heat/Power (kW)			
		Full load	Partial load	Hot standby	Partial load
SOE	Electrolyser	9.00	4.75	0.00	0.00
EH-A	Anode electrical heater	1.62	1.43	1.47	1.47
EH-C	Cathode electrical heater	0.43	0.18	0.07	0.22
HE-A	Anode heat exchanger	5.00	4.70	4.67	4.67
HE-C	Cathode heat exchanger	1.10	0.48	0.18	-
SG	Steam generator	2.30	1.10	0.39	-
EH-H2	Hydrogen electrical heater	0.04	0.02	0.01	-
CH	Chiller	-1.38	-0.50	-0.52	-

The solar field and thermal storage system were sized aiming that the number of hours in which the SOE has been working with heat directly discharged from the thermal storage vs. total hours is higher than 40%. It is found that the pressure at which water is evaporated in the steam generator plays a crucial role in the integration of solar heat (solar field, storage system, and steam generator). The pressure required in the electrolyser is limited to around 40 mbarg and must remain very stable. To ensure this condition, it is found that the water should be evaporated at a pressure higher than the required pressure in the SOE. This value should consider the pressure drop of the steam across all components between the steam generator and the SOE, and it should also account for a lamination process after the steam generator to prevent condensation.

Figure 4 shows the total monthly energy produced by the solar collector mounted horizontally, using the typical meteorological year (TMY) for Cuatro Vientos (Madrid), Spain [3], the nearest meteorological station to the plant location (approx. 11 km). The simulations resulted in a solar heat contribution for steam generation of 43%, corresponding to an annual heat production of 8700 kWh with a thermal efficiency of 23%. Regarding the KPIs related to the BoP of the SOE, a conversion efficiency of 38.7 kWh/kgH_2 and 84.4% (based on LHV) are obtained. For details of definition and values of calculated KPI see Table 5.

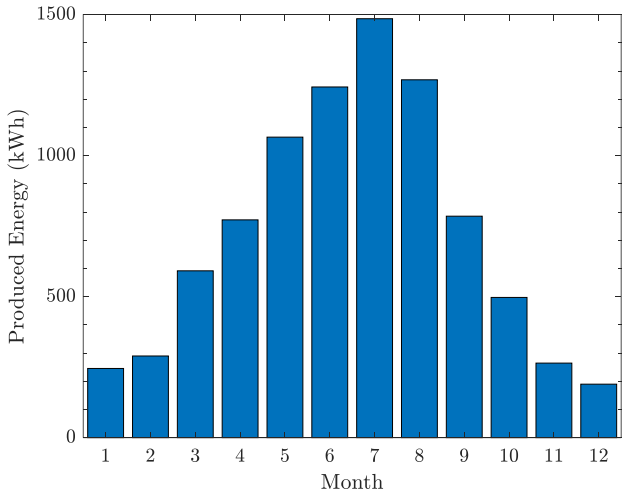

Fig. 4: Monthly thermal energy produced by the horizontally mounted solar collector for the location of Cuatro Vientos (Madrid), Spain.

Tab. 5: Key Performance Indicators obtained with EcosimPro simulation for the full-load operation mode 24/7

Key Performance (KPI)		Calculation	Simulation (Full load)
ID	**Definition**		
H_2 kg/day	Maximum hydrogen production rate at full-capacity	H_2_prod (kg/h) * 24 h/day	**5.8 kgH_2/day**
Eff %	Power-to-hydrogen energy conversion efficiency of heat-integrated SOE system (LHV basis)	(H_2_prod (kg/h)*LHVH_2)/(P_in_SOE + P_In_Anode_EH + P_In_Cathode_EH)	**84.4%**
Eff-w	Power-to-hydrogen conversion efficiency of the heat-integrated SOE system	(P_in_SOE + P_In_Anode_EH + P_In_Cathode_EH)/H_2_prod	**38.7 kWhe/kgH_2**
F-Solar	Hours in which the SOE has been driven with steam directly discharged from CST vs. total hours	(Total solar steam kWh_{th} used)/(Total steam kWh_{th} required)	**43%**

4. Conclusions

This work presents a design of a pilot plant that integrates a high-temperature Solid Oxide Electrolyser (SOE) with solar heat and power for hydrogen production. The solar field and thermal storage system were designed to ensure that the number of hours during which the SOE is supplied with heat directly discharged from the thermal storage relative to the total hours exceeds 40%. The energy and mass balance in all the components of the process flow diagram is obtained for full, partial, hot standby and night operation modes. It is found that the pressure at which water is evaporated in the steam generator plays a crucial role in the integration of solar heat (including the solar field, storage system, and steam generator). The pressure required in the electrolyser is limited to around 40 mbarg and must remain very stable. To meet this condition, it was determined that water must be evaporated at a pressure higher than the required pressure in the SOE. This value should account for the steam pressure drop across all components between the steam generator and the SOE, and it should also consider a throttling process after the steam generator to prevent condensation. Regarding the KPIs, a conversion efficiency of 38.7 kWh/kg H_2 and 84.4% (based on LHV) were achieved and a solar steam fraction of 43% is obtained considering a 24/7 operating strategy.

5. Acknowledgments

The authors thank the financial support and contributions from the GREENH2-CM project, funding entities Comunidad de Madrid and MCIN through the Recovery, Transformation, and Resilience Plan, financed by the European Union – NextGenerationEU (PRTR-C17.I1).

6. References

[1] GREENH2-CM - Strategic positioning of the Community of Madrid in R&D&i of green hydrogen and fuel cells. https://energia.imdea.org/en/porfolio/greenh2-cm-strategic-positioning-of-the-community-of-madrid-in-rdi-of-green-hydrogen-and-fuel-cells/ (16-05-2024).

[2] EcosimPro | PROOSIS - Modelling and Simulation Toolkits and Services. https://www.ecosimpro.com/ (16-05-2024).

[3] Repository of free climate data for building performance simulation. https://climate.onebuilding.org/ (20-05-2024).

Dynamic Energy Management Model: A Catalyst for Carbon Neutrality in Austrian Thermal Baths

Carina Seidnitzer-Gallien[1], Philipp Gradl[1] Xenia Bühne[1] and Michael Gumhalter[1]

[1] AEE Institute for Sustainable Technologies, Gleisdorf (Austria)

Abstract

Austrian thermal baths, significant energy consumers, primarily rely on fossil fuels, posing ecological and economic challenges. This research focuses on optimizing energy consumption by integrating renewable energy sources, such as deep geothermal energy, and enhancing efficiency through innovative technologies like heat pumps and dynamic optimization models. The performed baseline survey of thermal baths identified major energy consumers and potential areas for efficiency improvements. The developed Python-based dynamic simulation program uses Mixed Integer Linear Programming (MILP) to optimize the energy system, considering various energy sources, demands, and storage systems. Key strategies included waste heat utilization, efficiency enhancements in heating, ventilation, and cooling systems, and the integration of photovoltaic systems. The demonstration case in southeast Austria highlighted significant energy savings through the recovery of waste heat from thermal splashing water, air conditioning systems, and drinking water cooling. The optimized system configuration, featuring cascaded heat pumps and stratified storage systems, achieved substantial reductions in both heat and electricity demand. The results underscore the importance of dynamic simulation and optimization in achieving energy efficiency and sustainability in thermal bath operations. The research work provides a reference model for replication in other facilities, contributing to Austria's broader decarbonization goals.

Keywords: decarbonization, energy management system, renewables, heat pumps, thermal storages, dynamic optimization, Python simulation

1. Introduction

Austria, with its extensive thermal spa landscape comprising a total of 42 facilities, is not only a popular tourist destination in Europe but also one of the regions where the use of deep hydrothermal geothermal energy (depths greater than 400 meters in water-bearing layers) is at the forefront (Goldbrunner and Goetzl 2019). From an ecological perspective, thermal baths in Austria are significant energy consumers, still relying on fossil fuels like natural gas. However, since the increase in electricity and gas prices, these thermal spas have been striving for more energy-efficient operations. To achieve a transition away from fossil energy sources, it's essential to focus on major energy consumers, as the adoption of renewable energy in thermal spas is generally easier to implement compared to other urban areas (Goetzl 2022). The complex producer/consumer dynamics at a thermal spa site, with varying supply and demand profiles and external conditions, offer substantial potential for the efficient use of deep geothermal energy. This can be realized through innovative integration concepts involving heat pump technologies, efficiency enhancement measures within the internal energy system, and a real-time, innovative energy management system that provides flexibility with both the electricity and heat networks.

Energy Supply in Austrian Thermal Baths

The energy supply of Austrian thermal baths utilizes a combination of hydrothermal energy, biomass-based district heating, fossil fuels, and electricity. Most of the heat demand—60-70%—is dedicated to maintaining pool water temperatures, while 30-40% is used for hot water and heating requirements for thermal bath buildings, wellness facilities, and hotel complexes (Novakovits, 2018). Major electricity consumers include ventilation systems, which ensure optimal indoor air comfort, as well as cooling systems for hotel and spa operations. Overall, energy costs in Austrian thermal baths account for at least 20% of total costs, classifying this sector as "energy intensive." The volatility or increase in energy prices, particularly for electricity and fossil fuels like natural gas, poses significant challenges for these businesses, leading to substantial cost and price pressures. Decarbonizing thermal baths therefore requires a comprehensive approach that considers technological, economic, political, and societal factors.

© 2024. The Authors. Published by International Solar Energy Society
Selection and/or peer review under responsibility of Scientific Committee
10.18086/eurosun.2024.04.05 Available at http://proceedings.ises.org

Key strategies include:

- Reducing dependence on fossil fuels
- Implementing technological adjustments and conversions in heating, ventilation, and cooling systems
- Adapting existing infrastructure and integrating with future or existing electricity and heat networks
- Addressing cost pressures and exploring financing options
- Establishing clear regulatory frameworks to incentivize and support investments
- Enhancing public and stakeholder acceptance and awareness

Baseline Survey of Thermal Baths in Austria

The baseline survey confirms the energy-intensive nature of thermal baths. Table 1 below shows exemplary the heat and electricity consumption by energy source for two demonstration sites and the transfer site.

Table 1: Energy Consumption by Energy Source for Demonstration and Transfer Sites (Seidnitzer-Gallien et. al. 2024a)

Energy Consumption	Demo Case 1	Demo Case 2	Demo Case 3
Electricity	6 [GWh/a]	3,4 [GWh/a]	4 [GWh/a]
Biomass	-	6,4 [GWh/a]	4,5 [GWh/a]
Natural Gas	16 [GWh/a]	-	8,5 [GWh/a]

To reduce the high energy consumption and associated carbon footprint, a diverse combination of measures is planned, focusing on waste heat utilization in conjunction with heat pump technologies. Additionally, efficiency improvements in hot water preparation as well as ventilation and air conditioning systems will be implemented. These measures are intended to lay the groundwork for a complete decarbonization.

Aim and Methodology

The research work focuses on evaluating the current technical, energy, and environmental status of thermal spas in Austria. The goal is to identify realistic opportunities for decarbonization and energy transformation, while also developing innovative approaches such as the optimal utilization of renewable energy, maximizing energy efficiency, and integrating digital, predictive control and regulation systems. These strategies will be applied in real-world settings and will serve as reference models for replication in other thermal spa operations.

To achieve a sustainable transition to energy-efficient and renewable energy supply in Austrian thermal spas, an integrated methodological approach is employed.

- **Assessment of Energy Framework Conditions**: Initially, the basic energy data of the thermal spas were collected through a combination of surveys and a detailed energy audit. This assessment provided a comprehensive overview of the current energy consumption and existing energy use structures within the facilities.
- **Identification of Waste Heat and Efficiency Potentials**: Technical potentials were analyzed through targeted measurement series to identify possible sources of waste heat and areas with efficiency improvement potential. These analyses helped to recognize untapped energy sources and evaluate the efficiency of existing systems.
- **Energy Demand Simulation and PV System Analysis**: The optimization was based on a detailed energy demand simulation of the thermal spa's major consumers, created through a dynamic building simulation in IDA ICE. Additionally, simulations for the future use of a photovoltaic (PV) system were conducted to assess its integration into the energy system.
- **Comprehensive Energy System Optimization**: Finally, the entire energy system of the thermal spas was optimized using a Python-based dynamic simulation program, built on the optimization model of the Pyomo library. This model employed Mixed Integer Linear Programming (MILP) and distinguished four functional components: energy sources, energy demands, heat pumps (HPs), and energy storage systems. The core of this phase was the dynamic optimization of the energy system on a technical and energetic level, aimed at identifying the most energy-efficient system configuration and developing a sustainable, efficient overall system.

2. Demonstration Case

The demonstration case 2, situated in the southeast of Austria, is a significant energy consumer. It operates a geothermal well (depth: 498 m, production: 9 m³/h at 32°C) and is connected to a local district heating network. The annual heat demand is 6.4 GWh, and the electricity demand is 3.4 GWh. At the current energy system there is considerable potential to recover waste heat from thermal splashing water, climate cooling supply, and drinking water cooling. Establishing bidirectional use of the waste heat with the district heating network (for both heat and cold) aims to conserve biomass resources and enhance the heating plant's efficiency during summer and transitional operation.

Waste Heat Potential

Potential of Splashing Water: The daily backwash water generated by the thermal spa operation amounts to approximately 60 m³ at a temperature of 30°C. Before being discharged into the receiving waters, this water is cooled to around 9°C, allowing the residual energy of the thermal water to be fully utilized. This process enables the recovery of around 670 MWh per year of waste heat.

Potential of Cooling Water from Air Conditioning Systems: Waste heat from the cooling water of the air conditioning systems and the exhaust air from the ventilation systems offers a potential of approximately 1 GWh per year from both the spa and the hotel.

Potential of Drinking Water Cooling: The new drinking water source for the local supply, with a flow rate of 18 m³/h, must be cooled from 21.3°C to around 9°C before being introduced into the drinking water network. This energy source is available 24 hours a day, 365 days a year, providing a waste heat potential of 2.7 GWh per year.

Efficiency Measures

In parallel with identifying waste heat potentials, the overall energy demand for heating and electricity was analyzed for efficiency improvements. The analysis reveals that more efficient use of hot water systems (both treatment and customer facilities) could save 125 MWh per year for the spa and the connected hotel. Optimizing the system temperatures of the pool water heat exchangers aims to effectively supply the pools with water temperatures in the range of 32-38°C, making them usable. Furthermore, optimizing the ventilation systems with a heat recovery system enables near year-round dehumidification in the swimming hall using outdoor air. Overall, efficiency measures could reduce the heat demand by 884 MWh per year and the electricity demand by 150 MWh per year.

Derived Innovation Concept for Utilizing Potentials

A schematic overview (Figure 1) illustrates the elements integrated into the innovation concept. The local heating supply, provided by a biomass heating plant (BIOS), serves both the thermal spa and the hotel. The geothermal heat source, with temperatures of 32°C, is directed into the pools and heated to 34°C to 36°C. (Seidnitzer-Gallien et al., 2024b) The identified waste heat potentials from splashing water, the optimization of ventilation systems (including exhaust air and cooling water from air conditioning systems), and the required cooling of the drinking water source form the basis for utilizing an integrated heat pump system used at three temperature levels (30 °C splashing water; 20°C drinking water, 14°C climate cold water)

The plan involves implementing a cascaded use of two to three compression heat pumps to optimally utilize the different temperature levels and maximize the coefficient of performance (COP). The goal is to minimize the mixing of high and low return temperatures. Additionally, optimized stratified cold and heat storage systems are intended to enhance system efficiency and operational flexibility while ensuring high exergy efficiency.

For time-independent operation of the HPs from waste heat offer there will be installed a cold-water storage in between. A second water storage will be used to decouple the heat supply of the HPs and biomass heating plant from the consumers. Due to different operation modes of the HPs, the heat supply can occur at two distinct temperature levels, with the ejection of hot gas occurring at a higher temperature. Following the warm water storage is getting charged at 55°C and 70°C or 70°C and 80°C. The consumers require a temperature level of 70°C therefore the highest temperature layer of the thermal storage is around 70°C and any heat load at 80°C will be transferred to this layer as well. To ensure the coverage of the heat demand independently from the availability of waste heat and the operation of the HPs, the biomass heating plant is connected to the warm water storage. This allows the heating of returns from the thermal bath and district heating network from 45°C to 70°C, or the raising of the temperature level of the 55°C-water to the required 70°C. To enable a sustainable electricity supply too, a photovoltaic system will be installed above the thermal baths car park. This system will be used primarily to meet the electricity demand of the thermal

bath itself, with any additional generation being used to cover the demand of the HPs. In the event of insufficient solar energy generation, the current electrical demand will be met through grid-based electricity supply.

The deployment of cascaded heat pumps enables the utilization of water at temperatures between 40°C and 50°C from various sources, including wastewater from the thermal spa, waste heat from the cooling water, and heat from the drinking water source. An integrated smart control strategy will allow for high self-consumption of photovoltaic (PV) electricity generated by the thermal spa, hotel, and heating plant, or for grid-supportive operation. This heat is used to preheat both the thermal water and domestic hot water.

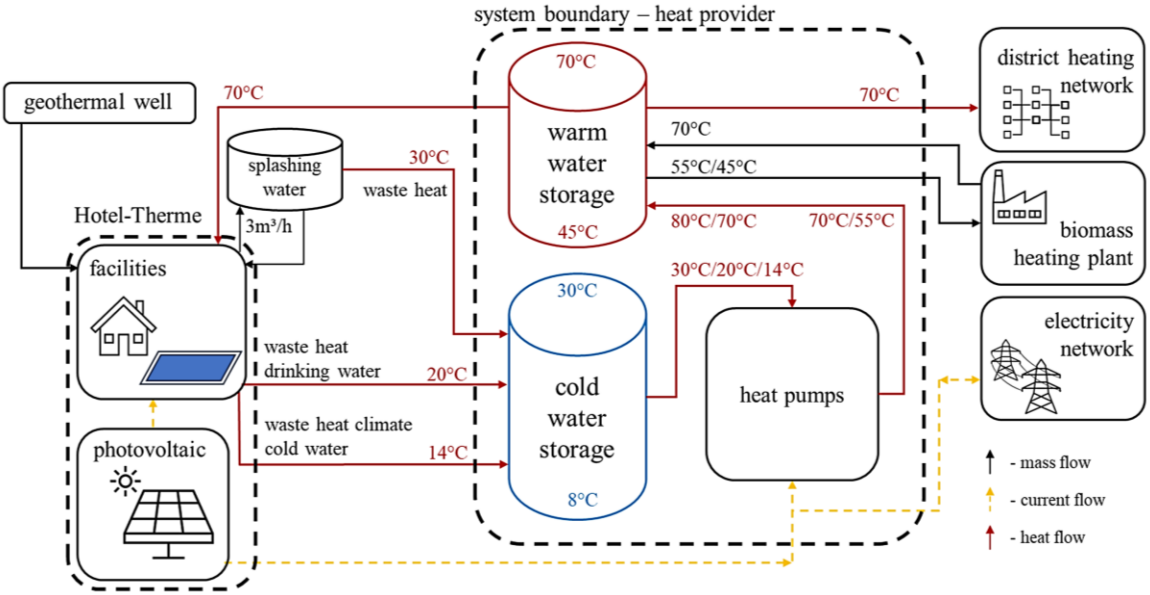

Figure 1: Simplified schematic overview of the innovative system concept at demo 1

The concept is further enhanced by expanding the connection between two heating plants (BIOW and BIOS) to enable bidirectional heat utilization. This allows waste heat from the thermal spa, using heat pumps, to also supply the second district heating grid (BIOW).

3. Dynamic Energy Management System

The development of a robust and efficient energy management system (EMS) is essential to effectively manage this complex system. This objective can be achieved through dynamic optimization using a Python-based programming tool. Dynamic modeling allows for the optimal configuration of the heat pumps and storage sizes, enabling efficient year-round control of the energy system. The model considers the different temperature levels and operating modes of the heat pumps, as well as the variable demands for cold and hot water. This ensures that the system can continuously adapt to changing conditions, minimize energy consumption, and maximize the use of available renewable energy sources.

The energy system was modeled with the optimization model built with the Pyomo library and distinguishes four functional components: sources, demands, HPs (heat pumps), and storages.

Technical and Operational Specifications

The utilization of the **waste heat sources** is contingent upon their availability. The new system will cool drinking water and feed it into the public drinking water network, thereby ensuring a waste heat capacity of up to 257 kW. Equally, the climate cold water always provides up to 500 kW. However, the waste heat from splashing water must be taken over night from 10 pm to 6 am when the thermal bath is closed to the public. Therefore, the water from the backwashing process is collected in a separate tank throughout the day, accumulating a volume of 60 m³.

Heat demand is met from the warm water storage. The biomass heating plant operates by drawing from the lower temperature levels in the storage and feeding heated water into the highest temperature zone. The biomass heating plants have a total capacity of 4 MW. The heat demand of the district heating network is defined based on measurement series from 2023, and the heat requirement of the thermal spa is simulated with the prospective efficiency measures with a comprehensive IDA ICE simulation.

The **electrical energy system** will also be expanded and made more sustainable, complementing the thermal energy improvements. A new 2 MW photovoltaic system will be installed at the thermal baths site. Any surplus electricity generated beyond the facility's needs will be used to power the thermal energy system, primarily the heat pumps. In case of a power outage, additional electricity will be sourced from the grid. The photovoltaic system's power generation is modeled using ASHRAE weather data in an IDA ICE simulation, while the thermal spas electricity demand data is based on measurements from 2023 and 2024.

Heat Pump Model

Each HP can choose from three different heat sources with different temperature levels. These temperature levels are 14°C, 20°C and 30°C. Regarding the condensation side, the heat can be released at 55°C with hot gas ejection at 70°C or 70°C with hot gas ejection at 80°C. These two options are labelled as operation modes. Each HP is capable of operating with every possible combination of the different operational points and modes. The schematic of the HP model can be seen in Figure 2.

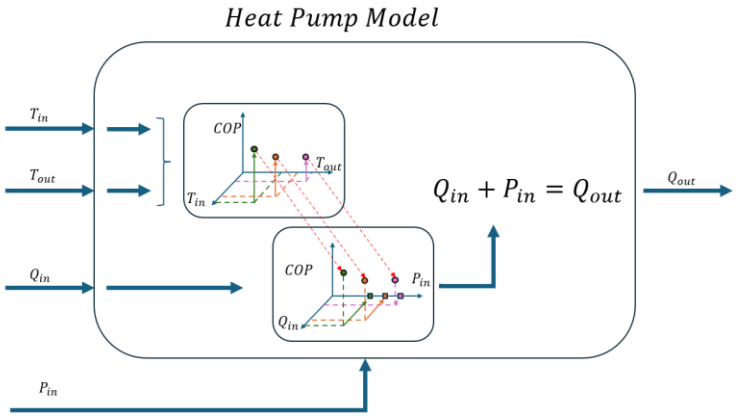

Figure 2: Schematic of the HP Model

Each pairing of inlet and outlet temperatures is defined as an operating point, with its own COP. A lower inlet temperature results in a lower COP, while a higher outlet temperature also leads to a lower COP. The optimizer can freely choose between these operating points. Each HP can switch between operating points in each timestep. The optimizer specifies an operating point for each timestep, and the HP model sets the associated COP. This COP dictates the electricity necessary to fulfill the heat demand. With a higher COP, more heat can be transferred from the cold side to the warm side with reduced electricity consumption.

Hot and Cold-water Storage Tank

The storages are implemented as layered storages (Figure 3). Each layer is defined by its own temperature level. Each layer can fully utilize the storage volume.

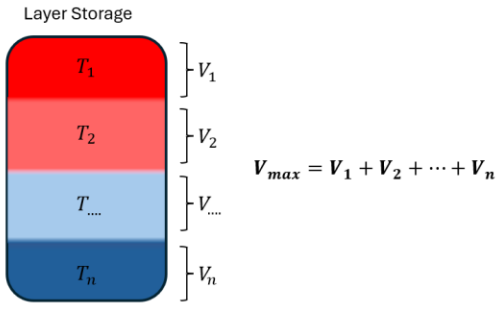

Figure 3: Schematic of the Layer Storage Model

Within the energy system, there are two separate storages: a cold-water storage and a hot water storage.

The cold-water storage has a capacity of 200 m³ and is consistently filled, always maintaining a constant volume of 200 m³. It has four different temperature levels. These temperature levels are 8°C, 14°C, 20°C and 30°C. The cold-water storage has four inlets. These inlets are the splashing water with a temperature of 30°C, the drinking water with a temperature of 20°C, the climate cold water at 14°C and cold water with a temperature of 8°C. This storage is connected to all HPs. All HPs can independently access all temperature levels at the same time. This cold-water

storage is used as a heat source for the HPs. If a HP accesses one heat level, the water from the heat level is not cooled down to 8°C. Instead, it is cooled down to the next lower heat level. For example, if one HP accesses water with a temperature level of 30°C it gets cooled down to 20°C. Therefore, the usable temperature difference for each HP is dependent on the temperature level it accesses.

$$V_{max} = V_{30}(t) + V_{20}(t) + V_{14}(t) + V_{8}(t) = 200\,m^3$$
$$V_{30}(t) = \dot{V}_{spw}(t) - \dot{V}_{HP\,30\to20}(t) + V_{30}(t-1)$$
$$V_{20}(t) = \dot{V}_{dw}(t) - \dot{V}_{HP\,20\to14}(t) + V_{20}(t-1)$$
$$V_{14}(t) = \dot{V}_{cw}(t) - \dot{V}_{HP\,14\to8}(t) + V_{14}(t-1)$$

There is one specific restriction for the cold-water storage. For cooling purposes, it must always contain at least 20% of the total storage capacity of 8°C water.

The energy system features a hot water storage with a capacity of 100 m³, consistently filled to maintain a constant volume throughout the entire timeseries. This storage unit operates at three distinct temperature levels: 45°C, 55°C, and 70°C. The HPs can increase the water temperature from 45°C to either 55°C or 70°C, but they cannot raise the temperature from 55°C to 70°C. This specific temperature increase can only be achieved using the biomass boiler.

The hot water storage is utilized to meet the 70°C demand of the energy system, which can be supplied by either the biomass boiler or the HPs. Both the biomass boiler and the HPs can operate simultaneously to fulfill this demand.

$$V_{max} = V_{70}(t) + V_{55}(t) + V_{45}(t) = 100\,m^3$$
$$V_{70}(t) = \dot{V}_{HP\,45\to70}(t) + \dot{V}_{BHP\,45\to70}(t) + \dot{V}_{BHP\,55\to70}(t) + V_{70}(t-1)$$
$$V_{55}(t) = \dot{V}_{HP\,45\to55}(t) + \dot{V}_{BHP\,45\to55}(t) + V_{55}(t-1)$$

The hot water storage must always contain at least 15 m³ of 70°C water for heating purposes.

Optimization Scenarios

The optimization model aims to determine the optimal HP configuration for the specified energy system. This configuration is characterized by two main parameters: the number of HPs and the power of each HP. Up to three HPs are considered. Multiple optimization runs are conducted to compare the objective values and identify the best configuration. The optimization process, which does not factor in the installation cost of each HP, seeks to maximize system revenue.

The impact of adding an extra HP or additional power is assessed by comparing the objectives of multiple runs. Significant differences in objectives suggest that such investments could be financially beneficial, while minimal differences indicate that additional power or an extra HP may not substantially reduce costs.

The HP configurations are determined for four representative weeks throughout the year, each representing a typical week for the thermal bath. The selected weeks start on the following dates:

1. 2023.01.22
2. 2023.04.01
3. 2023.07.01
4. 2023.08.22

The optimization is executed on an hourly basis. The means that there are 168 timesteps for each week.

4. Results

In total, over 5,000 scenarios with various heat pump (HP) configurations were calculated for several representative weeks throughout the year. These scenarios were designed to assess the impact of adjusting the maximum compressor power of each HP on the entire system's performance over the course of the year. Compressor power variations were specifically analyzed for four distinct representative weeks in 2023.

In the following plot (Figure 4), each axis represents the maximum available compressor power for a heat pump. The color of the dots indicates the objective values, with brighter dots representing better outcomes. It is important to note that the objective values are normalized for each representative week, meaning that values from different weeks cannot be directly compared across plots.

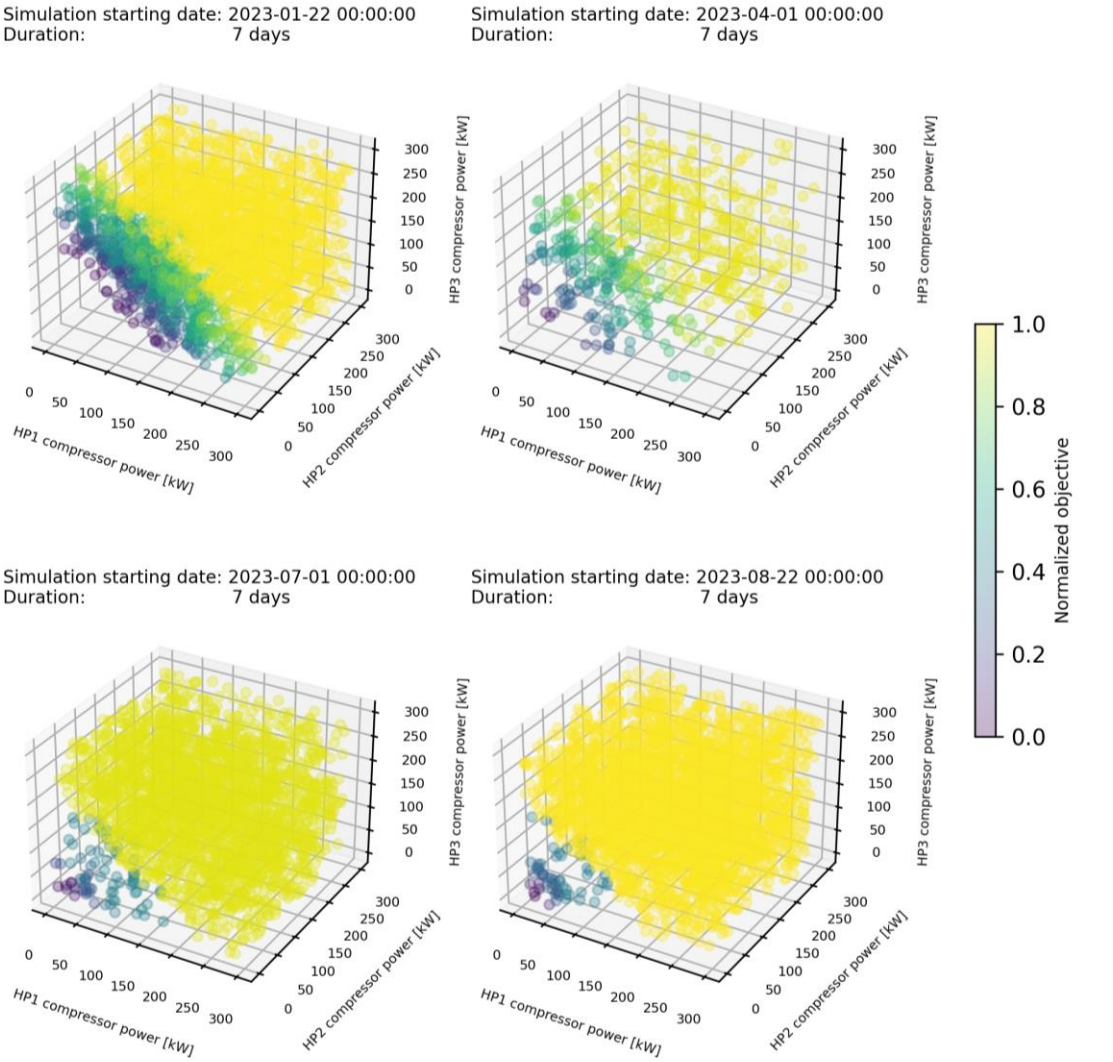

Figure 4: Impact HP power on energy system objective

These diagrams illustrate that the energy system gains more from larger heat pumps (HPs) in winter than in summer. They also suggest that increasing the HP size beyond a certain threshold offers no additional advantage.

Figure 5 depicts the relationship between the objective value and the maximum combined electrical power of the three HPs. It shows that improving the objective value by increasing HP power is only effective up to a certain point. Beyond this threshold, further increases in power yield no significant benefit.

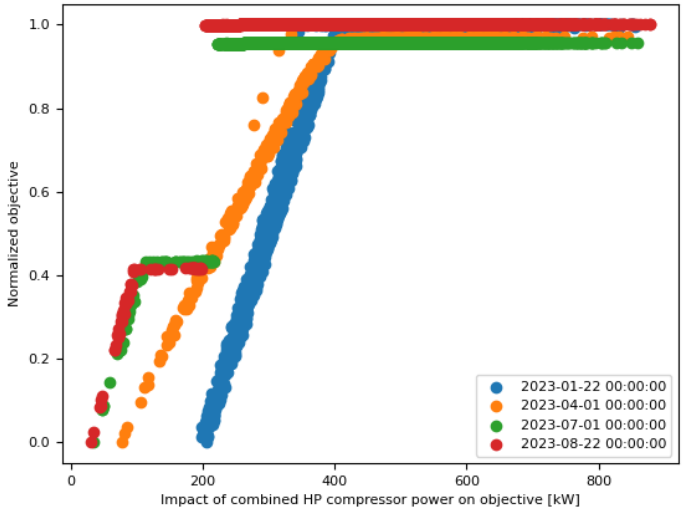

Figure 5: Effect of the combined compressor power of the three HPs on the normalized objective.

An analysis of the graph showing results from four representative weeks throughout the year indicates that the system gains no advantage from a combined maximum electrical power exceeding 400 kW for the three HPs. Furthermore, the results reflect only successful optimization runs, suggesting that a combined electrical power of at least 200 kW is necessary to meet winter demand. During the summer months, there is no benefit to having a combined power output above 200 kW. The minimum combined electrical power during the summer period is 100 kW. This indicates that the advantage of larger HPs is less pronounced in summer than in winter, as expected.

Based on data collected from over 5,000 configuration runs across multiple weeks during the year, one HP configuration emerged as particularly promising. For the subsequent run, the HPs will be configured as follows:

- HP1: 170 kW
- HP2: 100 kW
- HP3: 100 kW

The next phase of the analysis involves performing an optimization run over the course of a month, with January selected for this purpose. The resulting aggregated energy flows for this optimization run are depicted in Figure 6.

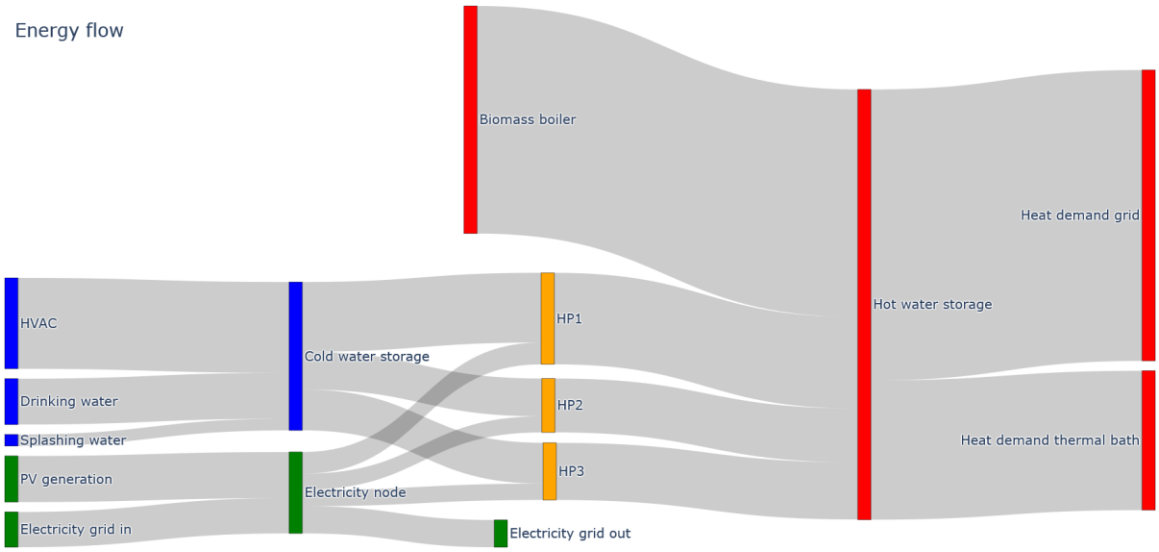

Figure 6: Energy flow of the system for the month January

As illustrated in the Sankey diagram above, the results of this run demonstrate that the HPs are capable of meeting approximately 47% of the heat demand in January. However, this percentage decreases during the winter months due to the higher heat demand, causing the HPs to frequently operate at their power limits to maintain this level of coverage. Additionally, the heat sources for these pumps are also constrained by power limitations. A similar month-long run was conducted for July, during which the HPs were able to fully meet the heat demand.

The following diagrams (Figure) provide an evaluation of the January optimization run results. The first diagram shows the supply from different energy sources. The waste heat from drinking water is fully utilized, and a significant portion of the waste heat from air conditioning is also harnessed. As per the specified requirements, the cooling of the splashing water is consistently maintained throughout the night. To meet the substantial heat demand during the winter period, the biomass boiler experiences significant fluctuations, reaching its maximum load.

To facilitate a more precise comparison of energy demand and supply, the second diagram depicts the heat demand of the thermal bath and the district heating network, as well as the excess electricity that cannot be utilized by the HPs.

The optimization run demonstrated that over the course of this month, the HP1 with the maximum electrical power of 170 kW operates for approximately 708 full load hours. The HP2 with 100 kW of electrical power operates with 714 full load hours, respectively. HP3, with a power of 100 kW, operates for 713 full load hours. Therefore, these three HPs are highly utilized while still providing comprehensive coverage of the heating demand.

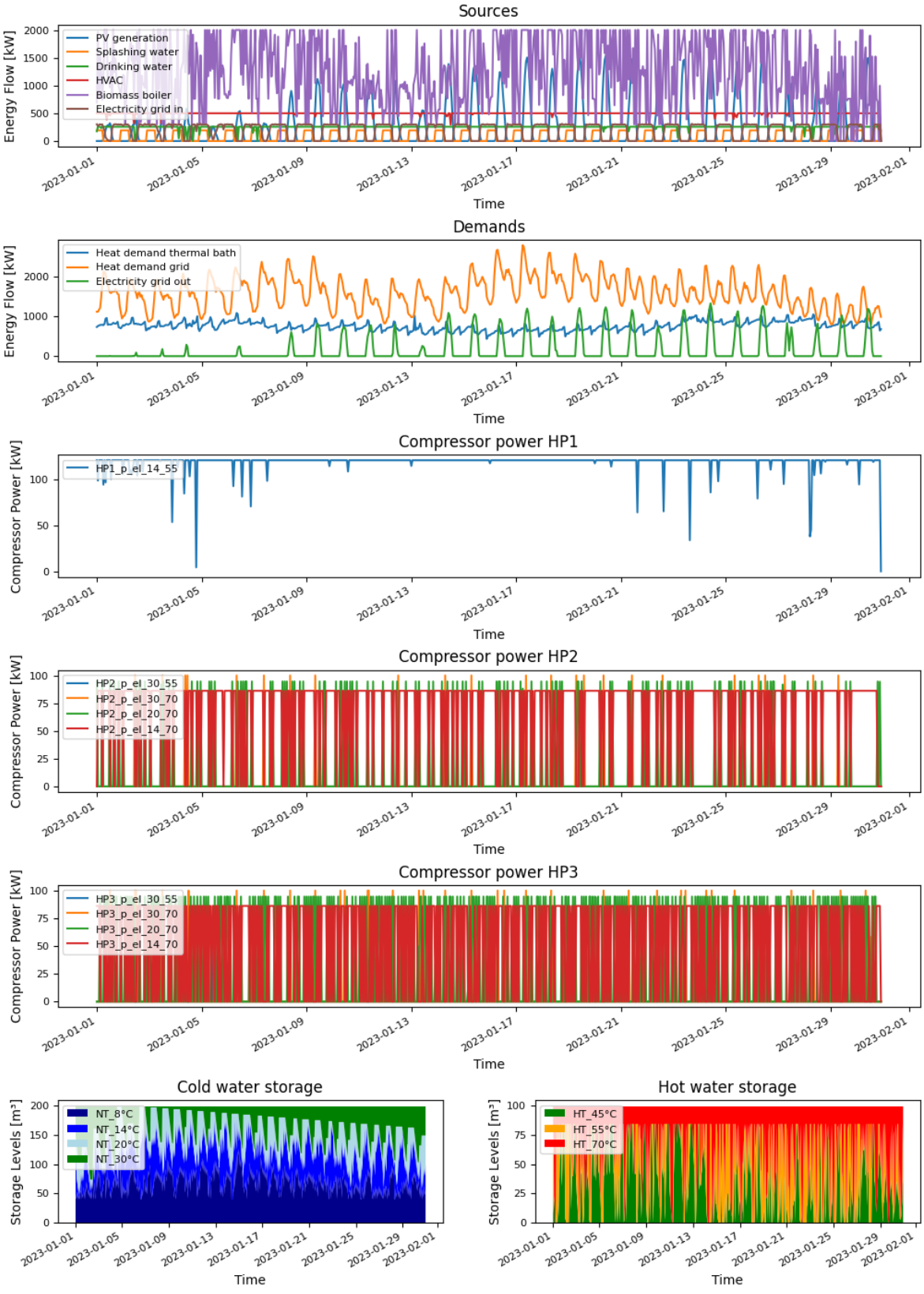

Figure 7: Results of the optimization run

Discussion & Conclusion

The exploration and implementation of innovative energy solutions in Austria's thermal bath facilities demonstrate significant potential for reducing carbon emissions and increasing energy efficiency. Through the optimization of existing infrastructure, utilization of untapped waste heat sources, and integration of renewable energy technologies, these facilities can play a pivotal role in the country's decarbonization efforts.

Especially, the heat pump (HP) configuration successfully met a significant portion of the heating demand during January, with each HP achieving over 700 full load hours. A similar performance was observed in July, where the

HPs operated extensively, accumulating 302, 469, and 480 full load hours for HP1, HP2, and HP3, respectively. The combined compressor power remained at 370 kW, below the previously defined limit of 400 kW, indicating the effectiveness of this configuration. However, further validation is needed through future optimization runs that include a cost model for the HPs.

Dynamic simulation and optimization play a main role in enhancing the overall efficiency and effectiveness of the energy system. By simulating various scenarios throughout the year, the model can account for fluctuating demands and environmental conditions, ensuring that the system operates at peak efficiency across different seasons. The ability to dynamically optimize HP configurations and energy flows allows for precise adjustments, minimizing energy consumption while maximizing the utilization of available renewable resources. This approach not only ensures reliable performance but also identifies the most cost-effective solutions, paving the way for sustainable energy management practices.

5. Outlook

The next phase will focus on refining the optimization model to autonomously determine the optimal installation power and number of HPs. To achieve this, price models for the initial costs of the HPs will be developed and integrated into the optimization process, enabling the model to independently identify the most efficient configuration.

Following the final dynamic optimization, detailed planning for the implementation of the demonstration site will be initiated. Simultaneously, the control strategy will be finalized, ensuring that the system operates efficiently under real-world conditions. The implementation phase will be closely monitored and accompanied by a dedicated optimization process to fine-tune system performance, ensuring that the goals of energy efficiency and sustainability are fully realized.

Through the integration of innovative technologies and optimization strategies, the project aims to revolutionize energy management in thermal bath complexes, paving the way for sustainable practices within the tourism industry.

6. Acknowledgments

The research works was carried out by the accompanying project GEO.MAT, which is funded by the Climate and Energy Fund and is carried out under the "Energy Model Region 2021" program.

The authors would like to thank the project partners Sonnentherme Lutzmannsburg, H2O-Hoteltherme, REDUCE Gesundheitsresort, BEST – Bioenergy and Sustainable Technologies, Büro für Erneuerbare Energie, Ing. Haas GmbH, StepsAhead Energiesysteme GmbH for their support.

7. References

Goldbrunner, J., Goetzl, G. (2019): Geothermal Energy Use, Country Update for Austria. In: Proceeding: European Geothermal Congress.

Goetzl, G. 2022. MUSE – Differences between deep and shallow geothermal energy, accessed on: 15.10.2023, https://geoera.eu/blog/muse-differences-between-deep-and-shallow-geothermal-energy/.

Novakovits, P. (2018): Entwicklung einer Methodik zur Erstellung eines Energieeffizienz-Benchmarks für Hotels sowie für Kur- und Gesundheitseinrichtungen anhand der Kurbad Tatzmannsdorf AG, Masterarbeit, Fachhochschule Burgenland, Pinkafeld.

Seidnitzer-Gallien, C., Bühne, X., Gumhalter, M. (2024a): CO2-freie Therme – Erhebung, Benchmarks und Konzepte zur Dekarbonisierung und Energietransformation. In: Proceeding e.nova International Conference, 2024, DOI: https://doi.org/10.57739/978-3-903207-89-9

Seidnitzer-Gallien, C., Stelzer R., Dragosits, S. (2024b): Use of waste heat potential and flexibility elements to speed up decarbonisation in Austrian thermal spas. In: Proceeding 3rd International Sustainable Energy Conference, 2024, DOI: https://doi.org/10.52825/isec.v1i.1262

05. Sustainable Energy Infrastructure and Electrification

Custom sizing and cost analysis of a PV-battery system: Dual-purpose application for residential load and agricultural water needs

Misagh Irandoostshahrestani, Patrick Turcotte, and Daniel R. Rousse

École de technologie supérieure, Université du Québec, Montréal, Canada

Abstract

This study conducts a technical and economic assessment of a solar water pumping system integrated with an electricity generation system used for a rural house and a farm. For the purpose of application, the location is Bandar-Abbas, a provincial capital in southern Iran. The study incorporates loss of power supply probability (LPSP) and water shortage probability (WSP) concepts along with users' tolerance levels for shortages. A custom code in MATLAB was developed, taking into account a particular energy usage pattern for a household and an irrigation water usage profile for a small-scale citrus farm. The results emphasize the substantial influence of LPSP and WSP thresholds on the system's size and cost. Notably, it was observed that increasing the LPSP tolerance from 0% to 3% could lower the levelized cost of energy (LCOE) by roughly 55% and reduce the WSP by about 36%. Hence, the key factor in such an installation is not technical, but rather human as the tolerance to the risk of service disruption is the key aspect that determines the overall cost, i.e., capital expenditure (CAPEX) and LCOE of a project.

Keywords: Solar water pumping, Photovoltaics, Loss of power supply, Water shortage

1. Introduction

Energy demand is growing due to increases in both population and per capita energy consumption (Key World Energy Statistics, 2021). In response, renewable energy sources are being increasingly adopted by both private and public sectors. Solar photovoltaic (PV) systems, first developed in 1954 by Chapin et al. (1954) have seen significant efficiency improvements.

One of the many applications of PV systems is water pumping and there are many studies in this particular field. However, it is worth noting that few studies focus on the dual application of residential load demand and agricultural water needs. For this combined application, Bhayo et al. (2019) examined a solar PV system designed to power a rural household's electricity requirements of 3.2 kWh per day. The study found instances where the system produced more energy than needed, which was then allocated for water pumping. It was shown that excess energy generation is common and can be redirected to secondary applications like water pumping. However, the study did not evaluate the tolerance level of the users in terms of water shortage probability (WSP) and loss of power supply probability (LPSP), and the effect of those factors on the sizing and cost of the system. In another study, Gualteros and Rousse (2021) developed an open-source software library designed to support various aspects of prefeasibility studies, system sizing, optimization, maintenance, and financial assessments. The software aimed to assist individuals with limited knowledge of solar water pumping systems in remote rural regions. They introduced the concept of WSP as a specific variation of LPSP to measure a community's tolerance for water shortages. The study demonstrated that this tolerance significantly impacts the system's size and cost.

The current study aims to examine technical and economic aspects of a PV-battery system for a farm by incorporating the concepts of LPSP and WSP. The objective is to demonstrate how the selection of appropriate values for LPSP and WSP can influence the overall system cost, highlighting that CAPEX and LCOE are highly dependent on the user-defined thresholds for these two parameters.

© 2024. The Authors. Published by International Solar Energy Society
Selection and/or peer review under responsibility of Scientific Committee
10.18086/eurosun.2024.05.01 Available at http://proceedings.ises.org

2. Methodology

2.1. Mathematical modelling

Equations (1) to (3) are utilized to calculate the output power of the PV array (Bhayo et al., 2019; Ibrahim et al., 2017; Bukar et al., 2019):

$$P_{PV}(t) = N_{PV} \times I_{PV}(t) \times V_{PV} \quad \text{(eq. 1)}$$

where the current of the panel and the effect of irradiation on the panel's temperature are defined as:

$$I_{PV}(t) = I_{PV,r} \times \left(\frac{G(t)}{G_{STC}}\right) \times (1 + \alpha \times (T_C(t) - T_{C,STC})) \quad \text{(eq. 2)}$$

$$T_C(t) = T_{amb} + \left(\left(\frac{NOCT - 20}{800}\right) \times G(t)\right) \quad \text{(eq. 3)}$$

The state of charge (SOC) of the batteries is determined using equations (4) and (5) (Bukar et al., 2019):

$$SOC_{Charging}(t) = SOC(t-1) \times (1 - \sigma) + \left(P_{PV}(t) - \left(\frac{P_l(t)}{\eta_{inv}}\right)\right) \times \eta_{bc} \quad \text{(eq. 4)}$$

$$SOC_{Disharging}(t) = SOC(t-1) \times (1 - \sigma) - \frac{\left(\left(\frac{P_l(t)}{\eta_{inv}}\right) - P_{PV}(t)\right)}{\eta_{bd}} \quad \text{(eq. 5)}$$

where σ represents the hourly self-discharge rate, and P_l indicates the load power. Additionally, η_{bc} and η_{bd} refer to the battery's charging and discharging efficiencies, respectively. The values for σ, η_{bc}, and η_{bd} are 0, 0.97, and 1, respectively (Bhayo et al., 2019).

Furthermore, the yearly loss of power supply probability (LPSP) and water shortage probability (WSP) are defined as:

$$LPSP = \frac{\sum_{t=1}^{t=8760} LPS(t)}{\sum_{t=1}^{t=8760} P_l(t)} \times 100 \quad \text{(eq. 6)}$$

$$WSP = \frac{\sum_{d=1}^{d=365} WS(d)}{\sum_{d=1}^{d=365} IWR(d)} \times 100 \quad \text{(eq. 7)}$$

For economic evaluations, the levelized cost of energy (LCOE) of the project was investigated in the study and is defined as (Bhayo et al., 2019):

$$LCOE_{\ Discounting} = \frac{\text{Life cycle cost}}{\sum_{t=0}^{Lifetime}\left(\frac{EP_t}{(1+r)^t}\right)} \quad \text{(eq. 8)}$$

where EP_t represents the annual electricity production. Here, the discount rate (r) was considered to be 15% as in the study by Nikzad et al., 2019 (Nikzad et al., 2019). The life cycle cost is defined as:

$$\text{Life Cycle Cost} = CAPEX_{0-PV} + CAPEX_{0-pump} + CAPEX_{0-else} + O_t + M_t + R_t + F_t \quad \text{(eq. 9)}$$

$CAPEX_0$ refers to the initial investment or capital expenditure for the components. The operational cost (O_t) and fuel cost (F_t) are assumed to be zero. Furthermore, the maintenance cost is considered to be 2% of the initial cost of the combined water pumping system and PV arrays (Bhayo et al., 2019; Li and Sun, 2018). The replacement cost for the lifetime of the project (30 years) is determined as follows (Bhayo et al., 2019):

$$R_t = CAPEX_{0-battery} \times \left(\sum_{i=1}^{i=5} \frac{1}{(1+r)^{5i}}\right) + CAPEX_{0-inverter} \times \left(\sum_{j=1}^{j=2} \frac{1}{(1+r)^{10*j}}\right) \quad \text{(eq. 10)}$$

To simulate pumping, it's necessary to determine π, the system's pumping power. The subsequent equation is used for this calculation:

$$\pi = \rho * g * \dot{V} * H \quad \text{(eq. 11)}$$

It is assumed that the water would be pumped directly from the pump to the farm, and no reservoir is used in the system. This set of equation is sufficient to carry out the results of the calculations presented in section 3.

2.2. Schematic of the system

The schematic of the system, including its main components, is shown in Fig. 1. As can be seen, the system provides electricity for a home and the batteries are used in case the generated energy is insufficient to meet demand. Finally, the pumping system is powered by energy exceeding domestic needs. It can partially or fully meet the farm's irrigation needs. The blue arrows represent AC current while the red ones are associated with the DC counterpart. Hence, Fig. 1 clearly illustrates that an AC water pump is used and that the house is also operating on alternative current. This is not a limitation and the rationale behind these choices is that the most efficient large-size water pumps are operating on AC and most residences involve AC appliances.

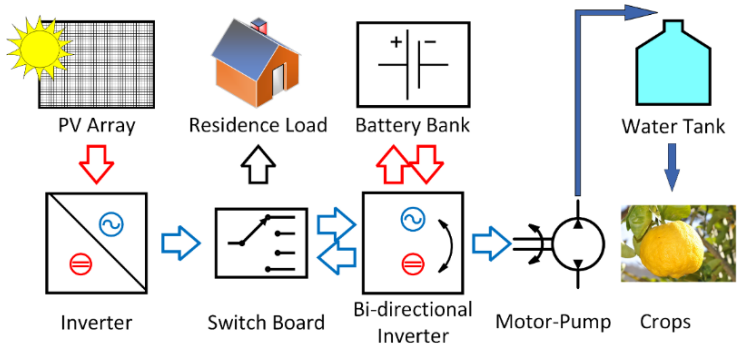

Fig. 1: Schematic of the dual-purpose electrification and water pumping system.

2.3. Algorithm of the study

The algorithm used in the design of the MATLAB code is depicted in Fig. 2. Initially, the algorithm determines the tilt angle for which the total annual irradiation is maximum. Then, it first takes in charge the load demand of the residence. When this electricity demand is met, the system starts charging the batteries, and finally, when there is still excess power, it is used to drive a pumping system. The motor pump is incorporated to provide water for a citrus farm with specific water irrigation requirements. The format of this conference paper does not allow a complete description of the algorithm as it would become overly lengthy. However, the interested reader should contact the authors for more details on the subject.

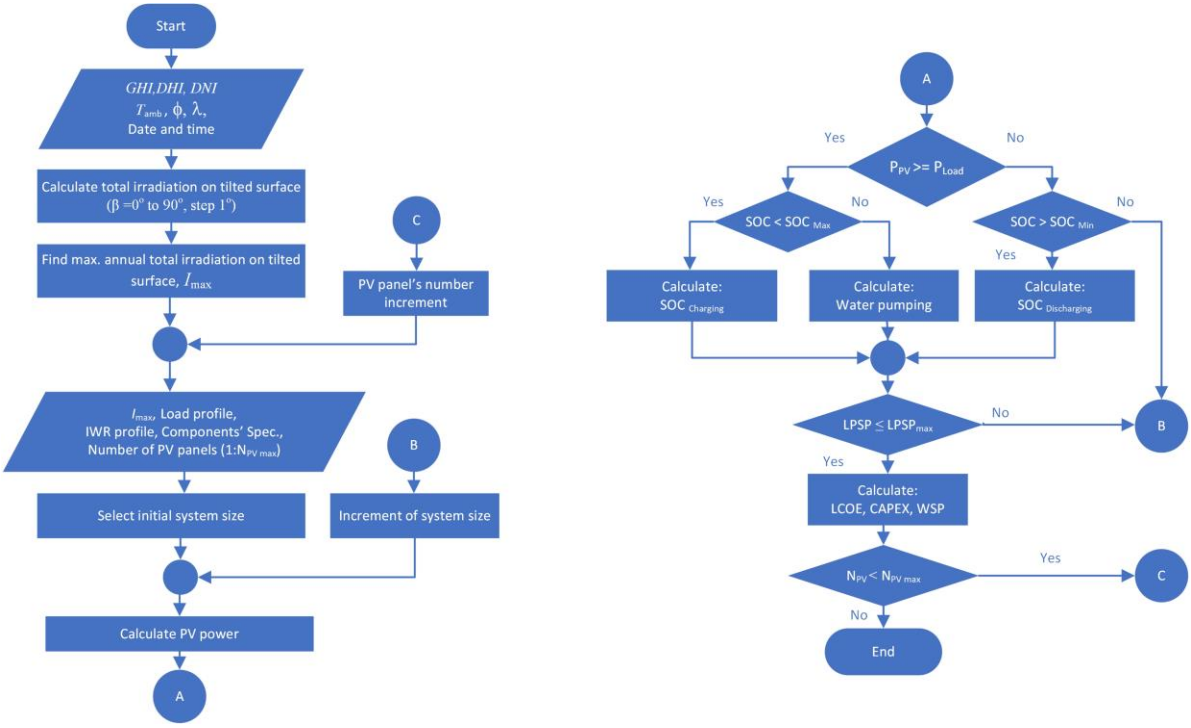

Fig. 2: The algorithm developed for the current study

2.4. Key component specifications

The specifications for all the main components are needed to provide a complete picture of the problem. These specifications are given in Appendix I, based on reference (Bhayo et al., 2019). Among other details, the batteries have a service life of 5 years, after which they are considered to have no residual or salvage value (Numbi and Malinga, 2017; Bhandari and Stadler, 2009; Ndwali et al., 2020). Furthermore, it is assumed that the inverters will have a service life of 10 years. The panels are anticipated to remain operational for the full 30-year term of the project without any performance loss, which is a rather optimistic assumption.

2.5. Case study

The city of Bandar-Abbas, the capital of Hormozgan province in Iran, is selected for the investigation. Bandar-Abbas is located in the southern part of the country. The Crop water requirement (CWR) and Irrigation water requirement (IWR) are shown in Fig. 3. The CWR reaches a maximum in summer with more than 250 mm of water needed while the IWR peaks at slightly more than 150. The needs are much less in winter.

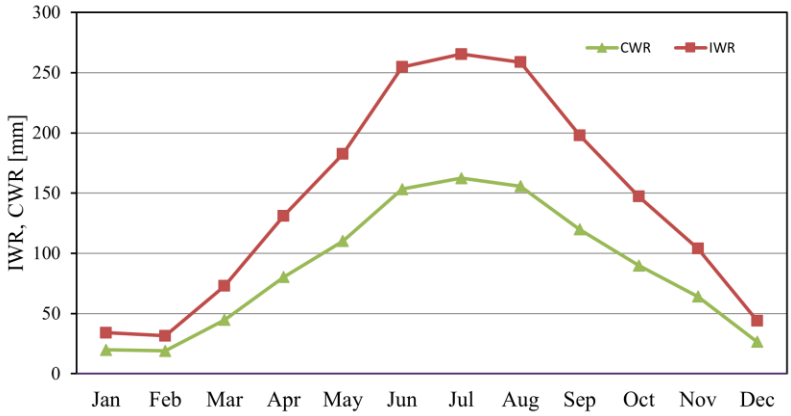

Fig. 3 Crop water requirement (CWR) and Irrigation water requirement (IWR) for a typical citrus orchard located in Bandar-Abbas, Iran (Bazrafshan et al., 2019).

A typical rural Iran electricity load profile for a house is shown in Fig. 5. The needs are basic with a lunchtime maximum of a bit more than 300 W between 12h and 14h and a 255 W consumption from 18h to 23h.

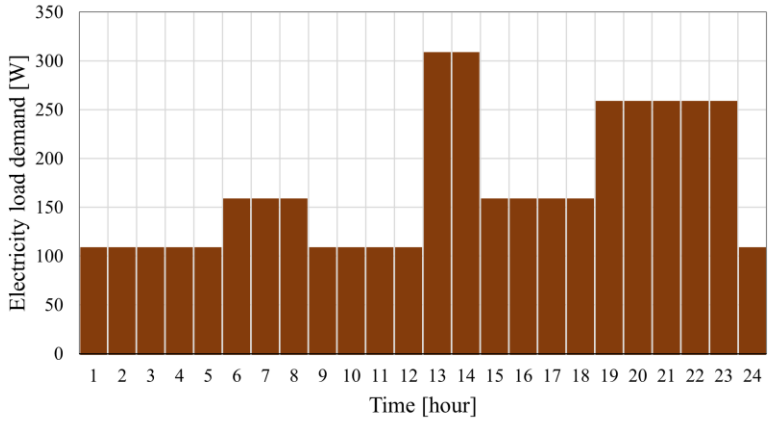

Fig. 4: Typical average hourly load profile in W as a function of the hour of the day used in the study.

3. Results and discussion

Selected simulation results for the proposed system are presented here, focusing on water shortage probability (WSP), levelized cost of energy (LCOE), and capital expenditure (CAPEX) across three loss of power supply probability (LPSP) scenarios. The initial objective is to find the optimal tilt angle for the south-facing panels. For this city, the optimal angle for maximizing total annual irradiation is about 17°, though angles between 10° and 28° offer similar performance.

The result is shown in Fig. 5 for a LPSP threshold of 0% (top), 1% (middle), and 3% (bottom). Please note

that the range of the Y-axis is not the same for the three plots in this figure.

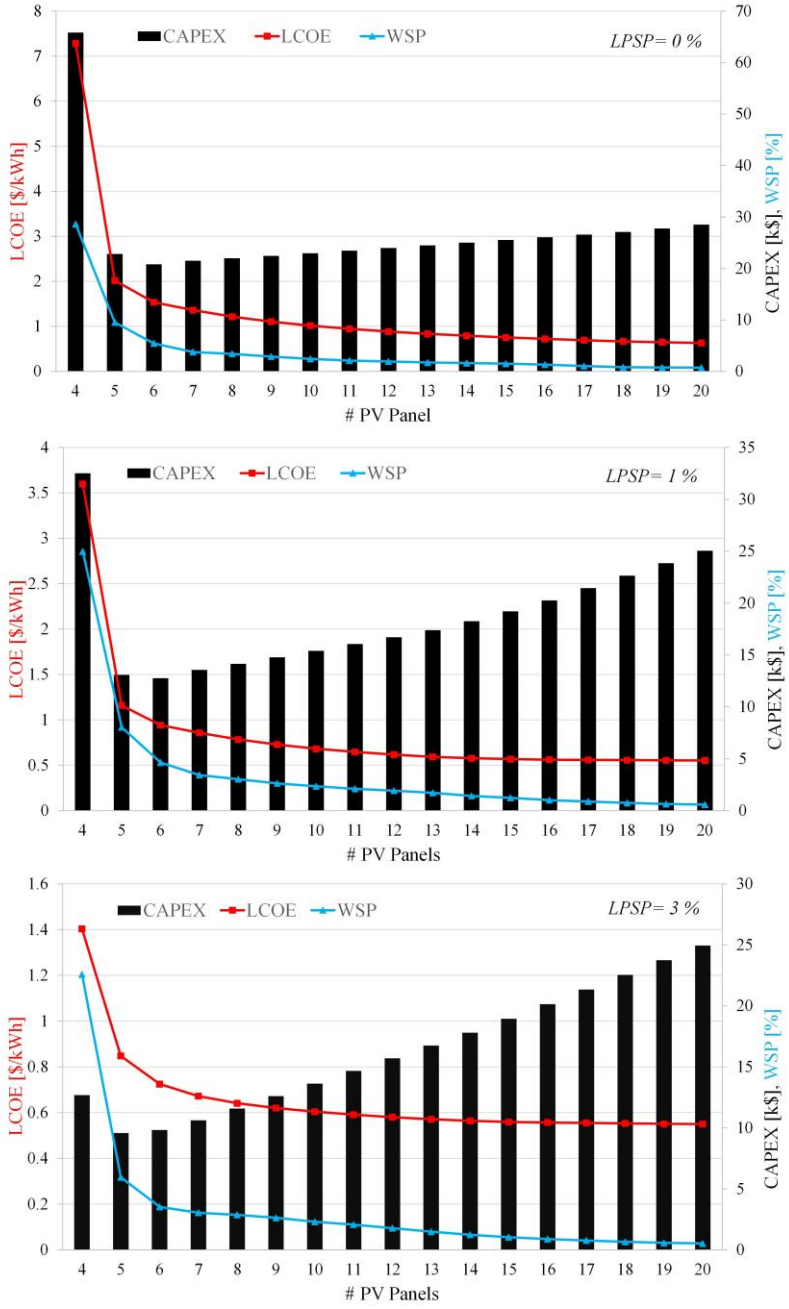

Fig. 5 : PV panel number versus CAPEX, WSP, and LCOE for different LPSP values.

LPSP=0% indicates 100% system reliability, providing uninterrupted electricity to the residence year-round. In this study, LPSP is set according to the tolerance of the house residents, and the minimum PV panel number and the capacity of the battery bank are determined based on this value. In LPSP=0%, a system with 4 panels involves a capital cost of $66,000, a WSP over 28%, and an LCOE above $7/kWh, largely due to the high battery capacity requirement. However, adding more panels quickly reduces both WSP and LCOE. The LCOE reaches around $1/kWh with 10 panels, beyond which further increases in panel numbers have little effect on LCOE but raise CAPEX.

Similar trends are seen with LPSP=1%, where 10 panels result in a 33% lower LCOE compared to LPSP=0%. A higher LPSP significantly reduces CAPEX; for example, CAPEX for a 10-panel system drops from $23,000 to $15,000 as LPSP increases from 0 to 1%.

When a larger tolerance is acceptable (LPSP=3% or about 263 hours per year), a 10-panel system shows a

40% LCOE reduction, with CAPEX as low as $14,000. It can be seen that the system's capital cost has a minimum value at different LPSP levels (6 panels for LPSP=0% and 1%, and 5 panels for LPSP=3%). This is because while adding panels increases system size and investment, a very low number of panels requires substantial battery capacity to meet LPSP thresholds, leading to high CAPEX driven by battery costs.

What this study does not mention is that when the situation requires it, the owner of the farm who tolerates a LPSP of 3% could lower his needs, he could postpone the use of water at the farm or distribute it at 80 or 90% of the curve presented in Fig. 3. He could use an alternative or complementary water storage tank for these hours only, etc.

4. Conclusion

In this paper, for the first time, the effects of the tolerance level of users in terms of WSP and LPSP (i.e., the reliability) on system size and price are evaluated for a dual-purpose hybrid PV-battery standalone system that produces electricity for a rural home and pumps water for a farm. It was shown that accepting a slight increase in the chance of power outages can significantly reduce the size of the system and its LCOE, with only a minor effect on the likelihood of water shortages. This indicates that communities or households with budget constraints might benefit from exploring additional measures to ensure they don't run out of water for irrigation. Finally, there is a point in the CAPEX versus PV panels number plot where additional increases in the number of panels result in only minor changes to WSP and LCOE. This occurs because the demand for battery storage rises significantly after reaching a certain number of panels, which are comparatively more affordable. It is expected that in a near future, when battery storage cost will decrease, the threshold shown in Fig. 5 will shift to the right.

5. References

Bazrafshan, O., Zamani, H., Ramezani Etedali, H., Dehghanpir, S., 2019, Assessment of citrus water footprint components and impact of climatic and non-climatic factors on them, Scientia Horticulturae, 250, 344-351.

Bhandari, R., Stadler, I., 2009, Grid parity analysis of solar photovoltaic systems in Germany using experience curves, Sol. Energy, 83, no. 9, 1634–1644.

Bhayo, B. A., Al-Kayiem, H. H., Gilani, S. I., 2019, Assessment of standalone solar PV-Battery system for electricity generation and utilization of excess power for water pumping, Solar Energy, 194,766-776.

Bukar, A., Tan, C., Lau, K., 2019, Optimal sizing of an autonomous photovoltaic/wind/battery/diesel generator microgrid using grasshopper optimization algorithm, Solar Energy,188, 685-696.

Chapin, P., Fuller, C., Pearson, G., 1954, A New Silicon p-n Junction Photocell for Converting Solar Radiation into Electrical Power, J. Appl. Phys, 25, no. 676.

Gualteros, S., Rousse, D. R., 2021, Solar water pumping systems: A tool to assist in sizing and optimization, Solar Energy, 225, 382-398.

Ibrahim, I., Khatib, T., Mohamed, A., 2017, Optimal sizing of a standalone photovoltaic system for remote housing electrification using numerical algorithm and improved system models, Energy, 126, 392-403.

"Key World Energy Statistics 2021," International Energy Agency, September 2021.

Li, H., Sun, Y., 2018, Operational performance study on a photovoltaic loop heat pipe solar assisted heat pump water heating system, Energy Build., 158, 861-872.

Ndwali, K., Njiri, J.G., Wanjiru, E.M., 2020, Multi-objective optimal sizing of grid connected photovoltaic batteryless system minimizing the total life cycle cost and the grid energy, Renew. Energy, 148, 1256–1265.

Nikzad, A., Chahartaghi, M., Ahmadi, M. H., 2019, Technical, economic, and environmental modeling of solar water pump for irrigation of rice in Mazandaran province in Iran: A case study, Journal of Cleaner Production, 239-118007.

Numbi, B. P., Malinga, S. J., 2017, Optimal energy cost and economic analysis of a residential grid-interactive solar PV system- case of eThekwini municipality in South Africa, Appl. Energy, 186, 28–45.

6. Appendix I: Key component specifications

The details presented here are provided for the researcher who would like to benchmark their results for the same problem. Here Tab.1 provides PV, batteries, inverter specifications and the details that pertains to the water system.

Tab. 1: Key component specifications

Feature	Value
PV panel specifications	
Maximum power	305W
Optimum voltage	32.70 V
Optimum current	9.33 A
Temperature coefficient	−0.37 % / °C
Nominal operating temperature	42 °C
Cost	201$
Battery specifications	
Nameplate voltage	12 V
Capacity	104 Ah
Service life	5 years
Cost	362$
PV inverter specifications	
Output power	2000 W
Efficiency	97 %
Service life	10 years
Cost	867 $
Bi-directional inverter specifications	
Output power	2200-2400W
Maximum efficiency	94 %
Service life	10 years
Cost	992 $
Pumping and storage system specifications	
O&M cost	0.02 of investment cost
Total head	8 m
Service life	30 years
Cost	2.4 $/W

Techno-Economic Analysis of a Stationary Battery Storage Operating on Frequency Regulation Markets in a Church Powered with PV System

Mohamad Koubar[1], Elaheh Jalilzadehazhari[1], Magnus Wessberg[2], Magdalena Boork[3], Johannes Wikstrom[3], and Joakim Munkhammar[1]

[1] Department of Civil and Industrial Engineering, Uppsala University, Lägerhyddsvägen 1, 75237, Uppsala, Sweden

[2] Department of Art History, Conservation, Uppsala University, Cramérgatan 3, 62153 Visby, Sweden

[3] The Church of Sweden, Dragarbrunnsgatan 71, 753 20 Uppsala, Sweden

Abstract

In Sweden, Svenska Kyrkan (the Church of Sweden) has over 3300 churches. A majority of the churches are electrically heated. The usage pattern of the church leads to a power peak during church heating, creating problems for the grid and the church organization through increased grid fees. Simultaneously, interest in deploying Battery Energy Storage Systems (BESSs) is growing. A significant challenge is determining the specific services the BESS should provide to maximize profits for the owner. For church load profiles, with the help of a battery, the church consumption peaks can be shaved. Additionally, when the Battery Energy Storage System (BESS) is not used for this purpose, it can instead be employed to support the grid through participation in the frequency regulation market. Frequency control services are activated in response to changes in the electricity grid frequency, with the BESS providing support during frequency fluctuations. The objective of this study is to investigate the economic value of installing BESS in a church powered by a PV system. Various frequency regulation services, with a focus on frequency containment reserve (FCR) are explored. The model operates on other energy markets, which are local flexibility and day-ahead markets. The inputs include selected services, feed-in and feed-out profiles, historical frequency data, and frequency regulation and energy market prices over the year 2023. The case study involves real data from Kila Church, equipped with a 60 kWp solar power system, located in mid-western Sweden. The economic metrics are net present value and payback period, whereas technical and environment metrics are the battery degradation and CO2 emissions equivalents, respectively. This study indicates that the investment in BESS is profitable if the BESS operates on frequency stability services together stacked with Peak Shaving (PS). The results show a 1.6-year payback period for a 120 kWh/60 kW BESS. A sensitivity analysis exploring future changes in prices of the frequency regulation market and BESS shows that Upward FCR for Disturbance (FCR-D Up) is more sensitive than Downward FCR for Disturbance (FCR-D Down) if a drop in the prices will occur in the future. Conclusively, BESS would be a beneficial investment for the churches and other commercial industrial load, from an economic, environmental, and societal perspective.

Keywords: Stationary Battery Storage, Frequency Regulation Markets, Ancillary Services, Techno-economic Analysis

1. Introduction

This In 2015, the United Nations launched Agenda 2030 to promote sustainable development through goals aimed at reducing poverty, addressing climate action, and ensuring affordable and reliable energy for all (Swedish UN Association, 2015). At the European level, the European Green Deal targets a 55% reduction in emissions by 2030 and aims for carbon neutrality by 2050 (European Comission, 2015). Additionally, the European Commission has implemented the REPowerEU plan in response to disruptions in fossil fuel imports, aimed at enhancing energy savings, diversifying energy supplies, and promoting clean energy (European Commission, 2022). Sweden has set a goal to achieve completely renewable electricity production by 2040 (IRENA, 2020). Consequently, wind and solar power capacities in Sweden have increased in recent years (Lindahl et al., 2022). However, these energy production technologies are weather-dependent, posing challenges for integrating them efficiently into the electric grid and ensuring power system stability. These objectives drive the growth of renewable energy production and

© 2024. The Authors. Published by International Solar Energy Society
Selection and/or peer review under responsibility of Scientific Committee
10.18086/eurosun.2024.05.02 Available at http://proceedings.ises.org

environmentally sustainable solutions, necessitating change. To advance these goals, the Church of Sweden has installed PV and battery storage systems and is leading pilot projects (The Church of Sweden, 2023). As one of the largest property owners in Sweden with over 20,000 buildings and extensive forest land, the Church of Sweden plays a crucial role in promoting the transition to renewables (in addition the total installed PV capacity in 2023 is 7.5 MW (The church of Sweden, 2024). It has set ambitious targets to achieve climate neutrality by 2030, focusing on sustainable development.

Globally, renewable energy generation capacity additions in 2023 exceeded 440 GW, with solar PV accounting for two-thirds of this capacity (IEA, 2023). The installed capacity of Battery Energy Storage System (BESS) integrated into the power sector globally doubled year-on-year from 2019 to 2023, reaching a total of 90 GW (65% utility-scale and 35% behind-the-meter) (European Commission, 2023). In Sweden, an estimated 3.5 GWh of BESS capacity is anticipated, according to the local newspaper "NyTeknik" (NyTeknik, 2024). Utility-scale battery storage refers to large systems connected directly to transmission or distribution networks, typically ranging from several hundred kWh to multiple GWh. In contrast, behind-the-meter battery storage systems are installed at residential, commercial, or industrial locations without direct grid connections.

Studies have explored utility-scale BESS operating on ASM alone or together with DAM (He G Chen Q Kang C Pinson P Xia Q, 2015). The BESS has been examined in the Ancillary Service Market (ASM) and Day-Ahead Market (DAM). either through a business case (Hameed Z Træholt C Hashemi S, 2023; Martins J Miles J, 2021) or using a Techno-Economical Analysis (TEA) framework (He G Chen Q Kang C Pinson P Xia Q, 2015) . It can also be a combination of operational bidding control and TEA (Merten et al., 2020). Behind-the-meter battery systems can operate similarly to utility-scale systems if aggregated as a virtual power plant. A virtual power plant is an aggregation of Behind The Meter (BTM) systems that can provide many of the same services as larger utility-scale systems (IEA, 2024). Additionally, BTM systems can offer services to consumers, such as frequency regulation and energy arbitrage, such as increasing self-consumption and self-sufficiency (Luthander et al., 2016), providing backup power (IRENA, 2019), enhancing energy resiliency, saving on electricity bills, and deferring demand change network investments. Thus, the increase operation of the battery could improve the economic value of BESS storage by staking multi-service and delivering the most value to customers and the grid.

For behind-the-meter battery storage, additional services beyond energy arbitrage include lowering electricity bills by taking advantage of variable tariffs or reducing peak demand, as well as increasing self-consumption and self-sufficiency of their systems (IEA, 2024). In this study the term BESS is referred to as BTM battery. Additionally, one of the focuses of this paper is on demand charge reduction, also known as Peak shaving (PS). PS and maximizing self-consumption and self-sufficiency have become increasingly interesting in recent years, as the battery's potential to reduce emissions and save costs through peak shaving and maximizing self-consumption is being recognized (Fares and Webber, 2017; Ollas et al., 2018; Oudalov et al., 2007). BTM batteries can also provide other services when connected to an aggregator. Investigating battery storage for more energy trading and frequency regulation can also be interesting (Merten et al., 2020). This study focuses on commercial and industrial loads and investigates the benefits of applying peak shaving when the BESS is connected to Local Flexibility Market (LFM), Frequency Regulation market (FRM), and DAM. Stacking services can increase the revenue streams and profitability of the BESS system (Berg K Resch M Weniger T Simonsen S, 2021; Braeuer et al., 2019).

Different country applications of industrial and commercial load PS, such as in Germany and Norway, have shown varying potential economic revenues compared to other cases. In the German case, the operation of the frequency market stacked with peak shaving increased the revenue. However, feasibility was only possible with the operation of the BESS on Frequency Containment Reserve (FCR) market (Braeuer et al., 2019). In Norway, feasibility increased with self-consumption and energy arbitrage; performing all possible services, including peak shaving and arbitrage, was feasible (Berg K Resch M Weniger T Simonsen S, 2021). Additionally, Shafique et al. (2021) investigated the connection between FRM, namely FCR Normal (FCR-N), and PS, showing the benefit of performing both in three Swedish case studies, with a return on investment of 24% in the case study for the year 2020 and around 13% PS achieved using real-time operation and prognosis modules. However, the authors did not evaluate other FRM like FCR for Disturbance (FCR-D) and did not estimate the individual effects of one service alone. Hjalmarsson et al. (2023) investigated the control operation of stacking Upwards FCR for Disturbance (FCR-D Up), DAM, and LFM, showing the optimization control possibility within one framework. This study explored the possibility of investigating different services, including FCR-D, the day-ahead market,

and a local flexibility market, in addition to peak shaving. To the best knowledge of the authors, a techno-economic assessment of these services combined with peak shaving has not been considered before, which is the focus of this study. This study has the following aims:

- Investigating the economic benefit of peak shaving using a load profile for a church generation and consumption profile.
- Assessing how stacking another service with peak shaving can increase the economic value of battery storage. The additional stacked services are LFM, FRM, and EA.
- Identifying the percentage price drop in the FRM and the battery storage investment cost at which the cash flow breaks even.

2. Methodology

This section outlines the techno-economic framework for the BESS, covering the simulation cases and key performance indicators. The framework is divided into two categories: BESS single services and BESS service stacking. The key performance indicators, which include economic, environmental, and technical metrics, are the outputs of the TEA.

2.1 Techno-economic framework overview

The operation of BESS can be categorized as a single service or service stacking. These services consist of peak shaving, local flexibility market, frequency regulation services, and energy arbitrage. The FCR involves five individual services, including FCR-D Up, FCR-D Down, and FCR-N, while energy arbitrage is on the DAM. In addition, maximizing self-consumption has used as well. The stacking of services has been combined with peak shaving. The goal of the peak shaving service is to reduce the cost for customers linked with energy storage to create cost savings in electricity bills (Chua et al., 2016). Additionally, there are three service stacking cases that include the operation of BESS for multiple services on the same day or hour. For example, Fig. 1 shows both the single and stacking operation. FCR-D operation includes both FCR-D Up and FCR-D Down operations in the same hour, while other services are operated exclusively for a complete hour, and other operations are not allowed in the same hour.

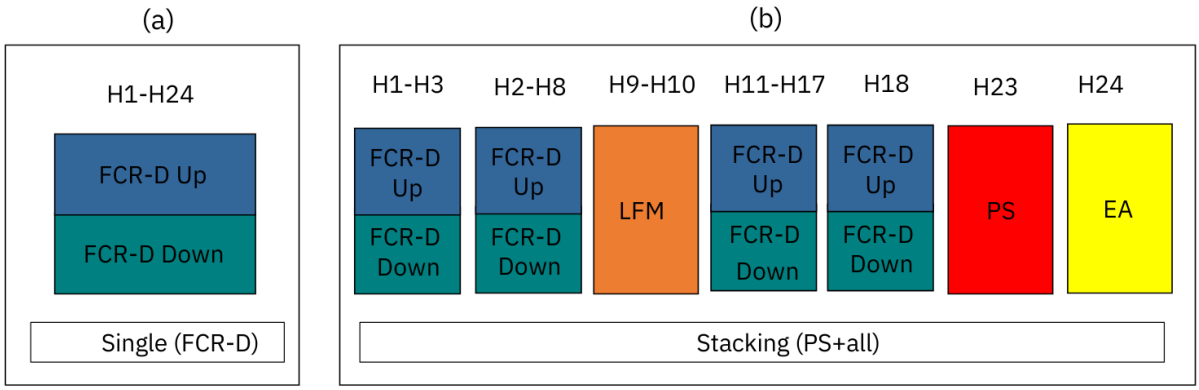

Fig. 1 Examples across various operational hours throughout the day: (a) illustrates the single service (FCR-D), while (b) depicts the stacking (All services).

The objective function for the BESS is economical. For peak shaving, the cost saving from the existing bill is considered as savings. Other objectives include the economic revenue from energy arbitrage, FRM, and LFM. Section 3.4 explains the markets input prices in the optimization. Section 3.2 explains each objective. Section 2.2 summarizes all the simulation scenarios conducted. The outputs of the optimization are then evaluated economically, technically, and environmentally. Economically, using the simple payback period and net present value calculation and annual savings of the base case; technically, through calculating the loss of capacity (LOC); and environmentally, by calculating CO2 emissions equivalents. Section 2.3 explains all the key performance indicators parameters for the TEA framework. The results of the TEA framework are shown in Section 4.1.

2.2 Simulation cases

The simulation cases were conducted on Kila Church and were split into two categories: BESS as a single service and BESS as a stacking service from A1-A5. For the single services, these included: self-consumption, peak shaving, energy arbitrage, and FRM (including FCR-N and FCR-D). For stacking, peak shaving was combined with the other services into four cases B1-B4. All the cases had the same PV system (60 kWp) and BESS (60 kW/120 kWh). The simulations were conducted for the year 2023. The simulation cases are shown in Tab. 1.

Tab. 1 Summary of simulation cases conducted on Kila Kyrka

Case No.	Service Type	Case Description	Fuse limit	PV size [kW]	BESS (P [kW], Cr)
R0	-	Base case no battery storage	63 A	60	-
BESS Single Service					
A1	SC	maximizing self-consumption	63 A	60	(60,0.5)
A2	PS	reducing peak electricity demand	63 A	60	(60,0.5)
A3	EA	Performing energy arbitrage	80 A	60	(60,0.5)
A4	FCRN	participates in FCR-N	80 A	60	(60,0.5)
A5	FCRD	participates in FCR-D	80 A	60	(60,0.5)
BESS Stacking Services					
B1	PS+EA	reducing electricity bill with arbitrage optimization.	80 A	60	(60,0.5)
B2	PS+EA+LFM	peak shaving and energy arbitrage including local energy markets.	80 A	60	(60,0.5)
B3	PS+FCRD	peak shaving and FCRD.	80 A	60	(60,0.5)
B4	PS+All	peak shaving, energy arbitrage and local energy market with FRM.	80 A	60	(60,0.5)

2.3 Key performance indicators

The key performance indicators of the cases are split into three categories: economical, technical, and environmental. The economic parameters include the annual savings relative to the base case without battery storage, net present value, *NPV*, and payback period, *PB*. The technical parameters include the battery capacity at the end of project life, E_{EOL}, equivalent cycle count, *EC*, and the relative battery usage, *RBU* (Berg et al., 2021). The environmental impact is calculated based on the amount of CO2 emissions equivalents, *CO2eq* per kWh, measured in tCO2eq. The key performance indicators parameters are estimated using the equations below:

$$NPV = \sum_{j=1}^{J} \frac{C_j}{(1+r)^j} \qquad (\boldsymbol{Eq.1})$$

$$PB = \sum_{j=1}^{PB} \frac{C_j}{(1+r)^j} = 0 \qquad (\boldsymbol{Eq.2})$$

$$E_{EOL} = (1 - LOC)E_N \qquad (\boldsymbol{Eq.3})$$

$$RBU = \frac{\sum_{d=1}^{D}\sum_{t=1}^{T} \mathbb{I}(P_{dch}^{cons}(t,d) \neq 0)}{8760} \qquad (\boldsymbol{Eq.4})$$

$$EC = \frac{\sum_{t=1}^{T} |E(t) - E(t-1)|}{2\,E_{net}} \qquad (\boldsymbol{Eq.5})$$

$$CO2_{eq} = \left(P_{ch}^{PV}(t,d) - P_{dch}^{load}(t,d)\right) PV_{eq} + \left(P_{ch}^{grid}(t,d) - P_{dch}^{grid}(t,d)\right) Grid_{eq}(\mathrm{t,d}) + E_N BESS_{eq}. \quad (\boldsymbol{Eq.6})$$

Eq. **1** represents the NPV, where C_j denotes the net cash flow at year j. J and r are the economic analysis period and the discount rate, respectively. Eq. **2** is used to determine the payback period of the BESS, where the payback period is the time taken for the cumulative discounted net cash flow to reach zero. The total BESS loss of capacity, LOC can be estimated using the semi-empirical model (Xu et al., 2018). The remaining energy capacity of the initial BESS energy capacity E_N at the end of the project E_{EOL} is estimated using Eq. **3**. Relative battery usage, RBU, is the estimate of the number of hours during which the BESS was used to cover a load, divided by the number of hours in a year as shown in Eq. **4** (Berg et al., 2021). EC can be estimated using Eq. **5**. The net energy storage capacity, E_{net}, is calculated by multiplying the allowable SOC limit by the rated energy capacity, E_N. E_{net} can be calculated as:

$$E_{net} = E_N(SOC_{max} - SOC_{min}) \quad (Eq.7)$$

Eq. **6** calculates CO2 emissions equivalents, $CO2_{eq}$, from battery operations, relative to a scenario without battery storage. it integrates contributions from solar and grid power with respective emissions which is the emissions of the Nordic energy mix. where E(t) is the energy at time t. $P_{ch}^{PV}(t,d)$ and $P_{ch}^{grid}(t,d)$ represent the charging power of the BESS from the PV system and the grid, respectively. $P_{dch}^{load}(t,d)$ and $P_{dch}^{grid}(t,d)$ refer to the discharge power from the battery to the load or to the grid. PV_{eq}, and $BESS_{eq}$ represent the associated emissions factors contributions from PV, and the BESS, respectively. $Grid_{eq}(t,d)$ is the emissions of the Nordic energy mix.

3. Models and inputs

3.1 Battery storage model

The BESS model is applied to the church load profile of year 2023. The BESS model consists of optimization, economic, degradation, and operational models. The operational model aims to identify the optimal service to operate the BESS by evaluating their potential in the DAM, LFM and FRM and peak shaving detailed further in Section 2.2.

Tab. 2 Summary of technical parameter of the BESS, PV, and the Load.

Technical Specifications	Value
BESS	
Power ratings (P_N) [kW]	60
Energy ratings (E_N) [kWh]	120
C-rate (C_r)	0.5
Allowable SOC (SOC_{min} – SOC_{max}) [%]	5 – 95
Charging efficiency (μ_{ch}) [%]	95
Discharging efficiency (μ_{dch}) [%]	95
BESS technology	LFP
BESS end-of-life criterion [%]	80
PV	
Nominal power [kW]	60
Annual residual PV energy [kWh]	24489
Profile type	Measured hourly data (2023)
Load	
Annual residual load energy [kWh]	62974
Profile type	Measured hourly data (2023)

The operational model aims to identify realistic operations with an energy management system for charging and discharging the battery while respecting the national technical requirements (ENTSO-E, 2023a). The outputs from the operation model feed into the economic and degradation models. The financial and technical assumptions of the BESS are provided in Tab. 2, where the physical quantities are in parentheses. The financial model calculates two main investment criteria NPV, and payback period. The degradation model is semi-empirical and has been formulated in ref. (Xu B Oudalov A Ulbig A Andersson G Kirschen DS, 2018). This model helps estimate the BESS's capacity loss over the economic analysis period.

3.2 Optimization model

This section focuses on optimization strategies where the objective varies across simulation cases. It encompasses four key terms: PS, used as a cost-saving term compared to the base case without a battery (case R0), similar to ref. (Shafique et al., 2021). Additionally, Energy Arbitrage (EA) and FCR-D, as modeled as in ref. (Argiolas L Stecca M Ramirez-Elizondo LM Soeiro TB Bauer P, 2022), are selected based on revenue optimization between these two markets. EA and LFM are employed similarly as described in ref. (Hjalmarsson et al., 2023) by assuming bids are sent a day ahead of the operation.

3.3 Case study

One of the churches with intermittent energy use is Kila church in Karlstad Sweden (59° 24' 36.36" N, 13° 30' 45.29" E), which since September 2022, has solar PV panels distributed on different direction and are connected to two inverters. Moreover, the church is also a pilot project to implement a battery storage system (The Church of Sweden, 2023). The technical requirement of the PV system as well as the load and BESS are shown in Table 2. The residual load and excess PV power is shown in Fig. 2.

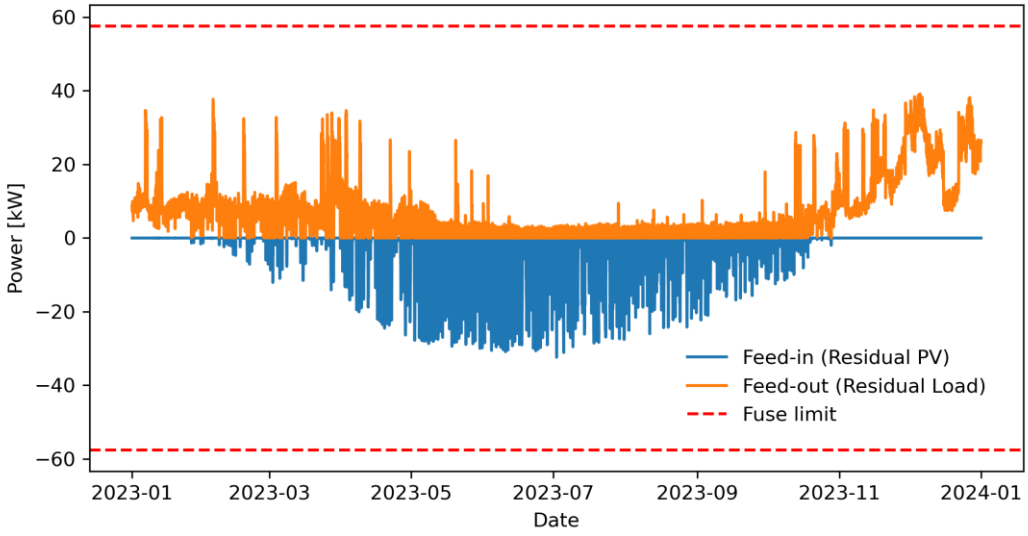

Fig. 2 Feed-in (residual PV power) and Feed-out (residual load) for the Kila church for the year 2023. Positive values are the residual consumption and negative values are the excess production.

3.4 Market prices

In the Nordic power network, electricity trading takes place on the Nord Pool market. This market consists of two types of auctions for power exchange: the DAM and the Intraday Market (Nord Pool, 2023). The spot prices for electricity in bidding area SE3 were chosen for the case study, where the case study is situated (see Section 3.3). The day-ahead and regulating prices were retrieved from ENTSO-E (European Network of Transmission System Operators for Electricity) Transparency Platform (ENTSO-E, 2023b, 2023c).The intraday market auction was not considered. LFM have been established and run as pilot projects in Sweden from 2021 to 2023 during the winter months (POWER CIRCLE, 2022). The data used are from CoordiNet in Uppland during Winter 2021/2022. The DSO is the main buyer of this flexibility the activation is considered 100% during the operation as the average activation is approximately 92% of the available data. The revenue from this market is split into capacity revenue and energy revenue (Real-time control of Battery storage for the Future Flexibility needs, 2022). The energy cost

of DAM buy and sell and local flexibility market is shown in Fig. 3. In Sweden, FRM trading takes place on a platform, provided by SvK, which is the only transmission system operator. The data used in this study are for the weighted average price of ASM. However, the pay-as-cleared mechanism was introduced on the 1st of February 2024 for Sweden. Historical prices for procured FCR capacity were retrieved from SvK's database Mimer (Mimer database, 2023) for the years 2021 to 2023. When operating on FCR-N, the resource must be capable of delivering the specified power for at least 1 hour, whereas, for FCR-D, it must sustain the specified power delivery for at least 20 minutes(Svenska Kraftnät, 2023).

(a)

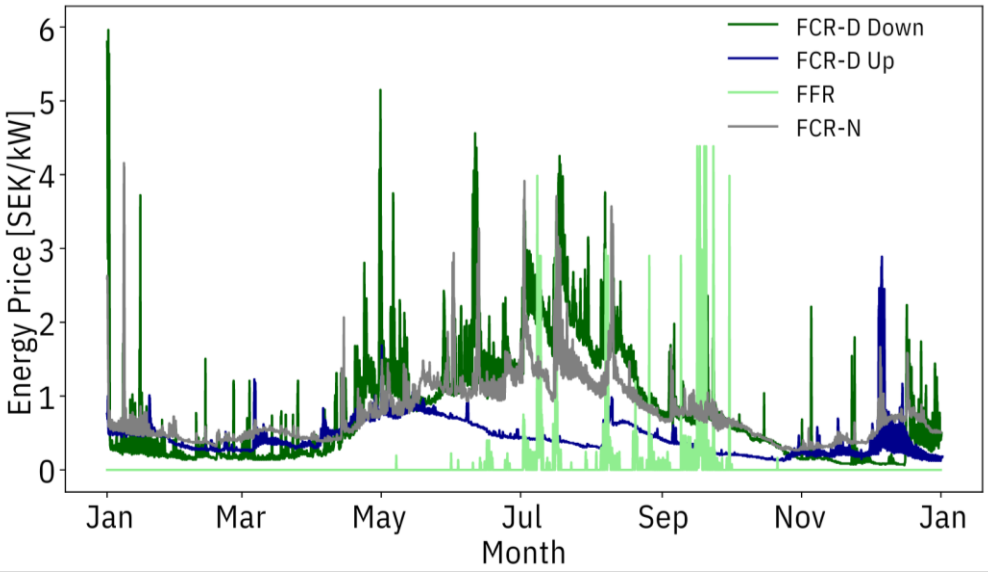

(b)

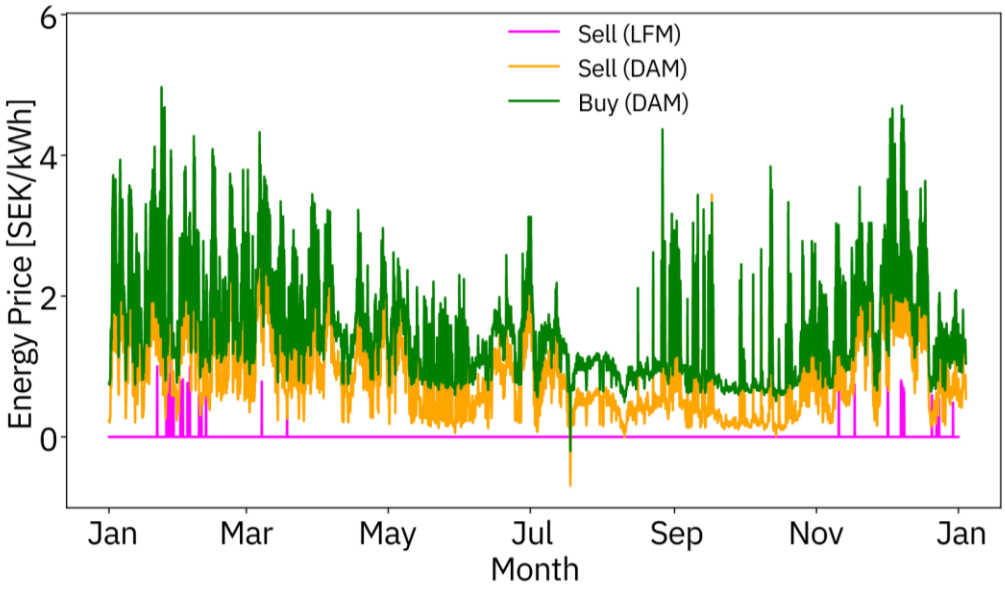

Fig. 3 (a) shows the ancillary services prices (b) shows the energy prices for selling and buying from day ahead market and local flexibility market (ENTSO-E, 2023; Mimer database, 2023; Svenska Kraftnät, 2023).

3.5 Emissions parameters

The CO2 emissions equivalents for the PV system, P Veq, are set to 25 gCO2eq/kWh, which was the emission value for PV in 2023 as shown in (Swedish Energy Agency, 2019). The battery's CO2 emissions equivalents are

derived from the Swedish Energy Agency and specified as the amount of CO2 emissions equivalents per installed kWh. Considering that the emission varied between 61 to 106 kgCO2eq per installed capacity, an average of 83.5 kgCO2eq/kWh is assumed in this study (Vattenfall, 2022). The total CO2 emissions equivalents for the Nordic energy mix, is weighted according to the production mix among the Nordic countries retrieved from the Electricity Map for the year 2023 over each hour (Electricity Map, 2023).

3.6 Distribution subscription tariff

The subscription tariff for Kila church is connected to a distribution network managed by Vattenfall Eldistribution. The N3 tariff was chosen for this study due to its lower feed-out fee compared to the other available tariffs. The tariff structure includes an energy fee and a power fee. The energy fee for consumption is based on usage during peak hours (6:00 to 22:00) in the winter months (January, February, March, November, and December), with off-peak pricing for other hours throughout the year. The power fee is based on the highest mean power each month. Electricity production incurs compensation, with higher rates during the winter (Vattenfall Distribution, 2023).

4. Results

The results section is composed of the key performance indicators on economic technical and environmental shown in 4.1. The sensitivity analysis on BESS cost and FCR-D market prices is shown in Section 4.2.

4.1 Key performance parameters results

The BESS has been simulated over the year 2023 and compared with the base case where the system does not have BESS. The simulations are split into two categories: A for single service, shown in Tab. 1, and B for stacking two or more services, shown in 0 Economically, investing in the BESS for only PS, SC, or EA is neither profitable nor feasible. However, operating on Frequency Regulation Service over the year 2023 is feasible with a 2.5-year payback period when operating on FCR-N and a 1.6-year payback period when operating on FCR-D. For the single services, economically and technically, FCR-D is more beneficial to operate on. Technically, the battery performed with a 13 % loss of capacity after 10-year period (LOC) when BESS operate on FCR-D. In contrast, FCR-N and Energy Arbitrage have the highest average peak. Regarding relative use, the battery's utilization is highest when operating on EA and results in the lowest CO2 emissions equivalents over one year when used for self-consumption.

Tab. 3 Summary of technical and economic metric results BESS single service year 2023.

Metric	A1	A2	A3	A4	A5
Economic metrics					
Net present value (*NPV*) [kSEK]	-514.6	-554.3	-533.7	1887.3	3764
Payback period (*PB*) [years]	N/A	N/A	N/A	2.5	1.6
Annual saving [kSEK]	13.95	6.6	17.6	303.5	505.5
Technical metrics					
Relative battery usage (*RBU*) [%]	19.4	26.5	37.3	0	0
Loss of capacity (*LOC*) [%]	14	13.3	16.7	16	13
Equivalent cycle count (*EC*) [cycle/year]	140.4	65.6	350	299	0.5
Average Peak [kW, month]	25.2	14.8	58	35.5	27
Environmental metrics					
CO2 emissions equivalents (*CO2eq*) [tCO2eq]	8.9	10.4	12.5	12.1	10

For stacking services, it is also economically non-feasible as the NPV is negative for cases B1 and B2, where the battery stacking involves peak shaving, energy arbitrage, and participation in the local flexibility market. The stacking of services has not significantly increased the operation; while some savings have been added to the service, they do not significantly contribute to economic feasibility. The equivalent cycles have increased for cases B1 and B2, while in cases B3 and B4, the operation is mostly FCR-D. it is clear that the average peak has decreased when multi-objective uses are applied, as in case B4 compared to A5. The CO2 emissions equivalents for cases B1 and B2 are the highest and are similar to operating only in A3, as the battery operates on arbitrage.

Tab. 4 Summary of technical and economic metric results with BESS stacking services year 2023.

Metric	B1	B2	B3	B4
Economic metrics				
Net present value (*NPV*) [kSEK]	-419.5	-298.5	3851.3	3970.3
Payback period (*PB*) [years]	N/A	N/A	1.6	1.6
Annual saving [kSEK]	30.1	43.3	524.8	538.6
Technical metrics				
Relative battery usage (*RBU*) [%]	33.8	41.2	0	0
Loss of capacity (*LOC*) [%]	16.5	16.5	13	13
Equivalent cycle count (*EC*) [cycle/year]	319.8	315.5	1	5
Average Peak [kW, month]	21.3	20.9	24.7	24.7
Environmental metrics				
CO2 emissions equivalents (*CO2eq*) [tCO2eq]	12.0	12.0	10.0	10.0

4.2 Sensitivity analysis

The sensitivity analysis assesses the impact of changes in FCR-D and battery prices on the feasibility of the BESS at the break-even investment point, where NPV equals 0. A break-even investment implies that while the investment does not generate profit, it also avoids losses for the investor. The sensitivity analysis examines price changes ranging from 1 to 90% drop in FCR-D prices as shown in Fig. 4. In addition, changes where FCR-D Down prices decrease are indicated in red, while FCR-D Up is shown in blue. FCR-D Up shows more sensitivity in the prices for the profitability of the BESS while FCR-D Down shows that it is more beneficial and more economical to operate on even for the high price of BESS market prices. Additionally, the figure illustrates that purchasing batteries at higher prices remains feasible in 2023. However, a significant drop in service prices in the future could challenge feasibility, as shown by a potential 90% decrease from 2010 to 2023 in battery prices (IEA, 2024), particularly with current BESS prices (including labor cost) needing to stay below 200 kSEK/kW, which is not expected in the foreseeable future.

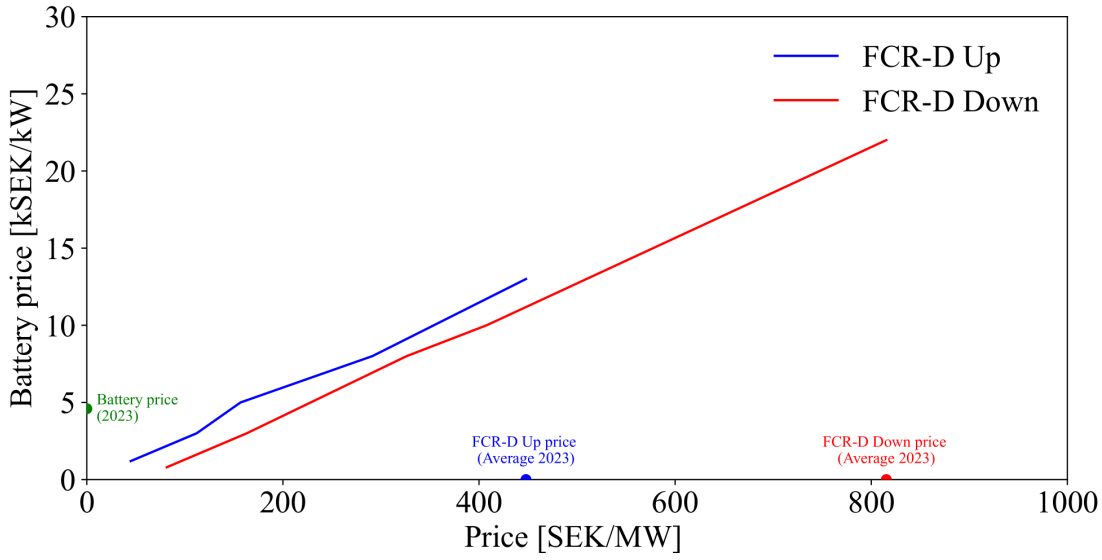

Fig. 4 Break even investments with sensitivity analysis for FCR-D prices and battery prices. Break-even investment means net present value equals zero.

5. Conclusion

In Sweden, the Church of Sweden (Svenska Kyrkan) owns more than 3,300 churches. A majority are used irregularly, typically only a few times a month, remaining unused between these sessions and A majority of the churches are electrically heated. This usage pattern results in electric peak power demand during church heating, posing challenges for both the electrical grid and the church organization due to higher grid fees. Many parishes have installed PV solar energy systems as part of the Church of Sweden's commitment to transitioning towards renewables, with goals set for climate neutrality by 2030. This study evaluated BESS operating various services including self-consumption, peak shaving, frequency regulation market, local flexibility market, and energy arbitrage. Stacking strategies included peak shaving, with FRM services encompassing FCR-N and FCR-D. Key performance indicators included technical metrics such as equivalent cycle count and loss of capacity, and economic metrics such as payback period and net present value, alongside environmental considerations like CO2 emissions equivalent.

The results indicate that battery operation is not economically feasible when BESS not operating on frequency regulation market. The highest annual average peaks were observed in FCR-N and energy arbitrage cases, while the lowest cycle and the highest NPV were associated with FCR-D operation. The lowest CO2 emissions equivalent were achieved with SC operations. For stacking FCR-D with other services, revenues are driven by FCR-D capacity revenue and the payback period was approximately 1.6 years, which is similar to the single service operation FCR-D. This shows that single service FCR-D and stacking other services with FCR-D is profitable during few hours of the year. Sensitivity analysis examined changes in both battery prices and FCR-D prices, revealing that a drop in FCR-D prices from 0 to 90% implies installing batteries with prices below 200 kSEK/kW, which is not feasible in the foreseeable future if a significant price drop occurs.

Future directions for this study could involve estimating the operation of churches combined with electric vehicle charging stations, and heating systems combined with BESS.

6. Acknowledgments

This work was is partly conducted within Solar Electricity Research Center Sweden (SOLVE) and forms part of the Swedish strategic research program StandUp for Energy. Also, the work was in part funded by the projects "Increased utilization of the grid with combined solar- and wind power parks", "Flexibility and energy efficiency in buildings with PV and EV charging" with grant number 50986-1, funded by the Swedish Energy Agency, and "Churches as flexibility resources in future power system" which funded by the Swedish Energy Agency and the Church of Sweden.

References

Argiolas L Stecca M Ramirez-Elizondo LM Soeiro TB Bauer P, 2022. Optimal Battery Energy Storage Dispatch in Energy and Frequency Regulation Markets While Peak Shaving an EV Fast Charging Station. IEEE Open Access Journal of Power and Energy 9, 374–385. https://doi.org/10.1109/OAJPE.2022.3198553

Berg K Resch M Weniger T Simonsen S, 2021. Economic evaluation of operation strategies for battery systems in football stadiums: A Norwegian case study. J Energy Storage 34, 102190. https://doi.org/https://doi.org/10.1016/j.est.2020.102190

Berg, K., Resch, M., Weniger, T., Simonsen, S., 2021. Economic evaluation of operation strategies for battery systems in football stadiums: A Norwegian case study ☆. J Energy Storage 34, 102190. https://doi.org/10.1016/j.est.2020.102190

Braeuer, F., Rominger, J., McKenna, R., Fichtner, W., 2019. Battery storage systems: An economic model-based analysis of parallel revenue streams and general implications for industry. Appl Energy 239, 1424–1440. https://doi.org/https://doi.org/10.1016/j.apenergy.2019.01.050

Chua, K.H., Lim, Y.S., Morris, S., 2016. Energy storage system for peak shaving. International Journal of Energy Sector Management 10, 3–18.

Electricity Map, 2023. CO2 emission hourly.
ENTSO-E, 2023a. Technical Requirements for Frequency Containment Reserve Provision in the Nordic Synchronous Area.
ENTSO-E, 2023b. Day-ahead Prices.
ENTSO-E, 2023c. Balancing Prices of Activated Balancing Energy.
European Comission, 2015. Summaries of EU legislation.
European Commission, 2023. REPORT FROM THE COMMISSION TO THE EUROPEAN PARLIAMENT AND THE COUNCIL Progress on Competitiveness of Clean Energy Technologies.
European Commission, 2022. REPowerEU: Joint European action for more affordable, secure and sustainable energy.
Fares, R.L., Webber, M.E., 2017. The impacts of storing solar energy in the home to reduce reliance on the utility. Nat Energy 2, 17001. https://doi.org/10.1038/nenergy.2017.1
Hameed Z Træholt C Hashemi S, 2023. Investigating the participation of battery energy storage systems in the Nordic ancillary services markets from a business perspective. J Energy Storage 58, 106464. https://doi.org/https://doi.org/10.1016/j.est.2022.106464
He G Chen Q Kang C Pinson P Xia Q, 2015. Optimal Bidding Strategy of Battery Storage in Power Markets Considering Performance-Based Regulation and Battery Cycle Life. IEEE Trans Smart Grid 7, 2359–2367. https://doi.org/10.1109/TSG.2015.2424314
Hjalmarsson, J., Wallberg, A., Flygare, C., Boström, C., Carlsson, F., 2023. Optimal scheduling of energy storage system in distribution grids using service stacking, in: 27th International Conference on Electricity Distribution (CIRED 2023). pp. 3077–3081. https://doi.org/10.1049/icp.2023.0907
IEA, 2024. Batteries and Secure Energy Transitions .
IEA, 2023. Renewable Energy Market Update Outlook for 2023 and 2024.
IRENA, 2020. Innovative solutions for 100% renewable power in Sweden.
IRENA, 2019. Innovation Landscape Brief: Utility-Scale Batteries.
Lindahl, J., Oller Westerberg, A., Berard, J., 2022. National Survey Report of PV Power Applications in Sweden 2021.
Luthander, R., Widén, J., Munkhammar, J., Lingfors, D., 2016. Self-consumption enhancement and peak shaving of residential photovoltaics using storage and curtailment. Energy 112, 221–231.
Martins J Miles J, 2021. A techno-economic assessment of battery business models in the UK electricity market. Energy Policy 148, 111938. https://doi.org/https://doi.org/10.1016/j.enpol.2020.111938
Merten, M., Olk, C., Schoeneberger, I., Sauer, D.U., 2020. Bidding strategy for battery storage systems in the secondary control reserve market. Appl Energy 268, 114951. https://doi.org/https://doi.org/10.1016/j.apenergy.2020.114951
Mimer database, 2023. Primary Regulation.
Nord Pool, 2023. Bidding Area.
NyTeknik, 2024. Unique mapping: Battery parks are increasing enormously – risk of over-establishment [WWW Document].
Ollas, P., Persson, J., Markusson, C., Alfadel, U., 2018. Impact of Battery Sizing on Self-Consumption, Self-Sufficiency and Peak Power Demand for a Low Energy Single-Family House With PV Production in Sweden, in: 2018 IEEE 7th World Conference on Photovoltaic Energy Conversion (WCPEC) (A Joint Conference of 45th IEEE PVSC, 28th PVSEC & 34th EU PVSEC). pp. 618–623. https://doi.org/10.1109/PVSC.2018.8548275
Oudalov, A., Cherkaoui, R., Beguin, A., 2007. Sizing and Optimal Operation of Battery Energy Storage System for Peak Shaving Application, in: 2007 IEEE Lausanne Power Tech. pp. 621–625. https://doi.org/10.1109/PCT.2007.4538388

POWER CIRCLE, 2022. Local flexibility markets.
Vattenfall, 2022. Real-time control of Battery storage for the Future Flexibility needs.
Shafique, H., Tjernberg, L.B., Archer, D.E., Wingstedt, S., 2021. Behind the Meter Strategies: Energy management system with a Swedish case study. IEEE Electrification Magazine 9, 112–119.
Svenska Kraftnät, 2023. Villkor för FCR (condition for FCR).
Swedish Energy Agency, 2019. Positiv minskning av klimatpåverkan i produktionen av elbilsbatterier.
Swedish UN Association, 2015. Agenda 2030 and the global goals.
The church of Sweden, 2024. Installed PV capacity 2023. Private communication.
The Church of Sweden, 2023. Stora vinster med batterilager (Great Benefits with Battery Storage) [WWW Document]. URL https://www.svenskakyrkan.se/karlstadsstift/stora-vinster-med-batterilager-i-svenska-kyrkor
Vattenfall, 2022. Elens ursprung och miljöpåverkan.
Vattenfall Distribution, 2023. Elnatspriser (Electricity Grid Prices).
Xu, B., Oudalov, A., Ulbig, A., Andersson, G., Kirschen, D.S., 2018. Modeling of lithium-ion battery degradation for cell life assessment. IEEE Trans Smart Grid 9, 1131–1140. https://doi.org/10.1109/TSG.2016.2578950
Xu B Oudalov A Ulbig A Andersson G Kirschen DS, 2018. Modeling of Lithium-Ion Battery Degradation for Cell Life Assessment. IEEE Trans Smart Grid 9, 1131–1140. https://doi.org/10.1109/TSG.2016.2578950

Enhancing Energy Transition on Campus: Implementing Thermal Accumulation Mechanisms for Flexibility

Pere A. Bibiloni[1], Jacinto Vidal[1], Vincent Canals[1], Yamile Diaz-Torres[1], Andreu Moià-Pol, Iván Alonso[1], Benito Mas[2] and Victor Marínez-Moll[1]

[1] Energy Engineering Group at the Department of Industrial Engineering and Construction / University of Balearic Islands, Palma (Spain)

[2] Technical and Infrastructure Service of the University of Balearic Islands, Palma (Spain)

Abstract

The University of the Balearic Islands has committed to reducing carbon emissions by 50% by 2030 and achieving net-zero emissions by 2050 through the United Nations' Race to Zero campaign. The UIB has developed a comprehensive strategy to enhance energy efficiency, electrify demand, and deploy 7.1 MW_p photovoltaic installations covering 113% of the campus's annual electricity consumption. The campus aims to minimize the excess hourly photovoltaic generation fed back into the distribution grid by deploying a new 4^{th}-5^{th} generation hybrid DHC network, powered by an HVAC plant based on heat pumps and chillers, with a thermal capacity of 4 MW_t and a dedicated storage system. Preliminary results, after analyzing multiple configurations of thermal energy storage systems for the HVAC system, demonstrate significant potential for reducing electrical surpluses through the deployment of a hybrid storage system. This system would include an 882 kWh_t thermal storage buffer and a 4,445 kWh_e battery storage system. The results show that the use of the proposed storage solution allows for a reduction in energy costs for cooling of between 89 to 95%, depending on the alternative considered.

Keywords: Photovoltaics, Energy Storage, Flexibility, District Heating and Cooling

1. Introduction

The European Union (EU) has established the Green Deal (Tsiropoulos et al., 2020) as a comprehensive roadmap to achieve climate neutrality by 2050, aiming to reduce greenhouse gas emissions and promote sustainable development. Decarbonization, a key focus area, seeks to reduce reliance on fossil fuels and promote renewable energy adoption. Despite traditional emphasis on sectors like manufacturing, it's crucial to recognize the role of academic institutions in this transition. The deployment of renewable energy on university campuses is essential for addressing climate change and reducing carbon emissions, providing sustainability and energy autonomy. University campuses are ideal places to install renewable infrastructure (Kalkan et al., 2011; Tu et al., 2015) such as solar panels and wind turbines, leveraging their large surface areas and available land. Although the initial construction of these systems is costly, the energy independence gained compensates for the costs over time, especially with government incentives. In this context, it's important to highlight the renewable energy projects undertaken by various universities (Elgqvist & VanGeet, 2017). Colorado State University took steps to install solar PV panels totaling 6.7MW between 2009 and 2015. At the same time, Arizona State University made significant strides by deploying both on-site (24.1 MW) and off-site (28.8 MW) solar PV panels. Additionally, across the University of California campuses, there is a collective capacity of 36 MW of solar PV panels, which contribute to generating over 52 million kWh of electricity. These initiatives demonstrate the commitment of academic institutions to transitioning towards sustainable energy sources. Additionally, it is essential to address carbon emissions related to university data centers, ensuring they come from renewable or carbon-free resources (University of Minnesota, 2023). Reducing energy consumption in institutions through the upgrade of older electrical infrastructures and implementation of more efficient systems is also crucial to making large-scale renewable energy more viable. However, ensuring the reliability of renewable energy, especially through the installation of backup systems like used generators, is important. Part of the renewable energy on university campuses can also come from carbon credits, although the primary

© 2024. The Authors. Published by International Solar Energy Society
Selection and/or peer review under responsibility of Scientific Committee
10.18086/eurosun.2024.05.03 Available at http://proceedings.ises.org

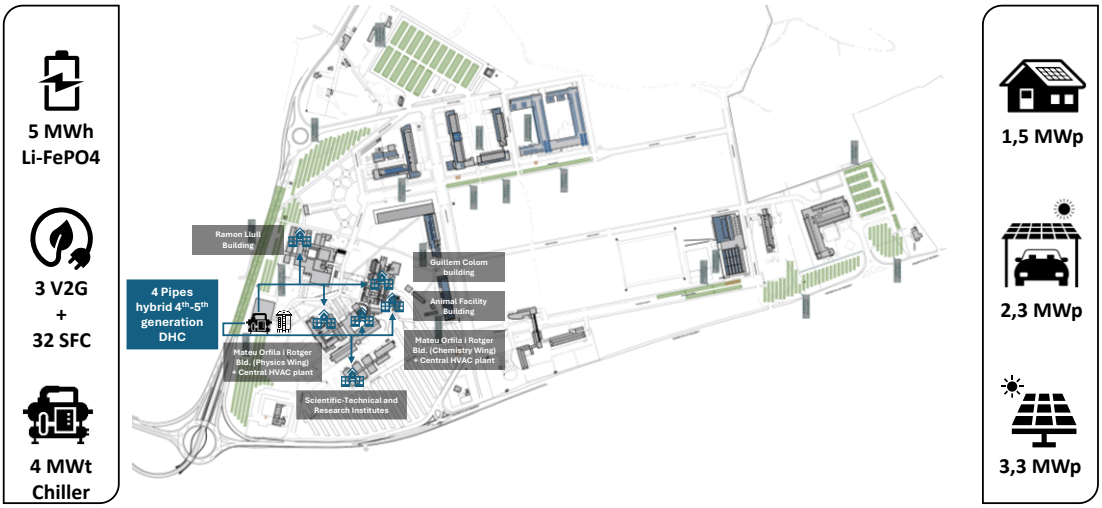

Fig. 1: Distribution of the renewable generation plants to be deployed at the UIB campus, located in Palma de Mallorca, Spain

goal should be to generate as much clean energy on-site as possible (Kiehle et al., 2023). Investing in renewable energy and carbon credits will help accelerate the transition to a more sustainable infrastructure and minimize long-term environmental impact. Furthermore, renewable energy universities are not only crucial for combating climate change but also attract future students concerned about the environment.

Due to the variable and weather-dependent nature of photovoltaic energy, integrating electric batteries is crucial to enhance self-consumption in buildings with photovoltaic systems. In the case of campuses, unused energy is stored in batteries for later use, such as during periods of low solar availability. This approach reduces dependence on both the electric grid and renewable energy sources, which are often uncontrollable and variable. Additionally, considering the price disparity between buying and selling energy to the grid, increasing self-consumption while reducing energy sales can be economically beneficial. Another strategy to improve self-consumption is to store excess energy in thermal form. If a thermal installation based on heat pumps already exists, additional components are not necessary; water tanks for energy storage and the thermal inertia of the building can be actively utilized (Zanetti et al., 2020). Some heat pump manufacturers are implementing solutions in their commercial products to boost system self-consumption. The control and optimization of integration between heat pumps and photovoltaic panels have been extensively studied in the literature (Péan et al., 2019).

The main objective of this study is to analyze, through simulations, various storage scenarios to meet the energy demand of a group of buildings on the university campus in the Balearic Islands, Spain. These buildings are interconnected through a district heating and cooling network (DHC) to serve as a flexibility mechanism and allow the valorization of photovoltaic surpluses derived from the deployment of a larges photovoltaic facilities and an electric storage system.

2. Case of study

The University of the Balearic Islands (UIB) joined the United Nations' Race to Zero campaign in 2021, committing to reduce carbon emissions by 50% by 2030 and achieve net-zero emissions by 2050. Additionally, UIB faced a significant increase in energy costs due to the Ukraine War, with energy costs rising by 281% between 2020 and 2022, reaching €3 million. In response to these challenges, UIB, with the assistance of various research groups, developed a strategy to reduce energy consumption and CO_2 emissions by improving building energy efficiency, electrifying demand, and deploying a set of photovoltaic installations to cover 113% of the campus's annual electricity consumption. Through projects developed under this strategy, UIB secured €20.8 million in competitive calls from the Mechanism for Recovery and Resilience (MRR), part of the EU's Next Generation EU funds aimed at supporting investment and reforms in Member States for sustainable and resilient recovery from the COVID-19 pandemic while promoting EU ecological and digital priorities.

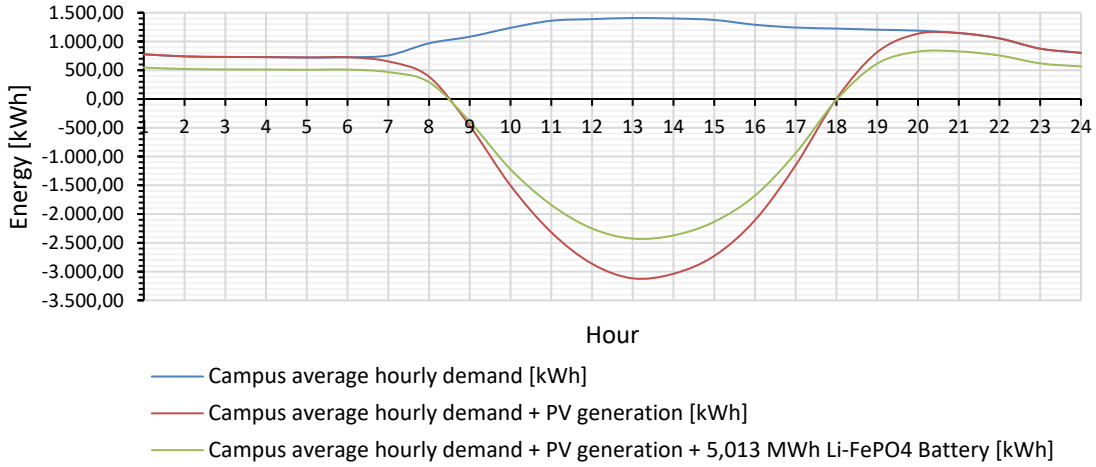

Fig. 2: Average hourly baseline curve of the energy demand at the UIB campus for different scenarios of photovoltaic and electric storage deployment.

Currently, 0.28 MWp of the projected 7.1 MWp of photovoltaic generation has been installed on campus in 18 locations. Fig. 1 illustrates PV plants distribution. Managing photovoltaic generation will require the deployment of demand management strategies and electric storage systems, as the campus's hourly demand varies widely between 0.75 MWh and 1.4 MWh, Fig. 2 blue line, peaking at 3 MWh. Furthermore, the campus's medium-voltage evacuation line is limited to 3 MW by the Distribution System Operator (DSO), leading simulations to predict that 37.5% of generation hours will result in surpluses exceeding 3 MWh, Fig. 2 red line. To address this issue, using hourly simulations of the expected photovoltaic generation and the actual campus demands across different years, it has been determined that deploying 5.3 MWh of Li-FePO4 batteries would reduce the annual hours with generation surpluses above 3 MWh to just 7.5%. Additionally, the campus has a thermal demand of over 10 MWt, with 5 of the 15 campus buildings connected to a 3rd generation district heating and cooling network supplied by a natural gas cogeneration plant located at 1.4 km in the "Parc Bit" technology park, Palma of Majorca, Spain, adjacent to the campus.

To address the remaining 7.5% of generation hours with surpluses exceeding 3 MW, the campus will need to self-limit its generation. To tackle this issue and considering that 60% of the campus's energy demand comes from air conditioning, this study analyzes the potential flexibility that would be provided by deploying a new HVAC plant with a capacity of at least 4 MW_t, using 4-pipe heat pumps capable of producing heating and cooling simultaneously. Accompanied by a storage system designed to operate on daily charge/discharge cycles, yet to be determined by this study, to supply 6 buildings to be interconnected in a new hybrid 4th – 5th generation DHC network to be deployed, Fig. 1. This plant will act as a manageable load for the generation/demand management. It is worth noting that UIB has recently secured an additional €3.6 million for the deployment of this new plant, thermal storage systems, and the new district network (Fig. 1).

3. Materials and Methods

The methodology developed for this work to optimize the storage deployment in the preliminary design of a 4th–5th generation hybrid DHC network is carried out in three phases. The first phase focuses on synthetically determining the HVAC demand of the buildings to be interconnected to a DHC network through thermal simulations using Energy Plus. The second phase involves analyzing and optimizing various storage solutions (both thermal and electrical) from a techno-economic perspective, with the aim of maximizing the use of excess photovoltaic generation for thermal energy production while minimizing the amount of energy fed back into the electrical grid. The third phase involves analyzing the operating costs of the storage configurations when they are running optimally, to determine the true operating expenses for each setup. This analysis goes beyond simply assessing whether the configurations can fully meet the HVAC demand with energy stored from excess photovoltaic generation; it also considers the deployment costs of the various configurations. It should be noted that this analysis does not consider the implementation costs of the different storage solutions to be deployed.

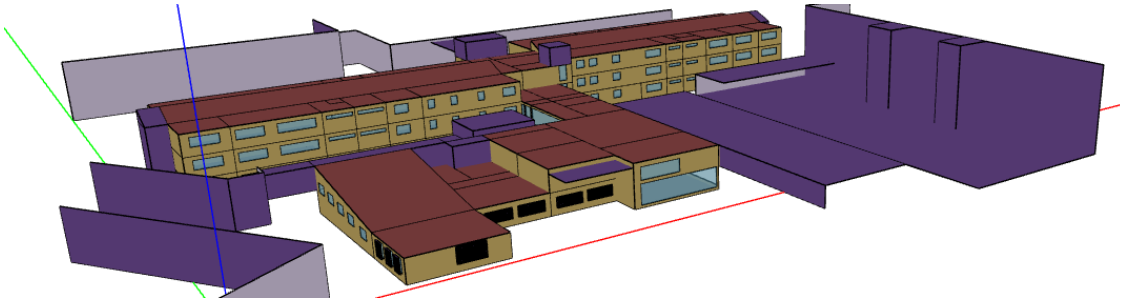

Fig. 3: 3D EnegyPlus model of the chemistry wing of the Mateu Orfila i Rotger building is created using OpenStudio.

The details of each of the three phases of the methodology are presented below.

3.1. HVAC Demand

Analyzing the energy consumption of buildings is a complex task that requires careful consideration of the interactions between the building itself, the HVAC system, and the surrounding environment. This process also involves developing effective mathematical and physical models for each of these elements. The dynamic nature of weather conditions, building operations, and the presence of multiple variables make computer-assisted design and operation essential for achieving high-performance buildings.

EnergyPlus (DOE, 2017), the official building simulation program of the United States Department of Energy, is widely used for energy simulation, load calculation, building performance analysis, energy efficiency, thermal balance, and mass balance. This program incorporates the best features of BLAST and DOE-2, along with new functionalities. It is capable of modeling heating, cooling, lighting, ventilation, and other energy flows, as well as the demand for domestic hot water in buildings. EnergyPlus is freely available and supported by the U.S. Department of Energy. Its extensive use within the scientific and technical communities, along with its robust capabilities and resources, are the primary reasons why EnergyPlus was selected as the simulation tool for estimating the thermal energy demand in this study's buildings. Additionally, EnergyPlus has been utilized in numerous other studies to estimate building energy consumption (Fumo et al., 2010; Mendes et al., 2024).

In this initial phase of the methodology, a 3D model of the buildings is created using OpenStudio (Heidarinejad et al., 2017), a suite of software tools that supports whole-building energy modeling with EnergyPlus to determine their HVAC demand. Additionally, the surrounding buildings were included in the models to accurately simulate the shadows they cast on each other (Fig. 3). It’s important to note that each building was studied separately, as they are independent from one another, and this approach also proved to be more computationally efficient. Regarding the properties of the building enclosures, the standards established in the Spanish Building Code NBE-CT-79 (Norma Básica de la Edificación, 1979), which was in effect at the time of construction of the analyzed buildings, were considered. For renovated buildings, the information provided in the engineering project was used. The different thermal zones of the buildings were identified through site visits, during which the temperature and humidity setpoints for each controllable space were recorded. As for the schedules and occupancy of offices and classrooms, these were based on data from a typical week of use for each building. Finally, to determine the internal loads of the various spaces, site visits were conducted, and after discussions with the responsible personnel, the internal thermal loads for each space were calculated.

3.2. Storage solution

The second phase of the methodology focuses on a techno-economic evaluation of various storage solutions for the preliminary design of a 4th–5th generation hybrid DHC network. This phase focuses on determining the thermal storage system (TES) necessary to meet the HVAC demand of the buildings using excess photovoltaic generation, applying statistical methodologies for a complete charge and discharge cycle of the storage deployed. It is important to note that while a discharge cycle can extend beyond a single day, in most cases, it typically aligns with a 24-hour cycle.

Specifically, to determine the optimal size and type of thermal storage system (TES) capable of handling a broad range of scenarios, rather than focusing on extreme or rare cases where excess energy from a single

charge/discharge cycle might allow for a higher discharge, a statistical approach has been chosen. All of this with the primary objective is to minimize the injection of excess photovoltaic generation into the electrical grid. The following assumptions were made:

- The storage capacity is considered unlimited.
- The plant's operation is divided into 'storage' and 'discharge' periods. Storage periods occur when there is excess electricity production from the photovoltaic system, while discharge periods occur when there is no such excess.
- Each storage period is followed by a discharge period.
- Energy stored during a 'storage' period can only be used in the next 'discharge' period.
- For each charge/discharge period, only the minimum value between the stored and discharged energy is considered.

This phase of the methodology involves determining, for a given period of the year—heating period (winter) and cooling period (summer)—the necessary storage for each complete charge and discharge cycle of the storage system. To do this, the method takes the hourly HVAC demand, obtained with EnergyPlus in the first phase of the methodology, and subtracts the potential thermal energy that could be generated with a heat pump or chiller, with a certain efficiency dependent on environmental conditions, using the excess photovoltaic generation available at that hour. The excess generated thermal energy is stored to meet the HVAC demand for the required period until net excess photovoltaic generation becomes available again. This period generally corresponds to a 24-hour cycle. However, if a day occurs without excess photovoltaic generation, this period will be extended, and consequently, the amount of thermal energy to be stored will increase to cover the thermal demand. After determining the set of charge and discharge cycles, a frequency diagram is generated based on the cycle's energy accumulated over the annual period. Finally, the most optimal storage solution is selected using the Pareto rule, based on the cumulative frequency of the cycles and the required storage energy. It should be noted that the hourly HVAC thermal demand can be met either through a thermal storage system, by using batteries that store electrical energy to generate the thermal demand with heat pumps or chillers at the time it is needed, or by hybrid solutions that combine both technologies.

3.3. Optimal operating energy cost evaluation

The third phase of the methodology focuses on determining the operating costs, based on the hourly cost of electricity that must be drawn from the grid, for a specific period of the year and a particular storage system configuration. This configuration is designed to meet HVAC demand during hours when there is no surplus photovoltaic generation. To ensure optimal performance, an optimization methodology for the hourly operation of the HVAC plant connected to the DHC network has been implemented. This phase of the methodology will be crucial in evaluating and comparing the effectiveness of the proposed storage solutions in terms of their operating costs.

Specifically, we utilized Pyomo (Hart et al., 2011), an open-source Python-based software package that offers a wide range of optimization capabilities for formulating, solving, and analyzing models. Pyomo is particularly useful for modeling structured optimization applications. It allows for the definition of general symbolic problems, the creation of specific problem instances, and the solving of these instances using both commercial and open-source solvers.

For optimizing the DHC system's operation, we modeled the heating and cooling production equipment at the central HVAC plant, which supplies the DHC network. This plant was represented as a heat pump or chiller responsible for primary production and a pump group that distributes the output through the DHC network connecting various buildings. To accomplish this, we employed Copper (Pacific Northwest National Laboratory, 2020), an open-source Python library package. Copper generates performance curves for building energy simulations, specifically designed for heating, ventilation, and air conditioning equipment. The software uses a genetic algorithm to adjust existing or aggregated performance curves to match specific design characteristics, including energy performance metrics at full and partial loads. Using Copper, we generated the performance curves for the air-to-water chiller, equipped with a variable-speed screw compressor and air-cooled condenser, based on the EnergyPlus model (entering condenser temperature). These curves follow a

quadratic function, resulting in a nonlinear optimization problem. To solve a real-world nonlinear programming (NLP) problem with many variables, as in the present work, the IPOPT algorithm was used. IPOPT (Kawajir et al., 2010) is an open-source solver that efficiently handles large-scale, full-space, interior-point (or barrier) nonlinear programming problems. Subsequently, Pyomo was used to describe the optimization model for the HVAC plant and DHC, based on a cost function aimed at minimizing the monetary cost of meeting the cooling thermal demand during the specified period. The model utilizes the average hourly electricity market prices in Spain for the year 2023 as a basis.

Every optimization system begins with a set of decision variables $\tilde{x}$ (eq. 1). In our case, there are seven, which are outlined below.

$$\tilde{x} = \langle x_1, x_2, x_3, x_4, x_5, x_6, x_7 \rangle \quad \text{(eq. 1)}$$

Where:

- $x_1(t)$: Electrical energy stored in the battery system over the last evaluation period (t), measured in kWh_e.
- $x_2(t)$: Thermal energy stored in the TES over the last evaluation period (t), measured in kWh_t.
- $x_3(t)$: Electrical energy discharged from the battery system to meet the thermal demand during a period (t), measured in kWh_e.
- $x_4(t)$: Thermal energy discharged from the TES during the evaluation period (t), measured in kWht.
- $x_5(t)$: Electrical energy stored in the battery during the evaluation period (t), measured in kWhe.
- $x_6(t)$: Thermal energy stored in the TES during the evaluation period (t), measured in kWht.
- $x_7(t)$: Electrical energy discharged from the battery system to meet the pumping demand during a period (t), measured in kWh_e.

These decision variables are integrated into a defined objective function $f(\tilde{x})$ by equation (eq. 2) between hours 1 and N, which must be minimized. In our case, the function is designed to optimize the system's storage to reduce the energy operating costs of the DHC network.

$$\begin{cases} f(\tilde{x}) = \sum_{t=1}^{N} \left(P_{el}[Thermal\ demand(t) - X4(t)] + P_{el}[X2(t)] + P_{el}[Pumping(t)] - X3(t) - X7(t) \right) \cdot \mathrm{AFP}(t) \\ Minimize\ \mathrm{f}(\tilde{x}) \end{cases} \quad \text{(eq. 2)}$$

Where:

- Thermal demand(t) represents the aggregated thermal demand of the buildings connected to the DHC network during a period (t), measured in kWh_t.
- $P_{el}[x(t)]$ returns the electrical energy associated with a specific thermal demand during a period (t), measured in kWh_e.
- P_{el}[Pumping] returns the electrical energy consumed by the DHC network's pumping system during a time period (t), measured in kWh_e.
- AFP(t): Average final price of the Spanish free electricity market over a period (t), measured in €/kWh_e.

In addition, the objective function (eq.2) incorporates a set of up to 4 bounds and 10 operational rules or constraints, which are detailed below.

1. The first bound (eq. 3) limits the charge/discharge rate of the battery system and the TES during the evaluation period (t).

$$\begin{cases} x_1(t) \leq 1000\ kWh_e \\ x_2(t) \leq 500\ kWh_t \\ x_3(t) \leq 1000\ kWh_e \\ x_4(t) \leq 500\ kWh_t \\ x_7(t) \leq 1000\ kWh_e \end{cases} \quad \text{(eq. 3)}$$

2. The second bound (eq. 4) is responsible for limiting the minimum and maximum capacity of the battery system during an evaluation period (t).

$$0\ kWh_e \leq x_5(t) \leq 4000\ kWh_e \quad \text{(eq. 4)}$$

Where:

- In this case, the maximum electrical storage in batteries has been set at 4 MWh_e.

3. The third bound (eq. 5) is responsible for limiting the minimum and maximum capacity of the TES during an evaluation period (t).

$$0\ kWh_t \leq x_6(t) \leq 750\ kWh_t \quad \text{(eq. 5)}$$

Where:

- In this case, the maximum thermal storage has been set at 0.75 MWh_t.

4. The fourth bound (eq. 6) states that if there are no excesses in photovoltaic generation, no energy can be stored in the battery system and/or in the TES during an evaluation period (t).

$$If\ PV_{Surplus}(t) = 0\ kWh_e \rightarrow \begin{cases} x_1(t) = 0\ kWh_t \\ x_2(t) = 0\ kWh_e \end{cases} \quad \text{(eq. 6)}$$

5. The first rule (eq. 7) states that the Li-FePO4 battery system may never discharge below the energy level accumulated in the previous evaluation period (t-1).

$$x_7(t) + x_3(t) \leq x_5(t-1) \quad \text{(eq. 7)}$$

6. The second rule (eq. 8) states that the thermal energy storage system (TES) cannot be discharged below the thermal energy accumulated in the previous evaluation period (t-1).

$$x_4(t) \leq x_6(t-1) \quad \text{(eq. 8)}$$

7. The third rule (eq. 9) limits the maximum thermal demand of the system by establishing that the HVAC thermal demand of the buildings plus the thermal energy stored in the TES must always be less than or equal to the maximum power of the HVAC equipment.

$$Thermal\ demand(t) + x_2(t) \leq power\ of\ the\ HVAC\ plant$$

- In this case, the maximum power of the HVAC plant has been set at 4 MW_{th}

8. The fourth rule (eq. 10) limits storage (thermal and electric) to the amount of energy associated with the electricity surpluses from photovoltaic generation system.

$$x_1(t) + P_{el}[x_2(t)] \leq PV_{Surplus}(t) \quad \text{(eq. 10)}$$

Where:

- $PV_{Surplus}$: Photovoltaic generation surpluses that must be fed into the distribution grid during the evaluation period (t), measured in kWh_e. These values were obtained from an hourly simulation of the installations conducted with PVSyst (Soualmia & Chenni, 2017).

9. The fifth rule (eq. 11) states that the electrical energy discharged from the battery system to meet the pumping demand must not exceed the pumping system's consumption during the evaluation period (t).

$$x_7(t) \leq P_{el}[Pumping(t)] \quad \text{(eq. 11)}$$

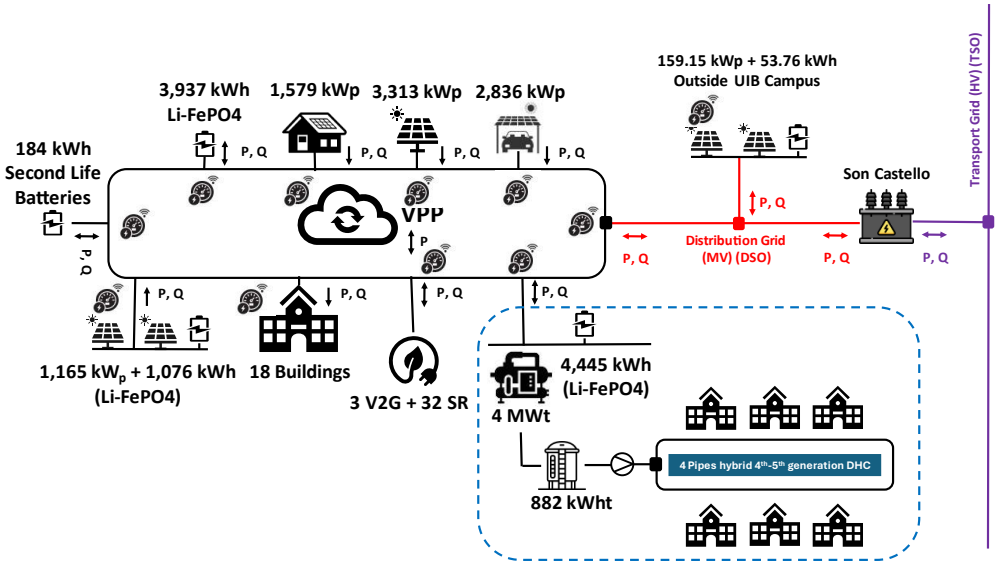

Fig. 4: Conceptual diagram of the DHC network to be implemented on the UIB campus as part of the ongoing renewable energy deployment project.

10. The sixth rule (eq. 12) is responsible for determining the state of charge of the battery system during the evaluation period (t).

$$x_5(t) = x_5(t-1) + x_1(t) \cdot 0.85 - (x_3(t) + x_7(t)) \quad \text{(eq. 12)}$$

Where:

- The factor 0.85 corresponds to the average efficiency of the battery system.

11. The seventh rule (eq. 13) is responsible for determining the state of charge of the TES system during the evaluation period (t).

$$x_6(t) = x_6(t-1) + x_2(t) \cdot 0.85 - \frac{x_4(t)}{0.85} \quad \text{(eq. 13)}$$

Where:

- The factor 0.85 to the average efficiency of the TES system

12. The eighth rule (eq. 14) states that the thermal energy discharged must be less than or equal to the thermal demand during an evaluation period (t).

$$x_4(t) \leq Thermal\ demand(t) \quad \text{(eq. 14)}$$

13. The nineth rule (eq. 15) states that the battery cannot be discharged more than the electrical energy discharged from the battery to meet the electrical demand to cover the thermal demand minus the thermal energy discharged from the TES during an evaluation period (t).

$$x_3(t) \leq P_{el}[Thermal\ demand(t) - x_4(t)] \quad \text{(eq. 15)}$$

14. The tenth rule (eq. 16) states that the electrical energy consumed from the excess photovoltaic generation must always be greater than or equal to 0 kWh_e during an evaluation period (t).

$$(P_{el}[Thermal\ demand(t) - x_4(t)] + P_{el}[x_2(t)] + P_{el}[Pumping(t)] - (x_3(t) + x_7(t)) \geq 0\ kWh_e \quad \text{(eq. 16)}$$

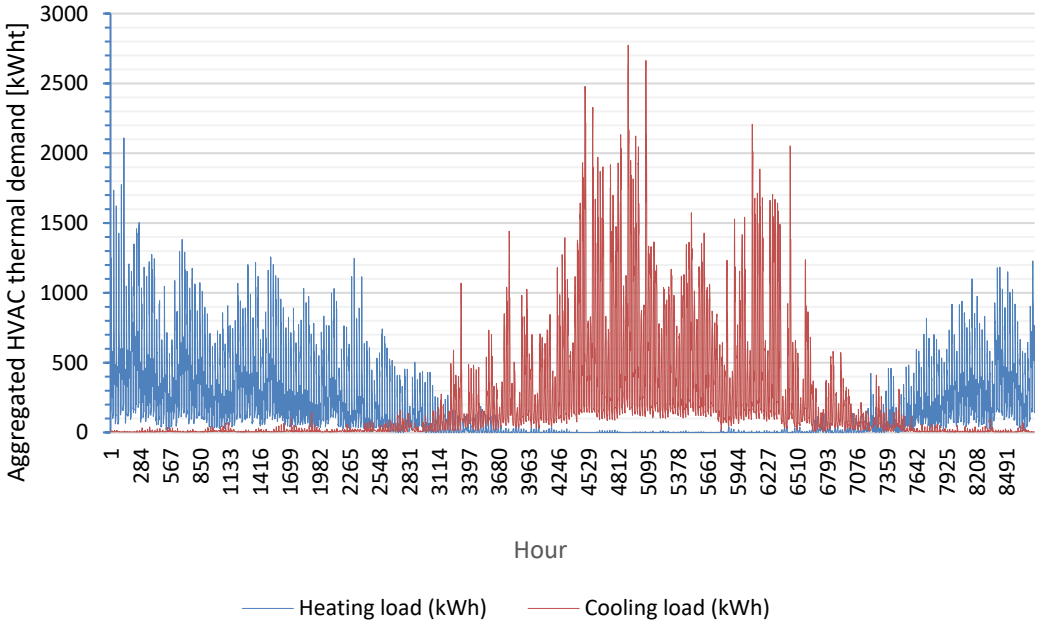

Fig. 5: Hourly total HVAC heating and cooling demand for the 6 buildings to be supplied by the 4th–5th generation hybrid DHC network being implemented.

4. Results and Discussion

In this section, we will present the results obtained by applying the methodology described in the previous section for the sizing of the preliminary design of the storage system for the 4th–5th generation hybrid DHC network, which is to be deployed on the University of the Balearic Islands campus, the case study addressed in this work (Fig. 4). It is important to note that this analysis has focused exclusively on the coverage of the cooling demand. Specifically, we will present the results obtained for the aggregated demand of the campus buildings under study. Subsequently, the procedure for the preliminary sizing of the DHC storage system to be deployed on the campus will be detailed (Fig. 4). Finally, the feasibility of the preliminary storage option chosen will be assessed based on an analysis of the annual operational energy costs, compared to the costs that would be incurred if the system were supplied by the energy service provider currently operating the existing third-generation network on campus. Additionally, the sensitivity of the proposed storage option to variations in the Coefficient of Performance (COP) and Energy Efficiency Ratio (EER) of the chillers to be installed will be examined.

4.1. HVAC Demand

This subsection presents the Energy Plus results of the aggregated heating and cooling demand for the six buildings that will be integrated into the DHC network to be deployed on the UIB campus. Specifically, Fig. 5 shows the hourly aggregated heating and cooling HVAC demand for the buildings under consideration, which include the Mateu Orfila i Rotger Building (Chemistry Wing), Mateu Orfila i Rotger Building (Physics Wing), Scientific-Technical and Research Institutes Building, Guillem Colom Casanovas Building, Animal Facility Building, and Ramon Llull Building. As illustrated in Fig. 5, the cooling demand between May 1 and October 31, 2023, ranges from 0 kWh to 2.8 MWh.

4.2. Storage solution

To determine the optimal storage capacity for the facility, based on the methodology outlined in the previous section, a frequency diagram evaluation for thermal energy storage was conducted. For this analysis, an Energy Efficiency Ratio (EER) of 2.5 was applied to the chillers converting surplus photovoltaic electricity into thermal energy, while the pumping energy consumption was estimated to account for 10% of the total HVAC electrical demand. This evaluation considers the number of complete charge and discharge cycles, which

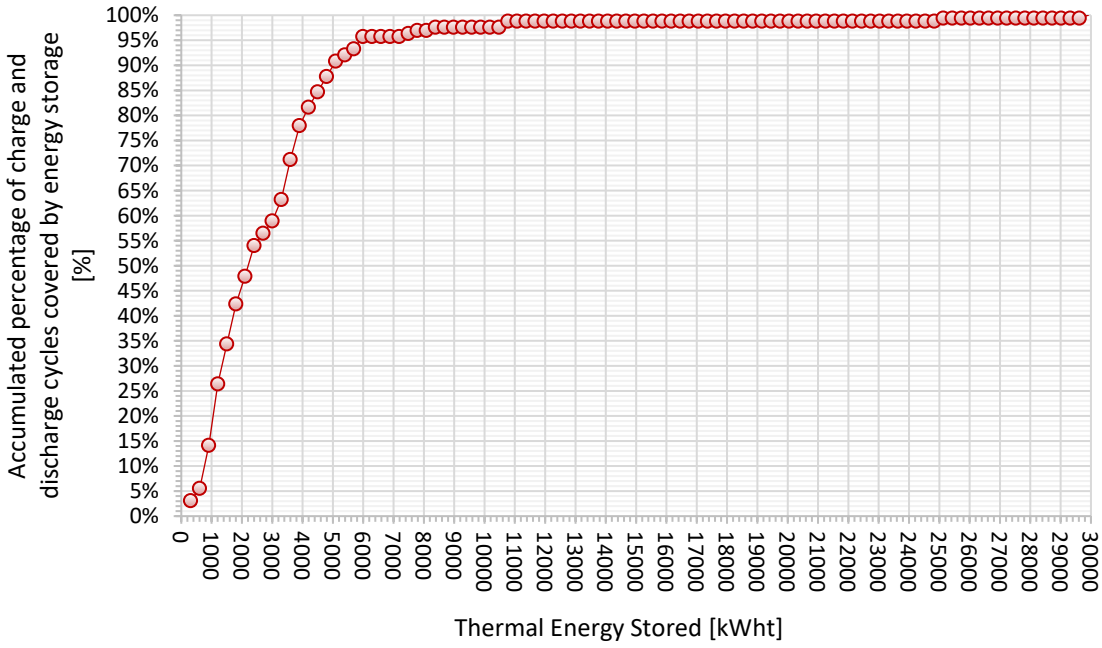

Fig. 6: Cooling thermal energy demand covered by storage during periods of net photovoltaic surpluses.

generally correspond to full days of the year when thermal storage can fulfill the entire daily cooling demand using surplus photovoltaic energy, without relying on the electricity grid. Fig. 6 illustrates this approach for meeting the hourly cooling needs of the 6 buildings that will be integrated into the DHC network.

The results in Fig. 6 indicate that with 4,000 kWh_e of thermal storage, 80% of the charge and discharge cycles for cooling the 6 buildings in 2023 would be covered. After conducting several simulations, it was determined that a hybrid storage solution, combining electrical and thermal storage, would be the most effective approach. This involves installing 4,000 kWh_e of Li-FePO4 batteries, which corresponds to a system with a storage capacity of 4,445 kWh_e, assuming a 90% depth of discharge, along with 750 kWh_t of thermal storage to serve as a buffer for the system. It's important to note that the thermal storage system was considered with an 85% depth of discharge, leading to an actual thermal storage capacity of 882 kWh_t.

This combination of 750 kWh_t of effective thermal storage and 4,000 kWh_e of electrical storage, which, with an EER of 2.5, allows for the generation of up to 10,000 kWh_t of thermal energy, can cover 98.8% of the charge and discharge cycles for cooling. Additionally, the proposed thermal storage solution on its own can cover 9.64% of the charge and discharge cycles without requiring the battery system's intervention.

Tab. 1: Sensitivity analysis of the operational energy costs for the proposed storage solution based on the chiller's EER.

Description	**Chiller with an average EER of 3.07**	**Chiller with an average EER of 3.72**	**Chiller with an everage EER of 5.17**
Electricity costs for the charge and discharge cycles not covered by the proposed storage solution:	2,725.66 €/year	2,113.04 €/year	1,454.63 €/year
Percentage reduction in electricity costs related to the storage solution, based on a reference cost of €2,725.66 per year:	0 %	22,48%	46,63%

4.3. Optimal operating energy cost evaluation

To evaluate the effectiveness of the preliminarily selected energy storage solution for the DHC network, we analyzed the energy costs associated with the charge and discharge cycles that the deployed storage system would not be able to cover. The analysis revealed that cooling costs would be as low as €2,725.66 per year,

based on a chiller system with an EER of 3.07, which is a conservative estimate for this type of equipment. This cost is only around a 11% of the cost of purchasing the required electric power if there were no storage in the new DHC network and a 5% of the cost of purchasing the same thermal energy from the existing 3rd generation DHC network with an external contractor. In those cases, the forecasted costs would have been 24381,11€ and 54490,80€ respectively.

Finally, to assess the sensitivity of the operational energy costs for the selected storage solution in relation to the Energy Efficiency Ratio (EER) of the chillers to be installed, an analysis was conducted considering different EER values for the chiller while operating the proposed storage system optimally. The results are presented in Tab. 1. The results in Tab.1 demonstrate that even a slight improvement in the EER can significantly reduce electricity costs associated with cooling. However, the reduction in energy costs does not follow a linear pattern with the increase in the chiller's EER. For example, a 68.4% increase in the Chiller average EER results in only a 46.63% reduction in energy costs using the proposed storage solution.

5. Conclusions and Future Work

The UIB is actively working to position itself as a leader in sustainability and environmental management through the deployment of a photovoltaic generation facility equipped with an electric storage system. Initial results suggest that introducing demand flexibility by deploying a 4th-5th generation hybrid DHC network, powered by a highly efficient HVAC plant equipped with a thermal storage system of no less than 882 kWh_t and 4,445 kWh_e of batteries, will effectively utilize excess photovoltaic generation to meet cooling demand. This strategy would greatly reduce the amount of surplus photovoltaic energy that needs to be fed back into the distribution grid, enabling the UIB to significantly minimize its dependence on grid electricity. Additionally, the results demonstrate a substantial reduction in energy costs associated with cooling, achieving a 486.43% decrease in the most conservative EER scenario for the chillers in the central HVAC plant under the proposed storage solution.

It is important to note that the work on defining the storage solution and the topology of the 4th-5th generation hybrid DHC network to be deployed represents an initial outline of the efforts being undertaken at the UIB as part of the institutional projects PIREP and PITEIB – 1/2023. Ultimately, these projects aim to explore net-zero energy scenarios and provide insights that could serve as guiding examples for other university campuses in the Mediterranean region, facilitating significant decarbonization of their facilities through the adoption of flexibility mechanisms such as thermal and electric storage systems.

6. Acknowledgments

This work has been carried out within the framework of a set of institutional projects at the University of the Balearic Islands, obtained through competitive funding calls. Specifically, this work is partially supported by the Plan to Promote the Recovery of Public Buildings (PIREP) through the PIREP Mateu Orfila and PIREP Ramon Llull projects, which aim to undertake sustainable rehabilitation actions for publicly owned and used buildings. These projects have been submitted by the regional government of the Balearic Islands (Directorate General of Housing and Architecture) to the Spanish Ministry of Transport and Sustainable Mobility and are financed under Spain's Recovery and Resilience Plan through the European Union's NextGenerationEU funds. At the same time, this work has been partially supported by the Investment Plan for Energy Transition in the Balearic Islands (PITEIB) through the PITEIB Innovadors - 1/2023 project. This project will enable the deployment of an innovative pilot project for a Virtual Power Plant on the UIB campus, allowing for the efficient control and management of energy resources. This project has been financed through a call by the Directorate General of Circular Economy, Energy Transition, and Climate Change of the regional government of the Balearic Islands, with funding from the Institute for the Diversification and Saving of Energy (IDAE) under Spain's Recovery and Resilience Plan, through the European Union's NextGenerationEU funds.

7. References

Norma Básica de la Edificación. (1979). NBE-CT-79. In *Condiciones Termicas de los Edificios*.

DOE. (2017). *EnergyPlus | EnergyPlus*. U.S. Department of Energy’s.

Elgqvist, E., & VanGeet, O. (2017). Campus Energy Approach, REopt Overview, and Solar for Universities. *NREL/PR-7A40-70252 Presented at the 2017 I2SL Annual Conference*. https://www.nrel.gov/docs/fy18osti/70252.pdf

Fumo, N., Mago, P., & Luck, R. (2010). Methodology to estimate building energy consumption using EnergyPlus Benchmark Models. *Energy and Buildings*, *42*(12), 2331–2337. https://doi.org/10.1016/j.enbuild.2010.07.027

Hart, W. E., Watson, J. P., & Woodruff, D. L. (2011). Pyomo: Modeling and solving mathematical programs in Python. *Mathematical Programming Computation*, *3*(3). https://doi.org/10.1007/s12532-011-0026-8

Heidarinejad, M., Mattise, N., Sharma, K., & Srebric, J. (2017). Creating Geometry with Basic Shape Templates in OpenStudio. *Procedia Engineering*, *205*, 1990–1995. https://doi.org/10.1016/j.proeng.2017.10.068

Kalkan, N., Bercin, K., Cangul, O., Morales, M. G., Saleem, M. M. K. M., Marji, I., Metaxa, A., & Tsigkogianni, E. (2011). A renewable energy solution for Highfield Campus of University of Southampton. *Renewable and Sustainable Energy Reviews*, *15*(6), 2940–2959. https://doi.org/10.1016/j.rser.2011.02.040

Kawajir, Y., Laird, C. D., & Waechter, A. (2010). Introduction to IPOPT: A tutorial for downloading, installing, and using IPOPT . *Most*. https://doi.org/http://web.mit.edu/ipopt_v3.8/doc/documentation.pdf

Kiehle, J., Kopsakangas-Savolainen, M., Hilli, M., & Pongrácz, E. (2023). Carbon footprint at institutions of higher education: The case of the University of Oulu. *Journal of Environmental Management*, *329*, 117056. https://doi.org/10.1016/j.jenvman.2022.117056

Mendes, V. F., Cruz, A. S., Gomes, A. P., & Mendes, J. C. (2024). A systematic review of methods for evaluating the thermal performance of buildings through energy simulations. *Renewable and Sustainable Energy Reviews*, *189*, 113875. https://doi.org/10.1016/j.rser.2023.113875

Pacific Northwest National Laboratory. (2020). *Copper*. Pacific Northwest National Laboratory. https://github.com/pnnl/copper?tab=readme-ov-file

Péan, T. Q., Salom, J., & Costa-Castelló, R. (2019). Review of control strategies for improving the energy flexibility provided by heat pump systems in buildings. *Journal of Process Control*, *74*, 35–49. https://doi.org/10.1016/j.jprocont.2018.03.006

Soualmia, A., & Chenni, R. (2017). Modeling and simulation of 15MW grid-connected photovoltaic system using PVsyst software. *Proceedings of 2016 International Renewable and Sustainable Energy Conference, IRSEC 2016*. https://doi.org/10.1109/IRSEC.2016.7984069

Tsiropoulos, I., Nijs, W., Tarvydas, D., & Ruiz Castello, P. (2020). Towards net-zero emissions in the EU energy system by 2050 – Insights from scenarios in line with the 2030 and 2050 ambitions of the European Green Deal. *Publications Office of the European Union*. https://doi.org/10.2760/081488

Tu, Q., Zhu, C., & McAvoy, D. C. (2015). Converting campus waste into renewable energy – A case study for the University of Cincinnati. *Waste Management*, *39*, 258–265. https://doi.org/10.1016/j.wasman.2015.01.016

University of Minnesota. (2023). *Twin Cities Climate Action Plan 2023*.

Zanetti, E., Aprile, M., Kum, D., Scoccia, R., & Motta, M. (2020). Energy saving potentials of a photovoltaic assisted heat pump for hybrid building heating system via optimal control. *Journal of Building Engineering*, *27*, 100854. https://doi.org/10.1016/j.jobe.2019.100854

Scenarios for Integration of Power to Heat Technology in Czech District Heating Systems

Nikola Pokorny[1], Vojtech Zavrel[2] and Jan Safranek[3]

[1] University Centre for Energy Efficient Buildings, Czech Technical University in Prague, Bustehrad

2 Faculty of Mechanical Engineering, Czech Technical University in Prague, Prague

3 Feramat Energies s.r.o., Prague

Abstract

The paper addresses the sustainability of the operation of existing district heating (DH) systems in the Czech Republic, which historically used primarily fossil fuel sources and currently are under transformation. The system integration of heat with electricity sector through power to heat (P2H) technologies allows for the efficient use of DH thermal capacity to store surplus renewable energy and can also offer additional support services to the electricity transmission system. Simulation study was performed in TRNSYS for three typical typologies of DH systems in the Czech Republic. Key performance indicators (KPIs) such as CO_2 emissions, non-renewable energy or the cost of heat produced by P2H technology were assessed.

Keywords: power to heat, P2H, district heating, high temperature heat pump, solar energy, photovoltaic plant

1. Introduction

To reduce CO_2 emissions in the power sector, EU is promoting renewable energy sources for power generation. Installation of new wind and photovoltaic plants is growing in many countries in the EU . Coupling of power and heat sectors can significantly contribute to both renewable energy integration and decarbonization (Bloess et al., 2018). Potential of P2H technology integration in DH system was evaluated in other studies in the Germany (Böttger et al., 2014) or in the Sweden (Schweiger et al., 2017) with specific results for every state. Technical P2H potential in Germany accounts 6 GW_{el} in 2015 and 20 GW_{el} in 2030. The P2H potential in Sweden was estimated from 0.2 to 8.6 TWh. In 2017, an overview of the status of P2H technology in DH systems in Europe was conducted (David et al., 2017). The analysis revealed that 149 units with capacities exceeding 1 MW were integrated into DH systems across Europe. For a greater number of installations, it is essential to analyse sources of low-potential heat in relation to areas served by DH systems, this approach was implemented in a study conducted for Denmark (Lund and Persson, 2016). Another review explores various configurations for integrating heat pumps into heating and cooling systems (Barco-Burgos et al., 2022). The review concludes that energy conversion approach through P2H technology has the potential to be a cost-effective solution, supporting the decarbonization of the DH sector. Other analyses focus on the economic perspective, for example, one study (Østergaard and Andersen, 2018) compares DH systems supplied by heat pumps using air, seawater, or groundwater as heat sources and examines three low-temperature DH schemes. Another study analyses the techno-economic potential of P2H technology in DH systems (Fambri et al., 2023), highlighting their role in enhancing electricity grid flexibility by absorbing surplus renewable energy and optimizing system efficiency. A case study, based on data from the DH and electricity network of the city of Turin in Italy, was analysed.

For now, potential of P2H technology in Czech Republic has not been deeply evaluated. In 2022, the heat supply in the Czech Republic was composed of 54% from coal-fired sources, 26% from gas, and 9.2% from biomass. So far, the only industrial heat pumps in the Czech Republic used on an industrial scale is in Decin (2 x 3.28 MW) for the DH system. Several projects for the use of electric boilers or low-potential heat in heat supply systems using heat pumps are expected to be implemented by 2030. Simultaneously, the capacities of fluctuating renewable electric energy sources (wind and solar power) is estimated to increase from 3.8 GW in 2024 to 11.5 GW in 2030. This paper deals with technology model focused on advanced methods of dynamic

© 2024. The Authors. Published by International Solar Energy Society
Selection and/or peer review under responsibility of Scientific Committee
10.18086/eurosun.2024.05.04 Available at http://proceedings.ises.org

simulation of DH systems with use of TRNSYS and PYTHON. Model is designed to be scalable to generate different KPIs for different P2H solution integration options for different scale of DH system while requiring the least number of inputs from heat distributor.

2. Model of different typologies of DH systems

Based on analysis of the available data of the DH systems in the Czech Republic in strategic documents, the typologies were divided to 6 categories depending on the declared total heat output of heat sources belong to the given DH system. The chosen scale represents all types of systems from the smallest, local or municipal heat networks, through small and medium-sized urban heat networks, to the largest urban or regional heat networks. The largest urban or regional DH systems have specific boundary conditions (temperatures higher than 150 °C) and usually the planning of new heat sources is more specific to every case. Due to this fact the three largest categories were not studied due to small potential of replication in national level. In any case, there is a statistically very significant number of relatively small DH systems in the Czech Republic. The focus of simulation study was on the typically most common three categories of DH systems, which cover approximately more than 70 % of DH systems in the Czech Republic and contributes approximately 39 % of the total heat supply. 3 typologies were selected for the general parametric study which represent:

- medium urban network with a combination of conventional and low-emission DH sources with a predominance of residential consumption (maximum **heat output 20 MW**, annual heat supply 180 TJ, length of DH system 15 km, winter temperature difference 95/65 °C, annual heat losses 10 %, fuel composition - 30% of coal, 30% of natural gas, 40% of biomass);
- small urban network with a predominance of low-emission DH sources with a predominance of residential consumption (maximum **heat output 10 MW**, annual heat supply 135 TJ, length of DH system 10 km, winter temperature difference 85/65 °C, annual heat losses 8 %, fuel composition – 70% of natural gas, 30% of biomass);
- small municipal network with a predominance of low-emission heat sources and residential consumption (**maximum heat output 5 MW**, annual heat supply 65 TJ, length of DH system 4 km, winter temperature difference 70/50 °C, annual heat losses 8 %, 40% of natural gas, 60% of biomass).

A detailed numerical model in TRNSYS was developed to evaluate technical KPIs such as CO_2 emissions, non-renewable energy or the cost of heat produced. Inputs for the model are following: location and climate data, the ratio of consumption profiles by category (industry, commercial, residential), the desired peak and off-peak temperatures and heat output in the DH system, the annual heat supply, length of the DH system, etc.). The model is designed to support various P2H scenarios integrating an industrial electric boiler, industrial air-to-water (bivalence limit temperature of 5 °C was considered) and water-to-water heat pump into a system with an existing fuel source. However, two scenarios of water-to-water heat pump were compared with heat extracted from river water (average annual water temperature 10 °C) and heat extracted from waste heat (average annual temperature 20 °C). In this study only heat pumps as a P2H technology were observed.

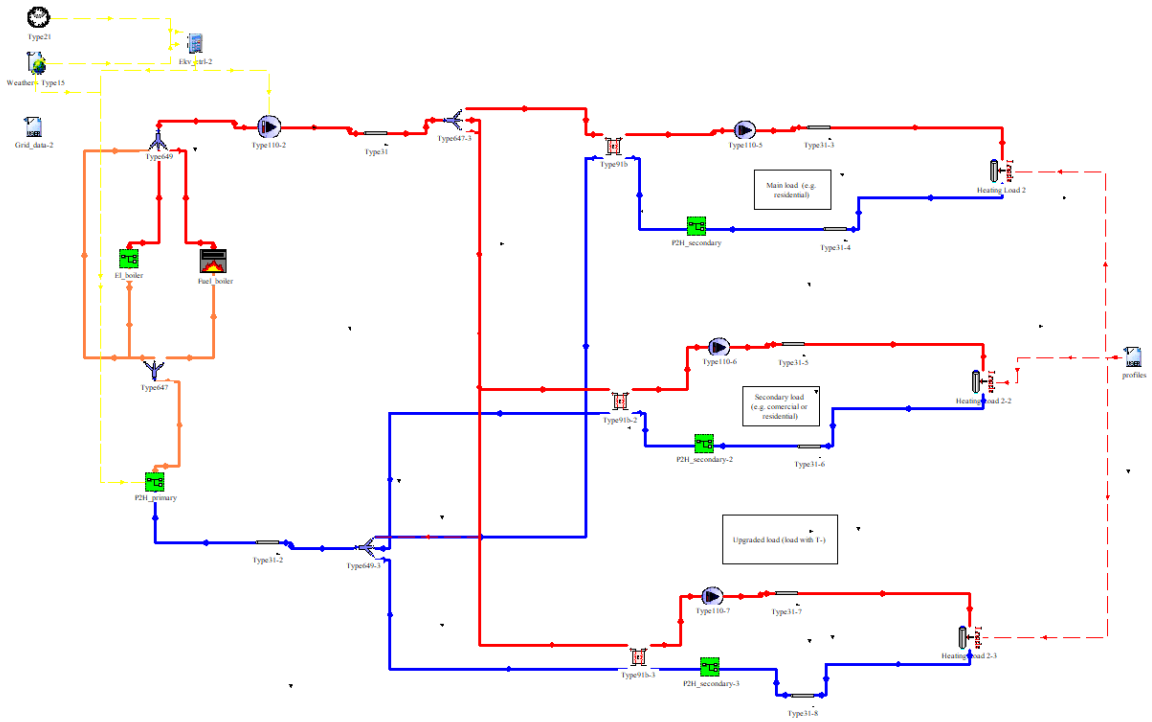

Fig. 1: Numerical model in TRNSYS simulation tool

P2H technologies are modelled based on performance maps for a wide range of boundary conditions. Heat pump considered for simulation used refrigerant R1234ze. The P2H technology is considered to be connected in series before fossil-based source of heat. The simulated operation of heat pumps within the DH systems is significantly influenced by the temperature level in the DH system. If the heat pump does not have sufficient capacity to deliver the required temperature, higher than the simulated return water temperature level, the device is switched off. In the P2H technology configuration, a storage tank with a specific volume of 0.15 $m^3.kW^{-1}$ is considered. Furthermore, the settings vary according to the type of heat pump for air-to-water and water-to-water. The model also provides information on electricity consumption divided into auxiliary (hydraulic pump consumption) and P2H technology consumption. Furthermore, electricity generation from renewable sources is also included in the simulation. In this study, a photovoltaic (PV) plant with a nominal capacity of 1 MW_p and 2 MW_p is considered. Annual specific electric production is 152 $kWh.m^{-2}.a^{-1}$. The progress of heat supply, water-to-air heat pump output and temperatures in DH system are in Fig. 2. The progress of the electricity consumption tied to the operation of the DH systems and the expected production from PV plant is shown in Fig. 3 for a typology with 20 MW heat output class. This figure also shows the considered carbon intensity profile of the grid (for Czech Republic), which is used to calculate the equivalent CO_2 emissions linked to the operation of P2H technology.

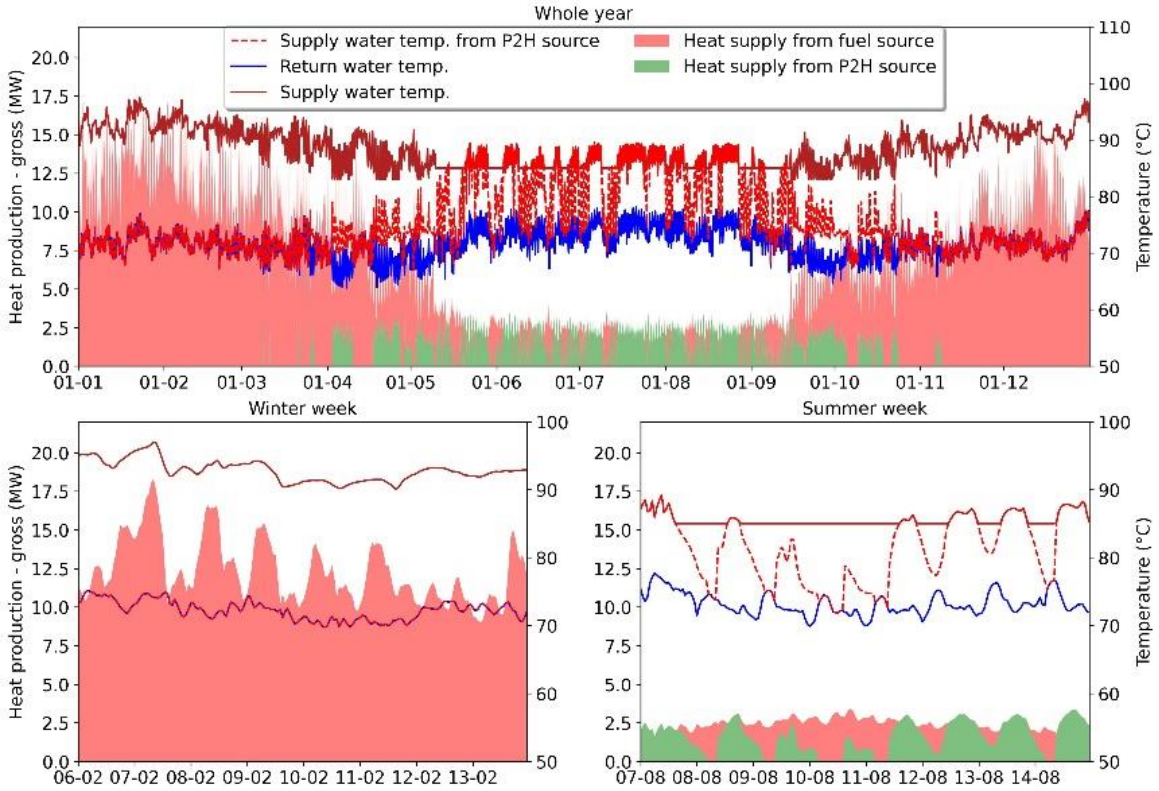

Fig. 2: Example of one typology (20 MW heat demand) and integration of air-to-water heat pump

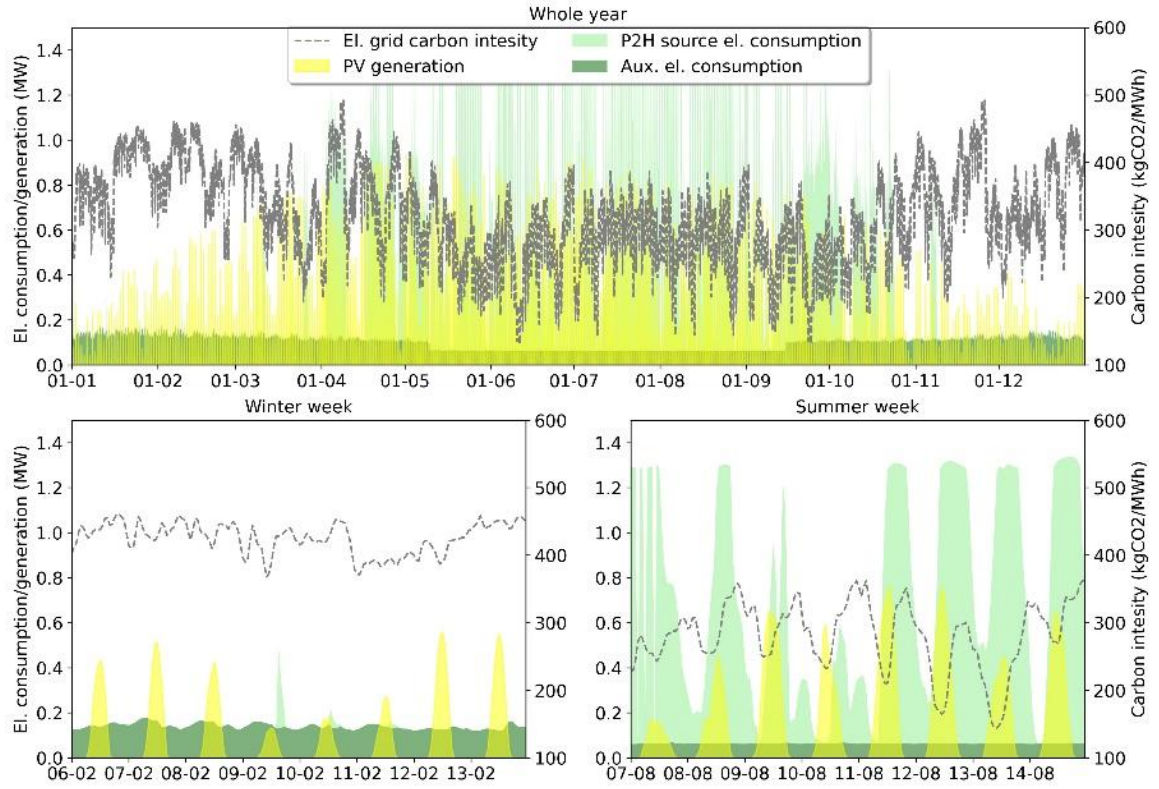

Fig. 3: Example of one typology (20 MW heat demand) and integration of air-to-water heat pump

3. Simulation results

Impact assessment of P2H technology integration into three typological DH systems in Czech Republic was done for nine different scenarios of P2H integration and PV production, see in Tab. 1. Energy delivered by

different sources is shown in Fig. 4. to 6. For two largest DH systems 2.4 MW installed thermal capacity of P2H technology was considered (for the smallest sized DH system 1.2 MW). In general, for all types of integration of the selected P2H technologies it can be stated that they are very sensitive to the temperature conditions in the DH systems. If there is a better-quality heat source on the evaporator side of the water-to-water HP (e.g. waste heat from waste-water treatment plant, data centre), the plant achieves sufficient capacity to partially cover the demand even for DH system at higher temperature levels and its operation does not need to be significantly limited. For low-temperature DH systems (from 60 to 85 °C), all types of heat pumps usually have sufficient capacity and achieve the maximum possible operating time. In Fig. 4. to 6. shows the change in the source composition on the total heat supply (including the inclusion of the combustion efficiency of the individual fuels).

Tab. 1: Scenarios of P2H integration into three typologies of DH systems

REF	Reference case
1	HP air-to-water
2	HP air-to-water with PV plant 1 MW_p
3	HP air-to-water with PV plant 2 MW_p
4	HP water-to-water (river)
5	HP water-to-water (river) with PV plant 1 MW_p
6	HP water-to-water (river) with PV plant 2 MW_p
7	HP water-to-water (waste heat)
8	HP water-to-water (waste heat) with PV plant 1 MW_p
9	HP water-to-water (waste heat) with PV plant 2 MW_p

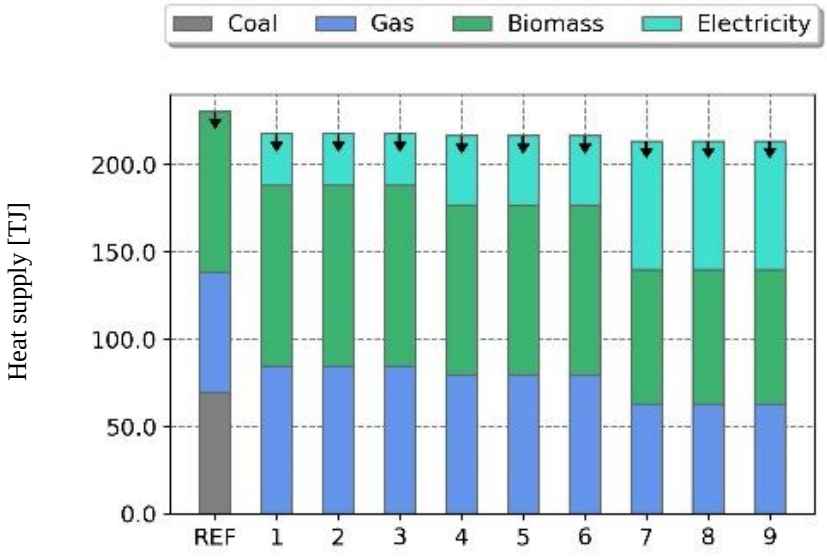

Fig. 4: Energy delivered by different sources – typology with heat output class 20 MW

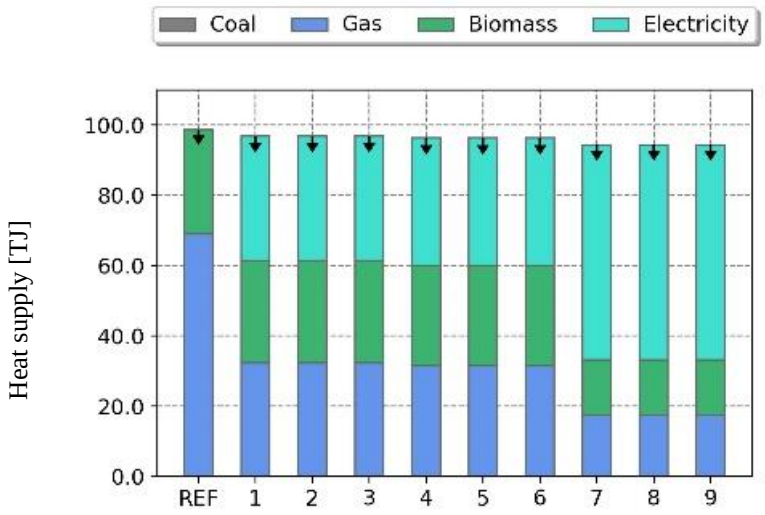

Fig. 5: Energy delivered by different sources – typology with heat output class 10 MW

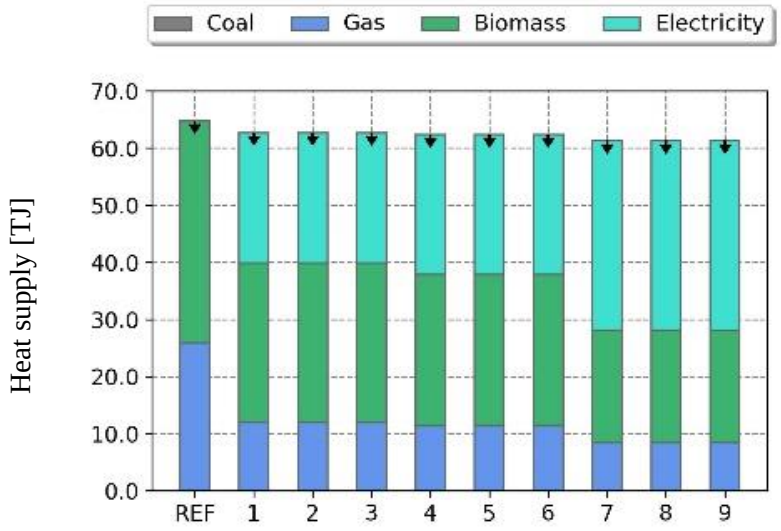

Fig. 6: Energy delivered by different sources - typology with heat output class 5 MW

Projected increase in electricity consumption, as well as consumption covered by local PV and possible export to the grid is shown in Fig. 7. to 9. PV generation is considered primarily for self-consumption within the DH system and PV plant. Self-consumption or possible export of PV generation is included in the evaluation of economic indicators (specific heat prices of P2H) and sustainability indicators (primary non-renewable energy, carbon intensity of DH system).

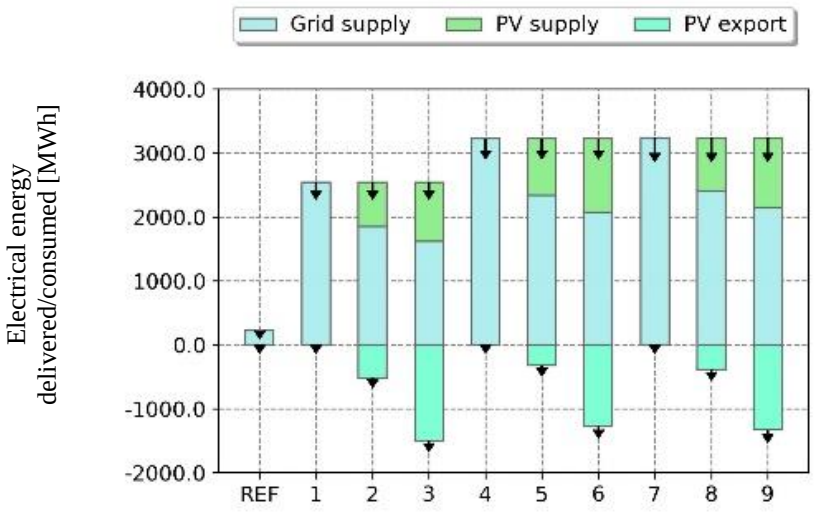

Fig. 7: Results of electricity consumption of P2H technology with fraction which is used and exported – typology with heat output class 5 MW

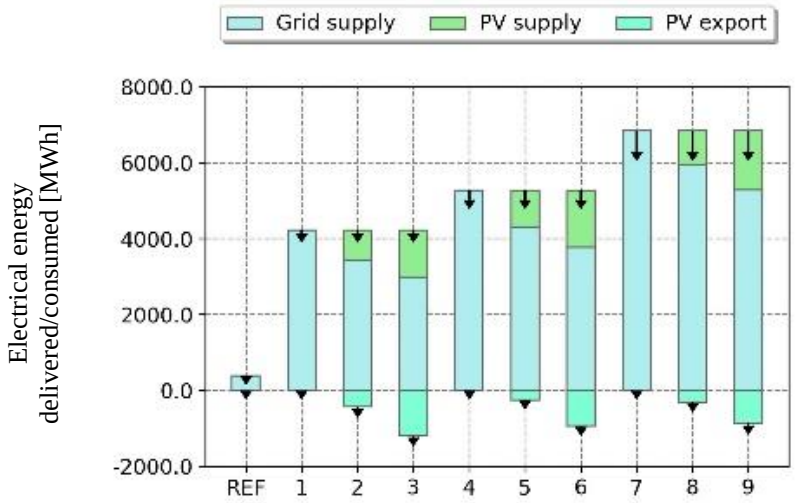

Fig. 8: Results of electricity consumption of P2H technology with fraction which is used and exported – typology with heat output class 10 MW

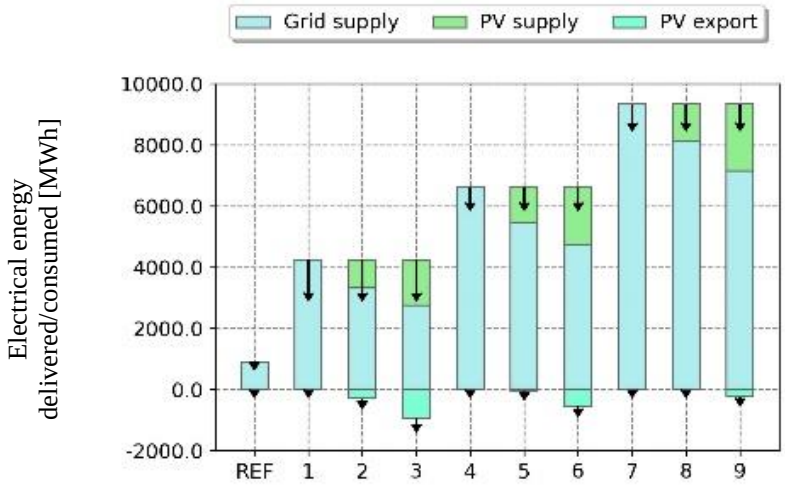

Fig. 9: Results of electricity consumption of P2H technology with fraction which is used and exported – typology with heat output class 20 MW

Detailed results are shown only for typology with 20 MW and 5 MW heat output class. Indicators related to annual coefficient od performance (COP), operating time, and fraction of electricity from PV used for P2H technology are shown in Tab. 2 and 3. All types of P2H technologies can be effectively combined with PV. Most cases show solar fraction from 13 to 35% of with a production utilisation of 61 to 100%. The results of combining with PV are mainly indicative in this study to evaluate the potential impact on the economics and sustainability of the operation. The integration of air-to-water heat pump is characterized by a relatively high COP in the range of 2.5 and 2.7. For this type of heat pump, it is necessary to assume a bivalence limit (in this case the heat pump is not operated at an outdoor air temperature below 5 °C), which in principle does not allow annual operation and the operating time of this type of heat pump will depend on the climatic conditions. Another factor limiting the efficient operation of these devices is mainly the temperature of the return water. For conservative operation without considering the interaction with the electricity grid (dynamic tariff, ancillary services), an operating time of this type of heat pump in the range of 4000 to 6000 hours can be considered, depending on the typology. Air-to-water heat pump is suitable as an efficient secondary source to cover off-season demand. The integration of water-to-water heat pump with river water as a source results in a lower annual COP in the range of 1.9 and 2.3. Due to the more stable temperature on the evaporator side with an average temperature of 10 °C, this type of heat pump allows year-round operation. Its operating time is mainly limited by the return water temperature. High return water temperatures do not allow operation with sufficient efficiency and can limit the operating hours to 6700 hours, almost to the level of operating hours of air-to-water pump. Due to the year-round operation, a higher share of the total heat production can be assumed. However, this share is limited by lower efficiency at certain times of the year and it may be more advantageous to use a bivalent peak source (e.g. natural gas).

Tab. 2: Summary of energy performance results - typology with heat output class 20 MW

	COP [-]	Operation period [h]	Coverage of heat production by P2H technology [%]	Solar fraction [%]	Use of PV production [%]
Ref	0	4056	13,7	0	0
1	2,5	4056	13,7	0	0
2	2,5	4056	13,7	22	76
3	2,5	6741	18,4	35	61
4	1,9	6741	18,4	0	0
5	1,9	6741	18,4	17	95
6	1,9	8751	34,5	28	77
7	2,4	8751	34,5	0	0
8	2,4	8751	34,5	13	100
9	2,4	8751	34,5	23	90

Tab. 3: Summary of energy performance results - typology with heat output class 5 MW

	COP [-]	Operation period [h]	Coverage of heat production by P2H technology [%]	Solar fraction [%]	Use of PV production [%]
Ref	0	0	0	0	0
1	2,7	6202	36,3	0	0
2	2,7	6202	36,3	27	57
3	2,7	6202	36,3	37	38
4	2,3	8697	39,3	0	0
5	2,3	8697	39,3	27	73
6	2,3	8697	39,3	36	47
7	3,1	8754	54,1	0	0
8	3,1	8754	54,1	25	67
9	3,1	8754	54,1	34	45

The integration of water-to-water heat pump with waste heat recovery achieves relatively high COP in the range of 2.4 and 3.1. Due to the constant and relatively high temperature 20 °C on the evaporator side, this

type of pump allows year-round operation with high efficiency. The operating hours stably reach values of 8751 to 8756 hours without limitation related to the temperature level of the return water. The high operating temperatures of the SCZT in this case are mainly reflected in a reduction of the COP. If suitable temperature conditions are provided, a heat supply with a high COP heating factor can be expected to enable the heat pump to effectively take a high share of heat production. For smaller municipal installations this configuration can be considered for installation as a single heat source without an additional peak source.

4. Conclusion

Taking into account the current carbon intensity of the electricity grid, P2H technology can clearly be considered as a low-emission solution, see in Tab. 4 and 5. The inclusion of the selected P2H technologies in the studied DH systems leads in most cases to a reduction of the carbon intensity of the delivered heat. As expected, the largest reductions can be achieved in the medium urban grid typology (20 MW) where the coal source has been shut down under this scenario. However, even for networks with a low-carbon source base, represented here by a small municipal network (5 MW), additional CO_2 reductions can be achieved by incorporating P2H technologies, especially if a combination with PV is considered. For recalculation of non-renewable energy, the available conversion efficiencies by energy carrier and the factors given by Czech legislation (Decree 264/2020 Coll.) were used. Emissions of CO_2 were evaluated based on factors related to IPCC emission factor database. For electricity, a dynamic annual intensity profile based on the efficiency of the electricity network in 2023 was used, based on the methodology for calculating the average carbon intensity in a given hour according to the resource utilisation available on the ENTSOE portal(ENTSOE, 2021). The prices of individual commodities and capital costs were determined according to the current market situation in 2023 and also include regulated components. The non-renewable energy consumption, carbon intensity (from 0.08 to 0.14 tCO_2/MWh), and cost of heat produced from P2H technology (from 36 to 81 EUR/MWh) were analyzed for two typologies.

This simulation study was focused on a simple integration of high temperature heat pumps into DH system. However, the developed model is suitable for analyses of the impact of temperature level changes in DH system, analysis of the profitability of operation according to spot prices, or analysis of operation for electricity network support services. Three analyzed typologies are small to medium scale DH systems where technical feasibility and stronger linkage between the DH distributor and the municipality can be assumed. The result of a large number of simulations will be used for design of simplified tool for communication of decarbonization plan between heat producer and municipality in Czech Republic.

Tab. 4: Summary of KPIs - typology with heat output class 20 MW

	Nonrenewable primary energy [TJ]	Carbon intensity of delivered heat [$tCO_{2,ekv}$/MWh]	Specific cost of heat production from P2H [EUR/MWh]
Ref	155,6	0,182	68
1	131,0	0,112	74
2	119,6	0,108	64
3	108,2	0,106	56
4	147,6	0,120	81
5	136,3	0,115	73
6	124,9	0,112	66
7	155,2	0,120	61
8	143,8	0,114	57
9	132,5	0,110	53

Tab. 5: Summary of KPIs - typology with heat output class 5 MW

	Non-renewable primary energy [TJ]	Carbon intensity of delivered heat [$tCO_{2,ekv}/MWh_t$]	Specific cost of heat production from P2H [EUR/MWh]
Ref	30,6	0,097	67
1	37,9	0,089	62
2	26,5	0,079	50
3	15,1	0,075	41
4	43,6	0,102	68
5	32,2	0,089	57
6	20,8	0,084	48
7	40,2	0,094	51
8	28,9	0,081	42
9	17,5	0,077	36

5. Acknowledgments

The analysis has been supported by Technology Agency of Czech Republic in the frame of research project TK04010294 Methodology for smart thermal grid planning: exemplary scenarios and coordination tools for Power2Heat system integration at the municipal level.

6. References

Barco-Burgos, J., Bruno, J.C., Eicker, U., Saldaña-Robles, A.L., Alcántar-Camarena, V., 2022. Review on the integration of high-temperature heat pumps in district heating and cooling networks. Energy 239, 122378. https://doi.org/10.1016/J.ENERGY.2021.122378

Bloess, A., Schill, W.P., Zerrahn, A., 2018. Power-to-heat for renewable energy integration: A review of technologies, modeling approaches, and flexibility potentials. Appl Energy. https://doi.org/10.1016/j.apenergy.2017.12.073

Böttger, D., Götz, M., Lehr, N., Kondziella, H., Bruckner, T., 2014. Potential of the Power-to-Heat technology in district heating grids in Germany, in: Energy Procedia. Elsevier Ltd, pp. 246–253. https://doi.org/10.1016/j.egypro.2014.01.179

David, A., Mathiesen, B.V., Averfalk, H., Werner, S., Lund, H., 2017. Heat Roadmap Europe: Large-Scale Electric Heat Pumps in District Heating Systems. Energies 2017, Vol. 10, Page 578 10, 578. https://doi.org/10.3390/EN10040578

ENTSOE, 2021. Power Flow Tool.

Fambri, G., Mazza, A., Guelpa, E., Verda, V., Badami, M., 2023. Power-to-heat plants in district heating and electricity distribution systems: A techno-economic analysis. Energy Convers Manag 276, 116543. https://doi.org/10.1016/J.ENCONMAN.2022.116543

Lund, R., Persson, U., 2016. Mapping of potential heat sources for heat pumps for district heating in Denmark | Enhanced Reader 129–138.

Østergaard, P.A., Andersen, A.N., 2018. Economic feasibility of booster heat pumps in heat pump-based district heating systems. Energy 155, 921–929. https://doi.org/10.1016/J.ENERGY.2018.05.076

Schweiger, G., Rantzer, J., Ericsson, K., Lauenburg, P., 2017. The potential of power-to-heat in Swedish district heating systems. Energy 137, 661–669. https://doi.org/10.1016/j.energy.2017.02.075

06. Thermal energy storage

Efficiency Analysis of An Integrated Cascade Sorption Energy Storage into A Solar DHW System

Nasrin Aliyari[1], Marco S. Fernandes[1], Adélio R. Gaspar[1]

[1] Univ Coimbra, ADAI, Department of Mechanical Engineering, Rua Luís Reis Santos, Pólo II, 3030-788 Coimbra, Portugal

Abstract

Sorption heat storage has garnered significant interest for its potential in long-term thermal energy storage, particularly in domestic hot water (DHW) systems. This paper explores the concepts and operating principles of single material and cascade thermochemical energy storage systems, focusing on their application in solar DHW production. Single material sorption systems store and release energy based on reversible physicochemical phenomena, while cascade systems utilize two different storage materials to optimize energy density and discharge temperature. The study assesses and compares the integration of salt-hydrates-based cascade sorption energy storage, specifically using $MgCl_2 \cdot 6H_2O$ and $SrBr_2 \cdot 6H_2O$, with a solar DHW system for a single-family dwelling in the distinct climates of Coimbra (Portugal) and Shiraz (Iran). The findings indicate that the cascade system can result in a 21% and 43% reduction in auxiliary energy demand respectively in Coimbra and Shiraz, thus significantly increasing the renewable energy share and enhancing energy efficiency in DHW systems.

Keywords: DHW, Thermal storage, Adsorption, Cascade System, Solar energy

1. Introduction

Sorption heat storage has generated much interest due to its potential for long-term thermal energy storage (Scapino *et al.*, 2017). It is a promising technology for enhancing the efficiency and sustainability of energy systems, particularly in the context of building applications. This method leverages the reversible chemical reactions between a sorbent material and water vapor to store and release thermal energy (Fernandes *et al.*, 2016). Salt hydrates, particularly, are highly effective sorbents due to their substantial energy storage densities and favorable thermodynamic properties (Yan and Zhang, 2022). For salt hydrate-based sorption heat storage, salt hydrates form new crystal structures by either dissociating or absorbing water molecules, thereby enabling the storage or release of thermal energy in the form of chemical bonds. The typical reaction can be represented as follows (Stitou *et al.*, 1997; Xu *et al.*, 2021):

$$MX \cdot xH_2O_{(s)} + yH_2O_{(g)} \leftrightarrow MX(x+y) \cdot H_2O_{(s)} + y\Delta H_r \qquad \text{(eq. 1)}$$

Where $MX \cdot xH_2O$ is a salt hydrate produced from the chemical salt MX and solvent H_2O. MX and H_2O constitute the working pair. ΔHr is the enthalpy of the chemical reaction. The operating principle of salt hydrate-based sorption heat storage can be classified into two charging (dehydration) and discharging (hydration) processes. When exposed to heat, salt hydrates undergo a dehydration process, with the desorption heat being stored in the sorbent using a chemical bond. During cooler periods, the stored energy is released as the salts rehydrate, providing a reliable and efficient source of heat. This technology is particularly advantageous for long-term thermal energy storage, as it can be charged during periods of excess energy (such as summer) and discharged during times of high energy demand (such as winter), thereby reducing reliance on auxiliary heating systems and improving overall energy efficiency.

The sorption storage system needs to provide the user with useful discharging temperature and energy storage density. To conciliate the requirement for high energy density and thermodynamic constraints like discharging and charging temperatures, it is possible to utilize two different thermochemical (storage) materials (TCM) in a cascade configuration (N'Tsoukpoe *et al.*, 2016) – one with higher energy storage density but unable to provide the useful discharging temperature (TCM1) and other that can provide the useful temperature level under the set discharging constraints but with lower storage density (TCM2). In the end, the system can satisfy the user with the desired discharging temperature while the overall energy storage density is between the

© 2024. The Authors. Published by International Solar Energy Society
Selection and/or peer review under responsibility of Scientific Committee
10.18086/eurosun.2024.06.01 Available at http://proceedings.ises.org

respective energy storage densities of the two materials.

The objective of this study is to assess the integration of single material sorption heat storage (Fig. 1a) with a solar DHW production system and compare its performance with a cascade configuration (Fig. 1b), by evaluating the system efficiency in reducing the auxiliary energy demand in relation to the conventional DHW system. The storage unit performs both charging and discharging processes at the same time and at every moment. This assessment is performed for the mild climate of Coimbra (Portugal) and the harsher climate of Shiraz (Iran).

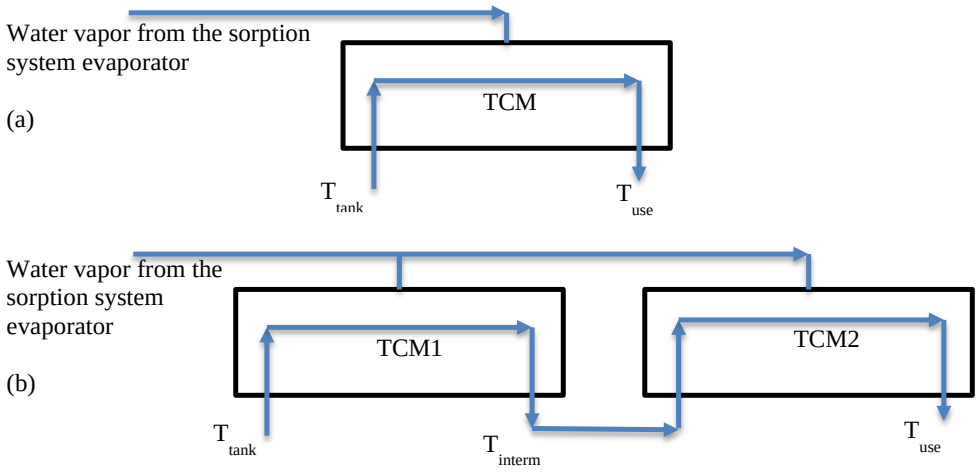

Fig. 1: (a) Single material heat storage configuration; (b) cascade heat storage configuration. T_{tank}, T_{use} and T_{interm} are the minimum outlet temperature of the tank, end-use temperature, and intermediate temperature.

2. Problem Description and Methodology

The auxiliary energy reduction percentage of the solar DHW sorption storage system in relation to the conventional system (without sorption storage) is calculated for two scenarios: (i) integration of a single-material sorption thermal storage, and (ii) integration of a cascade sorption thermal storage. The conventional solar DHW system (**Error! Reference source not found.**) is simulated in TRNSYS 18 to calculate the auxiliary heat (Q_{aux}) required during a year. The simulation is then performed for the integrated solar DHW system (**Error! Reference source not found.**) with single-material and cascade sorption thermal storage under the following thermodynamic constraints:

- For discharge, a minimum temperature of 55 °C has been defined to satisfy the need for DHW.
- The maximum output of the hot water tank has been set to 100 °C, which is adopted as the maximum charging temperature.
- The heat sink provides a condensation temperature of 22 °C and the low-temperature heat source an evaporation temperature of 10 °C.

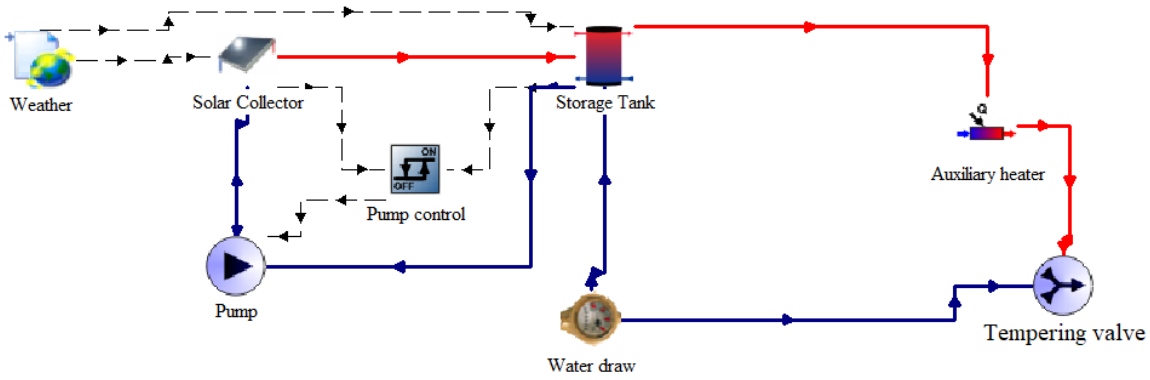

Fig. 2: Conventional solar DHW system.

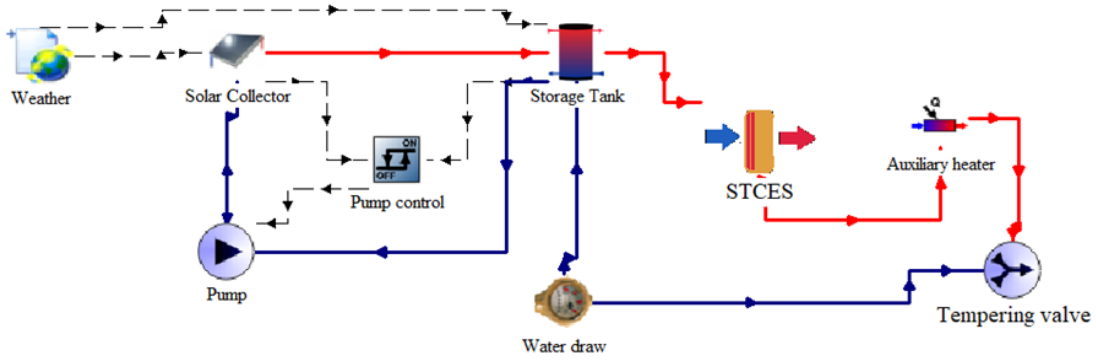

Fig. 3: Solar DHW system integrated with sorption storage unit.

In the conventional system, the outlet flow from the hot water tank, heated by solar energy, flows through the auxiliary heater, where, if the temperature is below the set point at the storage tank outlet, it is heated to reach the desired temperature. In the integrated DHW system with an energy storage unit, the outlet fluid flow from the storage tank first passes through the sorption storage unit (STCES), before entering the auxiliary heater. The thermal energy dynamics of the storage unit, consisting of two TCM, are simulated to manage simultaneous heat storage and release based on the inlet fluid temperature. When the fluid's temperature exceeds 55 °C, the system charges by storing heat in the TCMs, with the amount of stored heat being limited to predefined maximum values of each TCM. Conversely, when the temperature is lower than 55 °C, the system discharges by releasing stored heat to the fluid. The system continuously tracks the total stored, released, and remaining energy, ensuring accurate energy management within the storage unit. This method allows an understanding of the efficiency and behavior of the thermal energy storage system under varying operational conditions.

As for typical domestic hot water consumption patterns, Fuentes *et al.* (2018) provided information for different European countries, referring to a value of 0.04 $m^3\ day^{-1}\ person^{-1}$ for Portugal. **Error! Reference source not found.** illustrates a daily consumption pattern for a single-family of 4 people (0.16 $m^3\ day^{-1}$) considered for both Shiraz and Coimbra, for which the main consumption peaks occur in the morning and the

evening.

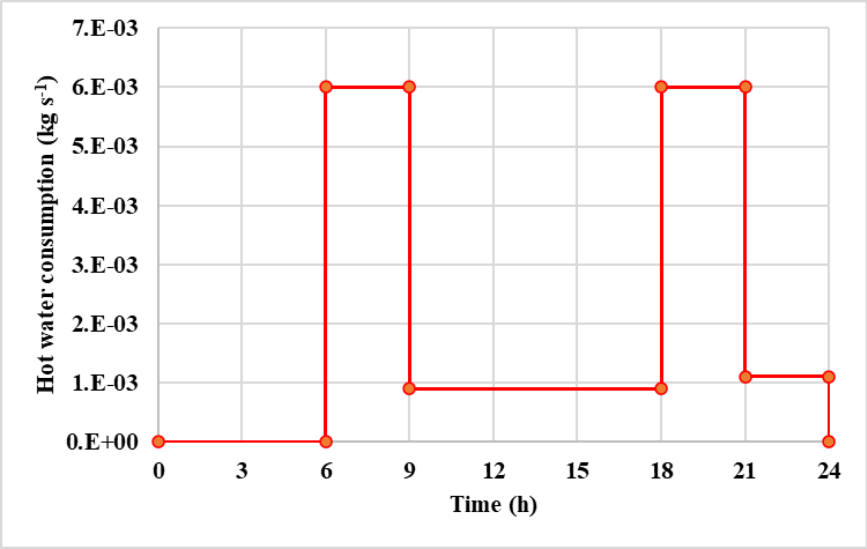

Fig. 4: Daily hot water consumption profile considered for a single-family of 4 people in Coimbra and Shiraz.

The primary task in designing a sorption thermal storage system is to select the appropriate material. Based on the previously mentioned thermodynamic constraints, the selection criteria for the main material are as follows:

- Under a condensation vapor pressure of 2600Pa (26 mbar) (corresponding to the water vapor pressure at 22 °C), the equilibrium temperature of the material should not exceed 100°C, to meet the maximum charging temperature requirement.
- Under an evaporator vapor pressure of 1200 Pa (12 mbar) (corresponding to the water vapor pressure at 10 °C), the equilibrium temperature of the salt should be above 55 °C, to fulfill the requirement of a discharging temperature of at least 55 °C.

The thermodynamics constraints are represented on the equilibrium curves diagram of salt hydrates, Fig. 5. To satisfy both charging and discharging constraints (no. 1 and no. 2), the equilibrium curve of the salt must intersect both the charging and discharging constraint areas. As a result, possible salt hydrates that could be used as primary salt are represented in Tab. 1. Although $Na_2S{\cdot}5\text{-}2H_2O$, with its large energy storage density (D_v), could be the best candidate, its main drawback is its toxicity. Among the other candidates, $MgCl_2{\cdot}6\text{-}4H_2O$ stands out due to its higher energy storage density and appropriate discharging temperature. Therefore, magnesium chloride has been selected as the storage material for the single-material storage system, with an energy storage density of 8.5×10^5 kJ, a charging temperature of 73.8 °C, and a discharging temperature of 60.5 °C.

Tab. 1: Possible salt hydrates to be used as primary salt.

Hydrated Salt	$MgCl_2{\cdot}6H_2O$	$SrCl_2{\cdot}2H_2O$	$Na_2S{\cdot}5H_2O$
Dehydrated Salt	$MgCl_2{\cdot}4H_2O$	$SrCl_2{\cdot}H_2O$	$Na_2S{\cdot}2H_2O$
$T_{melting}$ [°C]	117	100	70.8
T_{disch} [°C]	60.5	58	65.8
T_{charge} [°C]	73.8	70	77.9
D_v [kJ m^{-3}]	8.5×10^5	8.1×10^5	1.8×10^6

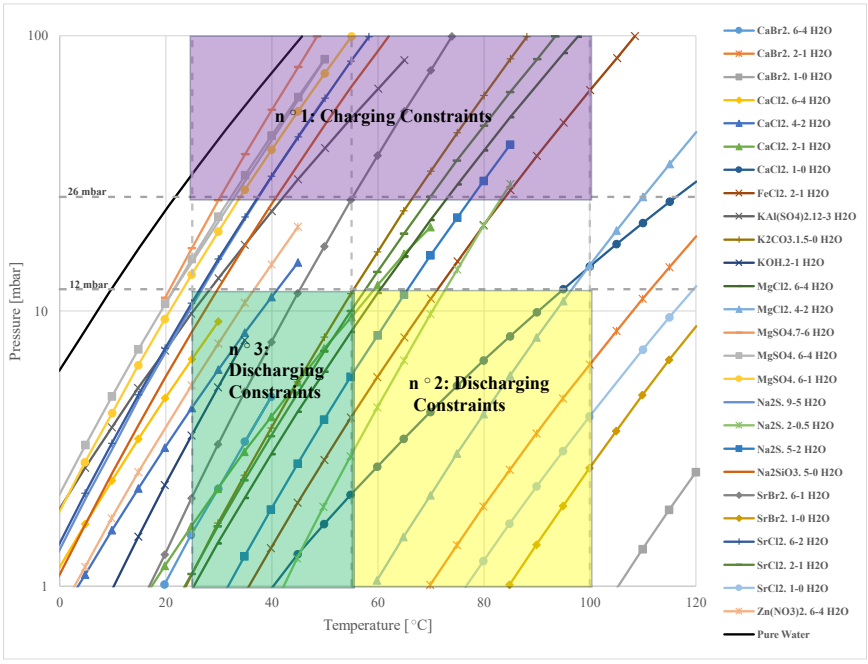

Fig. 5: Equilibrium curves for various solid-gas reactions involving salt hydrates and thermodynamic constraints. To satisfy both charging and discharging constraints (no. 1 and no. 2), the equilibrium curve of the salt must intersect both the charging and discharging constraint areas. Reference data for the equilibrium curves are provided by N'Tsoukpoe *et al.* (2014).

To design the cascade storage unit, it is assumed that the primary salt which can provide the required 55 °C has already been selected ($MgCl_2.6H_2O$), so the focus now shifts to identifying potential materials that could enhance the energy storage density of the process, as targeted by the cascading approach. To qualify:

- The secondary salt must offer a reaction with a higher energy storage density than that of the primary salt ($MgCl_2.6\text{-}4H_2O$, 8.5×10^5 kJ m^{-3}).
- Additionally, the material must meet the discharging constraint no. 3 (Fig. 5): under an evaporator vapor pressure of 1200 Pa (12 mbar), the salt's equilibrium temperature should exceed 25 °C, the minimum outlet temperature of the hot water tank.

Possible salt hydrates that meet these criteria and could be used as secondary salts are listed in Tab. 2. To enhance the energy storage density of the sorption heat storage system, $SrBr_2\cdot6\text{-}1H_2O$ emerges as the most suitable material due to its significantly higher energy storage density. So, strontium bromide is selected as the secondary salt.

Tab. 2: Possible salt hydrates to be used as secondary salt.

Hydrated Salt	$SrBr_2\cdot6H_2O$	$SrCl_2\cdot6H_2O$	$KAl(SO4)_2\cdot12H_2O$	$Na_2SiO_3\cdot5H_2O$
Dehydrated Salt	$SrBr_2\cdot1H_2O$	$SrCl_2\cdot2H_2O$	$KAl(SO4)_2\cdot3H_2O$	$Na_2SiO_3\cdot H_2O$
$T_{melting}$ [°C]	88.6	61.3	65	N.A.
T_{disch} [°C]	45.8	27	28.9	29.8
T_{charge} [°C]	55	37.8	42	43
D_v [kJ m^{-3}]	2.26×10^6	1.58×10^6	1.48×10^6	1.6×10^6

3. Results and discussion

3.1. Single material TCES system

The energy stored and released along with the remaining energy charts of the single material TCES system for Coimbra and Shiraz are shown in Fig. 6 and **Error! Reference source not found.**, respectively. Fig. 6a shows intermittent peaks for energy storage and release events around the middle of the year, particularly noticeable between 4380 hours (mid-year) and 6570 hours (three-quarters of the year) for Coimbra which are much less frequent and have lower magnitudes compared to Shiraz. Fig. 7a exhibits a much higher frequency and

magnitude for energy storage and release for Shiraz compared to Coimbra, indicating a more dynamic energy exchange. The peaks are more frequent and sustained, particularly notable towards the end of the year, which correlates with Shiraz's harsher climate and higher solar radiation levels.

According to Fig. 6b, for Coimbra, the energy released predominantly surpasses the energy stored towards the latter half of the year, leading to low remaining energy values, and the overall trend suggests sporadic energy storage and consistent energy release in the mid to late parts of the year. While for Shiraz, the remaining energy shows a significant rise starting around 3650 hours (roughly mid-year) and peaks around 7300 hours, followed by a gradual decline, Fig. 7b. This indicates substantial energy accumulation in the mid to late parts of the year, consistent with the higher solar energy input due to the climatic conditions of Shiraz. The fact that there is an amount of energy left in the reactor at the end of the year may indicate an oversized reactor design, however, a multiyear simulation would be required to understand how this remaining energy affects the next annual cycle.

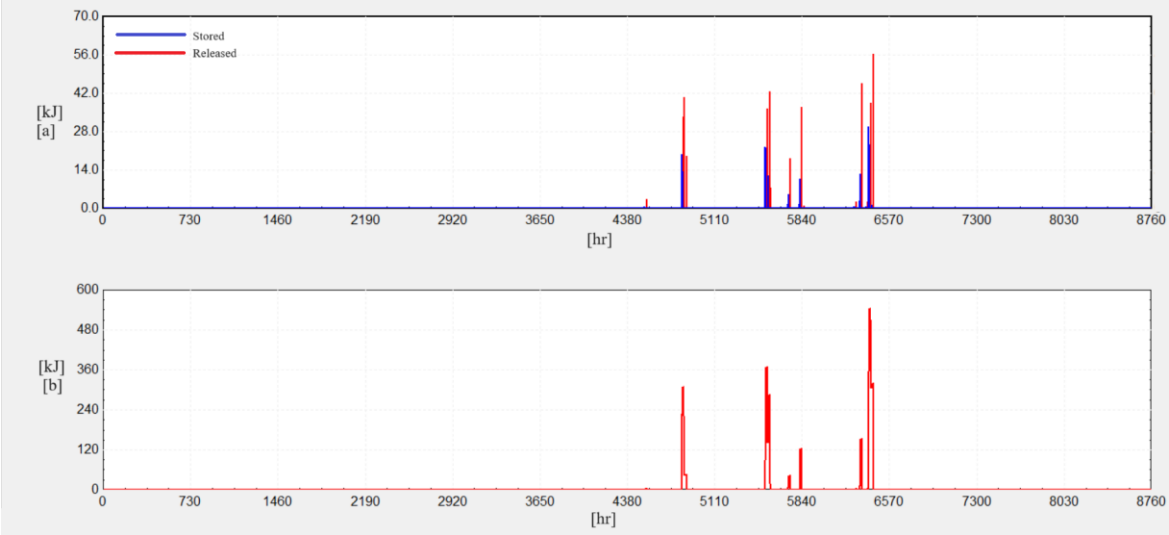

Fig. 6: (a) energy stored and released, and (b) remaining energy of single material TCES system in Coimbra.

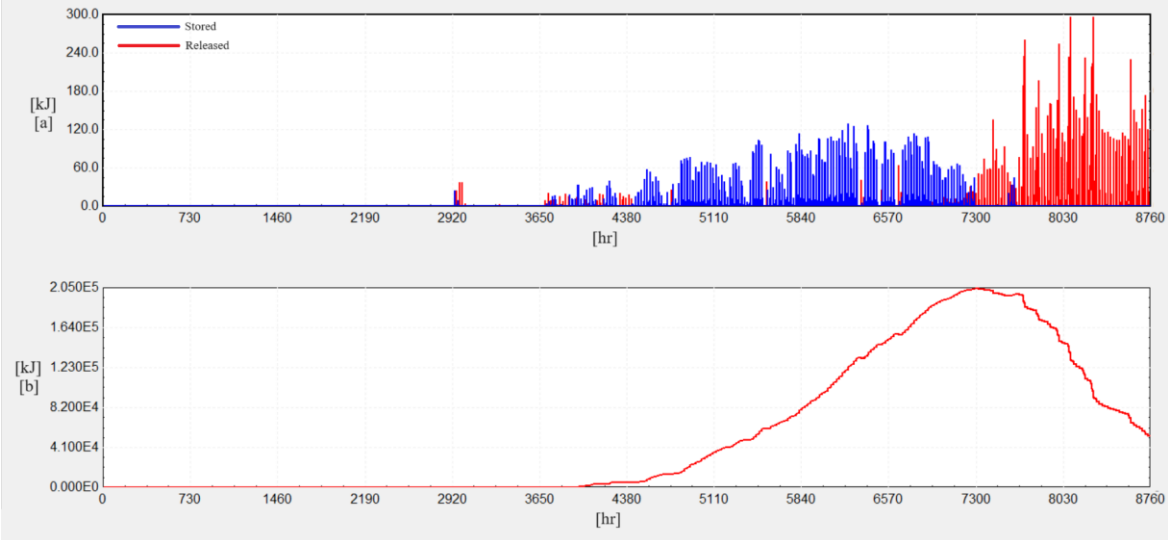

Fig. 7: (a) energy stored and released, and (b) remaining energy of single material TCES system in Shiraz.

The heat transfer rate of the auxiliary heater of the TCES system over a year are depicted for Coimbra and Shiraz in Fig. 8 and Fig. 9, respectively. According to Fig. 8, the auxiliary heater's activity is distributed throughout the year, with notable peaks in the first half. The heat transfer rate fluctuates significantly, reaching up to 3200 kJ h^{-1} frequently. This indicates a substantial need for auxiliary heating due to the inefficiency of

the TCES system. However, under Shiraz weather conditions, the auxiliary heater's activity is concentrated only in the first half of the year (Fig. 9). The heat transfer rate is generally lower compared to Coimbra, with peaks up to 3000 kJ h^{-1}, but less frequently. This suggests less reliance on the auxiliary heater overall, due to higher solar radiation, which also promotes a more effective energy storage in the latter half of the year.

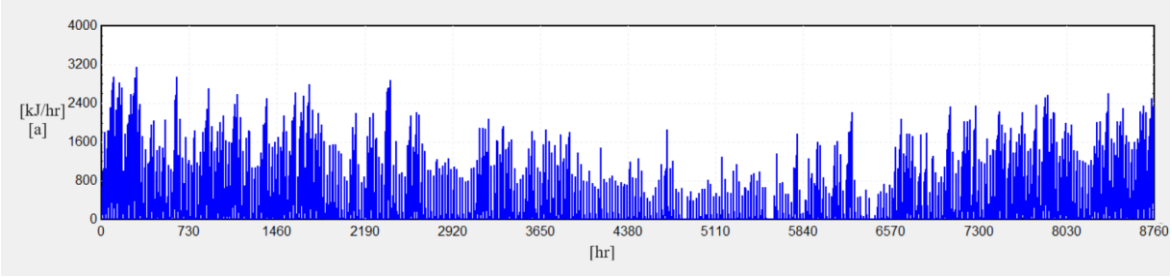

Fig. 8: Heat transfer rate of the auxiliary heater in case of single-material TCES system in Coimbra.

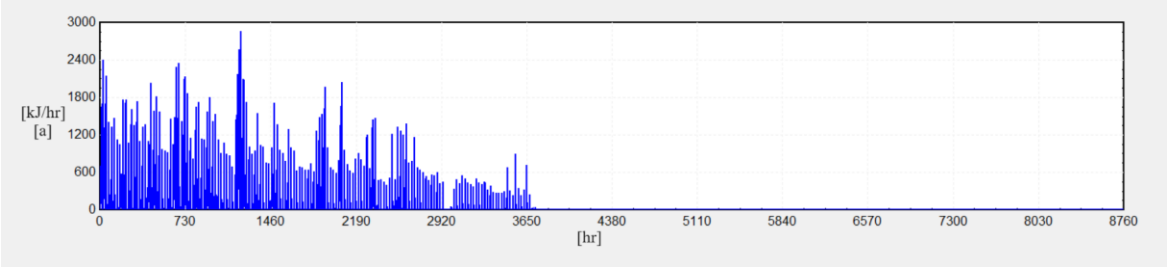

Fig. 9: Heat transfer rate of the auxiliary heater in case of single-material TCES system in Shiraz.

3.2. Cascade TCES system

Fig. 10 depicts the energy storage and release patterns, as well as the remaining energy trend of the cascade sorption energy storage using two thermochemical materials (TCMs): Strontium bromide ($SrBr_2$) and magnesium chloride ($MgCl_2$), for Coimbra during one year. Energy storage patterns are shown in Fig. 10a. For $SrBr_2$ (magenta), energy storage occurs frequently throughout the year with significant peaks, especially between 2000 and 6000 hours. The storage activity reaches up to 180 kJ, indicating substantial energy storage events during these periods. The activity diminishes after 7000 hours, suggesting a seasonal dependency in the latter part of the year. For $MgCl_2$ (yellow), energy storage events are rare and minimal compared to strontium bromide. The peaks are much lower, barely reaching above 60 kJ. This indicates that magnesium chloride is less effective or less utilized for energy storage in this climate.

Energy release patterns are shown in Fig. 10b. For strontium bromide (blue), the energy release is sporadic but notable throughout the year, with peaks up to 240 kJ. There is a consistent pattern of release, particularly between 2000-4500 hours and 6500-8760 hours, indicating a seasonal dependency in the middle part of the year. Also, this aligns with the periods of significant energy storage, indicating active use of stored energy. For magnesium chloride (red), similar to storage, energy release events for are minimal. The release peaks are infrequent and low, barely reaching 60 kJ. This further confirms that $MgCl_2$ plays a minor role in the energy management of the system.

The total remaining energy for strontium bromide shows a steady increase, peaking around 6500 hours at approximately 500,000 kJ (Fig. 10c). After peaking, there is a gradual decline towards the end of the year. This trend suggests efficient storage and gradual utilization of energy throughout the year. The remaining energy for magnesium chloride is negligible, consistent with the low storage and release activity observed. This confirms its minimal contribution to the overall energy storage system.

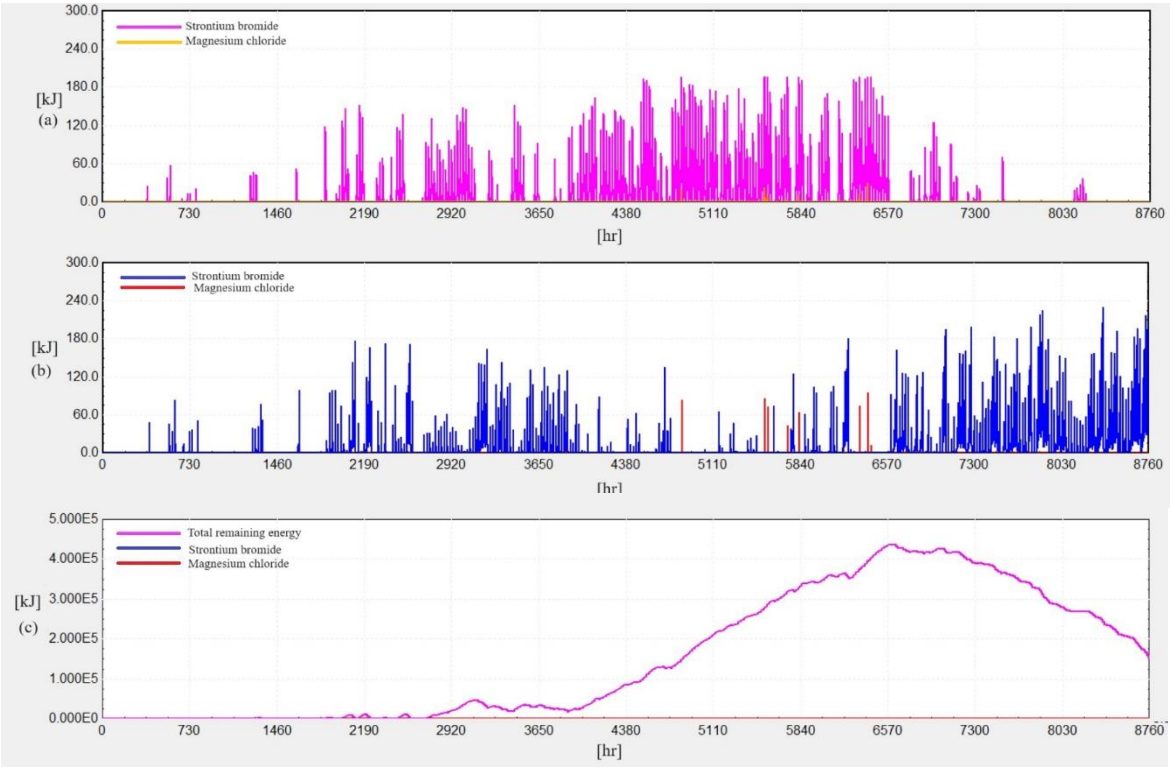

Fig. 10: (a) Energy storage, (b) release patterns, and (c) remaining energy trend of the cascade TCES using two TCMs: Strontium Bromide and Magnesium Chloride, for Coimbra during a year.

Regarding the effectiveness of TCMs, strontium bromide is highly effective in both storing and releasing energy, with substantial activity observed throughout the year. It shows a robust capacity to store energy and release it as needed, maintaining a high level of remaining energy. Magnesium chloride, on the other hand, is ineffective in this setup, with minimal storage and release activity. It has a negligible contribution to the total remaining energy, suggesting it is not suitable for the primary energy storage role in this system mainly due to its high charging temperature which limits its ability to store energy. Thus, the system heavily relies on $SrBr_2$ for energy storage and release, with active periods concentrated between 2000 and 7000 hours. This period represents seasons with significant temperature fluctuations requiring active energy management. The total remaining energy trend indicates efficient energy utilization, with a peak followed by a steady decline, ensuring energy availability throughout the year.

Fig. 11 depicts the energy storage and release patterns, as well as the remaining energy trend of the cascade sorption energy storage using two TCMs, for Shiraz during one year. Regarding the energy storage patterns, shown in Fig. 11a, for strontium bromide (magenta), energy storage occurs frequently throughout the year, with significant peaks, particularly in the second half of the year. The storage activity reaches up to 200 kJ, indicating substantial energy storage events during these periods. Activity diminishes somewhat after 7300 hours, suggesting a seasonal influence on energy storage needs. For magnesium chloride (orange), energy storage events are more frequent and higher compared to Coimbra, though still less than $SrBr_2$. Peaks in storage reach above 120 kJ, indicating a more active role for magnesium chloride in Shiraz compared to Coimbra. This suggests that $MgCl_2$ is more effective or more utilized for energy storage in this system in Shiraz.

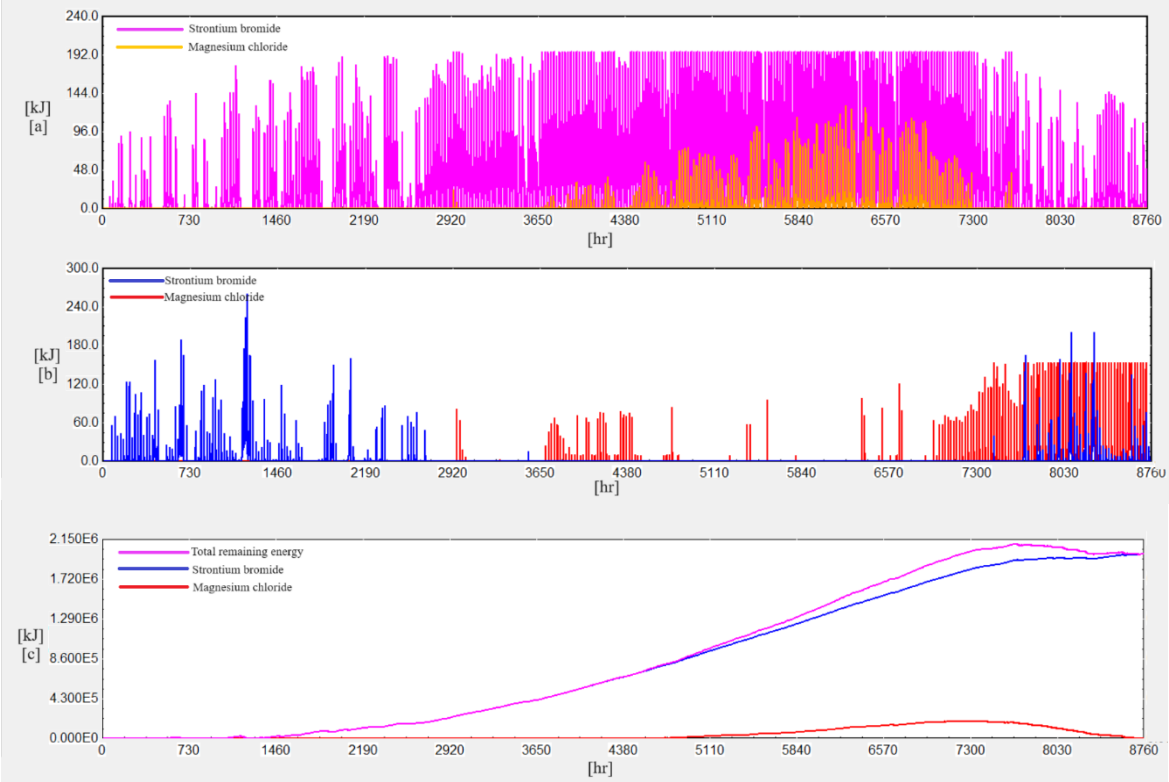

Fig. 11: (a) Energy storage, (b) release patterns, and (c) remaining energy trend of the cascade TCES using two TCMs: Strontium Bromide and Magnesium Chloride, for Shiraz during a year.

Energy release patterns are shown in Fig. 11b. For strontium bromide (blue), the energy release is consistent throughout the year with significant peaks, particularly in the first half of the year. Peaks reach up to more than 240 kJ, indicating active use of stored energy. For magnesium chloride (red), energy release events for are frequent and significant in the second half of the year. The release peaks often reach up to 180 kJ, indicating active involvement in energy management. This further suggests a significant role for $MgCl_2$ in the energy release process in Shiraz.

The total remaining energy for strontium bromide (Fig. 11c) shows a steady increase, peaking around 6500 hours at approximately 2,150,000 kJ. After peaking, there is a gradual decline towards the end of the year. This trend indicates efficient storage and gradual utilization of energy throughout the year. The remaining energy for magnesium chloride increases steadily but remains significantly lower than $SrBr_2$. Peaks at around 7000 hours and then shows a slight decline towards the end of the year. This confirms its supportive role in the overall energy storage system, though less dominant compared to strontium bromide.

Strontium bromide is thus highly effective in both storing and releasing energy, with substantial activity observed throughout the year. It shows a robust capacity to store energy and release it as needed, maintaining a high level of remaining energy. Magnesium chloride is more effective and utilized in Shiraz compared to Coimbra. It plays a significant role in both energy storage and release, especially in the second half of the year. Overall, the system in Shiraz utilizes both TCMs more effectively than in Coimbra, with active periods for both. The total remaining energy trend indicates efficient energy utilization, with peaks followed by a steady decline, ensuring energy availability throughout the year.

The heat transfer rate of the auxiliary heater in case of the cascade TCES system applied in Coimbra and Shiraz are shown in Fig. 12 and Fig. 13, respectively. The auxiliary heater's activity in Coimbra is high in the first half of the year, with peaks reaching up to 3200 kJ h^{-1}. There is a significant amount of auxiliary heating required between 0 and 3650 hours, indicating the need for additional heat to maintain the fluid temperature due to the low amount of stored energy in TCES system to do so. However, after 3650 hours, due to the hours the increasing amount of stored energy beside the seasonal influence, the activity of the auxiliary heater diminishes but still shows sporadic peaks until the end of the year.

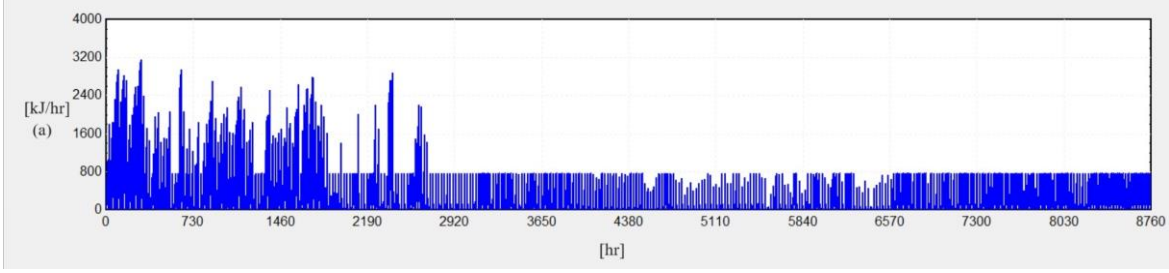

Fig. 12: Heat transfer rate of the cascade TCES system's auxiliary heater in Coimbra.

The auxiliary heater's activity in Shiraz is primarily concentrated in the first 2200 hours of the year, with peaks reaching up to 2400 kJ h^{-1}. After this initial period, the auxiliary heater's activity drops significantly, showing minimal peaks for the remainder of the year until a minor peak at the end. This suggests that Shiraz requires intense auxiliary heating only during a specific period of the year, likely due to distinct seasonal variations and the effectiveness of the thermal storage unit during the latter half of the year, after the TCES system is effectively charged.

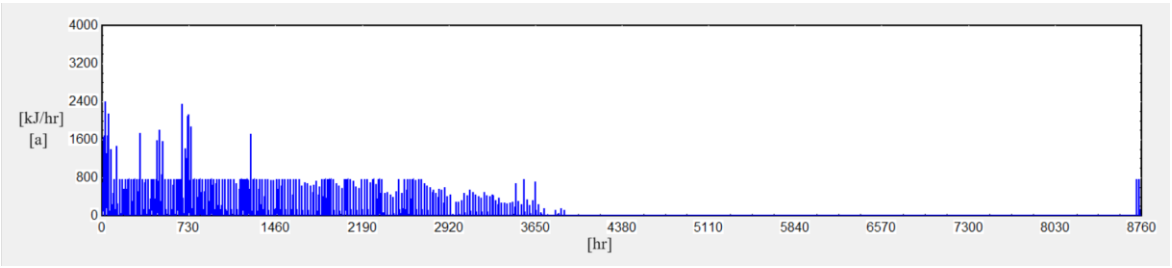

Fig. 13: Heat transfer rate of the cascade TCES system's auxiliary heater in Shiraz.

The performance of the single material and cascade thermochemical energy storage systems is evaluated in the two locations. The results are summarized in Tab. 3. They demonstrate the advantages of the cascade system in terms of auxiliary energy reduction in relation to the conventional system and energy storage capability.

Tab. 3: Performance of the single material and cascade thermochemical energy storage system.

System	Conventional		Single		Cascade	
Location	**Coimbra**	**Shiraz**	**Coimbra**	**Shiraz**	**Coimbra**	**Shiraz**
Ql (Energy rate to load from hot water tank) (kJ)	7.41E+06	9.18E+06	7.41E+06	9.18E+06	7.41E+06	9.18E+06
Qaux (Auxiliary heat supplied by heater) (kJ)	2.71E+06	7.25E+05	2.71E+06	5.27E+05	2.13E+06	4.13E+05
Qs (total stored heat in thermal storage unit) (kJ)	_	_	1.71E+03	2.11E+05	7.12E+05	2.73E+06
Qr (Total released heat from thermal storage unit) (kJ)	_	_	1.71E+03	1.58E+05	5.13E+05	3.84E+05
QS_$MgCl_2$ (Total stored heat in the reacor containing $MgCl_2$ hydrated salt) (kJ)	–	–	–	–	1.71E+03	2.27E+05
QS_$SrBr_2$ (Total stored heat in the reactor containing $SrBr_2$ hydrated salt) (kJ)	–	–	–	–	7.10E+05	2.51E+06

QR_$MgCl_2$ (Total released heat from the reacor containing $MgCl_2$ hydrated salt) (kJ)	–	–	–	–	1.71E+03	2.29E+05
QR_$SrBr_2$ (Total released heat from the reacor containing $SrBr_2$ hydrated salt) (kJ)	–	–	–	–	5.11E+05	1.55E+05
Auxiliary heat reduction percentage in relation to conventional system (%)	–	–	0.1	27.3	21.4	43.1

The cascade system in Coimbra achieved a 21.4% reduction in auxiliary energy demand in relation to the conventional system, compared to only 0.1% for the single material system. Similarly, in Shiraz, the cascade system showed a significant reduction of 43.1%, while the single material system achieved a 27.3% reduction. These results highlight the superior performance of the cascade system in optimizing energy storage and reducing auxiliary energy requirements.

The cascade system's ability to balance the thermodynamic constraints and user requirements allows it to perform more efficiently under varying climatic conditions. The integration of different storage materials in a cascade configuration enables the system to provide the necessary discharge temperature while maintaining a high energy storage density. This makes the cascade thermochemical energy storage system a more viable solution for solar DHW applications. Moreover, as seen in the case of Shiraz, where the system can consistently present a net positive storage rate in the hotter months, it can effectively improve the overall system’s performance, allowing, for example, the storage energy to be used to satisfy other requirements or to be seasonally stored.

Additionally, the analysis of two different TCMs indicates that selecting the primary material based on the local weather conditions and its charging temperature is more advantageous than selecting it based solely on its nominal storage density. In this study, for instance, the charging temperature of $MgCl_2 \cdot 6H_2O$, the primary salt, is approximately 73.8°C. However, in Coimbra, the outlet temperature of the hot water tank rarely reaches this value, rendering magnesium chloride less effective in this climate. Conversely, in Shiraz, where the climate is harsher and the outlet temperature of the hot water tank frequently exceeds the charging temperature of $MgCl_2 \cdot 6H_2O$, this salt proves to be more effective in the cascade system. Therefore, a more detailed analysis of how the charging temperature of the primary TCM impacts the efficiency of the cascade thermochemical energy storage integrated with DHW systems would be highly beneficial.

4. Conclusion

The study evaluates the performance of single material and cascade thermochemical energy storage systems integrated with solar domestic hot water (DHW) systems in different climatic conditions of Coimbra (Portugal) and Shiraz (Iran). The findings indicate that the cascade system, using a combination of $MgCl_2 \cdot 6H_2O$ and $SrBr_2 \cdot 6H_2O$, significantly reduces auxiliary energy demand by 21% in Coimbra and 43% in Shiraz, compared to conventional systems. This reduction underscores the cascade system's efficiency in optimizing energy storage and discharge temperatures. The single material system, while effective, demonstrated limited performance improvements, particularly in milder climates like Coimbra. The cascade configuration's ability to leverage the unique properties of different storage materials enables it to meet the energy demands more effectively, thus enhancing the renewable energy share and overall efficiency of the DHW systems. Additionally, the study highlights the importance of selecting primary thermochemical materials based on local climatic conditions as well as its charging temperature to maximize the system's efficiency, as evidenced by the varying effectiveness of $MgCl_2 \cdot 6H_2O$ in different environments. This comprehensive analysis confirms the viability of cascade thermochemical energy storage systems in improving solar DHW applications, promoting sustainable and efficient energy use. Future work should focus on multi-year simulations and the exploration of other material combinations to further optimize these systems.

5. Acknowledgments

The presented work is framed under the research projects 'AdsorSeason – Long-term adsorption solar thermal energy storage', funded by the Portuguese Foundation for Science and Technology (FCT) (ref. 2022.03339.PTDC, https://doi.org/10.54499/2022.03339.PTDC), and 'Associate Laboratory of Energy, Transports and Aerospace' (ref. UIDB/50022/2020, https://doi.org/10.54499/UIDB/50022/2020). FCT funds Marco S. Fernandes through researcher contract 2021.02975.CEECIND/CP1681/CT0002 (https://doi.org/10.54499/2021.02975.CEECIND/CP1681/CT0002).

6. References

Fernandes, M.S., Brites, G.J.V.N., Costa, J.J., Gaspar, A.R., Costa, V.A.F., 2016. Modeling and parametric analysis of an adsorber unit for thermal energy storage. Journal of Energy. 102, 83-94. https://doi.org/10.1016/j.energy.2016.02.014.

Fuentes, E., Arce, L., Salom, J., 2018. A review of domestic hot water consumption profiles for application in systems and buildings energy performance analysis. Journal of Renewable and Sustainable Energy Reviews. 81, Part 1, 1530-1547. https://doi.org/10.1016/j.rser.2017.05.229.

N'Tsoukpoe, K.E., Mazet, N., Neveu, P., 2016. The concept of cascade thermochemical storage based on multimaterial system for household applications. Journal of Energy and Buildings. 129, 138-149. https://doi.org/10.1016/j.enbuild.2016.07.047.

N'Tsoukpoe, K.E., Schmidt, T., Rammelberg, H. U., Watts, B. A., Ruck, W.K.L., 2014. A systematic multi-step screening of numerous salt hydrates for low temperature thermochemical energy storage, Journal of Applied Energy, 124, 1-16, https://doi.org/10.1016/j.apenergy.2014.02.053.

Scapino, L., Zondag, H. A., Van Bael, J., Diriken, J., Rindt, C.C.M., 2017. Sorption heat storage for long-term low-temperature applications: A review on the advancements at material and prototype scale. Journal of Applied Energy. 190, 920-948. https://doi.org/10.1016/j.apenergy.2016.12.148.

Stitou, D., Goetz, V., Spinner, B., 1997. A new analytical model for solid-gas thermochemical reactors based on thermophysical properties of the reactive medium, Chemical Engineering and Processing: Process Intensification, 36, Issue 1,29-43, ISSN 0255-2701, https://doi.org/10.1016/S0255-2701(96)04173-6.

Xu, J., Li, T., Yan, T., Chao, J., Wang, R., 2021. Dehydration kinetics and thermodynamics of magnesium chloride hexahydrate for thermal energy storage. Solar Energy Materials and Solar Cells.219, 110819, ISSN 0927-0248, https://doi.org/10.1016/j.solmat.2020.110819.

Yan, T., Zhang, H., 2022. A critical review of salt hydrates as thermochemical sorption heat storage materials: Thermophysical properties and reaction kinetics. Journal of Solar Energy. 242, 157-183, ISSN 0038-092X, https://doi.org/10.1016/j.solener.2022.07.002.

Assessment of Fin Thickness Influence on Melting and Solidification Processes Inside Longitudinally Finned Latent Thermal Energy Storage

Mateo Kirincic, Anica Trp, Kristian Lenic, Josip Batista

University of Rijeka, Faculty of Engineering, Department of Thermodynamics and Energy Engineering, Vukovarska 58, 51000 Rijeka, Croatia

Abstract

In the paper, series of numerical investigations have been performed in order to evaluate the influence of fin thickness on melting and solidification performance inside the shell-and-tube type longitudinally finned latent thermal energy storage (LTES). The LTES uses water as the heat transfer fluid (HTF) and RT 25 paraffin as the phase change material (PCM). Using experimentally validated mathematical model and numerical procedure, numerical investigations of PCM melting and solidification have been carried out for various fin thicknesses; 0.5 mm, 2 mm and 4 mm. Thermal energy stored in 8 h of charging, during which the PCM melts, and released in 12 h of discharging, during which the PCM solidifies, as well as melting and solidification rates, were compared. Time-wise variations of average liquid fractions and fin temperatures have been obtained for all configurations during melting and solidification processes. The results indicate that, due to increased fin capacity, thicker fins expedite melting/solidification rate. However, due to reduced amount of the PCM as the result of using thicker fins, less thermal energy can be stored in and released from the LTES. As indicated by the investigation, fin thickness is an influential geometry parameter which should be carefully selected in order to maximize the LTES thermal performance.

Keywords: Latent thermal energy storage, melting and solidification, fin thickness, numerical investigation.

1. Introduction

Thermal energy storage plays a crucial role in solar energy-based thermal systems. Since solar energy is only available during the day, thermal energy storage helps bridge the gap between solar energy availability and heating demand, thereby improving the efficiency of the thermal system. There are three types of thermal energy storage: sensible, latent, and thermochemical. In latent thermal energy storage (LTES) system, the heat acquired by solar collectors is transferred to a phase change material (PCM) through a heat transfer fluid (HTF) during the charging period (melting) and released during the discharging period (solidification). LTES are implemented in various fields of thermal engineering, e.g. domestic heating systems, refrigeration, solar-powered plants and processing facilities etc. However, a major downside of LTES technology is relatively low thermal conductivity of the PCMs, especially organics, which include paraffins and fatty acids, mostly used in low temperature HVAC systems. This hinders heat transfer, resulting in reduced charging/discharging power and less accumulated/released energy (Khan et al., 2016). To overcome this issue, several approaches can be adopted. Varying the LTES geometry parameters, such as increasing the LTES length/height, aspect ratios and tube diameters (Modi et al., 2023) or implementing fins results in increased heat transfer surface area and/or decreased PCM thickness (thus decreasing the PCM thermal resistance), which both increase the overall heat transfer. The PCM effective thermal conductivity can be enhanced by inserting high conductivity nanoparticles (Yu et al., 2023), foams (Fteiti et al., 2023) or matrices (Kumar and Saha, 2020) into the PCM. Due to their affordability and simplicity in design, manufacture and implementation process, the addition of fins is the most commonly used enhancement (Liu et al., 2012). A variety of fin designs has been investigated experimentally and numerically, and their geometry parameters have been optimized according to specified objectives.

Rathod and Banerjee (2015) have experimentally investigated charging and discharging performance enhancement in a shell-and-tube LTES using stearic acid as the PCM and water as the HTF. By installing three longitudinal fins, melting time has been reduced by up to 25%, while solidification time has been reduced by up to 44% in comparison to the plain tube configuration. Z. Khan and Z.A. Khan (2017) have experimentally

© 2024. The Authors. Published by International Solar Energy Society
Selection and/or peer review under responsibility of Scientific Committee
10.18086/eurosun.2024.06.02 Available at http://proceedings.ises.org

investigated LTES thermal performance during charging in a LTES with novel type longitudinal fins. Compared to the plain tube configuration, melting time and mean charging power have been enhanced by up to 70%. The effect of using eight longitudinal fins per tube on the charging/discharging process of shell-and-tube LTES was quantitatively compared by Kirincic et al. (2021a), assessing the performance of a finned design against a configuration without fins. The implementation of fins resulted in a significant enhancement of thermal performance throughout both the charging and discharging cycles. In comparison to the finless design, the addition of fins reduced melting/solidification time by 52%/43%. To examine the overall efficiency of the LTES, comprehensive LTES efficiency was defined as the ratio of stored/released thermal energy and the maximum LTES thermal capacity for the finless design. The finned design exhibited superior performance compared to the design without fins, as the chosen fin type and parameters did not notably decrease the amount of stored/released thermal energy while substantially promoting the heat transfer rate.

Yu et al. (2020) investigated the melting behavior of RT 58 paraffin in a horizontal LTES with eight non-uniformly distributed longitudinal fins. They performed an optimization of fin angle gradient and fin thickness gradient with the objective of minimizing melting time. For the optimized LTES configuration, a decrease in total melting time by 30.5% in comparison with the uniform fin configuration was observed. Yang et al. (2017) investigated the influence of radial fins on heat transfer in a shell-and-tube LTES which uses paraffin as the PCM and water as the HTF. The influence of fin number, fin thickness and fin spacing on heat transfer was assessed and a decrease in melting time by 65% compared to the equivalent time in the finless configuration was observed. Additionally, the authors noted that increasing fin number and fin thickness beyond a specific value can have a negative effect on heat transfer, as well as LTES heat storing/releasing capacity as the influence of natural convection and the amount of the PCM are both reduced.

In this paper, influence of fin thickness on LTES thermal performance during melting and solidification processes is numerically evaluated by comparing melting/solidification rates and energies stored in 8 h of charging and released in 12 h of discharging for LTES configurations with fin thicknesses of 0.5 mm, 2 mm and 4 mm.

2. Mathematical model and numerical solving

2.1 Physical problem and computational domain

Numerical investigation has been conducted on the PCM melting and solidification in a vertically oriented shell-and-tube LTES tank. The LTES tank consists of a 950 mm diameter outer shell and has a height of 1500 mm, with 19 concentric aluminum tubes with inner and outer diameters of 25 mm and 30 mm, respectively. Water is used as the HTF and flows through the tubes, entering the tank at the top. The PCM used is technical grade paraffin (RT 25), which fills the shell-side. During the charging process (daytime), hot HTF transfers heat to the PCM, causing it to melt and accumulate heat. During the discharging process (nighttime), the PCM solidifies and releases stored heat to the cold HTF. Each tube features eight equidistant longitudinal fins installed on the PCM-side. The fins are 66 mm wide with fin investigated thicknesses of 0.5, 2 and 4 mm.

Performed experimental investigations on low temperature organic PCM indicate that the melting process is non-isothermal, occurring within a narrow temperature range, while solidification is typically isothermal at a nearly constant temperature. These distinctions have been taken into account and thermophysical properties of the PCM used in the numerical investigation, based on the manufacturer's data sheet (Rubitherm GmbH, 2018), are given in Tab. 1.

The computational domain represents the smallest segment of the analyzed physical problem and encompasses all physical phenomena within the LTES tank. In the multi-tube LTES, thermal behavior in and around geometrically identical tubes is very similar, i.e. observing the physical phenomena in and around one HTF tube is sufficiently representative of the thermal behavior of the whole LTES. Regions of influence of each tube can be defined with circles circumscribed around each of them, with the diameter of the circles being equal to the tube pitch. Therefore, it is sufficient to investigate the heat transfer process around a single tube and its PCM annulus. Due to the tube geometry and physical symmetry, the investigated region can be further simplified so that includes one-eighth of a single tube, containing the corresponding HTF segment, tube

segment, halves of adjacent fins and its surrounding PCM annulus segment. The computational domain is divided into three subdomains: the HTF subdomain, the tube wall and fins subdomain, and the PCM subdomain. In Figure 1, tube configuration inside the LTES, a single tube and its surrounding PCM annulus, as well as the selected computational domain are shown.

Tab. 1. Thermophysical properties of the PCM

Property	PCM
Melting temperature range, °C	18-25
Solidification temperature, °C	25
Specific heat capacity, J/kgK	2000
Specific latent heat, J/kg	170000
Thermal conductivity, W/mK	0.2
Density, kg/m^3	820
Dynamic viscosity, Pa·s	0.0036
Thermal expansion coefficient, 1/K	0.001

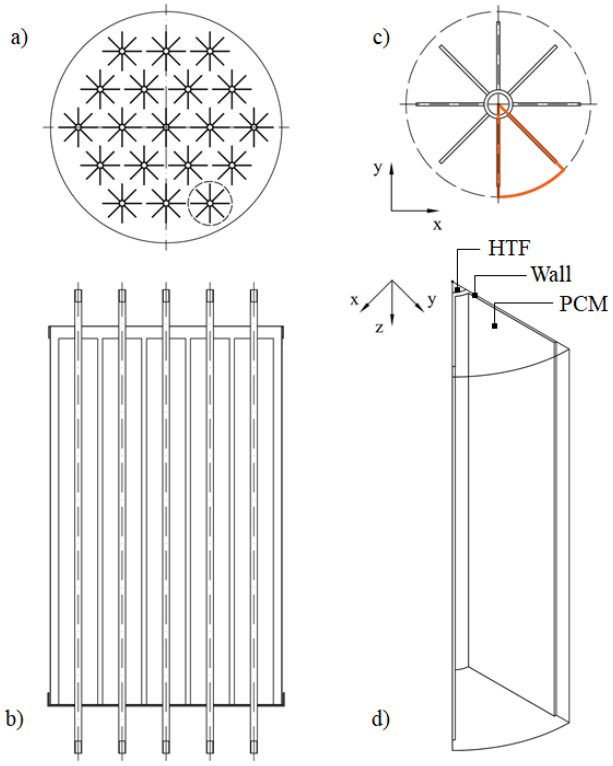

Fig. 1. Investigated LTES tank, a) top view, b) longitudinal cross-section view, c) transversal cross-section of a single finned tube with surrounding PCM annulus and denoted computational domain, d) selected computational domain in 3D view.

2.1 Governing equations, initial and boundary conditions

For the physical problem involving a transient conjugated problem that includes forced convection, conduction, and phase change heat transfer, including natural convection occurring in the liquid phase of the PCM, a 3D mathematical model has been developed. It uses the enthalpy formulation describe heat transfer during the melting and solidification of the PCM, where specific enthalpy is the calculated variable instead of temperature in the PCM energy equation. Natural convection in the liquid phase of the PCM significantly affects heat transfer during melting but has only a minor impact during solidification. Previous work by the

authors has shown that neglecting natural convection during solidification leads to a small error but significantly reduces computation time (Kirincic et al., 2021b). Therefore, in the current study, natural convection in the PCM subdomain is considered only during the melting process.

Several assumptions have been made regarding the physical properties, such as assuming constant thermophysical properties for all materials, homogeneous and isotropic PCM with equal physical properties in both solid and liquid phases, incompressible and laminar flow of the HTF and liquid PCM during melting (with both fluids considered as Newtonian). The operating conditions assume constant HTF inlet velocities and inlet temperatures, uniform initial temperature distributions throughout the computational domain for both charging and discharging analyses, and neglecting heat dissipation through the top and bottom of the LTES tank. Modeling of natural convection effects in the liquid PCM during melting has been included through the Boussinesq approximation.

The governing equations, based on these assumptions, are applied to each subdomain and are presented below. For concision, momentum equations have been condensed so that *i* represents x, y and z direction in their respective equations.

HTF

- continuity

$$\operatorname{div} \vec{\boldsymbol{w}} = 0 \qquad \text{(eq. 1)}$$

- momentum

$$\frac{\partial(\rho_{HTF} \cdot w_i)}{\partial t} + \operatorname{div}(\rho_{HTF} \cdot w_i \cdot \vec{\boldsymbol{w}}) = \frac{\partial p}{\partial i} + \operatorname{div}(\mu_{HTF} \cdot \operatorname{grad} w_i) \qquad \text{(eq. 2)}$$

- energy

$$\frac{\partial(\rho_{HTF} \cdot T)}{\partial t} + \operatorname{div}(\rho_{HTF} \cdot \vec{\boldsymbol{w}} \cdot T) = \frac{k_{HTF}}{c_{HTF}} \operatorname{div}(\operatorname{grad} T) \qquad \text{(eq. 3)}$$

Wall

- energy

$$div(\rho_w \cdot \vec{\boldsymbol{w}} \cdot T) = \frac{k_w}{c_w} \operatorname{div}(\operatorname{grad} T) \qquad \text{(eq. 4)}$$

PCM

- continuity

$$\operatorname{div} \vec{\boldsymbol{w}} = 0 \qquad \text{(eq. 5)}$$

- momentum

$$\frac{\partial(\rho_{PCM} \cdot w_i)}{\partial t} + \operatorname{div}(\rho_{PCM} \cdot w_i \cdot \vec{\boldsymbol{w}}) = \left(\rho_{PCM} - \rho_{0,PCM}\right) \cdot g_i - \frac{\partial p^*}{\partial i} + \operatorname{div}(\mu_{PCM} \cdot \operatorname{grad} w_i) + S_i \qquad \text{(eq. 6)}$$

Momentum sinks are incorporated to consider the velocity damping that occurs within the phase change region of the PCM (referred to as the "mushy zone"). The mushy zone is characterized as a porous region (Brent et al., 1988), and the formulations for the momentum sinks are based on the Carman-Kozeny equations, which describe flow through porous media:

$$S_i = \frac{(1-\gamma)^2}{\gamma^3+\varepsilon} \cdot A_{mush} \cdot w_i \qquad \text{(eq. 7)}$$

The intensity of velocity damping is dependent on A_{mush} [kg/m^{3}s], a morphological or „mushy zone" constant, which is usually a large number. In the present investigation, a value of 10^6 has been used. Dividing by zero is

prevented by including the parameter ε, a very small number, set in the expressions to 0.001. The parameter γ is the liquid fraction and it represents the porosity of a cell in the mushy zone. When the specific enthalpy in the PCM region is between H_s and H_l, liquid fraction is calculated as:

$$\gamma = \frac{H - H_s}{H_l - H_s} \quad \text{(eq. 8)}$$

H_s represents solidus specific enthalpy and has a value of $c_{PCM} \cdot T_s$ and H_l represents liquidus specific enthalpy, with the value of $c_{PCM} \cdot T_l + L$.

- energy

$$\frac{\partial(\rho_{PCM} \cdot H)}{\partial t} + \mathrm{div}(\rho_{PCM} \cdot \vec{\boldsymbol{w}} \cdot H) = \frac{k_{PCM}}{c_{PCM}} \mathrm{div}(\mathrm{grad}\, H) \quad \text{(eq. 9)}$$

Temperature is calculated from numerically obtained specific enthalpies in the following way:

$$H \leq H_s \rightarrow T = \frac{H}{c_{PCM}} \quad \text{(eq. 10)}$$

$$H_s \leq H \leq H_l \rightarrow T = T_s + (T_l - T_s) \cdot \frac{H - H_s}{c_{PCM} \cdot (T_l - T_s) + L} \quad \text{(eq. 11)}$$

$$H \geq H_l \rightarrow T = \frac{H - L}{c_{PCM}} \quad \text{(eq. 12)}$$

Equations (1)-(6) and (9) are solved when melting processes are simulated. When solidification processes are considered, governing equations regarding the PCM subdomain are reduced to the energy equation, describing conductive heat transfer:

$$\frac{\partial(\rho_{PCM} \cdot H)}{\partial t} = \frac{k_{PCM}}{c_{PCM}} \mathrm{div}(\mathrm{grad}\, H) \quad \text{(eq. 13)}$$

Equations (1)-(4) remain unchanged when solidification processes are investigated since they are governing equations for the HTF and wall subdomains.

In the initial moment, uniform temperature distribution throughout the computational domain is defined, below the solidus temperature in melting simulations and above solidification temperature in solidification simulations. Also, the HTF is assumed to be stationary, i.e. its velocity has been set to zero. It can be written:

$$T = T_{init};\ w_x = 0;\ w_y = 0;\ w_z = 0 \quad \text{(eq. 14)}$$

Boundary conditions are defined at the outer boundaries of the computational domain and at the boundaries between subdomains. The inlet boundary condition is specified at the HTF inlet, providing the inlet temperature and velocity values. The outlet boundary condition assumes fully developed fluid flow, where there is no variation in variables in the flow direction, and is applied at the HTF outlet.

At the top and bottom regions of the PCM and wall, adiabatic boundary conditions are applied, considering them to be perfectly insulated. In the fluid PCM subdomain (in melting simulations), the no-slip condition is also applied at these boundaries, indicating that the fluid velocity at the boundary is zero. Heat transfer by conduction is defined in the thin layer along the boundaries between the HTF and the wall, as well as between the PCM and the wall. Furthermore, at those boundaries, the no-slip condition is also applied in the HTF subdomain, as well as in the PCM subdomain in melting simulations. For the outer domain boundaries in the HTF, wall and PCM subdomains, symmetry boundary conditions are defined, assuming that the flow and temperature profiles are symmetrical with respect to these boundaries. A schematic of the boundary conditions has been provided in Fig. 2. In Fig. 2, asterisks (*) denote that the expression is only applied when natural convection is considered, i.e. in melting investigations.

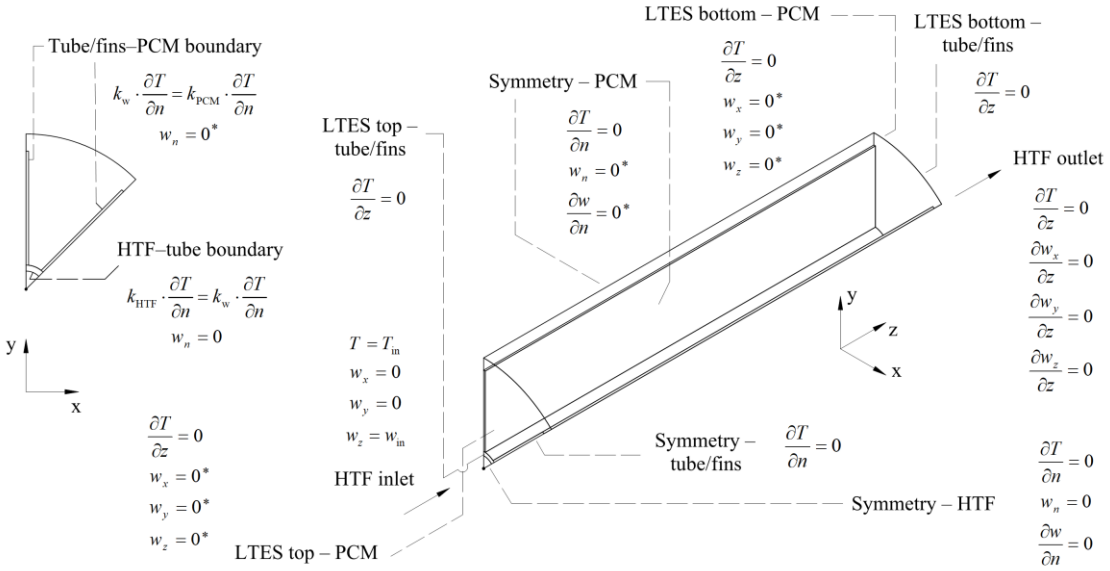

Fig. 2. Boundary conditions schematic in the xy plane and in 3D view

2.2 Numerical procedure

Numerical solution has been obtained by ANSYS Fluent numerical solver that uses the finite volume method (Versteeg and Malalasekera, 1995). Pressure and velocity fields have been coupled using the SIMPLE algorithm. Pressure Staggering Option scheme (PRESTO!) has been used to discretize pressure correction equations. Quadratic upwind scheme (QUICK) has been used to discretize convective terms in momentum and energy equations. Fully implicit discretization in time has been implemented. Under-relaxation factors of 0.3, 0.6 and 1 have been used for pressure, momentum and energy equations, respectively. Convergence criteria of 10^{-3} for continuity and 10^{-6} for momentum and energy equations have been used.

Temperature was coupled with specific enthalpy at the boundaries between the wall (tube and fins) and the PCM subdomains using a series of self-written user-defined functions (UDFs). Momentum sinks, as described in eq. (7), and the conversion of specific enthalpy to temperature according to eqs. (10)-(12) were implemented into the numerical procedure using UDFs. Mesh and timestep independence studies were previously performed (Kirincic et al., 2024a,b) and appropriate mesh size (268500 cells) and timestep (0.1 s) have been selected.

3. Experimental validation

Validation of the mathematical model and numerical procedure was performed through experimental measurements conducted on the constructed LTES tank with the specified geometry characteristics and fin thickness of 2 mm. The LTES tank used Rubitherm's RT 25 paraffin as the PCM and water as the HTF. To prevent heat dissipation to the surroundings, the tank was insulated with expanded rubber foam. The experimental measurements took place at the Laboratory for Thermal Measurements at the University of Rijeka, Faculty of Engineering.

The experimental setup consisted of a shell-and-tube LTES tank, water-water heat pump with hot and cold water supply tanks, a control valve, circulation pumps, temperature sensors, flow meters, and an automatic control system to maintain a constant water temperature at the LTES inlet. A full description of the experimental system can be found in Kirincic et al. (2021c). Temperature measuring was performed using thermocouples, with measurement uncertainty of 0.37 °C (Kirincic, 2021), placed at specific positions around selected tubes on the PCM-side of the tank, as well as at the water inlet and outlet. Measured temperatures were recorded and stored into computer memory at 10-second intervals through a LabView application, which received and processed data from the data acquisition unit. Parts of the experimental setup, as well as the positions of thermocouples around a single examined tube are shown in Fig. 3.

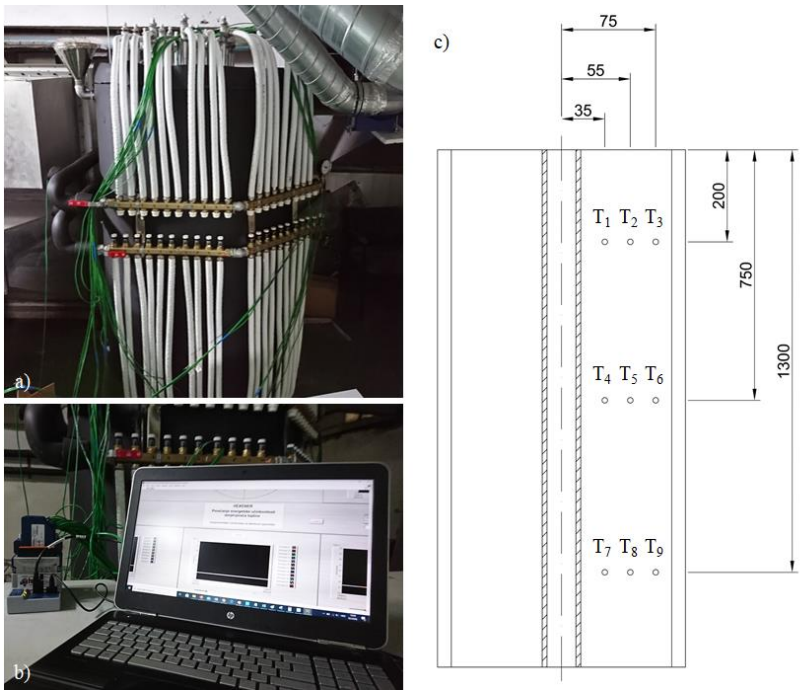

Fig. 3. Experimental setup, a) experimental LTES tank, b) data acquisition set and personal computer, c) thermocouples position and nomenclature

Experimental measurements were performed during the PCM melting and solidification processes for a variety of operating conditions. Validation was performed by comparing the PCM transient temperature variations obtained numerically with those obtained experimentally during both melting and solidification processes. In Fig. 4, a comparison of transient PCM temperature variations obtained experimentally and numerically during both melting and solidification processes at position T_3 is shown.

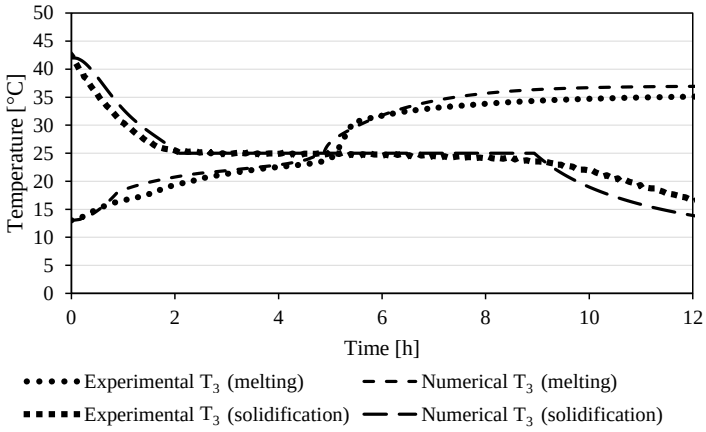

Fig. 4. Comparison of transient temperature variations during melting and solidification obtained experimentally and numerically at position T_3

The comparison was performed with the total HTF mass flow rate of 0.185 kg/s, which corresponds to an inlet velocity of 0.02 m/s through each tube. For the melting process, the HTF inlet temperature was 37 °C, while for the solidification process, the HTF inlet temperature was 10 °C. Initial temperatures of the PCM were uniform throughout the domain at the start of both melting and solidification experiments and were 13 °C and 42 °C, respectively. As evident from Fig. 4, good agreement between experimental and numerical results was observed for both melting and solidification processes. Additional comparisons, featuring different axial and radial positions and discussion of relative errors between experimental and numerical results, can be found in Kirincic et al. (2021b).

4. Numerical results and discussion

Influence of fin thickness (δ) on heat transfer during PCM melting and solidification processes has been numerically investigated by comparing thermal performances of three LTES configurations with different fin thicknesses; 0.5 mm, 2 mm and 4 mm. The numerical investigation has been performed with the HTF inlet velocity ($w_{HTF,in}$) of 0.02 m/s in both melting and solidification investigations. HTF inlet temperature ($T_{HTF,in}$) was 42 °C in melting investigations and 7 °C in solidification investigations. Initial temperature ($T_{PCM,init}$) was homogenous throughout the domain; 13 °C in melting investigations and 42 °C in solidification investigations. Since there is a slightly larger initial temperature difference between the HTF in the PCM in solidification investigations compared to melting investigations, LTES discharging capacity is approximately 5% larger as a result.

Thermal performances of LTES with different fin thicknesses have been assessed by comparing melting and solidification rates, through temperature and liquid fraction distributions, transient average liquid fraction variations and transient variations of average fin temperatures, as well as stored and released thermal energies in selected charging and discharging times for the PCM annulus surrounding a single HTF tube.

For investigated LTES configurations with selected fin thicknesses, temperature and liquid fraction distributions in the xy plane at z = 750 mm have been shown during melting in calculation times of 1, 3 and 5 h (Fig. 5) and during solidification in calculation times 2, 5 and 8 h (Fig. 6), while transient average variations of liquid fraction during melting and solidification have been shown in Fig. 7.

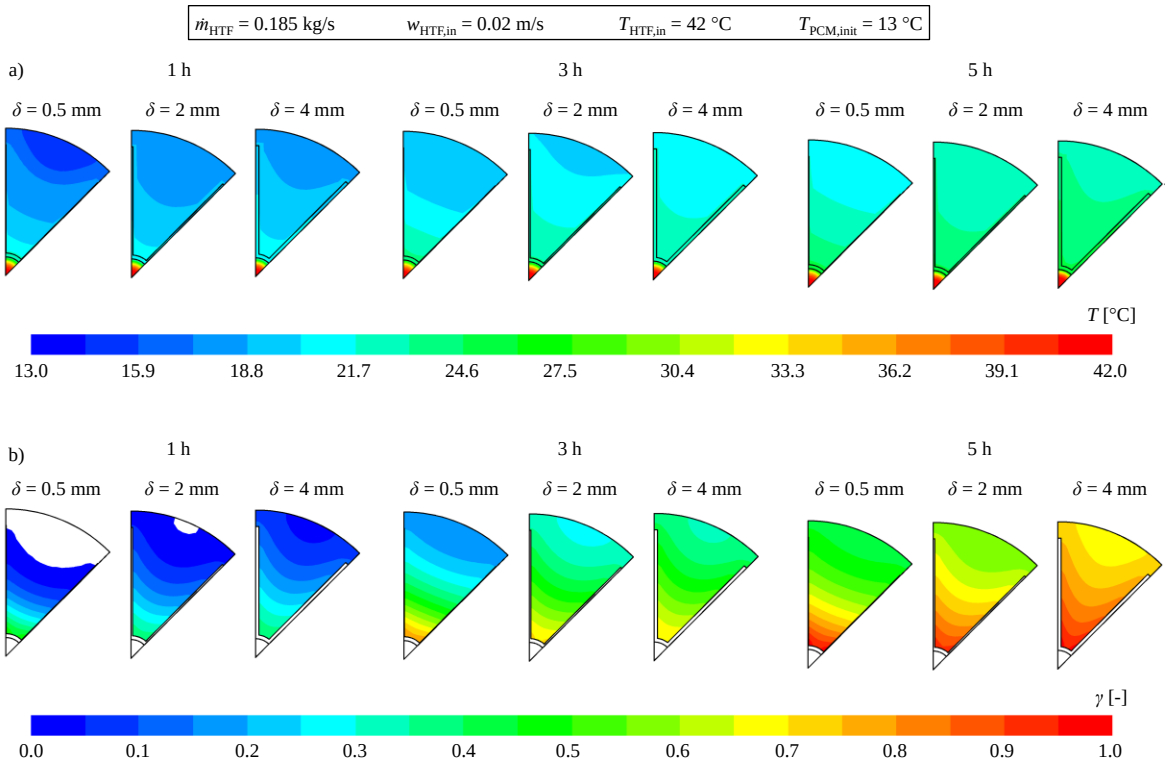

Fig. 5. Temperature (a) and liquid fraction (b) distributions obtained during melting in the xy plane at z = 0.75 m for LTES configurations with fin thicknesses of 0.5 mm, 2 mm and 4 mm

From the comparison of temperature and liquid fraction distributions of LTES configuration with different fin thicknesses in equivalent calculation times, it can be concluded that the most intense heat transfer for both melting and solidification processes is achieved for the largest fin thickness of 4 mm, while the least intense heat transfer is achieved for the smallest fin thickness of 0.5 mm. From liquid fraction distributions, a faster advancement of both the melting and solidification front can be seen in the configuration with the largest considered fin thickness. Similar can be observed from the variations of liquid fraction, from which melting and solidification times can be observed. Melting time for the LTES configurations with 4 mm, 2 mm and 0.5 mm fin thicknesses are 8.67 h, 9.17 h and 11.75 h, respectively, while solidification times for same

configurations are 12.89 h, 14.48 h and 16.64 h, respectively. The investigation also revealed that variations in fin thickness surface area modestly affect heat transfer, as they are increased by 1.5% and decreased by 1.1% in configurations with 4 mm and 0.5 mm compared to the 2 mm fin configurations, respectively. Significant difference in heat transfer is a result of a significantly larger heat capacity of thicker fins, which is directly linked to fin volume and consequently, its mass. For thicker fins, this results in higher average fin temperatures throughout the entire charging process and lower average fin temperatures throughout the discharging process. In order to illustrate that, transient variations of average fin temperatures during charging and discharging have been provided in Fig. 8.

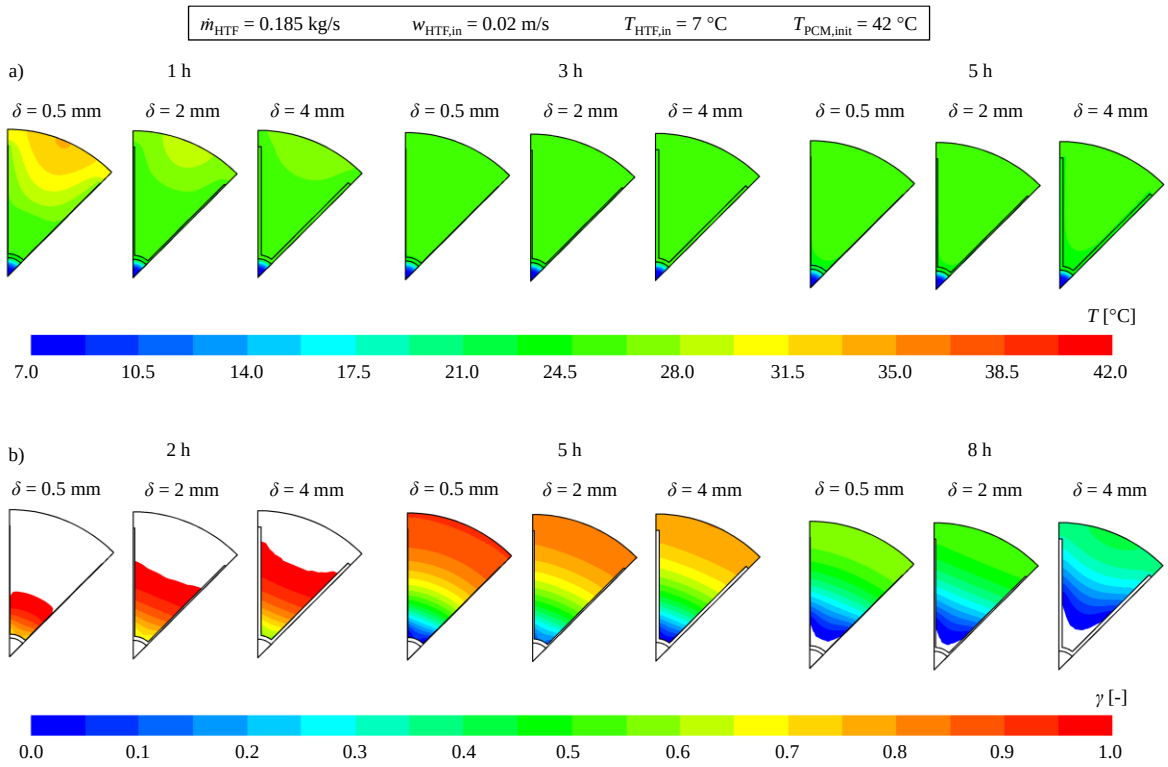

Fig. 6. Temperature (a) and liquid fraction (b) distributions obtained during solidification in the xy plane at z = 0.75 m for LTES configurations with fin thicknesses of 0.5 mm, 2 mm and 4 mm

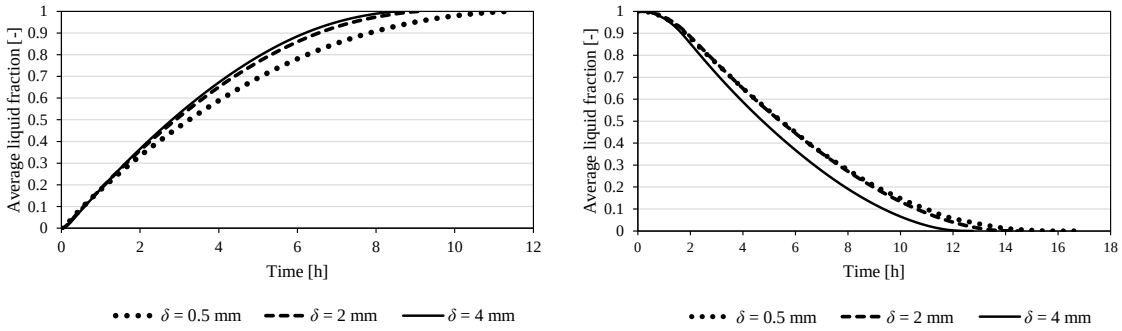

Fig. 7. Comparison of transient average liquid fraction variations during melting (left) and solidification (right) for LTES configurations with fin thicknesses of 0.5 mm, 2 mm and 4 mm

However, increasing fin thickness in a LTES of constant volume also means that the LTES thermal energy storing capacity reduces. For a single LTES tube and its surrounding PCM annulus, values of thermal energy stored in 8 h and released in 12 h have been given in Fig. 9. Stored and released thermal energies are calculated as a sum of sensible and latent thermal energies obtained for the PCM region surrounding the tube. It can be observed that in the 8 h of charging the most thermal energy is stored inside the LTES with 2 mm fin thickness,

6163.3 kJ. Due to lower fin heat capacity resulting in poorer heat transfer, less thermal energy is stored inside the LTES with 0.5 mm fin thickness, 6055.9 kJ. For the LTES with 4 mm fin thickness, 6059.7 kJ is stored in the equivalent charging time. Similarly, in 12 h of discharging, the most thermal energy is also released for the LTES with 2 mm thick fins, 6297.8 kJ, while for LTES configurations with 0.5 mm (6158.7 kJ) and 4 mm thick fins (6291.3 kJ), less thermal energy was released due to lower fin capacity which resulted in lesser heat transfer and reduced amount of the PCM, respectively. Even though thicker fins are beneficial for heat transfer, they decrease the amount of the PCM inside the LTES and result in less stored thermal energy.

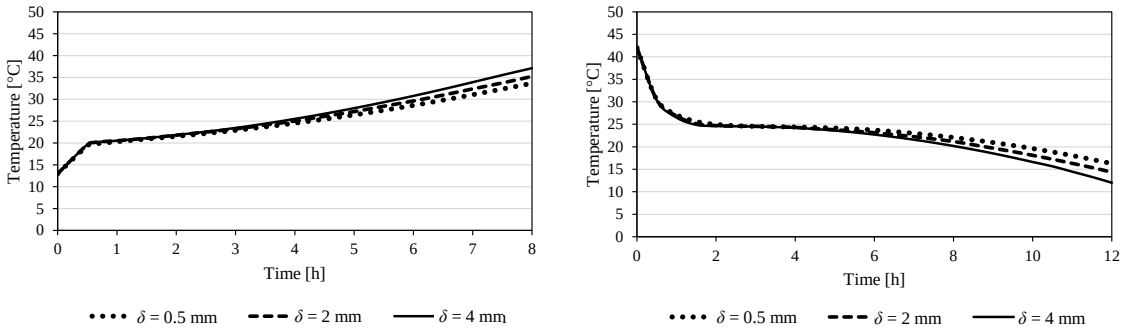

Fig. 8. Comparison of transient average fin temperatures variations during melting (left) and solidification (right) for LTES configurations with fin thicknesses of 0.5 mm, 2 mm and 4 mm

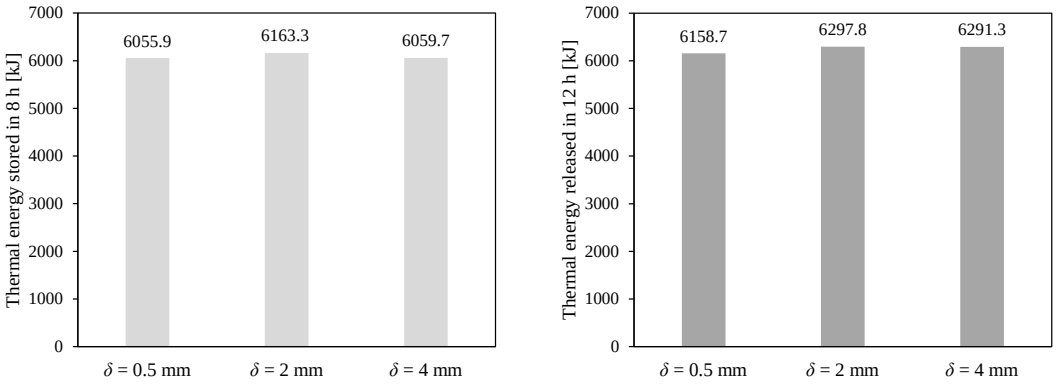

Fig. 9. Comparison of thermal energies stored during 8 h of charging (left) and released during 12 h of discharging (right) for LTES configurations with fin thicknesses of 0.5 mm, 2 mm and 4 mm

5. Conclusion

The paper presented the results of the numerical investigation of the influence of fin thickness on longitudinally finned LTES melting and solidification thermal performance. LTES configurations with fin thicknesses of 0.5 mm, 2 mm and 4 mm were investigated and it was observed from temperature and liquid fraction distributions, transient variations of average liquid fraction and average fin temperatures that thicker fins considerably expedite melting/solidification rate. However, thicker fins also reduce the amount of the PCM inside the LTES, which can result in reduced LTES thermal energy storing/releasing capacity. As observed from obtained stored/released thermal energies for analyzed fin thicknesses, the largest amount of thermal energy was stored/released for the configuration with 2 mm fin thickness. Based on the investigation, it is evident that fin thickness is an influential geometry parameter which needs to be selected carefully in order to enhance the LTES thermal performance.

6. Acknowledgments

This work has been supported in part by Croatian Science Foundation under the project HEXENER (IP-2016-06-4095) and in part by the University of Rijeka under the project numbers “uniri-iskusni-tehnic-23-180” and “uniri-mladi-tehnic-23-8”.

7. References

Brent, A.D., Voller, V.R., Reid, K.J., 1988. Enthalpy-porosity technique for modeling convection-diffusion phase change: application to the melting of a pure metal, Numerical Heat Transfer, 13 (3), 297–318.

Fteiti, M.A., Ghalambaz, M., Younis, O., Sheremet, M., Ismael, M., 2023. The influence of the metal foam layer shape on the thermal charging response time of a latent heat thermal energy storage system, Journal of Energy Storage, 58, 106284.

Khan, Z., Khan, Z., Ghafoor, A.., 2016. A review of performance enhancement of PCM based latent heat storage system within the context of materials, thermal stability and compatibility, Energy Conversion and Management, 115, 132–158.

Khan, Z., Khan, Z.A., 2017. Experimental investigations of charging/melting cycles of paraffin in a novel shell and tube with longitudinal fins based heat storage design solution for domestic and industrial applications, Applied Energy, 206, 1158–1168.

Kirincic, M., 2021. Experimental and numerical analysis of the latent thermal energy storage performance enhancement, PhD thesis, University of Rijeka, Faculty of Engineering, Rijeka, Croatia, (in Croatian).

Kirincic, M., Trp, A.., Lenic, K., 2021. Numerical evaluation of the latent heat thermal energy storage performance enhancement by installing longitudinal fins, Journal of Energy Storage, 42, 103085.

Kirincic, M., Trp, A., Lenic, K., 2021. Influence of natural convection during melting and solidification of paraffin in a longitudinally finned shell-and-tube latent thermal energy storage on the applicability of developed numerical models, Renewable Energy, 179, 1329–1344.

Kirincic, M., Trp, A., Lenic, K., Wolf, I., 2021. Experimental investigation on melting of paraffin in latent thermal energy storage, Proceedings of the 14th International Renewable Energy Storage Conference 2020 (IRES 2020), 193–198.

Kirincic, M., Trp, A., Lenic, K., Torbarina, F., 2024. Numerical analysis of the influence of geometry parameters on charging and discharging performance of shell-and-tube latent thermal energy storage with longitudinal fins, Applied Thermal Engineering, 236 (A), 121385.

Kirincic, M., Trp, A., Lenic, K., Batista, J., 2024. Latent thermal energy storage performance enhancement through optimization of geometry parameters, Applied Energy, 365, 123255.

Kumar, A., Saha, S.K., 2020. Experimental and numerical study of latent heat thermal energy storage with high porosity metal matrix under intermittent heat loads, Applied Energy, 263, 114649.

Liu, M., Saman, W., Bruno, F., 2012. Review on storage materials and thermal performance enhancement techniques for high temperature phase change thermal storage systems, Renewable and Sustainable Energy Reviews, 16, 2118–2132.

Modi, N., Wang, X., Negnevitsky, M., 2023. Numerical investigation into selecting the most suitable shell-to-tube diameter ratio for horizontal latent heat thermal energy storage, Energy for Sustainable Development, vol. 73, 188–204.

Rathod, M.K., Banerjee, J., 2015. Thermal performance enhancement of shell and tube Latent Heat Storage Unit using longitudinal fins, Applied Thermal Engineering, 75, 1084–1092.

Versteeg, H.K., Malalasekera, W., 1995. An Introduction to Computational Fluid Dynamics: The Finite Volume Method, Longman Scientific and Technical, Essex, England.

Yang, X., Lu, Z., Bai, Q., Zhang, Q., Jin, L., Yan, J., 2017. Thermal performance of a shell-and-tube latent heat thermal energy storage unit: Role of annular fins, Applied Energy, 202, 558–570.

Yu, C., Zhang, X., Chen, X., Zhang, C., Chen, Y., 2020. Melting performance enhancement of a latent heat storage unit using gradient fins, International Journal of Heat and Mass Transfer, 150, 119330.

Yu, D., Qiu, Y., Zhang, X., 2023. Role of nano-copper in discharging performance of latent heat storage unit, International Communications in Heat and Mass Transfer, 144, 106748.

RT 25 data sheet, Rubitherm GmbH, 2018.

List of symbols

A_{mush}	morphological constant (kg/m^{3}s)
c	specific heat capacity (J/kgK)
g	gravitational acceleration (m/s^2)
H	specific enthalpy (J/kg)
k	thermal conductivity (W/mK)
L	specific latent heat (J/kg)
$\dot{m}$	mass flow rate (kg/s)
p	pressure (Pa)
p^*	pressure reduced by hydrostatic component (Pa)
S	source term in momentum equations (N/m^3)
T	temperature (K)
t	time (s)
w	velocity (m/s)
x, y, z	spatial coordinates (m)
β	thermal expansion coefficient (1/K)
γ	liquid fraction (-)
δ	fin thickness (m)
ε	numerical constant (-)
μ	dynamic viscosity (Pa·s)
ρ	density (kg/m^3)

Subscripts

0	reference
HTF	heat transfer fluid
in	inlet
init	initial
l	liquidus
n	normal
PCM	phase change material
s	solidus
w	wall
x, y, z	spatial coordinates

Pilot facility for the study of thermal energy storage: Experiments and Theoretical model

A. Castro-Vizcaíno[1,2], K. Babul[3], M.S. Romero-Cano[1,2], J.L. Bosch[1,2], M.J. Ariza[1,2], J. Alonso-Montesinos[1,2], A.M. Puertas[1,2], B. Gil[4], S. Rosiek[4]

[1] Department of Chemistry and Physics, University of Almería, Ctra. Sacramento s/n, Almería, 04120, Spain

[2] CIESOL, Joint Centre of the University of Almería-CIEMAT, Ctra. Sacramento s/n, Almería, 04120, Spain

[3] Department of Energy Conversion Engineering, Wroclaw University of Science and Technology, Wybrzeze Wyspianskiego 27, Wroclaw, 50370, Poland

[4] Department of Thermodynamics and Renewable Energy Sources, Wroclaw University of Science and Technology, Wybreze Wyspianskiego 27, Wroclaw, 50370, Poland

Abstract

Thermal energy storage is a widely used solution to address the mismatch problems between energy availability and demand. However, research in this topic is still necessary to optimise the benefits of energy storage. For this purpose, many research groups have designed and built pilot facilities that allow the study of small pilot tanks for further optimization of storage parameters. Here, we present an experimental setup to study the charging and discharging of thermal energy in a storage tank intended for refrigeration. The facility consists of a chiller which cools down the heat transfer fluid (water/glycol mixture), an 80-litres inertia bath to enhance the chiller's cooling capacity, and a storage tank of 60 litres. A three-way valve allows to control the inlet storage tank temperature, and an electric heater is used with the purpose to study the tank discharging process. A theoretical model representing the energy balance equations for each pilot's components is also presented to rationalise the experimental results. The model reproduces satisfactorily the operation of the system and shows that even minimal thermal losses must be accounted for. Finally, the energy stored in the tank is calculated, showing that up to 30% of the inlet energy is dissipated to the environment, which was also represented by the developed theoretical model.

Keywords: Thermal energy storage, pilot facility, thermodynamic modelling

1. Introduction

The demand of energy for the development of our societies is continuously increasing during the last few decades, while this is in stark contrast with the necessity to reduce gas emissions. This combination has been the driving force for research in renewable energies and energy storage. Buildings is one of the sectors where the demand is increasing more rapidly, amounting to 132 exajoules in 2021, around 30% of the global energy consumption, according to the REN21 Global Status Report (Ren21, 2023), and around 75% of this demand is used for space heating and cooling. However, only 14% of the heating demand was covered with renewable energy in 2021, mainly due to the intermittency of the energy source and the mismatch between energy production and demand, in comparison to the easiness and fastness of fossil fuels-based technologies. Nevertheless, thermal energy storage is perfectly suited to cover this mismatch (Cabeza, 2022; Lizana, 2018).

Several strategies have been developed, but the most widely extended ones are storing the thermal energy in the form of temperature variations of a substance (sensible heat) or inducing a phase change in a so-called phase change material, PCM, (Alva, 2018). Although the use of thermal energy storing is common in many different applications, there are many aspects that need further research, such as the internal structure of the tanks, the control strategies, or the development of new materials. For this purpose, many researchers have designed pilot plants that allow the study of small storage systems. The analysis of the results from these

© 2024. The Authors. Published by International Solar Energy Society
Selection and/or peer review under responsibility of Scientific Committee
10.18086/eurosun.2024.06.03 Available at http://proceedings.ises.org

experiments is then up scaled into real applications, but this requires a deep understanding of the pilot facility. For instance, Koukou et al. (Koukou, 2020) built a prototype storage system based on PCMs, and with two different energy sources, solar and geothermal energy. Two different PCMs were tested, and the most stable output is proposed as optimal for their application. Weiss et al. (Weiss, 2021) studied numerically the stratification inside a tank to conclude that the idealised flow distribution misestimated the thickness of the thermocline and optimised the inlet location for their application. In refrigeration applications, Selvnes et al. (Selvnes, 2021) designed and tested a novel plates-in-tank storage unit, integrated in a pilot facility modelling industrial refrigeration systems based on CO_2. Even more, the combination of modelling and experiments improves the understanding of an actual facility, in particular for the analysis of heat losses in a storage tank, as performed by Mawire (Mawire, 2013). These few examples show that this field is still under development, mainly due to the many different processes involved in it.

In this work, we present a pilot facility for the study of a storage tank of 60 litres, aimed for the analysis of PCMs as storage medium for refrigeration (the whole system operates at sub-zero temperatures). It is composed of a chiller unit and a buffer, or inertia, bath of 80 litres, a heater, and the storage tank. In the present work and with the main goal to simplify the experiments, the storage tank does not contain PCMs, and only the heat transfer fluid (HTF) is used as storage medium. The system allows setting the mass flow rate and storage inlet temperature, as well the heater to simulate an external load to activate the tank discharging process. Moreover, a theoretical model is also presented, based on the energy balance of the main components of the facility, where most of the parameters are taken from the real experiment. The comparison of the model with the experiments shows that even minimal thermal losses must be considered in the storage design process, therefore its importance when we compare to the total energy stored in the tank were also presented.

This work is part of the European Life Programme project COOLSPACES 4 LIFE, aimed to test the viability of thermal PCM-based energy storage for a newly developed solar powered air conditioning system.

2. Materials and methods

2.1. Technical data

Figure 1 illustrates the pilot unit of the cooling system, which includes the inertia tank, an electric heater, two circulation pumps, two and three-way valves, and its corresponding piping. Panels (b) and (c) present the storage tank from side and top views, respectively. A glycol/water mixture (70/30) has been used as the heat transfer fluid (HTF). The cooling unit, has a cooling capacity rating of 1.7 kW and operates on a conventional vapour-compression refrigeration cycle. This is composed of a compressor, a condenser, an expansion valve, and an evaporator, along with the R449A refrigerant gas. Its temperature operating range varies from -40 ºC to +100 ºC and can withstand pressures up to 28 bars. The buffer tank has a storage capacity of 80 litres. An electric heater, is used to activate the storage tank discharging process, and has a power of up to 2 kW. The circulation pumps allows variable flow rates, varying the electricity power from 18 W to 191 W. The inertia tank and all conducting pipes are thermally isolated with a elastomeric insulating foam.

The right section of the experimental setup (c.f. Fig.1 c) presents a horizontal thermal storage tank that was designed for sensible or latent heat storage. This work focuses only on sensible heat storage operation conditions, while latent heat storage experimental results will be presented in the near future. The presented storage tank was designed within the COOLSPACES 4 LIFE project and manufactured by one of consortium partner Hedera Helix. Constructed from stainless steel, the tank's dimensions are 750 mm x 400 mm x 200 mm, with a total volumetric capacity of 60 litres. It is equipped with small observation windows to monitor the fluid dynamics. For precise temperature control, six holes have been integrated in one side of the tank, facilitating the insertion of six probe branches with racor connections to prevent HTF leaks. This design allows the accommodation of up to 32 probes. To mitigate fluid stratification, the tank incorporates eight fluid inlets, four at the upper level and four at a level immediately below, with an equivalent configuration at the tank outlet. An access gate is installed at the top of the tank, enabling the manipulation of internal probes and encapsulated phase change materials (EPCMs) for future experimental applications. Thermal insulation is provided by an external layer of polyurethane insulating foam surrounding the whole tank, except the observation windows and gate.

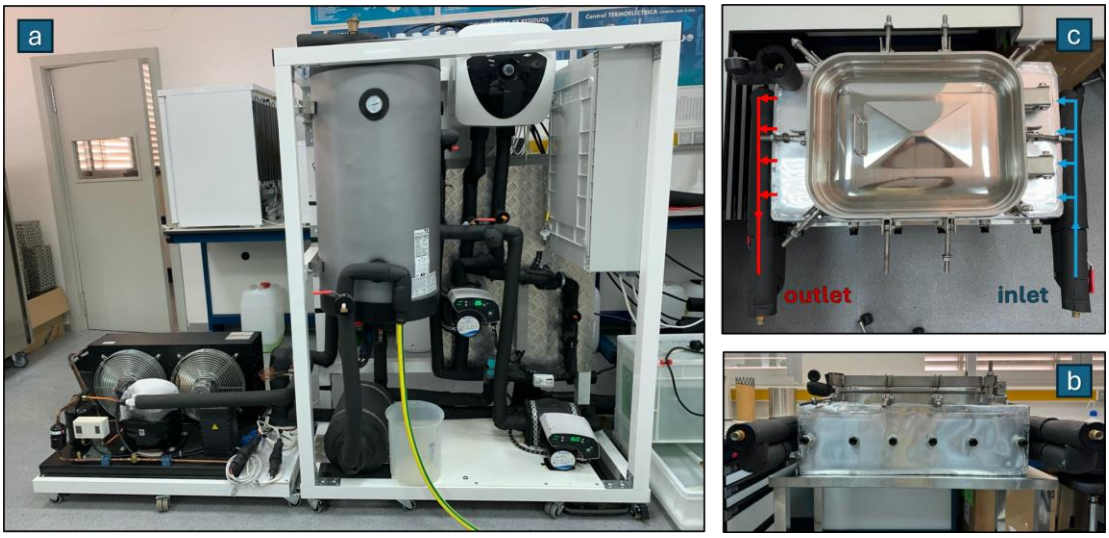

Fig. 2.1: Photograph of the experimental cooling setup with the buffer tank and the heater on the left and a top view of the horizontal storage tank on the right (c) along with a front view (b).

2.2. Operation mode

The presented in this work experimental set-up can operate in two different modes: charging mode, extracting heat from the storage tank, then cooling it down, as well discharging mode, where the cold fluid stored in the tank is circulated through an electrical resistance which simulates a constant energy demand. Thanks to that we can use this prototype for scaling up to a real storage system application in the air-conditioning building systems. Both operational modes are described in greater detail below:

Charging Mode:

This mode starts with the pre-cooling of the heat transfer fluid (HTF) that circulates through the entire system. This cooling is achieved by a heat exchanger in the chiller unit (refrigerant gas-glycol mixture), specifically the evaporator of the cycle. As the HTF cools, (negative) energy is accumulated in the buffer tank until it reaches the set point (T_{buffer}). Once the buffer tank is charged, the actual charging of the thermal storage tank begins, using the energy stored in the buffer tank while the chiller tries to keep its temperature to the set point. The temperature of the inlet to the storage tank (T_{inlet}) is fixed (above the temperature of the inertia bath) using the three-way valve, mixing the outlet of the storage and buffer tanks. This operational mode is designed to minimise the charging time. A hysteresis mechanism is used in the buffer tank to allow variations of the temperature around the set point without the chiller working.

Discharging Mode:

When the thermal storage tank is cold charged, it can be discharged using the heater. This operation mode involves circulating the HTF against a variable load resistance (fixed load during each test), thereby dissipating all the stored energy during the charging process and simulating a real discharging operation.

For both operation modes, the parameters that the user can modify include: buffer tank temperature, inlet temperature to the storage tank, system flow rate, power of the general pump, opening or closing of the three-way valve and the percentage of load offered by the resistance. The system flow rate is controlled by the power of the general pump and the two-way valve located at the storage tank outlet, which operates automatically based on the integrated control system. To control the inlet temperature to the storage tank, the three-way valve operates freely to regulate the water mixture between the storage tank outlet and the buffer tank outlet, thereby adjusting the temperature to the selected set value. When the system operates in discharging mode, the valve must be closed to 0% to prevent the controller from acting and to maintain HTF recirculation through the resistance without mixing the fluid with the buffer tank.

3. Model description

In order to model the experimental setup described previously, it is schematized as shown in Fig. 3.1. The approximation of subcooled liquids is used, where the change in enthalpy is written as $\Delta h = c_p \cdot \Delta T$ in the energy balance equation:

$$\frac{dE_{vc}}{dt} = \dot{Q} - \dot{W} + \sum_e \dot{m}_e h_e - \sum_s \dot{m}_s h_s \quad (1)$$

where E_{vc} stands for the energy in the control volume, $\dot{Q}$ and $\dot{W}$ correspond the heat and work exchanged through the boundaries, and $\dot{m}$ is the mass flow rate. The subindices *e* and *s* refer to "entering" and "leaving" the control volume.

Only the heat exchanger of the cooling unit is considered, with a cooling capacity $\dot{Q}_{cooler}$. Ideal mixing is assumed in both the *inertia bath* and the *storage tank*, and heat losses are assumed, proportional to the temperature difference with the ambient. The three-way valve is also included, with a control similar to the experimental setup, to achieve the target temperature entering the *tank*, T_{3a}. The heater is active only in the discharging mode and is characterised by the thermal power $\dot{Q}_{heater}$.

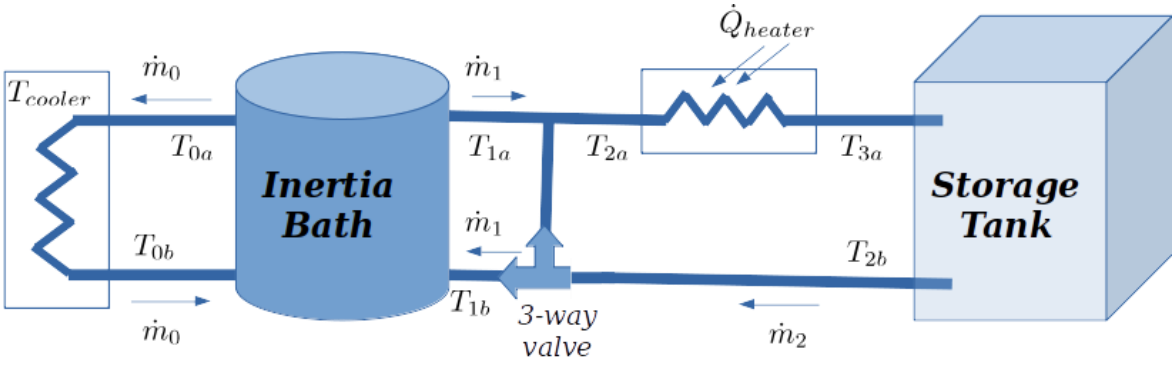

Fig. 3.1: Schematic representation of the experimental setup, with the variables for the model

The governing equations are therefore as follows:

- Cooler. The heat released by the refrigerant, at temperature T_{cooler}, is given by $\dot{Q}_{cooler} = k(T_{cooler} - T_{0a})$, where k is a heat transfer coefficient to be determined. Assuming that the cooler is in the stationary state, the temperature of the HTF leaving the cooler is:

$$T_{0b} = T_{0a} + \frac{k}{\dot{m}_0 c_{HTF}}(T_{cooler} - T_{0a}) \quad (2)$$

  with c_{HTF} the specific heat capacity of the HTF.

- Bath. The inflows with temperatures T_{0b} and T_{1b} mix, and the temperature of the outlets are equal, and identical to the bath temperature: $T_{0a} = T_{1a} = T_{bath}$. This is calculated as:

$$\frac{dT_{bath}}{dt} = \frac{\dot{m}_0}{m_{bath}}(T_{0b} - T_{bath}) + \frac{\dot{m}_1}{m_{bath}}(T_{1b} - T_{bath}) + \frac{\dot{Q}_{env}}{m_{bath} c_{HTF}} \quad (3)$$

  where m_{bath} is the HTF mass inside the bath. The heat loss to the environment is calculated as:

$$\dot{Q}_{env} = k_{env}(T_{bath} - T_{env}) \quad (4)$$

  with k_{env} a constant that controls the heat exchange.

- 3-way valve. This is used to fix the temperature T_{3a} in the charging mode. The opening of the valve is calculated as:

$$x_v = \frac{T^*_{tank} - T_{tank}}{T_{bath} - T_{tank}} \quad (5)$$

where T^*_{tank} is the set point of the tank; when x_v, calculated with this equation is larger than one, it is set to one. The mass flow rate entering the inertia bath from the storage tank is then set according to $\dot{m}_1 = x_v \cdot \dot{m}_2$.

In the discharging mode, in contrast, x_v is fixed $x_v = 0$, and the heater is connected.

- Heater. To model the electric resistance, only the heat flux to the HTF is considered:

$$T_{3a} = T_{2a} + \frac{\dot{Q}_{heater}}{\dot{m}_2 c_{HTF}} \quad (6)$$

where $\dot{Q}_{heater}$ is the heat transferred to the HTF per unit time, which is assumed to be equal to the power of the electric resistance.

- Storage tank. This reservoir is intended to store the energy, either using sensible heat (with HTF or another material), or latent heat with PCM; in our case, energy is stored in the HTF. The energy balance in the tank results in:

$$\frac{dT_{tank}}{dt} = \frac{\dot{m}_2}{m_{tank}}(T_{3a} - T_{tank}) + \frac{\dot{Q}_{env}}{m_{tank} c_{HTF}} \quad (7)$$

where the heat gain from the environment is calculated as in eq. (4), with the tank temperature instead of the bath temperature. The parameter k_{env} is similar in both cases, for simplicity, and is expected to be very small.

The system of equations formed by equations (2), (3), (4), (6), and (7) with the relation between the mass flow rates with x_v, is solved numerically, obtaining the evolution of all temperatures as a function of time, and allowing a direct comparison with the experiments. This requires the specification of T_{cooler}, k and k_{env}, which cannot be accessed experimentally, whereas the flow rates, mass of HTF in the bath, and power of the heater are taken from the experimental setup. The time step is set to δt = 1s, which was checked to be small enough not to influence the results.

4. Results

Fig. 4.1 shows the results of a single experiment and its comparison with the theoretical model presented in previous section. The initial part of the graph (for time below 150 min) shows the cooling of the inertia bath, until it reaches -8 ºC. At t = 150 minutes, the HTF is directed to the storage tank, while the primary loop keeps cooling the bath, as far as it is above the set point (-7 ºC with a hysteresis of 1.25 ºC in this experiment). At t = 300 minutes, the tank has been fully charged as noted by the outlet temperature, which is constant, and discharging process starts with the heater, with a power set to 2000 W. The 3-way valve is closed, and the inlet temperature raises notably.

The predictions of the model, without heat losses, are shown in Fig. 4.2, with T_{cooler} = -13 ºC and $k = 100\ W\ K^{-1}$. These parameters control the initial kinetics, i.e. the charging of the inertia bath, and only k_{env} remains to be determined, while all other parameters are taken from the experiment, including the operation times. At t = 150 min. the cold HTF from the bath is directed to the storage tank, and it charges until the inlet and outlet temperatures are equal. In this case, heat losses are not

considered, $k_{env} = 0$, and the inertia bath keeps its temperature when the storage tank is fully charged. This disagrees with the experiments of Fig. 4.1, where the inertia bath heats up slowly as soon as the cooler is disconnected.

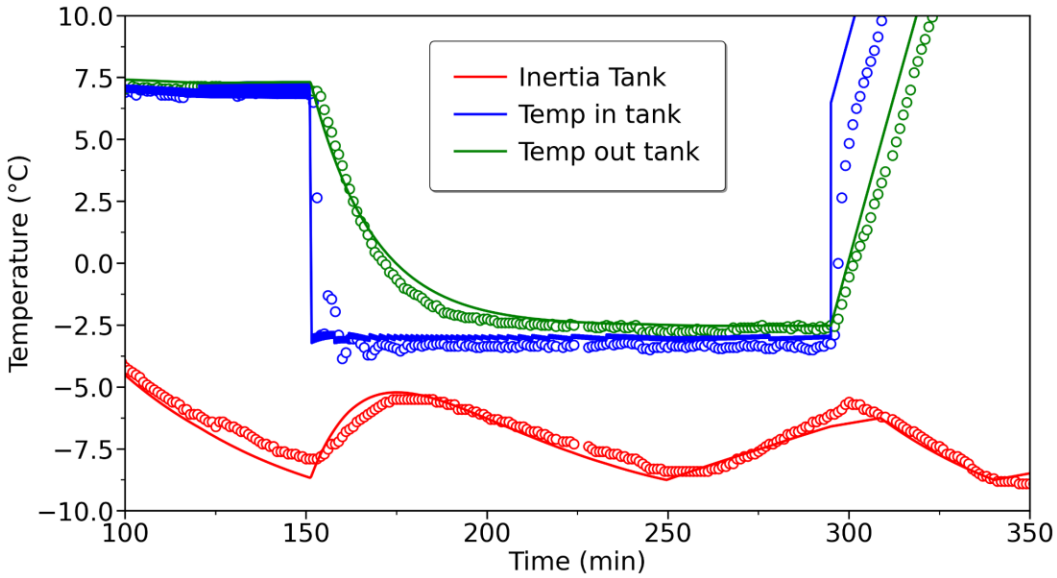

Fig. 4.1: Experimental evolution of the temperature in the inertia bath (red line), inlet and outlet to the storage tank (blue and green lines, respectively).

Therefore, heat losses must be included in the model, and the lines in Fig. 4.1 show the results for $k_{env} = 0.00125\ W\ K^{-1}$, which agree with the experiments (all other parameters are equal to the previous case). Notably, the value of the heat transfer coefficient is much smaller for the heat losses than for the heat exchanger in the cooler, as expected from the isolation of the pipes and reservoirs. It is interesting to note also that the outlet from the tank is in this case always slightly hotter than the inlet. The comparison of these results with Fig. 4.2 shows that heat losses, although minimal, are indeed relevant in the experimental system design, and the model provides an appropriate description of the processes involved in the operation of the experimental set up.

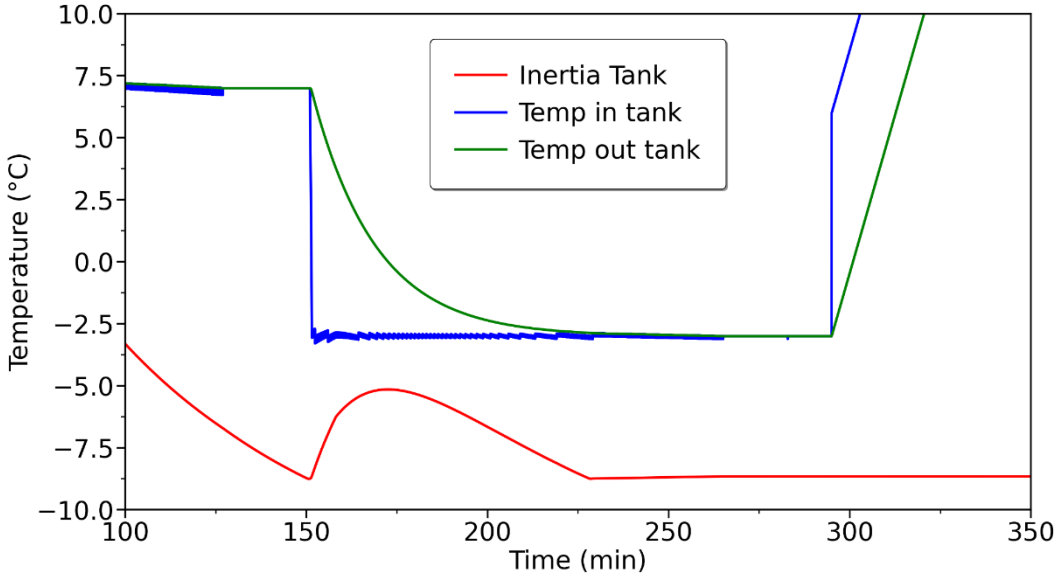

Fig. 4.2: Evolution of the temperature in the inertia bath (red line), inlet and outlet to the storage tank (blue and green lines, respectively) in the model, without heat losses.

On the other hand, when we analyze the energy stored in the tank, we can calculate the energy balance in the tank with the temperature of the inlet and outlet flows. In particular, for the storage tank, the total (negative) energy driven into tank is calculated as below:

$$E_{vc} = \int_{t_0}^{t_1} dt\, \dot{m}\, c_{HTF}(T_{3a} - T_{2b}) \tag{8}$$

A fraction of this energy is stored in the tank, whereas the rest is transferred to the environment (actually, because the energy is negative, the energy is gained from it).

Fig. 4.3 shows the evolution of the energy (in absolute value) for the same case as presented above, comparing the experiments and simulations. The horizontal line shows the energy that can be stored according to the change of HTP temperature:

$$Q = m_{tank} c_{HTF} \Delta T \tag{9}$$

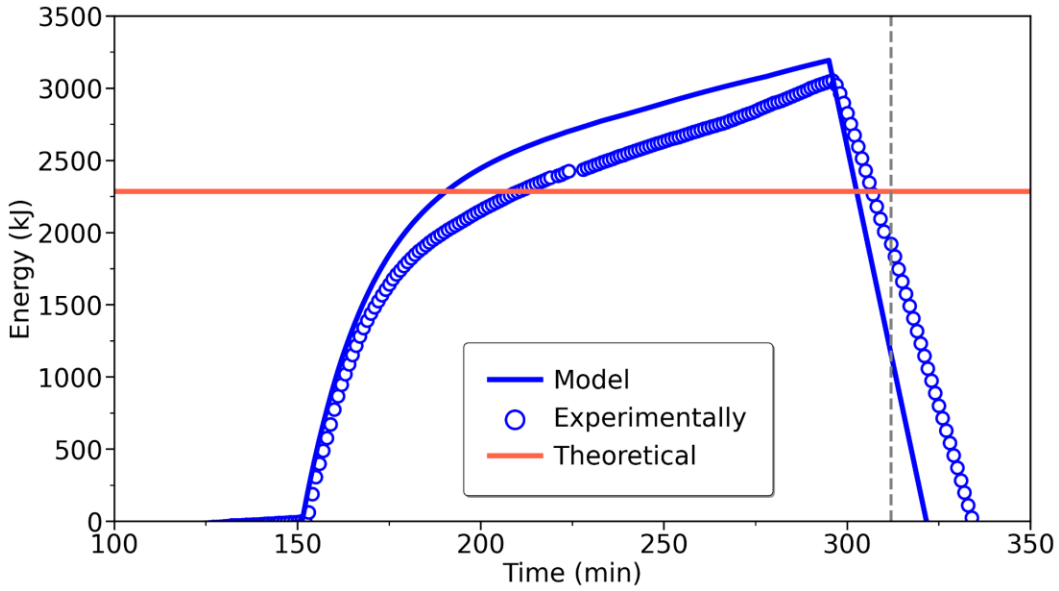

Fig. 4.3: Energy transferred into the storage tank, experimentally (circles) and from the model (line). The horizontal line represents the energy stored in the HTF according to eq. (9).

After the tank has been charging for 150 minutes, it is discharged with the heater, as mentioned above, and the energy in the tank starts decreasing. After 20 minutes, the outlet temperature reaches the initial temperature of the storage tank, 7 ºC (marked by the vertical line) in the figure. The difference between the energy when the discharging starts, and this point, is the energy that could be recovered in this experiment, which, in principle, should agree with the stored energy (horizontal line in the figure).

Fig. 4.4 shows the energy driven to the storage tank, calculated from the experiment and model, with the calculation of the sensible energy in the HTF, eq. (9), and the energy recovered experimentally during the discharging phase. This graph shows that in the model and experiments a large fraction of the energy introduced in the tank is dissipated to the environment, up to 30% in the experiments and up to 25% in the model, whereas the fraction of recovered energy is below the estimated store

energy. Notably, the model and experimental results follow the same trend, with small quantitative differences between them.

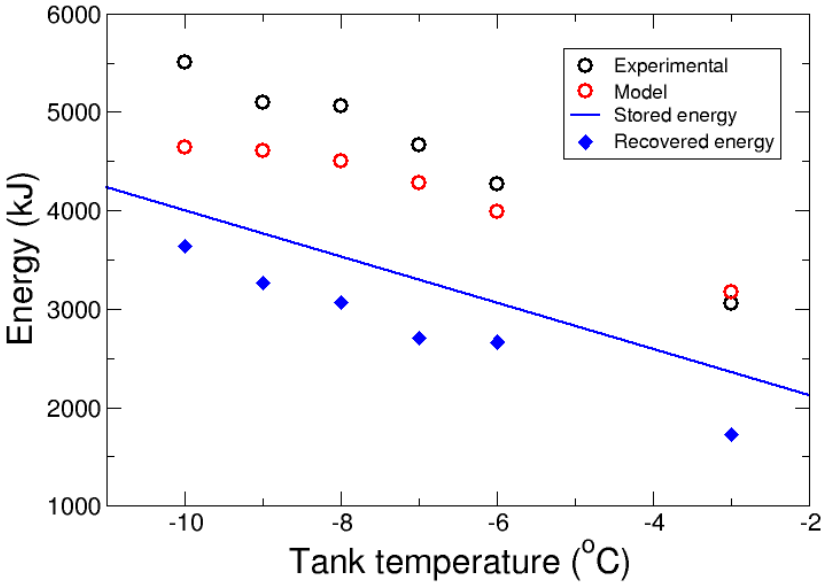

Fig. 4.4: Energy transferred into the storage tank, experimentally (black circles) and from the model (red circles), as a function of the set point tank temperature. The line represents the store capacity according to eq. (9), and the blue diamonds show the energy that is recovered.

5. Discussion and conclusions

Although the model presented here is very simple, and contains only a limited number of parameters, it provides an acceptable description of the presented pilot facility through the evolution of the temperatures in key locations, and the subsequent analysis of storage tank energy balance. Even more, it has led us to verify and quantify the heat gains from the environment that are necessary for a full interpretation of the experimental results. The prototype is now well understood, with all relevant parameters characterised properly, thus the model can be used to predict its behaviour in different circumstances.

In summary, we have presented a prototype cooling facility connected to a tank intended for thermal energy storage for refrigeration. A model describing the thermal balance of each its component has been used to rationalise the results, with a small number of adjustable parameters. The model has shown that thermal losses, although minimal, are relevant to interpret correctly the experimental results, allowing to calculate with good agreement between experiments and the model the amount of energy stored in the tank, and dissipated to the environment.

An attractive future work could consist of EPCMs introduction in this pilot storage tank to perform charging and discharging cycles with the main goal to gain knowledge for full scale tank operation, that are going to be installed in two institutional buildings in different locations: Almeria (Spain) and Wroclaw (Poland).

6. Acknowledgments

The COOLSPACES 4 LIFE project (LIFE20 CCM/PL/001607) is financed by the European Commission under the LIFE Programme and co-financed by the National Fund for Environmental Protection and Water Management in Poland (Project 2244/2021/WN01/OA-PO-LF/D).

Sabina Rosiek is most grateful for the financial support from the Polish National Agency for Academic Exchange, Polish Returns 2018 (https://nawa.gov.pl/en/), with the project identification number: 07PP/0001/19.

7. References

Alva, G., Lin, Y., Fang G., 2018. An overview of thermal energy storage systems. Energy, 144, 341-378.

Cabeza, M.L. (ed.), 2022. Encyclopedia of Energy Storage (four volumes). Elsevier. (See in particular the first volume for Thermal Energy Storage).

Koukou, M.K., Dogkas, G., Vrachopoulos, M.Gr., Konstantaras, J., Pagkalos, Ch., Stathopoulos, V.N., Pandis, P.K., Lymperis, K., Coelho, L., Rebola, A., 2020. Experimental assessment of a full scale prototype thermal energy storage tank using paraffin for space heating application. International Journal of Thermofluids, 1-2, 100003.

Lizana, J., Chacartegui, R., Barrios Padura, A., Ortiz, C., 2018. Advanced low-carbon energy measures based on thermal energy storage in buildings: A review.Renewable and Sustainable Energy Reviews, 82, 3705-3749.

Mawire, A., 2013. Experimental and simulated thermal stratification evaluation of an oil storage tank subjected to heat losses during charging. Applied energy, 108, 459-465.

REN21,2023. Renewables 2023 Global Status Report collection, Renewables in Energy Demand. ISBN 978-3-948393-07-6.

Selvnes, H., Allouche, Y., Hafnes, A., 2021. Experimental characterisation of a cold thermal energy storage unit with a pillow-plate heat exchanger design. Applied Thermal Engineering, 199, 117507.

Weiss, J., Ortega-Fernández, I., Müller, R., Bielsa, D., Fluri, Th., 2021. Improved thermocline initialization through optimized inlet design for single-tank thermal energy storage systems. Journal of Energy Storage 42, 103088.

Microwave Desorption for Flexible Sorption-Heat Storage Application

DI Dr Bernhard Zettl[1], MSc Nayrana Daborer-Prado[1], DI Gayaneh Issayan[1]

[1] University of Applied Sciences Upper Austria

Stelzhamer Straße 23, 4600 Wels, Austria

Abstract

Microwave desorption is a highly efficient method for thermochemical heat storage, surpassing conventional drying. Zeolite desorption experiments showed material-dependent efficiencies: 4ABF reached 70%, 13XBF 30%, and 4AK 15%, compared to a 30% maximum for conventional methods. Sample weight influenced performance, with 13XBF maintaining efficiency across 262g to 869g, though larger masses required longer drying times. The porous structure of 4ABF enhanced vapor transport, achieving superior results. Challenges included non-uniform heating and thermal runaway in samples over 700g, with hotspots exceeding 500°C. Microwave desorption's flexibility in power adjustment (100%, 75%, 50%) makes it a promising approach for sorption heat storage, requiring further optimization to mitigate risks and enhance scalability.

Keywords: Thermochemical heat storage, sorption heat storage, zeolite desorption, microwave desorption

1. Introduction

In order to achieve efficient thermo-chemical heat storage, it is necessary to utilize sorption storage materials that have undergone complete desorption. The rate of desorption is dependent upon the specific material in question, the temperature, the duration of the desorption process, and the process vapor pressure (in a vacuum or in an atmosphere). Mineral sorption materials (e.g., zeolite) necessitate high maximum desorption temperatures; insufficient desorption results in diminished reaction kinetics and energy yield during storage discharge. In contrast, hygroscopic salts require a meticulously regulated desorption process over time to prevent melting and the formation of solutions.

Microwave desorption, which involves the conversion of electromagnetic wave energy directly into heat within the storage material, represents a highly flexible energy conversion option for this application, like reported in Dinglsreiter (2000) and Kraus (2010). Studies demonstrate that microwave irradiation significantly enhances the desorption rate of water vapor from zeolites. For instance, Watanabe et al. (2009) observed a 2.22-fold increase in water desorption rate from zeolite 4A using microwave heating compared to conventional hot-air methods. Similarly, Zhang and Hu (2011) reported that microwave-assisted regeneration of zeolites 13X and 4A for water desorption achieved superior efficiency and speed relative to traditional techniques. These findings are corroborated by Yasin and Martin (2020), who highlighted the enhanced energy efficiency and accelerated desorption process facilitated by microwave heating, particularly in humidity control applications.

The process of heating zeolite using microwaves is initiated by the application of microwave energy, which triggers a series of chemical and thermal interactions within the zeolite structure. Initially, hydrated zeolite absorbs microwave energy through its adsorbed water, resulting in a temperature increase. The adsorbed water desorbs from the zeolite at temperatures between 150 and 250°C, completing its contribution to microwave absorption. At higher temperatures (300–400°C), the zeolite itself begins to absorb microwaves directly, with absorption efficiency increasing as the temperature rises. A critical threshold (approximately 400–500°C) may result in thermal runaway, depending on the cation composition of the zeolite lattice. For example, ion-exchanged 5A zeolite does not experience thermal runaway due to the absence of cations in specific lattice positions, unlike 4A zeolite (Thiebaut, 1988; Ogishi, 2001).

This paper presents a concept of a multimode microwave desorption process, offering an efficient and highly flexible desorption method for energy storage using fluctuating sources. To capture the special conditions of this process, a demonstration setup is being implemented to compare desorption via infrared and microwave heating. By leveraging findings from prior research, such as those by Watanabe et al. (2009), Zhang and Hu (2011), and Yasin and Martin (2020), this study aims to further optimize desorption efficiency and evaluate its scalability for practical applications.

© 2024. The Authors. Published by International Solar Energy Society
Selection and/or peer review under responsibility of Scientific Committee
10.18086/eurosun.2024.06.04 Available at http://proceedings.ises.org

2. Material and Methods

Several commercial materials were employed in the experimental investigations. Zeolites in granulated form, each exhibited distinctive behaviour contingent on their crystal structure, ion content, and binder content. The zeolites were procured from the supplier Chemiewerke Bad Köstritz: 4AK (1.6-2.5mm granules containing binder, LTA-Type, 0.4nm pore size), 13XK (1.6-2.5mm granules containing binder, Faujesite-Type, 0.9nm pore size), 13XBF (2.5-5mm granules, no binder, Faujesite-Type, 0.9nm pore size).

Two different measurement techniques were employed, including (a) a multimode microwave oven with a wave stirrer and internal weight measurement and temperature control, and (b) conventional drying in a hot air oven

Fig. 1: Multimode fixed-bed microwave oven with balance and power-meter (left), conventional hot-air drying oven (right)

A weighing device was incorporated into the design of the multimode microwave oven (Fig.1, left) in order to facilitate the monitoring and recording of the weight loss of the material sample. The magnetron has a maximum output of approximately 1000W, with typical conversion losses of 35%. The emitted wave has a frequency of 2.45GHz. An infrared temperature sensor is positioned above the material undergoing drying, allowing for the monitoring of the temperature. A power meter is employed to quantify the electrical power consumption of the microwave. Comparative measurements in a conventional drying oven (Fig. 1, right) are conducted to facilitate a comparison of the efficiency of the two desorption routes. The measurements in the drying oven were determined with other sample weights due to the size of the oven. The electrical power was only measured during the desorption process, and the heating of the empty oven was not taken into account in the efficiency comparison.

3. Results

3.1. Microwave batch heating

Several different experiments were carried out. Different types of zeolite were tested, different sample weights were used and finally the microwave power was varied. For analysis, both the material temperature and the material weight were recorded to evaluate the drying progress of the zeolites.

The figures below show the results.

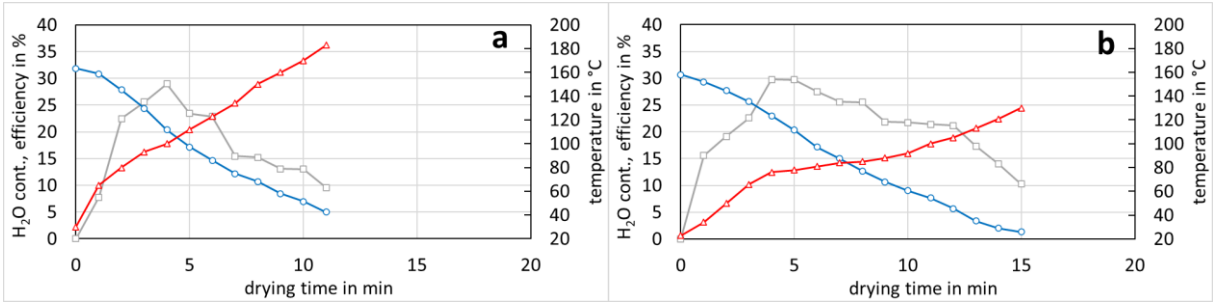

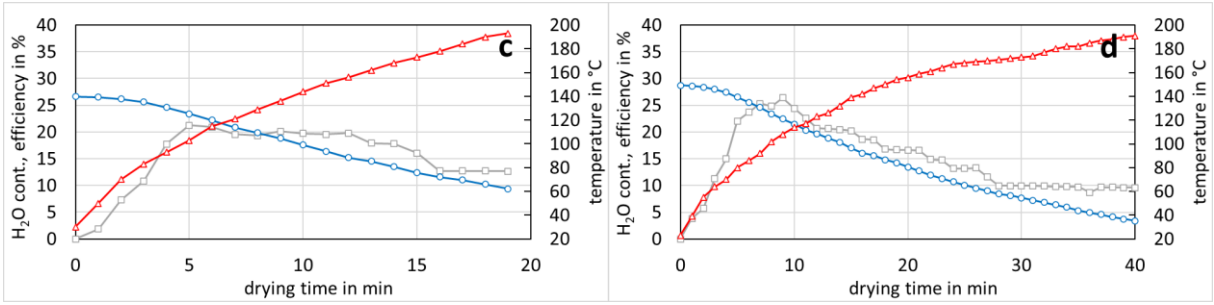

Fig. 2: Microwave desorption on 13XBF material with different masses: (a) 262g, (b) 408g, (c) 640g, (d) 869g. Material water fraction (blue) and drying efficiency (grey) refers to the left axis, material temperature (red) to the right axis.

In Fig 2 the material 13XBF was desorbed and the sample mass increased in steps from 262g to 869g. All weights are dry mass. The red line is the temperature of the material as measured by the infrared sensor, the blue line is the water content of the material as a percentage of the dry mass and the grey line is the drying efficiency.

The drying efficiency represents the current enthalpy per time required to cause the weight loss of the sample by desorption, compared to the total current power consumed.

The time required to heat and dry the material varies according to the weight of the material. The drying tests were carried out at a temperature of max. 200°C and the residual moisture of the material was determined in a conventional oven by heating (1h@350°C) and weighing. Heating of the zeolite fill was not always uniform; sometimes a hot spot pattern was formed, indicating that the wave-stirring function is inadequate. Prolonged heating (above 200°C) leads to thermal runaway in some areas of the material, the granules begin to glow, indicating temperatures >500°C.

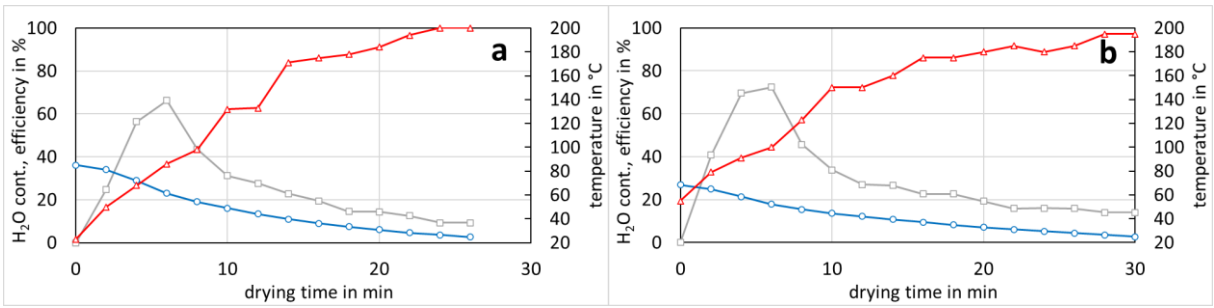

Fig. 3: Microwave desorption on 4ABF material with different masses: (a) 300g, (b) 550g. Material water fraction (blue) and drying efficiency (grey) refers to the left axis, material temperature (red) to the right axis.

In Fig. 3, 4ABF was desorbed. The drying efficiency is significantly higher for this material, with values of over 70% being achieved at times.

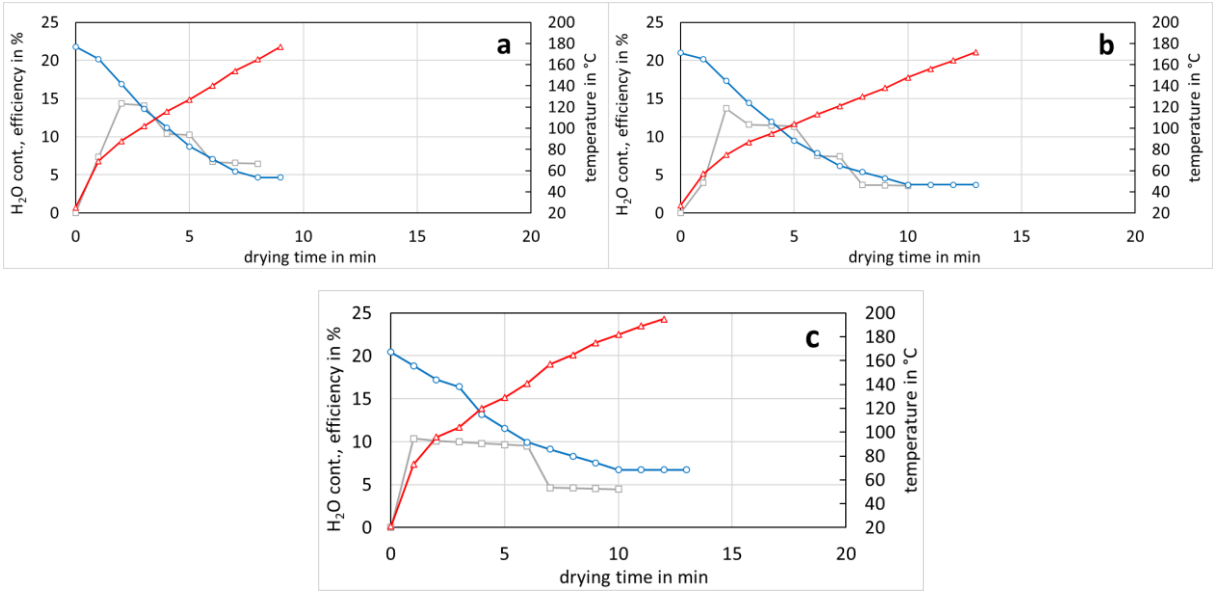

Fig. 4: Microwave desorption on 4AK material with similar masses but different microwave power: (a) 100% power, (b) 75% power, (c) 50% power. Material water fraction (blue) and drying efficiency (grey) refers to the left axis, material temperature (red) to the right axis.

In Fig. 4, the material 4AK was used, the microwave power was varied in this test. The sample mass of all measurements in Fig. 4 is 120g, the heating time is longer for lower powers, the drying efficiency is comparatively low for this material.

3.2 Conventional heating oven

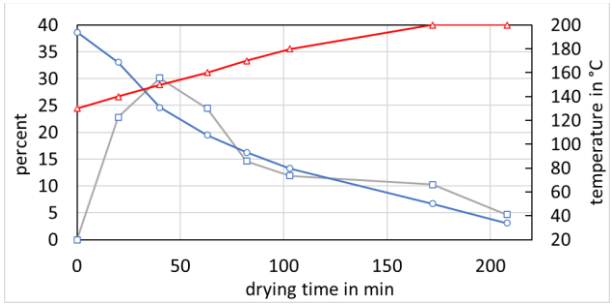

Fig. 5: Oven desorption of 13XBF material with a mass of 2800g. Material water fraction (blue) and drying efficiency (grey) refers to the left axis, material temperature (red) to the right axis.

To compare microwave drying with the conventional method, tests were carried out in a hot air oven. The weight of the sample was chosen to make good use of the space and electrical power of the oven and to avoid problems with moisture removal. The oven was preheated to 200° and from the time the sample was placed in the oven, the weight loss was determined by weighing at intervals and the drying efficiency was calculated.

4. Discussion

All tests show a temperature rise and mass loss due to desorption. The drying efficiency, defined as the ratio of the enthalpy required to cause sample weight loss through desorption to the total current power consumed, is initially low as the material heats up. Maximum drying efficiency is highly material-dependent, with values ranging from 15% for 4AK to 70% for 4ABF and 30% for 13XBF. However, at low material moisture levels, efficiency drops significantly and eventually reaches zero when no further drying is achieved. The ability to desorb a wide range of sorbent materials with high efficiency is a critical advantage of microwave drying, but it is contingent upon the specific zeolite structure and granule composition.

The granules 4AK and 4ABF, composed of identical zeolite crystals, differ in binder type: 4AK uses an attapulgite clay binder, while 4ABF incorporates an organic binder thermally converted into a porous zeolite-like structure. The BF-bonded materials exhibit significantly higher drying efficiencies due to enhanced vapor transport and faster desorption facilitated by the porous binder layer. When comparing 4ABF and 13XBF granules, the differing zeolite structures necessitate higher temperatures for 13X crystals than 4A crystals to achieve similar material moisture contents (Zettl et al., 2015).

Material quantity also influences the drying process. Larger quantities necessitate longer heating times, and for samples exceeding 700 g, temperature distribution fluctuations in the zeolite bed may lead to thermal runaway. However, for material quantities between 100 and 700 g, consistent temperature profiles, residual moisture values, and drying efficiencies are observed, apart from test duration.

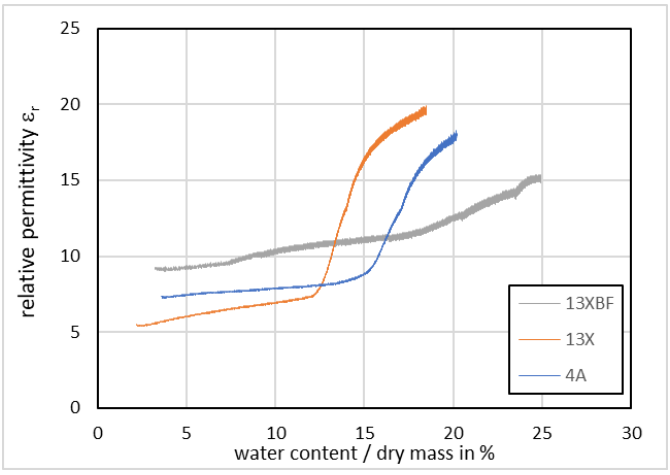

Fig. 6: Relative permittivity of commercial zeolites depending on material water content (Zettl et al. 2023)

The relative permittivity (dielectric conductivity) of zeolites varies with material water content and provides critical insights into absorption behaviour. Dielectric properties, including polarizability, ion oscillations, and water molecule displacement, are influenced by temperature and excitation frequency. Zettl et al. (2023) demonstrated a correlation between permittivity and humidity levels, showing that higher water content initially facilitates efficient microwave absorption. However, as desorption progresses and moisture decreases, permittivity declines, slowing temperature increases until thermal runaway thresholds are surpassed.

The experimental results corroborate the advantages of microwave heating observed in previous studies, such as its ability to accelerate desorption rates and enhance energy efficiency. Notably, our findings reveal material-dependent variations in drying efficiency, with 4ABF exhibiting significantly higher performance due to its porous binder structure. These results align with the reported improvements in desorption efficiency for similar materials (e.g., Zhang and Hu, 2011; Yasin and Martin, 2020), suggesting that microwave heating's volumetric and selective energy delivery plays a pivotal role.

However, challenges such as non-uniform heating patterns and thermal runaway risks persist, particularly in larger sample volumes. These issues resonate with findings by Nigar et al. (2019), who highlighted the influence of dielectric property changes and binder composition on heating behaviour. Addressing these through optimized system design, as suggested in prior research (e.g., Demir, 2013; Watanabe et al., 2009), and innovations in binder materials could further enhance the scalability and practicality of microwave-assisted desorption in energy storage applications.

The studies collectively emphasize the potential of microwave heating to achieve volumetric and selective heating, reducing cycle times and improving energy efficiency. Nonetheless, challenges such as thermal runaway, non-uniform temperature distribution, and material-specific performance variations persist. Addressing these through cavity optimization, binder innovations, and precise power control is vital for advancing the application of microwave desorption in thermochemical storage systems.

5. Conclusion

The study underscores the potential and challenges of employing microwave desorption in thermo-chemical heat storage applications, emphasizing its material-specific efficiency and operational characteristics. Key findings and numerical results from the experiments and referenced studies are summarized as follows:

Material-Specific Efficiency:

- Maximum drying efficiency varied significantly across zeolite types: 15% for 4AK, 30% for 13XBF, and 70% for 4ABF.
- BF bonded materials such as 4ABF have demonstrated superior drying efficiency due to the porous binder structure, which allows for faster vapor transport and desorption compared to conventional bonded materials using attapurgite clay as a binder.

Temperature and Moisture Dynamics:

- Microwave desorption exhibited a clear dependency on the zeolite structure. For instance, 13X crystals required higher temperatures (300–400°C) compared to 4A crystals (150–250°C) to achieve comparable residual moisture levels.
- At higher material temperatures (above 400°C), thermal runaway occurred in some samples, particularly those exceeding 700 g, emphasizing the need for careful temperature regulation.

Scale and Uniformity:

- Larger sample masses required extended heating times. Consistent drying efficiency and moisture reduction were observed for samples between 100 and 700 g, whereas 869 g samples exhibited non-uniform temperature distribution and thermal runaway.
- Comparison with conventional drying highlighted the superior energy efficiency of microwaves in smaller samples, though oven drying managed larger sample masses (e.g., 2800 g) more uniformly.

Permittivity and Dielectric Properties:

- The relative permittivity of zeolites decreased significantly as water content reduced, slowing desorption. For example, NaY zeolite exhibited a rapid temperature rise to 180°C within 5 minutes at 30 W microwave power, with its loss factor exponentially increasing above 200°C (Nigar et al., 2019).
- The permittivity changes align with reduced microwave absorption efficiency at lower moisture levels, a limitation for further optimization.

Microwave vs. Conventional Heating:

- Microwave heating consistently outperformed conventional methods in speed and energy efficiency, with faster desorption in zeolite 4A compared to hot-air drying.
- However, challenges such as non-uniform heating, partly low energy absorption efficiency, and thermal runaway risks were noted.

Implications and Recommendations

Microwave desorption proves advantageous in terms of speed, energy efficiency, and material-specific optimization for small-to-medium sample sizes. However, scaling up and ensuring uniform heating remain key challenges. Innovations in cavity design, power control, and binder composition are necessary to mitigate risks like thermal runaway and non-uniform heating. Addressing these will pave the way for efficient and scalable microwave-based desorption systems in thermo-chemical storage applications.

6. Acknowledgement

This work has been supported by the Government of Upper Austria in the project ‘COMPESTO – comprehensive energy storage’, Research Grant Wi-2022-600132/7-Au

7. References

Demir, H. (2013). Development of microwave-assisted zeolite-water adsorption heat pump. International Journal of Refrigeration. https://doi.org/10.1016/j.ijrefrig.2013.07.005

Dinglreiter, U. (2000). Adsorption, Heißgas- und Mikrowellendesorption bei Matrixadsorbern. Herbert Utz Verlag GmbH, München. ISBN 3-89675-899-3.

Kraus, M. (2010). Dynamische Adsorptionsphänomene in mikroporösen Wirt/Gast-Systemen unter dem Einfluss hochfrequenter elektromagnetischer Felder (Doctoral dissertation). University of Leipzig.

Kumja, M., Ng, C. K., Yap, C., Koyama, S., & Saha, B. B. (2009). Modeling of a novel desorption cycle by dielectric heating. Modern Physics Letters B, 23, 425–428. https://doi.org/10.1142/S0217984909018581

Nigar, H., Sturm, G. S. J., Garcia-Baños, B., Peñaranda-Foix, F. L., Catalá-Civera, J. M., Mallada, R., Stankiewicz, A., & Santamaría, J. (2019). Numerical analysis of microwave heating cavity: Combining electromagnetic energy, heat transfer, and fluid dynamics for a NaY zeolite fixed-bed. Applied Thermal Engineering, 155, 226–238. https://doi.org/10.1016/j.applthermaleng.2019.03.103

Ohgishi, T., Komarneni, S., & Bhalla, A. S. (2001). Mechanism of microwave heating of Zeolite A. Journal of Porous Materials, 8, 23–25. https://doi.org/10.1023/A:1009691313054

Thiebaut, J.-M., Akyel, C., Roussy, G., & Bosisio, R. G. (1988). Dehydration and dielectric permittivity measurements of a porous, inorganic material (13X Zeolite) heated with microwave power. IEEE Transactions on Instrumentation and Measurement, 37(1), 23–27. https://doi.org/10.1109/19.3667

Watanabe, F., Sumitani, K., Kashiwagi, T., Takagi, T., Huang, H., Hasatani, M., & Kobayashi, N. (2009). Influence of microwave irradiation on water-vapor desorption from zeolites. Kagaku Kogaku Ronbunshu, 35(5), 431–435. https://doi.org/10.1252/kakoronbunshu.35.431

Yasin, M. M., & Martin, C. F. (2020). Effect of microwave heating on the performance of Zeolite 13X for water vapor desorption in humidity control applications. Journal of Environmental Chemical Engineering, 8(3), 103378. https://doi.org/10.1016/j.jece.2020.103378

Zettl, B., Englmair, G., & Somitsch, W. (2015). An open sorption heat storage concept and materials for building heat supply. Energy Procedia, 73, 297–304. https://doi.org/10.1016/j.egypro.2015.07.705

Zettl, B., Kirchsteiger, H., Issayan, G., Wagner, W., & Resch, A. (2022). Development of a virtual sensor for state-of-charge evaluation of TCM energy storage. Proceedings of the Conference EUROSUN 2022.

Zhang, X., & Hu, Z. (2011). Microwave-assisted regeneration of zeolites 13X and 4A for water desorption. International Journal of Environmental Science and Technology, 8(1), 55–62. https://doi.org/10.1007/BF03326199

CFD analysis of a thermal storage tank driven by natural convection

Germilly Barreto[1], José González-Aguilar[1], Manuel Romero[1] and Alberto Giaconia [2]

[1]High Temperature Processes Unit, IMDEA Energy, Avda. Ramón de la Sagra 3, 28935, Móstoles, Spain

[2]ENEA, Casaccia Research Center, Via Anguillarese, 301, 00123 Rome, Italy

Abstract

This work addresses a numerical research on a concept of thermal energy storage tank by natural convection. The design of the tank comprises a single reservoir with molten salt and two indirect heat exchangers (thermal oil to molten salt) inside. For discharging, cold thermal oil circulates in the heat exchanger located at the top of the tank, and due to natural convection, the cooled molten salt moves to the bottom of the tank through an adiabatic channel. For charging, the hot thermal oil circulates through the bottom heat exchanger, heating the molten salt and causing it to move up through a second channel. To analyze this concept, a two-dimensional computational fluid dynamics (CFD) model is developed and used to investigate the storage system for different discharge and charge conditions of the heat exchangers. The mass flow rate of the molten salt in the channels, inlet and outlet temperatures of the heat exchangers, and temperature and velocity distribution in the tank are analyzed for different imposed resistance of the flow and discharge/charge rate of the heat exchangers. As main results, the pattern of the mass flow rate of the molten salt in the channels are identified, and its magnitude depends on the design of the heat exchanger, temperature, and heat sink/source. The evolution of the inlet and outlet temperature in the heat exchangers are key indicators to identify the discharge and charge duration of the thermal storage tank and assessing its potential to work as a thermocline system.

Keywords: thermal energy storage, natural convection, numerical modelling, CFD

1. Introduction

To foster the adoption of medium- and high-temperature solar thermal technologies, it is fundamental to implement low-cost thermal storage systems. For this reason, the possibility of using a single stratified tank containing molten salt and driven by natural convection is being analyzed. This concept might avoid costs associated with external pumping of molten salt and control. In this regard, Russo et al. (2018) analyzed this concept integrated into a plant with a solar field and an organic Rankine cycle using a simplified numerical approach. They found that controlling the mass flow rate of molten salt in the tank was necessary for the correct operation of the integrated system. On the experimental side, Gaggioli et al. (2020) conducted an experimental campaign to characterize this concept integrated with real operating conditions, analyzing both discharge and charge modes. For both modes, they found that while the storage system can maintain appropriate temperatures, the minimum temperature during discharge and the maximum temperature during charging were never reached. They concluded that this was related to the high speed of molten salt in the channels. Recently, Cagnoli et al. (2023) developed and validated a transient 2D axisymmetric computational fluid dynamics (CFD) model and used it to analyze the discharging and charging processes to determine heat losses and temperature distribution in the tank. They also investigated numerically the effect of the diameter of the internal channel on the performance of the tank, finding that decreasing the diameter leads to an increase in the temperature of the molten salt. Mostly, for analyzing thermal energy storage systems, particularly thermoclines, the key performance indicators include the time evolution of temperature distribution within tank and discharge/charge efficiency. For example, Shokrnia et al. (2024) employed a 2D axisymmetric CFD model validated with experiments to investigate performance improvement in the storage tank through the incorporation of phase change materials (PCM). Their modifications demonstrated a significant increase in storage capacity, discharge and charge efficiency, and improved temperature distribution. However, literature

© 2024. The Authors. Published by International Solar Energy Society
Selection and/or peer review under responsibility of Scientific Committee
10.18086/eurosun.2024.06.05 Available at http://proceedings.ises.org

on this thermal storage system concept consistently highlights the critical role of the mass flow rate within the channels. Detailed analyses to assess the behavior of this type of storage tank, where natural convection may promote undesirable flow patterns, are lacking in the literature. To address the gap of knowledge, this work develops a two-dimensional CFD model and uses it to analyze the discharging and charging cases for different working conditions of the heat exchangers. The flow rate of the molten salt in the channel, inlet and outlet temperature in the heat exchangers, and the distribution of temperature and molten salt velocity in the tank are assessed.

2. Thermal energy storage design

The main components and working principle for discharging and charging in this concept of thermal storage tank are presented in Figure 1. For discharging, cold thermal oil circulates in a heat exchanger located on the top of the tank (HEx1), which cools down the molten salt and increases its density. Due to natural convection, the cooled molten salt flows to the bottom of the tank through an adiabatic channel (a cylindrical shell crossing the thermocline layers in the vertical direction). For charging, the hot thermal oil (from a solar field) circulates in the heat exchanger at the bottom of the tank (HEx2), which heats up the molten salt and decrease its density. This causes the molten salt to rise to the top of the tank through the charge channel.

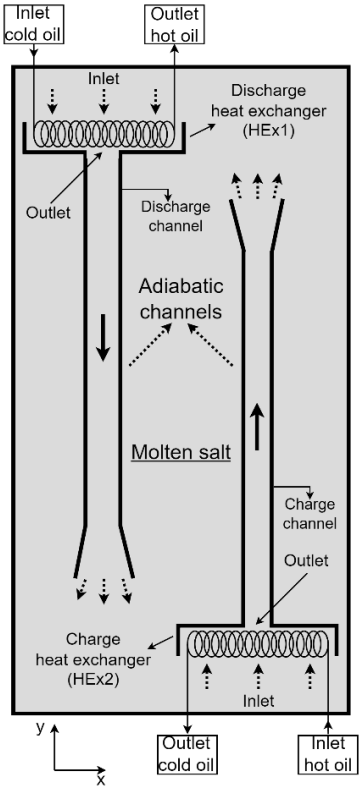

Fig. 1: Two-dimensional scheme of the thermal storage tank driven by natural convection.

3. Numerical modelling

The conservation equations for mass, momentum and energy were solved in Cartesian coordinates using finite element method (FEM) in COMSOL Multiphysics (v6.1),

$$\rho \frac{\partial}{\partial t} + \nabla \cdot (\rho \mathbf{u}) = 0 \qquad \text{(eq. 1)}$$

$$\rho \frac{\partial \mathbf{u}}{\partial t} + \rho(\mathbf{u} \cdot \nabla)\mathbf{u} = -p\nabla + \nabla \cdot \left(\mu(\nabla \mathbf{u} + (\nabla \mathbf{u})^T) - \frac{2}{3}\mu(\nabla \mathbf{u})\mathbf{I}\right) + \left(\rho - \rho_{ref}\right)\mathbf{g} - \mathbf{F} \qquad \text{(eq. 2)}$$

$$c_p \frac{\partial T}{\partial t} + \rho c_p \mathbf{u} \cdot \nabla T = \nabla \cdot (k \nabla T) + Q \qquad \text{(eq. 3)}$$

where ρ, c_p, μ and λ are the density, heat capacity, dynamic viscosity and thermal conductivity of the molten salt, **u** is the velocity vector, p is the pressure, T is the temperature, respectively, and **g** is the gravity acceleration. The heat exchangers are modelled considering a momentum sink **F** in the momentum conservation equation and a heat sink/source Q in the energy conservation equation. The heat sink (negative value) is used for simulate the discharge and a heat source (positive value) is used for the charge and expressed as,

$$Q = Q_0 + m\,t \qquad \text{(eq. 4)}$$

The following formulation for the momentum source is used in the heat exchanger domain:

$$\mathbf{F} = -C_1 \mu \mathbf{u} \qquad \text{(eq. 5)}$$

where C_1 is a momentum sink coefficient. The fluid considered in this study is the molten salt Hitec XL (Na/K/Ca nitrate), with the temperature dependence of its thermal and hydrodynamic properties modelled. The temperature dependence of the fluid density, heat capacity and dynamic viscosity are calculated using the correlations form the work of Giaconia et al. (2021).

3.1. Input parameters and boundary and initial conditions

The walls of the tank and channels are considered with non-slip boundary conditions for the fluid flow and as adiabatic for heat transfer. For discharge, the initial temperature of the tank is uniformly set to a hot temperature of 300 ℃, with a heat sink applied in the corresponding heat exchanger (HEx1), while the inlet of the charge heat exchanger (HEx2) is treated as a wall for fluid flow. For charge, the initial temperature of the tank is uniformly set to a cold temperature of 290 ℃, with a heat source applied in the corresponding heat exchanger (HEx2), while the inlet of the discharge heat exchanger (HEx1) is treated as a wall for fluid flow. Table 1 shows all the main parameters used in this analysis.

Tab. 1: Main geometric parameters of the thermal storage tank.

Description	Dimensions (cm)
Height of the tank	171
Width of the tank	80
Height of heat exchanger	8
Width of the heat exchanger	38
Width of the discharge channel	10
Width of the charge channel	6

4. Results

To check the robustness of the numerical model, the evolution of the computed inlet and outlet mass flow rates in the heat exchangers are compared and maximum difference of less than 5% were found. Figure 2 and Figure 4 show the temperature (℃) distribution and flow direction in the tank at 0, 4, 8, 12, and 16 min (from left to right) during the discharge (Figure 2) and charge (Figure 4). Figure 3 and 5 show the time evolution of the molten salt mass flow rate in the channel (figure on the right) and the inlet and outlet temperatures of the molten salt (figure on the right) in the discharge and charge heat exchangers, respectively. It is observed that for this type of thermal storage, the mass flow rate in the channel shows three main stages during discharging. The first stage consists of a rapid increase in the mass flow rate until it reaches a maximum value (within the first minute), followed by a decrease until a stable region is reached, and finally a third stage characterized by a more stable zone. This instability of the mass flow rate in the channel have also been raised in other works present in literature, such as the study of Gaggioli et al. (2020). Regarding the inlet and outlet temperatures, the outlet exhibits significant fluctuation due to the unstable flow in the channels.

Fig. 2: Temperature (°C) distribution and flow direction in the tank for different times during discharge (heat sink of 1 MW m^{-3} and no momentum sink in the heat exchanger).

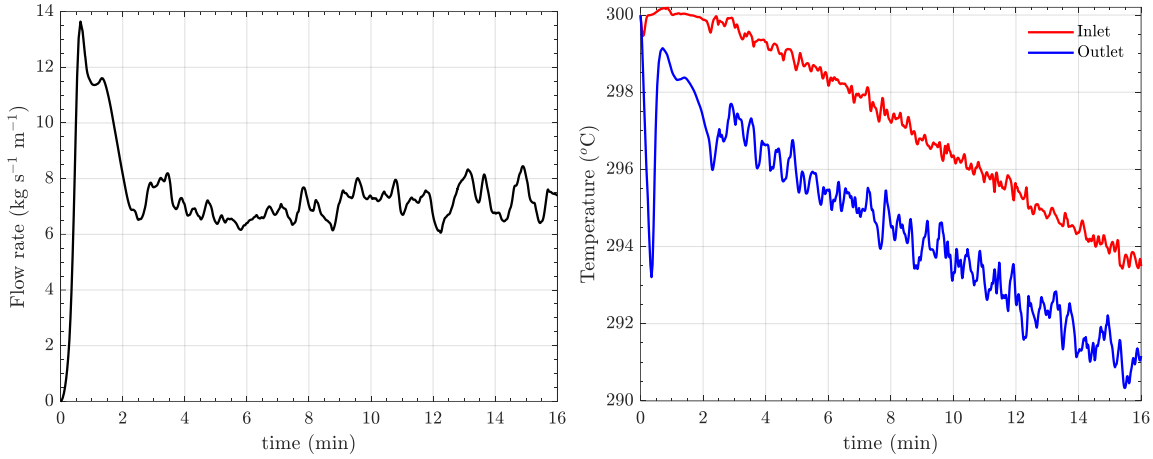

Fig. 3: (left) Mass flow rate of the molten salt in the discharging channel and (right) inlet and outlet temperatures of the molten salt at the cold heat exchanger (heat sink of 1 MW m^{-3} and no momentum sink in the heat exchanger).

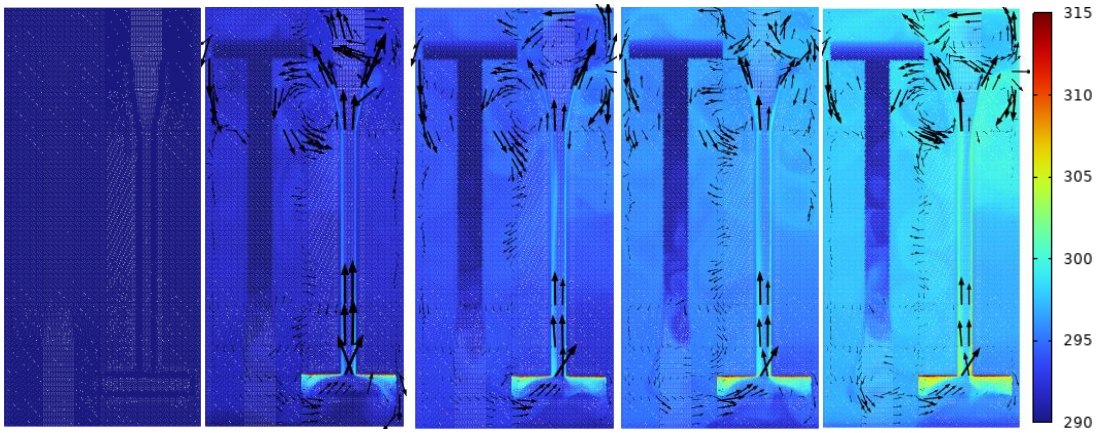

Fig. 4: Temperature (°C) distribution and flow direction in the tank for different times during charge (heat source of 1 MW m^{-3} and no momentum sink in the heat exchanger).

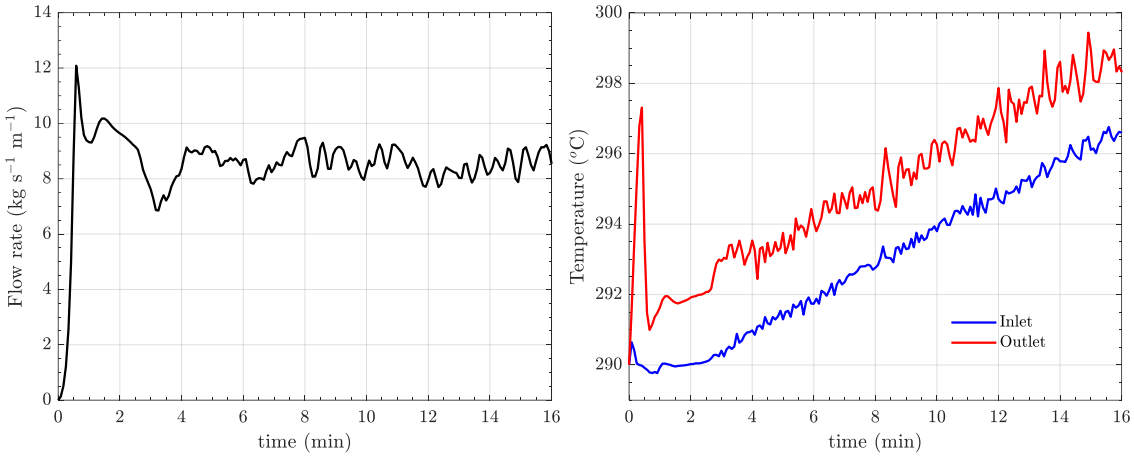

Fig. 5: (left) Mass flow rate of the molten salt in the charging channel and (right) inlet and outlet temperatures of the molten salt at the hot heat exchanger (heat source of 1 MW m^{-3} and no momentum sink in the heat exchanger).

4.1. Parametric analysis of discharge

In this section, a parametric analysis of the momentum sink coefficient C_1 and heat sink profiles during discharge of the thermal storage is presented. Figure 6 shows the evolution of the molten salt mass flow rate in the discharge channel for different momentum sink coefficient, while Figure 7 shows the corresponding inlet (left) and outlet (right) temperatures in the discharge heat exchanger. In both cases, a fixed heat sink of 1 MW m^{-3} was considered. The momentum sink coefficient introduces resistance to fluid flow in the discharge heat exchanger, resulting in a decrease in both the mass flow rate and its fluctuation within channel. This effect is directly correlated to the inlet and outlet temperatures in the heat exchanger, given a fixed heat sink. Although the different stages in the evolution of the mass flow rate in the channel remain, but lower peaks of mass flow rates are observed for higher momentum sink coefficients.

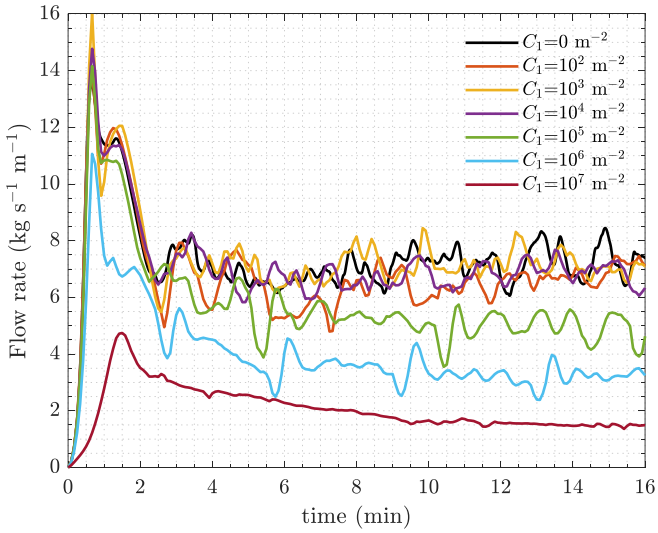

Fig. 6: Time evolution of the molten salt mass flow rate in the discharge channel for different momentum sink coefficient (heat sink, 1 MW m^{-3}).

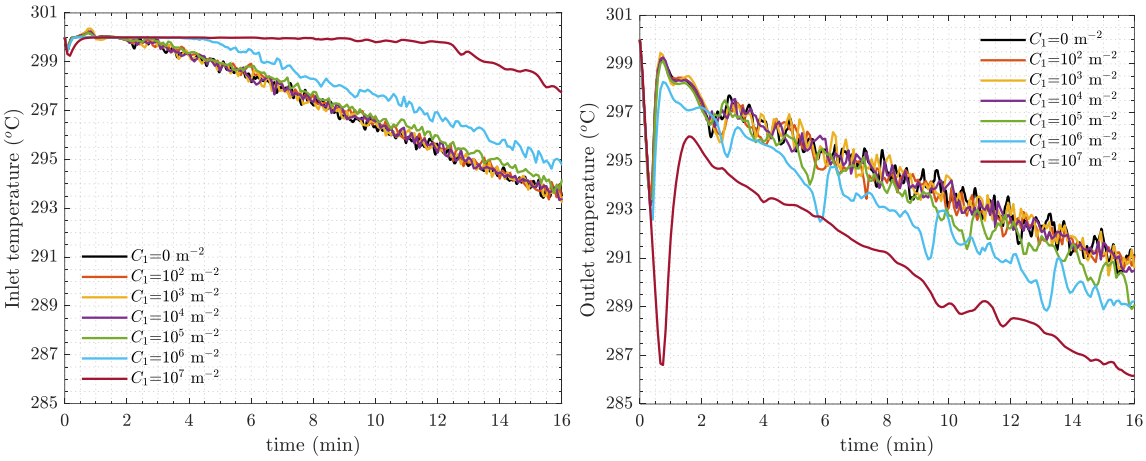

Fig. 7: Inlet (left) and outlet (right) temperatures in the discharge heat exchanger for different momentum sink coefficients (heat sink, 1 MW m^{-3}).

Regarding the use of different heat sink profiles for discharging, Figure 8 (left) shows the heat sink profiles used in the parametric analysis, while Figures 8 (right) shows the resulting evolution of the mass flow rate in the discharge channel, assuming a fixed momentum sink coefficient of 10^7 m^{-2}. Figure 9 presents the corresponding inlet (left) and outlet (right) temperatures in the discharge heat exchanger for the different heat sink profiles. It can be observed that increasing the slope of the discharging heat sink profile leads to more constant outlet temperature in the heat exchanger. This is an important finding, as demonstrates the potential of the thermal storage to behave as a typical thermocline system.

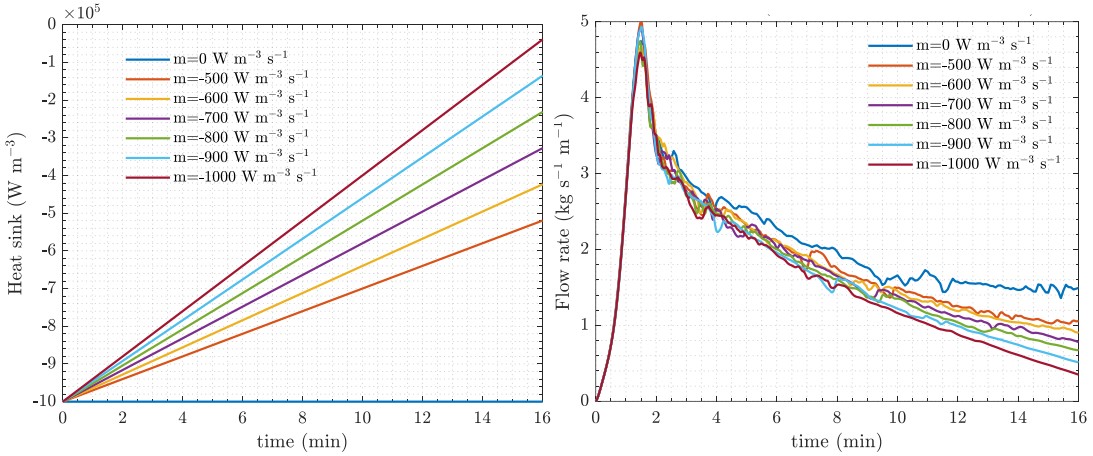

Fig. 8: Heat sink profiles (left) and the corresponding obtained mass flow rate (right) in the discharge channel ($C_1 = 10^7$ m^{-2}).

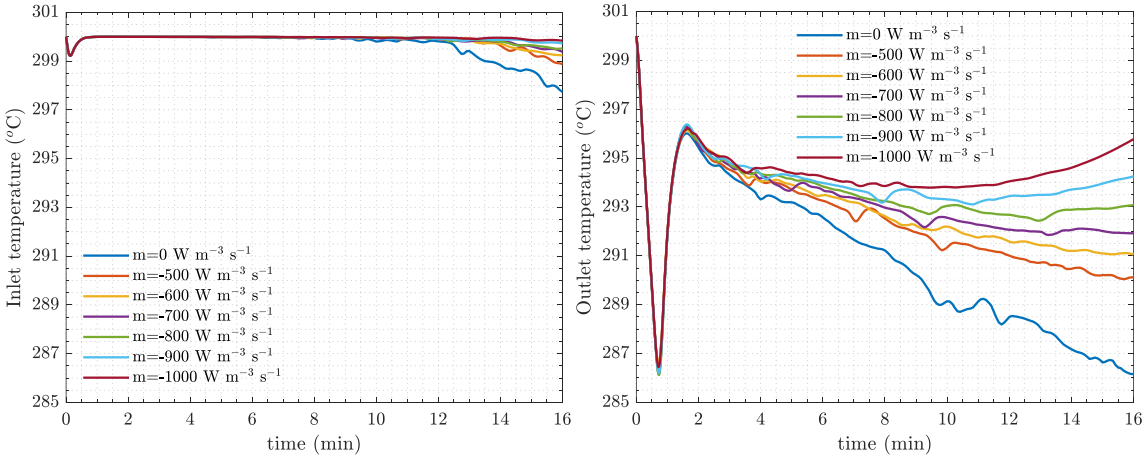

Fig. 9: Inlet (left) and outlet (right) temperatures in the discharge heat exchanger for different heat sink profiles ($C_1 = 10^7$ m^{-2}).

4.2. Parametric analysis of charge

For charging the tank, Figure 10 shows the evolution of the molten salt mass flow rate in the charge channel for different momentum sink coefficients, while Figure 11 illustrates the corresponding inlet (left) and outlet (right) temperatures in the heat exchanger. Both cases use a fixed heat source of 1 MW m^{-3}. The behavior is similar to that observed during discharge, with the peak of mass flow rate being less pronounced.

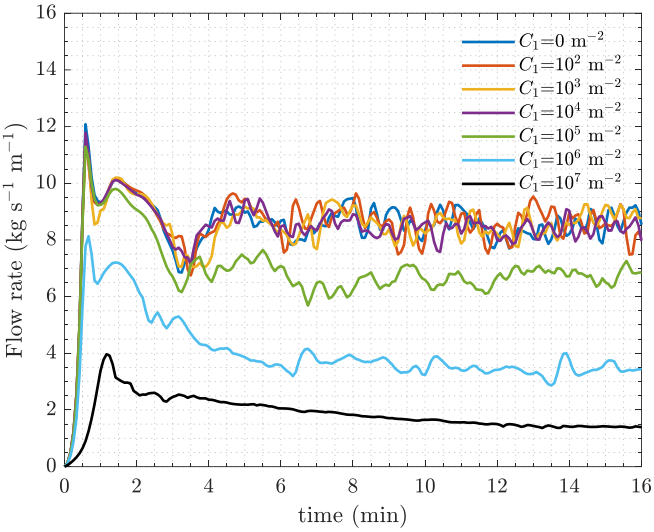

Fig. 10: Time evolution of the molten salt mass flow rate in the charge channel for different momentum sink coefficient (heat source, 1 MW m^{-3}).

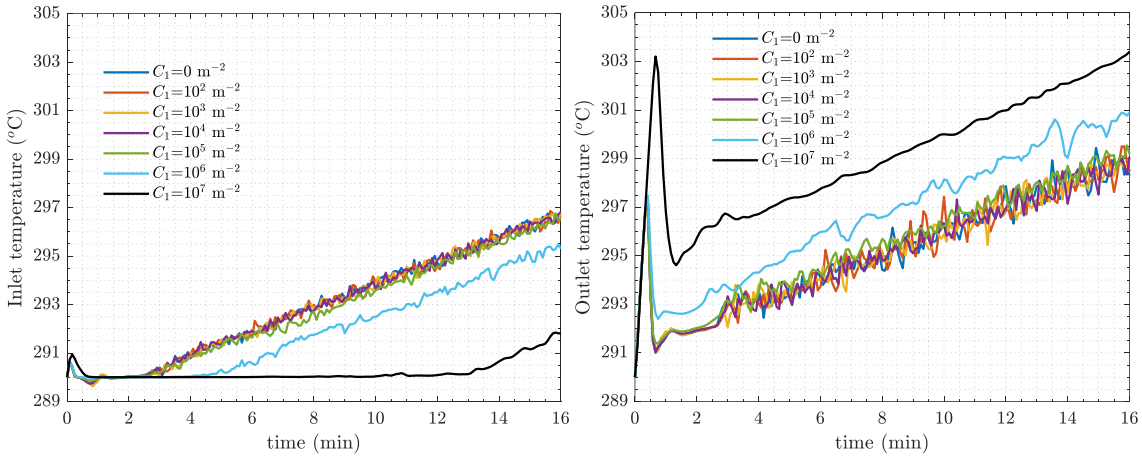

Fig. 11: Inlet (left) and outlet (right) temperatures in the charge heat exchanger for different momentum sink coefficients (heat source, 1 MW m^{-3}).

Regarding the heat source profile for charging, Figure 12 (left) shows the heat source profiles used in the parametric analysis, while Figures 12 (right) shows the resulted evolution of the mass flow rate in the charge channel, with a fixed momentum sink coefficient of 10^7 m^{-2}. Figure 13 shows the corresponding inlet (left) and outlet (right) temperatures in the charge heat exchanger for different heat source profiles. The same behavior observed in discharge mode is also present during charging, but the second stage of the decrease in the mass flow rate until a stable region less pronounced.

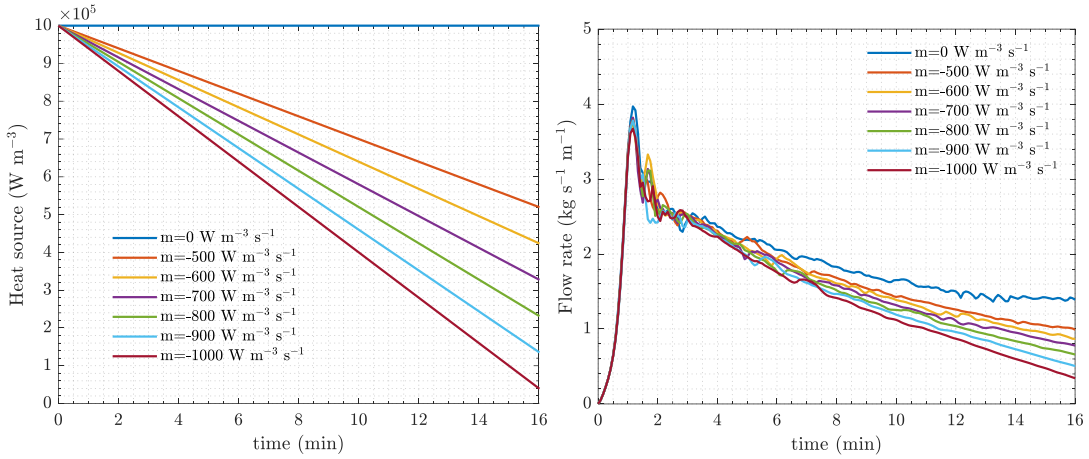

Fig. 12: Heat source profiles (left) and the obtained corresponding mass flow rate (right) in the charge channel ($C_1 = 10^7$ m^{-2}).

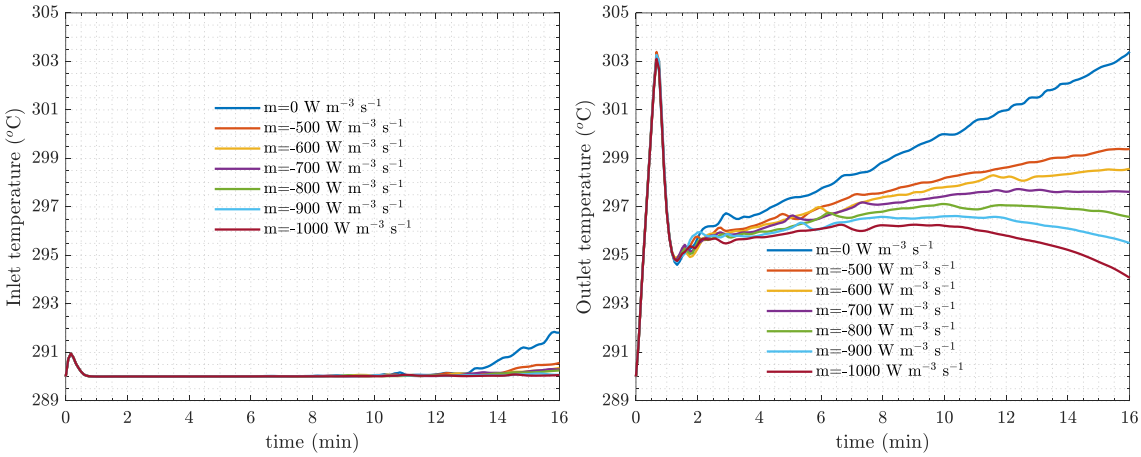

Fig. 13: Inlet (left) and outlet (right) temperatures in the charge heat exchanger for different heat sink profiles ($C_1 = 10^7$ m^{-2}).

5. Conclusions

This paper presents a numerical investigation of a concept for a thermal energy storage tank driven by natural convection. A two-dimensional CFD model is developed in COMSOL Multiphysics and used to analyze the storage concept in detail. First, a reference case with constant heat sink/source and no momentum sink in the heat exchanger is analyzed for both discharge and charge modes. It is observed that for this type of thermal storage, the mass flow rate in the channel exhibits three main stages during both discharge and charge. The first stage involves a rapid increase in the mass flow rate until it reaches a maximum value, followed by a decrease until a stable region is reached, and finally a third stage characterized by a more stable zone. The second stage is less significant in the charging case. The design of the heat exchanger plays a crucial role in the performance of this type of thermal storage, as it dictates the mass flow rate profile. From the analysis, it is found that a momentum sink coefficient of 10^7 and a heat sink slope of 800 W m^{-3} s^{-1} lead to a more constant outlet temperature of the molten salt in the discharge and charge heat exchangers, approaching behavior similar to that of a typical thermocline.

6. Acknowledgments

The authors would like to acknowledge the financial support and contributions from European Commission Horizon 2020 project PROMETEO (project reference number: 101007194) and the project partners' participation.

7. References

Cagnoli, M., Gaggioli, W., Liberatore, R., Russo, V., Zanino, R., 2023. CFD modelling of an indirect thermocline energy storage prototype for CSP applications. Solar Energy. 259, 86 - 98.

Gaggioli, W., Liberatore, R., Di Ascenzi, P., Mazzei, D., Russo, V., 2020. Experimental test of characterization of an innovative thermal energy storage system based on low melting molten salt thermocline tank integrated with an oil exchanger. SolarPACES 2019. 2303, 190012.

Giaconia, A., Tizzoni, A. C., Sau, S., Corsaro, N., Mansi, E., Spadoni, A., Delise, T., 2021. Assessment and Perspectives of Heat Transfer Fluids for CSP Applications. Energies. 14, 7486.

Russo, V., Mazzei, D., Liberatore, R., 2018. Thermal Energy Storage with Integrated Heat Exchangers Using Stratified Molten Salt System for 1 MWe CSP. SolarPACES 2017. 2033, 090025.

Shokrnia, M., Cagnoli, M., Gaggioli, W., Liberatore, R., Russo, V., Zanino, R., 2024.Geometrical and PCM optimization of a thermocline energy storage system. Journal of Energy Storage. 98, 113070.

State of charge estimation using regression models in a novel photovoltaic thermal storage system with macro-encapsulated phase change material

Yannick Krabben[1], Lorant Sztranyovszky[1], Philipp Roos[2], Florian Schaefer[2], Anabel Palacios[1] and Anastasia Stamatiou[1]

[1] Competence center for Thermal Energy Storage (CCTES), Institute of Mechanical Engineering and Energy Technology, School of Engineering and Architecture, Lucerne University of Applied Sciences and Arts, Horw (Switzerland)

[2] COWA Thermal Solutions AG, Root (Switzerland)

Abstract

Photovoltaic heat pump systems (PV-WP Systems) are becoming a standard for low-carbon building heating. In this framework, this work aims to optimize photovoltaic (PV) systems coupled with heat pumps (WP) by integrating a novel high-density thermal storage unit to address the mismatch between solar energy production and heating demands. Through a pilot setup featuring an 800 L storage tank equipped with multiple sensors, comprehensive data was collected over the 2022/2023 heating seasons in Switzerland. This dataset formed the base for the development and validation of state of charge (SoC) estimation models for latent thermal energy storage (LTES) systems. Challenges in defining SoC due to temperature differentials within the storage were addressed using both energy balance and machine learning approaches. The machine learning approach, leveraging regression techniques and ensemble algorithms, proved particularly effective, achieving a prediction accuracy with a deviation of less than 2.06 kWh for 95% of data points with a total storage capacity of 45 kWh. This approach enabled adaptive SoC predictions, enhancing the operational efficiency of the storage system without additional hardware. Further work will focus on redefining of these models to improve accuracy, explore scalability across different system configurations, and reduce computational demands to facilitate integration into existing energy management systems. This research indicates significant potential for advancing thermal energy storage technology in PV-WP systems, contributing to more sustainable building heating solutions.

Keywords: Photovoltaic systems, thermal energy storage, state of charge, latent heat, machine learning, energy efficiency

© 2024. The Authors. Published by International Solar Energy Society
Selection and/or peer review under responsibility of Scientific Committee
10.18086/eurosun.2024.06.06 Available at http://proceedings.ises.org

1. Introduction

Thermal energy storage systems (TES) are key-enabling technologies when it comes to enhancing the efficiency of renewable energy systems, particularly photovoltaic (PV) systems in building applications (Dong and Xu, 2023). TES systems work by storing excess thermal energy generated during periods of low demand and releasing it when energy demand is high, thereby balancing supply and demand. A traditional way of storing heat for the residential and commercial building sector has been hot water storage tanks, which are currently used in conventional building systems in Switzerland and Europe (Renz, 2020). An upcoming approach to storing large amounts of thermal energy is phase change materials (PCM), where the phase change of a material is utilized to absorb or release heat at a constant temperature. As a result, a larger amount of energy is stored with the same storage volume compared to conventional water storage tanks. There are different approaches to implementing PCM into heating systems to facilitate the heat exchange between water and PCM. A popular approach is through the macro-encapsulation of the PCM (Vérez *et al.*, 2021), where existing boiler systems in buildings are filled with capsules to increase the energy density in the storage tank and the building's consumption is increased (Jaradat *et al.*, 2024).

In this work, a new type of pilot system in the form of a hot water buffer storage is developed and integrated into the heating system of a single-family home. The buffer storage tank of the heating system is filled with PCM45 capsules from COWA Thermal Solutions (Maranda and Waser, 2024). These are incorporated into the storage tank as a bulk material, where the entire system is analyzed over two full heating periods (2022-2023). For comparison purposes, the 2022 heating period without the use of COWA capsules and the 2023 heating period with the use of the capsules.

One of the challenges in operating a storage tank with PCM is determining the state of charge (SoC). Unlike with water storage tanks (Kachalla and Ghiaus, 2024; Ritchie and Engelbrecht, 2022; Nemitallah *et al.*, 2023), in latent thermal energy storage (LTES) systems with encapsulated PCM the SoC cannot be determined directly from the pre-installed measurement equipment, as the progress of the phase change inside the capsules is unknown and takes place at a constant temperature. For LTES systems different approaches using additional equipment have been discussed in the literature. Energy balance approaches use an energy meter at the inlet and the outlet of the storage to constantly monitor the SoC and have been successfully used for systems with finned heat exchangers (HEX) (Zsembinszki *et al.*, 2020). However, the literature states that a reference state must be approached at certain intervals during the determination process to prevent the result from drifting. To overcome the challenge of drift, it has been shown that by inserting a small number of temperature sensors into the PCM and using mathematical models, the SoC, the state of the PCM and the temperature distribution can be reliably determined (Barz *et al.*, 2018). Another approach is to use regression models, which are used to fit a model that best describes the relationship between one or more predictor variables and a response variable (Maulud and Abdulazeez, 2020). The advantage is that once the model has been trained, no further measurement equipment is required and it can be applied directly to new systems. Bastida *et al.*, 2024 successfully demonstrated the determination of the SoC of a LTES module with internal counter-flow HEX by using a regression model. The model, built using MATLAB's deep learning toolbox (Hudson *et al.*, 2024) requires the current mass flow and temperature at the inlet of the storage tank and the past SoC. Jančík *et al.*, 2021 developed a simulation model using the mean liquid phase fraction method to determine the SoC of a LTES system filled with cylindrical capsules. Accurate results could be achieved using only the temperature and mass flow rate at the inlet of the LTES as input.

In residential buildings there is usually pre-installed measurement equipment available to monitor temperature and mass flow on the primary (charge) side. As the additional installation of measurement equipment on the secondary (discharge) side is a challenge, the aim of this work is to train a regression model that allows the SoC to be determined with the existing measurement equipment.

2. Filler Capsules and PCM Material

Capsules developed by COWA Thermal Solutions are used for the LTES system (Figure 1). The capsules achieve an approximate packing density of 62% in cylindrical boilers. The outer shell is made of polyethylene (PE) and each is filled with 0.109 L of PCM45 from COWA. The PCM45 is based on a sodium acetate mixture (Wang *et al.*, 2022). Figure 2 illustrates the thermal behavior of the PCM45 during charging and discharging, as determined by differential scanning calorimetry (DSC) (Fatahi and Claverie, 2022). The PCM45 has an approximate heat capacity when discharging of 190J/g in the temperature range of 47°C to 44°C.

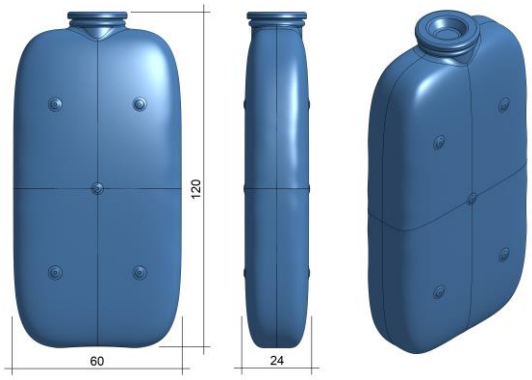

Figure 1: Geometry of the COWA Capsule, dimensions in millimeters.

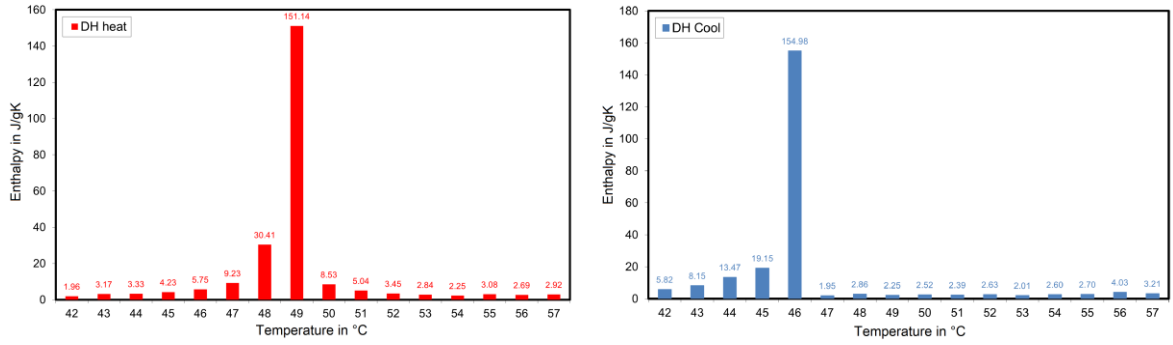

Figure 2: Charging (left) and discharging (right) behavior of the PCM45 measured by DSC.

3. Pilot Setup

The pilot setup is located in a single-family house with a rental apartment located on a sunny terrace in Pany (GR) in Switzerland (Figure 3) at an altitude of 1,178 meters. The house, built in 1988, has a photovoltaic (PV) system with 26 west-facing and 24 east-facing modules, covering a total area of 84.4 m² and providing 17 kWp of power. Surplus solar energy is used to charge a 7.7 kWh electrical battery to support off-grid operation. The heating system comprises an air-to-water heat pump (Oertli LSI 140 SHW-SG) with a thermal output of 5.7 - 15.8 kW, connected to an 800 L buffer tank and a 500 L hot water tank, both fitted with heating elements. The buffer tank is filled with 3550 COWA PCM45 Capsules (Figure 4) Key indicators of the pilot are:

- PV system: 17 kWp, 84.4 m², 26 modules west, 24 modules east.
- Estimated heat demand: 100 kWh/m²/year, energy reference area: 200 m².
- Electricity consumption: 4000 kWh/year.
- Hot water consumption: 180 Liters/day, heated from 16°C to 55°C.
- Heat pump efficiency with a seasonal performance factor (SPF) of 3.2.
- Heat pump output: 5.7 kWth to 15.8 kWth.
- Buffer tank (800 Liters) operating between 40°C and 52°C (up to 60°C with heating rod), providing a capacity of 11.2 kWh to 14 kWh (39.1 kWh with 3550 COWA Capsules, without heating rod)

Figure 3: Pilot building in Pany (GR), Switzerland.

Figure 4: Left 800L buffer boiler. Right: Inside-view of the buffer boiler 30% filled with COWA Capsules.

Figure 5 shows the comparison of the buffer boiler in heating period 1 (HP1) without the capsules and in heating period 2 (HP2) including the capsules. Two days were selected with comparable PV production, outside temperatures and heating requirements. By installing the capsules, it was possible to increase the building's heating self-sufficiency from 26% to 41.4% and the PV yield from 6679.4 kWh to 11050.8 kWh.

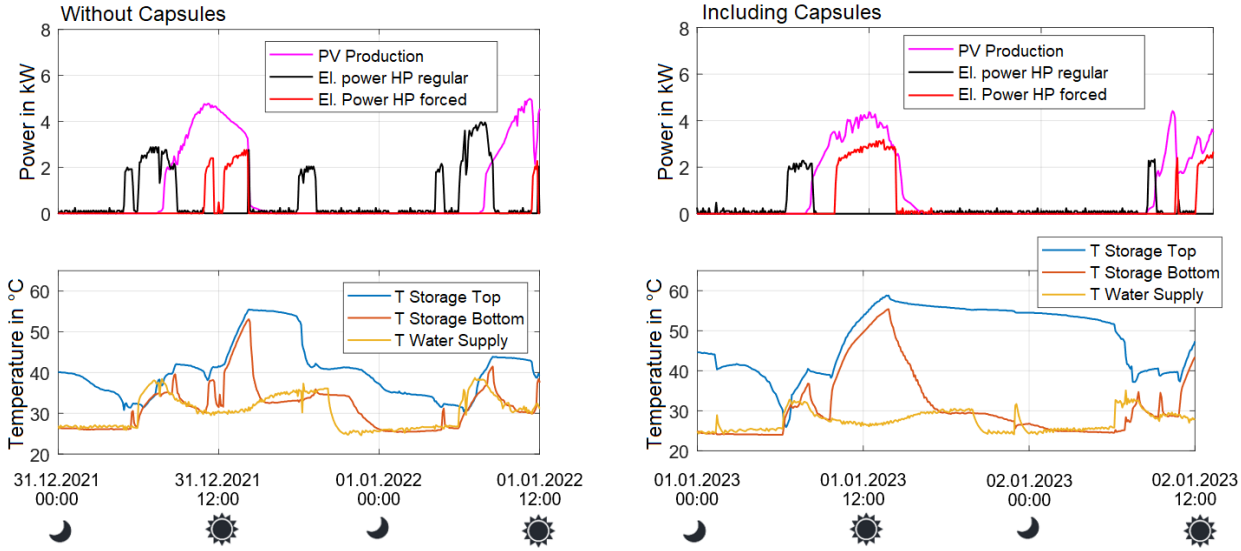

Figure 5: Comparison of two days of the HP1 and HP2 with similar PV production, heating loads and similar average outside temperature. Left: HP1 (2022) without capsules; Right: HP2 (2023) with COWA capsules.

4. State of Charge Determination

To overcome the limitations of direct measurements, a machine learning model was developed using MATLAB's Deep Learning Toolbox (Hudson *et al.*, 2024). The ensemble learning model, coupled with a Bayesian optimizer that varies the hyperparameters for each iteration, is used to estimate the SoC based on indirect measurements such as inlet and outlet temperatures and flow rates from the heat pump. The model was trained using data collected from the pilot installation (Figure 6), which included different operating scenarios over a heating season. The use of ensemble learning algorithms improved the model's ability to generalize across different operating conditions, significantly reducing prediction errors.

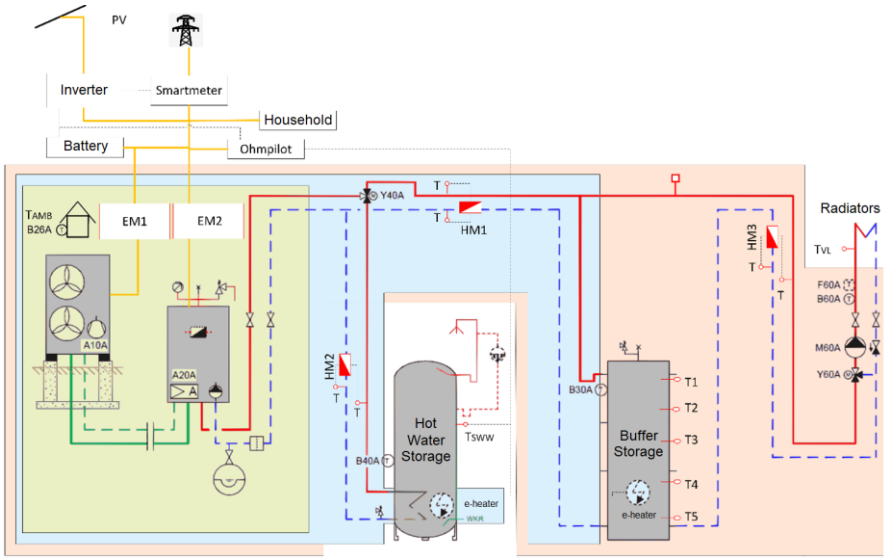

Figure 6: Diagram of the pilot plant with measuring equipment for determining the training data.

The experimental data was collected from COWA's pilot installation in Pany during the 2022/2023 heating season. Measurements were taken using two energy meters positioned at the inlet and outlet of the LTES, allowing for the calculation of an approximate SoC via an energy balance approach. Initially, storage losses were estimated based on the mean temperature of the LTES, a constant external temperature, and the thermal resistance of the insulation.
Despite subtracting the estimated losses from the measured energy difference between the inlet and outlet, the resulting SoC values exhibited an increasing trend, indicating additional unaccounted losses (Figure 7, blue curve). To address this, a baseline correction was applied by smoothing the energy balance curve using a 24-hour moving average, resulting in the adjusted baseline (Figure 7, red curve).

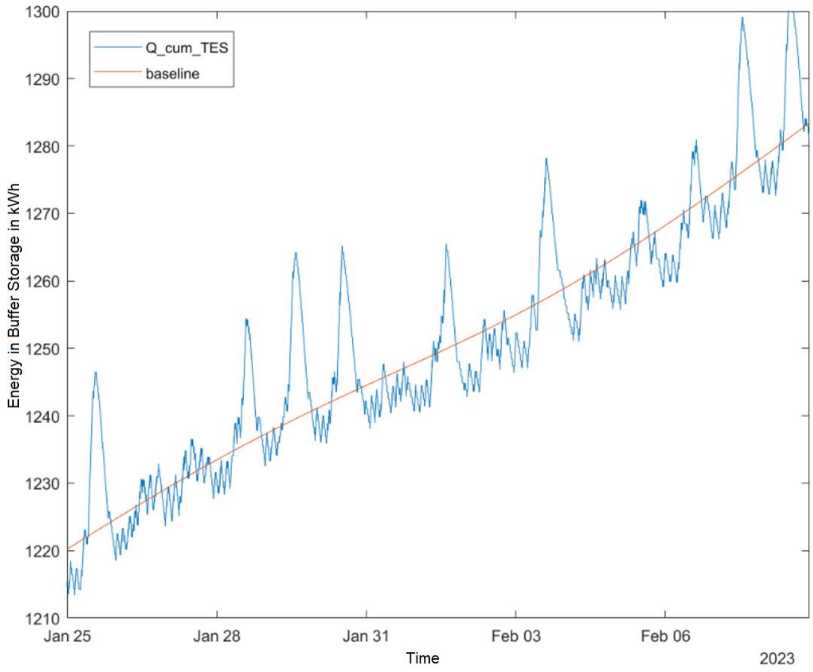

Figure 7: Trend of energy in buffer storage and baseline correction.

To mitigate errors introduced by averaging SoC over several days, four distinct periods of 3-4 days each were manually selected. Since only the change in accumulated energy was measured, the SoC values needed appropriate offsets relative to a reference state. Due to the LTES not reaching the reference state in two of the four periods, some uncertainty in the offsets was inevitable.
The dataset for model training and testing was expanded by incorporating storage history information. Using logical criteria, the end times of charging cycles were identified, leading to the creation of two additional variables: The temperature inside the storage tank at the end of the last charging cycle, and the time elapsed since the last charging cycle ended. These variables are viable for use in practical applications as well.

The complete dataset comprised the following variables:

True Response:

- Thermal energy stored in the LTES.

Predictors:

- Temperature measured at a fixed point inside the LTES.
- Mass flow of the heat pump.
- LTES charging inlet and outlet temperatures.
- Temperature inside the LTES at the end of the last charging cycle.
- Time elapsed since the end of the last charging cycle.

5. Results

The results (see Figure 8) demonstrate that the machine learning approach not only predicts the SoC with a high degree of accuracy but also adapts to various system behaviors without the need for additional hardware. The model achieved a prediction deviation of less than 2.06 kWh for 95% of the data points, with a root mean square error close to 1 kWh. These results indicate a promising direction for optimizing the management of thermal energy storage systems.
Furthermore, the integration of machine learning into the system's operational framework can allow real-time adjustments and optimizations, enhancing the overall efficiency of the thermal storage system. The increased autonomy from improved SoC predictions can enable more effective use of solar energy, reducing reliance on external energy sources and optimizing operational costs.

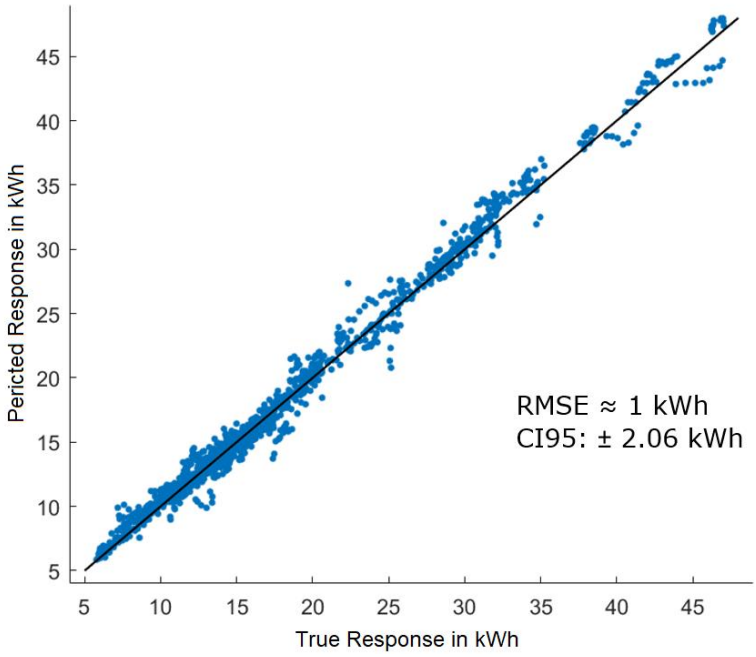

Figure 8: Comparison of Predicted Response and True Response of the SoC of the LTES using ¼ of the datapoints of HP2 as separated test data.

6. Conclusions

The model successfully demonstrated the potential of integrating advanced state of charge estimation techniques with photovoltaic thermal storage systems to enhance their efficiency and autonomy. The innovative use of machine learning for SoC estimation has proven to be a viable solution to the challenges traditionally associated with thermal energy storage systems, offering significant improvements in energy management and system performance. The work presented leads to the following conclusions:

- Improved Energy Efficiency: Incorporating PCM capsules into the thermal storage system significantly enhances the energy density and storage capacity, as demonstrated by the increased heating self-sufficiency from 26% to 41.4%.
- Enhanced PV Utilization: The integration of PCM capsules also improves photovoltaic yield, increasing from 6679.4 kWh to 11050.8 kWh, illustrating the potential for better utilization of solar energy in residential settings.
- Machine Learning for SoC Estimation: The developed machine learning model, leveraging MATLAB's Deep Learning Toolbox, effectively predicts the SoC with high accuracy, achieving a prediction deviation of less than 2.06 kWh for 95% of data points. Reducing the error in determining the true state of charge in the training data can potentially lead to an even greater reduction in the error in the actual prediction.
- Minimized Hardware Requirements: The model provides accurate SoC predictions using existing measurement equipment, avoiding the need for additional costly and complex sensors, making it a practical solution for residential applications.
- Scalability and Applicability: The methodology and findings from this study can be scaled and applied to similar residential setups, potentially leading to widespread improvements in energy efficiency and renewable energy utilization in buildings. However, it is very likely that a different model will need to be trained for different configurations of the system.

Future efforts will focus on refining the estimation models to further enhance their accuracy and reliability. Additional research will explore the scalability of the developed techniques to larger systems and different configurations, potentially broadening their applicability across various residential and commercial settings. Moreover, ongoing efforts will aim to reduce the computational demands of the models to facilitate their integration into existing energy management systems, making sustainable technology more accessible and practical for widespread adoption.

7. References

Barz, T. *et al.* (2018) 'State and state of charge estimation for a latent heat storage', *Control Engineering Practice*, 72(June 2017), pp. 151–166. doi:10.1016/j.conengprac.2017.11.006.

Bastida, H. *et al.* (2024) 'Discrete-time state-of-charge estimator for latent heat thermal energy storage units based on a recurrent neural network', *Applied Energy*, 371(October 2023), p. 123526. doi:10.1016/j.apenergy.2024.123526.

Dong, H., Xu, C. and Chen, W. (2023) 'Modeling and configuration optimization of the rooftop photovoltaic with electric-hydrogen-thermal hybrid storage system for zero-energy buildings: Consider a cumulative seasonal effect', *Building Simulation*, 16(10), pp. 1799–1819. doi:10.1007/s12273-023-1066-5.

Fatahi, H., Claverie, J. and Poncet, S. (2022) 'Thermal Characterization of Phase Change Materials by Differential Scanning Calorimetry: A Review', *Applied Sciences (Switzerland)*, 12(23). doi:10.3390/app122312019.

Hudson, M. *et al.* (2024) 'Deep Learning Toolbox™ User's Guide'. Available at: www.mathworks.com.

Jančík, P. *et al.* (2021) 'Experimental investigation and modelling of a laboratory-scale latent heat storage with cylindrical PCM capsules', *Scientific Reports*, 11(1), pp. 1–15. doi:10.1038/s41598-021-02705-1.

Jaradat, M. *et al.* (2024) 'Enhancing Energy Efficiency in Buildings through PCM Integration: A Study across Different Climatic Regions', *Buildings*, 14(1). doi:10.3390/buildings14010040.

Kachalla, I.A. and Ghiaus, C. (2024) 'Electric Water Boiler Energy Prediction: State-of-the-Art Review of Influencing Factors, Techniques, and Future Directions', *Energies*, 17(2). doi:10.3390/en17020443.

Maranda, S., Waser, R. and Worlitschek, J. (2024) *COWA Thermal Soulutions AG*. Available at: https://www.cowa-ts.com/.

Maulud, D. and Abdulazeez, A.M. (2020) 'A Review on Linear Regression Comprehensive in Machine Learning', *Journal of Applied Science and Technology Trends*, 1(2), pp. 140–147. doi:10.38094/jastt1457.

Nemitallah, M.A. *et al.* (2023) 'Artificial intelligence for control and optimization of boilers' performance and emissions: A review', *Journal of Cleaner Production*, 417(July), p. 138109. doi:10.1016/j.jclepro.2023.138109.

Renz, S. (2020) 'Heat Pump Market Development in Switzerland', *Heat Pumping Technologies MAGAZINE*, 38(1), pp. 19–22. Available at: https://heatpumpingtechnologies.org/publications/heat-pump-market-development-in-switzerland/.

Ritchie, M.J., Engelbrecht, J.A.A. and Booysen, M.J. (2022) 'Water Heaters'.

Vérez, D. *et al.* (2021) 'Experimental study on two pcm macro-encapsulation designs in a thermal energy storage tank', *Applied Sciences (Switzerland)*, 11(13). doi:10.3390/app11136171.

Wang, S. *et al.* (2022) 'Study on Performance Improvement of Sodium Acetate Trihydrate in Thermal Energy Storage System by Disturbance', *Processes*, 10(6). doi:10.3390/pr10061093.

Zsembinszki, G. *et al.* (2020) 'Evaluation of the State of Charge of a Solid / Liquid Storage Tank', *Energies*, 13,1425, pp. 1–26.

EFFECT OF ZINC OXIDE-WATER NANOFLUIDS ON THE THERMAL EFFICIENCY OF A FLAT PLATE SOLAR COLLECTOR – A COMPARATIVE ANALYSIS OF CENTRAL COMPOSITE DESIGN AND BOX BEHNKEN DESIGN

Mercy N.A.A Budu[1], Kevin N. Nwaigwe[1]

[1] University of Botswana, Gaborone (Botswana)

Abstract

Comparative analysis of response surface methodology (RSM) using central composite design (CCD) and box-Behnken design (BBD) in thermal efficiencies of a solar water heating system is undertaken. CCD and BBD were applied to data obtained from an experimental study that studied the effect of zinc oxide-water nanofluids on a pumped solar thermal system with a flat plate collector. The two methods were then compared in terms of the coefficient of determination and the P-values of the models. The results showed that Box Behnken Design yielded a model with a higher coefficient of determination (R2) of 85.88%, while Central Composite Design gave a coefficient of determination of 77.78%. It is concluded that the Box Behnken Design achieves a better-fitting model with fewer experimental runs. On the other hand, Central Composite Design gave a more accurate model that had a p-value of 0.007 in comparison to 0.097 for Box Behnken Design. Consequently, CCD is a better option when producing an accurate model while BBD is preferred for making models with a good fit.

Keywords: Central Composite Design, Box Behnken Design, Solar Thermal, Flat Plate, Efficiency

1. Introduction

Solar thermal systems have increasingly become popular in Southern Africa because of the copious amounts of solar irradiance received in the area. These systems have proven to be effective at heating water to ideal temperatures for residential and industrial use (Joubert, et al., 2016). However, there is still hesitancy in using solar thermal systems because most of them use backup heating elements to compensate for days with little solar irradiance (Gautum & Saini, 2020). The result is that consumers still end up using electricity to heat their water on cloudy days and in winter. In a bid to curb this, numerous studies have been carried out to maximize the thermal efficiency of these systems. Some of these studies utilize nanofluids as the working fluid of the system, mainly due to their superior thermophysical properties in comparison to other working fluids such as water and water-glycol mixtures (Shojaeizadeh, et al., 2015). Studies have shown that the use of nanofluids increases the efficiency of a flat plate solar collector (Amin, et al., 2015). A specific study done by Sindhuja et al. (2018) showed that nanoparticles can also be used in high temperature applications such as concentrated solar power absorbers. Furthermore, some researchers have employed optimization techniques to optimize the working parameters of these systems and an example of such is Response Surface Methodology (RSM).

Response Surface Methodology is a popular optimization technique used by engineers and scientists to achieve optimal process conditions without having to carry out numerous experiments. The advantages of this method include that it is precise, saves time, and produces models with satisfactory accuracy (Esfe, et al., 2016). It applies several mathematical and statistical relationships to design experiments, regress data, and find the target response specified by the researcher. According to Chollom et al. (2020), this method produces models that are either linear or quadratic depending on the established relationship between the dependent and independent variables of the experiment.

Central Composite Design is a design of experiments that involves five levels of two to ten factors. The levels for CCD are $+\alpha$,+1,0,-1, and $-\alpha$, where +1 and -1 are the cube points, 0 is the mid-point, and $-\alpha$ and $+\alpha$ are axial points. This design typically involves excessive combinations of factors and levels to model the data as accurately as possible (Rakić, et al., 2014). A study by Hatami & Jing (2017) successfully found the best wave profile of aluminium oxide-water nanofluids in a wavy direct absorber solar collector. The researchers

© 2024. The Authors. Published by International Solar Energy Society
Selection and/or peer review under responsibility of Scientific Committee
10.18086/eurosun.2024.06.07 Available at http://proceedings.ises.org

considered the amplitude of the wave and the number of waves as the independent variables of the experiment to optimize the Nusselt number of aluminium oxide-water nanofluid in the solar collector. With the use of CCD, authors were able to find the wave amplitude and number that yielded the highest Nusselt number. Another research by Ghasemi et al. (2021) employed CCD to simultaneously minimize pressure drop and maximize heat transfer in a mini channel heat sink. The explanatory variables were defined as the number of channels, mass flow rate, and channel diameter, with the response variables as the heat transfer rate between them and pressure drop. The research concluded that the optimal design consisted of four channels, a mass flow rate of 3 cm/s, and a channel diameter of 4mm, consequently, the desirability function of the optimization was 0.573.

Box Behnken Design (BBD) is another design of experiments that falls under Response Surface Methodology. It involves three levels, namely -1,0, and +1 and it gives a similar mathematical model to that produced by CCD. The main difference between the two is that CCD involves more experimental runs than BBD because it considers the axial points of the dataset instead of solely the cube points (Rakić, et al., 2014). This also implies that BBD has a lower degree of freedom in comparison to CCD which makes it less rotatable. BBD is preferred for applications whereby the range of favourable operating conditions has already been determined and the researcher now seeks to pinpoint the most optimal conditions. In a study to enhance thermal efficiency by optimizing the filling ratio, tilt angle, and dispersion mass fraction of the nanoparticles in an evacuated tube solar collector using the Box Behnken Design (Sarafraz, et al., 2019), the researchers were able to model the thermosyphon system using RSM and found out that a maximum thermal efficiency of 96.2% was achieved when the tilt angle was 48°, with a filling ratio of 0.65, and a mass fraction of 0.3. When validation was carried out, the RSM model had a margin of error of 1.5%, proving the accuracy of the RSM-generated model. As RSM involves different Designs of Experiments, this paper specifically presents Central Composite Design (CCD) and Box Behnken Design (BBD) in the context of optimization of a pumped solar thermal system with flat plate collectors, suitable for hot water preparation at the household/domestic level

2. Methodology

Experiments were conducted on an existing pumped solar thermal system with a flat plate collector and zinc oxide-water nanofluids were used as the working fluid for the system. The apparatus comprised a full port ball valve, a flat plate collector, two 100-litre storage tanks, a pump, piping, and pipe fittings. The pipes and storage tanks were all insulated to minimize thermal losses to the environment. The first portion of the experiment involved preparing the zinc oxide-water nanofluids at varying mass fractions ranging from 0.0% to 0.15%. Additionally, a concentration of 1.0% of sodium dodecyl sulphate (SDS) was used as a surfactant in the prepared nanofluids.

The mass flow rate of the working fluid was also varied at 0.0556 kg/s, 0.1667 kg/s, and 0.2778 kg/s to investigate the effect of mass flowrate on the thermal efficiency of the system, and this was controlled by a full port ball valve. To calculate the thermal efficiency, the inlet temperature, outlet temperature, and solar irradiance were recorded and used.

The experiments investigated mass flow rate, mass fraction, and irradiance as independent variables affecting the thermal efficiency of the system and Table 1 shows the allocated values for each level. Central Composite Design and Box Behnken Design were both used to generate tables for the design of experiments. Minitab software was used to generate the design tables for both methods and the same software was used to analyse the data obtained from the experiments. Central Composite Design yielded 20 experimental runs, and the alpha value was specified as one for a face-centred design. The design of experiments for Central Composite Design is illustrated in Table 2. The design was unblocked because there were no blocks for the data set obtained. Consequently, Box Behnken Design yielded 15 experiment runs for the three defined factors, and the design was also unblocked, similar to Central Composite Design. The design of experiments for Box Behnken Design is shown in Table 3. An Analysis of Variance (ANOVA) was then carried out on the model to determine the accuracy and correctness.

Tab 1: Specific values for each level of the three factors

Factor	Coded	Level		
		+1	0	-1
Mass Flowrate (kgs^{-1})	A	0.2778	0.1667	0.0556
Mass Fraction (%)	B	0.0	0.75	0.15
Irradiance (W/m^2)	C	64	486	908

Table 1: Design of experiments table for Central Composite Design generated by Minitab

Run	Blk	A	B	C
1	1	-1	-1	-1
2	1	1	-1	-1
3	1	-1	1	-1
4	1	1	1	-1
5	1	-1	-1	1
6	1	1	-1	1
7	1	-1	1	1
8	1	1	1	1
9	1	-1	0	0
10	1	1	0	0
11	1	0	-1	0
12	1	0	1	0
13	1	0	0	-1
14	1	0	0	1
15	1	0	0	0
16	1	0	0	0
17	1	0	0	0
18	1	0	0	0
19	1	0	0	0
20	1	0	0	0

Table 2: Design of experiments table for Box Behnken Design generated by Minitab

Run	Blk	A	B	C
1	1	-1	-1	0
2	1	1	-1	0
3	1	-1	1	0
4	1	1	1	0
5	1	-1	0	-1
6	1	1	0	-1
7	1	-1	0	1
8	1	1	0	1
9	1	0	-1	-1
10	1	0	1	-1
11	1	0	-1	1
12	1	0	1	1
13	1	0	0	0
14	1	0	0	0
15	1	0	0	0

3. Results and Discussion

To analyse the data obtained, Minitab software was used, and Response Surface Methodology was also applied for regression of the data. The data was used to generate surface plots from the two designs of experiments (Figure 1 and Figure 2). Table 4 presents the model summary for CCD, and Table 6 presents ANOVA for CCD. Similarly, Table 5 presents the model summary for BBD, and Table 7 presents ANOVA for BBD.

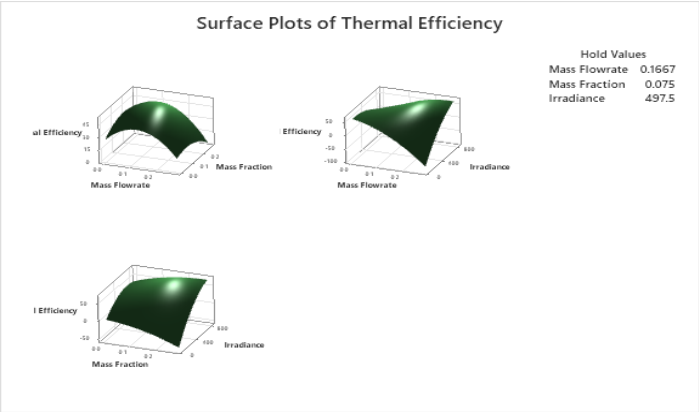

Fig. 1: Surface plots of thermal efficiency generated from CCD

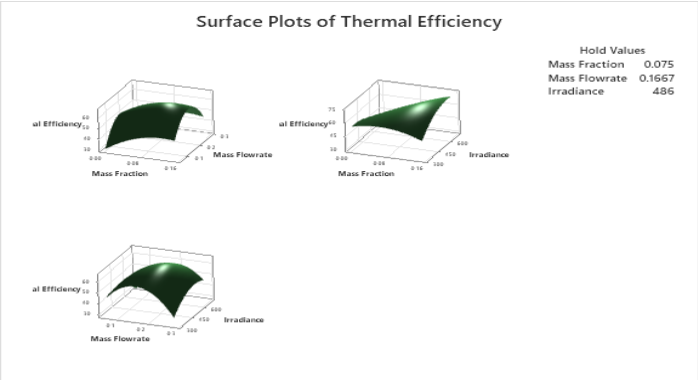

Fig. 2: Surface plots of thermal efficiency generated from BBD

Table 3: Model summary for CCD

S	R-sq	R-sq(adj)	R-sq(pred)
7.47560	77.78%	57.79%	0.00%

Table 4: Model summary for BBD

S	R-sq	R-sq(adj)	R-sq(pred)
7.89615	85.88%	60.46%	0.00%

Table 5: Analysis of Variance for CCD

Source	DF	Adj SS	Adj MS	F-Value	P-Value
Model	9	1956.48	217.387	3.89	0.023
Linear	3	800.29	266.763	4.77	0.026
Mass Fraction	1	481.84	481.835	8.62	0.015
Mass Flowrate	1	1.74	1.740	0.03	0.863
Irradiance	1	70.90	70.902	1.27	0.286
Square	3	459.24	153.078	2.74	0.099
Mass Fraction *Mass Fraction	1	2.68	2.679	0.05	0.831
Mass Flowrate *Mass Flowrate	1	290.54	290.539	5.20	0.046
Irradiance*Irradiance	1	41.35	41.354	0.74	0.410
2-Way Interaction	3	258.14	86.045	1.54	0.264
Mass Fraction*Mass Flowrate	1	37.11	37.110	0.66	0.434
Mass Fraction *Irradiance	1	128.40	128.399	2.30	0.161
Mass Flowrate *Irradiance	1	235.22	235.224	4.21	0.067
Error	10	558.85	55.885		
Total	19	2515.33			

Table 6: Analysis of variance for BBD

Source	DF	Adj SS	Adj MS	F-Value	P-Value
Model	9	1895.86	210.651	3.38	0.097
Linear	3	284.80	94.935	1.52	0.317
Mass Fraction	1	172.95	172.950	2.77	0.157
Mass Flowrate	1	1.50	1.503	0.02	0.883
Irradiance	1	2.25	2.254	0.04	0.857
Square	3	475.74	158.581	2.54	0.170
Mass Fraction*Mass Fraction	1	73.30	73.299	1.18	0.328
Mass Flowrate*Mass Flowrate	1	329.29	329.289	5.28	0.070
Irradiance*Irradiance	1	69.31	69.308	1.11	0.340
2-Way Interaction	3	168.88	56.293	0.90	0.502
Mass Fraction*Mass Flowrate	1	5.78	5.784	0.09	0.773
Mass Fraction*Irradiance	1	158.98	158.984	2.55	0.171
Mass Flowrate*Irradiance	1	39.83	39.829	0.64	0.460
Error	5	311.75	62.349		
Total	14	2207.61			

The regression outcomes for evaluating thermal efficiency of the system for both experimental designs – CCD and BBD, are presented. Equation 1 presents the regression outcome for CCD, while equation 2 presents the regression outcome for BBD.

$$\eta_{th} = 49.8 - 90\, m_i + 45\dot{m} - 0.0257H - 154 m_i(m_i) - 950\dot{m}(\dot{m}) - 0.000077\, H(H) - 317\, m_i(\dot{m}) + 0.485\, m_i(H) + 0.542\, \dot{m}(H) \quad \text{(eq.1)}$$

$$\eta_{th} = 3.5 - 116\, m_i + 388\, \dot{m} + 0.111\, H - 1123\, m_i(m_i) - 1554\dot{m}(\dot{m}) - 0.000223 H(H) - 146\, m_i(\dot{m}) + 0.824\, m_i(H) + 0.305\, \dot{m}(H) \quad \text{(eq.2)}$$

The Central Composite Design was able to accurately optimize the mass fraction, mass flow rate, and solar irradiance. The coefficient of determination (R^2) was found to be 77.78 %, while the values of adjusted R^2 and predicted R^2 were 57.79 % and 0.0% respectively. The coefficient of determination indicated that the model produced was a good fit for the data obtained from the experiment. The P-value of the model was found to be 0.023, which is lower than the standard F-value of 0.05 for a confidence level of 95%. This shows that the model produced is significant and can therefore be used to accurately predict the behaviour of the system under different conditions.

The Box Behnken Design was also able to optimize the mass fraction, mass flow rate, and solar irradiance. The coefficient of determination (R^2) was found to be 85.88 %, which is higher than that of the CCD model. This difference implies that the BBD model fits the data provided better than the CCD model. Additionally, the adjusted R^2 and predicted R^2 were 60.46% and 0.0% respectively. The coefficient of determination indicated that the model produced was also a good fit for the data obtained from the experiment. The P-value of the model was found to be 0.097, which is higher than the standard F-value of 0.05 for a confidence level of 95%. This shows that the model produced has a confidence level of at most 90% as opposed to the conventional 95%. It can be inferred that the CCD model is more significant and therefore has superior accuracy.

The two regression models show that mass flowrate has the most negative influence on thermal efficiency. This is backed up by the observations that in both Table 6 and &, this interaction is also amongst the most significant ones. Additionally, mass flowrate alone had the most positive effect on thermal efficiency, while irradiance is shown to have little effect on the output as the coefficients for both regression models are under 0.20.

4. Conclusion

CCD and BBD can both be used to effectively optimize thermal efficiency of a solar thermal system, as demonstrated in this study. Although the Box Behnken Design was found to surpass the Central Composite Design in terms of model fitting, the Central Composite Design produced a more accurate model. Both the models displayed the same patterns of significant factors and interactions in the regression models. However, Box Behnken Design was observed to be a more cost-effective and accurate method because it involves less runs and it still produces a model that is representative of the actual system.

5. Appreciation

This work was carried out under the auspices of the SOLTRAIN project – a regional initiative on capacity building and the demonstration of solar thermal systems in the Southern African region. For details, see www.soltrain.org

6. References

Amin, T. E., Roghayeh, G., Fatemeh, R. & Fatollah, P., 2015. Evaluation of nanoparticle shape effect on a nanofluid based flat-plate solar collector efficiency. Energy Exploration and Exploitation, pp. 659-676.

Chollom, M. et al., 2020. Comparison of response surface methods for the optimization of an upflow anaerobic sludge blanket for the treatment of slaughterhouse wastewater. Environmental Engineering Research, Volume 25, pp. 114-122.

Esfe, M. H. et al., 2016. The optimization of viscosity and thermal conductivity in hybrid nanofluids prepared with magnetic nanocomposite of nanodiamond cobalt oxide(ND-Co3O4) using NSGA-II and RSM. International Communications in Heat and Mass Transfer, pp. 128-134.

Gautum, A. & Saini, R., 2020. A review on technical, applications and economic aspect of packed bed solar thermal energy storage system. Journal of Energy Storage, Volume 27.

Ghasemi, E., Ranjbar, A., Hoseini, J. & Mohsenian, S., 2021. Design optimization and experimental investigation of CPU heat sink cooled by alumina-water nanofluid. Journal of Materials Research and Technology, Volume 15, pp. 2276-2286.

Hatami, M. & Jing, D., 2017. Optimization of Wavy Direct Absorber Solar Collector (WDASC) using Al2O3-water Nanofluid and RSM Analysis. Applied Thermal Engineering, Volume 121, pp. 1040-1050.

Joubert, E., Hess, S. & Niekerk, J. V., 2016. Large-scale solar water heating in South Africa: Status, barriers and recommendations. Renewable Energy, pp. 809-822.

Rakić, T. et al., 2014. Comparison of Full Factorial Design, Central Composite Design, and Box-Behnken Design in Chromatographic Method Development for the Determination of Fluconazole and Its Impurities. Analytical Letter, pp. 1334-1347.

Sarafraz, M. et al., 2019. Smart optimization of a thermosyphon heat pipe for an evacuated tube solar collector using response surface methodology (RSM). Physica A: Statistical Mechanics and its Applications, Volume 534.

Shojaeizadeh, E., Veysi, F. & Kamandi, A., 2015. Exergy efficiency investigation and optimization of an Al2O3–water nanofluid based Flat-plate solar collector. Energy and Buildings, pp. 12-23.

Sindhuja, M. et al., 2018. Electrodeposited Ni/SiC composite coating on graphite for high temperature solar thermal applications. Material Science for Energy Technologies, pp. 3-10.

01. PV Cell Technologies

Extruded Water Adsorbent APO-Tric for Adsorption Thermal Battery Utilizing Solar Energy

Alenka Ristić[1], Urška Mlakar[2], Suzana Mal[1], Franz Hengel[3], Wim van Helden[3], Uroš Stritih[2], Nataša Zabukovec Logar[1,4]

[1] National Institute of Chemistry Slovenia, Ljubljana, Slovenia

[2] Faculty of Mechanical Engineering, University of Ljubljana, Ljubljana, Slovenia

[3] AEE - Institute for Sustainable Technologies, Gleisdorf, Austria

[4] University of Nova Gorica, Nova Gorica

Abstract

An adsorption thermal battery utilizes the reversible adsorption and desorption of water on porous solids and is of particular interest in combination with solar thermal collectors. The efficiency of this technology depends on the performance of the adsorbents, which should have high water adsorption capacity and, consequently, a high energy storage density, stability under humid conditions, and fast kinetics of adsorption and desorption. New synthetic approaches and improved performance of the adsorbents and the systems are being studied to improve the energy storage performance. The microporous aluminophosphate APO-Tric adsorbent with chabazite structure was shaped into extrudes and granules on laboratory scale, showing higher water adsorption capacity of the extrudes in comparison to the granules. The APO-Tric extrudes were tested in 15 adsorption-desorption cycles between 40 °C and 90 °C at a water vapour pressure of 12.5 mbar and showed good hydrothermal stability under these conditions. Good mass balances between adsorbed and desorbed water were achieved in the sorption cycles. In all cycles, maximum temperatures from 53 to 57 °C were reached during adsorption.

Keywords: APO-Tric extrudes, water adsorption, hydrothermal stability, solar energy, thermal battery, test set up

1. Introduction

The adsorption thermal battery (*Zeng et al., 2023*) utilizes the reversible adsorption and desorption of water on porous solids and is of great interest as it represents an energy storage concept with great potential for the loss-free and long-term storage of thermal energy with high energy density, especially in combination with solar thermal collectors. It offers the possibility of reducing the consumption of fossil fuels for space heating in buildings and achieving net-zero scenarios.

The driving forces for the development of an efficient storage adsorbent with advanced properties are a high water adsorption capacity in the low relative pressure range, a low regeneration temperature of up to 100 °C, good adsorption kinetics and hydrothermal cycling stability under working conditions. New synthetic approaches, improved sorption properties of the adsorbents and the systems should be developed to improve the energy storage performance.

Thermally stable microporous adsorbents such as zeolites, aluminophosphates and metal-organic frameworks are often tested with water as the working fluid for thermal energy storage and/or transformation. (*Ristić,*

© 2024. The Authors. Published by International Solar Energy Society
Selection and/or peer review under responsibility of Scientific Committee
10.18086/eurosun.2024.06.08 Available at http://proceedings.ises.org

2022) Zeolites are microporous crystalline alkali or alkali-earth aluminosilicates with a 3D framework containing channels and/or cavities with pore openings of 0.3 to 0.8 nm. One of the advantageous properties for thermal energy storage applications is the strong hydrophilicity of zeolites, expressed as a Type I water isotherm, that depends on the Si/Al molar ratio of the zeolite framework, the framework structure type, the type and distribution of exchangeable extra-framework cation, structural defects and the distribution of possible surface silanol groups. (*Ng, Mintova, 2008*) However, the high affinity for water at low partial pressure affects on the desorption temperature in the heat storage cycle, i.e. high desorption temperatures above 300 °C are the result of the strong interactions between the charged framework and water molecules. The most frequently investigated zeolites with a high Al content as thermal energy storage materials are the commercially available zeolites A, X and, more recently, Y. (*Ristić, 2022; Schmit et al., 2024*) Microporous aluminophosphates have shown their advantages over zeolites in terms of lower charging/desorption temperature, higher water adsorption capacity and higher adsorption enthalpy. (*Ristić, 2022*) They have a weaker hydrophilic (water isotherm Type I) or hydrophobic-hydrophilic (water isotherm Type V) character depending on the chemical composition, structure type, framework defects and synthesis approach. The commercially available aluminophasphates AQSOA FAM Z02 (SAPO-34), AQSOA FAM Z05 (APO-5) and AQSOA FAM Z01 (FAPO-5) from Mitsubishi Plastics Ltd. (*Kakiuchi et al., 2005*) are more expensive than above listed zeolites, because expensive organic structural directing agents are used for their production. Of the aluminophosphates, SAPO-34 is the most widely investigated adsorbent for use in the adsorption thermal batteries application, with various energy storage densities being determined as a function of the working conditions. Henninger determined an energy storage density of 177 Wh kg^{-1} at an adsorption temperature of 40 °C and a water vapour pressure of 5.6 kPa as well as a desorption temperature of 95 °C and a water vapour pressure of 1.2 kPa. (*Henninger et al., 2010*) A study by Brancato and Frazzica showed a lower energy storage density (94 Wh kg^{-1}) at a desorption temperature of 90 °C and a water vapor pressure of 1.2 kPa and an adsorption temperature of 35 °C and a water vapor pressure of 4.2 kPa (*Brancato, Frazzica, 2018*). In contrast, a higher energy storage density of 196 Wh kg^{-1} was achieved by Palomba et al. (*Palomba et al., 2017*) under conditions of adsorption temperature (35°C), evaporation temperature (10 °C), desorption temperature (91 °C) and condensation temperature (15 °C) in an open system. In addition to energy storage density, the determination of cycling stability under humid conditions is another important objective in the development of aluminophosphate adsorbents for their use in solar energy storage. Two SAPO-34 prepared by different synthesis routes were tested in short-term adsorption-desorption cycles by Henninger et al. (*Henninger et al., 2011*). The tests were performed directly in a thermogravimetric apparatus that could cycle the adsorbent material between 140°C and 20°C at a water vapour pressure of 5.6 kPa and 1.2 kPa for the desorption and adsorption conditions, respectively, to monitor the change in water adsorption capacity. Frazzica presented the experimental protocol for the long term cycling stability of adsorbents for thermal energy storage applications under realistic operating conditions. SAPO-34 was tested between 90°C and 40°C at a water vapour pressure of 7.3 kPa. (*Frazzica, Brancato, 2018*) in a designed test rig. Freni et al. proposed a protocol to test the hydrothermal stability of adsorbent coatings on heat exchanger, which was carried out in a system with saturated and dry air over samples that were continuously cooled and heated to simulate typical cycles. The adsorption capacity was then checked in a thermogravimetric device to detect possible deterioration of the adsorption capacity. (*Freni et al, 2013*)

The water adsorbent APO-Tric has the same chabazite structure as SAPO-34, containing 3-dimensional interconnected pore system with pore openings of 0.38 nm and large ellipsoidal cavities of 0.84 nm. (*Baerlocher et al., 2007*) The adsorbent was developed by (*Ristić et al., 2012)*. It was found that a driving force for the water adsorption process (S-shaped water adsorption isotherm) was formation of highly ordered water clusters in the micropores, which was enabled by an optimal micropore diameter and, rapid and reversible changes in Al coordination associated with synthesis in a fluoride medium. The dehydration of this material is a very complex process and practically all the water can be desorbed at 95 °C, which is another important characteristic for its utilization. Recent calculations of the dynamics of the system by mimicking an in-house solar heat storage system, revealed a complex sorption/desorption dynamics. (*Krajnc et al., 2017*) One consequence of the sudden water uptake in a narrow pressure range was the immediate release of heat. The APO-Tric adsorbent (powder) can store 320 Wh kg^{-1} at working conditions of the adsorption temperature of 30 °C and desorption temperature of 100 °C at a water vapour pressure of 12.5 mbar, which is significantly

higher than the reported stored energy densities for SAPO-34s. The APO-Tric adsorbent is considered an expensive adsorbent when piperidine is used in its synthesis. However, a green synthesis using a low-cost ionic liquid was recently developed (*Mal et al., 2021*), which resulted in the preparation of APO-Tric powder with a more hydrophilic character and an improved water adsorption capacity of 5 %. The reuse of the spent ionic liquid was also confirmed, contributing to the reduction of toxicity and production costs of aluminophosphate synthesis. The powdered form in which these aluminophosphates are produced is not advantageous, as the thermal energy storage systems require compacted and shaped adsorbents, such as bodies a few millimetres in size, due to process requirements such as mechanical stability and mass transport. The powder material limits the separation of powder and gas phase, the permeability of the material and the handling in general and leads to clogging of the valves in the systems. Therefore, thermochemical adsorbent powders must be shaped for the utilization in the systems.

We present here a study on the influence of a shaping process on the water sorption properties of the adsorbent APO-Tric developed for a low temperature solar energy storage application. To this end, the hydrothermal cycling stability in the gravimetric adsorption analyzer and the mass transport in the laboratory test rig were investigated for the first time.

2. Materials and methods

The extruded APO-Tric, which was produced using a Caleva Multi Lab extruder (Dorset, UK) at the National Institute of Chemistry in Slovenia, was analysed by X-ray powder diffraction using the PANalytical X'Pert PRO diffractometer (Malvern Panalytical, Almelo, Netherlands) and nitrogen physisorption using Autosorb iQ3 (Quantachrome Instruments, Boynton Beach, FL, USA) to determine the structural properties. The isotherms of water adsorption at 25 °C and the adsorption/desorption cycles were determined using the automatic gravimetric water sorption analyser IGAsorp-XT (accuracy ± 0.1 µg) (Hiden Isochema Ltd., Warrington, UK). Hydrothermal stability (short term) of the small amount of the APO-Tric material (1 g) was determined by the same analyser using the modified sequential method (*Ocvirk et al., 2021; Frazzica, Brancato, 2018*), in which water uptake was measured at 40 °C under humid nitrogen gas flow (80 % relative humidity) and then dried at 90 °C with dry nitrogen flow.

The heat storage performance of a larger quantity of the adsorbent (150 g) was tested in a dedicated laboratory test rig at AEE INTEC in Austria. The test rig is placed in a vacuum vessel and can be divided in two main parts: the evaporator/condenser unit and the material block unit. The cooling system for heat sinks of both units is situated outside the vacuum vessel. Figure 1 shows a schematic representation of the setup, where the blue line represents a cooling fluid. The material block is a coated aluminum block with ribs, in between which the adsorption material is placed. Multiple adsorption-desorption cycles can be performed under vacuum conditions. The masses of the water reservoir and the material block are monitored during the process in order to check the mass balance. To sufficiently monitor adsorption-desorption cycles, temperature and pressure sensors together with mass balances were used.

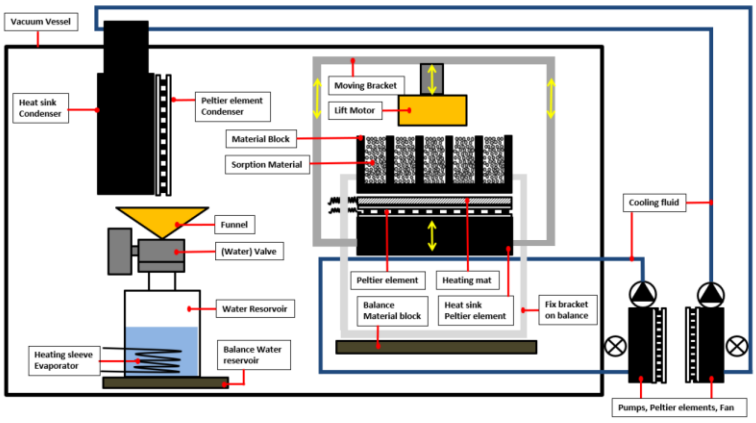

Figure 1: Schematic representation of the material test set up at AEE INTEC

3. Results

A new synthesis approach using cheap and recyclable reactants (*Mal et al., 2021*) has significantly reduced the production cost of the shaped aluminophosphate adsorbent. Figure 2 shows a comparison of the water adsorption isotherms of APO-Tric granules (spheres) and extrudes (cylinders), which illustrates the influence of the shaping process on the water uptake of the adsorbent.

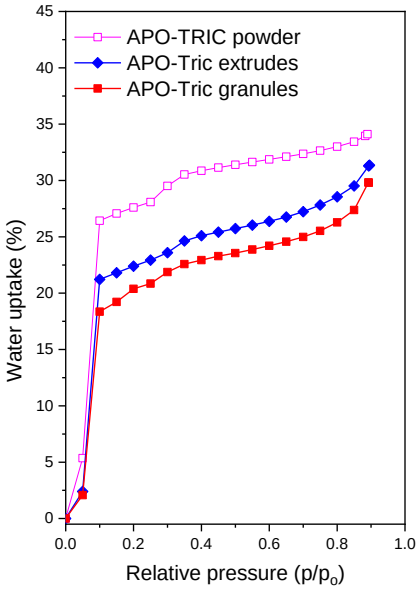

Figure 2: Water adsorption isotherms at 25 °C of shaped APO-Tric and powdered APO-Tric adsorbents

Figure 3 presents good cycling stability of the APO-Tric extrudes and a water loading lift as the difference between the amount of adsorbed water at 40 ºC and desorber water at 90 ºC at a water vapor pressure of 12.5 mbar. The small decrease (3%) in water uptake was observed after 15 adsorption/desorption cycles, which is consistent with the powdered sample. (*Ristić et al., 2012)*

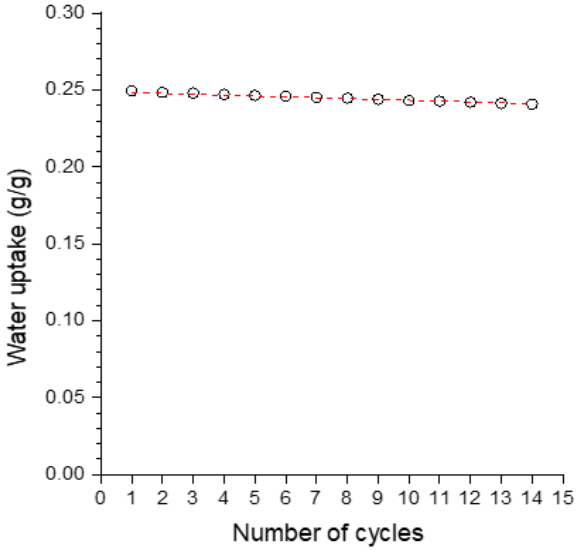

Figure 3: Cycling stability of APO-Tric extrudes of 15 cycles of adsorption and desorption between 40 °C and 90 °C at 12.5 mbar

The APO-Tric extrudes were used for the first time in experiments on a dedicated laboratory test rig. As these were the first experiments with the extrudes, extensive adsorption-desorption cycles were carried out to better understand both the processes with the new material and the interaction of the material in the system. Different conditions were used to find the optimal conditions. For example, the adsorption time was set at 10

hours. When the adsorption cycle started, the valve of the evaporator was opened and water vapour was adsorbed by the APO-Tric material, the temperature of the material initially increased and reached a maximum temperature of 53 °C, while it decreased to 31 °C at the end of the process. During adsorption, the mass of the evaporator decreased by 22.3 g and the mass of the adsorber increased by 22.8 g. With a difference of only 0.5 g, it can be concluded that the balance of masses in the adsorption cycle is very good. During adsorption, it was possible to achieve a temperature lift of 29 °C, starting from 24 °C, the temperature of the material at the beginning of adsorption, up to a maximum temperature of 53 °C, which was reached after 8 minutes. It was observed that the mass of the adsorber reached a maximum after 3 hours and 28 minutes. More detailed results obtained during adsorption are shown in Table 1. They show the time of the start and end of the adsorption cycle, the mass of the evaporator, the mass of the adsorber, the pressure change in the vacuum vessel, the temperature of the material and the temperature lift

Tab 1: Detailed results during the adsorption process

Time [h:min]	m_Evaporator [g]	m_Adsorber [g]	p_Vacuum [mbar]	T_APO-Tric [°C]	T_lift [°C]
15:59	1287	1508.8	3.46	24	29
03:11	1264.7	1531.6	27.21	53	
	-22.3	**22.8**			

Figure 4 shows one of the adsorption processes carried out at 15 °C and a pressure from 3.46 mbar.

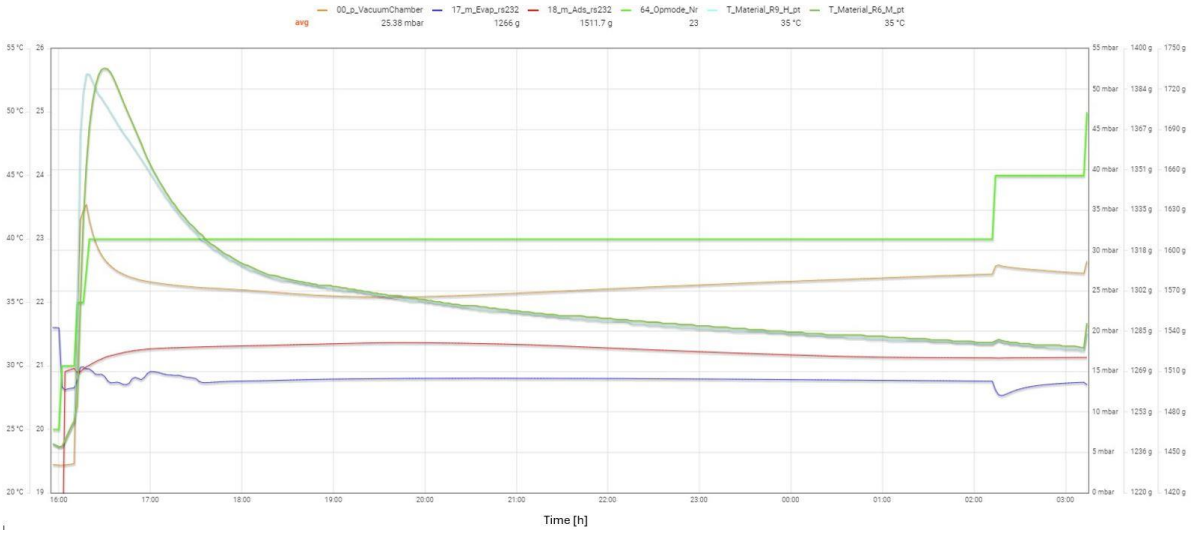

Figure 4: Monitoring of the adsorption at 15 °C and pressure starting at 3.46 mbar

When the adsorption was complete, the valve on the evaporator was closed and after 1 hour a desorption process began with the heating of the material to 100 °C. The water vapour desorbed from the material condensed on the surface of the condenser and collected in the water reservoir. The desorption process lasted 1 hour and 3 minutes. During this time, the temperature of the material changed from 31 °C to 105 °C and also reached the maximum temperature of 116.5 °C at the end of desorption. During desorption, 25.5 g of water was desorbed from the material, while 14.8 g of water was stored in the water reservoir. There is a difference in the mass balance between the adsorber and the water reservoir because the remaining water that condensed during desorption was still dripping into the funnel even though the valve was already closed (this can be seen in Figure 5 as a jump in the curve showing the mass of the evaporator at the end of desorption). Further results obtained during desorption can be found in Table 2.

Tab 2: Results during desorption temperature of 100 °C

Time [h:min]	m_Evaporator [g]	m_Adsorber [g]	p_Vacuum [mbar]	T_Material [°C]	T_lift [°C]
3:11	1264.7	1531.6	27.21	31	84
4:14	1279.5	1506.1	30.82	105	
	14.8	**-25.5**			

The monitoring of the desorption process is shown in Figure 5.

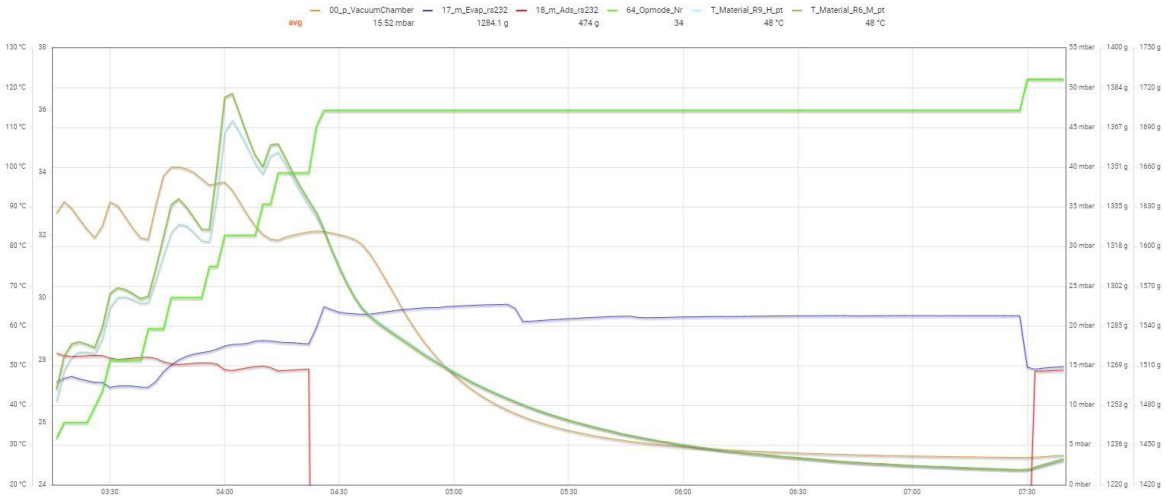

Figure 5: Monitoring of desorption at 100 °C and pressure starting at 27.21 mbar

The highest value of water uptake achieved during adsorption was 27.2 g, and 27.6 g of water vapour was desorbed during the associated desorption. This was achieved at an adsorption temperature of 15 °C and a pressure range of 3.36 mbar to 32.13 mbar. At the desorption temperature of 100 °C, a maximum pressure of 54.94 mbar was reached, which fell to 39.20 mbar by the end of desorption.

4. Conclusions

In order to develop and optimize TCMs and storage systems, a multi-level approach is required, ranging from the material level to the component and system level. When a new material is introduced into an existing pilot plant or system, extensive adsorption-desorption testing is required to determine the interaction between the material and the system.

In this work, newly developed extrudes of APO-Tric were investigated and tested in a 150-gramme laboratory test rig to demonstrate the potential of water adsorption for low-temperature heat storage applications. Due to the hydrophobic inorganic binder in the extrudates, the shaped materials were found to have lower water uptake than the powdered material. After 15 cycles with a small amount of the material (1 g), a 3% decrease in water uptake was observed, which is consistent with a decrease in specific surface area. The mass balance during adsorption was in good agreement in most tests, while larger mass differences were observed during desorption. Therefore, further analyses need to be carried out to determine the cause of the discrepancies in mass balance in some of the adsorption-desorption cycles.

5. Acknowledgments

We thank for the support of the Slovenian Research and Innovation Agency through the research program P1-0021 (Nanoporous Materials). The work is also a part of the IEA SHC TCP ES joint Tasks 67/40 »Compact Thermal Energy Storage: Materials within components within systems«. We also thank for Erasmus+ practicum exchange funding 612-5/2023-103 that enabled conducting the experiments in dedicated lab-test rig.

6. References

Baerlocher, Ch., McCusker, L.B., Olson, D. H., 2007. Atlas of zeolite framework types, Elsevier, Amsterdam.

Brancato, V., Frazzica, A. 2018. Characterisation and comparative analysis of zeotype water adsorbents for heat transformation applic,ations. Solar Energy Materials and Solar Cells, 180, 91–102.

Frazzica A., Brancato V., 2019. Verification of hydrothermal stability of adsorbent materials for thermal energy storage. Int J Energy Res., 43, 12, 6161-6170.

Freni A., Frazzica A., Dawoud B., Chmielewski S., Calabrese L., Bonaccorsi L., 2013. Adsorbent coatings for heat pumping applications: verification of hydrothermal and mechanical stabilities. Appl Therm Eng., 50, 2, 1658-1663.

Henninger, S.K., Schmidt, F.P., Henning, H.-M., 2010. Water adsorption characteristics of novel materials for heat transformation applications. Applied Thermal Engineering 30, 1692–1702.

Henninger S. K., Munz G., Ratzsch K-F., Schossig P., 2011 .Cycle stability of sorption materials and composites for the use in heat pumps and cooling machines. Renew Energy. 36, 11, 3043-3049.

Kakiuchi, H., Iwad, M., Shimooka, S., Ooshima, K., Yamazaki, M., Takewaki, T., 2005. Water vapour adsorbent FAM-Z02 and its applicability to adsorption heat pump. Kagaku Kogaku Ronbunshu, 31, 273-280.

Krajnc, A., Varlec, J., Mazaj, M., Ristić, A., Zabukovec Logar, N., Mali, G. 2017. Superior performance of microporous aluminophosphate with LTA topology in solar-energy storage and heat reallocation. Advanced energy materials, 7, 11, 1601815-1-1601815-8.

Mal, S., Ristić, A., Golobič, A., Zabukovec Logar, N., 2021. Tailoring water adsorption capacity of APO-Tric. Crystals, 11, 773.

Ng, E. P., Mintova, S., 2008. Nanoporous materials with enhanced hydrophilicity and high water sorption capacity. Microporous Mesoporous Mater, 114, 1–26.

Ocvirk, M., Ristić, A., Zabukovec Logar, N., 2021. Synthesis of mesoporous γ-alumina support for water composite sorbents for low temperature sorption heat storage. Energies, 14, 1-15.

Palomba, V., Vasta, S., Freni, A., 2017 Experimental testing of AQSOA FAM Z02/water adsorption system for heat and cold storage, Appl. Therm. Eng., 124, 967–974.

Ristić, A., Zabukovec Logar, N., Henninger, S.K., Kaučič, V., 2012. The performance of small-pore microporous aluminophosphates in low-temperature solar energy storage: the structure-property relationship, Adv. Funct. Mater. 22, 9, 1952–1957.

Ristić, A., 2022. Sorption material developments for TES applications, in Hauer, A. (Ed), Advances in energy storage: latest developments from R&D to the market. J. Wiley & Sons, Chichester, pp. 631-653.

Schmit, H., Schubert, T., Ristic, A., Velte-Schäfer, A., Hügenell, P., Füldner, G., Lävemann, E., Hiebler, S., 2024. Experimental determination of characteristic curves of two commercial zeolites and the composite of γ-Al2O3 and CaCl2 for sorption heat storage, J Energy Storage, 97, Part B, 113011.

Zeng, Z., Zhao, B., Wang, R., 2023. Water based adsorption thermal battery: Sorption mechanisms and applications, En. Stor. Mat., 54, 794-821.

06. Thermal energy storage

Optimized Thermodynamics and Building Physics of large-scale Thermal Energy Storage

Alice Tosatto[1], Fabian Ochs[1], Christoph Muser[2] and Franz Hengel[3]

[1] Unit of Energy Efficient Building, Universität Innsbruck, Innsbruck (Austria)

[2] Ingenieurbüro ste.p ZT-GmbH, Vienna (Austria)

[3] AEE Intec, Gleisdorf (Austria)

Abstract

Seasonal thermal energy storage (TES) systems are a key element to promote the increase of renewable energy in district heating networks. Their complex dynamic operation within the energy system as well as their interaction with the surrounding environment requires detailed planning and design. The TES envelope plays a key role: the TES efficiency and the temperature of the surrounding ground are strongly influenced by the thermal losses through the cover and walls. Numerical simulations are a fundamental step to define the baseline targets for the optimal TES performance. Materials testing are required to assess the effective performance of the selected materials under the specific TES operating conditions and to support the design of the specific envelope performance. The construction of mock-ups is a third element to verify the test results and to identify possible challenges in the real scale application. In this work, these three elements are mutually integrated to support the design and optimization of the final TES structure with particular attention in preventing the formation of convective heat flux within the insulation layer.

Keywords: Thermal energy storage, thermal losses, thermal insulation, porous insulation, numerical modelling, convective heat transfer

1. Introduction

The decarbonization of the building sector requires the integration in the energy system of renewable energy (RE) sources, traditionally characterized by high volatility, low density and often strong daily and seasonal oscillations. Alongside the transition of the energy generation systems, storage systems will gain increasing importance to ensure the stability of the energy supply and to increase the self-sufficiency of the communities, as it allows to decouple energy demand and generation (Golmohamadi et al., 2022).

In district heating (DH) networks, large-scale water-based thermal energy storage (TES) systems have been used to increase the share of RE. The two main construction solutions can be distinguished between tank TES (TTES) and pit TES (PTES) (Schmidt et al., 2018). TTES are of cylindrical shape and are usually freestanding; some examples are the TTES of Munich Ackermannbogen (see Fig. 1(a)) and Friedrichshafen (Ochs, 2009). PTES have a truncated pyramidal shape, generally present significantly larger volumes than TTES and can be considered the current state of the art of water-based TES, with the main examples being the PTES in Dronninglund, Marstal and the more recent Høje Taastrup in Denmark and new plant in Langkazi (Tibet, China) (International Energy Agency (IEA), 2024).

The successful application in Denmark has increased the interest in the use of this technology in other countries, but the local specific requirements (i.e., presence of groundwater, low space availability) need the implementation of specific solutions (i.e., lateral insulation, diaphragm walls, graphically presented in Fig. 1(b)) that can be cost demanding (Tosatto, Ochs, Dahash, & Muser, 2022). The TES planning and design requires the evaluation of these requirements at different levels, from the DH grid to the specific envelope element. In this phase, numerical simulations and experimental studies are an important resource.

This works aims to show the relevance and mutual connection between the different design steps for what concerns the TES envelope, highlighting how simulation studies can help to define the required parameters (i.e., thermal conductivity threshold, insulation thickness) and how the experimental investigations on the materials can support the specific design of the envelope. The case of buried TTES vertical walls is investigated here, as many of the existing applications of large-scale PTES are non-insulated, thus making the definition of reliable designs and

© 2024. The Authors. Published by International Solar Energy Society
Selection and/or peer review under responsibility of Scientific Committee
10.18086/eurosun.2024.06.09 Available at http://proceedings.ises.org

insulation concepts an important research gap to be filled. In the design of TES envelope, material degradation due to combined effects of moisture and high temperatures is a non-negligible aspect. Structural elements in concrete, polymeric liners, piping systems and insulation need to be designed to enable high performance and long life. When considering the insulation, the high costs involved for both the material and the installation call for a careful selection and design based on a deep knowledge of the heat transfer phenomena involved. The insulating bore pile wall (IBPW) concept developed within the "gigaTES" project (van Helden et al., 2021) opens several questions concerning the optimal insulation material to be applied, the construction process and the final costs. Far from being able to answer all of these questions, this work aims to highlight the most important aspects to be taken into account in the material selection and envelope design, considering the thermophysical phenomena involved.

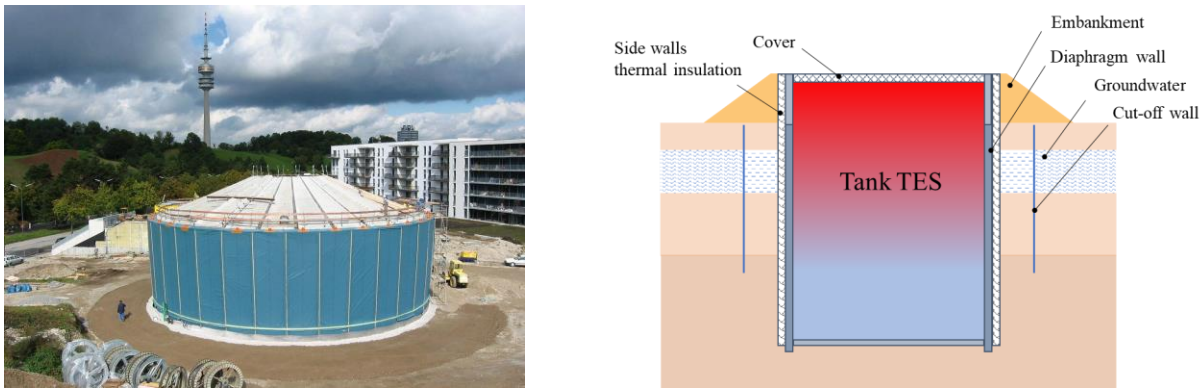

(a) **(b)**

Fig 1: (a) Freestanding TTES in Munich Ackermannbogen. (b) Sketch of the main elements of a buried TTES with lateral insulation.

In this work an integrated approach for the assessment of the TES envelope properties is suggested. Alongside standard material tests, mock-ups replicating the specific application of vertical insulation in buried TTES are considered. Following the existing approach that uses thermal response tests (TRT) to determine the thermal properties of the ground (useful for the design of ground source heat pumps) (Spitler & Gehlin, 2015), a similar solution is implemented to study the performance of vertical underground insulation. Mock-ups for TES lateral insulations are built on a lab scale (to test the approach) and are followed by tests on field-scale underground mock-ups.

2. Materials and their properties

Among the different types of insulation materials, bulk granular insulation is considered to be a suitable solution that can be used as TES insulation due to its ease of installation without the need for scaffolding, as the grains can be poured and adjusted to any geometric irregularity. Some examples applied in existing TES are foam glass gravel (FGG), expanded glass granules and perlite. However, the heat transfer that occurs within the TES envelope goes beyond the thermal conduction, as radiation and convection can concur to increase significantly the heat flux, depending on the material's characteristics (granules vs. panels, porosity, permeability) and conditions (upwards/ horizontal heat flux, temperature difference) (Drück et al., 2022; Ochs & Bianchi Janetti, 2018). Due to the presence of open porosity (i.e. voids between the grains) and large temperature difference, the use of bulk granular insulation can be unfavorable from the point of view of insulation performance in the presence of upward and horizontal heat flow (as in the TES cover and wall, respectively), since the formation of natural convective transfer (which occurs as a consequence of the air density gradient) would represent a non-negligible part of the total heat flow. The negative effects of natural convection on the effective performance of thermal insulation have been observed in large-scale TES (Ochs, 2009), but affect also the insulation of spherical cryogenic storage tanks (Taghavi et al., 2024), making this a relevant research topic for various applications.

When investigating the heat transfer within the insulation layers, alongside the energy balance equation (eq. 1), the momentum equation needs to be included to solve the velocity field of the fluid (i.e., the air within the insulation layer) related to the convective heat transfer. For the application in porous insulation materials, the Brinkman equation can be introduced (eq. 2) as it describes the momentum transport in porous media.

$$\left(\rho C_p\right)_{bulk}\frac{\partial T}{\partial t} = \nabla\cdot\left(\lambda_{bulk}\nabla T\right) - \left(\rho C_p\right)_{bulk} u\cdot\nabla T \qquad \text{(eq. 1)}$$

$$\rho\frac{du}{dt} = \nabla\cdot\left[-pI + \frac{\eta}{\psi_{macro}}\left(\nabla u + (\nabla u)^T\right) + \frac{2}{3}\frac{\eta}{\psi_{macro}}(\nabla u)I\right] + \rho g\beta(T - T_c) + \frac{\eta}{K_{bulk}}u \qquad \text{(eq. 2)}$$

In the presented equations, T is the material temperature ([K]), ρ_{bulk} ([kg/m^3]) and $C_{p,bulk}$ ([J/(kg·K)]) the bulk density and thermal capacity, λ_{bulk} ([W/(m·K)]) the bulk thermal conductivity, u the fluid velocity within the bulk ([m/s]), ρ ([kg/m^3]) the fluid density, p ([Pa]) the pressure, η ([Pa·s]) the fluid viscosity, ψ_{bulk} the bulk macro porosity, β the expansion coefficient ([1/K]) and K_{bulk} ([m^2]) the bulk permeability.

Taking into account these phenomena in the TES modelling is computationally intensive, but the design process can be divided into different steps, each one focusing on a specific aspect of the design, as simplified in Fig. 2. System models based on TRNSYS or Modelica/Dymola can be used to define the TES capacity and operation temperatures, while detailed models based on MATLAB/Simulink or COMSOL Multiphysics can provide more detailed information concerning the required insulation performance and distribution (Ochs et al., 2022). For the detailed design of the single envelope components, software tools like COMSOL Multiphysics, ANSYS and Delphin can be used to model the heat, fluid and moisture transport within the materials. This numerical analysis can go on both directions (i.e., system-to-component and component-to-system) as the information gained on one level can be used on the others and viceversa. Experimental investigations are an additional important support to extend the knowledge of the material properties, investigate the application on small mock-ups of the TES elements, and provide important indications for the design process.

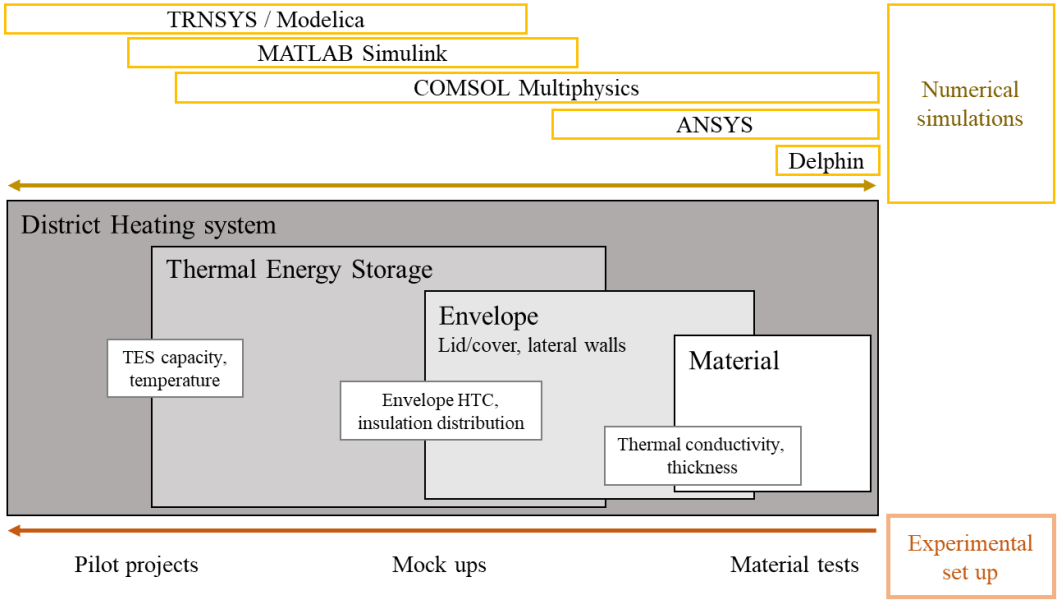

Fig. 2: Steps for the design of buried TES envelope.

3. Methodology

3.1. TES Numerical models

The integration of a buried TES within a DH systems is evaluated through the assessment of its performance under the expected operating conditions (i.e., charging/ discharging temperatures and profiles, seasonal/weekly operation). In this preliminary step, the surrounding ground (i.e., soil properties and stratification, presence of groundwater) can also be taken into account. Several numerical models are available for this type of evaluation (Ochs et al., 2022), depending on the degree of detail required and on the level of the analysis. This step is relevant to assess the general characteristics required from the TES envelope in terms of heat transfer coefficient (HTC). Many studies highlight the necessity to ensure a good performance of the insulation materials of the lateral walls, not only to improve the TES performance but also to reduce the impact on the surrounding ground and groundwater, depending on the material type (clay, sand, rock) but also on the groundwater depth and velocity (Dahash et al., 2021).

3.2. Assessment of materials' properties

Once the general requirements in terms of HTC are defined, the most suitable materials can be selected. The selection criteria for materials in this step include not only thermal conductivity, but also porosity, density, structure (panels, granules) and their attitude to absorb water. Material datasheets are an important source of information, but often the data are available for a limited range of temperatures, lower than the operation of the TES, that can reach 95 °C.

In order to assess the material behaviour at the specific operation conditions, and in particular the risk of natural convection development, three main approaches can be used: preliminary evaluations based on available data,

numerical modelling and material testing. Each one is to be considered complementary to the others, as they are able to provide different kind of information concerning the characteristics and performance of the material.

- *Preliminary assessment*. Alongside the material selection based on the properties available from the datasheets, a preliminary evaluation regarding the convection risk can be done using the Darcy-modified Rayleigh number presented in eq. 3 (Stephan et al., 2019), which defines the transition from conduction to convection (natural to turbulent) of the heat transfer in a porous material like thermal insulation.

$$Ra = \frac{g\,\beta_a}{\nu_a} \cdot \frac{L\,K\,\Delta T}{\alpha} \qquad \text{(eq. 3)}$$

  The single contributions on the development of convective heat flux depend on fluid characteristics (ν_a is the fluid kinematic viscosity, [m^2/s]), geometry and layout (L is the characteristic length [m], ΔT is the temperature difference between the two sides of the insulation [K]), and material characteristics (α thermal diffusivity [m^2/s], K material permeability [m^2]). Other factors are the gravitational acceleration (g, [m/s^2]) and the coefficient of thermal expansion (β_a, [1/K]). The Rayleigh number allows to assess for different materials and applications (i.e., temperature difference and material thickness) the role of convection. Its limit is the fact that it considers a 1D heat transfer, while the heat transfer through TES lateral walls and cover is 2D or even 3D. Moreover, the material permeability is often an unknown parameter, that can be estimated through empirical correlations (see eq. 4, Ergun correlation (Ochs, 2009)) or experimentally defined, and the thermal conductivity used to the define the thermal diffusivity depends on the material average temperature, which is usually much higher than the temperature used to define the nominal thermal conductivity in commercial datasheets.

$$K_{Ergun} = \frac{d_m^2 \cdot \psi^3}{A \cdot (1-\psi)^2} \qquad \text{(eq. 4)}$$

- *Material testing*. Material investigations in this step consist in laboratory investigations to assess the thermal conductivity using one- and two-plates guarded hot plate (GHP) devices (Adam et al., 2015). The two-plates GHP device allows defining the thermal conductivity without the influence of convection, while the one-plate GHP device, depending on its orientation, allows to assess the relevance of convection with respect to conduction. These investigations allow to define the relation between thermal conductivity and temperature, that can be used for the Rayleigh evaluation.

- *Numerical modelling*. The material-level numerical modelling of the conducted tests allows defining the material permeability (also required for the Rayleigh evaluation) from the comparison with the experimental results (Ochs et al., 2015). Available tools are Delphin, specialized for the investigation of the moisture transport, and COMSOL Multiphysics, which is a FE-based software, able to solve multiphysics phenomena.

3.3. Mock ups

The knowledge of the material properties supports the definition of cost-effective insulation design solutions. In the IBPW concept, this additional step is used to assess the effective performance of the insulating material. The IBPW concept for the TTES vertical walls consists of a series of ground bored cylindrical piles filled with granular insulation (Tosatto, Ochs, Dahash, Muser, et al. (2022)), as presented in Fig. 3(a). The combination of porous granular insulation, high temperature differences (i.e., between the TES and the surrounding ground) and heat flux orientation (horizontal) will most likely trigger the development of a convective plume within the pile, thus resulting in an overall poorer insulation performance. The study of mock-ups allows for the investigation of the structural stability of the granular material (required to allow the over-drillability of the piles) and the optimization of the construction process (i.e., material mixing and compaction). In addition, the building physics performance of the selected material in the specific application can be tested and verified, thus providing further insights for the design optimization.

In the definition of the IBPW concept, the mock-up investigation is divided in two phases, one with lab-scale tests and one with field tests. Two mock-ups of an insulating pile are built: a small (lab-scale) insulating pile (small mock up, sMU) and a higher (drilled) insulating pile (field mock up, fMU), with the characteristics presented in Tab. 1 and the geometry presented in Fig. 3(b). Both mock-ups have the same experimental configuration, with a measuring probe located vertically along the symmetry axis of the cylindrical pile, containing an electric heating band and temperature sensors; the voids in the measuring probe are filled with sand. Within the “gigaTES” project, the tested insulation material is FGG, both compacted and uncompacted.

Tab. 1: Characteristics of the IBPW investigated mock ups.

	Small mock up	Field mock up
Height, [m]	1	6
Diameter, [m]	0.5	0.9
Type	freestanding	buried
Location	climate chamber (UIBK, AT)	construction site (Vienna, AT)
Tested materials	uncompacted and compacted FGG	

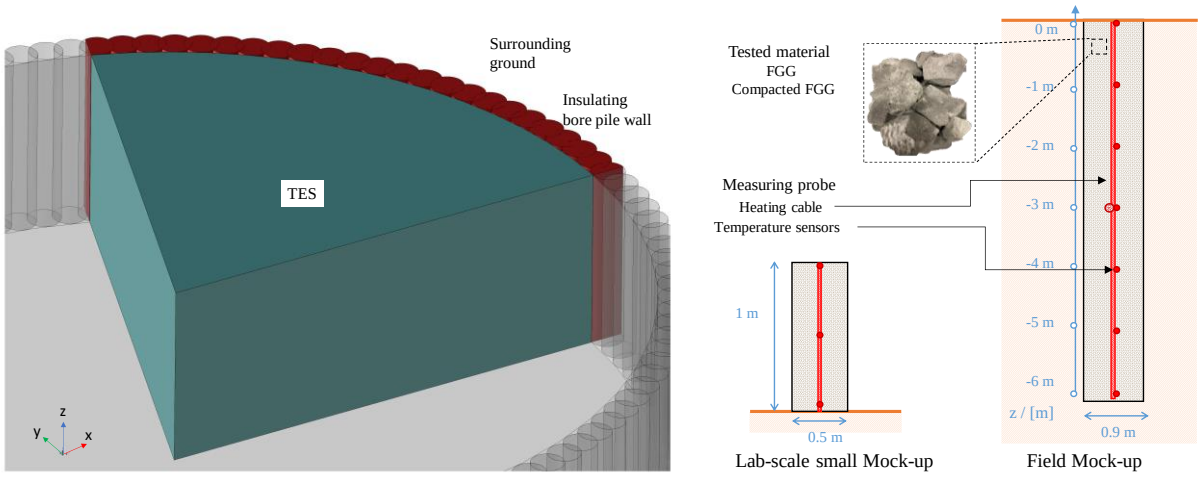

Fig. 3: Insulating bore pile solution for TES lateral walls. (a) Concept of the IBPW as lateral insulation. (b) Lab-scale and field mock-ups.

The testing procedure consists in a heating phase when the heating band is heated at a specific set point (80 to 90 °C to simulate TES operating temperatures), and a following cooling phase. The insulation performance of the investigated material is evaluated comparing the electric power required to maintain the given set point temperature and the profile of the temperature curve during the cooling phase. The experimental results are compared with numerical simulations, thus allowing to derive the apparent thermal conductivity and the permeability of the material at the specific conditions. Two numerical models are then implemented in COMSOL Multiphysics environment:

- a heat conduction model, which allows to assess the apparent thermal conductivity of the material. This simplified implementation of eq. 1 does not consider the convective term and is not able to capture all the involved phenomena, but provides a general evaluation concerning the insulation performance in terms of apparent thermal conductivity ($\lambda_{bulk,app}$, as from eq. 5), which considers both the heat transfer by conduction and convection.

$$\left(\rho C_p\right)_{bulk} \frac{\partial T}{\partial t} = \nabla \cdot \left(\lambda_{bulk,app} \nabla T\right) \qquad \text{(eq. 5)}$$

- a detailed model, able to consider also the convective heat transfer, combining the heat transfer (eq. 1) and the Brinkman equation (eq. 2), to estimate the bulk permeability.

The numerical models replicate the geometry and the boundary conditions of the two mock-ups and receive as input the (measured) electric power required by the heating band to maintain the desired set point temperature.

4. Results

4.1. TES numerical models

From existing studies based on numerical simulations of large-scale TES, HTC in the range of 0.2 W/(m^2·K) to 0.3 W/(m^2·K) are desirable to achieve sufficiently good TES storage efficiencies of 80-90 % depending on the TES volume and geometry. In presence of groundwater, lower overall HTCs are required (about 0.1 W/(m^2·K)), together with additional geotechnical measures such as the installation of cut-off walls at an appropriate distance, in order to limit the groundwater temperature exceedance (Dahash et al., 2021).

4.2. Assessment of materials' properties

Given the output of the TES numerical simulations, in presence of groundwater an HTC around 0.1 W/(m^2·K) is desirable. To maintain the insulation layer thickness below 1 m (to minimize the required volume and the amount of material required), this results in a required thermal insulation effective conductivity around 0.1 W/(m·K). The reference to the 'apparent' thermal conductivity (eq. 5) rather than to the nominal one is necessary in the evaluation of the HTC, as it considers the total heat transfer, considering the additional influence of radiation and convection. Nevertheless, the nominal thermal conductivity provided by manufacturers is a good starting point to select the most suitable materials.

4.2.1. Material testing

The lab tests allow to investigate the effect of temperature on the material thermal conductivity under controlled boundary conditions. Previous tests run on FGG, both compacted and uncompacted, using a large one-plate GHP device (oriented downwards to prevent the development of convection) showed already a preliminary distinction between the two (Adam et al., 2015). The better performance of the compacted FGG can be traced back to the reduced impact of the radiative heat transfer, due to the reduced space between the grains. However, grain size, porosity distribution, relative humidity, probe thickness and temperature have a major influence on the heat transfer mechanisms and therefore on the measurement results. Therefore, the effects of convection, radiation and conduction (both in solid and in fluid domains) can compensate each other, leading to a higher uncertainty in the measurements (estimated to be around 5 %). For example, Mustafa et al. (2023) reported an opposite observation in the investigation of FGG, with increasing values of thermal conductivity with increasing compaction rates, but the measurement results were in a similar range as the ones reported by Adam et al. (2015).

The thermal conductivity of the investigated materials is defined as a linear function of the average temperature according to eq. 6, from the results presented by Adam et al. (2015). The nominal reference values for the two coefficients λ_a and λ_b are defined from material tests (see Fig. 4) at specific measuring points and extrapolated to higher temperatures. In addition to FGG, perlite is considered in the analysis as a reference material where convection plays a negligible role. In this case, thanks to the lower dimensions of the grains, a smaller one-plate GHP device (Taurus TCA 300, Taurus Instruments GmbH) was used, resulting in a smaller error.

$$\lambda_{bulk} = \lambda_a + \lambda_b \cdot T \quad \text{(eq. 6)}$$

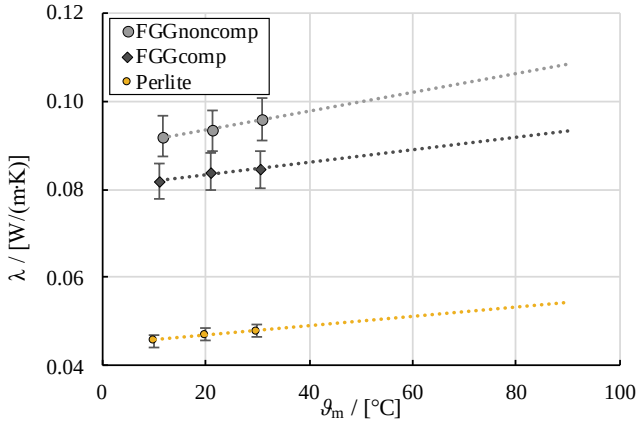

Fig. 4: Thermal conductivity for the investigated materials (FGG from (Adam et al., 2015)) as a function of the mean temperature.

4.2.2. Rayleigh number

The results provided by the material investigation (porosity, thermal conductivity as function of temperature), allow to derive a preliminary indication of the convection risk through the Rayleigh number. With the parameters presented in Tab. 2, the Rayleigh number is evaluated for the real scale application of the IBPW and for the two mock up solutions (sMU, and fMU). For this preliminary evaluation, the material permeability from the Ergun correlation (eq. 4) is used, while the fluid properties (i.e., air) are defined on the average temperature between the hot and the cold side.

Tab. 2: Input parameters for the evaluation of the Rayleigh number. The fluid properties are evaluated for the average temperature.

	Parameter	Perlite	FGG	Compacted FGG
Operation conditions	T (warm side) / [°C]	90		

	T (cold side) / [°C]	20		
	L / [m]	0.25 (sMU radius), 0.45 (fMU), 0.9 (IBPW)		
Insulation Material	λ / [W/(mK)]	λ(T_m) (Fig. 4)		
	ψ / [-]	0.48	0.38	0.15
	d_m / [m]	0.003	0.35	0.35
	K_{Ergun} / [m^2]	$2.4 \cdot 10^{-8}$	$1.16 \cdot 10^{-6}$	$7 \cdot 10^{-8}$
Fluid (air)	β / [1/K]	0.003		
	ρ / [kg/m^3]	1.075		
	c_p / [J/(kgK)]	1007		
	ν / [m^2/s]	$1.847 \cdot 10^{-5}$		

The resulting Rayleigh numbers, shown in Fig. 5, indicate that the influence of convection is expected to be more pronounced in the real scale application, since the main heat transfer occurs along the whole pile diameter, rather than along the radius (as in the two mock-ups where the heating cable is arranged axially). Considering the threshold of $Ra \approx 40$ proposed by Ochs et al. (2015) for the development of convection, the non-compacted FGG does not seem to be suitable for this specific application, while the compacted FGG solutions seem to be on the borderline, with the sMU below the convection risk threshold, and the larger structures (fMU and real scale IBPW) susceptible to the risk of convection development. An important element of uncertainty is in the assessment of the permeability of the porous bulk, which depends on the degree of compaction and its distribution, which may not be homogeneous within the probe.

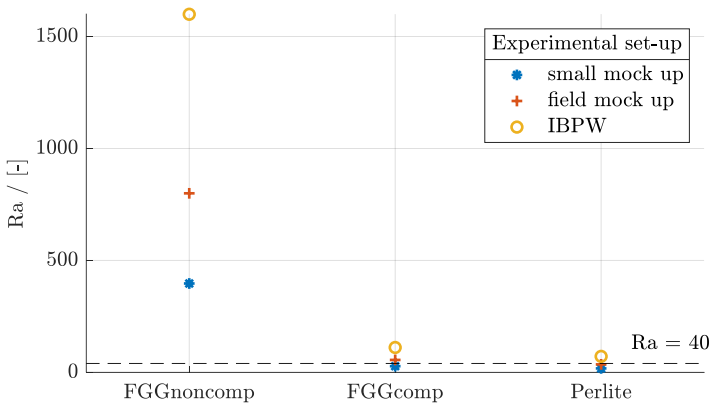

Fig. 5: Rayleigh number for the IBPW: small mock up, field tests and real scale application and threshold for the risk of convection.

4.3. Mock up

The investigation of the insulation material performance in a configuration similar to the final application helps to define the most suitable installation procedures and to evaluate potential challenges in this phase. In order to cross-check the results of the Rayleigh evaluation and to provide a reference test procedure for the IBPW, two mock-up solutions are investigated: a lab-scale sMU and a larger scale fMU.

The indicators used to assess the performance of the different configurations are:

- the effective electric power required to maintain the set point temperature (eq. 7). This is directly measured from the test and provides an immediate indicator (P_{el} is used as input in the implemented numerical model).

$$P_{eq} = \frac{P_{el}}{H_{pile} \cdot (T_{max} - T_{min})} \qquad \text{(eq. 7)}$$

- the apparent thermal conductivity of the material (eq. 5), resulting from the comparison between the measured temperatures and the numerical simulation results.
- the Rayleigh number, derived from the assessment of the bulk permeability with the detailed model.

A reference test using perlite in the sMU, is run to calibrate the numerical model and to provide a reference value for the FGG. Fig. 6 shows the geometry of the model implemented in COMSOL Multiphysics for the sMU; thanks to

the axial symmetry of the mock-up, the numerical model was built using a 2D axisymmetric geometry. Tab. 3 presents the properties of the probe materials defined with the reference test and used in the following simulations.

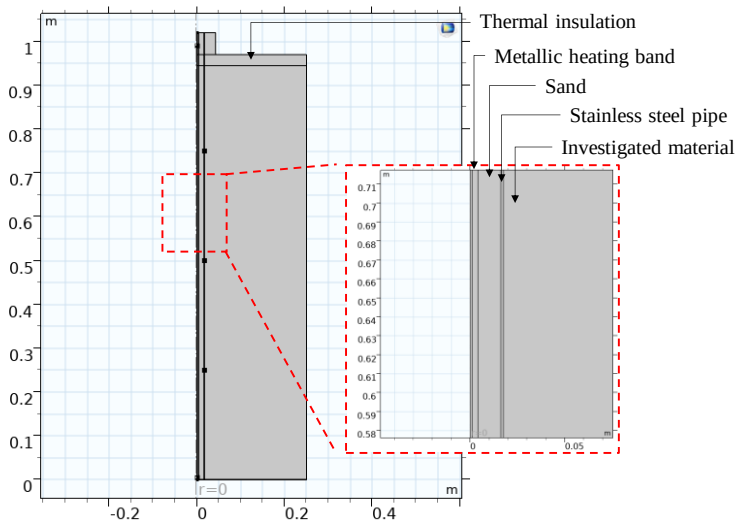

Fig. 6: Axisymmetric view of the sMU implemented in COMSOL Multiphysics.

Tab. 3: Probe parameters defined from model calibration.

Material	Thermal conductivity, λ [W/(m·K)]	Thermal capacity, ($\rho \cdot c_p$) [J/(kg·m^3)]
Metallic heating band	200	2.40e+06
Sand	1	1.26e+06
Stainless steel pipe	30	4.16e+06

The comparison between measured and simulated temperature curves of the mock ups allows to define the apparent thermal conductivity, by changing the coefficient $\lambda_{a,app}$ in the heat conduction model (see eq. 8), while in the detailed model with Brinkman equations the permeability K is evaluated, using the nominal λ_{bulk} from eq. 6.

$$\lambda_{app} = \lambda_{a,app} + \lambda_b \cdot T \qquad \text{(eq. 8)}$$

Fig. 7(a) presents the measured effective powers for the conducted tests and Fig. 7(b) the measured temperature profiles for the three investigated materials. From fig. 7(a) it is possible to see the better insulation performance of perlite, which has the lowest nominal thermal conductivity and requires a lower power to maintain the set point temperature of 90 °C during the heating phase compared to the uncompacted FGG, which shows the worst performance. From the temperature profiles in Fig. 7(b), the influence of convection in the uncompacted FGG is visible, with the upper temperature sensor measuring the highest temperatures, while perlite and compacted FGG measure higher temperatures in the central probe.

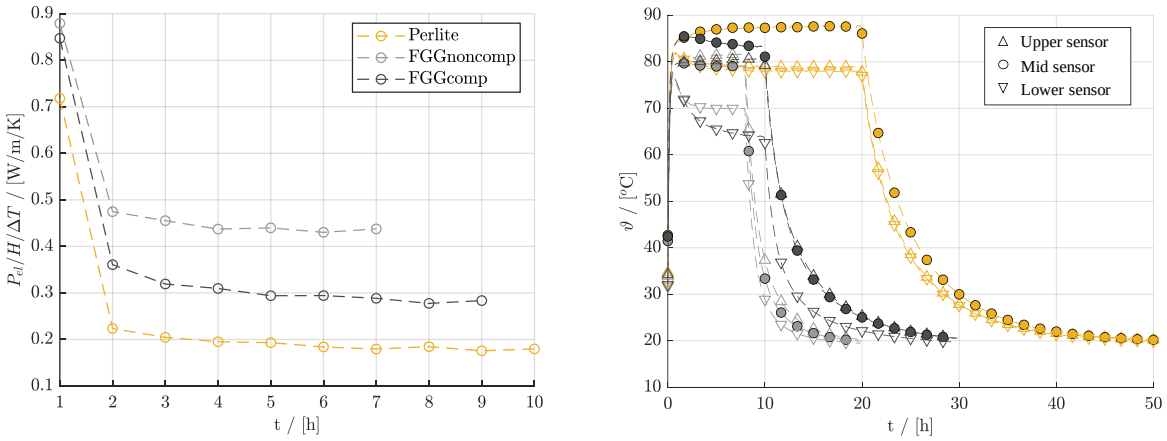

(a) **(b)**

Fig. 7: (a) Effective electric power required to maintain the set point temperature. (b) Measured temperature profiles.

For the assessment of the material apparent thermal conductivity, the measured temperature profiles are compared to the simulated ones. The results of the heat conduction model are presented in Fig. 8 for the sMU, for the reference measurement with perlite and the two FGG cases (non-compacted and compacted), for the mid sensor only, as border and 3D effects on the upper and lower sensor make it difficult to conclude on the respective simulation results.

It is possible to see that the pure heat conduction model is able to replicate quite well the behavior of the material in presence of low or negligible convective heat transfer. Therefore, the simulated temperature curves of perlite and compacted FGG are quite close to the measured values, with the best match with $\boldsymbol{\lambda_{a,app}}$=0.04 W/(m·K). In case of the perlite (used as reference measurement to calibrate the model), the uncertainty in the $\boldsymbol{\lambda_{a,app}}$ term is around 0.005 W/(m·K), which is considered acceptable taking into account the complexity of the geometry and the uncertainty in the properties of the insulating probe used in the numerical model.

In case of the non-compacted FGG, the curve which enables the best fit with the measured values is $\lambda_{a,app}$=0.2 W/(m·K), as already observed by Tosatto, Ochs, Dahash, Muser, et al. (2022). This means, that against a nominal thermal conductivity of around 0.09 W/(m·K) (see Fig. 4), the apparent conductivity, taking into account the effect of convection, is at least double. In the compacted FGG, material compaction, through the reduction of the bulk porosity, does not only reduce the convective heat transfer, but also the radiative, resulting in $\lambda_{a,app}$ of around 0.1 W/(m·K).

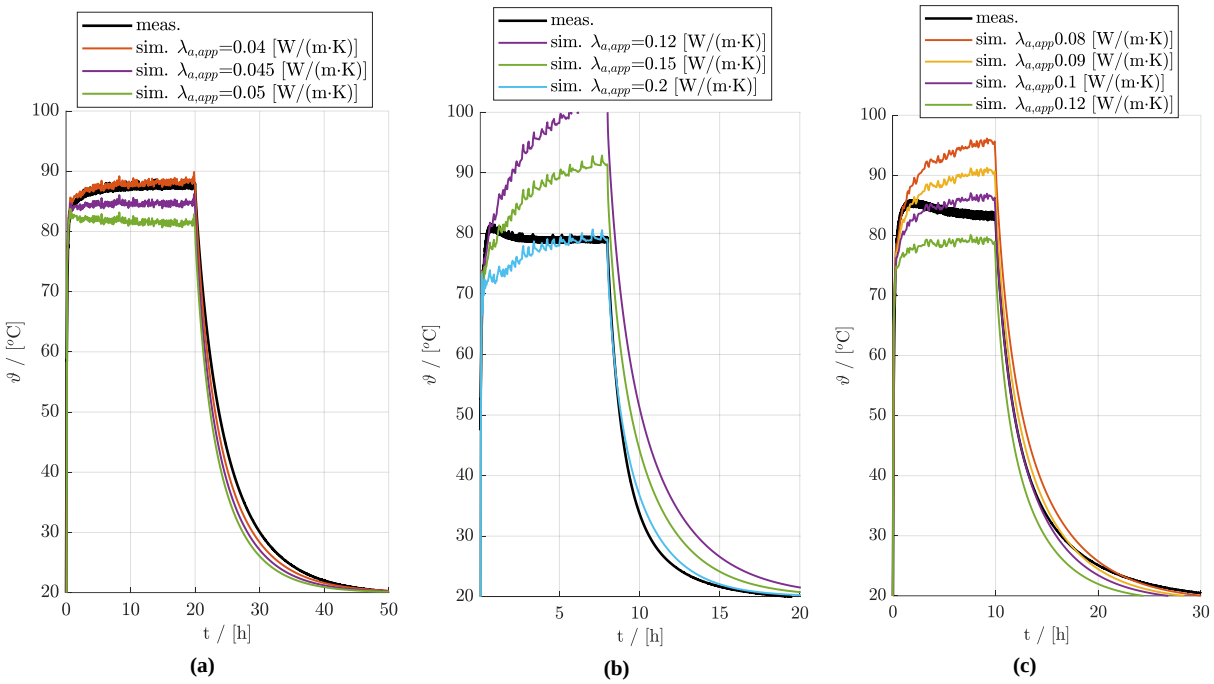

Fig. 8: Apparent thermal conductivity evaluation with heat conduction model. (a) Perlite (b) FGG non-compacted. (c) compacted FGG.

However, the heat conduction model alone is not able to capture the dynamics of the heat transfer. In porous media, thermal conductivity increases with increasing temperature as the air conductivity increases, but radiative heat transfer also plays a role as temperature differences increase, and air motion due to buoyancy results in an inhomogeneous radial and vertical temperature distribution. The use of a detailed model capable of simulating also the fluid motion is useful to investigate the effects of convection and to take into account the properties of the air. Fig. 9 presents the temperature profiles of the mid sensor, obtained with the detailed numerical model. It is possible to observe that this model allows to better capture the dynamics of the measurement, especially in the heating phase. The permeability that allows the best fit is $7 \cdot 10^{-7}$ m^2 in the case of the non-compacted FGG and $1 \cdot 10^{-7}$ m^2 in the case of the compacted FGG, which are comparable to the values derived empirically using the Ergun correlation (presented in Tab. 2). In the case of the sMUs, the results obtained in the preliminary evaluation using the Rayleigh number (Fig. 5) are then confirmed by the lab tests.

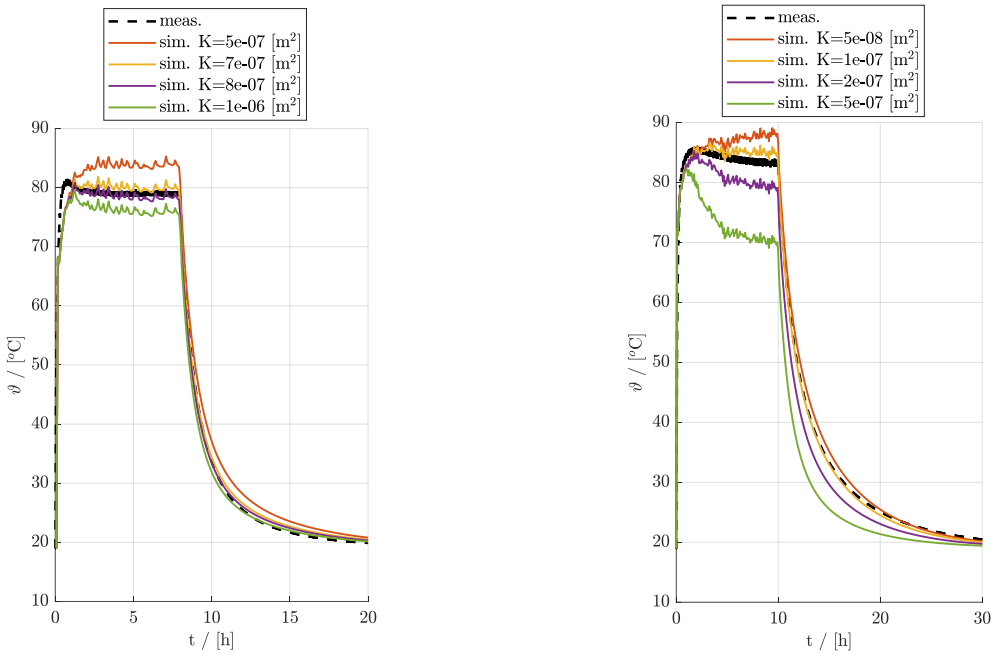

Fig. 9: Permeability evaluation with detailed numerical model. (a) FGG non-compacted. (b) compacted FGG.

The extension of the study on the field tests allows to investigate how the larger dimensions of the probe (both in terms of height and diameter), affect the development of convection, as suggested from the Rayleigh number evaluation. This is visible from the effective electric power required to maintain the set point temperature, presented in Fig. 10. The larger mass of the piles in the field tests require a longer heating phase to reach steady state conditions to compare the required powers. The compacted FGG configuration shows a better performance than the uncompacted one, but in the fMU it is worse than that observed in the sMU. This difference can be attributed to two main reasons: (1) in the sMU, homogeneous compaction is ensured as the FGG is compacted layer by layer under visual control, whereas in the fMU, different layers may have different degrees of compaction and therefore different permeability, (2) the larger radius of the fMU favors the development of the convective plume.

The field tests thus made it possible to observe how the construction procedure has an influence on the insulating performance of the material. Inhomogeneous compaction results in higher porosity along the vertical, thus favoring convection in already critical conditions (due to the larger dimensions).

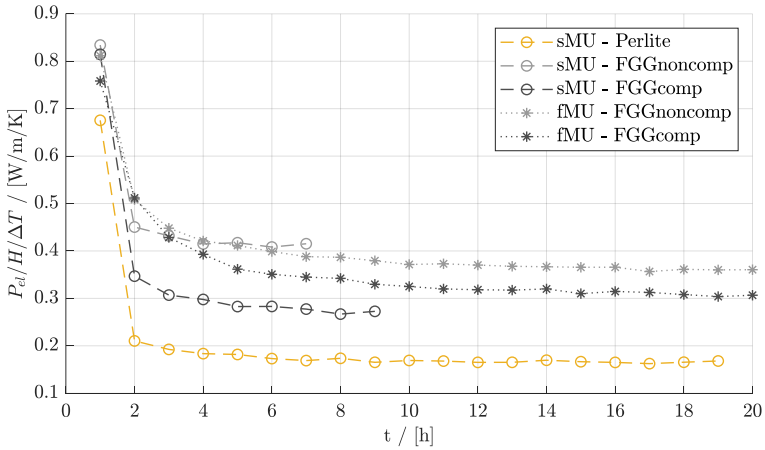

Fig. 10: Effective electric power required to maintain the set point temperature in the sMU and fMU.

5. Conclusions

In this work, the role of numerical studies and experimental studies is defined in supporting the design of the envelope and insulation of buried TES. Both can be divided in different steps, going from the smallest element (i.e., the material itself) to the component (i.e., the TES vertical wall or cover) to the system. Each of these steps is able to provide indications about the envelope requirements and the specific characteristics that the materials need to have, thus helping the designer selecting the ideal insulation material and ensuring that it performs as intended.

The specific case of IBPW is here presented as example. TES-level studies are able to define a range for the required HTC to ensure both a good TES performance (in terms of thermal losses) and prevent the groundwater overheating. Bulk insulation materials appear to be the most suitable for this kind of application, and the minimum required insulation thickness can be defined from their nominal thermal conductivities. The effective performance of these materials can however deviate from the one provided by the manufacturers' datasheets, as high temperatures and horizontal/upwards heat fluxes can trigger the development of convection, thus enhancing the local heat transfer. Targeted material testing and insulation mock ups are able to assess the performance of the materials under the TES operation conditions and to give indication about the optimal construction process. FGG is one of the most suitable materials for this application, thanks to its high structural stability and its good insulation performance. The large porosity within the FGG bulk makes it however prone to the development of convection in presence of high temperature difference and unfavorable heat transfer direction: material compaction can block the convection, but it may not be sufficient in the real-scale application, as observed both by theory analysis (Rayleigh number) and targeted material tests. The field tests confirmed the preliminary investigations with the Rayleigh number in terms of convection risk development and provided important insights on the structural stability of the insulation material to ensure the over-drillability. Further studies within the "ScaleUp" project are ongoing and investigate the possibility to mix different granular insulation materials with different granulometries to prevent the convection development.

6. Acknowledgments

This research was carried within the framework of the "ScaleUp" project led by Wien Energie and funded by the Austrian "Klima- und Energiefonds". Therefore, the authors wish to acknowledge the financial support for this work.

7. References

Adam, D., Andreatta, A., Feist, W., & Feix, J. (2015). Grundlagenforschung Glasschaumgranulatschüttungen als lastabtragender und wärmedämmender Baustoff - Berichte aus Energie- und Umweltforschung. In *Bundesministerium für Verkehr, Innovation und Technologie*.

Dahash, A., Ochs, F., Giuliani, G., & Tosatto, A. (2021). Understanding the interaction between groundwater and large-scale underground hot-water tanks and pits. *Sustainable Cities and Society*, *71*, 102928. https://doi.org/10.1016/j.scs.2021.102928

Drück, H., Bonk, N., Juschka, W., Ullmann, J., Lang, S., Gensbaur, M., Bestenlehner, D., Hübner, J., Reu, E., & Abel, S. (2022). *Erweiterung und Optimierung der solaren Nahwärmeversorgung Hirtenwiesen II in Crailsheim sowie Begleitforschung zu solarer Nahwärme und saisonaler Wärmespeicherung (CROW)*. 1–130.

Golmohamadi, H., Larsen, K. G., Jensen, P. G., & Hasrat, I. R. (2022). Integration of flexibility potentials of district heating systems into electricity markets: A review. *Renewable and Sustainable Energy Reviews*, *159*, 112200. https://doi.org/10.1016/J.RSER.2022.112200

International Energy Agency (IEA). (2024). *IEA ES TCP Task 39 - Large Thermal Energy Storages for District Heating. Deliverable A5 - List of LTES projects*. https://iea-es.org/task-39/deliverables/

Mustafa, W. S., Szendefy, J., & Nagy, B. (2023). Thermal Performance of Foam Glass Aggregate at Different Compaction Ratios. *Buildings*, *13*(7), 1844. https://doi.org/10.3390/buildings13071844

Ochs, F. (2009). *Modelling Large-Scale Thermal Energy Stores* [Univ. Diss.]. University of Stuttgart.

Ochs, F., & Bianchi Janetti, M. (2018). *Wärmeleitfähigkeit von Dämmstoffen in Abhängigkeit von Temperatur und Feuchtegehalt. In: Stephan, P., Mewes, D., Kabelac, S., Kind, M., Schaber, K., Wetzel, T. (eds) VDI-Wärmeatlas.* Springer Vieweg, Berlin, Heidelberg. https://doi.org/10.1007/978-3-662-52991-1_107-1

Ochs, F., Bianchi Janetti, M., & Klesnil, O. (2015). *Wärmeleitfähigkeit von Schüttungen aus Glasschaumgranulat: Messtechnische Analyse sowie Analytische und Numerische Modellierung*. http://www.aee-now.at/cms/fileadmin/downloads/projekte/store4grid/store4Grid Wärmeleitfähigkeit.pdf

Ochs, F., Dahash, A., Tosatto, A., Reisenbichler, M., O'Donovan, K., Gauthier, G., Kok Skov, C., & Schmidt, T. (2022). Comprehensive Comparison of Different Models for Large-Scale Thermal Energy Storage. *Proceedings of the International Renewable Energy Storage Conference 2021 (IRES 2021)*, 36–51. https://doi.org/10.2991/ahe.k.220301.005

Schmidt, T., Pauschinger, T., Sørensen, P. A., Snijders, A., Djebbar, R., Boulter, R., & Thornton, J. (2018). Design Aspects for Large-scale Pit and Aquifer Thermal Energy Storage for District Heating and Cooling. *Energy Procedia*, *149*, 585–594. https://doi.org/10.1016/j.egypro.2018.08.223

Spitler, J. D., & Gehlin, S. E. A. (2015). Thermal response testing for ground source heat pump systems—An historical review. *Renewable and Sustainable Energy Reviews*, *50*, 1125–1137. https://doi.org/10.1016/J.RSER.2015.05.061

Stephan, P., Kabelac, S., Kind, M., Mewes, D., Schaber, K., & Wetzel, T. (Eds.). (2019). *VDI-Wärmeatlas. Fachlicher Träger VDI-Gesellschaft Verfahrenstechnik und Chemieingenieurwesen* (12th ed.). Springer Vieweg Berlin, Heidelberg. https://doi.org/https://doi.org/10.1007/978-3-662-52989-8

Taghavi, M., Sharma, S., & Balakotaiah, V. (2024). Natural convection effects in insulation layers of spherical cryogenic storage tanks. *International Journal of Heat and Mass Transfer*, *220*. https://doi.org/10.1016/j.ijheatmasstransfer.2023.124918

Tosatto, A., Ochs, F., Dahash, A., & Muser, C. (2022). The Challenge of Planning and Constructing Large-Scale Hot Water TES for District Heating System: A Techno-Economic Analysis. *Proceedings of the International Renewable Energy Storage Conference 2021 (IRES 2021)*, 52–66. https://doi.org/https://doi.org/10.2991/ahe.k.220301.006

Tosatto, A., Ochs, F., Dahash, A., Muser, C., Kutscha-Lissberg, F., & Kremnitzer, P. (2022). Insulating piles for the cost-effective construction of very large-scale high temperature thermal energy storage. *Proceedings of the International Renewable Energy Storage Conference 2021 (IRES 2021)*, 67–77. https://doi.org/https://doi.org/10.2991/ahe.k.220301.007

van Helden, W., Leusbrock, I., O'Donovan, K., Reisenbichler, M., Riegler, T., Knabl, S., Wallner, G. M., Peham, L., Pugstaller, R., Muser, C., Drucker, P., Moser, M., Ochs, F., Tosatto, A., Dahash, A., & Bianchi Janetti, M. (2021). *Giga-scale thermal energy storage for renewable districts - Publishable final report*. https://www.gigates.at/index.php/en/publications/reports

07. Solar Thermal and PVT Collectors and Solar Loop Components

MODELING AND SIMULATION OF THE NATIONAL SOLAR THERMAL RESEARCH DEMONSTRATION FACILITY IN GWALPAHARI

Spiros Alexopoulos [1], Amitojsingh Arora [2], Zahra Mahdi [1]

[1] Solar-Institut Jülich of the FH Aachen University of Applied Sciences, Germany

[2] FH Aachen University of Applied Sciences, Germany

*Correspondence: Spiros Alexopoulos, alexopoulos@sij.fh-aachen.de

Abstract

To facilitate research in the renewable energy field, the Government of India in cooperation with the Indian Institute of Technology Bombay established a research demonstration facility on the campus of National Institute of Solar Energy. This 1 MW_e concentrated solar power facility uses parabolic trough collectors and linear Fresnel reflectors to concentrate solar energy and produce thermal energy which is used in the power block for electricity production. The article describes a simulation model of the facility for a steady state condition with and without the Fresnel reflectors and an additional one for the calculation of the annual energy production as well as the corresponding simulation results.

Keywords: Concentrated Solar Power, Parabolic Trough Collector, Linear Fresnel Reflector, Simulation

1. Introduction

India, as a tropical country, possesses significant solar energy resources, which can be harnessed for electricity generation via concentrated solar thermal technologies. In recognition of this potential, the Government of India (GoI) has launched an ambitious program within the Jawaharlal Nehru National Solar Mission (JNNSM) aimed at generating 40 GW of solar powered electricity until 2022 (Nehru, 2021). This initiative necessitates the development of essential knowledge, workforce training, and the requisite infrastructure.

To promote awareness, foster research, develop a simulation software and establish a demonstration facility for solar thermal power, the Indian Institute of Technology Bombay (IIT B) initiated a project in 2008, with financing from the Ministry of New and Renewable Energy (MNRE) under the GoI.

The concentrated solar power (CSP) facility uses parabolic trough collectors (PTC) and linear Fresnel reflectors (LFR) to concentrate solar energy and produce thermal energy, which is used in the power block to produce electricity. The article describes simulation models of the CSP facility in steady state condition and an alternative model for calculating the annual energy production together the corresponding simulation results.

2. System Description

A 1 MW_e research and demonstration solar thermal power plant has been established within the campus of the National Institute of Solar Energy (NISE), under the purview of the Ministry of New and Renewable Energy (MNRE), Government of India (GoI), situated in Gwalpaharai, Haryana, India. The power plant harnesses two distinct technologies, namely the Parabolic Trough Collector (PTC) technology and the Linear Fresnel Reflector (LFR) technology. The PTC field boasts a thermal capacity of 3 MW_{th}, while the LFR field has a capacity of 2 MW_{th}, ultimately resulting in a 1 MW_e electric output. For the PTC field, the Heat Transfer Fluid

© 2024. The Authors. Published by International Solar Energy Society
Selection and/or peer review under responsibility of Scientific Committee
10.18086/eurosun.2024.07.01 Available at http://proceedings.ises.org

(HTF) employed is Therminol VP 1 (Eastman Chemical Company, 2024) whereas the LFR field directly utilizes steam to facilitate the energy management process. A buffer thermal storage system is incorporated, allowing for a 30-minute storage period through a pressure vessel, designed for high temperature conditions (Nayak et. al., 2015). Figure 1 is a satellite image of the power plant at Gwalpahari.

Fig. 1: Satellite image of the power plant located at Gwalpahari (Google Maps, (2023))

The working fluid heated up by the PTC field, is stored in a high-temperature tank. Subsequently, it is conveyed to a heat exchanger, where it transfers its thermal energy to water, generating high-temperature steam. The cooled down HTF is then stored in a low-temperature vessel to maintain its circulation within the PTC solar field. The LFR field is responsible for producing saturated steam, which is extracted from the deaerator and released into the steam drum. These two loops interest over three heat exchangers. The high-temperature steam is directed into a steam turbine to generate mechanical power, which is then converted into electric power by an AC generator. The spent steam from the turbine is condensed through a condenser. A regeneration steam is also taken out of the turbine to optimize the overall efficiency.

3. Approach

Two different approaches were applied to model the performance of the facility. First model simulates the CSP facility for a steady state condition to investigate the peak performance of the system. For the second model, the annual production simulation is performed using SAM through various weather conditions of a typical year.

The steady state model was created in EBSILON® *Professional* by Iqony Soultions GmbH (STEAG, 2023), which is a specialized graphical software tool for the simulation and analysis of power plants. Components from the in-built library were used to conduct the steady state simulation. The model generated in EBSILON can be seen in Figure 2. The main components of this model are those of a simple Rankine cycle power plant, namely turbine, condenser, pump and generator as well as the CSP and LFR field as the heat source. Additional components such as heat exchangers, storage, deaerator and steam drum were also required which are shown in Figure 2.

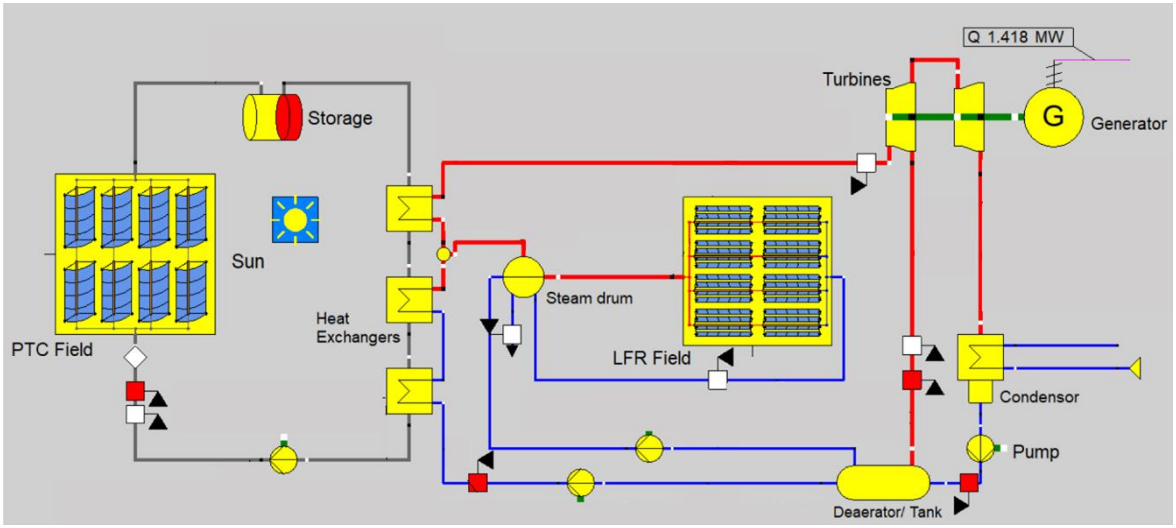

Fig. 2: Schematic diagram of the CSP demonstration facility in EBSILON® *Professional*

The plant utilizes two separate technologies for heat capture. The grey loop with the PTC field and storage on the left is utilizing Therminol VP1 as the HTF. The primary loop with the power block, condenser and deaerator and secondary loop with LFR field uses water/steam as the working medium. The steam flow from the LFR field is fed into the steam drum. While designing the simulation model, the loops were individually simulated and merged through the three cross flow heat exchangers, namely economizer, steam generator and the super heater. The saturated steam from the steam drum is merged with the primary loop before the superheater. There is also a regeneration stream bled into the deaerator at 2 bar and 0.15 $kg \cdot s^{-1}$. The deaerator then splits the water stream with 0.84 $kg \cdot s^{-1}$ towards the LFR via the steam drum. The input parameters of the steady state simulation are shown in Table 1.

Tab. 1: Key parameters of the steady state simulation

Component	Parameter	Value
PTC Field	HTF	Therminol VP1
	Input Temperature	237 °C
	Number of collectors	12
	Input pressure	17.5 bar
LFR Field	HTF	Water / Steam
	Input Temperature	256 °C
	Number of collectors	16
	Input pressure	44 bar
Turbine	Isentropic Efficiency	75 %
	Inlet temperature	364.2 °C
Mass flow rate	Therminol VP 1	8.53 $kg \cdot s^{-1}$
	Primary water steam loop	1.93 $kg \cdot s^{-1}$
	Secondary water steam loop	2.22 $kg \cdot s^{-1}$

As compared to the model of Nayak et. al. (2015) the deaerator has been substituted with a tank for

simplification. The loop with the PTC field is installed with two storage tanks, a high temperature tank (393 °C) and a low temperature tank (232 °C), to provide approx. 30 minutes of thermal energy backup and to homogenize the fluid flow. For this simulation, only one tank is used as a simplification for the steady state analysis. Additionally, in the sun component constant DNI of 600 $W \cdot m^{-2}$ and an ambient temperature of 23 °C is used as the weather parameter for the chosen location.

To simulate the annual yield, System Advisory Model (SAM), which is developed by the National Renewable Energy Laboratory (NREL) (System Advisor Model, 2023), is used. SAM is a software package that incorporates various renewable energy models and graphical analysis tools. To develop the annual model, two separate models, namely one only dependent on PTC field and second one with LFR field, were generated. Both the models are generated as a non-financial model. These models were individually simulated and then combined in the software. For both the models the weather data was imported by NREL's National Solar Radiation Database (NSRDB). This database is a collection of international weather data. For this project, DNI from the model SUNY from the METEOSAT IODC is accessed (NSRDB, 2023). The PTC field has an area of 8,175 m^2 and a storage of 30 mins, whereas the LFR field has an area of 7,020 m^2 without any storage.

4. Results and Discussion

The solar power plant was modeled, simulated and the steady state results were compared to the expected design values given by Nayak et al. (2015) and are depicted in Table 2. It is to be noted that the LFR is determined to be only adding heat primarily for phase change as at the pressure of 44 bars the input water flow is at the boiling point and is released into the steam drum with a quality of 55 %. From the comparison, it can be seen that the deviations of the individual field loops of the simulation to the design point are relatively low. These deviations can be explained by the approximation of the input values. The power block efficiency of the simulation model is 7 % more than the design vale, which is due to the optimistic assumption of the isentropic efficiency of the expansion vessel, which was taken in accordance with the values taken by Bhukta et.al (2016). The higher power block efficiency results in 5 % deviation in the overall plant efficiency and the higher net heat capture and increased net electricity output. The values are listed in Table 3.

Tab. 2: Comparison of the results of the simulation to the design model presented in (Nayak et. al., 2015)

Component	Parameter	Simulation	Design model
PTC Field	Net heat capture	3.235 MW_{th}	3.000 MW_{th}
	Output Temperature	397.0 °C	393.0 °C
	Efficiency	66 %	61 %
LFR Field	Net heat capture	2.038 MW_{th}	2.000 MW_{th}
	Output Temperature	256.1 °C	256.1°C
	Efficiency	48 %	47 %
Power block	Efficiency	27 %	20 %
Overall plant	Efficiency	16 %	11 %

The presented simulation model has been used for further research, including sensitivity analysis, dependence of the LFR field and scale up possibilities. The sensitivity analysis and the scale-up model simulation results are presented in (Arora, 2023) and discussed in (Alexopoulos et al., 2024).

Along with the steady state simulation using both PTC and LFR systems, a further simulation was done only with the PTC field to compare the outputs of the power plant for both cases and analyze the dependency of the system output on the LFR field. Figure 3 illustrates the simulation model without the LFR field.

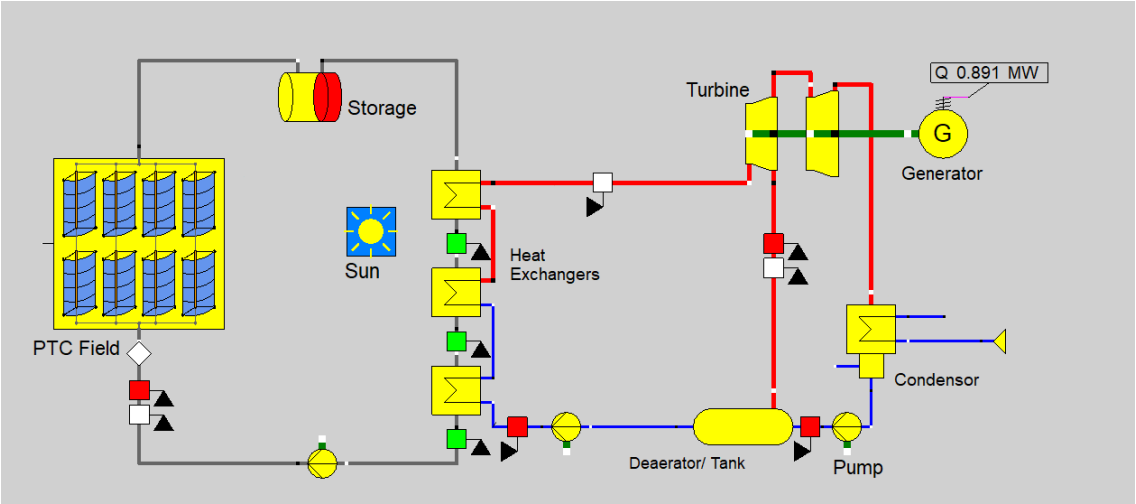

Fig. 3: Schematic diagram of the CSP demonstration facility without LFR module in EBSILON® *Professional*

To maintain the turbine input temperature of 350 °C from the design point, the flow rate of the water / steam cycle was decreased to 1.19 $kg \cdot s^{-1}$. Due to a lower total heat capture by only the PTC field, 39 % decrease in the net electric output is observed. The results from the simulation models with and without the LFR field are summarized in Table 3.

Tab. 3: Comparison of the results from the simulation models with and without the LFR field

Model	Mass flow in the primary loop	Total net heat capture	Net plant capacity
Original combined model	1.93 $kg \cdot s^{-1}$	5.273MW_{th}	1.418 MW_e
Only PTC Field	1.19 $kg \cdot s^{-1}$	3.235 MW_{th}	0.891 MW_e

For the annual simulation conducted by SAM, the monthly electric output is depicted in Figure 4. In the months of March, April and May, the output is higher than in the monsoon season of India in the months of June to August. The results show that due to the increased cloud cover in monsoon and therefore lack of direct sunlight, the output of the plant drastically decreases. Furthermore, due to ambient temperatures in the November to January averaging below the Therminol VP1 freezing point of 12 °C (Eastman Chemical Company, 2024), additional heat was required to defrost the HTF for nominal usage and therefore showing an additional dip in the net output energy.

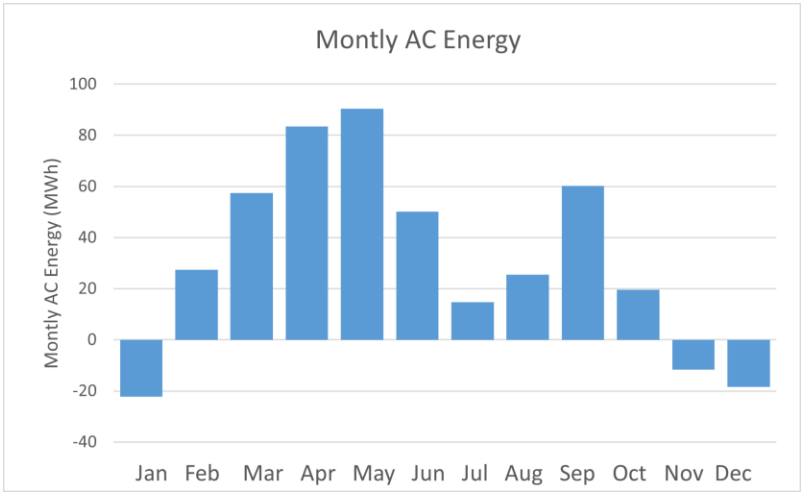

Fig. 4: Monthly electrical output of the power plant

5. Conclusion

The 1 MW_e power plant at the campus of NISE in Gwalpahari was simulated in EBSILON® *Professional* to conduct a steady state analysis and a comparison with the design point. This resulted in a minor deviation for the individual solar fields but 5 % deviation in the power block efficiency. These deviations resulted in a higher net output of the power plant than the design point. The steady state model was also simulated with only the PTC field to observe the dependance of the system on the LFR field. Due to a lower net heat capture, the output was 39 % lower than the combined model. An annual analysis was also done with SAM to check the output over the course of a year through various weather conditions. The annual simulation has shown that during the months with relatively higher DNI as compared to the monsoon months gave a comparable higher electric output. It was also to be noted that addition energy was required in winter to maintain the flow of Therminol VP1 as the ambient temperature was below its freezing point of 12 °C. A further DNI sensitivity analysis and also analysis of scale up possibilities are done in (Arora, 2023) and shown in (Alexopoulos et al, 2024).

6. Acknowledgments

This work was done in the framework of a thesis at Solar-Institut Jülich of the FH Aachen University of Applied Sciences.

7. References

Alexopoulos S; Arora A, Mahdi Z, 2024. Design, Simulation and Sensitivity Analysis of the National Solar Thermal Research Demonstration facility in Gwalpahari [Abstract], Proceedings of the SolarPACES 2024

Arora A., 2023. Simulation Analysis of the concentrated solar plant National Solar Thermal Research Demonstration facility in Gwalpaharai, India, Bachelor thesis at FH Aachen University of Applied Sciences

Bhutka, J., Gajjar, J. and Harinarayana, T, 2016. Modelling of Solar Thermal Power Plant Using Parabolic Trough Collector. *Journal of Power and Energy Engineering*, **4**, 9-25. doi: 10.4236/jpee.2016.48002

Eastman Chemical Company, 2024. Therminol VP-1 Heat Transfer Fluid. https://www.therminol.com/product/71093459 – Accessed on 06 July 2024 [Online]

Google Maps, 2023. https://www.google.com/maps – Accessed on 18 October 2023 [Online]

Jawaharlal Nehru National Solar Mission (Phase I, II and III), 2021. https://www.iea.org/policies/4916-jawaharlal-nehru-national-solar-mission-phase-i-ii-and-iii – Accessed on 21 September 2023 [Online]

Nayak, J K., Kedar, S eB., Banerjee, Rangan, Bandyopadhyay, S, Desai, N B., Paul, S, Kapila, A, 2015. A 1 MW national solar thermal research cum demonstration facility at Gwalpahari, Haryana, India. In: CURRENT SCIENCE 109 (2015), No. 8. https://www.researchgate.net/publication/283152474_A1_MW_National_Solar_Thermal_Research_Cum_Demonstration_Facility_at_Gwalpahari_Haryana_India – Accessed on 18 June 2023 [Online]

NREL, 2022. National Solar Thermal Power Facility CSP Project. https://solarpaces.nrel.gov/project/national-solar-thermal-power-facility – Accessed on 21 June 2023 [Online]

NSRDB, 2023. https://nsrdb.nrel.gov/ – Accessed on 5 August 2023 [Online]

STEAG, 2023. https://www.ebsilon.com/en/ – Accessed on 27 April 2023 [Online]

System Advisor Model, 2023. https://sam.nrel.gov/ – Accessed on 21 October 2023 [Online]

Fins vs No Fins: A Comparative Experimental Analysis of Novel Box-Channel Photovoltaic/Thermal Collector Prototypes for Ground Source Heat Pump Integration

Ellen Louise Nicholson[1], Francisco Beltran[1], Alonso Conejos Lopez[1], Nelson Sommerfeldt[1], Valentin Delachaux[2] and Mohammad Ali Jaafar[2]

[1] KTH Royal Institute of Technology, Stockholm (Sweden)

[2] DualSun, Marseille (France)

Abstract

This study compares the thermal performance of two novel box-channel PVT collectors, assessing the impact of fins in low temperature operating conditions. This work will contribute the understanding of how PVT collectors can be integrated with GSHPs for borehole regeneration in cold climates. The two prototype PVT collectors were tested simultaneously at an outdoor testing facility in Stockholm, Sweden. The outdoor testing environment allows for the analysis of a variety of different weather conditions under different fluid flow rates as well as different roof installations. It was found that the finned PVT collector displayed a potential annual thermal energy output 11% higher than that of the non-finned one at the optimal flow rate of 77 l/h m2. At the optimal flow rate, fluctuations in wind speed also significantly impacted the observed specific thermal energy of the PVTs, mainly the finned PVT collector, with an increase of 93% being observed due to a 2.5 m/s increase in wind speed.

Keywords: Solar PV/thermal, PVT collector, heat pump, thermal performance, fins

1. Introduction

In recent years, the integration of photovoltaic/thermal (PVT) collectors with ground source heat pumps (GSHP) has been the interest of many research studies. This is because of the system's ability to decarbonise domestic heating while also regenerating the borehole field (Sommerfeldt et al., 2020) and reducing their length and spacing needs (Sommerfeldt and Madani, 2019).

One key feature of these systems is the low working fluid temperature, allowing for simultaneous cooling of the PV panel as well as heat extraction from ambient air. This allows for an increase in both thermal and electrical efficiencies of the PVT collector.

While the sheet and tube absorber is the most prevalent in literature as well as among commercially available PVTs, studies show that collectors with a box-channel absorber design outperform those with sheet and tube absorbers (Herrando et al., 2019). This is because of the increased heat transfer area between the fluid and the absorber plate. The addition of fins to the back of the absorber further increases the heat transfer area between the low temperature fluid and the higher temperature ambient air (Giovannetti et al., 2019).

However, the addition of fins serves to increase the PVT collector mass and cost. Therefore, to obtain a better understanding of the trade-offs between increased thermal performance and the associated increase in collector cost, it is necessary to conduct a comparative analysis of a specific PVT collector with and without fins. While previous studies have assessed the performance of finned PVT collector designs, to the best knowledge of the authors, there has not been a study that concurrently compares the effect of fins on the same absorber design through outdoor laboratory experiments. The results of this study will help in refining the design of PVT collectors specifically for GSHP integration.

© 2024. The Authors. Published by International Solar Energy Society
Selection and/or peer review under responsibility of Scientific Committee
10.18086/eurosun.2024.07.02 Available at http://proceedings.ises.org

2. Objectives

The objective of this study is to compare two box-channel PVT collector prototypes, one finned and the other non-finned, under low operating temperatures and a wide range of ambient weather conditions. This will provide a better understanding of the effect of fins on energy and power outputs of PVT collectors. The aim of the work is achieved by answering the following research questions:

1. How do varying ambient weather conditions, such as wind and solar irradiance, affect the thermal output and U-value of the finned and non-finned designs?
2. How do varying flow rates of the working fluid impact the thermal performance of the finned and non-finned designs?
3. How do different roof installation types affect the thermal performance of the finned and non-finned designs?

3. Methods

The experiments performed are under outdoor dynamic conditions on a south facing testing array located at KTH Royal Institute of Technology, Stockholm, see the right panel of Figure 1. The testing facility includes two PVT collectors, identical apart from fins, designed specifically for heat pump integration. They consist of a harp-shaped box-channel absorber, with a manifold at either end for the inlet and outlet connection. The PVT design can be seen in Figure 2. Both PVTs are connected to a 12 kW variable speed HP with a 300 L cold storage tank, left of Figure 1. This allows for the simultaneous operation of the two PVTs with separate temperature and mass flow rate measurements from installed heat meters. The system diagram can be found in Figure 3. The HP can provide supply temperatures as low as -5°C during the summer, enabling low temperature operation. The collected heat is dissipated through a hot water tank and a 10 kW air-to-water heat exchanger. Ambient conditions at the collectors are measured by a weather station and a reference cell at the same tilt, 45°, as the PVT collectors.

Fig. 1: Left) Mechanical room containing the HP and hot and cold storage tanks, as well as the circulation pumps and their monitoring system. Right) Test rig with the PVT collectors being tested.

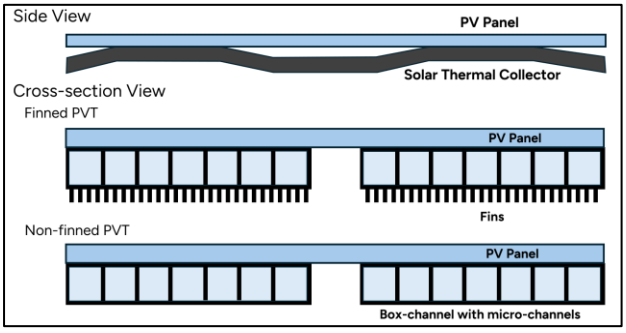

Fig. 2: Schematic of the prototype PVT absorbers, not to scale.

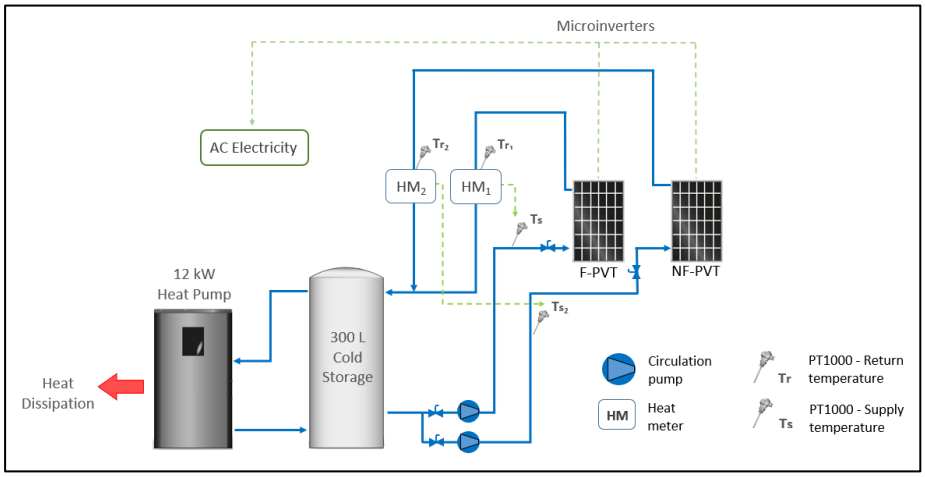

Fig. 3: System diagram of the testing rig.

Experiments are carried out over several days in spring 2024, between 11th March and 31st May, to obtain data in a variety of ambient conditions. This will allow for the investigation of the impact of ambient weather conditions, answering Question 1. The range of mass flow rates studied is approximately 50 to 100 l/h per meter^2, based on the manufacturer's recommended mass flow rate for the PVT collectors. This will provide data to answer Question 2. To answer Question 3, sheets of corrugated plastic and thin metal are used to construct side and back panels for the PVTs, see Figure 4. This final set of tests will be carried out at a constant flow rate of 51 l/h per m^2, however, as the tests are performed outdoors, a range of ambient conditions will be used.

Fig. 4: Left) Side panels attached behind the PV panel. Right) Back panel attached 14.5 cm behind the absorber of the PVT.

The mass flow rate along with the temperature difference between the inlet and outlet temperatures of the working fluid will be used to calculate the specific thermal power (W/m^2) of the PVT collectors. To compare the performance of the finned and non-finned designs, the thermal performance coefficients of the PVT collectors will be calculated using a simplified version of the specific thermal power output equation presented in ISO 9806:2017 for solar thermal collectors, see Equation 1. The coefficients and their errors are calculated using multivariable regression analysis.

$$\dot{q} = \eta_0 G + a_1(T_a - T_m) + a_3 u(T_a - T_m) - a_6 uG \qquad \text{(eq. 1)}$$

Additionally, the U-value of the PVTs will be calculated along with the potential annual thermal energy output per m^2. The U-value will be calculated at wind speeds of 1 m/s using Equation 2 below and the potential annual thermal energy output will be calculated by summing the hourly heat output of the PVT collectors. The hourly heat output is calculated using the obtained hourly thermal performance coefficients from the regression model, the monthly average mean brine temperature and hourly weather data of a typical meteorological year in Stockholm. The method is described in greater detail in Beltran et. al. (2024) and gives an estimation for the potential annual thermal energy output when a PVT is connected in series to a GSHP system in a Nordic climate.

$$U = a_1 + a_3 \times u \qquad \text{(eq. 2)}$$

4. Results

4.1. Result Validation

Tables 1 and 2 show the obtained thermal performance coefficients for the two prototype PVT collectors when considering different brine flow rates and different roof installation types, respectively. The calculated coefficient of determination of the regression, R^2, is also shown. Below in Figure 5, the empirical data can be seen for the baseline flow rate of 51 l/h per m^2 at different irradiance levels.

Tab. 1: Thermal performance coefficients for the finned and non-finned PVTs at the three flow rates tested.

Brine flow rate [l/h per m^2]	51		77		103	
Thermal performance coefficient	**Finned PVT**	**Non-finned PVT**	**Finned PVT**	**Non-finned PVT**	**Finned PVT**	**Non-finned PVT**
η_0	0.506	0.423	0.523	0.470	0.326	0.267
a_1	34.105	38.460	27.032	29.206	45.419	45.979
a_3	4.251	3.001	12.304	9.951	4.313	1.939
a_6	0.000	0.000	0.064	0.062	0.000	0.000
R^2	0.92	0.94	0.90	0.90	0.86	0.87

Tab. 2: Thermal performance coefficients for the finned and non-finned PVTs for the three roof installations tested.

Roof installation	Side panels		Back panels		Side and back panels	
Thermal performance coefficient	**Finned PVT**	**Non-finned PVT**	**Finned PVT**	**Non-finned PVT**	**Finned PVT**	**Non-finned PVT**
η_0	0.562	0.478	0.554	0.488	0.506	0.507
a_1	21.626	26.708	28.197	29.857	21.382	21.899
a_3	4.773	4.773	3.224	2.041	1.943	2.786
a_6	0.016	0.012	0.014	0.004	0.019	0.015
R^2	0.97	0.97	0.96	0.96	0.97	0.97

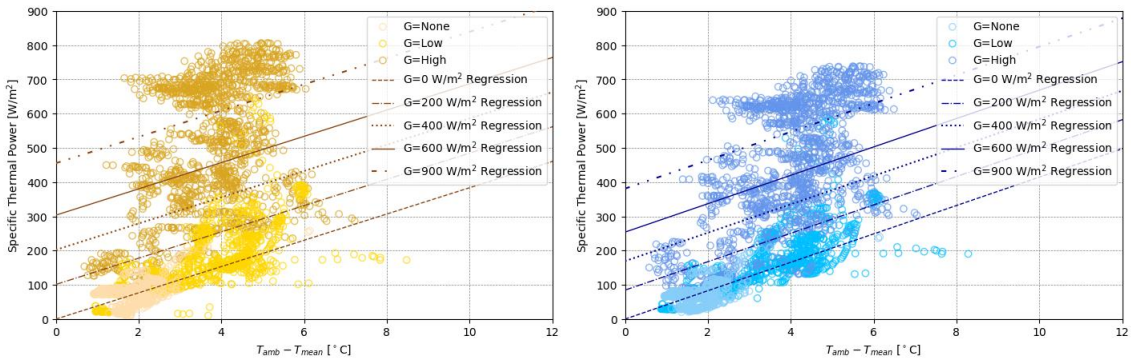

Fig. 5: Empirical data of the baseline flow rate of 51 l/h per m² with the corresponding regression line for the irradiance level for the finned PVT collector (yellow) on the left and the non-finned PVT collector (blue) on the right.

4.2. Ambient Weather Conditions

As the experiments were conducted outdoors between March and May of 2024, a broad range of ambient conditions was observed. This range is presented in Table 3.

Tab. 3: Range of ambient weather conditions experienced throughout experimental period.

Ambient Conditions	Unit	Minimum	Maximum
Irradiance	W/m²	0	1286
Wind speed	m/s	0	9.1
Ambient Temperature	°C	-4.1	28

In conjunction with previous literature, it was found that a higher irradiance level leads to a higher specific thermal power output of both PVT collectors as the thermal efficiency of the absorber is constant, see Figure 6.

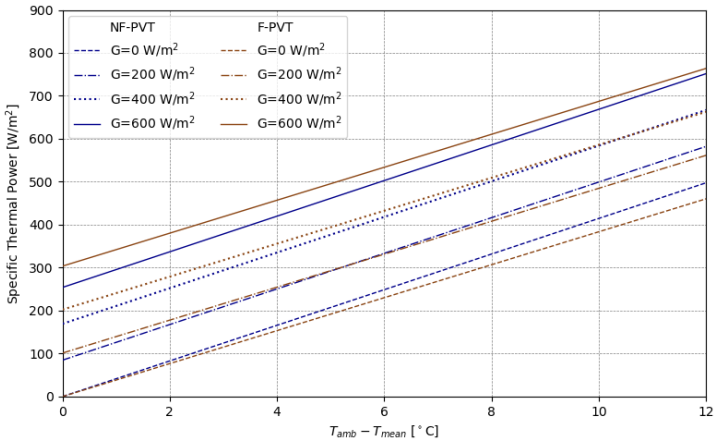

Fig. 6: Impact of increasing irradiance on the thermal performance of the non-finned (NF-PVT) and finned (F-PVT) PVT collector when using the baseline flow rate of 100 l/h per collector.

It can be seen from Figure 6 that at zero-irradiance the non-finned PVT collector has a higher specific thermal power than the finned collector. This is contrary to expectations but can be explained by a manufacturing defect on the non-finned PVT collector, resulting in a larger air gap between the PV panel and the absorber compared to that on the finned PVT collector. This will be discussed further in Section 5.

As with increasing irradiance, it was observed that increasing the wind speed improved thermal performance, see Figure 7. This is due to the greater airflow created around the PVTs, allowing for more efficient heat

transfer. This can also be seen in the increasing U-values as the wind speed increases, see Table 4. Here it is also possible to see that the non-finned PVT collector appears to perform better thermally than the finned PVT collector. As above, this will be discussed in more detail below. It was found that as irradiance increases, the impact of increasing wind decreases. This shows that the thermal performance of the PVT is more sensitive to irradiance than wind speed. Finally, it was observed that the finned PVT was more sensitive to changes in wind speed, with an increase in wind speed resulting in greater improvements to the thermal performance and U-value of the finned PVT than the non-finned one. This was expected as the fins provide more surface area for the absorber to interact with the ambient air (Giovannetti et al., 2019).

Tab. 4: Impact of increasing wind speed on U-value of finned and non-finned PVT collector using a flow rate of 51 l/h per m^2.

Wind speed [m/s]	**Finned PVT** [W/(m^{2}K)]	**Non-finned PVT** [W/(m^{2}K)]
0.5	36.23	39.96
1.5	40.48	42.96
3	46.86	47.46

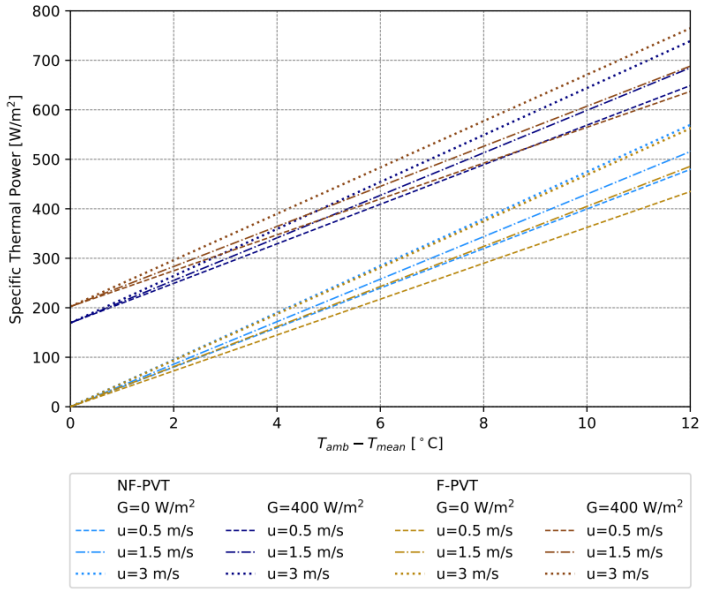

Fig. 7: Impact of increasing wind speed on the thermal performance of the non-finned (NF-PVT) and finned (F-PVT) PVT collector when using the baseline flow rate of 51 l/h per m^2 at two irradiance levels.

4.3. Flow Rate

When higher brine flow rates were used, it is possible to see how the thermal performance responded to the different ambient conditions described above.

As the mass flow rate of the brine was increased, the impact of increasing irradiance on the specific thermal power output of the PVT collectors was observed to decreased. This can be seen in Table 5. From this it is possible to see that the lowest flow rate is not fast enough to extract all the heat from the solar panel. However, the diminishing returns experienced at higher flow rates indicate the presence of an optimum flow rate for absorbing the solar thermal energy. It is also possible to see from Table 5 that the finned PVT collector displays higher improvements in specific thermal power than the non-finned PVT. This is due to a manufacturing defect resulting in better thermal contact between the PV panel and the absorber in the finned than the non-finned PVT collector. This will be discussed further in Section 5.

Tab. 5: Increase in the specific thermal power of both the finned and non-finned PVT collectors due to an increase in irradiance of 200 W/m².

Brine Flow Rate [l/h per m²]	**Finned PVT** [W/m²]	**Non-finned PVT** [W/m²]
51	101	85
77	92	82
103	65	53

When looking at the impact of increasing wind speed on the different flow rates it was found that there is an optimal flow rate at which increasing wind speed significantly increases the specific thermal power. As seen in Table 6, for the PVT collectors tested, this flow rate was 77 l/h per m². This significant increase is due to the relative velocity of the wind and the brine being at the optimal speed for heat transfer. Through further testing it might be possible to derive a model for the optimal brine flow rate based on the predicted wind speed and direction. It is also possible to see from Table 6 that the finned PVT collector is more sensitive to increases in wind speed that the non-finned PVT collector, as mentioned before.

Tab. 6: Percentage increase in the specific thermal power of both the finned and non-finned PVT due to an increase in wind speed of 2.5 m/s at both zero irradiance and 400 W/m².

Brine Flow Rate [l/h per m²]	**0 W/m²**		**400 W/m²**	
	Finned PVT	**Non-finned PVT**	**Finned PVT**	**Non-finned PVT**
51	+ 29 %	+ 19 %	+ 12 %	+ 9 %
77	+ 93 %	+ 73 %	+ 18 %	+ 12 %
103	+ 23 %	+ 10 %	+ 13 %	+ 7 %

Using the method described in Beltran et. al. (2024), it is possible to obtain the potential annual thermal energy output of each PVT collector, connected in series to a GSHP in a Nordic climate, at different flow rates. These can be seen in Table 7. The thermal performance coefficients used to calculate these annual thermal energies are given in Table 1. It is possible to see that under a typical meteorological year in Stockholm, the finned PVT collector produced more energy annually than the non-finned PVT collector. The amount by which the finned PVT collector thermally outperforms the non-finned one increases with increasing flow rate. This shows that a higher flow rate is more beneficial for a finned PVT collector than for a non-finned one.

Tab. 7: Potential annual thermal energy output of both the finned and non-finned PVT collector at the three tested flow rates.

Brine Flow Rate [l/h per m²]	**Finned PVT** [kWh/m²/yr]	**Non-finned PVT** [kWh/m²/yr]	**Finned vs Non-finned**
51	2161	2070	+ 0.4 %
77	2685	2427	+ 11 %
103	2360	2033	+ 16 %

4.4. Roof Installations

To evaluate the impact of different roof installations, the potential annual thermal energy output (following the same method as above) of the different scenarios was compared. This can be seen in Table 8. As the different roof installation types are all evaluated at the baseline flow rate of 51 l/h per m², the potential annual thermal energy output is compared to the baseline flow rate case. For all three cases, the roof installation caused the

PVT to perform worse thermally than the baseline with no obstruction to the airflow around the absorber. Nonetheless, the finned PVT collector produced more heat energy per m^2 than the non-finned. This again shows that the additional surface area provided by the fins is beneficial to heat exchange with the ambient, as the restriction of the airflow does not impact the finned PVT collector as much as the non-finned PVT collector.

Tab. 8: Annual thermal energy of both the finned and non-finned PVT collector at the three tested roof distances.

Roof Installation Type	Finned PVT [kWh/m²/yr]	Finned PVT Comparison to baseline	Non-finned PVT [kWh/m²/yr]	Non-finned Comparison to baseline	Finned vs Non-finned
Side Panels	2016	- 5 %	1906	- 8 %	+ 6 %
Back Panels	1840	- 15 %	1723	- 18 %	+ 7 %
Side and Back Panels	1451	- 33 %	1528	- 26 %	- 5 %

In the third configuration of roof installations, consisting of both the side and back panels, the finned PVT gives a lower potential annual thermal energy output when compared to the non-finned, see Table 8. However, Table 9 shows that the thermal performance coefficient a_1, the heat transfer coefficient, of the two PVT panels is similar, withing statistical error. This shows that in the absence of wind, as with both the side and back panels the airflow around the absorber is severely restricted, the two PVT collectors behave the same in terms of heat transfer with the ambient. This is expected as the fins should help with extracting heat from the ambient air, and so when there is no movement of the air the fins will not impact the efficiency of the PVT collector. The a_3 thermal performance coefficient, the wind dependence of heat transfer coefficient, shows that the non-finned PVT is more sensitive to changes in wind speed, contrary to previous findings. This could be an artefact of the multivariable regression overestimating the impact of wind due to the recorded wind speed by the weather station not being equal to the wind speed experienced by the absorber.

Tab. 9: Thermal performance coefficients of the finned and non-finned PVT for the roof installation of both side and back panels.

Thermal performance coefficient	Finned PVT	Non-finned PVT
a_1	21.382	21.899
a_3	1.943	2.786
a_6	0.019	0.015
R^2	0.97	0.97

5. Discussion

When comparing the two PVT collectors in terms of their annual thermal energy, the finned PVT always outperforms the non-finned PVT collector, apart from the roof installation with both side and back panels. This can be seen in Tables 7 and 8 above. This shows that for the typical ambient conditions found in Stockholm, the finned PVT collector has the potential to generate more thermal energy output annually. However, as the additional cost of adding the fins is not known, it is imperative to conduct an economic analysis to determine whether the additional heat gained justifies the extra costs and well as the additional weight.

From testing different roof installations, it is possible to see that the fins improve heat exchange with the ambient, as expected from the result of Chhugani et. al. (2020). This is because when specific roof installations are added, and airflow around the absorber is restricted, the potential annual thermal energy output of the

finned PVT collector decreases less with respect to the baseline than the potential annual thermal energy output of the non-finned PVT collector. This means that the finned PVT thermally outperforms the non-finned PVT collector under these conditions. Similarly, when wind speeds were increased, the finned PVT performed significantly better than the non-finned PVT collector. It was also observed that the specific thermal output of both collectors is very sensitive to wind speed, as previously found by Lammle and Munz (2022). To more accurately quantify the impact of wind, a longer testing period is needed. This additional data could enable the creation of a model that can provide the optimal flow rate for the predicted wind speed and direction.

As previous literature has found, it is extremely difficult to determine the optimal flow rate of an integrated PVT and GSHP system as there are many variables affecting the system's operation (Yan et. al., 2022). It has been widely agreed that increasing flow rate results in more heat being collected under constant ambient conditions. However, there are diminishing returns as flow rate increases with Abdul-Ganiyu et. al. (2021) finding that for a solar thermal collector in Ghana, flow rates above 227 l/h per m^2 do not result in additional heat gains. In the current study it was found the optimal flow rate was 77 l/h per m^2. This is much lower compared with Abdul-Ganiyu et. al.'s (2021) result, however this can be explained by the large difference in ambient temperature between the two locations.

When comparing the finned and non-finned PVT, this study found that the optimal flow rate is the same for both collectors. This is because of the large intervals used when testing different flow rates. However, as the two PVTs are affected differently by the ambient conditions, it is possible that the optimal flow rate for the two collectors is not the same. By testing a greater number of flow rates around the optimal flow rate of 77 l/h per m^2 it will be possible to determine the true optimum for each PVT collector as well as how rapidly changes in flow rate cause deviations from the maximum thermal performance. This will show if there is a range of optimal flow rates rather than a singular optimum. The data gathered could be used to incorporate the flow rate into the coefficient calculation, creating a model that considers flow rate as well as other ambient conditions such as irradiance and wind speed. This would help expand on Yan et. al. (2022) work. In addition to testing a greater number of flow rates, looking at the trade-offs between the larger specific thermal power gained by the larger flow rate and the increase in pumping power required could help determine a global optimum flow rate rather than a flow rate optimised for thermal performance of the PVT collector. In a previous study, Gomariz et. al. (2019) found that the lower cost of using 20 l/h per m^2 did not justify the loss in heat gains compared to the 80 l/h per m^2 flow rate for solar thermal collectors.

When comparing the two PVTs, some results contrary to what was expected from literature were found. These results were the generally higher a_1 thermal performance coefficient of the non-finned PVT collector, resulting in lower U-values for the finned PVT collector compared to the non-finned one, and the higher zero-loss efficiency of the finned PVT collector. This is the opposite to what was expected from the results of Beltran et. al. (2024) as well as Giovanetti et. al. (2019). Upon inspection of the PVTs it was determined that this was due to imperfect thermal contact between the PV panel and the absorber on the non-finned PVT. This resulted in less efficient thermal exchange between the PV panel and the absorber, lowering the zero-loss efficiency of the non-finned PVT collector compared to the finned PVT collector, and created an airgap between the PV panel and the absorber. This meant that there was more surface area exposed to ambient air for heat exchange, artificially increasing the a_1 thermal performance coefficient. This was exacerbated by the more exposed location of the non-finned PVT collector on the roof, allowing a greater airflow around the collector. Figure 8 provides thermal images of the two PVT collectors showing the identified imperfect thermal contact. While both PVT collectors experience this problem, the higher temperature of the "hot spot" on the non-finned PVT demonstrates worse thermal contact and so a larger airgap.

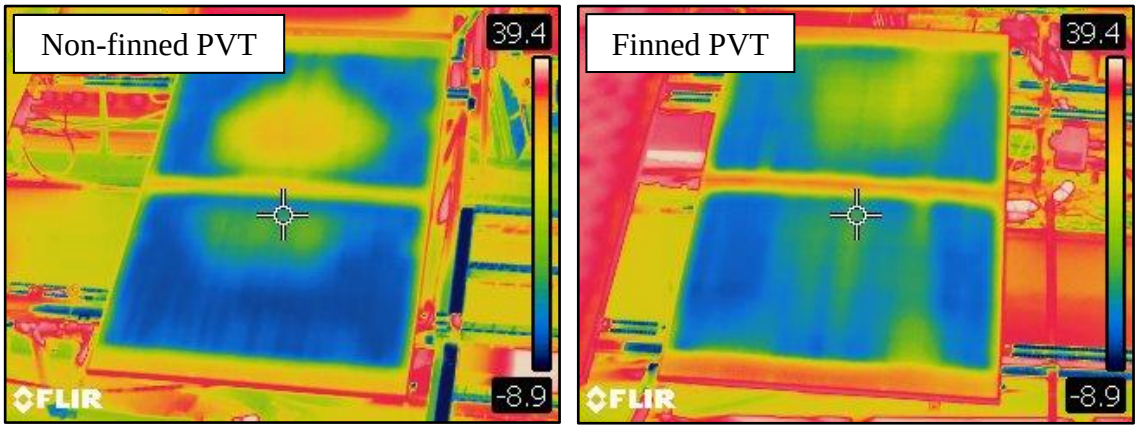

Fig. 8: Thermal images of the two PVT collectors (non-finned on the left and finned on the right) to show the imperfect thermal contact between the PV and the absorber, showing the larger airgap present in the non-finned PVT collector.

6. Conclusion

In conclusion, using the U-value, specific thermal power output and potential annual thermal energy output, the thermal performance of a finned and non-finned prototype PVT collector were compared. The PVTs were evaluated outdoors in Stockholm, simulating cold temperature operation for PVT integration with a GSHP system as a borehole regeneration mechanism. It was found that the finned PVT collector has an overall better thermal performance than the non-finned PVT collector. This can be seen by the finned PVT collector displaying potential annual thermal energy outputs 11% higher than that of the non-finned PVT collector at the optimal flow rate.

In general, higher levels of irradiance and wind speeds lead to improved values of specific thermal power output, with a 200 W/m^2 increase in irradiance resulting in increases in specific thermal power output of 92 W/m^2 for the finned PVT collector and 82 W/m^2 for the non-finned PVT collector. When considering irradiance, a higher flow rate is always desirable due to the higher specific thermal power output, however, the trade-off with increase pumping power needs to be determined. With increasing wind speeds, for optimal increase in performance, a balance between the wind speed and the brine flow rate must be found. In this study, the optimal flow rate was around 77 l/h per m^2. As mentioned above, each PVT collector was affected differently by the ambient conditions so to determine the optimal operating conditions the average ambient conditions need to be considered.

This study found that a higher flow rate appears to be more favourable for the finned PVT while the non-finned PVT performs thermally better at the lower flow rates. This can be seen by greater improvements in the finned PVT collector as flow rate increased compared to the non-finned one. However, to determine the true optimum, or if a range exists, smaller increments in flow rate need to be evaluated. When combined with the analysis of ambient conditions, a global optimal flow rate can be determined for the entire system.

The impact of restricting airflow around the absorber by adding different roof installations proved to decrease potential annual thermal energy output of both PVTs between 7% and 33%, with the non-finned thermally underperforming the most. This can be seen by the finned PVT collector's thermal performance coefficients resulting in a potential annual thermal energy output around 6% higher than the non-finned PVT collector. This further supports the found positive impact fins have on aiding heat transfer with the ambient. It can also be concluded than on a sloped roof, the addition of fins is beneficial as they allow for greater heat absorption. However, the fins will add weight to the PVT collector and so a full system analysis needs to be conducted to see if the additional heat gains justify the installation constraints.

Further work to this study includes a full techno-economic analysis to determine the financial feasibility of the addition of fins to the PVT absorber. This will show whether the additional heat absorbed justifies the additional cost. Secondly, the ambient conditions studied did not include cold climate weather patterns such as condensation, rain and frost. Therefore, to obtain a full picture of the operation of these two PVT collectors in cold climates further studies on these phenomena are needed. Lastly, as it was observed that the zero-loss efficiency and the a_1 thermal performance coefficient are sensitive to the thermal contact between the PV

panel and the absorber. This led to results that are contrary to what has been previously found in literature. However, based on the trends observed, even with the manufacturing defect, the fins increase heat exchange with the ambient. To provide more certainty in the results, a further study with multiple panels could be conducted to help quantify the impacts of manufacturing deviations.

7. Acknowledgments

This study was conducted as part of the Smart Renovation Strategies for Sustainable Electrification project (SmartReno SE - Project No. P2023-01509), funded by the Swedish Energy Agency under the ReBygg Program, for which the authors are grateful.

8. References

Abdul-Ganiyu, S., Quansah, D. A., Ramde, E. W., Seidu, R., Adaramola M. S., 2021. Study effect of flow rate on flat-palate water-based photovoltaic-thermal (PVT) system performance by analytical technique. Journal of Cleaner Production. 321, 128985. https://doi.org/10.1016/j.jclepro.2021.128985

Beltran, F., Sommerfeldt, N., Eskola, J., Madani, H., 2024. Empirical investigations of solar photovoltaic-thermal collectors for heat pump integration. Applied Thermal Engineering. 248 (B), 123175. https://doi.org/10.1016/j.applthermaleng.2024.123175

Chhugani, B., Pärisch, P., Kirchner, M., Littwin, M., Lampe, C., and Giovannetti, F., 2020. Model validation and performance assessment of unglazed photovoltaic-thermal collectors with heat pump systems, in EuroSun 2020 Proceeding. 10.18086/eurosun.2020.05.13

Giovannetti, F., Lampe, C., Kirchner, M., Littwin, M., Asenbeck, S., Fischer, S., 2019. Experimental Investigations on Photovoltaic-Thermal Arrays Designed for the Use as Heat Pump Source, in ISES Solar World Congress 2019 Conference Proceedings.

Gomariz, F. P., Cejudo Lopez J. M., Dominguez Munoz, F., 2019. An analysis of low flow for solar thermal system for water heating. Solar Energy. 179, 67-73. https://doi.org/10.1016/j.solener.2018.12.060

Herrando, M., Markides, C.N., Hellgardt, K., 2019. A comprehensive assessment of alternative absorber-exchanger designs for hybrid PVT-water collectors. Journal of Applied Energy. 235, 1583-1602. https://doi.org/10/1016/j.apenergy.2018.11.024

ISO, 2017. ISO9806: Solar Energy – Solar Thermal Collectors -Test Methods.

Lammle, M., Munz, G., 2022. Performance of Heat Pump Systems with PVT Collectors and Optimized Finned Heat Exchangers Integrated as Single Heat Source, in EuroSun 2022 Proceedings. 10.18086/eurosun.2022.07.06

Sommerfeldt, N., Beltran, F., Madani, H., 2020. Solar PVT for heat pumps: Collector development, systems integration, and market potential, in: BuildSIm-Nordiv 2020 Conference Proceedings.

Sommerfeldt, N., Madani, H., 2019. In-depth techno-economic analysis of PV/Thermal plus ground source heat pump systems for multi-family houses in a heating dominated climate. Sol. Energy 190, 44-62. https://doi.org/10.1016/j.solener.2019.07.080

Yan, B., Wu, Q., Chi X., Wu, C., Luo, P., Luo, Y., Zeng, P., 2022. Numerical and Experimental Investigation of Photovoltaic/Thermal Systems: Parameter Analysis and Determination of Optimum Flow. Sustainability. 14 (16), 10156. https://doi.org/10.3390/su141610156

EXPERIMENTAL STUDY ON HEAT TRANSFER FROM AMBIENT AIR IN ROW-INSTALLED PHOTOVOLTAIC-THERMAL (PVT) SOLAR COLLECTORS ON A FLAT ROOF

Summary

With climate change urging the transition to renewable energy sources, Photovoltaic-Thermal (PVT) solar collectors emerge as a promising decarbonized solution producing both electricity and heat. Our study evaluates the performance of PVT panels designed to be as the sole heat source of a brine to water Heat Pump (HP) system for buildings thermal needs. By focusing on the impact of the number of PVT panels in a single row on ambient air heat gain, experimental data reveal a significant influence of panel configuration on the heat exchange coefficient, with a noticeable decrease in heat loss as the number of panels increases, highlighting the critical role of PVT panel arrangement in system performance enhancement.

Keywords: Photovoltaic-Thermal (PVT), solar collector, Heat Pump (HP), heat transfer

1. Introduction

With the urgent need for decarbonized thermal solutions to reduce the scale of ongoing climate change, Photovoltaic-Thermal (PVT) solar collectors stand out for their dual role of producing renewable electricity and heat within a single component. They present a performant alternative as the sole heat source of a brine/water Heat Pump (HP) for thermal needs of buildings including mainly space heating (SH) and Domestic Hot Water (DHW). Indeed, in (Chhugani et al., 2023), it has been highlighted that this combination of PVT and HP with a well sized hot buffer storage and a floor heating can achieve higher overall energy performance than a reference system made up with the same area of PV panels and an air/water heat pump. In the terminology of solar-assisted heat pumps as reminded in (Jonas, 2023), this system configuration is classified as an “indirect” (the refrigerant fluid does not circulate in the panels) and “serial” (the PVT panels provide heat to the heat pump evaporator) combination.

The most critical feature in such system is the capability of PVT panels to recover heat from the ambient air. In (Jaafar et al., 2022), it has been shown that the higher this capability is, the more performant the system is. Indeed, when there is no irradiation (very cloudy day or night), PVT panels act solely as air/water heat exchangers. Then, numerous parameters, such as the distance from the panel to the roof, the roof pitch, the mounting system as well as the orientation of the installation in relation to the prevailing winds in the region, affect this capability.

This paper focuses on the impact of the number of PVT panels as a single row on the *ambient air heat gain* performance of the field. The end goal of this study is to provide valuable insights which can be used for optimizing the PVT field design to enhance the performance of a PVT-HP system.

2. Methodology

2.1. PVT panel prototype

Each of the PVT panels tested is made up with a standard PV panel with a mini-channel flow distribution heat exchanger mounted behind it (see Fig. 1). They were installed in a row in Z configuration (see Fig. 3).

© 2024. The Authors. Published by International Solar Energy Society
Selection and/or peer review under responsibility of Scientific Committee
10.18086/eurosun.2024.07.03 Available at http://proceedings.ises.org

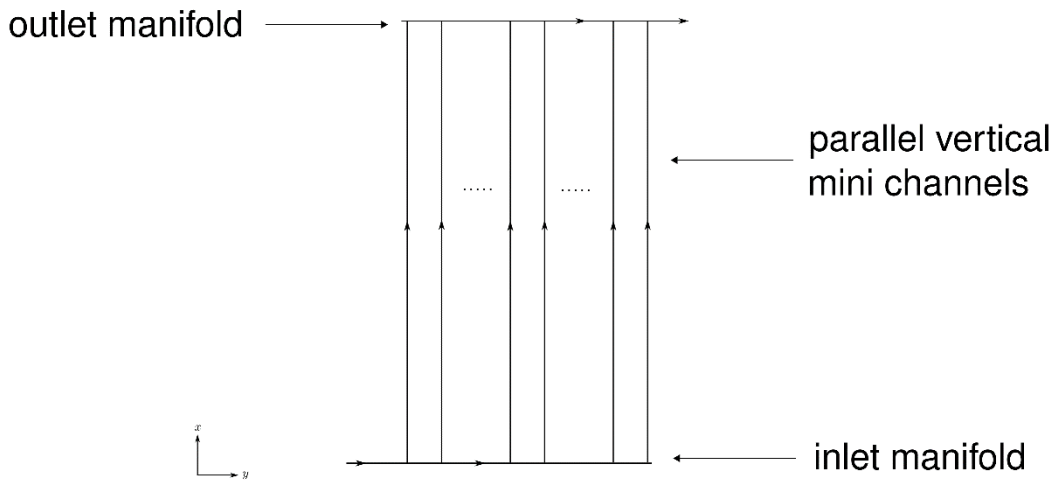

Fig. 1: Scheme of the tested PVT panel prototype

2.2. Test bench

The experimental set-up used for this study is shown in photo (see Fig. 2) and described on the diagram below (see Fig. 3). It consists mainly of a water tank filled with a mixture of water and glycol, whom temperature profile is estimated using two temperature probes installed in two immersion sleeves at the top and the bottom. For the PVT thermal power measurements, a flowmeter ($\dot{V}_{PVT}$) and two temperature probes are installed at the inlet ($T_{PVT,in}$) and the outlet ($T_{PVT,out}$). The overall pipes are insulated. The fluid circulation is insured using a water circulator which is controlled by a regulator through a PWM signal to ensure volume flowrate within a given range in the row of 1 to 8 PVT panels installed on a flat roof (see Fig. 1b). Of course, for each configuration, the flow rate in the row was set so that the flow rate per panel remained roughly the same. The regulator also controls an electrical heating resistance installed in the middle of the water tank with a hysteresis control strategy based on the temperature on its top side. Thus, the fluid temperature entering the PVT field is higher than the ambient air temperature, so the measured heat output is negative.

The assumption made here is that the heat loss (measured here) is equivalent to the heat gain (needed for HP combination) for the same absolute temperature difference between the PVT panel heat exchangers (in average) and the ambient air ($T_{PVT,m} - T_{amb}$). In theory, when free convection dominates, the movement of air around the panels is not symmetrical from one situation to another as it is described in (Incropera et al., 2013) for a hot flat plate and a cold flat plate. However, we assume that the potential variations of heat loss/gain by installing several panels in a row are similar. Moreover, it is important to note that the radiative heat transfers, from the sky and from behind the panel, are considered invariable from one panel to another so that the measured variations are only linked to the variations of convective heat transfer with ambient air (or of temperature distribution over the heat exchangers).

Fig. 1: (a) Photo of the test bench technical room (b) Photo of the row of PVT panels on the flat roof

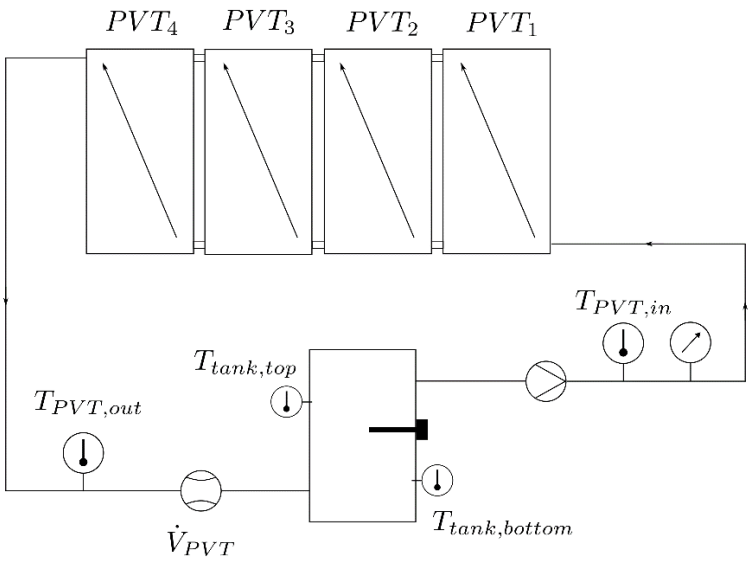

Fig. 3: Test bench diagram

2.3. Data filtering

When the electrical heating resistance of constant power (set before the test between 400 W and 2 kW depending on expected power in the coming conditions) switches off, inlet temperature drops drown then the resistance switches on again. We removed the data corresponding to this phenomenon with a 20-minute window around the local minimum inlet temperature (see grey boxes on Fig. 3). We also removed the first 10 minutes of each test sequence to avoid transient effects. Then we selected data with $G < 1\ W/m^2$ (night) and with flow rate in expected range. Finally, we resampled the data at a time step of 5 minutes and selected those that verify $T_{PVT,m} - T_{amb} \in [6\ ;\ 12]\ K$ and $u \in [0\ ;\ 3]\ m/s$.

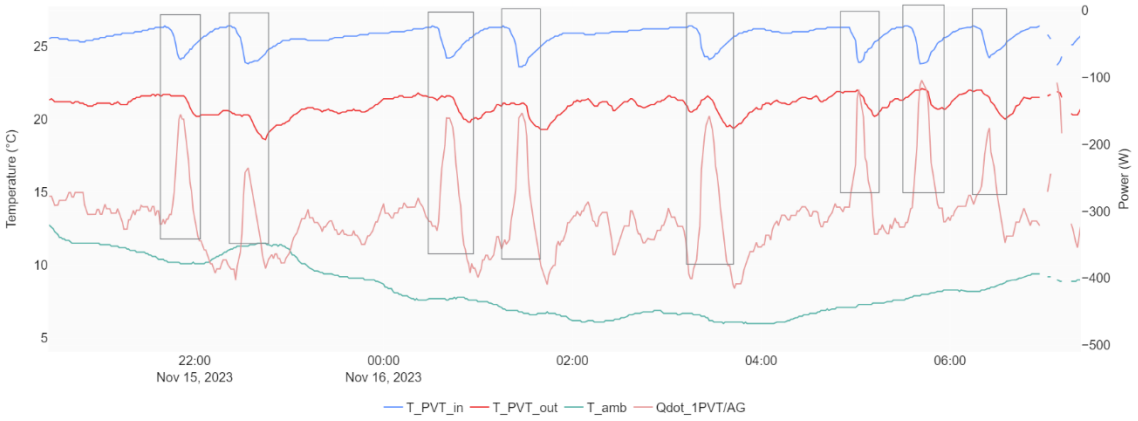

Fig. 4: Time series graph of a test night

2.4. Data analysis

As we study PVT panels heat gain/loss with their environment, the experiments were performed during the night. Then, for unglazed PVT technology, it is relevant to linearize the heat output of the panels in relation to the difference between the average temperature of the heat exchanger and the ambient temperature:

$$\dot{Q} = (\rho \dot{V}_{PVT}) C_p (T_{PVT,out} - T_{PVT,in}) = A_1(u)\,(T_{PVT,m} - T_{amb}) \qquad \text{(eq. 1)}$$

ρ stands for the density of the heat transfer fluid and C_p for its calorific capacity (here MPG 40%). By disregarding the influence of second and fourth order terms in $(T_{PVT,m} - T_{amb})$, by including the radiative heat transfer in A_1, so that we set the a_4 and a_7 coefficients relating to $G' = E_L - \sigma T_{amb}{}^4$ to 0, and by

defining $A_1(u)$ as $a_1 + a_3(u-3)$, we achieve the simplified version of the ISO 9806:2017 standard equation described in ("ISO/DIS 9806:2017 Solar energy — Solar thermal — Test methods," 2017).

In the following results section, we will present the results with two different approaches:

- Linearize $A_1(u)$ in this form: $a_1 + a_3(u-3)$ and get a_1 and a_3 coefficients with a linear least squares method (LLSQ).
- Find $A_1(u_m)$ for each wind range $[u_m - 0.1\ ;\ u_m + 0.1]$ for $u_m \in [0.1, 0.3, 0.5, 0.7 \dots]$

3. Results

3.1. Least squares method

We implemented a classic linear least squares method with the *linalg.lstsq* function of *NumPy* Python library to get a_1 and a_3 coefficients. We also performed 10,000 bootstrap resampling. For each bootstrap sample, we fitted the $a_1$and a_3 coefficients. By resampling our dataset with replacement, we generate a comprehensive distribution of coefficients estimates, allowing us to provide a quantitative measure of uncertainty: the standard deviation of $A_1(u)$ calculated with equation 2 and represented by the coloured band on Fig. 3.

$$\sigma_{A_1} = \sqrt{{\sigma_{a_1}}^2 + (u-3)^2 {\sigma_{a_3}}^2} \qquad \text{(eq. 2)}$$

As it is shown in figures 5 and 6 below, this multiple linear regression works well to estimate the thermal output of the PVT panels row.

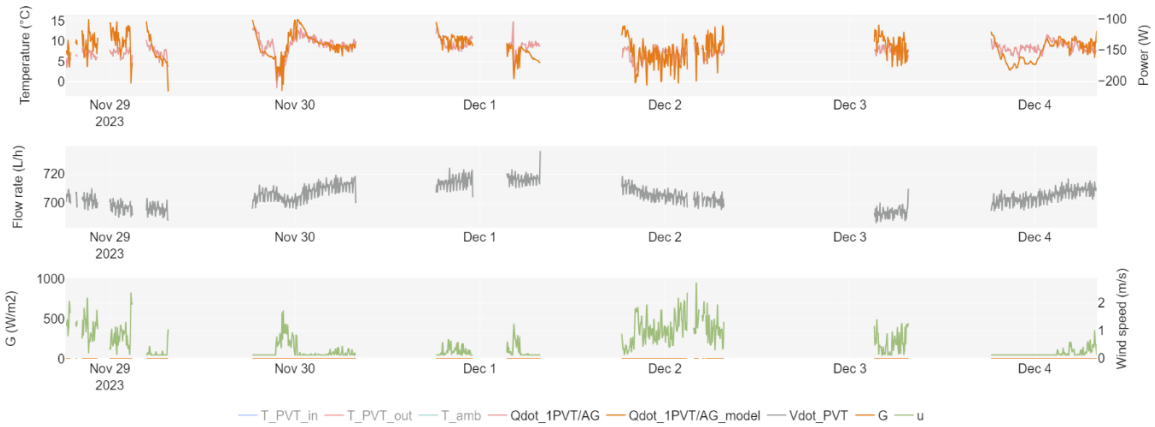

Fig. 5: Timeseries graph of test sequences for 6 panels in a row with the thermal output per collector gross area "Qdot_1PVT/AG" and the modelled one "Qdot_1PVT/AG_model"

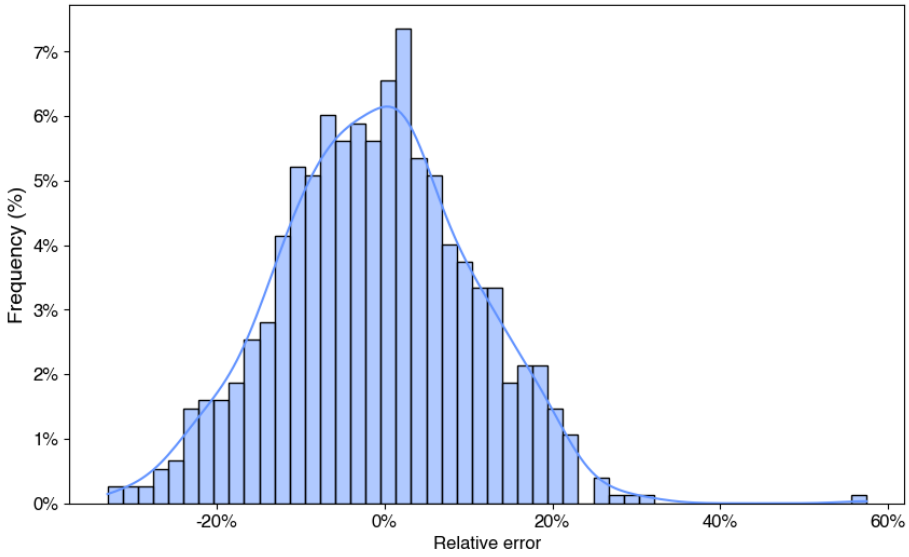

Fig. 6: Relative error between modelled and measured thermal output for 6 panels in a row

Finally, we compared the results from 1 to 8 panels in a row:

Tab. 1: Results obtained with least squares method on filtered data for 1 to 8 panels

Number of panels	Mean total flow rate	Mean flow rate per panel	Hours of data	b_1	a_3	MAE	MAE out of mean power
Unit	L/h	L/h	h	W/m^2K	$W/m^2K/(m/s)$	W	%
1	143	143	4.7	22.6	6.8	21	7%
2	220	110	26.0	19.8	5.0	22	9%
4	420	105	18.6	19.2	4.2	21	9%
6	704	117	62.3	15.3	6.0	14	9%
8	1013	127	28.1	13.9	6.4	8	7%

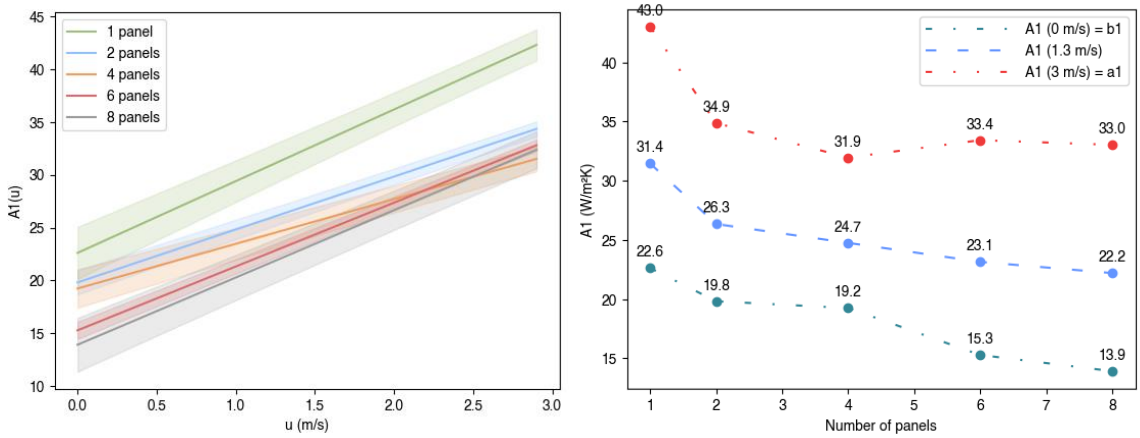

Fig. 7: Results obtained with least squares method on filtered data for 1 to 8 panels

In our test facility configuration, the obtained results show:

- For $u = 0\ m/s$, the heat loss coefficient ($b_1$in W/m^2K) decreases from 1 to 8 panels installed in the row. 2 and 4 panels have a performance decrease of about 15% compared to 1 panel.
- For $u = 1.3\ m/s$, there is a significant reduction from 1 to 2 panels (-16%) and then the reduction is roughly linear with a slope of $-0.8\ W/m^2K/panel$.
- For $u = 3\ m/s$, there is a reduction between 2 panels and 1 panel and then the heat loss coefficient looks stable until 8 panels.

3.2. Clustering by wind range

In this section, we cluster data by wind ranges $[u_m - 0.1\ ;\ u_m + 0.1]$ for $u_m \in [0.1, 0.3, 0.5, 0.7 \ldots]$ of for each cluster, a linear fit provided the corresponding $A_1(u_m)$ coefficient.

This analysis shows that we should be careful when comparing "performance" based on linearization of $A_1(u)$. It can lead to misinterpretation. Thus, we find that the A_1 values for wind speed higher than 2 m/s (resp. 1 m/s) are not relevant for the configuration with 6 panels in a row (resp. 8 panels in a row) because of a lack of data.

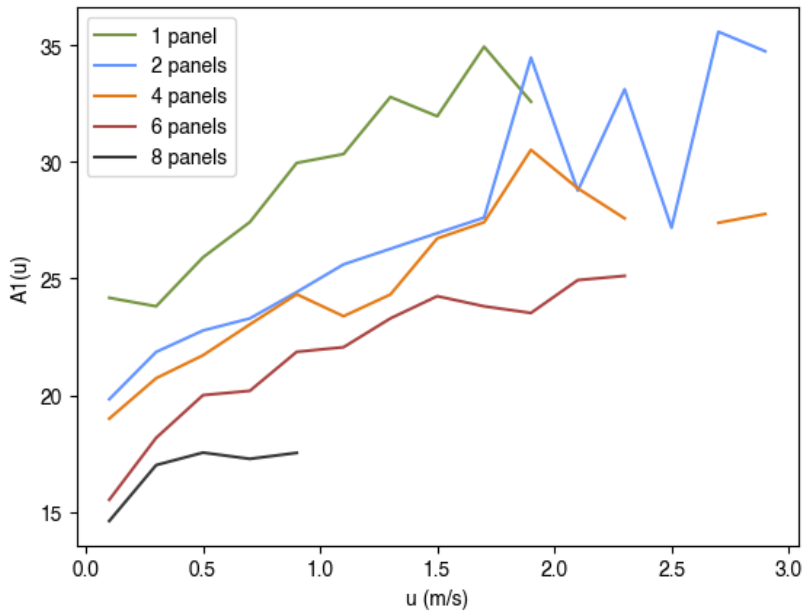

Fig. 8: $A_1(u_m)$ in each configuration

4. Discussion

4.1. Experimental bias

We should keep in mind that, due to the experimental set-up, the more panels there are, the lower the difference in temperature between the average on the exchangers and the ambient air (see Fig. 9). We can't rule out the hypothesis that this is at the root of some of the degradation of the heat loss coefficient by increasing the number of panels in the row.

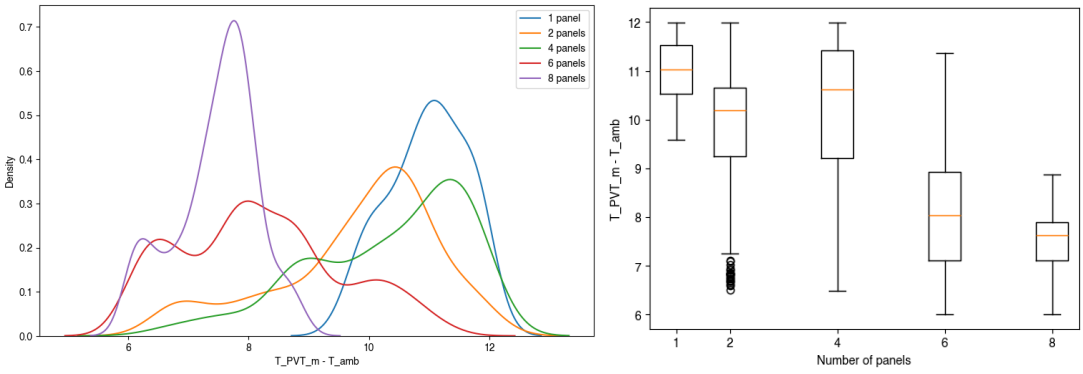

Fig. 9: (a) Distribution of T_PVT_m – T_amb in each configuration
(b) Boxplots of these distributions in each configuration

4.2. Flow distribution

Due to these PVT panels prototypes design, it is highly possible that the flow distribution would be uneven between them when installed in a row (in Z configuration). In (García-Guendulain et al., 2020), this kind of flow nonuniformity and thermal imbalances in solar collectors of similar design was studied. So far, we cannot quantify this nonuniformity in our experimental set-up, but it can be a source of reduction in thermal performance. Indeed, for PVT panels in which the flow rate would be too low, the mean heat exchanger temperature would be closer to ambient air temperature so that heat transfer would be lower.

We tried to measure the flow rate in each panel in this configuration and for each number of panels. To do this, we positioned flowmeters between consecutive panels at the inlet manifold. These experimental results confirm that there may be a significant flow distribution imbalance in this PVT panels row general design (manifolds and parallel mini-channels) but do not give any information on the original set-up (see Fig. 10). Indeed, the flow meters cause sharp drops in pressure in the inlet manifold so that the profile is reversed

compared with what is expected in such a Z configuration (the highest flow rates should be in the last panels): the hydraulic behaviour with flowmeters is significantly different from the configuration without.

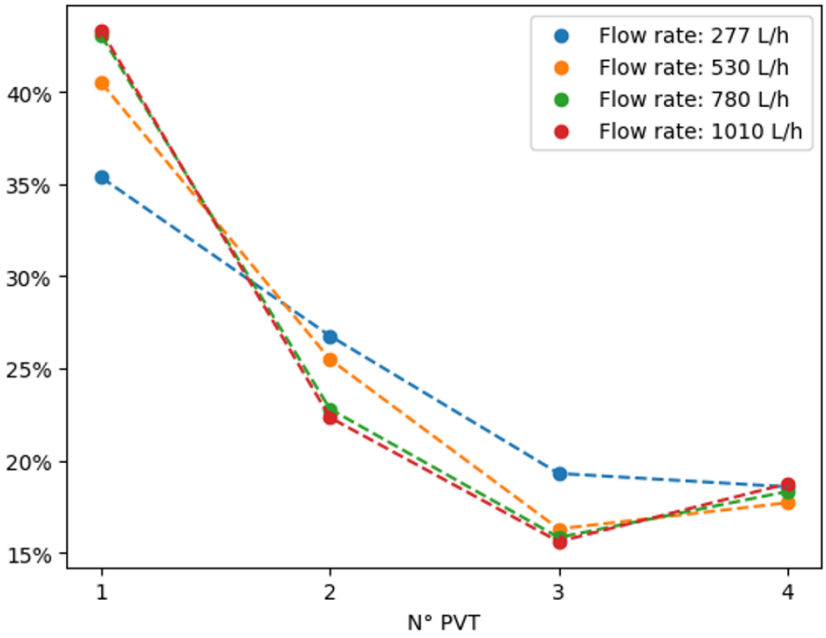

Fig. 10: measured flow distribution for 4 panels in a row in Z configuration with flowmeters between consecutive panels

4.3. Row geometry

The third possible explanation is the impact of the overall geometry on the shape and the temperature field of the airflow around the panels (including edge effects on the sides of the row corresponding to higher heat transfer).

5. Conclusion

Our research underscores the pivotal role of PVT panel configuration in enhancing the thermal performance of PVT-HP systems. The experimental analysis reveals that increasing the number of PVT panels in a single row significantly reduces the heat loss coefficient, thereby affecting overall system efficiency. This finding is crucial for the design and optimization of PVT fields, suggesting that careful consideration of panel arrangement can lead to substantial gains in energy performance. Besides, quantify the possible contribution of the heterogeneous flow distribution in the mini-channel heat exchangers is the subject of ongoing modelling and experimental work.

6. References

Chhugani, B., Pärisch, P., Helmling, S., Giovannetti, F., 2023. Comparison of PVT - heat pump systems with reference systems for the energy supply of a single-family house. Solar Energy Advances 3, 100031. https://doi.org/10.1016/j.seja.2022.100031

García-Guendulain, J.M., Riesco-Ávila, J.M., Picón-Núñez, M., 2020. Reducing thermal imbalances and flow nonuniformity in solar collectors through the selection of free flow area ratio. Energy 194, 116897. https://doi.org/10.1016/j.energy.2020.116897

Incropera, F.P., DeWitt, D.P., Bergman, T.L., Lavine, A.S. (Eds.), 2013. Fundamentals of heat and mass transfer, 7. ed., international student version. ed. Wiley, Hoboken, NJ.

ISO/DIS 9806:2017 Solar energy — Solar thermal — Test methods, 2017.

Jaafar, M.A., Chhugani, B., Brottier, L., 2022. Numerical Study of the Effect of Hybrid Solar Collectors on the Performances of the System Combining PVT With Heat Pumps, in: Proceedings of EuroSun 2022 - ISES and IEA SHC International Conference on Solar Energy for Buildings and Industry. Presented at the EuroSun 2022 - ISES and IEA SHC International Conference on Solar Energy for Buildings and Industry, International Solar Energy Society, Kassel, Germany, pp. 1–8. https://doi.org/10.18086/eurosun.2022.08.06

Jonas, D., 2023. Model-based Analysis of Solar and Heat Pump Systems for the Energy Supply of Residential Buildings.

ENERGY PERFORMANCE SIMULATION OF THE 52MW MINOS SOLAR TOWER PROJECT

Vasileios Katsaros[1], Hysenj Sadik[2], Rosie Christodoulaki[3], Michalis Karagiorgas[1], Vasiliki Drosou[3]

[1] Aspete/Greece, Athens

[2] Nur Energie Ltd/ United Kingdom, London

[3] CRES Solar Thermal Department/Greece, Athens

Summary

MINOS Concentrated Solar Power (CSP) project in Crete island, is a strategic investment in Greece that receives continued and increasing government support and is at the focus of public attention. It is the first CSP plant in Greece, and it aims to cover 10% of the island of Crete power demand. The system's capacity is equal to 52MW and a molten salt thermal energy storage of 5 hours capacity is also included. This work attempts to estimate the total electricity production and the annual performance of the MINOS project, through the development of a dedicated model in System Advisor Model (SAM) software. The findings of this feasibility study provide valuable insights into the annual electricity production and the efficiency of this CSP project, facilitating informed decision-making for stakeholders and investors interested in the development of solar tower projects.

Keywords: CSP, Solar Tower, electricity production, solar energy, concentrated solar collectors

1. Introduction

Solar tower systems, or central solar receiver systems, are based on the conversion and transfer of direct incident solar radiation into thermal energy. This thermal energy is absorbed by high temperature fluid, used as a heat transfer medium, and it is then collected by a working fluid and employed to drive a steam engine cycle for electricity generation which is finally being supplied to the grid [1].

More specifically, the direct incident solar radiation that reaches the earth surface is reflected by the heliostats/mirrors and concentrated onto the solar receiver which is located on the top of the solar tower. Each mirror is installed on an individual tracking system, so that each of them be able to track the sun's orbit. After the solar radiation reaches the solar receiver and is concentrated on a particular surface of the tower, thermal energy it is transferred as heat to a fluid that flows through a heat exchanger located behind the surface of the receiver. The fluid is heated and vaporized either directly or indirectly. The steam produced feeds a steam turbine to produce mechanical work on its rotor, where it drives a generator to produce electricity. After the steam leaves the exhaust section of the turbine, it enters a condenser, where it is cooled (water-cooled or air-cooled) and becomes saturated water. After that, the water is taken to the top of the tower to be heated and start another new cycle [2].

MINOS CSP solar tower is a CSP tower project with 5h storage and 52MW electricity capacity to be constructed in the island of Crete, Greece. The site is located on the island of Crete, in Sitia Municipality,

© 2024. The Authors. Published by International Solar Energy Society
Selection and/or peer review under responsibility of Scientific Committee
10.18086/eurosun.2024.07.04 Available at http://proceedings.ises.org

in the southeastern coastal area of Atherinolakos. The site is adjacent to the industrial zone of the Atherinolakos conventional power station, owned by the Public Power Corporation, and rated at 200Mwe [5]. Due to its proximity, the project will be easily connected with the electricity grid.

MINOS solar tower uses concentrated solar thermal technology and consists of 19,514 of sun-tracking mirrors which reflect the sun to the top of the Tower. The required adjustments of the mirrors during the sun's course within a day is performed automatically. A molten salt mixture is heated by the concentrated solar radiation and is stored in a tank on the ground. The heated salt is used to transfer its heat to water to generate steam which activates a steam turbine with a turning motion to generate electricity.

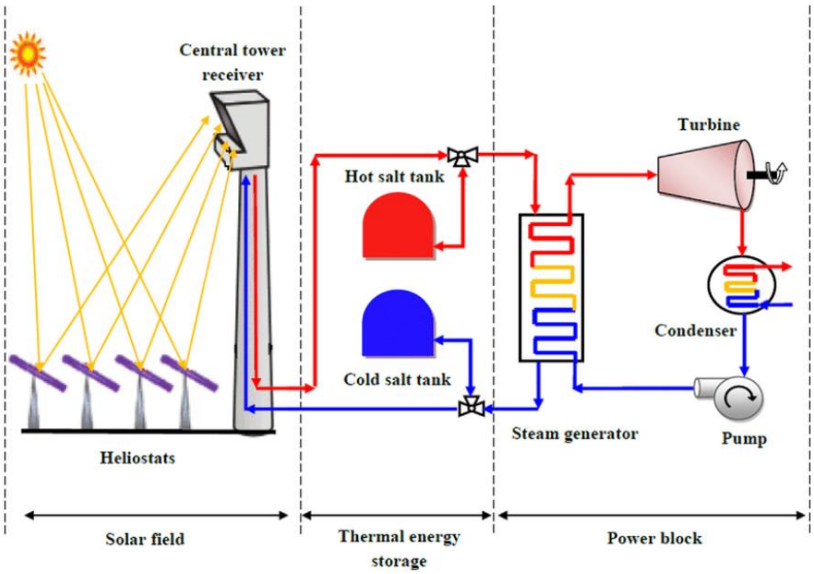

Figure 1 Schematic diagram of a solar tower power plant. (Source: https://www.researchgate.net/)

The plant is fully prepared for construction, and a 25-year Power Purchase Agreement (PPA) is set to be signed with a fixed tariff of €268/MWh. The project has been awarded a €42 million subsidy from the European Union through the NER300 program. Specifically, this subsidy offers an additional tariff of €115/MWh, which will be disbursed throughout the operational years until December 31, 2025.

Figure 2 Visualization of the MINOS CSP Solar Tower to be constructed in Crete, Greece (Source: https://www.nur-minos.com/)

2. Methodology

For the study of the concentrated solar power (CSP) system with thermal storage, meteorological data for the area were initially extracted from PVGIS in the form of a Typical Meteorological Year (TMY) file. Subsequently, key technical specifications of the system were collected, including those related to the solar tower, the heliostat field, the thermal storage, and the power cycle. The collected meteorological data and technical specifications were then entered the System Advisor Model (SAM) developed by the National Renewable Energy Laboratory (NREL). The purpose was to calculate the capacity factor, the performance of subsystems, the electrical energy production, and the energy consumption required for the operation of the system.

The fundamental equations used by SAM for calculating the results presented in this work, are as follows:

$$\text{Optical Efficiency (\%)} = \left(\frac{\text{Thermal energy Absorbed by receiver}}{\text{Incident Solar Energy on Heliostats}}\right) \times 100 \quad \text{(eq. 1)}$$

- Thermal Energy Absorbed by Receiver: The amount of heat absorbed by the tower's receiver.
- Incident Solar Energy on Heliostats: The total solar energy incident on the heliostats.

$$\text{Thermal efficiency (\%)} = \left(\frac{\text{Useful Thermal Energy output}}{\text{Thermal Energy Absorbed by Receiver}}\right) \times 100 \quad \text{(eq. 2)}$$

- Useful Thermal Energy Output: The heat utilized for energy production or storage.
- Thermal Energy Absorbed by Receiver: The amount of heat absorbed by the receiver.

$$\text{Power Cycle Efficiency (\%)} = \left(\frac{\text{Gross Electric Power Output}}{\text{Thermal Energy Input to Power Block}}\right) \times 100 \quad \text{(eq. 3)}$$

- Gross Electric Power Output: The electric power generated by the power cycle before subtracting parasitic consumptions.
- Thermal Energy Input to Power Block: The heat entering the power cycle for conversion into electrical energy.

$$\text{Capacity Factor (\%)} = \left(\frac{E_{actual}}{P_{max} \times T}\right) \times 100\% \quad \text{(eq. 4)}$$

- E_{actual} is the actual energy produced during the year in kilowatt-hours (kWh) or megawatt-hours (MWh).
- P_{max} is the maximum capacity of the solar power tower in kilowatts (kW) or megawatts (MW).
- T is the total number of hours in a year, representing the maximum time the plant could theoretically operate.

3. Solar radiation data

Atherinolakos is located in the southeast of Crete with a longitude/latitude of 26.14 E/35.014 N. With the use of PVGIS, a file (.tmy) of the annual solar radiation data of this area was created, with purpose of using it in the computational tool used for the simulation.

The solar irradiance data to be used takes into account the variability that occurs at short intervals, making the simulation results more accurate.

Based on PVGIS data, it is observed that for the month of June at 12 pm, the average value of direct solar radiation in the region is 819.66 W/m^2, while in the month of winter solstice the maximum value of direct incident radiation is 492.34 W/m^2 at 11:00 am. Also, the average value of daily direct radiation is 5.8

kWh/m^2 while the average value of diffuse radiation is 1.58 kWh/m^2. In addition, the average annual temperature of the area is 19.6 ^{o}C and the average wind speed during the year is 6.6 m/s [3].

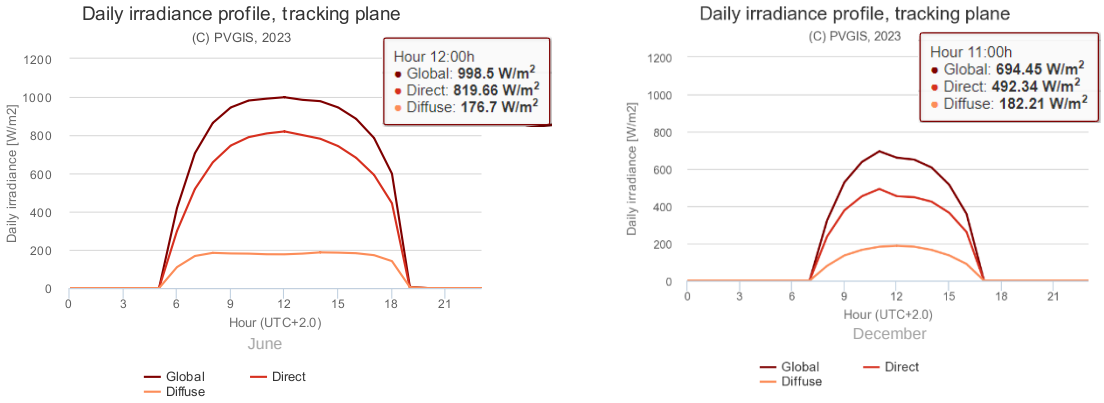

Figure 3 Average daily variation of solar radiation for the months of June and December (Source: https://re.jrc.ec.europa.eu/)

4. Technical Data

The basic technical characteristics of the MINOS project are provided by the company and are given in Table 1.

Table 1 Technical characteristics of MINOS project

Nominal power of the steam turbine	52 MW
Heliostats	19,514
Single heliostat area	20 m^2
Solar tower	
Tower height	200 m
Receiver height	16 m
Receiver diameter	8 m
Number of panels	20 m
Heat transfer fluid	molten salt
HTF hot temperature	565 C^o
HTF cold temperature	265 C^o
Storage system	
Storage type	2 tank
Tank height	12 h
Tank fluid minimum height	1 h
Tank diameter	17.7 m
Full load hours of storage	5 hours
Rankine cycle parameters	
Boiler operating pressure	120 bar
Condeser type	Air-cooled

The solar tower concentrating system with 5 hours thermal storage capacity, uses an external solar receiver to absorb heat and transfer it to the molten salts. The molten salts mixture is a composition of

60% NaNo3 and 40% KNO3 and it is used as heat transfer medium, flow through the hot salt tank to the heat exchanger and transfer the absorbed heat to the water (water boiler). The water state is changed to superheated steam at a constant pressure of 120 bar. During this process, the maximum temperature of the transferred fluid is 565 ºC and the minimum temperature is 265 ºC. The low temperature (cooled) salt is transferred, by the use of pumps, to the cold salt tank or to the inlet of the receiver for re-absorption of heat. Similarly, the saturated steam at the outlet of the steam turbine passes through the condenser and then it is transferred to the heat exchanger.

In order to produce power of 52 MWe at the steam turbine's (Rankine) outlet, the power of 124 MWt is required in the turbine's inlet given that the thermal efficiency of the cycle is 42%. Since the direct solar irradiance (DNI) in the area is known, the design point of the plant (Design Point) was set at 850 W/m^2. Considering the steam turbine's power requirements, the receiver's surface sized to be capable to absorb a thermal power up to 140 MWt, taking into account the heat losses occurring during the salt transportion.

The heliostatic field, which concentrates the solar radiation to the receiver, is consisted of 19,514 mirrors with the surface area of each mirror equals 20 m^2. Based on the zoning shown in Figure 44, the area covered by the heliostatic field is 390.28 acres, with the total land area required to install the system being 1,598.51 acres. In Fig.3 is shown the positioning of heliostats in the field, with the central solar tower as a reference point, taking into account the differences in altitude of the land.

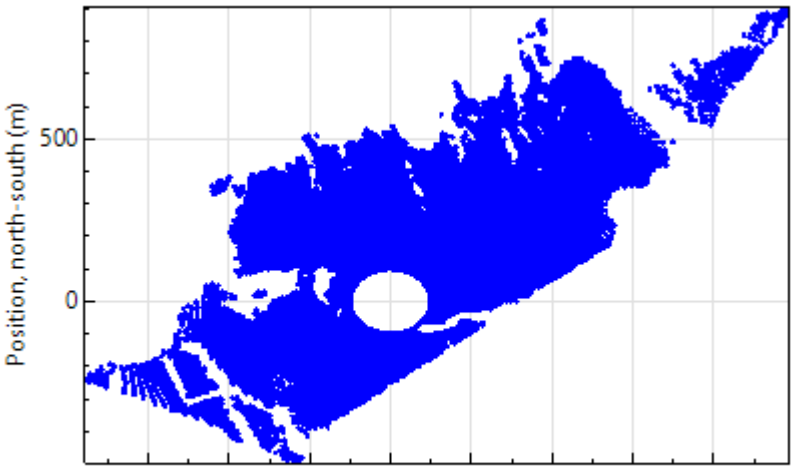

Figure 4 Positioning of heliostats in the MINOS field

Heliostat Properties

Heliostat width	4.48934	m
Heliostat height	4.5	m
Single heliostat area	20	m²
Image error (slope, single-axis)	1.53	mrad
Reflected image conical error	4.32749	mrad
Number of heliostat facets - X	1	
Number of heliostat facets - Y	1	
Heliostat focusing method	Flat	
Heliostat canting method	None	

Heliostat Operation

Heliostat stow/deploy angle	5	deg
Wind stow speed	15	m/s
Heliostat startup energy	0.025	kWe-hr
Design-point DNI	850	W/m²

Atmospheric Attenuation

Polynomial coefficient 0	0.006789	
Polynomial coefficient 1	0.1046	1/km
Polynomial coefficient 2	-0.017	1/km²
Polynomial coefficient 3	0.002845	1/km³
Average attenuation loss	4.3	%

Heliostat field multiple: 1

Cycle thermal efficiency: 0.42

Cycle thermal power: 124 MWt

Tower and Receiver

Land Area

Non-solar field land area	320	acres
Solar field land area multiplier	0.264	
Base land area	285.161	acres
Total land area	395	acres
Total heliostat reflective area	390,280	m²

Solar Field Layout Constraints

Max. heliostat distance to tower height ratio	9.52843	
Min. heliostat distance to tower height ratio	0.714285	
Tower height	200	m
Maximum distance from tower	1905.69	m
Minimum distance from tower	142.857	m

Mirror Washing

Water usage per wash	0.70	L/m²,aper.
Washes per year	63	

Heliostat field availability

Edit losses... | Constant loss: 0.0 % | Hourly losses: None | Custom periods: None

Curtailment and availability losses reduce the solar field output to represent component outages, soiling, or other events.

Mirror reflectance and soiling	0.9
Heliostat availability	0.98

Table 2 MINOS technical data for SAM tool calculations

Main technical parameters entered into SAM in order to simulate the system operation are presented in

System Design Parameters

Solar multiple	1.13	
Receiver thermal power	140.0	MWt
HTF hot temperature	565.0	°C
HTF cold temperature	265.0	°C

Tower and Receiver Dimensions

Solar field geometry optimization on the Heliostat Field page calculates new values for tower height, receiver height, and receiver diameter.

Tower height	200	m
Receiver height	16	m
Receiver diameter	8	m
Number of panels	20	

Receiver Heat Transfer Properties

Tube outer diameter	40	mm
Tube wall thickness	1.25	mm
Coating emittance	0.88	
Coating absorptance	0.94	
Heat loss factor	1	

Design and Operation

Minimum receiver turndown fraction	0.25	
Maximum receiver operation fraction	1.2	
Receiver startup delay time	0.2	hr
Receiver startup delay energy fraction	0.25	
Receiver HTF pump efficiency	0.850	
Maximum flow rate to receiver	372.351	kg/s

Materials and Flow

HTF type: Salt (60% NaNO3 40% KNO3)

Property table for user-defined HTF: Edit...

Material type: Stainless AISI316

Flow pattern: 1

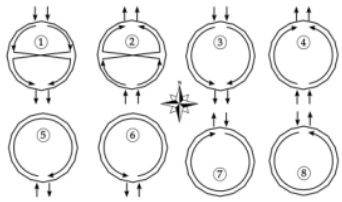

Receiver Flux Modeling Parameters

Maximum receiver flux	1000	kWt/m²
Estimated receiver heat loss	30.0	kWt/m²
Receiver flux map resolution	20	
Number of days in flux map lookup	8	
Hourly frequency in flux map lookup	2	hours

Piping Losses

Piping heat loss coefficient	10200	Wt/m
Piping length constant	0	m
Piping length multiplier	2.6	
Piping length	520	m
Total piping loss	5304	kWt

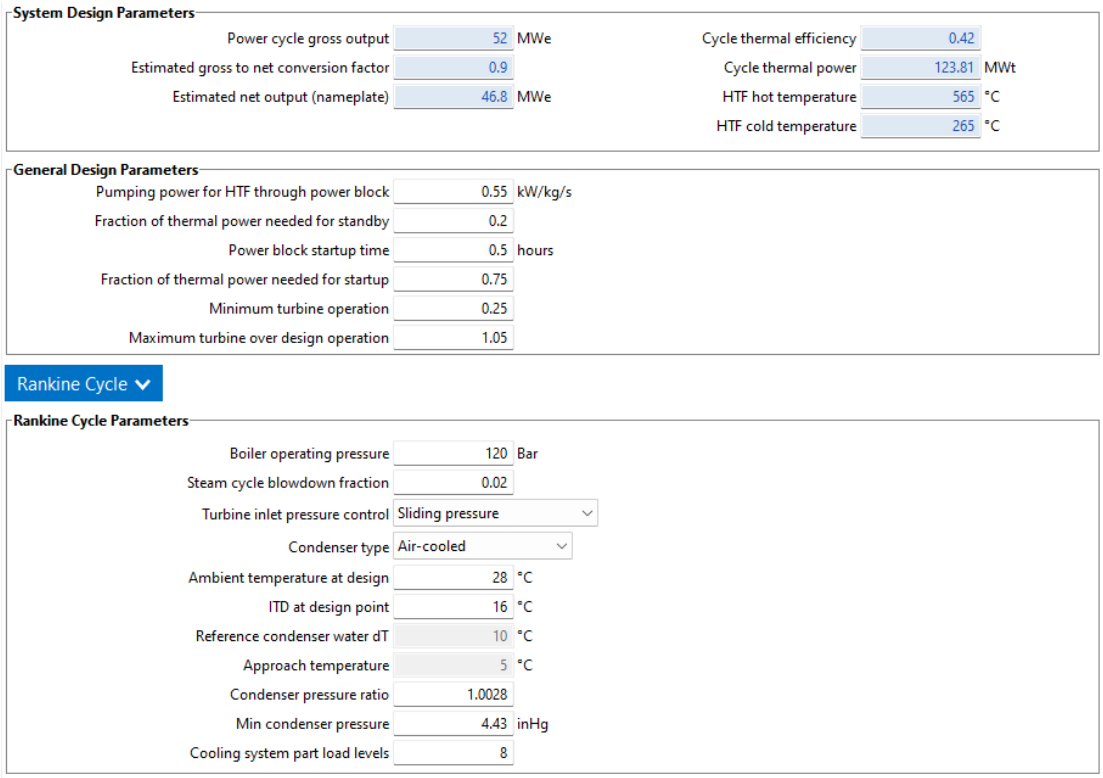

5. Results

The results selected to be presented after the SAM analysis, concern the system's Capacity Factor, the efficiency of the subsystems, the total electrical power of the system for electricity production and the consumptions required for its operation.

In a solar power tower system, the overall efficiency is influenced by three key factors. The optical efficiency pertains to the ability of the heliostats to collect and direct solar radiation towards the receiver. Proper alignment and reflectivity of the mirrors are critical for achieving high performance.

The thermal efficiency depends on how effectively the receiver converts the collected heat into usable thermal energy. Key factors include the design of the receiver and its ability to minimize thermal losses.

Finally, the power cycle efficiency depends on the system's ability to convert thermal energy into electrical energy.

In the chart below, the variation of the optical field efficiency, the power cycle efficiency and the thermal efficiency, during the year, are shown.

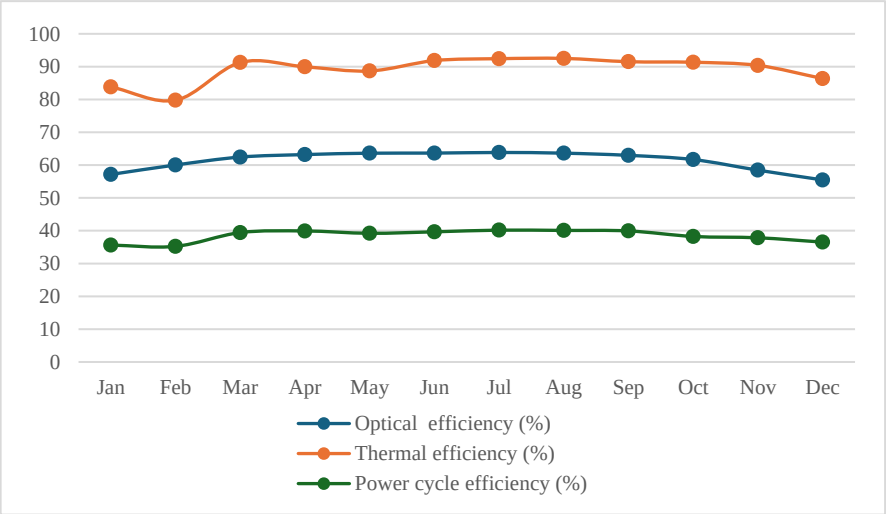

Figure 5 Monthly variation in optical efficiency, thermal efficiency, and power cycle efficiency

Table 3 System efficiency during the year

Month	Optical efficiency (%)	Thermal efficiency (%)	Power cycle efficiency (%)
Jan	57.14	83.83	35.62
Feb	60.03	79.76	35.23
Mar	62.44	91.27	39.43
Apr	63.2	89.95	39.92
May	63.62	88.68	39.21
Jun	63.65	91.84	39.66
Jul	63.84	92.42	40.17
Aug	63.63	92.5	40.08
Sep	62.96	91.5	39.93
Oct	61.68	91.33	38.25
Nov	58.45	90.37	37.84
Dec	55.47	86.37	36.53
Average	**61.34**	**89.15**	**38.49**

According to the analysis, the total energy produced and fed into the grid by the solar tower system with 5 hours of thermal storage is 109.26 GWh/y and the annual system capacity factor is 24.5%. Correspondingly, the annual consumption necessary for the operation of the system is 12 GWh/y.

Table 4 shows the monthly generated energy of the system as well as the electricity needed for the subsystems operation, necessary for the overall system's operation.

Table 4 Capacity factor and electricity produced and consumed by the solar power tower.

Month	System energy consumption (MWh)	Solar tower energy produced (MWh)	Capacity factor (%)
Jan	500.8	3,472.2	9.3
Feb	555.1	4,209	11.3
Mar	938.7	8,299	22.3
Apr	1,101	9,977.8	26.8
May	1,083.4	9,781.4	26.3
Jun	1,473.9	14,385.7	38.7
Jul	1,514.6	15,025.8	40.4
Aug	1,499.5	14,979.1	40.3
Sep	1,195.1	11,249.4	30.3
Oct	905.8	8,057.9	21.7
Nov	710.1	5,932.6	16
Dec	517.5	3,890.8	10.5
Sum	**11,995.6**	**109,260.70**	

The diagram below shows the monthly energy produced and consumed by the system during the year, after data analysis in SAM and taking into account the efficiency of the systems and.

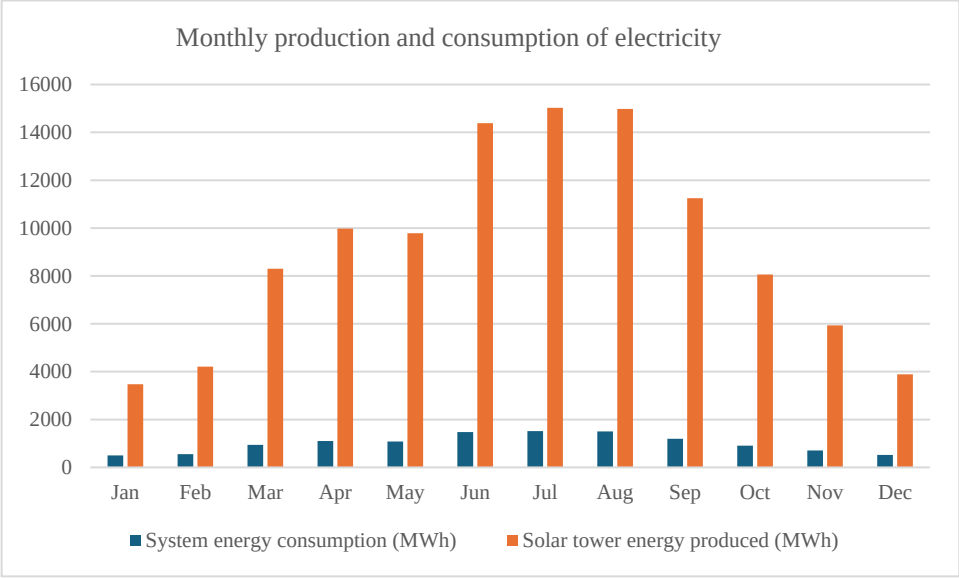

Figure 6 Electricity produced and consumed by the solar power tower.

Based on the electricity produced by the solar tower (values in Table 4), the variation of the capacity factor of the system during the year is presented in Fig7.

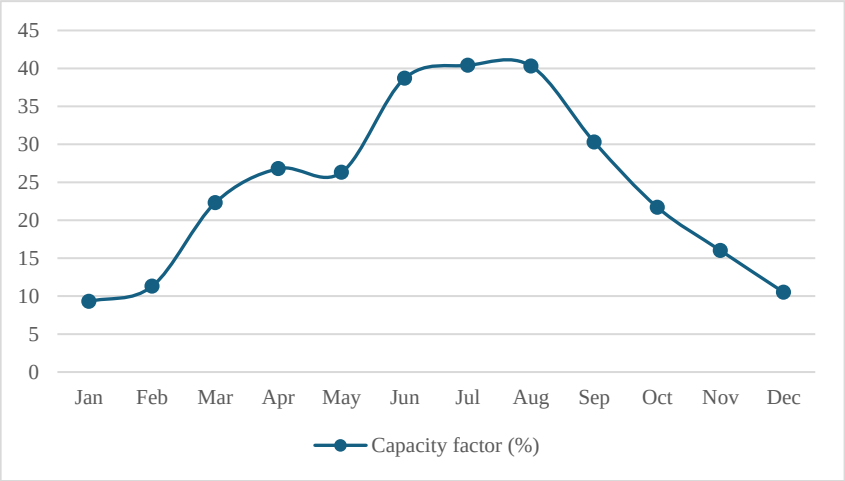

Figure 7 Monthly variation of the capacity factor

During the summer solstice period, where the amount of direct solar radiation is maximum, there is an increase in the system's capacity factor compared to the month of December when the winter solstice occurs. Particularly in July the capacity factor is increased from 10.50% to 40.4%. Regarding the generated electricity as a function of the system capacity factor, there is an increase in the summer months and a corresponding decrease in the winter months. This is also noticed by the energy consumed by the system during its operation in summer and winter period as well. In addition, it was found that the penetration rate of the system in electricity generated from RES and in total electricity production as well, for the island of Crete, peaks in the summer months. More specifically, the highest penetration of the system in electricity generated from renewable sources has occurred in the month of June with a percentage of 18.96%, while the system's contribution in total production (RES & conventional systems) is up to 8.62%.

According to a survey by ELSTAT in cooperation with CRES, each Greek household consumes 13,994 kWh per year [4]. The energy produced and fed into the grid by the solar tower system is sufficient to cover the demand of almost 7,800 households.

The electrical energy required for the solar tower's subsystems operation is up to 10.98%. A percentage of this amount of energy is generated from backup power plants and the rest of it from the system itself. It is worth mentioning that the energy required for the tower's subsystems operation, could cover the annual electricity demand of about 850 households. The energy needed for tower's subsystems operation could be mitigated using an independent renewable energy source whose operational needs would be negligible. Adopting solutions like this, would help to increase the amount of electricity fed into the grid from the solar tower system as well as to reduce the amount of energy needed to maintain the fluid's temperature over its critical lower value during the night.

6. Conclusions

In this paper, the simulation of the first ever designed concentrating solar-thermal system in Greece, with a capacity of 52MW, was presented. It is a pilot project while processes are underway to find a tenderer to construct and operate the project.

Through the simulation carried out for the solar tower power system, there were interesting outcomes regarding the system's contribution in meeting the energy needs for the island of Crete. The maximum performance of the system has occurred during the summer period where it is capable to feed the grid with an amount of energy equal to 15,025.8 MWh, while the system's capacity factor for the month of July is up to 40.4%. The electricity generated only from this system contributes significantly to the annual electricity demand, with the maximum contribution occurring in the month of July where the penetration

of the system is up to 8.62%. The total electricity generated from the system (109.26 GWh/y) is capable to meet the annual energy needs of about 7,800 households.

The simulation results were compared to the project calculations by the company and it was shown that SAM software is a reliable tool for modeling various renewable energy systems and more specifically concentrating solar thermal systems as analyzed in this paper.

Further research is needed on the design and sizing of an individual RES system to cover the energy requirements for the operation of the concentrated solar tower, since the electrical energy requirements for running the concentrated solar tower subsystems cannot be considered negligible. Furthermore, a financial study could be carried out regarding the system's sustainability (construction costs, operating costs, maintenance costs, life cycle of the various sub-units of the system).

7. References

1. James Wight, 19/03/2011, Zero Carbon Australia: We can do it. skepticalscience.com
2. Alvarez, Romero Manuel. Concentrating Solar Thermal Power. Chapter 2, Handbook of Energy Efficiency and Renewable Energy. Frank Keith. s.l.: Taylor & Francis Group, LLC, 2007.
3. PHOTOVOLTAIC GEOGRAPHICAL INFORMATION SYSTEM, Retrieved from: re.jrc.ec.europa.eu
4. GREEK STATISTICAL AUTHORITY, 29/10/2013, HOUSEHOLD ENERGY CONSUMPTION RESEARCH 2011-2012, PIRAEUS, Retrieved from: www.statistics.gr
5. NUR MINOS, 50MW CSP Project, Utilizing the sun's endless energy supply, Retrieved from: https://www.nur-minos.com/
6. National Renewable Energy Laboratory, SAM (System Advisor Model), Retrieved from: https://sam.nrel.gov/

Validation of a simulation model for parabolic trough collectors in a high-latitude district heating system

Frej Fogelström[1], Andrea Gambardella[2], Gireesh Nair[1], Benjamin Ahlgren[1,3], Itai Danielski[1], Truong Nguyen[1]

[1] Department of Applied physics and Electronics, Umeå University, Sweden

[2] Absolicon Solar Collector AB

[3] WSP Sverige AB

Abstract

Currently, companies in the solar heating sector may choose from a wide range of tools for modelling and simulating solar thermal power. However, due to the deviant design of some collectors, conventional simulation tools may be inadequate in correctly assessing the performance of such collectors. This study aims to test and validate an in-house simulation model for T160 PTC collectors developed by the company Absolicon Solar Collector AB by comparing measured data with simulated results. A solar district heating (SDH) plant in Härnösand, Sweden featuring 192 parabolic trough collectors (PTC) is used as a case study for the validation. Operational data such as weather data, solar heat production and collector loop/ambient temperatures were collected from the facilities of Absolicon. The data was compiled and simulated using a Python model developed for the T160 collectors. The study shows an acceptable correlation between simulated and measured data during periods with high DNI where a relatively high amount of heat is delivered to the district heating. Deviations are present during periods of low DNI and can be derived from inadequate assessments of heat losses from the piping of the installation in addition to inaccurate measurement data.

Keywords: PTC collectors, Simulation, Solar District Heating, Sweden

1. Introduction

As reported by Weiss and Spörk-Dür (2023), the world-wide annual solar thermal energy yield reached 442 TWh by the end of 2022 corresponding to approximately 153 million tons of CO_2-reduction if assumed to replace oil (Weiss and Spörk-Dür, 2023). During the same year, 41 new large-scale (>350 kW_{th}) solar heating plants for district heating, residential, commercial and public buildings were commissioned. However, implementations of SDH systems in upper Nordic regions are less common. Accordingly, there is also a scarcity of measured data from such installations.

As stated by the Swedish energy company organization Energiföretagen, the DH sector has a goal of a fully decarbonized heat supply by 2030 (Rydegran, 2023). Waste incineration constitutes approximately one-fifth of supplied energy and two-thirds of the total greenhouse gas emissions in the DH sector (Naturvårdsverket, 2024.). Increasing the effectiveness or reducing the amount of waste incineration can therefore be regarded as a priority to reach the 2030 goals. DH companies in Sweden have experienced a high increase in the costs of biofuels, where the prices for pellets and wood chips significantly have increased over the past few years (Selin and Vinterbäck, 2023). With biomass constituting approximately 47% of supplied energy in the DH sector (Khodayari, 2023), the increased cost of combustibles have increased the incentives for alternative heat sources in Sweden.

DH utilities in Sweden have started exploring the possibility of solar thermal (ST) as a viable addition to the fuel mix (Bergman, 2023). Further, an ongoing investigation as part of the IEA SHC Task 68 (IEA SHC, 2024) reports good synergies between biofuel boilers and collector fields, with solar production during summer effectively replacing boilers operating on reduced loads and low efficiencies. Additionally, the study shows DH companies reduce CO_2-impact and fuel price dependency while the boilers are subjected to reduced wear and tear. Despite recognized technical readiness, a knowledge gap exists among Swedish DH companies regarding function and feasibility of SDH systems.

© 2024. The Authors. Published by International Solar Energy Society
Selection and/or peer review under responsibility of Scientific Committee
10.18086/eurosun.2024.07.05 Available at http://proceedings.ises.org

For detailed design, installers of solar thermal typically use commercialized simulation software's like TRNSYS (especially with the TESS library) and Modelica (Gauthier, 2024). However, these software's may be limited in correctly assessing heat production from specially designed PTC collectors at higher latitudes (Absolicon Engineering department, 2024). This study aims to validate an in-house developed simulation tool by comparing measured and simulated data from Högslätten Solar Thermal Park in the city of Härnösand, Sweden.

2. Högslätten Solar Thermal Park

Serving as a SDH demonstration site for Absolicon Solar Collectors AB, Högslätten Solar Thermal Park is situated in the city of Härnösand (62˚ N) and consists of 192 PTC collectors with the optical efficiency of 76.4%. These collectors are connected to the DH network of the city and serve as a demonstration site for DH companies and industries. The plant was commissioned during autumn 2021 with continuous measurements of weather data and heat production. The collectors consist of 8 sub-circuits containing 24 collectors each. The collectors are mounted on a 1-axis tracking system with a solar central connected to the DH network located next to the collector field. As shown by technical parameters given in Table 1, the installation covers an area of 2 940 m^2 and has under its years of operation reached an annual heat production of approximately 329 MWh. Regulators on both collector and DH side control the temperatures in the collector loop and DH network. The plant is turned off between 1st November and 28st February to avoid unnecessary wear and tear from harsh weather conditions during winter season.

Table 1: Basic technical parameters for Högslätten Solar Thermal Park.

Technical parameter	Value	Unit
Aperture area	1 056	m^2
Total area of installation	2 940	m^2
No. of collectors	192	Pcs.
Collector type	Absolicon T160 PTC	-
Collector efficiency	76.4	%
Heat carrier fluid	Water with glycol	Type
Installed thermal power	0.74	MW
Heat production (year)	329	MWh/y
Specific production (year)	445	kWh/kW/y
Global horizontal irradiation	889.4	kWh/ m^2
CO_2 saving (year)[1]	65-189	tonnes/year

[1] Nguyen et al 2024

With the installation being commissioned in early autumn 2021, only a few weeks of measurement data is available from that year. The data used in the study was therefore collected for the years 2022-2024 (exemplary day shown in Figure 1) The temperatures were all collected from sensors at the collector side, while solar heat is measured at the DH side showing heat supplied to the DH network. At present, the installation only covers a small fraction (0.21%) of the annual heat demand in the municipality.

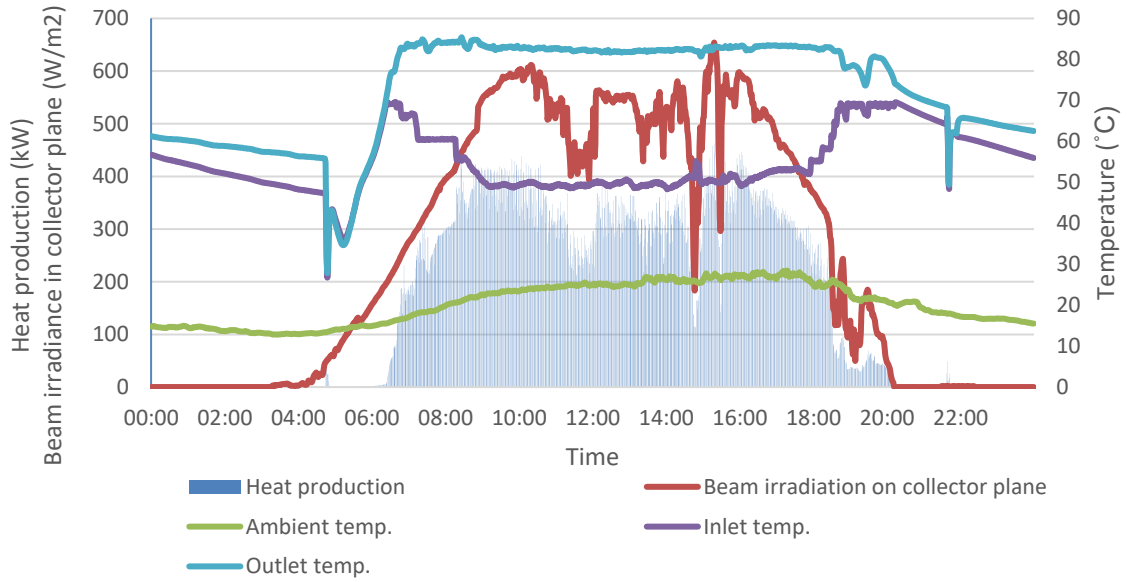

Figure 1. Measurement data during a specific day (2023-06-21) from the installation in Härnösand.

3. Methodology

3.1 Data pre-processing

Hourly measurement data on direct normal irradiation (DNI), diffuse radiation (DHI), outlet temperature, heat supplied to the DH network and ambient temperature was received from Högslätten's in-house monitoring client at the facilities of Absolicon in Härnösand. The data was divided into three separate simulation periods for 2022-2024: Simulation period 1- 1st March - 31st October 2022; Simulation period 2- 1st March - 31st October 2023; Simulation period 3 - 1st March - 6th May 2024 representing the actual periods of operation for the plant. Where inconsistent data was present during smaller time series, missing values were added using linear interpolation. Where the data was inconsistent for larger time series, missing hourly values were matched with similar data values from previous time series during the same month. Missing data points and substitution method for each of the simulation periods between 2022-2024 are presented in Table 2.

Table 2: Inconsistent measurement data and substitution method.

Interpolated		Matched from similar data series	
Date	**Time**	**Date**	**Time**
2022-07-31	06:00	2022-03-31	14:00-23:00
2022-08-31	05:00-06:00	2022-04-01	00:00-09:00
2023-03-26	02:00	2022-04-15	16:00-23:00
2023-08-30	12:00-15:00	2022-04-16	00:00-14:00
2023-10-29	02:00	2022-08-14	09:00-13:00
2024-03-31	02:00	2022-09-22	01:00-08:00

3.2. Simulation

Each data set was simulated using the in-house developed Python model for each of the simulation periods using hourly time steps. Three plot combinations were chosen for validation of simulated data; heat supplied to the DH network, outlet temperatures from the collector field and DNI/supplied heat to the DH network. Plots were created showing accumulated energy for each time step. For the outlet temperature, three separate plots during spring, summer and autumn were created for each simulation period to assess the correlation between simulated and measured data.

During the time of simulation, the U-values for the piping at Högslätten were not available why these were approximated from past projects and put in the model. Test simulations were conducted with past U-values before the value resulting in the closest mismatch between simulated and measured data was chosen (0.1 W/m, K).

3.2.1 Model function and inputs

Tilted surface radiation, row shading and collector heat output is calculated by defining functions from Mathematical Reference Compendium, TRNSYS 16: 'Solar radiation processor', 'Collector array shading' (Klein et al., n.d.) and the Solar Keymark quasi-dynamic model portrayed in ScenoCalc documentation (SolarHeatEurope, 2024). The model iterates defined functions over each time step from hourly measurement data (DNI, DHI, ambient temperature) plotting the result for simulated outlet temperatures and heat delivered to DH. The working principle of the model is shown in Figure 2.

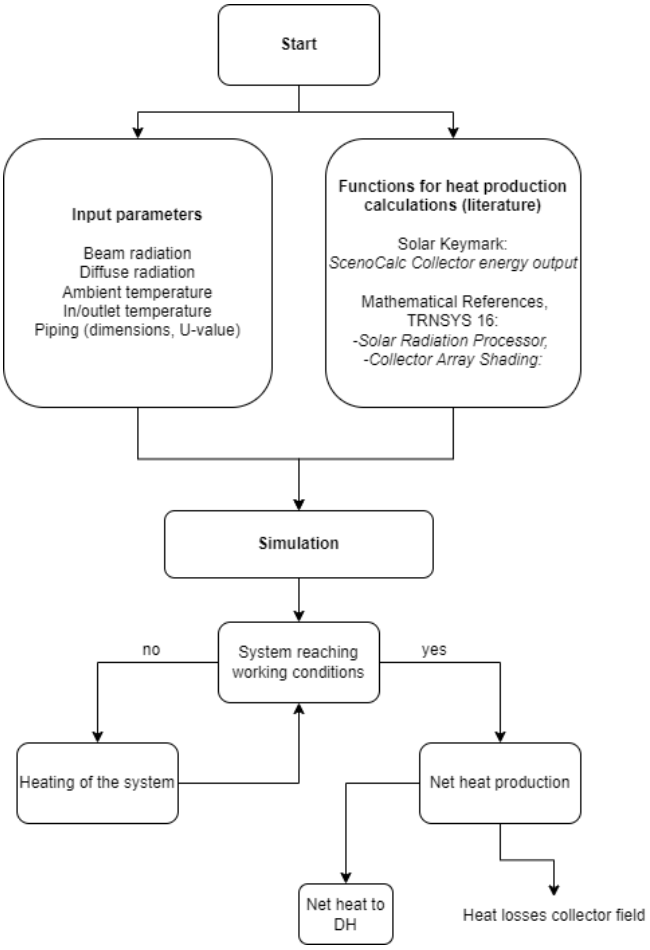

Figure 2. Schematic of the system simulation.

For fluid equations, thermodynamic relations and media properties, the Python library 'CoolProp' is used. Additionally, before heat can be supplied to the DH network, the model features a 'warm-up' function depending on ambient temperature, DNI and component properties during the start of heat production each day. The function describes the warmup of piping and system components to operational conditions until a steady state between heat carrier and system components is reached. It was created as a result from studies on actual/simulated heat production mismatches from commissioned plants and if neglected can result in a substantial shift in heat production during sunrise. Heat losses dependent on pipe dimensions as well as operational and ambient temperature are then calculated before final net heat delivered to DH is quantified and plotted.

The results are visualized in scatter plots, showing hourly accumulated heat supplied to the DH network. To further clarify the results, color mapping is used for different percentages of maximum measured DNI (0, 25, 50, 75, 100) during each simulation period showing active heat production relative measured Direct Normal Irradiance. The plots do not consider DHI as it has a negligible impact on the heat delivered from the T160 collectors. A reference line is given in each plot representing a 100% correlation between simulated and measured data. Obvious measurement

errors (simulated data 0) are marked in grey showing data points for which the input data is inconsistent/missing. To further clarify the difference between simulated and measured data, three additional plots are given showing accumulated monthly heat supplied to the DH network as well as the ratio between simulated and measured data over the time of day and relative measured DNI.

4. Results

4.1 Simulated and measured heat supplied to the DH network

The measured heat supplied to DH network was calculated to 281,42; 314,69; 34,10 MWh during Simulation period 1,2 and 3, respectively. Corresponding simulated results obtained during the same period were 206,13; 236,12; 23,87 MWh respectively, with the simulated annual results falling no more than 70% below corresponding measured values.

To give an indication on the spread of the datapoints for different values of measured DNI, a scatter plot is used (Figure 3,5,7) (light blue-blue-red-orange-yellow) representing data points of heat supplied at different levels of measured maximum DNI (0%, 25%, 50%, 75%, 100%) during each of the simulation periods. Figure 3-8 show the comparison of simulated and measured data.

4.1.1 Simulation period (1/3-31/10- 2022)

Comparison of simulated and measured data is shown in Figure 3.

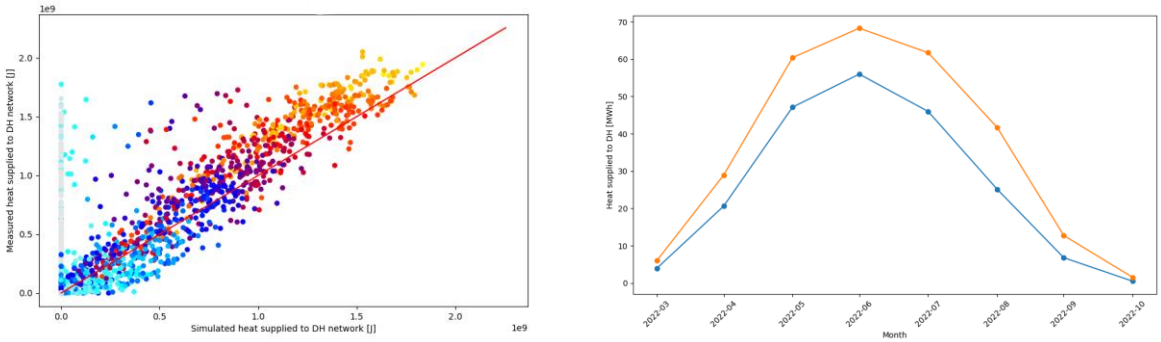

Figure 3. Simulated and measured hourly values for heat supplied to the DH network for Simulation period 1, 1/3-31/10 where the reference line (red) corresponds to a 100% match between simulated and measured data (left). Colours (light blue-red-yellow) indicate data points for different values of maximum measured DNI (0%, 25%, 50%, 75%, 100%) under the period. Measurement errors are marked in grey. Monthly comparison of simulated (blue) and measured (orange) heat supplied to the DH network (right).

The ratio simulated/measured heat supplied to the DH network relative time of day and DNI is shown in Figure 4.

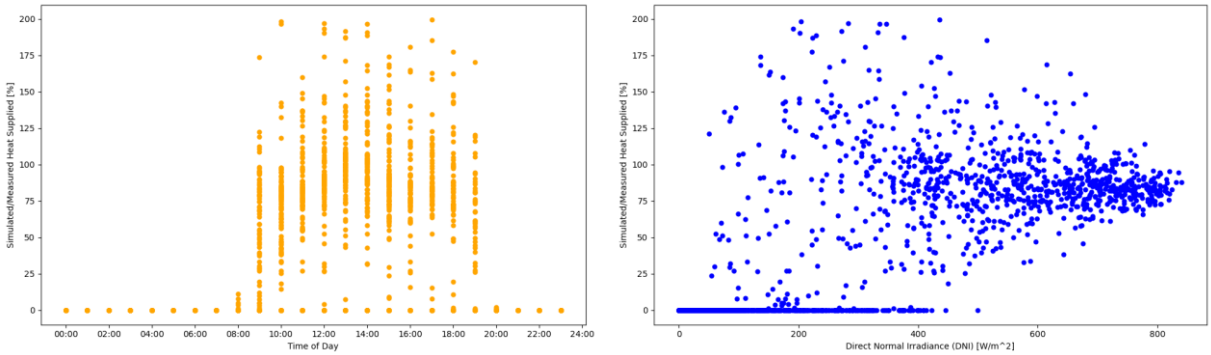

Figure 4. Simulated/measured heat (%) over the time of day (left) and relative measured DNI (right). Measurement errors occur where simulated/measured heat is zero at the bottom of the graphs.

4.1.2 Simulation period 2 (1/3-31/10- 2023)

Comparison of simulated and measured data is shown in Figure 5.

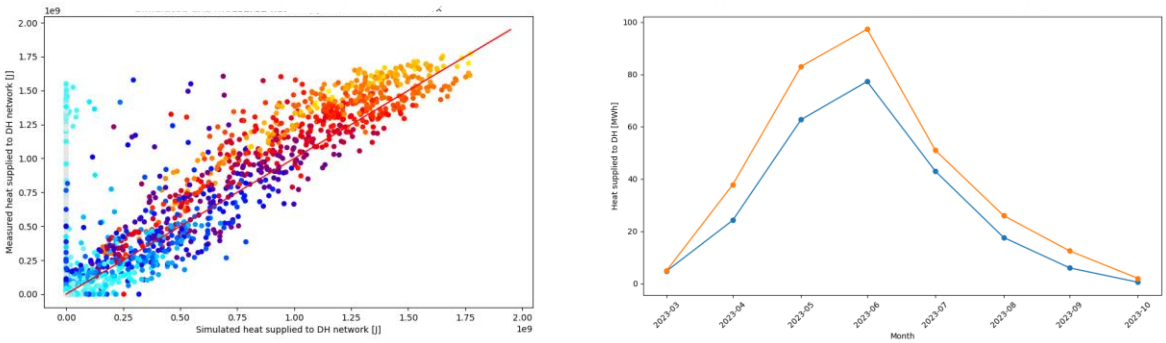

Figure 5. Simulated and measured hourly values for heat supplied to the DH network during Simulation period 2, 1/3-31/10 where the reference line (red) corresponds to a 100% match between simulated and measured data (left). Colours (light blue-red-yellow) indicate data points for different values of maximum measured DNI (0%, 25%, 50%, 75%, 100%) under the period. Measurement errors are marked in grey. Monthly comparison of simulated (blue) and measured (orange) heat supplied to the DH network (right).

The ratio simulated/measured heat supplied to the DH network relative time of day and DNI is shown in Figure 6.

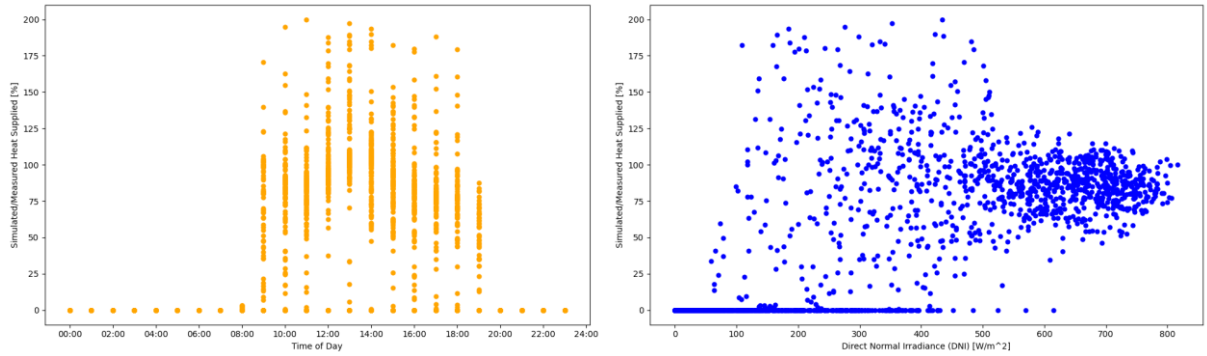

Figure 6. Simulated/measured heat (%) over the time of day (left) and relative measured DNI (right). Measurement errors occur where simulated/measured heat is zero at the bottom of the graphs.

4.1.3 Simulation period 3 (1/3-6/5- 2024)
Comparison of simulated and measured data during Simulation period 3 are shown in Figure 7.

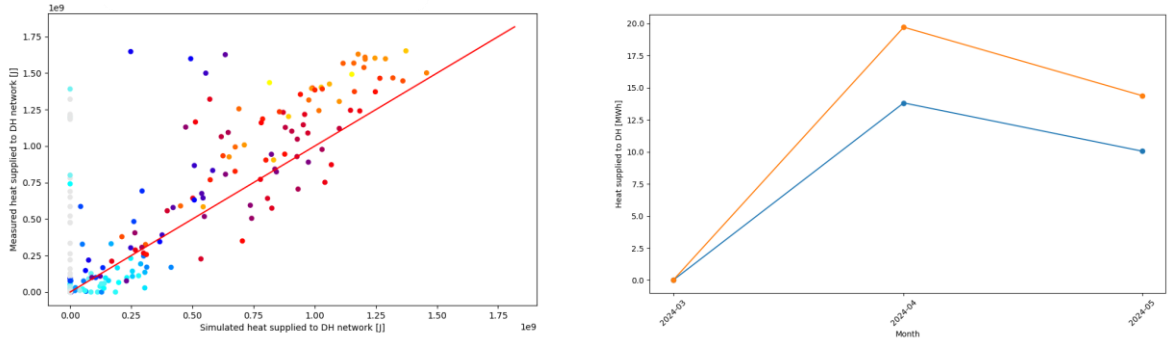

Figure 7. Simulated and measured hourly values for heat supplied to the DH network during Simulation period 3, 1/3-6/5 where the reference line (red) corresponds to a 100% match between simulated and measured data (left). Colours (light blue-red-yellow) indicate data points for different values of maximum measured DNI (0%, 25%, 50%, 75%, 100%) under the period. Measurement errors are marked in grey. Monthly simulated (blue) and measured (orange) heat supplied to the DH network (right).

The ratio simulated/measured heat supplied to the DH network relative time of day and DNI is shown in Figure 8.

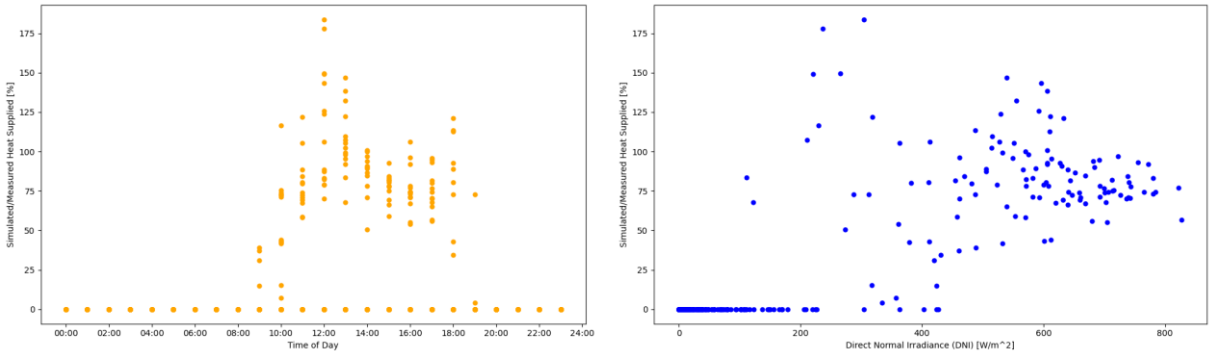

Figure 8. Simulated/measured heat (%) over the time of day (left) and relative measured DNI (right). Measurement errors occur where simulated/measured heat is zero at the bottom of the graphs.

A mismatch between simulated and measured data can be observed during simulation periods where simulated supplied heat is zero. This could be attributed to inconsistent or inaccurate input data, likely related to malfunctions or coverages of the irradiation sensors. A trend of scattered data points where measured supplied heat is higher than the simulated is present during all simulation periods. However, the colored scatterplot (Figure 3, 5, 7) reveal a trend where the deviation of data points decreases for values over 1 000 MJ.

The color mapping showing the amount of heat supplied to the DH network at different percentages of maximum DNI reveals the occurrence of lower values of heat supplied during high values of DNI. This is related to warm-up of system components, weather overcasts and thermal inertia of the system. Figure 4, 6 and 8 show the range of the mismatch between the data series decrease during the middle of the day and during periods with high DNI, correlating with the decreased deviation of data points (Figure 3, 5, 7) for high amounts of heat supplied.

4.2 Simulated and measured collector outlet temperatures

This section shows hourly collector outlet temperatures from Högslätten solar thermal park from a week during spring (April), summer (July) and autumn (October) for each of the simulation periods. The plateaus and tops in the graphs represent the operational hours of the collector field and the sinks accordingly the standby hours during nighttime.

4.2.1 Simulation period 1 (1/3-31/10- 2022)

The collector outlet temperatures during Simulation period 1 are shown in Figure 9.

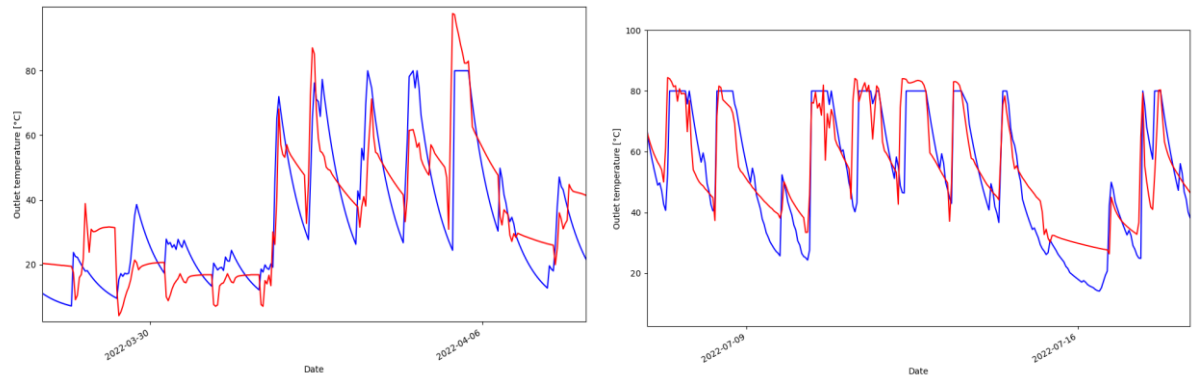

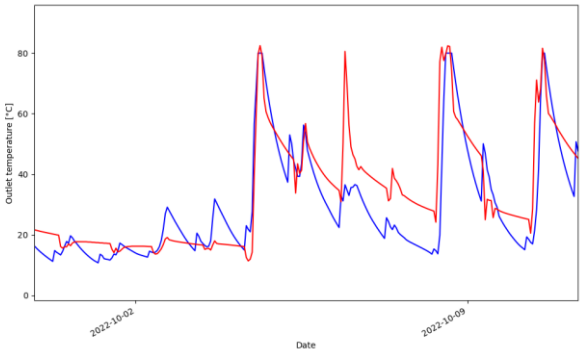

Figure 9. Simulated (blue) and measured (red) hourly outlet temperatures for April (left), July (right) and October (bottom) during Simulation period 1.

4.2.2 Simulation period 2 (1/3-31/10- 2023)
The collector outlet temperatures during Simulation period 2 are shown in Figure 10.

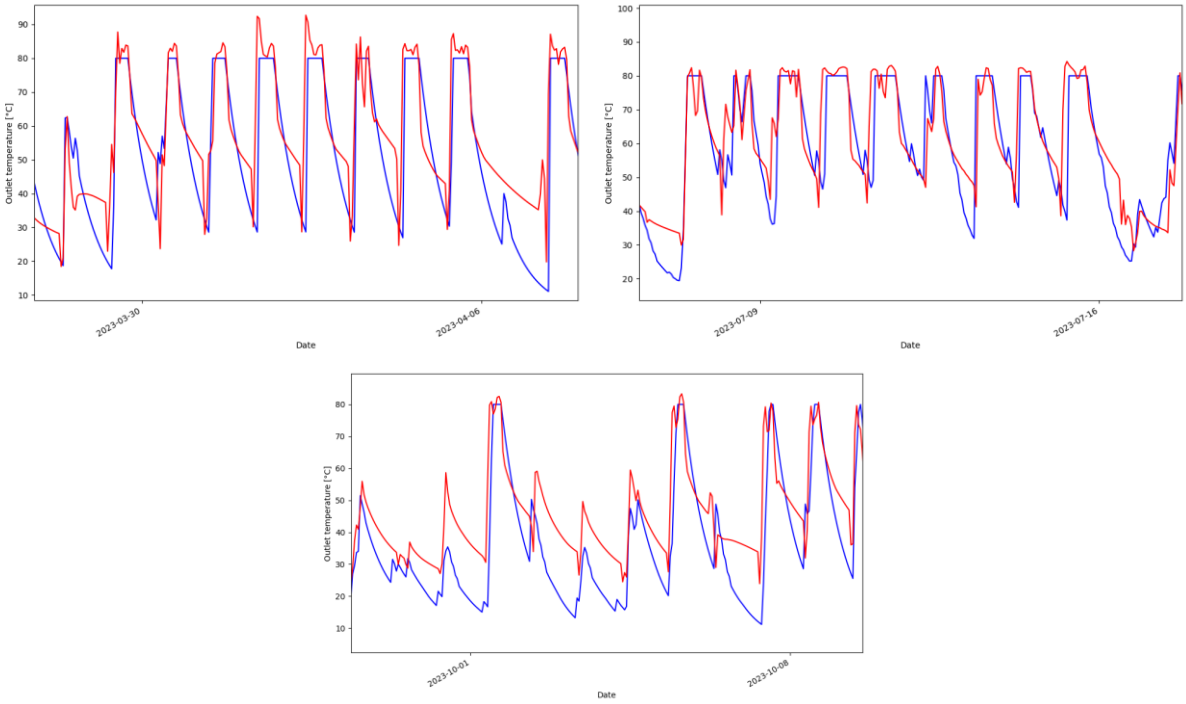

Figure 10. Simulated (blue) and measured (red) hourly outlet temperatures for April (left), July (right) and October (bottom) during Simulation period 2.

4.2.3 Simulation period 3 (1/3-6/5- 2024)
The collector outlet temperatures during Simulation period 3 are shown in Figure 11.

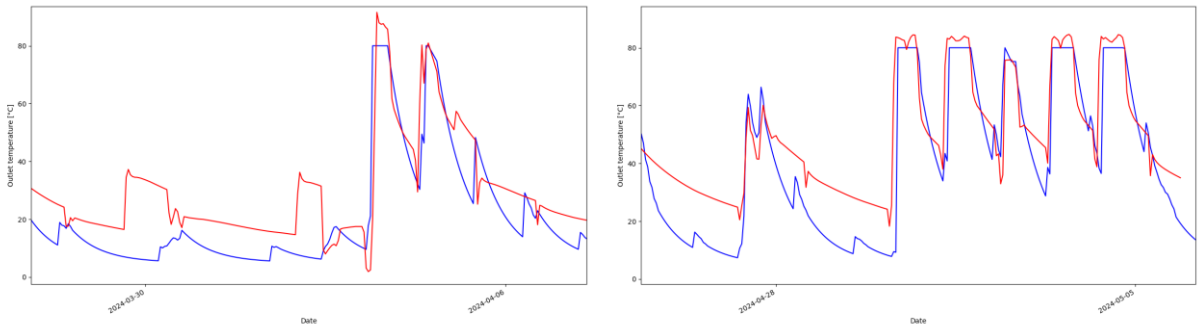

Figure 11. Simulated (blue) and measured (red) hourly outlet temperatures for April (left) and May (right) and October during Simulation period 3.

Figure 10-11 show a clearer overview of “pockets” forming between simulated and measured data in the lower temperature regions during nighttime. However, this trend disappears during operational hours in daytime where a general close correlation between simulated and measured data can be observed. The mismatch between the data series during nighttime could be related to the dissipation of heat during the installations non-commissioning hours and approximated U-values for the piping of the installation further discussed in section 5.

4.3 DNI and measured heat supplied to the DH network

To further evaluate the correlation between heat delivered to the DH network and available irradiation plots are created for each simulation period (Figure 12-13) showing measured DNI relative supplied heat to the DH network.

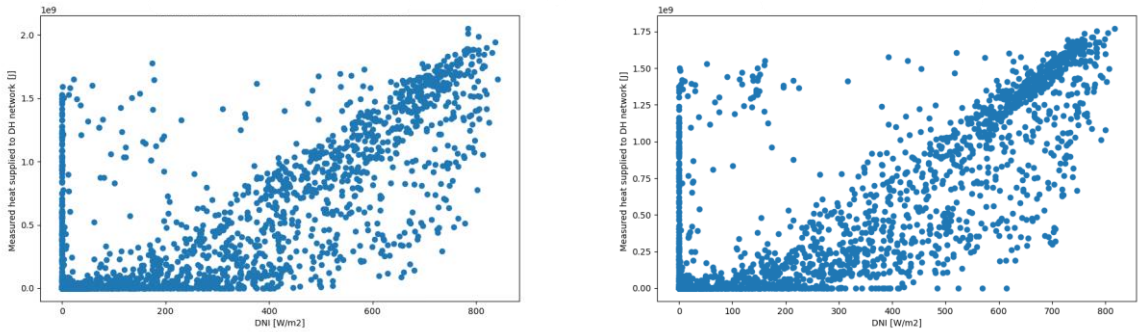

Figure 12. DNI and measured heat supplied to the DH network for Simulation period 1 (left) and 2 (right), 1/3-31/10.

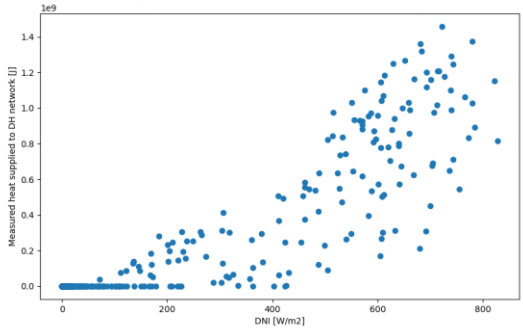

Figure 13. DNI and measured heat supplied to the DH network for Simulation period 3, 1/3-6/5.

Figure 12-13 show heat is delivered to the DH network during hours with low or no DNI and are hence measurement errors. Additionally, an accumulation of data points showing low or no measured heat for DNI between 0-400 W/m^2 can be observed. While a linear relationship between heat supplied and DNI is prominent during all simulation periods, a shift towards a trend with high DNI/low heat supplied is present during all simulation periods. The figures show all three periods have data in the complete DNI and measured heat range while featuring the same general trend and are thus comparable for analyses.

5. Discussion

5.1 Simulated and measured heat supplied to the DH network

As can be observed in Figure 3-8, data points with varying values on measured heat supplied to DH where the simulated values are zero are present during all simulation periods. A probable cause to this result is inaccurate input data used in the simulation model. For example, fluctuations and malfunctions of the irradiation sensors (bird feces, leaves, pollen etc.) at Högslätten have been reported that could contribute to incorrect measurements resulting in deviation of simulated and measured values. In addition, malfunctions on temperature sensors used to calculate heat supplied to the DH network have been reported on rare occasions.

The slight shift of data points above the reference line and mismatch of accumulated monthly data (Figure 3, 5, 7) where the measured results exceed the simulated for high values of heat supplied is affected by the defined U-value used for the piping of the solar field. During the study, U-values for the piping of Högslätten were not available and

were therefore approximated from earlier studies. In addition, simulations were carried out with varying U-values to achieve the best correlation between simulated and measured data. The magnitude of the heat losses from the piping is dependent on operational and ambient temperature and can be regarded as a dynamic variable. With the heat losses being determined from one approximated U-value during the simulations, the trend where measured values exceed the simulated results is explained by the simplification of the dynamic heat losses. Accordingly, inadequate assessments of heat losses for varying ambient and operational temperatures constitute the most prominent source of error in the simulation architecture. The monthly comparisons show an increased mismatch between the data series for months with high heat supplied, while the range of the mismatch clearly is reduced in the scatter plots during periods with high DNI/heat supplied. This is likely due to the higher number of days with heat production, resulting in "one-time" losses when the plant is cooling down and gets heated up respectively.

5.1.1 Ratio simulated/measured heat supplied to DH

The figures showing the ratio simulated/measured heat supplied to DH indicate a trend with a reduced number of outliers during high levels of DNI. Accordingly, in the case of simulated/measured heat supplied relative time of day, the same trend is present with the least number of outliers occurring during mid-day. It can therefore be concluded that the simulation model is most accurate during operational hours with high DNI. This correlates well with the results on simulated and measured outlet temperatures, where the mismatch is prominent during nighttime and negligible during daytime.

5.2 Simulated and measured collector outlet temperatures

As can be observed in Figure 9-11, there is generally a good correlation between simulated and measured collector outlet temperatures during operational hours for all simulation periods. Deviations are especially prominent during Simulation periods 2 and 3 where "pockets" are formed between simulated and measured data during non-operational hours. In most cases, the simulated data forms the pocket by assuming lower values relative the measured. With the pockets representing the outlet temperature during nighttime, the simulation model is accordingly not completely accurate during these time periods with the simulated dissipation of heat falling below the measured values.

During the initial test simulations with varying U-values (Section 3.1), the appearance of the pockets changed. However, while the pockets reduced in size for certain values, additional mismatches occurred during operational hours. Accordingly, the U-value used in the final simulations was derived from several iterations during the test phase. It can therefore be concluded that the U-values set in the model strongly affects the simulated temperatures. This is especially distinct during the first half of Simulation period 3 (Figure 11) where there is a consistent mismatch between simulated and measured data. In general, the correlation between simulated and measured data is increased during the installation's operational hours during daytime. The pockets and mismatch between simulated and measured data for low temperatures can partly be explained by the U-value used in the model being approximated for operational temperatures. To correctly assess heat losses from the pipes in the installation, convection occurring between the heat transfer fluid and the inside of the pipes in addition to ambient air and the surface of the pipes should be considered. Additional heat transfer mechanisms describing conduction through the pipes as well as heat radiation from the pipe surface to surroundings are all approximated into one U-value.

With the U-value representing all the above heat transfer mechanism during operational temperatures, it may be concluded that the increased mismatch between simulated and measured data during non-operational hours could be reduced by correctly assessing heat losses from the pipes in the collector field.

5.3 DNI and measured heat supplied to the DH network

In the case of DNI and measured heat supplied to the DH network, a trend similar to Figure 3-8 can be observed with accumulations of data points for measured heat supplied when the DNI is zero. This is a prominent source of error in the input data, where the irradiation sensors used at Högslätten could be malfunctioning. On a few occasions, bird feces or leaves have been reported to stick to the sensors further increasing the inaccuracy of the measurements.

Additional accumulations of data points can be observed close to the x-axis for values of DNI and no measured heat supplied to the DH network. This trend predominately occurs for DNI-values below 400 W/m^2. This is due to the generated heat being used to warm working parts of the installation in the mornings. Heat is supplied to the DH network when the difference between the temperature of the system components and heat carrier is reduced, enabling heat transport between the collector field and solar central. The "belly-shaped" area in the figures where low measured heat supplied and high DNI is present is related to the above phenomena, with heat supplied slowly

increasing with measured DNI as the system gradually heats up.

6. Conclusion

In this study, validation of a simulation model developed for T160 parabolic trough collectors is conducted by comparing simulated and measured data from Högslätten solar thermal park.

In the case of simulated and measured heat supplied to the DH network, deviating values mainly occur due to incorrect or inconsistent measurement data which may be attributed to occasional errors in the readings from irradiation sensors. The trend related to higher measured and lower simulated data points are most likely related to the approximation of U-values for the piping of the installation. The mismatch between simulated and measured collector outlet temperatures during standby hours in the nighttime can accordingly be derived from the same phenomena, where heat losses from the pipes vary with the temperature dependence of the U-value. With the plant cooling down during nighttime and systematically warms up during daytime, more elaborate functions are needed to assess the behaviour more accurately.

The study shows an acceptable correlation between simulated and measured data during operational hours where a relatively high amount of heat is delivered to DH. Deviating trends are consistent for all simulation periods, have the same appearance and can be derived from inaccurate measurement data or inadequate approximations of heat losses for varying operational temperatures. To further enhance the simulation model, the heat losses at varying operating and ambient temperatures need to be assessed more accurately.

The validation process facilitated Absolicon Solar Collector AB to fine tune their in-house simulation model.

7. Acknowledgments

The authors acknowledge the funding support of Absolicon Solar Collector AB, the Industrial Doctoral School of Umeå University and the Swedish Energy Agency for the projects “Soldriven fjärrvärme för hållbara städer” (project no. 50037-1) and RESILIENT Energisystem Kompetenscentrum” (project no. 52686-1).

The authors would also like to thank Ramez Shabani and Loick Bruand at Absolicon Solar Collectors AB for access to Absolicon servers and continuous support throughout the study.

8. References

Absolicon Engineering department, 2024. Absolicon HQ, Härnösand, Sweden.

Rydegran, E., 2023. Fjärrvärmens minskade koldioxidutsläpp - Energiföretagen Sverige [WWW Document]. Energiföretagen. URL https://www.energiforetagen.se/statistik/fjarrvarmestatistik/fjarrvarmens-koldioxidutslapp/ (accessed 1.10.24).

Gauthier, G., Project Manager, Plan Energi, Denmark. Personal communication 30th April 2024.

Bergman, H., Energy strategist, Härnösand Energi och Miljö, Sweden. Personal communication 6th June 2024

IEA SHC || Task 68 || Efficient Solar District Heating Systems [WWW Document], 2024. URL https://task68.iea-shc.org/ (accessed 7.3.24).

Klein, S.A., Duffie, J.A., Mitchell, J.C., Kummer, J.P., Thornton, J.W., Bradley, D.E., Arias, D.A., Beckman, W.A., Duffie, N.A., Braun, J.E., n.d. Mathematical Reference.

Naturvårdsverket, 2024. El och fjärrvärme, utsläpp av växthusgaser [WWW Document]. URL https://www.naturvardsverket.se/data-och-statistik/klimat/vaxthusgaser-utslapp-fran-el-och-fjarrvarme/ (accessed 12.21.23).

Nguyen, T., Danielski, I., Ahlgren, B., Nair, G., 2024. Effects of solar thermal energy on district heating systems: the case of parabolic trough collectors in a high latitude region. Sustainable Energy & Fuels.

Khodayari, R., 2023. Tillförd energi - Energiföretagen Sverige [WWW Document]. Energiföretagen. URL https://www.energiforetagen.se/statistik/fjarrvarmestatistik/tillford-energi/ (accessed 12.6.23).

Selin, M., Vinterbäck, J., 2023. Läget på energimarknaderna - Biodrivmedel och fasta biobränslen.

SolarHeatEurope, 2024. Description-of-ScenoCalc-v6.1.pdf [WWW Document]. Descr.--ScenoCalc-V61pdf. URL https://solarheateurope.eu/wp-content/uploads/2019/09/Description-of-ScenoCalc-v6.1.pdf (accessed 7.2.24).

Weiss, W., Spörk-Dür, M., 2023. Solar Heat Worldwide 2023. AEE- Institute for Sustainable Technologies, IEA Solar Heating and Cooling Programme, Graz, Austria.

Comparative Numerical Analysis of Middle-Temperature and High Temperature versions of High-Vacuum Flat-Plate Collectors: Assessing Performance in the Field.

Eliana Gaudino[1,3], Alessandro Anacreonte[2,3], Antonio Caldarelli[3], Francesco Di Giamberardino[4], Vittorio G. Palmieri[4], Roberto Russo[3] and Marilena Musto[2,3]

1 Department of Physics, University of Naples Federico II, Via Cintia - Complesso Monte S. Angelo Naples,80100, Italy.

2 Department of Industrial Engineering, University of Naples Federico II, P.le Tecchio, 80, Naples, Italy.

3 Institute of Applied Sciences and Intelligent Systems, National Research Council of Italy, Via Pietro Castellino 111, Napoli, 80131, Italy

4 TVP Solar SA,10 rue de Pré-de-la-Fontaine ZIMEYSA 1242 Satigny (GE) Switzerland

Abstract

High Vacuum Flat Plate Collectors (HVFPCs) stand as a highly promising solution for renewable thermal energy generation. At present, TVP-Solar exclusively manufactures HVFPCs tailored for middle-temperature (MT) applications, with a maximum operating temperature of 200 °C. Recent advancements have yielded optimized absorbers designed for HVFPCs, enabling them to attain elevated temperatures (HT) up to 300 °C via optimization of optical parameters, thus effectively ameliorating the prevailing radiative losses affecting HVFPCs. This study employs dynamic simulation to analyze the daily performance of an HVFPCs test field. Our primary objective is to compare the performance of MT and HT HVFPCs configurations within the field, operating at temperatures of 150, 200 and 250 °C. The results of the numerical analysis not only highlight the advantage of the optimized technology but also serve as a robust cornerstone for future undertakings, particularly in the formulation of advanced control strategies tailored for HT HVFPC-equipped fields.

Keywords: Solar Energy, Solar Thermal Collectors Field, High-Vacuum Flat-Plate Collectors, dynamic solar field simulations, Solar Field Performances

1. Introduction

The utilization of solar energy represents a straightforward and sustainable approach for producing thermal energy, catering to both domestic and industrial needs. Amongst the various solar energy technologies, Flat plate solar collectors (FPSCs) are the most established technology being the first FPC with a separate storage tank patented by William J. Bailey in 1910 (Schobert, 2014). FPCs consist of a dark absorber plate, typically made of metal or coated with a selective surface, enclosed within an insulated casing. The absorbed solar radiation heats the absorber plate, which in turn transfers the thermal energy to a circulating fluid, such as water or air (Benz and Beikircher, 1999). FPCs have emerged as structurally simple systems with low manufacturing costs (Karki et al., 2019) and minimal maintenance requirements, ensuring long-lasting operation. Another key advantage is their versatility, as they can be integrated into various building designs, both for new constructions and retrofitting existing structures (Al-Joboory, 2019). Their adaptability allows

© 2024. The Authors. Published by International Solar Energy Society
Selection and/or peer review under responsibility of Scientific Committee
10.18086/eurosun.2024.07.06 Available at http://proceedings.ises.org

for seamless incorporation into roofs, walls, or ground-mounted systems, enabling homeowners and building owners to harness solar energy without significantly altering the architectural aesthetics.

Despite their numerous advantages, FPCs have some drawbacks compared to other solar thermal technologies. They heave lower thermal efficiency compared to evacuated tube collectors and concentrating solar thermal (CST) devices because of the substantial convective heat losses that limit their maximum achievable delivery temperature for domestic applications (60-90 °C) (Kalogirou, 2004).

Evacuated tube collectors, which utilize a vacuum to minimize heat loss, can achieve higher operating temperatures and better thermal efficiency, particularly in colder climates.

A promising advancement in flat collector technology is the introduction of high vacuum flat plate collectors (HVFPCs) by TVPSolar ("TVP Solar, (2023)). These collectors feature a flat design where the space between the absorber, glass cover, and collector case is evacuated, effectively eliminating convective thermal losses. This reduction in convective losses, along with minimized conductive losses due to architectural enhancements, results in significantly higher efficiency compared to conventional FPSCs operating at middle temperatures. A recent study by (Gao et al., 2022), demonstrated that an efficiently optimized HVFPC field achieved a stable annual average thermal efficiency of up to 50% at 123 °C. These results are remarkable for renewable thermal energy generation at middle temperatures.

Researchers have been actively investigating further improvements in HVFPC technology in recent years, focusing particularly on the selective solar absorber (SSA), the critical component of HVFPCs responsible for capturing solar irradiation. The fundamental characteristic of SSAs is that exhibit high solar absorptance in the solar spectrum range and minimal thermal emittance in the infrared region but, for flat collectors operating at temperatures above 123°C, (Cao et al., 2014), demonstrated that thermal emittance assumes greater importance than solar absorptance in terms of SSA efficiency. However, the current Middle Temperature (MT) commercial version of HVFPCs, MT Power, employs a commercial SSA with optical properties optimized for operation at 100 °C.

(De Maio et al., 2022) have developed low-emissive SSAs specifically designed for HVFPCs, optimized to operate at higher temperatures, thereby paving the way for the development of HVFPCs for High Temperatures (HT) applications. The HT version of TVPSolar HVFPC considered in this study maintains the same structural characteristics while adopting an SSA developed, designed, and optimized to work at 300°C.

A comprehensive performance comparison between the MT and HT versions of TVPSolar HVFPCs was conducted using a dynamic simulation model of a TVPSolar test field, implemented in Simulink. After validating the model with experimental data, the simulation was utilized to evaluate the performance of the field equipped with HT and MT panels at various operating temperatures (150°C, 200°C, 250°C). The simulation employed hourly meteorological data from Cairo for the year 2019. The validated simulation model facilitated a thorough assessment of the comparative performance of the HT and MT solar panels under different operating conditions. By analyzing the system behavior at 150°C, 200°C, and 250°C, the study provided a detailed understanding of the energy output and efficiency of both panel types across a range of operating temperatures.

2. Experimental system and Model Description

The solar plant model (Fig. 1) replicates an existing test field located on the rooftop of TVP-Solar headquarters in Avellino, Italy. This test field comprises 25 arrays, each consisting of 7 MT panels mounted with a tilt angle (β) of 15° and an azimuth angle (γ) of 0°. The collectors in each array are connected in series using hose connectors and are interlinked through supply and return pipelines, while the arrays are connected in parallel. Additionally, there is a third pipe that functions as a pressure equalizer, balancing the pressure between the two main pipes to prevent flow reversal in certain rows due to pressure differentials. A vent valve is also incorporated into the system to release excess pressure when necessary. The solar field follows a single-side module format, with the pipelines running laterally through the field.

At ground level, the thermal block consists of two subsystems. Subsystem 1 primarily includes a pressurization pump, an expansion vessel, and a buffer tank. These components work together to adjust the flow rate and maintain the system pressure within the desired range of 0.6-1.0 MPa. Since the facility currently lacks a designated application, Subsystem 2 becomes crucial when the heat transfer fluid (HTF) reaches its target temperature. In this case, the HTF is channeled for cooling. This subsystem is equipped with a dry cooler and an electromagnetic three-way valve. When the HTF's temperature at the field outlet surpasses the set threshold, the valve redirects it to the dry cooler for cooling before recirculation.

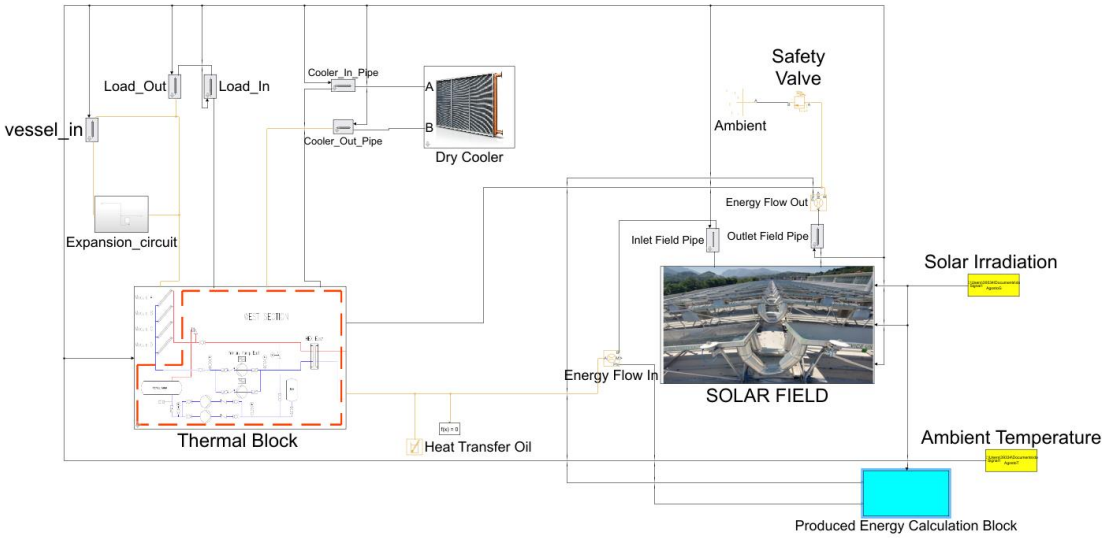

Figure 1 Simulink model of the HVFPCs Solar plant.

2.1 Mathematical Model of MT and HT HVFPCs

In this study, the instantaneous thermal power converted by each solar thermal collector and transferred to the heat transfer fluid (HTF) is modeled using the basic equation for solar thermal collector performance:

$$Q_c = \eta * A_c * G \tag{1}$$

This equation states that the power output (Q_c in Watts) is equal to the product of the collector efficiency (η), the collector surface area (A_c), and the incident solar irradiation (G) on the collector surface. The efficiency (η) of an HVFPC collector can be expressed as a function of the solar absorber optical properties, as shown in the following formula (Gaudino et al., 2023):

$$\eta_{th} = \alpha\tau f * IAM_\theta - \left\{\frac{\varepsilon_e(T_m)*\sigma[(T_m+273.15)^4-(T_{amb}+273.15)^4]}{G} * \frac{A_{abs}}{A_c} + \frac{k(T_m-T_{amb})^z}{G}\right\} \tag{2}$$

In this expression: α is the solar absorptance of the absorber surface, τ is the glass cover transmittance, *f* is the collector efficiency factor, which accounts for the difference between the HTF temperature and the average absorber temperature, *IAM* is the incidence angle modifier function, which describes the optical efficiency for a certain radiation incidence angle normalized by the optical efficiency at perpendicular irradiation (Lv et al., 2018), ε_e is the effective emittance of the absorber surface, T_m is the mean HTF temperature between field inlet and outlet, T_{amb} is the ambient temperature, A_{abs} is the absorber surface area, A_C is the collector surface area while *k* and *z* are constants related to the heat transfer characteristics of the collector. This comprehensive model captures the key factors that influence the thermal efficiency of the solar thermal collector, including optical, thermal, and geometrical parameters, allowing for a detailed performance analysis and optimization of the system.

For an HVFPC with the TVPSolar MT Power collector architecture, *k* and *z* were determined by a mathematical fit of experimental data (Gaudino et al., 2023) and equation (2) becomes:

$$\eta_{th} = \alpha\tau f * IAM_\theta - \left\{\frac{\varepsilon_e(T_m)*\sigma[(T_m+273.15)^4-(T_{amb}+273.15)^4]}{G} * \frac{A_{abs}}{A_c} + \frac{0.258(T_m-T_{amb})}{G}\right\} \tag{3}$$

The efficiency formula for the MT and HT versions of TVPSolar HVFPC, considered in this work, differs due to the optical properties of the solar absorbers adopted by each version. The coefficient of solar absorptance

and the effective emittance of the commercial selective absorber used in the MT version of TVPSolar HVFPC were obtained experimentally by calorimetric measurements taken under Sun and LED light (D'Alessandro et al., 2022). The coefficient of solar absorptance in the solar spectrum of the absorber adopted by the HT version of TVPSolar HVFPC was obtained through the integration of the spectral absorptivity, determined by applying Fresnel laws once the refractive index of the materials composing the multilayer stack was experimentally characterized using a Horiba Jobin Yvon - UVISEL spectroscopic ellipsometer ("Spectroscopic Ellipsometry - HORIBA). The simulated values closely matched the absorptance obtained by reflectance measurements using an integrating sphere.

Unlike the commercial absorber, which has an aluminum substrate, the SSA of the HT HVFPC is a multilayer deposited on a copper substrate with very low thermal emittance. Measuring the thermal emittance of the HT absorber required a highly precise methodology. The effective emittance of the HT absorber was determined using an improved calorimetric procedure, as detailed by (Gaudino et al., 2024b). The coefficients of solar absorptance for the MT and HT absorbers are listed in Table 1, while the effective emittances as a function of absorber temperature are shown in Fig. 2(a). Substituting the optical properties of the absorbers into equation (3), the efficiencies of the MT and HT versions of the TVPSolar HVFCs were obtained and are illustrated in Fig. 3(b).

Table 1 Solar absorptance values for MT and HT absorbers.

SSA	α
MT	0.95
HT	0.89

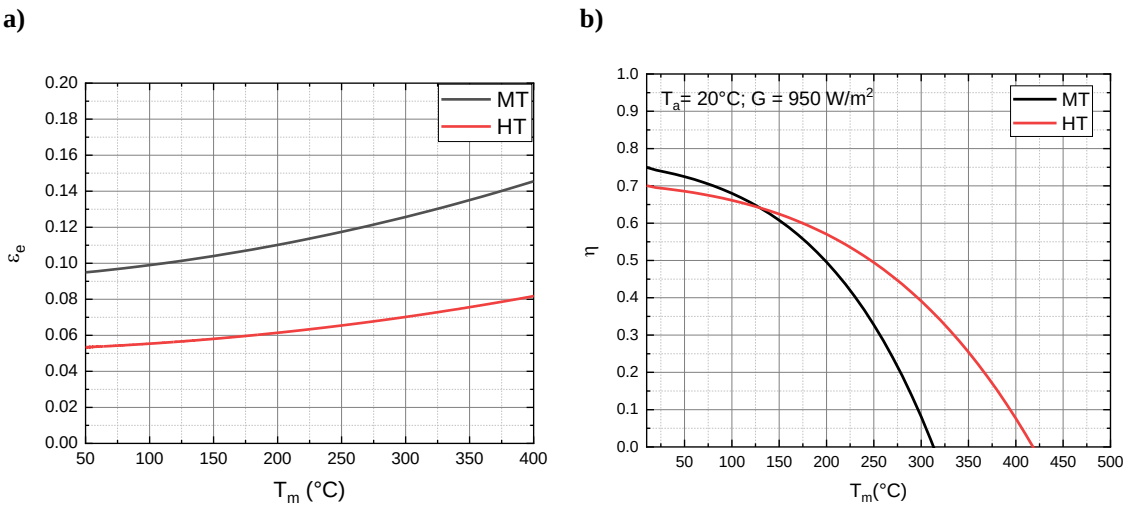

Figure 2 a) Effective thermal emittance as a function of absorber temperature for both MT and HT absorbers. b) Thermal efficiency curves of MT and HT HVFPCs as a function of absorber temperature, with an ambient temperature mantained at 20°C and solar irradiation of 950 W/m².

The efficiency of the HVFPC serves as the mathematical representation of a collector's performance within the Simulink model of the solar plant employed in this study.

As shown in Figure 2 b), the MT absorber exhibits higher thermal efficiency at lower temperatures compared to the HT absorber, which is more favorable at higher temperatures. Additionally, the HT absorber demonstrates a higher stagnation temperature, representing the maximum attainable absorber temperature (the equilibrium temperature between the absorbed and emitted power).

After formulating the mathematical representation of HVFPCs within the dynamic model, it was validated through experimental daily performance measurements.

2.2 Dynamic Solar HVFPCs field model validation

The performance measurements for validating the dynamic HVFPCs simulation model were carried out using the TVPSolar test field located in Avellino. It should be noted that the architectural constraints of the building roof influenced the structure of the installation.

The field is divided into two sections, each forming a 6° angle with the horizontal plane. Each set comprises seven panels: four on the east-facing surface and three on the west-facing surface. A comprehensive evaluation of plant performance must account for the varying orientations of the collectors within the arrays. The objective of the performance measurements was to monitor the solar field's daily productivity and efficiency. Water was the selected Heat Transfer Fluid (HTF), and the set-point temperature for each measurement day was determined accordingly.

To assess the field's performance, several parameters were measured, including HTF temperatures at the inlet and outlet of the solar field and dry cooler, HTF flow rates at the inlet of the solar field and dry cooler, solar irradiation, and ambient temperature. Solar irradiation was monitored separately on each side of the building roof using two pyranometers to capture localized variations in solar irradiation across the roof. The flow rate regulation took into account the average value of irradiation measured by the two pyranometers. The measurements were conducted when the solar irradiation (G) was greater than or equal to 150 W/m^2 to cover the full range of solar illumination.

Figure 3 (Gaudino et al., 2024a) displays the results obtained on July 9, 2023. The set-point temperature was maintained at 100 °C. The solar irradiation measurements were recorded from the east-facing pyranometer (G_{est}) and the west-facing pyranometer (G_{west}). The HTF flow rate (depicted in Figure 3 a)) is regulated to maintain the set-point temperature while providing a specific cooling power for the dry cooler. In Figure 3 b), P_{inc} represents the sum of solar power on the collectors positioned on the east-facing side of the roof (G_{est} * A_c * N_{C_est}) and the solar power incident on the collectors mounted on the west-facing side of the roof (G_{west} * A_c * N_{C_west}), where N_{C_est} and N_{C_west} are the number of collectors mounted on the east and west facing side of the roof, respectively. P_{conv} (W) represents the amount of power converted by the solar field while maintaining the set-point temperature. It is computed using the formula (4):

$$P_{conv} = \dot{m} * c_p * \Delta T \quad (4)$$

The simulation takes into account various input parameters, including the HTF mass flow rate, solar irradiation, ambient temperature, set-point temperature, and dry cooler air flow rate for controlling the cooling power. To maintain consistency with the actual case, water was used as the circulating HTF with the same flow rate.

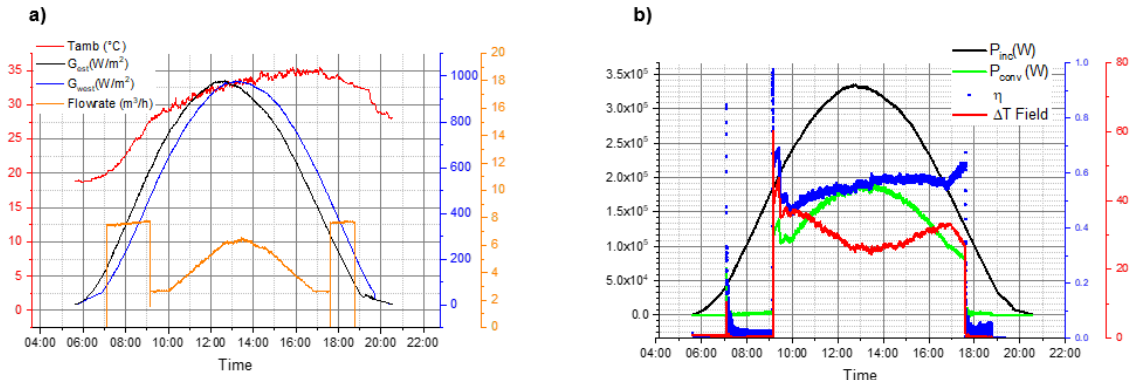

Figure 3 a)Acquired weather data, and flow rate b) Measured field performance parameters with a set point temperature equal to 100 °C.

Figure 4 provides a comparison between the daily experimental and numerical results of the HTF ΔT and average temperature T_m between the inlet and outlet of the solar field over time. The simulation accurately replicates the behaviour of the solar field, as the differences between the numerical and experimental

measurements are within a 4% margin during operational hours. These small deviations can be attributed to measurement uncertainties. Therefore, the comparison depicted in Fig. 4 demonstrates the fidelity of the numerical model in reproducing the performance of the analysed solar field.

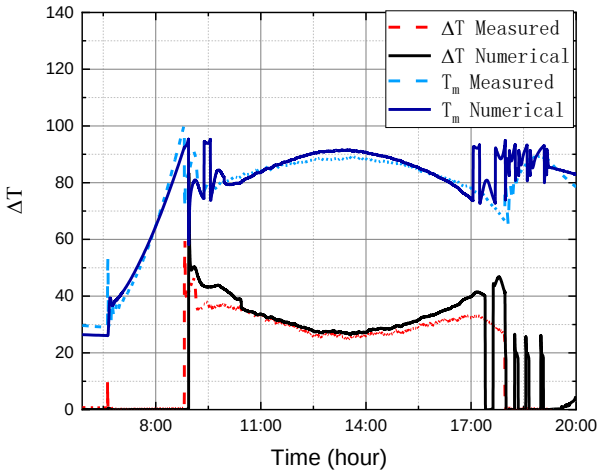

Figure 4 Comparison between experimental & numerical results: Measured ΔT (red dashed line) and the Tm (light blue dashed line) and comparison with simulation results (black and dark blue continuous line respectively)

3. Results & Discussion

Figure 5 presents a comparison of the monthly energy production between a medium temperature (MT) and a high temperature (HT) high-vacuum flat plate collector (HVFPC), operating at three different temperatures (Tm = 150, 200, and 250 °C). The data used in this comparison were the hourly irradiation and ambient temperature measurements from Cairo in 2019.

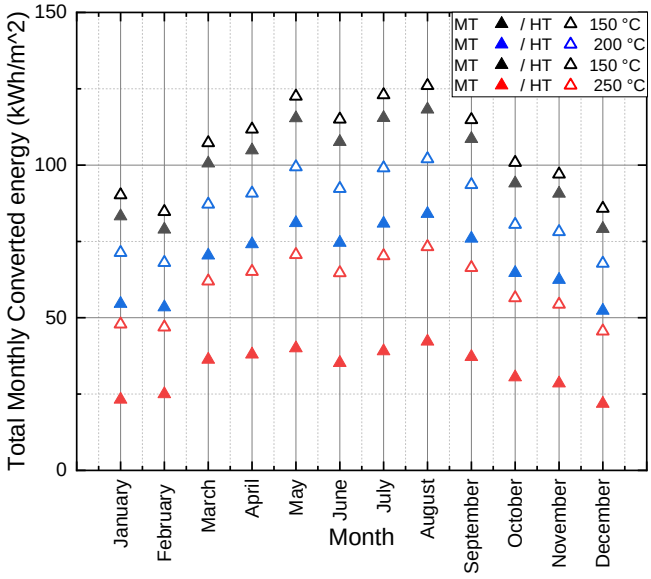

Figure 5 Comparison between monthly energy production of MT and HT version of a TVPSolar HVFPC

The difference in the projected annual energy production between the HT and MT HVFPCs varies depending on the operating temperature, as evident from the efficiency curves in Fig. 2 b). The maximum difference is observed at 250 °C, where the annual production of the HT collector is 724 kWh/m^2 compared to 397 kWh/m^2 for the MT HVFPC, resulting in an 82% increase in energy output.

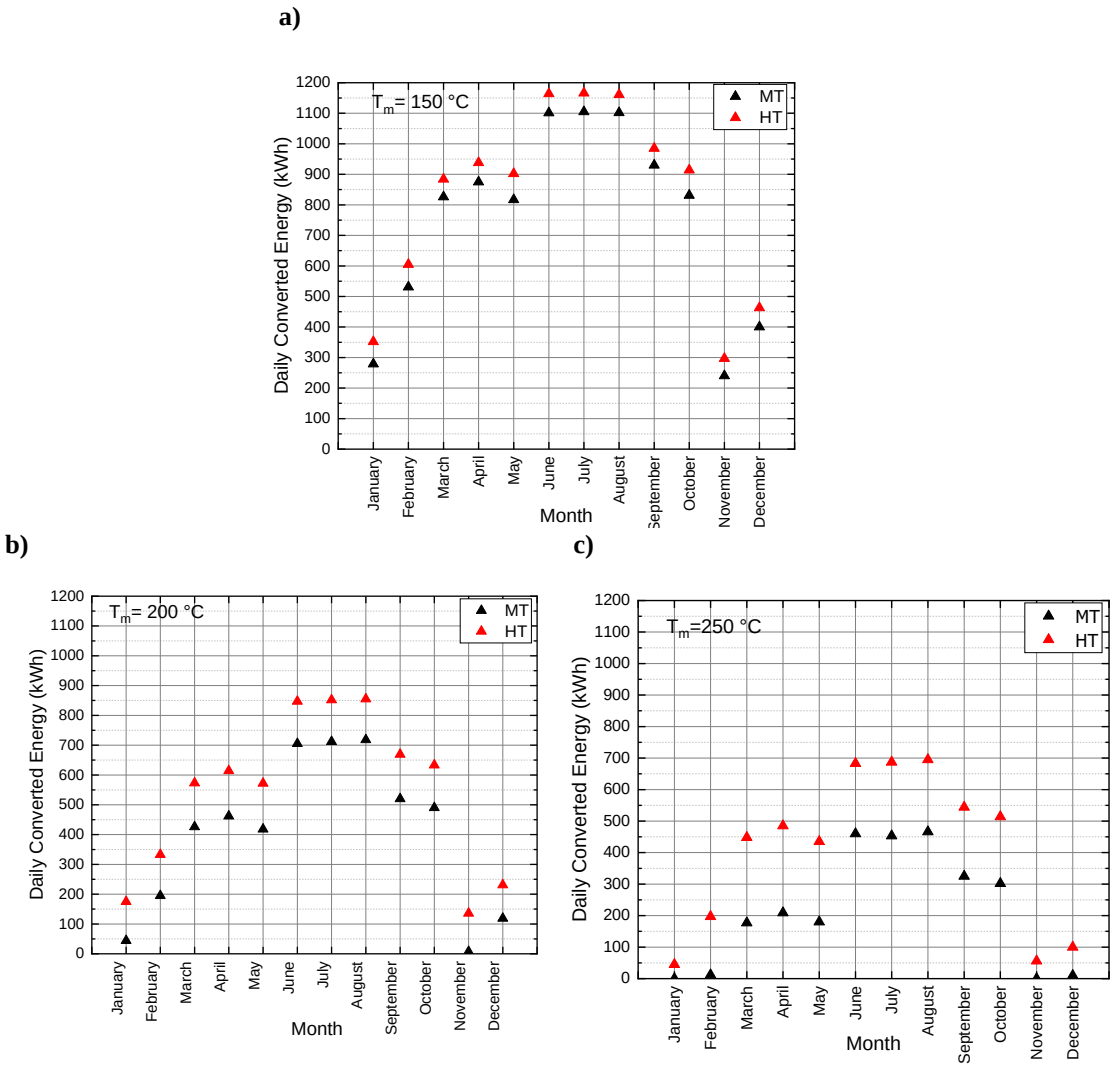

Figure 6 Numerical comparison between average daily energy production per month of MT and HT field for an operating temperature of a) 150 °C b) 200 °C and c) 250 °C

To further investigate the solar field performance, simulations were conducted to compare the daily energy production of MT and HT HVFPC fields, using diathermic oil (Xceltherm 500) as the heat transfer fluid and operating temperatures of 150, 200, and 250 °C. The input data for these simulations were the same irradiation and ambient temperature measurements from Cairo in 2019. The hourly data were averaged on a daily basis and then aggregated monthly to simulate the field performance through the monthly average day, as shown in Fig. 6.

It is important to note that using the monthly average day to represent the daily energy production is a conservative, pessimistic approximation of the field's performance. This approach underestimates the actual irradiation that could be obtained in a given month, as the monthly average day does not capture the full variability of the solar resource.

4. Conclusions

High-vacuum flat plate collectors represent the state-of-the-art technology for middle-temperature thermal energy generation. This technology can be further improved through the optimization of the solar absorber's spectral selectivity. In this paper, a numerical performance comparison between a solar field equipped with

commercial (MT) and optimized (HT) HVFPCs is presented.

The key difference between the MT and HT HVFPCs lies in the optical properties of the solar absorber. The numerical performance comparison was carried out using a dynamic simulation model implemented in Simulink and validated through daily experimental measurements conducted with a TVPSolar test field.

The comparison of the daily energy production per month, as shown in Fig. 6, demonstrates that by improving the solar absorber properties (HT version), the collector's performance can be significantly enhanced. At an operating temperature of 250 °C, the HT HVFPC can achieve the same energy output as the MT HVFPC operating at 200 °C.

Having an accurate simulation model of the solar field, particularly for HVFPCs with optimized absorbers, is advantageous for future advancements. The TVPSolar company plans to replace the MT HVFPCs in the test field with the optimized HT version and configure the system to achieve even higher temperatures. The availability of the simulation model will facilitate the assessment and development of these future enhancements.

5. Aknowledgment

This study was supported by the Eurostar Program powered by EUREKA and the European Community (Project ESSTEAM reference E! 115642).

6. References

Al-Joboory, H.N.S., 2019. Comparative experimental investigation of two evacuated tube solar water heaters of different configurations for domestic application of Baghdad- Iraq. Energy and Buildings 203, 109437. https://doi.org/10.1016/j.enbuild.2019.109437

Benz, N., Beikircher, T., 1999. HIGH EFFICIENCY EVACUATED FLAT-PLATE SOLAR COLLECTOR FOR PROCESS STEAM PRODUCTION1Paper presented at the ISES Solar World Congress, Taejon, South Korea, 24–29 August 1997.1. Solar Energy 65, 111–118. https://doi.org/10.1016/S0038-092X(98)00122-4

Cao, F., McEnaney, K., Chen, G., Ren, Z., 2014. A review of cermet-based spectrally selective solar absorbers. Energy Environ. Sci. 7, 1615. https://doi.org/10.1039/c3ee43825b

D'Alessandro, C., De Maio, D., Caldarelli, A., Musto, M., Di Giamberardino, F., Monti, M., Mundo, T., Di Gennaro, E., Russo, R., Palmieri, V.G., 2022. Calorimetric testing of solar thermal absorbers for high vacuum flat panels. Solar Energy 243, 81–90. https://doi.org/10.1016/j.solener.2022.07.039

De Maio, D., D'Alessandro, C., Caldarelli, A., Musto, M., Russo, R., 2022. Solar selective coatings for evacuated flat plate collectors: Optimisation and efficiency robustness analysis. Solar Energy Materials and Solar Cells 242, 111749. https://doi.org/10.1016/j.solmat.2022.111749

Gao, D., Li, J., Ren, X., Hu, T., Pei, G., 2022. A novel direct steam generation system based on the high-vacuum insulated flat plate solar collector. Renewable Energy 197, 966–977. https://doi.org/10.1016/j.renene.2022.07.102

Gaudino, E., Anacreonte, A., Caldarelli, A., Strazzullo, P., Musto, M., Bianco, N., Giamberardino, F., Iameo, R., Palmieri, V., Russo, R., 2024a. Impact of Collector Array Orientation on the Performance of a Flat Collectors Field for Middle-Temperature Applications. https://doi.org/10.46855/energy-proceedings-11166

Gaudino, E., Caldarelli, A., Russo, R., Musto, M., 2023. Formulation of an Efficiency Model Valid for High Vacuum Flat Plate Collectors. Energies. https://doi.org/10.3390/en16227650

Gaudino, E., Farooq, U., Caldarelli, A., Strazzullo, P., De Luca, D., Di Gennaro, E., Musto, M., Russo, R., 2024b. Thermal Emittance Measurement of Very Low-Emissive Materials for Solar Thermal Applications. https://doi.org/10.20944/preprints202405.0717.v1

Kalogirou, S.A., 2004. Solar thermal collectors and applications. Progress in Energy and Combustion Science 30, 231–295. https://doi.org/10.1016/j.pecs.2004.02.001

Karki, S., Haapala, K.R., Fronk, B.M., 2019. Technical and economic feasibility of solar flat-plate collector thermal energy systems for small and medium manufacturers. Applied Energy 254, 113649. https://doi.org/10.1016/j.apenergy.2019.113649

Lv, Y., Si, P., Rong, X., Yan, J., Feng, Y., Zhu, X., 2018. Determination of optimum tilt angle and orientation for solar collectors based on effective solar heat collection. Applied Energy 219, 11–19. https://doi.org/10.1016/j.apenergy.2018.03.014

Schobert, A.H., 2014. Energy and Society: An introduction, Seconda. ed. CRC Press, 600 Broken Sound Parkway,NW, Suite 300.

Spectroscopic Ellipsometry - HORIBA, (n.d.). https://www.horiba.com/en_en/products/scientific/surface-characterization/spectroscopic-ellipsometry/., n.d.

Performance Analysis of a Hybrid Solar-Geothermal Power Plant in México

Eduardo González-Mora[1], Álvaro Lentz-Herrera[2] and Ma. Dolores Durán-García[1]

[1] Facultad de Ingeniería, Universidad Autónoma del Estado de México, Toluca (México)

[2] Programa de Energía, Universidad Autónoma de la Ciudad de México, Ciudad de México (México)

Abstract

Solar energy integration with existing geothermal power plants offers a promising approach to enhance renewable energy output. Hybrid systems, particularly those combining parabolic trough collectors (PTC) with geothermal facilities, can improve the efficiency and sustainability of energy production. This study investigates the feasibility of incorporating PTCs into the Cerro Prieto geothermal power plant to boost steam quality and increase overall energy generation. Specifically, we compared two configurations: using Therminol VP1 as the heat transfer fluid (HTF) and employing direct steam generation (DSG). Our results indicate that both configurations successfully enhanced steam quality, with VP1 showing higher exergy efficiency and requiring a smaller solar field area; DSG achieved superior energy efficiency but faced significant pressure drops. These findings demonstrate that solar-geothermal hybrid systems can significantly improve plant performance by carefully selecting the appropriate HTF and optimizing system parameters. This research underscores the potential of such hybrid systems to advance renewable energy technologies, providing valuable insights for future energy planning and policy development.

Keywords: Solar-geothermal hybrid systems, Parabolic trough collectors, Direct Steam Generation, Therminol VP1

1. Introduction

At the end of 2022, the global geothermal installed capacity was 16 318 MW, distributed across thirty-two countries. This value accounts for 0.16% of the world's total installed electric capacity, which stood at 10 216 390 MW (Ritchie and Rosado, 2023). In 2021, these countries generated 96,552 GWh of electricity from geothermal sources, representing 0.34% of global electric generation. Mexico ranks among the top ten countries with the highest geothermal capacity, occupying the sixth position behind New Zealand and Kenya, which have similar installed capacities.

Mexico's geothermal installed capacity totals 1 001.9 MW, consisting of thirty-nine power units across five geothermal fields. Most units are single and double-flash condensing types, collectively providing 924 MW. Fifteen backpressure units, each with a capacity of 5 MW, contribute a combined total of 75 MW. Additionally, two binary ORC units, each with a capacity of 1.45 MW and manufactured by Ormat, remain installed in Los Azufres, though they have been non-operational for several years. The largest flash plants, located in the Cerro Prieto field, each have a capacity of 110 MW, featuring two 55 MW turbines manufactured by Toshiba. Cerro Prieto is the oldest and largest geothermal field in the country.

Although installed capacity remained unchanged over the past three years, electric generation decreased by 16%, from 5 375 GWh to 4 511.5 GWh, in 2021. This decline resulted from the shutdown of two power units in 2021: Unit 1 of Cerro Prieto III, with a capacity of 110 MWe, and Unit 17 of Los Azufres, with a capacity of 53.4 MWe (Gutiérrez-Negrin et al., 2023). Net geothermal electric generation accounted for 1.3% of the total electric generation in Mexico in 2021, which was 323 527 GWh.

In 2021, the electricity generated within the Baja California electric grid, home to the Cerro Prieto power

© 2024. The Authors. Published by International Solar Energy Society
Selection and/or peer review under responsibility of Scientific Committee
10.18086/eurosun.2024.07.07 Available at http://proceedings.ises.org

plants, amounted to 11 869.1 GWh. Of this, the geothermal units at Cerro Prieto generated 2 363.4 GWh, representing 19.9% of the total production. This isolated system, which includes major urban centers like Tijuana and Mexicali, relied on geothermal energy for its electricity needs, excluding self-supply, cogeneration, and imports from California, USA.

The Cerro Prieto geothermal field, owned by CFE (Comision Federal de Electricidad), is situated in northern Mexico, approximately 30 km south of the USA border, within the Ring of Fire. Spanning an area of approximately 20 km^2, with an additional 18 km2 allocated to the evaporation pond, Cerro Prieto comprises four distinct geothermal fields. Originally, Cerro Prieto I comprised five units with a total installed capacity of 180 MW. However, in 2011, four of these units, each with a capacity of 37.5 MW, were decommissioned, leaving only one operational unit with a capacity of 30 MW. Cerro Prieto II and III each boast a total installed capacity of 220 MW, powered by two identical units. The Cerro Prieto geothermal field encompasses more than 200 wells, varying in depth from 700 to 4,300 meters. At present, the installed capacity of the Cerro Prieto geothermal power plant amounts to 570 megawatts. The Cerro Prieto geothermal field features over 200 wells, with depths ranging from 700 to 4 300 m. Currently, the installed capacity of the Cerro Prieto geothermal power plant stands at 570 MW (Hernández Martínez et al., 2020).

In 2009, CFE proposed plans for Cerro Prieto V, a new plant comprising two 50 MW units, to increase Cerro Prieto's total capacity by 100 MW. However, following the earthquake in Mexicali in 2010, steam production was adversely affected, leading to the abandonment of the Cerro Prieto V project. Subsequently, with the permanent shutdown of the four Cerro Prieto I units in 2011, the geothermal field experienced a decline in steam production. Since then, CFE has been exploring various methods to augment energy generation.

The abundant solar radiation at Cerro Prieto, measured at 5.5 kW/m^2, surpassing the national average, presents a promising opportunity for solar energy utilization. In 2012, the installation of 5 MW power plants at Cerro Prieto incorporated four distinct technologies: polycrystalline panels with one and two-axis tracking systems, thin-film panels with a one-axis tracking system, and solar concentration panels with a two-axis tracking system. This initiative paved the way for a solar thermal plant to harness steam from wastewater discharged from the geothermal cooling towers, supplying steam to the Cerro Prieto pipeline grid for use in the steam turbines of the power plants. A water treatment facility must be installed to remove impurities from the blowdown before it enter the CSP plant and ensure the feedwater's quality (Miranda-Herrera, 2015).

2. Methodology

2.1. Overview for hybridization analysis

This study scrutinize the incorporation of commercial parabolic trough collectors (PTC) into the existing geothermal power plant Cerro Prieto to propose a solar-geothermal hybrid power plant. The hybridization looks to enhance the steam quality available in the geothermal wells as a function of the solar field size. To enhance the steam quality, we propose two configurations for the solar field employing two heat transfer fluids (HTF): thermal oil with a heat recovery steam generator (HRSG) and direct steam generation (DSG). For the thermal oil and HRSG (case 1), we use Therminol VP1 (VP1) as it is the standard HTF for solar power plants; while the DSG concept (case 2) employs the fluid available from the geothermal well. Both cases are shown in Fig. 1, while Table 1 depicts the geothermal well characteristics.

Tab. 1: Cerro Prieto geothermal well characteristics (Lentz and Almanza, 2006)

Parameter	Value
Pressure, (bar)	50
Temperature, (ºC)	263.9
Steam quality	0.2449
Mass flow rate, (kg/s)	46.17
Flash pressure, (bar)	10.5
Flash steam quality	0.3907

In México, Abengoa's successful deployment of the ASTR0 parabolic troughs (Fig. 2) in the integrated solar combined cycle Agua Prieta II informs the choice for the solar field, as this is the only CSP power plant in México. Table 2 summarizes the key parameters of the ASTR0 parabolic troughs.

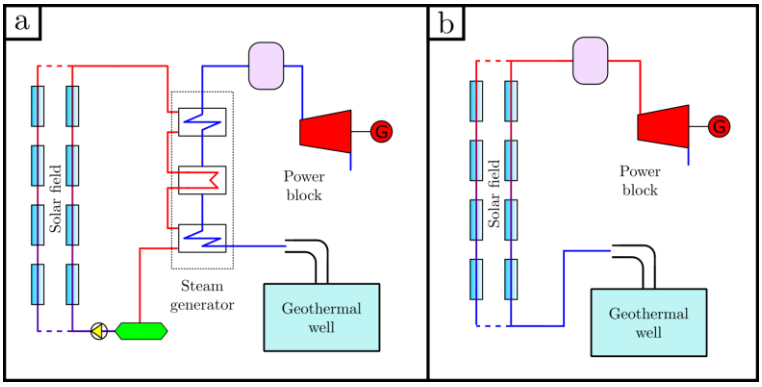

Fig. 1: Schematic diagram of the proposed systems for Cerro Prieto IV. (a) VP1 + HRSG (case 1). (b) DSG (case 2).

Tab. 2: Geometric parameters of the ASTR0 parabolic trough collector (ABENGOA, 2013)

Parameter	Value
Width, (m)	5.77
Focal length, (m)	1.71
Rim angle, (deg)	80.3
Receiver diameter, (m)	0.07

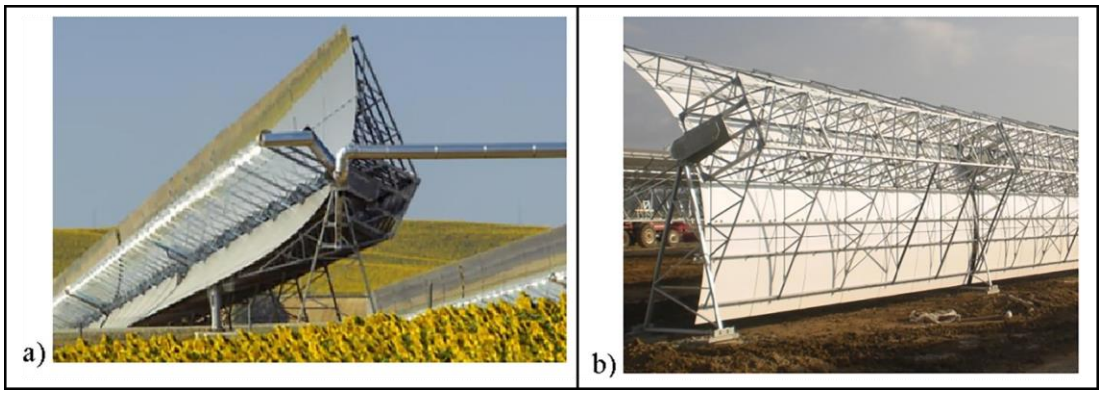

Fig. 2: Abengoa Solar ASTR0 collector (ABENGOA, 2013).

2.2. Evaluation procedure

Fig. 3. illustrates the calculation procedure for assessing the solar fields. The initial step involves the definition of the steam quality enhancement of the geothermal fluid before the flashing process. Following this determination, we proceed with the thermohydraulic characterization of the solar fields, which in this study, encompass PTC with VP1 and DSG. After analysing these solar fields setups, we consolidate the results into 5 functions that allow the evaluation as a function of the solar field size. These functions encompass:

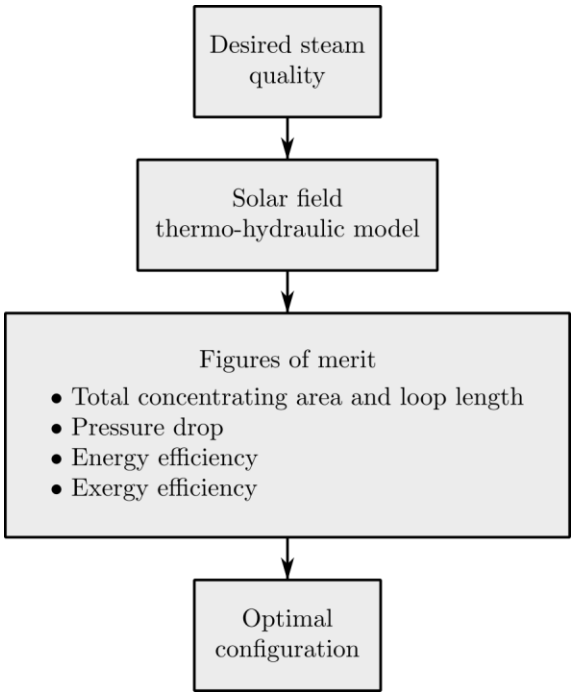

Fig. 3: Evaluation procedure.

- Steam quality enhancement: Increasing the quality of the stem delivered to the turbine is the main objective of the study. This process will be attained using the solar radiation to heat Therminol VP1 and a HRSG, or the DSG concept. One can define the desired steam quality and compute the thermal load to be delivered by the solar field:

$$\dot{Q}_{gain,HTF} = \dot{m}_{HTF}\left(h_{out,SF} - h_{in,SF}\right) \qquad \text{(eq. 1)}$$

- Total concentrating area and loop length: The loop size depends on the desired quality to be attained for the steam turbine. To determine the concentrating area they loop lengths are considered for mirror placement. In this study, the total concentrating area is solely associated with the mirrors, accounting the loops number N_{loop}, loop's length (L_{loop}) and the PTC width (W_{PTC}), as:

$$A_{SF} = N_{loop} L_{loop} W_{PTC} \qquad \text{(eq. 2)}$$

The loops number is determined by the mass flow rate within the receiver. It is suggested to maintain a turbulent flow (Re~10^5) to ensure efficient heat transfer between the receiver tube and the HTF.

- Pressure drop. Longer loops led to higher pressure drop, limited by the desired pressure in the flash tank to deliver the steam at the steam turbine. In the case of VP1, the pressure drop must be carefully traced to avoid any phase change.

- Energy and exergy efficiency: The solar field's energy efficiency can be evaluated by comparing the net thermal power transferred to the heat transfer fluid ($\dot{Q}_{gain,HTF}$) to the incident solar power on the net mirror area ($\dot{Q}_{inc}$). This calculation provides insight into the conversion of solar energy into usable thermal power, expressed as:

$$\eta_{I,SF} = \frac{\dot{Q}_{gain,HTF}}{\dot{Q}_{inc}} = \frac{\dot{m}_{HTF}\left(h_{out,SF} - h_{in,SF}\right)}{A_{SF} G_{bn}} \qquad \text{(eq. 3)}$$

The exergy efficiency of the solar field can be computed as the ratio of the fluid exergy increment ($\dot{E}x_{gain,HTF}$) to the exergy of solar radiation incident on the net mirror area ($\dot{E}x_{inc}$). This parameter provides insight into the solar field's effectiveness in transforming solar radiation into practical exergy in the form of thermal power, expressed as:

$$\eta_{II,SF} = \frac{\dot{E}x_{gain,HTF}}{\dot{E}x_{inc}} = \frac{\dot{m}_{HTF}(ex_{out,SF} - ex_{in,SF})}{A_{SF}\dot{E}x_{G_{bn}}} \quad \text{(eq. 4)}$$

The exergy associated with solar radiation has been extensively discussed in the literature, leading to different models and approaches to estimate it. Recently, researchers have made a progress in an improved model, addressing shortcomings in existing approaches (González-Mora et al., 2023). The model integrate the principles of endoreversible thermodynamics, accounting for external irreversibilities within the solar collector system. The exergy of solar radiation can be expressed as follows:

$$\dot{E}x_{G_{bn}} = G_{bn}\left[1 - \frac{1}{\xi}\left(\frac{T_a}{T_{sun}}\right)^4\right]\left(1 - \frac{\lambda_c T_0}{\lambda_c T_a + \xi\sigma T_{sun}^4 - \sigma T_a}\right) \quad \text{(eq. 5)}$$

where T_{sun} is the equivalent absolute temperature of the sun as a black-body (~5800 K), T_0 is the ambient temperature, ξ is the concentration acceptance product, λ_c is the thermal conductance per unit surface area of the environment, and σ is the Stefan-Boltzmann constant. The value of T_a is the solution of $\mathrm{d}\dot{E}x_{G_{bn}}/\mathrm{d}T_a = 0$. It can be demonstrated that in the limit case, Eq. 5 takes a value of $\dot{E}x = 0.8391AG_{bn}$ (González-Mora et al., 2023).

For the solar field using VP1 as HTF, the energy and exergy efficiency must consider the proper HRSG efficiency. The HRSG efficiencies can be determined considering the $T - \dot{Q}$ diagram in Fig. 4, and the total efficiency values are calculated as:

$$\eta_I = \eta_{I,SF}\eta_{I,HRSG} \quad \text{(eq. 6)}$$

$$\eta_{II} = \eta_{II,SF}\eta_{II,HRSG} \quad \text{(eq. 7)}$$

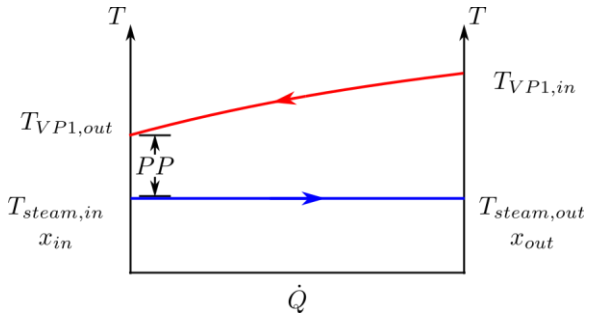

Fig. 4: Heat recovery steam generator $T - \dot{Q}$ diagram.

2.3. Details on solar field's thermohydraulic model

The present model employs the 'Homogeneous Equilibrium Model' approach with a 1D finite difference method, as described and validated by González-Mora and Durán-García (2023, 2024).The model applies a steady-state energy balance over the receiver (heat collector element, HCE), considering the direct normal solar irradiation, optical losses, thermal losses, and HTF gains. Unlike other models, the present model does not rely on the convective heat transfer coefficient (h) and the friction factor (f), enabling a faster computation time as no iterative processes are required to characterize the solar field. Fig. 5 displays the HCE for the parabolic trough, while Eqs. 8 shows the balance equations per unit length.

$$\begin{cases} \dot{q}'_{12,conv} = \dot{q}'_{23,cond} \\ \dot{q}'_{3,SolAbs} = \dot{q}'_{34,conv} + \dot{q}'_{34,rad} + \dot{q}'_{23,cond} + \dot{q}'_{38,cond} \\ \dot{q}'_{45,cond} = \dot{q}'_{34,conv} + \dot{q}'_{34,rad} \\ \dot{q}'_{45,cond} + \dot{q}'_{5,SolAbs} = \dot{q}'_{56,conv} + \dot{q}'_{57,rad} \\ \dot{q}'_{12,conv} = \frac{\dot{m}}{L_{HCE}}(h_{in} - h_{out}) \end{cases} \quad \text{(eq. 8)}$$

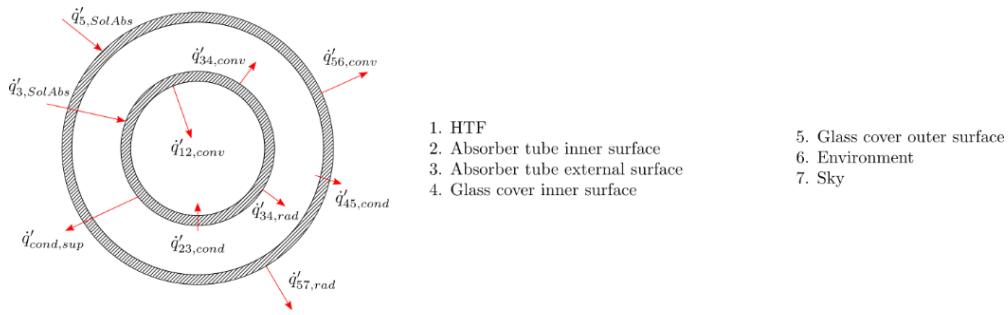

Fig. 5: Heat fluxes over the PTC receiver. Adapted from (González-Mora and Durán-García, 2024)**.**

The Eqs. 8 simplifies the absorption in the receiver and the glass cover as surface phenomena. In addition, it is assumed that temperatures, heat flows and thermodynamic properties are uniform in the whole cross section area. In this regard, one can express each heat flow as:

$$\begin{cases} \dot{q}'_{i,SolAbs} = IAM\rho_{PTC}(\alpha\tau)_i W G_{bn} \\ \dot{q}'_{ij,cond} = \frac{2\pi k_{ij}(T_i - T_j)}{\ln D_j/D_i} \\ \dot{q}'_{ij,rad} = \frac{\sigma\pi D_i\left(T_i^4 - T_j^4\right)}{\frac{1}{\varepsilon_i} + \frac{(1-\varepsilon_j)D_i}{\varepsilon_j D_j}} \\ \dot{q}'_{ij,conv} = f(\Delta T) \end{cases} \quad \text{(eq. 9)}$$

where IAM represents the incidence modifier angle, ρ_{PTC} is the mirror reflectance, $(\alpha\tau)_i$ is the product of the absorbance and transmittance of surface i, W_{PTC} is the PTC width, G_{bn} is the incident solar radiation in the normal direction, k is the surface conductivity, T is the temperature, D is the diameter, σ is the Stefan-Boltzmann constant, ε is the emittance. The subscripts i and j are used to identify each of the surfaces, as shown in Fig. (4b). It is important to note that the last equation in the set of Eqs. (9) implies a functional of the temperatures, for the purpose of avoiding the use of the convective coefficient.

To model the annulus between the absorber tube and the glass cover, free convection between two cylinders is considered, since the receiver is evacuated. The convection between the glass cover and the environment can be forced or natural, depending on the atmospheric conditions; for natural convection, the Churchill and Chu equation is used, while for forced convection the Žhukauskas equation is applied. Regarding convection between the absorber tube and the heat transfer fluid, there are two scenarios: the Pethukhov or Gnielinski equation for single-phase flow and the Gungor and Winterton correlation for two-phase flow.

For the DSG case, the flow pattern inside the receiver must be taken into account. It is suggested that PTC under DSG should operate within the annular-flow pattern (Zarza Moya, 2003) to enhance the heat transfer rate, avoid thermal stresses and attain higher efficiency. Consequently, we rely on the Taitel and Dukler diagram (1976) to characterize the flow pattern due to its ease of use, and high accuracy.

3. Results and discussion

The evaluation of the whole model is performed in an inhouse code. The flow from the wells has a low

concentration of salts (<2%); for this reason, it is possible to assume that the geothermal fluid behaves as water (Lentz and Almanza, 2006). In both proposed systems, solar field with VP1 and DSG, the steam quality enhancement after the flashing is modelled until reaching the saturated vapor condition, so the solar field, and the HRSG, should attain a steam quality of 0.9894 before the flashing. Doing this, we can retrieve the upper performance limits that will allow projections of several configurations for the geothermal power plant.

3.1. General considerations

A heat demand of 57.27 MW to be supplied to the geothermal fluid to attain the desired steam quality enhancement of saturated vapor. This heat demand must be supplied by the solar field, either with VP1 or DSG, respectively.

We fix some values regarding the VP1 in the steam generator, namely the temperature at the HSRG ($T_{VP,1}$) inlet and the pinch point (PP). We define $T_{VP,1}$ at 390ºC and PP at 20ºC and their pressure at 12 bar, to avoid any phase change of thermal oil. Applying an energy balance for the HRSG (see Fig. 4), recalling that $x_{in} = 0.2449$, $x_{out} = 0.9894$, and a pressure drop of 3 bar in both fluids, a typical value present in HRSG of CSP plants (Lippke, 1995).

Under these considerations, 208.3 kg/s of VP1 is required to meet the requirements. As stated in Section 2.2, a turbulent flow must be attained in the receiver. Consequently, we select 125 loops, each one with 1.667 kg/s flowing in the receiver tube with a Reynolds number high enough to keep a turbulent flow. With the VP1 thermal conditions, a 90.97% energy efficiency ($\eta_{I,HRSG}$) and 92.07% exergy efficiency ($\eta_{II,HRSG}$) are expected in the HRSG. For the DSG solar field, the 46.17 kg/s are distributed between 20 loops, with 2.308 kg/s per loop. This mass flow rate allows a proper annular flow as shown below.

3.2. Solar field behaviour

As stated in Section 2.2, we define four parameters to characterize the upper limits for the steam quality enhancement requirements related to the solar field (and the HRSG for VP1). These parameters define our figures of merit that relates loop size (and total concentrating area), pressure drop, energy efficiency and exergy efficiency. These figures of merit are plotted in Fig. 6.

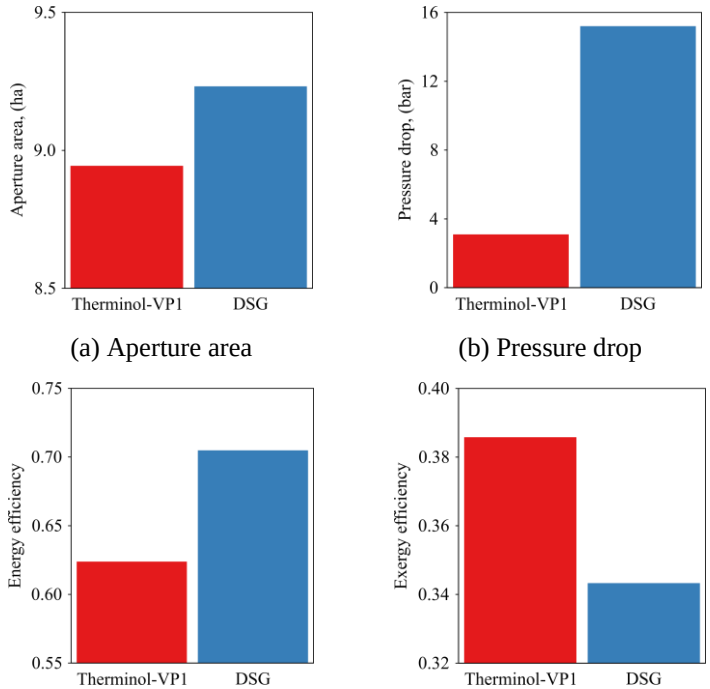

(a) Aperture area (b) Pressure drop

(c) Energy efficiency (d) Exergy efficiency

Fig. 5: Figures of merit

From Fig. 6, comparing VP1 and DSG, distinct differences in key performance metrics are retrieved. The area

required for VP1 is slightly smaller at 8.944 hectares compared to 9.232 hectares for DSG. However, the DSG configuration necessitates a significantly longer length of 796 meters, in contrast to the 120 meters required for Therminol VP1. When evaluating energy efficiency, DSG demonstrates a superior efficiency of 0.7049, surpassing VP1 efficiency of 0.6239. Conversely, VP1 exhibits higher exergy efficiency at 0.3858, while DSG registers a lower exergy efficiency of 0.3433. A notable distinction is observed in the pressure drop; DSG experiences a substantial pressure drop of 15.2 bar, whereas VP1 records a markedly lower pressure drop of 3.1 bar. It is important to note that the pressure drop for Therminol VP1 already includes the pressure drop in the HRSG. The low exergy value obtained in the DSG, stands for the high pressure drop along the loops. These results underscore the trade-offs between the two configurations, highlighting DSG's higher energy efficiency at the expense of greater pressure drop and area requirements, while Therminol VP1 offers a more compact and thermodynamically favorable alternative since the exergy efficiency is higher.

Upon characterizing the DSG in the solar field, we constructed the Taitel and Dukler diagram (Fig. 7) to identify the flow pattern inside the receiver tube. The operating conditions of pressure and mass flow rate ensured an annular flow throughout the entire boiling process, despite the high-pressure drop. This indicates that the boiling process can proceed without major complications, providing confidence in the system's operational stability and effectiveness.

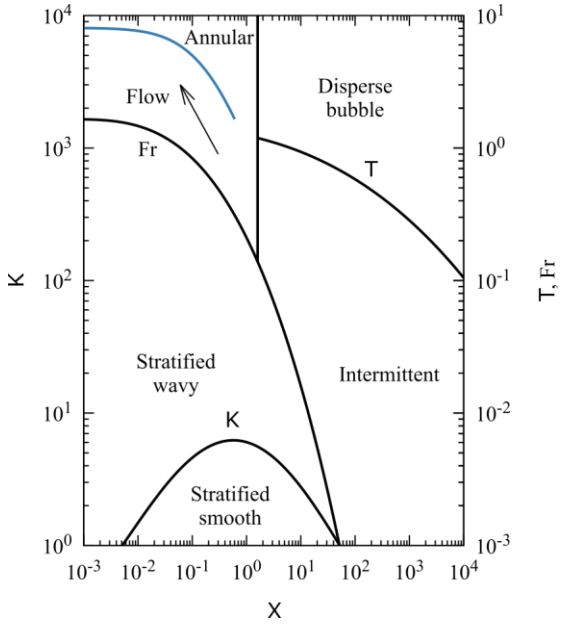

Fig. 7: Boiling process flow pattern

4. Conclusions

This study evaluated the feasibility of integrating parabolic trough collectors (PTC) with the Cerro Prieto geothermal power plant to enhance steam quality and increase energy production. The research focused on two configurations: using Therminol VP1 as the heat transfer fluid (HTF) and employing direct steam generation (DSG). We aimed to determine which configuration could effectively augment the geothermal plant's efficiency and output.

The study highlights the significant potential of solar-geothermal hybrid systems. Compared to DSG, using VP1 required a slightly smaller solar field area, demonstrating higher exergy efficiency. Conversely, DSG achieved superior energy efficiency but faced a considerable pressure drop. These results underscore the trade-offs between the two approaches regarding efficiency and operational challenges, indicating that both have distinct advantages and limitations depending on the specific operational goals and conditions.

The study demonstrated that both configurations could enhance steam quality to the desired levels, proving the concept's viability. The findings provide valuable insights into the performance metrics of hybrid solar-geothermal power plants, emphasizing the importance of selecting the appropriate HTF and optimizing system

parameters. In addition, the study confirmed that integrating PTCs into geothermal plants could significantly improve their performance, thus validating the potential for such hybrid systems.

PTC integration improves steam quality and offers a pathway to increase renewable energy output in regions with abundant solar resources. The enhanced steam quality can lead to higher electricity generation efficiency, making hybrid plants more competitive and reducing dependency on fossil fuels. This research sets a foundation for policymakers and industry stakeholders to consider hybrid solutions in future energy planning and development. Future research should explore long-term operational impacts, cost-benefit analysis, and scalability of the proposed hybrid systems. In addition, investigating other HTFs and advanced materials for PTCs could further optimize system performance and economic viability.

5. References

ABENGOA, 2013. A new generation of parabolic trough technology.

González-Mora, E., Durán-García, M.D., 2024. Alternative Approach for Thermo-Hydraulic Modeling of Direct Steam Generation in Parabolic Trough Solar Collectors. J Therm Sci Eng Appl 16, 1–12. https://doi.org/10.1115/1.4064819

González-Mora, E., Durán-García, M.D., 2023. Alternative Methodology for Modeling Direct Steam Generation in Parabolic Collectors: A Study Case in Northeast Mexico, in: 36th International Conference on Efficiency, Cost, Optimization, Simulation and Environmental Impact of Energy Systems (ECOS 2023). ECOS 2023, Las Palmas De Gran Canaria, Spain, pp. 1496–1506. https://doi.org/10.52202/069564-0136

González-Mora, E., Poudel, R., Durán-García, M.D., 2023. A practical upper-bound efficiency model for solar power plants. Journal of Non-Equilibrium Thermodynamics. https://doi.org/10.1515/jnet-2022-0080

Gutiérrez-Negrin, L., Izquierdo-Montoya, G., Canchola-Félix, I., 2023. Situation of geothermal energy in Mexico: country update, in: Proceedings of the World Geothermal Congress 2023. Beijin.

Hernández Martínez, E., Avitia Carlos, M.C.P., Cisneros Solís, J.I., Prieto Avalos, M.C.M. del C., 2020. Thermodynamic simulation and mathematical model for single and double flash cycles of Cerro Prieto geothermal power plants. Geothermics 83, 101713. https://doi.org/10.1016/j.geothermics.2019.101713

Lentz, Á., Almanza, R., 2006. Solar–geothermal hybrid system. Appl Therm Eng 26, 1537–1544. https://doi.org/10.1016/j.applthermaleng.2005.12.008

Lippke, F., 1995. Simulation of the part-load behavior of a 30 MWe SEGS plant. Sandia National Lab.(SNL-NM), Albuquerque, NM (United States).

Miranda-Herrera, C., 2015. Power Generation in Cerro Prieto Geothermal Field, in: World Geothermal Congress . Melbourne.

Ritchie, H., Rosado, P., 2023. Data Page: Geothermal energy capacity" [WWW Document]. Energy. URL https://ourworldindata.org/grapher/installed-geothermal-capacity (accessed 5.26.24).

Taitel, Y., Dukler, A.E., 1976. A model for predicting flow regime transitions in horizontal and near horizontal gas-liquid flow. AIChE Journal 22, 47–55. https://doi.org/10.1002/aic.690220105

Zarza Moya, E., 2003. Generación directa de vapor con colectores solares cilindro parabólicos. Proyecto DIrect Solar Steam (DISS). Universidad de Sevilla.

Computational Fluid Dynamics Optimization of a Heat Exchanger Design for Photovoltaic Thermal Retrofit Applications

Abel Climente García[1], Damu Murali[2], Iván P. Acosta-Pazmiño[1], María Herrando[3], Mario Morales-Hernández[4], Juan Pablo Santana [2] and João Gomes[2]

[1] MG Sustainable Engineering AB, Uppsala (Sweden)

[2] Department of Building Engineering, Energy Systems and Sustainable Science, University of Gävle, Gävle (Sweden)

[3] Instituto Tecnológico de Aragón (ITA), Zaragoza (Spain)

[4] Fluid Dynamics Technology Group, I3A, University of Zaragoza, Zaragoza (Spain)

Abstract

This paper investigates the geometrical optimization of a heat exchanger designed for retrofitting photovoltaic (PV) panels into PV-thermal (PVT) collectors to enhance their electrical efficiency and harness residual heat for supplementary purposes. Through computational fluid dynamics (CFD) simulations in Ansys-Fluent and Ansys Steady-state Thermal, an initial model is analyzed and optimized to develop three alternative models with improved electrical and thermal performance. The study focuses on varying geometrical aspects of the heat exchanger to evaluate their impact on defined Key Performance Indicators (KPIs), including pressure drop and fluid temperature gain. The results show that the increase in thermal efficiency may compromise homogeneous thermal flow distribution, emphasizing the need for a balance between thermal efficiency and uniform cooling distribution. This research provides valuable insights for optimizing thermal management designs in PV panel retrofit applications, contributing to advancing PV and PVT technologies and systems.

Keywords: Photovoltaics, Heat exchanger, Retrofitting, Computational fluid dynamics, Thermal management, Hybrid photovoltaic thermal (PVT) systems.

1. Introduction

Solar energy stands as a cornerstone within the realm of renewable energy, offering immense potential for sustainable power generation. Within the framework of photovoltaic (PV) cells, only a fraction of the incident solar radiation is directly converted into electrical energy. A significant portion of this solar irradiance is absorbed by the PV cells, leading to increased temperatures and subsequent reductions in panel efficiency and longevity. Recognizing the importance of mitigating this heat buildup, efforts have been directed towards the cooling of PV panels to enhance their electrical efficiency. In this regard, the cooling techniques explored so far can be classified into passive and active cooling mechanisms (Herrando et al. 2023). Passive cooling systems do not require additional power consumption to absorb the heat from PV panels. Heat pipes, phase change materials (PCMs), adding extended surfaces to the PV panel surface, among others are the commonly used passive cooling mechanisms. Alternatively, active cooling technologies use heat transfer fluids (HTFs) driven by external power-consuming devices like a fan or a pump to extract heat from the PV modules. One of the widely adopted active cooling strategies is the integration of thermal absorbers behind the PV panels, which gives rise to photovoltaic thermal (PVT) collectors.

PVT systems offer the dual benefits of generating thermal energy and electric power from the same aperture area thus making the renewable energy (RE) system more versatile (Chow, 2010 and Tripanagnostopoulos 2002). However, the effectiveness of the PVT system depends on how efficiently the heat energy can be absorbed. Among the various influencing factors, the design characteristics of the thermal absorber play a crucial role in determining the performance of the PVT system. Water-based PVT collectors are widely used as they are considered more efficient due to the high specific capacity of the heat transfer fluid. By water-based collectors, the authors also include water-glycol mixtures, one of the commonly used HTFs. Previous research has focused on the design and development of thermal absorbers for the water-based PVT collector, both in terms of the materials chosen and the overall geometrical specifications.

Various thermal absorber configurations have already been tested for PVT collectors. Among them, parallel

© 2024. The Authors. Published by International Solar Energy Society
Selection and/or peer review under responsibility of Scientific Committee
10.18086/eurosun.2024.07.08 Available at http://proceedings.ises.org

tubes (pipes) are widely explored due to their geometrical simplicity (Herrando et al., 2014) that can achieve TRLs of 9. Due to this high TRL level, this configuration is also used for many commercial PVT collectors (Herrando et al., 2023). It has already been reported that, in this configuration, the thermal energy that can be extracted depends upon the W/D ratio (where W is the distance between the pipes and D is the pipe diameter), the collector fin efficiency, and the tube bonding quality (Herrando et al., 2023). These parameters are, therefore, considered to be directly influencing the efficiency of the collector. In this regard, several design optimization efforts have been reported in the literature by altering these parameters (Herrando et al., 2019). Huang et al., 2001 conducted studies using different thermal absorber materials, such as aluminium and copper with thermally conductive adhesive between the PV panel and the thermal absorber. From the analysis, it was found that the PVT system performance could have been more satisfactory. One of the other conclusions was that the absorber plate should be in direct contact with the PV cells to ensure proper heat transfer. Convective heat transfer between the coolant and the channels needs to be maximized to enhance the performance of the thermal absorber. This can be achieved by reducing the pipe diameter, D, and by increasing the number of channels per unit width (W) (Ji et al., 2006). Following this investigation, He et al., 2006 concluded that by using a flat-box design, the key design factors such as the collector fin efficiency and the tube-bonding quality could be further improved. This design was later explored by several authors in which the W/D ratio was reduced to 1 by using square channels (Huang et al. 2001). It was found that such a design could improve the fin efficiency by increasing the heat transfer area between the absorber plate and the cooling fluid. One of the outcomes of these studies was that to collect more than 90% of the energy, it was essential to have a fluid layer thickness smaller than 10 mm (Cristofari et al., 2002).

Among the materials used for the thermal absorber, copper is widely used owing to its high thermal conductivity (Makki and Sabir 2015, Michael and Goic 2015). However, one of the disadvantages of metal-based thermal absorbers is that the overall system weight and cost increase. This is not recommended considering the additional requirement of supporting structures that would increase the installation as well as the maintenance costs. This drawback arising from the material perspective, however, can be mitigated using a polymer-based thermal absorber that would significantly reduce the system weight and cost. Additionally, they offer a special advantage in terms of design, as they can acquire layouts that would be very difficult and expensive using conventional materials. Despite these advantages of using polymer-based material for thermal absorbers, only a few studies (Cristofari et al., 2002, 2009) so far have reported using polycarbonate material for thermal absorbers. Even though the effectiveness of current heat exchangers in absorbing thermal energy is already proven, they frequently encounter challenges in achieving homogeneous thermal distribution across the backside surface of the PV panel. This uneven thermal distribution heightens the risk of developing hotspots within the panel, leading to decreased electrical efficiency (Nahar et al., 2019). Researchers in this area have already demonstrated that innovative configurations, designs, and materials could increase the overall efficiency, cost-effectiveness, and reliability of PVT collectors (Herrando et al., 2019).

Despite the promising prospects of PVT technologies, their optimal design and competitiveness for effective heat extraction still need to be improved, hindering their widespread adoption. Nevertheless, there is a growing need to try out novel configurations other than that of the parallel pipe design. Therefore, The present study intends to develop a polymer-based thermal absorber; hence, the proposed geometrical specifications, primarily the fluid domain, are designed to ensure uniform thermal distribution and maximized heat absorption from the PV panel. The selection of polymeric material is also aimed at reducing manufacturing costs by taking advantage of the economy of scale in producing polymeric elements, as opposed to copper and aluminium heat exchangers. However, it is important to highlight that for a fair comparison with the existing configurations at this developmental stage, all studies of this work have been carried out considering aluminium as the material of choice.

2. Methodology

The methodology employed in this study involves an initial comparative analysis focusing on varying two key geometrical aspects in the thermal absorber: i) orifice sizing and ii) orifice spacing, to identify trends and understand how these parameters influence the defined key performance indicators (KPIs). This initial phase aimed to establish a foundational understanding of the impact of primary geometric modifications on system performance. The KPIs are defined in Section 2.1.

Following identifying these trends, the methodology progressed to iteratively refining a model focused on optimizing thermal power output. This iterative process incorporated additional geometrical features, such as baffles and different orifice arrangements, to enhance thermal performance. Building upon the insights gained from these iterations, three distinct models were ultimately proposed. The first model was optimized for maximum thermal power output, ensuring the highest possible thermal energy capture and heat transfer. The second model focused on achieving thermal homogeneity, ensuring uniform temperature distribution and minimizing thermal gradients in the PV module. The third model represented a trade-off design, balancing thermal power output and thermal homogeneity to provide a versatile and practical solution.

2.1. Key Performance Indicators (KPIs)

KPIs are needed to provide numerical insights that validate the hypotheses of each design modification in the optimization of the thermal absorber. KPIs serve as quantifiable measures that evaluate the performance and efficiency of different geometric configurations and therefore flow distributions. The indicators chosen in this study are pressure drop, temperature gain, thermal absorber wall temperature, internal heat transfer coefficient, Nusselt number, temperature standard deviation, thermal power, and thermal and electric efficiency.

Temperature gain (ΔT) refers to the increase in the fluid's temperature as it passes through the thermal absorber. It is a direct measure of the thermal power captured by the system and is essential for evaluating the efficiency of the heat exchanger. If the flow rate is kept constant, a higher temperature gain indicates better thermal performance, contributing to higher thermal energy production. This indicator helps determine the capacity of the design to efficiently absorb and transfer heat from the PV panel to the working fluid.

The thermal absorber wall temperature **(**T_{wall}**)** is an important KPI that reflects the average temperature on the surface of the absorber in contact with the photovoltaic panel. This temperature provides information about the thermal load experienced by the absorber material and the cooling potential of the PV cells. It is necessary to maintain a reduced wall temperature level to increase the durability and longevity of the thermal absorber. Excessively high wall temperatures can lead to material degradation, while low temperatures may indicate poor thermal energy production.

The internal convective heat transfer coefficient (h_{conv}) quantifies the heat transfer efficiency between the absorber surface and the working fluid. A higher convection value signifies more effective heat transfer, contributing to higher thermal power extraction and better overall system performance. The internal heat transfer coefficient is calculated with eq. 1.

$$h_{conv}[W\,m^{-2}K^{-1}] = \frac{q}{T_{wall}-T_m} \quad \text{(eq. 1)}$$

where $q\ [W\,m^{-2}]$ refers to the heat collected by the absorber and T_m refers to the average temperature of the fluid between the inlet and outlet.

The Nusselt number (Nu) is a dimensionless number that characterizes the ratio of convective to conductive heat transfer within the fluid. It provides an overall understanding of convective heat transfer relative to conduction. A higher Nusselt number indicates improved convective heat transfer, often achieved through design features that induce turbulence. It is calculated with eq. 2.

$$Nu = \frac{h_{conv}\,L}{k} = \frac{h_{conv}\,D_h}{k} \quad \text{(eq. 2)}$$

where D_h refers to the hydraulic diameter of the absorber and k refers to the thermal conductivity of the heat transfer fluid.

The temperature standard deviation (σ_T) measures the variation in temperature within the surface of the PV panel that is in contact with the thermal absorber. It is a crucial indicator of thermal homogeneity, as a lower deviation indicates a more uniform temperature distribution. Achieving a low standard deviation is necessary to avoid hot spots affecting PV electrical production and ensure uniform thermal performance throughout the absorber. This KPI helps identify designs that balance heat absorption and distribution, optimizing both electrical production by evenly cooling the cells and thermal performance. It is defined with eq. 3.

$$\sigma_T[K] = \sqrt{\frac{\sum_{i=1}^{N}(T_i-\overline{T})^2}{N}} \quad \text{(eq. 3)}$$

where T_i refers to the temperature of each cell, $\overline{T}$ refers to the mean temperature value of the cells, and N refers to the number of cells considered in each simulation.

Thermal power ($P_{th}[W\ m^{-2}]$) measures the amount of heat transfer from the absorber to the working fluid per unit collection area. It is a key indicator of the system's ability to convert solar energy into usable thermal energy. It is defined in eq. 4.

$$P_{th}[W_{th}\ m^{-2}] = \dot{m}\ C_p\ \Delta T \frac{1}{A_c} \qquad \text{(eq. 4)}$$

where $\dot{m}$ and C_p refer to the mass flow rate and the specific heat capacity of the fluid, respectively, and A_c refer to the area of collection of the PV panel.

Subsequently, thermal efficiency ($\eta_{th}[\%]$) represents the proportion of incident solar energy that is successfully converted into thermal energy by the system. It is a measure instantaneous thermal performance of the collector. Is is obtained with eq. 5.

$$\eta_{th}[\%] = \frac{P_{th}}{G} \qquad \text{(eq. 5)}$$

where $G\ [W\ m^{-2}]$ refer to the solar irradiance that in this case is used as a contant heat flux boundary condition.

The parameters that relate electrical production with thermal performance are the photovoltaic efficiency ($\eta_{el}[\%]$), which describes how the efficiency of the PV panel changes with temperature and the electrical power production per unit area of collection $P_e\ [W\ m^{-2}]$. Their relationship is given by the following eq. 6 and eq. 7.

$$\eta_{el}[\%] = \eta_{PV,ref}\left[1 + \beta_0\left(T_{PV} - T_{PV,ref}\right)\right] \qquad \text{(eq. 6)}$$

$$P_{el}[W_{el}\ m^{-2}] = G\ \eta_{el} \qquad \text{(eq. 7)}$$

where $\eta_{PV,ref}$ refers to the reference PV efficiency at the reference temperature, β_0 is the temperature coefficient of the PV cells, T_{PV} refers to the temperature of the PV cells and $T_{PV,ref}$ refers to the reference temperature of the PV panel, equal to 298 K.

Lastly, the pressure drop is a critical indicator that measures the resistance encountered by the fluid as it flows through the thermal absorber. Therefore, it is indicative of the energy required to maintain fluid circulation, directly impacting the pumping power requirements of the system. The pressure drop characterization is commonly presented as a function of the flow rate in the thermal absorber. A lower pressure drop ($\Delta P[Pa]$) is desirable as it implies lower energy consumption for fluid movement, enhancing overall system efficiency and reducing initial investments.

2.2. CFD and Steady-State Thermal models.

For the geometrical design of the PVT retrofit, multiple CFD models were developed, enabling a detailed study of various aspects of fluid flow and heat transfer within the collector. The following sections present these models along with their underlying rationale: i) Half-retrofit model (fluid only), ii) Half-retrofit model with PV layer, and iii) Half-PV panel model.

2.3.1. Half-retrofit model (fluid only)

The half-retrofit models (fluid only) are used primarily to optimize the flow distribution of the designs. These models do not consider the attachment of any PV panel and the conversion of electricity in the heat flux boundary condition. The aim is to examine the trends of the flow under different geometry variations. The boundary conditions for these models are specified in Tab. 1. The material selected is aluminium for comparative purposes with thermal absorber geometries presented in the literature.

Tab. 1: Boundary conditions for the fluid flow in Fluent.

Fluid - Material	Water - Aluminium
Fluid flow-rate	0.035 kg/s
Pressure inlet	3 bar

Temperature inlet	293 K
Fluid domain thickness	6 mm
Solar irradiance / Heat flux	1000 W/m^2

2.3.2. Half-retrofit model with PV layer

The half-retrofit model with the PV layer involves a system coupling simulation using ANSYS Fluent and Steady-State Thermal modules. This model aims to calculate the nominal values of the PVT collector retrofit when operating under realistic conditions, such as electric and thermal power. The electrical properties of the PV panel taken as reference are 300 W_{el} of peak electrical power, 18.44% for the nominal PV cell efficiency, -0.39 %/K as power temperature coefficient, and 1.62 m^2 as gross area, representing a conventional c-Si PV panel. The thermal properties of the PV panel layers used as a reference in these simulations are presented in Tab. 2. These properties were introduced into the model as a single layer, using a weighted average value based on the thickness of each layer.

Tab. 2: PV panel layers properties considered.

Layer	Specific heat [J/kg K]	Density [kg/m3]	Conductivity [W/mK]	Thickness [mm]
Tempered Glass	779.70	2125	1.15	3.00
EVA (x2)	2098	950	0.35	0.50
Solar Cells (c-Si)	702	2330	124	0.26
TEDLAR	1200	1765	0.17	0.10

The boundary conditions for Fluent remain the same as in the fluid-only models, except for the heat flux value (reduced to consider the conversion of energy into electricity) and surface application, as mentioned in the previous section. Additionally, Tab. 3 presents the boundary conditions used for the Steady-State Thermal module, including convection and radiation losses characterized by the heat transfer coefficients. These boundary conditions are consistent with those established in reviewed studies from the literature (Herrando et al., 2023), aiming for the simulation results to be compared accordingly.

Tab. 3: Steady-state thermal boundary conditions.

Solar Irradiance / Heat flux	1000 W/ m^2
Ambient Temperature	25 ºC
Convective Heat Transfer Coefficient (Front)	4.79 W/ m^2 K
Convective Heat Transfer Coefficient (Back)	0.45 W/ m^2 K
Emissivity of Glass	0.86
Emissivity of Solar PV Cells	0.89

The electrical conversion consideration process begins by applying a Solar Irradiance of 1000 W/m² to determine the PV cell temperature. Once the PV cell temperature is determined, the corrected efficiency of the PV cells at this temperature is calculated with eq. 6. The calculated electrical efficiency is then subtracted from the initial 1000 W/m² solar irradiance to estimate the remaining heat flux available for the thermal conversion. This adjusted heat flux value is subsequently used to run the final simulation, providing a more accurate representation of the system's thermal behaviour after accounting for the electrical energy extracted by the PV module.

2.3.3. Half-PV panel model

The half-PV panel model is a Steady-State Thermal model in ANSYS, similar to the previous steady-state thermal model without including the Fluent part. This model considers only the PV panel layers without the heat exchanger and the fluid domain, serving as a reference to determine the temperature of the PV cells and

electrical efficiency without any cooling effect. It is used to compare the electrical performance improvements achieved by integrating the heat exchanger in the previous models.

3. Optimization towards energy production

Before delving into the optimization towards energy production, it is essential to address a key design consideration that significantly affects the overall configuration of the thermal absorber. It has been decided to split the model into two halves to overcome the problem posed by the junction boxes of next-generation PV panels. Modern PV panels, particularly those using medium-sized solar cells, are equipped with three junction boxes at the back. These junction boxes can obstruct the placement of the heat absorber and affect the heat transfer efficiency. Therefore, dividing the model into two identical sections allows the heat absorber to be placed above and below the junction boxes, ensuring an unobstructed path for heat transfer (see Fig. 1, right). This configuration allows the absorber to be connected without passing through the junction boxes. This strategic decision lays the foundation for the subsequent detailed optimization of energy production, ensuring effective management of the practical challenges of the installation. Fig. 1 shows a rendering of a conventional PV panel with three junction boxes and the possible configuration for the split retrofit.

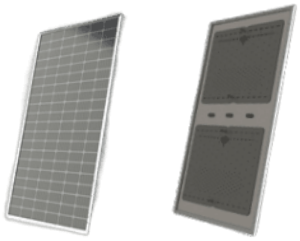

Fig. 1: Conventional PV panel and the possible configuration for the split retrofit.

3.1. Influence of flow distribution on thermal production

In this section, the influence of the flow distribution on the thermal output within the heat exchanger of the solar collector is discussed in more detail. The main objective is to improve the KPI related to the temperature gain. Firstly, a comparative approach is adopted, using half-collector (fluid only) simplified models with variations in the size and number of orifices, establishing the identified trends as a basis for developing the proposed orifice arrangements to maximize the temperature gain.

The simplified models (half collector and fluid only) present different orifice sizes (20 mm, 30 mm, 40 mm) and spacing, leading to different numbers of holes per row (3/4, 5/6, 7/8). For the different orifice sizes, an orifice spacing relative to 5/6 holes per row is considered, and on the other hand, for the different orifice spacing cases, an orifice size of 30 mm is considered. CFD simulations of these models have been carried out under the boundary conditions explained above, allowing trends to be observed and conclusions to be drawn on their impact on thermal output.

Tab. 4: Results of geometrical aspects and correlation of KPIs for thermal production (half collector, fluid only).

Model	T_1[K]	T_2[K]	$\Delta T[K]$
20 mm	293	303.3	10.3
30 mm	293	300.9	7.9
40 mm	293	298.4	5.4
3/4	293	302.3	9.3
5/6	293	299.7	6.7
7/8	293	298.1	5.1

The results presented in Tab. 3 show that reducing the size and number of holes benefits thermal output. Subsequently, based on the identified trends, an iterative adjustment of the hole layout is made to improve the temperature gain further, resulting in the optimal design to increase thermal output. Tab. 5 presents a description of the variations in the arrangement of the holes that were introduced to increase the temperature

gain and, therefore, the thermal production, taking as a basis a version (v1) that emulated the geometry of the original heat exchanger but with the hypothesis of a reduction in the size and number of holes introduced. It should be noted that the bridge between modules is a bypass with a height of 50 mm and a distance of 70 mm, which could be optimized to reduce the pressure drop and is excluded from this study.

Tab. 5: Description of the geometrical variations from v1 to v6 and results of the temperature gain for thermal production.

Model	Modifications with respect to the previous model	$\Delta T[K]$
v1	-	6.6
v2	Centred inlets and outlets (non-diagonal flow) to reduce the distance to opposite corners to be filled.	8.7
v3	Inclusion of a zone of high flow resistance in the centre, condensing the distance between holes locally, to create a tendency for the flow to avoid this zone and fill in the corners.	8.9
v4	Adjustment of the approximation of this zone to the inlet.	10.3
v5	Inclusion of flaps and a deflector at the outlet to improve the reach in the corners.	10.7
v6	Lengthening of the deflector to maximise corner outreach.	12.1
v7	Adaptation of the deflector to reduce pressure drop.	13.9

After analyzing the flow behaviour of each version, it is possible to identify the optimal orifice arrangements that maximize the temperature gain while maintaining or improving other critical KPIs and to propose a design oriented towards thermal production (Design A). Fig. 2 shows the first version (v1) and the final developed design (v7 – Design A), aimed at maximizing thermal output. Consequently, Fig. 3 shows a rendering of Design A, developed following these considerations (left), alongside its temperature field in a plane in the middle of the fluid domain (right). Moreover, the numerical results obtained regarding thermal output and their improvement with respect to the first conceptualized version are a temperature gain ($\Delta T[K]$) enhancement from 6.6 K in v1 to 13.9 K.

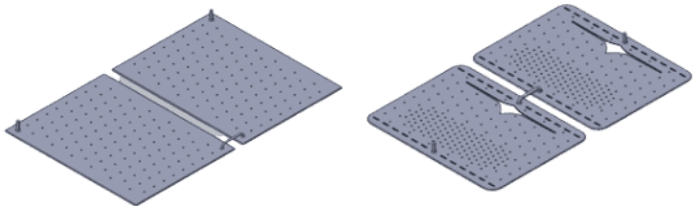

Fig. 2: First version (v1) and the final developed design (v7), aimed at maximizing thermal output.

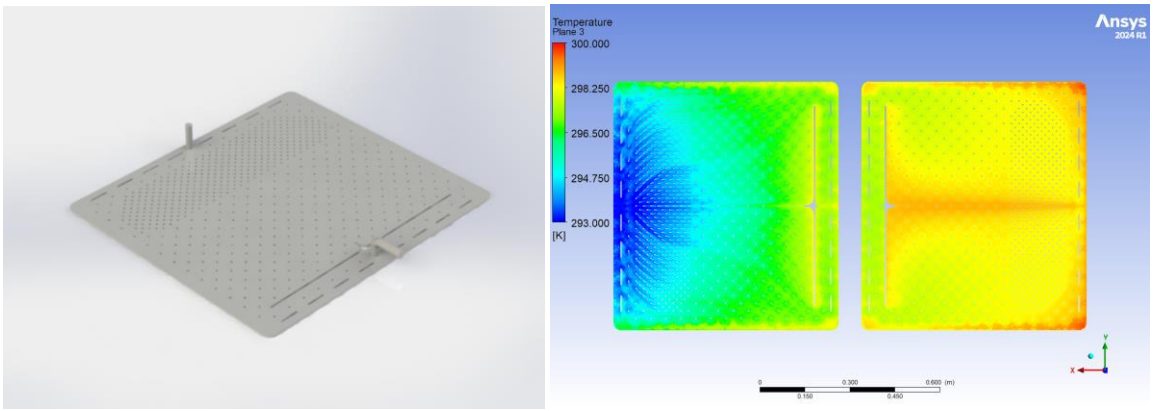

Fig. 3: Rendering of Design A (left), and its temperature field (right).

3.2. Influence of flow distribution on electrical production

The influence of the flow distribution on the electrical output is an important aspect of the design optimization process; the main objective in this respect is to reduce the wall temperature of the heat absorber, thus lowering

the operating temperature of the PV panel. This is essential because PV cells exhibit higher efficiency at lower temperatures, and minimizing their operating temperature can significantly improve the overall electrical output of the system.

To achieve this goal, the focus is on maximizing the Nusselt number and the convective heat transfer coefficient. These parameters are directly related to the efficiency of heat transfer from the absorber surface to the fluid. Higher values indicate more efficient cooling, which helps maintain lower temperatures for the PV panels.

One of the most effective ways to increase the Nusselt number and convection coefficient is to ensure a high fluid flow velocity and, therefore, increase the Reynolds number. A high flow velocity improves convective heat transfer, leading to more uniform and efficient cooling over the entire absorber surface. To achieve higher flow velocities, the design must incorporate reduced orifice spacing, facilitating a more turbulent and faster-moving fluid flow. Nevertheless, given the geometry, this becomes a trade-off against the amount of available surface for heat transfer and, thus, thermal output, as well as a tentative increase in pressure drop in the absorber. In this sense, Fig. 4 shows a rendering of Design B, developed following these considerations (left), alongside its temperature field in a plane in the middle of the fluid domain (right).

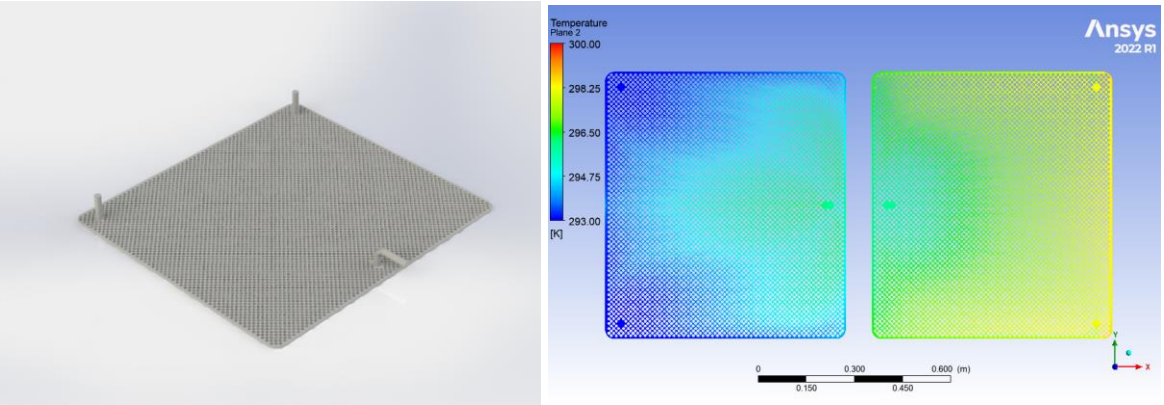

Fig. 4: Rendering of Design B (left), and its temperature field (right).

4. Optimization analyses

4.1 Identification of optimal geometric configurations

To propose a design that meets a coherent compromise between thermal power generation and electrical efficiency enhancement, iterative simulations and evaluations of different geometrical configurations are carried out. The aim is to identify a design that offers an acceptable compromise between maximum possible output temperature, thermal homogeneity and reduced pressure drop. This involves adjusting parameters such as orifice spacing and orifice arrangement. As explained in previous sections, smaller orifices with reduced orifice spacing can increase flow velocity and improve convective heat transfer alongside thermal homogeneity, leading to better cooling and lower wall temperatures, resulting in lower cell operating temperatures and, hence, higher electricity production from the panel attached to the heat exchanger.

However, this configuration may result in higher pressure drops and lower thermal output due to limited fluid flow. An optimized layout that ensures uniform flow distribution can help achieve thermal homogeneity and efficient heat transfer. In this regard, incorporating an accumulation zone at the inlet and outlet, alongside a discontinuous baffle, can effectively distribute the fluid evenly, minimize overheating zones, and ensure efficient heat extraction. This design induces a flow path that minimizes dead zones at corners and ensures uniform fluid movement over the entire surface of the heat exchanger, prioritizing. Analyzing the trends obtained in Section 3.1 about orifice dimensions and orifice spacing, Tab. 6 presents the main geometric considerations taken in this regard for the third and rest of the proposed designs. Fig. 5 shows a rendering of Design C proposed heat exchanger, together with the temperature map, where the objective is developing a model with an intermediate approach between wall cooling and thermal energy development. In turn, Tab. 7 presents the CFD results and compares them to the other models focused on different energy generation previously developed.

Tab. 6: Geometric considerations for the three proposed designs.

Parameter	Design A	Design B	Design C
Orifice size [mm]	5	9	7
Orifice spacing [mm]	50	15	20

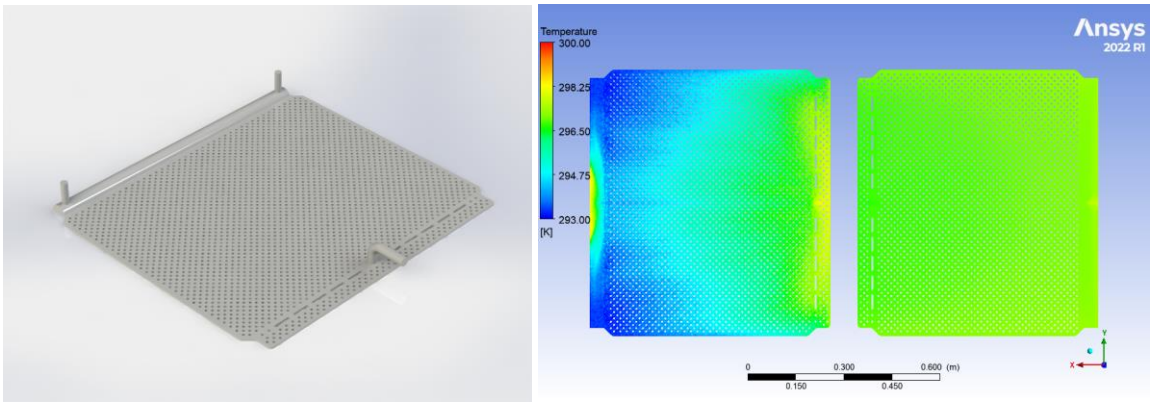

Fig. 5: Rendering of Design C (left), and its temperature field (right).

Tab. 7: CFD results performed on the three models.

Parameter	Design A	Design B	Design C
ΔT [K]	6.9	5.1	4.2
T_{wall} [K]	299.2	296.7	297.5
h_{conv} [W m^{-2} K^{-1}]	181.9	324.2	615.8
Nu	3.2	5.9	11.3
σ_T [K]	1.6	1.5	1.2
P_{th} [W m^{-2}]	604.8	450.2	372.2
η_{th} [%]	60	45	37
T_{PV} [K]	299.8	296.8	297.6
P_{el} [W m^{-2}]	183.1	185.3	184.7
η_{el} [%]	18.3	18.5	18.4
ΔP [Pa]	72	271	36

Tab. 8: Steady-State Thermal results for the half-PV panel model without cooling.

Parameter	Half-PV panel model
P_{el}[W m^{-2}]	144.1
η_{el}[%]	14.4
T_{PV}[K]	364.1

In addition, through multiparametric analysis, the pressure drop curve against flow rate was determined for Design A. Fig. 6 presents the curve, illustrating how increasing the flow rate leads to a corresponding rise in pressure drop. Given the similar geometric configurations and fluid dynamics principles applied across the other designs, it is expected that the pressure drop behaviour for these designs will follow a similar trend.

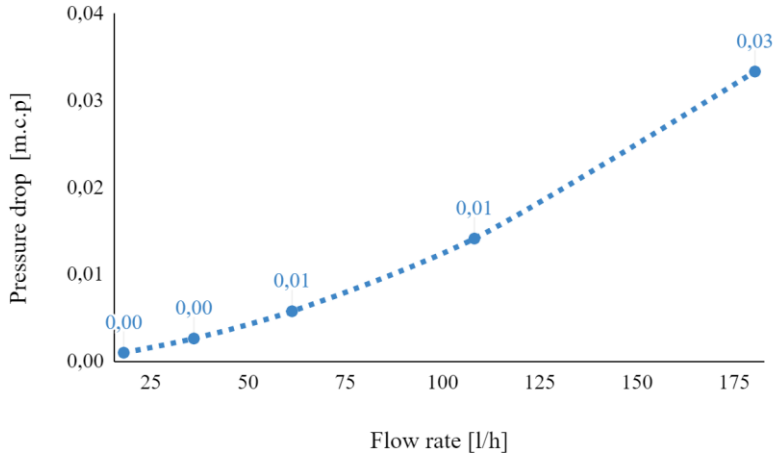

Fig. 6: Flow rate vs. Pressure drop for Design A.

4.2. Comparative analysis with different proposed configurations.

Three different designs were proposed for the polymeric heat exchanger to convert a PV panel into a PVT retrofit. The designs were tailored to address distinct objectives: enhancing electrical output by cooling the PV panel, maximizing thermal power generation, and a balanced trade-off design that aims to achieve both goals. The analysis evaluates each design's performance, providing insights into their suitability based on varying user demand profiles for electricity and heat. For the study, a conventional PV panel of 300W_{el} is chosen as a reference. Fig. 6 shows a visual comparison (not to scale) of CFD results between the different designs developed.

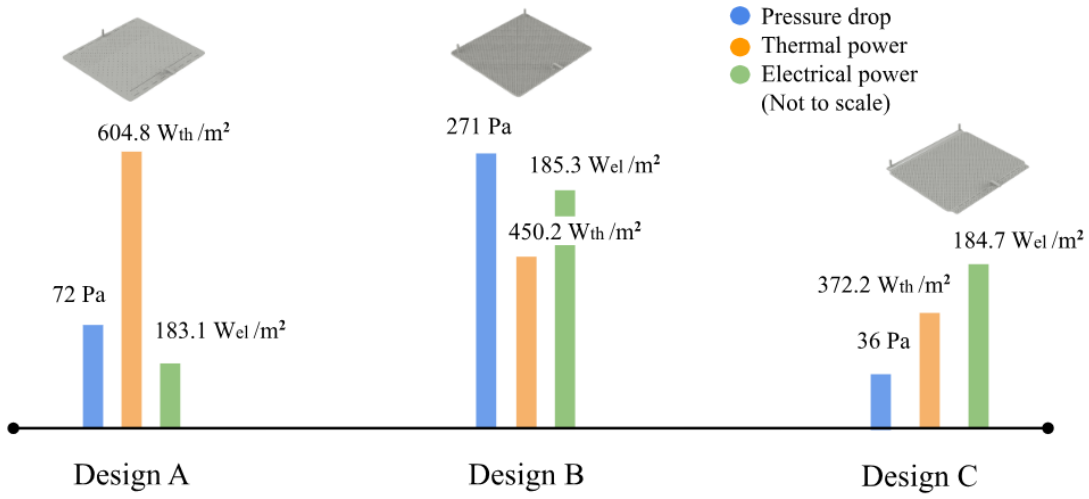

Fig. 7: Visual comparison (not to scale) of CFD results between the developed designs.

Design A focuses on maximizing thermal energy generation. This design features modifications that optimize the heat exchanger's performance in transferring solar thermal energy to the working fluid, enhancing the system's overall thermal output. The increased electrical output of this design is calculated as +21.3% compared to a PV-only panel, with a thermal power development of 604.8 W_{th} and a pressure drop of 72 Pa. This makes Design A suitable for applications where the primary demand is for heat, such as domestic hot water or low-grade industrial process heat.

On the other hand, Design B incorporates smaller flow channels by reducing orifice spacing to maximize the convective heat transfer coefficient and Nusselt values, which increases the cooling effect on the PV cells. This significantly reduces the PV cell temperature, leading to a noticeable relative improvement in electrical efficiency by up to +22.2%, compared to a PV-only panel. The design develops a thermal power output of 450.2 W_{th} and has a pressure drop of 271 Pa. The reduction in temperature correlates with an increase in electrical production, making this design ideal for scenarios where the primary demand is for electricity.

However, deeper analysis is needed to address the pressure drop and pumping requirements.

Lastly, Design C was initially conceived as an intermediate option between Design A and Design B, intending to balance the cooling of the PV panel and the generation of thermal energy. Although it was expected to be closer in performance to Design B due to similar orifice size and spacing, the inclusion of an accumulation zone in Design C led to a notable reduction in pressure drop. This adjustment resulted in a model with a significantly lower pressure drop (38 Pa) while achieving less thermal output (372.2 Wth /m^2) but similar electrical efficiency to those of Design B (184.7 Wth /m^2), representing an increased +21.7% electrical efficiency compared to a PV-only panel.

5. Discussion and conclusions

This study conducted an extensive comparative analysis of various geometrical configurations for a thermal absorber, focusing on KPIs such as pressure drop, temperature gain, thermal absorber wall temperature, convective heat transfer coefficient, Nusselt number, temperature standard deviation, thermal power, and electrical efficiency. The initial phase involved examining orifice sizing and spacing to identify performance trends. Based on these insights, a model was iteratively refined to optimize thermal power, proposing two additional models: one emphasizing thermal homogeneity and another balancing pressure drop reduction and homogeneity. The findings provide a comprehensive understanding of how geometric modifications affect absorber performance, guiding future design improvements. The results demonstrated an electrical enhancement of approximately +21.3%, +22.2% and +21.7% compared to the PV-only panel before retrofitting this solution into PVT systems. Additionally, the system provided a substantial energy surplus in the form of low-grade hot water, showing thermal efficiencies of 60%, 45% and 37%, representing thermal energy outputs of 604.8 W/m^2, 450.2 W/m^2, and 372.2 W/m^2 across the three different configurations. This thermal power development and electrical efficiency enhancement are two aims that could be tackled in the design phase and that depend on the user's specific needs. The choice between these designs should be guided by the particular user demand profile. Users with a higher electricity demand may prefer the electrical enhancement designs, as they maximize the PV panel's electrical efficiency. Conversely, users requiring more thermal energy should opt for the thermal power development design, which excels in heat generation.

Future work will explore further optimization of these models under varying operational and physical conditions, such as the integration of advanced polymeric materials or nanofluids as heat transfer fluid to enhance overall system efficiency, and experimental validation utilizing prototyping.

6. Acknowledgments

This study has been developed under the framework of the PVT4EU project, granted by the Clean Energy Transition Partnership Programme (project ID. CETP-2022-00403). The work is supported by national funds through Sweden: Swedish Energy Agency (P2023-00884); Denmark: Innovation Fund Denmark (3112-00010B); and Portugal: FCT- Fundação para a Ciência e a Tecnologia, I.P. This work is also supported by Spanish funds in the framework of the Juan de la Cierva Incorporación Fellowship awarded to Dr. María Herrando, funded by the Ministry of Science, Innovation and Universities (AEI) and cofounded by the EU (through the NextGeneration funds) [grant number IJC2020-043717-I].

The study was also supported by the Swedish Energy Agency (grant number 2021-036454)

7. References

Agathokleous, R.A., Ding, Y., Ekins-Daukes, N., Herrando, M., Huang, G., Kalogirou, S., Markides, C.N., Mousa, O.B., Otanicar, T., Taylor, R.A., Wang, K., 2023. A review of solar hybrid photovoltaic-thermal (PV-T) collectors and systems. *Progress in Energy and Combustion Science* 97, 101072. https://doi.org/10.1016/j.pecs.2023.101072

Chow, T.T., 2010. A review on photovoltaic/thermal hybrid solar technology. *Applied Energy* 87, 365–379. https://doi.org/10.1016/j.apenergy.2009.06.037

Cristofari, C., Notton, G., Canaletti, J.L., 2009. Thermal behavior of a copolymer PV/Th solar system in low flow rate conditions. *Solar Energy* 83, 1123–1138. https://doi.org/10.1016/j.solener.2009.01.008

Cristofari, C., Notton, G., Poggi, P., Louche, A., 2002. Modelling and performance of a copolymer solar water heating collector. *Solar Energy* 72, 99–112. https://doi.org/10.1016/s0038-092x(01)00092-5

Fudholi, A., Sopian, K., Yazdi, M.H., Ruslan, M.H., Ibrahim, A., Kazem, H.A., 2014. Performance analysis of photovoltaic thermal (PVT) water collectors. *Energy Conversion and Management* 78, 641–651. https://doi.org/10.1016/j.enconman.2013.11.017

Guarracino, I., Freeman, J., Ramos, A., Kalogirou, S.A., Ekins-Daukes, N.J., Markides, C.N., 2019. Systematic testing of hybrid PV-thermal (PVT) solar collectors in steady-state and dynamic outdoor conditions. *Applied Energy* 240, 1014–1030. https://doi.org/10.1016/j.apenergy.2018.12.049

He, W., Chow, T.-T., Ji, J., Lu, J., Pei, G., Chan, L.-S., 2006. Hybrid photovoltaic and thermal solar-collector designed for natural circulation of water. *Applied Energy* 83, 199–210. https://doi.org/10.1016/j.apenergy.2005.02.007

Herrando, M., Hellgardt, K., Markides, C.N., 2014. A UK-based assessment of hybrid PV and solar-thermal systems for domestic heating and power: System performance. *Applied Energy* 122, 288–309. https://doi.org/10.1016/j.apenergy.2014.01.061

Herrando, M., Markides, C.N., Huang, G., Otanicar, T., Mousa, O.B., Agathokleous, R.A., Ding, Y., Kalogirou, S., Ekins-Daukes, N., Taylor, R.A., Wang, K., 2023. A review of solar hybrid photovoltaic-thermal (PV-T) collectors and systems. *Progress in Energy and Combustion Science* 97, 101072. https://doi.org/10.1016/j.pecs.2023.101072

Herrando, M., Ramos, A., Zabalza, I., Markides, C.N., 2019. A comprehensive assessment of alternative absorber-exchanger designs for hybrid PVT-water collectors. *Applied Energy* 235, 1583–1602. https://doi.org/10.1016/j.apenergy.2018.11.024

Huang, B.J., Lin, T.H., Hung, W.C., Sun, F.S., 2001. Performance evaluation of solar photovoltaic/thermal systems. *Solar Energy* 70, 443–448. https://doi.org/10.1016/s0038-092x(00)00153-5

Ibrahim, A., Othman, M.Y., Sopian, K., Ruslan, M.H., Alghoul, M.A., Yahya, M., Zaharim, A., 2009. Performance of photovoltaic Thermal collector (PVT) with different absorbers design. **WSEAS Transactions on Environment and Development 5, 321–330.**

Makki, A., Omer, S., Sabir, H., 2015. Advancements in hybrid photovoltaic systems for enhanced solar cells performance. *Renewable & Sustainable Energy Reviews* 41, 658–684. https://doi.org/10.1016/j.rser.2014.08.069

Michael, J.J., S, I., Goic, R., 2015. Flat plate solar photovoltaic–thermal (PV/T) systems: A reference guide. *Renewable & Sustainable Energy Reviews* 51, 62–88. https://doi.org/10.1016/j.rser.2015.06.022

Nahar, A., Hasanuzzaman, M., Rahim, N.A., Parvin, S., 2019. Numerical investigation on the effect of different parameters in enhancing heat transfer performance of photovoltaic thermal systems. *Renewable Energy* 132, 284–295. https://doi.org/10.1016/j.renene.2018.08.008

Tripanagnostopoulos, Y., Nousia, Th., Souliotis, M., Yianoulis, P., 2002. Hybrid photovoltaic/thermal solar systems. *Solar Energy* 72, 217–234. https://doi.org/10.1016/s0038-092x(01)00096-2

Xu, P., Zhang, X., Shen, J., Zhao, X., He, W., Li, D., 2015. Parallel experimental study of a novel super-thin thermal absorber based photovoltaic/thermal (PV/T) system against conventional photovoltaic (PV) system. *Energy Reports* 1, 30–35. https://doi.org/10.1016/j.egyr.2014.11.002

Numerical study of the system specifications effect on the performance of a Brine/Water heat pump in combination with PhotoVoltaic Thermal solar

Mohamad Ali Jaafar[1] and Bharat Chhugani[2]

[1] Dualsun, Marseille (France)

[2] Institute for Solar Energy Research in Hamelin, Emmerthal (Germany)

Abstract

PhotoVoltaic Thermal (PVT) collectors are an exciting energy technology that produces both heat and electricity. They offer a very suitable source for brine-to-water heat pumps (HP), as PVT can be used as the direct heat source for the evaporator and additionally provide electricity for the compressor. The system combines HP and PVT to offer an efficient energy solution for the heat demands of buildings. However, there are still many uncertainties about the system design and configuration. The main goal of this paper is to study the effect of the different hydraulic configurations and the system specifications on the overall system performance. For instance, the numerical study in Strasbourg shows that a heat pump with a minimum temperature limit at the evaporator inlet of -15 °C enhances by 20 % the Seasonal Performance Factor (SPF) compared to a heat pump with a temperature limit of -10 °C. However, the maximum temperature limit has a negligeable impact on the system's performance. Moreover, it has also been shown that the self-consumed photovoltaic energy improves the overall system performance by 7 %.

Keywords: Photovoltaic thermal solar collectors (PVT), Heat pump (HP), energy system analysis, seasonal performance factor (SPF), numerical simulations, TRNSYS

1. Introduction

Heat Pumps (HP) coupled with Photovoltaic-Thermal (PVT) collectors are becoming more and more popular since they coproduce heat and electricity and enhance the overall system performance. Researchers and industries worldwide are studying and analyzing this combination to meet the thermal needs of buildings (Kazem et al., 2024). James et al. (2021) have concluded that PVT collectors are more efficient in combination with HP than solar thermal collectors. However, they identified future research needs relating to some limitations according to the different PVT configurations during freezing, snowfall, pressure drop and corrosion. Miglioli et al. (2023) highlighted that the integration of PVT to the evaporator side of the HP systems allows to increase the heat recovery by the heat source and then improving system performances, however, the distinction of solar and evaporator circuits would be relevant and flexible especially when a second heat source is used.

Moreover, Vaishak and Bhale (2019) have shown that the systems combining HP and PVT collectors are more energy efficient and reliable compared to other conventional and non-conventional energy resources for hot water applications. A detailed simulation study carried out by Chhugani et al. (2023) showed that PVT-heat pump systems can significantly contribute to reducing CO2 emissions compared to fossil heating systems and represent a promising, noise-free alternative to air-source heat pumps. Furthermore, they found that combining PVT collectors with ground-coupled heat pump systems allows 35% smaller dimensioning of Borehole Heat Exchangers (BHE) with lower CO2 emissions simultaneously.

Helbig et al. (2018) found that PVT collector designs with high heat loss coefficients (c1 and c2 according to ISO 9806) can work both as solar collectors and environmental heat exchangers and achieve a higher/better system efficiency with direct PVT-heat pump combinations compared to PVT collectors with lower heat loss coefficients. Jaafar et al. (2022) also showed numerically that the most influencing parameter on system performance is PVT collectors' first-order heat loss coefficient compared to other thermal coefficients.

© 2024. The Authors. Published by International Solar Energy Society
Selection and/or peer review under responsibility of Scientific Committee
10.18086/eurosun.2024.07.09 Available at http://proceedings.ises.org

The presented paper focuses on the effect of the different hydraulic configurations of the sink circuit and the different HP specifications on the overall performance of the system combining HP and PVT. First, it describes the system, and the numerical methodology used for this study. Then, the results are presented, comparing the different system scenarios, including different heating systems in the building and different HP specifications as maximum and minimum temperature limits at the evaporator and the compressor technology.

2. Methodology

The TRNSYS software is used for the present study. Several models (TRNSYS types) were developed and assembled to simulate HP and PVT systems, the details of the models are shown in Table 1. The PVT type used herein has been validated with experimental measurements (Chhugani, 2020). As shown in Figure 1, PVT is the single heat source of the HP that produces heat to cover the domestic hot water (DHW) and space heating (SH) needs of the building. The backup electric heater is located in the flow pipe of the heat pump. The mixing valve in front of the evaporator prevents too high temperatures from reaching the evaporator of the heat pump (set point of the mixing valve depends on the maximum temperature limit of the evaporator of the HP). The photovoltaic energy produced by PVT can be consumed directly by the HP compressor.

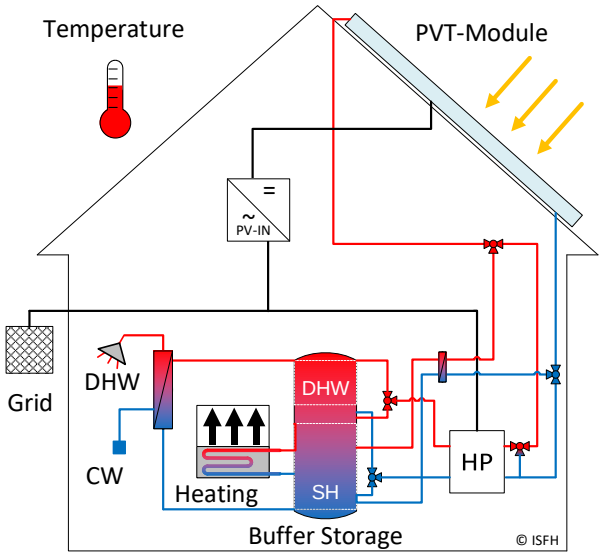

Fig. 1: The hydraulic schema of the system, including combi storage in the sink side

Tab 1: Various component models used for TRNSYS System simulations

Description	Documentation/Reference
Thermal building	TRNSYS Multi zone Building ("Multizone Building modeling with Type56 and TRNBuild," 2012)
PVT collector	Uncovered PVT (photovoltaic-thermal) collector (Stegmann et al., 2011)
Heat pump	Compressor heat pump model (Afjei and Wetter, 1997)
Thermal storage tank	Multiport thermal buffer Store tank model (Druck, 2006)
Radiator heating	Model for Radiator heating System for Buildings (Holst, 1996)

The simulation study investigates three distinct configurations of photovoltaic-thermal (PVT) systems integrated with heat pumps, as illustrated in Figure 2. All these configurations utilize PVT collectors as the sole heat source for the heat pumps, differing only in the hydraulic arrangement of the sink side. In the first configuration, a combi storage tank supplies space heating (SH) and domestic hot water (DHW) to the building, while the second configuration features two separate storage tanks, one for SH and the other for DHW. In the

third configuration, a single storage tank is used for DHW, and the SH system is directly connected to the heat pump.

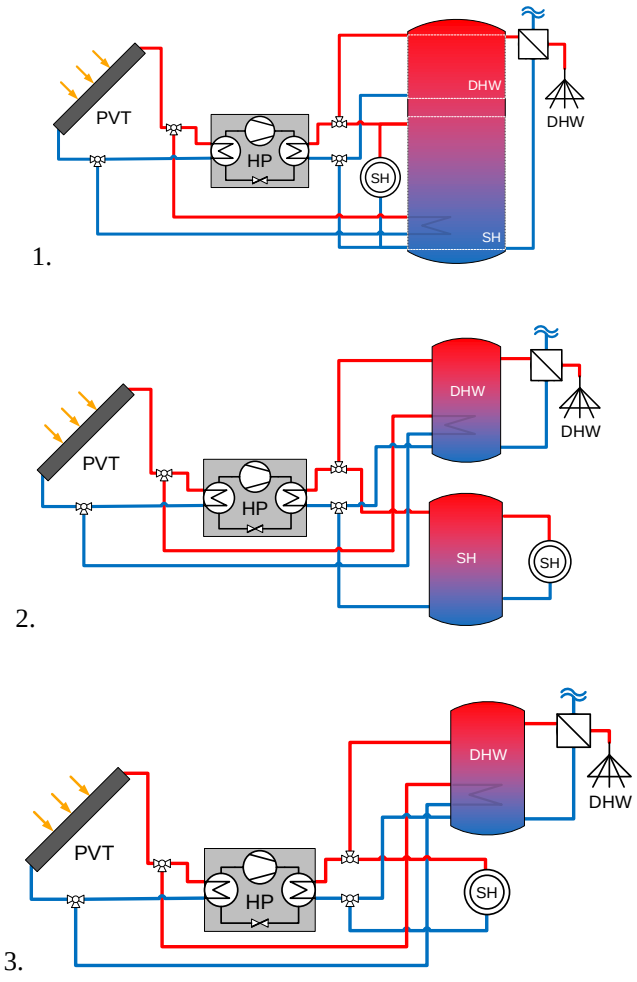

Fig. 2: The three investigated configurations of the sink side

The used building is a single-family house with a total surface of 140 m^2 and a space heating demand of 48 $kWh/m^2.a$. The external wall and the roof ceiling have a U-value construction of 0,28 and 0,19 $W/m^2.K$, respectively. The domestic hot water demand is 2141 kWh/a (150 L/day at 45 °C which corresponds to 3 people) and the daily domestic hot water profile is shown in Figure 3. A detailed description of the boundary conditions, load profiles, and building components (SFH45) is published in IEA Task 44 (Dott et al., 2013).

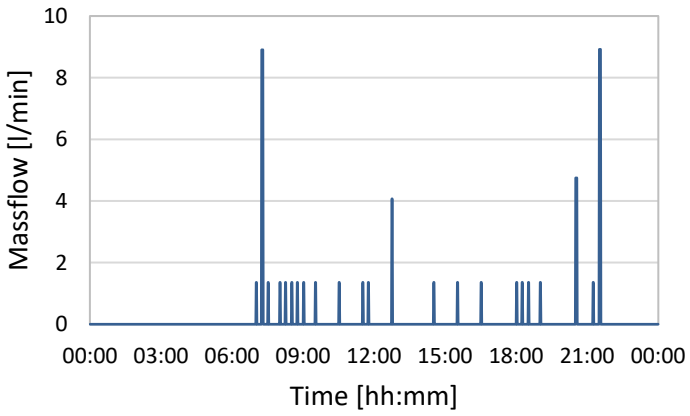

Fig. 3: Domestic hot water demand (DHW) of the building at 45°C

Additional to different configuration as shown in Figure 2, the building is also simulated with two different heating concepts: floor heating and radiator heating. Figure 4 shows the heating characteristic curves of the two different heating systems respect to flow temperature.

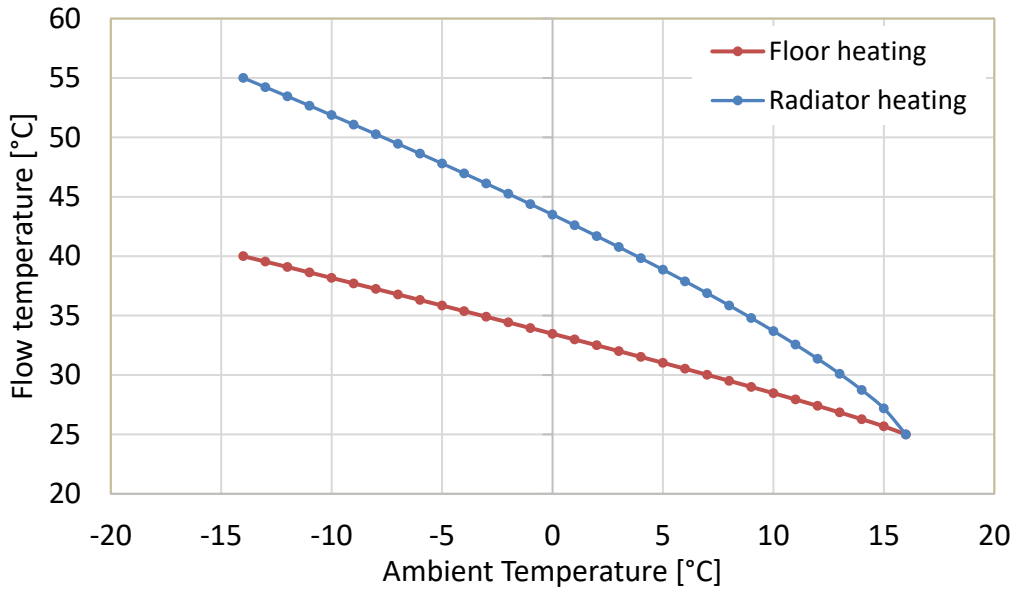

Fig. 4: Heating characteristic curves for floor and radiator heating

The simulated PVT collector, with a surface of 1.95 m² and photovoltaic peak power of 425 W, has the following thermal coefficients according to the Solar Keymark test. The parameters of the PVT collector are shown in Table 2. Additionally, in all the configurations of PVT to heat pump, the PVT collectors are regularly defrosted to account for model uncertainties below 0 °C as explained in (Chhugani, 2020).

Tab. 2: Thermal coefficients according to Solar Keymark certification (licence number 011-7S3219 P)

Coefficient	Description and [unit]	Value
η0,b	Optical efficiency [-]	0,38
c1	Heat loss coefficient [W/m²K]	37,44
c2	Temperature dependence of the heat loss coefficient [W/m²K²]	0
c3	Wind speed dependence heat loss coefficient [J/m³K]	7,31
c4	Sky temperature dependence of the heat loss coefficient [-]	0
c5	Effective thermal capacity [kJ/m²K]	29,46
c6	Wind speed dependence conversion factor [s/m]	0,046
c7	Wind speed dependence of IR radiation exchange [W/m²K⁴]	0
c8	Radiation losses [W/m²K⁴]	0
Kd	Incidence angle modifier for diffuse solar radiation [-]	0,98

The heat pump used is an inverter whose compressor speed depends on both heat demand in the building and the heat provided by the heat source (PVT) and their temperature levels. The flow rates on the source and the sink sides are controlled to maintain a temperature difference of 5 and 3 K, respectively. The thermal power of the HP is 9.1 kW B0/W35, and the thermal output of the heat pump at different inlet temperatures and different compressor speeds is shown in below Figure 5.

During the operation of the heat pump, the mean temperature of the PVT reduces until the power equilibrium of the evaporator and PVT. A simple and robust control strategy is implemented in the numerical model. The compressor speed is adapted firstly to meet heating or domestic hot water demand as well as to avoid cut-off of the compressor due to very high temperatures or very low temperatures on the evaporator side. The adaption is done according to the compressor envelope, as shown in Figure 6. The distinction is also made between

space heating and domestic hot water loading since the heat pump must provide heat at different temperature levels.

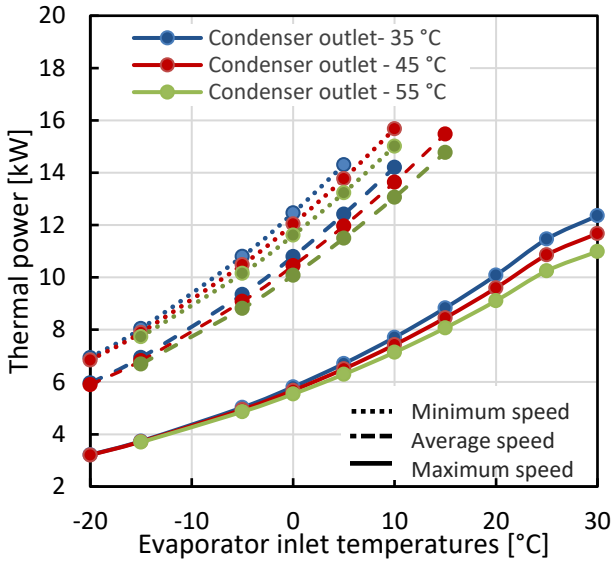

Fig. 5: Thermal output (y-axis) at different evaporator inlet temperatures (x-axis) for condenser outlet temperatures for the minimum, average and maximum compressor speed.

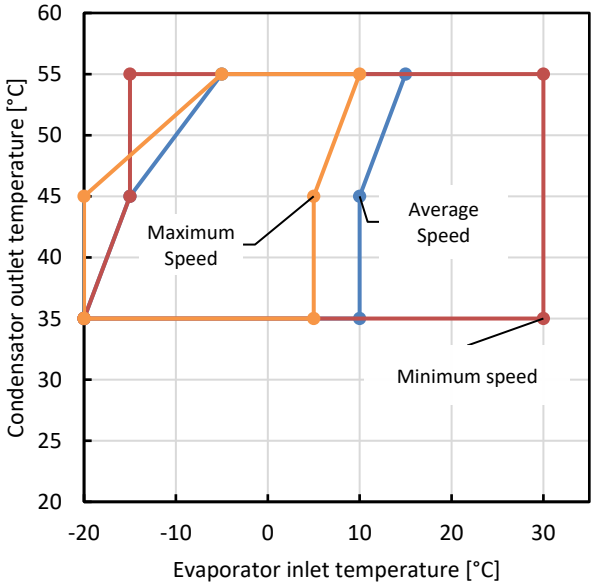

Fig. 6: Compressor envelope of the brine-water heat pump with different compressor speeds

For each system scenario, the thermal Seasonal Performance Factor (before storage) is defined as the ratio between the produced thermal energy and the consumed electric energy by the system. For a whole year of system operation, it can be calculated following this equation (Eq. 1):

$$SPF = \frac{\int (\dot{Q}_{HP} + \dot{Q}_{backup} + \dot{Q}_{PVT,Defrosting})\, dt}{\int (\dot{E}_{HP} + \dot{E}_{backup} + \dot{E}_{pump,defrosting})\, dt} \qquad \textit{Eq. 1}$$

$\dot{Q}$ stands for the supplied heat and $\dot{E}$ stands for the electric consumption of each component.

As an additional system indicator, the SPF_{Grid} considering the self-consumed photovoltaic energy by the heat pump is calculated following this equation (Eq. 2):

$$SPF_{Grid} = \frac{\int (\dot{Q}_{HP} + \dot{Q}_{backup} + \dot{Q}_{PVT,Defrosting})\, dt}{\int (\dot{E}_{HP} + \dot{E}_{backup} + \dot{E}_{pump,defrosting} - \dot{E}_{PV_el_self})\, dt} \qquad \textit{Eq. 2}$$

The difference between the indicators shows the enhancement in the system performance due to the photovoltaic energy produced by the PVT and at the time if the HP is running, it consumes this photovoltaic electricity. Otherwise, this energy is consumed by other electric equipment in the building (without household electricity) and rest of the electricity is sent to the grid. In all cases, this photovoltaic energy is a very important source of CO_2 emissions and money saver for the building owner.

All the simulations are performed with 10 PVT and a 9,1 kW (B0/W35) HP. The five studied parameters are detailed in the following:

- The sink circuit hydraulic configuration as shown in Figure 2: combi storage (560L used for both DHW and SH), double storages (one of 200L for DHW and another of 300L for SH) or only one storage for DHW (200L, the SH is connected directly to the condenser of the HP).
- The compressor technology: inverter or fixed-speed.
- Minimum and maximum temperature limits of the HP evaporator. When the temperature at the PVT outlet is lower than the minimum temperature limit, the HP is not allowed to provide heat to the system and the electric backup is activated. When the temperature at the PVT outlet is higher than the maximum temperature limit, the flow rate in the PVT circuit is reduced thanks to the mixing valve so that the temperature at the inlet of the evaporator does not exceed this maximum limit.
- The heating system used to distribute heat in the building is floor heating or water radiators (heating curves are illustrated in Figure 4).

3. Results

According to the above-described methodology, the obtained results of both SPF and SPF_{Grid} are provided in the following table:

Tab. 3: The obtained results according to the different system scenarios

Scenario	Hydraulic configuration	Compressor technology	T_{eva_min}	T_{eva_max}	Heating system	SPF	SPF_{Grid}
1	Combi storage	Inverter	-15 °C	+25 °C	Floor heating	3,6	3,87
2	Double storages	Inverter	-15 °C	+25 °C	Floor heating	3,55	3,8
3	One storage for DHW	Inverter	-15 °C	+25 °C	Floor heating	3,33	3,56
4	Combi storage	Inverter	-10 °C	+25 °C	Floor heating	2,8	2,99
5	Combi storage	Inverter	-5 °C	+25 °C	Floor heating	1,9	2,1
6	Combi storage	Inverter	-15 °C	+10 °C	Floor heating	3,55	3,79
7	Combi storage	Inverter	-10 °C	+20 °C	Floor heating	2,75	2,94
8	Combi storage	Inverter	-15 °C	+ 25 °C	Radiators	3,33	3,53
9	Combi storage	ON/OFF	-10 °C	+ 25 °C	Floor heating	2,56	2,73

The results of the influencing parameters are shown in Figure 7. These results show that no matter what the system specifications are, the SPF_{Grid} (orange markers) are, according to all the studied scenarios, higher by almost 7% than the thermal SPF (blue markers). This shows that the photovoltaic energy produced by the PVT enhances the system's overall performance, saving both money and CO_2 emissions. It is green electricity available by PVT at free to use and the smart control strategies can be applied here in the future to enhance more self-consumption, which increases the SPF_{Grid}. The rest of the photovoltaic energy can feed other electric equipment in the building, otherwise it can be sent back to the electrical grid. In all cases, it brings benefits to the building and the environment saving both money and CO_2 emissions. The following subsections discuss only thermal SPF according to each parameter studied.

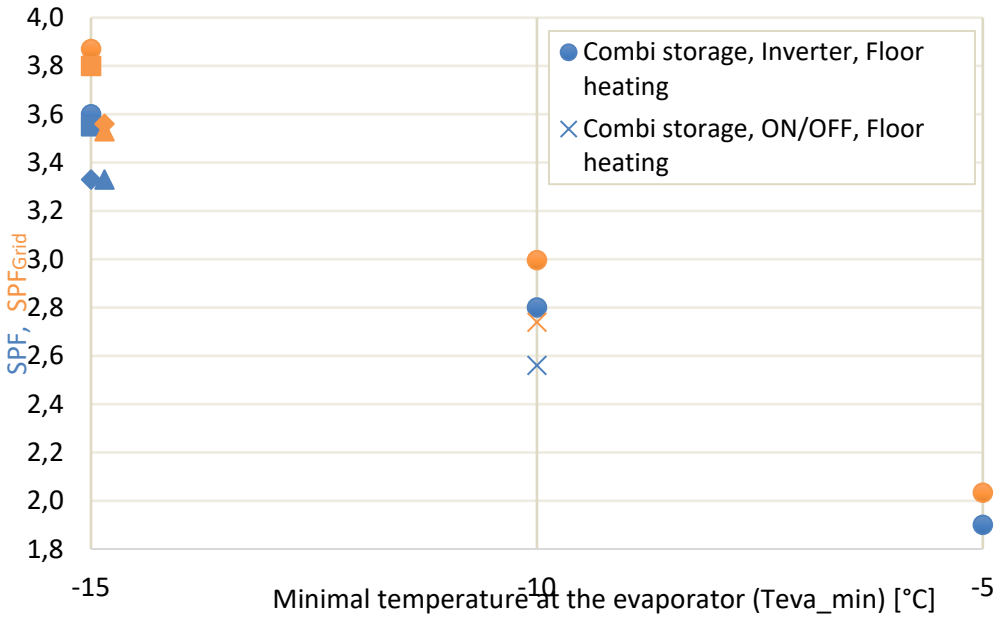

Fig. 7: The obtained results of the system performances SPF (blue markers) and SPF_{Grid} (orange markers)

3.1. Maximum temperature limit of the evaporator

When the PVT is directly connected to the evaporator of the HP, special attention must be given to the high temperatures that can be provided by the PVT, especially during summer and sunny times. When the temperature produced by the PVT exceeds the maximum temperature limit of the evaporator, which is a characteristic of the HP depending on both the used refrigerant inside the HP and the compressor operating map, the flow rate from the PVT is derived by the mixing valve so that the evaporator is protected. Although it is a critical topic in protecting HP operations, the results show that the maximum temperature limit on the evaporator side does not influence the overall system performance. The comparison between scenarios 1 (SPF = 3,6) and 6 (SPF = 3,55) and between scenarios 4 (SPF = 2,8) and 7 (SPF = 2,75) shows that the SPF is not really impacted (the system is more performant by less than 2% with higher maximum limits) when the maximum limit is decreased for both cases. It is worth mentioning that scenario 6 with +10°C represents the lowest maximum limit existing in the market of brine/water HP. The obtained result is normal for two reasons. The first is that it is a low-temperature application in which the HP does not require high temperatures to operate and provide heat in the building. The second is that the recorded average temperature at the outlet of the PVT is -1 °C, showing that temperatures that are too high are rarely observed, only during the summer season when there is no space heating demand in the building. Since the maximum temperature limit does not influence the system performance, the results according to it are not shown in Figure 7.

3.2. Minimum temperature limit of the evaporator

As for the maximum temperature limit, the minimum one is also a characteristic of the HP. However, the results show that it is a crucial parameter on the system performance: the SPF is significantly deteriorating when the minimum temperature limit increases. According to the obtained results, the system performance decreases by 22% when the minimum temperature limit passes from – 15 °C (SPF scenario 1 = 3,6) to – 10 °C (SPF scenario 4 = 2,8) and by 32% when it passes from – 10 °C (SPF scenario 4 = 2,8) to – 5 °C (SPF scenario 5 = 1,9). The impact of the minimum temperature limit can be clearly seen in Figure 7 where the horizontal axis shows the minimum temperature limit in the curve. For the exact system specifications, circle markers follow a decreasing curve when this limit increases. It has an average effect on system performance since the HP cannot run anymore, and the electric backup is activated when the temperature at the PVT outlet is lower than the minimum temperature limit of the evaporator. The minimum temperature limit is reached quicker when it is higher for the same heat source (same number of the same PVT) and the same heat demand. One must give special attention to this parameter when coupling HP with PVT.

3.3. Compressor technology (fixed or variable speed)

A variable speed, also called inverter, heat pump can adjust the speed of its compressor according to what happens in its surroundings: the heat source and the heat sink. It has many operation points according to the temperature levels in the evaporator and the condenser as well as to the heat demand. This technology is useful to save the overall electricity consumed and ensures a longer lifetime for the system with smooth and progressive HP start and stop. Numerical simulations have been performed to study the impact of this technology compared to the classic one: constant speed, also called ON/OFF, heat pump, which no matter what is happening in its surroundings, has only one compressor speed. The comparison between the scenarios 4 and 9 in Table 3 for a minimum temperature limit of – 10 °C of the evaporator shows that the inverter HP (SPF scenario 4 = 2,8) is more performant than a constant speed one (SPF scenario 9 = 2,56). This difference of almost 9% is also observed in Figure 7 for a minimum temperature limit of – 10 °C for the evaporator between the blue circle and the blue cross. The difference obtained is not as great as expected. This can be explained by the hydraulic configuration of the sink circuit, including a storage tank, which softens the impact of ON/OFF technology since the excess heat produced by the HP is stored for another time.

3.4. Hydraulic configuration of the sink circuit

Three different hydraulic configurations of the sink circuit between the heating system and the condenser of the HP are studied herein. All the configurations include storage for the domestic hot water. The SPF of configurations, including storage for the space heating (combi storage or double storage), are almost equal: 3,6 and 3,55 according to scenarios 1 and 2 in Table 3 and circle and square blue markers in Figure 7. The slight difference can be explained by the fact that the combi storage has less heat losses than the double storages overall the year since its surface is lower than the total surface of the double storages.

However, the configuration including only one storage for the DHW while the space heating is directly connected to the condenser of the HP has the lowest SPF (scenario 3 = 3,33 in Table 3, with the diamond blue marker in Figure 7) compared to the others. The deterioration of almost 7% in the SPF is explained by the fact that the space heating system has less thermal inertia with no heat storage, which causes many start and stop losses of the HP. At the beginning of each cycle, the compressor starts for a few seconds before the condenser produces heat in the space heating. These frequent starting cycles make the system consume electricity without being useful for longer than the configurations, including storage for the SH.

3.5. Heating system in the building

The impact of the heating system was studied for the same building. As expected, the obtained results show that the use of water radiators instead of the floor heating deteriorates by almost 7% the SPF of the system. The scenario 9 with water radiators has an SPF of 3,33 (blue triangle in Figure 7) lower than the SPF of the scenario 1 (blue circle in Figure 7) which is 3,6. This is obvious since the water radiators require higher temperature level to the HP condenser than the floor heating to distribute the same amount of heat in the building. The higher the gap between the evaporation and condensation temperatures, the less the HP is performant (see Figure 4).

4. Conclusions

The present paper investigated the different system specifications on the performance of the energy system combining brine/water heat pump with photovoltaic thermal solar collectors. The condenser of the heat pump produces heat to satisfy both domestic hot water and space heating of the building. The photovoltaic thermal solar collectors constitute the single heat source of the heat pump evaporator thanks to the back-side integrated heat exchanger and can feed the compressor with electricity thanks to the front-side photovoltaic cells. The concept is simple and performant, the photovoltaic thermal solar collectors use both the sun and the ambient air to extract heat from environment feeding the evaporator of the heat pump.

The numerical study presented herein was done using the TRNSYS software by combining the TYPES of the system components. For the same solar installation, the study investigated the system specifications, such as the heat sink hydraulic configuration and the heating system as well as the heat pump specifications, such as the compressor technology and both minimum and maximum temperature limits of the evaporator.

The simulations were performed for a well-insulated single-family house of 140 m² in Strasbourg (France).

The energy system is composed of 10 photovoltaic thermal solar collectors connected directly to the primary circuit of a 9.1 kW B0/W35 brine/water heat pump. Both thermal and grid seasonal performance factors have been estimated for each simulated scenario.

The results have shown the following:

- The photovoltaic energy produced by the solar collectors improves the system performance by 7 % no matter the other system specifications are.
- With space heating storage in the secondary circuit, the inverter compressor heat pump performs 9 % better than a fixed-speed heat pump. We think that this enhancement would be higher when the space heating system is directly connected to the heat pump condenser.
- The maximum temperature limit of the evaporator has no impact on the system performance. However, the minimum temperature limit is critical on the system performance. The thermal SPF of a heat pump with a – 15 °C of a minimum temperature of the evaporator is 3,6 while the SPF of a -10 °C and – 5 °C are 2,8 and 1,9, respectively.
- The presence of any type of water storage between the heat pump and the heating system in the building ensures a better system performance than the sink configuration without any storage.
- A floor heating system performs better than water radiators since the required flow temperature is lower.

5. References

Afjei, T., Wetter, M., 1997. Type 401, TRNSYS Compressor heat pump including frost and cycle losses, version 1.1.

Chhugani, B., 2020. Model Validation and Performance Assessment of Unglazed Photovoltaic-Thermal Collectors with Heat Pump Systems, in: Proceedings of the ISES EuroSun 2020 Conference – 13th International Conference on Solar Energy for Buildings and Industry. Presented at the EuroSun 2020, International Solar Energy Society, Online, pp. 1–12. https://doi.org/10.18086/eurosun.2020.05.13

Chhugani, B., Pärisch, P., Helmling, S., Giovannetti, F., 2023. Comparison of PVT - heat pump systems with reference systems for the energy supply of a single-family house. Solar Energy Advances 3, 100031. https://doi.org/10.1016/j.seja.2022.100031

Dott, R., Haller, M.Y., Ruschenburg, J., Ochs, F., Bony, J., n.d. A technical report of subtask C Report C1 Part B. Part B.

Druck, harald, 2006. TRNSYS Type 340, MULTIPORT Store - Model. Stratified fluid storage tank with four internal heat exchangers, ten connections for direct charge and discharge and an internal electrical heater.

Helbig, S., Kirchner, M., Giovannetti, F., Lampe, C., Littwin, M., Kastner, O., 2018. PVT-Kollektoren als bisolare Wärmepumpenquelle – Ein Simulationsvergleich zwischen Polysun und TRNSYS.

Holst, 1996. TRNSYS Models for Radiator Heating Systems.

Jaafar, M.A., Chhugani, B., Brottier, L., 2022. Numerical Study of the Effect of Hybrid Solar Collectors on the Performances of the System Combining PVT With Heat Pumps, in: Proceedings of EuroSun 2022 - ISES and IEA SHC International Conference on Solar Energy for Buildings and Industry. Presented at the EuroSun 2022 - ISES and IEA SHC International Conference on Solar Energy for Buildings and Industry, International Solar Energy Society, Kassel, Germany, pp. 1–8. https://doi.org/10.18086/eurosun.2022.08.06

James, A., Mohanraj, M., Srinivas, M., Jayaraj, S., 2021. Thermal analysis of heat pump systems using photovoltaic-thermal collectors: a review. J Therm Anal Calorim 144, 1–39. https://doi.org/10.1007/s10973-020-09431-2

Kazem, H.A., Chaichan, M.T., Al-Waeli, A.H.A., Sopian, K., 2024. A systematic review of photovoltaic/thermal applications in heat pumps systems. Solar Energy 269, 112299. https://doi.org/10.1016/j.solener.2023.112299

Miglioli, A., Aste, N., Del Pero, C., Leonforte, F., 2023. Photovoltaic-thermal solar-assisted heat pump systems for building applications: Integration and design methods. Energy and Built Environment 4, 39–56. https://doi.org/10.1016/j.enbenv.2021.07.002

Multizone Building modeling with Type56 and TRNBuild, 2012.

Stegmann, M., Bertram, E., Rockendorf, G., 2011. Model of an Unglazed Photovoltaic Thermal Collector Based on Standard Test Procedures, in: Proceedings of the ISES Solar World Congress 2011. Presented at the ISES Solar World Congress 2011, International Solar Energy Society, Kassel, Germany, pp. 1–9. https://doi.org/10.18086/swc.2011.19.30

Vaishak, S., Bhale, P.V., 2019. Photovoltaic/thermal-solar assisted heat pump system: Current status and future prospects. Solar Energy 189, 268–284. https://doi.org/10.1016/j.solener.2019.07.051

SOLAR THERMAL COLLECTORS AND THEIR COMPONENTS. RESULTS OF LONG-TERM EXPOSURE AT EXTREME TEST SITE

Summary

The reliability of solar thermal collectors is of great economic importance for suppliers, manufacturers and operators due to the long lifetimes demanded by the market. However, it is naturally strongly influenced by the specific climatic conditions at the installation site and is therefore difficult for the industry to estimate. The determination of the load factors for collectors and components under the conditions of the various extreme outdoor weathering locations offers the possibility of influencing the design of thermal solar collectors and components.

To quantify the ageing behavior of solar thermal collectors and their components, we exposed solar thermal flat plate collectors to locations in moderate as reference and with harsh conditions in tropical, alpine, arid and maritime climates. The performance of the solar thermal collectors was measured before and after the outdoor exposure. In order to quantify the influence of the soiling of the transparent cover, the collectors were measured without cleaning and after cleaning. After the performance test, the collectors were opened and subjected to a visual inspection. The effect of direct deposits on the absorber plate and the transparent cover were quantified using spectroscopic measurements.

In this paper we present the results of the latest collector measurements. An exposure time of ten years under stagnation conditions was achieved. This exposure time corresponds to approx. 50 - 100 years of real operation, depending on the location and the application.

Keywords: Solar thermal collectors, components, durability, degradation, optical characterization, thermal stress

1. Introduction

In the SpeedColl and SpeedColl2 [1] projects, a consortium consisting of Fraunhofer ISE and the University of Stuttgart has been working with industry representatives on the loads and resulting tests for solar thermal collectors and their components. As part of the joint project, solar thermal collectors and components were exposed to various climatic regions. The exposure locations were equipped with comprehensive load monitoring to continuously record environmental conditions relevant to ageing. The aim of the exposure was to uncover any weak points at an early stage and to improve the reliability of solar thermal systems in the long term. Ageing effects of components in flat-plate collectors are mainly determined by the temperature level and humidity in the collector. Recently, the trend towards systems with higher solar fractions has led to an increase in stagnation times and temperatures.

The locations are characterized by typical combinations of different stress factors, such as high UV radiation with mechanical wind and snow loads at the Zugspitze location, or strong irradiation at high temperatures and day-night differences at the desert location in Israel. At the maritime location on Gran Canaria, wind loads usually occur in addition to high humidity with a high content of salt aerosols [2].

For the investigation of the weather resistance of solar thermal materials and the analysis of macro- and microclimatic degradation factors, findings from outdoor weathering are indispensable. At the outdoor weathering sites of the SpeedColl 2 project, meteorological data was measured every minute in addition to collector-specific parameters such as absorber or adhesive joint temperatures. Load profiles were created from the recorded data. From the stress profiles, conclusions could be drawn about the effects of the combined stress factors such as UV radiation, humidity, temperature and corrosiveness on the test specimens, which were used for the development of adequate rapid tests.

© 2024. The Authors. Published by International Solar Energy Society
Selection and/or peer review under responsibility of Scientific Committee
10.18086/eurosun.2024.07.10 Available at http://proceedings.ises.org

2. Results

Three different solar thermal collectors types we exposed in various extreme climates while continuously monitoring the outdoor climatic conditions and the micro-climate inside the collector. Within the project, a complex quality assurance of the measured data was successfully defined and implemented. The highest absorber temperatures, up to 225 °C, were measured at the alpine exposure site [3]. The performance of the solar thermal collectors was measured in accordance with the test standard ISO 9806:2013 [4].

In Figure 1 exemplary the comparative performance curves for one solar thermal collector as reference before exposition and after 2.5 years, 7,5 years and 10,0. years of dry exposition (stagnation mode) and the relative deviation to reference at maritime exposition site Gran Canaria are shown. This Figure shows the collector efficiency after cleaning the transparent cover, where G is Global irradiance, $T_{fl,m}$ is the fluid mean temperature and T_{amb} the ambient temperature. The measured difference in collector efficiency before and after cleaning the transparent cover for the collector after 10.0 years of exposure was 17%.

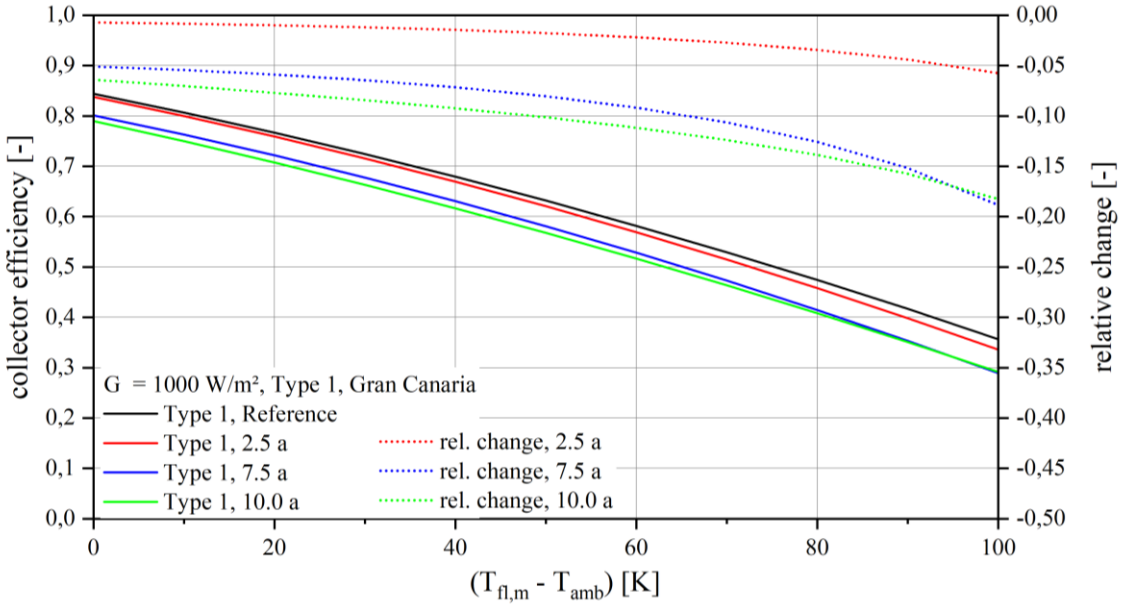

Figure 1 comparative performance test according to ISO 9806:2013 for reference before exposition and after 2.5 years and 7.5 years and 10.0 years of dry exposition and relative deviation to reference at maritime exposition site Gran Canaria

After the performance measurements, the collectors were opened and a visual inspection was carried out. Observed degradation effects were:

- soiling of the glass cover
- fogging on the inside of the glass cover
- partial weld seam detachment on absorber (figure 2)
- deformation of absorber with contact to glass cover
- corrosion on the collector frame, bottom plate and absorber
- increase in thermal conductivity of thermal insulation.

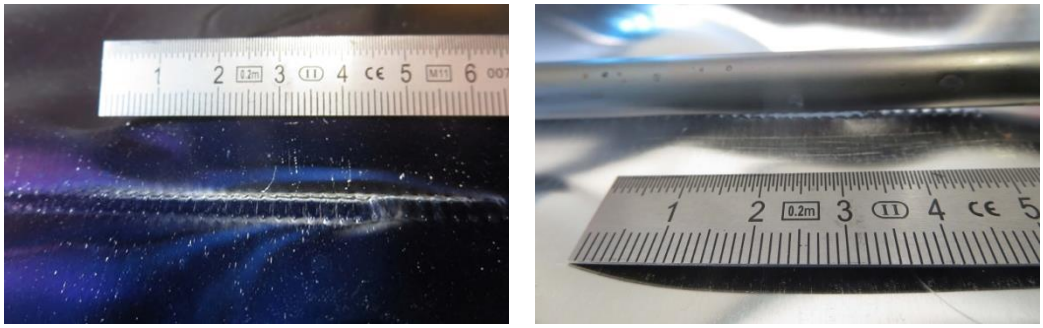

Figure 2 Absorber plate approx. 40 mm cracking on laser weld seam of the heat transfer pipe frontside (left) and backside (right) after 8.3 years of dry exposition at maritime exposition site Gran Canaria

The solar absorber was characterized as described in the standard testing in ISO 22975 [5].

In figure 3 three prepared pieces of the solar absorber not cleaned and cleaned after 7 years exposure mounted inside a solar thermal collector in stagnation mode are shown. Exemplary the collectors were of type 3 exposed at the alpine (Zugspitze, Germany), the maritime (Gran Canaria, Spain) and the arid climate (Negev, Israel). On the left side the picture of the prepared absorber are shown. On the right side the spectral reflectance measurements with the weighting functions normalized solar spectrum (AM 1.5) and normalized Planck spectrum (373 K) for emittance are shown.

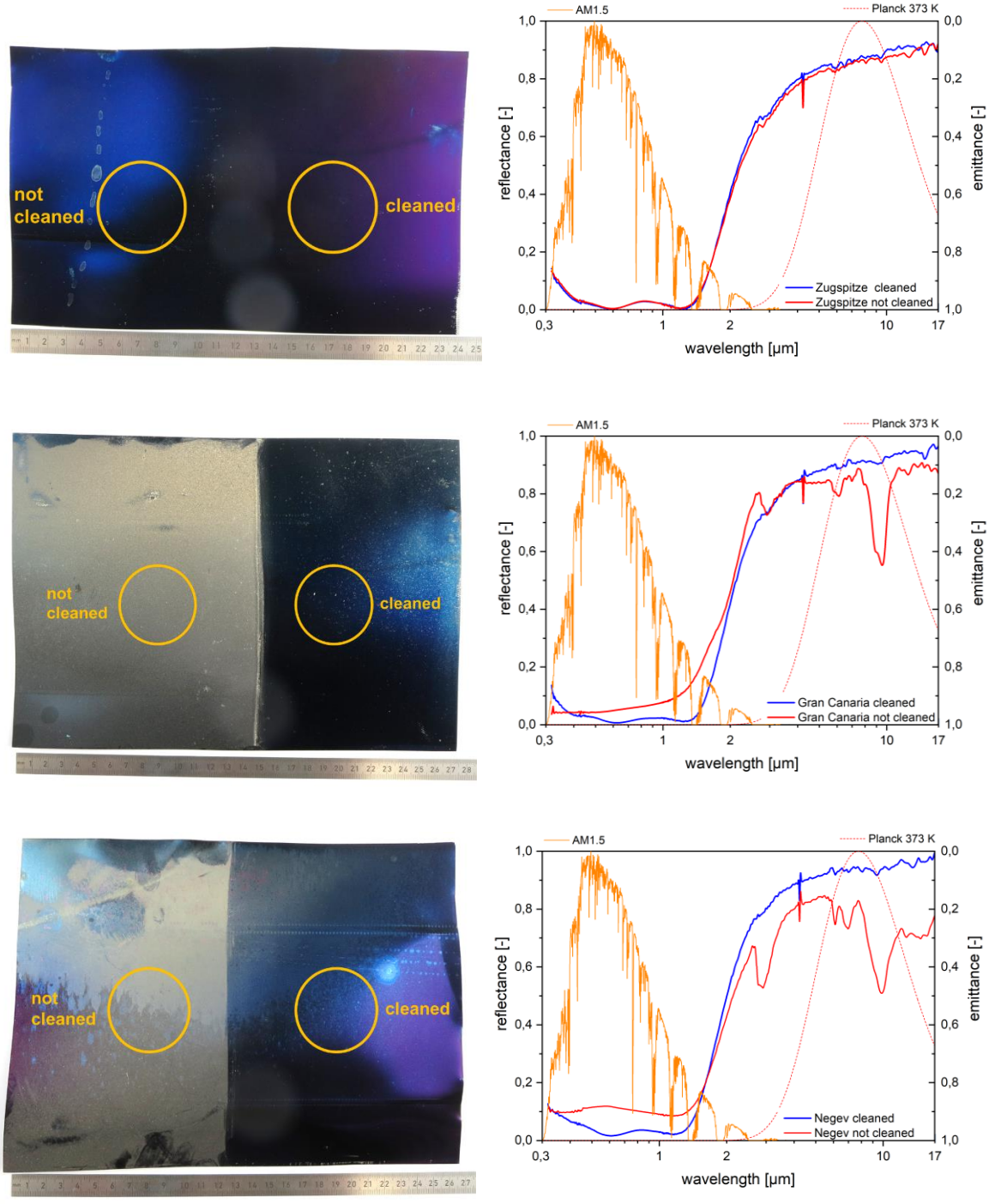

Figure 3 Left side the picture of the prepared absorber and measured reflectance of solar absorber not cleaned and cleaned after 7 years' exposure mounted inside a solar thermal collector in stagnation with weighting functions normalized AM 1.5 solar spectrum for reflectance and normalized Planck spectrum for 373 K for emittance.
Top: alpine (Zugspitze, Germany), middle: maritime (Gran Canaria, Spain), bottom arid climate (Negev, Israel)

In table 1 the values for the solar absorption (α [AM1.5]) with the weighting function of the solar spectrum AM 1.5 and the thermal emittance value (ε [373K]) with the weighting function of a Planck spectrum for 373 K for the not cleaned and cleaned spot are shown for the three different exposition sites alpine, maritime and arid. The differences ($\Delta\alpha$,$\Delta\varepsilon$) and the relative changes ($rel_{\Delta\alpha}$, $rel_{\Delta\varepsilon}$) are shown, too.

Type 3	α [AM1.5]		ε [373K]		$\Delta\alpha$	$\Delta\varepsilon$	$rel_{\Delta\alpha}$	$rel_{\Delta\varepsilon}$
	not cleaned	cleand	not cleaned	cleand	$\alpha_{cleaned} - \alpha_{not\ cleaned}$	$\varepsilon_{cleaned} - \varepsilon_{not\ cleaned}$	$\Delta\alpha / \alpha_{cleaned}$	$\Delta\varepsilon / \varepsilon_{cleaned}$
Zugspitze	0,956	0,957	0,126	0,110	0,001	-0,016	0,001	-0,140
Gran Canaria	0,874	0,954	0,288	0,077	0,080	-0,211	0,084	-2,758
Negev	0,848	0,935	0,268	0,054	0,087	-0,214	0,093	-3,985

Table 1 solar absorption and the thermal emittance value for the not cleaned and cleaned spot, differences and relative changes at exposition sites alpine (Zugspitze), maritime (Gran Canaria) and arid (Negev)

The results show a very different behavior in terms of the optical change of the absorber and the exposition site. The relative change of solar absorption and the thermal emittance are very small at the alpine exposition compared with the changes at the maritime and arid exposition.

To determine the influence of the collector performance degradation in terms of energy savings in a solar thermal system in a normal operating mode, system simulations were carried out using the TRNSYS simulation program and the reference system for domestic hot water heating [6] and reference combined system [7] as defined in IEA SHC TASK 54. The simulations were carried out at the Institute for Building Energetics, Thermotechnology and Energy Storage, Univ. of. Stuttgart, Germany. The observed performance degradation is in the range of 2% to 16 % in the proportionate primary energy saving (reference combined system Würzburg 15 m² flat plate collector).

Overall, even under the extreme conditions of the outdoor weathering test, due to the extreme climatic loads and the permanent stagnation over the entire exposure time, the collectors under consideration and their components show only low degradation effects, which suggests a very long service life under normal operating conditions.

3. Acknowledgements

The authors would like to thank the industrial partners and the German Federal Ministry for Economic Affairs and Energy (FKz. 0325969A) for their support and funding.

4. References

[1] Development of Accelerated Aging Tests for Solar Thermal Collectors and their Components www.speedcoll2.de

[2] Slamova, K., Duerr, I., Kaltenbach, T., Köhl, M., 2016. Degradation effects of maritime atmosphere on metallic components of solar collectors. Solar Energy Materials & Solar Cells 147, 246–254

[3] Kaltenbach, T., Heck, M., Kaaya, I., Standard testing of absorber surface durability according to ISO 22975–3 versus measured thermal and high-humidity stress of absorber surface at extreme test sites, Solar Energy Advances, Volume 3, 2023, 100042, ISSN 2667-1131

[4] ISO 9806:2013, Solar energy — Solar thermal collectors — Test methods

[5] ISO 22975 Part 3:2013, Solar Energy-Collector components and materials, Absorber surface durability

[6] Bachmann, S., Fischer, S. et al. (2018) Info Sheet A08: Reference System, Germany Solar Domestic Hot Water System for Single-Family House http://task54.iea-shc.org/Data/Sites/1/publications/A08-Info-Sheet--Ref-SF-SDHW-System--Germany.pdf

[7] Bachmann, S., Fischer, S. et al. (2018) Info Sheet A08: Reference System, Germany Solar Domestic Hot Water System for Single-Family House, A09-Info-Sheet--Ref-SF-Solar-Combisystem --Germany.pdf

Experimental Assessment of the Effects of Cold Climate Weather Patterns on Novel PVT Collector Designs for Low Temperature Heat Pump Integration

Alonso Conejos Lopez[1], Francisco Beltran[1], Ellen Nicholson[1], Nelson Sommerfeldt[1], Valentin Delachaux[2], Mohammad Ali Jaafar[2]

[1] KTH Royal Institute of Technology, Stockholm (Sweden)

[2] DualSun, Marseille (France)

Abstract

This study investigates the impact of cold climate weather patterns on the thermal performance of two novel designs of extruded photovoltaic thermal (PVT) collectors optimized for integration with low-temperature heat pumps. The study aims to provide a comprehensive understanding of how different weather conditions, including condensation, rainfall, frost formation, and snow, affect the thermal output of these systems. The study compares two PVT designs, one with fins attached to the thermal collector and another without, to determine the optimal configuration for maximizing efficiency under varying cold climate conditions. The results indicate significant differences in performance between the finned and non-finned designs, with the finned design showing up to 11% better thermal performance. A strong impact on the thermal performance of the PVT as a result of the different weather patterns was also observed, with up to 60% thermal gains from rainfall, and 21% thermal losses during defrosting. This research fills a critical gap in the understanding of PVT performance in cold climates and provides valuable insights that can be used to determine the appropriate control strategies for heat pumps to enhance system efficiency. The findings offer a valuable contribution to the development of more efficient renewable energy systems in regions with harsh winter conditions.

Keywords: Photovoltaic thermal, solar panel, heat pump, thermal performance, climate, condensation, rain, frost, snow.

1. Introduction

Photovoltaic Thermal (PVT) panels have been a rapidly growing technology in recent years due to their ability to collect thermal energy from a photovoltaic (PV) module, thus showing increased efficiency per unit area when compared to traditional solar PV panels. This is the case for two main reasons: the heat removed from the solar panel can be subsequently used for other applications such as heating domestic hot water, and the cooling of the photovoltaic panels increases their electrical efficiency (Aste *et al.*, 2014). One of the most interesting uses for the captured heat is when the system is coupled with a heat pump, with novel PVTs designed specifically for heat pump integration being used as the sole thermal input for the system in some cases (Beltrán *et al.*, 2023).

PVT collectors for heat pump integration are of particular interest in cold climate scenarios, where the low temperature of the working fluid for the heat pump makes it possible to collect heat from the panels and the surrounding air even at times of low or zero solar irradiance. This is particularly effective with the addition of metal fins to the backside of the PVT collectors, which have been proved to enhance the thermal capture capabilities of the system (Chow, 2010). However, cold climates can exhibit unpredictable weather patterns that affect the thermal performance of the PVT system, such as condensation, rain, frost formation and snow.

Some studies in the past have explored the effects that condensation has on the efficiency of PVTs, finding overall thermal gains associated to the phenomenon (Bertram *et al.*, 2010). Other studies have also started to explore the effects of frost formation on PVT panels, but they did not focus on the defrosting process, nor the heat losses associated with the presence of an ice layer on the thermal collector surface (Chhugani *et al.*, 2020). Rain and snow, however, have not received much attention in previous research and their effects remained largely unexplored. Therefore, further research in this area will be useful to understand how these weather patterns affect the thermal performance of the PVTs. The results from this study will help to shed some light on the optimal way to operate the heat pumps in combination with the PVT modules for cold climate operation,

© 2024. The Authors. Published by International Solar Energy Society
Selection and/or peer review under responsibility of Scientific Committee
10.18086/eurosun.2024.07.11 Available at http://proceedings.ises.org

as well as what PVT design characteristics increase thermal performance under such conditions.

2. Objectives

The objective of this study is to provide a detailed analysis of the effects of cold weather patterns on the thermal performance of two novel designs for extruded PVT collectors optimized for heat pump integration through experimental testing. The difference between the panels is a set of fins located on the thermal collector of one of the panels to increase its surface area. The experiments performed will provide a better understanding of how these two different collector designs perform in cold climate settings, as well as how big of an impact the weather patterns have on the system. Additionally, advancing the research for PVT with heat pump integration will provide an indication as to what the optimal operating parameters are in order to maximize the thermal performance of the system under such weather conditions. These objectives will be achieved by answering the following research questions:

1. How does condensation impact the thermal output of the PVTs?
2. How does rainfall impact the thermal output of the PVTs?
3. How does frost formation and defrosting impact the thermal output of the PVTs?
4. How does snow impact the thermal and electrical output of the PVTs? How much energy is required to shed the snow layer?
5. How do the finned and the non-finned PVT designs compare under these different weather conditions?

3. Methods

3.1. Test environment description

The experiments in this study were performed in an outdoor laboratory at KTH Royal Institute of Technology in Stockholm, Sweden. The system diagram for the testing equipment is shown in Fig. 1. The laboratory is equipped with a South-facing array of photovoltaic solar panels with thermal collectors attached to the back (PVTs) at an inclination of 45°. The panels are manufactured by DualSun, rated at 425W of electrical power, and have an extruded aluminium thermal collector attached to the back. The collectors are optimized for heat pump integration and use an adapted box-channel design with harp configuration, pressed mechanically to the back of the PV panel with springs. Fig. 2 shows the two collector designs, one with fins (finned) and one without (non-finned).

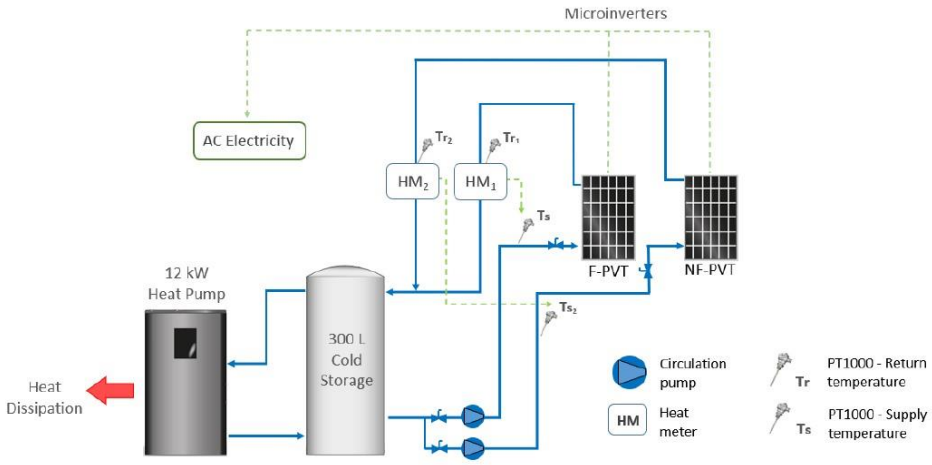

Fig. 1 Test bench system diagram.

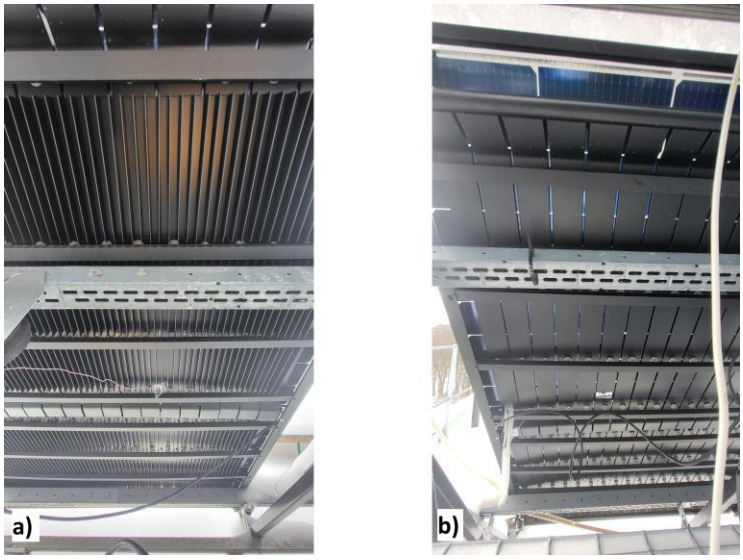

Fig. 2: a). Finned thermal collector and b). Non-finned thermal collector designs

The PVTs are connected via a set of pipes to a variable speed heat pump rated at 3-12kW (Thermia model Atlas 12 400V), which uses a mixture of ethylene glycol and water (volumetric ratio 1:3) as the working fluid and can reach temperatures as low as -10°C in the summer months. A set of LOWARA pumps circulates the fluid and allows to change the volumetric flow rate of the fluid. The panels are connected in two parallel loops, which allows for both of them to be run simultaneously and tested under the same conditions.

The system is also equipped with a variety of measuring devices that monitor the thermal performance of the system as well as the dynamic ambient conditions present at the outdoor laboratory. A set of 2Flow AB heat meters measure the thermal power generated by the PVTs and monitor the inlet and outlet temperatures of the working fluid. Additionally, a weather station located on-site provides accurate measurements on the atmospheric conditions, including ambient temperature, wind speed, wind direction, relative humidity, and dew point. A solar irradiance meter is also located next to the panels with the same tilt angle to measure the global solar irradiance in the plane of the array. Finally, eight different thermocouples can be used to measure the temperature distribution of the thermal collector during operation, or other useful measurements like the temperature of the rain.

3.2. Experiment setup

The experiments conducted in this study consist of different tests run on the PVT system with heat pump integration described in Section 3.1. during times when the PVTs were affected by condensation, rainfall, frost, or snow. A baseline model is also created during times where none of the weather patterns are present, and is used for comparison with the other experiments.

These tests are performed at normal operating conditions, unless required and stated otherwise. Normal operating conditions follow the indications from the PVT manufacturer and consist of a volumetric flow rate of 100 l/h per panel, and a PVT outlet temperature of 3 – 6 °C less than the ambient temperature. The experiments were conducted between March and May of 2024 in Stockholm, Sweden, so a range of atmospheric conditions representative of cold climates could be observed.

3.3. Data analysis

From the measurements obtained of the inlet and outlet temperature, as well as the flow rate of the working fluid, the thermal power for each panel is calculated following eq. 1:

$$\dot{q} = \frac{\frac{\dot{V}}{\rho(T_m)} c_p (T_{out} - T_{in})}{A_G} \qquad \text{(eq. 1)}$$

Where q̇ is the specific thermal power per unit area, V̇ is the fluid volumetric flow rate, ρ is the fluid density, T_m is the mean fluid temperature, c_p is the fluid specific heat capacity, T_{out} is the fluid temperature at the PVT outlet and T_{in} at the inlet, and A_G is the collector area.

According to the ISO standard 9806:2017, a polynomial regression can be used to model solar thermal

collectors under steady state conditions, while also considering the weather conditions (ISO, 2017). An adaptation of this formula used for this study is shown in eq. 2:

$$\dot{q} = \eta_0 G - a_1(T_m - T_a) - a_3 u(T_m - T_a) - a_6 uG \qquad \text{(eq. 2)}$$

Where η_0 is the zero loss efficiency, a_1 is the heat loss coefficient, a_3 is the wind speed dependence of the heat loss coefficient, a_6 is the wind speed dependence of the zero-loss efficiency, G is the perpendicular solar irradiance, T_a is the ambient temperature, and u is the surrounding air speed. These two equations combined are used to determine the thermal performance coefficients η_0, a_1, a_3, and a_6. These coefficients serve as a polynomial model to estimate what the thermal power should be under a different set of conditions, and a comparison between the measured and the modelled value is made. Finally, the coefficient of determination R^2 is calculated to determine how well the regression model fits the measured data, with a value of 1 being a perfect fit and 0 being no correlation between the model and measured data at all.

4. Results

4.1. Baseline model

The baseline model was created from data points collected during times where none of the weather patterns assessed in this study were present, and the data was filtered out if the conditions for condensation or frost were given, or if rain or snow were observed. The system was run at normal operating conditions during different times spanning the duration of the experimental part of the study, accumulating a total of 3408 data points (over 56 hours of cumulative data), to create a comprehensive model that could be used to compare the different patterns, as explained in section 3.3. The Baseline was divided into an overall baseline, and three cases with zero irradiance, low irradiance, and high irradiance, to better represent different moments of the day or atmospheric conditions. The thermal performance coefficients and coefficients of determination for all the baseline cases are displayed in Tab. 1. When looking at the total thermal energy produced by each type of PVT, the finned panel thermally outperformed the non-finned panel by about 6% overall, 4% for zero irradiance, 1% for low irradiance, and 8% for high irradiance.

Tab. 1: Baseline thermal performance coefficients and calculated coefficients of determination.

	Overall		**Zero Irradiance**		**Low Irradiance**		**High Irradiance**	
	Non-finned	Finned	Non-finned	Finned	Non-finned	Finned	Non-finned	Finned
η_0	0.42	0.51	0.00	0.00	0.29	0.38	0.42	0.52
a_1	38.46	34.11	37.65	36.12	45.41	39.49	36.41	29.13
a_3	3.00	4.25	2.68	4.59	0.08	2.45	4.68	5.51
a_6	0.00	0.00	0.00	0.00	0.00	0.01	0.00	0.00
R^2	0.94	0.92	0.49	0.48	0.70	0.64	0.83	0.80

4.2. Condensation

The condensation experiments were run when the atmospheric conditions allowed for the temperature at the collector surface to be below the dew point, but above freezing. When these conditions were met, the water molecules suspended in the air changed from gas to liquid phase. Fig. 3 shows the finned and non-finned panel at a time when condensation was present on the collector surface. These conditions occurred mainly in the spring months of April and May, on days of high humidity and warmer temperatures. Four separate experiments were conducted where condensation was successfully formed on the collector surface, with 4688 data points collected (over 78 hours of cumulative data after filtering). In order to maintain the conditions for as long as possible while preventing frost from forming, the fluid temperature was set to 1°C, while the volumetric flow rate was maintained at the recommended setting of 100 l/h per panel. The experiment was subdivided into times with zero irradiance (nighttime) and times with nonzero irradiance (daytime). The thermal performance coefficients and the calculated coefficients of determination are shown in the appendix in Tab. A1.

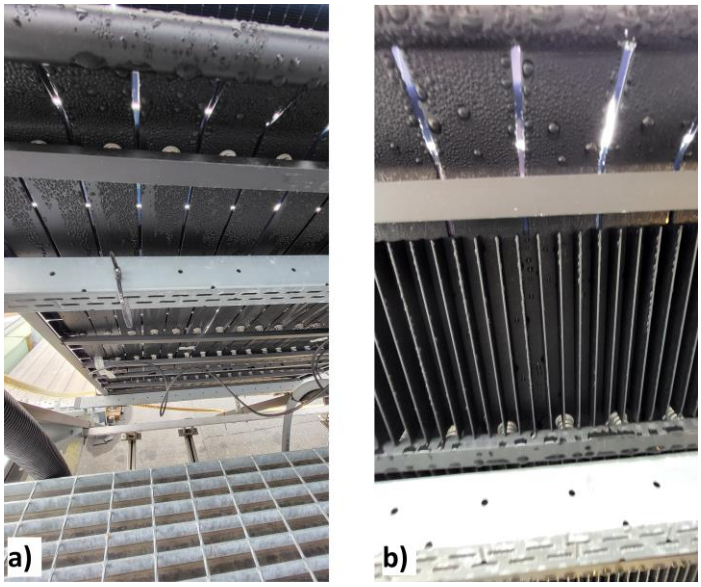

Fig. 3: Condensation forming on the collector surface for a) non-finned panel and b) finned panel.

When looking at the zero irradiance data for this experiment, the measured average specific heat output was around 3% lower than what the zero irradiance baseline model would have predicted for the same atmospheric conditions for the non-finned panel, and roughly 8% lower for the finned panel. The thermal power output of both panels was very similar, with the finned panel producing 0.5% less thermal energy than the non-finned panel.

For the nonzero irradiance data, the comparison to the baseline was made with the low irradiance baseline, as it was the one that best matched the irradiance conditions during the condensation experiments. With this comparison, the non-finned collector returned a heat losses similarly to the zero irradiance case, with a 4.4% reduction in average specific power output compared to the baseline model. However, the finned panel showed condensation gains of 1%. The finned panel also showed a small improvement in performance with respect to the non-finned panel, producing 6.3% more average specific thermal power, as well as better improvement with respect to the baseline.

4.3. Rain

The rain tests were conducted when rainfall was observed and recorded by the weather station present on-site. In addition to the power measurements, the amount of rainfall and the rain temperature were also recorded. However, the weather station was only able to measure rainfall surpassing 0.2mm per hour, so times when the rainfall amount was lower than that were discarded. Additionally, the weather station only records rainfall in 0.2mm increments, so in order to estimate the actual amount of rainfall at any given time, an average was made dividing the amount of rainfall in a specific time period by the length of said period. These experiments were conducted mainly in the spring months of April and May, accumulating 1333 data points collected (over 22 hours of cumulative data). These tests were run under normal operating conditions, and were subdivided into times with zero irradiance and times with nonzero irradiance. The thermal performance coefficients and the calculated coefficients of determination are shown in the appendix in Tab. A2. This experiment is an exception since it is not compared to the baseline model. Instead, the thermal performance coefficients from the condensation experiment are used to create a model following the same steps as for the baseline. This condensation model is used to compare the results from the rain experiment, since condensation is assumed to be present during such humid conditions as rainy weather.

For zero irradiance measurements, when comparing the heat output of the rain scenario to the regression model created from the condensation results, these experiments returned considerable heat gains. The non-finned panel showed an average specific heat output around 43% higher than the zero irradiance condensation model for the same atmospheric conditions, and the finned panel showed an increase in average specific heat of around 60% for the same case. The overall thermal power output of the finned panel is slightly higher than that of the non-finned panel, with around 10% more average specific power.

The heat gains of the measured data compared to the condensation regression with respect to rain temperature and rainfall amount are plotted in Fig. 4. During zero irradiance, times where rainfall occurred always generated heat gains, and the rain temperature was always measured to be higher than both ambient and mean operating fluid temperature. Fig. 4 a) shows that there is a positive correlation for both collector designs between higher rain temperatures and the heat gains compared to the modelled power, though the amount differs significantly between panels. When considering the amount of rainfall (Fig. 4 b), this shows a positive trend for the finned panel but a negative one for the non-finned panel.

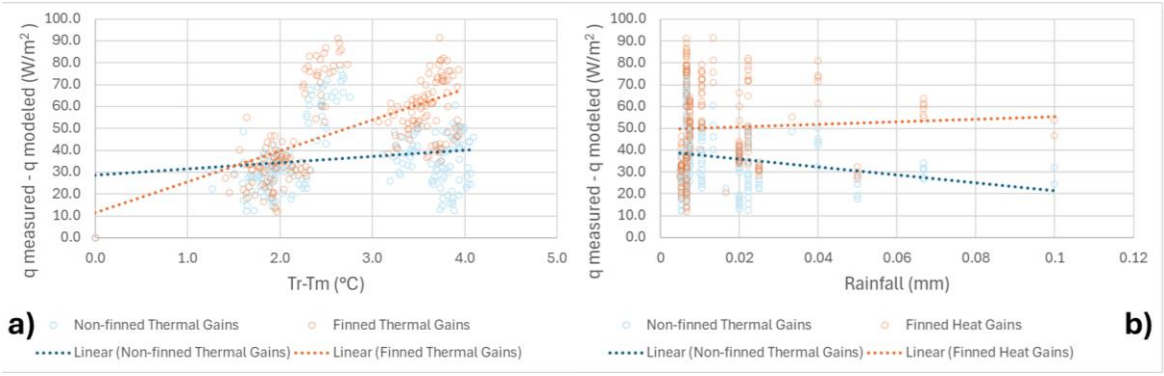

Fig. 4: Heat gains from rain compared to condensation regression during times of zero irradiance with respect to a) rain temperature, and b) rainfall amount.

For the nonzero irradiance measurements, when comparing the heat output of the rain scenario to the regression created from the condensation results, these experiments returned noticeable heat gains. The non-finned panel showed an average specific heat output around 25% higher than the nonzero irradiance condensation model for the same atmospheric conditions, and the finned panel showed gains of around 32% in the same case. These heat gains are, however, less significant than for the zero irradiance case. The overall power output of the finned panel is slightly higher than the non-finned panel, with around 7% more average specific power.

The heat gains of the measured data compared to the condensation regression with respect to rain temperature and rainfall amount are plotted in Fig. 5. During nonzero irradiance, there were times where the measured power was less than the modelled power with the condensation regression, even though the rain temperature was always measured to be higher than both ambient and mean operating fluid temperature. Results are inconsistent for both rain temperature and rainfall amount, with a weak correlation between these parameters and the heat gains, and even a slightly negative correlation in the case of rain temperature, which could be tied to the difference in $\eta 0$ coefficient for these experiments.

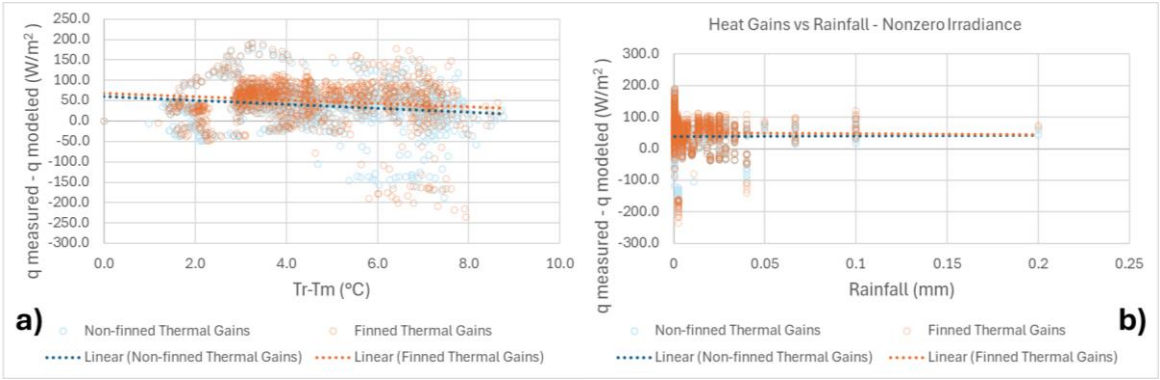

Fig. 5: Heat gains from rain compared to condensation regression during times of nonzero irradiance with respect to a) rain temperature, and b) rainfall amount.

4.4. Frost

The frost experiments were run when the atmospheric conditions allowed for the temperature at the collector surface to be below both the dew point and the freezing point. When these conditions were met, the water molecules suspended in the air changed from gas to solid phase, with some cases where the water would first condense into water droplets, then freeze. Fig. 6 shows the finned and non-finned panel at a time when frost

was present on the collector surface. These conditions occurred mainly in the late winter and early spring months of March and April, on nights of high humidity and cold temperatures. During the day, the frost then melted, and the phase change occurred in the opposite direction. Six separate experiments were conducted where frost was successfully formed on the collector surface with 4688 data points (over 102 hours of cumulative data).

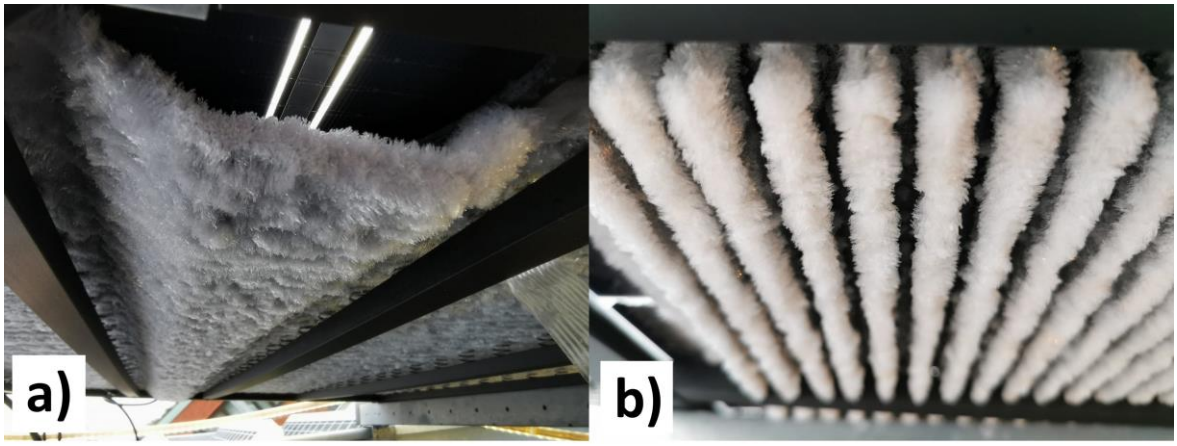

Fig. 6: Frost formation on the collector surface for a) non-finned panel and b) finned panel.

In order to maintain the frost formation conditions throughout the night, the fluid temperature was set to the minimum allowed (fluctuating between -9 to -6°C), while the volumetric flow rate was maintained at the recommended setting of 100 l/h per panel. After the sun came out and the temperature started to rise, the system was returned to normal operating conditions to allow for defrosting. The experiment was subdivided into times when frost was being formed, times when frost was present and had covered the full collector surface, and times when the panel was being defrosted. A camera was set up at the back of the finned PVT collector to monitor the different stages of the cycle. The thermal performance coefficients and the calculated coefficients of determination are shown in the appendix in Tab. A3. A comparison between the measured and modelled power for the finned panel during one of the experiments is seen in Fig. 7, outlining the different stages of the frost formation process. Both panels showed similar trends throughout all the frost experiments.

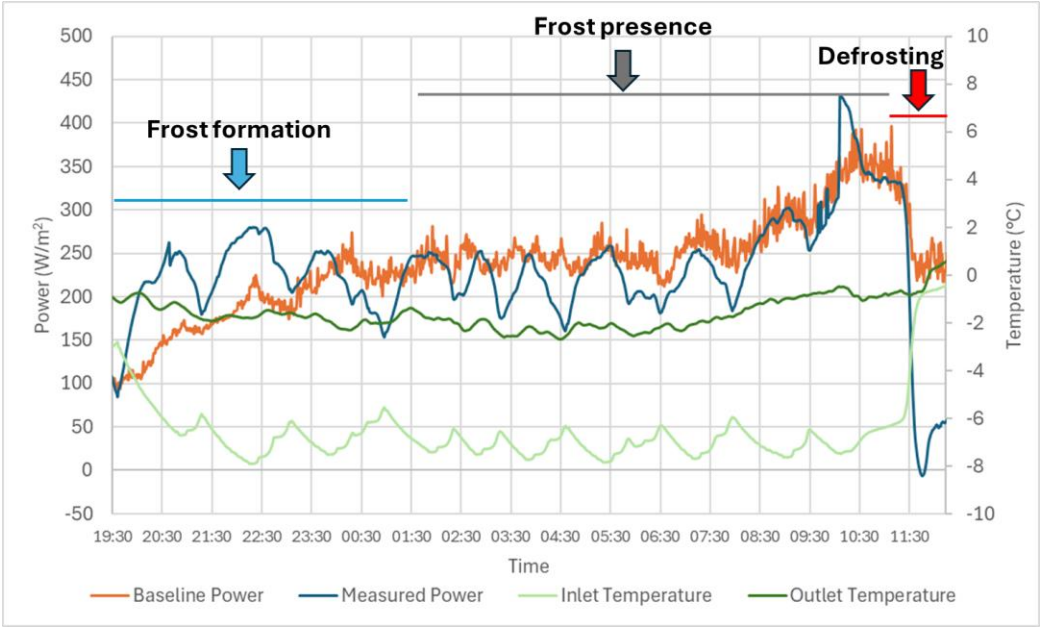

Fig. 7: Measured vs. baseline power over time for a frost formation experiment, finned collector.

When comparing the heat output of the frost formation stage to the zero irradiance baseline regression (frost formation occurred only at night), both collector designs showed heat gains of about 6%. During these times, the baseline model underestimates the power produced by the PVT, as shown in Fig.7. The overall power output of the finned panel is slightly higher than that of the non-finned panel, with around 6% more average

specific power.

For the comparison between the heat output of the frost presence stage and the overall baseline regression, both collectors showed a decline in specific thermal power, with around 18% for the non-finned panel and 15% for the finned panel. During these times, the baseline model overestimates the power produced by the PVT, as shown in Fig.7. The overall power output of the finned panel was slightly higher than the non-finned panel, with around 3% more average specific power.

Comparing the heat output of the defrosting stage to the overall baseline regression, both collectors showed a thermal performance decline, with a 21% decrease for the non-finned panel and 16% for the finned panel. During these times, the baseline model greatly overestimates the power produced by the PVT, as shown in Fig.7. The overall power output of the finned panel is noticeably higher than the non-finned panel, with around 7% more average specific power.

Additionally, a different experiment was conducted to test how different amounts of frost affected the thermal performance of the panel. The system was left running at the minimum temperature setting and an increased flow rate for over 48h until a substantial layer of frost was formed. A sample time from the start of the experiment, when the frost layer was thin, was compared to a time from near the end of the experiment, when the layer was considerably thicker. The results show that both collectors exhibit a thermal performance decline, with a decrease of about 33% for the non-finned panel and 51% for the finned panel at the end of the experiment. During this time frame at the end of the experiment the finned panel also produced around 9% less average specific thermal power than the non-finned panel. Finally, the system was returned to normal operating conditions (with the higher amount of frost still present) and compared against the baseline. Comparing the heat output of this part of the experiment to the overall baseline regression, both collectors showed a significant thermal performance decline, with a decrease in thermal power of about 43% for the non-finned panel and 34% for the finned panel. The overall power output of the finned panel is noticeably higher than the non-finned panel, with around 11% more average specific power.

4.5. Snow

The conditions for studying the impact of snow on the performance of the PVT were only given once during the experimental phase of this study, in the month of March, where a snow layer fully covered the front side of the panels and was allowed to shed naturally, as shown in Fig. 8. This test was run under normal operating conditions, and observed the time after the snowstorm stopped, until the snow layer was shed. Since only one camera was available to record the process and the shedding happened at different times for both panels, only the finned panel is observed for this experiment.

Fig. 8: Snow shedding process on the front side of the finned panel showing a) full snow cover, b) shedding start, and c) shedding end.

The layer of snow impacts both the thermal performance of the PVT, as some of the heat collected is directed towards shedding, and the electrical performance of the panel, since the sunlight is kept from reaching the surface of the panel by the layer of snow. The measured thermal power when compared to the overall baseline model returned losses of about 61%, equating to 1.12 kWh for the duration of the shedding process. In terms of electrical production, the panel produced only 123 Wh for the time frame of the experiment, while it was calculated that the panel should have produced 1141 Wh under the environmental conditions present during the test, had it been clean, which translates to an 89% reduction in electricity production. The timeline comparing measured and modelled electrical production is shown in Fig. 9, and the moments when the shedding starts at 12.30, and when it is mostly shed at 15.15 can be seen as spikes in the measured power line.

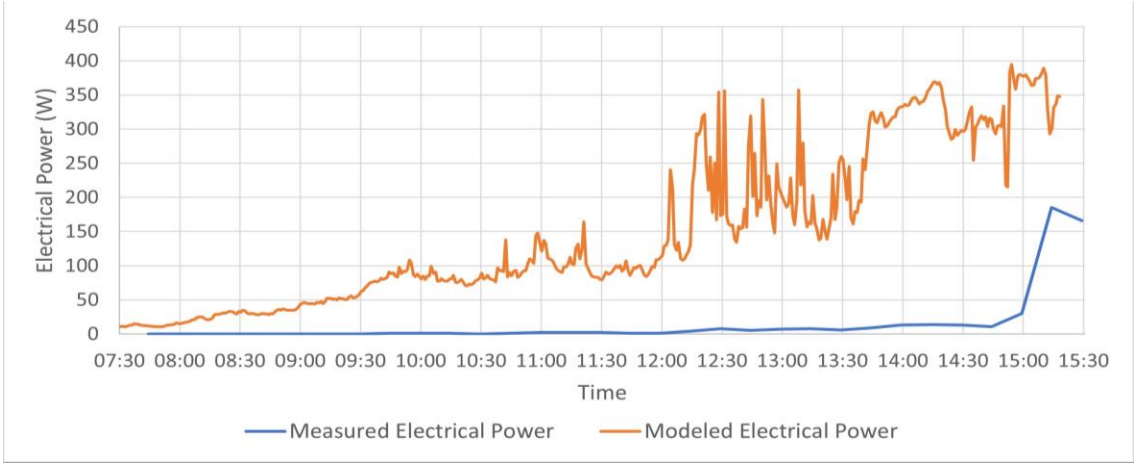

Fig. 9: Measured electrical power vs. modeled electrical power during snow shedding process.

5. Discussion

5.1. Baseline

The results obtained in this study are interesting for many reasons. In part, new findings on the effects of previously unexplored weather patterns like rain, snow, and even expanding the previous work done on frost formation serve to better understand how PVTs behave under these conditions. On the other hand, some of the expected results for previously explored phenomena like condensation formation do not match with those obtained in this study. This mismatch in the results might be caused by the way the baseline scenario was developed. The baseline is curated with a data set that has a much lower temperature difference between the ambient and the operating fluid than the other tests, following the specified guidelines for normal operation of the heat pump, while the different weather pattern experiments often operate outside of these conditions. As a result, it is possible that the baseline overestimates the heat loss coefficient $a1$, thus producing higher results in modelled power than expected when applied to situations when a much higher temperature difference is present. As a result, a direct numerical comparison between the baseline and the other experiments is inherently flawed, and these should be taken only as reference to observe trends.

The baseline did, however, provide useful information on the comparison between the finned and non-finned panel during normal operation, showing that the finned panel outperforms the non-finned panel, as is the case in most cases throughout the different experiments. However, the difference in average thermal output is not always as significant as one could expect, particularly for the low irradiance baseline scenario, where the finned panel only has a 1% increased thermal output. The finned panel is also more susceptible to effects of atmospheric conditions, showing higher dependence on the wind speed and irradiance levels than the non-finned panel.

5.2. Condensation

The condensation experiments returned surprising results, with this phenomenon netting thermal losses with respect to the baseline. From previous research, and following the laws of physics, it would be expected that condensation nets heat gains related to the phase change from gas to liquid (Betram *et al.*, 2010). The energy released during the phase change could be captured by the collector, and since the surface is slanted, the water droplets just slide off the panel, so the phase change is unidirectional. This difference in the results obtained could be due to the way the results are compared to the baseline, as explained previously. Looking at both panels, however, the finned panel does generally perform better than the non-finned panel as expected, which agrees with the results obtained by Chhugani *et al.* (2020).

5.3. Rain

The results from the rain experiment return the highest thermal gains among all, with up to 60% gains for the

finned panel during nighttime operation, which is to be expected since the rain temperature was measured to be higher than both ambient and fluid temperature at all times. The finned panel once again outperforms the non-finned panel for these experiments, being able to better take advantage of the warmer, more humid surrounding air. Regarding rainfall amount and rain temperature, it would be expected that higher values of both rainfall and temperature difference would net higher gains. However, only the rain temperature dependence of the zero irradiance case shows a clearly positive correlation. When the nonzero irradiance cases are observed, there seems to be no clear correlation between these parameters and the calculated thermal gains. A possible explanation is that once the system reaches a steady state, the rain has already incresed the output fluid temperature, and thus the average temperature of the working fluid, reducing the difference between rain temperature and mean fluid temperature, (X-axis in Fig. 4 and 5). Therefore, the highest thermal gains recorded, when the inlet and outlet fluid temperature difference is highest, correspond to moments when the mean fluid temperature has already risen, while the highest difference between rain temperature and mean operating fluid temperature will happen right at the start of rainfall, before the rain has affected the outlet fluid temperature and the system is not yet in steady state. With regards to rainfall amount, it is possible that a small amount of rainfall is enough to get the front side of the panel to match the rain temperature, therefore saturating as rainfall increases, which could explain the mostly flat trend lines when looking at heat gains in terms of rainfall amount.

An interesting observation is that the highest losses measured corresponded to times of higher measured irradiance. This could be due to the fact that the rain might be cooling down the panel, thus limiting the effect of the irradiance. This hypothesis is supported by the fact that the $\eta 0$ coefficient is almost 0 for the nonzero irradiance cases in the rain experiments, and up to 0.5 for the condensation regression. This is consistent with the explanation that a small amount of rainfall is enough to change the temperature of the front side of the panel. Regardless, it is clear that rain heat gains compared to the condensation scenarios are highest for cases with no irradiance, and are worst at cases with higher irradiance, where the effect of the rain and the sun are arguably counteracting each other.

5.4. Frost

Similarly to the condensation experiment, this scenario expects heat gains associated with the phase change from gas to solid as the water molecules in the air freeze onto the collector surface. This is supported by the early stages of the frost formation cycle, where heat gains are observed. However, during defrosting the phase change occurs in the other direction, and heat losses are sustained. However, there is only one phase change occurring in this stage since the water goes from solid to liquid, and then proceeds to drip off the panel. During the time the panel is fully covered until it starts to defrost, the results also show associated losses compared to the model. This could be the case because a layer of frost limits the heat exchange with the surrounding air. This hypothesis is further supported by the experiment where different layers of frost were compared, and a thicker layer of frost was found to have reduced performance compared to a thinner layer. Additionally, since the frost presence shows to negatively impact the thermal performance of the system, the longer this state is held, the more the overall thermal production through for the whole cycle.

In this experiment the finned panel once again outperformed the non-finned panel during the normal frost cycles, which is to be expected as a larger surface area leads to more frost forming on the collector. However, this can turn out to be a disadvantage, as the finned collector performed worse than the non-finned one while the thick layer of frost was present.

5.5. Snow

This experiment on the impact of snow showed how detrimental a snow layer can be to the overall performance of a PVT system, since it impacts not only the thermal performance but also the electricity production. Previous research on snow and PVTs focused on whether it is possible to actively shed the layer of snow from the panel by running the heat pump in reverse (Rahmatmand *et al.*, 2019). However, the system used for this study did not have that capability. Instead, the snow layer was allowed to shed naturally, and the thermal losses sustained during that period of time were assumed to be directed to melting the snow and the shedding process. Therefore, if the amount of energy required to actively shed the panel were the same as the losses associated with passive shedding (1.12 kWh), it would not be energy efficient to actively shed the panel in this case, since the expected electrical gains from doing so (1.02 kWh) would not cover the energy needed for the process.

Perhaps turning off the system until the snow has fully shed would be optimal.

6. Conclusion

The results from this study show that there is indeed a considerable impact from cold climate weather patterns on the thermal performance of PVTs. While condensation was expected to provide thermal gains as found in previous research, the opposite occurred for the experiments conducted in this study. Rain was the phenomenon with the highest calculated thermal gains, as the rain temperature was consistently above ambient, thus warming the panels. However, it seems that just a small amount of rainfall is enough to get a positive effect on thermal performance, and higher amounts of rainfall have diminishing returns. Frost formation showed varying results depending on the stage of the cycle: while the formation of frost generates some thermal gains, the defrosting stage and the presence of frost on the collector surface have detrimental effects on the thermal performance of the system. Finally, snow returned considerable energetic losses for both the thermal and electrical output of the system and, under the conditions experienced during the experiment, it is estimated that actively shedding the panel of the snow layer would not be energy efficient.

Comparing the finned and the non-finned PVT designs, the finned design showed better thermal performance than the non-finned design in almost every scenario. However, the difference in performance might not always be worth the extra steps during manufacturing, the heavier weight of the panel, or the increased cost. Additionally, the higher dependency on weather conditions of the finned panel lead to stronger negative effects in some of the scenarios that were tested, such as when a thick layer of frost was present.

Lastly, further work on this project would prove useful to improve the quality of the baseline and provide better comparisons, as well as to develop a more comprehensive database of all the weather patterns. It would also be beneficial to use the results obtained in this study to explore new parameters and control strategies for the heat pump to find the optimal mode of operation to increase the energy efficiency of the system when used in cold climates that present conditions such as the ones explored in this study.

7. Acknowledgments

This study was carried out under the project *Smart Renovation Strategies for Sustainable Electrification* (Project No. P2023-01509), funded by the Swedish Energy Agency (Energimyndigheten) as part of the ReBygg Program.

Special thanks to the people from the KTH department of Energy Technology, and to the project partner DualSun, who provided the PVTs used for the study.

8. References

Aste, N. del Pero, C. and Leonforte, F. (2014) 'Water flat plate PV–thermal collectors: A review', Solar Energy, 102, pp. 98–115. Available at: https://doi.org/10.1016/j.solener.2014.01.025.

Beltrán, F., Sommerfeldt, N. and Madani, H. (2023) 'Experimental testing of solar photovoltaic/thermal collector as a heat pump source under outdoor laboratory conditions.'

Bertram, E. Scheuren, J. Glembin, J. and Rockendorf, G. (2010) 'Condensation heat gains on unglazed solar collectors in heat pump systems,' pp. 1–8. 10.18086/eurosun.2010.07.02.

Chhugani, B. et al. (2020) 'Model Validation and Performance Assessment of Unglazed Photovoltaic-Thermal Collectors with Heat Pump Systems', in. Available at: https://doi.org/10.18086/eurosun.2020.05.13.

Chow, T.T. (2010) 'A review on photovoltaic/thermal hybrid solar technology', Applied Energy, 87(2), pp. 365–379. Available at: https://doi.org/10.1016/j.apenergy.2009.06.037.

ISO, (2017). ISO9806: Solar Energy – Solar Thermal Collectors -Test Methods.

Rahmatmand, A. Harrison, S. J. and Oosthuizen, P. H. (2019) 'Evaluation of removing snow and ice from photovoltaic-thermal (pv/t) panels by circulating hot water,' Solar Energy, vol. 179, pp. 226–235. Available at: https://doi.org/10.1016/j.solener.2018.12.053.

9. Appendix

9.1. Condensation

Tab. A1: Condensation thermal performance coefficients and calculated coefficients of determination.

	Zero Irradiance		Nonzero Irradiance	
	Non-finned	Finned	Non-finned	Finned
η_0	0.00	0.00	0.47	0.50
a_1	37.13	37.07	24.43	22.37
a_3	1.60	1.69	6.70	8.93
a_6	0.00	0.00	0.06	0.08
R^2	0.78	0.78	0.79	0.78

9.2. Rain

Tab. A2: Rain thermal performance coefficients and calculated coefficients of determination.

	Zero Irradiance		Nonzero Irradiance	
	Non-finned	Finned	Non-finned	Finned
η_0	0.00	0.00	0.02	0.00
a_1	51.71	57.45	45.52	48.95
a_3	1.63	2.71	5.09	6.43
a_6	0.00	0.00	0.00	0.00
R^2	0.94	0.94	0.89	0.87

9.3. Frost

Tab. A3: Frost thermal performance coefficients and calculated coefficients of determination.

	Frost formation		Frost Presence		Defrosting	
	Non-finned	Finned	Non-finned	Finned	Non-finned	Finned
η_0	0.00	0.00	0.00	0.00	0.04	0.00
a_1	41.71	44.00	34.42	33.10	33.42	35.92
a_3	1.16	2.12	1.86	4.18	3.95	4.64
a_6	0.00	0.00	0.00	0.00	0.02	0.00
R^2	0.82	0.81	0.83	0.81	0.94	0.90

Effect of Boundary Conditions on Glazed Flat-Plate Solar Collector Performance Test Results

Tomas Matuska and Viacheslav Shemelin

Czech Technical University in Prague, Prague (Czech Republic)

Abstract

This analysis investigates the effect of performance test boundary conditions on the glazed flat-plate solar collector performance test results. The current test standard allows for some variations in boundary conditions, which can lead to differences in thermal performance characteristics. This article focuses on variations in collector tilt angle, average air speed, solar irradiance at the collector plane, and heat transfer fluid flow rate. A series of experimental thermal performance evaluations of a specific flat-plate solar collector was conducted using an indoor solar simulator, following the ISO 9806 test standard under various boundary conditions. It was observed that differences in collector tilt angle and wind speed resulted in variations in thermal performance test results, especially under high values of reduced temperature difference. However, irradiance and heat transfer fluid flow rate variations did not yield significant differences in thermal performance test results. Subsequently, an annual simulation analysis was performed using ScenoCalc simulation software under various constant mean operating temperatures and the climatic conditions of Stockholm, Würzburg, and Athens. The results demonstrated that differences in test boundary conditions under the current test standard would not cause considerable differences in solar system energy output simulation results for the most common solar thermal system applications (pool heating, solar domestic hot water systems, and space heating). Conversely, differences in test boundary conditions could lead to significant disparities in energy output simulation results for high-temperature solar thermal applications, such as process heat thermal systems.

Keywords: solar thermal system, solar collector testing, simulation analysis, boundary conditions

1. Introduction

To design a solar thermal system, it is essential to know the thermal performance parameters of the solar flat-plate collector used in the system. Typically, the minimum information required includes the efficiency curve characteristics (η_0, a_1, and a_2) and the reference area (the collector gross area according to the ISO 9806 standard ("ISO 9806:2017. Solar energy — Solar thermal collectors — Test methods.," 2017)). However, a challenge arises because the testing procedure for thermal performance parameters allows for some variations in experimental boundary conditions as per the current standard. Specifically, the standard for indoor testing of glazed flat-plate solar collectors (using a solar simulator) under steady-state conditions states:

- The collector tilt angle is unspecified but should be included in the test protocol.
- The average air speed parallel to the collector plane should be maintained at 3 m s^{-1} ± 1 m s^{-1}.
- The hemispherical solar irradiance at the collector plane should exceed 700 W m^{-2}.

As a result, the thermal performance characteristics of the thermal collector, tested according to the valid standard under different boundary conditions, may vary. For instance, Müller-Schöll and Frei (2000) presented a method for calculating the uncertainty of the performance characteristic curve's parameters obtained during the performance test evaluation. In their work, the authors stated that slight deviations in the test boundary conditions of the same solar collector among different laboratories cause differences in the thermal performance testing results. Reddy (2011), in his comprehensive work, investigated the modelling process for engineers and scientists in detail and concluded that the difference in performance between the modelled on-site and obtained in laboratory conditions could be caused by many reasons. One of them is the difference between boundary conditions on-site and during the laboratory measurement. Mathioulakis et al. (2012) investigated the sources of uncertainty in solar system simulation results and concluded that any deviation in the collector test method can introduce additional uncertainty components to the final simulation results. Later, Sowmy et al. (2017) experimentally demonstrated that differences in test boundary conditions contribute to variations in thermal performance results.

© 2024. The Authors. Published by International Solar Energy Society
Selection and/or peer review under responsibility of Scientific Committee
10.18086/eurosun.2024.07.12 Available at http://proceedings.ises.org

This study aims to investigate the influence of boundary conditions under the valid standard ISO 9806 on the performance characteristics of glazed flat-plate solar collectors. Firstly, the reference boundary conditions and the investigated parameters were identified. Secondly, a series of experimental thermal performance tests were performed to investigate the effect of each investigated parameter individually. Then, the minimum and maximum possible thermal performance characteristic curve variants were derived. Finally, a simulation analysis was performed to understand the effect of the test boundary conditions on a glazed flat-plate solar collector's thermal performance.

2. Methodology

To investigate the effect of boundary conditions on the performance of glazed flat-plate solar collectors, the reference solar collector was experimentally tested to obtain its performance characteristics under different boundary conditions. An indoor solar simulator was utilised to perform a steady-state efficiency testing procedure, followed by a thermal performance evaluation conducted in accordance with the ISO 9806 standard. Fig. 1(a) demonstrates the solar simulator test loop, while Fig. 1(b) illustrates the analysed collector on the test stand during the experimental testing. Tab. 1 summarises the utilised sensor's type and their accuracy.

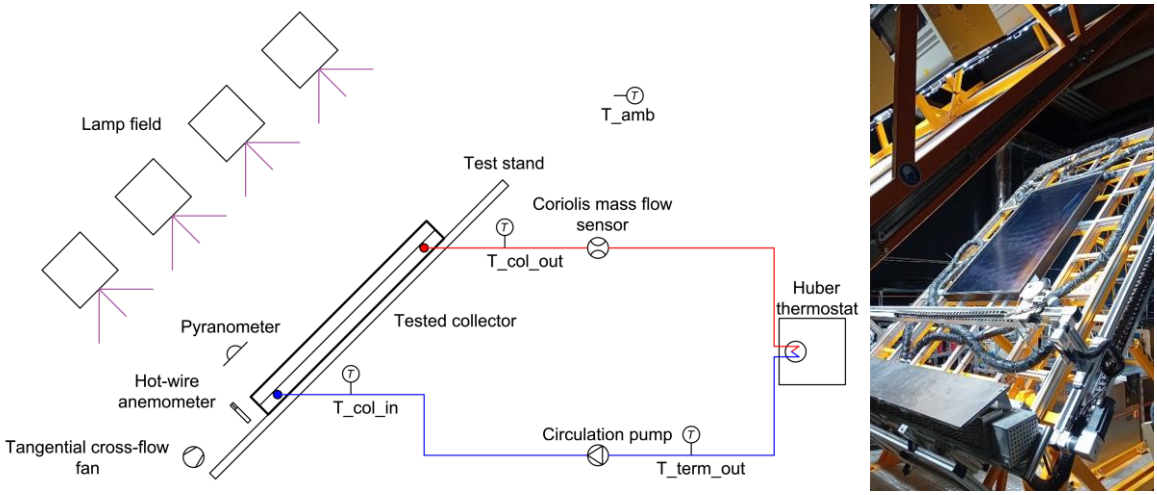

a) **b)**

Fig. 1: (a) The solar simulator test loop; (b) The analysed solar collector on the solar simulator test stand

Tab. 1: The sensors' type and their accuracy

Sensor	Manufacturer	Type	Accuracy
Temperature	TMG	PT100	± 0.05 K
Flow rate	Krohne	Coriolis mass flow sensor OPTIMASS 7000 T10	± 0.002%
Solar irradiation	Kipp & Zonen	Pyranometer SMP1 1 -A	± 1.4%
Wind velocity	Airflow Lufttechnik GmbH	Hot-wire anemometer D12-65V C	± 0.1 m/s

The effects of the following boundary conditions were analysed: collector tilt angle, solar irradiance at the collector plane, average air speed at the collector plane, and heat transfer fluid flow rate. The following conditions were considered as the reference boundary conditions for this investigation:

- Collector tilt angle of 45°,
- Hemispherical solar irradiance at the collector plane of 905 W m^{-2},
- Average air speed of 3 m s^{-1} at the collector plane,
- Heat transfer fluid flow rate of 72 kg m^{-2} h^{-1} of the collector gross area,
- Ambient air temperature of 18 °C.

It is worth noting that it is impossible to maintain the exact same values for the boundary condition parameters during the series of experimental tests. For instance, a solar irradiance homogeneity test was performed before each series of tests to ensure the homogeneity condition was fulfilled. Moreover, the average value of solar irradiance was determined for each test series during this test. Even though the lamps' position and power intensity were not changed, hemispherical solar irradiance at the collector plane may slightly differ (by a couple of watts). Therefore, the solar irradiance value, the heat transfer fluid flow rate value, and the ambient air temperature mentioned above are average values. Additionally, it should be emphasised that during all experimental tests, the actual values of these parameters did not vary by more than ±2% from the average values mentioned above.

To analyse the nature of the changes in the obtained thermal performance characteristics caused by different boundary conditions, a detailed validated model of a glazed flat-plate collector designed in TRNSYS simulation software was utilised (Shemelin and Matuska, 2017).

2.1. Effect of collector tilt angle

Firstly, the effect of the solar collector tilt angle was investigated. The reference setup conditions were applied, and the collector tilt angle was varied. The thermal performance evaluation was performed for seven tilt angles ranging from 0° to 90° with a 15° angle increment (see Fig. 2a). The results indicated a decrease in the thermal efficiency of the solar collector as the collector tilt angle decreased. This decline can be attributed to the increasing heat transfer by natural convection in the closed air gap between the absorber and the glazing. Increasing natural convection heat transfer significantly impacts the front-side heat loss and, consequently, the overall heat loss of the collector.

To confirm this, the heat transfer by convection in the closed gap between the absorber and the glazing was modelled using the detailed validated model of a glazed flat-plate collector. The obtained thermal resistance values of the convection heat transfer are plotted in Fig. 2b for various tilt angles (0°, 15°, 30°, …, 90°). The aim was to analyse the effect of the layer inclination angle on the natural convection heat transfer in the closed gap between the absorber and the glazing.

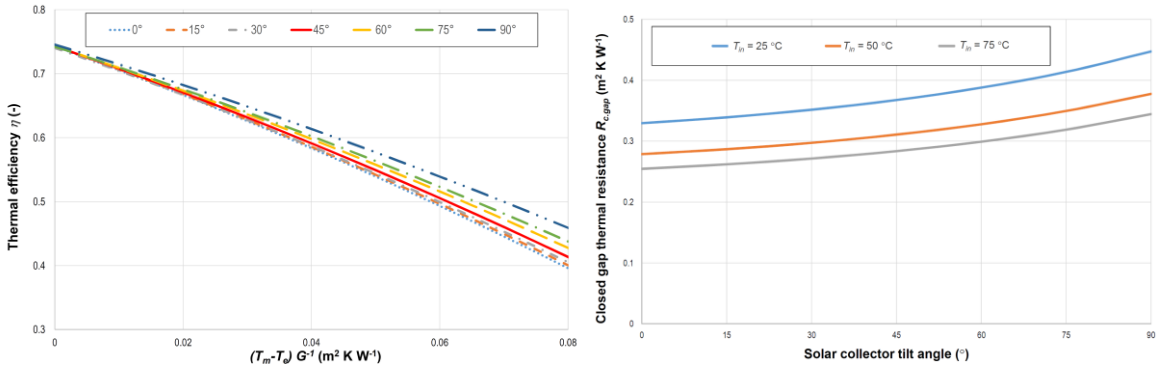

a) **b)**

Fig. 2: (a) The solar collector's thermal performance under different tilt angles; (b) The closed gap convection thermal resistance under different tilt angles and different mean operating temperatures

The results reveal a consistently increasing trend in the closed gap natural convection thermal resistance as the tilt angle of the collector increases. In the horizontal position, the thermal resistance is minimal, the heat transfer by convection is highest, and the solar collector has higher heat losses. In contrast, the vertical position minimises the heat losses (maximum thermal resistance); hence, the collector's thermal efficiency is higher. It can be noted that the thermal resistance through the air gap remains practically unchanged for low tilt angle values (0° to 30°). As a result, the efficiency curves are identical for collector inclinations ranging from 0° to 30°.

2.2. Effect of solar irradiance

Secondly, the effect of solar irradiance was analysed. The collector's thermal performance evaluation was performed for three solar irradiance levels. As mentioned before, the reference boundary condition for solar irradiance at the collector plane was 909 W m^{-2}. Then, the lamp positions were adjusted to increase solar irradiance at the collector plane to 1126 W m^{-2}. After that, the lamp field power was reduced by 14% (on

average) to decrease the solar irradiance to 827 W m^{-2}. It is worth noting that the irradiance homogeneity condition was fulfilled; the solar irradiance value at each measured point at the collector plane fell within a ±15% interval of the average irradiance at the collector plane. The obtained thermal performance characteristic curves under the different solar irradiance values are illustrated in Fig. 3. The figure indicates that there is no significant difference between the obtained thermal performance. Therefore, it is evident that the solar irradiance boundary condition specified in the test standard (the hemispherical solar irradiance at the collector plane should exceed 700 W m^{-2}) fully fulfils its purpose: following the standard leads to a specific solar collector performance result.

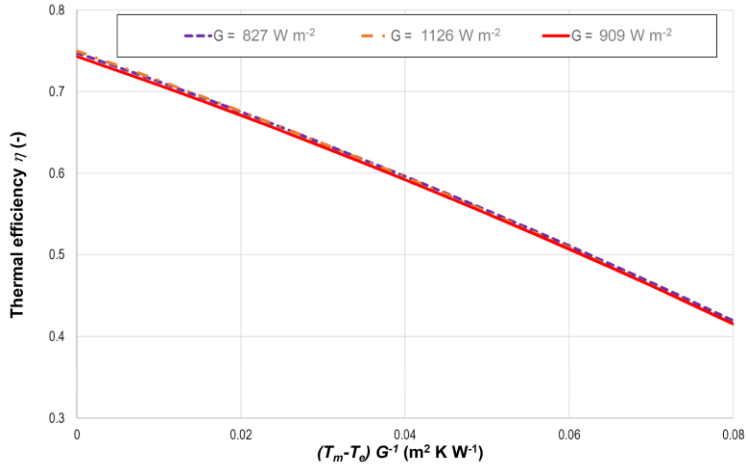

Fig. 3: The obtained thermal performance characteristic curves under different solar irradiances

2.3 Effect of wind speed

Thirdly, the effect of wind speed was investigated. The thermal efficiency evaluation based on the experimental test results was conducted for six wind speed velocities: 2 m s^{-1}, 3 m s^{-1}, and 4 m s^{-1} (according to the valid standard), as well as 0 m s^{-1}, 1.5 m s^{-1}, and 4.5 m s^{-1} to provide a complete understanding. The results of the evaluation are demonstrated in Fig. 4.

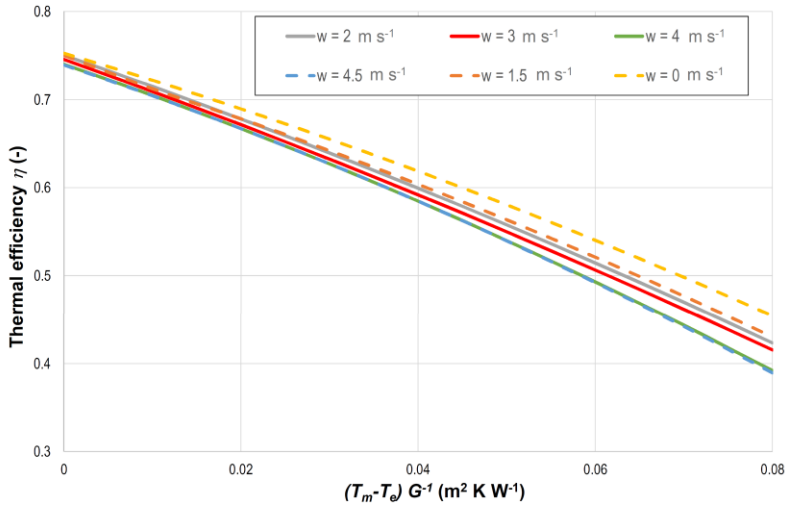

Fig. 4: The evaluated thermal performance characteristic curves under different wind speeds

The reference boundary conditions were applied, and only the artificial wind fan speed settings were changed to obtain different wind speeds. For the reference variant, the average wind speed at the collector plane was measured at 3 m s^{-1} (under 60% of fan power). The reduced and increased wind speed variants were achieved by decreasing and increasing fan power. Specifically, to achieve an average speed of 2 m s^{-1}, the fan's power was reduced to 43%; to achieve an average speed of 4 m s^{-1}, the power was increased to 86%. In addition, the performance evaluation procedure was also carried out for average wind speeds of 4.5 m s^{-1}, 1.5 m s^{-1}, and 0 m s^{-1}. Although these wind speeds no longer correspond to the current test conditions, the results can be helpful in analysing the effect of wind speed.

The effect of wind speed on the collector's thermal performance is significant for solar collectors with a high value of the collector front-side heat loss coefficient. The front-side heat loss coefficient depends on the closed-gap convection and thermal radiation between the absorber and the front-side glazing thermal resistances, the thermal resistance of the glazing itself, and the combined (wind and natural) convection and thermal radiation from the glazing's front-side thermal resistances. Therefore, to analyse the influence of wind speed on the collector's thermal performance, the combined convection thermal resistance has to be modelled. The problem is that more than 90 correlations can be applied to model the forced convection heat transfer coefficients (Palyvos, 2008). Around 35 of them, with some reservations, can be applied to model the forced convection heat transfer coefficients of a glazed flat plate collector (Shemelin and Matuška, 2023). Fig. 5a demonstrates the combined convection thermal resistance calculated using all of them, while Fig. 5b indicates the combined convection thermal resistance calculated using the most widely used correlations for solar collector performance modelling (Kumar et al., 1997; McAdams, 1954; Sharples and Charlesworth, 1998; Test et al., 1981; Wattmuff et al., 1977) together with the closed gap convection heat transfer resistance.

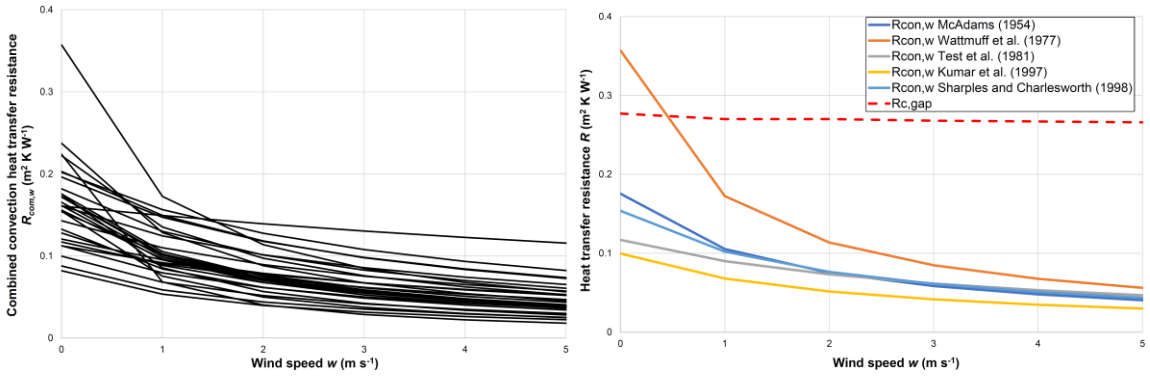

a) **b)**

Fig. 5: Combined convection heat transfer resistance calculated using (a) 35 correlations and (b) 5 widely used correlations in solar thermal modelling correlations

The modelling results indicated that under zero wind speed $w \rightarrow 0$ m s^{-1}, the combined convection heat transfer resistances reach their maximum values, and, more importantly, their values are comparable to the closed gap convection heat transfer resistance. As a result, it is evident that under such wind speeds, a solar collector's thermal performance also reaches its maximum. Under wind speeds in the range between 0 and 4 m s^{-1}, a decrease in thermal performance can be observed, caused by a decrease in the combined convection thermal resistance. The thermal efficiency remains the same under wind speeds higher than 4 m s^{-1}. This can be explained by the fact that changes in wind speed do not lead to significant changes in the combined convection heat transfer resistance at such speeds (see Fig. 5a). Moreover, these changes are insignificant considering the magnitude difference between the combined convection heat transfer resistance and the closed gap convection heat resistance (see Fig. 5b).

Therefore, the current standard sets the wind speed testing interval in the range between 2 and 4 m s^{-1}. Higher wind speeds do not significantly change thermal performance characteristic curves, while lower wind speeds do not adequately represent the on-site wind conditions. However, it is worth noting that even though there is no significant difference in thermal performance within the range between 2 and 4 m s^{-1} under low- and middle values of the reduced temperature difference, there is a considerable difference in thermal performance under high values of the reduced temperature difference.

2.4 Effect of heat transfer fluid flow rate

Moreover, the thermal performance efficiency test was also performed for three different values of the heat transfer fluid flow rates. The reference heat transfer fluid flow rate was 72 kg m^{-2} h^{-1}, while the reduced flow rate was 50% of the reference one, about 36 kg m^{-2} h^{-1}, and the increased flow rate was 150% of the reference flow rate, around 108 kg m^{-2} h^{-1}. The results of the testing are illustrated in Fig. 6.

Firstly, the tested variants with the reference and increased flow rates demonstrate similar thermal performance characteristic curves under the low value of the reduced temperature difference. Then, the increased flow rate variant showed higher thermal performance compared to the reference one. Finally, the reference variant demonstrated higher thermal performance compared to the increased flow rate variant under a relatively high

value of the reduced temperature difference. As for the reduced flow rate variant, it showed slightly lower thermal performance throughout the whole range of operating conditions. The Reynolds and average Nusselt numbers were further calculated using the detailed model to investigate this issue. The modelling results are illustrated in Fig. 7. It is worth noting that a considerable number of Nusselt number correlations describe the forced convection heat transfer process (Churchill and Ozoe, 1973; Colburn, 1964; Dittus and Boelter, 1985; Gnielinski, 1976; Hausen, 1943; Kakaç et al., 1987; Petukhov, 1970; Shah and London, 2014; Sieder and Tate, 1936; Sleicher and Rouse, 1975). As a result, the application of different equations leads to different results. In this work, the correlations initially presented by Shah (Shah and London, 2014) are utilised.

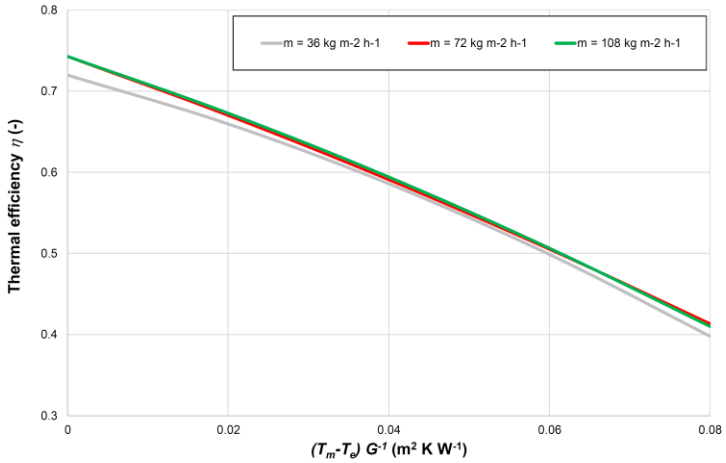

Fig. 6: The obtained thermal performance characteristic curves under different heat transfer fluid flow rates

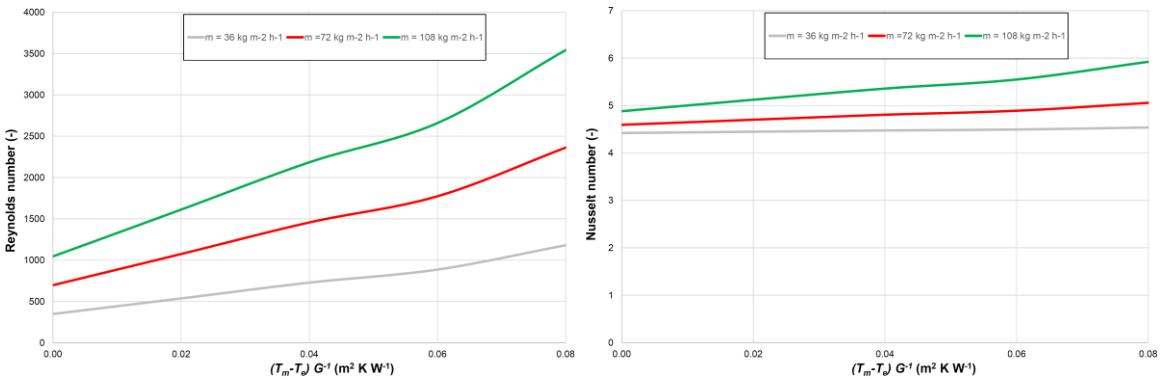

a) **b)**

Fig. 7: (a) Reynolds and (b) Nusselt number modelling results under considered operating conditions

These results show that under the considered operating conditions, the heat transfer fluid flow is primarily laminar (*Re* < 2300). For a few measured points, the flow proceeds to the transition zone between laminar and turbulent flow, where it is impossible to identify precisely whether it is laminar or turbulent. Considering these facts, the forced convection heat transfer correlations (for the fully developed flow and entrance region) initially presented by Shah were applied for calculation purposes (Shah and London, 2014). According to the calculation results, the reference variant and the increased flow rate variant outperform the reduced flow rate variant over the entire measured range. The higher Nusselt numbers eventually lead to a higher value of the forced convection heat transfer coefficient, resulting in higher energy performance. The modelling results, utilising the detailed validated flat-plate collector model, confirm this. Therefore, it can be concluded that inconsistent results during this series of experiments can be attributed to the measurement uncertainty caused by sensors' accuracy and the repeatability of readout values. Since the difference in thermal performance between analysed variants is minor, the measurement uncertainty can mix up with the results. Thus, it was decided not to include the flow rate parameter in the simulation analysis presented in the next chapter.

3. Simulation analysis

The experimental testing results mentioned above demonstrated that the collector tilt angle and wind speed considerably affect the tested collector's thermal performance. The thermal performance increases with increasing slope and decreasing wind speeds. According to the current standard, the maximum possible thermal efficiency will be the thermal characteristic curve obtained under a wind speed of 2 m s^{-1} and a collector's tilt angle of 0 degrees (variant MAX). Conversely, the minimum possible thermal efficiency will be the thermal characteristic curve obtained under a wind speed of 4 m s^{-1} and a collector's tilt angle of 90 degrees (variant MIN). These two variants were obtained using the experimental and simulation results from the detailed validated mathematical model. The thermal performance characteristic curve derived under the reference boundary conditions, with a wind speed of 4 m s^{-1} and a collector's tilt angle of 90 degrees, was selected as the reference variant RV. The efficiency characteristic curves of the compared variants are shown in Fig. 8.

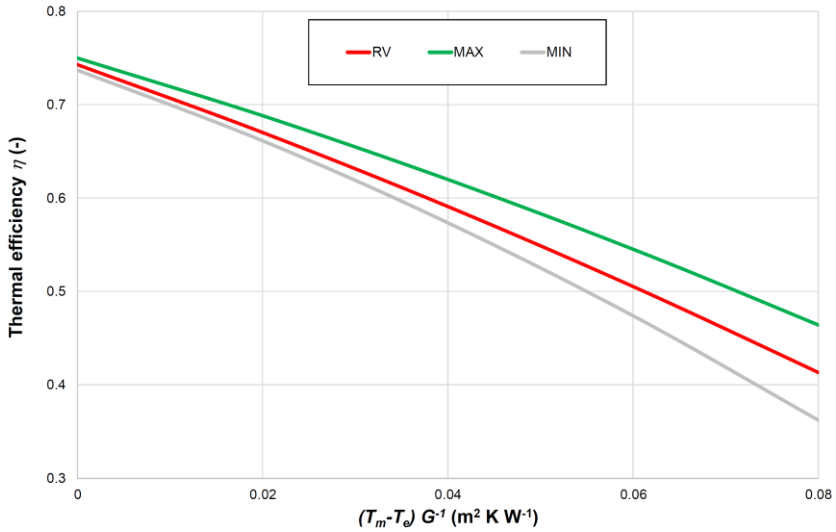

Fig. 8: The analysed thermal performance variants

The simulation analysis should be performed to understand the effect of the test boundary conditions on a glazed flat-plate solar collector's thermal performance. While the individual thermal performance characteristic curves demonstrate the variation in thermal performance under different boundary conditions, this is not a telling comparison because the collector's operating point moves along part of the presented efficiency curve in ordinary operation. Furthermore, the collector's heat transfer fluid operating temperature defines the operating region. Therefore, it was decided to perform a simulation analysis for different operating temperatures using ScenoCalc software.

To obtain a comprehensive understanding of the influence of boundary conditions on the performance results and, consequently, the solar system's performance simulation results, an annual simulation analysis was performed using ScenoCalc simulation software. This software allows the calculation of an annual solar collector's energy output using the obtained thermal performance characteristic curves under constant operating temperatures and different climatic conditions. To represent different solar collector applications, ranging from pool heating to process heat, the following constant collector mean operating temperatures were applied: 25 °C, 50 °C, 75 °C, and 100 °C. Moreover, to represent different climatic zones, the climatic conditions of Stockholm (Sweden), Würzburg (Germany), and Athens (Greece) were considered.

4. Results and discussion

The simulation results for the considered collector variants (MAX, MIN, and RV) under different operating temperatures and climatic conditions are presented in

Tab. 2. Additionally, the results for Stockholm and Athens climatic conditions are illustrated in Fig. 9.

The simulation results indicated that below the operating temperature of 50 °C, the difference between the simulated variants is not significant for all climatic conditions. Specifically, the annual solar collector's energy output varies between -5% and 10% if the reference boundary conditions are not met during the performance

evaluation test. In contrast, the simulation results demonstrated that for operating temperatures higher than 50 °C, the difference between the annual solar collector's energy output becomes significant. For instance, under the operating temperature of 100 °C and the climatic conditions of Würzburg, the simulated annual solar collector's energy output varies between -25% and +29%. The situation is also similar for the other climatic conditions.

Tab. 2: Simulation results under various operating temperatures and climate conditions

	Annual solar collector's energy output (kWh m^{-2})			
	25 °C	**50 °C**	**75 °C**	**100 °C**
Stockholm (Sweden), incident solar irradiation 1166 kWh m^{-2} (yearly)				
MIN	635 (-2%)	407 (-5%)	237 (-12%)	113 (-27%)
RV	645	429	271	154
MAX	670 (+4%)	472 (+10%)	319 (+18%)	201 (+30%)
Würzburg (Germany), incident solar irradiation 1228 kWh m^{-2} (yearly)				
MIN	685 (-1%)	435 (-5%)	250 (-13%)	122 (-25%)
RV	695	458	286	163
MAX	720 (+4%)	505 (+10%)	338 (+18%)	209 (+29%)
Athens (Greece), incident solar irradiation 1170 kWh m^{-2} (yearly)				
MIN	1109 (-1%)	773 (-3%)	487 (-9%)	251 (-22%)
RV	1121	799	537	319
MAX	1138 (+2%)	857 (+7%)	612 (+14%)	402 (+26%)

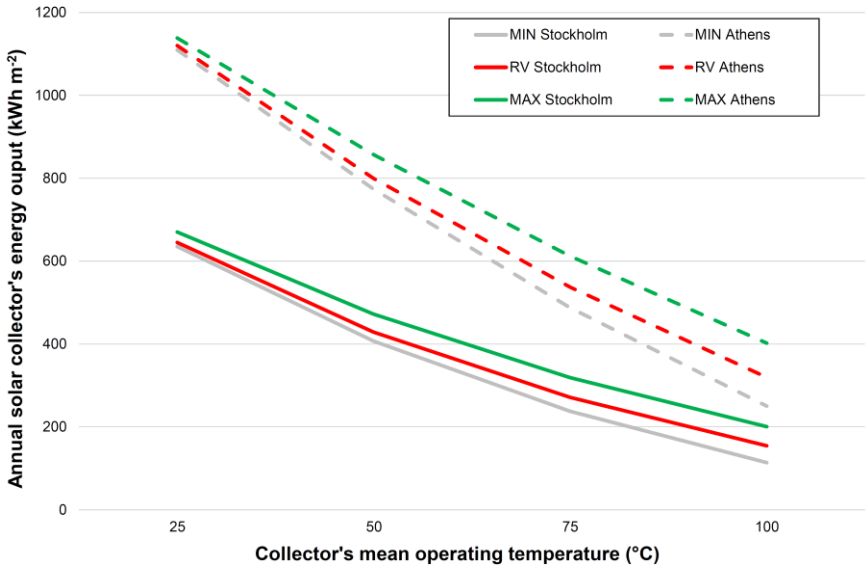

Fig. 9: Annual solar collector's simulation results under different operating and climatic conditions

To sum up, differences in test boundary conditions (under the valid standard) are unlikely to cause any considerable difference in the simulated annual solar collector's energy output during the design stage for systems such as solar pool heating systems or solar domestic hot water systems. In contrast, the annual solar collector's energy output difference is much more significant under the collector's mean temperature between 50 °C and 100 °C. Thus, for such systems (for instance, solar process heat systems), it is highly recommended that the boundary conditions under which the performance test was carried out be considered before performing the simulation analysis at the design stage. In any case, it is essential to emphasise that for such systems (with high operating temperatures), the differences in test boundary conditions will cause significant uncertainty in the energy simulation results.

5. Conclusion

This paper investigated the effect of boundary conditions on the performance evaluation test results of glazed flat-plate collectors. Firstly, the reference boundary conditions and the investigated parameters were identified. Secondly, a series of experimental thermal performance tests were performed to investigate the effect of each parameter individually. Then, the minimum and maximum possible thermal performance characteristic curves were derived. Finally, a simulation analysis was performed to understand the effect of the test boundary conditions on a glazed flat-plate solar collector's thermal performance. The following conclusions can be made:

- The experimental results demonstrated a negligible effect of solar irradiance and the heat transfer fluid flow rate (under the valid standard) on the solar collector's thermal performance.
- In contrast, wind speed and collector tilt angle during the performance evaluation test considerably affect the obtained thermal performance characteristic curves.
- The results showed that the difference in the test boundary conditions under the valid test standard would not cause any considerable difference in the solar system energy output simulation results performed at the design stage for the most common solar thermal system applications (pool heating, solar domestic hot water systems, and space heating).
- Conversely, the differences in test boundary conditions could lead to significant disparities in energy output simulation results for high-temperature solar thermal applications, such as process heat.

6. References

Churchill, S.W., Ozoe, H., 1973. Correlations for laminar forced convection in flow over an isothermal flat plate and in developing and fully developed flow in an isothermal tube. J. Heat Transfer 95, 416–419.

Colburn, A.P., 1964. A method of correlating forced convection heat-transfer data and a comparison with fluid friction. Int. J. Heat Mass Transf. 7, 1359–1384.

Dittus, F.W., Boelter, L.M.K., 1985. Heat transfer in automobile radiators of the tubular type. Int. Commun. Heat Mass Transf. 12, 3–22.

Gnielinski, V., 1976. New equations for heat and mass transfer in turbulent pipe and channel flow. Int. Chem. Eng. 16, 359–368.

Hausen, H., 1943. Darstellung des Warmeuberganges in Rohren durch verallgemeinerte Potenzbeziehungen. Z. VDI Beih. Verfahrenstech 4, 91–98.

ISO 9806:2017. Solar energy — Solar thermal collectors — Test methods., 2017.

Kakaç, S., Shah, R.K., Aung, W., others, 1987. Handbook of single-phase convective heat transfer. Wiley New York et al.

Kumar, S., Sharma, V.B., Kandpal, T.C., Mullick, S.C., 1997. Wind induced heat losses from outer cover of solar collectors. Renew. Energy 10, 613–616. https://doi.org/10.1016/S0960-1481(96)00031-6

Mathioulakis, E., Panaras, G., Belessiotis, V., 2012. Uncertainty in estimating the performance of solar thermal systems. Sol. Energy 86, 3450–3459. https://doi.org/10.1016/j.solener.2012.07.025

McAdams, W.H., 1954. Heat Transmission 3d Ed. McGraw-Hill, New York.

Müller-Schöll, C., Frei, U., 2000. Uncertainty analyses in solar collector measurement, in: Proceedings of the Eurosun Congress. Copenhagen, Denmark.

Palyvos, J.A., 2008. A survey of wind convection coefficient correlations for building envelope energy systems' modeling. Appl. Therm. Eng. 28, 801–808. https://doi.org/10.1016/j.applthermaleng.2007.12.005

Petukhov, B.S., 1970. Heat transfer and friction in turbulent pipe flow with variable physical properties. Adv. heat Transf. 6, 503–564.

Reddy, T.A., 2011. Applied Data Analysis and Modeling for Energy Engineers and Scientists. Springer US, Boston, MA. https://doi.org/10.1007/978-1-4419-9613-8

Shah, R.K., London, A.L., 2014. Laminar flow forced convection in ducts: a source book for compact heat exchanger analytical data. Academic press.

Sharples, S., Charlesworth, P.S., 1998. Full-scale measurements of wind-induced convective heat transfer

from a roof-mounted flat plate solar collector. Sol. Energy 62, 69–77.

Shemelin, V., Matuska, T., 2017. Detailed Modeling of Flat Plate Solar Collector with Vacuum Glazing. Int. J. Photoenergy 2017, 1–9. https://doi.org/10.1155/2017/1587592

Shemelin, V., Matuška, T., 2023. The effect of the wind conditions on the thermal performance of an unglazed solar thermal collector. Energy Reports 10, 2880–2888. https://doi.org/10.1016/j.egyr.2023.09.132

Sieder, E.N., Tate, G.E., 1936. Heat Transfer and Pressure Drop of Liquids in Tubes. Ind. Eng. Chem. 28, 1429–1435. https://doi.org/10.1021/ie50324a027

Sleicher, C., Rouse, M.W., 1975. A convenient correlation for heat transfer to constant and variable property fluids in turbulent pipe flow. Int. J. Heat Mass Transf. 18, 677–683.

Sowmy, D.S., Schiavon Ara, P.J., Prado, R.T.A., 2017. Uncertainties associated with solar collector efficiency test using an artificial solar simulator. Renew. Energy 108, 644–651. https://doi.org/10.1016/j.renene.2016.08.054

Test, F.L., Lessmann, R.C., Johary, A., 1981. Heat Transfer During Wind Flow over Rectangular Bodies in the Natural Environment. J. Heat Transfer 103, 262–267.

Wattmuff, J.H., Charters, W.W.S., Proctor, D., 1977. Solar and wind induced external coefficients for solar collectors. Coop. Mediterr. pour l'Energie Solaire, Rev. Int. d'Heliotechnique 2, 56.

Experimental Investigation of Large Area Transpired Solar Air Collectors

Lucio Mesquita[1], Gary Johnson[2], Ross Breton[2] and Stephen Harrison[2]

[1] Natural Resources Canada, CanmetENERGY-Ottawa, Ottawa (Canada)

[2] QSBR Innovations, Kingston (Canada)

Abstract

Single-pass transpired solar air systems are one of the most cost-effective solar thermal technologies available in the market due to their simplicity and robustness. While most experimental work in this area deals with small samples, the present work evaluates the performance of a large-area transpired solar air collector operating under natural atmospheric conditions. The collector array evaluated was unglazed and was equipped with a perforated metal absorber panel through which air was drawn and heated during operation. The absorber surface was coated with a spectrally-selective Low-e coating. Tests were performed between December 2023 and March 2024 at the Canadian National Solar Test Facility (NSTF) located in Mississauga, ON, Canada. During monitoring, the thermal performance of the installation was evaluated at two air flow rate conditions, typical of real installations. Although integrated into the building's wall, the system was not connected to the building ventilation system to allow for continuous operation for the study. This provided a level of operational independence that is usually not possible in field evaluations. The present work presents the results of the experiment with an analysis of the collector's efficiency as a function of ambient air temperature, wind speed and air flow rate.

Keywords: transpired collector, solar air heating, ventilation, perforated collector, solar thermal

1. Introduction

Transpired solar air systems are one of the most cost-effective solar thermal technologies available in the market due to their simplicity and robustness. Initially developed in the 1990's, several contributions in the literature have covered both theoretical and experimental investigations of the technology. Kutscher et al. (1991) developed an initial model with experimental validation through a small flat-plate sample. Brunger et al. (1999) evaluated several aspects of the technology, including description of demonstration projects, simulation and design tools and laboratory testing of small samples. Fleck et al (2002) measured the field performance of a large area transpired air collector, noting significant performance variation due to wind effects. However, the operational conditions related to suction air speed were not optimal during the experiments due to issues with one of the air blowers. Shukla et al (2012) reviewed the state-of-the-art of the technology.

While small samples have frequently been used for experimental study, they carry an inherent disadvantage. For example, the suction of air through the transpired surface causes a reduction of the boundary layer thickness, causing a reduction in convection losses. This effect, however, is difficult to capture when testing small samples. Small samples, however, do carry the advantage of being tested under controlled conditions with solar and wind simulators.

The motivation for the current work comes from a desire to better understand the performance of large scale transpired air solar collectors operating under real atmospheric conditions, and to study the relationship between small samples tested under steady-state conditions in simulated environments for rating purposes. The data captured during this investigation represents a significant source of information on the performance of these types of solar thermal collectors. This paper is an initial analysis of selected samples taken from the monitored data.

© 2024. The Authors. Published by International Solar Energy Society
Selection and/or peer review under responsibility of Scientific Committee
10.18086/eurosun.2024.07.13 Available at http://proceedings.ises.org

2. Experimental Description

2.1 Test System

For this experiment, a large-area transpired air solar collector array was installed at the National Solar Test Facility (NSTF) located in Mississauga, Ontario, Canada. The installed collectors were equipped with a spectrally-selective low-emittance surface coating. The collectors followed the building wall orientation of 53° SE. Although integrated into the building wall, the system was not connected to the building ventilation system and was "single pass". This provided a level of operational independence that is usually not possible in field evaluations.

The focus of this study is the single collector array equipped with the spectrally selective absorber surface. The overall specifications of the selective absorber collector array studied in this paper are given in Table 1. A close-up photograph of the perforated absorber surface is shown in Fig. 1. The cross-section surface profile and dimensions of the absorber sheet are shown, Fig. 2. Figures 3 and 4 show the collector array during and after installation.

Tab. 1: Solar Collector Array Specifications

Collector Type	Single-stage, unglazed, transpired absorber, air solar collector
Collector coating	Low-e Selective surface
Gross dimensions	9.255 m W x 10.58 m H (97.9 m^2)
Plenum depth	0.205 m
Outlet Port Size	1.83 m W x 1.22 m H
Absorber	Aluminum sheet (0.75 mm)
Absorptance, α	0.935 (SRCC, 2020)
Emittance, ε	0.025 (SRCC, 2020)

Fig. 1: Closeup of perforated aluminum selective surface.

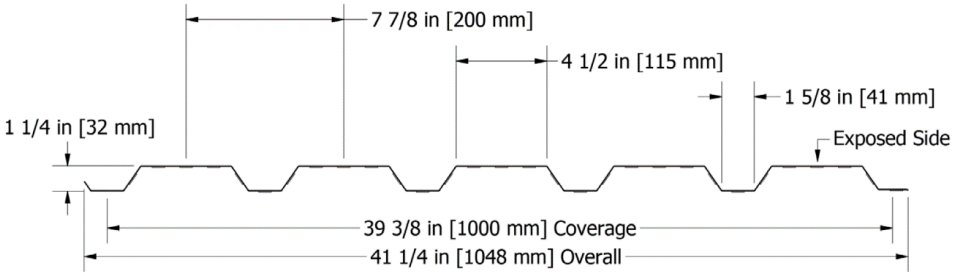

Fig. 2: Cross-section profile and dimensions of the absorber sheet.

Fig. 3: Transpired solar air collectors under construction at the Canadian National Solar Test Facility.

Fig. 4: Installed collectors. left: unglazed, selective surface model, right: two-stage black paint model.

2.2 Experimental configuration, Instrumentation and Data Acquisition

The assembled collector array was instrumented to monitor solar and infrared radiation incident on the collector's surface, horizontal direct and diffuse solar irradiance, barometric pressure, ambient air temperature and humidity, and wind speed and direction, Fig. 5.

During operation, outdoor ambient air was drawn through the solar collector's perforated absorber plate and directed through 20" diameter duct sections to the intake of a variable speed, centrifugal blower located in the building interior. The heated air exited the solar collector through an outlet manifold located in the upper periphery of the solar array. The outlet manifold directed the airflow through the building wall where the average outlet air temperature was measured by a 12-junction thermocouple array before it entered a flow nozzle to measure the volumetric flow rate. The pressure differential across the nozzle and duct air-temperature and pressure were recorded to calculate air mass flowrate. Thermocouples were installed on the back surface of the solar collector's absorber plate, and the exterior and interior surface of the wall behind the collector to estimate heat transmission through the wall.

Propeller/vane anemometers were installed on the rooftop and ahead of the panels to determine wind speed and direction. To measure total radiation (direct and diffuse) on the vertical wall, a PSP Pyranometer was mounted in the plane of the transpired panels, Fig. 6. A Precision infrared radiometer (PIR) was also mounted in the plane of the transpired panels. Global and Diffuse horizontal radiation were captured by an SPN1 Delta-T Pyranometer installed on a tower 15 m South of the panels. An ultrasonic anemometer was also placed at 2.5 meters directly in front of the panels to measure the U, V, and W components of wind velocity, Fig. 7. A temperature and humidity sensor was installed at ground level to measure local air properties at the site.

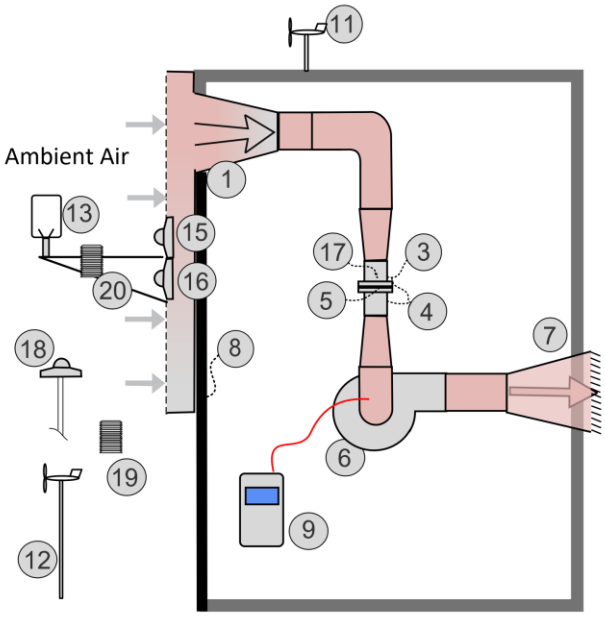

Fig. 5: Schematic of the experimental flow configuration, measurement points and instrumentation. Refer to Table 2 for the specifications of the numbered instrumentation.

All data was recorded by a PC running Windows 10® and LabVIEW 2020®. A "virtual instrument VI" was written specifically for the project. Values were stored at approximately 1-minute intervals during daylight hours and written as CSV (Excel) compatible data files for post analysis.

An Agilent data acquisition unit attached to the PC recorded raw sensor signals. An SPN1 Pyranometer transmitted both global and diffuse radiation as text values through an RS232 interface at polled intervals directly to LabVIEW.

The 3-axis ultrasonic anemometer components of the U, V, and W velocities were transmitted through an RS485 interface to the host computer/LabVIEW VI and captured at 4 Hz, then stored as daily numeric data files. The ultrasonic wind component values (U, V, W) were averaged over 1-minute intervals and stored.

Analysis and processing of the recorded data was performed using an MS Excel spreadsheet.

A photo of the interior of the building showing the wall directly behind the solar collector is shown in Figure 8. The ducting, hardware and measurement points are shown and numbered in the photo. Volumetric flowrates through the solar collector could be varied using a Variable Frequency Drive (VFD) to control blower motor frequency. Refer to Table 2 for the specifications of the indicated components.

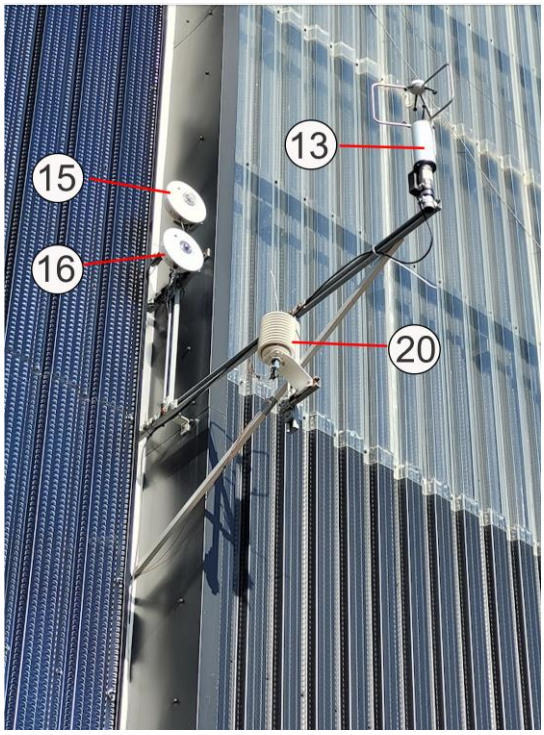

Fig. 6: Eppley PSP (15) and PIR (16) Pyranometers, ambient temperature sensors (20), and ultrasonic anemometer (13).

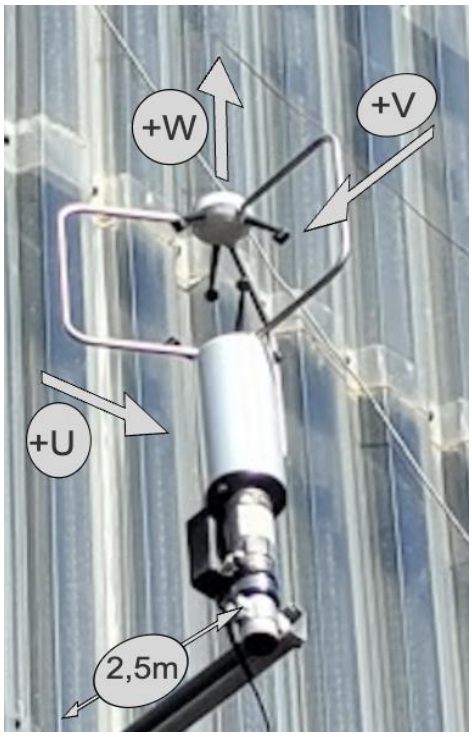

Fig. 7: 3-D Ultrasonic anemometer with direction of vectors U, V, and W relative to panel surface

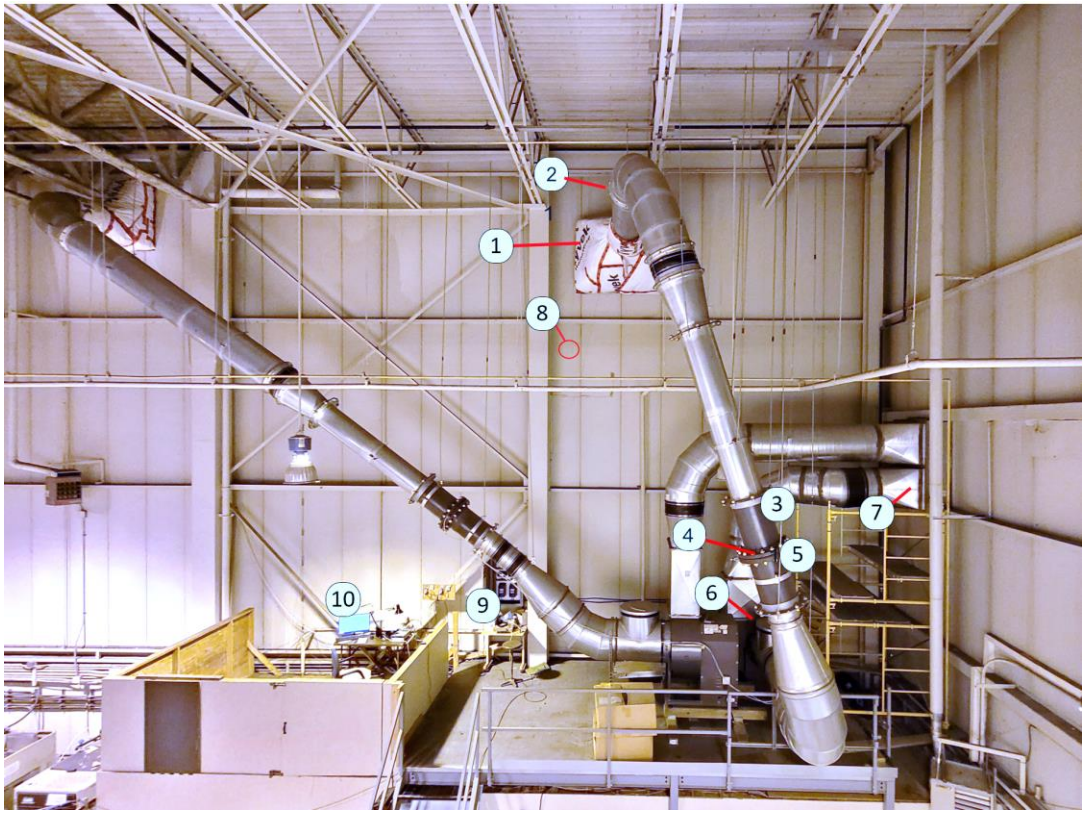

Fig. 8: Ducting for the system on the interior of the building showing the flow configuration and instrumentation. Outlet of the collector is at the top (1) . See Table 2 for the instrument specifications associated with the number tags.

Tab 2: Equipment and Instrumentation List

#	Instrument/equipment	Make/Model	Range	Accuracy*
1	Collector outlet manifold	NA	1.83 m x 1.22 m	-
2	Thermocouple array 2x6	Type T, thermocouple	-25 to 50˚C	±0.5 K
3	Static pressure selective	Vaisala PTB110	800 to 1100 hPa	±0.3 hPa
4	Δ pressure selective	Setra, model 264	0-250 Pa, 0-2.5 kPa	±1.0 % FS
5	Venturi	PIFS, MII# B14822	0.5 to 5 m^3 s^{-1}	±0.5 %
6	Blower	NA	-	-
7	Exhaust out of Bldg.	NA	NA	-
8	Wall temperatures	Type T, thermocouple	-25 to 50˚C	±0.5 K
9	Blower speed control	Lenze SMV	0 to 60 Hz	-
10	Data system	Agilent 34972a	-	-
11	Rooftop Wind monitor	Young, model 5103L	1 to 100 m s^{-1}, 360˚	±0.3 m s^{-1}, ±5°
12	Tower Wind monitor	Young, model 5103L	1 to 50 m s^{-1}, 360˚	±0.3 m s^{-1}, ±5°
13	Ultrasonic anemometer	Young, model 81000	0 to 40 m s^{-1}, 360˚	±3 %, ±5°
15	Wall Pyranometer	Eppley PSP	0.285 to 2.8 µm	±3 %
16	Infrared Radiometer	Eppley PIR	4 to 50 µm	±5 Wm^{-2}
17	Nozzle inlet Temp.	Type T, thermocouple	-25 to 50˚C	±0.5 K
18	Horizontal Pyranometer	Delta T SPN1-A3925	0.4 to 2.7 µm	±8 %
19	Temperature/humidity	Vaisala HMP155	-80 to 60ºC 0 to 100% RH	±1 %
20	Ambient temperature	Type T, thermocouple	-25 to 50˚C	±0.5 K

Note*: accuracy stated for typical operating conditions.

3. Results

3.1 Analyses of Results

Tests were performed from the 18th of December 2023 to the 24th of March 2024. Part way through the test period, the flowrate through the collector was adjusted to investigate the effects of array flow rate and suction velocity through the absorber surface. For this current study, specific clear days from the complete monitoring dataset were selected for detailed study. Each of the days selected was analyzed to determine the instantaneous power output over the course of daylong periods and to determine the total energy delivered during the day. Values of instantaneous and average daily efficiency were calculated. To determine the solar collector net power output, $\dot{Q}_{col}$ was calculated accounting for positive or negative heat gain through the back wall of the building, i.e.,

$$\dot{Q}_{col} = \left(\dot{m} \cdot Cp_m \cdot \Delta T \right) - \dot{Q}_{wall}, \text{ (W)} \qquad \text{(eq. 1)}$$

where $\dot{m}$ is the air mass flowrate (kg s^{-1}),

Cp_m = Specific heat capacity of moist air (kJ $kg^{-1}K^{-1}$)

$$\Delta T = T_{out} - T_a, \text{ (K)} \qquad \text{(eq. 2)}$$

where T_{out} is the temperature of the air exiting the collector (ºC), and

T_a is the temperature of the ambient air entering the collector (ºC).

$\dot{Q}_{wall}$ is the rate of heat transmission through the building wall into the solar collector air channel due to building heat loss.

$$\dot{Q}_{wall} = U_{wall} \cdot A_{col} \cdot \left(T_{building} - T_{eff} \right), \text{ (W)} \qquad \text{(eq. 3)}$$

U_{wall} is the thermal conductance of the wall (0.6 W m^{-2} K^{-1}, (Coenen, 2016), A_{col} is the collector surface area (97.9 m^2), and $(T_{building} - T_{eff})$ is the temperature difference between the building interior and the effective air

temperature in the solar collector air channel (K). Daily values of collected energy were calculated by numerically integrating the measured data over the course of daylong periods, i.e.,

$$Q_{day} = \frac{1}{1000} \cdot \int_{sunrise}^{sunset} \dot{Q}_{col}\, dt \qquad \text{(eq. 4)}$$

where Q_{day} is the total solar energy delivered to the building over a daylong period in kJ or expressed in kWh as $Q_{day,kWh} = Q_{day}/ 3600$.

It is important to determine the collector array's thermal efficiency to allow product comparisons and design improvements. The instantaneous efficiency (expressed as a percentage) for the solar collector was calculated as:

$$\eta_{wall} = 100 \cdot \frac{\dot{Q}_{col}}{(G_i + Ms) * A_{col}} \qquad \text{(eq. 5)}$$

where G_i = Total incident solar radiation on the surface of the collector (W m^{-2}), and

Ms = Net radiant emissive power from the surface of the solar wall (W m^{-2}).

It is worth noting that the calculated value of Ms was effectively zero due to the fact that the solar collector's emittance was very low (0.025) and the surroundings adjacent to the installation were usually snow covered during the monitoring period.

The daily efficiency for the solar collector wall was calculated as a percentage, i.e.,

$$\eta_{daily} = 100 \cdot \frac{Q_{day}}{(H_i/1000) * A_{col}} \qquad \text{(eq. 6)}$$

where H_i is the total irradiance striking surface of the solar collector absorber over the course of a day in J m-2.

3.2 Experimental Results

For this current study, specific days were chosen for detailed analysis, representative of the solar collector's performance at two system flow rates. Typical results for one of the days (March 23rd, 2024) are shown below in Figures 8 to 11. The flow rate through the solar collector was a nominal 2.65 ±0.05 kg s^{-1} and the wind speed was 0.9±0.3 m s^{-1} on that day. Figure 9 shows the variation of collector efficiency over the day. The plot shows unrealistic solar efficiencies in the early morning, most likely due to heat transmission through the building wall when the solar radiation was very low. The rise in effective efficiency later in the day is most likely due to the release of stored heat in the collector and building wall. The plots shown for the 23rd show the effects of the collector's orientation directed to the east of south (53^{o} SE), Fig. 10. This explains why solar irradiance on the wall is skewed toward the morning hours, while the global horizontal irradiance is centered around "solar" noon. Solar irradiance on the wall suddenly drops to a low value as the sun moved behind the building's wall.

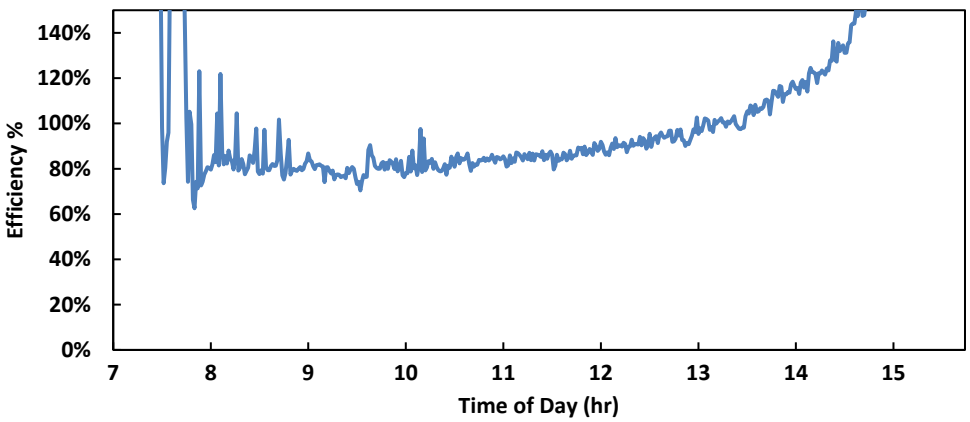

Fig. 9: Apparent Solar collector Efficiency as measured over March 23, 2024.

Figures 11 shows the daily variation of collector inlet and outlet temperatures, and Figure 12 shows the corresponding power output of the collector and cumulative energy.

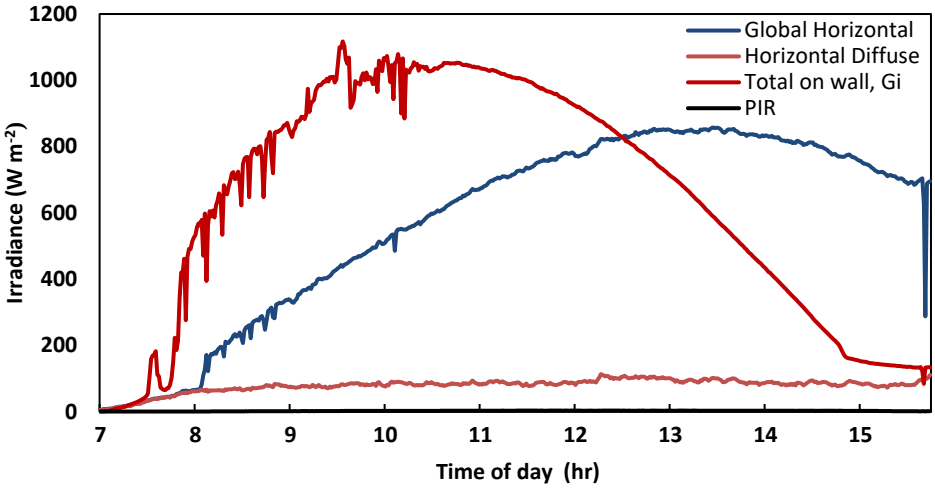

Fig. 10: Solar Irradiance measured over the course of March 23rd, 2024

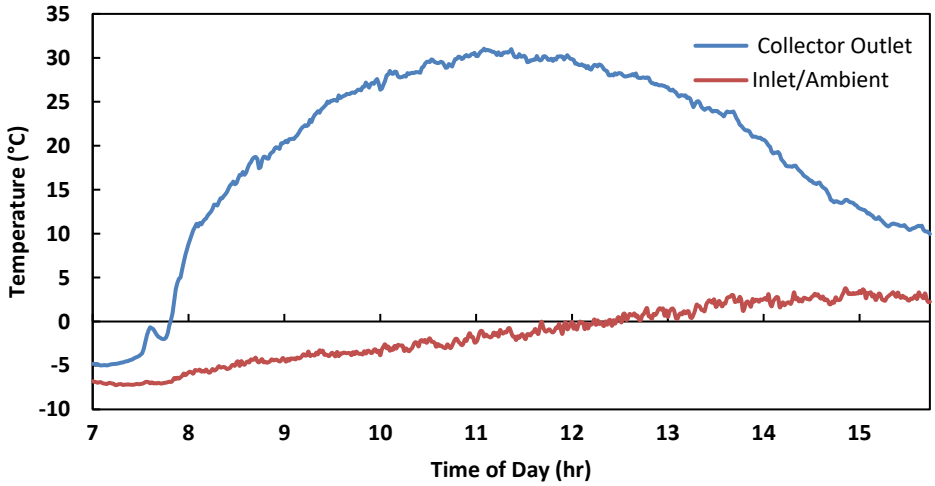

Fig. 11: Inlet and outlet temperatures for the solar collector as measured over the course of March 23rd, 2024. The ambient air temperature in front of the solar collector is taken as the inlet temperature.

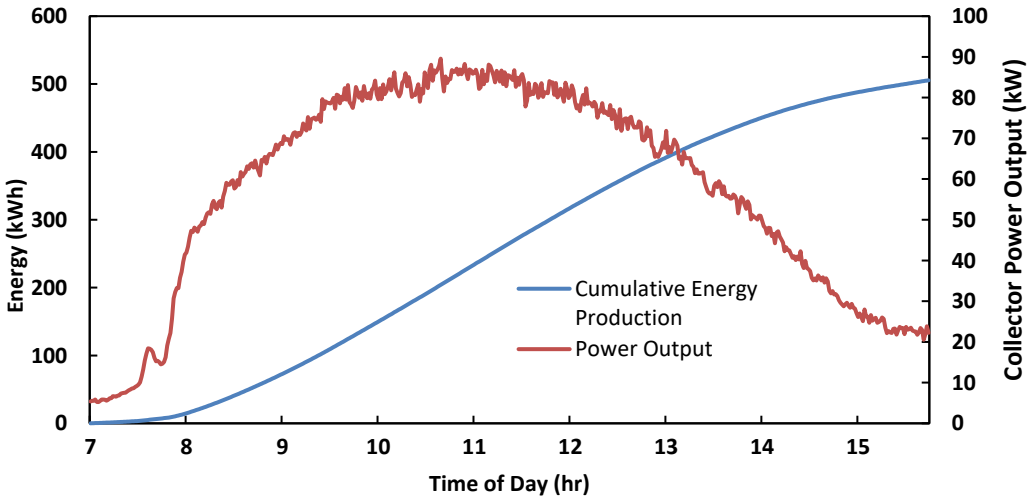

Fig. 12: Cumulative energy and power measured over the course of March 23rd, 2024

A good indication of instantaneous collector efficiency may be obtained by taking the values when the solar collector is operating in a more steady-state condition centered around the peak irradiance time period, e.g., between 10:00 and 11:00 am. Considering this region shown in Figure 9, the collector efficiency is seen to be above 80%. This high value is indicative of the low convective loss as ambient air is drawn through the collector and the Low-e absorber coating that reduces thermal radiation exchange with the surrounding environment. As the temperature of the solar collector increased over the day, the rate of heat transmission through the wall was reduced to insignificant values.

3.2.1 Daily Energy Delivered and Daily Collector Efficiency for Selected Days

To further illustrate the performance of the collector array, total energy delivered over the course of the day was calculated for 5 days with high solar irradiance (i.e., clear days). The daily solar energy delivered to the building and average daily efficiency for the 5 days is given in Table 3 and plotted in Figures 13 and 14.

Tab. 3: Summary of energy production and efficiency for clear days

High Solar Days	Average Daily Ambient Air Temperature (°C)	Average solar Irradiance on solar collector (W m^{-2})	Array Energy Production over Day (kWh)	Average Daily Efficiency	Average Flow Rate Kg s^{-1} m^{-2}
23-Mar	-0.5	487	551	82%	2.70
24-Mar	-2.5	584	454	85%	2.75
13-Mar	16	383	413	83%	2.50
15-Jan	-10	471	270	70%	2.44
26-Feb	5.8	596	328	81%	3.83
11-Mar	4.20	544	317	70%	2.33

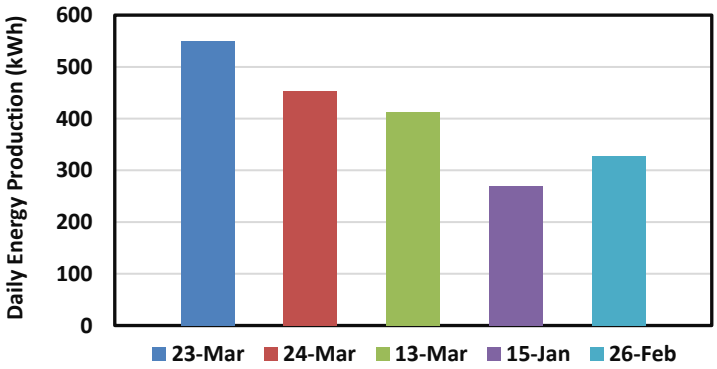

Fig. 13: Summary of energy production for selected clear days

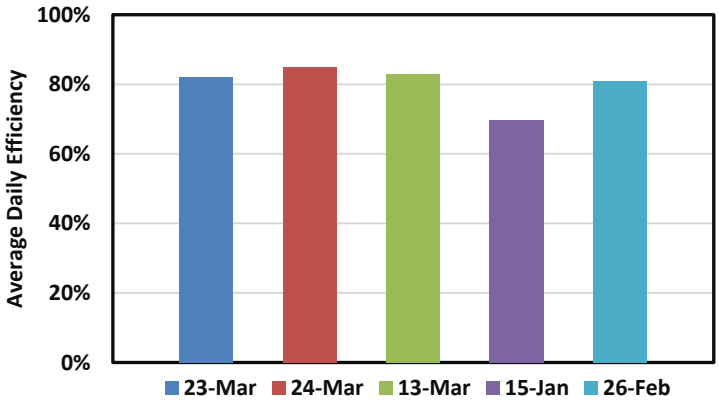

Fig. 14: Summary of collector efficiency for selected clear days

4. Discussion of Results

From the limited results shown if this paper, it is evident that transpired solar air systems operate at high efficiency when drawing ambient air. This is particularly advantageous if industrial or institutional applications require large quantities of fresh air. Currently there are no widely accepted test protocols to evaluate large-scale transpired solar collectors. In their absence, small scale samples have been tested under standard laboratory conditions allowing products to be listed for sale in certain jurisdictions.

In the case considered, a scaled version of the transpired solar collector with low emittance absorber was previously tested under laboratory conditions (SRCC, 2020, Fraunhofer, 2020) in a solar simulator facility. Tests were conducted under steady-state conditions according to the general requirements of ISO 9806. Consequently, these test conditions imposed during this standard test sequence, differed from those experienced in the field installation, including the ambient and inlet temperatures, solar irradiance intensity, and wind direction and velocity and characteristics (e.g., turbulence). A summary of the major differences between the standard test sequence and the test conditions experienced during this field trial are given below in Table 4.

Tab. 4: Comparison of test ISO- 9806 test conditions with large-scale tests

ITEM	ISO 9806 Standard Laboratory Test Sequence	NSTF large-Scale collector
Angle of tilt	45 ˚ to horizontal	Vertical
Infrared losses/gains	Higher effective sky temp due to simulator lamps and surroundings temperatures	Colder effective sky and surroundings temperatures
Wind direction	Scroll up from bottom of collector	Random, Turbulent
Ratio of Aperture to Gross collector area	Aperture = 2.43, Gross= 2.56 m^2 (Ratio = 0.95)	Negligible
Area of panel	Small, 2.56 m^2	Large, 98 m^2
Ambient air temperature	298 K (25ºC)	253 to 293 K (-20 to 20ºC)

The monitored test data obtained at the National Solar Test Facility show that the flow conditions adjacent to the large solar collector array were highly complex, with the various components of the air flow velocity varying rapidly in time, consistent with a turbulent flow condition. An example plot of air flow direction and velocity is shown in Figure 15, as measured using the three-axis ultrasonic wind transducer located at approximately 2.5 meters from the solar collector surface. The effects of turbulence intensity on unglazed transpired solar air collectors have been investigated in earlier studies (Fleck et al., 2002) and will be the focus future studies based on the data measured on the large collector array at the NSTF. The full wind data set was recorded at high frequency (4 times per second) to capture the rapid changes in velocity. It is also expected that the effects of wind on solar collector performance will depend on the air flow velocity through the solar collector as higher suction velocities at the surface may also affect boundary layer development and heat loss from the collector surface.

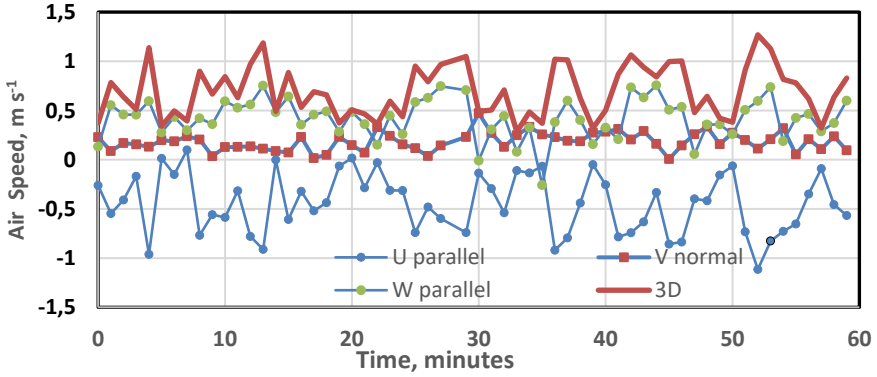

Fig. 15: Plot of 1-minute averages of the vector components of wind speed, as measured with the 3-axis ultrasonic wind transducer located in front of the collector surface, shown for a one hour-long period, i.e., 12 to 1 pm on January 15th, 2024. The vector sum is also shown, labeled 3D, and calculated as the root-mean square of the three velocity vectors. This plot illustrates the variability of the wind direction and velocity adjacent to the test wall.

4.1 Comparison with Previous Test Data

As an initial comparison, the NSTF monitored data was compared with standard laboratory results published by SRCC (SRCC, 2020) and based on tests conducted on a scaled collector sample according to the general requirements of the ISO 9806 (ISO 9806, 2017) test procedure. To facilitate this comparison, NSTF outdoor data was selected from "high irradiance" and "quasi-steady-state" periods at near-normal incidence angles. As ambient air temperatures were not the same, the data was compared to a performance characteristic derived from the laboratory test results and plotted as a function of the temperature difference between ambient inlet air temperature, Ta, and the average of the collector inlet and outlet air temperatures, Tm.

The results of this comparison are show in Figure 16, where the solid line indicates the approximate performance characteristic derived from the laboratory testing of the scaled sample (SRCC, 2020). The data points shown on the graph were derived from the NSTF monitored data taken on the large-scale solar collector. It may be seen that at higher flow rates and lower values of (Tm-Ta) the results correspond well. However, at higher values of (Tm-Ta) the output per unit area for the large-scale collector are higher than the laboratory derived result. These results suggest that the airflow associated with wind velocity around the large-scale collector differ from those experienced during laboratory testing. As well, the large-scale collector would have lower edge effects including heat losses, when compared to the small sample. One would expect that at higher collector flowrates through the perforated absorber plate, heat transfer would be greater, but the overall temperature rise, and resultant Tm would be lower. This would increase overall efficiency but at the cost of a lower delivery temperature to the building.

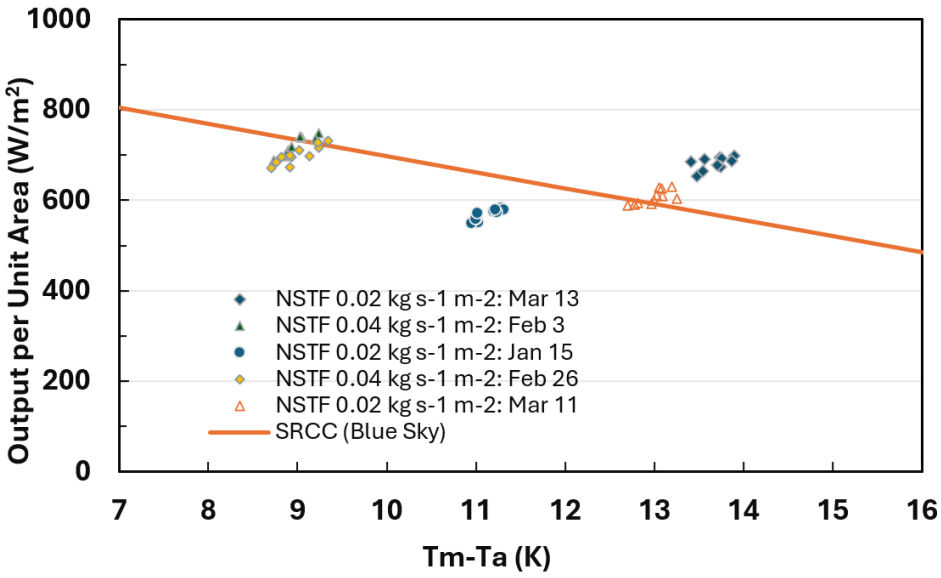

Fig. 16: Comparison of data selected from the large collector test at the NSTF with a performance characteristic derived from standard test results conducted on scaled samples (SRCC, 2020).

5. Conclusions

An extensive data set on the performance of a large scale transpired air solar collector has been collected under real atmospheric conditions. High level monitoring and data acquisition was used to record both the atmospheric and thermal performance data. The preliminary results have shown that the transpired collector with low emittance absorber coating can achieve high thermal efficiency while delivering solar preheated air.

The preliminary results indicate that differences in predicted performance exist between the large-scale installations and tests conducted on scaled samples and these increase at higher values of (Tm-Ta).

While this project has obtained significant data on the performance of transpired solar collectors, additional analysis is required to fully quantify the effects of the various variables. The results also indicate that the development of an appropriate test standard for transpired solar air collectors should be undertaken. With this in mind, a future endeavour will focus characterizing the performance of the large-scale transpired collector installation through regression analysis conducted on the monitored data, similar to that proposed for outdoor dynamic testing liquid-based solar collectors in ISO 9806.

6. Acknowledgments

The authors gratefully acknowledge the financial support of Natural Resources Canada through the Office of Energy Research and Development – Energy Innovation Program (EIP).

7. References

Brunger, A.P., Cali, A., Kutscher, C.F., Dymond, C.S., Pfluger, R., McClenahan, D., Kokko, J. and Hollick, J., 1999. Low cost, high performance solar air-heating systems using perforated absorbers. IEA International Energy Agency Solar Heating and Cooling Task 14 report – Air Systems Working Group.

Coenen, M., Exova Canada Inc., NRCan Report, 2016. Evaluation of Foam Insulation from the NSTF Lab Wall for Thermal Properties in Accordance with ASTM C518-15.

Fleck, B.A., Meier, R.M. and Matović, M.D., 2002. A field study of the wind effects on the performance of an unglazed transpired solar collector. Solar energy, 73(3), pp.209-216.

Fraunhofer-Institut für Solare Energiesysteme ISE, 2020. Test report according to EN 12975-1:2006+A1:2010 /EN ISO 9806:2017, Report KTB: 2020-02-k2.

ISO 9806:2017, 2017. International Standards Organization. Solar energy – Solar thermal collectors – Test Methods. https://www.iso.org/standard/67978.html, accessed August 1, 2024.

Kutscher, C.F., Christensen, C. and Barker, G., 1991. Unglazed transpired solar collectors: an analytic model and test results. In Proceedings of ISES Solar World Congress (Vol. 2, pp. 1245-1250).

Shukla, A., Nkwetta, D.N., Cho, Y.J., Stevenson, V. and Jones, P., 2012. A state of art review on the performance of transpired solar collector. Renewable and Sustainable Energy Reviews, 16(6), pp.3975-3985.

SRCC, Solar Rating and Certification Corporation. 2020. Report OG-100 ICC-SRCC Certified Solar Air Heating Collector #10002111. https://solar-rating.org/, accessed August 1, 2024.

Performance Comparison of a Transpired Air Solar Collector with Low-E Surface Coating

Stephen Harrison[1], Anh Kiet Nguyen[2], Gary Johnson[2] and Lucio Mesquita[3]

[1] Queen's University, Mechanical and Materials Engineering, Kingston (Canada)

[2] QSBR Innovations, Kingston (Canada)

[3] Natural Resources Canada, CanmetENERGY-Ottawa, Ottawa (Canada)

Abstract

Transpired air solar collectors are often used to preheat ventilation-air in commercial buildings. Outdoor air is drawn through a perforated, unglazed metal absorber and delivered to a building space in a single pass. Until recently, high-emittance absorber coatings were commonly used, making them susceptible to radiant thermal losses to the surrounding environment. The recent development of durable, low-emittance coatings has allowed manufacturers to offer these surfaces on their unglazed products. This study compares the performance of two transpired solar air collectors: one with a high-emittance absorber coating and the other with a low-emittance coating. Results indicate that, the low-emittance surface coating significantly increased both the efficiency and delivery air temperature compared to the collector with the high-emittance surface coating.

Keywords: Unglazed Transpired Solar Air Collector, Low-emittance Absorber

1. Introduction

The use of transpired solar collectors to preheat ventilation-air represents one of the most cost-effective solar energy applications. Primarily used on commercial buildings, outdoor air is drawn through a perforated, unglazed metal absorber and delivered to a building space in a single pass (Badache et al. 2013). Until recently, high-emittance absorber coatings were commonly used, making them susceptible to radiant thermal losses to the surrounding environment. However, the development of durable, low-emittance coatings has allowed manufacturers to offer these surfaces on their unglazed products. This study compares the thermal performance of two transpired solar air collectors: one with a high-emittance surface coating as a baseline and the other with a highly spectrally selective low-emittance coating.

Geometrically identical collector samples were installed side-by-side on a south-facing vertical wall and operated under natural environmental conditions during 2023 and 2024's winter. Both collectors were operated under typical airflow conditions, and ambient and collector temperatures, incident solar energy and wind intensity were monitored in real-time. *Shukla et al (2012) reviewed the state-of-the-art of the technology.*

2. Description of Experimental Measurements

Geometrically identical collector samples were installed side-by-side on a south-facing vertical wall and operated under natural environmental conditions during the winter of 2023 and 2024. Both collectors were operated under typical airflow conditions, and ambient and collector temperatures, incident solar energy and wind intensity were monitored in real-time.

2.1 Test Samples

The two collectors used in the test were constructed of commercially available, unglazed transpired solar thermal air collector panels with perforated aluminum absorber plates. The panels were attached to identical insulated boxes specially constructed by the manufacturer for this study. The assembled test samples were identical except for the surface coatings. One used a non-selective painted surface (SRCC, 2016), and the other,

© 2024. The Authors. Published by International Solar Energy Society
Selection and/or peer review under responsibility of Scientific Committee
10.18086/eurosun.2024.07.14 Available at http://proceedings.ises.org

a (0.025) low-emittance surface coating, (SRCC, 2020; Fraunhofer, 2020). The thermal-optical properties and dimensions of the two samples tested are given in Table 1. Figure 1 shows the cross-section profile dimensions of the test samples' absorber sheets. A close-up view of the absorber surface of the selective absorber surface showing the surface perforations for airflow is shown in Figure 2. Both collector samples had identical absorber geometries and perforations.

The collectors were mounted vertically on a south-facing wall, Fig. 3. A 5 cm rigid foam insulation was placed behind each collector to reduce heat loss through the back surface.

Tab. 1: Properties of samples tested

Sample	Absorptance, α	Emittance, ε	Base material (0.75 mm thick)	Dimensions (L x W x H)
Selective	0.935	0.025	Perforated Aluminium sheet	2.44 x 1.03 x 0.20 (m)
Non-selective	0.95	0.95*	Perforated Aluminium sheet	2.44 x 1.03 x 0.20 (m)

*Note. Estimated value

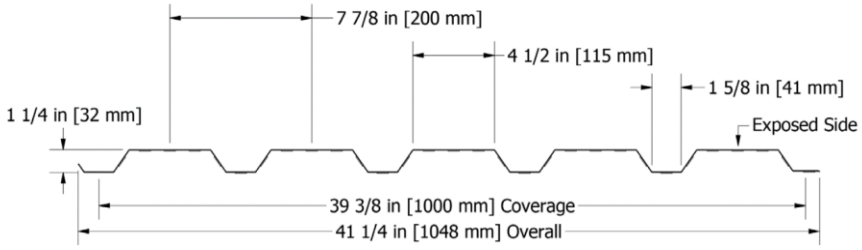

Fig. 1: Cross-section profile dimensions of the test samples' absorber sheets

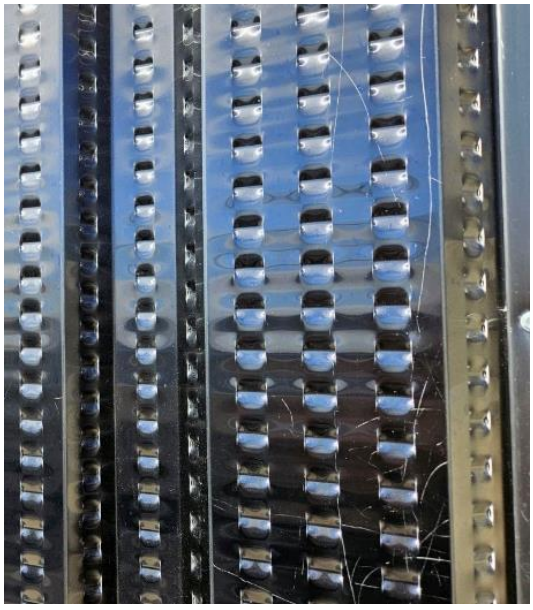

Fig. 2: A close-up view of the absorber surface showing the surface perforations for airflow

Fig. 3: Collectors mounted vertical on the building's south-facing wall.

2.2 Experimental Configuration and Instrumentation

During testing, the collectors were mounted vertically on a south-facing wall at the Solar Calorimetry Laboratory, Queen's University, located in Kingston Ontario. Canada (44.23° N, 76.49° W). The geometrically identical collector samples were installed side-by-side on a south-facing vertical wall and operated under natural environmental conditions during the winter of 2023 and 2024. Both collectors were operated under the same airflow conditions. Ambient and collector temperatures, collector volumetric flowrate, incident solar energy, barometric pressure and wind intensity were monitored in real-time.

Each solar collector sample was connected to a separate air-flow circuit, instrumented to measure the instantaneous power output of each sample, Fig. 4. All instrumentation had current calibration certifications, traceable to secondary standards. During operation ambient air was drawn through the collectors" perforated absorber plates by centrifugal blowers. Various flowrates could be set by varying the blower's speed using variable frequency (VFD) controls.

Air exited each solar collector through a 10 cm diameter opening located at its top-center, through the wall and into a blower. Inside the building, temperature & humidity sensors and laminar flow elements were used to measure collected energy.

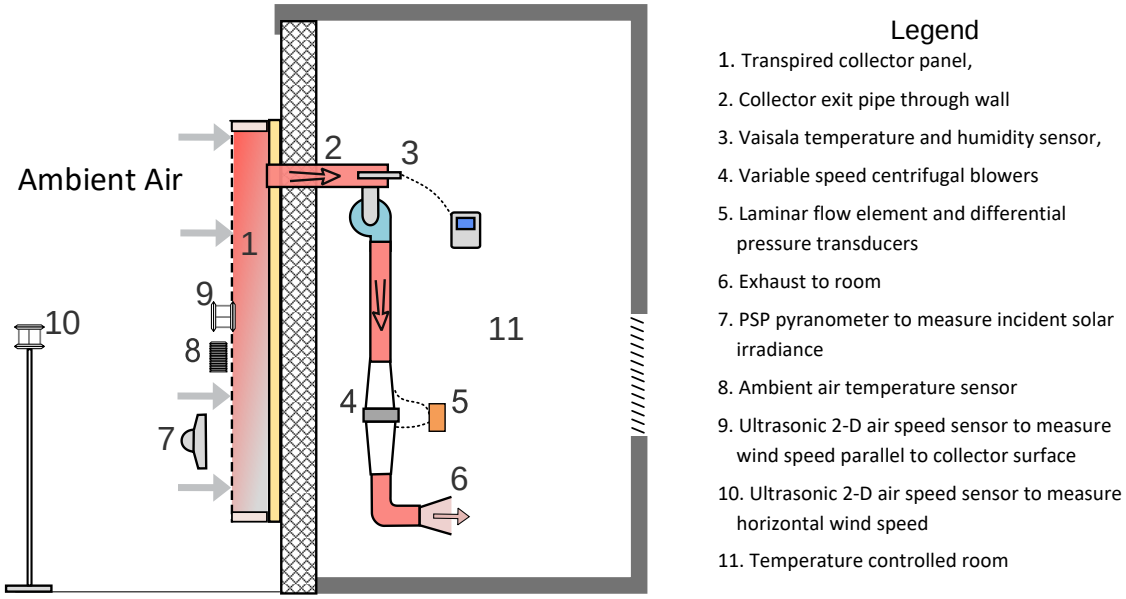

Fig. 4: Schematic of the of one of the test flow circuits showing monitoring points

With this setup, the incoming air was directed through the sensors and the laminar flow element, and into a temperature-controlled space, Fig. 4. Two pyranometers were mounted vertically between the collectors to measure solar radiation and two ultrasonic wind transducers were mounted vertically, parallel with the collector surface. An additional ultrasonic sensor was mounted in front of the collectors, to measure ambient air temperatures, wind speeds, and wind direction. In addition, there was a propeller anemometer placed approximately 15 m from the collectors to measure the overall wind speed at the test location.

All experimental data for both systems was recorded in real time ever 30 seconds with a Campbell Scientific CR1000 data acquisition system. Campbell Scientific data acquisition software Loggernet IV® was used to process and display the data in real time, Fig. 5.

The collectors were monitored over multiple days and weather conditions during the months of March and April 2023, and the winter of 2024. The two collectors were set to run at different air flow rates consisting of 45 CFM, 80 CFM, 105 CFM, and 185 CFM. Data collected during this time was analyzed to compare the thermal performance of the non-selective and selective surface collectors.

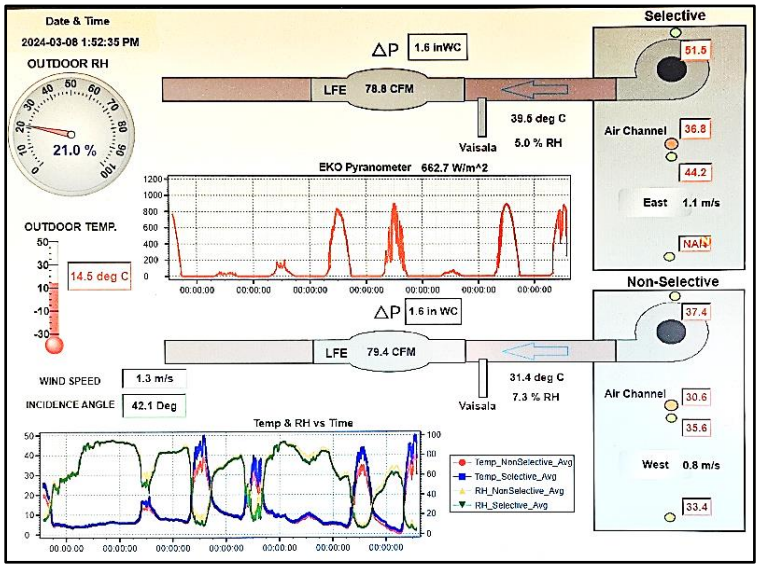

Fig. 5: Screenshot of data monitoring software

3. Results & Discussions

3.1 Analyses of Results

Tests were performed from the 18th of December 2023 to the 24th of March 2024. During the monitoring period, the flowrate through the collectors was adjusted to investigate the effects of array flow rate and suction velocity through the absorber surface. To compare the performance of the solar collectors, the raw data for each collector was processed in MS Excel to determine the instantaneous power output over the course of daylong periods and to determine the total energy delivered during the day. Values of instantaneous and average daily efficiency were calculated. To determine the solar collector net power output, $\dot{Q}_{col}$ was calculated accounting for positive or negative heat gain through the back wall of the building, i.e.,

$$\dot{Q}_{col} = \left(\dot{m} \cdot Cp_m \cdot \Delta T \right) \text{(W)} \qquad \text{(eq. 1)}$$

where $\dot{m}$ is the air mass flowrate (kg s^{-1}),

Cp_m = Specific heat capacity of moist air (kJ $kg^{-1}K^{-1}$)

$$\Delta T = T_{out} - T_a, \text{ (K)} \qquad \text{(eq. 2)}$$

where T_{out} is the temperature of the air exiting the collector (ºC), and

T_a is the temperature of the ambient air entering the collector (ºC).

The values of Cp_m, $\dot{m}$ and the density of air were calculated at the average temperature of the air entering and exiting the solar collectors.

Daily values of collected energy were calculated by numerically integrating the measured data over the course of daylong periods, i.e.,

$$Q_{day} = \frac{1}{1000} \cdot \int_{sunrise}^{sunset} \dot{Q}_{col}\, dt \qquad \text{(eq. 3)}$$

where Q_{day} is the total solar energy delivered to the building over a daylong period in kJ or expressed in kWh as

$Q_{day,kWh} = Q_{day} / 3600$.

The instantaneous efficiency (expressed as a percentage) for the solar collector was calculated as:

$$\eta_{wall} = 100 \cdot \frac{\dot{Q}_{col}}{(G_i) * A_{col}} \qquad \text{(eq. 4)}$$

where G_i = Total incident solar radiation on the surface of the collector (W m^{-2}), and

The daily efficiency for the solar collector wall was calculated as a percentage, i.e.,

$$\eta_{daily} = 100 \cdot \frac{Q_{day}}{(H_i/1000) * A_{col}} \qquad \text{(eq. 5)}$$

where H_i is the total irradiance striking surface of the solar collectors' absorber over the course of a day in J m^{-2}.

3.2 Experimental Results

Day-long periods were selected from the full data set for detailed analysis and the results. Example plots of power output for each collector non-selective (high-emittance) and selective absorbers (low-emitance) are plotted for both a clear and overcast day in Fig. 3 and Fig. 4.

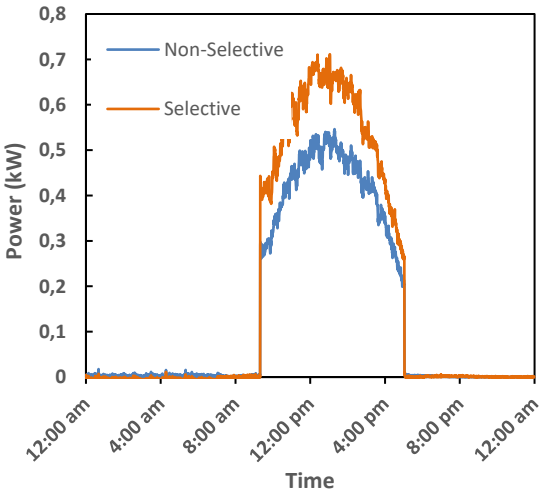

Fig. 6: Delivered Power vs Time for Clear Sky Day, April 1st, 2023, ambient air temperature = 4ºC, (9:00 am to 5:00 pm)

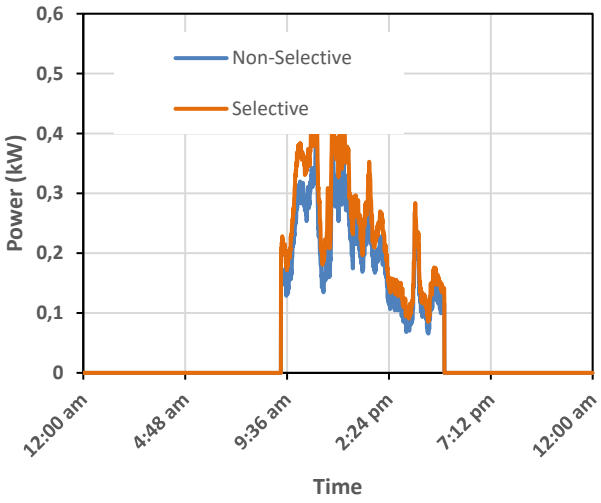

Fig. 7: Delivered Power vs Time for Cloudy Day, April 11, 2023, ambient air temperature = 8ºC, (9:00 am to 5:00 pm)

To evaluate how the selective and non-selective solar collectors performed, the daily energy delivered by the two collectors was compared under four different flow rates: 45 CFM, 80 CFM, 105 CFM, and 185 CFM. Plots showing the daily energy delivered by each of the collectors is compared for different air flow rates are shown below in Figs. 8 to Fig. 15. The ratio of the energy delivered by the low-emittance collector relative to the non-selective collector are also shown

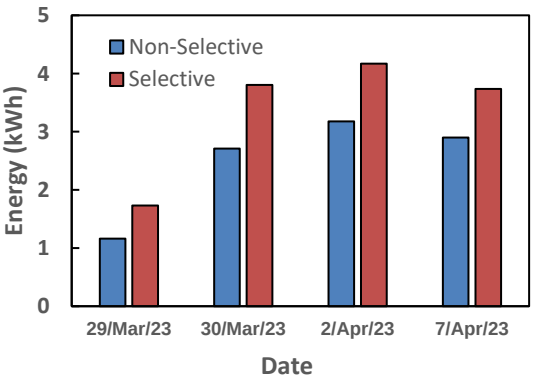

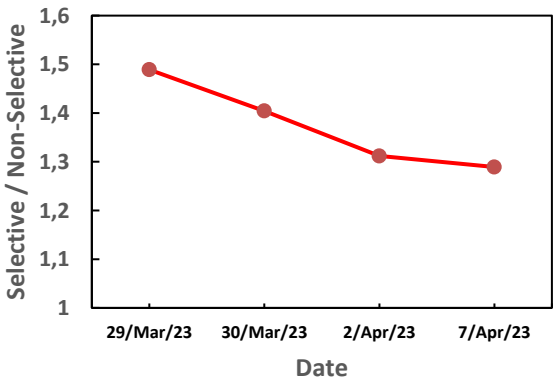

Fig. 9: Ratio of daily energy delivered for collector with selective absorber coating (i.e., low-emittance) relative to the non-selective (i.e., high-emittance)

Fig. 8: Comparison of collector energy delivered per day at 0.02 m^3s^{-1} (45 CFM) or 0.0084 $m^3s^{-1}m^{-2}$

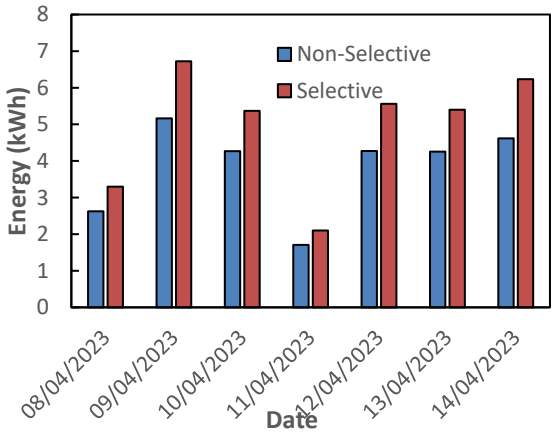

Fig. 10: Comparison of collector energy delivered per day at 0.038 m^3s^{-1} (80 CFM) or 0.015 $m^3s^{-1}m^{-2}$

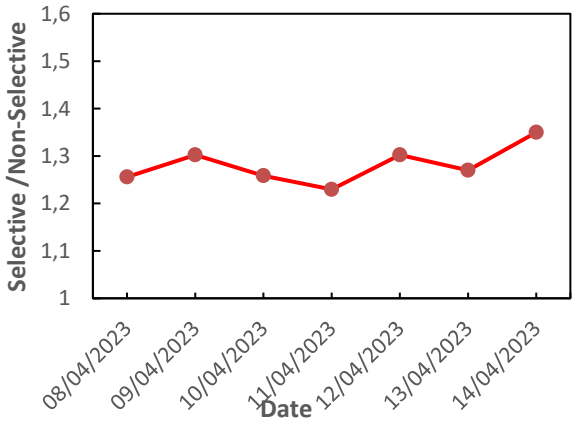

Fig. 11: Ratio of daily energy delivered for collector with selective absorber coating (i.e., low-emittance) relative to the non-selective (i.e., high-emittance)

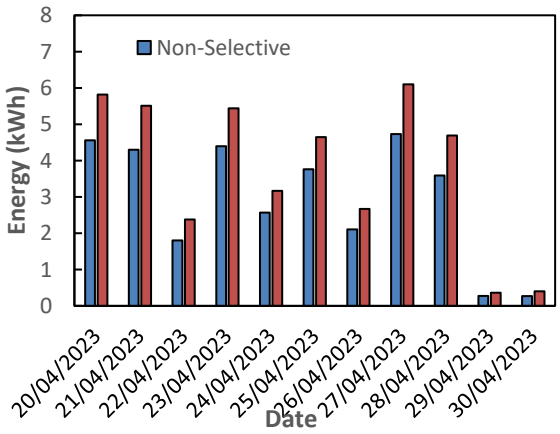

Fig. 12: Comparison of collector energy delivered per day at 0.050 m^3s^{-1} (105 CFM) or 0.02 $m^3s^{-1}m^{-2}$

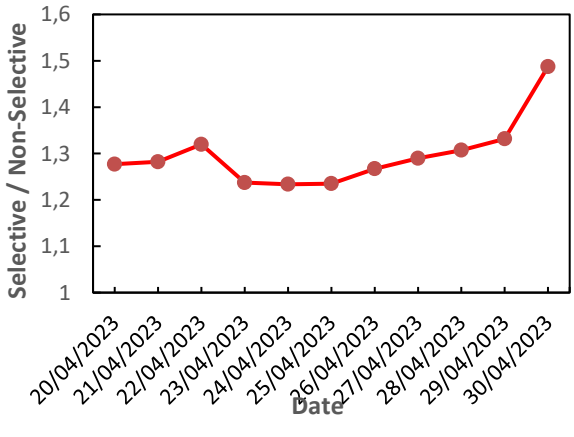

Fig. 13: Ratio of daily energy delivered for collector with selective absorber coating (i.e., low-emittance) relative to the non-selective (i.e., high-emittance)

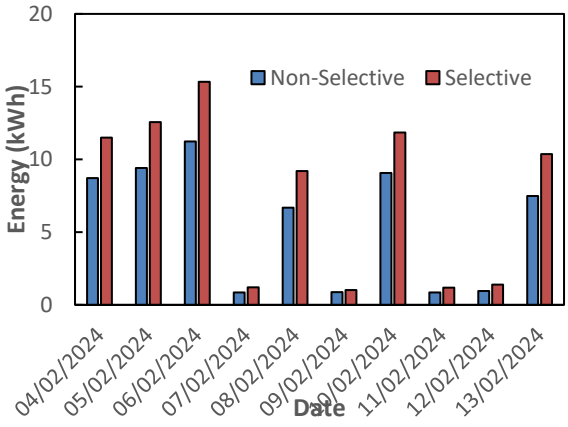

Fig. 15: Ratio of daily energy delivered for collector with selective absorber coating (i.e., low-emittance) relative to the non-selective (i.e., high-emittance)

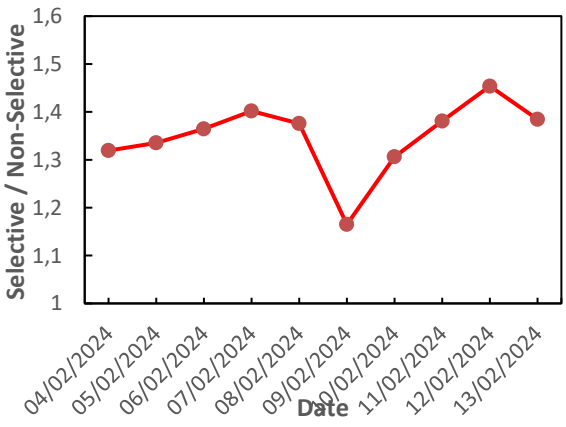

Fig. 14: Comparison of collector energy delivered per day at 0.087 m^3s^{-1} (185 CFM) or 0.035 $m^3s^{-1}m^{-2}$

In addition to the daily energy delivered, the efficiencies of the two solar air collectors are also compared with respect to the air flow rates, as illustrated in Figs. 16 and 17. The data used for the efficiency calculation were taken from clear sky sunny days, with the time frame at noon when the solar incidence angle is at its minimum.

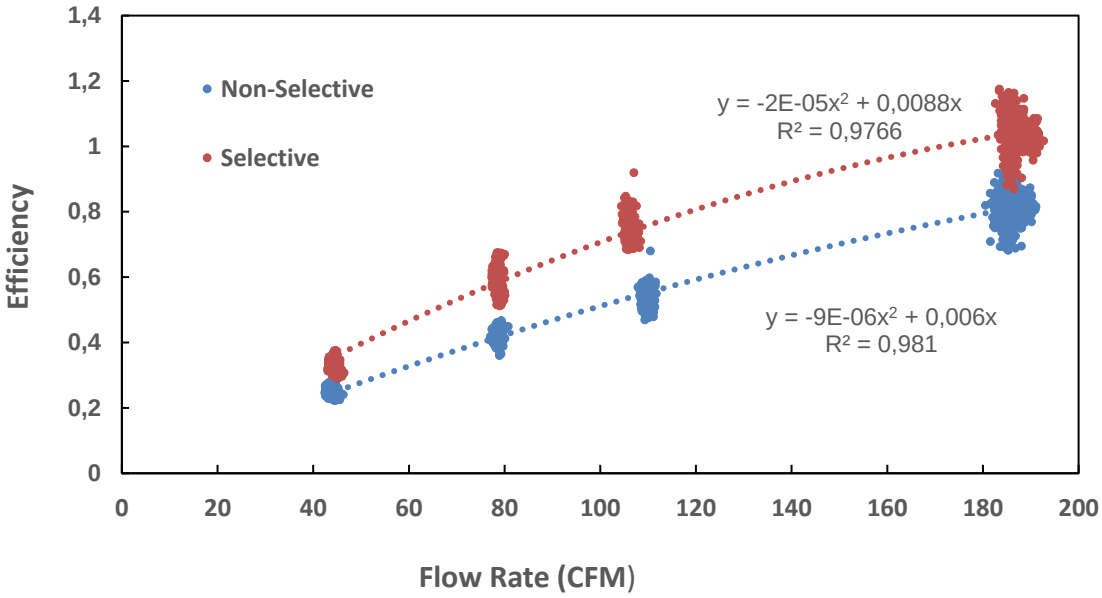

Fig. 16: Efficiencies of the two Solar Air Collectors at different Flow Rates

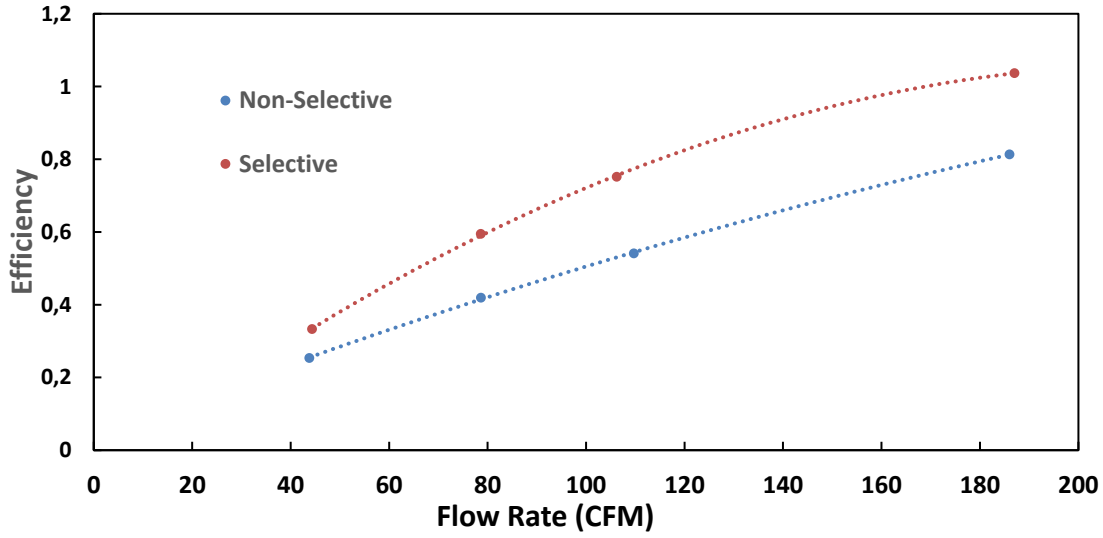

Fig. 17: Efficiencies of the two Solar Air Collectors at different Flow Rates (Average Values)

4. Conclusion

By comparing the energy delivered by the two solar air collectors, results indicated that the solar air collector with the low- emittance surface coating operated at higher efficiency and delivered air at higher temperature as compared to the collector with high-emissivity coating. Specifically, depending on operational conditions,

the energy ratios of the two collectors show that the solar collector with low emissivity surface coating delivered approximately 1.2 - 1.5 times the energy as the identical non-selective collector.

5. Acknowledgments

The authors gratefully acknowledge the financial support of Natural Resources Canada through the Office of Energy Research and Development – Energy Innovation Program (EIP). Collector samples were provided by Trigo Energies.

6. References

Badache, M., Rousse, D. R., Hallé, S., & Quesada, G., 2013. Experimental and numerical simulation of a two-dimensional unglazed transpired solar air collector. Solar Energy, 93, 209-219.

Shukla, A., Nkwetta, D.N., Cho, Y.J., Stevenson, V. and Jones, P., 2012. A state of art review on the performance of transpired solar collector. Renewable and Sustainable Energy Reviews, 16(6), pp.3975-3985.

SRCC, Solar Rating and Certification Corporation. 2016. Report OG-100 ICC-SRCC Certified Solar Air Heating Collector #. https://solar-rating.org/, accessed August 1, 2024.

SRCC, Solar Rating and Certification Corporation. 2020. Report OG-100 ICC-SRCC Certified Solar Air Heating Collector #10002111. https://solar-rating.org/, accessed August 1, 2024.

Fraunhofer-Institut für Solare Energiesysteme ISE, 2020. Test report according to EN 12975-1:2006+A1:2010 /EN ISO 9806:2017, Report KTB: 2020-02-k2.

How does the thermal characteristics of PVT panels influence the performance of PVT heat pump systems

Mark Dannemand[1], Svend Erik Mikkelsen[2], Elsabet Nielsen[1] and Simon Furbo[1]

[1] Technical University of Denmark, Department of Civil and Mechanical Engineering, Kgs. Lyngby (Denmark)

[2] Racell, Albertslund (Denmark)

Abstract

The effect of the thermal efficiency of hybrid photovoltaic – thermal (PVT) collectors was evaluated in system simulations where PVT collectors were used as source for a heat pump. The demand represented space heating and domestic hot water usage for a single-family house located in Denmark. With the presented system and demands it turned out that the value for the optical performance of the thermal absorber for the PVT collector had only marginal effect on the overall yearly system performance. An increase of the heat loss coefficient from 14.5 W m^{-2} K^{-1} to 58 W m^{-2} K^{-1} resulted in 1.7% higher electricity production of the solar cells due to lower PVT collector temperatures and 2% less electricity purchased from the grid due to higher COP in the heat pump caused by higher inlet temperatures to the heat pump in periods without solar radiation. The main effect of varying the different thermal characteristics was the minimum temperatures in the PVT collectors, which affect the heat pump performance and COP. The largest risk is that the brine temperature at the inlet to the heat pump will drop below the limits of the heat pump causing it to switch off and run only on direct electrical heating.

Keywords: : PVT assisted heat pump, system performance, thermal efficiency, Polysun simulation.

1. Introduction

Hybrid photovoltaic – thermal (PVT) collectors can be used as source for liquid/liquid heat pumps in heating systems in buildings (Dannemand et al., 2017). Benefits of using PVT collectors as the source for the heat pump include potential synergistic effect of combining PV and thermal collectors, better usage of limited roof space, potentially increased electrical output of solar cells due to cooling, avoiding noise from a ventilator in an air to water heat pump system, lower installation cost compared the ground sourced heat pumps, high heat pump efficiency without a soil based loop and better esthetics (Dannemand et al., 2020a).

The desired characteristics of the PVT collectors, when used as a source for the heat pump, will be different compared to the desired characteristics of traditional solar thermal (PVT) collectors where high efficiency and high temperatures are beneficial. When the PVT collector is the main source of the heat pump, it will operate in periods without solar radiation e.g. during night time to cover the heat demand (Dannemand et al., 2017). Therefore, insulation and front glass covers are no go in order to extract as much heat from the surrounding ambient air as possible when the sun does not shine. The mean collector temperature will be below the ambient air temperature during periods without significant solar irradiance e.g. at night. In this case the optical efficiency is less relevant and the "heat loss coefficient" from the collector efficiency expression will be the most influential parameter governing the heat gain to the collector.

As with all heating systems, low-cost components and systems are desired (Sifnaios et al., 2021). Potentially simple, less efficient collectors, produced at lower cost, can work well as source for heat pumps (Dannemand et al., 2020b)

Utilization of PVT panels in systems for heating with or without heat pumps has been the focus of the IEA SHC task 60 in the years 2018 to 2020 (Hadorn, n.d.).

2. Aim and scope

Current research aims to elucidate how the thermal characteristics, optical efficiency and heat loss coefficient,

© 2024. The Authors. Published by International Solar Energy Society
Selection and/or peer review under responsibility of Scientific Committee
10.18086/eurosun.2024.07.15 Available at http://proceedings.ises.org

of a PVT collector will affect the yearly performance of a PVT heat pump system. Further, the relation between the PVT collector area and the thermal performance is elucidated. Apart from the thermal performance, emphasis is placed on the temperatures in the PVT collectors because some liquid-liquid heat pumps have a relatively narrow allowed temperature span for inlet to the evaporator which may cause the heat pump to go to fail mode and run on direct electricity when the inlet temperature drops below a limit.

3. Method

The simulation software Polysun was used to perform parameter variations for optical efficiency and heat loss coefficient in a PVT assisted heat pump system. The performance evaluation was based on the yearly values of how much electricity was produced and how much was purchased from the grid. Besides the electrical consumption over the year, the temperature in the PVT collectors was evaluated in order to assess if the inlet temperature of the brine to the heat pump exceeded the limit of the heat pump.

The simulated demands of the building were 10.000 kWh per year for space heating, 2600 kWh for domestic hot water and 3500 kWh for electrical appliances. Weather data for Copenhagen, Denmark was used. The characteristics of a “Delta” heat pump from the manufacturer Metro Therm was applied. This heat pump has been developed with PVT collectors in mind to allow for a temperature range of the brine from -15 ºC to 50 ºC. The Delta heat pump has a nominal capacity of 4.7 kW and is suitable for smaller houses. Fig. 1 shows the schematics of the PVT heat pump system.

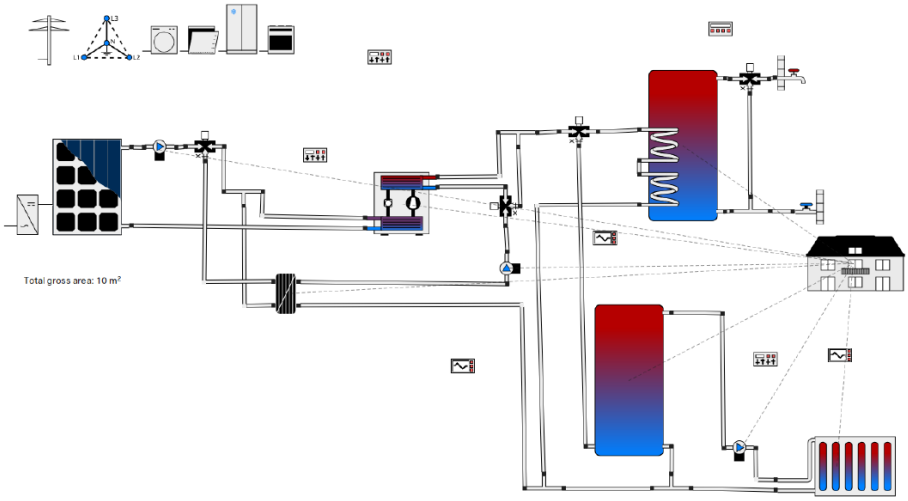

Fig. 1: Schematic of PVT heat pump system in Polysun.

The system had buffer tanks of 100 liters for domestic hot water and in the space heating loop. A 10 m^2 PVT collector area was used for the simulation in the reference model. The panels are facing south with a tilt of 45°.

The PVT collector model in Polysun does not account for condensation on the collector surface and possible ice formation on the collector when brine fluid is below 0 ºC, therefore this effect is not considered in the analysis. Eq.1 shows the collector efficiency expression based on the ISO 9806 standard terminology where only the coefficients that are used in Polysun are included.

$$\dot{Q} = A_G \left[\eta_{0,b} K_b(\Theta_L, \Theta_T) G_b - a_1(\vartheta_m - \vartheta_a) - a_3 u\,(\vartheta_m - \vartheta_a) + a_4(E_L - \sigma T_m^4) - a_5 \left(\frac{d\vartheta_m}{dt}\right) - a_6 u G - a_7 u(E_L - \sigma T_m^4)\right] \quad \text{(eq. 1)}$$

In Polysun other terminology for the coefficients is used as shows in Tab. 1.

Tab. 1 shows the applied characteristics of the PVT panel in the reference model and for the variations. The characteristic of the reference panel represents an uninsulated PVT collector or PVT WISC. The effects of the optical efficiency Eta0 and the heat loss coefficient b1/b3 were evaluated separately in the parameter analysis.

Tab. 1: Reference and variations for PVT collector characteristics for parameter variation.

Thermal efficiency coefficient		Unit	Reference value	Variation 1	Variation 2	Variation 3
ISO 9806	Polysun					
η0	Eta0 (turbulent)	-	0.55	0.33	0.77	-
a1	b1	W m^{-2} K^{-1}	14.5	7.25	29	58
a3	b2	W s m^{-3} K^{-1}	4.5	2.25	9	18

The PV STC nominal efficiency was 0.21.

PVT collector area variations between 5 m^2 and 40 m^2 were used.

4. Results

4.1. Optical efficiency

Increasing Eta0 from 0.55 to 0.77 resulted in 2.2 % (45 kWh) less electricity production; 0.5 % (50 kWh) higher thermal energy to the system and 0.5% (26 kWh) more electricity purchased from the grid.
Reducing Eta0 from 0.55 to 0.33 resulted in 1.1% (21 kWh) higher electricity production; 0.5% (48 kWh) less thermal energy to the system and 0.1 % (7 kWh) less electricity purchased from the grid. Fig 2 shows the energy amounts as functions of Eta0.

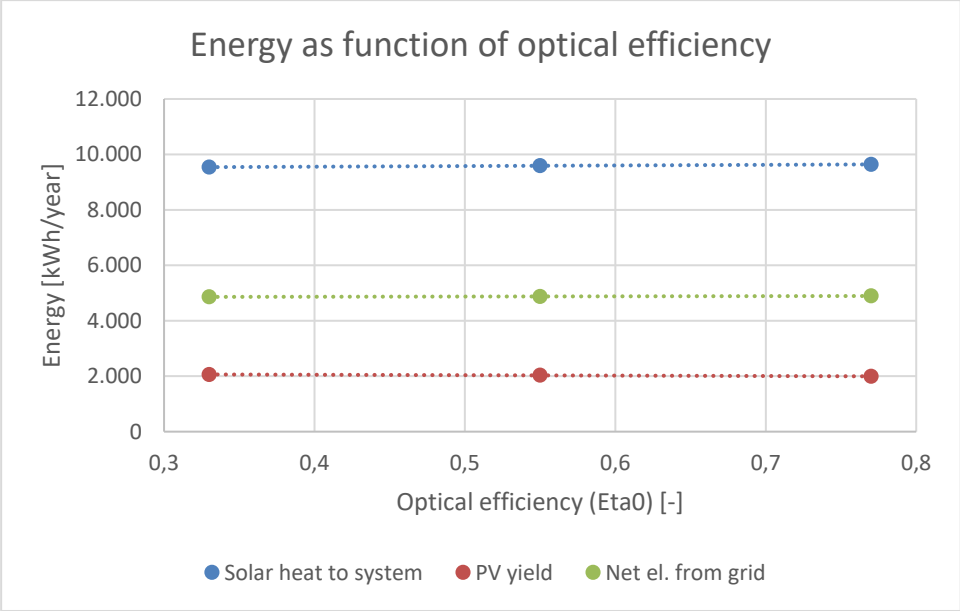

Fig. 2: Energy as a function of optical efficiency.

Fig **3** shows the simulated PVT collector temperatures. It can be seen that the minimum temperature is not affected by Eta0 but the maximum temperature is dependent on Eta0 especially in the summer months. Eta0 of 0.77 resulted in a maximum temperature in the PVT panel exceeding 50 ºC, which is the limit for the heat pump considered in these simulations.

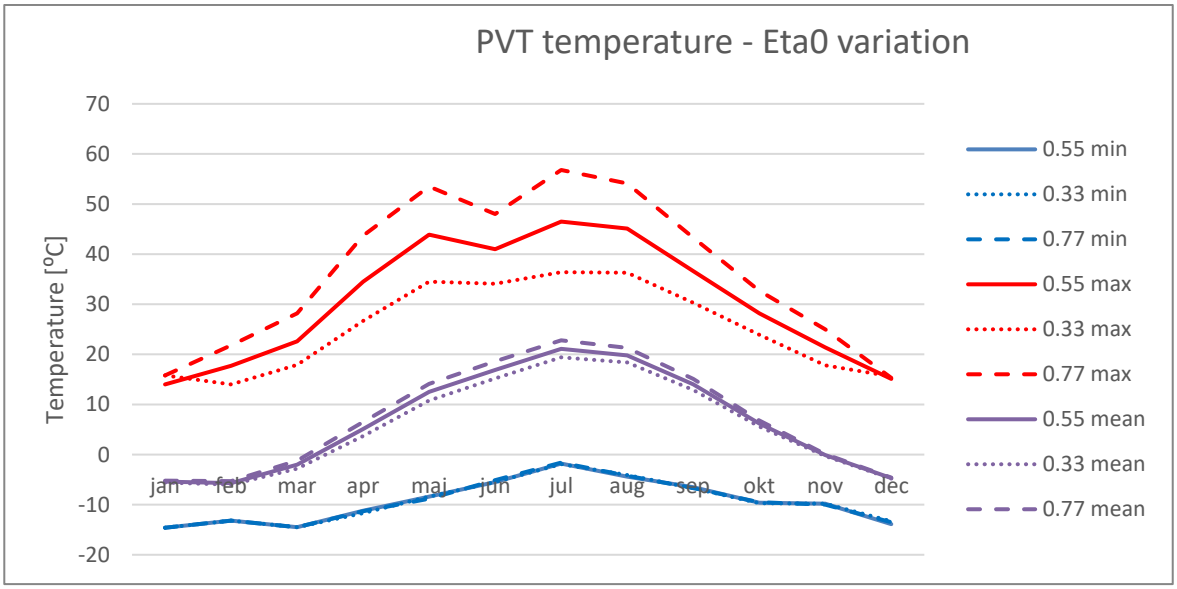

Fig. 3: Minimum and maximum temperatures in the PVT collector for different optical efficiencies.

4.2. Heat loss coefficient

Increasing the heat loss coefficient A1 from 14.5 W m^{-2} K^{-1} to 58 W m^{-2} K^{-1} resulted in 6 % (576 kWh) higher thermal energy to the system, due to better performance in periods without solar radiation; 1.7 % (35 kWh) higher electricity production of the solar cells due to lower panel temperature and 2 % (110 kWh) less electricity was purchased from the grid. Fig 4 shows the energy amounts for different heat loss coefficients.

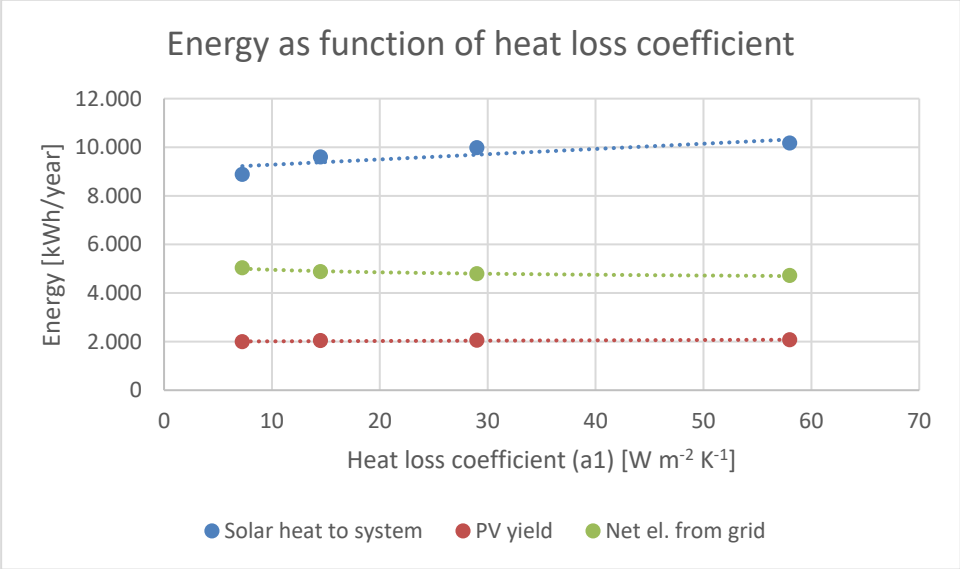

Fig. 4: Energy as function of heat loss coefficient.

Fig. 5 shows the minimum, mean and maximum temperatures in the PVT collector for various heat loss coefficients during operation over the year. It indicates that a low heat loss coefficient may increase maximum temperatures and reduce minimum temperatures exceeding the limits of the heat pump.

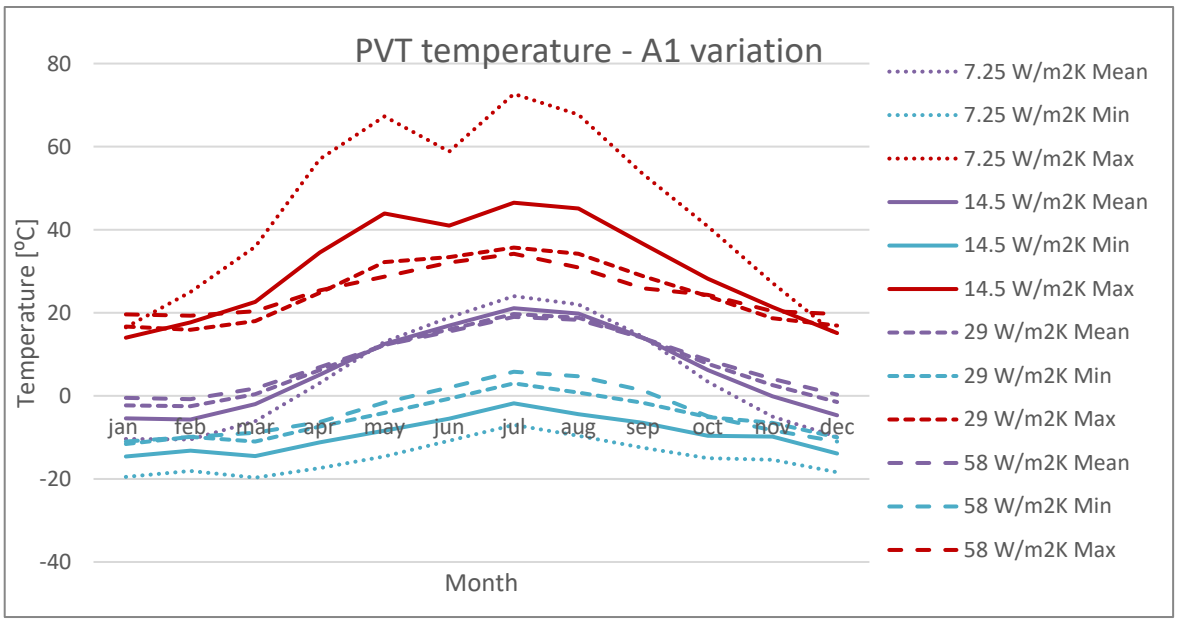

Fig. 5: Minimum and maximum temperatures in the PVT collector for different heat loss coefficients.

Considering the yearly thermal performance, it is desired to have a low optical efficiency and high heat loss coefficient, quite the opposite of what is desired for a traditional solar heating system.

4.3. Collector area

Fig. 6 shows the net purchased electricity from the grid over the year as a 2function of the PVT panel area. With approximately 29 m^2 PVT, the purchased and sold electricity to and from the grid balances out over the year, however, in this scenario, a majority of the needed electricity in the winter period is purchased from the grid and a large amount of PV generated electricity is sold to the grid in the summer period. The optimal PVT collector area depends on the electricity price and the feed in tariffs. With the current prices the economically optimal PVT area is likely a smaller PVT area due to very low feed in tariffs.

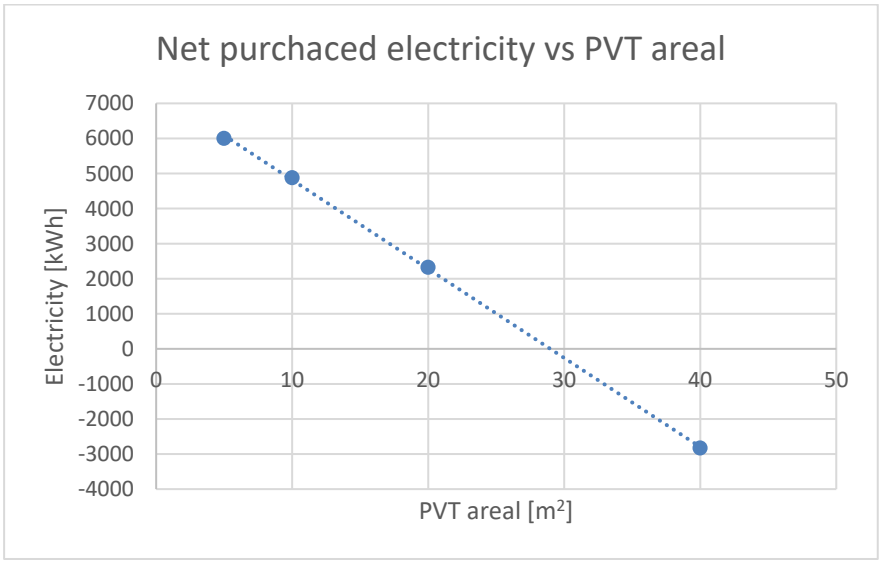

Fig. 6: Net purchased electricity from the grid as function of PVT collector area.

Comparing the PVT collector temperatures in systems with different PVT collector areas showed that the maximum temperature in the PVT array was not affected by the collector area. The mean and minimum temperatures were however highly affected by the PVT collector area. This indicates that for a given heat demand and a given heat pump there is a minimum collector area which is required to avoid that the

minimum limit of the brine will be reached for the heat pump. Fig. 7 shows the minimum, mean and maximum temperatures in the PVT collectors for different collector areas.

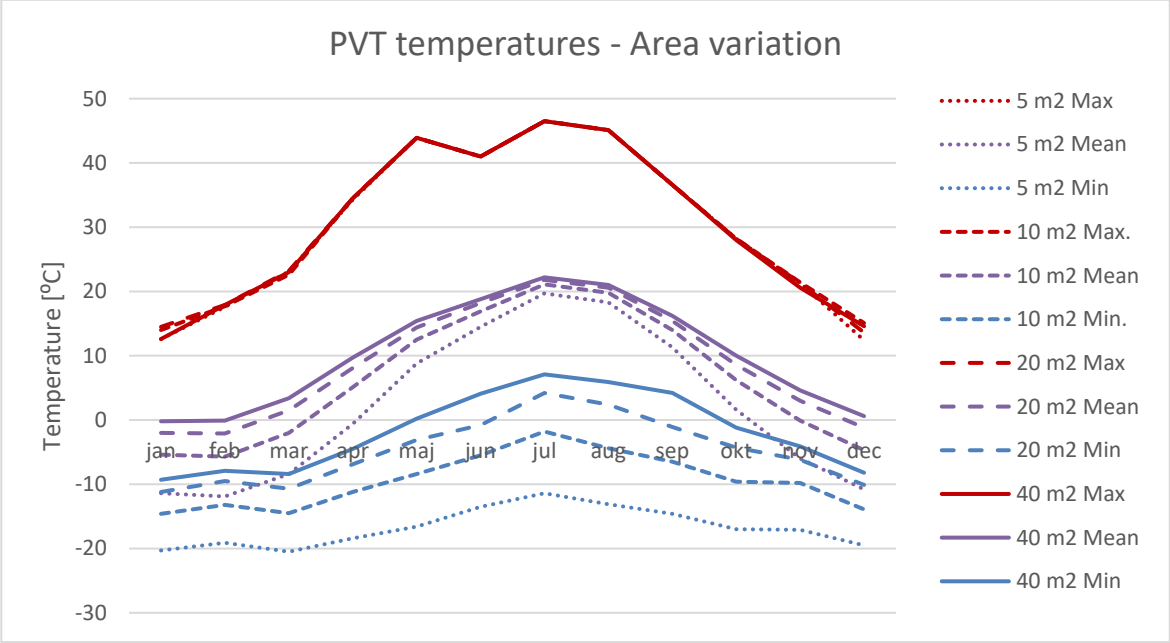

Fig. 7: Minimum, mean and maximum temperatures in the PVT collector for different collector areas.

Fig. 8 shows a comparison of PVT collector temperatures of the reference 10 m² PVT system compared to a 5 m^2 array with double heat loss coefficient. It shows that with a higher heat loss coefficient even a 5 m² PVT area may be sufficient as source for the heat pump and will not exceed the lower limit of the heat pump.

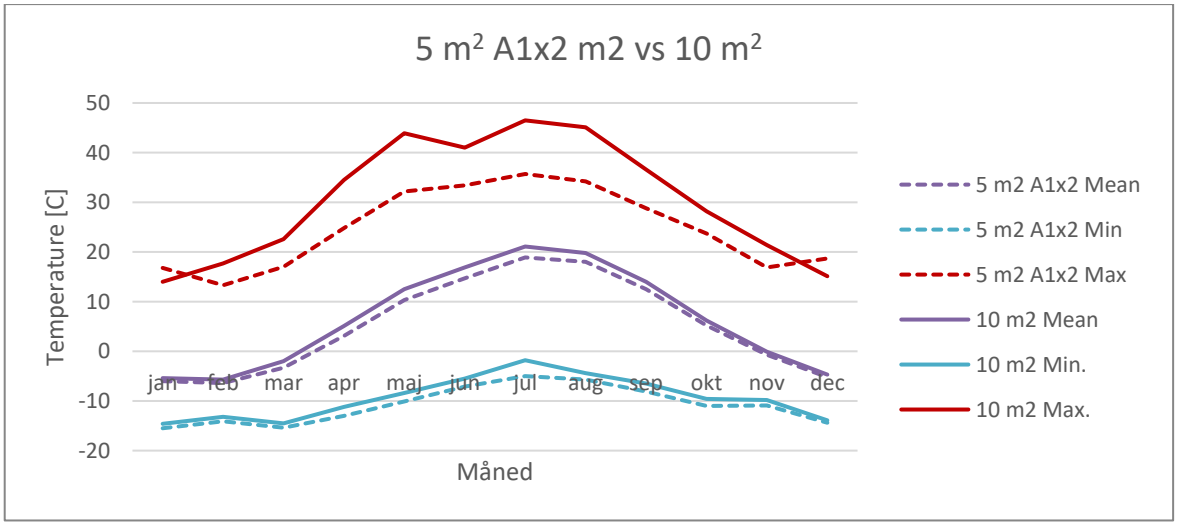

Fig. 8: Minimum, mean and maximum temperatures in the PVT collector for the reference 10 m2 array and 5 m2 with double heat loss coefficient.

5. Conclusions

The investigations showed that varying the optical efficiency of the thermal characteristics only had a minor effect on the yearly performance of the system. The heat loss coefficient had slightly more impact on the system performance. It turned out that the heat loss coefficient to some extent affected the temperature in the PVT panels and a large heat loss coefficient resulted in lower panel temperatures in summer, which improved electricity output slightly. During the winter period, large heat loss coefficients resulted in higher inlet temperatures to the heat pump. With a low heat loss coefficient, the collector outlet temperature reached -20 ºC in some periods, which was beyond the limits of the heat pump.

It can be concluded that for PVT heat pump systems, high heat loss coefficient will slightly improve the yearly performance and reduce the maximum temperature in the panel in summer and increase the minimum temperature in the panel in winter, which will give better operating conditions for the heat pump and potentially allow for heat pumps with a more narrow allowed temperature range to be integrated with PVT panels.
Ice formation and condensation on the PVT panels was not considered in this analysis. Investigations regarding the effect of condensation and ice formation on the thermal and electrical performance are recommended.

6. Acknowledgments

Thie research projects “integrated Triple energy Building elements”, “IEA Task 66 Subtask C ledelse” and “EUDP 2020-I IEA Solar Energy Buildings” were funded by the Danish Energy Agency through the EUDP program grant no: 64022-1036, 134-21020 and 64020-1071. We thank our partners in Racell for the collaboration.

7. Nomenclature and symbols

Quantity	Symbol	Unit
Gross area of collector	A_G	m^2
Heat loss coefficient	α_1	$W\ m^{-2}\ K^{-1}$
Wind speed dependence of heat loss coefficient	α_3	$J\ m^{-3}\ K^{-1}$
Sky temperature dependence of heat loss coefficient	α_4	-
Effective thermal capacity	α_5	$J\ m^{-2}\ K^{-1}$
Wind speed dependence of peak collector efficiency	α_6	$m^{-1}\ s$
Wind speed dependence of infrared radiation exchange	α_7	$W\ m^{-2}\ K^{-4}$
Heat loss coefficient (polysun)	b1	$W\ m^{-2}\ K^{-1}$
Wind speed dependence of heat loss coefficient (polysun)	b2	$J\ m^{-3}\ K^{-1}$
Stefan- Boltzmann constant	σ	$W\ m^{-2}\ K^{-4}$
Longwave irradiance	E_L	$W\ m^{-2}$
Hemispherical solar irradiance	G	$W\ m^{-2}$
Global solar irradiance at the collector plane	G_t	$W\ m^{-2}$
Beam irradiance	G_b	$W\ m^{-2}$
Diffuse irradiance	G_d	$W\ m^{-2}$
Incidence angle modifier for diffuse solar radiation	K_d	-
Incidence angle modifier for direct solar irradiance	K_b	-
Incidence angle modifier	K_ϑ	-
Incidence angle modifier coefficient	b_0	-
Air speed	u	$m\ s^{-1}$
Peak collector efficiency based on G_b	$\eta_{0,b}$	-
Mean temperature of heat transfer fluid	ϑ_m	°C
Ambient air temperature	ϑ_α	°C
Incidence angle	θ_i	°
Transversal angle of incidence	θ_T	°

8. References

Dannemand, M., Furbo, S., Perers, B., Kadim, K., Mikkelsen, S.E., 2017. Performance of a Solar Heating System with Photovoltaic Thermal Hybrid Collectors and Heat Pump, in: The IAFOR International Conference on Sustainability, Energy & the Environment – Hawaii 2017.

Dannemand, M., Sifnaios, I., Jensen, A.R., Furbo, S., 2020a. Experimental investigation and characterization of faÇade integrated pvt collectors with and without insulation, in: Proceedings of the ISES Solar World Congress 2019 and IEA SHC International Conference on Solar Heating and Cooling for Buildings and Industry 2019. International Solar Energy Society, pp. 1752–1759. https://doi.org/10.18086/swc.2019.35.02

Dannemand, M., Sifnaios, I., Tian, Z., Furbo, S., 2020b. Simulation and optimization of a hybrid unglazed solar photovoltaic-thermal collector and heat pump system with two storage tanks. Energy Convers Manag 206. https://doi.org/10.1016/j.enconman.2019.112429

Hadorn, J.-C., n.d. SHC Task 60 | Application of PVT Collectors [WWW Document]. Solar Heating and cooling programme, International Energy Agency. URL https://task60.iea-shc.org/ (accessed 6.25.24).

Sifnaios, I., Jensen, A.R., Dannemand, M., Dragsted, J., 2021. Demonstration of a domestic photovoltaic-thermal (PVT)-heat pump system, performance simulation, and economic analysis for different climates, in: Proceedings - ISES Solar World Congress 2021. International Solar Energy Society, pp. 588–599. https://doi.org/10.18086/swc.2021.26.03

ESTIMATION OF DUST ACCUMULATION IN PARABOLIC TROUGH CONCENTRATORS USING AERIAL LASER REFLECTION

Salvador Robles-Velázquez[1], Manuel I. Peña-Cruz[2,*], Marcelino Sánchez-González[3]

1 Centro de Investigaciones en Optica, A.C. Unidad Aguascalientes, Prol. Constitución 607, Fracc. Reserva Loma Bonita, 20200, Aguascalientes, Aguascalientes. México.

2 CONAHCYT - Centro de Investigaciones en Optica, A.C. Unidad Aguascalientes, Prol. Constitución 607, Fracc. Reserva Loma Bonita, 20200, Aguascalientes, Aguascalientes, México.

3 Centro Nacional de Energías Renovables, Ciudad de la Innovación 7, 31621 Sarriguren, Navarra, España.

Abstract

Solar thermal energy has a high capacity to supply a large part of the planet's energy demand. However, it is necessary to increase its efficiency and performance, as well as improve operation and maintenance (O&M) processes; since these systems are strongly affected by dust deposition, mainly parabolic trough plants. This work analyzes the deposition of dust on the transparent covers of the absorber tubes of parabolic trough collectors and the energy loss associated with it. An optical methodology is developed based on analyzing transmittance of the receiver in different dirt scenarios using a point laser and subsequently, the reflectance of a linear laser on the transparent cover of the absorbent tube captured by a camera mounted on an aerial vehicle; thus relating the luminous intensity to the amount of dust deposited and establishing an energy loss criterion.

Keywords: Dust deposition, Parabolic trough, concentrating solar energy, drones.

1. Introduction

Dust collection in concentrated solar power (CSP) plants presents significant challenges, primarily due to its impact on system efficiency and lifetime. Dust buildup on the mirrors and solar receivers, crucial components for concentrating sunlight, can significantly reduce the amount of solar energy captured, leading to a decrease in the plant's originally estimated total energy output. This reduction in efficiency necessitates frequent, resource-intensive cleaning, especially in arid regions where water scarcity further complicates maintenance efforts. Furthermore, abrasive dust particles can cause surface degradation over time, increasing maintenance costs and potentially shortening the lifespan of optical components. Therefore, the need for effective dust mitigation strategies is crucial to maintaining the efficiency and cost-effectiveness of solar technology (Maghami et al., 2016).

Studies have increasingly focused on quantifying the impact of dust accumulation on optical efficiency, revealing that dirt accumulation can significantly degrade the performance of solar collectors (Hachicha et al., 2019). Niknia et al. (2012) highlighted that dust accumulation on parabolic trough concentrators adversely affects both reflectance and transmittance, which are critical for the efficiency of solar receivers. Zhao et al., (2020) examines the impact of dust accumulation on a linear Fresnel reflector, finding that dust density increases while relative reflectivity decreases over time, with a 9.4% drop in reflectivity for every 1 g/m² increase in dust.

Several factors contribute to the loss of efficiency in solar collectors due to dust accumulation, including the geographical location of the solar plant, the orientation and position of the collectors, nearby facilities like highways or factories that might contribute to dust levels, the frequency of rainfall in the area, and the prevailing wind conditions (Deffenbaught et al., 1986). Each of these factors plays a role in determining how quickly dust builds up on the collectors and how severely it impacts performance (Usamentiaga et al., 2020).

To overcome these challenges, various cleaning methods and equipment have been developed to maintain the cleanliness of CSP systems (Bergwon J.F. 1981). For example, Fernández et al., (2014) optimizes cleaning methods for solar reflectors in CSP plants under semi-desert conditions, finding that demineralized water with a brush is most effective, achieving up to 98.8% efficiency, while steam cleaning is less effective, and adding detergent offers no significant benefit. These findings underscore the importance of regular monitoring and cleaning to preserve the optimal performance of CSP plants.

© 2024. The Authors. Published by International Solar Energy Society
Selection and/or peer review under responsibility of Scientific Committee
10.18086/eurosun.2024.07.16 Available at http://proceedings.ises.org

In response to these challenges, this work uses laser technology mounted on a Remote Piloted Aircraft (RPA) system to detect dust deposition levels on parabolic trough (PT) solar receivers. First, by study how increasing levels of dust deposited on a PT receiver affect light transmittance over time. Second, by impinging a laser beam onto the solar concentrator in an experimental campaign that provides valuable information on the relationship between laser reflected light intensity and energy loss caused by dust deposition. These innovative approaches offer the potential to develop more accurate and effective dust mitigation strategies, ultimately improving the performance and longevity of CSP plants.

2. Materials and Methods

This project introduces an optical system which consists of a laser mounted on a Remotely Piloted Aircraft (RPA) to evaluate dust deposition and surface conditions of parabolic trough receivers in solar power plants. The innovative approach focuses on characterizing the collectors based on varying levels of dirt accumulation, with the goal of establishing a link between dust buildup and consequent energy losses. By quantifying the transmittance losses on the receiver tube at different levels of dirt accumulation, the project provides a detailed understanding of how dust impacts the efficiency of solar energy collection.

The system operates by directing a linear laser beam onto the receiver tube during night-time conditions, capitalizing on the hypothesis that dust particles scatter light. This scattering effect is expected to influence the reflectance measured by the system, allowing for precise assessments of dust-related degradation in optical performance. The night-time testing is particularly significant as it minimizes the interference of ambient light, thereby enhancing the accuracy of the laser-based measurements. The project's findings could lead to more efficient maintenance schedules and improved cleaning strategies, ultimately contributing to the optimized performance of solar power plants by reducing energy losses caused by dust accumulation.

2.1 Transmittance validation phase

The methodology begins with an experimental validation phase, in which a 550 nm laser (see Tab. 1 for technical characteristics) was directed towards the glass cover of the solar receiver of a PT collector. The transmittance of the laser light when passing through the glass cover with different levels of dirt was measured using a calibrated radiometer. Additionally, and as a reference, this same measurement was carried out outside the glass cover, as a way of determining the base value of radiative flux incident by the laser.

Table 1. Laser technical data

Laser characteristics	
Model	Z-LASER-ZM
Type	Clase 1M
Operating voltaje	5-30 V
Operating current	300-400 mA
Wavelength	532 ; 635-685 nm
Weight	85 g

Fig. 1 depicts the technical arrangement for the experimental setup of the validation phase measuring the transmittance of the glass cover of the PT receiver over time. Additionally, the optical system is able to move along the receiver tube, allowing the identification and analysis of average dirt levels. This approach provides a detailed assessment of how surface contamination affects solar energy collection efficiency.

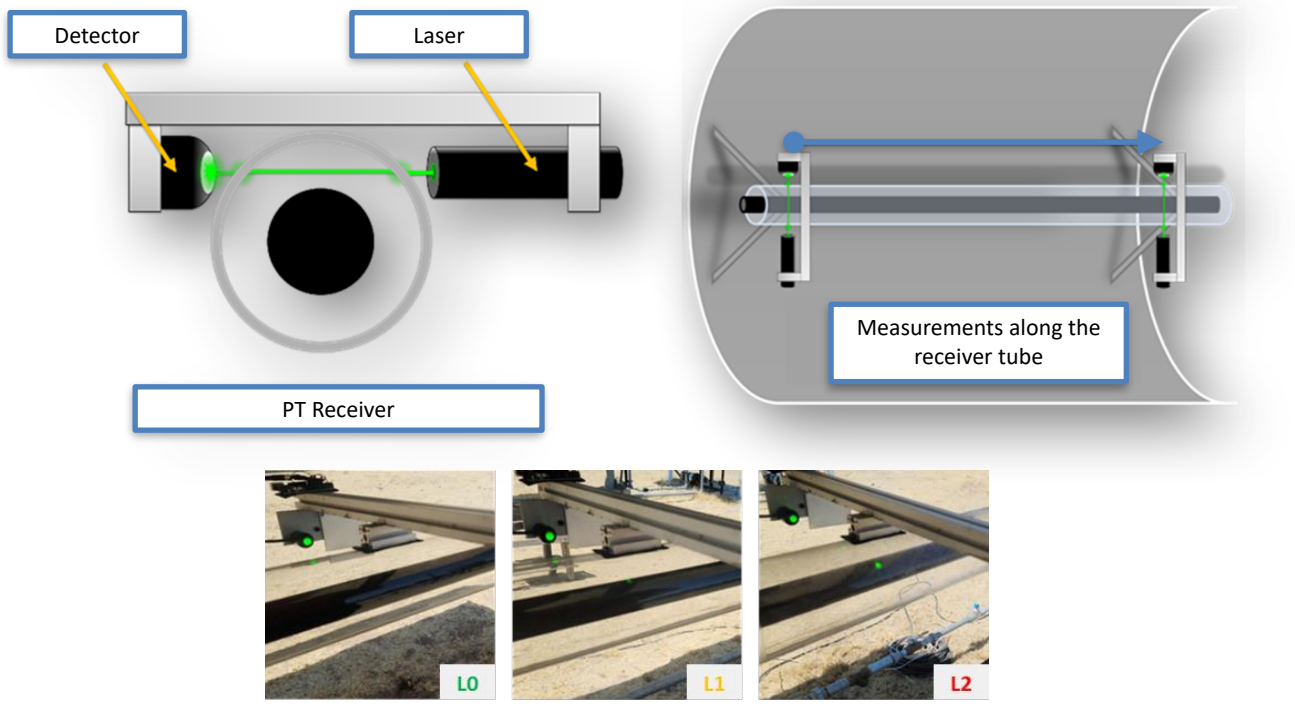

Fig. 1: Experimental setup for measuring transmittance of the parabolic trough receiver over time.

An experimental campaign was carried out over 60 consecutive days, in which dust was allowed to settle on the solar receiver in order to accurately assess the different levels of dirt that were accumulating over time. According to Deffenbaught et al., (1986), the transmittance decreases considerably after the first month of exposure to the outdoors. Therefore, it was decided to divide the accumulation of dirt into three levels. Level L0 represents a recently cleaned receiver. Level L1 represents a receiver that has been outdoors for 15 days. Finally, after two months, an extreme dirt level of L2 is considered (See Tab. 2).

Tab. 2: Levels of dust depositions according to the days without cleaning.

Dust deposition level	**L0**	**L1**	**L2**
Days without cleaning	0	15	60

Fig. 2 provides a visual representation of dust accumulation on the solar receiver over the course of the 60-day experimental campaign. The image clearly illustrates the progressive buildup of dust over time, highlighting the increasing opacity of the solar receiver surface as the days pass. Each segment of the receiver displays varying degrees of dust deposition, making differences in cleanliness readily apparent. These variations in dust levels are critical as they directly impact the receiver's ability to effectively concentrate and convert solar energy.

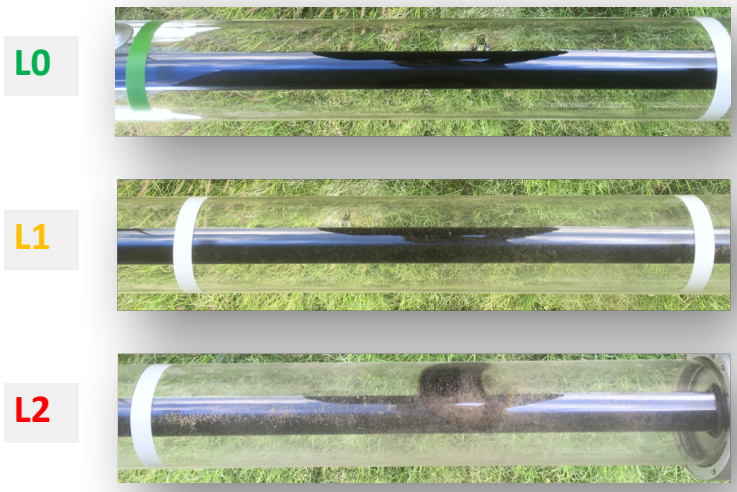

Fig. 2: Levels of dust accumulation along the experimental campaign.

2.2 RPA laser reflectance system

The Remotely Piloted Aircraft system, (RPA), consists of a pilot-controlled controller, a DJI Matrice 100 and a Zenmuse Z3 camera. Several support designs were created to adapt the laser to the RPA, addressing the critical issue of weight restrictions. To minimize any impact on battery performance, a design was developed that weighs just 48 grams, ensuring that the RPA´s efficiency remains unaffected. Fig.3 depicts the methodology used to sweep the receiver tube of the PT concentrator with the laser.

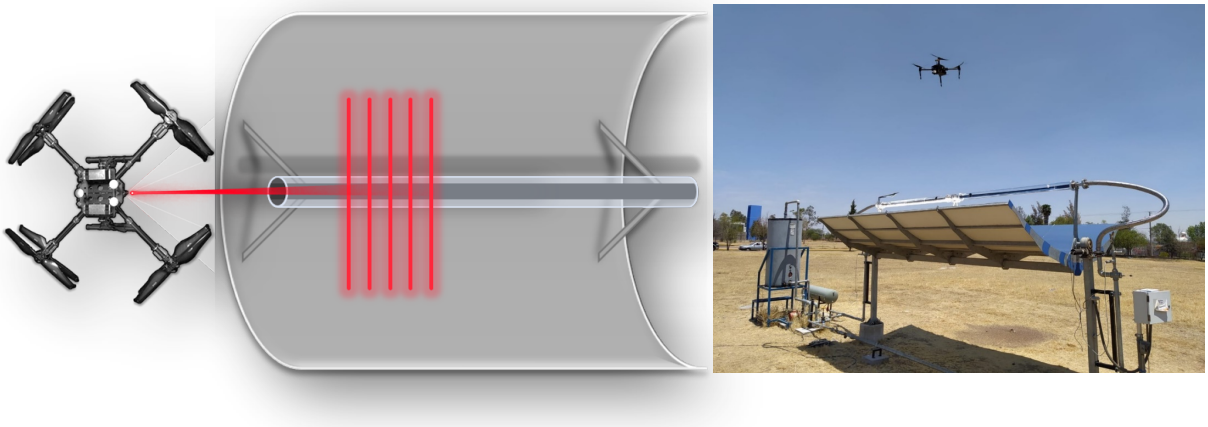

Fig. 3. Graphical representation of the RPA system and the laser system flying over the PT concentrator for the experimental campaign (left). Actual RPA system and PT concentrator.

Two types of flights were conducted to assess the system's performance. The first, a moderate flight, involved a test flight with various maneuvers within the designated flight test area of approximately 3,500 m², without any predetermined sequence. The second type was a static flight, in which the drone remained stationary at a height of 10 meters. This static flight allowed for a focused evaluation of the system's stability and precision in capturing data without the influence of movement, providing a controlled environment to validate the accuracy of the optical measurements. These two flight scenarios were essential for determining how well the system could perform under both dynamic and static conditions, offering insights into the operational flexibility and reliability of the technology in real-world applications (See Tab. 3).

Tab. 3: RPA flight estimated times from 90% to 30% of battery.

Flight type	Moderate flight		Static flight	
	W/o Laser	W/ laser	W/o Laser	W/ laser
Duration (sec)	593	583	602	555

3. Results and discussion

This section presents the results obtained throughout the 60-day experimental campaign. Initially, the results of the average transmittance measured on the receiver tube are presented and then the analysis of the images obtained from the RPA campaign is performed.

3.1 Transmittance validation results

From the analysis campaign of the transmittance obtained from the incident laser on the glass cover of the receiver, operating intervals can be determined (see Tab. 4). For example, it is determined that the glass cover of the solar receiver presents levels above 93% when compared to the reference value of transmittance (when this is measured outside the glass cover). From 15 days to two months the transmittance decreases to 86 ±7% on average, and once it approaches two months of outdoor exposure, it decreases to an average of 79%.

Tab. 4: Estimates of mean transmittance by the level of dust deposition on the collector tube.

Dust deposition level	L0	L1	L2
Transmittance relative to reference (%)	> 93	86 ±7	< 79

It is worth noting that the experimental campaign was carried out in months with little rainfall. However, the strong wind currents and morning dew cause dust to settle on the receiver. Although these data are a particular case for the location, they serve as evidence that long periods of time produce substantial dust accumulations that affect the performance of solar technology.

3.2 RPA reflectance results

From the drone overflight over the parabolic trough collectors, the reflectance profile of the solar receivers was obtained. In Fig. 4, the incidence of the laser is shown for each level of dust deposition in the receiver tube. In it, a visual image is included, a broken blue line that represents the line where the luminous intensity is measured (called segmentation), and the result of the analysis with color representations corresponding to the levels of dust deposition. A plot representing the accumulation of dust on the receiver is also depicted in accordance with the previously determined levels of dirt.

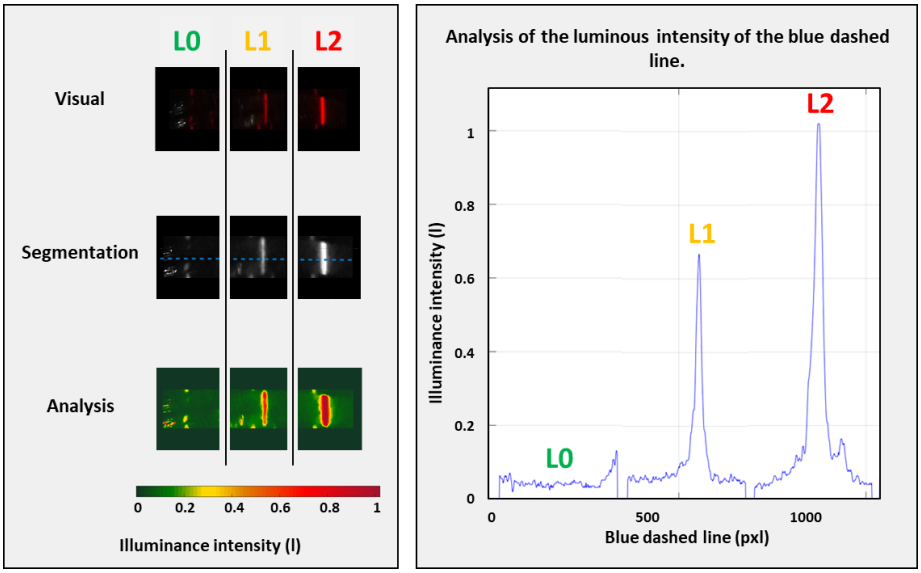

Fig. 4. Reflectance analysis of the aerial optical system on the solar receiver of the parabolic trough concentrator. Details of the methodology are shown in the left. An intensity plot is shown in the right.

Fig. 4 illustrates the luminous intensity (I) along the blue dashed line, correlating with different levels of dust accumulation (L0, L1, L2) on the receiver surface. The intensity profile shows a clear progression from L0 to L2, where L0 represents the cleanest state with the lowest intensity peaks, indicating minimal dust accumulation. As the dust levels increase (L1 and L2), the peaks in the intensity graph become more pronounced, with L2 showing the highest intensity peak, reflecting the greatest amount of dust accumulation. This suggests that as more dust accumulates, the reflectivity of the laser is increased by the scattering of the dust particles. Although the L2 level shows saturation, this case represents an extreme scenario where dust accumulation is already very significant. However, one of the strengths of this system is its adaptability; the operational conditions can be adjusted to meet the specific needs and circumstances of the user. This flexibility is a key advantage, as it allows the system to be fine-tuned for different environmental conditions and levels of dust accumulation. For example, in situations where dust levels are lower or where precision is more critical, the system's sensitivity can be increased to detect even minimal changes in dust deposition. Conversely, in harsher environments where dust accumulation is more pronounced, the system can be adjusted to prevent saturation and ensure accurate measurements. This adaptability also means that the system can be integrated into a variety of solar energy facilities, regardless of their geographical location or the specific environmental challenges. Whether in arid desert regions with frequent dust storms or in more temperate climates with occasional dust accumulation, the system can be calibrated to provide reliable and actionable data. This ensures that solar power plants can maintain optimal efficiency and reduce energy losses due to dust, ultimately leading to better performance and lower operational costs.

4. Conclusions

As shown by the results of the experimental campaign, it was found that there is a direct correlation between the dust accumulated in the parabolic trough receivers and the transmittance/reflectance generated by the incidence of a laser on it. It is possible to determine the operating conditions of the system by measuring the transmittance by shining a laser on the glass cover of the receiver and measuring it by a radiometer; subsequently, it is possible to quantify that the greater the accumulation of dust, the greater the reflectance of the incidence of a laser captured by a camera mounted on an aerial vehicle.

Significant advances have been made in the research and development of an RPA that allows for the rapid and effective estimation of dust accumulation in solar thermal plants. It was determined that adding the optical elements necessary to carry out this experiment does not represent a significant cost for the time and

quality of flight of an RPA with the characteristics presented here. Finally, the main hypothesis regarding the visualization of dust on transparent materials using a laser has proven to be promising, particularly in low-light conditions, where very evident variations in the intensity of dust accumulation on the receivers were observed. In addition, this developed methodology has the advantage of being fast, economical, programmable and, when operated at night, it does not interfere with the operating conditions of the solar plant.

Among the results obtained are the following:

- A dust accumulation analysis methodology was successfully developed using an RPA.
- The necessary hardware was developed to implement the methodology in the RPA without compromising airworthiness.
- Three types of dirt were characterized, ranging from the most typical cases of dirt to extreme cases.
- The necessary software was developed to perform real-time signal processing, which is configurable according to the needs and specifications of potential users.

Future research will focus on quantifying the thermal energy losses directly attributable to varying levels of dust accumulation on solar collectors and establishing a clear correlation with the optical losses identified in this study. By integrating thermal performance metrics with the optical data, the goal is to create a comprehensive model that predicts how dust affects overall system efficiency in concentrated solar power (CSP) plants. This model will consider not only the immediate impact of reduced reflectance and transmittance but also the long-term effects of dust on thermal energy conversion efficiency. Additionally, future experiments may involve real-time monitoring of both optical and thermal losses under different environmental conditions, allowing for the development of predictive maintenance strategies and optimized cleaning schedules. This work will contribute to enhancing the reliability and cost-effectiveness of CSP technology by minimizing energy losses due to environmental factors.

5. References

Bergwon, J. F. K., 1981. Cleaning strategies for Parabolic-Trough Solar-Collector Fields; Guideline for decisions. Sandia National Laboratories.

Deffenbaught, D. M., Green, S. T., and Svedeman, S. J., 1986. The effect of dust accumulation on line-focus parabolic trough solar collector performance. Solar Energy, 36(2), pp. 139-146.

Fernández, A., Álvarez-Rodrigo, L., Martínez-Arcos, L., Aguiar, R., and Márquez-Payés, J. M., 2014. Study of different cleaning methods for solar reflectors used in CSP plants. Energy Procedia, 49, pp. 80-89. doi: 10.1016/j.egypro.2014.03.009.

Hachicha, A. A., Al-Sawafta, I., and Ben Hamadou, D., 2019. Numerical and experimental investigations of dust effect on CSP performance under United Arab Emirates weather conditions. Renewable Energy, 143, pp. 263-276. doi: 10.1016/j.renene.2019.04.144.

Maghami, M. R., Hizam, H., Gomes, C., Radzi, M. A., Rezadad, M. I., and Hajighorbani, S., 2016. Power loss due to soiling on solar panel: A review. Renewable and Sustainable Energy Reviews, 59, pp. 1307-1316. doi: 10.1016/j.rser.2016.01.044.

Niknia, I., Yaghoubi, M., and Hessami, R., 2012. A novel experimental method to find dust deposition effect on the performance of parabolic trough solar collectors. International Journal of Environmental Studies, 69(2), pp. 233-252. doi: 10.1080/00207233.2012.664810.

Usamentiaga, R., Fernández, A., and Carús, J. L., 2020. Evaluation of dust deposition on parabolic trough collectors in the visible and infrared spectrum. Sensors (Switzerland), 20(21), pp. 1-20. doi: 10.3390/s20216249.

Zhao, X., Chen, Z., Yan, S., Ming, T., Wu, Z., and Ma, R., 2020. Influence of Dust Accumulation on the Solar Reflectivity of a Linear Fresnel Reflector. Journal of Thermal Science. doi: 10.1007/s11630-020-1379-y.

Study of the Impact of Automatic Backflush on Direct SDHW Thermosyphon Systems

Ben Stinson[1], Stephen J. Harrison[2], Joseph Breton[1], Anh Kiet Nyugen[1]

[1]QSBR Innovations Inc. Kingston (Canada)

[2]Queen's University, Dept. of Mechanical and Materials Engineering. Kingston (Canada)

Abstract

Thermosyphon solar water heaters are often deployed in regions where freezing ambient conditions do not occur, allowing potable water from the storage tank to be directly circulated through the solar collectors. In many regions "hard water" conditions exist where dissolved minerals can deposit on hot surfaces within the solar collector's flow tubes, restricting the flow of water and resulting in increasing collector temperatures. A recent development aims to alleviate this condition by introducing a novel flow configuration and valving system that reverses the flow of cold "mains" water through the solar collectors each time hot water is drawn from the system. This flushes the collector, and the regular introduction of cooler "mains" water significantly reduces the potential of hardwater scaling in the solar collectors. This study investigates the effect of this flow reversal on the energy delivered to the end user through a side-by-side comparison of two thermosyphon solar systems; one with the backflush feature and one without.

Keywords: thermosyphon, backflush, valve, SDHW

1 Introduction

Thermosyphon solar water heaters have existed for over a century as an inexpensive and simple method to heat domestic water and other process fluids (Ragheb, 2014). These systems typically consist of solar thermal collectors that circulate water from elevated thermal storage during charging. A feature of thermosyphon systems is the low parasitic energy consumption, as buoyancy forces in heated solar collectors cause the circulation of water, to and from an elevated thermal storage. Most of these systems are deployed in regions where freezing ambient conditions do not occur, allowing potable water from the storage tank to be directly circulated through the solar collectors. In many regions, however, "hard water" conditions exist where dissolved minerals in the water supply can deposit on hot surfaces within the solar collector's flow tubes, restricting the flow of water and resulting in increasing collector temperatures (Arunachala et al., 2009). If this condition is allowed to continue, flow through the solar collectors will be restricted such that solar collectors stagnate, potentially damaging the system components and causing systems to over-temperature.

A recent development aims to alleviate this condition by introducing a novel flow configuration and valving system that reverses the flow of cold "mains" water through the solar collectors each time hot water is drawn from the system. This configuration allows a thermosyphon system to provide heat normally while reversing the flow direction within the collector when there is a draw of hot water, Fig. 1. This flushes the system, and the regular introduction of cooler "mains" water significantly reduces the potential of hardwater scaling in the solar collectors. This approach was previously applied to backflushing plate style heat exchanger (Harrison, 2005). This study investigates the effect of flow reversal in thermosyphon solar systems on the energy delivered to the end user, through a side-by-side comparison of two thermosyphon solar systems; one with the backflush feature and one without.

2 Methodology

Two identical direct thermosyphon systems were set up, one with the flow reversal (automatic backflush) feature and the other without, as a baseline system, Fig. 2. Programmed hot-water draws were made on the systems at regular intervals. The systems were controlled with an NIST DA system to draw water from the thermosyphon tanks using a United States Department of Energy specified draw schedule of 120 liters/day (Tab. 1). The equation used for calculating delivered energy can be found below, (eq.1).

© 2024. The Authors. Published by International Solar Energy Society
Selection and/or peer review under responsibility of Scientific Committee
10.18086/eurosun.2024.07.17 Available at http://proceedings.ises.org

Each system was supplied by mains water and included a 110 L horizontally mounted tank on top of the collector. Each tank contained a temperature probe, containing 8 thermocouples, to measure temperatures vertically at 5 cm intervals. This allowed measurement of the degree of stratification and the impact of backflushing on stratification within the tank. No diffusers or baffles were used on the inlet water pipes to aid stratification. The system also included a pyranometer and other thermocouples to measure the inlet, outlet, and ambient conditions.

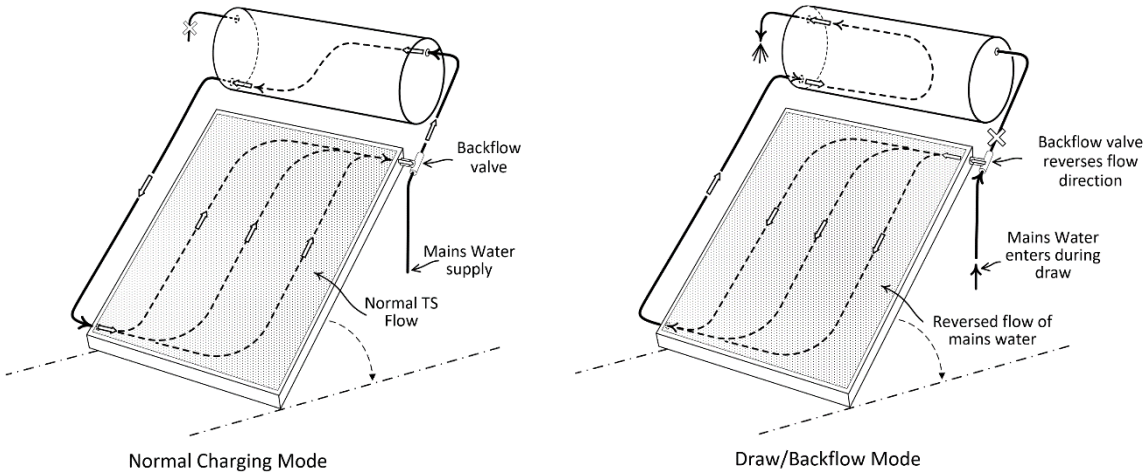

Fig. 1: Illustration of backflush operation during charge and discharge operation.

Check valves on the inlet to each system were installed and a 10-minute delay was set between the hot water withdrawal from each system to prevent mixing and to allow each system to receive full mains pressure and flow. Each draw consisted of three parts: (1) a pre-draw that flushed the exterior mains line, thus cooling the water and ensuring similar inlet water temperatures for both systems; (2) a draw from the backflush system and (3) an identical draw from the baseline system. A Supervisory Control and Data Acquisition (SCADA) system was set up in LABVIEW™ to gather data, view current conditions, and change system operating parameters as required. This setup allows a high degree of versatility, and users can change the automatic draw schedule on an hourly basis.

The system was set up in the summer of 2023 and operated until late October. It was then drained for the winter and restarted in May 2024. The energy performance results are from the 2023 testing period and the impact of higher flow rates were taken from the 2024 testing period. The system is currently operating under varied operating conditions.

Fig. 2: Installation of identical thermosyphon domestic hot water heaters installed for testing.

2.1 Energy Calculation Equation

$$Q = \int \dot{Q}.dt = \int \dot{m}.c_w.(T_{delivered} - T_{mains\ in}).dt \qquad \text{(eq. 1)}$$

where: Q: is the energy delivered (kJ) over the draw period

$\dot{Q}$ is the power delivered (kW) over the draw period

$\dot{m}$ is the mass flow rate of water (kg/s), calculated from water volumetric flow rate ($\dot{V}$) and density

$T_{delivered}$ is the water temperature at the outlet (°C)

$T_{mains\ in}$ is the water temperature at the inlet (°C)

c_w is the specific heat capacity of water (kJ/kg. K)

T is the time interval between each reading (i.e. scan rate). In this DA system, *t*=0.5s

The density and specific heat capacity of water are calculated based on the water average temperature. $((T_{delivered} + T_{mains\ in}) / 2)$.

Tab. 1: U.S Department of Energy small draw profile in liters, (L).

Draw Schedule												
Time (h:mm)	0:00	1:00	2:00	3:00	4:00	5:00	6:00	7:00	8:00	9:00	10:00	11:00
Draw Volume (L)	0	0	0	0	0	1.82	10.91	12.73	10.91	7.28	7.28	5.46
Draw Schedule												
Time (h:mm)	12:00	13:00	14:00	15:00	16:00	17:00	18:00	19:00	20:00	21:00	22:00	23:00
Draw Volume (L)	5.46	3.64	1.82	3.64	5.46	5.46	7.28	9.09	7.28	5.46	5.46	3.64

3 Results

Over a 23-day testing period, the results showed a 0.12% increase in the energy output from the system equipped with the automatic backflush feature when compared to the baseline thermosyphon system, Fig. 3. The results of this test indicate that the automatic backflush valve configuration had no apparent impact on the delivered energy when subjected to daily hot water draws consistent with normal usage patterns. A review of delivery hot water temperatures and stratification temperatures in the hot water tanks indicated insignificant differences between the system equipped with automatic backflush and the baseline system.

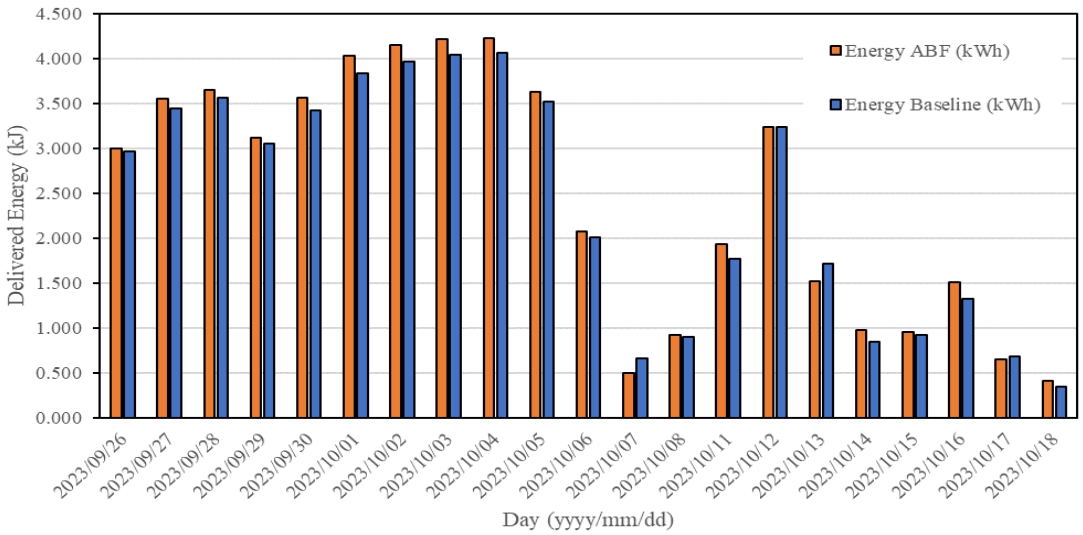

Fig. 3: Comparison of daily energy delivered by the ABF and baseline thermosyphon systems over a 22-day period.

It was also observed that the backflush operation had no significant impact on the thermosyphon flow rate as compared to the baseline, Fig. 4 & 5, and the system had no issue restarting its buoyancy-driven flow after a backflush, as seen in the IR pictures of a 1-minute backflush at 0.26-liter s^{-1} (16 liters/min). At the end of the backflush, the collector resumed its thermosyphon flow in 1-2 minutes under optimal solar irradiance conditions (clear sunny day, at 11:30 am, with approximately 1000 W/m^2), Fig. 6.

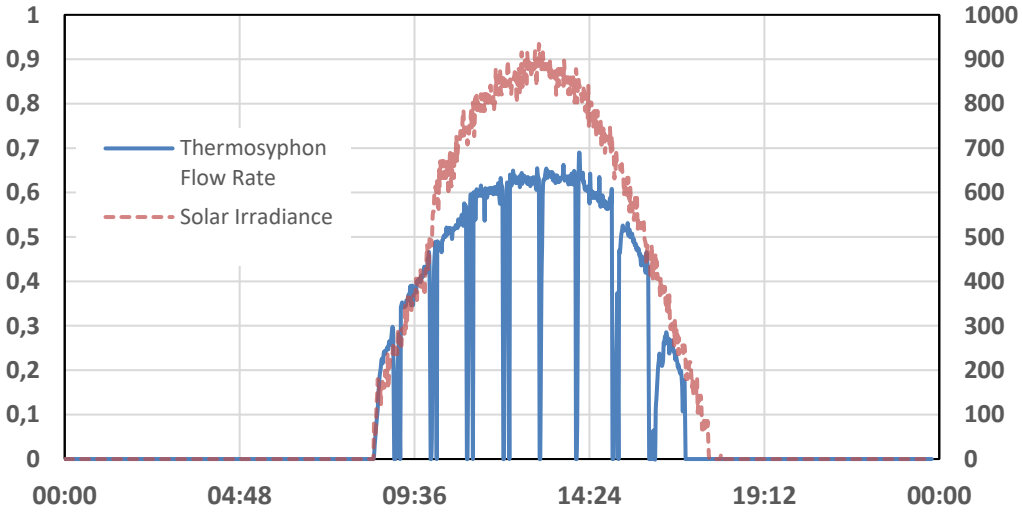

Fig. 4: Thermosyphon flow rate (liters/min) & solar irradiance (W/m^2) vs. time (sunny clear sky). Automatic Backflush valve installed and draw profile during operation.

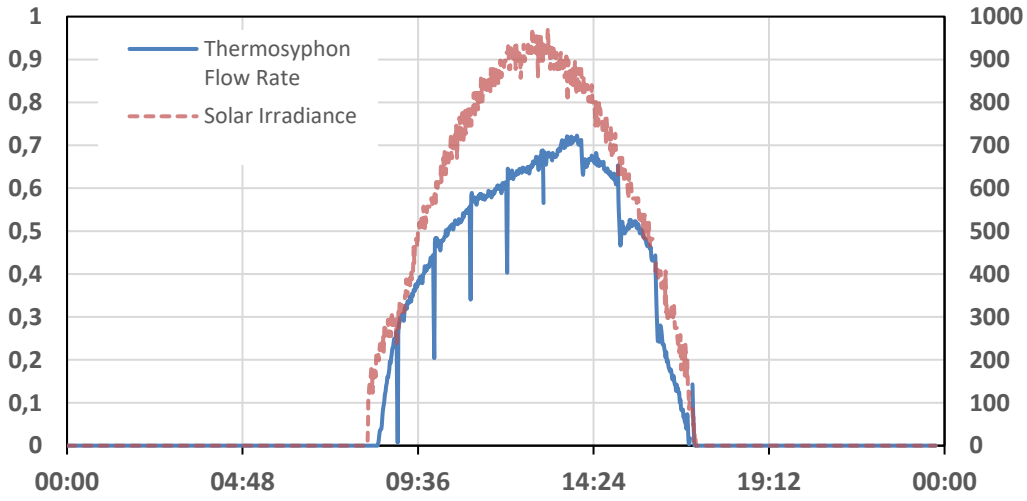

Fig. 5: Thermosyphon flow rate (liters/min) and solar irradiance (W/m^2) vs. time (clear sunny day) without Automatic Backflush valve installed and draw profile during operation.

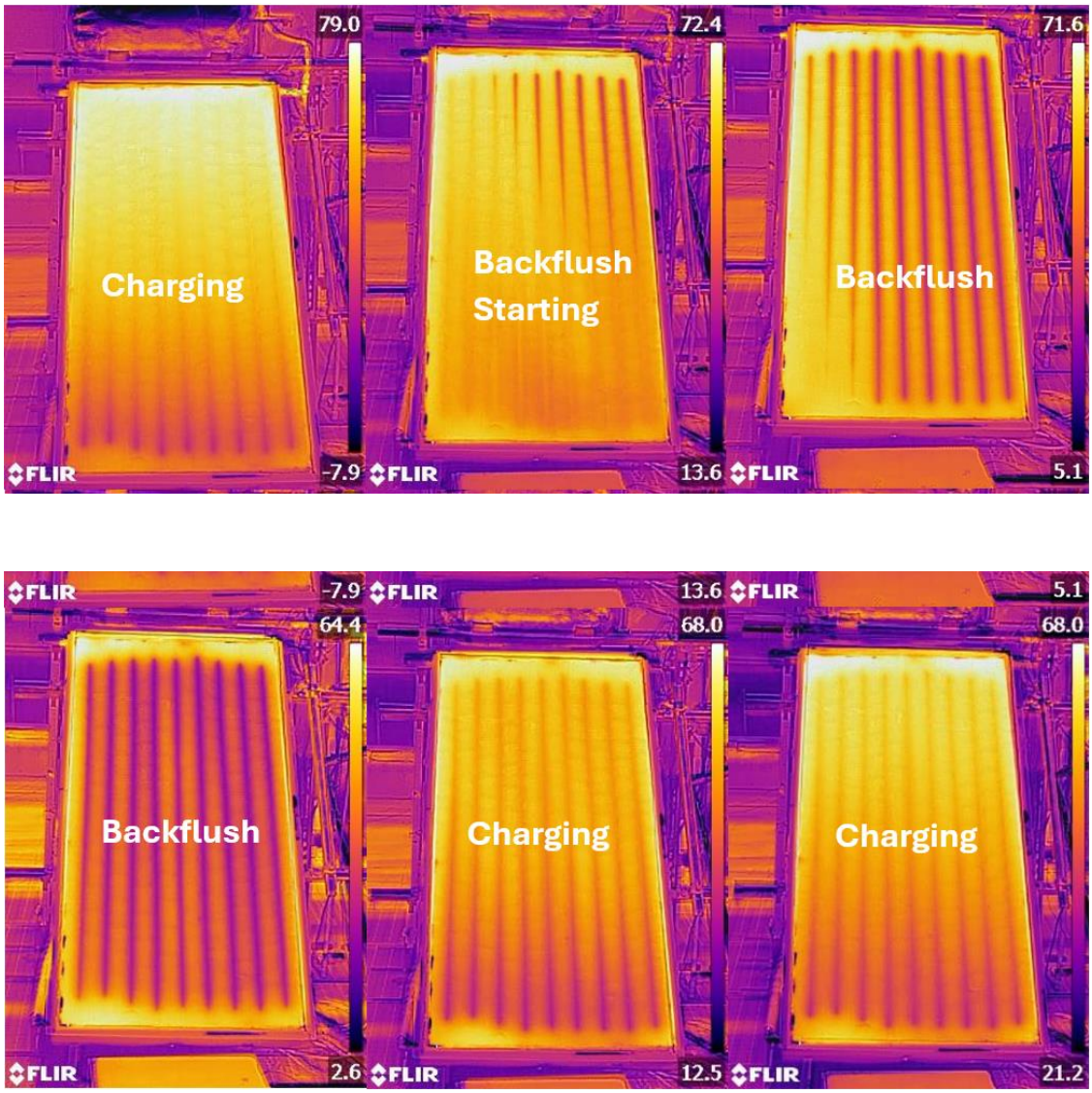

Fig. 6: Backflush through a solar thermal collector with an IR camera. The draw was conducted at 6L/min for one minute. The total time of the test was 4 minutes.

Stratification in the tank was also a key indicator of the energy performance, and thus, the temperatures in the tanks were compared. Tests were conducted at 2 flow rates: 0.1 liters s^{-1} (6 liters/min) Fig. 7 & 8 and 0.166-liters s^{-1} (10 liters/min), Fig. 9 & 10. The results indicated that backflushing had virtually no impact on the stratification in the tank at 0.1 liters s^{-1} (6 liters/min). At 0.166 liters s^{-1} (10 liters/min), there is minimal impact, but with a less than 1% difference in energy delivered in a 24-hour period.

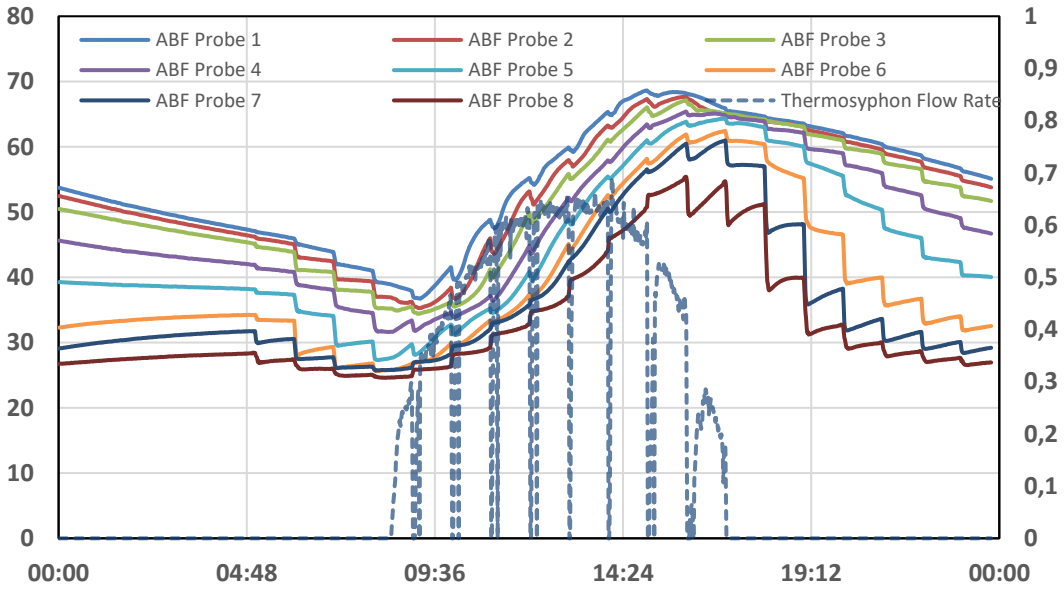

Fig. 7: Tank temperatures (°C) in the backflush system with thermosyphon flow rates shown on the right under high solar irradiance conditions with a draw flow rate of 0.1 liters s^{-1} (6 liters/min). The spikes represent hourly draws/backflushes as per DOE. Draw profile.

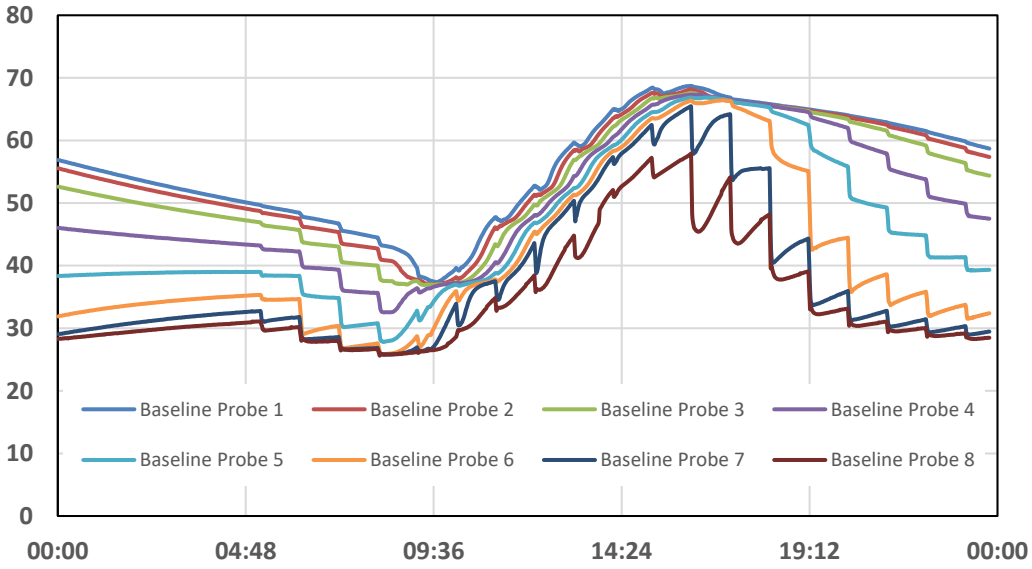

Fig. 8: Baseline thermosyphon tank temperatures (°C) vs. Time under high solar irradiance with a flow rate of 0.1 liters s^{-1} (6 liters/min).

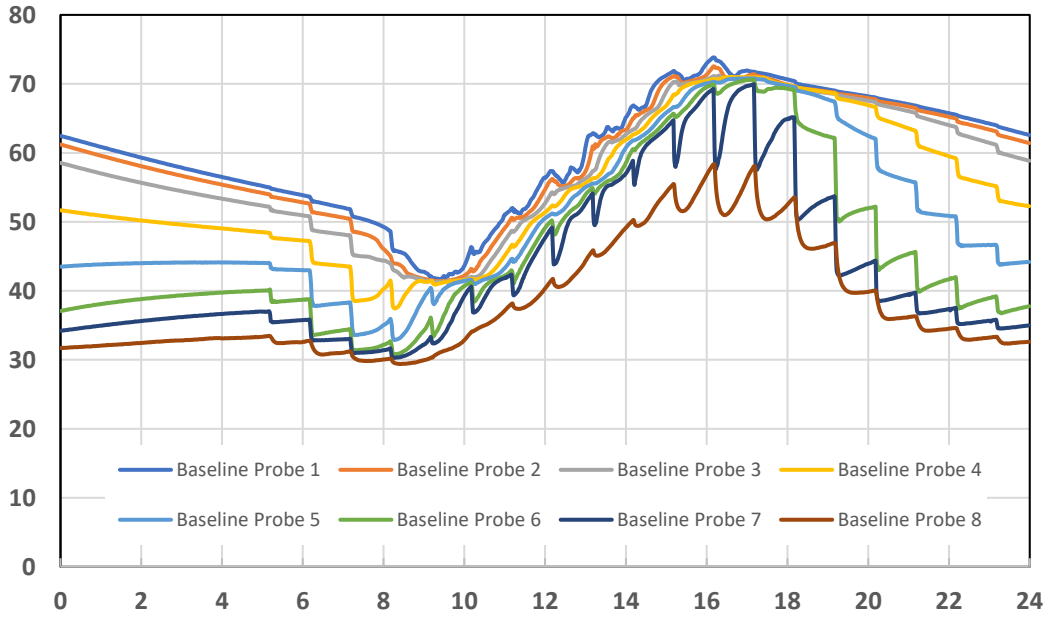

Fig. 9: Baseline thermosyphon tank temperatures (°C) vs. Time under high solar irradiance with a flow rate of 0.1 liters s^{-1} (6 liters/min).

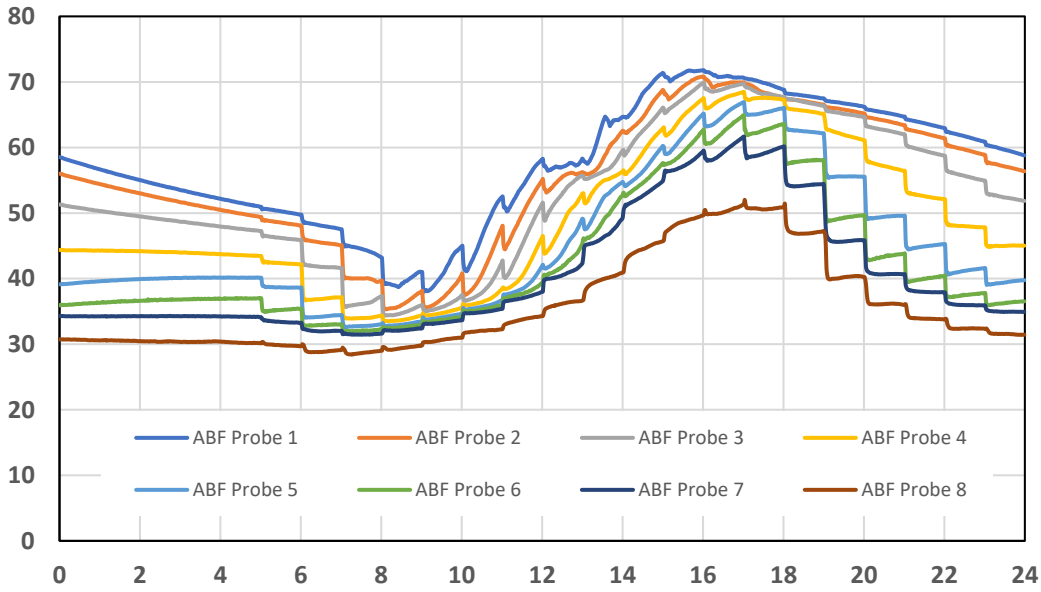

Fig. 10: ABF thermosyphon tank temperatures (°C) and the impact of backflush on tank stratification at 0.166 liters s^{-1} (10 liters/min) draw

4 Discussion

This study investigated the impact of backflushing on the energy performance of direct solar thermosyphon systems to prevent scale and fouling inside the solar collector. Analysis of the inlet and outlet temperatures as shown in Figure 3), the thermosyphon flow rate in Figures 4 and 5, and tank stratification and flow rates Figures 7 and 8. The results show a negligible impact on the energy performance of the overall system, including maintaining tank stratification and restarting of the buoyancy driven flow.

Hardwater scaling in solar thermal collectors has been known to cause a reduction in system performance due to reduced heat transfer and flow rates, and potential system failure when not addressed (Arunachala et al., 2009). Backflushing heat exchangers prevent the build-up of scale has been shown to be an effective for heat exchangers (Harrison, 2005 & Al Nasser et al.,), yet little was known on the system impact of backflushing solar thermal collectors.

This study was carried out under controlled laboratory conditions. While every effort was made to simulate typical draw patterns, further testing in 'real world' conditions or 'field studies' should be undertaken to fully understand the impact of backflushing the solar thermal collector, when a draw of hot water occurs. Despite the limitations, this initial study has yielded positive results for maintaining the performance of solar thermosyphon systems, in that no significant impact was observed on the energy output from a system using automatic backflush.

5 Conclusion

While backflushing has been shown to prevent the formation of scale in heat exchangers no work to the author's knowledge, has been conducted on backflushing of solar thermal collectors and its impact on system performance. This is a key topic for future research, given the need of more renewable energy technologies, like solar thermal, and the simplicity and availability of direct thermosyphon systems. These systems are expected to perform reliably for several decades and, in regions with moderate to hard water, scaling will negatively impact the system's performance over time. Backflushing these systems will help to maintain their rated energy performance.

The results of this study indicate that backflushing a solar thermal collector has little to no effect on the energy performance of a direct thermosyphon solar thermal system. Analysis of the temperatures, flow rates and flow volumes indicate that reversing the flow of water through the solar thermal collector during a draw of hot water from the storage tank has no impact on the energy production of the system compared to an identical system without a flow reversal function. Further testing under real world conditions to validate the findings and a field trial with different sized systems and anticipated draw volumes should be considered in the future to help validate these findings.

6 Acknowledgments

The authors wish to acknowledge the support of QSBR Innovations and Neoperl GmbH. in this study.

7 References

Al Nasser, W.N., 2016. Effect of Silica Nanoparticles to Prevent Calcium Carbonate Scaling Using an in Situ Turbidimeter, Chemical Engineering Research and Design, Volume 110, 98-107.

Arunachala et al., 2009. Performance Analysis of Solar Flat Plate Collectors in Scaling Environment, International Journal of Sustainable Energy, 33, 192-202.

Harrison, S., 2005. Passive Heat Exchanger Anti-Fouling for Solar DHW Systems, Proceedings of ISEC 2005, International Solar Energy Conference, August 6-12, 2005, Orlando, Florida, USA.

Ragheb, M., 2014. Solar thermal power and energy storage historical perspective. Nuclear Power Engineering, 52.

FIELD EVALUATION OF NAKED ENERGY'S VIRTU SOLAR THERMAL AND HYBRID PVT COLLECTORS IN COMMERCIAL ENERGY SYSTEMS

Maria Zagorulko[1], Dr. Alexander Mellor[1], Dr. Adrian Murrell[1]

[1] Naked Energy Limited, Crawley (United Kingdom)

Abstract

In this communication, we provide an overview of Naked Energy's Virtu solar thermal and hybrid photovoltaic thermal (PVT) technology, showcasing its application in various commercial settings. We share field data from customer sites, including office buildings, leisure centers, supermarkets, and student residences, to highlight the real-world performance and system integration of Virtu products. Our discussion covers how these installations meet different heating and power needs while contributing to carbon reduction efforts. We also introduce Naked Energy's Clarity monitoring platform, which tracks and analyzes system performance to help optimize operations. Lastly, we offer a preview of upcoming projects that will incorporate interseasonal heat storage, further expanding the potential of Virtu technology in supporting the transition to sustainable energy.

Keywords: solar thermal, PVT, field data, monitoring, industry

1. Introduction

Decarbonizing heat is a crucial step in addressing global greenhouse gas emissions. Heat generation is a major contributor to these emissions, so finding commercially viable solutions to reduce this impact is essential. Decarbonizing heat can also improve energy security and offer economic benefits through lower fuel costs and increased efficiency. In this context, the commercialization of solar thermal technologies is a key step towards achieving sustainable energy goals.

Naked Energy is a company dedicated to developing, manufacturing, and supplying the Virtu product family, which includes VirtuHOT solar thermal collectors and VirtuPVT hybrid heat and power collectors. Back in 2018, we introduced this technology at its early stage to this conference, sharing field results from a small-scale pilot (Murrell et. al., 2018) [1]. By 2022, we provided a progress update at the joint Eurosun-IEA meeting. As of 2024, we have over 100 commercial and industrial (C&I) scale installations featuring Virtu products in nine countries. This paper recaps the certified Virtu product family and highlights its unique features. We will present field data and integration insights from several recent projects, including an office block, a student residence, a leisure center, a supermarket and a cardboard manufacturing plant. Additionally, we will preview an upcoming project that includes interseasonal storage elements.

This study aims to showcase the growing adoption of solar thermal technologies through the commercialization of Virtu products. By highlighting the scalability and efficiency of Virtu technology, we demonstrate how these innovations are being utilized across various sectors to help decarbonize heat. The increasing number of installations and diverse applications of Virtu products show the technology's effectiveness in real-world settings.

This paper provides insights into several applications where solar thermal technology decarbonizes all or part of the heating demand. Through detailed analysis of recent projects, we illustrate the practical benefits and performance of Virtu products in different environments. These case studies not only highlight the technology's capabilities but also offer valuable lessons on integration and optimization, paving the way for broader adoption and future advancements in solar thermal energy.

© 2024. The Authors. Published by International Solar Energy Society
Selection and/or peer review under responsibility of Scientific Committee
10.18086/eurosun.2024.07.18 Available at http://proceedings.ises.org

2. Methodology

To evaluate the performance and impact of the Virtu product family, we aggregated real performance data in kilowatt-hours (kWh) of both thermal and electrical energy using our innovative monitoring platform, Clarity24-7. This platform allows us to collect continuous data from our installations, providing detailed insights into their operation and efficiency. The data is anonymized to ensure privacy and confidentiality, while still allowing us to analyze the general use cases for our collectors.

3. Results and Discussion

3.1. System Description

Thermal-only module: The solar thermal collector, VirtuHOT, comprises an optimally designed aluminium absorber inside a vacuum-filled glass tube. It is used to generate heat while being installed on building roofs. With integrated reflectors, a low profile, and a tubular design, it maximizes space efficiency and energy capture. The product, tested by TUV Rheinland and certified under DIN CERTCO (EN 12975-1:2006, EN ISO 9806:2017), achieves peak power production of 400 Wp. An exemplar setup of the product is shown in Figure 1.

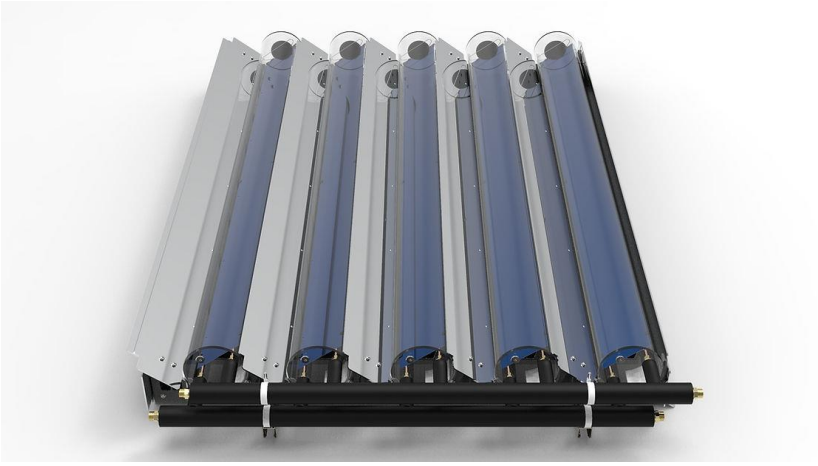

Figure 1. Fully kitted VirtuHOT array

Hybrid Module: The VirtuPVT module consists of photovoltaic cells laminated to a heat exchanger inside a vacuum-filled glass tube. It generates both heat and electricity and can be installed on building roofs, facades and the ground. With integrated reflectors, a low profile and a tubular design, it optimizes space usage and energy capture. The VirtuPVT module integrates PERC-Si PV cells to achieve a thermal capacity of 275 Wp and an electrical capacity of 75 Wp. Both products are designed and manufactured by Naked Energy [2], a British design and engineering firm leading global innovation in solar thermal and solar PVT. An exemplar setup of the hybrid product is shown in Figure 2.

Figure 2. Fully kitted VirtuPVT array

3.2. Field data review

VirtuPVT system, heating & powering the office building:

The Active Office in the UK, equipped with 40 VirtuPVT tubes, provides space heating and hot water for office use. The system, which heats the main thermal store alongside a heat pump, operates at a fluid outlet temperature of 70°C and is installed on a vertical facade. The performance data shows (Figure 3.) that the system delivers stable energy output year after year, despite some seasonal fluctuations due to changes in irradiance. On average, the system produces 2,663 kWh/year of thermal energy and 1,458 kWh/year of electrical energy, which is in line with the predicted values. This reliable performance highlights the effectiveness of VirtuPVT technology in supplying decarbonized heat and power to office buildings.

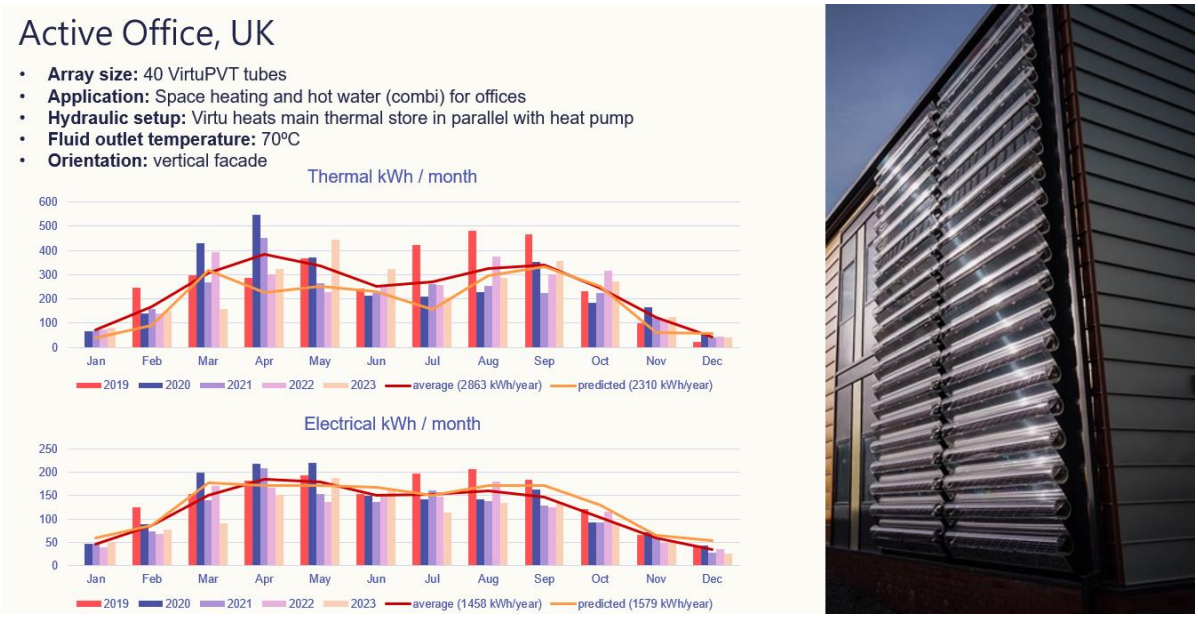

Figure 3. Field data (2019-2023) from the vertical façade array at the Active Office in Swansea, UK

Hybrid system, heating the student residence:

The Halls of Residence in the UK feature 75 VirtuHOT tubes and 60 VirtuPVT tubes for preheating hot water for student accommodations. Installed on a sloped roof, the system operates with a mean fluid temperature of 60°C. The 2023 performance data shows strong thermal and electrical outputs, generating 27,302 kWh/year of thermal energy and 3,185 kWh/year of electrical energy, both exceeding the predicted values of 23,367 kWh/year and 3,361 kWh/year, respectively. This performance (Figure 4.) highlights the system's ability to efficiently meet the hot water demands of a large residential facility, demonstrating the reliability and effectiveness of Virtu technology in such applications.

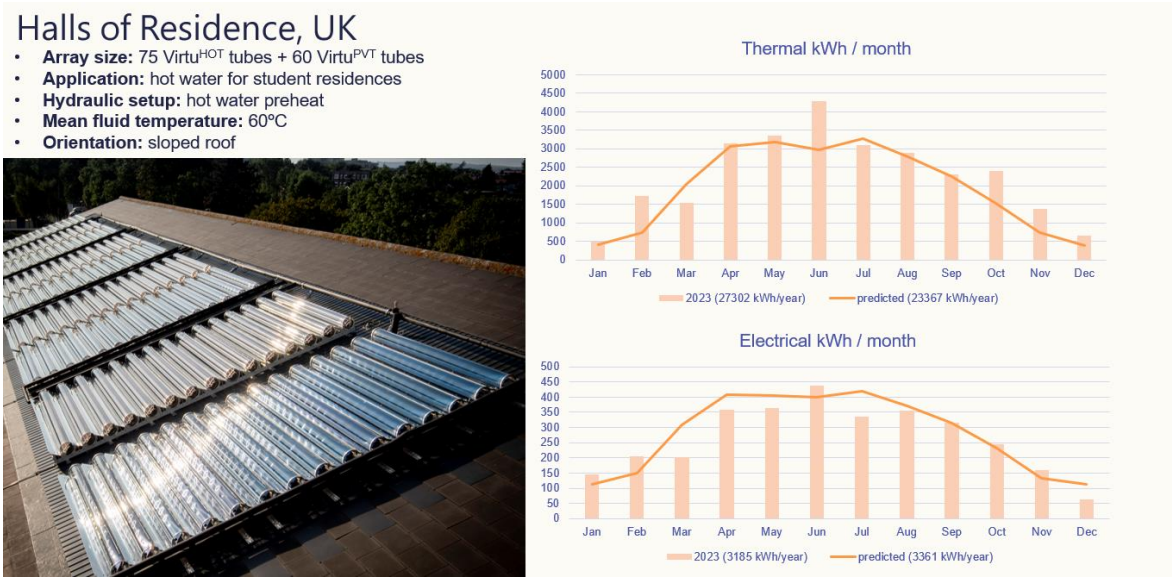

Figure 4. Field data (2023) from the sloped roof array at the student accommodation, UK

VirtuHOT system, heating the leisure center:

The Leisure Centre in the UK, equipped with 420 VirtuHOT tubes, heats its swimming pool via a heat exchanger. Installed on a flat roof (Figure 5.) with a 45° southwest orientation and partial shading from a parapet, the system operates with a mean fluid temperature of 45°C. The thermal output, as shown in the chart, peaks in June and closely aligns with the predicted 82 MWh for the season. Despite some shading and irradiance variations, the system delivered 80 MWh of thermal energy in 2023, demonstrating the effectiveness of VirtuHOT technology in meeting the heating demands of the facility.

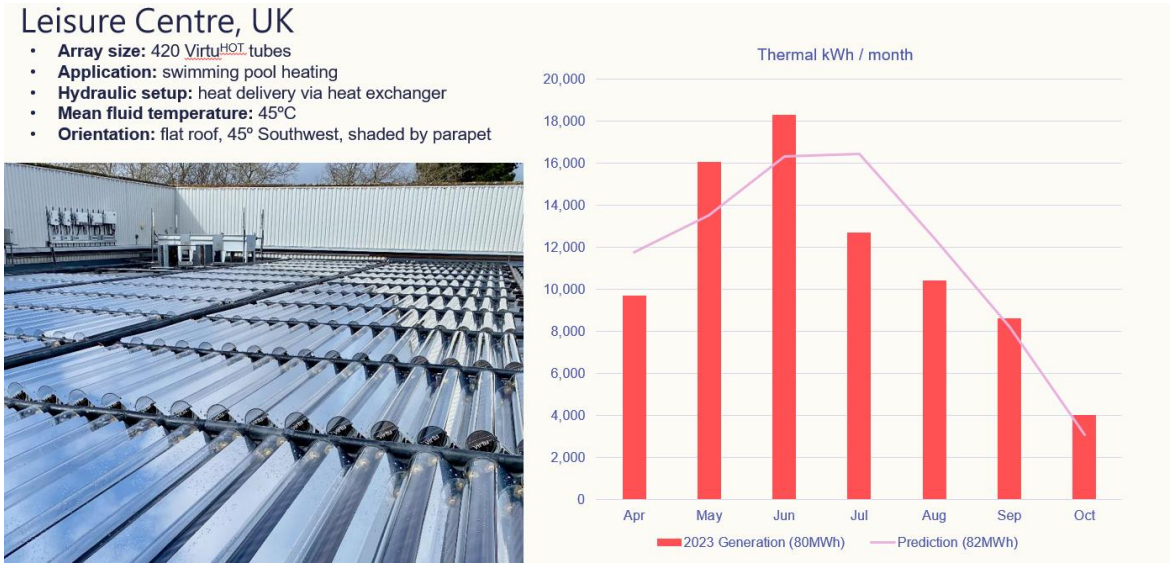

Figure 5. Field data (2023) from the flat roof array at a leisure centre, UK

Hybrid system, heating & powering a supermarket:

The supermarket in the UK uses 5 VirtuPVT and 5 VirtuHOT tubes for preheating hot water in the staff room. Installed on a flat roof, the system operates at a mean fluid temperature of 30°C. Due to mis-calibration, no thermal data is available before June 2022, and post-May 2023 data is missing due to research activities. Despite these issues, the system delivered (Figure 6.) an average of 2,945 kWh/year of thermal energy and 283 kWh/year of electrical energy, exceeding predictions, showing the effectiveness of Virtu technology even with operational disruptions.

Figure 6. Field data (2023) from the sloped roof array at the student accommodation, UK

Upcoming hybrid project, heating & powering a manufacturing facility:

This upcoming project in Figure 7. for Naked Energy exemplifies the extensive integration of VirtuPVT and VirtuHOT technology in a large-scale commercial setting. The building will entirely replace its gas demand by the end of Phase 3, relying solely on a combination of Virtu solar collectors and a ground source heat pump (GSHP) system for both heating and cooling. The graph illustrates the expected monthly energy generation versus demand, showcasing how Virtu systems will meet the building's year-round energy needs. The design also incorporates interseasonal storage, which allows excess summer heat to be stored and utilized during cooler months, ensuring balanced energy supply throughout the year. This project highlights Naked Energy's commitment to providing comprehensive, sustainable energy solutions that cater to both heating and cooling demands in large-scale commercial applications.

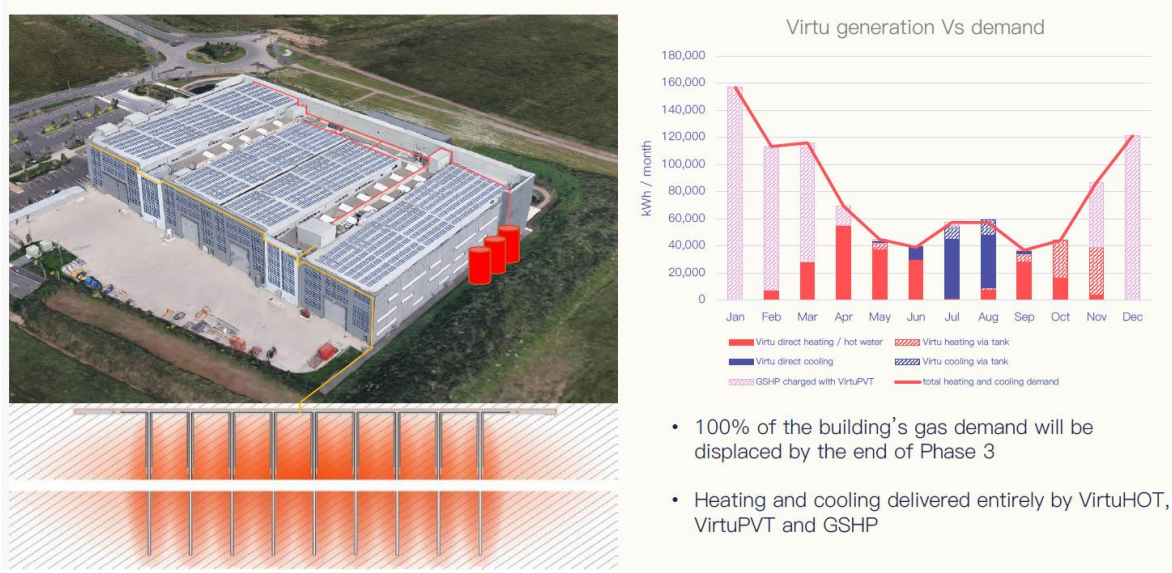

Figure 7. An upcoming project featuring interseasonal storage elements.

4. Conclusions

The presented results showcase the plethora of applications of VirtuHOT and VirtuPVT, where the solar thermal systems are delivering useful, decarbonized heat and power in buildings with varied applications, installation geometries and heating demands. From the national library to an office block, a student residence, a leisure center, a supermarket, and a cardboard manufacturing plant, the data demonstrates the versatility and effectiveness of Virtu technology. These findings underscore the scalability and adaptability of our solar thermal solutions, reinforcing their crucial role in the ongoing efforts to decarbonize heat across diverse sectors.

5. References

[1] S. P. C. W. A. M. A. A. N. J. E.-D. Adrian Murrell, "Development and Field Testing of a Novel Hybrid PV-Thermal Solar," in *Eurosun*, Papperswil, 2018.

[2] "Naked Energy," 30 7 2024. [Online]. Available: https://nakedenergy.com/ .

Quantifying The Environmental Implications Of Solar Thermal Technologies: A Comprehensive Examination Of Life Cycle Impacts And Payback Periods

Maria Zagorulko[1], Dr. Alexander Mellor[1], Dr. Adrian Murrell[1]

[1] Naked Energy Limited, Crawley (United Kingdom)

Abstract

This study evaluates the sustainability of solar technologies though life-cycle analysis (LCA). A comparison is made of the embedded carbon of solar thermal evacuated tubes and hybrid photovoltaic thermal (PVT) evacuated tubes and these are compared to photovoltaic (PV) panels. The solar thermal collector VirtuHOT is found to have the lowest embedded carbon (0.172 $kgCO_2eq$ /Wp), followed by the hybrid collector VirtuPVT (0.344 $kgCO_2eq$ /Wp), and both are significantly lower than published data for PV panels (0.81 $kgCO_2eq$ /Wp). VirtuHOT exhibits an average carbon payback period of 1.25 years, whereas VirtuPVT collectors require 3.25 years. While the hybrid PVT collector exhibits this longer carbon payback period due to the PV element and associated manufacturing and disposal intensities of silicon, its embedded carbon remains lower or comparable to that of PV modules utilizing the same carbon-intensive PERC silicon cells. This research addresses a gap in the existing literature on life cycle analysis of solar thermal technologies.

Keywords: solar thermal technology, sustainability, life cycle analysis, PVT collectors, evacuated collectors, embedded carbon

1. Introduction

With increasing governmental focus on environmental sustainability, there is an urgent need to assess the environmental impacts of technologies marketed as renewable and beneficial for the energy transition. Most comparisons of Renewable Energy products focus on quantifying the energy production (in J or kWh) and show how much CO2 each product therefore saves compared to burning fossil fuels. However, to make a more accurate assessment of total carbon displacement it is essential also to take account of the carbon budget for manufacturing the product (the Embedded Carbon) and other carbon generated throughout the whole life cycle of the product. Accurate comparisons therefore require product Life Cycle Analysis (LCA) studies that are holistic and transparent.

This research is becoming more and more relevant given the expansion in usage of green building certification systems such as LEED (Leadership in Energy and Environmental Design) or BREEAM (Building Research Establishment Environmental Assessment Method). These frameworks evaluate the full carbon footprint of buildings and require manufacturers of renewable products to calculate and declare their embedded carbon. Manufacturers who adhere to reporting standards inevitably broaden their market reach in an economy increasingly driven by sustainability.

In this study LCA analyses have been undertaken of both solar thermal and hybrid photovoltaic-thermal (PVT) collectors. This research represents one of the first commercial lifecycle evaluations of these technologies, offering valuable insights for consumers and real estate developers considering the integration of low-carbon solutions into their projects, for applications such as water and space heating. We examine the entire lifecycle of these technologies, from production through to disposal, with a particular focus on environmental impacts such as embedded carbon and greenhouse gas emissions.

© 2024. The Authors. Published by International Solar Energy Society
Selection and/or peer review under responsibility of Scientific Committee
10.18086/eurosun.2024.07.19 Available at http://proceedings.ises.org

Review of existing literature has revealed a significant gap in the life cycle assessments of solar thermal technologies. A notable exception is the work by Ardente et. al. (2005) [1] from the University of Palermo, who conducted an in-depth LCA of a flat plate solar thermal collector. Their research covered emissions and energy requirements throughout the lifecycle, including production, raw material delivery, installation, maintenance, disposal and transportation. The study also assessed the CO_2 and energy payback times, which were both under two years, demonstrating the significant environmental benefits of solar thermal technology given its typical service life of 25 to 30 years. Despite this important study, there remains a lack of available LCA data for major solar thermal manufacturers globally as well as comparative assessments of the environmental impacts of solar thermal collectors versus photovoltaic panels.

2. Methodology

2.1.System description

Thermal-only module: The solar thermal collector, VirtuHOT, is designed and manufactured by Naked Energy Ltd. It comprises an optimally designed aluminium absorber inside a vacuum-filled glass tube. It is used to generate heat in the range 40-120˚C and is usually installed on building roofs. With integrated reflectors, a low profile, and a modular design, it maximizes space efficiency and energy density. The product, tested by TUV Rheinland and certified under DIN CERTCO (EN 12975-1:2006, EN ISO 9806:2017), achieves peak power production of 400 Wp. An exemplar setup of the product is shown in Figure 1.

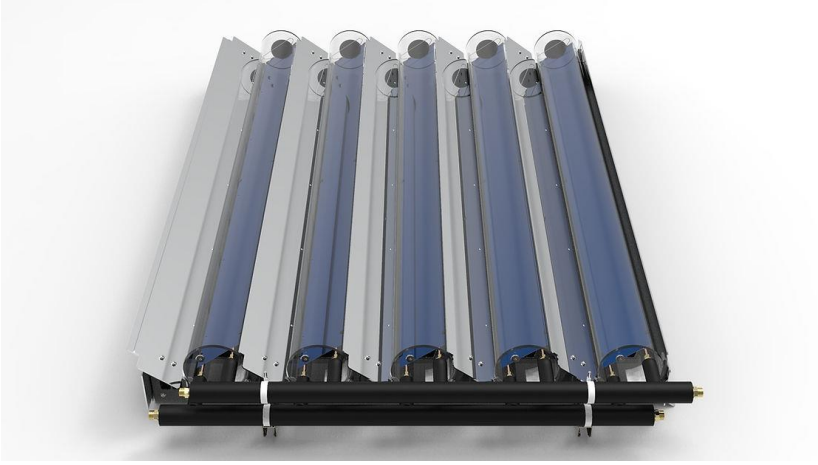

Figure 1. Fully kitted VirtuHOT array

Hybrid Module: The VirtuPVT module consists of photovoltaic cells laminated to a heat exchanger inside a vacuum-filled glass tube. It generates both heat and electricity and can be installed on building roofs, facades and the ground. It shares the same mounting frame and fluid connections as VirtuHOT, with the addition of electrical connectors. The VirtuPVT module integrates PERC-Si PV cells to achieve a thermal capacity of 275 Wp and an electrical capacity of 75 Wp. Both products are designed and manufactured by Naked Energy [2], a British design and engineering firm leading global innovation in solar thermal products and renewable heating systems. An exemplar setup of the hybrid product is shown in Figure 2.

Figure 2. Fully kitted VirtuPVT array

2.2. LCA scope

The lifecycle analysis (LCA) of both products was conducted in accordance with EN 15804+A2 and ISO 14025 / ISO 21930 standards, as outlined in the Whole Life-Cycle Carbon Assessments Guidance [3]. The method calculates the CO2 contribution from every component in the product, based on its weight, material type and production processes, including the manufacturing of raw materials, packaging and ancillary materials during the manufacturing and packaging stages (A1-A3 stages of LCA). Table 1. can be used for referencing different LCA stages. Fuel usage by machines, waste handling, material losses and electricity transmission losses are also considered. Key components of the solar thermal collectors, such as photovoltaic cells, absorber plates and glass tubes, are manufactured in different countries and assembled at two facilities, in the UK and the EU.

Table 1. Life cycle stages utilised in environmental analysis

Product stage			Assembly stage		Use stage							End of life stage				Beyond the system boundaries		
A1	A2	A3	A4	A5	B1	B2	B3	B4	B5	B6	B7	C1	C2	C3	C4	D		
x	x	x	x	x	MND	MND	MND	MND	MND	MND	MND	x	x	x	x	x		
Raw materials	Transport	Manufacturing	Transport	Assembly	Use	Maintenance	Repair	Replacement	Refurbishment	Operational energy use	Operational water use	Deconstr./demol.	Transport	Waste processing	Disposal	Reuse	Recovery	Recycling

Modules not declared = MND. Modules not relevant = MNR.

The materials utilized include borosilicate glass, aluminium, high-density polyethylene and copper, with electricity being the primary energy source for manufacturing. Greenhouse gas emissions (GHG) are approximated from proper waste management practices, directing plastic waste to incineration, and recycling glass and metal waste streams. Transportation impacts (A4-A5 stages) from the production plant to the building site are evaluated, considering fuel exhaust emissions and related infrastructure impacts. The end-of-life stage (C1-C4, D) involves assessing energy consumption during de-construction, waste transportation to treatment centers and waste treatment processes such as recycling and incineration with energy recovery. Benefits from material and energy recovery, including the displacement of virgin material production and electricity and heat production, are accounted for.

The use phase (B1-B7) is not covered in this study as, once installation is complete, no additional energy or materials are required for maintenance. Our methodology adheres to strict cut-off criteria, ensuring the inclusion of all relevant modules and processes mandated by reference standards. Additionally, allocations are made according to reference standards and applied product category rules (PCR), ensuring accurate representation of data where separate measurement is not feasible.

2.3. Assessment method

The environmental analysis and impact calculation were performed using OneClickLCA software. OneClickLCA [4] is a comprehensive tool for lifecycle assessment, offering robust data analysis capabilities and alignment with international standards. It facilitates detailed environmental impact assessments across various phases of a product's lifecycle. Data for stages A2, A3, A4, A5, as well as for C1 and C2, were collected using presented values from the product supply chain. In contrast, data for stages A1, C3, and C4 were obtained through theoretical approximation.

2.4. Functional and declared units

The results of the lifecycle analysis are presented in $kgCO_2$ per declared unit (one vacuum tube collector), with the hybrid PVT collector at 19.99 kg and the solar-thermal collector at 18.19 kg per declared unit. The declared unit encompasses the total weight of the collector, including all auxiliary components such as the frame, reflector, and manifold. To facilitate the comparison of global warming potential (GWP) between solar thermal collectors and photovoltaic modules, the evaluated embedded carbon is converted to $kgCO_2$ per functional unit (Wp). For VirtuPVT, the functional unit is presented to be 1 Wp of combined thermal and electrical capacities while for VirtuHOT the functional unit is 1 Wp of thermal capacity.

This study includes a comparison that is based on work by Müller A. et.al. (2021) , [5] conducted at the Fraunhofer Institute, which focused on two single crystalline PV modules: one manufactured in China and one in the EU. For this study, we compare the environmental impact of the Virtu products to the glass-backsheet (G-BS) module

manufactured in China. The G-BS module studied has similar peak performance values to the Virtu products and a comparable value chain, making it suitable for comparison. The declared unit of this study has been converted to a functional unit of Wp to align with the specimens studied by Müller A. et.al. (2021), ensuring an accurate and relevant comparison of environmental impacts.

2.5. Payback on embedded carbon

The payback on embedded carbon is calculated using the following formula:

$$CP = \frac{Embedded\ carbon\ of\ 1\ declared\ unit\ in\ kgCO_2}{Abated\ carbon\ of\ 1\ declared\ unit\ in\ kgCO_2/year} \quad \text{(eq. 1)}$$

The abated carbon for thermal-only is determined using the equation:

$$Abated\ carbon = E_{th} \times I_{th} \quad \text{(eq. 2)}$$

where $\mathbf{E_{th}}$ is the geographically estimated thermal energy in kWh produced annually (values from the DIN CERTCO specification sheet), and $\mathbf{I_{th}}$ is the carbon intensity of the replaced heat source ($kgCO_2eq/kWh$). For this study, the heat source replaced is assumed to be natural gas with a carbon intensity of 0.210 $kgCO_2eq/kWh$.

The abated carbon for 1 declared unit of VirtuPVT is determined using the equation:

$$Abated\ carbon = E_{th} \times I_{th} + E_{el} \times I_{el} \quad \text{(eq. 3)}$$

where $\mathbf{E_{el}}$ refers to the geographically estimated electrical energy produced annually, expressed in kilowatt-hours (kWh), and $\mathbf{I_{el}}$ refers to the carbon intensity of the electricity source being replaced, measured in kilograms of CO2 equivalent per kilowatt-hour ($kgCO_2eq/kWh$).

Energy modelling considers four key locations that are used in the Solar Keymark certification (DIN CERTCO), including Athens, Greece; Davos, Switzerland; Stockholm, Sweden; and Wurzburg, Germany. For each location, two circulating fluid temperatures, 25°C and 50°C, are investigated. The results of this analysis are presented in subsection 3.3. An average value for Carbon Payback is then calculated for each product, based on the locations of VirtuHOT and VirtuPVT installations currently installed across Europe. These values are then compared to the Carbon Payback of a PV module manufactured in China, as analysed by Müller A. et.al., (2021).

3. Results and discussion

3.1. Global Warming Potential (GWP) of Virtu product line

The components level analysis of the PVT collector yielded a total embedded carbon value of 122 $kgCO_2$ per declared unit, while the thermal-only collector showed an embedded carbon of 69 $kgCO_2$ per declared unit. The pie charts depicting the GWP breakdown for solar thermal technologies provide a visual comparison. Figure 3. highlights the lower emissions associated with the thermal-only collector, particularly attributable to the absorber plate and other components. In contrast, Figure 4. showcases the hybrid PVT collector's higher emissions, primarily attributed to the inclusion of PERC Silicon Cells and associated components. These visual representations underscore the importance of selecting appropriate collector configurations to minimize environmental impacts effectively.

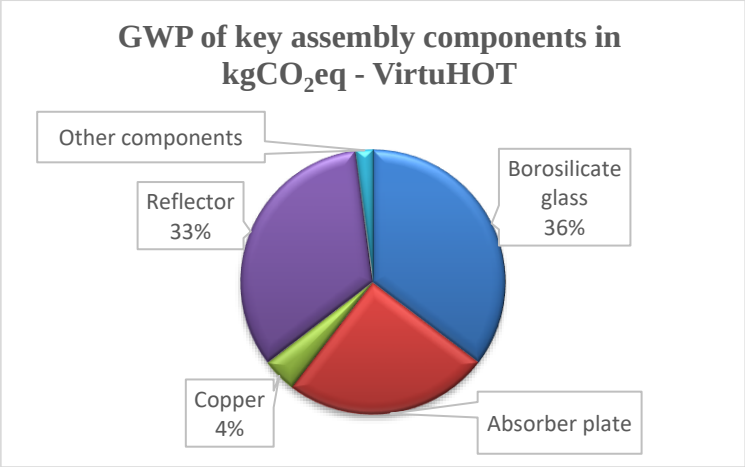

Figure 3. Global Warming Potential (GWP) in $kgCO_2$ of key components in VirtuHOT

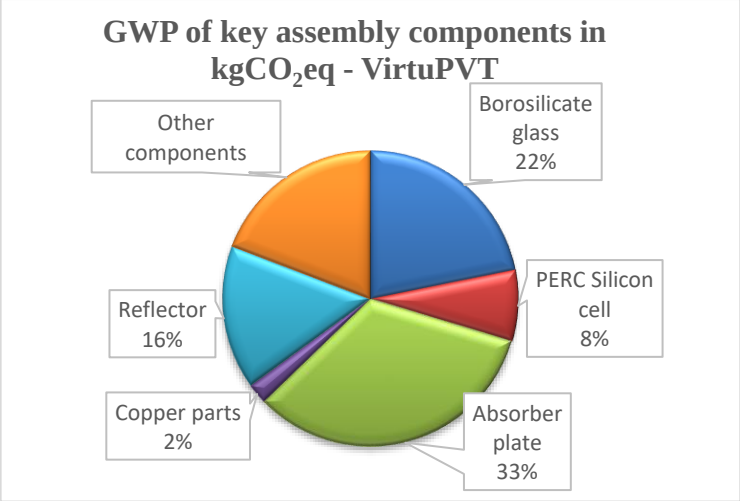

Figure 4. Global Warming Potential (GWP) in $kgCO_2$ of key components in VirtuPVT

Thermal-Only Collector (VirtuHOT)

For the thermal-only collector, the majority of the GWP is attributed to the borosilicate glass enclosure, which accounts for 36% of the total GWP. The integrated reflector also significantly contributes, comprising 33% of the total GWP. These high proportions are primarily due to the emissions from transportation of some components within the supply chain. The combined global warming potential of sea-freight and road freight from China to the United Kingdom has significantly increased the embedded carbon within the VirtuHOT product.

Additionally, the aluminium-copper absorber plate contributes 17.25 $kgCO_2$ to the embedded carbon within the VirtuHOT collector. The high intensity within this part is attributed to the energy-intensive process of aluminium sheet rolling. This highlights the importance of considering both transportation and manufacturing processes when evaluating the environmental impacts of solar thermal technologies.

Hybrid PVT Collector (VirtuPVT)

When examining the VirtuPVT data, the aluminium heat exchanger plate has a larger mass than the VirtuHOT absorber, since a thicker substrate is needed to support the PV cells and ensure temperature uniformity. Consequently, the embedded carbon for this part doubles to 40.25 $kgCO_2$eq. Similar to the VirtuHOT's carbon intensity, the borosilicate glass encapsulant and the reflector account for substantial portions of the total embedded GWP, at 22% and 16%, respectively. Given the commonality in the value chains, these results were expected.

Interestingly, the PERC-Si cells account for only 8% of the total GWP of VirtuPVT, which equates to 9.76 $kgCO_2$eq. Despite the fact that the sourcing and formation of silicon cells are highly carbon and energy-intensive processes, in this case, the proportional mass of silicon in the declared unit is under 1% of the total mass. This finding is significant as it indicates that the inclusion of PERC-Si cells in the PVT collector does not substantially increase the overall GWP.

In the sourcing and manufacturing stages (A1-A3) of the LCA, the VirtuPVT module requires approximately 557 kWh of energy, significantly higher than the 291 kWh needed for the VirtuHOT collector. The increased energy demand for the VirtuPVT module is largely due to the energy-intensive processes involved in producing the aluminium-copper heat plate, specifically the extrusion and rolling of aluminium, which contribute an additional 44% to the overall energy consumption. Additionally, the inclusion of PERC silicon PV cells in the VirtuPVT module raises the energy requirement by 25%. The production of these PV cells is energy-intensive, involving steps such as polysilicon ingot formation, Czochralski processing and subsequent wafer cutting and etching. These processes collectively account for the higher energy consumption associated with the VirtuPVT module compared to the VirtuHOT collector.

3.2. Environmental impacts per Wp of nominal power

When evaluated on the basis of CO_2 per Wp of nominal power, the results of the embedded carbon assessments reveal interesting contrasts between the various solar collector technologies. Specifically, the hybrid PVT collector and the thermal-only collector exhibited significantly lower embodied carbon values when compared to a generic PV module. The hybrid PVT collector demonstrated an embedded carbon of 0.344 $kgCO_2$ equivalent per Wp, while the thermal-only collector exhibited an even lower value at 0.172 $kgCO_2$ equivalent per Wp. In contrast, the generic PV module registered a higher embedded carbon of 0.81 $kgCO_2$ equivalent per Wp,.

Table 2. Embodied Carbon Comparison of Solar Collector Technologies

Collector Type	Embodied Carbon ($kgCO_2eq/Wp$)
Hybrid PVT Collector	0.344
Thermal-Only Collector	0.172
PV Module	0.81

Table 2 summarizes these results and highlights the superior environmental performance of solar thermal technologies. While the PVT collector and the thermal-only collector may exhibit differences in their specific embedded carbon values, both significantly outperform the generic PV module. These findings hold substantial implications, particularly within the context of the imperative to mitigate carbon footprints in energy systems. The lower embodied carbon of solar thermal collectors underscores their promising role as sustainable energy solutions.

A comparison of the presented LCA results with the Global Warming Potential (GWP) of PV panels, utilizing the IPCC 2013 100-year method for two distinct types of solar modules (Müller A. et.al., 2021) accentuates the superiority of solar thermal technologies. One module is a glass-backsheet sc-Si PERC module with specifications of P = 366 Wp and η = 19.79%, produced in China. The other module is a glass-glass sc-Si PERC module with specifications of P = 359 Wp and η = 19.40%, produced in the EU. The aforementioned table only considers the PV module made in China, which is representative of the PVT's geographical value chain.

Particularly noteworthy is the significantly lower embedded carbon per Wp exhibited by the hybrid PVT collector, rendering it an especially attractive alternative to PV. These findings underscore the potential of solar thermal technologies to significantly contribute to sustainable energy transition.

3.3. Payback on embedded carbon

Considering carbon payback periods across various geographical locations, including Athens, Davos, Stockholm and Wurzburg, reveals insightful data as presented in Table 3.

Table 3. Payback on embedded carbon for VirtuHOT

	Athens		Davos		Stockholm		Wurzburg	
Fluid Temperature (˚C)	25	50	25	50	25	50	25	50
Thermal Yield, E_{th} (kWh/year)	567	474	439	355	314	244	353	277
Carbon Abatement ($kgCO_2$/year)	119	99.5	92.2	74.6	65.9	51.2	74.1	58.2
Carbon Payback (years)	0.69	0.82	0.89	1.10	1.24	1.60	1.11	1.41

Athens has the shortest carbon payback period due to its high solar irradiance and warmer climate, resulting in higher thermal yields and greater carbon abatement. In contrast, Stockholm, with its cooler climate and lower solar irradiance, exhibits the longest payback period due to reduced thermal yields and less carbon abatement.

Higher fluid temperatures (50°C) consistently decrease thermal yield and carbon abatement, extending the payback periods across all locations. Davos, characterized by a cooler alpine climate, and Würzburg, with a moderate climate, show intermediate payback periods, reflecting the impact of regional climate conditions.

For VirtuPVT, in Table 4., the analysis has taken into account the carbon intensity of the grid in the equivalent geographical locations.

Table 4. Payback on embedded carbon for VirtuPVT

	Athens		**Davos**		**Stockholm**		**Wurzburg**	
Fluid Temperature (˚C)	25	50	25	50	25	50	25	50
Thermal Yield, E_{th} (kWh/year)	362	217	238	132	177	92	203	107
Electrical Yield, E_{el} (kWh/year)	103	94	91	83	63	58	70	64
Carbon intensity of the grid ($kgCO_2/kWh$)	0.448	0.448	0.357	0.357	0.012	0.012	0.314	0.314
Carbon Abatement ($kgCO_2$/year)	122	87.5	82.5	57.4	37.9	20.0	64.6	42.6
Carbon Payback (years)	1.07	1.49	1.59	2.28	3.46	6.55	2.03	3.08

The VirtuPVT system's carbon payback period is shorter in locations with higher grid carbon intensity and better solar conditions, such as Athens, and longer in areas with lower grid carbon intensity and less favorable conditions, like Stockholm.

In summary, regions with higher solar irradiance and warmer climates, like Athens, have shorter carbon payback periods, while cooler, less sunny regions, like Stockholm, have longer periods. The efficiency of solar energy conversion and the operating fluid temperature are key factors in these variations.

Overall, the payback periods for the VirtuPVT and VirtuHOT systems are short compared to the their service lifetime. While thermal-only collectors demonstrate an average payback period of approximately 1.25 years, PVT collectors require an average of about 3.25 years to offset their embedded carbon. This indicates that, despite regional variations in payback periods, the long-term environmental benefits of PVT collectors generally outweigh their initial carbon costs.

4. Conclusions

The life cycle analysis of the VirtuHOT and VirtuPVT collectors demonstrates an interesting and environmentally important benefit of solar thermal technologies compared to generic PV modules. The thermal-only collector, VirtuHOT, and the hybrid VirtuPVT collector both exhibit significantly lower embedded carbon per Wp than standard PV modules (manufactured in China), highlighting their potential for reducing carbon footprints in energy systems. Notably, the thermal-only collector demonstrates the lowest embedded carbon, particularly due to the optimized design and lower material use. In contrast, the hybrid PVT collector, while offering both thermal and electrical outputs, shows a slightly higher embedded carbon due to the additional PV components, yet still remains significantly more environmentally favorable compared to typical PV technologies.

The results emphasize the importance of careful material selection and design optimization in minimizing environmental impacts. The detailed component level analysis reveals that the borosilicate glass enclosure and integrated reflector contribute substantially to the embedded carbon total, particularly due to the transportation emissions involved in the supply chain. For the PVT collector, the energy-intensive processes associated with the aluminium heat exchanger and the PV cell silicon components are also significant contributors and would be targets for future improvement.

In terms of payback on embedded carbon, both products show favorable results, with VirtuHOT offering a shorter payback period than VirtuPVT, due in large part to its lower initial carbon footprint. However, the benefits of

VirtuPVT, which include electrical generation capabilities, provide a broader scope of carbon offset opportunities, particularly in regions with high grid carbon intensity.

The study also identifies key areas for future research. Specifically, more detailed investigation into the use phase (operation and maintenance) of solar thermal technologies is necessary to fully understand their long-term environmental impacts. Additionally, obtaining supplier specific data on the sourcing and manufacturing processes of constituent parts will enhance the accuracy of the analysis. This will not only refine the understanding of the environmental impacts but also inform strategies for further reducing the carbon footprint of these renewable technologies. The ongoing development of solar thermal technology, along with improved data transparency and material efficiency throughout the product life cycle, offers significant potential for future technology applications.

5. References

[1] B. G. C. M. L. B. V. Ardente F, "Life cycle assessment of a solar thermal collector," *Renewable Energy*, pp. 1031-54, 2005. Available from: https://doi.org/10.1016/j.renene.2004.09.009

[2] "Naked Energy," 30 7 2024. [Online]. Available: https://nakedenergy.com/ .

[3] "Whole Life-Cycle Carbon Assessments guidance," 8 03 2024. [Online]. Available: https://www.london.gov.uk/publications/whole-life-cycle-carbon-assessments-guidance.

[4] "Product carbon footprint," 31 7 2024. [Online]. Available: https://oneclicklca.com/en-gb/software/manufacturing/product-carbon-footprint

[5] F. L. R. C. H. S. M. M. N. D. Müller A, "A comparative life cycle assessment of silicon PV modules: Impact of module design, manufacturing location and inventory," *Solar Energy Materials and Solar Cells*, 2021. Available from: https://doi.org/10.1016/j.solmat.2021.111277

08. Solar Air Conditioning and Refrigeration

First experimental investigations of a facade-integrated adsorption system for solar cooling

Olaf Boeckmann[1], Simon Weber[2], Andreas Schedler[3], Micha Schaefer[1]

[1] Institute for Building Energetics, Thermotechnology and Energy Storage, University of Stuttgart (Germany)

[2] Institute for Acoustics and Building Physics, University of Stuttgart (Germany)

[3] Institute for Building Construction, University of Stuttgart (Germany)

Abstract

In this work, a novel facade-integrated adsorption system for solar cooling is investigated experimentally with a first prototype. This system consists of an evaporator, which is installed as cooling ceiling, a condenser and an adsorber. To precisely measure the achieved cooling power rates, the system is tested with an almost adiabatic test chamber, which is placed in an air-conditioned laboratory, and the evaporator is installed as cooling ceiling into the chamber. The adsorber are designed as panel-shaped elements and are mounted in standard facade frames on load cells in the laboratory. The adsorber is regenerated by an infrared heater. The first experimental tests reveal minimum evaporator temperatures of around 6 °C and the outer bottom of the evaporator can be maintained below 10 °C for over 15 hours.

Keywords: Solar Energy, Thermal Energy Storage, Adsorption Chiller, Cooling Ceiling, Building Energy Systems

1. Introduction

Due to its high demand for resources and energy, the building sector accounts for almost 40% of the global carbon dioxide emissions (United Nations Environment Programme 2020). Therefore, in order to achieve the ambitious climate protection goals, it is essential to reduce the required amount of building material in the construction of future buildings as well as to operate these lightweight buildings more energy efficiently or, if possible, energy self-sufficiently. Against this background, a novel, facade-integrated adsorption system for solar cooling of lightweight buildings is being developed within the Collaborative Research Centre 1244 at the University of Stuttgart. The proposed adsorption system combines the functionality of energy storage and cold production, with minimum occupation of inner building space. After detailed simulations of a reference case confirmed the general functionality of the proposed cooling system (Boeckmann et al. 2024), a first prototype was setup in an air-conditioned laboratory. This work introduces the prototype set-up and presents first measurement results.

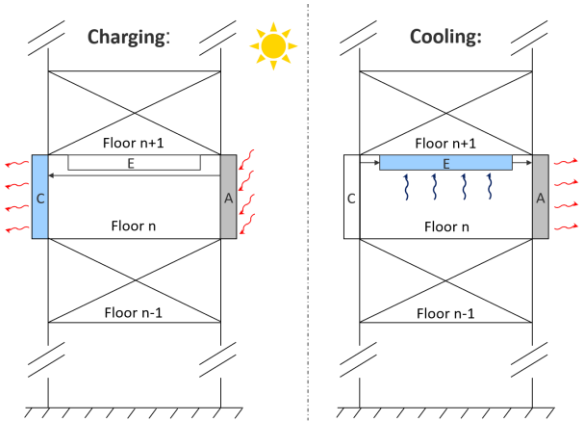

Figure 1: Cross-section view and operating principle of a high-rise building equipped in floor n (exemplarily) with the facade-integrated adsorption system for solar cooling. The main components are: A-adsorber, C-condenser, E-evaporator. The regeneration phase, in which the reactor is heated up by solar irradiation, is shown on the left-hand side and the cooling phase on the right-hand side. The colored arrows indicate the main heat fluxes during the two phases. (Boeckmann et al. 2024)

Adsorption-based cooling is a highly researched cooling technology (Chauhan et al. 2022) and current experimental research addresses the heat transfer design of the adsorber (Wang et al. 2022), the applied working pairs (Allouhi et al. 2015; Cabeza et al. 2017), the influence of thermal operation conditions (Liang et al. 2023) as well as the operation

© 2024. The Authors. Published by International Solar Energy Society
Selection and/or peer review under responsibility of Scientific Committee
10.18086/eurosun.2024.08.01 Available at http://proceedings.ises.org

under real conditions (Bujok et al. 2022; Mat Wajid et al. 2021). However, the work of (Hallström et al. 2014) is the only work know to the authors in which the solar thermal collector and the adsorber are integrated into one component. This element was not designed for the integration into the facade and cooling could only be produced during the night.

The adsorption system consists of the three components adsorber, condenser and evaporator, refer to **Figure *1***. The adsorber and the condenser are integrated as panel-shaped elements into the building facade. The particular challenge lies in the efficient absorption of solar irradiation by the adsorber during the regeneration phase and the sufficiently high heat release to the ambient during cooling operation. The evaporator is installed as a cooling ceiling in the building. For cooling, the evaporator is connected to the previously regenerated adsorber, whereby the cooling power can be controlled by throttling the vapor mass flow.

This work aims to provide a detailed description of the developed experimental setup, including detailed descriptions of the three main components adsorber, condenser and evaporator as well as the installed sensors, the introduction of the test chamber, in which the system is tested and the heating system to regenerate the adsorber. The prototype is designed based on the previous simulation studies partially presented in (Boeckmann et al. 2024). Finally, the successful installation is demonstrated through first cooling operations with the system.

The paper is organized as follows: In Section 2, the experimental setup is introduced and the experimental procedure is presented in Section 3. The experimental results are shown and discussed in Section 4 and finally, the study is concluded in Section 5.

2. Experimental setup

2.1 Adsorber

The adsorber is panel-shaped with dimensions of 890 mm height, 1100 mm width and 87 mm depth. The design scheme of the adsorber is given in Figure 11. It is enclosed by a metal casing at the back as well as the sides and by a metal absorber sheet at the outer face and is vertically attached to a facade of the building or to a wall in this experimental setup, respectively. To ensure mechanical stability, which is one of the main challenges with flat-shaped low-pressure constructions, metallic pins are used as known from evacuated solar thermal collector, refer to Figure 2 (left). These add only little mass and thermal bridges. The adsorber is filled with the granular adsorbent zeolite 13X, while a mesh separates the adsorbent from an adjacent vacuum gap, see Figure 2 (right). This allows for a good distribution of the vapor inside the adsorber. The adsorber is thermally well insulated towards the building's envelope by 20 mm vacuum insulation panels on the back and the sides of the casing. Three ISO-KF16 in-/outlets for the water vapor are integrated into the back of the adsorber with the central one being used in the studies of this work. Metal fins are integrated into the zeolite packed bed to overcome the heat transport limitations of the adsorbent.

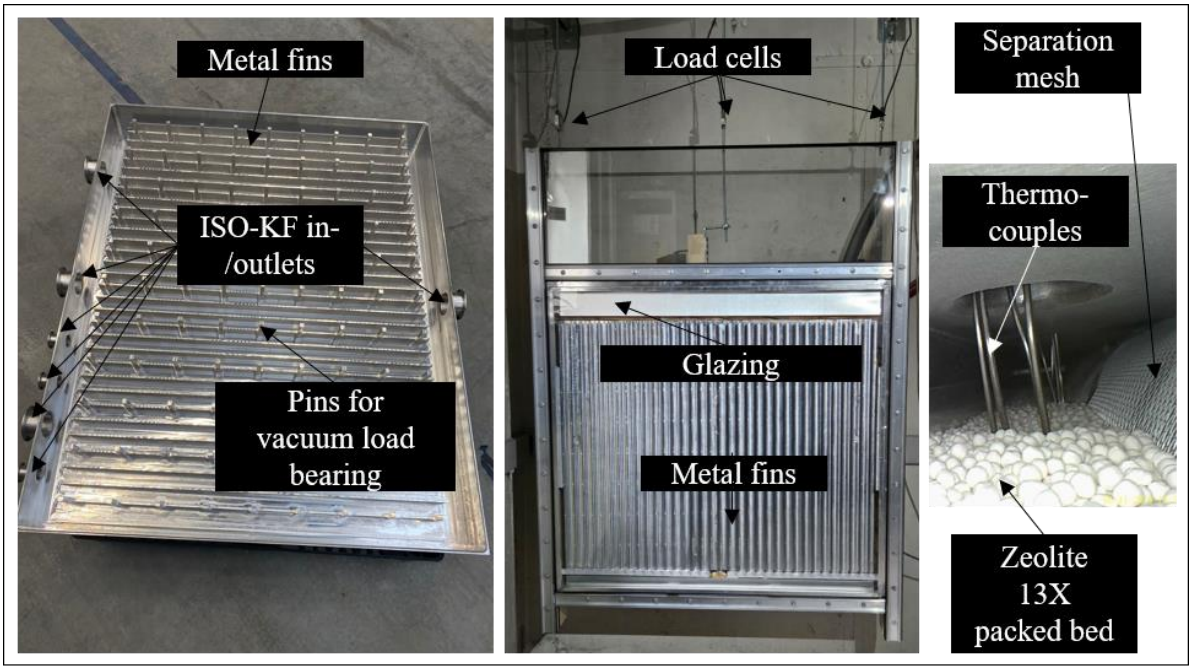

Figure 2: Photo documentation of the adsorber. Left: The inside of the adsorber during the manufacturing. The metal fins, which are integrated into the zeolite packed bed, and the pins for vacuum load bearing are visible. Middle: The adsorber installed into the facade frame and mounted on loads cells in the laboratory. Right: Insight into the filled adsorber with a borescope.

In order to efficiently absorb the solar irradiation during the regeneration phase, the outer adsorber surface face is covered by a metal absorber sheet as well as a low iron float glass, with a Ug-Value of 5,8 W/m^{2}K and a g-Value of 91 %, shown in Figure 2 (middle). Between the absorber sheet and the glazing, there is an air channel, which is closed by a flap during the regeneration phase, while it is open during the cooling phase to efficiently transfer the released heat of adsorption to the ambient by free air convection through the air gap channel (Greiner et al. 2022). To enhance the heat release in the cooling phase, the absorber sheet is equipped with vertical metal fins in the air gap to increase the heat transfer surface. This structure was simulation-based analyzed in (Greiner et al., 2022) and supplemented with variant studies.
On the top of the adsorber, three ISO-KF25 inlets allow for the vacuum tight feed through of thermocouple sensors into the zeolite packed bed. Further three ISO-KF 50 inlets at the top as well as one ISO-KF 50 inlet at the bottom allow to fill/release the adsorbent into/from the adsorber.
The adsorber is integrated into a standard facade construction in order to test the components properties under nearly building conditions and to demonstrate the possibility of integration. This is the Stabalux AK-H system, a mullion-transom construction made of laminated timber with an aluminum attachment.

2.2 Condenser

The condenser is panel-shaped and has the same dimensions as the adsorber (890 mm height, 1100 mm width and 87 mm depth). The design scheme of the condenser is shown in Figure 12. Similar to the adsorber, the condenser is enclosed by a metal casing and is attached vertically to the facade of the building or to the outer wall of the test chamber in this experimental setup, respectively, see Figure 3 (left). Internal metal fins are included to enhance heat transport to the ambient, and thus, improve the condensation rate. Furthermore, theses fins ensure mechanical stability. The backside of the condenser is thermally insulated by 20 mm vacuum insulation panels. In the regeneration phase, vapor flows from the adsorber into the condenser and condenses on the metal fins or the water surface, releasing the heat of condensation to the fins or the water, respectively. The heat is then conducted through the internal fins to the external fins, where it is emitted to the ambient air. Furthermore, the water phase is in direct contact to the outer wall and heat is being transferred to the ambient through the outer wall.
Similar to the adsorber, the condenser is installed into the same facade construction.

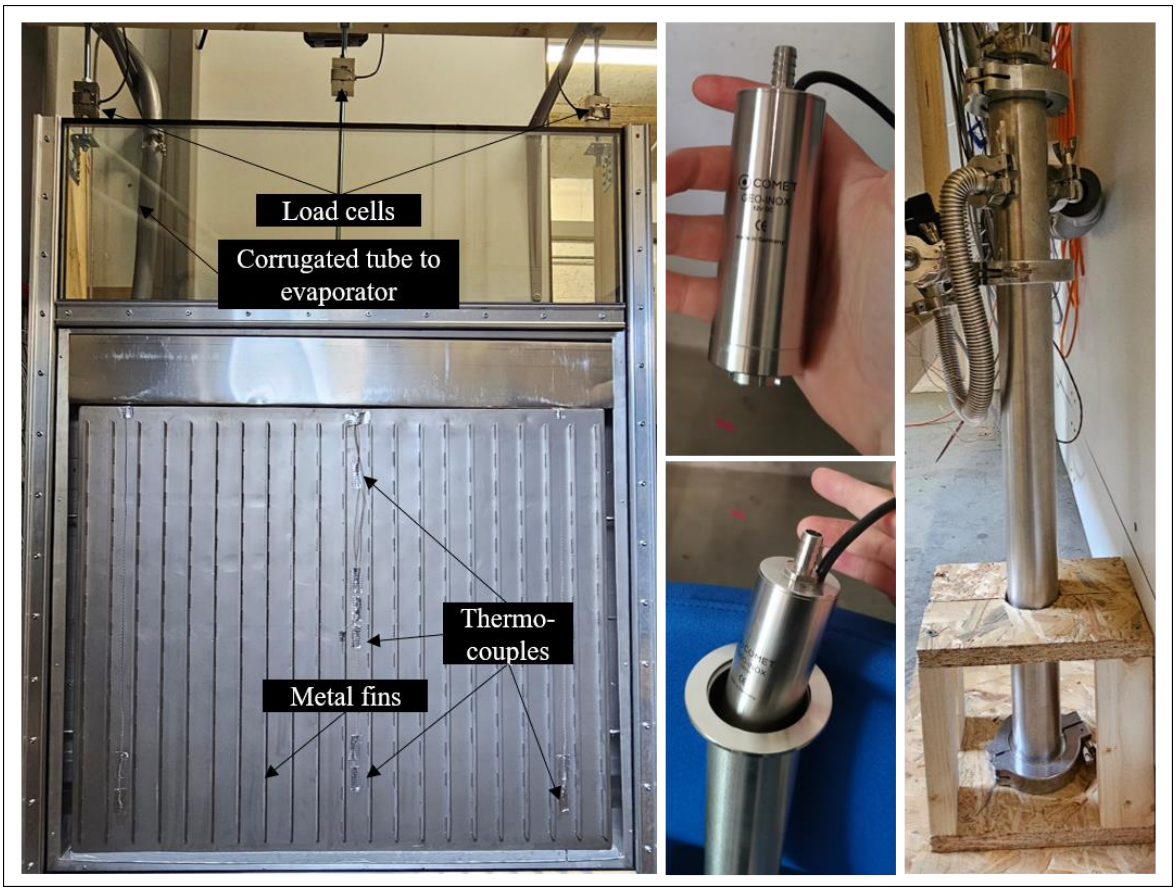

Figure 3: Left: Photo documentation of the condenser installed into the facade frame mounted on load cells in the laboratory. Middle and right: Vacuum-tight pump realized by installing a submersible pump into vacuum tubes.

2.3 Evaporator

The quadratic evaporator with a side length of 1000 mm and a height of 67 mm is also enclosed by a metal casing. It is installed as a cooling ceiling inside the building or into the test chamber in this experimental study, refer to Figure 4 (left). The applied box-shaped configuration is a very simple configuration, chosen in this work to determine the potential of the system with respect to the cooling rate. Nevertheless, more complex solutions such as pipe coils or active ventilation are possible and could be investigated in the future works. Vapor is extracted from the evaporator by the adsorption in the adsorber during the cooling phase, which reduces the pressure in the evaporator. Thus, evaporation is induced and the remaining water is cooled due to extracted heat of evaporation. The water then cools the metallic bottom sheet of the evaporator, which is in direct contact with the air inside the room.
In Figure 4 (right) the top of the evaporator with the sensors as well as the ISO-KF16 in-/outlets can be seen.

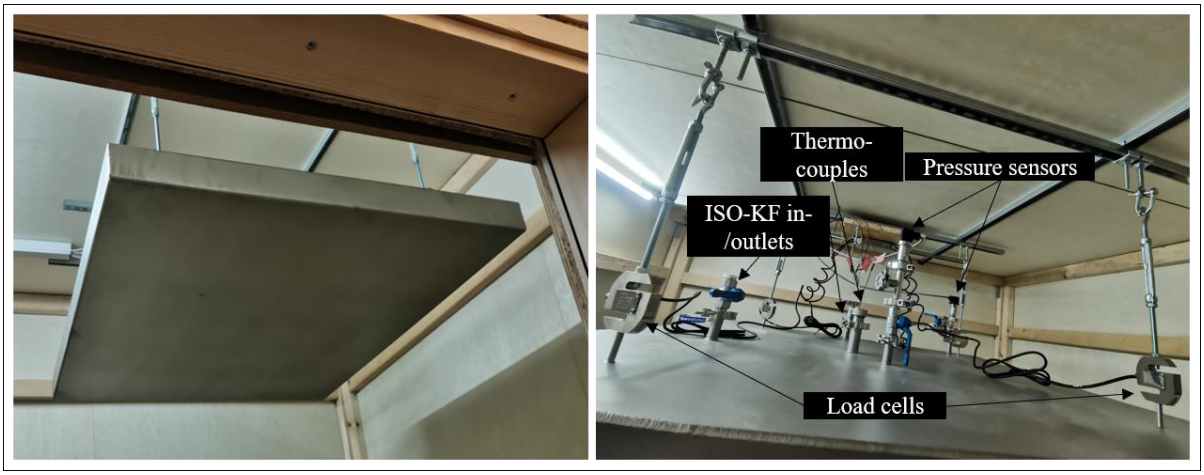

Figure 4: Photo documentation of the evaporator. Left: The evaporator installed as cooling ceiling into the test chamber. Right: View on the top of the evaporator with sensors.

2.4 Couplings

The components are connected with vacuum-tight corrugated tubes, which offer a certain flexibility. Valves are installed to open and close the connections between the components and a controllable throttle is used between evaporator and adsorber to control the inlet pressure of the adsorber, which allows to set the adsorption rate and thus the evaporation rate. This allows to control the evaporator temperature. An overview of all connections and valves is given in the hydraulic diagram in Figure 5.
The condensed water is pumped from the condenser to the evaporator using a vacuum tight pump, see Figure *3* (middle and right). This is realized by integrating a 12 V submersible pump into a 50 mm ISO-KF50 tube and feed a 10 mm hose through a corrugated tube into the evaporator. The electrical connection of the pump is enabled by vacuum tight electrical feed through.

2.5 Sensors

Three variables are measured for the components: Temperature, pressure and weight. The latter is measured via load cells and allows to calculate the water vapor flow between the components. Furthermore, current water uptake of the adsorber can be estimated by the weight measurements. For the temperature, thermocouple sensors are fed into the vacuum components via special feedthroughs and a reduced measuring grid is used. For all components the temperature distribution over the height is measured at four points. For both evaporator and condenser these points cover water as well as vapor phase. Additionally, for the adsorber the temperature distribution in width and depth between the fins is measured with four sensors each. The pressure is measured at the vapor inlet of all components as well as at one additional position for condenser and evaporator. In order to measure the vapor distribution inside the vacuum gap of the adsorber, two additional pressure sensors are installed over the height. Furthermore, all outer surfaces are equipped with thermocouples. An overview of all installed pressure sensors as well as thermocouples inside the components is shown in Figure 5.
An automation station with a programmable logic controller (PLC) is used for logging measurements, control, regulation and model identification of the system.

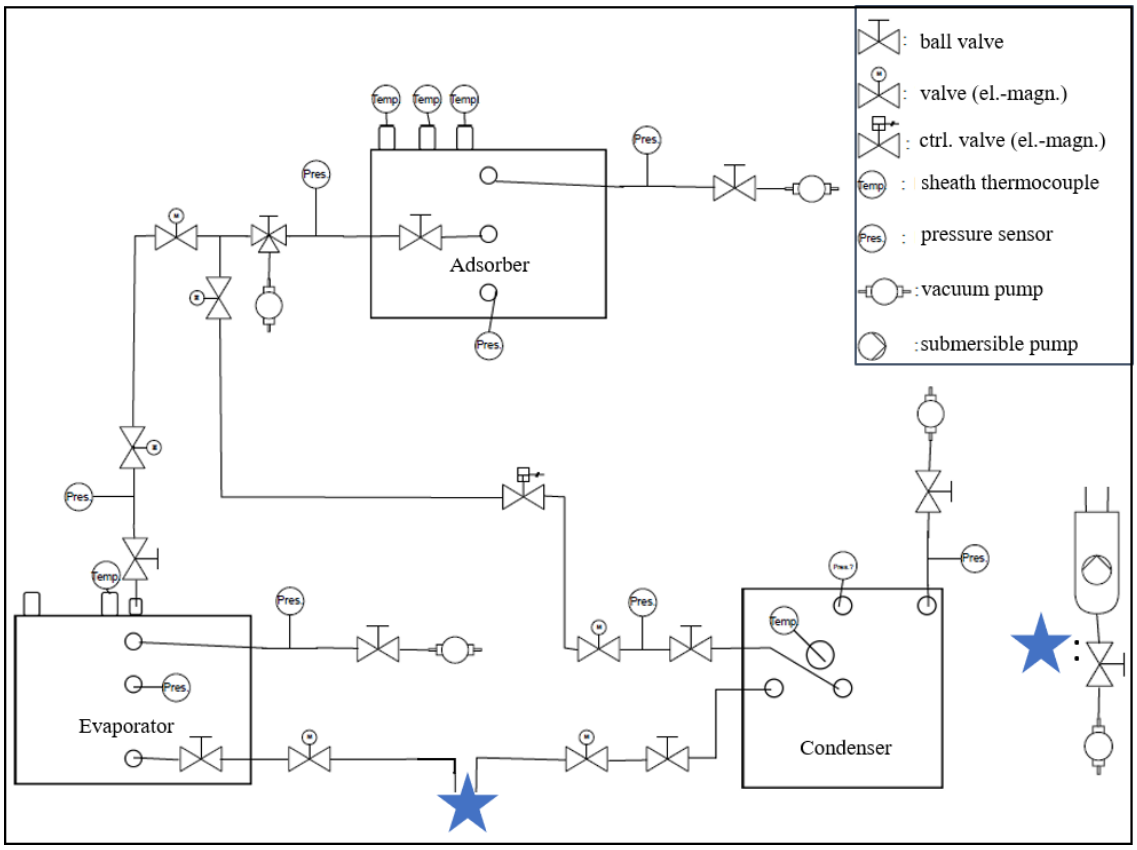

Figure 5: Left: Hydraulic diagram of the adsorption cooling system.

2.6 Test chamber

The adsorption cooling system is tested in a chamber with a multi-layer insulation concept, in which the evaporator is placed, refer to Figure 6. The wall structure consists (from outside to inside) of a layer of 8 mm thick High Pressure Laminate (HPL), 100 mm mineral wool, 18 mm oriented strand board (OSB), 20 mm vacuum insulation panel and 12 mm multiplex board. Each boundary layer temperature between the wall layers is recorded by two thermocouples. This resolves the heat dissipation through the side walls and the ceiling element. To measure the cooling capacity of the evaporator, the insulated room is brought to a constant temperature by supplying a continuously adjustable heating power. The room temperature is measured with a network of 12 measuring points at different heights and surface points using precise resistance thermometers. The heating power is delivered to the room air by an electric heating system. To identify the actual heat input into the test chamber, the electrical power provided to the heating system is measured. Homogeneous room air is achieved by a uniform flow provided by a controllable fan.

2.7 Heating system for regeneration

The adsorption system is regenerated by heating up the adsorber to desorb water vapor from the zeolite packed bed. In the laboratory setup this is done by an infrared heating system, which consists of heating wires in a thermally insulated construction, see Figure 7. The inside of the heating system fits perfectly the outer dimensions of the adsorber to reduce heat losses. The heating wires are resistance wires of the material kanthal 1.4765 with a diameter of 1.5 mm and a specific resistance of 0.7745 Ω/m. A total length of 34 m is used to reach thermal power rates up to 2000 W with a maximum voltage of 230 V possible. A voltage controller allows for continuous setting of the required thermal power.

Figure 6: Pictures of the thermally high insulated test chamber. Left: Outside of the chamber with 100 mm mineral wool. Middle: 20 mm vacuum insulation panels installed to the inside of the chamber. Right: Inner top layer of 12 mm multiplex board.

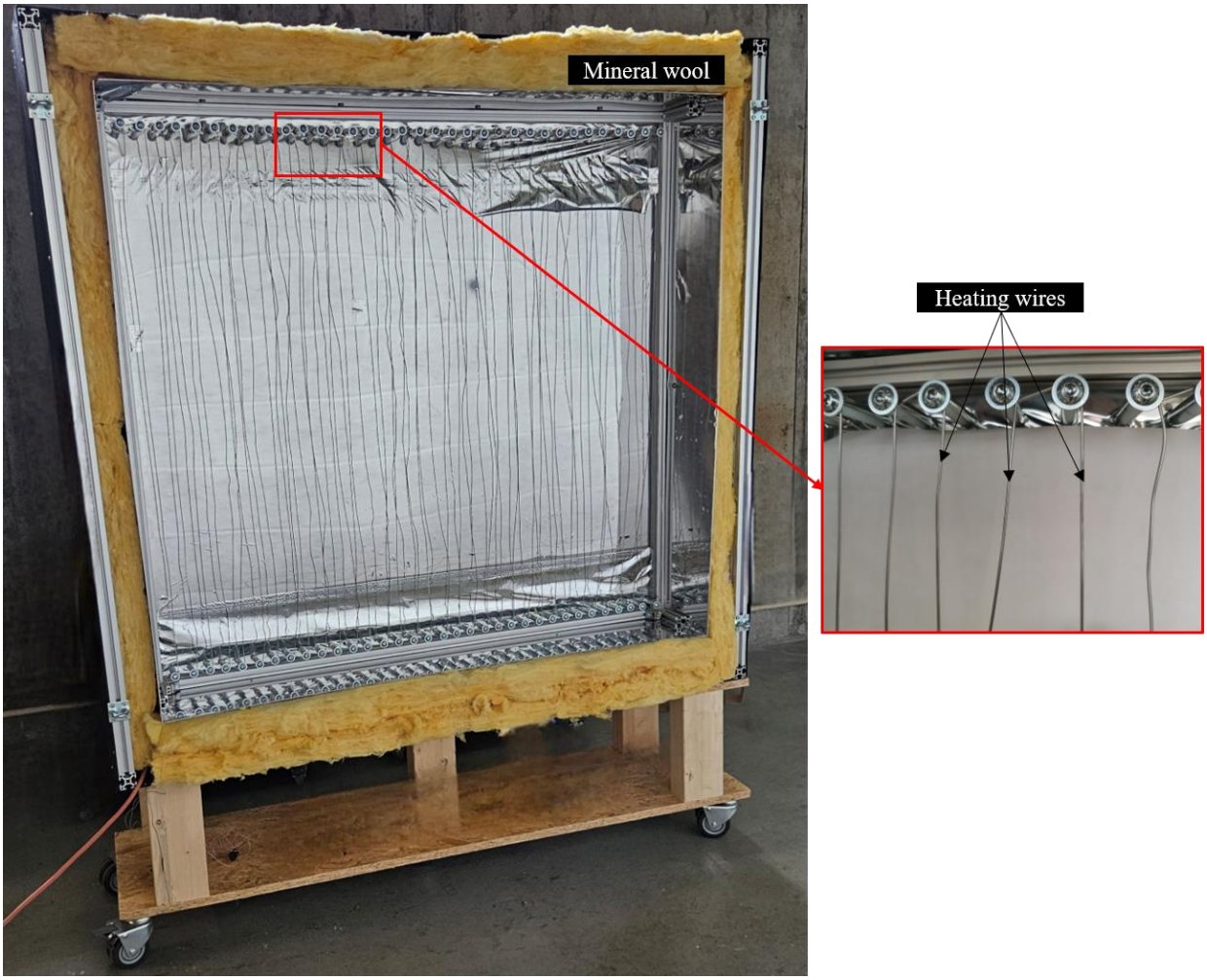

Figure 7: Pictures of the heating system for the regeneration of the adsorber. Left: Full heating system with insulation. Right: Detail of the heating wires.

3. Experimental procedure

3.1 Initial leak test

The three components adsorber, condenser, evaporator are evacuated after installation into the laboratory setup and leak tests are performed for more than 60 h to check if no leaks raised during the transport of the components or the installation. This further ensures that the system is vacuum tight and minimizes the risks for issues due to inert gases in the low-pressure system during the operation.

3.2 Cooling tests

The first cooling tests are performed after commissioning of the system with the new adsorbent zeolite 13X. For this reason, the water uptake levels are lower as in the later operation. Nevertheless, these tests allow to test the system under ideal regeneration conditions.

The cooling tests start with the connection of the adsorber and the evaporator, which immediately induces both adsorption of vapor and thus, evaporation in the evaporator. To investigate the full potential of the adsorption system, the temperature control of the evaporator is not applied. The temperatures of the vapor and water inside the evaporator as well as the temperature distribution in the test chamber are measured.

4. Results and discussion

4.1 Initial leak test

The results of the initial leak test can be seen in Figure 8. For each component the data of two pressure sensors are evaluated. It is found that all components are free of any leaks as there are no significant pressure increases over time. The pressure levels inside the evaporator and condenser are almost constant since they are tested empty and the small differences between the two sensors are within the measurement inaccuracies.

The leak test of the adsorber is done after it was filled with zeolite 13X and before the final complete evacuation. Thus, some gas molecules were still inside, which explains the slightly higher pressure levels compared to the condenser and evaporator as well as the higher fluctuations due to ad-/desorption processes. Nevertheless, it is clearly found that the adsorber is vacuum-tight and the differences between the two pressure sensors are within the measurement inaccuracies.

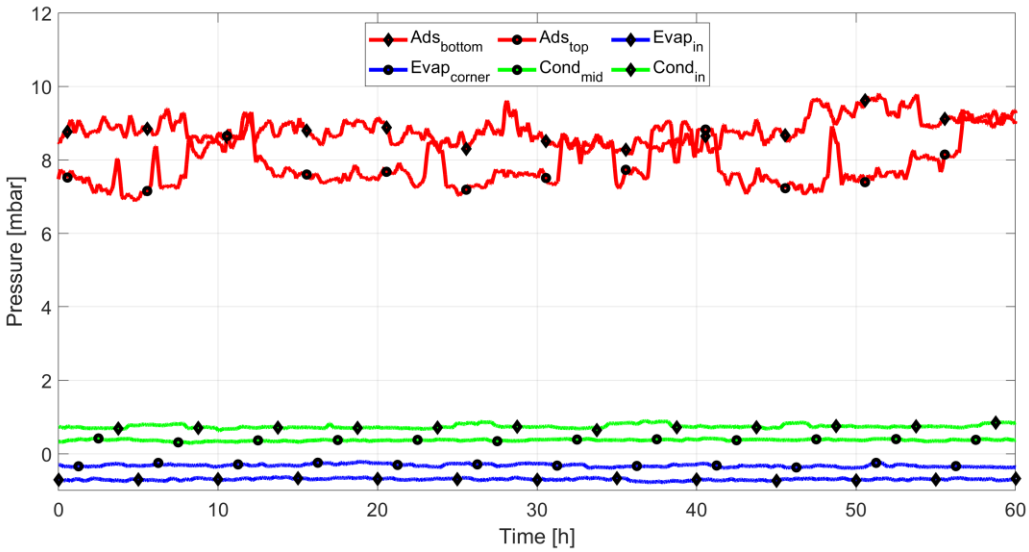

Figure 8: Evolution of the pressures inside the three components adsorber (red), condenser (green) and evaporator (blue) over time during the initial leak tests.

4.2 Cooling tests

Three cooling tests are performed during the commissioning of the novel developed facade integrated adsorption system for solar cooling. The first two tests take only around 1.5 hours, while the third test was performed over 24 hours. The results of the last test are shown in Figure , where the blue curve is the temperature at the central outer bottom of the evaporator and red as well as the green curves are the measurement data of the four sheath thermocouples that are fed into the evaporator.

It is found that a minimal temperature of around 6 °C was reached inside the evaporator. The bottom of the evaporator, which is in contact with the room to be cooled, is cooled down to below 9 °C and this a temperature

below 10 °C can be maintained for more than 15 h. Furthermore, a stable stratification of the water temperature can be seen with the minimum temperature close to the bottom and the highest temperature at the top. This is favorable since the vapor pressure inside the evaporator is mainly influenced by the temperature at the top of the water phase. High pressure levels increase the adsorption rate and thus lead to a higher evaporation.

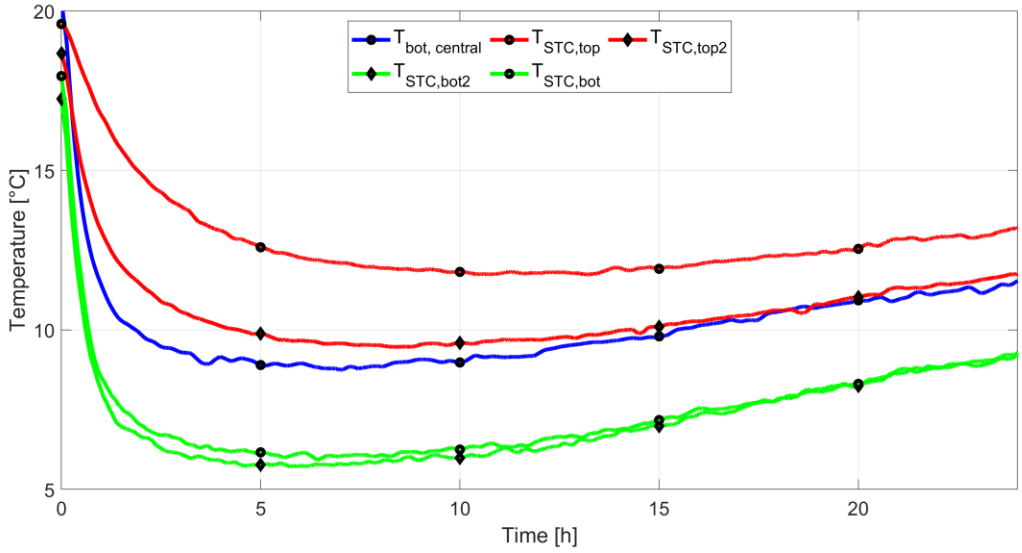

Figure 9: Evolution of temperatures at the central outer bottom (blue) and inside the evaporator over time during the 24h commissioning test.

The comparison of the temperature at the central outer bottom of the evaporator for the three tests shows similar cooling decreases, see Figure 10. The first test was stopped after approximately 1 hour, when the evaporator had reached 14 °C.

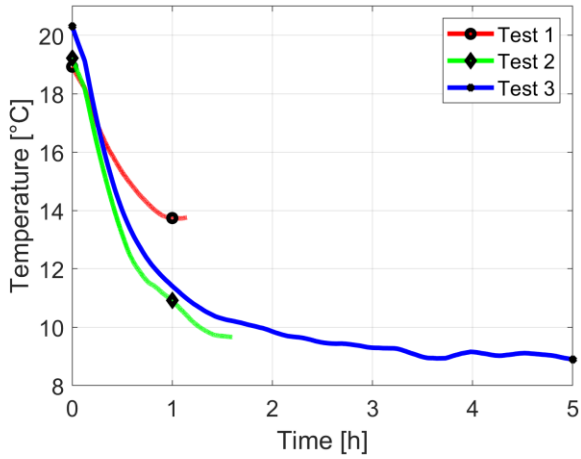

Figure 10: Evolution of bottom temperatures of the evaporator during three commissioning tests.

5. Conclusion and Outlook

In this work, the experimental setup of a novel facade-integrated adsorption system for solar cooling of buildings as well as first measurement results are presented.

The initial leakage tests confirmed that the system is vacuum tight as no pressure increases are found inside the main components adsorber, condenser and evaporator. Furthermore, it is found that minimum pressure levels below 1 mbar are reached by the evacuation process.

The first cooling tests with highly desorbed adsorbent zeolite 13X prove the practical functionality of the proposed cooling system. Minimum evaporator temperatures of around 6 °C are found and the outer bottom of the evaporator could be maintained below 10 °C for over 15 hours.

The future work will start with the regeneration process and will perform experiments with full daily cycles under various ambient conditions as well as different control strategies. Furthermore, the experimental results will be used to validate the simulation models.

6. Acknowledgements

The authors thank the Deutsche Forschungsgemeinschaft (DFG, German Research Foundation) for funding this work within the Collaborative Research Center CRC1244 ‘Adaptive skins and structures for the built environment of tomorrow, subproject C06, under SFB1244-279064222.

7. References

Allouhi, A.; Kousksou, T.; Jamil, A.; El Rhafiki, T.; Mourad, Y.; Zeraouli, Y. (2015): Optimal working pairs for solar adsorption cooling applications. In: *Energy* 79, S. 235–247. DOI: 10.1016/j.energy.2014.11.010.

Boeckmann, Olaf; Marmullaku, Drin; Schaefer, Micha (2024): Dyanmic modeling and simulation of a facade-integrated adsorption system for solar cooling of lightweight buildings. In: *Energies*.

Bujok, Tomasz; Sowa, Marcin; Boruta, Piotr; Mika, Łukasz; Sztekler, Karol; Chaja, Patryk Robert (2022): Possibilities of Integrating Adsorption Chiller with Solar Collectors for Polish Climate Zone. In: *Energies* 15 (17), S. 6233. DOI: 10.3390/en15176233.

Cabeza, Luisa F.; Solé, Aran; Barreneche, Camila (2017): Review on sorption materials and technologies for heat pumps and thermal energy storage. In: *Renewable Energy* 110, S. 3–39. DOI: 10.1016/j.renene.2016.09.059.

Chauhan, P. R.; Kaushik, S. C.; Tyagi, S. K. (2022): Current status and technological advancements in adsorption refrigeration systems: A review. In: *Renewable and Sustainable Energy Reviews* 154, S. 111808. DOI: 10.1016/j.rser.2021.111808.

Greiner, Andreas; Böckmann, Olaf; Weber, Simon; Ostermann, Martin; Schaefer, Micha (2022): CoolSkin - A Novel Facade Design for Sustainable Solar Cooloing by Adsorption. In: *JFDE* 10 (2), S. 39–56. DOI: 10.47982/jfde.2022.powerskin.3.

Hallström, Olof; Füldner, Gerrit; Spahn, Hans-Joseph; Schnabel, Lena; Salg, Frank (2014): Development of Collector Integrated Sorption Modules for Solar Heating and Cooling: Performance Simulation. In: *Energy Procedia* 48, S. 67–76. DOI: 10.1016/j.egypro.2014.02.009.

Liang, Jingkang; Zhao, Wenkui; Wang, Yunfeng; Ji, Xu; Li, Ming (2023): Effect of cooling temperature on the performance of a solar adsorption chiller with the enhanced mass transfer. In: *Applied Thermal Engineering* 219, S. 119611. DOI: 10.1016/j.applthermaleng.2022.119611.

Mat Wajid, Norhayati; Zainal Abidin, Abdul Murad; Hakemzadeh, Mirhamed; Jarimi, Hasila; Fazlizan, Ahmad; Fauzan, Mohd Faizal et al. (2021): Solar adsorption air conditioning system – Recent advances and its potential for cooling an office building in tropical climate. In: *Case Studies in Thermal Engineering* 27, S. 101275. DOI: 10.1016/j.csite.2021.101275.

United Nations Environment Programme (2020): 2020 Global Status Report for Buildings and Construction.

Wang, Zepeng; Yuan, Zhongxian; Du, Chunxu; Liu, Yimo; Wang, Jie (2022): Performance of solar adsorption cooling system with internal finned vacuum tube bed. In: *Case Studies in Thermal Engineering* 34, S. 102063. DOI: 10.1016/j.csite.2022.102063.

Appendix

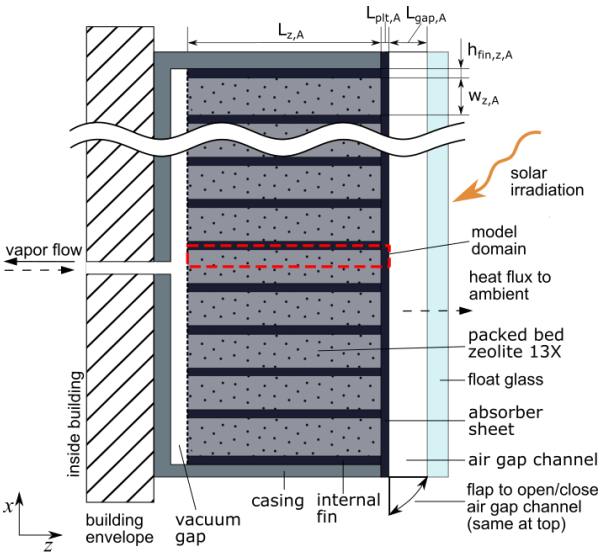

Figure 11: Design scheme of the adsorber (cross-section side view). The scheme is not to scale as the height is approximately 0.9 m, while the width in z-direction is only approximately 9 cm. The absorber sheet is equipped with metal fins inside the air gap channel (not depicted). (Boeckmann et al. 2024)

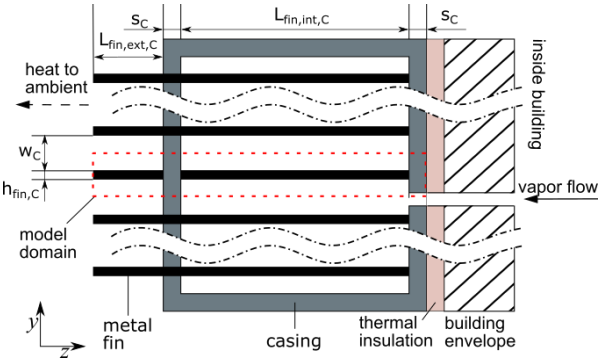

Figure 12: Design scheme of the condenser (cross-section top view). The scheme is not to scale as the width in y-direction is approximately 1.1 m, while the depth in z-direction is only approximately 9 cm. (Boeckmann et al. 2024)

Towards designing and evaluating solar cooling integrated façades in office buildings

Hamza Hamida[1], Alejandro Prieto[2], Lourdes Beneito[3], Thaleia Konstantinou[1] and Ulrich Knaack[1]

[1] Department of Architectural Engineering + Technology, Faculty of Architecture and the Built Environment, Delft University of Technology, Julianalaan 134, 2628BL Delft, the Netherlands

[2] School of Architecture, Diego Portales University, República Av. 180, 8370074, Santiago, Chile

[3] School of Architecture, Department of Construction, Facilities and Structures, University of Navarra, Campus Universitario Universidad de Navarra, Pamplona, 31009, Navarra, Spain

Abstract

The present research proposes a framework to design and evaluate façade products integrating solar cooling technologies (SCTs), applied in an office building in a Southern Europe region. The building comprises various types of façade elements, such as opaque walls, glazed curtain walls, overhangs, and balconies. Key regulatory measures were implemented considering national energy saving regulations. The results represent annual energy consumption (kWh/m^2/year) and the average daily cooling demand in Summer Design Week (kWh/day) of the simulated base model. This energy consumption lies within range of a previously simulated generic office and the average annual energy consumption of office blocks. Potential scenarios for integrating SCTs were outlined and evaluated using the solar fraction (SF) as an indication to measure the potential performance of the system based on nominal efficiencies, providing an initial reference of its ability to meet cooling demands, an essential step in early design stages. Scenarios per configuration related to double-effect chillers with evacuated tubes collectors and water-cooled vapor compression chiller and photovoltaic (PV) panels were the only one having an SF value of 1 or more, meaning that they can be able to handle the required cooling demand. Future steps should consider a second level of technical evaluation of scenarios having SF values of 1 or more, which should involve aspects related to how to physically integrate the technology, considering compactness and space usability and also maintenance requirements, among other relevant criteria.

Keywords: Semi-arid climate, thermal envelope, solar fraction, PV panels

1. Introduction

Cooling demands in the built environment have been estimated to have a dramatic increase in the coming decades as a result of climate change and the growth in the global population (Enteria and Sawachi, 2020; Sahin and Ayyildiz, 2020; Santamouris, 2016). Accordingly, this demand increase can lead to a rise in the use of cooling systems depending on energy generated in power plants in order to meet thermal comfort requirements (Santamouris, 2016). Consequently, supporting the use of cooling systems relying on renewable energy is becoming more important to reduce greenhouse gas (GHSs) emissions generated from energy consumed by conventional cooling systems. Therefore, the façade integration of solar active cooling technologies can have an important role in minimizing the use of conventional cooling systems since façades are usually highly exposed to solar radiation. Hence, solar energy can be harvested through the façade in order to drive cooling systems (Prieto et al., 2017).

The integration of solar active technologies in facades can be defined as "building envelope systems that include elements using and/or controlling solar radiation to deliver self-sufficient solar renewable electric and/or thermal energy needed to generate cooling effect in a particular indoor environment" (Hamida et al., 2023c). It should be noted that providing design approaches to professionals who lack the experience with such technologies can have a vital role in enabling the widespread application (Saini and Weiss, 2023). Hence,

© 2024. The Authors. Published by International Solar Energy Society
Selection and/or peer review under responsibility of Scientific Committee
10.18086/eurosun.2024.08.02 Available at http://proceedings.ises.org

this study presents initial findings of an ongoing research aiming to propose a framework supporting designers at early stages to design and evaluate façade products integrating solar cooling technologies to meet the cooling demand of a particular building. The framework proposition is based on a "research through design" methodology considering the development of design alternatives and their evaluation with respect to relevant design criteria.

The framework focuses on designing and evaluating such façade products for office buildings located in Southern European climates. The Spanish context has been selected with a focus on Madrid as a case study, which had as a cold semi-arid climate according to Koppen Geiger classification (Del Ama Gonzalo et al., 2023). Spain is ranked as the third country in the European Union (EU), after Malta and Cyprus, in terms of cooling demands. The increase in temperatures in the country has resulted in a greater demand for cooling systems. In addition, the Spanish cooling demand has raised by around 2.6 times during the last four decades (Inspain News, 2023). Furthermore, Spain tends to have large office market and investments. The country had total of €728 million invested on the offices in the first half of year 2023. Madrid accounted total of €471 million (65% of total office investment) (Cushman & Wakefield, 2023). In addition, Madrid city had the greatest share (40%) of European business and professional services which can have a direct relation with office demand (Savills Commercial Research, 2023).

2. Research Methods

To propose a framework for designing and evaluating SCIFs, this study is based on a "research through design" strategy. Therefore, the adopted strategy for the proposed framework is based on gathering and organizing relevant information needed to design and evaluate solar cooling integrated facades considering the definition of (Hamida et al., 2023c).

2.1. Key Design Stages

The aim of the research is to support designers at early key design stages to design a suitable product able to meet the cooling demand. This is due to the fact that having proper design can avoid many issues as well as ensure proper assembly and operation (Hamida et al., 2023a, 2023b). There are various ways and categorizations of design and construction stages that are available in the literature, including RIBA workplan for all disciplines on the construction industry (RIBA, 2020), integrated design and construction processes for new building construction and renovation projects identified by (Oliveira and Melhado, 2011), key phases associated with zero-energy residential building renovation (Prieto et al., 2023), and the façade design and construction processes associated with the curtain wall industry that were identified by (Klein, 2013). Hence, it is essential to have key identified design stages that can be used for proposing the framework through the case study. A total of four stages have been identified, namely (i) conception and strategic definition, (ii) preparation and briefing, (iii) façade technological selection, and (iv) architectural design. This paper presents results related to the conception and strategic definition as well as part of the preparation and briefing, as indicated throughout the paper.

2.1.1. Conception and Strategic Definition

The key outcomes of this stage include the establishment of possibilities related to integrating solar cooling technologies into the façade by taking into account different requirements and considerations, namely legal prerequisites as well as the building requirements. The legal prerequisites consider national guidelines related to energy savings. The building requirements consider that the definitions of solar active cooling integrated façades include having a self-sufficient solar renewable electric and/or thermal energy needed to generate cooling effect in a particular indoor environment (Hamida et al., 2023c). To obtain possibilities of façade integration as a main outcome of the conception and strategic definition phase, a set of three steps should be followed:

- Establishment of reference building model: The establishment of the reference building requires detailed descriptions of different aspects, such as geometry, location, occupancy profile, set-point temperatures. Such reference building can be considered as a benchmark for investigating different scenarios (Ochs et al., 2020). Accordingly, it was essential to identify constant and variable parameters to define the basis of the reference model (Ferrari and Zanotto, 2016). Therefore, key

inputs should include the project characteristics (building size and location). Hence, main tools considered were data collection and market survey, which involved identifying the two main aspects needed to establish the base model. The first one includes assumptions of constant parameters which are climate contexts, internal heat loads (occupancy schedule and density based on the number of people per square meter), heating, cooling, and air-conditioning (HVAC), and air infiltration. The second one includes construction characteristics of the thermal envelope elements according to national energy saving guidelines.

- Assessment of energy performance of reference model: Considering the established base model, assessing its performance was carried through performing different sets of dynamic energy simulations using DesignBuilder 7.0.2.006, which is a graphical interface software of EnergyPlus. Such sets of simulations aim to assess the energy and cooling demands and compare the building energy performance with relevant data, and determine and select the suitable building base model. Energy simulations considered all thermal zones to assess the building energy performance at four different orientations, which included orienting the building main entrance to the North (N), South (S), East (E), and West (W) directions.
- Identification of possibilities for façade integration: The identification of such possibilities took into account relevant technologies to be involved in the process of generating and evaluating scenarios with respect to different criteria. The possibilities for integrating technologies into the façade are identified based on determination of key configurations of selected technologies and establishment of matrix of possibilities for integrating technologies into the façade.

2.1.2. Preparation and Briefing

This phase aimed to assess the technical and economic feasibility of the generated possibilities, and to determine functional requirements. This study provides the initial findings related to the pre-feasibility technical evaluation of different scenarios, which is based on assessing the product performance and efficiency and the ability to meet user cooling requirements. Considering that the definitions of solar active cooling integrated façades indicated by (Hamida et al., 2023c), it is essential to have a particular indicator that takes into account different aspects. These aspects include the delivered solar renewable electric and/or thermal energy, the generated cooling effect in a particular indoor environment, and the cooling demand in such environment. One of the commonly used measurements considering such aspects while enable evaluating the technical feasibility of product applicability is based on calculating the Solar Fraction (SF) (Noaman et al., 2022; Prieto et al., 2018a). Two main parameters are divided, namely cooling effect delivered by the selected technology and cooling demand of a particular indoor environment as shown in equation 1. Equation 2 and table 1 indicate the detailed calculations for all parameters needed to assess the SF. The SF value was assessed considering daily solar availability as key input and daily cooling demands during the summer design week, which involves the most crucial period in summer season according to the weather data file.

$$SF = SCOOL_{out}/COOL_{req} \quad \text{(eq. 1)}$$

$$SCOOL_{out} = SOL_{input} \times SOL_{arry} \times COP_{solarsys} \times COP_{coolsys} \quad \text{(eq. 2)}$$

2.2. Solar Cooling Technologies

This study aimed to involve relevant options for both of solar electrically-driven and thermally- driven technologies, which are involved in the process of generating and evaluating scenarios with respect to design criteria. For electrically-driven systems, the use of Photovoltaic (PV) for cooling through coupling it with conventional heating, ventilation, and air conditioning (HVAC) systems provide advantages related construction simplicity and high efficacy. Furthermore, the maturity and advancement of PV technologies was considered as a key factor supporting the widespread integration of electrically-driven solar cooling technologies into façades (Hamida et al., 2023a). For thermally-driven technologies, solar absorption cooling was identified to be a relevant option as it is a mature technology and has a high growth rate compared to other thermally-driven systems (Alsagri et al., 2020). In addition, solar absorption chillers are globally popular in the market of solar cooling technologies. This is because of their high coefficient of performance (COP) values compared to other technologies (Alahmer and Ajib, 2020). Furthermore, solar absorption cooling technologies were found to have relevant technical feasibility at different climate contexts (Prieto et al., 2018a, 2018b).

Tab. 1: Assessment of pre-technical feasibility (Noaman et al., 2022; Prieto et al., 2018a)

Item	Parameter						SF
	$COOL_{req}$	**SOL_{input}**	**SOL_{arry}**	**$COP_{solarsys}$**	**$COP_{coolsys}$**	**$SCOOL_{out}$**	
Description	Average daily cooling demand in summer design week of a particular indoor environment	The average daily solar radiation availability on a particular location/orientation considering the month of summer design week.	Designed area for collection	Efficiency of the applied solar collection system, that can be either PV panels or solar thermal collectors (STCs)	Coefficient of performance of the cooling technology	Cooling effect delivered by the selected technology to a specific indoor environment, represents heat removed by cooling technology	Solar fraction of the designed façade system
Unit	kWh/day	kWh/m^2/day	m^2	Unitless	Unitless	kWh/day	Unitless
Assessment Method	Use of dynamic energy simulation software, such as DesignBuilder 7.0.2.006	Use of dynamic energy simulation techniques, such as the System Advisor Model (SAM) 2023.12.17 software	Calculation of the amount of the installed units of PV or STC	Published technical reports/case studies	Published technical reports/case studies	By using eq. 2	By using eq. 1
Notes	Having an SF value of 100% and more indicates that the system can be able to handle the required cooling demand						

2.3. Standards and Regulations

It is crucial to include key aspects in the decision-making process for integrating technologies into building façades. According to (Prieto et al., 2017), the design and development of solar cooling integrated façades are only worth pursuing when all other passive measures are unable to meet indoor requirements. Accordingly, the study aims to reduce cooling demand using relevant guidelines as a first step. Hence, his study considers the Spanish energy saving regulations to optimize the building design by implementing necessary passive measures to lower energy demand (CTE, 2022a). Although some researchers used the Passive House Standard, (Borrallo-jiménez et al., 2022) indicated that applying the Passive House standard could not provide competitive benefits related to improving the building energy performance when it is compared to the local Spanish regulations. It should be noted that the efficiency improvement of the European building sector has been identified to be addressed by two main instruments, namely the Energy Performance of Building Directives (EPBD) and also the Energy Efficiency Directives (EED) (de Arriba Segurado, 2021). The Spanish Technical Building Code, El Código Técnico de la Edificación (CTE), contributes to transporting such directives into the legal system by modifying the Basic Document, Documento Básico (DB-HE) (CTE, 2022b). Such document provides rules and procedures allowing basic energy saving requirements to be met.

2.4. Building Case

The consideration of a typical building case in a particulier context contribute to demonstrating the framework

applicability from practical point of view. Taking into account that the building industry is fragmented with various construction materials and systems, (Ebbert, 2010) sorted various office façade typologies in Western Europe systematically in a matrix in order to have an insight into the functions of different façade types so that various façade refurbishment strategies can be developed and applied. However, many of existing office buildings tend to have a combination of various façade types and elements, such curtain walls, double façades, shading devices and overhangs. This makes the consideration of a particular façade typology can be a challenging task since every project is unique. Accordingly, proposing the framework by considering a generic typical office with various façade types and elements is an essential to demonstrate its applicability in practice through determining different possibilities for façade integration. Hence, the selected building case in a generic office 5-story building. Each floor has a hight of 4.2 m. The ground floor has its own layout in terms of sizes and numbers of thermal zones and spaces functions, such as office areas and storerooms, while first and second floors have similar layouts. The third, fourth, and fifth floors have similar layouts. The key characteristics of this building are that they take into account the common features of newly constructed office buildings in major European cities (Costanzo and Donn, 2017). Majority of the external walls consist of glazed units attached to a concrete structure, although the backside of the building are opaque walls. The building presents flat concrete roof surfaces that are bitumised. Table 2 and Figure 1 provide an overview of the selected building case for framework proposition.

Tab. 2: Overview of the selected building case for framework proposition

Item	Description	Values
Altitude	Altitude with respect to sea level	655 m
Ground floor area	Ground has its own same layout	2695.68 m^2
First/second floor area	First and second floors have same layout and sizes	2851.2 m^2
Third/Fourth/fifth floor area	Third, fourth and fifth floors have same layout and sizes	1866.24 m^2
Gross floor area	Sum of all floor areas	13996.8 m^2
Floor height	All floors have an equal hight	4.2 m
Window-to-Wall Ratio (WWR)	Proportion of exterior glazed walls	55%

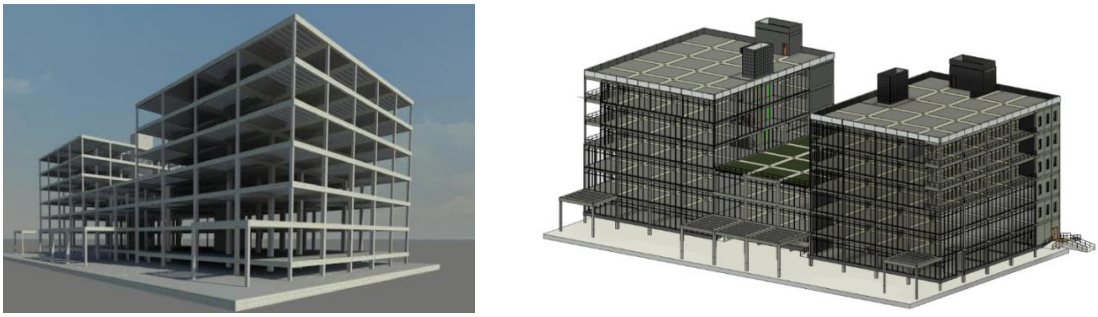

Fig. 1: Selected building case

3. Results

This section presents the findings of the conception and strategic definition phase (sections 3.1) as well as part of the preparation and briefing phase (sections 3.1). Hence, section 3.1 provides the results of the established reference model, and also identified possibilities for façade integration. On the other hand, section 3.2 shows findings of assessing the technical feasibility of generated possibilities based on the SF values.

3.1. Conception and Strategic Definition

As indicated in section 2.1.1, the key outcomes of this stage include the establishment of possibilities to integrate solar technologies into the façade by taking into account different requirements, legal and building prerequisites and specifications. The legal requirements in this study were considered based on Spanish guidelines related to energy savings (CTE, 2022a). Table 3 shows the building and façade characteristics, including Window-to-Wall ratio (WWR), of the reference model when considering different orientation of the building main entrance.

Tab. 3: WWR and thermal zones of simulated base case scenarios

Item		**Orientation of the Building Main Entrance**			
		N	**S**	**E**	**W**
WWR	Total	0.55	0.55	0.55	0.55
	North	0.84	0.01	0.71	0.71
	South	0.01	0.84	0.71	0.71
	East	0.71	0.71	0.84	0.01
	West	0.71	0.71	0.01	0.84
Number of thermal zones in the ground floor	Ground has its own layout	15 zones			
Number of thermal zones in the 1st /2nd floor area	First and second floors have the same layout	14 zones			
Number of thermal zones in the 3rd/4th /5th floor area	Third, fourth and fifth floors have the same layout	10 zones			
Total Number of thermal zones	Sum of all zones	73 zones			
Spaces functions		Generic office areas, storerooms, toilets, dining rooms, and light plant rooms			

Figure 2 shows simulation outcomes that include the annual building energy use intensity while Figure 3 indicates the building average daily cooling demand in summer design week of (COOLreq) (kWh/day). The results of the simulated base model revealed considering all orientations ranged between 227.02 and 230.96 [kWh/m^2/year] for orienting the building main entrance to the North and South, respectively. These values were compared with other values in literature to have an initial validation of simulated reference base case. Considering the simulated office case by (Cortiços and Duarte, 2022) at different European climates considering Spanish energy savings requirements, the annual energy consumption in Madrid was estimated to be between 192.2 and 242.23 [kWh/m^2]. Considering this range of energy consumption, the building energy consumption simulated base case lies within this range.

According to simulation outcomes, it is shown that the orientation of the main entrance to the north, where opaque façade on the south side as well as shaded balconies are on the Ease and west sides, resulted in the lowest building energy use intensity and cooling demand intensity in both of yearly and summer design week time periods. On the other hand, orienting the building main entrance to the north had the highest energy and cooling demand. Hence, orienting the building main entrance has been selected as the building base case for generating and evaluating the scenarios.

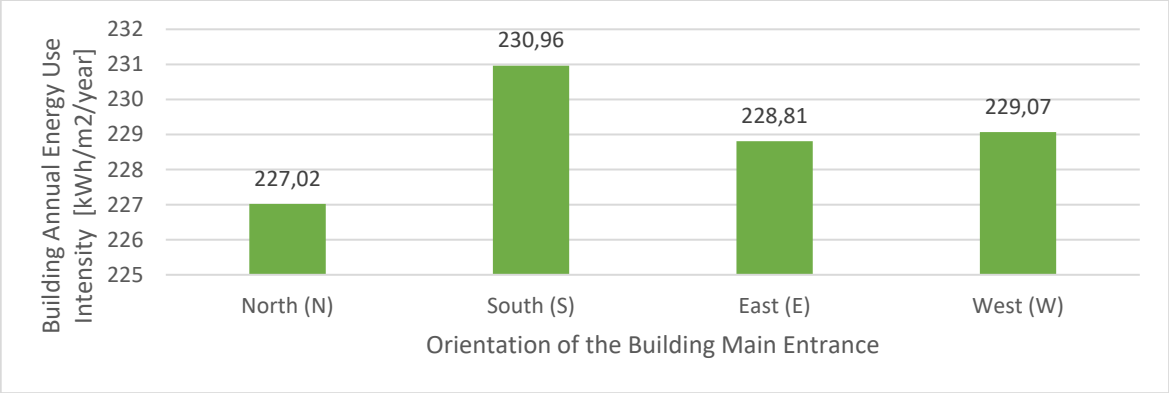

Fig. 2: Building annual energy use intensity according to the orientation of the building main entrance

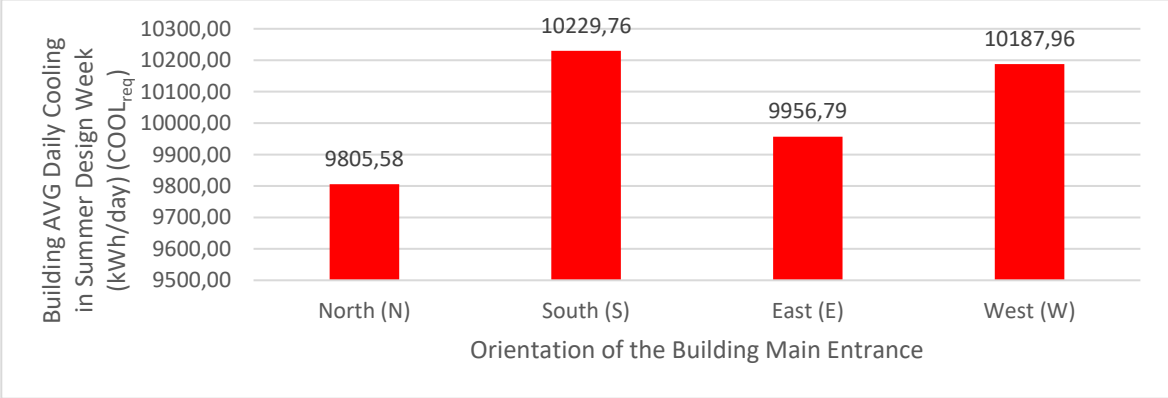

Fig. 3: Building average daily cooling demand in Summer Design Week (COOLreq) according to the orientation of the building main entrance

Based on the selected reference model, the identification of such possibilities took into account relevant technologies to be involved in the process of generating and evaluating scenarios with respect to different criteria, namely SF in the present paper. The generation of scenarios was based on the establishment of matrix of possibilities for integrating both technologies into the façade, which facilitated estimating SOL_{arry} (Table 5). It also considered different configurations of solar cooling technologies, which facilitate determining the $COP_{solarsys}$ $COP_{coolsys}$ of components related to both technologies (Table 5) (Alahmer and Ajib, 2020; Ayou and Coronas, 2020; Cortiços and Duarte, 2022; Mugnier et al., 2017; Prieto et al., 2018a).

Tab. 4: Matrix of possibilities for integrating both technologies into the façade

Envelope Possibilities	Scenarios Per Configuration and Key Design Features	Graphical Representation
A. Rooftops only	A.I. Installing solar collection devices on rooftops with a particular tilt angel (30°) and orientation (S), and different use factors (0.25, 0.40, 0.50, and 0.60)	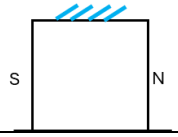
B. Façade only	B.I. Only vertical attachment of solar collection devices along the external layer of the opaque façades (Backside of the building-opposite to the main entrance)	
	B.II. Same as B.I with additional overhangs on the top of window of the first floor dining rooms for installing the collector at different tilt angles (60°, 30°, and 0°)	

Tab. 4: Matrix of possibilities for integrating both technologies into the façade (cont.)

Envelope Possibilities	Scenarios Per Configuration and Key Design Features	Graphical Representation
B. Façade only	B.III. Same as B.II with additional vertical attachment of solar collection devices along the external layer of balcony rails and roofs	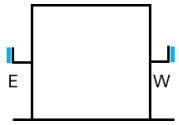
C. Rooftops & Façade	C.I. Combination of A.I and B.I	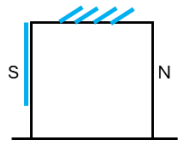
	C.II. Combination of A.I and B.II	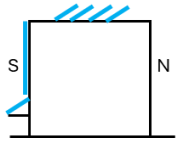
	C.III. Combination of A.I and B.III	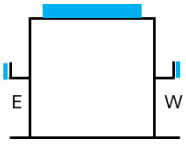

Tab. 5: Key information required to generate scenarios

Item	Thermally Driven Technology			Electrically Driven Technology
	Single-effect (SE) absorption chillers and flat-plate collectors (FPCs)	Single-effect (SE) absorption chillers and evacuated tubes collectors (ETCs)	Double-effect (DE) absorption chillers and evacuated tubes collectors (ETCs)	Water-cooled vapor compression chiller (VCC) and PV panel
$COP_{coolsys}$	0.70	0.70	1.20	2.60
$COP_{solarsys}$	0.60	0.65	0.65	0.22

3.2. Preparation and Briefing

This phase aimed to assess the technical feasibility of the generated possibilities in Table 4, to determine the technical feasible scenarios having an SF value 1 or more. To assess such feasibility, two key steps were considered, namely assessing of solar energy input to the system and then assessing the SF value of each scenario considering Table 2.

3.2.1. Assessment of Solar Energy Input to the Façade System

This step aimed at assessing solar energy input to the façade system through considering different physical positioning of the solar collection devices in the building envelope, such as rooftops, vertical facades or overhangs. The assessment was carried out by estimating the average daily solar radiation availability on a particular location/orientation (SOL_{input}) (kWh/m^2/day) considering the month of summer design week of Madrid, July. Such assessment was performed using the simulation tool of System Advisor Model (SAM) 2023.12.17 software and the EnergyPlus weather file of Madrid, which is the same file used on DesignBuilder 7.0.2.006 software. Figure 4 provides the daily average solar irradiation of 90^o, 60^o, 30^o, and 0^o tilted plane, respectively, for the summer design month of Madrid.

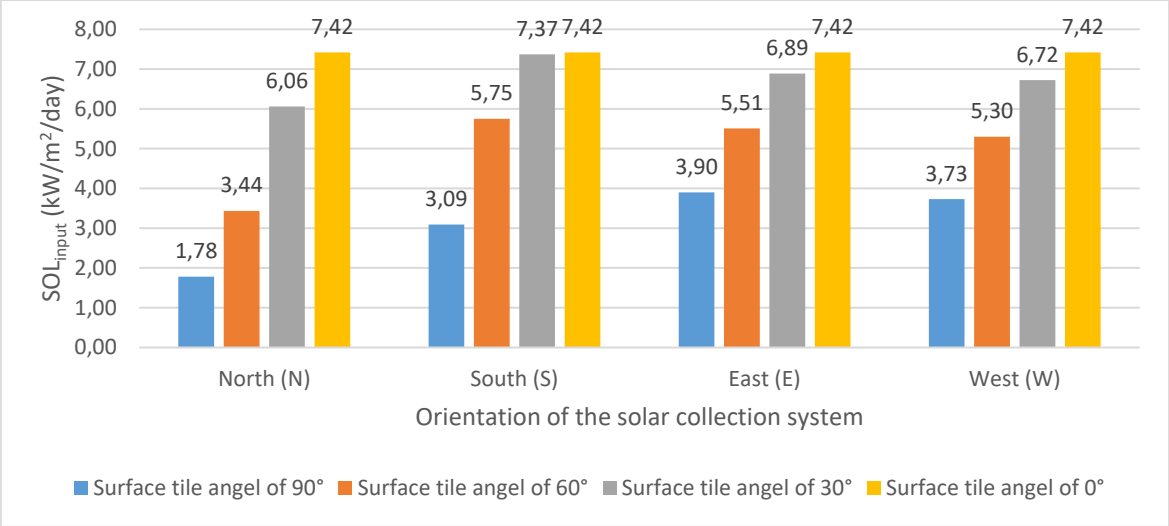

Fig. 4: SOL$_{input}$ at different orientations of the solar collection system considering the month of summer design week

3.2.2. Assess the Product Technical Feasibility based on the SF

Considering key parameters required to assess the SF (Table 1), assessed SOL$_{array}$ of solar collection devices of different scenarios (Table 4), efficiencies considered for different components of technologies (COP$_{solarsys}$ and COPc$_{oolsys}$) (Table 5), and assessed solar energy input to the façade system (Figure 4), the SF values for all scenarios were assessed. The results of assessing the SF values of the three main envelope possibilities, namely rooftops only (A), facades only (B), and also rooftops & façade (C) are shown in Figures 5, 6 and 7, respectively. As mentioned in Table 2, having an SF value of 100% and more indicates that the system can be able to handle the required cooling demand. Hence, it is shown that some of the scenarios per configuration related to DE absorption chillers and ETCs (thermally driven) and water-cooled VCC and PV panel (electrically driven) were the only one having an SF value of 1 or more. Furthermore, only DE absorption chillers and ETCs were able to meet the cooling requirements by considering only rooftops installations. However, none of all configurations were able to meet the cooling requirements using façade installations only, such as opaque, overhang, and balconies installations.

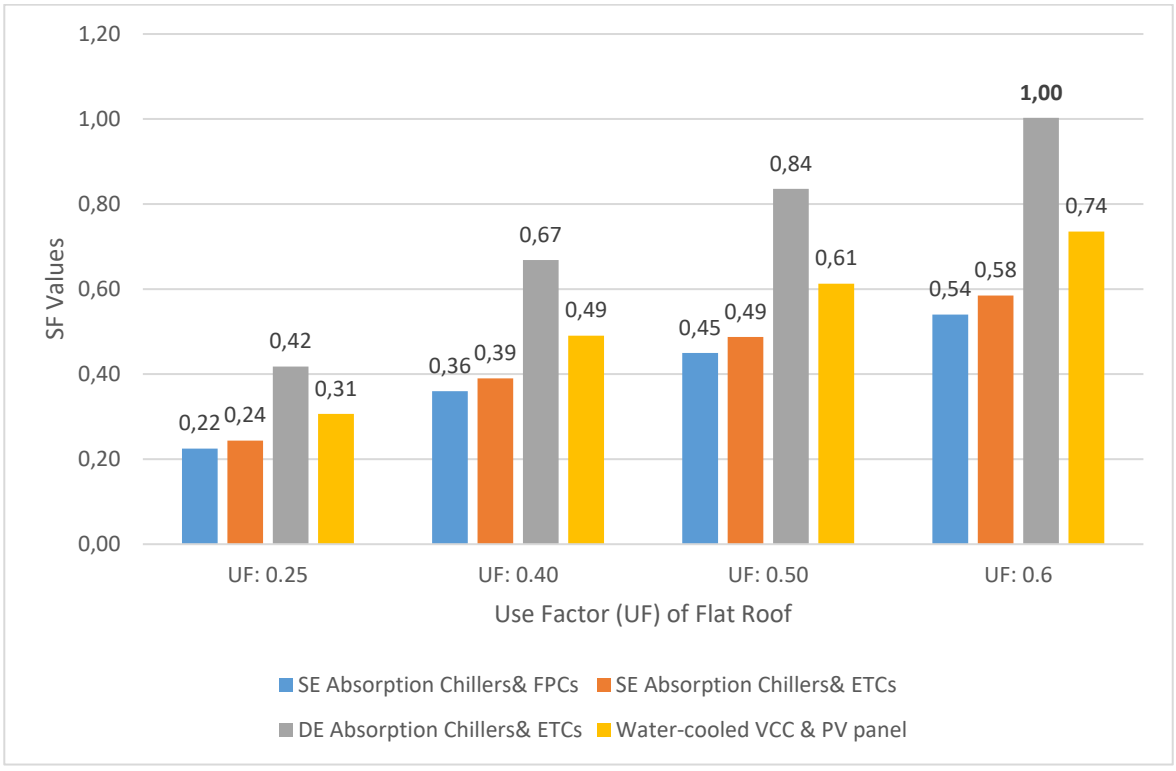

Fig. 5: Results of assessing the product technical feasibility for rooftops only (A) based on the SF

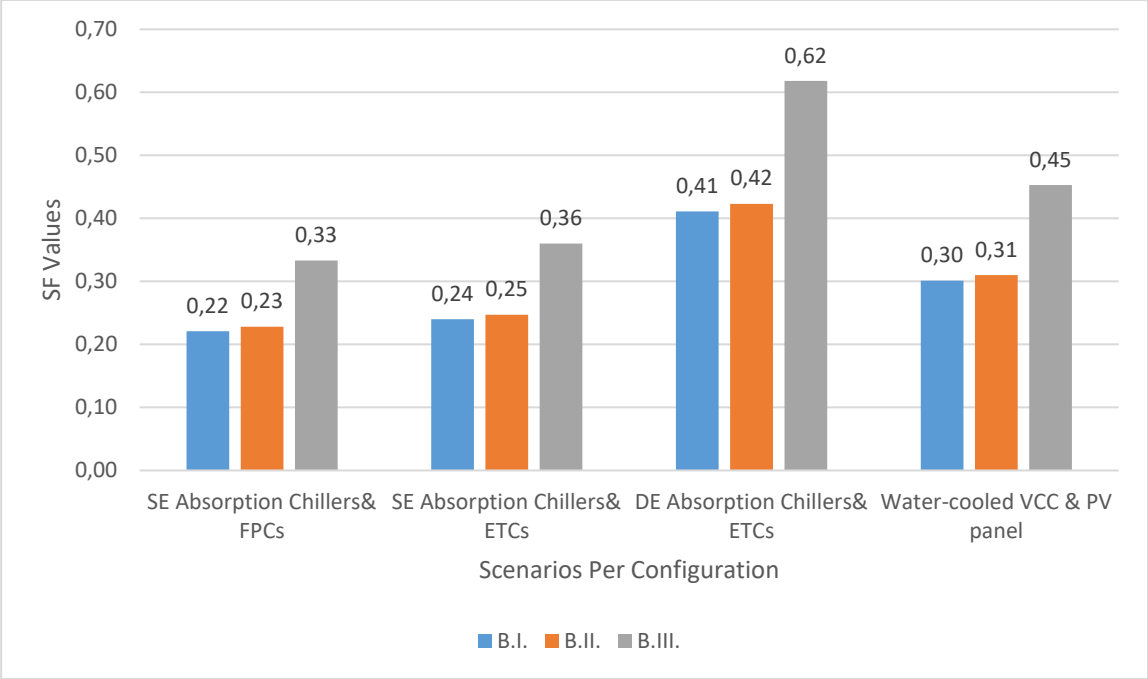

Fig. 6: Results of assessing the product technical feasibility for façades only (B) based on the SF

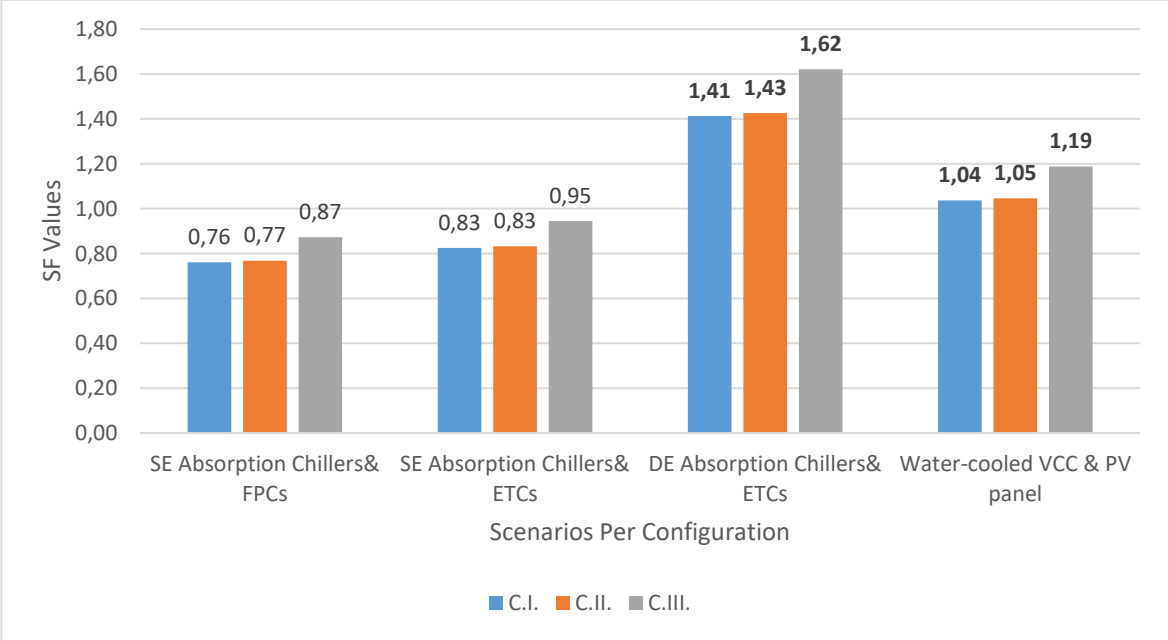

Fig. 7: Results of assessing the product technical feasibility for rooftops and façades (C) based on the SF

4. Conclusion

The present research aims to propose a framework to guide the architectural integration of solar cooling technologies (SCTs) in an office building with various façade types, located in Southern Europe. Key regulatory measures were implemented considering national energy saving guidelines. The results represent annual energy consumption (kWh/m^2/year) and the average daily cooling demand in Summer Design Week (kWh/day) of the simulated base model. This energy consumption lies within range of a previously simulated generic office and the average annual energy consumption of office blocks. Potential scenarios for integrating SCTs were outlined and evaluated using the SF as an indication to measure the product performance and

efficiency and its ability to meet cooling demand represent as essential step during early design stages. The SF value was assessed considering daily solar availability as key input and daily cooling demands during the summer design week, which involves the most crucial period in summer season according to the weather data file. Such step helps the decision regarding what type of technology and components could be selected for a second level of technical evaluation. Scenarios per configuration related to double-effect chillers with evacuated tubes collectors (thermally driven) and water-cooled vapor compression chiller and PV panel (electrically driven) were the only one having an SF value of 1 or more. Future steps should consider a second level of technical evaluation of scenarios having SF values of 1 or more involving aspects related to how to integrate the technology, which may consider the compactness and space usability, assemble and connections, and maintenance requirements. Once this second level is carried out, economic feasibility aspects can be considered to evaluate and compare pre-defined potential scenarios at a higher level of detail.

5. References

Alahmer, A., Ajib, S., 2020. Solar cooling technologies: State of art and perspectives. Energy Convers. Manag. 214, 112896.

Alsagri, A.S., Alrobaian, A.A., Almohaimeed, S.A., 2020. Concentrating solar collectors in absorption and adsorption cooling cycles : An overview. Energy Convers. Manag. 223, 113420.

Ayou, D.S., Coronas, A., 2020. New developments and progress in absorption chillers for solar cooling applications, Applied Sciences.

Borrallo-jiménez, M., Lopezdeasiain, M., Esquivias, P.M., Delgado-trujillo, D., 2022. Energy & Buildings Comparative study between the Passive House Standard in warm climates and Nearly Zero Energy Buildings under Spanish Technical Building Code in a dwelling design in Seville , Spain. Energy Build. 254, 111570 Contents.

Cortiços, N.D., Duarte, C.C., 2022. Energy efficiency in large office buildings post-COVID-19 in Europe's top five economies. Energy Sustain. Dev. 68, 410–424.

Costanzo, V., Donn, M., 2017. Thermal and visual comfort assessment of natural ventilated office buildings in Europe and North America. Energy Build. 140, 210–223.

CTE, 2022a. Documento Básico HE: Ahorro de energía.

CTE, 2022b. Presentation [WWW Document]. El Código Técnico la Edif. URL https://www.codigotecnico.org/QueEsCTE/Presentacion.html (accessed 12.11.23).

Cushman & Wakefield, 2023. Cushman & Wakefield MarketBeat reports analyse quarterly: Offices Q2 2023.

de Arriba Segurado, P., 2021. Energy renovation of buildings in Spain and the EU: Lessons learned and main recommendations. ODYSSEE-MURE Policy Briefs 1–6.

Del Ama Gonzalo, F., Moreno Santamaría, B., Montero Burgos, M.J., 2023. Assessment of Building Energy Simulation Tools to Predict Heating and Cooling Energy Consumption at Early Design Stages. Sustainability 15, 1920.

Ebbert, T., 2010. Re-Face: Refurbishment strategies for the technical improvement of office façades. Delft University of Technology.

Enteria, N., Sawachi, T., 2020. Air Conditioning and Ventilation Systems in Hot and Humid Regions. In: Enteria, N., Awbi, H., Santamouris, M. (Eds.), Building in Hot and Humid Regions: Historical Perspective and Technological Advances. Springer Nature Singapore Pte Ltd., pp. 205–219.

Ferrari, S., Zanotto, V., 2016. Chapter 5: Defining Representative Building Energy Models. In: Ferrari, S., Zanotto, V. (Eds.), Building Energy Performance Assessment in Southern Europe. Springer, pp. 61–77.

Hamida, H., Konstantinou, T., Prieto, A., Klein, T., 2023a. Solar Cooling Integrated Façades: Key perceived enabling factors and prospects of future applications. J. Build. Eng. 76, 107355.

Hamida, H., Konstantinou, T., Prieto, A., Klein, T., 2023b. Data underlying the publication: Solar Cooling Integrated Façades: Key perceived enabling factors and prospects of future applications. [WWW Document]. 4TU.ResearchData. URL https://doi.org/10.4121/bead775f-2674- 477a-85b5-cf8446291348.v1 (accessed 10.2.23).

Hamida, H., Konstantinou, T., Prieto, A., Knaack, U., 2023c. Solar Cooling Integrated Façades : Towards investigating product applicability. In: 8th International ICARB Conference 2023. Edinburgh, pp. 58–70.

Inspain News, 2023. Cooling demand in Spain multiplied by increasing heat [WWW Document]. Inspain News. URL https://inspain.news/cooling-demand-in-spain-multiplied-by-increasing-heat/ (accessed 12.5.23).

Klein, T., 2013. Integral Facade Construction: Towards a new product architecture for curtain walls. Delft University of Technology.

Mugnier, D., Neyer, D., White, S.D., 2017. The Solar Cooling Design Guide: Case Studies of Successful Solar Air Conditioning Design. Ernst & Sohn.

Noaman, D.S., Moneer, S.A., Megahed, N.A., El-ghafour, S.A., 2022. Integration of active solar cooling technology into passively designed facade in hot climates. J. Build. Eng. 56, 104658.

Ochs, F., Magni, M., Venturi, E., de Vries, S., Hauer, M., Bonato, P., Taveres- Cachat, E., Venus, D., Geisler-Moroder, D., Abdelnour, N., 2020. Design Guidelines: Deliverable DC. 3, IEA SHC TASK 56 | Building Integrated Solar Envelope Systems for HVAC and Lighting.

Oliveira, L.A., Melhado, S.B., 2011. Conceptual model for the integrated design of building façades. Archit. Eng. Des. Manag. 7, 190–204.

Prieto, A., Armijos-moya, T., Konstantinou, T., 2023. Renovation process challenges and barriers: addressing the communication and coordination bottlenecks in the zero-energy building renovation workflow in European residential buildings. Archit. Sci. Rev. ISSN.

Prieto, A., Knaack, U., Auer, T., Klein, T., 2017. Solar Coolfacades: Framework for the Integration of Solar Cooling Technologies in the Building Envelope. Energy 137, 353–368.

Prieto, A., Knaack, U., Auer, T., Klein, T., 2018a. Feasibility study of self-sufficient solar cooling fa ade applications in different warm regions. Energies 11, 121693718.

Prieto, A., Knaack, U., Klein, T., Auer, T., 2018b. Possibilities and Constraints for the Widespread Application of Solar Cooling Integrated Façades. J. Facade Des. Eng. 6, 010–018.

RIBA, 2020. Plan of Work 2020.

Sahin, G., Ayyildiz, F.V., 2020. Chapter 14: Climate Change and Energy Policies: European Union-Scale Approach to a Global Problem. In: Qudrat-Ullah, H., Asif, M. (Eds.), Dynamics of Energy, Environment and Economy: A Sustainability Perspective. Springer Nature Switzerland AG, pp. 295 – 320.

Saini, P., Weiss, W., 2023. Design guidelines.

Santamouris, M., 2016. Cooling the buildings – past, present and future. Energy Build. 128, 617–638.

Savills Commercial Research, 2023. European Office Outlook.

Modelling and Analysis of Building Optimisation and Solar thermal Cooling Technology in Nepal

Michael Strobel[1,2], Uli Jakob[1,2]

[1] Universität Innsbruck, Innsbruck (Austria)

[2] Dr. Jakob energy research GmbH & Co. KG, Weinstadt (Germany)

Abstract

Space cooling and air conditioning becomes more important as the energy demand for cooling increases rapidly and the increasing frequency and intensity of heat waves become threats, entailing that cooling is not only a matter of comfort, but of health. The demand for cooling appliances in Nepal is rising sharply, which is due to both the effects of global warming and the growing purchasing power of the population. This study investigates treatment of space cooling demand for an office building the humid subtropical climate of Nepal using TRNSYS18 simulation software. Different measures to lower the building cooling energy demand through building optimisation are considered in the first place and then the coverage of cooling demand by solar-based cooling systems. Results show, that the annual sensible cooling demand can be cut by 50% through building optimisation. A solar thermally driven absorption chiller is capable to keep the indoor air temperature below 30 °C at 96% of the time with a maximum temperature of 34.6 °C with a $SEER_{th}$ of 0.79. Adding an electric driven vapour compression chiller increases this number to 100% with a maximum indoor temperature of 29.6 °C and a reduced $SEER_{th}$ for the absorption unit at 0.67. The electric efficiency of the hybrid system on the other hand is characterised by an $SEER_{el}$ of 14.51.

Keywords: Building Optimisation, Building Energy Performance, Solar Cooling, Solar Thermal, Simulation

1. Introduction

The months from July 2023 to June 2024 have been the hottest 12 contiguous months in history and mark the first timeframe that the average surface temperature is 1.5°C above the pre-industrial period (copernicus programme 2024). This ongoing global warming causes heat waves to become more extreme, to occur more often and to last longer (Chen et al. 2023). Moreover, cities and urban areas, where 55% of world population live (UNDP 2018), are even more exposed to the danger of heat waves due to the urban heat island effect (Ranasinghe et al. 2023). This climatic development combined with socioeconomic trends of growing world population and increasing economic power in countries of the global south cause cooling energy demand to increase (IEA 2018). These developments underline the relevance of space cooling for both indoor comfort in hot climate, but also for health reasons. “Air conditioning is slowly moving from a luxury product to a necessity.” says the head Hannah Ritchie, head of the research service Our World in Data (Ritchie 2024).

Nepal is a country which is strongly affected by all of these influences. The population is growing and urbanizing, the economic power is rising and the country experiences intense heat waves. There are not reliable data on the previous development of the Nepalese cooling demand, but the cooling demand market index (CDMI) (Strobel et al. 2023) for Nepal is expected to grow from 2020 until 2050 by additional 200% to 335%. As a result, the demand for cooling appliances, primarily electric driven single split air conditioners (AC), grows rapidly. The import of AC units into the country has increased by 44% until mid-2024 compared to the year before (Prasain 2024). Nepal was struck by a heat wave in summer 2023, causing schools to shut down and crop fields to wither (Lekhanath Pandey 2023). One important point to tackle these problems and challenges is to optimise buildings in the first place, to create safe spaces from heat and to decrease the energy demand for cooling appliances.

The project Building Energy Efficiency in Nepal (BEEN) is dedicated to contribute to these challenges, to support the uptake of energy efficient planning at building design phase, support the increase of renewable energies and energy efficient HVAC technologies and create a groundwork of future standards in this field. This project is funded by the European Commission (EC) under the switchasia project. It includes training activities for experts and the assistance in decision making to optimise building in concrete cases, both residential and non-residential uses. This

© 2024. The Authors. Published by International Solar Energy Society
Selection and/or peer review under responsibility of Scientific Committee
10.18086/eurosun.2024.08.03 Available at http://proceedings.ises.org

work covers the investigation of the impact of building optimisation measures on the cooling demand and additionally provide an overview of a solar thermally driven cooling system using an absorption chiller. This system is then adapted to a hybrid system including a vapour compression chiller.

2. Methodology

There are different options of solar cooling system designs for space cooling purpose. Systems differ in driving energy type (thermal or electric), in ventilation integration and central or decentralised solutions or even concrete activation. The system selection must correspond to the user needs, building quality, cooling demand and economic aspects. The influence of both the building design and construction and the design of a solar cooling solution are modelled in this study for an exemplary building.

The building investigated is an office building with operation only during the day from 10:00 until 17:00 for six days a week. The building has four floors, a square base with a length of 40.6 m and a square courtyard with a length of 17.4 m in the middle, see Figure 1. The stairways and corridors go around the courtyard and have access to each outside façade of the building. The office spaces are located in each corner of the building. All floors are designed the same, except that the ground floor has an additional entry zone facing West. The building is modelled in SketchUp with in total 26 zones. The offices account for a total area of 3,060 m² and the traffic area for about 2,530 m². A high occupancy rate is taken into consideration with 10 m² for each employee and additionally heating loads of 6 W/m² from lighting and 7 W/m² from technical equipment.

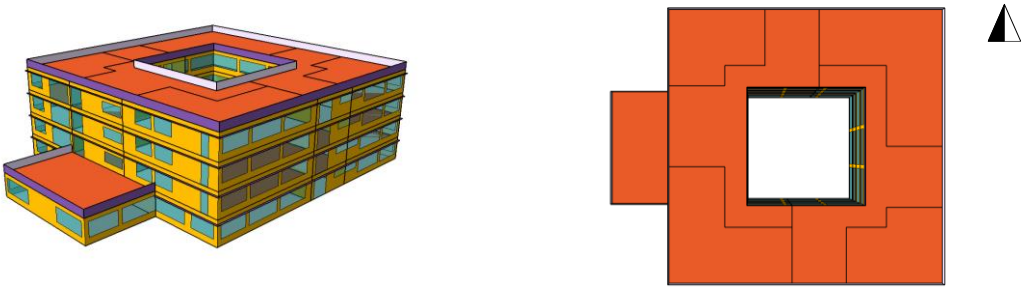

Figure 1: 3D model of the investigated building with showing the building geometry and the different zones.

The climate used for the analysis represents the humid subtropical climate in Nepal of low elevation. The temperatures reach values exceeding 40 °C in April and humidity peaks from June to August due to the monsoon season with an absolute humidity of up to 26 g/kg. The essential building energy demand in this region is cooling, both sensible and latent. In addition to the hot and humid climate, the internal heat gains from persons, lighting and technical equipment increase the demand cooling in the office building. Night ventilation has limited opportunities in this climate and region, as the outdoor temperature doesn't fall below 20°C from April to September.

The first step of the investigation targets the optimisation of the building envelope to reduce the cooling load in the first place. The building has a window-to-wall ratio (WWR) of 45% on the outer facades and 54% on the inner surfaces facing the courtyard. Except for some exceptions, all windows start at 1.2 m above the ground. This is beneficial to reduce the solar heat gain without losing substantial solar radiation to light the room. The façades have a fixed 0.3 m long overhang right above the windows along the total length of the building. This overhang is useful to block solar radiation when the sun is at low zenith angle, but not useful to block solar radiation when the sun is a high zenith angle, especially on the Eastern and Western façade in the morning and in the evening. Each zone in the building has transmission heat fluxes to the neighbouring zones. The offices are accessed through the traffic zones, causing air coupling between an office zone and the neighbouring hallway. The air change between an office and the neighbouring hallway is set to be 200 m³/h, considering a door of about 2.2 m² to be open for 15 min per hour at an air speed of 0.1 m/s. The stairways in the building are open, giving the opportunity for air to flow between freely between the 4 floors of the building. Table 1 gives information on the building envelope quality and the changes through the optimisation measures. The measures do not include any changes in the building's architecture, but instead focus on measures that can be applied to existing buildings in retrofit activities, primarily insulating the roof on the outer surface and change of windows with additionally external shading systems, e.g., automated raff store.

Table 1: Overview of building envelope quality and infiltration for the building of current state and for the optimised case.

Element	Current state	Optimised
External wall	Brick wall with plaster layers U-value: 2.04 W/m²K	Brick wall with plaster layers U-value: 2.04 W/m²K
External roof	15 cm RCC with tiles as a cover U-value: 3.50 W/m²K	Same construction, but 5 cm polystyrene (λ=0.04 W/mK) added between RCC and tiles with plaster U-value: 0.64 W/m²K
Infiltration	1.2 (Offices) 1.2 (Hallways)	0.6 (Offices) 0.6 (Hallways)
Window	Clear single glazing U-value: 5.69 W/m²K; g-value: 0.82	Argon-filled double glazing U-value: 1.46 W/m²K; g-value: 0.52
External shading	Not applied	External shading Shading factor: 0.8 if solar irradiance exceeds 140 W/m²

The building and cooling system simulation are modelled in TRNSYS18 simulation software. This software was used as the building can be individually modelled, different zones and operations are used and the materials and layers of construction elements can be adapted. Furthermore, it offers a large library of technical components (types) to integrate in the set-up of a solar HVAC system. Table 2 shows a list of essential system elements used in the simulation and the TRNSYS types used for modelling.

Table 2: Overview of simulation elements and used TRNSYS types in the simulation.

Simulation element	TRNSYS type	Simulation element	TRNSYS type
Building	Type56	Cooling coil	Type124
Solar thermal collector	Type71	Sorption wheel	Type716
Hot water storage	Type156	Water-to-air heat exchanger	Type753d
Absorption chiller	Type107	Air-to-air exchanger	Type760
Pumps	Type110	Solar PV module	Type103a
Water-to-water heat exchanger	Type91	Air cooled vapour compression chiller	Type655

The target of the system design is to reach an energy efficient space cooling system using mainly solar thermal energy. Evacuated tube collectors are used to harness solar energy and provide heat to a hot water storage, capable of storing heat up to 120 °C pressurised hot water. The evacuated tube collector specifications are based on a product available in the Indian market (THERMOMAX HP400, (Kingspan 2019)) with α_1 at 1.18 W/m²K and α_2 at 0.0095 W/m²K². The 300 collectors have each a collector area of 2 m² and are placed on the flat roof of the building. The heat from the collectors is provided to the hot water tank via an internal heat exchanger. The buffer tank provides heat at a temperature of 90 °C to an absorption chiller. The chiller operation stops when the temperature of heat supply falls below 75 °C. The chiller operation is derived from a hot water driven single effect absorption chiller (AbCh) using Lithium bromide (LiBr) as absorbent. The product which was used as guidance is also available on the Indian market (THERMAX 5G series, (Thermax)). The absorption chiller is modelled using TRNSYS type107, making use of a customised external data file indicating the performance map of the chiller with a rated COP of 0.8. The set-point temperature of the chiller is 10 °C.

For the case of no or not sufficient solar heat available for the absorption chiller and also for the times of peak cooling demand, an additional electric vapour compression chiller (VCC) is integrated in an adapted version of system to serve as a back-up. The system was investigated and modelled with and without this back-up to assess its impact and necessity. The VCC turns on, if the AbCh does not reach to cool the refrigerant in the cooling coil cycle below 15 °C. The cold from the AbCh and the VCC is supplied via heat exchanger to a refrigerant circuit, which is connected to the cooling coil. The cold is provided to the office rooms via a centralised ventilation system which also provides

fresh air. The fresh air demand is based on the number of persons present during the operation and is set at 8,400 m³/hr. This is the fixed air supply from outdoor to indoor during operation. The inlet air temperature during cooling operation is set at minimum 20 °C to avoid discomfort at the ventilation outlets in the offices. If the supply of cold fresh air is not sufficient to keep the office rooms below 26 °C, circulation of room air is considered to cool down more air and provide more cold to the room. The maximum amount of circulated air is set at 60,000 m³/hr, leading to a maximum air change per hour of 6.2 1/hr for the office spaces. The hallways are not ventilated. The schedule to run the cooling systems starts in the morning at 08:00, even though the occupation starts at 10:00. This way, the cooling system uses the available solar radiation to cool down the building mass in the morning. This morning cooling makes only use of air circulation.

The humid climate at the location requires dehumidification of the fresh air to avoid condensate in the room and to increase comfort. A sorption wheel is installed at the inlet of the fresh air. The exhaust air in the flow is additionally heated with solar heat from the hot water tank. This increases the dehumidification of the fresh air. A schematic of the system is pictured in Figure 2 with water and refrigerant flows in thinner lines and air flows in bigger lines on the right side.

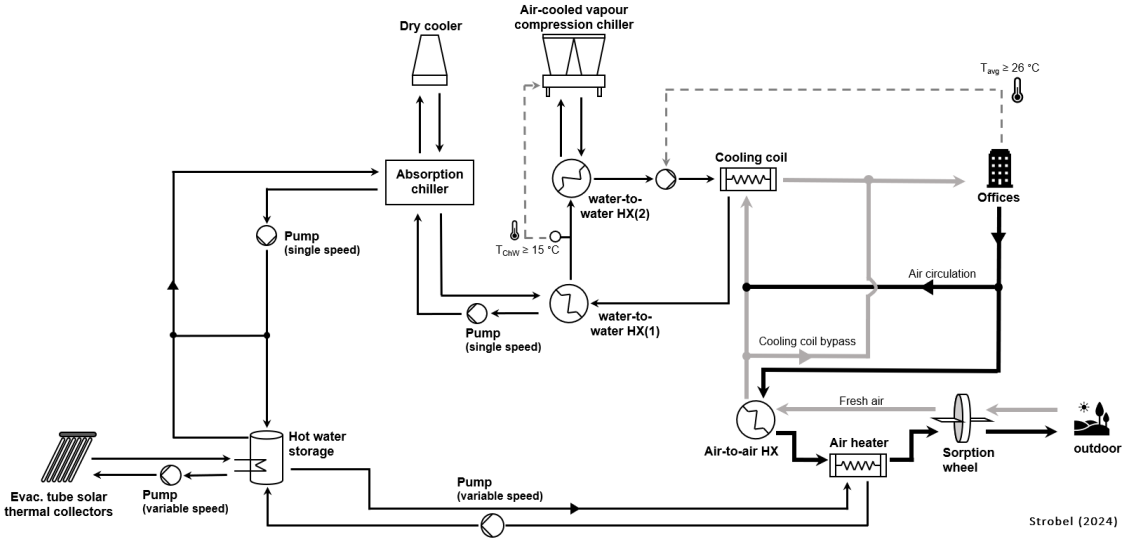

Figure 2: Scheme of the solar cooling system with a VCC as a back-up.

Figure 3 shows the representation of the system in the TRNSYS18 simulation software.

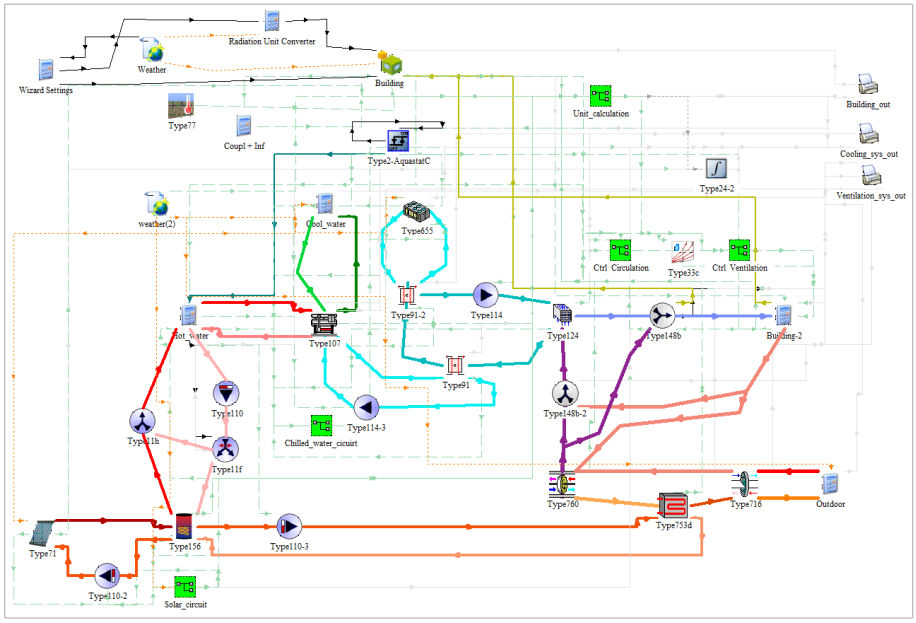

Figure 3: TRNSYS deck of the solar thermal cooling system

3. Results

This chapter provides the results on both the building optimisation and its impact on the cooling energy demand as well as on the design and results of the investigated solar cooling system with and without back-up. The cooling systems are sized for the optimised building case only.

Four individual measures (see Table 1: external roof insulation, double glazed coated windows, reduced infiltration, and external movable shading) are applied to optimise the thermal performance of the building. The not-optimised building has 10,707 cooling degree hours at a base temperature of 26 °C for the average office temperature during 2,191 hours of operation during the year. This number is reduced to 8,650 cooling degree hours for the optimised version, marking a reduction of 20%. A comparison between the number of hours during occupation of the average office temperature above different temperature levels is presented in Figure 4(a). It shows, that the highest total and relative impact for higher temperatures above 32 °C. Figure 4 (b) on the right shows the sensible cooling demand for both cases separated into the zones of offices and of hallways for different operation schedules of cooling. First of all, the optimisation leads to a massive reduction of about 50% in cooling demand. Secondly, the cooling demand is lowest when only the office zones are treated (circled). An active cooling of the offices at night time and on Sundays to a temperature of 28 °C limits the heating of the building mass and causes an increase in cooling energy demand of 31% for the non-optimised building and 11% in the optimised case. Treating the hallways at 28 °C during the time of building operation causes an increase in total cooling demand by 54% for the building of current state and 35% for the optimised building. In this case however, the cooling demand for the office spaces is slightly reduced compared to the office cooling only version, as the heat gains from the hallways through air coupling is reduced. These results show that the definition of cooling operation already has major affects in the cooling energy demand.

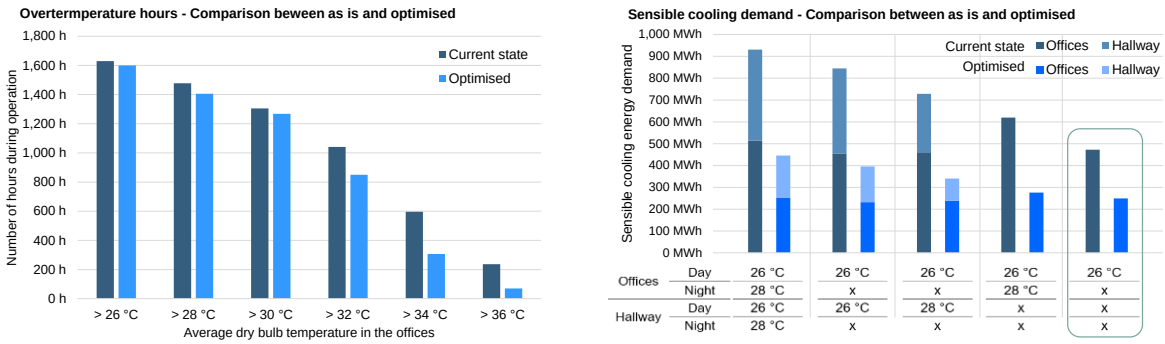

Figure 4: Results of building optimisation through envelope retrofitting. Comparison of over temperature hours (a) and the sensible cooling energy demand for offices and hallways at different operation typologies (b).

For the further studies, a cooling demand schedule is set focussing only on the office spaces during the time of operation, marked with the lowest sensible cooling demand, see Figure 4 (b). The maximum sensible cooling demand results in 312 kW_{th}. Given a desired maximum relative humidity at 60%, the maximum latent cooling load results in 328 kW_{th}. The maximum simultaneous total cooling demand is 603 kW_{th}. Based on this, the AbCh is has a cooling capacity of 400 kW_{th}, whereas the additional VCC has a capacity of 200 kW_{th}.

Hot water storage

A hot water storage is placed between the solar thermal collectors and the absorption chiller to increase flexibility for fluctuation of solar radiation throughout the day and to store heat for the operation during days of low radiation in general. The AbCh unit has a chilling capacity of 400 kW_{th} at design point with a COP of 0.8. Based on this, the hot water demand is at about 500 kW_{th}. A sensitivity analysis of the hot water storage is performed to estimate the impact of the thermal storage on the operation of the sorption chiller. The sensitivity analysis covers storage volumes in different sizes: 5 m³, 10 m³, 30 m³, 100 m³ and 300 m³. The different storages sizes are assessed based on their impact on the operation of the absorption chiller. The results of this sensitivity analysis are shown in Table 3 below.

The size of the hot water storage tank is set at 30 m³ for the further investigation of the system. This size is capable to store about 1,500 kWh heat in a temperature range between 75 °C and 120 °C, enough to drive the chiller for three hours.

Table 3: Results of sensitivity analysis on hot water storage size and impact on absorption chiller

Storage size	**5 m³**	**10 m³**	**30 m³**	**100 m³**	**300 m³**
Storage energy capacity [kWh]	260	520	1,559	5,196	15,587
Hours of AbCh operation	1,492	1,586 (+6%)	1,672 (+12%)	1,814 (+22%)	1,848 (+24%)
AbCh Heat consumed [kWh]	267,355	296,326	309,774	355,131	363,568
AbCh Cold provided [kWh]	209,005	228,812	241,501	276,231	281,062

Indoor air quality

The indoor air quality is analysed for four cases, for the building current state and for the optimised building and each with two cooling systems: only solar thermal cooling via AbCh and the hybrid system with VCC as a back-up. Figure 5 shows both the average indoor air quality of the office spaces (blue) and the supply air quality from the ventilation system entering the room for all 2,191 hours of annual operation in the offices.

Th upper diagrams (a) and (b) show the air qualities for the building of current state. It shows that the cooling system is not correctly sized to maintain comfortable air quality throughout the year with maximum temperatures of 36 °C for the solar cooling system only and 33.9 °C for the case with VCC back-up. Of course, this situation would change if the corresponding cooling system was larger and not designed for the optimised building already, but a comparison on different sized cooling systems is not targeted.

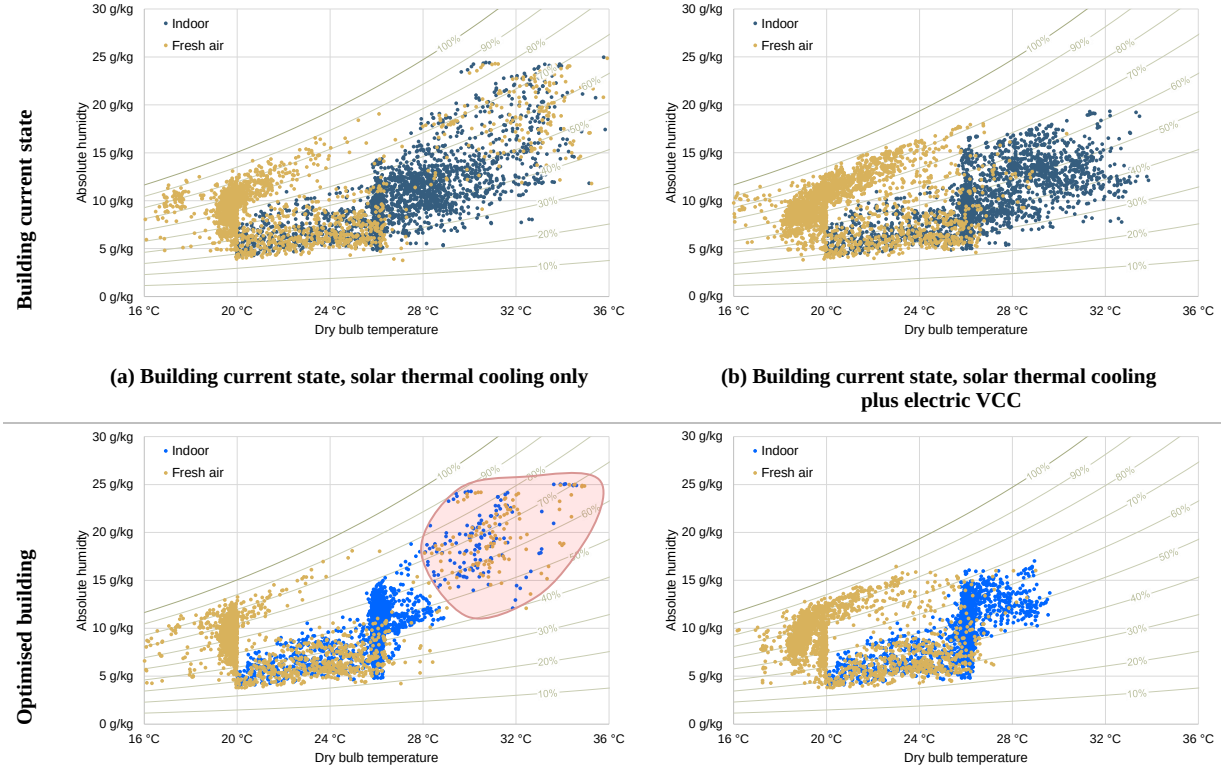

(a) Building current state, solar thermal cooling only

(b) Building current state, solar thermal cooling plus electric VCC

(c) Optimised building, solar thermal cooling only

(d) Optimised building, solar thermal cooling plus electric VCC

Figure 5: Psychrometric diagrams showing comparison of dry bulb temperature and humidity for indoor air and fresh air supply for the four investigated cases.

The lower two diagrams (c) and (d) in Figure 5 show the results of the two cooling systems for the optimised building. The diagram on the left shows that during many hours of operation, the fresh air supply is maintained at 20 °C and indoor temperature at 26 °C. However, there are several hours in the year where both the fresh air and the indoor air temperature exceed 30 °C, marked with a red circle. The reason for this is the lack of solar heat, hence no operation of the AbCh. This challenge is solved with the integration of a VCC as a back-up. The corresponding diagram (d) shows that there are no situations where the indoor air temperature exceeds 30 °C.

For the last case (d) of Figure 5, there is an additional overview given in Figure 6 showing the listed average office air temperature and the temperature of the 16 offices zones in the building and the ambient temperature for the 2,191

hours of annual operation considered. The figure shows that there is difference of up to 5 K air temperature between the different zones. This is due to the different orientation and the impact of the floor level. The diagram shows the system is capable of keeping the average indoor air temperature at 26 °C even in cases when the outdoor temperature is at 40 °C.

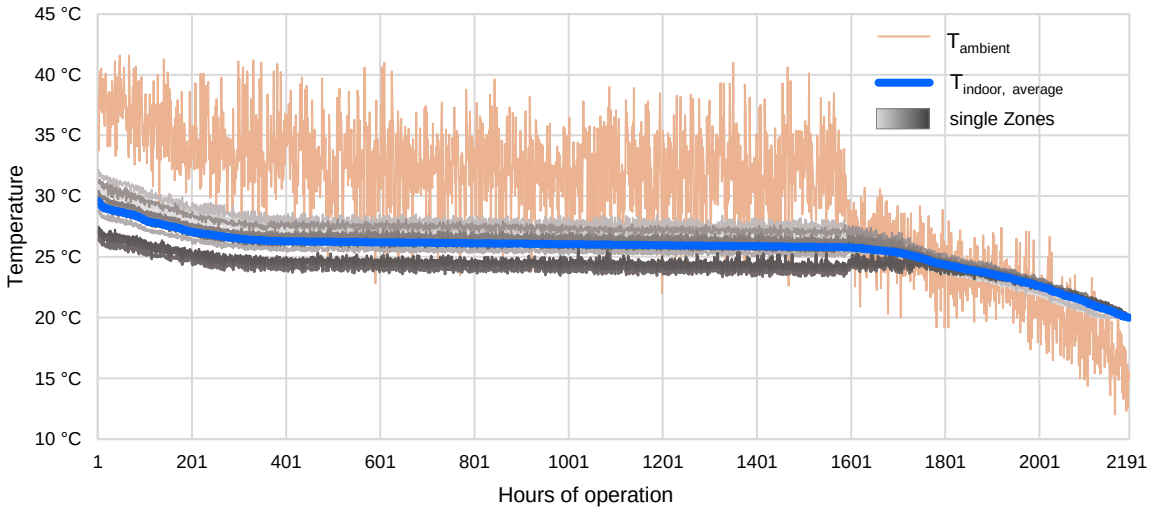

Figure 6: Listing of dry bulb temperature of average office temperature (blue) the individual zone and the outdoor temperature (orange).

Energy analysis

The energy analysis covers only the performance of the cooling system for the optimised building. Figure 7 shows the monthly cold provided from the AbCh (yellow bar), from the VCC (green bar), and the monthly average for the COP for the AbCh. Integrating the VCC into the system has three essential effects: (i) more cold is generated in total (+ 11.7%), (ii) the AbCh generates less cold, especially in the summer time from June to September and (iii) the monthly average COP of the AbCh drops in the named months. The reason for this behaviour is that the VCC supports to cool down the room air, causing the exhaust air to be cooler. Thus, the AbCh operates with lower chilled water temperatures, while the indoor comfort is increased.

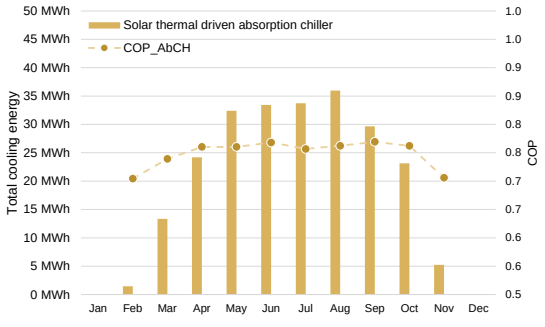

(a) Monthly cooling energy supply from absorption chiller only

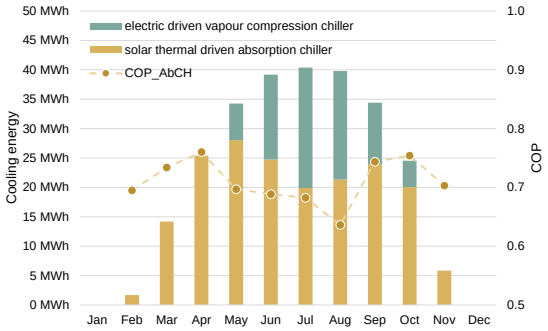

(b) Monthly cooling energy supply from hybrid system

Figure 7: Comparison of monthly average COP and cold provided from AbCh only and hybrid system including a VCC for the optimised building

The thermal seasonal energy efficiency ratio ($SEER_{th}$) of the AbCh is at 0.79 for the solar only system and at 0.67 for the AbCh in the hybrid system. This difference is due to the reason, that with the help of the VCC the temperature in the offices is kept at cooler and more comfortable level than in the solar only case. Hence, AbCh is not in the position to cool the refrigerant from e.g. 25 °C down to 21 °C, but from 19 °C down to 15 °C. This comes together with the hot outdoor weather conditions and thus high cooling water temperatures. Figure 7 (b) shows that the VCC is providing cold especially from June to September. This is the season of high humidity in the climate, showing the increased impact latent cooling demand. The VCC consumes around 18 MWh_{el} electricity with a $SEER_{el}$ of 4.17. The electric $SEER_{el}$ of the total hybrid system however is at 14.5, which highlights the system efficiency of this hybrid system.

Following Figure 8 shows the course of the solar energy yield (q_collector), the thermal capacities of the AbCh hot water supply (AbCh_HW), the heat dissipation through the dry cooler (q_AbCh_CW), the cooling power of the chiller (q_AbCh_ChW), the cooling power of the VCC (q_VCC_ChW) as well as the energy stored in the hot water storage (Q_storage) for three exemplary days in September.

At the start of the first day, 18th of September, the hot water storage is discharged and no heat is available to drive the AbCh. Additionally, this day is characterised by low solar radiation of maximum 110 W/m², not enough to run the evacuated tube collectors to reach the minimum of 90 °C. For this day, the VCC runs all day with a break at 11:00 whereas the AbCh does not run at all. The VCC on this day is enough to cool the building and to keep an average temperature in the office spaces at around 26 °C. In the morning of the 19th the VCC start operating to provide the morning cooling before building occupation while the solar collector field generates heat at 400 kW, thanks to low tank temperatures and high solar radiation of up to 1,000 W/m². This solar heat is capable to drive the absorption chiller throughout the day and partly even charge the hot water storage. In the afternoon of the 19th, the solar yield decreases and the storage gets discharged. This day is characterised by hot ambient temperature of up to 35 °C, causing the COP of the AbCh to go down to 0.6. The VCC is still not needed in this case, as the AbCh capable of providing cold below 15 °C. During the last day shown, the solar collector field can again charge the storage in the morning until 10:00 in the morning. In the afternon, the solar collector field does not provide enough solar heat, but the stored heat from the storage is enough to drive the AbCh until the end of day. During this day, the back-up VCC is not necessary for cooling.

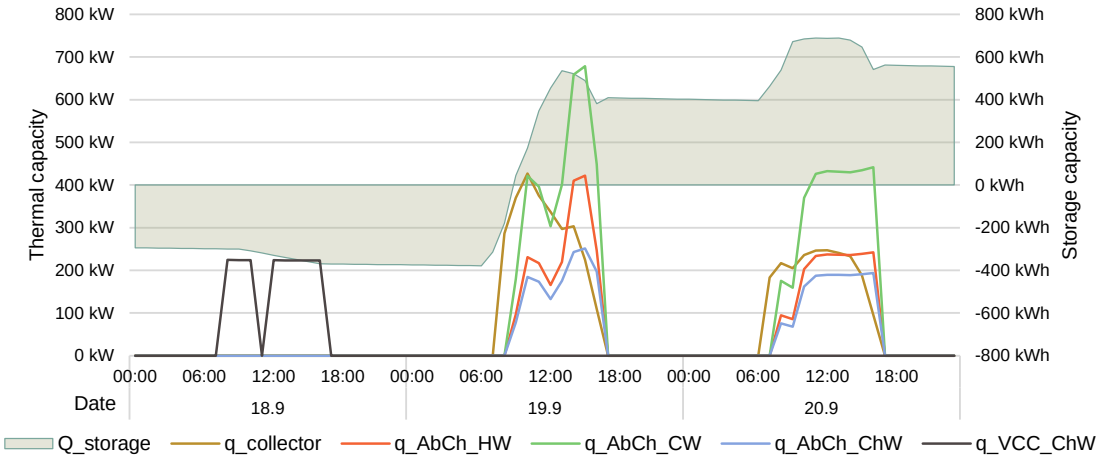

Figure 8: Comparison of thermal capacity and storage capacity for three days in September. The operation of the VCC depends on the solar radiation and the energy level of the hot water storage.

4. Conclusion

This study covers the reduction and of cooling demand of an office building via building optimisation and the sustainable and efficient supply of cold and fresh air via solar-assisted ventilation to the office rooms. The building optimisation shows great effect on the sensible cooling demand, leading to reduction between 47% and 53%, depending on the desired cooling operation. This shows that the optimisation of a building is crucial when cooling is required. The optimisation allows a size reduction of the cooling system of about 50%.

The analysis of the temperature and air quality shows that the solar only system is operating well, but is not capable to cover all days of the year, leaving several hours of occupation to temperatures of 30 °C and higher. This is especially the case for the not-optimised building, for which the investigated cooling system is not correctly sized. For the optimised building the hybrid systems consisting of a 400 kW absorption chiller (AbCh) and a back-up 200 kW vapour compression chiller (VCC) is a good combination to drastically reduce the number of hot hours during occupation and to avoid indoor temperatures above 30 °C at all. The solar thermally driven absorption chiller alone is capable to provide cold for up to 89 % of the time. This highlights that a back-up is necessary to ensure user comfort at all time. If no VCC is installed, the $SEER_{th}$ is higher and reaches 0.79. In the hybrid system, the user comfort increases. The cold provided by the AbCh decreases by 20%, whereas the heat consumption decreases only marginally, as the AbCh operates at lower chilled water temperatures and high ambient temperatures, resulting in a lower COP. The chilled water temperature is lower due to the work of the VCC. The AbCh has a $SEER_{th}$ of 0.67 for

the hybrid case whereas the VCC has a $SEER_{el}$ of 4.17. electric efficiency of the total hybrid system is characterised by a $SEER_{el}$ of 14.51.

Further investigation for a full system assessment is necessary to comprehensively compare different solar cooling systems, especially thermal losses through pipes. Another important aspect to assess the future potential of solar thermal cooling systems in Nepal is the economic aspects. Along with this study, an economic comparison was targeted, but there is currently a lack of sources covering the Nepalese market.

5. Acknowledgement

This research received funding under Building Energy Efficiency in Nepal (BEEN) project by European Commission under the SWITCH-Asia-promoting sustainable consumption and production program, contract number ACA/2021/428-648.

6. References

Chen, D.; Rojas, M.; Samset, B. H.; Cobb, K.; Diongue Niang, A.; Edwards, P. et al. (2023): Climate Change Information for Regional Impact and for Risk Assessment. In Intergovernmental Panel on Climate Change (Ed.): Climate Change 2021 – The Physical Science Basis: Cambridge University Press, pp. 1767–1926.

copernicus programme (2024): Surface air temperature for June 2024. Edited by ECMWF. European Commission. Available online at https://climate.copernicus.eu/surface-air-temperature-june-2024, updated on July 2024, checked on 7/8/2024.

IEA (2018): The Future of Cooling. International Energy Agency (IEA); OECD. Paris. Available online at www.iea.org/reports/the-future-of-cooling, checked on 7/8/2024.

Kingspan (2019): Product data sheet Thermomax HP400. Edited by Solarsense UK. Available online at https://www.solarsense-uk.com/wp-content/uploads/2019/05/Thermomax-HP400-Data-Sheet.pdf, updated on May 2019, checked on 8/9/2024.

Lekhanath Pandey (2023): Nepal struggles with blistering heat wave. Edited by Deutsche Welle (DW). Kathmandu. Available online at https://www.dw.com/en/nepal-struggles-with-blistering-heat-wave/a-65941491, updated on 6/16/2023, checked on 7/28/2024.

Prasain, Krishana (2024): From hills to Tarai, heatwaves push demand for ACs https://kathmandupost.com/money/2024/05/30/from-hills-to-tarai-heatwaves-push-demand-for-acs. Import of ACs has increased by 43.62 percent to Rs2.93 billion in the first 10 months of the current fiscal year, government data show. https://kathmandupost.com/money/2024/05/30/from-hills-to-tarai-heatwaves-push-demand-for-acs. Edited by The Kathmandu Post. Available online at https://kathmandupost.com/money/2024/05/30/from-hills-to-tarai-heatwaves-push-demand-for-acs, updated on 5/30/2024, checked on 7/8/2024.

Ranasinghe, R.; Ruane, A. C.; Vautard, R.; Arnell, N.; Copola, E.; Cruz, F. A. et al. (2023): Framing, Context, and Methods. In Intergovernmental Panel on Climate Change (Ed.): Climate Change 2021 – The Physical Science Basis: Cambridge University Press, pp. 147–286.

Ritchie, Hannah (2024): How can the world reduce deaths from extreme heat? Edited by OurWorldInData.org. Available online at https://ourworldindata.org/how-can-the-world-reduce-deaths-from-extreme-heat, updated on 7/22/2024, checked on 7/28/2024.

Strobel, Michael; Jakob, Uli; Streicher, Wolfgang; Neyer, Daniel (2023): Spatial Distribution of Future Demand for Space Cooling Applications and Potential of Solar Thermal Cooling Systems. In *Sustainability* 15 (12), p. 9486. DOI: 10.3390/su15129486.

Thermax: Product data sheet Thermax 5G series. Edited by Trane Belgium. Available online at https://www.tranebelgium.com/files/product-doc/307/en/TECH-5G-ENG.pdf, checked on 8/9/2024.

UNDP (2018): World Urbanization Prospects: The 2018 Revision, Online Edition. Edited by United Nations, Department of Economic and Social Affairs, Population Division.

Ice-slurry production for solar-ice systems using supercooling with an in-stream crystallizer

Ann-Katrin Thamm[1], Kevin Erb[1], Ignacio Gurruchaga[1], Daniel Carbonell[1,2]

[1]SPF Institut fur Solartechnik, OST – Ostschweizer Fachhochschule, Oberseestr. 10, CH-8640 Rapperswil, Switzerland
[2]DCarbo Energy Consulting S.L. 08182, Barcelona, Spain.

Abstract

Using ice slurry produced from supercooled water with an in-stream crystallizer opens a new path for solar-ice systems, increasing efficiency and reducing investment cost compared to ice-on-coil systems. Power needs are decoupled from the stored energy since the heat exchangers are not evenly distributed in the ice storage vessel but directly placed as the heat pump evaporator, which depends on the heat pump capacity and not on the ice storage volume. The novel ice storage design can serve as a heat source for a heat pump, where its evaporator is used to supercool water below 0 °C, or for refrigeration. The supercooled water at a temperature around −2 °C, maintained in a meta-stable liquid state, is triggered to nucleate in an in-stream crystallizer. The current design of the ice crystallizer allows for continuous operation of the system and scalability. Experimental results obtained with a gasketed plate heat exchanger used to supercool water and an in-stream crystallizer operated at a power of up to 6.5 kW are presented.

Keywords: supercooling, ice slurry, solar-ice, ice storage, in-stream, crystallizer

1. Introduction

In the near future the European energy system will include a lot of heat pumps to supply residential buildings with heating and cooling (Lyons, et al., 2023). However, which heat sources these heat pumps will use will depend on many factors such as regulations and social acceptance including the noise of fans for Air Source Heat Pumps (ASHP) as well as aesthetics, ground water regulations, wastewater availability, etc. Thus, to cover many local and regional needs, several heat sources for heat pumps need to be considered. Solar-ice systems, combining solar thermal collectors, a heat pump and an ice storage solution, are promising candidates for supplying heating demands to buildings in heating dominated climates with enough solar radiation in winter. The ice storage can serve as a heat source for the heat pump in periods of insufficient amount of direct heat from the solar thermal collectors, e.g. during night or days with low irradiation. During times of high irradiation, excess heat, not required for the heat pump, can be used to regenerate the ice storage and can also provide heat for domestic hot water or space heating (Carbonell, et al., 2016). In this context, a solar-ice systems is usually considered as an alternative to Ground Source Heat Pumps (GSHP) since it can achieve the same efficiency with the additional benefit of not needing to drill boreholes. When compared to GSHP, a solar-ice system offers an often-missed benefit: it does not need further regeneration in the long term since it regenerates on a yearly basis.

Most of the ice storages installed in Europe, used in solar-ice systems or for refrigeration, are based on coil heat exchangers and are known as ice-on-coil storages (Nelson, et al., 1996). An anti-freeze solution is circulating in tubes embedded into the storage-vessel, serving as heat exchanger. Ice is formed on the outer surface of the tubes, acting as a growing insulating layer due to the low thermal conductivity of ice, limiting the amount of ice per unit surface area of the heat exchanger (Carbonell, et al., 2022). Thus, the tubes need to be distributed along the storage volume coupling power and capacity needs. Consequently, the cost for the heat exchanger scales with capacity of the ice storage.

In order to keep the heat transfer area free of ice, two concepts have been proposed earlier at our institute: the thermal de-icing approach (Philippen, et al., 2012; Carbonell, et al., 2015) and an ice slurry concept (Carbonell, et al., 2020). While the thermal de-icing concept still needs an indeed reduced number of heat

© 2024. The Authors. Published by International Solar Energy Society
Selection and/or peer review under responsibility of Scientific Committee
10.18086/eurosun.2024.08.04 Available at http://proceedings.ises.org

exchangers in the storage, the slurry concept decouples ice generation and storage volume avoiding continuous ice growth on the heat exchanger surface, while the produced slurry remains pumpable (Kauffeld, et al., 2005). Possibilities to avoid that ice grows at the heat exchanger surface completely, are based on slurry concepts using direct contact evaporation with a refrigerant (Wijeysundera, et al., 2004), water vacuum freezing (Honke, et al., 2015) or supercooling (Tanino & Kozawa, 2001). The second possibility to keep the surface free of ice is to continuously remove it from the surface, e.g. by fluidized beds (Pronk, et al., 2003), supercooled water jets (Mouneer, et al., 2010), blowing compressed air (Zhang, et al., 2008) or using scrapers (Stamatiou, et al., 2005). The latter is the most common method in commercial ice slurry systems nowadays and uses mechanically scraped-surface heat exchangers, where ice is formed on a cold surface and is then removed continuously by a rotating mechanical arm that scrapes ice from a cylindrical barrel. The scraper design, having a mechanical component, requires high operation and maintenance cost, and has limited potential for scale up due to the mechanical constrains of the rotating-scraping arm.

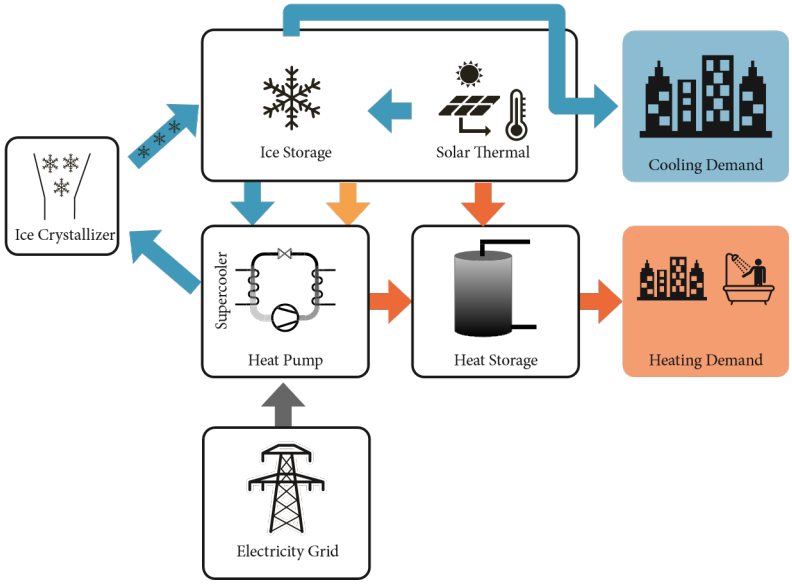

Figure 1: General scheme of a solar ice-slurry system using the supercooling approach.

To reduce installation and maintenance cost as well as improving energy efficiency and reliability of the ice storage implemented in a solar-ice system, a passive concept for ice slurry production based on the supercooling method (see Fig. 1) was proposed earlier in Carbonell et al. (2020). In Gurruchaga et al. (2023a) the investment costs of solar-ice slurry systems were estimated to be between 8 % to 11 % lower than the reference ice-on-coil system in Bilbao and between 14 % to 17 % lower in Zurich. The heat generation costs in ct/kWh were between 7 % to 12 % lower for the slurry version. Moreover, the system is conceived such that the used heat exchanger is always free of ice and thus a higher efficiency compared to the ice-on-coil method for large ice fractions can be reached. Arenas-Larranaga et al. (2024) numerically demonstrated the system performance of such solar-ice slurry systems for several European climates and two multi-family buildings using natural refrigerant heat pumps with supercooling evaporators.

Besides numerical simulations, a hardware-in-the-loop Concise Cycle Test (Haberl, et al., 2022) was used to validate in the laboratory the autonomous operation of a solar-ice slurry system and assessed its performance during a whole year using an accelerated system test methodology (Gurruchaga, et al., 2023b). Specifically, a 10 kW CO_2 heat pump with a coated supercooler-evaporator developed in Carbonell et al. (2022) was tested with a complete system including hydraulics, thermal storages, electrical battery, inverter and an autonomous control. To provide the appropriate dynamic boundary conditions for the system, the solar thermal collectors, PV and building demands were simulated and emulated. The system was working continuously efficiently and reliable for two consecutive weeks. However, key parts of the ice slurry system i.e., the in-stream ice crystallizer and storage vessel, were simulated and emulated due to lack of reliable devices at the appropriate

power needs. In the current work, a working and scalable crystallizer is demonstrated experimentally in the laboratory with a power of 6.5 kW as one of the missing pieces of the complete solar ice-slurry system.

1.1. Ice slurry generation using supercooling approach

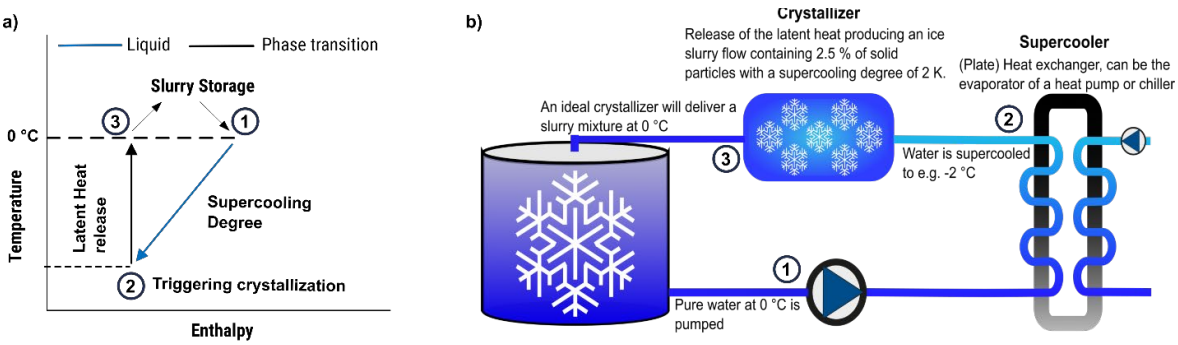

Figure 2: a) Temperature as a function of enthalpy using supercooling for ice slurry production. b) Conceptual visualisation of the supercooling concept. a) and b) are linked via points 1 to 3: Pure liquid water at a temperature of 0 °C (1), is pumped into the supercooler, where it is supercooled and remains in a metastable liquid state (2). The supercooled water is crystallized in an in-stream crystallizer, releasing sensible heat into latent heat, and is pumped into the storage vessel as slurry (3).

The supercooling concept with an in-stream crystallizer to produce ice slurry is visualised in Fig. 2 b), while Fig. 2 a) shows the temperature as a function of system enthalpy during the process. Both are linked via the indicated state points 1 to 3. Liquid water at a temperature of 0 °C is pumped from the storage vessel (state point 1) into a standard plate heat exchanger - the supercooler - where it undergoes supercooling, e.g. to a temperature of −2 °C and stays in a metastable liquid phase (state point 2). The supercooling degree is defined as the difference between the melting temperature T_m and the meta-stable liquid water temperature T_{wat} in Kelvin: $\Delta T_{sup}=T_m-T_{wat} > 0$ K. After the supercooler, the stored sensible heat is transformed into latent heat triggered by the nucleation mechanism placed in-stream inside the crystallizer. The conversion from sensible to latent heat leads to a mass ice fraction on the fluid flow of approximately 2.5 % at a supercooling degree of 2 K. Thus, the slurry will leave the crystallizer with a temperature of 0 °C (state point 3), which prevents the piping system of being clogged as the freezing potential has been exhausted, i.e. all sensible heat is converted into latent heat during the phase change from supercooled water to ice inside the crystallizer. After the in-stream crystallizer, the slurry is pumped into the storage vessel. For the system to work, phase separation between solid and liquid must be guaranteed in the storage vessel, as no ice crystals should be pumped into the supercooler, where they would cause a freezing event immediately. For this, the relatively large density difference between ice and water is beneficial. On top of that, the storage vessel is equipped with some internal design to guarantee proper phase separation inside the vessel.

Due to the instability of the supercooling method, attributed to the fact that ice nucleation in supercooled water has a stochastic nature (Kauffeld, et al., 2005), not a single system using the supercooling approach has been installed in Europe nowadays, contrary to Japan, where several companies made use of the method in air-conditioning (Tanino & Kozawa, 2001; Kozawa, et al., 2005; Kurihara & Kawashima, 2001) more than 20 years ago. For the concept to work, three main challenges need to be solved: i) reliable supercooling of the water needs to be achieved in the heat exchanger and maintained downstream of it before entering the crystallizer; ii) the supercooled water needs to be crystallized in a defined location, in our case in the in-stream crystallizer, without causing blockage in the hydraulics downstream and avoiding upstream ice propagation into the supercooler and iii) produced ice slurry needs to be stored in the vessel with a high mass ice fraction avoiding even small ice particles from being pumped into the supercooler where they would cause crystallization.

While challenge i) has been a research topic in Europe since years (Saito & Okawa, 1994; Faucheux, et al., 2006; Bédécarrats, et al., 2010; Ernst & Kauffeld, 2016) without finding a working scalable solution, Japanese companies seem to use the supercooling approach since the beginning of the 21st century (Nagato, 2001; Kozawa, et al., 2005). However, public literature lacks giving details about the used supercooler and their stability. Just recently, Carbonell et al. (2022) demonstrated the possibility to use very compact coated brazed

plate heat exchangers as supercoolers for residential heat pumps. The ones with icephobic coatings improved the supercooling degree with respect to the non-coated reference one and reached in average supercooling degrees in the range of 3 K to 4 K for water mass flow rates of 1000 kg/h.

The efficient and reliable generation of ice slurry (challenge ii) was identified as one of the “last unravelled mysteries” by Kauffeld & Gund (2019). Successful release of supercooling potential ready for application in the kW to MW scale is - to our knowledge - only reported from researches in Japan: Tanino & Kozawa (2001) and Mito et al. (2001) proposed a free-falling stream of supercooled water into the ice storage, initiating nucleation through collision with a surface. The same researchers reported about a crystallizer where the supercooled fluid was continuously bombarded with ultrasonic waves to trigger nucleation and to prevent ice from adhering to walls (Tanino, et al., 2000). Upstream ice propagation can be avoided by using a warm laminar flow at the inside of the pipe wall according to them (Mito, et al., 2002).

In the following, we propose a solution for reliable slurry generation from supercooled water with the design of a scalable “in-stream-crystallizer”, operated at a power of 6.5 kW for almost 3 h, using an average supercooling degree of 1.75 K at a mass flow rate of 3200 kg/h. The proper separation of ice and water in the slurry storage vessel, challenge iii), will be addressed in future research work and is currently solved by using two storage vessels connected in series, one is filled with the produced slurry, and the water for the supercooler is sucked from the second storage which is free of ice for longer time periods.

2. Material and Methods

The constructed experimental set-up is described in section 2.1, followed by a short description about the tools for experimental control and data acquisition in section 2.2. Next, the test procedure to evaluate the reachable supercooling degree of heat exchangers is identified in section 2.3 and last, the development of the crystallizer used for slurry generation is explained in section 2.4.

2.1. Experimental Set-up

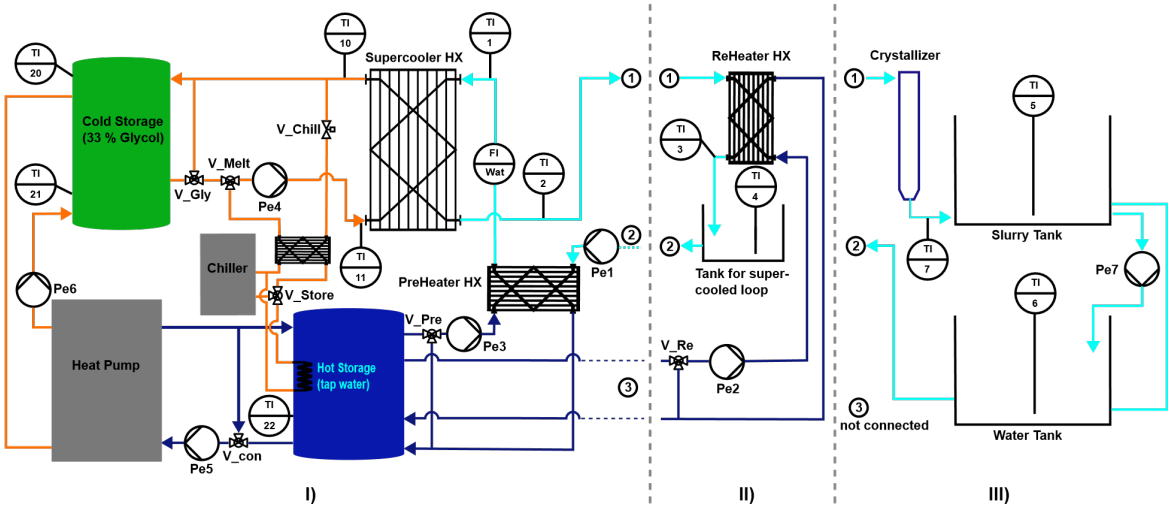

Figure 3: Schematic diagram of the experimental set-up, orange loop: glycol, cyan: supercooled loop, dark blue: tap water. I) Shared components for both supercooler and crystallizer testing. II) components for supercooler testing plugged into I) on ports 1, 2 and 3 (loop III not used). III) Components for crystallizer testing, plugged into I) via 1 and 2, 3 not connected (loop II not used).

The developed set-up (see Fig. 3) can be used for two types of experiments: the *supercooler testing* (loop part I and II) aiming at the evaluation of reachable supercooling temperatures for different mass flow rates without producing ice slurry and the *crystallizer development* testing (loop part I and III) for producing the ice slurry. Loop part I) shows the shared loop for supercooler and crystallizer testing: a heat pump operates between the hot storage (blue in Fig. 3), filled with tap water, and cold storage (green), filled with 33 % Glycol. The temperature in the cold storage (TI20 and TI21) is the control temperature for the heat pump to turn on and charge the glycol storage to the desired negative temperature. Cold glycol from the cold storage is pumped into

the supercooler, controlling TI11 (T_{GlyIn}) with Pe4 and the mixing valve V_{Gly}. If ice in the supercooler needs to be melted, hot glycol, supplied from the chiller, and connected with V_{melt} and V_{Chill}, pumped with Pe4, can be used. In both type of experiments, the water in the supercooled loop (cyan in Fig. 3) is pumped (Pe1) from the storage into the PreHeater, a brazed plate heat exchanger used to control the inlet temperature TI1 (T_{WatIn}) of the supercooler. The hot side of the PreHeater is connected to the hot storage and the temperature can be controlled with Pe3 and V_{Pre}. The mass flow rate in the supercooled loop is measured with a Coriolis mass flow meter (Fl Wat). Pumped water is supercooled in the supercooler to a temperature TI2 (T_{WatOut}) and, depending on the type of the experiment, entering into the ReHeater for supercooler tests (loop part II) or into the crystallizer (loop part III) for controlled release of supercooling potential.

During supercooler tests, the supercooled water, in a metastable liquid state, leaving the supercooler is directly pumped into the ReHeater (see Fig. 3 part II) with only ≈ 300 mm of pipe in between the two heat exchangers. In the ReHeater the supercooled water is reheated to a temperature of 0°C, measured with temperature sensor TI3 (T_{Reheat}) and controlled by Pe2 and V_{Re}, supplied with water from the hot storage. This guarantees that no blockage of the piping system occurs before entering the storage vessel and avoids supercooling of the storage vessel content. During supercooler tests, a small storage vessel with a maximum capacity of 110 l allows for fast heating and cooling of the water in the supercooled loop.

For experimental analysis of the crystallizer, a device to release the supercooling potential in a controlled manner in a determined place, called in-stream crystallizer, is mounted after the supercooler instead of the ReHeater (see Fig. 3 part III). There, nucleation is triggered on the supercooled water forming ice slurry with a temperature of 0 °C, consisting of ice particles and liquid water with a solid mass content on the mass flow rate of less than 3 %. The produced slurry leaves the crystallizer and is fed into one of the two 1m^3 storage vessels, which are connected in series, while the ice-free water being pumped (Pe1) into the supercooler is sucked from the “ice-free” storage. Level compensation between the two storage vessels is guaranteed by a direct connection and a pump (Pe7).

2.2. Experimental control, measurements and calculation of power

The experimental control, including data acquisition, is realized using a CompactDAQ from National Instruments (NI) that establishes the communication between the computer with the in-house programmed LabView GUI and the I/O hardware modules. Used I/O modules are digital or analog modules from Wago with two to four channels each, used to control valves, pumps, heat pump and chiller. Signals from the PT100 temperature sensors, immersed into the flow, are received by 8-channel temperature input modules from NI with a precision of ± 0.03 K. During supercooler tests, the immersed temperature sensor TI2, measuring the outlet water temperature of the supercooler, is replaced by a calibrated PT100 surface sensor attached to the outlet stainless steel fitting of the supercooler to avoid obstacles in the supercooled flow. Calibration was done according to the procedure described earlier (see Carbonell et al. (2022)), but linear fit could be realized in a wider temperature range from 0.4 °C to −4 °C. The mass flow rate in the supercooled loop is measured with a Coriolis mass flow meter (precision of ± 0.15 %). Software detects freezing events, which block the hydraulic system, by a change in the mass flow rate and stops the test run, i.e. turns off pumps Pe1, Pe2, Pe3 and Pe4 as well as chiller and closes valves, in case of a blockage to avoid damage to components and allows for automated deicing of components. The supercooling power, i.e. the capacity stored in the supercooled water as sensible heat, which is converted into latent heat by inducing nucleation, can be calculated from the (indirect) measured quantities, supercooling degree, ΔT_{sup} in K, the mass flow rate of the supercooled water $\dot{m}$ in kg/h and using the specific heat of water c_P in J/(kg K) as:

$$P = \frac{Q}{t} = \frac{\dot{m} \cdot c_p \cdot \Delta T_{sup}}{t} \qquad \text{(Eq. 1)}$$

2.3. Supercooler Test Procedure

A commercial gasketed plate heat exchanger, called supercooler, with stainless steel plates is tested using part I and II of the set-up presented in Fig. 3. The water in the storage of the supercooled loop (filled with ≈ 80 l of water) is cooled down to a temperature between 0 °C and 0.1 °C. After, the test is started by keeping the glycol temperature T_{GlyIn} in the inlet of the supercooler constant at −0.4 °C for 15 min, resulting in a water

outlet temperature T_{WatOut} of approx. −0.1 °C. Next, the temperature of the glycol is decreased in steps of 0.2 K per 0.5 min. Consequently, the water outlet temperature is following the decrease in temperature. T_{GlyIn} is decreased until a "freezing" event is detected by the control program. This is achieved by monitoring the pump power required to establish the desired mass flow rate in the hydraulic system (water side): a freezing event causes an increase in the required pump power to keep the mass flow rate stable due to the increase of resistance in the hydraulic system. When the program detects a freezing event, the test is stopped and the last measured supercooling degree is taken as the achieved one for this test run. Deicing of the heat exchanger is realized by heating up the glycol flow causing a melting of the ice on the water side after some time. The water in the supercooled loop (including the water in the storage) is heated to 8 °C and a new test run can be started. During the test run the supercooled water is heated up to $T_{ReHeat} \approx 0.1$ °C after the supercooler to prevent a supercooling of the storage; the water temperature at the inlet of the supercooler T_{WatIn} is kept constant at ≈ 0.4 °C with the PreHeater during the whole test run to provide stable conditions. The achievable supercooling degree is measured 15 times for each of the water mass flow rates of 2000 kg/h, 2500 kg/h and 3000 kg/h.

To obtain comparable results the supercooled loop needs to be degassed before starting the test sequence as air bubbles present in the piping system are known to act as nucleating agents and thus to cause freezing events from previous experiments. The transparent piping system allows to detect air bubbles by eye with sufficient illumination. For every new test campaign, i.e. when a heat exchanger is replaced, fresh water at room temperature is filled into the system and the pump is started. At high pump speeds the flow is strong enough to carry away most of the air in the system. As the ability of water to absorb air is higher at lower temperatures, the water inside the supercooled loop is heated to 40 °C and constantly pumped through the loop for one night (12 hours). During this time air gets released from the water and accumulates into the open storage vessel. After roughly 12 h the water is cooled to room temperature. Repeated on/off sequences of the pump from 0 % to 100 % pump power are executed to carry away air accumulated inside dead zones of the loop. This process is supported by a valve mounted at the end of the inlet pipe (immersed into the water storage) that can be opened and closed while the pump is running, assisting the removal of air. The procedure is repeated until no air bubbles are visible in the pipes and at the inlet of the storage. Another visual check for air bubbles is done after cooling the water in the supercooled loop to 10 °C. If no air is visible, the system is ready for the supercooler tests under stable conditions.

2.4. Crystallizer Development and Test Procedure

Supercooled water, free of ice, is entering a vertically mounted in-stream crystallizer (Fig. 3 loop part III), made from transparent PVC-U, at the top of it, through a tangential inlet with reduced pipe diameter to accelerate the flow velocity (see Fig. 4 A and E). This serves as a barrier for growing ice crystals at the pipe wall upstream, into the direction of the supercooler as the force of the water on ice particles growing at the pipe wall is increased. Initially, crystallization is triggered via ultrasonic transducers attached to the external wall of the in-stream crystallizer but are turned off as soon as first ice nuclei exist inside the crystallizer. Afterwards, the nucleation process is self-sustaining due to the adhesion of very small ice crystals to upper part of the crystallizer pipe wall; ice crystals are flushed away from the wall as soon as the resistance to the water is larger as the adhesion to the wall. The dimensions of the crystallizer are such that the whole amount of stored sensible heat at a supercooling degree of 2 K and a mass flow rate of 3200 kg/h is transformed into latent heat inside the crystallizer. To ensure this was the case, pretests with an open crystallizer end, fed directly into the storage vessel, allowed to insert a temperature sensor (PT100) from the bottom to measure the slurry temperature at various positions with the aim to determine the necessary length of the device. Due to the tangential inlet, a swirl motion is introduced in the fluid flow (see Fig. 4 A), which is beneficial for mixing of ice and supercooled water and therefore the release of supercooling is further enhanced (compared to a pure axial flow). Furthermore, the possibility to use a reduction piece at the outlet of the in-stream crystallizer is strongly related to the structure of the produced ice crystals. If they agglomerate to big ice chunks inside the crystallizer, it will be more difficult for them to enter and go through the reduction. To avoid the agglomeration a higher rotational velocity component is preferable limiting the maximal diameter of the in-stream crystallizer. The outlet reduction piece is essential for being able to mount the crystallizer at any place after the supercooler

- potentially far away from the storage vessel, as the produced ice slurry can then easily be transported through a piping system consisting of various elbow pieces and pipe sections.

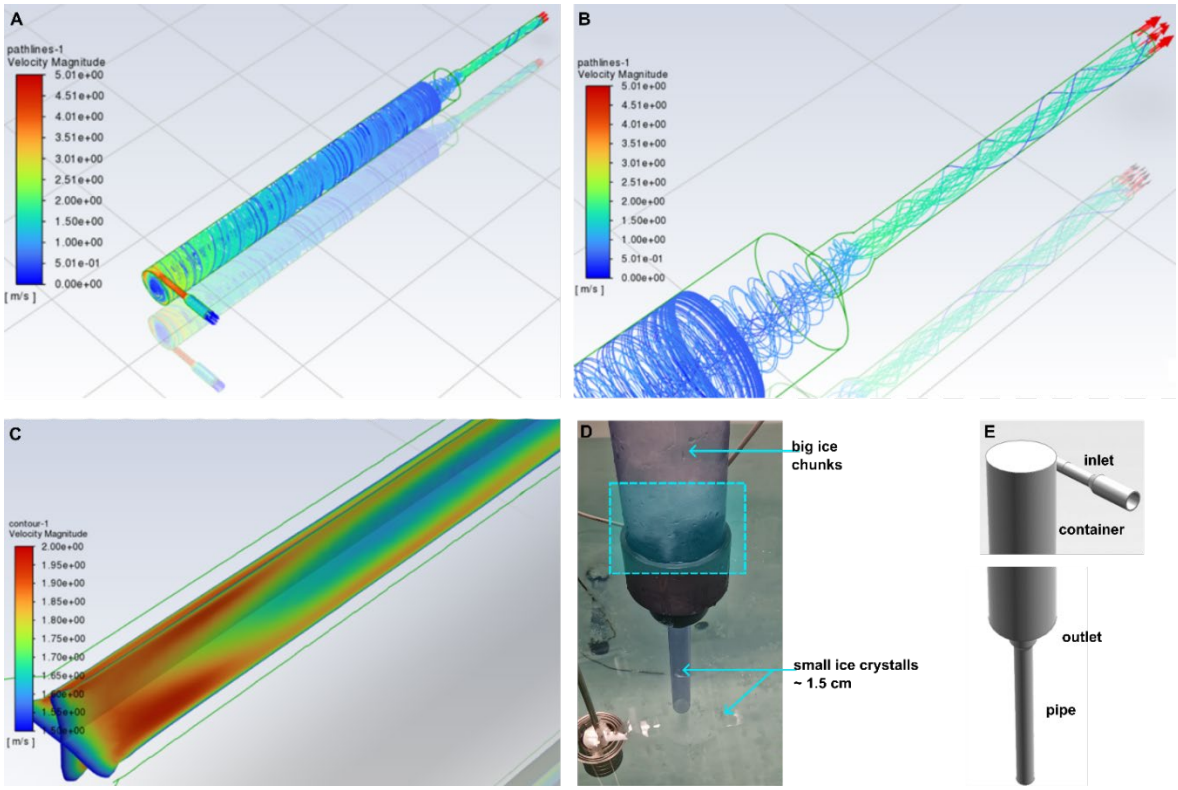

Figure 4: A: CFD simulation of a single-phase fluid (water) inside the crystallizer, showing a velocity profile of the flow (velocities given according to color bar). B: Zoom to the outlet region. C: Velocity profile in the pipe after outlet reduction, showing a fast stabilizing of the flow velocities inside the pipe. D: Photograph of the crystallizer with mounted outlet reduction and pipe, slurry fed into the storage. The cyan marked area is the area of suction effect causing a trenching of the ice crystals into smaller particles. E: CAD drawing of the crystallizer showing inlet, main crystallizer pipe, outlet and pipe.

A three-dimensional steady-state monophasic CFD model was developed to analyse the flow behaviour in the in-stream crystallizer and helped to understand the ice-slurry biphasic flow behaviour (despite the single-phase simplification) inside the crystallizer due to reduced ice content (less than 3 %). The reduction piece mounted to the outlet of the in-stream crystallizer causes a region of suction effect just above the outlet reduction and an acceleration of the fluid in this region (see Fig. 4 B). Bigger ice chunks, produced inside the in-stream crystallizer, are trenched into smaller particles in the region just above the outlet reduction (see Fig. 4 D) because of the acceleration of the flow and the arising suction. In addition, CFD simulations gave insight into the flow stabilization after the reduction piece at the outlet (see Fig. 4 C): the simulation shows that the flow inside the pipe, mounted after the reduction, is stabilizing within the first centimetres of the thin pipe, i.e. the velocity profile does not change over length of the pipe. To be able to freely mount the crystallizer in the set-up, a 90° elbow was mounted below the outlet reduction guiding the flow from vertical into horizontal direction and feeding it into one of the two installed 1 m^3 storage vessels. To fulfil all the above-described requirements the crystallizer was built step by step: first, it was tested with an open end mounted into the storage vessel. Second, the reduction piece was mounted and tested into the storage vessel. Third, the thin pipe was mounted into the reduction and cut to the appropriate length as described above and tested in the vessel. Forth, the elbow was mounted and tested into the vessel. Fifth, the crystallizer was removed from the storage vessel and mounted into the piping system.

For testing the crystallizer, the water enters the supercooler with a temperature between 0.5 °C to 1 °C and is supercooled to a stable temperature between −1.6 °C to −2.0 °C at a constant water mass flow rate (kept constant by the control program by adjusting the power of the pump). The PreHeating of the water before entering the supercooler enables stability under a broad range of working conditions melting potentially contained ice particles in the water flow. After the supercooler, the water releases its latent potential in the

crystallizer forming a slurry. Initial nucleation is triggered by ultrasonic waves at 50 kHz emitted from two to four ultrasonic transducers operated at a power of 25 W each. They are mounted to the outside of the crystallizer and the ultrasonic signal is applied for some seconds until first crystals are visible inside the crystallizer. The generated slurry is pumped though some pipes and is introduced into the storage vessel through an inlet mounted to one of the sidewalls and directed onto the center of the bottom of the storage. The feeding towards the bottom causes a wide spreading of the ice crystals, as they hit the bottom with a high velocity (1.5 m/s), before the crystals are rising by buoyancy to the highest reachable free space inside the storage vessel, unoccupied with ice yet. A crystallizer test run is considered successful if no blockage occurred in the system and if the production of slurry needs to be stopped due to a full storage, which is visible in the measurement data of the pump power and the mass flow rate (see Figure 6 B).

3. Results and Discussion

First, experimental results quantifying the supercooling degrees achieved for different water mass flow rates between 2000 kg/h to 3000 kg/h in gasketed heat exchangers are presented in section 3.1. Second, temperature and mass flow rate measurements for a successful crystallizer test with a power of 6.5 kW are shown and discussed in section 3.2.

3.1. Supercooler Test Results

Fig. 5 A) shows temperature measurements of a single test run at a mass flow rate of 2500 kg/h where the temperature of the glycol T_{GlyIn} in the supercooler (blue line) was decreased in steps of 0.2 K per 0.5 min. Water is entering into the supercooler at a temperature of 0.4 °C (T_{WatIn}, pink line). The green line is the temperature of the supercooled water leaving the supercooler T_{WaOut}, which is reheated in the ReHeater to 0 °C (T_{Reheat}, brown line). The lowest reached supercooling temperature in this test was −5.0 °C and is one of the points in Fig. 5 B) as indicated with the arrow. Fig. 5 B) summarizes results for supercooling tests performed with the supercooler and with water mass flow rates of 2000 kg/h (red), 2500 kg/h (green) and 3000 kg/h (blue). The data points correspond to the achieved supercooling temperature of single test runs, as shown in Fig. 5 A), with the average value for each mass flow rate given as the height of the corresponding bars.

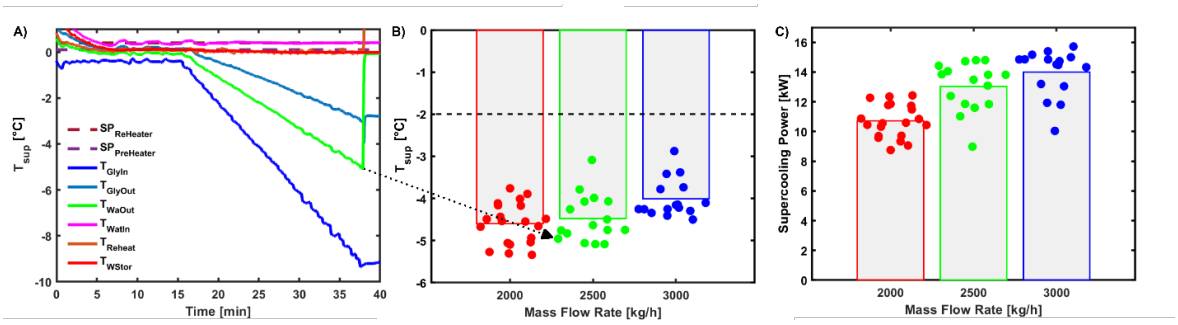

Figure 5: A) Single supercooler test-run at a water mass flow rate of 2500 kg/h with the decrease of the glycol temperature (blue line) in steps of 0.2 K per 0.5 min. The minimum supercooling temperature, which is measured at the outlet of the supercooler (T_{WaOut}, green line) is one of the points in the bar plot (B) summarizing the reached supercooling temperatures for the three evaluated different mass flow rates: 2000 kg/h = red, 2500 kg/h = green, 3000 kg/h = blue. Each point corresponds to the achieved supercooling temperature of a single test run. The bar heights give the average supercooling temperature achieved per mass flow rate. C) Comparison of corresponding supercooling power for each measurement run for water mass flow rates of 2000 kg/h, 2500 kg/h and 3000 kg/h. Each point corresponds to the power for the achieved supercooling temperature of a single test run. The bar heights give the average power achieved per mass flow rate.

The average supercooling temperature decreased from 4.6 °C ± 0.5 °C at a mass flow rate of 2000 kg/h to 4 °C ± 0.4 °C at a mass flow rate of 3000 kg/h. The spread between the highest and the lowest supercooling temperature for the same mass flow rate is 1.6 K for the mass flow rates of 2000 kg/h and 3000 kg/h, while it is 2 K for the mass flow rate of 2500 kg/h and is attributed to the stochastic nature of the freezing of supercooled water. All freezing events were detected for supercooling temperatures smaller than −2.9 °C. Despite the accelerated testing methodology used here is not the same than in our previous work (Carbonell, et al., 2022)

and results cannot be compared one to one, current results show that with large enough heat exchanger surfaces we can operate reliable at a reasonable supercooling temperature of −2 °C (dashed horizontal line in Fig. 5 B) without using icephobic coatings, provided the water quality is high and remains constant. However, the influence of water quality has not been assessed properly and will be topic of future research.

Fig. 5 C) shows the corresponding supercooling power delivered in the supercoolers from the tests of Fig. 5 B), calculated according to Eq. 1. For a mass flow rate of 3000 kg/h, an average supercooling power of 14 kW was reached.

3.2. Crystallizer Results

Temperature measurements of a successful test-run of the crystallizer with a supercooling power of 6.5 kW, operated for 3 h, at a mass flow rate of 3200 kg/h are shown in Fig. 6 A). Water was entering into the supercooler at a temperature of 1.0°C (T_{WatIn}, red line) and was supercooled to (in average) −1.75 °C (T_{WaOut}, blue line) using glycol at an average temperature of −4.5 °C (T_{GlyIn}, orange line). Slurry was continuously produced inside the crystallizer (see Figure 7 A) from the point marked with the black dashed line in Fig. 6 A) when nucleation was triggered by applying ultrasonic waves from the transducers for some seconds. The temperature of the storage filled with slurry was around 0 °C (T_{WStor}, yellow line) during the whole test, while the storage temperature of the second storage connected in series and free of ice was around 0.25 °C (upper = green, $T_{WatTank4}$; lower = purple, $T_{WatTank5}$). Fluctuations of the glycol temperature around the set-point of −4.5 °C are clearly visible in the data and are a result of the experimental control, as the glycol temperature in the inlet of the supercooler is controlled by a mixing valve (V_{Gly} in Fig. 3) with a PID-controller, determining the ratio of the glycol extracted from the cold storage into the glycol loop.

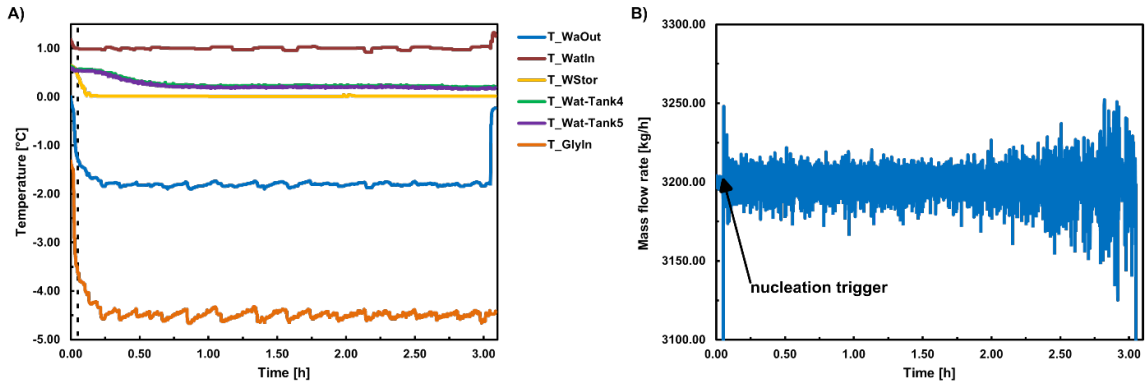

Figure 6: A) Measured temperature data for a successful 3 h test run at an average supercooling temperature of −1.75 °C (blue line, T_{WaOut}). The black dashed line marks initial triggering of nucleation by ultrasonic waves. Water is pre-heated to 1.0 °C before entering the supercooler (red line, T_{WatIn}). The temperature in the storage vessel filled with slurry is very close to zero during the whole test run (yellow line, T_{WStor}). The temperature in the second storage vessel (ice-free) is around 0.25 °C during the test run (upper = green, $T_{WatTank4}$; lower = purple, $T_{WatTank5}$). B) Mass flow rate with an average of 3200 kg/h for the same test run. The arrow marks the initial nucleation by ultrasound, the black dashed line marks the beginning of strong fluctuations in the mass flow rate due to high ice content in the storage vessel.

The PID controller is tuned as good as possible, while the temperature of the glycol in the storage is also dependent on the status of the heat pump (running or off). The fluctuations of the glycol temperature have an influence on the supercooling temperature in the water loop, which can be seen in the fluctuations of T_{WaOut} signal (blue line). However, the amplitude of fluctuations in the supercooled water temperature is less distinct as in the glycol temperature. Nevertheless, the fluctuations in the supply temperature (glycol) and the so caused fluctuations in the supercooling temperature are not causing any issue in the slurry production inside the crystallizer indicating a sign for the robustness of the device.

Fig. 6 B) shows the signal of the mass flow rate measurement, where the black arrow marks the triggering of initial nucleation by ultrasound. Starting at a time of ≈ 2.1 h, indicated with the black dashed line, the mass flow rate starts to fluctuate stronger which can be attributed to the filling of the 1m^3 ice storage with ice particles. The produced ice particles introduced into the vessel towards a central spot at the bottom (see Fig. 7 B) are distributed almost randomly inside the storage vessel, with some asymmetry caused by the suction

of the pump. With time, the storage vessel is filled with ice from top to bottom, as introduced ice particles rise due to buoyant forces. When most of the vessel is filled with ice, new ice particles start to accumulate close to the slurry-inlet into the storage as no space is left for ice particles to move around. Thus, pressure increases and the pump power needs to be increased too, to keep the same mass flow rate, which is realised by the experimental control. The increase in pump power causes an increase in mass flow rate, likely above the set-point value, and can brush aside the accumulated ice in front of the inlet resulting in a small free space around the inlet until it is covered by more ice particles. This process leads to a pulsing effect until complete blockage. The phases of "slightly blocked" vessel slurry inlet are therefore visible in the mass flow rate by fluctuations.

A "freeze alarm" was detected after almost 3 h and could be attributed to an ice formation in the supercooler itself (no complete blockage), likely caused by an ice particle entering the supercooler, and visible in the rise of the T_{WaOut} signal to 0 °C, mounted after the supercooler. By visual investigation it could be observed that ice particles moved into the former "ice-free" second storage due to the "full" ice slurry storage (see Fig. 7 C) from where they can be easily pumped to the supercooler. After finishing the test, a manual check of the ice consistency in the ice slurry storage revealed a lower packing density in top layers, which were filled in the beginning of the test-run, when ice crystals entering the storage were able to rise more freely. In comparison, the ice in lower layers, also around the inlet, was packed with a higher density and almost down to the bottom. However, the theoretically produced ice mass during this time with the used operational parameters is around 200 kg, occupying a volume of 0.23 m^3, which is 23 % of the complete slurry storage volume (one tank), making clear that the introduction of slurry into the vessel needs to be improved.

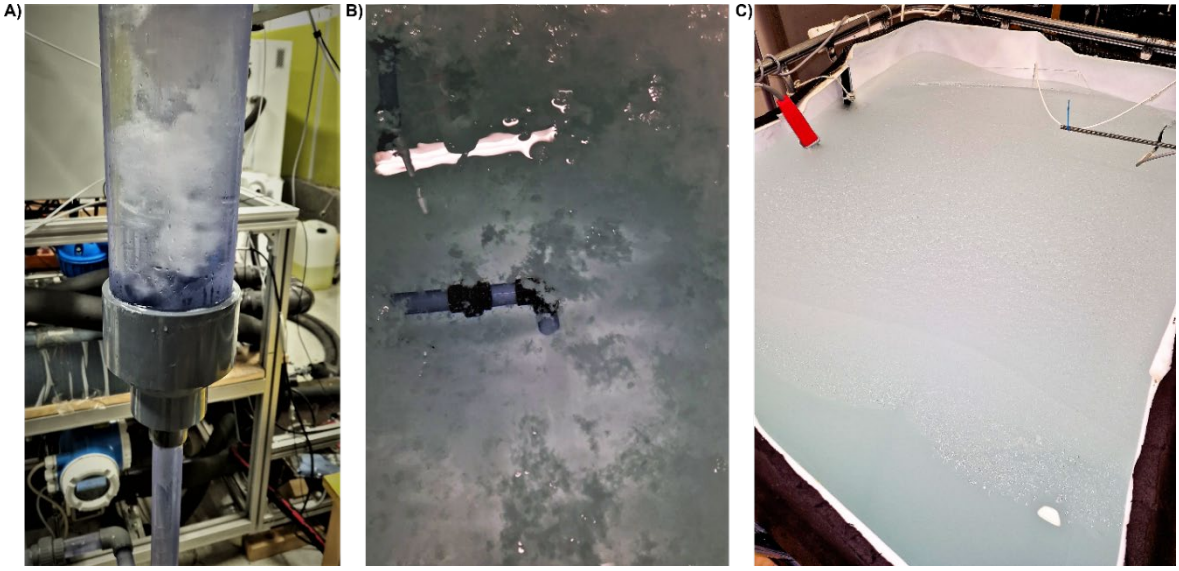

Figure 7: Photographs of A) the slurry generation inside the crystallizer, B) the produced slurry entering the storage vessel and C) the full storage vessel at the end of test-run as presented in Fig. 6.

4. Conclusion

This paper presents experimental developments and results for the reliable and continuous generation of ice slurry from an in-stream crystallizer using the supercooling method at a power of up to 6.5 kW.

The possibility to use gasketed plate heat exchangers reaching supercooling degrees suitable for ice slurry production between −1.5 °C and −2.5 °C without the need of icephobic coatings was shown. This possibility could decrease fabrication and installation cost of the technology as well as avoidance of coating degradation, decreasing thus maintenance needs. Gasketed plate heat exchangers are a suitable solution for large scale applications such as industrial processes. However, these type of heat exchangers are typically not suitable for residential heat pumps since they are too large. Moreover, the influence of the water quality is unclear at this stage as well as the question if icephobic coatings could provide a more stable system using tap water, likely with an increasing number of particles that could be expected after long term operation and that could trigger heterogeneous nucleation in the system. The effect of water quality on supercooling stability and the possible

increase of operation stability by using icephobic coatings, assuming a growing number of particles in the system with operation time, will be topic of further research in near future.

The development of the in-stream ice crystallizer, demonstrated at a mass flow rate of 3200 kg/h and an average supercooling degree of 1.75 K can become a breakthrough technology for energy storage paving the way to provide energy flexibility at low cost. However, to implement this technology at large scale, the scalability needs to be proven and optimisation needs to be conducted. To obtain more accurate and detailed insights into the in-stream crystallizer, further development of CFD modelling using multi-scale biphasic simulation is planned for near future, helping to realise the up-scaling of the crystallizer in an optimised configuration.

In this paper, two of the defined three challenges for the proposed ice slurry technology have been addressed and solutions for the supercooling and the continuous crystallisation have been presented. Nevertheless, the low maximum mass ice fraction achieved of approximately 23 % compared to the expected value of approximately 50 % (Kauffeld, et al., 2005) clearly shows that the third challenge remains to be investigated further. A better separation of solid particles and liquid water would allow to increase reliability as well as lowering the water inlet temperature into the supercooler to increase performance of the technology by reducing heat losses. Thus, the aforementioned third challenge of a proper separation of ice and water in the storage vessel needs to be content of future research work, before the proposed method is ready to be implemented into the field.

5. Acknowledgments

The authors thank the US Department of Energy (Solar Energy Technology Office) [Award Number DEEE0009814] and the Swiss Departement of Energy (SFOE) [Grant Number SI502570-01] for financial support.

We thank Alfred Brunner for support in the electrical and software control as well as Bruno Füchslin and Ramon Mattle for help in building the experimental set-up.

6. References

Arenas-Larranaga, M., Gurruchaga, I., Carbonell, D. & Martin-Escudero, K., 2024. Performance of solar-ice slurry systems for residential buildings in european climates. Energy and Buildings, Volume 307.

Bédécarrats, J.-P., David, T. & Castaing-Lasvignottes, J., 2010. Ice slurry production using supercooling phenomenon. International Journal of Refrigeration, 33(1), p. 196–204.

Carbonell, D. et al., 2020. Slurry-Hp II - Development of a supercooling ice slurry heat pump concept for solar heating applications, Bern: Institut für Solartechnik SPF for Swiss Federal Office of Energy (SFOE), Research Programme Heat Pumps and Refrigeration.

Carbonell, D., Philippen, D., Granzotto, M. & Haller, M. Y., 2016. Simulation of a solar-ice system for heating applications. System validation with one-year of monitoring data. Energy and Buildings, 127(0), p. 846 – 858.

Carbonell, D., Philippen, D., Haller, M. Y. & Frank, E., 2015. Modeling of an ice storage based on a de-icing concept for solar heating applications. Solar Energy, Volume 121, pp. 2-16.

Carbonell, D. et al., 2022. Development of supercoolers for ice slurry generators using icephobic coatings. Internationa Journal of Refrigeration, Volume 144, pp. 90-98.

Ernst, G. & Kauffeld, M., 2016. Influence of the wall surface roughness on the supercooling degree of water flowing inside a heat exchanger. Karlsruhe, Germany, International Journal of Refrigeration (IRR).

Faucheux, M., Muller, G., Havet, M. & LeBait, A., 2006. Influence of surface roughness on the supercooling degree : Case of selected water/ethanol solutions frozen on aluminium surfaces. International Journal of Refrigeration, Volume 29, p. 1218–1224.

Gurruchaga, I. et al., 2023a. Potential benefits of TRI-HP systems around Europe, s.l.: Deliverable 7.10 TRI-HP: Trigeneration systems based on heat pumps with natural refrigerants and multi renewable sources, Horizon 2020 research and innovation programme under grant agreement N. 814888.

Gurruchaga, I. et al., 2023b. Demonstrated energetic performance and cost competitiveness of tri-hp systems, s.l.: Deliverable 7.9 TRI-HP: Trigeneration systems based on heat pumps with natural refrigerants and multi renewable sources, Horizon 2020 research and innovation programme under grant agreement N. 814888.

Haberl, R. et al., 2022. Concise cycle test methods to evaluate heating/cooling systems with multiple renewable sources. s.l., CLIMA 2022 conference.

Honke, M., Safarik, M. & Herzog, R., 2015. R718 turbo chillers and vacuum ice generation - two applications of a new generation of high speed, high capacity R718 centrifugal compressors. s.l., 24th International Congress of Refrigeration.

Kauffeld, M. & Gund, S., 2019. Ice slurry − History, current technologies and future developments. International Journal of Refrigeration, Volume 99, p. 264–271.

Kauffeld, M., Kawaji, M. & Egolf, P., 2005. Handbooks on Ice Slurries: Fundamentals and Engineering. Paris: International Institute of Refrigeration (IIR).

Kozawa, Y., Aizawa, N. & Tanino, M., 2005. Study on ice storing characteristics in dynamic-type ice storage system by using supercooled water.: Effects of the supplying conditions of ice-slurry at deployment to district heating and cooling system. International journal of refrigeration, 28(1), pp. 73-82.

Kurihara, T. & Kawashima, M., 2001. Dynamic ice storage system using super cooled water. introductions of heat pump and thermal storage unit for commercial use. Osaka, Japan, Proceedings of the 4th Workshop on Ice Slurries of the IIR, pp. 61-69.

Lyons, L. et al., 2023. Clean energy technology observatory: Heat pumps in the european union - 2023 status report on technology development, trends, value chains and markets, s.l.: Publications Office of the European Union, Luxembourg.

Mito, D., Mikami, Y., Tanino, M. & Kozawa, Y., 2002. A New Ice Slurry Generator by Using Actively Thermal-hydraulic Controlling both Supercooling and Releasing of Water. s.l., Proceedings of the 5th Workshop on Ice Slurries of the IIR, pp. 185-196.

Mito, D., Tanino, M., Kozawa, Y. & Okamura, A., 2001. Application of a dynamic ice-type storage system to the intermittent cooling process in the food industry.

Mouneer, T. A., El-Morsi, M. S., Nosier, M. A. & Mahmoud, N. A., 2010. Heat transfer performance of a newly developed ice slurry generator: A comparative study. Ain Shams Engineering Journal, 1(2), pp. 147-157.

Nagato, H., 2001. A dynamic ice storage system with a closed ice-making device using supercooled water. Osaka, Japan, Proceedings of the 4th Workshop on Ice Slurries of the IIR, pp. 97-103.

Nelson, D. J., Vick, B. & Yu, X., 1996. Validation of the algorithm for ice-on-pipe brine thermal storage systems. ASHRAE Transactions, Volume 102, p. 55–62.

Philippen, D. et al., 2012. Development of a heat exchanger that can be de-iced for the use in ice stores in solar thermal heat pump systems. Rijeka and Opatija, International Solar Energy Society (ISES).

Pronk, P., Meewisse, J. M., Ferreira, C. A. I. & Witkamp, G. J., 2003. Ice slurry production with a circulating fluidized bed heat exchanger. Washington D.C., International Congress of Refrigeration.

Saito, A. & Okawa, S., 1994. Fundamental research on initiation of freezing of supercooled water on heat transfer surface. Brighton, United Kingdom, 10th International Heat Transfer Conference, p. 121–126.

Stamatiou, E., Meewisse, J. W. & Kawaji, M., 2005. Ice slurry generation involving moving parts. International Journal of Refrigeration, 28(1), pp. 60-72.

Tanino, M. & Kozawa, Y., 2001. Ice-water two-phase flow behavior in ice heat storage systems. International Journal of Refrigeration, 24(7), p. 639–651.

Tanino, M., Kozawa, Y., Mito, D. & Inada, T., 2000. Development of active control method for supercooling releasing of water. Proceedings of the 2nd Workshop on Ice Slurries of the IIR, Volume 127.

Wijeysundera, N. E., Hawlader, M. N. A., Andy, C. W. B. & Hossain, M. K., 2004. Ice-slurry production using direct contact heat transfer. International Journal of Refrigeration, 27(5), pp. 511-519.

Zhang, X. J. et al., 2008. Performance improvement of vertical ice slurry generator by using bubbling device. Energy Conversion and Management, 49(1), pp. 83-88.

Disclaimer

This report was prepared as an account of work sponsored by an agency of the United States Government. Neither the United States Government nor any agency thereof, nor any of their employees, makes any warranty, express or implied, or assumes any legal liability or responsibility for the accuracy, completeness, or usefulness of any information, apparatus, product, or process disclosed, or represents that its use would not infringe privately owned rights. Reference herein to any specific commercial product, process, or service by trade name, trademark, manufacturer, or otherwise does not necessarily constitute or imply its endorsement, recommendation, or favouring by the United States Government or any agency thereof. The views and opinions of authors expressed herein do not necessarily state or reflect those of the United States Government or any agency thereof.

Developing and demonstrating innovative solutions for renewable and waste heat-driven cooling technologies in industries: the RE-WITCH project

Christian SCHWEIGLER[1], Felix ZIEGLER[2], Walter MITTELBACH[3], Matteo CALÒ[3,8], Andrea BAELZ[4], Stefan PETERSEN[5], José Luis CORRALES[6], Maider EPELDE[6], Salvatore VASTA[7], Alessio SAPIENZA[7], Andrea FRAZZICA[7]

[1]Hochschule München Munich (Germany)
[2]Technische Universität Berlin Berlin (Germany)
[3]Sorption Technologies GmbH Freiburg, (Germany)
[4]BS Nova Apparatebau GmbH Siegen (Germany)
[5]Factor4Solutions GmbH Berlin (Germany)
[6]Tecnalia Research & Innovation Derio (Spain)
[7]CNR ITAE Messina (Italy)
[8]Politecnico di Torino, Department of Energy Turin (Italy)

Abstract

The present work introduces a research project funded by the European Commission under the Horizon Europe program, focusing on the development and demonstration of innovative cooling technologies for industrial applications, which can be driven by low-grade waste heat and solar thermal collectors. Aiming at increased compactness and reduced cost, an adsorption chiller based on a novel internal cycle configuration will be developed. For simultaneous heating and cooling with increased temperature lift and for supply of cooling at two separate temperature levels, advanced absorption chiller concepts will be applied, based on a hybrid absorption/compression cycle and a twin evaporator/absorber configuration, respectively.

Keywords: absorption, adsorption, industrial cooling, solar thermal, waste heat

1. Introduction

In 2022, the industrial sector in the EU was responsible for 25.1% of the final energy consumption, which totalled 10,900 TWh. This energy demand was primarily met by electricity (33.3%) and fossil fuels (48.4%), leading to a significant dependence on these resources, most of which are imported from non-EU countries (Eurostat, 2022). Approximately 150 TWh/year of electricity is consumed for process cooling, particularly in industries such as food and beverage, tobacco, and light chemicals, where cooling can account for up to 50% of a company's total electricity consumption (Rehfeldt, 2016). The market is largely dominated by electricity-powered vapour compression chillers due to their commercial availability and reliability, which restricts the adoption of thermally driven technologies to a niche segment. However, there is about 300 TWh/year of technically available waste heat from industrial processes in the EU, with roughly 35% classified as low-grade waste heat (below 200°C). Additionally, direct solar heating (SHIP) is becoming more attractive for its sustainability, technical, and economic benefits, although it is not yet widely implemented (Kumar, 2019).
Under the "Climate, Energy and Mobility" component of the Horizon Europe programme, a consortium of 27 partners is collaborating on the RE-WITCH project ("Renewable and Waste Heat Valorisation in Industries via Technologies for Cooling Production and Energy Harvesting") to develop and demonstrate innovative thermally-driven cooling and heating technologies for industrial processes. This includes introducing a next-generation adsorption chiller based on a novel internal cycle and component design. Advanced absorption chiller concepts, which use a hybrid absorption/compression cycle and a twin evaporator/absorber configuration, will be applied for simultaneous heating and cooling with increased temperature lift and cooling supply at two separate temperature levels. These thermally activated cooling systems will be powered by low-

© 2024. The Authors. Published by International Solar Energy Society
Selection and/or peer review under responsibility of Scientific Committee
10.18086/eurosun.2024.08.05 Available at http://proceedings.ises.org

grade (<100°C) waste heat from industrial processes or high-efficiency solar thermal collectors, providing both process cooling and useful heat for industrial operations.
The project involves analyzing typical applications in key industrial sectors such as food and beverage or pharmaceuticals and conducting detailed modelling of industrial processes with integrated thermal cooling systems for optimized techno-economic integration. The performance of these thermally driven cooling systems will be evaluated and demonstrated in four real installations across Europe in the following settings:

- A brewery located in Poland. In this case, the cooling demand is related to the need to cool down the wort from 98 °C to 8 °C, for the fermentation process. This is accomplished through two two-stage cooling process, using an ammonia vapour compression chiller, with a total capacity of 200 kW. The demonstration campaign will be based on the waste heat recovery from wastewater around 80°C, to drive the innovative adsorption chiller with an installed cooling capacity of 200 kW, to provide cooling down to 5°C. Moreover, a solar collector field with a heating capacity in the range of 50-70 kW will be integrated, to provide up to 100°C to the process and to complement the driving heat for the cooling provision. The demonstrative system is expected to work in parallel with the existing cooling facilities in order to provide energy saving service: preliminary estimations foresee an electricity saving of up to 64 MWh with 800 production cycles per year.
- A dairy industry located in Spain. The portion of the plant interested in the RE-WITCH system integration has on average a cooling demand ranging from 700 to 1500 kW, at temperatures between -6 and 0 °C, with a total electric consumption of 24 GWh/y. At the same time, there is a need for heating, for cleaning at 60°C, with a yearly energy demand of 6.8 GWh. The installation will aim to demonstrate the partial replacement of the existing technology with the innovative hybrid absorption cooling and heating device. A solar field of 80-100 m2 solar collectors will be integrated with renewable heat from the biomass plant to provide up to 110°C and 50-160 kW, to drive the hybrid absorption/compression heat pump with a peak cooling capacity of around 100 kW, providing cooling down to 3°C (in parallel to the existing ammonia chillers) and up to 250 kW of process heating at 60°C. The proposed integration shall be able to save up to 90 MWh/y electric and 830 MWh/y natural gas, with associated 225 t/year of CO2 emissions saved.
- A bio-refinery located in Greece. The cooling demand is at two different temperature levels, namely, 10 °C for process cooling and 20 °C to maintain the digester temperature during hot days in summer. For this reason, the demonstration campaign will integrate an absorption chiller being able to provide both temperature levels at the same time. The system will exploit waste heat recovery from CHP around 99°C, to drive a dual evaporator/absorber chiller, 40 kWc at 10°C and up to 400 kWc at 20/25°C in parallel. Around 30 kWth of solar collectors will be integrated to provide up to 99 °C to the process and to complement the driving heat for the cooling provision Moreover, when there is excess cooling production, this will be used in the post-digester to improve its performance. The system implementation aims to provide up to 3.5 GWh/y of cooling and increase plant productivity by 5-10% by maintaining the optimal digester's temperature.
- The integration of an air compressor and adsorption chiller system in a pharmaceutical industry, in Germany, specialized in the development, analytics, and contract manufacturing of medicinal products. The new facility will feature a 225 kW water-cooled air-compression system, providing waste heat to an 80 kW adsorption chiller. This chiller will generate chilled water for production and laboratory use, feeding into the central cooling system designed for 500 kW nominal capacity at 10/15°C. The system is expected to meet 1.5 GWh of annual cooling demand, with an electricity requirement of 375 MWh per year. The adsorption chiller will operate on base-load compressors, achieving 7,500 hours of operation annually and saving 110 MWh of electricity, equivalent to 29% of the cooling system's energy consumption. This translates to a reduction of 50 tons of CO_2 emissions annually. Pre-assembled in a container, the system includes a hybrid cooler with 230 kW nominal capacity, while BIM-based engineering and monitoring tools optimize its operation. The demonstration highlights significant energy and environmental savings, with high replication potential across industries requiring compressed air and heating/cooling solutions.

In each case, solar thermal collector systems will supplement the driving heat input from the industrial

environment.

2. RE-WITCH most relevant innovations

The RE-WITCH project will develop and validate innovative cooling technologies to be driven by low-grade heating sources, such as onsite waste heat and renewable heat from solar thermal collectors. Specifically, three different cooling technologies will be designed, tested at laboratory scale, and demonstrated in real industrial plants:

- A novel adsorption chiller technology, based on a patented solution by Sorption Technologies GmbH company (German patent, 2019), aims at overcoming most of the issues of previous adsorption chiller designs, by applying a novel internal cycle concept by switching the refrigerant flow (i.e. water) in liquid phase, thus making use of smaller valves (thanks to the higher density of the liquid compared to vapor) and applying direct evaporation and condensation inside the adsorber module instead of the conventional heat exchanger design. The target of the project will be the improvement of the core components design (i.e. refrigerant pumps, heat exchangers, module architecture), focusing on the increasing of the chiller compactness This will lead to higher thermal efficiency (thermal cooling COP 0.65) and electric efficiency (electric cooling COP >20). allowing to meet an expected compactness >17 kW/m3 and the easiness in stacking adsorption modules to meet the industrial cooling demand, being able to be driven by heat at temperature varying from 75 to 90 °C.
- A hybrid absorption/compression cooling and heating technology. The hybridization concept will be based on the integration of a mechanical vapor compressor, between the evaporator and absorber of a single-stage absorption chiller. The development will start from previous design validated at lab-scale, as reported in **Error! Reference source not found.** (Schweigler, 2019). The mechanical compression serves for an increase of the pressure level of the absorber, allowing for an increase of the temperature level of heat rejection, usually limited by the risk of crystallization of the LiBr/water solution. The developed concept will be able to provide cooling simultaneously, at around 3/5°C, and heating up to 60°C, thus covering two different requirements for industrial cooling and heating. Under these operating conditions, the thermal cooling COP, is expected being around 0.65-0.70, while the thermal heating COP, reaches up to 1.75. At the same time, the electric consumption will be very limited, being the cooling electric COP, up to 9 and the heating electric COP up to 23.
- An absorption chiller able to provide, by means of the same working cycle, two different temperature levels of useful cooling to the consumer. The integration of a second evaporator-absorber pair will start from the existing design of LiBr/water absorption chillers by the company BS-NOVA and will be adapted to allow the chiller to serve two different chilling temperatures. Specifically, in the demonstration campaign of the project, the target cooling temperatures will be 10 °C and 20 °C, with different capacities, namely, 40 kW and 400 kW respectively.

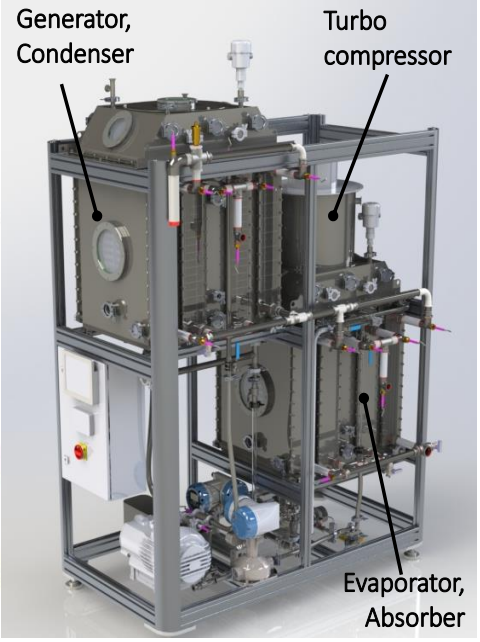

Figure 1: Design of the lab-scale hybrid chiller (Schweigler, 2019).

Regarding the onsite renewables, the project will rely on the integration of the innovative high vacuum flat plate solar thermal collectors, designed, and manufactured by the Swiss company TVP Solar (TVP Solar. 2024). These collectors can provide heating power in a temperature range between 80 °C and 180 C, at the highest conversion efficiency on the market for non-concentrating collectors technology. This technology will be then employed both as the driving source of the sorption cooling devices as well as to provide direct heating to the industrial plant. The optimization of the system operation will be guaranteed by dedicated control and management algorithms developed and implemented in each demonstration site.

3. The “RE-WITCH way”: the innovative aDsorption chiller

In recent decades, adsorption chillers using water as a refrigerant and solid sorbents like Silica Gel or Zeolites have been developed and utilized in commercial applications to provide chilled water. The fundamental operation of these chillers relies on the cyclic loading and unloading of the solid sorbent in the adsorber and desorber, respectively. By alternating the operation of two reactors filled with sorbent material, continuous cooling power is maintained. This process requires an appropriate valve system to switch the refrigerant flow between the reactors and the evaporator/condenser. Previously, various configurations known as “1st and 2nd Generation” adsorption chillers have been developed. This publication introduces a novel 3rd Generation adsorption chiller:

- 1st Generation Adsorption Chillers (Mayekawa, Bry-Air, SorTech): The refrigerant vapor flows from the desorber to the condenser and from the evaporator to the adsorber through valves integrated between the compartments, offering high flexibility but necessitating complex and expensive vacuum systems.
- 2nd Generation Adsorption Chillers (SorTech/Fahrenheit): These feature a simpler vacuum system by combining each adsorber with a heat exchanger that serves as both evaporator and condenser. Vapor exchange between the adsorber and heat exchanger occurs without valves, simplifying the vacuum system but resulting in significant thermal losses during cycling.
- 3rd Generation Adsorption Chillers (Sorption Technologies): This system, based on a patented solution (see the patent by Mittelbach, 2019), distributes the refrigerant in the liquid phase, alternately connecting each adsorber with the evaporator or condenser loop. The refrigerant evaporates/condenses directly inside the adsorber. Using liquid-phase water, with its higher density,

allows for smaller valves and components, and separating the heat exchangers mitigates the thermal losses encountered in the 2nd generation.

As in the previous solutions, the 3rd Generation includes two equal modules which alternate in adsorption/desorption by properly controlling a system of valves in the refrigerant loops and in the external loops, as shown in Figure 2, thus providing a constant cooling effect. The project's objective is to enhance the design of core components, such as refrigerant pumps, heat exchangers, and module architecture, to achieve a more compact chiller. This will result in higher thermal efficiency (thermal cooling COP ≈ 0.65) and greater electric efficiency (electric cooling COP >20).

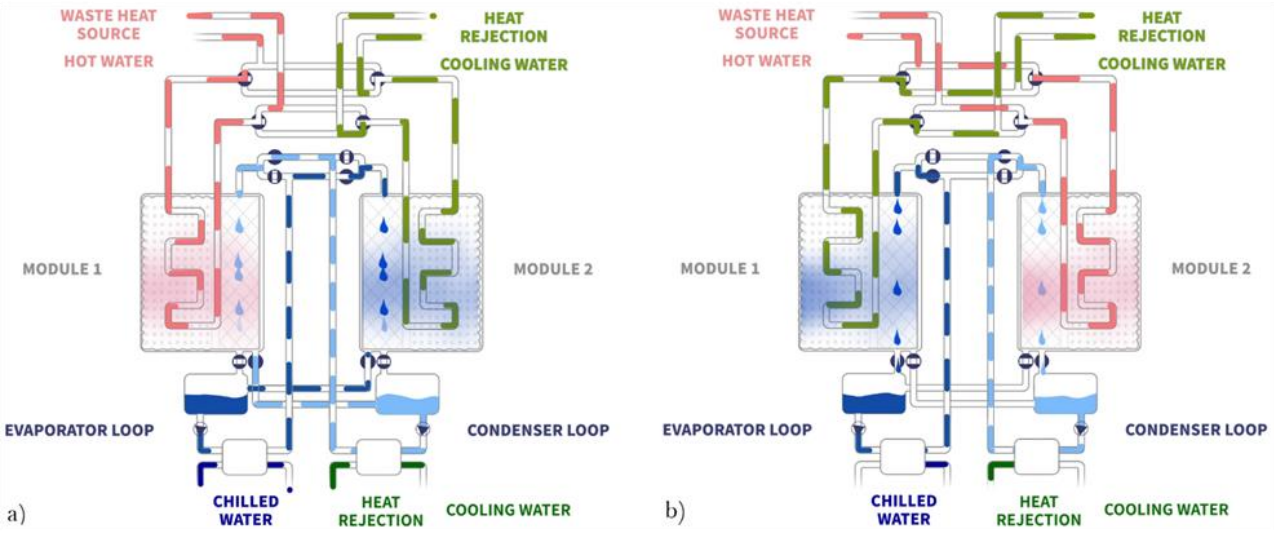

Figure 2: During the first phase, Module 1 is connected to the condenser loop, allowing the solid sorbent to unload, while Module 2 is connected to the evaporator loop, where the solid sorbent absorbs water; the cooling effect is harnessed through the evaporator loop heat exchanger (a). In the second phase, the roles of Module 1 and Module 2 are reversed, with Module 1 connecting to the evaporator loop and Module 2 to the condenser loop, thereby continuing to provide cooling power from the evaporator loop heat exchanger (b).

4. The “RE-WITCH way”: the innovative aBsorption chiller

Absorption chillers utilizing the LiBr-water working pair are well-developed and easily applicable in industrial settings. However, all sorption cooling devices face stringent temperature restrictions: in simple commercially available units, the waste heat temperature and chilling temperature limit the attainable reject heat temperature. This restriction reduces the capability to implement heat pumps that simultaneously provide cooling and useful heat output. For example, if the reject heat is required at around 60°C, standard designs driven by low-temperature waste heat will not suffice. The RE-WITCH project addresses these limitations by implementing advanced absorption cycles that decouple the thermodynamic states of the components. This allows for the provision of cooling at a low temperature (T0), heat output at a medium temperature (T1), and consumption of driving heat at a high temperature (T2) (Figure 3, left). These limitations are due to the equilibrium data of the water/lithium bromide working fluid pair and the potential crystallization of the mixture at states with low water content (Figure 3, right).

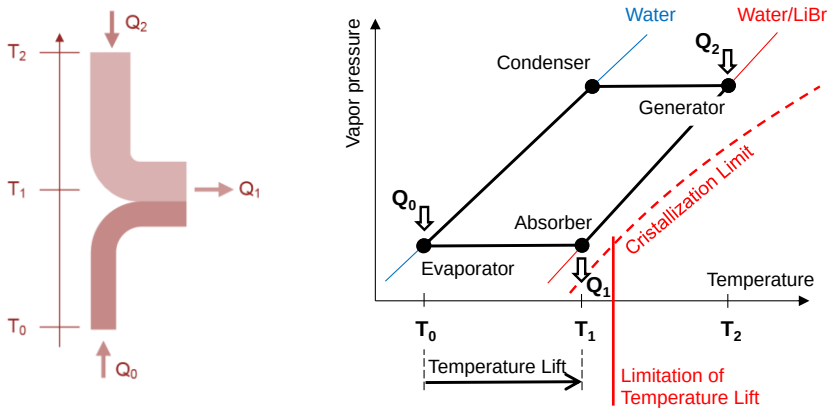

Figure 3: Temperature levels and heat flows of a sorption heat pump (left). Process parameters (internal pressure and temperature) of the standard absorption heat pump cycle (right). Limitation of the operational envelope by the crystallization limit of the sorbent solution.

4.1. Absorption Chiller with dual evaporator design

An absorption chiller featuring two evaporator/absorber pairs will enable the chiller to provide cooling at two different temperatures simultaneously, each with specified capacities (Figure 4). This configuration is distinct from the conventional twin design, which involves two evaporators connected to a single chilled water loop and two absorbers connected to a single cooling water loop. Typically, the solution flows are arranged in series from one absorber to the next to achieve larger temperature glides and avoid crystallization.

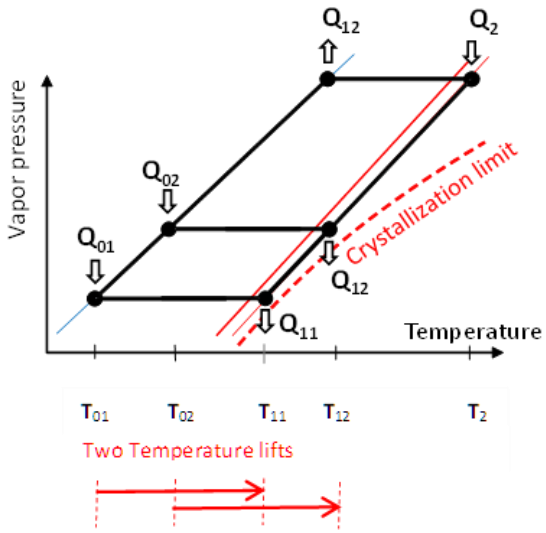

Figure 4: A schematic of the dual-evaporator layout

In the proposed design, each evaporator operates independently to accommodate different temperatures and cooling capacities. The solution flow and cooling water can be arranged either in parallel or in series, based on specific needs and technical constraints, ensuring design flexibility. Beyond the apparatus design, the project will focus on optimizing and controlling the operation.

The dual evaporator chiller will be designed for a demonstration case in Greece, providing cooling for two consumers at 10°C and 20°C, 40 and 400 kW respectively. An alternative to this concept would be installing two chillers operating almost in parallel. However, by directing the absorbing solution to either absorber in varying quantities, the proposed design makes more efficient use of the heat transfer surfaces. It will be demonstrated that cooling capacities and temperatures can be individually adjusted while maintaining cycle efficiency near the nominal COP value.

4.2. Hybrid Absorption/Compression Chiller

Integrating a mechanical vapour compressor between the evaporator and absorber of a single-stage absorption

chiller creates a hybrid chiller. This configuration, powered by mechanical energy supplied to the vapour compressor, achieves an increased temperature lift while maintaining the thermal efficiency of the hybrid cycle, as shown in Figure 5.

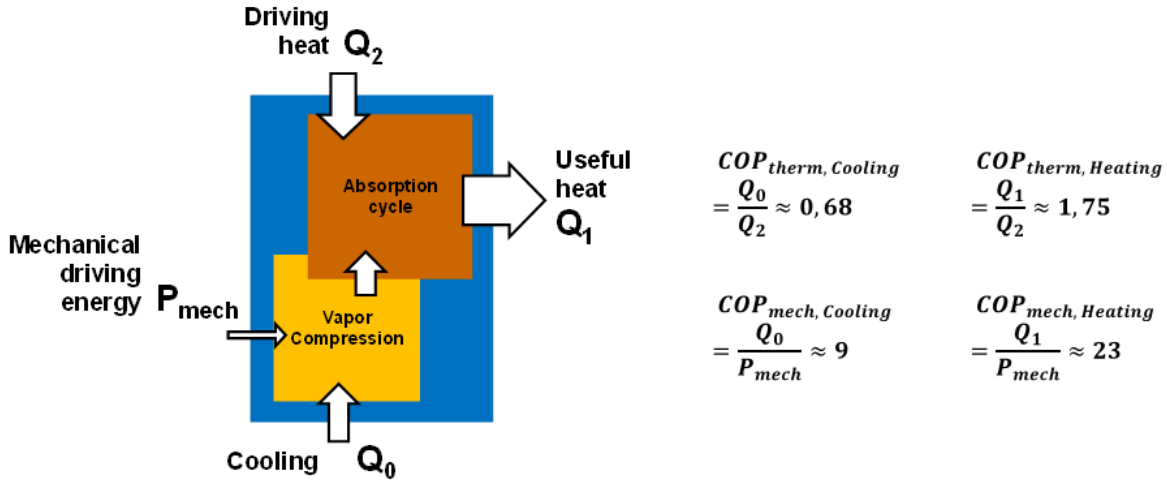

Figure 5: Hybrid absorption/compression chiller/heat pump: Energy flow scheme and COP for thermal and mechanical efficiency

The mechanical compression raises the pressure level of the absorber, which in turn elevates the temperature level of heat rejection within the crystallization limit of the sorbent solution (see Figure 6, left). This hybrid absorption/compression cycle with a high-temperature lift offers significant potential for heat recovery and simultaneous cooling and heating in industrial settings. Compared to a standard absorption chiller, the hybrid absorption/compression chiller provides a substantially higher temperature lift, as illustrated in Figure 6, right.

The development will build on a proof of concept demonstrated by a lab-scale test plant (Schweigler, 2019). For the industrial environment of a dairy plant in Spain, the hybrid cycle will be designed to provide a chilled water outlet temperature at the evaporator of 5°C and heat sanitary hot water from 15°C to 60°C using heat output from the absorber and condenser.

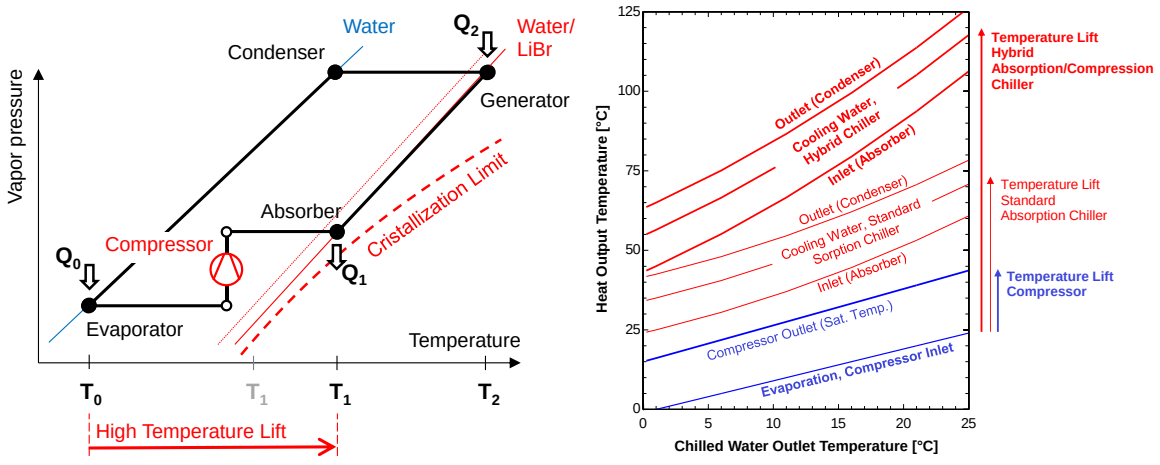

Figure 6: Hybrid absorption/compression chiller/heat pump with vapour compressor between evaporator and absorber (left). Increased temperature lift of the Hybrid chiller/heat pump compared to the standard absorption cycle (right).

5. RE-WITCH's expected impacts

The expected impact of RE-WITCH, with respect to solar energy exploitation, is profound and wide-ranging. Indeed, the integration of solar heat into the proposed systems (see the demos description in Section 1) enables

a solar cooling configuration that will lead to significant energy and fuel savings, and improve energy efficiency in the selected industrial processes. By harnessing renewable solar energy to drive cooling systems, the project aims to drastically reduce electric consumption for industrial cooling, thereby cutting down on greenhouse gas emissions and other pollutants. This shift towards solar cooling will lessen the dependency on traditional energy sources, enhancing the integration of renewable energy both at the industrial level and within the EU energy system.

Specific outcomes include the demonstration of solar cooling technologies across four industrial sectors in Europe, proving their viability and efficiency in real-world applications. This will not only validate the technology but also highlight its potential for substantial primary energy savings and CO2 emission reductions. By focusing on solar cooling, the project aligns with the EU's strategic plan for sustainable energy use, promoting clean energy solutions that are "100% Made in the EU."

Further, the project supports the development of a circular and clean economy by leveraging renewable energy for cooling purposes. Long-term projections indicate significant energy savings and GHG emission reductions by 2050, with the potential to cover 25% of the EU's industrial cooling demand through solar cooling technologies. Additionally, this shift is expected to create approximately 1,500 new direct and 4,000 indirect jobs by 2035, accompanied by substantial industrial investments.

6. References

- Eurostat 2020

  (https://ec.europa.eu/eurostat/statistics-explained/index.php?title=Final_energy_consumption_in_industry_-_detailed_statistics#Paper.2C_pulp_and_printing_industry)

- German patent, November 2019 (DE 10 2020 129 341 A1), extended to an international (PCT) application.

- Kumar L., et al. 2019. Global advancement of solar thermal energy technologies for industrial process heat and its future prospects: A review. Energy Conversion and Management.

- Rehfeldt M., et al. 2016. A bottom-up estimation of heating and cooling demand in the European industry. ECEEE Industrial Summer Study Proceedings.

- Schweigler C. et al. 2019. Flexible Heat Pump or Chiller with Hybrid Water/LiBr Absorption/Compression Cycle. International Journal of Refrigeration.

- TVP Solar products, 2024 (https://www.tvpsolar.com/products.html)

Solar Cooling for the Sunbelt Regions – Final results from IEA-SHC Task 65

Paul Kohlenbach[1*], Uli Jakob[2], Salvatore Vasta[3], Wolfgang Weiss[4] and Daniel Neyer[5,6]

[1] BHT Berliner Hochschule für Technik, Berlin (Germany)

[2] Dr. Jakob energy research GmbH & Co. KG, Weinstadt (Germany)

[3] CNR - ITAE, Messina (Italy)

[4] ergsol Inc., Portland/OR (USA)

[5] Neyer Brainworks GmbH, Bludenz (Austria)

[6] University of Innsbruck, Innsbruck (Austria)

* Corresponding author, kohlenbach@bht-berlin.de

Abstract

The IEA SHC Task 65 "Solar Cooling for the Sunbelt Regions" started in July 2020 and has been focusing on innovations for affordable, safe and reliable Solar Cooling systems for the Sunbelt regions. The Task 65 finished in June 2024. Its innovative approach was the adaptation of existing concepts/technologies to the Sunbelt regions using solar energy, either solar thermal or solar PV. This paper presents the comprehensive Task 65 results of the different activities carried out in the last four years as well as the research highlights. In Subtask A (Adaptation) climatic conditions, applications, components and systems have been investigated and adapted tools and systems for sun belt countries have been developed. A GIS-based tool is now available for the global identification of possible solar cooling locations, taking into account technical as well as socio-economic factors. Subtask B (Demonstration) put the focus on design guidelines, performance indicators and standardization. An analysis of multiple case studies has been undertaken and lessons learned have been compiled. In Subtask C (Assessment & Tools), design tools have been analysed as well as assessment mechanisms have been developed. A variety of tools for solar cooling design is available. Subtask D (Dissemination) focused mainly on distributing the Task 65 results, but also developed new roadmaps for sunbelt countries with regard to the implementation of solar cooling systems. Financing models have been analyzed and recommendations for policy makers are given as a result.

Keywords: Solar thermal cooling, PV cooling, Sunbelt regions, IEA SHC Task 65

1. Introduction

Air-conditioning accounts for nearly 20% of the total electricity demand in buildings worldwide and is growing faster than any other consumption in buildings (IEA, 2018). The undisputed rationales for the increase are global economic and population growth and thus rising standards of living. Growth in the demand of cooling is especially driven by countries with high temperatures. Three emerging countries (India, China, Indonesia) contribute to more than half of the annual growth rates. If no measures are taken to counteract this increase, space cooling demand could triple by 2050. In some countries, peak load caused by air conditioning does reach a share of >70% of the total electricity consumption on hot days (IEA, 2018). With an increase in cooling demand comes the increase in the cost of electricity and summer blackouts, which have been attributed to the large number of conventional air conditioning systems running on electricity. As the number of vapor compression chillers for AC purposes increase globally, so do AC-related greenhouse gas emissions, both from direct leakage of high GWP refrigerant, such as HFCs, and from indirect emissions related to fossil fuel derived electricity consumption. Solar air-conditioning is intuitively a well-suited alternative, because the demand for air-conditioning correlates quite well with the availability of solar energy. Interest in solar air-conditioning has grown steadily over the last years. The latest numbers of worldwide installations in 2023 showed nearly 2,000 systems (IEA SHC, 2023). Solar air-conditioning can be achieved by (i) operating a vapor compression air-conditioner with electricity generated by solar photovoltaic cells or by (ii) using solar thermal heat to run a thermally driven sorption chiller. Both these technologies can be used with or without a storage option, such as batteries or thermal storage units.

© 2024. The Authors. Published by International Solar Energy Society
Selection and/or peer review under responsibility of Scientific Committee
10.18086/eurosun.2024.08.06 Available at http://proceedings.ises.org

2. Methodology

The know-how on solar cooling technologies (both thermal and PV) in OECD countries (Europe, US, Australia, etc.) is already quite comprehensive thanks to more than twenty years of research and commercial activities on the subject. However, very few efforts have been made to adapt and transfer this knowhow to sunbelt countries e.g. in Africa, in the MENA region or in Asia. The sunbelt countries are located between the 20th and 40th degree of latitude in the northern and southern hemisphere and typically contribute to the global increase in demand for air conditioning (AC) since they are mostly located in hot and/or humid climates. In such climates solar cooling can play an important role in energy savings for AC. Further, all sunbelt countries are in regions of the world with high annual solar irradiation. Therefore, the IEA Task 65 "Solar Cooling for the Sunbelt Regions" focused on innovations for affordable, safe and reliable cooling systems for the sunbelt regions worldwide. It covers the small to large size segment of cooling and air conditioning (between 2 kW and 5,000 kW). The implementation/adaptation of components and systems for the different boundary conditions is forced by cooperation with industry and with support of selected target countries like India and UAE through Mission Innovation (MI) Innovation Community on "Affordable Heating and Cooling of Buildings" (MI IC7, 2023).

2.1 Task 65 structure

The Task is organized into four main activities, aka subtasks, derived from the described focus areas above. Figure 1 shows the subtask titles and work packages of each subtask.

Figure 1. Structure and work packages of Task 65 (IEA SHC, 2024)

2.2. Key objectives

The key objectives of IEA SHC Task 65 were to adapt, verify and promote solar cooling as an affordable and reliable solution in the rising cooling demand across sunbelt countries. Existing solar AC technologies have been analyzed, adapted to the specific boundaries and optimized in terms of investment and operating cost and their environmental impact (e.g. solar fraction). They have been compared and benchmarked against reference technologies with regard to a life cycle cost base. Task65 wanted to contribute to solar cooling becoming a reliable part of the future cooling supply in sunbelt regions. After the recent completion of IEA SHC Task 65 the following key objectives have been achieved:

- Supporting the development of solar cooling technologies on component and system level adapted for the boundary conditions of Sunbelt (tropical, arid, etc.) with regard to affordability, safety and reliability in medium to large scale (2 kW-5,000 kW) capacities
- Adapting existing tools for assessing technology and economics of solar AC systems
- Comparing the economic and financial viability of different cooling options with a life-cycle cost-benefit

analyses (LCCBA) model.

- Applying the LCCBA model to assess case studies and use cases from subtasks A and B to draw conclusions and recommendations for solar cooling technology and market development and policy design.
- Pre-assessing the 'bankability' of solar cooling investments with financial KPIs.
- Finding boundary conditions (technical/economic) under which solar cooling is competitive against fossil-driven systems and different renewable solutions.
- Establishing a technical and economic data base to provide a standardized assessment of demo (or simulated) use cases.
- Accelerating the market creation and development through communication and dissemination activities.

3. Results and analysis

3.1 Final results of Subtask A – Adaptation

Designing effective solar cooling systems in sunbelt regions requires a comprehensive understanding of the prevailing climatic conditions as well as a holistic approach considering a wide range of climatic factors. By tailoring systems to these conditions and promoting sustainable practices, a region can harness its abundant solar resources for efficient and eco-friendly cooling solutions. The following sections report the results that have been achieved in Subtask A.

A1: Climatic Conditions & Applications

Generally, the suitability of (solar) cooling systems and the specific applications thereof are highly contingent on the geographical location. To establish region-specific prerequisites for solar cooling systems, leveraging geographical data is a logical approach. This necessitates the utilization of a Geographic Information System (GIS), which possesses the capability to acquire, store, validate, and visualize data associated with Earth's surface coordinates. Most pertinent geographical data essential for this purpose can readily be sourced from various outlets, including solar radiation statistics, climate records, population demographics, and more. In the initial phase (Activity A1) of this project, GIS software was employed to amalgamate geographical data in a manner conducive to ascertaining localized reference conditions for solar cooling systems within Sunbelt regions. The data sources used in this study consist of multiple layers, with each layer containing data on specific topics or numerical values. These data layers are extensive, comprising 145 million grid cells and having a size of approximately 1.5 gigabytes each. The analysis took into account various conditions and sources, including geographic areas requiring cooling (spanning latitudes between 48°N and 44°S), different solar irradiances (DNI, GHI, DIF) and photovoltaic power potential (PVOUT), population density and settlement levels, climate zones based on the Köppen–Geiger climate classification system, water availability, assessment of market risk through Environmental Social Governance (ESG) factors, and considerations of Purchasing Power Parity (PPP) and Gross Domestic Product (GDP). These data sources and conditions played a crucial role in conducting the comprehensive analysis (Figure 2).

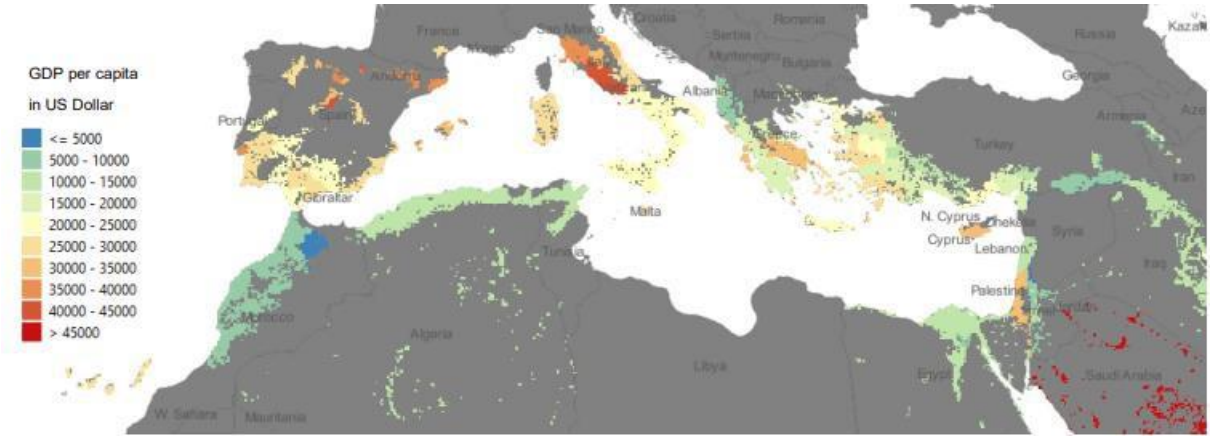

Figure 2. The Mediterranean region was used to identify the potential for a specific Solar Cooling System in building cooling applications. The analysis was conducted on a 10km raster grid, taking into account the Gross Domestic Product (GDP) levels. (Gurtner et.al, 2023).

The prospects for further investigation and improvement of the methodology encompass refining the method to provide specific regional or country-level insights for better result quality, conducting a more precise analysis of industrial areas and population distribution to identify clusters of large buildings showcasing cooling network potential, incorporating additional data sources like cooling degree days and energy prices to increase the significance of results by considering economic factors, expanding the study to encompass various building types (residential, commercial, hospital, university, etc.) to enhance its overall value in assessing cooling network potential, applying the methodology's principles to other renewable energy technologies for heating and electricity supply, and exploring the development of interactive web-based maps for improved user exploration, providing flexibility in presenting information according to specific needs and details. These considerations outline potential directions for refining and extending the methodology in future research and applications. Further details can be found in the published Task 65 A1 final report (Gurtner et. al, 2023).

A2-B1 & A3: Adapted Components and Systems

The Sunbelt regions feature diverse climates with critical factors like temperature, humidity, and dust presence. These factors affect the design and performance of solar cooling systems. Reliable data on these conditions is essential for selecting or adapting components to specific markets. Documenting available components is crucial for promoting solar cooling. Activity A2-B1 focused on documenting components, including collectors (photovoltaic, thermal, etc.), storage units, chillers, and heat rejection systems. This documentation combines climatic conditions and typical applications for effective technical adaptation. It considers the Köppen climate classification (see Figure 3), categorizing climates into five main groups (A, B, C, D, E) to qualitatively assess systems and components in the involved countries.

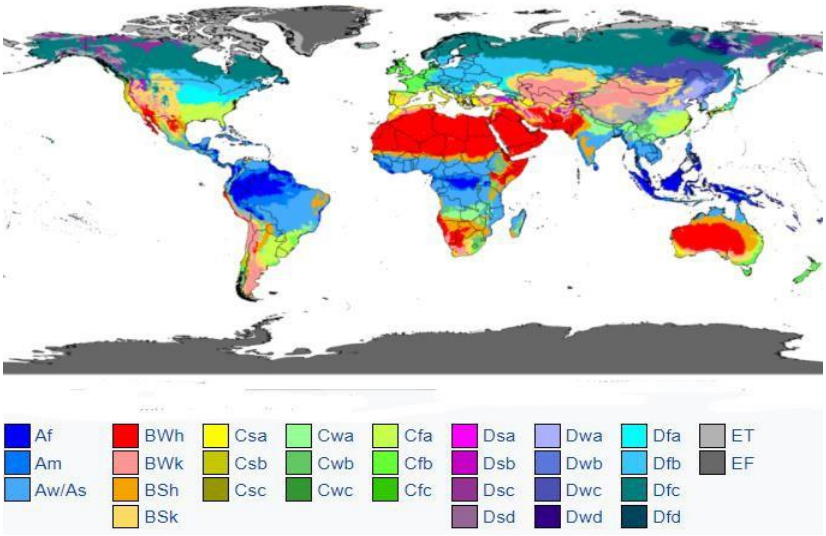

Figure 3. Köppen–Geiger climate map used for data classification (Beccali et.al, 2024)

This study analyzes various components used in solar cooling technologies and their relationships with factors like solar collector type, climatic zone, application, and adapted components (Beccali et. al, 2024). Solar cooling has the potential to decarbonize countries in the Sunbelt region effectively. With rising cooling demands in these areas, selecting the right components and analyzing existing projects can enhance its impact. During Task 65, 32 projects from 18 Sunbelt countries have been analysed, considering their demographic distribution, see Figure 4. The Köppen-Geiger climate classification was used to categorize these into climate zones, which is crucial for choosing cooling systems and solar collectors. The majority of projects analysed are in hot desert and hot semi-arid climates. About 50% of projects are in the implementation phase, 18% are operational, and 25% are in the concept phase. Evacuated tube collectors are popular in simulations, while flat plate and Fresnel collectors are common in implemented projects. Solar cooling systems are often installed in public buildings (34%) and domestic buildings (25%), with potential applications in food preservation and process industries.

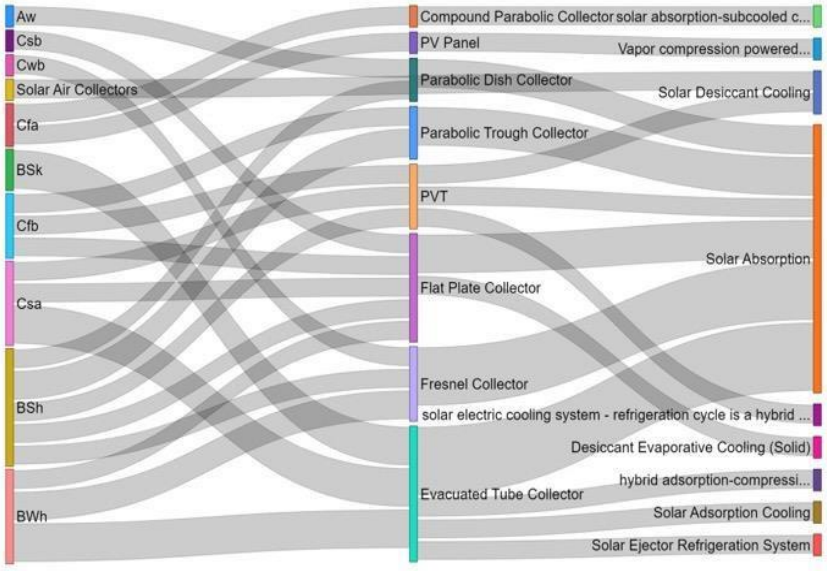

Figure 4. Representation of weather profile with solar collector and solar cooling technology used (Beccali et.al, 2024)

The results show that thermal storage units, along with auxiliary heating systems, play a vital role in meeting cooling requirements during periods of minimal or zero solar radiation, particularly at night. The cooling demand in public buildings like offices and educational institutions is primarily concentrated during daytime hours, leading to a reduced need for these components. In contrast, cooling demand may extend throughout the entire day and night for domestic applications (such as villa houses and multi-family buildings) and the process industry. Cold backup components, including vapor compression systems, are employed to extend the cooling capacity even when the solar cooling system is not active. Furthermore, Figure 4 provides valuable insights into the relationship between climate classifications, the types of solar collectors used, and the choice of solar cooling systems. Noteworthy observations from this analysis include:

1. In regions characterized by hot desert climates (BWh), Fresnel and evacuated tube collectors are often preferred for harnessing solar energy.
2. For areas with Hot summer Mediterranean (Csa) and Tropical and subtropical steppe (BSk) climates, evacuated tube collectors are commonly chosen.
3. Solar absorption cooling emerges as the most prevalent solar cooling technology, followed by PV-assisted cooling and ejector cooling.

A4: Building and Process Optimization Potential

The primary objective of Activity A4 was to assess the potential of energy-efficient buildings and processes in Sunbelt regions, both for new and existing structures. This involved studying other related projects and examining the integration of solar cooling into retrofitted HVAC systems. Integrating solar cooling into existing HVAC systems can be complex, especially concerning refrigerants and cold distribution methods. The aim was to identify the best technical solutions from both technical and economic perspectives. However, not all the planned analyses yielded useful data, leading to adjustments in the workflow. Some research projects and IEA EBC projects were reviewed, but it was found that there are limited recent projects focusing on the application of solar cooling systems in buildings. Nevertheless, the information gathered can serve as a foundation for assessing the potential energy savings achievable through the implementation of solar cooling systems. The initial phase of Activity A4 involved collecting and analyzing data from various buildings to assess the potential for energy-efficient building processes in Sunbelt regions. This assessment pertained to both new constructions and existing structures. One particular challenge addressed in this study is the integration of solar cooling into pre-existing HVAC systems. This integration presents hurdles related to refrigerants and cold distribution. Additionally, the study explored the application of cold delivery systems to reduce drafts in air-based systems and improve thermal comfort within

buildings. The data used in this analysis are sourced from (i) a research programme belonging to EU Horizon 2020 named "POI ENERGIA 2014e2020" (Beccali et. al, 2015) and (ii) selected completed projects from IEA's Energy in Building and Communities Programme (https://iea-ebc.org/). In cases where no necessary data were obtained through the primary data collection efforts, a comprehensive analysis of relevant literature was conducted. This approach effectively filled in the missing data gaps. By reviewing existing research papers, reports, and studies relevant to the field, valuable insights and information that enriched the research findings were accessed. The literature review revealed that global space cooling significantly contributes to the energy consumption of the building sector, accounting for approximately 16% of the final energy consumption in 2021. Furthermore, projections indicate that global electricity usage for space cooling could triple from 2020 to 2050. This trend is particularly prominent in rapidly developing countries like India and Indonesia, which experience cooling-intensive climates. To address these challenges, efforts have focused on providing efficient and environmentally friendly cooling solutions grounded in three fundamental principles: building energy efficiency, system energy efficiency, and renewable primary energy supply. Combining these principles results in cost-effective and sustainable cooling solutions that enhance user comfort and mitigate greenhouse gas emissions, benefiting the environment and climate. The outcomes of this study underscore the multifaceted nature of achieving energy efficiency in Sunbelt regions, especially concerning solar cooling and building processes (Bonomolo et. al, 2023). These findings emphasize the importance of robust data analysis, considering a range of factors that impact energy consumption and cooling demands in different building contexts. Further details can be found in the published A4 final report (Bonomolo and Strobel, 2023).

A5: Standardisation Activities

The Activity A5 covered two main aspects, which can be found in the published A5 final report (Vasta and Sapienza 2024):

1. Standardization and Definition of Key Performance Indicators (KPIs): The aim was to establish standardized definitions to create a unified language for solar cooling. KPIs are pivotal in assessing and comparing different solutions and technologies within the field. Given the diverse nature of solar cooling systems and components and their current limited adoption in energy systems, it is crucial to develop a precise and comprehensive set of KPIs. A selection process has been devised to choose appropriate KPIs, with seven base KPIs identified initially, which will be expanded to encompass materials, components, and systems.

2. Examination of Existing Standards and Regulations: Activity A5 investigated the present state of standardization and regulation concerning solar heating and cooling across Sunbelt countries. Various countries and international bodies have already formulated standards covering performance testing, system design, equipment specifications, safety requirements, and installation practices for solar heating and cooling systems. Prominent organizations in this realm include ISO, CEN, ASHRAE, among others. The Australian Standard AS5389 was deemed most suitable for solar cooling in the Sunbelt region, offering a comprehensive framework for the design, installation, operation, and maintenance of solar heating and cooling systems. However, AS5389 does not specifically address solar cooling systems in the Sunbelt region. To adapt it, several modifications were proposed, including additional design considerations, guidelines for cooling load calculation, recommendations for solar collector selection, guidance on thermal energy storage, and measures for evaluating system performance tailored to the Sunbelt region's needs. These adaptations aim to align the existing standard with the specific requirements and challenges of solar cooling systems in the Sunbelt region.

3.2 Final results of Subtask B – Demonstration

Solar thermal cooling has a long history (with first commercial examples having been built in the 1990's), however a real commercial market did not establish itself anywhere in the world. Roughly 2,000 solar (thermal) cooling systems exist worldwide. Most of them can be declared as customized, early-stage systems. PV supported cooling developed in the recent years, mainly driven by the cost decrease for PV modules in the recent decade. PV cooling has become the dominant type of solar cooling system globally due to its simplicity in installation and low cost. No robust numbers exist for installed PV cooling systems globally, but, as an example, several millions of these systems are in operation in Australia alone. The technology for both solar thermal and solar PV cooling is

commercially available worldwide. However, mostly economic reasons are still preventing solar cooling from gaining a wider global market uptake, especially in Sunbelt regions with lower purchasing power. One important approach for introducing these technologies into Sunbelt countries is a wide range of demonstrations locally. It must be assured that solar cooling is seen as technically reliable, economically viable (reasonable), and smart.

B1: Show Cases on System and Component Level

A number of installed projects was examined in order to find the constituent elements employed in different solar cooling technologies and their relationships with various variables, including type of solar collector, climate zone, application, and the components integrated into the systems. Solar cooling stands as a promising and efficient means of contributing to decarbonization efforts in nations within the Sunbelt region. Considering the expected increase in cooling needs within these nations, there is a substantial opportunity in identifying the best components and conduct comprehensive evaluations of existing/ongoing projects. This approach is expected to help expanding the scope of solar cooling and amplify its overall influence significantly. The research undertaken in this work package encompasses 31 studies conducted in 18 countries located in the Sunbelt region. Figure 5 illustrates the demographic distribution of these projects.

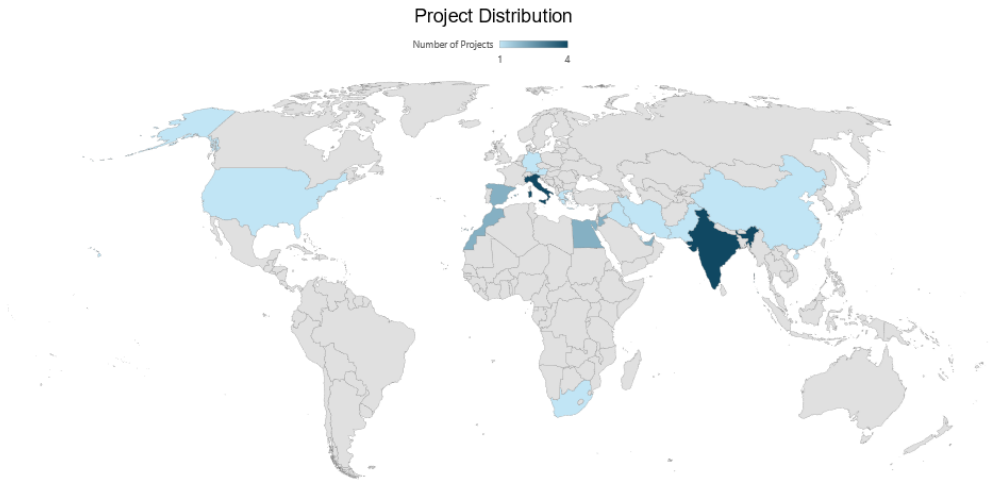

Figure 5. Case studies located in the Sunbelt region (Beccali et al., 2024)

The studies conducted included a diverse range of project types. Among these, 50% of the projects are currently in the implementation phase, 25% of the projects are in conceptual phase, 19% are in operation and have attained established outcomes, 3% are validated concepts and the remaining 3% are projects that have been modelled using simulation tools like TRNSYS, Python, Matlab, or other mathematical modeling techniques. Additionally, the study also includes published works featuring laboratory experiments and simulations validated by real-time building energy usage. This mixed approach ensures a comprehensive and varied analysis. The analysis shows that evacuated tube collectors are utilized in 30% of the analyzed projects, while both flat plate collectors and Fresnel collectors are equally prominent at 17% each. The research also indicates that Fresnel collectors and flat plate collectors are the most commonly chosen options in executed projects, whereas evacuated tubes are predominant in simulation projects. Examining the distribution of different solar collectors across various temperature profiles provides valuable insights into their suitability for different scenarios. Evacuated tube collectors find extensive application across three distinct climate regions: BSk (Cold semi-arid), BWh (Hot desert climates), and Csa (Hot-summer Mediterranean climate). Similarly, flat plate collectors are suitable for a range of five different profiles, spanning from Hot Desert (BWh) to Warm-summer Mediterranean climates (Csb). With regard to buildings the analysis shows that in the majority of the examined cases, solar cooling systems are installed in public buildings (34%), including offices, schools, and university buildings, enabling direct utilization of solar energy during daytime hours. Domestic buildings (25%) appear to be the next most studied due to prevalent requirements for improved indoor comfort in the Sunbelt region. The third most studied application (19%) includes indoor test facilities and process industry. The remaining applications include district cooling, food processing and preservation and highrise buildings.

B2: Design Guidelines

This work package included the collection of design and system integration guidelines for solar cooling projects. For this purpose, a comprehensive questionnaire was created that goes into detail about various solar cooling components, design, sizing and other sub-systems such as heat rejection unit and cold distribution system. Data from 10 case studies are collected and presented showing the performance of solar cooling systems with varying boundary conditions. Additionally, three different case studies, each with their own scope and unique characteristics, are discussed. The summary is as follows:

- Industrial cooling offers significant opportunities for solar thermal cooling applications. Such systems can achieve a high solar fraction and thus significantly reduce CO2 emissions compared to conventional electricity-powered chillers.
- The integration of solar PV with vapor compression chillers as an emerging solution for decarbonization of cooling systems. A comparative analysis considering different load and weather profiles suggests that solar PV cooling can result in lower levelized cost of cooling compared to solar thermal.
- Hybrid chillers emphasizes the potential of combining electrical and thermal chillers. Both simulation and practical results indicate a significant reduction in electricity consumption when using the topping cycle of an adsorption chiller.

In summary, these case studies highlight the transformative potential of cooling solutions. As technology advances and policies evolve, the adoption of such systems will play a critical role in shaping a greener and more energy efficient cooling future.

B3-C3: This work packages had not been finished at the time of writing of this publication, please refer to Task65 webpage (https://task65.iea-shc.org/) for a future publication of report B3-C3.

B4: Standardized Solar Cooling Kits

The activity B4 focused on the standardization of solar cooling kits presents experiences from 11 component and/or system suppliers of solar cooling kits, which adapted/investigated their products/concepts for Sunbelt region conditions. Moreover, several findings on system adaptations for Sunbelt regions are collected and analyzed from manufacturers, equipment providers, solar system providers and researchers. The essential findings/results of the published B4 report (Weiss et. al 2024) are:

- Eight different products/concepts adapted to the constraints of the Sunbelt regions are presented, including information on Sunbelt specific adaptations or experiences.
- Use of medium-temperature solar systems to operate two-stage absorption chillers to increase competitiveness.
- Cleaning collector systems when dust contamination happens can reduce typical performance by 20% per month. Therefore, it is recommended to clean the system every 14 days, which will then result in an average performance loss of only 5%.
- Lack of knowledge of design guidelines including the effects of part load conditions and techno-economic boundary conditions.
- Heat rejection systems in dry climates present significant challenges

B5: Lessons Learned (Technical and Non-Technical)

Activity B5 involved identifying and documenting lessons learned, both technical and non-technical, to create a summary for dissemination in Subtask D. The primary objective was to collect trustworthy data and gain valuable insights from various stakeholders. A survey was conducted to gather information on stakeholder’s requirements, expectations, and specific circumstances that may prompt the utilization of solar cooling. The survey's primary objective was to identify crucial factors influencing the adoption of solar cooling technologies across different applications and regions. The gathered information was then analyzed to better comprehend the challenges, needs, and desires of the stakeholders involved. The results obtained from the questionnaire showed that solar cooling technologies are highly valued and important, but their market transformation requires collaboration across various

sectors. Engaging with stakeholders, including government agencies, industry players, research institutions, and consumers, is crucial for creating a supportive ecosystem for solar cooling. GIS software aids in effective planning and deployment, while technical training programs build capacity and expertise in the industry. Demonstrating the technical and economic viability of solar cooling and reducing reliance on the electrical grid can promote adoption. A multi-faceted strategy involving awareness-raising, market acceptance, and accelerated penetration can make solar cooling a sustainable solution for cooling needs. This approach contributes to climate change mitigation, economic growth, and energy security.

3.3 Final results of Subtask C – Assessment and Tools

The concurrent technical, economic and financial assessment of solar cooling options is of high importance in each stage of the life cycle of a project, starting with comparison of different technology options and pre-design, detailed planning, optimizing of operation but also for policy design with proven concepts. In all life cycle phases, it is crucial to have corresponding tools that deliver the necessary information and key performance indicators for the different stakeholder. The KPIs need to take into consideration economic, financial, social and environmental issues as well as other 'Multiple Benefits'. Tools and their specific outputs permit to provide guidance on optimized system design and implementation and show the level of quality of both the most critical components and systems.

C1: Design Tools and Models

The work involved reviewing and adapting tools and models for technical and financial assessment and design for solar cooling and the project phases from pre-feasibility to simulation to monitoring. The main focus is the documentation of the tools and their specific application to provide measured data for validating the tools and the adaptation of selected ones for Sunbelt countries. Three approaches were used to evaluate tools used worldwide and within this IEA SHC Task. Firstly, a generic literature research in Web of Science (WoS), secondly interviews and questionnaires among the IEA SHC Task Expert, and thirdly interactive questionnaires during Task expert meetings. A total of 1,216 documents were identified as a result of the search in WoS. The initial data gathered provided a general idea of which components are being used and which software is being implemented. Based on the information provided by the task participants, the following software are currently being implemented in their applications/research: MATLAB, Meteonorm + Excel tool, TRNSYS, EES, and Phyton. This is also reflected in the third evaluation of tools. All software tools are commercially available and are ready to be used. Further details can be found in the published C1 final report (Daborer-Prado et. al, 2023).

C2: Database for Technical and Economic Assessment

Activity C2 was aimed at creating a comprehensive database of technical and economic data for solar cooling components and Sunbelt countries, supporting extensive assessments and providing insights into future scenarios. This database should establish a solid framework for sensitivity analyses and future scenario planning for solar cooling concepts. The IEA SHC Task 53 databases (IEA SHC, 2018) form the basis for the economic analysis of solar cooling systems (entire system, ST or PV based, including all main components already installed). An internal Task 65 expert survey has been conducted to further refine cost and technical figures for the database. The data base is comprehensive and listing every item here is not possible. As an example, technical components listed include:

- Solar sources: Flat plate collector, Evacuated tube collector, Photovoltaic
- Heat sources: Natural gas, Combined heat and power, Heat pump and reversible heat pump, Absorption heat pump and reversible absorption heat pump, District heating, Natural gas boiler, Condensing natural gas boiler, Electrical heater, Oil boiler, pellet boiler
- Cold sources: Air- or water-cooled vapor compression chiller, Single effect absorption chiller, Double effect absorption chiller, Adsorption chiller, District cooling
- Heat rejection: Wet cooling tower, Dry cooling tower, Hybrid cooling tower
- Storage: Hot water storage, Cold water storage, Battery storage

These components can be used as reference system or as part of the solar heating and cooling system. Please refer

to Task65 webpage (https://task65.iea-shc.org/) for a future publication of report C2.

C3-B3: Assessment mechanism / C4: Benchmarking/Sensitivity analysis

These work packages had not been finished at the time of writing of this publication, please refer to Task65 webpage (https://task65.iea-shc.org/) for a future publication of both reports C3-B3 and C4.

3.4 Final results of Subtask D – Dissemination

A wide penetration of solar cooling in Sunbelt countries is not only depending on the accomplishment of technical barriers. Non-technical barriers often have a critical role. Financing, policy advise, and dissemination/communication of success stories are among the important activities to overcome also non-technical barriers. The focus is on the implementation of target specific promotion activities based on the collected results, upgrade of material for dissemination for external communication, the implementation of knowledge transfer measures towards the technical stakeholders, the development of instruments and their provision for policy makers.

D1: Task65 Website and Publications

A website included into the IEA SHC portal has been created, see https://task65.iea-shc.org/. It firstly presents the Task purpose and activities and secondly the Task results. It also lists all Task participants and observers. Finally, in the near future the website will also host an online best practice collection webpage, presenting the system concepts, state of the art of cooling markets, the main lessons learned and the entire technical and economic KPIs. The website will further act as an archive of the Task's collective work results. Several publications about Task 65 and the experts work related to the different activities have been published: EuroSun 2020, FotoVolt 10/2021, SWC 2021, APSRC 2021, ISEC 2022, EuroSun 2022, APSRC 2022, s@ccess 2023, ICR 2023, SWC 2023, EusroSun 2024). For a comprehensive list please visit https://task65.iea-shc.org/news.

D2: Policy Advice and Financing Models

Solar cooling solutions typically require high upfront capital expenditures. They may also be perceived as risky by potential clients due to their complexity or unfamiliarity with solar cooling technologies. These and other non-technical barriers underscore the importance of developing client- and service-oriented solar cooling solutions for greater market penetration – in particular in the sunbelt regions. However, a common language in this interdisciplinary developmental area is missing, which limits effective communication and collaboration among stakeholders. The aim of this work package was to establish a common understanding of technical terms and core concepts in economics and financing that are necessary for the development of successful business and financing models for solar cooling. The following topics are covered:

1. Business Models vs. (Third Party) Financing.
2. Basic Financing Options for Solar Cooling Investments.
3. Business Models including Third Party Financing for solar cooling investments and services.
4. Life-Cycle Cost-Benefit Analyses to support Business Model development and financing solutions.

This work shall serve as a basis for better informed discussions among technical and non-technical stakeholders from various disciplines, which are crucial for advancing client-oriented financing and business models to achieve greater market penetration of solar cooling solutions. Further details can be found in the published D2 final report (Bleyl 2024).

D3: Roadmaps for Solar Cooling in Sunbelt Countries

Activity D3 was dedicated to provide guidelines and recommendations on the development of roadmaps and policy recommendations to accelerate and spread the development of solar cooling technologies. A literature review provided information and compared exemplary roadmaps and documents on cooling demand and solar technologies, respectively. The review results identify promising methods and possibilities in roadmap and implementation plan formulation. Furthermore, existing roadmap manuals and analyses and Task 65 results are introduced to provide background information and to collect input for new roadmap and policy recommendations.

The screening and review outcomes indicate that a linkage between the solar cooling technologies and their potential field of application on a national scale, directly targeting the most fruitful operation, is promising. As a final result of Activity D, an adapted and updated process recommendation on the roadmap development following a step-by-step approach has been developed. Additionally, a list of policy recommendations is delivered as potential guidance for policy makers to promote solar cooling technologies on a national level. Further details can be found in the published D3 final report (Strobel & Jakob, 2024).

D4: Booklet

A comprehensive summary in the form of a booklet will be published later in 2024.

D5: Workshops

The goal of work package D5 was to organise four half-day workshops dedicated to the industrial players (manufacturers and installers, consultants, policy makers) in sunbelt countries. This goal has been exceeded by far since 11 workshops have been organised and conducted altogether during the four-year period of Task 65. 567 participants have been recorded. Detailed information on the individual workshops as well as workshop agendas can be found in the published final report on D5 (Kohlenbach and Jakob, 2024).

D6: Stakeholder Engagement

A multitude of intermediate and final results has been generated during Task 65 and part of its activity was to ensure efficient communication of these results to all interest groups. Stakeholders from sunbelt countries have been selected as a specific interest group. These include end-users, industry, researchers, operators, policy makers etc. Work package D6 was tailored to this specific audience with a focus on knowledge transfer towards the different stakeholder groups in sunbelt countries. The following three steps have been implemented in order to achieve this:

1. **Identifying key stakeholders** around the sunbelt countries
2. **Involving stakeholders** through one-to-one meetings, workshops and conferences in their countries.
3. **Inviting stakeholders** to participate in demonstration projects

The process of identification firstly included collecting 90 individuals and organisations from the total observer list of Task 65. Secondly, a first email has been sent to 44 individuals and organisations in sunbelt countries identified from this collection. Thirdly, a second email and a questionnaire were sent to 19 individuals and organisations which expressed interest to proceed further. The analysis of questionnaire feedback provided a comprehensive list of topics of interest for stakeholders in sunbelt countries, Finally, 5 individuals and organisations expressed interest to get further involved in Task 65 goals. Invitations to workshops, conferences and personal one-to-one meetings were sent to all stakeholders interested during the following involvement/invitation phase of the process. The uptake on workshops was excellent with 63% of stakeholders participating in one or more workshops. Conference participation could not be quantified due to lack of participant statistics from each conference. Meetings were not requested by stakeholders despite opportunities for such being offered by Task 65 leaders whenever possible. Invitations to participate in demonstration projects have been continuously offered to Task 65 participants from the stakeholder group and three project proposals have been submitted together with Task65 experts and stakeholders from sunbelt countries. Detailed information on the process and the results can be found in the published final report on D6 (Kohlenbach and Jakob, 2024a).

4. Conclusions and outlook

In Subtask A (Adaptation) climatic conditions, applications, components and systems have been investigated and adapted tools and systems for sun belt countries have been developed. A GIS-based tool is now available for the global identification of possible solar cooling locations, taking into account technical as well as socio-economic factors. Subtask B (Demonstration) put the focus on design guidelines, performance indicators and standardization. An analysis of multiple case studies has been undertaken and lessons learned have been compiled. In Subtask C (Assessment & Tools), design tools have been analysed as well as assessment mechanisms have been

developed. A variety of tools for solar cooling design is available. Subtask D (Dissemination) focused mainly on distributing the Task 65 results, but also developed new roadmaps for sunbelt countries with regard to the implementation of solar cooling systems. Financing models have been analyzed and recommendations for policy makers are given as a result.

5. References

Beccali, M., Bonomolo, M., Ciulla, G., Galatioto, A. & Lo Brano, V. (2015). Improvement of energy efficiency and quality of street lighting in South Italy as an action of Sustainable Energy Action Plans. The case study of Comiso (RG). In Energy 92, pp. 394–408. DOI: 10.1016/j.energy.2015.05.003

Beccali, M., Bonomolo, M., Martorana, F., Alex Baby, B., Pellegrini, M., & Vasta, S. (2024). *Show cases on system and component level & adapted components*. SHC Task 65: Solar Cooling for the Sunbelt Regions, Subtask A: Adaptation & B: Demonstration. Report D-A2-B1. International Energy Agency. https://doi.org/10.18777/ieashc-task65-2024-0001

Bleyl, J. (2024). *Business Models and Financing Options for Solar Cooling*. SHC Task 65: Solar Cooling for the Sunbelt Regions, Subtask D: Dissemination. Report D-D2. International Energy Agency. https://doi.org/10.18777/ieashc-task65-2024-0004

Bonomolo, M., Jakob, U., Neyer, D., Strobel, M., & Vasta, S. (2023). Integration of solar cooling systems in buildings in Sunbelt region: An overview. *Buildings*, 13(9), 2169. https://doi.org/10.3390/buildings13092169

Bonomolo, M., & Strobel, M. (2023). *Building and process optimization potential*. SHC Task 65: Solar Cooling for the Sunbelt Regions, Subtask A: Adaption. Report D-A4. International Energy Agency. https://doi.org/10.18777/ieashc-task65-2023-0003

Daborer-Prado, N., Neyer, D., Aye, L., Jakob, U. (2023). *Design tools and models*. SHC Task 65: Solar Cooling for the Sunbelt Regions, Subtask C: Assessment and Tools. Report D-C1. International Energy Agency. https://doi.org/10.18777/ieashc-task65-2023-0004

Gurtner, R., Schmetzer, T., & Riepl, M. (2023). *Climatic conditions & applications*. SHC Task 65: Solar Cooling for the Sunbelt Regions, Subtask A: Adaption. Report D-A1. International Energy Agency. https://doi.org/10.18777/ieashc-task65-2023-0002

IEA, 2018. The Future of Cooling. Opportunities for energy efficient air conditioning. IEA Publications, International Energy Agency.

IEA, 2019. The Future of Cooling in Southeast Asia. IEA Publications, International Energy Agency.

IEA SHC, 2023. Solar Heat Worldwide – Global Market Development and Trends in 2022 – Detailed Market Figures 2021, Edition 2023. IEA SHC Publications, International Energy Agency.

IEA SHC, 2024. https://task65.iea-shc.org/subtasks. Last accessed Aug 8th 2024.

IEA SHC, 2018. https://task53.iea-shc.org/publications. Last accessed Aug 8th 2024.

Kohlenbach, P. & Jakob, U. (2024). *Summary Report of Task Workshops & Trainings*. SHC Task 65: Solar Cooling for the Sunbelt Regions, Subtask D: Dissemination. Report D-D5. International Energy Agency. https://doi.org/10.18777/ieashc-task65-2024-0007

Kohlenbach, P. & Jakob, U. (2024a). *Summary Report on List of Stakeholders and Activities*. SHC Task 65: Solar Cooling for the Sunbelt Regions, Subtask D: Dissemination. Report D-D6. International Energy Agency. https://doi.org/10.18777/ieashc-task65-2024-0008

MI IC7, 2023. Innovation community on affordable heating and cooling of buildings (IC7). Mission Innovation Initiative, last accessed 25.10.2023, http://mission-innovation.net/platform/innovation-community-ic7/.

OECD, 2017. World Energy Outlook 2017. Paris: OECD Publishing. https://ebookcentral. proquest.com/lib/gbv/detail.action?docID=5160837[Manuscript submitted for publication]

Strobel, M. & Jakob, U. (2024). *Roadmaps for Solar Cooling in Sunbelt Countries*. SHC Task 65: Solar Cooling for the Sunbelt Regions, Subtask D: Dissemination. Report D-D3. International Energy Agency. https://doi.org/10.18777/ieashc-task65-2024-0005

Vasta, S., & Sapienza, A. (2024). *Standardization activities*. SHC Task 65: Solar Cooling for the Sunbelt Regions, Subtask A: Adaptation. Report D-A5. International Energy Agency. https://doi.org/10.18777/ieashc-task65-2024-0003

Weiss, W., Jakob, U., Weiss, M. & Cuamba, B. (2024). *Standardized Solar Cooling Kits*. SHC Task 65: Solar Cooling for the Sunbelt Regions, Subtask B: Demonstration. Report D-B4. International Energy Agency. https://doi.org/10.18777/ieashc-task65-2024-0006

09. Sustainable and Solar Energy Transition

Simulation model for autonomous energy planning for Milos island

Spiros Alexopoulos[1] and George Mathew[2]

[1] Solar-Institut Jülich of the FH Aachen University of Applied Sciences, Germany, Jülich (Germany)

[2] FH Aachen University of Applied Sciences, Jülich (Germany)

Abstract

A new project to generate electricity on a selected remote Greek island with a population of around 5,000 inhabitants has been developed, using only renewable energy sources (RES) and energy storage systems. This new energy plan was made taking into account the framework of the clean energy transition for islands, for the island of Milos in the Aegean Sea and compared with the current energy coverage. The electricity demand coverage needs on this island are met by using conventional fuels with the operation of diesel engines. Appropriate software was selected and used for the optimisation and creation of energy systems. For the energy study of the island, integrated simulation models were created both for the current total energy supply and for different scenarios of the newly developed energy planning.

Keywords: energy transition, clean energy, remote island, simulation model, renewable energy system (RES), storage system

1. Introduction

In Greece, there are a considerable number of remote islands, most of which are not interconnected with the mainland electricity grid of Greece. It is very common that such remote places with high potential for usage of renewable energy systems aren't being fully taken advantage of. On the contrary, the Public Power Corporation (PPC) uses autonomous thermal power plants to meet the needs of the Aegean islands (PPC 2020). These plants require large quantities of either light (diesel) or heavy (fuel oil) oil to operate, with correspondingly high carbon dioxide emissions.

A new project to generate electricity on the selected remote Greek island Milos with a population of around 5,000 inhabitants has been developed, using only renewable energy sources (RES) and energy storage systems. This article describes this new concept for an energy system for Milos island in Greece and the simulations which ran with an software application. The simulations results are then compared with the current supply of energy in the island.

2. Description of current situation

According to IPTO 2020 the majority of the island's energy is provided by diesel generators and imported electricity via underwater cables from Independent Power Transmission Operator (IPTO). The Public Power Corporation (PPC 2020) uses according to Kaldellis and Zafirakis 2007 autonomous thermal power plants (CHPs) to meet the needs of the Aegean and Ionian islands.

The majority of the island's energy is provided by PV panels, wind turbines, diesel generators and imported electricity via underwater cables from Independent Power Transmission Operator (IPTO 2020). However, out of these four sources, the main one being used are the diesel generators. The diesel generators on the island provide a consistent source of power, but they are costly to operate and maintain, and their emissions contribute to air pollution and climate change. Furthermore, the island's reliance on imported electricity exposes it to price fluctuation and supply problems (Mathew 2023).

Table 1 shows a list of the available and running diesel generators on Milos Island.

© 2024. The Authors. Published by International Solar Energy Society
Selection and/or peer review under responsibility of Scientific Committee
10.18086/eurosun.2024.09.01 Available at http://proceedings.ises.org

Tab. 1: List of diesel generators on Milos Island as described in HEDNO 2022

No.	Generator	Capacity [MW]
1	G3	5.0
2	G4	5.0
3	G5	5.0
4	G7	1.5
5	G8	1.5

It is important to note that the five generators with a total capacity of 18 MW can produce more than the required demand of the island. These generators are switched on and off according to the real-time electricity demand.

Additionally there exist some small-scale PV systems and a wind turbine which are already installed on Milos Island, and are considered in order to prepare the current energy concept. The installed PV in the island according to HEDNO 2023 include PV arrays with a capacity of 0.5 MW, roof PV with an installed capacity of 74 kW and tracking PV systems of 120 kW. One wind turbine, with a rotor at a height of 50 m, is operating at the island with a total installed capacity of 2.6 MW.

Fig. 1 shows the current energy system model in Milos island.

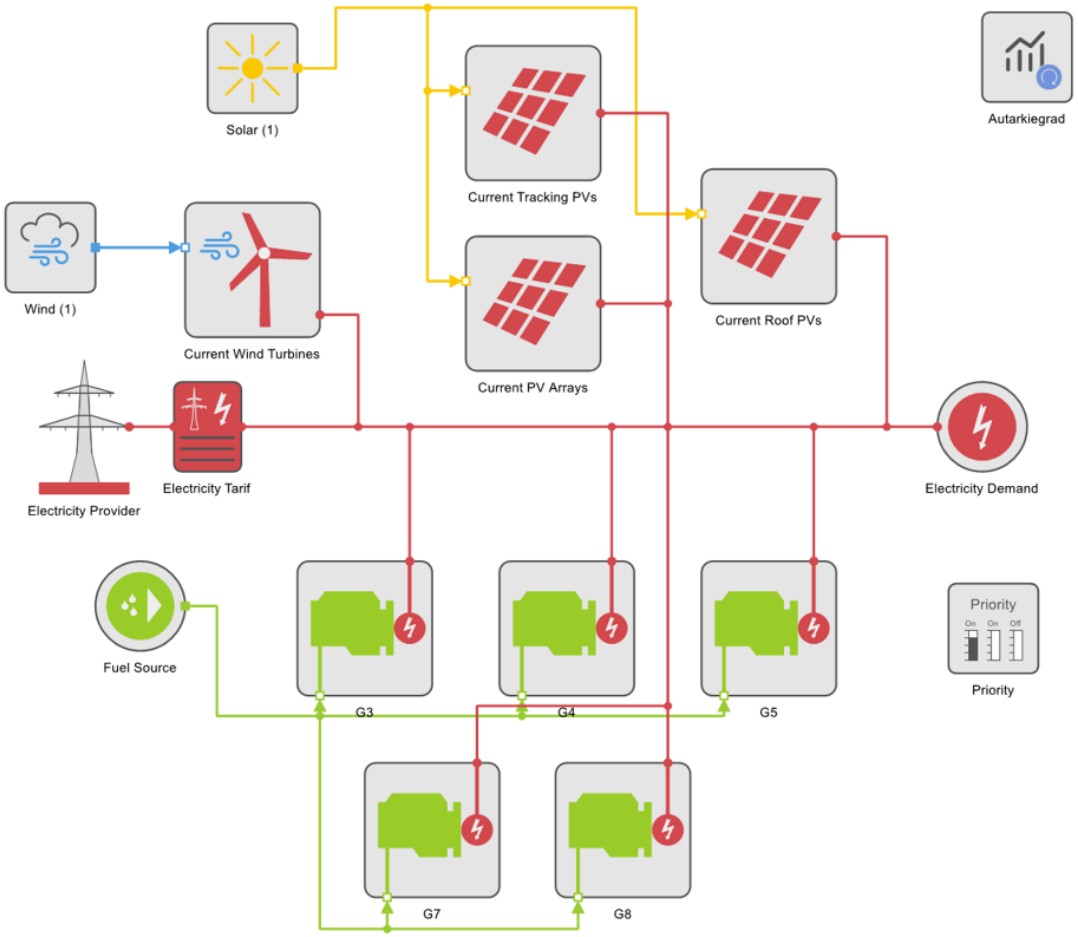

Fig. 1: Current energy system model in the island of Milos

This model was created by selecting the required components from the component library of the software tool and linking every input and output accordingly. Each of the components in the model can be configured with

the respective technical data. In Milos, most of the electricity comes from the diesel generators, a small percentage from the PVs and the wind turbine.

Also, an electricity grid provider, even though it is not used yet, is added to the concept since very soon the island will be connected to the main grid. The project, which concerns the interconnection of Milos with the mainland Electricity Transmission System, is part of the fourth and final phase of the interconnection of the Cyclades. The implementation of the project, including the installation of the 150 kV high voltage submarine cables, is expected to be completed in 2026.

Fig. 2 shows a typical summer electricity demand curve on Milos island. This is different to winter months as in these months the amount of tourists is decreasing.

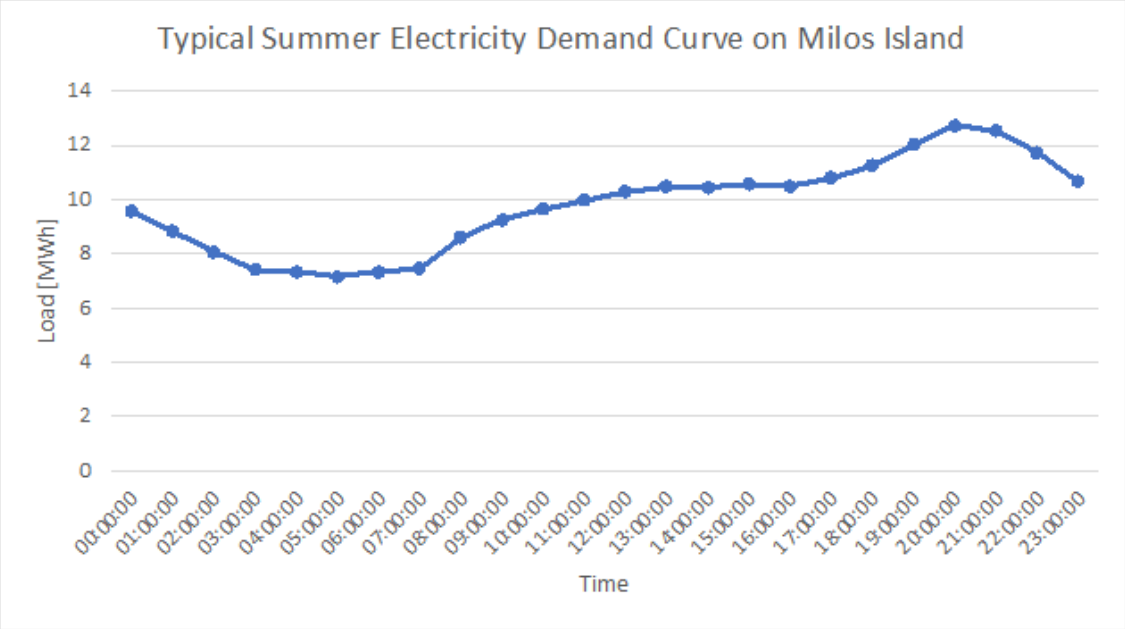

Fig. 2: Summer energy demand curve in Milos Island according to HEDNO 2022

In the winter time the energy demand for a characteristic day does not exceed 5 MWh and takes values between 2.5-5 MWh.

3. New concept for energy production in Milos

It is important to describe first the potential of renewable energy sources. This is followed by the new energy planning with the aim of 100% renewable energy use and modelling with appropriate software.

3.1. Renewable energy potential

It is a fact that the vast majority of the remote Aegean islands are characterised by a very high solar, but also a remarkable wind potential. The choice of renewable energy technologies is illustrated by a potential analysis which focuses on the location of the island and therefore the impact on the potential potential returns.

Regarding the solar potential Milos receives enough of sunlight throughout the year, making it an ideal location for the installation of solar panels (Greeka 2023). According to measurements of the National Meteorological Service (EMY), the Centre for Renewable Energy Sources (KAPE) and other services, the relative solar potential for the remote Aegean islands ranges according between 1500 and 1850 kWh/m^2 in the horizontal plane, while the average wind speed is between 7 and 9.5 m/s.

Fig. 3 shows according to Kaldellis 2021 the solar and wind energy potential for Greece. As can be derived from this figure the solar potential for Milos is the highest in Greece with annual solar radiation values of 1650 kWh/m² and annual mean wind speed at 30 m of more than 5.3 m/s. The average daily solar irradiance in Milos Island varies depending on the time of year, but it is generally around 5,5 kWh/m²/day during the winter months and 8 kWh/m²/day during the summer months (NASA 2018).

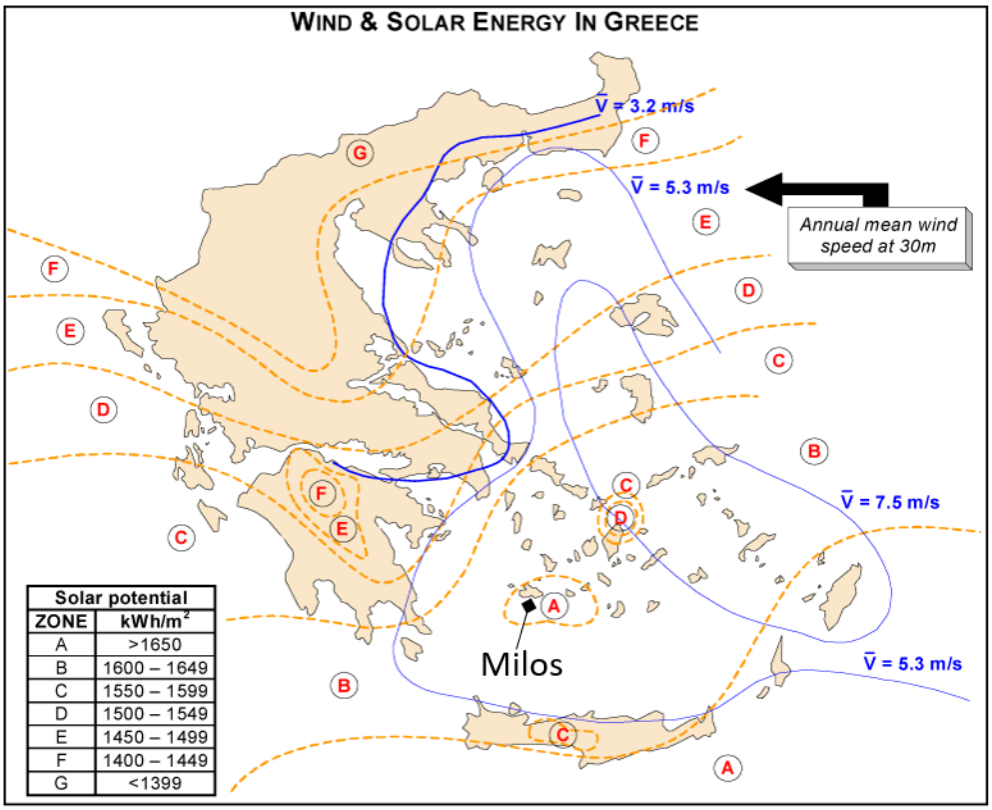

Fig. 3: Solar and wind energy potential for Greece, according to Kaldellis 2021

The average wind speed on Milos Island is around 6-7 m/s, with maximum wind speeds reaching up to 22 m/s at 10 m (NASA 2018). Milos also features a harsh and hilly terrain with several elevated locations that are exposed to the wind. These topography features generate high wind speeds and turbulence, making wind energy generation ideal.

3.2. New concept

Taking into account the pressing need to meet the island's energy needs without further use of conventional and therefore polluting fuels, the prospects for the development of a new energy system on the island, based mainly on the exploitation of the available solar and wind potential and the use of energy storage systems, are proposed and explored.

The main difficulty in drawing up an energy plan is that renewable energy production is always linked to storage, as it fluctuates throughout the day and the seasons. Generating electricity with photovoltaic and wind power systems is a way to make up for the use of conventional forms of energy in the long term.

The new concept envisages a combination of these two types of energy production technologies, as they work well together. In winter, wind speeds are high, so more electricity is produced than wind power, and in summer, solar power is high while wind power is lower, so the two are balanced throughout the year. For energy security, storage is also added to ensure that energy is available during the dark phase or in case of problems with the systems.

3.3 Simulation model development

Appropriate software was selected and used for the optimisation and creation of energy systems. For the energy study of the island, integrated simulation models were created both for the current total energy supply and for different scenarios of the newly developed energy planning.

The authors used the TOP Energy software, as it has a number of advanced features, which are mentioned in Schwarzkopf 2022:

- the possibility of carrying out economic and ecological evaluation
- the freedom to design and test new ideas
- the integration of solvers that help to find the right economic, ecological and energy optimum

Fig.4 shows the concept with new PV arrays, wind turbines and a battery for Milos island.

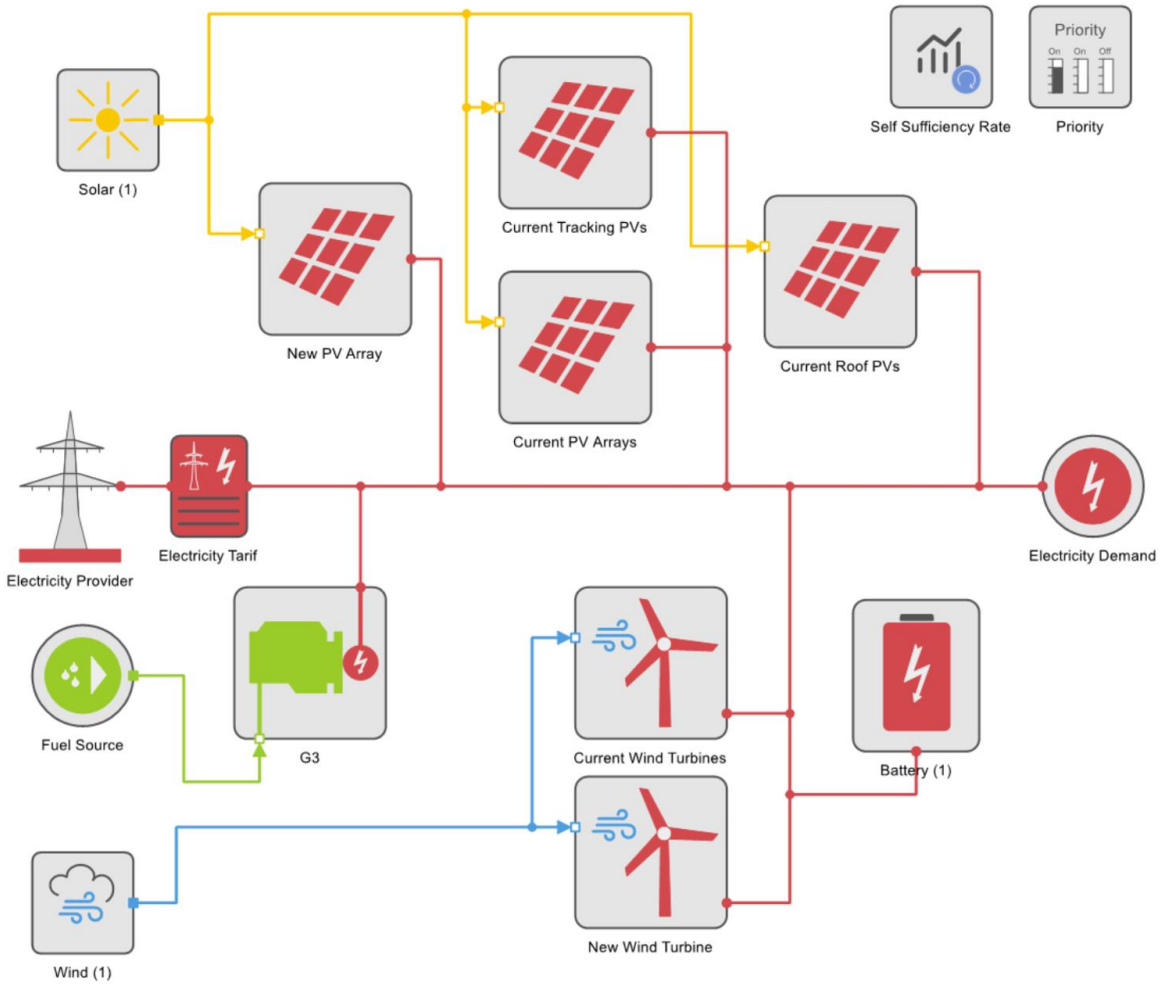

Fig. 4: Model of new energy concept for Milos Island

The new energy concept includes new PV arrays with an installed capacity of 17.5 MW and a wind turbine from Vestas with an installed capacity of 8 MW. For reasons of security of energy supply, the G3 diesel generator set of 5 MW is considered additionally but is only activated when no other sources and the battery are available. The battery was chosen to have a capacity of 433 MWh, which was not yet optimized. The priority is also configured so that the renewable energy sources are set as the main source of electricity.

The energy comparison is carried out using real data describing hourly step by hour the production of the renewable energy plants for a full year of operation. The climate impact is presented on the basis of a CO_2 balance and taking into account the reduction of fuel requirements.

4. Simulation results

Fig. 5 further shows the division of power production of the new energy concept. According to this pie chart most of the energy production comes from the new PV and wind turbine installation.

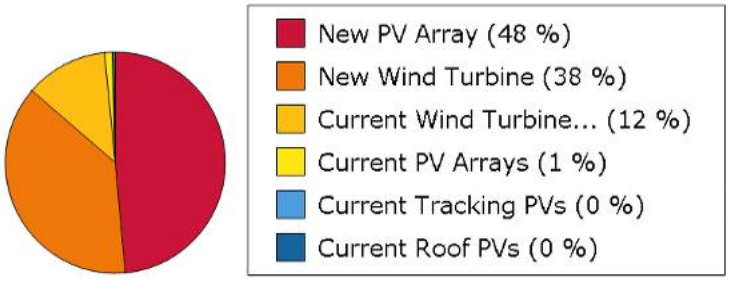

Fig. 5: Milos electricity production from different RES

To get a better overview of the results, Fig. 6 depicts the power output and compares it to the demand. The yearly electricity production was 59.3 GWh.

The stacked bars represent the energy being produced and the line represents the energy demand. It is noticeable here that the demand line is always lower than the sum of the bars, this means that enough energy is produced to cover the demand. The leftover energy will be stored in the battery and saved for usage in the next time period.

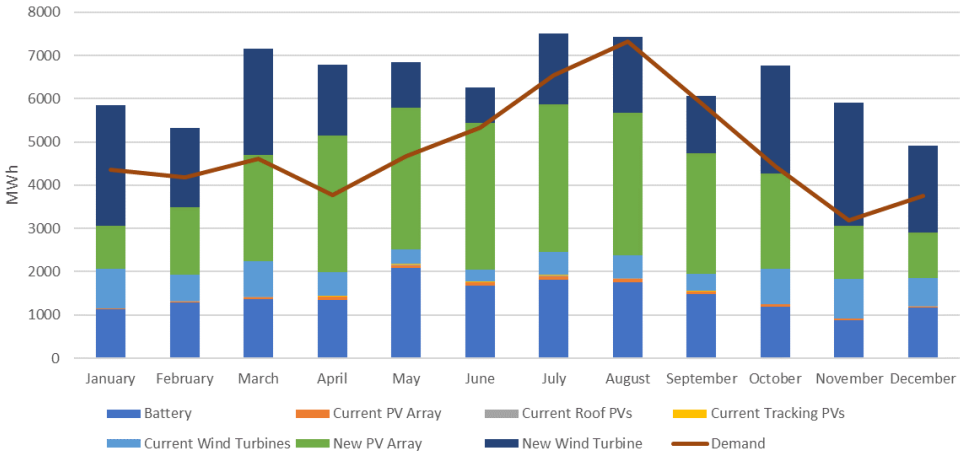

Fig. 6: Monthly production Milos concept

The main objective when implementing renewable energy sources is to lower the emissions of carbon dioxide. The currents sources of energy in Milos island still include diesel as a source, which has a high CO_2-emission factor of 1.1. With the simulations, it was possible to completely eliminate the usage of diesel and replace it with sustainable sources. The simulation results provided that an amount of 1,520 t CO_2/a can be saved, when the new concept is implemted.

The self-sufficiency rate for the new concept that was simulated is 100%. This means that the electricity demand for each island could be fully covered by the planned renewable energy sources.

5. Conclusion and future steps

A new project for the production of electricity on a selected remote Greek island with a population of less than 5,000 inhabitants has been developed for the island of Milos in the Cyclades, using only renewable energy sources (RES).

The electricity demand coverage needs on this island are so far covered by the use of conventional fuels with the operation of diesel engines. Taking into account the pressing need to meet the energy needs of the island without further use of these conventional and therefore polluting fuels, the prospects of developing a new energy system on the island, based mainly on the exploitation of the available solar and wind potential and the use of energy storage systems, were explored.

This article focused more on a small-scale location of an island, but it is generally also possible to implement the same techniques for larger scale locations or cities and ultimately lower CO_2-emissions. The energy planning is on a purely theoretical level and was done in the context of an undergraduate thesis. Next steps of optimization will be carried out in order to define a new energy planning for the island of Milos, which will be 100% based on RES.

In less than 2 years, in the year 2026, the island will be connected to the 150 kV HV submarine cable grid. Therefore the whole calculations will change and this should be considered in future energy concept analysis for the island of Milos.

6. Acknowledgments

The authors would like to thank at this point the TOP Energy team for their assistance and software support. The main author would like to thank Prof. J.K. Kaldellis for his scientific contributions in form of publications

in the field of remote island energy planning for Greece, which provided very useful basic informations about the RES potential and the energy concepts in this paper.

7. References

Geography of Milos island |Greeka 2023. [online] Greekacom. Available at: https://www.greeka.com/cyclades/milos/geography/ [Accessed 22 Apr. 2023].

Hedno (2023). *StartPage*. [online] HEDNO. Available at: https://deddie.gr/en/ [Accessed 12 May 2023]

Interconnection of Cyclades Phase D Santorini-Folegandros-Milos-Serifos. [online] IPTO. 2020 Available at: https://www.admie.gr/en/node/113968 [Accessed 22 Apr. 2023].

IPTO (2020). *Interconnection of Cyclades Phase D Santorini-Folegandros-Milos-Serifos*. [online] IPTO. Available at: https://www.admie.gr/en/node/113968 [Accessed 22 Apr. 2023].

Kaldellis J.K., Zafirakis D., 2007. Present Situation and Future Prospects of Electricity Generation in Aegean Archipelago Islands, Energy Policies Journal, Vol.35 (9), pp.4623-4639.

Kaldellis J.K., 2021. Supporting the Clean Electrification for Remote Islands: The Case of the Greek Tilos Island Energies 2021, 14, 1336.

Mathew G., 2023. Alternative renewable energy concepts for Moti and Milos Island Bachelor thesis FH Aachen University of Applied Sciences 2023

NASA, 2023. ArcGIS Web Application. [online] Nasa.gov. 2018 Available at: https://power.larc.nasa.gov/data-access-viewer/ [Accessed 23 Apr. 2023].

HEDNO, 2022. Publication of NII Daily Energy Planning Data. [online] Available at: https://deddie.gr/en/themata-tou-diaxeiristi-mi-diasundedemenwn-nisiwn/leitourgia-mdn/dimosieusi-imerisiou-energeiakou-programmatismou/ [Accessed 22 Apr. 2023].

PPC, 2020. Annual production plan of autonomous power stations. Technical Report prepared by Island Production Department of Greek Public Power Corporation, Athens, Greece.

Schwarzkopf I., 2022. Autarke Energie- und Klimaschutzkonzepte für ausgewählte kleine deutsche und griechische Inseln Bachelorarbeit FH Aachen University of Applied Sciences 2022

Critical Analysis on the Renewable Heating and Cooling plans in Croatia, Germany, Greece, Poland and Portugal

Rosa Christodoulaki[1], Leopoldo Micò[2], Hrvoje Dorotić[3], Rita Ehrig[4], Joana Fernandes[5], Marek Tobiacelli[6] and Vassiliki Drosou[1]

[1] Centre for Renewable Energy Sources and Savings, Athens (Greece)

[2] Solar Heat Europe, Bruxelles (Belgium)

[3] Energetski Institut Hrvoje Pozar, Zagreb (Croatia)

[4] Deutsche Energie-Agentur Gmbh, Berlin (Germany)

[5] Agencia para a Energia, Lisboa (Portugal)

[6] Krajowa Agencja Poszanowania Energii Spolka Akcyjna, Warszawa (Poland)

Corresponding author: christodoulaki@cres.gr

Abstract

Heat is half of the total energy demand; far more than that required for fuel, transport and electricity. Despite this, only 10% of the heat worldwide is generated from renewable energy sources. The decarbonisation of heating and cooling is therefore of utmost importance for the energy transition. The REDI4Heat project supports the decarbonization of heating and cooling and provides assistance for the implementation of the EU Directives and national regulations. This work presents the main results, concerning the assessment of the EU heating and cooling policy framework and the national regulations in Croatia, Germany, Greece, Poland and Portugal. The study begins with the analysis of the heating and cooling demand, the existing regulations and the decarbonization targets and the progress. Then, the barriers for the further deployment of the renewable heating and cooling in each country are identified and recommendations and priority actions for faster decarbonization are proposed. This study reveals that establishing an effective legal framework, making clean heating and cooling accessible to all, addressing the local dimension of H&C, prioritizing energy efficiency measures, making more data available and overcoming technical obstacles could tackle the remaining barriers in the way of a transition to renewable heating and cooling.

Keywords: National Energy and Climate Plans, Decarbonisation, Heating and Cooling, Energy Efficiency, Renewable Heating and Cooling

Introduction

Heating and Cooling (H&C) represents half of EU energy consumption. The decarbonisation of the sector is critical to achieve the EU legally binding targets of 55% reduction of greenhouse gas emissions by 2030 and climate neutrality by 2050, which are enshrined in the EU Climate Law (EC d). More importantly nowadays, the uptake of renewable and efficient H&C technologies reduces Europe's dependence on energy imports, increasing energy security and contributing to the objectives of REPowerEU (EC i).

Nonetheless, fossil fuels still remain by far the dominant energy sources for H&C, while the share of renewables was only 23% in 2021 and is not increasing fast enough, despite the effects of the energy crisis triggered by the Russian invasion in Ukraine.

Therefore, it is of paramount importance that the EU and its Member States step up their efforts to decarbonize H&C. To this end, specific targets for 2030 and 2050 have been set up by the EU and the Member States, accompanied by policies and regulations, both at EU and national level. In this sense, the National Energy and Climate Plans (NECPs) (EC f) and their ongoing revision are key to translate EU policies and targets into national legislation and concrete actions. Member States were due to submit the draft revision by June 2023 and receive

© 2024. The Authors. Published by International Solar Energy Society
Selection and/or peer review under responsibility of Scientific Committee
10.18086/eurosun.2024.09.02 Available at http://proceedings.ises.org

feedback and recommendations by the European Commission by December 2023, with the updated version due by 2024.

The REDI4Heat European project provides technical assistance to Member States and local authorities for the implementation of the relevant EU Directives, such as the Renewable Energy Directive (RED), the Energy Performance of Buildings Directive (EPBD) and the Energy Efficiency Directive (EED), and the National Climate and Energy Plans (NECP). The present work focuses on the H&C sector of the five target countries participating in the REDI4Heat project (Croatia, Germany, Greece, Poland, Portugal) and aims at assessing their current H&C plans and the uptake of RES and EE technologies, with the view to identify the challenges and to propose priority actions for the wide deployment of renewable H&C solutions.

1. Analysis of EU Framework

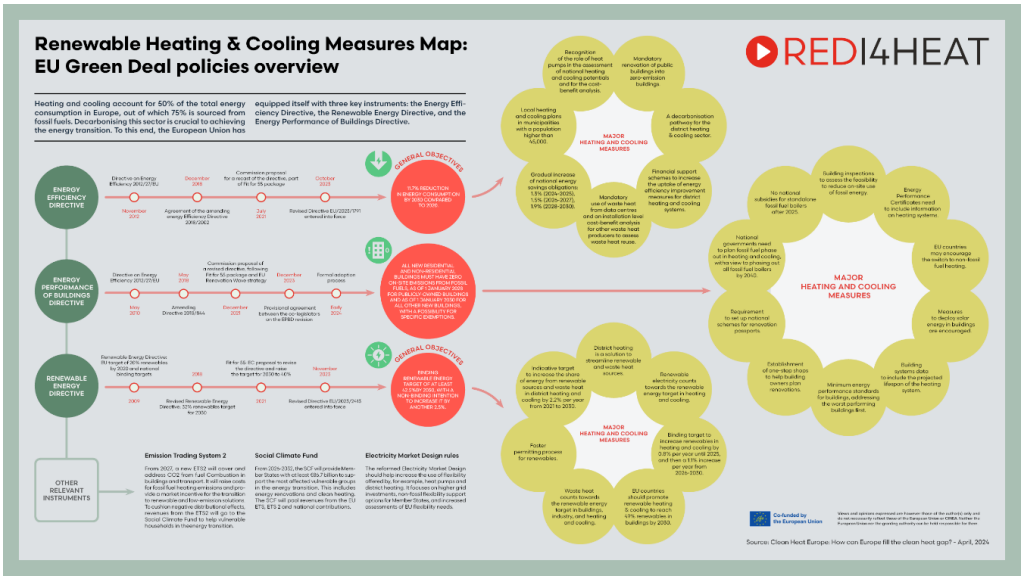

Fig. 1: Mapping of the new Renewable Heating and Cooling measures (REDI4Heat European project)

This analysis refers to the comparison of articles relevant to heating and cooling in the Energy Efficiency Directive (EED), the Renewable Energy Directive (RED) and the Energy Performance of Buildings Directive (EPBD). A map has been produced (Fig. 1) that visualizes in one page all the new RHC measures and three high level policy briefings for RED, EED and EPBD, that are all available at the REDI4Heat project website. For the EED, relevant articles are 25 and 26 and for the RED the relevant articles are 3, 15, 15b, 15c, 22a, 23, 24 and 29.

1.1. EED

The analytical comparison between the old (2018) and new (2023) EED showed that there are four new important provisions: Alignment of the comprehensive heating and cooling assessment with the NECPs, the requirement for local heating and cooling planning for towns and cities with more than 45,000 inhabitants, the redefinition of the efficiency criteria for district heating networks and the stronger consideration for waste heat and recommendation for data centres to connect. Furthermore, the SWOT analysis highlighted better synergies between the EED articles and the RED articles, the obligatory nature of certain provisions with precise deadlines (especially for the definition of heat networks), local planning, as well as the definition of heat networks as efficient that will potentially unlock public and private investments.

However, the analysis revealed important weaknesses and in particular:

- The lack of specifications regarding exceptions, criteria and sometimes, timelines. And this in a context where Member States still have a large margin of maneuver to interpret the text during its transposition in the two years following publication.
- An increased risk of disparity between Member States both on the share of renewables in heat networks,

in particular on the issues of considering waste heat, and on the way of making local heating and cooling plans.
- The capacity and skills of Member States to achieve the outlined targets.
- The indicative character of certain key targets which might not serve as a strong driver to the Member States to be achieved.
- The timetables are too tight and the Member States risk not having time to carry out their study for this revision in 2024 and will therefore have to delay them.

To sum up, the EED can make a major contribution for all Member States to achieve the 2030 targets and set their path towards carbon neutrality by 2050. However, two important parameters may jeopardize this contribution; the degree of freedom that MS have in interpreting the text when transposing it into national law and the technical and financial support mechanisms that will be adopted to enable these measures.

1.2. RED

The 2023 revision of the RED has significantly increased its overall ambition, as well as the sectoral efforts for heating and cooling. Certainly, the energy crisis triggered by the Russian invasion of Ukraine played a crucial role, with the EU facing the consequences of its reliance on imported fossil fuels in terms of energy security and affordability for its citizens and businesses. Nonetheless, especially regarding heating and cooling, the new measures introduced are far from sufficient to meet the urgency of the climate challenge, as demonstrated by the SWOT analysis, and should therefore be considered as an encouraging starting point. The new RED set some important targets for renewable sources, including:

- The headline target for the share of renewables in the EU energy mix in 2030 (article 3), was raised to 42.5%, more than ten percentage points higher than the previous one.
- The sectoral target for the share of renewables in heating and cooling (article 23) was made binding; while the target per se is close to a business-as-usual scenario, its mandatory nature is a crucial step to ensure compliance by Member States.
- The new indicative target for the share of renewables in buildings in 2030 (article 15a) was set at 49%.
- The new indicative target for the share of renewables in industry (article 22a), requiring an average annual increase of 1.6% for the periods 2021-2025 and 2026-2030.
- The target for the share of renewable energy in district heating, while maintained indicative (non-binding), was raised from a 1% average annual increase to 2.2%.

The new RED has also introduced several articles aimed at streamlining and accelerating permitting procedures for renewable energy installations, through the identification of renewable acceleration areas and dedicated measures for specific technologies. These new articles are included through a targeted amendment presented by the Commission in May 2022, as part of the REPowerEU package, to speed up the deployment of renewable technologies and reduce dependency on Russian fossil fuels.

1.3. NECP

The qualitative assessment implemented for the NECPs in the five REDI4Heat Member States (EL, DE, HR, PL and PT) showed that the NECP vary strongly concerning the content, the structure and the quality of drafting across MS and that the Member States are making real efforts to reach EU targets for 2030 and beyond. It also revealed though that the outlined specific strategies often lack clear measures to reach individual targets and timelines and often, there is a need for the targets and strategies to become stricter. One of the biggest challenges seems to be the phase-out of fossil fuels, since clear and strict measures are lacking. Furthermore, local heating and cooling planning is not properly addressed, along with the related support measures that would help local authorities towards this direction. Last but not least, more efforts are needed concerning the easing of administrative procedures and support to connect to DHC networks.

2. Assessment of Target Countries

2.1. Croatia

The total final energy consumption (TFEC) for H&C was 3,253 ktoe in 2018, with 8% increasing tendency for 2030. The share of RES in the H&C sector was 36.5% in 2018, however the projected number for 2030 is almost the same, so basically no growth in RES H&C is expected.

Croatia claims that it meets the requirements set out in Article 23 of the Renewable Energy Directive (RED) II, as more than 60% of the district heating (DH) networks are supplied by cogeneration of heat and power (CHP) systems. Though, their fuel source is not specified.

The RES target in the H&C sector has been increased from 38.1% to 47.1% in the draft revision of the Croatian NECP (EC a). The most important measures for the H&C sector in the NECP are: the upgrade of the DH systems through insulation, RES integration (mainly geothermal, solar thermal and heat pumps) and boilers replacement with CHP systems; the wide renovation of public and private buildings with replacement of old heating systems; the CO_2 emission tax for non-ETS stationary sources emitting more than 30tn CO_2 annually; the provision of financial incentives for the development of RES projects for thermal needs (mainly geothermal and biomass) and the participation in the Covenant of Mayors program for reducing emissions by 40%.

Solid biomass is the dominant source of RES, since it covers the 45% of the heating loads in households, followed by natural gas boilers (20%) and electric heaters. However, most of the biomass devices are traditional wood stoves, which are inefficient and uncontrolled and result in high particle emissions. For this reason, a reduction of biomass and an increase in heat pumps is expected in the upcoming years. Today, in Croatia the potential of heat pumps is largely untapped and the market is dominated by air-to-air heat pumps, used mainly for cooling in the coastal region. In continental Croatia, heat pumps are installed in refurbished and newly built buildings. District heating in Croatia has 10% share in the RES H&C sector and it is supplied by natural gas CHP systems. The 80% of the total DH systems are in the City of Zagreb. Decarbonisation of DH systems is a key measure for the NECP and the most promising technology is deep geothermal whose exploration has already secured finance.

2.2. Germany

The TFEC for the H&C sector was 109 Mtoe in 2018 (REDI4Heat). The share of RES in the H&C sector was 13.6 % in 2018 and the projected number for 2030 is 24.2%, so a fair growth is expected.

The targets for the H&C sector in the 2019 NECP are (EC f): reduction of GHG emissions at least 55% by 2030 compared to 1990 levels; 30% RES in gross energy consumption by 2030 and 30% reduction of primary energy consumption by 2030 and 50% by 2050 compared to 2008. Other national goals include: achievement of climate neutrality by 2045 and 50% increase of RES heat by 2030. The recent Renewable Heating Act (EC h) mandates a 65% RES heat share for all new heating system installations and an extensive subsidy program is released, supporting heat pumps and the decarbonisation of district heating networks. Specific measures tackling energy poverty should be highlighted, since the energy poverty risk has been increased from 14.5% in 2021 to 25.2% in 2022 (iwkoeln).

The uptake of RES and EE in Germany is still hindered by several obstacles, including regulations, initial costs and lack of skilled labor. According to projections, a mild increase in the use of biomass and waste heat is foreseen between 2020 and 2030 (from 13 to 14 Mtoe), while other RES are expected to experience a more robust growth, from 2 to 6 Mtoe (Climate Change Laws a).

Biomass boilers are broadly available, with 14 million boilers being installed in Germany in 2023 (umweltbundesamt). Heat pumps are already installed in every third new building today and this number is expected to increase in the coming years. However, more support programs and campaigns are needed to accelerate the uptake. The main obstacles are long delivery times and lack of skilled labor. Solar thermal is widely deployed in Germany, with 15.5 GWth of installed capacity in 2022 (Solar Heat Europe). The 2019 NECP (EC f) foresees that solar thermal production will grow from 900 ktoe in 2020 to more than 2000 ktoe by 2030. While the residential market remains the main segment, the use of solar thermal in district heating and industrial processes is growing rapidly. Geothermal energy only accounts for 4% of RES in Germany (zdf). Currently, there

are only 42 deep geothermal plants in Germany with very limited capacities (geothermie).

2.3. Greece

The TFEC for the H&C sector in Greece was 5 Mtoe in 2018, with a 30.18% share of RES in the H&C sector. The latter is expected to reach 43% in 2030. With a share of 60%, biomass is the dominant RES technology in the H&C sector in 2018, followed by heat pumps (21%) and solar thermal (18%). A substantial growth in RES heat is expected, almost 114%, until 2030. This growth is not expected to be covered by biomass. Solar thermal technology will cover part of this growth, since the projection is a 39% increase by 2030. Notably, the RES share in the DHC sector is expected to be decreased; from 43 ktoe in 2020 to 39 ktoe in 2030.

The targets for the H&C sector in the 2023 draft revision of the Greek NECP (EC e) include 54% reduction in GHG emissions compared to 1990; 45% share of RES in final gross energy consumption; 46% share of RES in heating & cooling and 44%-49% increase in energy efficiency. Available information indicates that these targets will be slightly higher in the updated NECP that will be submitted in 2024. Further specific measures for H&C are outlined, including:

- wide energy upgrade of the building stock. The annual share of renovation in residential buildings will increase to 1.4% in 2030 (from 0.8% today) and will reach 1.7% in 2050, contributing to the renovation of 43% of residential buildings.
- wide deployment of heat pumps: 17% of residential buildings are expected to meet thermal needs by heat pumps by 2030 and 91% by 2050.
- promotion of decarbonised H&C, such as solar thermal systems and heat pumps.
- mixing of 12-15% biomethane in the natural gas transmission system.
- deduction in income tax for H&C investments with solar thermal, biogas/biomass, geothermal and heat pumps. The deduction is 10% of qualifying project costs up to a maximum of 3,000€ (Greek Law 4399/2016).
- subsidies and tax breaks for investments in RES H&C by private enterprises or social co-operatives.

Particular attention has to be paid in the energy poverty issue. Greece has particularly high levels of energy poverty due to low incomes and high energy needs stemming from old energy-inefficient housing (EC c); 65% of the country's buildings were constructed prior to 1980 (EU Climate-ADAPT), with practically no thermal protection systems.

From 2010 to 2021, renewable H&C increased from 50 PJ to 67.5 PJ and from 19% to 31.1% of total H&C demand. This growth was driven mainly by increased use of heat pumps (from 3 PJ to 18.3 PJ), of solar thermal (from 10 PJ to 12.7 PJ) and biogas (from 0.1 PJ to 1.4 PJ). The use of solid biomass for H&C declined from 45 PJ in 2011 to 34.7 PJ in 2021. However, solid biomass still accounts for the largest share of renewables in H&C (51.4% in 2021), followed by heat pumps (27.1%), solar thermal (18.8%), and biogas (2.1%). It has to be mentioned that Greece has the highest use of solar thermal heating among the International Energy Agency country members, as it covers 5% of demand in buildings, compared to the IEA average of 0.6%.

Biomass in the H&C sector corresponded to 868 ktoe, (54% of the total renewable H&C mix of the country) (Eurostat). Out of this, the largest share is attributed to households as direct consumption (646 ktoe) followed by industry (130 ktoe). Solid biomass is the predominant renewable energy source for residential heating and is currently used in the form of firewood (in older appliances), pellets or agrobiomass, mainly as residues connected to the olive industry. Unfortunately, in the latest version on the NECP there are no major provisions for biomass and this represents a missed opportunity.

Regarding heat pumps, higher penetration of air conditioning units in residences and increase of cooling demand was shown in 2021, when the electricity covered 50% of total energy demand from buildings: 36% for residential buildings and 83% for service sector buildings. Wide electrification is expected to further increase the heat pumps share in the residential sector to 47% in 2030 and to 81% in 2050. Support measures for the electrification of heating demand are already taken (subsidies, loans, tax breaks).

As for solar thermal, Greece is a global leader, being among the top 5 countries by installed capacity per 1,000

inhabitants in 2023 (IEA b). In 2021, the installed capacity in operation was 3,606 MWth, representing 5,152,200m^2 of solar thermal collectors' area. The solar thermal market in Greece, which started 40 years ago, is still growing, by 18% in 2021 and 17% in 2022.

Exploitation of geothermal energy for heating and cooling purposes is limited and no major provisions exist in the latest version on the NECP. DH in Greece is also limited with 5 installations relying on lignite and natural gas. The decommissioning of the lignite factories has raised public debate on the operation of DH networks. Due to climate conditions, this technology is not expected to gain significant growth in the forthcoming years.

2.4. Poland

The TFEC for H&C amounted to 37.7 Mtoe in 2018 and the projections show a decrease of almost 11% from 2020 to 2030. The share of RES in the H&C sector was 14.5% in 2018 and is expected to grow to 28.4% in 2030. With a share of 97.4%, biomass was the main renewable technology in the sector in 2018; its use is expected to increase by 7.7% by 2030, compared to 2020. Heat pumps and solar energy are expected to increase largely by 2030, compared to 2020, by 195% and 371% respectively. DH energy amounted to 2670 ktoe in 2015. The share of RES in the DH sector was only 2% in 2015 (coal was 90%) but it will increase to 29% by 2030. Poland has a wide set of regulations on H&C:

- Increase energy efficiency standards for boilers and thermal insulation,
- Promote the use of RES in all buildings.
- Upgrade of heating plants, support for high-efficiency CHP plants,
- Promote energy-efficient and low-carbon DH, upgrade and expand the DH network.
- Especially for new buildings, the WT2021 Technical Guidelines have been released, which limit the annual primary energy consumption of designed buildings to 70 kWh/m^2. This requirement cannot be met without covering, at least partially, the energy demand for heating with RES.

In Poland, energy poverty rates are high. In 2022, the amendment of the Energy Law included the definition of energy poverty (CEE Bankwatch)."Poland's Energy Policy until 2040" aims to reduce energy poverty to 6% by 2030. However, Poland lacks a comprehensive, unified strategy to tackle energy poverty, despite substantial funding allocated for vulnerable groups.

Biomass and waste heat accounts for almost 90% of the share of RES in H&C and will continue to perform well in households. With 2.4 MWth of cumulative installed capacity in 2022, Poland is the 6th largest European market for solar thermal. In Poland, a solar collector produces 100% of the hot water in the summer (a storage tank is required) and can supplement the energy from the primary source to some extent during the rest of the year. Solar collectors are considered as a complementary source to the primary source. The heating energy production from solar thermal is expected to grow from 45ktoe in 2015 to 426ktoe in 2030 and 564ktoe in 2040 (Climate Change Laws database b). Heat pumps are becoming increasingly popular in households, though low winter temperatures can affect the efficiency of air-source heat pumps. Geothermal energy has not been exploited so far, but an upward trend is expected.

2.5. Portugal

The TFEC for the H&C sector was almost 6.2 Mtoe in 2018 and the projections show a decrease of 7.4% from 2020 to 2030. The share of RES in the H&C sector was 41.2% in 2018 and it is expected to grow to 47% by 2030. Bioenergy is the dominant renewable in the sector and its consumption is expected to remain stable until 2030. Energy supplied from heat pumps and solar thermal remains constant over the next decade. Portugal does not expect to deploy DH networks. Specifically on H&C, the main policy instruments are:

- Development of professional training programs for the technicians and installers,
- Wide building renovation strategy, including integration of energy efficiency and RES "easy win" solutions,
- Promotion of RES H&C systems, such as solar thermal systems, biomass boilers and hybrid systems,
- Development of a National Action Plan to accelerate the uptake of heat pumps in buildings and industry,

with the framework of the EU Heat Pumps Action Plan,

- Establishment of the requirements for the improvement of the buildings energy performance and regulation of the Energy Certification System for buildings.

As regards the H&C sector, energy efficiency measures and electrification of consumption are stepped up (EC g). In this context, the share of RES in H&C may be increased, but it should be noted that Portugal is one of the countries of the European Union where it may not be possible to increase the share of renewable energy sources by 1.3% or 1.1% per year in the H&C sector, in accordance with Directive (EU) 2018/2001. However, given that renewable gases, such as biomethane and renewable hydrogen, are expected to play a greater role by 2030, this outlook could change in the short to medium term.

Portugal is in the top 5 of EU countries for the inability to keep home adequately warm (EC c), therefore it experiences substantial energy poverty. The Long-Term Strategy to Combat Energy Poverty, approved in January 2024, will monitor the evolution of the energy poverty at the national level, through the creation of the National Energy Poverty Observatory. Also, in the framework of the National Strategy, action plans to combat energy poverty will be developed and proposed to the government, with a periodicity of 10 years, that will be reviewed every 3 years.

Heat pumps represent a small fraction of the market since they have high upfront costs and their integration to the existing poorly insulated buildings limit their effectiveness. Solar Thermal has a strong presence, especially in single family houses. The use of solar thermal is indirectly incentivised by the national obligation for new buildings. However, the installation procedures and licences acquisition for existing buildings is a challenging issue that hinders the new installations. Biomass and geothermal systems are present but not widespread and this is not expected to change in the future. DH systems will also not experience any growth or upgrade.

3. Challenges and Priority Actions

3.1. Unambitious RES targets

The figure below shows the share of RES in the EU Member States in 2020 in comparison to the targets set for 2030. Importantly, not all Member States set a sectoral target for renewable energy (the ones with no target are indicated with a 0%); following the latest revision of the Renewable Energy Directive, such sectoral target will become mandatory, as required by article 23.

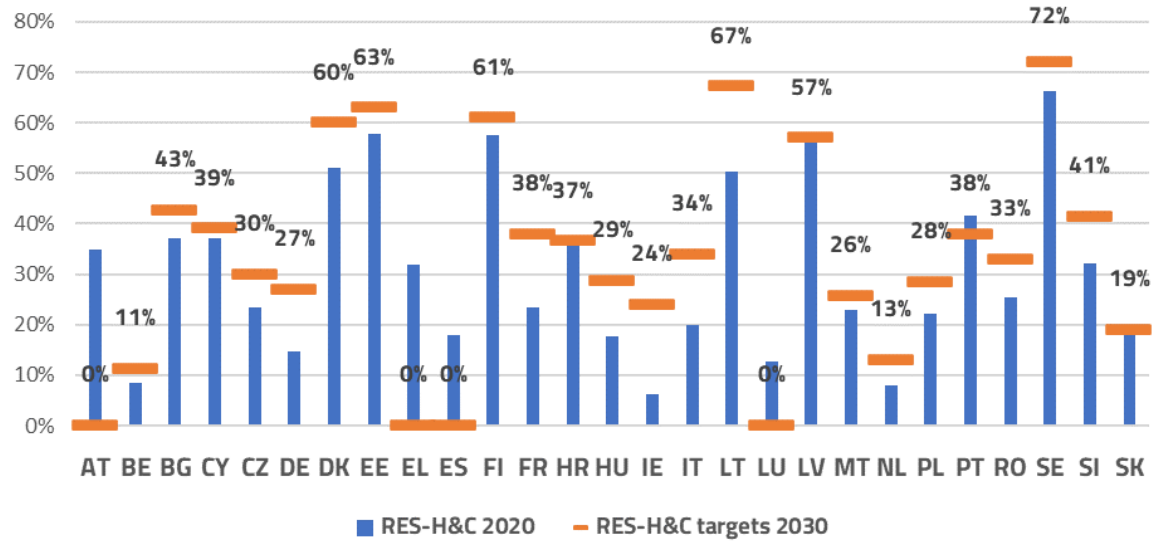

Fig. 2: Share of RES in EU Member States in 2020 (blue) in comparison to the targets for 2030 (orange)

The graph shows that the 2030 targets are unambitious and often reflect a business-as-usual scenario. More

specifically, there are 4 countries without RES targets for H&C at all and there are 17 countries with RES targets lower than 40%. The draft revisions of the NECPs seem to confirm this tendency. While the energy crisis and the political efforts to reduce EU dependency on Russian fossil fuels triggered a significant increase in the RES targets in electricity and transport, this increase is significantly more modest for H&C.

3.2. Ineffective legal framework for H&C

The decarbonisation of H&C should be a top priority for EU, national, and local policymakers, considering it represents the lion's share of Europe's energy consumption. Furthermore, the recent energy crisis has highlighted the urgent need for transitioning into RES solutions that are reliable and secure. However, the sector is still dominated by fossil fuels.

The European Commission addressed this issue with the proposal to revise the Renewable Energy Directive that was tabled in July 2021, with several new or revised provisions on H&C. Notably, a proposal for binding national targets for renewable energy in H&C by 2030 was presented and adopted with the final text published in October 2023. While the binding nature of the target is important, the target itself (0.8 additional percentage points per year between 2021 and 2025, 1.1 between 2026 and 2030) remains disappointingly low.

Special attention has to be paid in the NECPs, which tend to focus on matters that are directly in the hands of central governments. Most NECPs dedicate limited space and few specific measures to the H&C sector. In fact, the parts on H&C are often scattered and split between the chapters on the renewable energy and energy efficiency dimensions, as well as significantly shorter than the sections on electricity, renewable gases, or transport.

A stronger link between the NECPs and the Comprehensive Assessments on efficient H&C required by the Energy Efficiency Directive should be also established, in line with the revised text of article 25 of the EED. This would help provide a more holistic approach of the national actions undertaken to decarbonise the H&C sector, which is overall missing in many draft revisions of the NECPs submitted so far.

An appropriate regulatory framework and the selection of right policies are a prerequisite for a successful transition towards decarbonising H&C. An easy solution would be to make measures legally binding. But this is risky, since mandating RES and EE may hinder people's comprehension of their real value to the environment and public health. Smarter, indirect solutions are needed, such as public campaigns and publicity, financial incentives, new building standards, increasing market availability, redirecting carbon revenue to vulnerable groups. In all cases, deploying measures at various policy levels should be strongly coordinated to ensure coherence between all measures and to avoid contradictory measures, leading to confusion and limited implementation.

3.3. Lack of Local H&C planning

Every region has different climatic conditions, geology, infrastructure, building types and condition, occupancy profile patterns and available energy sources. What works in a Greek city will probably not work in a Polish town. Therefore, H&C planning should happen not only at national level, but also at regional and local level and policies should cater also for settlings below 45.000 inhabitants. In this aspect, more than half of European countries will require a new legislative framework and a new support system for both Regions and Cities. With Regions and Municipalities being often understaffed, this support should include training and upskilling of their personnel, providing guidance and resources to help Municipalities of all sizes draw up a sound and functional plan. More importantly, the effectiveness of these local plans should be monitored, regularly assessed, ensuring mitigation measures in case of misalignments.

3.4. Just H&C transition

Today 41.5 million Europeans, 9.3% of the EU's population, cannot adequately warm their housing (The Cool Heating Coalition). Among the poor, 1 in 5 suffers cold at home, as they tend to live in the worst-performing homes with the highest heating costs. Therefore, making RES H&C accessible to all consumers should be the core intent of any policy action. However, in 2023, only 9 Member States provided a suitable level of energy efficiency subsidies in low-income households (The Cool Heating Coalition). Even though RES costs are falling as they become more widely available, there is still urgent need to support low-income consumers in accessing these technologies. Policies adopted should serve low-income households first and foremost, from a ring-fenced share

of EU and national funds, leaving no one behind.

3.5. Energy efficiency first

The cleanest energy is the one which is not used (EC b). In other terms, reduction of energy demand should be prioritized over the supplying the demand with low emission sources. Higher energy sufficiency can be achieved, among others, through insulation, tree planting, shading, upgrade of equipment, connecting to DH networks, de-steaming in industries, smart energy management and last but not least, through awareness raising campaigns on the methods to improve thermal comfort.

3.6. More data

During the research work in REDI4Heat, the partners revealed a lack of energy-related and spatial data across the target countries. The granularity of available data also varies, with potential misalignments and discrepancies affecting the reliability of findings. Lack of data availability and poor data quality pose significant challenges in analysing and assessing the H&C sector. This obstructs the decision-making process, the identification of policy priorities and the development of new proposals that are meaningful. Good practices are found in Germany, where energy utilities are obliged to share their data in open access databases. The data is then used to evaluate the quality and impact of the plans.

4. Conclusions

The EU heating and cooling policy framework is undisputedly a major contributor for the speed of the energy transition and the path towards carbon neutrality. The new updated EED and RED Directives are moving in this direction, however, especially for the heating and cooling sector, there are still crucial parameters that may jeopardize this contribution; such as the degree of freedom that MS have in interpreting the EU texts when transposing it into national law and the selection of the support mechanisms to enable these measures.

The analysis of the NECPs in the five MS has shown that the MS are making real efforts to reach EU targets for 2030 and beyond. It also revealed though that the outlined specific strategies often lack clear measures to reach individual targets and timelines and often, there is a need for the targets and strategies to become stricter. One of the biggest challenges seems to be the phase-out of fossil fuels, since clear and strict measures are lacking. Furthermore, local heating and cooling planning is not properly addressed, along with the related support measures that would help local authorities towards this direction. Last but not least, more efforts are needed concerning the easing of administrative procedures and support to connect to DHC networks.

On the other hand, RES H&C technologies, such as biomass, solar thermal, heat pumps and DH are ready to drive the decarbonisation efforts. Thanks to their different strengths, these solutions can address the different market needs in different countries; moreover, their combination can often maximise their efficiency and minimize their limitations for the individual installation and/or the energy system as a whole. Their main barriers are higher upfront costs and lack of awareness for the society and the public authorities. Energy transition requires overcoming these barriers and therefore, policymakers should play an active role in the uptake of renewable H&C solutions and the decarbonisation of the H&C sector, which accounts for half of the EU's energy consumption.

5. Acknowledgments

This research was funded by the European Project 101077369 — LIFE21-CET-POLICY-REDI4HEAT.

6. References

CEE Bankwatch Network, Tackling energy poverty in EU Member States https://bankwatch.org/publication/tackling-energy-poverty-in-eu-member-states (last accessed 30/07/2024)

Climate Change Laws of the World database a, Integrated National Energy and Climate Plan for Germany, https://climate-laws.org/document/integrated-national-energy-and-climate-plan-for-austria_7ce0 (last accessed

30/07/2024)

Climate Change Laws of the World database b, Integrated National Energy and Climate Plan for the Republic of Croatia, https://climate-laws.org/document/integrated-national-energy-and-climate-plan-for-the-republic-of-croatia_ab2d (last accessed 30/07/2024)

European Climate Adaptation Platform Climate-ADAPT, Country profiles: Greece, https://climate-adapt.eea.europa.eu/en/countries-regions/countries/greece (last accessed 17/05/2024)

European Commission a, Croatia Draft Updated NECP 2021-2030, https://commission.europa.eu/publications/croatia-draft-updated-necp-2021-2030_en (last accessed 04/06/2024)

European Commission b, Energy Efficiency First principle, https://energy.ec.europa.eu/topics/energy-efficiency/energy-efficiency-targets-directive-and-rules/energy-efficiency-first-principle_en (last accessed 04/07/2024)

European Commission c, Energy Poverty Advisory Hub, An inclusive energy transition: citizen engagement for affordable and sustainable energy solutions, https://energy-poverty.ec.europa.eu/observatory/publications/inclusive-energy-transition-citizen-engagement-affordable-and-sustainable (last accessed 30/07/2024)

European Commission d, European Climate Law, https://climate.ec.europa.eu/eu-action/european-climate-law_en (last accessed 30/07/2024)

European Commission e, Greece - Draft Updated NECP 2021-2030, https://commission.europa.eu/publications/greece-draft-updated-necp-2021-2030_en (last accessed 30/07/2024)

European Commission f, National energy and climate plans, https://commission.europa.eu/energy-climate-change-environment/implementation-eu-countries/energy-and-climate-governance-and-reporting/national-energy-and-climate-plans_en (last accessed 05/06/2024)

European Commission g, Portugal - Draft Updated NECP 2021-2030 https://commission.europa.eu/publications/portugal-draft-updated-necp-2021-2030_en (last accessed 30/07/2024)

European Commission h, Renewable Energy Recast to 2030 (RED II), https://joint-research-centre.ec.europa.eu/welcome-jec-website/reference-regulatory-framework/renewable-energy-recast-2030-red-ii_en (last accessed 05/06/2024)

European Commission i, REPowerEU, https://commission.europa.eu/strategy-and-policy/priorities-2019-2024/european-green-deal/repowereu-affordable-secure-and-sustainable-energy-europe_el (last accessed 12/07/2024)

Eurostat, https://ec.europa.eu/eurostat/data/database (last accessed 01/04/2024)

Greek Ministry of Economy, Development and Tourism, Law 4399/2016, Regulatory framework for the establishment of state aid schemes for private investments for the regional and economic growth of the country, https://www.law-services.gr/wp-content/uploads/2017/01/Amoiridis_New_Development_Law_4399_2016_new.pdf (last accessed 23/04/2024)

https://www.geothermie.de/aktuelles/geothermie-in-zahlen.html

https://www.iwkoeln.de/studien/ralph-henger-maximilian-stockhausen-gefahr-der-energiearmut-waechst.html

https://www.umweltbundesamt.de/themen/klima-energie/erneuerbare-energien/erneuerbare-energien-in-zahlen#waerme

https://www.zdf.de/nachrichten/politik/geothermie-energie-erdwaerme-deutschland-olaf-scholz-100.html

International Energy Agency a, Renewable Energies Heat Act https://www.iea.org/policies/1526-renewable-energies-heat-act (last accessed 30/07/2024)

International Energy Agency b, Solar Heating and Cooling Technology Collaboration Programme, Solar Heat Worldwide 2024, https://www.iea-shc.org/solar-heat-worldwide (last accessed 30/07/2024)

REDI4Heat European project, https://redi4heat.ehpa.org/ (last accessed 30/07/2024)

Solar Heat Europe, Solar Thermal Market Outlook 2023/2024, https://solarheateurope.eu/publications/market-statistics (last accessed 30/07/2024)

The Cool Heating Coalition, Just right: eight policy recommendations for sustainable, renewable and affordable heating and cooling by 2040, https://coolheatingcoalition.eu/knowledge_hub/just-right-policy-recommendations-sustainable-renewable-affordable-heating-cooling/ (last accessed 04/07/2024)

Evaluation of an Indirect Solar Dryer with Integrated Heat Exchanger

Henrik Davidsson[1], Tandin Jamtsho[1,2], Dechen Om[1,3] and Martin Andersson[4]

[1] Lund University Dep. of Building & Environmental Technology, Lund (Sweden)

[2] College of Science and Technology, Phuentsholing (Bhutan)

[3] Jigme Namgyel Engineering College, Dewathang (Bhutan)

[4] Lund University Dep. of Energy Sciences, Lund (Sweden)

Abstract

Solar drying, utilizing solar energy to extract moisture from foodstuff, is a highly effective method for extending the shelf life of for instance fruits and vegetables. The utilization of solar dryers brings numerous benefits, e.g., it reduces reliance on fossil fuels and electricity and establishing an environmentally sustainable and relatively cheap option for food preservation. In this research we present key findings from measurements perform on a solar dryer with a built-in heat exchanger. Our solar dryer was constructed with the goal to keep it both as simple and as cheap as possible. The results show that the dryer outperforms open sun drying while simultaneously protecting the food stuff from the surrounding environment. Filling the dryers with more trays, and consequently more food, increases the difference in drying rate between the trays, which could be a concern for the end user as more attention needs to be paid to the drying process. This problem clearly indicates where future research must be carried out, i.e. in reducing this uneven drying. Future testing using multiple mixing fans or altering the airflow direction created by the internal fan could lead to a more even drying process.

Keywords: solar drying, measurements, indirect solar dryer

1. Introduction

Solar drying, utilizing solar energy to extract moisture from foodstuff, is a highly effective method for extending the shelf life of fruits. The utilization of solar dryers brings numerous benefits. It reduces reliance on fossil fuels and electricity, establishing an environmentally sustainable option. Solar drying preserves the natural qualities of fruits, including flavour, colour, and nutrient content, enhancing their nutritional value. Implementing solar dryers has the potential to significantly reduces post-harvest losses and boosts farmers' income. This paper presents measurements of a solar dryer with a built-in low-cost heat exchanger. Incorporating a heat exchanger along with the solar collector has potential to improve the dryer's efficiency. The heat exchanger preheats the incoming air, using the heat from the outgoing moist air from the dryer. Using heat recovery for small scale solar dryers is not common in the literature. However, it has been mentioned in earlier work, for instance in (Ghasemkhani et al., 2016) or in (Atalay et al. 2017) where external heat exchangers were used. However, these heat exchangers are more complex and would increase the price of the solar dryer. Adding complex heat exchangers also increases the risk of high pressure drop which in turn leads to larger and more expensive fans for the dryer. It 's therefore of great importance to try to use simple, low cost heat exchangers with a relatively low pressure drop.

Traditionally, open sun drying is used to dry for instance fruits and vegetables. However, this method has several disadvantages such as long drying time (Singh, 2011), dust contamination and losses related to animal

© 2024. The Authors. Published by International Solar Energy Society
Selection and/or peer review under responsibility of Scientific Committee
10.18086/eurosun.2024.09.03 Available at http://proceedings.ises.org

intrusion (Moses et al., 2013). Furthermore, the texture and colour of the product may also change (Chaatouf et al., 2021). Solar drying using various kinds of protecting structures where the food is placed can result in a safer drying process. These dryers are often divided in two different categories, direct dryers, and indirect dryers. The direct type dryers are built in such way that the food stuff is directly hit by the solar radiation while the indirect dryers use the principle of heating the air indirectly and then transferring the heated air to some type of drying chamber where the food is placed (Aacharya, 2024).

One of the main limitations in this work is that the dryer has only been tested indoors using a solar simulator. Thus, effect from wind, varying solar irradiation, dust accumulation etc. is not included in this research. Furthermore, drying has only been carried out using apples as produce. Fruit or vegetables with lower moisture content, such as leafy greens, could show somewhat different results as the temperature in the dryer will be slightly higher.

2. Method

The constructed solar dryer is illustrated in Fig 1. The incoming fresh air, forced through the dryer using an external fan, comes in from below (1) and passes through the heat exchanger (2) placed at the bottom of the dryer. After the heat exchanger the air is passed through the absorber (3) and further into the drying chamber passing through water bottles (4) used for storing heat. Storing heat gives the possibility to prolong the drying time even after the sun has set. The heated air is then passed over the different trays (5) in the dryer before it is let out at via the chamber exhaust (6) and finally to the hot side of the heat exchanger with the exhaust at the back of the dryer (7). An internal fan (8) between the two sections of the dryer moves air in the same direction as the external fan. This fan is set for maximum airflow at all times. Figure 2 shows a photo of the solar dryer. The two chambers and the placement of the fruit are shown in the figure. The intention with the internal fan is to increase the airflow in the drying chamber without increasing the net flow through the entire dryer. This is done in order to increase the convective heat transfer from the air to the foodstuff at the same time as a high airflow will reduce temperature differences inside the dryer. Without the internal fan the risk is higher to have hot dry air from the absorber hitting the first tray, while as the air moves over the different trays it picks up moisture and consequently drops in temperature. This leads to the last tray, in the airflow direction, getting cold moist air and thus consequently low drying rate. This uneven drying rate can cause difficulties for the user as the food is not dried to desired levels all at once.

Measurements were carried out using an indoor solar simulator at Lund University in Sweden. The irradiation, at approximately 900 W/m², from the simulator can be considered to be parallel light due to reflectors arrangement in the simulator. No diffuse radiation hit the dryer during the experiments. Airspeed was measured using a Testo 416 with a precision of 0,1 m/s. The airspeed, and thus also the airflow, was measured in a long duct connected to the inlet of the dryer. Temperatures were measured using thermocouples connected to a Campbell Scientific Cr 1000 logger and an AM 16/32 multiplexer. Three thermocouples were placed at the inlet to the dryer (inlet cold side of the heat exchanger), inlet to the absorber (outlet at the cold side of the heat exchanger), absorber outlet, heat storage, drying chamber outlet (inlet at hot side of the heat exchanger) and at the dryer outlet (outlet at the hot side of the heat exchanger). Five thermocouples were installed at the different trays in the drying chamber. Experiments were carried out using five or nine trays of food. All measurements were performed using apples as drying object. All sensors were tested in boiling water and at ice/water mixture to discard faulty sensors. Measurements were taken every 30 seconds and averaged to minute values stored in the logger and downloaded to a computer for data treatment.

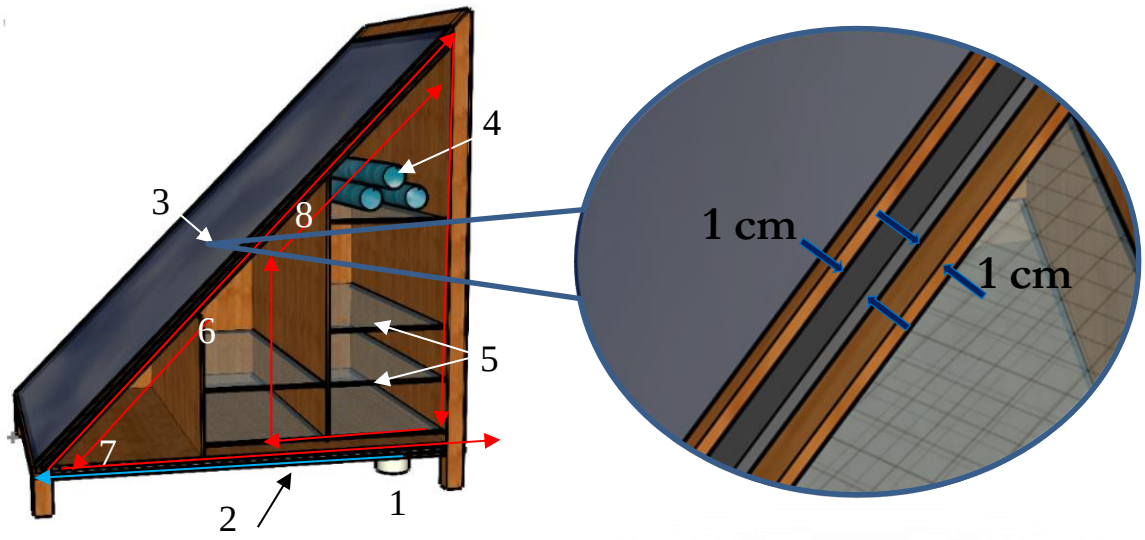

Fig. 1: Illustration of the solar dryer. The heat exchanger is placed at the bottom of the dryer. Airflow is indicated by the arrows. Blue arrows indicate cold air while the red arrows indicate warmer air. The zoom-in to the right shows the absorber separated 1 cm both to the glass cover and to the wooden backside.

Fig. 1 shows a zoom in on the absorber. The distance between the absorber and the glazing as well as the distance to the wooden structure of the drying chamber is 1 cm per side, see Fig 1. Allowing double passage, both front and back of the absorber results in a larger heat transfer surface and thus a higher heat transfer. The heat exchanger in the bottom of the dryer has the same measurements, 1 cm per side of the separating plastic sheet. The trays are made from simple mosquito net on a wooded frame. The heat storage bottles are old, recycled soda bottles. The entire dryer is made using as cheap material as possible in order to achieve a low production cost. All edges that could result in air leakage was sealed using duct tape.

Fig. 2, left, shows a photo of the solar dryer. The two chambers are indicated. The right side in Fig 2 shows a photo of apple slices to be dried in the drier.

Fig. 2: Left: Photo of the solar dryer. The two chambers are indicated in the photo. Right: Photo showing the placement of apples on the trays.

Measurements were taken with the external fan producing different airflows into the dryer in the range of 10 l/s to 20 l/s. The built in heat exchanger was evaluated by measuring the temperatures in and out at the cold and the hot side. The average of cold and hot side temperature heat recovery efficiency, η_{cold} and η_{hot} was investigated. Eq. 1 and Eq 2. was used for the calculations regarding temperature heat recovery efficiency.

$$\eta_{cold} = \frac{T_{out,cold} - T_{in,cold}}{T_{in.hot} - T_{in,cold}} \quad \text{(eq. 1)}$$

and

$$\eta_{hot} = \frac{T_{in,hot} - T_{out,hot}}{T_{in.hot} - T_{in,cold}} \quad \text{(eq. 2)}$$

where T is the temperature. The subscript *in* and *out* is used for inlet and outlet temperature while the subscript *cold* and *hot* is used to indicate the cold side and the hot side of the heat exchanger.

The efficiency of the absorber was calculated using Eq. 3.

$$\eta_{abs} = \frac{f_m \cdot C_p \cdot \Delta T}{I \cdot A} \quad \text{(eq. 3)}$$

where f_m is the mass flow, C_p is the specific heat for air, ΔT is the temperature increase for the air in the absorber section, I is the radiation and A is the glazed area for the absorber. The absorber efficiency was measured as an average over the first three hours of operation. This means that the initial time when the absorber, the glazing and the solar drying construction is heating up, parts of the solar heat is used for this. Thus, the maximum efficiency is higher than the average efficiency stated in the result section.

For comparative reason, simultaneous measurements were carried out where trays with apples were placed outside the dryer, one in the radiation from the lamp and one tray in the shade. All experiments were carried out inside a laboratory. Thus, no wind was present during the experiments. One investigation was carried out where the average weight of a drying tray with fruit was measured every hour for eight hours straight. Another investigation looked at the ratio of drying rates between the highest and lowest drying rates among the different trays. For this, two different internal fans were used, a smaller and a larger fan. The exact flow from the two fans is now known. It should be noted that it is difficult to determine the airflow inside the drying chamber as the flow profile is far from well established. Experiments were carried out using the standard five trays and one set with an increased number of trays. In this case nine trays were used.

3. Results and discussion

Fig. 3 shows the efficiency of the heat exchanger for different flows. As can be seen the efficiency higher for the low airflows. The efficiency for the low flow is around 70 % and reduces to approximately 50 % for the higher flow around 20 l/s.

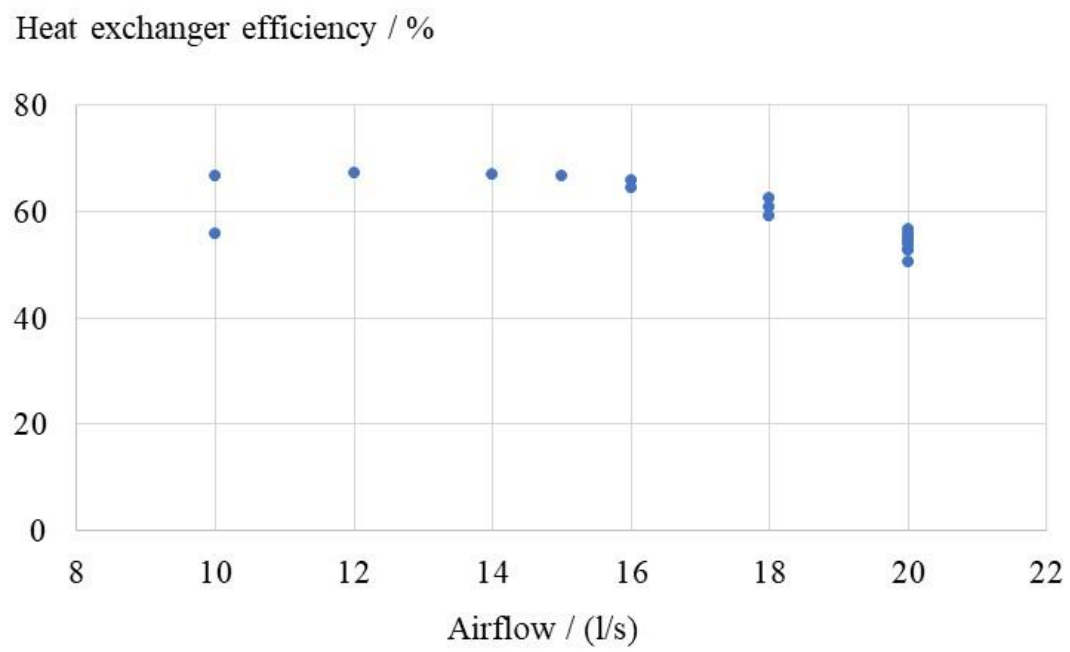

Fig. 3: Heat exchanger efficiency as a function of airflow to the dryer.

Fig. 4 shows the absorber efficiency for two different airflow settings, 10 l/s and 20 l/s. After approximately one hour the absorber efficiency is stable around 60 % for the 20 l/s airflow and somewhat below 40 % for the 10 l/s airflow. The increase in efficiency over the first hour is explained by solar drier heating up from a cold initial condition. As parts of the heat is used to heat the drier less heat is available for heating the air and thus the efficiency of the absorber appears low in the beginning of the day.

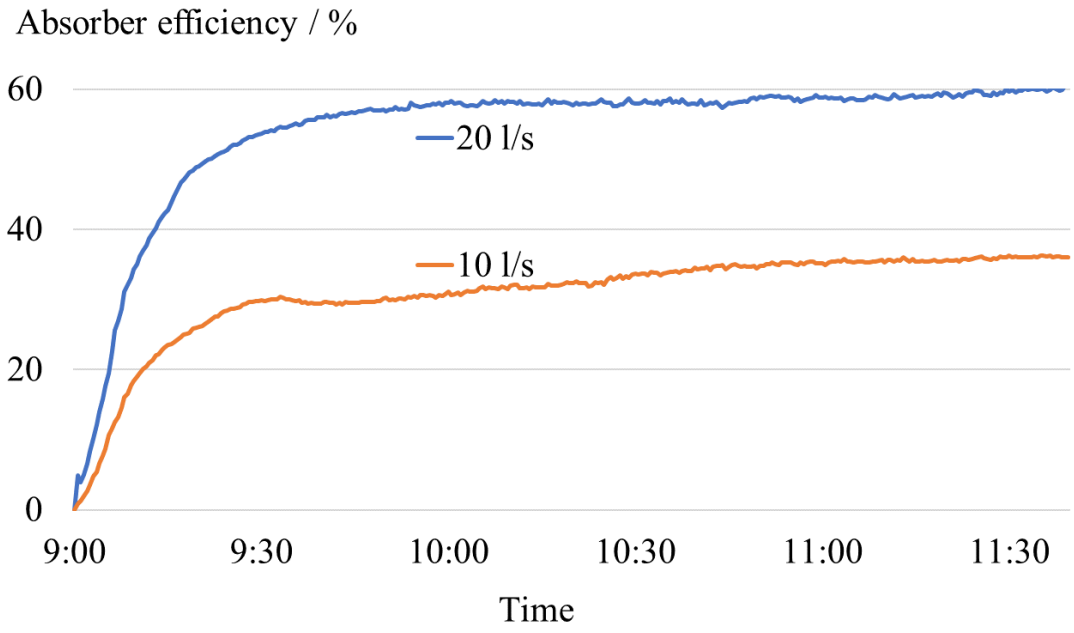

Fig. 4: Absorber efficiency as a function of time. The orange line is for 10 l/s airflow through the dryer and the blue line is for 20 l/s.

The absorber efficiency is shown in Fig. 5. The y-axis shows the efficiency as a function of airflow. As can be seen the efficiency is higher for the higher flows. The experiments performed with the larger internal fan are indicated with red circles. The lower efficiencies might depend on a change in airflow due to higher pressure in the drying chamber. This was however not investigated. The results from the different heat transfer processes, i.e. the heat transfer in the heat exchanger and from the absorber, are contradicting in how the flow to the dryer should be controlled. High flow leads to an effective heat transfer from the absorber to the air but a lower heat recovery rate in the heat exchanger.

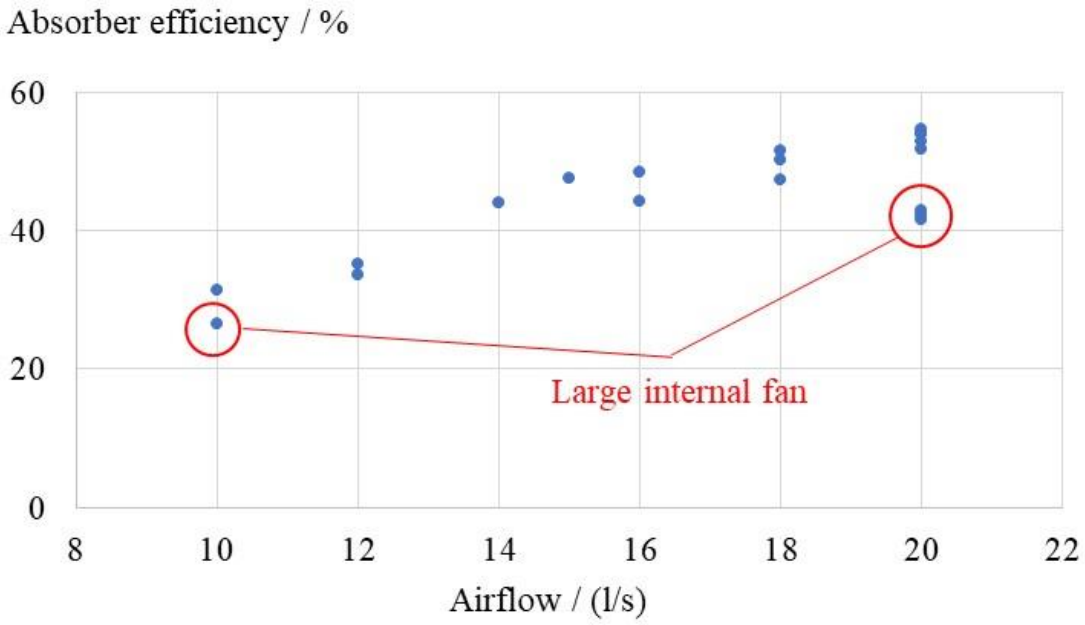

Fig. 5: Absorber efficiency as a function of airflow to the dryer.

Results from apple drying are shown in Fig 6. The y-axis shows the total weight of the fruit. For the solar dryer cases using different airflow from the external fan the average weight of the trays is used to represent the weight. The red, grey, and yellow lines show the weight measured every hour for different external flows, 10 l/s, 15 l/s and for 20 l/s. The difference in drying rate between the different airflows are small. The weight of the fruits using open solar drying with the fruits under the solar simulator lamp is shown in green colour while open drying where the fruit was placed in shade is shown in blue colour. The largest difference in drying rate is for the open drying placed in shade. However, also the open drying placed in the radiation shows significantly lower drying performance compared to the solar dryers. It should be noted that the open solar drying placed in the radiation from the lamp, appears to flatten out at a significantly higher moisture content. This phenomenon was not further evaluated. It should be noted that one possible measurement mistake was removed from the analysis for the “Open sun drying”. The point is indicated in Fig 6 with a green star.

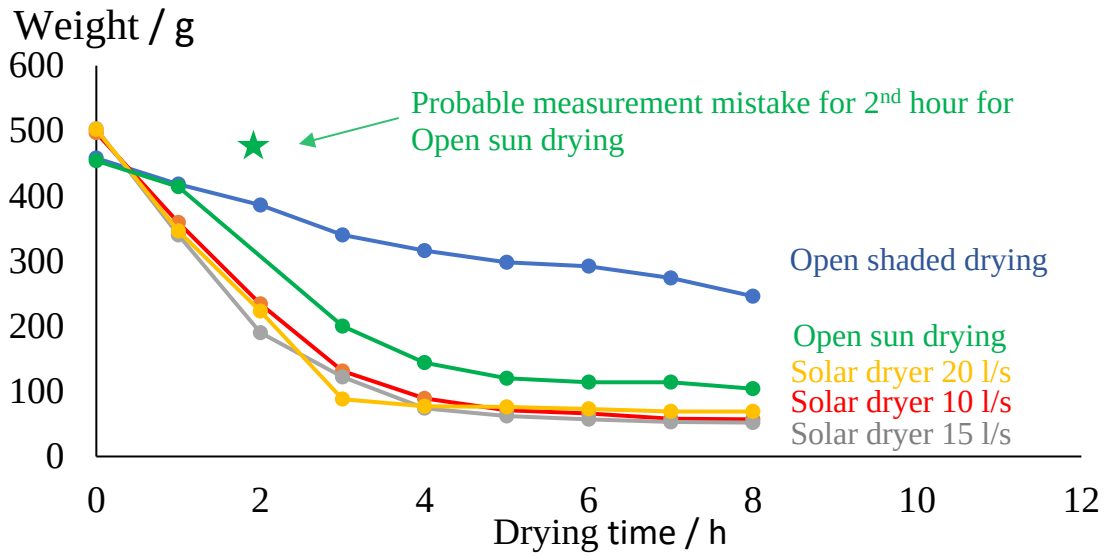

Fig. 6: Drying rates for different types of solar drying and different airflows. The green line is for open sun drying, the blue line is for open shaded drying while the red, grey and yellow lines are for different airflows, 10 l/s, 15 l/s, and 20 l/s.

Fig. 7 shows the variation of drying rate among the different trays inside the dryers. The blue bar shows the highest drying rate during a specific set-up while the red bar shows the lowest drying rate for the same set-up. Using a larger internal fan reduces the difference between the trays. When more trays are introduced into the dryer the difference between the highest and lowest drying rate increases significantly.

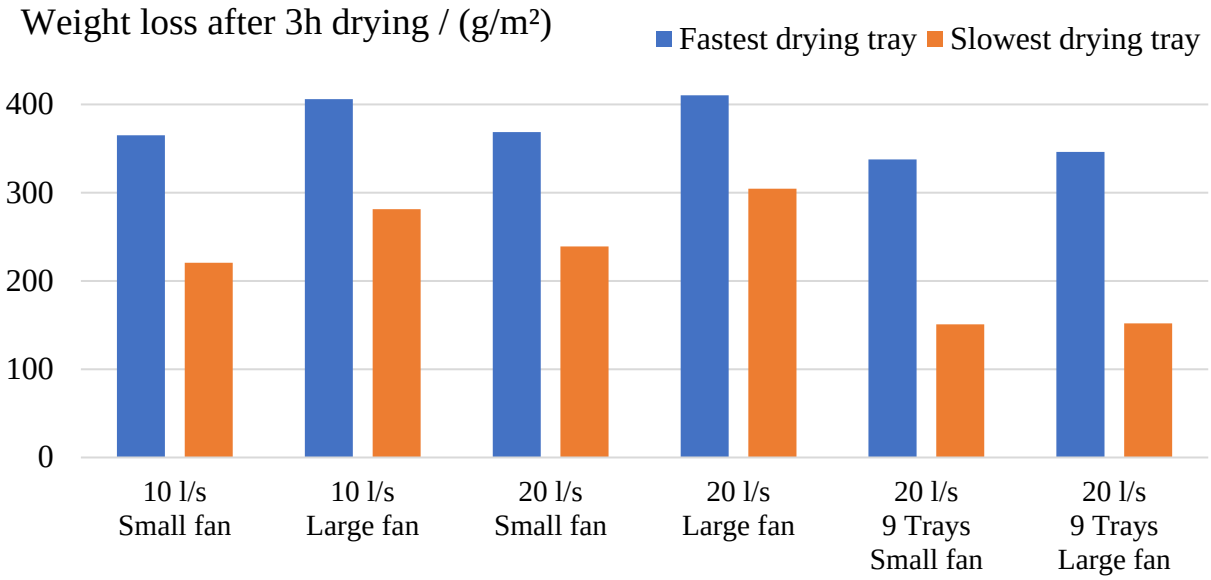

Fig. 7: Total drying during 3 h. In blue is the total weight loss for the fastest drying tray and in orange is the total weight loss for the slowest drying tray.

Table 1 shows the ratio between the fastest drying tray and the slowest drying tray. Having a larger internal fan both increases the drying rate at the same time as it reduces the difference in drying rate between the trays. Increasing the number of trays makes the difference in drying rate worse. Furthermore, using the larger fan does not offset the drying rate difference when loading the dryer with nine trays rather than only five.

Table 1. Ratios between fastest and slowest drying trays in the drying chamber.

Flow / (l/s)	Internal fan size	Number of trays	Ratio of drying rate (Fastest / Slowest)
10	Small fan	5	1,65
10	Large fan	5	1,44
20	Small fan	5	1,54
20	Large fan	5	1,35
20	Small fan	9	2,24
20	Large fan	9	2,28

Fig. 8 shows a typical temperature distribution in the dryer during drying. The specific temperatures captured in the figure is from a drying case using 20 l/s. The measurement was taken at 12:00 midday. The incoming air is at 22 °C. After passing the heat exchanger the temperature has increased to 28 °C. After passing the absorber the temperature reaches 52 °C. Inside the dryer temperature drops as moisture is removed from the food stuff. The average temperature in the dryer is between 32 °C to 37 °C. The temperature at the outlet from the drying chamber, i.e. the inlet to the hot side of the heat exchanger is at 36 °C. After passing the heat exchanger the temperature is at 28 °C. The higher temperature drop on the cold side of the heat exchanger could be due to leakage in the dryer, resulting in lower outlet flow from the dryer compared to inlet flow. This would then lead to a higher temperature drop on the hot side of the heat exchanger. Using Eq. 1 and Eq. 2 gives an average temperature efficiency of 50 % for the heat exchanger. This is almost as high as the efficiency for the absorber as presented in Fig. 4. However, the actual temperature gain, and thus energy gain, is much higher for the absorber than for the heat exchanger. This is partly an effect of the rather efficient drying inside the drying chamber. The higher the drying rate is the colder outlet temperature from the drying chamber and thus less heat to recover in the heat exchanger. The results could differ depending on what type of food is being dried. Fruit and vegetables that dries slower, for instance due to skin or shell on the fruit, could then result in a higher outlet temperature. This could in turn be interpreted as the heat exchanger being more effective.

Fig. 8: Temperature distribution in the dryer.

4. Conclusions

Increasing the airflow through the dryer has mixed consequences for the different parts in the dryer. The heat exchanger works less optimal for higher flows. However, the absorber parts work better for higher flows as the higher airflow through the absorber moves the heat from that section into the drying chamber. Furthermore, the measurements show that varying the external fan between 10 l/s to 20 l/s only has a smaller effect on the actual drying rate. However, the drying rate is higher when using a solar dryer compared to open sun drying. Running the dryer with the external fan at 20 l/s slightly reduces the difference in drying rate between the trays compared to using only 10 l/s from the external fan. Using a larger internal fan also reduces the difference. However, filling the dryers with more trays, and consequently more food, increases the difference in drying rate between the trays. This could be a large concern for the end user as more attention needs to be paid to the drying process. This problem clearly indicates where future research must be carried out, i.e. in reducing this uneven drying. Furthermore, the dimensions for the heat exchanger and the solar absorber have potential for future improvements. Other techniques for enhancing the heat transfer rate such as introducing a non smooth surfaces on the absorber could also lead to higher efficiency for the absorber.

The low heat transfer from the heat exchanger is mainly due to temperature loss inside the drying chamber. As the energy in the dryer is used for drying the food the temperature is reduced. This effects the heat transfer in a negative way for the heat exchanger, even if the efficiency in relative terms is high. However, a deeper test of the dryer should be carried out using leafy vegetables and fruits and vegetables with skin or shell. The slower drying in terms of moisture supply to the drying air could lead to a higher temperature in the drier. In such cases the heat exchanger might be more suitable as part of a solution.

5. Acknowledgments

The Swedish Research Council is acknowledged for funding of the research project “Solar Food: Reducing post-harvest losses through improved solar drying", 2020-04071”.

6. References

Ananta Aacharya, Christian Rissler, Bivek Baral, Tshewang Lhendup, Martin Andersson, Henrik Davidsson 2024. Development of a novel solar dryer with an incorporated heat exchanger. Solar Energy Volume 269. https://doi.org/10.1016/j.solener.2024.112327

Halil Atalay, Mustafa Turhan Çoban, Olcay Kıncay, Modeling of the drying process of apple slices:Application with a solar dryer and the thermalenergy storage system, Energy Volume 134, 1 September 2017, Pages 382-391, https://doi.org/10.1016/j.energy.2017.06.030

Chaatouf, D., Salhi, M., Raillani, B., Amraqui, S., Mezrhab, A., 2021. Assessment of a heat storage system within an indirect solar dryer to improve the efficiency and the dynamic behavior. J. Energy Storage 41, 102874. https://doi.org/10.1016/j.est.2021.102874

Ghasemkhani, H., Keyhani, A., Aghbashlo, M., Rafiee, S., 2016. Improving exergetic performance parameters of a rotating-tray air dryer via a simple heat exchanger. Appl. Therm. Eng. 94, 13–23. https://doi.org/10.1016/j.applthermaleng.2015.10.114

Moses, J.A., Jayas, D.S., Alagusundaram, K., 2013. Resistance to airflow through bulk grains, oilseeds and other agricultural products - A Review. J. Agric. Eng. 50, 1–13.

Singh, P.L., 2011. Silk cocoon drying in forced convection type solar dryer. Appl. Energy 88, 1720–1726. https://doi.org/10.1016/j.apenergy.2010.11.016

TECHNO-ECONOMIC EVALUATION FOR JOINT PRODUCTION OF ELECTRICITY AND GREEN HYDROGEN WITH HYBRID CONCENTRATED SOLAR POWER (CSP) AND PHOTOVOLTAIC (PV) TECHNOLOGIES COUPLED WITH PEM ELECTROLYZERS

Roberto Leiva-Illanes[1,2,3,4], Guillermo Herrera[1,4], German Amador[1,2,4], Cynthia Herrera[1]

[1] Grupo de Investigación de Energía, Agua y Sostenibilidad, Universidad Técnica Federico Santa María, Viña del Mar (Chile)

[2] Grupo de Investigación de Motores y Combustibles Alternativos, Universidad Técnica Federico Santa María, Valparaíso (Chile)

[3] Departamento de Mecánica, Universidad Técnica Federico Santa María, Viña del Mar (Chile)

[4] Departamento de Ingeniería Mecánica, Universidad Técnica Federico Santa María, Valparaíso (Chile)

Abstract

A techno-economic analysis is conducted on integrating PEM electrolyzers and solar power plants, including a Concentrated Solar Power (CSP) and Photovoltaic (PV) plant in northern Chile. The methodological approach is based on production analysis through four alternatives: PV and PEM (Case 1), CSP and PEM (Case 2), a hybrid case of CSP, PV, and PEM (Case 3), and the same hybrid case but with a higher capacity PEM plant (Case 4). SAM software is used to create solar plant models, while Python is used to model the PEM electrolysis plant and perform system integration. The economic evaluation aims to calculate the levelized cost of electricity (LCOE) and the levelized cost of hydrogen (LCOH). Results yield a minimum LCOH of 5,76 USD/kg H_2 and a maximum of 6,63 USD/kg H_2 for the current scenario (2024), while for the future scenario (2030), values range between 2,86 and 4,26 USD/kg H_2. The configuration that achieved the lowest LCOE and LCOH was Case 1. In all evaluated cases, green hydrogen production costs exceed 2 USD/kg H_2, both in the current and future scenarios. Therefore, green hydrogen is not economically competitive with gray hydrogen under these conditions. However, as electricity prices and electrolyzer investment costs decrease, and efficiency improves, green hydrogen could become competitive. These results provide valuable insights for decision-making regarding solar hydrogen production policies.

Keywords: PEM electrolyzer, CSP, PV, LCOE, LCOH, hydrogen.

1. Introduction

Green hydrogen emerges as a prominent energy vector to contribute to the decarbonization of the planet [1]–[3], and Chile positions itself with the potential to lead its production thanks to its abundant solar resources [4], [5]. However, the cost of hydrogen produced using solar energy remains high due to high investment costs, limited operating hours, and the price of solar energy itself [6].

To harness solar energy, there are two main types of solar technologies: photovoltaic (PV) solar plants and concentrated solar power (CSP) plants. The former has a low investment cost, but its production is intermittent and limited by fluctuations in solar resources. One solution is electrical energy storage, though this comes with high investment costs. On the other hand, a CSP plant can incorporate a thermal energy storage (TES) system at a lower cost, allowing for controlled energy dispatch and a higher capacity factor. A hybrid CSP and PV plant has the advantage of achieving a high capacity factor, where the PV plant operates during sunlight hours, while the CSP plant stores the generated thermal energy for use when solar radiation is not available, thus mitigating the effects of variability in solar production under intermittent conditions.

Currently, global hydrogen production has reached 95 Mton H_2/year, with 83% of this being produced from fossil fuels, followed by production via oil and gasoline reforming at 16%. This type of hydrogen is referred to as grey hydrogen and emits approximately 1,2 Mton CO_2/year [2]. Carbon-free hydrogen production accounts for only 0,7% of total production [3]. This carbon-free hydrogen can be obtained through electrolysis. PEM (Polymer Electrolyte Membrane) electrolyzers use an electrolyte composed of a thin polymer membrane, which facilitates the conduction of hydrogen protons (H+) due to its composition of sulfonic acid functional groups (−SO3OH). This membrane is notable for its high efficiency, high oxidative stability, and good durability [7]. PEM electrolyzers are capable of operating at much higher current densities compared to alkaline electrolyzers; however, these high current densities

© 2024. The Authors. Published by International Solar Energy Society
Selection and/or peer review under responsibility of Scientific Committee
10.18086/eurosun.2024.09.04 Available at http://proceedings.ises.org

require very specific materials such as platinum, iridium, and ruthenium, which increase production costs [8]. On the other hand, when coupled with a renewable energy source, PEM electrolyzers exhibit a good dynamic response to fluctuations in electrical supply [9], which is not observed with other types of electrolyzers

In recent years, several studies have been published on hydrogen production using solar energy. These research works evaluate three main electrolysis technologies: alkaline, proton exchange membrane (PEM), and solid oxide. Regarding the associated solar technology, photovoltaic (PV) technology is the most commonly used, closely followed by concentrated solar power (CSP). In this context, Rosenstiel et al. [10] evaluated hydrogen production via a hybrid (CSP-PV) plant with an alkaline electrolyzer, obtaining an LCOH of 4,04 USD/kg H2 for Morocco, a location with an annual direct normal irradiation of 2518 kWh/m^2. Moraga et al. [11] evaluated three configurations: CSP, PV, and CSP-PV in northern Chile, with an annual direct normal irradiation of 3000 kWh/m^2. The results showed that the LCOH reaches its minimum value for the PV-ALK configuration, with a value of 2,38 USD/kg H_2. Grube et al. [12] studied hydrogen production using four technologies: CSP/PEM, CSP/SOE, PV/PEM, and PV/SOE. The results indicated that the minimum LCOH is obtained with the CSP/SOEC configuration, with a value of 5,02 USD/kg H_2. Gallardo et al. [4] evaluated CSP and PV technologies separately with PEM and ALK electrolyzers, with these plants located in the Atacama Desert. The minimum LCOH obtained was 2,2 USD/kg H_2 with the PV-ALK technology. On the other hand, Yang et al. [13] proposed a model for the PV-PEM electrolysis system, detailing the voltage-current characteristics of both the PV cell and the PEM electrolyzer. Tebibel et al. [14] compared hydrogen production using PV technology through three electrolysis processes: PEM, methanol, and hybrid sulfur. Gallardo et al. [15] proposed a methodology for the optimal sizing of grid-connected PV-PEM systems, with results ranging between 5,9 and 11,3 USD/kg H_2. Xiang et al. [16] evaluated the LCOH for PV and nuclear technology in China, showing that by 2050, the PV-PEM technology could achieve an LCOH of 0,1154 USD/kg H_2. Nasser et al. [17] studied hydrogen production using different pathways: PV, wind, and a Rankine cycle with waste heat, obtaining an LCOH of 6,45 USD/kg H_2 for the PV case. Bhandari et al. [18] obtained an LCOH of 6,79 USD/kg H2 and 8,57 USD/kg H_2 for the PV-ALK and PV-PEM cases, respectively, for a global radiation of 3,23 kWh/m^2/day. Rezaei et al. [19] examined the sensitivity of LCOH produced by a PV plant, demonstrating the importance of careful site selection to achieve a high PV capacity factor. Finally, Jaradat et al. [20] discussed the potential for green hydrogen production in Jordan through a PV solar system using ALK and PEM

In summary, some articles have focused on the design of integrated systems using optimization functions to achieve the minimum Levelized Cost of Hydrogen (LCOH) [10], [15], while others have considered the design of CSP and PV plants using fixed design capacities [11], [12], [16], [21]. This study evaluates the integration of solar power generation technologies, CSP and/or PV, coupled with a PEM electrolyzer, operating in off-grid mode, to produce green hydrogen in a region with high solar radiation

2. Methodology

Green hydrogen production through solar energy is evaluated in northern Chile, one of the regions with the highest solar irradiance in the world. CSP and PV power plants are configured, along with PEM electrolyzers, which are modeled using specialized software to obtain the hourly annual production of each output. Subsequently, the levelized costs of electricity and hydrogen are calculated, and the main variables are analyzed for sensitivity to determine the optimal configuration. Two scenarios are evaluated: one for the present (2024) and one for the future (2030).

Three configurations (Figure 1) were modeled and evaluated considering four analysis alternatives. The first configuration, Case 1, includes PV and PEM; the second configuration, Case 2, involves CSP and PEM; the third configuration, Case 3, is a hybrid system comprising CSP, PV, and PEM; and finally, Case 4 is the same hybrid configuration (CSP, PV, and PEM) but with a higher capacity PEM plant.

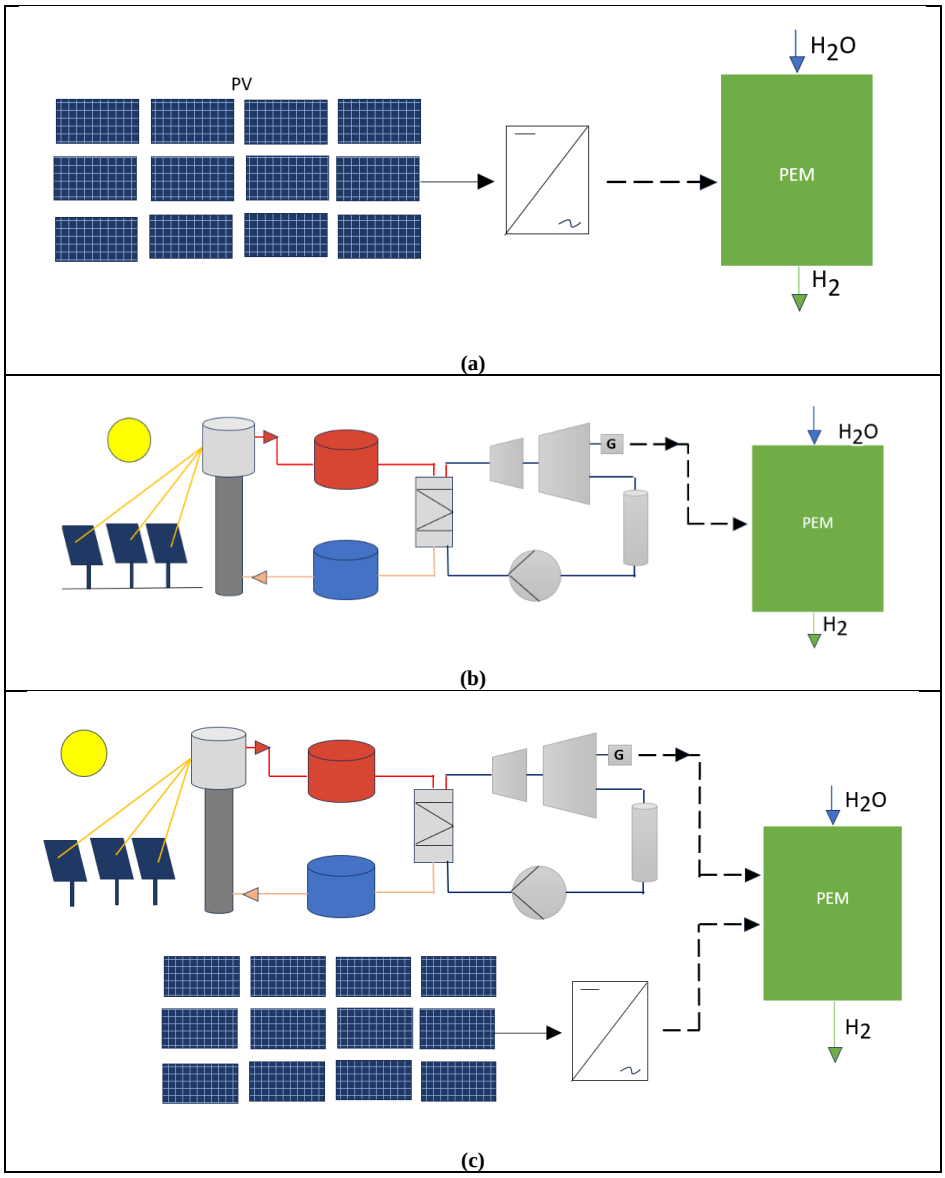

Fig. 1: Configurations evaluated a) PV and PEM, b) CSP and PEM. c) hybrid plant (CSP, PV and PEM)

SAM software [22] is used for modeling solar plants (CSP and PV), while Python programming language [23] is utilized for modeling PEM electrolysis plants and model integration, to determine the annual hourly production of electricity and hydrogen. The economic evaluation aims to calculate the levelized cost of energy (LCOE) and the levelized cost of hydrogen (LCOH). Two temporal scenarios are considered, a current scenario and a future one.

The location of the plants under evaluation is in the Antofagasta region of northern Chile (22,81 °S, 69,51 °W), at 1525 meters above sea level, 3 kilometers from “Atacama I / Cerro Dominador” [24]. This site has high irradiation levels: 3724 kWh/(m² year) of direct normal irradiation and 2580 kWh/(m² year) of global horizontal irradiation [5]. This site is chosen due to its high radiation values, making it an attractive location for evaluating a new CSP and PV project in the area

Design and Modeling of the CSP and PV System. The modeled CSP plant has a nominal capacity of 19,9 MW, with 15 hours of TES, a solar multiple of 2,5, 2625 heliostats of 118,8 m², a 140 m tower, an 8,89 m receiver, operating with HTF at 565 °C, and an evaporative-type condenser. The PV plant, on the other hand, has a nominal capacity of 20 MW, with 81840 Yingli Solar YL245-29b modules, 20 inverters with 98,5% efficiency, and a capacity of 500 kWac.

The PEM electrolyzer was modeled using the methodology outlined in [25], where the hydrogen flow at the outlet is determined using Equation 1

$$\dot{N}_{H2out} = \frac{J}{2 \cdot F} \qquad \text{(eq. 1)}$$

where J is the density current density and F is the Faraday constant.

The power consumed by the electrolyzer is determined by Equation 2

$$W = I \cdot n_{cell} \cdot V_{cell} \quad \text{(eq. 2)}$$

where I is the current consumed by the electrolyzer, n_{cell} is the number of cells, and V_{cell} is the cell voltage.

The cell voltage is calculated by Equation 3

$$V_{cell} = V_0 + V_{act} + V_{ohm} \quad \text{(eq. 3)}$$

where V_0 is the reversible voltage, V_{act} is the activation voltage y V_{ohm} is the ohmic overpotential.

Finally, the efficiency of the electrolyzer is calculated with Equation 4.

$$\eta_{PEM} = \frac{\dot{N}_{H2out} \cdot HHV_{H2}}{W} \quad \text{(eq. 4)}$$

where HHV_{H2} is the higher heating value of hydrogen.

In Cases 1, 2, and 3, an 18 MW electrolyzer was considered, whereas in Case 4, a 35 MW electrolyzer was used.

The parameters employed in the PEM cell model are presented in Table 1.

Tab. 1: Main parameters used in the PEM cell model [25].

Parameter	Value	Unit
Operating pressure	1,0	Atm
Operating temperatura	353	K
Reference Temperature	298,15	K
Anode activation energy	76	kJ/mol
Cathode activation energy	18	kJ/mol
Water content at the anode membrane interface	14	-
Water content at the cathode membrane interface	10	-
Membrane thickness	100	μm
Specific electrical consumption	54	kWh/kg H_2

For hydrogen compression, the energy required to store the produced hydrogen was determined using Equation 5.

$$L_{e,spec} = \frac{C_{pH2} \cdot \Delta T_{12}}{\eta_m \cdot \eta_e} = \frac{T_1 \cdot \left(\beta^{\frac{k-1}{k}} - 1\right)}{\eta_m \cdot \eta_e} \quad \text{(eq. 5)}$$

where $L_{e,spec}$ is the specific electrical consumption for the compression, C_{pH2} is the specific heat of hydrogen, T_1 and T_2 are the input and output temperatures respectively, η_m y η_e are the mechanical and electrical efficiency correspondingly, β is the compression ratio, and k is the isentropic coefficient. Mechanical and electrical efficiency are considered to be 70% and 90% respectively [4], and hydrogen is compressed from 20 bar to 350 bar.

The Levelized Cost of Energy (LCOE) represents the total cost of constructing and operating a power plant, divided by the total energy production over the plant's evaluation period. It is determined using Equation 6.

$$LCOE = \frac{CAPEX + \sum_{i=1}^{n} \frac{OPEX_i}{(1+t)^i}}{\sum_{i=1}^{n} \frac{E_i \cdot (1-d)^i}{(1+t)^i}} \quad \text{(eq. 6)}$$

where $CAPEX$ is the investment cost, $OPEX$ is the operational cost, n is the evaluation period, t is the disount rate, E_i is the annual energy production, and d is the annual degradation factor.

The LCOE of a hybrid CSP and PV plant is obtained by Equation 7 [26]

$$LCOE_{HYB} = \frac{LCOE_{PV} \cdot E_{PV} + LCOE_{CSP} \cdot E_{CSP}}{E_{PV} + E_{CSP}} \qquad \text{(eq. 7)}$$

The Levelized Cost of Hydrogen (LCOH) represents the average cost of hydrogen production, accounting for both capital and operational expenses. It is calculated by Equation 8

$$LCOH = \frac{CAPEX + \sum_{i=1}^{n} \frac{OPEX_i}{(1+t)^i}}{\sum_{i=1}^{n} \frac{H_i \cdot (1-d)^i}{(1+t)^i}} = \qquad \text{(eq. 8)}$$

where H_i is the annual production of hydrogen.

Tables 2, 3, and 4 present the cost structures of the evaluated plants (CSP, PV, and PEM), respectively. These data were used to conduct the economic evaluations.

Tab. 2: Cost structure of the CSP plant [6], [22], [27]

Costs	Parameter	Value (2024)	Value (2030)	Unit
Direct	Site improvements	16	10	USD/m^2
	Heliostat field	122	50	USD/m^2
	Solar tower	95.000	75.000	USD/m
	receiver	39.335.054	28.711.717	USD
	TES (Thermal Energy Storage)	22	10	USD/kWh
	Power block	1.100	700	USD/kW
	Balance of plant	340	340	USD/kW
	Contingency	5	2	%
Indirect	EPC (Engineering, procurement, and construction)	10	10	%
O&M	Fixed costs	66	66	USD/kW
	Variable costs	3,5	3,5	USD/MWh

Tab. 3: Cost structure of the PV plant [22], [28]–[30]

Costs	Parameter	Value (2024)	Value (2030)	Unit
Direct	Modules	0,3	0,17	USD/W_{dc}
	Investors	0,05	0,05	USD/W_{ac}
	Balance of plant	0,27	0,15	USD/W_{dc}
	Installation	0,11	0,11	USD/W_{dc}
	Contingency	3	1	%
Indirect	EPC	0,08	0,08	USD/W_{dc}
O&M	Fixed costs	15	8,1	USD/kW/year

Tab. 4: Cost structure of PEM plant [4], [31], [32]

Element	Parameter	Value (2024)	Value (2030)	Unit
PEM	CAPEX	1.100	650	USD/kW
	Stack replacement	65.000	90.000	h
Compressor	$CAPEX_{Comp}$	3.900	3.900	USD/kW
	$OPEX_{Comp}$	4	4	% $CAPEX_{Comp}$
Storage	$CAPEX_{Storage}$	500	500	USD/kg H_2
	$OPEX_{Storage}$	2	2	% $CAPEX_{Storage}$
EPC & O&M	$CAPEX_{EPC}$	3	3	% $CAPEX$

The economic parameters used for calculating the LCOE and LCOH include a 20-year time horizon, a discount rate of 7%, and a degradation rate of 0,2% per year for the CSP plant and 0.6% per year for the PV plant

3. Results and discussion

The CSP plant was validated using data from the Gema Solar plant [33] located in Seville, Spain, while the PV plant was validated with data from the Adrar Solar plant [34] located in Adrar, Algeria. Finally, the electrolyzer was validated with data from Ioroi et al. [35].

Table 5 presents the results of the annual electricity production (E), the capacity factor (cf) of the power plants, the annual hydrogen production (H), the annual water consumption of the electrolyzer (H_2O), and the levelized costs of electricity and hydrogen for 2024 and 2030. Case 4 produces the largest amount of hydrogen due to its higher electricity production and larger electrolyzer capacity; however, it does not result in the lowest levelized costs. Results yield a minimum LCOH of 5,76 USD/kg H_2 and a maximum of 6,60 USD/kg H_2 for the current scenario, while for the future scenario, values range between 2,86 and 4,26 USD/kg H_2. The minimum LCOE and LCOH in both scenarios are achieved in Case 1. Therefore, Case 1 is the most recommended, despite having a lower capacity factor and lower hydrogen production

Tab. 5: Results of electricity, hydrogen, LCOE and LCOH

Case	E kWh/year	cf %	H kg H_2/year	H_2O kg H_2O/year	LCOE USD/MWh		LCOH USD/kg H_2	
					2024	2030	2024	2030
Case 1	54.825.847	31,3	974.886	8,773,974.1	37,30	15,74	5,76	2,86
Case 2	150.207.389	86,2	2.610.582	23,495,240.1	85,15	57,04	6,60	4,26
Case 3	186.616.790	53,4	2.665.916	23,993,244.9	79,14	50,18	6,37	3,94
Case 4	205.033.237	58,7	3.640.271	32,762,440.8	72.36	45.99	6,37	3,88

The LCOH values for both 2024 and 2030 are not competitive compared to the costs of hydrogen produced from fossil fuels (grey hydrogen), which range from 1,2 to 2,3 USD/kg H_2 [2], [36]. According to the IEA, the current LCOH for green hydrogen ranges between 3 and 7,5 USD/kg H_2 [1], while IRENA estimates it to be between 4 and 5 USD/kg H_2 for a PV system in Chile [37]. By 2030, there will be a significant reduction in costs; however, they do not fall below 2 USD/kg H_2

Figure 2 presents the breakdown of the LCOH for all cases. In Case 1, which has the lowest LCOH, the distribution in the 2024 scenario is 51,1%, 36,4%, 12,0%, and 0,5% for CAPEX, energy consumption, O&M, and water consumption, respectively. For the 2030 scenario, the distribution is 52,6%, 30,9%, 15,4%, and 1,1%, respectively

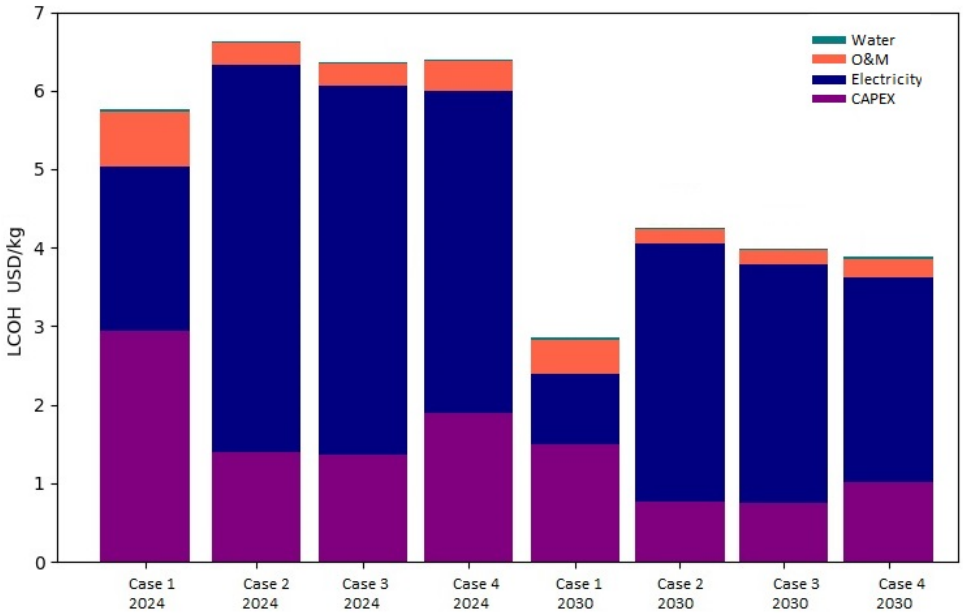

Fig. 2: Breakdown of the levelized cost of hydrogen.

A sensitivity analysis is conducted to quantify the impact of varying key parameters on the LCOH. The selected parameters are the LCOE and CAPEX of the PEM electrolyzer, both of which were varied within a range of ±10% of their base values, to proceed with the new calculation of the LCOH. The results are shown in Figure 3. From an economic standpoint, it has been identified that none of the solar hydrogen production pathways achieve costs below 2 USD/kgH_2 in the current scenario (2024). Therefore, it can be concluded that it is currently challenging for green hydrogen to compete economically with fossil fuel-based hydrogen production. While this situation would persist into 2030, the sensitivity analysis reveals that simply reducing the cost of energy and/or the cost of investment would allow achieving grey hydrogen levels.

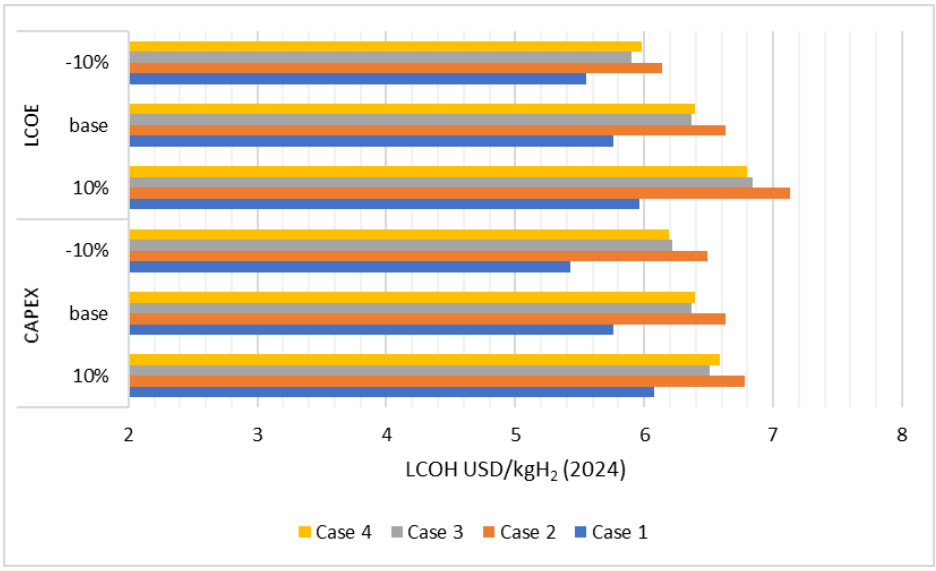

(a)

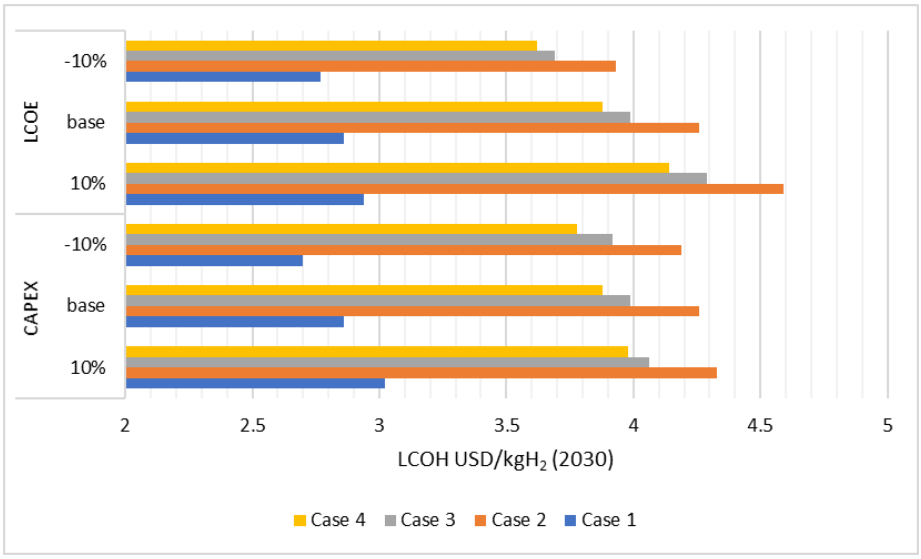

(b)

Fig. 3: Sensitivity analysis a) Current scenario (2024), b) Future scenario (2030)

4. Conclusions

The technical and economic feasibility of hydrogen production from solar energy was assessed, integrating a CSP plant, PV, and PEM electrolyzer operating in off-grid mode. Four cases were evaluated considering three configurations: Case 1 involves PV-PEM, Case 2 CSP-PEM, Case 3 is a hybrid CSP-PV-PEM, and the final case is similar to Case 3 but with a larger PEM plant.

The production of green hydrogen in all evaluated cases exceeds 2 USD/kg H_2, both for the current (2024) and future (2030) scenarios. Therefore, under these conditions, green hydrogen is not economically competitive with grey hydrogen. However, as electricity prices and electrolyzer investment costs decrease and efficiency improves, green hydrogen could become competitive.

The configuration that achieves the minimum LCOH is Case 1, which integrates a PV plant with an electrolyzer. Increasing the capacity factor of the PV plant, without increasing investment costs, could further reduce the LCOH; the same would apply to the CSP plant.

A hybrid solar plant offers complementary or additional benefits, such as greater stability and reliability in hydrogen production, as it is more flexible and less dependent on daily and seasonal variations in solar resources. However, the high investment costs of this technology result in a higher LCOH compared to a PV-PEM plant but lower than a CSP-PEM plant.

The residual heat from the CSP and PV plants could be utilized for cogeneration, using this heat to preheat the water for the PEM plant, thereby increasing system efficiency and potentially reducing the LCOH.

Future work will evaluate the performance of the plants in cogeneration mode and analyze the transient operation of the electrolyzer in more detail

5. Acknowledgments

This research work was funded by project PID2301-UTFSM and GIEAS (Grupo de Investigación en Energía, Agua y Sostenibilidad) of UTFSM.

6. References

[1] IEA, “The Future of Hydrogen,” 2019. doi: 10.1787/1e0514c4-en.

[2] IRENA, “International Trade and Green Hydrogen,” *Int. Trade Green Hydrog.*, 2023, doi: 10.30875/9789287075635.

[3] IEA, “Global Hydrogen Review 2023,” 2023. doi: 10.1787/cb2635f6-en.

[4] F. I. Gallardo, A. Monforti Ferrario, M. Lamagna, E. Bocci, D. Astiaso Garcia, and T. E. Baeza-Jeria, “A Techno-Economic Analysis of solar hydrogen production by electrolysis in the north of Chile and the case of exportation from Atacama Desert to Japan,” *Int. J. Hydrogen Energy*, vol. 46, no. 26, pp. 13709–13728, 2021, doi: 10.1016/j.ijhydene.2020.07.050.

[5] Ministerio de Energía, “Explorador Solar.” 2024. [Online]. Available: http://solar.minenergia.cl/inicio

[6] Office of Energy Efficiency and Renewable Energy, “2030 Solar Cost Targets.” https://www.energy.gov/eere/solar/articles/2030-solar-cost-targets (accessed Mar. 24, 2024).

[7] A. Ursúa and P. Sanchis, “Static-dynamic modelling of the electrical behaviour of a commercial advanced alkaline water electrolyser,” *Int. J. Hydrogen Energy*, vol. 37, no. 24, pp. 18598–18614, 2012, doi: 10.1016/j.ijhydene.2012.09.125.

[8] W. Xu and K. Scott, “The effects of ionomer content on PEM water electrolyser membrane electrode assembly performance,” *Int. J. Hydrogen Energy*, vol. 35, no. 21, pp. 12029–12037, 2010, doi: 10.1016/j.ijhydene.2010.08.055.

[9] D. S. Falcão and A. M. F. R. Pinto, “A review on PEM electrolyzer modelling: Guidelines for beginners,” *J. Clean. Prod.*, vol. 261, 2020, doi: 10.1016/j.jclepro.2020.121184.

[10] A. Rosenstiel, N. Monnerie, J. Dersch, M. Roeb, R. Pitz-paal, and C. Sattler, “Electrochemical hydrogen production powered by pv/csp hybrid power plants: A modelling approach for cost optimal system design,” *Energies*, vol. 14, no. 12, 2021, doi: 10.3390/en14123437.

[11] F. Moraga, M. T. Cerda, F. Dinter, and F. Fuentes, “Techno-Economic Analysis of the Integration of Large-Scale Hydrogen Production and a Hybrid CSP+PV Plant in Northern Chile,” *SolarPACES Conf. Proc.*, vol. 1, pp. 1–8, 2023, doi: 10.52825/solarpaces.v1i.669.

[12] T. Grube *et al.*, “A techno-economic perspective on solar-to-hydrogen concepts through 2025,” *Sustain. Energy Fuels*, vol. 4, no. 11, pp. 5818–5834, 2020, doi: 10.1039/d0se00896f.

[13] Z. Yang, J. Lin, H. Zhang, B. Lin, and G. Lin, “A New Direct Coupling Method for Photovoltaic Module-PEM Electrolyzer Stack for Hydrogen Production,” *Fuel Cells*, vol. 18, no. 4, pp. 543–550, 2018, doi: 10.1002/fuce.201700206.

[14] H. Tebibel and R. Medjebour, “Comparative performance analysis of a grid connected PV system for hydrogen production using PEM water, methanol and hybrid sulfur electrolysis,” *Int. J. Hydrogen Energy*, vol. 43, no. 6, pp. 3482–3498, 2018, doi: 10.1016/j.ijhydene.2017.12.084.

[15] F. Gallardo, J. García, A. Monforti Ferrario, G. Comodi, and J. N. Chiu, “Assessing sizing optimality of OFF-GRID AC-linked solar PV-PEM systems for hydrogen production,” *Int. J. Hydrogen Energy*, vol. 47, no. 64, pp. 27303–27325, 2022, doi: 10.1016/j.ijhydene.2022.06.098.

[16] P. Xiang, K. Jiang, J. Wang, C. He, S. Chen, and W. Jiang, “Evaluation of LCOH of conventional technology, energy storage coupled solar PV electrolysis, and HTGR in China,” *Appl. Energy*, vol. 353, no. PA, p. 122086, 2024, doi: 10.1016/j.apenergy.2023.122086.

[17] M. Nasser and H. Hassan, “Techno-enviro-economic analysis of hydrogen production via low and high temperature electrolyzers powered by PV/Wind turbines/Waste heat,” *Energy Convers. Manag.*, vol. 278, no. November 2022, p. 116693, 2023, doi: 10.1016/j.enconman.2023.116693.

[18] R. Bhandari and R. R. Shah, “Hydrogen as energy carrier: Techno-economic assessment of decentralized hydrogen production in Germany,” *Renew. Energy*, vol. 177, pp. 915–931, 2021, doi: 10.1016/j.renene.2021.05.149.

[19] M. Rezaei, A. Akimov, and E. M. A. Gray, “Economics of solar-based hydrogen production: Sensitivity to financial and technical factors,” *Int. J. Hydrogen Energy*, vol. 47, no. 65, pp. 27930–27943, 2022, doi: 10.1016/j.ijhydene.2022.06.116.

[20] M. Jaradat, O. Alsotary, A. Juaidi, A. Albatayneh, A. Alzoubi, and S. Gorjian, “Potential of Producing Green Hydrogen in Jordan,” *Energies*, vol. 15, no. 23, pp. 1–21, 2022, doi: 10.3390/en15239039.

[21] R. Boudries, “Techno-economic study of hydrogen production using CSP technology,” *Int. J. Hydrogen Energy*, vol. 43, no. 6, pp. 3406–3417, 2018, doi: 10.1016/j.ijhydene.2017.05.157.

[22] NREL, “System Advisor Model (SAM).” 2024.

[23] Python Software Foundation, “Python programming language.” [Online]. Available: https://www.python.org/

[24] SolarPACES, “Atacama I / Cerro Dominador. PV CSP Project.” https://solarpaces.nrel.gov/project/atacama-i-cerro-dominador-110mw-csp-100mw-pv (accessed Aug. 16, 2024).

[25] M. Ni, M. K. H. Leung, and D. Y. C. Leung, “Energy and exergy analysis of hydrogen production by a proton exchange membrane (PEM) electrolyzer plant,” *Energy Convers. Manag.*, vol. 49, no. 10, pp. 2748–2756, 2008, doi: 10.1016/j.enconman.2008.03.018.

[26] L. Bousselamti and M. Cherkaoui, “Modelling and Assessing the Performance of Hybrid PV-CSP Plants in Morocco: A Parametric Study,” *Int. J. Photoenergy*, vol. 2019, 2019, doi: 10.1155/2019/5783927.

[27] J. A. Gacitúa, R. Palma-Behnke, J. M. Cardemil, M. T. Cerda, F. Godoy, and F. Dinter, “Assessing the synergy between a seawater pumping system for mining facilities and the cooling system of a CSP plant in Northern Chile,” *J. Clean. Prod.*, vol. 346, no. February, p. 131052, 2022, doi: 10.1016/j.jclepro.2022.131052.

[28] C. Parrado, A. Girard, F. Simon, and E. Fuentealba, “2050 LCOE (Levelized Cost of Energy) projection for a hybrid PV (photovoltaic)-CSP (concentrated solar power) plant in the Atacama Desert, Chile,” *Energy*, vol. 94, pp. 422–430, 2016, doi: 10.1016/j.energy.2015.11.015.

[29] A. Zurita *et al.*, “State of the art and future prospects for solar PV development in Chile,” *Renew. Sustain. Energy Rev.*, vol. 92, no. November 2017, pp. 701–727, 2018, doi: 10.1016/j.rser.2018.04.096.

[30] W. J. Cole *et al.*, “SunShot 2030 for Photovoltaics (PV): Envisioning a Low-cost PV Future,” 2017. [Online]. Available: https://www.nrel.gov/docs/fy17osti/68105.pdf%0Ahttp://www.osti.gov/servlets/purl/1392206/

[31] R. Dufo-López, J. M. Lujano-Rojas, and J. L. Bernal-Agustín, “Optimisation of size and control strategy in utility-scale green hydrogen production systems,” *Int. J. Hydrogen Energy*, vol. 50, pp. 292–309, 2024, doi: 10.1016/j.ijhydene.2023.08.273.

[32] S. Krishnan *et al.*, “Present and future cost of alkaline and PEM electrolyser stacks,” *Int. J. Hydrogen Energy*, vol. 48, no. 83, pp. 32313–32330, 2023, doi: 10.1016/j.ijhydene.2023.05.031.

[33] F. De Andalucía, *System Advisor Model (SAM) Case Study : Gemasolar*. pp. 1–6.

[34] S. Bentouba, M. Bourouis, N. Zioui, A. Pirashanthan, and D. Velauthapillai, “Performance assessment of a 20 MW photovoltaic power plant in a hot climate using real data and simulation tools,” *Energy Reports*, vol. 7, pp. 7297–7314, 2021, doi: 10.1016/j.egyr.2021.10.082.

[35] T. Ioroi, K. Yasuda, Z. Siroma, N. Fujiwara, and Y. Miyazaki, “Thin film electrocatalyst layer for unitized regenerative polymer electrolyte fuel cells,” *J. Power Sources*, vol. 112, no. 2, pp. 583–587, 2002, doi: 10.1016/S0378-7753(02)00466-4.

[36] IRENA, “Green Hydrogen Cost Reduction,” 2020. doi: 10.1002/er.8645.

[37] IRENA, *“Hydrogen from renewable power: Technology outlook for the energy transition (2018)”, IRENA, available at https://www.irena.org/publications/2018/Sep/Hydrogen-from-renewable-power [Accessed : 29-Nov.-2019]*, no. September. 2018. [Online]. Available: www.irena.org

SOLAR HYDROGEN PRODUCTION: TECHNO-ECONOMIC EVALUATION OF CONCENTRATED SOLAR POWER PLANT AND HIGH-TEMPERATURE ELECTROLYSIS INTEGRATION

João H. S. Martins [1], Timo Roeder [1,2], Andreas Rosenstiel [1,2] and Nathalie Monnerie [1]

[1] German Aerospace Center (DLR), Institute of Future Fuels, Cologne (Germany)

[2] RWTH Aachen University, Faculty of Mechanical Engineering, Chair for Solar Fuel Production, Aachen (Germany)

Abstract

High-temperature electrolysis systems produce hydrogen with high electrical efficiency, but require additional thermal energy for steam generation. Thus, this study explores the thermal and electrical integration of a concentrated solar power (CSP) plant with a high-temperature electrolysis system. Medium-temperature heat (above 150 °C) from the solar plant can be used for water evaporation during steam electrolysis, reducing the electrical energy demand compared to low-temperature alternatives. The techno-economic performance of this integration is evaluated through quasi-dynamic numerical simulations for a 50 MW plant in Morocco. The model includes a parametric analysis to optimize the levelized cost of hydrogen (LCOH) by varying the solar multiple and storage capacity. Additionally, the solar-to-fuel efficiency and capacity factor are evaluated, with comparisons to other CSP- and photovoltaic-powered electrochemical hydrogen production pathways. Under current cost assumptions, the optimal configuration (solar multiple of 2.29 and storage capacity of 10.7 hours) results in an LCOH of 7.88 EUR kg^{-1}. In a 2030 cost scenario, a similar configuration yields an LCOH of 4.83 EUR kg^{-1}, a capacity factor of 48 %, and a solar-to-fuel efficiency over 12 %. Finally, the sensitivity analysis identifies the most critical economic parameters influencing the LCOH, and highlights further research needs to bring this integration concept closer to competing technologies.

Keywords: Parabolic trough collectors, Solid oxide electrolysis cell, Thermal energy storage, Solar hydrogen production, Thermal and electrical integration

1. Introduction

Global hydrogen use reached 95 Mt in 2022, predominantly for refining and industrial processes. Virtually all of this was produced through processes such as steam methane reforming, which generates significant greenhouse gas (GHG) emissions. Nonetheless, hydrogen is also recognized as a promising sustainable energy carrier with the potential to bridge gaps in the temporal and spatial availability of renewable energy. Beyond the energy sector, hydrogen and its derivatives hold great promise for replacing fossil fuels and decarbonizing sectors such as aviation, shipping, and hard-to-abate industries like steel, cement, and fertilizer production (IEA, 2022). To realize this potential, hydrogen production must be driven by low-carbon energy sources, notably solar and wind, requiring further technological advancements to become cost-competitive with conventional processes.

Moreover, renewable hydrogen plays a pivotal role in the European Union's (EU) policy for energy transition, achieving net-zero emissions, and fostering sustainable development in the frame of the EU Green Deal. The EU's REPowerEU Strategy sets an ambitious target of producing 10 Mt of hydrogen domestically and importing an additional 10 Mt by 2030. By 2050, the aim is for renewable hydrogen to meet approximately 10 % of the EU's energy needs, enabling significant decarbonization of energy-intensive industrial processes and the transport sector (European Commission, 2020). Furthermore, Braun et al. (2023) estimate that nearly half of the EU's projected hydrogen demand of 25.9 Mt in 2050 could be met through imports from the Middle East and North Africa (MENA) region. Countries such as Morocco, Algeria, Tunisia, Libya, Egypt, and Saudi Arabia are identified as key partners, given their renewable energy potential, low production costs, geographic proximity to Europe, and established cross-regional infrastructure.

© 2024. The Authors. Published by International Solar Energy Society
Selection and/or peer review under responsibility of Scientific Committee
10.18086/eurosun.2024.09.05 Available at http://proceedings.ises.org

In terms of solar energy, the three main methods for producing hydrogen are electrochemical, photochemical, and thermochemical (Haussener, 2022). The electrochemical pathway – mainly using alkaline (AEC) or proton exchange membrane electrolysis cells (PEMEC), compatible with electricity from concentrated solar power (CSP), photovoltaics (PV), or hybrid CSP/PV systems – is the most mature, boasting the highest maturity, as highlighted by the IEA (2022). Rosenstiel et al. (2021) compared these three solar-driven systems for providing electricity to an AEC, finding that PV and hybrid systems achieve comparable levelized costs of hydrogen (LCOH), as low as 3.42 and 2.61 EUR kg^{-1} in present and outlook scenarios for Morocco, respectively, while the CSP/PV system using solar power towers (SPT) demonstrates a significantly higher capacity factor Moreover, CSP and hybrid systems offer a key advantage over PV systems by delivering lower lifetime GHG emissions (Edenhofer et al., 2011).

Within the electrochemical pathway, using solar heat and electricity for high-temperature electrolysis (HTE) with solid oxide electrolysis cells (SOECs) shows promise for improving efficiency and reducing hydrogen production costs (Seitz et al., 2017). SOECs can split water with lower total energy demands and operate at temperatures between 700–1000 °C by combining heat and electricity (Laurencin and Mougin, 2015). Figure 1 illustrates the thermodynamic energy demand of the water-splitting reaction for typical operating temperature ranges of low-temperature electrolysis (LTE) and HTE. Conducting the reaction at temperatures exceeding the evaporation point of water, by providing thermal energy to the process, decreases the total enthalpy change ΔH inside the electrolyzer by the heat of evaporation ΔH_{evap}, thereby reducing the associated electrical energy consumption and potentially lowering hydrogen costs. Additionally, higher temperatures reduce cell resistance, enabling electrical efficiencies above 90 %. Since CSP facilities can cost-effectively supply renewable electricity and medium- to high-temperature heat for extended periods, due to their compatibility with thermal energy storage (TES) systems, their energy streams can complement SOEC operating conditions. Despite these benefits, research on integrating CSP with the-SOEC systems is still limited in both literature and industrial applications.

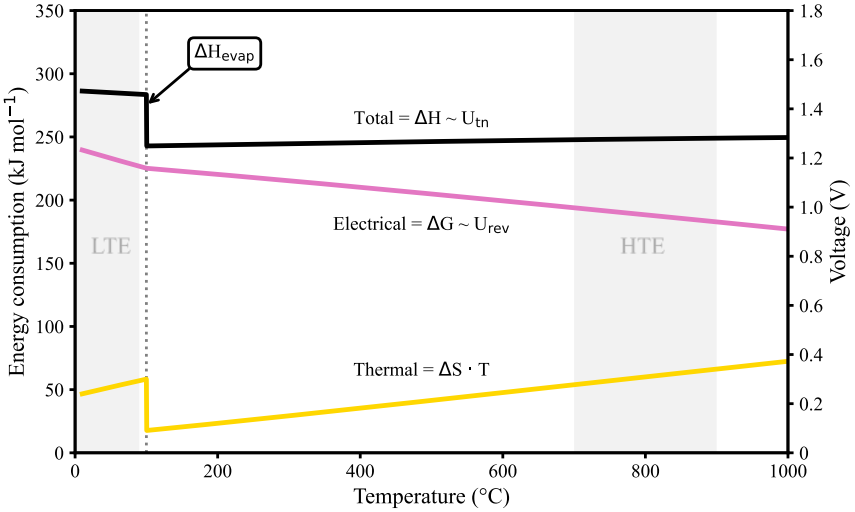

Fig. 1: Total energy demand of water splitting reaction at elevated temperature. U_{tn} = thermoneutral cell voltage; U_{rev} = reversible cell voltage. While LTEs usually operate under 100 °C, HTEs operate between 700–900 °C.

To address this, Immonen and Powell (2023) proposed three concepts for integrating solar energy with HTE-SOEC systems: (i) using PV and electrical heaters to meet both the electrical and thermal demands of the process; (ii) combining grid electricity with concentrated solar thermal (CST); and (iii) using CST and PV to meet the process's power and heat demands, respectively. Their study found similar LCOHs for all approaches, around 2.96 EUR kg^{-1} in the USA, and concluded that achieving higher capacity factors, potentially through TES integration, is essential for meeting more ambitious cost targets, such as the Hydrogen Shot from the United States Department of Energy – of 1 USD kg^{-1} (~ 0.93 EUR kg^{-1}) until the 2030s (DOE, 2023). Seitz et al. (2017) also explored a concept combining CST with SOECs modeled in Spain, achieving LCOHs of 3.67 EUR kg^{-1} with TES and 5.33 EUR kg^{-1} without TES. Another relevant study by Muhammad et al. (2024) carried simulations in EBSILON Professional to assess a CSP-SPT model to supply, under nominal conditions, 1–8 MW of electricity to an SOEC system, reporting LCOHs in the range of 5.64–8.23 EUR kg^{-1} in Western

Australia. However, comprehensive studies evaluating the simultaneous provision of electricity and heat to an HTE-SOEC system exclusively by a CSP plant are still in the early stages, highlighting the need for further investigation, which this paper aims to address.

In this context, our study presents a techno-economic assessment (TEA) of electrically and thermally integrating a CSP plant using parabolic trough collectors (PTCs) with an HTE-SOEC system. We estimate the associated capacity factor, solar-to-fuel (STF) efficiency, and LCOH, comparing it to hydrogen production via electrochemical routes powered by CSP and/or PV listed above. To achieve this, we modeled and simulated the proposed hydrogen production plant over a typical meteorological year in Morocco, given the expected importance of MENA region in the European hydrogen supply chain.

2. Hydrogen plant description

The design, modeling and annual simulation of this solar-driven hydrogen production concept was performed by integrating two main process blocks – solar and electrochemical. The coupling was carried by combining built-in and user-defined macro components in EBSILON® Professional (STEAG, 2022) and Aspen Plus (AspenTech, 2021), enabling the evaluation of the hydrogen production plant under design and off-design conditions, as well as parametric analysis to be carried out to obtain the optimal LCOH, given various combinations of solar multiple and TES capacity. Figure 2 presents a simplified block diagram showing this integration and the main mass and energy flows.

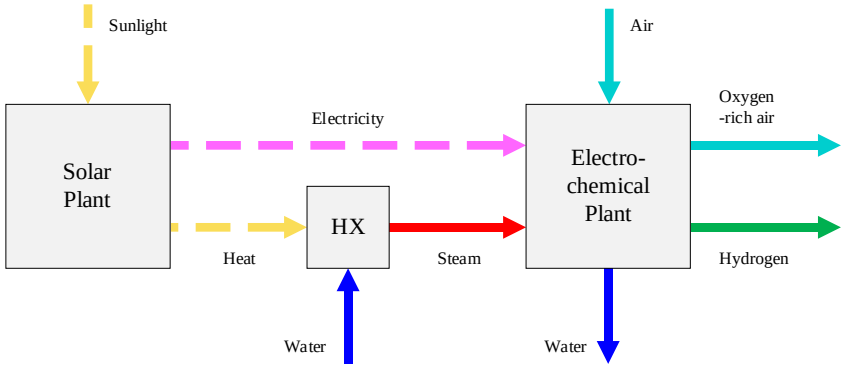

Fig. 2: Simplified scheme of the electrical and thermal integration of solar and electrochemical plants for hydrogen production. Full and dotted lines represent mass and energy streams, respectively. HX = heat exchanger.

The integrated model requires the characteristics of the solar and electrochemical sections as input, as well as the geographical and meteorological conditions of the selected site, here Ouarzazate in Morocco – where the world's largest CSP facility, the Noor Complex, is located (Thonig et al., 2023). Table 1 summarizes the important site parameters.

Tab. 1: Main geographical and meteorological parameters of the selected site (Meteotest, 2007). GHI = global horizontal irradiance; DNI = direct normal irradiance.

Parameter	Ouarzazate, MAR	Unit
Geographical coordinates	30.93; -6.90	° [*latitude*; *longitude*]
Elevation above sea level	1 140	m
Annual cumulative irradiation	2 123; 2 518	kWh m^{-2} [*GHI*; *DNI*]
Annual average ambient temperature	18.88	°C
Annual average wind speed	3.29	m s^{-1}

The outputs of the numerical model are the profile of the heat and electricity dispatch from the CSP-PTC plant, as well as the water demand and hydrogen production of the HTE-SOEC system. For simplicity, the following technical assumptions were considered:

- Quasi-dynamic simulations with hourly timestep considered;
- Pressure drop and thermal losses in the piping are neglected;
- Thermal losses in the TES are neglected;
- An ideal linear HTE-SOEC partial load behavior is assumed; and
- Energy demand for hydrogen separation and further compression is neglected.

2.1. Solar plant

The solar plant layout is based on Andasol-1, the first commercial CSP-PTC facility to operate in Europe, and detailed by Feldhoff et al. (2012) and NREL (2013). It mainly consists of three hydraulic circuits: a synthetic oil circuit heated by the parabolic trough solar field; a molten salt circuit consisting of two indirectly integrated tanks for sensible heat storage, and a water/steam circuit for a conventional Rankine cycle. The main parameters of the solar plant are presented in Table 2.

Tab. 2: Nominal parameters of the solar plant for a SM=1 and storage capacity of one full-load hour.

Parameter	Value	Unit
Solar field		
SCA model	Eurotrough ET150	-
Number of SCAs	294	-
SCA dimensions	5.76; 150.00	m [*width*; *length*]
SCA aperture area	864.00; 817.43	m² [*gross*; *net*]
Optical efficiency at design	74.73	%
Thermal efficiency at design	93.37	%
Solar field efficiency at design	69.77	%
HTF	Therminol VP-1	-
HTF temperature	290; 395	°C [*inlet*; *outlet*]
HTF pressure	5; 3.5	MPa [*inlet*; *outlet*]
Peak optical efficiency	75	%
Thermal energy storage		
HSM	Solar Salt	-
HSM temperature	385; 282	°C [*hot tank*; *cold tank*]
HSM mass capacity in each tank	3 600 000	kg
HSM mass flow rate at discharging	1 000	kg s^{-1}
State of charge at beginning of simulation	50	%
Power block		
Steam temperature at turbine	373; 41	°C [*inlet*; *outlet*]
Water temperature at condenser	20; 36.5	°C [*inlet*; *outlet*]
Steam pressure at turbine	10; 0.008	MPa [*inlet*; *outlet*]
Steam pressures at extractions	4; 1.7; 0.6; 0.25; 0.12; 0.06	MPa [*extraction 1 to 6*]
Thermal energy demand	147	MW
Electric output	54.1; 50	MW [*gross*; *net*]
Thermal efficiency	38.1	%
Generator efficiency	96.00	%

The model for the solar field comprises a series of solar collector assemblies (SCA) of PTCs. They are used to increase the temperature of the Therminol VP-1 up to 395 °C, since this heat transfer fluid (HTF) suffers thermal degradation at higher temperatures. The sizing of the solar plant followed the design point method, described by Wang (2019). For a solar multiple $SM = 1$ – i.e., when solar field aperture area equals the area required to absorb the heat to run the power block in nominal conditions – a thermal capacity of 147 MW is required to achieve the electricity production of 54.1 MW gross and 50 MW net. This capacity was chosen to align with the scale of numerous existing installations, particularly in Spain (Thonig et al., 2023), ensuring practical implementation. This approach facilitates seamless integration with current CSP infrastructure, as only the SOEC system, including the heat exchanger, would need to be installed. CSP-PTC plants, with their modular design, offer simpler scalability than SPT plants and can potentially benefit from even larger capacities. However, while scaling up these plants could lead to cost reductions through economies of scale, this aspect is beyond the scope of the current study and will be addressed in the future.

The heat absorbed in the solar field can be stored in the TES using a heat storage medium (HSM) hydraulic circuit, composed of two tanks where Solar Salt – a mixture of 60 wt% of sodium nitrate ($NaNO_3$) and 40 wt% of potassium nitrate (KNO_3) – is kept at 385 °C and 282 °C in the hot and cold tanks, respectively. The resultant process flow diagram is shown ahead in Figure 4.

Finally, the power block is composed of a conventional Rankine cycle with steam input at 373 °C and 10 MPa, with net electrical capacity of 50 MW. The generator coupled to the steam turbine produces the electricity dispatched to the HTE system in addition to the electricity demanded by the balance of the plant (BOP) equipment, i.e., the pumps, compressors and electric heaters.

2.2. Electrochemical system

The electrolyzer design is based on a commercial model, the Sunfire-HyLink SOEC (Sunfire, 2021), modeled under thermoneutral operation, so lowest degradation rates are achievable (Lang et al., 2020) and heat can be efficiently recuperated, limiting the amount of external heat input for the superheating the HTE input streams (Petipas et al., 2014). The modeling of the electrolysis system was done in ASPEN Plus to integrate heat from the CSP plant efficiently, and was designed to reduce electrical requirements and enhance heat recovery from the electrolysis outlet streams. The HTE system is composed mainly of the SOEC, and a series of components such as heat exchangers, air compressors, electric heaters and gas coolers, responsible for providing air and steam at 820 °C and 0.6 MPa, as well as separating the hydrogen from the steam/hydrogen mixture at its outlet, while recuperating part of the heat from the outlet gases.

The results of the ASPEN Plus are used in the EBSILON Professional for the time series analysis. For the calculation of the electrical energy an electrical heater efficiency of 95 % (Kanthal, 2023) and a pumping and compressing efficiency of 98 % for the reagent gases of the electrolysis is assumed. Furthermore, the electrolysis efficiency is assumed to be 95.7 % for an isothermal operation at a steam conversion rate of 70 % (Tomberg et al., 2023). Then, the electrolysis system and thermal energy demands were calculated to match the net electric load for a conventional 50 MW CSP-PTC plant.

Once electricity and steam are produced, they are directed to the HTE system, which requires electricity, steam, air, and hydrogen inputs, as shown in Figure 2. The design point conditions for the HTE system are showed in Table 3. For off-design operation, when electricity and steam are provided in partial load, it was considered linear behavior, assuming that even in part load operation, a share of the electrolyzer stacks is operated in nominal conditions. For the inactive stacks, a hot standby mode is considered, in which an electrical demand equivalent to 8.2 % of their nominal requirement is used to avoid temperature drop during inactivity. Since during these periods of inactivity, the CSP plant is unable to provide the input for the hot standby mode, it is provided by the connection with the electrical grid.

Tab. 3: Nominal parameters of the electrochemical plant.

Parameter	Value	Unit
Total electrical input	50	MW
SOEC electrical demand	47.27	MW
Electric heater demand	2.34	MW
BOP electrical demand	0.40	MW
SOEC temperature	850; 820	°C [*inlet*; *outlet*]
Steam/water mass flow rate	2.486; 0.746	kg s^{-1} [*inlet*; *outlet*]
Air mass flow rate	8.303; 2.099	kg s^{-1} [*inlet*; *outlet*]
Air mass flow rate	0.058; 0.424	kg s^{-1} [*inlet*; *outlet*]
Net hydrogen production rate	0.366	kg s^{-1}
Steam conversion rate	70	%
SOEC nominal efficiency	95.7	%
SOEC electricity demand on hot standby mode	8.2	% nominal demand
SOEC electricity demand at end of life	105	% nominal demand
H_2 content at SOEC inlet steam-H_2 stream	10	mol%
O_2 content at SOEC outlet O_2-rich air stream	40	mol%

2.3. Operation strategy

To represent the operation of the hydrogen production plant in multiple conditions throughout a typical year, the plant control model developed in EBSILON at the EbsScript interface accounted for five operation modes. The decision tree of the operation strategy is summarized in Figure 3.

Those steps are carried for each timestep of the simulation and decide the operation of the solar field, TES, power block, and the electrical and thermal dispatch from the CSP plant to the HTE-SOEC system. Moreover, the dispatch strategy was modeled to run the hydrogen plant in full-load as long as possible.

- Mode 1: the solar field charges the TES and supplies heat and electricity to the HTE. Hydrogen is produced in full- or part-load and the TES's state of charge (SoC) increases;
- Mode 2: the available heat is not enough to simultaneously charge the TES and power the HTE, thus the HTE is prioritized. Hydrogen is produced in full- or part-load and the TES's SoC is unaltered;
- Mode 3: due to low solar irradiance, the solar field is supported by the TES in supplying heat and electricity to the HTE. Hydrogen is produced in full- or part-load and the TES's SoC decreases;
- Mode 4: the solar irradiance in the solar field is insufficient to drive the process and the TES is not completely discharged. Thus, heat and electricity are supplied to the electrolysis exclusively by the TES. Hydrogen is produced in full- or part-load and the TES's SoC decreases;
- Mode 5: the solar irradiance in the solar field is insufficient to drive the process and the TES is completely discharged. Hydrogen is not produced and the TES's SoC stays at its minimum.

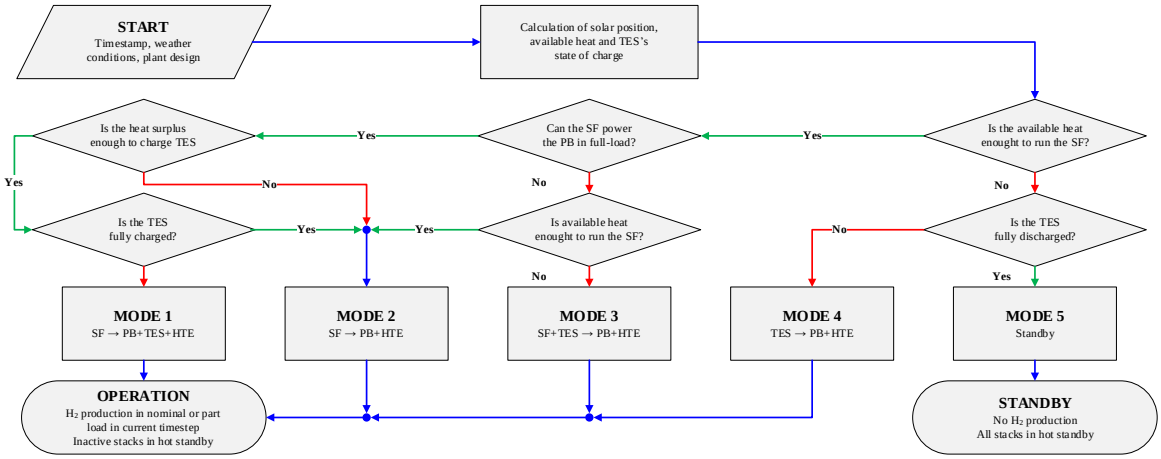

Fig. 3: Visual scheme of the operation strategy decision. SF = solar field; PB = power block.

2.4. Parametric analysis

To complement the modeling of the plant, a parametric analysis evaluates how changing input variables affects the output of a model. In this study, the focus was on how varying the solar field size – given by the solar multiple – and TES capacity influences the process KPIs. The analysis involved simulating various combinations of SMs (ranging from 1 to 4) and TES capacities (ranging from no storage to 18 hours of equivalent full load operation). After that, those discrete results undergo through an interpolation algorithm to obtain continues values for all KPIs, which are used to identify the plant configurations with the highest capacity factor, STF efficiency and, above all, the lowest LCOH – which indicates the most cost-effective configuration for the hydrogen production plant.

3. Techno-economic modeling

The methodology used for the techno-economic analysis largely follows the approach outlined by Albrecht et al. (2017). Key performance indicators (KPI) are established to assess the efficiency, energy conversion, and economic viability of the hydrogen production process, alongside the economic boundary conditions that define our analysis.

3.1. Key performance indicators

The primary KPIs evaluated include the capacity factor (CF), solar-to-fuel efficiency (η_{STF}) and the LCOH. The capacity factor reflects how effectively the process operates relative to its maximum potential output. It is calculated as the ratio between the actual hydrogen output $\sum_{t=1}^{n} H_{2,t}$ and the theoretical maximum output over a given period if the process were running at full capacity $H_{2,design}$. Given the assumption of process

degradation, this calculation extends across the entire plant lifetime n of 25 years. The contribution of each year is denoted by the subscript t.

$$CF = \frac{\text{Actual H}_2\text{ output [kg]}}{\text{Theoretical maximum H}_2\text{ output [kg]}} = \frac{\sum_{t=1}^{n} H_{2,t}}{8760 \cdot n \cdot H_{2,design}}\ [-] \quad \text{(eq. 1)}$$

The STF efficiency η_{STF} is defined as the ratio of the energy content of the produced fuel, based on the lower heating value of hydrogen LHV_{H_2}, to the incident solar energy in the solar field Q_{solar} plus the auxiliary electricity from the grid E_{aux}. Similar to the capacity factor, it was calculated throughout the plant lifetime.

$$\eta_{STF} = \frac{\text{Total energy stored at the produced H}_2\text{ [J]}}{\text{Total energy provided to the process [J]}} = \frac{\sum_{t=1}^{n} H_{2,t} \cdot LHV_{H_2}}{\sum_{t=1}^{n} (Q_{solar,t} + 2.5 \cdot E_{aux,t})}\ [-] \quad \text{(eq. 2)}$$

Finally, the LCOH is the cost the per-unit of producing hydrogen, considering all capital, operational, and maintenance expenses over the facility's lifetime. Here it was calculated using the cash flow method. The detailed procedure for this calculation and definitions of engineering, procurement, and construction (EPC) costs, capital expenditure (CAPEX), operating expenditure (OPEX), and interest rate i are further described by Dersch et al. (2020), containing detailed cost parameters for 2018 and 2030 for different locations.

$$LCOH = \frac{\text{Total life cycle costs [EUR]}}{\text{Total life cycle H}_2\text{ production [kg]}} = \frac{\sum_{t=0}^{n} (CAPEX_t + OPEX_t)(1+i)^{-t}}{\sum_{t=1}^{n} (H_{2,t})(1+i)^{-t}}\ [\text{EUR kg}^{-1}] \quad \text{(eq. 3)}$$

The process STF efficiency, capacity factor, heat, electricity and hydrogen production results from the time series calculations from EBSILON are used for performing the TEA, in which the CAPEX and fixed annual OPEX are used for the LCOH calculation. This LCOH is then used as the main performance indicator for the comparison with other hydrogen production technologies.

3.2. Cost assumptions

The main cost parameters used for the TEA calculations are summarized in Table 4. It is noteworthy that the costs and energy demand for hydrogen compression are neglected, while an annual interest rate of 7.5 % and a plant lifetime of 25 years are assumed.

Tab. 4: Cost parameters considered for the TEA in 2023 and 2030 scenarios.

Parameter	2023	2030	Unit
Direct EPC costs			
Solar field	247	150	EUR m^{-2} aperture
Thermal energy storage	49	24	EUR kWh^{-1}
Power block	935	638	EUR kW^{-1}
High-temperature electrolyzer	3 270	1 566	EUR kW^{-1}
Indirect EPC costs			
Engineering, management, EPC services	5	2	% total EPC
Profit margin and contingencies	10	6	% direct EPC
Owner's costs			
Infrastructure (grid connection, roads, etc.)	5 550 000	5 550 000	EUR
Project development	4	2	% total EPC
Additional owner's cost	3	2	% total EPC
Specific land cost	0.93	0.93	EUR m^{-2} land
Running costs			
Annual CSP O&M cost	1.5	1.5	% CSP direct EPC
Annual HTE O&M cost	32.5	12.5	EUR kW^{-1}
SOEC stack replacement cost	$f(CF)$	$f(CF)$	EUR kW^{-1}
SOEC stack durability	$f(CF)$	$f(CF)$	a
Annual insurance cost	0.7	0.7	% direct EPC
Electricity cost	93	93	EUR MWh^{-1}
Water costs	2	2	EUR m^{-3}

The cost assumptions for the CSP plant were obtained from the study by Dersch et al. (2020), which presents the costs for the components of a CSP-PTC plant and its site-specific costs when implemented in several countries. The costs were adjusted to Morocco using a price index of 42, as well as local and global cost shares. Moreover, all costs are converted to EUR_{2023} using the Chemical Engineering Plant Cost Index (CEPCI). Finally, the average exchange rate of the reference year for converting costs between USD and EUR.

The total SOEC system investment cost is calculated with a methodology from a previous study (Roeder et al., 2024). Its cost calculation method considers cost development predictions from Böhm et al. (2020) and stack lifetime development expectations from various studies and reports. Thus, the year of the stack replacement and the individual costs as a function of process capacity factor (or full load hours) and project lifetime is calculated. Additionally, annual operation and maintenance (O&M) costs for the electrolysis system are considered as in Smolinka et al. (2018). The O&M costs are considered to be constant throughout the project lifetime because, they are considered for the whole HTE system.

4. Simulation results and discussion

The key findings from the simulation of the integrated hydrogen production process are presented below. The plant integration is first examined, with a focus on how the solar and electrochemical systems were combined. Next, the capacity factor and solar-to-fuel efficiency are discussed, highlighting how operational conditions affect system performance. Finally, the levelized cost of hydrogen (LCOH) is analyzed, followed by a sensitivity analysis to identify the factors most influencing this critical indicator.

4.1. Plant integration

The outcome of the design of the integrated process is presented in Figure 4, which shows the schematic process diagram. In the presented concept, the solar and electrochemical systems are integrated through a heat exchanger that extracts heat from the synthetic oil at the outlet of the power block at a temperature around 290 °C, in line with the simplified diagram shown in Figure 2. In addition, the main parameters from the simulation of the heat exchanger used for steam generator are contained in Table 5.

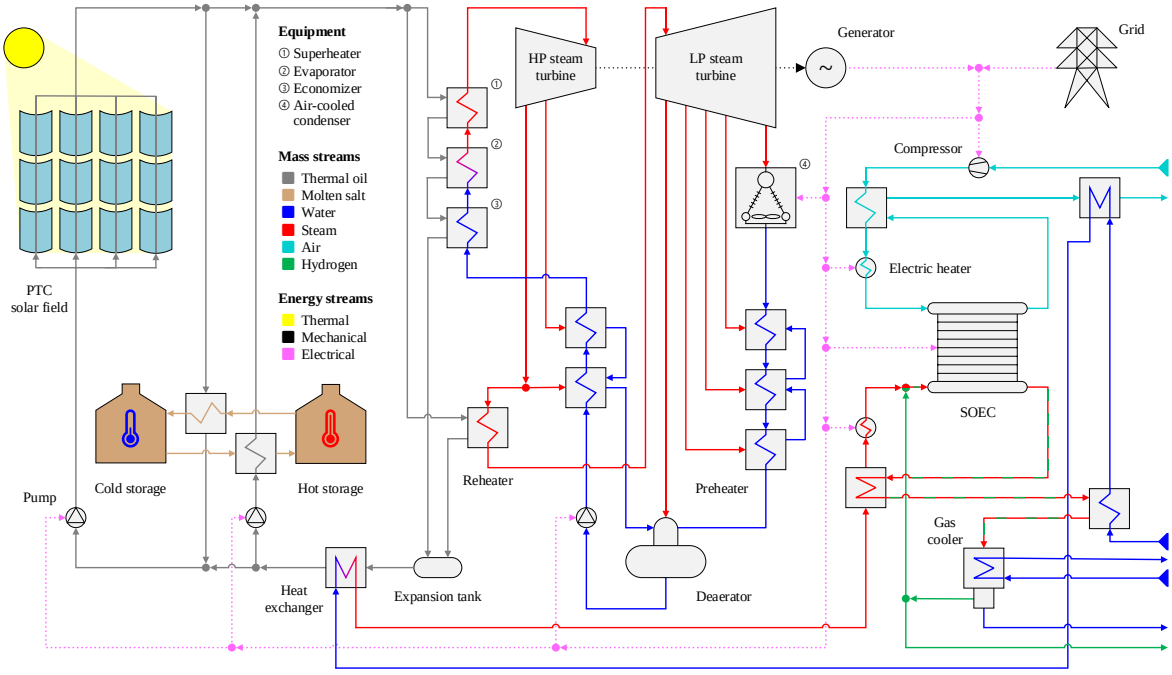

Fig. 4: Scheme of the thermal and electrical integration between PTC-CSP plant and HTE-SOEC system for solar hydrogen production, highlighting main equipment, mass and energy streams. Grid connection is used only for SOEC hot standby. LP = low pressure; HP = high pressure.

After the steam generation, electricity is used to reach the water-splitting temperature around 850 °C under SOEC thermoneutral operation, which is favorable for long stack lifetimes (Lang et al., 2020). This choice simplifies the combined operation of the power block with the HTE, which requires proportional amounts of

steam and electricity for hydrogen production. In addition, this integration position does not interfere with the water/steam cycle, which can significantly change the operating point and performance of the steam turbine. Furthermore, this solution has the potential to be retrofitted into existing CSP-PTC plant, requiring only minor changes in the system design.

Tab. 5: Parameters of the integrated steam generator.

Parameter	Value	Unit
Thermal oil temperature	292; 286	°C [*inlet*; *outlet*]
Water/steam temperature	95; 200	°C [*inlet*; *outlet*]
Thermal oil pressure	1.5; 1.45	MPa [*inlet*; *outlet*]
Water/steam pressure	0.65; 0.6	MPa [*inlet*; *outlet*]
Water/steam mass flow rate at design	4.67	kg s^{-1}
Thermal energy demand	9.463	MW

4.2. Capacity factor

The capacity factors resulting from the process simulation are shown in Figure 5 (a) and (b), reflecting the CSP-HTE performance for 2023 and 2030, respectively. With expected improvements in SOEC durability over time, the average SOEC lifetime is expected to increase for the future scenario, which leads to lower electrical demand and/or reduced hydrogen output, causing a slight increase in the process capacity factor from 61.75 % in 2023 to 62.20 % in 2030. The maximum capacity factor is achieved with a combination of 18 hours of storage capacity and a solar multiple of approximately 3.4.

These results align with the known relationship between storage capacity and solar multiple, indicating that both must be increased proportionally to achieve higher capacity factors. Otherwise, the solar field cannot provide sufficient heat for disproportionate large storage systems, or the excess heat from an oversized solar field cannot be efficiently stored.

4.3. Solar-to-fuel efficiency

Similar to the results for the capacity factor, the values for the STF efficiency are summarized in Figure 5 (c) for 2023 and (d) for 2030. It is observed that the peak efficiency values do not align with the highest capacity factors, and are generally achieved for combinations of intermediate solar multiples and storage capacities. While higher solar multiples and larger storage can enhance the plant's ability to produce hydrogen consistently, they can also lead to inefficiencies, such as excess heat that cannot be effectively converted or stored. This discrepancy occurs because optimizing for continuous operation and maximizing output does not always match the conditions that yield the highest conversion efficiency. For example, the process may be less efficient when powered by heat from the TES due to lower temperatures when compared to the heat provided directly by the solar field, and during part-load conditions, where power block efficiency decreases at lower steam mass flow rates, temperatures, or pressures.

In our simulations it was obtained similar maximum efficiencies for 2023 and 2030, about 12 % for a combination of solar multiple of 2.41 and 5.51 hours of storage. The value is slightly increased in 2030 mainly due to reduced degradation expected for the SOEC stacks, resulting in a lower average specific electrical consumption by the stacks over their lifetime. This improvement for the future scenario could be further improved if enhancements of the CSP performance (e.g., higher HTF temperature, more efficient power blocks and/or SCAs) are considered.

4.4. Levelized cost of hydrogen

Finally, the results of the LCOH for various combinations of solar multiple and storage capacity are presented in Figure 5 (a) for 2023 and (b) for 2030. We considered it as the most important indicator, since it allows comparison with other hydrogen production processes and cost targets. For the 2023 scenario, which includes higher specific costs for purchasing and maintaining the solar and electrochemical components of the plant and decreased durability of the stacks in the HTE-SOEC system, the minimum LCOH is significantly higher compared to the 2030 scenario. The 2030 scenario benefits from more favorable technical and economic conditions. Specifically, for 2023, the lowest achieved LCOH is 7.88 EUR kg^{-1} with a solar multiple of 2.29 and 10.65 hours of storage. In contrast, for 2030, the LCOH decreases to 4.83 EUR kg^{-1} with a solar multiple of 2.35 and the same storage capacity.

The analysis also suggests that storage capacities exceeding 18 hours could potentially lead to even lower LCOHs. However, due to their extensive size, storage capacities beyond that were not evaluated in this study, and could be the subject of future studies. Additionally, improvements in CSP plant performance and economy of scale factor for component costs could further reduce the LCOH. These factors were not included in our study but could further lower the optimal LCOH, especially if larger storage and more extensive solar fields were used.

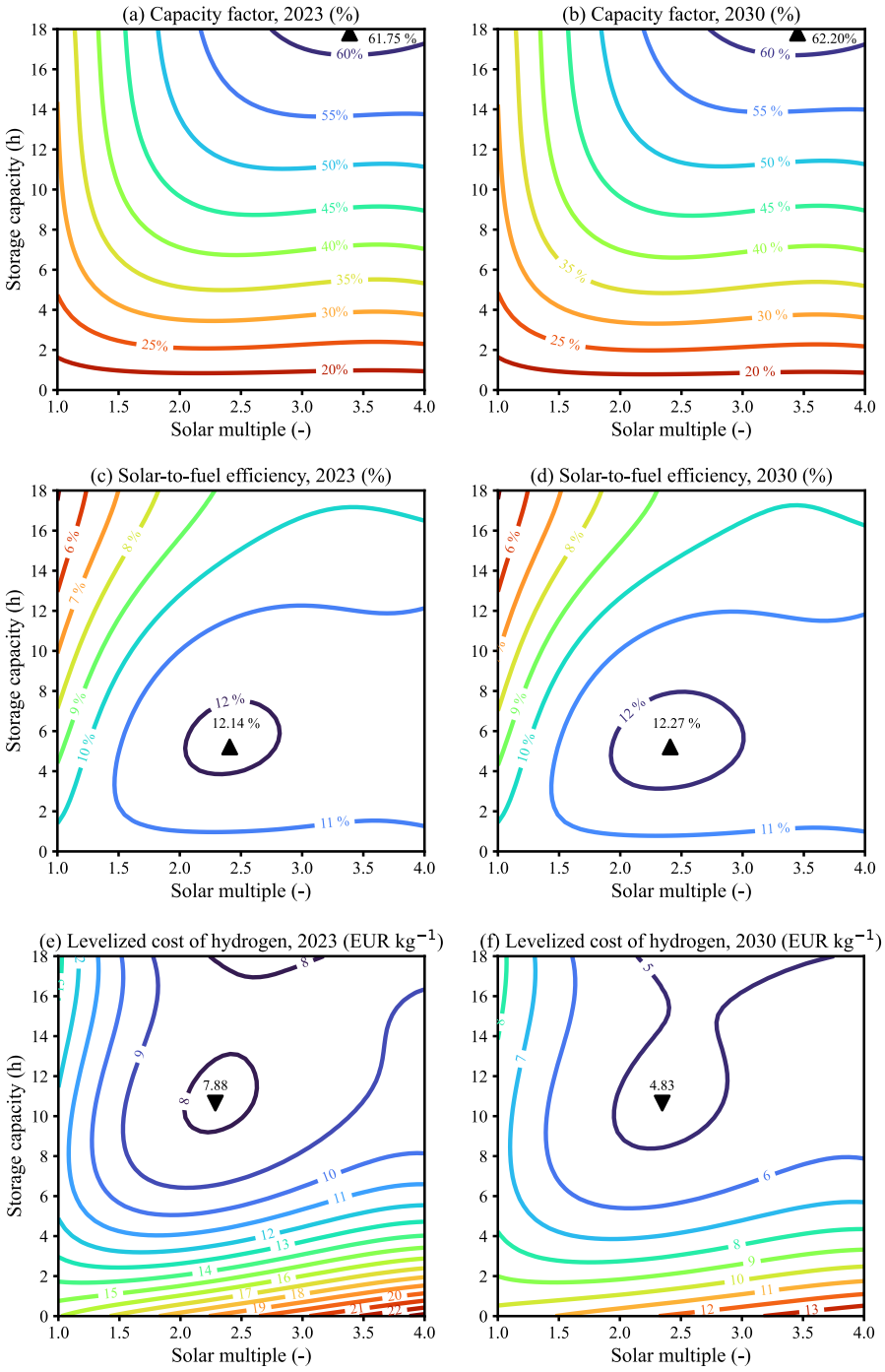

Fig. 5: Isolines for the key performance indicators of the process according to different combinations of solar multiple and storage capacity considering current (2023) and future (2030) assumptions. Capacity factor for 2023 (a) and 2030 (b); Solar-to-fuel efficiency using hydrogen's LHV for 2023 (c) and 2030 (d); and levelized cost of hydrogen for 2023 (e) and 2030 (f).

Compared to the literature reviewed in the introduction section, which reports LCOHs ranging from 2.61 to 8.23 EUR kg^{-1}, our model yields comparable results for both current and future scenarios, but costs remain higher than the lowest LCOH identified. Nevertheless, this direct comparison is not simple, as relevant disparities are present in LCOH calculation methods, site-specific meteorological conditions, and differing

economic assumptions, including the use of different base years for economic analyses. Since our study adjusts cost assumptions for inflation, it is expected to produce less competitive but realistic results. Further improvements in the process, TEA methodology, and comparisons under consistent boundary conditions could provide clearer insights into the advantages and disadvantages of each process.

4.5. Sensitivity analysis

After the parametric analysis, a sensitivity analysis was conducted to further explore how varying key input variables affect the LCOH. Figure 6 presents a detailed sensitivity analysis, showing the impact of nine variables on LCOH for both 2023 and 2030 scenarios. These variables include interest rates, cost of components, O&M, and utilities.

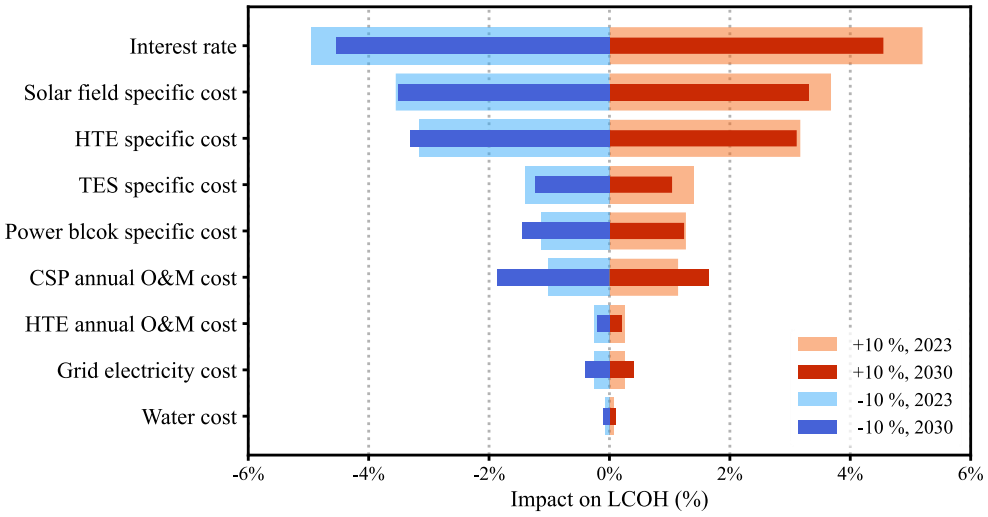

Fig. 6: Sensitivity of the LCOH on the variation of selected input variables in ±10 % considering the 2023 and 2030 scenarios.

It was found that while sensitivity patterns remain consistent between the 2023 and 2030 scenarios, the impact range for some variables varies more significantly. The most significant influence on LCOH is the interest rate; reducing it by 10 % results in a 4.6 % decrease in LCOH for 2023 and a 5 % decrease for 2030. Fluctuations in the interest rate beyond this are common, underscoring its importance in evaluating the cost-effectiveness of this capital-intensive technology. For example, if the interest rate changes from 7.5 % (the value considered in our study) to 5 %, the LCOH decreases to 6.61 EUR kg^{-1} for 2023 and 4.13 EUR kg^{-1} for 2030. Following interest rates, the next most relevant parameters identified were the specific costs of the solar field and the HTE system, reinforcing the significant influence of the uncertainties in cost projections of both systems to the quality of such TEA studies.

After interest rates, the specific costs of the solar field and the HTE system emerge as the most critical parameters, highlighting how uncertainties in the cost projections of both systems can significantly impact the quality of TEA studies and make direct comparisons with literature challenging.

Conversely, variables such as the water, grid electricity and the O&M costs for the HTE and CSP systems exhibit less significative impact on LCOH in both scenarios. The bars representing these variables are comparatively short, indicating that changes in these factors have a relatively small effect on the overall LCOH.

5. Conclusions and outlook

This study provides a comprehensive techno-economic analysis of integrating a concentrated solar power (CSP) plant using parabolic trough collectors and high-temperature electrolysis using solid oxide electrolysis cells for hydrogen production, focusing on Ouarzazate, Morocco. Through numerical simulations in EBSILON Professional and ASPEN Plus, we assessed the performance, efficiency, and costs of this system, uncovering several key findings and possibilities for further research.

Effective thermal and electrical integration between the CSP plant and the electrolysis system was evident from the schematic process flow diagram and performance parameters, demonstrating promising efficiency

and cost-effectiveness. The system achieved a peak capacity factor of approximately 61.75 % in 2023, projected to slightly rise to 62.20 % by 2030, reflecting anticipated improvements in electrolysis cell durability. Although the peak solar-to-fuel efficiency peak, around 12 %, did not correspond with the highest capacity factors, it highlighted the need for a trade-off between continuous operation and efficiency. Simultaneously, the levelized cost of hydrogen (LCOH) decreased significantly from 7.88 EUR kg^{-1} in 2023 to 4.83 EUR kg^{-1} by 2030, demonstrating the economic benefits of technological advancements and enhanced system performance and economics. Finally, the sensitivity analysis revealed that factors like interest rates and solar field and electrolysis cells specific costs play a big role in the LCOH due to the process capital intensity.

Future research ought to explore several areas aiming to further optimize the synergies of solar and high-temperature electrolysis systems. Integrating photovoltaic systems to the CSP plant could enhance energy output and efficiency by providing additional low-cost electricity and increasing thermal energy storage temperatures. Additionally, using solar power towers in CSP plants could offer both electricity and higher-temperature heat, potentially improving operational efficiency and reducing even more the electrolysis electrical consumption. Moreover, comparing this production pathway with alternative hydrogen production methods, evaluating the impact of scale, location, and technological advancements of CSP on future scenarios will be crucial for refining cost predictions and enhancing economic feasibility assessment, potentially make it even more attractive and able to outperform competitor technologies, and therefore will follow in next studies. Finally, a life-cycle assessment of such system could potentially shed light not only its economic benefits but also its environmental advantages, leveraging one of the key strengths of CSP and CST technologies. Addressing these aspects will advance efficient and cost-effective hydrogen production, leveraging solar energy sustainably.

6. Acknowledgments

Financial support from DLR's basic funding for the project NeoFuels is gratefully acknowledged.

7. References

Albrecht, F.G., König, D.H., Baucks, N., Dietrich, R.-U., 2017. A standardized methodology for the techno-economic evaluation of alternative fuels – A case study. Fuel 194, 511–526. doi: 10.1016/j.fuel.2016.12.003.

AspenTech, 2021. Aspen Plus Version 12.1. Aspen Technology Inc, Bedford, USA.

Böhm, H., Zauner, A., Rosenfeld, D.C., Tichler, R., 2020. Projecting cost development for future large-scale power-to-gas implementations by scaling effects. Applied Energy 264, 114780. doi: 10.1016/j.apenergy.2020.114780.

Braun, J., Frischmuth, F., Gerhardt, N., Pfennig, M., Schmitz, R., Wietschel, M., Carlier, B., Réveillère, A., Warluzel, G., Wesoly, D., 2023. Clean Hydrogen Deployment in the Europe-MENA Region from 2030 to 2050.

Dersch, J., Dieckmann, S., Hennecke, K., Pitz-Paal, R., Taylor, M., Ralon, P., 2020. LCOE reduction potential of parabolic trough and solar tower technology in G20 countries until 2030, in: SOLARPACES 2019: International Conference on Concentrating Solar Power and Chemical Energy Systems, Daegu, South Korea. 1–4 October 2019. AIP Publishing, 120002. doi: 10.1063/5.0028883.

DOE, 2023. U.S. National Clean Hydrogen Strategy and Roadmap. U.S. Department of Energy, Washington, USA. https://www.hydrogen.energy.gov/library/roadmaps-vision/clean-hydrogen-strategy-roadmap (accessed on Nov 2024).

Edenhofer, O., Pichs-Madruga, R., Sokona, Y., Seyboth, K., Matschoss, P., Kadner, S., Zwickel, T., Eickemeier, P., Hansen, G., Schlömer, S., Stechow, C. von (Eds.), 2011. IPCC Special Report on Renewable Energy Sources and Climate Change Mitigation. Cambridge University Press, Cambridge, United Kingdom and New York, NY, USA.

European Commission, 2020. A hydrogen strategy for a climate-neutral Europe, Brussels, Belgium. https://eur-lex.europa.eu/legal-content/EN/TXT/?uri=CELEX:52020DC0301 (accessed on Nov 2024).

Feldhoff, J.F., Schmitz, K., Eck, M., Schnatbaum-Laumann, L., Laing, D., Ortiz-Vives, F., Schulte-Fischedick, J., 2012. Comparative system analysis of direct steam generation and synthetic oil parabolic

trough power plants with integrated thermal storage. Solar Energy 86, 520–530. doi: 10.1016/j.solener.2011.10.026.

Haussener, S., 2022. Solar fuel processing: Comparative mini-review on research, technology development, and scaling. Solar Energy 246, 294–300. doi: 10.1016/j.solener.2022.09.019.

IEA, 2022. Global Hydrogen Review 2022. International Energy Agency, Paris, France.

Immonen, J., Powell, K.M., 2023. Hydrogen from solar? A rigorous analysis of solar energy integration concepts for a high temperature steam electrolysis plant. Energy Conversion and Management 298, 117759. doi: 10.1016/j.enconman.2023.117759.

Kanthal, 2023. Flow Heaters - Information. Kanthal AB. https://www.kanthal.com/en/products/air-heaters/flow-heaters/ (accessed on Jan 2024).

Lang, M., Raab, S., Lemcke, M.S., Bohn, C., Pysik, M., 2020. Long-Term Behavior of a Solid Oxide Electrolyzer (SOEC) Stack. Fuel Cells 20, 690–700. doi: 10.1002/fuce.201900245.

Laurencin, J., Mougin, J., 2015. High-Temperature Steam Electrolysis, in: Godula-Jopek, A. (Ed.), Hydrogen Production. Wiley, pp. 191–272.

Meteotest, 2007. Meteonorm Version 6.1. Meteotest AG, Bern, Switzerland.

Muhammad, H.A., Naseem, M., Kim, J., Kim, S., Choi, Y., Lee, Y.D., 2024. Solar hydrogen production: Technoeconomic analysis of a concentrated solar-powered high-temperature electrolysis system. Energy 298, 131284. doi: 10.1016/j.energy.2024.131284.

NREL, 2013. System Advisor Model (SAM) Case Study: Concentrating Solar Power (CSP) Physical Trough Andasol-1. Boulder, USA.

Petipas, F., Brisse, A., Bouallou, C., 2014. Benefits of external heat sources for high temperature electrolyser systems. International Journal of Hydrogen Energy 39, 5505–5513. doi: 10.1016/j.ijhydene.2014.01.179.

Roeder, T., Rosenstiel, A., Monnerie, N., Sattler, C., 2024. Impact of expected cost reduction and lifetime extension of electrolysis stacks on hydrogen production costs. International Journal of Hydrogen Energy. doi: 10.1016/j.ijhydene.2024.08.015.

Rosenstiel, A., Monnerie, N., Dersch, J., Roeb, M., Pitz-Paal, R., Sattler, C., 2021. Electrochemical Hydrogen Production Powered by PV/CSP Hybrid Power Plants: A Modelling Approach for Cost Optimal System Design. Energies 14, 3437. doi: 10.3390/en14123437.

Seitz, M., Storch, H. von, Nechache, A., Bauer, D., 2017. Techno economic design of a solid oxide electrolysis system with solar thermal steam supply and thermal energy storage for the generation of renewable hydrogen. International Journal of Hydrogen Energy 42, 26192–26202. doi: 10.1016/j.ijhydene.2017.08.192.

Smolinka, T., Wiebe, N., Sterchele, P., Palzer, A., Lehner, F., Jansen, M., Kiemel, S., Miehe, R., Wahren, S., Zimmermann, F., 2018. IndWEDe: Industrialisierung der Wasserelektrolyse-Industrie in Deutschland. Freiburg, Germany.

STEAG, 2022. EBSILON®Professional Version 16.00. STEAG Energy Services GmbH, Zwingenberg, Germany.

Sunfire, 2021. Sunfire-HyLink SOEC Factsheet. Sunfire GmbH. https://www.sunfire.de/en/hydrogen (accessed on Jan 2024).

Thonig, R., Gilmanova, A., Lilliestam, J., 2023. CSP.guru 2023-07-01. Zenodo. doi: 10.5281/zenodo.8191855.

Tomberg, M., Heddrich, M.P., Ansar, S.A., Friedrich, K.A., 2023. Operation strategies for a flexible megawatt scale electrolysis system for synthesis gas and hydrogen production with direct air capture of carbon dioxide. Sustainable Energy Fuels 7, 471–484. doi: 10.1039/D2SE01473D.

Wang, Z., 2019. General Design of a Solar Thermal Power Plant, in: Design of Solar Thermal Power Plants. Elsevier, pp. 117–224.

Thermal performance of a solar box cooker with forced convection heating and sensible heat storage

Ashmore Mawire[1], Sunita Mahavar[1, 2]

[1]Material Science, Innovation and Modelling Research (MaSIM) Research Focus Area, Department of Physics, North-West University (Mafikeng Campus), Private Bag X2046, Mmabatho 2735, South Africa

[2]Solar Energy Research Laboratory, Department of Physics, University of Rajasthan, Jaipur 302004, India

Abstract

A solar box cooker using a 12 V DC fan in the forced convection mode is experimentally evaluated. The experimental tests use two black stainless steel cooking pots with and without storage. The storage system consists of a glass bowl with 500 g of granite, and one pot is placed inside the glass bowl. The experimental tests are carried out for a 10-hour interval. The first part of the experiments involves testing without any load for 4 hrs to establish the stagnation temperatures. The second part of the experiment consists of loading the cooking pots with 1 litre of water for 6 hrs. The pots with and without storage are tested simultaneously in the solar cooker. Experimental results without the fan blowing and without the load show that the highest temperatures for the storage and non-storage cases are around 142 and 123 ^{o}C, respectively. For the case of forced convection using the fan without the load, the corresponding maximum temperatures in the cooking pots are around 156 and 135 ^{o}C, respectively. During the 6 hrs water heating cycle, maximum temperatures attained for the storage and non-storage cases are 92 and 81 ^{o}C without the fan. These maximum temperatures are comparable to the forced convection maximum temperatures of 93 and 82 ^{o}C, achieved at about the same time. The first figure of merits (F_1) for the storage case with and without the fan of 0.121 and 0.110 ^{o}C/(W/m^2) is greater than those of the non-storage case of 0.102 and 0.092 ^{o}C/(W/m^2), respectively. Using the fan results in an improvement of the first figure of merit. The storage case shows better performance in terms of the higher cooking temperatures achieved and the higher first figure of merits; however, there is no advantage to using forced convection when the pots are loaded after achieving higher temperatures in the no-load tests.

Keywords: Forced convection, Sensible heat storage, Solar box cooker, Thermal performance

1. Introduction

Solar cookers are environmentally friendly cooking devices that use the sun's energy, thus reducing greenhouse gas emissions [1]. The three main types of solar cookers are concentrating solar cookers, panel cookers, and box cookers. Box and panel cookers achieve lower operating temperatures than concentrating solar cookers, but they are safer and do not need too much operator intervention, like consistently tracking the sun and ensuring that food is not burnt [2]. Panel cookers are usually limited to smaller cooking pots and have lower efficiencies than box solar cookers. In terms of the compromise between safety, reasonable cooking size, cost, ease of use, and acceptable cooking temperatures, the box solar cooker is a viable option compared to the other options.

As with all solar cookers, box cookers cannot operate optimally under low solar radiation conditions, and their cooking speed and temperatures are low. Recent work has focused on incorporating thermal energy storage (TES) with solar box cookers to improve their off-sunshine performance [3-8]. Goyal and Eswaramoorthy [3] presented theoretical and experimental results of a solar box cooker with sensible heat storage. Their results showed that using marble as the storage material made cooking possible at night. Verma et al. [4] developed an analytical model for a solar box cooker with sensible heat storage. The results revealed that the storage should be charged for the whole solar period but for an optimal period, which is valuable for storing thermal energy. Cuce [5] presented an experimental investigation of a box solar cooker using Bayburt stone as the TES material. Bayburt stone was suitable for s efficient and continuous solar cooking. Cooking A multi-criteria decision-making technique for an optimal section of phase change materials (PCMs) for a solar box cooker was presented by Anilkumar et al. [6]. Erythritol was recommended as the most suitable PCM for a solar box cooker with storage. Coccia et al. [7] also investigated the use of erythritol in a solar box cooker. They found

© 2024. The Authors. Published by International Solar Energy Society
Selection and/or peer review under responsibility of Scientific Committee
10.18086/eurosun.2024.09.06 Available at http://proceedings.ises.org

that erythritol extended the average load cooling time, in the range of 125–100 °C, to around 351 % compared to the case without storage. Although latent heat storage using PCM provides a more significant energy storage density than sensible heat storage, its main drawbacks are the cost, low thermal conductivity and degradation after numerous charging and discharging cycles. Thus, sensible heat storage is more viable in terms of cost. A viable sensible heat TES material is granite, used in recent solar thermal applications because of its cheapness, non-toxic nature, and availability worldwide [8-12].

A method to improve heat transfer and operating temperatures in a solar box cooker uses a heat circulation fan, which has yet to be explored [13]. To improve the thermal performance of solar box cookers, a forced convection solar cooking mode using a 12 V DC fan powered by a battery charged with a 30 W solar panel is presented. This paper considers two black stainless cooking pots with and without heat storage. The heat storage material used is granular pebbles. The paper aims to investigate the effect of forced convection on the solar cooking process for cooking pots with and without storage. The novel aspect of the study is comparing solar cooking pots with and without storage in a forced convection mode, which has rarely been reported. The storage material is also enclosed in a glass bowl to reduce heat losses, and this has yet to be investigated.

2. Experimental method

The experimental setup showing two cooking pots inside a solar box cooker is shown in Figure 1. All pots are made of stainless steel, and they are painted black. One pot is enclosed in a glass bowl containing 500 g of granite as the sensible heat storage material. The capacity of the pots is 1 litre. The dimensions and specifications of the solar box cooker, cooking pots, glass bowl and storage material are shown in Table 1. A 12 V DC fan is driven by a 12 V 7 Ah battery that is charged by a 30 W solar panel (not shown in Figure 1). The battery is charged with a maximum power point tracking (MPPT) charge controller. The fan runs continuously for 10 hrs during the experimental test period when testing forced convection heating. The first four (4) hours of the experimental tests involve heating the pots without the load to establish the stagnation temperatures. After that, the next six (6) hours are water heating tests with one litre of water placed in each pot. Experimental tests are conducted with and without the fan to compare natural and forced convection heating. Two K-type thermocouples measure the temperatures in the pots during the experimental tests. Another K-type thermocouple measures the ambient temperature. Global solar radiation is measured using a Kipp and Zonen CMP11 pyranometer. All thermocouples and the pyranometer outputs are connected to the channels of a Sefram DAS 240 datalogger, which records the experimental data at 10 s intervals.

Table 1: Dimensions and specifications of the solar box cooker and associated experimental components

Parameter	Value
Length of box cooker (m)	0.590
Width of box cooker (m)	0.540
Height of box cooker (m)	0.250
Area of glass glazing (m^2)	0.207
Aluminium reflector area (m^2)	0.230
Diameter of cooking pot (m)	0.130
Height of the pot (m)	0.100
Volume of the pot (m^3)	0.001
Material of pot	Stainless steel
Volume of glass bowl (m^3)	0.025
Storage material	Granite
Storage mass (kg)	0.500
Specific heat capacity of granite (J/kgK) [9]	798

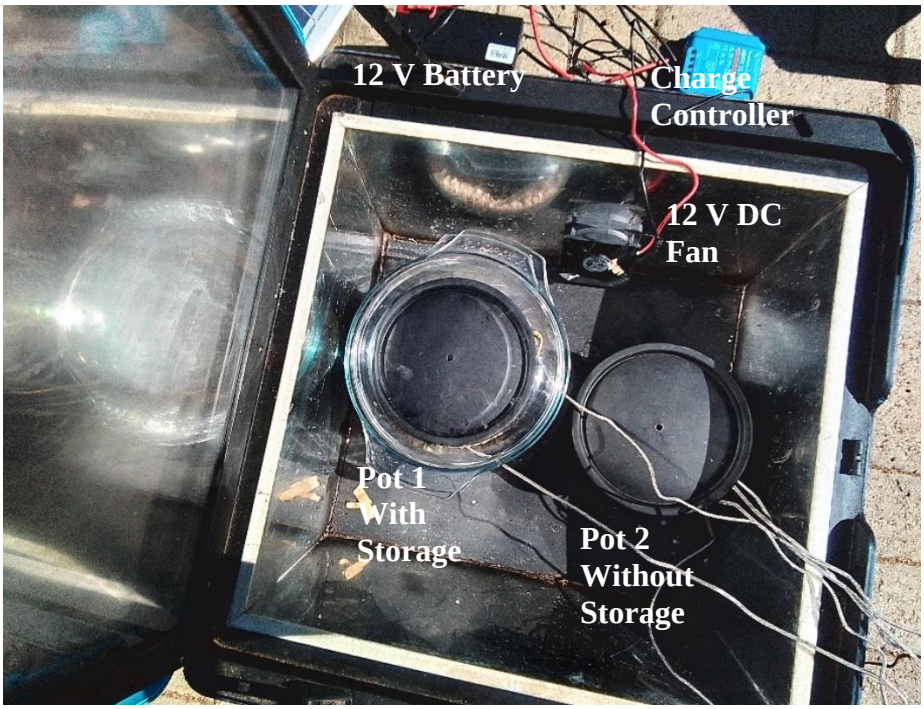

Figure 1: Experimental setup of the solar cooking experiments showing the storage and non-storage cooking pots, the 12 V DC fan, the charge controller, and the 12 V battery.

3. Thermal analysis

To evaluate the solar box cookers with and without storage around the cooking pot, the first figure of merit (F_1) proposed by Mullick et al. [14] and also used in Refs. [3, 12] is utilized. It is defined as:

$$F_1 = \frac{T_{abs} - T_{amb}}{I} \tag{1}$$

, where T_{abs} is the stagnation temperature of the absorber (empty pot in this case), T_{amb} is the ambient temperature and I is the solar radiation. Average values towards the end of the heating tests were considered in the experiments. Other important quantities, such as the thermal efficiency and the second figure of merit (F_2), were not considered as the load was only added after peaking solar radiation conditions had elapsed. These parameters are usually evaluated under load conditions at intervals of ±2 hrs from solar noon. It was not possible to calculate the second figure of merit and the water heating (thermal) efficiency using an empty pot during stagnation temperature heating tests. These parameters will be presented in future work since the aim of the study was limited to understanding the effect of forced convection on the temperatures of a solar box cooker with and without heat storage surrounding the cooking pot.

Another important parameter that could be derived from the experiments was the cooking power after loading the pots with water. It is expressed as [3]:

$$P_W = \frac{m_w \left(T_{Wf} - T_{Wi}\right)}{\Delta t} \tag{2}$$

, where m_w is the mass of the heated water, T_{Wf} is the final maximum water temperature achieved, T_{Wi} is the ininitial water temperature and Δt is the time interval to from the initial to the maximum water temperatures.

4. Results and discussion

Figure 2 (A, B) shows experimental solar heating tests with and without using the fan for a 10-hour test period on 9 March 2024 (without fan) and on 10 March 2024 (with fan). The average solar radiation for the test using the fan (740 W/m^2) is comparable to that without using the fan (772 W/m^2). The maximum temperature

achieved for the natural heating test using the pot with storage is around 142 ºC compared to 123 ºC for the pot without storage. This suggests that the glass bowl with storage reduces heat losses compared to the pot without storage. Higher temperatures are achieved for the forced convection case using the fan during the first four hours of heating compared to the case without the fan. The maximum temperatures achieved by the storage and non-storage pots are around 156 and 135 ºC, respectively. These results suggest that forced convection in the solar box improves the heat transfer rate, resulting in higher temperatures. During the 6 hrs water heating cycle, maximum temperatures attained for the storage and non-storage cases are 92 and 81 ºC without the fan. These maximum temperatures are comparable to the forced convection maximum temperatures of 93 and 82 ºC, achieved at about the same time. The results suggest that forced convection is insignificant when the pot is fully loaded to its maximum capacity.

Additionally, the pots without forced circulation show slightly higher temperatures at the end of the testing period. This suggests the fan tends to cool the surrounding air when solar radiation values become low. The temperature difference between the storage and non-storage case is more significant during forced convection heating, suggesting that this mode of operation is more beneficial to the case with storage since it is circulated more in the storage medium.

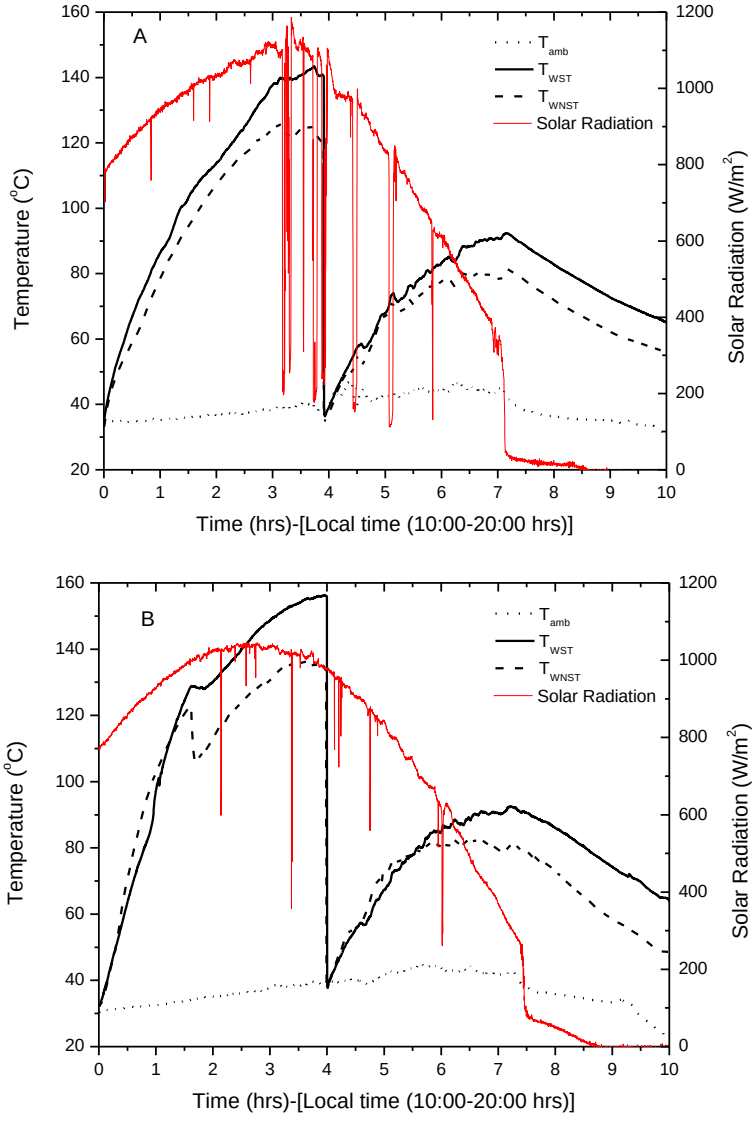

Figure 2: Experimental results of solar heating tests (A) without forced convection (no fan) and (B) using the fan (forced convection).

The first figures of merit obtained for the storage case with and without the fan are 0.121 and 0.110 $^oC/(Wm^2)$, respectively, showing better performance for forced convection. Similarly, the forced convection mode for the non-storage case shows a higher first figure of merit of 0.102 $^oC/(W/m^2)$ compared to 0.092 $^oC/(W/m^2)$ for the case without a fan. The storage case with a glass bowl reduces heat losses, showing higher first-of-merit values compared to the non-storage case. The values of the first merit obtained in the experiments are higher or comparable to related recent work on solar box cookers with sensible heat storage [3, 12] F_1 values obtained by Saxena et al. [12] in the range of 0.011-0.012 $^oC/(W/m^2)$ are much lower than those presented in this paper of 0.092-0.121 $^oC/(W/m^2)$. On the otherhand the F_1 value of 0.1325 $^oC/(W/m^2)$ obtained by Goyal and Eswaramoorthy [3] is slightly greater but comparable to the maxmimum F_1 value of 0.121 $^oC/(W/m^2)$ obtained in this work. The water heating powers for the cases without the fan are 19.0 and 16. 6 W, respectively, for the non-storage and storage cases. These water heating powers are comparable to the cases with fan of 20.5 and 16.0 W, respectively. A direct comparision of the water heating power values with work presented in Refs. [3, 12[is not possible since the authors calculated the water heating power during the solar heating period unlike our case where we first achieved maximum stagnation temperatures and then added water. Although the forced convention mode shows higher temperatures and the first figures of merits compared to the mode without the fan during no-load conditions, there is no advantage of using forced convection when the pots are loaded after achieving higher temperatures in the no-load tests. This is because similar temperatures are obtained after loading the pots with water, regardless of the higher no-load temperatures obtained with forced convection. These similar temperatures resulted in almost similar water heating powers.

5. Conclusion

Experimental results of solar heating tests with and without forced convection have been presented for storage and non-storage cases for a solar box cooker. The main conclusions of the experimental tests were:

1. Experimental results without the fan blowing and without the load showed that the highest temperatures achieved for the storage and non-storage cases are around 142 and 123 ^oC; the case of forced convection without the load showed higher temperatures of 156 and 135 ^oC, respectively. Higher temperatures were achieved with the storage case.
2. For the case of water heating after the no-load heating, the maximum temperatures attained for the storage and non-storage cases using the fan were 93 and 82 ^oC. These maximum temperatures were comparable to the water heating tests without the fan, where the storage and non-storage cases achieved maximum temperatures of 93 and 82 ^oC, respectively.
3. The first figure of merits (F_1) for the storage case with and without the fan of 0.121 and 0.110 $^oC/(W/m^2)$ were greater than those of the non-storage case of 0.102 and 0.092 $^oC/(W/m^2)$, respectively. The first figure of merit improved with storage and an air-circulating fan.
4. The water heating powers for the cases without the fan were 19.0 and 16. 6 W, respectively, for the non-storage and storage cases. These water heating powers were comparable to the cases with fans of 20.5 and 16.0 W, respectively.
5. Although the cases with the fan showed higher no-load temperatures and higher first-figure merits, there was no advantage of using the fan during water heating tests after stagnation temperature tests since almost similar maximum water temperatures were obtained. These similar temperatures resulted in almost similar water heating powers.

6. References

1. Lentswe K, Mawire A, Owusu P, Shobo A. (2021). A review of parabolic solar cookers with thermal energy storage. Heliyon 7 (10), e08226.
2. Arunachala UC, Kundapur A. (2020). Cost-effective solar cookers: A global review. Solar Energy 207, 901-916.
3. Goyal RK, Eswaramoorthy M. (2023). Theoretical and experimental analysis of box-type solar cooker with sensible heat storage. Solar Energy 268, 112273.

4. Verma S, Banerjee S, Das R. (2022). A fully analytical model of a box solar cooker with sensible thermal storage. Solar Energy 233, 531-542.

5. Cuce PM. (2018). Box type solar cookers with sensible thermal energy storage medium: A comparative experimental investigation and thermodynamic analysis. Solar Energy 166, 432-440.

6. Anilkumar BC, Maniyeri R, Anish S. (2021). Optimum selection of phase change material for solar box cooker integrated with thermal energy storage unit using multi-criteria decision-making technique. Journal of Energy Storage 40, 102807.

7. Coccia G, Aquilanti A., Tomassetti S, Comodi G, Di Nicola G. (2020). Design, realization, and tests of a portable solar box cooker coupled with an erythritol-based PCM thermal energy storage. Solar Energy 201, 530-540.

8. Li B, Ju F. (2020). Thermal stability of granite for high-temperature thermal energy storage in concentrating solar power plants. Applied Energy 138, 409-416.

9. Lugolole R, Mawire A, Lentswe KA., Okello D, Nyeinga K. (2018). Thermal performance comparison of three sensible heat thermal energy storage systems during charging cycles. Sustainable Energy Technologies and Assessments 30, 37-51.

10. Lugolole R., Mawire A, Okello D, Lentswe KA, Nyeinga K, Shobo AB (2019). Thermal performance comparison of three sensible heat thermal energy storage systems during charging cycles. Sustainable Energy Technologies and Assessments 35, 117-130.

11. Zhang S, Li Y, Yan Y (2024). Hybrid sensible-latent heat thermal energy storage using natural stones to enhance heat transfer: Energy, exergy, and economic analysis. Energy 286, 129530.

12. Saxena A, Joshi SK., Gupta P, Tirth V, Suryavanshi A, Singh DB, Sethi M. (2023). An experimental comparative analysis of the appropriateness of different sensible heat storage materials for solar cooking. Journal of Energy Storage 61, 106761.

13. Misra R, Aseri TK (2012). Thermal performance enhancement of box-type solar cooker: a new approach. International Journal of Sustainable Energy 31, 107-118.

14. Mullick S, Kandpal T, Saxena A (1987). Thermal test procedure for box-type solar cookers. Solar Energy 39, 353-360.

QUANTUM DOT AS A MECHANISM TO SUPRESS CHARGE RECOMBINATION IN POLYMER SOLAR CELL

Genene Tessema Mola[a*] and Abiodun Kazeem Ogundele[a]

[a] *School of Chemistry & Physics, University of KwaZulu-Natal, Scottsville (South Africa)*

Abstract

Effective light trapping mechanisms in thin film polymer solar cells (PSC) are leveraged by employing group II-VI semiconductor quantum dots. Core-shell semiconductor quantum dots ($Cd_xS/Zn_{1-x}S$ SQD) were synthesised via the microwave irradiation method. The SQDs were incorporated into the electron transport layer of PTB7:PC71BM blend PSC to assist in light trapping and charge collection processes. The measured device parameters suggest that the inclusion of SQD has significantly enhanced the solar cell's power conversion efficiency (PCE) due to improved energy transfer, exciton generation, and charge collection processes in PSCs. Moreover, the performances of the solar cells are found to be dependent on the concentration of SQD in the transport layer. Hence, the best efficiency recorded was 7.13% at an optimal concentration of 0.375 wt.%, which is an increment in PCE by nearly 23%.

Keywords: Quantum Dots, Polymer Solar cell, Solar Energy,

© 2024. The Authors. Published by International Solar Energy Society
Selection and/or peer review under responsibility of Scientific Committee
10.18086/eurosun.2024.09.07 Available at http://proceedings.ises.org

1.1 Introduction

Solar energy remains one of the cleanest, and most desirable alternative sources of energy to replace those environmentally unfriendly yet depleted fossil fuels to reduce global greenhouse gases (Ritchie & Roser, 2023). A vast amount of solar energy, radiated from the Sun per hour could have been enough to fulfil the energy demand for the world population for a year, but unfortunately, it is under-utilized and accounts for only about 4.5% of global electricity generation today, according to the International Energy Agency (IEA). This is due to various reasons ranging from cumbersome manufacturing processes, high cost of solar cell fabrication, and knowledge gaps on renewable energy sources. Interestingly, organic solar cells (OSC) are cost-effective, lightweight, solution-processable and suitable for roll-to-roll production making them more attractive from an economic perspective with the power conversion efficiencies (PCEs) currently stands over 20%, which is comparable to several to inorganic solar cell technologies (Guo et al., 2023). However, OSCs still suffer from a shortfall in photons to energy conversion efficiencies because of inherent inadequacies and challenges like environmental instability, low charge transport properties, non-robust temperature tolerance, narrow absorption range, competitive market, facelift cost etc. (Li et al., 2019; Ma et al., 2020).

This study demonstrates the application of microwave-synthesised core-shell semiconductor quantum dot (SQD) ($Cd_xS/Zn_{1-x}S$) in the electron transport layer of an inverted thin film polymer solar cell (TFPSC) containing photo-active layer blends of poly[[4,8–bis[(2-ethylhexyl)oxy]benzo[1,2-b']dithiophene-2,6-diyl][3-fluoro-2-[(2-ethyl hexyl)-carbonyl]thieno[3,4-b]thiophenediyl]]:[6,6]-phenyl C_{71} butyric acid methyl ester (PTB7:PC71BM). The SQD materials ($Cd_xS/Zn_{1-x}S$) with medium energy bandgap core and wide bandgap shell were used in the electron transport layer of TFPSC to assist in improving light trapping in the medium. These combined effects of core-shell SQD can be used to broaden optical absorption spectra leading to high light trapping resulting in an improved solar cell performance.

1.2 Synthesis of Semiconductor Quantum Dots

The bottom-up synthesis method involving two precursors was employed here designed by Soltani *et al.*, Shi *et al.*, and Rafea *et al (Rafea et al., 2009; Shi et al., 2011; Soltani et al., 2012)* . The core-shell SQD was synthesised via a two-step path: synthesis of core (Cd_xS) followed by the shell's growth ($Zn_{1-x}S$). 1.33265 g of Cadmium acetate was dissolved in a beaker containing 100 mL of ethylene glycol to obtain 0.05 M, thiol-stabilized with 4 mL thioglycolic acid followed by addition of 0.56343 g (75 mmol) of thioacetamide. The reaction was allowed to stir for about 10 min at about 5000 rpm. The reaction was then transferred into Russel Hobbs (Model no. RHEM21L) domestic microwave with an output power of 700W, the reaction was made to follow a working cycle of 30% for 25 minutes. The second precursor was achieved via the same process with lower concentrations, 0.54873 g (25 mmol) of zinc acetate was dissolved in a beaker containing ethanol, stirred for ten minutes at a speed of 5000 rpm, and later transferred to a microwave oven following a similar working cycle used for the core precursor. The precursors were added dropwise and allowed to disperse uniformly using a sonication bath for 60 min at 40ºC. The final precipitates were cooled to room temperature and centrifuged for about 10 min at a speed of 4000 rpm. This was followed by re-dispersing in deionized water and ethanol several times to remove the excess ionic remnants. Eventually, the SQD was dried in a vacuum oven at 60ºC for 24 h and its morphology was later subjected to various characterisation techniques.

1.3 J-V Characteristics of the Devices

An inverted device architecture composed of different layers of materials shown in Fig. 1a is employed in the current investigation. The current density-voltage (J-V) characteristics data under illumination conditions were measured from the fabricated solar cells are provided in Table 1. The data clearly shows an increase in the measured photocurrent as the result of the inclusion of SQD in the charge transport layers at different concentrations. Furthermore, the performance of the devices is found to be dependent on the concentration of the SQD in the medium. The best device performance found was PCE = 6.62% at the concentration of 0.375 wt%. This is growth in PCE by nearly 16% compared to the reference cell. Furthermore, the influence SQD on charge generation/recombination processes were analysed using generated photocurrent (J_{ph}) and effective voltage (V_{eff}) as presented in Fig. 1d to deduce exciton dissociation efficiency, charge collection efficiency, and saturation current (J_{sat}). The latter was used to determine the maximum exciton generation ($G_{max} = J_{sat}/_{qL}$). The probabilities of charge dissociation (η_{diss}) and collection (η_{coll}) of the pristine and modified

devices were determined by evaluating ($^{J_{ph}}/_{J_{sat}}$) under short circuit and maximum power output area of the curve, respectively. The device with 0.375 wt.% exhibited the highest probability of dissociation and collection of charges with magnitude of 94.71% and 69.9%, respectively as provided in Table 2.

Table 1: The Thin film Polymer solar cells' parameters for devices with/without SQD devices in ETL

ZnO:/$Cd_xS/Zn_{1-x}S$	V_{oc} (V)	$J_{sc}\,(mAcm^{-2})$	FF (%)	PCE (%)	$R_s(\Omega)$	$R_{SH}\,(K\Omega)$
Pristine	0.69 ± 0.01	15.49 ± 0.18	52.59 ± 1.04	5.70 ± 0.08	291.5	8.78
0.125 wt.%	0.63 ± 0.01	17.90 ± 0.93	53.30 ± 1.04	6.62 ± 0.08	234.2	8.68
0.375 wt.%	0.65 ± 0.02	18.95 ± 0.55	54.62 ± 1.62	7.01 ± 0.12	229.2	8.82
0.625 wt.%	0.64 ± 0.04	14.33 ± 0.04	52.00 ± 1.43	4.81 ± 0.08	514.1	10.1

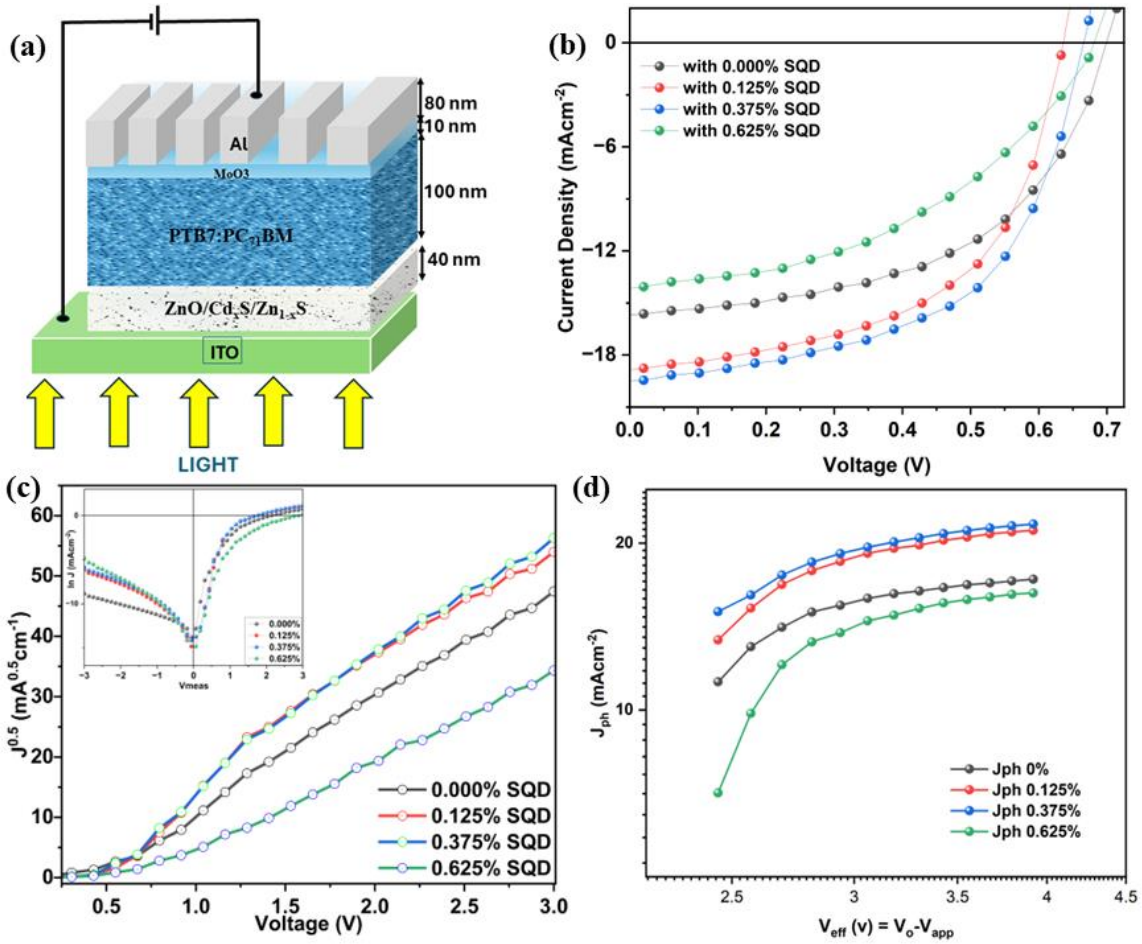

Fig. 1. (a) Inverted device architecture of PSC with modified ETL (b) J-V graphs under illumination & (c) $J^{0.5}$-V graphs under dark conditions (inset SCLC) (d) J_{ph} vs. V_{eff} for TFPSCs pristine and modified ETL devices.

Table 2: Charge transport parameters of TFPSCs w/wo SQD in electron transport layer

ZnO/$Cd_xS/Zn_{1-x}S$	$\mu_l(cm^2S^{-1}V^{-1})$	γ (cm V^{-1})	$G_{max}(m^{-3}s^{-1})$	η_{diss} (%)	η_{coll} (%)
Pristine	3.02×10^{-6}	-6.58×10^{-5}	1.08×10^{27}	85.9	66.1
0.125 wt.%	4.12×10^{-6}	-1.76×10^{-4}	1.32×10^{27}	89.3	66.9
0.375 wt.%	4.36×10^{-6}	-1.29×10^{-4}	1.35×10^{27}	94.7	70.0
0.625 wt.%	1.44×10^{-6}	-7.67×10^{-6}	1.02×10^{27}	87.8	62.1

Importantly, all SQD incorporated devices showed enhanced dissociation efficiency, underscoring the positive impacts of the SQD doped into the ETL buffer layer. On the other hand, the impact of SQD on the charge transport processes were investigated using the measured space charge limited current (SCLC) taken without the influence photons generated current. The Mutt-Gurney charge transport equation eq (1) is used to compare with the SCLC data to be able to derive the transport parameters. The low field mobility (μ_l), which is a

measure of charge carriers' movement in the TFPSCs under low electric field conditions and activation factor (γ) can be determined by an equation of the form:

$$J = {}^{9}/_{8}\ \varepsilon_o \varepsilon_r \mu_l\, {V^2}/_{L^3}\, e^{0.89\gamma\sqrt{{V}/{L}}}, \qquad (1)$$

where $\varepsilon_r = 3.5$ is the relative permittivity of PTB7:PC71B, ε_o is the permittivity of free space ($= 8.85 \times 10^{-12}\ m^{-3}kg^{-1}s^4A^2$), L(~ 150 nm) is the distance between the aluminium and ITO electrodes (see Fig 1a). The linear fittings of $J^{0.5}$ against V (obtained under dark conditions) as shown in Fig. 1c were eventually used to determine the values of the low field mobility for pristine devices and SQD-modified devices. The results of the analysis suggest that indeed the charge mobility in the medium has improved by a factor of 1.4 at the optimum SQD concentration in ETL compared to the reference cell.

4. Conclusion

Core-shell ternary semiconductor quantum dots ($Cd_xS/Zn_{1-x}S$) were employed as a mechanism for light trapping in an inverted TFPSC whose photoactive layer is composed of PTB7:PC71BM blend. The devices with the modified electron transport layer showed significant improvement in power conversion efficiency and device stability compared to the reference cell. The investigation results suggest that the improved device performances depend on SQD concentration in the ETL. The optimum SQD concentration for the best device performance recorded was 0.375 wt.%, which resulted in PCE of 7.01%, which is an increase of 23.4% compared to the reference cell. Such enhanced solar cell performance was attributed to the improved excitons generation, and effective light trapping in the absorber medium. This study showed the characteristic synergy inherent in semiconductor quantum dots in improving the various metrics of thin film polymer solar cells ultimately leading to better device parameters and environmental stability.

References

Guo, C., Fu, Y., Li, D., Wang, L., Zhou, B., Chen, C., Zhou, J., Sun, Y., Gan, Z., & Liu, D. (2023). A Polycrystalline Polymer Donor as Pre-Aggregate toward Ordered Molecular Aggregation for 19.3% Efficiency Binary Organic Solar Cells. *Advanced Materials*, *35*(41), 2304921.

Li, K., Wu, Y., Tang, Y., Pan, M. A., Ma, W., Fu, H., Zhan, C., & Yao, J. (2019). Ternary blended fullerene-free polymer solar cells with 16.5% efficiency enabled with a higher-LUMO-level acceptor to improve film morphology. *Advanced energy materials*, *9*(33), 1901728.

Ma, Q., Jia, Z., Meng, L., Zhang, J., Zhang, H., Huang, W., Yuan, J., Gao, F., Wan, Y., & Zhang, Z. (2020). Promoting charge separation resulting in ternary organic solar cells efficiency over 17.5%. *Nano Energy*, *78*, 105272.

Ogundele, A. K., & Mola, G. T. (2022). Ternary atoms alloy quantum dot assisted hole transport in thin film polymer solar cells. *Journal of Physics and Chemistry of Solids*, *171*, 110999.

Rafea, M. A., Farag, A., & Roushdy, N. (2009). Structural and optical characteristics of nano-sized structure of Zn0. 5Cd0. 5S thin films prepared by dip-coating method. *Journal of Alloys and Compounds*, *485*(1-2), 660-666.

Ritchie, H., & Roser, M. (2023). What are the safest and cleanest sources of energy? *Our World in Data*.

Shi, J., Liang, Z., Lu, X., Tong, Y., Su, C., & Liu, H. (2011). The roles of defect states in photoelectric and photocatalytic processes for Zn x Cd 1− x S. *Energy & Environmental Science*, *4*(2), 466-470.

Soltani, N., Saion, E., Erfani, M., Bahrami, A., Navaseri, M., Rezaee, K., & Hussein, M. Z. (2012). FACILE SYNTHESIS OF ZnS/CdS AND CdS/ZnS CORE-SHELL NANOPARTICLES USING MICROWAVE IRRADIATION AND THEIR OPTICAL PROPERTIES. *Chalcogenide Letters*, *9*(9).

Xia, Y., Nguyen, T. D., Yang, M., Lee, B., Santos, A., Podsiadlo, P., Tang, Z., Glotzer, S. C., & Kotov, N. A. (2011). Self-assembly of self-limiting monodisperse supraparticles from polydisperse nanoparticles. *Nature nanotechnology*, *6*(9), 580-587.

Zhou, P., Lan, W., Gu, J., Zhao, M., Wang, Z., Liao, Y., Liu, Y., Pu, H., Ding, J., & Wei, B. (2020). High-efficiency organic photovoltaic cells with an antimony quantum sheet modified hole extraction layer. *IEEE Journal of Photovoltaics*, *11*(1), 111-117.

Optimizing energy and economic performance of solar-biomass systems for rural district heating: a technical and financial analysis

Xavier Jobard[1], Stefano Pauletta[1*], Alexis Duret[1] et Quentin Francois[1]

[1] HEIG-VD, Yverdon-Les-Bains (Switzerland)

Abstract

This article investigates the integration of large-scale solar thermal fields with biomass boilers for district heating (DH) in rural areas, aligning with the principles of 4th Generation DH. Using TRNSYS 17 software, the technical and economic aspects of this integration were analyzed. The technical assessment revealed high specific solar productivities over 850 kWh.m^{-2} for small solar fractions and a corresponding optimum specific volume of the Thermal Energy Storage (TES). The economic analysis demonstrated the viability of solar installations in various scenarios, with the potential for levelized costs of heat (LCOH) to be under 100 CHF/MWh. Overall, the study concludes that integrating solar thermal systems with wood chip boilers is technically feasible and financially advantageous. However, careful consideration of system configuration and financing is necessary for sustainable and high-performance solutions, ensuring optimal resource utilization and economic viability.

Keywords: Solar district heating, evacuated flat plate collectors, biomass boiler, economic assessment, levelized cost of heat.

***corresponding author stefano.pauletta@heig-vd.ch**

1. Introduction

District Heating Networks (DHNs) play a crucial role in advancing the adoption of renewable energy sources and harnessing local heat resources, such as low-temperature waste heat, making them an essential component of sustainable urban and rural energy strategies (Jessen et al., 2014; Tschopp et al., 2022). Traditionally, DHNs have relied heavily on fossil fuels and high distribution temperatures, due to reasons linked to the energy source, the transfer substation design and the type of serviced building and its heating system. But the high temperature regime typically adopted in the majority of DHN currently in operation (120 to 90°C) is not particularly favorable to the integration of lower temperature energy and local heat sources. Integrating renewable sources like solar, geothermal and biomass energy into DH networks can significantly improve its energy efficiency and sustainability (Jodeiri et al., 2022), but it requires, among other interventions, lowering the DHN operating temperatures to maximize the renewable energy share, which in turn can further improve the DH network efficiency as distribution heat losses are reduced. Modern buildings, furthermore, feature lower heating energy needs and are often compatible to the lower temperature regimes due to larger heat distribution systems. For example, from the house radiators of the past, needing supply temperatures in the 70-60°C range, nowadays, for new constructions, subfloor heating is frequently adopted, with supply temperatures typically around 38°C (Quiquerez et al., 2013).

In this context, the evolution towards the 4th Generation District Heating (4GDH) would mark a significant shift (Lund et al, 2014). These modern networks operate at lower temperatures, typically between 30-50°C, enhancing their ability to integrate diverse renewable energy sources, including solar thermal, geothermal, and waste heat from industrial processes. These lower operating temperatures not only reduce heat losses, but also align with the increased efficiency of contemporary building heating systems, paving the way for more resilient and eco-friendly energy infrastructures and communities (Jenssen et al., 2014). In this framework, Ruesch et al. (2020) have investigated the potential for low-cost solar heat production and integration with biomass in Switzerland, with specific configurations achieving costs competitive with those of fossil fuels. The report underscores the ecological benefits of using solar thermal energy to offset biomass use during summer, thus conserving wood resources for winter when renewable alternatives are limited. Similar conclusions are obtained by Jobard et Duret (2022) through numerical simulation, confirming that integrating solar heat production can reduce startup cycles for wood boilers, though marginal increases may occur during mid-season.

© 2024. The Authors. Published by International Solar Energy Society
Selection and/or peer review under responsibility of Scientific Committee
10.18086/eurosun.2024.09.08 Available at http://proceedings.ises.org

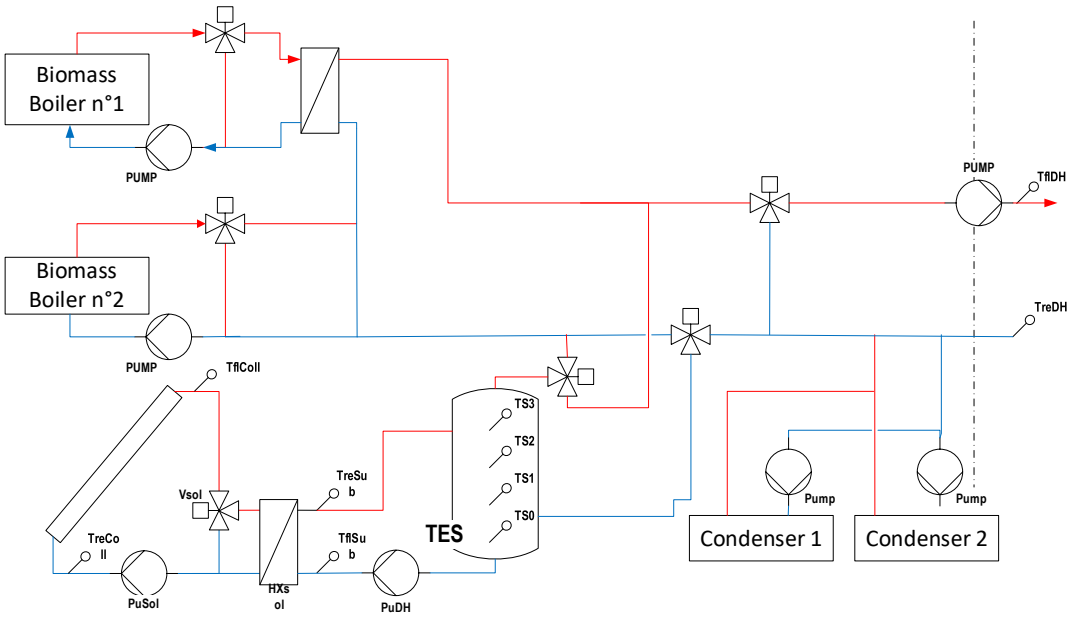

Figure 1: Simplified hydraulic diagram of the hybrid biomass-solar DH plant under study.

This paper aims at investigating the technical and economic performance of large-scale solar thermal plants combined with biomass boilers for DHNs in rural areas, by extending the analysis presented in Jobard et Duret (2022) to the case of evacuated flat solar collectors. In order to provide more realistic estimations, the original numerical model of the plant developed under TRNSYS and adopted to determine the impact of solar energy on the biomass boiler operability, was integrated with a TRNSYS model of a solar field made of 400 evacuated flat plate solar collectors manufactured by TVP Solar SA. This latter model, validated on the monitoring data of the SDH plant of Geneva, has been extrapolated to the lower operating temperatures typical of the 4th generation DH to precisely estimate the performance figures required for the economic analysis.

2. Methodology

The energy optimization and the investigation of the economic performance of solar-biomass systems for rural district heating has been carried out through a technical, economic and financial analysis. The technical analysis adopted TRNSYS 17 software to model a district heating power station made of 2 wood-fired boilers, each equipped with a flue gas condenser, integrated to a solar thermal plant and a thermal energy storage (TES), see Figure 1. The numerical model for the wood-fired section of the plant equipped with a TES was validated in a previous study by Jobard et Duret (2022), while the solar field model validation has been described by Duret et al. (*in press*).

Several plant configurations were investigated to optimize the renewable heat production by varying the solar array size and the TES volume. A final economic analysis investigated the investment and operating costs in 3 scenarios selected based on their respective solar fraction. A series of key performance indicators was then computed to allow an economic comparison among the selected scenarios.

The technical assessment was based on the computation of a series of technical indicators (see CEA, 2018), in particular:

- The solar annual yield (Q_0,), which is the quantity of solar thermal energy collected by the power plant during 1 year of operation and injected into the TES or the DH, expressed usually in [MWh/y] or [kWh/y].
- The specific solar yield or specific heat production (spQ_0), computed as the ratio between the solar annual yield and the total aperture area of the solar collectors (i.e. the aperture area is the area through which light can enter the collector); it is expressed in [kWh/m^2/y].
- The solar fraction (*SFr*), which is an indicator representing the fraction of the total energy consumption satisfied by solar thermal energy. It is defined as the ratio between solar energy production

(in, e.g., [MWh/an]) and the total energy consumption of the plant in the same period (also in [MWh/an]); it is expressed in [%].

To carry out the economic analysis, on the other hand, the capital expenditures (CAPEX), or the investment costs, were considered, together with the plant operational expenditures (i.e., OPEX). A series of assumptions was made for the financial parameters of the economic analysis, like the nominal discount rate, the system lifetime, the market price for the auxiliary electricity consumption, the selling price for the heat injected by the plant on the DH network and energy price inflation rate. To assess the economic viability for each scenario, the following key performance indicators, selected again from CEA (2018), were computed:

- The levelized cost of heat (LCOH), which is defined as the constant energy price in real terms required for the revenues generated from the project to be sufficient to obtain an internal rate of return equal to the discount rate. When using nominal figures, this indicator returns the average nominal price required trough the project's life to generate the required nominal return (Aldersey-Williams et Rubert, 2019). The calculation formula is as follow:

$$LCOH = \frac{CAPEX + \sum_{t=1}^{n} \frac{OPEX}{(1+r)^t}}{\sum_{t=1}^{n} \frac{Q_0 (1-d)^t}{(1+r)^t}} \qquad \text{(eq. 1)}$$

where CAPEX includes all the investment costs incurred at the beginning of the project (i.e., year 0); OPEX are the operational expenditures at year t; r is the nominal discount rate; Q_0 is the annual heat delivered by the power plant to the DH network in year *0* expressed in [MWh/y]; d is the rate of panel degradation, in [%/y]; t is the year under consideration; n is the plant's lifetime, in [y].

- The Payback Period (*PP*), which is the time needed to make the project profitable and to recover the initial investment. Expressed in [y], it gives the number of years after which the project's Net Present Value (NPV) becomes positive.
- The Profitability Index (*PI*), which measures the profitability of an investment. It corresponds to the value created for each euro spent on the investment and it is expressed in [%]. It is computed as the rate between the sum of discounted future cash flow and the initial investment.
- The Internal Rate of Return (*IRR*), which evaluates the profitability of an investment and is commonly adopted to compare investments projects. It is the discount rate at which the net present value (NPV) of all future cash flows (both incoming and outgoing) equals zero.

By comparing the scenarios based on these KPIs, it is possible to gain an insight of the overall profitability of each system and rank them based on their LCOH.

3. Simulation setup

The model developed under TRNSYS makes use of specific "types", computational modules dedicated to performing the simulation of a particular plant component or process. Figure 2a and Figure 2b show the TRNSYS model for the complete plant and for the solar part, respectively. Among the adopted types, it is

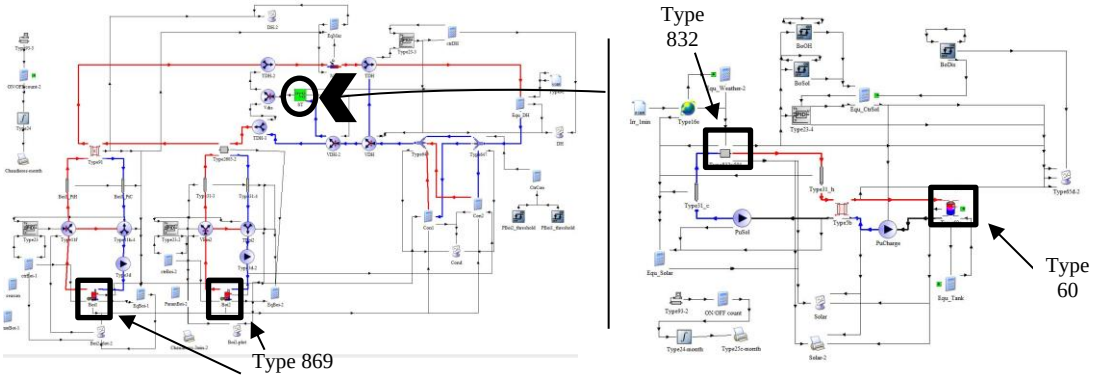

a) Overall TRNSYS model b) TRNSYS model for the solar field and TES

Figure 2: (a) General TRNSYS model for the hybrid biomass-solar DH plant; (b) TRNSYS model adopted for the solar field and integrated in the general model as a macro (black circle in (a)).

Table 1: Main characteristics of the modelled DH network

Modelled DH network parameter	Value
Annual total heat production, in [MWh/an]	5'830
Annual consumption for DHW production, in [%]	30
Nominal heating power @ -11°C, in [MW]	1.6
Nominal power for DHW production, in [kW]	400
No-heat temperature, in [°C]	16
Distribution heat losses, in [%]	10

worth noting the adoption of type 869 for the biomass boiler, type 832 for the solar collector and type 60 for the TES. The reader can refer to Jobard et Duret (2022) to find the detailed description of the TRNSYS model based on the DH network of the town « Les-Ponts-de-Martel », exploited since 2007 and located in Switzerland. On the other hand, the solar field model is derived from the one of the solar DH plant of Geneva, equipped with TVP Solar SA evacuated collectors. Duret et all (*in press*) describe in detail the numerical model and its validation against measurement data acquired at a 1-per-minute sampling rate. The validated model has been then extrapolated to the case of the "Les-Ponts-de-Martel" DH, in which the solar field operates at lower temperatures (i.e., while the Geneva operates at 95-80°C in summer, the temperature regime of the rural DH under consideration in the same season is as low as 70-45°C). Table 1 resumes the main features of the modelled DH network. For the current study, the meteorological data were derived by the service provided by MeteoSwiss, the Swiss Federal Office of Meteorology and Climatology, while the DH temperature and power profiles were taken directly from the monitoring data of the DH network of Les-Ponts-des-Martel.

4. Technical assessment

Once developed, the simulation model was used to evaluate the overall performance of the hybrid plant for several values of solar field aperture area, TES volume and solar fraction. Figure 3 shows the simplified but systematic procedure adopted to preliminary dimension the solar field and TES volume based on a target solar fraction value (Hiris 2022). For a given energy consumption, depending from the assumed solar fraction, the specific yield of solar collectors is estimated at an average value of 875 or 750 kWh/m^2/y, which allow grossily

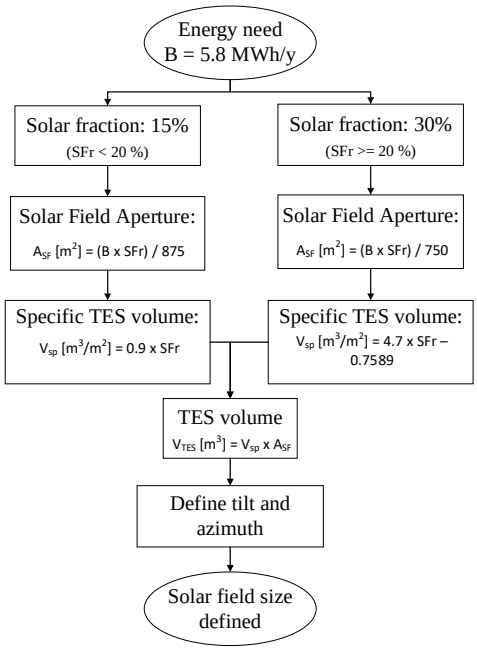

Figure 3: Simplified procedure followed for sizing the solar field area and the TES volume from a target solar fraction

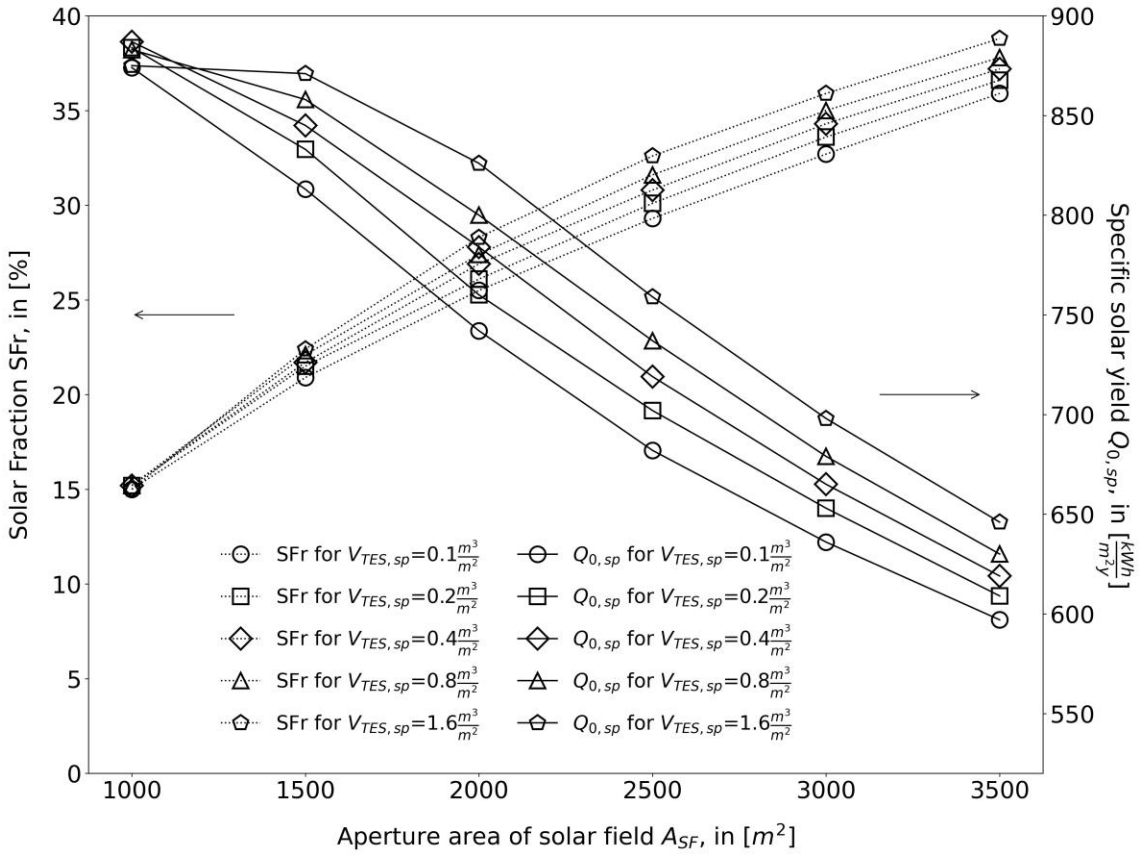

Figure 4: Solar fraction and specific heat productivity for different solar array sizes and specific storage capacities obtained by TRNSYS simulation.

estimating the solar field area required. Once simulated, each configuration has been categorized by the corresponding collector area (A_{SF}, in [m^2]), the resulting specific solar yield ($Q_{0,sp}$ in [kWh/m^2]) and solar fraction (*SFr*, in [%]), and the ratio between the TES volume and the field surface (i.e. or specific TES volume, $V_{TES,sp}$ in [m^3/m^2]). For the different modelled configurations, Figure 4 shows the resulting annual solar fraction and specific productivity as a function of the total field area and the TES specific volume. Solar array size varies between 1000 and 3500 m^2, while the studied range of specific storage capacities is between 0.1 and 1.8 m^3/m^2. As shown, high specific solar productivities are obtained for small solar fractions and small collector areas, as all the solar energy collected in the field can be dispatched to the DHN. For higher solar fractions, in particular during summer and at low load conditions, a larger part of solar energy cannot be readily dispatched to the DHN and needs to be stored in the TES, with increasing production temperatures, or even to be wasted to avoid stagnation. As a consequence, the specific productivity declines. For a given solar field size, furthermore, there exist an optimal value for the specific storage volume above which there is no significant increase in productivity of the solar field, as it can be inferred by the plateau in the specific productivity up to 1500 m^2 at high specific TES volume ratio and its decrease in value from a TES specific volume of 0.8 m^3/m^2 to 1.6 m^3/m^2, shown in Figure 4.

5. Economic analysis

The hybridization of wood-based DH networks with solar thermal energy has several advantages, already mentioned beforehand. But different field-TES combinations have different profitability, which is understandably an important driver of the investment decision-making process. To investigate how the technical features of a solar-hybridization project of an existing biomass plant affect its profitability, an economic model based on discounted cash flow analysis was compiled and a sensitivity analysis on the *LCOH* was carried out. Three scenarios of interest were finally selected for further analysis and the relevant KPI introduced in section 2 were compared.

Table 2: Costs of piping between solar field and DH network

Conduit diameter, in [mm]	Linear cost, in [CHF / m]
80	478
100	616
125	762
150	914
200	1091

Table 3: Assumptions made for the cost calculations related to connection piping.

Parameter	Value
In-pipe water speed, in [m/s]	1
Forward – return temperature difference, in [K]	30
Specific pic power of solar field under nominal conditions, in [W/m^2]	700

5.1 Economic model for KPI calculations

For the purpose of building an economic model and compute the KPI introduced beforehand (i.e, *LCOH*, *PP* and *PI*), only the investments on the solar field, the TES, the control system and the solar piping for connection to the DH were taken into account. Conversely, costs related to adaptations to the wood-fueled boiler circuits, costs or benefits due to wood storage in summer, costs due to land or space acquisition or rent were not taken into account.

The investment and installation costs for the solar field (solar collectors, supports, hydraulic components, control system, heat exchanger, i.e. the solar field CAPEX, noted CAP_{SF}) were estimated with eq. 2, based on private communications with technical partners of the HEIG-VD and for Switzerland.

$$CAP_{SF} = 2682\ {A_{SF}}^{0.826} \qquad \text{(eq. 2)}$$

In eq. 2, CAP_{SF} is the solar field capital expenditure, in [CHF], and A_{SF} the solar field aperture area, in [m^2]. The TES system was estimated, on the other hand, trough eq. 3, as a linear extrapolation of the trend derived from several offers obtained on the Swiss market for off-ground water-based TES tank volumes from 25 up to 300 m^3.

$$CAP_{TES} = 540.9 V_{TES} + 9045.3 \qquad \text{(eq. 3)}$$

In eq.3, CAP_{TES} is the TES capital expenditure, in [CHF], and V_{TES} the TES useful volume, in [m^3].

The costs for the connecting conduits between solar field and DH network were estimated based on values provided by the Swiss Association of DH Networks (ASCAD) shown in Table 2, and based on the assumptions reported by Table 3. To complete the picture, operating expenditures were estimated conservatively by summing up 1%/y of the total solar field CAPEX and the costs due to the electricity consumption of the auxiliary equipment and pumps. Electrical consumption was evaluated by adopting an annual COP value for the solar field of 100 MWh_{th}/MWh_e, about 30% higher than the annual mean encountered on the SolarCADII and reported by Duret et al. (2022). The economic model was completed by a series of assumptions made on the main economic/financial parameters of the model, shown in Table 4.

A sensitivity analysis of 30 cases was carried out with the aim of observing the evolution of the LCOH as a function of the size of the solar array and the storage volume, as shown in Figure 5. The analysis was carried

Table 4: Values adopted for the main parameters of the economic analysis.

Economic model parameter	Value
Solar plant service life, in [y]	25
Solar field yield degradation, in [%/y]	0.8
Solar plant COP, in [MWh_{th}/MWh_e]	100
Electricity price at t=0, in [CHF/MWh]	200
Heat selling price at t=0, in [CHF/MWh]	120
Annual energy price increase, in [%]	3
Nominal discount rate, in [%]	5.2

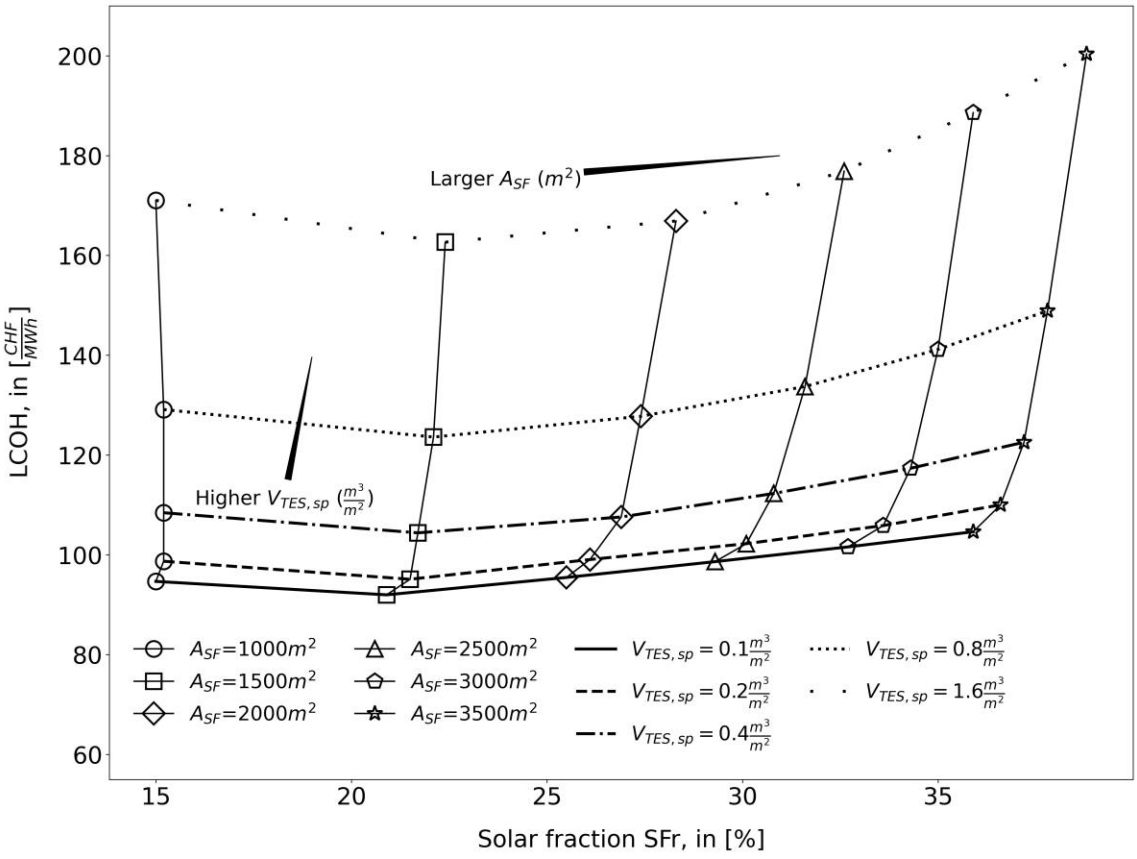

Figure 5: LCOH for a hybrid biomass-solar plant as a function of the solar fraction, the size of the solar array and the storage volume.

out by varying the solar field area in 500 m² steps between 1000 m² and 3500 m², and assuming values for the specific TES volumes of. 0.1, 0.2, 0.4, 0.8 and 1.6 m^3/m^2. As shown in Figure 5, for a given specific TES volume, the LCOH as a function of solar aperture area show a minimum after which any increase in the solar surface is less than optimal. An increase in specific TES volume, on the other hand, affects the LCOH negatively as it is shown from all the curves derived for ratios bigger than 0.1 m^3/m^2. When the increase in the size of the storage volume allows increasing the solar fraction, there are gains in solar heat production but these are offset by the higher investment costs for the purchase of the larger storage. In order to reduce investment and LCOH, it is preferable to opt for small-scale storages.

5.2 Study cases and KPI comparison

In Figure 5, the minimum value of the LCOH for the simulated DH network is found at about 92 CHF/MWh for a solar fraction of about 21%, featured by a 1500 m^2 solar field, equipped with a TES volume of 150 m^3. Three scenarios among those taken into account for the sensitivity analysis were then selected around this optimal case. The three scenarios refer to the same DH network consumption, but they feature differences in solar field area and TES volume. The analysis compared a hybrid plant made of a 1000 m^2 solar field equipped with a 135 m^3 TES to solutions consisting of a 1500 m^2 solar field equipped with 300 m^3 TES and a 2320 m^2 solar field equipped with a 1500 m^3 TES. As such, the scenarios featured specific TES volumes of 0.135, 0.2 and 0.64 m^3/m^2, respectively., while Table 5 shows the values of the main KPIs computed for the three scenarios. As shown, scenario 1 and scenario 2 feature similar values of LCOH, while scenario 3 shows the highest value. This latter scenario, in fact, is equipped with a TES that features a specific volume of about 0.64 m^3/m^2, much higher than the others, whilst also featuring the lowest specific productivity. The much larger size of TES volume allows to cover about 30 % of the energy consumption, but the profitability of the project is affected by its costs, as it is shown by the IRR values evaluated at the heat selling price (including energy inflation) and according to the values shown in section 2.

Table 5: KPI values computed for the three scenarios.

Parameter	Scenario 1	Scenario 2	Scenario 2
Solar field aperture area, in [m^2]	1000	1500	2320
TES Volume, in [m^3]	135	300	1500
Yearly solar yield, in [MWh/y]	855	1'227	1'733
Specific yearly solar yield, in [kWh/m^2/y]	855	818	747
Solar fraction, in [%]	14.7	21	29.7
CAPEX, in [CHF]	980'700	1'412'580	2'573'162
LCOH, in [CHF/MWh]	105.3	105.6	135.5
NPV @ selling price, in [CHF]	679'210	968'775	706'304
PP @ selling price, in [y]	12.4	12.5	18.2
PI @ selling price, in [y]	1.69	1.68	1.27
IRR @ selling price, in [%]	11.4	11.3	7.8

5.3 Impact of business model on the LCOH.

Based on the type of adopted business model, the same solution of solar energy integration may have a different economic impact on the overall cost of heat. To address this question, the following two business models were analyzed in reference to the case featuring the lowest value of LCOH:

- The owners of the DH network and plant are members of the rural community and they are reunited as a "Cooperative".
- The DH network and plant are owned by an ESCO (Energy Service Company) external to the rural community.

To evaluate the impact on the energy bill of the DH customers, heat costs from the biomass plant (i.e., 87 CHF/MWh in 2019 for the DHN of " Les-Ponts-de-Martel") and from the solar plant can be weighted according to eq. 4 to estimate the mean heat cost issued by the hybrid plant.

$$LCOH_{mean} = \mathrm{LCOH}_{SF} * SolarFraction + (1 - \mathrm{SolarFraction}) * \mathrm{LCOH}_{biomass} \quad \text{(eq. 4)}$$

In the "Cooperative" case, the aim of the owners is to have the lowest possible cost for the energy that the DH produces and distributes, as they are not interested in a real margin (apart from a small fee meant to pay for operating and managing the energy system). In this case, as there's no interest in having a positive NPV, the LCOH for solar heat can be taken equal to the minimal LCOH (92 CHF/MWh). By assuming 87 CHF/MWh for the biomass heat and 21% for the solar fraction, it can be calculated that the rural community will have access to heat at an average price of 88.05 CHF/MWh. This figure is 1.08 CHF/MWh higher than the biomass-only case, but adding the solar field has many benefits, among others the reduction of the number of cycles featured by the biomass boilers in one year, impacting emissions particularly in summer (Jobard et Duret, 2022).

In the ESCO scenario, on the other hand, the investing and operating entity is a private company, which creates value by charging for the supply of energy to its customers and it is constrained to provide a return to its investors. One may consider, for example, that the ESCO is only willing to invest in projects that have a PP value of 15 years or lower (i.e., corresponding to a heat cost of 128 CHF/MWh). In this case, the solar heat cost is substantially larger than the LCOH, as the ESCO requires a margin to compensate its investors for the risk undertaken and service its debt. In this case, the average selling price for the DH heat can be computed at 95 CHF/MWh. In this latter case, the cooperative would disburse 7-8 CHF/MWh more than for the biomass-only production managed by the Cooperative itself, highlighting the importance of collaboration between stakeholders to achieve balanced financial objectives.

6. Conclusions

This study highlights the technical and financial viability of the integration of solar thermal technology with wood chip boilers. Such an addition can enhance energy efficiency, reduce CO2 emissions, and optimize costs. In particular, it analyses the technical and economic performances of the integration of a large-scale solar thermal field with biomass boilers for district heating (DH) in rural areas, as aligned with the principles of 4th Generation DH for sustainable energy systems. The technical analysis shows that combining solar thermal energy with existing boilers significantly boosts renewable heat production, with a potential optimal solar fraction of about 21 % for the chosen location, Les-Ponts-Des-Martel, a small rural village in Switzerland. Financially, the study confirms that most configurations are economically feasible, with careful consideration of solar field size, storage volume, and associated costs. An optimal TES volume can be identified with respect to the target solar fraction and the surface of the solar field. Two financing scenarios were furthermore explored: one involving cooperative members as investors, which keeps heat costs stable and close to the break-even point, and another with third-party investors, which provides financial gains while maintaining reasonable consumer costs. Overall, the study supports the integration of solar thermal systems, provided that the optimal plant configuration and financing scheme are selected.

7. Acknowledgments

We express our sincere gratitude to the Swiss Federal Office of Energy (SFOE) for their financial support of this research (Project N.SI/502569). and to the cooperative des “Marais-rouge” for providing the DHN data.

8. References

Quiquerez, L., Cabrera S., Jose D., Hollmuller, P., (2013) Températures de distribution de chauffage du parc immobilier genevois. Archive Ouverte UNIGE, https://archive-ouverte.unige.ch/unige:27989.

Lachal, Bernard MarieJenssen, T., König, A., & Eltrop, L. (2014). Bioenergy villages in Germany: Bringing a low carbon energy supply for rural areas into practice. *Renewable Energy*, *61*. https://doi.org/10.1016/j.renene.2012.08.014

Klein, S. A., Beckman, W. A., Mitchell, J. W., & Duffie, J. A. (2014). TRNSYS 17 Mathematical Reference. In Trnsys 17 (Vol. 4).

Lund, H., Werner, S., Wiltshire, R., Svendsen, S., Thorsen, J. E., Hvelplund, F., Mathiesen, B. V. (2014). 4th Generation District Heating (4GDH). Integrating smart thermal grids into future sustainable energy systems. In Energy (Vol. 68, pp. 1–11). Elsevier Ltd. https://doi.org/10.1016/j.energy.2014.02.089

Winterscheid, C., Dalenbäck, J. O., & Holler, S. (2017). Integration of solar thermal systems in existing district heating systems. Energy, 137. https://doi.org/10.1016/j.energy.2017.04.159

CEA (2018) D2.3. Key Performance Indicators to evaluate the integration of solar heating in industrial processes; D2.3 SHIP2FAIR ID GA 792276; http://ship2fair-h2020.eu/wp-content/uploads /2018/12/SHIP2FAIR_D2.3_KPI_CEA.pdf

Aldersey-Williams, J., & Rubert, T. (2019). Levelised cost of energy – A theoretical justification and critical assessment. Energy Policy, 124. https://doi.org/10.1016/j.enpol.2018.10.004

Ilie, A., Vișa, I. (2019). Hybrid solar-biomass system for district heating. E3S Web of Conferences, 85. https://doi.org/10.1051/e3sconf/20198504006

Ruesch, F., Caflisch, M., Haller, M. (2020). BioSolFer Integration von Solarwärme in Biomasse Fernwärmenetze, www.ost.ch/fileadmin/dateiliste/3_forschung_dienstleistung/institute/spf/forschung/ projekte/biosolfer_schlussbericht_2020.pdf

Tschopp, D., Tian, Z., Berberich, M., Fan, J., Perers, B., Furbo, S. (2020). Large-scale solar thermal systems in leading countries: A review and comparative study of Denmark, China, Germany and Austria. Applied Energy, 270(January), 114997. https://doi.org/10.1016/j.apenergy.2020.114997

Duret, A., Jobard, X., Pauletta, S., Demonchy, G. (2022). Performance Monitoring of an 800m^2 Solar Thermal

Plant with Evacuated Flat Plate Collectors coupled to a DHN. Proceedings of EuroSun 2022 - ISES and IEA SHC International Conference on Solar Energy for Buildings and Industry, 1–10. https://doi.org/10.18086/eurosun.2022.04.02

Hiris, D. P., Pop, O. G., & Balan, M. C. (2022). Preliminary sizing of solar district heating systems with seasonal water thermal storage. Heliyon, 8(2). https://doi.org/10.1016/j.heliyon.2022.e08932

Jobard, X., Duret, A. (2022). Operability of District Heating Plants Combining a Large-Scale Solar Thermal Field and Condensing Wood Chip Boilers – a Case Study in Switzerland. Proceedings of EuroSun 2022 - ISES and IEA SHC International Conference on Solar Energy for Buildings and Industry, 1–11. https://doi.org/10.18086/eurosun.2022.04.03

Jodeiri, A. M., Goldsworthy, M. J., Buffa, S., & Cozzini, M. (2022). Role of sustainable heat sources in transition towards fourth generation district heating – A review. In *Renewable and Sustainable Energy Reviews* (Vol. 158). https://doi.org/10.1016/j.rser.2022.112156

Duret, A., Jobard, X., Pauletta, S., Lasvaux, S., Frossard, M., Demonchy, G. (*in press*). Dynamic Simulation and Life Cycle Analysis of a 784m^2 Solar Thermal Plant with Evacuated Flat Plate Collectors coupled to a DHN. J. Thermal Sciences.

Feasibility study of a solar desalination unit for small isolated communities

Daniel R. Rousse, Vincent Deblock, Misagh Irandoostshahrestani, and Patrick Turcotte

École de technologie supérieure, Université du Québec, Montréal (Canada)

Abstract

Population growth and changing consumption patterns are intensifying the use of fresh water worldwide. While large-scale, expensive desalination solutions do exist, there is still a need for low-cost solutions for populations located far from major centers and in financial need. The main objective of the project is to design a low-cost and low-environmental footprint solar-powered seawater desalination unit and to verify its performance using a custom numerical simulation tool. The second objective is to provide a summary economic analysis to target the potential cost of water production when the single-basin still is compared with a double-basin still with similar characteristics. This numerical study of two types of solar stills – without technological improvements such as fins, sponges, etc. – shows that the production per m² of the two solar stills remains relatively low. Nevertheless, when ground space is available, simple solar stills appear to be robust, resilient, and cheaper solutions as a source of drinking water.

Keywords: Feasibility study, low-cost desalination units, simple solar still.

1. Introduction

In 2015, 17 Sustainable Development Goals (SDGs) were proposed by the United Nations (UN). In particular, SDG 6 aims to "ensure access to sustainably managed water and sanitation services for all". Although fresh water is a vital element for survival, this resource represents only 2.5% of all water on Earth, compared to the 97.5% occupied by salt water, which is unsuitable for human consumption. The issues surrounding water continue to grow (WHO, 2017). On the one hand, the amount of fresh water available is decreasing, whether through global warming, which accelerates evaporation, causes glaciers to melt and raise sea levels, or through water pollution linked to human activities, mainly industrial, agricultural, and domestic discharges. On the other hand, demographic pressure leads to an increase in needs, and therefore in consumption (UN, 2020). This gap between supply and demand, known as water scarcity or water stress, poses many risks, such as the transmission of diseases like cholera, premature deaths, migratory movements or conflicts directly related to access to water (WHO, 2019). Alongside this crisis, fossil energy sources commonly used to help with water pumping, treatment, and desalination are becoming increasingly expensive and emit greenhouse gases that intensify global warming, amplifying the problem (Al-Shayji, 2018). Moreover, technologies involving processes such as osmosis (direct or reverse), electrodialysis, nanofiltration, or ion exchange, even when operated using renewable energies, are often too expensive for many communities. In this context, the solar still is an ideal source of fresh water for both drinking and agriculture in remote areas. There are many types of solar stills; the simplest and most proven is the basin type (Bloemer et al., 1961).

However, among the many variations of solar basins, several involve technologies designed to increase performance. Indeed, since the 1960s study by Bloemer et al. (1961) cited by Malik et al, (1982), which indicates that only about 31% of the incoming radiation is used to evaporate the distillate (while cover reflection (11%) and absorption (5%), ground and edge losses (2%), radiative losses from the basin water to cover (26%), internal convection (8%), re-evaporation of distillate and other losses (17%) complete the balance), researchers tried in many ways to improve this 60 years old threshold. To improve solar basins, fins, sophisticated absorbing materials, multi-basin stills, phase-change materials, storage tanks, hybridation, nanocomposites, adjacent solar pond, specific configurations, floating plates, perforated plates, cascades, glass treatments, double glass, etc. were proposed (Panchal and Mohan, 2017) (Velmurugan and Srithar, 2011).

Indeed, these improvements lead to increases in efficiency. But when space is available, is it the efficiency gains that matter?

The main objective of the project reported in this article is to design a solar-powered seawater desalination unit to

© 2024. The Authors. Published by International Solar Energy Society
Selection and/or peer review under responsibility of Scientific Committee
10.18086/eurosun.2024.09.09 Available at http://proceedings.ises.org

reduce costs and environmental footprint and verify its performance using a numerical simulation tool. The unit, basically designed to avoid any fancy technological improvements such as those mentioned above, will be used to produce drinking water for small, isolated communities (i.e. communities that are not connected to a reliable drinking water distribution system, and for which drinking water supply options are limited and/or expensive) located on the seafront. The sole comparison is carried out between the single- and double-basin to discuss productivity in $kg\ m^{-2}$ per unit time and unit cost in $\$CA\ m^{-3}$ per unit time

2. Brief literature review

2.1. Desalination processes

There are two main families of desalination processes: those with a phase change of the water, and those without. This review, due to limited space, can only mention a few references to available technologies and instead offers references on the state of desalination in the world. Table 1 and Table 2 list some of the studies reviewed in preparation for this article.

Tab. 1: Phase change desalination processes

Process	Reference
Multiple Effect Distillation	Guimard, 2019, Liponi et al., 2020
Flash Distillation by Successive Expansions	Nannarone et al., 2017, Darawsheh et al., 2019
Vapor Compression	Lara, 2005, Bahar et al., 2004
Freezing	Kadi & Janajreh, 2017, Mandri, 2011
Membrane Distillation	Saadat et al., 2018, Lawson & Lloyd, 1997
Direct Solar Desalination	Chauhan et al., 2021, Arunkumar et al., 2019

Tab. 2: Desalination processes without phase change

Process	Reference
Reverse osmosis	Kim et al., 2019, Shafagnat, Eslami & Baneshi. 2023
Electrodialysis	Akther, Habib & Qamar, 2018, Sedighi et al., 2023
Nanofiltration	Wafi et al., 2019, Yadav, Karki & Ingole, 2022
Direct osmosis	McCutcheon et al., 2019, Qasim et al., 2015
Ion exchange	Subban & Gadgil, 2019, Wang et al., 2020

2.2. Direct Solar Desalination

To provide an overview of the current situation of desalination in the world, a few recent studies can be recommended, including those by Eke et al. (2020), Ghazi et al., (2022), Janaireh et al., (2023), Jones et al., (2019), Li et al., (2023) and Ray et al., (2023). More specifically, Aboulfotoh et al. (2023) investigated the effectiveness of a solar still for desalination to produce fresh water for small and rural communities in Zagazig, Egypt. They studied the effect of variations in water depth, salinity, and cover angle on the still's water production. Not surprisingly, it was shown that reducing water depth and salinity, along with increasing the cover angle in winter, increased water output. Removing chloride and total dissolved solids, the still demonstrated high efficiency in producing water. The developed theoretical models predicted the still's thermal performance with good agreement compared to experimental data. Furthermore, the economic analysis showed that the solar still is more cost-effective than commercially available water. In He et al. (2024), water scarcity in rural regions was studied by introducing a solar-powered electrodialysis reversal system used for desalination. It was showed that the system can harnesses 77% of available solar energy. They evaluated this technology for a village-scale case study in India and they concluded that water production costs can decrease by 22%. The authors declared that this technology can be a reasonable alternative to fossil fuel-powered reverse osmosis systems.

2.3. Recent reviews

However, the important thing to remember about current literature reviews is that, due to the preponderant importance of water for humanity and the growing supply difficulties discussed in the introduction, this field is experiencing exceptional research activity, as evidenced by the 46 review articles and 246 research articles reported in Solar Energy alone (with term: desalination) in 2022, 2023, and 2024 (by 2024-08-06).

3. Methodology

3.1. Location

To choose a location to simulate the desalination system among the 15 non-landlocked countries most exposed to the risk of water stress, the method used was a multi-criteria comparison of different countries according to three indicators:

1) water stress, related to freshwater withdrawals as a proportion of available resources. This is SDG 6 indicator 6.4.2 (clean water and sanitation) managed by the World Resources Institute;
2) the Human Development Index (HDI). Created by the United Nations Development Programme (UNDP), it takes into account three criteria: life expectancy at birth, GDP/capita, and level of education;
3) the mortality rate attributed to unsafe water, sanitation, or hygiene. This is SDG 3 indicator 3.9.2 (good health and well-being) managed by the WHO (WHO, 2019).

After a multi-criteria analysis (not presented here), the study showed that Eritrea obtains the highest average score, particularly due to the lowest HDI and the highest, by far, mortality rate attributed to insufficient water supply, inadequate sanitation or unsanitary hygiene. As a result, the modeling is carried out for the city of Assab, located in southern Eritrea. Its latitude is 13°01' North, its longitude is 42°44' East, while its standard meridian is 45°.

3.2. Meteorological and oceanic data

The climate in Assab is hot and dry, with average temperatures between 25 and 35°C. Four different sources of weather data were selected for comparison:

1) an EPW file provided on the Climate.OneBuilding website (Lawrie & Crawley, 2019);
2) hourly data from the European Commission's website (European Commission, 2019);
3) the SoDa website (HELIOCLIM-3 ARCHIVES *DEMO*, 2006);
4) daily data from the RETScreen tool (NRCan, 2016).

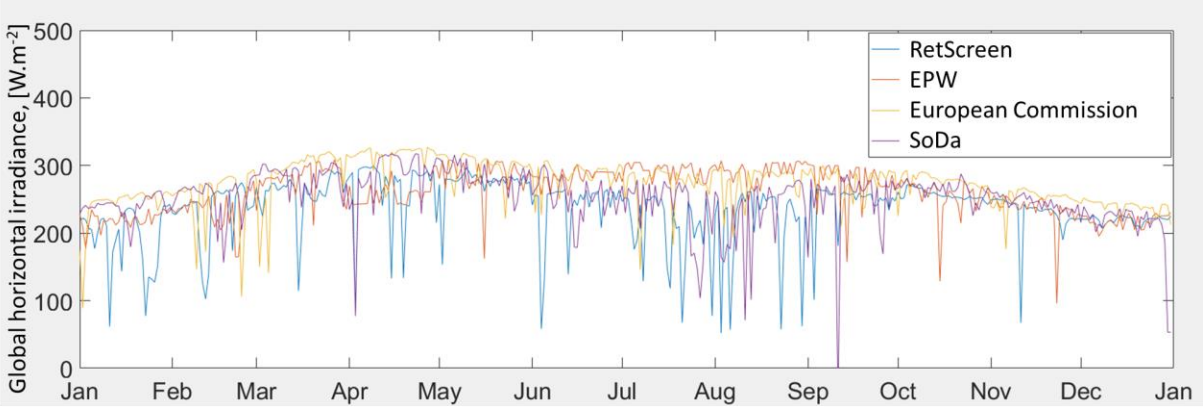

Fig.1: Yearly variations of the average daily global horizontal irradiance in Assab, Erytrea, from four different sources

The EPW has been kept for simulations, as it can easily be read by TRNSYS to obtain irradiance on an inclined plane.

To estimate the contribution that a solar still can make to the drinking water production of an isolated community, the 2020 edition of *Domestic water quantity, service level and health* was used as a reference (Howard et al., 2020). 50 litres/day/person are recommended as the minimum volume to ensure medium health risk (Optimum: 100 litres/day/day optimal low risk, Basic: 20 litres/day/person basic high risk) by Omarova et al. (2019). The basic 20 litres per person daily should be considered partly sufficient for beverages and food but not for hygiene purposes.

In desalination, it is mostly important to retrieve the characteristics of the local seawater (salinity and properties) as these will have an impact on the operation of the system. The use of the CoolProp library (Bell et al., 2014) allows quick access to these properties, which depend on salinity in addition to pressure and temperature.

3.3. Energy balance

Among the technologies previously cited, direct solar desalination in basin is the most appropriate for small, isolated communities located by the sea when cost matters. Two types of basins are studied: Figure 2 schematically illustrate

the heat transfers associated with the conventional single-stage (left) and two-stage (right) basins with single glazing. In both cases, the horizontal surface area of the collector is 2m x 0.5m or 1m^2 footprint.

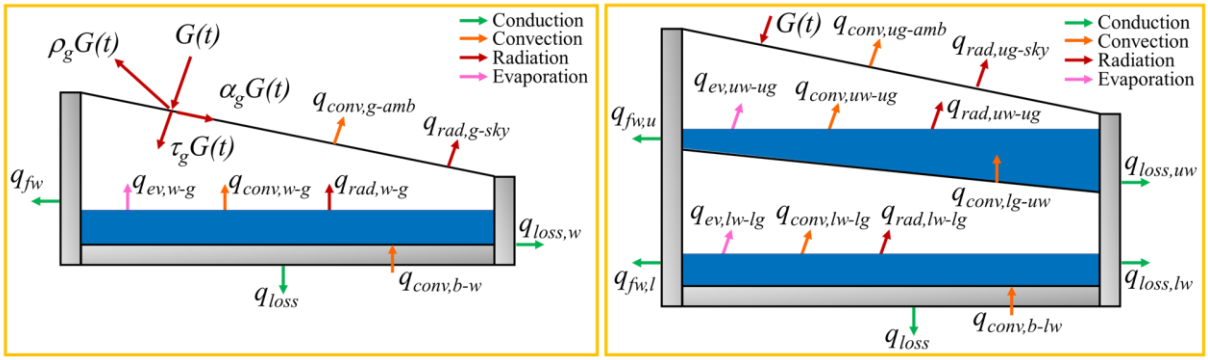

Fig.2: Energy balance on the investigated still configurations: single-basin (left); double basin (right)

The energy balance on the glazed cover (g-index) of the conventional single-basin still (Figure 2, left) is:

$$m_g cp_g \frac{dT_g}{dt} = I_T(t)\alpha_g A_g + q_{conv,w-g} + q_{ev,w-g} + q_{rad,w-g} - q_{conv,g-amb} - q_{rad,g-sky} \quad \text{(eq.1)}$$

This balance at the surface of the salt water (index w) is:

$$m_w cp_w \frac{dT_w}{dt} = I_T(t)\tau_g \alpha_w A_w + q_{conv,b-w} - q_{conv,w-g} - q_{ev,w-g} - q_{rad,w-g} - q_{fw} - q_{f,w} \quad \text{(eq.2)}$$

The balance sheet on the volume of the basin (index b) is:

$$m_b cp_b \frac{dT_b}{dt} = I_T(t)\tau_g \tau_w \alpha_b A_b - q_{conv,b-w} - q_{loss} \quad \text{(eq.3)}$$

In these equations and figures, subscripts *ev*, *conv*, and *rad* refer to evaporation, convection, and radiation while *loss*, *amb*, *g*, *sky*, *w*, *b*, and *fw*, pertain to losses to the ground and walls, ambient air, glass, surroundings, water, basin, and feed water, respectively. Subscripts *l* and *u* refer to the lower and upper basin of the double basin still.

Each of the terms is familiar to the heat transfer analyst and the reader wishing to obtain the entire mathematical model involving 49 equations is invited to contact the authors. A similar balance can be explained for the two-stage basin shown in Figure 1, right.

3.4. Production and efficiency

The average annual daily productivity results of the desalination system are obtained in kg.m^{-2}.d^{-1}, which then makes it possible to determine the floor area needed to support an entire community.

Equations (4) and (5) provide the hourly productivity, in kg.m^{-2}.h^{-1}, for the single- and double-basin stills, respectively.

$$\dot{m}''_h = 3600 \times \frac{q_{ev,w\text{-}g}}{A_w h_{fg}} \quad \text{(eq.4)}$$

$$\dot{m}''_h = 3600 \times \left(\frac{q_{ev,lw-lg}}{A_{lw} h_{fg}} + \frac{q_{ev,uw-ug}}{A_{uw} h_{fg}} \right) \quad \text{(eq.5)}$$

The daily unit production, in kg.m^{-2}, is simply the cumulative sum of equation (4) or (5) over 24 hours. The daily recovery efficiency of the ponds is defined for the two types of ponds such as:

$$\eta_d = 100 \times \frac{\sum_1^{24} \dot{m}''_h h_{fg}}{\sum_1^{24} I_T(t)\Delta t} \quad \text{(eq.6)}$$

3.5. Simplifying assumptions

In addition, it is important to specify the assumptions made during the implementation for the two types of basins (Fig.2):

- There are no air leaks and the stills are waterproof.
- The window is supposed to be clean.
- Water vapor and dry air act as ideal gases.
- There are no temperature gradients along the vertical axis, the temperature is considered uniform in the chamber and initially the temperatures of all surfaces are equal to the ambient temperature.
- The surfaces of the water and the basin are of equal dimensions.

- Conduction is neglected in the glass and in the absorbent plate, due to their low thicknesses, and condensation only takes place on the inner surface of the glass.
- For a deep basin, the reduction in water mass due to evaporation is negligible. However, in a shallow basin, the effect of the mass of evaporated water on performance is significant. It is therefore assumed that the evaporated mass is continuously replaced and that the volume of water in the basin is thus constant. The water replaced is assumed at atmospheric temperature and it exchanges heat with the water in the basin.

These assumptions are appropriate for this feasibility study and also allow for consistency with the literature, so that different studies can be compared with each other more rigorously. Nevertheless, the impact and actual accuracy of these simplifying assumptions should be reassessed in future studies.

3.6. Implementation details

For each still, the mathematical model was developed and then implemented in MATLAB. This model makes it possible to solve the systems of ordinary differential equations partially presented above, to obtain the temperatures of the different components of the solar still (glass-g, water-w, and the absorbent plate of the basin-b) and to deduce its instantaneous and cumulative productivity as well as its efficiency as a function of time.

Usually, it is advisable to use the *ode45 solver*, based on an explicit Runge-Kutta formula (of order 4 and 5), more specifically the Dormand-Prince method. This method uses six function evaluations to compute precise fourth- and fifth-order solutions. The difference between these solutions is then considered the error of the solution. However, this solver is not recommended in the case of a so-called "stiff" system of differential equations. This is more of a qualitative notion than a quantitative one, and it means that sensitivity to the parameters of the equations makes it difficult to solve by explicit numerical methods. This is due to the fact that the *ode45s solver* would need a very small time step to ensure the stability of the solution, but over a high time interval, which would result in a long computation time. It is then recommended to use the *ode15s solver*, which also integrates the system of differential equations according to a given time interval and initial conditions. But this solver is implicit, usually based on a variable-order numerical differentiation formula, or on an inverse differentiation formula. This solver calculates the solution at time $t + \Delta t$ taking into account the value of the function in t and $t + \Delta t$. This method also uses a variable time step, which therefore makes it possible to reduce computation times (Shampine & Reichelt, 1997).

3.7. Irradiance calculation

The driving force behind the system is the irradiance, G_T in W.m^{-2}, which hits the sloping glass surface. The classical equations of radiative transfer are implemented in TRNSYS. This software is used to feed the MATLAB code. The theory and equations for radiation models are not reproduced here since they are standard. However, it is important to note that the data extracted from TRNSYS show that the Perez, Reidl, and Hay Davis models differ by up to 3.8% from the isotropic model (overshoot). Since the sunshine data values predicted with the latter are lower, the sizing will be conservative regardless of the type of desalination unit simulated.

3.8. Cost evaluation

For a community with limited financial means, it is also important to study the economic viability of a solar still throughout its lifespan to justify the interest in this potential solution. The cost of water produced in a solar still depends on several parameters, mainly the initial investment (CAPEX), the costs of operation (OPEX), maintenance, storage and repair, the lifespan of the still, and its freshwater production capacity. Usually, seawater desalination involves high operating costs due to a large energy cost. However, in the case of the solar stills, the energy is drawn directly from solar radiation. The operation and maintenance (O&M) costs of the solar stills must be as low as possible to meet the objectives set at the beginning of the study. It is interesting to compare the cost of the solar still with other approaches, to estimate its possible economic interest. Other possible options include the delivery of fresh water from a conventional source, or the use of another desalination technique.

The specific cost of freshwater production, CPL in \$.litres^{-1}, can be found with equation (7).

$$CPL = \frac{CAPEX \times \left[\frac{i(1+i)^N}{(1+i)^N - 1}\right](1 + x_{\%}) - y_{\%} \times CAPEX \times \frac{i}{(1+i)^N - 1}}{1000 \times \frac{\dot{M}_a''}{\rho_w} \times A} \quad \text{(eq. 7)}$$

The denominator of equation (7) denotes the average annual production, in litres.y^{-1}, which can be expressed as a function of the annual mass production per unit area, $\dot{M}_a''$, the density of the water, ρ_w, as well as the surface area of

the solar basin studied, A.

The first term (on the left-hand side) of the numerator refers to the fixed annual costs or FAC, in $\$.y^{-1}$, which is expressed as a function of the CAPEX of the solar basin studied, in \$, the interest rate i and the estimated lifetime of the system, N, in years. That is $FAC = CAPEX \times [f(i, N)]$. The term $x_{\%}$ indicates that the annual operation and maintenance costs or $O\&M$, in $\$.y^{-1}$, are expressed as a percentage of the annual fixed costs. $O\&M = x_{\%} \times CAPEX \times [f(i, N)]$

The last term (on the right-hand side) of the numerator refers to the annual residual value or ARV of the solar still studied, expressed in terms of RV, the residual value of the solar still at the end of its lifetime, in \$, and a sinking fund factor. Here, RV is expressed as a percentage of the CAPEX of the solar still studied, i.e. $RV = y_{\%} \times CAPEX$.

This concludes the partial presentation of the methodology used in this study. The following section presents selected results obtained from the simulations carried out on the two solar stills.

4. Selected results

As part of this project, the solar basin will be south oriented, towards the equator. The azimuth angle γ is equal to the magnetic declination δmag, in the opposite sign. As the latter is close to zero, a zero azimuth is chosen. Since the drinking water requirements are assumed to be constant throughout the year, and because we are close to the equator, the value of the slope β angle is equal to the value of the latitude φ to induce optimal irradiance throughout the year. The inclination must also be large enough to allow the condensed water to flow, which is the case here. September 20 and December 21 were selected for the simulations, as these days respectively provide strong and low sunlight on the inclined plane of the simulated solar stills. With these parameters chosen, TRNSYS can then extract and read the supplied .EPW file and output the irradiance on the inclined plane for the two selected typical days and according to five different models. For example, on September 20, a maximum at 11:00 is observed between 1020 $W.m^{-2}$ (isotropic model) and 1035 $W.m^{-2}$ (Perez 1999 model). On December 21, a maximum at 12:00 was observed between 790 $W.m^{-2}$ (isotropic model) and 820 $W.m^{-2}$ (Perez 1999 model).

4.1. Validation of the formulation and implementation

Before looking at the results obtained from the use of the implemented MATLAB models, it is worth comparing the results of the numerical simulations with a few references, when possible. Here, validation is carried out using experimental data (Table 3) from a paper published in 2021 (Raj Kamal et al., 2021) as well as theoretical data (Table 4) from a paper published in 2009 (El-Sebaii et al., 2009). These two papers deal in particular with a conventional single-glazed solar still (Figure 2), the first being tested from 9:30 to 16:00, in Tamil Nadu, India, and the second being simulated over 24 hours with meteorological data from the city of Jeddah, Saudi Arabia.

The relative difference E, in %, between the external data X and the calculated data Y is estimated using equation (8), where the two variables X and Y can designate the temperature of the still, T_b, the water, T_w, the glass, T_g, or the instantaneous and cumulative daily productivity, $\dot{M}''_d$.

$$E_t = |X_t - Y_t| \,/\, \left[\frac{X_{max}+Y_{max}}{2}\right] \times 100 \qquad \text{(eq.8)}$$

The relative difference was computed every 30 minutes from 9h30 to 16h00 for comparison with experimental data from (Raj Kamal et al., 2021) and from 7h00 to 18h30 for comparison with the theoretical calculations of (El-Sebaii et al., 2009).

Tab.3: Comparison with experimental and theoretical data from Raj Kamal et al., 2021 and El-Sebaii et al., 2009, respectively.

Source	Relative difference	T_g [°C]	T_w [°C]	T_b [°C]	$\dot{M}''_d$ [kg m^{-2} h^{-1}]
		E [%]	E [%]	E [%]	E [%]
Raj Kamal et al., 2021	Average	7.77	11.05	10.37	10.25
	Standard deviation	5.14	8.86	8.47	10.32
El-Sebaii et al., 2009	Average	1.47	1.82	2.15	1.65
	Standard deviation	0.77	1.65	2.09	1.90

The adequacy with the first study is correct with maximum deviations of 10%, while this maximum does not exceed 2% in the case of the results proposed in El-Sebaii et al. (2009). The values for the 4 variables were always higher in the morning and lower in the afternoon when compared to the experimental data. This could suggest a different weather on those days in Tamil Nadu, India than that embedded in the data file and a relative inertia of the still structure to heat up. The discrepancies with the experimental study by Raj Kamal et al. (2021) could also be explained

in different ways: 1) some values are collected from graphical readings, which leads to an error in the result; 2) information was omitted from the article, such as the depth of the basin (which has an influence) or whether the irradiance provided is on a horizontal or inclined plane; 3) the properties of materials such as insulation have also been estimated due to the lack of full citation in the article; 4) the reality on the real site may compromise some assumptions made for the simulation, such as the absence of leaks or the absence of conduction in the glass or the absorbent plate.

Nevertheless, these results validate the correct formulation and implementation of the model.

4.2. Some results for Assab, Erytrea

Table 5 provides a summary of the data required to conduct the simulations and for the reader who would like to benchmark their own method relative to this one.

Tab 5: Main technical characteristics of the simulated stills

System	Parameter	Value	System	Parameter	Value
Location	φ	13.00°	**Still water**	e_w	0.02 m
	L_{loc}	42.74°		α_w	0.05
	L_{st}	45°		τ_w	0.9
	ρ_g	0.2		ε_w	0.95
Global	L	2 m		x	0.035
	l	0.5 m	**Absorbing plate**	cp_b	871 J $kg^{-1}K^{-1}$
	H	0.20 m		e_b	0.0015 m
	γ	0°		α_b	0.9
Glass	β	13°		ρ_b	2719 kg m^{-3}
	cp_g	840 J $kg^{-1}K^{-1}$	**Insulation**	L_{is}	0.08 m
	e_g	0.003 m		k_{is}	0.04 W $m^{-1}K^{-1}$
	α_g	0.05	**Other**	P_{ref}	101325 Pa
	τ_g	0.88		g	9.81 m s^{-2}
	ε_g	0.90		σ	5.67e-08 W m^{-2} K^{-4}

4.3. Daily production and conversion efficiency

Figure 3 and Figure 4 present the daily evolution of the instantaneous and cumulative productivity of the two types of solar stills for the two days that were studied. Concerning the conventional basin, its maximum productivity is 0.89 $kg.h^{-1}.m^{-2}$ around noon on 20 September, with a total daily production of 6 $kg.m^{-2}$, compared to 3.8 $kg.m^{-2}$ for 21 December. On September 20, its production began between 6:30 and 7:00 and ended around 19:45. As for the double-stage still, its maximum productivity is 0.93 kg h^{-1} m^{-2} around 1:30 p.m. on September 20, with a total daily production of 7.9 $kg.m^{-2}$, compared to 4.7 $kg.m^{-2}$ for December 21. On September 20, its production begins between 6:30 and 7:00 and ends around 20:00. for the lower basin, and from 9:00 to 21:00. for the upper basin. Basin 2 shows an increase in daily production of 31.7% compared to Basin 1 for 20 September and 23.7% for 21 December.

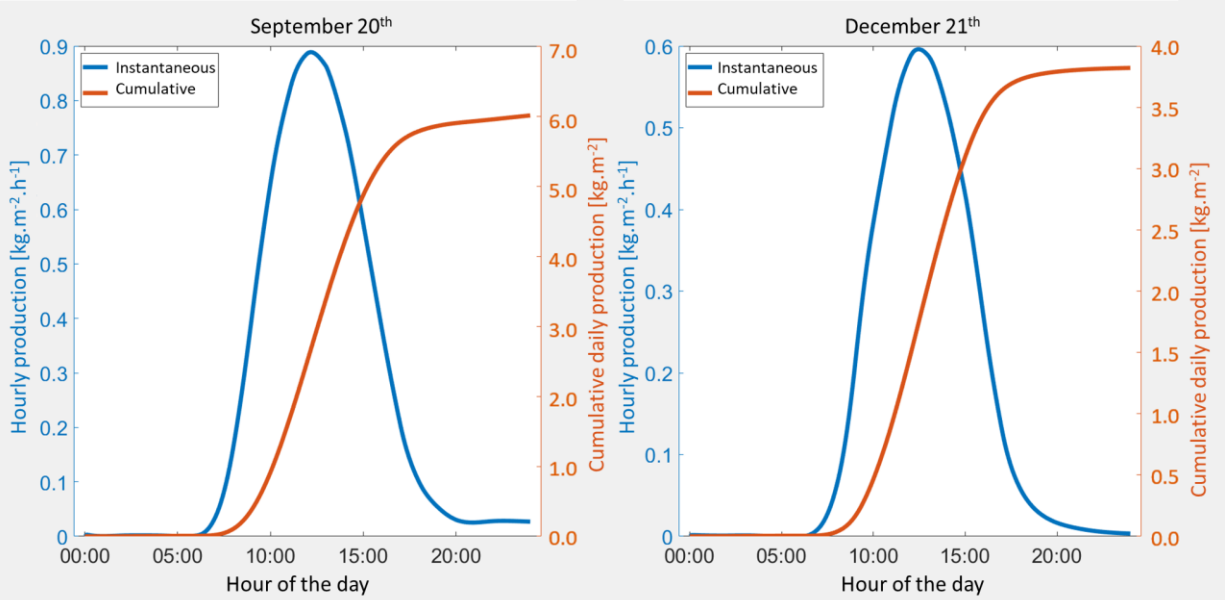

Fig.3: Daily evolution of productivity for the conventional still

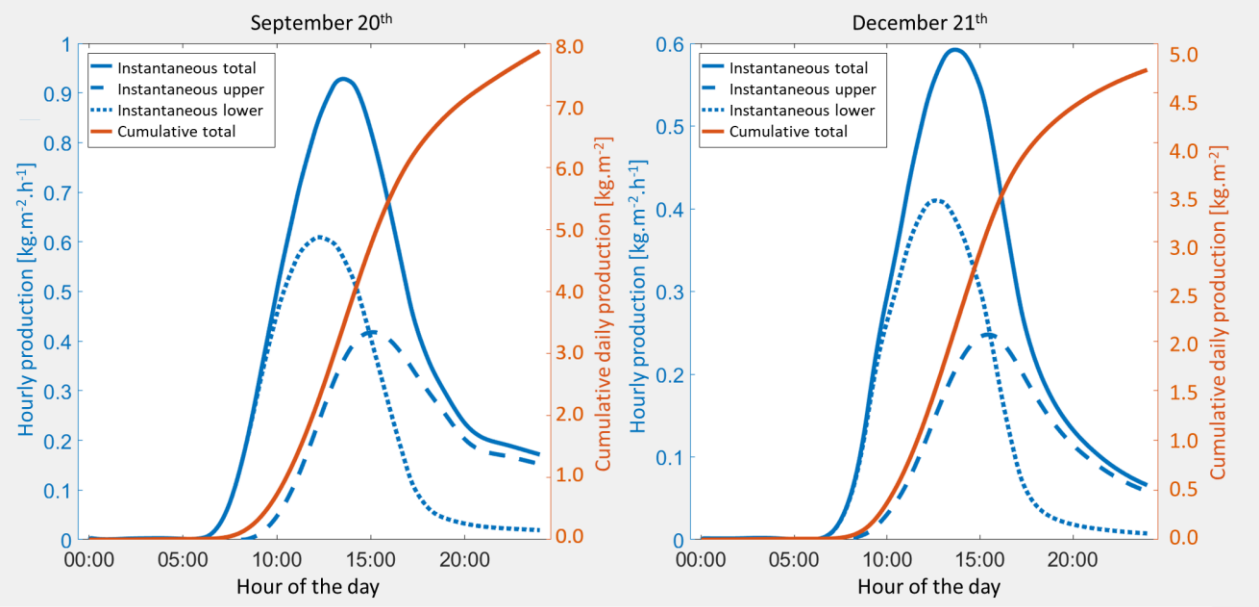

Fig.4: Daily evolution of productivity for the two-stage still

Variations in the conversion efficiency of the two stills were also determined (Figure 5). The conventional single-basin still shows a yearly average value of 49%, while the double-basin counterpart has an average efficiency of 61%. In both cases, the maximum values are observed during the late summer and early fall periods. The peaks observed at the end of June can be explained by abnormally high ambient temperatures for these days, sometimes approaching 50°C. This consequently promotes the heat exchange of the upper basin of the double-basin still with the upper glass cover. This results in a considerable production surplus compared to the standard basin which loses more of this energy to the environment.

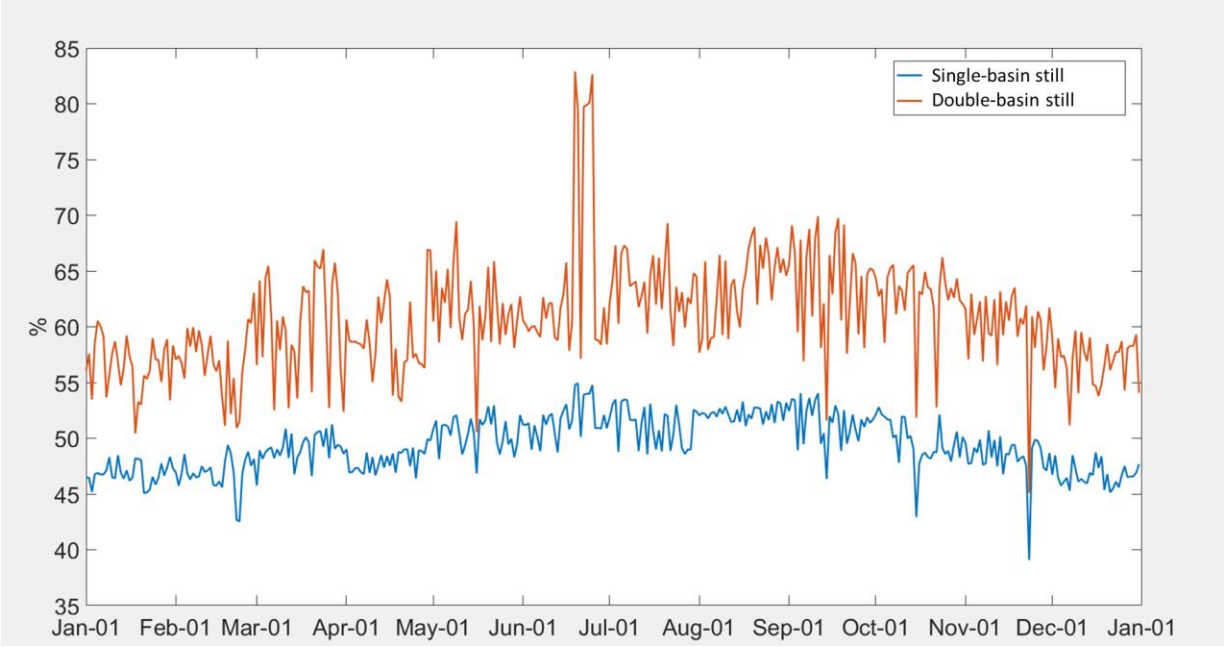

Fig 5: Variations in daily efficiencies during the year: blue – single-basin still; orange – double-basin still.

4.4. Brief parametric study

The graphs presented here concern the conventional basin (Figure 2, left) for a variation in the thickness of the insulation and the depth of the water admitted to the latter. Figure 6 shows the evolution of daily freshwater productivity for the day of September 20 as a function of the thickness of the insulation (left) and the depth of the basin (right). It can be seen that production increases significantly when the insulation thickness is increased by up to 4 cm. Beyond that, the increase continues, but less markedly, and it ends up being negligible when this thickness is greater than 6 cm. This suggests that care must be taken to avoid making the still too expensive with respect to the water production gain. On the left-hand side of Figure 6, when the depth of the water increases in the basin, the daily

production decreases significantly almost linearly. For example, a 33% drop is observed when the depth increases from 2 to 10 cm. It is probably this parameter that explains the predictions lower than the measurements in Table 3 (Raj Kamal et al. 2021) as the authors do not specify this parameter.

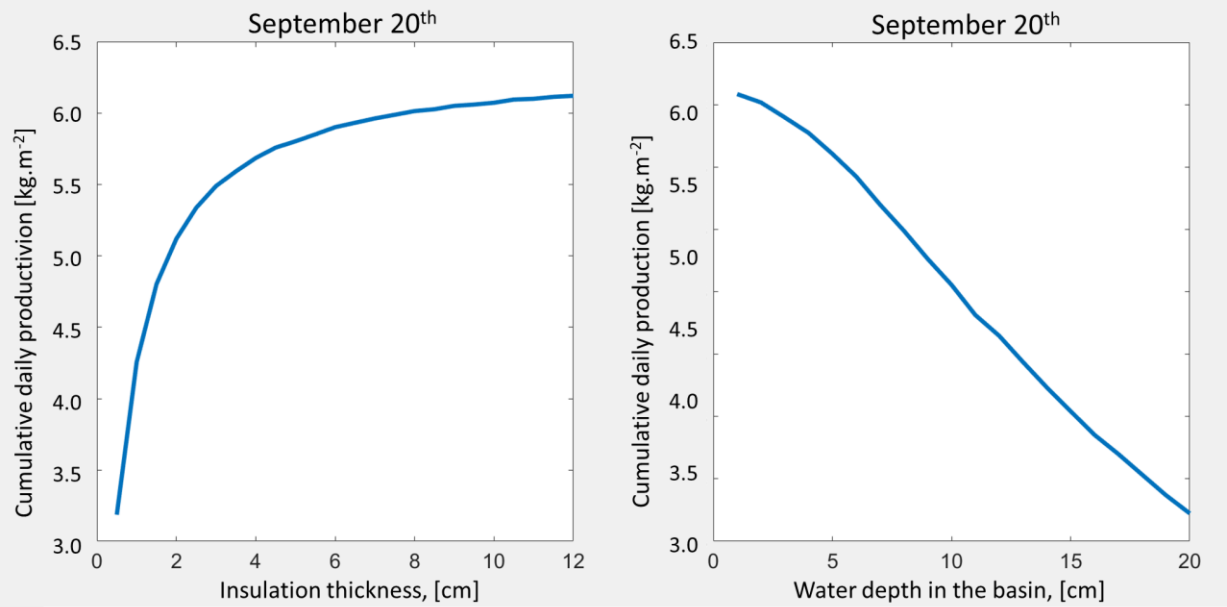

Fig. 1 : Variation in daily production as a function of insulation thickness (left) and water depth (right) in the single-basin still.

4.5. Economic results

The estimated material (glass, absorbing plate, insulation, ply-wood, structure, paint, tank, sealant, pipes, gutters, hardware) and labor costs for the simulated basins are CA$200 for the conventional still and CA$295 for the two-stage still. These benchmark costs were obtained by consulting with suppliers in Montreal, Canada and assuming very low production. Thus, unit costs could decrease with greater production and design optimization, for both types of stills. With an estimated lifespan of 10 years and a residual value of 20% of CAPEX for both types of basins, a specific cost of 21.2 $CA.m^{-3} for the conventional solar basin is obtained compared to 25.5 $CA.m^{-3} for the two-stage solar basin. Table 6 summarizes the results.

Tab 6: Annual economic results for the two simulated stills

Item (for a 1 m^2 still)	Single-basin still	Double-basin still
Annual fixed costs, [$]	35.41	52.3
Annual O&M costs, [$]	5.30	7.80
Annual residual value, [$]	2.28	3.37
Annual water production, [m^3]	1.80	2.22
Specific costs, [$.m^{-3}]	21.20	25.50

To validate the results, an equation-solving package originally proposed with the 4th edition of the classic heat transfer textbook *Fundamentals of Heat and Mass Transfer* (Incropera and Dewitt, 1996) (Interactive Heat Transfer, IHT 4.0) was used. The software has been used to estimate the annual water production based upon the global cumulated average daily radiative energy over a square meter from the EPW database, the yearly average conversion efficiency calculated with the MATALB model for the single-basin still (49%), and the water properties functions embedded within IHT. The annual amount of water calculated is 3.3% lower (1.743 m^3 vs 1.796 m^3) than the above result (Table 6).

5. Discussion

5.1. Technical and economic feasibility

For either solar still model investigated here, this type of approach seems technically viable to provide a solution for producing drinking water for remote communities by the sea. It is suitable for an isolated area, as there is usually no running water distribution system, or even any other option to get water, other than the use of unhealthy and/or remote sources, or the purchase of bottles at high prices. However, the production per m^2 of the two types of solar

basins remains relatively low, and this could represent a significant area when considering meeting the needs of a family. Large open spaces are needed, since in Assab the production of 1795 litres.m^{-2} of surface per year (approximatively 4.91 litres daily on average) by the conventional still unit means that at least 4 m^2 of surface is required to satisfy basic needs and 10 m^2 for intermediate needs of one person (Omarova et al., 2019). This may call for efficiency improvements. The double-basin model was compared with the single-basin model; the average conversion efficiency increased from 49% to 61%. However, the specific cost for each cubic meter of fresh water rose from 21.20 $CA to 25.50 $CA. Therefore, is it worth injecting technologies to improve the yield?

The answer seems to be no. However, to confirm it, we need to consider the premises of this article. The technological and financial resources of the target communities are limited. Furthermore, it is assumed that there is sufficient space to install several collectors close to each other or even per house. While this could be possible in Assab, where the solar resource is abundant, particular care should be taken in extrapolating this study to other locations.

Nevertheless, even if it were possible to increase the conversion efficiency to 100% by technological means, i.e. all available solar energy would be used (without loss) to evaporate the water from the brine and no water loss would occur, the surface area required could not be divided by a factor greater than 2 as the efficiency is very near 50% with the prescribed characteristics of the still.

Consequently, if ground space is available, the simplest solar basin appears to be a robust and resilient solution as a source of drinking water, if only in addition to another main source. It would then free up some of the time spent by people fetching and transporting clean water in many communities, especially by women and children.

6. Conclusion

Given that 97.5% of all water on earth is salty, that freshwater resources are under increasing pressure, that water is becoming increasingly polluted, that the world's population is growing, and that financial disparities are exacerbating, we need to find cheap, resilient, robust, and reliable solutions to produce drinking water for the world's remote and poorest populations. In this context, several areas of the world rely on high-tech solutions such as osmosis (direct or reverse), electrodialysis, nanofiltration, or ion exchange, to produce water for villages and cities. However, these technologies are often too expensive for many remote and poor communities. In this context, the solar still could be considered as a solution for the production of fresh water. But as these low-tech solutions basically have low yields, is it worth trying to improve them with sophisticated technologies?

This study attempted to answer that question. First, it simulates a single-basin still unit and compares its production with that of a double-basin still unit involving the same thermo-mechanical characteristics and properties. The article shows that while the double-basin still unit offers better productivity than the conventional one, it nevertheless involves a higher specific cost due to the increase in its manufacturing cost.

In general, the conversion efficiency ratio of a solar basin remains relatively low (here 49% for the basic single-basin) and the technology therefore requires large areas to fully meet the needs of a community. In addition, it has a high specific cost compared to other technologies. But, the isolation and size of the communities are often obstacles to other options that require significant production to be profitable, making the solar basin a possible solution for isolated communities of small sizes.

7. Acknowledgments

The authors thank Mr. Michel Trottier for his unwavering financial support of the research group's activities and the FRQ-NT and NSERC organizations for the public funding granted to the t3e research group.

8. References

Aboulfotoh, A., et al., 2023, Optimizing solar distillation to meet water demand for small and rural communities, Desalination and Water Treatment, 292, 10-22.

Akhter, M., Habib, G., & Qamar, S. U., 2018. Application of Electrodialysis in Waste Water Treatment and Impact of Fouling on Process Performance. Journal of Membrane Science & Technology, 08(02). https://doi.org/10.4172/2155-9589.1000182

Al-Shayji, K., & Aleisa, E., 2018. Characterizing the fossil fuel impacts in water desalination plants in Kuwait: A Life Cycle Assessment approach. Energy, 158, 681-692.

Arunkumar, T., Raj, K., Dsilva Winfred Rufuss, D., Denkenberger, D., Tingting, G., Xuan, L., & Velraj, R., 2019, A review of efficient high productivity solar stills. Renewable and Sustainable Energy Reviews, 101, 197-220. https://doi.org/10.1016/j.rser.2018.11.013

Bahar, R., Hawlader, M. N. A., & Woei, L. S., 2004, Performance evaluation of a mechanical vapor compression desalination system. Desalination, 166, 123-127. https://doi.org/10.1016/j.desal.2004.06.066

Bell, I. H., Wronski, J., Quoilin, S., & Lemort, V., 2014, Pure and Pseudo-pure Fluid Thermophysical Property Evaluation and the Open-Source Thermophysical Property Library CoolProp. Industrial & Engineering Chemistry Research, 53(6), 2498-2508. https://doi.org/10.1021/ie4033999

Bloemer, J. W., Collins, R. A., & Eibling, J. A., 1961, Study and evaluation of solar seawater stills, OSW Report No.60 PB111934

Chauhan, V. K., Shukla, S. K., Tirkey, J. V., & Singh Rathore, P. K., 2021, A comprehensive review of direct solar desalination techniques and its advancements. Journal of Cleaner Production, 284, 124719. https://doi.org/10.1016/j.jclepro.2020.124719

Darawsheh, I., Islam, Md., & Banat, F., 2019, Experimental characterization of a solar powered MSF desalination process performance. Thermal Science and Engineering Progress, 10, 154-162. https://doi.org/10.1016/j.tsep.2019.01.018

Duffie, J. A., & Beckman, W. A., 2013, Solar Engineering of Thermal Processes. 4th edition, Wiley, 928 p.

Eke, J., Yusuf, A., Giwa, A., & Sodiq, A., 2020, The global status of desalination: An assessment of current desalination technologies, plants and capacity. Desalination, 495 (2020) 114633

El-Sebaii, A. A., Al-Ghamdi, F.S., Al-Hazmi, A. S. Faidah, A. S., 2009, Thermal performance of a single basin solar still with PCM as a storage medium. Applied Energy, 86 7 1187-1195

European Commission., 2019, JRC Photovoltaic Geographical Information System (PVGIS, https://re.jrc.ec.europa.eu/pvg_tools/en/tools.html#PVP

Ghazi Z.M., Rizvi, S.W.F., Shahid, W.M., Abdulhameed, A.M., Saleem, H., Zaida, S.J., 2022, An overview of water desalination systems integrated with renewable energy sources, Desalination, 542 116063

Guimard, L., 2019, Étude du comportement et modélisation d'une installation de dessalement d'eau de mer par distillation soumise à des régimes transitoires [Université de Lyon]. https://tel.archives-ouvertes.fr/tel-02091474/document

He, W., et al., 2024, Flexible batch electrodialysis for low-cost solar-powered brackish water desalination, Nature Water volume, 2, 370–379.

HELIOCLIM-3 ARCHIVES *DEMO*., 2006, SoDa - Solar radiation Data. http://www.soda-pro.com/web-services/radiation/helioclim-3-archives-for-free

Howard, G., Bartram, J., Williams, A., Overbo, A., Fuente, D., & Geere, J.-A., 2020, Domestic water quantity, service level and health (p. 76, World Health Organization. https://www.globalwaters.org/sites/default/files/domestic_water_quantity.pdf

Janajreh, I., Zhang, H., El Kadi, K., Ghaffour, N., 2023, Freeze desalination: Current research development and future prospects, Water Research 229 119389

Jones, E., Qadir, M., van Vliet, M.T.H., Smakhtin, V., Kang, S., 2019 The state of desalination and brine production: A global outlook. Science of The Total Environment, 657 (2019) 1343-1356.

Kadi, K. E., Janajreh, I., 2017, Desalination by Freeze Crystallization : An Overview. Environmental Engineering, 8.

Kim, J., Park, K, Yang, D.R., Hong, S., 2019, A comprehensive review of energy consumption of seawater reverse osmosis desalination plants. Applied Energy, 16.

Lara, Jorge R., 2005, An advanced vapor-compression desalination system, Ph.D. thesis, Texas A&M University

Lawrie, L. K., & Crawley, D. B., 2019, Development of Global Typical Meteorological Years (TMYx, http://climate.onebuilding.org/default.html

Lawson, K. W., & Lloyd, D. R., 1997, Membrane distillation. Journal of Membrane Science, 124(1), 1-25. https://doi.org/10.1016/S0376-7388(96)00236-0

Li, Y. and 6 other authors, 2023, Desalination by membrane pervaporation: A review, Desalination, 547 116223

Liponi, A., Wieland, C., & Baccioli, 2020, A. Multi-effect distillation plants for small-scale seawater desalination : Thermodynamic and economic improvement. Energy Conversion and Management 205 112337

Malik, M.A.S., Tiwari, G.N., Kumar, A. and Sodha, M.S., 1982, Solar Distillation: A Practical Study of a Wide

Range of Stills and Their Optimum Design, Construction and Performance. Pergamon Press, Oxford.

Mandri. Y., 2011, Étude paramétrique du procédé de dessalement de l'eau de mer par congélation sur paroi froide [Université Claude Bernard - Lyon I]. https://tel.archives-ouvertes.fr/tel-00831277/document

McCutcheon, J., Xia, L., Bui, N.-N., 2019, Forward Osmosis. In J. Kucera (Éd.), Desalination (p. 209-243, John Wiley & Sons, Inc. https://doi.org/10.1002/9781119407874.ch5

Nannarone, A., Toro, C., Sciubba, E., 2017, Multi-Stage Flash Desalination Process : Modeling and Simulation. SAN DIEGO, 13.

Omarova, A., Tussupova, K., Hjorth, P., Kalishev, M., & Dosmagambetova, R., 2019, Water supply challenges in rural areas: a case study from Central Kazakhstan. International journal of environmental research and public health, 16(5), 688.

Panchal, H., Mohan. I., 2017, Various methods applied to solar still for enhancement of distillate output, Desalination, 415 76-89.

Qasim, M., Darwish, N.A., Sarp, S., Hilal, N., 2015, Water desalination by forward (direct) osmosis phenomenon: A comprehensive review, Desalination 374 47-69.

Raj Kamal, M. D., Parandhaman, B., Madhu, B., Magesh Babu, D., Sathyamurthy, R., 2021, Experimental analysis on single and double basin single slope solar still with energy storage material and external heater. Materials Today: Proceedings, S2214785320401610

RNCan, 2022, RETScreen Expert (8.1.0.44) [Computer software]. Ressources Naturelles Canada.

Saadat, A. H. M., Islam, M. S., Islam, M. S., Parvin, F., & Sultana, A., 2018, Desalination Technologies for Developing Countries: A Review. Journal of Scientifc Researh, 10 (1) DOI:10.3329/jsr.v10i1.33179.

Sedighi, M., Mahdi Behvand Usefi, M. Fauzi Ismail, A., Mostafa G. 2023. Environmental sustainability and ions removal through electrodialysis desalination: Operating conditions and process parameters, Desalination 549 (2023) 116319

Shafagnat, A.H., Eslami, M. Baneshi, M., (2023) Techno-enviro-economic study of a reverse osmosis desalination system equipped with photovoltaic-thermal collectors, ATE 218(2023) 119289

Shampine, L. F., Reichelt, M. W., 1997, The MATLAB ODE Suite. SIAM Journal on Scientific Computing, 18(1), 1-22. https://doi.org/10.1137/S1064827594276424

Ray, S.S., Verma, R.K., Singh, A., Ganesaoillais, M., Kwon, Y.N., 2023, A holistic review on how artificial intelligence has redefined water treatment and seawater desalination processes, Desalination, 547 (2023) 116221.

Subban, C. V. Gadgil, A.J., 2019, Electrically regenerated ion-exchange technology for desalination of low-salinity water sources. Desalination 465 (2019) 38-43.

UN, World Water Development Report., 2020, World Water Development Report (UN WWDR 2020): Water and Climate Change https://www.unwater.org/publications/world-water-development-report-2020/

Velmurugan, V., Srithar, K., 2011, Performance analysis of solar stills based on various factors affecting the productivity—A review, RSER 15 1294-1304

WHO, World Health Organization., 2017, Guidelines for drinking-water quality. https://www.who.int/publications/i/item/9789241549950

WHO, World Health Organization., 2019) GHO | By category | Burden of disease—SDG 3.9.2—Mortality rate attributed to unsafe water, unsafe sanitation and lack of hygiene (exposure to unsafe Water, Sanitation and Hygiene for All (WASH), WHO; World Health Organization. Updated 2022-11-07 https://apps.who.int/gho/data/node.main.INADEQUATEWSH?lang=en

Yadav, D., Karki, S., Ingole, P. G., 2022) Current advances and opportunities in the development of nanofiltration (NF) membranes in the area of wastewater treatment, water desalination, biotechnological and pharmaceutical applications, Journal of Environmental Chemical Engineering, 10 (2022) 108109

Wafi, M. K., Hussain, N., El-Sharief Abdalla, O., Al-Far, M. D., Al-Hajaj, N. A., & Alzonnikah, K. F. 2019. Nanofiltration as a cost-saving desalination process. SN Applied Sciences, 1(7), 751. https://doi.org/10.1007/s42452-019-0775-y

Wang, Z., Tain, S., Niu J., Kong, W., Lin, J., Hao, X., Guian, G., 2020) An electrochemically switched ion exchange process with self-electrical-energy recuperation for desalination, Separation and Purification Technology 239 116521.

Enhancement of a photovoltaic drinking water pumping system design software tool

Patrick Turcotte, Daniel R. Rousse and Misagh Irandoostshahrestani

École de Technologie Supérieure, Montréal (Canada)

Abstract

Easy access to safe, drinkable water is an essential requirement for societal growth and betterment. With the human population increasing and current climate changes, this key resource is becoming increasingly difficult to access in many locations across the globe, especially in areas without an electrical power grid. Solar-powered pumps are a good tool to help address this problem in many cases; however, taking into account all the parameters (water consumption, total dynamic head, local irradiance, etc.) to reach the cheapest design that satisfies requirements can be challenging. *pvpumpingsystem* is an open-source tool to assist in the design process and the determination of the model, number, and arrangement of photovoltaic panels, pump model, and reservoir capacity. This tool was recently enhanced to accommodate more detailed water consumption profiles and more realistic MPPT (Maximum Power Point Tracking) behaviour; the impacts of these new features on simulation results are the focus of the study described herein. The new consumption profiles have a significant impact (up to +/- 40% change to the load loss probability). The simulations also showed that using an MPPT with the perturb & observe algorithm, widely available in commercial devices, increases water output by as much as 6.7%. However, the detailed MPPT model did not affect results significantly compared to a generic 94% MPPT efficiency coefficient.

Keywords: software enhancement, photovoltaic, MPPT, pumping, drinking water.

1. Introduction

Easy access to clean water, safe for human consumption and basic sanitation needs, is an essential requirement for human comfort, growth, and betterment. WHO data for 2021 indicates that 771 million people don't have access to safe water sources within a 15-minute walking radius (WHO, 2021), and with the human population growing and current climate changes, this key resource is becoming increasingly scarce and difficult to access in many locations across the globe (Urama and Ozor, 2010), compounding health issues tied to contaminated water consumption (IHME, 2019) and an increased workload, often on women and girls (Boone et al., 2011). Pumping water from aquifers is, in many cases, a good solution to help address this problem; however, manual pumping seldom provides sufficient quantities and limits the depth at which water can be retrieved (Ghoneim, 2006). The common solution is to use pumps powered by fossil fuel engines (Quansah et al., 2016), but the recurrent and increasing costs of fuel, dependency on a steady fuel supply, and environmental impacts render this approach less than ideal. Electric pumps powered by photovoltaic solar panels address all those issues, and since pumped water can be stored in simple reservoirs, the intermittent nature of that form of renewable energy is easily addressed. Many studies demonstrate that, despite higher upfront costs, a solar-powered solution is significantly less expensive in the long term in many locations (Xie et al., 2021). A basic diagram of such a system is illustrated in Fig. 1.

However, designing such a system so that it adequately addresses the needs of the target community while taking into account all the parameters (total dynamic head, local irradiance, etc.) and keeping it as affordable as possible is not a simple problem. To help with this task, a bespoke software tool was developed to iterate through various solutions and assist in the selection of the best-suited option: *pvpumpingsystem* is an open-source and (to the best of our knowledge) unique software package written in the Python language by Tanguy Lunel and Sergio Gualteros (Gualteros and Rousse, 2021). Its initial version offered limited options for water consumption profiles and made use of a highly simplified maximum power point tracking system (MPPT)

© 2024. The Authors. Published by International Solar Energy Society
Selection and/or peer review under responsibility of Scientific Committee
10.18086/eurosun.2024.09.10 Available at http://proceedings.ises.org

implementation; the objectives of this project are to add support for detailed water consumption profiles and for an accurate MPPT model, and then study the impact of those changes on the results obtained.

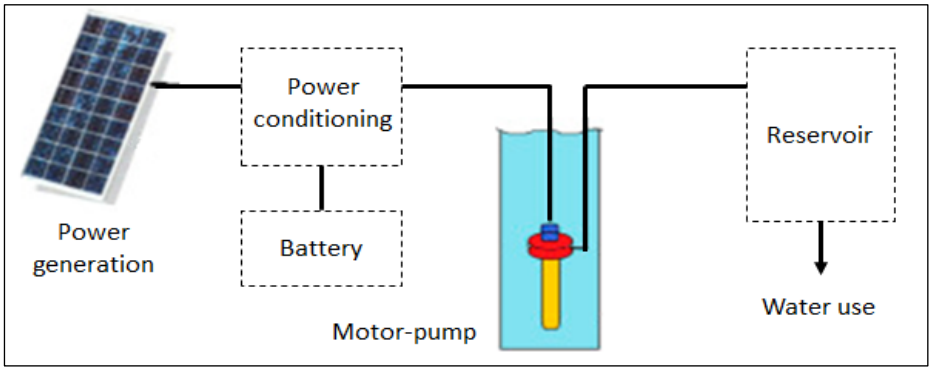

Fig. 1: Basic diagram of a photovoltaic pumping system (Lunel, 2020)

2. Methodology and implementation

In most articles studied in the literature, a community's basic water needs vary greatly according to the time of year (+/- 10% to 30% of the average daily demand for the year) (Andey and Kelkar, 2009). This is mostly due to seasonal changes (dry vs. rainy season, warm vs. cooler season), which impact both the availability of surface water and the daily quantity required. Therefore, a water consumption model that relies on a constant daily value throughout the year is missing a key factor. To address this, two consumption models were added: the first allows the selection of a community's daily water requirements for each month of a year, and the second allows the selection of a community's daily water requirements for each day of a year. Combined with *pvpumpingsystem*'s already-existing feature which allows the selection of hourly water requirements for each hour of a day, this provides a flexible way of inputting the target community's water consumption, leading to a more realistic simulation. This was directly implemented in the software package through an expansion of the existing functions.

Three water consumption profiles were used in simulations for comparison:

- Scenario 1: constant 120 $L.h^{-1}$ (2880 $L.d^{-1}$) water consumption throughout the year, suitable for a population of about 25 to 100 people (Gleick, 1996) (WHO, 2003) (Singh and Turkiya, 2013). This is the reference/control scenario.
- Scenario 2: constant daily water consumption of 2880 $L.d^{-1}$ throughout the year with a variable hourly consumption (nil during nighttime, peaks around 8h00, 12h00, and 18h00), as illustrated in Fig. 2. This is the first new scenario, making use of the new features in *pvpumpingsystem*, reflecting variations throughout the day but neglecting seasonal factors.
- Scenario 3: constant daily water consumption for each month (higher from April to July, lower from October to February), illustrated in Fig. 3, with a variable hourly consumption (nil during nighttime, peaks around 8h00, 12h00, and 18h00), illustrated in Fig. 4. This is the second new scenario, making use of the new features in *pvpumpingsystem*, reflecting variations throughout the day and possible seasonal factors, and the one closest to what a real-world consumption profile could be.

All three scenarios amount to the same water consumption for the whole year, namely 1,051,200 litres.

Those scenarios were combined with PVGIS meteorological data for the year 2005 for five locations: near Tunis (Tunisia, 36°N 10°E), Aswan (Egypt, 24°N 33°E), Nairobi (Kenya, 1°S 36°E), Lima (Peru, 12°S 77°W), and Madrid (Spain, 40°N 3°W). It should be noted that the monthly water consumption profiles used in all scenarios are generic examples and do not reflect actual local needs. Identical system configurations were used for all locations, namely:

- 5 Canadian Solar CS5C 80M solar panels in a serial arrangement;
- Simulated basic MPPT with 96% efficiency;
- Sun Pumps SCB-10-150-120 BL (Kou modelisation) (Kou et al., 1998) pump/motor assembly;
- Plastic piping (100m length, 0.05m diameter);

- 20m total dynamic head.

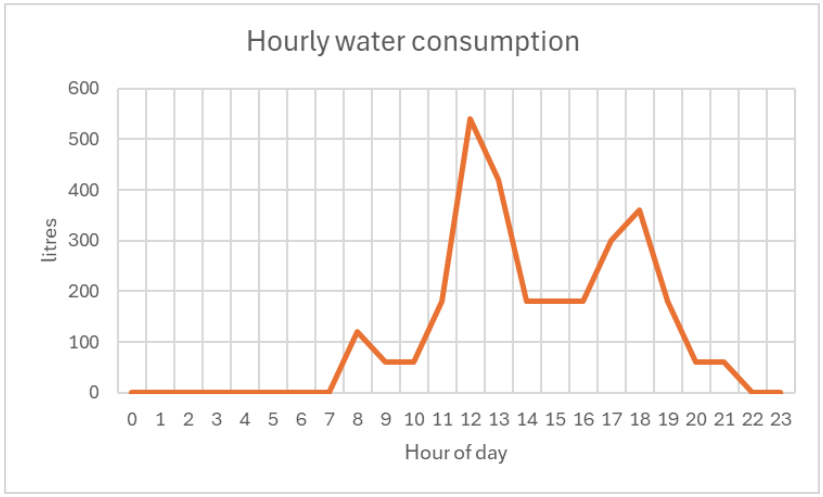

Fig. 2: Hourly water consumption for each hour of the day for Scenario 2

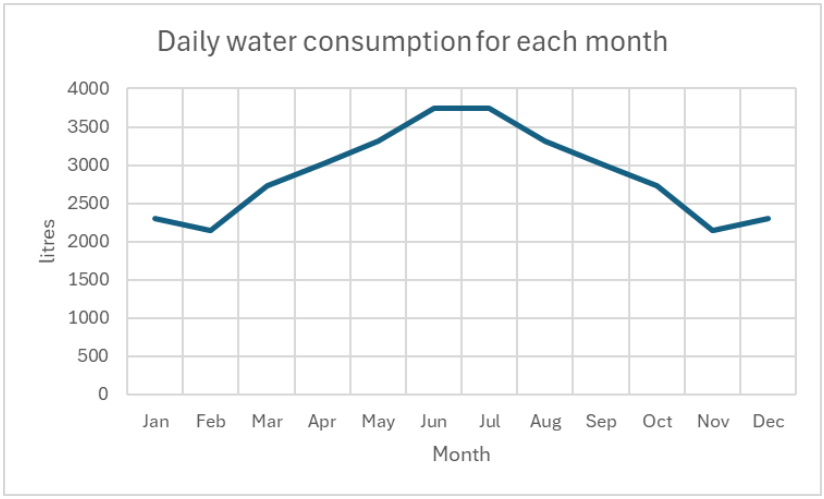

Fig. 3: Daily water consumption for each month of the year for Scenario 3

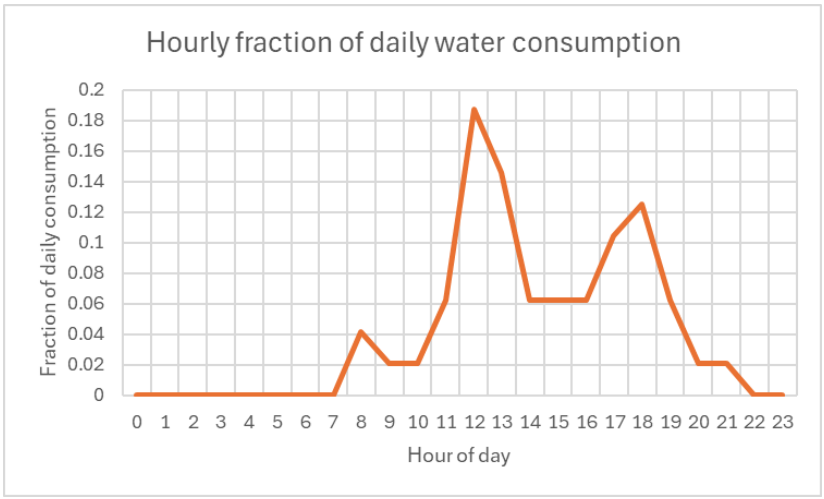

Fig. 4: Fraction of the daily water consumption for each hour of the day for Scenario 3

Solar panel azimuth was due south for the northern hemisphere and due north for the southern hemisphere; tilt was equivalent to the local latitude, although the best slope is usually slightly higher for most latitudes (Memme and Fossa, 2022).

MPPT systems are often combined with solar panels to maximize their power output (Elgendy et al., 2008), therefore increasing the quantity of water pumped (Oi et al., 2009) (Allouhi et al., 2019). This is achieved by dynamically adjusting the load presented to a panel's electrical outputs so that it produces the maximum power available under the current operating conditions. This specific optimal load is susceptible to change based on environmental conditions like solar irradiance (intensity and distribution on the panels) and panel temperature (Podder et al., 2019). Therefore, most MPPTs dynamically seek the maximum power point (MPP) through various algorithms (Subudhi and Pradhan, 2012). The most popular of these in commercial implementations are perturb & observe (P&O) and incremental conductance (IC) (Podder et al., 2019), because of their simplicity and acceptable performance under most conditions.

The basic MPPT model in *pvpumpingsystem* was implemented by taking the maximum theoretical available power supplied by the solar panels under current irradiance and temperature conditions and applying an efficiency factor (usually between 94% and 96%) to determine the power available at the motor. To achieve a more faithful simulation, the following elements were added:

- A control circuit using a basic perturb-and-observe (P&O) algorithm (Elgendy et al., 2011), with a customizable duty cycle step size (default value 0.01) and execution frequency (default value 100Hz); and
- A detailed buck-boost DC-DC conversion circuit (Amri and Ashari, 2015) model operating at a 1kHz switching frequency, using linear extrapolation of the various components sampled at 100kHz.

The P&O algorithm modifies the duty cycle of the buck-boost circuit by a step value at each iteration and compares the current power output of the solar panels to the power output of the previous iteration. If the power output increased, it is assumed that the change brought the solar panels closer to their MPP, and the same step change is applied to the duty cycle at the next iteration. If the power output decreased, it is assumed that the change brought the solar panels further from their MPP, and the sign of the step change is flipped (multiplied by -1) before applying it to the duty cycle at the next iteration. The algorithm's flowchart is illustrated in Fig. 5.

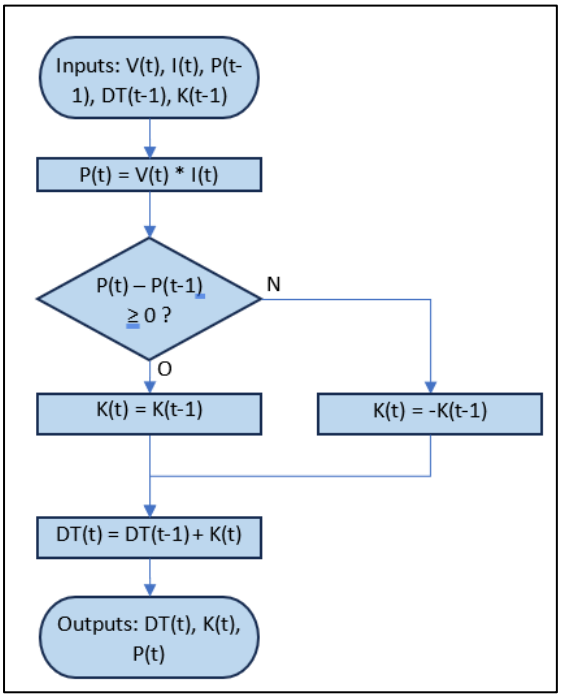

Fig. 5: The Perturb & Observe MPPT algorithm

In this flowchart, V is the voltage at the solar panels' output, I is the current at the solar panels' output, DT is the duty cycle of the buck-boost conversion circuit, K is the step change of the duty cycle, t is the algorithm's current execution cycle, and t-1 is the algorithm's previous execution cycle.

The main advantages of the P&O algorithm are its simplicity and speed of execution (Ahmad et al., 2019). However, since it is always "chasing" the MPP, it tends to induce harmonics in the power supply that can be detrimental to the load's behaviour (Elgendy et al., 2009). Furthermore, it is vulnerable to "false MPPs", i.e. a

local maximum that is not the true maximum of the power curve (Tsang and Chan, 2015). Nevertheless, because of the simplicity of the setup and in the context of this study, it was deemed an adequate choice, especially since it is widely used in commercial products.

The buck-boost conversion circuit, illustrated in Fig. 6, was modeled through nodal and loop analysis of its components in both its operational states (closed transistor and open transistor, as illustrated in Fig. 7), which lead to the following equations:

Closed transistor:

$$I_L(t) = I_L(0) + \frac{dI_L}{dt} * \Delta t \quad \text{(eq. 1)}$$

$$V_C(t) = V_C(0) + \frac{dV_C}{dt} * \Delta t \quad \text{(eq. 2)}$$

$$V_R(t) = \frac{V_C(t)}{R_C+R} + V_C(t) \quad \text{(eq. 3)}$$

Open transistor:

$$I_L(t) = I_L(0) + \frac{dI_L}{dt} * \Delta t \quad \text{(eq. 4)}$$

$$V_C(t) = V_C(0) + \frac{dV_C}{dt} * \Delta t \quad \text{(eq. 5)}$$

$$V_R(t) = V_C(t) + \left(R_C * C * \frac{dV_C}{dt}\right) \quad \text{(eq. 6)}$$

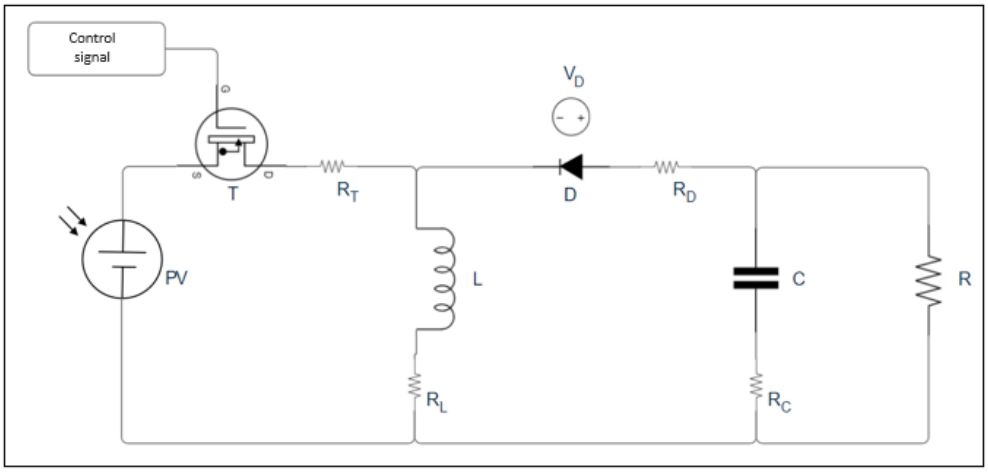

Fig. 6: The buck-boost circuit diagram

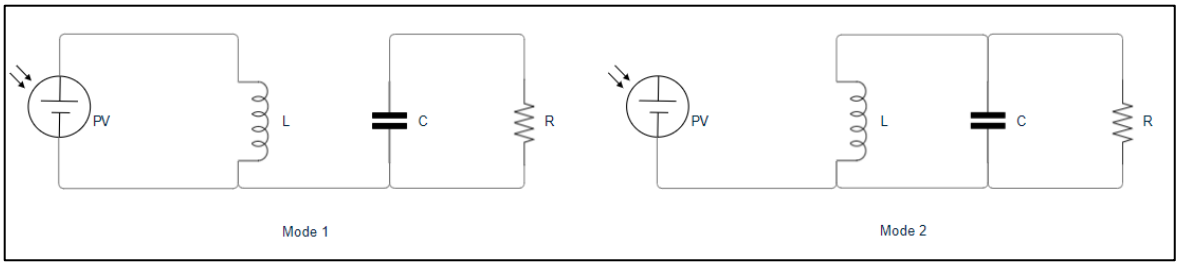

Fig. 7: The buck-boost circuit diagram in closed transistor mode (1) and open transistor mode (2)

The behaviour of the simulated buck-boost circuit was successfully compared to the results of an identical simulation in MATLAB/SIMULINK to verify its accuracy.

This detailed MPPT model was added to *pvpumpingsystem* through an expansion of the existing MPPT module. To determine its impacts, three scenarios were combined with PVGIS meteorological data for the year

2005 for the five locations previously selected (Tunis, Aswan, Nairobi, Lima and Madrid):

- Scenario 4: no MPPT.
- Scenario 5: simplified basic MPPT with a 96% efficiency.
- Scenario 6: detailed MPPT with P&O algorithm and simulated buck-boost circuit, making use of the new features added to *pvpumpingsystem*.

3. Results and discussion

Tab. 1 presents the Load Losses Probability (LLP, here equivalent to the Water Shortage Probability, i.e., the fraction of the year during which a water shortage is experienced) for each scenario for the five locations:

Tab. 1: Load Losses Probability/Water Shortage Probability, for three different types of water consumption profiles.

Location	Scenario 1 (Constant consumption)	Scenario 2 (Constant monthly, variable hourly)	Scenario 3 (Variable monthly, variable hourly)
Tunis	0.0958	0.0578	0.0397
Aswan	0.0031	0.0010	0.0001
Nairobi	0.0816	0.0473	0.0611
Lima	0.2523	0.2067	0.2326
Madrid	0.1280	0.0930	0.0729

The use of hourly consumption profiles significantly impacts the LLP, lowering it by 20% to 66%. This is because the daily profile used heavily skews the water consumption towards daytime, when the solar resource is available to power the pump. The addition of monthly consumption profiles, which skews the water consumption towards the April to July period, has a significant impact as well, but this impact can be positive (lower LLP) or negative (higher LLP). This negative impact is explained by a combination of geographical mismatch (in the southern hemisphere, the solar resource is lower in the April-July period, while the consumption profile used demands more water during those months) and local meteorological characteristics. However, since the monthly consumption profile used is generic and does not reflect actual local data, these values are purely illustrative of the possible impact of the use of such scenarios and do not indicate real-world performance.

For the MPPT simulation, Tab. 2 presents the total water pumped for the year (in litres) for each scenario for the five locations:

Tab. 2: Total yearly water production, [litre], for the cases of no MPPT, a basic MPPT and a detailed MMPT.

Location	Scenario 4 (No MPPT), [litre]	Scenario 5 (Basic MPPT), [litre]	Scenario 6 (Detailed MPPT), [litre]
Tunis	2,488,034	2,645,250	351,514
Aswan	3,384,703	3,611,701	611,402
Nairobi	2,708,110	2,869,420	463,955
Lima	1,969,246	2,088,440	304,650
Madrid	2,560,211	2,736,773	424,482

As expected, using the basic MPPT model increases significantly the volume of water pumped in a year, since more power is extracted from the solar resource. However, the detailed MPPT model led to dramatically reduced values; this is explained by a flaw in the initial design. Buck-boost converters leave the power source in an open circuit during their complementary duty cycle period (open transistor), which leads to a very significant loss in average available power and total energy available to the pump's motor when solar panels are used, and therefore in total pumped water.

Furthermore, it was observed that the execution time of the various simulations differed greatly according to the scenario; running on a standard Intel Core i5-8365U processor with 16 GB RAM, the Scenario 4

simulations took on average 10 seconds, the Scenario 5 took on average 2 seconds, and the Scenario 6 more than 2 hours, after code optimisations. This is explained by the very high number of iterations required by the conversion circuit simulation (1,000,000 iterations per simulated second) to produce accurate results.

4. Conclusions

As stated in the introduction, the objectives of this project were to add support for detailed water consumption profiles and for an accurate MPPT model, and then study the impact of those changes on the results obtained from the *pvpumpingsystem* software. The results clearly indicate that the use of more detailed water consumption profiles has significant impacts on the results provided by *pvpumpingsystem*. Of course, this means that data needs to be collected for the targeted community, ideally at least over a year; the more precise the data, the more accurate the results. It should also be taken into account that increased accessibility to water usually leads to an increase in consumption.

As for the detailed MPPT model, the flaw in the original design renders it unusable as is for *pvpumpingsystem* simulations. Nevertheless, further simulations and extrapolations have indicated that for simple solar panel configurations and normal operational conditions, the basic MPPT model with a 94% efficiency provides power outputs that match detailed simulations sufficiently well to supply reliable results. Since execution time is much shorter compared to the detailed MPPT model, it makes the basic MPPT model a better option for simulations. A different power conversion circuit topology (Ćuk, for example) could be simulated to verify this extrapolation, and could be the subject of a subsequent project.

5. References

Ahmad et al., 2019: Ahmad, R., Murtaza, A. F., & Sher, H. A. (2019). Power tracking techniques for efficient operation of photovoltaic array in solar applications–A review. Renewable and Sustainable Energy Reviews, 101, 82-102.

Allouhi et al., 2019: Allouhi, A., Buker, M. S., El-Houari, H., Boharb, A., Amine, M. B., Kousksou, T., & Jamil, A. (2019). PV water pumping systems for domestic uses in remote areas: Sizing process, simulation and economic evaluation. Renewable Energy, 132, 798-812.

Amri and Ashari, 2015: Amri, B., & Ashari, M. (2015). The comparative study of Buck-boost, Cuk, Sepic and Zeta converters for maximum power point tracking photovoltaic using P&O method. *2015 2nd International Conference on Information Technology, Computer, and Electrical Engineering (ICITACEE)* (pp. 327-332), Semarang, 16-18 October 2015. IEEE.

Andey and Kelkar, 2009: Andey, S. P., & Kelkar, P. S. (2009). Influence of intermittent and continuous modes of water supply on domestic water consumption. Water Resources Management, 23(12), 2555-2566.

Boone et al., 2011: Boone, C., Glick, P., & Sahn, D. E. (2011). Household water supply choice and time allocated to water collection: Evidence from Madagascar. Journal of Development Studies, 47(12), 1826-1850.

Elgendy et al., 2008: Elgendy, M. A., Zahawi, B., & Atkinson, D. J. (2008). Analysis of the performance of DC photovoltaic pumping systems with maximum power point tracking. *4th IET International Conference on Power Electronics, Machines and Drives (PEMD 2008)* (pp. 426-430), York, 2-4 April 2008. IET.

Elgendy et al., 2009: Elgendy, M. A., Zahawi, B., Atkinson, D. J., & Giaouris, D. (2009). Dynamic behaviour of DC motor-based photovoltaic pumping systems under searching MPPT algorithms. *2009 International Conference on Power Engineering, Energy and Electrical Drives* (pp. 413-418), Lisbon, 18-20 March 2009. IEEE.

Ghoneim, 2006: Ghoneim, A. A. (2006). Design optimization of photovoltaic powered water pumping systems. Energy conversion and management, 47(11-12), 1449-1463.

Gleick, 1996: Gleick, P. H. (1996). Basic water requirements for human activities: Meeting basic needs. Water international, 21(2), 83-92.

Gualteros and Rousse, 2021: Gualteros, S., & Rousse, D. R. (2021). Solar water pumping systems: A tool to

assist in sizing and optimization. Solar Energy, 225, 382-398.

IHME, 2019: IHME (2019). Global burden of disease 2019. https://vizhub.healthdata.org/gbd-results/ (last retrieved 2024-08-12)

Kou et al., 1998: Kou, Q., Klein, S. A., & Beckman, W. A. (1998). A method for estimating the long-term performance of direct-coupled PV pumping systems. Solar Energy, 64(1-3), 33-40.

Lunel, 2020: Lunel, T. (2020). A flexible, genuine software for the simulation and sizing of photovoltaic pumping systems. Master thesis, École de Technologie Supérieure.

Memme and Fossa, 2022: Memme, S., & Fossa, M. (2022). Maximum energy yield of PV surfaces in France and Italy from climate based equations for optimum tilt at different azimuth angles. Renewable Energy, 200, 845-866.

Motahhir et al., 2020: Motahhir, S., El Hammoumi, A., & El Ghzizal, A. (2020). The most used MPPT algorithms: Review and the suitable low-cost embedded board for each algorithm. Journal of cleaner production, 246, 118983.

Oi et al., 2009: Oi, A., Anwari, M., & Taufik, M. (2009). Modeling and simulation of photovoltaic water pumping system. *2009 Third Asia International Conference on Modelling & Simulation* (pp. 497-502), Bundang, 25-29 May 2009. IEEE.

Podder et al., 2019: Podder, A. K., Roy, N. K., & Pota, H. R. (2019). MPPT methods for solar PV systems: a critical review based on tracking nature. IET Renewable Power Generation, 13(10), 1615-1632.

Quansah et al., 2016: Quansah, D. A., Adaramola, M. S., & Mensah, L. D. (2016). Solar photovoltaics in sub-Saharan Africa–addressing barriers, unlocking potential. Energy Procedia, 106, 97-110.

Singh and Turkiya, 2013: Singh, O., & Turkiya, S. (2013). A survey of household domestic water consumption patterns in rural semi-arid village, India. GeoJournal, 78(5), 777-790.

Subudhi and Pradhan, 2012: Subudhi, B., & Pradhan, R. (2012). A comparative study on maximum power point tracking techniques for photovoltaic power systems. IEEE transactions on Sustainable Energy, 4(1), 89-98.

Tsang and Chan, 2015: Tsang, K. M., & Chan, W. L. (2015). Maximum power point tracking for PV systems under partial shading conditions using current sweeping. Energy conversion and management, 93, 249-258.

Urama and Ozor, 2010: Urama, K. C., & Ozor, N. (2010). Impacts of climate change on water resources in Africa: the role of adaptation. African Technology Policy Studies Network, 29(1), 1-29.

WHO, 2003: World Health Organization (WHO), The right to water (2003). https://www2.ohchr.org/english/issues/water/docs/Right_to_Water.pdf (last retrieved 2024-08-12)

WHO, 2021: World Health Organization (2021). Progress on household drinking water, sanitation and hygiene 2000-2020: five years into the SDGs. https://www.who.int/publications/i/item/9789240030848 (last retrieved 2024-08-12)

Xie et al., 2021: Xie, H., Ringler, C., & Mondal, M. A. H. (2021). Solar or diesel: a comparison of costs for groundwater-fed irrigation in sub-Saharan Africa under two energy solutions. Earth's Future, 9(4), e2020EF001611.

10. Solar Resources and Energy Meteorology

Study of intra-hour direct normal irradiance variability effects on hourly WRF-Chem outputs

Daniel Perez-Astudillo[1], Dunia Bachour[1] and Christos Fountoukis[1]

[1] Qatar Environment and Energy Research Institute, HBKU, Doha (Qatar)

Abstract

Reliable and accurate solar resource information can be obtained, ideally, through direct ground measurements of the incoming solar irradiance; however, greater temporal and spatial coverages require most of the time some sort of modelling, commonly by directly deriving irradiance from satellite imaging or through physical, empirical, or numerical models. Operationally running the Weather Research and Forecasting (WRF) model provides the current values of irradiance as well as forecasts up to a few days ahead, and great efforts are being made to reduce the relatively high uncertainties from these models. While NWP models can provide forecasts at hourly intervals, which is relatively high for some applications, for solar radiation applications this temporal resolution cannot correctly capture the intra-hour variability and can be a source of errors especially during changing atmospheric conditions, in which hourly averages do not necessarily reflect representative enough conditions, particularly in the case of direct (or beam) normal irradiance, which is especially sensitive to clouds and aerosols. A study is presented here on the effects of intra-hour (within the hour) variability of beam radiation for cloud- and aerosol-variable conditions, in the use of hourly values in the advanced WRF-Chem model to predict beam irradiances in desert conditions.

Keywords: WRF-Chem, direct normal irradiance, solar irradiance variability

1. Introduction

Numerical weather prediction (NWP) models are useful tools not only for "traditional" meteorological applications, but also, increasingly, for solar resource applications. The NWP outputs, either as forecasts or modelling of cloudiness, directly impact the modelled solar radiation at ground level, and NWPs are also able to model and forecast solar irradiance, although usually with high uncertainties. The inclusion of better aerosol and aerosol transport treatment, for instance in the WRF-Chem model, in which recent advances have explored improvements in the modelling of global horizontal irradiance (G) and beam or direct normal irradiance (Gb), the latter a more challenging component of solar radiation given its high sensitivity to not only clouds but also (even in clear-sky, or cloudless, conditions) aerosols.

Apart from aerosol treatment, an additional source of uncertainty in the modelling is the temporal variability of solar radiation. Meteorological parameters such as air temperature, barometric pressure and relative humidity are typically not highly variable over short periods of time, and modelling at hourly resolutions is sufficient in most cases; accordingly, NWP outputs are obtained at hourly resolutions. Solar radiation, on the other hand, can vary even within few seconds, especially in cloudy conditions, and changes are even larger in Gb, for which even a small passing cloud reduces Gb to zero during the time the sun is behind the cloud; similarly, varying aerosols have a large effect on Gb. High-resolution ground Gb measurements are commonly collected as 1-minute averages of higher-frequency samples, and as such are able to capture a more realistic picture of Gb; when these are averaged over one hour and compared to hourly averages from the WRF model, the latter have the disadvantage of missing those details. In this work, we present a study of the effect, on WRF-Chem model (Fast et al, 2005) results, of the variability of Gb within hourly intervals in a mostly cloudless location, but with high and variable aerosol loads (mainly due to airborne desert dust); cloudy and cloudless skies are included in order to try to identify the effects of aerosols. The hourly averages of ground-measured Gb are compared to the corresponding outputs from the WRF-Chem model as a function of the variability of the ground-measured 1-minute Gb values within the hour.

© 2024. The Authors. Published by International Solar Energy Society
Selection and/or peer review under responsibility of Scientific Committee
10.18086/eurosun.2024.10.01 Available at http://proceedings.ises.org

2. Methodology

The site of this study is Doha, Qatar (25° N, 51° E), namely a desert location, in which clear skies are the common conditions, but with periods of cloudiness and rain during winter and occasionally scattered throughout the year. Airborne desert sand is, however, present throughout the year, with frequent sandstorms especially around summer months, when temperature and humidity also increase.

Direct normal irradiance is measured at this site with a high-quality monitoring station equipped with a Kipp and Zonen CHP-1 pyrheliometer mounted on a sun tracker, which also hosts two pyranometers measuring global horizontal and (with a shading assembly) diffuse horizontal irradiances (G and Gd, respectively). These irradiances are sampled every second and the 1-minute averages are saved. Since these 3 components are available, BSRN quality checks (Long and Dutton, 2010) are applied to filter the 1-minute Gb data used here for studying variability and for averaging over each hour.

A three-dimensional atmospheric meteorology-chemistry model, namely WRF-Chem, with a triple-nesting configuration over the region of interest, focusing particularly on the hot desert climate, is employed here to simulate Gb, considering an advanced treatment of aerosols.

Several metrics are explored to characterise the variability of Gb within each hour:

- Range (difference between the maximum and minimum values within the interval).
- Standard deviation.
- Inter-quartile range, IQR (range of the middle half of the data --Q1 to Q3-- in the interval).

To obtain the inter-quartile range, or IQR, the (ground-measured) 1-minute Gb values within each hour are first sorted by Gb and divided into quartiles; note that, in this study, a minimum of 5 usable minutes (passing quality checks and with SZA<90 deg) were required within each hour in order to assign an IQR. Q1 is the lower quartile or 25th percentile, Q2 is the median or 50th percentile, and Q3 is the upper quartile or 75th percentile. Then,

$$IQR = Q3 - Q1 \qquad \text{(eq. 1)}$$

In addition, the clearness index Kt and the sun's zenith angle SZA are obtained for each of the hours included in this study. Kt is defined as:

$$K_t = \frac{G}{G_{TOA}} \qquad \text{(eq. 2)}$$

where G_{TOA} is the extra-terrestrial, or top-of-the-atmosphere, global horizontal irradiance, that is, the light coming from the sun, projected on a horizontal plane, before crossing the earth's atmosphere. The clearness index provides an indication on the cloudiness at the considered instant or interval; however, there is no wide consensus yet as to an objective definition of clear-skies (see e.g. Ruiz-Arias and Gueymard, 2023, and references therein). The sun's zenith angle is measured from the vertical overhead, corresponding to 0 degrees, with the horizontal corresponding to 90 degrees, and is calculated here using an implementation of NREL's SolPos v.2 algorithm (NREL, 2001).

The differences between (time-) coincident pairs of hourly values of measured and WRF-Chem-modelled Gb are analysed in the following section, as function of Kt, SZA and of the variability metrics listed above, for all daytime hours, i.e. hours in which average SZA<90 degrees. Note that in Figures 2 to 7 the (hourly) data are presented binned in x and y, and the colour scales on the right side denote the number of (hourly) entries within each bin.

3. Results

3.1. Selected data

Data from four months are studied here. These months are May, July and August 2022, and February 2023. These cover different sky conditions throughout the year, from winter to summer, and days with sunny, cloudy

and dusty conditions, resulting in a good variety of both smooth and variable solar conditions. Note that in all figures, the months are shown in order from February to August, to reflect winter to summer progression, although the included February corresponds to the calendar year after that of the other months.

3.2. Hourly beam irradiance

For a general view on the measured and modelled values, Figure 1 shows the profiles of hourly Gb, from both sources, throughout the four months; Figure 2 shows the same data in scatter plots, in bins of 10 W/m^2. Gb is very sensitive to atmospheric conditions, mainly clouds and aerosols, to a higher degree than global irradiance; therefore, relatively larger dispersions are commonly seen in comparisons of measured and modelled (not only physical models like WRF but also from satellite-based models) Gb.

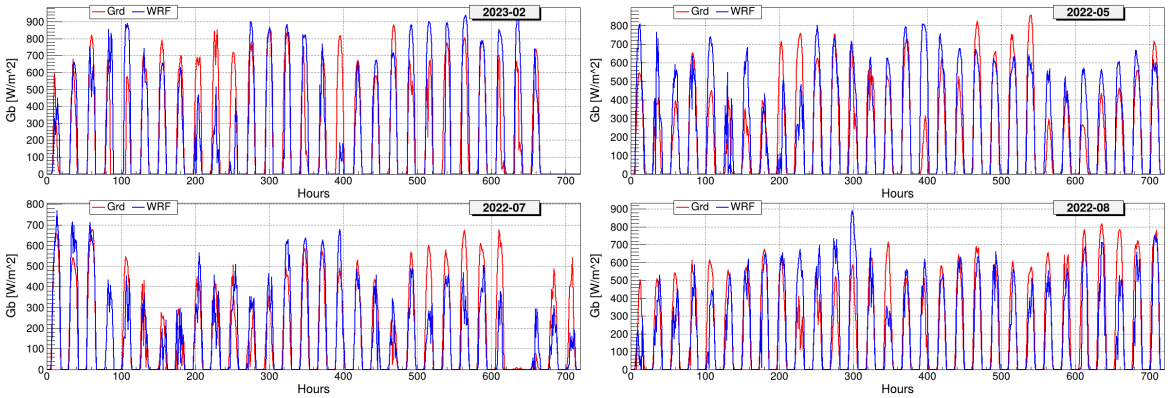

Fig. 1: Daily profiles of (red) measured and (blue) modelled hourly Gb in the studied months.

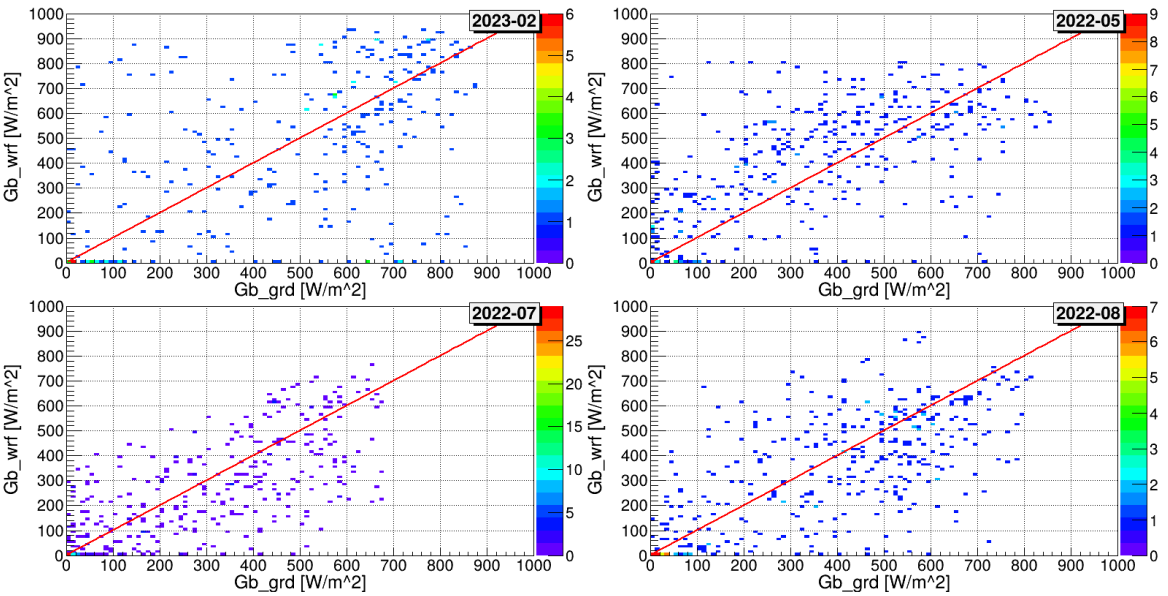

Fig. 2: Comparison of measured (x-axis) and modelled (y-axis) hourly Gb in the studied months. The colour scales indicate the number of entries in each bin (10 W/m^2 in both x and y).

3.3 Differences as function of clearness index and of sun zenith angle

Figure 3 shows the differences in WRF-Chem-modelled to ground-measured Gb as function of SZA for all daytime hours (SZA<90) of the considered months. Note that in February for this location the SZA does not go below 30 degrees at any hourly average (in other words, hourly averages of solar elevation stay below 60 degrees above the horizon). Somewhat larger differences can be seen around mid-elevations but on average there is no clear dependency on SZA.

The differences as function of Kt are shown in Figure 4. It can be seen that WRF-Chem tends to underestimate

Gb at the higher clearness values, from around 0.6-0.7 on. This suggests that WRF-Chem works better under cloudy skies than under clear skies, which may seem counterintuitive, but can be understood by noting the influence of high aerosol loads in the region, which affect Gb more clearly in the absence of clouds, indicating the need for a better inclusion of aerosols in WRF-Chem.

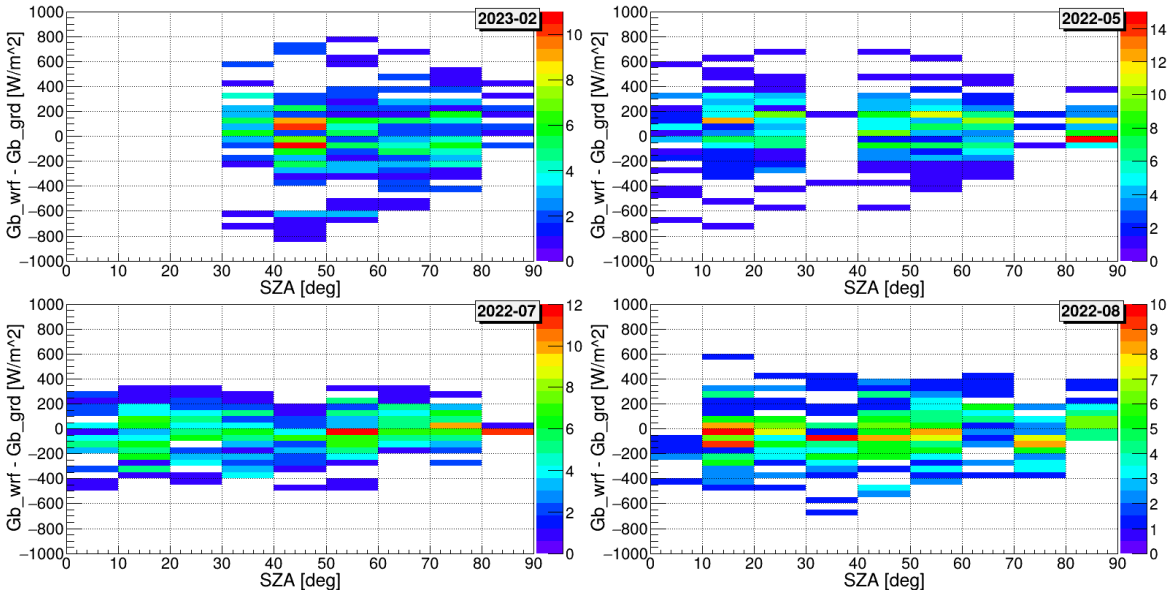

Fig. 3: Differences in Gb as function of solar zenith angle, per month.

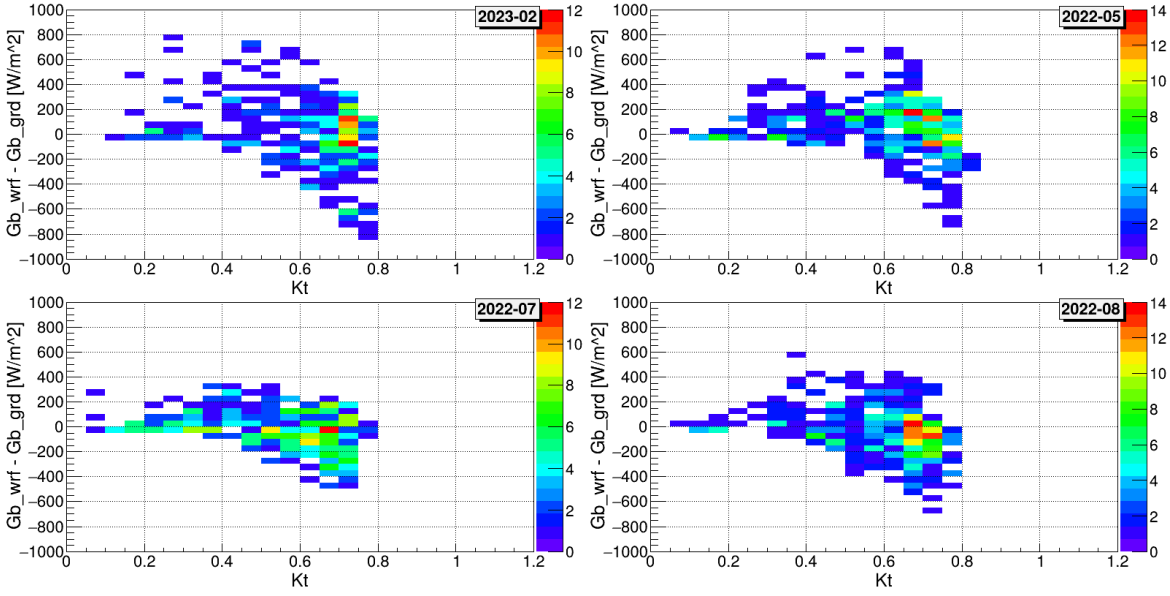

Fig. 4: Differences in Gb as function of clearness index, per month.

3.4 Differences by variability

In order to look for model deviations due to intra-hour variability, Figures 5, 6 and 7 show the model-to-measurement differences in Gb as function of the range, standard deviation and inter-quartile range, respectively, of the 1-minute measured Gb within the hour (see definitions in Section 2).

Comparing the spread of data along the x-axis across the months, larger variations in Gb can be found, as expected, in February, due to increased cloudiness and unstable weather during winter in Qatar. Along the y-axis, the differences between WRF-Chem and measurements appear generally less widespread in summer, particularly in July, and a dependency on the variability metrics (x-axis) is not clear, although an indication

towards overestimation can be seen at higher variabilities during August; a possible explanation for this overestimation could be too few shallow convection clouds in the WRF-Chem simulation.

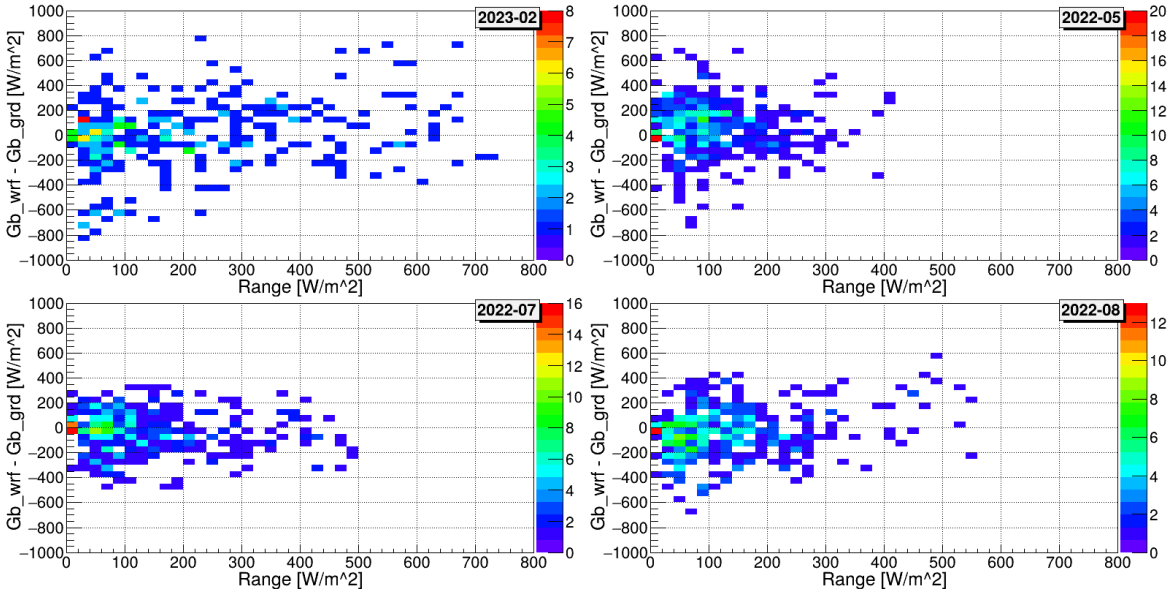

Fig. 5: Differences in Gb as function of the range of 1-min Gb within the hour, per month.

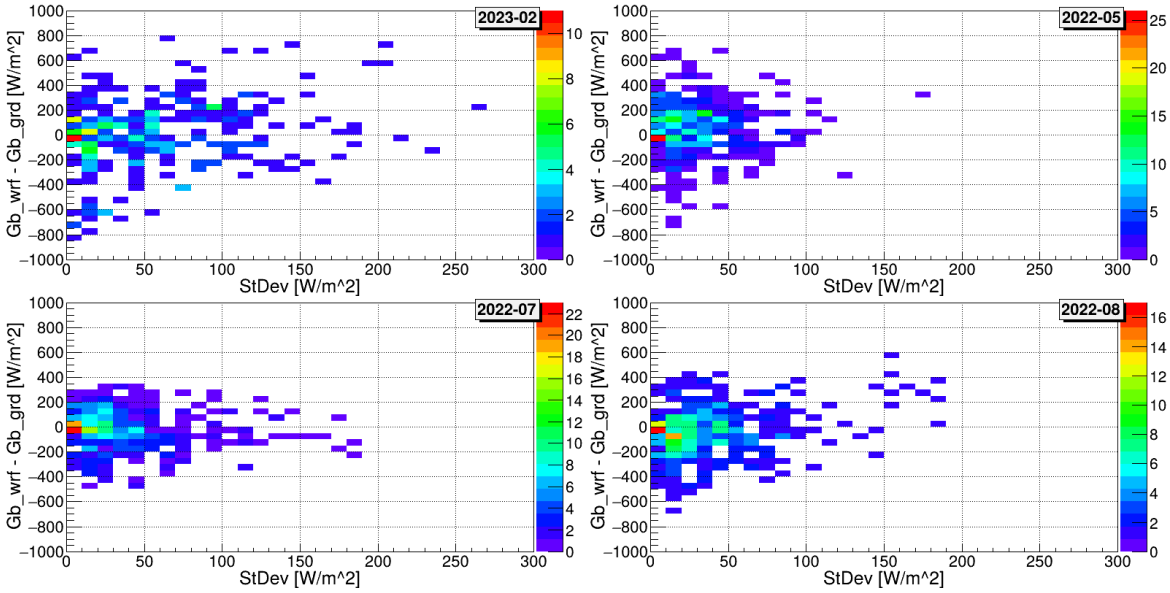

Fig. 6: Differences in Gb as function of the standard deviation of 1-min Gb within the hour, per month.

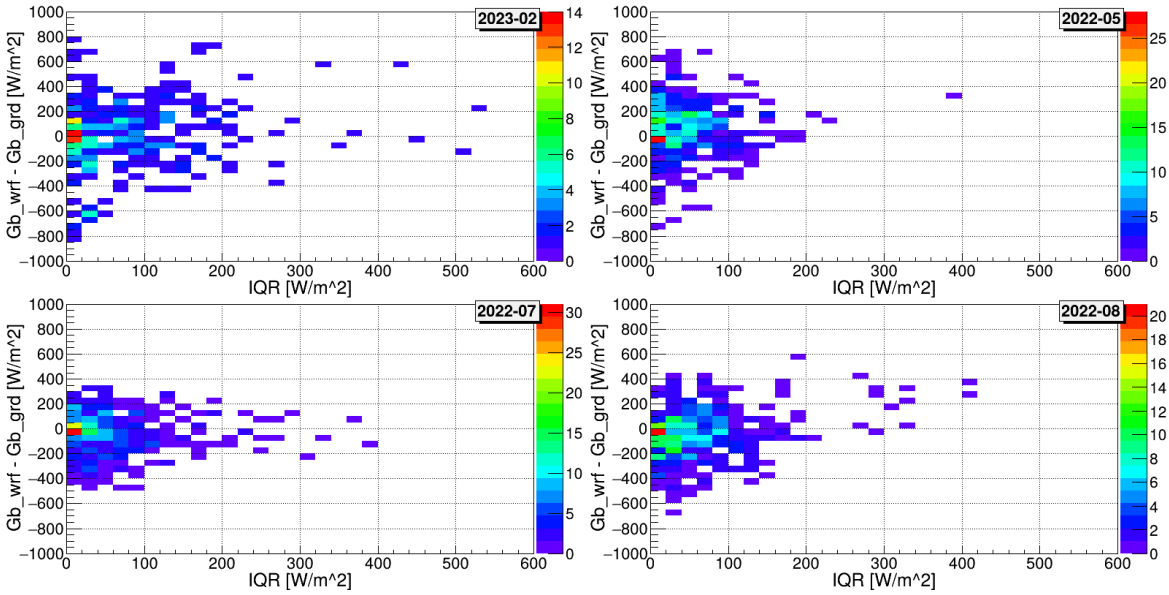

Fig. 7: Differences in Gb as function of the inter-quartile range of 1-min Gb within the hour, per month.

To provide a clearer view on any dependencies, Figures 8, 9 and 10 show the same variables as Figures 5, 6 and 7, namely difference in hourly modelled vs measured Gb as function of range, standard deviation and IQR of the 1-minute ground measurements, respectively, but presented in a different form. The points, which represent the averages along the y-axis for each x-axis bin, are shown with standard errors (standard deviation divided by sqrt(n); for the n 1-hour entries along the y-axis on that x-axis bin). From these figures, the increased overestimation in WRF-Chem Gb, i.e. positive differences, is more clearly seen at the higher values of variability, especially at higher standard deviation and IQR values and more notably in August. On the other hand, underestimation of Gb can be seen throughout but seems more prevalent than overestimation at low variabilities.

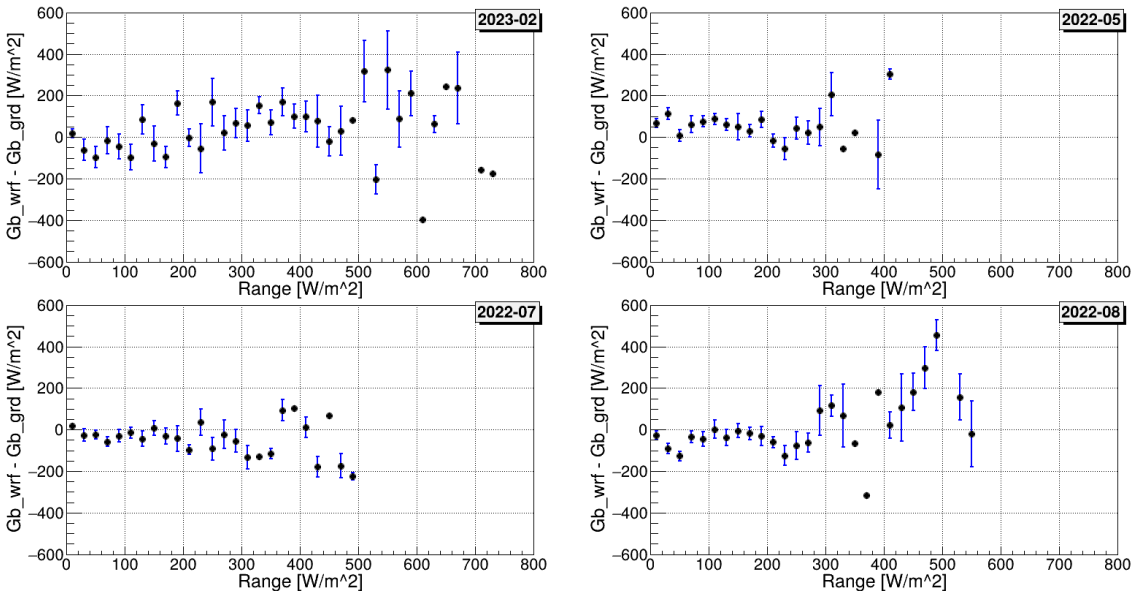

Fig. 8: Means and std error of differences in Gb as function of the range of 1-min Gb within the hour, per month.

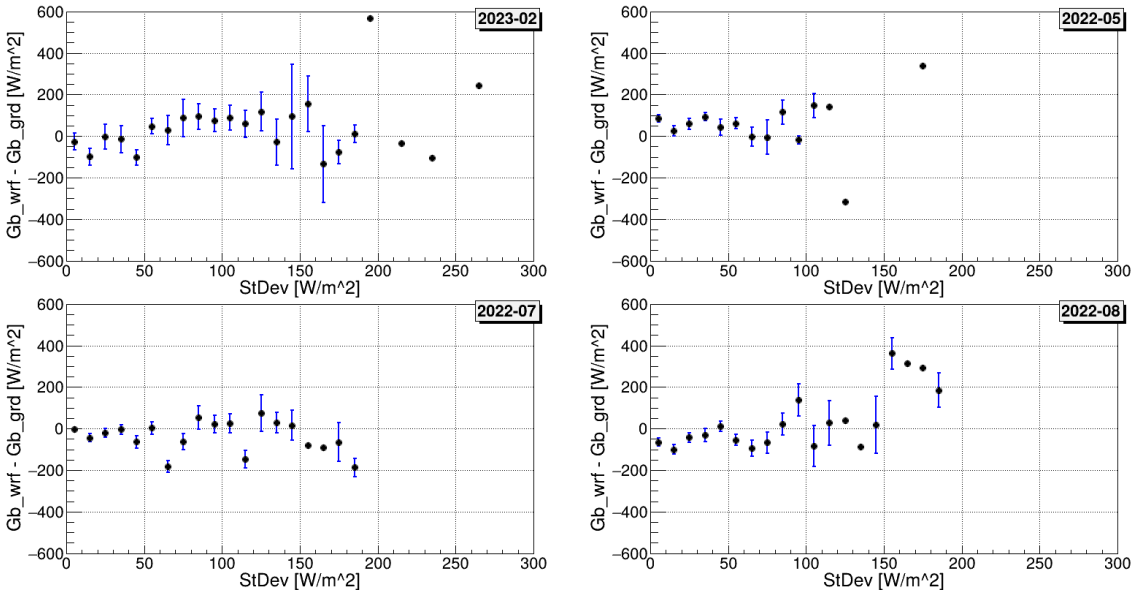

Fig. 9: Means and std error of differences in Gb as function of the standard deviation of 1-min Gb within the hour, per month.

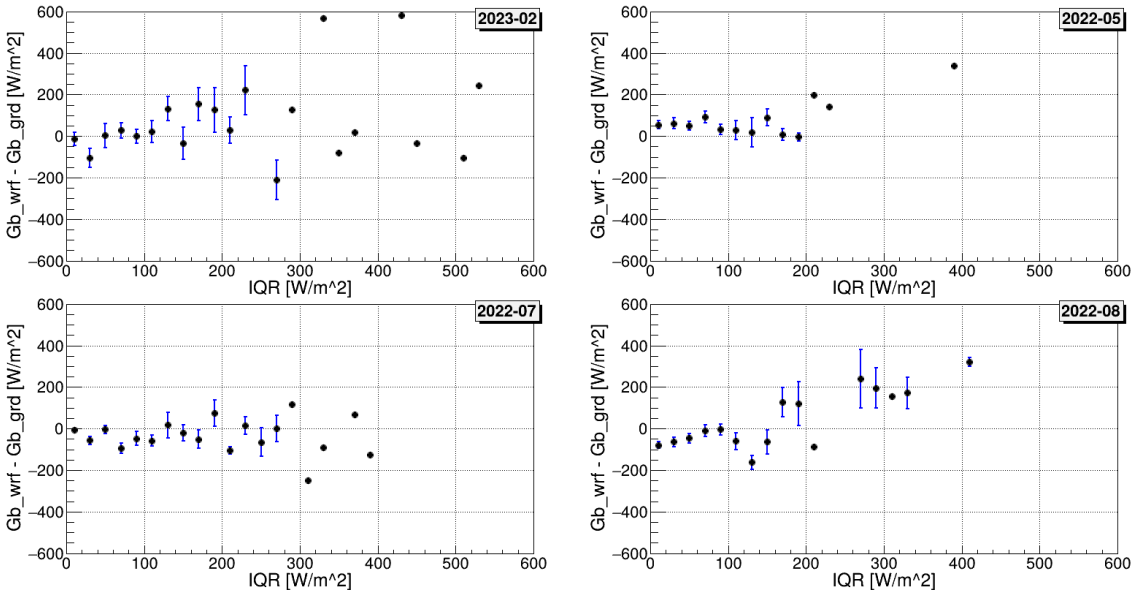

Fig. 10: Means and std error of differences in Gb as function of the inter-quartile range of 1-min Gb within the hour, per month.

4. Conclusions

Numerical weather prediction models, such as WRF, are valuable tools to obtain insight not only on meteorological information, but also on solar resources at ground level. Beam or direct irradiance is particularly challenging for models, given its high sensitivity to most atmospheric components, from clouds (as the case of global irradiance) to aerosols (which affect global irradiance to a smaller degree). As aerosol measurements are generally scarce, models using this information (from WRF to satellite models for solar irradiance) have higher uncertainty in the derivation of direct than for global irradiance. An additional complication is the usually high temporal variability of atmospheric aerosol contents, with even higher impact in regions, such as deserts, with large aerosol loads; WRF models work with comparatively larger temporal resolutions (hourly or three-hourly), which may not be able to capture these rapid changes, further increasing uncertainty. The study presented here covers 4 months with varying sky conditions, from winter to summer, sunny to rainy and dusty, in a desertic location, and shows that the WRF-Chem model, at hourly level, results in higher errors in direct irradiance, as compared to the corresponding ground measurements, when the

cloudiness is lower (indicating the effect or aerosols on solar radiation) and at high irradiance variabilities (based on the 1-minute ground measurements), mainly as measured through the standard deviation and the inter-quartile range of the 1-minute measurements within each hour. These results underline a need for a better treatment of aerosol inputs in the model, which currently can be summarised in two limitations: the temporal resolution of the aerosol inputs (usually only one or a couple of values per day are available), and the processing of the aerosols in the model itself; these shortcomings are currently being addressed in WRF-Chem by additional research at QEERI.

5. Acknowledgments

Research reported in this work was supported by the Qatar Research Development and Innovation Council (Grant: ARG01-0503-230061). The content is solely the responsibility of the authors and does not necessarily represent the official views of Qatar Research Development and Innovation Council.

6. References

Fast, L.D., Gustafson, Jr. W. I., Easter, R.C., Zaveri, R.A., Barnard, J.C., Chapman, E.G., Grell, G.A., 2005. Evolution of ozone, particulates, and aerosol direct forcing in an urban area using a new fully-coupled meteorology, chemistry, and aerosol model, J. Geophys. Res. (111), D21305. doi:10.1029/2005JD006721

Long, C.N., Dutton, E.G. 2010. Available online at https://epic.awi.de/id/eprint/30083/1/BSRN_recommended_QC_tests_V2.pdf (last accessed 7/Aug/2024).

NREL, 2001. The code, references, and an online calculator are available at https://www.nrel.gov/grid/solar-resource/solpos.html (last accessed 7/Aug/2024).

Ruiz-Arias, J.A., Gueymard, C.A., 2023. CAELUS: Classification of sky conditions from 1-min time series of global solar irradiance using variability indices and dynamic thresholds. Solar Energy 263, 111895. DOI: 10.1016/j.solener.2023.111895

Evaluation of aerosol optical depth for further assimilation into WRF-Chem simulations

Dunia Bachour[1], Daniel Perez-Astudillo[1], and Christos Fountoukis[1]

[1] Qatar Environment and Energy Research Institute, HBKU, Doha (Qatar)

Abstract

WRF-Chem is a powerful simulation tool for modeling atmospheric parameters and processes that influence solar radiation reaching the Earth's surface. By integrating aerosols and their interactions with radiation, WRF-Chem provides estimates of solar radiation reaching the surface that can be used as valuable information for solar energy forecasting. However, the prediction of solar radiation comes with high uncertainties related to the high variability of atmospheric components, especially aerosols in clear-sky conditions. In this contribution, the aerosol optical depth (AOD) parameter is used to represent the optical property of aerosols. AOD derived from WRF-Chem and a reanalysis model (CAMS) are evaluated in comparison to ground AOD data. The resulting analysis will server to correct the forecasted WRF-Chem AOD products and thus the prediction of solar radiation based on additional analysis of AOD data in a region with mostly cloudless conditions in general, but with the presence of aerosols and airborne desert dust throughout the year.

Keywords: WRF-Chem, aerosols, AOD, CAMS, direct normal irradiance

1. Introduction

The WRF-Chem model is a powerful numerical weather prediction (NWP) simulation tool for modeling atmospheric parameters and processes that influence solar radiation reaching the Earth's surface. It is a coupled model combining the weather forecasting capabilities from the Weather Research and Forecasting (WRF) model, as well as chemical transport capabilities that simulate the emissions, transport, and transformation of atmospheric gases and aerosols. WRF-Chem can be used as a valuable tool for solar radiation forecasting, with somehow large uncertainties, however, due to variability in clouds, in general, and in aerosols when clouds are absent (Ruiz-Arias et al., 2013). These uncertainties are even more pronounced on the direct solar radiation component, given its high sensitivity to the optical properties of the atmosphere, mainly coming from aerosols in cloud-free conditions (Gueymard, 2012). Among several parameters used to describe the aerosol optical properties, the aerosol optical depth (AOD) is commonly used to quantify the extinction of solar radiation by aerosols. AOD is acquired by ground-based sun photometers, such as the worldwide network of sun photometers provided by the AErosol Robotic NETwork (AERONET). Ground observations offer localized data of high quality; however, they are usually not available for long periods and suffer from data gaps. Other alternatives for AOD data retrieval are satellite products such as the Moderate Resolution Imaging Spectroradiometer (MODIS), or models such as NWP and global atmospheric chemistry models. Recently, atmospheric models, using data assimilation and reanalysis from satellite or ground observations, provide continuous time-series of AOD data with relatively high temporal resolution. The Modern-Era Retrospective analysis for Research and Applications, version 2 (MERRA-2), developed at NASA, and the Copernicus Atmosphere Monitoring Service (CAMS) model, developed at the European Centre for Medium-range Weather Forecasting, are two examples of reanalysis models widely used in solar resource applications to derive AOD data.

In this contribution, AOD derived from CAMS and WRF-Chem model will be evaluated in comparison to ground AOD data, to assess the reliability of the derived data in Doha, Qatar, a region characterized by high concentrations of atmospheric dust. The results of the analysis will be used to study a possible correction on WRF-Chem AOD products in high aerosol loads conditions, which may improve WRF-Chem performance in predicting solar radiation when further analysis of AOD data is performed.

© 2024. The Authors. Published by International Solar Energy Society
Selection and/or peer review under responsibility of Scientific Committee
10.18086/eurosun.2024.10.02 Available at http://proceedings.ises.org

2. Methodology

A high-precision monitoring station equipped with thermopile sensors is used here to collect ground-measurements of the direct, global and diffuse components of solar radiation.

At the same site, a sun photometer is used to derive ground AOD data, based on a spectrally selective detector measuring the spectral extinction of the direct radiation from the top of the atmosphere to the radiation at the earth surface for several wavelengths. The total optical depth is derived following the Lambert-Beer equation and AOD is derived from the total optical depth after removing the contribution of the other extinctions including the molecular scattering, ozone and other trace gas absorptions. To conform with satellite-derived data, the 500 nm channel is used here; this is also the closest wavelength to the representative wavelength (550 nm) of the scattering properties of aerosols in the atmosphere.

In this study, the three-dimensional WRF-Chem meteorology-chemistry model was implemented over the Arabian Peninsula, with a focus on enhanced grid resolution specifically for Qatar. The model simulated three primary processes: the emission of atmospheric components (both gases and aerosols), their transport, and their physicochemical transformations in the atmosphere. It was applied to the Middle East region using a 3-D grid system within a two-way nesting configuration, allowing communication between three domains with varying grid resolutions, all of which ran concurrently (Fountoukis et al., 2022). Aerosol concentration data moved in and out of all computational domains during model integration. The parent domain utilized a 50 km × 50 km grid resolution, while the intermediate nested domain (centered on the Arabian Desert) used a resolution of 10 km × 10 km. The third domain, covering Qatar, was resolved at 2 km × 2 km. The GOCART (Georgia Institute of Technology–Goddard Global Ozone Chemistry Aerosol Radiation and Transport) aerosol scheme was employed in all simulations, alongside the RACM (Regional Atmospheric Chemistry Mechanism) scheme for chemistry. The HTAP (Hemispheric Transport of Air Pollution emissions; http://www.htap.org/) anthropogenic emissions were used, featuring a grid resolution of 0.1° × 0.1°. Dust emissions were simulated using the US Air Force Weather Agency (AFWA) scheme, which incorporates the MB95 dust emission parameterization with typical airborne dust size distributions. Initial conditions for all pollutant concentrations are taken based on typical measurements of air quality in the region.

AOD is also derived from the reanalysis products CAMS. The CAMS Radiation Service v4.6 all-sky irradiation is used to derive 1-minute AOD values at 550 nm as the sum of all available optical depth products, and from these, hourly-averaged AOD values are calculated.

The statistical parameters used to compare the modeled and ground AOD data are the mean bias error (Bias) and the root mean square error (RMSE). For each entry, the difference and its square between the estimated (AOD WRF and AOD CAMS) and measured (AOD Ground) at the same time stamps (t) are calculated for the corresponding period. Then, these differences and their squares are summarized to determine the corresponding bias and root mean square error. The values are also expressed in relative values with respect to the mean values calculated from the measured AOD. Equations 1 to 6 are used to determine the statistical parameters where N is the total number of considered values.

$$\Delta_{(t)} = AODestimated_{(t)} - AODground_{(t)} \quad \text{(eq.1)}$$

$$Bias = \frac{\sum_1^N \Delta_t}{N} \quad \text{(eq.2)}$$

$$RMSE = \sqrt{\frac{\sum_1^N {\Delta_t}^2}{N}} \quad \text{(eq.3)}$$

$$mean\ AOD = \frac{\sum_1^N AODground(t)}{N} \quad \text{(eq.4)}$$

$$rBias = \frac{Bias}{mean\ AOD} \quad \text{(eq.5)}$$

$$rRMSE = \frac{RMSE}{mean\ AOD} \quad \text{(eq.6)}$$

3. Results

3.1 Ground AOD

To quantify and study the range of AOD values seen in Doha's conditions, we study in figure 1 the hourly variations of AOD derived by the sun photometer for a period of ~one year, showing all months consecutively excluding August due to the unavailability of processed data for this month at the time of analysis. Note that the months are shown in order from January until December for clarity, although the included January and February corresponds to year 2023 while the other months are in year 2022. The blue lines on the figure correspond to the beginning of a new month. For some months AOD variation is confined within a defined band, while for other months the variation is more obvious with an observed high range (between 0.3 and 1.4 in July for instance). The observed AOD mean is ~ 0.5 with a standard deviation of 0.27, indicating a dynamic fluctuation of AOD in the region with a more turbid atmosphere in the summer season. This variation in AOD induces a pronounced variation in solar radiation; when simulating the beam normal irradiance component with SMARTS2 (Simple Model of the Atmospheric Radiative Transfer of Sunshine) model, the maximum is reduced by ~ 5 % when AOD is 0.1, and by ~ 50 % when AOD is equal to 1, with respect to AOD = 0 (Bachour et al., 2023).

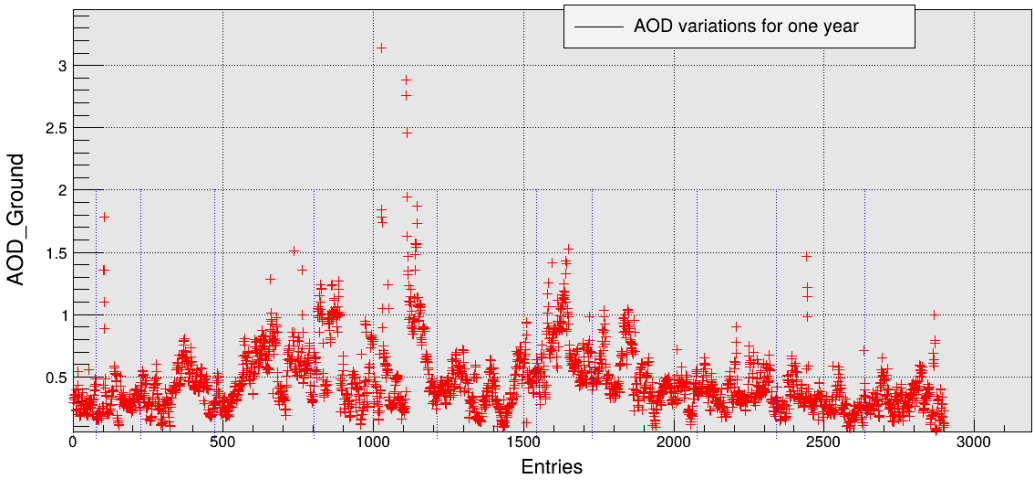

Figure 1. Variations of hourly AOD through one year, measured by a sun photometer in Doha, Qatar.

3.2 Model-derived AOD

Hourly AOD data were also derived from the CAMS reanalysis database and WRF-CHEM. Figure 2 shows an example of the normalized frequency distributions of AOD from these models in comparison with the ground data for two months: May, and July 2022.

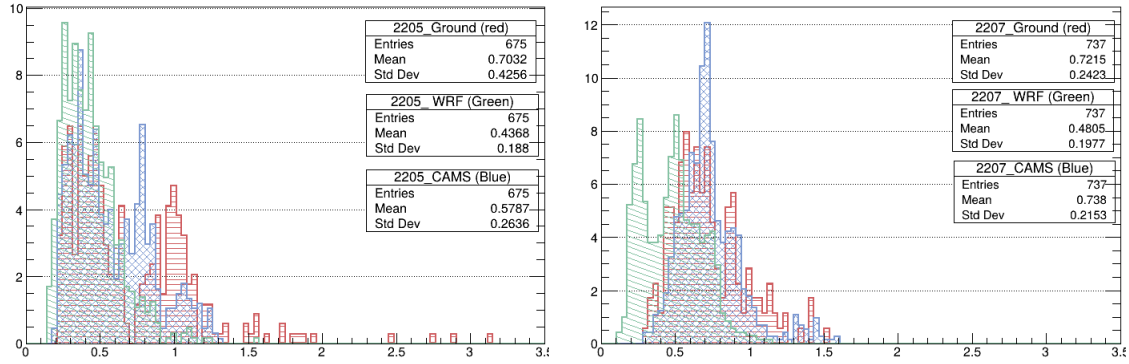

Figure 2. Normalized frequency distribution (in %) of hourly AOD per month.

Looking to the overall distribution, AOD values obtained from CAMS (blue line) agree partially with AOD obtained from the ground (red line), with differences observed mainly in the tail part of the two histograms, where higher AOD values are being captured by the ground measurements. AOD values between 0.7 and 1 are frequent in the CAMS data; AOD higher than 1, values attributed to local dust events, are observed in the

ground measurements. For WRF-Chem, the distribution of modeled AOD (green line) does not conform with the ground-derived values, with an observed underestimation. A clear discrepancy is seen towards the low AOD values where WRF-Chem reports very low values with high frequency (even for other months not shown here), which may not be possible in the turbid atmosphere of Doha. WRF-Chem is clearly not able to capture high AOD values, with mean values significantly lower than those derived by the sun photometer, highlighting the model limitations when predicting AOD in Doha's desert environment (Fountoukis et al., 2020), and the need to reconfigure or correct the model with new parameters based mainly on AOD, in order to improve the ability of WRF-CHEM to predict local dust events in a desert environment, consequently improving the prediction of solar radiation in a desert location with high aerosol loads.

To examine the comparison in more detail, the profile of the hourly AOD data from the 3 sources is plotted at the same time stamps for two one-month periods (May and July of 2022): CAMS and ground data in Figure 3, WRF-Chem and ground data in Figure 4. The data of the x-axis, labeled as 'entries' in the plots, are chronologically sorted but they are not consecutive in time, and they include commonly available AOD data from both sources at the same timestamp. The dotted red vertical lines are plotted to discern the first entry of a new day. The statistical comparison with the ground data is reported in table 1 for CAMS and table 2 for WRF-Chem; the mean bias error (Bias) and the root mean square error (RMSE) are determined, respectively, by calculating the differences and their squares between the modeled and ground AOD values at the same time stamps, and their corresponding mean Bias and RMSE and their relative values (rBias, rRMSE) with respect to the mean values of AOD-Ground. The number of data points in the comparison is also shown in the tables.

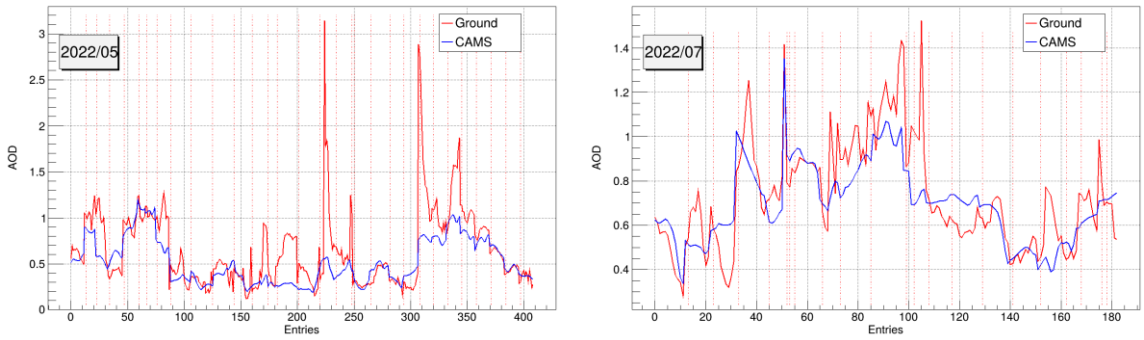

Figure 3. Hourly AOD variations of CAMS in comparison with ground data in Doha, Qatar.

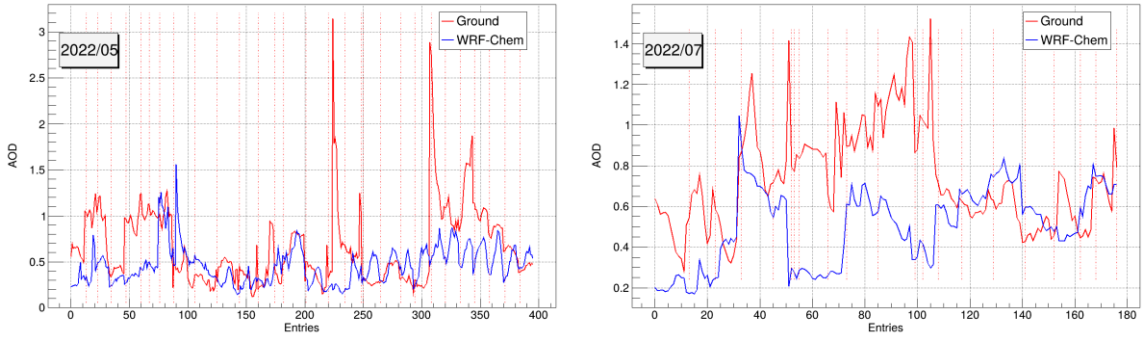

Figure 4. Hourly AOD variations of WRF-Chem in comparison with ground data in Doha, Qatar.

Table 1. Comparison of AOD CAMS and ground.

MONTH	BIAS	RBIAS (%)	RMSE	RRMSE (%)	DATA POINTS
05/22	-0.15	-20.81	0.34	49.2	340
07/22	-0.03	-4.44	0.16	22.4	176
09/22	-0.04	-8.27	0.12	25.28	322
02/23	0.03	7.95	0.22	66.99	145

Table 2. Comparison of AOD WRF-Chem and ground.

MONTH	BIAS	RBIAS (%)	RMSE	RRMSE (%)	DATA POINTS
05/22	-0.23	-31.69	0.49	68.51	327
07/22	-0.22	-30.51	0.38	51.87	170
09/22	-0.2	-41.81	0.29	59.75	322
02/23	-0.09	-29.10	0.26	79.43	145

From figures 3 and 4, it is observed that CAMS captures better the local variability observed in the ground data, with larger discrepancies observed in WRF-Chem data. However, high AOD values observed in the ground data are not properly modeled by either CAMS or WRF-Chem. When comparing the statistics for each of the months in tables 1 and 2, CAMS is mostly underestimating the AOD values with a relative bias less than 10 % except for May. For WRF-Chem the AOD values are underestimated for all the months and the relative RMSE is considerably high.

3.3 Data validation

The solar radiation measurement is used For AOD data validation; the measured direct component, Gb, is compared with a clear-sky Gb (Gb_cs) calculated with the European Solar Radiation Atlas (ESRA) clear-sky model, with a Linke turbidity value of 1 to get the maximum Gb representing a perfectly clear atmosphere free from any aerosols or water vapor. This component is then reduced by the AOD parameter to obtain Gb_cs, which quantifies the reduction in solar radiation caused by aerosols. See Equation 1 for more details, where m is the air mass and AOD is the value derived from ground, CAMS, and WRF-Chem.

Gb_cs = Gb-ESRA (max) * Exp (-m*AOD) (Eq.1)

Figure 5 shows an example of 3 daily profiles of measured (red line) and modeled Gb, as described previously. It is observed that Gb modeled using ground AOD data as input follows the measured Gb, while Gb modeled using AOD from CAMS and WRF-Chem deviates from the measured Gb with a significant overestimation due to an underestimation of AOD values. For a broader validation, the scatter plot of one month of data between the measured and modeled Gb shows a reasonably good agreement when using AOD data derived from the ground measurement (Bachour et al., 2023).

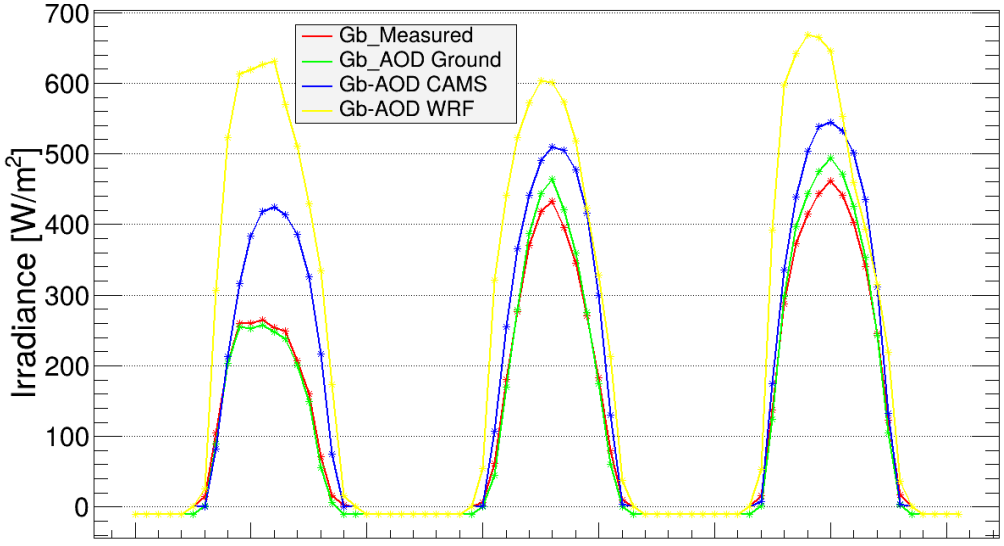

Figure 5. Daily profiles of measured and clear-sky DNI.

3.4 Data filtering

Although the processing of the sun photometer data includes a cloud screening algorithm that identifies cloudy periods and flags the corresponding AOD data, some days with relatively high AOD values identified from figures 3 and 4 will be further analysed to eliminate the possibility of outliers in the ground AOD data, which

may indicate cloud contamination and thus inaccurate ground AOD values. For this analysis, the direct solar radiation component Gb measured by a solar monitoring station located close to the sun photometer will be analysed. Although it is not straightforward to distinguish between the attenuation in Gb caused by clouds or aerosols without using additional data, days with clouds exhibit a profile with sharp decreases and recoveries as compared to the aerosol effects that tend to cause a more gradual reduction in irradiance throughout the day. Following this assumption, all days identified as days with possible clouds contamination are removed.

In addition, the cumulative distribution of the ground AOD has been analysed for each of the month; it was noted that AOD values less than 0.1 are extremely rare (<1% for all the studied months), and 0.14 are also quite rare (<1% for the studied months except for Feb, when it was ~ 3.5%). Table 3 shows the comparison excluding the suspected cloudy days. In addition to the exclusion of cloudy periods, tables 4 and 5 show the same parameters excluding also AOD data with values less than a fixed threshold: 0.1 in table 4 and 0.14 in table 5; only months with changes are reported.

Table 3. Statistical parameters between AOD WRF-Chem and ground, excluding cloudy periods.

Month	Bias	rBias	RMSE	rRMSE	Data Points
05/22	-0.22	-31.44	0.49	68.71	308
07/22	-0.16	-23.28	0.33	48	127
09/22	-0.19	-39.71	0.27	55.95	299
02/23	-0.02	-8.8	0.16	55.79	108

Table 4. Statistical parameters between AOD WRF-Chem and ground, excluding cloudy periods and AOD<0.1 .

MONTH	BIAS	RBIAS	RMSE	RRMSE	DATA POINTS
02/23	-0.02	-5.85	0.15	54.41	104

Table 5. Statistical parameters between AOD WRF-Chem and ground, excluding cloudy periods and AOD<0.14

MONTH	BIAS	RBIAS	RMSE	RRMSE	DATA POINTS
09/22	-0.19	-39.48	0.27	55.37	285
02/23	0.01	-0.1	0.15	49.85	76

From the bias values of the WRF-Chem, the model tends to underestimate the AOD values consistently. To keep consistency among all months, only periods with AOD values less than 0.1, seen only in WRF-Chem data, were eliminated as it is not ‘physically’ possible (not seen in the ground measurements during these months) in Doha’s conditions.

3.5. Correction of WRF-Chem AOD data

Since the WRF-Chem data consistently underestimated AOD, the bias correction method is used to improve forecasting results. This method consists of determining a mean bias error of the data within a certain period and using it to correct the forecasted results. The bias is calculated using the data of three months analysed together and used to correct the data of the remaining month (table 6).

Table 6. Statistical parameters for the comparison of ground and WRF-Chem AOD, using the bias correction method.

MONTH	BIAS	RBIAS	RMSE	RRMSE	DATA POINTS
05/22	-0.03	-5.47	0.42	64.25	356
07/22	-0.03	-4.47	0.28	42.10	131
09/22	-0.07	-14.15	0.2	41.84	317
02/23	0.14	50.44	0.21	73.59	107

While the bias of the forecasted data has been reduced for most of the tested months, their relative RMSE hasn't improved much, and the applied correction amplified the errors for February. This means that it is not adequate to apply the same correction on the forecasted results without considering some sort of data clustering based on data distribution similarity, or data seasonality. As a first attempt, looking to the frequency distribution of AOD WRF-Chem, a certain similarity is observed between months 5 and 7 (wider range with a relatively high mean of AOD values) compared to months 9 and 2 which show a somehow narrower distribution with lower mean AOD values. However, month 9 has a higher mean AOD value and exhibits

higher AOD variations than month 2. Table 7 shows the results of the bias correction method determined with the data of one month (i.e. month 5 and 9) and validated using the data of the similar month respectively (i.e. month 7 and 2), and vice versa. The errors for 5 and 7 are reduced, however the errors in months 9 and 7 are high as expected, suggesting the use of another correction factor for winter months with low AOD values.

Table 7. Statistical parameters for the comparison of ground and WRF-Chem AOD, using the bias correction method.

MONTH	BIAS	RBIAS	RMSE	RRMSE	DATA POINTS
05/22	-0.02	-2.47	0.42	64.06	356
07/22	-0.04	-5.37	0.29	42.2	131
09/22	-0.17	-35.87	0.25	53.27	317
02/23	0.16	59.6	0.22	80.15	107

Other correction methods are tested here and consist of finding a possible fit between two datasets, as will be defined in Figures 6 and 7, to check if errors improve compared to the bias correction method. Figure 6 shows an example of a scatter plot between AOD ground and WRF-Chem, with the x-axis presenting the WRF-Chem data and the y-axis presenting the ground data. The black line indicates the one-to-one line, while the red line represents the linear fit function found between the data, determined in the range 0 to 1.5 to eliminate some outliers, which might help the fit function to better represent the relation between the two datasets. Figure 7 shows the scatter plot between the point-by-point bias of WRF-Chem and ground AOD (y-axis) and AOD WRF-Chem (x-axis), and the fit function is shown with a solid red line. Following the same method discussed in the bias correction method, the fit functions are determined using the data of three months and validated using the data of the remaining month.

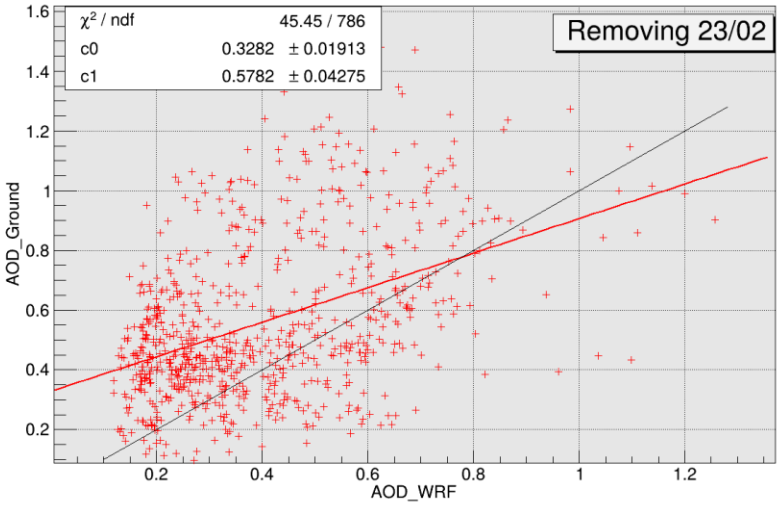

Figure 6. Scatter plot between measured and WRF-Chem AOD.

The linear fit function parameters (c0, c1) are determined from figure 6, in this case using the three months (5,7,9), and applied to correct AOD_WRF of month 2. The fit function is shown in equation 2. Table 8 shows the results of applying this correction on all forecasted AOD_WRF, alternating the used/removed months to have all possible combinations.

AOD_ground = c0 + c1 * (AOD_WRF) (Eq.2)

Table 8. Statistical parameters for the comparison of ground and WRF-Chem AOD, using the linear fit correction.

MONTH	BIAS	RBIAS	RMSE	RRMSE	DATA POINTS
05/22	-0.09	-13.69	0.42	63.89	356
07/22	-0.09	-12.58	0.27	39.87	131
09/22	-0.01	-3.18	0.17	37.21	317
02/23	0.2	70.68	0.23	82.3	107

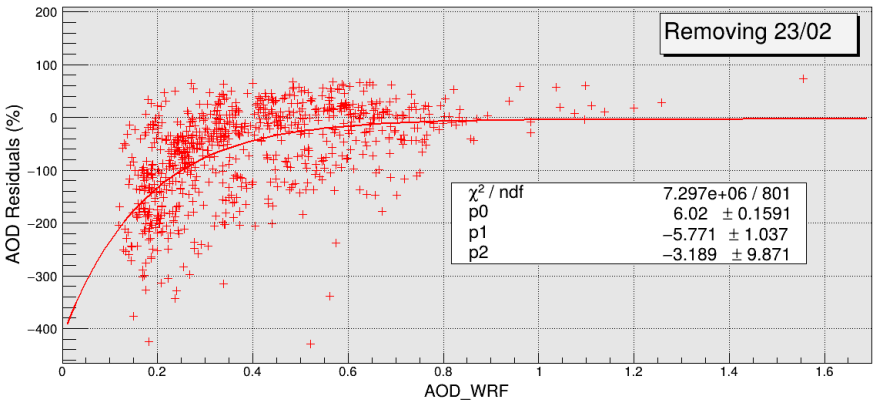

Figure 7. Scatter plot between bias and WRF-Chem AOD.

Figure 7 is used to determine the fit function between the residuals PR (as percentage of AOD_WRF), and AOD_WRF, following the formula shown in equation 3. The residuals are the differences between each AOD_WRF value and the corresponding ground-derived AOD.

$$PR = P2 - Exp\ (P0 + P1 * (AODWRF_{Chem})) \qquad \text{(Eq. 3)}$$

P2, P0, P1 are the fit parameters determined from the scatter plot using the data of three months. The correction is then applied on the remaining month comparing the calibrated WRF-chem AOD with ground data (table 9).

Table 9. Statistical parameters for the comparison of ground and WRF-Chem AOD, using the residuals correction.

MONTH	BIAS	RBIAS	RMSE	RRMSE	DATA POINTS
05/22	-0.26	-40.37	0.51	78.2	356
07/22	-0.22	-32.62	0.39	56.88	131
09/22	-0.30	-64.94	0.36	76.79	317
02/23	-0.12	-43.94	0.18	65.39	107

The results of the linear fit on AOD show a somewhat similar improvement as seen in the bias correction method; in some months the relative RMSE is even lower, thus reducing the dispersion of WRF-Chem data compared to the ground data, however the bias of the month of Feb is amplified similarly to the previous method, suggesting the need of aggregating the data by season following the sky turbidity level as discussed previously. The correction determined from the fitting of the residuals failed to improve the errors and in fact worsened them. This was expected looking to the wide band of data dispersion around the fit line (figure 7), reflected in the errors associated to the parameters of the fit (shown in the statistics box on the plot), mainly for P2.

4. Conclusions

Among different parameters used to quantify the aerosols, AOD is used to account for the attenuation of the solar radiation in the atmospheric column due to aerosols, and AOD quantification, whether short- or long-term, is required in many applications such as climate change, air quality, and solar radiation. Due to the high dynamicity of the aerosols in the atmosphere, AOD obtained by ground measurements remains the reference method for deriving reliable data with high temporal resolution, and models based on satellite observations and reanalysis databases provide AOD data with high uncertainties, mainly in regions with high aerosol loads.

In this contribution, AOD (with hourly temporal resolution) is quantified with a sun photometer deployed in Doha, Qatar to obtain ground-derived AOD data and evaluate the AOD products obtained from CAMS and WRF-Chem model. CAMS model data show relatively good agreement with the ground data. However, the assessment of the WRF-based data shows non-conformity and high discrepancy with the ground data, leading to the suggestion of correction methods to WRF-Chem reducing the errors of the forecasted values. By considering AOD post correction into WRF-Chem simulation process, the accuracy and reliability of the solar radiation prediction can be improved, mainly in region characterized by high concentrations of atmospheric dust.

5. Acknowledgments

Research reported in this work was supported by the Qatar Research Development and Innovation Council (Grant: ARG01-0503-230061). The content is solely the responsibility of the authors and does not necessarily represent the official views of Qatar Research Development and Innovation Council.

6. References

Ruiz-Arias, J.A., Dudhia, J., Santos-Alamillos, F.J., Pozo-Vázquez, D., 2013. Surface clear-sky shortwave radiative closure intercomparisons in the Weather Research and Forecasting model. Journal of Geophysical Research: Atmospheres 118, 9901–9913. DOI: 10.1002/jgrd.50778

Gueymard, C. A., 2012. Temporal variability in direct and global irradiance at various time scales as affected by aerosols. Solar Energy 86 (12), 3544–3553. DOI: 10.1016/j.solener.2012.01.013

Bachour, D., Perez-Astudillo., Fountoukis, C., Sanfilippo, A., 2023. Aerosols estimation in arid region for solar resource applications. EU PVSEC 2023 Conference Proceedings, 020364-001 - 020364-006. ISBN: 3-936338-88-4. DOI: 10.4229/EUPVSEC2023/4CO.9.4

Fountoukis, C., Harshvardhan, H., Gladich, I., Ackermann, L., Ayoub, M.A., 2020. Anatomy of a severe dust storm in the Middle East: Impacts on aerosol optical properties and radiation budget. Aerosol and Air Quality Research, 20, 155-165. DOI: 10.4209/aaqr.2019.04.0165.

Fountoukis, C., Mohieldeen, Y., Pomares, L., Gladich, I., Siddique, A., Skillern, A., Ayoub, M.A., 2022. Assessment of High-resolution Local Emissions and Land-use in Air Quality Forecasting at an Urban, Coastal, Desert Environment. Aerosol Air Qual. Res. 22, 220001. DOI: 10.4209/aaqr.220001

Climate Adjustment of Photosynthetically Active Radiation Estimates Using Site Adaptation Technique

Francisco Ferrera-Cobos[1], Ousmane Wane[1, 2], Ana A. Navarro[1], Cecilia Popovich[3], Gustavo H. Ribeiro da Silva[4], María Navarro Llorens[5], Luisa Gouveia[6, 7], Luis F. Zarzalejo[1] and Rita X. Valenzuela[1]

[1] CIEMAT Energy Department, Renewable Energy Division, Madrid (Spain)

[2] E.T.S.I. Agronómica, Alimentaria y Biosistemas, Universidad Politécnica de Madrid, Madrid (Spain)

[3] Laboratorio de Estudios Básicos y Biotecnológicos en Algas (LEBBA). Centro de Recursos Naturales Renovables de la Zona Semiárida (CERZOS) CONICET-UNS, Departamento de Biología, Bioquímica y Farmacia (UNS), Bahía Blanca (Argentina)

[4] Department of Environmental and Civil Engineering, São Paulo State University (UNESP), São Paulo (Brazil)

[5] Grupo de Ingeniería metabólica Departamento de Bioquímica y Biología Molecular, Universidad Complutense de Madrid, Madrid (Spain)

[6] LNEG UBB - Laboratório Nacional de Energia e Geologia IP. - Unidade de Bioenergia e Biorrefinarias, Lisboa, (Portugal)

[7] GreenCoLab - Green Ocean Technologies and Products Collaborative Laboratory, CCMAR, University of Algarve, Campus de Gambelas, Faro, (Portugal)

Abstract

In this work, a local adjustment is proposed for photosynthetically active radiation (PAR) estimates at several locations around the world with different Köppen-Geiger climate classes, resulting in a climate adjustment for PAR estimates. For adjustment, a site adaptation technique was used for each of the climates (hemiboreal, semi-arid, mediterranean, oceanic, and tropical) represented in this study. Remote sensing PAR data from thirteen locations were collected from the Copernicus CAMS global greenhouse gas reanalysis (EGG4) dataset to be used as initial PAR estimates, while observed PAR data from the same locations were also collected to perform the local adjustment. The results evidenced good fitting for four out of five climates; conversely, the semi-arid climate had to be divided into two subclimates (hot and cold semi-arid) to obtain good results. After division, the best results were obtained for the cold semi-arid and mediterranean climates. In the hot semi-arid climate, the results were contradictory, since it had the worst determination coefficient and the second-best MBE and RMSE among all climates. These results suggest that PAR is affected by local climatic and atmospheric conditions.

Keywords: Photosynthetically Active Radiation, PAR, Modelling

1. Introduction

Photosynthetically Active Radiation (PAR) is the portion of solar radiation whose wavelength is located between $4 \cdot 10^{-7}$ m and $7 \cdot 10^{-7}$ m. It is the range of the solar spectrum that plants use to perform photosynthesis, and it is the visible range for the human eye as well. PAR can be expressed as the photosynthetic photon flux density measured in µmol s^{-1} m^{-2} or as the energy flux density measured in W m^{-2}. In this work, the term PAR refers to the energy flux density and is expressed as W m^{-2}.

Despite its many applications, for example in estimating biomass growth or in calculating gross and primary production (Iasimone et al., 2018; Pinker et al., 2010; Trofimchuk et al., 2019; Wu et al., 2009), PAR is not as

© 2024. The Authors. Published by International Solar Energy Society
Selection and/or peer review under responsibility of Scientific Committee
10.18086/eurosun.2024.10.03 Available at http://proceedings.ises.org

commonly measured as other solar components. When ground PAR data are not available, satellite-derived PAR estimates are a good option to consider because they usually cover long time periods and the entire surface of the world.

PAR is strongly dependent on local atmospheric and climatic conditions (Ferrera-Cobos et al., 2020a). Consequently, PAR models also depend on the data used to train the models. Previous studies addressed PAR modelling, analysing climatology and meteorological conditions (Ferrera-Cobos et al., 2020b; García-Rodríguez et al., 2021; Wang et al., 2021).

Site adaptation is a process in which the long-term time series of a modelled variable is improved in accuracy by using the short-term observations of the variable. It is often used when the variable is the irradiance or one of the components of the irradiance, employing mathematical adjustments to perform the site adaptation process (Ferrera-Cobos et al., 2020b; Mazorra Aguiar et al., 2019; Polo et al., 2016).

This work presents a climate adjustment for satellite-derived PAR estimates from 13 locations around the world, covering five different climates according to their Köppen-Geiger clasification. The adjustment was performed using a site adaptation technique.

2. Materials and Methods

Satellite-derived PAR data from 13 locations were collected from the Copernicus CAMS global greenhouse gas reanalysis (EGG4) (Agustí-Panareda et al., 2023) dataset from 2013 to 2020 along with ground PAR observations from the GEOPAR network, AMERIFLUX (Yepez, 2020), CERZOS CONICET-UNS, São Paulo State University and Helsinki University-Viikki Campus (https://osf.io/e4vau/), overlapping at least one year in that time span from the same 13 locations. The daily average was calculated for both data sets.

Thirteen locations, covering five climates according to the Köppen-Geiger climate classification (hemiboreal climate, semi-arid climate, mediterranean climate, oceanic climate, and tropical climate), provided PAR ground data. More details of each location can be found in the Tab. 1. Tropical (Aw) and subtropical (Cfa) climates were combined into a single class named tropical, while the climate subgroup Bsks was classified as a Mediterranean climate.

For local climate adjustment, this work used a site adaptation technique for each of the climates represented in this study. Site adaptation consisted of a fitting between remote sensing data and observed data. In this case, satellite-derived PAR estimates were fitted using ground-observed PAR data from the radiometric stations listed in Tab. 1 and Fig. 1.

Tab. 1. Locations. Positive degrees indicate north latitude or east longitude.

Country	Location	Latitude	Longitude	Altitude (m)	Köppen-Geiger classification	Climate type
Spain	Tabernas	37.092	-2.364	491	Bskw	Semiarid
México	Alamos	26.997	-108.789	367	Bsh	Semiarid
Spain	Albacete	39.041	-2.082	698	Bsks	Mediterranean
Spain	Salamanca	40.978	-5.715	777	Bsks	Mediterranean
Spain	Lubia	41.601	-2.508	1099	Bsks	Mediterranean
Spain	Córdoba	37.857	-4.803	91	Csa	Mediterranean
Spain	Zaragoza	41.727	-0.814	226	Bsks	Mediterranean
Spain	Lugo	42.995	-7.541	447	Csb	Oceanic
Spain	Villaviciosa	43.476	-5.441	6	Cfb	Oceanic
Spain	Vitoria	42.854	-2.622	520	Csb	Oceanic
Argentina	Bahía Blanca	-38.678	-62.232	42	Cfa	Tropical
Brasil	Baurú	-22.351	-49.033	610	Aw	Tropical
Finland	Helsinki	60.225	25.017	8	Dfb	Hemiboreal

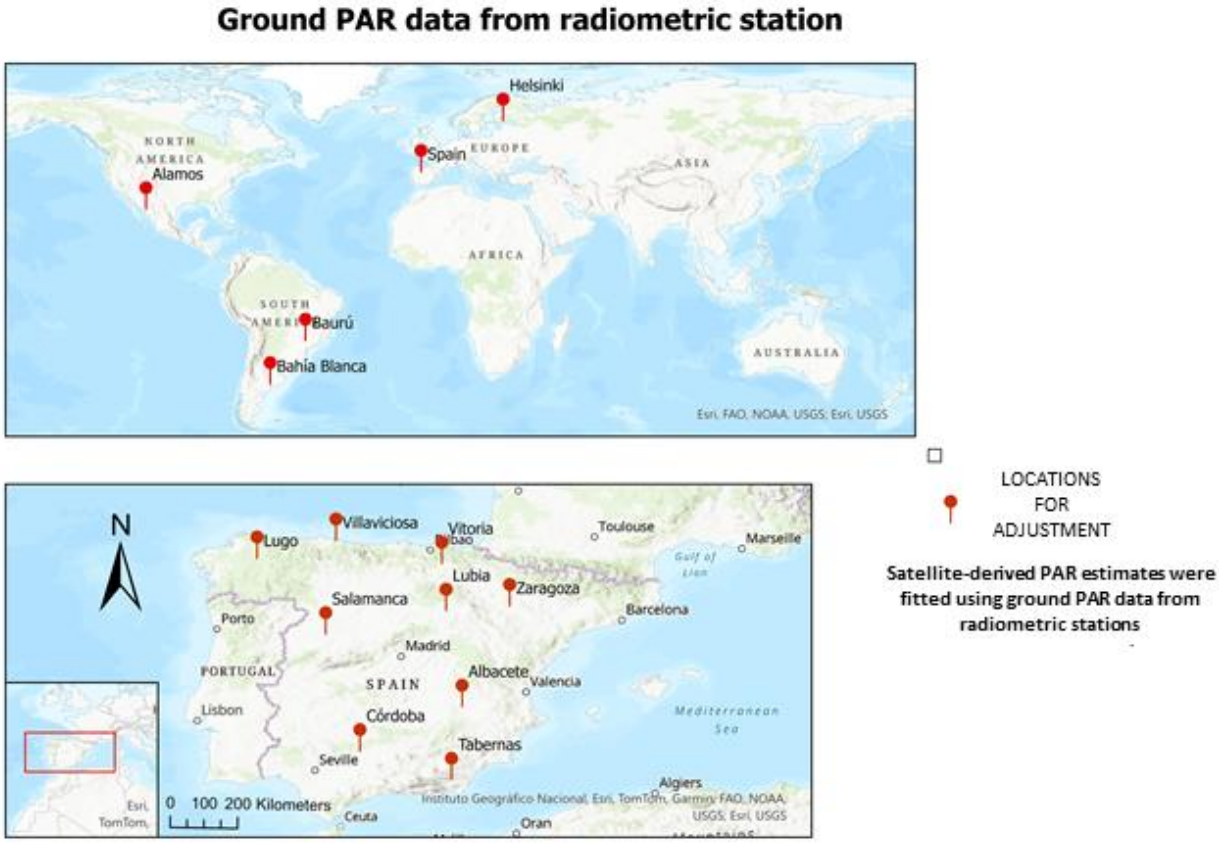

Fig. 1. Locations used in this work.

All data from the 13 locations were classified according to their Köppen-Geiger class. As there were some similar climate classes, the climatic classification was simplified into the following five groups.

- Hemiboreal
- Semi-arid
- Mediterranean
- Oceanic
- Tropical

A linear regression between the PAR satellite-derived data and the PAR ground observations was used to perform site adaptation for each of the climates, as illustrated in eq. 1. This method implies the use of observed data to refine satellite estimates.

$$y_{local} = a \cdot x_{satellite} + b \qquad \text{(eq. 1)}$$

Where the slope of the linear regression is a, the intercept is b, y_{local} refers to the ground-observed data, $x_{satellite}$ indicates the satellite-derived data.

In this work, this methodology is applied to PAR data. Therefore, the ground-observed PAR data is used as y_{local}, whereas the satellite-derived PAR data is used as $x_{satellite}$. To perform the training of the models, the fittings were conducted for each of the groups of PAR data (hemiboreal climate, semiarid climate, mediterranean climate, oceanic climate, and tropical climate) allowing us to obtain the corresponding parameters a and b for each of the climates. These parameters can be used to estimate PAR in a location with the same climate, using PAR satellite-derived data from this location, as eq. 2 shows. Thus, using eq. 2 we can obtain local climate-based PAR estimates from satellite-derived data.

The mathematical expression of the resulting PAR model derived from the linear regressions is shown in eq. 2.

$$PAR_{adjusted} = a \cdot PAR_{satellite} + b \qquad \text{(eq. 2)}$$

To eliminate outliers, the data were previously checked and filtered. Any data whose ratio between ground-observed PAR and satellite-derived PAR differed more than 40% from the mean of the dataset ratio were dismissed.

The corresponding PAR data for each of the climates were randomly divided 70/30 into two groups. The first group, which contained 70% of the data, was used to train the models and obtain the parameters a and b for each climate. The remaining data were subsequently used to validate the models.

3. Results

The preliminary results training the models showed good correlations in all climates except in the semi-arid case, where the R^2 was 0.563. Furthermore, two different data groups can be observed in Fig. 2, since the scatterplot between the measured and remote-sensing PAR shows a 'V' shape. As a consequence, semi-arid climate was divided into two subclasses: Cold Semi-arid and Hot Semi-arid. After division, the R^2 numbers improved significantly, from 0.563 to 0.918 and 0.801, respectively. The statistics MBE (mean bias error) and RMSE (root mean squared error) improved as well in the cold semi-arid climate. In contrast, these statistics showed worse numbers in the hot semi-arid climate. Interestingly, the slopes obtained differ significantly from the cold to the hot semi-arid climate (1.20 to 1.67).

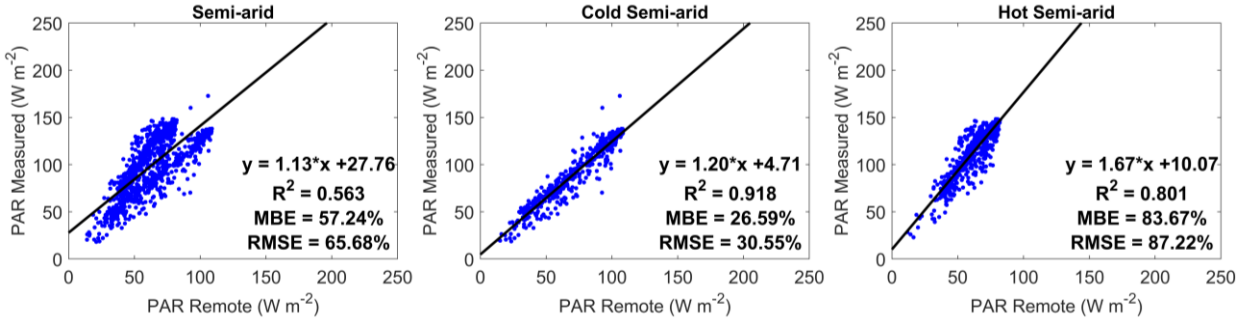

Fig. 2. Training models for semi-arid climates

Fig. 3 illustrates the results of training the models, with the semi-arid climate divided into two subclasses.

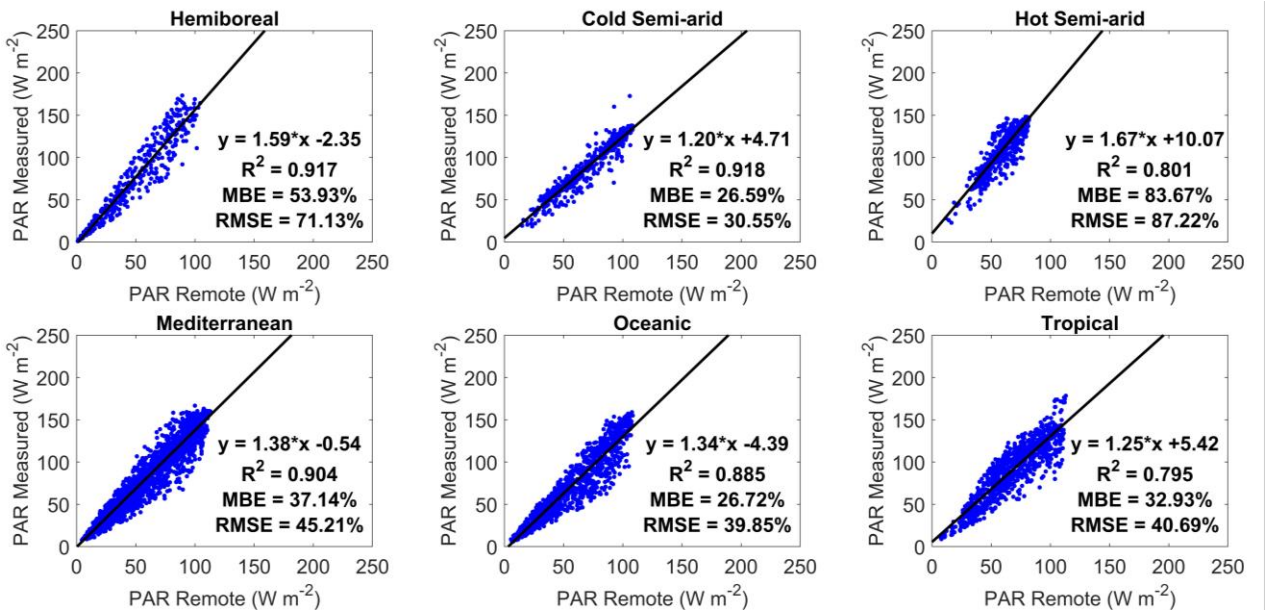

Fig. 3. Results of the training process for each climate.

Interestingly, all climates showed good correlations, the worst being tropical, where the R^2 was 0.795. Although MBE and RMSE did not show numbers lower than 26%. It is also noticeably that the slopes vary from one climate to another; the highest slope is for the hot semi-arid climate, and the lowest slope is for the cold semi-arid climate. The remaining slopes range between these two extremes. Thus, according to these results, the model adjustment for each climate is illustrated in Tab. 2.

Tab. 2. Model expressions for each climate.

Climate type	Model expression
Hemiboreal	$PAR = 1.59 \cdot PAR_{satellite} - 2.35$
Cold Semi-arid	$PAR = 1.20 \cdot PAR_{satellite} + 4.71$
Hot Semi-arid	$PAR = 1.67 \cdot PAR_{satellite} + 10.07$
Mediterranean	$PAR = 1.38 \cdot PAR_{satellite} - 0.54$
Oceanic	$PAR = 1.34 \cdot PAR_{satellite} - 4.39$
Tropical	$PAR = 1.25 \cdot PAR_{satellite} + 5.42$

The expressions for the adjusted models were validated using the remaining 30% of the data that were not used in the training process. Fig. 4 shows the validation results.

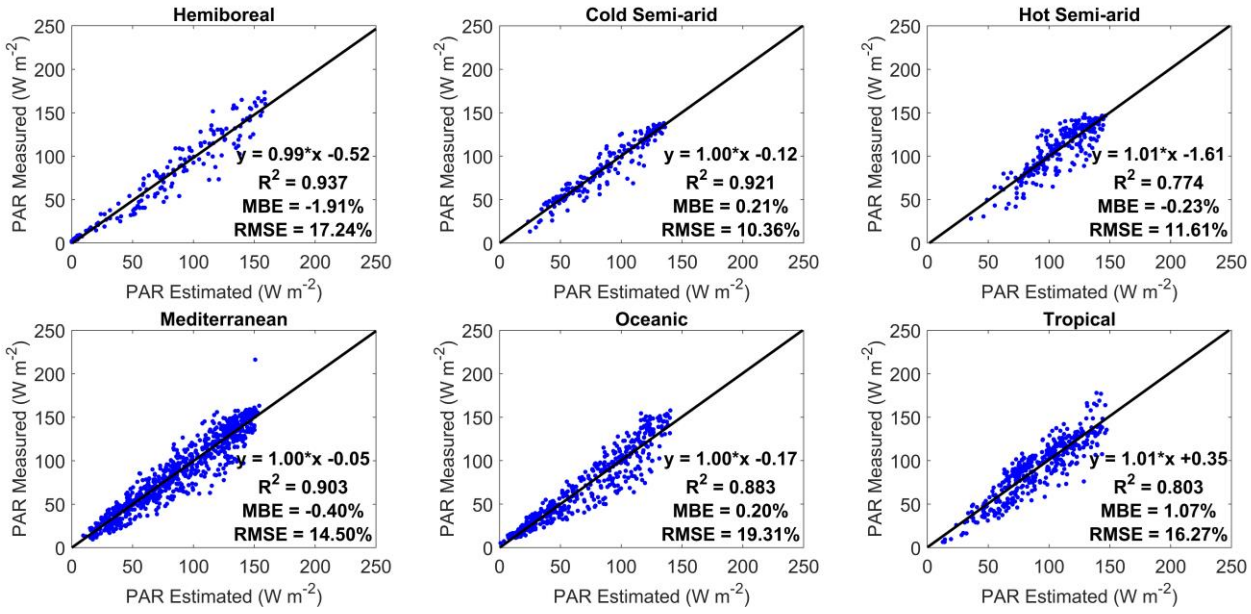

Fig. 4. Results of the validation process for each climate.

The results indicate a good performance of the models, as all slopes range from 0.99 to 1.01, and a good determination coefficient, as the lowest R2 is 0.774 and three of them are above 0.9. The MBE in absolute value is below 2% in all cases. However, the worst statistics obtained were RMSE, which in no case was lower than 10%. Model adjustment seems to perform better in dry and stable weather climates such as cold semi-arid or Mediterranean climates. Models obtained worse results in climates where precipitations are more common, such as tropical or oceanic. Interestingly, the error statistics in the hot semi-arid climate are good, despite having the worst R^2. In fact, its MBE and RMSE (-0.23% and 11.61%, respectively) are the second lowest among all climates under study. This climate is only covered by one location, thus local perturbations or disturbances cannot be ruled out, and further research is needed to understand and improve the model adjustment in this climate.

4. Conclusions

A local adjustment was proposed for photosynthetically active radiation (PAR) estimates in 13 locations around the world with five different climate types. The proposed methodology develops local models using satellite-derived and ground-observed PAR data. Merging data from sites with the same climatic features enable to develop models based on their climatic classification. Therefore, these models can also be used to estimate PAR in other locations whose climate is the same. The estimates provided by the proposed models are a useful tool for obtaining PAR data at locations where no ground observed data are available and can be of interest for energy balance in ecosystem calculations, biomass production models, agrofood industry, etc. that need PAR data as input.

The statistical results showed a good correlation between the adjusted satellite-derived PAR estimates using the proposed method and the ground-measured PAR data at the locations studied. The type of semi-arid climate initially showed a poor correlation; indeed, two groups of data could be observed. This made it necessary to divide the semiarid climate type into two classes (hot semiarid and cold semiarid) to obtain good fitting results, supporting the idea that PAR is strongly dependent on local climatic and atmospheric conditions. The best results were obtained for the cold semi-arid and mediterranean climates. This good performance of the models in the cold semi-arid and mediterranean climates was expected, as both are usually dry and stable weather climates, so that the satellite-derived estimates are normally more accurate and so does the model adjustment proposed. Noticeably, the results in the hot semi-arid climate are shocking. On the one hand, it had the worst determination coefficient among all climates, and nevertheless its MBE and RMSE are the second best. This could be explained due to local disturbances as this climate is only covered by one location. These results suggest that PAR is affected by local atmospheric conditions, and further research in this field is needed.

5. Acknowledgements

This research was funded by the Spanish Ministry of Science and Innovation (MCIN/AEI/10.13039/501100011033) and the European Union ‘Next Generation EU”/PRTR, TEDDY (TED2021-130366B-I00). The authors also acknowledge the CYTED-Ibero American Programme on Science and Technology for Development (RED RENUWAL P320RT0005 CYTED). Satellite data were downloaded from the Copernicus Atmosphere Monitoring Service (CAMS) Atmosphere Data Store (ADS), particularly global greenhouse gas reanalysis (EGG4) (https://ads.atmosphere.copernicus.eu/cdsapp#!/dataset/cams-global-ghg-reanalysis-egg4?tab=overview) (accessed in February 2022). We acknowledge the following AmeriFlux sites for their data records: MX-Aog (Alamos). In addition, funding for AmeriFlux data resources was provided by the U.S. Department of Energy’s Office of Science. The authors also acknowledge Dr. Pedro Aphalo for the Viikki (Helsinki) PAR data.

6. References

Ferrera-Cobos, F., Vindel, J.M., Valenzuela, R.X., González, J.A., 2020a. Analysis of Spatial and Temporal Variability of the PAR/GHI Ratio and PAR Modeling Based on Two Satellite Estimates. Remote Sens (Basel) 12, 1262. https://doi.org/10.3390/rs12081262

Ferrera-Cobos, F., Vindel, J.M., Valenzuela, R.X., González, J.A., 2020b. Models for estimating daily photosynthetically active radiation in oceanic and mediterranean climates and their improvement by site adaptation techniques. Advances in Space Research 65, 1894–1909. https://doi.org/10.1016/j.asr.2020.01.018

García-Rodríguez, A., Granados-López, D., García-Rodríguez, S., Díez-Mediavilla, M., Alonso-Tristán, C., 2021. Modelling Photosynthetic Active Radiation (PAR) through meteorological indices under all sky conditions. Agric For Meteorol 310, 108627. https://doi.org/10.1016/j.agrformet.2021.108627

Iasimone, F., Panico, A., De Felice, V., Fantasma, F., Iorizzi, M., Pirozzi, F., 2018. Effect of light intensity and nutrients supply on microalgae cultivated in urban wastewater: Biomass production, lipids accumulation and settleability characteristics. J Environ Manage 223, 1078–1085. https://doi.org/10.1016/j.jenvman.2018.07.024

Mazorra Aguiar, L., Polo, J., Vindel, J.M., Oliver, A., 2019. Analysis of satellite derived solar irradiance in islands with site adaptation techniques for improving the uncertainty. Renew Energy 135, 98–107. https://doi.org/10.1016/j.renene.2018.11.099

Pinker, R.T., Zhao, M., Wang, H., Wood, E.F., 2010. Impact of satellite based PAR on estimates of terrestrial net primary productivity. Int J Remote Sens 31, 5221–5237. https://doi.org/10.1080/01431161.2010.496474

Polo, J., Wilbert, S., Ruiz-Arias, J.A., Meyer, R., Gueymard, C., Súri, M., Martín, L., Mieslinger, T., Blanc, P., Grant, I., Boland, J., Ineichen, P., Remund, J., Escobar, R., Troccoli, A., Sengupta, M., Nielsen, K.P., Renne, D., Geuder, N., Cebecauer, T., 2016. Preliminary survey on site-adaptation techniques for satellite-derived and reanalysis solar radiation datasets. Solar Energy 132, 25–37. https://doi.org/10.1016/j.solener.2016.03.001

Trofimchuk, O.A., Petikar, P. V., Turanov, S.B., Romanenko, S.A., 2019. The influence of PAR irradiance on yield growth of Chlorella microalgae. IOP Conf Ser Mater Sci Eng 510. https://doi.org/10.1088/1757-899X/510/1/012017

Wang, C., Du, J., Liu, Y., Chow, D., 2021. A climate-based analysis of photosynthetically active radiation availability in large-scale greenhouses across China. J Clean Prod 315, 127901. https://doi.org/10.1016/j.jclepro.2021.127901

Wu, C., Niu, Z., Tang, Q., Huang, W., Rivard, B., Feng, J., 2009. Remote estimation of gross primary production in wheat using chlorophyll-related vegetation indices. Agric For Meteorol 149, 1015–1021. https://doi.org/10.1016/j.agrformet.2008.12.007

Yepez, E.A., 2020. AmeriFlux BASE MX-Aog Alamos Old-Growth tropical dry forest, Ver. 1-5, AmeriFlux AMP, (Dataset). https://doi.org/10.17190/AMF/1756414

The Aerosol Effect on Direct Normal Irradiance in a Dust-Rich Hot, Desert Climate

Christos Fountoukis, Dunia Bachour, Daniel Perez-Astudillo

Qatar Environment and Energy Research Institute (QEERI), Hamad Bin Khalifa University, Doha, Qatar

Abstract

This study investigates how the spatial and temporal variations in atmospheric aerosols impact Direct Normal Irradiance (DNI) in a region affected by desert dust intrusions. We employ a three-dimensional atmospheric meteorology-chemistry model (WRF-Chem) with a triple-nesting configuration over the Middle East, focusing particularly on the hot desert climate of the Arabian Peninsula. We analyze data of solar radiation covering five-month periods (May-September), which represent both dry and humid summertime conditions in the region. These data are used to evaluate the model's performance. By implementing an advanced prognostic treatment of aerosols, the model demonstrates significantly improved accuracy in predicting DNI. The influence of aerosols on DNI is particularly pronounced in areas affected by human activities, such as large cities, as well as those experiencing desert dust intrusions. In these regions, aerosol-induced attenuation of DNI can exceed 70%, corresponding to a reduction of nearly 6 kWh m^{-2} per day.

Keywords: WRF, WRF-Chem, anthropogenic emissions, desert particles

1. Introduction

Qatar benefits from an abundance of sunlight throughout the year, receiving about 6.1 kWh/m² of solar energy per day (Perez-Astudillo et al., 2022), making it one of the top locations worldwide for solar potential. This high level of solar irradiation throughout the year makes Qatar a prime candidate for solar PV energy projects. The country's annual Global Horizontal Irradiation (GHI), essential for solar photovoltaic (PV) applications, is approximately 2100 kWh/m². According to Qatar's National Research Strategy and Energy Development Action Plan, one of the primary objectives is to implement large-scale PV projects. By the end of 2022, Qatar had achieved 800 MW of utility-scale PV capacity, and it aims to generate over 20% of its total electricity from solar energy by 2030. This transition is expected to contribute to a reduction of up to 26 million metric tons of CO2 equivalent by that year. Considering Qatar's demographic profile and energy requirements, solar energy, especially through distributed residential and commercial PV systems, can significantly aid in meeting the country's solar adoption targets. This approach can lower infrastructure costs and boost energy security. Furthermore, incorporating distributed PV generation into smart grids can improve grid adaptability, manage the variability of renewable energy sources, and decrease peak demand via demand response programs. This not only fortifies grid resilience but also enhances national energy security. Moreover, shifting to solar energy for electricity generation can conserve natural gas, Qatar's primary electricity source, offering potential economic benefits through gas savings for international trade or downstream industrial development.

As the use of solar energy applications increases, accurate forecasting of solar irradiance is essential. Ensuring the precise forecasting of solar irradiance is paramount for reducing grid integration expenses and enhancing the management of electricity grids. Nonetheless, unlike wind power, the prediction of solar insolation still comes with significant errors. A variety of modeling techniques, such as statistical models, satellite data-based models, sky cameras, and numerical weather prediction (NWP) models, are conventionally employed for forecasting DNI. The selection of a modeling approach depends on the forecast timeframe. NWP models are the favored tool for DNI prediction from 6 hours up to several days in advance. These models integrate a radiative transfer model (RTM) to dynamically forecast DNI by simulating the troposphere. Mesoscale NWP models offer benefits as they cover smaller geographic areas (ranging from urban to regional) and are

© 2024. The Authors. Published by International Solar Energy Society
Selection and/or peer review under responsibility of Scientific Committee
10.18086/eurosun.2024.10.04 Available at http://proceedings.ises.org

computationally efficient while incorporating detailed physics compared to global large-scale NWP models. They are particularly suitable for solar irradiance predictions due to their advanced shortwave solar radiation parameterizations (Ruiz-Arias et al., 2013). However, the dynamic behavior of atmospheric aerosols presents a significant challenge for solar radiation forecasts due to the complex and uncertain aerosol radiative forcing. Specifically, uncertainties in the subgrid-scale variability of clouds and the high temporal and spatial variability of atmospheric aerosol concentrations complicate the accuracy of solar radiation predictions. NWPs often inadequately represent complex cloud microphysics and non-deterministic aerosol patterns.

2. Methodology

Solar radiation data utilized in this research were gathered from the high-precision monitoring station operated by the Qatar Environment and Energy Research Institute (QEERI) in Doha (25.33ºN, 51.43ºE). This station is equipped with thermoelectric sensors manufactured by Kipp & Zonen, mounted on a Solys2 sun tracker with a sun sensor kit for precise tracking. GHI and DHI are measured using two CMP11 pyranometers fitted with CVF 3 ventilation units, while DNI is measured using a CHP1 pyrheliometer. The WRF-Chem version 4.5 (Weather Research Forecasting with Chemistry, Fast et al. (2006) three-dimensional meteorology-chemistry model was utilized over the Arabian Peninsula region, with a high grid resolution specifically over Qatar (Fountoukis et al., 2022). The model simulates three fundamental components: emissions of atmospheric constituents (both gases and aerosol particles), their transport, and physicochemical transformations. Employing a two-way nesting configuration, the WRF-Chem model operates across three domains at varying grid resolutions, with information regarding species concentrations exchanged between domains throughout the model integration process. The parent domain adopts a 50 km × 50 km grid resolution, while the intermediate nested domain, focused on the Arabian Desert, employs a 10 km × 10 km resolution. The third domain is configured over the Qatar region with a resolution of 2 km × 2 km. This nesting capability enables WRF-Chem to efficiently cover large geographical areas where regional pollutant transport, such as dust, is significant, while also offering fine resolution in specific areas to capture small-scale features.

3. Results and discussion

Typically, NWPs either disregard atmospheric particles entirely or adopt overly simplified aerosol approaches, frequently resulting in inaccuracies in cloud cover location and duration and substantial biases in solar irradiance projections. In the Arabian Peninsula, elevated temperatures for much of the year lead to cloud-free atmospheric conditions owing to swift cloud dissipation. However, aerosol concentrations persistently remain high due to frequent dust events and other urban emissions (Fountoukis et al., 2016, 2020, 2022; Tsiouri et al., 2015; Prakash et al., 2015). Therefore, accounting for aerosol effects in radiation modules is imperative for mitigating solar irradiance prediction inaccuracies in this region. In this study, we employ WRF-Chem to simulate Direct Normal Irradiance (DNI) in Qatar and the broader Middle East, incorporating an advanced prognostic treatment of aerosols (Fountoukis et al., 2020). Our model's performance is assessed against in-situ measurements, and we investigate the impact of aerosol presence on our predictions.

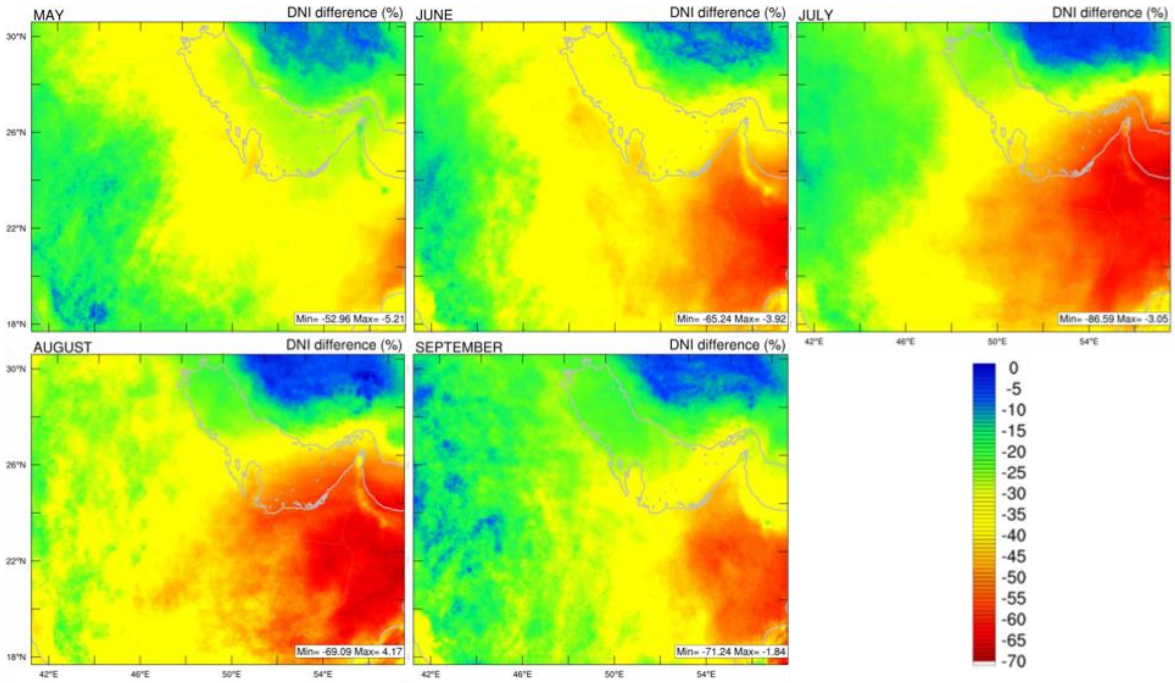

Fig. 1: Average monthly aerosol effect on DNI (%) simulated for the period May – September over the Arabian Peninsula.

Figures 1 and 2 depict the monthly average influence of aerosols on Direct Normal Irradiance (DNI) across the Arabian Peninsula and Qatar, respectively. This influence is assessed by computing the percentage (%) difference between two WRF-Chem DNI forecasts: one with detailed aerosol representation and another assuming no aerosols. The most significant percentage differences are observed in the eastern part of the Arabian Peninsula, with values decreasing by as much as -70%. This translates to a reduction of about 5-6 kWh m^{-2} per day.

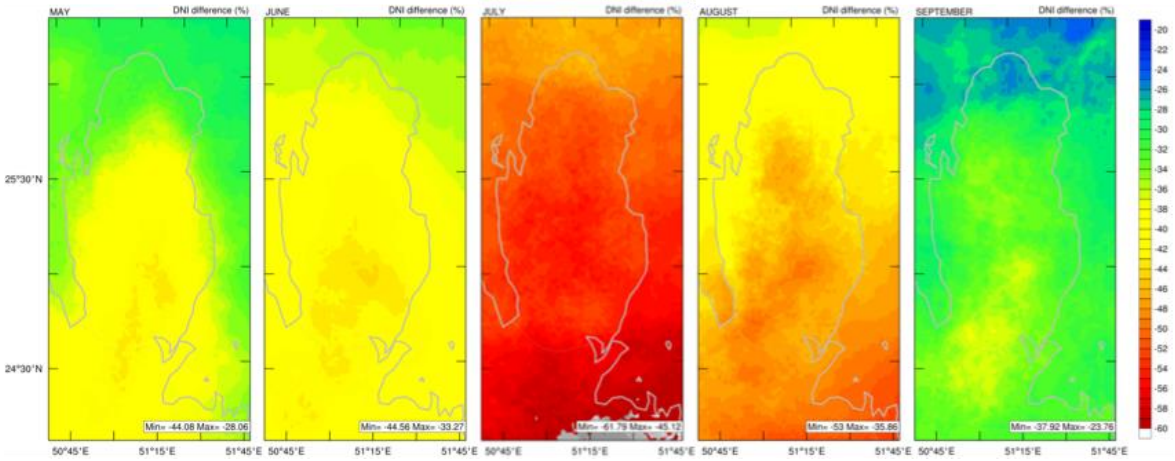

Fig. 2: Aerosol effect on DNI (%) as a monthly mean predicted for the period May – September over the state of Qatar.

This region often experiences dust storms, as noted in prior research (Roshan et al., 2019). Situated downstream of the well-known North Westerly (Shamal) winds, this area is susceptible to dust intrusions originating from the Fertile Crescent region of Iraq and Syria, as well as the deserts of Saudi Arabia, which are directed towards the Eastern Arabian Peninsula and the Arabian Gulf. The Asir Mountains in southwestern Saudi Arabia play a significant role in dust dispersal across the Arabian Peninsula. Their elevation increases the volume of dust transported over and eastward of the mountains into the Eastern Arabian Peninsula.

Notably, the most significant reductions are observed in July and August among the five months studied, coinciding with higher atmospheric relative humidity levels. This increased humidity also impacts the predicted aerosol optical depths by the model, as shown in Figure 3, which illustrates the elevated levels of AOD during the humid months in Qatar.

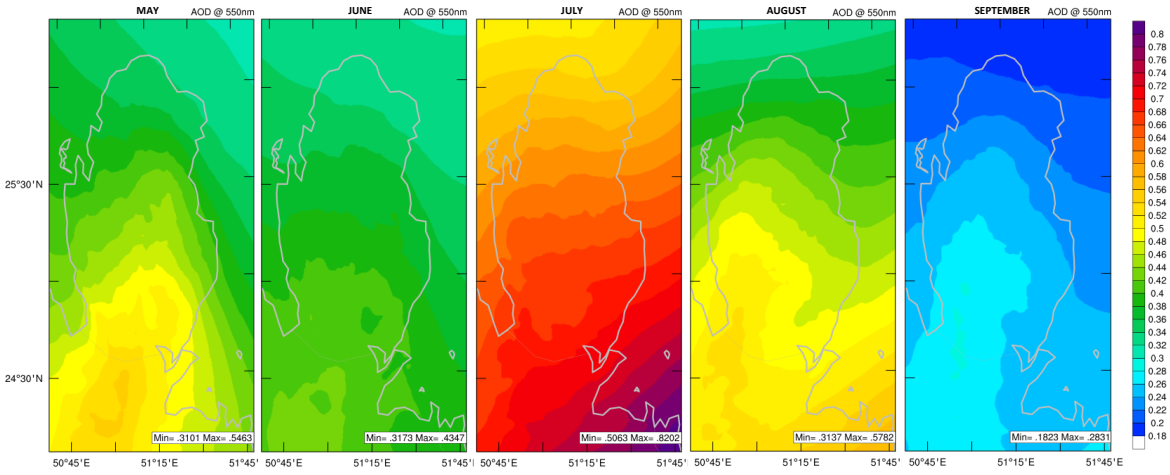

Fig. 3: Aerosol optical depth predicted as a monthly mean for the period May – September over the state of Qatar.

The model's performance significantly improves when incorporating the prognostic treatment of aerosols compared to the observed DNI values. Including comprehensive aerosol physics and chemistry enables the model to accurately replicate the observed DNI in Qatar throughout all studied months, resulting in a 30-40% reduction in the model's relative root mean square error. Figure 4 shows such a comparison for the period of June.

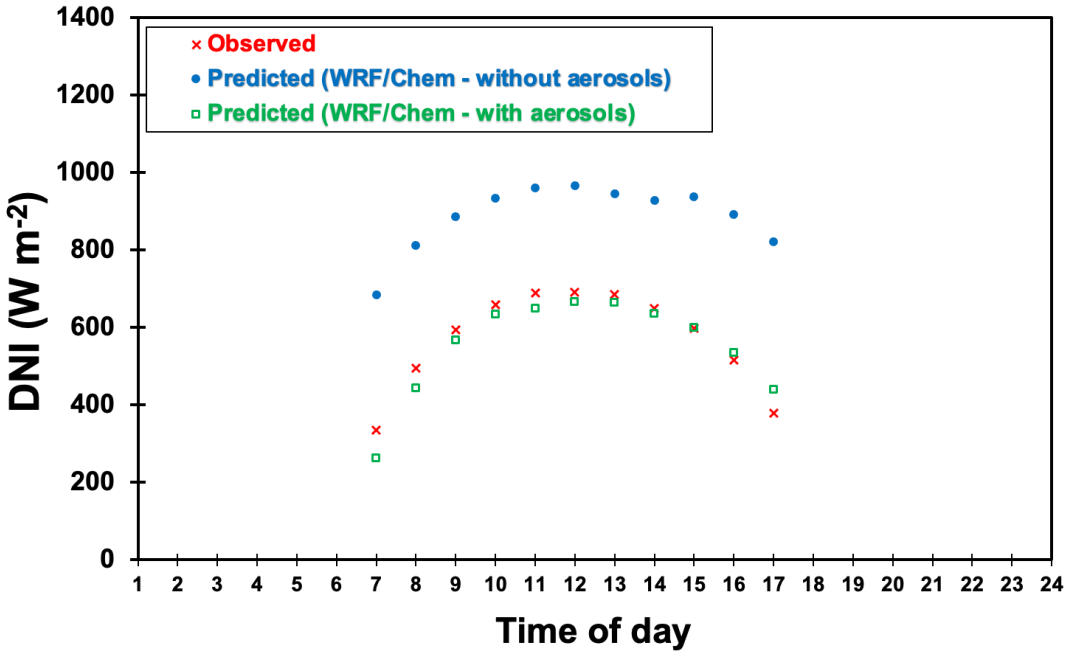

Fig. 4: Average diurnal profile of DNI (W/m^2) during the month of June for the location of QEERI's solar station in Doha, Qatar.

Acknowledgements

Research reported in this work was supported by the Qatar Research Development and Innovation Council (Grant: ARG01-0503-230061). The content is solely the responsibility of the authors and does not necessarily represent the official views of Qatar Research Development and Innovation Council.

4. References

Fast, L.D., Gustafson, Jr. W. I., Easter, R.C., Zaveri, R.A., Barnard, J.C., Chapman, E.G., Grell, G.A., 2005. Evolution of ozone, particulates, and aerosol direct forcing in an urban area using a new fully-coupled meteorology, chemistry, and aerosol model, J. Geophys. Res. (111), D21305. doi:10.1029/2005JD006721.

Fountoukis, C., Ackermann, L., Ayoub, M.A., Gladich, I., Hoehn, R.D., Skillern, A., 2016. Impact of atmospheric dust emission schemes on dust production and concentration over the Arabian Peninsula. Model. Earth Syst. Environ. 2 (115), doi:10.1007/s40808-016-0181-z.

Fountoukis, C., Harshvardhan, H., Gladich, I., Ackermann, L., Ayoub, M.A., 2020. Anatomy of a severe dust storm in the Middle East: Impacts on aerosol optical properties and radiation budget, Aerosol and Air Quality Research, 20, 155-165, doi: 10.4209/aaqr.2019.04.0165

Fountoukis, C., Mohieldeen, Y., Pomares, L., Gladich, I., Siddique, A., Skillern, A., Ayoub, M.A., 2022. Assessment of High-resolution Local Emissions and Land-use in Air Quality Forecasting at an Urban, Coastal, Desert Environment, Aerosol and Air Quality Research, 22 (6), https://doi.org/10.4209/aaqr.220001.

Perez-Astudillo, D., D. Bachour, A. Sanfilippo, H. Al-Hajri. Management and Operation of Qatar's Solar Radiation Monitoring Network. EuroSun 2022 Proceedings. DOI: 10.18086/eurosun.2022.15.06

Prakash, P.J., Stenchikov, G., Kalenderski, S., Osipov, S., Bangalath, H., 2015. The impact of dust storms on the Arabian Peninsula and the Red Sea, Atmos. Chem. Phys. 15, 199-222. doi:10.5194/acp-15-199-2015.

Roshan, D.R., M. Koc, R. Isaifan, M.Z. Shahid, C. Fountoukis, Aerosol Optical Thickness over Large Urban Environments of the Arabian Peninsula—Speciation, Variability, and Distributions, Atmosphere, 10 (5), 228, 2019.

Ruiz-Arias, J.A., Dudhia, J., Santos-Alamillos, F.J., Pozo-Vazquez, D., 2013. Surface clear-sky shortwave radiative closure intercomparisons in the Weather Research and Forecasting model, J. Geophys. Res. Atmos. 118 (2013) 1-13, http://dx.doi.org/10.1002/jgrd.50778.

Tsiouri, V., Kakosimos, K.E., Kumar, P., 2015. Concentrations, sources and exposure risks associated with particulate matter in the Middle East Area - a review, Air. Qual. Atmos. Health 8, 67-80, doi:10.1007/s11869-014-0277-4.

Assessing the Impact of Diffuse Fraction Estimation on Ground Albedo Modeling

Juan M. Rodríguez-Muñoz, Rodrigo Alonso-Suárez, Italo Bove and Gonzalo Abal

Laboratorio de Energía Solar, Universidad de la República (Uruguay)

Abstract

Ground reflectivity or albedo is required for the estimation of the solar irradiance incident on an inclined surface. The ground is frequently modeled as a constant albedo diffuse reflector and this is inadequate for several solar energy applications, particularly for bifacial PV power plant yield estimation. Recent advances have categorized albedo models according to their complexity, with bivariate models -those incorporating the zenith angle and diffuse fraction- performing better. In a previous study, Rodríguez-Muñoz et al. (2022) evaluated six albedo models and confirmed that bivariate models were the most accurate. However, they also highlighted the need for measurements of both global and diffuse solar irradiance to apply these models. For simplicity, empirical diffuse fraction models can be used instead of using diffuse irradiance measurements. This study builds upon prior research by assessing the impact of employing empirical diffuse fraction models on albedo estimation. To assess this, measurements were conducted over the course of approximately one year at an experimental site with soil and climate conditions representative of the Pampa Húmeda region in South America. The results indicate that incorporating these models into albedo estimation slightly degrades performance, but still outperforms constant and univariate models. Thus, a bivariate albedo model combined with diffuse fraction estimates represents an effective balance between accuracy and simplicity.

Keywords: ground albedo, diffuse fraction, bifacial PV.

1. Introduction

Solar energy applications require estimating global solar irradiance on surfaces of arbitrary orientation, which includes three components: direct irradiance, diffuse irradiance from the sky, and irradiance reflected from nearby surfaces. Traditional transposition models typically focus only on ground reflection, assuming it to be hemispherical and isotropic reflecting surface with constant albedo. This assumption is generally sufficient when the reflected component constitutes a small portion of the total incident irradiance, as in many solar energy applications. However, this assumption is less suitable for bifacial photovoltaic panels, which are more sensitive to ground reflection. These panels can generate up to 15% more energy annually than conventional panels on typical albedo soils, and up to 30% more on highly reflective soils (Yusufoglu et al., 2014). The increasing adoption of this technology suggests it will soon dominate the market (Kopecek & Libal, 2021). This trend has motivated the advancement of more sophisticated albedo models that take into account solar geometry, cloud cover, and the characteristics of the surrounding terrain.

These models fall into three categories of increasing complexity. The first category (I) includes models that assume that the ground is a diffuse hemispherical isotropic reflector with a constant albedo. Variations in these models arise from different methods for assigning this constant value (Liu & Jordan, 1960; Gueymard, 1987; Psiloglou & Kambezidis, 2009). The second category (II) includes models that introduce some specular component in the reflected ground irradiance, thus treating albedo as a univariate function of the solar zenith angle (Nkemdirim, 1972; Temps & Coulson, 1977; Dickinson, 1983; Psiloglou & Kambezidis, 2009; Tuomiranta et al., 2021). The third category (III) includes models that further refines the previous by incorporating cloudiness information (through the diffuse fraction) into the albedo calculation (Temps & Coulson, 1977; Gueymard, 1987; Gardner & Nadeau, 1988; Ineichen et al., 1990; Chiodetti et al., 2016; Tuomiranta et al., 2021). These latter models require measurements of both global and diffuse horizontal irradiance, whereas the simpler models in the first two categories only need global irradiance.

Comparative performance of these models across different soils and climates has been explored in the literature (Ineichen et al., 1990; Psiloglou & Kambezidis, 2009; Tuomiranta et al., 2021). Early studies recommended using constant, locally measured albedo values based on terrain characteristics (Ineichen et al., 1990). However, more recent research, such as Tuomiranta et al. (2021), which evaluated 26 albedo models at 26 sites, reports significant

© 2024. The Authors. Published by International Solar Energy Society
Selection and/or peer review under responsibility of Scientific Committee
10.18086/eurosun.2024.10.05 Available at http://proceedings.ises.org

benefits of using bivariate models. Their findings also suggest that relying on constant albedo values from databases can introduce significant errors, highlighting the need for local model adaptation to reflect typical conditions accurately.

Given the importance of local adaptation, Rodríguez-Muñoz et al. (2022) evaluated the performance of six pre-existing models for estimating green grass albedo using data from a site in the Pampa Húmeda region in South America (Salto, Northwest of Uruguay). Two models from each category were selected based on Tuomiranta et al. (2021). The best-performing model was identified both globally and within each category. The models' coefficients were determined through random sampling and cross-validation using albedo measurements from the Solar Energy Laboratory at the University of the Republic of Uruguay (LES-UdelaR). The most accurate models were those in the third category, which are bivariate and depend on the Sun position in the sky and the diffuse fraction. However, these models are more complex to implement and calibrate locally, as they require the additional measurement of horizontal diffuse irradiance (DHI) for the calculation of the diffuse fraction, $f_d = \mathrm{DHI}/\mathrm{GHI}$, where GHI is the horizontal global solar irradiance. Datasets with DHI are less common than those with GHI, since the accurate measurement of the diffuse component requires precise solar tracking for blocking the direct and circumsolar components and this implies frequent maintenance.

An alternative approach to simplify the implementation of bivariate albedo models is the use of empirical diffuse fraction models. These models estimate the diffuse fraction through empirical correlations based on geometrical calculations and global irradiance data, such as the solar zenith angle and clearness index, thus eliminating the need for measurements of diffuse solar irradiance (Abal et al., 2017; Yang, 2022). This study aims to assess the impact on model performance when using empirical diffuse fraction models instead of diffuse solar irradiance measurements.. Specifically, it considers two locally adjusted diffuse fraction models in combination with two bivariate locally adjusted albedo models. The performance of these combinations was assessed using one year of quality-controlled albedo measurements collected at LES-UdelaR, which were independent of the data used in the previous work (Rodríguez-Muñoz et al., 2022). The coefficients of the albedo models were updated due to minor differences in grass height at the site, compared to the previous campaign.

This paper is organized as follows: The next section provides an overview of the models under consideration (both for albedo and diffuse fraction), details the dataset used, outlines the quality control procedures, and describes the performance indicators for model comparison. This is followed by a presentation and analysis of the results. The final section summarizes the main conclusions of this study.

2. Methodology

2.1. Albedo models

The albedo or reflectance of a surface is the fraction of global solar irradiance that is reflected by it. The albedo of the ground, assumed horizontal, is defined as:

$$\rho_g = \frac{G_g}{G_h} \tag{1}$$

where G_g is the irradiance reflected by the ground (to the entire hemisphere) and G_h is the global solar irradiance on a horizontal plane. This parameter depends on various factors: solar altitude, cloudiness, changes due to local climate or human actions (e.g., changes in the surrounding terrain or grass height due to maintenance). The simplest model assumes the ground to be a diffuse hemispherical isotropic reflector with constant albedo independent of the aforementioned variables. The albedo can be obtained from generic databases for different soil types (Liu & Jordan, 1960; Gueymard, 1987) or estimated from experimental measurements, this latter being the recommended procedure (Ineichen et al., 1990; Tuomiranta et al., 2021).

Although this work focuses on bivariate models (category III), it will also include category I and II models to provide a better framework and baseline for comparison, working with a total of four albedo models. The first model considered in this work the arithmetic mean albedo,

$$model\ 1: \rho_g = \frac{1}{n}\sum \rho_i \tag{2}$$

where ρ_i represents the i-th albedo measurement out of n measurements. This model belongs to category I and is considered in Psiloglou & Kambezidis (2009) and Tuomiranta et al. (2021).

The second model in this work corresponds to that proposed by Tuomiranta et al. (2021)

$$model\ 2: \rho_g = \rho_n \times \frac{1 + b_1}{1 + b_1 cos\theta_z} \quad (3)$$

This univariate model depends on the solar zenith angle, θ_z, and has two adjustable parameters: ρ_n and b_1. Is based on the previous work of Dickinson (1983) and involves the restriction: $b_1 \in [0, 2]$, indicating that albedo is an increasing function of the solar zenith angle. This directional model is in category II.

Although there exist other models in categories I and II, the models selected for this study offer the highest performance within their categories for the specific ground and climate conditions considered here. This is supported by the findings of Tuomiranta et al. (2021) and Rodríguez-Muñoz et al. (2022).

The third and fourth models are bivariate and belong to category III. Specifically, the third model extends the second model and as proposed by Tuomiranta et al. (2021). It incorporates cloud cover presence through the diffuse fraction f_d and features three adjustable parameters. This approach allows for separate consideration of reflections from both direct and diffuse solar irradiance:

$$model\ 3: \rho_g = (1 - f_d) \times \rho_{bn} \times \frac{1 + b_1}{1 + b_1 cos\theta_z} + f_d \times \rho_d \quad (4)$$

where ρ_{bn}, b_1, and ρ_d are the adjustable parameters. The parameters ρ_{bn} and ρ_d represent the albedo for beam solar irradiance and diffuse solar irradiance, respectively. The restriction $b_1 \in [0, 2]$ is maintained, and the condition $\rho_{bn} \leq \rho_d$ is added.

The fourth and final model has a similar structure, and was initially proposed by Rodríguez et al. (2022). It builds on Gueymard's (1987) model for inclined surfaces, but has been adapted and simplified for horizontal surfaces. It integrates both the zenith angle and the diffuse fraction into a simplified expression with five adjustable parameters:

$$model\ 4: \rho_g = (1 - f_d) \times \left[\rho_n + e^{b_1 + b_2\theta_z + b_3\theta_z^2}\right] + f_d \times \rho_d \quad (5)$$

where ρ_n represents the albedo for direct normal irradiance under pure isotropy conditions, and ρ_d is the albedo for diffuse irradiance. The parameters b_1, b_2, and b_3 control how the albedo varies with the solar zenith angle. This model has five adjustable parameters in total.

2.2. Diffuse fraction models

As mentioned in the introduction, category III models require two experimental measurements: GHI and DHI. This work explores the cost -in terms of accuracy- of replacing the DHI measurements with a locally adjusted phenomenological model to estimate DHI from GHI.

Numerous phenomenological models for diffuse fraction estimation are used worldwide (see Yang (2022) for a comprehensive review). However, these models often require locally adapted coefficients to perform with acceptable accuracy in different climates. For convenience and simplicity, we selected two of the simplest and best performing models from Abal et al. (2017), which also used data from a site in Salto.

The first model, referred here as RA2s (Ruiz Arias et al., 2010), has a dependence on air mass (or solar zenith angle) and on the clearness index (or GHI), as shown in Eq. (6). The second model, referred here as SO2, is the historical model introduced in Skartveit and Olseth (1987). It has a more complicated structure than RA2s but ultimatley depends on the solar altitude (or solar zenith angle) and the clearness index. Both models, were previously evaluated with locally adjusted coefficients for the Salto site, have a relative RMSD of 16.9% and 16.6% of the measured diffuse fraction, respectively and negligible mean bias (Abal et al. (2017)). As mentioned, both are bivariate and require the clearness index ($k_t = GHI/S_C\ F_n cos(\theta_z)$, a normalized version of the GHI defined below) and the solar zenith angle, which can be calculated from site position and local time information.

The RA2s model is given by the following expression:

$$RA2s\ model: f_d = a_0 + a_1 \times e^{-exp(a_2 + a_3 k_t + a_4 k_t^2 + a_5 m)} \quad (6)$$

where k_t is the clearness index defined as $k_t = G_h/G_{0h}$, where $G_{0h} = S_c F_n cos(\theta_z)$ is the solar irradiance on a horizontal surface at the top of the atmosphere (with a solar constant Sc = 1361 W/m^2 and F_n the orbital factor). The parameter *m* represents the air mass and is calculated from the zenith angle including corrections for sphericity and refraction (Young 1994). The RA2s model has six adjustable parameters: a_0, a_1, a_2, a_3, a_4, a_5.

The SO2 model is shown below,

$$SO2\ model: f_d = \begin{cases} 1 & k_t < k_a \\ f(k_t, \alpha_s) & k_a \le k_t \le \alpha k_b(\alpha_s) \\ f(\alpha k_t, \alpha_s) & k_t > \alpha k_b(\alpha_s) \end{cases} \quad (7)$$

with,

$$\begin{aligned} f(k_t, \alpha_s) &= 1 - (1 - d_1)\left[a\sqrt{K} + (1 - a)K^2\right], \\ K(k_t, \alpha_s) &= \frac{1}{2}\left\{1 + sin\left[\pi\left(\frac{k_t - k_a}{k_b - k_a} - \frac{1}{2}\right)\right]\right\}, \\ k_b(\alpha_s) &= r + sexp\left(\frac{-\alpha_s}{\alpha_0}\right), \\ d_1(\alpha_s) &= r' + s'exp\left(\frac{-\alpha_s}{\alpha_0}\right), \end{aligned} \quad (8)$$

where α_s is the solar altitude and the complementary angle of the zenith angle, and α_0=0.291. This model also has six adjustable parameters: a, k_a, r, s, r′, and s′.

The locally determined parameters for both models, specific to the location of this work (Salto), can be found in Abal et al. (2017).

2.3 Experimental data and quality control

The experimental data for this study was collected at the Solar Energy Laboratory of the University of the Republic of Uruguay (LES-UdelaR, from its Spanish name), located in a semi-rural area near the city of Salto (latitude: 31.28°S, longitude: 57.92°W, altitude: 60 m above sea level). LES is located in the Pampa Húmeda climate region, classified as Cfa (warm temperate, humid, with hot summers) according to the updated Köppen-Geiger classification (Peel et al., 2007). The data results from a setup deviced specifically to measure ground albedo and set spans approximately one year, from January 2023 to January 2024. It includes global horizontal irradiance (G_h or GHI), solar irradiance reflected by the ground with no tilt (G_g), diffuse horizontal irradiance (G_d or DHI), and normal incidence solar irradiance (G_b or DNI) recorded at one-minute intervals.

Fig. 1a: Albedo measurement setup, including G_h and G_g sensors (both instruments on the right; the others are for inclined solar irradiance, not used in this study).

Fig. 1b: SOLYS2 system with G_d and G_b sensors.

Fig. 1: Installation of measuring instruments.

The ground under study is covered mainly by green grass, and its albedo was calculated using Eq. (1) with measurements of G_g and G_h. These measurements were taken with Kipp & Zonen CMP6 pyranometers positioned 1.2 meters above the ground, using a special support shown in Fig. 1a (both equipment at the right). Horizontal diffuse solar irradiance, G_d, was measured with a Kipp & Zonen CMP10 ventilated pyranometer with a shading ball,

mounted on a SOLYS2 tracking system (Fig. 1b), located about 30 meters from the previous setup. Direct normal irradiance was measured with a Kipp & Zonen CHP1 pyrheliometer on the same tracking system, primarily for quality control. All pyranometers are maintained daily and calibrated twice a year against the LES secondary standard, which is traceable to the World Standard Group in the World Radiation Center in Davos, Switzerland. Data were recorded every minute and averaged over ten-minute intervals to account for spatial mismatch between measurements and to account for rapid irradiance variations due to specific cloud formations.

The diurnal dataset (N=22282 records) was subjected to a series of quality control filters based on the Baseline Solar Radiation Network guidelines (BSRN; McArthur (2005)). The quality control process is summarized in Table 1 and Fig. 2. Each filter is applied on diurnal records, independently from the rest, except for the last one. The first four filters (F1 to F4) apply upper and lower limits to the solar irradiance measurements, G, as follows:

$$b \leq G \leq S_c p(cos\theta_z)^a + c \quad (9)$$

where G represents each solar irradiance component and parameters *p*, *a*, *b*, and c were determined locally for each filter through visual inspection. Filter F5 imposes a lower limit on solar altitude, $\alpha_s > 10°$, excluding measurements affected by significant directional errors (low solar altitudes). Filter F6 checks that G_h, G_d, and G_b satisfy the closure relation:

$$G_h = G_b cos\theta_z + G_d \quad (10)$$

with an 8 % tolerance from the average G_h. Filter F7 imposes an upper limit on the diffuse fraction, ensuring that f_d <1.03, with a 3 % tolerance to allow for experimental error. Filter F8 eliminates data points with low clearness index and low diffuse fraction, typically linked to errors under heavy overcast conditions and low irradiance. Filter F9 sets a loose upper limit on the clearness index, with $k_t < 1$. Filter F10 ensures albedo measurements are within the theoretical range $0 \leq \rho_g \leq 1$. Finally, Filter F11 is a statistical filter that removes outliers, defined as albedo data not meeting the condition $\left|\rho_g - \overline{\rho}_g\right| \leq 3\sigma$, where $\overline{\rho}_g$ and σ represent the mean and standard deviation of albedo measurements in the corresponding interval. This filter is applied independently in data bins defined by 10-degree zenith angle intervals, following the application of filters F1 to F11. At the end of this process, approximately 43 % of the original data was discarded, with 14 % removed due to solar altitude (F5). Table 1 provides details on each filter's conditions, the variables affected, the number of passing data points, and those discarded.

Tab. 1: Detail of the filtering process applied to the diurnal measurements

Filter	condition	variable	output	% discarded
F1	Eq. (9)	G_h	20749	6.9
F2	Eq. (9)	G_d	18304	17.9
F3	Eq. (9)	G_b	21724	2.5
F4	Eq. (9)	G_d	19930	10.6
F5	$\alpha_s > 10°$	all	19102	14.3
F6	Eq. (10)	G_h, G_d, G_b	18549	16.8
F7	$f_d < 1.03$	G_h, G_d	16860	24.3
F8	$k_t < 0.20$ & $f_d > 0.80$	G_h, G_d	21313	4.4
F9	$k_t < 1$	G_h	22269	0.0
F10	$0 \leq \rho_g \leq 1$	G_g, G_h	19866	10.8
F11	$\left\|\rho_g - \overline{\rho}_g\right\| \leq 3\sigma$	G_g, G_h	15949	28.4
all	-	all	12698	43.0

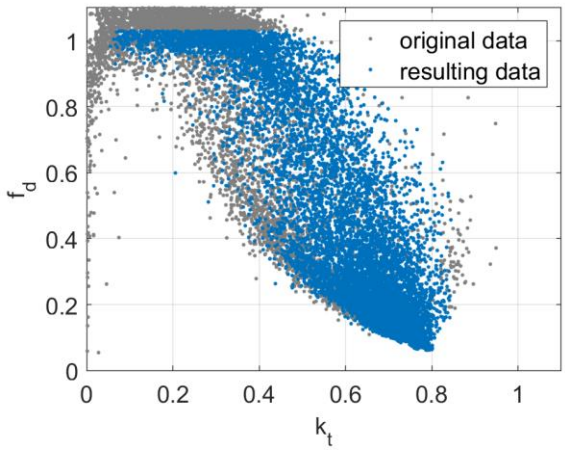

Fig. 2a: Diffuse fraction vs clearness index.

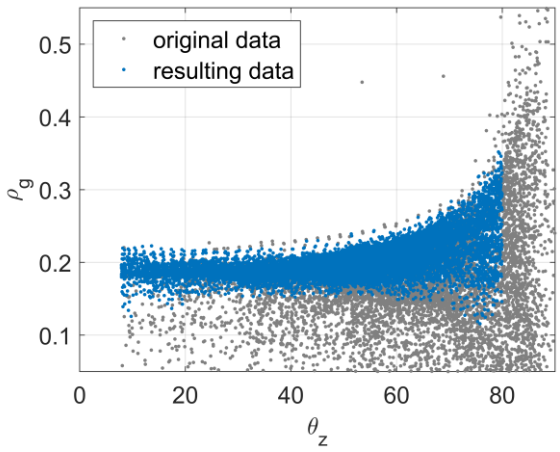

Fig. 2b: Albedo vs zenith angle.

Fig. 2: Result of the filtering procedure: original data in gray and data resulting from the filtering procedure in blue (those that pass all filters).

2.3 Methodology and performance indicators

The methodology employed in this work has three parts. First, the filtered dataset was employed to update the coefficients of the previously described albedo models. For Model 1, the arithmetic mean of the albedo measurements was calculated using Eq. (2). For Models 2 to 4, regression algorithms were utilized to minimize the mean squared error between measured and modeled albedo. For this part, the measured diffuse fraction was used for Models 3 and 4, without imposing any optimization parameter constraints. In the second part of the study, the performance of the diffuse fraction models RA2a and SO2 was evaluated. Finally, in the third part, the performance of Models 3 and 4 was reassessed using diffuse fraction estimates derived from the RA2a and SO2 models.

The coefficients from previous work (Rodríguez-Muñoz et al, 2022) were not utilized due to differences in the experimental setup and grass height, which may influence the albedo. Efforts were made to maintain a relatively constant grass height in a broad circle around the setup throughout the year, but the data may contain seasonal trends, since different amounts of rainfall and air temperature between summer and winter may seasonally affect the albedo of the grass. To update model coefficients and performance indicators, random sampling and cross-validation were employed, with 60% of the data utilized for training and 40% for validation. To ensure the consistency of the results, the 60/40 split was repeated 1,000 times, and the final results are the average of the coefficients and the performance indicators, respectively.

The model performance was evaluated using three indicators: mean bias deviation (MBD), root mean squared deviation (RMSD), and Kolmogorov-Smirnov integral (KSI). These are defined as follows:

$$MBD = \frac{1}{n}\sum_{i=1}^{n}(\hat{y}_i - y_i), \qquad RMSD = \left[\frac{1}{n}\sum_{i=1}^{n}(\hat{y}_i - y_i)^2\right]^{1/2}, \qquad KSI = \int_0^1 \left|\hat{F}(y) - F(y)\right| dy, \tag{11}$$

where y_i represents the reference value (albedo measurement), $\hat{y}_i$ is the model estimate, and $F(y)$ and $\hat{F}(y)$ are the cumulative probability distributions of y_i and $\hat{y}_i$, respectively. These metrics share the same units as y_i, making them dimensionless for albedo measurements. They can also be expressed relatively (rMBD, rRMSD, and rKSI) as a percentage of the mean measurement value. Each indicator provides unique information about the model's accuracy: MBD shows the average bias of the estimates, RMSD gauges the spread of the estimation errors, and KSI quantifies the statistical distance between the cumulative distributions of measurements and estimates. In order to provide a unified representation of these indicators, the Combined Performance Indicator (CPI) has been defined, integrating the three metrics into a single one:

$$CPI = \frac{1}{3}(|rMBD| + rRMSD + rKSI) \tag{12}$$

A similar global indicator has been proposed in Gueymard (2014) and has been successfully used in evaluating diffuse fraction models (Abal et al., 2017) and correction factors for diffuse irradiance measurements (Rodríguez-Muñoz et al., 2021).

3. Results

3.1 Locally adjusted albedo models performance

Table 2 shows the locally adjusted coefficients for the albedo models. As mentioned before, the values presented in this table correspond to the average of the 1000 iterations of the sampling and cross-validation procedure.

Tab. 2: Coefficients for locally adjusted models.

Model	coefficients				
	ρ_n/ρ_{nb}	b_1	b_2	b_3	ρ_d
1 - Arithmetic average, Eq. (2)	0.2021	-	-	-	-
2 - Tuomiranta et al. (2021), Eq. (3)	0.1651	0.0039	-	-	-
3 - Tuomiranta et al. (2021), Eq. (4)	0.1692	0.9406	-	-	0.1862
4 - Modified Gueymard (1987), Eq. (5)	0.1618	-3.5233	-0.0209	0.0005	0.1859

The standard deviations of the coefficients were also calculated, which turned out to be at least 30 times smaller than the averages, the small variability indicates the robustness of the models and the adjustment methods. The parameters of the models from Tuomiranta et al. (2021) models satisfy the constraints $b_1 \in [0, 2]$ and $\rho_{bn} \leq \rho_d$, indicating that these constraints do not need to be imposed during the parameter adjustment procedure, at least for the data used in this particular study. The values of the coefficients ρ_n, ρ_{nb}, and ρ_d are slightly lower than those previously adjusted by Rodríguez-Muñoz et al. (2022). For instance, in the case of model 1, the average value decreased from 0.2209 to 0.2021. This discrepancy is likely due to differences in soil humidity or grass height, as investigated by Dickinson (1983), which found that albedo values are inversely proportional to grass height. The coefficients describing the variation of albedo with the zenith angle, b_1, b_2, and b_3, remain practically unchanged from those reported in Rodríguez-Muñoz et al. (2022).

The performance indicators for the four models are shown in Table 3 as a percentage of the mean albedo value, $\overline{\rho}_g = 0.2021$. The indicators and overall ranking are similar to those presented in Rodríguez-Muñoz et al. (2022). All models show a mean bias close to zero (<1%). Based on rRMSD, the models are ranked from worst to best from 1 to 4. Based on rKSI, they are ranked 1, 2, 4, and 3, while based on the combined indicator CPI, they are ranked 1, 2, 4, and 3. In general, model performance improves with complexity: bivariate models (3 and 4) perform best, followed by univariate models (2), and the constant model (1) performs worst. Category III models (bivariate) perform similarly. Model 3 performs slightly best according to CPI, followed closely by model 4. Although Model 4 has the lowest rRMSD, this does not compensate for the difference in rKSI (statistical similarity of distributions). The difference in performance is small enough to consider them with similar accuracy.

Tab. 3: Performance indicators for the four albedo models, expressed as a percentage of the mean measurement value, $\overline{\rho}_g = 0.2021$.

Model	Relative performance indicators (%)			
	rMBD	rRMSE	rKSI	CPI
1 - Arithmetic average, Eq. (2)	0.0	12.2	8.9	7.0
2 - Tuomiranta et al. (2021), Eq. (3)	-0.7	9.4	2.6	4.0
3 - Tuomiranta et al. (2021), Eq. (4)	0.0	8.3	1.7	3.3
4 - Modified Gueymard (1987), Eq. (5)	0.0	7.9	2.6	3.5

Complementing the previous analyses, Fig. 3 shows the comparison of albedo measurements with model estimates in ρ_g vs. θ_z plots. Model 2 (Fig. 3a) generally describes the increasing behavior of albedo with solar zenith angle but does not capture the data scatter due to variations in cloud conditions. Model 3 (Fig. 3b) on the other hand, captures both the zenith angle dependence and the cloud condition dependence. Model 4 shows a similar behavior o its plot is omitted.

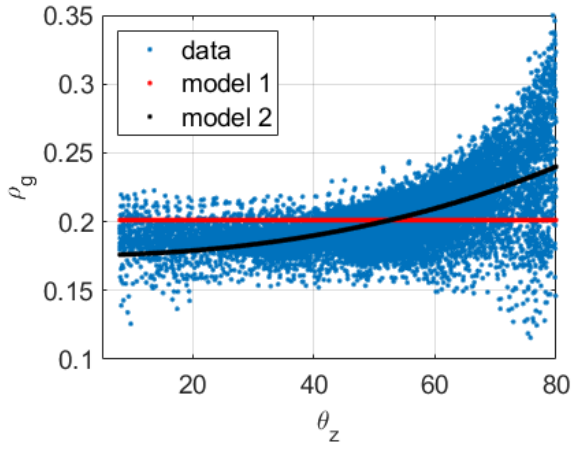

Fig. 3a: Model 1 and 2.

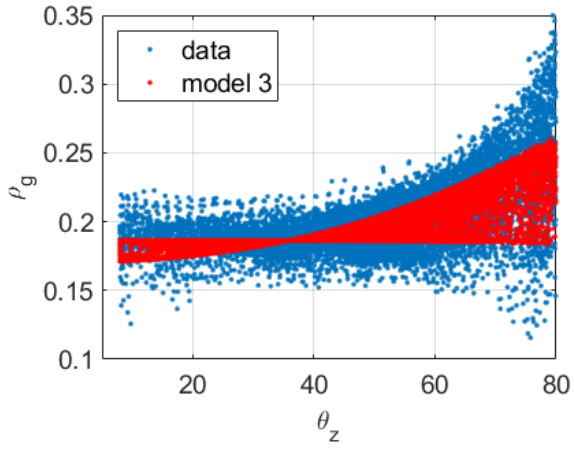

Fig. 3b: Model 3.

Fig. 3: Comparison between albedo measurements and estimates from different models.

3.2 Diffuse fraction model performance

As mentioned in the introduction, there is a plethora of phenomenological models for estimating the diffuse fraction from clearness index, solar zenith angle and other variables. A comprehensive review considering the performance of 140 published models against quality 1-minute data from 54 sites worldwide was published in 2016 (Gueymard and Ruiz-Arias, 2016). This work assessed the models with their original coefficients, which were derived from diverse datasets under different climatic conditions. Furthermore, several coefficients were derived from hourly datasets and used for 1-minute estimation of diffuse fraction. A more recent review (Yang 2022) considered 10 of the best diffuse fraction models against a 1-min dataset with five years of 1-min data from several sites worldwide. In this case, the coefficients where adjusted by grouping the data by broad climate zones, making for 5 or 6 sets of coefficients covering the whole globe. If anything, this search for a "quasi-universal" diffuse fraction model strongly suggests to us that there is no such thing. For a good performance, a diffuse fraction model must be adjusted to local data.

Tab. 4: Performance indicators for the for the two diffuse fraction models, expressed as a percentage of the mean measurement value, $\overline{f}_d = 0.3710$.

Model	Relative performance indicators (%)			
	rMBD	rRMSD	rKSI	CPI
RA2s	-7.7	33.4	10.1	17.1
S02	-11.5	33.5	12.3	19.1

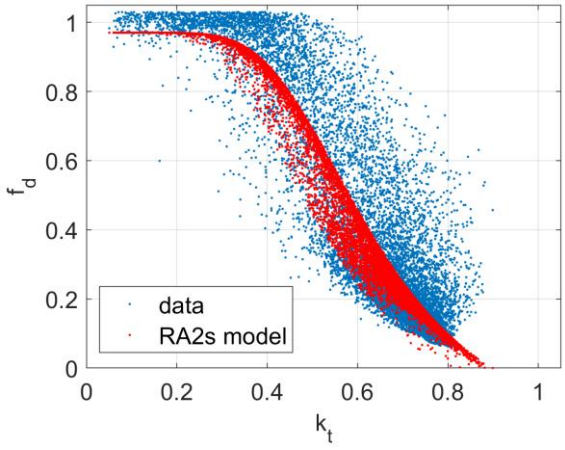

Fig. 4a: RA2s model.

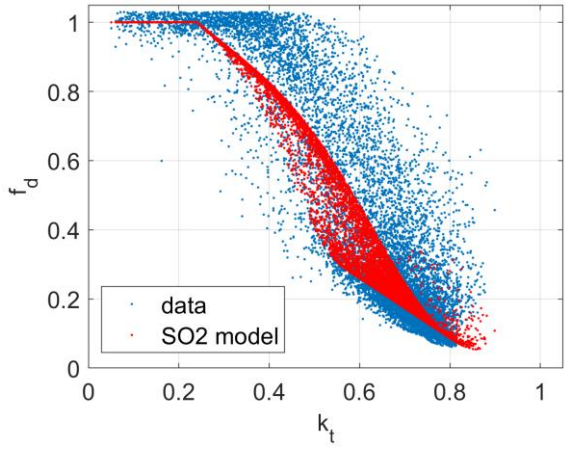

Fig. 4b: S02 model.

Fig. 4: Comparison between diffuse fraction measurements and estimates from different models.

Both models for diffuse fraction chosen for this work (RA2s Eq. (6) and SO2 Eq. (7)) are selected for its relative simplicity (they ultimately depend on the clearness index and the solar zenith angle) and because local adjusted sets for their coefficients are available for the site of interest in this work (Abal et al., 2017). These models estimate 10-minute diffuse fraction with rRMSD of about 33% and some underestimation is apparent in Fig. 4 and in the negative mean bias reported in Table 4. This may be due to the fact that coefficients adjusted to horuly data are being used on 10-min data. However, in the context of this paper, the interest is to evaluate the impact on accuracy of the albedo estimates of using even diffuse fraction models. To this objective, using poor diffuse fraction models is useful, as it may provide an upper value for the cost in terms of accuracy of the albedo estimates.

3.3 Impact of diffuse fraction estimation on bivariate albedo models

In this section, the impact of using phenomenological diffuse fraction models in combination with bivariate albedo models is evaluated. In this regard, Table 5 shows the performance indicators for the bivariate models considering three different scenarios, which differ in the way f_d is treated. In the first scenario, the experimental measurement of the diffuse fraction is used as a baseline (as in Table 3). In the second and third scenarios, f_d is estimated using the RA2s and SO2 models, respectively. The results show that the use of the phenomenological diffuse fraction models leads to a slight decrease in the performance metrics, with the smallest impact on rRMSD, followed by rMBD and rKSI. The models for the baseline scenario are unbiased, and they acquire small biases when diffuse fraction models are used. A negative bias in the fd estimation models translates to negative bias in albedo model 4 (subestimation of albedo) and to a positive bias in model 3 (overestimation of albedo). However, in both cases the mean biases are small, under 1%. Interestingly, the rRMSD (i.e., dispersion) of these models is almost unaffected by the use of diffuse fraction models. The performance of models 3 and 4 with f_d estimation still exceeds that of categories I and II, demonstrating the feasibility of combining empirical diffuse fraction models with category III ground albedo models when diffuse irradiance measurements are not available.

Tab. 5: Performance indicators for the four albedo models across three different scenarios, expressed as a percentage of the mean measurement value, $\overline{\rho}_g = 0.2021$.

Model	Approach for f_d	Relative performance indicators (%)			
		rMBD	rRMSD	rKSI	CPI
3 - Tuomiranta et al. (2021), Eq. (4)	Experimental (baseline)	0.0	8.3	1.7	3.3
	RA2s	0.3	8.3	1.9	3.5
	SO2	0.5	8.3	2.0	3.6
4 - Modified Gueymard (1987), Eq. (5)	Experimental (baseline).	0.0	7.9	2.6	3.5
	RA2s	-0.7	8.0	2.9	3.9
	SO2	-0.5	7.9	2.7	3.7

Complementing the previous analysis, Fig. 5 shows the rMBD and rRMSD for the best model 3 in scenarios 1 and 2, categorized by the cosine of the zenith angle ($\cos\theta_z$, *x* axis) and the clearness index (k_t, *y* axis). The clearness index correlates with the diffuse fraction and allows to distinguish between different sky conditions. Three different conditions can be identified: clear sky ($k_t > 0.6$), partly cloudy sky ($0.6 > k_t > 0.2$), and overcast sky ($k_t < 0.2$). These plots show under which sky conditions the performance of the model decreases. The results for the other cases are similar. The graphs use the same color scale to facilitate comparison, although in some cases the scale is saturated to ensure adequate visualization.

In Rodríguez-Muñoz et al. (2022), besides the general superiority of the category III models over the category I and II models, it was shown that they also exhibit a more homogeneous behavior when discriminating between sky conditions (diffuse fraction and solar elevation), i.e., the rRMSD and rMBE matrices are more uniform. This characteristic is maintained when diffuse fraction models are introduced, as can be seen in Fig. 5c and Fig. 5d. In these figures, it can be observed that the matrices do not change significantly in the range of the cosine of the zenith angle greater than 0.3, i.e. zenith angles less than about 70°, where the solar irradiance is higher. For zenith angles greater than 70°, more significant differences are observed, especially under clear sky conditions (kt > 0.6). It is also important to note that in these conditions the solar irradiance is lower, since these data correspond to the moment close to sunrise and sunset. Therefore, if the metrics were weighted by solar irradiance, the impact of diffuse fraction

models would be even smaller.

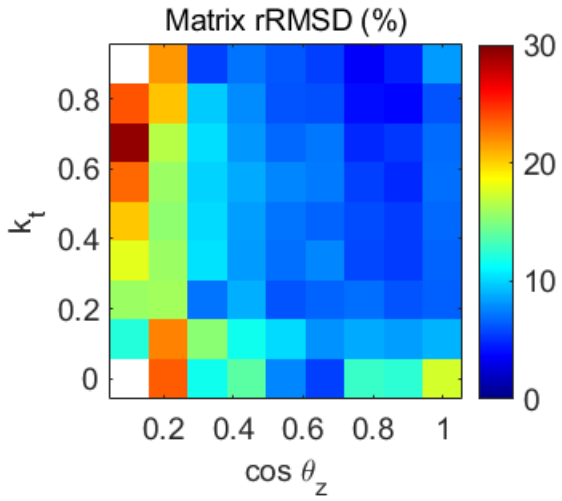

Fig. 5a: Model 3.

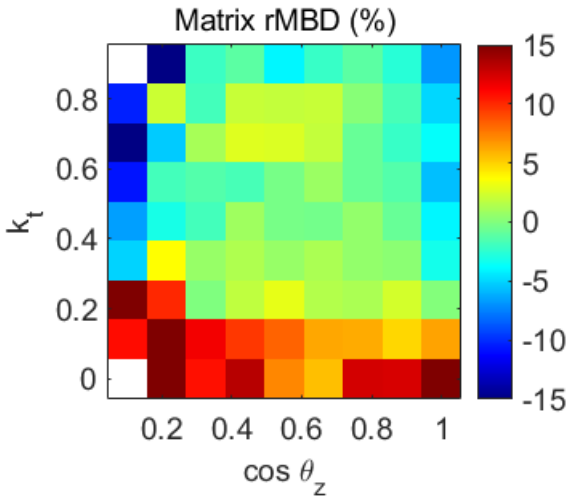

Fig. 5b: Model 3.

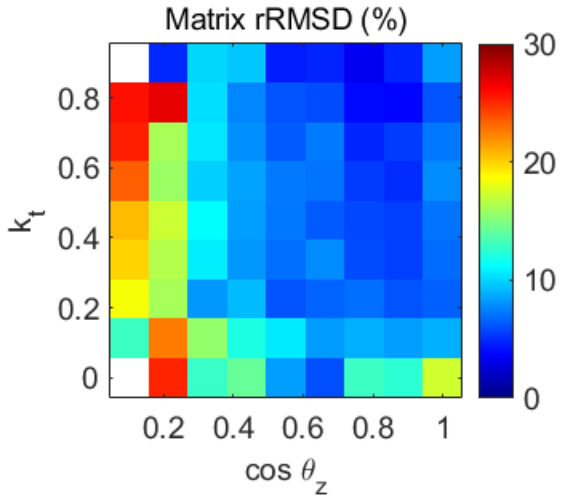

Fig. 5c: Model 3 combined with RA2s.

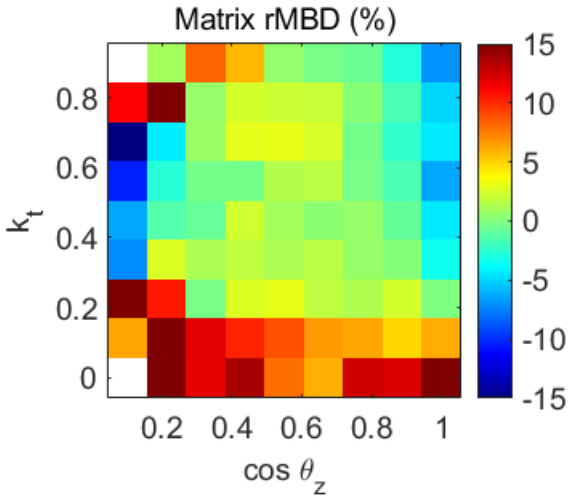

Fig. 5d: Model 3 combined with RA2s.

Fig. 5: rMBD and rRMSD matrix for the first and second scenario for model 3, expressed as a percentage of the mean measurement value, $\overline{\rho}_g = 0.2021$. The scale of the figures is the same to facilitate comparison. The white regions indicate that no data is available for that condition.

In the previous analysis, the coefficients adjusted for the specific site were used for the diffuse fraction models. The use of the original coefficients was also evaluated, but these results are not shown in this article because they are very similar. This reinforces the earlier conclusion: using empirical diffuse fraction models in conjunction with bivariate albedo models represents a robust option when diffuse solar irradiance measurements are not available.

4. Conclusions

The coefficients of four empirical albedo models for grass representative of the Pampa Húmeda region of South America were updated. The model coefficients were slightly lower than in the previous work (Rodríguez-Muñoz et al. 2022), probably due to differences in grass height between the measurement campaigns. Similarly, the performance indicators were very similar, and the conclusions regarding model performance are consistent with previous studies. The bivariate models show the best performance, followed by the univariate models and finally the constant models.

While the bivariate models perform better, their implementation is more challenging as they require two solar irradiance measurements: global and diffuse on a horizontal plane. In this context, with the aim of simplifying the implementation of these models, the impact of using empirical diffuse fraction models as a substitute for diffuse solar

irradiance measurements was evaluated, eliminating the need for one measurement. Despite the slight decrease in performance when diffuse fraction models are included, their superiority over categories I and II is evident. This supports the viability of combining empirical diffuse fraction models with category III albedo models, potentially creating a fourth category with performance between categories II and III while maintaining simplicity of implementation. These conclusions are considered valid regardless of whether the original coefficients or the locally adjusted coefficients are used for the diffuse fraction models, providing robustness to the models in this fourth category.

5. Acknowledgments

The authors thank the Sectoral Commission for Scientific Research (CSIC) of the University of the Republic for financial support through its R&D Groups program.

6. References

Abal, G., Aicardi, D., Alonso-Suárez, R., y Laguarda, A. (2017). Performance of empirical models for diffuse fraction in Uruguay. Solar Energy, 141:166–181.

Chiodetti, M., Lindsay, A., Dupeyrat, P., Binesti, D., Lutun, E., Radouane, K., y Mousel, S. (2016). PV bifacial yield simulation with a variable albedo model. En Proceedings of the EU PVSEC 2021.

Dickinson, R. E. (1983). Land surface processes and climate—surface albedos and energy balance. En Saltzman, B., editor, Theory of Climate, volumen 25 de Advances in Geophysics, pp. 305–353. Elsevier.

Gardner, C. L., y Nadeau, C. (1988). Estimating south slope irradiance in the arctic—a comparison of experimental and modeled values. Solar Energy, 41(3):227–240.

Gueymard, C. (1987). An anisotropic solar irradiance model for tilted surfaces and its comparison with selected engineering algorithms. Solar Energy, 38(5):367–386.

Gueymard, C. (2014). A review of validation methodologies and statistical performance indicators for modeled solar radiation data: Towards a better bankability of solar projects. Renewable and Sustainable Energy Reviews, 39:1024–1034.

Gueymard, C.A. and Ruiz-Arias, J.A. (2016), Extensive worldwide validation and climate sensitivity analysis of direct irradiance predictions from 1-min global irradiance, Solar Energy 128: pp 1-30.

Ineichen, P., Guisan, O., y Perez, R. (1990). Ground-reflected radiation and albedo. Solar Energy, 44(4):207–214.

Kopecek, R., y Libal, J. (2021). Bifacial photovoltaics 2021: Status, opportunities and challenges. Energies, 14(8).

Liu, B. Y., y Jordan, R. C. (1960). The interrelationship and characteristic distribution of direct, diffuse and total solar radiation. Solar Energy, 4(3):1–19.

McArthur, L. (2005). Baseline Surface Radiation Network (BSRN) Operations Manual. Td-no. 1274, wrcp/wmo, World Meteorological Organization (WMO). www.wmo.org.

Nkemdirim, L. C. (1972). A note on the albedo of surfaces. Journal of Applied Meteorology (1962-1982), 11(5):867–874.

Peel, M. C., Finlayson, B. L., y Mcmahon, T. A. (2007). Updated world map of the Köppen-Geiger climate classification. Hydrology and Earth System Sciences Discussions, 11:1633–1644. https://doi.org/10.5194/hess-11-1633-2007

Psiloglou, B., y Kambezidis, H. (2009). Estimation of the ground albedo for the Athens area, Greece. Journal of Atmospheric and Solar-Terrestrial Physics, 71(8):943–954.

Rodríguez-Muñoz, J. M., Monetta, A., Alonso-Suárez, R., Bove, I., y Abal, G. (2021). Correction methods for shadow-band diffuse irradiance measurements: assessing the impact of local adaptation. Renewable Energy, 178:830–844.

Rodríguez Muñoz, J. M., Alonso-Suárez, R., Bove, I., y Abal, G. (2022). Evaluación de seis modelos empíricos para estimar albedo del suelo en la Pampa Húmeda. En: Avances en Energías Renovables y Medio Ambiente, vol. 26, p. 357-368.

Ruiz-Arias, J. A., Alsamamra, H., Tovar-Pescador, J., y Pozo-Vázquez, D. (2010). Proposal of a regressive model for the hourly diffuse solar radiation under all sky conditions. Energy Conversion and Management, 51(5):881–893.

Skartveit, A., y Olseth, J. A. (1987). A model for the diffuse fraction of hourly global radiation. Solar Energy, 38(4):271–274.

Temps, R. C., y Coulson, K. (1977). Solar radiation incident upon slopes of different orientations. Solar Energy, 19(2):179–184.

Tuomiranta, A., Alet, P.-J., Ballif, C., y Ghedira, H. (2021). Worldwide performance evaluation of ground surface reflectance models. Solar Energy, 224:1063–1078.

Yang, D. (2022). Estimating 1-min beam and diffuse irradiance from the global irradiance: A review and an extensive worldwide comparison of latest separation models at 126 stations. Renewable and Sustainable Energy Reviews, 159:112195.

Young, A., 1994, "Air mass and refraction," Applied Optics, 33(6), pp. 1108-1110.

Yusufoglu, U. A., Lee, T. H., Pletzer, T. M., Halm, A., Koduvelikulathu, L. J., Comparotto, C., Kopecek, R., y Kurz, H. (2014). Simulation of energy production by bifacial modules with revision of ground reflection. Energy Procedia, 55:389–395. Proceedings of the 4th International Conference on Crystalline Silicon Photovoltaics (SiliconPV 2014).

11. Solar Energy Advances

A minute-resolution downscaling algorithm for high-resolution global irradiance time series

D. Almpantis[1], **H. Davidsson**[2], **M. Andersson**[1]

[1] Department of Energy Sciences, Lund University, Lund, 221 00, Sweden

[2] Division of Energy and Building Design, Lund University, Lund, 221 00, Sweden

Abstract

Numerous studies have demonstrated the significant impact of the resolution of solar irradiation data on the outcomes of hourly production models. Accurate integration of photovoltaic (PV) systems sometimes demands a high-resolution global horizontal irradiance (GHI) time series to capture the rapid fluctuations in PV power output induced by swift irradiance changes. Most of the available databases provide data at hourly resolution, leading to a lack of accuracy in PV simulations. Those existing hourly averages of global horizontal irradiance in open sources fail to represent this volatility adequately, especially when PV systems are coupled with fast ramp rate technologies. In the present work, an easy-to-use algorithm is implemented to synthesize highresolution GHI time series from hourly averaged and clear sky irradiance datasets. By employing Linear interpolation, a technique that helps to achieve the desired time resolution and afterward computing critical factors, the algorithm identifies periods characterized by short-term weather phenomena, thus creating a highresolution time series that accurately represents these dynamics. Avoiding the probabilistic components and machine learning techniques conserves computational power and reduces calculation time, but this comes at the cost of reduced fidelity in reproducing the results. Improving accuracy in PV simulations is not always directly related to reproducing real phenomena, but enhancing the amount of information contained in the data is sufficient. This study's approach enhances user-friendliness and facilitates seamless integration into existing energy modeling frameworks, aiming for representation with sub-hourly time steps. The algorithm's effectiveness is demonstrated by applying the model to hourly averaged data to revert them to a one-minute time step, and finally comparing the synthetically produced one-minute GHI data to the original measured data. The comparative analysis between synthesized and measured data demonstrated a strong agreement, with normalized mean bias error (MBE) values ranging between 1.8% and 9.6% and normalized root mean square error (NRMSE) values between 2.7% and 16.1%, depending on weather conditions. Additionally, the coefficient of determination (R2) consistently remained above 0.64. Successful algorithm validation makes our algorithm suitable for use in meteorological datasets and locations, with similar climatic characteristics.

Keywords: Global horizontal irradiance; Solar integration; Downscaling synthesis; Minute time resolution; Data validation; Solar-to-hydrogen coupling

---

The paper was published in Solar Energy Advances as part of the EuroSun 2024 select papers.

https://doi.org/10.1016/j.seja.2024.100076

Selective transmission and absorption in oxide-based nanofluid optical filters for PVT collectors

Mohit Barthwal[1 2] and Mohit Barthwal[1 3]

[1] Indian Institute of Technology Delhi, New Delhi, India ,Rice

[2] University, Houston, TX, USA

[3] Indian Institute of Technology Delhi (IITD)-Abu Dhabi, Abu Dhabi, United Arab Emirates

Abstract

The division of the solar spectrum in a photovoltaic thermal (PVT) collector serves a dual purpose for separate heat and electricity applications. One part of the spectrum is used for generating electricity, which prevents the excessive temperature increase of the photovoltaic cells, while the other part facilitates a thermal gain. This concept is termed as spectral beam splitting (SBS). In this work, the implementation of SBS in a PVT collector using a nanofluid-based optical filter is investigated. An optical model, based on Rayleigh scattering, is developed to analyze various oxide-based nanofluids for SBS. The purpose of the model is to determine the transmittance and absorbance of ZnO, Fe3O4, and SiO2-based nanofluids across the solar spectrum range of 300 nm to 2500nm. The model takes into account the complex refractive indices of the particles and base fluids to determine the scattering, extinction, and absorption efficiencies of the nanofluids being studied. The oxide-based nanofluids outperformed the polypyrrole and Cu9S5-based nanofluids in terms of spectral transmission and absorption of sunlight. Water, de-ionized water, and ethylene glycol are used as base fluids. The nanoparticle-base fluid duos determine the agglomeration and size of the particles in the nanofluid and hence affect their optical properties. Therefore, ZnO-based nanofluids are synthesized in-house to correlate the effects of agglomeration and particle size on the optical properties of the nanofluids derived from the developed theoretical model. Using ethylene glycol as a base fluid has a significant impact on reducing agglomeration, resulting in smaller and more stable nanoparticles, in comparison to using de-ionized water. Furthermore, the influence of particle size, dispersion in the base fluid, and optical length on the optical properties of the nanofluid are examined. It is concluded that adjusting the size (dispersion), concentration, and optical length of the particles can allow for the efficient use of the solar spectrum to generate both electrical and thermal energy.

Keywords: Photovoltaic thermal, Spectral beam splitting, Optical filter, Nanofluid, Rayleigh scattering

The paper was published in Solar Energy Advances as part of the EuroSun 2024 select papers.

https://doi.org/10.1016/j.seja.2024.100078

Turning weakness into strength - A feasibility analysis and comparison of datacenter deployment in hot and cold climates

Michael Chrysostomou[1 3], Nicholas Christofides[2], Stelios Ioannou [3]

[1] MIEEK Larnaca, St. Anargyron 58, Larnaca, 6302, Cyprus

[2] Frederick University, Nicosia, Cyprus

[3] University of Central Lancashire, Pyla, Larnaca, Cyprus

Abstract

Datacenters are major components of the Information and Communication Technologies (ICT) responsible for storing, processing and transmitting enormous amounts of data every second. The significance and importance of datacenters in the world economy can be identified from studies which report that in 2023, datacenter infrastructures consumed a total of 4 % of global electricity and contributed 3–5% of global carbon emissions, whereas between the years of 2017–2021, datacenters added $2.1 trillion to the U.S. Gross Domestic Product (GDP). A big portion of energy supplied in datacenters is consumed by the required cooling systems hence companies do not favor developments in hot climate countries. However, due to environmental and climate change concerns along with the steep increase of energy production costs in recent years made the industry look for alternatives. This work includes an in-depth feasibility and comparative study of datacenter construction and operation in hot and cold European countries and addresses the environmental impact of photovoltaics integration in the electrical supply system. The study considers cost parameters (land, operating expenses, photovoltaic system, etc.), the net present cost and levelized cost of energy which are different for each European country under investigation. Furthermore, for every country under consideration, the PV generation was simulated using the PVsyst software which includes multiple meteorological databases, whereas the feasibility analysis was simulated using the HOMER Pro software which integrates components, resources and economic calculations. An elaborate analysis of the results knocks down the common belief that datacenters have lower operational and running expenses in cold climates because of lower cooling requirements. On the contrary, this study shows that hot climates with high solar radiation levels may favor the operation of datacenters by providing 45 % higher green energy and 35 % lower CO2 emissions, whereas the cooling cost is only 5 % higher. In addition, the break-even period for the photovoltaic system in Southern European countries with hot climates is 3–4 times faster.

Keywords: Datacenter deployment, Hot and cold climates, Hybrid PV supply systems

The paper was published in Solar Energy Advances as part of the EuroSun 2024 select papers.

https://doi.org/10.1016/j.seja.2024.100068

A quality control scheme for solar irradiance measurements on facades in urban environments

Nesrin Irmak Köker[1], Martina Giorio[1], Gabriele Lobaccaro[1], Gilles Desthieux[2], Peter Gallinell[2], Bjørn Petter Jelle[1], Mattia Manni[1]

[1] Department of Civil and Environmental Engineering, Faculty of Engineering, Norwegian University of Science and Technology (NTNU), 7491 Trondheim, Norway

[2] Haute école du paysage d'ingénierie et d'architecture de Genève, (HEPIA), University of Applied Sciences and Arts Western Switzerland (HES-SO), 1202 Geneve, Switzerland

Abstract

The increasing prominence of digital tools for city-scale solar analysis emphasizes the need for validation methodologies, which include urban environmental monitoring and data quality control. This study addresses this gap by introducing a quality control scheme for solar irradiance measurements, using a typical street canyon in Geneva (Switzerland) as a case study. The developed quality control scheme is replicable and effectively addresses challenges posed by the built environment, distinguishing it from existing methods that mostly apply to measurements from unobstructed sensors. The experimental data used in this study were retrieved from the monitoring system installed on two opposing facades of the street canyon case study, as well as a nearby weather station. Measurements were recorded from December 22nd, 2022, to December 19th, 2023, at a one-minute time resolution. Five quality checks – nighttime check, range limit tests, precipitation check, shadow detection, and consistency check - were defined to identify the potential flaws and disturbances in the dataset so that these data points could be flagged accordingly. The results consist of reliable solar irradiance data over one year, which can be used in the future for validating a new component for modeling façade solar potential within the Grand Geneva Area Solar Cadaster.

Keywords: Global tilted irradiance, Solar radiation Data quality control, Building façade, Shadow detection, Urban monitoring

The paper was published in Solar Energy Advances as part of the EuroSun 2024 select papers.

https://doi.org/10.1016/j.seja.2024.100083

Combining expansion turbines, heat pumps, and low-temperature solar heat for enhanced primary energy savings in gas pressure regulating stations

Y. Louvet[1], S. Ahlgrimm[2] , F. Pag[1], K. Vajen[1]

[1] University of Kassel, Institute of Thermal Engineering, Kurt-Wolters Straße 3, Kassel 34109, Germany
[2] Stadtwerke Rostock AG, Schmarler Damm 5, Rostock 18069, Germany

Abstract

According to previous studies, gas pressure regulating and metering stations (GPRMS) in Germany account for a primary energy consumption between 1.4 and 2.0 TWh/a for the preheating of natural gas flowing through. This work assesses the potential of reducing this consumption through the combined use of expansion turbines, heat pumps, and solar thermal collectors. For this purpose, operation data of 57 GPRMS of a German gas network operator are used to design systems combining in different scenarios two and three of these technologies in each GPRMS. Using an in-house model developed in Python the 57 systems are simulated over one year with an hourly time step. The results show a potential for the installation of expansion turbines with a total capacity of 3.57 MWel, leading, combined with the renewable heating technologies, to a reduction of more than 99 % of the original gas consumption for gas preheating. The results are then extrapolated to the whole country using scaling factors, showing a potential for feeding-in between 510 and 1,140 GWh/a of surplus electricity into the grid, on top of the almost complete elimination of the gas consumption for gas preheating. In total, the use of the complete technical potential available would lead to net primary energy savings between 1,710 and 3,650 GWh/a and net CO2 emissions reductions between 470 and 1,010 kt/a. Overall, this work demonstrates that the combination of expansion turbines and heat pumps technically allows an almost complete decarbonation of the operation of GPRMS in Germany. In addition, significant amounts of electricity could be fed into the grid, especially during the winter months, which would contribute to decarbonise the electricity mix of the country. The amount of electricity fed into the grid can be increased with the additional use of low-temperature solar thermal systems. To exploit this potential in the future, current regulations should be adapted and targeted support programmes launched.

Keywords: Gas pressure regulating and metering station, Expansion turbine, Heat pump, Solar heat for industrial processes, Potential analysis

---

The paper was published in Solar Energy Advances as part of the EuroSun 2024 select papers.

https://doi.org/10.1016/j.seja.2024.100075

Multisectoral decarbonisation strategies in Punta Arenas, Chile: A multi-renewable technologies approach

Iván Muñoz[1] and Francisco Fuentes[1]

[1] Fundación Fraunhofer Chile Research, Santiago, Chile

Abstract

This study evaluates multisectoral energy planning to decarbonize Punta Arenas, Chile, transitioning from fossil fuels to renewable energies by 2050. Scenarios aligned with the Carbon Neutral 2050 (CN2050) plan, developed under the Long-Term Energy Planning (PELP) program by the Chilean Ministry of Energy, were assessed using EnergyPLAN. In 2019, Punta Arenas emitted 1.32 million tonnes of carbon dioxide equivalent (CO_2eq), projected to rise to 2.2 million tonnes by 2050 under a business-as-usual (BAU) scenario, with annual costs of 947 million euros. Implementing PELP CN2050 measures reduces emissions to 1.2 million tonnes and costs to 560 million euros, demonstrating that decarbonization can be achieved alongside economic savings. This validates the PELP CN2050 plan's effectiveness, highlighting that renewable energy integration supports sustainability and economic benefits. Reductions are achieved through energy efficiency, technological changes, and integrating renewable energies—particularly wind and solar thermal—in industrial, transport, and residential sectors. Electrification and green hydrogen for motive, thermal, and transport applications are crucial. Two cases were evaluated: importing green hydrogen or producing it locally via renewable-powered electrolysers. Sensitivity analyses increasing wind capacity from 13 MW to 310 MW showed that higher renewable integration reduces CO_2eq emissions and costs, indicating a negative abatement cost. Further decarbonization could be achieved by incorporating cogeneration, district heating, and synthetic fuels.

Keywords: Multisectoral energy planning, Decarbonisation of cities,Energy efficiency, Integration of renewable energies, Wind energy, Solar thermal energy, Electrification, Green hydrogen, EnergyPlan©

The paper was published in Solar Energy Advances as part of the EuroSun 2024 select papers.

https://doi.org/10.1016/j.seja.2024.100087

Industrial solar heat potential in Chile: A technical-economic analysis

Diego Naranjo[1], Francisco Fuentes[1], Iván Muñoz[1]

[1] Fundación Fraunhofer Chile Research, Santiago, Chile

Abstract

This paper presents a comprehensive techno-economical potential analysis for integrating solar heat for industrial processes (SHIP) in Chile. Utilizing TRNSYS software for simulation and Python for data analysis, the study evaluates the levelized cost of heat (LCoH) and solar fraction for various industrial sectors across different regions of the country. The findings indicate that regions such as Coquimbo, Antofagasta, and Metropolitan exhibit high solar fractions and competitive LCoH values, particularly in hot water production. The central zone, especially the Metropolitan region, demonstrates significant potential for steam generation, achieving an average solar fraction of 50 % and producing 295 GWh/year of solar thermal energy. Validation with real-world data demonstrated an average error margin of 21 %, underscoring the developed heat load calculation model's reliability. The study concluded that SHIP is a viable solution for reducing energy costs and greenhouse gas emissions in Chile. It has the potential to displace over 3,500 GWh/year of fossil fuel energy in the considered productive sectors. These findings highlight the strategic importance of supporting SHIP implementation through favorable policies and investments.

Keywords: Solar heat for industrial processes, TRNSYS, Techno-economical potential, Levelized cost of heat, Chile

The paper was published in Solar Energy Advances as part of the EuroSun 2024 select papers.

https://doi.org/10.1016/j.seja.2024.100082

Characteristic load curves of positive energy districts

Fabian Ochs[1], Alice Tosatto[1], Elisa Venturi[1], Samuel Breuss[1], Mara Magni[1], Georgios Dermentzis[1], Carsten Wemhoener[2]

[1] University of Innsbruck, Innsbruck, Austria

[2] OST, Rapperswil, Switzerland

Abstract

The decarbonization of the building sector is linked to the electrification of buildings, thus, increasing the stress on the electric grid. The concept (or vision) of positive energy districts (PEDs) aims at supporting the energy transition in cities by fostering the development of both, planning processes and tools as well as technologies. Furthermore, the goal is to raise awareness about sustainable cities and to showcase the feasibility to reach a positive energy balance on the district level. While with improved efficiency of buildings, with heat pumps (HP) and on-site PV, a net positive energy balance is possible for new buildings, in existing or in high-density districts, reaching a positive energy balance on the footprint of the district is very challenging. Using a real case study from Austria and different archetype PEDs, electric load and supply curves are generated by means of dynamic simulation and are characterized with the aim to support decision-making in terms of minimum required energy efficiency level, HP system concepts and renewable energy integration. Even if the net energy balance is achieved, a significant gap in winter remains that has to be covered by the grid. Addressing the mismatch between energy demand in winter and RE generation in summer (so-called winter gap) is crucial for building a sustainable, affordable and resilient energy system. The grid stress cannot be relevantly reduced by increasing on-site PV and on-site storage but instead can be significantly limited by efficiency measures (electric peak load reduction by ca. 50 %) and is one of the most relevant KPIs to evaluate and optimize PEDs on the path to or transforming districts into PEDs.

Keywords: Positive energy district, Energy efficiency, Heat pump, Load curve, Renewable energy, Energy storage, Flexibility, Winter gap, Peak load

The paper was published in Solar Energy Advances as part of the EuroSun 2024 select papers.

https://doi.org/10.1016/j.seja.2024.100081

Oversizing solar heating plants in industry: A cost-effective solution to increase solar fractions

Felix Pag[1], Mateo Jesper[1], Klaus Vajen[1], Ulrike Jordan[1]

1 University of Kassel, Institute of Thermal Engineering, Kurt-Wolters-Str. 3, 34125 Kassel, Germany

Abstract

Numerous studies have demonstrated the significant impact of the resolution of solar irradiation data on the outcomes of hourly production models. Accurate integration of photovoltaic (PV) systems sometimes demands a high-resolution global horizontal irradiance (GHI) time series to capture the rapid fluctuations in PV power output induced by swift irradiance changes. Most of the available databases provide data at hourly resolution, leading to a lack of accuracy in PV simulations. Those existing hourly averages of global horizontal irradiance in open sources fail to represent this volatility adequately, especially when PV systems are coupled with fast ramp rate technologies. In the present work, an easy-to-use algorithm is implemented to synthesize high-resolution GHI time series from hourly averaged and clear sky irradiance datasets. By employing Linear interpolation, a technique that helps to achieve the desired time resolution and afterward computing critical factors, the algorithm identifies periods characterized by short-term weather phenomena, thus creating a high-resolution time series that accurately represents these dynamics. Avoiding the probabilistic components and machine learning techniques conserves computational power and reduces calculation time, but this comes at the cost of reduced fidelity in reproducing the results. Improving accuracy in PV simulations is not always directly related to reproducing real phenomena, but enhancing the amount of information contained in the data is sufficient. This study's approach enhances user-friendliness and facilitates seamless integration into existing energy modeling frameworks, aiming for representation with sub-hourly time steps. The algorithm's effectiveness is demonstrated by applying the model to hourly averaged data to revert them to a one-minute time step, and finally comparing the synthetically produced one-minute GHI data to the original measured data. The comparative analysis between synthesized and measured data demonstrated a strong agreement, with normalized mean bias error (MBE) values ranging between 1.8% and 9.6% and normalized root mean square error (NRMSE) values between 2.7% and 16.1%, depending on weather conditions. Additionally, the coefficient of determination (R) consistently remained above 0.64. Successful algorithm validation makes our algorithm suitable for use in meteorological datasets and locations, with similar climatic characteristics.

Keywords: Global horizontal irradiance, Solar integration, Downscaling synthesis, Minute time resolution, Data validation, Solar-to-hydrogen coupling

---

The paper was published in Solar Energy Advances as part of the EuroSun 2024 select papers.

https://doi.org/10.1016/j.seja.2024.100071

Design and modeling of PV-integrated Double Skin Facades and application to retrofit buildings

Somil Yadav[1], Caroline-Hachem Vermette[2], Md.Nadim Heyat Jilani[2], Gilles Desthieux [3]

[1] Department of Civil and Infrastructure Engineering, Indian Institute of Technology, Dharwad, India

[2] Department of Building, Civil and Environmental Engineering, Concordia University, Montreal, Canada

[3] Haute École du Paysage d'Ingénierie et d'Architecture de Genève (HEPIA), University of Applied Sciences and Arts Western Switzerland (HES-SO), Switzerland

Abstract

Double Skin Façade (DSF) system comprises two glazing layers with a ventilated cavity. Integrating photovoltaic (PV) modules within the outer layer of DSFs offers an efficient method for electricity generation. Current tools for modeling and analyzing DSF systems are complex and resource-intensive, lacking the capability to evaluate the performance of innovative PV-DSF systems during the early design stage. This study develops a mathematical model to evaluate the electrical and thermal performance of PV-DSF systems, considering architectural design elements such as PV color and relative orientation. Based on an energy balance approach, the model is particularly suited for designing PV-DSF systems in heritage buildings, which often have color and relative orientation constraints. The model is applied to assess the performance of PV-DSF systems with conventional clear glass PV and colored front glass PV modules under the climatic conditions of Montreal, Canada. Results indicated that conventional clear glass PV module exhibit higher PV cell temperature than colored PV modules due to greater transmissivity, with peak temperature differences at noon of 5.5 °C, 6.2 °C, and 6.5 °C for orange, blue, and gray PV modules, respectively. On the contrary, the influence of PV's color front glass on room air temperature is non-significant. Furthermore, the optimal orientation for maximum energy yield is not always south-facing; it depends on the hourly distribution of the beam, diffuse solar irradiation, and ambient air temperature. For Montreal, west-facing DSFs produce more electrical and thermal energy on a summer design day because the hourly distribution of beam radiation is skewed towards afternoon hours.

Keywords: Double skin façade, PV-DSF systems, Coloured PV modules, Energy balance approach, Early design stage, Mathematical model

---

The paper was published in Solar Energy Advances as part of the EuroSun 2024 select papers.

https://doi.org/10.1016/j.seja.2024.100067

A

Abal, G.
Assessing the Impact of Diffuse Fraction Estimation on Ground Albedo Modeling **987**

Abbas, R.
ASTEP Project: Status And Progress At 2024 . . . . . **470**
Hybrid Steam Generation for Industry Using Linear Fresnel Solar Collectors and High... . . . . . **478**

Acosta-Pazmiño, I.P.
Computational Fluid Dynamics Optimization of a Heat Exchanger Design for Photovoltaic... . . . . . **699**

Agirre, M.E.
Developing and demonstrating innovative solutions for renewable and waste heat-driven... . . . . . **846**

Ahlgren, B.
Validation of a simulation model for parabolic trough collectors in a high-latitude... . . . . . **670**

Ahlgrimm, S.
Combining expansion turbines, heat pumps, and low-temperature solar heat for enhanced... . . . . . **1004**

Akar, S.
Parabolic Trough Collector Cost Update for Industrial Process Heat in The United... . . . . . **457**

Alexopoulos, S.
Modeling and Simulation of the National Solar Thermal Research Demonstration Facility... . . . . . **634**
Simulation model for autonomous energy planning for Milos island **867**

Aliyari, N.
Efficiency Analysis of An Integrated Cascade Sorption Energy Storage into A Solar... . . . . . **547**

Almpantis, D.
A minute-resolution downscaling algorithm for high-resolution global irradiance time... . . . . . **1000**

Alonso, I.
Enhancing Energy Transition on Campus: Implementing Thermal Accumulation Mechanisms... . . . . . **524**

Alonso-Suárez, R.
Assessing the Impact of Diffuse Fraction Estimation on Ground Albedo Modeling **987**

Amador, G.
Techno-Economic Evaluation For Joint Production Of Electricity And Green Hydrogen... . . . . . **894**

Andersson, H.D.a.M.
A minute-resolution downscaling algorithm for high-resolution global irradiance time... . . . . . **1000**

Andersson, M.
Evaluation of an Indirect Solar Dryer with Integrated Heat Exchanger **885**

Androutsopoulos, A.
ASTEP Project: Status And Progress At 2024 . . . . . **470**

Arora, A.
Modeling and Simulation of the National Solar Thermal Research Demonstration Facility... . . . . . **634**

Astudillo, D.P.
Study of intra-hour direct normal irradiance variability effects on hourly WRF-Chem... . . . . . **958**

Athienitis, A.
Air-based BIPV/T for Low-arctic Applications **1**

Auer, T.
A Parametric Study: Impact of Thermal Mass on Summer Overheating for Residential... . . . . . **33**
Integration of Weather and Emission Predictive Control (WEPC) into Building Energy... . . . . . **46**

B

Babul, K.
Pilot facility for the study of thermal energy storage: Experiments and Theoretical... . . . . . **571**

Bachour, D.
Evaluation of aerosol optical depth for further assimilation into WRF-Chem simulations **966**
Study of intra-hour direct normal irradiance variability effects on hourly WRF-Chem... . . . . . **958**
The Aerosol Effect on Direct Normal Irradiance in a Dust-Rich Hot, Desert Climate **982**

Baelz, A.
Developing and demonstrating innovative solutions for renewable and waste heat-driven... . . . . . **846**

Bampi, B.B.
Model Predictive Control of a Heat Pump System Integrated with PVT Collectors and... . . . . . **58**

Barbero, R.
ASTEP Project: Status And Progress At 2024 . . . . . **470**

Baril, D.
Air-based BIPV/T for Low-arctic Applications **1**

Barnetche, M.
ASTEP Project: Status And Progress At 2024 . . . . . **470**

Barreto, G.
CFD analysis of a thermal storage tank driven by natural convection **587**
Pilot plant for hydrogen production using high-temperature solid oxide electrolyser... . . . . . **489**

Barthwal, M.
Selective transmission and absorption in oxide-based nanofluid optical filters for... . . . . . **1001**

Batista, J.
Assessment of Fin Thickness Influence on Melting and Solidification Processes Inside... . . . . . **559**

Belda, A.
Sizing an Electrical Storage in Combination with Thermochemical Storage for a PVT-Driven... . . . . . **176**

Beltran, F.
Experimental Assessment of the Effects of Cold Climate Weather Patterns on Novel... . . . . . **725**
Fins vs No Fins: A Comparative Experimental Analysis of Novel Box-Channel Photovoltaic/Thermal... . . . . . **640**
Techno-Economic Comparison of Different Solar Photovoltaic/Thermal (PVT) Absorber... . . . . . **146**

Beneito, L.
Towards designing and evaluating solar cooling integrated façades in office buildings **812**

Berberich, M.
Integrating Concentrated Solar Thermal in District Heating - A Simulation Study in... . . . . . **398**

Bibiloni, P.A.
Enhancing Energy Transition on Campus: Implementing Thermal Accumulation Mechanisms... . . . . . **524**

Bockelmann, F.
Energy concepts with high solar fraction for multi-family houses **154**

Boeckmann, O.
First experimental investigations of a facade-integrated adsorption system for solar... . . . . . **802**

Boork, M.
Techno-Economic Analysis of a Stationary Battery Storage Operating on Frequency Regulation... . . . . . **512**

Bove, I.
Assessing the Impact of Diffuse Fraction Estimation on Ground Albedo Modeling **987**

Breton, J.
Study of the Impact of Automatic Backflush on Direct SDHW Thermosyphon Systems **780**

Breton, R.
Experimental Investigation of Large-Area Transpired Solar Air Collectors **747**

Breuss, S.
Characteristic load curves of positive energy districts **1007**

Brütting, M.
Thermal Characterization of Single Greening Components and Green Roofs **110**

Budu, M.N.A.A.
Effect of zinc oxide-water nanofluids on the thermal efficiency of a flat plate solar... . . . . . **604**

Bühne, X.
Dynamic Energy Management Model: A Catalyst for Carbon Neutrality in Austrian Thermal... . . . . . **494**

Bulut, Y.
Quantifying the effect of radiator capacity on hybrid heat pump performance using... . . . . . **165**

C

Camacho, M.J.A.
Pilot facility for the study of thermal energy storage: Experiments and Theoretical... . . . . . **571**

Canals, V.
Enhancing Energy Transition on Campus: Implementing Thermal Accumulation Mechanisms... . . . . . **524**

Cano, M.S.R.
Pilot facility for the study of thermal energy storage: Experiments and Theoretical... . . . . . **571**

Capiello, F.L.
Integrating Radiative Cooling and Chilled Ceilings in Buildings: A Simulation Study... . . . . . **262**

Carbonell, D.
Slurry Production for Solar-Ice Systems using Supercooling and a Flow-based Crystallizer **833**

Carlucci, S.
Occupant feedback on indoor humidity assessment **88**

Castell, A.
Potential thermal energy storage technologies for radiative cooling implementation... . . . . . **240**

Castro, A.
Pilot facility for the study of thermal energy storage: Experiments and Theoretical... . . . . . **571**

Chèze, D.
Energy Performance and Environmental Impact of Solar Photovoltaic, Thermal and Hybrid... . . . . . **196**

Chhugani, B.
Numerical Study of the Effect of the System Specifications on the Performance of... . . . . . **711**

Chong, A.
Integration of Weather and Emission Predictive Control (WEPC) into Building Energy... . . . . . **46**

Christodoulaki, R.
ASTEP Project: Status And Progress At 2024 . . . . . **470**
Critical Analysis on the Renewable Heating and Cooling plans in Croatia, Germany,... . . . . . **874**
Energy Performance Simulation of the 52mW Minos Solar Tower Project **659**

Christofides, N.
Turning weakness into strength - A feasibility analysis and comparison of datacenter... . . . . . **1002**

Chrysostomou, M.
Turning weakness into strength - A feasibility analysis and comparison of datacenter... . . . . . **1002**

Cimmino, L.
Integrating Radiative Cooling and Chilled Ceilings in Buildings: A Simulation Study... . . . . . **262**

Coca-Ortegón, A.
Sizing an Electrical Storage in Combination with Thermochemical Storage for a PVT-Driven... . . . . . **176**

Cofré-Toledo, J.
Potential thermal energy storage technologies for radiative cooling implementation... . . . . . **240**

D

Daborer-prado, N.
Mathematical modelling of an Innovative Ice Storage system **187**
Microwave Desorption for Flexible Sorption-Heat Storage Application **580**

Danielski, I.
Validation of a simulation model for parabolic trough collectors in a high-latitude... . . . . . **670**

Dannemand, M.
How does the thermal characteristics of PVT panels influence the performance of PVT... . . . . . **766**

Davidsson, H.
Evaluation of an Indirect Solar Dryer with Integrated Heat Exchanger **885**

Deblock, V.
Feasibility study of a solar desalination unit for small isolated communities **937**

Dehner, H.
Sensitivity Analysis of Solar District Heating Systems **432**

Delachaux, V.
Experimental Assessment of the Effects of Cold Climate Weather Patterns on Novel... . . . . . **725**
Experimental Study on Heat Transfer from Ambient Air in Row-installed Photovoltaic-thermal... . . . . . **651**
Fins vs No Fins: A Comparative Experimental Analysis of Novel Box-Channel Photovoltaic/Thermal... . . . . . **640**

Dermentzis, G.
Characteristic load curves of positive energy districts **1007**
Evaluation of positive energy districts with district heating and heat pumps **409**

Desthieux, G.
A quality control scheme for solar irradiance measurements on facades in urban environments **1003**
Design and modeling of PV-integrated Double Skin Facades and application to retrofit... . . . . . **1009**

Díaz-Torres, Y.
Enhancing Energy Transition on Campus: Implementing Thermal Accumulation Mechanisms... . . . . . **524**

Djebbar, R.
Solar Radiant Floor and Sub-Surface Ground Heat Exchanger Thermal Storage System:... ... **250**

Doroti, H.
Critical Analysis on the Renewable Heating and Cooling plans in Croatia, Germany,... ... **874**

Dott, R.
Development of a new generation of cold district heating systems with water as heat... ... **371**

Drosou, V.
Critical Analysis on the Renewable Heating and Cooling plans in Croatia, Germany,... ... **874**
Energy Performance Simulation of the 52mW Minos Solar Tower Project ... **659**

Drück, H.
Development of a new generation of cold district heating systems with water as heat... ... **371**

Dubhashi, V.
Quantifying the effect of radiator capacity on hybrid heat pump performance using... ... **165**

Durán-García, M.D.
Performance Analysis of a Hybrid Solar-Geothermal Power Plant in México ... **690**

Duret, A.
Optimizing energy and economic performance of solar-biomass systems for rural district... ... **927**

E

Ehrig, R.
Critical Analysis on the Renewable Heating and Cooling plans in Croatia, Germany,... ... **874**

Engelmann, P.
Propane-based heat pump solutions for existing multi family houses – requirements... ... **70**

Erb, K.
Slurry Production for Solar-Ice Systems using Supercooling and a Flow-based Crystallizer ... **833**

F

Famiglietti, A.
Hybrid Steam Generation for Industry Using Linear Fresnel Solar Collectors and High... ... **478**

Fan, J.
Domestic hot water heating with direct electricity from PV panels and the grid ... **285**
Yearly thermal performances of Danish solar heating plants ... **360**

Fares, H.
Energy Performance and Environmental Impact of Solar Photovoltaic, Thermal and Hybrid... ... **196**

Fernandes, J.
Critical Analysis on the Renewable Heating and Cooling plans in Croatia, Germany,... ... **874**

Fernandes, M.S.
Efficiency Analysis of An Integrated Cascade Sorption Energy Storage into A Solar... ... **547**

Fernández, B.G.
Energy Building Sustainability by Optimized Daylight Tubes ... **12**

Fernández-Balbuena, A.A.
Energy Building Sustainability by Optimized Daylight Tubes ... **12**

Ferrera-Cobos, F.
Climate Adjustment of Photosynthetically Active Radiation Estimates Using Site Adaptation... . . . . . ***975***

Fogelström, F.
Validation of a simulation model for parabolic trough collectors in a high-latitude... . . . . . ***670***

Fountoukis, C.
Evaluation of aerosol optical depth for further assimilation into WRF-Chem simulations ***966***
Study of intra-hour direct normal irradiance variability effects on hourly WRF-Chem... . . . . . ***958***
The Aerosol Effect on Direct Normal Irradiance in a Dust-Rich Hot, Desert Climate ***982***

Frazzica, A.
Developing and demonstrating innovative solutions for renewable and waste heat-driven... . . . . . ***846***

Frison, L.
Model Predictive Control of a Heat Pump System Integrated with PVT Collectors and... . . . . . ***58***

Fuentes, F.
Industrial solar heat potential in Chile: A technical-economic analysis ***1006***
Multisectoral decarbonisation strategies in Punta Arenas, Chile: A multi-renewable... . . . . . ***1005***

Furbo, S.
Domestic hot water heating with direct electricity from PV panels and the grid ***285***
How does the thermal characteristics of PVT panels influence the performance of PVT... . . . . . ***766***
Yearly thermal performances of Danish solar heating plants ***360***

G

Gallinell, P.
A quality control scheme for solar irradiance measurements on facades in urban environments ***1003***

Gambardella, A.
Validation of a simulation model for parabolic trough collectors in a high-latitude... . . . . . ***670***

García, A.C.
Computational Fluid Dynamics Optimization of a Heat Exchanger Design for Photovoltaic... . . . . . ***699***

Garcia, M.A.
Energy Building Sustainability by Optimized Daylight Tubes ***12***

Gaspar, A.R.
Efficiency Analysis of An Integrated Cascade Sorption Energy Storage into A Solar... . . . . . ***547***

Gaudino, E.
Comparative Numerical Analysis of Middle-Temperature and High Temperature versions... . . . . . ***681***

Ge, H.
Air-based BIPV/T for Low-arctic Applications ***1***

Geagea, T.
Enhancing Thermal Performance of Roofs Within Heavy-Weight Thermal Mass Residential... . . . . . ***22***

Georgii, M.
Monitoring an innovative cold district heating network with decentralized heat pumps... . . . . . ***310***

Giaconia, A.
CFD analysis of a thermal storage tank driven by natural convection ***587***

Giganda, J.L.C.
Developing and demonstrating innovative solutions for renewable and waste heat-driven... . . . . . **846**

Gil, B.
Pilot facility for the study of thermal energy storage: Experiments and Theoretical... . . . . . **571**

Giorio, M.
A quality control scheme for solar irradiance measurements on facades in urban environments **1003**

Gölles, M.
Predictive Rule-Based Control Strategy for Optimizing the Operation of Solar District... . . . . . **382**

Gomes, J.
Computational Fluid Dynamics Optimization of a Heat Exchanger Design for Photovoltaic... . . . . . **699**

Gonzalez-Aguilar, J.
CFD analysis of a thermal storage tank driven by natural convection **587**
Pilot plant for hydrogen production using high-temperature solid oxide electrolyser... . . . . . **489**

González-Mora, E.
Performance Analysis of a Hybrid Solar-Geothermal Power Plant in México **690**

Gottkehaskamp, B.
A Parametric Study: Impact of Thermal Mass on Summer Overheating for Residential... . . . . . **33**
Integration of Weather and Emission Predictive Control (WEPC) into Building Energy... . . . . . **46**

Gouveia, L.
Climate Adjustment of Photosynthetically Active Radiation Estimates Using Site Adaptation... . . . . . **975**

Gradl, P.
Dynamic Energy Management Model: A Catalyst for Carbon Neutrality in Austrian Thermal... . . . . . **494**
Providing Flexibility for District Heating Grids with Thermally Activated Building... . . . . . **208**

Gumhalter, M.
Dynamic Energy Management Model: A Catalyst for Carbon Neutrality in Austrian Thermal... . . . . . **494**
Providing Flexibility for District Heating Grids with Thermally Activated Building... . . . . . **208**

Gurruchaga, I.
Slurry Production for Solar-Ice Systems using Supercooling and a Flow-based Crystallizer **833**

H

Hafner, B.
Development of a new generation of cold district heating systems with water as heat... . . . . . **371**

Hamida, H.
Towards designing and evaluating solar cooling integrated façades in office buildings **812**

Harrison, S.
Experimental Investigation of Large-Area Transpired Solar Air Collectors **747**
Performance Comparison of a Transpired Air Solar Collector with Low-E Surface Coating **758**
Study of the Impact of Automatic Backflush on Direct SDHW Thermosyphon Systems **780**

Heck, M.
Solar Thermal Collectors and their Components. Results of Long-term Exposure at Extreme... . . . . . **721**

Helden, W.v.
Extruded Water Adsorbent APO-Tric for Adsorption Thermal Battery Utilizing Solar... . . . . . **613**

Hengel, F.
Extruded Water Adsorbent APO-Tric for Adsorption Thermal Battery Utilizing Solar... . . . . . ***613***
Optimized Thermodynamics and Building Physics of large-scale Thermal Energy Storage ***621***

Hepf, C.
A Parametric Study: Impact of Thermal Mass on Summer Overheating for Residential... . . . . . ***33***
Integration of Weather and Emission Predictive Control (WEPC) into Building Energy... . . . . . ***46***

Herrando, M.
Computational Fluid Dynamics Optimization of a Heat Exchanger Design for Photovoltaic... . . . . . ***699***

Herrera, C.
Techno-Economic Evaluation For Joint Production Of Electricity And Green Hydrogen... . . . . . ***894***

Huber, P.
Development of a new generation of cold district heating systems with water as heat... . . . . . ***371***

Hysenj, S.
Energy Performance Simulation of the 52mW Minos Solar Tower Project ***659***

I

Ibarra, M.
ASTEP Project: Status And Progress At 2024 . . . . . ***470***

Ioannou, S.
Turning weakness into strength - A feasibility analysis and comparison of datacenter... . . . . . ***1002***

Irandoostshahrestani, M.
Custom sizing and cost analysis of a PV-battery system: Dual-purpose application... . . . . . ***505***
Enhancement of a photovoltaic drinking water pumping system design software tool ***949***
Feasibility study of a solar desalination unit for small isolated communities ***937***

Issayan, G.
Microwave Desorption for Flexible Sorption-Heat Storage Application ***580***

J

Jaafar, M.A.
Experimental Assessment of the Effects of Cold Climate Weather Patterns on Novel... . . . . . ***725***
Experimental Study on Heat Transfer from Ambient Air in Row-installed Photovoltaic-thermal... . . . . . ***651***
Fins vs No Fins: A Comparative Experimental Analysis of Novel Box-Channel Photovoltaic/Thermal... . . . . . ***640***
Numerical Study of the Effect of the System Specifications on the Performance of... . . . . . ***711***

Jakob, U.
Developing and demonstrating innovative solutions for renewable and waste heat-driven... . . . . . ***846***
Modelling and Analysis of Building Optimisation and Solar thermal Cooling System... . . . . . ***824***
Solar Cooling for the Sunbelt Regions – Final results from IEA-SHC Task 65 . . . . . ***854***

Jalilzadehazhari, E.
Techno-Economic Analysis of a Stationary Battery Storage Operating on Frequency Regulation... . . . . . ***512***

Jamtsho, T.
Evaluation of an Indirect Solar Dryer with Integrated Heat Exchanger ***885***

Jaureguizar, M.
Energy Building Sustainability by Optimized Daylight Tubes ***12***

Jelle, B.P.
A quality control scheme for solar irradiance measurements on facades in urban environments **1003**

Jesper, M.
Oversizing solar heating plants in industry: A cost-effective solution to increase... . . . . . **1008**

Jiao, Q.
Research And Analysis Of Solar Heat Pump Performance **216**

Jiao, X.
Research And Analysis Of Solar Heat Pump Performance **216**

Jilani, M.N.H.
Design and modeling of PV-integrated Double Skin Facades and application to retrofit... . . . . . **1009**

Jobard, X.
Optimizing energy and economic performance of solar-biomass systems for rural district... . . . . . **927**

Johnson, G.
Experimental Investigation of Large-Area Transpired Solar Air Collectors **747**
Performance Comparison of a Transpired Air Solar Collector with Low-E Surface Coating **758**

Jordan, U.
Oversizing solar heating plants in industry: A cost-effective solution to increase... . . . . . **1008**
Two case studies for renewable district heating with solar fraction 70 % **421**

K

Kaltenbach, T.
Solar Thermal Collectors and their Components. Results of Long-term Exposure at Extreme... . . . . . **721**

Karagiorgas, M.
Energy Performance Simulation of the 52mW Minos Solar Tower Project **659**

Karsbergen, V.v.
Space Heating and Cooling Demand of Buildings in the Perspective of Climate Change... . . . . . **82**

Kasturi, P.
Simulation of a Photovoltaic-Thermal (PV-T) Air Source Heat Pump (ASHP) System for... . . . . . **228**

Katsaros, V.
Energy Performance Simulation of the 52mW Minos Solar Tower Project **659**

Kemp, R.
Quantifying the effect of radiator capacity on hybrid heat pump performance using... . . . . . **165**

Khamidov, D.
Model Predictive Control of a Heat Pump System Integrated with PVT Collectors and... . . . . . **58**

Kirincic, M.
Assessment of Fin Thickness Influence on Melting and Solidification Processes Inside... . . . . . **559**

Knaack, U.
Towards designing and evaluating solar cooling integrated façades in office buildings **812**

Kohlenbach, P.
Solar Cooling for the Sunbelt Regions – Final results from IEA-SHC Task 65 . . . . . **854**

Köker, N.I.
A quality control scheme for solar irradiance measurements on facades in urban environments **1003**

Konstantinou, T.
Towards designing and evaluating solar cooling integrated façades in office buildings ***812***

Körner, W.
Thermal Characterization of Single Greening Components and Green Roofs ***110***

Koubar, M.
Techno-Economic Analysis of a Stationary Battery Storage Operating on Frequency Regulation... . . . . . ***512***

Krabben, Y.
State of charge estimation using regression models in a novel photovoltaic thermal... . . . . . ***596***

Kurup, P.
Parabolic Trough Collector Cost Update for Industrial Process Heat in The United... . . . . . ***457***

Kusyy, O.
Two case studies for renewable district heating with solar fraction 70 % ***421***

Kyprianou, I.
Occupant feedback on indoor humidity assessment ***88***

L

Lamaison, N.
Improved Pre-calculation of Solar Thermal Production for Milp-based Optimization... . . . . . ***444***

Lara, Y.
Sizing an Electrical Storage in Combination with Thermochemical Storage for a PVT-Driven... . . . . . ***176***

Leiva-Illanes, R.
Techno-Economic Evaluation For Joint Production Of Electricity And Green Hydrogen... . . . . . ***894***

Lenic, K.
Assessment of Fin Thickness Influence on Melting and Solidification Processes Inside... . . . . . ***559***

Lentz-Herrera, Á.E.
Performance Analysis of a Hybrid Solar-Geothermal Power Plant in México ***690***

Lichtenegger, K.
Predictive Rule-Based Control Strategy for Optimizing the Operation of Solar District... . . . . . ***382***

Llorens, M.N.
Climate Adjustment of Photosynthetically Active Radiation Estimates Using Site Adaptation... . . . . . ***975***

Lobaccaro, G.
A quality control scheme for solar irradiance measurements on facades in urban environments ***1003***

Logar, N.Z.
Extruded Water Adsorbent APO-Tric for Adsorption Thermal Battery Utilizing Solar... . . . . . ***613***

Lopez, A.C.
Experimental Assessment of the Effects of Cold Climate Weather Patterns on Novel... . . . . . ***725***
Fins vs No Fins: A Comparative Experimental Analysis of Novel Box-Channel Photovoltaic/Thermal... . . . . . ***640***

López, A.M.P.
Pilot facility for the study of thermal energy storage: Experiments and Theoretical... . . . . . ***571***

Louvet, Y.
Combining expansion turbines, heat pumps, and low-temperature solar heat for enhanced... . . . . . ***1004***

Lozano, I.
Sizing an Electrical Storage in Combination with Thermochemical Storage for a PVT-Driven... . . . . . ***176***

Luparelli, A.
Occupant feedback on indoor humidity assessment ***88***

M

Magni, M.
Characteristic load curves of positive energy districts ***1007***
Evaluation of positive energy districts with district heating and heat pumps ***409***

Mahavar, S.
Thermal performance of a solar box cooker with forced convection heating and sensible... . . . . . ***917***

Mahdi, Z.
Modeling and Simulation of the National Solar Thermal Research Demonstration Facility... . . . . . ***634***

Mal, S.
Extruded Water Adsorbent APO-Tric for Adsorption Thermal Battery Utilizing Solar... . . . . . ***613***

Manni, M.
A quality control scheme for solar irradiance measurements on facades in urban environments ***1003***

Marco, J.M.
Potential thermal energy storage technologies for radiative cooling implementation... . . . . . ***240***

Martinopoulos, G.
Sizing an Electrical Storage in Combination with Thermochemical Storage for a PVT-Driven... . . . . . ***176***

Martins, J.H.S.
Solar Hydrogen Production: Techno-Economic Evaluation of Concentrated Solar Power... . . . . . ***904***

Martorell, I.
Integrating Radiative Cooling and Chilled Ceilings in Buildings: A Simulation Study... . . . . . ***262***

Mas, B.
Enhancing Energy Transition on Campus: Implementing Thermal Accumulation Mechanisms... . . . . . ***524***

Mathew, G.
Simulation model for autonomous energy planning for Milos island ***867***

Matuska, T.
Comparison of Solar Systems with Seasonal Storage for Renewable Heat Production for... . . . . . ***391***
Effect of Boundary Conditions on Glazed Flat-Plate Solar Collector Performance Test... . . . . . ***737***

Mawire, A.
Thermal performance of a solar box cooker with forced convection heating and sensible... . . . . . ***917***

Medrano, M.
Integrating Radiative Cooling and Chilled Ceilings in Buildings: A Simulation Study... . . . . . ***262***
Potential thermal energy storage technologies for radiative cooling implementation... . . . . . ***240***

Mehnert, S.
Solar Thermal Collectors and their Components. Results of Long-term Exposure at Extreme... . . . . . ***721***

Mellor, A.
Field Evaluation of Naked Energy's Virtu Solar Thermal and Hybrid PVT Collectors... . . . . . ***788***
Quantifying The Environmental Implications Of Solar Thermal Technologies: A Comprehensive... . . . . . ***793***

Mesquita, L.
Experimental Investigation of Large-Area Transpired Solar Air Collectors **747**
Performance Comparison of a Transpired Air Solar Collector with Low-E Surface Coating **758**
Solar Radiant Floor and Sub-Surface Ground Heat Exchanger Thermal Storage System:... . . . . . **250**

Micò, L.
Critical Analysis on the Renewable Heating and Cooling plans in Croatia, Germany,... . . . . . **874**

Mikkelsen, S.E.
How does the thermal characteristics of PVT panels influence the performance of PVT... . . . . . **766**

Miller, C.
Integration of Weather and Emission Predictive Control (WEPC) into Building Energy... . . . . . **46**

Miró, R.V.
Integrating Radiative Cooling and Chilled Ceilings in Buildings: A Simulation Study... . . . . . **262**

Mittelbach, W.
Developing and demonstrating innovative solutions for renewable and waste heat-driven... . . . . . **846**

Mlakar, U.
Extruded Water Adsorbent APO-Tric for Adsorption Thermal Battery Utilizing Solar... . . . . . **613**

Moià-Pol, A.
Enhancing Energy Transition on Campus: Implementing Thermal Accumulation Mechanisms... . . . . . **524**

Mola, G.T.
Quantum Dot as a Mechanism to Supress Charge Recombination in Polymer Solar Cell **923**

Moll, V.M.
Enhancing Energy Transition on Campus: Implementing Thermal Accumulation Mechanisms... . . . . . **524**

Monnerie, N.
Solar Hydrogen Production: Techno-Economic Evaluation of Concentrated Solar Power... . . . . . **904**

Monteleone, W.
Comparative study on small-scale HPs for decentral DHW preparation in multi-family... . . . . . **273**

Montesinos, J.A.
Pilot facility for the study of thermal energy storage: Experiments and Theoretical... . . . . . **571**

Morales-Hernández, M.
Computational Fluid Dynamics Optimization of a Heat Exchanger Design for Photovoltaic... . . . . . **699**

Mselle, B.
Potential thermal energy storage technologies for radiative cooling implementation... . . . . . **240**

Munkhammar, J.
Techno-Economic Analysis of a Stationary Battery Storage Operating on Frequency Regulation... . . . . . **512**

Muñoz, I.
Industrial solar heat potential in Chile: A technical-economic analysis **1006**
Multisectoral decarbonisation strategies in Punta Arenas, Chile: A multi-renewable... . . . . . **1005**

Muñoz, J.
ASTEP Project: Status And Progress At 2024 . . . . . **470**

Murali, D.
Computational Fluid Dynamics Optimization of a Heat Exchanger Design for Photovoltaic... . . . . . **699**

Murrell, A.
Field Evaluation of Naked Energy's Virtu Solar Thermal and Hybrid PVT Collectors... . . . . . **788**
Quantifying The Environmental Implications Of Solar Thermal Technologies: A Comprehensive... . . . . . **793**

Muser, C.
Optimized Thermodynamics and Building Physics of large-scale Thermal Energy Storage **621**

N

Nair, G.
Validation of a simulation model for parabolic trough collectors in a high-latitude... . . . . . **670**

Naranjo, D.
Industrial solar heat potential in Chile: A technical-economic analysis **1006**

Navarro, A.A.
Climate Adjustment of Photosynthetically Active Radiation Estimates Using Site Adaptation... . . . . . **975**

Neyer, D.
Solar Cooling for the Sunbelt Regions – Final results from IEA-SHC Task 65 . . . . . **854**

Nguyen, A.K.
Performance Comparison of a Transpired Air Solar Collector with Low-E Surface Coating **758**

Nguyen, T.
Validation of a simulation model for parabolic trough collectors in a high-latitude... . . . . . **670**

Nicholson, E.L.
Experimental Assessment of the Effects of Cold Climate Weather Patterns on Novel... . . . . . **725**
Fins vs No Fins: A Comparative Experimental Analysis of Novel Box-Channel Photovoltaic/Thermal... . . . . . **640**

Nielsen, E.
Domestic hot water heating with direct electricity from PV panels and the grid **285**
How does the thermal characteristics of PVT panels influence the performance of PVT... . . . . . **766**
Yearly thermal performances of Danish solar heating plants **360**

Nienborg, B.
Model Predictive Control of a Heat Pump System Integrated with PVT Collectors and... . . . . . **58**
Propane-based heat pump solutions for existing multi family houses – requirements... . . . . . **70**

Nikolopoulos, N.
Sizing an Electrical Storage in Combination with Thermochemical Storage for a PVT-Driven... . . . . . **176**

Nissim, R.
S.A.P.I.EN.T.E Experimental Test Facility For Full-Scale Testing Of New Configurations... . . . . . **297**

Nwaigwe, K.N.
Effect of zinc oxide-water nanofluids on the thermal efficiency of a flat plate solar... . . . . . **604**

Nyugen, A.K.
Study of the Impact of Automatic Backflush on Direct SDHW Thermosyphon Systems **780**

O

Ochs, F.
Characteristic load curves of positive energy districts **1007**
Comparative study on small-scale HPs for decentral DHW preparation in multi-family... . . . . . **273**
Evaluation of positive energy districts with district heating and heat pumps **409**
Optimized Thermodynamics and Building Physics of large-scale Thermal Energy Storage **621**
Space Heating and Cooling Demand of Buildings in the Perspective of Climate Change... . . . . . **82**

Ogundelea, A.K.
Quantum Dot as a Mechanism to Supress Charge Recombination in Polymer Solar Cell **923**

Om, D.
Evaluation of an Indirect Solar Dryer with Integrated Heat Exchanger **885**

Orozaliev, J.
Monitoring an innovative cold district heating network with decentralized heat pumps... . . . . . **310**
Two case studies for renewable district heating with solar fraction 70 % **421**

P

Pag, F.
Combining expansion turbines, heat pumps, and low-temperature solar heat for enhanced... . . . . . **1004**
Oversizing solar heating plants in industry: A cost-effective solution to increase... . . . . . **1008**

Palacios, A.
State of charge estimation using regression models in a novel photovoltaic thermal... . . . . . **596**

Palma, A.L.
S.A.P.I.EN.T.E Experimental Test Facility For Full-Scale Testing Of New Configurations... . . . . . **297**

Papadopoulos, P.
Occupant feedback on indoor humidity assessment **88**

Papageorgiou, D.
Developing and demonstrating innovative solutions for renewable and waste heat-driven... . . . . . **846**

Pauletta, S.
Optimizing energy and economic performance of solar-biomass systems for rural district... . . . . . **927**

Peña-Cruz, M.
Estimation of Dust Accumulation in Parabolic trough Concentrators using Aerial Laser... . . . . . **773**

Perez-Astudillo, D.
Evaluation of aerosol optical depth for further assimilation into WRF-Chem simulations **966**
The Aerosol Effect on Direct Normal Irradiance in a Dust-Rich Hot, Desert Climate **982**

Peter, M.
Energy concepts with high solar fraction for multi-family houses **154**

Pierrès, N.L.
Energy Performance and Environmental Impact of Solar Photovoltaic, Thermal and Hybrid... . . . . . **196**

Pietra, B.D.
S.A.P.I.EN.T.E Experimental Test Facility For Full-Scale Testing Of New Configurations... . . . . . **297**

Platzer, W.
Solar Thermal Collectors and their Components. Results of Long-term Exposure at Extreme... . . . . . **721**

Pokorny, N.
Scenarios for Integration of Power to Heat Technology in Czech District Heating Systems **536**

Popovich, C.
Climate Adjustment of Photosynthetically Active Radiation Estimates Using Site Adaptation... . . . . . **975**

Potonik, J.
Deep Learning Techniques for Prediction of Non-visual Luminous Content of Cellular... . . . . . **98**

Prieto, A.
Towards designing and evaluating solar cooling integrated façades in office buildings **812**

R

Rakshit, D.
Achieving Sustainable Buildings: Balancing Energy Efficiency and Comfort through... . . . . . **322**
Selective transmission and absorption in oxide-based nanofluid optical filters for... . . . . . **1001**

Reim, M.
Thermal Characterization of Single Greening Components and Green Roofs **110**

Ristic, A.
Extruded Water Adsorbent APO-Tric for Adsorption Thermal Battery Utilizing Solar... . . . . . **613**

Robles-Velázquez, S.
Estimation of Dust Accumulation in Parabolic trough Concentrators using Aerial Laser... . . . . . **773**

Rodenbücher, B.
Propane-based heat pump solutions for existing multi family houses – requirements... . . . . . **70**

Rodríguez-Muñoz, J.M.
Assessing the Impact of Diffuse Fraction Estimation on Ground Albedo Modeling **987**

Roeder, T.
Solar Hydrogen Production: Techno-Economic Evaluation of Concentrated Solar Power... . . . . . **904**

Romero, J.
A Parametric Study: Impact of Thermal Mass on Summer Overheating for Residential... . . . . . **33**

Romero, M.
CFD analysis of a thermal storage tank driven by natural convection **587**
Pilot plant for hydrogen production using high-temperature solid oxide electrolyser... . . . . . **489**

Roos, P.
State of charge estimation using regression models in a novel photovoltaic thermal... . . . . . **596**

Rosenstiel, A.
Solar Hydrogen Production: Techno-Economic Evaluation of Concentrated Solar Power... . . . . . **904**

Rosiek, S.
Pilot facility for the study of thermal energy storage: Experiments and Theoretical... . . . . . **571**

Rousse, D.
Enhancement of a photovoltaic drinking water pumping system design software tool **949**

Rousse, D.R.
Custom sizing and cost analysis of a PV-battery system: Dual-purpose application... . . . . . **505**
Feasibility study of a solar desalination unit for small isolated communities **937**

Rovira, A.
ASTEP Project: Status And Progress At 2024 . . . . . ***470***

S

Safranek, J.
Scenarios for Integration of Power to Heat Technology in Czech District Heating Systems ***536***

Saldaña, J.L.B.
Pilot facility for the study of thermal energy storage: Experiments and Theoretical... . . . . . ***571***

Sánchez-González, M.
Estimation of Dust Accumulation in Parabolic trough Concentrators using Aerial Laser... . . . . . ***773***

Santana, J.P.
Computational Fluid Dynamics Optimization of a Heat Exchanger Design for Photovoltaic... . . . . . ***699***

Sapienza, A.
Developing and demonstrating innovative solutions for renewable and waste heat-driven... . . . . . ***846***

Sauer, C.
Monitoring an innovative cold district heating network with decentralized heat pumps... . . . . . ***310***

Schäfer, F.
State of charge estimation using regression models in a novel photovoltaic thermal... . . . . . ***596***

Schmelzer, C.
Monitoring an innovative cold district heating network with decentralized heat pumps... . . . . . ***310***
Two case studies for renewable district heating with solar fraction 70 % ***421***

Schwarz, J.S.
Simulation of a Photovoltaic-Thermal (PV-T) Air Source Heat Pump (ASHP) System for... . . . . . ***228***

Schweigler, C.
Developing and demonstrating innovative solutions for renewable and waste heat-driven... . . . . . ***846***

Segreto, M.
S.A.P.I.EN.T.E Experimental Test Facility For Full-Scale Testing Of New Configurations... . . . . . ***297***

Seidnitzer-Gallien, C.
Dynamic Energy Management Model: A Catalyst for Carbon Neutrality in Austrian Thermal... . . . . . ***494***

Shemelin, V.
Effect of Boundary Conditions on Glazed Flat-Plate Solar Collector Performance Test... . . . . . ***737***

Silva, G.H.R.d.
Climate Adjustment of Photosynthetically Active Radiation Estimates Using Site Adaptation... . . . . . ***975***

Simón-Allué, R.
Sizing an Electrical Storage in Combination with Thermochemical Storage for a PVT-Driven... . . . . . ***176***

Solano, J.P.
ASTEP Project: Status And Progress At 2024 . . . . . ***470***

Solé, C.
Potential thermal energy storage technologies for radiative cooling implementation... . . . . . ***240***

Sommerfeldt, N.
Experimental Assessment of the Effects of Cold Climate Weather Patterns on Novel... . . . . . **725**
Fins vs No Fins: A Comparative Experimental Analysis of Novel Box-Channel Photovoltaic/Thermal... . . . . . **640**
Techno-Economic Comparison of Different Solar Photovoltaic/Thermal (PVT) Absorber... . . . . . **146**

Sourek, B.
Comparison of Solar Systems with Seasonal Storage for Renewable Heat Production for... . . . . . **391**

Stamatiou, A.
State of charge estimation using regression models in a novel photovoltaic thermal... . . . . . **596**

Stinson, B.
Study of the Impact of Automatic Backflush on Direct SDHW Thermosyphon Systems **780**

Streicher, W.
Space Heating and Cooling Demand of Buildings in the Perspective of Climate Change... . . . . . **82**

Stritih, U.
Extruded Water Adsorbent APO-Tric for Adsorption Thermal Battery Utilizing Solar... . . . . . **613**

Strobel, M.
Modelling and Analysis of Building Optimisation and Solar thermal Cooling System... . . . . . **824**

Studtrucker, M.
Thermal Characterization of Single Greening Components and Green Roofs **110**

Sztranyovszky, L.
State of charge estimation using regression models in a novel photovoltaic thermal... . . . . . **596**

T

Talke, M.
A Parametric Study: Impact of Thermal Mass on Summer Overheating for Residential... . . . . . **33**

Tamm, S.
Integrating Concentrated Solar Thermal in District Heating - A Simulation Study in... . . . . . **398**

Thamm, A.
Slurry Production for Solar-Ice Systems using Supercooling and a Flow-based Crystallizer **833**

Thornton, J.
Solar Radiant Floor and Sub-Surface Ground Heat Exchanger Thermal Storage System:... . . . . . **250**

Thür, A.
Space Heating and Cooling Demand of Buildings in the Perspective of Climate Change... . . . . . **82**

Tobiacelli, M.
Critical Analysis on the Renewable Heating and Cooling plans in Croatia, Germany,... . . . . . **874**

Torio, H.
Simulation of a Photovoltaic-Thermal (PV-T) Air Source Heat Pump (ASHP) System for... . . . . . **228**

Tosatto, A.
Characteristic load curves of positive energy districts **1007**
Optimized Thermodynamics and Building Physics of large-scale Thermal Energy Storage **621**

Trp, A.
Assessment of Fin Thickness Influence on Melting and Solidification Processes Inside... . . . . . **559**

Tsimpoukis, A.
Sizing an Electrical Storage in Combination with Thermochemical Storage for a PVT-Driven... . . . . . **176**

Tuñon, G.H.
Techno-Economic Evaluation For Joint Production Of Electricity And Green Hydrogen... . . . . . **894**

Turcotte, P.
Custom sizing and cost analysis of a PV-battery system: Dual-purpose application... . . . . . **505**
Enhancement of a photovoltaic drinking water pumping system design software tool **949**
Feasibility study of a solar desalination unit for small isolated communities **937**

U

Uhl, A.
Propane-based heat pump solutions for existing multi family houses – requirements... . . . . . **70**

Unterberger, V.
Predictive Rule-Based Control Strategy for Optimizing the Operation of Solar District... . . . . . **382**

V

Vajen, K.
Combining expansion turbines, heat pumps, and low-temperature solar heat for enhanced... . . . . . **1004**
Monitoring an innovative cold district heating network with decentralized heat pumps... . . . . . **310**
Oversizing solar heating plants in industry: A cost-effective solution to increase... . . . . . **1008**
Two case studies for renewable district heating with solar fraction 70 % **421**

Valencia, S.
A Review of the Coherence of Strategies to Optimize Photovoltaic Systems within the... . . . . . **122**

Valenzuela, R.X.
Climate Adjustment of Photosynthetically Active Radiation Estimates Using Site Adaptation... . . . . . **975**

Vasta, S.
Developing and demonstrating innovative solutions for renewable and waste heat-driven... . . . . . **846**
Solar Cooling for the Sunbelt Regions – Final results from IEA-SHC Task 65 . . . . . **854**

Vázquez-Moliní, D.
Energy Building Sustainability by Optimized Daylight Tubes **12**

Venturi, E.
Characteristic load curves of positive energy districts **1007**
Evaluation of positive energy districts with district heating and heat pumps **409**

Verma, R.
Achieving Sustainable Buildings: Balancing Energy Efficiency and Comfort through... . . . . . **322**

Vermette, C.
Design and modeling of PV-integrated Double Skin Facades and application to retrofit... . . . . . **1009**

Vidal, J.
Enhancing Energy Transition on Campus: Implementing Thermal Accumulation Mechanisms... . . . . . **524**

Vilà, R.
Potential thermal energy storage technologies for radiative cooling implementation... . . . . . **240**

Volk, P.
Two case studies for renewable district heating with solar fraction 70 % **421**

W

Wagner, C.
Mathematical modelling of an Innovative Ice Storage system **187**
Sensitivity Analysis of Solar District Heating Systems **432**

Walter, J.
Investigation of the Influence of Instantaneous Water Heaters on the Efficiency of... . . . . . **334**

Wane, O.
Climate Adjustment of Photosynthetically Active Radiation Estimates Using Site Adaptation... . . . . . **975**

Weiglein, C.
Thermal Characterization of Single Greening Components and Green Roofs **110**

Weinläder, H.
Thermal Characterization Of Living Wall Systems **134**
Thermal Characterization of Single Greening Components and Green Roofs **110**

Weismann, S.
Development of a Hybrid Collector for an Innovative Energy Supply System Using Molecular... . . . . . **346**
Thermal Characterization of Single Greening Components and Green Roofs **110**

Weiss, A.
Solar Radiant Floor and Sub-Surface Ground Heat Exchanger Thermal Storage System:... . . . . . **250**

Weiss, W.
Solar Cooling for the Sunbelt Regions – Final results from IEA-SHC Task 65 . . . . . **854**

Wemhoener, C.
Characteristic load curves of positive energy districts **1007**

Werner, F.
Monitoring an innovative cold district heating network with decentralized heat pumps... . . . . . **310**

Wessberg, M.
Techno-Economic Analysis of a Stationary Battery Storage Operating on Frequency Regulation... . . . . . **512**

Wijhe, A.v.
Quantifying the effect of radiator capacity on hybrid heat pump performance using... . . . . . **165**

Wikstrom, J.
Techno-Economic Analysis of a Stationary Battery Storage Operating on Frequency Regulation... . . . . . **512**

Wissocq, T.
Improved Pre-calculation of Solar Thermal Production for Milp-based Optimization... . . . . . **444**

Wolfrath, E.
Thermal Characterization of Single Greening Components and Green Roofs **110**

Wurtz, E.
Energy Performance and Environmental Impact of Solar Photovoltaic, Thermal and Hybrid... . . . . . **196**

Y

Yadav, S.
Design and modeling of PV-integrated Double Skin Facades and application to retrofit... . . . . . ***1009***

Z

Zagorulko, M.
Field Evaluation of Naked Energy's Virtu Solar Thermal and Hybrid PVT Collectors... . . . . . ***788***
Quantifying The Environmental Implications Of Solar Thermal Technologies: A Comprehensive... . . . . . ***793***

Zarzalejo, L.F.
Climate Adjustment of Photosynthetically Active Radiation Estimates Using Site Adaptation... . . . . . ***975***

Zavrel, V.
Scenarios for Integration of Power to Heat Technology in Czech District Heating Systems ***536***

Zettl, B.
Microwave Desorption for Flexible Sorption-Heat Storage Application ***580***

Ziegler, F.
Developing and demonstrating innovative solutions for renewable and waste heat-driven... . . . . . ***846***